Isolation of Small Molecular Weight Bioactive Compounds and Polysaccharides from Seaweeds (Phaeophyceae and Rhodophyceae)

Thesis submitted in partial fulfillment of the requirement for the degree of

DOCTOR OF PHILOSOPHY

in

CHEMISTRY

Submitted to

MANGALORE UNIVERSITY

By

Ms. TIMA ANTONY

(Ref. No. MU/EXB/Ph.D./CR.84/Chem./2017-18/E.13, dated 07-07-2017)

Guided By

Dr. KAJAL CHAKRABORTY

Senior Scientist (Organic Chemistry),

Marine Biotechnology Division, Central Marine Fisheries Research Institute (CMFRI)

Under the Faculty of Science and Technology

MANGALORE UNIVERSITY

MANGALAGANGOTHRI – 574 199

Dakshina Kannada Dist. Karnataka, India

भारतीय कृषि अनुसंधान परिषद

केन्द्रीय समुद्री मात्स्यिकी अनुसंधान संस्थान

[कृषि अनुसंधान एवं शिक्षा विभाग, कृषि मंत्रालय,भारत सरकार]

Indian Council of Agricultural Research

Central Marine Fisheries Research Institute

[Department of Agricultural Research and Education, Ministry of Agriculture, Govt. of India]

पोस्ट बोक्स सं.1603, एरणाकुलम नोर्त पी.ओ.,कोच्ची–682018, केरल, भारत

Post Box No.1603, Ernakulam North P.O., Kochi - 682018, Kerala, India

JANUARY 2020

भारतीय कृषि अनुसंधान परिषद
Indian Council of Agricultural Research
केन्द्रीय समुद्री मात्स्यिकी अनुसंधान संस्थान
Central Marine Fisheries Research Institute
(कृषि अनुसंधान एवं शिक्षा विभाग, केन्द्र कृषि एवं किसान कल्याण मंत्रालय, भारत सरकार)
(Department of Agricultural Research and Education, Ministry of Agriculture and Farmers' Welfare, Govt. of India)
पोस्ट बोक्स सं. 1603, एरणाकुलम नोर्थ पी.ओ., कोच्ची - 682 018, केरल, भारत
Post Box No. 1603, Ernakulam North P.O., Kochi - 682 018, Kerala, India
Phone: 91 484 2394867/2391407, Fax: 91 484 2394909/2396685, Email: director@cmfri.org.in, Web: www.cmfri.org.in
CMFRI Platinum Jubilee - Celebrating 70 years of Excellence in Research

Dr. Kajal Chakraborty

Senior Scientist (Organic Chemistry)

Certificate

*This is to certify that this thesis entitled "**Isolation of Small Molecular Weight Bioactive Compounds and Polysaccharides from Seaweeds (Phaeophyceae and Rhodophyceae)**" submitted by **Ms. TIMA ANTONY**, Research Fellow of Marine Biotechnology Division of Central Marine Fisheries Research Institute, for the award of the degree of Doctor of Philosophy in Chemistry is the result of bonafide research work carried out by her in the Marine Biotechnology Division of Central Marine Fisheries Research Institute in Chemistry, Kochi-682018, under my guidance and direct supervision. I further certify that this thesis or part thereof has not previously formed the basis for the award of any degree, diploma and associateship of any other University or Institution.*

Kajal Chakraborty

Place: Kochi

Date:

Declaration

*I do hereby declare that the thesis entitled "**Isolation of Small Molecular Weight Bioactive Compounds and Polysaccharides from Seaweeds (Phaeophyceae and Rhodophyceae**" is an authentic record of research work carried out by me under the guidance and supervision of Dr. Kajal Chakraborty, Senior Scientist (Organic Chemistry), Marine Biotechnology Division, Central Marine Fisheries Research Institute, Kochi-682018 and the same has not previously formed the basis for the award of any degree or diploma.*

Whenever the work described is based on the findings of other researchers, due acknowledgement is made in keeping with the general practice of reporting scientific observations. However, errors and unintentional oversights, if any are regretted.

TIMA ANTONY

Place: Kochi

Date:

Acknowledgements

First and foremost, all praise, honour and glory to my Lord Jesus Christ for His richest grace and mercy for the accomplishment of this research work successfully. You have given me the power to believe in myself and pursue my dreams. You have given me the strength and confidence to face all my difficult situations and hardships throughout my journey. I express my sincere gratitude and thanks to God for giving me strength, wisdom, health and luck to accomplish this endeavor. I could never have done this without the faith I have in you, the Almighty.

I would like to express my special appreciation and thanks to my Research supervisor and Guide Dr. Kajal Chakraborty, Senior Scientist (Organic Chemistry), Central Marine Fisheries Research Institute, you have been a tremendous mentor for me. I would like to thank you for giving me the proper guidance and the priceless support. I will always be obliged to you for your valuable advices and suggestions at times when I needed them the most. Thank you sir for enhancing my interest and widening my research path. I still remember the efforts he has put in for providing me all the facilities in lab for carrying out the experiments and above all, for the valuable time he has invested on me to clarify my doubts and the moral support granted for the fulfillment of my thesis. I will always be debted to you for the fanatical concern you have shown during the intricate situations.

I wish to place in record, my deep sense of respect and gratitude to Dr. A. Gopalakrishnan, Director, Central Marine Fisheries Research Institute for providing all the necessary facilities and support required to carry out my research work. I am extremely grateful to him for equipping me with a peaceful and positive atmosphere throughout my research period.

I express my sincere thanks to Dr. Vijayagopal Pananghat, Head of the Department, Marine Biotechnology Division, Central Marine Fisheries Research Institute for his constant encouragement and the support granted to complete my research activities in his prestigious

department. I take this opportunity to show my courtesy towards Dr. Bobby Ignatius, Principal Scientist and Head of HRD Cell of CMFRI for extending me all the necessary support regarding the doctoral work. I have great pleasure in expressing my gratitude and obligations to the scientists of Marine Biotechnology Division, Dr. N. K. Sanil, Dr. Sandhya Sukumaran and Dr. M. A. Pradeep. I will be indebted to Late. Mr. Nandakumar Rao, Mrs. G. Shylaja (Technical Officers, CMFRI) , Dr. M.P. Paulton (Senior Technical Officer), Mrs. P. Vineetha, SIC librarian, library support staff, staff members of the HRD Cell, the canteen, security personnel and all the employees of CMFRI, Kochi, for their kindhearted service and support bestowed on me throughout my research life.

I am grateful to the staffs of Sophisticated Analytical Instrument Facility (SAIF), Indian Institute of Technology (IIT), Chennai, Tamil Nadu especially, Dr. S.S.Bhattacharya, Head of SAIF, Dr. C. Baby (Technical officer), Mr. V. Srinivasan, Mr and. R. Sathiyamoorthi and the staffs of Sophisticated Test and Instrumentation Centre (STIC), Cochin University of Science and Technology (CUSAT) for their honest support and help in providing the spectroscopic and analytical experimental results.

I thank my intimate colleagues Vinaya K.K, Soumya Salas, Soumya Krishnan, Minju Joy, Fasina Makkar, Anusree Maneesh, Vamshi Krishna Raola, Dexy Joseph, Anjaly Thambi, Archana M K, Prima Francis, Shubhajit Dhara, Silpa KK, Vishnupriya and Suji Chandru, for the stimulating discussions, valuable feedbacks, co-operation and for all the fun we have had in the last four years. I wish to thank all other research scholars of CMFRI for a mesmerizing research life.

I would like to acknowledge the people who mean world to me, my parents and siblings for the selfless efforts, sacrifices and their endless prayers. Thank you appacha and amma for showing faith in me and giving me the opportunity to nurture my wings to fly behind my dreams. I would like to pay my special concern and love to my elder sister, brother-in -law and her family, for their creative criticisms, moral support and everlasting inspiration throughout the entire course of work.

Words fail to express my deep sense of gratitude towards my loving Chettayi, Mr.Nikhil Jose, for his understanding, patience, and the support he has given for me to accomplish this endeavor. I value his concern, support and encouragement at all times, good and bad.

I feel extremely privileged to show my appreciation to my family, and all those who put selfless efforts.

Finally I wish to thank all

Tima Antony

Place: Cochin

Date:02/01/2020

Dedicated to my. . . .

Lord Jesus Christ

Beloved parents &Family

ABSTRACT

Seaweeds were consumed as staple food items of the cuisines in many Asian countries, and are considered as essential components of a healthy diet. The pharmacological potential of ethyl acetate-methanol (EtOAc-MeOH) extract of ten species of seaweeds belonging to the subclasses Dictyotophycidae, Rhodymeniophycidae, and Corallinophycidae against progressive lifestyle diseases was determined by various *in vitro* models. Among the studied species, the organic extracts of *Gracilaria salicornia* and *Padina tetrastromatica* exhibited potential dipeptidyl-peptidase-4 inhibiting activity (IC_{50} ~ 0.03 mg mL^{-1}) and angiotensin converting enzyme-I inhibitory property (ACE-I) (IC_{50} 0.12 mg mL^{-1}) compared to those displayed by other studied species. The organic extracts of *G. salicornia* and *P. tetrastromatica* also displayed significantly greater attenuation properties against pro-inflammatory cyclooxygenase-2 and 5-lipoxygenase (IC_{50} 0.98-1.34 mg mL^{-1}, $P < 0.05$) compared to those derived from other species (IC_{50} 1.99-5.02 mg mL^{-1}). The nuclear magnetic resonance-guided dereplication of organic extracts of the studied seaweed species recognized the co-linearity between the bioactive potential and downfield electronegative functionalities. These results recognized the significance of the organic extracts of *G. salicornia* and *P. tetrastromatica* to isolate compounds for functional food applications against oxidative stress and induced diseases, such as diabetes, hypertension, and inflammation.

Phytochemical investigation on the biologically active compounds of seaweed *G. salicornia* (family Gracilariaceae) guided to the separation of a previously unreported abeo-labdane class of diterpenoid. The compound was characterized as methyl-16(13→14)-abeo-7-labdene-(12-oxo) carboxylate (**1**) by extensive spectroscopic experiments, and comparison with the related compounds. The studied compound registered significantly greater activities against pro-inflammatory 5-lipoxygenase (IC_{50} 2.33 mM) than that exhibited by non-steroidal anti-inflammatory agent ibuprofen (IC_{50} 4.51 mM, $P<0.05$). Likewise, this compound exhibited comparable radical quenching (1, 1-diphenyl-2-picryl-hydrazil) activity (IC_{50} 1.97 mM) as standard antioxidant agent α-tocopherol (IC_{50} 1.49 mM).

Carbolytic enzyme-associated cascades have been considered as potential curative target in attenuating diabetic mellitus pathogenesis. Two oleanene class of triterpenoids characterised as 24(4→23), 27(8→26), 30(20→29)-tris-abeo-olean-(12-oxo)-1,15,22-triene-methyl hept-5-enoate (**2**) and 24(4→23)-abeo-olean-(12-oxo)-3,5-diene-deconoate (**3**) with potential inhibitory activities against the starch digestive enzymes α-glucosidase and α-amylase,

were purified from the organic extract of intertidal red seaweed *G. salicornia* (family Gracilariaceae). Structural interpretation of compounds was carried out by detailed spectroscopic analysis, and their antioxidant/anti-diabetic potentials were assessed. Inhibitory potential of abeo-oleanene derivative (**3**) towards the starch digestive enzymes, α-glucosidase (IC_{50} 0.29 mM) and α-amylase (IC_{50} 0.32 mM) were greater than those displayed by its abeo-oleanene chemotype **2** (IC_{50} 0.34-0.40 mM). The molecular modelling studies were performed to designate the α-amylase and α-glucosidase inhibitory mechanism of oleanene analogues, and the comparison of docking parameters suggested that compound **3** exhibited least binding energy of -10.04 and -9.84 kcal mol^{-1} towards α-amylase and α-glucosidase respectively, and those results were corroborated with its greater inhibition potential against carbolytic enzymes. These results demonstrated that abeo-oleanene derivative (**3**) might constitute prospective anti-hyperglycaemic pharmaceutical candidate to moderate the likelihood of type-II diabetes.

The 5-lipoxygenase-associated cascade has appeared as potential therapeutic target in attenuating inflammatory pathologies. Progression and pathophysiology of inflammation have also shown potential involvement of oxidative stress and inflammatory pathways. Three drimane sesquiterpene quinols, characterised as 3-(hept-3^6-enyloxy)- decahydro-4,6a,12a,12b-tetramethyl-1*H*-benzo[*a*]xanthene-4,10,12-triol (**4**), 13-[[2-(hexyloxy)-2,5,5,8a-tetramethyldecahydro-1-naphthalenyl](methoxy)methyl]benzenol (**5**), and 1-butoxy-4,4,11b,11c-tetramethyl-decahydrobenzo[*kl*]xanthen-10-ol (**6**) were purified from the organic solvent extract of intertidal marine macroalga *Gracilaria salicornia*, obtained from the southeast coastal region of Indian peninsular. The 1*H*-benzo[a]xanthene-triol derivative (**4**) registered potential activities against pro-inflammatory 5-lipoxygenase (IC_{50} 1.7 mM) and free radicals (IC_{50} 1.3-1.5 mM). The *in silico* molecular modelling studies to designate 5-lipoxygenase inhibitory mechanism of the studied analogues and the comparison of docking parameters attributed that the drimane sesquiterpene **4** exhibited least binding energy of -12.30 kcal mol^{-1}, and showed effective hydrogen bonding interactions with the catalytic site of the enzyme. The higher electronic parameters and permissible hydrophobic-hydrophilic balance of the drimane sesquiterpene bearing 1*H*-benzo[*a*]xanthene-triol moiety (**4**) appeared to constitute significant roles towards the attenuation of pro-inflammatory 5-lipoxygenase. Putative biosynthetic pathway of the studied compounds involving cyclisation of farnesyl diphosphate and carbocationic rearrangement through a battery of enzyme-mediated cascade validated their structural attributions. These results demonstrated that the drimane-type sesquiterpenoids with 1*H*-benzo[*a*]xanthene-triol framework could be used as a potential therapeutic agent for the treatment of 5-lipoxygenase-mediated inflammatory pathologies.

Phytochemical investigation on biologically active compounds of an intertidal red seaweed *G. salicornia* (family Gracilariaceae) guided to the separation of two previously undisclosed *2H*-chromenyl derivatives. The compounds were characterised as 4'-[10'-[7-hydroxy-2,8-dimethyl-6-(pentyloxy)-2*H*-chromen-2-yl]ethyl]-3',4'-dimethyl-cyclohexanone (**7**) and 3'-[10'-(8-hydroxy-5-methoxy-2,6,7-trimethyl-2*H*-chromen-2-yl)ethyl]-3'-methyl-2'-methylene cyclohexyl butyrate (**8**) by extensive spectroscopic experiments. The studied metabolites recorded prospective bioactivities against 5-lipoxygenase (IC_{50} < 2.50 mM), whereas their selectivity indices were significantly greater (~ 1) than ibuprofen (0.89) (p < 0.05), which attributed higher anti-inflammatory selectivity of 2*H*-chromenyl compounds against inducible cyclooxygenase-2 than its constitutive pro-inflammatory isoform of cyclooxygenase-1. The radical scavenging potential of **8** against oxidants, 2,2-diphenyl-1-picrylhydrazyl and 2,2'-azino-bis-3 ethylbenzothiozoline-6-sulfonic acid were higher (IC_{50} < 1.35 mM) than standard antioxidant, α-tocopherol (IC_{50} 1.42-1.79 mM). The greater hydrogen bond interactions and binding affinity of **8** (-7.35 kcal mol^{-1}) bearing *2H*-chromenyl ethyl-3'-methyl-4'-methylenecyclohexyl butyrate moiety with 5-lipoxygenase, along with higher electronic properties and permissible hydrophobic-hydrophilic balance, manifested towards its greater anti-inflammatory activity than **7**.

The inflammation pathology is an orchestrated biological process and the dual inhibition of pro-inflammatory enzymes 5-lipoxygenase and cyclooxygenase-2 has been found to be an effective approach against inflammation. This study involves the characterisation of two previously undescribed spiro[5.5]undecanes, 3-(hydroxymethyl)-7-(methoxymethyl)-3,11-dimethyl-9-oxospiro[5.5]undec-4-en-10-methylbutanoate (**9**) and 4-ethoxy-11,11-dimethyl-7-methylene-8-(propionyloxy)spiro[5.5]undec-2-en-10^3,10^5-dihydroxytetrahydro-2*H*-pyran-10-carboxylate (**10**) with potential anti-inflammatory properties, from seaweed *Gracilaria salicornia* by extensive-spectroscopic-experiments. These metabolites recorded prospective bioactivities against 5-lipoxygenase (IC_{50} < 2.80 mM), whereas their selectivity indices were significantly greater (~1) than ibuprofen (0.89) (p<0.05), which attributed selective anti-inflammatory potencies of the studied spiro[5.5]undecane derivatives against inducible cyclooxygenase-2 than constitutive cyclooxygenase-1. Radical scavenging potential of spiro[5.5]undec-2-en-10^3,10^5-dihydroxytetrahydro-2*H*-pyran-10-carboxylate analogue (**10**) against oxidants, 2,2-diphenyl-1-picrylhydrazyl and 2,2'-azino-bis-3 ethylbenzothiozoline-6-sulfonic acid were found to be greater (IC_{50} < 1.25 mM) than commercial standard, α-tocopherol (IC_{50} 1.42-1.79 mM). The greater hydrogen-bonding interactions and binding affinity of **10** (-10.13 kcal/mol) with 5-LOX appropriately corroborated its prospective anti-inflammatory activity.

5-Lipoxygenase (5-LOX)/cyclooxygenase-2 (COX-2) were found to be the two major inducible pro-inflammatory enzymes catalysing the rate-limiting stage in the development of pro-inflammatory prostaglandins/thromboxanes by COX-2 pathway and leukotrienes by 5-LOX pathway. Instantaneous quenching of COX-2/5-LOX-associated cascade is an important therapeutic objective in the attenuation of inflammatory pathologies. Two polyether triterpenoids, characterised as 15-(octahydro-7-(4,5-dihydro-3-methoxy-2,6-dimethyl-2*H*-pyran-6-yl)-10-methylpyrano[3,2-b]pyran-14-yl)-18-(19-methyl-23-methyleneoxepan-19-yl)pent-15-en-18-ol (**11**) and tetrahydro-6-(hexahydro-13-((tetrahydro-18-(23-hydroxy-23-methylheptan-19-yl)-15-methylfuran-15-yl)methyl)-10-methyl-2*H*-furo[3,2-b]pyran-7-yl)-2,2,6-trimethyl-2*H*-pyran-3-yl butyrate (**12**) were isolated from the organic extract of the marine macroalga, *Gracilaria salicornia* harvested from southeast-coastal zones of Indian peninsular. Polyether analogue bearing trimethyl-2*H*-pyran-3-yl butyrate moiety (**12**) disclosed potent attenuation properties against 5-LOX (IC_{50} 1.89 mM) and COX-2 (IC_{50} 1.87 mM) enzymes. *In-silico* molecular docking methods designated the anti-inflammatory mechanisms of isolated compounds and their comparison of docking factors assigned that the polyether **2** displayed the smallest binding energy of -10.29 and -10.96 kcal mol^{-1} in COX-2 and 5-LOX active sites, respectively and designated competent hydrogen-bonding associations with the enzymatic catalytic regions. Greater electronic factors along with lesser steric bulk of the polyether **12** bearing furanyl-furo[3,2-b]pyran-2*H*-pyran moiety was found to have noteworthy functional roles to attenuate the inflammatory enzymes. Proposed bio-synthetic origin leading to the polyether analogues comprising the cyclization of squalene epoxides through the sequences of enzyme-catalysed cascade corroborated their structural attributions. These reports designated that polyether triterpenoid enclosing furanyl-furo[3,2-b]pyran-2*H*-pyran skeleton might be considered as a prospective anti-inflammatory therapeutic source to alleviate COX-2 and 5-LOX-mediated inflammatory pathologies.

Three macrolides bearing the carbon framework of oxabicyclo[21.3.1]heptacosa-ene-diones (**13** and **14**) and oxabicyclo[19.3.1]pentacosa-ene-dione (**15**) were isolated and characterised from the organic extract of the intertidal red seaweed *G. salicornia* (family Gracilariaceae), which were named as compounds **13**-**15**. These natural macrolides were conformationally pre-organised ring structure providing diverse functionalities, and their potential bioactive properties led to the development of pharmacophores with anti-inflammatory properties. The 21-membered pyran-enclosed compound **14** displayed greater cyclooxygenase-2 (IC_{50} COX-2 1.13 mM) inhibitory activity than those exhibited by the 21-membered aryl compound **13** and 19-membered compound **15** (IC_{50} COX-2 ~1.2 mM). The attenuating potential of the studied compounds against pro-inflammatory enzyme, 5-lipoxygenase (IC_{50}

LOX < 1.5 mM) was significantly greater than that displayed by the non-steroidal anti-inflammatory ibuprofen (IC_{50} 4.5 mM), whereas the selectivity indices exhibited by salicornolides against cyclooxygenase-2 was significantly higher (1.18-1.41, $P < 0.05$) when compared to that of ibuprofen (SI 0.43) attributing the greater selectivity profile of the former towards inducible pro-inflammatory mediators than the latter. The minimal binding energy of compound **14** (-9.64 kcal mol^{-1}), a greater number of hydrogen-bonds and lesser inhibitory constant (Ki 85.15 nM) might be responsible for effective binding towards 5-lipoxygenase, and that could attribute its greater anti-inflammation potential than those displayed by other compounds. The putative biosynthetic cascade initiated by malonate-acyl carrier protein unambiguously confirmed the structural attributions of the titled macrocyclic lactones. The undescribed compounds **13**-**15** from seaweed *Gracilaria salicornia* attenuating pro-inflammatory 5-lipoxygense might be considered as prospective natural anti-inflammatory leads for pharmaceutical applications.

Two previously unreported xenicane class of novaxenicin-type xenicin diterpenoids (**1**-**2**) bearing cyclonona[*d*]furo [2,3-*b*]pyrandiol and three xeniolide-type diterpenoids with unprecedented octahydrocyclonona[*c*]pyran-3(1*H*)-one backbones (**3**-**5**) were separated from the organic extract of the intertidal seaweed *Padina tetrastomatica* (family Dictyotaceae), collected from southern India. The compounds were deduced to bear a xenicane moiety with a 2-oxabicyclo[7.4.0]tridecane cyclic system. The structures of these specialized metabolites were attributed based on the extensive nuclear magnetic resonance spectral analyses, and comparison of related compounds. Xeniolide type diterpenes (**3**-**5**) registered significantly greater attenuation potential against pro-inflammatory 5-lipoxygenase (IC_{50} ~ 2.04 mM) than that exhibited by non-steroidal anti-inflammatory drug ibuprofen (IC_{50} 4.50 mM, $P < 0.05$). The xeniolide derivative octahydro-1,7-dihydroxy-4-(4^1-hydroxy-4^2-methylpropyl)-6-(6^1-hydroxy-6^2-propenyl)-10-methyl-cyclonona[*c*]pyran-3(*1H*)-one (**5**) exhibited comparable antioxidant activity (DPPH IC_{50} 1.73 mM) along with standard antioxidative agent α-tocopherol (IC_{50} < 2 mM). *In silico* molecular modelling studies were performed to designate the 5-lipoxygenase inhibitory mechanism of the xenicanes, and the comparison of docking parameters suggested that the xeniolide derivative **5** exhibited least binding energy of −11.56 kcal mol^{-1}, and that was corroborated with its greater inhibition potential against the pro-inflammatory enzyme. These results demonstrated that the xeniolide-type diterpenoids with previously unreported *δ*-lactone cyclononane framework might constitute promising anti-inflammatory leads with pro-inflammatory 5-lipoxygenase enzyme inhibitory activities.

New dolabellanes {6-methoxy-dolabella-8(17),12-diene-10*β*,18-diol (**6**), 3-methoxy-dolabella-12(18)-ene-4*β*-ol (**7**), 3-methoxy-dolabella-10,18(19)-diene-5α,8*β*-diol (**8**)} and

dolastanes {2,7-dimethoxy-14α-hydroxy-dolasta-1(15),9-diene (**9**) and 4,7-dimethoxy-9*β*,14α-dihydroxy-dolasta-1-ene (**10**)} were identified from brown seaweed *Padina tetrastomatica* (family Dictyotaceae), collected from the southeast coast of India. Compounds **6**-**8** were found to possess dolabellane skeleton with [9.3.0] cyclotetradecane framework whereas, **9**-**10** were composed of tricyclic diterpenes with linear arrangement of six-seven-five fused alicyclic rings. Compounds **8** and **10** registered greater antioxidative activities (IC_{50} ≤0.63 mg/mL) than other analogues (IC_{50} ≥0.65 mg/mL), whereas their attenuating potentials against carbolytics α-amylase and α-glucosidase (IC_{50} ~0.12-0.14 mg/mL) were comparable with those displayed by acarbose (IC_{50} 0.14-0.12 mg/mL). Bioactive potentials of titled compounds were assessed by electronic and lipophilic parameters. The lesser binding energies of **8** (-9.71 kcal/mol) and **10** (-8.59 kcal/mol) through molecular docking demonstrated their effective hydrogen bonding interactions with α-amylase. Thus, dolabellanes and dolastanes might be used as anti-diabetic and antioxidant leads to reduce the risk of hyperglycaemia.

ABBREVIATIONS

^{1}D NMR	-	One Dimensional NMR
^{1}H NMR	-	Proton Nuclear Magnetic Resonance
$^1O_2$	-	Singlet Oxygen
2D NMR	-	Two Dimensional NMR
5-LOX	-	5-Lipoxygenase
AA	-	Arachidonic Acid
$ABTS^+$	-	2, 2-Azino-Bis-3ethylbenzothiozoline-6-Sulfonic Acid
Ac_2O	-	Acetic anhydride
ACE	-	Angiotensin Converting Enzyme
AI	-	Atherogenicity Index
AIP	-	Atherogenic Index of Plasma
ALP	-	Alkaline Phosphatase
ALT	-	Alanine aminotransferase
ANOVA	-	Analysis of Variance
AST	-	Aspartate aminotransferase
BSA	-	Bovine Serum Albumin
CC	-	Column Chromatography
COSY	-	Correlation Spectroscopy
COX	-	Cyclooxygenase
DCM	-	Dichloromethane
DDT	-	Dithiothreitol
DEAE	-	Diethylaminoethyl
DEPT	-	Distortionless Enhancement by Polarization Transfer
DHA	-	Docosahexaenoic acid
DMSO	-	Dimethyl Sulfoxide
DPPH	-	1,1-Diphenyl-2-Picrylhydrazyl
EDTA	-	Ethylenediaminetetra Acetic Acid

EI-MS	-	Electron Ionisation Mass Spectra
EtOAc	-	Ethyl Acetate
FAPGG	-	*N*-(3-[2-furyl] acryloyl)-Phe-Gly-Gly
FC	-	Flash Chromatography
FFA	-	Free Fatty Acid
FT-IR	-	Fourier Transform Infra Red
GAE	-	Gallic Acid Equivalence
GC-MS	-	Gas Chromatography-Mass Spectrometry
GPPN	-	Gly-Pro-p-Nitroanilide
GPx	-	Glutathione Peroxidase
GSH	-	Glucocorticoid Suppressible Hyperaldosteronism
GSH	-	Reduced Glutathione
H_2O_2	-	Hydrogen Peroxide
HAT	-	Hydrogen Atom Transfer
HMBC	-	Heteronuclear Multiple Bond Correlation
HPLC	-	High-Performance Liquid Chromatography
HRESIMS	-	High Resolution Electro Spray Mass Spectroscopy
HSQC	-	Heteronuclear Single Quantum Coherence
IC_{50}	-	Inhibition Concentration at 50 %
m/z	-	Mass-to-Charge Ratio
MDA	-	Malondialdehyde/Malonaldehyde
MDAEQ	-	Malondialdehyde Equivalent
MeI	-	Methyl Iodide
MeOH	-	Methanol
MNP	-	Marine Natural Products
NaOH	-	Sodium Hydroxide
NMR	-	Nuclear Magnetic Resonance
NOESY	-	Nuclear Overhauser Effect Spectroscopy
NSAIDs	-	Non-Steroidal Anti-inflammatory Drugs
O_2^-	-	Superoxide Anion
OH·	-	Hydroxyl Radical

PBS	-	Phosphatase Buffered Saline
PCA	-	Principal Component Analysis
PDA	-	Photodiode Array
PGs	-	Prostaglandins
PMAAs	-	Partially Methylated Alditol Acetates
ppm	-	Parts Per Million
PTLC	-	Preparative Thin Layer Chromatography
PUFA	-	Poly Unsaturated Fatty Acid
QSAR	-	Quantitative Structure Activity Relationship
R_f	-	Retardation Factor
RID	-	Refractive Index Detector
RMSD	-	Root Mean Square Deviation
ROS	-	Reactive Oxygen Species
RP-HPLC	-	Reverse Phase High-Performance Liquid Chromatography
R_t	-	Retention Time
RT	-	Room Temperature
SD	-	Standard Deviation
SEM	-	Scaning Electron Microscope
SOD	-	Superoxide Dismutase
SPSS	-	Statistical Program for Social Sciences
TBA	-	Thiobarbituric Acid
TBARS	-	Thiobarbituric Acid Reactive Species
TLC	-	Thin Layer Chromatography
TPC	-	Total Phenolic Content
UV-VIS	-	Ultra Violet-Visible

LIST OF CONTENTS

SL. NO. **TITLE**

CHAPTER 1: INTRODUCTION

1.1 Background
1.2 Marine environment as a potential source of bioactive compounds……...
1.3 Bioactive potentials of seaweeds and their secondary metabolites……
1.3.1 Major classification of seaweeds……..
1.3.2 Distribution and diversity of seaweeds in Indian coastline……
1.3.3 Pharmacological importance of seaweeds …….
1.4 Free radicals in the defense mechanism……..
1.4.1 Impact of free radicals in the defense mechanism
1.4.2 Free radicals induced various chronic disorders…….
1.5 Seaweeds and their metabolites combat oxidative stress induced life style disorders……..
1.5.1 Seaweeds and their metabolites as natural alternative to combat various oxidative stress induced life style disorders……
1.5.2 Role of seaweeds belonging to the class of Phaeophyceae and Rhodophyceae in the oxidative stress defense mechanism…….
1.6 Objectives……
1.7 Thesis outline……..

CHAPTER 2: REVIEW OF LITERATURE

2.1 Background…….....
2.2 Marine ecosystem as a source of bioactives……
2.3 Seaweeds as a source of bioactives…….
2.3.1 Secondary metabolites derived from seaweeds.…….
2.3.1.1 Terpenoids……...
2.3.1.2 Phenolic compounds…….....
2.3.1.3 Steroids…….
2.3.1.4 Alkaloids…….
2.3.1.5 Lipids and Fatty acid derivatives……
2.3.1.6 Protein and peptides……
2.3.1.7 Polysaccharides……...
2.4 An outline of bioactive secondary metabolites derived from seaweeds belonging to Rhodophyceae and Phaeophyceae …….
2.4.1 Bioactive secondary metabolites derived from seaweeds belonging to the class Rhodophyceae…….
2.4.2 Bioactivities secondary metabolites derived from seaweeds belonging to the class Phaeophyceae…….
2.5 Over all morphological features of the seaweeds belonging to Rhodophyceae and Phaeophyceae ……
2.5.1 Morphology and distribution of *Gracilaria* species …….....

2.5.3 Morphology and distribution of *Padina* species …….....
2.6 Conclusions…….

CHAPTER 3: SCREENING OF BIOACTIVE POTENTIALS OF CRUDE SOLVENT EXTRACTS FROM RED AND BROWN SEAWEEDS (RHODOPHYCEAE AND PHAEOPHYCEAE)

3.1 Background.……
3.2 Materials and methods……
3.2.1 Chemicals, reagents and solvents…..……..
3.2.2 Materials of seaweed and depiction of work area……..
3.2.3 Preparation of organic extracts from seaweeds……..
3.2.4 Instrumentation……...
3.2.5 Analysis of pharmacological activities of EtOAc:MeOH crude solvent extracts……
3.2.5.1 Determination of total phenolic content…….
3.2.5.2 *In vitro* antioxidant activities……...
3.2.5.2a 1,1-Diphenyl-2-picryl hydrazil (DPPH) radical scavenging activitity……
3.2.5.2b 2,2'-Azino-bis-3-ethylbenzothiozoline-6-sulfonic Acid ($ABTS^{+}$) radical scavenging activitity……...
3.2.5.2c Hydrogen peroxide (H_2O_2) scavenging activities……...
3.2.5.2d Ferrous ion chelating (Fe^{2+} ion) activity……..
3.2.5.2e Thiobarbituric acid-reactive species (TBARS) formation inhibitory activity……
3.2.5.3 *In vitro* anti-inflammatory activities……...
3.2.5.3a Cyclooxygenases (COX) inhibition assay……...
3.2.5.3b 5-Lipoxygenase (5-LOX) inhibition assay……..
3.2.5.4 *In vitro* antidiabetic activities…….....
3.2.5.4a α -Amylase inhibition assay……
3.2.5.4b α-Glucosidase inhibition assay……
3.2.5.4c Dipeptidyl peptidase-4 (DPP-4) inhibition assay……
3.2.5.5 *In vitro* antihypertensive activities…….....
3.2.5.5a Angiotensin converting enzyme-I (ACE-I) inhibitory activity... …….
3.2.6 Statistical analysis……...
3.3 Results and discussion……
3.3.1 Bioactive potentials and correlation analysis of the organic extracts of seaweeds
3.3.1.1 Total phenolic content and antioxidant activities……
3.3.1.2 Antioxidant activities……..
3.3.1.3 Anti-diabetic activities……
3.3.1.4 Antihypertensive and anti-inflammatory activities…….....
3.3.2 Spectroscopic characterization of solvent extracts …….
3.4 Conclusions…….

CHAPTER 4: ISOLATION AND CHARACTERIZATION OF BIOACTIVE LEADS FROM RED SEAWEED (RHODOPHYCEAE) *GRACILARIA SALICORNIA*

4.1 Background.……
4.2 Materials and methods……

4.2.1 Instrumentation, chemicals and reagents……
4.2.2 Chromatographic purification techniques …….....
4.2.2.1 Purification by column chromatography ……
4.2.2.2 Purification by flash chromatography…….
4.2.2.3 Purification by High pressure liquid chromatography (HPLC) ……
4.2.2.4 Percentage of purity assessment by thin layer chromatography and analytical HPLC……..
4.2.3 Spectrophotometric and spectroscopic analysis……
4.2.4 Chromatographic purification of pure compounds and bioactive potentials of sub-column fractions from *G. salicornia* …….
4.2.5 Physicochemical description of bioactive-leads isolated from EtOAc-MeOH extract of *G. salicornia*
4.2.5.1 Physicochemical description of compound **1** ...…….
4.2.5.2 Physicochemical description of compound **2**…….
4.2.5.3 Physicochemical description of compound **3**…….
4.2.5.4 Physicochemical description of compound **4**…….
4.2.5.5 Physicochemical description of compound **5**…….
4.2.5.6 Physicochemical description of compound **6** ……
4.2.5.7 Physicochemical description of compound **7**…….
4.2.5.8 Physicochemical description of compound **8**…….
4.2.5.9 Physicochemical description of compound **9**…….
4.2.5.10 Physicochemical description of compound **10**……
4.2.5.11 Physicochemical description of compound **11**……
4.2.5.12 Physicochemical description of compound **12**……
4.2.5.13 Physicochemical description of compound **13**……
4.2.5.14 Physicochemical description of compound **14**……
4.2.5.15 Physicochemical description of compound **15**……
4.2.6 Assessment *in vitro* of bioactive potentials……
4.2.6.1 *In vitro* antioxidant assays……..
4.2.6.2 1,1-Diphenyl-2-picryl hydrazil (DPPH) radical scavenging activities……..
4.2.6.3 2,2'-Azino-bis-3-ethylbenzothiozoline-6-sulfonic Acid ($ABTS^{+}$) radical scavenging activities……...
4.2.7 *In vitro* anti-inflammatory assays
4.2.7.1 Cyclooxygenases (COX) inhibition properties……...
4.2.7.2 5-Lipoxygenase (5-LOX) inhibition properties……..
4.2.8 *In vitro* anti-diabetic activities…….....
4.2.8.1 α-Amylase inhibition assay…….
4.2.8.2 α-Glucosidase inhibition assay……
4.2.8.3 Dipeptidyl peptidase-4 (DPP-4) inhibition assay……
4.2.9 Structure-activity correlations of bioactive leads isolated from EtOAc-MeOH extract of *G. salicornia* ……...
4.2.10 Molecular modelling experiments ……..
4.2.11 Statistical analyses……..
4.3 Results and discussion…….
4.3.1 Chromatographic fractionation, bioactive potentials and spectroscopic analyses
4.3.1.1 Chromatographic fractionation, bioactive potentials and spectroscopic analyses

of intermediate fractions from EtOAc:MeOH extract of *G. salicornia* ……
4.3.2 Spectroscopic characterization of bioactive compounds derived from EtOAc-MeOH extract of *G. salicornia*……
4.3.3 Isolation of bioactive secondary metabolites from EtOAc:MeOH extract of *G. salicornia*…….
4.3.4 Spectroscopic analyses of bioactive secondary metabolites isolated from EtOAc:MeOH extract of *G. salicornia*……...
4.3.4.1 Structural characterization of labdane diterpene derivatives (**1**) ……
4.3.4.2 Structural characterization of oleanane triterpene derivatives (**2-3**) ……
4.3.4.2a Structural characterization of compound **2**…….
4.3.4.2b Structural characterization of compound **3**…….
4.3.4.3 Structural characterization of drimane diterpene derivatives (**4-6**) ……
4.3.4.3a Structural characterization of compound **4**……..
4.3.4.3b Structural characterization of compound **5**……..
4.3.4.3c Structural characterization of compound **6**……..
4.3.4.3 Structural characterization of 2*H*-chromenyl derivatives (**7-8**) …….
4.3.4.3a Structural characterization of compound **7**…….
4.3.4.3b Structural characterization of compound **8**…….
4.3.4.4 Structural characterization of spiro compounds (**9-10**) …….
4.3.4.4a Structural characterization of compound **9**…….
4.3.4.4b Structural characterization of compound **10**……...
4.3.4.5 Structural characterization of polyether derivatives (**11-12**) …….
4.3.4.5a Structural characterization of compound **11**……...
4.3.4.5b Structural characterization of compound **12**……...
4.3.4.6 Structural characterization of macrolide derivatives (**13-15**) ……
4.3.4.7 Structural characterization of compound **13** …….
4.3.4.7a Structural characterization of compound **14**……..
4.3.4.7b Structural characterization of compound **15**……...
4.3.5 Pharmacological potentials of secondary metabolites isolated from EtOAc-MeOH extract of *G. salicornia;* antioxidant, anti-inflammatory and antidiabetic properties…….
4.3.6 Structure-activity correlation analyses of bioactives isolated from EtOAc-MeOH extract of *G. salicornia*……...
4.3.7 *In silico* molecular docking analysis of bioactives isolated from *G. salicornia*
4.4 Conclusions…….

CHAPTER 5: ISOLATION AND CHARACTERIZATION OF BIOACTIVE LEADS FROM BROWN SEAWEED *PADINA TETRASTROMATICA*

5.1 Background.……
5.2 Materials and methods……
5.2.1 Instrumentation, chemicals and reagents……
5.2.2 Chromatographic purification techniques …….....
5.2.2.1 Purification by column chromatography…….
5.2.2.2 Purification by flash chromatography…….
5.2.2.3 Purification by High pressure liquid chromatography (HPLC) …….

5.2.2.4 Percentage of purity assessment by thin layer chromatography and analytical HPLC……...
5.2.3 Spectrophotometric and spectroscopic analysis……..
5.2.3.1 UV-Visible spectrophotometric analysis……
5.2.3.2 Fourier transform infrared (FTIR) spectroscopy……
5.2.3.3 Mass spectroscopic (MS) analysis…….
5.2.3.4 Nuclear magnetic resonance (NMR) spectroscopic analysis…….
5.2.4 Chromatographic purification of pure compounds from *P. tetrastromatica*……
5.2.5 Analysis of physicochemical parameters of pure bioactive compounds from EtOAc:MeOH extract of *P. tetrastromatica*…….....
5.2.5.1 Analysis of physicochemical parameters of compound **1** …….
5.2.5.2 Analysis of physicochemical parameters of compound **2**…….
5.2.5.3 Analysis of physicochemical parameters of compound **3**…….
5.2.5.4 Analysis of physicochemical parameters of compound **4**…….
5.2.5.5 Analysis of physicochemical parameters of compound **5**…….
5.2.5.6 Analysis of physicochemical parameters of compound **6**…….
5.2.5.7 Analysis of physicochemical parameters of compound **7**…….
5.2.5.8 Analysis of physicochemical parameters of compound **8**…….
5.2.5.9 Analysis of physicochemical parameters of compound **9**…….
5.2.5.10 Analysis of physicochemical parameters of compound **10**……
5.2.6 Assessment of *in vitro* of bioactive potentials……
5.2.6.1 *In vitro* antioxidant assays……...
5.2.6.2 1,1-Diphenyl-2-picryl hydrazil (DPPH) radical scavenging activities……...
5.2.6.3 2,2'-Azino-bis-3-ethylbenzothiozoline-6-sulfonic Acid ($ABTS^{+}$) radical scavenging activities……...
5.2.7 *In vitro* anti-inflammatory assays……
5.2.7.1 Cyclooxygenases (COX) inhibition properties……...
5.2.7.2 5-Lipoxygenase (5-LOX) inhibition properties …….
5.2.8 *In vitro* anti-diabetic activities…….....
5.2.8.1 α-Amylase inhibition assay…….
5.2.8.2 α-Glucosidase inhibition assay……
5.2.8.3 Dipeptidyl peptidase-4 (DPP-4) inhibition assay……
5.2.9 The structure-activity relationship analyses of secondary metabolites isolated from EtOAc:MeOH extract of *P. tetrastromatica*……..
5.2.10 *In silico* molecular modeling……..
5.2.11 Statistical analyses……..
5.3 Results and discussion……
5.3.1 Chromatographic fractionation, bioactive potentials and spectroscopic analyses
5.3.1.1 Chromatographic fractionation, bioactive potentials and spectroscopic analyses of intermediate fractions from EtOAc:MeOH extract of *P. tetrastromatica* ……
5.3.2 Spectroscopic analyses of intermediate fractions from EtOAc:MeOH extract of *P. tetrastromatica* ……
5.3.3 Isolation of bioactive secondary metabolites from EtOAc:MeOH extract of *P. tetrastromatica* …….
5.3.4 Spectroscopic analyses of bioactive secondary metabolites isolated from

EtOAc:MeOH extract of *P. tetrastromatica* ……..
5.3.4.1 Structural characterization of xenicane diterpene derivatives (**1**-**5**) ……
5.3.4.1a Structural characterization of compound **1**……
5.3.4.1b Structural characterization of compound **2**……
5.3.4.1c Structural characterization of compound **3**……
5.3.4.1d Structural characterization of compound **4**……
5.3.4.1e Structural characterization of compound **5**……
5.3.4.2 Structural characterization of dolabellane and dolastane diterpene derivatives (**6**-**10**) …….
5.3.4.2a Structural characterization of compound **6**……
5.3.4.2b Structural characterization of compound **7**……
5.3.4.2c Structural characterization of compound **8**……
5.3.4.2d Structural characterization of compound **9**……
5.3.4.2e Structural characterization of compound **10**……..
5.3.5 Pharmacological potentials of secondary metabolites isolated from EtOAc-MeOH extract of *P. tetrastromatica;* antioxidant, anti-inflammatory and antidiabetic properties……
5.3.5.1 Antioxidative properties of bioactives isolated from EtOAc:MeOH extract of *P. tetrastromatica*……
5.3.5.2 Anti-inflammatory properties of bioactives isolated from EtOAc:MeOH extract of *P. tetrastromatica*……..
5.3.5.3 Anti-diabetic properties of bioactives isolated from EtOAc:MeOH extract of *P. tetrastromatica*……
5.3.6 Structure-activity correlation analyses of bioactives isolated from EtOAc:MeOH extract of *P. tetrastromatica*……
5.3.7 *In silico* molecular docking analysis of bioactives isolated from *P. tetrastromatica*……
5.4 Conclusions…….

CHAPTER 6: EXTRACTION, PURIFICATION AND STRUCTURAL CHARACTERIZATION OF POLYSACCHARIDES FROM SEAWEEDS (PHAEOPHYCEAE AND RHODOPHYCEAE)AND PHARMACOLOGICAL APPLICATIONS

6.1 Background……
6.2 Materials and methods……
6.2.1 Collection and processing of seaweed materials……....
6.2.2 Chemicals, reagents and instrumentation……
6.2.3 Extraction, isolation and purification of sulfated polysaccharide from red seaweed *G. salicornia*……
6.2.4 Composition analysis of polysaccharide fractions……..
6.2.4.1 Determination of total carbohydrate content……...
6.2.4.2 Determination of uronic acid content……..
6.2.4.3 Determination of sulfate content…….
6.2.4.4 Determination of protein content……
6.2.5 Analysis of monosaccharide composition……...

6.2.6 Preparation of sulfated polysaccharide based silver nano composite
6.2.7 Pharmacological activities of polysaccharide fractions, pure polysaccharide and polysaccharide based nano composite…….
6.2.7.1 *In vitro* antioxidant activities……...
6.2.7.1.1 1,1-Diphenyl-2-picryl hydrazil (DPPH) and 2,2-azino-bis-3-ethylbenzothiozoline-6- sulfonic acid ($ABTS^{+}$) radical scavenging activities…...
6.2.7.2 *In vitro* antidiabetic activities……..
6.2.7.2.1 α-Amylase inhibition assay……
6.2.8.2.2 α-Glucosidase inhibition assay……
6.2.8.2.3 Dipeptidyl peptidase-4 (DPP-4) inhibition assay……
6.2.7.3 *In vitro* anti-osteoporotic activities…….
6.2.7.3.1 Alkaline phosphatase inhibitory activity…….
6.2.7.3.2 Cytotoxicity analysis by MTT assay on mesenchymal cells……..
6.2.8 Spectroscopic analysis of sulfated polysaccharide derived from *G. salicornia*…
6.2.9 Glycosidic linkage pattern analysis of sulfated polysaccharide derived from *G. salicornia*…….
6.2.10 Statistical analysis……...
6.3 Results and discussion…….
6.3.1 Extraction, purification, yield and chemical composition analysis of the seaweed derived sulfated polysaccharide……..
6.3.2 Structural characterization of sulfated polysaccharide……
6.3.3 Fourier transform infrared spectral (FT-IR) analysis of ……
6.3.4 NMR spectroscopic analysis……...
6.3.5 Pharmacological properties of sulfated polysaccharide…….
6.3.5.1 *In vitro* antioxidant activities……...
6.3.5.2 *In vitro* antidiabetic activities……..
6.3.5.3 *In vitro* anti-osteoporotic activities…….
6.3.6 Structural characterization of sulfated polysaccharide by methylation analysis……
6.3.7 Structural elucidation and Glycosidic linkage analysis reductive cleavage method using mass, NMR and FT-IR spectroscopic methods……
6.4 Conclusions…….

CHAPTER 8: SUMMARY…….
REFERENCES ……..…….
PUBLICATIONS ……...……..

TABLE CAPTIONS

Table 1. Percentage yield, phenolic contents and pharmacological activities of the organic extracts of seaweeds belonging to Dictyotophycidae, Rhodymeniophycidae and Corallinophycidae

Table 2. Type and integral values of protons obtained from the 1H-NMR of the organic extracts of seaweeds belonging to the subclasses Dictyotophycidae (phylum Ochrophyta), Rhodymeniophycidae and Corallinophycidae (phylum Rhodophyta).

Table 4.1.: Yield and bioactivities (antioxidant, anti-inflammatory and antidiabetic) of sub-fractions from EtOAc-MeOH extract of *G. salicornia*

Table 4.10: NMR spectroscopic data[a] of 24(4→23)-abeo-olean-(12-oxo)-3,5-diene-deconoate (**3**) isolated from red seaweed *G. salicornia*

Table 4.13: NMR spectroscopic data of compound (**6**), 1-butoxy-4,4,11b,11c-tetramethyl-1,2,3,3a,4,5,6,6a,11b,11c-decahydrobenzo[kl]-xanthen-10-ol (**6**)isolated from red seaweed *G. salicornia*

Table 4.14: NMR spectroscopic data of compound (**7**), 4'-[10'-[7-Hydroxy-2,8-dimethyl-6-(pentyloxy)-*2H*-chromen-2-yl]ethyl]-3',4'-dimethyl-cyclohexanone (**7**) isolated from red seaweed *G. salicornia*

Table 4.15: NMR spectroscopic data of compound (**8**), 3'-[10'-(8-Hydroxy-5-methoxy-2,6,7-trimethyl-*2H*-chromen-2-yl)ethyl]-3'-methyl-2'-methylene cyclohexyl butyrate (**8**) isolated from red seaweed *G. salicornia***Table 4.16:** NMR spectroscopic data of compound (**9**), 3-(hydroxymethyl)-7-(methoxymethyl)-3,11-dimethyl-9-oxospiro[5.5]undec-4-en-10-methylbutanoate (**9**) isolated from red seaweed *G. salicornia*

Table 4.17: NMR spectroscopic data of compound (**10),** 4-ethoxy-11,11-dimethyl-7-methylene-8-(propionyloxy)spiro[5.5]undec-2-en-10^3,10^5-dihydroxytetrahydro-*2H*-pyran-10-carboxylate (**10**) isolated from red seaweed *G. salicornia*

Table 4.18: NMR spectroscopic data of compound (**11),** 15-(Octahydro-7-(4,5-dihydro-3-methoxy-2,6-dimethyl-*2H*-pyran-6-yl)-10-methylpyrano[3,2-b]pyran-14-yl)-18-(19-methyl-23-methyleneoxepan-19-yl)pent-15-en-18-ol (**11**) isolated from red seaweed *G. salicornia*

Table 4.19: NMR spectroscopic data of compound (**12),** tetrahydro-6-(hexahydro-13-((tetrahydro-18-(23-hydroxy-23-methylheptan-19-yl)-15-methylfuran-15-yl)methyl)-10-methyl-*2H*-furo[3,*2-b*]pyran-7-yl)-2,2,6-trimethyl-*2H*-pyran-3-yl (**12**) isolated from red seaweed *G. salicornia*

Table 4.2.: Yield and bioactivities of (antioxidant, anti-inflammatory and antidiabetic) sub-column fractions derived from EtOAc-MeOH extract of *G. salicornia*

Table 4.20: NMR spectroscopic data of compound (**13),** 3-acetyl-14-(furanyl)-11-methyl-15-(15^3-methylbutyloxy)-8-oxabicyclo-[21.3.1]heptacosa-11,23,25,27 tetraene-7,18-dione (**13**) isolated from red seaweed *G. salicornia*

Table 4.21: NMR spectroscopic data of compound (**14),** (2E,12E,14E)-10-acetyl-9-isopentyl-2-methyl-5,16,23^1-trioxa-bicyclo[21.3.1]-heptacosa-2,12,14-triene-6,19-dione (**14**) isolated from red seaweed *G. salicornia*

Table 4.22: NMR spectroscopic data of compound (**15),** (2Z,5E,16E)-8-hydroxy-20-isobutyl-16-methyl-7,14-dioxa-bicyclo[19.3.1]-pentacosa-2,5,16-triene-10,23-dione (**15**) isolated from red seaweed *G. salicornia*

Table 4.23.: *In vitro* antioxidant, anti-inflammatory and antidiabetic {radical scavenging, cyclooxygenase-1 & 2 (COX-1 & 2) and 5-lipoxygenase (5-LOX)) and α-amylase/glucosidase} activities of compounds (**1-15**) isolated from EtOAc-MeOH extract of *G. salicornia* against commercial standard, tocopherol (T), ibuprofen (I) and acarbose (A)

Table 4.24: Molecular descriptors (electronic, steric and hydrophobic)[†] of compound **1** from *G. salicornia*

Table 4.25: Molecular descriptors (electronic, steric and hydrophobic)[†] of compounds **2**-**3** from *G. salicornia*
Table 4.26: Molecular descriptors (electronic, steric and hydrophobic)[†] of compounds **4**-**6** from *G. salicornia*
Table 4.27: Molecular descriptors (electronic, steric and hydrophobic)[†] of compounds **7**-**8** from *G. salicornia*
Table 4.28: Molecular descriptors (electronic, steric and hydrophobic)[†] of compounds **9**-**10** from *G. salicornia*
Table 4.29: Molecular descriptors (electronic, steric and hydrophobic)[†] of compounds **11**-**12** from *G. salicornia*
Table 4.3.: Yield and bioactivities of (antioxidant, anti-inflammatory and antidiabetic) sub-column fractions derived from EtOAc-MeOH extract of *G. salicornia*
Table 4.30: Molecular descriptors (electronic, steric and hydrophobic)[†] of compounds **13**-**15** from *G. salicornia*
Table 4.31: The binding energy, docking score, inhibition constant, intermolecular energy and torsional free energy between the ligands (compounds **1**) and the active sites of 5-lipoxygenase
Table 4.32: The binding energy (B.E), inhibition constant (IC), intermolecular energy (I.E) and torsional free energy (T.E) between the ligands (compounds **2**-**3**) and the active sites of carbolytic enzymes α-glucosidase and α-amylase.
Table 4.33: The binding energy, docking score, inhibition constant, intermolecular energy and torsional free energy between the ligands (compounds **4**-**6**) and the active sites of 5-lipoxygenase
Table 4.34: The binding energy, docking score, inhibition constant, intermolecular energy and torsional free energy between the ligands (compounds **7**-**8**) and the active sites of 5-lipoxygenase.
Table 4.35: The binding energy, inhibition constant, intermolecular energy and torsional free energy between the ligands (compounds **9**-**10**) and the active sites of pro-inflammatory enzyme 5-LOX
Table 4.36: The binding energy, inhibition constant, intermolecular energy and torsional free energy between the ligands (compounds **11**-1**2**) and the active sites of pro-inflammatory enzymes 5-LOX
Table 4.37: The binding energy, inhibition constant, intermolecular energy and torsional free energy between the ligands (compounds **13**-**15**) and the active sites of pro-inflammatory enzyme 5-LOX
Table 4.4.: Yield and bioactivities (antioxidant, anti-inflammatory and antidiabetic) of sub-fractions from EtOAc-MeOH extract of *G. salicornia*
Table 4.5.: Yield and bioactivities (antioxidant, anti-inflammatory and antidiabetic) of sub-fractions from EtOAc-MeOH extract of *G. salicornia*
Table 4.6.: Yield and bioactivities (antioxidant, anti-inflammatory and antidiabetic) of sub-fractions from EtOAc-MeOH extract of *G. salicornia*
Table 4.7.: Yield and bioactivities (antioxidant, anti-inflammatory and antidiabetic) of sub-fractions from EtOAc-MeOH extract of *G. salicornia*
Table 4.8: NMR spectroscopic data[a] of methyl-16(13→14)-abeo-7-labdene-(12-oxo) carboxylate (**1**) isolated from red seaweed *G. salicornia*
Table 4.9: NMR spectroscopic data[a] of 24(4→23), 27(8→26), 30(20→29)-tris-abeo-olean-(12-oxo)-1,15,22-triene-methyl-hept-5-enoate (**2**) isolated from red seaweed *G. salicornia*

FIGURE CAPTIONS

Figure 1.1.: The percentage share of seaweeds along with different classes of marine organisms
Figure 1.2.: The percentage share of different seaweeds in the classification
Figure 1.3.: The major collection spots in Indian coastline
Figure 1.4.: The distribution of seaweeds in coastal region of India
Figure 1.5.: ROS induce oxidative damage to proteins, lipids and DNA
Figure 1.6.: Enzymatic and non-enzymatic antioxidants in seaweeds.
Figure 2.1.: Number of marine bioactive compounds isolated in the periods of 1965-2016 (Alves et al., 2018)
Figure 2.2.: The distribution of different marine living forms by phylum (Blunt *et al*., 2002)
Figure 2.3.: The Distribution of marine living forms between the various phyla isolated over the period of 1971-2015 (Blunt *et al*., 2017)
Figure 2.4.: Distribution of the seaweed secondary metabolites isolated per year (Blunt et al., 2009) and coupled with data from the same authors (Blunt et al., 2010, 2011, 2017 & 2018)
Figure 2.5.: Percentage diversity of the seaweeds and approximate proportion of secondary metabolites identified from seaweeds belonging to three major classes, Rhodophyceae, Phaeophyceae and Chlorophyceae over the period of 2000 - 2018 (approximate proportions of secondary metabolites assembled from Faulkner (2000 - 2002) and Blunt et al. (2003 - 2018).
Figure 2.6.: Thallus of *Gracilaria species* belonging to the family Gracilariaceae (Rhodophyta, Gracilariales)
Figure 2.7.: Thallus of *Padina species* is belonging to the family Dictyotaceae (Phaeophyta, Dictyotales)
Figure 3.1.: Representative photograph of sample collection site located between 8º48′ N, 78º9′ E and 9º14′ N, 79º14′ E at Gulf of Mannar of Mandapam region
Figure 3.10.: ^{1}H NMR spectrum of EtOAc-MeOH extract of *G. salicornia*
Figure 3.11.: ^{1}H NMR spectrum of EtOAc-MeOH extract of *P. tetrastromatica*
Figure 3.12.: ^{1}H NMR spectrum of EtOAc-MeOH extract of *G. canaliculata*
Figure 3.13.: ^{1}H NMR spectrum of EtOAc-MeOH extract of *G. corticata*
Figure 3.14.: ^{1}H NMR spectrum of EtOAc-MeOH extract of *H. edulis*
Figure 3.15.: ^{1}H NMR spectrum of EtOAc-MeOH extract of *A. fragilissima*
Figure 3.16.: ^{1}H NMR spectrum of EtOAc-MeOH extract of *P. pedrochei*
Figure 3.17.: ^{1}H NMR spectrum of EtOAc-MeOH extract of *S. filamentosa*
Figure 3.18.: ^{1}H NMR spectrum of EtOAc-MeOH extract of *H. dilatata*
Figure 3.19.: ^{1}H NMR spectrum of EtOAc-MeOH extract of *P. hornemannii*
Figure 3.2.: Representative photograph of four seaweeds, *P. tetrastromatica, G. salicornia, G. canaliculata and G. corticata* selected for the pharmacological screening
Figure 3.20.: ^{13}C NMR spectrum of EtOAc-MeOH extract of *G. salicornia*
Figure 3.21.: ^{13}C NMR spectrum of EtOAc-MeOH extract of *P. tetrastromatica*
Figure 3.22.: ^{13}C NMR spectrum of EtOAc-MeOH extract of *G. canaliculata*
Figure 3.23.: ^{13}C NMR spectrum of EtOAc-MeOH extract of *G. corticata*
Figure 3.24.: ^{13}C NMR spectrum of EtOAc-MeOH extract of *H. edulis*
Figure 3.25.: ^{13}C NMR spectrum of EtOAc-MeOH extract of *A. fragilissima*
Figure 3.26.: ^{13}C NMR spectrum of EtOAc-MeOH extract of *P. pedrochei*
Figure 3.27.: ^{13}C NMR spectrum of EtOAc-MeOH extract of *S. filamentosa*
Figure 3.28.: ^{13}C NMR spectrum of EtOAc-MeOH extract of *H. dilatata*
Figure 3.29.: ^{13}C NMR spectrum of EtOAc-MeOH extract of *P. hornemannii*
Figure 3.3.: Representative photograph of six seaweeds, *G. corticata, P. pedrochei, H. dilatata, S. filamentosa, P. hornemannii and A. fragilissima* selected for the pharmacological screening
Figure 3.30.: FTIR spectrum of EtOAc-MeOH extract of *G. salicornia*
Figure 3.31.: FTIR spectrum of EtOAc-MeOH extract of *P. tetrastromatica*

Figure 3.32.: FTIR spectrum of EtOAc-MeOH extract of *G. canaliculata*
Figure 3.33.: FTIR spectrum of EtOAc-MeOH extract of *G. corticata*
Figure 3.34.: FTIR spectrum of EtOAc-MeOH extract of *H. edulis*
Figure 3.35.: FTIR spectrum of EtOAc-MeOH extract of *A. fragilissima*
Figure 3.36.: FTIR spectrum of EtOAc-MeOH extract of *P. pedrochei*
Figure 3.37.: FTIR spectrum of EtOAc-MeOH extract of *S. filamentosa*
Figure 3.38.: FTIR spectrum of EtOAc-MeOH extract of *H. dilatata*
Figure 3.39.: FTIR spectrum of EtOAc-MeOH extract of *P. hornemannii*
Figure 3.4.: FTIR spectra of the organic extracts of *G. salicornia*-TA1, *P. tetrastromatica*-TA2, *G. canaliculata*-TA3, *G. corticata*-TA4, *H. edulis*-TA5, *A. fragilissima*-TA6, *P. pedrochei*-TA7, *S. filamentosa*-TA8, *H. dilatata*-TA9, and *P. hornemannii*-TA10.
Figure 3.5.: ^{1}H-NMR spectra of the organic extracts of (A) *G. salicornia*, (B) *P. tetrastromatica*, (C) *G. canaliculata*, (D) *G. corticata*, and (E) *H. edulis*. The spectra were vertically stacked according to their decreasing order of activities.
Figure 3.6.: ^{1}H-NMR spectra of the organic extracts of (F) *A. fragilissima*, (G) *P. pedrochei*, (H) *S. filamentosa*, (I) *H. dilatata*, and (J) *P. hornemannii*. The spectra were vertically stacked according to their decreasing order of activities
Figure 3.7.: ^{13}C-NMR spectra of the organic extracts of (A) *G. salicornia*, (B) *P. tetrastromatica*, (C) *G. canaliculata*, (D) *G. corticata*, and (E) *H. edulis*. The spectra were vertically stacked according to their decreasing order of activities.
Figure 3.8.: ^{13}C-NMR spectra of the organic extracts of (F) *A. fragilissima*, (G) *P. pedrochei*, (H) *S. filamentosa*, (I) *H. dilatata*, and (J) *P. hornemannii*. The spectra were vertically stacked according to their decreasing order of activities.
Figure 3.9.: Loading plot diagram (various components, PC1 and PC2 in the rotated space) of antioxidant activities vs anti-inflammatory, anti-diabetic and anti-hypertensive activities of the organic extracts of the studied seaweeds.
Figure 4.1.: The red seaweed *G. salicornia* of collected from the southeast coastline of the Indian sub-continent Gulf of Mannar region; between 8º48' N, 78°9' E and 9°14' N, 79°14' E)
Figure 4.10.: Key ^{1}H-^{1}H COSY (bold face bonds), selected HMBC (black coloured double barbed arrows) correlations of methyl-16(13→14)-abeo-7-labdene-(12-oxo) carboxylate
Figure 4.10.: ^{13}C-NMR spectrum of methyl-16(13→14)-abeo-7-labdene-(12-oxo) carboxylate (**1**)
Figure 4.100.: FTIR spectrum of 4'-[10'-[7-Hydroxy-2,8-dimethyl-6-(pentyloxy)-*2H*-chromen-2-yl]ethyl]-3',4'-dimethyl-cyclohexanone (7)
Figure 4.101.: ^{1}H NMR spectrum of 4'-[10'-[7-hydroxy-2,8-dimethyl-6-(pentyloxy)-*2H*-chromen-2-yl]ethyl]-3',4'-dimethyl-cyclohexanone (7)
Figure 4.102.: ^{13}C NMR spectrum of 4'-[10'-[7-hydroxy-2,8-dimethyl-6-(pentyloxy)-*2H*-chromen-2-yl]ethyl]-3',4'-dimethyl-cyclohexanone (7)
Figure 4.103.: ^{135}DEPT spectrum of 4'-[10'-[7-hydroxy-2,8-dimethyl-6-(pentyloxy)-*2H*-chromen-2-yl]ethyl]-3',4'-dimethyl-cyclohexanone (7)
Figure 4.104.: HSQC spectrum of 4'-[10'-[7-hydroxy-2,8-dimethyl-6-(pentyloxy)-*2H*-chromen-2-yl]ethyl]-3',4'-dimethyl-cyclohexanone (7)
Figure 4.105.: ^{1}H-^{1}H COSY (bold face bonds), and selected HMBCs (double-barbed arrows), correlations of 4'-[10'-[7-Hydroxy-2,8-dimethyl-6-(pentyloxy)-*2H*-chromen-2-yl]ethyl]-3',4'-dimethyl-cyclohexanone (**7**)
Figure 4.106.: ^{1}H-^{1}H COSY spectrum of 4'-[10'-[7-Hydroxy-2,8-dimethyl-6-(pentyloxy)-*2H*-chromen-2-yl]ethyl]-3',4'-dimethyl-cyclohexanone (7)
Figure 4.107.: HMBC spectrum of 4'-[10'-[7-hydroxy-2,8-dimethyl-6-(pentyloxy)-*2H*-chromen-2-yl]ethyl]-3',4'-dimethyl-cyclohexanone (7)
Figure 4.108.: NOESY (double-barbed arrows), correlations of 4'-[10'-[7-hydroxy-2,8-dimethyl-6-(pentyloxy)-*2H*-chromen-2-yl]ethyl]-3',4'-dimethyl-cyclohexanone (7)

Figure 4.109.: NOESY (double-barbed arrows), correlations of 4'-[10'-[7-hydroxy-2,8-dimethyl-6-(pentyloxy)-*2H*-chromen-2-yl]ethyl]-3',4'-dimethyl-cyclohexanone (7)
Figure 4.11.: ^{1}H-^{1}H COSY correlation spectrum of methyl-16(13→14)-abeo-7-labdene-(12-oxo) carboxylate (**1**)
Figure 4.110.: EI-MS spectrum of 4'-[10'-[7-hydroxy-2,8-dimethyl-6-(pentyloxy)-*2H*-chromen-2-yl]ethyl]-3',4'-dimethyl-cyclohexanone (7)
Figure 4.111.: Tentative mass fragmentation pattern of 4'-[10'-[7-hydroxy-2,8-dimethyl-6-(pentyloxy)-*2H*-chromen-2-yl]ethyl]-3',4'-dimethyl-cyclohexanone (7)
Figure 4.112.: UV spectrum of 3'-[10'-(8-hydroxy-5-methoxy-2,6,7-trimethyl-*2H*-chromen-2-yl)ethyl]-3'-methyl-2'-methylene cyclohexyl butyrate (**8**)
Figure 4.113.: HPLC chromatogram of 3'-[10'-(8-Hydroxy-5-methoxy-2,6,7-trimethyl-*2H*-chromen-2-yl)ethyl]-3'-methyl-2'-methylene cyclohexyl butyrate (**8**)
Figure 4.114.: HRESIMS of 3'-[10'-(8-hydroxy-5-methoxy-2,6,7-trimethyl-*2H*-chromen-2-yl)ethyl]-3'-methyl-2'-methylene cyclohexyl butyrate (**8**)
Figure 4.115.: FTIR spectrum of 3'-[10'-(8-hydroxy-5-methoxy-2,6,7-trimethyl-*2H*-chromen-2-yl)ethyl]-3'-methyl-2'-methylene cyclohexyl butyrate (**8**)
Figure 4.116.: ^{1}H NMR spectrum of 3'-[10'-(8-hydroxy-5-methoxy-2,6,7-trimethyl-*2H*-chromen-2-yl)ethyl]-3'-methyl-2'-methylene cyclohexyl butyrate (**8**)
Figure 4.117.: ^{13}C NMR spectrum of 3'-[10'-(8-hydroxy-5-methoxy-2,6,7-trimethyl-*2H*-chromen-2-yl)ethyl]-3'-methyl-2'-methylene cyclohexyl butyrate (**8**)
Figure 4.118.: ^{135}DEPT NMR spectrum of 3'-[10'-(8-hydroxy-5-methoxy-2,6,7-trimethyl-*2H*-chromen-2-yl)ethyl]-3'-methyl-2'-methylene cyclohexyl butyrate (**8**)
Figure 4.119.: HSQC spectrum of 3'-[10'-(8-hydroxy-5-methoxy-2,6,7-trimethyl-*2H*-chromen-2-yl)ethyl]-3'-methyl-2'-methylene cyclohexyl butyrate (**8**)
Figure 4.12.: HMBC correlation spectrum methyl-16(13→14)-abeo-7-labdene-(12-oxo) carboxylate (**1**)
Figure 4.120.: ^{1}H-^{1}H COSY (bold face bonds), and selected HMBCs (double-barbed arrows), correlations of 3'-[10'-(8-hydroxy-5-methoxy-2,6,7-trimethyl-*2H*-chromen-2-yl)ethyl]-3'-methyl-2'-methylene cyclohexyl butyrate (**8**)
Figure 4.121.: ^{1}H-^{1}H COSY spectrum of 3'-[10'-(8-hydroxy-5-methoxy-2,6,7-trimethyl-*2H*-chromen-2-yl)ethyl]-3'-methyl-2'-methylene cyclohexyl butyrate (**8**)
Figure 4.122.: HMBC spectrum of 3'-[10'-(8-hydroxy-5-methoxy-2,6,7-trimethyl-*2H*-chromen-2-yl)ethyl]-3'-methyl-2'-methylene cyclohexyl butyrate (**8**)
Figure 4.123.: NOESY (double-barbed arrows), correlations of 3'-[10'-(8-hydroxy-5-methoxy-2,6,7-trimethyl-*2H*-chromen-2-yl)ethyl]-3'-methyl-2'-methylene cyclohexyl butyrate (**8**)
Figure 4.124.: ^{1}H NMR spectrum of 3'-[10'-(8-hydroxy-5-methoxy-2,6,7-trimethyl-*2H*-chromen-2-yl)ethyl]-3'-methyl-2'-methylene cyclohexyl butyrate (**8**)
Figure 4.125.: EI-MS spectrum of 3'-[10'-(8-hydroxy-5-methoxy-2,6,7-trimethyl-*2H*-chromen-2-yl)ethyl]-3'-methyl-2'-methylene cyclohexyl butyrate (**8**)
Figure 4.126.: Tentative mass fragmentation pattern of 3'-[10'-(8-hydroxy-5-methoxy-2,6,7-trimethyl-*2H*-chromen-2-yl)ethyl]-3'-methyl-2'-methylene cyclohexyl butyrate (**8**)
Figure 4.127.: Structures of spiro[5.5]undecane compounds (**9**-**10**) isolated from the seaweed *G. salicornia*. The representative image of the thalli of *G. salicornia* was shown.
Figure 4.128.: UV spectrum of 3-(hydroxymethyl)-7-(methoxymethyl)-3,11-dimethyl-9-oxospiro[5.5]undec-4-en-10-methylbutanoate (**9**)
Figure 4.129.: HPLC chromatogram of 3-(hydroxymethyl)-7-(methoxymethyl)-3,11-dimethyl-9-oxospiro[5.5]undec-4-en-10-methylbutanoate (**9**)
Figure 4.13.: HSQC spectrum methyl-16(13→14)-abeo-7-labdene-(12-oxo) carboxylate (**1**)
Figure 4.130.: ESIMS spectrum of 3-(hydroxymethyl)-7-(methoxymethyl)-3,11-dimethyl-9-oxospiro[5.5]undec-4-en-10-methylbutanoate (**9**)

Figure 4.131.: FTIR spectrum of 3-(hydroxymethyl)-7-(methoxymethyl)-3,11-dimethyl-9-oxospiro[5.5]undec-4-en-10-methylbutanoate (**9**)
Figure 4.132.: ^{1}H-NMR spectrum of 3-(hydroxymethyl)-7-(methoxymethyl)-3,11-dimethyl-9-oxospiro[5.5]undec-4-en-10-methylbutanoate (**9**)
Figure 4.133.: ^{13}C-NMR spectrum of 3-(hydroxymethyl)-7-(methoxymethyl)-3,11-dimethyl-9-oxospiro[5.5]undec-4-en-10-methylbutanoate (**9**)
Figure 4.134.: ^{135}DEPT spectrum of 3-(hydroxymethyl)-7-(methoxymethyl)-3,11-dimethyl-9-oxospiro[5.5]undec-4-en-10-methylbutanoate (**9**)
Figure 4.135.: HSQC spectrum of 3-(hydroxymethyl)-7-(methoxymethyl)-3,11-dimethyl-9-oxospiro[5.5]undec-4-en-10-methylbutanoate (**9**)
Figure 4.136.: ^{1}H-^{1}H COSY (bold face bonds), and selected HMBCs (double-barbed arrows), correlations of 3-(hydroxymethyl)-7-(methoxymethyl)-3,11-dimethyl-9-oxospiro[5.5]undec-4-en-10-methylbutanoate (**9**)
Figure 4.137.: ^{1}H-^{1}H COSY spectrum of 3-(hydroxymethyl)-7-(methoxymethyl)-3,11-dimethyl-9-oxospiro[5.5]undec-4-en-10-methylbutanoate (**9**)
Figure 4.138.: HMBC spectrum of 3-(hydroxymethyl)-7-(methoxymethyl)-3,11-dimethyl-9-oxospiro[5.5]undec-4-en-10-methylbutanoate (**9**)
Figure 4.139.: NOESY (double barbed arrows) correlations of 3-(hydroxymethyl)-7-(methoxymethyl)-3,11-dimethyl-9-oxospiro[5.5]undec-4-en-10-methylbutanoate (**9**)
Figure 4.14.: Key NOESY correlations (double headed arrows) of methyl-16(13→14)-abeo-7-labdene-(12-oxo) carboxylate.
Figure 4.140.: NOESY spectrum of 3-(hydroxymethyl)-7-(methoxymethyl)-3,11-dimethyl-9-oxospiro[5.5]undec-4-en-10-methylbutanoate (**9**)
Figure 4.141.: EI-MS spectrum of 3-(hydroxymethyl)-7-(methoxymethyl)-3,11-dimethyl-9-oxospiro[5.5]undec-4-en-10-methylbutanoate (**9**)
Figure 4.142.: Tentative mass fragmentation pattern of 3-(hydroxymethyl)-7-(methoxymethyl)-3,11-dimethyl-9-oxospiro[5.5]undec-4-en-10-methylbutanoate (**9**)
Figure 4.143.: UV spectrum of 4-ethoxy-11,11-dimethyl-7-methylene-8-(propionyloxy)spiro[5.5]undec-2-en-10^{3},10^{5}-dihydroxytetrahydro-*2H*-pyran-10-carboxylate (**10**)
Figure 4.144.: HPLC chromatogram of 4-ethoxy-11,11-dimethyl-7-methylene-8-(propionyloxy)spiro[5.5]undec-2-en-10^{3},10^{5}-dihydroxytetrahydro-*2H*-pyran-10-carboxylate (**10**)
Figure 4.145.: HRESIMS spectrum of 4-ethoxy-11,11-dimethyl-7-methylene-8-(propionyloxy)spiro[5.5]undec-2-en-10^{3},10^{5}-dihydroxytetrahydro-*2H*-pyran-10-carboxylate (**10**)
Figure 4.146.: FTIR spectrum of 4-ethoxy-11,11-dimethyl-7-methylene-8-(propionyloxy)spiro[5.5]undec-2-en-10^{3},10^{5}-dihydroxytetrahydro-*2H*-pyran-10-carboxylate (**10**)
Figure 4.147.: ^{1}H-NMR spectrum of 4-ethoxy-11,11-dimethyl-7-methylene-8-(propionyloxy)spiro[5.5]undec-2-en-10^{3},10^{5}-dihydroxytetrahydro-*2H*-pyran-10-carboxylate (**10**)
Figure 4.148.: ^{13}C-NMR spectrum of 4-ethoxy-11,11-dimethyl-7-methylene-8-(propionyloxy)spiro[5.5]undec-2-en-10^{3},10^{5}-dihydroxytetrahydro-*2H*-pyran-10-carboxylate (**10**)
Figure 4.149.: ^{135}DEPT spectrum of 4-ethoxy-11,11-dimethyl-7-methylene-8-(propionyloxy)spiro[5.5]undec-2-en-10^{3},10^{5}-dihydroxytetrahydro-*2H*-pyran-10-carboxylate (**10**)
Figure 4.15.: NOESY spectrum of methyl-16(13→14)-abeo-7-labdene-(12-oxo) carboxylate (**1**).
Figure 4.150.: HSQC spectrum of 4-ethoxy-11,11-dimethyl-7-methylene-8-(propionyloxy)spiro[5.5]undec-2-en-10^{3},10^{5}-dihydroxytetrahydro-*2H*-pyran-10-carboxylate (**10**)
Figure 4.151.: ^{1}H-^{1}H COSY spectrum of 4-ethoxy-11,11-dimethyl-7-methylene-8-(propionyloxy)spiro[5.5]undec-2-en-10^{3},10^{5}-dihydroxytetrahydro-*2H*-pyran-10-carboxylate (**10**)
Figure 4.152.: ^{1}H-^{1}H COSY (bold face bonds), and selected HMBCs (double-barbed arrows), correlations of 4-ethoxy-11,11-dimethyl-7-methylene-8-(propionyloxy)spiro[5.5]undec-2-en-10^{3},10^{5}-dihydroxytetrahydro-*2H*-pyran-10-carboxylate (**10**)
Figure 4.153.: HMBC spectrum of 4-ethoxy-11,11-dimethyl-7-methylene-8-(propionyloxy)spiro[5.5]undec-2-en-10^{3},10^{5}-dihydroxytetrahydro-*2H*-pyran-10-carboxylate (**10**)

Figure 4.154.: NOESY correlations (double barbed arrows) of 4-ethoxy-11,11-dimethyl-7-methylene-8-(propionyloxy)spiro[5.5]undec-2-en-10^3,10^5-dihydroxytetrahydro-*2H*-pyran-10-carboxylate (**10**)

Figure 4.155.: EI-MS spectrum of 4-ethoxy-11,11-dimethyl-7-methylene-8-(propionyloxy)spiro[5.5]undec-2-en-10^3,10^5-dihydroxytetrahydro-*2H*-pyran-10-carboxylate (**10**)

Figure 4.156.: Tentative mass fragmentation pattern of 4-ethoxy-11,11-dimethyl-7-methylene-8-(propionyloxy)spiro[5.5]undec-2-en-10^3,10^5-dihydroxytetrahydro-*2H*-pyran-10-carboxylate (**10**)

Figure 4.157.: Structural representations of (**A**) 3-methoxy-2,6-dimethyl-3,4-dihydro-2*H*-pyranyl-(6-(7-(10-methyl-octahydropyrano[3,2-*b*]pyranyl)-14-((19-methyl-23-methyleneoxepan)-(15-pentene-18-ol)) (**11**) and (**B**) 14-(15-methyltetrahydrofuranyl)-(18-(23-(hydroxy-23-methylheptanyl)-10-methylhexahydro-2*H*-furo-[3,2-*b*]pyranyl))-2,2,6-trimethyltetrahydro-2*H*-pyran-3- butyrate (**12**) purified from *G. salicornia*. (**D**) The characteristic of thalli (leaf-like structures) of *G. salicornia* was presented.

Figure 4.158.: UV spectrum of 15-(octahydro-7-(4,5-dihydro-3-methoxy-2,6-dimethyl-*2H*-pyran-6-yl)-10-methylpyrano[3,2-b]pyran-14-yl)-18-(19-methyl-23-methyleneoxepan-19-yl)pent-15-en-18-ol (**11**)

Figure 4.159.: HPLC chromatogram of 15-(octahydro-7-(4,5-dihydro-3-methoxy-2,6-dimethyl-*2H*-pyran-6-yl)-10-methylpyrano[3,2-b]pyran-14-yl)-18-(19-methyl-23-methyleneoxepan-19-yl)pent-15-en-18-ol (**11**)

Figure 4.16.: EI-MS spectrum of methyl-16(13→14)-abeo-7-labdene-(12-oxo) carboxylate (**1**)

Figure 4.160.: HRESIMS spectrum of 15-(octahydro-7-(4,5-dihydro-3-methoxy-2,6-dimethyl-*2H*-pyran-6-yl)-10-methylpyrano[3,2-b]pyran-14-yl)-18-(19-methyl-23-methyleneoxepan-19-yl)pent-15-en-18-ol (**11**)

Figure 4.161.: FTIR spectrum of 15-(octahydro-7-(4,5-dihydro-3-methoxy-2,6-dimethyl-*2H*-pyran-6-yl)-10-methylpyrano[3,2-b]pyran-14-yl)-18-(19-methyl-23-methyleneoxepan-19-yl)pent-15-en-18-ol (**11**)

Figure 4.162.: ^{1}H NMR spectrum of 15-(octahydro-7-(4,5-dihydro-3-methoxy-2,6-dimethyl-*2H*-pyran-6-yl)-10-methylpyrano[3,2-b]pyran-14-yl)-18-(19-methyl-23-methyleneoxepan-19-yl)pent-15-en-18-ol (**11**)

Figure 4.163.: ^{13}C NMR spectrum of 15-(octahydro-7-(4,5-dihydro-3-methoxy-2,6-dimethyl-*2H*-pyran-6-yl)-10-methylpyrano[3,2-b]pyran-14-yl)-18-(19-methyl-23-methyleneoxepan-19-yl)pent-15-en-18-ol (**11**)

Figure 4.164.: ^{135}DEPT spectrum of 15-(octahydro-7-(4,5-dihydro-3-methoxy-2,6-dimethyl-*2H*-pyran-6-yl)-10-methylpyrano[3,2-b]pyran-14-yl)-18-(19-methyl-23-methyleneoxepan-19-yl)pent-15-en-18-ol (**11**)

Figure 4.165.: HSQC spectrum of 15-(octahydro-7-(4,5-dihydro-3-methoxy-2,6-dimethyl-*2H*-pyran-6-yl)-10-methylpyrano[3,2-b]pyran-14-yl)-18-(19-methyl-23-methyleneoxepan-19-yl)pent-15-en-18-ol (**11**)

Figure 4.166.: ^{1}H-^{1}H COSY (bold face bonds) and selected HMBCs (double-barbed arrows) correlations of 15-(Octahydro-7-(4,5-dihydro-3-methoxy-2,6-dimethyl-*2H*-pyran-6-yl)-10-methylpyrano[3,2-b]pyran-14-yl)-18-(19-methyl-23-methyleneoxepan-19-yl)pent-15-en-18-ol (**11**)

Figure 4.167.: ^{1}H-^{1}H COSY spectrum of 15-(octahydro-7-(4,5-dihydro-3-methoxy-2,6-dimethyl-*2H*-pyran-6-yl)-10-methylpyrano[3,2-b]pyran-14-yl)-18-(19-methyl-23-methyleneoxepan-19-yl)pent-15-en-18-ol (**11**)

Figure 4.168.: HMBC spectrum of 15-(octahydro-7-(4,5-dihydro-3-methoxy-2,6-dimethyl-*2H*-pyran-6-yl)-10-methylpyrano[3,2-b]pyran-14-yl)-18-(19-methyl-23-methyleneoxepan-19-yl)pent-15-en-18-ol (**11**)

Figure 4.169.: NOESY correlations (double headed arrows) of 15-(octahydro-7-(4,5-dihydro-3-methoxy-2,6-dimethyl-*2H*-pyran-6-yl)-10-methylpyrano[3,2-b]pyran-14-yl)-18-(19-methyl-23-methyleneoxepan-19-yl)pent-15-en-18-ol (**11**)

Figure 4.17.: Tentative mass fragmentation pattern of methyl-16(13→14)-abeo-7-labdene-(12-oxo) carboxylate (**1**)

Figure 4.170.: NOESY spectrum of 15-(octahydro-7-(4,5-dihydro-3-methoxy-2,6-dimethyl-*2H*-pyran-6-yl)-10-methylpyrano[3,2-b]pyran-14-yl)-18-(19-methyl-23-methyleneoxepan-19-yl)pent-15-en-18-ol (**11**)

Figure 4.171.: EI-MS spectrum of 15-(octahydro-7-(4,5-dihydro-3-methoxy-2,6-dimethyl-*2H*-pyran-6-yl)-10-methylpyrano[3,2-b]pyran-14-yl)-18-(19-methyl-23-methyleneoxepan-19-yl)pent-15-en-18-ol (**11**)

Figure 4.172.: Mass fragmentation pattern of 15-(octahydro-7-(4,5-dihydro-3-methoxy-2,6-dimethyl-*2H*-pyran-6-yl)-10-methylpyrano[3,2-b]pyran-14-yl)-18-(19-methyl-23-methyleneoxepan-19-yl)pent-15-en-18-ol (**11**)

Figure 4.173.: UV spectrum of tetrahydro-6-(hexahydro-13-((tetrahydro-18-(23-hydroxy-23-methylheptan-19-yl)-15-methylfuran-15-yl)methyl)-10-methyl-*2H*-furo[3,2-b]pyran-7-yl)-2,2,6-trimethyl-*2H*-pyran-3-yl (**12**)

Figure 4.174.: HPLC chromatogram of tetrahydro-6-(hexahydro-13-((tetrahydro-18-(23-hydroxy-23-methylheptan-19-yl)-15-methylfuran-15-yl)methyl)-10-methyl-*2H*-furo[3,2-b]pyran-7-yl)-2,2,6-trimethyl-*2H*-pyran-3-yl (**12**)

Figure 4.175.: HRESIMS spectrum of tetrahydro-6-(hexahydro-13-((tetrahydro-18-(23-hydroxy-23-methylheptan-19-yl)-15-methylfuran-15-yl)methyl)-10-methyl-*2H*-furo[3,2-b]pyran-7-yl)-2,2,6-trimethyl-*2H*-pyran-3-yl (**12**)

Figure 4.176.: FTIR spectrum of tetrahydro-6-(hexahydro-13-((tetrahydro-18-(23-hydroxy-23-methylheptan-19-yl)-15-methylfuran-15-yl)methyl)-10-methyl-*2H*-furo[3,*2-b*]pyran-7-yl)-2,2,6-trimethyl-*2H*-pyran-3-yl (**12**)

Figure 4.177.: ^{1}H NMR spectrum of tetrahydro-6-(hexahydro-13-((tetrahydro-18-(23-hydroxy-23-methylheptan-19-yl)-15-methylfuran-15-yl)methyl)-10-methyl-*2H*-furo[3,*2-b*]pyran-7-yl)-2,2,6-trimethyl-*2H*-pyran-3-yl (**12**)

Figure 4.178.: ^{13}C NMR spectrum of tetrahydro-6-(hexahydro-13-((tetrahydro-18-(23-hydroxy-23-methylheptan-19-yl)-15-methylfuran-15-yl)methyl)-10-methyl-*2H*-furo[3,*2-b*]pyran-7-yl)-2,2,6-trimethyl-*2H*-pyran-3-yl (**12**)

Figure 4.179.: ^{135}DEPT spectrum of tetrahydro-6-(hexahydro-13-((tetrahydro-18-(23-hydroxy-23-methylheptan-19-yl)-15-methylfuran-15-yl)methyl)-10-methyl-*2H*-furo[3,*2-b*]pyran-7-yl)-2,2,6-trimethyl-*2H*-pyran-3-yl (**12**)

Figure 4.18.: Structural representations of (**A1**) 24(4→23), 27(8→26), 30(20→29)-tris-abeo-olean-(12-oxo)-1,15,22-triene-methyl hept-5-enoate (**1**) and (**A2**) 24(4→23)-abeo-olean-(12-oxo)-3,5-diene-deconoate (**2**) isolated from *G. salicornia*. (**A3**) Representative photograph of thalli of the red seaweed *G. salicornia*.

Figure 4.180.: HSQC spectrum of tetrahydro-6-(hexahydro-13-((tetrahydro-18-(23-hydroxy-23-methylheptan-19-yl)-15-methylfuran-15-yl)methyl)-10-methyl-*2H*-furo[3,*2-b*]pyran-7-yl)-2,2,6-trimethyl-*2H*-pyran-3-yl (**12**)

Figure 4.181.: ^{1}H-^{1}H COSY (bold face bonds) and selected HMBCs (double-barbed arrows), correlations of tetrahydro-6-(hexahydro-13-((tetrahydro-18-(23-hydroxy-23-methylheptan-19-yl)-15-methylfuran-15-yl)methyl)-10-methyl-*2H*-furo[3,*2-b*]pyran-7-yl)-2,2,6-trimethyl-*2H*-pyran-3-yl (**12**)

Figure 4.182.: ^{1}H-^{1}H COSY spectrum of tetrahydro-6-(hexahydro-13-((tetrahydro-18-(23-hydroxy-23-methylheptan-19-yl)-15-methylfuran-15-yl)methyl)-10-methyl-*2H*-furo[3,*2-b*]pyran-7-yl)-2,2,6-trimethyl-*2H*-pyran-3-yl (**12**)

Figure 4.183.: HMBC spectrum of tetrahydro-6-(hexahydro-13-((tetrahydro-18-(23-hydroxy-23-methylheptan-19-yl)-15-methylfuran-15-yl)methyl)-10-methyl-*2H*-furo[3,*2-b*]pyran-7-yl)-2,2,6-trimethyl-*2H*-pyran-3-yl (**12**)

Figure 4.184.: HMBC spectrum of tetrahydro-6-(hexahydro-13-((tetrahydro-18-(23-hydroxy-23-methylheptan-19-yl)-15-methylfuran-15-yl)methyl)-10-methyl-*2H*-furo[3,2-b]pyran-7-yl)-2,2,6-trimethyl-*2H*-pyran-3-yl (**12**)

Figure 4.185.: NOE spectrum of tetrahydro-6-(hexahydro-13-((tetrahydro-18-(23-hydroxy-23-methylheptan-19-yl)-15-methylfuran-15-yl)methyl)-10-methyl-*2H*-furo[3,2-b]pyran-7-yl)-2,2,6-trimethyl-*2H*-pyran-3-yl (**12**)

Figure 4.186.: EI-MS spectrum of tetrahydro-6-(hexahydro-13-((tetrahydro-18-(23-hydroxy-23-methylheptan-19-yl)-15-methylfuran-15-yl)methyl)-10-methyl-*2H*-furo[3,2-b]pyran-7-yl)-2,2,6-trimethyl-*2H*-pyran-3-yl (**12**)

Figure 4.187.: Mass fragmentation pattern m of tetrahydro-6-(hexahydro-13-((tetrahydro-18-(23-hydroxy-23-methylheptan-19-yl)-15-methylfuran-15-yl)methyl)-10-methyl-*2H*-furo[3,2-b]pyran-7-yl)-2,2,6-trimethyl-*2H*-pyran-3-yl (**12**)

Figure 4.188.: Structural representations of 3 macrolides (**13-15**) along with the characteristic of thalli (leaf-like structures) of *G. salicornia* were presented.

Figure 4.189.: UV spectrum of 3-acetyl-14-(furanyl)-11-methyl-15-(15^3-methylbutyloxy)-8-oxabicyclo-[21.3.1]heptacosa-11,23,25,27 tetraene-7,18-dione (**13**)

Figure 4.19.: UVspectrum of 24(4→23), 27(8→26), 30(20→29)-tris-abeo-olean-(12-oxo)-1,15,22-triene-methyl hept-5-enoate **(2)**

Figure 4.190.: HPLC chromatogram of 3-acetyl-14-(furanyl)-11-methyl-15-(15^3-methylbutyloxy)-8-oxabicyclo-[21.3.1]heptacosa-11,23,25,27 tetraene-7,18-dione (**13**)

Figure 4.191.: HRESIMS spectrum of 3-acetyl-14-(furanyl)-11-methyl-15-(15^3-methylbutyloxy)-8-oxabicyclo-[21.3.1]heptacosa-11,23,25,27 tetraene-7,18-dione (**13**)

Figure 4.192.: FTIR spectrum of 3-acetyl-14-(furanyl)-11-methyl-15-(15^3-methylbutyloxy)-8-oxabicyclo-[21.3.1]heptacosa-11,23,25,27 tetraene-7,18-dione (**13**)

Figure 4.193.: ^{1}H NMR spectrum of 3-acetyl-14-(furanyl)-11-methyl-15-(15^3-methylbutyloxy)-8-oxabicyclo-[21.3.1]heptacosa-11,23,25,27 tetraene-7,18-dione

Figure 4.194.: ^{13}C NMR spectrum of 3-acetyl-14-(furanyl)-11-methyl-15-(15^3-methylbutyloxy)-8-oxabicyclo-[21.3.1]heptacosa-11,23,25,27 tetraene-7,18-dione (**13**)

Figure 4.195.: ^{135}DEPT NMR spectrum of 3-acetyl-14-(furanyl)-11-methyl-15-(15^3-methylbutyloxy)-8-oxabicyclo-[21.3.1]heptacosa-11,23,25,27 tetraene-7,18-dione (**13**)

Figure 4.196.: HSQC spectrum of 3-acetyl-14-(furanyl)-11-methyl-15-(15^3-methylbutyloxy)-8-oxabicyclo-[21.3.1]heptacosa-11,23,25,27 tetraene-7,18-dione (**13**)

Figure 4.197.: ^{1}H-^{1}H COSY (bold face bonds) and HMBC (double-barbed arrows) correlations of 3-acetyl-14-(furanyl)-11-methyl-15-(15^3-methylbutyloxy)-8-oxabicyclo-[21.3.1]heptacosa-11,23,25,27 tetraene-7,18-dione (**13**)

Figure 4.198.: ^{1}H-^{1}H COSY spectrum of 3-acetyl-14-(furanyl)-11-methyl-15-(15^3-methylbutyloxy)-8-oxabicyclo-[21.3.1]heptacosa-11,23,25,27 tetraene-7,18-dione (**13**)

Figure 4.199.: ^{1}H-^{1}H COSY (bold face bonds) and HMBC (double-barbed arrows) correlations of 3-acetyl-14-(furanyl)-11-methyl-15-(15^3-methylbutyloxy)-8-oxabicyclo-[21.3.1]heptacosa-11,23,25,27 tetraene-7,18-dione (**13**)

Figure 4.2.: Schematic representation of purification of fractions and compounds from the EtOAc-MeOH extract of *G. salicornia*. CC- column chromatograph

Figure 4.20.: HPLC chromatogram of 24(4→23), 27(8→26), 30(20→29)-tris-abeo-olean-(12-oxo)-1,15,22-triene-methyl hept-5-enoate (**2**)

Figure 4.200.: NOE (double-barbed green coloured arrows for α-orientation and blue coloured arrows for β orientations) correlations of 3-acetyl-14-(furanyl)-11-methyl-15-(15^3-methylbutyloxy)-8-oxabicyclo-[21.3.1]heptacosa-11,23,25,27 tetraene-7,18-dione (**13**)

Figure 4.200.: NOESY spectrum of 3-acetyl-14-(furanyl)-11-methyl-15-(15^3-methylbutyloxy)-8-oxabicyclo-[21.3.1]heptacosa-11,23,25,27 tetraene-7,18-dione (**13**)

Figure 4.201.: EI-MS spectrum of 3-acetyl-14-(furanyl)-11-methyl-15-(15^3-methylbutyloxy)-8-oxabicyclo-[21.3.1]heptacosa-11,23,25,27 tetraene-7,18-dione (**13**)

Figure 4.202.: Tentative mass fragmentation pattern of 3-acetyl-14-(furanyl)-11-methyl-15-(15^3-methylbutyloxy)-8-oxabicyclo-[21.3.1]heptacosa-11,23,25,27 tetraene-7,18-dione (**13**)

Figure 4.203.: UV spectrum of (2E,12E,14E)-10-acetyl-9-isopentyl-2-methyl-5,16,23[1]-trioxa-bicyclo[21.3.1]-heptacosa-2,12,14-triene-6,19-dione (**14**)
Figure 4.204.: HPLC chromatogram of (2E,12E,14E)-10-acetyl-9-isopentyl-2-methyl-5,16,23[1]-trioxa-bicyclo[21.3.1]-heptacosa-2,12,14-triene-6,19-dione (**14**)
Figure 4.205.: HRESIMS spectrum of (2E,12E,14E)-10-acetyl-9-isopentyl-2-methyl-5,16,23[1]-trioxa-bicyclo[21.3.1]-heptacosa-2,12,14-triene-6,19-dione (**14**)
Figure 4.206.: FTIR spectrum of (2E,12E,14E)-10-acetyl-9-isopentyl-2-methyl-5,16,23[1]-trioxa-bicyclo[21.3.1]-heptacosa-2,12,14-triene-6,19-dione (**14**)
Figure 4.207.: ^{1}H NMR spectrum of (2E,12E,14E)-10-acetyl-9-isopentyl-2-methyl-5,16,23[1]-trioxa-bicyclo[21.3.1]-heptacosa-2,12,14-triene-6,19-dione (**14**)
Figure 4.208.: ^{13}C NMR spectrum of (2E,12E,14E)-10-acetyl-9-isopentyl-2-methyl-5,16,23[1]-trioxa-bicyclo[21.3.1]-heptacosa-2,12,14-triene-6,19-dione (**14**)
Figure 4.209.: ^{135}DEPT NMR spectrum of (2E,12E,14E)-10-acetyl-9-isopentyl-2-methyl-5,16,23[1]-trioxa-bicyclo[21.3.1]-heptacosa-2,12,14-triene-6,19-dione (**14**)
Figure 4.21.: HRESIMS of 24(4→23), 27(8→26), 30(20→29)-tris-abeo-olean-(12-oxo)-1,15,22-triene-methyl hept-5-enoate **(2)**
Figure 4.210.: HSQC spectrum of (2E,12E,14E)-10-acetyl-9-isopentyl-2-methyl-5,16,23[1]-trioxa-bicyclo[21.3.1]-heptacosa-2,12,14-triene-6,19-dione (**14**)
Figure 4.211.: ^{1}H-^{1}H COSY (bold face bonds) and HMBC (double-barbed arrows) correlations of (2E,12E,14E)-10-acetyl-9-isopentyl-2-methyl-5,16,23[1]-trioxa-bicyclo[21.3.1]-heptacosa-2,12,14-triene-6,19-dione (**14**)
Figure 4.212.: ^{1}H-^{1}H COSY spectrum of (2E,12E,14E)-10-acetyl-9-isopentyl-2-methyl-5,16,23[1]-trioxa-bicyclo[21.3.1]-heptacosa-2,12,14-triene-6,19-dione (**14**)
Figure 4.213.: HMBC spectrum of (2E,12E,14E)-10-acetyl-9-isopentyl-2-methyl-5,16,23[1]-trioxa-bicyclo[21.3.1]-heptacosa-2,12,14-triene-6,19-dione (**14**)
Figure 4.214.: NOESY (double-barbed green coloured arrows for α-orientation and blue coloured arrows for β orientations) correlations of (2E,12E,14E)-10-acetyl-9-isopentyl-2-methyl-5,16,23[1]-trioxa-bicyclo[21.3.1]-heptacosa-2,12,14-triene-6,19-dione (**14**)
Figure 4.215.: NOE spectrum of (2E,12E,14E)-10-acetyl-9-isopentyl-2-methyl-5,16,23[1]-trioxa-bicyclo[21.3.1]-heptacosa-2,12,14-triene-6,19-dione (**14**)
Figure 4.216.: EI-MS spectrum of (2E,12E,14E)-10-acetyl-9-isopentyl-2-methyl-5,16,23[1]-trioxa-bicyclo[21.3.1]-heptacosa-2,12,14-triene-6,19-dione (**14**)
Figure 4.217.: Tentative mass fragmentation pattern of (2E,12E,14E)-10-acetyl-9-isopentyl-2-methyl-5,16,23[1]-trioxa-bicyclo[21.3.1]-heptacosa-2,12,14-triene-6,19-dione (**14**)
Figure 4.218.: UV spectrum of (2Z,5E,16E)-8-hydroxy-20-isobutyl-16-methyl-7,14-dioxa-bicyclo[19.3.1]-pentacosa-2,5,16-triene-10,23-dione (**15**)
Figure 4.219.: HPLC chromatogram of (2Z,5E,16E)-8-hydroxy-20-isobutyl-16-methyl-7,14-dioxa-bicyclo[19.3.1]-pentacosa-2,5,16-triene-10,23-dione (**15**)
Figure 4.22.: FT-IR of 24(4→23), 27(8→26), 30(20→29)-tris-abeo-olean-(12-oxo)-1,15,22-triene-methyl hept-5-enoate **(2)**
Figure 4.220.: FTIR spectrum of (2Z,5E,16E)-8-hydroxy-20-isobutyl-16-methyl-7,14-dioxa-bicyclo[19.3.1]-pentacosa-2,5,16-triene-10,23-dione (**15**)
Figure 4.221.: ^{1}H NMR spectrum of (2Z,5E,16E)-8-hydroxy-20-isobutyl-16-methyl-7,14-dioxa-bicyclo[19.3.1]-pentacosa-2,5,16-triene-10,23-dione (**15**)
Figure 4.222.: ^{13}C NMR spectrum of (2Z,5E,16E)-8-hydroxy-20-isobutyl-16-methyl-7,14-dioxa-bicyclo[19.3.1]-pentacosa-2,5,16-triene-10,23-dione (**15**)
Figure 4.223.: ^{135}DEPT spectrum spectrum of (2Z,5E,16E)-8-hydroxy-20-isobutyl-16-methyl-7,14-dioxa-bicyclo[19.3.1]-pentacosa-2,5,16-triene-10,23-dione (**15**)
Figure 4.224.: HSQC spectrum of (2Z,5E,16E)-8-hydroxy-20-isobutyl-16-methyl-7,14-dioxa-bicyclo[19.3.1]-pentacosa-2,5,16-triene-10,23-dione (**15**)

Figure 4.225.: ^{1}H-^{1}H COSY (bold-faced bonds) and HMBC (double-barbed arrows) correlations of (2Z,5E,16E)-8-hydroxy-20-isobutyl-16-methyl-7,14-dioxa-bicyclo[19.3.1]-pentacosa-2,5,16-triene-10,23-dione (**15**)

Figure 4.226.: HMBC spectrum of (2Z,5E,16E)-8-hydroxy-20-isobutyl-16-methyl-7,14-dioxa-bicyclo[19.3.1]-pentacosa-2,5,16-triene-10,23-dione (**15**)

Figure 4.227.: HMBC spectrum of (2Z,5E,16E)-8-hydroxy-20-isobutyl-16-methyl-7,14-dioxa-bicyclo[19.3.1]-pentacosa-2,5,16-triene-10,23-dione (**15**)

Figure 4.228.: NOESY (double-barbed green coloured arrows for α-orientation and blue coloured arrows for β orientations) correlations of (2Z,5E,16E)-8-hydroxy-20-isobutyl-16-methyl-7,14-dioxa-bicyclo[19.3.1]-pentacosa-2,5,16-triene-10,23-dione (**15**)

Figure 4.229.: NOESY spectrum of (2Z,5E,16E)-8-hydroxy-20-isobutyl-16-methyl-7,14-dioxa-bicyclo[19.3.1]-pentacosa-2,5,16-triene-10,23-dione (**15**)

Figure 4.23.: ^{1}H-NMR of 24(4→23), 27(8→26), 30(20→29)-tris-abeo-olean-(12-oxo)-1,15,22-triene-methyl hept-5-enoate **(2)**

Figure 4.230.: NOESY spectrum of (2Z,5E,16E)-8-hydroxy-20-isobutyl-16-methyl-7,14-dioxa-bicyclo[19.3.1]-pentacosa-2,5,16-triene-10,23-dione (**15**)

Figure 4.231.: Tentative mass spectrum of (2Z,5E,16E)-8-hydroxy-20-isobutyl-16-methyl-7,14-dioxa-bicyclo[19.3.1]-pentacosa-2,5,16-triene-10,23-dione (**15**)

Figure 4.232.: Closer view of molecular binding interactions of compound **1** in the catalytic site of protein 5-LOX

Figure 4.233.: Closer view of molecular binding interactions of (**A1**) 24(4→23), 27(8→26), 30(20→29)-tris-abeo-oleanene **2** and (**A2**) 24(4→23)-abeo-oleanene **3** derivatives in the catalytic site of protein *α*-glucosidase along with molecular binding interactions of (**B1**) 24(4→23), 27(8→26), 30(20→29)-tris-abeo-oleanene **2** and (**B2**) 24(4→23)-abeo-oleanene **3** derivatives in the catalytic site of *α*-amylase as deduced from its molecular modeling simulations.

Figure 4.234.: Closer view of molecular binding interactions of the drimane sesquiterpene quinols in the catalytic site of (**A-C**) 5-lipoxygenase (5-LOX) as deduced from the molecular docking simulation experiment. The molecular docking analysis of ligands (studied sesquiterpene analogues **4-6**) and pro-inflammatory 5-LOX showed two hydrogen bonds (displayed as red and blue-coloured lines with amino acyl residues of Lys^{441} and Arg^{438} with bond distances of 3.370 and 3.030 Å, respectively) in the active binding site. The compounds **4** and **6** showed one hydrogen bonded interactions with amino acyl residues Gly^{150} and Lys^{441} with molecular distances of 2.790 Å and 2.915 Å, respectively.

Figure 4.235.: Closer view of molecular binding interactions of the compounds **7**-**8** (**A** and **B**) in the catalytic site of 5-lipoxygenase (5-LOX) as deduced from the molecular docking simulation experiment. The molecular docking analysis of ligands (compound, **8**) and pro-inflammatory 5-LOX showed six hydrogen bonds (displayed as red and blue-coloured lines) with amino acyl residues of Ser^{522}, Lys^{521}, Lys^{527} and Ser^{628} with bond distances of 2.743, 3.640, 3.117, 2.792, 2.668, and 3.075 Å in the active binding site. The compound **7** showed two hydrogen-bonded interactions with amino acid residues of Gln^{534} and Gln^{497} with molecular distances of 2.883, 3.046 Å, respectively**Figure 4.236.:** Closer view of molecular binding interactions of the spiro[5.5]undecanes (A and B) in the catalytic site of 5-lipoxygenase (5-LOX) as deduced from the molecular docking simulation experiment. The molecular docking analysis of ligands (**10**) and pro-inflammatory 5-LOX showed four hydrogen bonds (displayed as red and blue-coloured lines) with amino acyl residues of GLN^{437} (2-hydrogen bonds), $ARG^{438}$and ASP^{442} with bond distances of 3.126, 3.146, 2.737 and 3.181 Å in the active binding site. The compound **9** showed two hydrogen-bonded interactions with amino acid residues of ARG^{438} with molecular distances of 3.089 Å.

Figure 4.237.: Closer view of molecular binding interactions of compound (**11**) in the and 5-lipoxygenase (5-LOX) (**A**1-**A2**) catalytic site as obtained from molecular docking. Closer view of molecular

binding interactions of the compound (**12**) in the 5-lipoxygenase (5-LOX) (**B**1-**B2**) catalytic sites as obtained from molecular docking.

Figure 4.238.: Closer image of molecular docking interactions of compounds **13**-**15** (**A**-**C**) in the 5-LOX catalytic site as obtained by docking experiment. The docking analysis of compound **13** and pro-inflammatory 5-LOX showed three hydrogen-bonds (displayed as red and blue-coloured lines with amino-acyl residues of ASP^{442} And Arg^{438} with bond distances of 2.870, 3.139 and 4.077 Å) in binding site. Compound **14** displayed five hydrogen-bonds with amino acid residues of Lys^{254}, Asp^{290}, Arg^{438} and Arg^{520}, with molecular distances of 2.702, 2.914, 3.435, 3.049, and 2.393 Å. Compound **15** showed two hydrogen-bonds with amino acid residues of Asp^{285} and Leu^{244}, with molecular distances of 3.172 and 2.846 Å.

Figure 4.24.: ^{13}C NMR of 24(4→23), 27(8→26), 30(20→29)-tris-abeo-olean-(12-oxo)-1,15,22-triene-methyl hept-5-enoate **(2)**

Figure 4.25.: ^{135}DEPT spectrum of 24(4→23), 27(8→26), 30(20→29)-tris-abeo-olean-(12-oxo)-1,15,22-triene-methyl hept-5-enoate **(2)**

Figure 4.26.: HSQC spectrum of 24(4→23), 27(8→26), 30(20→29)-tris-abeo-olean-(12-oxo)-1,15,22-triene-methyl hept-5-enoate **(2)**

Figure 4.27.: ^{1}H-^{1}H COSY (bold-face bonds), and selected HMBC (double-barbed arrows) correlations of 24(4→23), 27(8→26), 30(20→29)-tris-abeo-olean-(12-oxo)-1,15,22-triene-methyl hept-5-enoate (**2**) isolated from *G. salicornia*.

Figure 4.28.: ^{1}H-^{1}H COSY spectrum of 24(4→23), 27(8→26), 30(20→29)-tris-abeo-olean-(12-oxo)-1,15,22-triene-methyl hept-5-enoate **(2)**

Figure 4.29.: HMBC spectrum of 24(4→23), 27(8→26), 30(20→29)-tris-abeo-olean-(12-oxo)-1,15,22-triene-methyl hept-5-enoate **(2)**

Figure 4.3.: Structure of methyl-16(13→14)-abeo-7-labdene-(12-oxo) carboxylate isolated from *G. salicornia* (family Gracilariaceae), (B) representative photograph of thalli of red seaweed *G. salicornia*

Figure 4.30.: NOESY spectrum of 24(4→23), 27(8→26), 30(20→29)-tris-abeo-olean-(12-oxo)-1,15,22-triene-methyl hept-5-enoate (**2**)

Figure 4.31.: NOE correlations of 24(4→23), 27(8→26), 30(20→29)-tris-abeo-olean-(12-oxo)-1,15,22-triene-methyl-hept-5-enoate (**2**) isolated from *G. salicornia*.

Figure 4.32.: EI-MS spectrum of 24(4→23), 27(8→26), 30(20→29)-tris-abeo-olean-(12-oxo)-1,15,22-triene-methyl-hept-5-enoate (**2**) isolated from *G. salicornia*.

Figure 4.32.: EI-MS spectrum of 24(4→23), 27(8→26), 30(20→29)-tris-abeo-olean-(12-oxo)-1,15,22-triene-methyl-hept-5-enoate (**2**)

Figure 4.34.: UVspectrum of 24(4→23)-abeo-olean-(12-oxo)-3,5-diene-deconoate (**3**)

Figure 4.35.: HPLC chromatogram of 24(4→23)-abeo-olean-(12-oxo)-3,5-diene-deconoate (**3**)

Figure 4.36.: HRESIMS spectrum of 24(4→23)-abeo-olean-(12-oxo)-3,5-diene-deconoate (**3**

Figure 4.37.: FT-IR spectrum of 24(4→23)-abeo-olean-(12-oxo)-3,5-diene-deconoate (**3**)

Figure 4.38.: ^{1}HNMR spectrum of 24(4→23)-abeo-olean-(12-oxo)-3,5-diene-deconoate (**3**)

Figure 4.39.: ^{13}C NMR spectrum of 24(4→23)-abeo-olean-(12-oxo)-3,5-diene-deconoate (**3**)

Figure 4.4.: UV spectrum of methyl-16(13→14)-abeo-7-labdene-(12-oxo) carboxylate (**1**)

Figure 4.40.: ^{135}DEPT spectrum of 24(4→23)-abeo-olean-(12-oxo)-3,5-diene-deconoate (**3**)

Figure 4.41.: HSQC spectrum of 24(4→23)-abeo-olean-(12-oxo)-3,5-diene-deconoate (**3**

Figure 4.42.: ^{1}H-^{1}H COSY (bold-face bonds), selected HMBC (double-barbed arrows) correlations of 24(4→23)-abeo-olean-(12-oxo)-3,5-diene-deconoate (**3**)

Figure 4.43.: ^{1}H-^{1}H COSY spectrum of 24(4→23)-abeo-olean-(12-oxo)-3,5-diene-deconoate (**3**)

Figure 4.44.: HMBC spectrum of 24(4→23)-abeo-olean-(12-oxo)-3,5-diene-deconoate (**3**)

Figure 4.45.: NOE (single headed arrows) correlations of 24(4→23)-abeo-olean-(12-oxo)-3,5-diene-deconoate (**3**)

Figure 4.46.: NOE spectrum of 24(4→23)-abeo-olean-(12-oxo)-3,5-diene-deconoate (**3**)

Figure 4.47.: EI-MS spectrum of 24(4→23)-abeo-olean-(12-oxo)-3,5-diene-deconoate (**3**)

Figure 4.48.: Tentative mass fragmentation pattern of 24(4→23)-abeo-olean-(12-oxo)-3,5-diene-deconoate (**3**)
Figure 4.49.: Structural representations of (**A**) 3-(hept-3^6-enyloxy)-decahydro-4,6a,12a,12b-tetramethyl-1*H*-benzo[*a*]xanthene-4,10,12-triol (compound **4**), (**B**) 13-[[2-(hexyloxy)-2,5,5,8a-tetramethyldecahydro-1-naphthalenyl](methoxy)methyl]benzenol (compound **5**), and (**C**) 1-butoxy-4,4,11b,11c-tetramethyl-decahydrobenzo[*kl*]xanthen-10-ol (compound **6**) isolated from red seaweed *G. salicornia*. (**D**) The representative photograph of thalli (leaf-like structures) of *G. salicornia*.
Figure 4.5.: HPLC chromatogram of methyl-16(13→14)-abeo-7-labdene-(12-oxo) carboxylate (**1**)
Figure 4.50.: UV spectrum of 3-(Hept-3^6-enyloxy)-2,3,4,4a,5,6,6a,12,12a,12b-decahydro-4,6a,12a,12b-tetramethyl-*1H*-benzo[a]xanthene-4,10,12-triol (**4**)
Figure 4.51.: HPLC chromatogram of 3-(Hept-3^6-enyloxy)-2,3,4,4a,5,6,6a,12,12a,12b-decahydro-4,6a,12a,12b-tetramethyl-*1H*-benzo[a]xanthene-4,10,12-triol (**4**)
Figure 4.52.: HRESIMS spectrum of 3-(Hept-3^6-enyloxy)-2,3,4,4a,5,6,6a,12,12a,12b-decahydro-4,6a,12a,12b-tetramethyl-*1H*-benzo[a]xanthene-4,10,12-triol (**4**)
Figure 4.53.: FTIR spectrum of 3-(Hept-3^6-enyloxy)-2,3,4,4a,5,6,6a,12,12a,12b-decahydro-4,6a,12a,12b-tetramethyl-*1H*-benzo[a]xanthene-4,10,12-triol
Figure 4.54.: FTIR spectrum of 3-(Hept-3^6-enyloxy)-2,3,4,4a,5,6,6a,12,12a,12b-decahydro-4,6a,12a,12b-tetramethyl-*1H*-benzo[a]xanthene-4,10,12-triol
Figure 4.55.: ^{13}C-NMR spectrum of 3-(Hept-3^6-enyloxy)-2,3,4,4a,5,6,6a,12,12a,12b-decahydro-4,6a,12a,12b-tetramethyl-*1H*-benzo[a]xanthene-4,10,12-triol (**4**)
Figure 4.56.: DEPT spectrum of 3-(Hept-3^6-enyloxy)-2,3,4,4a,5,6,6a,12,12a,12b-decahydro-4,6a,12a,12b-tetramethyl-*1H*-benzo[a]xanthene-4,10,12-triol (**4**)
Figure 4.57.: HSQC spectrum of 3-(Hept-3^6-enyloxy)-2,3,4,4a,5,6,6a,12,12a,12b-decahydro-4,6a,12a,12b-tetramethyl-*1H*-benzo[a]xanthene-4,10,12-triol (**4**
Figure 4.58.: ^{1}H-^{1}H COSY (bold face bonds), and selected HMBCs (double-barbed arrows), correlations of 3-(Hept-3^6-enyloxy)-2,3,4,4a,5,6,6a,12,12a,12b-decahydro-4,6a,12a,12b-tetramethyl-*1H*-benzo[a]xanthene-4,10,12-triol (**4**)
Figure 4.59.: ^{1}H-^{1}H COSY spectrum of 3-(Hept-3^6-enyloxy)-2,3,4,4a,5,6,6a,12,12a,12b-decahydro-4,6a,12a,12b-tetramethyl-*1H*-benzo[a]xanthene-4,10,12-triol (**4**)
Figure 4.6.: HRESIMS spectrum of methyl-16(13→14)-abeo-7-labdene-(12-oxo) carboxylate (**1**)
Figure 4.60.: NOE spectrum of 3-(Hept-3^6-enyloxy)-2,3,4,4a,5,6,6a,12,12a,12b-decahydro-4,6a,12a,12b-tetramethyl-*1H*-benzo[a]xanthene-4,10,12-triol (**4**)
Figure 4.61.: DEPT spectrum of 3-(Hept-3^6-enyloxy)-2,3,4,4a,5,6,6a,12,12a,12b-decahydro-4,6a,12a,12b-tetramethyl-*1H*-benzo[a]xanthene-4,10,12-triol (**4**)
Figure 4.62.: NOE correlations of 3-(hept-3^6-enyloxy)-2,3,4,4a,5,6,6a,12,12a,12b-decahydro-4,6a,12a,12b-tetramethyl-1*H*-benzo[a]xanthene-4,10,12-triol (**4**)
Figure 4.63.: EI-MS spectrum of 3-(Hept-3^6-enyloxy)-2,3,4,4a,5,6,6a,12,12a,12b-decahydro-4,6a,12a,12b-tetramethyl-*1H*-benzo[a]xanthene-4,10,12-triol (**4**)
Figure 4.64.: Mass fragmentation pattern of 3-(Hept-3^6-enyloxy)-2,3,4,4a,5,6,6a,12,12a,12b-decahydro-4,6a,12a,12b-tetramethyl-*1H*-benzo[a]xanthene-4,10,12-triol (**4**)
Figure 4.66.: UV spectrum of 13-[[2-(Hexyloxy)-2,5,5,8a-tetramethyldecahydro-1-naphthalenyl](methoxy-)-methyl]-benzenol (**5**)
Figure 4.67.: HPLC chromatogram of 13-[[2-(Hexyloxy)-2,5,5,8a-tetramethyldecahydro-1-naphthalenyl](methoxy-)-methyl]-benzenol (**5**)
Figure 4.68.: HRESIMS spectrum of 13-[[2-(Hexyloxy)-2,5,5,8a-tetramethyldecahydro-1-naphthalenyl](methoxy-)-methyl]-benzenol (**5**)
Figure 4.69.: FTIR spectrum of 13-[[2-(Hexyloxy)-2,5,5,8a-tetramethyldecahydro-1-naphthalenyl](methoxy-)-methyl]-benzenol (**5**)
Figure 4.7.: FT-IR spectrum of methyl-16(13→14)-abeo-7-labdene-(12-oxo) carboxylate (**1**)

Figure 4.70.: ^{1}H-NMR spectrum of 13-[[2-(Hexyloxy)-2,5,5,8a-tetramethyldecahydro-1-naphthalenyl](methoxy-)-methyl]-benzenol (**5**)
Figure 4.71.: ^{13}C-NMR spectrum of 13-[[2-(Hexyloxy)-2,5,5,8a-tetramethyldecahydro-1-naphthalenyl](methoxy-)-methyl]-benzenol (**5**)
Figure 4.72.: ^{135}DEPT spectrum of 13-[[2-(Hexyloxy)-2,5,5,8a-tetramethyldecahydro-1-naphthalenyl](methoxy-)-methyl]-benzenol (**5**)
Figure 4.73.: HSQC spectrum of 13-[[2-(Hexyloxy)-2,5,5,8a-tetramethyldecahydro-1-naphthalenyl](methoxy-)-methyl]-benzenol (**5**)
Figure 4.74.: ^{1}H-^{1}H COSY spectrum of 13-[[2-(Hexyloxy)-2,5,5,8a-tetramethyldecahydro-1-naphthalenyl](methoxy-)-methyl]-benzenol (**5**)
Figure 4.75.: ^{1}H-^{1}H COSY (bold face bonds), and selected HMBCs (double-barbed arrows), correlations of 13-[[2-(Hexyloxy)-2,5,5,8a-tetramethyldecahydro-1-naphthalenyl](methoxy-)-methyl]-benzenol (**5**)
Figure 4.76.: HMBC spectrum of 13-[[2-(Hexyloxy)-2,5,5,8a-tetramethyldecahydro-1-naphthalenyl](methoxy-)-methyl]-benzenol (**5**)
Figure 4.77.: NOE correlations of 13-[[2-(Hexyloxy)-2,5,5,8a-tetramethyldecahydro-1-naphthalenyl](methoxy-)-methyl]-benzenol (**5**)
Figure 4.77.: NOE spectrum of 13-[[2-(Hexyloxy)-2,5,5,8a-tetramethyldecahydro-1-naphthalenyl](methoxy-)-methyl]-benzenol (**5**)
Figure 4.78.: EI-MS spectrum of 3-(Hept-3^{6}-enyloxy)-2,3,4,4a,5,6,6a,12,12a,12b-decahydro-4,6a,12a,12b-tetramethyl-*1H*-benzo[a]xanthene-4,10,12-triol (**5**)
Figure 4.8.: ^{1}H-NMR spectrum of methyl-16(13→14)-abeo-7-labdene-(12-oxo) carboxylate (**1**)
Figure 4.80.: Mass fragmentation pattern of 3-(Hept-3^{6}-enyloxy)-2,3,4,4a,5,6,6a,12,12a,12b-decahydro-4,6a,12a,12b-tetramethyl-*1H*-benzo[a]xanthene-4,10,12-triol (**5**)
Figure 4.81.: UV spectrum of 1-butoxy-4,4,11b,11c-tetramethyl-1,2,3,3a,4,5,6,6a,11b,11c-decahydrobenzo[kl]-xanthen-10-ol (**6**)
Figure 4.82.: HPLC chromatogram of 1-butoxy-4,4,11b,11c-tetramethyl-1,2,3,3a,4,5,6,6a,11b,11c-decahydrobenzo[kl]-xanthen-10-ol (**6**)
Figure 4.83.: HRESIMS spectrum of 1-butoxy-4,4,11b,11c-tetramethyl-1,2,3,3a,4,5,6,6a,11b,11c-decahydrobenzo[kl]-xanthen-10-ol (**6**)
Figure 4.84.: FTIR spectrum of 1-butoxy-4,4,11b,11c-tetramethyl-1,2,3,3a,4,5,6,6a,11b,11c-decahydrobenzo[kl]-xanthen-10-ol (**6**)
Figure 4.85.: ^{1}H-NMR spectrum of 1-butoxy-4,4,11b,11c-tetramethyl-1,2,3,3a,4,5,6,6a,11b,11c-decahydrobenzo[kl]-xanthen-10-ol (**6**)
Figure 4.86.: ^{13}C-NMR spectrum of 1-butoxy-4,4,11b,11c-tetramethyl-1,2,3,3a,4,5,6,6a,11b,11c-decahydrobenzo[kl]-xanthen-10-ol (**6**)
Figure 4.87.: ^{135}DEPT spectrum of 1-butoxy-4,4,11b,11c-tetramethyl-1,2,3,3a,4,5,6,6a,11b,11c-decahydrobenzo[kl]-xanthen-10-ol (**6**)
Figure 4.88.: HSQC spectrum of 1-butoxy-4,4,11b,11c-tetramethyl-1,2,3,3a,4,5,6,6a,11b,11c-decahydrobenzo[kl]-xanthen-10-ol (**6**)
Figure 4.89.: ^{1}H-^{1}H COSY (bold face bonds), and selected HMBCs (double-barbed arrows) of 1-butoxy-4,4,11b,11c-tetramethyl-1,2,3,3a,4,5,6,6a,11b,11c-decahydrobenzo[kl]-xanthen-10-ol (**6**)
Figure 4.9.: ^{13}C-NMR spectrum of methyl-16(13→14)-abeo-7-labdene-(12-oxo) carboxylate (**1**)
Figure 4.90.: ^{1}H-^{1}H COSY spectrum of 1-butoxy-4,4,11b,11c-tetramethyl-1,2,3,3a,4,5,6,6a,11b,11c-decahydrobenzo-[kl]-xanthen-10-ol (**6**)
Figure 4.91.: HMBC spectrum of 1-butoxy-4,4,11b,11c-tetramethyl-1,2,3,3a,4,5,6,6a,11b,11c-decahydrobenzo[kl]-xanthen-10-ol (**6**)
Figure 4.92.: NOE (double barbed arrows) correlations of 1-butoxy-4,4,11b,11c-tetramethyl-1,2,3,3a,4,5,6,6a,11b,11c-decahydrobenzo[kl]-xanthen-10-ol (**6**)
Figure 4.93.: NOESY spectrum of 1-butoxy-4,4,11b,11c-tetramethyl-1,2,3,3a,4,5,6,6a,11b,11c-decahydrobenzo[kl]-xanthen-10-ol (**6**)

Figure 4.94.: EI-MS spectrum of 1-butoxy-4,4,11b,11c-tetramethyl-1,2,3,3a,4,5,6,6a,11b,11c-decahydrobenzo[kl]-xanthen-10-ol (**6**)
Figure 4.95.: Mass fragmentation pattern of 1-butoxy-4,4,11b,11c-tetramethyl-1,2,3,3a,4,5,6,6a,11b,11c-decahydrobenzo[kl]-xanthen-10-ol (**6**)
Figure 4.96.: Structures of 2*H*-chromenyl derivatives (**7**-**8**) isolated from the seaweed *Gracilaria salicornia*. The representative photograph of the thalli of *G. salicornia* was shown
Figure 4.97.: UV spectrum of 4'-[10'-[7-Hydroxy-2,8-dimethyl-6-(pentyloxy)-*2H*-chromen-2-yl]ethyl]-3',4'-dimethyl-cyclohexanone (7)
Figure 4.98.: HPLC chromatogram of 4'-[10'-[7-hydroxy-2,8-dimethyl-6-(pentyloxy)-*2H*-chromen-2-yl]ethyl]-3',4'-dimethyl-cyclohexanone (7)
Figure 4.99.: HRESIMS spectrum of 4'-[10'-[7-Hydroxy-2,8-dimethyl-6-(pentyloxy)-*2H*-chromen-2-yl]ethyl]-3',4'-dimethyl-cyclohexanone (7)
Figure 5.1.: The brown seaweed *P. tetrastromatica* of collected from the southeast coastline of the Indian sub-continent Gulf of Mannar region; between 8º48' N, 78°9' E and 9°14' N, 79°14' E)
Figure 5.10.: ^{135} DEPT NMR spectrum of 12-ethenyl-3a,6,9,10,11,12,12a,12b-octahydro-1-(1^2-hydroxy-1^2-methyl-propyl)-cyclonona[*d*]furo[2,3-*b*]pyran-6,10-diol **(1)**
Figure 5.101.: DEPT spectrum of 3-methoxy-dolabella-12(18)-ene-4β-ol (**7**)
Figure 5.102.: ^{1}H-^{1}H COSY spectrum of 3-methoxy-dolabella-12(18)-ene-4β-ol (**7**)
Figure 5.103.: HSQC spectrum of 3-methoxy-dolabella-12(18)-ene-4β-ol (**7**)
Figure 5.104.: HMBC spectrum of 3-methoxy-dolabella-12(18)-ene-4β-ol (**7**)
Figure 5.105.: Prominent ^{1}H-^{1}H COSY, and selected HMBC correlations of 3-methoxy-dolabella-12(18)-ene-4β-ol (**7**). The key ^{1}H-^{1}H COSY couplings were represented in bold face bonds. The key HMBC couplings have been represented by double barbed arrows.
Figure 5.106.: NOESY of 3-methoxy-dolabella-12(18)-ene-4β-ol (**7**)
Figure 5.107.: Prominent NOE correlations of 3-methoxy-dolabella-12(18)-ene-4β-ol (**7**). NOESY relations are represented by double-tailed arrows**Figure 5.108.:** EI-MS spectrum of 3-methoxy-dolabella-12(18)-ene-4β-ol (**7**)
Figure 5.109.: EI-MS spectrum of 3-methoxy-dolabella-12(18)-ene-4β-ol (**7**)
Figure 5.11.: HSQC spectrum of 12-ethenyl-3a,6,9,10,11,12,12a,12b-octahydro-1-(1^2-hydroxy-1^2-methyl-propyl)-cyclonona[*d*]furo[2,3-*b*]pyran-6,10-diol **(1)**
Figure 5.110.: UVspectrum of 3-methoxy-dolabella-10,18(19)-diene-5α,8β -diol (**8**)
Figure 5.111.: HPLC chromatogram of 3-methoxy-dolabella-10,18(19)-diene-5α,8β -diol (**8**)
Figure 5.112.: HRESIMS of 3-methoxy-dolabella-10,18(19)-diene-5α,8β -diol (**8**)
Figure 5.113.: FTIR spectrum of 3-methoxy-dolabella-10,18(19)-diene-5α,8β -diol (**8**)
Figure 5.114.: ^{13}C NMR spectrum 3-methoxy-dolabella-10,18(19)-diene-5α,8β -diol (**8**)
Figure 5.114.: ^{1}H NMR spectrum 3-methoxy-dolabella-10,18(19)-diene-5α,8β -diol (**8**)
Figure 5.115.: DEPT spectrum spectrum 3-methoxy-dolabella-10,18(19)-diene-5α,8β -diol (**8**)
Figure 5.116.: ^{1}H-^{1}H COSY spectrum 3-methoxy-dolabella-10,18(19)-diene-5α,8β -diol (**8**)
Figure 5.117.: HSQC spectrum 3-methoxy-dolabella-10,18(19)-diene-5α,8β -diol (**8**)
Figure 5.118.: HMBC spectrum 3-methoxy-dolabella-10,18(19)-diene-5α,8β -diol (**8**)
Figure 5.119.: Prominent ^{1}H-^{1}H COSY, and selected HMBC correlations of 3-methoxy-dolabella-10,18(19)-diene-5α,8β-diol (**8**). The key ^{1}H-^{1}H COSY couplings were represented in bold face bonds. The key HMBC couplings have been represented by double barbed arrows.
Figure 5.12.: ^{1}H-^{1}H COSY spectrum of 12-ethenyl-3a,6,9,10,11,12,12a,12b-octahydro-1-(1^2-hydroxy-1^2-methyl-propyl)-cyclonona[*d*]furo[2,3-*b*]pyran-6,10-diol **(1)**
Figure 5.120.: NOESY spectrum 3-methoxy-dolabella-10,18(19)-diene-5α,8β -diol (**8**)
Figure 5.121.: Prominent NOE correlations of 3-methoxy-dolabella-10,18(19)-diene-5α,8β -diol (**8**). NOESY relations are represented by double-tailed arrows
Figure 5.122.: EI-MS spectrum 3-methoxy-dolabella-10,18(19)-diene-5α,8β -diol (**8**)
Figure 5.123.: Tentative mass fragmentation pattern of 3-methoxy-dolabella-10,18(19)-diene-5α,8β -diol (8)

Figure 5.124.: UVspectrum of 2,7-dimethoxy-14α-hydroxy-dolasta-1(15),9-diene (**9**)
Figure 5.125.: HPLC chromatogram of 2,7-dimethoxy-14α-hydroxy-dolasta-1(15),9-diene (**9**)
Figure 5.126.: HRESIMS of 2,7-dimethoxy-14α-hydroxy-dolasta-1(15),9-diene (**9**)
Figure 5.127.: FTIR spectrum of 2,7-dimethoxy-14α-hydroxy-dolasta-1(15),9-diene (**9**)
Figure 5.128.: ^{1}H NMR spectrum of 2,7-dimethoxy-14α-hydroxy-dolasta-1(15),9-diene (**9**)
Figure 5.129.: ^{13}C NMR spectrum of 2,7-dimethoxy-14α-hydroxy-dolasta-1(15),9-diene (**9**)
Figure 5.13.: HMBC spectrum of 12-ethenyl-3a,6,9,10,11,12,12a,12b-octahydro-1-(1^{2}-hydroxy-1^{2}-methyl-propyl)-cyclonona[*d*]furo[2,3-*b*]pyran-6,10-diol **(1)**
Figure 5.130.: DEPT spectrum of 2,7-dimethoxy-14α-hydroxy-dolasta-1(15),9-diene (**9**)
Figure 5.131.: ^{1}H-^{1}H COSY spectrum of 2,7-dimethoxy-14α-hydroxy-dolasta-1(15),9-diene (**9**)
Figure 5.132.: HSQC spectrum of 2,7-dimethoxy-14α-hydroxy-dolasta-1(15),9-diene (**9**)
Figure 5.133.: HMBC spectrum of 2,7-dimethoxy-14α-hydroxy-dolasta-1(15),9-diene (**9**)
Figure 5.134.: Prominent ^{1}H-^{1}H COSY, and selected HMBC correlations of 2,7-dimethoxy-14α-hydroxy-dolasta-1(15),9-diene (**9**). The key ^{1}H-^{1}H COSY couplings were represented in bold face bonds. The key HMBC couplings have been represented by double barbed
Figure 5.135.: NOESY spectrum of 2,7-dimethoxy-14α-hydroxy-dolasta-1(15),9-diene (**9**)
Figure 5.136.: Prominent NOE correlations of 2,7-Dimethoxy-14α-hydroxy-dolasta-1(15),9-diene (**9**). NOESY relations are represented by double-tailed arrows
Figure 5.137.: EI-MS spectrum of 2,7-Dimethoxy-14α-hydroxy-dolasta-1(15),9-diene**Figure 5.138.:** Tentative mass fragmentation pattern of 2,7-dimethoxy-14α-hydroxy-dolasta-1(15),9-diene (**9**)
Figure 5.138.: Tentative mass fragmentation pattern of 2,7-dimethoxy-14α-hydroxy-dolasta-1(15),9-diene (**9**)
Figure 5.139.: UVspectrum of 4,7-dimethoxy-9β ,14α-dihydroxy-dolasta-1-ene (**10**)
Figure 5.14.: Prominent ^{1}H-^{1}H COSY, and selected HMBC correlations of 12-ethenyl-3a,6,9,10,11,12,12a,12b-octahydro-1-(1^{2}-hydroxy-1^{2}-methyl-propyl)-cyclonona[*d*]furo[2,3-*b*]pyran-6,10-diol **(1)**. The key ^{1}H-^{1}H COSY couplings were represented in bold face bonds. The key HMBC couplings have been represented by double barbed arrows.
Figure 5.140.: HPLC chromatogram of 4,7-dimethoxy-9β ,14α-dihydroxy-dolasta-1-ene (**10**)
Figure 5.141.: HRESIMS of 4,7-dimethoxy-9β ,14α-dihydroxy-dolasta-1-ene (**10**)
Figure 5.142.: ^{13}C NMR spectrum of4,7-dimethoxy-9β ,14α-dihydroxy-dolasta-1-ene (**10**) **Figure 5.142.:** HSQC spectrum of 4,7-dimethoxy-9β ,14α-dihydroxy-dolasta-1-ene (**10**)
Figure 5.142.: ^{1}H-^{1}H COSY spectrum of4,7-dimethoxy-9β ,14α-dihydroxy-dolasta-1-ene (**10**)
Figure 5.142.: DEPT spectrum of4,7-dimethoxy-9β ,14α-dihydroxy-dolasta-1-ene (**10**)
Figure 5.142.: FTIR spectrum of4,7-dimethoxy-9β ,14α-dihydroxy-dolasta-1-ene (**10**)
Figure 5.143.: ^{1}H NMR spectrum of4,7-dimethoxy-9β ,14α-dihydroxy-dolasta-1-ene (**10**)
Figure 5.143.: HMBC spectrum of4,7-dimethoxy-9β ,14α-dihydroxy-dolasta-1-ene (**10**)
Figure 5.144.: Prominent ^{1}H-^{1}H COSY, and selected HMBC correlations of 4,7-dimethoxy-9β ,14α-dihydroxy-dolasta-1-ene (**10**). The key ^{1}H-^{1}H COSY couplings were represented in bold face bonds. The key HMBC couplings have been represented by double barbed arrows.
Figure 5.145.: NOESY spectrum of 4,7-dimethoxy-9β ,14α-dihydroxy-dolasta-1-ene (**10**)
Figure 5.146.: Prominent NOE correlations of 2,7-dimethoxy-14α-hydroxy-dolasta-1(15),9-diene (**10**). NOESY relations are represented by double-tailed arrows
Figure 5.147.: EI-MS spectrum of 4,7-dimethoxy-9β ,14α-dihydroxy-dolasta-1-ene (**10**)
Figure 5.148.: Tentative mass fragmentation pattern of 4,7-dimethoxy-9β ,14α-dihydroxy-dolasta-1-ene (**10**)
Fig. 5.149.: Closer view of molecular binding interactions of the xenicane derivatives **1** (**A**) and **2** (**B**) in the catalytic site of protein LOX-5 as deduced from its molecular modeling simulations. The xenicanes **1** and **2** exhibited one hydrogen bond interaction with amino residues Arg411 and Arg438 in the enzyme active site with molecular distances of 3.011 Å and 2.740 Å, respectivel

Figure 5.152.: Prominent NOE correlations of 12-ethenyl-3a,6,9,10,11,12,12a,12b-octahydro-1-(1^2-hydroxy-1^2-methyl-propyl)-cyclonona[*d*]furo[2,3-*b*]pyran-6,10-diol **(1)**. NOESY relations are represented by double-tailed arrows

Figure 5.150.: Closer view of molecular binding interactions of the xeniolide derivatives **3** (**A**), **4** (**B**), and **5** (**C**) in the catalytic site of protein LOX-5 as deduced from its molecular modelling simulations. The xeniolide **5** showed three hydrogen bonded interactions with amino acid residues, one hydrogen bonded with Lys441 (2.799 Å), and two with Gln434 (2.860 and 2.886 Å). Compound **5** displayed greater number of hydrogen bond interactions with amino acyl residues than those recorded by **3** and **4**.

Figure 5.151. Closer view of molecular binding interactions of compounds **8** (**A1**-**A2**) and **10** (**B1**-**B2**) in the catalytic site of protein *α*-amylase deduced from molecular modeling simulations.

Figure 5.16.: NOE correlations of 12-ethenyl-3a,6,9,10,11,12,12a,12b-octahydro-1-(1^2-hydroxy-1^2-methyl-propyl)-cyclonona[*d*]furo[2,3-*b*]pyran-6,10-diol **(1)**.

Figure 5.17.: EI-MS spectrum of 6-methoxy-dolabella-8(17),12-diene-10β ,18-diol (**1**)

Figure 5.18.: Tentative mass fragmentation pattern of 6-methoxy-dolabella-8(17),12-diene-10β ,18-diol (**1**)

Figure 5.19.: UVspectrum of 1,2,5,5a,6,9,10,11,12,12a-decahydro-11(11^2-hydroxypropyl)-2-[(*E*)-2^1-propenyl] cyclonona[*d*]-furo[2,3-*b*]pyran-9,12-diol (**2**)

Figure 5.2.: Schematic representation of purification of fractions and compounds from the EtOAc-MeOH extract of *G. salicornia*.CC-column chromatography

Figure 5.20.: HPLC chromatogram of 1,2,5,5a,6,9,10,11,12,12a-decahydro-11(11^2-hydroxypropyl)-2-[(*E*)-2^1-propenyl] cyclonona[*d*]-furo[2,3-*b*]pyran-9,12-diol (**2**)

Figure 5.21.: HRESIMS of 1,2,5,5a,6,9,10,11,12,12a-decahydro-11(11^2-hydroxypropyl)-2-[(*E*)-2^1-propenyl] cyclonona[*d*]-furo[2,3-*b*]pyran-9,12-diol (**2**)

Figure 5.22.: FTIR spectrum of 1,2,5,5a,6,9,10,11,12,12a-decahydro-11(11^2-hydroxypropyl)-2-[(*E*)-2^1-propenyl] cyclonona[*d*]-furo[2,3-*b*]pyran-9,12-diol (**2**)

Figure 5.23.: ^{1}H NMR spectrum of 1,2,5,5a,6,9,10,11,12,12a-decahydro-11(11^2-hydroxypropyl)-2-[(*E*)-2^1-propenyl] cyclonona[*d*]-furo[2,3-*b*]pyran-9,12-diol (**2**)

Figure 5.24.: ^{13}C NMR spectrum of 1,2,5,5a,6,9,10,11,12,12a-decahydro-11(11^2-hydroxypropyl)-2-[(*E*)-2^1-propenyl] cyclonona[*d*]-furo[2,3-*b*]pyran-9,12-diol (**2**)

Figure 5.25.: ^{135}DEPT NMR spectrum of 1,2,5,5a,6,9,10,11,12,12a-decahydro-11(11^2-hydroxypropyl)-2-[(*E*)-2^1-propenyl] cyclonona[*d*]-furo[2,3-*b*]pyran-9,12-diol (**2**)

Figure 5.26.: HSQC spectrum of 1,2,5,5a,6,9,10,11,12,12a-decahydro-11(11^2-hydroxypropyl)-2-[(*E*)-2^1-propenyl] cyclonona[*d*]-furo[2,3-*b*]pyran-9,12-diol (**2**)

Figure 5.27.: Prominent ^{1}H-^{1}H COSY, and selected HMBC correlations of 1,2,5,5a,6,9,10,11,12,12a-decahydro-11(11^2-hydroxypropyl)-2-[(*E*)-2^1-propenyl] cyclonona[*d*]-furo[2,3-*b*]pyran-9,12-diol (**2**). The key ^{1}H-^{1}H COSY couplings were represented in bold face bonds. The key HMBC couplings have been represented by double barbed arrows.

Figure 5.28.: ^{1}H-^{1}H COSY spectrum of 1,2,5,5a,6,9,10,11,12,12a-decahydro-11(11^2-hydroxypropyl)-2-[(*E*)-2^1-propenyl] cyclonona[*d*]-furo[2,3-*b*]pyran-9,12-diol (**2**)

Figure 5.29.: HMBC spectrum of 1,2,5,5a,6,9,10,11,12,12a-decahydro-11(11^2-hydroxypropyl)-2-[(*E*)-2^1-propenyl] cyclonona[*d*]-furo[2,3-*b*]pyran-9,12-diol (**2**)

Figure 5.3.: Bioactive secondary metabolites isolated from *P. tetrastromatica* (family Dictyotaceae) and representative photograph of thalli of brown seaweed *P. tetrastromatica*

Figure 5.30.: HMBC spectrum of 1,2,5,5a,6,9,10,11,12,12a-decahydro-11(11^2-hydroxypropyl)-2-[(*E*)-2^1-propenyl] cyclonona[*d*]-furo[2,3-*b*]pyran-9,12-diol (**2**)

Figure 5.31.: NOESY spectrum of 1,2,5,5a,6,9,10,11,12,12a-decahydro-11(11^2-hydroxypropyl)-2-[(*E*)-2^1-propenyl] cyclonona[*d*]-furo[2,3-*b*]pyran-9,12-diol (**2**)

Figure 5.32.: EI-MS spectrum of 1,2,5,5a,6,9,10,11,12,12a-decahydro-11(11^2-hydroxypropyl)-2-[(*E*)-2^1-propenyl] cyclonona[*d*]-furo[2,3-*b*]pyran-9,12-diol (**2**)

Figure 5.33.: Tentative mass fragmentation pattern of 1,2,5,5a,6,9,10,11,12,12a-decahydro-11(11^2-hydroxypropyl)-2-[(*E*)-2^1-propenyl] cyclonona[*d*]-furo[2,3-*b*]pyran-9,12-diol (**2**)

Figure 5.34.: UVspectrum of 4-(4^1,4^2-dihydroxypropyl)-4,4a,5,6,7,8,11,11a-octahydro-8,11-dihydroxy-7-methyl-6-(6^1-methyl-6^2-propenyl)-cyclonona[*c*]pyran-3-(1*H*)-one (**3**)

Figure 5.35.: HPLC chromatogram of 4-(4^1,4^2-dihydroxypropyl)-4,4a,5,6,7,8,11,11a-octahydro-8,11-dihydroxy-7-methyl-6-(6^1-methyl-6^2-propenyl)-cyclonona[*c*]pyran-3-(1*H*)-one (**3**)

Figure 5.36.: HRESIMS of 4-(4^1,4^2-dihydroxypropyl)-4,4a,5,6,7,8,11,11a-octahydro-8,11-dihydroxy-7-methyl-6-(6^1-methyl-6^2-propenyl)-cyclonona[*c*]pyran-3-(1*H*)-one (**3**)

Figure 5.37.: FTIR spectrum of 4-(4^1,4^2-dihydroxypropyl)-4,4a,5,6,7,8,11,11a-octahydro-8,11-dihydroxy-7-methyl-6-(6^1-methyl-6^2-propenyl)-cyclonona[*c*]pyran-3-(1*H*)-one (**3**)

Figure 5.38.: ^{1}H NMR spectrum of -(4^1,4^2-dihydroxypropyl)-4,4a,5,6,7,8,11,11a-octahydro-8,11-dihydroxy-7-methyl-6-(6^1-methyl-6^2-propenyl)-cyclonona[*c*]pyran-3-(1*H*)-one (**3**)

Figure 5.39.: ^{13}C NMR spectrum of 4-(4^1,4^2-dihydroxypropyl)-4,4a,5,6,7,8,11,11a-octahydro-8,11-dihydroxy-7-methyl-6-(6^1-methyl-6^2-propenyl)-cyclonona[*c*]pyran-3-(1*H*)-one (**3**)

Figure 5.4.: Xenicane class of xenicins (**1**-**2**) bearing cyclonona[*d*]furo[2,3-*b*]pyrandiol and three xeniolide-type diterpenoids with octahydrocyclonona[*c*]pyran-3(1*H*)-one backbones (**3**-**5**) isolated from the seaweed *Padina tetrastromatica*.

Figure 5.40.: ^{135}DEPT NMR spectrum of 4-(4^1,4^2-dihydroxypropyl)-4,4a,5,6,7,8,11,11a-octahydro-8,11-dihydroxy-7-methyl-6-(6^1-methyl-6^2-propenyl)-cyclonona[*c*]pyran-3-(1*H*)-one (**3**)

Figure 5.41.: HSQC spectrum of 4-(4^1,4^2-dihydroxypropyl)-4,4a,5,6,7,8,11,11a-octahydro-8,11-dihydroxy-7-methyl-6-(6^1-methyl-6^2-propenyl)-cyclonona[*c*]pyran-3-(1*H*)-one (**3**)

Figure 5.42.: ^{1}H-^{1}H COSY of 4-(4^1,4^2-dihydroxypropyl)-4,4a,5,6,7,8,11,11a-octahydro-8,11-dihydroxy-7-methyl-6-(6^1-methyl-6^2-propenyl)-cyclonona[*c*]pyran-3-(1*H*)-one (**3**)

Figure 5.43.: Prominent ^{1}H-^{1}H COSY, and selected HMBC correlations of 4-(4^1,4^2-dihydroxypropyl)-4,4a,5,6,7,8,11,11a-octahydro-8,11-dihydroxy-7-methyl-6-(6^1-methyl-6^2-propenyl)-cyclonona-[*c*]-pyran-3-(1*H*)-one (**3**). The key ^{1}H-^{1}H COSY couplings were represented in bold face bonds. The key HMBC couplings have been represented by double barbed arrows

Figure 5.44.: HMBC spectrum of 4-(4^1,4^2-dihydroxypropyl)-4,4a,5,6,7,8,11,11a-octahydro-8,11-dihydroxy-7-methyl-6-(6^1-methyl-6^2-propenyl)-cyclonona[*c*]pyran-3-(1*H*)-one (**3**)

Figure 5.45.: Prominent NOE correlations of 4-(4^1,4^2-dihydroxypropyl)-4,4a,5,6,7,8,11,11a-octahydro-8,11-dihydroxy-7-methyl-6-(6^1-methyl-6^2-propenyl)-cyclonona[*c*]pyran-3-(1*H*)-one (**3**). NOESY relations are represented by double-tailed arrows

Figure 5.46.: NOESY spectrum of 4-(4^1,4^2-dihydroxypropyl)-4,4a,5,6,7,8,11,11a-octahydro-8,11-dihydroxy-7-methyl-6-(6^1-methyl-6^2-propenyl)-cyclonona[*c*]pyran-3-(1*H*)-one (**3**)

Figure 5.47.: EI-MS spectrum of 4-(4^1,4^2-dihydroxypropyl)-4,4a,5,6,7,8,11,11a-octahydro-8,11-dihydroxy-7-methyl-6-(6^1-methyl-6^2-propenyl)-cyclonona[*c*]pyran-3-(1*H*)-one (**3**)

Figure 5.48.: Tentative mass fragmentation pattern of 4-(4^1,4^2-dihydroxypropyl)-4,4a,5,6,7,8,11,11a-octahydro-8,11-dihydroxy-7-methyl-6-(6^1-methyl-6^2-propenyl)-cyclonona[*c*]-pyran-3-(1*H*)-one (**3**)

Figure 5.49.: UVspectrum of 4,4a,5,6,7,8,11,11a-octahydro-7-hydroxy-6-(6^2-hydroxy-6^3-butenyl)-4-(4^1-hydroxypropyl)-11-methoxy-8-methyl-cyclonona[*c*]pyran-3-(1*H*)-one (**4**)

Figure 5.5.: UVspectrum of 12-ethenyl-3a,6,9,10,11,12,12a,12b-octahydro-1-(1^2-hydroxy-1^2-methyl-propyl)-cyclonona[*d*]furo[2,3-*b*]pyran-6,10-diol **(1)**

Figure 5.50.: HPLC chromatogram of 4,4a,5,6,7,8,11,11a-octahydro-7-hydroxy-6-(6^2-hydroxy-6^3-butenyl)-4-(4^1-hydroxypropyl)-11-methoxy-8-methyl-cyclonona[*c*]pyran-3-(1*H*)-one (**4**)

Figure 5.51.: HRESIMS of 4,4a,5,6,7,8,11,11a-octahydro-7-hydroxy-6-(6^2-hydroxy-6^3-butenyl)-4-(4^1-hydroxypropyl)-11-methoxy-8-methyl-cyclonona[*c*]pyran-3-(1*H*)-one (**4**)

Figure 5.52.: FTIR of 4,4a,5,6,7,8,11,11a-octahydro-7-hydroxy-6-(6^2-hydroxy-6^3-butenyl)-4-(4^1-hydroxypropyl)-11-methoxy-8-methyl-cyclonona[*c*]pyran-3-(1*H*)-one (**4**)

Figure 5.53.: ^{1}H-NMR of 4,4a,5,6,7,8,11,11a-octahydro-7-hydroxy-6-(6^2-hydroxy-6^3-butenyl)-4-(4^1-hydroxypropyl)-11-methoxy-8-methyl-cyclonona[*c*]pyran-3-(1*H*)-one (**4**)

Figure 5.54.: ^{13}C-NMR of 4,4a,5,6,7,8,11,11a-octahydro-7-hydroxy-6-(6^2-hydroxy-6^3-butenyl)-4-(4^1-hydroxypropyl)-11-methoxy-8-methyl-cyclonona[*c*]pyran-3-(1*H*)-one (**4**)
Figure 5.55.: DEPT spectrum of 4,4a,5,6,7,8,11,11a-octahydro-7-hydroxy-6-(6^2-hydroxy-6^3-butenyl)-4-(4^1-hydroxypropyl)-11-methoxy-8-methyl-cyclonona[*c*]pyran-3-(1*H*)-one (**4**)
Figure 5.56.: HSQC spectrum of 4,4a,5,6,7,8,11,11a-octahydro-7-hydroxy-6-(6^2-hydroxy-6^3-butenyl)-4-(4^1-hydroxypropyl)-11-methoxy-8-methyl-cyclonona[*c*]pyran-3-(1*H*)-one (**4**)
Figure 5.57.: COSY spectrum of 4,4a,5,6,7,8,11,11a-octahydro-7-hydroxy-6-(6^2-hydroxy-6^3-butenyl)-4-(4^1-hydroxypropyl)-11-methoxy-8-methyl-cyclonona[*c*]pyran-3-(1*H*)-one (**4**)
Figure 5.58.: HMBC spectrum of 4,4a,5,6,7,8,11,11a-octahydro-7-hydroxy-6-(6^2-hydroxy-6^3-butenyl)-4-(4^1-hydroxypropyl)-11-methoxy-8-methyl-cyclonona[*c*]pyran-3-(1*H*)-one (**4**)
Figure 5.59.: Prominent ^{1}H-^{1}H COSY, and selected HMBC correlations of 4,4a,5,6,7,8,11,11a-Octahydro-7-hydroxy-6-(6^2-hydroxy-6^3-butenyl)-4-(4^1-hydroxypropyl)-11-methoxy-8-methyl-cyclonona[*c*]pyran-3-(1*H*)-one (**4**). The key ^{1}H-^{1}H COSY couplings were represented in bold face bonds. The key HMBC couplings have been represented by double barbed arrows.of
Figure 5.6.: HPLC chromatogram of 12-ethenyl-3a,6,9,10,11,12,12a,12b-octahydro-1-(1^2-hydroxy-1^2-methyl-propyl)-cyclonona[*d*]furo[2,3-*b*]pyran-6,10-diol **(1)**
Figure 5.60.: NOESY spectrum of 4,4a,5,6,7,8,11,11a-octahydro-7-hydroxy-6-(6^2-hydroxy-6^3-butenyl)-4-(4^1-hydroxypropyl)-11-methoxy-8-methyl-cyclonona[*c*]pyran-3-(1*H*)-one (**4**) **Figure 5.61.:** Prominent NOE correlations of 4,4a,5,6,7,8,11,11a-octahydro-7-hydroxy-6-(6^2-hydroxy-6^3-butenyl)-4-(4^1-hydroxypropyl)-11-methoxy-8-methyl-cyclonona[*c*]pyran-3-(1*H*)-one (**4**). NOESY relations are represented by double-tailed arrows
Figure 5.62.: EI-MS spectrum of 4,4a,5,6,7,8,11,11a-octahydro-7-hydroxy-6-(6^2-hydroxy-6^3-butenyl)-4-(4^1-hydroxypropyl)-11-methoxy-8-methyl-cyclonona[*c*]pyran-3-(1*H*)-one (**4)**
Figure 5.63.: Tentative mass fragmentation pattern of 4,4a,5,6,7,8,11,11a-octahydro-7-hydroxy-6-(6^2-hydroxy-6^3-butenyl)-4-(4^1-hydroxypropyl)-11-methoxy-8-methyl-cyclonona[*c*]pyran-3-(1*H*)-one (**4)**
Figure 5.64.: UVspectrum of 4,4a,5,6,7,8,11,11a-octahydro-1,7-dihydroxy-4-(4^1-hydroxy-4^2-methylpropyl)-6-(6^1-hydroxy-6^2-propenyl)-10-methyl-cyclonona[*c*]pyran-3(1*H*)-one (**5**)
Figure 5.65.: HPLC chromatogram of 4,4a,5,6,7,8,11,11a-octahydro-1,7-dihydroxy-4-(4^1-hydroxy-4^2-methylpropyl)-6-(6^1-hydroxy-6^2-propenyl)-10-methyl-cyclonona[*c*]pyran-3(1*H*)-one (**5**)
Figure 5.66.: HRESIMS of 4,4a,5,6,7,8,11,11a-octahydro-1,7-dihydroxy-4-(4^1-hydroxy-4^2-methylpropyl)-6-(6^1-hydroxy-6^2-propenyl)-10-methyl-cyclonona[*c*]pyran-3(1*H*)-one (**5**)
Figure 5.67.: FTIR spectrum of 4,4a,5,6,7,8,11,11a-octahydro-1,7-dihydroxy-4-(4^1-hydroxy-4^2-methylpropyl)-6-(6^1-hydroxy-6^2-propenyl)-10-methyl-cyclonona[*c*]pyran-3(1*H*)-one (**5**)
Figure 5.69.: ^{1}H NMR of 4,4a,5,6,7,8,11,11a-octahydro-1,7-dihydroxy-4-(4^1-hydroxy-4^2-methylpropyl)-6-(6^1-hydroxy-6^2-propenyl)-10-methyl-cyclonona[*c*]pyran-3(1*H*)-one (**5**)
Figure 5.7.: FTIR of 12-ethenyl-3a,6,9,10,11,12,12a,12b-octahydro-1-(1^2-hydroxy-1^2-methyl-propyl)-cyclonona[*d*]furo[2,3-*b*]pyran-6,10-diol **(1)**
Figure 5.7.: HRESIMS of 12-ethenyl-3a,6,9,10,11,12,12a,12b-octahydro-1-(1^2-hydroxy-1^2-methyl-propyl)-cyclonona[*d*]furo[2,3-*b*]pyran-6,10-diol **(1)**
Figure 5.70.: ^{13}C-NMR of 4,4a,5,6,7,8,11,11a-octahydro-1,7-dihydroxy-4-(4^1-hydroxy-4^2-methylpropyl)-6-(6^1-hydroxy-6^2-propenyl)-10-methyl-cyclonona[*c*]pyran-3(1*H*)-one (**5**)
Figure 5.71.:DEPT spectrum of 4,4a,5,6,7,8,11,11a-octahydro-1,7-dihydroxy-4-(4^1-hydroxy-4^2-methylpropyl)-6-(6^1-hydroxy-6^2-propenyl)-10-methyl-cyclonona[*c*]pyran-3(1*H*)-one (**5**)
Figure 5.72.: HSQC of 4,4a,5,6,7,8,11,11a-octahydro-1,7-dihydroxy-4-(4^1-hydroxy-4^2-methylpropyl)-6-(6^1-hydroxy-6^2-propenyl)-10-methyl-cyclonona[*c*]pyran-3(1*H*)-one (**5**)
Figure 5.73.: ^{1}H-^{1}H COSY spectrum of 4,4a,5,6,7,8,11,11a-octahydro-1,7-dihydroxy-4-(4^1-hydroxy-4^2-methylpropyl)-6-(6^1-hydroxy-6^2-propenyl)-10-methyl-cyclonona[*c*]pyran-3(1*H*)-one (**5**)
Figure 5.74.: Prominent ^{1}H-^{1}H COSY, and selected HMBC correlations of 4,4a,5,6,7,8,11,11a-octahydro-1,7-dihydroxy-4-(4^1-hydroxy-4^2-methylpropyl)-6-(6^1-hydroxy-6^2-propenyl)-10-

methyl-cyclonona[*c*]pyran-3(1*H*)-one (**5**). The key ^{1}H-^{1}H COSY couplings were represented in bold face bonds. The key HMBC couplings have been represented by double barbed arrows.

Figure 5.75.: HMBC spectrum of 4,4a,5,6,7,8,11,11a-octahydro-1,7-dihydroxy-4-(4^{1}-hydroxy-4^{2}-methylpropyl)-6-(6^{1}-hydroxy-6^{2}-propenyl)-10-methyl-cyclonona[*c*]pyran-3(1*H*)-one (**5**)

Figure 5.76.: Prominent NOE correlations of 4,4a,5,6,7,8,11,11a-octahydro-1,7-dihydroxy-4-(4^{1}-hydroxy-4^{2}-methylpropyl)-6-(6^{1}-hydroxy-6^{2}-propenyl)-10-methyl-cyclonona[*c*]pyran-3(1*H*)-one (**5**). NOESY relations are represented by double-tailed arrows

Figure 5.77.: NOESY spectrum of 4,4a,5,6,7,8,11,11a-octahydro-1,7-dihydroxy-4-(4^{1}-hydroxy-4^{2}-methylpropyl)-6-(6^{1}-hydroxy-6^{2}-propenyl)-10-methyl-cyclonona[*c*]pyran-3(1*H*)-one (**5**)

Figure 5.78.: EI-MS spectrum of 4,4a,5,6,7,8,11,11a-octahydro-1,7-dihydroxy-4-(4^{1}-hydroxy-4^{2}-methylpropyl)-6-(6^{1}-hydroxy-6^{2}-propenyl)-10-methyl-cyclonona[*c*]pyran-3(1*H*)-one (**5**)

Figure 5.79.: Tentative mass fragmentation pattern of 4,4a,5,6,7,8,11,11a-octahydro-1,7-dihydroxy-4-(4^{1}-hydroxy-4^{2}-methylpropyl)-6-(6^{1}-hydroxy-6^{2}-propenyl)-10-methyl-cyclonona[*c*]-pyran-3(1*H*)-one (**5**)

Figure 5.8.: ^{1}H NMR spectrum of 12-ethenyl-3a,6,9,10,11,12,12a,12b-octahydro-1-(1^{2}-hydroxy-1^{2}-methyl-propyl)-cyclonona[*d*]furo[2,3-*b*]pyran-6,10-diol **(1)**

Figure 5.80.: The structures of 6-methoxy-dolabella-8(17),12-diene-10β,18-diol (**6**), 3-methoxy-dolabella-12(18)-ene-4β-ol (**7**), 3-methoxy-dolabella-10,18(19)-diene-5α,8β-diol (**8**), 2,7-dimethoxy-14*α*-hydroxy-dolasta-1(15),9-diene (**9**), and 4,7-dimethoxy-9β,14*α*-dihydroxy-dolasta-1-ene (**10**) isolated from *P. tetrastromatica*. Representative photograph of the thalli (leafy structures) of *P. tetrastromatica* was shown**Figure 5.81.:** UVspectrum of 6-methoxy-dolabella-8(17),12-diene-10β ,18-diol (**6**)

Figure 5.82.: HPLC chromatogram of 6-methoxy-dolabella-8(17),12-diene-10β ,18-diol (**6**)

Figure 5.83.: HRESIMS of 6-methoxy-dolabella-8(17),12-diene-10β ,18-diol (**6**)

Figure 5.84.: FTIR spectrum of 6-methoxy-dolabella-8(17),12-diene-10β ,18-diol (**6**)

Figure 5.85.: ^{1}H NMR spectrum of 6-methoxy-dolabella-8(17),12-diene-10β ,18-diol (**6**)

Figure 5.86.: ^{13}C NMR spectrum of 6-methoxy-dolabella-8(17),12-diene-10β ,18-diol (**6**)

Figure 5.87.: DEPT spectrum of 6-methoxy-dolabella-8(17),12-diene-10β ,18-diol (**6**)

Figure 5.88.: ^{1}H-^{1}H COSY spectrum of 6-methoxy-dolabella-8(17),12-diene-10β ,18-diol (**6**)

Figure 5.89.: HSQC spectrum of 6-methoxy-dolabella-8(17),12-diene-10β ,18-diol (**6**)

Figure 5.9.: ^{13} C NMR spectrum of 12-ethenyl-3a,6,9,10,11,12,12a,12b-octahydro-1-(1^{2}-hydroxy-1^{2}-methyl-propyl)-cyclonona[*d*]furo[2,3-*b*]pyran-6,10-diol **(1)**

Figure 5.90.: HMBC spectrum of 6-methoxy-dolabella-8(17),12-diene-10β ,18-diol (**6**)

Figure 5.91.: Prominent ^{1}H-^{1}H COSY, and selected HMBC correlations of 6-methoxy-dolabella-8(17),12-diene-10β ,18-diol (**6**). The key ^{1}H-^{1}H COSY couplings were represented in bold face bonds. The key HMBC couplings have been represented by double barbed arrows**Figure 5.92.:** NOESY spectrum of 6-methoxy-dolabella-8(17),12-diene-10β ,18-diol (**6**)

Figure 5.93.: Prominent NOE correlations of 1 6-methoxy-dolabella-8(17),12-diene-10β ,18-diol (**6**). NOESY relations are represented by double-tailed arrows

Figure 5.94.: EI-MS spectrum of 6-methoxy-dolabella-8(17),12-diene-10β ,18-diol (**6**) **Figure 5.95.:** Tentative mass fragmentation pattern of 6-methoxy-dolabella-8(17),12-diene-10β ,18-diol (**6**)

Figure 5.96.: UVspectrum of 3-methoxy-dolabella-12(18)-ene-4β-ol (**7**)

Figure 5.97.: HPLC chromatogram of 3-methoxy-dolabella-12(18)-ene-4β-ol (**7**)

Figure 5.98.: HRESIMS of 3-methoxy-dolabella-12(18)-ene-4β-ol (**7**)

Figure 5.99.: ^{1}H NMR spectrum of 3-methoxy-dolabella-12(18)-ene-4β-ol (**7**) **Figure 5.100.:** ^{13}C NMR spectrum of 3-methoxy-dolabella-12(18)-ene-4β-ol (**7**)

Figure 5.99.: FTIR of 3-methoxy-dolabella-12(18)-ene-4β-ol (**7**)

Figure 6.1.: The brown seaweed *P. tetrastromatica* collected from the southeast coastline of the Indian sub-continent Gulf of Mannar region; between 8º48’ N, 78°9’ E and 9°14’ N, 79°14’ E)

Figure 6.1.: The red seaweed *G. salicornia* collected from the southeast coastline of the Indian sub-continent Gulf of Mannar region; between 8º48’ N, 78°9’ E and 9°14’ N, 79°14’ E)

Figure 6.10.: NOESY spectrum of hydrolyzed polysaccharide analogue
Figure 6.11.: ESI-MS Spectrum of polysaccharide analogue
Figure 6.12.: ^{1}H NMR spectrum of methylated polysaccharide analogue after hydrolysis
Figure 6.13.: ^{13}C NMR spectrum of methylated polysaccharide analogue after hydrolysis
Figure 6.14.: DEPT^{135} spectrum of methylated polysaccharide analogue after hydrolysis
Figure 6.15.: ^{1}H-^{1}H COSY NMR spectrum of methylated polysaccharide analogue after hydrolysis
Figure 6.16.: HSQC spectrum of methylated polysaccharide analogue after hydrolysis
Figure 6.17.: HMBC spectrum of methylated polysaccharide analogue after hydrolysis
Figure 6.18.: NOESY spectrum of methylated polysaccharide analogue after hydrolysis
Figure 6.19.: ^{1}H NMR spectrum of acetylated polysaccharide analogue
Figure 6.20.: ^{13}C NMR spectrum of acetylated polysaccharide analogue
Figure 6.21.: DEPT^{135} spectrum of acetylated polysaccharide analogue
Figure 6.22.: COSY spectrum of methylated polysaccharide analogue
Figure 6.23.: HSQC spectrum of methylated polysaccharide analogue**Figure S24.** HMBC spectrum of methylated polysaccharide analogue**Figure S25**. NOESY spectrum of methylated polysaccharide analogue
Figure 6.27.: UV chromatogram of polysaccharide-silver nano composite (AgNPC) at different time intervals, 30, 60 and 120 minutes
Figure 6.28.: FTIR spectrum of polysaccharide-silver nano composite (Ag-NPC)
Figure 6.29.: XRD of polysaccharide-silver nano composite (AgNPC) at different time intervals, 30, 60 and 120 minuteS
Figure 6.3.: FTIR spectrum of hydrolyzed polysaccharide analogue
Figure 6.4.: ^{1}H NMR spectrum of hydrolyzed polysaccharide analogue
Figure 6.4.: Elution profile of polysaccharide solutions isolated from *G. salicornia* through DEAE Cellulose
Figure 6.5.: ^{13}C NMR spectrum of hydrolyzed polysaccharide analogue
Figure 6.5.: Monosaccharide composition analysis of polysaccharide analogue
Figure 6.6.: DEPT^{135} spectrum of hydrolyzed polysaccharide analogue
Figure 6.7.: ^{1}H-^{1}H COSY NMR spectrum of hydrolyzed polysaccharide analogue
Figure 6.8.: HSQC spectrum of hydrolyzed polysaccharide analogue
Figure 6.9.: HMBC spectrum of hydrolyzed polysaccharide analogue

CHAPTER 1
INTRODUCTION

Contents

1.1 Background
1.2 Marine environment as a potential source of bioactive compounds
1.3 Bioactive potentials of seaweeds and their secondary metabolites
1.4. Impact of free radicals in the defense mechanism
1.5 Seaweeds and their metabolites as natural alternative to combat various oxidative stress induced life style disorders
1.6 Objectives
1.7 Thesis outline

1.1. Background

In recent years, marine organisms have been attracted much attention to the natural product chemists due to their phenomenal biodiversity, and were considered to be prolific natural resources of structurally diverse pharmacologically active lead molecules. The bioactives derived from the marine organisms were found to represent useful leads in the production of pharmaceutical and functional food agents. Numerous novel compounds with interesting bioactivities and chemical organizations were developed from the marine organisms during the last decades (El Gamal, 2010). Since then, the recognition on untapped potential of the marine biodiversity, the mining of potential bioactive compounds, research and commercialization of high value compounds were exponentially increased during the later part of the 20th century. These led to the surge in investments on marine bio-source based research, ultimately boosted the number of publications, patents and marketing the products derived from marine source (Ypsita & Archana 2009). A unique set of bioactive compounds were found to be derived from marine based resources, such as marine plants, animals, microalgae, and seaweeds (otherwise termed as marine macroalgae).

The most interesting phyla with respect to pharmacologically active marine compounds include the abundantly available seaweed species, among which the brown and red seaweeds (belonging to the classes Phaeophyceae and Rhodophyceae, respectively) are potential sources of bioactive substances (Blunt et al., 2018; Blunt et al., 2017). Seaweeds are valuable sources of

bioactive compounds and could be introduced for the preparation of novel functional ingredients in food and also a good approach for the treatment or prevention of chronic inflammatory diseases (Carroll et al., 2019). Approximately, 271 genera and 1153 species of marine algae, including forms and varieties have been enumerated till date from the Indian waters. Seaweeds are macroscopic algae (non-flowering stem less water plant) found attached to the solid bottom substrate of rocks, dead corals, pebbles, shells and other plant materials. The seaweeds spread along the Indian coastline and its nine maritime states and islands {Gujarat-1700, Maharashtra-572, Goa-104, Karnataka-280, Kerala-560, Tamil Nadu-980, Andhra Pradesh-960, Orissa-432, West Bengal-280, Andaman and Nicobar Islands-1500 (approx.), Lakshadweep Islands-120 (approx.) in km} (Pati et al., 2016).

Seaweeds are among the most inexhaustible sources with varied chemical moieties of pharmacological potentials. They exist in each marine environmental zone, from the region of intertidal to abyssal, yielding a larger range of structures of chemical entities than any other group of marine algae. Other sources of marine bioactive entities with therapeutic activities are ascidians, bryozoans, cnidarians, molluscs and sponges (Figure 1.1.). Seaweeds are also considered as the valuable source with particular interest and gradually become the focus of area of natural products research (Lordan, Ross, & Stanton 2011). On seaweeds, especially seaweeds belonging to the class of Rhodophyceae and Phaeophyceae were found to contribute significantly, and have been extensively distributed in the marine habitats.

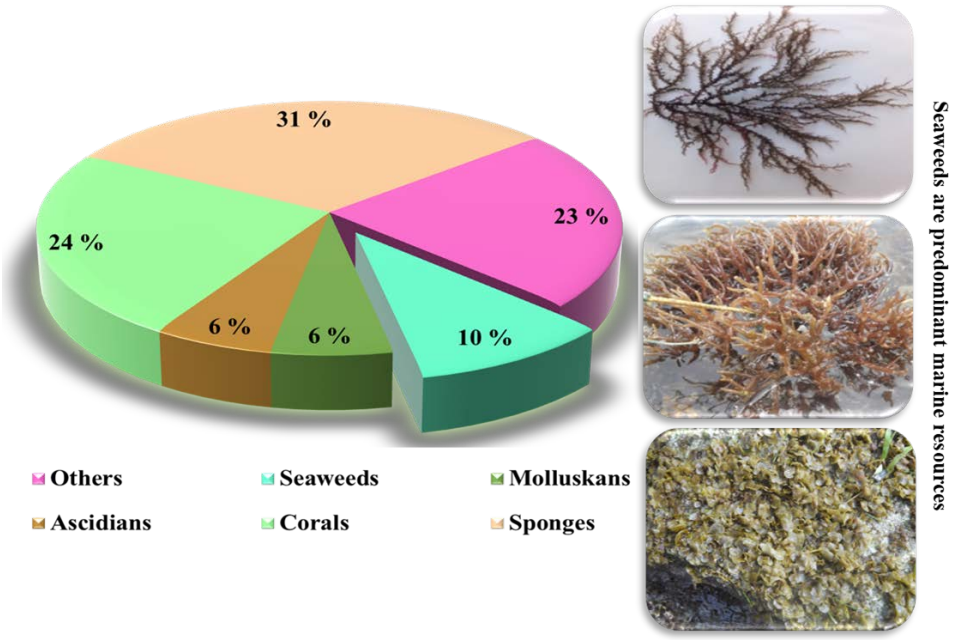

Figure 1.1.: The percentage share of seaweeds along with different classes of marine organisms

Seaweeds play an essential biological and ecological role in the marine environment. They provide a substantial contribution in primary production and make habitat for benthic communities in marine ecosystem (Mann, 1973; Williams & Smith, 2007). Seaweeds were utilized as food source in earlier times. Even though, their wide ranging nutritional status greatly contributes to industries due to its richness in micronutrients and vitamins. Therefore, around 220 species of seaweeds exhibited their commercial value. Around 200 species of seaweeds upsurge the international economy by the production of phycocolloids and food products (Bixler and Porse 2011; FAO 2013). Since the richness in nutrients, polyphenols, polysaccharides and small molecular weight bioactive compounds, the estimates from 2005 revealed that the production of seaweeds was increased to 1.3 and 14.8 million tonnes by capture and aquaculture, respectively. The production of seaweeds have doubled to 30.4 million tonnes with 29.4 and 1.1 million tonnes by culture and capture sectors as per the reports on 2015. It was estimated that the global demand of seaweeds has been increasing with rises in usage beyond traditional applications (Rebours et al., 2014; Hafting et al., 2015). The reports revealed that around 45000 species were widely distributed round the world (Bequette &France 1997). The presence of highly diverse bioactive phytochemical constituents in seaweeds registered their biomedical application from 17th century, these bioactivities including antioxidant, anti-inflammatory, anti-diabetic and hypocholesterolemic activity (Frestedt et al. 2009; Ravikumar and Kathiresan 1993). The seaweeds are unlike plants, not possessed roots, stems and real leaves, are grouped mainly into three on the basis of their content of pigments and structural characteristics, namely Rhodophyceae (Red seaweeds), Phaeophyceae (brown seaweeds), and Chlorophyceae (green seaweeds) (Mouritsen, 2013).

The seaweeds contain a large assemblage of species that predominate in the coastal shelf areas of Indian subcontinent

Seaweeds exhibited high biodiversity with more than 10,000 species (Philips 2001; Ang et al 2013). It was assessed that around 1800 of different brown species, 6200 of red species and 1800 of green species were found in the marine ecosystem. Among which, red seaweed species were found to be more diverse. The brown seaweed species were found as the largest group among them. In seaweeds, most of them are possessed soft tissues along with greater or lesser degree of calcification. The calcium layer formation in these seaweeds was found to be controlled by the presence of polysaccharide in their cell walls. The distribution of seaweeds in marine environment is varied for different group of seaweeds. The red species of seaweeds are grown at extreme depth, normally 30 meters down. The green seaweed species are bloomed in water surface and brown species are found to be in between, according to the optimal conditions such as temperature, light and content of nutrients. The combined effect of seaweed species is massive in global ecosystem. Seaweeds along with phytoplankton produce 90 % of oxygen and 80 % of the organic material on Earth (Mouritsen, 2013).

The seaweeds contain minerals ten times greater than that of terrestrial plants, whereas, they were found to be endowed with different types of trace elements and vitamins along with about 45-75 % carbohydrates and fibers, 7-35 % proteins, < 5 % fats, and a large number of different vitamins (Mouritsen, 2013). The carbohydrates and monosaccharide combinations in seaweeds are varied among the red, green, and brown species (Mouritsen, 2013). They were also found to contain essential amino acids. In general, these seaweed species have been widely utilized for polysaccharides and low molecular weight bioactive compounds by the pharmaceutical and functional food industries. However, most of the species belonging to the class of Rhodophyceae and Phaeophyceae were not broadly explored for their biochemical and pharmacological potentials. The significance of these species belonging to the class of Rhodophyceae and Phaeophyceae as potential bioactive source has been known in recent times, and their pharmaceutical potential started to attract substantial attention.

1.2 Marine environment as a potential source of bioactive compounds

The marine ecosystem consisted of almost 2,00,000 species of invertebrates and algae, representing an unexploited diverse resource of novel bioactive chemicals with pharmaceutical potential, which could use in the treatment of various prevalent disorders. In last few decades, the bioactive potentials of marine natural products (MNP) have captivated by research field. The importance of marine environment began to reveal by the isolation of spongothymidine and spongouridine from the marine sponge *Tethya crypta* and led to the development Cytarabine (an antileukemia agent) and Vidarabine (an antiviral agent), respectively. The pharmacological

approaches associated with MNPs included various novel chemical entities targeted to specific diseases and molecular targets, which were accelerated with sustained progresses in technology to isolate and characterize skeletal structures of MNP components (Hemant & Kritarth, 2018).

Marine derived bioactive compounds have the potencies to serve as prospective alternatives against deadly diseases. These compounds varied structurally and biologically, and around 30,000 compounds with distinctive structures and diverse pharmacological potentials were identified from the marine source. The seaweeds extracts from *Hypnea muciformis*, low molecular weight fucoidans from *Laminaria japonica* were found to be exhibited antioxidative, anti-inflammatory, anti-apoptotic effects and hepatoprotective activities (Nair, Weiskirchen, & Al-Musharafi, 2014). Several steroid entities such as polyoxygenated steroid contignasterol with anti-inflammatory properties isolated from marine organisms *Petrosia contignata, Xestospongia bergquisicta and Clathria lissosclera,* which hinders aggregation of platelets (Nair, Weiskirchen, & Al-Musharafi, 2014). The reports revealed that peptides identified from different marine protein hydrolysates could act as potential antioxidants (Nair, Weiskirchen, & Al-Musharafi, 2014). They were isolated from the marine organisms, such as squid, tuna, and sea cucumber, and exhibited higher antioxidative potentials than α-tocopherol. Similarly, oligosaccharides from *Apostichopus japonicus* found to be showed *in vitro* radical scavenging properties. These bioactive compounds from marine organisms were used in nutraceutical and pharmaceuticals, or substituted as synthetic antioxidants (Nair, Weiskirchen, & Al-Musharafi, 2014). Marine derived polysaccharides possessed various pharmaceutical, medical, and biotechnical applications, which were used in the fabrication of biomaterials for wound dressings and scaffolds. Marine-based chitosan from shrimp and crab shells used in the production of gels for the drug delivery of insulin and growth factors. These microgels used in the reduction of glucose level in blood thereby used in the treatment of type-1 diabetes. The fish oil rich in polyunsaturated fatty acids showed anti-oxidative effect. The novel components in fish oil supplements beneficial in liver pathophysiology (Nair, Weiskirchen, & Al-Musharafi, 2014).

Seaweeds were reported to be rich in bioactive entities, such as fibers, peptides, proteins, sulfated polysaccharides, phlorotannins, sulfolipids, carotenoids, vitamins, minerals, fatty acids and antioxidants (Khalid et al., 2018). They are used in gelling and thickening agents in the pharmaceutical and food industries. The potential effect of seaweeds is recently utilized in complementary medicine also (Khalid et al., 2018). Seaweed derived bioactive components and the functional food ingredients with potential health benefits are an emerging area of research. Various nutraceutical or functional food supplements and biomedical products from seaweeds provide a myriad of benefits for human health and multiple life threatening diseases, and

therefore, are the attractive options for the pharmaceutical and healthcare industry. The seaweeds of red, brown and green displayed prominent therapeutic activities for the management of degenerative-metabolic diseases, such as antiobesity, anticancer, antidiabetic, antihypertensive, antihyperlipidemic, anticoagulant, antioxidant, anti-inflammatory, thyroid stimulating, immunomodulatory, tissue healing properties, antiviral, antibacterial, neuroprotective, antifungal, and antiestrogenic potencies (Khalid et al., 2018). The various seaweed species belonging to marine origin represent potentially unexploited sources of bioactives with pharmacological and medicinal properties.

1.3 Bioactive potentials of seaweeds and their secondary metabolites

Novel secondary bioactive metabolites from these ocean herbs are attracting attention because of the growing demand for new compounds of 'marine natural' origin, having potential applications in pharmaceutical fields, and concerns about the toxic effects by synthetic drugs and their derivatives. The rich diversity of seaweeds belonging to the classes Phaeophyceae and Florideophyceae represents an untapped reservoir of bioactive compounds with valuable pharmaceutical and biomedical use. Seaweed derived functional food ingredients have potential pharmaceutical advantages, and is endowed with pluralities of bioactivities against different diseases (Carroll et al., 2019; Blunt et al., 2018; Blunt et al., 2017).

1.3.1 Major classification of seaweeds

In marine world, the divisions of algae include four groups, namely, Plantae, Bacteria, Protozoa and Chromista. They exhibited distinct size and morphology, which lead to the formation of unicellular organisms to micro algae. Their colony was found to be consisted of large groups of macrophytes and seaweeds. On the basis of size seaweeds are divided into two: microalgae (phytoplankton) and macroalgae (seaweed) with 5000 and 6000 species, respectively (Ravikumar et., 1993). Seaweeds are located in littoral habitats or rocks. They propagate in surface of coastal waters and in depth of sea regions up to the distance of 180 m. The most common classification of seaweeds was on the basis of the content of their characteristic pigments. These macroscopic algae are classified in to three groups, namely, brown (Phaeophyceae), red (Rhodophyceae) and green (Chlorophyceae) seaweeds, respectively.

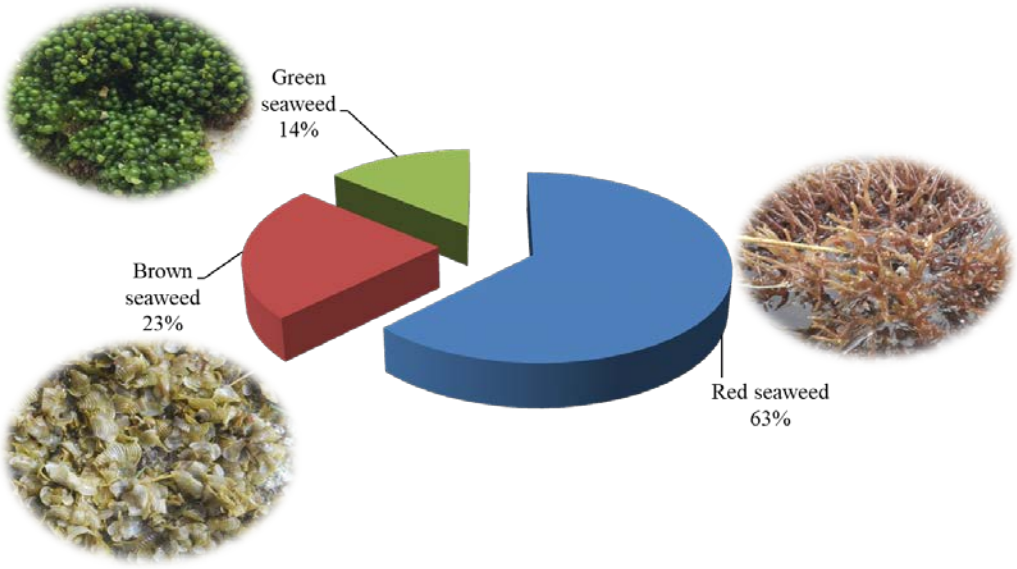

Figure 1.2..: Major classification of seaweeds

The presence of natural pigment fucoxanthin was found to be responsible for brown coloration of brown (Phaeophyceae) seaweeds. The dominance of pigments phycocyanin and phycoerythrin on other pigments chlorophyll, xanthophylls and carotene provides red color to the red (Rhodophyceae) seaweeds (Figure 1.2). The concentration of chlorophyll and related components in green (Chlorophyceae) seaweeds provide green color as in the plants (Khalid et al., 2018).

1.3.2 Distribution and diversity of seaweeds in Indian coastline

The Indian coastline is distributed up to 7000 km, which harbors a great diversity of seaweed species (Sahoo et al., 2003). The flora of seaweeds is greatly diversified in India and includes tropical seaweed species along with subtropical species. Among the various marine algal species, 1153 taxa of algae are reported, among which 271 genera have been estimated from the India. Most of these seaweed species are located in the rocky areas, coral reefs mudflats, lagoons and estuaries, Indian coastal region deliver ideal habitations for these seaweeds (Rao & Mantri, 2006). Indian coastline consisted of a total of 42 coastal stations along with 14 Gulf of Mannar islands. These regions include a total of 282 species of seaweeds. Among which, species of 80 seaweeds belong to Chlorophyta, 56 belong to Phaeophyceae and a total of 146 seaweeds belong to Rhodophyta (Ganesan, 2019). The seaweed-rich beds are located in the southern coastal regions, which are Gulf of Mannar, Mahabalipuram, Tuticorin, Tiruchendur, Kanyakumari and Kerala, along with the eastern coast of Visakhapatnam. The western coast incudes the region Veraval and Gulf of Kutch. Seaweeds are also found to be rich

in Lakshadweep Andaman and Nicobar Islands (Domettila et al., 2013). India is considered as the 12 mega-biodiversity realms in the world. The stocks of seaweed as 97,400 tonnes wet wt. were recorded from Tamil Nadu coast, 7500 tonnes wet wt. at the region of Andhra Pradesh coast, and 19,345 tonnes wet wt. throughout the islands of Lakshadweep (Kaliaperumal and Kalimuthu 1997). The diversity of seaweeds in these regions were further updated by Oza and Zaidi (2001) and documented as 434, 216, and 194 species of red, green, and brown seaweeds, respectively from a total of 844 species of total seaweeds (Figure 1.3-1.4). The Gujarat and Tamil Nadu coasts (Jha et al. 2009) were known as two large maritime states, where 366 species of seaweed were estimated, which nearly half is of total seaweed diversity in India.

Figure 1.3.: The major collection spots in Indian coastline

According to Domettila et al., in south-west coast of Indian waters, especially in Muttom coastal zone, a total of 38 species were reported due to the occurrences of intertidal rocky reefs, among which 19 species reported from the class of Florideophyceae (50 % of the total), 11 species reported from Phaeophyceae (28.9 %), while the remaining species were reported from Bryopsidophyceae (10 %) and Ulvophyceae (11 %) (Domettila et al., 2013). At the west coast of India, in particular in Maharashtra coast, the species diversity was found maximum during pre- and post- monsoon periods. Of 19 species of seaweeds, 15 families and 13 orders were documented from the Uran coast, among which, 7 species were found to belong to Rhodophyta and Chlorophyta. Varied diversity of seaweeds was recorded from three sites. Among these seaweeds, 36.8 % belonged to Rhodophyta and Chlorophyta, whereas 10.5 % were reported from Cyanobacteria and Ochrophyta, and remaining 5.2 % were reported from

Charophyta (Pawar, 2017). The coastline of Gujarat, particularly the Gulf of Kachchh extended up to 1000 km (includes 42 islands) was reported to harbor about 198 species, and among them a total of 109 belonged to Rhodophyta species, 54 belongs to Chlorophyta species, and 35 belong to Phaeophyceae species. Seaweeds of 130 species were reported from Gulf of Kachchh, whereas a total of 93 and 14 species were reported from Kalubhar Island and Narara Island, respectively (Ganesan et al., 2019).

A photo of seaweed harvest

In the southeast coastal region of Indian peninsular, the coastline of Tamil Nadu is extended to 1076 km long including 13 districts and 15 ports. It covers the region of the Bay of Bengal, Arabian Sea, and the Indian Ocean. Species of different seaweed genera were found in these regions, such as *Chaetomorpha, Ulva, Grateloupia* and *Bryopsis.* The central Tamil Nadu coast includes Palk Bay, which is in deltaic region. Several species of *Gracilaria* are dominant in this region. The Gulf of Mannar situated in the southern region of Tamil Nadu is extended up to 1 m, and support the growing of species, such as *Sargassum, Hypnea*, *Ulva* and *Acanthophora.* All these coastal regions together support the diversity of seaweeds in the Indian coastline with great economic value.

Figure 1.4.: Distribution of seaweeds as large assemblage of species predominating in the coastal shelf areas of Indian subcontinent

1.3.3 Pharmacological importance of seaweeds

Edible seaweeds have become a good source of food and alternative medicine in the Asian countries, and in the western countries they are used for many industrial applications in food (Suleria et al., 2016), cosmetics and pharmaceuticals. Traditionally, indigenous people, notably in Japan and throughout the South Pacific use seaweed supplements as a remedy for arthritis. Pluralities of studies on bioactive compounds from seaweeds exhibiting antitumor, antileukaemic, antibacterial and antiviral activities have been reported worldwide (Lorenzo-Morales et al., 2019; Yang et al., 2019).

The demand of seaweeds has been increased from the previous periods towards the nutrition, medical and healthy diet, and is the leading target in the formulation of foods and pharmaceuticals. Seaweeds from the natural origin are capable to provide bioactives for the production of novel substances with pharmaceutical and medicinal applications. Seaweed derived bioactive components and the functional food ingredients with potential health benefits are an emerging area of research. Various nutraceutical or functional food supplements and biomedical products from seaweeds provide a myriad of benefits for human health and multiple life threatening diseases, and therefore, are the attractive options for the pharmaceutical and healthcare industry. Novel secondary bioactive metabolites from these ocean herbs are attracting attention because of the growing demand for new compounds of 'marine natural' origin, having potential applications in pharmaceutical fields, and concerns about the toxic effects by synthetic drugs and their derivatives.

Since seaweeds are widely utilized as functional foods, they are highly exploited for their nutritional potentials. The significance of seaweeds as an essential source of functional ingredients in the marine ecosystem is increased because of their diverse origin, richness and universal obtainability. These are regarded as the reservoir of various bioactives and sulfated polysaccharides with pharmaceutical and bio-medical applications (Frestedt et al., 2009). The biomedical application of components in seaweeds includes antioxidant properties, anti-inflammatory activities, anticoagulant activities, antimicrobial activities, antiviral activities, anti-tumour activities and hypocholesterolemic activities (Frestedt et al., 2009). The bioactivities of seaweeds were due to the presence of numerous secondary metabolites. These bioactivities were broadly approved due to their potential health benefits. Most of these biological components include natural pigments (NPs), polyunsaturated fatty acids (PUFAs), lipids, proteins and polysaccharides. The content of bioactive compounds in the seaweeds are influenced by nutrients, CO_2 availability, light, pH, contaminants, temperature, salinity, and biotic relations (Stengel et al., 2011).

Seaweeds are considered as one of the abundant resources of naturally occurring antioxidants amongst the various marine organisms. These antioxidants protect the living cells

from the damage caused by attack of reactive oxygen species (ROS) on macromolecules, such as DNA, lipids and proteins leading to the development of prevalent disorders of cancer, diabetes, aging, and neurodegenerative diseases (Khalid et al., 2018). These can be prevented by various classes of natural and potent antioxidants, such as fucoxanthin, phycoerythrobilin, chlorophyll-a and their derivatives present in the seaweeds. The seaweed *Enteromorpha prolifera* was found to display strong antioxidant potentials due to the content of chlorophyll-a and related compounds, pheophorbidea, and phenolics (Khalid et al., 2018). Fucoxantin and their derivatives from seaweed *Undaria pinnatifida* were found to be the alternative for synthetic antioxidatives in various nutraceuticals and pharmaceutical formulations (Khalid et al., 2018). The presence of two hydroxyls in the ring structure of fucoxanthin were found to be attenuate the formation of ROS, which could also exhibit cytoprotective effect induced by H_2O_2 thereby effecting the suppression of ROS (Heo et a, 2008). The isolated phycoerythrobilin from *Porphyra* sp. also demonstrated potential antioxidant activity. Seaweeds could be used as a rich source of natural antioxidants with potential application in the food industry as well as cosmetic and pharmaceutical areas (Pangestuti & Kim, 2011).

The brown seaweed-derived polysaccharides were considered to be used as an alternate source for the production of anticoagulants than red and green seaweeds (Matsubara, 2004). There were various reports on the anticoagulant activities of the sulfated polysaccharides (SPs) (Mestechkina & Shcherbukhin, 2010). The sulfated galactan from red seaweeds and sulfated fucoidans from brown seaweeds were recognized with greater anticoagulant activities, which were due to presence of sulfate content, the sulfation position, and nature of the monosaccharide moieties. The SPs, xyloarabinogalactans, sulfated galactan, from the species of *Codium fragile*, *Codium cylindricum*, and *Monostroma nitidum* yielded higher anticoagulant activity than heparin (Khalid et al., 2018).

The large number of metabolites from the seaweeds also exhibited activities against inflammation along with and antioxidant properties (Khalid et al., 2018). Mainly, seaweeds derived fatty acids and marine terpenes, with structural entities ranged from the aliphatic groups of linear chains to complex polycyclic functionalities exhibiting potential activity against inflammation. A polysaccharide from *Aphanothece sacrum* produce an epicutaneous effect on 2,4,6-picryl chloride induced allergies by decreasing the production of pro-inflammatory cytokine (Ngatu et al., 2012). Phlorotannins from seaweeds also showed anti-inflammation effect (Khalid et al., 2018). The extract of red edible seaweed, *Porphyria dentate* has been used in the treatment of inflammatory diseases from previous decades due to their rich content of phenolics, such as catechol, rutin and hesperidin. Cyclic dipeptides, diketopiperazine, terpenes and steroids are the classes of anti-inflammatory compounds, which were found ubiquitously in

the seaweeds. Alkaloids isolated from the seaweeds showed to possess prospective anti-inflammatory properties (Khalid et al., 2018). The genus *Padina* belonging to the class, Phaeophyceae (brown seaweeds) are recognized active against some pathogen microbes, antioxidant and inflammation (Marques et al., 2012). Due to their different and unique living condition, the brown seaweed *Padina* sp., was found to be considered as a source of new chemical structures from seaweeds. Among the seaweeds belonging to class of Rhodophyceae (red seaweeds), genus *Gracilaria* was found to be a prospective candidate due to their capability to get high yields of the commercially valuable extracts. These were found to be a rich source of phycocolloids, such as agar and galactans. The prospective seaweeds for commercial phycocolloid extractions were reported as *G. confervoides*, *G. dura*, *G. chilensi*, and *G. secundata* (De Almeida et al., 2011). These seaweeds were also used in the production of bioactive metabolites, such as eicosanoids and prostanoids, which are derived through oxidative pathways of arachidonic acid and eicosapentaenoic acids from C_{20} polyunsaturated fatty acid (PUFA) metabolism (De Almeida et al., 2011). The pharmacophores, such as lipids, steroids, variety of compounds like alpha linolenic acid, gamma linolenic acid, glycolipids, 5-dehydro avenasterol, fucosterol, myristic acid, desmosterol, and 5-alpha-24(S)-ethyl-cholestane-3-beta-6-beta-diol are also abundant in this genus (De Almeida et al., 2011). Seaweeds are valued resources of bioactive metabolites, and could be used for the production of novel functional constituents in food and prevention of chronic disorders.

1.4 Free radicals in the defense mechanism

The exposure of regular and common biochemical reactions from the dietary-xenobiotics to the environment lead to the development of reactive oxygen species (ROS). These were found to be responsible for the oxidative stress in different pathophysiological states. As a consequence of these oxidative stress inductions, the cellular composition appeared to undergo alterations, which could result in chronic disease conditions (Nimse & Pal, 2015). The free radicals, such as hydroxyl radical ($^{\bullet}OH$), superoxide anion ($O_2^{\bullet-}$), non-free-radical entities like hydrogen peroxide (H_2O_2), singlet oxygen ($^1O_2$) are classified examples of ROS. The biological reactions, such as phosphorylation of protein, stimulation of several transcriptional factors, immunity, apoptosis, and differentiation, are reliant on the production of low level of ROS. When production of ROS increases, they show detrimental effects on the biomolecules (Pizzino et al., 2017). The production of ROS takes place in the mitochondria, during the pathophysiological condition, whereas $O_2^{\bullet-}$ can be generated by the cellular respiration, by pro-inflammatory cyclooxygenases (COX) and lipoxygenases (LOX), through the pathway of arachidonic acid and by inflammatory. The cells organize an antioxidant

defensive system on the basis of enzymatic constituents like superoxide dismutase-SOD, catalase-CAT, and glutathione peroxidase-GPx, to defend themselves from the cellular damage caused by the ROS (Figure 1.5) (Pizzino et al., 2017). ROS are produced by enzyme reactions those involved in the respiration, phagocytosis, synthesis of prostaglandin, and cytochrome P_{450} system. The free radical superoxide ($O_2^{\bullet-}$) is produced by the action of enzymes, such as xanthine oxidase, NADPH oxidase, and peroxidases (Pizzino et al., 2017). These superoxide radicals then lead to the generation of more free radicals, such as hydroxyl radical ($OH^{\bullet}$), hydrogen peroxide, hypochlorous acid (HOCl) and peroxynitrite ($ONOO^-$). The non-radical H_2O_2 is produced by the action of enzyme amino acid oxidase and enzyme xanthine oxidase. The most reactive hydroxyl radicals (OH•), are formed by the action of $O_2^{\bullet-}/H_2O_2$ with Fe^{2+}/Cu^{+}. Nitric oxide radicals (NO•), are synthesized by the oxidation of arginine to citrulline through enzyme nitric oxide synthase (NOS) (Pizzino et al., 2017).

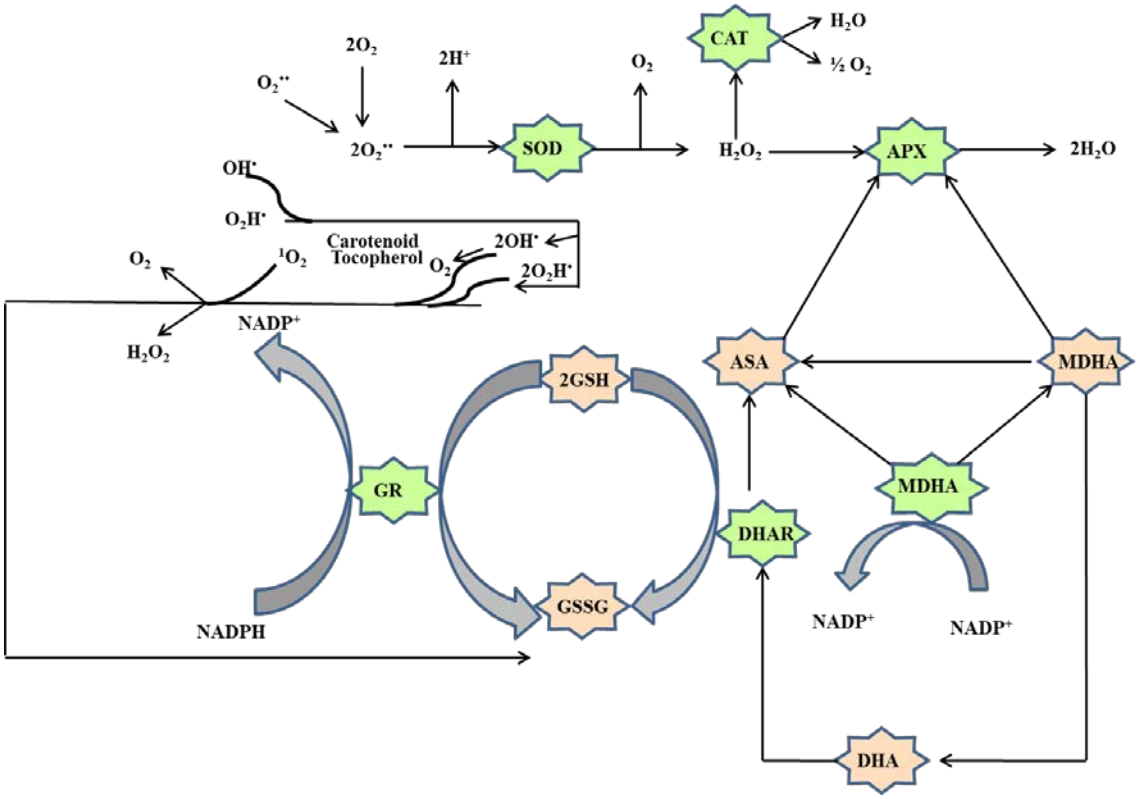

Figure 1.5.: Enzymatic and non-enzymatic antioxidants in seaweeds.

The electron transfer or higher energy exposure to molecular oxygen (O_2) were found to propagate the generation of reactive ROS (Nimse & Pal, 2015). The excess level of these ROS species in the defense mechanisms could cause peroxidation effect on lipids, oxidation of normal proteins and nucleic acids, inhibition of enzymes, finally leading to the death of the

unstressed cells. The oxidative stress could be efficiently neutralized by increasing the level of cellular defense with the aid of antioxidants (Lobo et al., 2010). The disproportionate equilibrium among the free radicals (FR), reactive oxygen species (ROS) and the defense mechanisms were deduced to lead to the state of oxidative stress. The normal metabolism of the body requires oxidant and antioxidant functionalities in the same proportion to maintain the transduction and the regulation of signals for the cellular functions (Sharma, 2014).

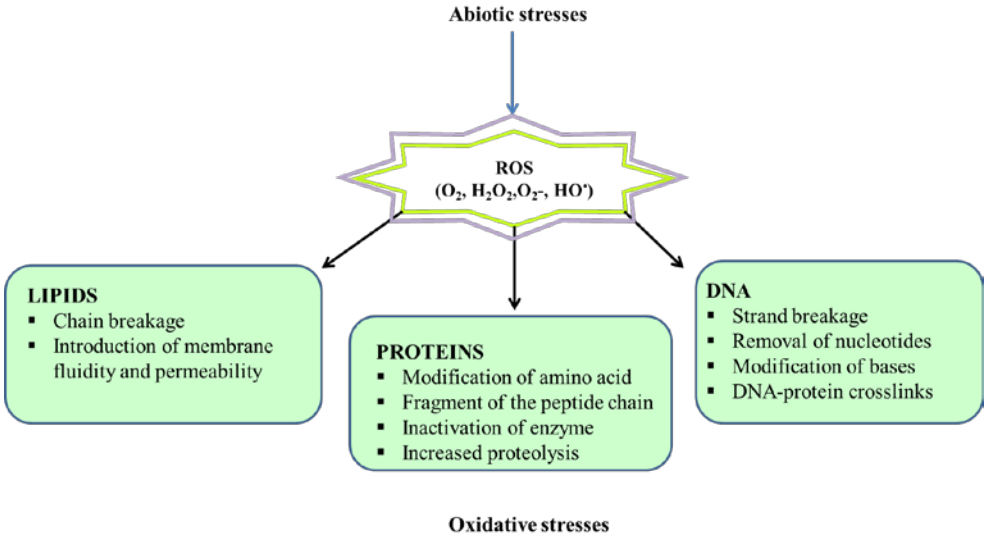

Figure 1.6.: ROS induce oxidative damage to proteins, lipids and DNA

Free radicals react with various biomolecules, especially they attack the polyunsaturated fatty acids (PUFA) in the cell wall membrane (Figure 1.6). The oxidative damage occuring in PUFA moieties could lead to the peroxidation of lipids through the intermediate free radical species, such as fatty acid peroxyl radical, lipid hydroperoxides etc. In particular, they propagate the chain reaction, which in turn lead to the formation of more free radicals and then towards the destruction of cellular system (Nimse & Pal, 2015). The action on free radicals, such as hydroxyls (•OH) on carbohydrates functionalities could lead to the abstraction of hydrogen atom from the molecule, and which in turn forms carbon centered free radicals. This destructs the molecular chain in carbohydrate molecules and finally produces the oxiradicals as a result of neutrophil activation, thus leading to inflammation of synovial fluid in the joints and cause rheumatoid arthritis (Sharma, 2014). The free radical actions on the cellular constituents generate the numerous pathological conditions, such as cancer, cardiovascular disorders, neurological diseases, diabetes conditions, ischemia, other chronic diseases and ageing (Sharma, 2014). These diseases can be categorized by the mitochondrial oxidative stress-induced disorders and inflammatory oxidative stress induced diseases, respectively. The shifting of the

thiol or disulphide redox state by pro-oxidants, damaging glucose regulation and mitochondrial oxidative stress were found to result in the pathophysiological situations leading to cancer and diabetes mellitus (Sharma, 2014). In inflammatory oxidative conditions, the greater action of either NAD(P)H oxidase or xanthine oxidase-induced the generation of ROS and finally leading to atherosclerosis and chronic inflammation, ischemia and reperfusion injury (Sharma, 2014).

1.4.2 Free radicals induced various chronic disorders

Oxidative stress destructs the critical balance between the free radical generation and antioxidant defense mechanisms. This imbalance damages the biological molecular species including nucleic acids, lipids, and proteins (Sharma, 2014). The occurrence of oxidative stress on infected tissues produce activation of radical generating enzymes, such as lipogenase, xanthine oxidase, cyclooxygenase, and lead to the initiation of phagocytes, release of Fe^{2+}, Cu^{2+}, or a disturbance in the electron transport chains of oxidative phosphorylation, making excess ROS. The ROS involved in the complications of age-related disease, diabetes mellitus, and neurodegenerative disorders (Sharma, 2014).

The DNA damage by oxidative stress is one of the reasons of cancer development. The activation of oncogene during the process of oxidative stress led to chromosomal abnormalities and then to cancer. Chemical carcinogenesis was reported to occurr by the oxidation of DNA by products, such as hydrolyzed DNA bases (Valko et al., 2004, 2006, 2007). The development of these kinds of adducts causing mutation of genes and hinders the cell growth by altering the physiological characteristics. Oxidative stress causes alteration in the structure of DNA, for instance, modification of lesions of sugar and base, cross-linkages in DNA-protein, breaking of DNA strands, and modification of base-free sites. The peroxidation of lipids due to oxidative stress also could play an important role in different types of cancer (Valko et al., 2004, 2006, 2007).

Oxidative stress was considered to be one of the preliminary causes of multifactorial etiologies associated with the cardiovascular disease risk factors (CVDs), such as hypertension, hypercholesterolaemia, unbalanced diet, diabetes, and stress (Bahorun ey al., 2006; Chatterjee et al., 2007; Ceriello et al., 2008). Oxidative stress also triggers atherosclerosis, and also was found to cause oxidation of LDL leading to the accumulation of lipid. Oxidative stress also leading to the diseased conditions such as ischemia, hypertension cardiomyopathy, congestive heart failure, and cardiac hypertrophy (Bahorun et al., 2006; Chatterjee et al., 2007; Ceriello et al., 2008). Oxidative stressed conditions were also associated with the neurological disorders and oxidative damage leading to neuron loss to progression of amyotrophic lateral sclerosis (ALS), Alzheimer's disease (AD), Parkinson's disease, depression, memory loss, and multiple

sclerosis (Pizzino et al., 2017). Oxidants were found to enhance the inflammation pathologies and activating several kinases pathways/NF-kappa β transcription, which in turn was found to lead to asthma, chronic obstructive pulmonary disease, and local chronic inflammation (Pizzino et al., 2017).

1.5 Seaweeds and their metabolites combat oxidative stress induced life style disorders

Seaweed-derived bioactive components with potential health benefits are an emerging area of research. Seaweeds have a long tradition as a food source in Asian countries, being part of the Western diet only to a limited extent. In 2014, production of seaweeds through mariculture (44% of all aquaculture) was estimated at about 27 million tons wet weight, registering annual growth rate of 8% and valued at 7 billion US$ (FAO 2016).

1.5.1 Seaweeds and their metabolites as natural alternative to combat various oxidative stress induced life style disorders

Seaweeds constitute a major share of marine flora, and they were reported to possess structurally diverse compounds of various bioactivities endowed with antihypertensive, anti-inflammatory, and anti-carcinogenic activities. These species grows in extremely hostile saline habitats, and evolved a number of specialized biochemical mechanisms to withstand salt-triggered oxidative stress conditions, which is governed by multiple biochemical mechanisms facilitating cell homeostasis and retention of water ability. However, the absence of oxidative damage in the structural components, deterrence of predation, and the ability to reproduce successfully suggest that their cells are the storehouse of bioactive metabolites with potential pharmacological properties. Therefore, these marine floras are considered as valuable sources of bioactive compounds with potential pharmacological significance.

Seaweeds are considered as a rich source of antioxidant components and bioactives. They were found to produce highly bioactive compounds as a part of their survival of harsh and stressful surroundings (Pinteus et al., 2017). There were several reports on oxidative-stress inhibiting effect of seaweeds, especially *in vitro* and in human issues. For instance, the seaweed species *Acanthophora spicifera*, *Padina tetrastromatica* and *Ulva lactuca* collected from the Gulf of Mannar exhibited effective antioxidant activities than standard drug alpha-tocopherol. The reports also revealed the greater antioxidant effect of methanolic extract of *Gracilaria* sp. than that of tocopherol by H_2O_2 scavenging assay method (Athiperumalsami et al. 2010).

Similar reports were documented on seaweeds, *Saccharina japonica* and *Sargassum horneri* oils by Sivagnanam et al. (2015).

The inhibitory effect on oxidative stress induced diseases and antioxidant potencies of phenolic components from seaweeds have been previously recorded (Kadam et al., 2016; Nakai et al., 2006). The polyphenol rich seaweed *Sargassum muticum* exhibited antioxidant effect along with anti-proliferative and anti-angiogenic properties Namvar et al. (2013). This species has been introduced for prevention of cancer Namvar et al. (2013). The seaweeds polyphenol were found to enhanced activities of different enzymes, such as glutathione peroxidase, catalase, and superoxide dismutase (Sanchez et al., 2018).

In recent days, development of value-added products, functional food candidates, nutraceuticals, and pharmaceutical leads from these underutilized seaweed species for commercial utilization has gained significance. Seaweeds are the natural bounty of the great Ocean, and these invaluable marine herbs are gifted with extraordinary medicinal properties (Pangestuti et., 2011; Ahn et al., 2012; Jin et al., 2006). Studies on seaweeds revealed that they are prospective source of micro/macro bioactive molecules along with large number of antioxidants, such as heterogeneous diverse group of polyphenols. Owing to the presence of rich content of polyphenolic compounds and phlorotannins in the seaweeds, inclusion of seaweeds and their metabolites in the daily diet has been linked with a reduced risk of different chronic diseases, including cancer, metabolic and neurodegenerative disorders and CVDs. The bromophenols, phenolic acids, and flavonoids were found to be rich in green and red seaweeds while phlorotannins were deduced to be the dominant polyphenolic compounds present in brown seaweeds as good antioxidants (Lee & Kim, 2013).

The seaweeds, *Undaria pinnatifida*, *Palmaria palmate*, *Porphyra columbina* and *Porphyra yezoensis* reported antioxidant effects, thereby exhibiting the positive impact on hypertension, cholesterol and diabetes mellitus. In addition, seaweed *Ishige okamurae Yendo* showed defense mechanism against the UV-radiation (Lee & Kim, 2013). Antioxidant components isolated and identified from this species was reported to enhance its antioxidant activity along with anti-inflammation/antidiabetic potential (Lee & Kim, 2013). Seaweeds *Ecklonia cava*, *Polysiphonia morrowii*, *Dictyopteris undulata*, *Sargassm micracanthum*, and *Sargassum macrocarpum* exhibited free radical-quenching activity. Electron donors from the seaweeds were found to react with the free radicals to form more stable products, which in turn could terminate the radical chain reactions (Lee & Kim, 2013). The seaweeds were found to neutralize the toxicity of the ROS generated from activated phagocytes, thereby reducing the formation of superoxide anions and maintained the redox homeostasis in the cellular metabolic system (Lee & Kim, 2013).

1.5.2 Role of seaweeds belonging to the class of Phaeophyceae and Rhodophyceae in the oxidative stress defense mechanism

Oxidative stress has considered being involved in pathophysiological states of many prevalent disorders. Seaweeds provided two defensive approaches for survival of effect on ROS before the impairment on cellular biological constituents. The seaweeds and seaweed derived extracts were reported to possess various pharmacological activities as a promising source of bioactive secondary metabolites with greater pharmaceutical potentials (Smith et al., 2004). Seaweeds are found to be rich in anti-oxidative metabolites, like various pigments, carotenoids, polyphenolic compounds and complex structural polysaccharides. Majority of these compounds were registered greater bioactive potentials like antioxidants. For instance, secondary metabolite phylopheophytin derived from *Eisenia bicyclis* (Cahyana et al., 1992), phlorotannin derived *Sargassum kjellamanianum* (Yan et al., 1996), fucoxanthin reported from *Hijikia fusiformis* (Yan et al., 1999), sulfated polysaccharide isolated from seaweed *Laminaria japonica* (Wang et al., 2008) and mycosporin-amino acids derived from red seaweeds (Nakayama et al., 1999). These metabolites were revealed their inhibition potential against peroxide chain initiation and decomposition, inhibition of proton abstraction, scavenging of free radicals, binding and reduction of metal ions. Therefore, seaweeds are considered as the alternative resource for natural antioxidants. Moreover, seaweed polyphenols are capable to inhibit peroxidation of lipids and chelation of metal ions. Polyphenolic metabolites including glycosylated flavanols, flavanols, and gallocatechin bearing chromenyl ring, catechin, and their derivatives have reported from seaweeds (Yoshie et al., 2003). Phenolic compounds greater antioxidant activities were identified from *Petalonia binghamiae* (Murakami et al., 2002). Potent antioxidants like phlorotannins have been reported seaweed *Ecklonia stolonifera* and E. (Kang et al., 2003). Bioactive metabolites isolated from *Turbinaria sp* were also possessed potential antioxidant a agents (Chakraborty et al., 2013; Zubia et al., 2009).

Antioxidant potential has been isolated from different species of seaweeds belonging to the class of Rhodophyceae, Phaeophyceae, and Chlorophyceae. Especially, extracts from seaweed species belong to Rhodophyceae and Phaeophyceae, and their bioactive metabolites exhibit significant role in oxidative stress defense mechanism (Lee et al., 2013).

1.6 Objectives

Based on this, the objectives of the Thesis are as follows:

1. To screen the extracts/fractions from the seaweeds belonging to the classes Phaeophyceae and Rhodophyceae from the marine and coastal ecosystems for antihypertensive, anti-inflammatory, antidiabetic and antioxidant activities.
2. To isolate the small molecular weight lead molecules and substituted polysaccharides from the extracts/fractions of the seaweeds *Padina tetrastromatica* and *Gracilaria salicornia* belonging to the classes Phaeophyceae and Rhodophyceae, respectively by various physical/chromatographic techniques, coupled with evaluation of biological activities using selective antidiabetic, anti-inflammatory, antihypertensive and antioxidant assays against different pharmacological models.
3. To characterize the purified compounds by exhaustive spectroscopic experiments.
4. To predict the biological properties by chemiinformatic tools, structure-activity relationship analyses and generation of database of potential lead molecules.

1.7 Thesis outline

On the basis of the above objectives, the current Thesis is classified into a total of seven chapters. The importance of this study on the bioactive potentials of the selected seaweeds, along with objectives was discussed in the introductory chapter (Chapter **1**). The detailed review of the studies was based on the significance of seaweeds as antioxidative, antidiabetic, antihypertensive and anti-inflammatory bioactive sources along with the characterized bioactive compounds and their medicinal values were envisaged in the Chapter **2**. Chapter **3** described the *in vitro* evaluation of the antioxidant, anti-diabetic and anti-inflammatory potentials of the organic extracts of seaweeds *Padina tetrastromatica* and *Gracilaria salicornia* belonging to the classes Phaeophyceae and Rhodophyceae, respectively. The isolation and characterization of secondary metabolites responsible for antioxidant, antidiabetic and anti-inflammatory activities from *Padina tetrastromatica* and *Gracilaria salicornia* were described in Chapter **4** and Chapter **5**, respectively. The isolation and characterization of the polysaccharides responsible for antidiabetic and anti-inflammatory activities from *Padina tetrastromatica* and *Gracilaria salicornia* were described in Chapter **6**. The summary and conclusion of the work and major research findings from the current study were detailed in Chapter **7**.

CHAPTER 2

REVIEW OF LITERATURE

Contents

2.1 *Background*

2.2 *Marine ecosystem as a source of bioactives*

2.3 *Seaweeds belonging to the class Rhodophyceae and Phaeophyceae: Specialized morphological features*

2.4 *Seaweeds as prolific source of bioactive metabolites*

2.5 *Specialized bioactive secondary metabolites of seaweeds belonging to Rhodophyceae and Phaeophyceae*

2.6 *Conclusions*

2.1. Background

The extensive extraction on marine biomes for identification and characterization of potential candidates of the therapeutics has significantly increased since past few decades. Consequently, diverse classes of compounds, which have substantial pharmaceutical potencial were developed as novel types of drug targets (Chojnacka, 2012; Pinto et al., 2012). Marine bioactive components and the functional food ingredients having potential applications in pharmaceutical fields with potential health benefits demonstrated to possess advantageous as functional food with added health benefits, and are attracting attention because of the growing demand for new compounds of 'marine natural' origin. The most interesting phyla with respect to pharmacologically active marine compounds include the abundantly available seaweed species occuring in te rocky layer of tidal/intertidal region of coastal waters, wherein the brown and red seaweeds (belonging to the classes Phaeophyceae and Rhodophyceae, respectively) are potential sources of bioactive substances (Carroll et al., 2019; Blunt et al., 2018; Blunt et al., 2017). Seaweeds are valuable sources of bioactive compounds and could be introduced for the preparation of novel functional ingredients in food and also a good approach for the treatment or prevention of chronic inflammatory diseases. Seaweeds have drawn relevant attention in recent years in the search for beneficial health properties, and showed great potential as anti-inflammatory, antimicrobial, antiviral and anti-tumor drugs (Chojnacka, 2012; Pinto et al., 2012). Due to these significant bioactive potentials, pharmaceutical industries are more

interestingly focused towards the seaweeds for the exploration of new drug targets. The value of extraction of seaweeds is also utilized by biochemical and medicinal fields of research.

In earlier 1950s, the application of seaweeds was constrained to the folk and traditional medications (Lincoln et al., 1991). Seaweed has long been part of the traditional diet of coastal communities. It is widely consumed in East Asia, particularly in Japan, China and Korea. Studies demonstrated that in Japan, the rate of mortality is less and hence their life expectancies are very high. It is reasonable to evaluate this result, because Japanese are regular consumers of seaweeds. After 1980s, bioactives with pharmacological potencies were discovered from seaweeds (Mayer & Lehmann, 2000). There were about 3200 new bioactive compounds reported from seaweeds. According to the estimation by 1977-1987, seaweeds occupied about 35 % of the newly discovered phytochemical constituents, followed by 29 % of sponges and 22 % of cnidarians (Kelecom, 2002).

Recently, much attention has been paid by the consumers toward natural bioactive compounds as functional ingredients in foods, and hence, seaweeds could be alternative sources for synthetic ingredients that can contribute to consumer's well-being, by being a part of new functional foods and pharmaceuticals. Majority of secondary metabolites isolated from seaweeds' structures have identified as the class of chemistries of fatty acid derivatives, hydroxyl unsaturated fatty acid derivatives, glycolipids, polysaccharides, steroid skeletal structures, phenolics and terpenes (Plaza et al. 2010; Karthikryan et al., 2010). Previous reports also suggested that the antioxidant, antibiotic or antifungal properties of bioactive metabolites isolated from seaweeds belonged to the class of halogenated diterpenoid and triterpenoids with bromine, chlorine and iodine substitutions (Bhagavathy et al. 2011). Recently, about 15 million mg of seaweeds products has been produce around the world. Among which, a small portion of about 250,000 mg of extracts were reported to be manufactured from seaweeds (Bhagavathy et al., 2011). However, utilization of seaweed extracts was increased globally because those can be easily made into the bioactive products (Bhagavathy et al., 2011). Besides the bioactive small molecular weight compounds, seaweeds were found to possess hydrocolloids, such as agar, carrageenan, and algin, which have exponentially increased the industrial value of seaweeds (Omar et al., 2017). Several studies have been carried out on extracts and pure bioactive leads acquired from red, brown and green seaweeds for evaluating the bioactive potencies against various disease targets (Omar et al., 2017).

2.2. Marine ecosystem as a source of bioactives

The oceans cover about 70% of the planet surface and holds high biodiversity; even though very few species have been explored or used for pharmaceutical purposes. The bioactive

metabolites of marine origin have attracted the attention of medical practitioners and scientists for the past few decades, because several of these chemicals exhibit pronounced pharmacological activities. The exploration on marine environment has been began at the period of 1970, and exhibited a dynamic increase during the 1980s, whereas during the past two decades it has reached to the optimum level of utilization according to estimation between the periods 2000-2018 (Alves et al., 2018). It was revealed that the bioactive natural metabolites with marine origin have effectively contributed towards the production of functional foods, nutraceuticals, medicinal, hydrocolloids and cosmetic industries (Alves et al., 2018). The distinct and unique chemistries of marine natural products (MNPs) include small molecular weight bioactives, such as terpenes, steroids, polyphenolic compounds, fatty acid derivatives and high molecular weight polysaccharides and oligosaccharides along with marine biotoxins. The number of bioactive compounds isolated from marine ecology in the periods of 1965-2016 was represented by the Figure 2.1 (Alves et al., 2018).

Seaweeds are one of the predominant oceanic flora, and these invaluable marine herbs are considered as a prolific source of bioactive compounds as they are able to produce a great variety of secondary metabolites characterized by a broad spectrum of extraordinary medicinal properties. These species grows in extremely hostile saline habitats, and evolved a number of specialized biochemical mechanisms to withstand salt-triggered oxidative stress conditions, which is governed by multiple biochemical mechanisms facilitating cell homeostasis and retention of water ability. However, the absence of oxidative damage in the structural components, deterrence of predation, and the ability to reproduce successfully suggest that their cells are the storehouse of bioactive metabolites with potential pharmacological properties. Therefore, these marine floras are considered as valuable sources of bioactive compounds with potential pharmacological significance.

Fig. 2.1. A photo of seaweed harvest

The marine environment included more than 2 lakhs of species of seaweeds and invertebrates from the 15 representative phyla of marine organisms (Figure 2.2) (Blunt *et al*., 2017). This estimation was found to be represented a minor percentage from the total estimated species that have yet to be exposed. The marine habitat represents an essentially untapped source of organisms for identification of new drug targets with pharmacological potencies (Blunt *et al*., 2002; Blunt *et al*., 2015; Blunt *et al*., 2016; Blunt *et al*., 2017; Blunt *et al*., 2018). The distribution of marine living forms between the various phyla isolated over the period of 1971-2016 was represented by the Figure 2.3 (Blunt *et al*., 2017). The secondary metabolites produced from different marine organisms displayed potencies like pharmaceutical leads, these were supposed to form as a part of evolutionary change. Because majority of these marine organisms are believed to be located in complex habitats, and these immobile living forms only possessed simple defensive mechanisms, they have produced biochemical components as a part of defensive strategies to hinder other entities settling on them. The identification of novel bioactive components with marine origin has established greater prospective to utilize them against various disease targets (Blunt *et al*., 2002; Blunt *et al*., 2015; Blunt *et al*., 2016; Blunt *et al*., 2017; Blunt *et al*., 2018). Exploration on the basis these unique habitats from the marine environments provided underexplored sources for detection of unique chemicals with therapeutic properties. Marine organisms are particularly attracted attention since they correlated with the traditional therapeutical schemes of a natural drug resource, and therefore, they found their utilization for development of pharmacolophore and drug candidates over the past few decades, and were considered as an untapped reservoir of novel bioactive leads for future.

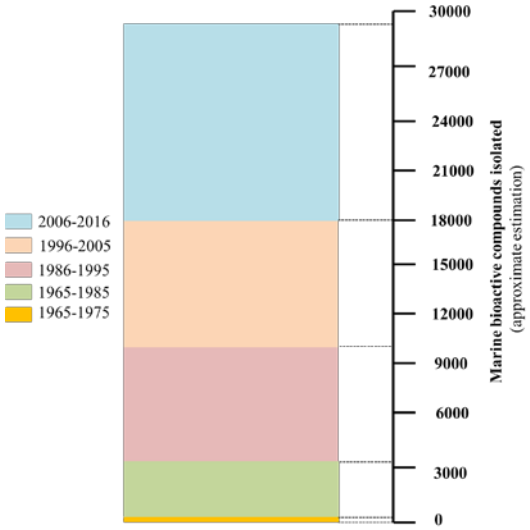

Figure 2.2.: Number of marine bioactive compounds isolated in the periods of 1965-2016 (Alves et al., 2018)

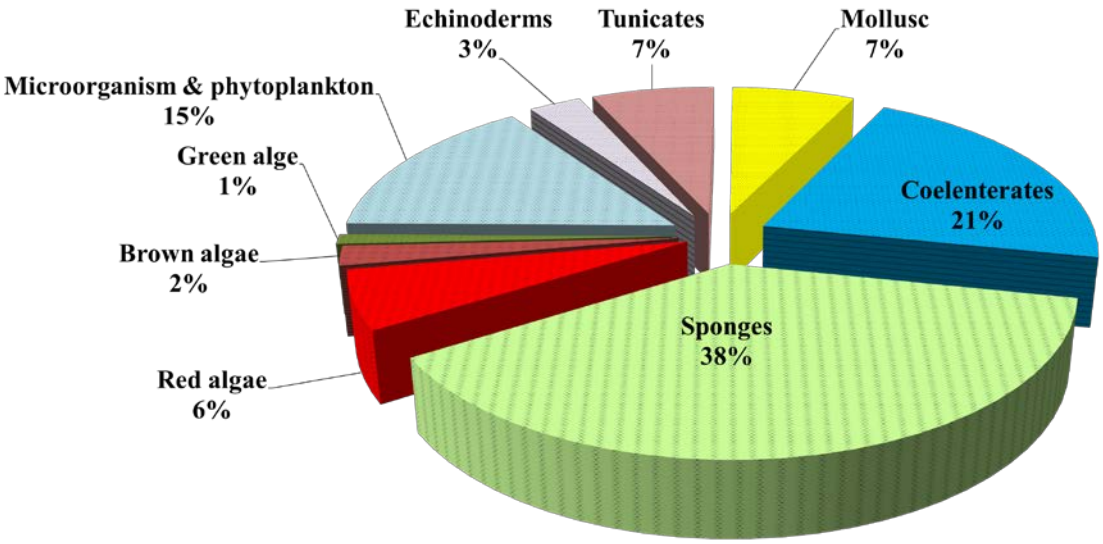

Figure 2.2.: The distribution of different marine living forms by phylum (Blunt *et al*., 2002)

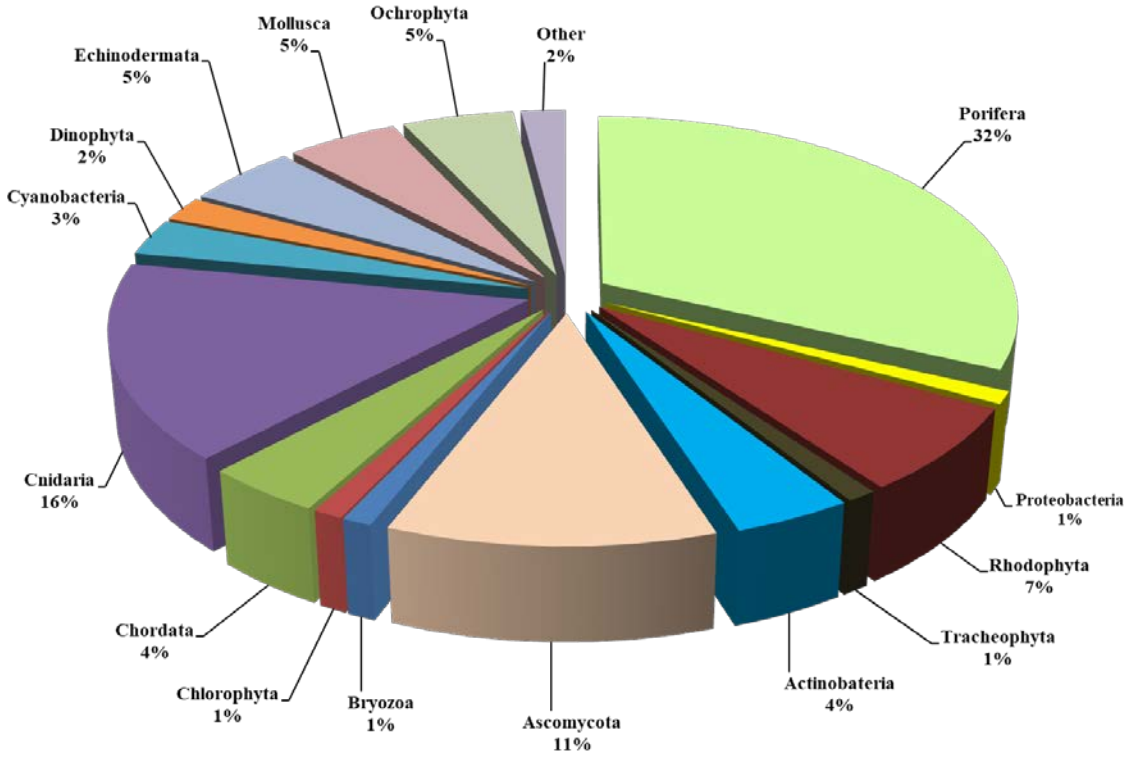

Figure 2.3.: The Distribution of marine living forms between the various phyla isolated over the period of 1971-2015 (Blunt *et al*., 2017)

2.3. Seaweeds as prolific source of bioactive metabolites

Seaweeds are considered as one of the leading producers of bioactive compounds among the various marine living forms (Bhadury et al., 2004). They can lead to the formation of broad array of secondary metabolites with prominent bioactive potentials. Seaweeds contain a large assemblage of species that predominate in the coastal shelf areas of Indian subcontinent. Seaweeds are rich source of secondary metabolites like halogenated compounds, alcohols, aldehydes, steroids, alkaloids, polysaccharides, fatty acid derivatives and terpenoids, and have therapeutic and functional food applications (Smit, 2004). Seaweeds and their extracts are estimated as the treasure-trove of potentially active components. Their utilities in nutrition and medicines were recognized during the past decades, and are valued now-a-days, for the production of novel biogenic products, functional food, fertilizer, fodder, and as source of medicaments (Kolanjinathan et al., 2014). They have found their usefor the industrial productions of hydrocolloids, and have been continuously explored by the Asian countries for food and pharmaceuticals. They are not possessed any true leaves, stem, and root. Seaweeds produce a diverse array of secondary metabolites, which play pivotal roles as therapeutic agents to alleviate undesirable pathophysiological conditions due to inflammation, diabetes, and other oxidative stress-induced diseases. The different groups of seaweeds belonging to the classes Rhodophyceae (red seaweeds), Phaeophyceae (brown seaweeds) and Chlorophyceae (green seaweeds) were contributed to bioactive marine natural products as primary producers and therefore, seaweeds were constituted as highly productive and dynamic groups among the various phyla in the marine ecosystem (Kolanjinathan et al., 2014). Bioactive compounds generated from the seaweeds were varied according to the environmental characteristics, such as competition for habitat, growing surfaces, and protection from predators. Therefore, different types of biologically active compounds derived from same species possessed varying bioactivities due to their geographical zone, habitat and climatic parameters. According to the reports obtained from 1977-2002 by D. J Faulkner, seaweeds are rich renewable resources of various secondary biogenic compounds (Faulkner, 1977). Estimation by Faulkner revealed that seaweeds consisted of more than 440 bioactives, along with the approximate number of 250 and 30 compounds were identified from the red and green seaweeds, respectively (Faulkner, 2002). Afterwards, Blunt et al. picked up these sequences and published updated data on MNP every year (up to 2018). The Figure 2.4 represented number MNP identified by the last 11 years showing that the number compounds isolated from seaweeds nearly reached to twice than the first 40 years (Brodie et al., 2007). From the reports, red and brown seaweeds have attracted by scientific research field because of their higher abundance of highly bioactive compounds from these groups. Majority of these bioactive compounds belonging to the classes of terpenes,

sterols, polyphenolics, lipids, macrolides and cytotoxic compounds, isolated from seaweeds have been reported to possess various pharmacological potencies, such as antimicrobial, antioxidant, anti-inflammatory, anticoagulant, antidiabetic, anti-proliferative, and anti-angiogenesis properties (Blunt et al., 2009; Blunt et al., 2010; Blunt et al., 2011; Blunt et al., 2017 ; Blunt et al., 2018).

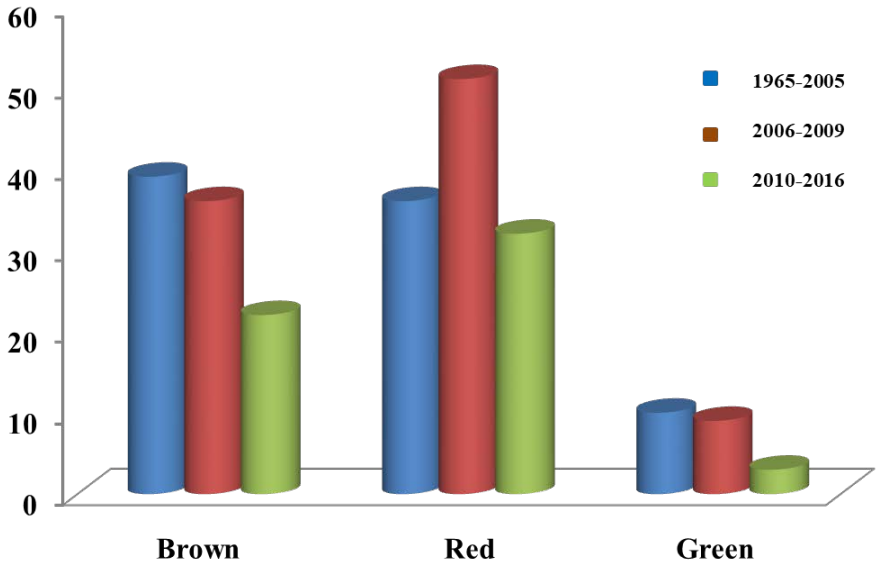

Figure 2.4.: Distribution of the seaweed secondary metabolites isolated per year (Blunt et al., 2009) and coupled with data from the same authors (Blunt et al., 2010, 2011, 2017 & 2018)

Recently, seaweeds are widely extracted for various polysaccharides due to their higher commercial values. The polysaccharides like alginate and agar extensively extracted from brown and red seaweeds, respectively, by the phycocolloid industry (Kolanjinathan et al., 2014). Seaweed polysaccharides, agar and carrageenan from the red seaweeds are utilized as gelling and thickening agents by the food industry, and are also used for preparing medium for growth of microorganisms (Kolanjinathan et al., 2014). Additionally, cell wall polysaccharides, such as fucoidans, ulvans and xylans isolated from the classes of Phaeophyceae, Chlorophyceae, and Rhodophyceae, respectively, were used as the functional food ingredients. Moreover, storage polysaccharides like laminarin, floridean starch from brown and red seaweeds are used as dietary fibers. Many of these soluble polysaccharides have documented to exhibit hypoglycemic and hypocholesterolemic activities (Kolanjinathan et al., 2014). The sulfated fucoidans from brown seaweeds found to display bioactive properties, such as anticancer, anti-proliferative, anti-thrombotic, anti-coagulant, anti-viral, anti-complementary, and anti-inflammatory agent. Furthermore, seaweeds were found to be rich reservoir of minerals, macro and micro elements,

and vitamins (Kolanjinathan et al., 2014). Hence, vitamin B rich brown seaweeds have been used as tradition remedy for thyroid goiters. The seaweeds were also found to contain proteins, fatty acids and lipids; whereas higher protein content was obtained from green and red seaweeds. The omega 3 and omega 6 polyunsaturated fatty acids obtained from seaweeds were found as effective therapy for cardiovascular diseases, diabetes, and osteoarthritis. The higher level of α-linolenic acid found in green seaweeds and fatty acids like eicosapentaenoic acid and arachidonic acid in red and brown seaweeds also raised the value of seaweeds and seaweed extracts (Kolanjinathan et al., 2014).

2.3.1 Secondary metabolites derived from seaweeds

In recent years, studies of marine natural product have yielded a considerable number of drug candidates (Yin et al., 2019; Xie et al., 2018; Koutsaviti et al., 2019; Lorenzo-Morales et al., 2019; Yang et al., 2019; Carroll et al., 2019; Blunt et al., 2018; Blunt et al., 2017). Marine bioactive components and the functional food ingredients with potential health benefits demonstrated to possess advantageous as functional food with added health benefits. Novel secondary bioactive metabolites from the red and brown seaweeds are attracting attention because of the growing demand for new compounds of 'marine natural' origin, having potential applications in pharmaceutical fields. The bioactive secondary metabolites identified from the seaweed included broad array of biochemical compounds, which were found to possess different classes of chemistries, including terpenes, sterols, polyphenols, acetogenins and others. The overview on seaweeds reveled that nine thousand species of seaweeds have been widely distributed into three classes according to their concentration of pigments, namely Rhodophyta, Phaeophyta, and Chlorophyta (or the red, brown, and green seaweeds, respectively) (Blunt et al., 2009; Blunt et al., 2010; Blunt et al., 2011; Blunt et al., 2017; Blunt et al., 2018). Percentage diversity of the seaweeds and approximate proportion of secondary metabolites identified from the seaweeds belonging to three major classes, Rhodophyceae, Phaeophyceae and Chlorophyceae, over the period of 2000 to 2018, was represented by the Figure 2.5 {approximate proportions of secondary metabolites assembled from Faulkner (2000 - 2002) and Blunt et al. (2003 - 2018)}. The diversity of various secondary metabolites have showed that several bioactivities along with potential therapeutic benefits like antidiabetic, antihypertensive, antihyperlipidemic, antioxidant, anti-inflammatory, antibacterial, and immunomodulatory properties. The red seaweed species are constituted as one of the dynamic source of halogenated secondary metabolites including terpenenoids, C_{15}-acetogenins, polyketide derivatives, alkaloids, phenolic compounds and peptide derivatives. Moreover, red seaweeds are found as major resources of hydrocolloids, such as agar, sulfated cell wall polysaccharides,

nucleic and shikimic acid analogues. With wide range of bioactive compounds, red seaweeds were associated with various pharmacological properties (Blunt et al. 2018). The halogenated terpene derivatives obtained from Rhodophyta were synthesized as a part of chemical defensive mechanisms against herbivores. The brown seaweeds are producers of structurally different compounds derived from isoprene-entities. Besides the terpenoids class of chemistries, they were found to produce cell wall polysaccharides, polyphenolic compounds, pigments, with numerous biological potentials (Pinto et al., 2012). Additionally, by the enzymatic modifications of fatty acid long chains, synthesized cyclic/acyclic volatile hydrocarbon analogues with number of carbons ranging from C_8 to C_{11}. The secondary metabolites derived from the green seaweed species are the least representative groups in marine natural metabolites. The representative classes of these compounds are the derivatives of isoprenoid entities. Like other seaweed species, amino acid-analogues, phycocolloids and shikimate-analogues were reported from these species. The cyclic peptides were examples of the most prominent class of compounds isolated from the green seaweed species (Pinto et al., 2012).

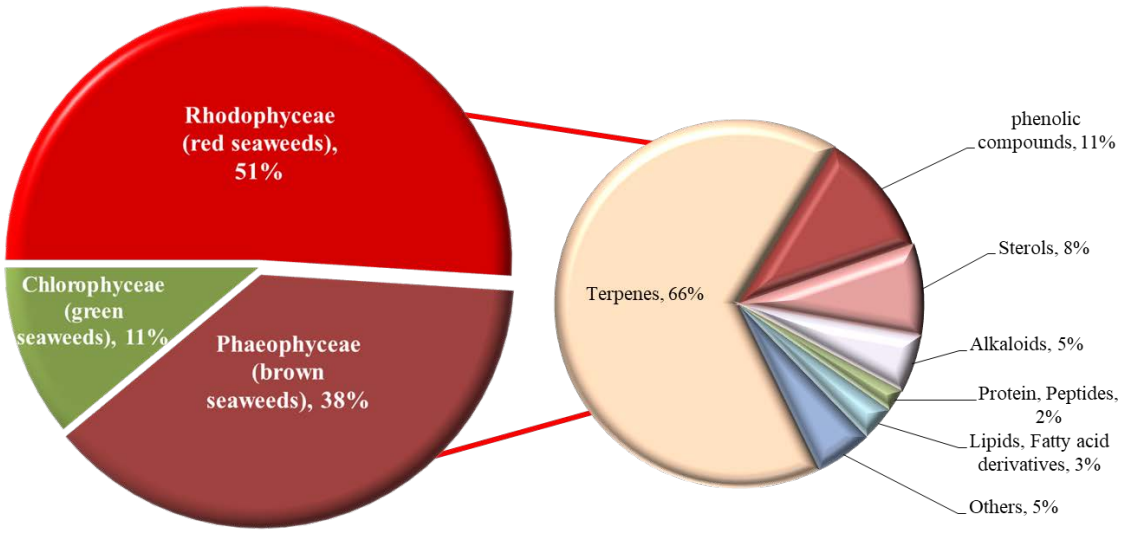

Figure 2.5.: Percentage diversity of the seaweeds and approximate proportion of secondary metabolites identified from seaweeds belonging to three major classes, Rhodophyceae, Phaeophyceae and Chlorophyceae over the period of 2000 - 2018 (approximate proportions of secondary metabolites assembled from Faulkner (2000 - 2002) and Blunt et al. (2003 - 2018).

2.3.1.1 Terpenoids

Terpenoids constitute one of the domineering classes of secondary metabolites; which are derived from the isoprene entity with five numbers of carbons oriented in a head to tail/tail

to tail fashion, with various functionalities at different positions. Structural modifications and assemblage of isoprene entities leads to the development of diverse and novel compounds with unique chemistries and bioactivities. These bioactive compounds varied structurally from ten-membered volatile hydrocarbons to forty-membered polyenes (Soltani, 2016). Their diversification includes monoterpenes, sesquiterpenes, diterpenes, sesterpenes and triterpenes with two, three, four, five and six isoprene entities, respectively. Terpenoids are synthesized from the mevalonic (MV) acid pathway through the two isomers of five carbon building blocks, namely, dimethylallyl diphosphate (DMAPP) and isopentenyl diphosphate (IPP) by the assemblage of precursors of ten, fifteen and twenty carbons, such as geranyl diphosphate (5C, GPP), neryl diphosphate (10C, NPP), farnesyl diphosphate (15C, FPP), geranylgeranyl diphosphate (20C, GGPP), and nerylneryl diphosphate (20C, NNPP) along with prenyltransferases. These ten, fifteen and twenty carbon substrates, on reaction with terpene synthases, produce cyclic/acyclic terpene class of olefins/alcohols through the series of regio/stereo selective reactions. The natural bio-synthesis of interesting chemistries of terpenoid structures were found to occur through the different combinations of terpene synthases with various enzymes, such as P450 enzymes through different chemical reactions, namely glycosylation, methylations, acylations, oxidations or peroxidation (Soltani, 2016). The pharmaceutical significance of these economically and traditionally dominant terpenoids started from the primitive times, and due to their wide range of medical applications, they were used to alleviate numerous disorders. These metabolites also possessed wide range of industrial applications and chemoecological functions (Gross and Konig, 2006). Marine organisms harvest a wide variety of unique class of terpenoids, differentiated by structural characteristic features. Some of the predominant marine taxa, such as algae and invertebrates are produced interesting structures with various functionalities (Gross and Konig, 2006; Blunt et al., 2005).

Three cytotoxic sesquiterpenes **1**-**3** with halogenated functionality has been reported from *Laurencia* species, which were found to exhibit cytotoxic property towards tumour cell line (Faulkner, 1996). A sesquiterpene class of cytotoxic peroxide majapolene **4** was reported from the red seaweed *Laurencia majuscula* from the Philippine. The derivative of this sesquiterpene, majapolone **5** and majapolols **6**-**10** were reported as diastereomers (Faulkner, 1996).

1 $R^1=R^2=H$
2 $R^1=Br$; $R^2=H$
3 $R^1=H$; $R^2=Br$

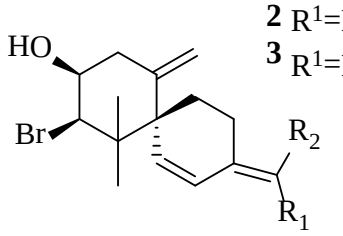

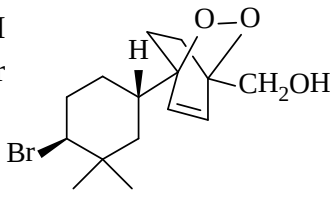

4

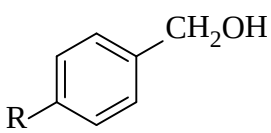

5
R=a

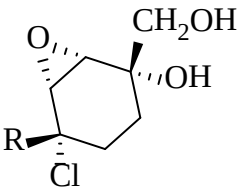

8 R=a

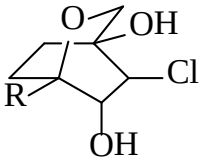

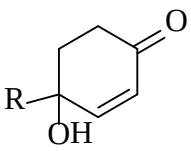

6

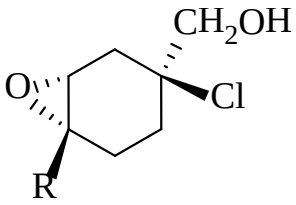

9 R=a

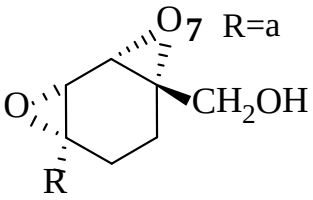

7 R=a

10 R=a

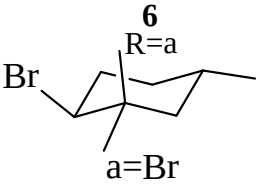

The meroditerpenoids, namely, a series of nahocols and isonahocols **11-13** and **14-15**, were isolated from *Sargassum autumnale* from Japan, and were endothelin antagonists. The meronorsesquiterpenes, cystomexicones **16** and **17** along with 4-(5-hydroxy-2-methoxy-3-methylphenyl)-butan-2-one **18** were identified from the brown species *Cystoseira abies marina* (from Tenerife) (Faulkner, 2000). Halogenated terpenes, pantopyranoids **19-21**, pantoisofuranoids **22-24**, pantoneurotriols **25-26** along with monoterpenes with linear structures, such as compounds **27-28** and pantoneurines **29-30** were recorded from the red seaweed species of *Pantoneura plocamioides (*from Antarctica) (Faulkner, 2000). Four moncyclic diterpenes **31-34** were reported from *Caulerpa trifaria* (from Tasmania) (Faulkner, 2002). A new brown seaweed derived meroterpenoid schimperiol **35** was separated from *Stypopodium schimperi*. The sesquiterpenes, such as zonarol **36** and isozonarol **37** were derived from seaweed *Dictyopteris zonaroides* (Faulkner, 2002).

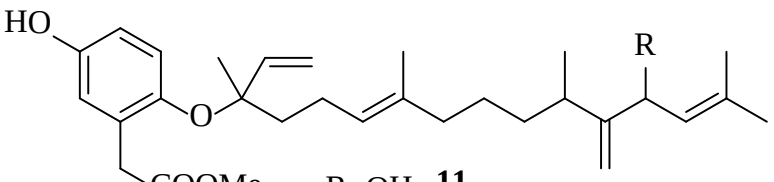

R=OH **11**
R=H **12**

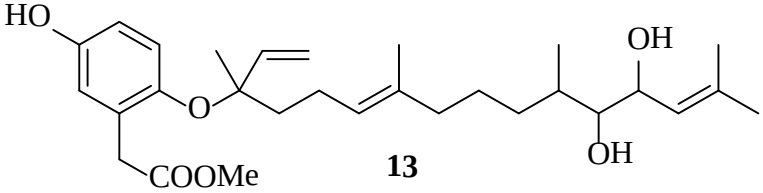

13

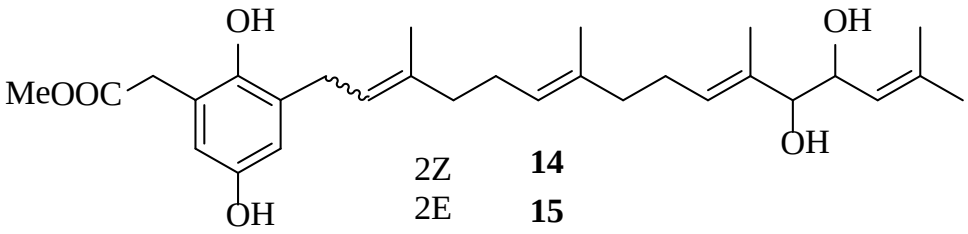

2Z **14**
2E **15**

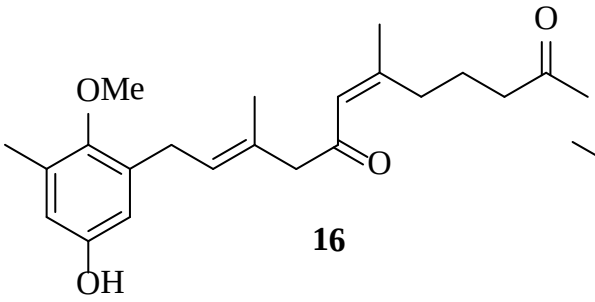

16

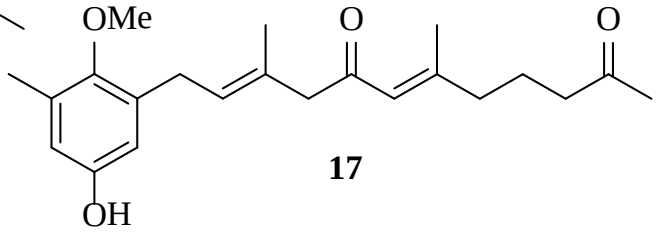

17

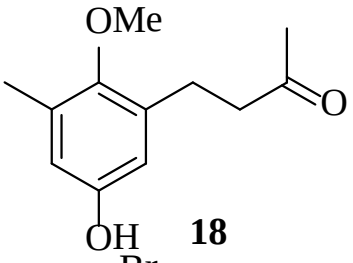

18

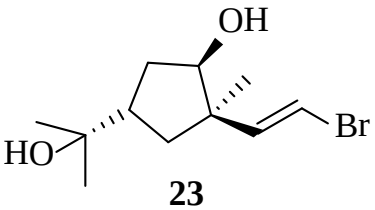

23

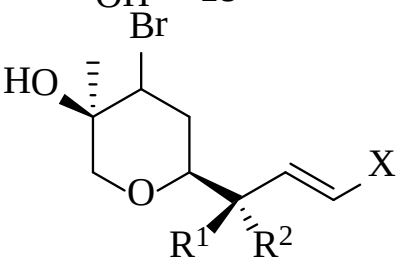

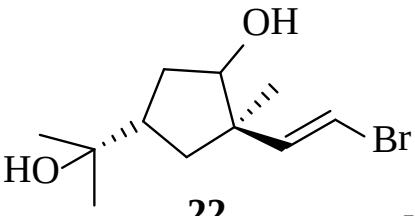

22

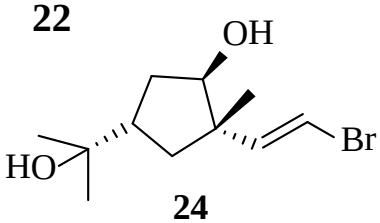

24

19 R^1=OH; R^2=Me; X=Br
20 R^1=Me; R^2=OH; X=Cl
21 R^1=OH ; R^2=Me; X=Cl

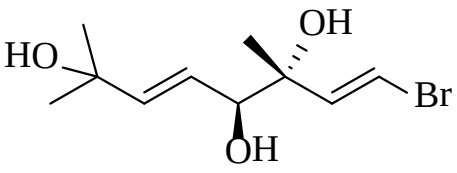

25

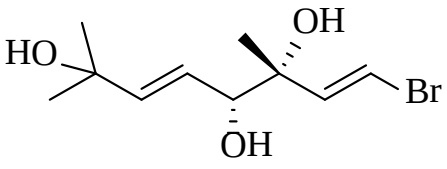

26

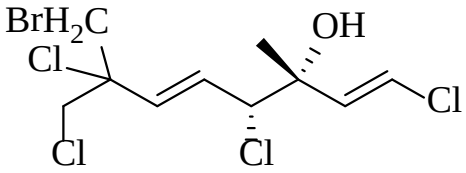

28

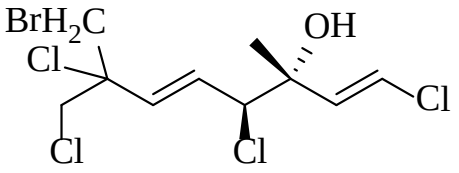

27

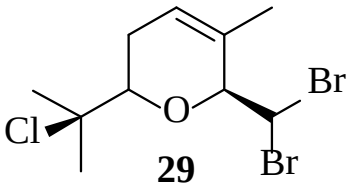

29

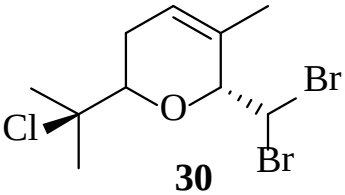

30

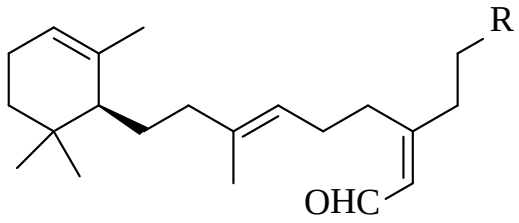

32 R=CHO

33 R=CH_2OAc

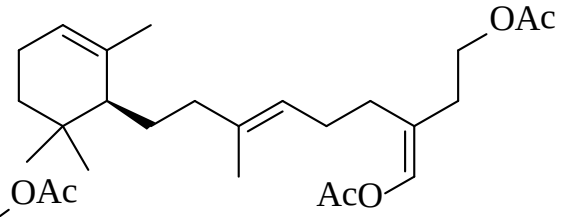

31

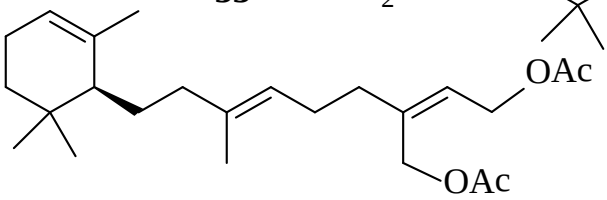

34

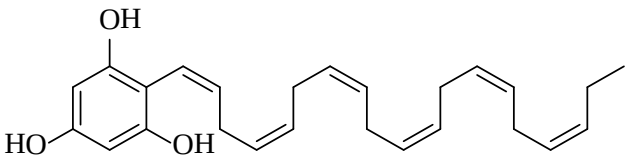

35

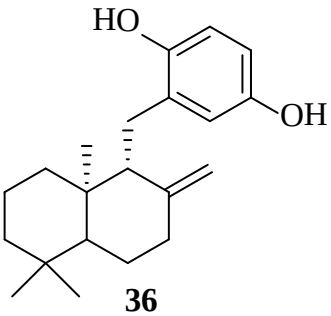

36

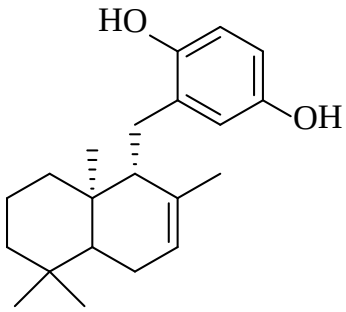

37

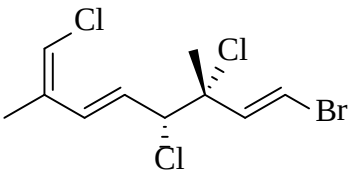

38

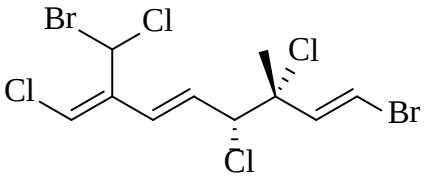

39

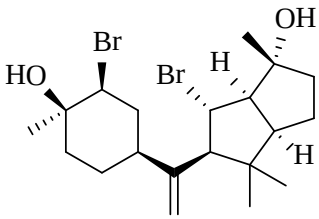

40

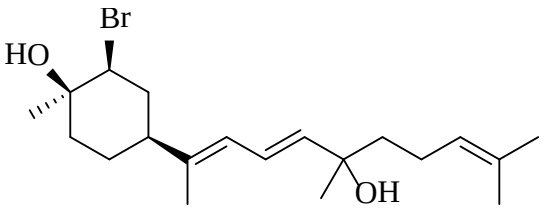

41

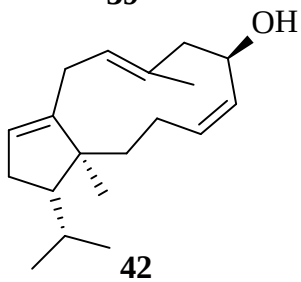

42

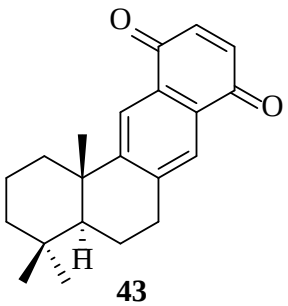

43

The polyhalogenated monoterpenes **37** and **38** were reported from an Eastern Tasmanian red seaweed *Plocamium cartilagineum*. The diterpenes neorogioldiol **39**, rogioldiol D **40** and $O^{11},^{15}$-cyclo-14-bromo-14,15-dihydrorogiol-3,11-diol **41**, were identified from *Laurencia microcladia* (Faulkner, 2002). A hydroclathrol **42**, dolabellane diterpene and enantio specific sesquiterpene benzoquinone (+)-cyclozonarone **43** were identified from the brown seaweeds *Hydroclathrus tenuis* and *Dictyopteris undulata*, respectively. New acyclic diterpenes **44-47** was documented from the seaweed *Bifurcaria bifurcata* (from the Atlantic coast of Morocco). The sesquiterpene 8-bromochamigren-1-en **48** was isolated from the red seaweed *Laurencia majuscula* (from the South China Sea) (Blunt et al., 2003). Novel antibacterial halogenated sesquiterpenes analogues, pannosanol **49** and pannosane **50** were isolated from red seaweed *Laurencia pannosa* (from Malaysia) (Blunt et al., 2003).

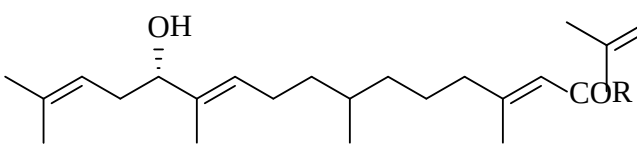

44 R=OMe
45 R=H

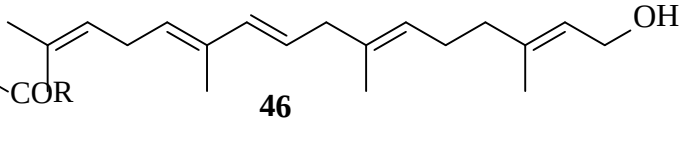

46

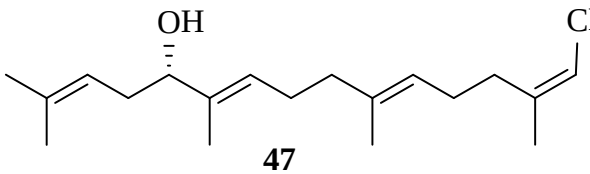

47

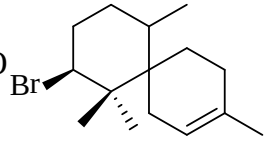

48

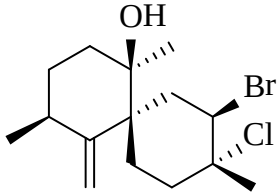

49

Five brominated sesquiterpenes isopalisol **51**, luzonensol **52**, luzonensol acetate **53**, luzonensin **54** and (3*Z*,6*E*)-1-bromo-2-hydroxy-3,7,11-trimethyldodeca-3,6,10-triene **55**, and a bromoditerpene 3-bromobarekoxide **56** were isolated from the seaweed species *Laurencia. luzonensis* (from Okinawan waters) (Blunt et al., 2003). Sesquiterpenes, such as scopariol **57** with reorganized chamigrane skeletal structure, isorigidol **58**, is a β-chamigrene, which were isolated from *L. scoparia* (collected from Brazilian waters). Squalene-derived four triterpenes pseudodehydrothyrsiferol **59**, martiriol **60**, dioxepandehydrothyrsiferol **61** as well as 16-epihydroxydehydrothyrsiferol **62** were isolated from *L. viridis* (Canary Islands) (Blunt et al., 2003). Another sesquiterpene, Calenzanol **63**, with novel ring system was obtained from of *L. microcladia* (Elba Island in the Mediterranean). The sesquiterpene with halogenation (6R,9R,10S)-10-bromo-9-hydroxychamigra-2,7(14)-diene **64** was derived from the Okinawan red seaweed *L. majuscula*. These compounds were found to exhibit prospective antibacterial activity (Blunt et al., 2003). Brominated diterpenes, Prevezols A **65** and B **66** were isolated from *L. obtusa* that was collected from the Greek waters. Bomotriterpene polyether analogues, armatols A-F **67-72** were identified from *Chondria armata* collected from the Indian Ocean. The homosesquiterpenic acids **73-76**, are polyhalogenated terpenes, which were isolated from *P. cartilagineum* (from the Mediterranean). Similarly, bromoditerpenes, sphaerolabdiene-3,14-diol **77** and bromosphaerone **78**, were isolated from a collection of *Sphaerococcus coronopifolius* from the Atlantic coast of Morocco (Blunt et al., 2003).

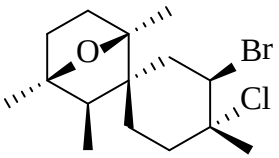

50

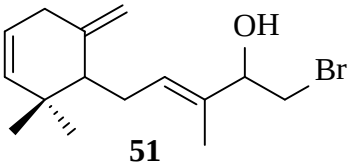

51

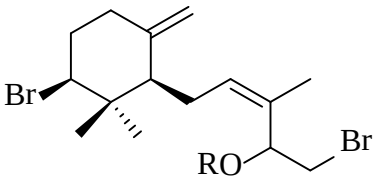

52 R=H
53 R=Ac

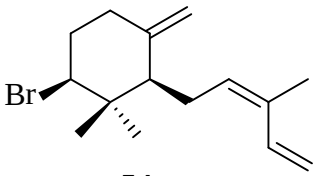

54

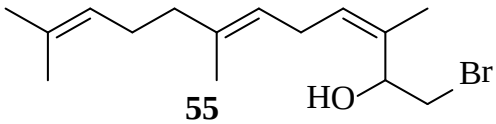

55

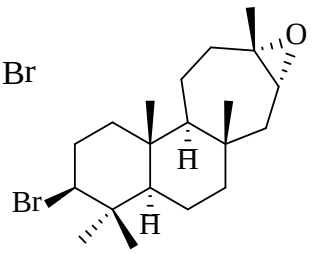

56

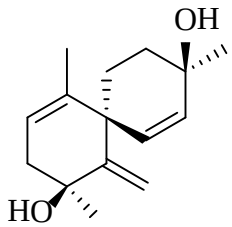

57

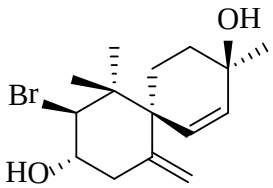

58

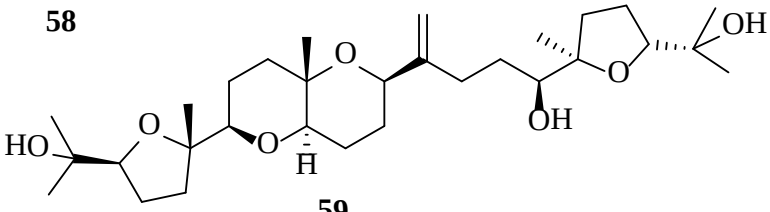

59

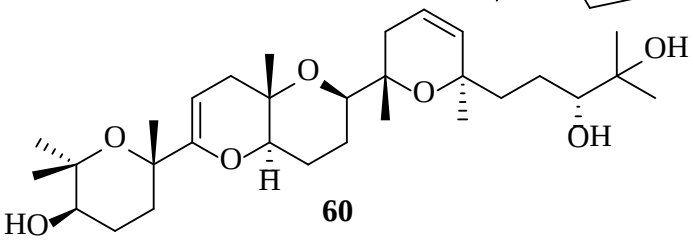

60

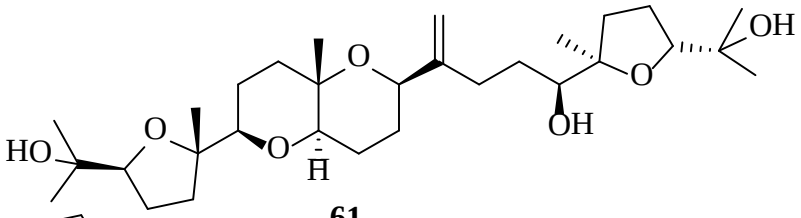

61

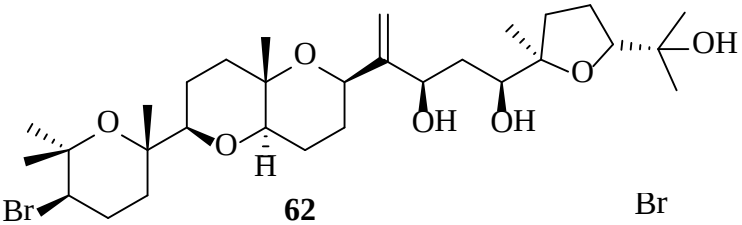

62

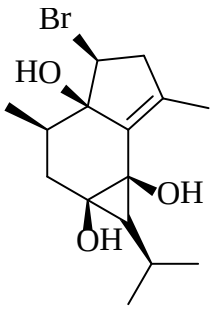

63

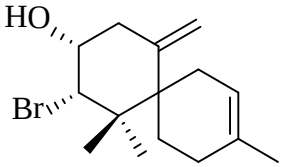

64

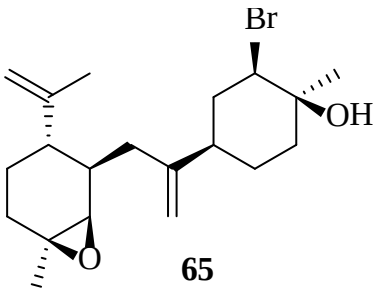

65

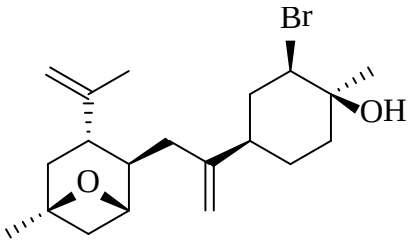

66

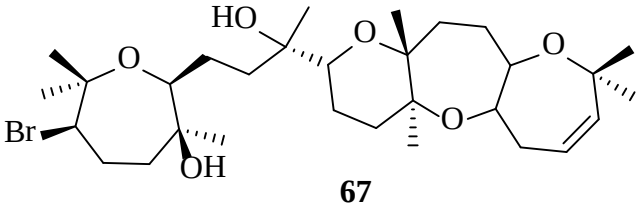

67

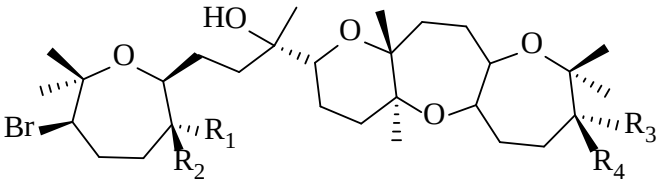

68 R_1=Me, R_2=OH, R_3=Br, R_4=H
69 R_1=OH, R_2=Me, R_3=Br, R_4=H
70 R_1=Me, R_2=OH, R_3=H, R_4=H
71 R_1=OH, R_2=Me, R_3=H, R_4=Br

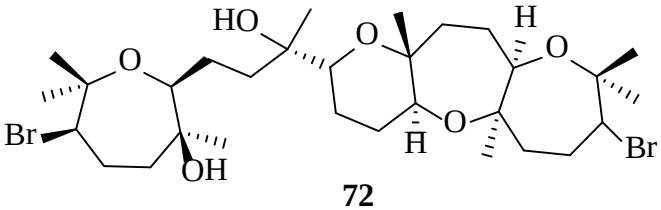

72

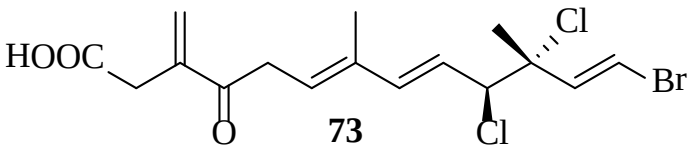

73

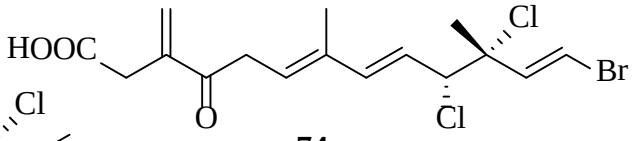

74

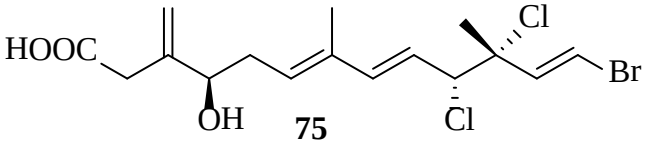

75

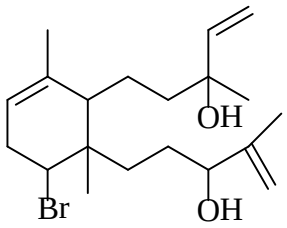

77

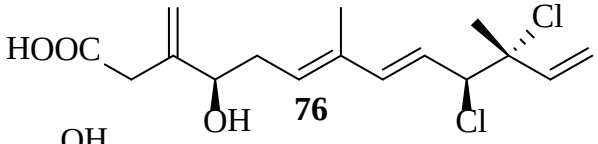

76

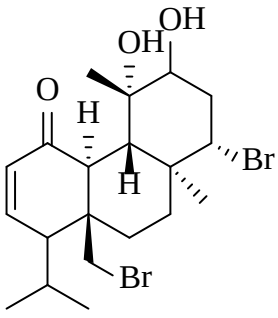

78

A diterpenoid, Stypolactone **79**, with weak *in vitro* cytotoxicity against the A-549 and H-116 cell lines, was identified from the brown seaweed *Stypopodium zonale* (Blunt et al., 2004). Novel diterpenoids, namely, dictyterpenoids A-B **80-81** have been derived from the seaweed *Dilophus okamurae*, which was harvested from the Coast of Japan Sea, and exhibited antifeedant activity (Blunt et al., 2004). Chilean red seaweed of *Plocamium cartilagineum* yielded a monoterpene, Prefuroplocamioid **82,** which is a linear polyhalohydroxylated monoterpenes, **83** and halogenated monoterpenes **84** and **85-88**. The species *L. obtusa* obtained from Coco, Cayo Cuba yielded oxachamigrene sesquiterpene **89** and 5-acetoxyoxachamigrene

90 (Blunt et al., 2004). The diterpenoids, such as seco-dolastane dichotone **91**, dichotodione **92**, dichototetraol **93** and dichopentaol **94**, and the related enone dolastane dichotenones A **95** and B **96** were reported from *D. dichotoma* collected from the Coast of Arabian Sea (Blunt et al., 2005). Novel diterpene dictyocrenulol **97** was yielded from the brown seaweed *Dictyota crenulata* obtained from the Easter Island. Other sets of terpenes like calenzanane sesquiterpene, debromoisocalenzanol **98**, indene-type sesquiterpene **99** were reported from *L. microcladia* collected from the coast of Elba Island (Blunt et al., 2005). The red seaweed *L. obtusa* collected from Bademli, Turkey was found to containsesquiterpenes, **100-103** along with the snyderol derivatives **104** and **105** (Blunt et al., 2005). *Laurencia perforata*, harvested from the Australian coast, was considered as the source of the sesquiterpenes 4-hydroxy-1,8-epi-isotenerone **106** and two 3-epi-perforenone A derivatives, **107** and **108**. Red seaweed *L. obtusa* harvested from the Greece yielded brominated diterpenes **109** and **110**. The red seaweed, *Portieria hornemanni*, was reported to yield monoterpenes **111-115** with potential bioactive properties (Blunt et al., 2005).

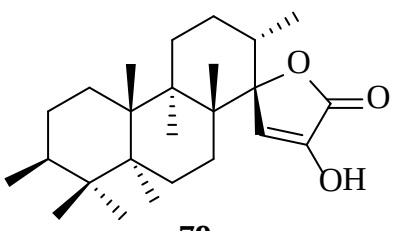

79

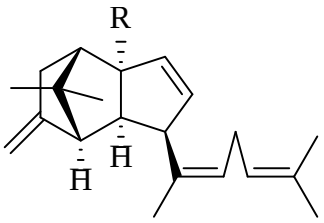

80 R=CHO
81 R=CH_2OH

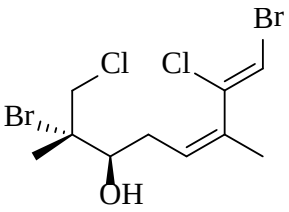

82

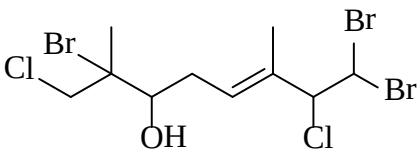

83

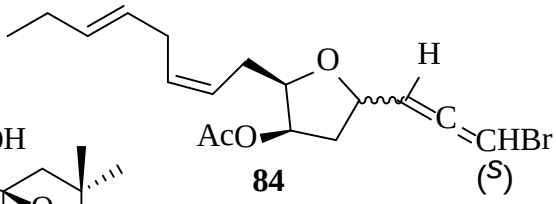

84 (S)

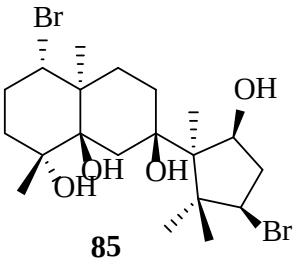

85

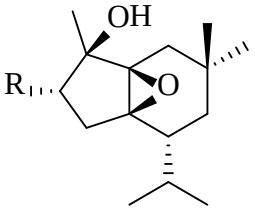

86 R=Cl
87 R=Br

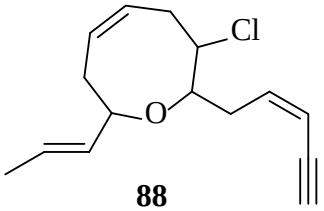

88

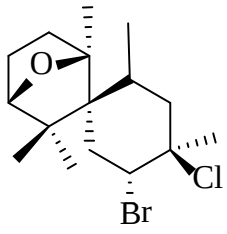

90

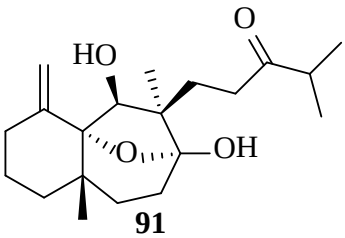

91

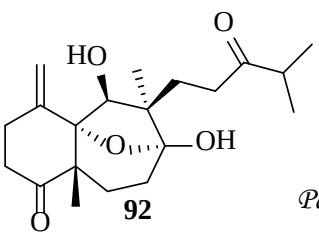

92

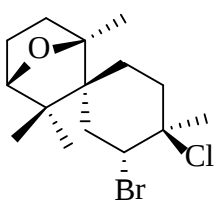

89

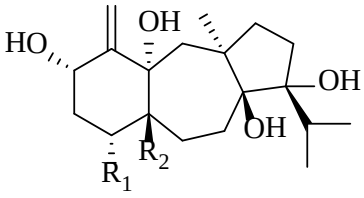

93 R=Me
94 R=CH_2OH

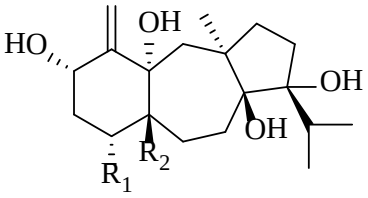

95

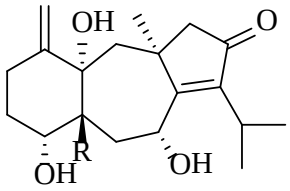

96 R=Me
97 R=OAc

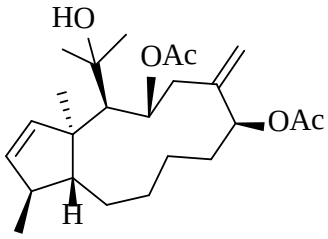

98 R=Me
99 R=OAc

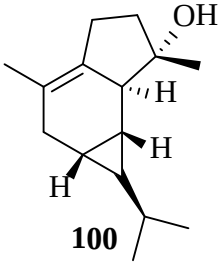

100

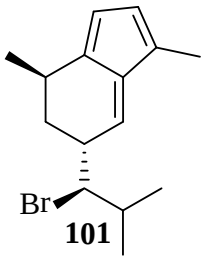

101

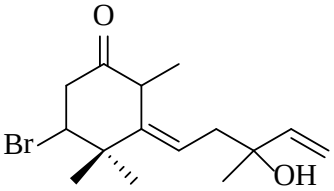

102

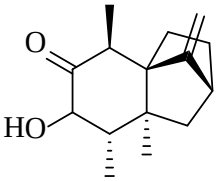

103

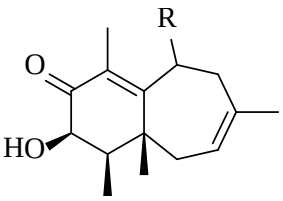

104 R=OH
105 R=H

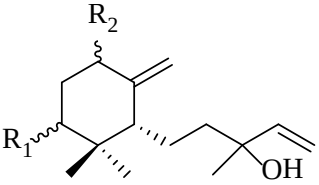

106 R_1=αBr, R_2=βBr
107 R_1=βBr, R_2=αBr

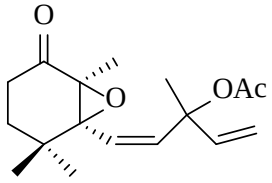

108

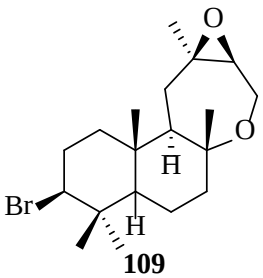

109

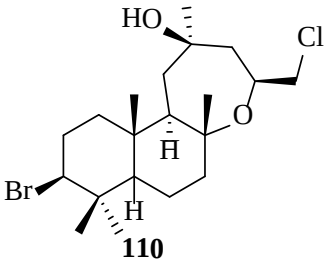

110

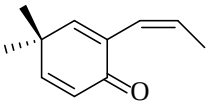

114 R=Br
115 R=Cl

The organic extract of the species *Bifurcaria bifurcate*, collected from the Atlantic coast of Morocco, yielded two trihydroxylated diterpenes **116** and **117**. The diterpenes, isopachydictyolal **118**, 4a-acetyldictyodial **119**, dichotenols A-C **120-122**, and dolabelladiene derivative **123** were reported from *Dictyota dichotoma* and *Dictyota linearis*, respectively

(Blunt et al., 2006). The brown seaweed *Stypopodium flabelliforme* collected from Papua New Guinea, yielded bioactive meroditerpenoids, such as 2β,3α-epitaondiol **124**, flabellinol **125**, flabellinone **126**, stypotriolaldehyde **127** stypohydroperoxide **128**, which displayed cytotoxic activity along with regulation of calcium concentrations in the cells (Blunt et al., 2007). Red seaweed *L. microcladia* collected from North Aegean Sea was found to be contain cuparene sesquiterpenes **129-131**. These were found as cytotoxic against the cancer cell lines. Other set of cuparene sesquiterpenes Laureperoxide **132**, 10-bromoisoaplysin **133**, isodebromolaurinterol **134** and 10-hydroxyisolaurene **135** were identified from the Chinese red seaweed *L. okamurai* (Blunt et al., 2007). A perhydroazulene diterpene, dictyol J **136** was identified from *D. dichotoma*. These compounds displayed algicidal activity to the bloom formation. Monoterpenes with halogenation **137-139** has been derived from *P. hornemannii* collected from Madagascar. These were found as moderate inhibitors of DNA methyl transferase-1 (Blunt et al., 2008). The bromine bearing diterpenes, 10-hydroxykahukuene B **140**, sesquiterpenes, such as 9-deoxyelatol **141** and isodactyloxene A **142** and halogenated sesquiterpenes **143** and **144** were afforded from Chinese *L. mariannensis.* The aromatic-sesquiterpene analogues **145**, **146** and **147**, cyclolaurane sesquiterpene **148** and sesquiterpene alcohol **149** were reported from *L. okamurai* obtained from China (Blunt et al., 2009). Selinane terpenes **150** and **151**, the brominated sesquiterpenoids were obtained from Chinese *Dictyopteris divaricate*. A brominated neorogioltriol **152**, exhibited analgesic property, was afforded from *L. glandulifera* (Greece) (Blunt et al., 2010). Diterpenoids, xenicanes **153** and **154** were obtained from the seaweed *Dictyota ciliolata* (Morocco). A special category of sesquiterpene hydroquinones peyssonoic acid A **155** and B **156** were characterized from *Peyssonnelia* species (Fiji). The compounds were found to inhibit the growth of the marine algal bacterial-pathogen (Blunt et al., 2012). From *Dictyota sp.* (France), dictyotadimer A **157** was isolated**,** which was an unusual diterpenoid dimer (Blunt et al., 2013). Chamigranes laurecomin sesquiterpene A-D **158-162** were obtained from *L. composita* (China), and among which, Laurecomin B was found to exhibit antifungal activity (Blunt et al., 2014). Meroditerpenoids with antioxidant activities, namely cystodione A-F **163-168** were identified from *Cystoseira usneoides* (Gibraltar Strait). The sesquiterpenes belonging to chamigrane class; yicterpene A **169** and B **170** were identified from *L. composita* (China) (Blunt et al., 2015).

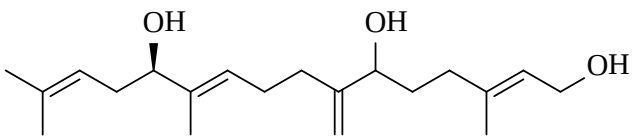

116

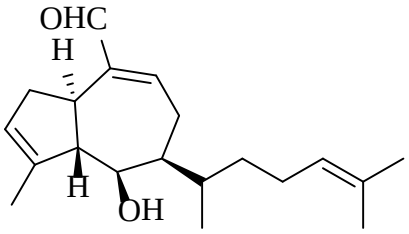

118

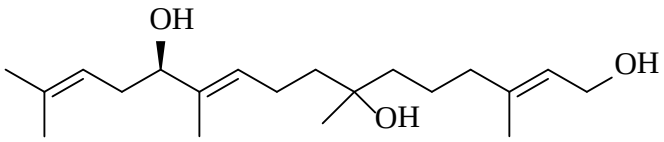

117

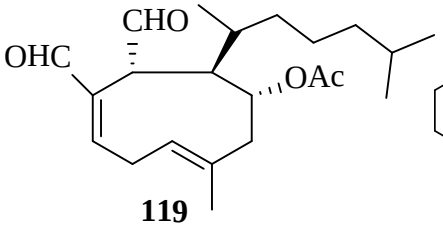

119

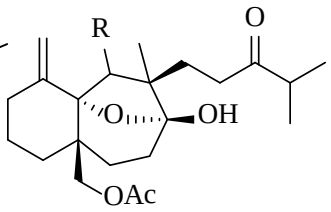

120 R=H
121 R=OH

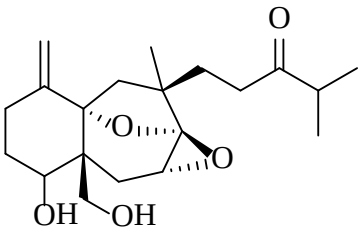

122

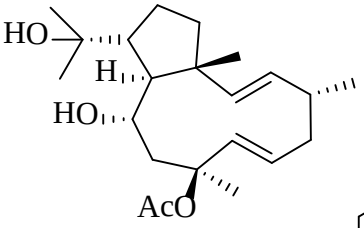

123

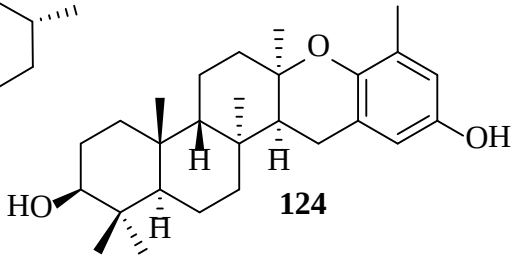

124

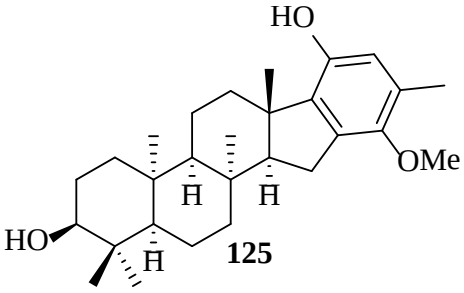

125

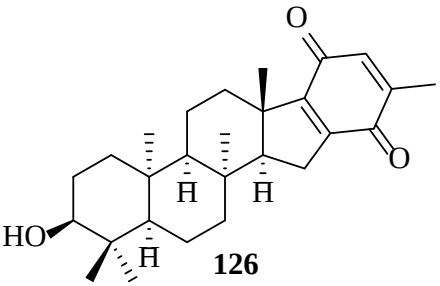

126

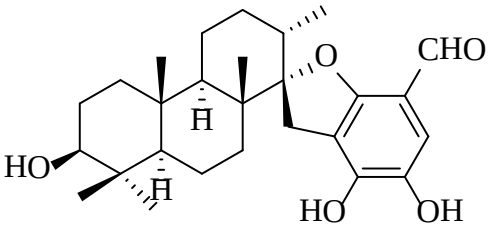

127

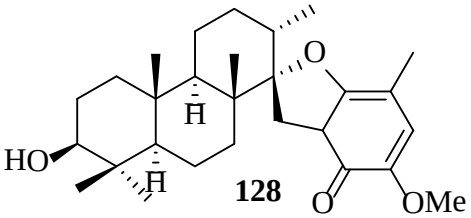

128

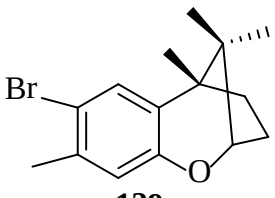

129

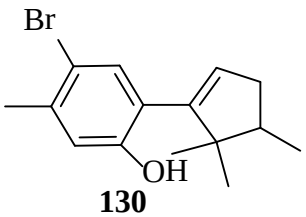

130

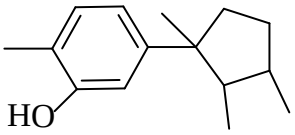

131

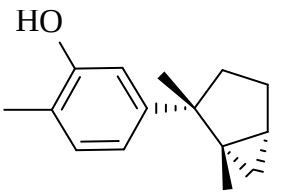

134

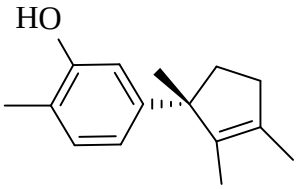

135

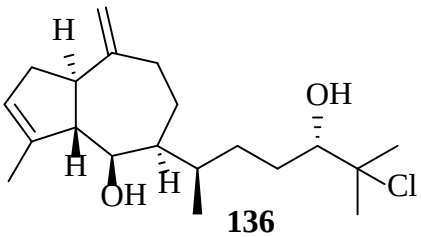

136

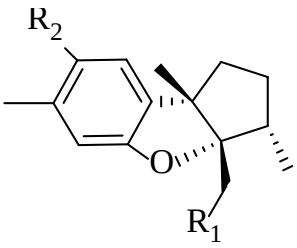

132 $R_{1=}OOH$, R_2=Br
133 R_1=R_2=Br

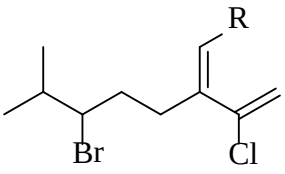

137 R=Br
138 R=Cl

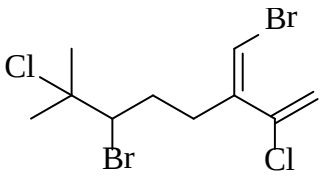

139

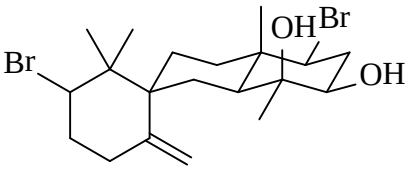

140

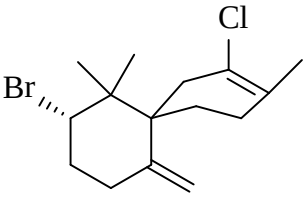

141

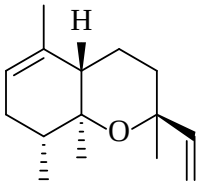

142

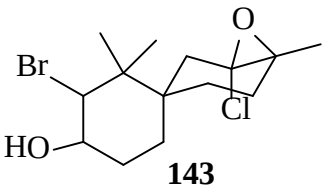

143

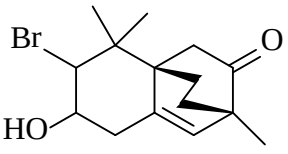

144

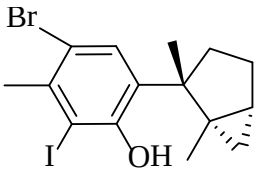

145

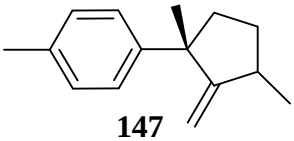

147

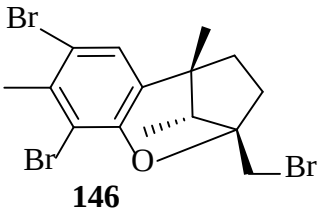

146

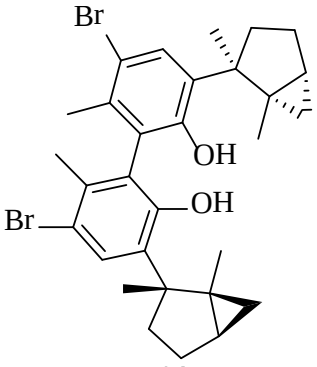

148

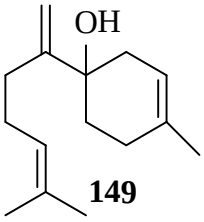

149

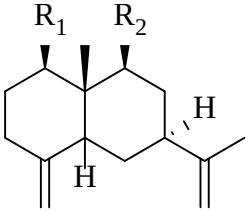

150 R_1=Br, R_2=H
151 R_1=H, R_2=Br

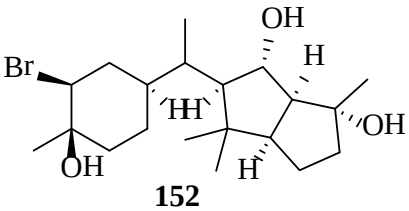

152

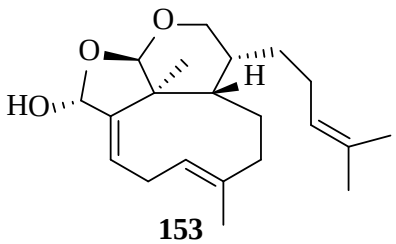

153

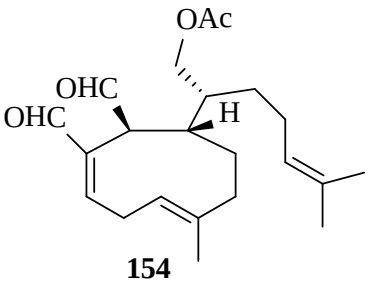

154

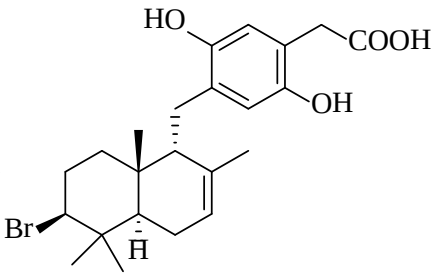

155

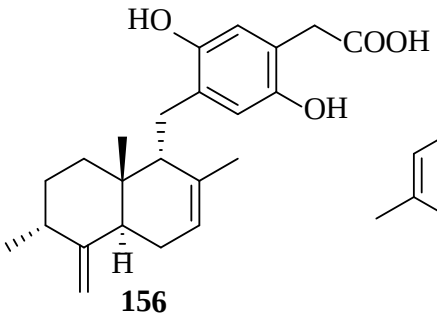

156

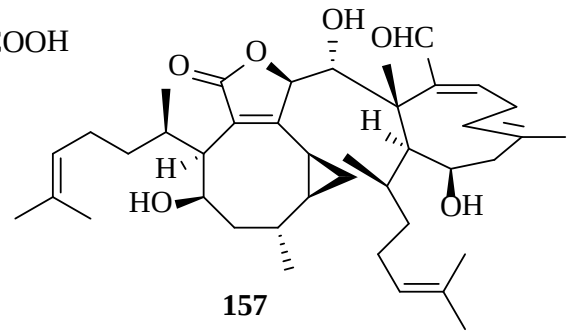

157

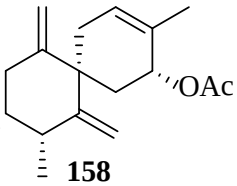

158

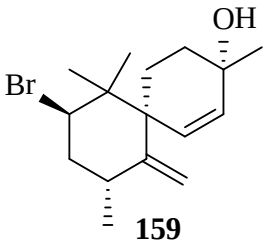

159

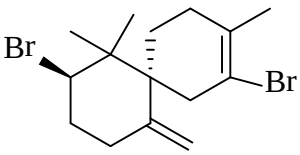

160

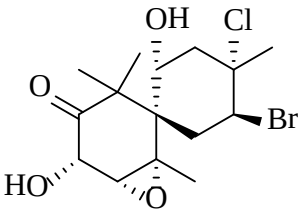

161

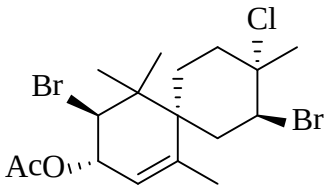

162

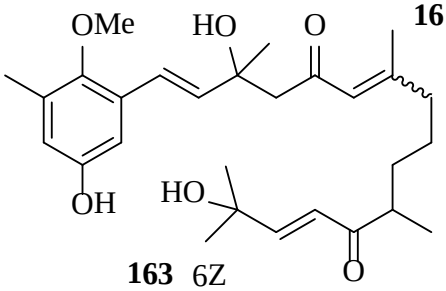

163 6Z
164 6E

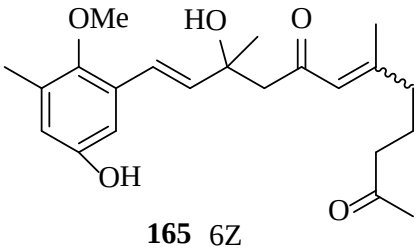

165 6Z
166 6E

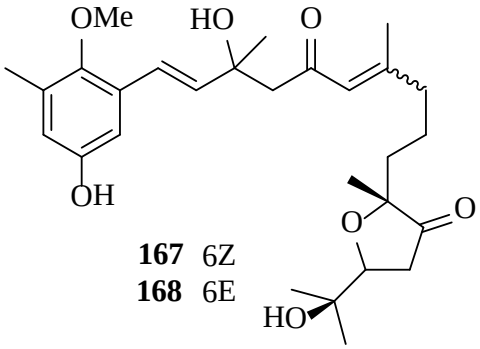

167 6Z
168 6E

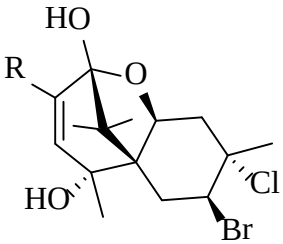

169 R=Cl
170 R=Br

2.3.1.2 Phenolic compounds

Polyphenolic compounds are considered as secondary metabolites derived by the combinations of aromatic benzene ring with more than one hydroxyl entities linked directly to the aromatic rings along with other functional moieties (Generali et al., 2019). A wide range of bioactive phenolic compounds have been identified from different marine living sources with varying structural peculiarities and bioactivities, including small molecular weight compounds to high molecular weight polymers. Phenolic compounds are used against various diseased targets due to their antioxidant potentials (Freile-Pelegrín and Robledo, 2013). Around 8000 phenolic secondary metabolites are presently known, and most of them were found to belong to the marine resources, especiallybof seaweed origin (Freile-Pelegrín and Robledo, 2013). These promising bioactive leads were biosynthesized in seaweeds by two major primary synthetic pathways, such as the acetate and shikimate pathways, and were found to produce phenolic acids to complex phlorotannins analogues (PHT). The polymerization of phloroglucinol (PG) units via the acetate-malonate/polyketide pathway leads to the formation of phlorotannins and these analogues restricted to the brown seaweeds. PHT metabolites are found to be detected in the cytoplasm, and these act as primarily constituents of the cell wall and thereby, found to act in early developmental stages to adult plants. On the basis of linkage pattern of the PG units, along with the number and the orientation of hydroxyl moieties, PHT metabolites were classified as phlorethols and fuhalols, fucols, fucophlorethols, and eckols. Among the various secondary metabolites, phenolics were considered as good free radical scavengers and reducing agents, which could interact actively with the living systems (Generali et al., 2019). They were found to exhibit potential pharmaceutical and nutraceutical application. The high concentration of polyphenolic analogues in seaweed species contributes towards the antioxidant potencies, which can reduce oxidative stress induced damages to health (Generali et al., 2019). During oxidative stress circumstances, destruction of biomolecules due to lipid peroxidation were found to be inhibited by polyphenolic metabolites and thereby, reduce the risk associated with cardiovascular diseases (CVDs) and cancers, and neurodegenerative diseases and diabetes (Freile-Pelegrín and Robledo, 2013). Phenolic terpenoids secondary metabolites have been identified from red and brown seaweeds. Phenolic compounds of meroditerpenoids including plastoquinones, chromanols, and chromenes are present in brown seaweeds. Diterpenes and sesquiterpenes obtained from the red seaweeds are examples of polyphenolic compounds. The presence of diterpene-benzoate macrolides from seaweeds also contributed towards the large number of polyphenolic compounds (Freile-Pelegrín and Robledo, 2013).

Bromophenols (BPs) are one of the phenolic compounds derived from red seaweeds with potential antioxidant activity. For example, BPs **171-175**, which were identified from the

species of red seaweeds *Symphyocladia latiuscula* displayed DPPH radical scavenging potencies. BPs identified from the brown seaweed *Leathesia nana*, **176-180,** exhibited cytotoxic properties against various cell lines of human cancer (Liu et al., 2011). Phlorotannins of eckol-type, **181-182**, **183-187** and **188** were identified from the brown seaweeds *Eisenia bicyclis* and *E. arbores*, respectively. Among which, **181** and **182** exhibited substantial inhibitory potential against the carbolytic enzymes. Compound **189** displayed inhibitory action on histamine discharge (Peng et al., 2015). Fuhalol-type phlorotannins, **190** and **191**, were isolated by the ethanolic extraction of the brown seaweed *Carpophyllum angustifolium*. The fucophlorethols **192-196** were derived from the seaweeds *Sargassum spinuligerum* and *Cystophora torulosa* (Peng et al., 2015). Three phlorethols **197-200** were isolated from *Sargassum spinuligerum.* A novel bromophenol **201** was identified from *Vertebrata lanosa* collected from Norway. These were found to exhibit prospective antioxidant potencies (Blunt et al., 2015). The brown seaweed *Ishige foliacea* obtained from the Jeju Island, yielded a phlorotannin octaphlorethol A **202**. This was known to exhibit antidiabetic potential by the regulation of glucose uptake. The seaweed *Ecklonia cava* also from Jeju Island yielded a new antioxidant 2,7″-phloroglucinol-6,60-bieckol **203** (Blunt et al., 2013). From the Korean species, *S. siliquastrum* (collected from Jeju Island), three sargachromanols **204-206** were isolated. These compounds displayed inhibition against radical-oxygen entities and up-regulate the level of glutathione. The Korean species, such as *Sargassum yezoense*, yielded a novel meroterphenol A-D **207-210** with potential bioactive properties. These were known to regulate energy metabolism via the activation peroxisome proliferator-activated-receptor-gamma (PPARg) (Blunt et al., 2013). The antioxidant phlorotannin, diphlorethohydroxycarmalol **211** was derived from the Japanese seaweed *Ishige okamurae.* This compound also acted as potential inhibitor of carbolytic enzymes, and thereby used to treat diabetes. The bromophenol **212** was isolated from the Chinese *Polysiphonia urceolata.* Novel nitrogen containing bromophenolic compound, colensolide A **213** was identified from *Osmundaria colensoi* (New Zealand) (Blunt et al., 2010). A new chromene, sargothunbergol A **214** with free radical scavenging activity was reported from *Sargassum thunbergii* (Youngdo Is., Busan, Korea). Bromophenols **215-217,** with C–N coupled with nucleoside base analogues were reported from the seaweed *Rhodomela confervoides* (China). Brominated tyrosine analogue **218**, bromophenols **219-221** were isolated from *Polysiphonia urceolata* (China). Brominated bis-phenols **221-223** with potent free radical scavenging potential were derived from the seaweed *Symphyocladia latiuscula* (China). Compounds **224** and **225**, bis(2,3,6-tribromo-4,5-dihydroxyphenyl)methane ether and 2,3,6-tribromo-4,5-dihydroxybenzyl methyl were identified from *Symphyocladia latiuscula* (China), as potential radical scavengers. Novel callophycoic acids A-H **226-233**, diterpene-phenols,

callophycols A and B **234** and **235**, were identified from the seaweed species *Callophycus serratus* (Fiji), whereas some of them exhibited antimalarial, antibacterial, antifungal and antitumour activity.

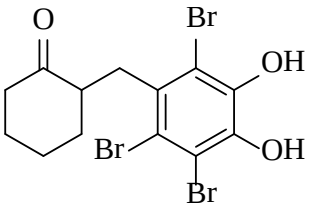

171

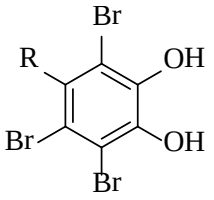

172 R=CH_2OH
173 R=CH_2OCH_3
174 R=CH_3
175 R=CHO

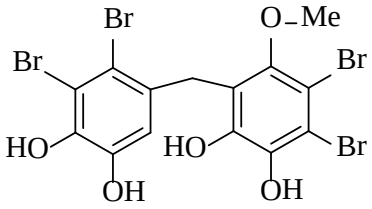

176

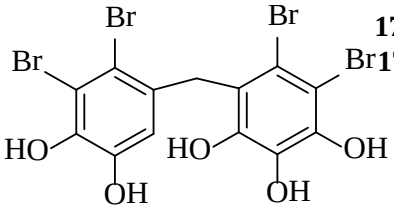

177

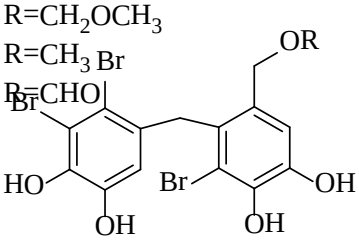

178 R=Et
179 R=Me

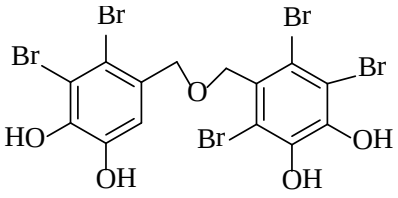

180

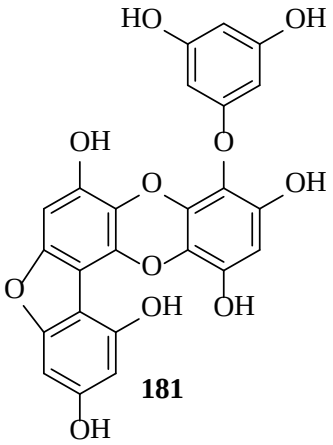

181

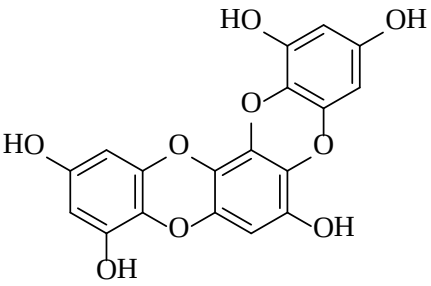

182

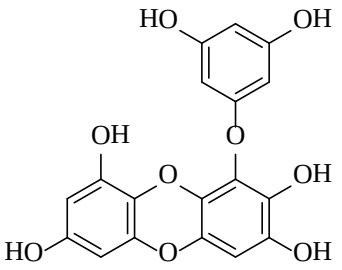

183

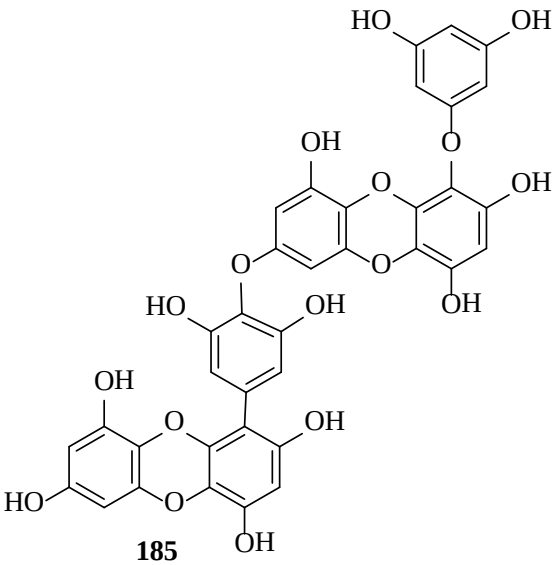

185

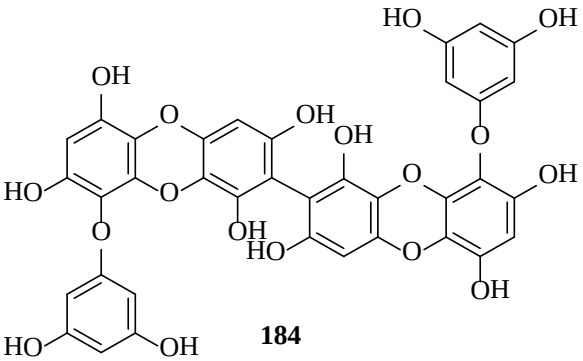

184

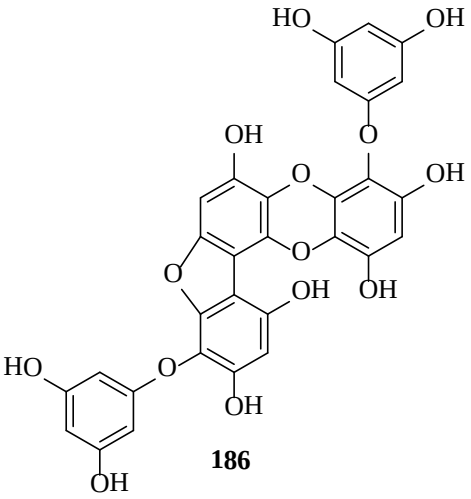

186

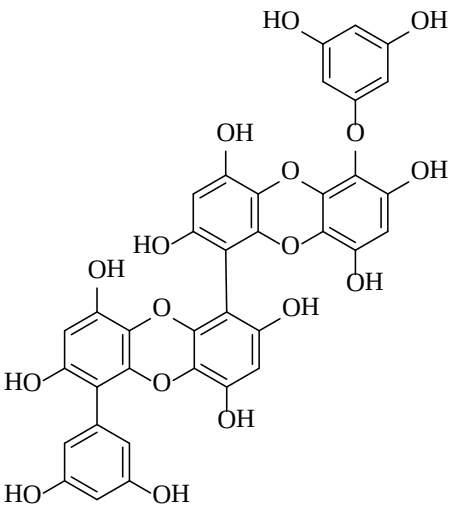

187

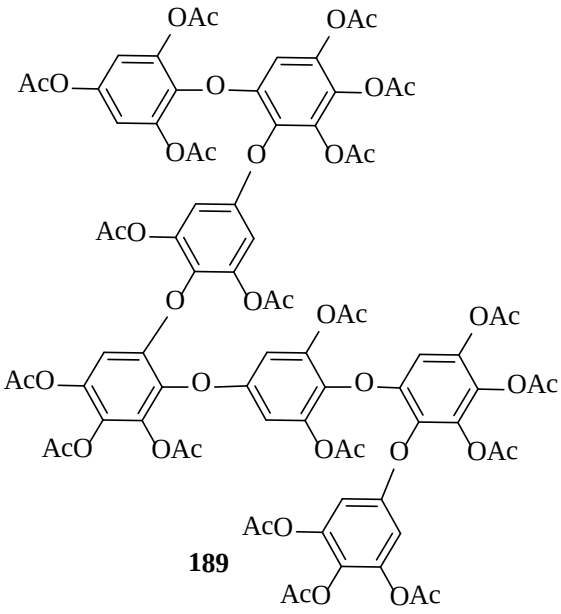

189

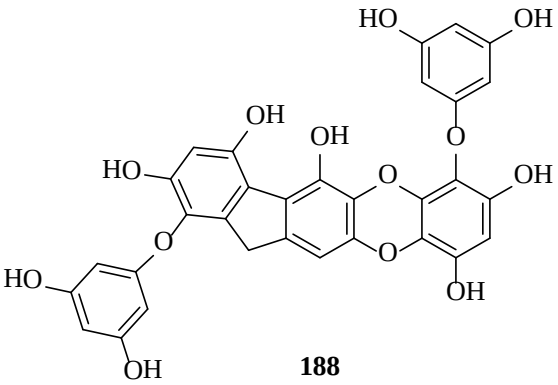

188

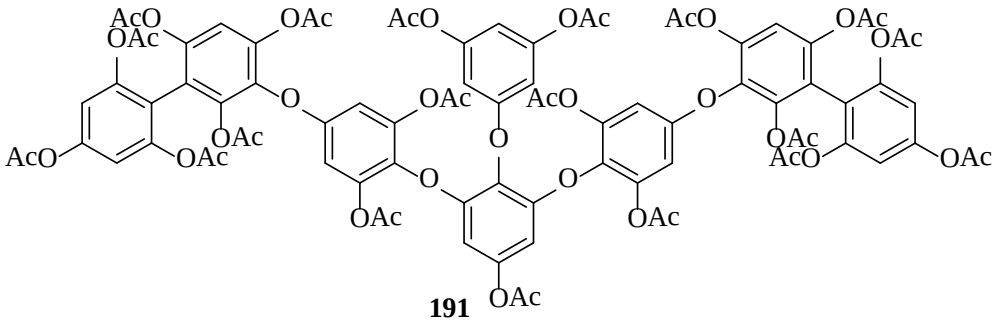

191

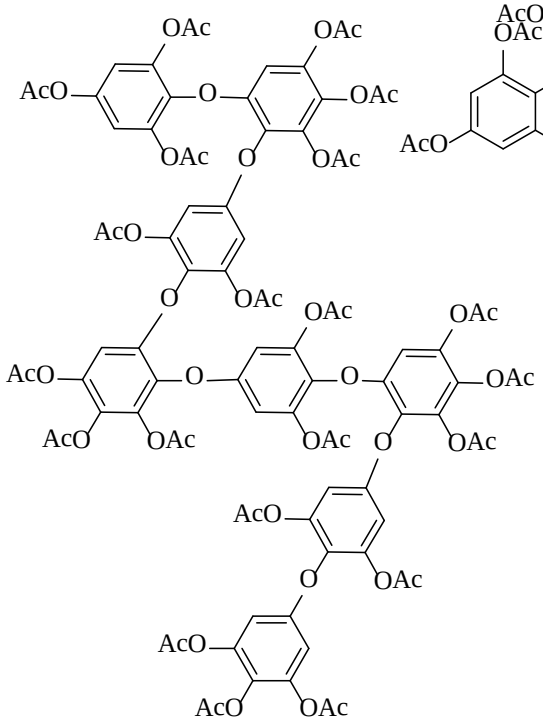

190

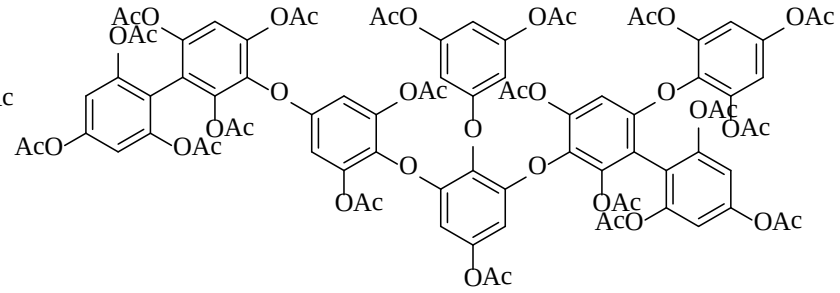

192

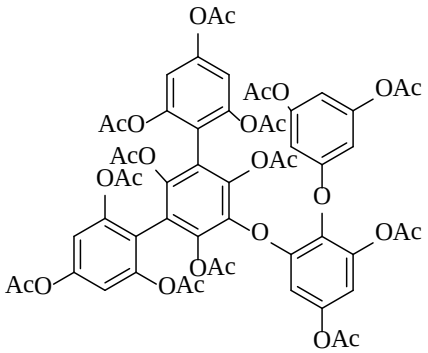

194

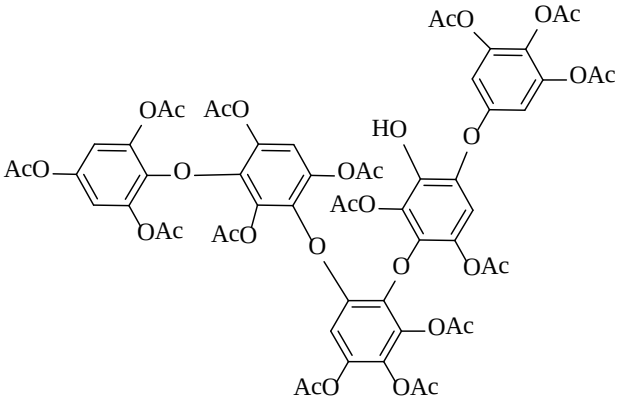

193

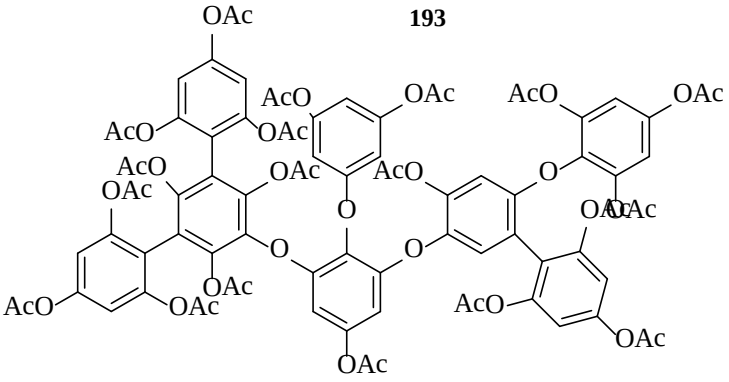

195

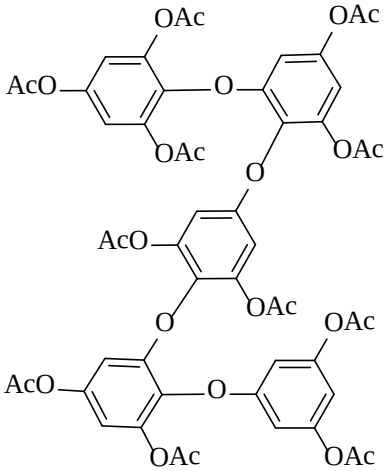

196

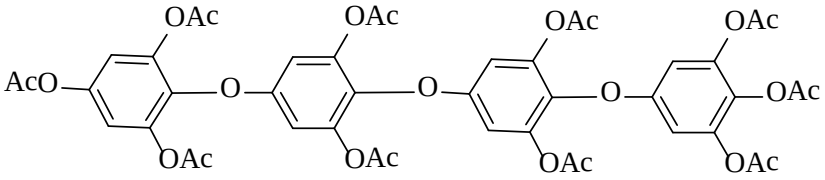

197

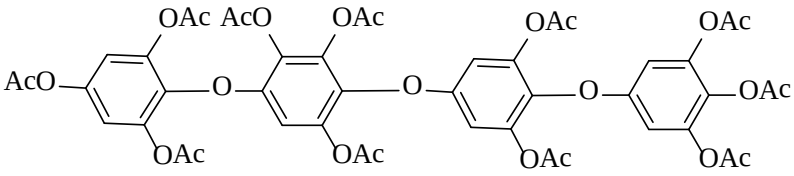

198

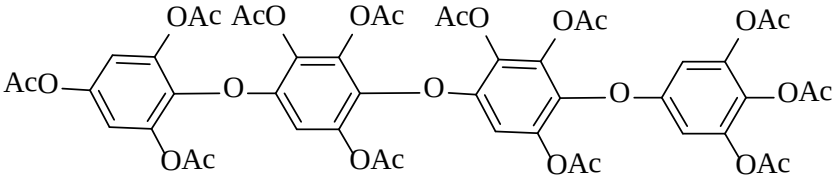

199

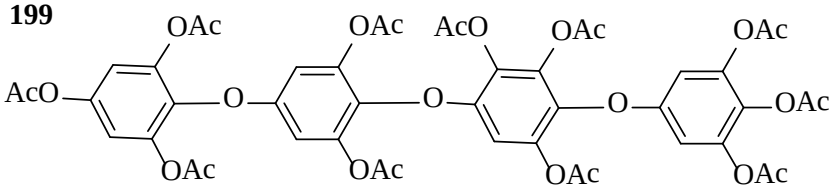

200

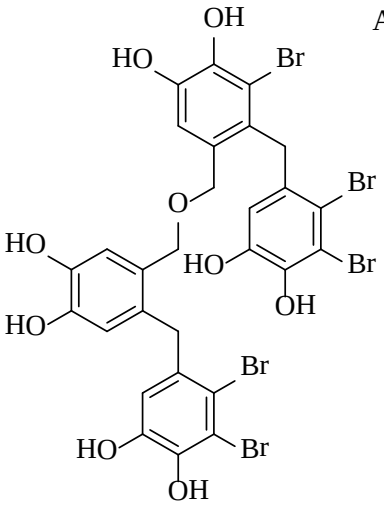

201

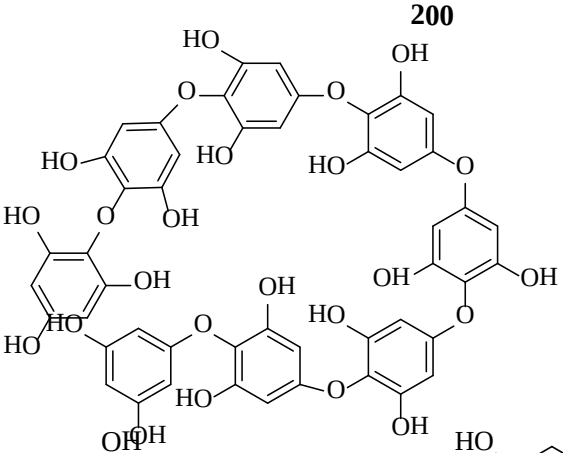

202

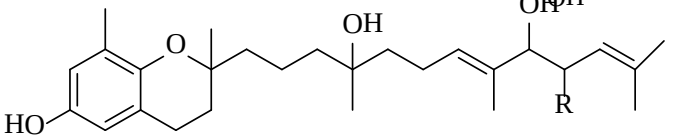

204 R=

205 R=

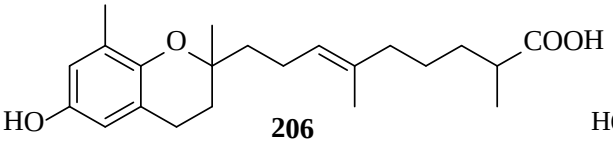

206

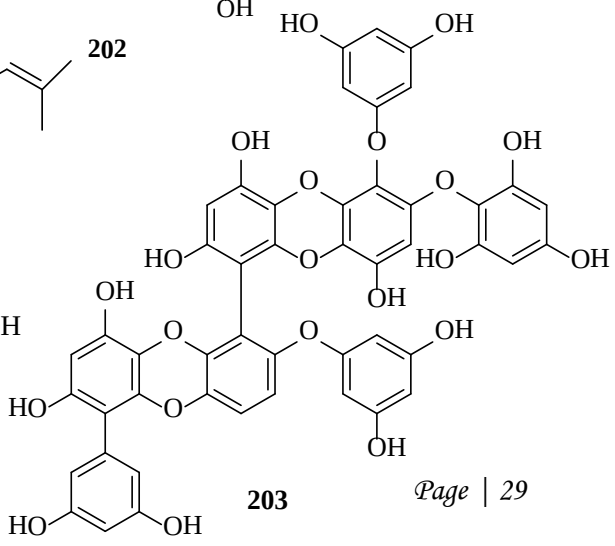

203

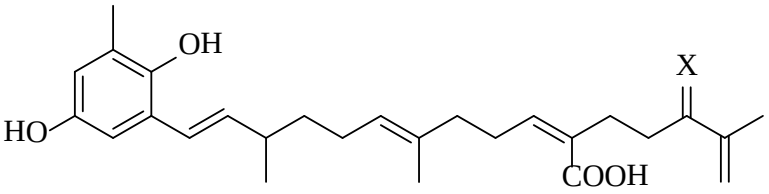

207 X= H, OH
208 X=O

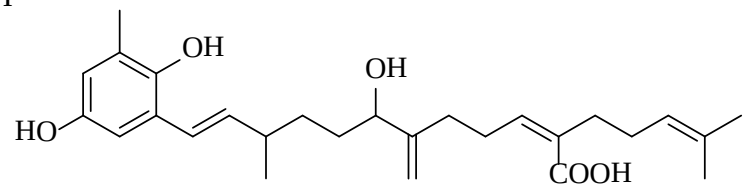

209

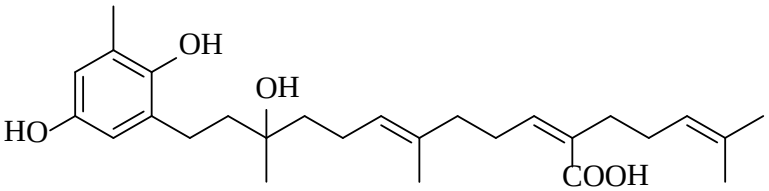

210

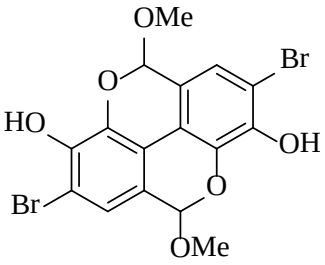

212

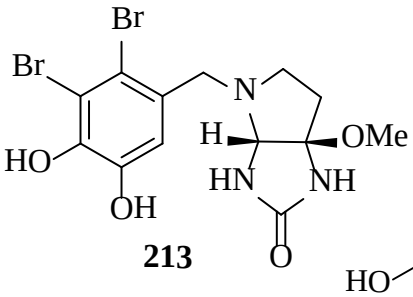

213

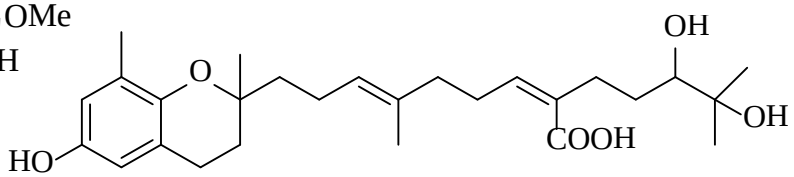

214

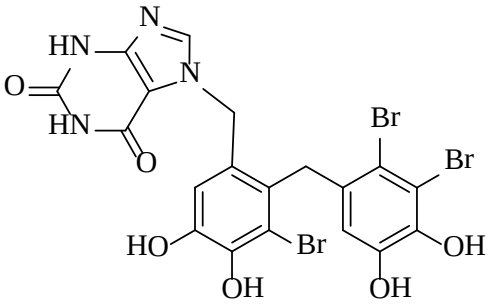

215

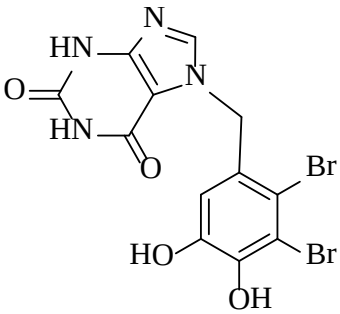

216

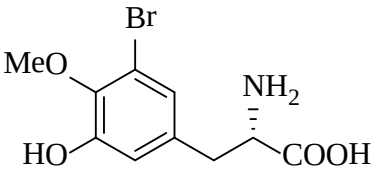

218

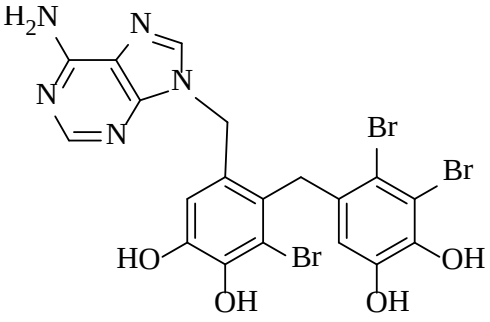

217

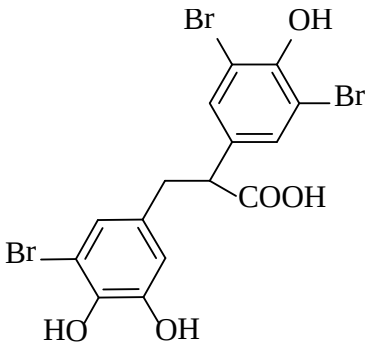

219

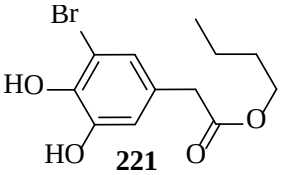

221

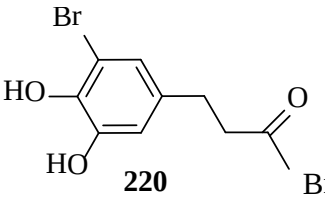

220

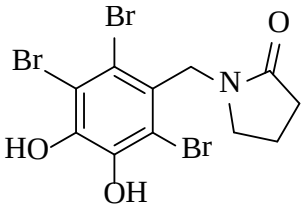

222

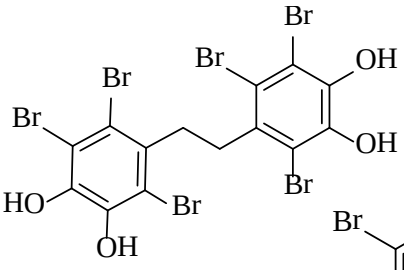

223

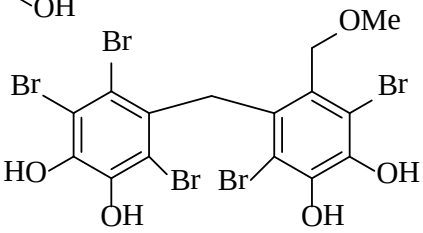

224

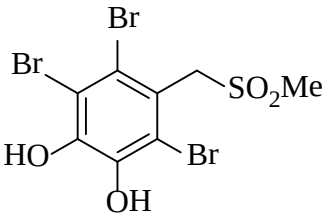

225

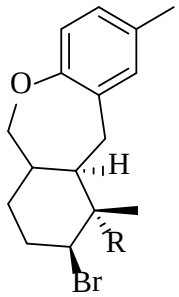

226 R= a
227 R=b

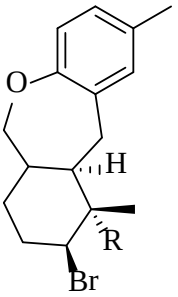

228 R= a
229 R=b

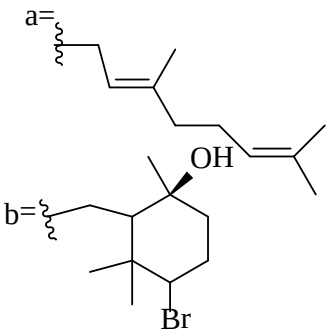

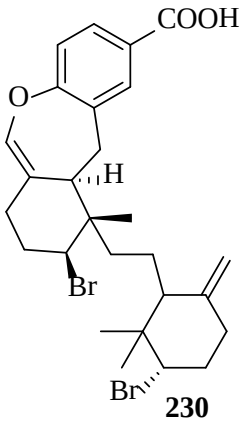

230

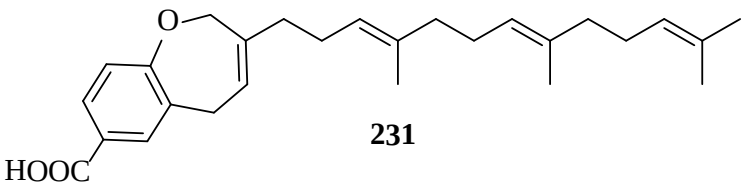

231

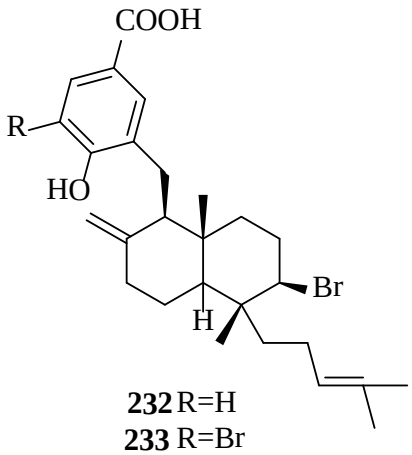

232 R=H
233 R=Br

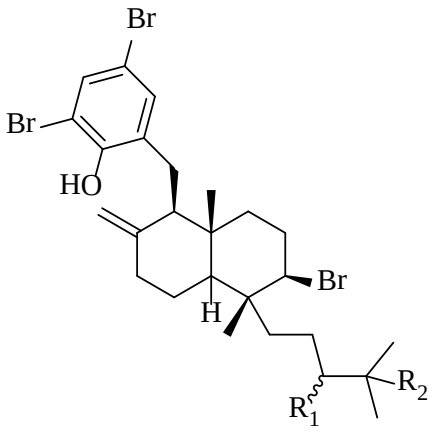

234 R_1=Br, R_2=Cl
235 R_1=Cl, R_2=Br

2.3.1.3 Steroids

Steroids are characteristic triterpene compounds with peculiar orientation of four rings of cyclo alkanes linked to each other. These were found to be derived by the cyclization of bio-precursor squalene along with a series of rearrangements including unsaturation, and substitution. Hundreds of steroidal skeletons were found to be identified from distinct marine living forms. Among which, the seaweed-derived steroids were considered to possess four different carbon skeletons, such as C26, C27, C28, and C29. The majority of red seaweeds were found to possess the carbon skeletons of C27 and C28 steroids, with small percentage of C29 steroids. Brown seaweeds were predominantly comprised of C29 steroids in higher percentage (Peng et al., 2015). These classes of terpenes were found to interact with various metabolic and physiological functions by binding with the steroid receptors (Sultan et al., 2015). Seaweeds have been considered as one of the major sources characteristic sterols with variations in the attached side chains and core skeleton (Peng et al., 2015).

The bioactive oxygenated cholesterols, such as clerosterols **235-237** were reported from green seaweed *Codium arabicum* (Faulkner, 1996). Two novel steroids, namely (20*S*)-3β,20-dihydroxyergosta-5,24(28)-dien-16-one **238** and 3β-hydroxyergosta-5,24(28)-dien-16-one **239** were obtained from the brown seaweed *Cystophora brownie*, originally harvested from the coastal location of South Australia . A cytotoxic steroid, 16β-hydroxy-5α-cholestane-3,6-dione **240** was reported from the red seaweed *Jania rubens* (collected from Tunisia) (Faulkner, 2002). A derivative of stigmastadiendiol **241** has been derived from *Laurencia majuscula* (from the South China Sea) (Blunt et al., 2003). A novel steroid, iyengadione **242** and two steroidal glycosides, iyengarosides A **243** and B **244** with moderate antibacterial activity were derived from the green seaweed *Codium iyengarii* from the coast of the Arabian Sea. A novel sterol 24-norchola-5,22-dien-3β-ol **245** has been isolated from the *Cystoseira crinite*, a brown seaweed collected from the Mediterranean region of Turkey (Blunt et al., 2004). Two new

pharmacologically active sterols **246** and **247** were separated from the seaweed *S. carpophyllum* harvested from the South China Sea. the sterol **112** isolated from seaweed exhibited cytotoxic activity against cancer cell lines. A sterol, stigmast-5,23,25-triene **248** was isolated from the seaweed *S. polycystum* harvested from North China Sea (Blunt et al., 2004). Red seaweed *Porphyridium cruentum* was found to yield inseparable mixture of steroids **249** and **250** from their sulfoglycolipidic fraction (Blunt et al., 2004).

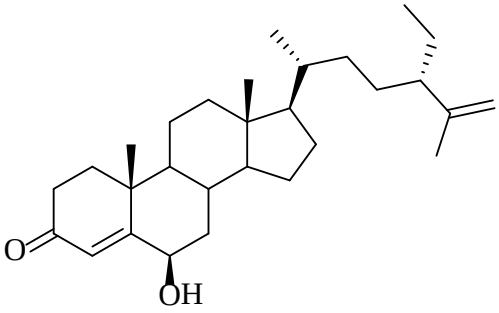

235

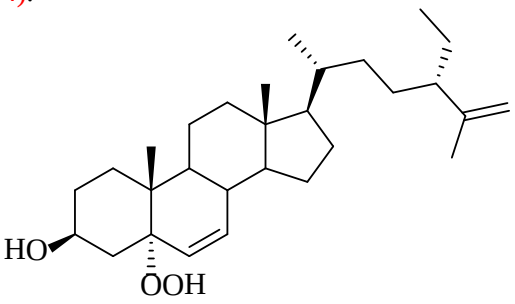

236

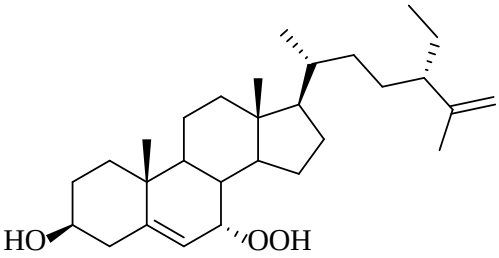

237

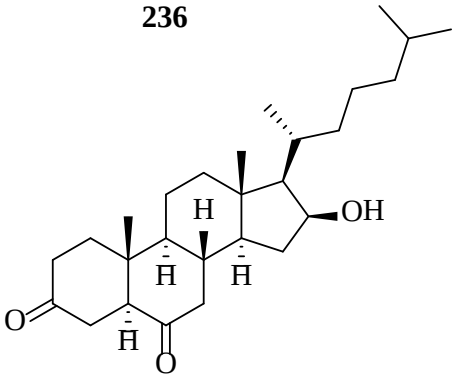

238

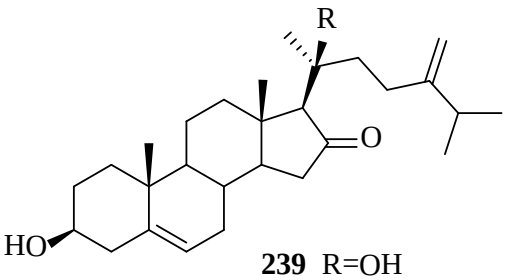

239 R=OH
240 R=H

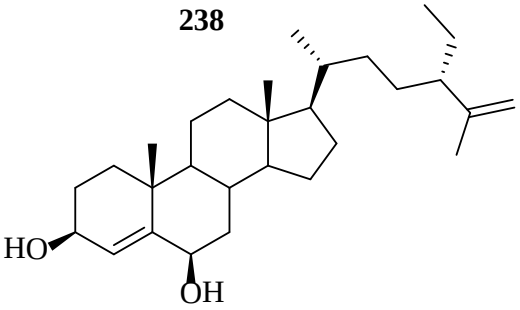

241

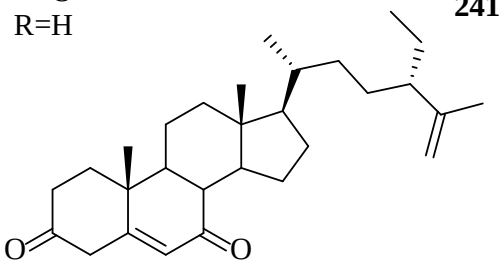

242

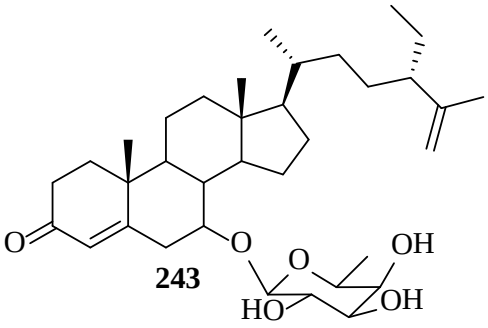

243

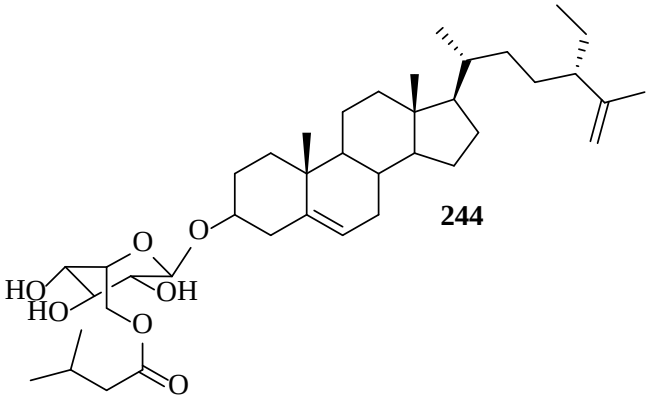

244

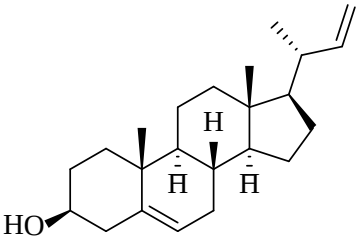

245

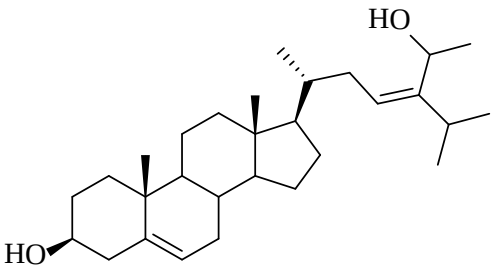

246

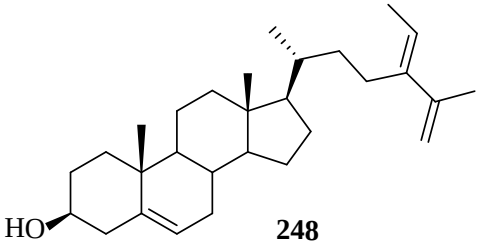

248

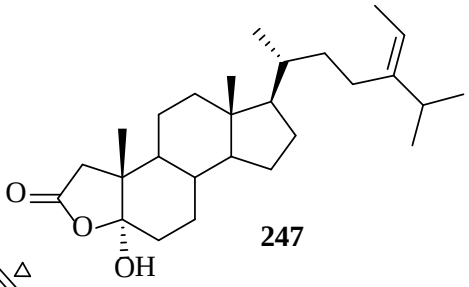

247

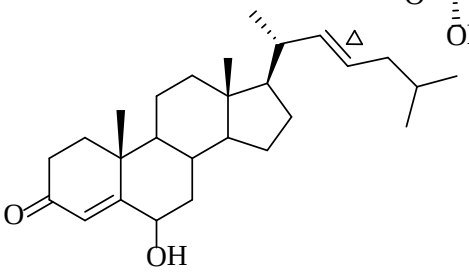

249 △ Saturated
250

2.3.1.4 Alkaloids

Alkaloids are cyclic, nitrogen containing secondary metabolites along with halogenation at different positions, and were reported to form as the part of their defensive mechanism. The presence of alkaloids in seaweeds is considered as relatively rare when compared with other terrestrial sources. However, these characteristic structural skeletons identified from the seaweeds mainly belonged to the halogenated alkaloids, indole and phenyl ethylamine groups. Among the different types of seaweeds, red seaweeds are considered as the most prominent source of alkaloids than green seaweeds, whereas least percentage of alkaloids are found in the brown seaweeds (Güven et al., 2013). .

The indole alkaloidal structures of chondriamide **251** and 3-indoleacrylamide **252** were identified with anthelmintic sactivitie, from the seaweed species, *Chondria atropurpurea* (Faulkner, 2000). Bromoindole alkaloids **253** and **254** were identified from the red seaweed *Laurencia similis* collected from China (Blunt et al., 2010). The indole alkaloid, jolynamine **255** was identified from *Jolyna laminaroides* collected from the coast of Karachi (Blunt et al., 2013). The new antifungal chloro-bisindole **256** metabolite was isolated from green seaweed *Caulerpa racemosa* (China) (Blunt et al., 2014). Halogenated alkaloids **257** was derived from the red seaweed *Laurencia brongniartii* harvested from the Caribbean and Okinawan sea (Güven et al., 2013). The alkaloid compounds **258** and **259** were identified from a red alga *Laurencia decumbens* collected from the Weizhou Island (China). The alkaloids **260**-**267** were identified from a red seaweed *Laurencia similis* harvested from Malaysia and China, respectively (Güven et al., 2013). Polyhalogenated bis-indole alkaloids **268** and **269** were identified from the green seaweeds *Chaetomorpha basiretorsa* and *Laurencia similis* harvested in China (Güven et al., 2013).

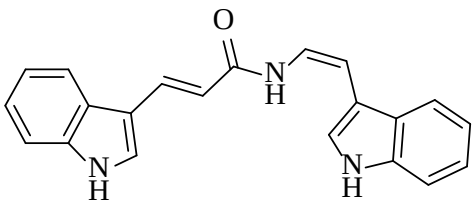

251

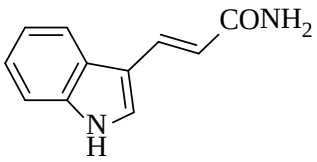

252

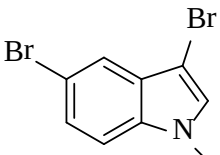

253

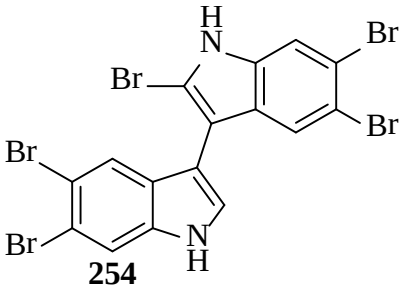

254

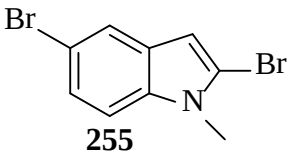

255

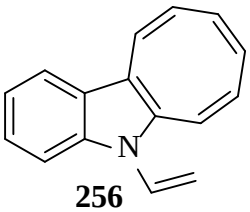

256

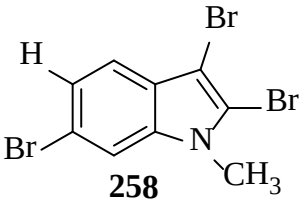

258

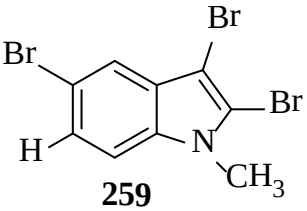

259

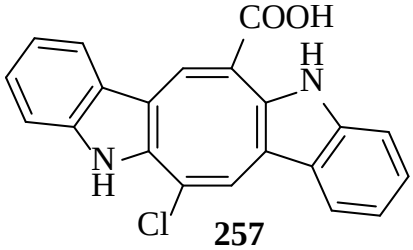

257

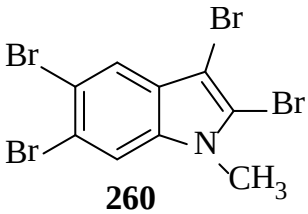

260

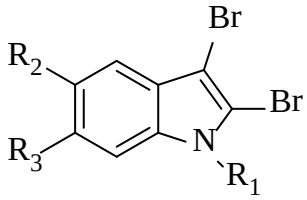

261 R_1=H; R_2=Br; R_3=Br
262 R_1=CH_3; R_2=Br; R_3=Br

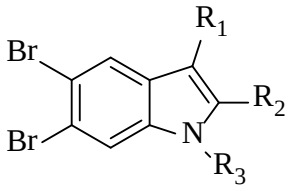

263 R_1=H; R_2=Br; R_3=H
264 R_1=Br; R_2=Br; R_3=H

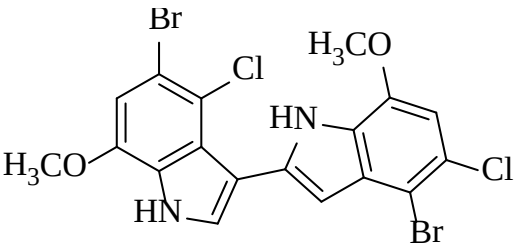

268

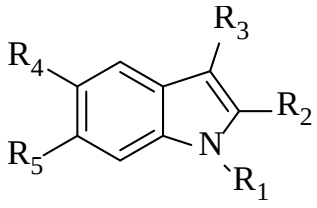

265 R_1=H; R_2=H; R_3, R_4, R_5=Br
266 R_1=CH_3; R_2=H; R_3, R_4, R_5=Br
267 R_1=CH_3; R_4=H; R_2 R_3, R_5=Br

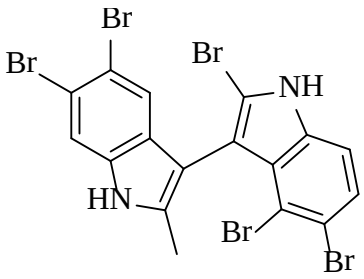

269

2.3.1.5 Lipids and fatty acids

Seaweeds are comprised of lower percentage of lipids (~5%), and thereby, they can be utilized for health benefits, such as source of food and nutrition due to the less content of energy (Peng et al., 2015). However, polyunsaturated fatty acids (PUFAs), such as eicosapentaenoic acid (EPA) and arachidonic acid (AA) were found to occupy the half of the portion of the lipids (Peng et al., 2015). The PUFAs were found to comprise greater than 18 carbons, which are essential to the nutritional benefits in human (Stengel et al., 2011). Glycoglycerolipids are significant class of membrane proteins with one or more sugar entities, which are attached to the glycerol-lipids via glycosidic bonds. These glycerol-lipids were considered to inhibit tumour cell generation (Stengel et al., 2011). Furthermore, they were found to be capable to normalize blood pressure and decrease the risk of various disorders, such as diabetes, cardiovascular diseases, and osteoporosis. Seaweed lipids and their constituents, such as phospho- and glycolipids have received greater attention owing to their prospective applications in food,

pharmaceutical, and cosmetic industries. Lipid levels and their composition in seaweeds were reported to vary according to their habitat and growth conditions (Stengel et al., 2011).

A novel polyunsaturated fatty acid, (42,72, 9E, 11E, l3 Z,16 Z,19Z)-docosaheptaenoic acid **270**, was reported from the seaweed species, *Anadyomene stellata* harvested from Florida (Faulkner, 1996). The fatty acids with methoxyl functionality, and named as 9-methoxypentadecenoic acid **271**, 9-methoxyheptadecenoic acid **272**, 13-methoxyheneicosanoic acid **273** and 15-methoxytricosanoic acid **274**, were reported from the Sicilian red seaweed species of *Schizymenia dubyi* (Faulkner, 2000). Four fatty acid derived oxylipins, named as (5R,6S,7E,9E,11Z,14Z)-5,6-dihydroxyicosa-7,9,11,14-tetraenoic acid **275**, (5R,6S,7E,9E,11Z,14Z,17Z)-5,6-dihydroxyicosa-7,9,11,14,17-pentaenoic acid **276**, (6E,8Z,11Z,14Z)-5-hydroxyicosa-6,8,11,14-tetraenoic acid **277**, and (6E,8Z,11Z,14Z,17Z)-5-hydroxyicosa-6,8,11,14,17-pentaenoic acid **278** were characterized from the red seaweed, *Rhodymenia pertusa* (Faulkner, 2002). A mixture of nitrogenous glycerolipids **279-281** was identified from the green seaweed *Ulva fasciata* from the Coast of India.

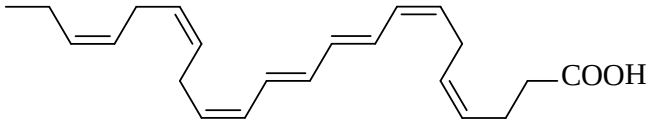

270

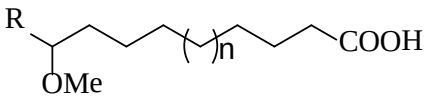

271 R=C_6H_{13}; n=1
272 R=C_8H_{17}; n=1
273 R=C_8H_{17}; n=5
274 R=C_8H_{17}; n=7

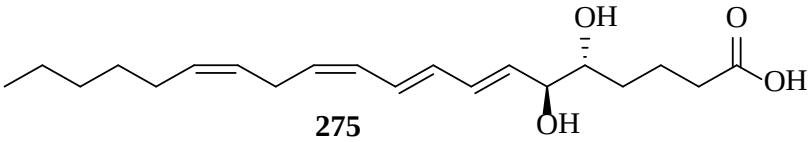

275

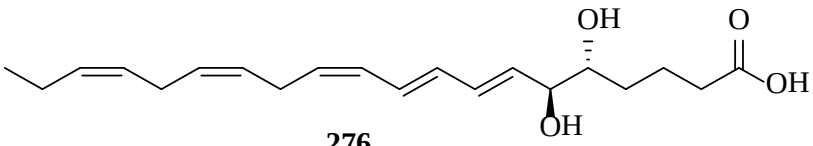

276

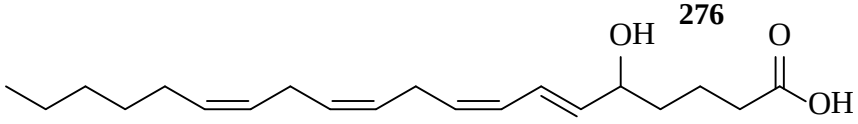

277

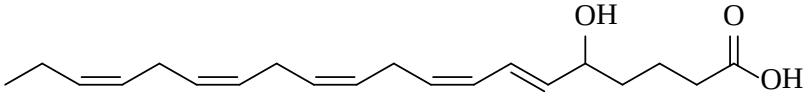

278

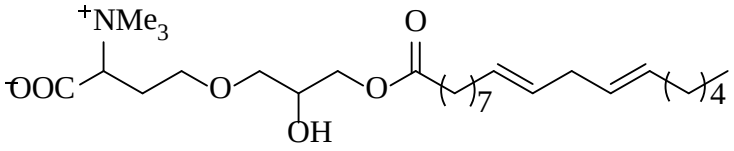

279

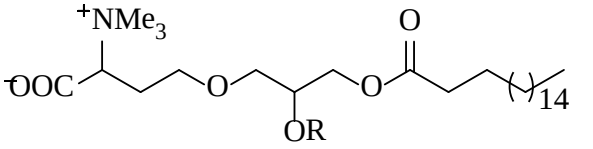

280 R=H
281 R=CO$(CH_2)_{14}CH_3$

2.1.3.6 Protein and peptides

Proteins extracted from the seaweeds were known to play prominent roles in cellular level, and they occurred in different range of forms at various locations of cells, like cell wall constituent, as enzymes, and linked to carbohydrates and pigments (Stengel et al., 2011). The distribution of proteins in seaweeds was varied by fluctuations induced by surroundings. The proteins identified from seaweed exhibited multiple bioactivities, such as the pepsin isolated from *Porphyra yezoensis* species were reported to have blood sugar reducing effect, cholesterol lowering, antioxidative activity, ACE-inhibitory potential, anti-mutagenic, inhibition effect on calcium precipitation, and activate hepatic functions (Stengel et al., 2011). In free existing form, they were found to bind with carbohydrates entities, glycoproteins, pigments, and proteoglycans; and further activating the formation of wide array of proteinaceous analogues in seaweeds. Seaweed proteins were considered as the richest source of dietary-proteins, amino acids, enzymes, peptides and bioactive lectins. The percentage of protein in seaweeds was found as almost in the range of 10-47 % of their dry weight (Stengel et al., 2011). Among the seaweeds, red seaweeds were consisted of protein around ~ 47 % dry weight; green and brown seaweeds ~26 % and ~15 % dry weight, respectively. Proteins isolated from the seaweeds possessed higher degree of digestibility. The seaweeds proteins, such as phycobiliproteins and lectins displayed several bioactivities including, anti-inflammatory, antibiotic, anti-HIV, cytotoxic, lowering pain sensitivity, anti-hypertensive activities and inhibition of platelet aggregation (Stengel et al., 2011). The depsipeptide, namely kahalalide O **282**, was isolated from the green seaweed *Bryopsis sp* (Faulkner, 2002). Two cyclic peptides such as lipopeptides mebamamide A **283** and B **284** were isolated from *Derbesia marina* (Blunt et al., 2017).

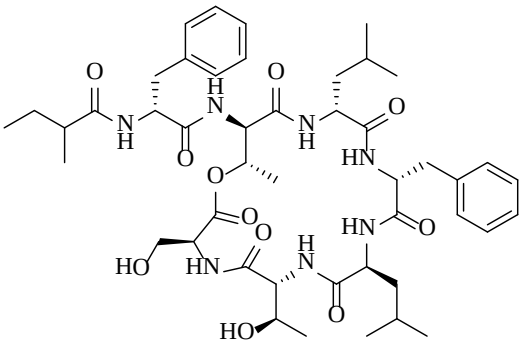

282

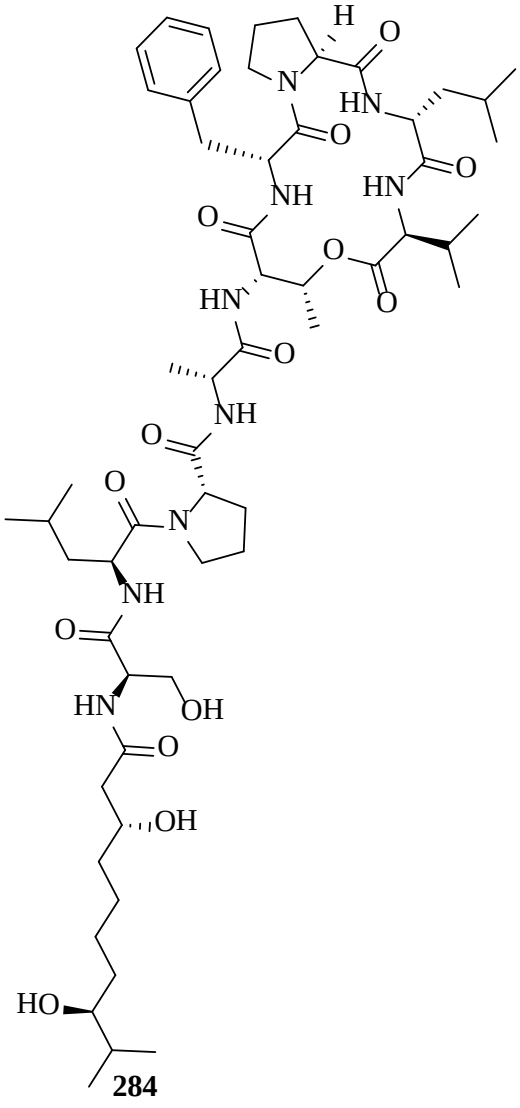

284

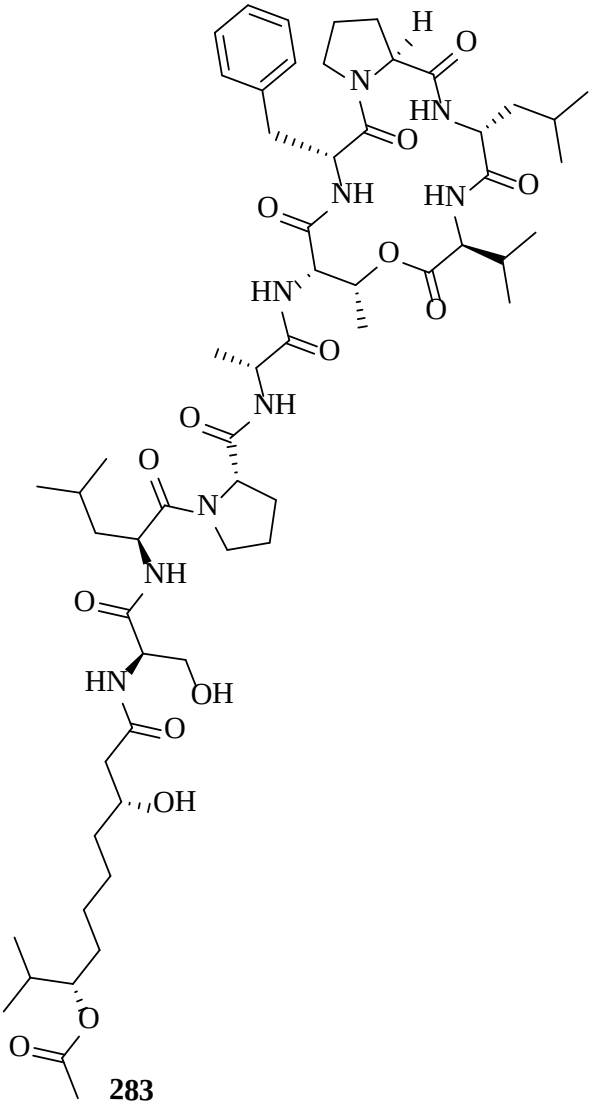

283

2.1.3.6 Polysaccharides

The polysaccharides derived from seaweeds are composed of comparatively few in numbers, even though they were found to be linked in infinite number of combination by different possible linkages with monosaccharide entities, resulting in the wide array of oligosaccharide building-blocks with structural complexities. The structural-diversity of polysaccharide analogues could be further improved by the series of chemical reactions, such as sulfation, methylation and acetylation (Wijesekara et al., 2011). Moreover, the polysaccharides derived from seaweeds were encompassed with various metabolic activities; for example, they could act as either a cell wall constituent or a storage lead molecule, and were found to be endured with several structural modifications during their formation cycle (Craigie, 1990). Because of these complex and unique structural features with multiple bioactive functionalities, seaweed polysaccharides were comprehensively exploited by food, nutraceutical, and pharmaceutical industries (Rinaudo, 2007). The physical properties of polysaccharides like solubility (Lahaye and Kaeffer, 1997), colloidal properties and gelling strength were found to be varied depending on their chemical structures. For example, the commercially relevant red seaweed phycocolloids, such as agar-agar and carrageenan **285-287** exhibited linear structures; linear galactose and anhygrogalactose repeating units of α(1→3)-(D-galactose) found in carrageenan along with sulfation at various positions and α(1→3) β (1→4)-(L-galactose) found in agars with partially methylated structures (Michel et al., 2006). Agar hydrocolloids with greater gel strength were observed in red seaweed of *Gelidium sp* (Rinaudo, 2007). Other commercially important polysaccharide alginate **288**, obtained from the brown seaweeds, also displayed particular variations in gelling strength depending on their percentage of monosaccharide units, D-mannuronic acid (M) to L-guluronic acid (G) and anionic properties (Rinaudo, 2007). Physical properties along with binding peculiarities in polysaccharides resulted in potential bioactivities, for instance, ulvan polysaccharide from green seaweeds were bound to bile acids and produce anti-hyperlipidemic effect (Yu et al., 2003).

Sulfated polysaccharides obtained from various species of seaweeds were reported to possess antioxidant potency. For instance, sulfated fucan **289** that was identified from *Fucus vesiculosus* displayed higher ferric reducing and superoxide radical scavenging properties (Jiao et al., 2011). Fucan obtained from *L. japonica* exhibited hydroxyl and superoxide radical scavenging potentials (Jiao et al., 2011). This polysaccharide also found to reduce LDL-cholesterol/triglycerides and increase HDL-cholesterol in rat model of hyperlipidemia (Jiao et al., 2011). Sulfated polysaccharide isolated from the seaweed *S. wightii* decreased hyperlipidemia in plasma (Jiao et al., 2011). The fucans reported from *S. polycystum* showed to inhibit the biosynthesis of cholesterol and triglycerides in serum (Raghavendran et al., 2005).

Sulfated galactoporphyrin from *Porphyra sp.* was reported to possess antitumor, hypotensive and anti-cholesterol activity (Raposo et al., 2015). The polysaccharide derived from *Gelidium crinale* displayed prospective anticoagulant activity (Pereira et al., 2005). The hydrocolloids, such as sulfated-agarans and hybrid DL-galactans, which were reported from *Pterocladia capillacea*, exhibited antiviral potential (Pujol et al., 1996). Sulfated-agarans and galactans extracted from the seaweed *Aghardiella tenera* showed antiviral potential (Raposo et al., 2015). The sulfated polysaccharide from *Gracilaria caudate* was found to exhibit potential antioxidant activity (Costa et al., 2010), whereas the sulfated agar and galactan isolated from *G. corticata* showed antiviral potential (Mazumder et al., 2002).

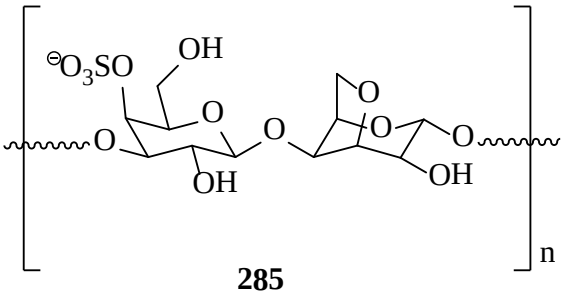

285

κ-carrageenam

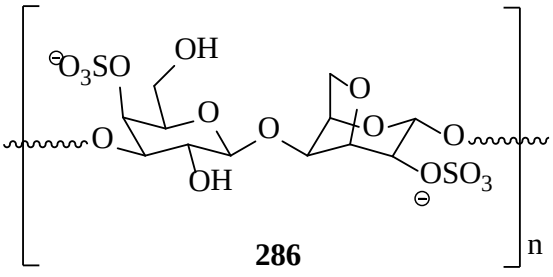

286

ι-carrageenam

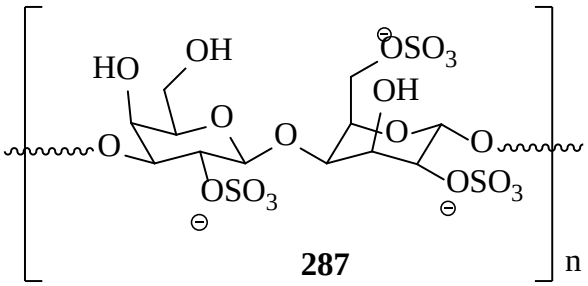

287

λ-carrageenam

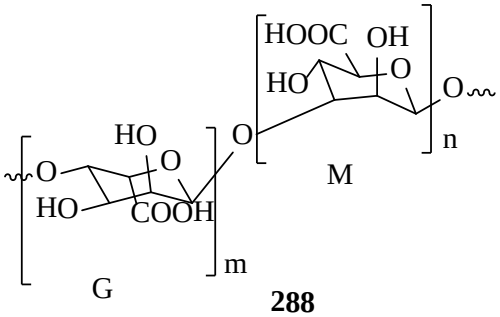

M

G

288

Repeating monosaccharide units of alginate

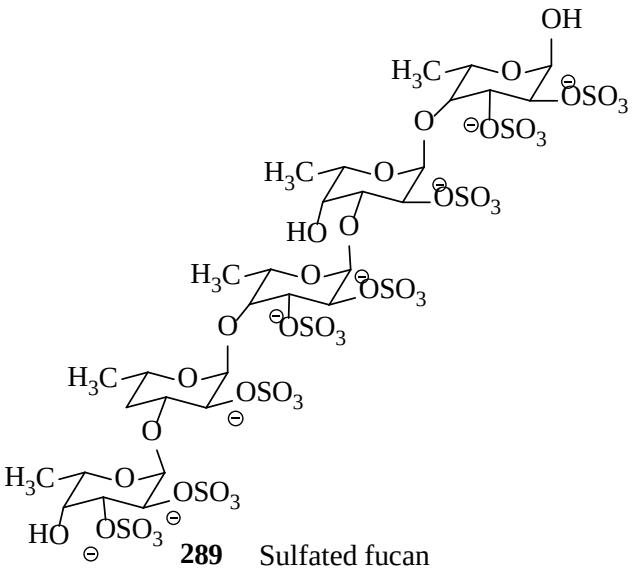

289 Sulfated fucan

2.4 Specialized bioactive secondary metabolites of seaweeds belonging to Rhodophyceae and Phaeophyceae

2.4.1 Bioactive secondary metabolites derived from seaweeds belonging to the class Rhodophyceae

Seaweeds belonging to the class of Rhodophyceae (red seaweeds, 98 %) are dynamic source of halogenated secondary metabolites, extending from terpenes, indoles, peptides, acetogenins phenolic compounds, and polyketides to volatile hydrocarbons with halogenation (Cabrita et al., 2010; Fujii et al., 2011). Furthermore, the red seaweeds produce large number of sulfated hydrocolloids (as cell wall material), and acid derivatives of nucleic and shikimate entities (Wijesekara et al., 2011; Güven et al., 2010). A wide range of pharmacological potencies were known to be related with red seaweed metabolites, such as anti-inflammatory, cytotoxic, antibacterial, antiproliferative, antifungal, antifouling, antiviral, insecticidal ichthyotoxic and antifeedant properties.

Related to applications of red seaweeds, the extracts acquired from the seaweed species *Digenea simplex* (Rhodomelaceae, Ceramiales) were utilized as a vermifuge for last dedades as the traditional medicament of Eastern region of the Asian countries (Pei-Gen & Shan-Lin, 1986). Further phytochemical analysis directed towards the separation of Kainic (KA) amino acid, recognized as the potentially active analogue in this seaweed extract, was performed. The later studies led to the re-discovery of anthelmintic KA amino acid **290**, which was found to be potential neuro-active and neuronal-glutamate-receptors (Hopkins et al., 2000; Sakai et al., 2005). The structural characteristics of KA were found to be associated with other neuronal amino acids, like domoic amino acid, separated from the extract of red seaweed *Chondria armata*, as an anthelmintic analogue (Sakai et al., 2005). Presently, kainoid derivatives have been utilized in neuro-biological study as a standardized reagent, and were found to play significant role in the treatment of neuro-physiological syndromes, such as Parkinson, Alzheimer and epilepsy (Higa & Kuniyoshi, 2000; Smit, 2004). In spite of pharmaceutical usages, the earlier studies on seaweed natural products were concentrated on halogenated secondary-metabolites, like the monoterpene analogue halomon **291**, which was identified from the species of red seaweed *Portieria hornemanni* (Clardy & Walsh, 2004; Fuller et al., 1992). This terpene displayed specific cytotoxic activity towards the tumor cells of renal, brain, and colon, and was used for the development of preclinical drug of cancer. Furthermore, halomon **291** analogue has been recognized as one of the promising secondary metabolites of seaweeds. Bicyclic diterpene, laurenditerpenol **292** was constituted as one of the potential halogenated

analogues from red seaweed. The isolation of laurenditerpenol **292** was carried out by the bioassay-assisted separation of the lipidic extract obtained from the red seaweed *Laurencia intricata*, and was found to be the first seaweed natural product that prevented the transcription factor induced by hypoxia; and as a tumor cell line-specific molecular drug target towards the development of cancer drug candidate (Chittiboyina et al., 2007; Jung & Im, 2008; Nagle & Zhou, 2009). Moreover, *Laurencia*, belonging to the family, Rhodomelaceae is the comprehensively extracted genus in the Rhodophyta phylum, and has been extensively studied over the last few years. This extensive exploration led towards the characterization of diverse array of bioactive lead molecules, such as the cytotoxic diterpene brasilenol **293**, calicladol (triterpene) **294**, antibacterial C-15 acetogenine analogues, and laurencin **295**. Additionally, with reference to red seaweed analogues, there are extensive researches related to the sulfated polysaccharides with antiviral properties (Luescher-Mattli, 2003; Campo et al., 2009). The carrageenans **285-287** were found to be the prominent sulfated-polygalactans from the red seaweeds. These polysaccharide analogues displayed potential immunomodulatory properties (Luescher-Mattli, 2003). In addition, carrageenan derived from the other families, such as *Tichocarpacea* and *Gigartinaceae*, also showed anticoagulant, antioxidant, and antithrombic properties (Sokolova et al., 2011).

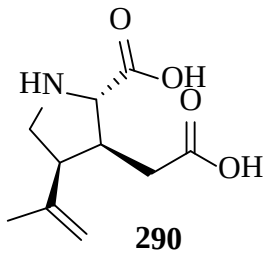

290

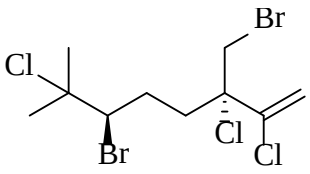

291

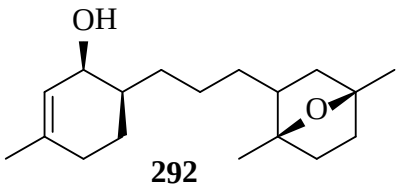

292

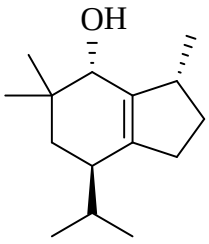

293

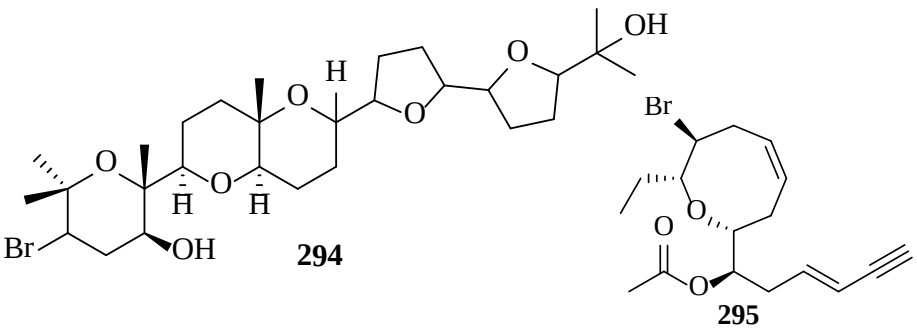

294 **295**

2.4.2 Bioactive secondary metabolites derived from seaweeds belonging to the class Phaeophyceae

The phylum Phaeophyta (brown seaweeds), which are known to be prolific producers of bioactive metabolites, was reported to produce derivatives of isoprene entities, as one of the

predominant bioactive metabolites (McClintock & Baker, 2001). Besides the large number of unique structures of terpenoids biosynthesized by the brown seaweeds, the volatile hydrocarbons, fucan polysaccharides, phlorotannins and fucoxanthins along with bioactivities, such as antioxidant, antibiotic, antifungal, antiviral, and anti-cancer activities, were also reported (Folmer et al., 2010). The major volatile metabolites derived from the brown seaweeds were recognized as cyclic or acyclic, which arose from the modification of long chain fatty acids. These compounds and their decomposition products were involved in chemical defense mechanism. For example, dictyotene **296**, which is an algal pheromone, was isolated from *Dictyota sp*., , and was used in the chemical defensive system (McClintock & Baker, 2001; Rui & Boland, 2010).

Bioactive phenolic compounds were recognized as one of the significant bioactive leads from brown seaweeds. For instance, phlorotannins isolated from brown seaweeds of family Laminariaceae, and these tannin derivatives were resulted by the polymerization of phloroglucinol moieties (Thomas & Kim, 2011; Wijesinghe & Jeon, 2011). Most of these compounds are used in the formulation of pharmacophores due to their bioactive potencies including antioxidant, anti-inflammatory, antihypertensive, antitumor, antidiabetic, and anti-allergic activities (Thomas & Kim, 2011). Currently, alginate **288** and some of the phlorotannin metabolites, such as, dieckol **297** and fucoxanthins **298** were used as the promising potentials for anti-aging and whitening formulations due their photo-oxidative stress and tyrosinase inhibitory properties (Heo et al., 2009; Li et al., 2009; Wijesinghe & Jeon, 2011). Recently, the antiviral diterpene **299** and antioxidant diterpene amijiol acetate **300** were reported from the brown seaweeds *Dictyota menstrualis* and *Dictyota dichotoma*, respectively (Cavalcanti et al., 2011; Ayyad et al. 2011). Antioxidative diterpene with 2,6-cycloxenicane moiety **301**, was reported from *Dilophus fasciola* and *Dilophus spiralis* (Ioannou et al., 2009). The cytotoxic bisprenylated quinol **302**, antiviral dolastane diterpenes, and anti-diabetic phlorotannins were reported from *Sporochnus comosus*, *Canistrocarpus cervicornis* and *Ecklonia stolonifera*, respectively (Oveden et al. 2011; Vallim et al., 2010; Moon et al., 2011). Polysaccharide fucoidans with antiviral activity were isolated from the brown seaweed *Cladosiphon okamuranus* (Phaeophyceae) (Hidari et al. 2008).

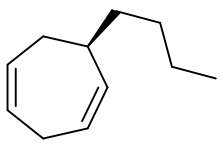

296

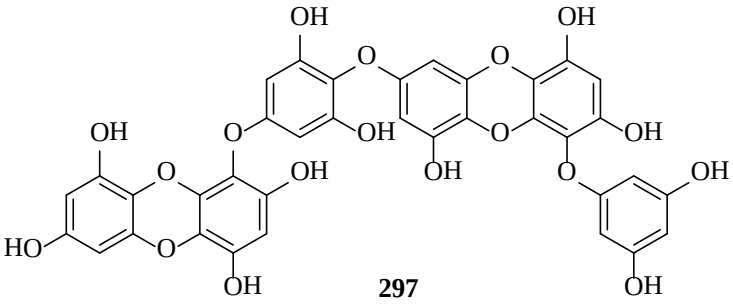

297

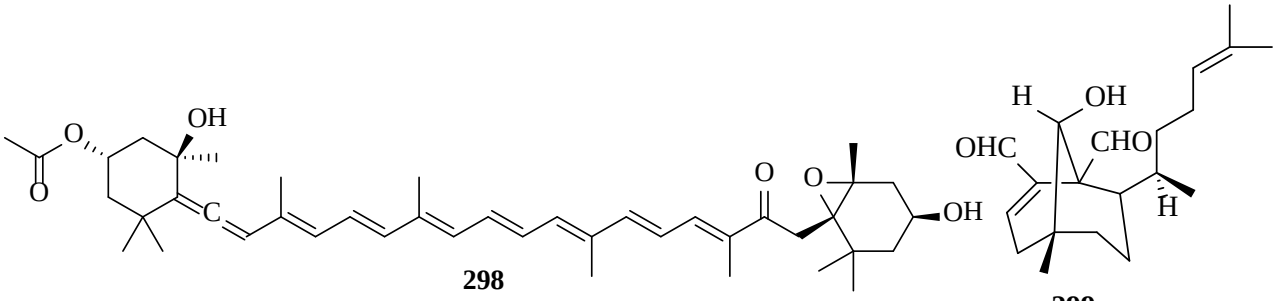

298 **299**

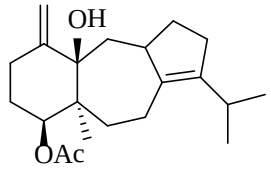

300

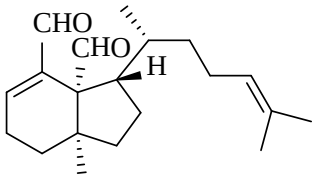

301

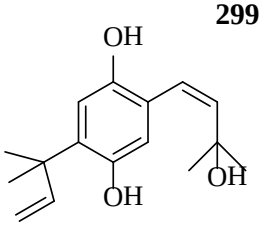

302

2.5 *Seaweeds belonging to the class Rhodophyceae and Phaeophyceae: Specialized morphological features*

Seaweeds were found to exhibit distinct morphological and physiological characteristics. Certain species of larger seaweeds possess complex structural features with specialized tissues that offer assistance to transport photosynthetic products and nutrients (Mouritsen, 2013). These largest seaweeds are found to appear ~50 meters long, while other category of smallest seaweeds appeared in few millimeters in size. The cells present in seaweeds also found in different size; in some of the species of seaweeds they can be measured more than one centimeter. The different organelles present in these large cells are responsible for the development of proteins, and to provide assistance for the cell functioning and their growth. Among the three major groups of seaweeds, all of them were found to contain pigments along with chlorophyll; whereas the characteristic colors of seaweeds are resulted from the percentage of extra pigments (Mouritsen, 2013).

The red seaweeds belong to the class of Rhodophyceae, which is a morphologically diverse class of photosynthetic-protists. Most of the red seaweed species were found as marine, excluding some of the fresh water species, for example, Batrachospermum (Yoon et al., 2017). Their morphology diverges from unicellular to complex multicellular species along with filamentous, pseudoparenchymatous, parenchymatous sheets, ribbons and lace-like features. These distinct eukaryotic seaweeds were found to appear in red colour due to the presence of pigments phycocyanin and phycoerythrin along with chlorophyll A. These well-established seaweeds possess uni/multiseriate filaments, and could also appeared in branched or unbranched forms with foliose thalli (blade-like). Some of the red seaweed species are found in erect and

crustose forms, and calcified. The red seaweeds have non-stacked thylakoids in their plastids, and they lack centrioles and flagella (Yoon et al., 2017).

Seaweeds belonging to the class Phaeophyceae (brown seaweeds) are much like plants, and generally appeared with three distinguishable parts. These seaweeds are found as exclusively marine, and characterized with brown colour due to the presence of dominant pigment fucoxanthin. They have layered cell wall with cellulose in the inner layer algin, and fucoidans is found in outer layer. The holdfast, which is a root-like structural part, is found in the bottom providing support to sustain in their habitat. Along with the root-like holdfast, seaweeds have stipe (or stem) and the leaf-like blades. The stipe makes the connection between the holdfast and blades (Mouritsen, 2013). The shape and number of blades are varied in different species. The blades have distinctive midribs in certain types of seaweeds. The long stipe in brown seaweeds provides assistance for blades to stand on the surface of the water, to absorb sufficient light, and consequently to perform photosynthesis. Some of the brown seaweeds have air containing bladders, which support them to stand on the surface of water to access light. Most of these bladders are in fifteen centimeter of height (Mouritsen, 2013).

2.5.1 Morphology and distribution of Gracilaria species

Gracilaria sp. belongs to the family of Gracilariaceae (Rhodophyta, Gracilariales) (Figure 2.6). This species consisted of solitary entities linked to the substratum, and was connected by holdfast; which appeared as decumbent and branched. The holdfast of *Gracilaria sp.*is found to appear as crust or disc, and which developed more than one erect axis. The thalli are found as segmented. Thalli are observed as erect- to prostrate structure or from terete- to widely flatten, which may be found as cylindrical and irregularly branched. These thalli are appeared in green, olive, and red to purple with some of the species possessed soft, smooth, and dentate structure. The thalli of *Gracilaria sp.* have divided into three kinds of tissues, such as epidermis, cortex, and medulla (Guiry & Guiry 2011). The irregularly branched thalli possessed robust arrangement and restricted throughout body, whereas the stipe of this species is cylindrical.

*Gracilaria sp.*was recognized in 1830 by Greville, and it was constituted as the third biggest genus in Rhodophyceae group along with more than 150 species around the world. Almost twenty eight species of *Gracilaria* have been derived from Indian coastline (Sahoo et al., 2001). These species of seaweeds can grow in saline water in the depth of 5-34 ppt. *Gracilaria sp.* is mostly harvested for the production of phycocolloid, agar, which provide > 50 % supply of agar in the total production of the world.

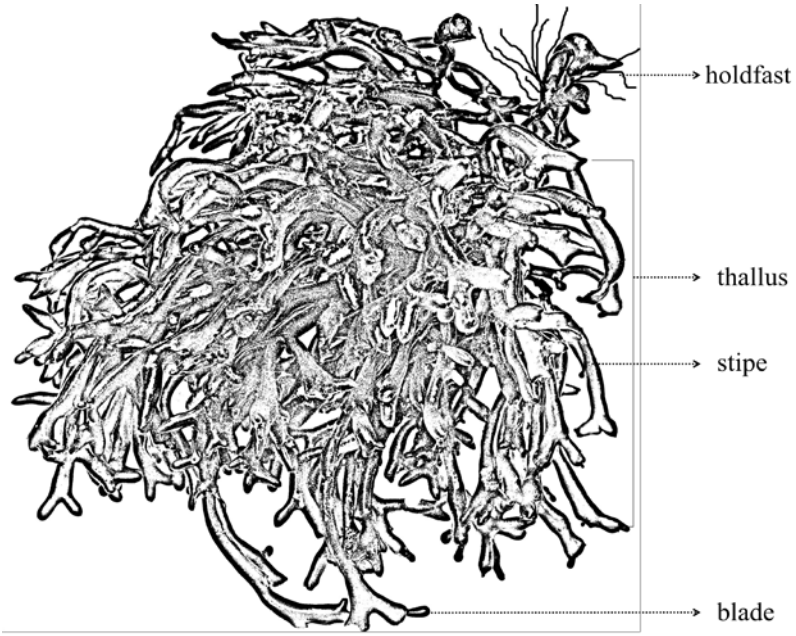

Figure 2.6.: Thallus of *Gracilaria sp.*belonging to the family Gracilariaceae (Rhodophyta, Gracilariales)

2.5.2 Morphology and distribution of *Padina* species

The *Padina sp.* belongs to the family Dictyotaceae (Phaeophyta, Dictyotales) (Figure 2.7), which is structurally featured by calcareous and flatten-fan-shaped thalli. They have possessed 2-3 or more than 3 stacked layers of parenchymatous-cells (Okazaki et al. 1986, van den Hoek, Mann and Johns 1995). The deposition of calcium carbonate/lime stone on the surface of flatten and fan-shaped thalli is considered as one of the distinctive characteristics of this species. The deposition of calcium is varied from species, and may occur either in a single surface or both surfaces. Certain species of *Padina* is lacked with calcium deposition, for instance, *P. arboresens* (Okazaki et al. 1986) and *P. glabra* (Wynne and De Clerck, 1999). The circinately coiled shape of distal margin is other notable peculiarity of *Padina sp.*, which can protect the apical cells (Bold and Wynne 1978). The division of the apical cells in this species led to the growth and their life cycle, which found as isomorphic and diplohaplontic (van den Hoek, Mann and Johns 1995). *Padina sp.* are found in pale brown/yellowish brown colour in appearance. They are smooth in bottom and relatively brittle on the top, which are grown in cluster or twisted shape. They have 5-6 stacked cell-layers, linked with stupose and holdfast, which is measured 2-4 mm in diameter. The margin of thallus is simple or irregularly divided.

Padina sp. is widely distributed in the world and around thirty two species were distributed throughout the tropical and temperate region of the sea (Guiry 2005). Among which, a total of 18 species are distributed in the Asiatic water bodies. These economically relevant

seaweeds are widely used as the source of polysaccharides, such as algin, which can be used as the functional food ingredient (Zaneveld, 1955) and fertilizer (Trono 2002, Soe-Htun 2005).

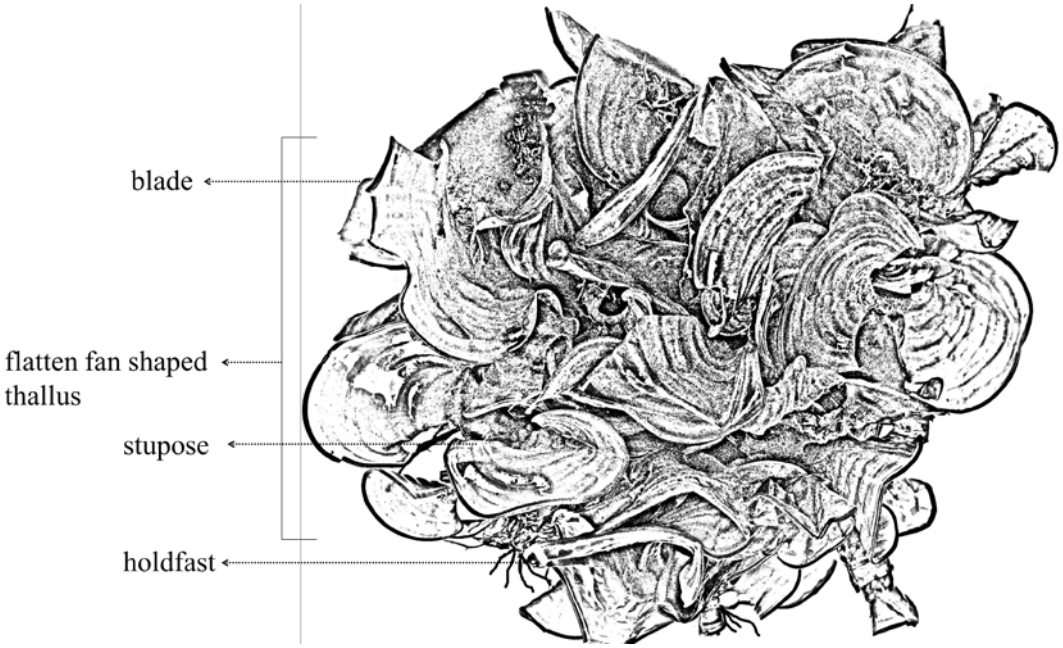

Figure 2.7.: Thallus of *Padina sp.* belonging to the family Dictyotaceae (Phaeophyta, Dictyotales)

2.6 Conclusion

The bioactive potencies of seaweeds, especially belonging to the classes of Rhodophyceae and Phaeophyceae directed towards the isolation of lead molecule with wide array of applications in food, medicinal, nutraceutical and pharmaceutical fields is extremely large, and has been directed towards the comprehensive extraction of novel bioactive compounds. In light of this, the present review properly corroborated those seaweeds, particularly of Rhodophyta and Phaeophyta as dynamic and promising candidates for identification, structural interpretation and bioactivity analysis of the seaweed-derived secondary metabolites, so as to reveal new natural entities with antioxidative, anti-inflammatory, and anti-diabetic potential.

CHAPTER 3

SCREENING OF BIOACTIVE POTENTIALS OF CRUDE SOLVENT EXTRACTS FROM RED AND BROWN SEAWEEDS (RHODOPHYCEAE AND PHAEOPHYCEAE

Contents

3.1 Background
3.2 Materials and methods
3.3 Results and discussion
3.4 Conclusions

3.1 Background

Seaweeds have established an adaptive stratagem for their endurance in the competitive surrounds by the development of enormous array of secondary metabolic analogues, and they can act as biologically as well as chemically dynamic defensive schemes against numerous life style disorders (Cardozo et al., 2007). Researches on natural-product-chemistry and chemical defensive systems of seaweeds documented the presence of bioactive lead molecules with prominent pharmacological activities (Faulkner, 2002). Phlorotannins and polyphenols from seaweeds have revealed their activities against proliferation of cancer cells (Kwon et al., 2007) and produce some effects on anti-inflammatory and anti-diabetic responses (Kim et al., 2009). Bioactive components in seaweeds were recognized to modulate glucose-induced oxidative stress and their ability to control the presence of starch-digestive enzymes (Lee et al., 2008). Potential side effects attributed to the synthetic drugs, demanded naturally obtained potential bioactive components for curing of persistent metabolic syndromes. Therefore, consumption and addition of these seaweeds might be increased their food and pharmaceutical applications**.**

Bioactive constituents of seaweeds also revealed their nutritional and bioactive properties against various life style diseases, which include hypertension, diabetes mellitus and inflammation (Joshipura et al., 2001; Maneesh and Chakraborty, 2017; Maneesh and Chakraborty, 2018; Antony and Chakraborty, 2019; Chakraborty et al., 2019). Bioactive

components of seaweeds also act as the inhibitor of angiotensin-I converting enzyme (ACE), which secrete the angiotensin-II vasoconstrictor (Curtiss et al., 1978). The potential side effects produced by the commercial ACE-inhibitors upsurges the demand of naturally occurring homologues (Atkinson and Robertson, 1979). Specific constituents of seaweeds were found to function as chemical intermediaries, which control the stimulations associated with mammalian defense mechanism and produces inflammatory deregulators (Thanh-Sang et al., 2012).

The present study evaluated the pharmacological potentials of ten different seaweeds belonging to the subclasses Dictyotophycidae (phylum Ochrophyta), Rhodymeniophycidae and Corallinophycidae (phylum Rhodophyta) collected from the southeast coastal areas of Indian Peninsular, using different *in vitro* models. The ethyl acetate-methanol (EtOAc-MeOH) extracts of various seaweeds were analyzed for various pharmacological potentials, such as anti-oxidant, anti-diabetic, anti-hypertension, and anti-inflammatory properties. The current study also described the nuclear magnetic resonance-guided spectroscopic de-replication of the prominent functional group fingerprints in the EtOAc-MeOH extracts of different seaweeds, and to correlate their presence with the bioactivities.

3.2 Materials and Methods

3.2.2 Chemicals, reagents and solvents

The chemicals used in this study include regents, solvents and solutions, which were acquired from Sigma-Aldrich Chemicals Co. Inc. (St. Louis, MO) and E-Merck (Darmstadt, Germany). Different buffers and solutions for screening studies were freshly made as and when required. All essential enzymes for biological assays were obtained from Sigma-Aldrich Chemicals Co. Inc. (St. Louis, MO). In detail, the chemicals include bases, acids for this such as Folin-Ciocalteu (F-C) reagent, Sodium carbonate/Na_2CO_3, potassium persulfate/$K_2S_2O_8$ ferrous sulphate/$FeSO_4$, sodium hydroxide/NaOH, ferrozine, diacetate of leuco-2,7-dichlorofluoresce, hematin, phenol, Gly-Pro-p-nitroanilide, N-(3-[2-furyl]acryloyl)-Phe-Gly-Gly/FAPGG, acids such as arachidonic acid, acetic acid, linoleic acid, 3,5-dinitrosalicylic acid were obtained from Sigma-Aldrich (St. Louis, MO). Furthermore, commercial standards, free radicals and non-free radicals for the *in vitro* anti-oxidative analysis such as 1,1-diphenyl-2-picryl-hydrazil/DPPH, 2,2'-azino-bis-3-ethylbenzothiozoline-6-sulfonic acid diammonium salt/$ABTS^+$, malondialdehyde, thiobarbituric acid/TBA, gallic acid, hydrogen peroxide/H_2O_2 were acquitted from Sigma-Aldrich (St. Louis, MO). The reagents for buffer preparations such as potassium phosphate buffer, sodium phosphate buffer, tris-buffer, were acquired from E-Merck (Darmstadt, Germany)/HiMedia (Pennsylvania, USA). Enzymes for biological assays such as

dipeptidyl peptidase-4/DPP-4 (from porcine-kidney), angiotensin converting enzyme-1/ACE-1 (from rabbit-lung), cyclooxygenase-1/COX-1 (from sheep), cyclooxygenase-2/COX-2 (human recombinant), 5-lipoxygenase/5-LOX (from soybean) were procured from Sigma-Aldrich (St. Louis, MO). The other enzymes, α-amylase (from porcine-pancreas) and α-glucosidase (from yeast) were procured from Sisco Research Laboratories (Mumbai, India). All glass wares were procured from Borosil (India).

3.2.2 Materials of seaweed and depiction of work area

The seaweeds used in this study were obtained from the southeast coastal areas of Peninsular India. The seaweeds belonging to the subclasses Dictyotophycidae (*Padina tetrastromatica* Hauck) (Figure 3.1), Rhodymeniophycidae {*Gracilaria salicornia* (C. Agardh) E. Y. Dawson (Figure 3.2), *Gracilaria canaliculata* Sonder, *Hydropuntia edulis* (S.G.Gmelin) Gurgel & Fredericq, *Gracilaria corticata* (J. Agardh) J. Agardh, *Palisada pedrochei* J.N.Norris, *Halymenia dilatata* Zanardini, *Spyridia filamentosa* (Wulfen) Harvey and *Portieria hornemannii* (Lyngbye) P.C. Silva} and Corallinophycidae {*Amphiroa fragilissima* (Linnaeus) J.V. Lamouroux} were collected. The collection site was located between 8º48′ N, 78º9′ E and 9º14′ N, 79º14′ E at Gulf of Mannar of Mandapam region (Figure 3.3). The seaweeds were initially washed with tap water to eliminate sand and unwanted constituents, and thoroughly washed with distilled water. The wet seaweeds were dried at room temperature, and stored in airtight containers for further experiments.

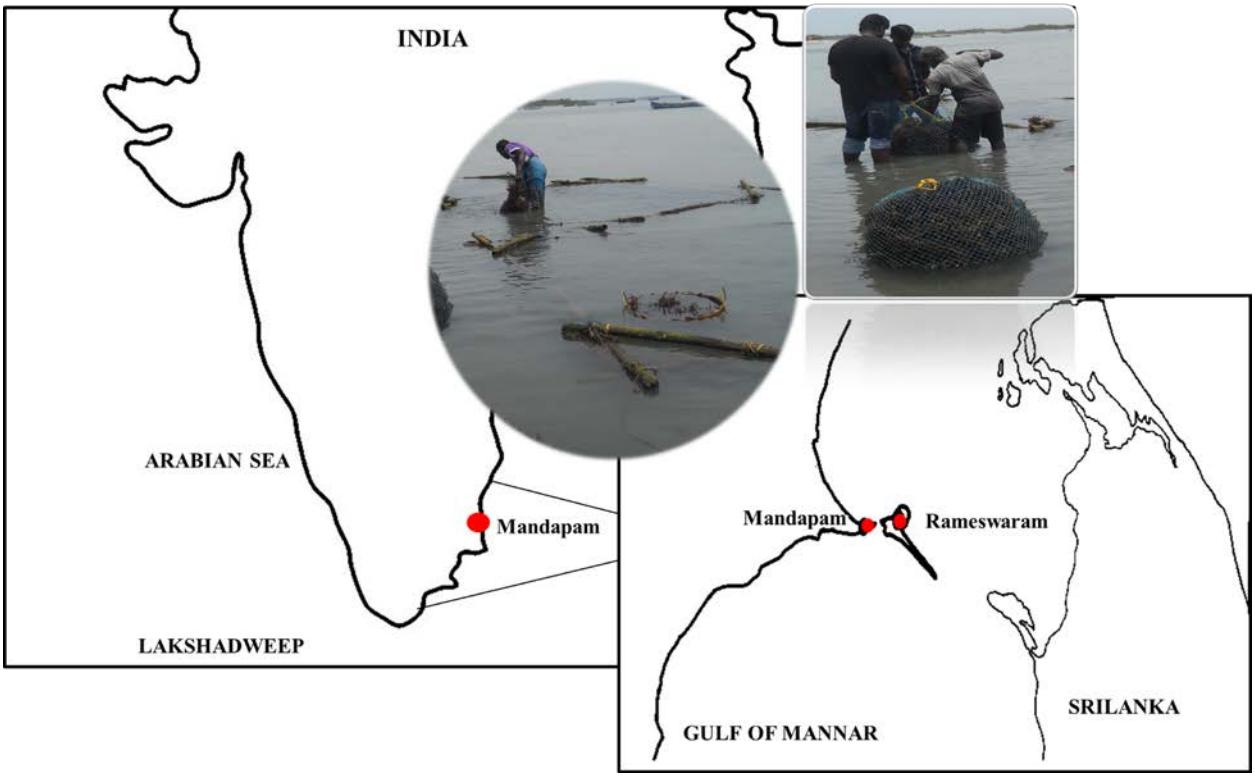

Figure 3.1.: Representative photograph of sample collection site located between 8º48′ N, 78º9′ E and 9º14′ N, 79º14′ E at Gulf of Mannar of Mandapam region

Figure 3.2.: Representative photograph of four seaweeds, *P. tetrastromatica, G. salicornia, G. canaliculata and G. corticata* selected for the pharmacological screening

Gracilaria corticata
Subclass Rhodymeniophycidae
Order Gracilariales
Family Gracilariaceae
Genus *Gracilaria*

Palisada pedrochei
Subclass Rhodymeniophycidae
Order Ceramiales
Family Rhodomelaceae
Genus *Palisada*

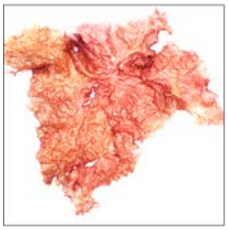

Halymenia dilatata
Subclass Rhodymeniophycidae
Order Halymeniales
Family Halymeniaceae
Genus *Halymenia*

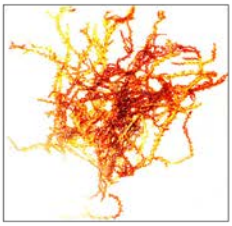

Spyridia filamentosa
Subclass Rhodymeniophycidae
Order Ceramiales
Family Callithamniaceae
Genus *Spyridia*

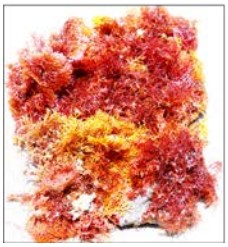

Portieria hornemannii
Subclass Rhodymeniophycidae
Order Gigartinales
Family Rhizophyllidaceae
Genus *Portieria*

Amphiroa fragilissima
Subclass Corallinophycidae
Order Corallinales
Family Lithophyllaceae
Genus *Amphiroa*

Figure 3.3.: Representative photograph of six seaweeds, *G. corticata, P. pedrochei, H. dilatata, S. filamentosa, P. hornemannii and A. fragilissima* selected for the pharmacological screening

3.2.3 Preparation of organic extracts from seaweeds

The dried seaweeds (1 kg) were powdered and were extracted with solvent *n*-hexane (700 mL) at 45 °C to remove pigments. Likewise, the second extraction of seaweed residues were carried out with acidified ethyl acetate-methanol (EtOAc-MeOH, 1:1 v/v) (700 mL x 3) mixture at 70 °C. The extracts obtained were pooled together, and filtered by Whatman No-1 filter paper. Filtrates were collected and evaporated by rotary vacuum concentrator to get the crude organic extracts. The EtOAc-MeOH extracts derived from seaweeds belonging to the subclass Dictyotophycidae was found to possess higher yield (~8.1 g) followed by subclasses Rhodymeniophycidae and Corallinophycidae (~6.5-7.8 g), in descending order. The extracts of seaweeds were stored in refrigerator (4-6 °C) until further use.

3.2.4 Instrumentation

Varian Cary 50 ultra-violet-visible (UV-VIS) spectrophotometer (Varian Cary, USA) was used for spectrophotometric analysis of samples. The Fourier transform infrared spectral (FTIR) analysis was carried out by Perkin-Elmer Series 400 FTIR spectrophotometer with an air-cooled deuterated triglycine sulfate (DTGS) detector within the scan range of 4000 and 400 cm^{-1}

by using KBR pellets, and the spectra were acquired with 32 scans with the spectral resolution of 4 cm (Figure 3.4). Bruker AVANCE III 500 MHz (AV 500) nuclear magnetic resonance (NMR) spectrometer (Bruker, Karlsruhe, Germany) used for the spectroscopic characterization of organic extracts. Appropriate dilutions of EtOAc-MeOH extracts prepared in NMR tubes (Norell, 5 mm OD and 7 inches length) with deuterated solvent ($CDCl_3$). Tetramethylsilane (TMS; Cortec, Paris, France) was used as the reference standard (δ 0 ppm). Each NMR spectra was referenced with TMS signal and residual solvent signal of $CDCl_3$. The chemical shift values were expressed in ppm, and were examined for specific regions, such as δ_H 1.0-2.0 (corresponding to saturated hydrocarbons, RCH_3, R_2CH_2 and R_3CH), δ_H 2-2.5 {representing acetyl ($RC(=O)CH_3$)/alkanoates of alkyl functionality (R_1O (O=)C-CH_2R)/alkyl amine substitutions (CH_3NR_2)}, δ_H 2.8-3.5 (signifying methoxyl moieties (CH_3-O-)/halides of alkyl groups (X-CH_2R)/substituted alkanol (CH_2OHR)}, δ_H 4-6 {indicating olefinic ($RCH=CHR_1$)/alkanoates of aryl functionalities ($CH_3O(O=)CCH_2R$)}, those at δ_H 6.5-8.5 {specifying aromatic protons (Ar-H)} (Figure 3.5 & 3.6).

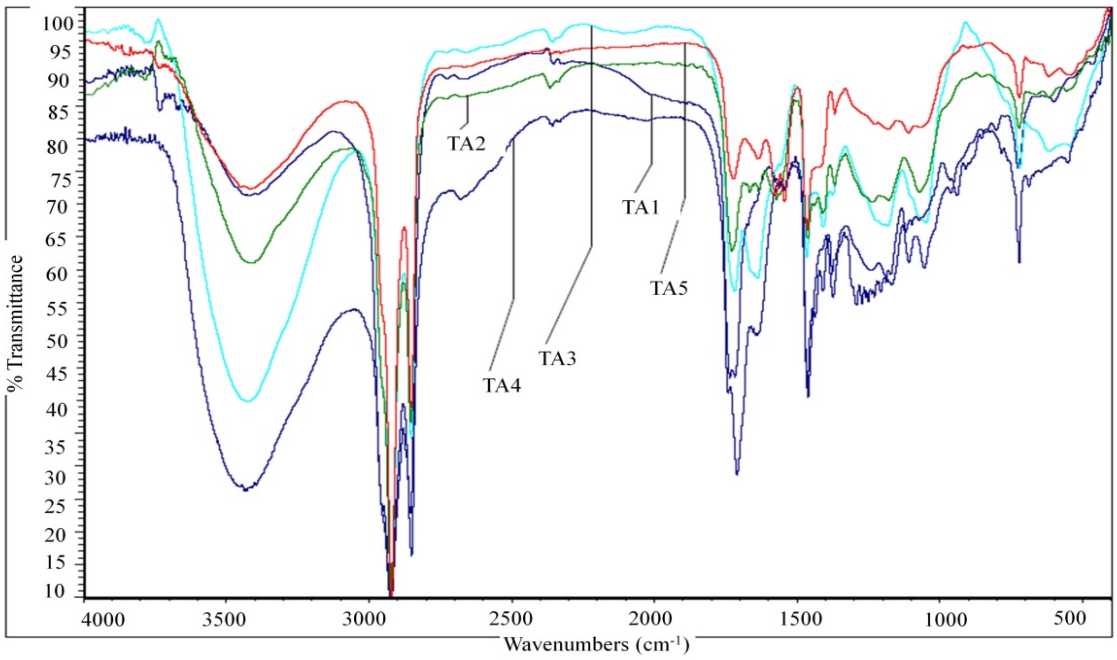

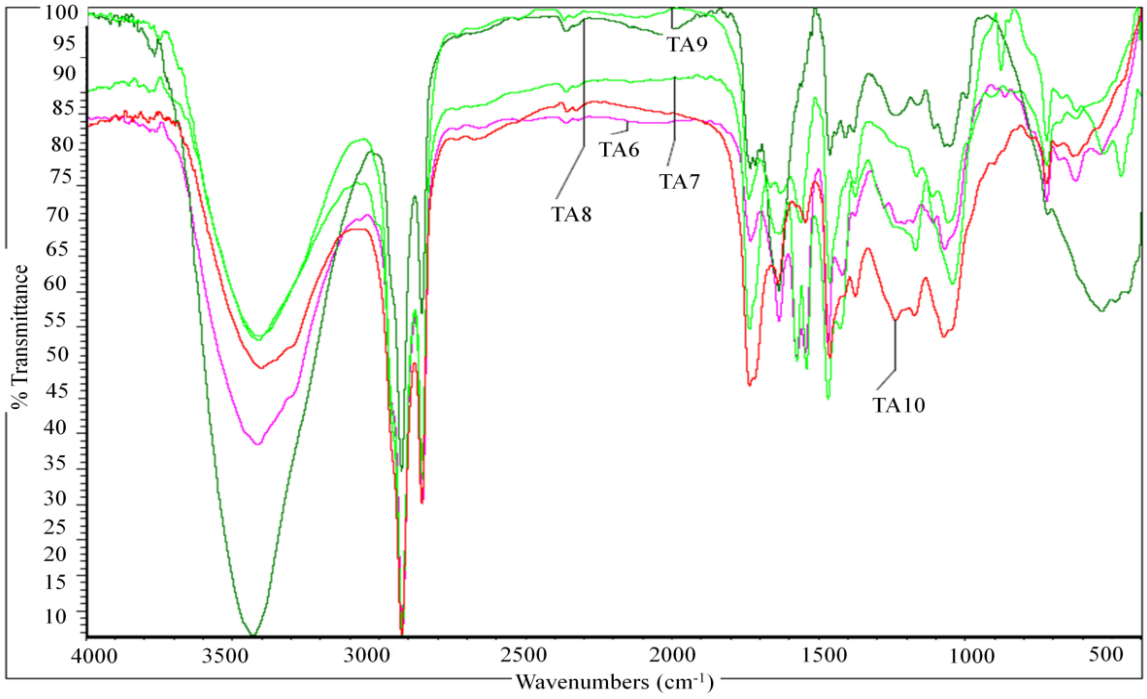

Figure 3.4.: FTIR spectra of the organic extracts of *G. salicornia*-TA1, *P. tetrastromatica*-TA2, *G. canaliculata*-TA3, *G. corticata*-TA4, *H. edulis*-TA5, *A. fragilissima*-TA6, *P. pedrochei*-TA7, *S. filamentosa*-TA8, *H. dilatata*-TA9, and *P. hornemannii*-TA10.

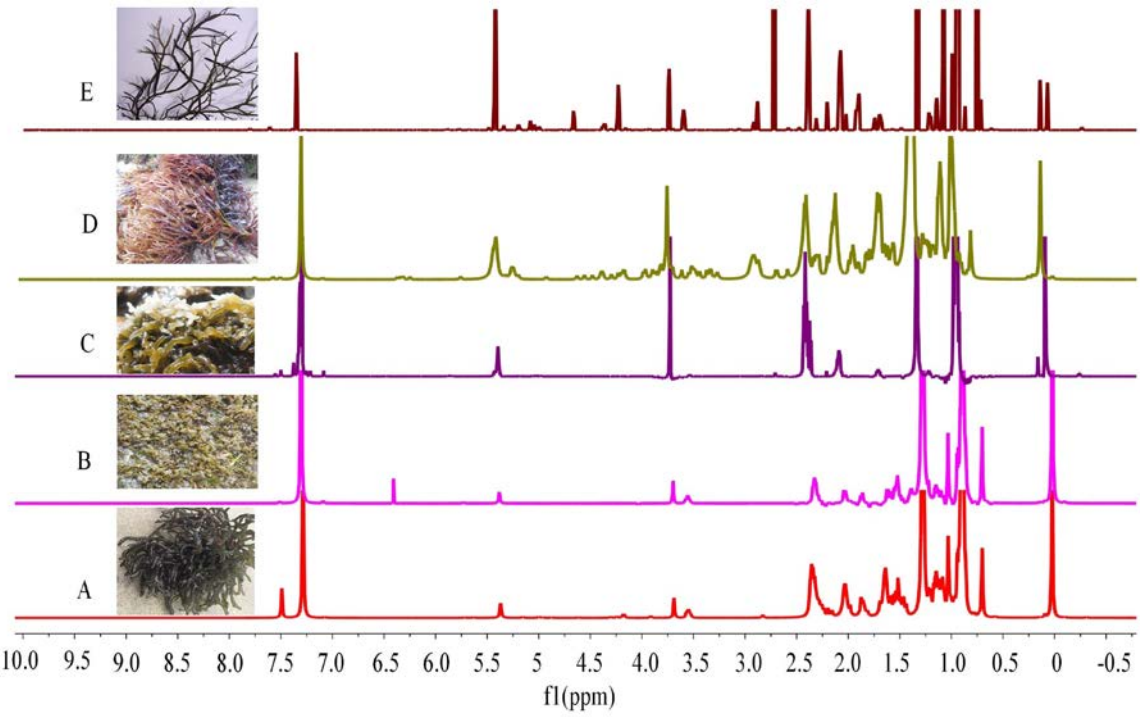

Figure 3.5.: ^{1}H-NMR spectra of the organic extracts of (A) *G. salicornia*, (B) *P. tetrastromatica*, (C) *G. canaliculata*, (D) *G. corticata*, and (E) *H. edulis*. The spectra were vertically stacked according to their decreasing order of activities.

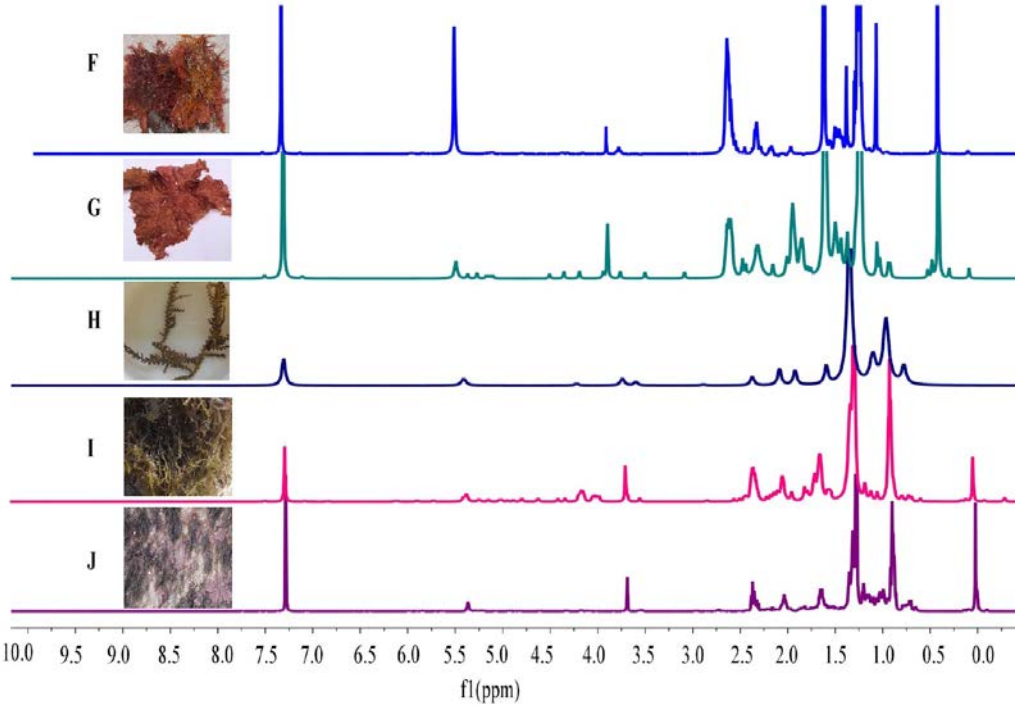

Figure 3.6.: ^{1}H-NMR spectra of the organic extracts of (F) *A. fragilissima*, (G) *P. pedrochei*, (H) *S. filamentosa*, (I) *H. dilatata*, and (J) *P. hornemannii*. The spectra were vertically stacked according to their decreasing order of activities

The chemical shift values at δ_H 9-10 represented the presence of the aldehyde proton in the proton NMR spectra. Integration of these distinct regions displayed the number of protons corresponding to these regions. Likewise, carbon signals in ^{13}C-NMR spectra were investigated. The different regions at δ_C 10-40 (aliphatic), δ_C 45-70 (alkoxy carbon; RCH_2OR_1), δ_C 70-80 {alkanoates of alkyl functionality ($R_1O(O=)CCH_2R$)}, δ_C 110-140 (functionalities of olefins), δ_C 140-160 (aromatic), δ_C 160-180 {ester alkanoate carbon atoms, $R_1O(O=)CR$}, and δ_C 180-210 (carbonyl carbon) were considered from the ^{13}C-NMR spectra (Figure 3.7 & 3.8).

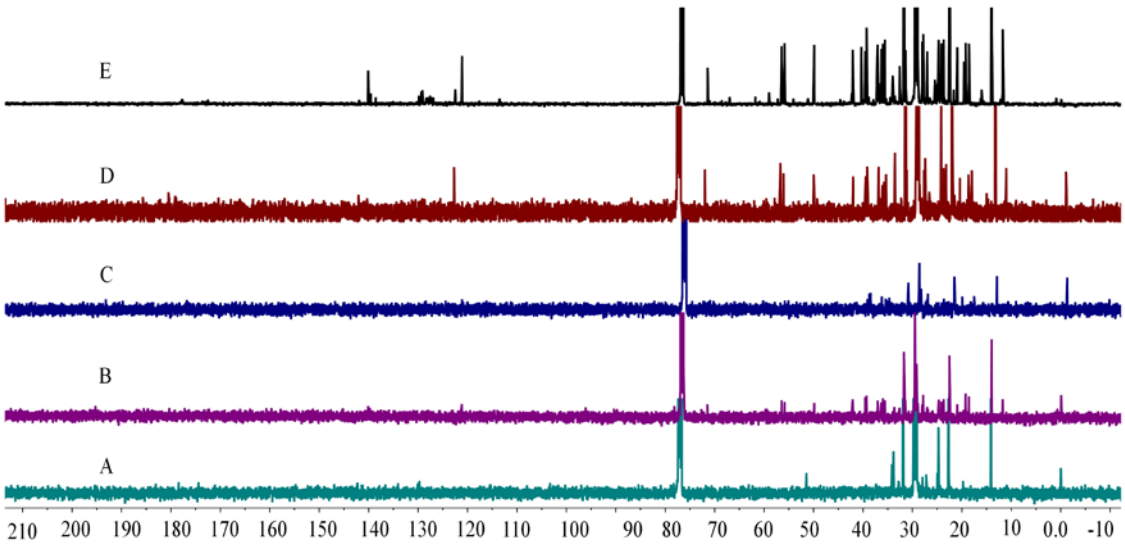

Figure 3.7.: ^{13}C-NMR spectra of the organic extracts of (A) *G. salicornia*, (B) *P. tetrastromatica*, (C) *G. canaliculata*, (D) *G. corticata*, and (E) *H. edulis*. The spectra were vertically stacked according to their decreasing order of activities.

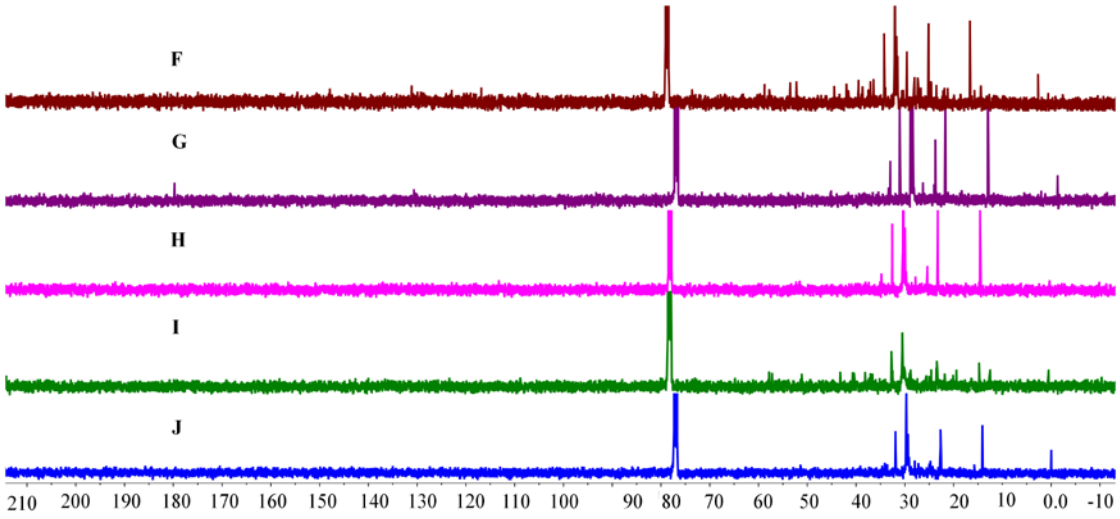

Figure 3.8.: ^{13}C-NMR spectra of the organic extracts of (F) *A. fragilissima*, (G) *P. pedrochei*, (H) *S. filamentosa*, (I) *H. dilatata*, and (J) *P. hornemannii*. The spectra were vertically stacked according to their decreasing order of activities.

3.2.5 Analysis of pharmacological activities of EtOAc:MeOH crude solvent extracts

3.2.5.1 Determination of total phenolic content

The Folin-Ciocalteu colorimetric method (Wojdylo et al., 2007) with suitable modification was used for the determination of total phenolic content (TPC) of the EtOAc-MeOH organic extracts of the seaweed samples (10 mg mL^{-1}) (nine red seaweeds and one brown seaweed) by using a UV-VIS spectrophotometer (Varian Cary 50, Palo Alto, CA, USA). In

detail, the EtOAc-MeOH organic extracts of the seaweed samples (10 mg) in methanol (1 mL) were added into the vial containing Folin-Ciocalteu (F-C) reagent of 5 mL. The mixture obtained was mixed with 4 mL sodium carbonate (0.7 M) solution, and allowed for incubation for 120 min (at 25 °C). The absorbance of the mixture was measured at 760 nm along with blank solution, methanol. The results obtained were evaluated with aid of standard curve procured from different concentrations of commercial standard gallic acid (0.2 to 0.005 mg mL^{-1}) with the equation y=mx+c. Finally, the TPC in EtOAc-MeOH organic extracts of the seaweed samples was estimated as milligram of gallic acid equivalents (mg GAE)/g of the organic extracts.

TPC was estimated with the equation: (mg GAE)/g = (x*w)/v

Where, 'x' is the concentration of mg/g gallic acid equivalent, 'w' is the weight of sample in gram, and 'v' is the volume of the extract.

3.2.5.2 In vitro antioxidant activities

3.2.5.2a 1,1-Diphenyl-2-picrylhydrazil (DPPH) radical scavenging activity

Radical scavenging activities of the organic extracts of the seaweeds against active free radical DPPH was evaluated according to an established method (Wojdylo et al., 2007) by using a UV-VIS spectrophotometer (Varian Cary 50, Palo Alto, CA, USA). Initially, the various concentrations (0.1-1.0 mg mL^{-1}) of organic extracts of the seaweeds were prepared by serial dilution of stock solutions. The equal volumes of various concentration of the organic extracts and DPPH (0.1 mM) in methanol (1.0 mL) were mixed with each other. The mixture was agitated properly, and kept for incubation at room temperature for 30 min in dark. The absorbance of coloured mixture formed was recorded at 517 nm along with blank solution (methanol) and control (1.0 mL of DPPH solution-methanol) after 20 min. The experiment was repeated to obtain triplicate results. The estimation of percentage inhibition along with the IC_{50} values were carried out for different concentrations of DPPH-extract reaction mixtures.

Percentage of radical (DPPH) scavenging activity (%) was calculated by the following equation, (%) = $(A_0-A_1)/A_0$ x 100, wherein, A_0 is the absorbance of control and A_1 is the absorbance of the sample. From the plot of scavenging activity of free radicals, IC_{50} values of (mg mL^{-1}) the organic extracts were calculated. IC_{50} is the concentration, at which the samples inhibits 50 % of radical scavenging activities.

3.2.5.2b 2,2[1]-Azino-bis-3-ethylbenzothiozoline-6-sulfonic acid ($ABTS^+$) radical scavenging activity

Radical scavenging activity of the EtOAc-MeOH organic extracts of the seaweeds against active free radical $ABTS^+$ was evaluated according to an established method (Wojdylo et al., 2007). In brief, the stock solution of $ABTS^+$ radical was prepared by the addition of 7 mM of $ABTS^+$ into the 2.45 mM of potassium persulfate solution. The mixture was allowed to stand for 16 h at room temperature in dark. The methanol was added to the concentrated $ABTS^+$ stock solution to get the absorbance of diluted solution as ~0.70 at 734 nm. The organic extracts of the seaweeds (0.1 mL) of various concentrations (0.1-1.0 mg mL^{-1}) was mixed with 5 mL of diluted $ABTS^+$. The absorbance of resulted coloured mixtures was measured at 734 nm along with the blank solution (methanol) by using a UV-VIS spectrophotometer (Varian Cary 50, Palo Alto, CA, USA). The estimation of percentage inhibition along with the IC_{50} values was carried out for different concentration of $ABTS^+$-extract reaction mixtures.

Percentage of radical ($ABTS^+$) scavenging activity (%) was calculated by following equation, (%) = $(A_0\text{-}A_1)/A_0$ x 100, wherein, A_0 is the absorbance of control and A_1 is the absorbance of the sample. From the plot of scavenging activity of free radicals, IC_{50} values of (mg mL^{-1}) the organic extracts were calculated. IC_{50} is the concentration at which samples inhibits 50 % of radical scavenging activities.

3.2.5.2c Hydrogen peroxide scavenging activities

Hydrogen peroxide (H_2O_2) scavenging abilities of the EtOAc-MeOH organic extracts of seaweeds were assayed by the established method with appropriate modifications (Gulcin et al., 2003). Initially, the various concentrations (0.1-1.0 mg mL^{-1}) of organic extracts of seaweeds were prepared in methanol by serial dilution of stock solutions (1 mg mL^{-1}). Thereafter, the H_2O_2 (40 mM) solution was made in phosphate (pH 7.4) buffer. Various concentrations of 3.0 mL of seaweed extracts were measured out into a vial containing 3.0 mL of H_2O_2 solution. The mixture was agitated thoroughly and allowed to stand for incubation for 10 min. The absorbances of different concentrations of seaweed extracts, blank (phosphate buffer), and control (H_2O_2-methanol mixture were measured at 230 nm after 10 min with UV-VIS spectrophotometer. The experiment was repeatedly carried out to obtain triplicate results and IC_{50} (mg mL^{-1}) values were recorded for various concentrations of H_2O_2-organic extract reaction mixtures from the calculation of percentage inhibition.

The percentage of H_2O_2 scavenging activity was determined and recorded as IC_{50} values. The percentage H_2O_2 scavenging activity (%) was found to be, $(A_0\text{-}A_1)/A_0$ x 100, where, A_0 = absorbance of control and A_1 = the absorbance of the sample.

3.2.5.2d Ferrous ion chelating activity

The ferrous ion chelating abilities of the organic extracts of seaweed samples were estimated according to the established method (Gulcin et al., 2003). The different concentrations (0.1 to 1.0 mg mL^{-1}) of organic seaweed extracts of 1 mL was mixed with equal volumes of 0.313 mM ferrozine reagent (1.0 mL) and 0.125 mM of $FeSO_4$ (1 mL). The solutions were mixed properly and kept for 10 min for the equilibration. The absorbances of solutions, such as organic extracts of seaweeds, blank solution (methanol) and control ($FeSO_4$-ferrozine mixture) were measured at 562 nm after 10 min of incubation, using a UV-VIS-spectrophotometer. The experiments were carried out repeatedly to obtain the triplicate values of results. The percentage inhibition and IC_{50} (mg mL^{-1}) values were recorded for various concentrations of reaction mixtures.

The percentage of chelation (%) was determined as, $(A_0-A_1)/A_0$ x 100, whereas A_0 = Absorbance of control, A_1 = Absorbance of sample.

3.2.5.2e Thiobarbituric acid-reactive species formation inhibitory activity

The lipid peroxidation inhibiting activity of the EtOAc-MeOH organic extracts was assessed by thiobarbituric acid reactive species (TBARS) assay (Kulisic et al., 2004). The lyophilized powder of *Perna viridis* L. (green mussel) was used as the lipid source (model system) in this assay. The organic extracts of seaweed samples (2 mg mL^{-1}) were incubated with 10 mg of lyophilized powder of green mussel meat. A total of 2 mL of ice cold acetic acid (pH 3.6, 20 % v/v) solution was added into the incubation mixture to terminate the reaction. Thiobarbituric acid (TBA) (2 mL, 0.78 % w/v in acetic acid solution) was added to the above reaction mixture and incubated at 95 ºC for 45 min. The reaction mixture was allowed to cool to room temperature and kept for centrifugation at 8000 rpm for 10 min. The formation of malondialdehyde was monitored spectrophotometrically by measuring the absorbance at 532 nm, and the results were expressed as mM of malondialdehyde equivalent compounds formed per kg sample (MDAEQ/kg sample).

3.2.5.3 In vitro anti-inflammatory activities

3.2.5.3a Cyclooxygenases (COX) inhibition assay

Bioactive assays using pro-inflammatory enzymes cyclooxygenases (COX-1/2) were used to recognize the anti-inflammatory activities of the EtOAc-MeOH organic extracts of seaweeds (Larsen et al., 1996). The leuco-2,7-dichlorofluorescein diacetate (5 mg) was incubated with NaOH solution (1 M, 50 µL) at room temperature for 10 min, for the formation of the hydrolysates. The hydrolysed reaction mixture was mixed with HCl (1 M, 30 µL) for the

production of 1-dichlorofluorescein (1-DCF). The excess NaOH present in the reaction mixture was neutralized with HCl, and the resulting 1-DCF was diluted with 0.1 M tris-HCl buffer (pH 8). The cyclooxygenase isoforms (COX-1/2) were made into soluble in 0.1 M tris-HCl buffer. The different concentrations of organic extracts of seaweed samples (0.1-1.0 mg mL^{-1}) were incubated with the pro-inflammatory enzymes in the presence hematin for 5 min at room temperature. The premixed solutions of 1-DCF, arachidonic acid and phenol were poured into the prepared enzyme-seaweed organic extract mixture for the initialization of the reaction, which led to formation of final reaction mixture (with volume 1 mL of 0.1 M tris-HCl buffer). The absorbances were measured at 502 nm for different concentrations of the reaction mixtures by using a spectrophotometer. The experiments were repeated to get triplicate values of results. The percentage inhibition was calculated for different concentrations of reactions mixture and which were recorded to obtain the final IC_{50} (mg mL^{-1}) values.

The results were expressed as percentage (%) inhibition of the enzymes, $(Ab_0-Ab_1)/Ab_0$ x 100, whereas Ab_0=Absorbance of control, Ab_1=Absorbance of sample, and the results were calculated as IC_{50} (mg mL^{-1}), the concentration at which samples inhibits 50 % of enzyme activities.

3.2.5.3b 5-Lipoxygenase (5-LOX) inhibition assay

The 5-lipoxygenase (5-LOX) inhibitory potential of the EtOAc-MeOH organic extracts of seaweeds was evaluated by the established method (Baylac and Racine 2003). The different concentrations of organic extracts of seaweed samples were prepared (0.1-1.0 mg mL^{-1}) in the mixture of DMSO and Tween 20 (29:1, w/w, 50 µL). The pre-heated 0.1 M, potassium phosphate buffer (2.95 mL; pH 6.3) and linoleic acid (48 µL) were added into the reaction mixture and mixed properly. Ice-cold potassium phosphate buffer (12 µL) was poured into the mixture after the addition of pro-inflammatory 5-LOX enzyme of 100 U. The absorbances of the reaction mixtures, control (DMSO-Tween 20), and blank solution (potassium phosphate buffer) were measured at 234 nm by a UV-Visible spectrophotometer, for different concentrations of the reaction mixtures. The experiments were repeated to get triplicate values of results. The percentage inhibition was calculated for different concentrations of reactions mixtures and which were recorded to obtain the final IC_{50} (mg mL^{-1}) values.

The results were expressed as percentage (%) inhibition of the enzymes, $(Ab_0-Ab_1)/Ab_0$ x 100, whereas Ab_0=Absorbance of control, Ab_1=Absorbance of sample, and the results were calculated as IC_{50} (mg mL^{-1}), the concentration at which samples inhibits 50 % of enzyme activities.

3.2.5.4 In vitro antidiabetic activities

3.2.5.4a α -Amylase inhibition assay

Inhibitory activities of the organic extracts against *α*-amylase were used for assessing their anti-diabetic properties (Hamdan and Afifi, 2004). The test solutions of organic extracts of seaweed samples with different concentrations (0.1-1.0 mg mL^{-1}) were prepared by serial dilution. The test solutions of equal volumes were added into the 0.20 mM, phosphate buffer (pH 6.9) containing enzyme, *α*-amylase (0.5 mg mL^{-1}). The reaction mixtures were subjected for incubation at 25 °C for 10 min. Furthermore, pre-incubated reaction mixture was mixed with 0.02 M phosphate buffer (pH 6.9) containing 1 % starch solution, and allowed to stand for 10 min at 25°C. The reaction mixture was warmed with 3, 5 dinitrosalicylic acid (1.0 mL) under boiling the water bath for 5 min to terminate the reaction, and allowed to cool to room temperature. The absorbances of various concentrations of reaction mixtures were measured out at 540 nm after the dilution with double distilled water. The experiments were repeated to get triplicate values of results. The percentage inhibition was calculated for different concentrations of reactions mixture, and were recorded to obtain the final IC_{50} (mg mL^{-1}) values.

The results were expressed as percentage (%) inhibition of the enzymes, $(Ab_0-Ab_1)/Ab_0$ x 100, Ab_0=Absorbance of control, Ab_1=Absorbance of sample, and the results were calculated as IC_{50} (mg mL^{-1}), the concentration at which samples inhibits 50 % of enzyme activities.

3.2.5.4b α-Glucosidase inhibition assay

Inhibitory potentials of the EtOAc-MeOH organic extracts of seaweeds against *α*-glucosidase enzyme were used for analyzing their anti-diabetic properties (Hamdan and Afifi, 2004). The organic extracts of various concentrations (0.1-1.0 mg mL^{-1}) were prepared in 0.2 M, tris-HCl buffer (500 µL, pH 8). The test solutions were pre-incubated with 500 µL of starch solution (2 % w/v) at 37 °C for 5 min, and then incubated with enzyme (1 U/mL) prepared in 0.2 M tris-HCl (pH 8.0) at 37 °C for 10 min. The reaction mixture was warmed with 3,5 dinitrosalicylic acid (1.0 mL) under the boiling water bath for 2 min to terminate the reaction and allowed to cool to room temperature. The absorbances of various concentrations of reaction mixtures were measured at 540 nm after dilution with double distilled water. The experiments were repeated to get triplicate values of readings. The percentage inhibition was calculated for different concentrations of reactions mixtures, and were recorded to obtain the IC_{50} (mg mL^{-1}) values.

The results were expressed as percentage (%) inhibition of the enzymes, $(Ab_0-Ab_1)/Ab_0$ x 100, whereas Ab_0=Absorbance of control, Ab_1=Absorbance of sample, and the results were calculated as IC_{50} (mg mL^{-1}), the concentration at which samples inhibits 50 % of enzyme activities.

3.2.5.4c Dipeptidyl peptidase-4 (DPP-4) inhibition assay

The dipeptidyl peptidase-4 (DPP-4) inhibitory potencies of EtOAc-MeOH organic extracts of seaweed samples were carried out by established method (Kojima *et al*., 1980). The organic extracts of samples with various concentrations (0.1-1.0 mg mL^{-1}) in 50 mM tris-HCl buffer (pH 7.5) was mixed with 15 µL of DPP-4 enzyme (0.05 U/mL) in 100 mM tris-HCl buffer (pH 8). The mixture was subjected for incubation at 37°C for 30 min. The Gly-Pro-p-nitroanilide (50 µL, 1.4 mM) in tris-HCl buffer (0.2 M) was added and incubated for 30 min at 37°C. The absorbances of various concentrations of reaction mixtures were measured at 405 nm by using a UV-VIS spectrophotometer (Varian Cary 50, Palo Alto, CA, USA). The experiments were repeated to get triplicate values of readings. The percentage inhibition was calculated for different concentrations of reactions mixture and which were recorded to obtain the IC_{50} (mg mL^{-1}) values.

The results were expressed as percentage (%) inhibition of the enzymes, $(Ab_0-Ab_1)/Ab_0$ x 100, whereas Ab_0=Absorbance of control, Ab_1=Absorbance of sample, and the results were calculated as IC_{50} (mg mL^{-1}), the concentration at which samples inhibits 50% of enzyme activities.

3.2.5.5 In vitro antihypertensive activities

3.2.5.5a Angiotensin converting enzyme-I (ACE-I) inhibitory activity

Determination of anti-hypertensive potentials of the EtOAc-MeOH organic extracts of the studied seaweeds was conducted with ACE-I inhibiting activity (ACE-I from rabbit lung, 20 µL, 20 mu) (Udenigwe et al., 2009). The organic extracts of seaweed samples (0.2-0.5 mg) were mixed with 20 mU of ACE-1 (1 U/mL, 20 µL) enzyme. The 50 mM tris-HCl buffer (pH 7.5) containing 0.5 mM FAPGG (1 mL) and 0.3 M sodium chloride were added to the enzyme-sample mixtures and the decrease in absorbances were found at 345 nm against the reagent blank (distilled water) by using a UV-VIS spectrophotometer (Varian Cary 50, Palo Alto, CA, USA).

The results were expressed as percentage (%) inhibition of the enzymes, $(Ab_0-Ab_1)/Ab_0$ x 100, where Ab_0=Absorbance of control, Ab_1=Absorbance of sample, and the results

were calculated as IC_{50} (mg mL^{-1}), the concentration at which samples inhibits 50% of enzyme activities.

3.2.6 Statistical analysis

The variances (ANOVA) between various results were analyzed by Statistical Program for Social Science (SPSS, ver. 13.0, SPSS Inc., Quarry Bay, HK), and was used for assessing the significant differences between the means. The significant differences were represented as $P < 0.05$, and the readings were presented as mean of triplicates ± standard deviation. Principal component analysis (PCA) was used to recognize the mean variances in the data set.

3.3 Results and Discussion

3.3.1 Bioactive potentials of the organic extracts of seaweeds

Pharmacological properties, such as antioxidant, anti-diabetic, anti-inflammatory and anti-hypertensive potentials of the organic extracts of the studied seaweeds were assessed with various *in vitro* bio-assays (Table 3.1), and the activities were statistically correlated.

3.3.1.1 Total phenolic content (TPC)

The TPC contents were found to vary from 0.06 to 2.02 mg GAE g^{-1} of extract (Table 3.1), and that the seaweeds of subclass Dictyotophycidae possessed higher amount of polyphenols than seaweeds of subclasses Rhodymeniophycidae and Corallinophycidae. Amongst the selected seaweeds, the TPC was significantly greater for the organic extracts of *P. tetrastromatica* (Dictyotophycidae) (2.02 mg GAE g^{-1}) and *G. salicornia* (Rhodymeniophycidae) (1.57 mg GAE g^{-1}) than those displayed by other studied seaweeds (1.2-0.06 mg GAE g^{-1}). Previous reports of literature deduced that the phenolic compounds could possess important bioactivities, such as antioxidant, anti-inflammatory, anti-tumour, and anti-viral properties (Novoa et al., 2011; Thomas and Kim, 2011; Wijesinghe and Jeon, 2012).

3.3.1.2 Antioxidant activities

The organic extracts acquired from different seaweeds belonging to the subclasses Dictyotophycidae, Rhodymeniophycidae and Corallinophycidae were evaluated for their antioxidant properties using scavenging activity of free radicals ($ABTS^{+}$, DPPH and H_2O_2). Among various organic extracts, that of *P. tetrastromatica* displayed greater scavenging ability on DPPH radicals (IC_{50} 0.39 mg mL^{-1}) followed by those obtained from *G. salicornia* (IC_{50} 0.42

mg mL^{-1}), *G. canaliculata* (0.53 mg mL^{-1}), and *G. corticata* (0.55 mg mL^{-1}), in descending order. The $ABTS^+$ free radical scavenging activities of the organic extract of the studied seaweeds varied considerably (IC_{50} 0.66-0.98 mg mL^{-1}) (Table 3.1). Notably, the organic extract of seaweed *P. tetrastromatica* exhibited higher $ABTS^+$ radical scavenging activity (IC_{50} 0.66 mg mL^{-1}), whereas among seaweeds belonging to Rhodymeniophycidae, *G. salicornia* (IC_{50} 0.78 mg mL^{-1}) showed potential $ABTS^+$ radical scavenging activity (Table 3.1). The organic extract of the seaweed, *P. tetrastromatica* (IC_{50} 0.18 mg mL^{-1}) displayed greater hydrogen peroxide radical scavenging activity followed by those obtained from the seaweeds belonging to the subclasses Rhodymeniophycidae and Corallinophycidae (Table 3.1). The organic extracts of seaweeds, *G. salicornia* (IC_{50} 0.19 mg mL^{-1}), *G. corticata* (IC_{50} 0.24 mg mL^{-1}), *G. canaliculata* (IC_{50} 0.20 mg mL^{-1}), and *H. edulis* (IC_{50} 0.22 mg mL^{-1}) displayed greater peroxyl radical scavenging potential than those obtained from other studied species of seaweeds (IC_{50} > 0.25 mg mL^{-1}) (Table 3.1).

The antioxidant activities of the EtOAc-MeOH extracts of seaweeds were analyzed by principal component analysis (PCA), whereas PC1 and PC2 contributed 45.21 and 39.65 % towards the studied bioactivities (Figure 3.9). The DPPH and $ABTS^+$ radical scavenging activities of the organic extracts appeared in the same quadrant in the PCA diagram. High loading of DPPH as well as $ABTS^+$ scavenging activities on PC1 revealed that EtOAc-MeOH extracts of seaweeds belonging to the subclasses Dictyotophycidae and Rhodymeniophycidae were potential antioxidants.

The inhibitions of lipid peroxide formation of the organic extracts of the studied seaweeds were displayed in Table 3.1. The TBARS formation inhibitory effects of EtOAc-MeOH extract of *P. tetrastromatica* was 58.86 mM MDAEQ/kg, whereas that of *G. salicornia* was 51.96 mM MDAEQ kg^{-1}. Besides *G. salicornia*, the organic extracts of seaweeds *G. corticata* (49.64 mM MDAEQ kg^{-1}), *G. canaliculata* (46.45 mM MDAEQ kg^{-1}), and *H. edulis* (48.23 mM MDAEQ kg^{-1}) exhibited significantly higher inhibition of TBARS formation than those derived from the seaweeds belonging to the subclasses Rhodymeniophycidae and Corallinophycidae.

The metal binding property of the seaweeds could be identified from their ferrous ion chelating activities (Table 3.1). Amongst the studied seaweeds, the ferrous ion chelating efficiency was significantly greater for the organic extract of *P. tetrastromatica* (IC_{50} 0.13 mg mL^{-1}) and decreased in the order, *G. salicornia* (IC_{50} 0.15 mg mL^{-1}) > *H. edulis* (IC_{50} 0.24 mg mL^{-1}) > *G. canaliculata* (IC_{50} 0.25 mg mL^{-1}).

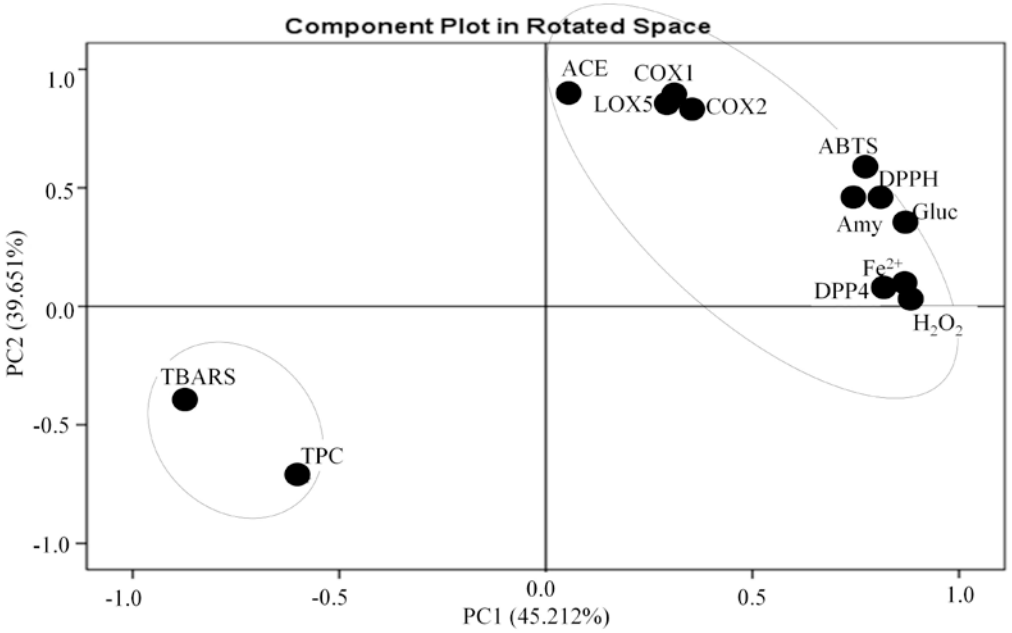

Figure 3.9.: Loading plot diagram (various components, PC1 and PC2 in the rotated space) of antioxidant activities vs anti-inflammatory, anti-diabetic and anti-hypertensive activities of the organic extracts of the studied seaweeds.

DPPH is a highly potent free radical that is used to find out the reducing power due to the presence of phenolic components, and hydrogen atom donating ability of antioxidants (Cho et al., 2011). The higher DPPH scavenging ability of seaweeds *P. tetrastromatica* (IC_{50} 0.39 mg mL^{-1}) and *G. salicornia* (IC_{50} 0.42 mg mL^{-1}) might be correlated with their greater TPC contents in the organic extracts. Earlier reports suggested that seaweeds of the subclass Dictyotophycidae showed greater DPPH radical scavenging activity than that exhibited by seaweeds of subclasses Rhodymeniophycidae and Corallinophycidae (Matsukawa et al., 1997). The antioxidant activity of the EtOAc-MeOH extracts of the studied seaweeds were also investigated by the non-radical species of hydrogen peroxide and that the scavenging activity of H_2O_2 recognized the reducing power of antioxidants against active radicals formed by the H_2O_2 during its reaction. The peroxyls were found to be potentially reactive oxidizing radicals that could act with the bioactive molecules resulting in the development of other radical species, such as alkoxy radicals. As the peroxyl radicals are the conveyors of the chain reaction, they oxidize polyunsaturated fatty acid (PUFA) molecules and begin new chains, inducing lipid peroxides that could be, fragmented to yet more radicals (Esterbauer and Porter, 1990). In this direction, the TBARS assay was used to deduce the inhibitory activity of antioxidants against free radical generation leading to lipid peroxidation. This assay indicated the formation of malondialdehyde as stable end product from oxidative degradation of unsaturated fatty acids. It has been

postulated that the presence of polyphenolic components might be responsible to hinder lipid peroxidation resulting in termination of free radical chain reactions (Karawita et al., 2005).

The metal binding property of the seaweeds could be identified from the ferrous ion chelating activity (Table 3.1). The iron in reduced form (Fe^{2+}) appeared to decompose the lipid hydroperoxides into radicals, such as peroxyls and alkoxyls, which make peroxidation of lipids, and could abstract hydrogen and extend the lipid peroxidation reaction (Costa et al., 2011). Therefore, the chelators of Fe^{2+} ion could be recommended as active lipid peroxidation inhibitors. The Fe^{2+} ion chelating activity of brown seaweed *Scytosiphon lomentaria* was previously reported (Kuda et al., 2005), and the studies revealed that the phenolic components in the polar solvent extracts of seaweeds of subclass Dictyotophycidae might be potential chelators of heavy metals (Wang et al., 2012). The Fe^{2+} chelating capabilities of the organic extracts of the seaweeds were also demonstrated by the existence of different kinds of non-phenolic compounds (Kuda et al., 2009). The negative correlation between TPC and Fe^{2+} chelating abilities might appropriately demonstrate the functional role of non-phenolic antioxidant components in the studied seaweeds.

The content of phenolic compounds in the seaweeds was varied from 2.02 mg GAE g^{-1}(*P. tetrastromatica*) to 0.06 mg GAE g^{-1} (*H. dilatata*) mg GAE g^{-1}. The phenolic contents in the organic extracts of *P. tetrastromatica* and *G. salicornia* extract (> 1.5 mg GAE g^{-1}) were significantly greater ($p < 0.05$) compared with those of the other species (< 1.25 mg GAE g^{-1}). The presence of phenolic group of compounds could be attributed to be one of the predominant reasons of antioxidant potential in the studied seaweed species (Rocha et al., 2018). Previous reports of literature demonstrated the functional roles of polyphenols and antioxidants as anticancer metabolites and growth suppressors of the cancer cells (Rocha et al., 2018). Among various brown seaweeds *Ecklonia cava* Kjellman and *Ecklonia stolonifera* Okamura displayed moderate antiproliferative activity against breast cancer cell lines, MCF-7 and MDA-MB-231 (Rocha et al., 2018). The red seaweeds belonging to the species of *Gracilaria* including *G. tenuistipitata*, *G. corticata* and *G. verrucosa* were found to exhibit cytotoxic potential against oral squamous carcinoma cells, HepG2, MCF7 and HeLa cancer cells (Yeh et al., 2012; Narasimhan et al., 2013; Dewi et al., 2018).

Table 1. Percentage yield, phenolic contents and pharmacological activities of the organic extracts of seaweeds belonging to Dictyotophycidae, Rhodymeniophycidae and Corallinophycidae

	A. fragillissima	*H. edulis*	*G. salicornia*	*G. corticata*	*P. pedrochei*	*S. filamentosa*	*P. hornemannii*	*H. dilatata*	*P. tetrastromatica*	*G. canaliculata*
Yield (%)	0.63±0.01^{a}	0.74±0.02^{b}	0.75±0.02^{b}	0.70±0.01^{c}	0.65±0.01^{a}	0.71±0.02^{c}	0.67±0.02^{a}	0.60±0.02^{d}	0.81±0.01^{e}	0.71±0.02^{c}
Total phenolics†	0.09±0.01^{a}	1.23±0.01^{b}	1.57±0.01^{c}	0.98±0.02^{d}	0.06±0.01^{a}	0.76±0.02^{e}	1.03±0.01^{f}	0.100±0.01^{a}	2.02±0.01^{g}	1.00±0.01^{dfh}
Antioxidant activities‡										
DPPH radical scavenging	0.72±0.01^{a}	0.62±0.01^{b}	0.42±0.01^{c}	0.55±0.01^{d}	0.59±0.01^{bde}	0.64±0.01^{bf}	0.78±0.01^{g}	0.75±0.01^{ag}	0.39±0.01^{ch}	0.53±0.01^{di}
$ABTS^{+}$ radical scavenging	0.98±0.01^{a}	0.93±0.01^{b}	0.78±0.01^{c}	0.81±0.01^{cd}	1.02±0.01^{a}	0.97±0.01^{ab}	0.89±0.01^{be}	0.98±0.01^{ab}	0.66±0.01^{f}	0.87±0.01^{eg}
Fe^{2+} ion chelating	0.33±0.02^{a}	0.24±0.01^{b}	0.15±0.01^{c}	0.33±0.02^{a}	0.45±0.02^{d}	0.90±0.02^{e}	0.43±0.02^{df}	0.89±0.01^{eg}	0.13±0.02^{ch}	0.25±0.01^{bi}
H_2O_2 scavenging	0.21±0.02^{a}	0.22±0.01^{a}	0.19±0.01^{a}	0.24±0.02^{abc}	0.29±0.02^{b}	0.30±0.02^{bc}	0.31±0.02^{bd}	0.28±0.01^{be}	0.18±0.02^{a}	0.20±0.01^{a}
Lipid peroxidation‡ inhibition	38.52±0.01^{a}	48.23±0.01^{b}	51.96±0.01^{c}	49.64±0.01^{d}	35.6±0.01^{e}	36.9±0.01^{f}	31.61±0.01^{g}	32.87±0.01^{h}	58.86±0.01^{i}	46.45±0.01^{j}
Anti-inflammatory activities‡										
COX-1 inhibition	4.99±0.01^{a}	2.91±0.01^{b}	1.01±0.01^{c}	2.99±0.01^{d}	4.04±0.01^{e}	3.01±0.01^{df}	2.01±0.01^{g}	3.04±0.01^{dh}	1.23±0.01^{i}	2.92±0.01^{bj}
COX-2 inhibition	5.01±0.01^{a}	3.01±0.01^{b}	1.02±0.01^{c}	3.01±0.01^{bd}	4.03±0.01^{e}	2.98±0.01^{bf}	1.99±0.01^{g}	3.00±0.01^{bh}	1.34±0.01^{i}	2.00±0.01^{bj}
5-LOX inhibition	5.02±0.01^{a}	2.98±0.01^{b}	0.98±0.01^{c}	3.02±0.02^{bd}	4.01±0.01^{e}	3.04±0.02^{df}	2.03±0.01^{g}	3.02±0.01^{bfh}	1.28±0.01^{i}	2.01±0.01^{gj}
Anti-diabetic activities‡										
α-Amylase inhibition	0.87±0.02^{a}	0.79±0.01^{b}	0.50±0.01^{c}	0.54±0.02^{cd}	0.61±0.02^{e}	0.77±0.02^{bf}	0.81±0.02^{bg}	0.95±0.02^{h}	0.45±0.02^{ci}	0.70±0.01^{j}
α-Glucosidase inhibition	0.73±0.02^{a}	0.63±0.02^{b}	0.45±0.02^{c}	0.53±0.0^{2d}	0.64±0.02^{b}	0.73±0.02^{a}	0.83±0.02^{f}	0.82±0.02^{fg}	0.40±0.02^{ch}	0.65±0.02^{bc}
DPP-IV inhibition	0.05±0.01^{a}	0.06±0.01^{a}	0.03±0.01^{a}	0.06±0.01^{a}	0.08±0.01^{ab}	0.05±0.01^{a}	0.08±0.01^{a}	0.17±0.01^{c}	0.02±0.01^{ad}	0.07±0.01^{a}
Anti-hypertensive activities‡										
ACE-I inhibition	0.62±0.02^{a}	0.18±0.01^{b}	0.09±0.01^{c}	0.20±0.02bd	0.21±0.02^{be}	0.24±0.02^{bf}	0.22±0.02^{bg}	0.23±0.02^{bh}	0.12±0.02^{ci}	0.19±0.01^{bj}

†Total phenolic contents were determined at 5 mg mL^{-1}, and presented as mg of gallic acid equivalence (GAE) g^{-1}.

‡The IC_{50} values were expressed as mg mL-1. Lipid peroxidation inhibitory (TBARS assay) was expressed as mM MDAEQ kg^{-1}.

The samples were analyzed in triplicate (n = 3) and expressed as mean ± standard deviation. Means followed by the different superscripts (a-j) within the same row indicate significant difference ($P < 0.05$).

3.3.1.3 Anti-diabetic activities

The organic extracts of seaweeds belonging to subclasses Dictyotophycidae, Rhodymeniophycidae and Corallinophycidae were evaluated for their attenuating properties against carbolytic enzymes *α*-amylase and *α*-glucosidase. The EtOAc-MeOH extracts of seaweed *P. tetrastromatica* exhibited greater attenuating properties against *α*-amylase (IC_{50} 0.45 mg mL^{-1}) than those obtained from other studied seaweed species (Table 3.1). Likewise, the organic extracts of *P. tetrastromatica* and *G. salicornia* exhibited significantly higher *α*-glucosidase inhibiting activity (IC_{50} ~0.4 mg mL^{-1}) than other studied seaweeds. The DPP-IV inhibitory potentials of the organic extracts of *P. tetrastromatica* (IC_{50} 0.02 mg mL^{-1}) and *G. salicornia* (IC_{50} 0.03 mg mL^{-1}) were considerably higher than those exhibited by other seaweed species (Table 3.1).

Diabetic mellitus is a chronic metabolic disease, and was found to occur because of insufficiency of insulin secretion or resistance (Nickavar and Yousefian, 2011). The complex starch degrading enzyme *α*-amylase was reported to perform major functional role in the hydrolysis of 1, 4-glycosidic linkages of various simple oligosaccharides, and the enzyme *α*-glucosidase additionally decomposes the disaccharides into smaller moieties for the intestinal absorption. The inhibitions of these enzyme activities were considered to be effective to reduce absorption of glucose to the blood (Hara et al., 1990).

3.3.1.4 Anti-hypertensive and anti-inflammatory activities

The organic extract of *G. salicornia* and *P. tetrastromatica* exhibited considerably greater anti-hypertensive activities as displayed by the higher ACE-I (IC_{50} 0.09 and 0.12 mg mL^{-1}, respectively; $P < 0.05$) inhibiting potential than those exhibited by other seaweeds (Table 3.1). The organic extracts *P. tetrastromatica* and *G. salicornia* exhibited greater attenuation properties against 5-LOX (IC_{50} 1.28 and 0.98 mg mL^{-1}, respectively) compared to the other studied seaweed species belonging to Rhodymeniophycidae (*H. edulis, G. canaliculata, G. corticata, P. hornemannii, P. pedrochei, S. filamentosa, H. dilatata*) and Corallinophycidae (*A. fragilissima*) (IC_{50} > 2 mg mL^{-1}) (Table 3.1). The organic extracts of seaweeds exhibited a positive correlation on PCA analyses, and was demonstrated by the co-linearity between antioxidative properties and ACE-I inhibitory activities. Notably, the organic extracts of *P. tetrastromatica* and *G. salicornia* exhibited higher duel COX-2 and 5-LOX inhibiting activity compared to the other studied seaweed species belonging to Rhodymeniophycidae and Corallinophycidae.

3.3.2 Spectroscopic fingerprinting of functional groups

The EtOAc-MeOH extracts obtained from the seaweeds displayed characteristic chemical shift values and corresponding integrals in the spectra (Figure 3.10-3.19, Table 3.2). The characterization of the signature peaks from the ^{1}H-NMR spectra was performed in an effective manner by a deconvolution method of the whole range of the ^{1}H-NMR spectra, whereas the algorithm of peak analysis and global spectral deconvolution untangled the transitions in ^{1}H-NMR spectra of the constitutive components. The ^{1}H-NMR spectra of the organic extracts of *P. tetrastromatica* and *G. salicornia* documented the occurrence of higher proton integrals at δ_H 4-6, which might be due to the occurrence of protons connected with the olefinic and the parent hydride group of alkyl alkanoates {$RCH_2C(=O)OCH_3$}. The signals at the region δ_C 125-135 might be assigned to the olefinic carbon atoms. Furthermore, the intense signals at δ_C160-180 in the ^{13}C-NMR spectra were assigned owing to the existence of alkanoate carbon atom of esters {$RC(=O)OR_1$} in the organic extracts of *P. tetrastromatica* and *G. salicornia*. The EtOAc-MeOH extracts of *P. tetrastromatica* and *G. salicornia* displayed prominent ^{13}C-NMR signals at δ_C 173, which could be attributed to the carbonyl groups. The ^{1}H-NMR spectra of the organic extracts of *G. salicornia* and *A. fragilissima* displayed common peaks in the range of δ_H 6.0-8.5, which could be associated with the aromatic traces. The characteristic peaks at δ_H 2.2-3 and δ_H 3.3-4.0 in the ^{1}H-NMR spectra of the organic extract of seaweeds might be attributed to the presence of benzylic groups (Ar-CH_3) and ether (R-O-CH_3) functional groups. The characteristic proton signals in the region δ_H 2.74-2.92 might be attributed to superimposed >CH_2 bis-allylic protons, which was deduced to be more important in the organic extracts of *P. tetrastromatica* and *G. salicornia,* belonging to the subclasses Dictyotophycidae and Rhodymeniophycidae, respectively. The signals owing to bis-allylic groups might also demonstrate the ubiquity of the unsaturated fatty acids in these seaweed extracts. The ^{1}H-NMR spectra obtained from the organic extracts of *P. tetrastromatica* and *G. salicornia* also earned well resolved, deshielded signals at about δ_H 5.0-5.3, which presumably explained the existence of oligosaccharide units. These assignments were furthermore evaluated by the ^{13}C-NMR spectra (Figure 3.20-3.29), which were acquired from the EtOAc-MeOH extracts of the seaweed species contemplated in this study. The organic extracts of *P. tetrastromatica* and *G. salicornia* exhibited very intense signals at δ_H 2.8-3.5, which might be associated with the electronegative groups, such as alkoxy/alkyl halide/functionalized hydride of the substituted alkanols. The signals at δ_C 45-70 and δ_C 70-80 in the ^{13}C-NMR spectra, might be due to the alkoxy carbon (RCH_2OR_1), and the carbons connected to the parent hydride group of alkyl alkanoates {$RCH_2C(=O)OCH_3$}, respectively. The organic extracts of the seaweeds did not show the occurrence of the intense aromatic carbon residues (at δ_C 142), with the exclusion of those obtained from *P. tetrastromatica* and *G. salicornia*.

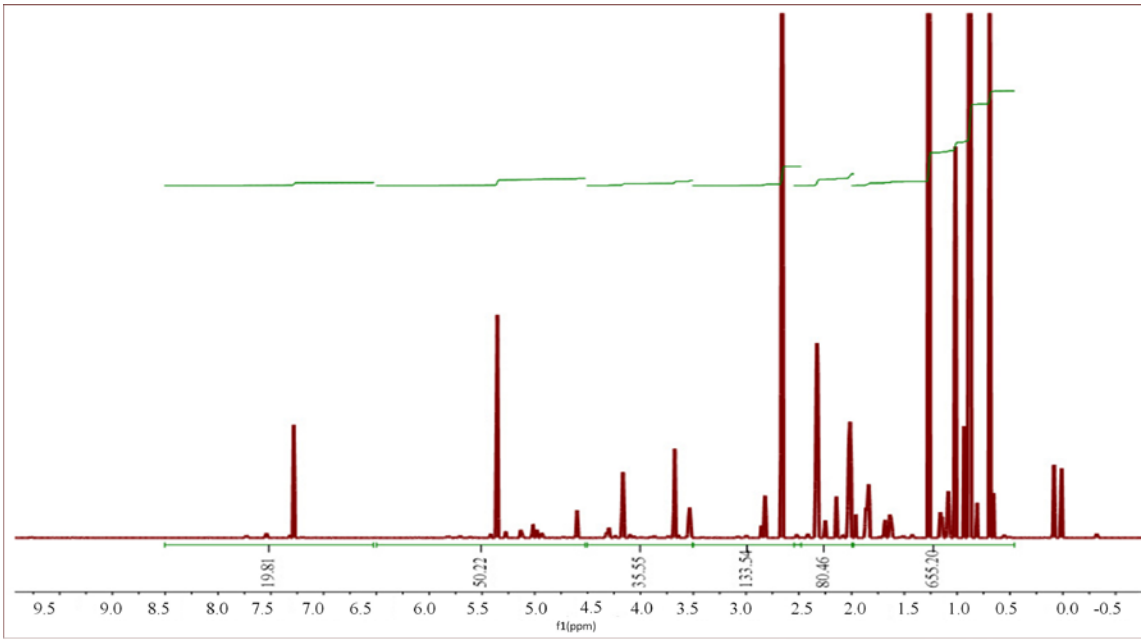

Figure 3.10.: ^{1}H NMR spectrum of EtOAc-MeOH extract of *G. salicornia*

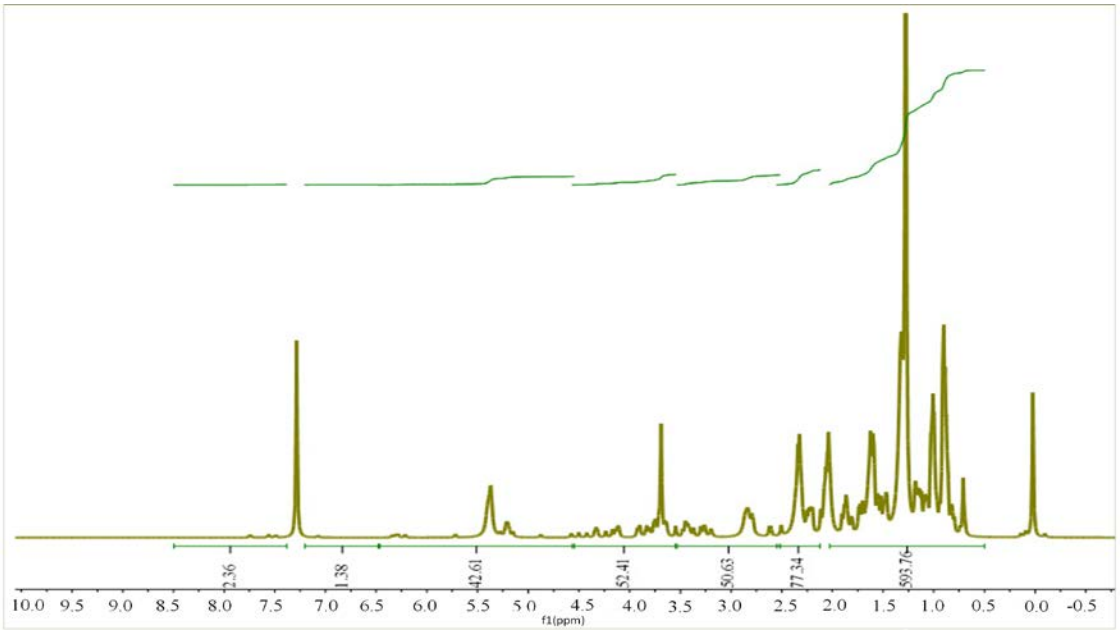

Figure 3.11.: ^{1}H NMR spectrum of EtOAc-MeOH extract of *P. tetrastromatica*

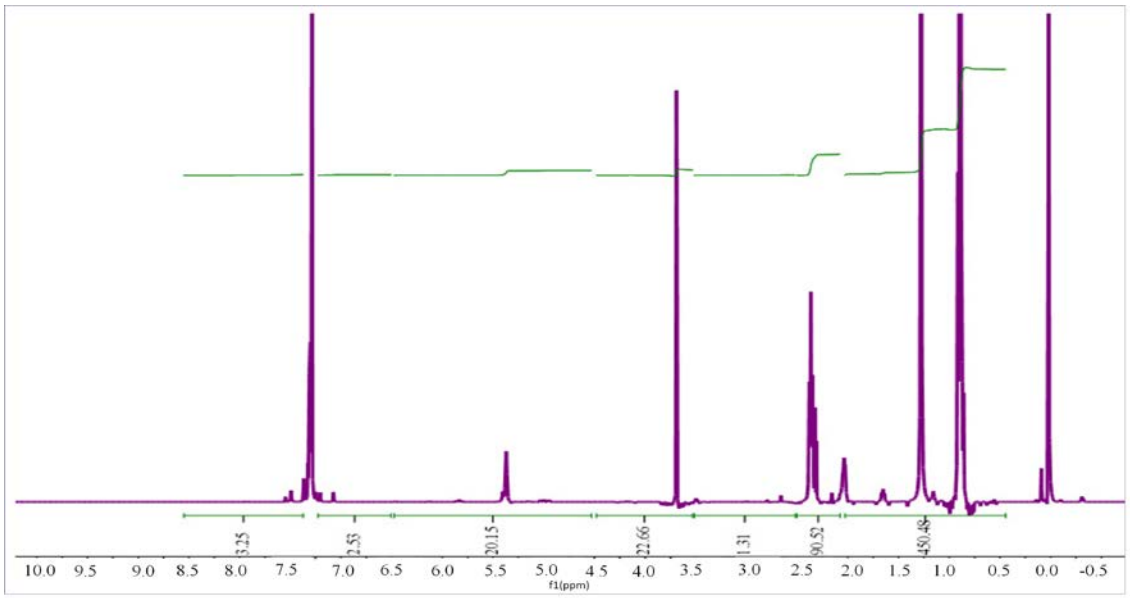

Figure 3.12.: ^{1}H NMR spectrum of EtOAc-MeOH extract of *G. canaliculata*

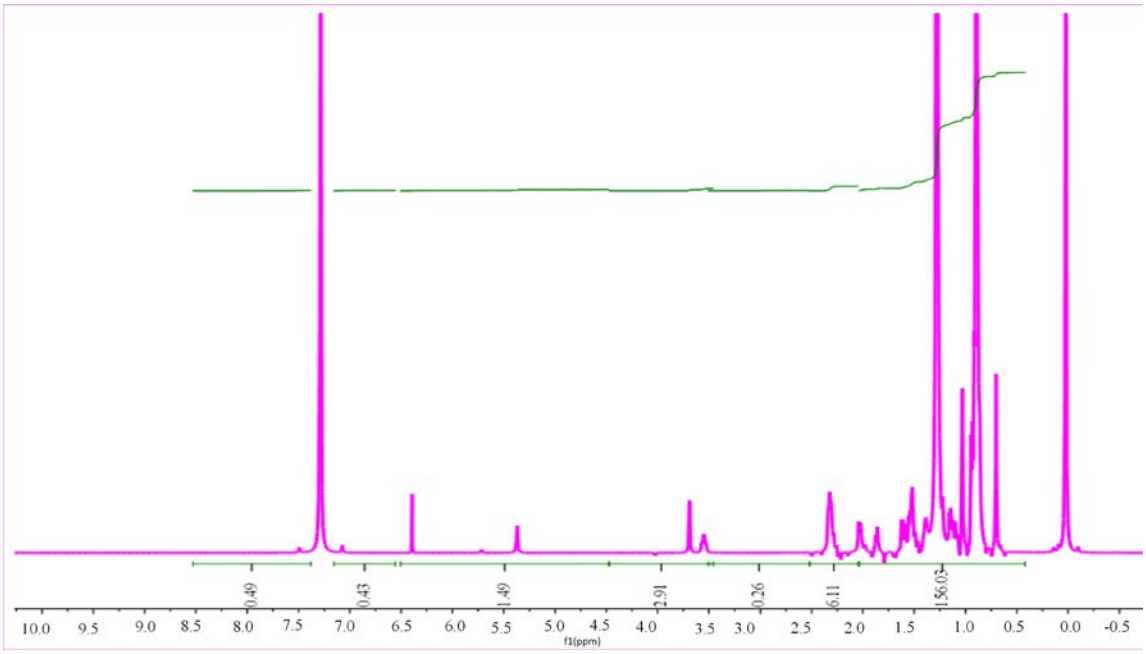

Figure 3.13.: ^{1}H NMR spectrum of EtOAc-MeOH extract of *G. corticata*

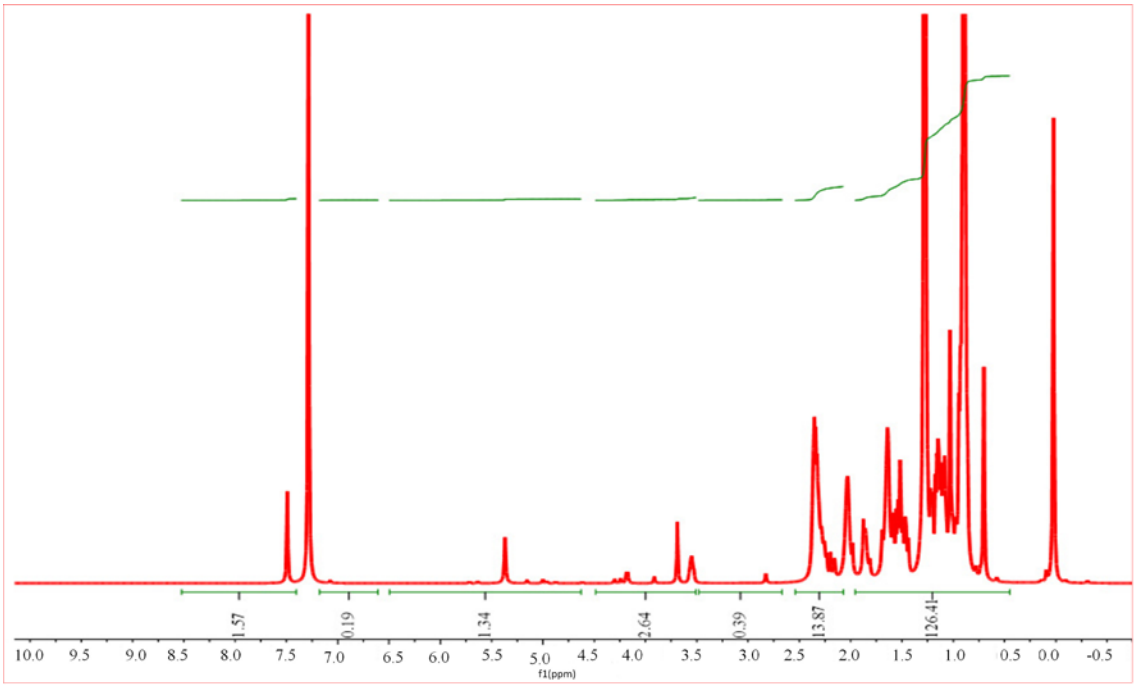

Figure 3.14.: ^{1}H NMR spectrum of EtOAc-MeOH extract of *H. edulis*

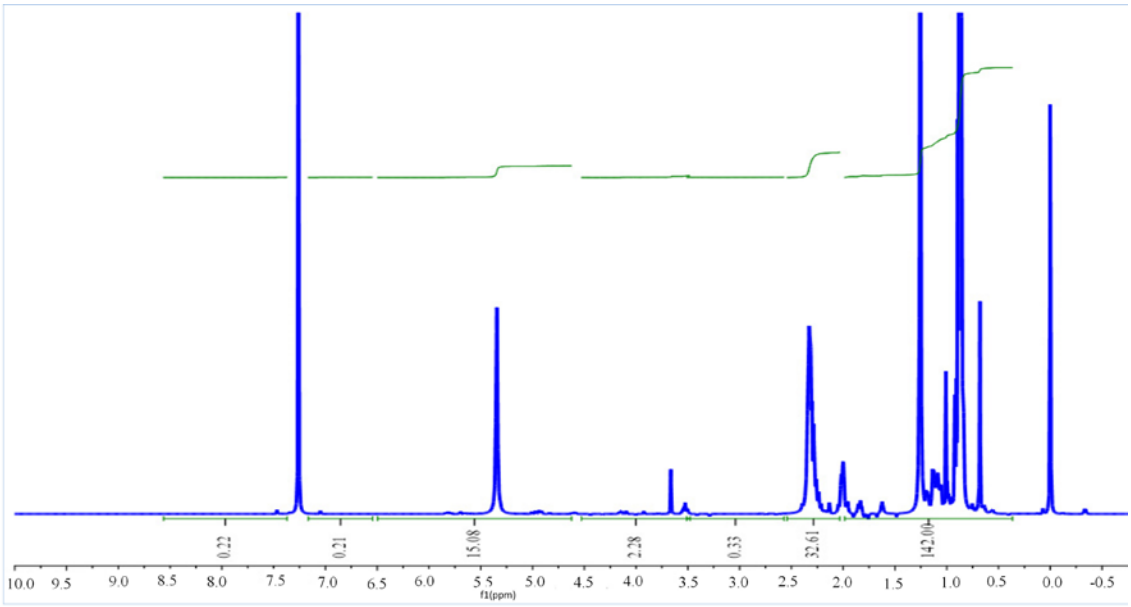

Figure 3.15.: ^{1}H NMR spectrum of EtOAc-MeOH extract of *A. fragilissima*

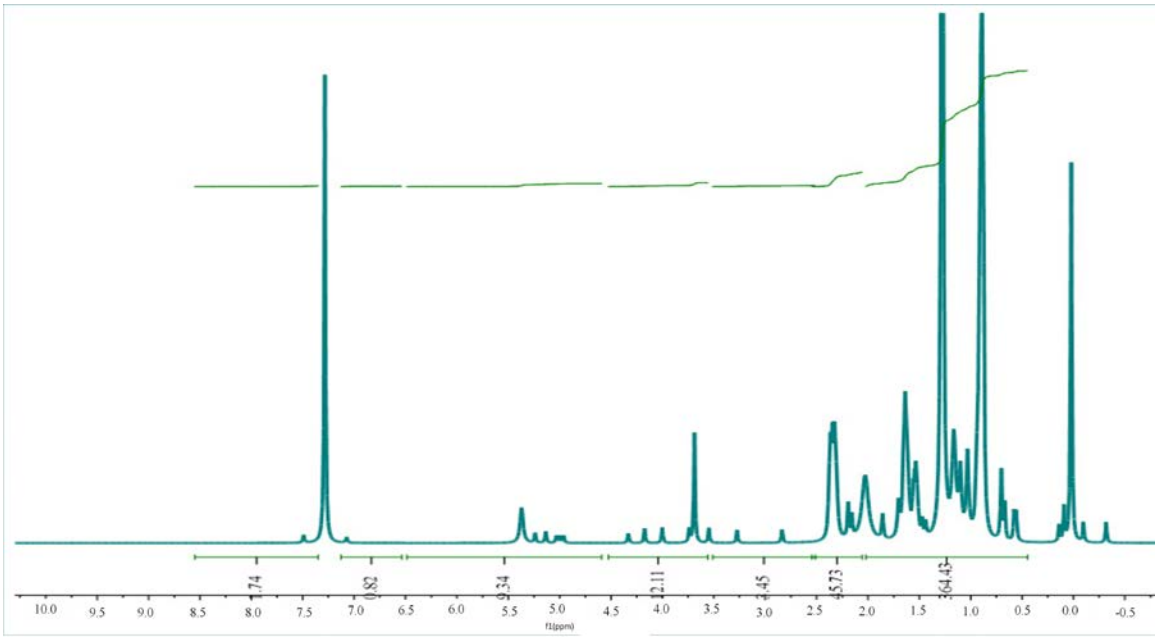

Figure 3.16.: ^{1}H NMR spectrum of EtOAc-MeOH extract of *P. pedrochei*

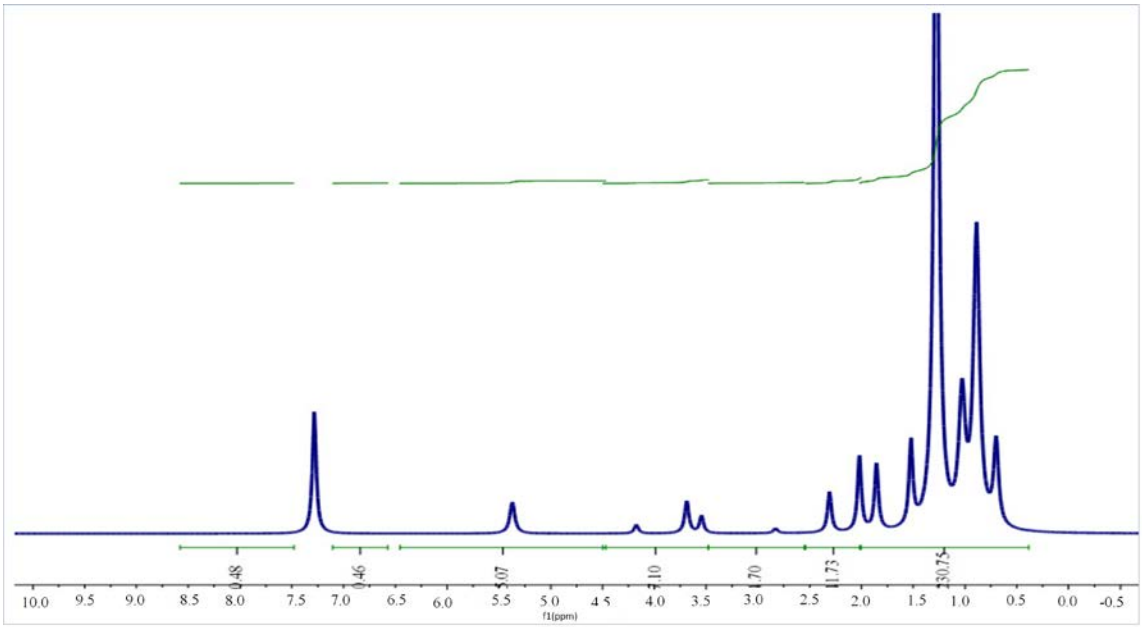

Figure 3.17.: ^{1}H NMR spectrum of EtOAc-MeOH extract of *S. filamentosa*

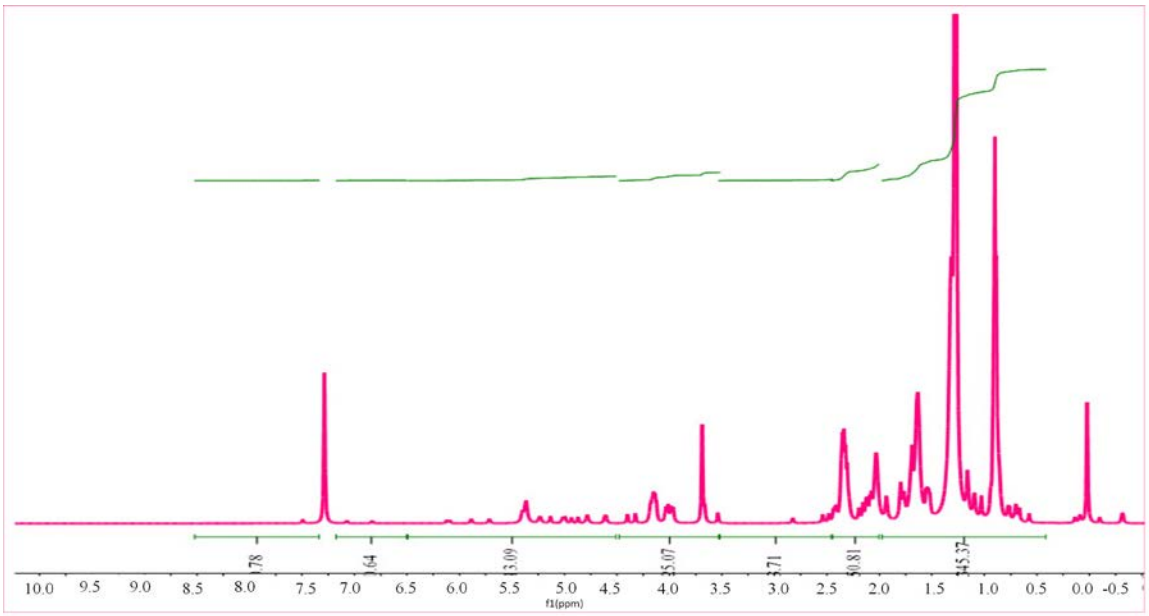

Figure 3.18.: ^{1}H NMR spectrum of EtOAc-MeOH extract of *H. dilatata*

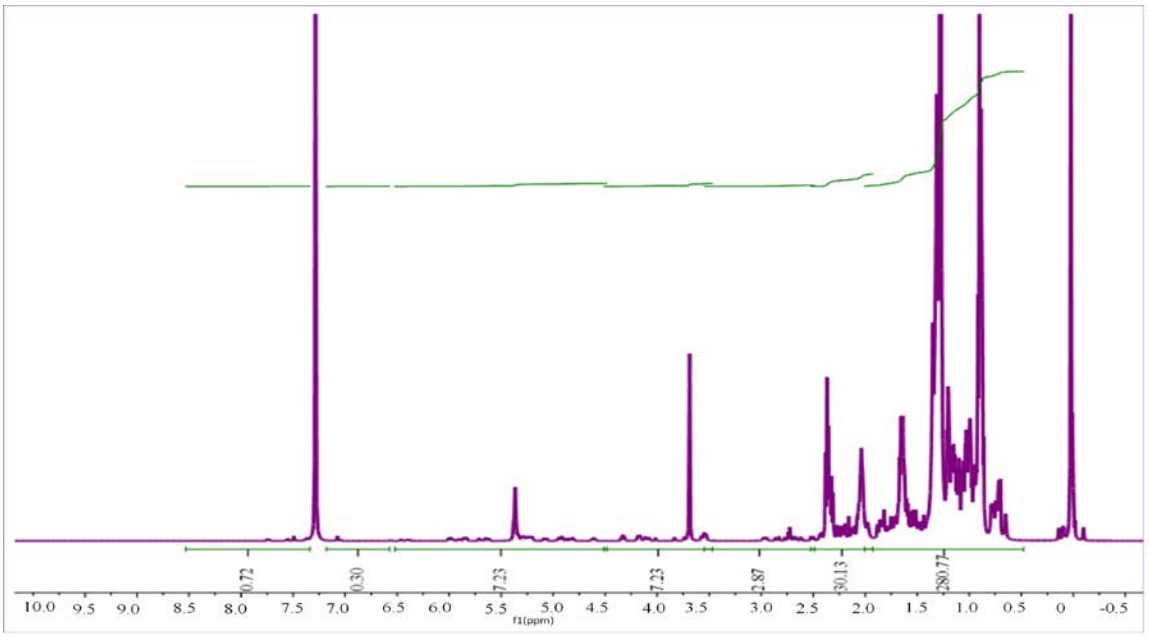

Figure 3.19.: ^{1}H NMR spectrum of EtOAc-MeOH extract of *P. hornemannii*

Table 2. Type and integral values of protons obtained from the 1H-NMR of the organic extracts of seaweeds belonging to the subclasses Dictyotophycidae (phylum Ochrophyta), Rhodymeniophycidae and Corallinophycidae (phylum Rhodophyta).

Seaweeds	**Integral values of protons (∑H) at the specified region (δ_H) of ^{1}H NMR spectra***					
	δ_H 0.5-2.0[a]	**2.0-2.5**[b]	**2.5-3.5**[c]	**3.5-4.5**[d]	**4.5-6.0**[e]	**6.5-8.5**[f]
G. salicornia	665.2	80.46	133.54	35.55	50.22	19.81
P. tetrastromatica	593.76	77.34	50.63	52.41	42.61	3.74
G. canaliculata	450.48	90.52	1.31	22.66	20.15	5.78
G. corticata	364.43	45.73	3.45	12.11	9.34	2.56
H. edulis	345.37	50.81	3.71	25.07	13.09	1.42
A. fragilissima	280.77	30.13	2.87	7.23	7.23	1.08
P. pedrochei	230.75	11.73	1.70	7.10	5.07	0.94
S. filamentosa	156.03	6.11	0.26	2.91	1.49	0.92
H. dilatata	142.00	32.61	0.39	2.28	15.08	0.43
P. hornemannii	126.41	13.87	0.33	2.64	1.34	1.76

[*]The protons signals appeared in the ^{1}H-NMR spectra of seaweeds were integrated to acquire the ratio of number of protons in selected regions.

[a] Saturated hydrocarbons

[b] CH_2=CH-CH_3/RC(=O)CH_3/RCH_2C(=O)OR_1/Ar-CH_3

[c] OCH_3/R-CH_2-X/R-CH_2-OH

[d] Anomeric (due to polysaccharides)

[e] RCH=CHR_1/RCH_2C(=O)OCH_3

[f]Ar-H

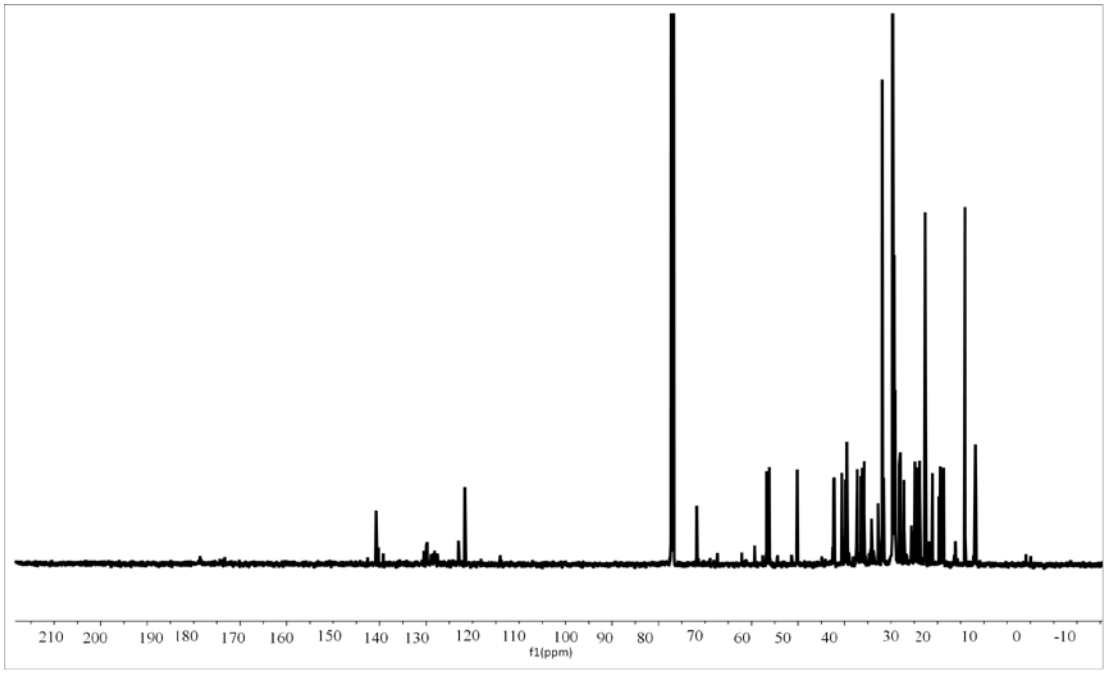

Figure 3.20.: ^{13}C NMR spectrum of EtOAc-MeOH extract of *G. salicornia*

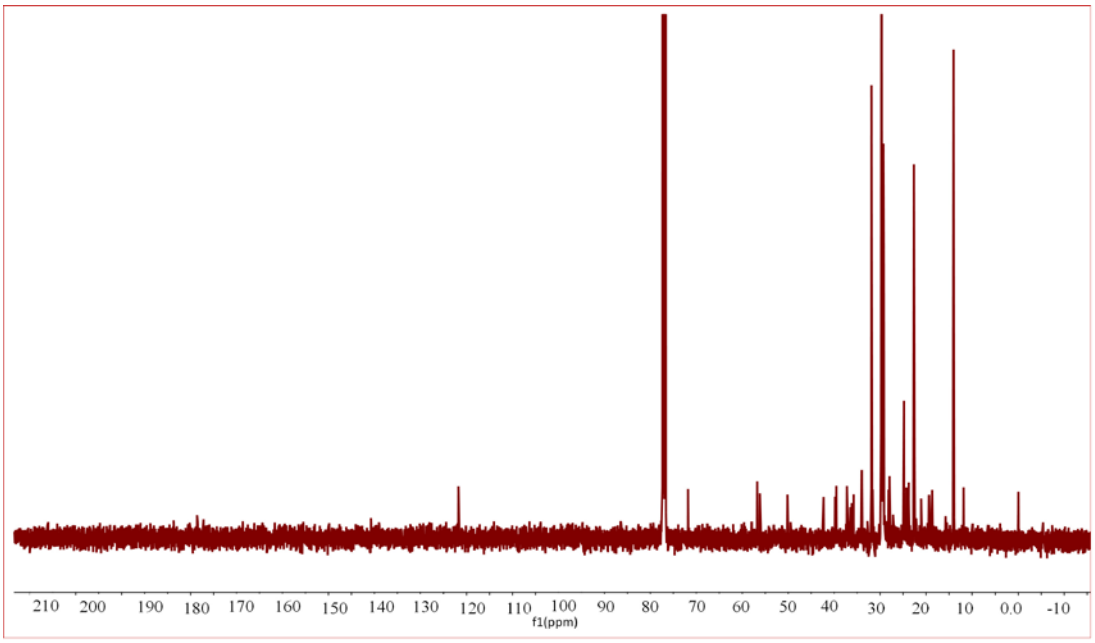

Figure 3.21.: ^{13}C NMR spectrum of EtOAc-MeOH extract of *P. tetrastromatica*

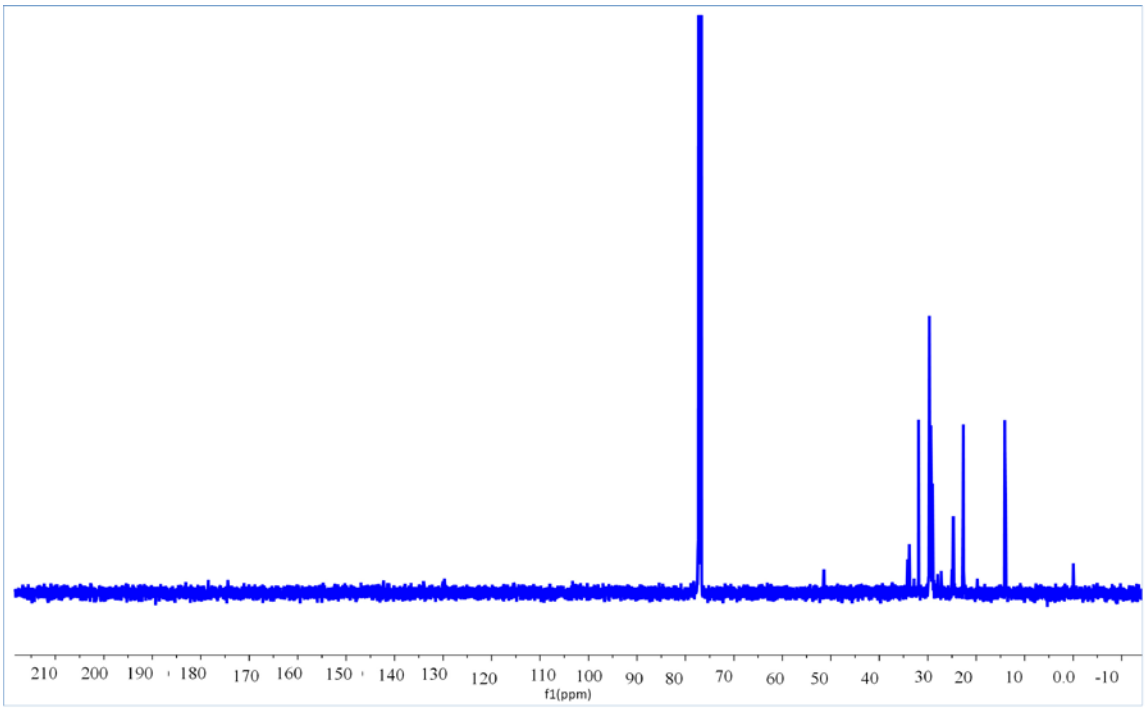

Figure 3.22.: ^{13}C NMR spectrum of EtOAc-MeOH extract of *G. canaliculata*

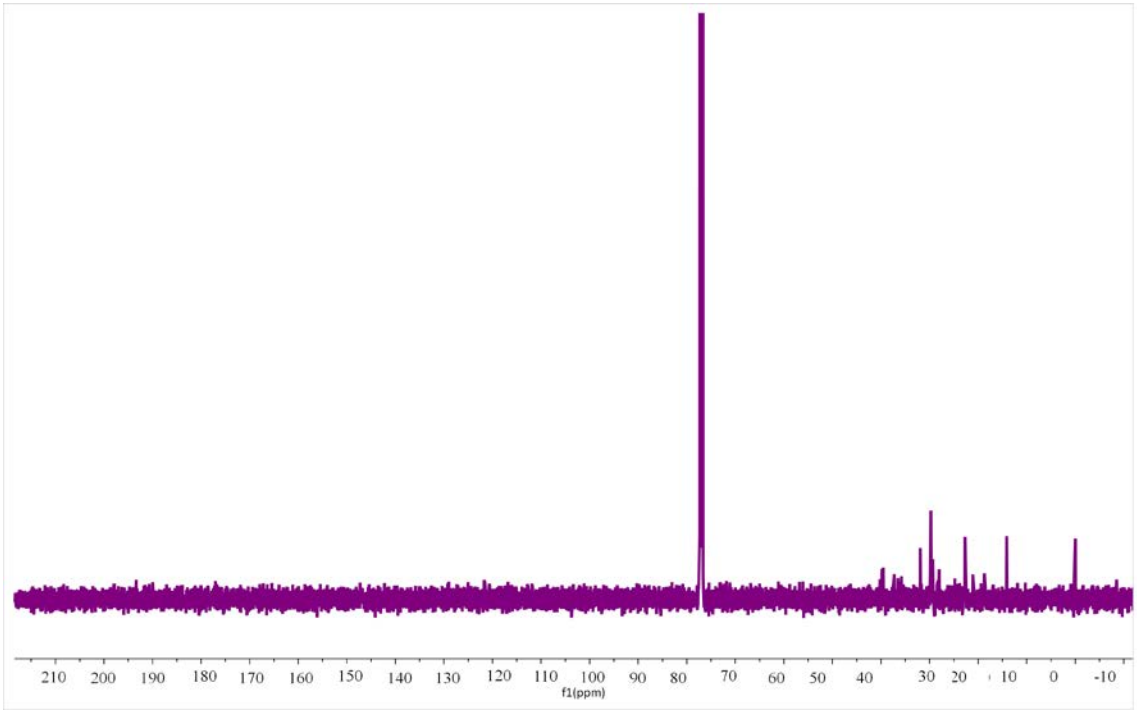

Figure 3.23.: ^{13}C NMR spectrum of EtOAc-MeOH extract of *G. corticata*

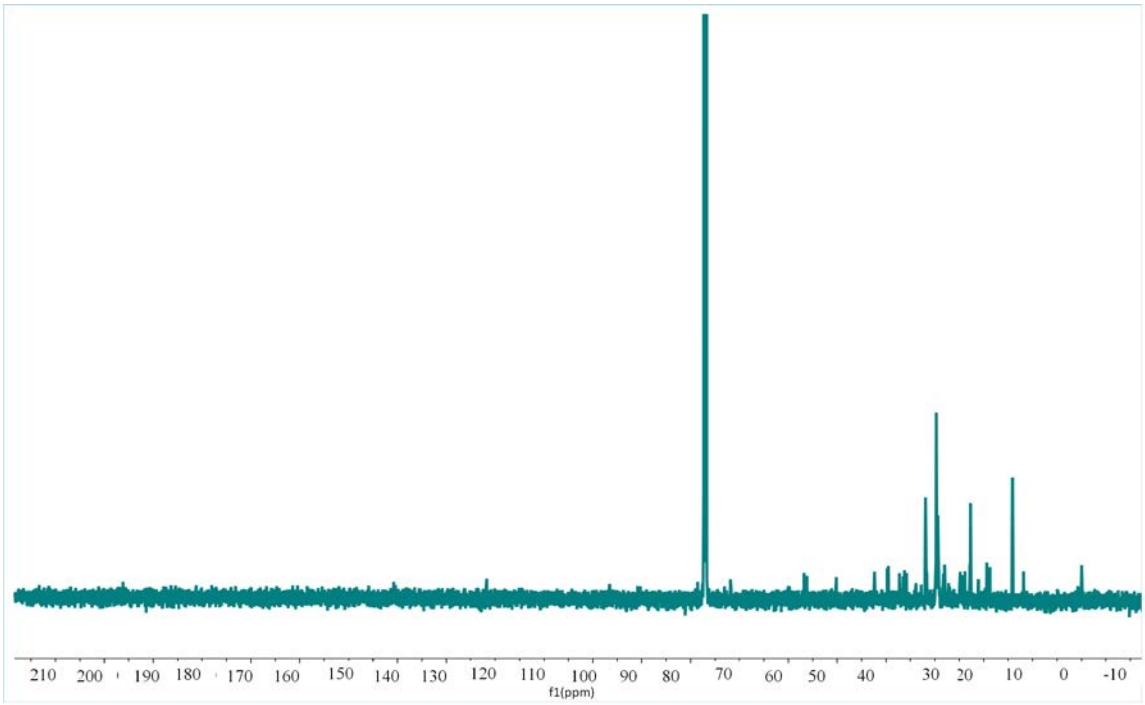

Figure 3.24.: ^{13}C NMR spectrum of EtOAc-MeOH extract of *H. edulis*

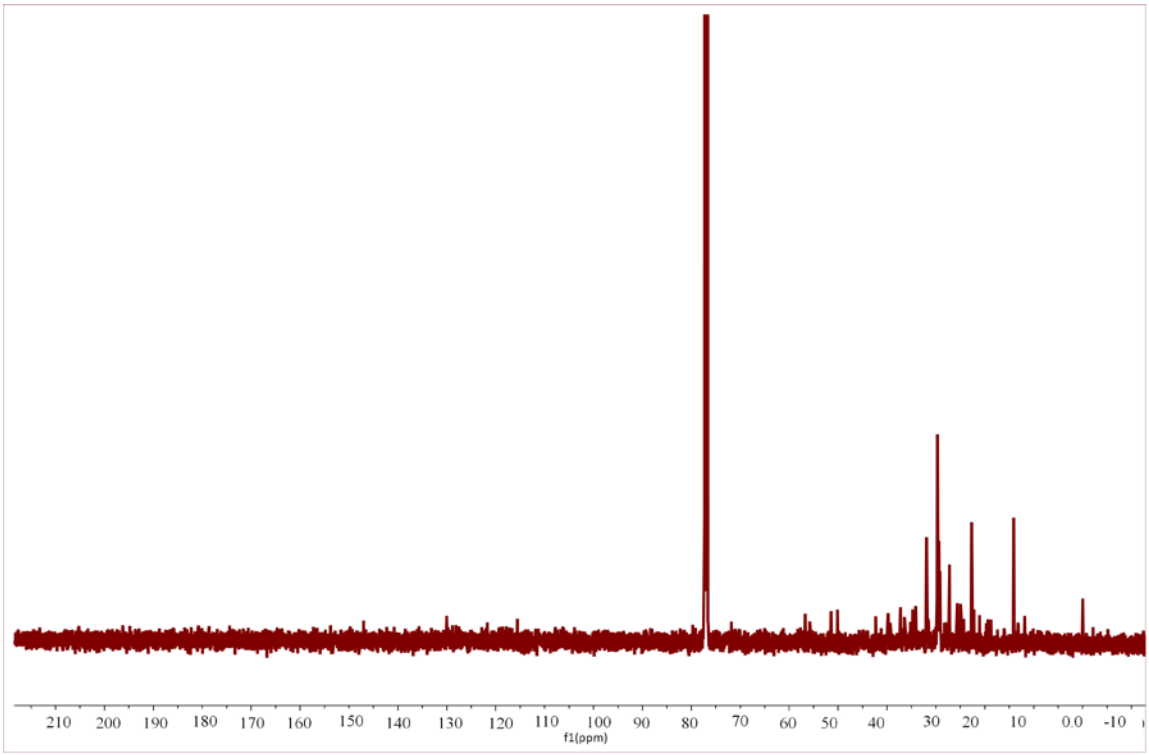

Figure 3.25.: ^{13}C NMR spectrum of EtOAc-MeOH extract of *A. fragilissima*

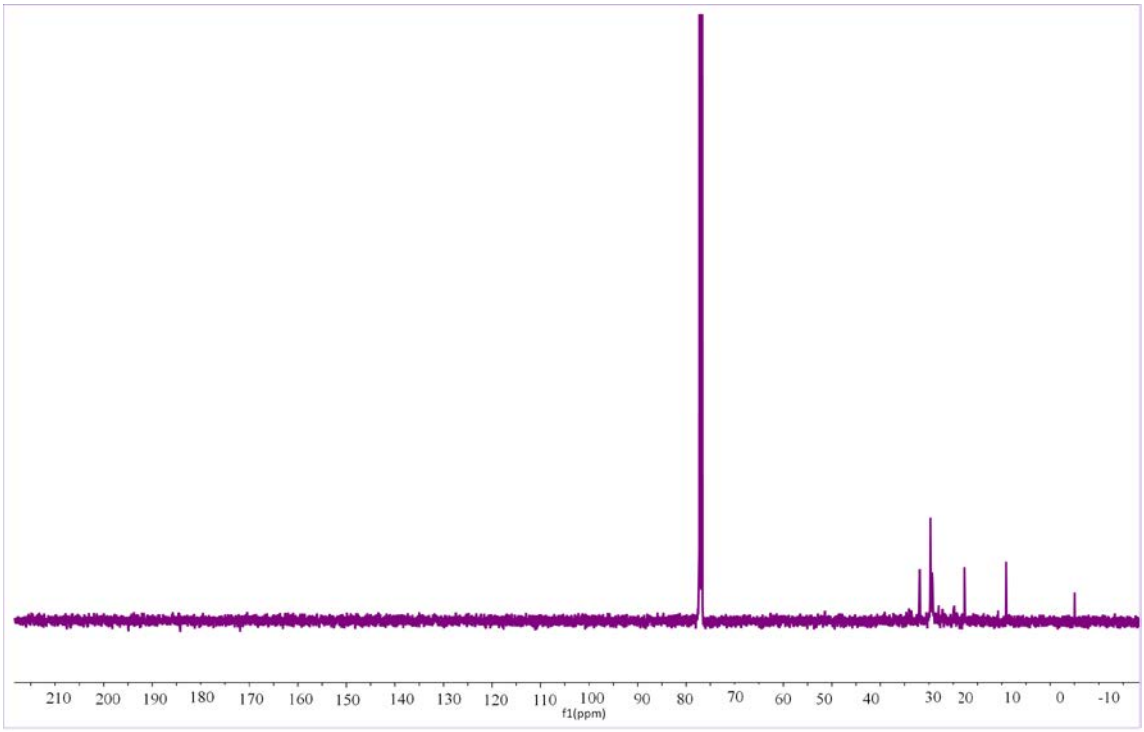

Figure 3.26.: ^{13}C NMR spectrum of EtOAc-MeOH extract of *P. pedrochei*

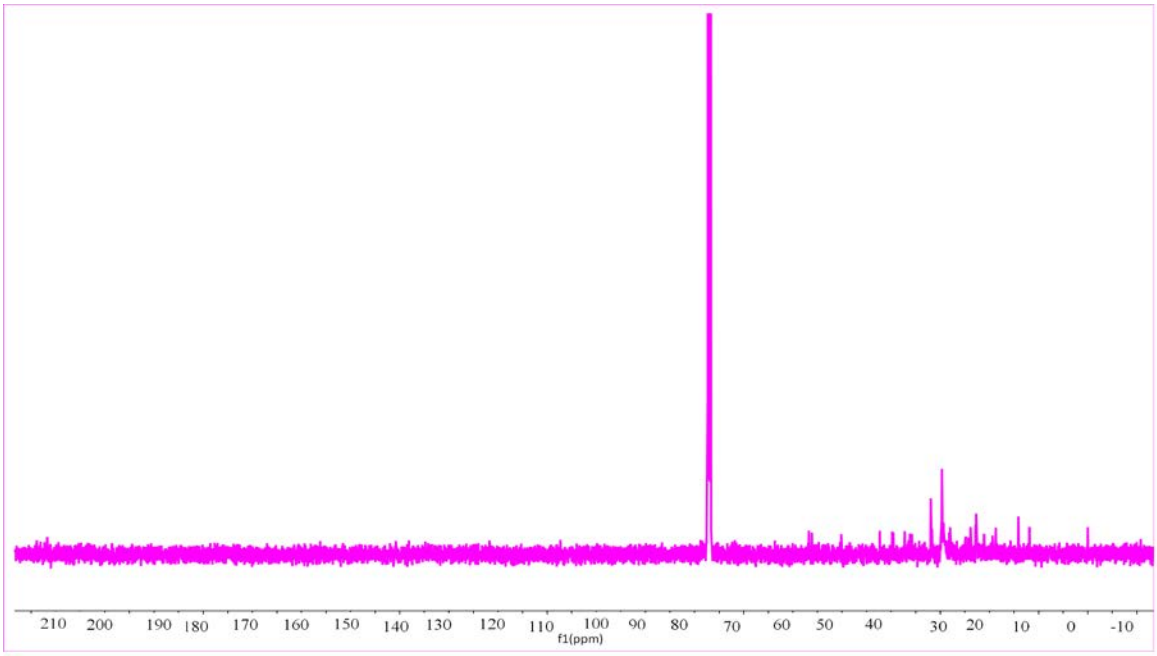

Figure 3.27.: ^{13}C NMR spectrum of EtOAc-MeOH extract of *S. filamentosa*

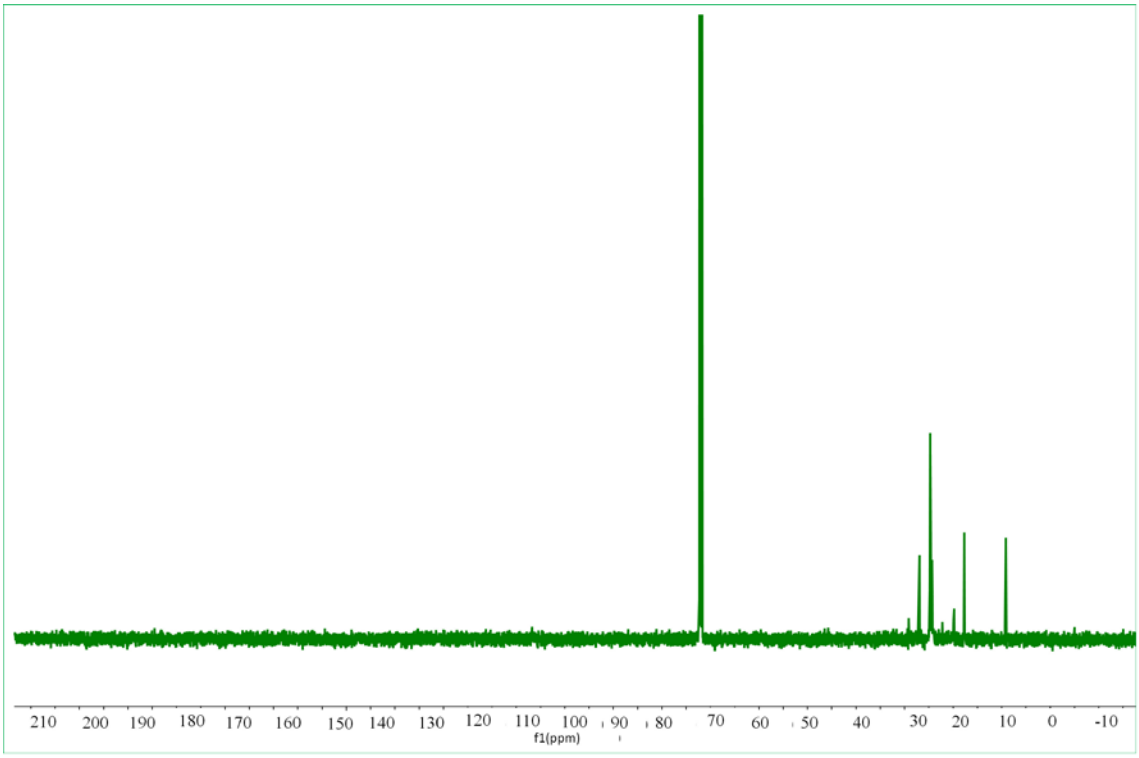

Figure 3.28.: ^{13}C NMR spectrum of EtOAc-MeOH extract of *H. dilatata*

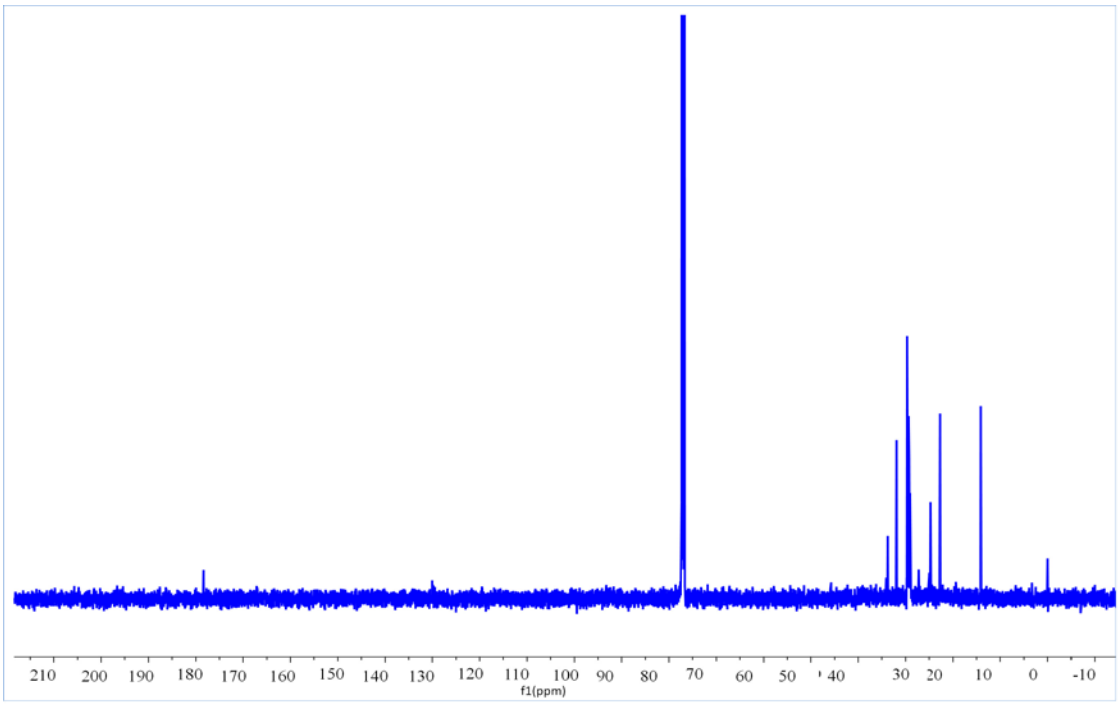

Figure 3.29.: ^{13}C NMR spectrum of EtOAc-MeOH extract of *P. hornemannii*

The proton integrals in the downfield section of the ^{1}H-NMR spectra at about δ_H 2-2.5 and 4.5-6.5 were feeble for *H. edulis* (ΣH 80.46 and 50.22, respectively) and *P. hornemannii* (ΣH 13.87 and 1.34, respectively), and comparatively lesser bioactivities of the organic extracts of these seaweeds described that these functional groups could be responsible for the studied pharmacological properties. Conversely, the organic extracts of *P. tetrastromatica* and *G. salicornia* showed greater proton integrals in the low-field region of the ^{1}H-NMR spectra, which might be attributed to the higher bioactivities of these seaweeds. A substantial co-linearity was observed to prevail among the electronegative groups in the downfield position of ^{1}H-NMR spectra *vis-a-vis* anti-diabetic and anti-inflammatory activities of the organic extracts of the seaweeds *P. tetrastromatica* and *G. salicornia*.

The NMR fingerprinting analyses were appropriately corroborated with those of infra-red (IR) spectral data. Characteristic IR traces at 1732 and 1724 cm^{-1} could be attributed to the C=O stretching frequencies of aldehydes or saturated aliphatic groups (Figure 3.30-3.39). Strong band appeared at 1540 cm^{-1} in the organic extract of *G. salicornia* might represent the occurrence of carbonyl functionalities, whereas the band at 1373 cm^{-1} have shown coupled C-O and O-H stretching frequencies.

The ^{1}H-NMR approach of de-replication could quickly lead to a conclusion of the types and number of protons that might be associated with the bioactive components present in the extracts. The presence of electronegative functionalities in the organic extracts of *G. salicornia, G. canaliculata* and *P. tetrastromatica* might be attributed to potential pharmacological activities as also corroborated by the *in vitro* bioactivity assays. Integrative spectroscopic analyses of the organic extracts of the seaweed species assessed the pattern of the resonances to differentiate the constitution of signals and intensities of moieties of the likely structural classes involved. In general, the organic extracts of *P. tetrastromatica* and *G. salicornia* displayed significantly greater proton integrals than other studied seaweeds in the downfield region of the spectra. It is apparent that the electronegative groups harbored by the organic extracts of these species, and those present in the downfield space of the ^{1}H-NMR and ^{13}C-NMR spectra, might structure strong electrostatic linkage with the Zn^{2+} ion present in the ACE-I enzyme active site that might explain the potential ACE-I activity (Ledesma et al., 2003). Positive correlation between the ACE-I inhibitory and Fe^{2+}chelation activities of the organic extracts of *P. tetrastromatica* and *G. salicornia* might also explain the functional role of Fe^{2+} ion chelating components to induce the anti-hypertensive properties.

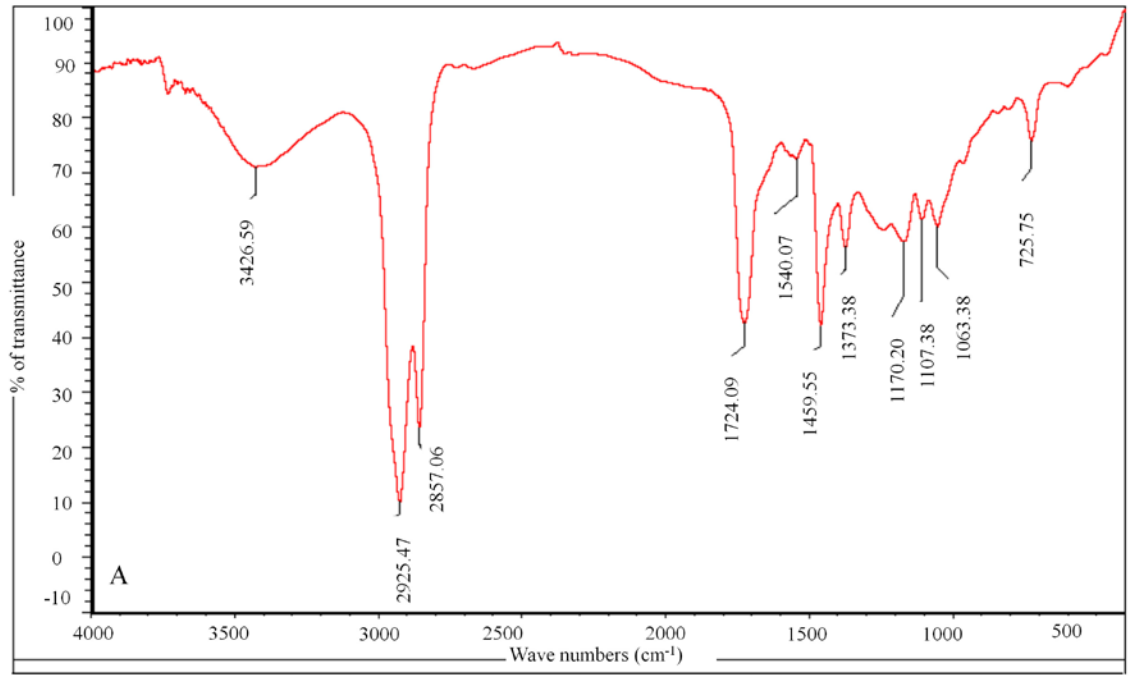

Figure 3.30.: FTIR spectrum of EtOAc-MeOH extract of *G. salicornia*

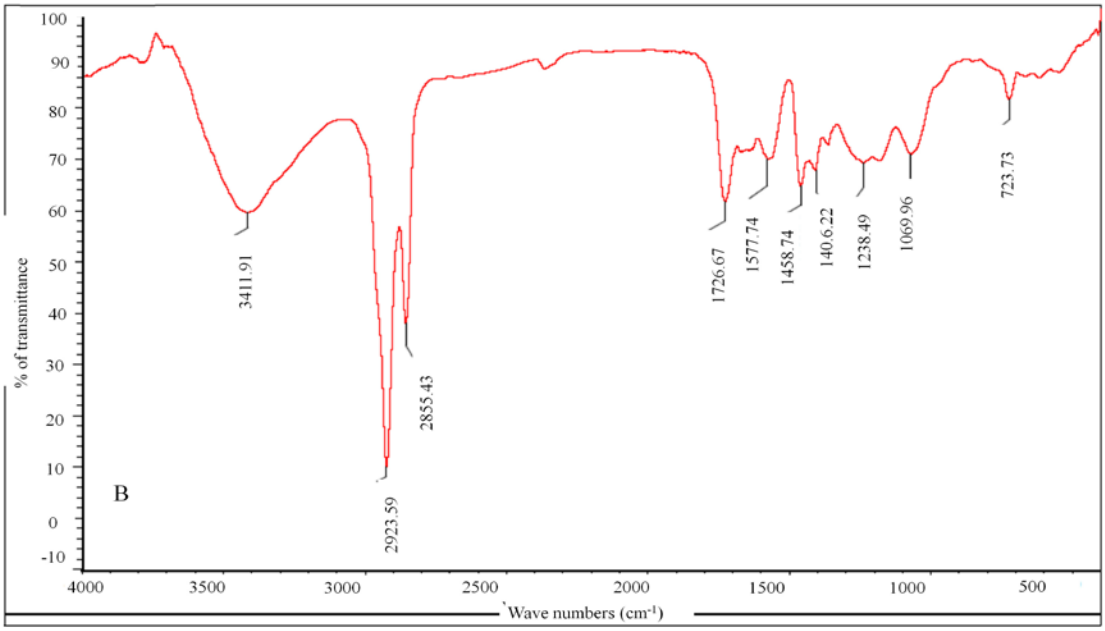

Figure 3.31.: FTIR spectrum of EtOAc-MeOH extract of *P. tetrastromatica*

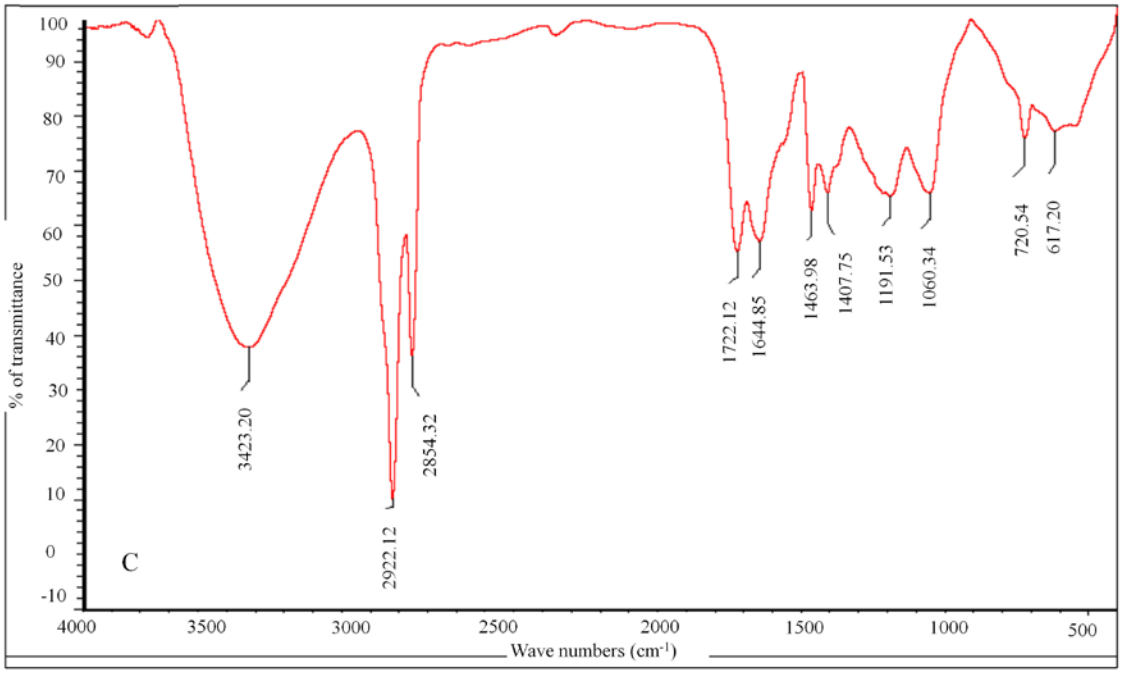

Figure 3.32.: FTIR spectrum of EtOAc-MeOH extract of *G. canaliculata*

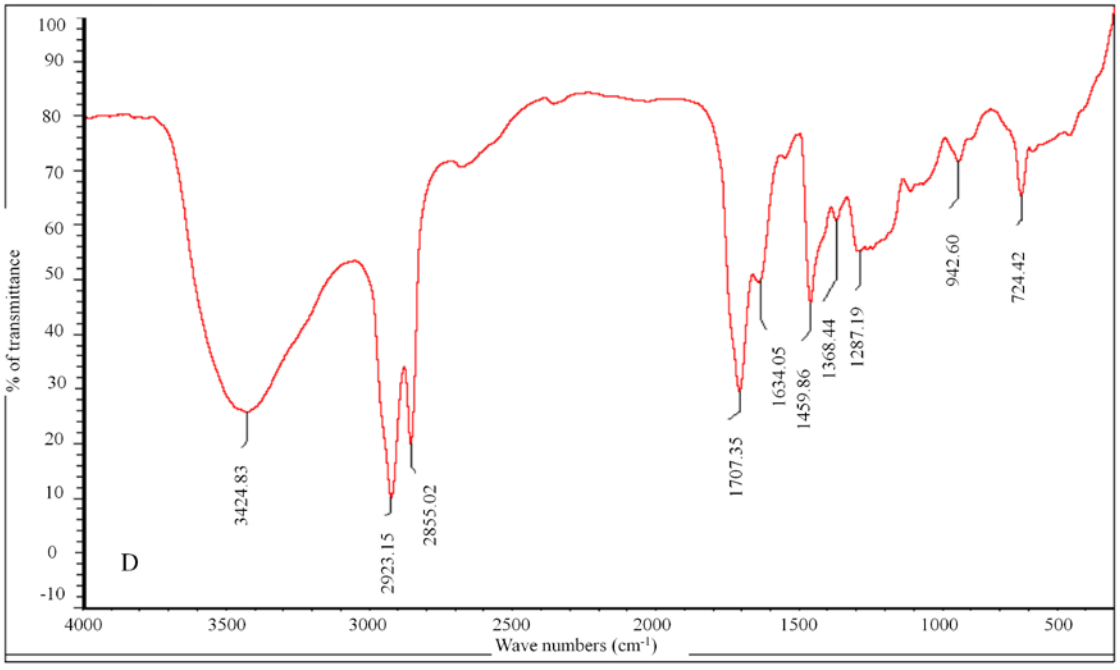

Figure 3.33.: FTIR spectrum of EtOAc-MeOH extract of *G. corticata*

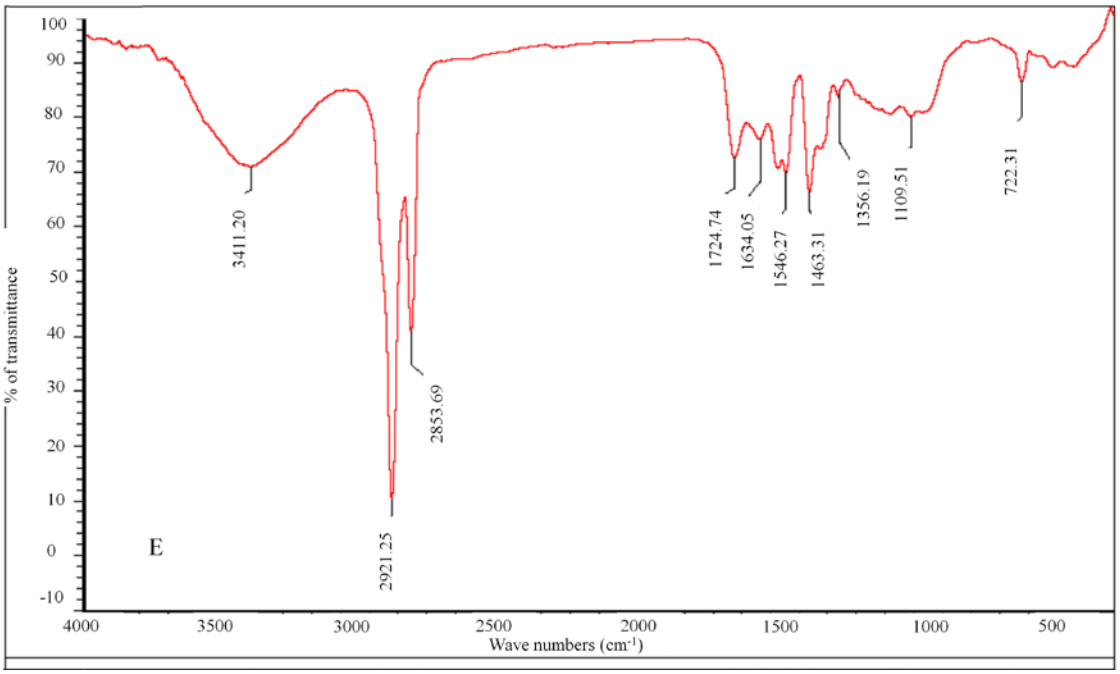

Figure 3.34.: FTIR spectrum of EtOAc-MeOH extract of *H. edulis*

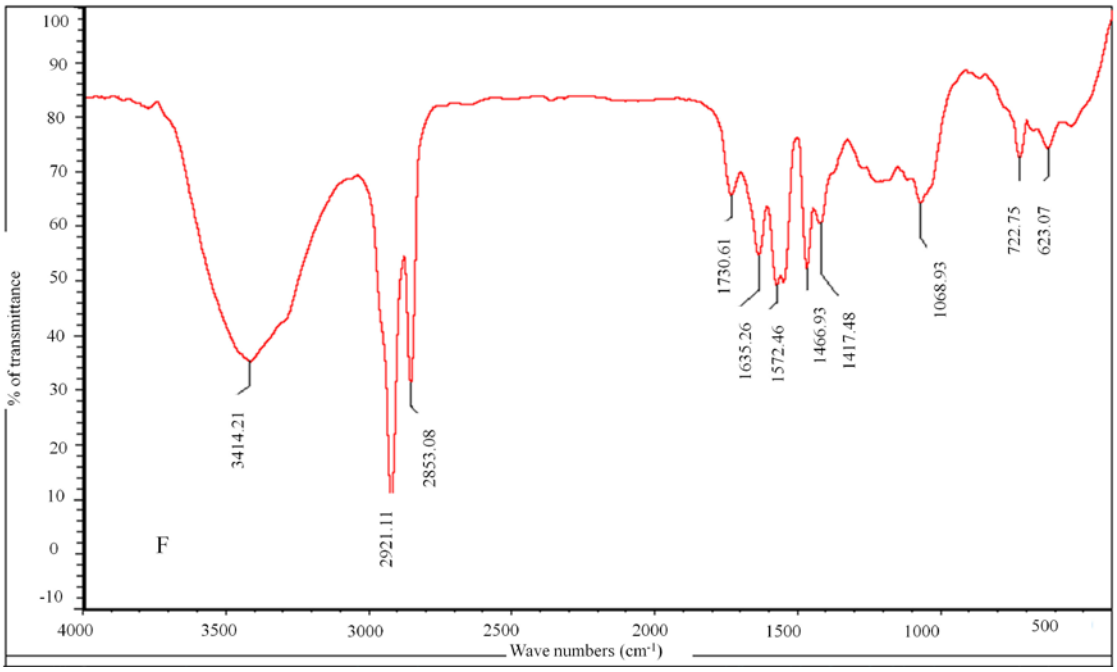

Figure 3.35.: FTIR spectrum of EtOAc-MeOH extract of *A. fragilissima*

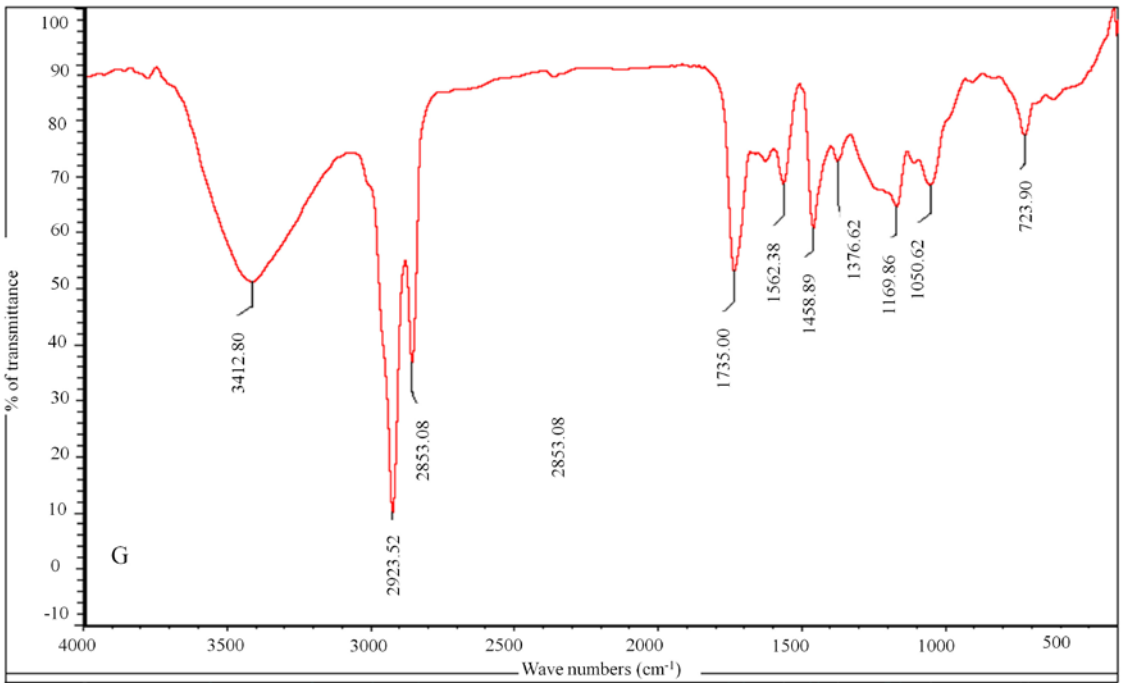

Figure 3.36.: FTIR spectrum of EtOAc-MeOH extract of *P. pedrochei*

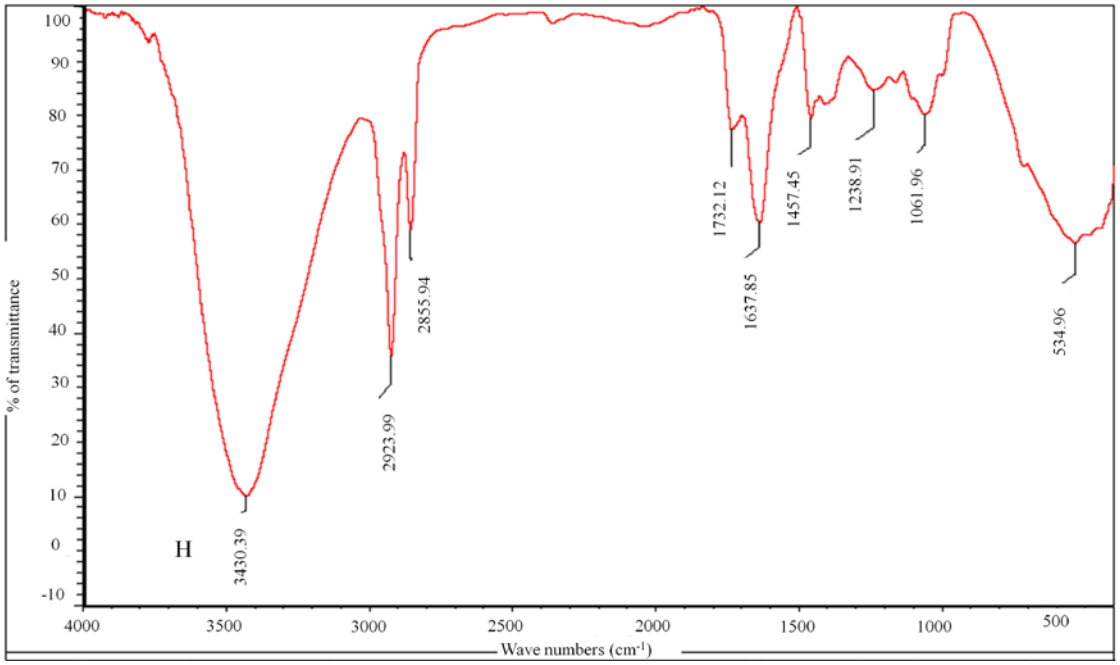

Figure 3.37.: FTIR spectrum of EtOAc-MeOH extract of *S. filamentosa*

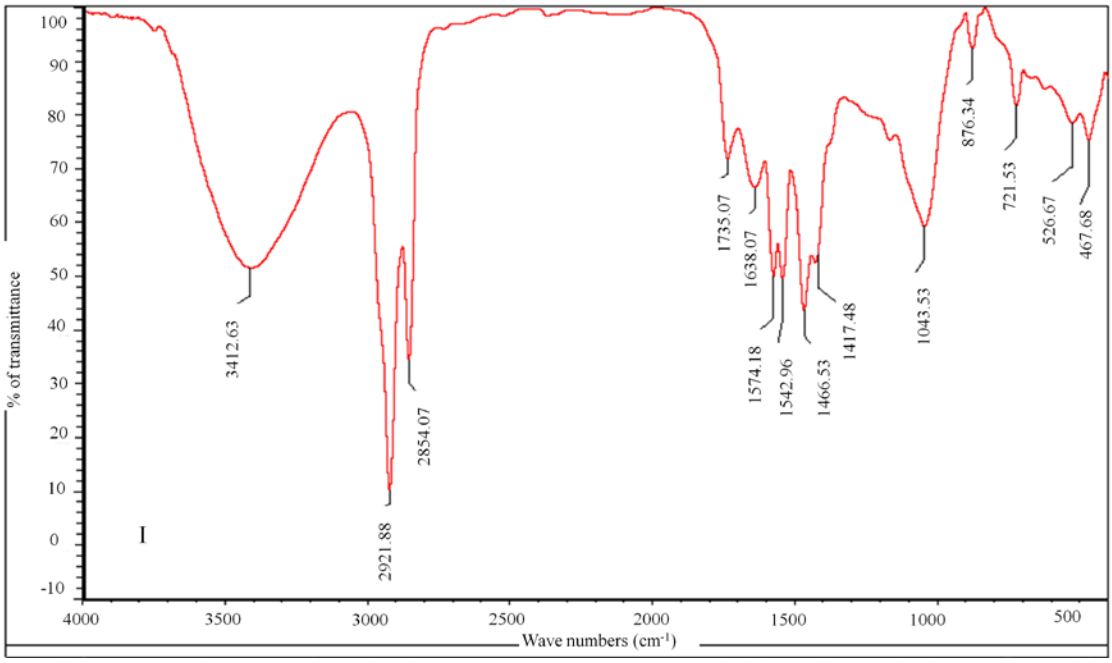

Figure 3.38.: FTIR spectrum of EtOAc-MeOH extract of *H. dilatata*

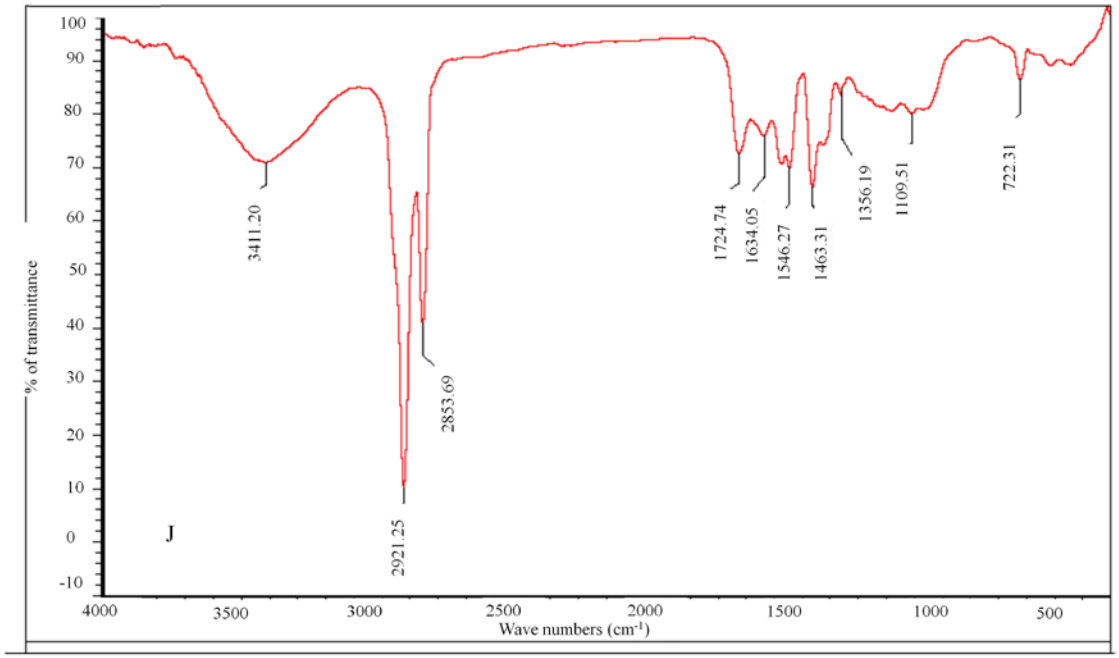

Figure 3.39.: FTIR spectrum of EtOAc-MeOH extract of *P. hornemannii*

3.4 Conclusions

A total of ten different seaweeds belonging to the subclasses Dictyotophycidae, Rhodymeniophycidae and Corallinophycidae collected from the Gulf of Mannar of Peninsular India were screened for *in vitro* antioxidant, anti-diabetic, anti-inflammatory and anti-hypertensive activities. Among various seaweeds considered in the present study, those belonging to the subclasses Dictyotophycidae and Rhodymeniophycidae displayed considerably greater pharmacological potentials. In particular, the organic extracts of *G. salicornia* and *P. tetrastromatica* registered significantly greater pharmacological properties than those derived from other studied seaweeds. This study also disclosed that the spectral fingerprinting could quickly deduce the signal pattern of the resonances, and conclusions could be drawn as to the likely structural classes involved in the organic extracts of the studied seaweeds. The present study recognized that the seaweeds *G. salicornia* and *P. tetrastromatica* might be promising candidates to isolate high value compounds for pharmacological use and their application as functional foods.

CHAPTER 4

ISOLATION AND CHARACTERIZATION OF BIOACTIVE LEADS FROM RED SEAWEED (RHODOPHYCEAE) *GRACILARIA SALICORNIA*

Contents

4.1 Background
4.2 Materials and methods
4.3 Results and discussion
4.4 Conclusions

4.1 Background

Seaweeds are prospective marine bioresources to isolate secondary metabolites with varied structural patterns and bio-activities, particularly, and have been considered as promising sources of new antioxidants (Ito and Hori, 1989). Antioxidants are found to be played significant role in the inhibition or scavenging of free radicals, and thus they can protect the organs from degenerative disorders and infections (Garcia et al., 2012). Generally, the formation of reactive oxygen species (ROS) surpasses the anti-oxidative defensive mechanism of the cells, and thereby, they can attack the structure and functions of biological molecules, such as lipids, carbohydrates, and proteins. These metabolic dysfunctions lead to the biological and physiological abnormalities in the cells, leading to the pathogenesis of type-2 diabetes, inflammation, cancer, cardiovascular disorders, and aging (Garcia et al., 2012). Antioxidants are able to donate electrons to the reactive radical species and convert them to harmless functionalities, and therefore, are endowed with potential applications in pharmaceutical and functional food. Notably, the bioavailability of natural antioxidants was found to be substantially greater related to the synthetic antioxidant molecules (Chioma, 2016; Athukorala et al., 2006). The chemical constituents present in seaweeds, such as terpenoids, amino acid derivatives, halogenated compounds, oxygenated cyclic/non-cyclic compounds and alkanes could potentially make them more attractive source of structurally and biologically novel potential metabolites than other marine living forms (Mtolera et al., 2010). Among various seaweeds, red seaweeds

were comprised large number of terpenoids, polyphenols, polysaccharides, proteins and peptides with bioactive potentials. The whole seaweeds of Rhodophyta have been used as traditional food, while polysaccharides and high value bioactive compounds were extracted for various properties including functional food, pharmaceutical and biotechnological applications.

Previous records on bioactive metabolites from seaweeds revealed the presence of various classes of secondary metabolites, namely macrocyclic compounds, diterpenoids, polyethers, triterpenoids, heterocyclic compounds, spiro compounds and polyketides, with bioactive potencies (Blunt et al., 2015). The α-pyrone macrolides, neurymenolides A and B were isolated from seaweed, *Neurymenia fraxinifolia* (Stout et al., 2009) and 2,6-disubstituted pyran-4-one along with 6-substituted pyran-2-one macrolides were documented from *Phacelocarpus labillardieri* (Kazlauskas et al., 1982). The macrolide, methyl-2-(12-oxo-7-phenyl-8-vinyl-1-oxa-4,9-cyclododecadien-3-yl)-acetate was reported from seaweed, *Sargassum wightii* (Maneesh and Chakraborty, 2017) with potent antioxidant and anti-inflammatory pluralities. An antibacterial macrolide, 7-*O*-methyl-5′-hydroxy-3’-heptenoate-macrolactin was reported from seaweed-associated bacteria, *Bacillus subtilis* (Chakraborty et al., 2014). Structurally diverse skeletons of drimane sesquiterpenes, such as sesquiterpene hydroquinones have been isolated from red seaweed *Peyssonnelia sp*. (Lane et al., 2010). The cytotoxic squalene-derived polyethers were identified from the red seaweed belonging to the genera of *Chondria* and *Laurencia* (family Rhodomelaceae) (Pacheco et al., 2011; Pacheco et al., 2010). Polyether compound, thyrsiferol was isolated from *Laurencia thyrsifera*, and further examples of polyether metabolites were reported from green seaweed *Botryococcus brauniis* (Faulkner, 2002; Blunt et al., 2011). Dehydrothyrsiferol was found to be another example of this polyether series, identified from *Laurencia pinnatifida* in the Canary Islands of Spain. Fatty acyl polyether okadaic acid with protein phosphatase inhibitory property was characterised from *Prorocentrum sp*. (Cohen et al., 1990). The non-halogenated rearranged spiro-compound, 1,4,9-trimethyl-5-methylidenespiro[5.5]undec-1,7-diene-4,9-diol and halogenated spiro-fused compounds, such as 2-bromo-1,1,9-trimethyl-5-methylidenespiro[5.5]undec-7-ene-3,9-diol and 2-bromo-9-bromomethylidene-1,1-dimethyl-5-methylene spiro [5.5]undec-7-ene were previously reported from a red seaweed, *Laurencia scoparia* with bio-potentials (Davyt et al. 2001). The halogenated and nonhalogenated spiro-compounds, which were classified as compositacins, were reported from the red seaweed, *Laurencia composita* (Yu et al., 2017). Chromenols have been derived from the seaweed *Desmarestia menziesii* (Davyt et al., 1997). Chromenyl metabolites, such as benzopyrans or benzopyrones were reported from the seaweeds *Sargassum micracanthum* and *Sargassum siliquastrum* (Iwashima et al., 2005; Jang et al., 2005). Labdane bicyclic diterpenoids were reported from seaweeds with broad range of biological activities

(Singh 1999; Demetzos & Dimas 2001; Hanson 2000; Hanson 2001; Hanson 2002; Blunt et al., 2006). Oleanane triterpenoids with anti-diabetic properties were characterised from *Sambucus adnata* (Sasaki et al., 2011) and *Astilbe koreana* (Na et al., 2006). The inhibitory potencies of fridooleanene triterpenoids against α-amylase and α-glucosidase were previously reported from the seaweed *Sargassum wightii* (Maneesh and Chakraborty, 2017). Although these classes of secondary metabolites deserve special consideration because of their targeted therapeutic potentials, very few studies were reported with the anti-diabetic activities of naturally-derived triterpenoids (Nazaruk and Borzym-Kluczyk, 2015).

Among the red seaweeds, the genus *Gracilaria* was found as the most promising candidate due to their ability to provide high yields and biosynthesizing commercially significant bioactive compounds and extracts (De Almeida et al., 2011). The species *G. asiatica* documented the presence of terpene *cis* and *trans*-phytol (Sims et al., 1976). Various types of lactone compounds were derived from *G. confervoides* (Nagai et al., 1997; Nagai et al., 1996). The compounds, such as polycavernoside B-B2, and polycavernoside A2-A3 have been identified from *G. crassa* (Yotsu-yamashita et al., 1993; Yotsu-yamashita et al., 1995). The protein, R-phycoerythrin were reported from two species, namely *G. salicornia* (D'agnolo et al., 1994) and *G. longa* (Talarico et al., 1978). The steroids and prostaglandins were isolated from red seaweeds *G. coronopifolia* and *G. crassa*, respectively (De Almeida et al., 2011). Commercially important agar, carrageenan and esterified polysaccharides were reported from seaweeds, *G. confervoides*, *G. dura*, *G. chilensi*, and *G. secundata* (De Almeida et al., 2011).

The significant and attractive phyla in terms of their pharmacologically active MNPs comprise the abundantly available seaweed species, among which the red seaweeds are potential sources of bioactive substances (Makkar and Chakraborty, 2019; Makkar and Chakraborty, 2018). Pluralities of investigations on bio-active components from seaweed demonstrating antiviral, antibacterial, antitumor and antileukaemic properties were reported worldwide. The rich diversity of red seaweeds particularly belonging to *Gracilaria sp.* along the coastline of South Indian subcontinent represents an unexploited source of bio-compounds with valuable biomedical as well as pharmaceutical use, although these species was not comprehensively studied to identify/characterize the bio-active leads (Makkar and Chakraborty, 2018). The seaweed of genus *Gracilaria sp*. are abundantly available in the coastal peninsular India with more than 300 reported species, and were recognized in industrial seaweed biotechnology due to the commercial product phycocolloid widely used in food, pharmaceutical and cosmetic industries (Makkar and Chakraborty, 2017; Andriamanatoanina et al., 2007; Francavilla et al., 2013). It has been documented that the organic extracts of *Gracilaria* sp. (family Gracilariaceae) comprised bioactive secondary metabolites along with anti-inflammatory, antioxidant,

antidiabetic and antimicrobial potentials (Bansemir et al. 2006, Makkar & Chakraborty 2018b, Makkar and Chakraborty 2018c). Among different species of the genus *Gracilaria*, *Gracilaria salicornia* (C. Agardh) E.Y. Dawson was found to be ubiquitous in the coastal waters of Indian peninsular, although the species was not extensively studied to characterize the bioactive leads. Since initial studies carried out in our laboratory provided us with promising leads, the current study is envisaged the isolation followed by characterization of bioactive secondary metabolites from the ethyl acetate/methanol (1:1 v/v) extract of *Gracilaria salicornia* by repeated chromatographic separation methods. The bioactive secondary metabolites characterized were grouped under different classes of chemistries, namely abeo-labdane class of diterpenoid (**1**), oleanene class of triterpenoids (**2**-**3**), drimane-associated quinols (**4**-**6**), 2*H*-chromenyl compounds (**7**-**8**), spiro-fused analogues (**9**-**10**), squalene polyether metabolites (**11**-**12**), and macrolides enclosing ether functionalities (**13**-**15**). These compounds were characterized through comprehensive spectroscopic techniques. Pharmacological properties were analyzed by various *in-vitro* antioxidant/anti-inflammatory/antidiabetic methods. The physico-chemical factors of the studied analogues were used to substantiate the chemistries of structures with their respective biological properties. Various physicochemical parameters were used to validate the structure-activity relationships of the titled compounds, and *in-silico* mode of attenuating potential against various enzymes was conducted by molecular docking analysis to corroborate the anti-inflammatory/antidiabetic potentials of the studied metabolites (**1**-**15)**.

4.2 Materials and methods

4.2.1 Chemicals and reagents

The chemicals used in this study include regents, solvents and solutions, which were acquired from Sigma-Aldrich Chemicals Co. Inc. (St. Louis, MO) and E-Merck (Darmstadt, Germany). Different buffers and solutions for screening studies were freshly made as and when required. All essential enzymes for biological assays were obtained from Sigma-Aldrich Chemicals Co. Inc. (St. Louis, MO). All analytical and spectroscopic graded reagents/solvents were purchased from E-Merck (Darmstadt, Germany) and Sigma-Aldrich Chemical Company, Inc. (Missouri, USA).

4.2.2 Chromatographic purification techniques and spectroscopic instrumentation analysis

4.2.2.1 Purification by column chromatography

Initially, the adsorbent dry silica gel of various mesh size, namely 60-120, 100-200, and 230-400 mesh (E-Merck, Germany) were packed with non-polar mobile phase (*n*-hexane) in vertically placed glass columns of different length and diameter (100 cm x 8 cm; 50 cm x 4 cm; 20 cm x 1.5 cm, Borosil, India), as found appropriate. The organic extracts of seaweed samples was made into slurry with silica (60-120 mesh size, 5 g) and loaded into the glass column. The components in the extracts were eluted by using different solvents with increasing order of polarity (*n*-hexane; dichloromethane; ethyl acetate and methanol). The sequential fractions were separately collected for further analysis.

4.2.2.2 Purification by flash chromatography

The organic extracts/fractions obtained from seaweed samples were separated by flash (Biotage AB SP1-B1A, Sweden) chromatographic technique using a silica column of 230-400 mesh size (Biotage Ref. No. 12 + M. Si). The organic extracts/fractions were loaded into the column in the form of slurry with silica gel. The sequential elution of components with desired wave length in the organic extracts/fractions was carried out using the non-polar mobile phase. The separation of fractions was monitored by the chromatograph, and they were collected separately.

4.2.2.3 Purification by high pressure liquid chromatography

The preparatory high pressure liquid chromatograph (PHPLC) system (Shimadzu Corporation, Nakagyo-ku, Japan) connected with a bonded reverse phase C_{18} (RP C_{18}) column (Shimadzu; Luna 250 mm X 14.0 mm, 5 μm) fitted with binary gradient pump (Shimadzu LC-20AP), column oven (CTO-20AC, Shimadzu), photodiode array detector (SPD-M20A, Kyoto, Japan) and a controller (CBM-20A, Shimadzu) were used for fine purification of the compounds. The injection volume was 2 mL and the column temperature retained at 40 °C. The various percentages of MeOH and acetonitrile were utilized as mobile phases with 6-8 mL/min flow rate. The absorbance was recorded between the range of 200-800 nm wavelengths and the mobile phase was comprised of various proportions of MeOH and acetonitrile with 1 mL/min flow rate.

The samples were filtered through the solid phase extraction cartridges (SPE; 55 mm, 70 Å, Strata C_{18}-E; Phenomenex, California, USA) and PTFE syringe filter (0.20 μm, Sartorius, Germany) prior to the injection to the analytical HPLC (AHPLC) and preparatory HPLC (PHPLC) systems, as and when deemed appropriate.

4.2.2.4 Purity assessment by thin layer chromatography and analytical HPLC

The purity of fractions was monitored by thin layer chromatography (TLC) and analytical high pressure liquid chromatography (AHPLC). The pure isolated fractions were spotted on the thin layer aluminium sheets (silica GF_{254}; E-Merck, Germany) by using capillary tubes after dissolved in small volume of desired solvents to analyse the presence of various components in the isolated fractions based on their R_f, retention factors (ratio of distance moved by component spot and solvent front). The various solvents with increasing polarity were used as the mobile phase (*n*-hexane; dichloromethane; ethyl acetate and methanol). The spots of the individual components were visualised in the 254 and 366 nm wavelengths by the UV lamp (Cole-Parmer, India).

An analytical HPLC system (Shimadzu Corporation, Nakagyo-ku, Japan) bonded with the reverse phase C_{18} (RP-C_{18}) column (Phenomenex, Torrance, California, USA; Luna 250 mm X 4.6 mm, 5 μm) fitted to binary gradient pump (Shimadzu LC-20AD), column oven (CTO-20A, Shimadzu), photodiode array detector (SPD-M20A, Kyoto, Japan) and a controller (CBM-20A, Shimadzu) were used to analyze the purity of isolated compounds. The injection-volume was 20 μL, and the column temperature was maintained at 40 °C. The fractions were eluted with mobile phases, such as methanol and acetonitrile in different proportions with a flow rate 1 mL/min in between the wavelengths 200-800 nm.

The samples were filtered through the solid phase extraction cartridges (SPE; 55 mm, 70 Å, Strata C_{18}-E; Phenomenex, California, USA) and PTFE syringe filter (0.20 μm, Sartorius, Germany) prior to the injection to the AHPLC/PHPLC system(s).

4.2.2.5 Spectrophotometric and spectroscopic analysis

The UV-spectrophotometric analyses were carried out using a Varian-Cary 50 UV/VIS spectrophotometer (Varian Cary 50, Palo Alto, CA) as well as micro-plate reader (Thermo Scientific™ Multiskan™ GO, USA). The quartz cuvettes (dimension 1:1:4.5 cm) and 96-well plates (Thermo Fisher Scientific; China) were used for measuring the absorbances of the samples. The infrared spectrum of the studied compounds was reported among 4000-400 cm^{-1} using KBR pellets through Perkin-Elmer Series 2000 FT-IR (Fourier-transform-infrared) spectrometer (Waltham, MA). The samples were mixed with KBr pellets, and the pressure was applied on them to make it transparent. The readings were recorded as % transmittance. Optical rotation was analysed in methanol by using a Perkin-Elmer 341 polarimeter.

The nuclear magnetic resonance (NMR) analyses {^{1}H-proton-500 MHz; ^{13}C-carbon-125 MHz; DEPT; ^{1}H-^{1}H COSY-; HSQC; HMBC; NOESY} were carried out through Bruker Avance DPX 500 MHz spectrometer (Rheinstetten, Germany) using deuterated chloroform

($CDCl_3$). The NMR data were attained by BrukerTopSpin™ 2 software and MestReNova-7.1.1-9649 (Mestrelab Research S.L.) was used for data processing. The mass spectrometric analyses were documented through Perkin-Elmer Clarus 680 gas chromatograph-mass spectrometer (GC-MS) functioning with the electron-impact (EI) method (Waltham, MA). A Bruker Daltonic micro-TOF series high-resolution-mass-spectrometer (HRMS) (GmbH; Germany) operating in positive mode electrospray ionisation {ESI-MS, $[M+H]^+$} has been used for high-resolution-mass-spectroscopy. The organic solvents extracts were concentrated using rotary vacuum evaporating instrument (IKA Werke GmbH & Co., Germany). All analytical and spectroscopic graded reagents/solvents were purchased from E-Merck (Darmstadt, Germany) and Sigma-Aldrich Chemical Company, Inc. (Missouri, USA).

4.2.3 Preparation of crude solvent extracts from red seaweed G. salicornia

The leaves (thalli) of red seaweed *G. salicornia* (voucher specimen number AC.3.1.1.4) was harvested during the low spring tides in the inter-monsoon wet period of March, 2017 from Mandapam (Gulf of Mannar region; between 8º48’ N, 78°9’ E and 9°14’ N, 79°14’ E) on the southeast coastline of the Indian sub-continent. The samples were identified by a marine algologist Dr. Chellaiah Periyasamy of Aquaculture Foundation of India, Madurai, and were deposited in the project repository under the accession number of GS. 1.4.2.1. The samples were subjected to repetitive washing with tap water and dehydrated at room temperature for 4 days. Dried leaves of seaweed were powdered (~1000 g) before being extracted with the solvent ethyl acetate (EtOAc) and methanol (MeOH) (1:1, v/v, 750 mL) at 50 °C for 3 h under reflux. The extracts were filtered over Whatman No. 1 filter paper using sodium sulfate (~ 115 g) and evaporated using a rotary vacuum evaporator (IKA Werke GmbH & Co., Germany) below 55 °C to obtain the crude extract (35 g) of *G. salicornia*. The extract was utilized for various chromatographic fractionations to yield the bioactive metabolites.

Figure 4.1.: The red seaweed *G. salicornia* of collected from the southeast coastline of the Indian sub-continent Gulf of Mannar region; between 8º48' N, 78°9' E and 9°14' N, 79°14' E)

4.2.4 Chromatographic purification of pure compounds and bioactive potentials of sub-column fractions from G. salicornia

The EtOAc-MeOH fraction (33.0 g) of *G. salicornia* was subjected for vacuum liquid chromatography (over silica gel, 60-120 mesh) and eluted primarily with 100% *n*-hexane to remove pigmentous and waxy type materials. The polarity of the mobile phase was gradually increased from, *n*-hexane (*n*-hex) to ethyl acetate (EtOAc) and then to methanol (MeOH) {*n*-hex: EtOAc (8:2 to 1: 9; v/v) and EtOAc: MeOH (9:1 to 3:7; v/v)} to obtain a total of 20 column fractions, such as GS_1-GS_{20}, respectively (Figure 4.2). The crude extract was mixed with silica (5 g, 60-120 mesh) to make a slurry before being packed into the glass column of dimension, 100 cm x 8 cm, which was enclosed with adsorbent silica gel (60-120 mesh). The bioactivities of the fractions were checked, and based on the results seven fractions (GS_2, GS_4, GS_7, GS_8, GS_{12}, GS_{13} and GS_{15}) were selected for further purifications. The column fractions were subjected for the analysis of antioxidant, anti-inflammatory and antidiabetic activities. The fraction GS_2 obtained by eluting with 30 % EtOAc was fractionated using *n*-hexane/EtOAc/MeOH on 230-400 mesh sized silica to afford 3 fractions ($GS_{2\text{-}1}$ – $GS_{2\text{-}3}$). The fraction $GS_{2\text{-}1}$ (30 % EtOAc:*n*-hexane) was found to be pure, which was further purified to homogeneity by preparative HPLC on octadecylsilane (C_{18}) bonded column using the solvent system of MeOH (methanol) / (water) H_2O (3:2, v/v) to yield the compound **TG_1** (0.86 mg), which was found to be homogeneous on

TLC plate (*n*-hexane:EA, 9:1 v/v) and reverse phase HPLC (MeOH/H_2O, 2:1 v/v), with 100% purity. The fraction GS_4 obtained by eluting with 50 % EtOAc:*n*-hexane was sub-fractionated on a preparatory RP-C_{18} HPLC system {using solvent system of (methanol) MeOH/ acetonitrile (MeCN, 2:1 v/v)} to yield the compounds, **TG_2** (0.83 mg) and **TG_3** (0.88 mg), which were homogeneous after TLC (EtOAc:*n*-hexane, 1:19 v/v) and RP-C_{18} HPLC (MeCN/MeOH, 1:2 v/v). The fraction GS_7 obtained with 5 % MeOH elution was subjected to the silica gel chromatography using *n*-hexane/EtOAc/MeOH solent system to afford six pooled fractions (GS_{7-1} - GS_{7-6}) on the basis of TLC (*n*-hexane:EtOAc, 8:2 v/v) as well as RP-C_{18} HPLC (3:2 MeOH/MeCN v/v) analyses. The fraction GS_{7-2-2} on repeated chromatographic/PHPLC purification techniques (by using the solvent gradient of MeOH/MeCN, 2:1 v/v) on a RP-C_{18} bonded-phase adsorbent yielded the compound **TG_4** (112 mg). The fraction GS_{7-2-3} on repeated HPLC purification techniques yielded compound **TG_5** (115 mg) and **TG_6** (108 mg), which were homogeneous after TLC (EtOAc/*n*-hexane, 1:19 v/v) and RP-C_{18} HPLC (MeCN/MeOH, 1:2 v/v). The fraction GS_8 on repeated chromatographic/HPLC purifications over octadecylsilane (C_{18}) bonded column with MeOH/MeCN (3:2, v/v) yielded compound **TG_7** (102 mg) and **TG_8** (98 mg), respectively, which were found to be homogeneous after TLC (*n*-hexane:EtOAc, 8:2 v/v) and RP-HPLC (MeOH/CH_3CN, 3:2 v/v).

The fraction GS_{12} obtained by eluting with 15 % MeOH, was subjected to further purification using *n*-hexane/EtOAc/MeOH on flash Biotage 230-400 mesh sized silica (25+M) to afford a total of 5-fractions (GS_{3-1} - GS_{3-5}). The fraction GS_{3-4} was further fractionated by flash chromatographic purification with *n*-hexane/EtOAc/MeOH as eluting solvent system to yield five sub-fractions, such as, GS_{3-4-1} - GS_{3-4-5}. The potentially active column sub-fraction $GS_{3-4-3,}$ was then fractionated with MeOH/MeCN solvent system (3:7, v/v) by reverse phase preparative HPLC over octadecylsilane (C_{18}) bonded column yielding **TG_9** (96 mg) and **TG_{10}** (103 mg), which were homogeneous after TLC (*n*-hexane:EtOAc, 8:2 v/v) and RP-HPLC (MeOH/MeCN, 3:7 v/v). The fraction GS_{13} obtained by eluting with 20 % MeOH on further purification using *n*-hexane/EtOAc/MeOH on flash Biotage 230-400 mesh sized silica (25+M) afforded a total of 4 fractions (GS_{13-1} - GS_{13-4}). The fraction GS_{13-4} was further fractionated by flash chromatographic purification with *n*-hexane/EtOAc/MeOH as eluting solvent system to yield five sub-fractions, named as GS_{13-4-1} - GS_{13-4-5}. The fraction, GS_{13-4-3} was found to contain two major compounds, which were purified by PHPLC (MeOH/MeCN, 1:1 v/v) fractionations on reverse phase C_{18} stationary phase to obtain two pure compounds **TG_{11}** (94 mg) and **TG_{12}** (128 mg), whereas their purities were checked through TLC (EtOAc/*n*-hexane, 1:9 v/v)/ RP-C_{18} HPLC (MeCN/MeOH, 1:1 v/v). Another active fraction GS_{15} was chromatographically fractionated by *n*-hexane/EtOAc/MeOH to yield three sub-fractions designated as, GS_{15-6-1} - GS_{15-6-3}. The

fractions, $GS_{15\text{-}6\text{-}1}$ and $GS_{15\text{-}6\text{-}2}$ were purified by repetitive RP-C_{18} bonded-phase column of HPLC by using binary gradient elution of MeOH and MeCN (3:2 v/v) to afford compounds **TG_{13}** (123 mg), **TG_{14}** (120 mg) and **TG_{15}** (107 mg), respectively, and were homogenous in TLC/RP-HPLC. The purities of the studied compounds were checked through TLC (EtOAc/n-hexane, 1:19 v/v) experiment and RP-C_{18} HPLC using binary gradient elution of MeCN/MeOH (1:2 v/v).

The repetitive bioassay guided fractionation of EtOAc-MeOH extract of *G. salicornia* along with the yield and bioactive potentials of the intermediate fractions were represented in Tables 4.1-4.7.

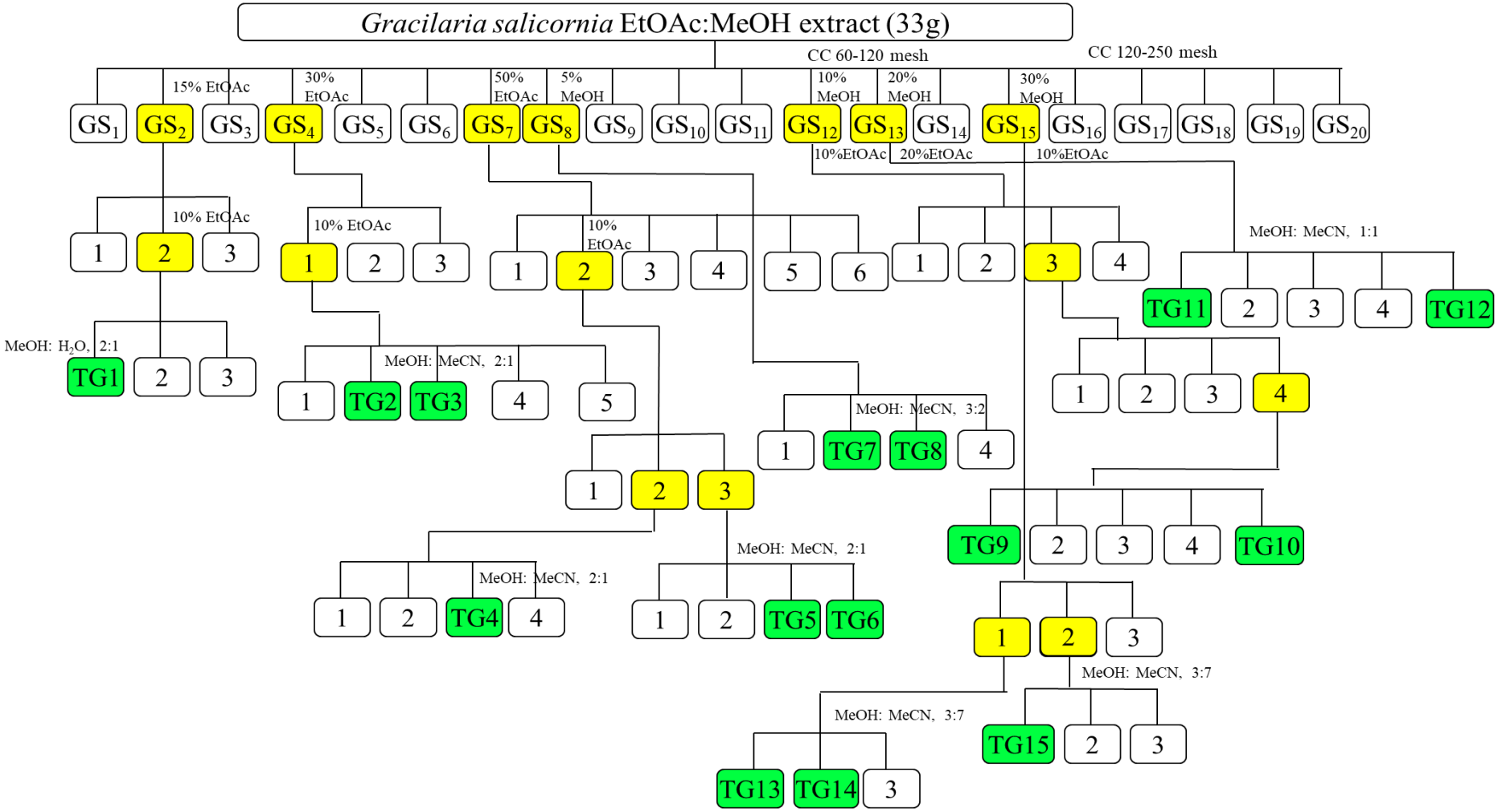

Figure 4.2.: Schematic representation of purification of fractions and compounds from the EtOAc-MeOH extract of *G. salicornia*. CC- column chromatograph

4.2.5 Physicochemical description of bioactive-leads isolated from EtOAc-MeOH extract of G. salicornia

4.2.5.1 Physicochemical description of compound-1 (TG_1)

Methyl-16(13→14)-abeo-7-labdene-(12-oxo)carboxylate; Yellowish-white amorphous powder; UV (MeOH) λ_{max}, log ε: 242 (2.35) nm; R_f: 0.81 (*n*-hexane:EtOAc, 9:1 v/v); R_t (HPLC, MeOH/H_2O, 2:1 v/v): 3.4 min; FTIR (KBr, cm^{-1}) υ_{max}: 840.76, 892.05 (=C-H_δ), 1172.96 (C-O_υ), 1377.46 (C-H_ρ), 1463.15 (CH_δ), 1644.13 (C-C_υ), 1725.25 (C-O_υ), 1736.25 (C=O_υ) 2854.11, 2925.88 (C-H_υ); ^{1}H NMR (500 MHz, MeOH; δ in ppm): δ_H 1.54 (1H, t, J=5.5 Hz), 1.30 (1H, t, J=4.2 Hz), 1.54 (1H, m), 1.42 (1H, m), 2.19 (1H, t, J=5.0 Hz), 1.88 (1H, t, J=4.2 Hz), 1.98 (1H, t, J=3.54 Hz), 1.79 (1H, t, J=5.1 Hz), 1.98 (1H,t, J=5.7.1 Hz), 5.55 (1H, t, J=6.6 Hz), 2.21 (1H, t, J=5.5 Hz), 2.37 (1H, dd, J=10.9, 6.5 Hz), 2.28 (1H, dd, J=12.7, 5.4 Hz), 2.30 (2H, d, J=6.5 Hz), 1.99 (1H,m), 0.79 (3H, d, J=6.0 Hz), 0.87 (3H, d, J=6.1 Hz), 1.14 (3H, s), 1.38 (3H, s), 0.63 (3H, s), 3.46 (3H,s); ^{13}C NMR (125 MHz, MeOH; δ in ppm): δ_C ^{13}C NMR (125 MHz, MeOH δ in ppm): δ_C 38.6 (CH_2), 20.8 (CH_2), 38.2 (CH_2), 42.9 (C), 44.6 (CH), 23.5 (CH_2), 124.8 (CH), 135.9 (C), 45.1 (CH), 39.2 (C), 41.3 (CH_2), 203.2 (C), 54.8 (CH_2), 24.1 (CH), 16.2 (CH_3), 17.9 (CH_3), 19.6 (CH_3), 17.9 (CH_2) 167.6 (C), 10.9 (CH_3), 69.7 (CH_3); ^{1}H-^{1}H COSY, and HMBC data were presented in Table 4.8; EI-MS *m/z*: calcd. for $C_{21}H_{34}O_3$ 334.2508; HRESIMS *m/z* found 335.2589 $[M+H]^+$, calcd for $C_{21}H_{35}O_3$ 335.2586 (Δ 0.08 ppm).

4.2.5.2 Physicochemical description of compound-2 (TG_2)

24(4→23), 27(8→26), 30(20→29)-tris-abeo-olean-(12-oxo)-1,15,22-triene-methyl hept-5-enoate; Pale yellow oily; UV_{MeOH} λ_{max} (log ε): 244 (2.91) nm; TLC {silica-GF(254); EtOAc/*n*-hexane, 1:19 v/v} R_f: 0.38; R_t (RP-C_{18} HPLC, MeOH/MeCN 2:1, v/v): 3.41 min; FTIR thin film (KBr) ν_{max} (bending *δ*, stretching *v*, rocking *ρ*): 2930 (C-H_v), 1730 {(-C(=O)-O-)$_v$}, 1726 (C=O_v), 1458 (C=C_v), 1406 (C-H_δ), 1238 (C-H_ρ), 1069 (C-C_v), 723 (C-H_δ) cm^{-1}; ^{1}H NMR (500 MHz, MeOH; δ in ppm): δ_H 5.32 (1H, d, J = 10.3 Hz), 5.28 (1H, dt, J = 8.9, 7.6 Hz), 1.77 (1H, t, J = 4.9 Hz), 2.01(1H, t, J = 4.9 Hz), 1.62 (1H, m), 1.30 (1H, m), 1.51 (1H, m), 1.28 (1H, m), 1.55 (1H, m), 1.26 (1H, m), 1.33 (1H, td, J = 6.8, 5.2 Hz), 1.66 (1H, td, J = 5.8, 5.5 Hz), 2.22 (1H, d, J = 8.6 Hz), 2.27 (1H, d, J = 8.0 Hz), 2.75 (1H, d, J = 6.7 Hz), 5.34 (1H, d, J = 12.1 Hz), 5.30 (1H, d, J = 13.0 Hz), 2.77 (1H, m), 1.65 (1H, m), 1.56 (1H, m), 1.93 (1H, m), 5.29 (1H, t, J = 14.0 Hz), 5.33 (1H, d, J = 12.7 Hz), 1.53 (2H, m), 0.80 (3H, t, J = 4.2 Hz), 1.32 (3H, s), 1.25 (2H, d, J = 3.7 Hz), 0.78 (3H, t, J = 4.9 Hz), 3.60 (2H, s), 1.52 (2H, m), 0.82 (3H, t, J = 5.0 Hz), 1.63 (2H, t, J = 4.7 Hz), 1.58 (2H, m), 2.20 (2H, m), 5.26 (1H, dt, J = 11.7 Hz), 5.25 (1H, m),

2.05 (3H, d, J = 9.2 Hz); ^{13}C NMR (125 MHz, MeOH; δ in ppm): δ_C 130.2 (CH), 127.8 (CH), 31.8 (CH_2), 33.9 (CH), 52.3 (CH), 29.0 (CH_2), 28.9 (CH_2), 29.7 (CH), 47.9 (CH), 46.8 (C), 39.3 (CH_2), 193.7 (C), 56.7 (CH), 34.4 (C), 130.5 (CH), 127.7 (CH), 43.5 (C), 31.9 (CH), 31.7 (CH_2), 37.2 (CH), 132.0 (CH), 127.5 (CH), 24.7 (CH_2), 12.2 (CH_3), 19.7 (CH_3), 29.8 (CH_2), 11.8 (CH_3), 65.7 (CH), 29.1 (CH_2), 13.1 (CH_3), 179.4 (C), 25.6 (CH_2), 26.9 (CH_2), 33.2 (CH_2), 129.7 (CH), 128.0 (CH), 14.2(CH_3) [135]DEPT, COSY, HSQC, and HMBC data data were presented in Table 4.9; EI-MS *m/z*: calcd. for $C_{37}H_{54}O_3$ 546.4073. HRESIMS *m/z* found 547.4155 $[M+H]^+$, calcd for $C_{37}H_{55}O_3$ 547.4151 (Δ 0.07 ppm)

4.2.5.3 Physicochemical description of compound-3 (TG$_3$)

24(4→23)-Abeo-olean-(12-oxo)-3,5-diene-deconoate; Yellowish oily; UV_{MeOH} λ_{max} (log ε): 247.24 (2.92) nm; TLC {silica-GF(254); EtOAc /*n*-hexane, 1:19 v/v} R_f: 0.40; R_t (RP-C_{18} HPLC, MeOH:MeCN 2:1, v/v): 2.91 min; FTIR thin film (KBr) ν_{max}: 2924 (C-H_v), 1734 {(-C(=O)-O-)$_v$}, 1634 (C-O_v), 1546 (C=C_v), 1463, 1356 (C-H_δ), 1109 (C-C_v), 722 (C-H_δ); ^{1}H NMR (500 MHz, MeOH; δ in ppm): δ_H 1.42 (1H, dt, J = 13.9, 5.9 Hz) , 1.15 (1H, dt, J = 11.8, 7.8 Hz), 2.03 (1H, dt, J = 11.2, 6.2 Hz), 1.72, 5.82(1H, t, J = 11.7 Hz), 2.00 (1H, d, J = 8.2 Hz), 1.75 (1H, d, J = 5.0 Hz), 1.70 (1H, t, J = 7.2 Hz), 2.33 (1H, dd, J = 10.8, 3.2 Hz), 2.07 (1H, dd, J = 9.9, 2.6 Hz), 2.30 (1H, d, J = 12.9 Hz), 1.59 (1H, dt, J = 10.9, 6.3 Hz), 1.35 (1H, dt, J = 11.9, 5.9 Hz), 1.60 (1H, dt, J = 10.9, 5.9 Hz), 1.38 (1H, dt, J = 11.2, 4.9 Hz), 1.62 (1H, m), 1.20 (1H, t, J = 4.9 Hz), 1.43 (1H, t, J = 4.0 Hz), 1.61 (1H, dt, J = 11.0, 4.8 Hz), 1.34 (1H, dt, J = 10.0, 4.0 Hz), 1.56 (1H, dt, J = 10.9, 4.7 Hz), 1.36 (1H, dt, J = 10.5, 4.0 Hz), 2.13 (2H, q, J = 5.7 Hz), 1.06 (3H, t, J = 6.9 Hz), 1.33 (3H, s), 1.04 (3H, s), 1.08 (3H, s), 1.10 (3H, s), 0.88 (3H, s), 0.96 (3H, s), 1.62 (2H, t, J = 10.9 Hz), 1.20 (2H, m), 1.43 (2H, m), 1.61 (2H, m), 1.34 (2H, m), 1.56 (2H, m), 1.36 (2H, m), 2.13(2H, m), 1.06 (2H, m), 1.33 (2H, m), 1.04 (2H, m), 1.08 (2H, m), 1.10 (2H, m), 0.88 (2H, m), 0.96 (2H, m), 2.34 (2H, m), 1.63 (2H, m), 1.29 (2H, m), 1.23 (2H, m), 1.28 (2H, m), 1.32 (2H, m), 1.30 (2H, m), 1.31 (2H, m), 0.84 (3H, t, J = 7.3 Hz); ^{13}C NMR (125 MHz, MeOH; δ in ppm): δ_C 30.5 (CH_2), 24.7 (CH_2), 132.2 (C), 128.8 (C), 139.2 (C), 130.9 (CH), 34.0 (CH_2), 42.7 (C), 43.4 (CH), 31.4 (C), 36.9 (CH_2), 213.1(C), 51.9 (CH), 38.8 (C), 29.4 (CH_2), 37.0 (CH_2), 33.4 (C), 41.4 (CH), 37.7 (CH_2), 28.0 (C), 33.9 (CH_2), 34.3 (CH_2), 19.1 (CH_2), 19.9 (CH_3), 20.8 (CH_3), 19.7 (CH_3), 19.4 (CH_3), 22.8 (CH_3), 30.2 (CH_3), 30.1 (CH_3), 176.1 (C), 26.7 (CH_2), 26.4 (CH_2), 29.2 (CH_2), 29.5 (CH_2), 29.6 (CH_2) , 29.3 (CH_2), 31.8 (CH_2), 22.6 (CH_2), 14.0 (CH_3); [135]DEPT, COSY, HSQC, and HMBC data were presented in Table 4.10; EI-MS *m/z*: calcd. for $C_{40}H_{64}O_3$ 592.2485. HRESIMS *m/z* found 593.4938 $[M+H]^+$, calcd for $C_{40}H_{65}O_3$ 593.4934 (Δ 0.06 ppm).

4.2.5.4 Physicochemical description of compound-4 (TG_4)

3-(Hept-3^6-enyloxy)-2,3,4,4a,5,6,6a,12,12a,12b-decahydro-4,6a,12a,12b-tetramethyl-*1H*-benzo[a] xanthene-4,10,12-triol; Pale yellow oil; $[\alpha]^{25}_D$ +58.9 (*c* 0.1, CH_3OH); UV_{MeOH} λ_{max} (log ε): 278 (3.44) nm; TLC (Si-GF_{254} 15 mm; EtOAc/*n*-hexane, 1:19 v/v) R_f: 0.38; R_t (HPLC-RP-C_{18}, MeCN/MeOH, 1:2 v/v): 3.241 min; FTIR thin film (ν_{max} in cm^{-1}; bending δ, stretching ν, rocking ρ): 3420 (O-H_ν), 3029 (C-$H_{\nu\ (aromatic)}$), 2855 (C-H_ν), 1625 (C=C_ν),1559 (C=$C_{\delta\ (aromatic)}$), 1460 (C-H_δ), 1373 ca(C-H_ρ), 1112, 1076 (-C-O-C_ν), 856 (C-$H_{\delta\ (aromatic)}$), 724 (C-H_δ); ^{1}H-NMR (500 MHz, MeOH; δ in ppm): δ_H 1.43 (1H, t, J = 12.0 Hz), 1.23 (1H, t, J = 12.1 Hz), 1.96 (1H, m), 1.56 (1H, m), 2.80 (1H, t, J = 9.8 Hz), 1.53 (1H, dd, J = 1.5, 12.1 Hz), 1.73 (1H, m), 1.45 (1H, m), 1.70 (1H, td, J = 12.5, 3.4 Hz), 1.37 (1H, td, J = 12.5, 3.0 Hz), 6.81 (1H, d, J = 13.4 Hz), 6.61 (1H, d, J = 13.8 Hz), 6.51 (1H, s), 4.68 (1H, s), 1.15 (3H, s), 1.42 (3H, s), 0.88 (3H, s), 0.83 (3H, s), 3.69 (2H, t, J = 8.6 Hz), 1.55 (2H, m), 1.21 (2H, m), 1.33 (2H, m), 2.04 (2H, m), 5.82 (1H, m), 5.01 (1H, dd, J = 3.4, 16.7 Hz), 4.94 (1H, dd, J = 3.4, 12.2 Hz); ^{13}C-NMR (125 MHz, MeOH; δ in ppm): δ_C 37.0 (CH_2), 24.7 (CH_2), 84.6 (CH), 73.9 (C), 68.7 (CH), 21.7 (CH_2), 33.4 (CH_2), 81.6 (C), 146.5 (C), 119.0 (CH), 119.1 (C), 140.9 (C), 115.2 (CH), 126.3 (C), 65.5 (CH), 61.0 (C), 42.8 (C), 22.6 (CH_3), 23.9 (CH_3), 14.1 (CH_3), 19.6 (CH_3), 71.1 (CH_2), 31.9 (CH_2), 26.7 (CH_2), 29.6 (CH_2), 33.8 (CH_2), 139.2 (CH), 114.0 (CH_2), DEPT, COSY, HSQC and HMBC were presented in Table 4.11; EI-MS *m/z* calcd. for $C_{28}H_{42}O_5$ 458.3032. HRESIMS *m/z* found 459.3114 $[M+H]^+$, calcd for $C_{28}H_{43}O_5$ 459.3110 (Δ 0.08 ppm)

4.2.5.5 Physicochemical description of compound-5 (TG_5)

13-[[2-(Hexyloxy)-2,5,5,8a-tetramethyldecahydro-1-naphthalenyl](methoxy-)-methyl]-benzenol; Yellowish oil; $[\alpha]^{25}_D$ +53.2 (*c* 0.1, CH_3OH); UV_{MeOH} λ_{max} (log ε): 281 (3.82) nm; TLC (Si-GF_{254} 15 mm; EtOAc/*n*-hexane, 1:19 v/v) R_f: 0.40; R_t (HPLC-RP-C_{18}, MeCN/MeOH, 1:2 v/v): 3.811 min; FTIR thin film (ν_{max}, cm^{-1}): 3402 (O-H_ν), 3028 (C-$H_{\nu\ (aromatic)}$), 2923, 2855 (C-H_ν), 1634 (C=C_ν), 1550 (C=$C_{\delta\ (aromatic)}$), 1540 (C=C_ν), 1459, 1372 (C-H_δ), 1239, 1070 (C-C_ν), 1120, 1070 (-C-O-C_ν), 850 (C-$H_{\delta\ (aromatic)}$), 723 (=C-H_δ); ^{1}H-NMR (500 MHz, MeOH; δ in ppm): δ_H 1.92 (1H, d, J = 8.0 Hz), 1.77 (1H, m), 1.56 (1H, m), 1.62 (1H, m), 1.42 (1H, m), 0.88 (1H, dd, J = 1.8, 12.2 Hz), 1.50 (1H, td, J = 13.5, 4.1 Hz), 1.17 (1H, td, J = 12.9, 4.2 Hz), 1.75 (1H, m), 1.07 (1H, m), 1.51 (1H, t, J = 12.0 Hz), 1.12 (1H, t, J = 12.0 Hz), 1.22 (3H, s), 1.03 (3H, s), 1.00 (3H, s), 1.02 (3H, s), 4.39 (1H, d, J = 8.2 Hz), 3.37 (3H, s), 6.28 (1H, s), 6.35 (1H, d, J = 12.1 Hz), 7.08 (1H, t, J = 13.2 Hz), 6.23 (1H, d, J = 13.1 Hz), 3.69 (2H, m), 1.53 (2H, m), 1.31 (2H, m), 1.34 (2H, m), 1.33 (2H, m), 0.94 (3H, t, J = 6.7 Hz); ^{13}C-NMR (125 MHz, MeOH; δ in ppm): δ_C 65.7 (CH), 72.4 (C), 39.3 (CH_2), 19.6 (CH_2), 55.0 (CH), 32.7 (C), 45.0 (CH_2), 19.3 (CH_2), 39.4 (CH_2), 37.2 (C), 22.5 (CH_3), 29.7 (CH_3), 29.3 (CH_3), 16.3

(CH_3), 82.7 (CH), 58.9 (CH_3), 154.3 (C), 113.0 (CH), 144.0 (C), 123.7 (CH), 128.4 (CH), 113.1 (CH), 65.0 (CH_2), 31.9 (CH_2), 25.6 (CH_2), 33.7 (CH_2), 22.7 (CH_2), 14.1 (CH_3); DEPT, COSY, HSQC, and HMBC were presented in Table 4.12; EI-MS *m/z* calcd. for $C_{28}H_{46}O_3$ 430.3447. HRESIMS *m/z* found 431.3528 $[M+H]^+$, calcd for $C_{28}H_{47}O_3$ 431.3525 (Δ 0.06 ppm)

4.2.5.6 Physicochemical description of compound-6 (TG_6)

1-Butoxy-4,4,11b,11c-tetramethyl-1,2,3,3a,4,5,6,6a,11b,11c-decahydrobenzo[kl]-xanthen-10-ol; Yellowish oil; $[\alpha]^{25}_D$ +55.6 (*c* 0.1, CH_3OH); UV_{MeOH} λ_{max} (log ε): 283 (4.97) nm; TLC (Si-GF_{254} 15 mm; EtOAc/*n*-hexane, 1:19 v/v) R_f: 0.43; R_t (HPLC-RP-C_{18}, MeCN/MeOH, 1:2 v/v): 4.204 min; FTIR thin film (ν_{max}, cm^{-1}): 3412 (O-H_ν), 3026 (C-$H_{\nu\,(aromatic)}$), 2921, 2854 (C-H_ν), 1638 (C=C_ν), 1560 (C=$C_{\delta\,(aromatic)}$), 1574, 1542 (C=C_ν), 1466, 1417 (C-H_δ), 1115, 1043 (-C-O-C_ν), 876, 854 (C-$H_{\delta\,(aromatic)}$), 721 (=C-H_δ); ^{1}H-NMR (500 MHz, MeOH; δ in ppm): δ_H 3.88 (1H, t, J = 9.2 Hz), 1.81 (1H, m), 1.60 (1H, m), 1.57 (1H, m), 1.31 (1H, m), 1.21 (1H, dd, J = 1.9, 12.1 Hz), 1.20 (1H, td, J = 13.2, 4.1 Hz), 1.51 (1H, td, J = 13.2, 4.3 Hz), 1.84 (1H, t, J = 12.7 Hz), 1.70 (1H, t, J = 12.9, 4.2 Hz), 3.20 (1H, t, J = 9.2 Hz), 6.26 (1H, d, J = 13.1 Hz), 6.20 (1H, d, J = 13.2 Hz), 6.31 (1H, s), 1.00 (3H, s), 0.98 (3H, s), 1.37 (3H, s), 1.15 (3H, s), 3.44 (2H, t, J = 9.8 Hz), 1.50 (2H, m), 1.43 (2H, m), 0.88 (3H, t, J = 6.8 Hz); ^{13}C-NMR (125 MHz, MeOH; δ in ppm): δ_C 78.1 (CH), 29.6 (CH_2), 22.7 (CH_2), 52.3 (CH), 37.2 (C), 42.2 (CH_2), 24.4 (CH_2), 81.0 (CH), 139.9 (C), 118.1 (CH), 121.7 (CH), 155.9 (C), 115.1 (CH), 128.7 (C), 45.4 (C), 39.3 (C), 28.8 (CH_3), 29.3 (CH_3), 22.6 (CH_3), 12.8 (CH_3), 74.6 (CH), 31.9 (CH_2), 18.7 (CH_2), 14.1 (CH_3); DEPT, COSY, HSQC, and HMBC were presented in Table 4.13; EI-MS *m/z* calcd. for $C_{24}H_{36}O_3$ 372.2664. HRESIMS *m/z* found 373.3746 $[M+H]^+$, calcd for $C_{24}H_{37}O_3$ 373.3742 (Δ 1.0 ppm)

4.2.5.7 Physicochemical description of compound-7 (TG_7)

4'-[10'-[7-Hydroxy-2,8-dimethyl-6-(pentyloxy)-*2H*-chromen-2-yl]ethyl]-3',4'-dimethyl-cyclohexanone; Yellowish-oil; UV $\lambda_{max\ MeOH}$ (log ε 2.91): 270 nm; $[\alpha]^{26}_D$ -20.4° ($CHCl_3$, c0.016); TLC (silica GF_{254}; *n*-hexane:EtOAc, 8:2 v/v) R_f: 0.65; R_t (HPLC, MeOH/CH_3CN, 3:2 v/v): 2.93 min; FTIR (KBr, cm^{-1}) υ_{max}: 840, 858 (C-$H_{(aromatic)}$), 892 (=C-H_δ), 1114, 1078 (-C-O-C-), 1377 (C-H_p),1457 (C-H_δ), 1562 (C=$C_{(aromatic)}$), 1637 (C=C), 1644 (C-C_υ), 1727 (C-O_υ), 1732 (C=O_υ), 2855, 2923 (C-H_υ), 3027 (C-$H_{(aromatic)}$), 3430 (O-H);^{1}H NMR (500 MHz, $CDCl_3$; δ in ppm): δ_H 6.07 (1H, d, J = 13.2 Hz), 6.33 (1H, d, J = 7.8 Hz), 6.21 (1H, s), 1.54 (3H, s), 2.35 (3H, s), 2.10 (1H, dd, J = 7.2, 5.8 Hz), 1.95 (1H, dd, J = 7.1, 5.9 Hz), 1.64 (1H, m), 1.82 (1H, dt, J = 7.3, 6.2 Hz), 1.68 (1H, dt, J = 7.1, 6.0 Hz), 2.49 (1H, dt, J = 6.8, 6.0 Hz), 2.43 (1H, dt, J = 7.1, 6.0 Hz), 1.14 (3H, d, J = 7.1 Hz), 1.20 (3H, s), 1.34 (1H, dt, J = 6.8, 5.9

Hz), 1.23 (1H, dt, J = 6.9, 5.7 Hz), 1.73 (2H, dd, J = 7.1, 6.3 Hz), 4.09 (2H, t, J = 9.8 Hz), 1.71(2H, m), 1.36 (2H, m), 1.39 (2H, m), 1.04 (3H, t, J = 5.4 Hz); ^{13}C NMR (125 MHz; $CDCl_3$; δ in ppm): δ_C 75.0 (C), 130.1 (CH), 128.4 (CH), 113.1 (C), 110.5 (CH), 142.8 (C), 148.6 (C), 114.8 (C), 148.6 (C), 24.8 (CH_3), 14.1 (CH_3), 213.9 (C), 39.4 (CH_2), 37.4 (CH), 32.9 (C), 36.8 (CH_2), 37.2 (CH_2), 22.6 (CH_3), 22.7 (CH_3), 32.8 (CH_2), 36.8 (CH_2), 65.5 (CH_2), 27.9 (CH_2), 29.7 (CH_2), 24.4 (CH_2), 19.7 (CH_3).^{1}H-^{1}H COSY, HSQC and HMBC data were presented in Table 4.14; EI-MS *m/z* calcd for $C_{26}H_{38}O_4$ 414.2770. HRESIMS *m/z* found 415.2852 $[M+H]^+$, calcd for $C_{26}H_{39}O_4$ 415.2848 (Δ 0.09 ppm).

4.2.5.8 Physicochemical description of compound-8 (TG$_8$) **3'-[10'-(8-Hydroxy-5-methoxy-2,6,7-trimethyl-*2H*-chromen-2-yl)ethyl]-3'-methyl-2'-methylene cyclohexyl butyrate**

Pale yellowish oil; UV $\lambda_{max\ MeOH}$ (log ε 2.43): 264 nm; $[\alpha]^{26}_D$ -21.6° ($CHCl_3$, c0.014); TLC (silica GF_{254}; *n*-hexane:EtOAc, 8:2 v/v) R_f: 0.35; R_t (HPLC, MeOH/CH_3CN, 3:2 v/v): 3.70 min; FTIR (KBr, cm^{-1}) υ_{max}: 857 (C-$H_{(aromatic)}$), 876, 893 (=C-H_δ), 1077, 1113 (O-C-O_υ), 1377 (C-H_p), 1466 (C-H_δ), 1574 (C=$C_{(aromatic)}$), 1638 (C=C_υ), 1728 (C-O_υ), 1735 (C=O_υ), 2854, 2921 (C-H_υ), 3027 (C-$H_{(aromatic)}$), 3412 (O-H); ^{1}H NMR (500 MHz; $CDCl_3$; δ in ppm); δ_H 6.20 (1H, d, J = 12.8 Hz), 6.79 (1H, d, J = 11.8 Hz), 3.73 (3H, s), 1.60 (3H, s), 2.39 (3H, s), 2.31(3H, s), 4.14 (1H, d, J = 7.2 Hz), 1.46 (2H, dt, J = 6.9, 4.3 Hz), 1.39 (2H, m), 1.94 (2H, dt, J = 5.2, 4.0 Hz), 5.19 (2H, s), 1.10 (3H, s), 1.33 (1H, dt, J = 9.3, 5.6 Hz), 1.28 (1H, dt, J = 9.8, 5.1 Hz), 1.74 (2H, dd, J = 7.8, 5.9 Hz), 2.17 (2H, d, J = 7.9 Hz), 1.72 (2H, m), 0.91 (3H, t, J = 6.9 Hz); ^{13}C NMR (125 MHz; $CDCl_3$; δ in ppm); δ_C 83.17 (C), 127.8 (CH), 120.9 (CH), 111.5 (C), 148.7 (C), 56.8 (CH_3), 114.1 (C), 123.3 (C), 143.5 (C), 142.8 (C), 24.2 (CH_3), 13.8 (CH_3), 12.5 (CH_3), 71.4 (CH), 154.3 (C), 42.2 (C), 42.0 (CH_2), 18.7 (CH_2), 31.8 (CH_2), 104.2 (CH_2), 22.5 (CH_3), 39.5 (CH_2), 35.8 (CH_2), 175.4 (C), 34.9 (CH_2), 18.7 (CH_2), 14.2 (CH_3); ^{1}H-^{1}H COSY, HSQC and HMBC data were presented in Table 4.15; EI-MS *m/z* calcd for $C_{27}H_{38}O_5$ 442.2719. HRESIMS *m/z* found 443.2800 $[M+H]^+$, calcd for $C_{27}H_{39}O_5$ 443.2797 (Δ 0.06 ppm)

4.2.5.9 Physicochemical description of compound-9 (TG$_9$)

3-(Hydroxymethyl)-7-(methoxymethyl)-3,11-dimethyl-9-oxospiro[5.5]undec-4-en-10-methylbutanoate; Colourless oily; $[\alpha]^{20}_D$ -52.0° (*c*0.04, $CHCl_3$); UV_{MeOH} λ_{max} (log ε): 247 (4.02) nm (Figure S21); TLC {silica-GF(254); EtOAc/*n*-hexane, 2:18 v/v} R_f: 0.45; R_t (HPLC-RP-C_{18}, MeOH:MeCN 1:2, v/v): 4.42 min; FTIR thin film (KBr) ν_{max} (bending *δ*, stretching *ν*, rocking *ρ*): 722 (=C-H_δ), 1068 (C-O_υ), 3114 (=C-H_ν), 1471, 1466 (C-H_υ), 1078 (-C-O-C), 2853, 2921 (C-H_δ), 1572, 1635 (C=C), 1716, 1736 (C=O_υ), 3414 (O-H); ^{1}H NMR (500

MHz; $CDCl_3$; δ in ppm); δ_H 1.70 (2H, t, 3.5 Hz), 1.77 (2H ,t, 3.8 Hz), 4.52 (1H, d, 7.6 Hz), 2.16 (1H, t, 4.2 Hz), 2.09 (2H, d, 9.6 Hz), 4.41(1H, d, 10.5 Hz), 2.82 (1H, d, 7.5 Hz), 0.88 (3H, d, 8.2 Hz), 3.69 (2H, d, 3.5 Hz), 1.33 (3H, d, 11.3 Hz), 3.37 (2H, s), 2.00 (2H, d, 8.1 Hz), 2.37 (1H, t, 3.5 Hz), 0.81 (3H, t, 3.5 Hz), 0.86 (3H, t, 3.5 Hz), 3.20 (3H, s);^{13}C NMR (125 MHz; $CDCl_3$; δ in ppm); δ_C 29.6 (CH_2), 31.9 (CH_2), 37.2 (C), 128.4 (CH), 133.0 (CH), 41.2 (C), 31.6 (CH), 36.6 (CH_2), 203.5 (C), 94.9 (CH), 32.6 (CH), 22.4 (CH_3), 50.0 (CH_2), 24.7 (CH_3), 72.4 (CH_2), 179.6 (C), 39.3 (CH_2), 33.7 (CH), 19.3 (CH_3), 19.6 (CH_3), 55.03 (CH_3). DEPT, COSY, HSQC, and HMBC data were presented in Table 4.16. EI-MS *m/z*: calcd. for $C_{21}H_{34}O_5$ 366.2406. HRESIMS (positive mode) *m/z*: found 367.4999 $[M+H]^+$, calcd. for $C_{21}H_{35}O_5$ 367.4996 $[M+H]^+$ (Δ 0.08 ppm).

4.2.5.10 Physicochemical description of compound-10 (TG_{10})

4-Ethoxy-11,11-dimethyl-7-methylene-8-(propionyloxy)spiro[5.5]undec-2-en-10^3,10^5-dihydroxytetrahydro-*2H*-pyran-10-carboxylate: Colourless oily; $[\alpha]^{20}_D$ -53.0° (*c*1.13, $CHCl_3$); UV_{MeOH} λ_{max} (log ε): 270 (3.32) nm; TLC {silica-GF(254); EtOAc/*n*-hexane, 1:19 v/v} R_f: 0.48; R_t (HPLC-RP-C_{18}, MeOH:MeCN 1:2, v/v): 3.35 min; FTIR thin film (KBr) ν_{max} (bending *δ*, stretching *ν*, rocking *ρ*): 722 (=C-H_δ), 3111 (=C-H_υ), 1109, 1156 (C-O_δ), 1356, 1463 (C-H_δ), 1463 (C-H_δ), 1546, 1634 (C=C_υ), 1724, 1746 (C=O_υ)$_{ester,}$ 2853, 2921 (C-H_υ), 3411 (O-H); ^{1}H NMR (500 MHz; $CDCl_3$; δ in ppm); δ_H 2.03 (1H, d, 4.8 Hz), 1.79 (1H, d, 4.8 Hz), 5.36 (1H, t, 7.1 Hz), 5.13 (1H, t ,8.3 Hz), 3.98 (1H, m), 1.62 (2H, d, 6.3 Hz), 4.00 (1H, t, 8.3 Hz), 1.93 (2H, m), 4.15 (1H, t, 5.3 Hz), 0.88 (3H, s), 0.87 (3H, s), 4.35 (1H, t, 12.6 Hz), 4.33(1H, t, 12.5 Hz), 4.18 (1H, t, 5.8Hz), 2.12 (2H, t, 6.8 Hz), 3.68 (1H, m), 2.10 (2H, t), 5.23 (1H, t, 5.5 Hz), 2.30 (2H ,m), 0.99 (3H, t, 4.1 Hz), 3.30 (2H, m), 0.89 (3H, t, 4.3 Hz); ^{13}C NMR (125 MHz; $CDCl_3$; δ in ppm); δ_C 31.92 (CH_2), 126.07 (CH), 132.97 (CH), 75.27 (CH), 39.61 (CH_2), 32.35 (C), 141.81 (C), 68.38 (CH), 33.65 (CH_2), 72.67 (CH), 36.90 (C), 16.49 (CH_3), 16.03 (CH_3), 119.45 (CH_2), 162.75 (C), 72.50 (CH), 39.66 (CH_2), 70.72 (CH), 37.66 (CH_2), 101.64 (CH), 172.15 (C), 27.99 (CH_2), 14.13 (CH_3), 65.64 (CH_2), 15.77 (CH_3). DEPT, COSY, HSQC, HMBC data were presented in Table 4.17; EI-MS *m/z*: calcd. for $C_{25}H_{38}O_8$ 466.2567. HRESIMS (positive mode) *m/z*: found 467.2648 $[M]^+$, calcd. for $C_{25}H_{39}O_8$ 467.2645 $[M+H]^+$ (Δ 0.06 ppm).

4.2.5.11 Physicochemical description of compound-11 (TG_{11})

15-(Octahydro-7-(4,5-dihydro-3-methoxy-2,6-dimethyl-*2H*-pyran-6-yl)-10-methylpyrano[3,2-b]pyran-14-yl)-18-(19-methyl-23-methyleneoxepan-19-yl)pent-15-en-18-ol; Colourless oil; $[\alpha]^{25}_D$ +9.8 (*c*0.18, CH_3OH); UV_{MeOH} λ_{max} (log ε): 240 (3.30) nm; TLC {Si-GF_{254} 15 mm; EtOAc/*n*-hexane, 1/9, v/v} R_f: 0.41; R_t (HPLC RP-C_{18}, MeOH:MeCN, 1:1, v/v):

3.28 min; FTIR thin film (KBr) ν_{max} (cm^{-1}) (bending δ, stretching υ, rocking ρ): 581 (=C-H_{δ}), 1044 (C-O-C_{υ}), 1372, 1455 (C-H_{υ}), 2854, 2925 (C-H_{δ}), 3390 (O-Hυ); ^{1}H NMR (500 MHz; $CDCl_3$; δ in ppm); δ_H 2.28 (3H,s), 1.97 (1H,t,4.2 Hz), 1.87 (1H ,t, 4.2 Hz), 1.76 (1H, t, 4.2 Hz), 1.96 (1H, t, 4.2 Hz), 3.61 (1H, t, 4.3 Hz), 1.72 (1H, m), 1.60 (1H, m), 1.82 (1H, t, 5.0 Hz), 1.52 (1H, t, 4.9 Hz), 3.05 (1H, t, 4.3 Hz), 1.91 (1H, m), 1.62 (1H, m), 1.74 (2H, m), 4.14 (1H, t, 4.3 Hz), 1.99 (2H, t, 4.2 Hz), 1.42 (2H, m), 3.78 (1H, t, 4.7 Hz), 1.54 (2H, t, 4.3 Hz), 1.38 (2H, m), 1.95 (2H, t, 6.2), 4.01 (1H, d, 8.2 Hz), 3.93 (1H, d, 8.3 Hz), 1.41 (3H, s), 1.33 (3H, s), 5.33 (1H, d, 10.0 Hz), 5.18 (1H, d, 9.3 Hz), 1.28 (3H, s), 5.36 (1H, d, 9.3 Hz), 5.17 (1H, d, 9.3 Hz), 3.68 (3H, s).^{13}C NMR (125 MHz; $CDCl_3$; δ in ppm); δ_C 20.3 (CH_3), 129.4 (C), 137.1 (C), 21.5 (CH_2), 24.6 (CH_2), 81.4 (C), 80.9 (CH), 22.3 (CH_2), 39.1 (CH_2), 77.1 (C), 78.8 (CH), 24.48 (CH_2), 25.7 (CH_2), 75.3 (CH), 147.0 (C), 29.3 (CH_2), 31.6 (CH_2), 74.1 (CH), 81.4 (C), 35.0 (CH_2), 21.8 (CH_2), 31.0 (CH_2), 143.2 (C), 72.4 (CH_2), 24.3 (CH_3), 19.3 (CH_3), 114.5 (CH_2), 18.82 (CH_3), 114.0 (CH_2), 60.0 (CH_3). [135]DEPT, COSY, HSQC, and HMBC data were presented in Table 4.18; EI-MS *m/z*: calcd. for $C_{30}H_{48}O_6$ 504.3451. HRESIMS (positive mode) *m/z*: found 505.3533 $[M+H]^+$, calcd. for $C_{30}H_{49}O_6$ 505.3529 (Δ 0.07 ppm)

4.2.5.12 Physicochemical description of compound-12 (TG_{12})

Tetrahydro-6-(hexahydro-13-((tetrahydro-18-(23-hydroxy-23-methylheptan-19-yl)-15-methylfuran-15-yl)methyl-10-methyl-*2H*-furo[3,2-b]pyran-7-yl)-2,2,6-trimethyl-*2H*-pyran-3-yl; Colourless oil; $[\alpha]^{25}_{D}$ +10.3 (*c*0.18, CH_3OH); UV_{MeOH} λ_{max} (log ε): 242 (3.23) nm; TLC {Si-GF_{254} 15 mm; EtOAc/*n*-hexane, 1/9, v/v} R_f: 0.45; R_t (HPLC RP-C_{18}, MeOH:MeCN 1:1, v/v): 3.18 min; FTIR ν_{max} (cm^{-1}): 720 (=C-H_{δ}), 1043 (C-O-C_{υ}), 1239, 1376 (C-H_{δ}), 2852, 2922 (C-H_{υ}), 3383 (O-Hυ); ^{1}H NMR (500 MHz; $CDCl_3$; δ in ppm); δ_H 1.24 (3H, s), 4.10 (1H, t, 4.2 Hz), 1.73 (1H, m), 1.99 (1H, m), 1.62 (1H, t, 4.3 Hz), 1.40 (1H, t, 4.3 Hz), 3.69 (1H, t, 6.2 Hz), 1.72 (1H, m), 1.44 (1H, m), 1.83 (1H, t, 5.2 Hz), 1.58 (1H, t, 5.2 Hz), 3.33 (1H, t, 9.2 Hz), 2.05 (1H, t, 6.4 Hz), 1.87 (1H, t, 6.5 Hz), 3.56 (1H, m), 1.50 (2H, d, 6.8 Hz), 2.01 (2H, t, 4.2 Hz), 1.75 (2H, m), 3.67 (1H, m), 1.92 (1H, m), 1.34 (2H, m), 1.30 (2H, m), 1.47 (2H, m), 1.19 (3H, s), 1.26 (3H,s), 1.29 (3H, s), 1.28 (3H, s), 1.31 (3H, s), 0.99 (3H, d, 7.2 Hz), 1.17 (3H, s), 2.33 (2H, t, 6.8 Hz), 1.77 (2H, m), 0.92 (3H, t, 4.1 Hz); ^{13}C NMR (125 MHz; $CDCl_3$; δ in ppm); δ_C 27.5 (CH_3), 83.9 (C), 71.5 (CH), 21.3 (CH_2), 30.3 (CH_2), 32.6 (C), 90.4 (CH), 22.3 (CH_2), 39.6 (CH_2), 81.4 (C), 80.5 (CH), 38.6 (CH_2), 65.2 (CH), 46.3 (CH_2), 79.5 (C), 36.0 (CH_2), 29.3 (CH_2), 79.1 (CH), 36.7 (CH), 33.9 (CH_2), 22.0 (CH_2), 42.6 (CH_2), 78.9 (C), 28.8 (CH_3), 26.3 (CH_3), 21.1 (CH_3), 17.3 (CH_3), 26.9 (CH_3), 18.1 (CH_3), 28.5 (CH_3), 167.9 (C), 36.6 (CH_2), 18.8 (CH_2), 13.9 (CH_3).[135]DEPT, COSY, HSQC, and HMBC data were presented in Table 4.19; EI-

MS *m/z*: calcd. for $C_{34}H_{60}O_7$ 580.4339. HRESIMS (positive mode) *m/z*: found 581.4420 $[M+H]^+$, calcd. for $C_{21}H_{61}O_3$ 581.4417 (Δ 0.05 ppm).

4.2.5.13 Physicochemical description of compound-13 (TG_{13})

3-acetyl-14-(furanyl)-11-methyl-15-(15[3]-methylbutyloxy)-8-oxabicyclo-[21.3.1]heptacosa-11,23,25,27 tetraene-7,18-dione. Pale yellow oily; $[\alpha]^{22}_D$ -118.6° (*c* 0.25, $CHCl_3$); UV (EtOAc) λ_{max} (log ε): 232 (4.315) nm; TLC (Si-GF254; EtOAc:*n*-hexane, 1/19 v/v) R_f: 0.42; RP-C_{18} HPLC R_t: 4.90 min (232 nm) (MeCN/MeOH, 1:2 v/v); FTIR (KBr, cm^{-1}) ν_{max}: 925/974 (alkene C-H_δ), 1085 (C-O-C_ν), 1220 (C-H_ρ), 1440 (C-H_δ), 1715 (C-CO-C_ν), 1735 (-C(=O)-O-), 2939/3009 (C-H_ν); ^{1}H NMR (500 MHz, $CDCl_3$; δ in ppm) δ_H 2.94 (1H, dd, 11.1, 6.8 Hz), 2.64 (1H, dd, 11.0, 6.5 Hz), 2.75 (1H, m), 2.69 (1H, m), 1.41 (1H, m), 1.72 (1H, m), 1.64 (1H, m), 2.28 (2H, m), 4.31 (2H, t, 7.8 Hz), 2.34 (2H, t, 7.6 Hz), 5.19 (1H, t, 6.2 Hz), 2.42 (2H, m), 2.85 (1H, m), 3.16 (1H, m), 1.80 (2H, m), 2.50 (2H, t, 7.8 Hz), 2.44 (2H, t, 7.9 Hz), 1.55 (2H, m), 1.61 (2H, m), 2.58 (2H, t, 5.8 Hz), 7.02 (1H, d, 7.4 Hz), 7.53 (1H, t, 7.6 Hz), 7.01 (1H, d, 7.6 Hz), 7.07 (1H,s), 1.96 (3H, s), 1.82 (3H, s), 6.08 (1H, d, 1.3Hz), 6.43 (1H, t, 2.9 Hz), 7.71 (1H, d, 1.6 Hz), 3.39 (2H, t, 7.9 Hz), 1.45 (2H, m), 1.76 (1H, m), 0.98 (3H, d, 5.1 Hz), 0.97 (3H, d, 5.3 Hz); ^{13}C NMR (125 MHz, $CDCl_3$; δ in ppm) δ_C 137.6 (C), 35.8 (CH_2), 54.0 (CH), 27.3 (CH_2), 24.1 (CH_2), 32.8 (CH_2), 177.2 (C), 65.5 (CH_2), 39.8 (CH_2), 130.9 (C), 128.4 (CH), 25.8 (CH_2), 43.3 (CH), 81.4 (CH), 24.7 (CH_2), 34.7 (CH_2), 213.3 (C), 40.1 (CH_2), 25.30 (CH_2), 29.6 (CH_2), 34.3 (CH_2), 148.5 (C), 126.8 (CH), 128.8 (CH), 126.1 (CH), 133.8 (CH), 210.6 (C), 30.5 (CH_3), 16.7 (CH_3), 154.9 (C), 109.3 (CH), 111.3 (CH), 140.5 (CH), 72.1 (CH_2), 40.6 (CH_2), 24.0 (CH), 23.8 (CH_3), 23.6 (CH_3) ^{1}H-^{1}H COSY, HSQC, and HMBC data were presented in Table 4.20; EI-MS *m/z* found 606.4 $[M]^+$. HRESIMS *m/z* calcd. for $C_{38}H_{55}O_6$ 607.3999, found 607.4003 $[M+H]^+$ (Δ = 0.6 ppm).

4.2.5.14 Physicochemical description of compound-14 (TG_{14})

(2E,12E,14E)-10-acetyl-9-isopentyl-2-methyl-5,16,23[1]-trioxa-bicyclo[21.3.1]-heptacosa-2,12,14-triene-6,19-dione. Pale yellow oily; $[\alpha]^{22}_D$ -125.5° (*c* 0.18, $CHCl_3$); UV (EtOAc) λ_{max} (log ε): 237 (4.985) nm; TLC (Si-GF254; EtOAc:*n*-hexane, 1/19 v/v) R_f: 0.38; RP-C_{18} HPLC R_t: 4.30 min (237 nm) (MeCN/MeOH, 1:2 v/v); FTIR (KBr, cm^{-1}) ν_{max}: 929 (alkene C-H_δ), 1046/1119/1192 (C-O-C_ν), 1354 (C-H_ρ), 1492 (C-H_δ), 1717 (C-CO-C_ν), 1742 (-C(=O)-O-), 2923/2799 (C-H_ν)**:** ^{1}H NMR (500 MHz, $CDCl_3$; δ in ppm), δ_H 4.78 (1H, m), 5.54 (1H, t, 6.4 Hz), 4.90 (2H, d,10.1 Hz), 2.30 (2H, t, 7.5 Hz), 1.77 (2H, m), 1.75 (1H, m), 2.33 (1H, m), 2.37 (2H, m), 5.81 (1H, m), 5.34 (1H, t,12.1 Hz), 5.05 (1H, t,11.0 Hz), 6.37 (1H, d,11.1 Hz), 4.36

(2H, m), 2.92 (2H, t, 4.8 Hz), 2.49 (1H, m), 2.43 (1H, m), 1.68 (1H, m), 1.56 (1H, m), 1.53 (1H, m), 1.25 (1H, m), 3.65 (1H, m), 1.72 (2H, m), 1.66 (2H, m), 1.80 (2H, m), 1.82 (3H, s), 1.37 (2H, m), 1.33 (2H, m), 1.62 (1H, m), 0.97 (3H, d, 6.3 Hz), 0.93 (3H, d, 5.2 Hz), 2.00 (3H, s); ^{13}C NMR (125 MHz, $CDCl_3$; δ in ppm), δ_C 85.0 (CH), 142.3 (C), 125.1 (CH), 66.4 (CH), 177.3 (C), 32.5 (CH_2), 28.0 (CH_2), 32.1 (CH), 53.1 (CH), 29.6 (CH_2), 135.4 (CH), 133.6 (CH), 109.0(CH), 145.0 (CH), 69.9 (CH_2), 41.9 (CH_2), 213.4 (C), 42.8 (CH_2), 19.2 (CH_2), 34.5 (CH_2), 80.3 (CH), 30.4 (CH_2), 24.7 (CH_2), 31.8 (CH_2), 13.8 (CH_3), 29.2 (CH_2), 37.3 (CH_2), 29.9 (CH), 23.8 (CH_3), 24.0 (CH_3), 209.3 (C), 31.7 (CH_3); ^{1}H-^{1}H COSY, HSQC and HMBC data were presented in Table 4.21; EIMS *m/z* found 530.7 $[M]^+$;HRESIMS *m/z* calcd. for $C_{32}H_{51}O_6$ 531.3686, found 531.3690 $[M+H]^+$ (Δ = 0.7 ppm).

4.2.5.15 Physicochemical description of compound-15 (TG_{15})

(2Z,5E,16E)-8-hydroxy-20-isobutyl-16-methyl-7,14-dioxa-bicyclo[19.3.1]-pentacosa-2,5,16-triene-10,23-dione. Yellow oily; $[\alpha]^{22}_D$ -124.2° (*c* 0.18, $CHCl_3$); UV (EtOAc) λ_{max} (log ε): 234 (4.985) nm; TLC (Si-GF254; EtOAc:*n*-hexane, 1/19 v/v) R_f: 0.42; RP-C_{18} HPLC R_t: 5.30 min (234 nm) (MeCN/MeOH, 1:2 v/v); FTIR (KBr, cm^{-1}) ν_{max}: 935 (alkene C-H_δ), 1098 (C-O-C_ν), 1377 (C-H_ρ), 1460 (C-H_δ), 1703 (C-CO-C_ν), 2856, 2922 (C-H_ν) 3426 (O-H_ν); ^{1}H NMR (500 MHz, $CDCl_3$; δ in ppm), δ_H 2.49 (1H, m), 5.59 (1H, dd, 6.9, 6.9 Hz), 5.82 (1H, m), 2.64 (2H, t, 7.1 Hz), 5.88 (1H, m), 5.98 (1H, d, 11.1 Hz), 5.62 (1H, m), 3.15 (1H, dd, 5.6,12.3 Hz), 2.84 (1H, dd, 5.3,12.1 Hz), 2.48 (1H, t, 4.5 Hz), 2.44 (1H, t, 4.8 Hz), 1.73 (2H, m), 3.50 (2H, m), 4.38 (1H, d, 9.3 Hz), 5.43 (1H, t, 5.8 Hz), 2.02 (1H, m), 1.98 (1H, m), 1.42 (1H, m), 1.13 (1H, m), 1.49 (1H, m), 1.80 (1H, m), 2.34 (2H, d, 6.8 Hz), 2.31 (2H, d, 6.1 Hz), 1.90 (2H, t, 5.9 Hz), 1.82 (3H, s), 1.25 (2H, t, 6.9 Hz), 1.64 (1H, m), 1.97 (3H, d, 5.9 Hz), 0.98 (3H, d, 6.2 Hz); ^{13}C NMR (125 MHz, $CDCl_3$; δ in ppm), δ_C 41.4 (CH), 136.4 (CH), 121.6 (CH), 34.6 (CH_2), 126.8 (CH), 144.8 (CH), 96.1 (CH), 49.4 (CH_2), 213.2 (C), 38.2 (CH_2), 24.7 (CH_2), 74.5 (CH_2), 80.6 (CH_2), 137.1 (C), 123.1 (CH), 25.0 (CH_2), 32.1 (CH_2), 34.1 (CH), 37.4 (CH), 47.1 (CH_2), 214.2 (C), 45.7 (CH_2), 36.6 (CH_2), 14.8 (CH_3), 43.3 (CH_2), 26.5 (CH), 23.3 (CH_3), 22.8 (CH_3). ^{1}H-^{1}H COSY, HSQC, and HMBC were presented in Table 4.22; EIMS *m/z* found 460.3 $[M]^+$; HRESIMS *m/z* calcd. for $C_{28}H_{45}O_5$ 461.3267, found 461.3270 $[M+H]^+$ (Δ = 0.6 ppm).

4.2.6 Evaluation of bioactive potencies

4.2.6.1 *In-vitro* antioxidative activities

4.2.6.1a 1, 1-Diphenyl-2-picryl-hydrazil radical/ $DPPH^{\bullet}$ scavenging activity

The estimation of antioxidant potencies of various fractions and pure compounds derived from the EtOAc-MeOH extracts of *G. salicornia* was carried out by *in vitro* $DPPH^{\bullet}$ scavenging assay. The details were described under the section 3.2.5.2a of Chapter 3.

4.2.6.1b 2,2′-Azino-bis-3-ethylbenzothiozoline-6-sulfonic acid diammonium salt/ $ABTS^{+\bullet}$ radical scavenging assay

The determination of antioxidant potencies of various fractions and pure compounds derived from the EtOAc-MeOH extracts of *G. salicornia* was carried out by *in vitro* $ABTS^{+\bullet}$ scavenging assay. The details were described under the section 3.2.5.2b of Chapter 3.

4.2.6.2 *In-vitro* anti-inflammation assays

4.2.6.2a Cyclooxygenases- (COX1/2) inhibition assay

The anti-inflammation bioactive potential of various fractions and pure compounds identified from the EtOAc-MeOH extracts of *G. salicornia* were evaluated by using the pro-inflammatory enzyme, cyclooxygenases (COX-1/2) inhibition assay. The methodology was detailed under the section 3.2.5.3a of Chapter 3.

4.2.6.2b 5-Lipoxygenase/5-LOX inhibition assay

The anti-inflammation bioactive potential of various fractions and pure compounds identified from the EtOAc-MeOH extracts of *G. salicornia* were evaluated by using the pro-inflammatory enzyme 5-lipoxygenase (5-LOX) inhibition assay. This was described under the section 3.2.5.3b of Chapter 3.

4.2.7 Structure-activity correlations of bioactive leads isolated from EtOAc-MeOH extract of G. salicornia

The structure-bioactivity-correlation investigations were carried out by utilising different molecular factors like octanol-water partition-coefficient (log P_{ow}-hydrophobicity); electronic (Pl-polarisability; topological polar surface area-tPSA) and steric (MV-molar volume; P-parachor; MR-molar refractivity) (Lipinski 2000) through ACD-ChemSketch (Advanced Chemistry Development, Inc., Toronto, Canada; ver. 12.0) and ChemDraw-Ultra (Cambridge Soft Corporation, USA; ver. 12.0) softwares.

4.2.8 *Molecular modelling experiments*

In-silico molecular modeling analysis of the bioactive compounds derived from seaweed *G. salicornia* was conducted by the software Auto-Dock-4 (ver. 1.5.6). The fractionated

compounds were drawn using ACD/Chem-sketch and were made into Molfiles before being converted to the PDB format (Open Babel, GUI 2.4.1). The X-ray crystal structures of 5-LOX (PDB 3V99, resolution 2.25 Å), α-glucosidase (PDB 3A4A, resolution 1.6 Å) and α-amylase (PDB 1HNY, resolution 1.8 Å) were acquired from the Protein Data Bank (www.pdb.org) and conformationally oriented (Swiss-Pdb Viewer, ver. 4.1.0) (Gilbert et al., 2012; Brayer et al., 1995; Yamamoto et al., 2010). The docking analyses were conducted by the molecular algorithm, which was run by Cygwin I-II. After auto docking, the RMSD data (root mean square deviation) was documented, and the conformations were oriented with the aid of docking parameters. Finally, molecular docking analyses were visualized using the Chimera software developed by University of California, San Francisco (USCF Chimera, ver. 1.11.2).

4.2.9 Statistical analysis

The entire sets of data were presented in triplicates along with their mean ± standard deviation. One-way analysis of variance (ANOVA; Statistical Program for Social Sciences, USA, ver. 13.0) was used to analyze the significant differences ($P \leq 0.05$) among the means of results.

4.3. Results and discussion

4.3.1. Chromatographic purification of pure compounds and bioactive potentials of sub-column fractions from G. salicornia

The organic extract of *G. salicornia* (33 g) was fractionated by extensive chromatographic fractionation. Initially, the slurry of the crude extract was made with the silica gel of mesh size 60-120 mesh (5 g), and it was packed into a glass column (100 cm x 4 cm) for chromatographic purification. The separation of compounds was carried out with solvents of increasing polarity (*n*-hexane; EtOAc and MeOH) to collect a total of 20 fractions. These fractions were subjected for subsequent chromatographic purification after TLC (*n*-hexane: EtOAc) along with RP C_{18}-HPLC experiments. The fractions that were reported higher percentage yield (> 9 %) on the basis of the dry weight of EtOAc-MeOH extract of *G. salicornia*, were subjected to repeated purification. The pooled homogeneous column fractions were assessed for their bioactive potencies to analyze their inhibition potentials against the carbolytic enzymes (α-amylase and α-glucosidase), pro-inflammatory cyclooxygenases (COX-1/COX-2) and lipoxygenases (5-LOX) along with free-stable-radicals ($DPPH^{\bullet}$ and $ABTS^{+\bullet}$). The fractions with greater bioactive potential were subjected to further downstream-purification. Further bioassay-guided chromatographic separation of major intermediate column fractions

were resulted in seven classes of previously undescribed bioactive compounds (a total of fifteen compounds). The fractionation, yield and bioactive potentials (antioxidative, ant-inflammatory and anti-diabetic) of the secondary metabolites isolated from the EtOAc-MeOH extract of *G. salicornia* was represented in Tables 4.1-4.7 in detail.

Table 4.1.: Yield and bioactivities (antioxidant, anti-inflammatory and antidiabetic) of sub-fractions from EtOAc-MeOH extract of *G. salicornia*

Fractions	***Yield (in %)**	**Bioactivity (IC_{50} in mg mL^{-1})**					
		Antioxidant		**Anti-inflammatory**		**Antidiabetic**	
		#DPPH	**#ABTS**	**#COX-2**	**#5-LOX**	**#α-amylase**	**#α-glucosidase**
GS_1	0.70	1.98^{a}±0.02	2.01^{a}±0.03	2.71^{a}±0.02	2.51^{a}±0.02	2.81^{a}±0.02	2.33^{a}±0.03
GS_2	**9.79**	**1.03^{b} ±0.02**	**1.05^{b}±0.04**	**1.02^{b}±0.02**	**1.01^{b}±0.03**	2.78^{b}±0.03	2.01^{b}±0.03
GS_3	0.97	2.10^{c}±0.03	2.22^{c}±0.05	2.11^{c}±0.03	2.54^{a}±0.04	2.56^{c}±0.06	2.21^{c}±0.03
GS_4	**11.79**	**1.05^{b}±0.03**	**1.08^{b}±0.07**	2.24^{d}±0.05	2.05^{c}±0.03	**0.92^{d}±0.03**	**0.94^{d}±0.06**
GS_5	0.58	2.21^{d}±0.06	2.87^{c}±0.03	2.41^{e}±0.03	2.59^{d}±0.05	2.68^{e}±0.06	2.48^{e}±0.01
GS_6	0.70	2.77^{e}±0.05	3.01^{d}±0.06	2.19^{f}±0.06	2.22^{e}±0.02	2.57^{c}±0.03	2.36^{f}±0.03
GS_7	**11.15**	**0.87^{f}±0.02**	**0.98^{e}±0.06**	**1.01^{b}±0.06**	**1.04^{b}±0.06**	2.87^{f}±0.06	3.01^{g}±0.02
GS_8	**11.79**	**1.03^{b}±0.04**	**0.99^{e}±0.03**	**1.03^{b}±0.04**	**1.02^{b}±0.04**	2.67^{e}±0.06	3.12^{h}±0.06
GS_9	1.70	3.01^{g}±0.02	3.21^{f}±0.03	2.34^{g}±0.06	2.88^{f}±0.03	2.79^{b}±0.03	3.08^{i}±0.07
GS_{10}	3.12	3.33^{h}±0.03	3.48^{g}±0.05	2.26^{h}±0.07	2.93^{g}±0.01	3.12^{g}±0.06	3.14^{h}±0.03
GS_{11}	3.06	3.51^{i}±0.04	3.65^{h}±0.06	2.47^{i}±0.03	2.49^{h}±0.02	3.02^{h}±0.03	2.87^{j}±0.02
GS_{12}	**11.79**	**0.96^{j}±0.02**	**1.06^{b}±0.05**	**1.04^{b}±0.05**	**1.05^{b}±0.03**	2.88^{f}±0.06	2.03^{b}±0.03
GS_{13}	**12.06**	**0.91^{k}±0.03**	**0.97^{e}±0.06**	**0.97^{j}±0.03**	**0.95^{i}±0.02**	2.63^{j}±0.05	2.04^{b}±0.02
GS_{14}	0.79	2.17^{k}±0.08	2.25^{i}±0.07	2.68^{k}±0.06	2.80^{j}±0.08	2.82^{a}±0.06	2.50^{e}±0.06
GS_{15}	**12.15**	**0.82^{l}±0.03**	**0.85^{j}±0.01**	**0.86^{l}±0.04**	**0.88^{k}±0.04**	2.69^{e}±0.06	2.09^{bk}±0.06
GS_{16}	1.45	2.89^{m}±0.06	2.98^{j}±0.03	2.72^{a}±0.01	2.79^{l}±0.01	3.89^{k}±0.02	2.20^{c}±0.07
GS_{17}	0.79	3.02^{g}±0.07	3.12^{k}±0.05	2.69^{a}±0.02	2.53^{a}±0.05	3.76^{l}±0.03	2.23^{c}±0.05
GS_{18}	1.00	2.27^{n}±0.05	2.58^{l}±0.04	2.73^{a}±0.03	2.56^{a}±0.04	3.65^{m}±0.06	2.41^{k}±0.02
GS_{19}	0.70	2.63^{o}±0.02	2.78^{m}±0.03	2.75^{a}±0.01	2.63^{d}±0.07	3.25^{n}±0.07	2.30^{a}±0.04
GS_{20}	0.67	2.84^{p}±0.03	2.86^{c}±0.06	2.86^{m}±0.06	2.71^{m}±0.02	3.13^{g}±0.06	2.99^{l}±0.05

*The yield of major sub-column fractions calculated based on the crude EtOAc-MeOH extract (33.0 g of dry weight). The values were tabulated in triplicate (n=3) and indicated as

mean±standard deviation. Significant differences were expressed as superscripts (a-p) within column ($p < 0.05$).

[#]The IC_{50} values were calculated in mg mL^{-1}

Table 4.2.: Yield and bioactivities of (antioxidant, anti-inflammatory and antidiabetic) sub-column fractions derived from EtOAc-MeOH extract of *G. salicornia*

Fractions	Bioactivity (IC_{50} in mg mL^{-1})						*Yield
	Antioxidant		Anti-inflammatory		Antidiabetic		
	#DPPH•	#$ABTS^{•+}$	#COX-2	#5-LOX	#α-amylase	#α-glucosidase	in %
GS_{2-1}	1.09^{a} ±0.02	1.12^{a}±0.02	1.02^{a}±0.02	1.01^{a}±0.03	2.08^{a}±0.03	2.02^{a}±0.03	7.66
GS_{2-2}	**0.97^{b}±0.03**	**0.98^{b}±0.03**	**0.92^{b}±0.03**	**0.94^{b}±0.04**	**2.06^{a}±0.06**	**2.11^{b}±0.03**	**1.60**
GS_{2-3}	1.04^{b} ±0.02	1.05^{c} ±0.02	1.06^{c}±0.02	1.03^{a}±0.03	2.04^{a}±0.03	2.13^{b}±0.03	1.42
GS_{2-2-1}	**0.87^{c}±0.06**	**0.89^{d}±0.06**	**0.78^{e}±0.03**	**0.73^{c}±0.05**	**2.32^{b}±0.06**	**2.18^{c}±0.1**	**0.31**
GS_{2-2-2}	1.08^{a}±0.05	1.01^{c}±0.05	1.09^{c}±0.06	1.02^{a}±0.02	2.17^{c}±0.03	2.16^{c}±0.03	0.06
GS_{2-2-3}	1.01^{b}±0.02	1.04^{c}±0.02	1.07^{c}±0.06	1.04^{a}±0.06	2.12^{c}±0.06	2.93^{d}±0.02	0.04

*The yield of sub-column fractions calculated based on the crude EtOAc-MeOH extract (33.0 g of dry weight). The values were tabulated in triplicate (n=3) and indicated as mean±standard deviation. Significant differences were expressed as superscripts (a-d) within column ($p < 0.05$). #The IC_{50} values were calculated in mg mL^{-1}

Table 4.3.: Yield and bioactivities of (antioxidant, anti-inflammatory and antidiabetic) sub-column fractions derived from EtOAc-MeOH extract of *G. salicornia*

Fractions	Bioactivity (IC_{50} in mg mL^{-1})						*Yield
	Antioxidant		Anti-inflammatory		Antidiabetic		
	#DPPH$^{\bullet}$	#ABTS$^{\bullet+}$	#COX-2	#5-LOX	#α-amylase	#α-glucosidase	in %
GS_{4-1}	**$1.03^{a}\pm0.03$**	**$1.02^{a}\pm0.03$**	**$1.18^{a}\pm0.03$**	**$1.17^{a}\pm0.04$**	**$1.03^{a}\pm0.06$**	**$1.01^{a}\pm0.03$**	**8.55**
GS_{4-2}	$1.05^{a}\pm0.03$	$1.07^{b}\pm0.03$	$1.21^{a}\pm0.05$	$1.25^{b}\pm0.03$	$1.11^{b}\pm0.03$	$1.09^{b}\pm0.06$	1.10
GS_{4-3}	$1.10^{b}\pm0.03$	$1.11^{b}\pm0.03$	$1.12^{b}\pm0.05$	$1.27^{b}\pm0.03$	$1.12^{b}\pm0.03$	$1.10^{a}\pm0.06$	0.99
GS_{4-1-1}	$1.05^{ab}\pm0.06$	$1.06^{a}\pm0.06$	$2.22^{c}\pm0.03$	$2.39^{c}\pm0.05$	$1.05^{a}\pm0.06$	$1.04^{a}\pm0.01$	0.07
GS_{4-1-2}	**$0.87^{c}\pm0.05$**	**$0.89^{b}\pm0.05$**	**$2.18^{c}\pm0.06$**	**$2.23^{d}\pm0.02$**	**$0.68^{c}\pm0.03$**	**$0.65^{c}\pm0.03$**	**0.36**
GS_{4-1-3}	**$0.84^{c}\pm0.02$**	**$0.85^{b}\pm0.02$**	**$2.11^{d}\pm0.06$**	**$2.15^{e}\pm0.06$**	**$0.69^{c}\pm0.06$**	**$0.63^{c}\pm0.02$**	**0.35**
GS_{4-1-4}	$1.04^{a}\pm0.05$	$1.10^{b}\pm0.05$	$2.12^{d}\pm0.06$	$2.14^{e}\pm0.02$	$2.62^{d}\pm0.03$	$2.59^{d}\pm0.03$	0.06
GS_{4-1-5}	$1.09^{bd}\pm0.05$	$1.08^{b}\pm0.05$	$2.20^{c}\pm0.06$	$2.25^{d}\pm0.02$	$2.52^{e}\pm0.03$	$2.48^{e}\pm0.03$	0.05

*The yield of sub-column fractions calculated based on the crude EtOAc-MeOH extract (33.0 g of dry weight). The values were tabulated in triplicate (n=3) and indicated as mean±standard deviation. Significant differences were expressed as superscripts (a-e) within column ($p < 0.05$). #The IC_{50} values were calculated in mg mL^{-1}

Table 4.4.: Yield and bioactivities (antioxidant, anti-inflammatory and antidiabetic) of sub-fractions from EtOAc-MeOH extract of *G. salicornia*

Fractions	Bioactivity (IC_{50} in mg mL^{-1})						*Yield
	Antioxidant		Anti-inflammatory		Antidiabetic		
	#DPPH•	#ABTS•+	#COX-2	#5-LOX	#α-amylase	#α-glucosidase	in %
GS_{7-1}	1.04^{a} ±0.02	1.10^{a} ±0.02	1.02^{a}±0.02	1.03^{a}±0.03	2.37^{a}±0.03	2.51^{a}±0.03	0.99
GS_{7-2}	**1.02^{a}±0.03**	**1.03^{b}±0.03**	**0.99^{b}±0.03**	**0.96^{b}±0.04**	**2.59^{b}±0.06**	**2.63^{b}±0.03**	**8.27**
GS_{7-3}	1.10^{b}±0.03	1.11^{a}±0.03	1.05^{a}±0.05	1.05^{a}±0.03	2.23^{c}±0.03	2.31^{c}±0.06	0.82
GS_{7-4}	1.08^{b}±0.06	1.09^{a}±0.06	1.04^{a}±0.03	1.06^{ac}±0.05	2.48^{d}±0.06	2.54^{a}±0.01	0.57
GS_{7-5}	1.11^{b}±0.05	1.08^{a}±0.05	1.03^{a}±0.06	1.01^{a}±0.02	2.67^{e}±0.03	2.68^{b}±0.03	0.98
GS_{7-6}	1.12^{b}±0.02	1.13^{a}±0.02	1.01^{a}±0.06	1.02^{a}±0.06	2.83^{f}±0.06	2.85^{c}±0.02	1.11
GS_{7-2-1}	1.02^{a}±0.06	1.07^{a}±0.03	1.05^{ac}±0.03	1.09^{c}±0.05	2.08^{g}±0.06	2.04^{d}±0.01	1.01
GS_{7-2-2}	**0.98^{c}±0.05**	**1.04^{b}±0.06**	**0.97^{b}±0.06**	**0.92^{b}±0.02**	**2.17^{h}±0.03**	**2.03^{d}±0.03**	**1.29**
GS_{7-2-3}	**0.97^{c}±0.02**	**1.02^{b}±0.06**	**0.96^{b}±0.06**	**0.93^{b}±0.06**	**2.18^{h}±0.06**	**2.16^{e}±0.02**	**1.56**
$GS_{7-2-2-1}$	1.05^{a}±0.02	1.12^{a}±0.06	1.02^{a}±0.06	1.07^{c}±0.06	2.13^{h}±0.06	2.21^{f}±0.02	0.08
$GS_{7-2-2-2}$	1.06^{a}±0.05	1.10^{a}±0.06	1.06^{a}±0.06	1.02^{a}±0.02	2.07^{i}±0.03	2.20^{f}±0.03	0.06
$GS_{7-2-2-3}$	**0.72^{d} ±0.02**	**0.81^{c}±0.02**	**0.73^{c}±0.02**	**0.72^{d}±0.03**	**2.06^{hi}±0.03**	**2.19^{f}±0.03**	**0.38**
$GS_{7-2-2-4}$	1.11^{b}±0.03	1.06^{b}±0.03	1.08^{c}±0.03	1.04^{a}±0.04	2.10^{i}±0.06	2.18^{f}±0.03	0.08
$GS_{7-2-3-1}$	1.09^{b}±0.03	1.05^{b}±0.05	1.05^{a}±0.05	1.05^{a}±0.03	1.98^{j}±0.03	2.07^{d}±0.06	0.05
$GS_{7-2-3-2}$	1.07^{b}±0.06	1.01^{b}±0.03	1.07^{c}±0.03	1.08^{c}±0.05	1.99^{j}±0.06	2.09^{d}±0.01	0.04
$GS_{7-2-3-3}$	**0.76^{d}±0.05**	**0.83^{c}±0.06**	**0.74^{d}±0.06**	**0.73^{d}±0.02**	**2.01^{k}±0.03**	**2.06^{d}±0.03**	**0.39**
$GS_{7-2-3-4}$	**0.75^{d}±0.02**	**0.86^{c}±0.06**	**0.76^{d}±0.06**	**0.75^{d}±0.06**	**2.03^{k}±0.06**	**2.01^{d}±0.02**	**0.38**

*The yield of sub-column fractions calculated based on the crude EtOAc-MeOH extract (33.0 g of dry weight). The values were tabulated in triplicate (n=3) and indicated as mean±standard deviation. Significant differences were expressed as superscripts (a-k) within column ($p < 0.05$). #The IC_{50} values were calculated in mg mL^{-1}

Table 4.5.: Yield and bioactivities (antioxidant, anti-inflammatory and antidiabetic) of sub-fractions from EtOAc-MeOH extract of *G. salicornia*

Fractions	Bioactivity (IC_{50} in mg mL^{-1})						*Yield
	Antioxidant		Anti-inflammatory		Antidiabetic		
	#DPPH$^{\bullet}$	#ABTS$^{\bullet+}$	#COX-2	#5-LOX	#α-amylase	#α-glucosidase	in %
GS_{8-1}	1.03^{a}±0.06	1.04^{a}±0.03	1.01^{a}±0.04	1.02^{a}±0.05	2.26^{a}±0.06	2.18^{a}±0.01	1.15
GS_{8-2}	**0.89^{b}±0.05**	**0.93^{b}±0.06**	**0.87^{b}±0.07**	**0.85^{b}±0.07**	**2.57^{b}±0.03**	**2.16^{a}±0.03**	**0.31**
GS_{8-3}	**0.88^{b}±0.02**	**0.91^{b}±0.06**	**0.86^{b}±0.03**	**0.83^{b}±0.02**	**2.53^{b}±0.06**	**2.49^{b}±0.02**	**0.38**
GS_{8-4}	1.08^{c}±0.02	1.06^{cd}±0.06	1.02^{a}±0.05	1.03^{a}±0.07	2.63^{c}±0.06	2.51^{b}±0.02	1.36
GS_{12-1}	1.07^{c}±0.05	1.10^{d}±0.06	1.11^{c}±0.05	1.09^{c}±0.04	2.51^{b}±0.03	2.63^{c}±0.03	1.5
$GS_{12.-2}$	1.06^{c} ±0.02	1.12^{d}±0.02	1.10^{c}±0.01	1.08^{c}±0.02	2.23^{a}±0.03	2.20^{a}±0.03	3.68
$GS_{12.-3}$	**1.12^{d}±0.03**	**1.05^{c}±0.03**	**1.04^{a}±0.03**	**1.06^{ac}±0.01**	**2.25^{a}±0.06**	**2.28^{d}±0.03**	**5.51**
$GS_{12-.4}$	1.16^{d}±0.03	1.14^{d}±0.05	1.06^{ac}±0.07	1.04^{a}±0.06	2.01^{d}±0.03	2.14^{a}±0.06	2.60
$GS_{12-.3-1}$	1.15^{d}±0.06	1.16^{d}±0.03	1.05^{a}±0.03	1.07^{ac}±0.01	2.32^{e}±0.06	2.33^{d}±0.01	1.92
$GS_{12-.3-2}$	1.10^{d}±0.05	1.18^{de}±0.06	1.08^{ac}±0.06	1.10^{c}±0.02	2.07^{f}±0.03	2.09^{e}±0.03	2.08
GS_{12-3-3}	1.09^{c}±0.02	1.08^{a}±0.06	1.09^{c}±0.08	1.11^{c}±0.06	2.12^{g}±0.06	2.13^{a}±0.02	2.18
GS_{12-3-4}	**1.01^{a}±0.06**	**1.02^{a}±0.03**	**0.99^{e}±0.03**	**1.01^{a}±0.03**	**2.03^{d}±0.06**	**2.08^{e}±0.01**	**1.78**
$GS_{12-3-4-1}$	**0.87^{b}±0.05**	**0.89^{f}±0.06**	**0.78^{f}±0.02**	**0.76^{e}±0.02**	**2.58^{b}±0.07**	**2.47^{b}±0.02**	**0.37**
$GS_{12-3-4-2}$	1.01^{a}±0.06	1.07^{a}±0.04	1.03^{a}±0.03	1.04^{a}±0.01	2.61^{c}±0.07	2.59^{f}±0.02	0.08
$GS_{12-3-4-3}$	1.02^{a}±0.02	1.01^{a}±0.02	1.05^{a}±0.04	1.03^{a}±0.01	2.52^{b}±0.04	2.48^{b}±0.05	0.04
$GS_{12-3-4-4}$	1.04^{a}±0.02	1.06^{a}±0.05	1.07^{a}±0.05	1.01^{a}±0.04	2.73^{h}±0.04	2.70^{g}±0.04	0.06
$GS_{12-3-4-5}$	**0.86^{b}±0.01**	**0.87^{f}±0.07**	**0.75^{f}±0.06**	**0.73^{e}±0.07**	**2.67^{i}±0.04**	**2.68^{h}±0.07**	**0.35**

*The yield of sub-column fractions calculated based on the crude EtOAc-MeOH extract (33.0 g of dry weight). The values were tabulated in triplicate (n=3) and indicated as mean±standard deviation. Significant differences were expressed as superscripts (a-i) within column ($p < 0.05$). #The IC_{50} values were calculated in mg mL^{-1}

Table 4.6.: Yield and bioactivities (antioxidant, anti-inflammatory and antidiabetic) of sub-fractions from EtOAc-MeOH extract of *G. salicornia*

Fractions	Bioactivity (IC_{50} in mg mL^{-1})						*Yield
	Antioxidant		Anti-inflammatory		Antidiabetic		
	#DPPH$^{\bullet}$	#$ABTS^{\bullet+}$	#COX-2	#5-LOX	#α-amylase	#α-glucosidase	in %
$GS_{13\text{-}1}$	**$0.82^{a}\pm0.05$**	**$0.84^{a}\pm0.05$**	**$0.72^{a}\pm0.05$**	**$0.70^{a}\pm0.04$**	**$2.53^{a}\pm0.05$**	**$2.50^{a}\pm0.06$**	**0.36**
$GS_{13\text{-}2}$	$1.03^{b}\pm0.08$	$1.05^{b}\pm0.03$	$1.04^{b}\pm0.02$	$0.99^{b}\pm0.02$	$2.54^{a}\pm0.05$	$2.51^{a}\pm0.02$	1.50
$GS_{13\text{-}3}$	$1.05^{b}\pm0.03$	$1.07^{b}\pm0.02$	$1.06^{b}\pm0.06$	$1.02^{a}\pm0.01$	$2.57^{a}\pm0.05$	$2.49^{a}\pm0.02$	0.80
$GS_{13\text{-}4}$	$1.06^{b}\pm0.04$	$1.08^{b}\pm0.06$	$1.07^{b}\pm0.05$	$1.05^{c}\pm0.05$	$2.28^{b}\pm0.03$	$2.26^{b}\pm0.07$	0.02
$GS_{13\text{-}5}$	**$0.80^{a}\pm0.04$**	**$0.81^{a}\pm0.02$**	**$0.71^{a}\pm0.04$**	**$0.70^{a}\pm0.03$**	**$2.31^{b}\pm0.04$**	**$2.30^{b}\pm0.07$**	**0.34**

*The yield of sub-column fractions calculated based on the crude EtOAc-MeOH extract (33.0 g of dry weight). The values were tabulated in triplicate (n=3) and indicated as mean±standard deviation. Significant differences were expressed as superscripts (a-b) within column ($p < 0.05$). #The IC_{50} values were calculated in mg mL^{-1}

Table 4.7.: Yield and bioactivities (antioxidant, anti-inflammatory and antidiabetic) of sub-fractions from EtOAc-MeOH extract of *G. salicornia*

Fractions	Bioactivity (IC_{50} in mg mL^{-1})						*Yield
	Antioxidant		Anti-inflammatory		Antidiabetic		
	#DPPH$^{\bullet}$	#ABTS$^{\bullet+}$	#COX-2	#5-LOX	#α-amylase	#α-glucosidase	in %
$GS_{15.-1}$	**1.05^{a}±0.04**	**1.09^{bd}±0.03**	**1.05^{a}±0.05**	**1.04^{a}±0.01**	**2.37^{a}±0.03**	**2.32^{a}±0.07**	**6.43**
$GS_{15.-2}$	**1.07^{a}±0.02**	**1.10^{d}±0.06**	**1.03^{a}±0.05**	**1.01^{a}±0.01**	**2.27^{b}±0.06**	**2.22^{b}±0.04**	**8.56**
$GS_{15.-3}$	1.11^{b}±0.06	1.12^{d}±0.03	1.01^{a}±0.03	1.00^{a}±0.05	2.18^{c}±0.06	2.08^{c}±0.04	3.27
$GS_{15.-1-1}$	**0.70^{c}±0.05**	**0.72^{f}±0.06**	**0.62^{b}±0.06**	**0.60^{b}±0.02**	**2.28^{b}±0.03**	**2.21^{b}±0.03**	**0.36**
$GS_{15.-1-2}$	**0.69^{c} ±0.02**	**0.71^{b}±0.02**	**0.60^{b}±0.02**	**0.59^{b}±0.03**	**2.31^{a}±0.03**	**2.18^{b}±0.03**	**0.34**
$GS_{15.-1-3}$	1.12^{b}±0.03	1.14^{c}±0.03	1.02^{a}±0.03	0.99^{a}±0.04	2.36^{a}±0.06	2.33^{c}±0.03	0.21
$GS_{15.-2-1}$	**0.71^{c}±0.03**	**0.72^{d}±0.05**	**0.65^{b}±0.05**	**0.63^{b}±0.03**	**2.41^{a}±0.03**	**2.38^{c}±0.06**	**0.33**
$GS_{15.-2-2}$	1.09^{b}±0.06	1.11^{e}±0.03	1.04^{a}±0.03	1.02^{a}±0.05	2.38^{a}±0.06	2.26^{b}±0.01	0.18
$GS_{15.-2-3}$	1.10^{b}±0.05	1.13^{f}±0.06	1.03^{a}±0.06	1.04^{a}±0.02	2.35^{a}±0.03	2.31^{a}±0.03	0.10

*The yield of sub-column fractions calculated based on the crude EtOAc-MeOH extract (33.0 g of dry weight). The values were tabulated in triplicate (n=3) and indicated as mean±standard deviation. Significant differences were expressed as superscripts (a-f) within column ($p < 0.05$). #The IC_{50} values were calculated in mg mL^{-1}

4.3.2 *Spectroscopic characterization of bioactive compounds derived from EtOAc-MeOH extract of G. salicornia*

The sequential chromatographic purification of EtOAc-MeOH crude extract of *G. salicornia* was led to the identification of bioactive secondary metabolic analogues. The structural interpretation of these lead molecules carried out using the nuclear magnetic resonance (NMR) analyses {^{1}H-proton-500 MHz; ^{13}C-carbon-125 MHz; DEPT; ^{1}H-^{1}H COSY; HSQC; HMBC; NOESY} using deuterated solvents along with mass spectrometric analyses (GC-EI-MS/HRESIMS), infrared spectrum analysis (FT-IR) (reported among 4000-400 cm^{-1}) and UV-spectrophotometric analyses. The isolated secondary metabolic analogues were categorized under the different classes of chemistries, namely abeo-labdane class of diterpenoid (**1**), oleanene class of triterpenoids (**2-3**), drimane-associated quinols (**4-6**), 2*H*-chromenyl compounds (**7-8**), spiro-fused analogues (**9-10**), squalene polyether metabolites (**11-12**), and macrolides enclosing ether functionalities (**13-15**).

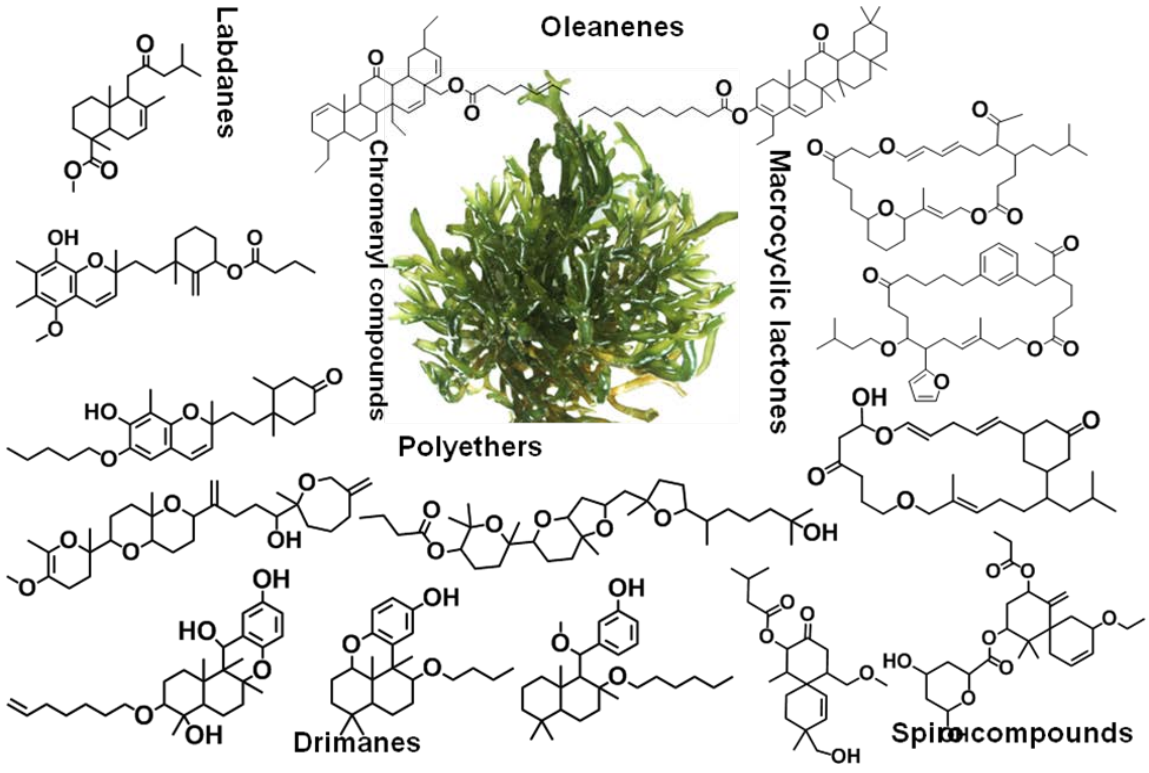

4.3.2.1 *Structural characterization of abeo-labdane class of diterpenoid derivative (Compound 1)*

Diterpenoids are large classes of bioactive leads assembled by isoprene moieties, with prominent functional and structural diversity (Hanson 2002). Labdanes are one of the predominant bicyclic diterpenoids in seaweeds with broad range of biological activities (Singh

1999, Demetzos & Dimas 2001, Hanson 2000, Hanson 2001, Hanson 2002, Blunt et al. 2006). The basic carbon frame work of labdane could be oriented into a decalin fused system C(1)-C(10) and a six-carbon branched side chain at C(9) {(C(11)-C(16), with C(16) connected to C(13)}. The remaining four methyl carbons from C(17)-C(20) were attached at C(8), C(40) {with C(18) and C(19) being attached}, and C(10) of the decalin system, respectively. The majority of labdanes were present in *trans* configuration at the C(5):C(10) junction of the ring, whereas labdanes with a *cis* orientation of C(5):C(10) ring junction were identified to a much lesser extent. On the basis of the ring junction stereochemistry, labdanes were further categorized by their orientations stereochemistries at C(9) and C(10). Subsequently, the classifications of labdane framework were defined as 'normal-', 'ent-', 'syn-', and 'syn–ent-', based on the configuration of the ring junctions and the substituents at C(9) and C(10) (Peters 2010, Demetzos & Dimas 2001, Tran et al. 2017).

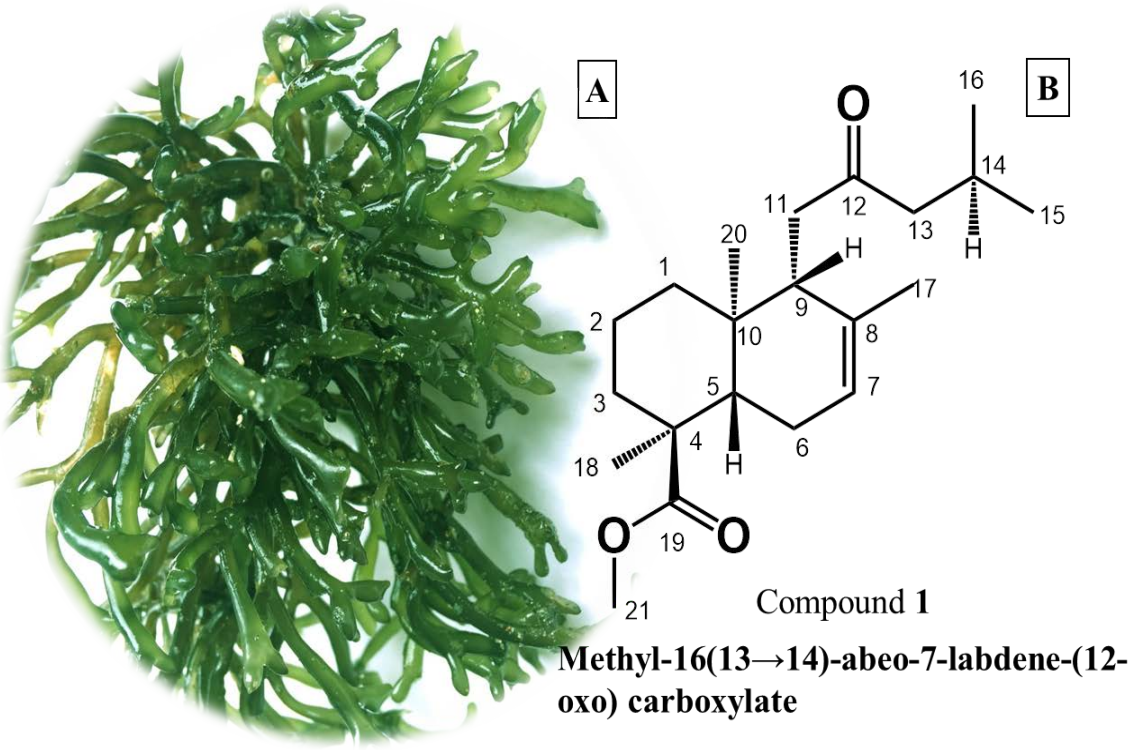

Compound **1**

Methyl-16(13→14)-abeo-7-labdene-(12-oxo) carboxylate

Figure 4.3.: Structure of methyl-16(13→14)-abeo-7-labdene-(12-oxo) carboxylate isolated from *G. salicornia* (family Gracilariaceae), (B) representative photograph of thalli of red seaweed *G. salicornia*

It has been documented that the organic extracts of *Gracilaria* sp. (family Gracilariaceae) comprised bioactive secondary metabolites along with anti-inflammatory, antioxidant, and antimicrobial potentials (Bansemir et al. 2006, Makkar and Chakraborty 2018b, Makkar and Chakraborty 2018c). The labdanes, 2α-hydroxy-8(17), 12 E, 14-labdatriene and 3β, 6β, 13α-trihydroxy 8(17), 12E, 14-labdatriene were isolated from brown seaweed *Sargassum wightii* (Maneesh et al., 2017) along with Venustanol from red seaweed *Laurencia venusta* (Suzuki et al. 1988; Suzuki et al. 2002). Here, we have characterized a 16(13→14)-abeo-labdene class of diterpenoid, namely methyl-16(13→14)-abeo-7-labdene-(12-oxo) carboxylate from the EtOAc-MeOH (ethyl acetate-methanol) extract of *G. salicornia* collected from the southern coast of Indian peninsular (Figure 4.3). The pharmacological activities were evaluated by various *in vitro* anti-inflammatory and antioxidant assays.

4.3.2.1a Structural characterization of Compound 1(TG_1)

Methyl-16(13→14)-abeo-7-labdene-(12-oxo) carboxylate

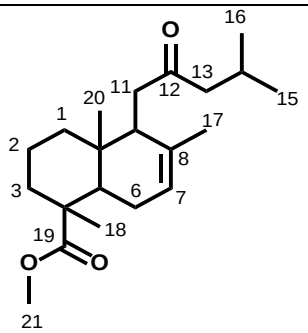

Sample yield	0.31% (> 99% purity, RP-C18 HPLC)
Physical description	Yellowish-white amorphous
Molecular formula	$C_{21}H_{34}O_3$
Molecular mass	334.2508

The abeo-labdane class of diterpenoid derivative, methyl-16(13→14)-abeo-7-labdene-(12-oxo) carboxylate was isolated as yellowish-white amorphous compound. The compound (**1**) has exhibited UV absorbance (UV (MeOH) λ_{max}) at 242 nm (Figure 4.4). The homogeneity of the compound was ascertained by HPLC data on a bonded phase octadecylsilane (C_{18}) stationary phase (HPLC, MeOH/H_2O, 2:1 v/v) with R_t: 3.4 min (Figure 4.5).

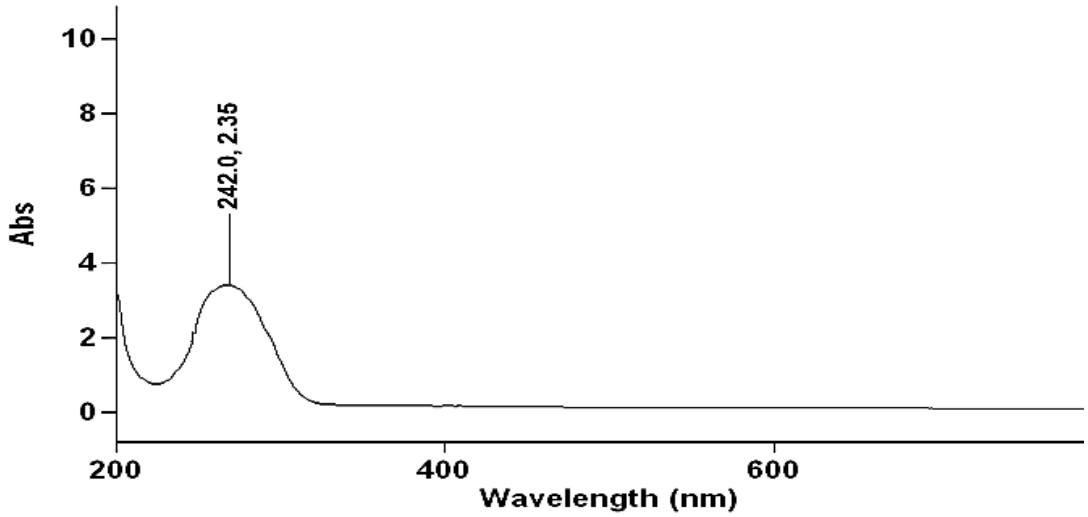

Figure 4.4.: UV spectrum of methyl-16(13→14)-abeo-7-labdene-(12-oxo) carboxylate (**1**)

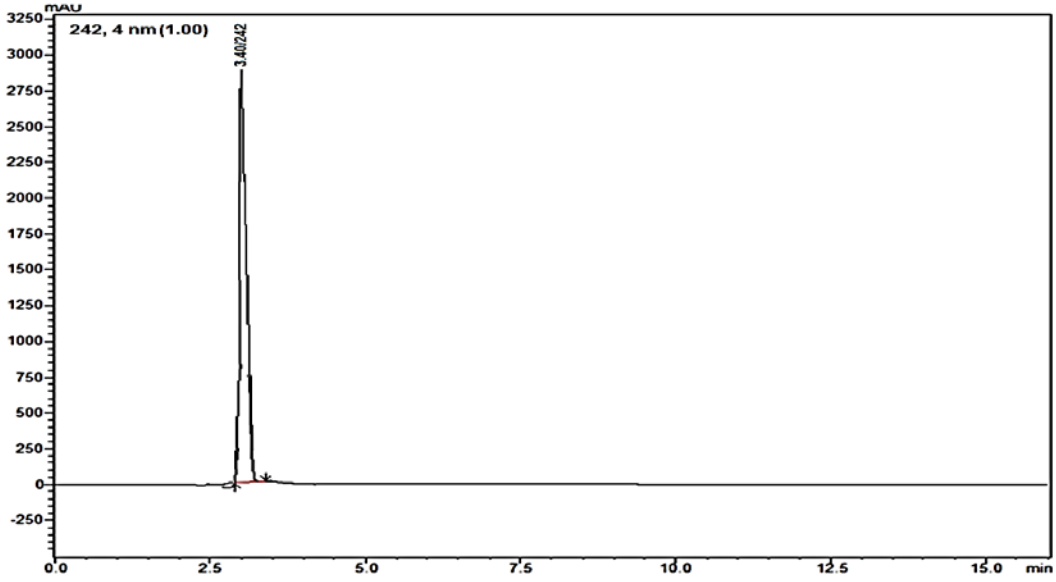

Figure 4.5.: HPLC chromatogram of methyl-16(13→14)-abeo-7-labdene-(12-oxo) carboxylate (**1**)

The chromatography-based fractionation of EtOAc-MeOH organic extract of *G. salicornia* afforded methyl-16(13→14)-abeo-7-labdene-(12-oxo) carboxylate as a homogeneous compound with greater than 99% purity. The ESI-MS (positive) experiment displayed a pseudo-molecular ion peak at m/z 335.2589 (HRESIMS *m/z* calcd 335.2586 [$M+H^+$]) (Figure 4.6), while the molecular formula $C_{21}H_{34}O_3$, implying five unsaturation degrees, was associated with one olefinic bond and two each of cyclic systems and carbonyl moieties based on integrative ^{13}C NMR-MS spectroscopic experiments.

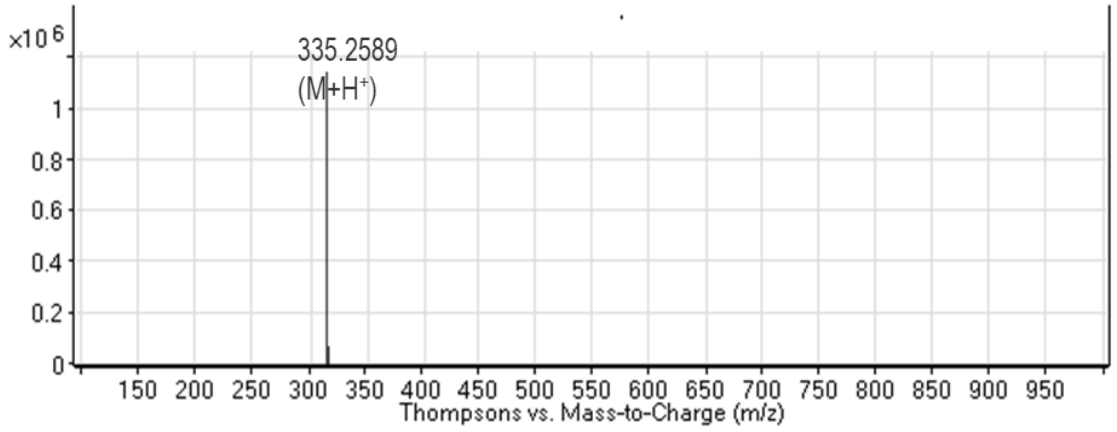

Figure 4.6.: HRESIMS spectrum of methyl-16(13→14)-abeo-7-labdene-(12-oxo) carboxylate (**1**)

The FTIR absorption bands at 1735 and 1725cm^{-1} indicated the presence of carbonyl and ester moieties, respectively (Figure 4.7). The ^{13}C NMR spectrum along with $DEPT_{135}$ analysis deduced 21 carbon signals in the studied compound (Table 4.8) including the signals due to five quaternary carbons (δ 42.41, δ 135.93, δ 39.27, δ 203.27, and δ 167.73), three sp^3 methines (δ 44.70, δ 124.87, δ 45.18, and δ 24.16), and one sp^2 methine (δ 124.87) other than six sp^3 methylene signals (δ 38.65, δ_C 20.85, δ 38.26, δ 23.54, δ 41.32 and δ 54.80) suggesting the structural features of labdane diterpene skeleton (Tran et al., 2017).

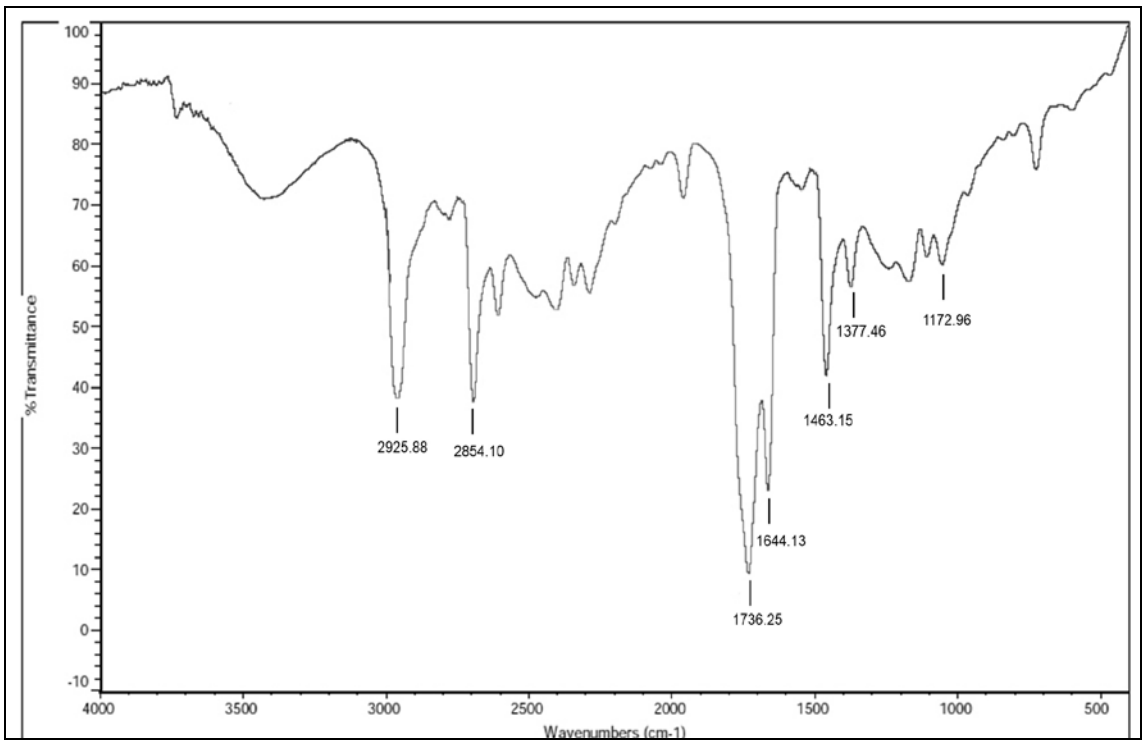

Figure 4.7.: FT-IR spectrum of methyl-16(13→14)-abeo-7-labdene-(12-oxo) carboxylate (**1**)

In addition, the analyses of the ^{13}C NMR spectrum designated the occurrence of one each of ketone group and ester functionality at δ 124.87 and 167.63, respectively. The ^{1}H NMR spectrum demonstrated five methyl groups at δ 0.79 (3H, d, J=6.0 Hz); δ 0.87 (3H, d, J=6.1 Hz); δ 1.14 (3H, s); δ 1.38 (3H, s), δ 0.63 (3H, s) (one angular methyl moiety), and δ 3.46 (3H, s) which were similar to labdane-type diterpenoid skelton (Suzuki et al., 1988; Chakraborty et al., 2010; Suzuki et al., 2002; Tran., 2017; Maneesh et al., 2017) (Figure 4.8-4.10).

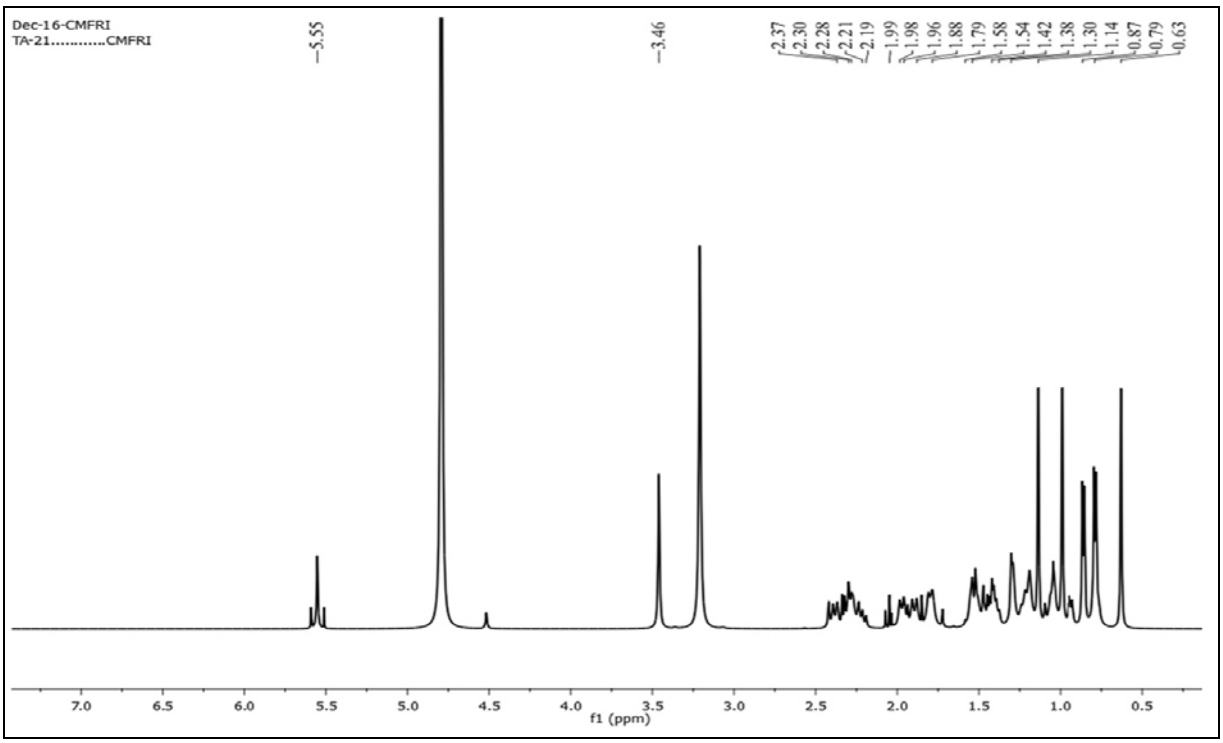

Figure 4.8.: ^{1}H-NMR spectrum of methyl-16(13→14)-abeo-7-labdene-(12-oxo) carboxylate (**1**)

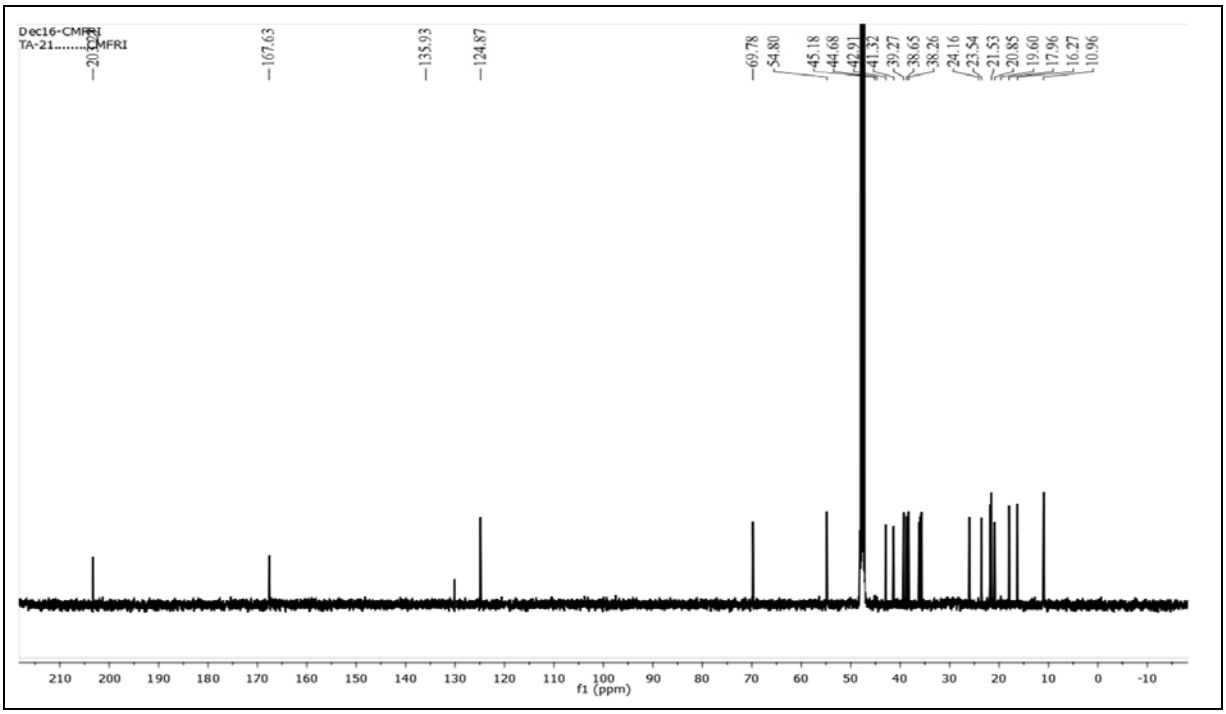

Figure 4.9.: ^{13}C-NMR spectrum of methyl-16(13→14)-abeo-7-labdene-(12-oxo) carboxylate (**1**)

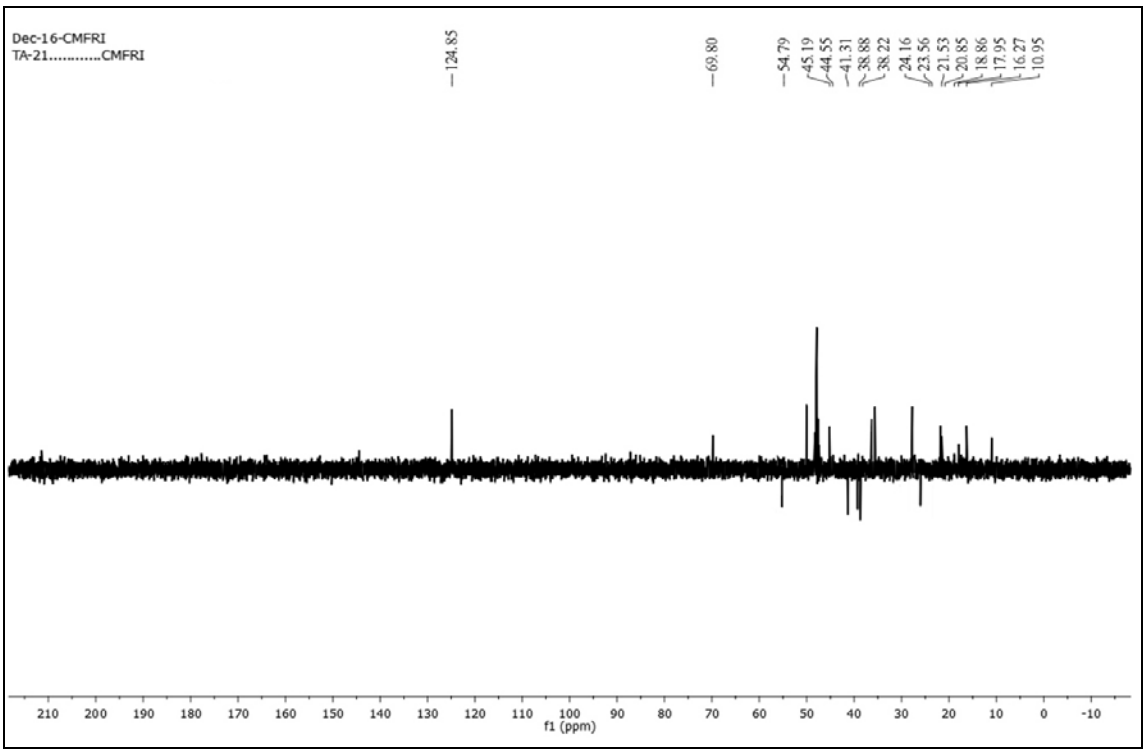

Figure 4.10.: ^{13}C-NMR spectrum of methyl-16(13→14)-abeo-7-labdene-(12-oxo) carboxylate (**1**)

A methyl singlet was apparent at δ 0.79, and this was confirmed by the ^{1}H-^{1}H COSY correlations between δ 0.79/1.96. The ^{1}H-^{1}H COSYs between the δ 1.54/1.42/2.18 along with HMBCs between δ1.54/20.85; 1.42/20.85; 1.54/39.27; 2.18/42.91; 1.98/39.27 revealed the occurrence of C_6-ring in the studied compound. Similarly, ^{1}H-^{1}H COSYs between δ 1.98/1.78/5.55 along with HMBCs between δ 1.98/23.54; 5.55/13.5.93; 2.18/135.93/39.27 demonstrated the second C_6-ring (Figure 4.10). The assembly of these ^{1}H-^{1}H COSYs and HMBCs led to the formation bicyclic decalin system in 16(13→14)-abeo-labdene. Hence, the positions of carbons in this decalin system were disposed from C-1 to C-10 continuously. The ^{1}H NMR data demonstrated the occurrence of an alkenic proton at δ 5.55(1H, t, J=6.6 Hz), exhibiting HSQC with the carbon at δ 124.87, and HMBCs with δ 135.93 and 44.68 (Figure 4.11-4.13). These assignments explained the occurrence of olefinic bond in decalin system between C(7)-C(8). The NMR spectrum of ^{13}C in combination with DEPT$_{135}$ exhibited six more carbon resonances, and which were attached at C-9 of the decalin system as corroborated by their 2D NMR spectral data. The ^{1}H-^{1}H COSYs from H-9/11(δ 2.21/2.37), H-13/14/15and H-14/16 and HMBCs between H-9/C-11, H-11/C-12, H-13/C-12 and H-14/C-12 appropriately explained the substitution of side chain 5-methyl-3-hexanone at C-9. The carbonyl functionality

(C=O) was attached to decalin system by long range correlation between H-9/C-12. The HMBCs from H-3 to C-19 described the occurrence of ester functionality at C-4. The HMBCs between H-9/C-8 and H-17/C-8 confirmed the presence of methyl functionality at C-8. Similarly, the substitution of methyl protons (H-20) was explained by the HMBCs between H-20/C-10. These attributions were specific features of labdanes (Suzuki et al. 1988; Chakraborty et al. 2010; Suzuki et al. 2002; Tran 2017; Maneesh et al. 2017).

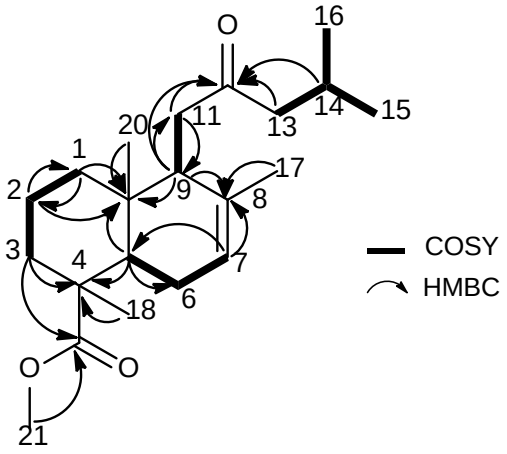

Figure 4.10.: Key ^{1}H-^{1}H COSY (bold face bonds), selected HMBC (black coloured double barbed arrows) correlations of methyl-16(13→14)-abeo-7-labdene-(12-oxo) carboxylate

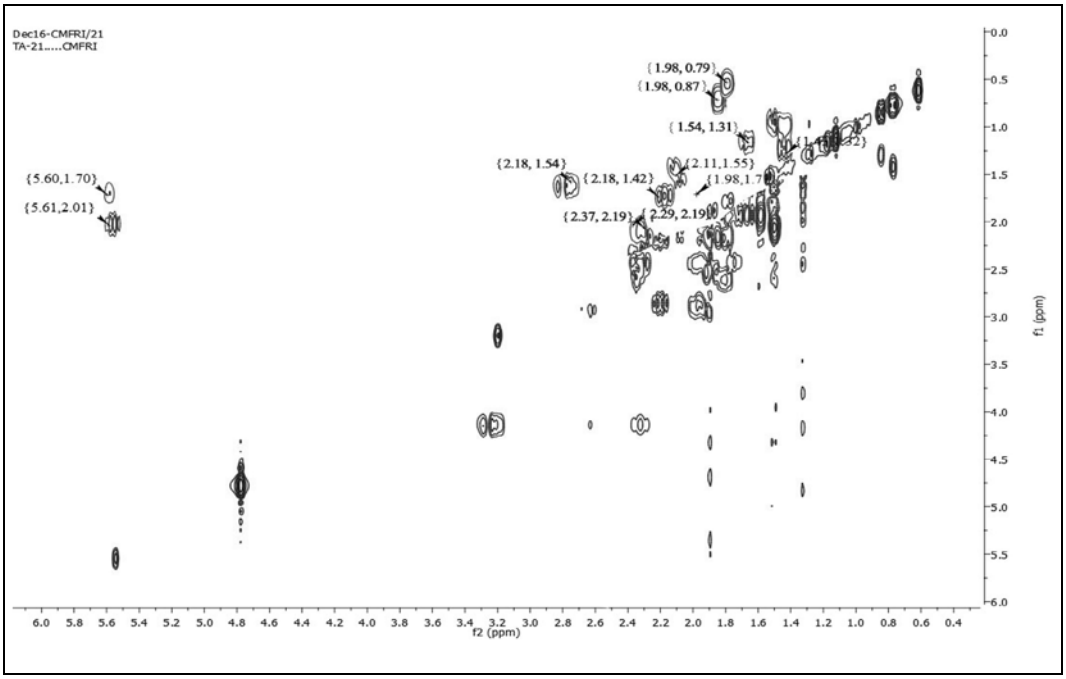

Figure 4.11.: ^{1}H-^{1}H COSY correlation spectrum of methyl-16(13→14)-abeo-7-labdene-(12-oxo) carboxylate (**1**)

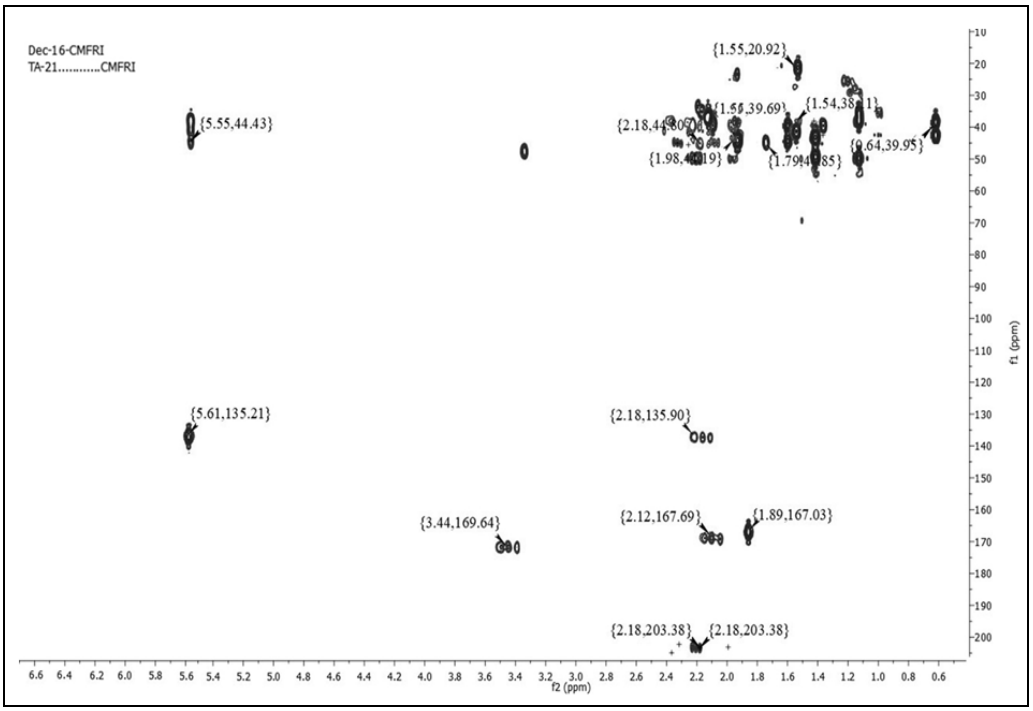

Figure 4.12.: HMBC correlation spectrum methyl-16(13→14)-abeo-7-labdene-(12-oxo) carboxylate (**1**)

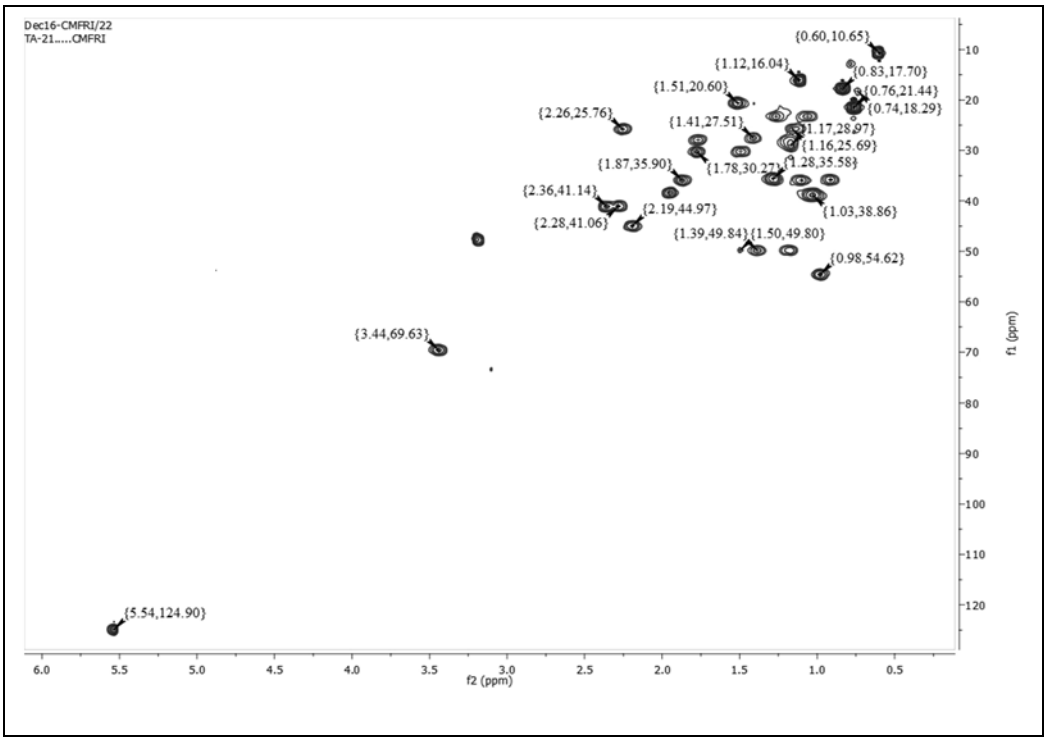

Figure 4.13.: HSQC spectrum methyl-16(13→14)-abeo-7-labdene-(12-oxo) carboxylate (**1**)

Table 4.8: NMR spectroscopic data[a] of methyl-16(13→14)-abeo-7-labdene-(12-oxo) carboxylate (**1**) isolated from red seaweed *G. salicornia*

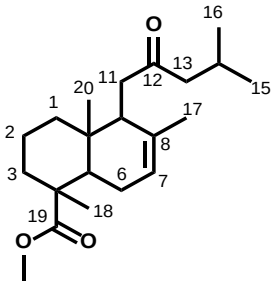

Compound **1**. Methyl-16(13→14)-abeo-7-labdene-(12-oxo)-carboxylate

Type of C	C. No.	^{13}C NMR	^{1}H NMR	int., mult., J in Hz[b]	COSY	HMBC
CH_2	1	38.65	1.54	t, J=5.5Hz	H-2	C-2, 10
			1.30	t, J=4.2Hz	-	-
CH_2	2	20.85	1.54	m	H-3	C-1, 10
			1.42	m	-	-
CH_2	3	38.26	2.19	t, J=5.0Hz	-	C-4, 19
			1.88	t, J=5.0Hz	-	-
C	4	42.91	-	-	-	-
CH	5	44.68	1.98	t, J=3.54Hz	H-6	C-4, 6, 10
CH_2	6	23.54	1.79	t, J=5.1Hz	H-7	-
			1.98	t, J=5.7.1Hz	-	-
CH	7	124.87	5.55	t, J=6.6Hz	-	C-5, 8
C	8	135.93	-	-	-	-
CH	9	45.18	2.21	t, J=5.5Hz	H-11	C-8, 10, 11, 12
C	10	39.27	-	-	-	-
CH_2	11	41.32	2.37	dd, J=10.9, 6.5 Hz	-	C-9, 12
			2.28	dd, J=12.7, 5.4Hz	-	-
C	12	203.27	-	-	-	-
CH_2	13	54.80	2.30	d, J=6.5Hz	H-14	C-12
CH	14	24.16	1.99	m	H-15, 16	C-12
CH_3	15	16.27	0.79	d, J=6.0Hz	-	-
CH_3	16	17.96	0.87	d, J=6.1 Hz	-	-
CH_3	17	19.60	1.14	s	-	C-8
CH_3	18	17.96	1.38	s	-	C-4
C	19	167.63	-	-	-	-
CH_3	20	10.96	0.63	s	-	C-10
CH_3	21	69.78	3.46	s	-	C-19

[a]NMR spectra were recorded using a Bruker AVANCE III 500 MHz (AV 500) spectrometer (Bruker, Karlsruhe, Germany) in MeOH as aprotic solvent at ambient temperature with TMS as the internal standard (δ 0 ppm). [b]Values in ppm, multiplicity and coupling constants (*J*= Hz) were indicated in parentheses. Multiplicities were allocated by [135]DEPT NMR spectrum. The assignments were made with the aid of the COSY, HSQC, HMBC and NOESY experiments.

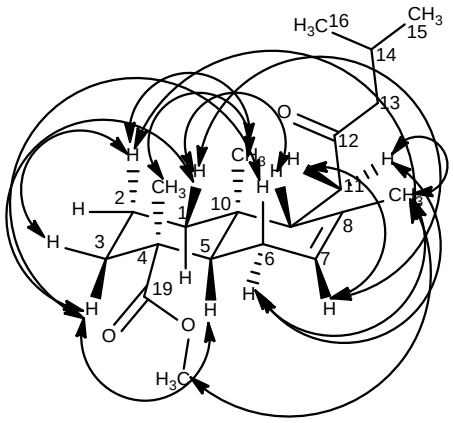

Figure 4.14.: Key NOESY correlations (double headed arrows) of methyl-16(13→14)-abeo-7-labdene-(12-oxo) carboxylate.

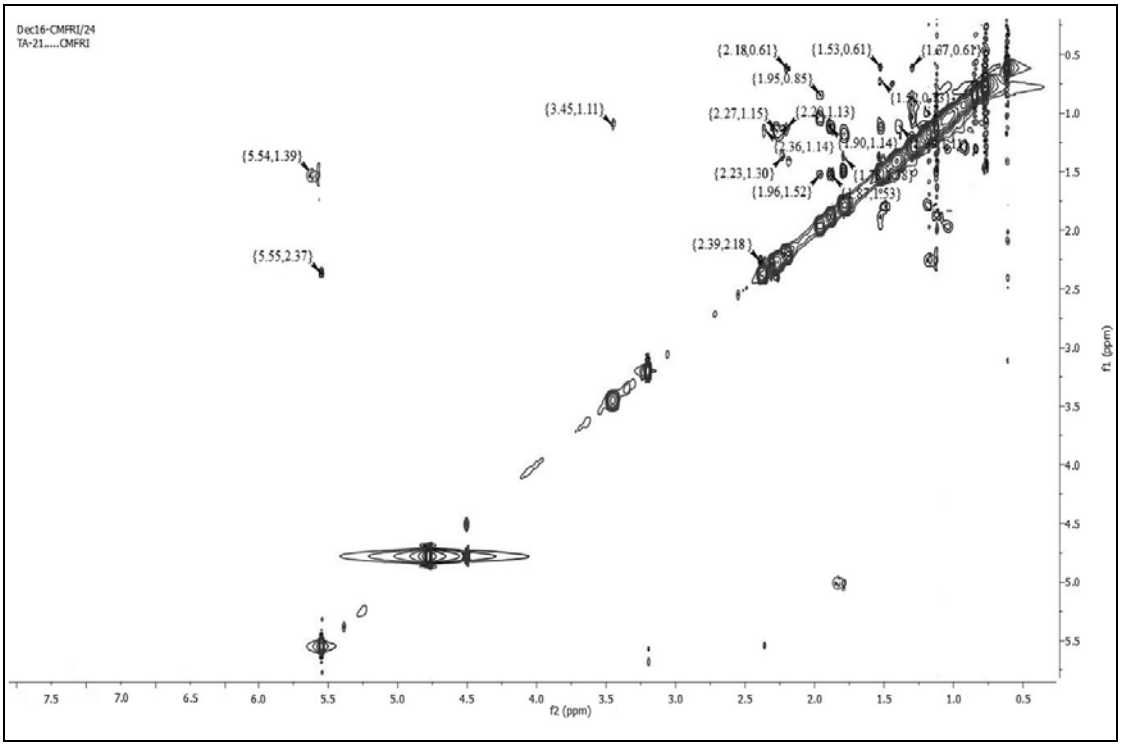

Figure 4.15.: NOESY spectrum of methyl-16(13→14)-abeo-7-labdene-(12-oxo) carboxylate (**1**).

The relative stereochemistries over the rigid bicyclic system of labdane was explained by NOESY experiment (Figure 4.14 & 4.15), whereas NOEs of H-2 (δ 1.54) with H-18 (δ 1.38) and H-20 (δ 0.63) recognized the axial arrangement of the β-face of the decalin frame work, as also supported by previous report of literature (Maneesh et al. 2017). The

spatial arrangement of protons at H-20/H-18 (δ 0.63/1.37), H-17/H-6 (δ 1.53/1.87), H-2/H-3 (δ 1.54/1.88), H-2/H-20 (δ 1.54/0.63), H-17/ H-3 (δ 1.14/1.88), H-6/H-11 (δ 1.79/2.27), H-2/H-17 (δ 1.54/1.79), H-17/H-11 (δ 1.14/2.28) and H-7/H-2 (δ 1.14/3.46) corroborated the β-alignment of these groups in decalin system. NOEs were exhibited between H-6/H-3 (δ 1.79/2.19), H-5/H-3 (δ 1.98/2.19), H-1/H-9 (δ 1.30/2.21), H-1/H-3 (δ 1.30/2.19), H-11/H-7 (δ 2.37/5.55) and H-1/H-7 (δ 1.30/5.55) suggesting that the protons were oriented at the α-face of the compound. These assignments were corroborated the occurrence of *trans*-decalin system with ester and ketone functionalities at C-4 and C-12.

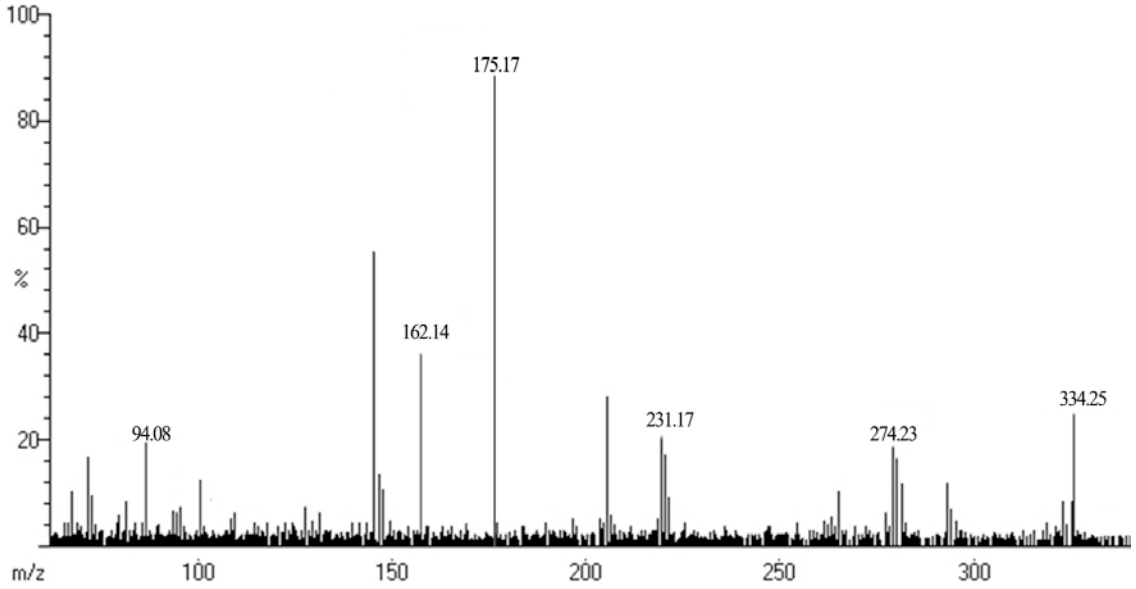

Figure 4.16.: EI-MS spectrum of methyl-16(13→14)-abeo-7-labdene-(12-oxo) carboxylate (**1**)

The FTIR spectrum displayed absorption signals corresponding to these functionalities. The molecular ion peak at m/z 335 (**a**) ($[M+H]^+$) performed an elimination of the side chain by the cleavage of bond, C4-C19 and the reorganization of bonds led to the formation of olefinic bond between C4 and C5 resulting in the fragment peak at *m/z* 274 (**b**). Exclusion of $C_6H_{11}O^+$ ion and radical methyl led to the formation of mass fragments **d** and **e** (*m/z* 175 and 162, respectively). The radical cation **d** also performed a rearrangement mechanism specific to labdane-type diterpenoid to form **f** with the *m/z* 94. The molecular ion peak at *m/z* 175 was found to be the base peak (Figure 4.16 & 4.17). On the basis of these detailed spectral data, the structure of compound was interpreted as 16(13→14)-abeo-7-labdene.

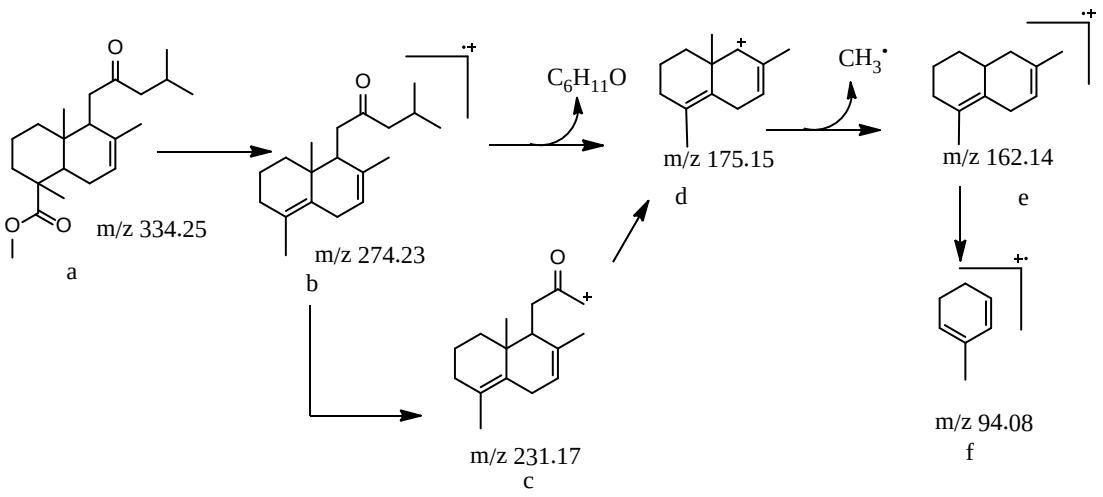

Figure 4.17.: Tentative mass fragmentation pattern of methyl-16(13→14)-abeo-7-labdene-(12-oxo) carboxylate (**1**)

Bio-assay assisted chromatographical purification of the EtOAc-MeOH extract of *G. salicornia* yielded a labdane diterpenoid, characterized as methyl-16(13→14)-abeo-7-labdene-(12-oxo) carboxylate. This ester and ketone functionalities enclosed these type of compounds can be used to develop as targeted bioactive templates.

4.3.2.2 Structural characterization of oleanane class of triterpenoid derivatives (Compounds 2-3)

Triterpenoids, which constitute a wide range of biogenetically derived structurally divergent class of natural compounds resulting from thirty-carbon squalene or analogues precursors, were found to possess potential anti-hyperglycaemic properties (Nazaruk and Borzym-Kluczyk, 2015; Hill and Connolly, 2012). Most of these compounds are tetracycles (6-6-6-5), pentacycles {6-6-6-6-5(6)}, although mono-, bi-, tri-, hexacyclic and acyclic class of triterpenoids were identified from naturally occurring resources (Ruzicka, 1963). Triterpenoids are ubiquitous in marine organisms, such as in seaweeds (Cen-Pacheco et al., 2010), and more than 20,000 triterpenoid metabolites and their variants belonging to oleanane, ursane, lanostane, dammarane, lupane, hopane, along with their pharmacological potential, were characterised (Hill and Connolly, 2012; Laszczyk 2009). Pentacyclic oleanene triterpenoids derived from natural sources were found to be pharmacologically active compounds that were found to lessen the likelihood of postprandial hyperglycaemia by obstructing the functionalities of starch digestive

enzymes (Lee et al., 2017). Oleanane triterpenoids with anti-diabetic properties were characterised from *Sambucus adnata* (Sasaki et al., 2011) and *Astilbe koreana* (Na et al., 2006). The inhibitory potencies of fridooleanene triterpenoids against α-amylase and α-glucosidase were previously reported from the seaweed *Sargassum wightii* (Maneesh and Chakraborty, 2017). Although these classes of secondary metabolites deserve special consideration because of their targeted therapeutic potentials, very few studies were reported with the anti-diabetic activities of naturally-derived triterpenoids (Nazaruk and Borzym-Kluczyk, 2015).

Here, characterized two previously unreported triterpenoids of oleanane class of chemistries from the ethyl acetate-methanol (EtOAc-MeOH) extract of *G. salicornia* collected from the southeast coastal region of Indian peninsular. The studied compounds were designated as 24(4→23), 27(8→26), 30(20→29)-tris-abeo-olean-(12-oxo)-1,15,22-triene-methyl hept-5-enoate (**2**) and 24(4→23)-abeo-olean-(12-oxo)-3,5-diene-deconoate (**3**) by extensive spectroscopic experiments (Figure 4.18).

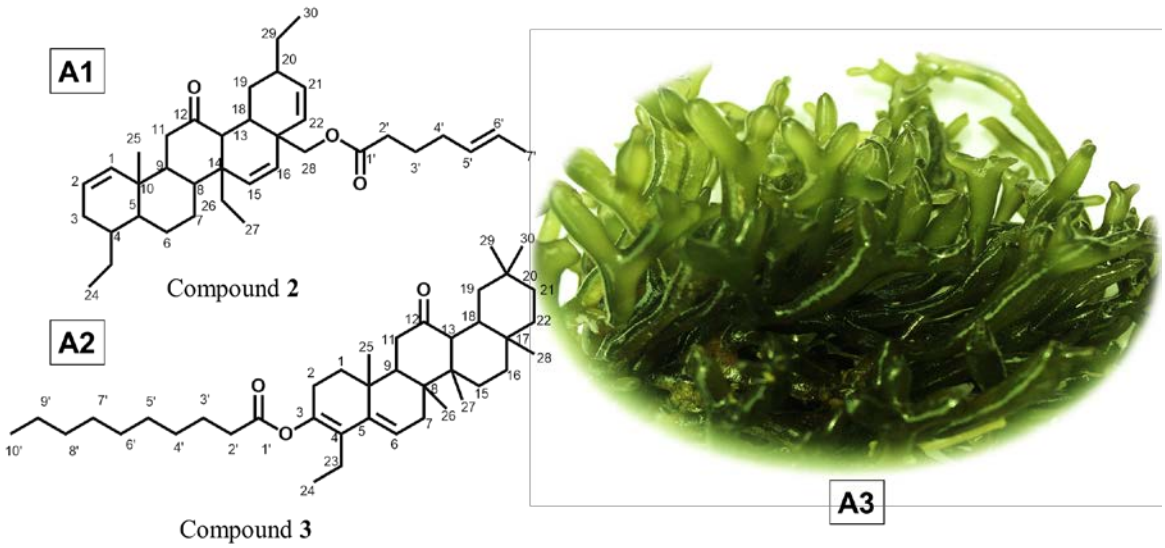

Figure 4.18.: Structural representations of (**A1**) 24(4→23), 27(8→26), 30(20→29)-tris-abeo-olean-(12-oxo)-1,15,22-triene-methyl hept-5-enoate (**1**) and (**A2**) 24(4→23)-abeo-olean-(12-oxo)-3,5-diene-deconoate (**2**) isolated from *G. salicornia*. (**A3**) Representative photograph of thalli of the red seaweed *G. salicornia*.

4.3.2.2a Structural characterization of Compound 2

24(4→23), 27(8→26), 30(20→29)-tris-abeo-olean-(12-oxo)-1,15,22-triene-methyl hept-5-enoate (2)

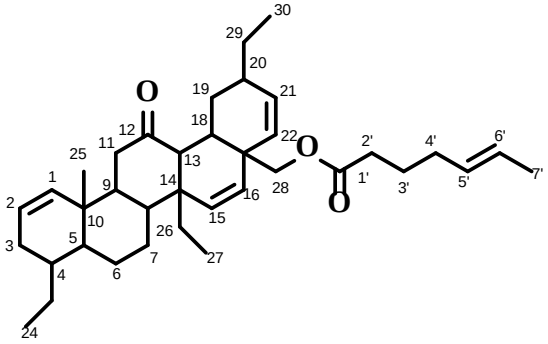

Sample yield	0.29% (> 99% purity, RP-C18 HPLC)
Physical description	Pale yellow oily
Molecular formula	$C_{37}H_{54}O_3$
Molecular mass	546.4073

The abeo-labdane class of diterpenoid derivative, 24(4→23), 27(8→26), 30(20→29)-tris-abeo-olean-(12-oxo)-1,15,22-triene-methyl hept-5-enoate (**2**) was isolated as yellowish-white amorphous compound. The compound (**2**) has exhibited UV absorbance (UV (MeOH) λ_{max}) at 244 nm (Figure 4.19.). The homogeneity of the compound was ascertained by HPLC data on a bonded phase octadecylsilane (C_{18}) stationary phase (HPLC, MeOH/MeCN, 2:1 v/v) with R_t: 3.41 min (Figure 4.20.).

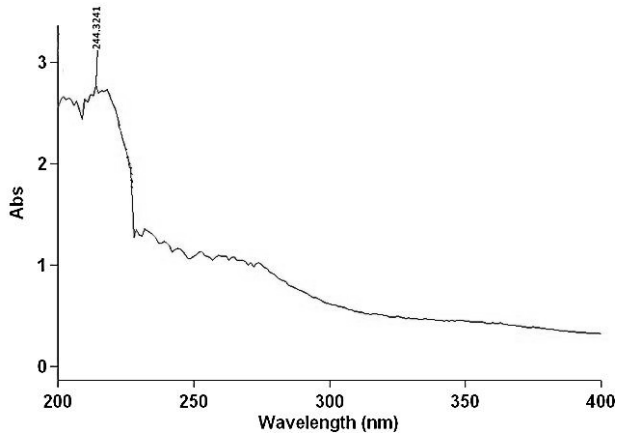

Figure 4.19.: UVspectrum of 24(4→23), 27(8→26), 30(20→29)-tris-abeo-olean-(12-oxo)-1,15,22-triene-methyl hept-5-enoate **(2)**

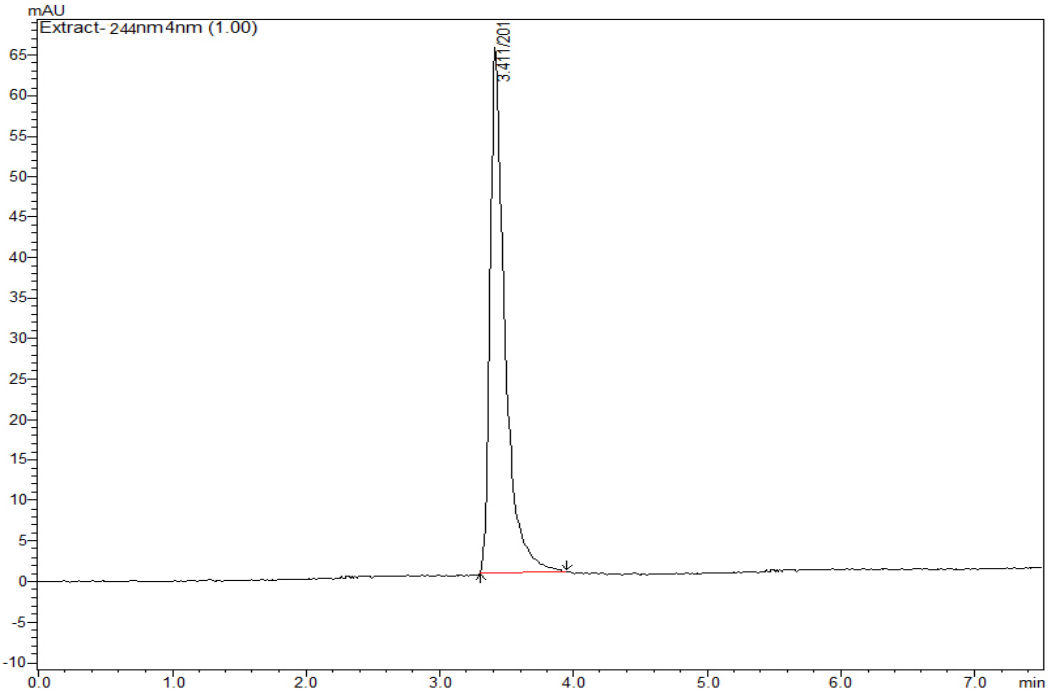

Figure 4.20.: HPLC chromatogram of 24(4→23), 27(8→26), 30(20→29)-tris-abeo-olean-(12-oxo)-1,15,22-triene-methyl hept-5-enoate (**2**)

Repeated column chromatographic fractionation of *G. salicornia* yielded compound (**2**) as an yellow oily substance, which was characterised as 24(4→23), 27(8→26), 30(20→29)-tris-abeo-olean-(12-oxo)-1,15,22-triene-methyl hept-5-enoate (**2**). The HRESIMS experiment displayed the molecular ion peak at *m/z* 547.4155 $[M+H]^+$, (Figure 4.21), which along with NMR-IR spectroscopic analyses deduced its molecular formula as $C_{37}H_{55}O_3$ (Table 4.8).

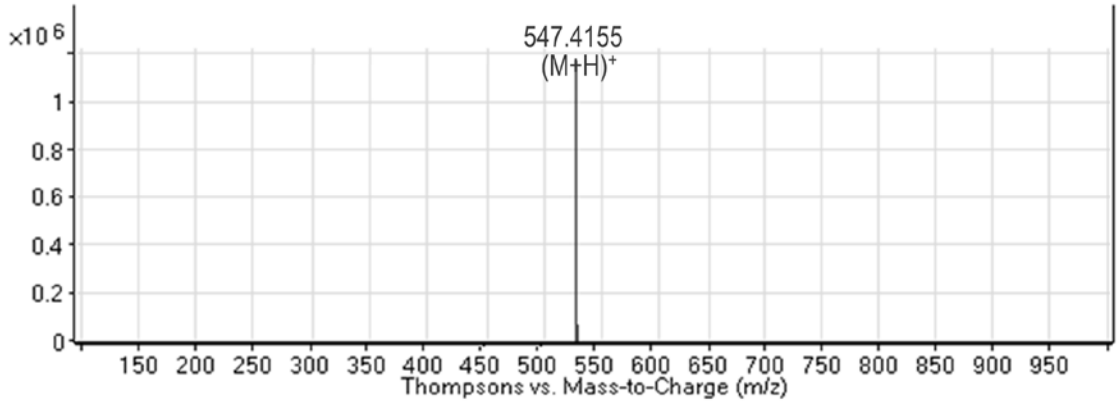

Figure 4.21.: HRESIMS of 24(4→23), 27(8→26), 30(20→29)-tris-abeo-olean-(12-oxo)-1,15,22-triene-methyl hept-5-enoate **(2)**

The FTIR signals at 1730 and 1726 cm^{-1} attributed the probable existence of ester and carbonyl functionalities, respectively (Figure 4.22). The ^{1}H NMR spectrum illustrated the occurrence of six deshielded olefinic hydrogens at δ 5.32, 5.28, 5.34, 5.30, 5.29, 5.33, 5.26, and 5.25. In addition, the shielded methyls (appeared as triplets) at δ 0.80, 0.78 and 0.82 suggested the presence of methyl substitutions on triterpenoid system (Figure 4.23). The ^{13}C NMR, ^{135}DEPT along with HSQC spectrum with of **(2)** disclosed 37 carbon traces, encompassing five methyls (δ 12.2, 11.8, 19.7, 13.1, 14.2), twelve sp^3 methylenes (δ 31.8, 29.0, 28.9, 39.3, 31.7, 4.7, 29.8, 65.7, 29.1, 25.6, 26.9, 33.2), eight sp^2 methines (δ 130.2, 127.8, 130.5, 127.7, 132.0, 127.5, 129.7, 128.0), seven sp^3 methines (δ 33.9, 52.3, 29.7, 47.9, 56.7, 31.9, 37.2), and five quaternary carbons (δ 46.8, 34.4, 43.5), including two carbonyls (δ 193.7, 179.4) (Figure 4.24-4.26).

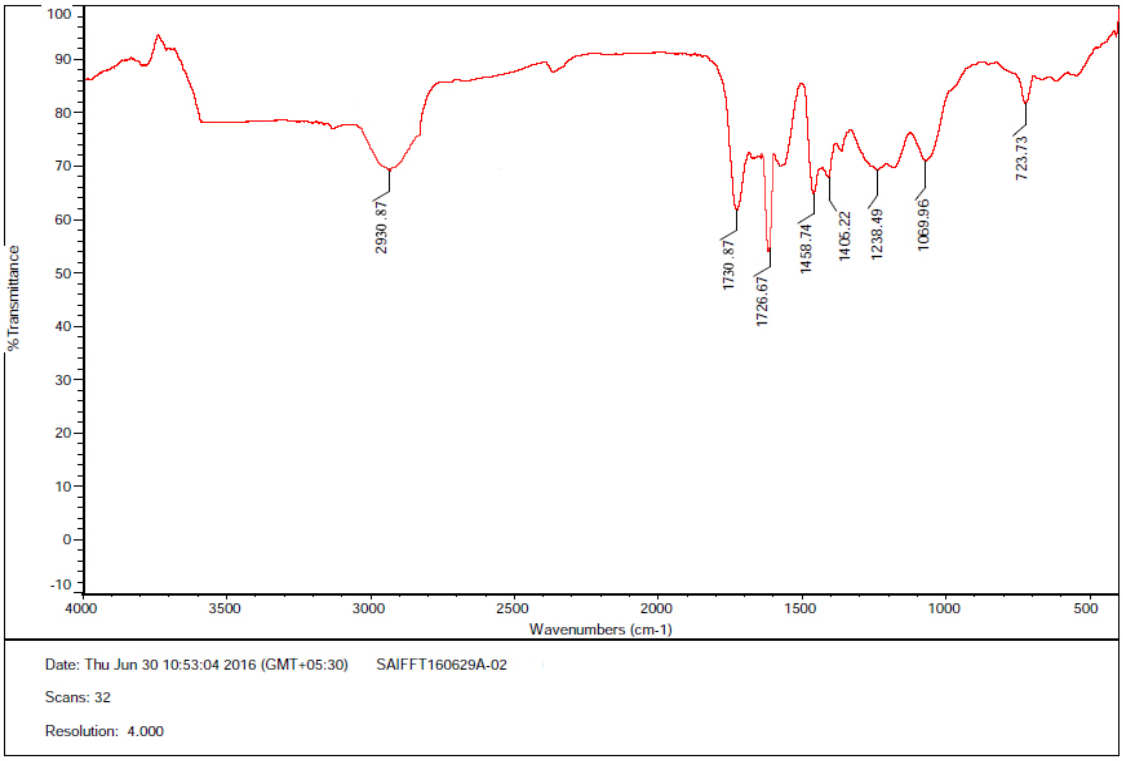

Figure 4.22.: FT-IR of 24(4→23), 27(8→26), 30(20→29)-tris-abeo-olean-(12-oxo)-1,15,22-triene-methyl hept-5-enoate **(2)**

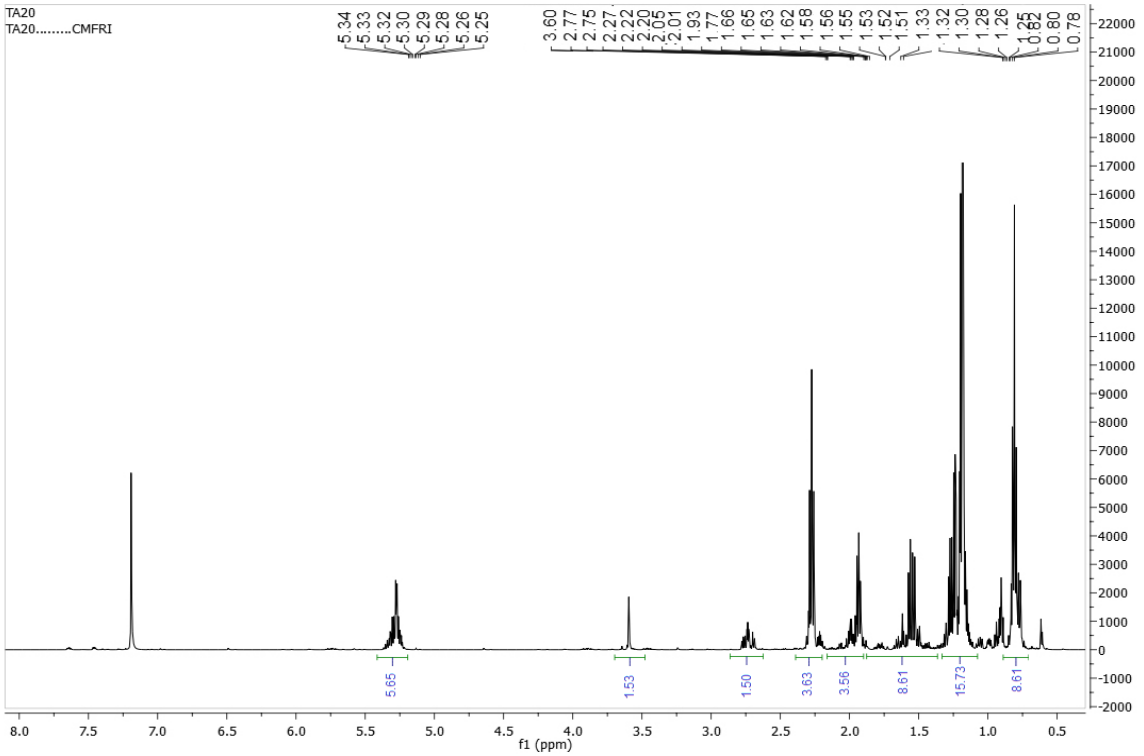

Figure 4.23.: ^{1}H-NMR of 24(4→23), 27(8→26), 30(20→29)-tris-abeo-olean-(12-oxo)-1,15,22-triene-methyl hept-5-enoate **(2)**

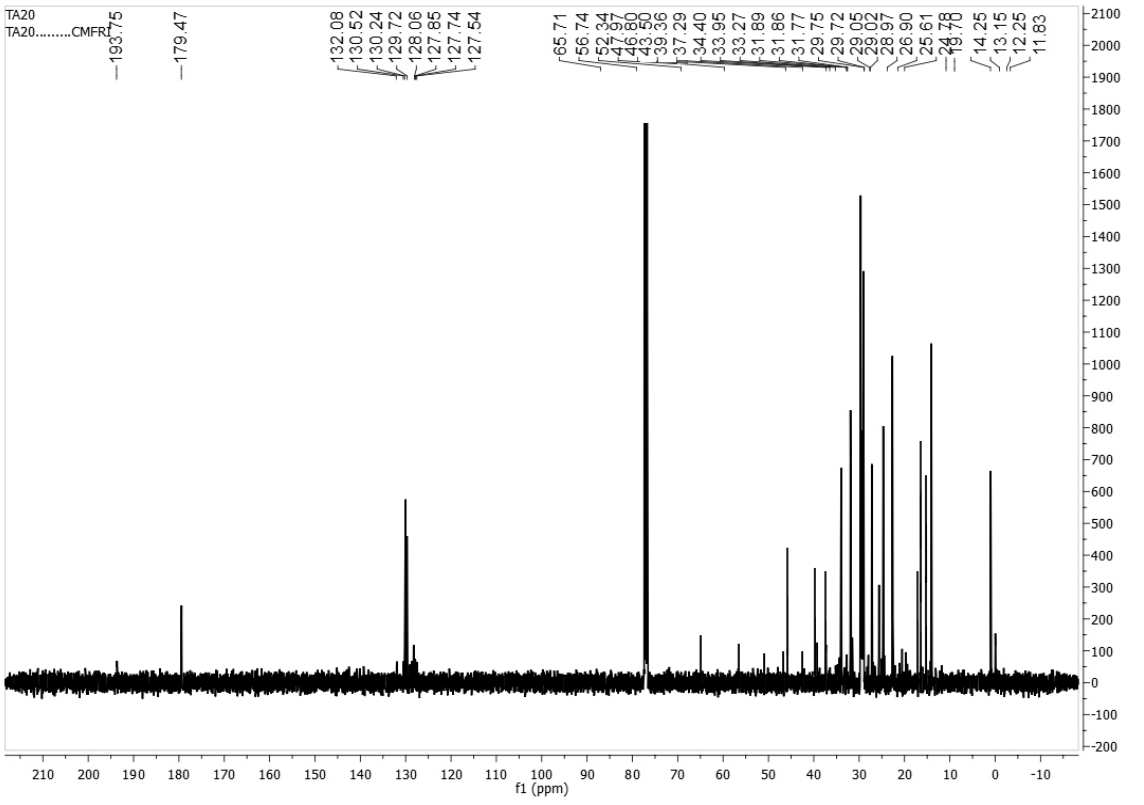

Figure 4.24.: ^{13}C NMR of 24(4→23), 27(8→26), 30(20→29)-tris-abeo-olean-(12-oxo)-1,15,22-triene-methyl hept-5-enoate **(2)**

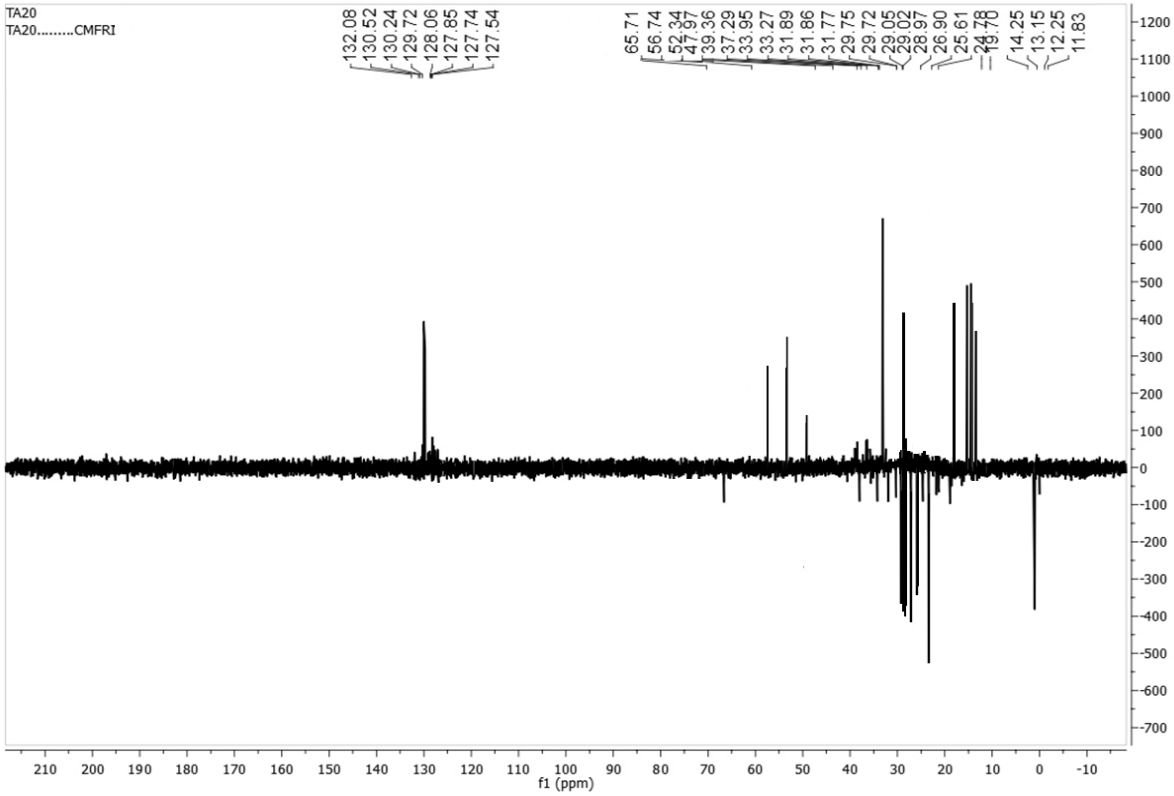

Figure 4.25.: ^{135}DEPT spectrum of 24(4→23), 27(8→26), 30(20→29)-tris-abeo-olean-(12-oxo)-1,15,22-triene-methyl hept-5-enoate **(2)**

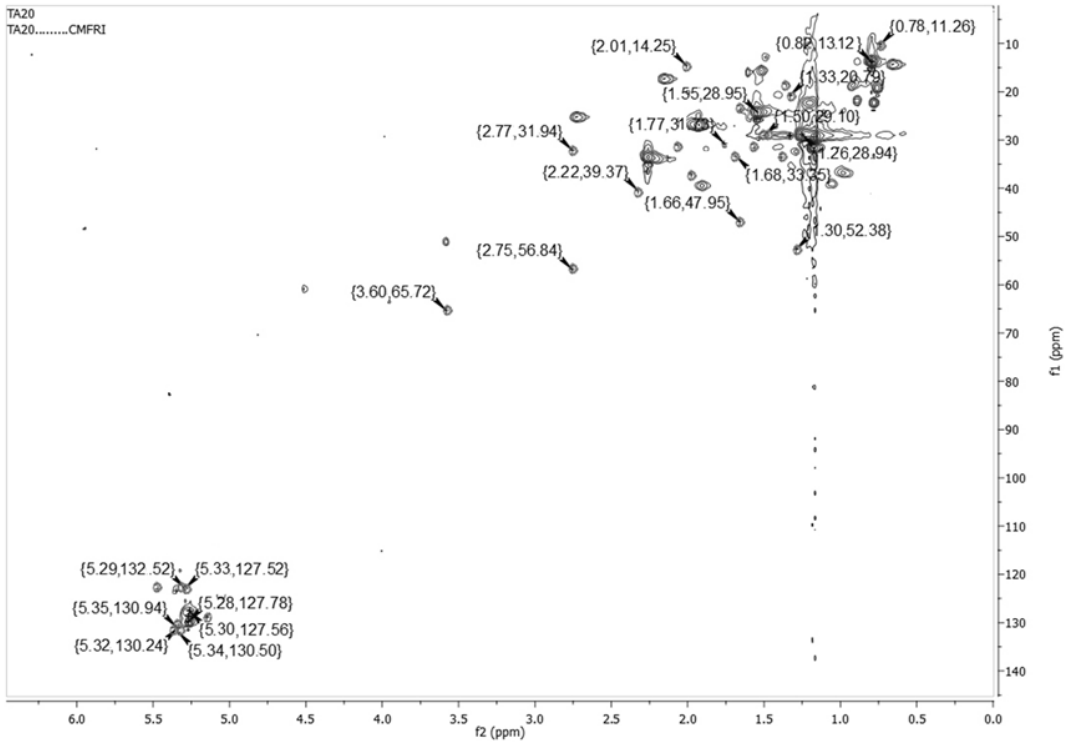

Figure 4.26.: HSQC spectrum of 24(4→23), 27(8→26), 30(20→29)-tris-abeo-olean-(12-oxo)-1,15,22-triene-methyl hept-5-enoate **(2)**

The intense ^{1}H-^{1}H COSY spectrum of compound **2** demonstrated the occurrence of spin networks between (CH-δ5.28) (arbitrarily assigned as H-2)-(CH_2-δ 1.77) (H-3)-(CH-δ1.62) (H-4)-(CH-δ1.30) (H-5)-(CH_2-δ1.51) (H-6)-(CH_2-δ1.26) (H-7)-(CH-δ1.33) (H-8)-(CH-δ1.66) (H-9)-(CH_2-δ2.22) (H-11) and (CH_2-δ1.65) (H-19)-(CH-δ 1.93) (H-20)-(CH-δ5.29) (H-21), which supported the partial skeleton of pentacyclic ring in the triterpenoid (Figure 4.27 & 4.28). The HMBC interactions from CH-1 (δ 5.32) to CH-2 (δ 127.8) and C-10 (δ 46.8) determined the occurrence of olefinic bond at C-1 (δ 5.32/δ 130.2) and C-2 (δ 5.28/δ 127.8) (Figure 4.29). The HMBC interactions between CH-15 (δ 5.34) to C-14 (δ 34.4) and those from CH-16 (δ 5.30) to C-15 (δ 130.5), C-17 (δ 43.5) assigned an olefinic bond at C-15 (δ 5.34/130.5) and C-16 (δ 5.30/δ 127.7). Likewise, HMBCs from CH-20 (δ 1.93) and CH-21 (δ 5.29) to C-22 (δ 127.5) and from CH-22 (δ 5.33) to C-17 (δ 43.5) ascribed the occurrence of an olefinic bond between CH-21 (δ 5.29/δ132.0) and CH-22 (δ 5.33/δ 127.5). This attribution was in agreement with the presence of olefinic bond in the E-ring system (Maneesh and Chakraborty, 2017). Other HMBC correlations from CH-5 (δ 1.30) to C-10 (δ 46.8), C-9 (δ 47.9); from CH_2-6 (δ 1.51) to C-5 (δ 52.3); from CH-8 (δ 1.33) to C-13 (δ 56.7); CH-13 (δ 2.75) to C-18 (δ 31.9), C-14 (δ 34.4) and from CH-18 (δ 2.77) to C-19 (δ 31.7), C-17 (δ 43.5) were persistent with the pentacyclic

skeleton of triterpenoid, (**2**). The long range couplings from CH-9 (δ 1.66), CH-13 (δ 2.75) and CH_2-11 (δ 2.22) to C-12 (δ 193.7) revealed the C-12 keto functionality in (**2**). This was comparable with the previously reported compound, dihydroxyolean-12-one, in which the chemical shift of C-12 was found to be δ 208 due to the presence of neighbouring hydroxyl group at C-11 (δ 71.8) (Da Rocha et al., 2015). No electronegative functionalities were apparent adjacent to keto group at C-12, hence it recorded lower chemical shift value in the present compound.

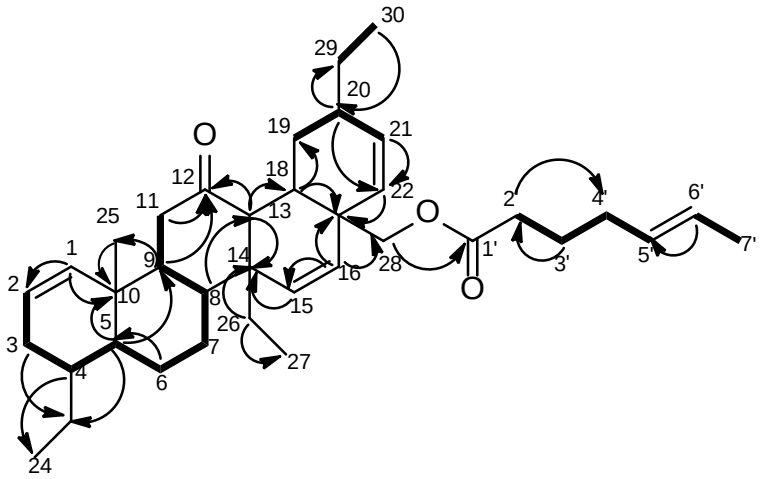

Figure 4.27.: ^{1}H-^{1}H COSY (bold-face bonds), and selected HMBC (double-barbed arrows) correlations of 24(4→23), 27(8→26), 30(20→29)-tris-abeo-olean-(12-oxo)-1,15,22-triene-methyl hept-5-enoate (**2**) isolated from *G. salicornia*.

These NMR assignments together with earlier reported values (Da Rocha et al., 2015; Huang et al., 2013; Maneesh and Chakraborty, 2017) substantiated the presence of pentacyclic triterpenoid bearing olean-(12-oxo)-1,15,22-triene framework. The typical oleanene skeleton enclosed seven tertiary methyls in the range of δ 0.7 to δ 1.25 at C-4, C-10, C-8, C-14, C-17 and C-20 positions (Da Rocha et al., 2015; Maneesh and Chakraborty, 2017), whereas the titled compound comprised of only one tertiary methyl at C-10. The position of tertiary methyl (CH_3-25) at C-10 was ascertained through the HMBCs from CH-9 (δ 1.66) to CH_3-25 (δ 19.7) and CH_3-25 (δ 19.7) to C-10 (δ 46.8), which was comparable with the earlier reports (Da Rocha et al., 2015).

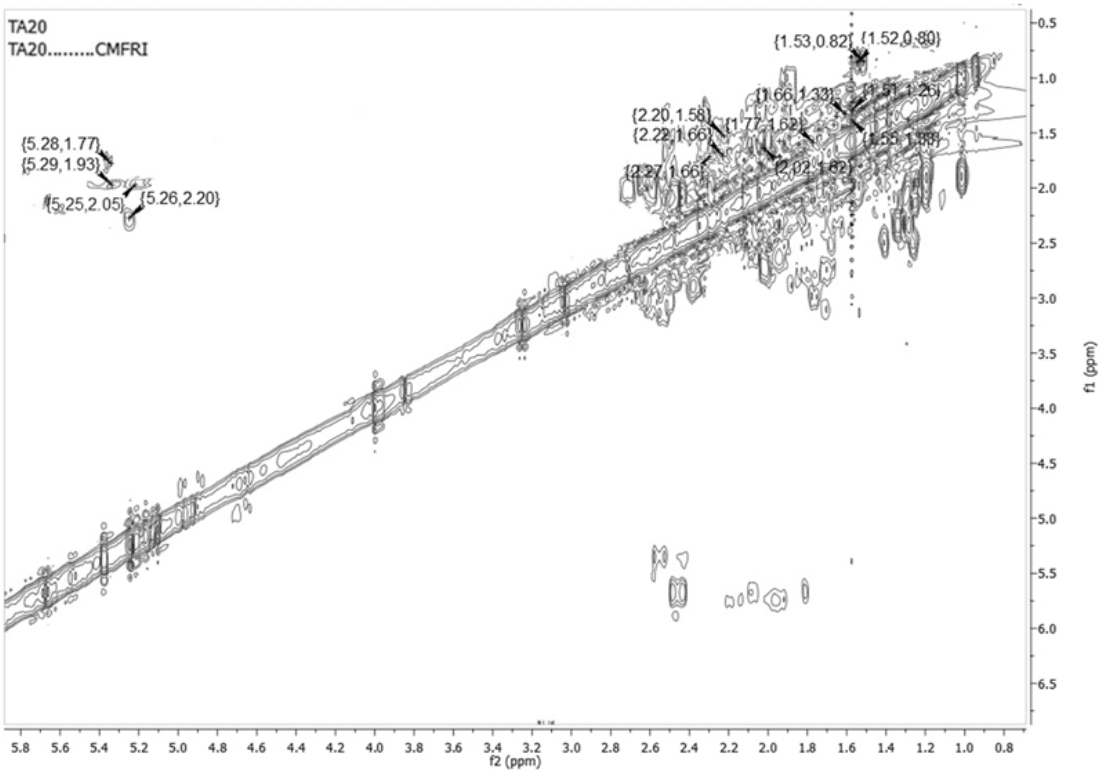

Figure 4.28.: ^{1}H-^{1}H COSY spectrum of 24(4→23), 27(8→26), 30(20→29)-tris-abeo-olean-(12-oxo)-1,15,22-triene-methyl hept-5-enoate **(2)**

The angular methyl at C-4 (CH_3-24) in the basic oleanene framework was shifted to C-23, which was affirmed by the HMBC connections from CH_2-3 (δ 1.77) to CH_2-23 (δ 24.7); CH-4 (δ 1.62) to CH_3-24 (δ 12.2) and CH-5 (δ 1.30) to CH_2-23 (δ 24.7). The methyl at C-8 (CH_3-27) was shifted to C-26, which was corroborated by the HMBCs from CH_2-26 (δ 1.25) to CH_3-27 (δ 11.8), C-14 (δ 34.4) (Fig. 2). Similarly, one of the gem dimethyl groups at C-20 (CH_3-30) was shifted to C-29, and was confirmed through the HMBC couplings from CH_3-30 (δ 0.82) to CH-20 (δ 37.2) and COSY couplings from (CH_2-δ 1.52) (H-29)-(CH_3-δ 0.82) (H-30). Therefore, the titled compound was classified as tris-abeo-oleanene triterpenoid, (**2**) which was named as 24(4→23), 27(8→26), 30(20→29)-tris-abeo-olean-(12-oxo)-triene. The typical angular methyl at C-17 (CH_3-28) was found to be deshielded in the present compound when compared to the previously reported chemical shift values (CH_3-28, δ 28.43/0.84) (Da Rocha et al., 2015), which was found to be δ 65.7/3.60 (CH_2-28). This higher chemical shift was typical for the oxygenated protons, and its HMBC coupling to δ179.4 (C-1') along with HMBC from CH-16 (δ 5.30) to CH_2-28 (δ 65.7) suggested the presence of an ester linkage in which oxygen was directly bonded to the sp^3 methylene at δ 3.60. The spin systems from (CH_2-δ 1.63)

(arbitrarily assigned as H-2')-(CH_2-δ 1.58) (H-3')-(CH_2-δ 2.20) (H-4')-(CH-δ 5.26) (H-5') and (CH-δ 5.25) (H-6')-(CH_3-δ 2.05) (H-7') along with HMBCs from CH_2-2' (δ 1.63) to CH_2-4' (δ 33.2); CH_2-3' (δ 1.58) to CH_2-2' (δ 25.6) and CH-6' (δ 5.25) to CH-5' (δ 129.7) appropriately supported the presence of methyl hept-5-enoate chain at C-17. The titled compound was structurally related to previously reported oleanenes (Da Rocha et al., 2015; Huang et al., 2013; Maneesh and Chakraborty, 2017; Oramas-Royo et al., 2010) besides the dissimilarities recognized in the positions of alkenes, tertiary methyls, ester linkages along with absence of hydroxyl functionalities.

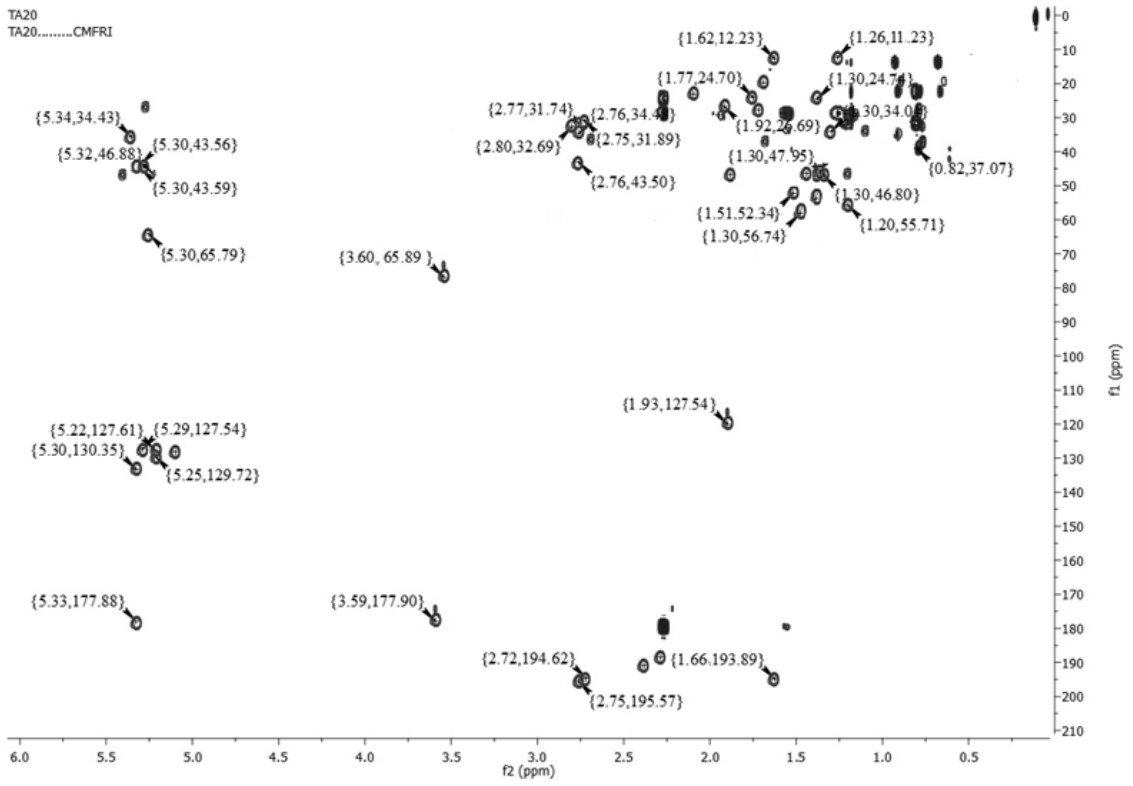

Figure 4.29.: HMBC spectrum of 24(4→23), 27(8→26), 30(20→29)-tris-abeo-olean-(12-oxo)-1,15,22-triene-methyl hept-5-enoate **(2)**

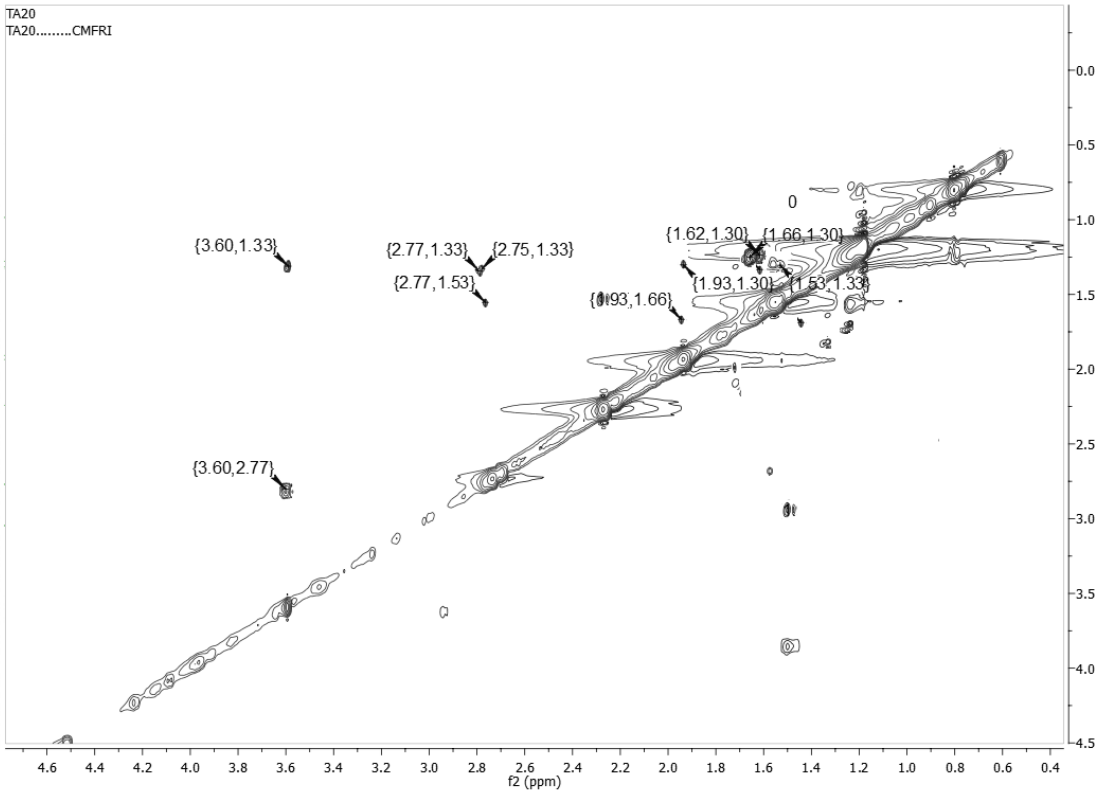

Figure 4.30.: NOESY spectrum of 24(4→23), 27(8→26), 30(20→29)-tris-abeo-olean-(12-oxo)-1,15,22-triene-methyl hept-5-enoate (**2**)

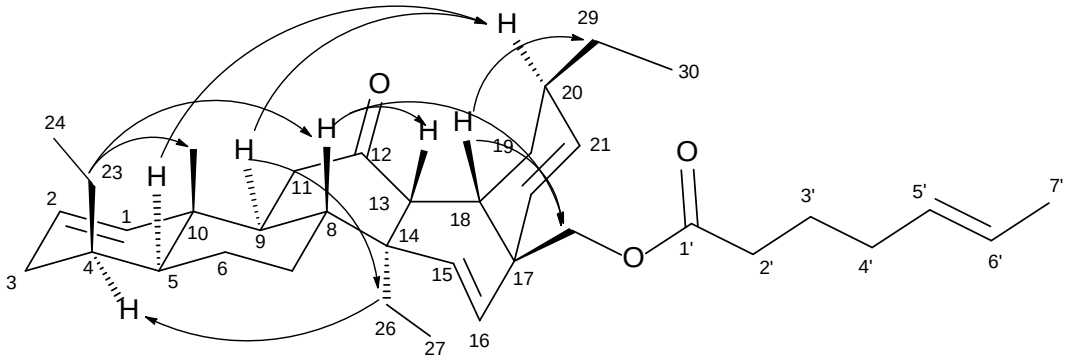

Figure 4.31.: NOE correlations of 24(4→23), 27(8→26), 30(20→29)-tris-abeo-olean-(12-oxo)-1,15,22-triene-methyl-hept-5-enoate (**2**) isolated from *G. salicornia*.

The relative stereochemistry of the chiral centres at δ 33.9 (C-4), 52.3 (C-5), 29.7 (C-8), 47.9 (C-9), 56.7 (C-13), 31.9 (C-18) and 37.2 (C-20) were deduced from nuclear overhauser

effect spectroscopy (NOESY) (Figure 4.30 and 4.31). The proton at chiral centre, δ 1.62 (assigned as CH-4) exhibited NOE with the proton (angular methyl) at δ 1.30 (H-5) that were α-aligned (Wang et al., 2014). The α-disposition of protons at H-4, H-5, H-9 and H-20 were inferred by the NOE correlations between H-5 (δ 1.30)/H-9 (δ 1.66) and H-9 (δ 1.66)/H-20 (δ 1.93). On the contrary, the protons at δ 1.32 (H-25), δ 2.75 (H-13), δ 1.33 (H-8), and δ 2.77 (H-18) were positioned at the β-surface of reference plane, which were inferred by NOE correlations between H-25 (δ 1.32)/H-13 (δ 2.75), H-8 (δ 1.33)/H-18 (δ 2.77) and H-8 (δ 1.33)/H-13 (δ 2.75), The trans- and cis-intersection of ABCD and DE parts were reinforced by their stereochemical attributions (Koay et al., 2013).

Table 4.9: NMR spectroscopic data[a] of 24(4→23), 27(8→26), 30(20→29)-tris-abeo-olean-(12-oxo)-1,15,22-triene-methyl-hept-5-enoate (**2**) isolated from red seaweed *G. salicornia*

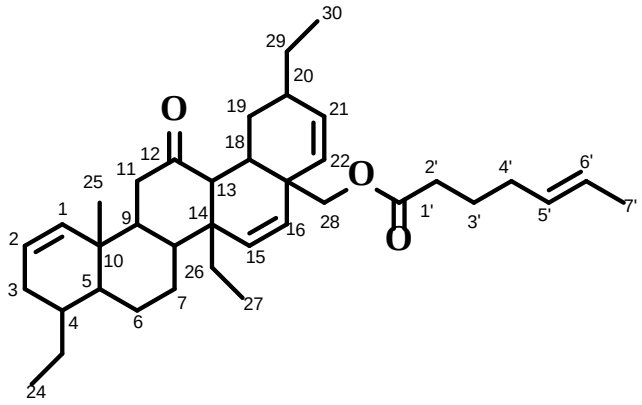

Compound 2……24(4→23), 27(8→26), 30(20→29)-tris-abeo-olean-(12-oxo)-1,15,22-triene-methyl-hept-5-enoate (**2**)

Type	C. No.	^{13}C NMR	^{1}H. No. (int., mult., J in Hz)[b]	^{1}H NMR	COSY	HMBC
CH	1	130.2	1H, d, J = 10.3 Hz	5.32	-	C-2,10
CH	2	127.8	1H, dt, J = 8.9, 7.6 Hz	5.28	H-3	-
CH_2	3	31.8	1H, t, J = 4.9 Hz	1.77	H-4	C-23
			1H, t, J = 4.9 Hz	2.01	-	-
CH	4	33.9	1H, m	1.62	H-5	C-24
CH	5	52.3	1H, m	1.30	H-6	C-23,9,10
CH_2	6	29.0	1H, m	1.51	H-7	C-5
			1H, m	1.28	-	-
CH_2	7	28.9	1H, m	1.55	H-8	-
			1H, m	1.26	-	-
CH	8	29.7	1H, td, J = 6.8, 5.2 Hz	1.33	H-9	C-13
CH	9	47.9	1H, td, J = 5.8, 5.5 Hz	1.66	H-11	C-12,25
C	10	46.8	-	-	-	-
CH_2	11	39.3	1H, d, J = 8.6 Hz	2.22	-	C-12
			1H, d, J = 8.0 Hz	2.27	-	-

C	12	193.7	-	-	-	-
CH	13	56.7	1H, d, J = 6.7 Hz	2.75	-	C-12,14,18
C	14	34.4	-	-	-	-
CH	15	130.5	1H, d, J = 12.1 Hz	5.34	-	C-14
CH	16	127.7	1H, d, J = 13.0 Hz	5.30	-	C-15,17,28
C	17	43.5	-	-	-	-
CH	18	31.9	1H, m	2.77	-	C-19,17
CH_2	19	31.7	1H, m	1.65	H-20	-
			1H, m	1.56	-	-
CH	20	37.2	1H, m	1.93	H-21	C-29,22
CH	21	132.0	1H, t, J = 14.0 Hz	5.29	-	C-22
CH	22	127.5	1H, d, J = 12.7 Hz	5.33	-	C-17
CH_2	23	24.7	2H, m	1.53	-	-
CH_3	24	12.2	3H, t, J = 4.2 Hz	0.80	-	-
CH_3	25	19.7	3H, s	1.32	-	C-10
CH_2	26	29.8	2H, d, J = 3.7 Hz	1.25	-	C-14,27
CH_3	27	11.8	3H, t, J = 4.9 Hz	0.78	-	-
CH_2	28	65.7	2H, s	3.60	-	C-1'
CH_2	29	29.1	2H, m	1.52	H-30	-
CH_3	30	13.1	3H, t, J = 5.0 Hz	0.82	-	C-20
C	1'	179.4	-	-	-	-
CH_2	2'	25.6	2H, t, J = 4.7 Hz	1.63	H-3'	C-4'
CH_2	3'	26.9	2H, m	1.58	H-4'	C-2'
CH_2	4'	33.2	2H, m	2.20	H-5'	-
CH	5'	129.7	1H, dt, J = 11.7 Hz	5.26	-	-
CH	6'	128.0	1H, m	5.25	H-7'	C-5'
CH_3	7'	14.2	3H, d, J = 9.2 Hz	2.05	-	-

[a]NMR spectra were recorded using a Bruker AVANCE III 500 MHz (AV 500) spectrometer (Bruker, Karlsruhe, Germany) in $CDCl_3$ as aprotic solvent at ambient temperature with TMS as the internal standard (δ 0 ppm).

[b]Values in ppm, multiplicity and coupling constants (J = Hz) were indicated in parentheses. Multiplicities were allocated by ^{135}DEPT NMR spectrum.

The assignments were made with the aid of the COSY, HSQC, HMBC and NOESY experiments.

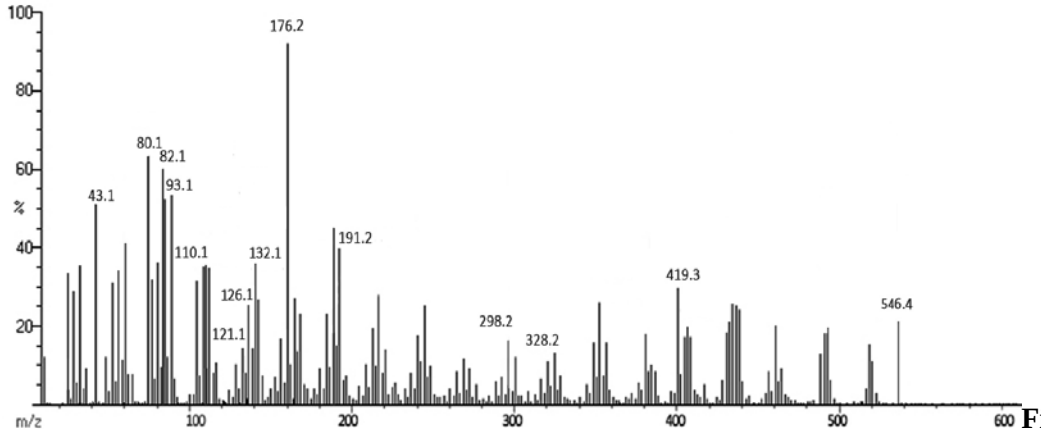

Figure 4.32.: EI-MS spectrum of 24(4→23), 27(8→26), 30(20→29)-tris-abeo-olean-(12-oxo)-1,15,22-triene-methyl-hept-5-enoate (**2**) isolated from *G. salicornia*.

The structural elucidation of **2** was corroborated by the mass spectral experiment wherein the molecular ion at 546.4 (1a) experienced the exclusion of methyl-hept-5-enoate to result 24(4→23), 27(8→26), 30(20→29)-tris-abeo-olean-(12-oxo)-1,15,22-triene (1b, m/z 419.3). The latter along with 1a underwent retro-Diels-Alder (rDA) rearrangement yielding the fragments m/z 126.1 (1c), 176.2 (1g), and 328.2 (1k). The spectroscopic experiments along with previous reports of literature unambiguously constructed of complete framework of oleanene triterpenoid, 24(4→23), 27(8→26), 30(20→29)-tris-abeo-olean-(12-oxo)-1,15,22-triene-methyl hept-5-enoate (1). The ion peak at 176.2 (1g) was considered as the base peak (Fig. S12). These analyses suggested its molecular formula as $C_{37}H_{54}O_3$ enclosing eleven indices of hydrogen deficiencies associated with six olefinic bonds (comprising four alkenes and two carbonyls) and five ring systems. The spectroscopic experiments along with previous reports of literature unambiguously constructed of complete framework of oleanene triterpenoid, 24(4→23), 27(8→26), 30(20→29)-tris-abeo-olean-(12-oxo)-1,15,22-triene-methyl hept-5-enoate (**2**) (Figure 4.32 & 4.33).

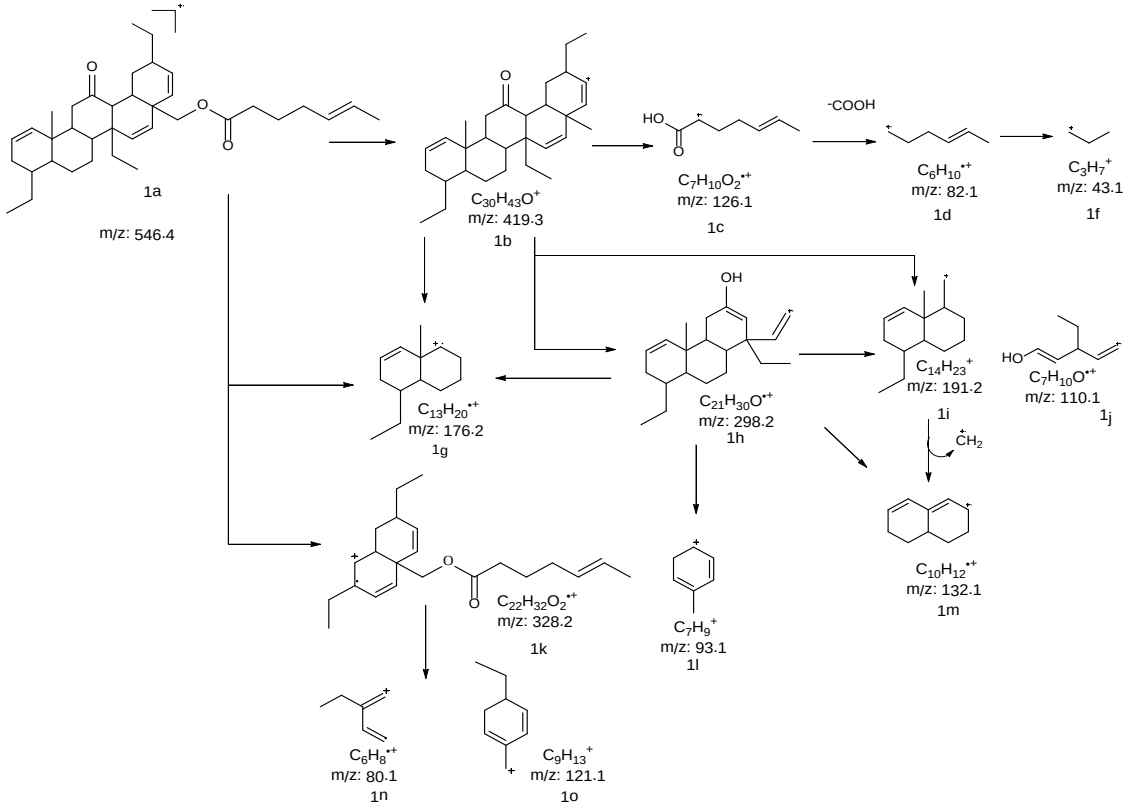

Figure 4.32.: EI-MS spectrum of 24(4→23), 27(8→26), 30(20→29)-tris-abeo-olean-(12-oxo)-1,15,22-triene-methyl-hept-5-enoate (**2**)

4.3.2.2b Structural characterization of Compound 3

24(4→23)-Abeo-olean-(12-oxo)-3,5-diene-deconoate	
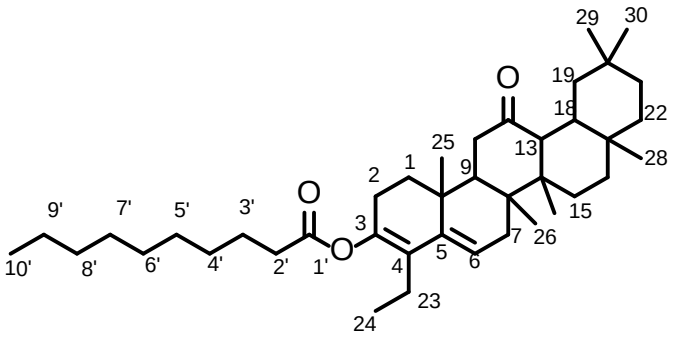	
Sample yield	0.30% (> 99% purity, RP-C18 HPLC)
Physical description	Yellowish oily
Molecular formula	$C_{40}H_{64}O_3$
Molecular mass	592.2485

The abeo-oleanane class of triterpenoid derivative, 24(4→23)-abeo-olean-(12-oxo)-3,5-diene-deconoate (**3**) was isolated as yellowish oily compound. The compound (**3**) has exhibited UV absorbance (UV (MeOH) λ_{max} at 247 nm (Figure 4.34.). The homogeneity of the compound was ascertained by HPLC data on a bonded phase octadecylsilane (C_{18}) stationary phase (HPLC, MeOH/MeCN, 2:1 v/v) with R_t: 2.91 min (Figure 4.35.).

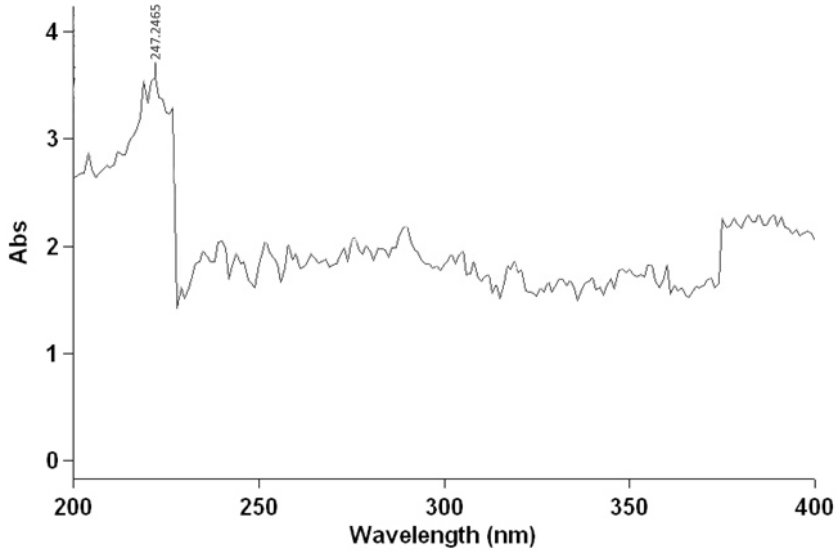

Figure 4.34.: UVspectrum of 24(4→23)-abeo-olean-(12-oxo)-3,5-diene-deconoate (**3**)

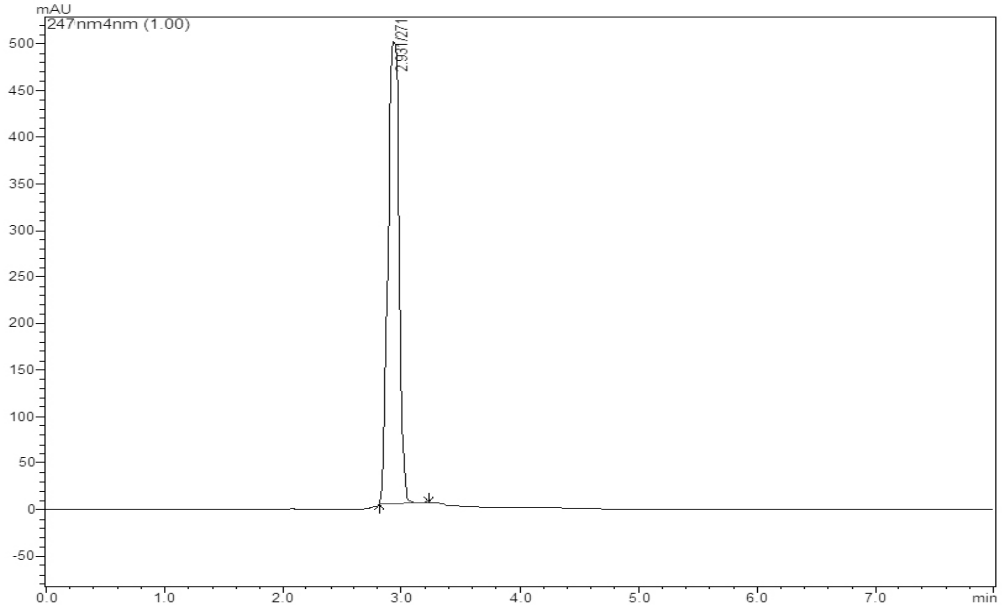

Figure 4.35.: HPLC chromatogram of 24(4→23)-abeo-olean-(12-oxo)-3,5-diene-deconoate (**3**)

Repeated column chromatographic purification of the crude of *G. salicornia*, yielded compound **3** as yellowish oily, which was characterised as 24(4→23)-abeo-olean-(12-oxo)-3,5-diene-deconoate (**3**). The HRESIMS experiment displayed the molecular ion peak at *m/z* 593.4938 $[M+H]^+$, (Figure 4.36) which along with NMR-IR spectroscopic analyses deduced its molecular formula as $C_{40}H_{65}O_3$ (Table 4.10).

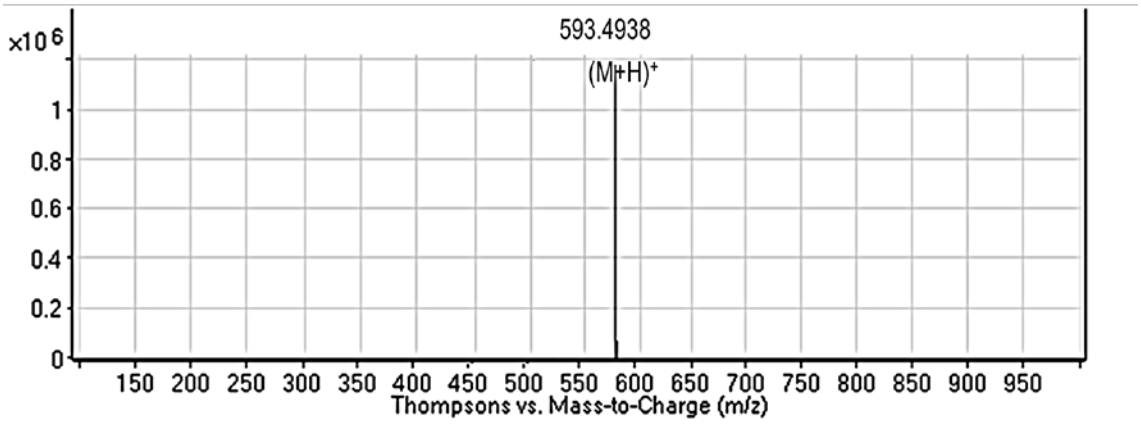

Figure 4.36.: HRESIMS spectrum of 24(4→23)-abeo-olean-(12-oxo)-3,5-diene-deconoate (**3**)

The FTIR vibrations at 1734 and 1634 cm^{-1} recognised the existence of ester and carbonyl functionalities, respectively (Figure 4.37). The ^{13}C along with ^{135}DEPT spectrum of **3** displayed the presence of forty carbon signals, including eight methyl groups (δ 19.9, δ 20.8, δ 19.7, δ 19.4, δ 22.8, δ 30.2, δ 14.0), eighteen sp^3 methylenes (δ 30.5, δ 24.7, δ 34.0, δ 36.9, δ 29.4, δ 37.0, δ 37.7, δ 33.9, δ 34.3, δ 19.1, δ 26.7, δ 26.4, δ 29.2, δ 29.5, δ 29.6, δ 29.3, δ31.8, δ 22.6), one sp^2 methine (δ 130.9), three sp^3 methines (δ 43.4, δ 51.9, δ 41.4), and ten quaternary carbons (δ 128.8, δ 132.2, δ 139.2, δ 42.7, δ 31.4, δ 38.8, δ 33.4, δ 28.0) including two carbonyl carbons (δ 213.1, δ 176.1). The presence of one olefinic hydrogen was apparent at δ 5.82, which exhibited HSQC correlation with δ 130.9 (Figure 4.38 - 4.41).

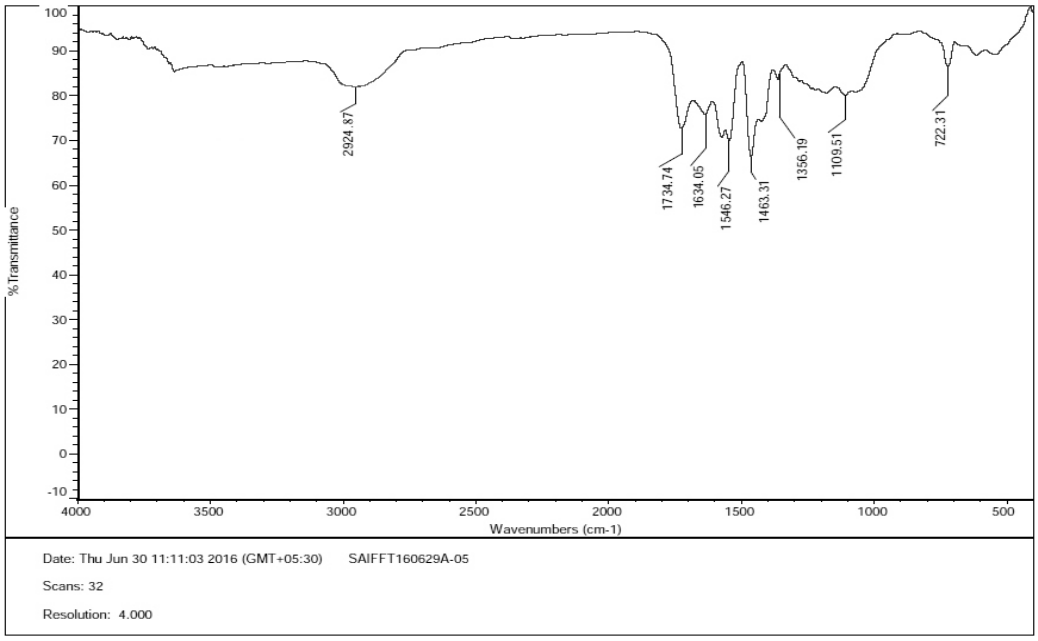

Figure 4.37.: FT-IR spectrum of 24(4→23)-abeo-olean-(12-oxo)-3,5-diene-deconoate (**3**)

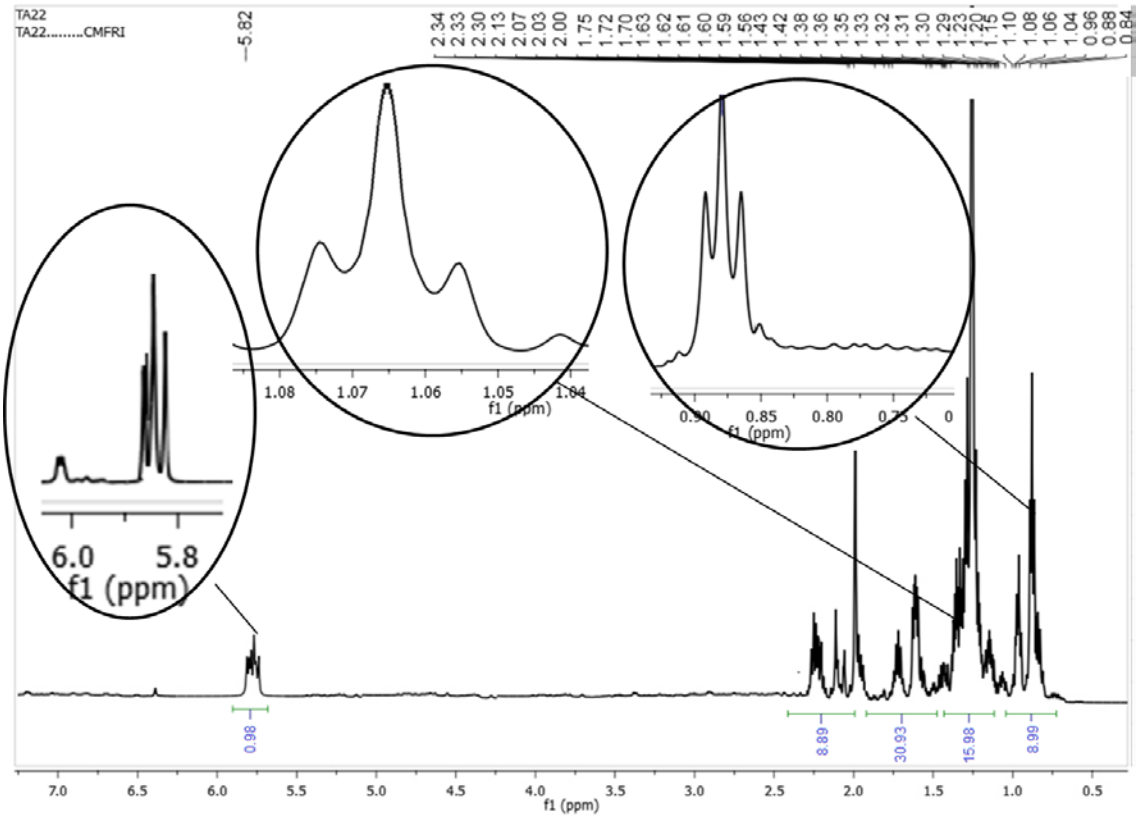

Figure 4.38.: [1]HNMR spectrum of 24(4→23)-abeo-olean-(12-oxo)-3,5-diene-deconoate (**3**)

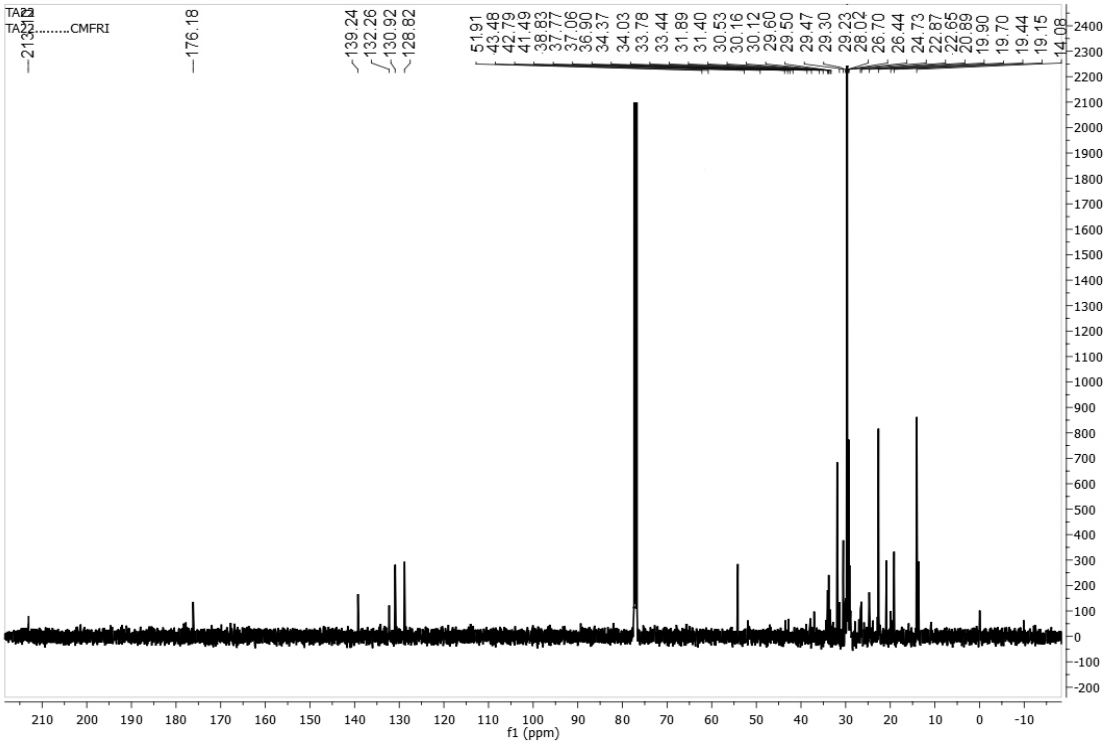

Figure 4.39.: ^{13}C NMR spectrum of 24(4→23)-abeo-olean-(12-oxo)-3,5-diene-deconoate (**3**)

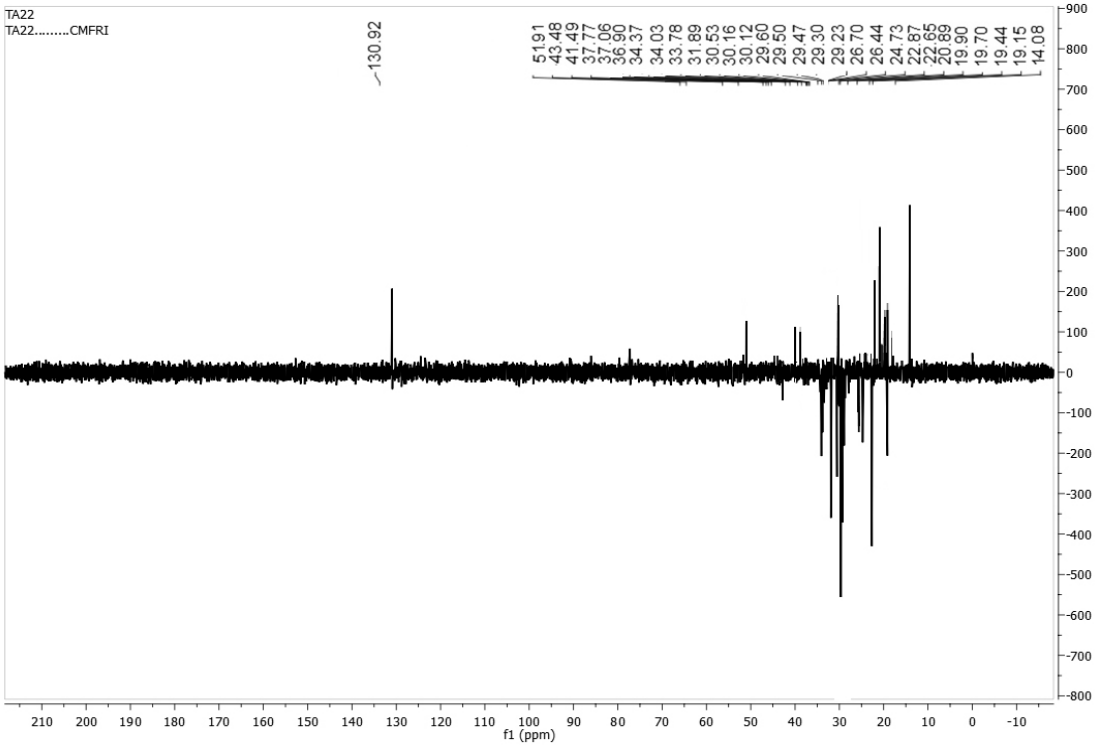

Figure 4.40.: ^{135}DEPT spectrum of 24(4→23)-abeo-olean-(12-oxo)-3,5-diene-deconoate (**3**)

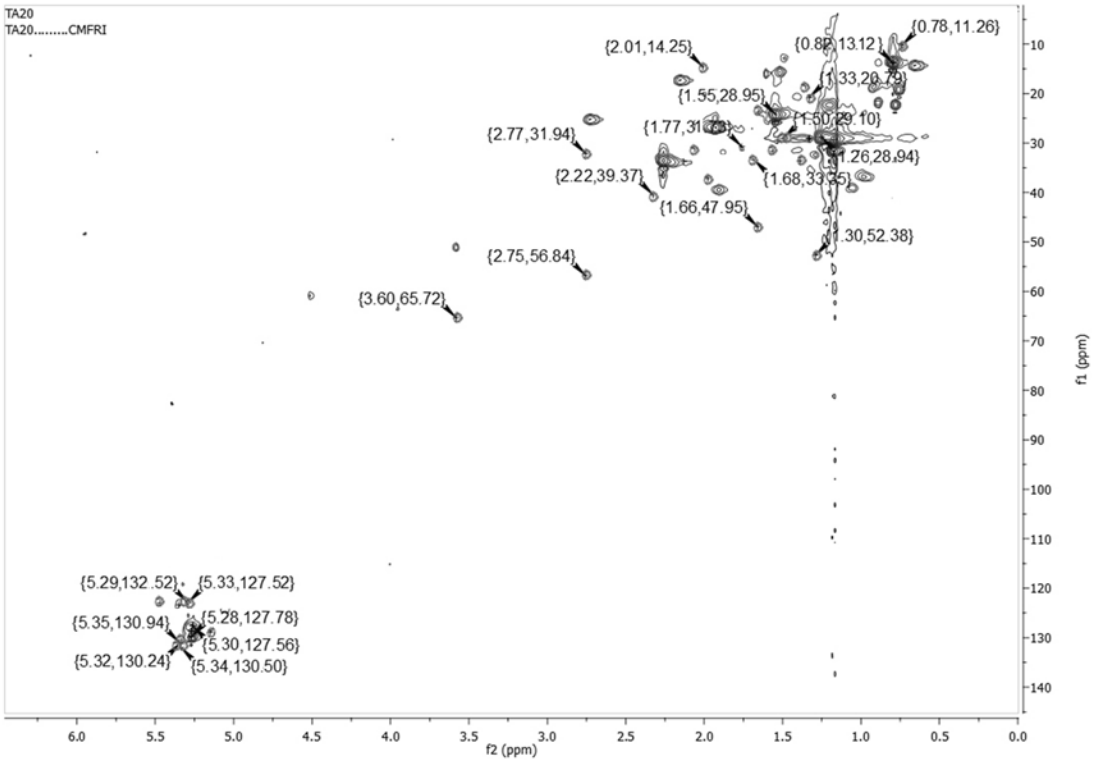

Figure 4.41.: HSQC spectrum of 24(4→23)-abeo-olean-(12-oxo)-3,5-diene-deconoate (**3**)

The ^{1}H-^{1}H COSY experiment put forward the occurrence of three spin networks, which were found to be (CH_2-δ 1.42) (arbitrarily assigned as H-1)-(CH_2-δ 2.03) (H-2); (CH-δ 1.70) (H-9)-(CH_2-δ 2.33) (H-11) and (CH-δ 2.30) (H-13)-(CH-δ 1.62) (H-18)-(CH_2-δ 1.20) (H-19) suggesting the partial fragments of pentacyclic ring in the triterpenoid (Figure 4.42 & 4.43). The HMBC interactions from CH_2-2 (δ 2.03) to C-4 (δ 128.8), C-3 (δ 132.2) determined the occurrence of tetrasubstituted olefinic bond at C-3 (δ 132.2) and C-4 (δ 128.8) and HMBCs from CH-6 (δ 5.82) to C-5 (δ 139.2), C-7 (δ 34.0) attributed a trisubstituted olefinic bond at C-5 (δ 139.2) and C-6 (δ 5.82/130.9) (Figure 4.44). Other HMBC correlations from CH_2-1 (δ 1.42) to C-10 (δ 31.4), C-5 (139.2); CH_2-2 (δ 2.03) to C-1 (δ 30.5); CH_2-7 (δ 2.00) to C-8 (δ 42.7); CH-9 (δ 1.70) to C-8 (δ 42.7), C-10 (δ 31.4), C-11 (δ 36.9); CH-13 (δ 2.30) to C-8 (δ 42.7) and C-14 (δ 38.8); CH_2-15 (δ 1.59) to C-14 (δ_C38.8) and C-16 (δ_C37.0); CH_2-16 (δ_H1.60) to C-17 (δ_C33.4); CH-18 (δ_H1.62) to C-17 (δ 33.4); CH_2-19 (δ 1.20) to C-17 (δ 33.4); CH_2-21 (δ 1.61) to C-20 (δ 28.0) and CH_2-22 (δ_H1.56) to C-21 (δ_C33.9) appropriately supported the complete structure of pentacyclic triterpenoid, **3**. The long range couplings from both CH_2-11 (δ 2.33) and CH-13 (δ 2.30) to C-12 (δ 213.1) deduced the C-12 keto functionality in **3**, whereas the attributions were comparable with the previously reported compound, trihydroxyolean-12-one in which the chemical shift of C-12 was found to be δ 212 (Da Rocha et al., 2015). These NMR

assignments in comparison with earlier reported chemical shift values (Da Rocha et al., 2015; Maneesh and Chakraborty, 2017) substantiated the presence of pentacyclic triterpenoid bearing olean-(12-oxo)-3,5-diene skeleton.

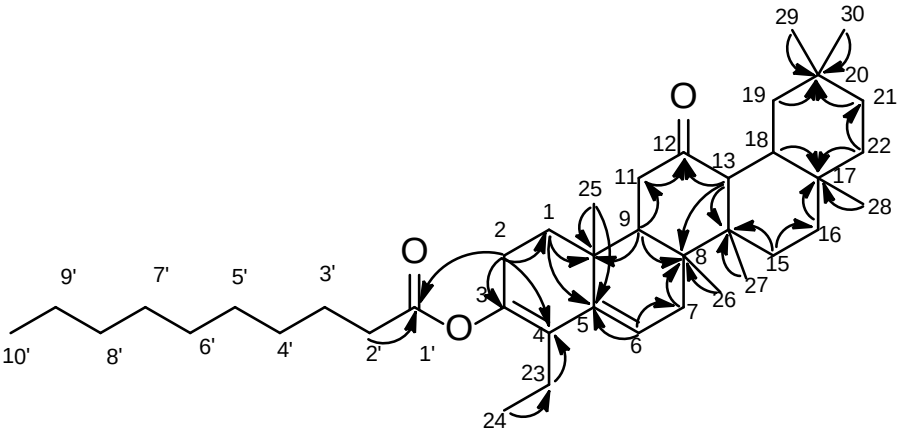

Figure 4.42.: ^{1}H-^{1}H COSY (bold-face bonds), selected HMBC (double-barbed arrows) correlations of 24(4→23)-abeo-olean-(12-oxo)-3,5-diene-deconoate (**3**)

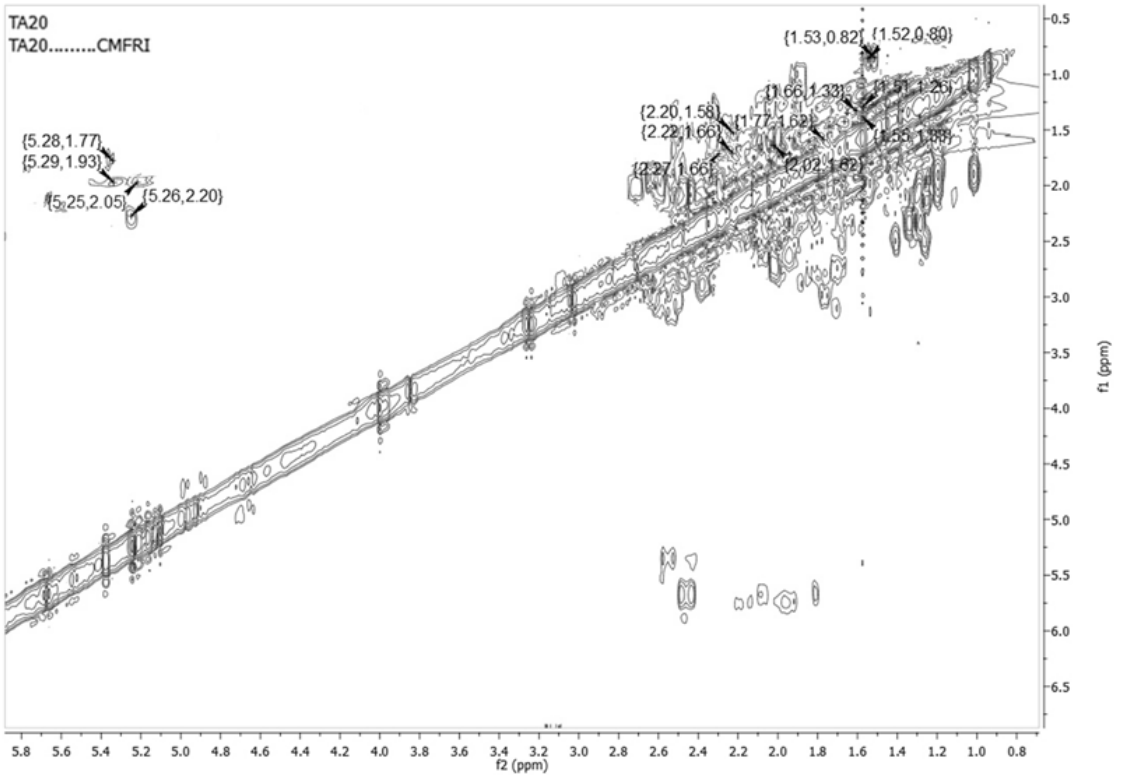

Figure 4.43.: ^{1}H-^{1}H COSY spectrum of 24(4→23)-abeo-olean-(12-oxo)-3,5-diene-deconoate (**3**)

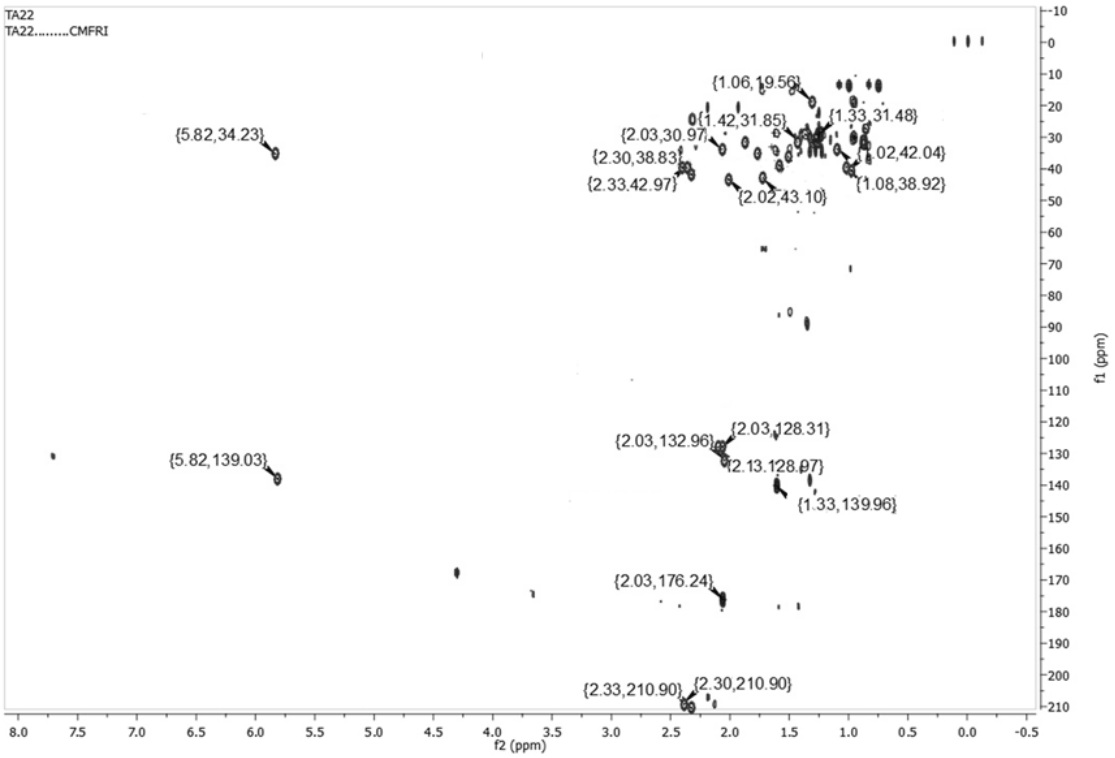

Figure 4.44.: HMBC spectrum of 24(4→23)-abeo-olean-(12-oxo)-3,5-diene-deconoate (**3**)

The distinctive oleanene framework comprised of seven angular methyls in the δ 0.7 to δ 1.25 range at C-4 (CH_3-23, CH_3-24), C-10 (CH_3-25), C-8 (CH_3-26), C-14 (CH_3-27), C-17 (CH_3-28) and C-20 (CH_3-29, CH_3-30) positions (Da Rocha et al., 2015; Maneesh and Chakraborty, 2017), whereas the titled compound comprised of six tertiary methyls at δ 1.33 (s), δ 1.04(s), δ 1.08 (s), δ 1.10 (s), δ 0.88 (s) and δ 0.96 (s). The position of tertiary methyl, δ 1.33 (s) (CH_3-25) at C-10 was ascertained through HMBCs from δ 1.33 to δ 31.4 (C-10), δ 139.2(C-5) and the HMBC correlations between δ 1.04 to δ 42.7 (C-8) suggested the position of tertiary methyl, δ 1.04 (s) (CH_3-26) at C-8. Similary, the HMBC couplings from δ 1.08 to δ 38.8 (C-14) and that from δ 1.10 (CH_3-28) to δ 33.4 (C-17) confirmed the presence of angular methyl substitutions of CH_3-27 at C-14 and CH_3-28 at C-17, respectively. The gem dimethyls (CH_3-29, CH_3-30) at C-20 were confirmed by the long range relations of δ 0.88 and 0.96 to δ 28.0 (C-20). These six typical angular methyls were comparable with earlier reported chemical shifts of basic oleanene skelton (Da Rocha et al., 2015; Hassan et al., 2012). One of the gem dimethyl groups at C-4 (CH_3-24) was shifted to C-23, and this assignment was corroborated through the HMBC couplings from CH_2-23 (δ 2.13) to C-4 (δ 128.8) and CH_3-24 (δ 1.06) to C-23 (δ 19.1). Due to the methyl shift at C-4, the titled compound was classified as abeo oleanene triterpenoid, **3** which was named as 24(4→23)-abeo-olean-(12-oxo)-3,5-diene. The COSY spin systems (CH_2-δ 2.34)

(H-2')-(CH_2-δ 1.63) (H-3')-(CH_2-δ 1.29) (H-4')-(CH_2-δ 1.23) (H-5')-(CH-δ 1.28) (H-6')-(CH_2-δ 1.32) (H-7')-(CH_2-δ 1.30) (H-8')-(CH_2-δ 1.31) (H-9')-(CH_3-δ 0.84) (H-10') attributed the presence of a linear side chain with nine carbon atoms. The HMBCs from CH_2-2 (δ 2.03) to C-1' (δ 176.1) and CH_2-2' (δ 2.34) to C-1' (δ 176.1) supported the presence of a ester linkage attached to the nine alkyl membered linear chain, which was classified as deconoate. The previous reports of 3-(stearyloxy)olean-12-ene enclosed 18-membered alkyl ester group in which the chemical shift at CH-3 was found to be δ 80.51/4.52, and the chemical shift of ester carbonyl at C-1' was found to be δ 173.55 (Da Rocha et al., 2015). Herein, the chemical shift of ester carbonyl at C-1' was found to be δ 176.1 and this increase in the chemical shift was due to the direct attachment of oxygen end of the ester carbonyl to an alkenic quarternary carbon at C-3. The compound, **3** was structurally correlated to previously reported oleanenes (Da Rocha et al., 2015; Huang et al., 2013; Maneesh and Chakraborty, 2017) beside the differences recorded in the dispositions of alkenes, ester linkages and presence of abeo tertiary methyls along with absence of hydroxyl functionalities.

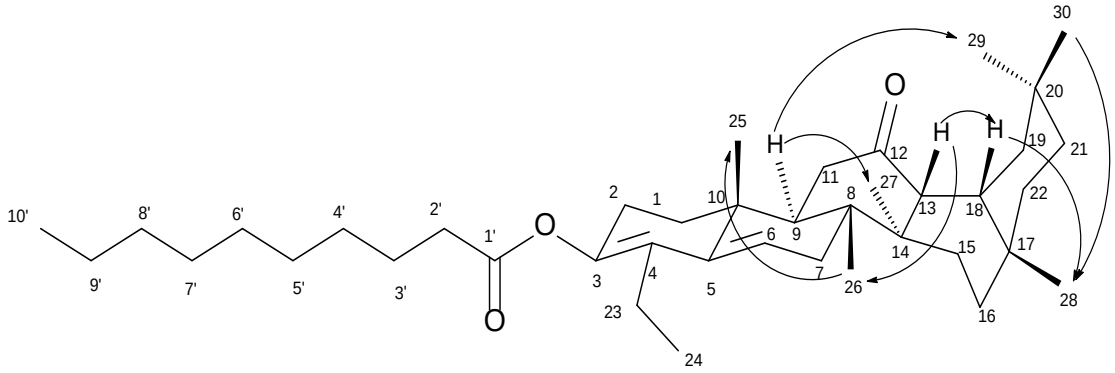

Figure 4.45.: NOE (single headed arrows) correlations of 24(4→23)-abeo-olean-(12-oxo)-3,5-diene-deconoate (**3**)

The relative stereochemistry of chiral centres at δ 43.4 (C-9), 51.9 (C-13) and 41.4 (C-18) were worked out by nuclear overhauser effect spectroscopic (NOESY) experiments. The proton at δ 2.30 (assigned to CH-13) exhibited NOE correlation with the angular methyl proton at δ 1.04 (H-26) and δ 1.62 (H-18) (Figure 4.45 & 4.46) that was positioned in the β-plane (Wang et al., 2014). In addition, the β-disposition of chiral protons H-18, H-25, H-26, H-28 and H-30 were inferred by the NOE association between H-25 (δ 1.33)/H-26 (δ 1.04), H-26 (δ 1.04)/H-13(δ 2.30), H-13 (δ 2.30)/H-18 (δ 1.62), H-18 (δ 1.62)/H-28 (δ 1.10) and H-28 (δ 1.10)/H-30 (δ 0.96). These assessments were in agreement with the alignments of methyl

functionalities at C-10, C-8 and C-20, as described in the previous reports of literature (Wang et al., 2014).

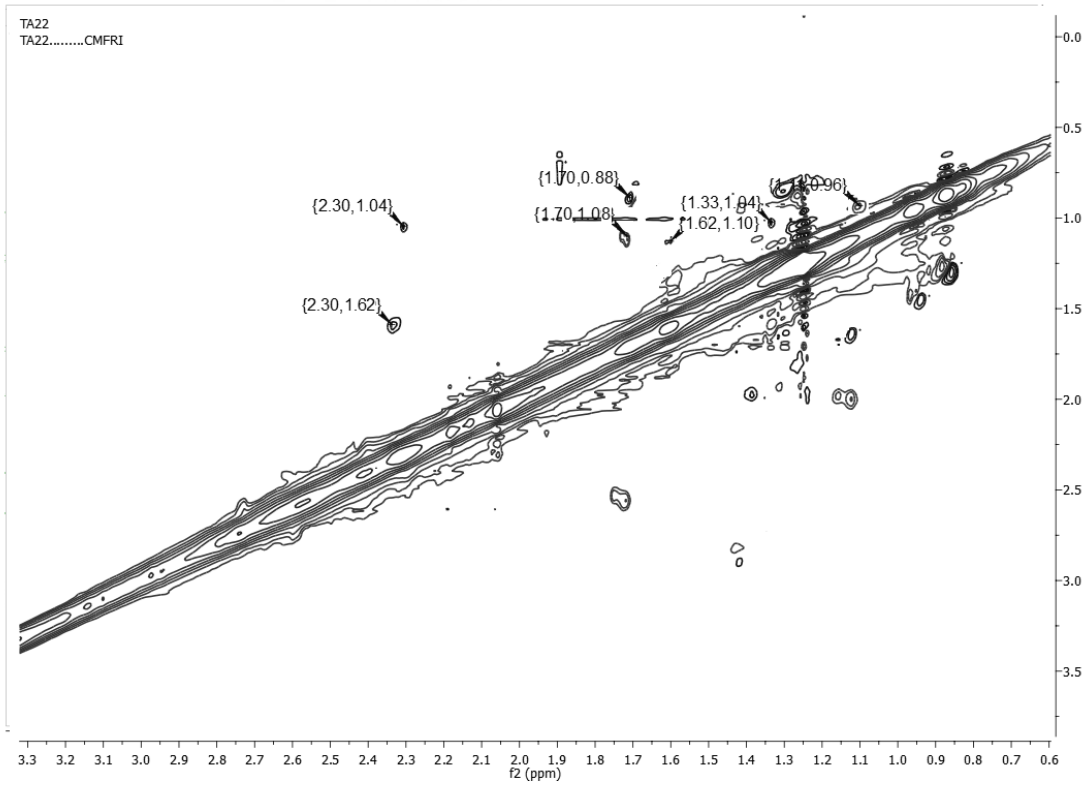

Figure 4.46.: NOE spectrum of 24(4→23)-abeo-olean-(12-oxo)-3,5-diene-deconoate (**3**)

Conversely, the proton at the chiral centre, δ 1.70 (assigned as CH-9) exhibited NOE correlation with the proton at δ 0.88 (H-29) that was disposed in the α-face. The other proton at δ_H1.08 (H-27) was found to be α-aligned. The trans-, cis-coincidence of ABCD and DE skeletons were substantiated by stereochemical attributions (Koay et al., 2013).

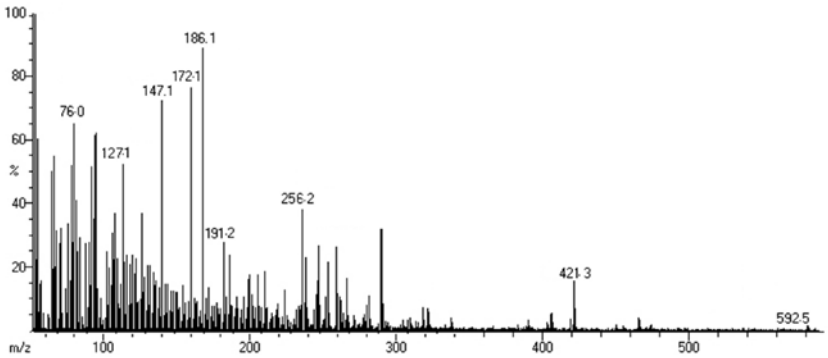

Figure 4.47.: EI-MS spectrum of 24(4→23)-abeo-olean-(12-oxo)-3,5-diene-deconoate (**3**)

Table 4.10: NMR spectroscopic data[a] of 24(4→23)-abeo-olean-(12-oxo)-3,5-diene-deconoate (**3**) isolated from red seaweed *G. salicornia*

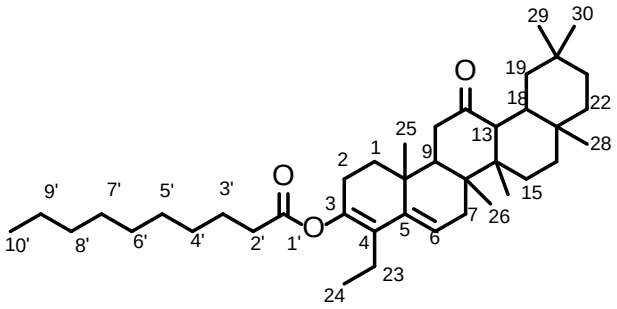

Compound **3**……...24(4→23)-abeo-olean-(12-oxo)-3,5-diene-deconoate (**3**)

Type	C. No.	^{13}C NMR	^{1}H. No. (int., mult., *J* in Hz)[b]	^{1}H NMR	COSY	HMBC
CH_2	1	30.5	1H, dt, J = 13.0, 6.5 Hz	1.42	H-2	C-10, 5
			1H, dt, J = 13.9, 5.9 Hz	1.15	-	-
CH_2	2	24.7	1H, dt, J = 11.8, 7.8 Hz	2.03	-	C-1,3,4,1'
			1H, dt, J = 11.2, 6.2 Hz	1.72	-	-
C	3	132.2	-	-	-	-
C	4	128.8	-	-	-	-
C	5	139.2	-	-	-	-
CH	6	130.9	1H, t, J = 11.7 Hz	5.82	-	C-5,7
CH_2	7	34.0	1H, d, J = 8.2 Hz	2.00	-	C-8
			1H, d, J = 5.0 Hz	1.75	-	-
C	8	42.7	-	-	-	-
CH	9	43.4	1H, t, J = 7.2 Hz	1.70	H-11	C-8,10,11
C	10	31.4	-	-	-	-
CH_2	11	36.9	1H, dd, J = 10.8, 3.2 Hz	2.33	-	C-12
			1H, dd, J = 9.9, 2.6 Hz	2.07	-	-
C	12	213.1	-	-	-	-
CH	13	51.9	1H, d, J = 12.9 Hz	2.30	H-18	C-12,8,14
C	14	38.8	-	-	-	-
CH_2	15	29.4	1H, dt, J = 10.9, 6.3 Hz	1.59	-	C-14,16
			1H, dt, J = 11.9, 5.9 Hz	1.35	-	-
CH_2	16	37.0	1H, dt, J = 10.9, 5.9 Hz	1.60	-	C-17
			1H, dt, J = 11.2, 4.9 Hz	1.38	-	-
C	17	33.4	-	-	-	-
CH	18	41.4	1H, m	1.62	H-19	C-17
CH_2	19	37.7	1H, t, J = 4.9 Hz	1.20	-	C-20
			1H, t, J = 4.0 Hz	1.43	-	-
C	20	28.0	-	-	-	-
CH_2	21	33.9	1H, dt, J = 11.0, 4.8 Hz	1.61	-	C-20
			1H, dt, J = 10.0, 4.0 Hz	1.34	-	-
CH_2	22	34.3	1H, dt, J = 10.9, 4.7 Hz	1.56	-	C-21,17
			1H, dt, J = 10.5, 4.0 Hz	1.36	-	-
CH_2	23	19.1	2H, q, J = 5.7 Hz	2.13	-	C-4
CH_3	24	19.9	3H, t, J = 6.9 Hz	1.06	-	C-23
CH_3	25	20.8	3H, s	1.33	-	C-10,5

CH_3	26	19.7	3H, s	1.04	-	C-8
CH_3	27	19.4	3H, s	1.08	-	C-14
CH_3	28	22.8	3H, s	1.10	-	C-17
CH_3	29	30.2	3H, s	0.88	-	C-20
CH_3	30	30.1	3H, s	0.96	-	C-20
C	1'	176.1	-	-	-	-
CH_2	2'	26.7	2H, t, J = 10.9 Hz	2.34	H-3'	C-1'
CH_2	3'	26.4	2H, m	1.63	H-4'	-
CH_2	4'	29.2	2H, m	1.29	H-5'	-
CH_2	5'	29.5	2H, m	1.23	H-6'	-
CH_2	6'	29.6	2H, m	1.28	H-7'	-
CH_2	7'	29.3	2H, m	1.32	H-8'	-
CH_2	8'	31.8	2H, m	1.30	H-9'	-
CH_2	9'	22.6	2H, m	1.31	H-10'	-
CH_3	10'	14.0	3H, t, J = 7.3 Hz	0.84	-	-

[a]NMR spectra were recorded using a Bruker AVANCE III 500 MHz (AV 500) spectrometer (Bruker, Karlsruhe, Germany) in $CDCl_3$ as aprotic solvent at ambient temperature with TMS as the internal standard (δ 0 ppm).

[b]Values in ppm, multiplicity and coupling constants (J = Hz) were indicated in parentheses. Multiplicities were allocated by ^{135}DEPT NMR spectrum.

The assignments were made with the aid of the COSY, HSQC, HMBC and NOESY experiments.

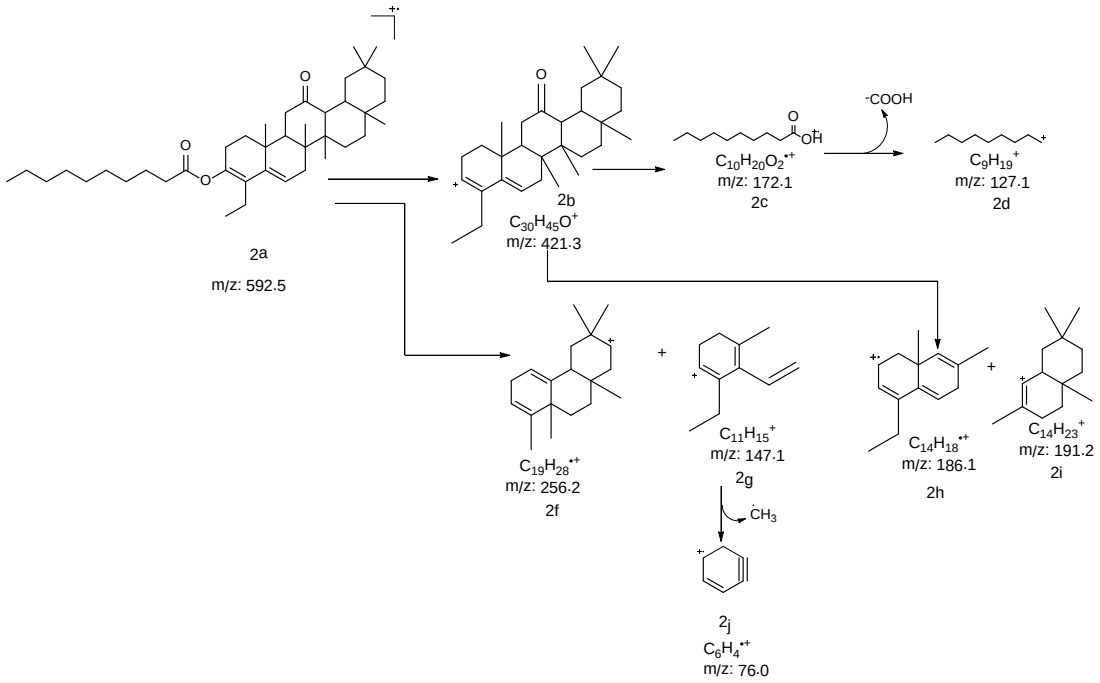

Figure 4.48.: Tentative mass fragmentation pattern of 24(4→23)-abeo-olean-(12-oxo)-3,5-diene-deconoate (**3**)

The structural elucidation of **3** was corroborated by the mass spectral data wherein the molecular ion (*m/z* 592.5, 2a) experienced the exclusion of 2c to yield abeo-24(4→23)-olean-(12-oxo)-3,5-diene (2b) with *m/z* 421.3. The fragment, 1a underwent retro-Diels-Alder (rDA) rearrangement to afford the mass fragments 2h and 2i (*m/z* 186.1 and 191.2, respectively). The ion peak at 186.1 (2h) was considered as the base peak) (Figure 4.47 & 4.48). These analyses deduced its molecular formula as $C_{40}H_{64}O_3$ enclosing nine indices of hydrogen deficiencies, which were associated with five ring systems and four olefinic bonds (comprising two carbonyls and two alkenes). The spectroscopic experiments along with previous reports of literature unambiguously characterised the oleanene triterpenoid as 24(4→23)-abeo-olean-(12-oxo)-3,5-diene-deconoate (**3**).

The organic extract of *G. salicornia* was fractionated by repeated chromatographic techniques to obtain two unprecedented abeo-oleanene analogues. The isolated compounds, 24(4→23), 27(8→26), 30(20→29)-tris-abeo-oleanene moiety (**2**) and 24(4→23) abeo-oleanene framework (**3**) bearing ester and keto- carbonyl functionalities along with olefinic bonds. These functional groups present in the studied analogues contributed towards the various bioactivities of these compounds (**2-3**)**.**

4.3.2.3 Structural characterization of drimane class of diterpenoid derivative (Compounds 4-6)

Red seaweeds (phylum Rhodophyta) were found to be the important sources of pharmacologically active sesquiterpenes, and these algae received greater attention due to their capability to biosynthesise structurally diverse skeletons of sesquiterpenes, such as sesquiterpenoid quinols (Lane et al., 2010; Sali et al., 2018).

The present work described the purification and characterisation of three previously unreported drimane-associated quinols from the organic solvent extract of *G. salicornia* collected from the southeast coastal region of Indian peninsular. The studied compounds, which were designated as 3-(hept-3^6-enyloxy)-decahydro-4,6a,12a,12b-tetramethyl-1*H*-benzo[*a*]xanthene-4,10,12-triol (**4**), 13-[[2-(hexyloxy)-2,5,5,8a-tetramethyldecahydro-1-naphthalenyl](methoxy)methyl]benzenol (**5**), and 1-butoxy-4,4,11b,11c-tetramethyl-decahydrobenzo[*kl*]xanthen-10-ol (**6**) (Figure. 4.4.) were characterised by extensive spectroscopic experiments. The pharmacological activities were assessed by different selective *in vitro* assays. The physicochemical parameters of these compounds were utilised to corroborate their structural features with their bioactive potentials.

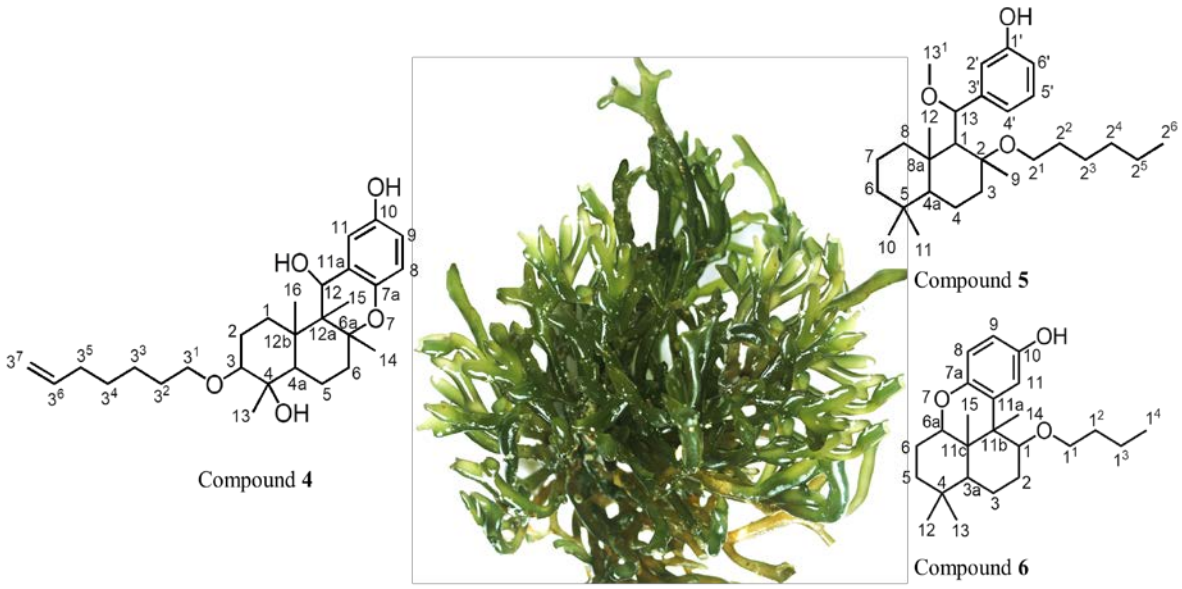

Figure 4.49.: Structural representations of (**A**) 3-(hept-3^6-enyloxy)-decahydro-4,6a,12a,12b-tetramethyl-1*H*-benzo[*a*]xanthene-4,10,12-triol (compound **4**), (**B**) 13-[[2-(hexyloxy)-2,5,5,8a-tetramethyldecahydro-1-naphthalenyl](methoxy)methyl]benzenol (compound **5**), and (**C**) 1-butoxy-4,4,11b,11c-tetramethyl-decahydrobenzo[*kl*]xanthen-10-ol (compound **6**) isolated from red seaweed *G. salicornia*. (**D**) The representative photograph of thalli (leaf-like structures) of *G. salicornia*.

4.3.2.3a Structural characterization of Compound 4

3-(hept-3^6-enyloxy)-decahydro-4,6a,12a,12b-tetramethyl-1*H*-benzo[*a*]xanthene-4,10,12-triol

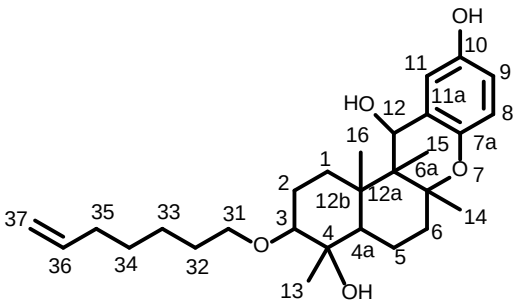

Sample yield	0.33% (> 99% purity, RP-C18 HPLC)
Physical description	Pale yellow oil
Molecular formula	$C_{28}H_{42}O_5$
Molecular mass	458.3032

The drimane class of diterpenoid derivative, 3-(Hept-3^6-enyloxy)-2,3,4,4a,5,6,6a,12,12a,12b-decahydro-4,6a,12a,12b-tetramethyl-*1H*-benzo[a]-xanthene-4,10,12-triol was isolated as yellowish-white amorphous compound. The compound (**4**) has exhibited UV absorbance (UV (MeOH) λ_{max}) at 278 nm (Figure 4.50.). The homogeneity of the compound was ascertained by HPLC data on a bonded phase octadecylsilane (C_{18}) stationary phase (HPLC, MeCN/MeOH, 1:2 v/v) with R_t: 3.24 min (Figure 4.51.).

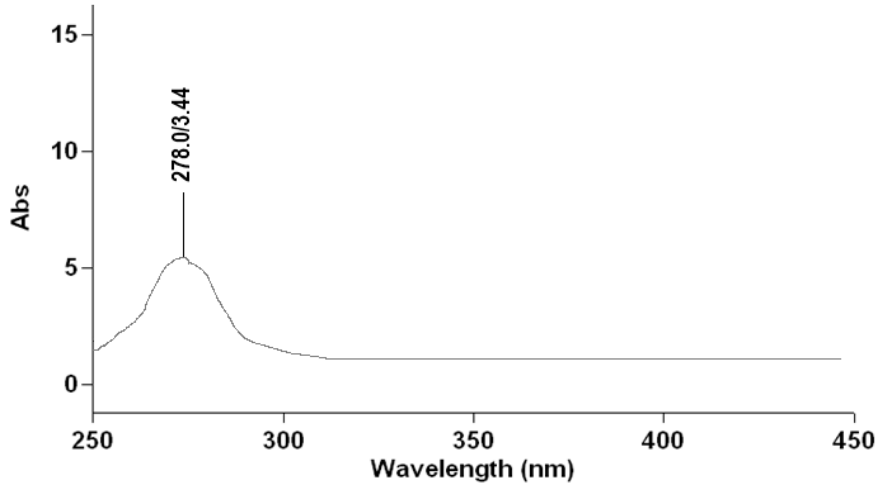

Figure 4.50.: UV spectrum of 3-(Hept-3^6-enyloxy)-2,3,4,4a,5,6,6a,12,12a,12b-decahydro-4,6a,12a,12b-tetramethyl-*1H*-benzo[a]xanthene-4,10,12-triol (**4**)

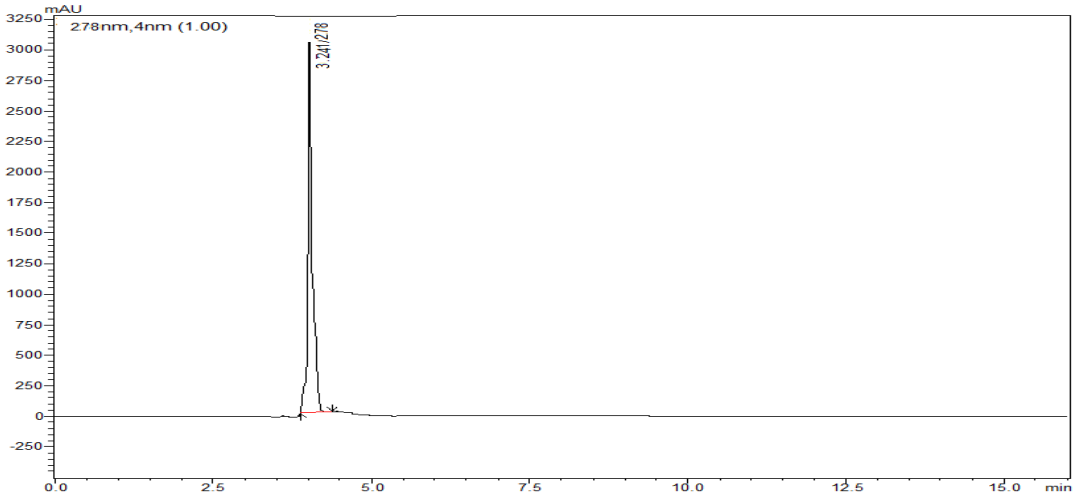

Figure 4.51.: HPLC chromatogram of 3-(Hept-3^6-enyloxy)-2,3,4,4a,5,6,6a,12,12a,12b-decahydro-4,6a,12a,12b-tetramethyl-*1H*-benzo[a]xanthene-4,10,12-triol (**4**)

Repeated column chromatographic fractionation of *G. salicornia* yielded drimane sesquiterpene quinol class of compound, **4** that was characterised as 3-(hept-3^6-enyloxy)-2,3,4,4a,5,6,6a,12,12a,12b-decahydro-4,6a,12a,12b-tetramethyl-1*H*-benzo[*a*]xanthene-4,10,12-triol. The mass spectroscopic experiment displayed its molecular ion peak at *m/z* 458 $[M]^+$, which corroborated its molecular formula of $C_{28}H_{42}O_5$. It showed eight indices of hydrogen deficiencies associated with one each of olefinic bond and benzene along with three rings. The HRESIMS experiment displayed the molecular ion peak at *m/z* 459.3114 $[M+H]^+$, (Figure 4.52.) which along with NMR-IR spectroscopic analyses deduced its molecular formula as $C_{28}H_{43}O_5$ $[M+H]^+$ (Table 4.11).

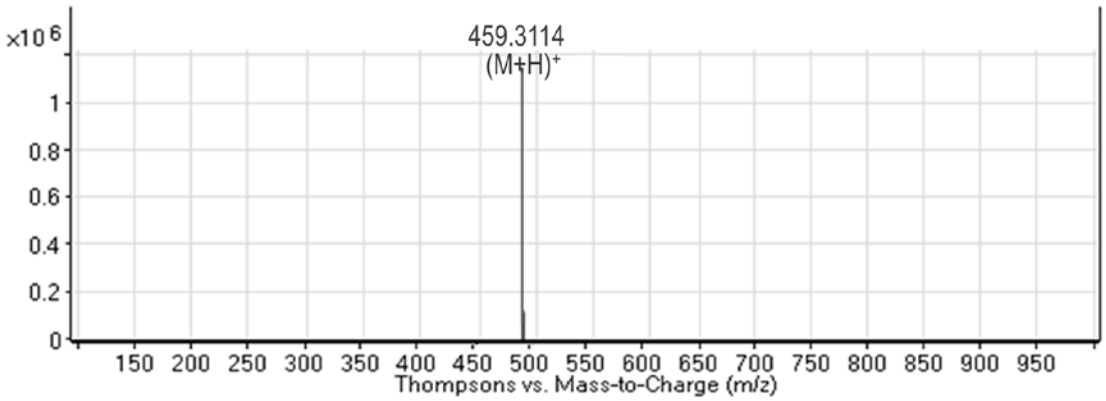

Figure 4.52.: HRESIMS spectrum of 3-(Hept-3^6-enyloxy)-2,3,4,4a,5,6,6a,12,12a,12b-decahydro-4,6a,12a,12b-tetramethyl-*1H*-benzo[a]xanthene-4,10,12-triol (**4**)

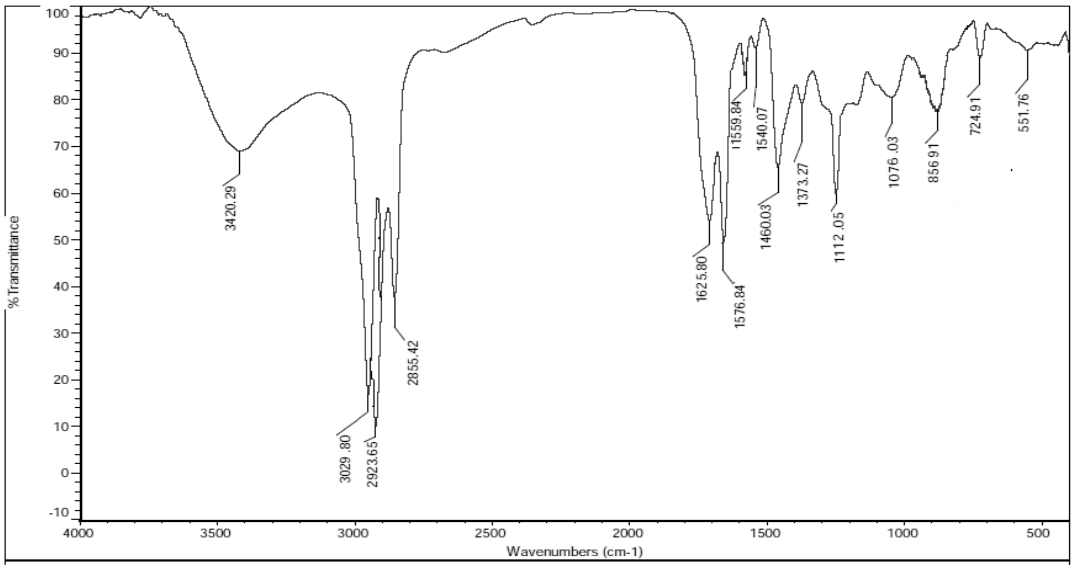

Figure 4.53.: FTIR spectrum of 3-(Hept-3^6-enyloxy)-2,3,4,4a,5,6,6a,12,12a,12b-decahydro-4,6a,12a,12b-tetramethyl-*1H*-benzo[a]xanthene-4,10,12-triol

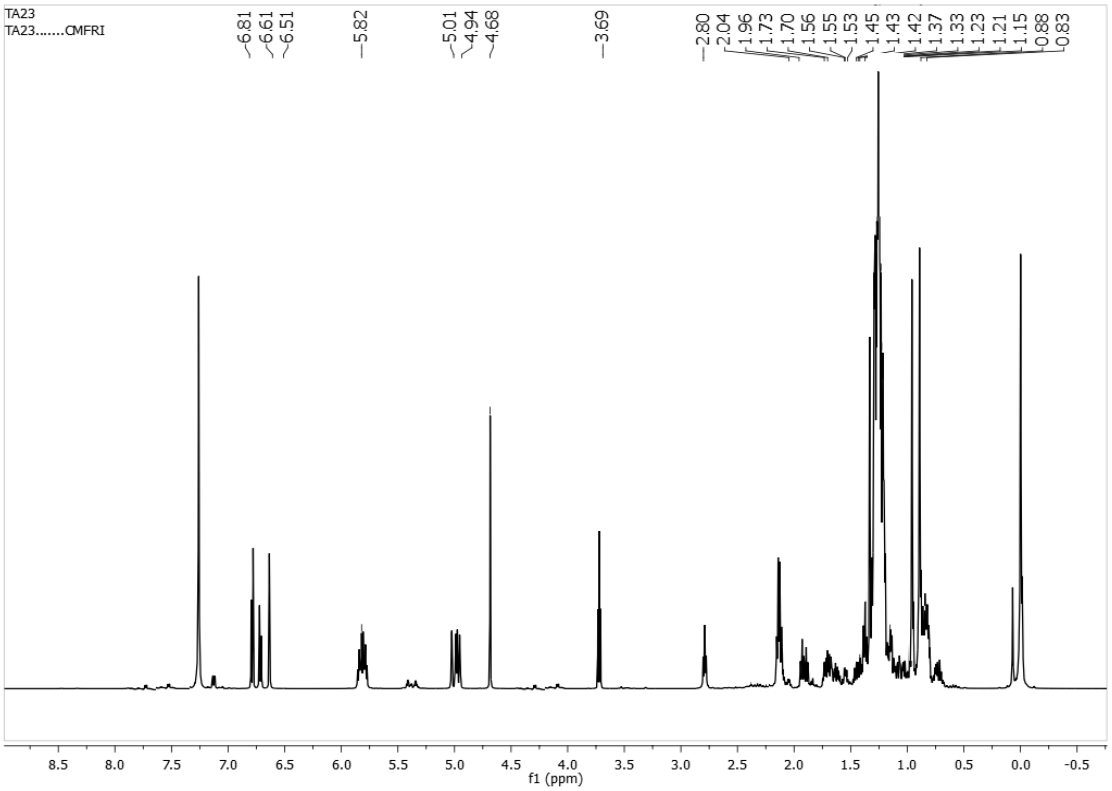

Figure 4.54.: FTIR spectrum of 3-(Hept-3[6]-enyloxy)-2,3,4,4a,5,6,6a,12,12a,12b-decahydro-4,6a,12a,12b-tetramethyl-*1H*-benzo[a]xanthene-4,10,12-triol

The FTIR absorption peaks of **4** at 3420, 856, 1559 and 1112-1076 cm^{-1} indicated the occurrences of hydroxyl, C-H aromatic, C=C aromatic and ether functionalities, respectively (Figure 4.53). The ^{1}H-NMR spectrum of **1** showed singlet signals for tertiary methyls at δ 1.42, 1.15, 0.88 and 0.83, which suggested the tetra-methyl substitution in **4**. The ^{1}H-NMR spectrum indicated the presence of six deshielded protons at δ 5.82, 5.01, 4.94, 6.81, 6.61 and 6.51, which might be associated with the olefinic and aromatic groups (Figure 4.54).

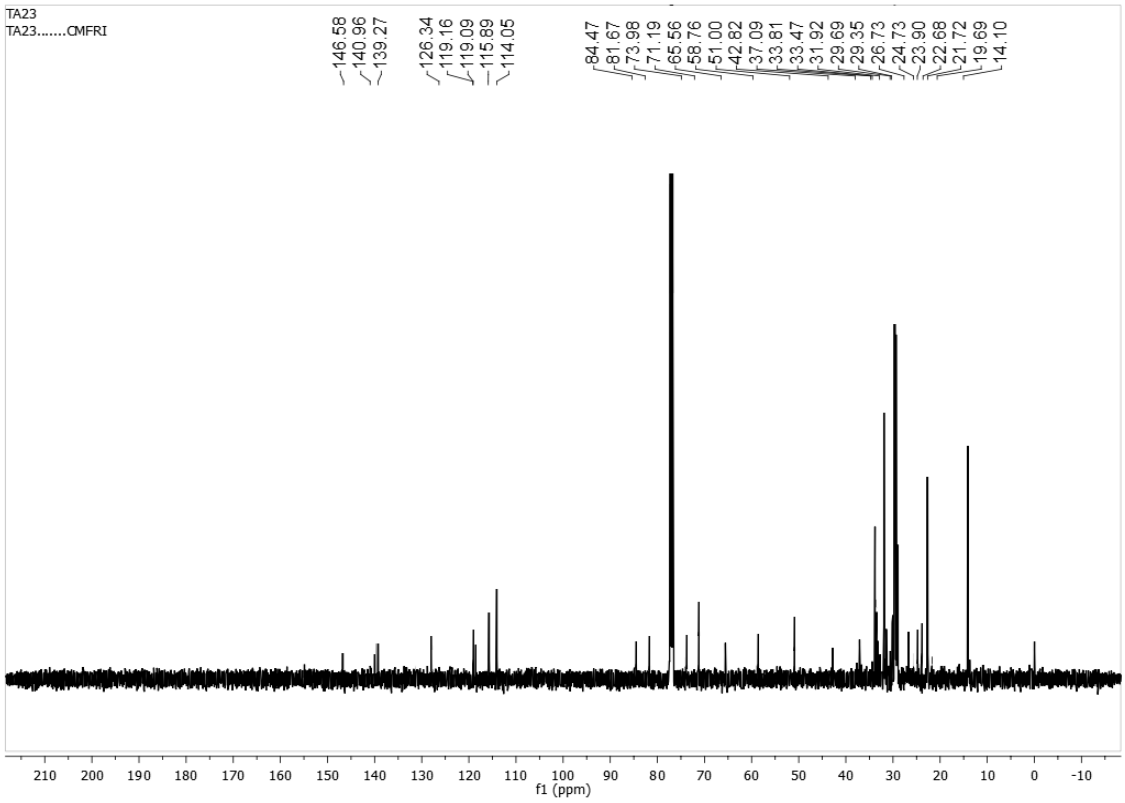

Figure 4.55.: ^{13}C-NMR spectrum of 3-(Hept-3^{6}-enyloxy)-2,3,4,4a,5,6,6a,12,12a,12b-decahydro-4,6a,12a,12b-tetramethyl-*1H*-benzo[a]xanthene-4,10,12-triol (**4**)

The ^{13}C-NMR, DEPT$_{135}$ along with HSQC spectra displayed 28 signals comprised of four methyls (δ 23.9, 22.6, 14.1, 19.6), nine sp^3 methylenes (δ 37.0, 24.7, 21.7, 33.4, 71.1, 31.9, 26.7, 29.6, 33.8), one sp^2 methylene (δ 114.0), four sp^2 methine (δ 139.2, 119.0, 119.1, 115.2), three sp^3 methines (δ 84.6, 58.7, 65.5) and seven non-protonated carbons (δ 73.9, 81.6, 51.0, 42.8, 126.3, 146.5, 140.9) (Figure 4.55-4.57). The COSY spectrum of **4** represented the occurrence of two individual spin systems: I δ (1.23)-(1.56)-(2.80) and II δ (1.53)-(1.73)-(1.37), which was assigned from H-1 to H-3 and H-4 to H-6, respectively (Figure 4.58 & 4.59). These spin systems were further connected by HMBC correlations from CH_2-1 (δ 1.23) to C-12b (δ 42.8); CH-3 (δ 2.80) to C-4 (δ 73.9); CH-4a (δ 1.53) to C-4 (δ 73.9) and CH_2-6 (δ 1.70) to C-6a (δ 81.6), C-12a (δ 51.0), which supported the bicyclic framework of **4** (Figure 4.60).

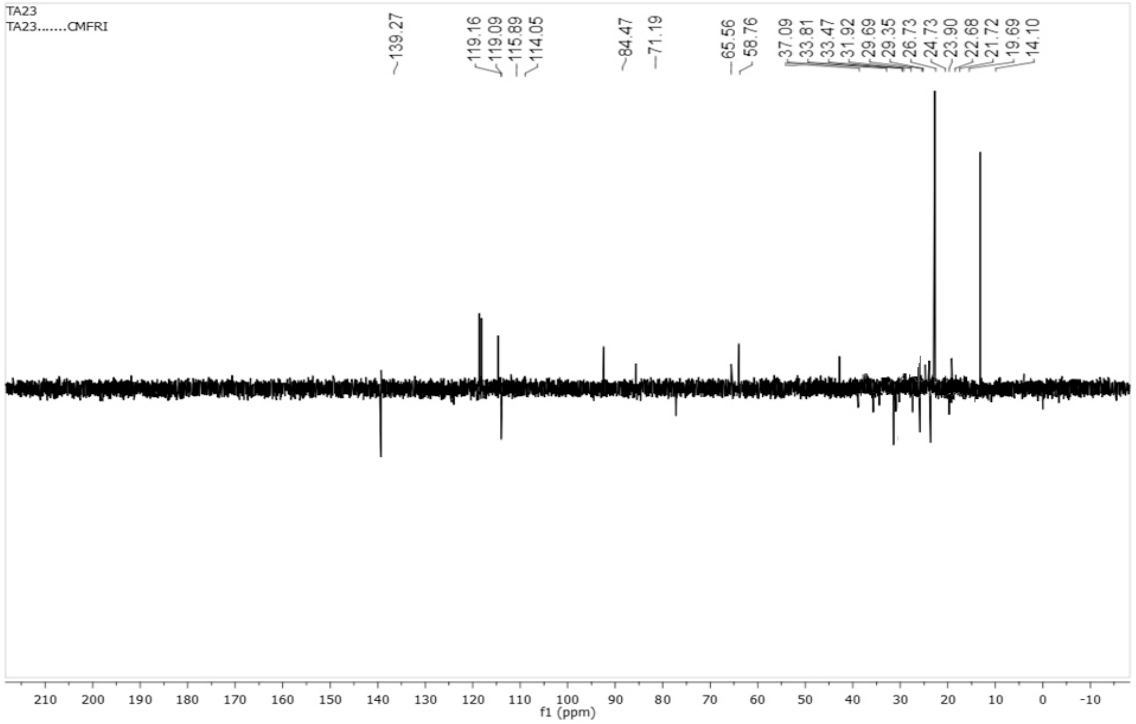

Figure 4.56.: DEPT spectrum of 3-(Hept-3[6]-enyloxy)-2,3,4,4a,5,6,6a,12,12a,12b-decahydro-4,6a,12a,12b-tetramethyl-*1H*-benzo[a]xanthene-4,10,12-triol (**4**)

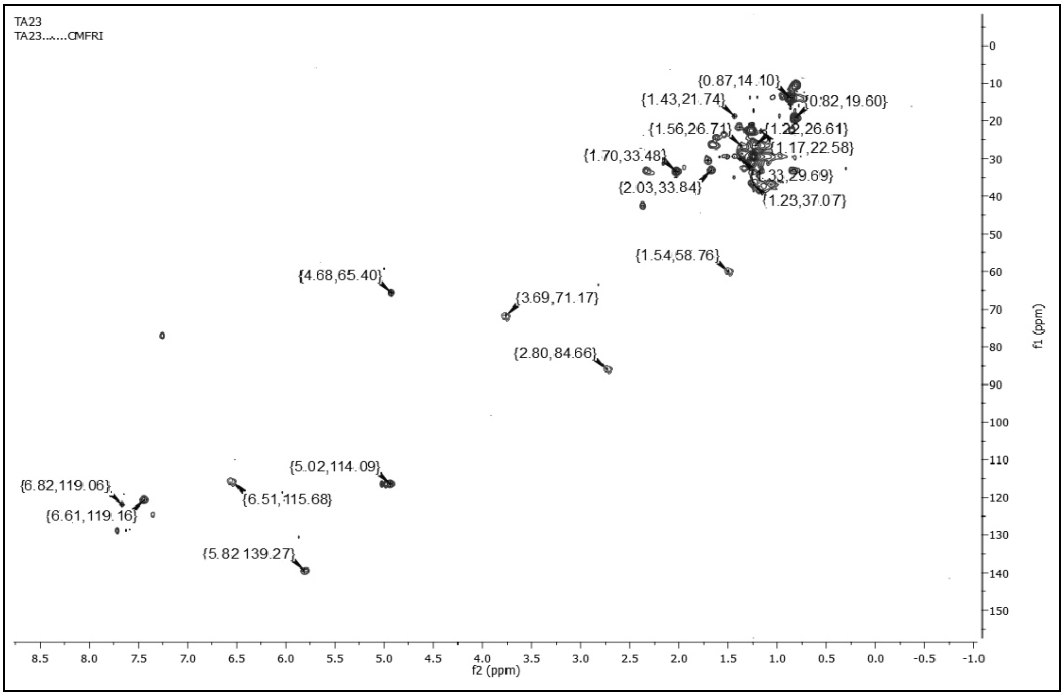

Figure 4.57.: HSQC spectrum of 3-(Hept-3[6]-enyloxy)-2,3,4,4a,5,6,6a,12,12a,12b-decahydro-4,6a,12a,12b-tetramethyl-*1H*-benzo[a]xanthene-4,10,12-triol (**4**)

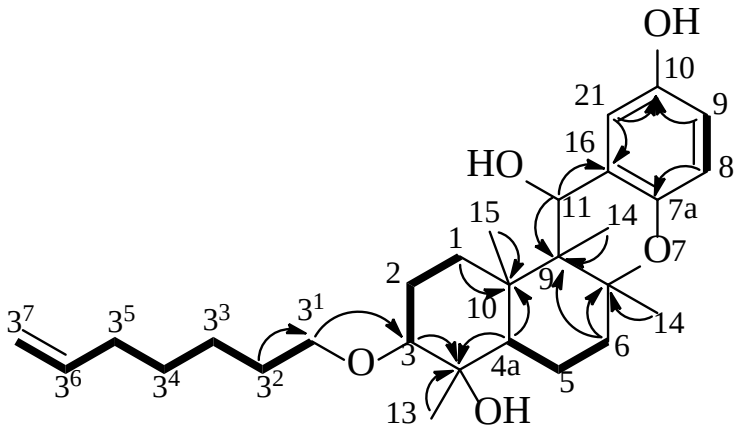

Figure 4.58.: ^{1}H-^{1}H COSY (bold face bonds), and selected HMBCs (double-barbed arrows), correlations of 3-(Hept-3^6-enyloxy)-2,3,4,4a,5,6,6a,12,12a,12b-decahydro-4,6a,12a,12b-tetramethyl-*1H*-benzo[a]xanthene-4,10,12-triol (**4**)

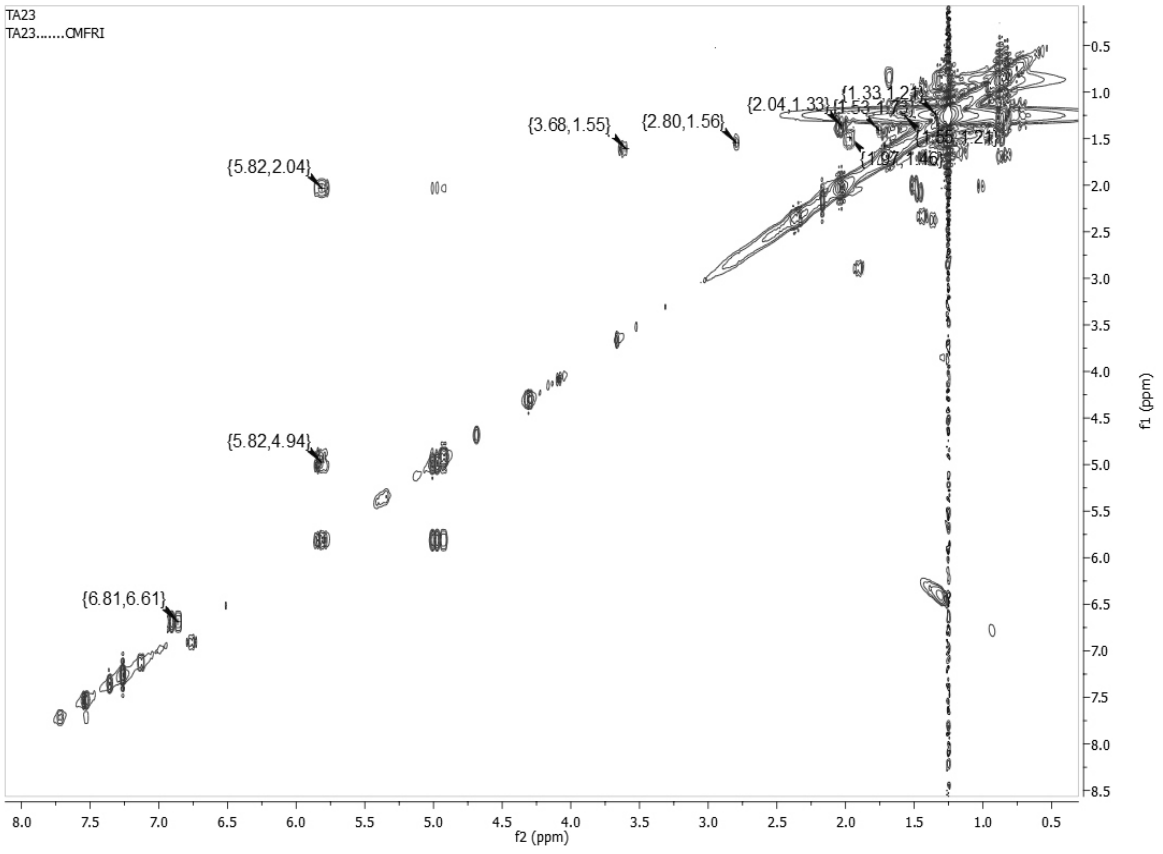

Figure 4.59.: ^{1}H-^{1}H COSY spectrum of 3-(Hept-3^6-enyloxy)-2,3,4,4a,5,6,6a,12,12a,12b-decahydro-4,6a,12a,12b-tetramethyl-*1H*-benzo[a]xanthene-4,10,12-triol (**4**)

Other HMBCs from CH_3-14 (δ 1.42) to C-6a (δ 81.6); CH_3-13 (δ 1.15) to C-4 (δ_C 73.9); CH_3-15 (δ 0.88) to C-12 (δ 51.0) and CH_3-16 (δ 0.83) to C-12b (δ 42.8) confirmed the attachment of four singlet methyl carbons at C-6a, C-4, C-12a, and C-12b, respectively, which appropriately corroborated the presence of bicyclic framework of drimane sesquiterpenoid. The three protons at δ 6.5-6.8 of **4** showed that aromatic ring might be trisubstituted and the COSY correlations from δ (6.81)-(6.61) (H-8 to H-9) along with singlet aromatic signal at δ 6.51 suggested that it might be in the meta-para fused relationship with the basic framework of **4**. The greatly deshielded quaternary carbon at δ 146.5 was related to the hydroxyl attached to the benzene ring.

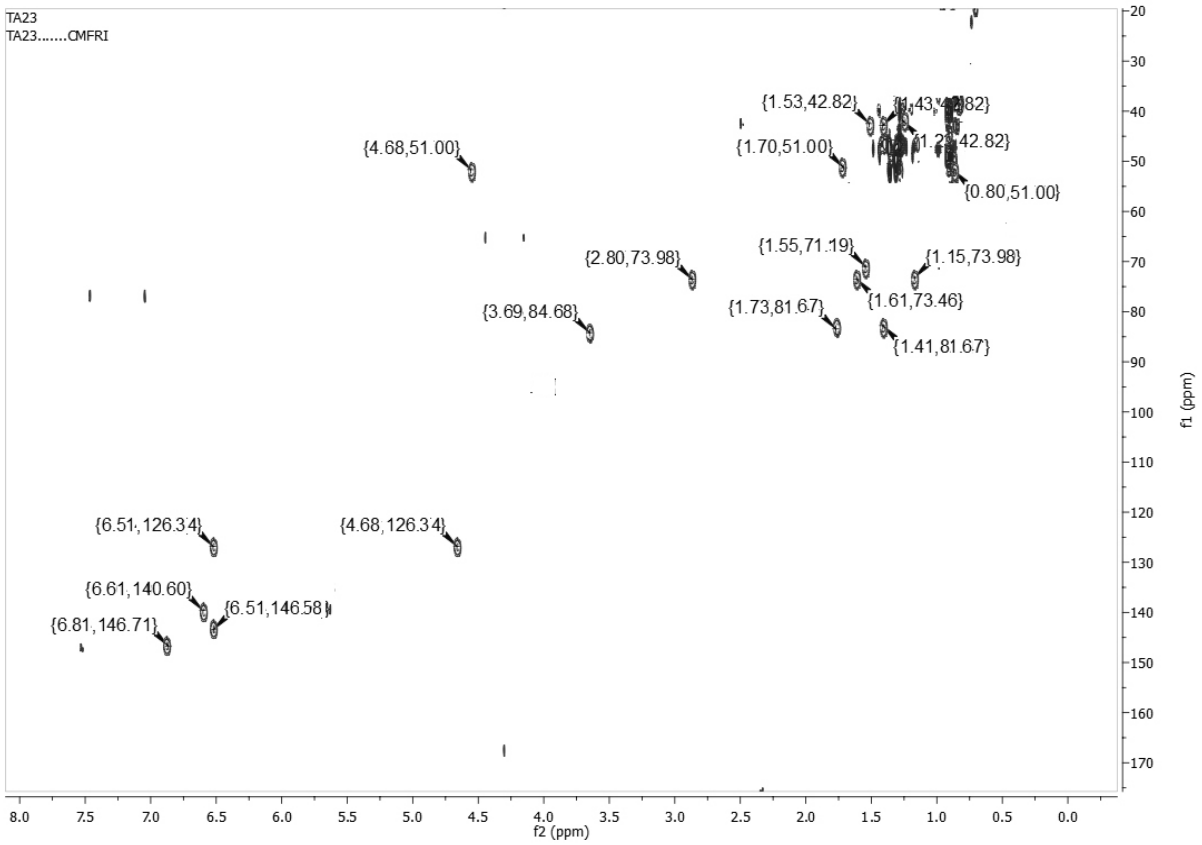

Figure 4.60.: NOE spectrum of 3-(Hept-3^6-enyloxy)-2,3,4,4a,5,6,6a,12,12a,12b-decahydro-4,6a,12a,12b-tetramethyl-*1H*-benzo[a]xanthene-4,10,12-triol (**4**)

The highly deshielded singlet proton at δ 4.68 exhibited HMBCs to C-12a (δ 51.0) of the drimane sesquiterpenoid and to C-11a (δ 126.3) of the aromatic ring. The deshielded signals at C-3 (δ 84.6), C-4 (δ 73.9), C-6a (δ 81.6), C-10 (δ 140.9) and C-12 (δ 65.5) in the ^{13}C-NMR spectrum and absence of any carbonyl absorbances in IR spectrum of **1** were accounted for

oxygenated functional groups, such as hydroxyl or ether. The greatly deshielded oxygenated quaternary carbon at δ 146.5 revealed that one of the oxygen atoms might form an ether bridge from drimane sesquiterpenoid to the aromatic ring system. These attributions recognized the occurrence of a quinol moiety in **4**, and suggested the association of drimane-quinol framework (benzo-xanthene) of sesquiterpene **4**. These spectroscopic assignments suggested the resemblance of compound **4** with the previously reported drimane sesquiterpene quinols and quinons (Mitome et al., 2003; Jiao et al., 2015; Hagiwara et al., 2015; Perez-Garcia et al., 2005; Hui et al., 2015; Cao et al., 2004). The greatly deshielded olefinic groups at δ 5.01, 4.94/δ 114.0 and δ 5.82/δ 139.2 with higher coupling constants (J=12.2-16.7) suggested the possibilities of a terminal monosubstituted vinylic group at -CH(3^6)=CH_2(3^7). The spin system from δ (3.69)-(1.55)-(1.21)-(1.33)-(2.04)-(5.82)-(4.94) suggested the linear arrangement of protons from H-3^1 to H-3^7, which was identified as hept-3^6-enyloxy chain. The strong HMBC coupling from CH_2-3^1 (δ 3.69) to C-3 (δ 84.6) appropriately delineated the attachment of hept-3^6-enyloxy at C-3 (δ 84.6) of the substituted drimane framework as an ether linkage.

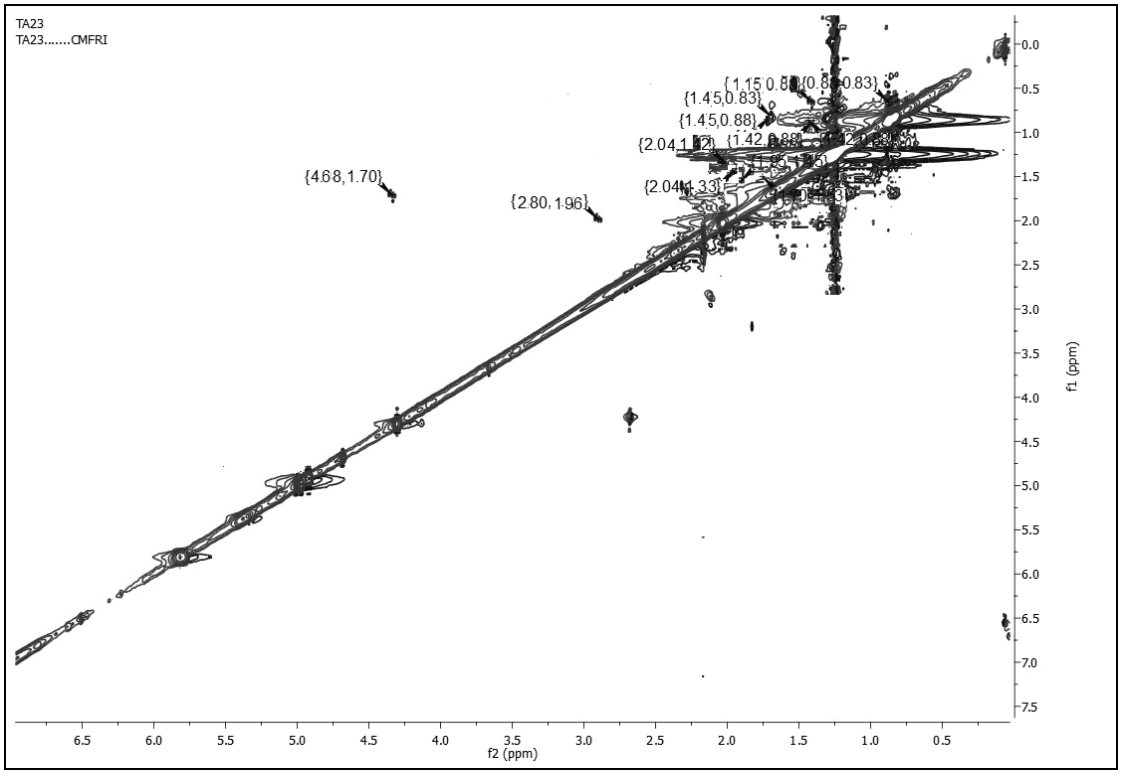

Figure 4.61.: DEPT spectrum of 3-(Hept-3^6-enyloxy)-2,3,4,4a,5,6,6a,12,12a,12b-decahydro-4,6a,12a,12b-tetramethyl-*1H*-benzo[a]xanthene-4,10,12-triol (**4**)

Relative stereochemistries of chiral centers at C-3, C-4, C-4a, C-6a, C-12a, C-12, and C-12b in **4** were assigned by NOESY experiments (Figure 4.61 & 4.62). The NOESY correlations between δ 1.96 (Hβ-2)/2.80 (H-3)/1.45 (Hβ-5); δ 1.15 (H-13)/0.83 (H-16)/1.45 (Hβ-5)/0.88 (H-15)/1.42 (H-14) attributed that these protons were coordinated in the same plane of reference, and hence, were arbitrarily assigned as β-oriented. Deshielded proton signals at δ 4.68 (H-12)/1.70 (Hα-6)/1.53 (H-4a) were found to be opposite to the β-oriented protons, and thus were arbitrarily attributed as α-aligned.

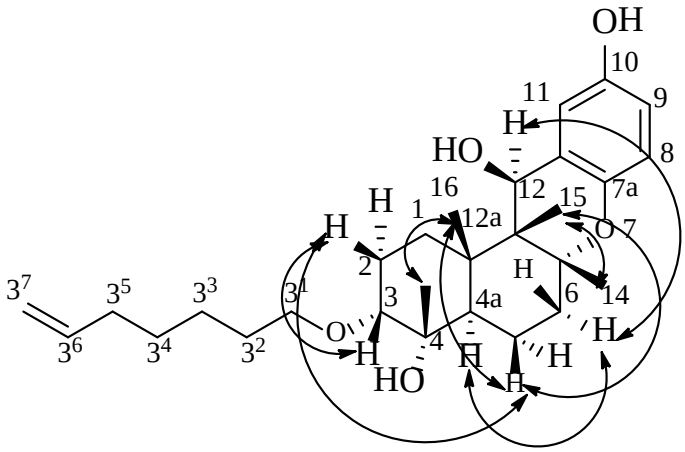

Figure 4.62.: NOE correlations of 3-(hept-3^6-enyloxy)-2,3,4,4a,5,6,6a,12,12a,12b-decahydro-4,6a,12a,12b-tetramethyl-1*H*-benzo[a]xanthene-4,10,12-triol (**4**)

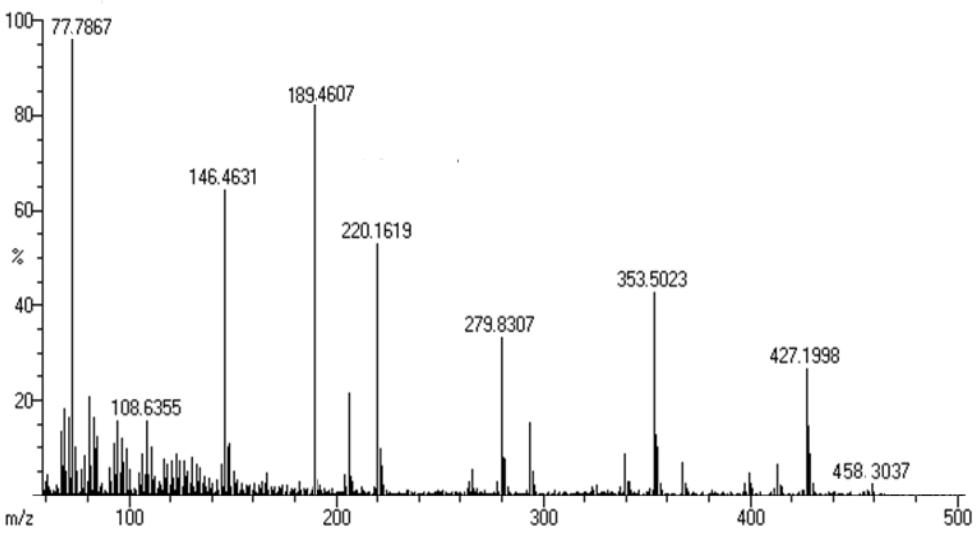

Figure 4.63.: EI-MS spectrum of 3-(Hept-3^6-enyloxy)-2,3,4,4a,5,6,6a,12,12a,12b-decahydro-4,6a,12a,12b-tetramethyl-*1H*-benzo[a]xanthene-4,10,12-triol (**4**)

Table 4.11: NMR spectroscopic data of compound (**4),** 3-(Hept-3^6-enyloxy)-2,3,4,4a,5,6,6a,12,12a,12b-decahydro-4,6a,12a,12b-tetramethyl-*1H*-benzo[a]-xanthene-4,10,12-triol (**4**)

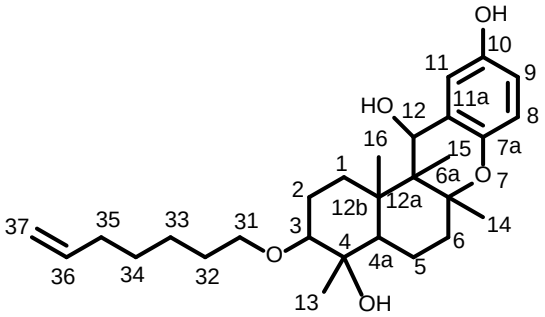

Compound **4**……3-(Hept-3^6-enyloxy)-2,3,4,4a,5,6,6a,12,12a,12b-decahydro-4,6a,12a,12b-tetramethyl-*1H*-benzo[a]-xanthene-4,10,12-triol (**4**)

C. No.	^{13}C-NMR	H. int., mult., J in Hz‡	^{1}H-NMR	COSY	HMBC
1	37.0	1H, t, J = 12.0 Hz	1.43	H-2	C-12b
		1H, t, J = 12.1 Hz	1.23	-	-
2	24.7	1H, m	1.96	H-3	-
		1H, m	1.56	-	-
3	84.6	1H, t, J = 9.8 Hz	2.80	-	C-4
		-	-	-	-
4	73.9	-	-	-	-
4a	58.7	1H, dd, J = 1.5, 12.1 Hz	1.53	H-5	C-4
5	21.7	1H, m	1.73	H-6	-
		1H, m	1.45	-	-
6	33.4	1H, td, J = 12.5, 3.4 Hz	1.70	-	C-6a,12a
		1H, td, J = 12.5, 3.0 Hz	1.37	-	-
6a	81.6	-	-	-	-
7a	146.5	-	-	-	-
8	119.0	1H, d, J = 13.4 Hz	6.81	H-9	C-7a
9	119.1	1H, d, J = 13.8 Hz	6.61	-	C-10
10	140.9	-	-	-	-
11	115.2	1H, s	6.51	-	C-11a,10
11a	126.3	-	-	-	-
12	65.5	1H, s	4.68	-	C-12a,11a
12a	51.0	-	-	-	-
12b	42.8	-	-	-	-
13	22.6	3H, s	1.15	-	C-4
14	23.9	3H, s	1.42	-	C-6a
15	14.1	3H, s	0.88	-	C-12a
16	19.6	3H, s	0.83	-	C-12b
3^1	71.1	2H, t, J = 8.6 Hz	3.69	H-3^2	C-3
3^2	31.9	2H, m	1.55	H-3^3	C-3^1
3^3	26.7	2H, m	1.21	H-3^4	-
3^4	29.6	2H, m	1.33	H-3^5	-

3^5	33.8	2H, m	2.04	H-3^6	-
3^6	139.2	1H, m	5.82	H-3^7	-
3^7	114.0	1H, dd, J = 3.4, 16.7 Hz	5.01	-	-
		1H, dd, J = 3.4, 12.2 Hz	4.94	-	-

‡ Values in ppm, multiplicity and coupling constants (J= Hz) were indicated in parentheses. Multiplicities were allocated by ^{135}DEPT NMR spectrum.

The assignments were made with the aid of the COSY, HSQC, HMBC and NOESY experiments.

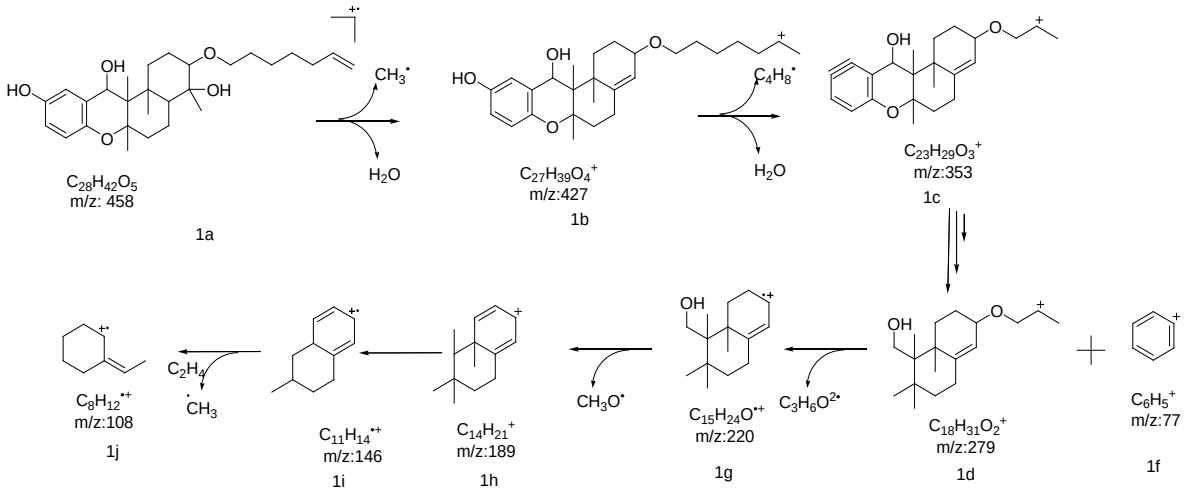

Figure 4.64.: Mass fragmentation pattern of 3-(Hept-3^6-enyloxy)-2,3,4,4a,5,6,6a,12,12a,12b-decahydro-4,6a,12a,12b-tetramethyl-*1H*-benzo[a]xanthene-4,10,12-triol (**4**)

The structural assignments of **4** were corroborated by mass spectral experiment, wherein the molecular ion peak at *m/z* 458 (1a) experienced the removal of a methyl-radical and H_2O to result $C_{27}H_{39}O_4^{\bullet+}$ (1b) with *m/z* 427. The elimination of $C_4H_8^{\bullet}$ and H_2O from 1b could result in the formation of $C_{23}H_{29}O_3^+$ with *m/z* 353 (1c). The fragment, 1c appeared to undergo further series of fragmentation to yield the mass fragments at *m/z* 77, 220, 189, 146, and 108. The base peak of the compound **4** was found at *m/z* 77, which was found to correspond to the phenyl cation ($C_6H_5^+$) (Figure 4.63 & 4.64). The 1D and 2D NMR assignments along with mass spectroscopic data unambiguously constructed the structure of the drimane sesquiterpene with substituted 1*H*-benzo[*a*]xanthene-4,10,12-triol moiety (**4**).

4.3.2.3b Structural characterization of Compound 5

13-[[2-(Hexyloxy)-2,5,5,8a-tetramethyldecahydro-1-naphthalenyl](methoxy-)-methyl]-benzenol

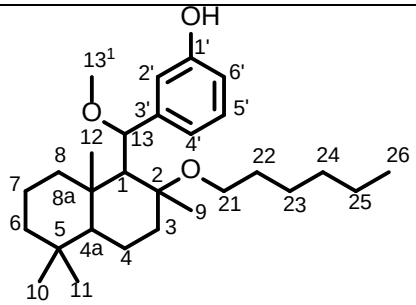

Sample yield	0.35 % (> 99% purity, RP-C18 HPLC)
Physical description	Yellowish oil
Molecular formula	$C_{28}H_{46}O_3$
Molecular mass	430.3447

The drimane class of diterpenoid derivative, 13-[[2-(Hexyloxy)-2,5,5,8a-tetramethyldecahydro-1-naphthalenyl](methoxy-)-methyl]-benzenol was isolated as yellowish-white amorphous compound. The compound (**5**) has exhibited UV absorbance (UV (MeOH) λ_{max}) at 281 nm (Figure 4.65). The homogeneity of the compound was ascertained by HPLC data on a bonded phase octadecylsilane (C_{18}) stationary phase (HPLC, MeCN/MeOH, 1:2 v/v) with R_t: 3.81 min (Figure 4.66).

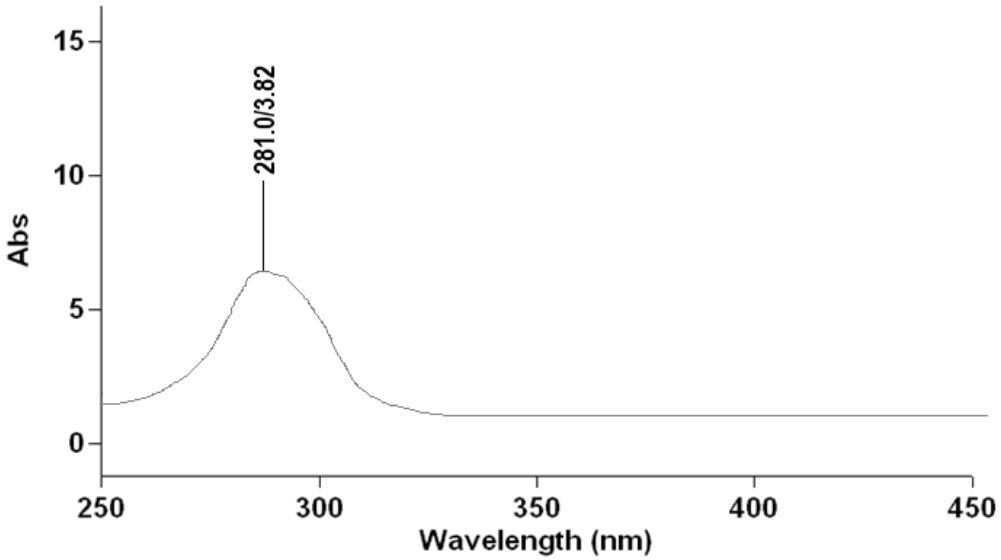

Figure 4.66.: UV spectrum of 13-[[2-(Hexyloxy)-2,5,5,8a-tetramethyldecahydro-1-naphthalenyl](methoxy-)-methyl]-benzenol (**5**)

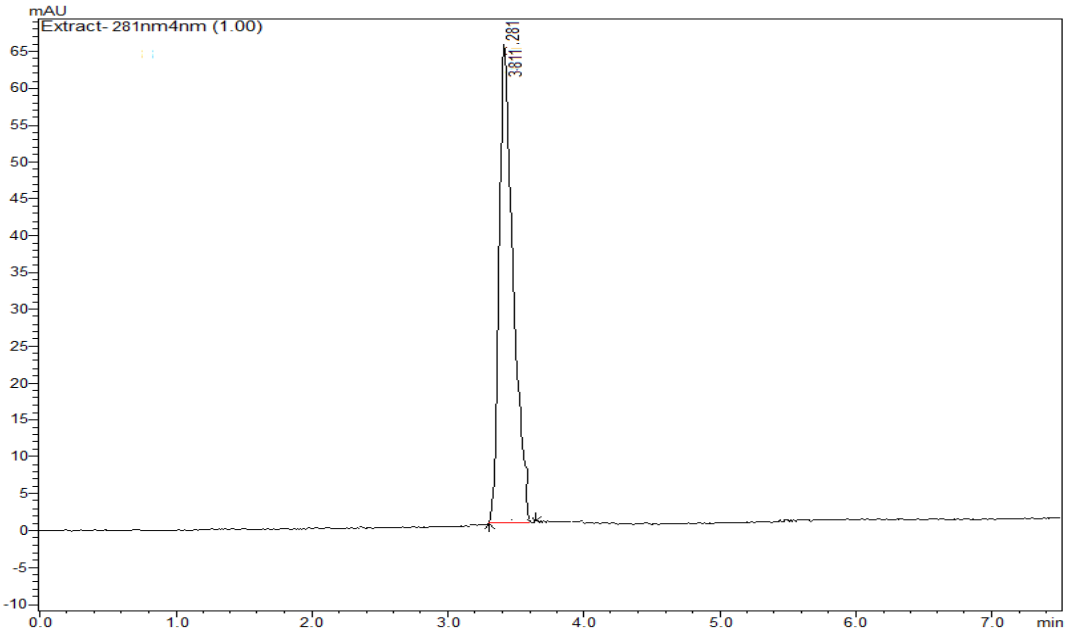

Figure 4.67.: HPLC chromatogram of 13-[[2-(Hexyloxy)-2,5,5,8a-tetramethyldecahydro-1-naphthalenyl](methoxy-)-methyl]-benzenol (**5**)

Repeated silica-gel column fractionation of the solvent extract of *G. salicornia* yielded substituted drimane derivative, **5** that was characterised as 13-[[2-(hexyloxy)-2,5,5,8a-tetramethyldecahydro-1-naphthalenyl](methoxy)methyl]benzenol. The molecular formula of **2** was inferred as $C_{28}H_{46}O_3$, using integrated mass (*m/z* 430) and comprehensive NMR data (Table 1, S1). Its six degrees of unsaturation was corroborated for two cyclic rings and aromatic ring. The HRESIMS experiment displayed the molecular ion peak at *m/z* 431.3528 $[M+H]^+$, (Figure 4.68) which along with NMR-IR spectroscopic analyses deduced its molecular formula as $C_{28}H_{47}O_3$ $[M+H]^+$ (Table 4.12).

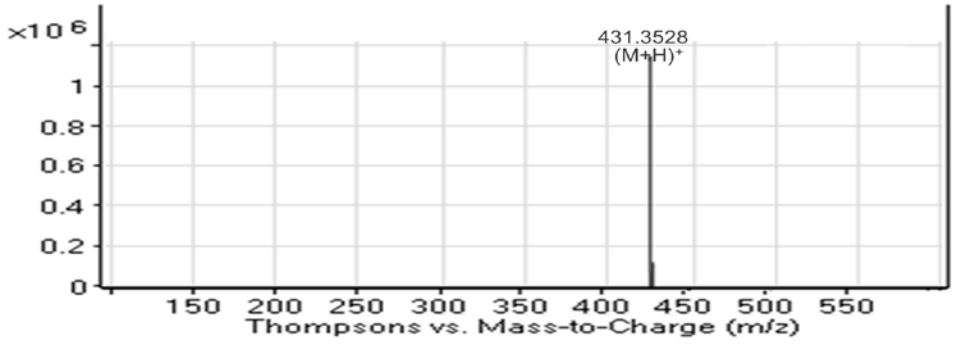

Figure 4.68.: HRESIMS spectrum of 13-[[2-(Hexyloxy)-2,5,5,8a-tetramethyldecahydro-1-naphthalenyl](methoxy-)-methyl]-benzenol (**5**)

The FTIR absorption peaks at 3402, 3028, 850, 1550 and 1120-1070 cm^{-1} suggested the probable presence of hydroxyl, aromatic and ether functionalities in the compound **5** (Figure 4.69). The ^{1}H-NMR spectrum of the studied compound showed singlet signals for four tertiary methyls at δ 1.22, 1.03, 1.00 and 1.02, which suggested the presence of tetramethyl groups (Figure 4.70).

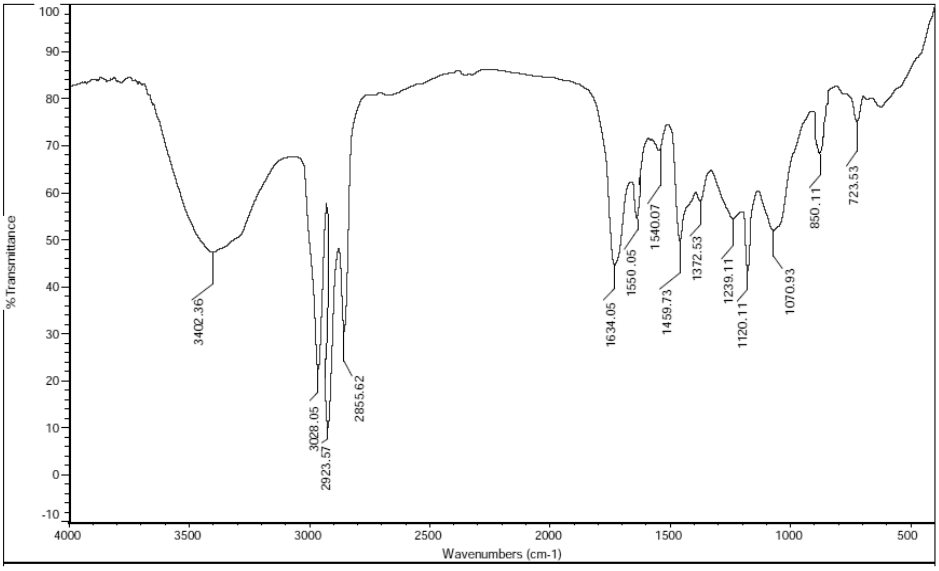

Figure 4.69.: FTIR spectrum of 13-[[2-(Hexyloxy)-2,5,5,8a-tetramethyldecahydro-1-naphthalenyl](methoxy-)-methyl]-benzenol (**5**)

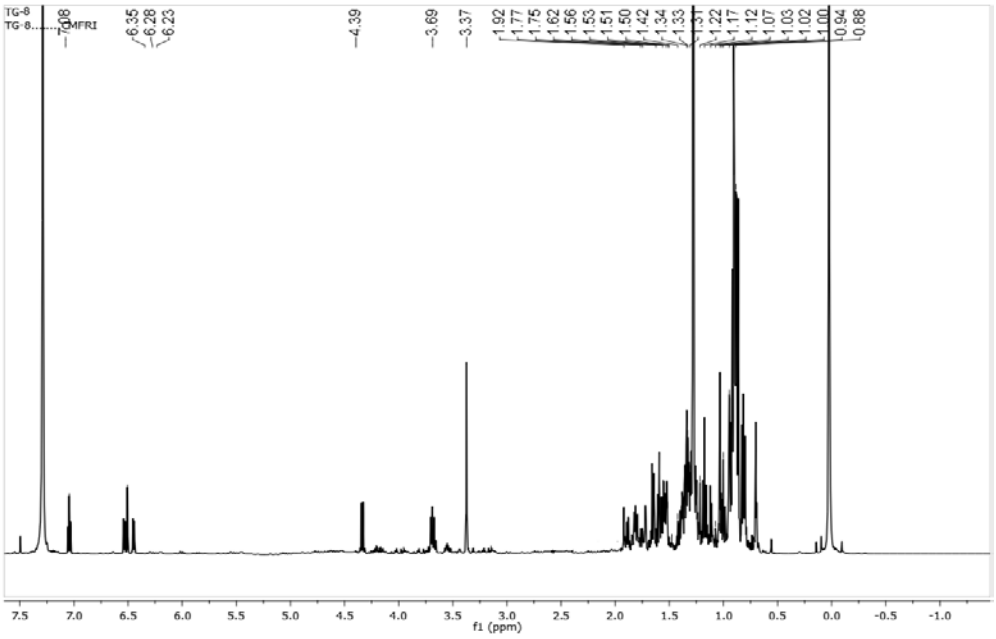

Figure 4.70.: ^{1}H-NMR spectrum of 13-[[2-(Hexyloxy)-2,5,5,8a-tetramethyldecahydro-1-naphthalenyl](methoxy-)-methyl]-benzenol (**5**)

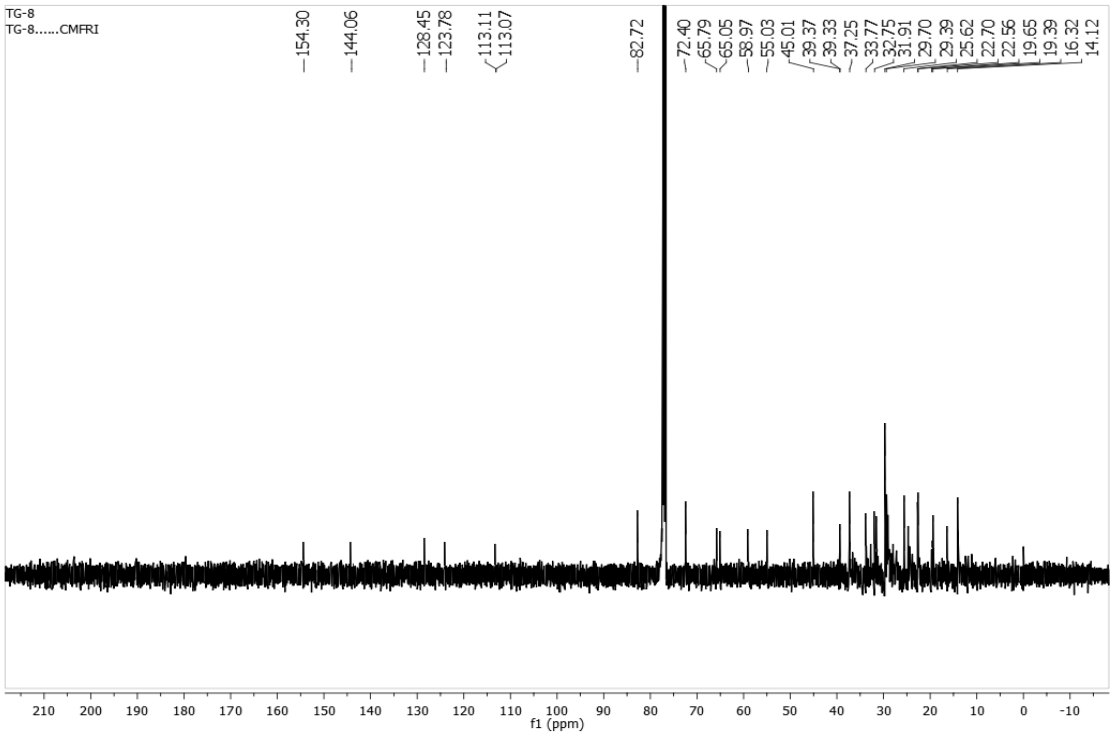

Figure 4.71.: ^{13}C-NMR spectrum of 13-[[2-(Hexyloxy)-2,5,5,8a-tetramethyldecahydro-1-naphthalenyl](methoxy-)-methyl]-benzenol (**5**)

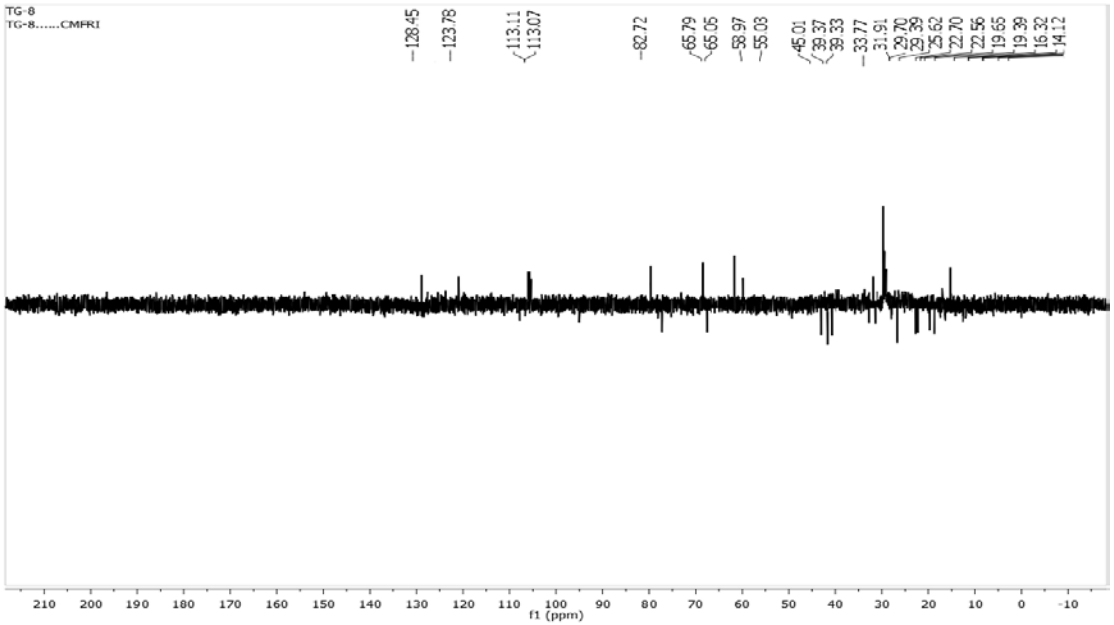

Figure 4.72.: ^{135}DEPT spectrum of 13-[[2-(Hexyloxy)-2,5,5,8a-tetramethyldecahydro-1-naphthalenyl](methoxy-)-methyl]-benzenol (**5**)

The spectrum also indicated the presence of four aromatic hydrogens at δ 6.35, 7.08, 6.23 and 6.28. The deshielded protons at δ 3.69 and 3.37 might be associated with an oxygenated functionality, such as ether linkage. The ^{13}C-NMR along with DEPT$_{135}$ spectra of **5** displayed the presence of 28 carbon signals, including six methyls (δ 22.5, 29.7, 29.3, 16.3, 14.1, 58.9), ten sp^3 methylenes (δ 39.3, 19.3, 45.0, 19.6, 39.4, 65.0, 31.9, 25.6, 33.7, 22.7), three sp^3 methines (δ 55.0, 65.7, 82.7), four sp^2 methines (δ 123.7, 128.4, 113.1, 113.0), and five quaternary carbons (δ 32.7, 72.4, 37.2, 144.0, 154.3) (Figure 4.71 & 4.72). These data was further supported by HSQC spectrum analysis (Figure 4.73).

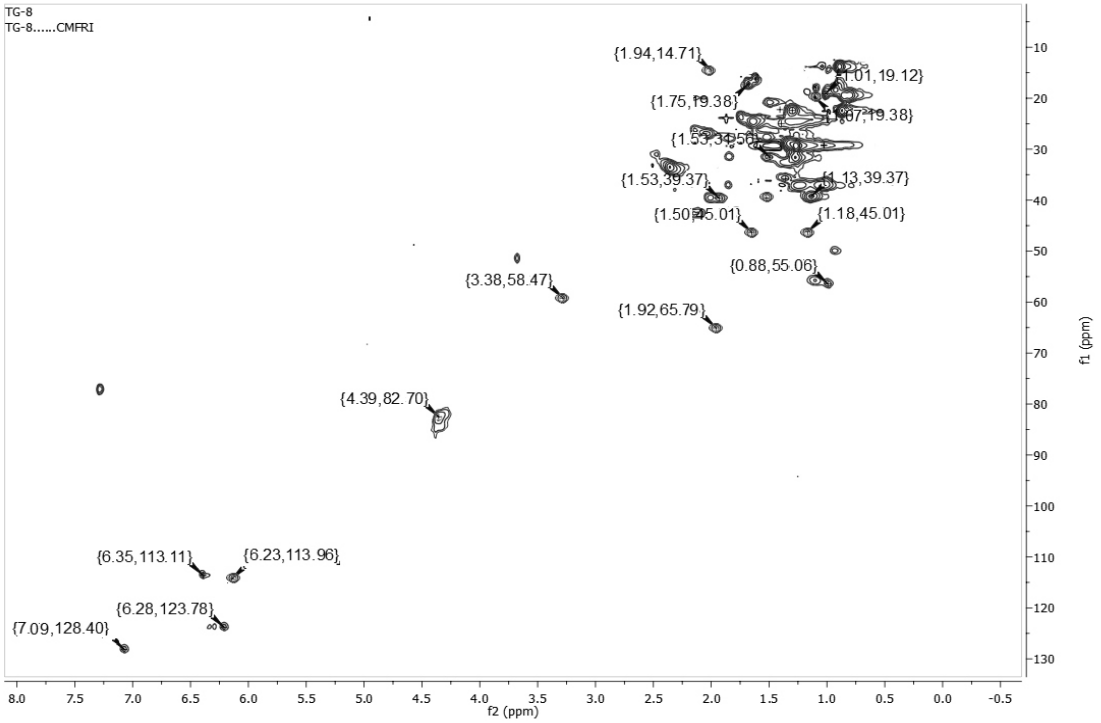

Figure 4.73.: HSQC spectrum of 13-[[2-(Hexyloxy)-2,5,5,8a-tetramethyldecahydro-1-naphthalenyl](methoxy-)-methyl]-benzenol (**5**)

The COSY spectrum of **5** suggested the presence of spin systems, such as δ (1.51)-(1.75)-(1.50) and δ (0.88)-(1.42)-(1.77), which corresponds to the partial structure of bicyclic ring from H-8/H-7/H-6 and H-4a/H-4/H-3, respectively (Figure 4.74 & 4.75). The HMBCs from CH_3-9 (δ 1.22) to C-2 (δ_C 72.4); CH_3-10 (δ 1.03) and CH_3-11 (δ1.00) to C-5 (δ 32.7); and from CH_3-12 (δ 1.02) to C-8a (δ 37.2) demonstrated the methyl substitutions at C-2, C-5 and C-8a (Figure 4.76).

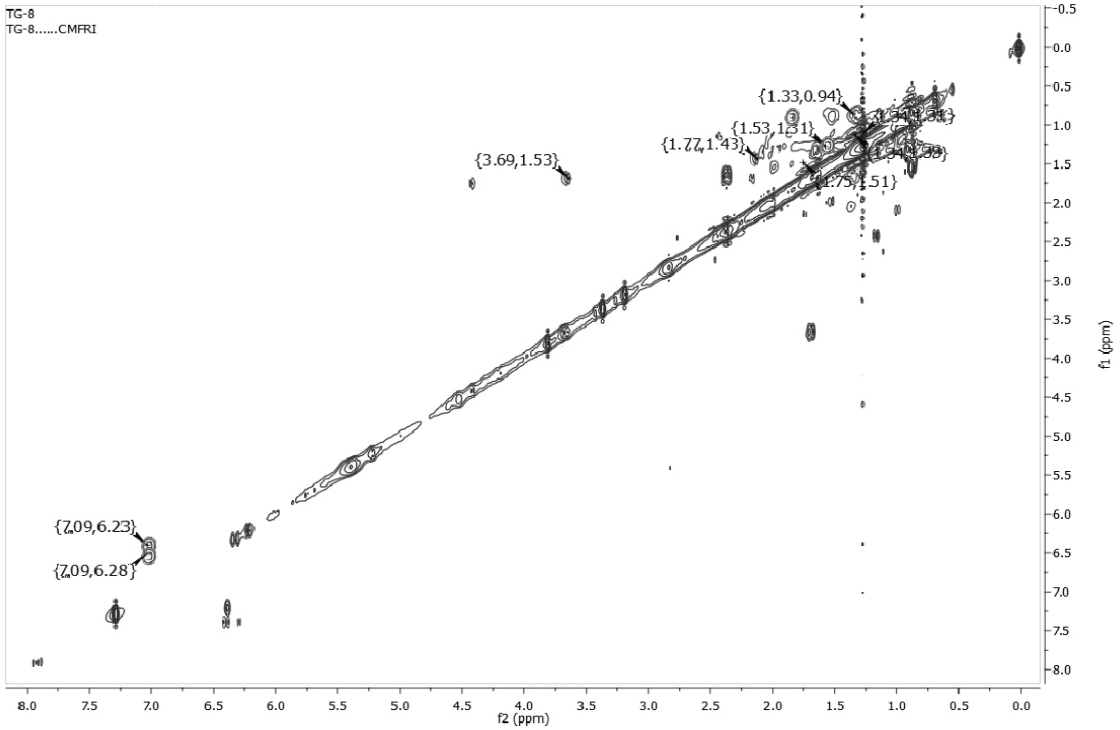

Figure 4.74.: ^{1}H-^{1}H COSY spectrum of 13-[[2-(Hexyloxy)-2,5,5,8a-tetramethyldecahydro-1-naphthalenyl](methoxy-)-methyl]-benzenol (**5**)

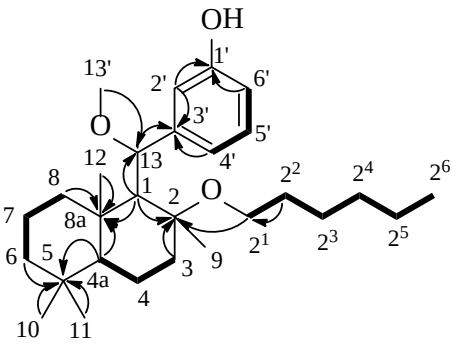

Figure 4.75.: ^{1}H-^{1}H COSY (bold face bonds), and selected HMBCs (double-barbed arrows), correlations of 13-[[2-(Hexyloxy)-2,5,5,8a-tetramethyldecahydro-1-naphthalenyl](methoxy-)-methyl]-benzenol (**5**)

The NMR spectroscopic investigations along with previous studies suggested the basic skeleton of **5** as a drimane sesquiterpenoid (Hui et al., 2015; Cao et al., 2004). The aromatic region of the proton spectrum exhibited an integral four in which one singlet, two doublets and one triplet were accounted. The greatly deshielded carbon signal at δ 154.3 (assigned as C-1') supported the presence of hydroxylated functionality at that position. The spin systems among the aromatic protons from δ (6.35)-(7.08)-(6.23) {H-4'/H-5'H-6'} suggested the

occurrence of 1,3-disubstituted aromatic ring. The HMBC correlations from CH-4' (δ 6.35) to C-3' (δ 144.0); from CH-6' (δ 6.23) to C-1' (δ 154.3) and CH-2' (δ 6.28) to C-3' (δ 144.0), C-1' (δ 154.3) attributed the possibilities of hydroxylated aromatic ring system. The strong HMBCs from δ 4.39 (H-13) to δ 144.0 (C-3') of benzene ring supported the attachment of hydroxybenzene to methine of the driamane skeleton located at C-13 position. Other spin systems from δ (3.69)-(1.53)-(1.31)-(1.34)-(1.33)-(0.94) assigned the continuous linear chain of hexane from H-2^1 to H-2^6 in which H-2^1 was found to be oxygenated, hence named as hexyloxy chain, the latter was linked at C-2 of the basic drimane skeleton as it recorded strong HMBCs from CH-2^1 (δ 3.69) to C-2 (δ 72.4). On the basis of 1D and 2D experimental data, the basic core of compound **5** strongly resembled to the quinol associated drimane sesquiterpene system (Perez-Garcia et al., 2005).

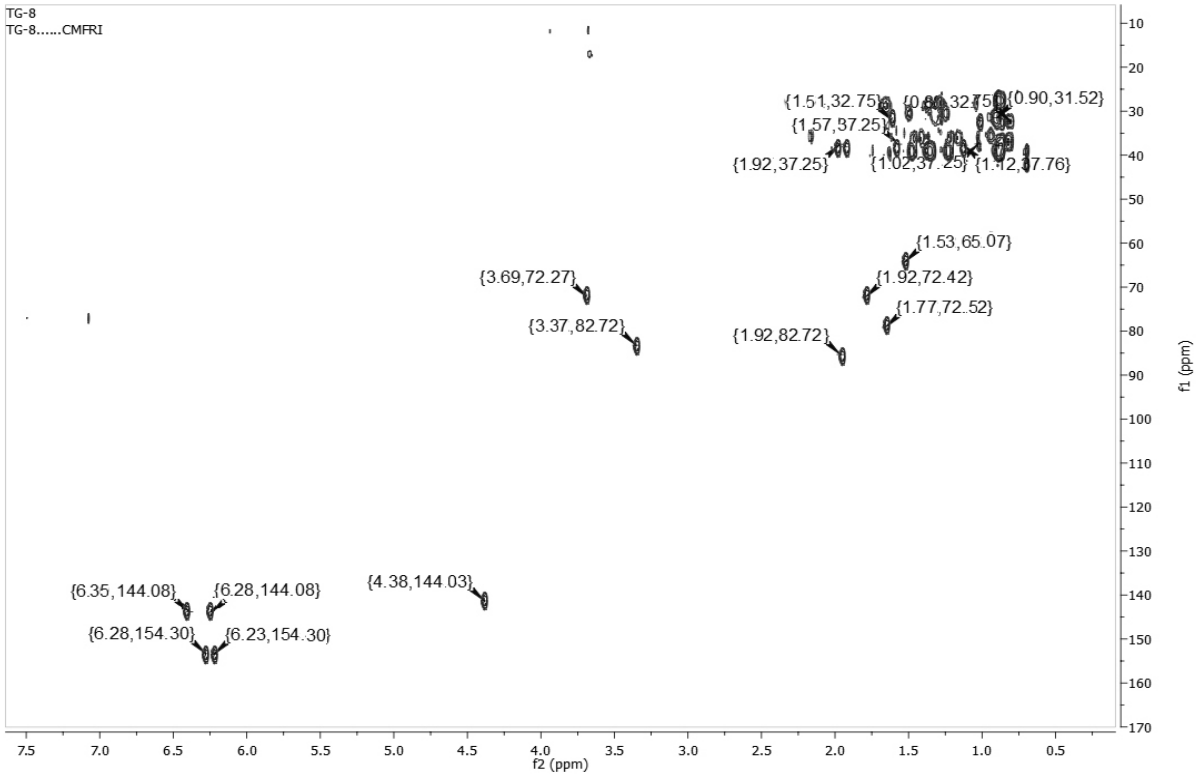

Figure 4.76.: HMBC spectrum of 13-[[2-(Hexyloxy)-2,5,5,8a-tetramethyldecahydro-1-naphthalenyl](methoxy-)-methyl]-benzenol (**5**)

Relative stereochemistries of the chiral centers at C-1, C-2, C-4a, C-5, C-8a and C-13 in **2** were assigned by NOESY experiments (Figure 4.77 & 4.78). The NOESY spectrum demonstrated that the protons δ 1.02 (H-12)/1.42 (Hβ-4)/1.22 (H-9) and δ 1.42 (Hβ-4)/1.03 (H-

10) displayed similar spatial correlations, and these protons were located in identical molecular reference plane, thus arbitrarily assigned as β-oriented. The NOESY correlations at δ 4.39 (H-13)/1.00 (H-11)/0.88 (H-4a), 1.17 (Hα-6), 1.92 (H-1) were found to be trans oriented to the β-protons, and therefore, assigned as α-protons.

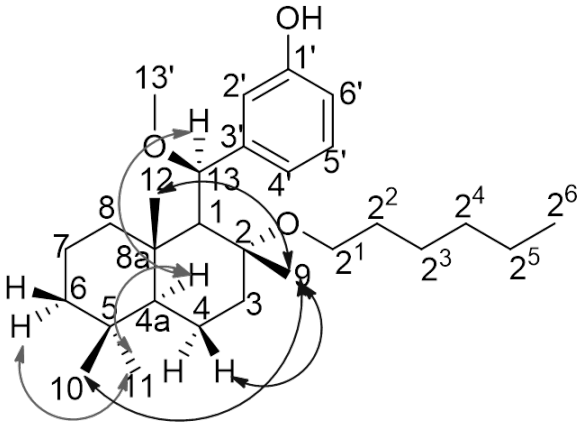

Figure 4.77.: NOE correlations of 13-[[2-(Hexyloxy)-2,5,5,8a-tetramethyldecahydro-1-naphthalenyl](methoxy-)-methyl]-benzenol (**5**)

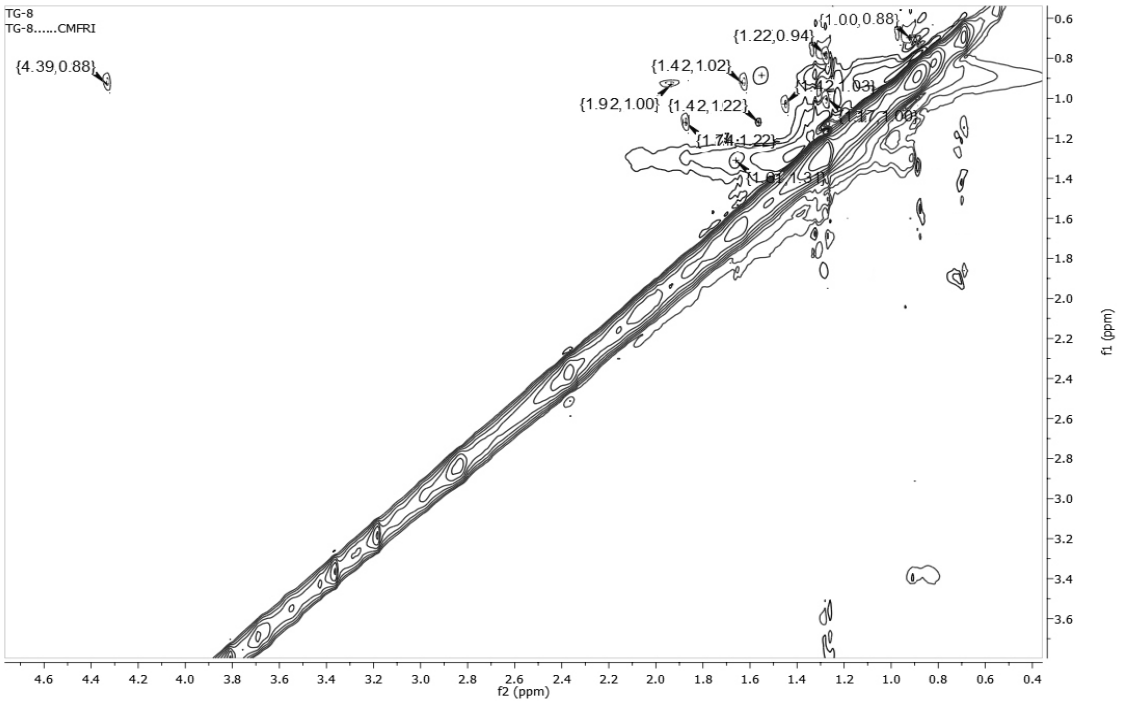

Figure 4.77.: NOE spectrum of 13-[[2-(Hexyloxy)-2,5,5,8a-tetramethyldecahydro-1-naphthalenyl](methoxy-)-methyl]-benzenol (**5**)

Table 4.12: NMR spectroscopic data of 13-[[2-(Hexyloxy)-2,5,5,8a-tetramethyldecahydro-1-naphthalenyl](methoxy-)-methyl]-benzenol (**5**)

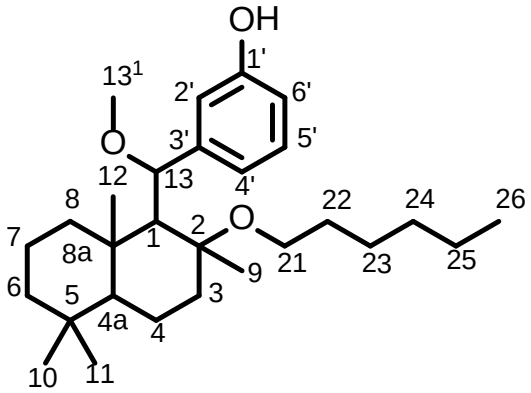

Compound **5**…….13-[[2-(Hexyloxy)-2,5,5,8a-tetramethyldecahydro-1-naphthalenyl](methoxy-)-methyl]-benzenol (**5**)

C. No.	^{13}C -NMR	H. int., mult., J in Hz‡	^{1}H-NMR	COSY	HMBC
1	65.7	1H, d, J = 8.0 Hz	1.92	-	C-2,8a,13
2	72.4	-	-	-	-
3	39.3	1H, m	1.77	H-4	C-2
		1H, m	1.56	-	-
4	19.6	1H, m	1.62	H-4a	-
		1H, m	1.42	-	-
4a	55.0	1H, dd, J = 1.8, 12.2 Hz	0.88	-	C-5,8a
5	32.7	-	-	-	-
6	45.0	1H, td, J = 13.5, 4.1 Hz	1.50	H-7	C-5
		1H, td, J = 12.9, 4.2 Hz	1.17	-	-
7	19.3	1H, m	1.75	H-8	-
		1H, m	1.07	-	-
8	39.4	1H, t, J = 12.0 Hz	1.51	-	-
		1H, t, J = 12.0 Hz	1.12	-	C-8a
8a	37.2	-	-	-	
9	22.5	3H, s	1.22	-	C-2
10	29.7	3H, s	1.03	-	C-5
11	29.3	3H, s	1.00	-	C-5
12	16.3	3H, s	1.02	-	C-8a
13	82.7	1H, d, J = 8.2 Hz	4.39	-	C-3’
13^1	58.9	3H, s	3.37	-	C-13
1’	154.3	-	-	-	-
2’	113.0	1H, s	6.28	-	C-1’,3’
3’	144.0	-	-	-	-
4’	123.7	1H, d, J = 12.1 Hz	6.35	H-5’	C-3’
5’	128.4	1H, t, J = 13.2 Hz	7.08	H-6’	-
6’	113.1	1H, d, J = 13.1 Hz	6.23	-	C-1’
2^1	65.0	2H, m	3.69	H-2^2	C-2
2^2	31.9	2H, m	1.53	H-2^3	-
2^3	25.6	2H, m	1.31	H-2^4	-

2^4	33.7	2H, m	1.34	H-2^5	-
2^5	22.7	2H, m	1.33	H-2^6	-
2^6	14.1	3H, t, J = 6.7 Hz	0.94	-	-

‡ Values in ppm, multiplicity and coupling constants (J= Hz) were indicated in parentheses. Multiplicities were allocated by ^{135}DEPT NMR spectrum.

The assignments were made with the aid of the COSY, HSQC, HMBC and NOESY experiments.

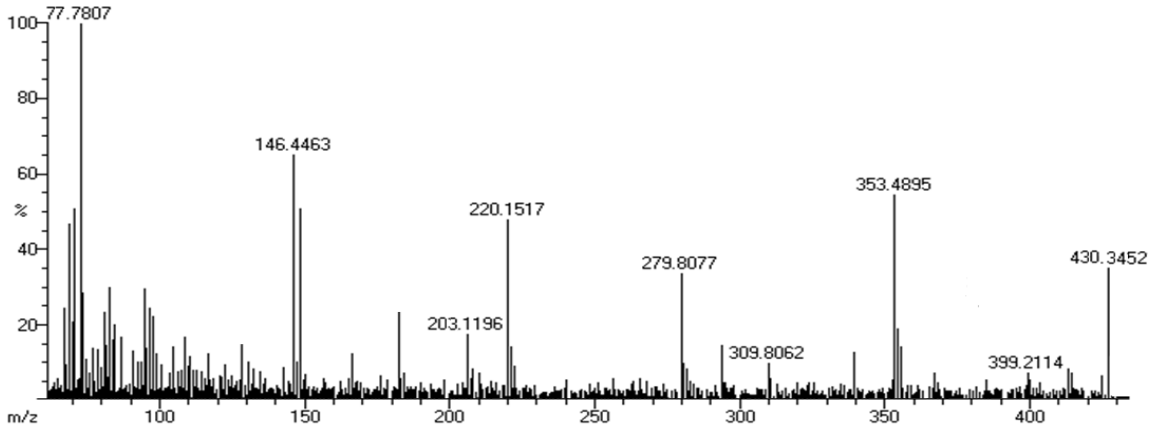

Figure 4.78.: EI-MS spectrum of 3-(Hept-3^6-enyloxy)-2,3,4,4a,5,6,6a,12,12a,12b-decahydro-4,6a,12a,12b-tetramethyl-*1H*-benzo[a]xanthene-4,10,12-triol (**5**)

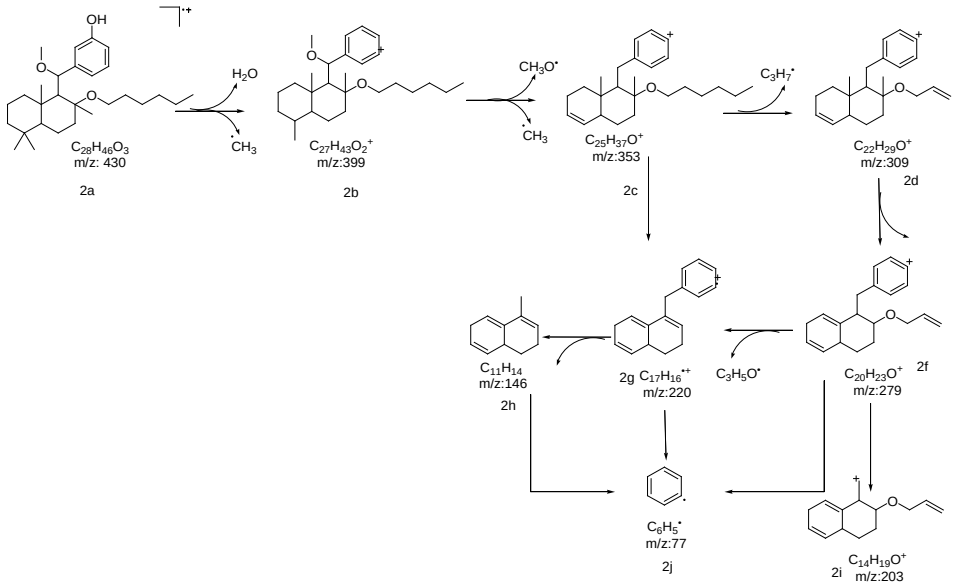

Figure 4.80.: Mass fragmentation pattern of 3-(Hept-3^6-enyloxy)-2,3,4,4a,5,6,6a,12,12a,12b-decahydro- 4,6a,12a,12b-tetramethyl-*1H*-benzo[a]xanthene-4,10,12-triol (**5**)

The structure elucidation of **5** was corroborated by the mass spectral experiment, wherein the molecular ion peak at *m/z* 430 (2a) experienced the removal of a methyl-radical and H_2O to yield $C_{27}H_{43}O_2^{\bullet+}$ (2b) with *m/z* 399. The elimination of $CH_3O^{\bullet}$ and $^{\bullet}CH_3$ from 2b resulted in the formation of $C_{25}H_{37}O^{\bullet+}$ with *m/z* 353 (2c). The fragment at *m/z* 309 (2d) underwent further series of fragmentation to result *m/z* 77 (2j) as the base peak, which was found to correspond the phenyl radical ($C_6H_5^{\bullet}$) (Figure 4.79 & 4.80). The NMR assignments along with mass spectroscopic data unambiguously constructed the structure of drimane sesquiterpene with substituted [(naphthalenyl)(methoxy)methyl]benzenol framework of the studied compound (**5**).

4.3.2.3c Structural characterization of Compound 6

1-Butoxy-4,4,11b,11c-tetramethyl-1,2,3,3a,4,5,6,6a,11b,11c-decahydrobenzo[kl]-xanthen-10-ol

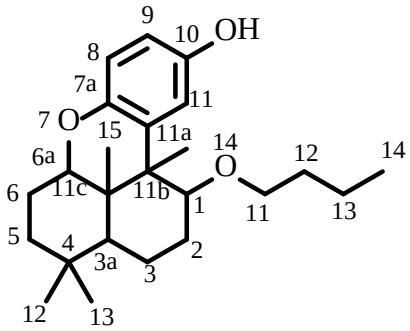

Sample yield	0.32 % (> 99% purity, RP-C18 HPLC)
Physical description	Yellowish oil
Molecular formula	$C_{24}H_{36}O_3$
Molecular mass	372.2664

The drimane class of diterpenoid derivative, 1-butoxy-4,4,11b,11c-tetramethyl-1,2,3,3a,4,5,6,6a,11b,11c-decahydrobenzo[kl]-xanthen-10-ol (**6**) was isolated as yellowish-white amorphous compound. The compound (**6**) has exhibited UV absorbance (UV (MeOH) λ_{max}) at 283 nm (Figure 4.81.). The homogeneity of the compound was ascertained by HPLC data on a bonded phase octadecylsilane (C_{18}) stationary phase (HPLC, MeCN/MeOH, 1:2 v/v) with R_t: 4.20 min (Figure 4.82.).

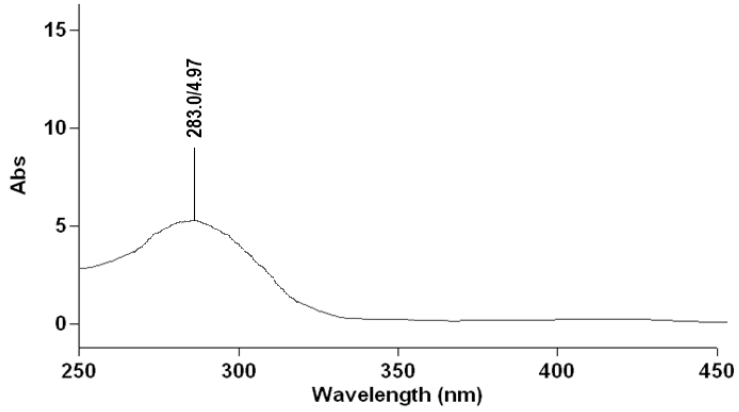

Figure 4.81.: UV spectrum of 1-butoxy-4,4,11b,11c-tetramethyl-1,2,3,3a,4,5,6,6a,11b,11c-decahydrobenzo[kl]-xanthen-10-ol (**6**)

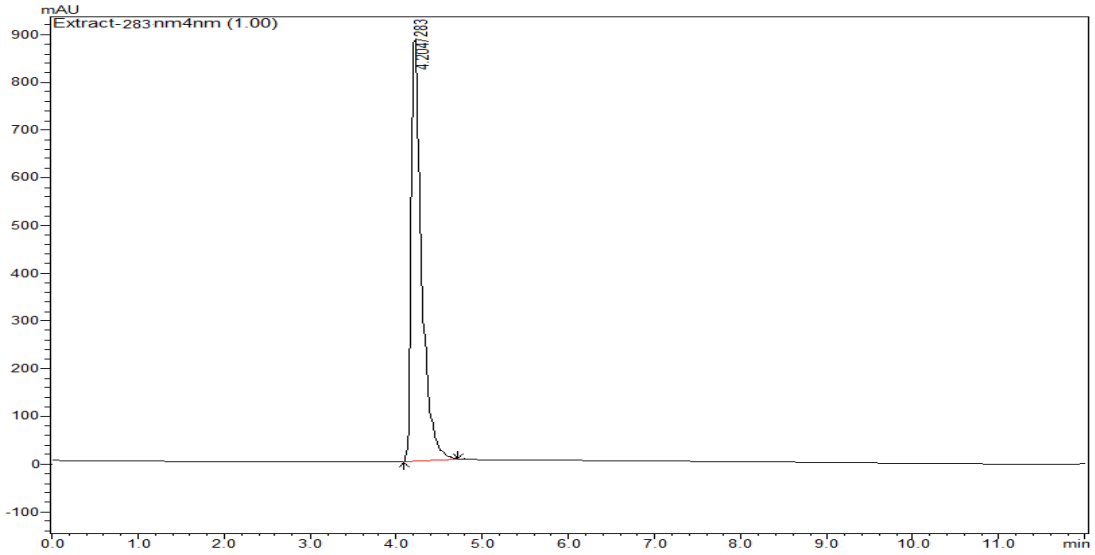

Figure 4.82.: HPLC chromatogram of 1-butoxy-4,4,11b,11c-tetramethyl-1,2,3,3a,4,5,6,6a,11b,11c-decahydrobenzo[kl]-xanthen-10-ol (**6**)

Repeated chromatographic fractionation of the organic solvent extract of *G. salicornia* resulted to substituted drimane derivative, **6** that was characterised as 1-butoxy-4,4,11b,11c-tetramethyl-1,2,3,3a,4,5,6,6a,11b,11c-decahydrobenzo[*kl*]xanthen-10-ol. The molecular formula of **5** was inferred as $C_{24}H_{36}O_3$, using integrated mass (*m/z* 372) and NMR experiments (Table 4.13). Its seven degrees of unsaturations were corroborated to three ring systems and one aromatic ring. The HRESIMS experiment displayed the molecular ion peak at *m/z* 373.3746 $[M+H]^+$, (Figure 4.83).

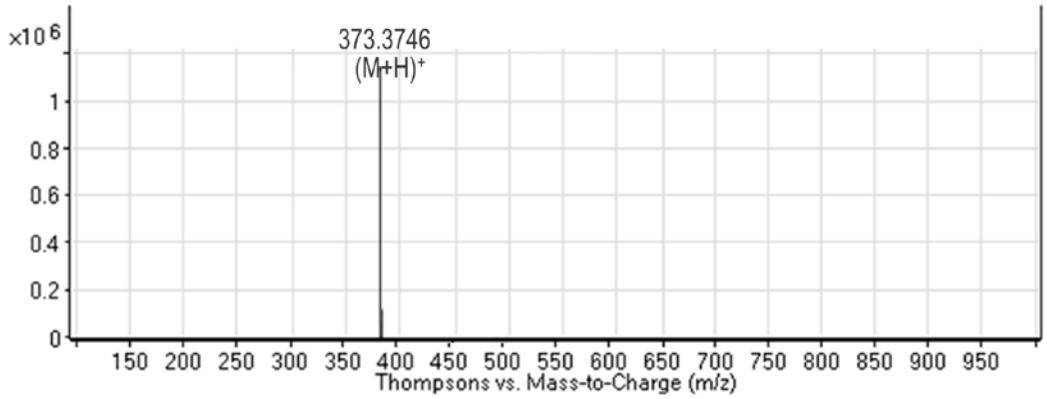

Figure 4.83.: HRESIMS spectrum of 1-butoxy-4,4,11b,11c-tetramethyl-1,2,3,3a,4,5,6,6a,11b,11c-decahydrobenzo[kl]-xanthen-10-ol (**6**)

The FTIR absorption peaks at 3412, 3026, 854, 1560 and 1115-1043 cm^{-1} assigned the occurrences of hydroxyl, aromatic and ether functionalities (Figure 4.84). The ^{1}H-NMR showed signals of four tertiary methyls at δ 1.37, 1.00, 0.98 and 1.15, which were typical of the drimane sesquiterpene framework (Hagiwara et al., 2015) (Figure 4.85).

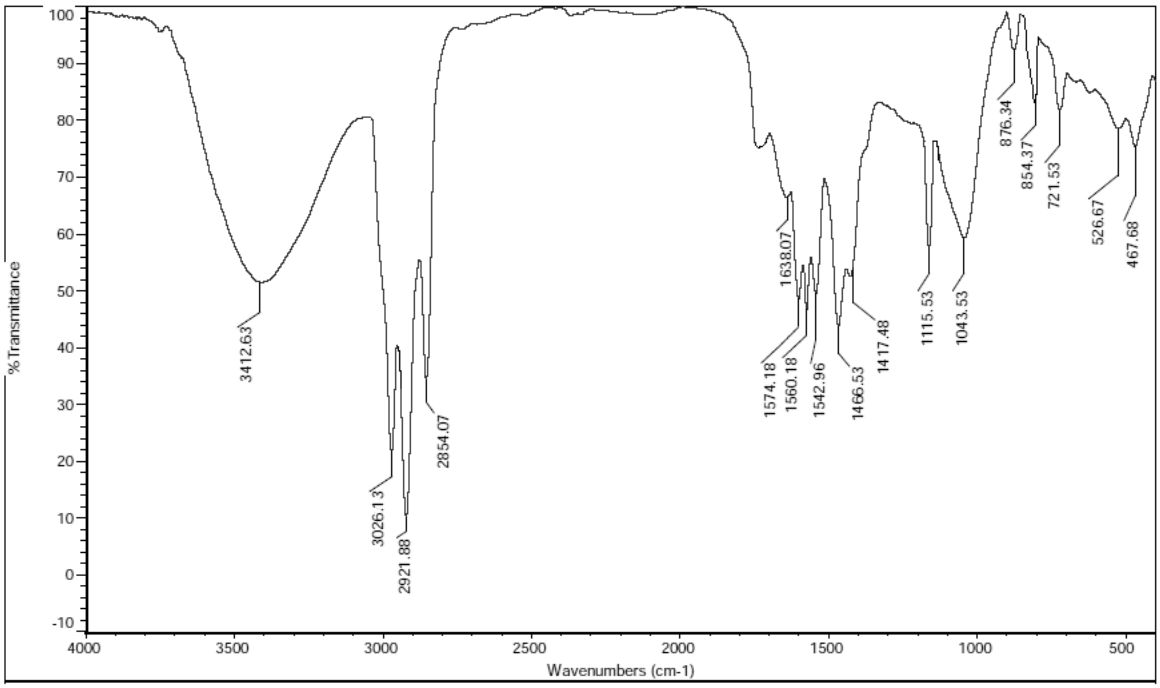

Figure 4.84.: FTIR spectrum of 1-butoxy-4,4,11b,11c-tetramethyl-1,2,3,3a,4,5,6,6a,11b,11c-decahydrobenzo[kl]-xanthen-10-ol (**6**)

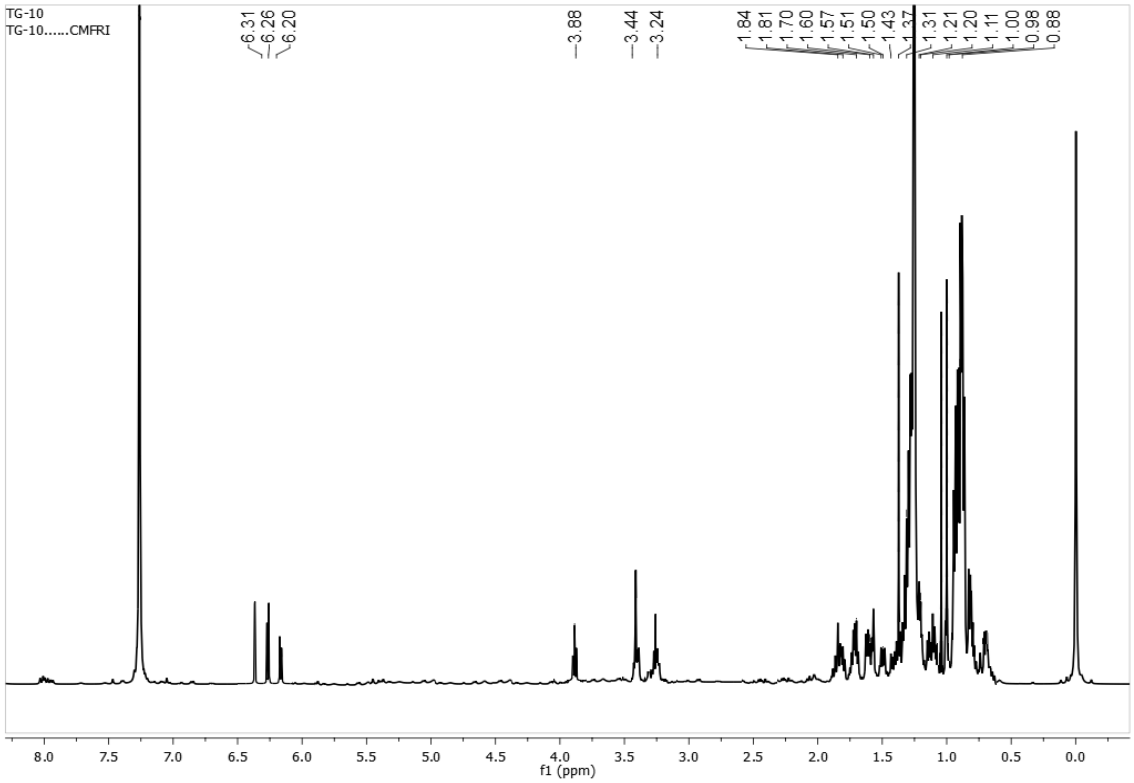

Figure 4.85.: ^{1}H-NMR spectrum of 1-butoxy-4,4,11b,11c-tetramethyl-1,2,3,3a,4,5,6,6a,11b,11c-decahydrobenzo[kl]-xanthen-10-ol (**6**)

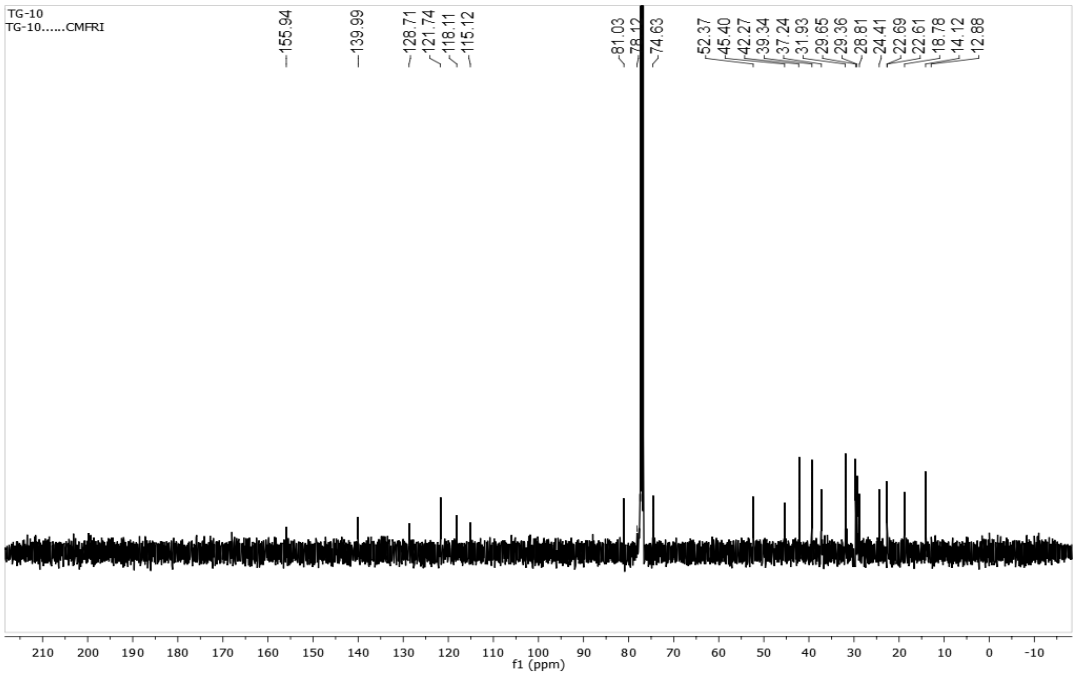

Figure 4.86.: ^{13}C-NMR spectrum of 1-butoxy-4,4,11b,11c-tetramethyl-1,2,3,3a,4,5,6,6a,11b,11c-decahydrobenzo[kl]-xanthen-10-ol (**6**)

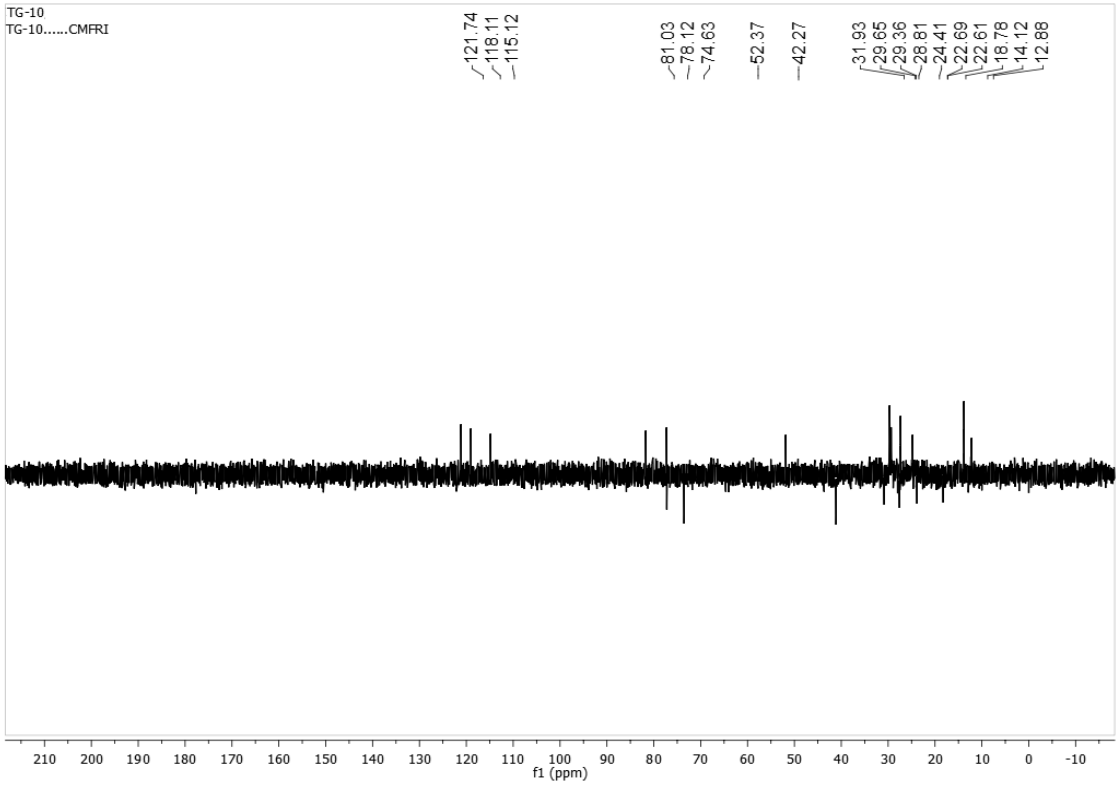

Figure 4.87.: ^{135}DEPT spectrum of 1-butoxy-4,4,11b,11c-tetramethyl-1,2,3,3a,4,5,6,6a,11b,11c-decahydrobenzo[kl]-xanthen-10-ol (**6**)

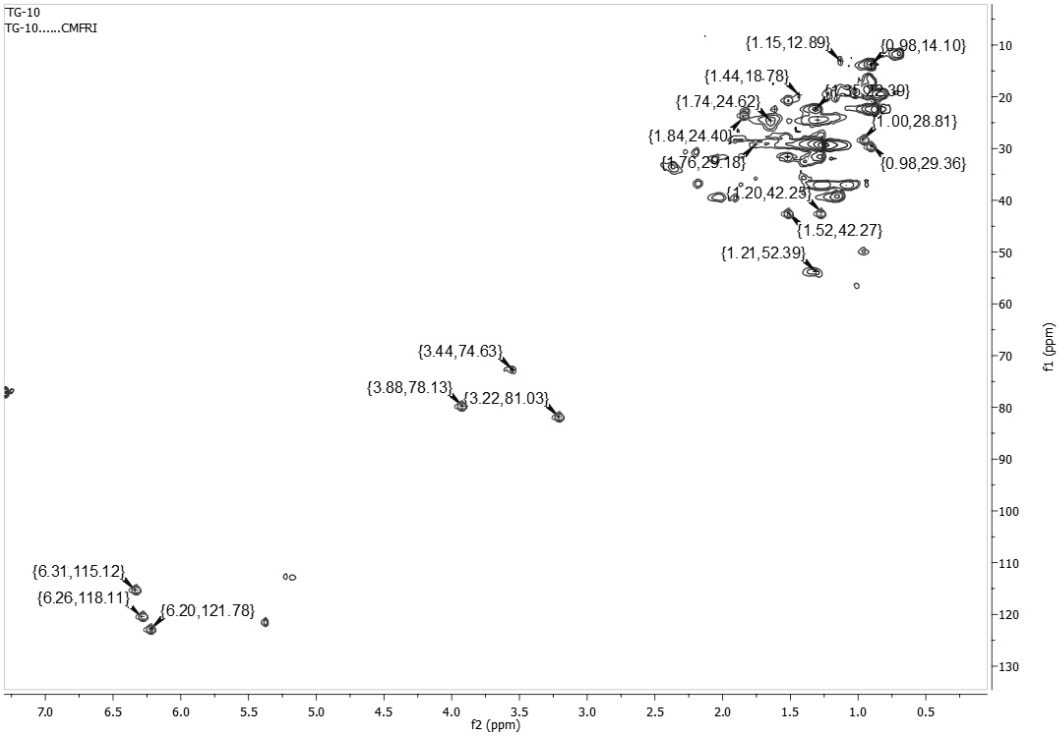

Figure 4.88.: HSQC spectrum of 1-butoxy-4,4,11b,11c-tetramethyl-1,2,3,3a,4,5,6,6a,11b,11c-decahydrobenzo[kl]-xanthen-10-ol (**6**)

The spectrum also indicated the presence of three aromatic hydrogens at δ 6.31, 6.26, and 6.20. In addition, a methyl triplet at δ 0.88 suggested the occurrence of terminal methyl substitution. The ^{13}C-NMR along with DEPT$_{135}$ spectra of **6** displayed the presence of 24 carbon signals, including five methyls (δ 22.6, 28.8, 29.3, 12.8, 14.1), seven sp^3 methylenes (δ 24.4, 42.2, 22.7, 29.6, 74.6, 31.9, 18.7), three each of sp^3 methines (δ 81.0, 78.1, 52.3) and sp^2 methines (δ 115.1, 118.1, 121.7) along with six quaternary carbons (δ 37.2, 45.4, 39.3, 128.7, 139.9, 155.9) (Figure 4.86 & 4.87). These data were further corroborated by HSQC spectral information (Figure 4.88).

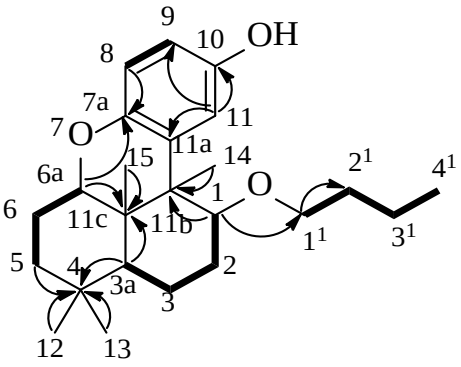

Figure 4.89.: ^{1}H-^{1}H COSY (bold face bonds), and selected HMBCs (double-barbed arrows) of 1-butoxy-4,4,11b,11c-tetramethyl-1,2,3,3a,4,5,6,6a,11b,11c-decahydrobenzo[kl]-xanthen-10-ol (**6**)

The COSY spectrum of **6** assigned the occurrences of four individual spin units, I: δ (3.20)-(1.84)-(1.51) and II: δ (1.21)-(1.57)-(1.81)-(3.88), which were accounted for the partial structure of the bicyclic ring; III: δ (6.26)-(6.20) corresponding to the aromatic ring part, and IV: δ (3.44)-(1.50)-(1.43)-(0.88) was accounted for the presence of butoxy chain (Figure 4.89 & 4.90). The HMBC correlations from CH-6a (δ 3.20) to C-11c (δ 39.3); from CH_2-5 (δ 1.20) and CH-3a (δ 1.21) to C-4 (δ 37.2); from CH-3a (δ 1.21) to C-11c (δ 39.3) and from CH-1 (δ 3.88) to C-11b (δ 45.4) appropriately suggested the complete structure of bicyclic drimane skeleton (Figure 4.91). Other key HMBCs were assigned from CH_3-12 (δ 1.00) and CH_3-13 (δ 0.98) to C-4 (δ 37.2); from CH_3-15 (δ 1.15) to C-11c (δ 39.3) and from CH_3-14 (δ 1.37) to C-11b (δ 45.4), which attributed the methyl substitutions at C-4, C-11c and C-11b. The greater deshielded signal at δ 155.9 was found to be due to the aromatic hydroxyl, whereas the aromatic proton integral of three suggested the possibility of trisubstituted aromatic ring in **6**. Other HMBCs from CH-11 (δ 6.31) to C-11a (δ 128.7), C-9 (δ 121.7), C-10 (δ 155.9) and from CH-8 (δ 6.26) to C-7a (δ 139.9) attributed to the occurrence of hydroxybenzene ring functionality.

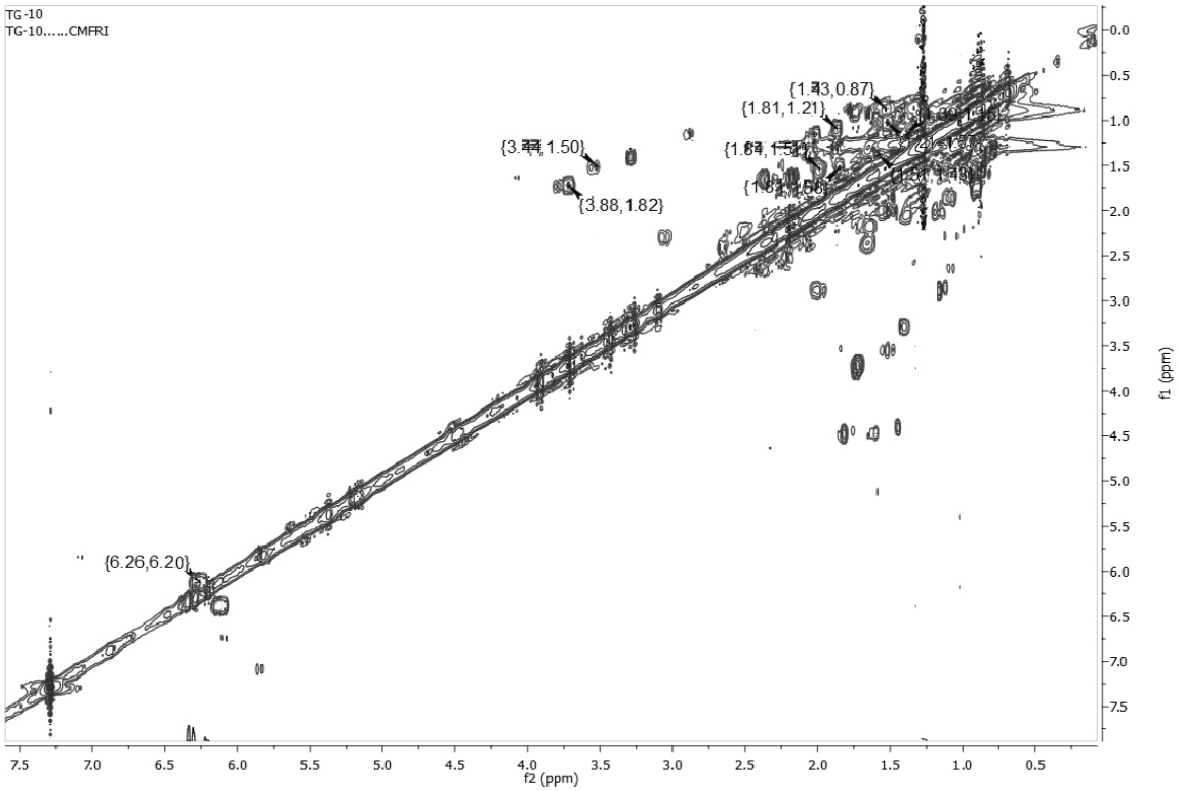

Figure 4.90.: ^{1}H-^{1}H COSY spectrum of 1-butoxy-4,4,11b,11c-tetramethyl-1,2,3,3a,4,5,6,6a,11b,11c-decahydrobenzo-[kl]-xanthen-10-ol (**6**)

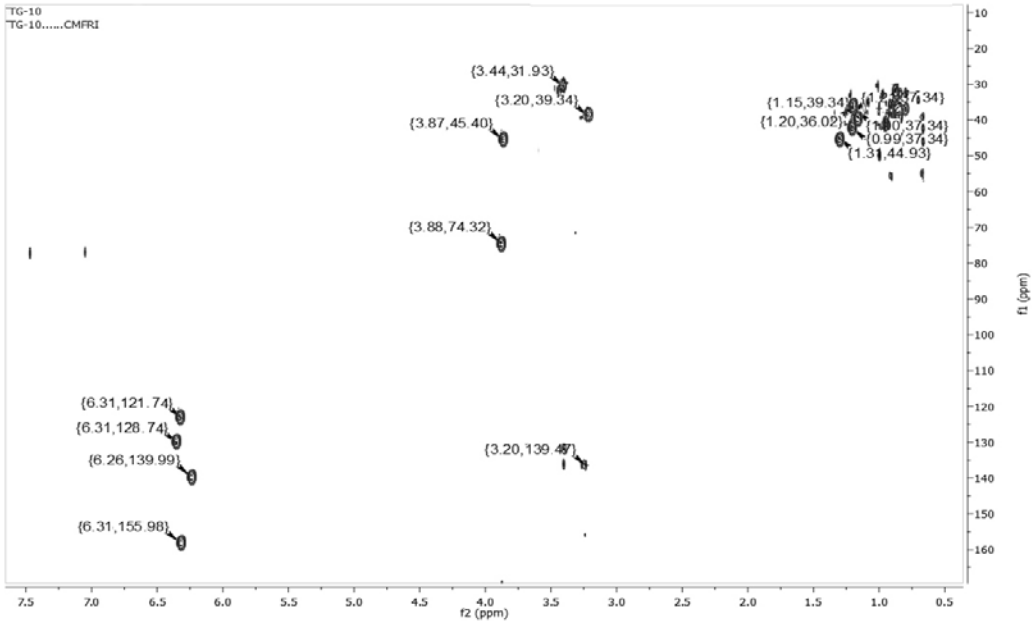

Figure 4.91.: HMBC spectrum of 1-butoxy-4,4,11b,11c-tetramethyl-1,2,3,3a,4,5,6,6a,11b,11c-decahydrobenzo[kl]-xanthen-10-ol (**6**)

The strong HMBC correlation from CH-6a (δ 3.20) to C-7a (δ 139.9) supported the attachment of drimane skeleton to the aromatic ring through an ether linkage. The butoxy side chain was attached at C-1 of the quinol associated drimane sesquiterpene, and this attribution was confirmed through strong HMBCs from CH-1 (δ 3.88) to C-1^1 (δ 74.6). The compound **6** was structurally related to the previously reported quinol fused drimane sesquiterpenes (Mitome et al., 2003; Hagiwara et al., 2015) and compound **4** except the dissimilarities perceived in the NMR signals due to the ether substitutions of the tetracyclic core, and also in the position and number of the methyl functionalities.

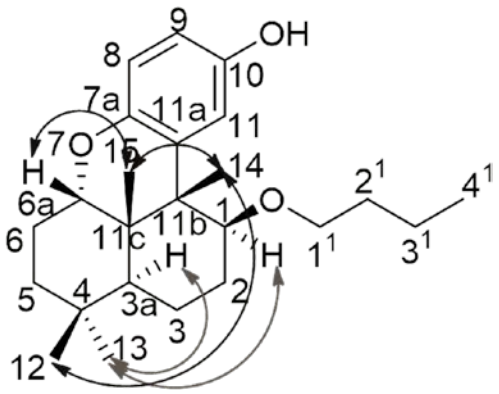

Figure 4.92.: NOE (double barbed arrows) correlations of 1-butoxy-4,4,11b,11c-tetramethyl-1,2,3,3a,4,5,6,6a,11b,11c-decahydrobenzo[kl]-xanthen-10-ol (**6**)

The relative stereochemistries of the chiral centers at C-1, C-3a, C-4, C-6a, C-11b, and C-11c in **6** were designated through NOESY experiments (Figure 4.92 & 4.93). The NOESY correlations between δ 3.20 (H-6a)/1.15 (H-15)/1.37 (H-14)/1.00 (H-12) were found to be in the identical plane of symmetry, and therefore, were arbitrarily attributed as β-faced protons. Similarly, NOE correlations were exhibited by the proton at δ 0.98 (H-13) with those at δ 3.88 (H-1) and 1.21 (H-3a). These were found to be situated at the opposite plane of the β-protons, and thus, were assigned as α-disposed.

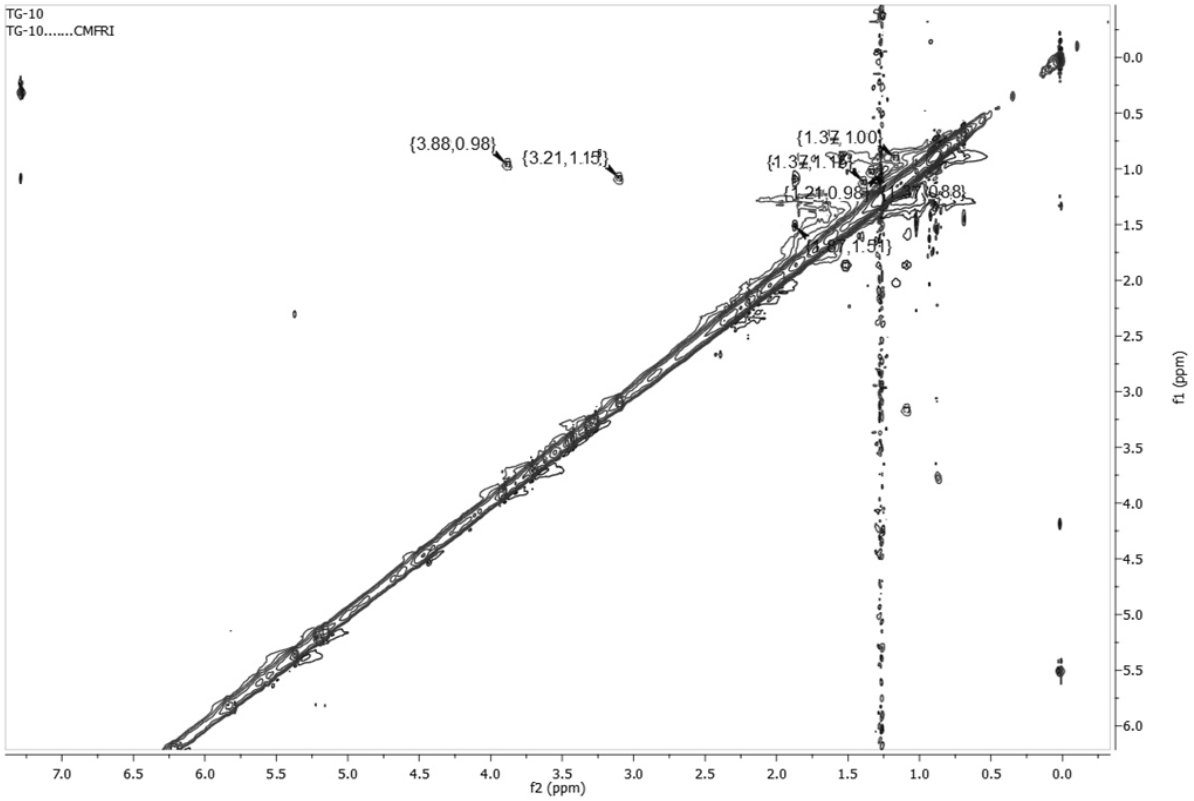

Figure 4.93.: NOESY spectrum of 1-butoxy-4,4,11b,11c-tetramethyl-1,2,3,3a,4,5,6,6a,11b,11c-decahydrobenzo[kl]-xanthen-10-ol (**6**)

Table 4.13: NMR spectroscopic data of compound (**6**), 1-butoxy-4,4,11b,11c-tetramethyl-1,2,3,3a,4,5,6,6a,11b,11c-decahydrobenzo[kl]-xanthen-10-ol (**6**)isolated from red seaweed *G. salicornia*

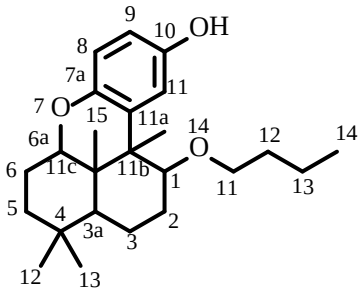

Compound **6** …….1-Butoxy-4,4,11b,11c-tetramethyl-1,2,3,3a,4,5,6,6a,11b,11c-decahydrobenzo[kl]-xanthen-10-ol (**6**)

C. No.	^{13}C-NMR	H. int., mult., J in Hz‡	^{1}H -NMR	COSY	HMBC
1	78.1	1H, t, J = 9.2 Hz	3.88	H-1	C-11b,1[1]
2	29.6	1H, m	1.81	H-3	-
		1H, m	1.60	-	-
3	22.7	1H, m	1.57	H-3a	-
		1H, m	1.31	-	-

3a	52.3	1H, dd, J = 1.9, 12.1 Hz	1.21	-	C-4,11c
4	37.2	-	-	-	-
5	42.2	1H, td, J = 13.2, 4.1 Hz	1.20	H-6	C-4
		1H, td, J = 13.2, 4.3 Hz	1.51	-	-
6	24.4	1H, t, J = 12.7, Hz	1.84	H-6a	-
		1H, t, J = 12.9, 4.2 Hz	1.70	-	-
6a	81.0	1H, t, J = 9.2 Hz	3.20	-	C-11c,7a
7a	139.9	-	-	-	-
8	118.1	1H, d, J = 13.1H	6.26	H-9	C-7a
9	121.7	1H, d, J = 13.2Hz	6.20	-	-
10	155.9	-	-	-	-
11	115.1	1H, s	6.31	-	C-11a,9,10
11a	128.7	-	-	-	-
11b	45.4	-	-	-	-
11c	39.3	-	-	-	-
12	28.8	3H, s	1.00	-	C-4
13	29.3	3H, s	0.98	-	C-4
14	22.6	3H, s	1.37	-	C11b
15	12.8	3H, s	1.15	-	C-11c
1^1	74.6	2H, t, J = 9.8 Hz	3.44	-	
1^2	31.9	2H, m	1.50	-	
1^3	18.7	2H, m	1.43	-	
1^4	14.1	3H, t, J = 6.8 Hz	0.88	-	

‡ Values in ppm, multiplicity and coupling constants (J= Hz) were indicated in parentheses. Multiplicities were allocated by ^{135}DEPT NMR spectrum.

The assignments were made with the aid of the COSY, HSQC, HMBC and NOESY experiments.

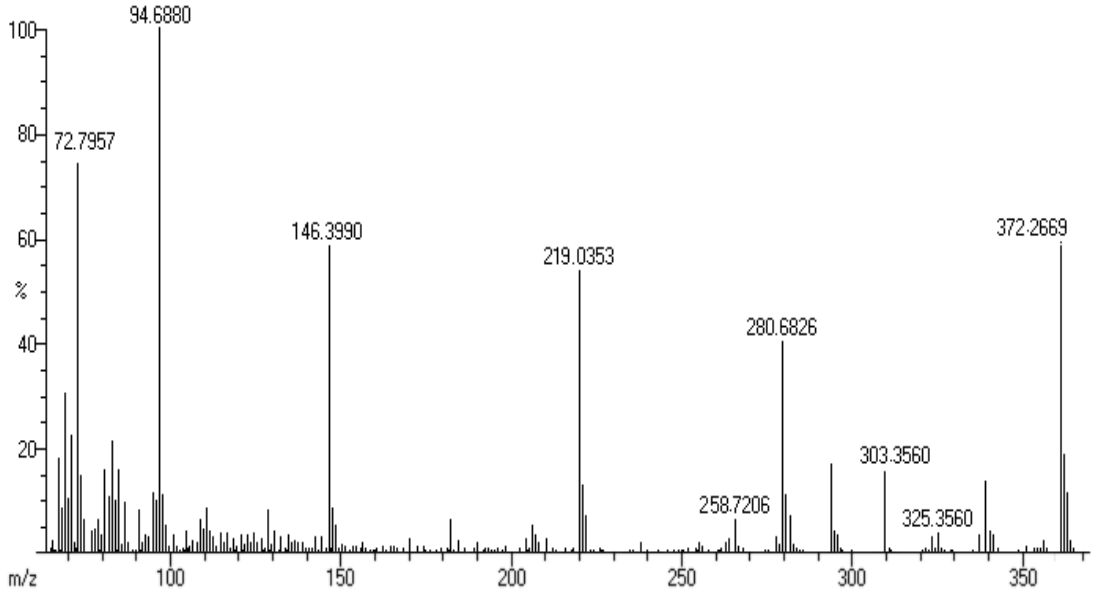

Figure 4.94.: EI-MS spectrum of 1-butoxy-4,4,11b,11c-tetramethyl-1,2,3,3a,4,5,6,6a,11b,11c-decahydrobenzo[kl]-xanthen-10-ol (**6**)

The structure elucidation of **3** was corroborated by the mass spectral experiment, wherein the molecular ion peak at *m/z* 372 (3a) experienced the elimination of a $C_2H_5^{\bullet}$ radical and H_2O to result the mass fragment $C_{22}H_{29}O_2^{+}$ (3b) with *m/z* 325. The removal of $C_2H_5O^{\bullet}$ from the latter could result in the formation of $C_{20}H_{24}O^{\bullet+}$ with *m/z* 280 (3c). The fragment (3d) with *m/z* 258 appeared to undergo further series of fragmentation to yield *m/z* 94, which was considered as the base peak (Figure 4.94 & 4.95).

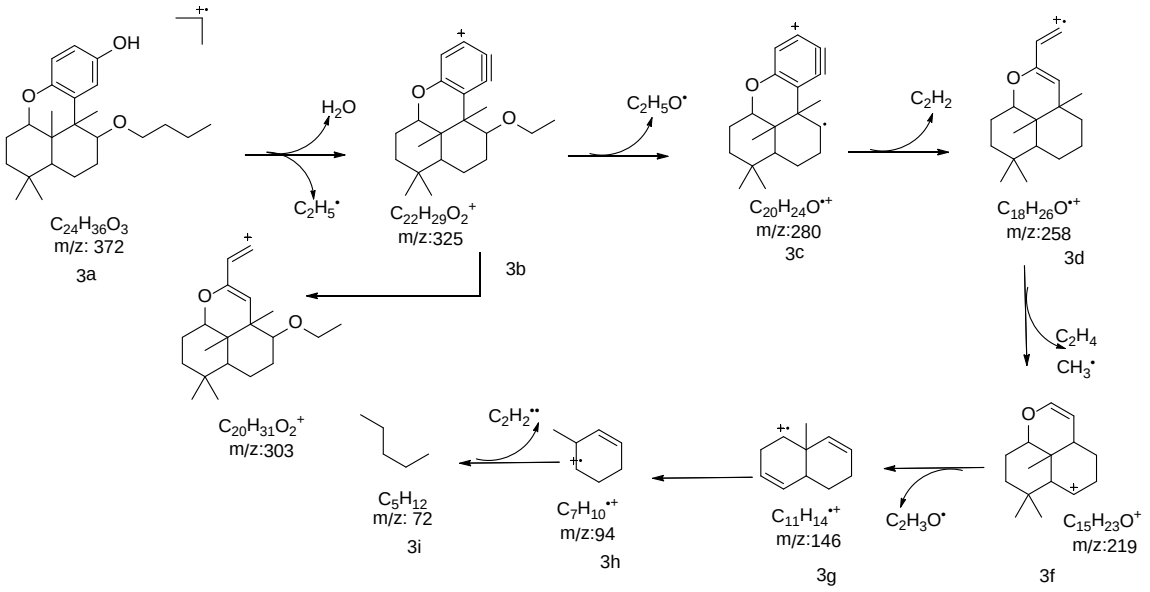

Figure 4.95.: Mass fragmentation pattern of 1-butoxy-4,4,11b,11c-tetramethyl-1,2,3,3a,4,5,6,6a,11b,11c-decahydrobenzo[kl]-xanthen-10-ol (**6**)

The organic solvent extract of the intertidal red saeweed, *G. salicornia* was fractionated by repeated techniques of chromatography to obtain three unprecedented drimane sesquiterpene quinol analogues. The isolated compounds, (**4**-**6**) were found to be bearing hydroxyl, benzene, ether and olefinic functionalities. Therefore, these metabolites can be used for the further analysis of biological activities.

4.3.2.4 Structural characterization of 2H-chromenyl derivative (Compounds 7-8)

Chromene analogues with natural and synthetic origin were identified as valuable pharmacophores exhibiting potential antioxidant (Milan et al. 2011) and anti-inflammatory (Nitin et al. 2012) activities. These oxygen heterocycles recognized greater attention due to their wide occurrence and broad pharmaceutical significance. Chromene analogues were found to constitute the basic backbone of bioactive polyphenols, alkaloids, tocopherols, flavonoids, and anthocyanins (Ren et al., 2011). Anti-inflammatory and antioxidative chromenyls with furanyl-2*H*-chromenyl and isochromenone derivatives were isolated and characterized from the marine organisms (Joy and Chakraborty, 2017a; Joy and Chakraborty, 2018). Bioactive secondary metabolites bearing oxygen heterocyclic analogues and sargachromanol A-P were recorded from the marine organisms (Jang et al. 2005, Joy & Chakraborty, 2017b). There were reports on the occurrences of chromenyl metabolites or chromenone-based skeletons, such as benzopyrans or benzopyrones from seaweeds (Davyt et al. 1997; El-Beih et al. 2007; Hwa et al. 2005; Iwashima et al. 2005). The natural chromene derivative (benzopyran), α-tocopherol possessing the 6-hydroxychromenol motif is a commonly used antioxidant agent with lipid peroxidation properties (Kindleysides et al. 2012, Birringer et al. 2018).

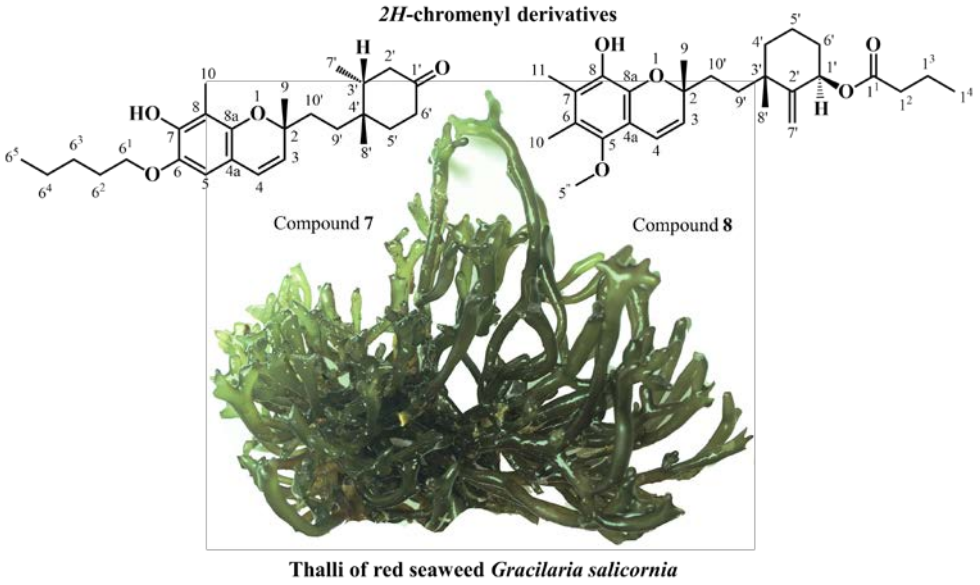

Figure 4.96.: Structures of 2*H*-chromenyl derivatives (**7**-**8**) isolated from the seaweed *Gracilaria salicornia*. The representative photograph of the thalli of *G. salicornia* was shown

Phytochemical investigation on red seaweeds reported different biological activities (Makkar and Chakraborty 2017a; Makkar and Chakraborty 2017b). It has been documented that the organic extracts of *Gracilaria* sp. (family Gracilariaceae) comprised bioactive secondary metabolites along with anti-inflammatory and antioxidant potentials (Antony and Chakraborty 2018; Makkar and Chakraborty 2018a; Makkar and Chakraborty 2018b. The current work described the separation and characterisation of chromene class of compounds, 4'-[10'-[7-hydroxy-2,8-dimethyl-6-(pentyloxy)-*2H*-chromen-2-yl]ethyl]-3',4'-dimethyl-cyclohexanone (**7**) and 3'-[10'-(8-hydroxy-5-methoxy-2,6,7-trimethyl-*2H*-chromen-2-yl)ethyl]-3'-methyl-2'-methylene cyclohexyl butyrate (**8**) from the EtOAc-MeOH (ethyl acetate-methanol) extract of *G. salicornia* collected from the southern coast of Indian peninsular (Figure 4.96).

4.3.2.4a Structural characterization of Compound 7

4'-[10'-[7-Hydroxy-2,8-dimethyl-6-(pentyloxy)-*2H*-chromen-2-yl]ethyl]-3',4'-dimethyl-cyclohexanone

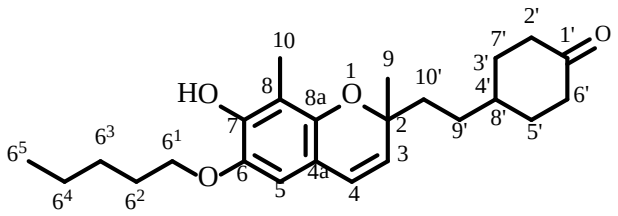

Sample yield	0.30% (> 99% purity, RP-C18 HPLC)
Physical description	Yellowish oil
Molecular formula	$C_{26}H_{38}O_4$
Molecular mass	414.2775

The *2H*-chromenyl derivative, 4'-[10'-[7-hydroxy-2,8-dimethyl-6-(pentyloxy)-*2H*-chromen-2-yl]ethyl]-3',4'-dimethyl-cyclohexanone was isolated as yellowish oil. The compound (**7**) has exhibited UV absorbance (UV (MeOH) λ_{max}) at 270 nm (Figure 4.97). The homogeneity of the compound was ascertained by HPLC data on a bonded phase octadecylsilane (C_{18}) stationary phase (HPLC, MeCN/MeOH, 3:2 v/v) with R_t: 2.93 min (Figure 4.98).

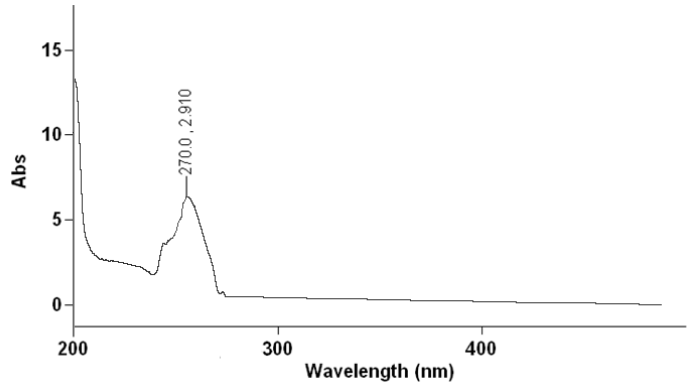

Figure 4.97.: UV spectrum of 4'-[10'-[7-Hydroxy-2,8-dimethyl-6-(pentyloxy)-*2H*-chromen-2-yl]ethyl]-3',4'-dimethyl-cyclohexanone (7)

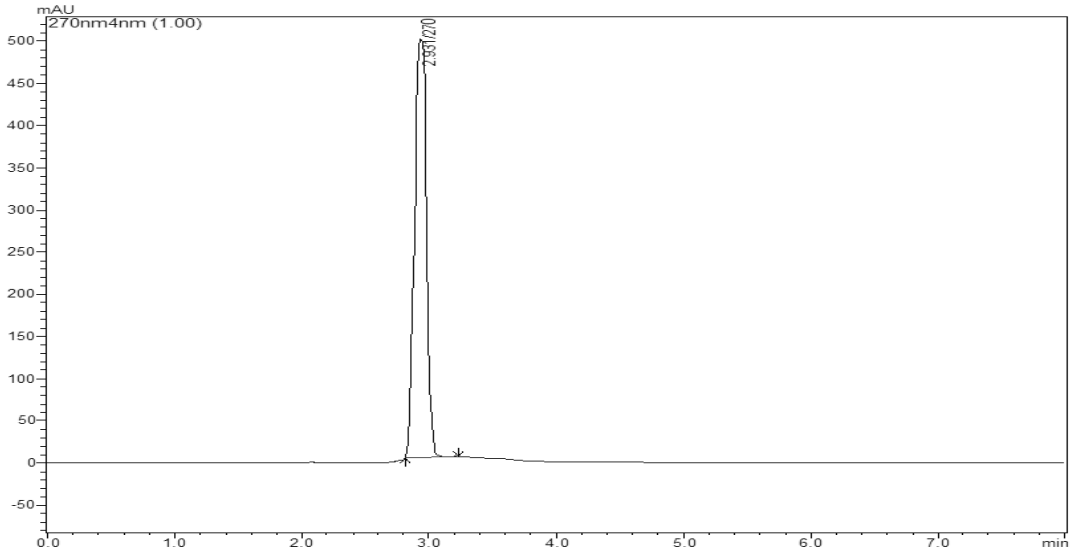

Figure 4.98.: HPLC chromatogram of 4'-[10'-[7-hydroxy-2,8-dimethyl-6-(pentyloxy)-*2H*-chromen-2-yl]ethyl]-3',4'-dimethyl-cyclohexanone (7)

Bioassay-assisted chromatographic fractionation of organic extract of *G. salicornia* yielded 4'-[10'-[7-hydroxy-2,8-dimethyl-6-(pentyloxy)-2*H*-chromen-2-yl]ethyl]-3',4'-dimethyl-cyclohexanone (**7**) as a yellowish oily substance, with about 99 % purity. The mass spectroscopic experiment displayed the molecular ion peak at *m/z* 414, which along with integrative NMR-IR spectroscopic experiments deduced its molecular formula as $C_{26}H_{38}O_4$ (Table 4.14). The HRESIMS experiment displayed the molecular ion peak at *m/z* 415.2852 $[M+H]^+$, (Figure 4.99).

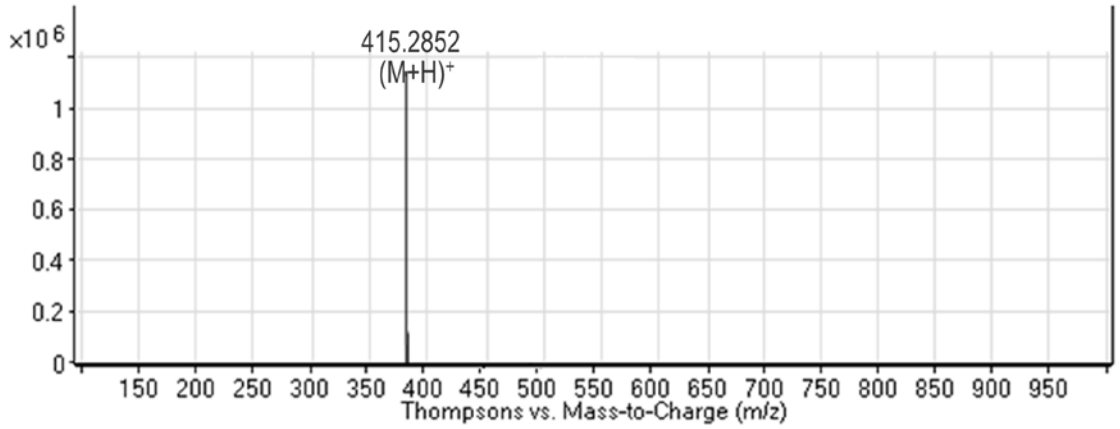

Figure 4.99.: HRESIMS spectrum of 4'-[10'-[7-Hydroxy-2,8-dimethyl-6-(pentyloxy)-*2H*-chromen-2-yl]ethyl]-3',4'-dimethyl-cyclohexanone (7)

The FTIR absorption peaks at 3430, 1727, 1732 and 1562 indicated the occurrences of hydroxyl, ether, carbonyl and aromatic ($C=C_{(aromatic)}$) functionalities, respectively (Figure 4.100). The ^{1}H-NMR experiments showed signals corresponding to methyl groups at δ 1.54 (3H, s), δ 2.35 (3H, s), δ 1.20 (3H, s) and δ 1.14 (3H, d, J=7.1Hz). The spectrum indicated the presence of greatly deshielded hydrogens at δ 6.07 (1H, d, J = 13.2 Hz), δ 6.33 (1H, d, J = 7.8 Hz) and δ 6.21 (1H, s), which might be related to alkene or aromatic protons (Figure 4.101).

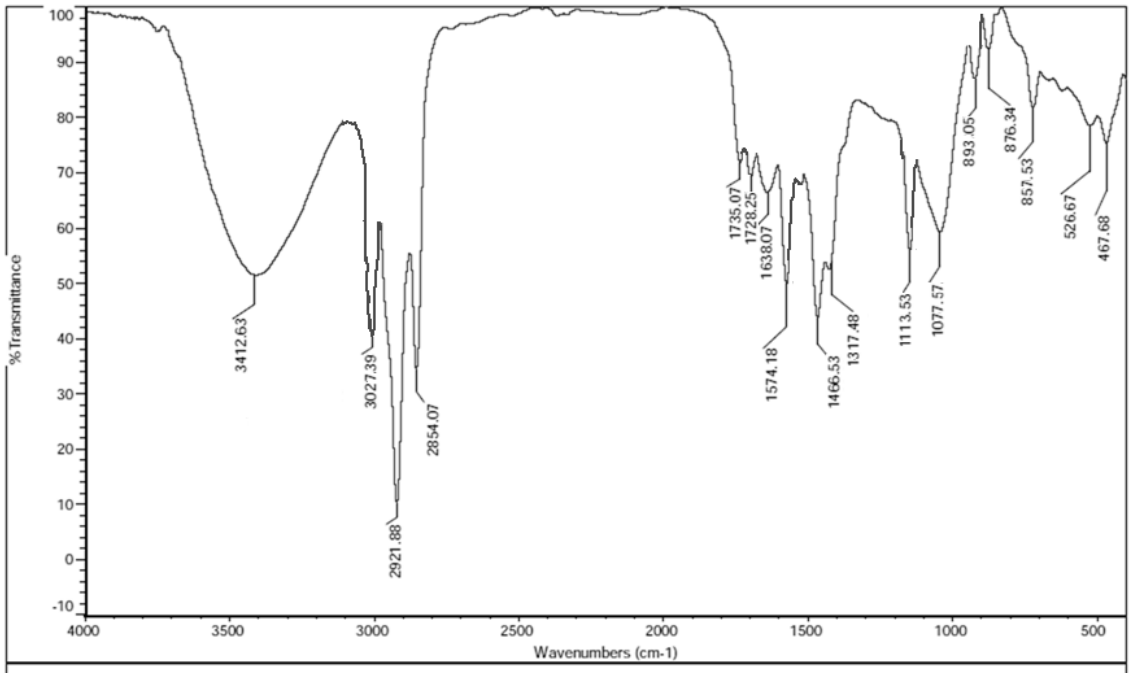

Figure 4.100.: FTIR spectrum of 4'-[10'-[7-Hydroxy-2,8-dimethyl-6-(pentyloxy)-*2H*-chromen-2-yl]ethyl]-3',4'-dimethyl-cyclohexanone (7)

The ^{13}C NMR spectrum along with $DEPT_{135}$ analysis deduced 26 carbon signals in the studied compound including the signals due to eight quaternary carbons (δ 75.00, δ 113.13, δ 142.82, δ 148.65, δ 148.67, δ 114.85, δ 32.99 and δ 213.90), one sp^3 methine (δ 37.43), and three sp^2 methine (δ 130.14, δ 128.46 and δ 110.56) other than nine sp^3 methylene signals (δ 36.81, δ 32.80, δ 36.84, δ 37.29, δ 39.37, δ 65.54, δ 27.99, δ 29.71 and δ 24.48) and five methyl groups (δ 24.81, δ 14.14, δ 22.64, δ 22.74 and δ 19.76) (Figure 4.102 & 4.103). In addition, the analyses of the ^{13}C NMR spectrum designated the occurrence of one each of ketone (δ 213.90) and two oxygenated functionalities (δ 75.00, δ 148.67, δ 142.82 and δ 65.54). These data were corroborated by HSQC spectral assignments (Figure 4.104).

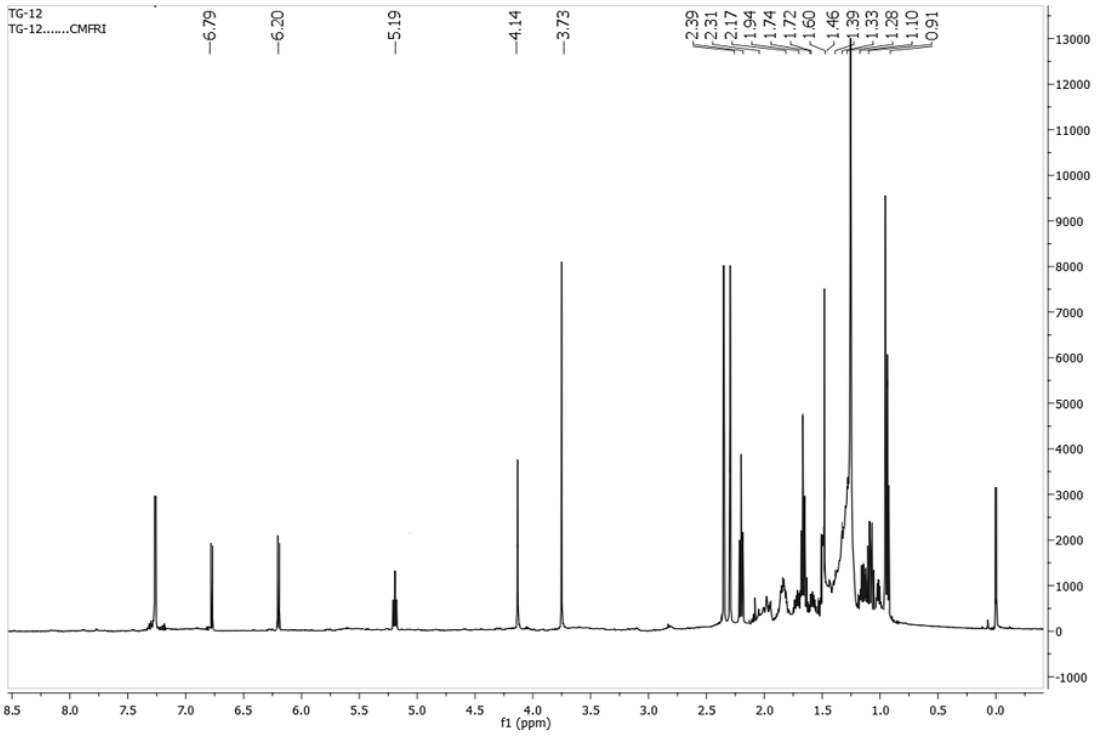

Figure 4.101.: ^1H NMR spectrum of 4'-[10'-[7-hydroxy-2,8-dimethyl-6-(pentyloxy)-*2H*-chromen-2-yl]ethyl]-3',4'-dimethyl-cyclohexanone (7)

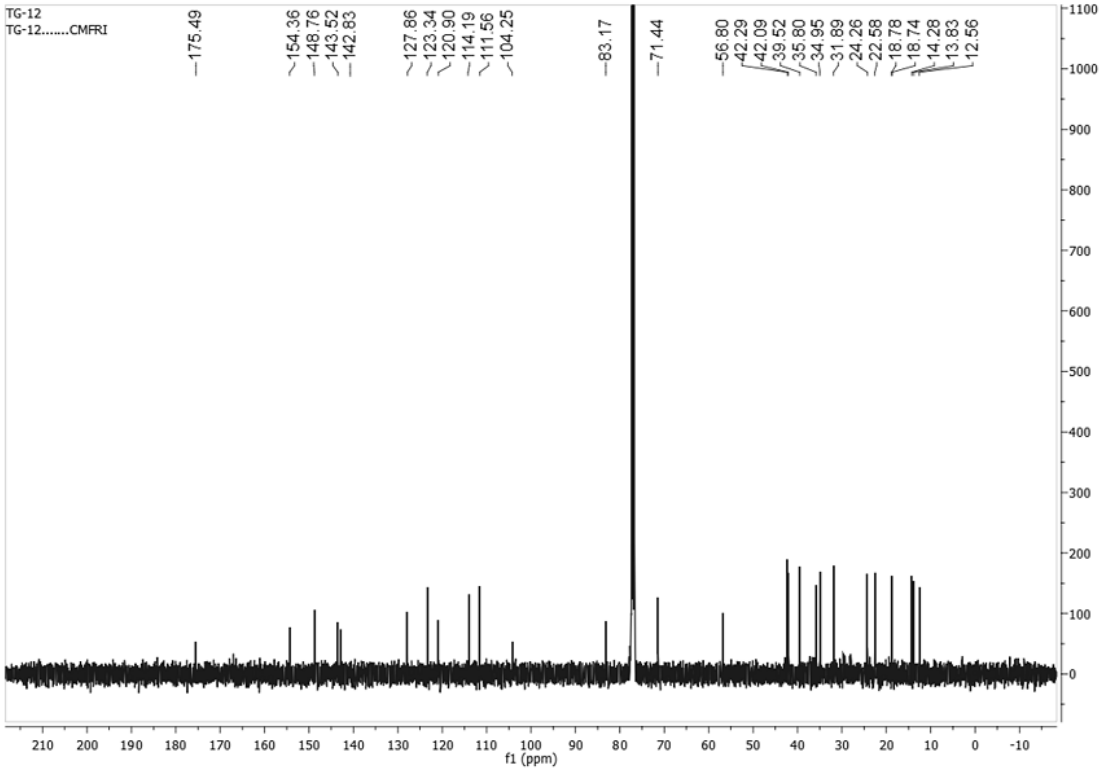

Figure 4.102.: ^{13}C NMR spectrum of 4'-[10'-[7-hydroxy-2,8-dimethyl-6-(pentyloxy)-*2H*-chromen-2-yl]ethyl]-3',4'-dimethyl-cyclohexanone (7)

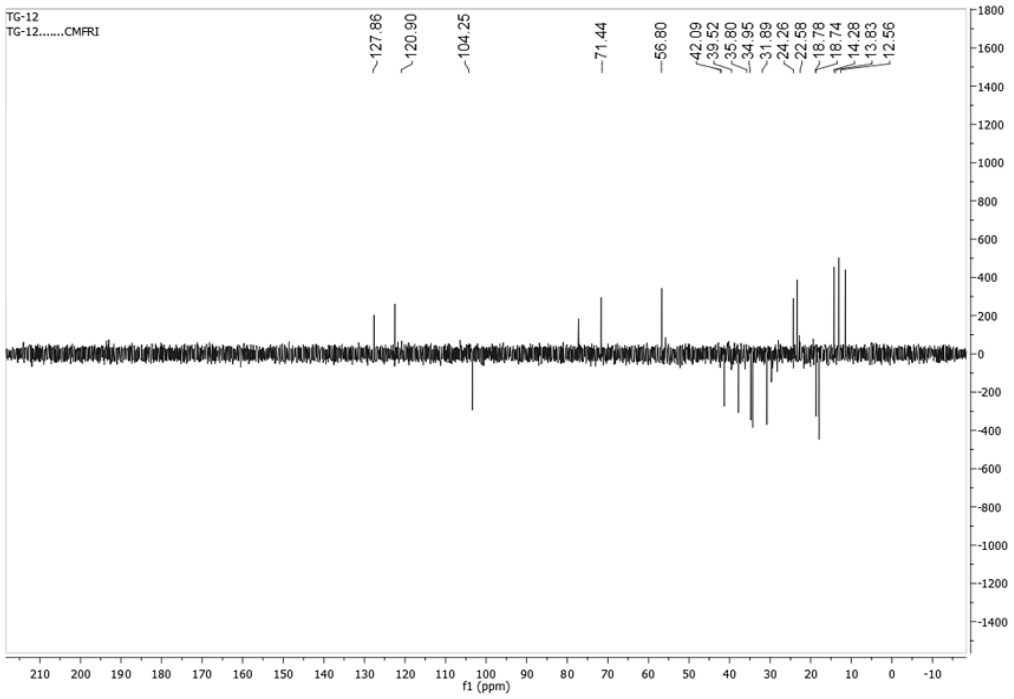

Figure 4.103.: ^{135}DEPT spectrum of 4'-[10'-[7-hydroxy-2,8-dimethyl-6-(pentyloxy)-*2H*-chromen-2-yl]ethyl]-3',4'-dimethyl-cyclohexanone (7)

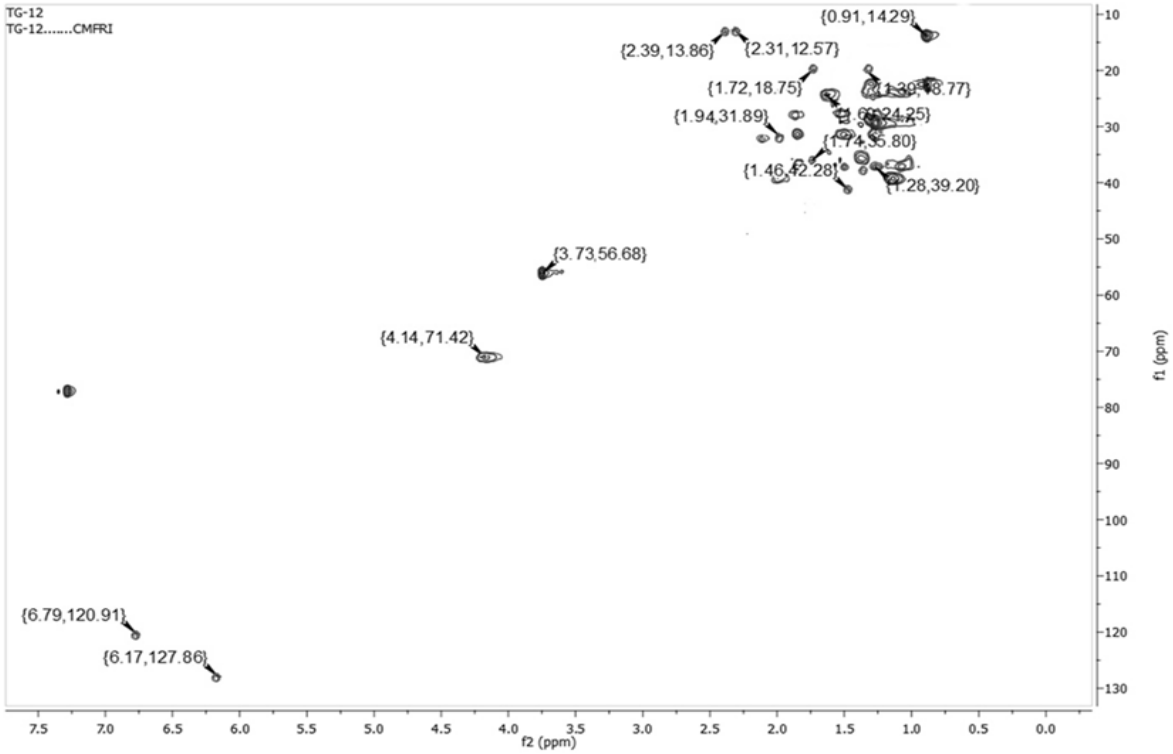

Figure 4.104.: HSQC spectrum of 4'-[10'-[7-hydroxy-2,8-dimethyl-6-(pentyloxy)-*2H*-chromen-2-yl]ethyl]-3',4'-dimethyl-cyclohexanone (7)

The partial structure of the studied compound was constructed with help of ^{1}H-^{1}H COSY correlations along with previous literature reports (Davyt et al. 1997; Ovenden et al. 2011). The ^{1}H-^{1}H COSY spectrum of **7** represented the occurrence of five individual spin systems: I (CH_3-δ 1.04)-(CH_2-δ 1.39)-(CH_2-δ 1.36)-(CH_2-δ 1.71)-(CH_2-δ 4.09); II (CH-δ 6.33)-(CH-δ 6.07); III (CH_2-δ 1.73)-(CH_2-δ 1.34); IV (CH_2-δ 2.49)-(CH_2-δ 1.82) and V (CH_2-δ 2.10)-(CH-δ 1.64)-(CH_3-δ 1.14). The positions of nine carbon signals in the studied compound were assigned from C-2 to C-10, which resembled the typical chromene bicyclic system (Hwa et al. 2005) (Figure 4.105 & 4.106). The remaining positions were assigned from 1' to 10' and 6^1 to 6^5, which represented substitutions on chromenyl merosesquiterpenoid framework. The HMBC correlations from CH_2-6^2-(δ 1.71) to C-6^1-(δ 65.54); CH_2-6^1-(δ 4.09) to C-6-(δ 142.82); CH-5-(δ 6.21) to C-6-(δ 142.82)/C-7-(δ 148.65)/C-4a (δ 113.13), and CH-4-(δ 6.33) to C-4a-(δ 113.13)/C-8a-(δ 148.67)/C-3-(δ 130.14) supported the bicyclic ring of chromene framework (Figure 4.107).

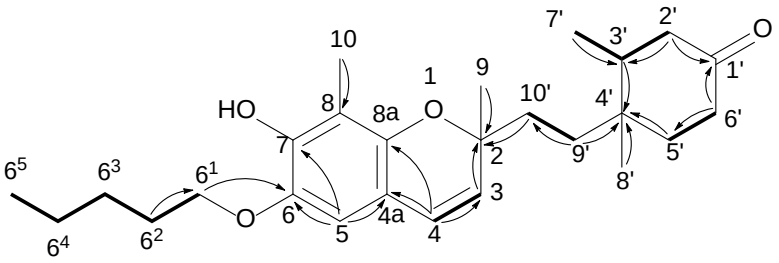

Figure 4.105.: ^{1}H-^{1}H COSY (bold face bonds), and selected HMBCs (double-barbed arrows), correlations of 4'-[10'-[7-Hydroxy-2,8-dimethyl-6-(pentyloxy)-*2H*-chromen-2-yl]ethyl]-3',4'-dimethyl-cyclohexanone (**7**)

This spectroscopic information appropriately explained the chromenyl system, and confirmed the attachment of oxygenated substitution, 6-pentyloxy at C-6-(δ 148.82). Other key HMBCs were apparent from CH-3-(δ 6.07) to C-2-(δ 75.00); CH_2-10'-(δ 1.73) to C-2-(δ 75.00); CH_2-9'-(δ 1.34) to C-10'-(δ 36.81)/C-4'-(δ 32.99); CH_2-5'-(δ 1.82) to C-4'-(δ 32.99); CH_2-6'-(δ 2.49.) to C-5'-(δ 36.84)/C-1'-(δ 213.90); and CH_2-2'-(δ 2.10) to C-1'-(δ 213.90)/C-3'-(δ 37.43), which suggested the presence of spin units-II, III, IV, and V. These spectroscopic assignments appropriately explained the fusion of bicyclic chromene system, and the connectivity between the carbons from C-1 to C-10 in **7**. The remaining HMBCs from CH_3-10-(δ 2.35) to C-8-(δ 114.85), CH_3-9-(δ 1.54) to C-2 (δ 75.00), CH_3-8'-(δ 1.20) to C-4'-(δ 32.99) and CH_3-7'-(δ1.14) to C-3'-(δ 37.43) confirmed the attachment of methyl carbons at C-8, C-2, C-4' and C-3', respectively.

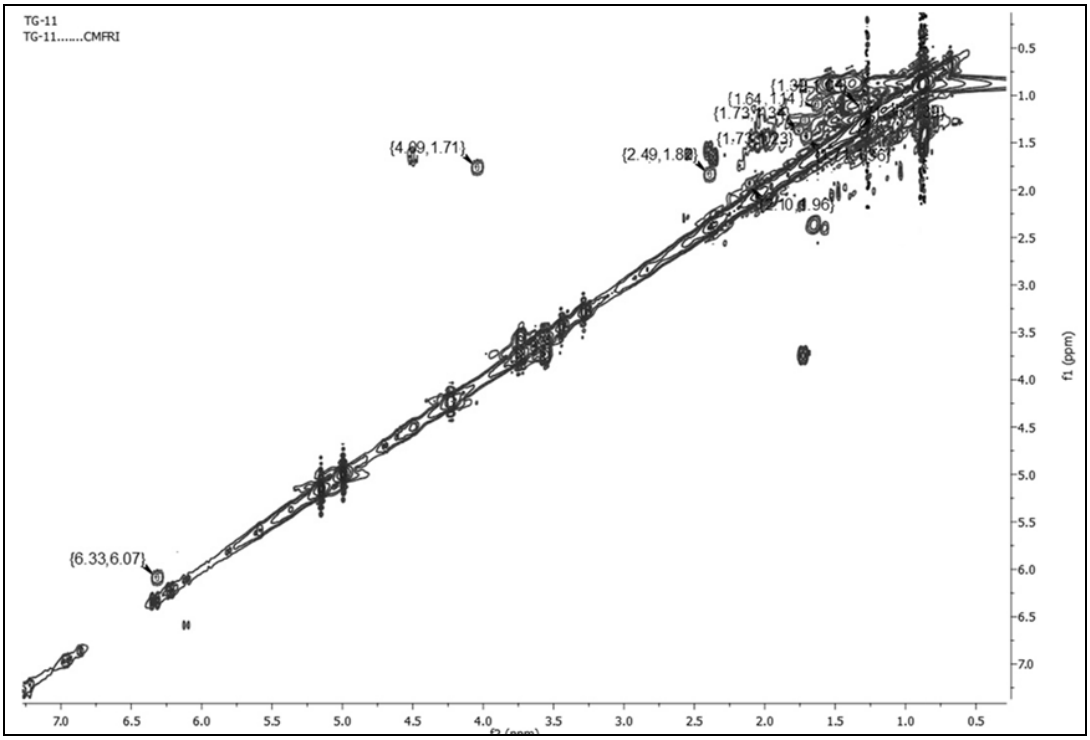

Figure 4.106.: ^{1}H-^{1}H COSY spectrum of 4'-[10'-[7-Hydroxy-2,8-dimethyl-6-(pentyloxy)-*2H*-chromen-2-yl]ethyl]-3',4'-dimethyl-cyclohexanone (7)

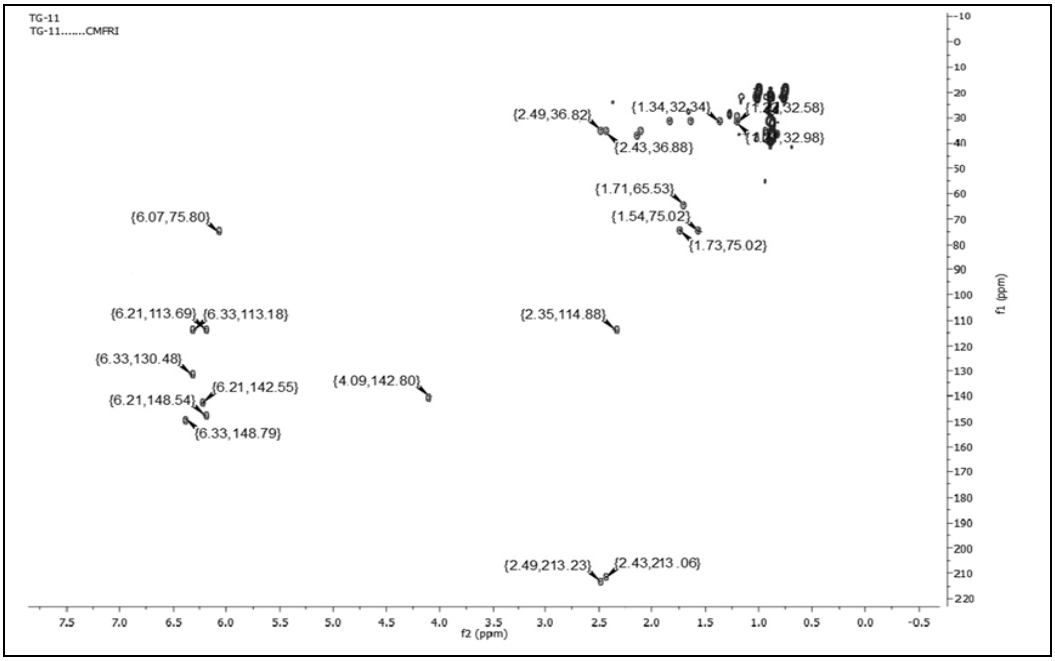

Figure 4.107.: HMBC spectrum of 4'-[10'-[7-hydroxy-2,8-dimethyl-6-(pentyloxy)-*2H*-chromen-2-yl]ethyl]-3',4'-dimethyl-cyclohexanone (7)

Table 4.14: NMR spectroscopic data of compound (**7**), 4'-[10'-[7-hydroxy-2,8-dimethyl-6-(pentyloxy)-*2H*-chromen-2-yl]ethyl]-3',4'-dimethyl-cyclohexanone (**7**) isolated from red seaweed *G. salicornia*

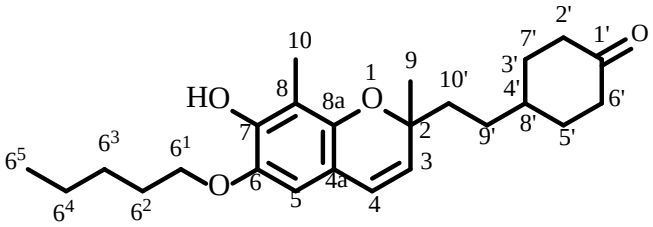

Compound **7** ……. 4'-[10'-[7-hydroxy-2,8-dimethyl-6-(pentyloxy)-*2H*-chromen-2-yl]ethyl]-3',4'-dimethyl-cyclohexanone (**7**)

Type	**C. No.**	**^{13}C NMR**	**H. No. (int., mult., J in Hz)[b]**	**^{1}H NMR**	**COSY**	**HMBC**
-	-	-	-	-	-	-
C	2	75.00	-	-	-	-
CH	3	130.14	1H, d, J = 13.2 Hz	6.07	H-4	C-2
CH	4	128.46	1H, d, J = 7.8 Hz	6.33	-	C-3,4a,8a
C	4a	113.13	-	-	-	
CH	5	110.56	1H, s	6.21	-	C-4a,7,6
C	6	142.82	-		-	
C	7	148.65	-	-	-	
C	8	114.85	-	-	-	
C	8a	148.67	-	-	-	
CH_3	9	24.81	3H, s	1.54	-	C-2
CH_3	10	14.14	3H, s	2.35	-	C-8
C	1'	213.90	-	-	-	-
CH_2	2'	39.37	1H, dd, J = 7.2, 5.8 Hz	2.10	H-3'	C-1',3'
	-	-	1H, dd, J = 7.1, 5.9 Hz	1.95	-	
CH	3'	37.43	1H, m	1.64	H-7'	C-4'
C	4'	32.99	-	-	-	
CH_2	5'	36.84	1H, dt, J = 7.3, 6.2 Hz	1.82	H-6'	C-4'
			1H, dt, J = 7.1, 6.0 Hz	1.68	-	
CH_2	6'	37.29	1H, dt, J = 6.8, 6.0 Hz	2.49	-	C-5',1'
	-	-	1H, dt, J = 7.1, 6.0 Hz	2.43	-	
CH_3	7'	22.64	3H, d, J = 7.1 Hz	1.14	-	C-3'
CH_3	8'	22.74	3H, s	1.20	-	C-4'
CH_2	9'	32.80	1H, dt, J = 6.8, 5.9 Hz	1.34	-	C-10',4'
	-	-	1H, dt, J = 6.9, 5.7 Hz	1.23	-	
CH_2	10'	36.81	2H, dd, J = 7.1, 6.3 Hz	1.73	H-9'	C-2
CH_2	6^1	65.54	2H, t, J = 9.8 Hz	4.09	H-6^2	C-6
CH_2	6^2	27.99	2H, m	1.71	H-6^3	C-6^1
CH_2	6^3	29.71	2H, m	1.36	H-6^4	-
CH_2	6^4	24.48	2H, m	1.39	H-6^5	-
CH_3	6^5	19.76	3H, t, J = 5.4 Hz	1.04	-	-

[a]NMR spectra were recorded using a Bruker AVANCE III 500 MHz (AV 500) spectrometer (Bruker, Karlsruhe, Germany) in $CDCl_3$ as aprotic solvent at ambient temperature with TMS as the internal standard (δ 0 ppm).

[b]Values in ppm, multiplicity and coupling constants (J = Hz) were indicated in parentheses.
Multiplicities were allocated by [135]DEPT NMR spectrum.
The assignments were made with the aid of the COSY, HSQC, HMBC and NOESY experiments.

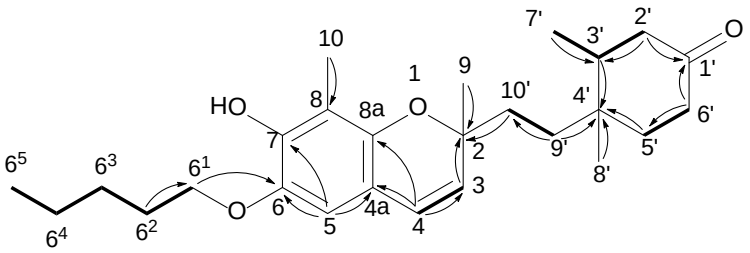

Figure 4.108.: NOESY (double-barbed arrows), correlations of 4'-[10'-[7-hydroxy-2,8-dimethyl-6-(pentyloxy)-*2H*-chromen-2-yl]ethyl]-3',4'-dimethyl-cyclohexanone (7)

The relative stereochemistries of protons attached to chiral carbon at C-3' (δ 37.43) and other methyl protons at C-10 (14.14), C-9 (24.81) and C-8' (22.74) were explained with nuclear overhauser effect spectroscopic (NOESY) experiments (Figure 4.108 & 4.109). The methyl proton at δ 1.14 (assigned to H-7' on C-3) exhibited NOEs with proton at δ 1.23 (H-9'α), which were oriented in α-side of **7**. Conversely, other protons in β-face of the molecule, particularly those of H-9, H-10, H-3', H-8', and H-9'β were deduced by NOE relationships between H-10 (δ 2.35)/H-9 (δ 1.54), H-9 (δ 1.54)/H-9'β (δ 1.34), H-9 (δ 1.54)/H-8' (δ 1.20) and H-3' (δ 1.64)/H-8' (δ 1.20).

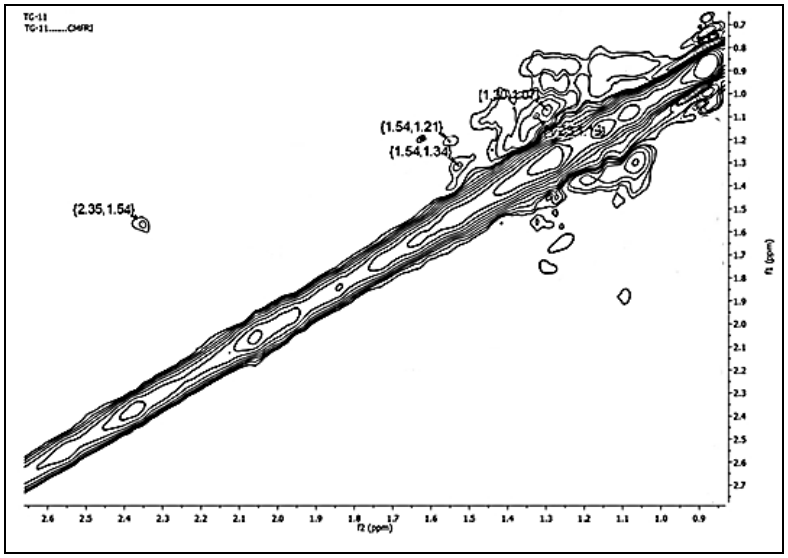

Figure 4.109.: NOESY (double-barbed arrows), correlations of 4'-[10'-[7-hydroxy-2,8-dimethyl-6-(pentyloxy)-*2H*-chromen-2-yl]ethyl]-3',4'-dimethyl-cyclohexanone (7)

The molecular ion peak at *m/z* 414 (**a**) $[M]^+$ underwent an elimination of $C_5H_{12}O$ moiety and the reorganization of bonds led to a fragment peak at *m/z* 327 (**b**). Further fragmentation of the latter led to the formation of mass fragments, **c** and **d** (*m/z* 174 and 152, respectively). The radical cation, **c** also performed a rearrangement mechanism to form **f** and **g** with the *m/z* 131 and 77, respectively. The mass fragment at *m/z* 77 ($C_6H_6^+$) was found to be the base peak. These detailed spectral data unambiguously interpreted the structure of the isolated compound as 4'-[10'-[7-hydroxy-2,8-dimethyl-6-(pentyloxy)-2*H*-chromen-2-yl]ethyl]-3',4'-dimethyl-cyclohexanone (**7**) (Figure 4.110 & 4.111).

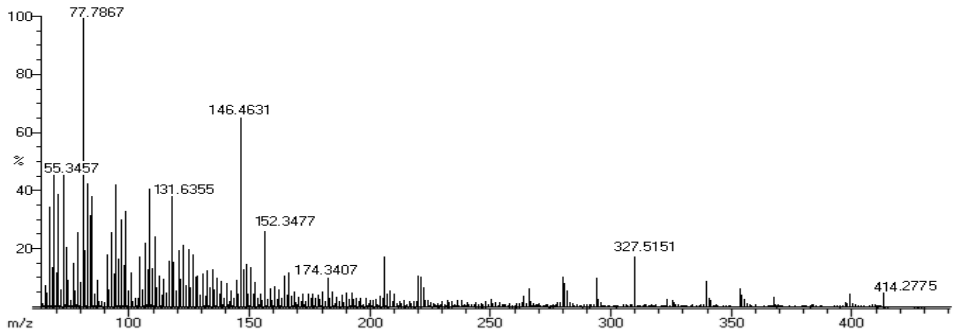

Figure 4.110.: EI-MS spectrum of 4'-[10'-[7-hydroxy-2,8-dimethyl-6-(pentyloxy)-*2H*-chromen-2-yl]ethyl]-3',4'-dimethyl-cyclohexanone (7)

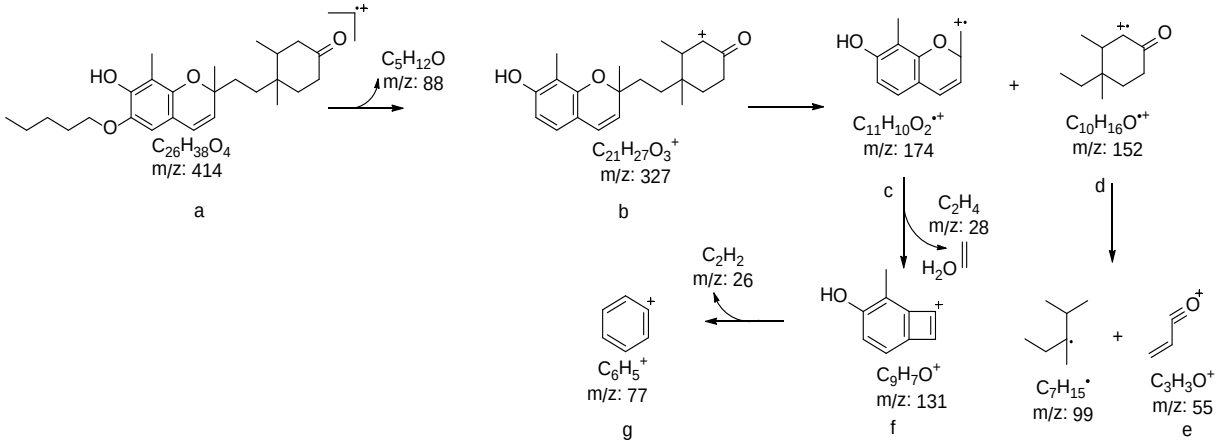

Figure 4.111.: Tentative mass fragmentation pattern of 4'-[10'-[7-hydroxy-2,8-dimethyl-6-(pentyloxy)-*2H*-chromen-2-yl]ethyl]-3',4'-dimethyl-cyclohexanone (7)

4.3.2.4b Structural characterization of Compound 8

3'-[10'-(8-Hydroxy-5-methoxy-2,6,7-trimethyl-*2H*-chromen-2-yl)ethyl]-3'-methyl-2'-methylene cyclohexyl butyrate

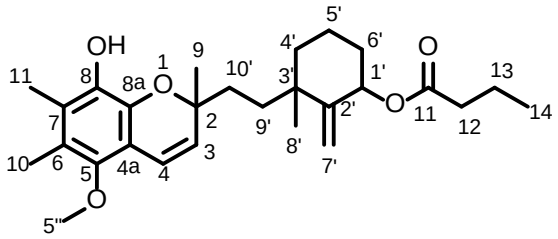

Sample yield	0.37% (> 99% purity, RP-C18 HPLC)
Physical description	Pale yellowish oil
Molecular formula	$C_{27}H_{38}O_5$
Molecular mass	442.2724

The *2H*-chromenyl derivative, 3'-[10'-(8-Hydroxy-5-methoxy-2,6,7-trimethyl-*2H*-chromen-2-yl)ethyl]-3'-methyl-2'-methylene cyclohexyl butyrate was isolated as yellowish oil. The compound (**8**) has exhibited UV absorbance (UV (MeOH) λ_{max}) at 264 nm (Figure 4.112). The homogeneity of the compound was ascertained by HPLC data on a bonded phase octadecylsilane (C_{18}) stationary phase (HPLC, MeCN/MeOH, 3:2 v/v) with R_t: 3.70 min (Figure 4.113).

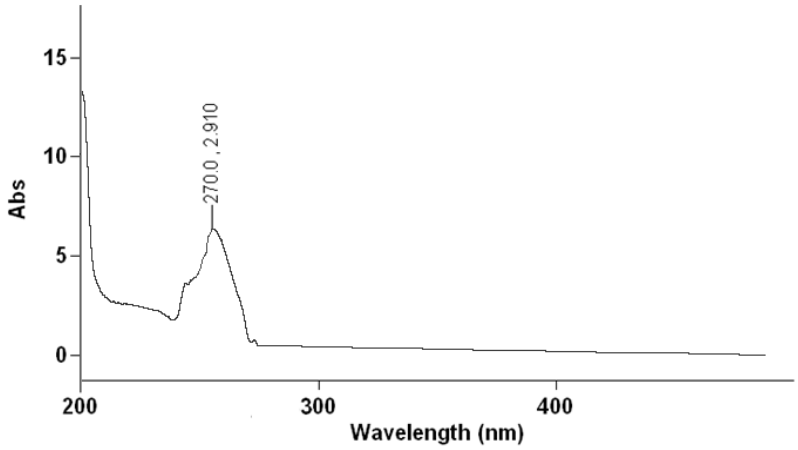

Figure 4.112.: UV spectrum of 3'-[10'-(8-hydroxy-5-methoxy-2,6,7-trimethyl-*2H*-chromen-2-yl)ethyl]-3'-methyl-2'-methylene cyclohexyl butyrate (**8**)

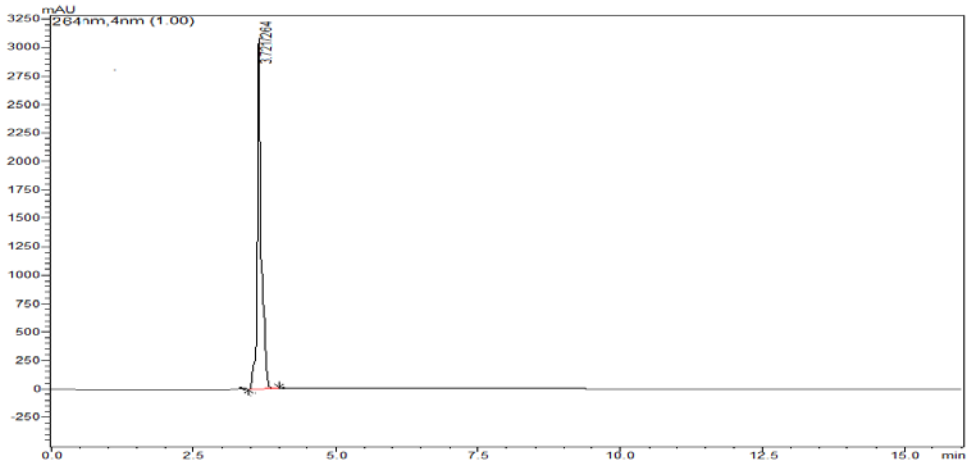

Figure 4.113.: HPLC chromatogram of 3'-[10'-(8-Hydroxy-5-methoxy-2,6,7-trimethyl-*2H*-chromen-2-yl)ethyl]-3'-methyl-2'-methylene cyclohexyl butyrate (**8**)

The chromatography-based fractionation of EtOAc-MeOH extract of *G. salicornia* afforded the titled compound as a pale yellowish oily substance. The EI-MS experiment displayed the molecular ion peak at *m/z* 442 along with integrative NMR-IR spectroscopic experiments were deduced its molecular formula as $C_{27}H_{38}O_5$ (Table 4.15). The HRESIMS experiment displayed the molecular ion peak at *m/z* 443.2797 $[M+H]^+$, (Figure 4.114).

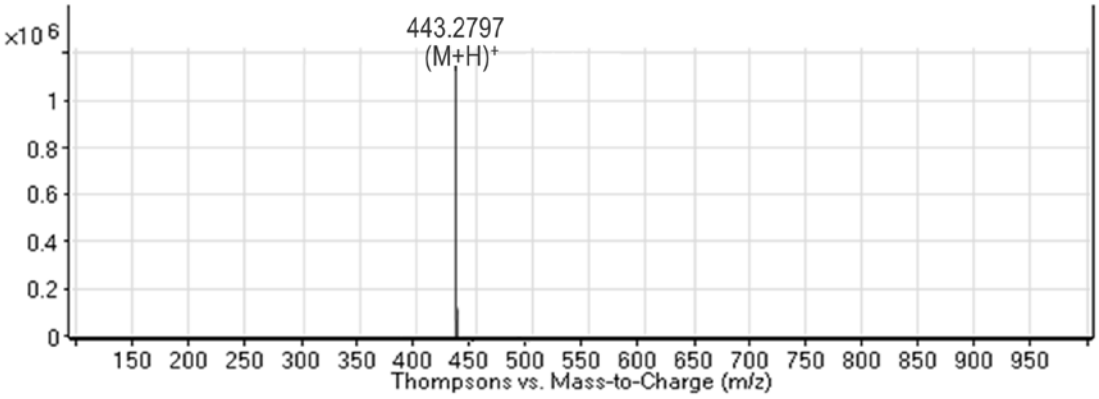

Figure 4.114.: HRESIMS of 3'-[10'-(8-hydroxy-5-methoxy-2,6,7-trimethyl-*2H*-chromen-2-yl)ethyl]-3'-methyl-2'-methylene cyclohexyl butyrate (**8**)

The FTIR absorption peaks at 3412, 1728, 1735 and 1574 assigned the occurrences of hydroxyl, ether, carbonyl and aromatic ($C=C_{(aromatic)}$) moieties, respectively (Figure 4.115). The ^{1}H-NMR experiments showed signals corresponding to methyl groups at δ 3.73 (3H, s), δ 2.39 (3H, s), δ 2.31 (3H, s), δ 1.60 (3H, s), and δ 0.91 (3H, t, J = 6.9 Hz). The spectrum also indicated the presence of three olefinic hydrogens at δ 6.20 (1H, d, J = 12.8 Hz), δ 6.79 (1H, d, J

= 11.8 Hz) and δ 5.19 (2H, s) (Figure 4.116). The ^{13}C NMR spectrum along with $DEPT_{135}$ analysis deduced 27 carbon signals in compound **8** including the signals due to ten quaternary carbons (δ 83.17, δ 111.56, δ 148.76, δ 114.19, δ 123.34, δ 143.52, δ 142.83, δ 42.29, δ 154.36 and δ 175.49), one sp^3 methine (δ 71.44) and two sp^2 methine (δ 127.86 and δ 120.90) other than seven sp^3 methylene signals (δ 35.80, δ 39.52, δ 31.89, δ 18.78, δ 42.09, δ 34.95 and δ 18.74), one sp^2 methylene (δ 104.25) signal and six methyl groups (δ 24.26, δ 13.83, δ 12.56, δ 56.80, δ 22.58 and δ 14.28) (Figure 4.117 and 4.118). In addition, the analyses of ^{13}C NMR spectrum designated the occurrence of one each of ester (δ 175.49) and two oxygenated functionalities (δ 83.17, δ 142.83, and δ 148.76). These spectral data were further supported by HSQC data (Figure 4.119).

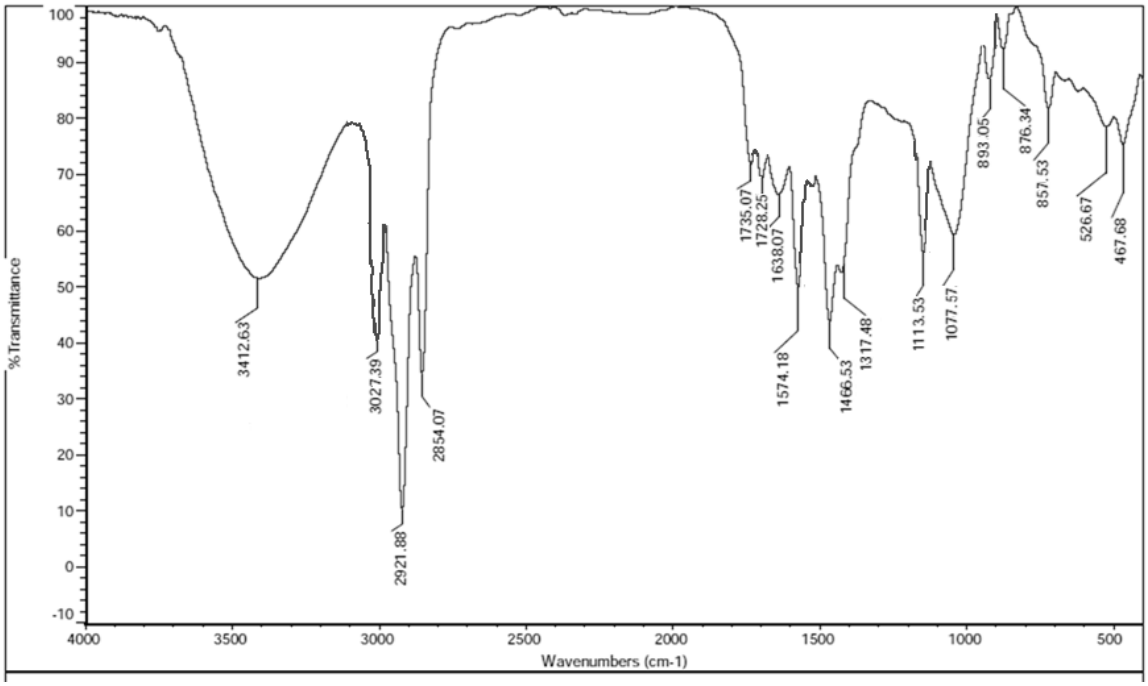

Figure 4.115.: FTIR spectrum of 3'-[10'-(8-hydroxy-5-methoxy-2,6,7-trimethyl-*2H*-chromen-2-yl)ethyl]-3'-methyl-2'-methylene cyclohexyl butyrate (**8**)

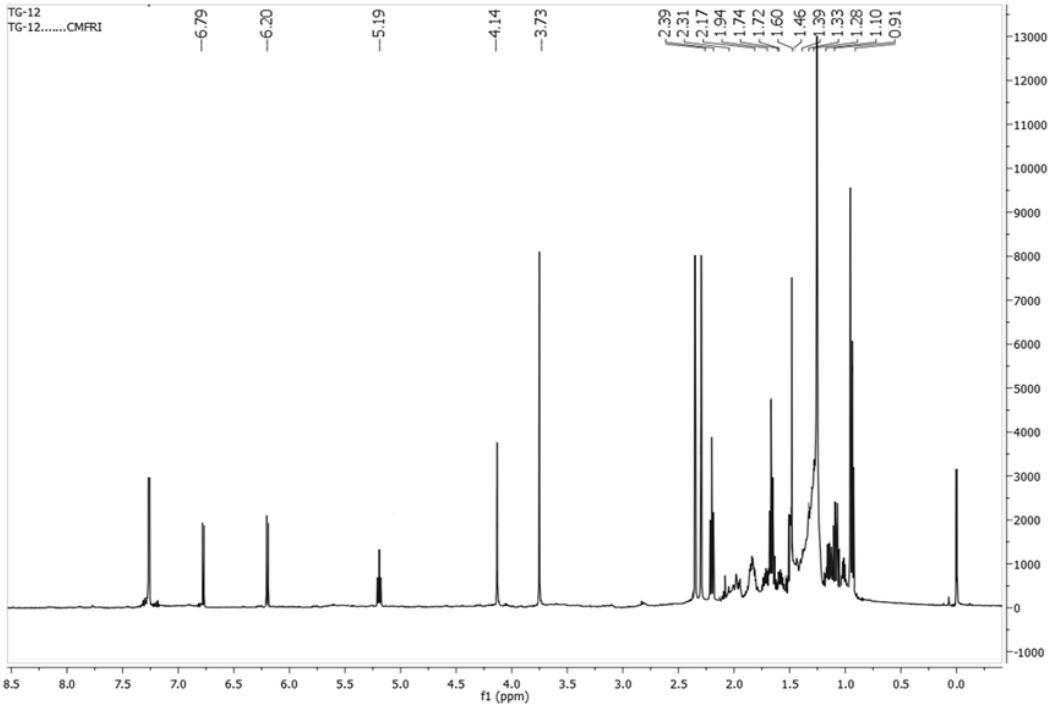

Figure 4.116.: ^{1}H NMR spectrum of 3'-[10'-(8-hydroxy-5-methoxy-2,6,7-trimethyl-*2H*-chromen-2-yl)ethyl]-3'-methyl-2'-methylene cyclohexyl butyrate (**8**)

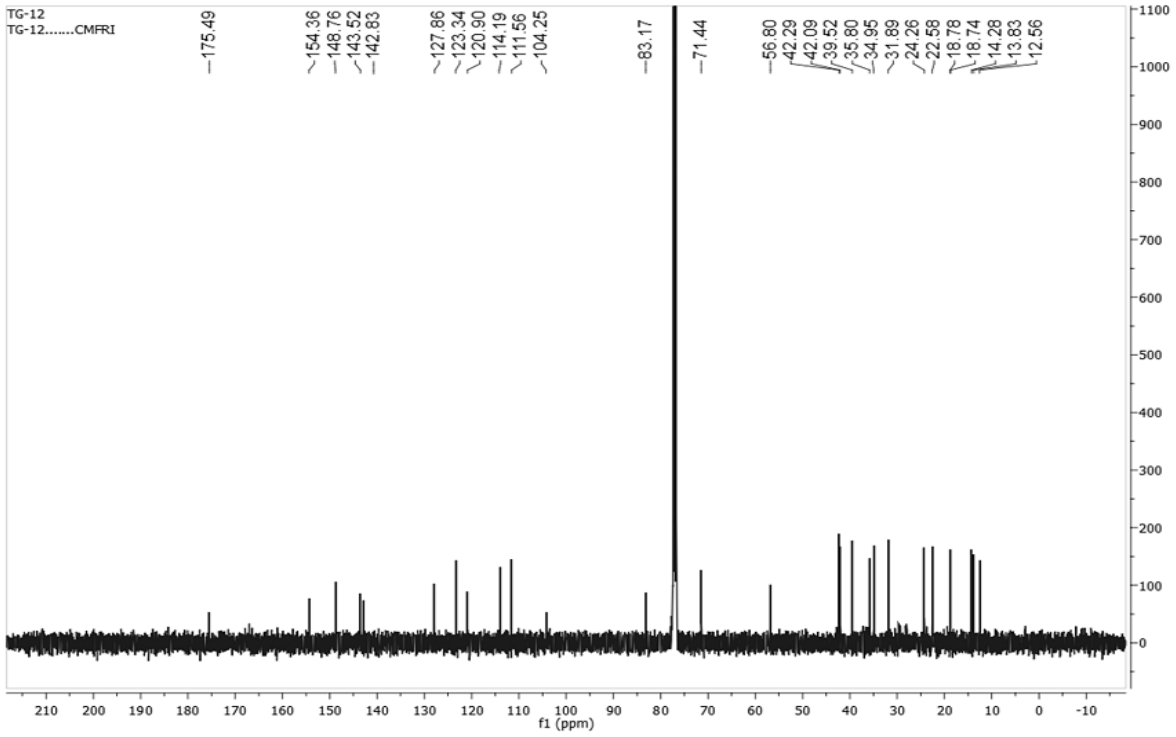

Figure 4.117.: ^{13}C NMR spectrum of 3'-[10'-(8-hydroxy-5-methoxy-2,6,7-trimethyl-*2H*-chromen-2-yl)ethyl]-3'-methyl-2'-methylene cyclohexyl butyrate (**8**)

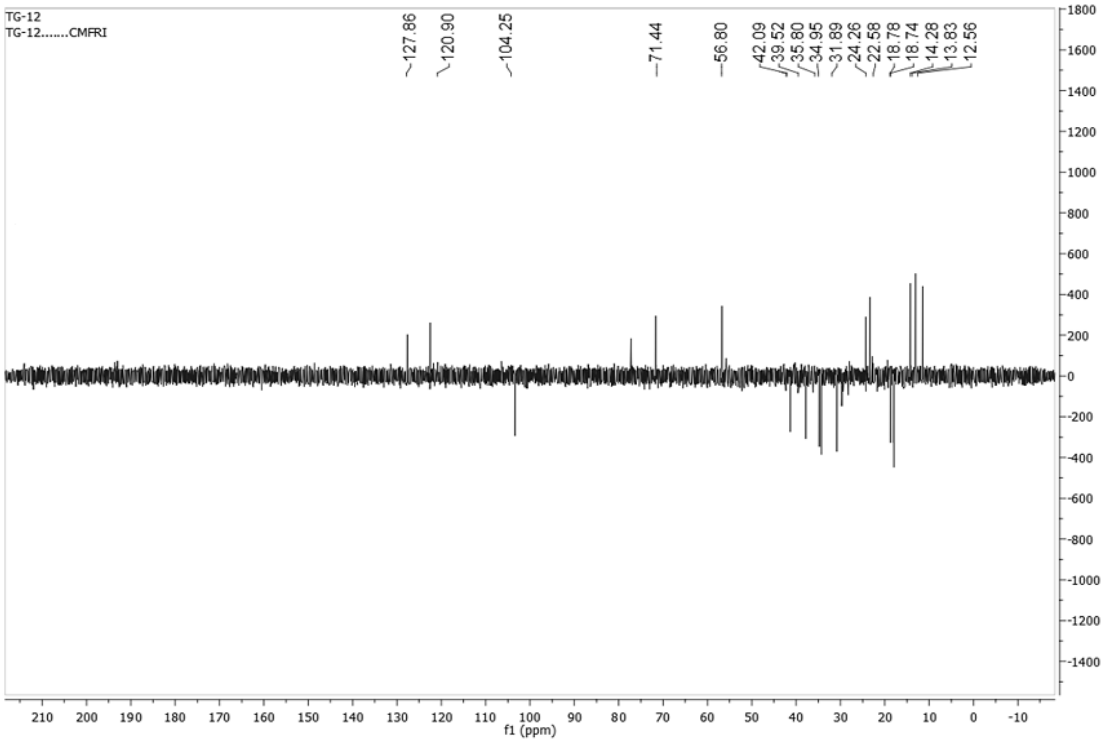

Figure 4.118.: [135]DEPT NMR spectrum of 3'-[10'-(8-hydroxy-5-methoxy-2,6,7-trimethyl-*2H*-chromen-2-yl)ethyl]-3'-methyl-2'-methylene cyclohexyl butyrate (**8**)

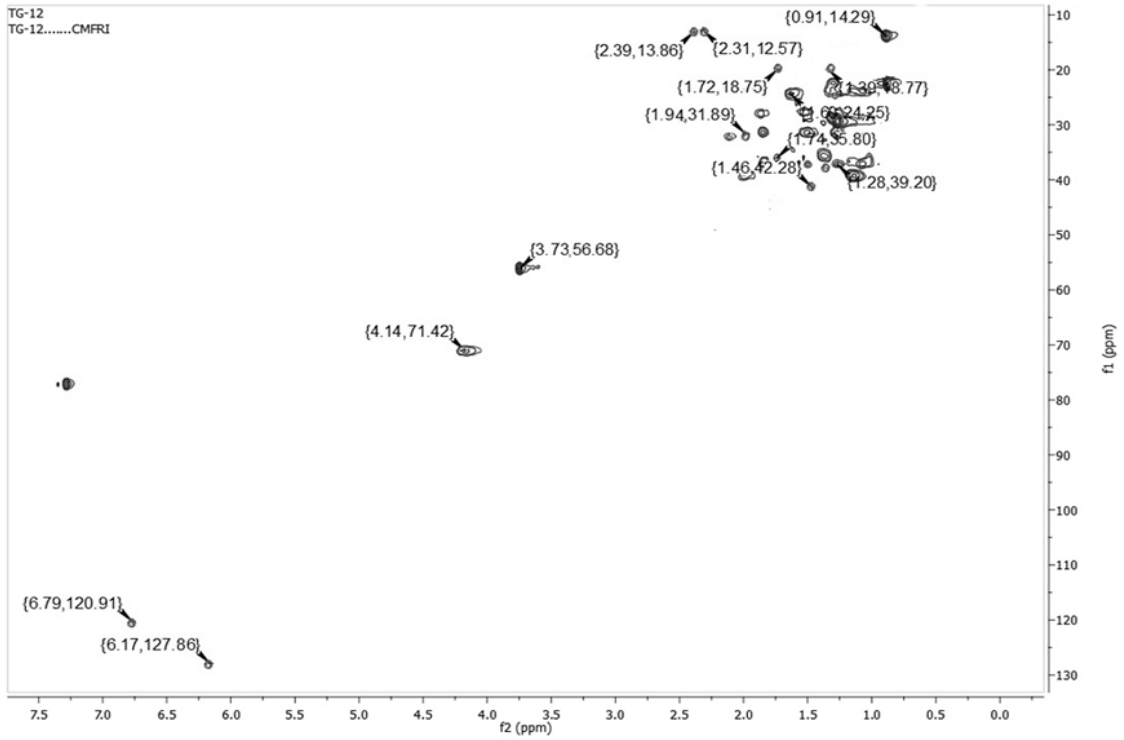

Figure 4.119.: HSQC spectrum of 3'-[10'-(8-hydroxy-5-methoxy-2,6,7-trimethyl-*2H*-chromen-2-yl)ethyl]-3'-methyl-2'-methylene cyclohexyl butyrate (**8**)

The partial structures of the studied compound were constructed with help of 1D NMR and ^{1}H-^{1}H COSY correlations along with previously reports of literature (Davyt et al. 1997; Iwashima et al. 2005; Ovenden et al. 2011). ^{1}H-^{1}H COSY spectrum of **8** assigned the occurrence of four individual spin systems: I (CH-δ 6.20)-(CH-δ 6.79); II (CH_2-δ 1.74)-(CH_2-1.33); III (CH_2-δ 1.46)-(CH_2-δ 1.39)-(CH_2-δ 1.94)-(CH-δ 4.14); and IV (CH_2-δ 2.17)-(CH_2-δ 1.72)-(CH-δ 0.91). The positions of nine carbon signals in the studied compound were assigned from C-2 to C-10, which resembled the typical chromene bicyclic system with methyl substitutions (Figure 4.120 & 4.121). The remaining positions were assigned from 1' to 10' and 1^{1} to 1^{4}, which represented the substitutions on chromenyl framework of **8**. HMBC correlations from CH-4-(δ 6.79) to C-4a-(δ 111.56)/C-5-(δ 148.76)/C-8a-(δ 142.83) and CH-3-(δ 6.20) to C-2-(δ 83.17) assigned the position of highly deshielded alkenic protons in the bicyclic ring of chromene framework (Figure 4.122). Other key HMBCs were apparent from CH_2-10'-(δ 1.74) to C-2-(δ 83.17); CH_2-9'-(δ 1.33) to C-10'-(δ 35.80)/C-3'-(δ 42.29); CH_2-4'-(δ 1.46) to C-3'-(δ 42.29)/C-2'-(δ 154.36); CH-1'-(δ 4.14) to C-2'-(δ 154.36); CH_2-6'-(δ 1.94) to C-5'-(δ 18.78); CH_2-1^{3}-(δ 1.72) to C-1^{2}-(δ 34.95), which suggested the presence of spin units-II, III, and IV. These spectroscopic assignments appropriately explained the fusion of the bicyclic chromene system, and the connectivity between the carbons from C-1 to C-8 in chromene ring system. The remaining HMBCs from CH_3-11-(δ 2.31) to C-7-(δ 123.34), CH_3-10-(δ 2.39) to C-6 (δ 114.19), CH_3-5"-(δ 3.73) to C-5-(δ 148.76), CH_3-9-(δ 1.60) to C-2-(δ 83.17), CH_3-8'-(δ 1.10) to C-3'-(δ 42.29) and CH_3-7'-(δ 5.19) to C-2'-(δ 154.36) confirmed the attachment of methyl carbons at C-7, C-6, C-5 (-O-CH_3), C-2, C-3' and C-2', respectively.

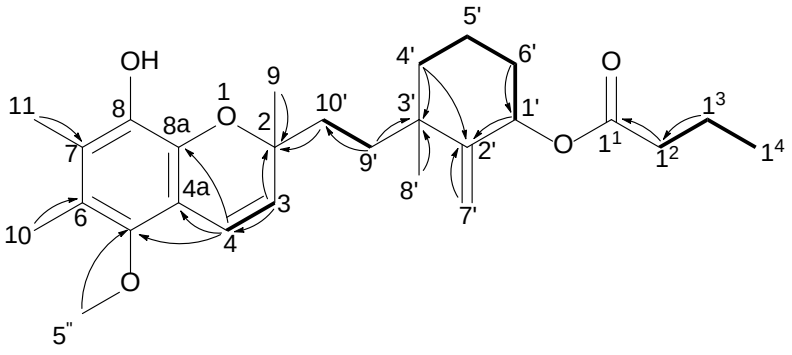

Figure 4.120.: ^{1}H-^{1}H COSY (bold face bonds), and selected HMBCs (double-barbed arrows), correlations of 3'-[10'-(8-hydroxy-5-methoxy-2,6,7-trimethyl-*2H*-chromen-2-yl)ethyl]-3'-methyl-2'-methylene cyclohexyl butyrate (**8**)

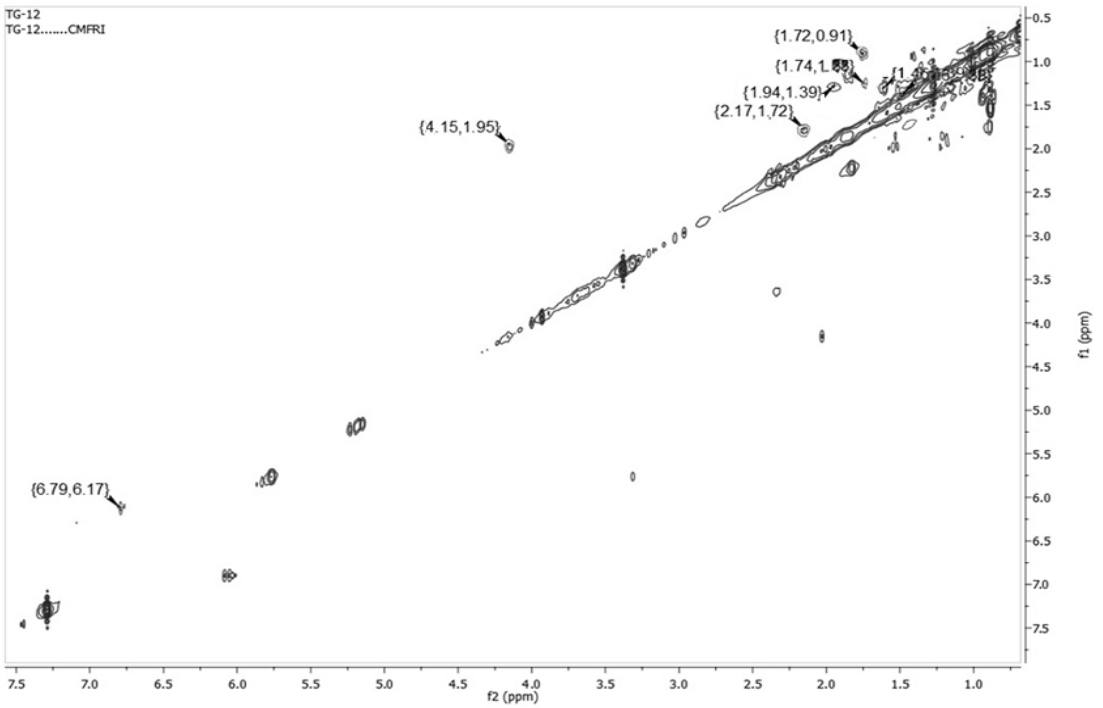

Figure 4.121.: ^{1}H-^{1}H COSY spectrum of 3'-[10'-(8-hydroxy-5-methoxy-2,6,7-trimethyl-*2H*-chromen-2-yl)ethyl]-3'-methyl-2'-methylene cyclohexyl butyrate (**8**)

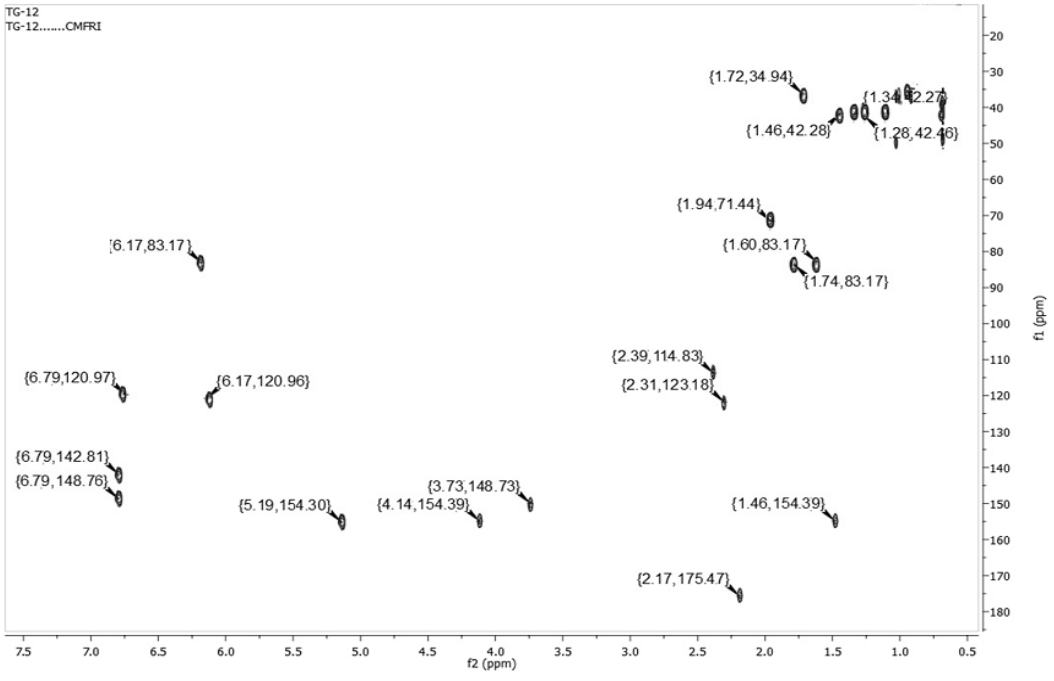

Figure 4.122.: HMBC spectrum of 3'-[10'-(8-hydroxy-5-methoxy-2,6,7-trimethyl-*2H*-chromen-2-yl)ethyl]-3'-methyl-2'-methylene cyclohexyl butyrate (**8**)

Table 4.15: NMR spectroscopic data of compound (**8**), 3'-[10'-(8-hydroxy-5-methoxy-2,6,7-trimethyl-*2H*-chromen-2-yl)ethyl]-3'-methyl-2'-methylene cyclohexyl butyrate (**8**) isolated from red seaweed *G. salicornia*

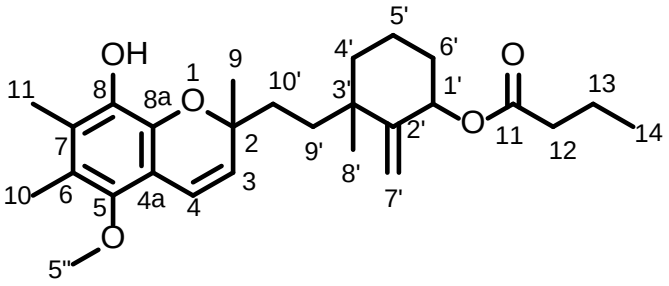

Compound **8** ……3'-[10'-(8-hydroxy-5-methoxy-2,6,7-trimethyl-*2H*-chromen-2-yl)ethyl]-3'-methyl-2'-methylene cyclohexyl butyrate (**8**)

Type	**C. No.**	**^{13}C NMR**	**H. No. (int., mult., J in Hz)[b]**	**^{1}H NMR**	**COSY**	**HMBC**
-	-	-	-	-	-	-
C	2	83.17	-	-		
CH	3	127.86	1H, d, J = 12.8 Hz	6.20	H-4	C-2,4
CH	4	120.90	1H, d, J = 11.8 Hz	6.79	-	C-4a, 8a,5
C	4a	111.56	-	-	-	-
C	5	148.76	-	-	-	-
CH_3	5''	56.80	3H, s	3.73	-	C-5
C	6	114.19	-	-	-	-
C	7	123.34	-	-	-	-
C	8	143.52	-	-	-	-
C	8a	142.83	-	-	-	-
CH_3	9	24.26	3H, s	1.60	-	C-2
CH_3	10	13.83	3H, s	2.39	-	C-6
CH_3	11	12.56	3H, s	2.31	-	C-7
CH	1'	71.44	1H, d, J = 7.2 Hz	4.14	H-6'	C-2'
C	2'	154.36	-	-	-	-
C	3'	42.29	-	-	-	-
CH_2	4'	42.09	2H, dt, J = 6.9, 4.3 Hz	1.46	-	C-2',3'
CH_2	5'	18.78	2H, m	1.39	H-4'	-
CH_2	6'	31.89	2H, dt, J = 5.2, 4.0 Hz	1.94	H-5'	C-1'
CH_2	7'	104.25	2H, s	5.19	-	C-2'
CH_3	8'	22.58	3H, s	1.10	-	C-3'
CH_2	9'	39.52	1H, dt, J = 9.3, 5.6 Hz	1.33	-	C-10',3'
			1H, dt, J = 9.8, 5.1 Hz	1.28	-	-
CH_2	10'	35.80	2H, dd, J = 7.8, 5.9 Hz	1.74	H-9'	C-2
C	1^1	175.49	-	-	-	-
CH_2	1^2	34.95	2H, d, J = 7.9 Hz	2.17	H-1^3	C-1^1
CH_2	1^3	18.74	2H, m	1.72	H-1^4	C-1^2
CH_3	1^4	14.28	3H, t, J = 6.9 Hz	0.91	-	-

[a]NMR spectra were recorded using a Bruker AVANCE III 500 MHz (AV 500) spectrometer (Bruker, Karlsruhe, Germany) in $CDCl_3$ as aprotic solvent at ambient temperature with TMS as the internal standard (δ 0 ppm).

[b]Values in ppm, multiplicity and coupling constants (*J* = Hz) were indicated in parentheses. Multiplicities were allocated by [135]DEPT NMR spectrum.

The assignments were made with the aid of the COSY, HSQC, HMBC and NOESY experiments.

The relative stereochemistries of protons attached to chiral carbon at C-1' (δ 71.44) and other methyl protons at C-9, C-8', C-10 and C-11 were explained with nuclear overhauser effect spectroscopic (NOESY) experiments (Figure 4.123 & 4.124). The signal of proton at chiral centre, δ 1.28 (assigned to H-9'α) exhibited NOEs with methylene proton at δ 4.14 (H-1'), which were oriented in the α-side of the compound. Conversely, the other protons in β-face of the molecule, particularly those of H-9, H-8', H-11, H-10 and H-9' were deduced by NOE relationships between H-11 (δ 2.31)/H-9 (δ 1.60), H-10 (δ 2.39)/H-9 (δ 1.60), H-9 (δ 1.60)/H-8' (δ 1.10) and H-9'β (δ 1.33)/H-8' (δ 1.10).

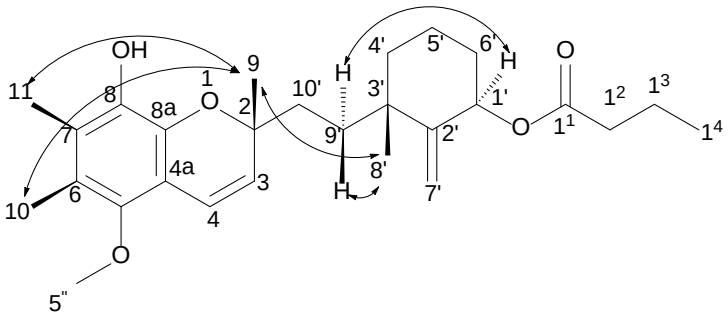

Figure 4.123.: NOESY (double-barbed arrows), correlations of 3'-[10'-(8-hydroxy-5-methoxy-2,6,7-trimethyl-*2H*-chromen-2-yl)ethyl]-3'-methyl-2'-methylene cyclohexyl butyrate (**8**)

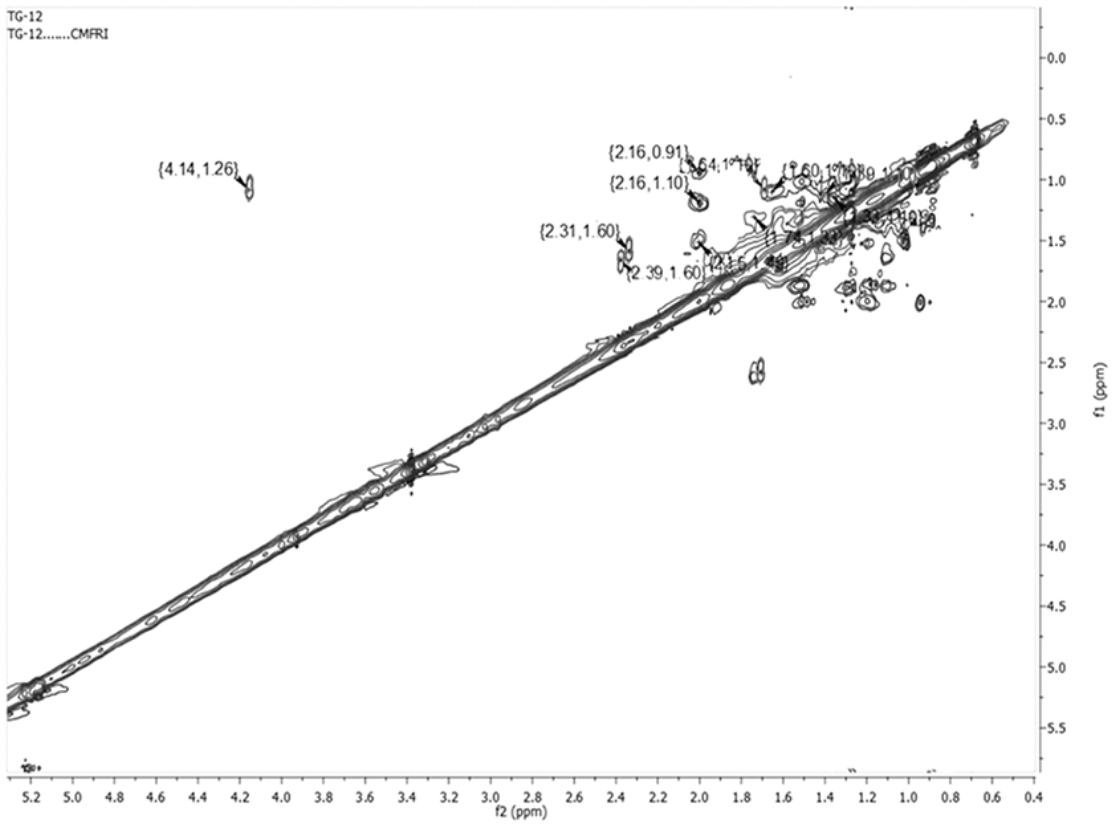

Figure 4.124.: ^{1}H NMR spectrum of 3'-[10'-(8-hydroxy-5-methoxy-2,6,7-trimethyl-*2H*-chromen-2-yl)ethyl]-3'-methyl-2'-methylene cyclohexyl butyrate (**8**)

The molecular ion peak at *m/z* 442 (**a**) $[M]^+$ underwent elimination of $C_4H_8O_2$ moiety and further rearrangement led to a fragment peak at *m/z* 370 (**b**). Further fragmentation of (**b**) led to the formation of radical cation **c** (*m/z* 352). The fragment ion **c** performed a rearrangement to form **d** and **g** (with *m/z* 218 and 135, respectively), whereas the latter led to the formation of **e** (with *m/z* 175) upon further fragmentation. The base peak at *m/z* 77 (**f**) ($C_6H_6^+$) appeared to form upon fragmentation of the mass fragment at *m/z* 175 (Figure 4.125 & 4.126). These detailed spectroscopic data unambiguously attributed the structure of isolated compound was as 3'-[10'-(8-hydroxy-5-methoxy-2,6,7-trimethyl-2*H*-chromen-2-yl)ethyl]-3'-methyl-2'-methylene cyclohexyl butyrate (**8**).

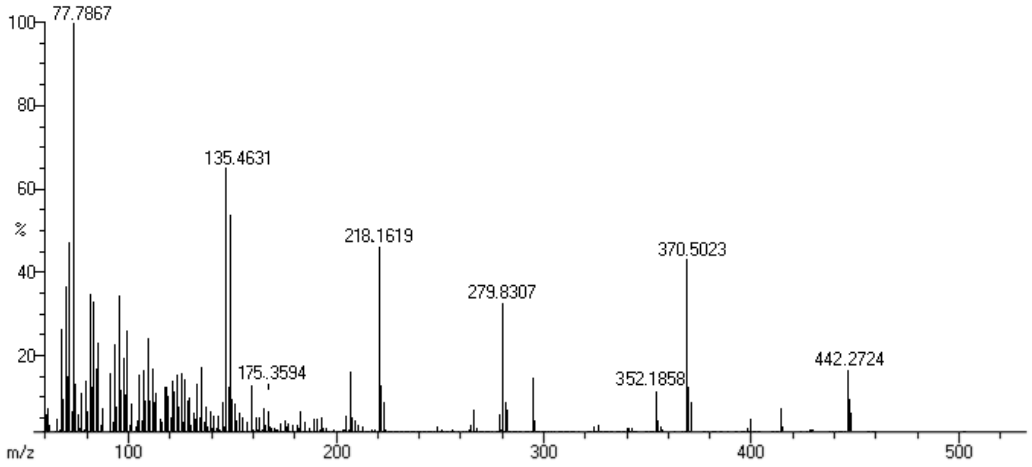

Figure 4.125.: EI-MS spectrum of 3'-[10'-(8-hydroxy-5-methoxy-2,6,7-trimethyl-*2H*-chromen-2-yl)ethyl]-3'-methyl-2'-methylene cyclohexyl butyrate (**8**)

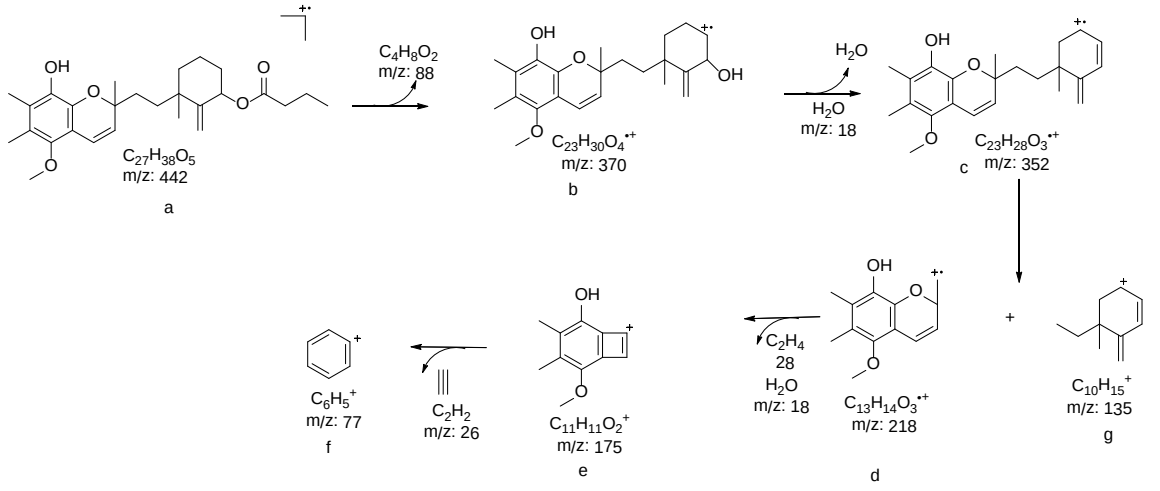

Figure 4.126.: Tentative mass fragmentation pattern of 3'-[10'-(8-hydroxy-5-methoxy-2,6,7-trimethyl-*2H*-chromen-2-yl)ethyl]-3'-methyl-2'-methylene cyclohexyl butyrate (**8**)

Bioassay-assisted repeated chromatographic fractionation of the organic extract of red seaweed, *G. salicornia* yielded two chromenyl derivatives, which were characterised as 4'-[10'-[7-hydroxy-2,8-dimethyl-6-(pentyloxy)-2*H*-chromen-2-yl]ethyl]-3',4'-dimethyl-cyclohexanone (**7**) and 3'-[10'-(8-hydroxy-5-methoxy-2,6,7-trimethyl-2*H*-chromen-2-yl)ethyl]-3'-methyl-2'-methylene cyclohexyl butyrate (**8**) using comprehensive spectroscopic techniques. This is considered as the first report of *2H*-chromenyl derivatives from *G. salicornia*.

4.3.2.5 Structural characterization of spiro-compound derivative (Compounds 9-10)

Spiro frameworks were represented as a significant class of naturally occurring compounds characterised with highly potent bioactive properties and has been known to be present in various phytochemicals with their wide range of pharmacological applications (Leonid et al. 2012). These spirocyclic compounds are of recent interest due to their remarkable conformational features and their structural implications on biological systems and were largely found in various biologically active natural products and pharmaceuticals (Bartoli et al. 2011). The stereochemistries of spiranes with six-membered rings have been extensively studied (Cismas et al. 2005). The non-halogenated rearranged spiro-compound, 1,4,9-trimethyl-5-methylidenespiro[5.5]undec-1,7-diene-4,9-diol and halogenated spiro-fused compounds, such as 2-bromo-1,1,9-trimethyl-5-methylidenespiro[5.5]undec-7-ene-3,9-diol and 2-bromo-9-bromomethylidene-1,1-dimethyl-5-methylene spiro [5.5]undec-7-ene were previously reported from a red seaweed, *Laurencia scoparia* with bio-potentials (Davyt et al. 2001). Also, the halogenated and nonhalogenated spiro-compounds, which were classified as compositacins, were reported from red seaweed, *Laurencia composita* (Yu et al. 2017). In order to access the versatile motifs of spiro-compounds with unique structural features, it has become one of the prominent research areas to the natural product chemists.

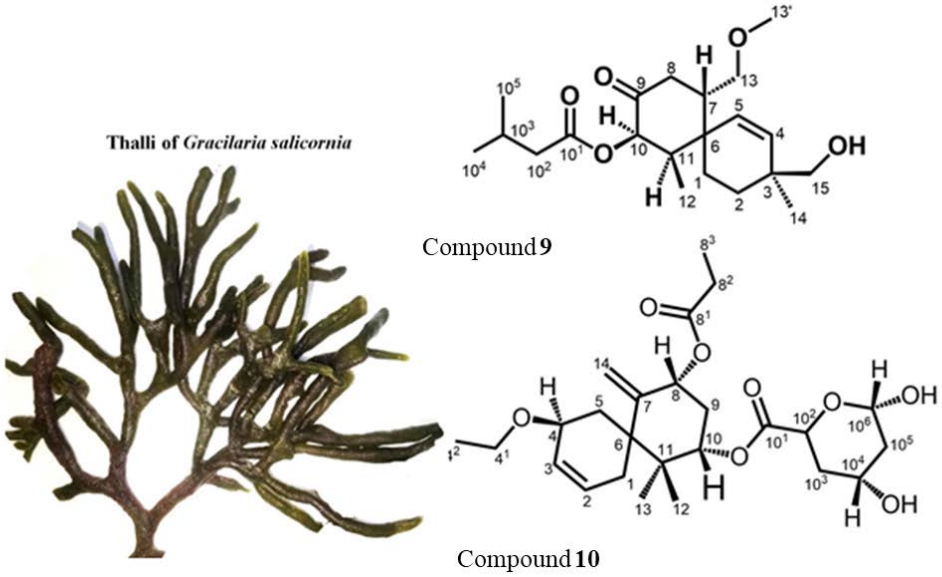

Figure 4.127.: Structures of spiro[5.5]undecane compounds (**9**-**10**) isolated from the seaweed *G. salicornia*. The representative image of the thalli of *G. salicornia* was shown.

In the present study, the organic ethyl acetate-methanol (EtOAc-MeOH) extract of *G. salicornia* collected from southern coastline of Indian peninsular was fractionated by repeated chromatographic techniques, which resulted in the identification of two unprecedented spiro-fused analogues, 3-(hydroxymethyl)-7-(methoxymethyl)-3,11-dimethyl-9-oxospiro[5.5]undec-4-

en-10-methylbutanoate (**9**) and 4-ethoxy-11,11-dimethyl-7-methylene-8-(propionyloxy)spiro[5.5]undec-2-en-10^3,10^5-dihydroxytetrahydro-*2H*-pyran-10-carboxylate (**10**) through the extensive spectroscopic experiments (Figure 4.127).

4.3.2.5a Structural characterization of Compound 9

3-(Hydroxymethyl)-7-(methoxymethyl)-3,11-dimethyl-9-oxospiro[5.5]undec-4-en-10-methylbutanoate

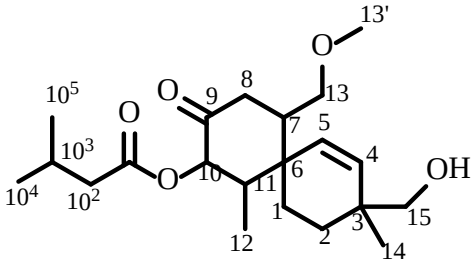

Sample yield	0.36 % (> 99% purity, RP-C18 HPLC)
Physical description	Colourless oily
Molecular formula	$C_{21}H_{34}O_5$
Molecular mass	366.2406

The spiro-compound, 3-(hydroxymethyl)-7-(methoxymethyl)-3,11-dimethyl-9-oxospiro[5.5]undec-4-en-10-methylbutanoate was isolated as colourless oil. The compound (**9**) has exhibited UV absorbance (UV (MeOH) λ_{max}) at 247 nm (Figure 4.128). The homogeneity of the compound was ascertained by HPLC data on a bonded phase octadecylsilane (C_{18}) stationary phase (HPLC, MeOH/ MeCN , 1:2 v/v) with R_t: 4.42 min (Figure 4.129).

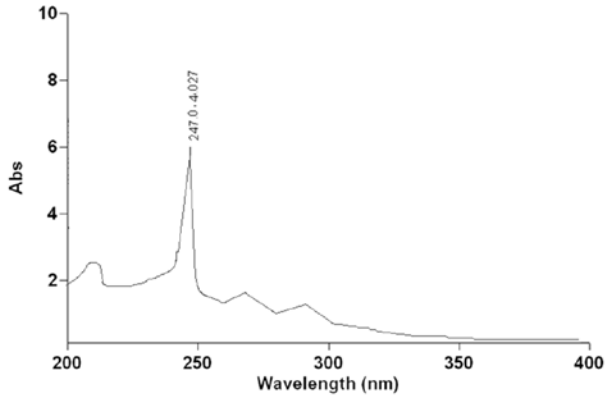

Figure 4.128.: UV spectrum of 3-(hydroxymethyl)-7-(methoxymethyl)-3,11-dimethyl-9-oxospiro[5.5]undec-4-en-10-methylbutanoate (**9**)

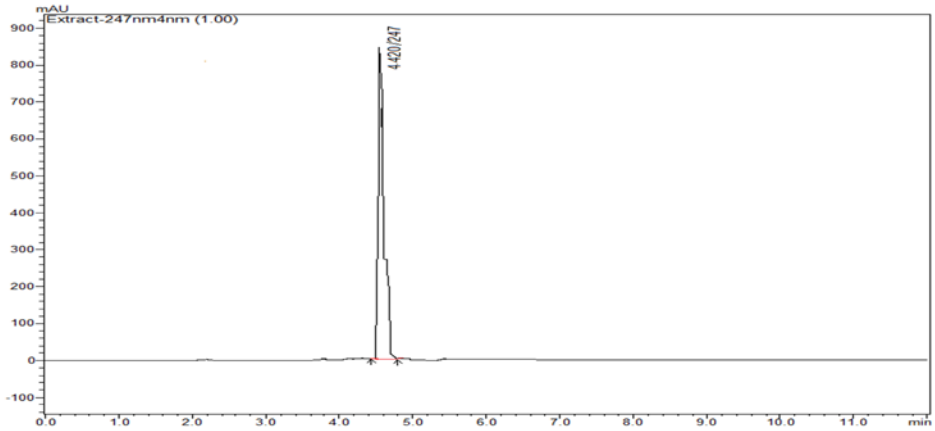

Figure 4.129.: HPLC chromatogram of 3-(hydroxymethyl)-7-(methoxymethyl)-3,11-dimethyl-9-oxospiro[5.5]undec-4-en-10-methylbutanoate (**9**)

Bioactivity-guided chromatographic purification using reverse phase preparative HPLC of the organic extract of *G. salicornia* yielded 3-(hydroxymethyl)-7-(methoxymethyl)-3,11-dimethyl-9-oxospiro[5.5]undec-4-en-10-methylbutanoate (**9**) as a colourless oily substance. The molecular ion peak was analyzed by mass spectroscopic (electrosparay ionization method; Bruker Daltonic, GmbH, Germany) experiment and its molecular ion peak was observed at *m/z* 367.4996 $[M+H]^+$ (Figure 4.130). The mass spectroscopy along with integrative NMR-IR experiments deduced the molecular formula of **9** as $C_{21}H_{34}O_5$ (Table 4.16), which was indicative of five sites of unsaturation.

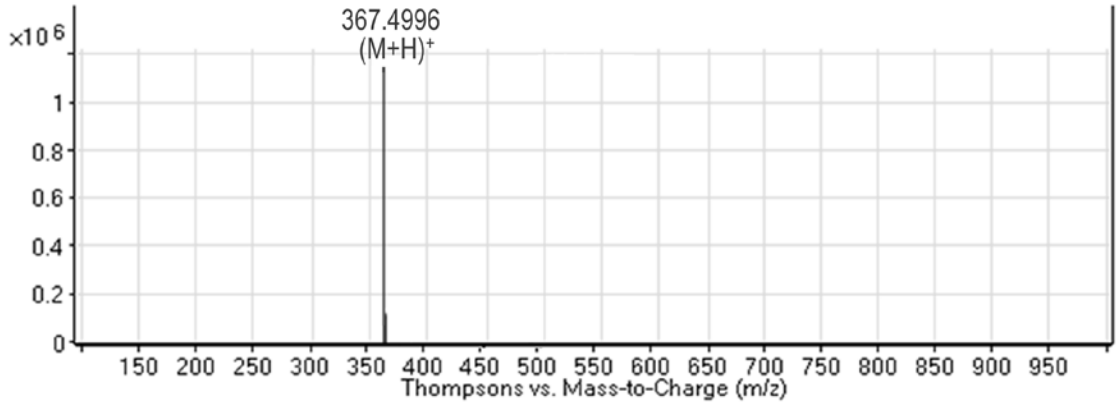

Figure 4.130.: ESIMS spectrum of 3-(hydroxymethyl)-7-(methoxymethyl)-3,11-dimethyl-9-oxospiro[5.5]undec-4-en-10-methylbutanoate (**9**)

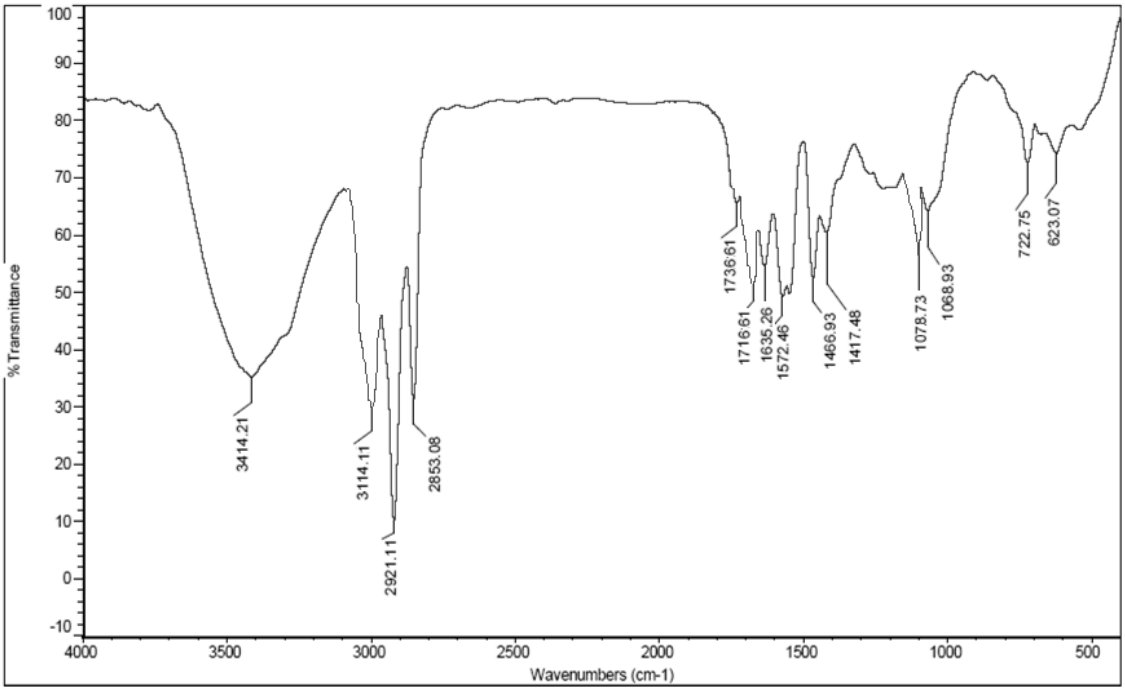

Figure 4.131.: FTIR spectrum of 3-(hydroxymethyl)-7-(methoxymethyl)-3,11-dimethyl-9-oxospiro[5.5]undec-4-en-10-methylbutanoate (**9**)

The FTIR spectrum of **9** exhibited absorption peaks at 3414, 1068, 1716 and 1736 cm^{-1} that might correspond to hydroxyl (-OH), ether (-C-O-C), carbonyl (-C=O) and ester {-O-(C=O)-} functionalities, respectively (Figure 4.131). The ^{13}C-NMR spectrum of **9** showed the signals for 21 carbons. The types of the carbon signals determined from DEPT spectrum were five methyls, six each of methylenes and methines (two olefinic), along with four non-protonated carbons (one each of carbonyl and carbonyl ester groups). The ^{1}H spectrum of **9** displayed signals at δ 5.24 and 4.52 due to the olefinic protons. Doublets at δ 4.41, 3.69 and singlets at δ 3.37 and 3.20 were assigned to protons, which were geminal to the oxygen atom, whereas nine well-resolved signals, each attributed to one of the remaining aliphatic protons, were recorded at δ 1.70-2.82. Four shielded protons at δ 0.81, 0.86, 0.88 and 1.33 were accounted for the methyl protons in **9**. In compound **9**, the chemical shifts for five methyls, four sp^3 methines, two sp^2 methines, six sp^3 methylenes and four quaternary carbons were identified by exhaustive ^{1}H/^{13}C/DEPT experiments(Figure 4.132-1.134). The ^{13}C exhibited highly deshielded resonances for four protonated carbons at δ 94.97, 50.09, 55.03 and 72.40, which might be directly attached to oxygen. The sp^2 protons with highly deshielded resonance at δ 4.52

and 5.24 with doublets were bonded to the carbons at δ 128.45 and 133.09, respectively, as inferred from the HSQC spectrum (Figure 4.135).

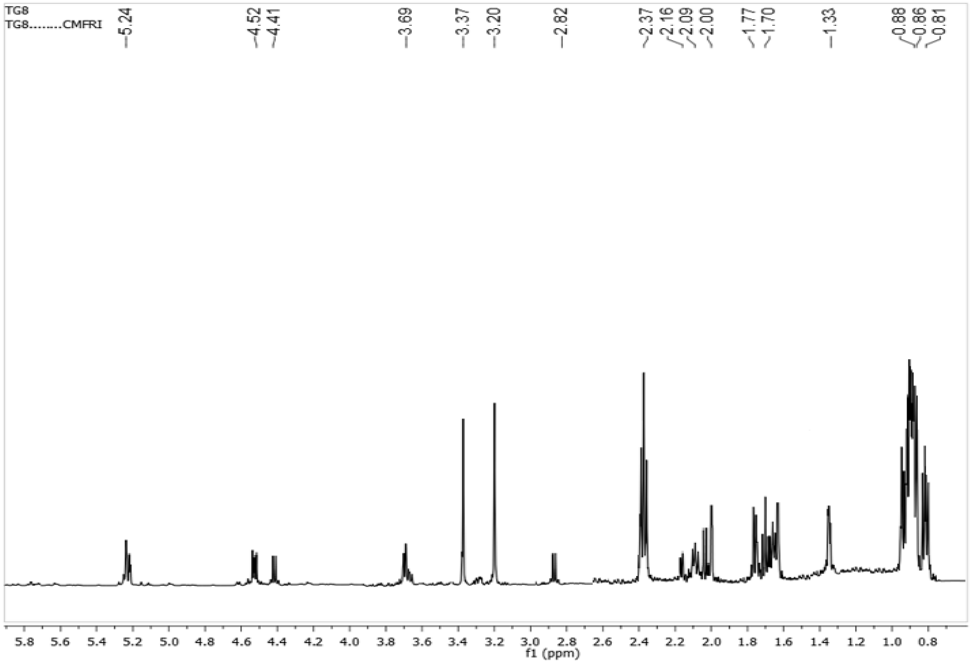

Figure 4.132.: ^{1}H-NMR spectrum of 3-(hydroxymethyl)-7-(methoxymethyl)-3,11-dimethyl-9-oxospiro[5.5]undec-4-en-10-methylbutanoate (**9**)

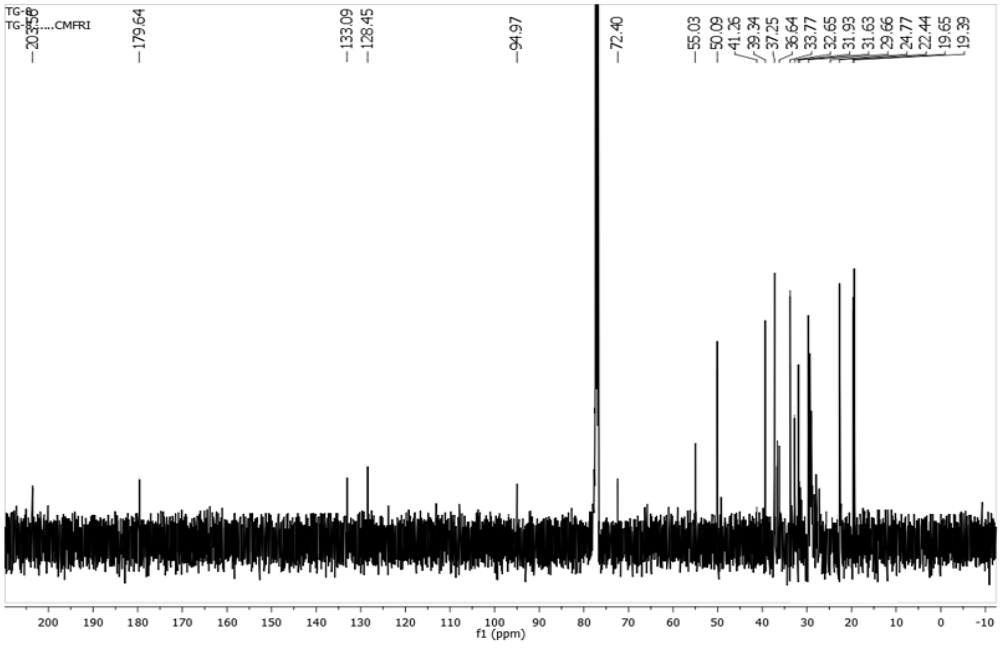

Figure 4.133.: ^{13}C-NMR spectrum of 3-(hydroxymethyl)-7-(methoxymethyl)-3,11-dimethyl-9-oxospiro[5.5]undec-4-en-10-methylbutanoate (**9**)

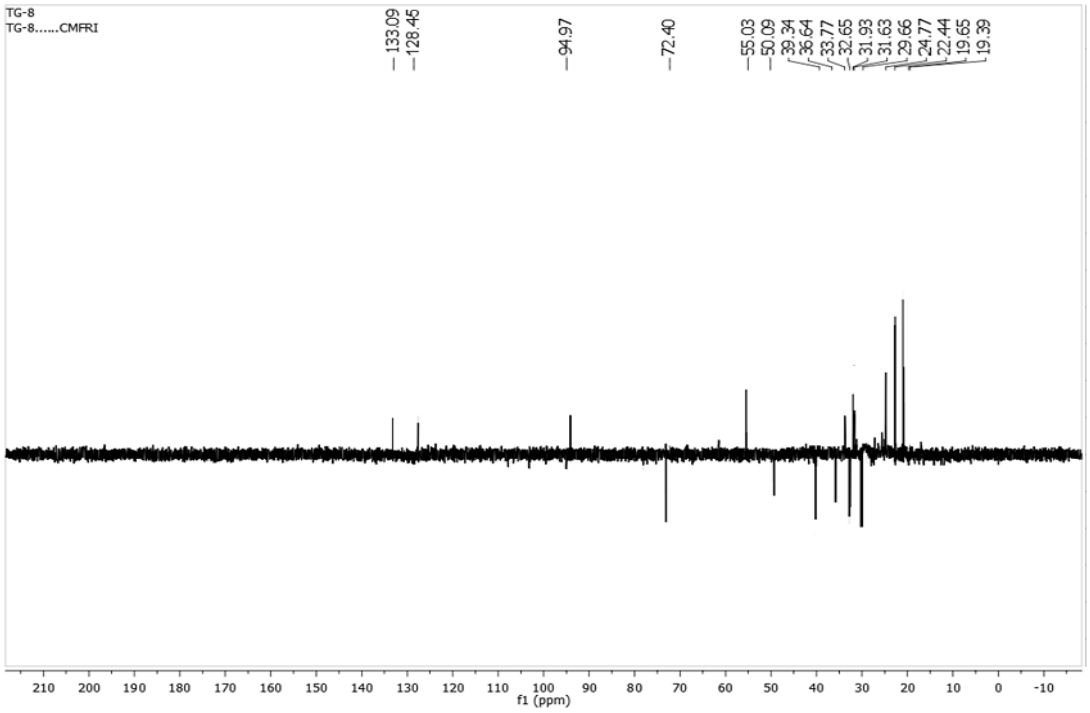

Figure 4.134.: [135]DEPT spectrum of 3-(hydroxymethyl)-7-(methoxymethyl)-3,11-dimethyl-9-oxospiro[5.5]undec-4-en-10-methylbutanoate (**9**)

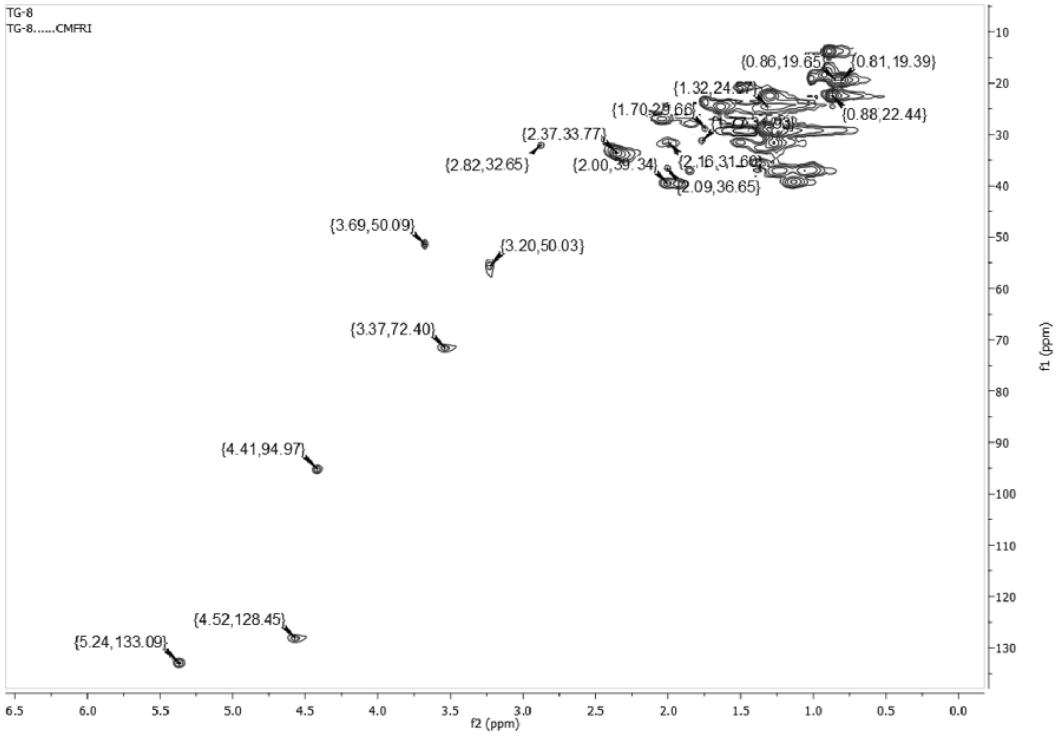

Figure 4.135.: HSQC spectrum of 3-(hydroxymethyl)-7-(methoxymethyl)-3,11-dimethyl-9-oxospiro[5.5]undec-4-en-10-methylbutanoate (**9**)

Besides these, COSYs from δ 4.52 (assigned at H-4) to δ 5.24 (H-5) and HMBCs from δ 4.52 (H-4) to δ 37.25 (C-3) and δ 5.24 (H-5) to δ 128.45 (C-4) confirmed the presence of olefinic carbons at C-4 and C-5, and quaternary carbon at C-3 (Figure 4.136-4.138). These were further attributed by HMBC correlations between H-2 and C-3 {δ 1.77 (H-2)/37.25 (C-3); -CH_2-C} and H-1 and C-2 {δ 1.70 (H-1)/31.93 (C-2)}. The HMBCs from the methyl proton at H-14 (δ 1.33) and methylene proton at H-15 (δ 3.37) to the shielded non-protonated carbon at C-3 (δ 37.25) confirmed the linkage of methyl and hydroxymethyl at C-3 of cyclohexene ring. These attributions established the partial structure of 3-hydroxymethyl-3-methyl cyclohexene ring in the compound. Similarly, HMBCs from H-7 (δ 2.16) to δ 36.64 (C-8), H-8 (2.09) to highly deshielded carbon, C-9 (δ 203.56) along with the HMBC linkages of H-10 (δ 4.41) to carbons at C-9 (δ 203.56), C-11 (δ 32.65) confirmed the presence of carbonyl group in the bicyclic frame work in the nearby position of C-8 (-CH_2). The previously reported spiro-compound, compositacin C enclosed carbonyl at C-10 with carbon signal of about δ 205, and this carbon shift was comparable with the present compounds with carbonyl at C-9 (δ 203.56) (Yu et al. 2017). Moreover, the COSY correlations from δ 2.09 (H-8)/2.06 (H-7)/3.69 (H-13) {H-8/H-7/H-13} and from δ 4.41 (H-10)/2.82 (H-10)/0.88 {H-12/H-10/H-12} together with the HMBCs from δ 0.88 (H-12) to δ 32.65 (C-11); δ 3.69 (H-13) to δ 2.16 (C-7), 55.03 (C-13') attributed to the partial structure of methoxymethyl-12-methylcyclohexanone ring system in **9**. The partial structure of 3-hydroxymethyl-3-methyl cyclohexene and 7-methoxymethyl-11-methyl cyclohexanone rings were spiro fused at C-6, which was confirmed through the HMBCs from H-5 to C-6 {δ 5.24 (H-5)/41.26 (C-6); =CH(5)-C(6)<}, H-1 to C-6{1.70 (H-1)/41.26 (C-6); -CH_2-CH_2-C-}, H-7 to H-11 {δ 2.16 (H-7)/41.26 (C-6)} and from H-11 to C-6 {2.82 (H-11)/41.26 (C-6); -CH-C-CH-}.

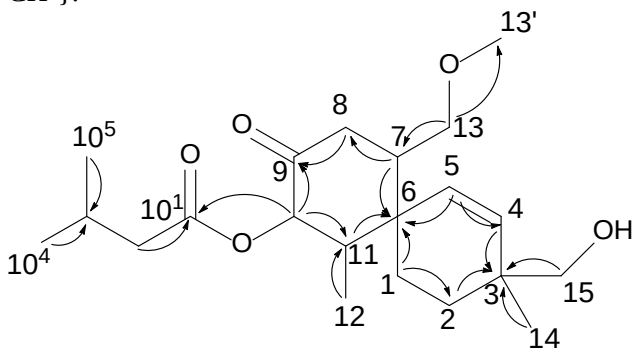

Figure 4.136.: ^{1}H-^{1}H COSY (bold face bonds), and selected HMBCs (double-barbed arrows), correlations of 3-(hydroxymethyl)-7-(methoxymethyl)-3,11-dimethyl-9-oxospiro[5.5]undec-4-en-10-methylbutanoate (**9**)

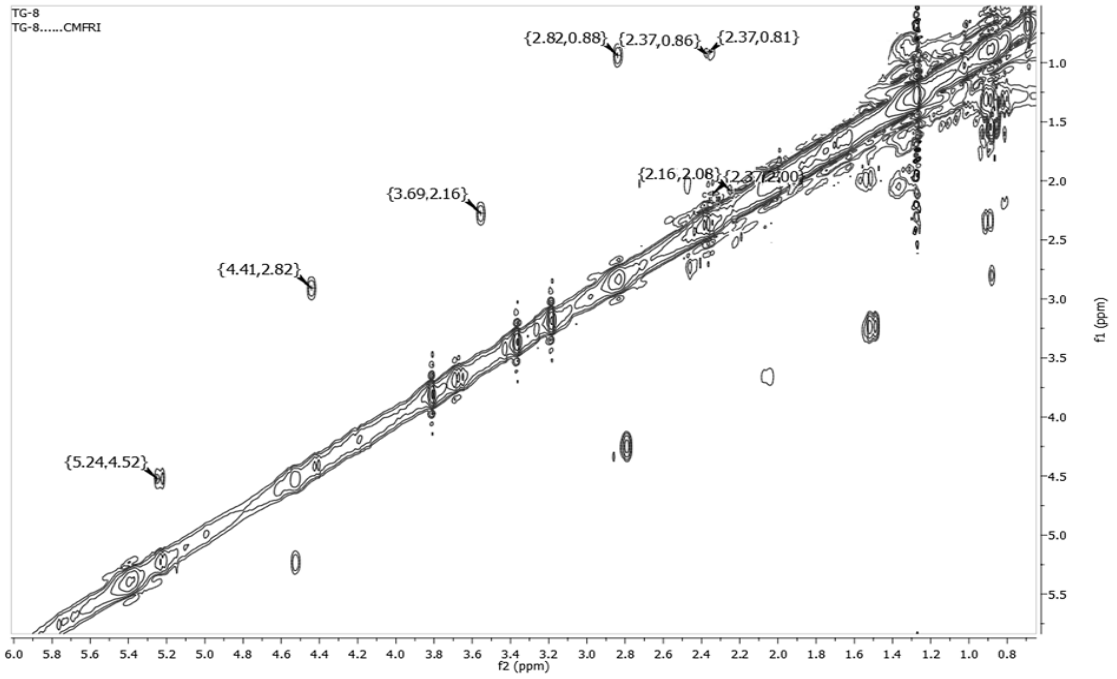

Figure 4.137.: ^{1}H-^{1}H COSY spectrum of 3-(hydroxymethyl)-7-(methoxymethyl)-3,11-dimethyl-9-oxospiro[5.5]undec-4-en-10-methylbutanoate (**9**)

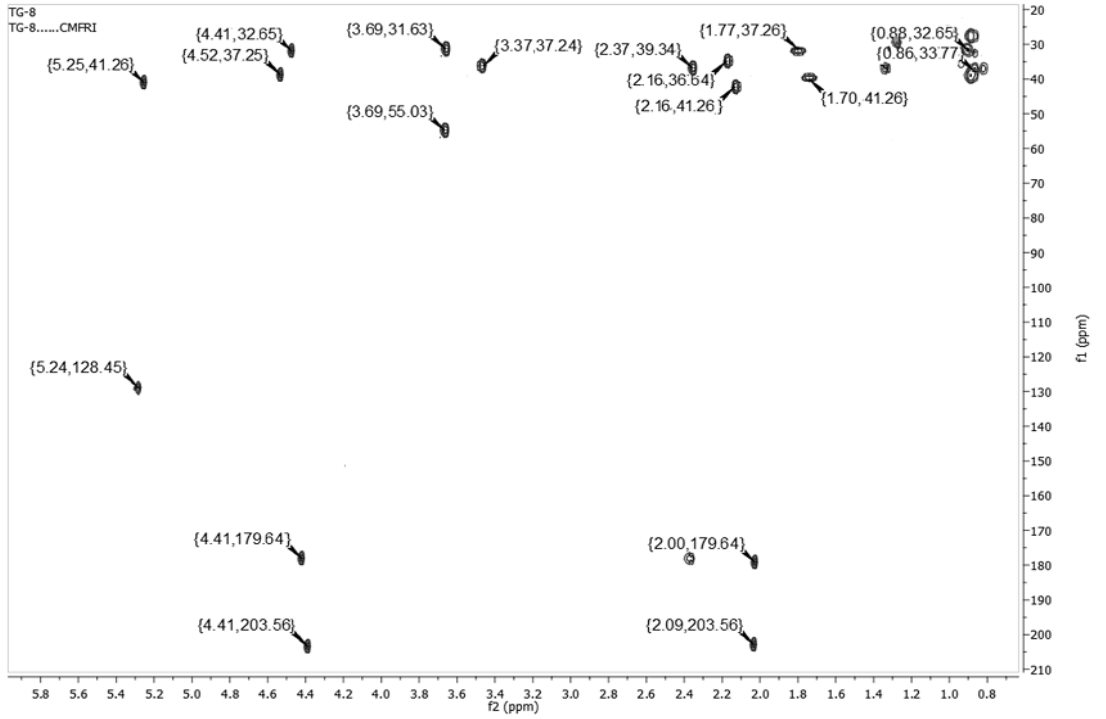

Figure 4.138.: HMBC spectrum of 3-(hydroxymethyl)-7-(methoxymethyl)-3,11-dimethyl-9-oxospiro[5.5]undec-4-en-10-methylbutanoate (**9**)

The titled compound **9** was supported by the previous reports of spiro[5.5]undecane derivatives (Davyt et al. 2001; Ji et al. 2007; Suzuki et al. 2001). The COSY couplings from δ 2.00 (H-10^2)/2.37 (H-10^3)/0.81 (H-10^4), 0.86 (H-10^5) along with ^{1}H-^{13}C HMBCs, such as δ 2.00 (H-10^2) to δ 179.64 (C-10^1); δ 2.37 (H-10^3) to δ 39.34 (C-10^2); δ 0.81 (H-10^4) to δ 33.77 (C-10^3) and δ 0.86 (H-10^5) to δ 33.77 (C-10^3) confirmed the ester side chain assignment. The long bond ^{1}H-^{13}C HMBCs from H-10 to C-10^1 of ester carbonyl {δ 4.41 (H-10)/179.64 (C-10^1)} suggested the attachment of ester carbonyl part of 3-methylbutanoate at C-10 of cyclohexanone ring. Notably, the olefinic group at δ 4.52 (H-4), 5.24 (H-5) recorded lesser coupling constants (J) of 7.6 and 5.5 Hz, respectively, and therefore, the configuration of these olefinic groups in oxospiro[5.5]undecen-4-ene was ascertained as cis oriented in the cyclohexene ring. Thus, the compound **9** was deduced to possess a rearranged bicyclic skeleton of cyclohexanone ring spiro-fused to substituted cyclohexene framework, and was found to possess a spiro[5.5]undecane skeleton.

Table 4.16: NMR spectroscopic data of compound (**9**), 3-(hydroxymethyl)-7-(methoxymethyl)-3,11-dimethyl-9-oxospiro[5.5]undec-4-en-10-methylbutanoate (**9**) isolated from red seaweed *G. salicornia*

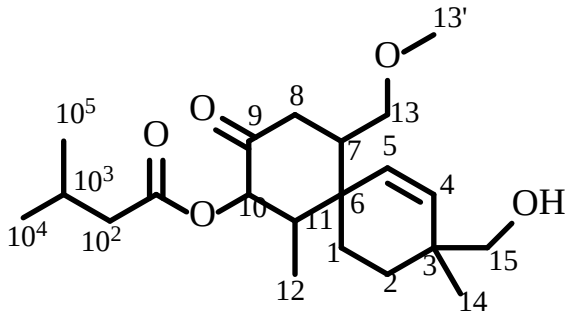

Compound **9…….**3-(Hydroxymethyl)-7-(methoxymethyl)-3,11-dimethyl-9-oxospiro[5.5]undec-4-en-10-methylbutanoate (**9**)

C. No.	^{13}C	^{1}H(int.,mult.,J in Hz)[b]	^{1}H-^{1}H COSY	HMBC
1	29.66	1.70(2H,t,3.5 Hz)	-	C-2,6
2	31.93	1.77(2H,t,3.8 Hz)	-	C-3
3	37.25	-	-	-
4	128.45	4.52(1H,d,7.6 Hz)	H-5	C-3
5	133.09	5.24(1H,t,8.5 Hz)	-	C-4,6
6	41.26	-	-	-
7	31.63	2.16(1H,t,4.2 Hz)	H-8, H-13	C-6, 8
8	36.64	2.09(2H,d,9.6Hz)	-	C-9
9	203.56	-	-	-

10	94.97	4.41(1H,d,10.5 Hz)	H-11	C-9,11,10^1
11	32.65	2.82(1H,d,7.5 Hz)	H-12	C-6
12	22.44	0.88(3H,d,8.2 Hz)	-	C-11
13	50.09	3.69(2H,d,3.5 Hz)	-	C-7,13'
14	24.77	1.33(3H,d,11.3 Hz)	-	C-3
15	72.40	3.37(2H,s)	-	C-3
10^1	179.64	-	-	-
10^2	39.34	2.00(2H,d,8.1 Hz)	H-10^3	C-10^1
10^3	33.77	2.37(1H,t,3.5 Hz)	H-10^4, H-10^5	C-10^2
10^4	19.39	0.81(3H,t,3.5 Hz)	-	C-10^3
10^5	19.65	0.86(3H,t,3.5 Hz)	-	C-10^3
13'	55.03	3.20(3H,s)	-	-

[a] NMR spectra recorded using Bruker AVANCE III 500 MHz (AV 500) spectrometers.

[b] Values in ppm, multiplicity and coupling constants (J = Hz) are indicated in parentheses.

Assignments were made with the aid of the ^{1}H-^{1}H COSY, HSQC, HMBC and NOESY experiments.

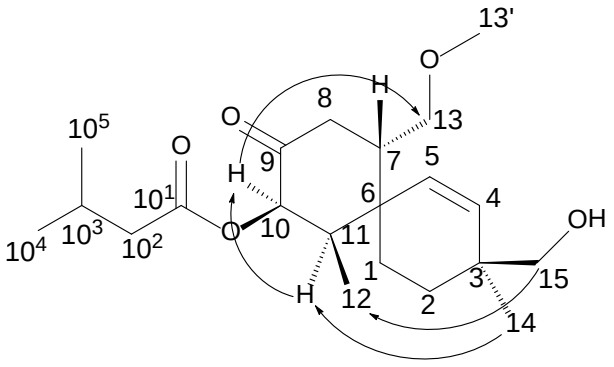

Figure 4.139.: NOESY (double barbed arrows) correlations of 3-(hydroxymethyl)-7-(methoxymethyl)-3,11-dimethyl-9-oxospiro[5.5]undec-4-en-10-methylbutanoate (**9**)

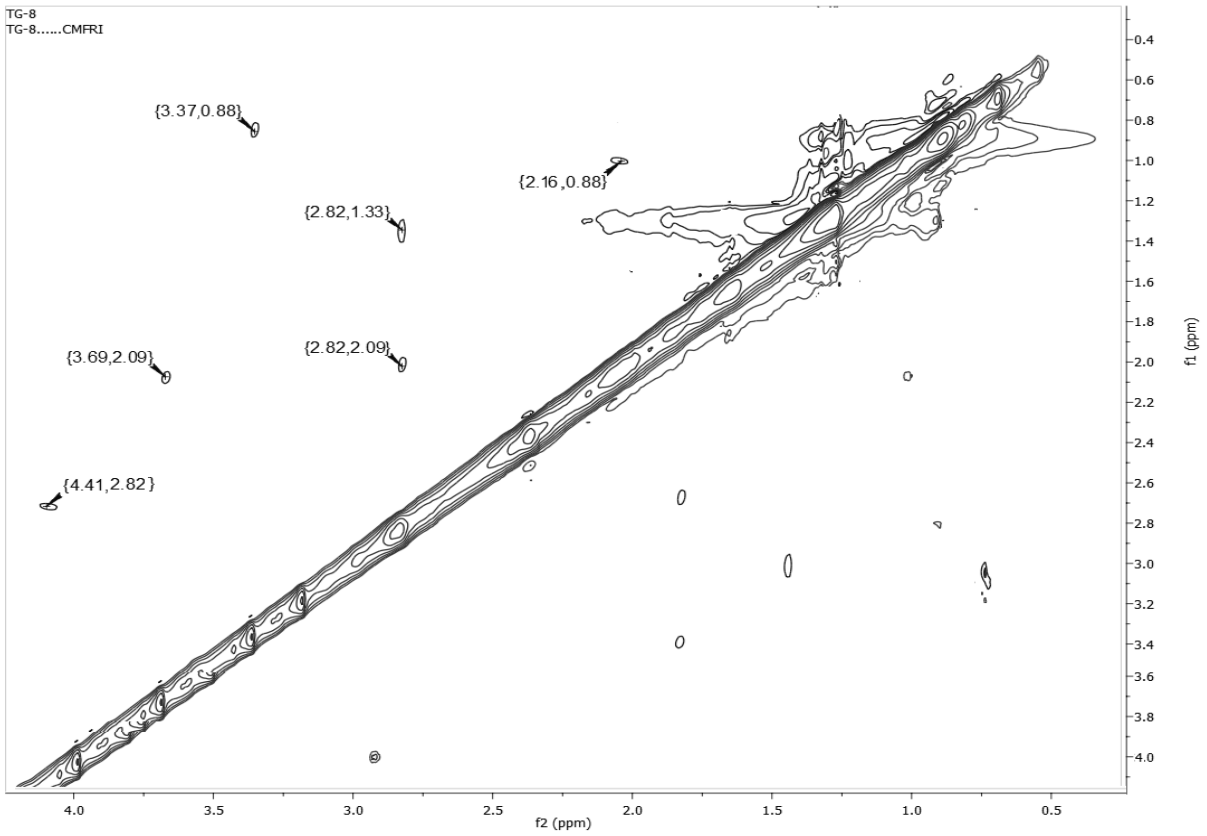

Figure 4.140.: NOESY spectrum of 3-(hydroxymethyl)-7-(methoxymethyl)-3,11-dimethyl-9-oxospiro[5.5]undec-4-en-10-methylbutanoate (**9**)

Relative stereochemistries of the protons chiral centers, mainly at C-3, C-7, C-10 and C-11 were deduced by extensive NOESY experiments (Figure 4.139-4.140). The NOE correlations from δ 1.33 (H-14)/2.82 (H-11)/4.41 (H-10) confirmed the equiplaner alignment of these protons in their close proximity, and these were arbitrarily allocated in the α-direction with reference to its molecular plane of symmetry. The NOE correlation from δ 2.16 (H-7)/0.88 (H-12) attributed that these protons were aligned opposite to α-protons, and therefore, assigned as β-oriented. Therefore, the 7-methoxymethyl at C-7 was α-directed being trans to the β-proton at C-7, whereas the hydroxymethyl was β-oriented being trans to the α-proton at C-3.

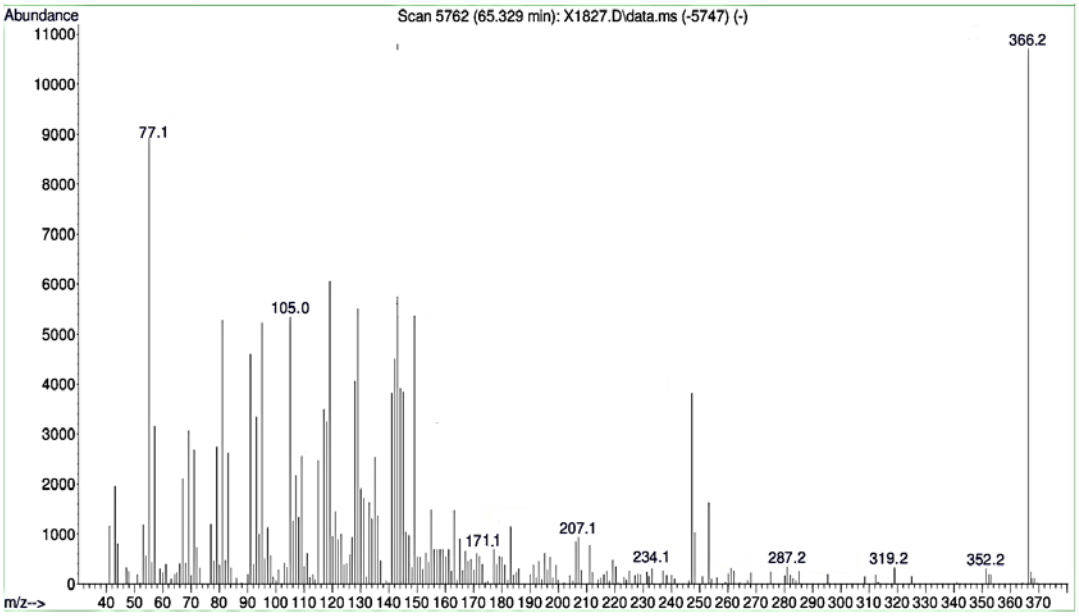

Figure 4.141.: EI-MS spectrum of 3-(hydroxymethyl)-7-(methoxymethyl)-3,11-dimethyl-9-oxospiro[5.5]undec-4-en-10-methylbutanoate (**9**)

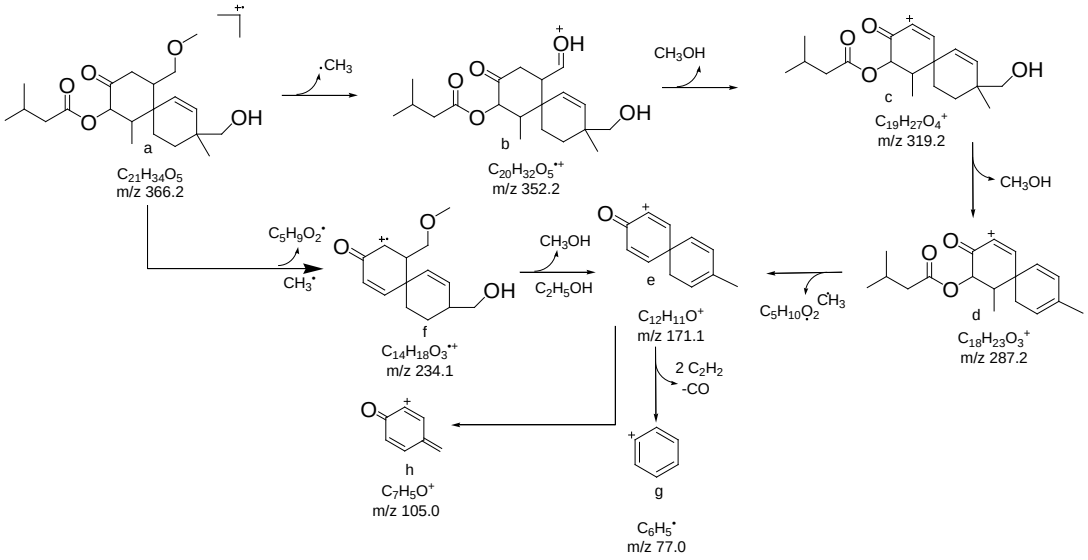

Figure 4.142.: Tentative mass fragmentation pattern of 3-(hydroxymethyl)-7-(methoxymethyl)-3,11-dimethyl-9-oxospiro[5.5]undec-4-en-10-methylbutanoate (**9**)

The molecular ion peak at *m/z* 366 (**a**) $[M]^+$ underwent an elimination of methyl and $C_5H_9O_2^{\bullet}$ along with reorganization of bonds leading to the fragment peaks at *m/z* 352 (**b**) and 234 (**f**). Further fragmentation of (**b**) led to the formation of mass fragment, **c** at *m/z* 319. The radical cation, **c** also performed an elimination of methanol radical ion leading to a rearrangement mechanism to yield **d**. The mass fragment (**f**) at *m/z* 234 was also led to the

formation of **e** and then to **h** (*m/z* 105). The fragment at *m/z* 77 was found to be the base peak (Figure 4.141-4.142).

4.3.2.5b Structural characterization of Compound 10

4-Ethoxy-11,11-dimethyl-7-methylene-8-(propionyloxy)spiro[5.5]undec-2-en-10^3,10^5-dihydroxytetrahydro-*2H*-pyran-10-carboxylate

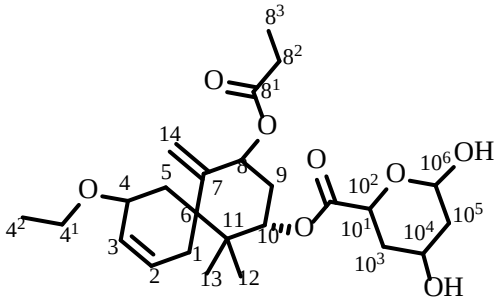

Sample yield	0.34% (> 99% purity, RP-C18 HPLC)
Physical description	Colourless oily
Molecular formula	$C_{25}H_{38}O_8$
Molecular mass	466.2567

The spiro-compound derivative, 4-ethoxy-11,11-dimethyl-7-methylene-8-(propionyloxy)spiro[5.5]undec-2-en-10^3,10^5-dihydroxytetrahydro-*2H*-pyran-10-carboxylate was isolated as colourless oil. The compound (**10**) has exhibited UV absorbance (UV (MeOH) λ_{max}) at 270 nm (Figure 4.143). The homogeneity of the compound was ascertained by HPLC data on a bonded phase octadecylsilane (C_{18}) stationary phase (HPLC, MeOH/MeCN , 1:2 v/v) with R_t: 3.35 min (Figure 4.144).

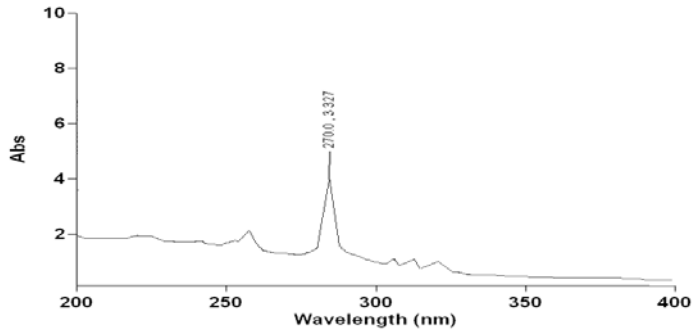

Figure 4.143.: UV spectrum of 4-ethoxy-11,11-dimethyl-7-methylene-8-(propionyloxy)spiro[5.5]undec-2-en-10^3,10^5-dihydroxytetrahydro-*2H*-pyran-10-carboxylate (**10**)

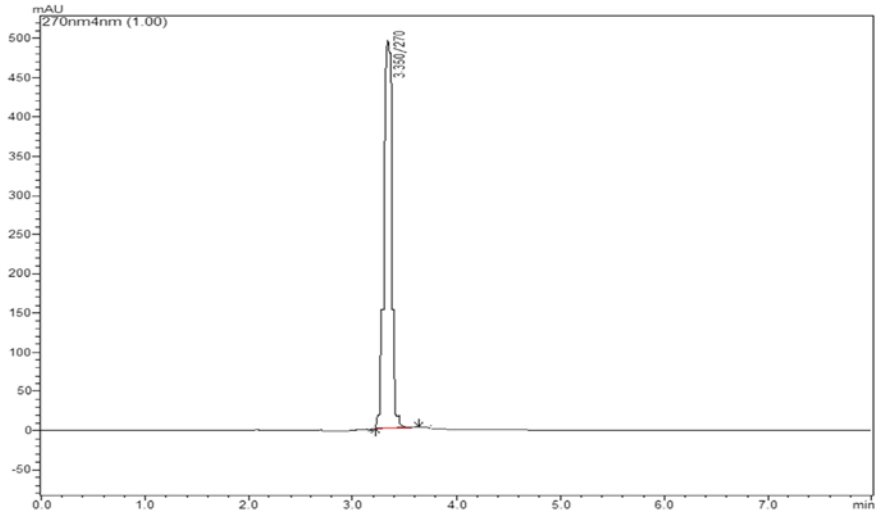

Figure 4.144.: HPLC chromatogram of 4-ethoxy-11,11-dimethyl-7-methylene-8-(propionyloxy)spiro[5.5]undec-2-en-10^3,10^5-dihydroxytetrahydro-*2H*-pyran-10-carboxylate (**10**)

The chromatographic fractionation of the organic extract of *G. salicornia* yielded 4-ethoxy-11,11-dimethyl-7-methylene-8-(propionyloxy)spiro[5.5]undec-2-en-10^3,10^5-dihydroxytetrahydro-2*H*-pyran-10-carboxylate (**10**) as a colourless oily substance. The molecular ion peak was observed at *m/z* 467.2645 $[M+H]^+$ (Figure 4.145). The mass spectroscopy along with integrative NMR-IR experiments deduced the molecular formula of **10** as $C_{25}H_{38}O_8$ (Table 4.17), which was indicative of six sites of unsaturation.

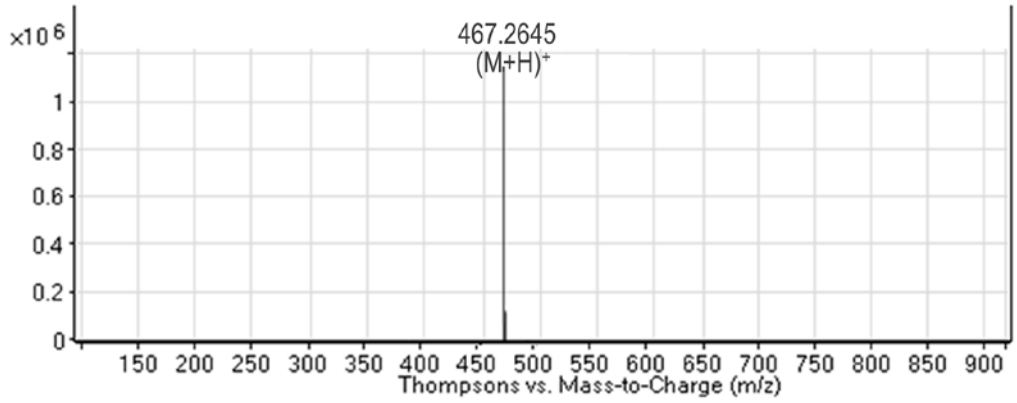

Figure 4.145.: HRESIMS spectrum of 4-ethoxy-11,11-dimethyl-7-methylene-8-(propionyloxy)spiro[5.5]undec-2-en-10^3,10^5-dihydroxytetrahydro-*2H*-pyran-10-carboxylate (**10**)

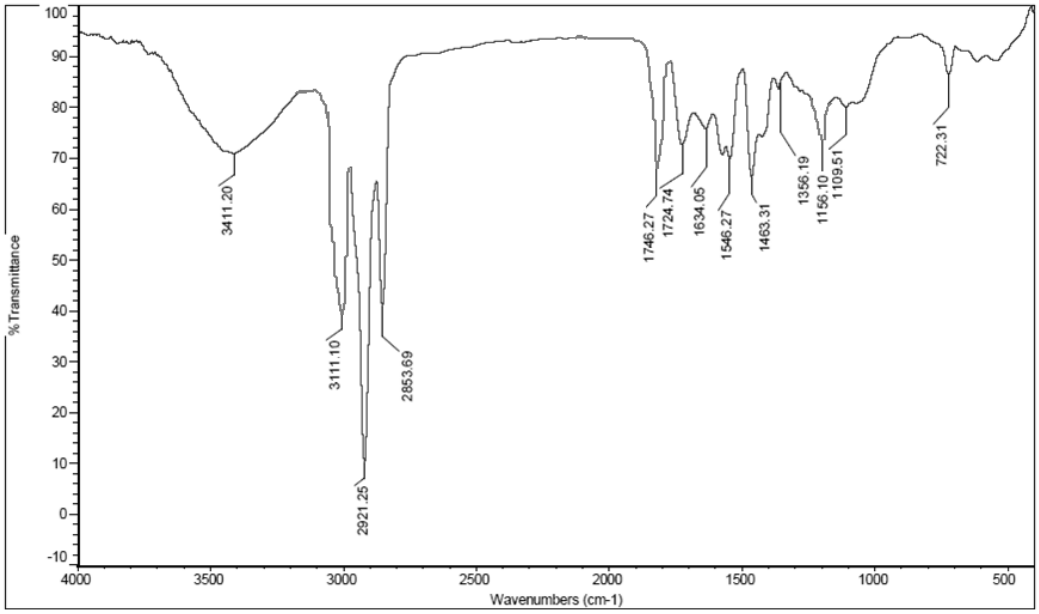

Figure 4.146.: FTIR spectrum of 4-ethoxy-11,11-dimethyl-7-methylene-8-(propionyloxy)spiro[5.5]undec-2-en-10^3,10^5-dihydroxytetrahydro-*2H*-pyran-10-carboxylate (**10**)

The FTIR spectrum of **10** exhibited the presence of absorption peaks at 3411, 1109 and 1746 cm^{-1} that might correspond to the hydroxyl (-OH), ether (-C-O-C) and ester {-O-(C=O)-} functionalities, respectively (Figure 4.146). The ^{13}C-NMR spectrum of **10** showed signals for 25 carbons. The type of carbon signals determined from DEPT spectrum were of four methyls, seven sp^3 methylene, one sp^2 methylene (exocyclic), six sp^3 methine, two sp^2 methines (one olefinic) and five non-protonated carbons (two ester groups).

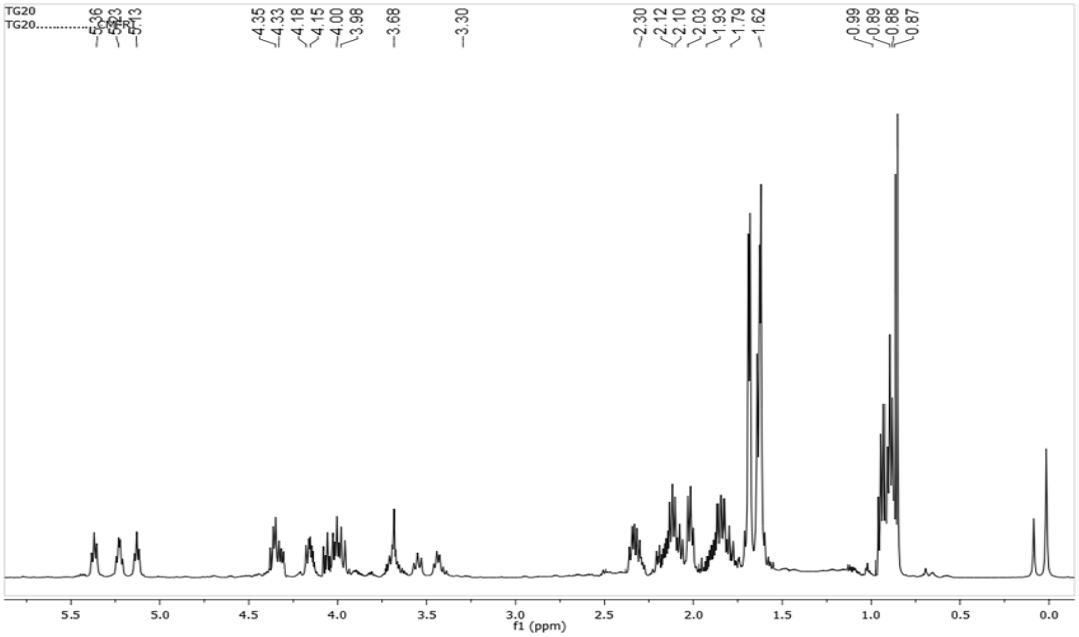

Figure 4.147.: ^{1}H-NMR spectrum of 4-ethoxy-11,11-dimethyl-7-methylene-8-(propionyloxy)spiro[5.5]undec-2-en-10^{3},10^{5}-dihydroxytetrahydro-*2H*-pyran-10-carboxylate (**10**)

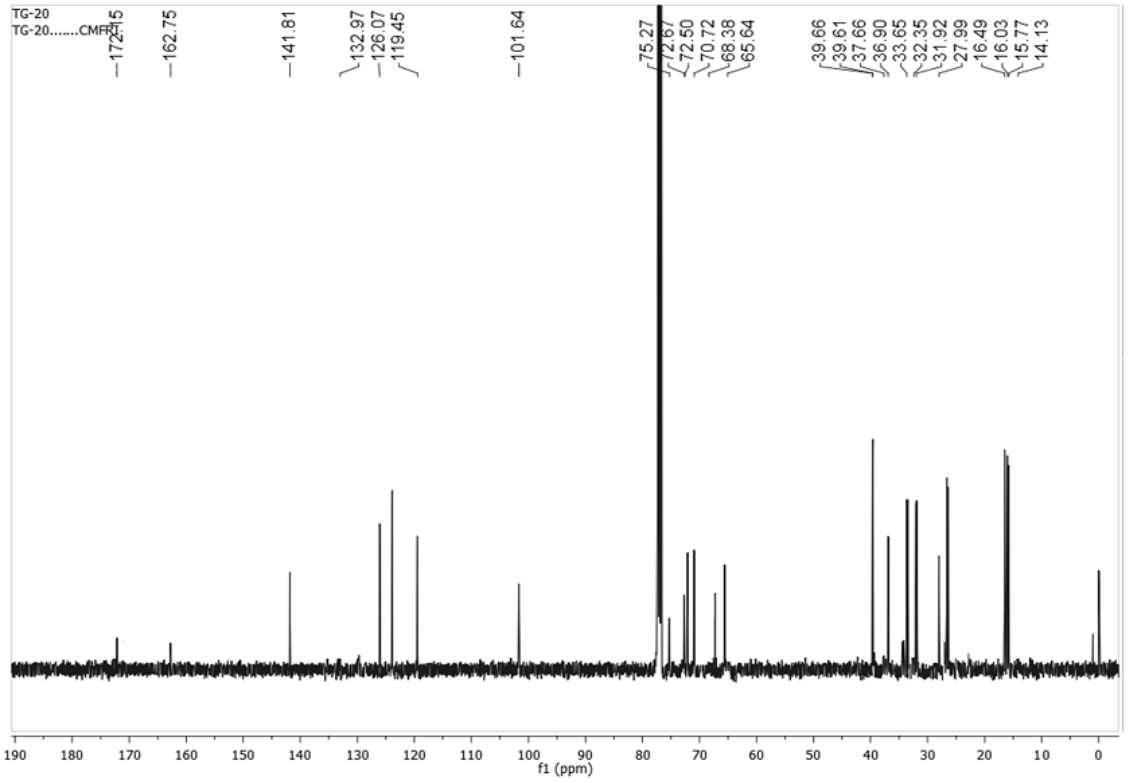

Figure 4.148.: ^{13}C-NMR spectrum of 4-ethoxy-11,11-dimethyl-7-methylene-8-(propionyloxy)spiro[5.5]undec-2-en-10^{3},10^{5}-dihydroxytetrahydro-*2H*-pyran-10-carboxylate (**10**)

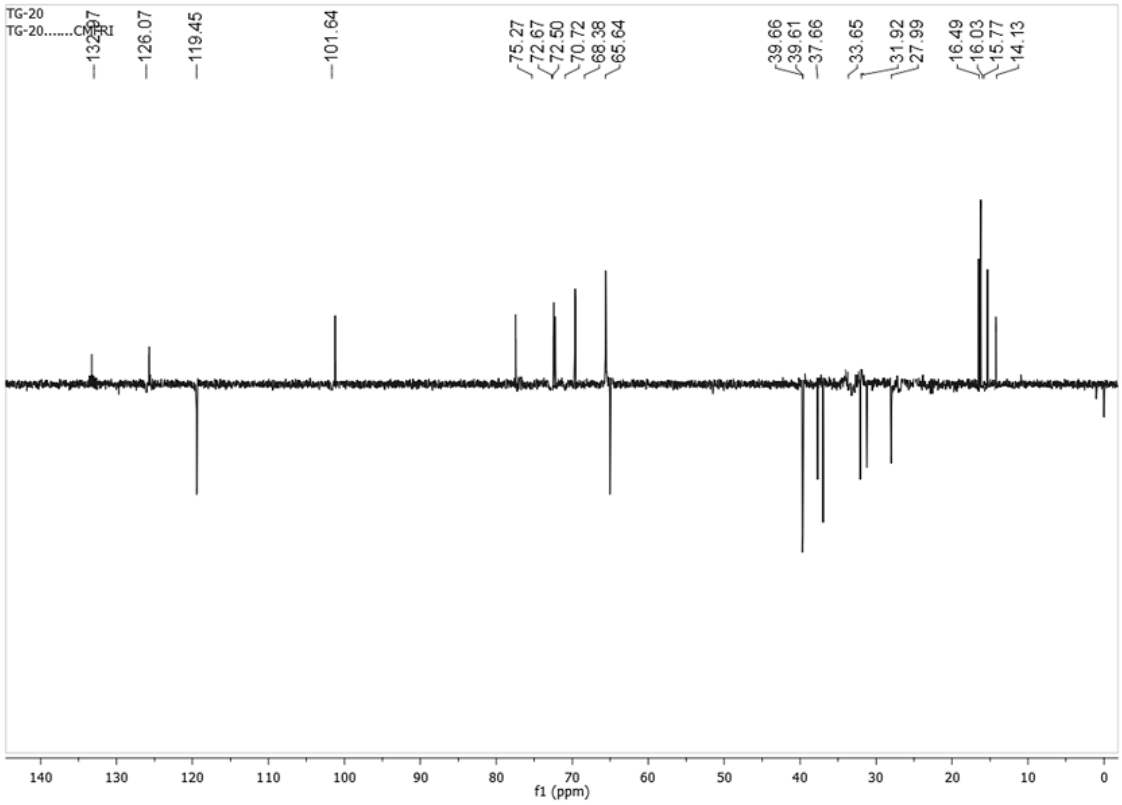

Figure 4.149.: ^{135}DEPT spectrum of 4-ethoxy-11,11-dimethyl-7-methylene-8-(propionyloxy)spiro[5.5]undec-2-en-10^{3},10^{5}-dihydroxytetrahydro-*2H*-pyran-10-carboxylate (**10**)

The ^{1}H-NMR spectrum of **10** displayed signals at δ 5.36 and 5.13 due to olefinic protons. Triplets at δ 4.00, 4.15, 4.18, 5.23 and multiplets at δ 3.30, 3.98 were assigned to protons geminal to the oxygen atom, whereas seven well-resolved signals, each attributed to one of the remaining aliphatic protons, appeared at δ 1.62-2.30. The chemical shift values at δ 0.87, 0.88, 0.89 and 0.99 were assigned to methyls in **10**. The ^{13}C-NMR of **10** displayed highly deshielded resonances for four protonated carbons at δ 75.27, 65.64, 72.50 and 101.64, which were directly attached to oxygen (Figure 4.147-4.149). The sp^{2} protons with highly deshielded resonance at δ 5.36 and 5.13 with triplets were bonded to the carbons at δ 126.07 and 132.97, respectively as inferred from the HSQC spectrum (Figure 4.150). Besides these, COSY correlations from H-1 to H-2; H-2 to H-3; H-3 to H-4 and H-4 to H-5 attributed to the presence of olefinic carbons (C-2 and C-3), and therefore, ascertained the partial portion of cyclohexene ring in **10** {δ 1.79 (assigned at H-1)/5.36 (H-2)/5.13 (H-3)/3.98 (H-4)/1.62 (H-5); -CH_2-CH=CH-CH-CH_2} (Figure 4.151 & 4.152). These attributions were further supported by the HMBC correlations between the H-1 and C-2 {δ 1.79 (H-1)/126.07 (C-2); CH_2-CH=}, H-3 and

C-2/C-4 {δ 5.13 (H-3)/126.07 (C-2)/75.27 (C-4); >CH=CH-CH<} and H-5 to C-4 {δ 1.62 (H-5)/75.27 (C-4); CH_2-CH<}.

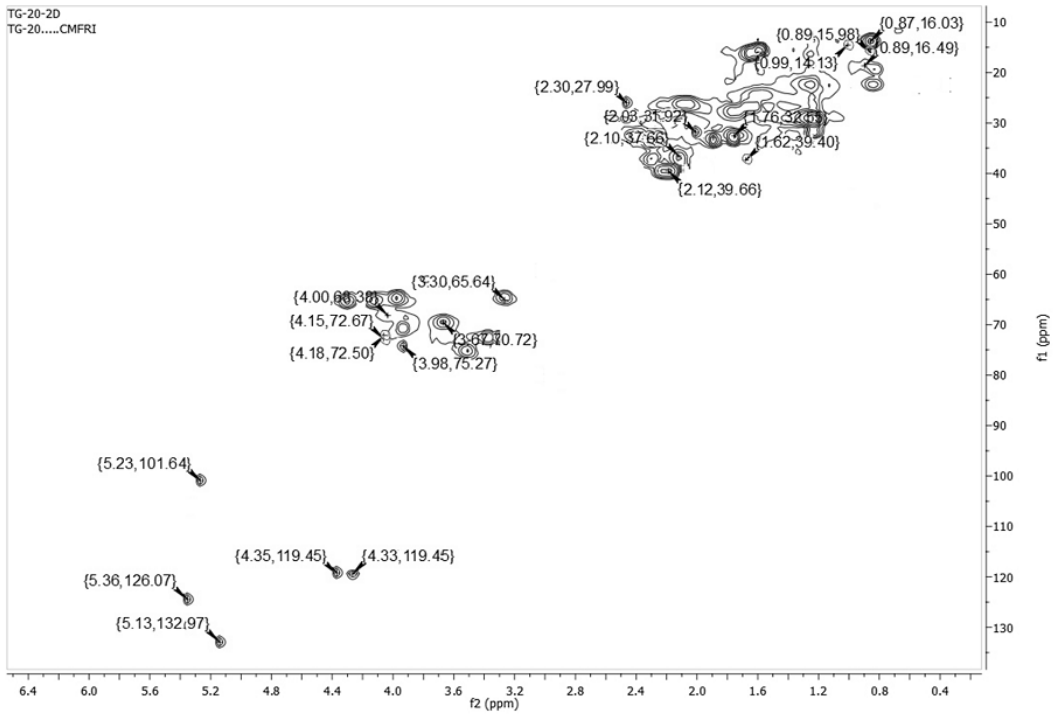

Figure 4.150.: HSQC spectrum of 4-ethoxy-11,11-dimethyl-7-methylene-8-(propionyloxy)spiro[5.5]undec-2-en-10^3,10^5-dihydroxytetrahydro-*2H*-pyran-10-carboxylate (**10**)

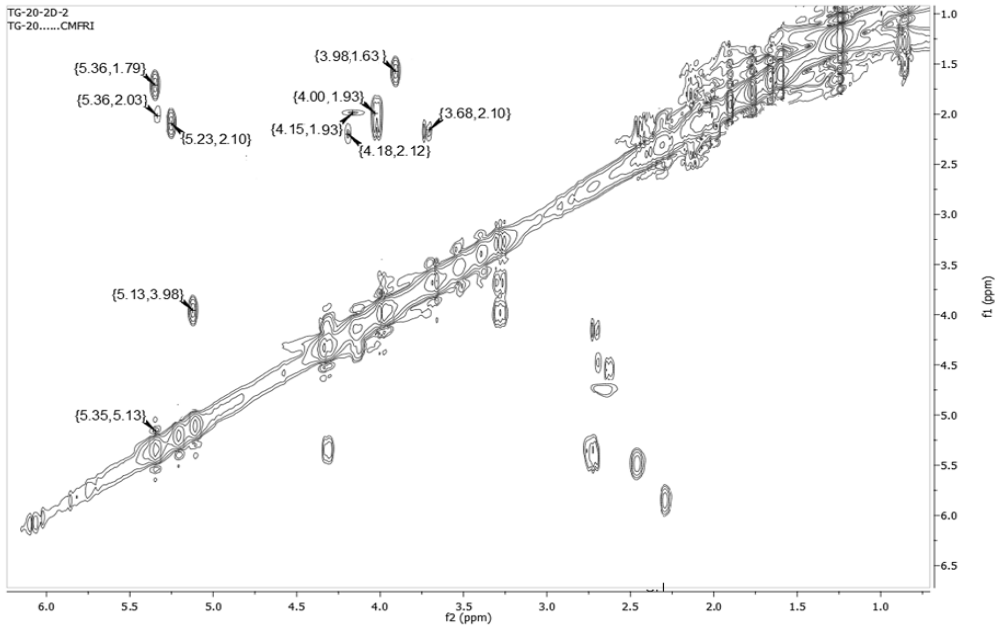

Figure 4.151.: ^{1}H-^{1}H COSY spectrum of 4-ethoxy-11,11-dimethyl-7-methylene-8-(propionyloxy)spiro[5.5]undec-2-en-10^3,10^5-dihydroxytetrahydro-*2H*-pyran-10-carboxylate (**10**)

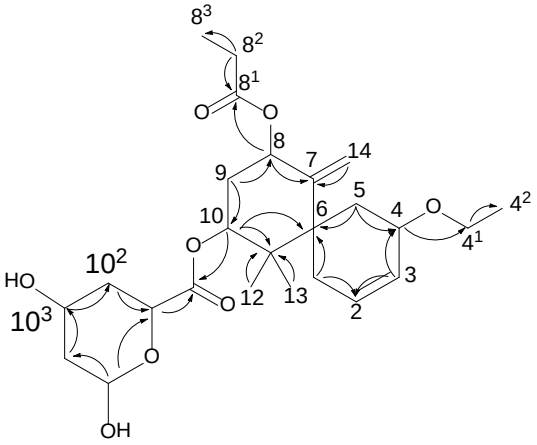

Figure 4.152.: ^{1}H-^{1}H COSY (bold face bonds), and selected HMBCs (double-barbed arrows), correlations of 4-ethoxy-11,11-dimethyl-7-methylene-8-(propionyloxy)spiro[5.5]undec-2-en-10^{3},10^{5}-dihydroxytetrahydro-*2H*-pyran-10-carboxylate (**10**)

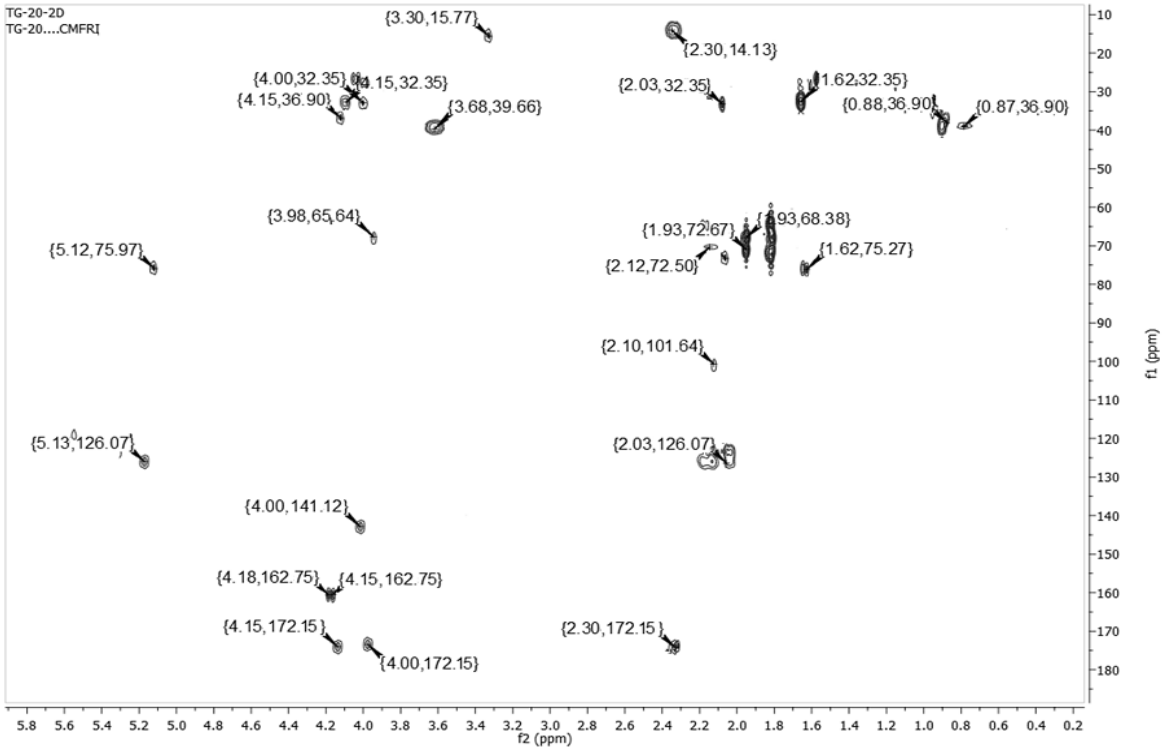

Figure 4.153.: HMBC spectrum of 4-ethoxy-11,11-dimethyl-7-methylene-8-(propionyloxy)spiro[5.5]undec-2-en-10^{3},10^{5}-dihydroxytetrahydro-*2H*-pyran-10-carboxylate (**10**)

The signals at δ 3.98 (H-4) and 3.30 (H-4^{1}) displaying HSQC correlation with δ 75.27 and 65.64, respectively were geminal to oxygen atom in the ether linkage {-CH(O)CH_2}. The proton signal at δ 4.18 (H-10^{2}) and 5.23 (H-10^{6}) displayed HSQC correlation with the

carbon traces at δ 72.50 and 101.64, respectively that were geminal to oxygen atom in pyran ring {-CH(O)CH-}. The previously reported spiro-compound, 1,4,9-trimethyl-5-methylidenespiro[5.5]undec-1,7-diene-4,9-diol bearing the exocyclic double bond between C-7 and C-14 with a chemical shift of δ 154.6 (C-7) and δ 110.2 (C-14) along with hydroxylated non-protonated carbon at δ 72.5 were comparable with the chemical shifts of **10** {δ 141.81 (C-7); δ 119.45 (C-14); δ 68.38 (C-8)} (Davyt et al. 2001). The lower chemical shift of δ 68.38 at C-8 in the titled compound might be due to the presence of protonated carbon and the derivatisation of hydroxyl group at C-8, whereas in the reported 1,4,9-trimethyl-5-methylidenespiro[5.5]undec-1,7-diene-4,9-diol (**10**), the C-8 position was found as non-protonated carbon with a hydroxyl group (Davyt et al. 2001). COSY spin systems between H-10^2/H-10^3/H-10^4/H-10^5/H-10^6 {δ 4.18 (H-10^2)/2.12 (H-10^3)/3.68 (H-10^4)/2.10 (H-10^5)/5.23 (H-10^6); -CH-CH_2-CH-CH_2-CH-} along with HMBCs from H-10^2 to C-10^1 {δ 4.18 (H-10^2)/162.75 (C-10^1)}, H-10^3 to C-10^2 {δ 2.12 (H-10^3)/72.50 (C-10^2)}, H-10^4 to C-10^3 {δ 3.68 (H-10^4)/39.66 (C-10^3)}, H-10^5 to C-10^4 {δ 2.10 (H-10^5)/70.72 (C-10^4)}, H-10^6 to C-10^5/C-10^1 {δ 5.23 (H-10^6)/37.66 (C-10^5)/162.75 (C-10^1)} attributed to the ester-linked side chain of 10^4,10^6-dihydroxytetrahydro-2H-pyran-10^2-carboxylate.

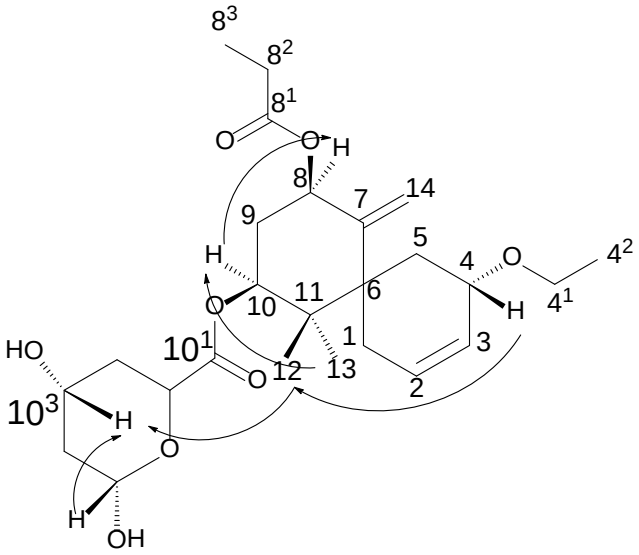

Figure 4.154.: NOESY correlations (double barbed arrows) of 4-ethoxy-11,11-dimethyl-7-methylene-8-(propionyloxy)spiro[5.5]undec-2-en-10^3,10^5-dihydroxytetrahydro-*2H*-pyran-10-carboxylate (**10**)

The attachment of 10^4,10^6-dihydroxytetrahydro-2H-pyran-10^2-carboxylate side chain at C-10 of cyclohexane ring was confirmed by the strong HMBCs from H-10 to C-10^1 {δ 4.15

(H-10)/162.75 (C-10^1); -CH-O-(C=O)}. The partial structure of 4-ethoxy cyclohexene and 10^3,10^5-dihydroxytetrahydro-*2H*-pyran-10-carboxylate attached 11,11-dimethyl-7-methylene-8-(propionyloxy) cyclohexane were spiro-fused at C-6, which confirmed through the HMBCs from H-1 to C-6 {δ 1.79 (H-1)/32.35 (C-6)}, H-5 to C-6 {δ 1.62 (H-5)/32.35 (C-6)}, H-8 to C-6 {δ 4.00 (H-8)/32.35 (C-6)} and H-10 to C-6 {4.15 (H-10)/32.35 (C-6)} (Figure 4.153). The assignment of spiro moiety in **10** was explained on the basis of previous literatures of spiro[5.5]undecane derivatives (Davyt et al. 2001; Ji et al. 2007; Yu et al. 2017). Notably, the olefinic group at δ 5.36 (H-2) and 5.13 (H-3) recorded higher coupling constants (J) of 7.1 and 8.3 Hz, respectively, and therefore, the configuration of these olefinic group in oxospiro[5.5]undecen-2-ene was ascertained as cis oriented. The relative stereochemistries of the chiral centers, mainly at C-4, C-8, C-10, C-11, C-10^4 and C-10^6 were deduced by extensive NOESY experiments. NOE correlations between δ 0.87 (H-13) (methyl proton)/4.15 (H-10)/4.00 (H-8) appropriately confirmed the equiplaner alignment of these protons in their close proximity and these were arbitrarily allocated in α-direction with reference to its molecular plane of symmetry. The NOE correlation between δ 3.98 (H-4)/0.88 (H-12)/3.68 (H-10^4)/5.23 (H-10^6) attributed that these protons were aligned opposite to α-protons, and therefore, assigned as β-oriented.

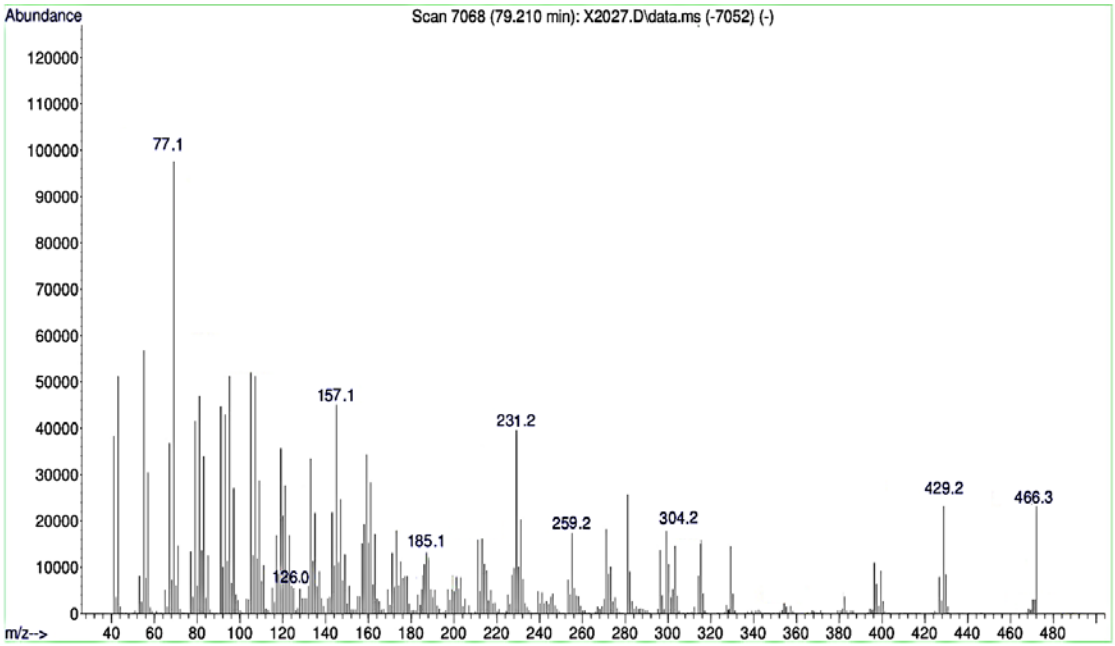

Figure 4.155.: EI-MS spectrum of 4-ethoxy-11,11-dimethyl-7-methylene-8-(propionyloxy)spiro[5.5]undec-2-en-10^3,10^5-dihydroxytetrahydro-*2H*-pyran-10-carboxylate (**10**)

Table 4.17: NMR spectroscopic data of compound (**10),** 4-ethoxy-11,11-dimethyl-7-methylene-8-(propionyloxy)spiro[5.5]undec-2-en-10^3,10^5-dihydroxytetrahydro-*2H*-pyran-10-carboxylate (**10**) isolated from red seaweed *G. salicornia*

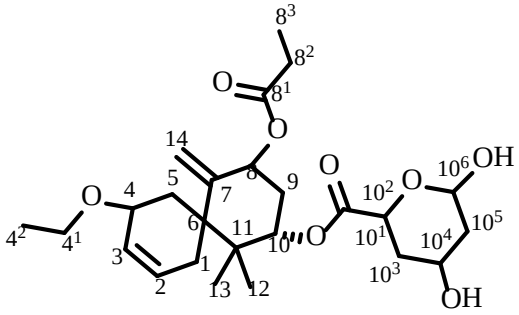

Compound **10**……4-Ethoxy-11,11-dimethyl-7-methylene-8-(propionyloxy)spiro[5.5]undec-2-en-10^3,10^5-dihydroxytetrahydro-*2H*-pyran-10-carboxylate (**10**)

C. No.	**^{13}C**	**^{1}H(int.,mult.,*J* in Hz)[b]**	**^{1}H-^{1}H COSY**	**HMBC**
		2.03(1H,*d*,4.8 Hz)		
1	31.92	1.79(1H,*d*,4.8 Hz)	H-2	C-2,6
2	126.07	5.36(1H,*t*,7.1 Hz)	H-3	-
3	132.97	5.13(1H,*t*,8.3 Hz)	H-4	C-2,4
4	75.27	3.98(1H,*m*)	H-5	C-4^1
5	39.61	1.62(2H,*d*,6.3 Hz)	-	C-4,6
6	32.35	-	-	-
7	141.81	-	-	-
8	68.38	4.00(1H,*t*,8.3 Hz)	H-9	C-7, 6,8^1
9	33.65	1.93(2H,*m*)	H-10	C-8,10
10	72.67	4.15(1H,*t*,5.3 Hz)	-	C-11,6,10^1,8^1
11	36.90	-	-	-
12	16.49	0.88(3H,*s*)	-	C-11
13	16.03	0.87(3H,*s*)	-	C-11
14	119.45	4.35(1H,*t*,12.6 Hz)	-	-
		4.33(1H,*t*,12.5 Hz)	-	-
10^1	162.75	-	-	-
10^2	72.50	4.18(1H,*t*,5.8Hz)	H-10^3	C-10^1
10^3	39.66	2.12(2H,*t*,6.8 Hz)	H-10^4	C-10^2
10^4	70.72	3.68(1H,*m*)	H-10^5	C-10^3
10^5	37.66	2.10(2H,*t*)	H-10^6	C-10^6, 10^2
10^6	101.64	5.23(1H,*t*,5.5 Hz)	-	-
8^1	172.15	-	-	-
8^2	27.99	2.30(2H,*m*)	-	C-8^3, 8^1
8^3	14.13	0.99(3H,*t*,4.1 Hz)	-	-
4^1	65.64	3.30(2H,*m*)	-	-
4^2	15.77	0.89(3H,*t*,4.3 Hz)	-	-

[a] NMR spectra recorded using Bruker AVANCE III 500 MHz (AV 500) spectrometers.

[b] Values in ppm, multiplicity and coupling constants (J = Hz) are indicated in parentheses. Assignments were made with the aid of the ^{1}H-^{1}H COSY, HSQC, HMBC and NOESY experiments.

The molecular ion peak at *m/z* 466 (**a**) $[M]^{+}$ underwent elimination of water molecule and reorganization of bonds leading to a fragment at *m/z* 429 (**b**). Further elimination radical cation at *m/z* 126 led to the formation of fragment, **c** (*m/z* 304). The radical cation, **c** also performed an elimination of neutral molecule $C_3H_6O_2$ and led to the formation of **d** at *m/z* 231. The further fragmentation of **d**, and fragment **f** at *m/z* 259 was formed from (**a**) leading to the formation of **e** at *m/z* 185. The latter on further mass fragmentation led to the formation of **g** at *m/z* 157 and then to **h** at *m/z* 77, which was deduced to be the base peak (Figure 4.156).

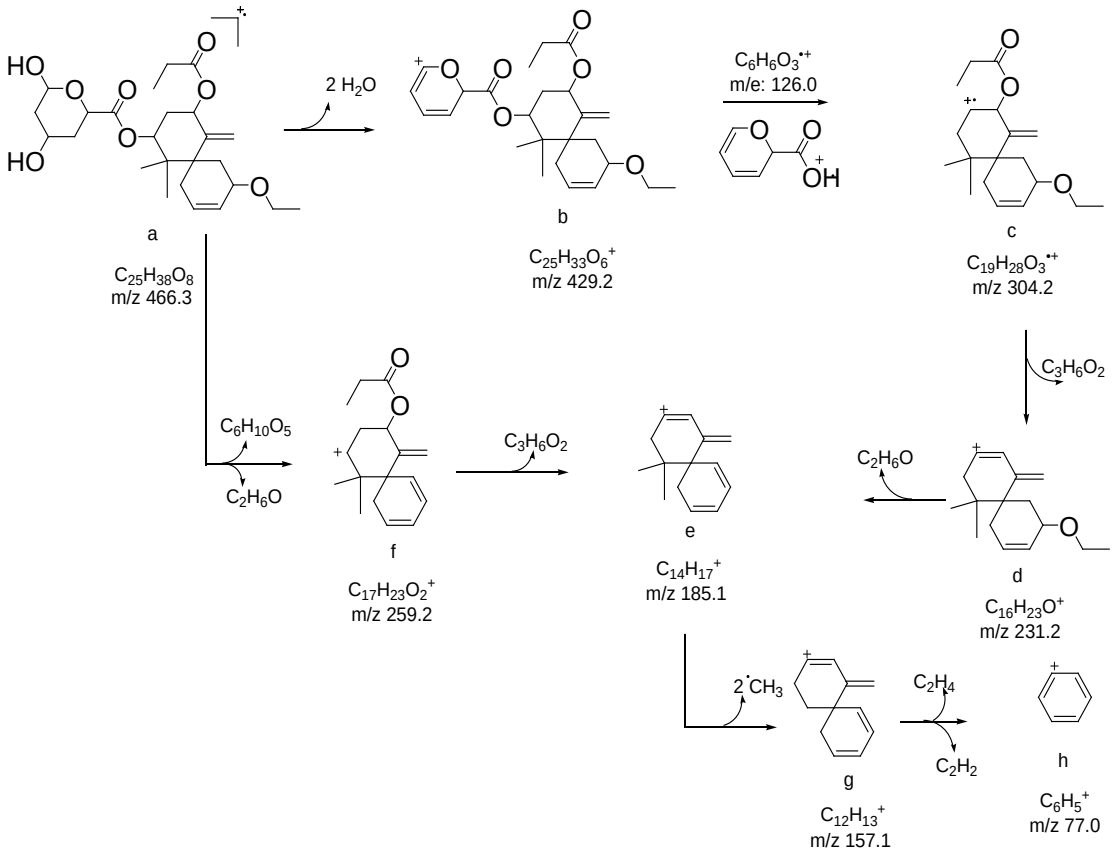

Figure 4.156.: Tentative mass fragmentation pattern of 4-ethoxy-11,11-dimethyl-7-methylene-8-(propionyloxy)spiro[5.5]undec-2-en-10^{3},10^{5}-dihydroxytetrahydro-*2H*-pyran-10-carboxylate (**10**)

4.3.2.6 Structural characterization of polyether derivatives (Compounds 11-12)

Seaweeds comprise an abundant and heterogeneous group of marine organisms, and obtained greater attention in the exploration of bioactive components to formulate newer pharmacophores as well as healthy diets (Qi et al., 2005; Ibanez et al., 2012). They were found to produce specialised secondary metabolites characterised by broad spectra of biological activities (Yuan et al., 2005). In particular, the seaweeds belonging to the *Gracilaria* genus, which has been ubiquitous on the coast of peninsular India, was considered to be one of the extensively studied for various pharmacological properties among those belonging to the family of Rhodophyceae (Cragg et al., 2009; Faulkner, 2002). Among the bioactive metabolites derived from the seaweed, the polyether components comprehended the distinctive group disclosing wide-diversity of chemistries and pharmacological properties, like ion-channel stoppers, stimulating neurotransmitter release, enzyme quenchers, and effective cytotoxicities (Faulkner, 2002; Blunt et al., 2011). The most valuable class of marine natural products (MNPs) includes polyether components that are structurally spiro or *trans*-fused systems of rings of diverse frameworks with potential bioactivities against various pharmaceutical targets. Their bio-genetic formations were found to be originated in the fatty acids or terpenoid derivatives (Fernandez et al., 2000). Polyether group of macrolides were ubiquitous in the marine organisms, for example, Halichondrin-B, isolated from the sponge *Halichondria okadai* and another polyether macrolide, theopederins isolated from the marine sponge *Theonella spp*., were found to possess anti-carcinogenic properties (Carte, 1996; Fuestani et al., 1992). The cytotoxic squalene-derived polyethers were identified from the red seaweeds belonging to the genera of *Chondria* and *Laurencia* (family Rhodomelaceae) (Pacheco, 2011; Pacheco et al., 2010). Historically, the explorations of these components have been initiated with the identification of thyrsiferol isolated from *Laurencia thyrsifera*, and further examples of polyether metabolites were reported from various marine organisms including green alga *Botryococcus brauniis*, sponges belonging to the family *Axinellidae* and mollusk *Dolabella auricularia* (Faulkner, 2002; Blunt et al., 2011; Pacheco et al., 2010). Thyrsiferol consisted of a middle *trans* fused pyrano-pyran fragment, attached bromo-ether ring and aliphatic side-chain bonding the middle part to the *trans* tetrahydrofuran unit (Fernandez et al., 2000). Dehydrothyrsiferol was found to be another example of this polyether series, identified from *Laurencia pinnatifida* in the Canary Islands of Spain. Its skeleton was formed by the chemical modification of thyrsiferolm and that differed by a double bond between C15-C28 position (end vinylic) in dehydrothyrsiferol, whereas thyrsiferol enclosed methyl and hydroxyl in the similar position (C15) (Gonzalez et al., 1984). Fatty acyl polyether Okadaic acid with protein phosphatase inhibitory property was characterised

from *Prorocentrum spp*. (Cohen et al., 1990). An anti-microbial polyether macrolide, Goniodomin-A, which was identified and characterised from the dinoflagellate *Goniodoma pseudogoniaulax* (Murakami et al., 1988), was found to exhibit anti-angiogenic activities via inhibition of actin reorganization in endothelial cells (Abe et al., 2002).

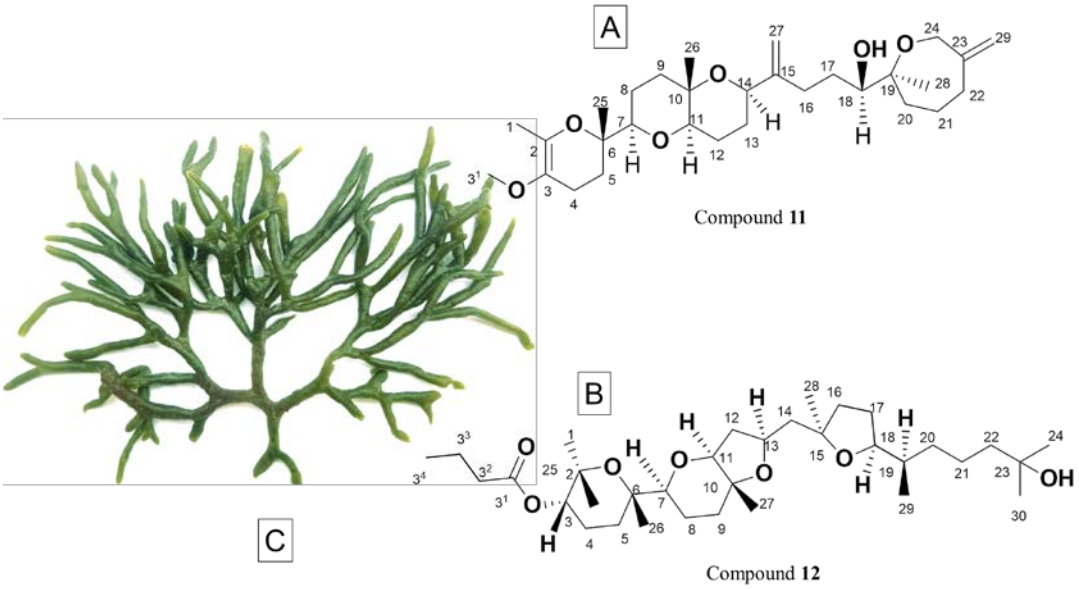

Figure 4.157.: Structural representations of (**A**) 3-methoxy-2,6-dimethyl-3,4-dihydro-2*H*-pyranyl-(6-(7-(10-methyl-octahydropyrano[3,2-*b*]pyranyl)-14-((19-methyl-23-methyleneoxepan)-(15-pentene-18-ol)) (**11**) and (**B**) 14-(15-methyltetrahydrofuranyl)-(18-(23-(hydroxy-23-methylheptanyl)-10-methylhexahydro-2*H*-furo-[3,2-*b*]pyranyl))-2,2,6-trimethyltetrahydro-2*H*-pyran-3- butyrate (**12**) purified from *G. salicornia*. (**D**) The characteristic of thalli (leaf-like structures) of *G. salicornia* was presented.

The significant and attractive phyla in terms of their pharmacologically active MNPs comprise the abundantly available seaweed species, among which the red seaweed are potential sources of bioactive substances (Makkar and Chakraborty, 2019; Makkar and Chakraborty, 2018) Pluralities of investigations on bio-active components from these seaweed demonstrating antiviral, antibacterial, antitumor, and antileukaemic properties were reported world-wide. Traditionally, natives of Japan and South-Pacific utilise seaweed supplements as arthritic remedies. The rich diversity of red seaweeds particularly belonging to *G. salicornia* along the coastline of South Indian subcontinent represents an unexploited source of bio-compounds with valuable biomedical as well as pharmaceutical use, although this species was not comprehensively studied to identify/characterise the bio-active leads (Makkar and Chakraborty,

2018; Since the initial studies carried out in our laboratory provided us with promising ideas; the current study has envisaged the isolation followed by characterisation of two formerly unreported squalene polyether metabolites from the ethyl acetate-methanol (EtOAc-MeOH) extract of *G. salicornia*. The studied compounds were designated as 15-(octahydro-7-(4,5-dihydro-3-methoxy-2,6-dimethyl-2*H*-pyran-6-yl)-10-methylpyrano[3,2-b]pyran-14-yl)-18-(19-methyl-23-methyleneoxepan-19-yl)pent-15-en-18-ol (**11**) and tetrahydro-6-(hexahydro-13-((tetrahydro-18-(23-hydroxy-23-methylheptan-19-yl)-15-methylfuran-15-yl)methyl)-10-methyl-2*H*-furo[3,2-b]pyran-7-yl)-2,2,6-trimethyl-2*H*-pyran-3-yl butyrate (**12**) (Figure 4.157) by comprehensive spectroscopic experiments.

4.3.2.6a Structural characterization of Compound 11

15-(Octahydro-7-(4,5-dihydro-3-methoxy-2,6-dimethyl-*2H*-pyran-6-yl)-10-methylpyrano[3,2-b]pyran-14-yl)-18-(19-methyl-23-methyleneoxepan-19-yl)pent-15-en-18-ol

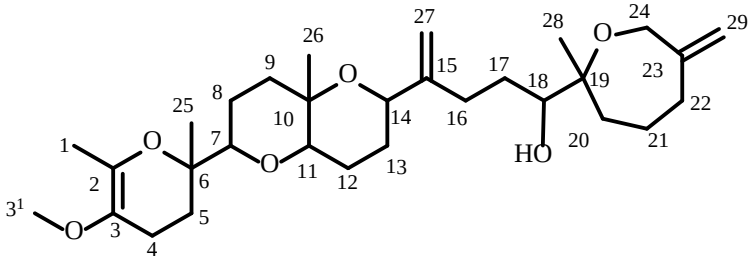

Sample yield	0.35% (> 99% purity, RP-C18 HPLC)
Physical description	Colourless oil
Molecular formula	$C_{30}H_{48}O_6$
Molecular mass	504.3451

The polyether derivative, 15-(octahydro-7-(4,5-dihydro-3-methoxy-2,6-dimethyl-*2H*-pyran-6-yl)-10-methylpyrano[3,2-b]pyran-14-yl)-18-(19-methyl-23-methyleneoxepan-19-yl)pent-15-en-18-ol was isolated as Colourless oil. The compound (**11**) has exhibited UV absorbance (UV (MeOH) λ_{max}) at 240 nm (Figure 4.158). The homogeneity of the compound was ascertained by HPLC data on a bonded phase octadecylsilane (C_{18}) stationary phase (HPLC, MeOH/MeCN, 1:2 v/v) with R_t: 3.28 min (Figure 4.159).

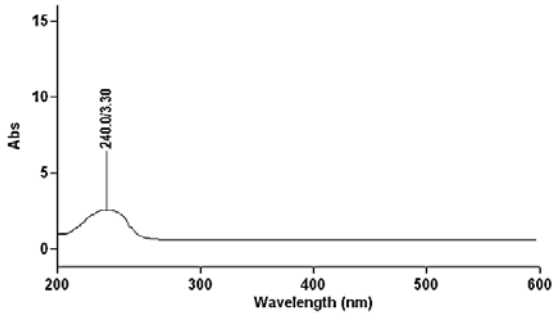

Figure 4.158.: UV spectrum of 15-(octahydro-7-(4,5-dihydro-3-methoxy-2,6-dimethyl-*2H*-pyran-6-yl)-10-methylpyrano[3,2-b]pyran-14-yl)-18-(19-methyl-23-methyleneoxepan-19-yl)pent-15-en-18-ol (**11**)

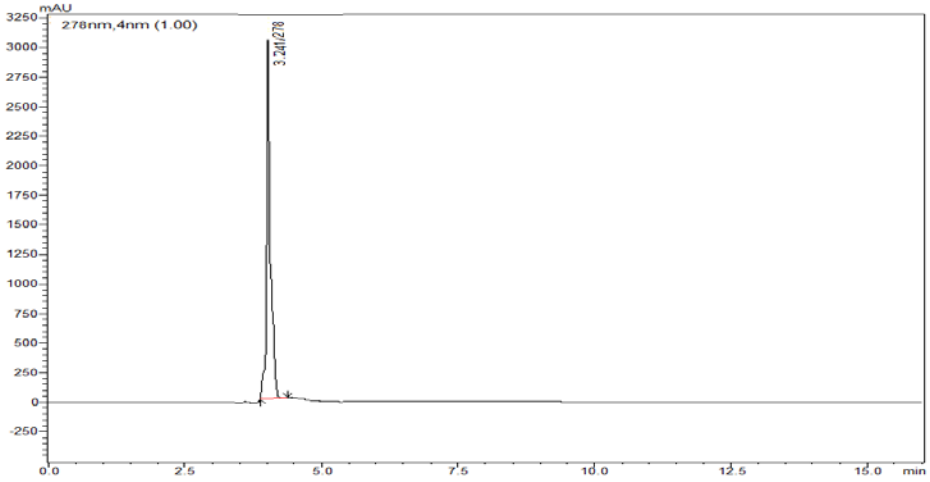

Figure 4.159.: HPLC chromatogram of 15-(octahydro-7-(4,5-dihydro-3-methoxy-2,6-dimethyl-*2H*-pyran-6-yl)-10-methylpyrano[3,2-b]pyran-14-yl)-18-(19-methyl-23-methyleneoxepan-19-yl)pent-15-en-18-ol (**11**)

Bioactive potential-assisted chromatographic purification of the organic extract of *G. salicornia* afforded a previously undisclosed polyether derivative, **11**, which was identified as 15-(octahydro-7-(4,5-dihydro-3-methoxy-2,6-dimethyl-2*H*-pyran-6-yl)-10-methylpyrano[3,2-b]pyran-14-yl)-18-(19-methyl-23-methyleneoxepan-19-yl)pent-15-en-18-ol. The molecular ion peak was analysed by HRESIMS (positive mode) registered $[M+H]^+$ at *m/z*: found 505.3533 (Figure 4.160).

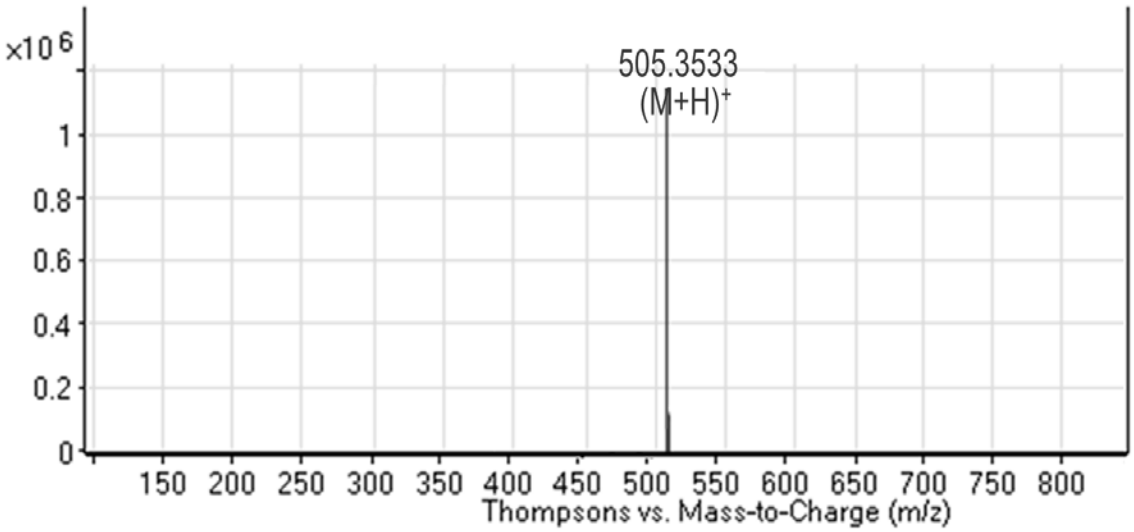

Figure 4.160.: HRESIMS spectrum of 15-(octahydro-7-(4,5-dihydro-3-methoxy-2,6-dimethyl-*2H*-pyran-6-yl)-10-methylpyrano[3,2-b]pyran-14-yl)-18-(19-methyl-23-methyleneoxepan-19-yl)pent-15-en-18-ol (**11**)

The FTIR of **11** reported the occurrence of absorption peaks at 3390 cm^{-1} and 1044 cm^{-1}, which specified the possibilities of hydroxyl (-OH) and ether (-C-O-C) groups, respectively (Figure 4.161). The combined mass-NMR-IR techniques deduced the molecular formula of **11** as $C_{30}H_{48}O_6$, which indicated its seven sites of unsaturations (Table 4.18). The ^{13}C NMR spectrum of **11** showed signal for 30 carbon atoms and the types of the carbon signals were determined from its ^{135}DEPT spectrum, which were found to be five methyls (δ 20.33, 24.37, 19.38, 18.82, 60.01), twelve sp^3 methylenes (δ 21.57, 24.63, 22.33, 39.13, 24.48, 25.74, 29.35, 31.66, 35.08, 21.82, 37.08, 72.42), two sp^2 methylenes (δ 114.50, 114.01), four sp^3 methines (δ 80.93, 78.80, 75.32, 74.15) and seven non-protonated carbons (δ 129.48, 137.14, 81.49, 77.13, 147.00, 81.44, 143.29). The highly deshielded ^{13}C NMR resonances observed at δ 81.49 (assigned at C-6), 80.93 (C-7), 77.13 (C-10), 78.80 (C-11), 75.32 (C-14), 74.15 (C-18), 81.44 (C-19), 72.42 (C-24) and 60.01 (C-3^1) were found to be related to the oxygen attached protonated carbons. ^1H NMR of **11** revealed the proton chemical shifts at δ 5.33/5.18 and δ 5.36/5.17 due to the olefinic protons; triplet signals at δ 3.61, 3.05, 4.14, 3.78; doublets at δ 4.01/3.93 and singlets at δ 3.68 (which might be adjacent to the oxygen atom), 1.41, 1.33, 1.28, and 2.28. The three shielded singlet protons at δ 1.41, 1.33 and 1.28 were accounted for the methyl protons directly attached to quaternary carbons in compound **11** and the slightly deshielded singlet proton at δ 2.28 was accounted for the methyl attached to non-protonated deshielded carbon atom (Figure 4.162-4.164).

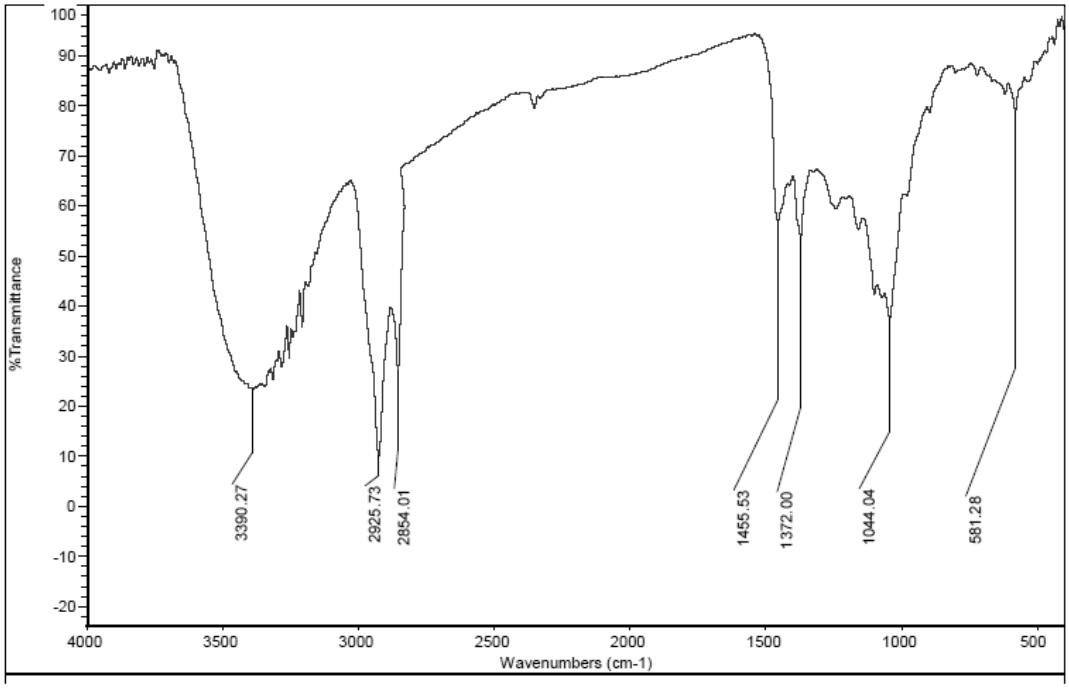

Figure 4.161.: FTIR spectrum of 15-(octahydro-7-(4,5-dihydro-3-methoxy-2,6-dimethyl-*2H*-pyran-6-yl)-10-methylpyrano[3,2-b]pyran-14-yl)-18-(19-methyl-23-methyleneoxepan-19-yl)pent-15-en-18-ol (**11**)

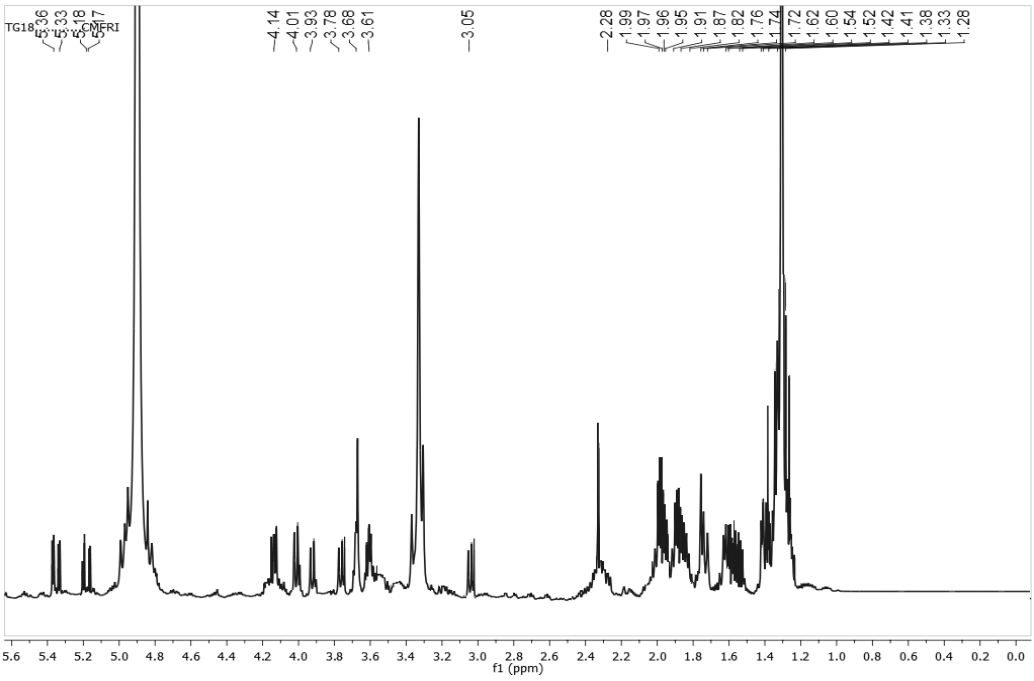

Figure 4.162.: ^{1}H NMR spectrum of 15-(octahydro-7-(4,5-dihydro-3-methoxy-2,6-dimethyl-*2H*-pyran-6-yl)-10-methylpyrano[3,2-b]pyran-14-yl)-18-(19-methyl-23-methyleneoxepan-19-yl)pent-15-en-18-ol (**11**)

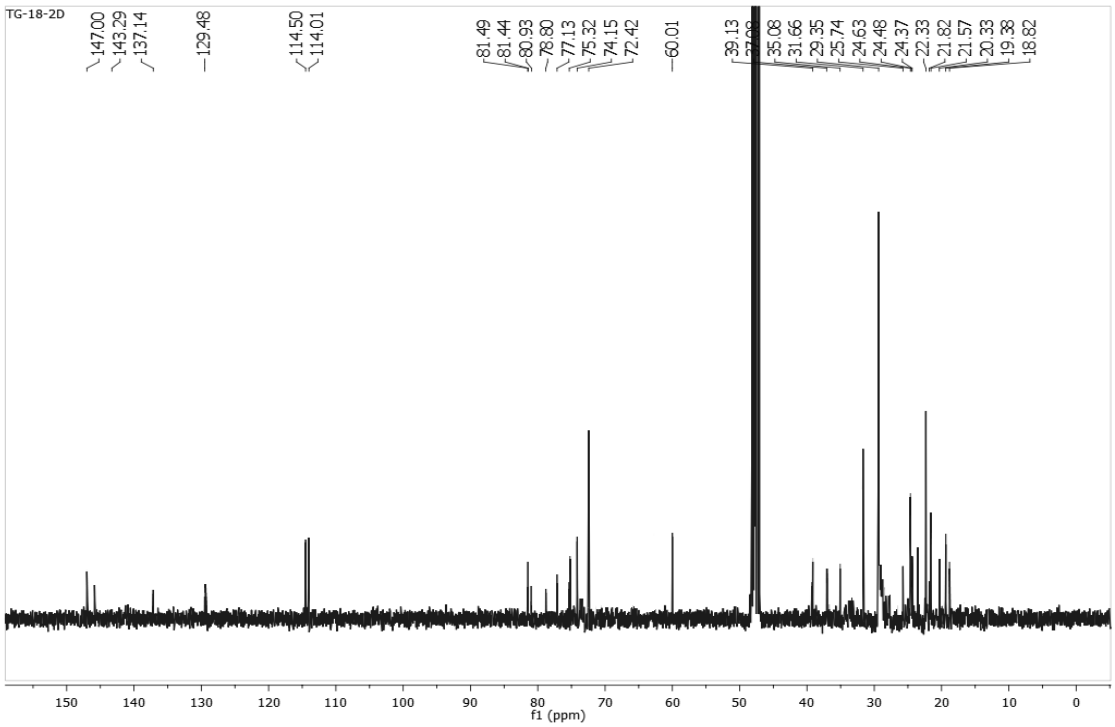

Figure 4.163.: ^{13}C NMR spectrum of 15-(octahydro-7-(4,5-dihydro-3-methoxy-2,6-dimethyl-*2H*-pyran-6-yl)-10-methylpyrano[3,2-b]pyran-14-yl)-18-(19-methyl-23-methyleneoxepan-19-yl)pent-15-en-18-ol (**11**)

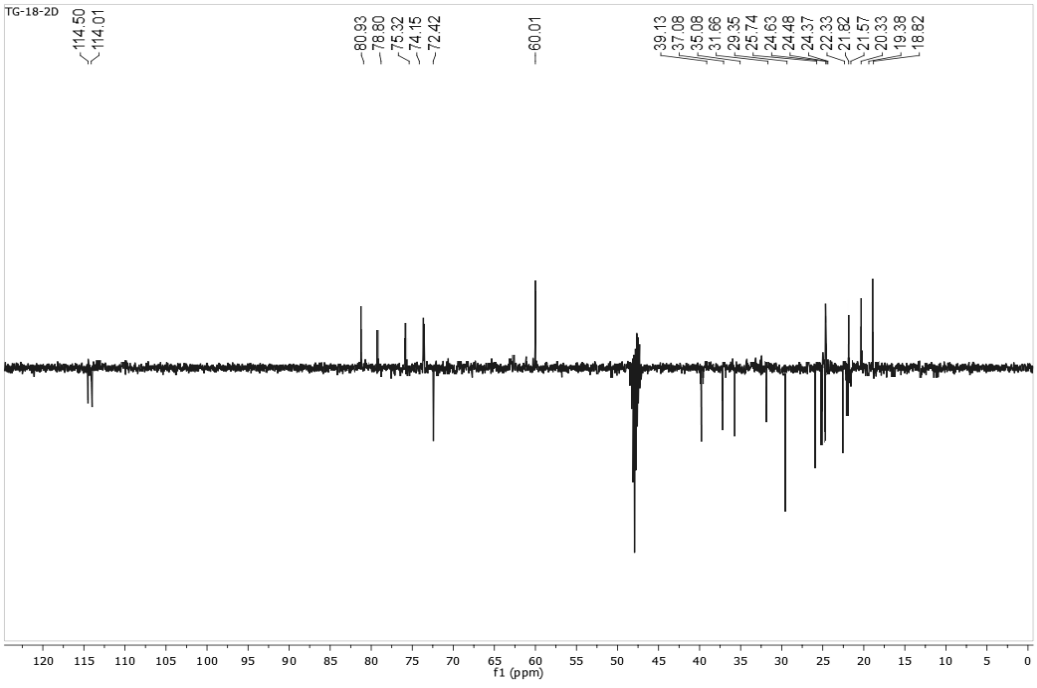

Figure 4.164.: ^{135}DEPT spectrum of 15-(octahydro-7-(4,5-dihydro-3-methoxy-2,6-dimethyl-*2H*-pyran-6-yl)-10-methylpyrano[3,2-b]pyran-14-yl)-18-(19-methyl-23-methyleneoxepan-19-yl)pent-15-en-18-ol (**11**)

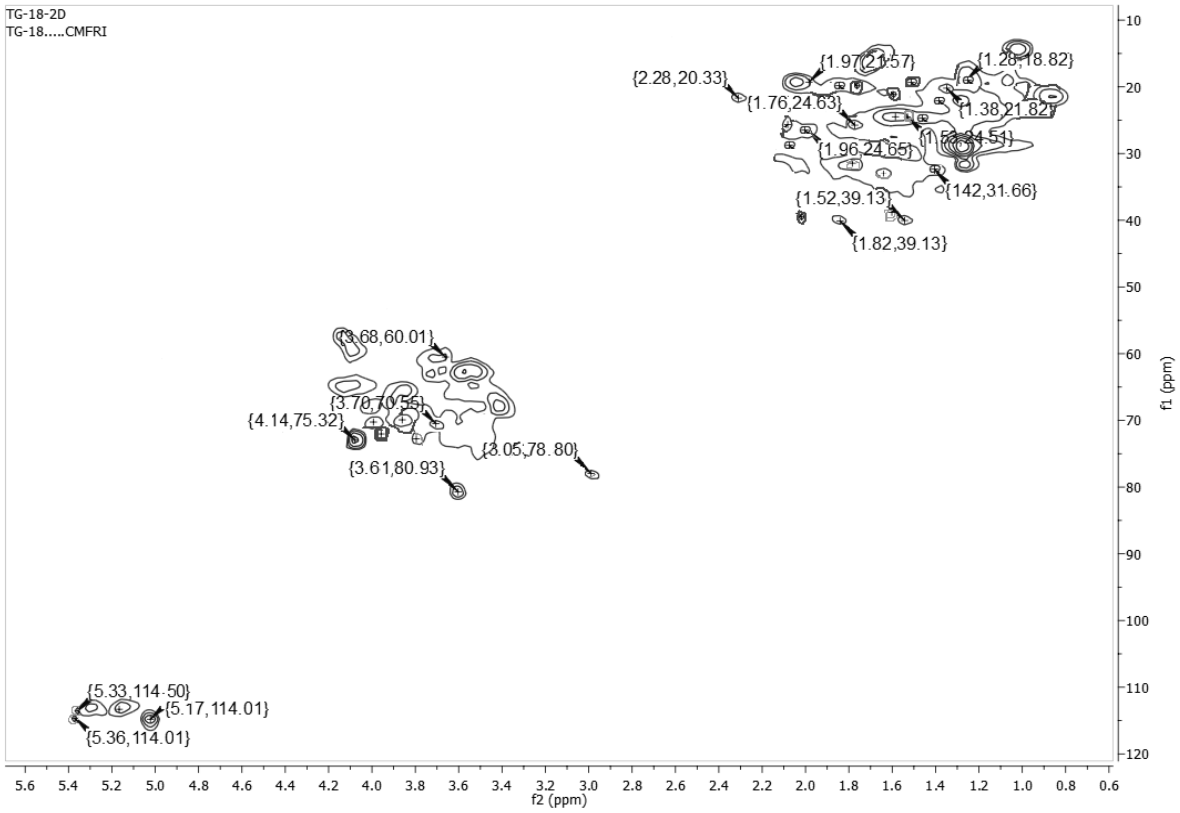

Figure 4.165.: HSQC spectrum of 15-(octahydro-7-(4,5-dihydro-3-methoxy-2,6-dimethyl-*2H*-pyran-6-yl)-10-methylpyrano[3,2-b]pyran-14-yl)-18-(19-methyl-23-methyleneoxepan-19-yl)pent-15-en-18-ol (**11**)

All these attributions established the ether substitutions in the titled compound and the chemical shift values were comparable with squalene-derived halogenated polyethers, such as dehydrothyrsiferol, 22-hydroxy-15(28)-dehydrovenustatriol and iuboli isolated from red seaweed, *Laurencia viridis*. The sp^2 protons with greatly deshielded resonance at δ 5.33/5.18 and δ 5.36/5.17 having doublet splitting were bonded to the carbons at δ 114.50 (H-27) and δ 114.01 (H-29), respectively, as inferred from the HSQC spectrum (Figure 4.165). Highly deshielded non-protonated carbons at δ 129.48 and 81.49 attributed the presence of oxygen between C-2 and C-6 carbon atoms.

The COSY conjunctions between δ 1.97 (H-4)/1.76 (H-5) and HMBC correlations from δ 1.97 (H-4) to δ 24.36 (C-5), 137.14 (C-3); δ 1.76 (H-5) to δ 81.49 (C-6); δ 2.28 (H-1) to δ 129.48 (C-5), 137.14 (C-3); δ 1.41 (H-25) to δ 81.49 (C-6) and δ 3.68 (H-3^1) to δ 137.14 (C-3) appropriately assigned the partial structure of **11** as 4,5-dihydro-3-methoxy-2,6-dimethyl-2H-pyran. Similarly, compound **11** exhibited COSY correlations δ 3.61 (H-7)/1.72 (H-8)/1.82 (H-9) and from δ 3.05 (H-11)/1.91 (H-12)/1.74 (H-13)/4.14 (H-14) (Figure 4.166 & 4.167). These COSY fragments were further connected by the HMBC correlations from δ 1.72 (H-8) to δ 80.93

(C-7); δ 1.82 (H-9) to δ 22.33 (C-8), 77.13 (C-10); δ 3.05 (H-11) to δ 77.13 (C-10), 24.48 (C-12), 80.93 (C-7); δ 1.74 (H-13) to δ 75.32 (C-14).

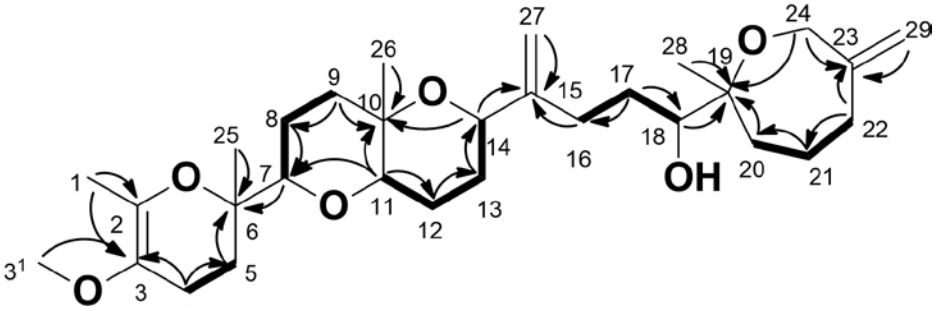

Figure 4.166.: ^{1}H-^{1}H COSY (bold face bonds) and selected HMBCs (double-barbed arrows) correlations of 15-(Octahydro-7-(4,5-dihydro-3-methoxy-2,6-dimethyl-*2H*-pyran-6-yl)-10-methylpyrano[3,2-b]pyran-14-yl)-18-(19-methyl-23-methyleneoxepan-19-yl)pent-15-en-18-ol (**11**)

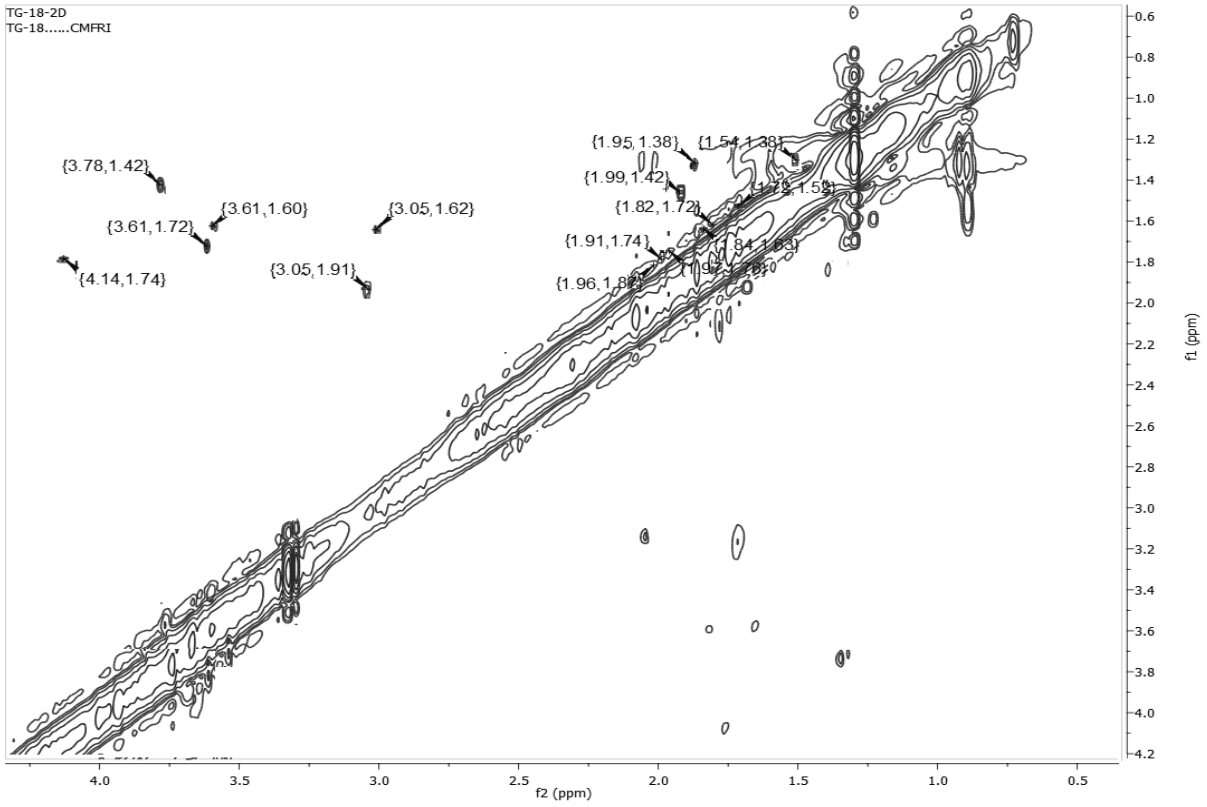

Figure 4.167.: ^{1}H-^{1}H COSY spectrum of 15-(octahydro-7-(4,5-dihydro-3-methoxy-2,6-dimethyl-*2H*-pyran-6-yl)-10-methylpyrano[3,2-b]pyran-14-yl)-18-(19-methyl-23-methyleneoxepan-19-yl)pent-15-en-18-ol (**11**)

These attributed the presence of octahydro-10-methylpyrano[3,2-b]pyran part in compound **11**. The attachment of octahydro-10-methylpyrano[3,2-b]pyran at C-6 of 4,5-dihydro-3-methoxy-2,6-dimethyl-2*H*-pyran was assigned through HMBC from δ 3.61 (H-7) to δ 81.49 (C-6) (Figure 4.168). Besides these, another COSY spin system from δ 1.54 (H-20)/1.38 (H-21)/1.95 (H-22) along with HMBC correlations from δ 1.54 (H-20) to δ 81.44 (C-19); δ 1.38 (H-21) to δ 35.08 (C-20); δ 1.95 (H-22) to δ 21.82 (C-21), 143.29 (C-23); δ 1.28 (H-28) to δ 81.44 (C-19); δ 4.01 (H-24) to δ 143.29 (C-23), 81.44 (C-19) and from exocyclic alkenic proton at δ 5.36 (H-29) to δ 143.29 (C-23) ascribed the seven-membered ring named as 19-methyl-23-methyleneoxepane. The characteristic signals at δ 74.9 (C-6) in the brominated pyran ring, δ 3.08 (H-7)/86.7 (C-7), 72.9 (C-10), 3.43 (H-11)/78.9 (C-11), 4.28 (H-14)/72.5 (C-14) in pyrano[3,2-b]pyran ring and δ 3.52 (H-18)/76.2 (C-18) for the hydroxylated methine of pentenol chain reported for dehydrothyrsiferol and iuboli (Pacheco, 2011) were comparable with the studied compound. The titled compound recorded characteristic signals at δ 81.49 (C-6) in the brominated pyran ring (unsaturated pyran), δ 3.61 (H-7)/80.93 (C-7), 77.13 (C-10), 3.05 (H-11)/78.80 (C-11), 4.14 (H-14)/75.32 (C-14) in pyrano[*3,2-b*]pyran ring and δ 3.78 (H-18)/74.15 (C-18) for the hydroxylated methine of pentenol chain. An exocyclic vinylic linkage at C-27 was directly bonded to non-protonated carbons at δ 147.00 (C-15) as obtained through HMBC correlations from δ 5.33 (H-27) to δ 147.00 (C-15), which was comparable with the exocyclic alkene assigned at >C(15)=CH_2(28) in a previously reported compound, dehydrothyrsiferol with chemical shifts of δ 151 (C-15) and δC 109/δ 4.88, 5.05 (C-28) (Pacheco, 2011). Also, other HMBCs from δ 1.42 (H-17) to δ 29.35 (C-16), δ 74.15 (C-18) and from δ 1.99 (H-16) to δ 147.00 (C-15) along with COSY spin system from H-16/H-17/H-18 {δ 1.99 (H-16)/1.42 (H-17)/3.78 (H-18)} ascribed the presence of a linear chain named as pent-15-en-18-ol. The octahydro-10-methylpyrano[*3,2-b*]pyran and 19-methyl-23-methyleneoxepane fragments were connected through the pent-15-en-18-ol chain, and the assignment was established through strong HMBCs from δ 4.41 (H-14 of pyrano[3,2-b]pyran) to δ 147.00 (C-15 of pentenol) and from δ 3.78 (H-18 of pentenol) to δ 81.44 (C-19 of methyleneoxepane). The compound dehydrothyrsiferol enclosed octahydro-methylpyrano[3,2-b]pyran, bromo-tetrahydro trimethyl-2*H*-pyran, connecting linkage pentenol and tetrahydro-hydroxypropanyl enclosed methylfuranyl at C-18 and the compound, iuboli was found to be similar to dehydrothyrsiferol except the presence of tetrahydro-trimethyl-2*H*-pyranol at C-18 (Pacheco et al., 2010). In short, these previously reported halogenated polyether derivatives enclosed seven-membered and five-membered rings at the C-18 position of the pent-15-en-18-ol chain (Pacheco, 2011; Pacheco et al., 2010), whereas the present compound enclosed a seven-membered ring. The titled compound was similar to the previously reported thyrsiferol except for the presence of methyl and hydroxyl

functionalities at C-15 and the tetrahydro-hydroxypropanyl methylfuranyl part at C-18 in thyrsiferol (Pacheco et al., 2010), whereas the studied compound **11** enclosed terminal vinylic moiety at C-15 and methyl-23-methyleneoxepan-19-yl ring at C-18

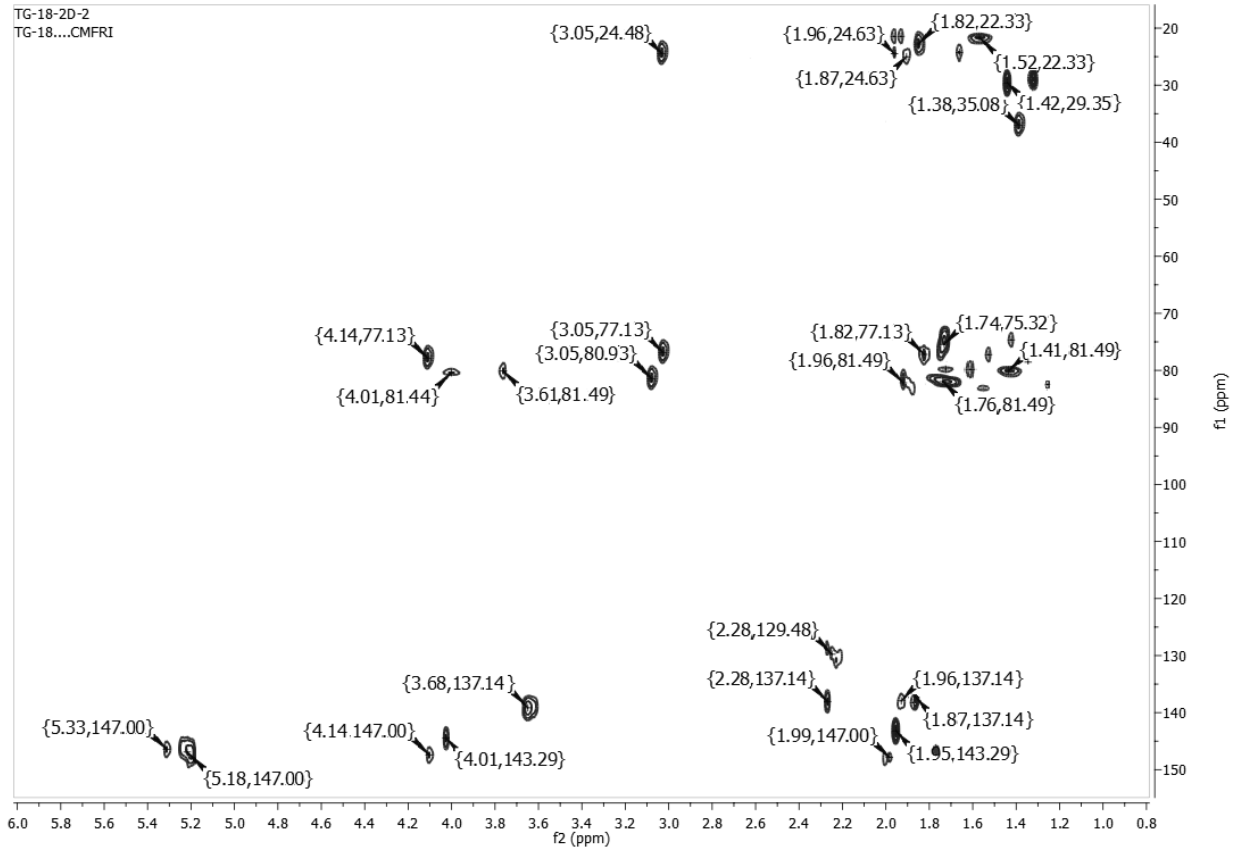

Figure 4.168.: HMBC spectrum of 15-(octahydro-7-(4,5-dihydro-3-methoxy-2,6-dimethyl-*2H*-pyran-6-yl)-10-methylpyrano[3,2-b]pyran-14-yl)-18-(19-methyl-23-methyleneoxepan-19-yl)pent-15-en-18-ol (**11**)

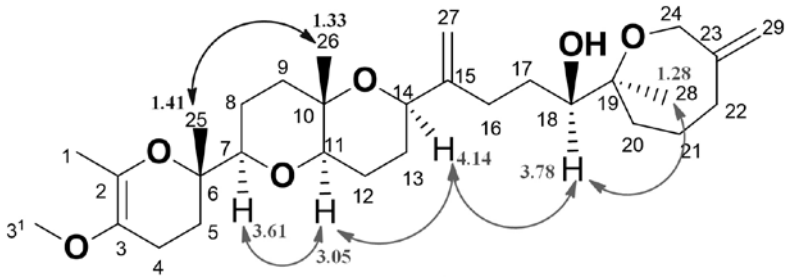

Figure 4.169.: NOESY correlations (double headed arrows) of 15-(octahydro-7-(4,5-dihydro-3-methoxy-2,6-dimethyl-*2H*-pyran-6-yl)-10-methylpyrano[3,2-b]pyran-14-yl)-18-(19-methyl-23-methyleneoxepan-19-yl)pent-15-en-18-ol (**11**)

Table 4.18: NMR spectroscopic data of compound (**11),** 15-(octahydro-7-(4,5-dihydro-3-methoxy-2,6-dimethyl-*2H*-pyran-6-yl)-10-methylpyrano[3,2-b]pyran-14-yl)-18-(19-methyl-23-methyleneoxepan-19-yl)pent-15-en-18-ol (**11**) isolated from red seaweed *G. salicornia*

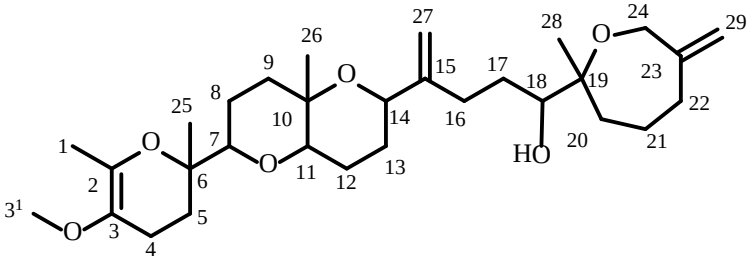

Compound **11** ……..15-(Octahydro-7-(4,5-dihydro-3-methoxy-2,6-dimethyl-*2H*-pyran-6-yl)-10-methylpyrano[3,2-b]pyran-14-yl)-18-(19-methyl-23-methyleneoxepan-19-yl)pent-15-en-18-ol (**11**)

C. No.	**^{13}C**	**^{1}H (int.,mult., *J* in Hz)[b]**	**^{1}H-^{1}H COSY**	**HMBC**
1	20.33	2.28 (3H,s)	-	C-2,3
2	129.48	-	-	-
3	137.14	-	-	-
4	21.57	1.97 (1H,t,4.2 Hz)	H-5	C-3,5
		1.87 (1H,t,4.2 Hz)	-	C-3,5
5	24.63	1.76 (1H,t,4.2 Hz)	-	C-6
		1.96 (1H,t,4.2 Hz)	-	C-6
6	81.49	-	-	-
7	80.93	3.61 (1H,t,4.3 Hz)	H-8	C-6
8	22.33	1.72 (1H,m)	H-9	C-7
		1.60 (1H,m)	-	-
9	39.13	1.82 (1H,t,5.0 Hz)	-	C-8,10
		1.52 (1H,t,4.9 Hz)	-	C-8
10	77.13	-	-	-
11	78.80	3.05 (1H,t,4.3 Hz)	H-12	C-10,12,7
12	24.48	1.91 (1H,m)	H-13	-
		1.62 (1H,m)	-	C-13
13	25.74	1.74 (2H,m)	H-14	C-14
14	75.32	4.14 (1H,t,4.3 Hz)	-	C-15,10
15	147.00	-	-	-
16	29.35	1.99 (2H,t,4.2 Hz)	H-17	C-15
17	31.66	1.42 (2H,m)	H-18	C-16,18
18	74.15	3.78 (1H,t,4.7 Hz)	-	C-19
19	81.44	-	-	-
20	35.08	1.54 (2H,t,4.3 Hz)	H-21	C-19
21	21.82	1.38 (2H,m)	H-22	C-20
22	37.08	1.95 (2H,t)	-	C-21,23
23	143.29	-	-	-
24	72.42	4.01 (1H,d,8.2 Hz)	-	C-23,19
		3.93 (1H,d,8.3 Hz)	-	-
25	24.37	1.41 (3H,s)	-	C-6

26	19.38	1.33 (3H,s)	-	C-10
27	114.50	5.33 (1H,d,10.0 Hz)	-	C-15
		5.18 (1H,d,9.3 Hz)	-	C-15
28	18.82	1.28 (3H,s)	-	C-19
29	114.01	5.36 (1H,d,9.3 Hz)	-	C-23
		5.17 (1H,d,9.3 Hz)	-	-
3^1	60.01	3.68 (3H,s)	-	C-3

[a]NMR spectra recorded using Bruker AVANCE III 500 MHz (AV 500) spectrometers.

[b]Values in ppm, multiplicity and coupling constants (J = Hz) are indicated in parentheses.

Assignments were made with the aid of the ^{1}H-^{1}H COSY, HSQC, HMBC and NOESY experiments. The stereo-chemical orientations in the structures were represented by wedge-faced and dash-faced bonds based on NOESY spectra.

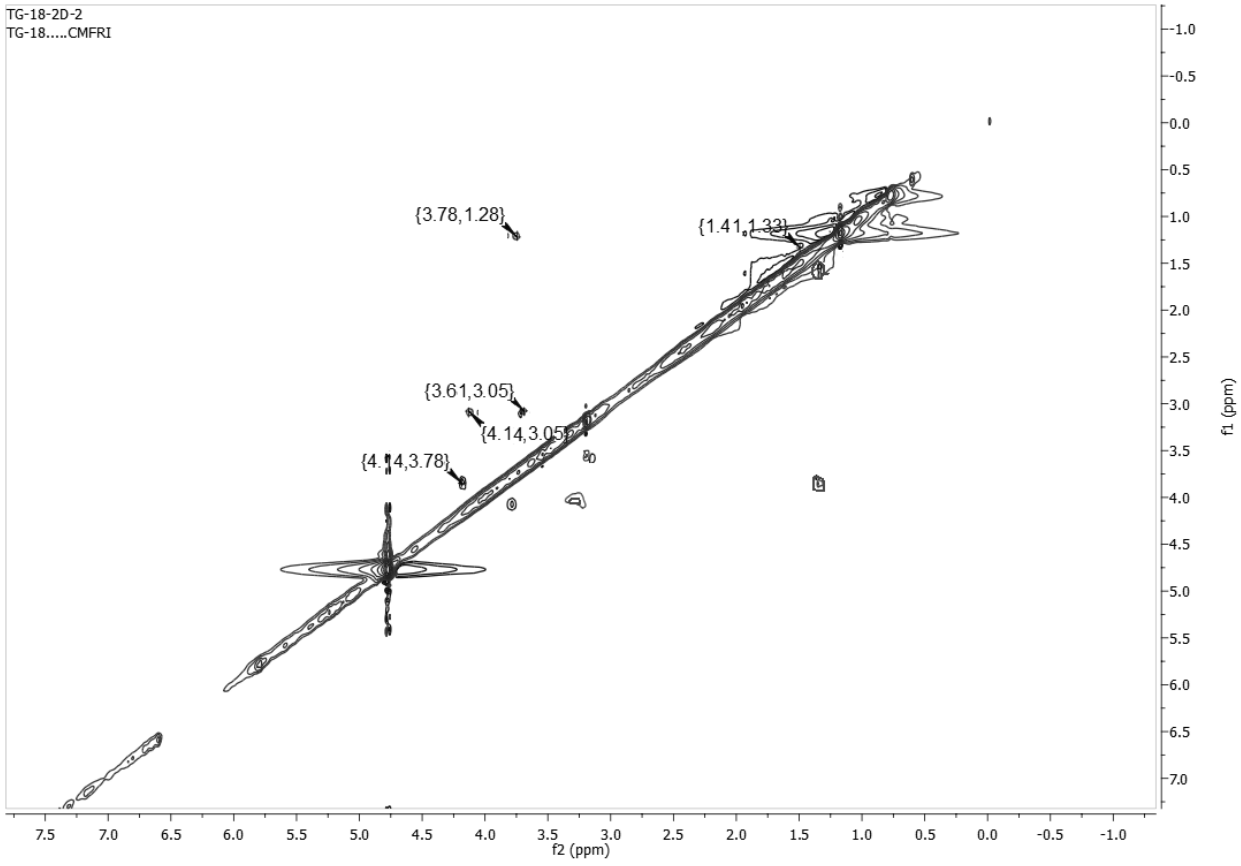

Figure 4.170.: NOESY spectrum of 15-(octahydro-7-(4,5-dihydro-3-methoxy-2,6-dimethyl-*2H*-pyran-6-yl)-10-methylpyrano[3,2-b]pyran-14-yl)-18-(19-methyl-23-methyleneoxepan-19-yl)pent-15-en-18-ol (**11**)

The relative stereo-chemical alignments of protons in the chiral centers, mainly at C-6, C-10, C-11, C-14, C-18, and C-19 were assigned through comprehensive NOESY experimentations (Figure 4.169 & 4.170). The NOE correlations from δ 3.61 (H-7)/3.05 (H-11)/4.14 (H-14)/3.78 (H-18)/1.28 (H-28) confirmed the equiplaner alignment of these protons in their close proximity and these were arbitrarily allocated in the α-direction with regard to its molecular plane of symmetry. The methyl protons δ 1.41 (H-25) and 1.33 (H-26) were positioned opposite to the α-protons, and therefore, allocated as β-oriented. The squalene-derived polyethers from L. viridis registered β-orientations for methyls at C-26, C-27, and 18-OH and α-orientations for the protons at H-7, H-11, H-14 and Me-29 (Pacheco, 2011; Pacheco et al., 2010), which were comparable to the present compound.

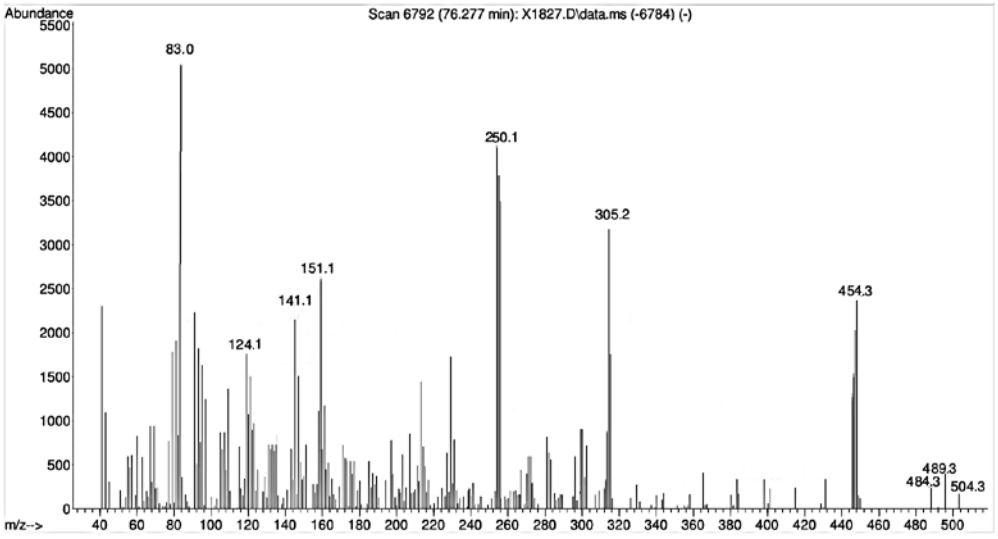

Figure 4.171.: EI-MS spectrum of 15-(octahydro-7-(4,5-dihydro-3-methoxy-2,6-dimethyl-*2H*-pyran-6-yl)-10-methylpyrano[3,2-b]pyran-14-yl)-18-(19-methyl-23-methyleneoxepan-19-yl)pent-15-en-18-ol (**11**)

The complete structural characterisation of **11** were further substantiated by mass spectral experiments, wherein the ion peak at *m/z* 504 (a) experienced methyl-radical removal and H_2O removal to form fragments $C_{29}H_{45}O_6^+$ (b) with *m/z* 489 and $C_{30}H_{44}O_5^{\bullet+}$ with *m/z* 484 (c), respectively. The elimination of CH_3OH and H_2O from (a) resulted in the formation of $C_{29}H_{42}O_4^{\bullet+}$ with *m/z* 454 (d). The fragment (d) underwent a further sequence of fragmentations to obtain the fragments at *m/z* 305 (e), which on further fragmentation resulted in the fragment $C_{15}H_{22}O_3^{\bullet+}$ with *m/z* 250 (h). The fragment (h) then directed to fragmented peaks at *m/z* 141 (g) and *m/z* 83 (i). The base peak of **11** was obtained at *m/z* 83 corresponding to $C_5H_7O^+$ (Figure 4.171-4.172).

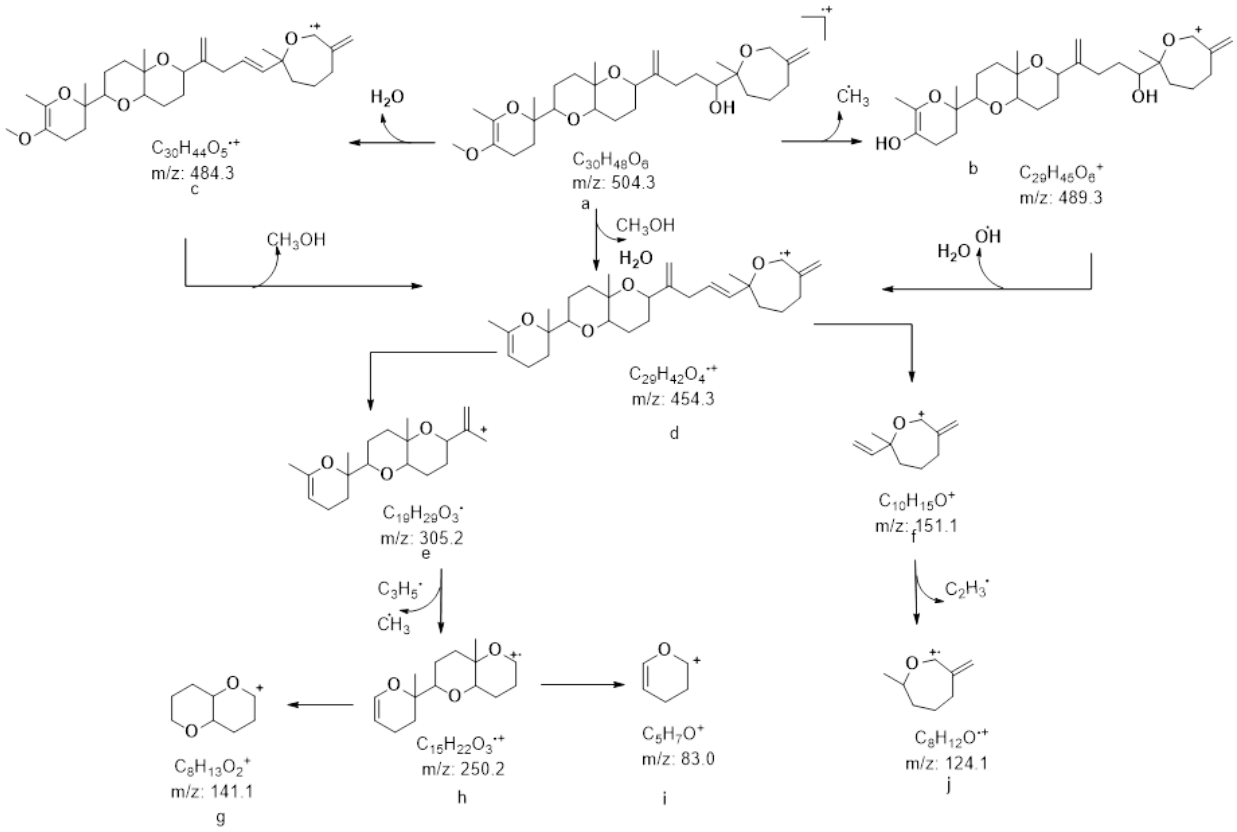

Figure 4.172.: Mass fragmentation pattern of 15-(octahydro-7-(4,5-dihydro-3-methoxy-2,6-dimethyl-*2H*-pyran-6-yl)-10-methylpyrano[3,2-b]pyran-14-yl)-18-(19-methyl-23-methyleneoxepan-19-yl)pent-15-en-18-ol (**11**)

4.3.2.6b Structural characterization of Compound 12

Tetrahydro-6-(hexahydro-13-((tetrahydro-18-(23-hydroxy-23-methylheptan-19-yl)-15-methylfuran-15-yl)methyl)-10-methyl-*2H*-furo[3,2-b]pyran-7-yl)-2,2,6-trimethyl-*2H*-pyran-3-yl

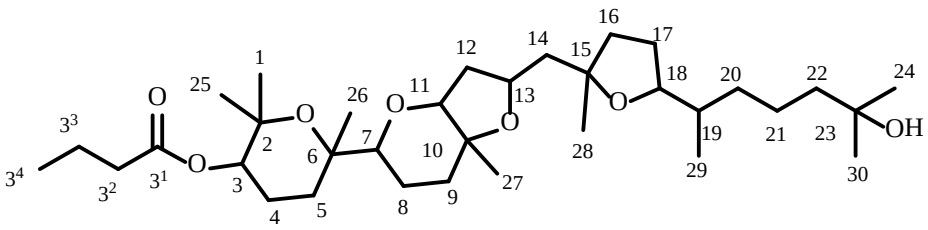

Sample yield	0.33% (> 99% purity, RP-C18 HPLC)
Physical description	Colourless oily
Molecular formula	$C_{34}H_{60}O_7$
Molecular mass	580.4339

The polyether derivative, tetrahydro-6-(hexahydro-13-((tetrahydro-18-(23-hydroxy-23-methylheptan-19-yl)-15-methylfuran-15-yl)methyl)-10-methyl-*2H*-furo[3,2-b]pyran-7-yl)-2,2,6-trimethyl-*2H*-pyran-3-yl was isolated as Colourless oil. The compound (**12**) has exhibited UV absorbance (UV (MeOH) λ_{max}) at 242 nm (Figure 4.173). The homogeneity of the compound was ascertained by HPLC data on a bonded phase octadecylsilane (C_{18}) stationary phase (HPLC, MeOH/MeCN, 1:1 v/v) with R_t: 3.18 min (Figure 4.174).

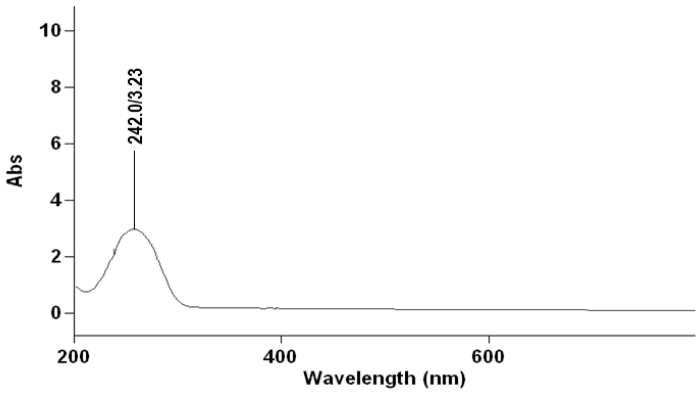

Figure 4.173.: UV spectrum of tetrahydro-6-(hexahydro-13-((tetrahydro-18-(23-hydroxy-23-methylheptan-19-yl)-15-methylfuran-15-yl)methyl)-10-methyl-*2H*-furo[3,2-b]pyran-7-yl)-2,2,6-trimethyl-*2H*-pyran-3-yl (**12**)

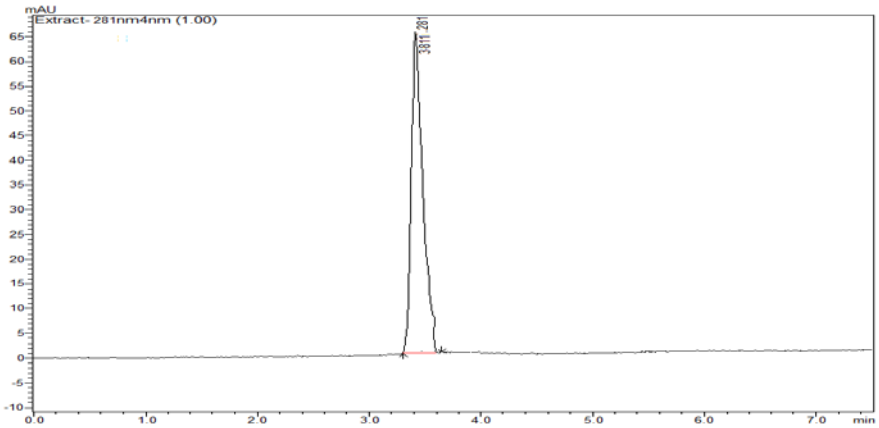

Figure 4.174.: HPLC chromatogram of tetrahydro-6-(hexahydro-13-((tetrahydro-18-(23-hydroxy-23-methylheptan-19-yl)-15-methylfuran-15-yl)methyl)-10-methyl-*2H*-furo[3,2-b]pyran-7-yl)-2,2,6-trimethyl-*2H*-pyran-3-yl (**12**)

Bioactivity-based chromatographic purification of the organic extract of *G. salicornia* afforded a previously undisclosed polyether derivative, characterised as tetrahydro-6-(hexahydro-13-((tetrahydro-18-(23-hydroxy-23-methylheptan-2-yl)-15-methylfuran-15-yl)methyl)-10-methyl-2*H*-furo[3,2-b]pyran-7-yl)-2,2,6-trimethyl-2*H*-pyran-3-yl butyrate (1**2**). The molecular ion peak has been analysed by HRESIMS (positive mode) spectroscopic experiment, and its molecular $[M+H]^+$ ion peak has been recorded at *m/z* 581.4420 (Figure 4.175). The integrative EIMS-NMR-IR techniques deduced the molecular formula of **12** as $C_{34}H_{60}O_7$, indicative of five sites of unsaturation (Table 4.19).

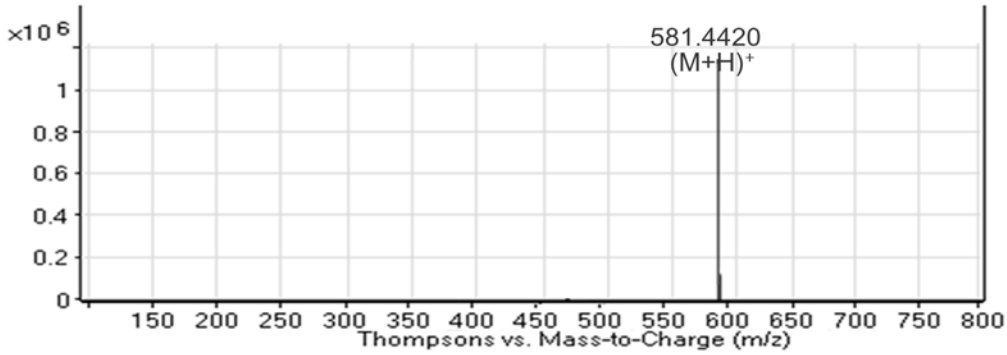

Figure 4.175.: HRESIMS spectrum of tetrahydro-6-(hexahydro-13-((tetrahydro-18-(23-hydroxy-23-methylheptan-19-yl)-15-methylfuran-15-yl)methyl)-10-methyl-*2H*-furo[3,2-b]pyran-7-yl)-2,2,6-trimethyl-*2H*-pyran-3-yl (**12**)

The FTIR spectrum of **12** registered absorption peaks at 3383 and 1043 cm^{-1}, which represented hydroxyl (-OH) and ether (-C-O-C) groups, correspondingly (Figure 4.176). The ^{13}C NMR of **12** registered 34 carbon atoms and the types of the carbon signals were determined from the ^{135}DEPT spectrum. It was deduced to include nine methyls (δ 27.58, 28.88, 26.39, 21.11, 17.31, 26.94, 18.13, 28.53, 13.99), thirteen sp^3 methylenes (δ 21.38, 30.32, 22.32, 39.67, 38.65, 46.37, 36.06, 29.34, 33.97, 22.04, 42.61, 36.61, 18.85), six sp^3 methines (δ 71.52, 90.49, 80.50, 65.26, 79.17, 36.72), and six non-protonated carbons (δ 83.98, 82.62, 81.42, 79.53, 78.93, 167.92). The ^{13}C NMR exhibited highly deshielded resonances for eight carbons observed at δ 71.52 (assigned at C-3), 82.62 (C-6), 90.49 (C-7), 81.42 (C-10), 80.50 (C-11), 65.26 (C-13), 79.17 (C-18) and 78.93 (C-23), which might be attributed to hydroxyl, ether and ester substitutions in the studied compound **12**, and these values were further corroborated by previous literature (Pacheco, 2011). ^1H NMR spectrum of **12** displayed deshielded proton signals at δ 4.10, 3.69, 3.33, 3.56 and 3.67 that were assigned to protons adjacent to the oxygen atoms. Seven shielded singlet protons at δ 1.19, 1.24, 1.26, 1.28, 1.29 and 1.31 were accounted for the methyls

in compound **12** (Figure 4.177-4.179). These attributions were corroborated by HSQC spectral analysis (Figure 4.180).

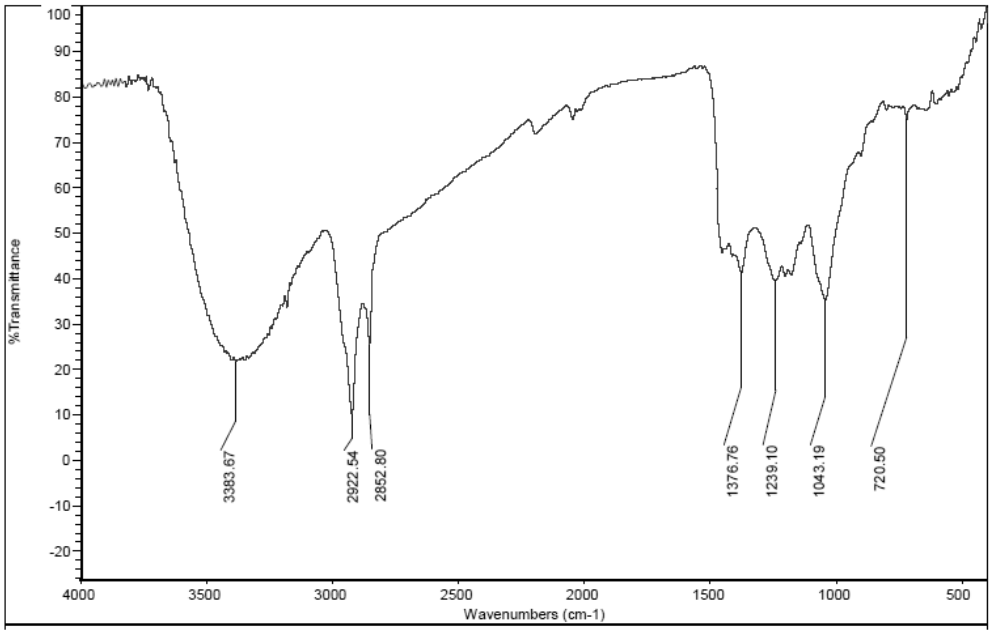

Figure 4.176.: FTIR spectrum of tetrahydro-6-(hexahydro-13-((tetrahydro-18-(23-hydroxy-23-methylheptan-19-yl)-15-methylfuran-15-yl)methyl)-10-methyl-*2H*-furo[3,*2-b*]pyran-7-yl)-2,2,6-trimethyl-*2H*-pyran-3-yl (**12**)

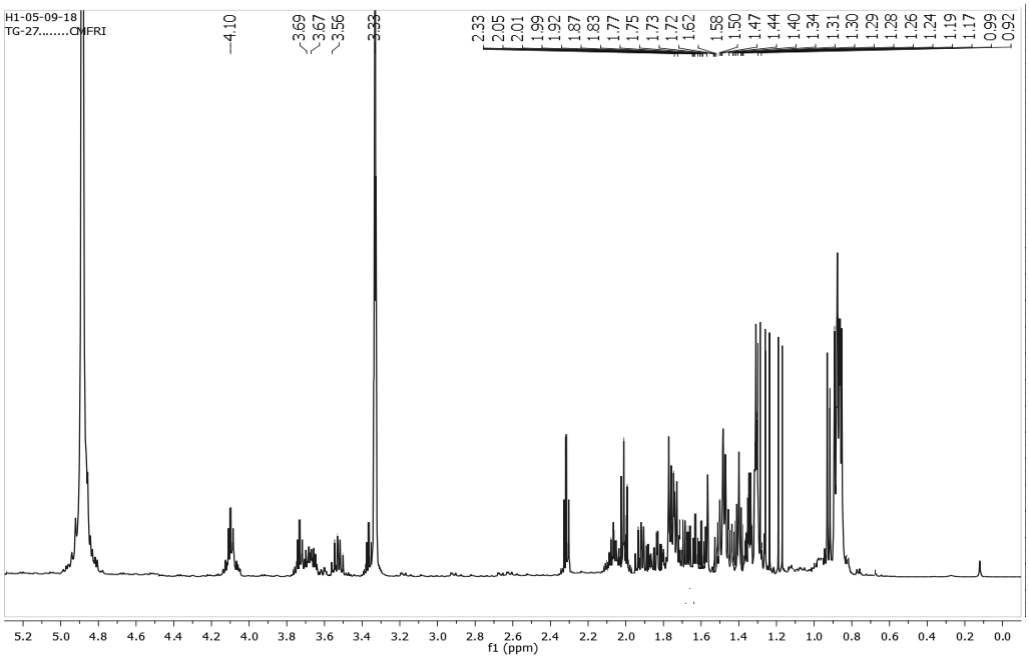

Figure 4.177.: ^{1}H NMR spectrum of tetrahydro-6-(hexahydro-13-((tetrahydro-18-(23-hydroxy-23-methylheptan-19-yl)-15-methylfuran-15-yl)methyl)-10-methyl-*2H*-furo[3,*2-b*]pyran-7-yl)-2,2,6-trimethyl-*2H*-pyran-3-yl (**12**)

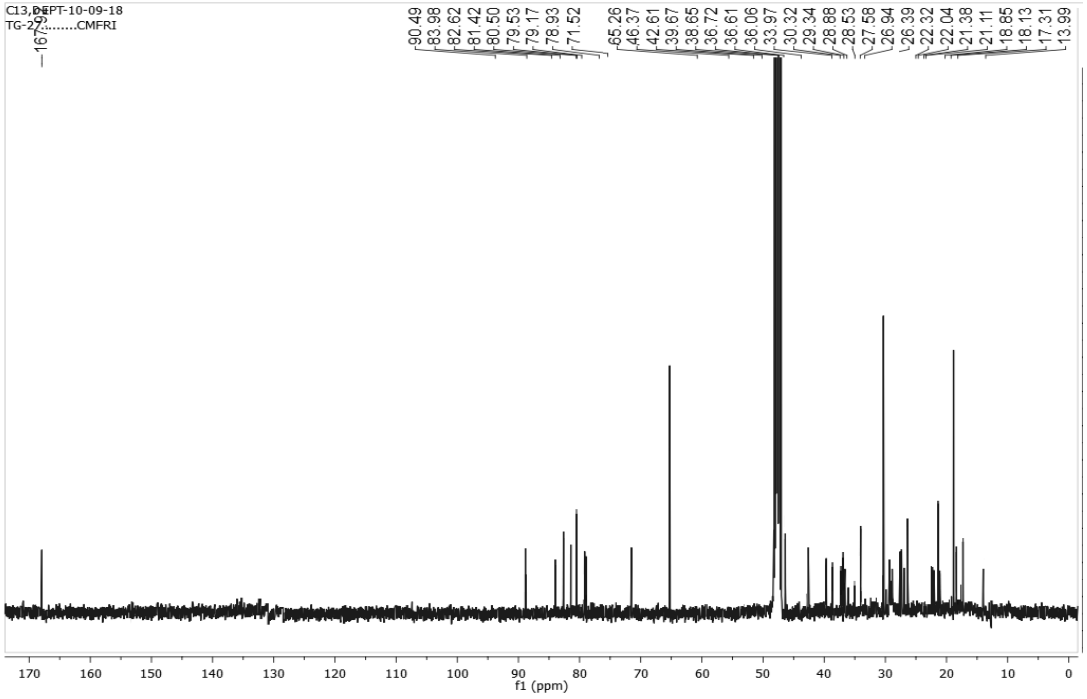

Figure 4.178.: ^{13}C NMR spectrum of tetrahydro-6-(hexahydro-13-((tetrahydro-18-(23-hydroxy-23-methylheptan-19-yl)-15-methylfuran-15-yl)methyl)-10-methyl-*2H*-furo[3,*2-b*]pyran-7-yl)-2,2,6-trimethyl-*2H*-pyran-3-yl (**12**)

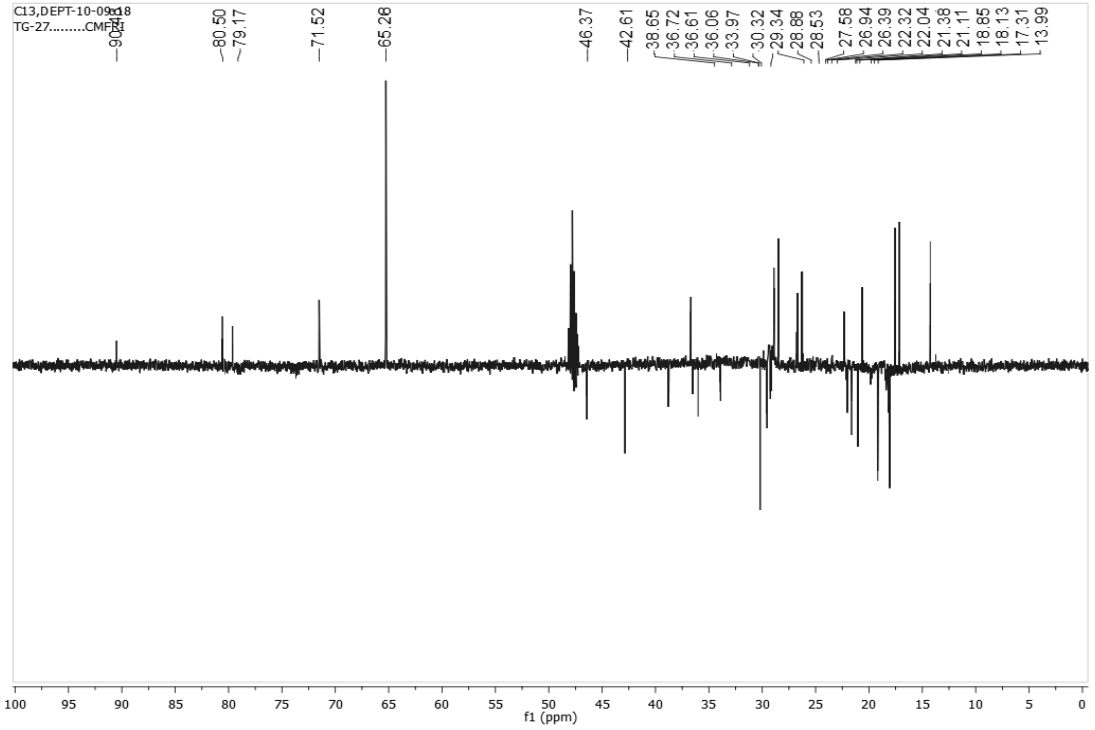

Figure 4.179.: ^{135}DEPT spectrum of tetrahydro-6-(hexahydro-13-((tetrahydro-18-(23-hydroxy-23-methylheptan-19-yl)-15-methylfuran-15-yl)methyl)-10-methyl-*2H*-furo[3,*2-b*]pyran-7-yl)-2,2,6-trimethyl-*2H*-pyran-3-yl (**12**)

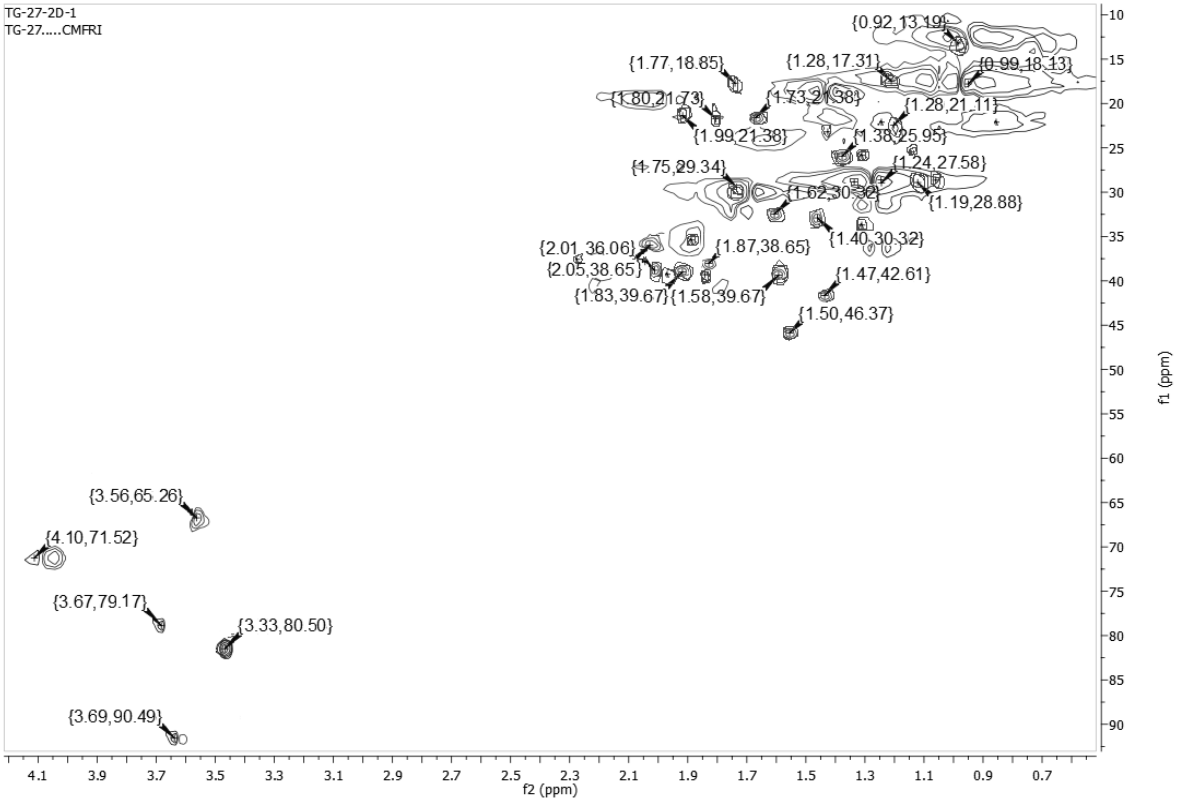

Figure 4.180.: HSQC spectrum of tetrahydro-6-(hexahydro-13-((tetrahydro-18-(23-hydroxy-23-methylheptan-19-yl)-15-methylfuran-15-yl)methyl)-10-methyl-*2H*-furo[3,*2-b*]pyran-7-yl)-2,2,6-trimethyl-*2H*-pyran-3-yl (**12**)

The COSY spin unit from δ 4.10 (H-3)/1.73 (H-4)/1.40 (H-5) and HMBC correlations from δ 4.10 (H-3) to δ 83.98 (C-2); δ 1.62 (H-5) to δ 82.62 (C-6); δ 1.24 (H-3) to δ 83.98 (C-2); δ 1.26 (H-25) to δ 83.98 (C-2) and δ 1.29 (H-6) to δ 82.62 (C-6) ascribed the presence of tetrahydro-2,2,6-trimethyl-*2H*-pyran moiety in the studied compound (Figure 4.181-4.183). The ^{1}H-^{1}H COSYs among δ 2.33 (H-3^{1})/1.77 (H-3^{2})/0.92 (H-3^{3}) along with HMBCs from δ 2.33 (H-3^{2}) to δ 167.92 (C-3^{1}) supported the occurrence of the butyrate side chain, which was directly attached at C-3 of tetrahydro-2,2,6-trimethyl-*2H*-pyran through the HMBCs from δ 4.10 (H-3) to ester carbonyl at δ 167.92 (C-3^{1}). Similarly, compound **12** exhibited COSYs like δ 3.69 (H-7)/1.72 (H-8)/1.58 (H-9) and δ 3.33 (H-11)/2.05 (H-12)/3.56 (H-13). These COSY fragments were further connected by the HMBC correlations from δ 1.72 (H-8) to δ 90.49 (C-7); H-9 to both C-8/C-10 {δ 1.83 (H-9) to δ 22.32 (C-8)/81.42 (C-10)}; H-11 to both C-10/C-7 {δ 3.33 (H-11) to δ 81.42 (C-10)/90.49 (C-7)}; H-12 to both C-11/C-13 {δ 2.05 (H-12) to δ 80.50 (C-11)/65.26 (C-13)} and from δ 3.56 (H-13) to δ 81.42 (C-10), which attributed the presence of 10-methyl-2*H*-furo[3,2-b]pyran. The attachment of furo[3,2-b]pyran at C-6 of tetrahydro-2,2,6-trimethyl-2*H*-pyran was ascribed through HMBCs from δ 3.69 (H-7) to δ 82.62 (C-6). Another

tetrahydro-furanyl ring was formed through COSYs from δ 2.01 (H-16)/1.75 (H-17)/3.67 (H-18), and which was extended with a seven-membered linear side chain at C-18 through the COSYs from δ 3.67 (H-18)/1.92 (H-19)/1.34 (H-20)/1.30 (H-21)/1.47 (H-22) along with δ 1.92 (H-19)/0.99 (H-29).

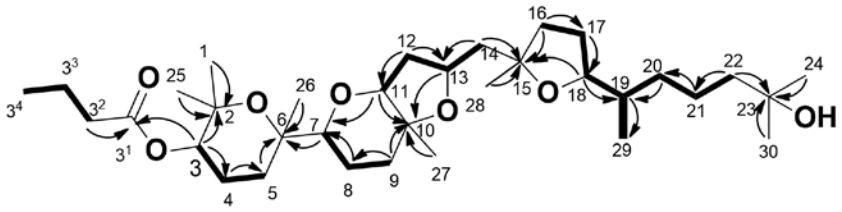

Figure 4.181.: ^{1}H-^{1}H COSY (bold face bonds) and selected HMBCs (double-barbed arrows), correlations of tetrahydro-6-(hexahydro-13-((tetrahydro-18-(23-hydroxy-23-methylheptan-19-yl)-15-methylfuran-15-yl)methyl)-10-methyl-*2H*-furo[3,*2-b*]pyran-7-yl)-2,2,6-trimethyl-*2H*-pyran-3-yl (**12**)

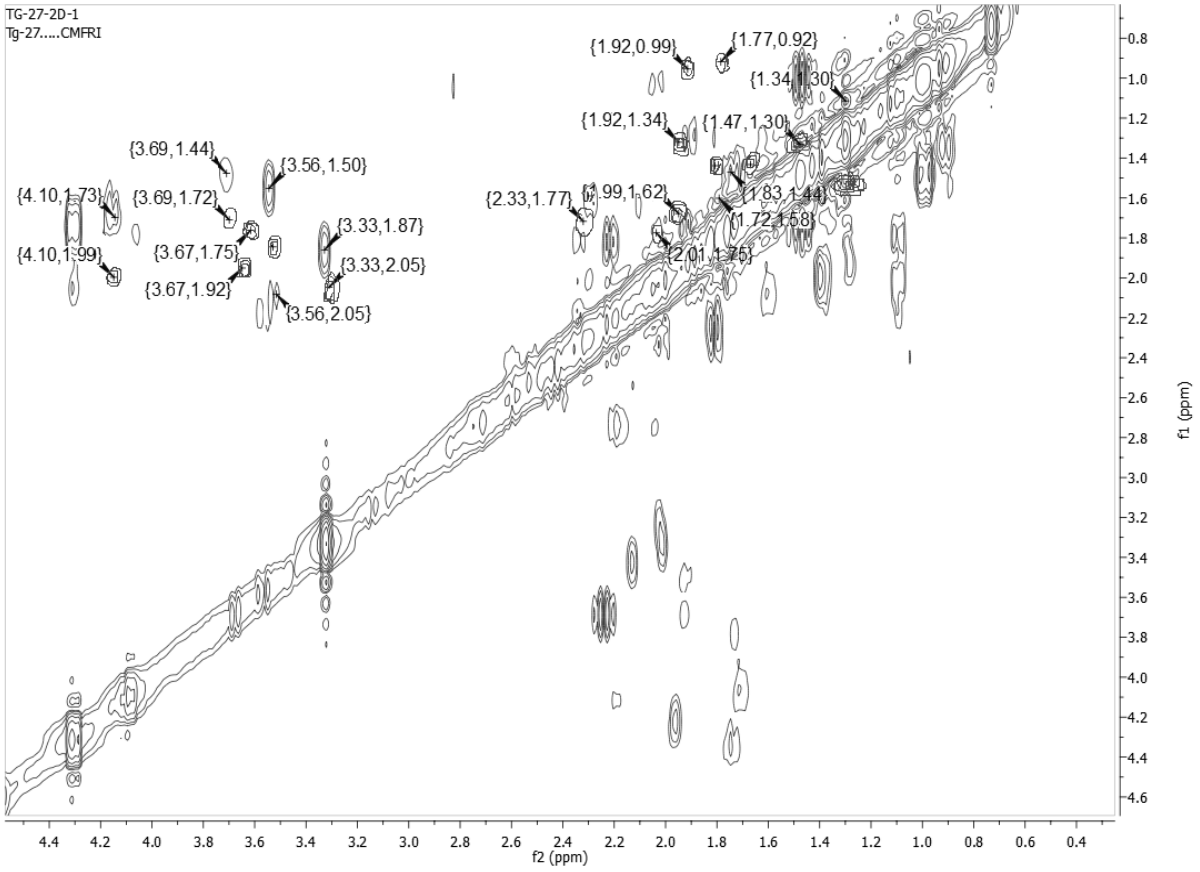

Figure 4.182.: ^{1}H-^{1}H COSY spectrum of tetrahydro-6-(hexahydro-13-((tetrahydro-18-(23-hydroxy-23-methylheptan-19-yl)-15-methylfuran-15-yl)methyl)-10-methyl-*2H*-furo[3,*2-b*]pyran-7-yl)-2,2,6-trimethyl-*2H*-pyran-3-yl (**12**)

Further, the HMBCs from δ 2.01 (H-16) to δ 79.53 (C-15); δ 3.67 (H-18) to δ 79.53 (C-15); H-12 to both δ 1.92 (H-19) to δ 18.13 (C-29); δ 1.47 (H-22) to δ 78.93 (C-23); δ 1.19 (H-24) to δ 78.93 (C-23), and from δ 1.31 (H-28) to δ 79.53 (C-15) appropriately established the partial structure of tetrahydro-18-(23-hydroxy-23-methylheptan-19-yl)-15-methylfuran group. The tetrahydro-furanyl ring with linear side chain enclosing 22-hydroxy-15(28)-dehydrovenustatriol was previously reported (Pacheco, 2011), and the chemical shifts were comparable with the titled compound. The 10-methyl-2*H*-furo[3,2-b]pyran ring and tetrahydro-18-(23-hydroxy-23-methylheptan-19-yl)-15-methylfuran group were connected through a methylene linkage, which was assigned by the strong HMBCs from the methylene proton at δ 1.50 located at H-14 to methine carbon at δ 65.26 (C-13 of furo[3,2-b]pyran) and to the non-protonated carbon at δ 79.53 (C-15 of furan enclosed side chain).

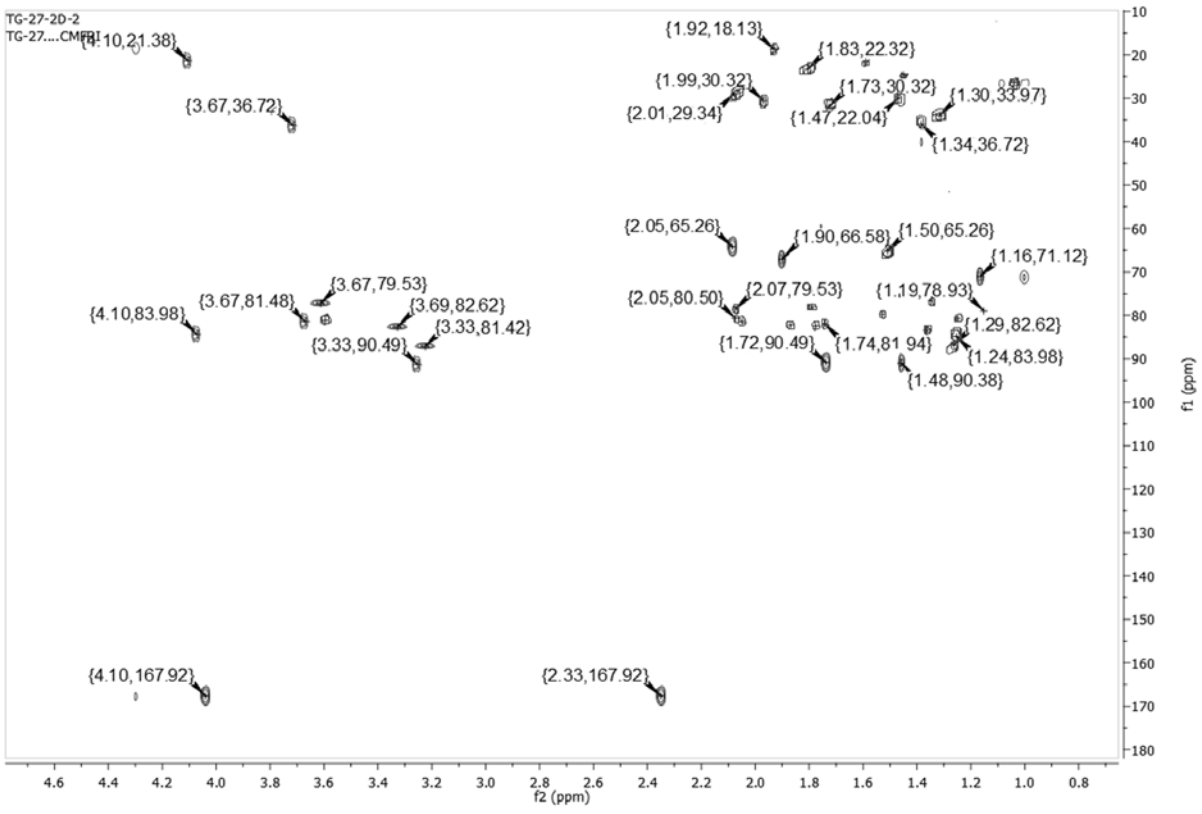

Figure 4.183.: HMBC spectrum of tetrahydro-6-(hexahydro-13-((tetrahydro-18-(23-hydroxy-23-methylheptan-19-yl)-15-methylfuran-15-yl)methyl)-10-methyl-*2H*-furo[3,*2-b*]pyran-7-yl)-2,2,6-trimethyl-*2H*-pyran-3-yl (**12**)

The spiro-dehydrovenustatriol enclosed trimethyl pyran with bromine at C-3 with chemical shifts of δ 1.28 (H-1)/29.7 (C-1), 74.9 (C-2), 3.90 (H-3)/59.1 (C-3), 74.8 (C-6); spiro-fused tetrahydro-furano-tetrahydro-pyran at C-11 with chemical shift signals at δ 72.9 (C-10), 109.9 (C-11); methyl tetrahydro-furan with chemical shifts at δ 84.6 (C-19), 1.60-2.01 (H-20)/35.0 (C-20), 1.77 (H-21)/24.7 (C-21), 3.76 (H-22)/86.7 (C-22) and a propan-2-ol end with chemical shift signals at δ 70.6 (C-23), 1.11 (H-24)/25.4 (C-24), 1.20 (H-30)/28.2 (C-30) (Pacheco et al., 2010) were apparent. Similarly, the present compound enclosed trimethyl pyran with ester linkage at C-3 with chemical shifts of δ 1.24 (H-1)/27.58 (C-1), 83.98 (C-2), 4.10 (H-3)/71.52 (C-3), 82.62 (C-6), and the greater chemical shifts at C-3 was due to the presence of highly electronegative groups like ester. It enclosed fused tetrahydro-furano-tetrahydro-pyran at C-10 and C-11 positions, and therefore, the chemical shift at C-11 was appeared to be lower (δ 80.50) when compared to spiro-fused compound spiro-dehydrovenustatriol (Pacheco et al., 2010). The chemical shifts of methyl tetrahydro-furan were found at δ 79.53 (C-15), 2.01 (H-16)/36.06 (C-16), 1.75 (H-17)/29.34 (C-17), 3.67 (H-18)/79.17 (C-18) and propan-2-ol end were found at δ 78.93 (C-23), 1.19 (H-24)/28.88 (C-24), 1.17 (H-30)/28.53 (C-30), which were comparable to the previously reported spiro-dehydrovenustatriol (Pacheco, 2011; Pacheco et al., 2010).

Table 4.19: NMR spectroscopic data of compound (**12),** tetrahydro-6-(hexahydro-13-((tetrahydro-18-(23-hydroxy-23-methylheptan-19-yl)-15-methylfuran-15-yl)methyl)-10-methyl-*2H*-furo[3,*2-b*]pyran-7-yl)-2,2,6-trimethyl-*2H*-pyran-3-yl (**12**) isolated from red seaweed *G. salicornia*

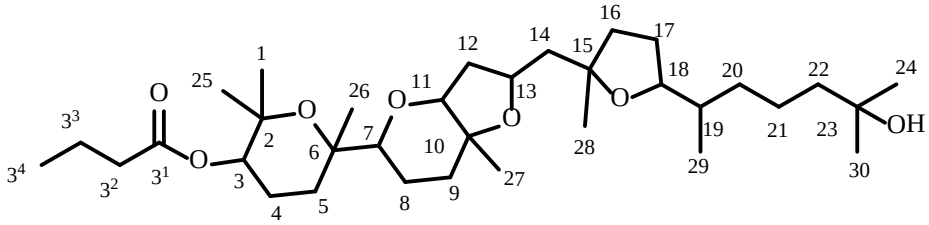

Compound **12**……. tetrahydro-6-(hexahydro-13-((tetrahydro-18-(23-hydroxy-23-methylheptan-19-yl)-15-methylfuran-15-yl)methyl)-10-methyl-*2H*-furo[3,*2-b*]pyran-7-yl)-2,2,6-trimethyl-*2H*-pyran-3-yl (**12**)

C. No.	**^{13}C**	**^{1}H (int.,mult., J in Hz)^{b}**	**^{1}H-^{1}H COSY**	**HMBC**
1	27.58	1.24 (3H,s)	-	C-2

2	83.98	-	-	-
3	71.52	4.10 (1H,t,4.2 Hz)	H-4	C-2,4,3[1]
4	21.38	1.73 (1H,m)	H-5	C-5
		1.99 (1H,m)	-	-
5	30.32	1.62 (1H,t,4.3 Hz)	-	C-6
		1.40 (1H,t,4.3 Hz)	-	-
6	82.62	-	-	-
7	90.49	3.69 (1H,t,6.2 Hz)	H-8	C-6
8	22.32	1.72 (1H,m)	H-9	C-7
		1.44 (1H,m)	-	-
9	39.67	1.83 (1H,t,5.2 Hz)	-	C-8,10
		1.58 (1H,t,5.2 Hz)	-	-
10	81.42	-	-	-
11	80.50	3.33 (1H,t,9.2 Hz)	H-12	C-7,10
12	38.65	2.05 (1H,t,6.4 Hz)	H-13	C-11,13
		1.87 (1H,t,6.5 Hz)	-	-
13	65.26	3.56 (1H,m)	H-14	C-10
14	46.37	1.50 (2H,d,6.8 Hz)	-	C-13,15
15	79.53	-	-	-
16	36.06	2.01 (2H,t,4.2 Hz)	H-17	C-15,17
17	29.34	1.75 (2H,m)	H-18	C-18
18	79.17	3.67 (1H,m)	H-19	C-19,15
19	36.72	1.92 (1H,m)	H-20, H-29	C-29
20	33.97	1.34 (2H,m)	H-21	C19
21	22.04	1.30 (2H,m)	H-22	C-20
22	42.61	1.47 (2H,m)	-	C-21,23
23	78.93	-	-	-
24	28.88	1.19 (3H,s)	-	C-23
25	26.39	1.26 (3H,s)	-	C-2
26	21.11	1.29 (3H,s)	-	C-6
27	17.31	1.28 (3H,s)	-	C-10
			-	-
28	26.94	1.31 (3H,s)	-	C-15
29	18.13	0.99 (3H,d,7.2 Hz)	-	-
			-	-
30	28.53	1.17 (3H,s)	-	C-23
3^1	167.92	-	-	-
3^2	36.61	2.33 (2H,t,6.8 Hz)	H-3^3	C-3^1
3^3	18.85	1.77 (2H,m)	H-3^4	-
3^4	13.99	0.92 (3H,t,4.1 Hz)	-	-

[a]NMR spectra recorded using Bruker AVANCE III 500 MHz (AV 500) spectrometers.

[b]Values in ppm, multiplicity and coupling constants (J = Hz) are indicated in parentheses.

Assignments were made with the aid of the ^{1}H-^{1}H COSY, HSQC, HMBC and NOESY experiments. The stereo-chemical orientations in the structures were represented by wedge-faced and dash-faced bonds based on NOESY spectra.

Relative stereo-chemical representations of the protons at the chiral points, mainly at C-2, C-3, C-6, C-7, C-10, C-11, C-13, C-15, C-18, and C-19 were corroborated via NOESYs

(Figure 4.184-4.185). The NOE correlations between δ 1.24 (H-1)/3.69 (H-7)/3.33 (H-11)/3.56 (H-13)/1.31 (H-28)/3.67 (H-18) and δ 1.31 (H-28)/1.92 (H-19) attributed the equi-planer arrangement of protons, and that these protons were arbitrarily aligned towards the α-direction with respect to its molecular plane of symmetry. The proton at δ 4.10 (H-3) and methyl protons at 1.26 (H-25), 1.29 (H-26) and 1.28 (H-27) were aligned opposite to the α-protons, and hence, allocated as β-oriented.

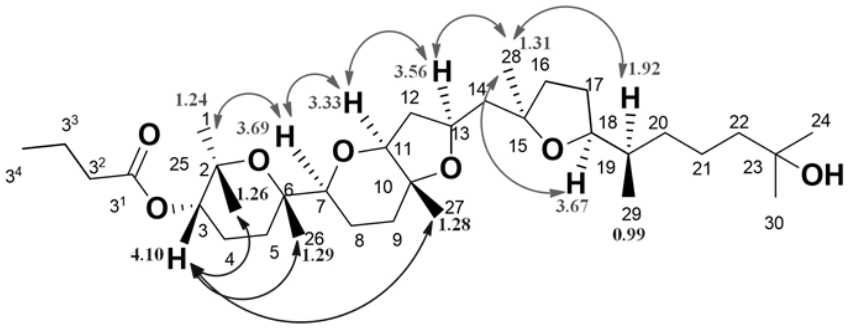

Figure 4.184.: HMBC spectrum of tetrahydro-6-(hexahydro-13-((tetrahydro-18-(23-hydroxy-23-methylheptan-19-yl)-15-methylfuran-15-yl)methyl)-10-methyl-*2H*-furo[3,2-b]pyran-7-yl)-2,2,6-trimethyl-*2H*-pyran-3-yl (**12**)

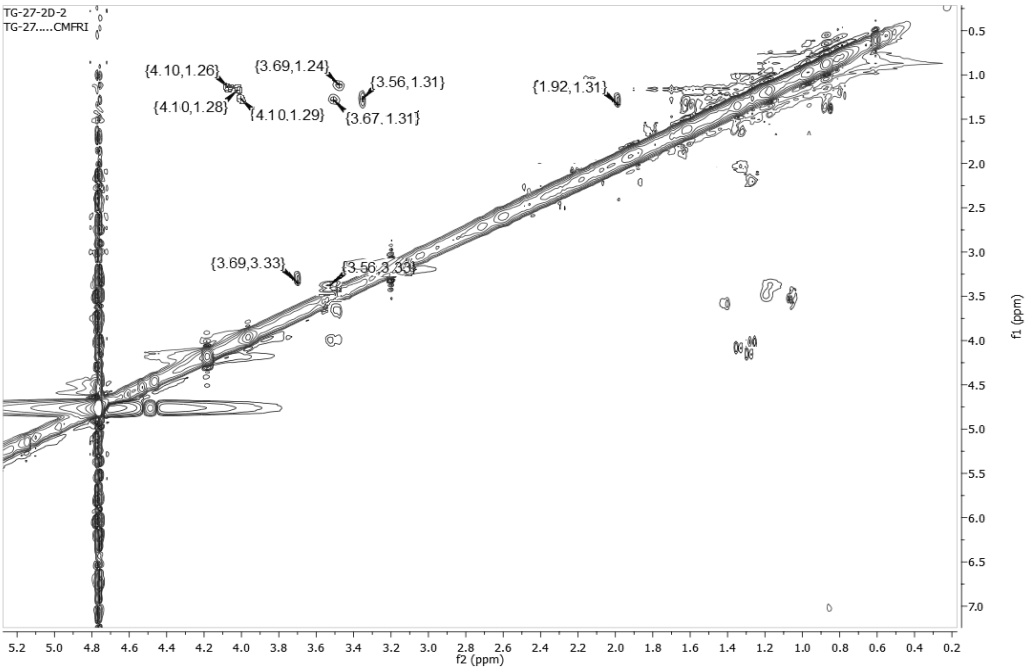

Figure 4.185.: NOE spectrum of tetrahydro-6-(hexahydro-13-((tetrahydro-18-(23-hydroxy-23-methylheptan-19-yl)-15-methylfuran-15-yl)methyl)-10-methyl-*2H*-furo[3,2-b]pyran-7-yl)-2,2,6-trimethyl-*2H*-pyran-3-yl (**12**)

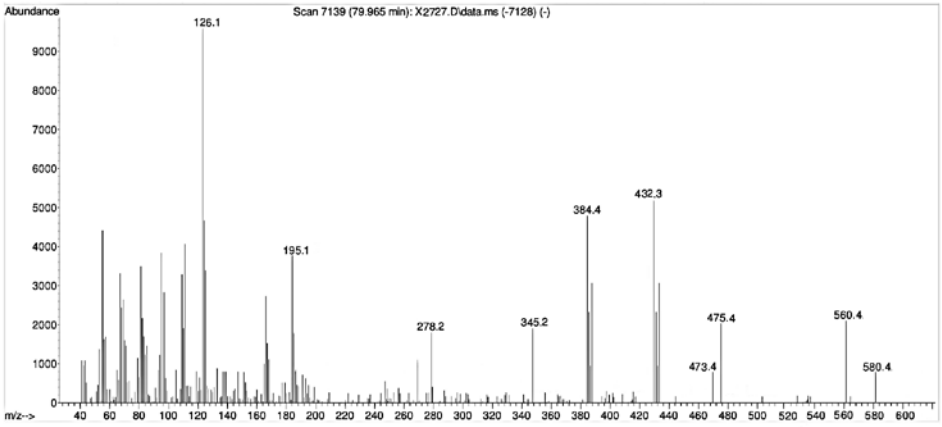

Figure 4.186.: EI-MS spectrum of tetrahydro-6-(hexahydro-13-((tetrahydro-18-(23-hydroxy-23-methylheptan-19-yl)-15-methylfuran-15-yl)methyl)-10-methyl-*2H*-furo[3,2-b]pyran-7-yl)-2,2,6-trimethyl-*2H*-pyran-3-yl (**12**)

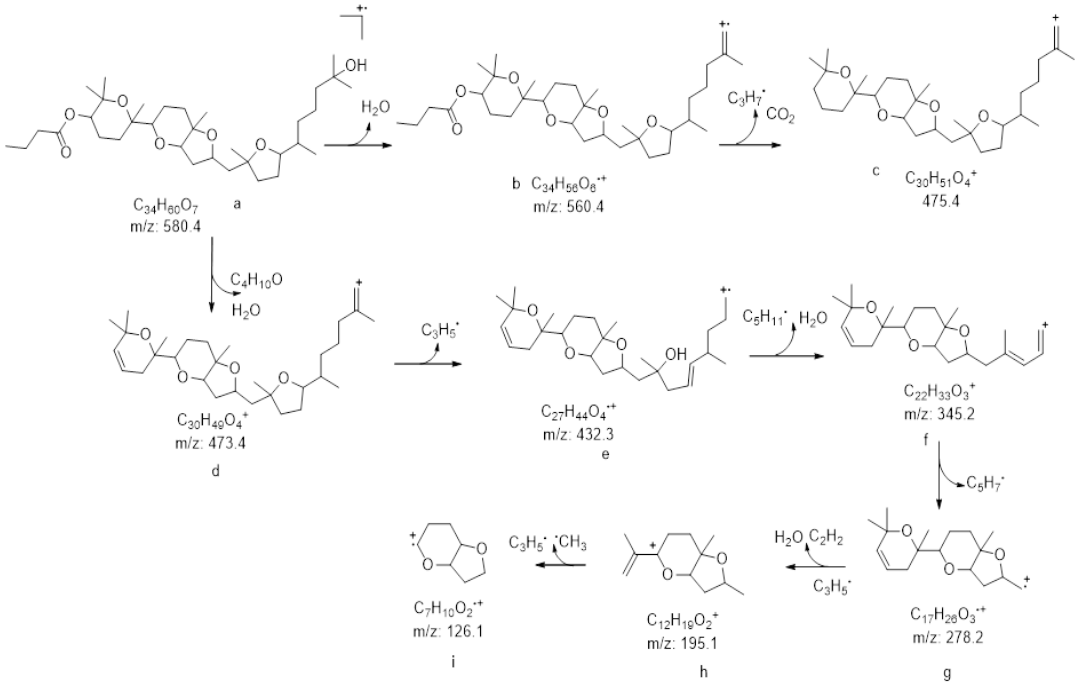

Figure 4.187.: Mass fragmentation pattern m of tetrahydro-6-(hexahydro-13-((tetrahydro-18-(23-hydroxy-23-methylheptan-19-yl)-15-methylfuran-15-yl)methyl)-10-methyl-*2H*-furo[3,2-b]pyran-7-yl)-2,2,6-trimethyl-*2H*-pyran-3-yl (**12**)

The structural assignments of **12** recorded molecular ion peak at *m/z* 580 (a) that could undergo elimination of water to result in the fragment of $C_{34}H_{56}O_6^{\bullet+}$ with *m/z* 560 (b). The elimination of $C_4H_{10}O$ and water from (a) might result in a fragment at $C_{30}H_{49}O_4^+$ with *m/z* 473 (d), whereas the elimination of $C_3H_7^+$ and CO_2 from (b) led to $C_{30}H_{51}O_4^+$ formation with *m/z* 475 (c). The fragment (d) underwent further series of fragmentation to yield the mass fragments at *m/z* 432 (e), 345 (f), 278 (g), 195 (h), and 126 (i). The base peak of **12** was reported at *m/z* 126 corresponding to $C_7H_{10}O_2^{+\cdot}$ (Figure 4.186-4.187).

The sequential chromatographic fractionation of EtOAc-MeOH extract of the seaweed, *G. salicornia* led to the identification of two previously unreported polyether analogues, 3-methoxy-2,6-dimethyl-3,4-dihydro-2*H*-pyranyl-(6-(7-(10-methyl-octahydropyrano[3,2-*b*]pyranyl)-14-((19-methyl-23-methyleneoxepan)-(15-pentene-18-ol)) (**11**) and 14-(15-methyltetrahydrofuranyl)-(18-(23-(hydroxy-23-methylheptanyl)-10-methylhexahydro-2*H*-furo-[3,2-*b*]pyranyl))-2,2,6-trimethyltetrahydro-2*H*-pyran-3- butyrate (**12**). The polyether triterpenoid possessing furanyl, pyranyl along with other oxygenated functionalities can be used to design as potential pharmacophore leads for use against various pathophysiologies.

4.3.2.7 Structural characterization of macrolide derivatives (Compounds 13-15)

Macrolides were recognized as a class of polyketide or polyene macrocyclic chemistries, which were identified as important sources of pharmacophores (Mishra and Tiwari, 2011; Blunt et al., 2013). Almost 100,000 natural derived secondary metabolites were identified previously, and among those, approximately 3 % were found to be macrocyclic compounds (Driggers et al., 2008). A significant number of marine polyketide or ether enclosed macrolides were isolated from various marine organisms, such as sponges (Uemura et al., 1985), mollusks (Chakraborty et al., 2019), seaweeds (Murakami et al., 1991) and seaweed-associated microorganisms (Chakraborty et al., 2014). Most of the naturally occurring macrocyclic metabolites were found to contain only carbon atoms in their ring skeletons like isoprenoids with or without unsaturations (Wessjohann et al., 2005). However, the macrocyclic lactones or ethers with more than ten-membered ring systems containing alkene, ester, ether or hydroxyl moieties were identified as significant pharmacophores (Molinski, 2009). These exhibited higher molecular weights (in the range of 450-850 g mol^{-1}), even though the greater numbers of proton-bond donors, higher polarizabilities along with their lesser number of rotatable bonds than their respective acyclic metabolites could enhance their bio-potencies and bio-availabilities through the effective interactions in the active binding sites of the targeted proteins (Driggers et al., 2008; Marsault and Peterson, 2011). The macrolides could be classified as polyketide derivatives that

typically enclosed multiple carbonyl functionalities, which might be responsible for its various bio-potencies like anti-inflammatory, antioxidant, anti-bacterial etc. (Chakraborty et al., 2017; Maneesh and Chakraborty, 2018). Therefore, macrocyclic lactone scaffolds were used as therapeutics due to its structural features than that of typical small-molecular therapeutics (Driggers et al., 2008). The α-pyrone macrolides, neurymenolides A and B were isolated from the seaweed, *Neurymenia fraxinifolia* (Stout et al., 2009). The 2,6-disubstituted pyran-4-one along with 6-substituted pyran-2-one macrolides were characterised from *Phacelocarpus labillardieri* (Kazlauskas et al., 1982). The macrolide, methyl-2-(12-oxo-7-phenyl-8-vinyl-1-oxa-4,9-cyclododecadien-3-yl)-acetate was reported from the brown seaweed, *Sargassum wightii* (Maneesh and Chakraborty, 2017) with potential antioxidant and anti-inflammatory activities. An antibacterial macrolide, 7-*O*-methyl-5′-hydroxy-3'-heptenoate-macrolactin was reported from seaweed-associated bacterium, *Bacillus subtilis* (Chakraborty et al., 2014).

Among various marine organisms, seaweeds were considered as one of the significant sources of specialised bioactive metabolites (Stout et al., 2009). The search for pharmacophores with active anti-inflammatory/antioxidant potentials from *G. salicornia* obtained from the south-east-coastline areas of Indian peninsular resulted in the isolation of three macrolides enclosing ether functionalities, (Figure. 4.188). The studied compounds were classified as 3-acetyl-14-(furanyl)-11-methyl-15-(15^3-methylbutyloxy)-8-oxabicyclo[21.3.1] heptacosa-11,23,25,27-tetraene-7,18-dione (**13**), (2*E*,12*E*,14*E*)-10-acetyl-9-isopentyl-2-methyl-5,16,23^1-trioxa-bicyclo[21.3.1]heptacosa-2,12,14-triene-6,19-dione (**14**) and (2*Z*,5*E*,16*E*)-8-hydroxy-20-isobutyl-16-methyl-7,14-dioxa-bicyclo[19.3.1]pentacosa-2,5,16-triene-10,23-dione (**15**) through comprehensive spectroscopic techniques.

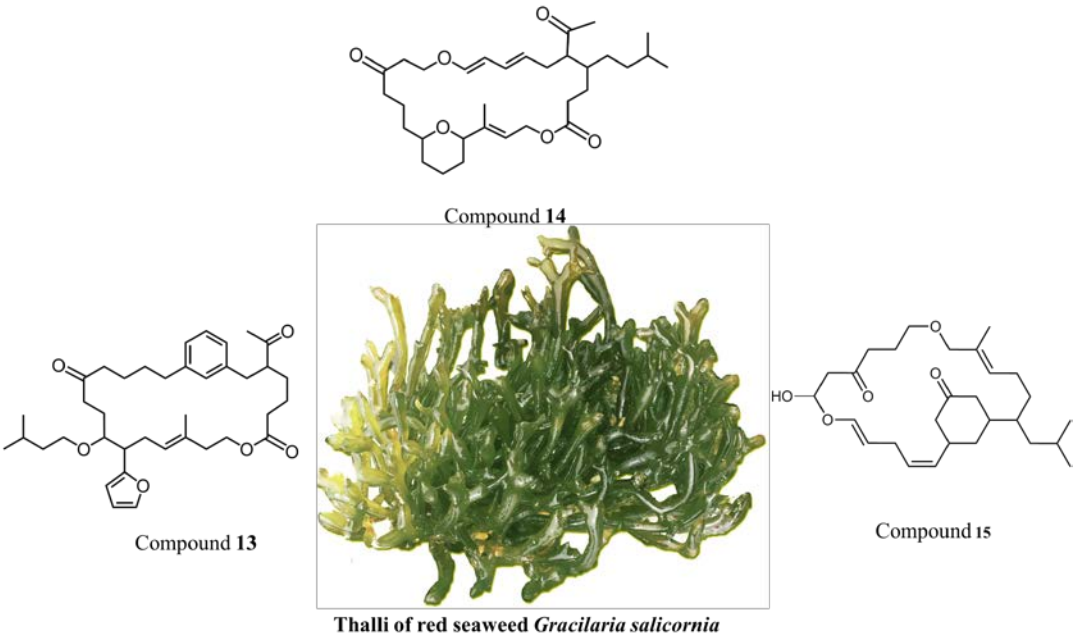

Figure 4.188.: Structural representations of 3 macrolides (**13-15**) along with the characteristic of thalli (leaf-like structures) of *G. salicornia* were presented.

4.3.2.7a Structural characterization of Compound 13

3-Acetyl-14-(furanyl)-11-methyl-15-(15^3-methylbutyloxy)-8-oxabicyclo-[21.3.1]heptacosa-11,23,25,27 tetraene-7,18-dione

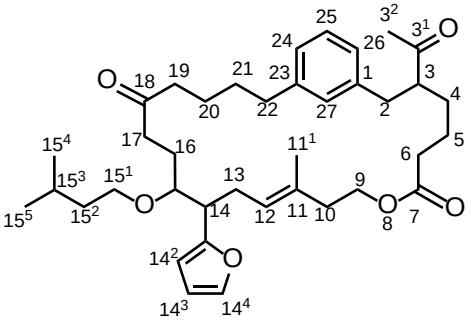

Sample yield	0.37% (> 99% purity, RP-C18 HPLC)
Physical description	Pale yellow oily
Molecular formula	$C_{38}H_{55}O_6$
Molecular mass	606.3920

The macrolide derivative, 3-acetyl-14-(furanyl)-11-methyl-15-(15^3-methylbutyloxy)-8-oxabicyclo-[21.3.1]heptacosa-11,23,25,27 tetraene-7,18-dione was isolated as pale yellow oil. The compound (**13**) has exhibited UV absorbance (UV (MeOH) λ_{max}) at 232 nm (Figure 4.189). The homogeneity of the compound was ascertained by HPLC data on a bonded phase octadecylsilane (C_{18}) stationary phase (HPLC, MeCN/MeOH, 1:2 v/v) with R_t: 4.90 min (Figure 4.190).

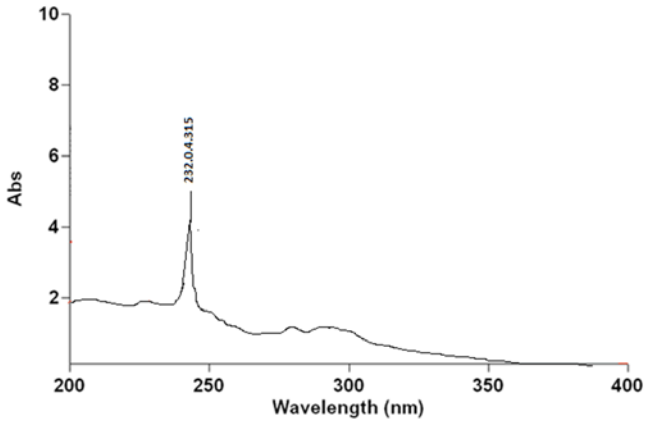

Figure 4.189.: UV spectrum of 3-acetyl-14-(furanyl)-11-methyl-15-(15[3]-methylbutyloxy)-8-oxabicyclo-[21.3.1]heptacosa-11,23,25,27 tetraene-7,18-dione (**13**)

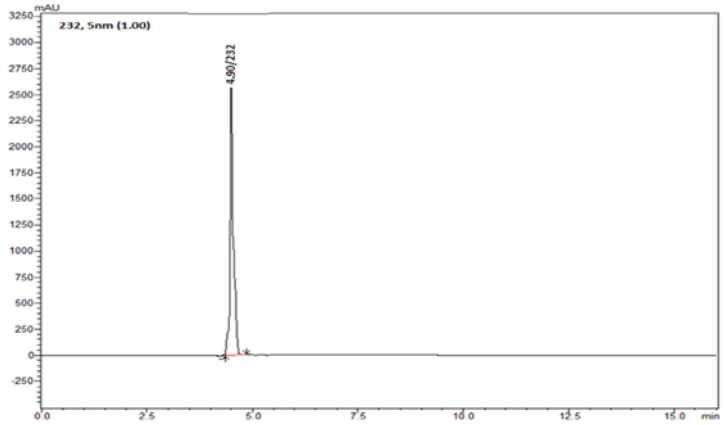

Figure 4.190.: HPLC chromatogram of 3-acetyl-14-(furanyl)-11-methyl-15-(15[3]-methylbutyloxy)-8-oxabicyclo-[21.3.1]heptacosa-11,23,25,27 tetraene-7,18-dione (**13**)

The first in the series of macrolides, 3-acetyl-14-(furanyl)-11-methyl-15-(15[3]-methylbutyloxy)-8-oxabicyclo[21.3.1] heptacosa-11,23,25,27-tetraene-7,18-dione (**13**) was acquired as a pale yellow oily substance with the molecular formula of $C_{38}H_{54}O_6$. This was ascertained by its molecular ion peak at *m/z* 606.4 $[M]^+$ along with HRESIMS data {*m/z* 607.4003 $[M+H]^+$} (Figure 4.191) that were in agreement with one/two dimensional NMR data (Table 4.20). The FTIR spectrum of compound **13** exhibited peaks at 3009/2939, 1735 and 1715 cm^{-1}, which confirmed the occurrences of C-H stretching, ester stretching (-C(=O)-O-) and C=O stretching (carbonyl), respectively (Figure 4.192).

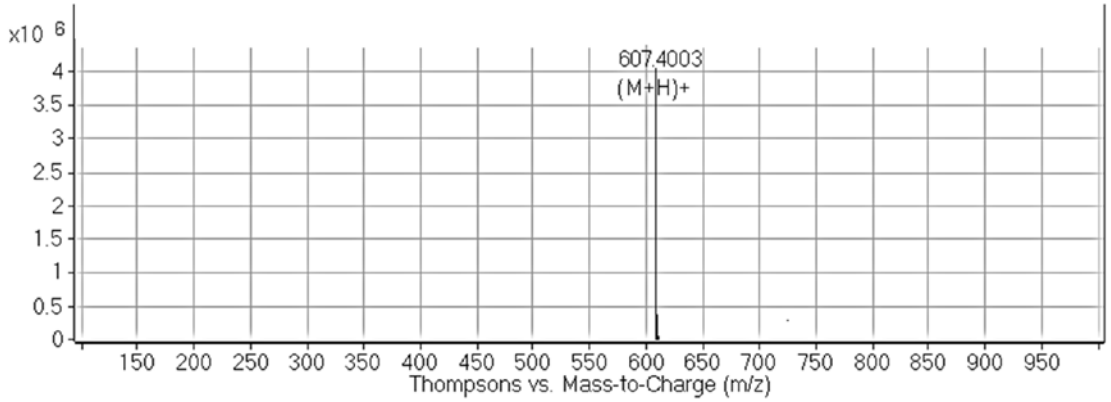

Figure 4.191.: HRESIMS spectrum of 3-acetyl-14-(furanyl)-11-methyl-15-(15^3-methylbutyloxy)-8-oxabicyclo-[21.3.1]heptacosa-11,23,25,27 tetraene-7,18-dione (**13**)

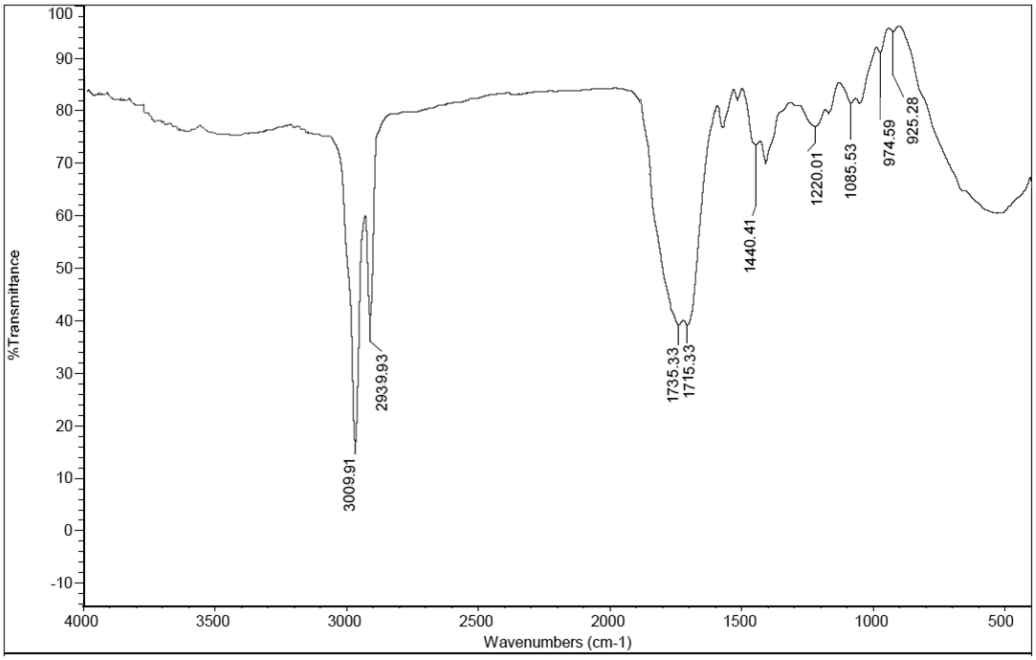

Figure 4.192.: FTIR spectrum of 3-acetyl-14-(furanyl)-11-methyl-15-(15^3-methylbutyloxy)-8-oxabicyclo-[21.3.1]heptacosa-11,23,25,27 tetraene-7,18-dione (**13**)

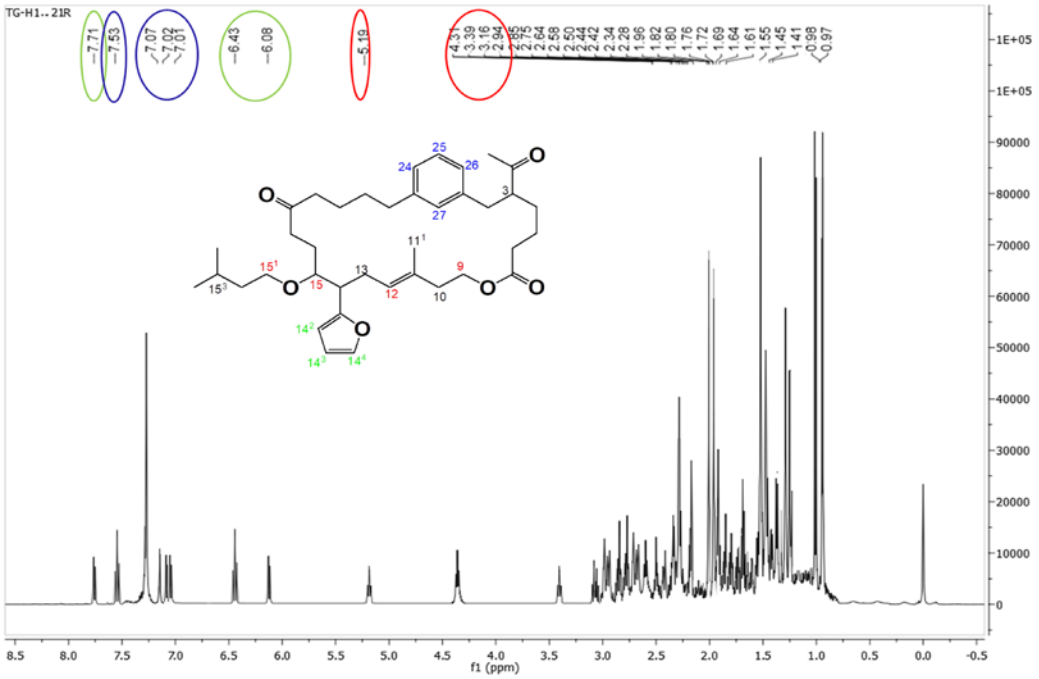

Figure 4.193.: ^{1}H NMR spectrum of 3-acetyl-14-(furanyl)-11-methyl-15-(15^{3}-methylbutyloxy)-8-oxabicyclo-[21.3.1]heptacosa-11,23,25,27 tetraene-7,18-dione

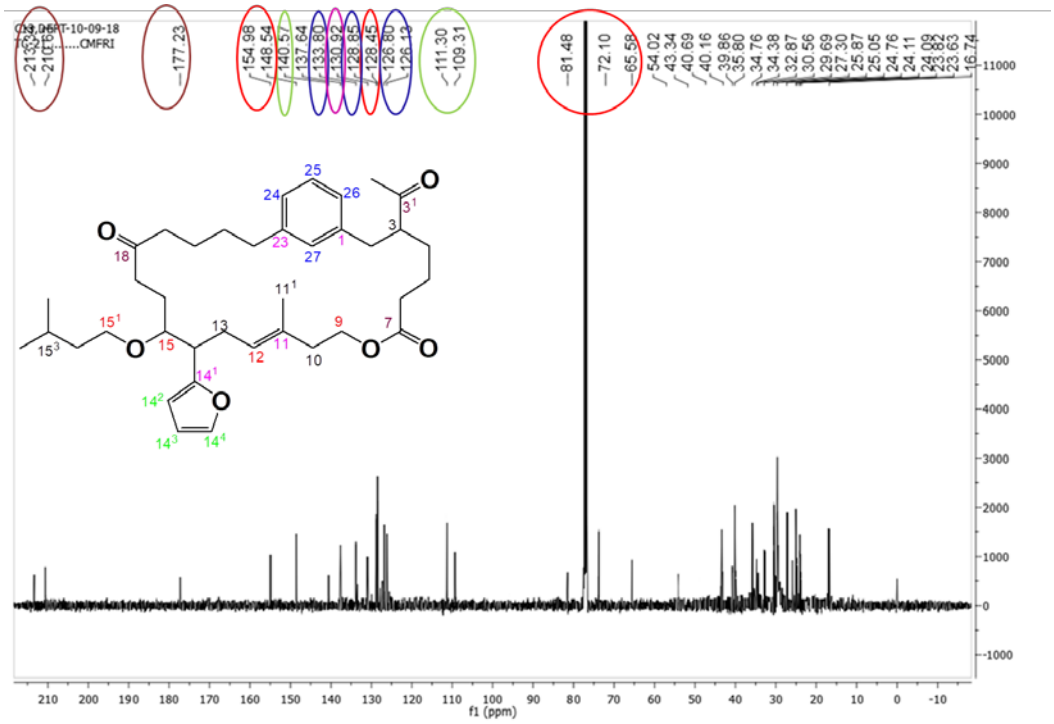

Figure 4.194.: ^{13}C NMR spectrum of 3-acetyl-14-(furanyl)-11-methyl-15-(15^{3}-methylbutyloxy)-8-oxabicyclo-[21.3.1]heptacosa-11,23,25,27 tetraene-7,18-dione (**13**)

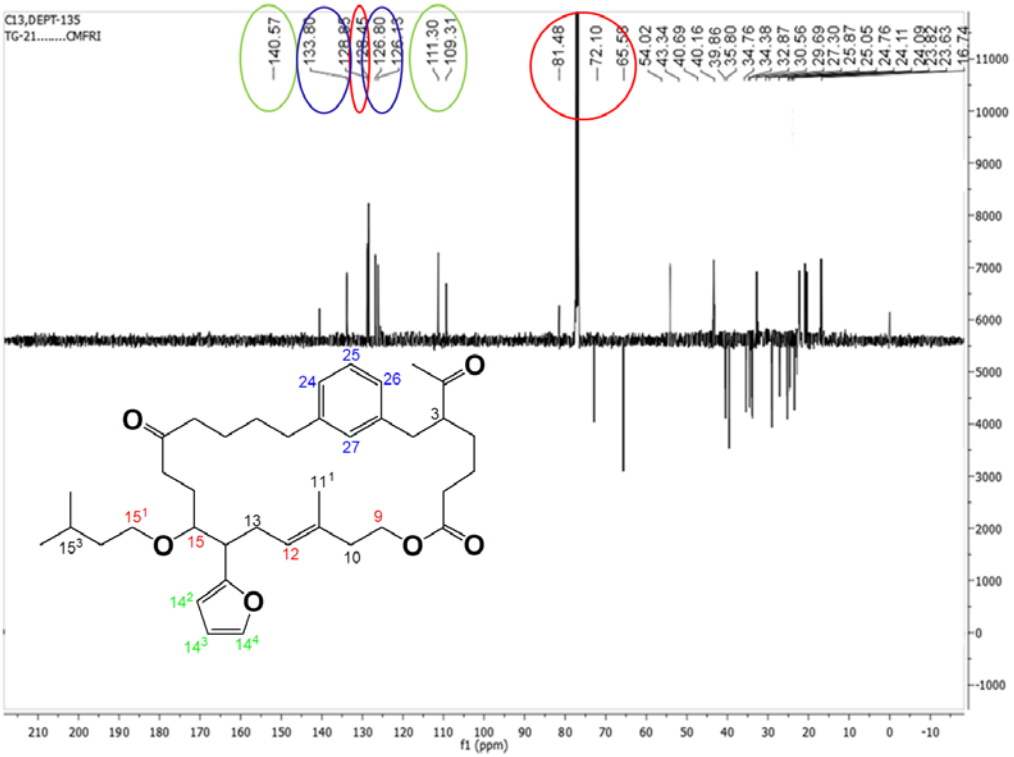

Figure 4.195.: ^{135}DEPT NMR spectrum of 3-acetyl-14-(furanyl)-11-methyl-15-(15^{3}-methylbutyloxy)-8-oxabicyclo-[21.3.1]heptacosa-11,23,25,27 tetraene-7,18-dione (**13**)

The proton (^{1}H NMR) and carbon NMR (^{13}C NMR) with DEPT spectra documented fifteen sp^{3} methylenes, twelve methines, four sp^{3} methyls along with seven quaternary carbons (two carbonyl carbons, one ester carbon and four sp^{2} carbons) (Figure 4.193). The ^{13}C NMR along with DEPT data recorded peaks at δ 177.23 corresponding to ester carbonyl {-C=O)-O-} and signals at δ 213.34 and 210.63 attributed to keto (-C=O) functionality. The sp^{2} methine groups at δ 7.02/126.80, 7.53/128.85, 7.01/126.13, 7.07/133.80, 6.08/109.31, 6.43/111.30 and 7.71/140.57 along with sp^{2} quaternary carbons at δ 137.64, 148.54 and 154.98 attributed the presence of two aromatic functionalities in compound **13** (Figure 4.194 & 4.195). These were also supported by the HSQC spectral data (Figure 4.196).

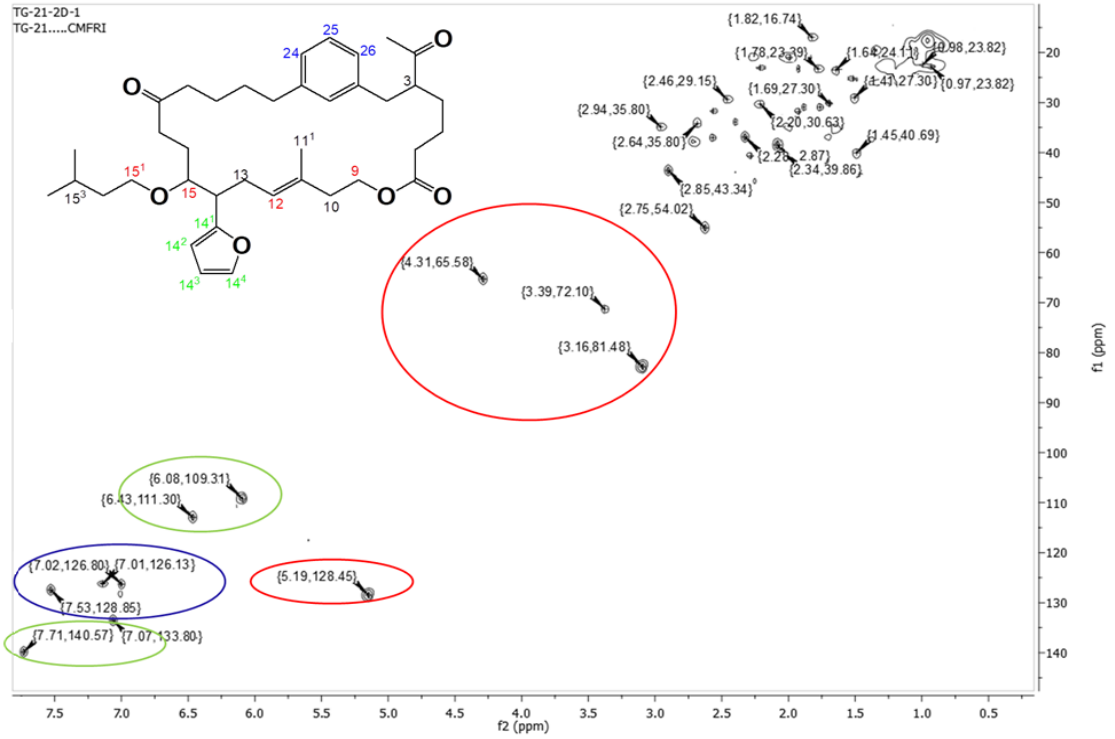

Figure 4.196.: HSQC spectrum of 3-acetyl-14-(furanyl)-11-methyl-15-(15^3-methylbutyloxy)-8-oxabicyclo-[21.3.1]heptacosa-11,23,25,27 tetraene-7,18-dione (**13**)

One of the aromatic ring skeletons were found to be benzene through the COSY (^{1}H-^{1}H) spin unit from δ 7.02/7.53/7.01 along with long-range-HMBCs observed from δ 7.02 to δ 148.54; δ 7.53 to δ 126.13 and δ 7.07, δ 7.01 to δ 148.54, which suggested the presence of a disubstituted aryl ring. The previously reported macrolactone bearing monosubstituted aryl ring as an attachment exhibited ^{13}C NMR peaks in the region of δ 129-132 (^{1}H NMR in the region of δ 7.0-7.8) with one aryl quaternary carbon at δ 132.29 (Maneesh and Chakraborty, 2017). Herein, two aryl quaternary carbons were recorded (δ 148.54, 137.64), and four proton integrals including one singlet (δ 7.0-7.5) appropriately confirmed the presence of disubstituted aryl functionality in compound **13**. Another aromatic ring skeleton was proposed as furan through COSY relations from δ 6.08/6.43/7.71 along with long-range HMBCs from δ 6.08 to δ 154.98, 111.30; δ 6.43 to δ 140.57 and δ 7.71 to δ 154.98 (Figure 4.197-4.199). Previously reported monosubstituted furan enclosed chromene recorded the quaternary carbon at δ 152.12 (Joy and Chakraborty, 2017), which was comparable to the quaternary carbon of furan ring system at δ 154.98 in present compound.

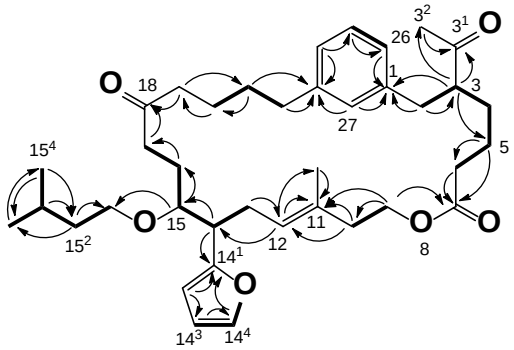

Figure 4.197.: ^{1}H-^{1}H COSY (bold face bonds) and HMBC (double-barbed arrows) correlations of 3-acetyl-14-(furanyl)-11-methyl-15-(15^{3}-methylbutyloxy)-8-oxabicyclo-[21.3.1]heptacosa-11,23,25,27 tetraene-7,18-dione (**13**)

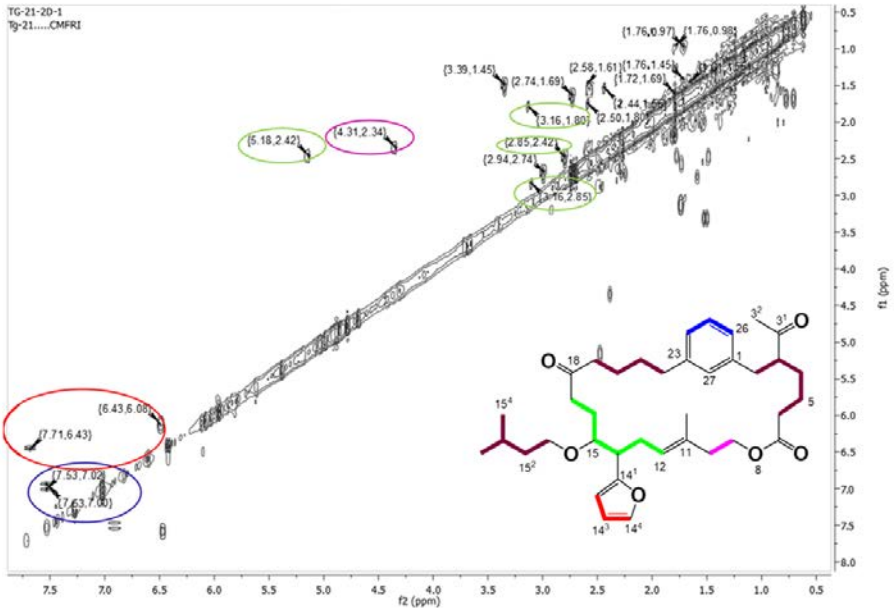

Figure 4.198.: ^{1}H-^{1}H COSY spectrum of 3-acetyl-14-(furanyl)-11-methyl-15-(15^{3}-methylbutyloxy)-8-oxabicyclo-[21.3.1]heptacosa-11,23,25,27 tetraene-7,18-dione (**13**)

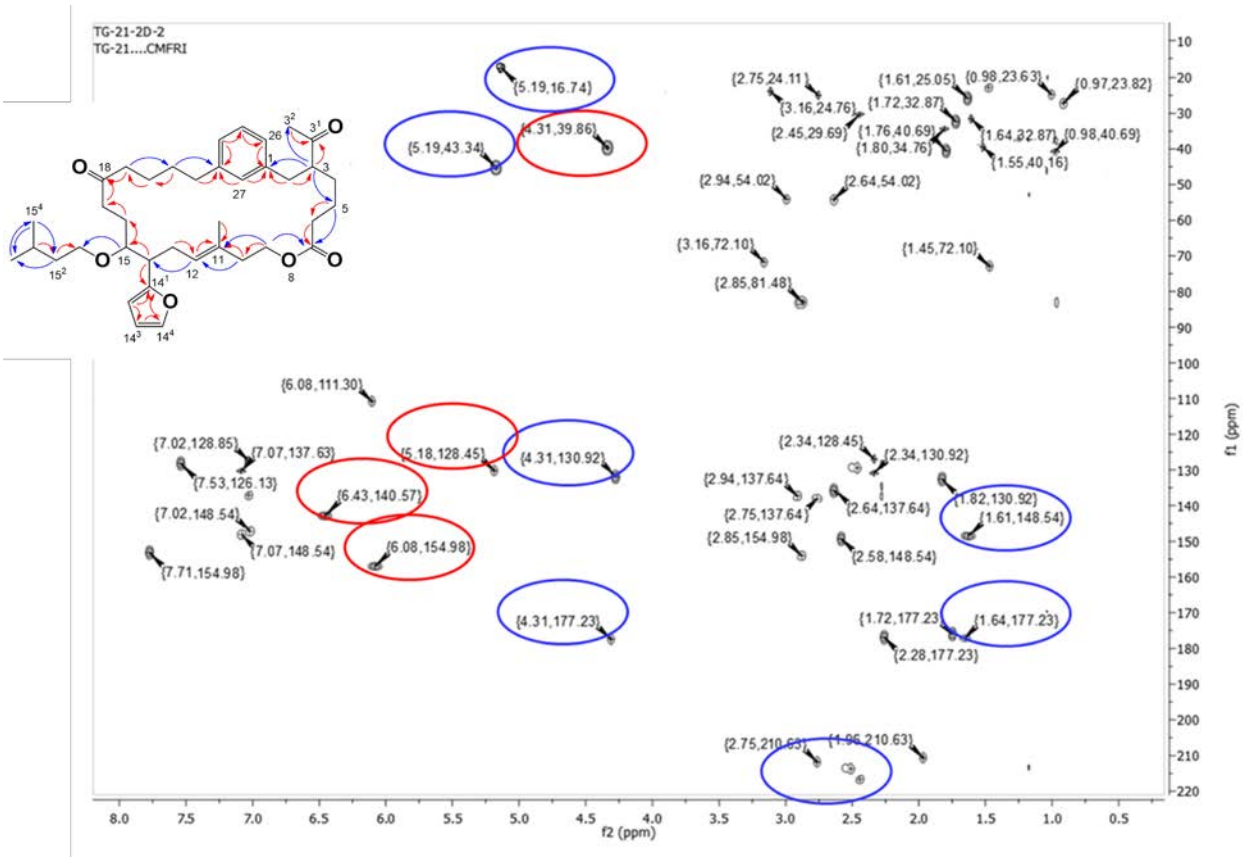

Figure 4.199.: ^{1}H-^{1}H COSY (bold face bonds) and HMBC (double-barbed arrows) correlations of 3-acetyl-14-(furanyl)-11-methyl-15-(15^{3}-methylbutyloxy)-8-oxabicyclo-[21.3.1]heptacosa-11,23,25,27 tetraene-7,18-dione (**13**)

The COSY correlations from δ 2.94, 2.64 (assigned at H-2)/2.75 (H-3)/1.69, 1.41 (H-4)/1.72, 1.64 (H-5)/2.28 (H-6); δ 4.31 (H-9)/2.34 (H-10); δ 5.19 (H-12)/2.42 (H-13)/2.85 (H-14)/3.16 (H-15)/1.80 (H-16)/2.50 (H-17) and δ 2.44 (H-19)/1.55 (H-20)/1.61 (H-21)/2.58 (H-22) were found to be the fragments of 21-membered macrocyclic ring skeleton. The relatively deshielded chemical shifts of methylene proton at δ 4.31 (at δ 65.58, HSQC) were found to reside near to an oxygen functionality of ester moiety (δ 177.23). This attribution was furthermore confirmed with the chemical shifts documented for methylenes (δC 65.58/δH 4.22-4.31) near to ester carbonyl moiety present in the aryl enclosed macrocyclic compound (Maneesh and Chakraborty, 2017). Further, the position of ester carbonyl functionality at δ 177.23 (C-7) was supported by HMBCs from δ 2.28 (H-6) and 4.31 (H-9) to δ 177.23, which designated the presence of respective ester carbonyl between C-6 and C-9 positions in the 21-membered macrocyclic ring. Similarly, the carbonyl carbon at δ 213.34 was positioned between C-17 and C-19 position of the macrocyclic ring through HMBCs from δ 2.44 (H-19) and 2.50 (H-17) to δ

213.34. The HMBC cross-peaks from δ 2.94 (H-2), 7.01 (H-26), 7.07 (H-27) to δ 137.64 (C-1) and from δ 2.58 (H-22) to δ 148.54 (C-23) appropriately assigned that the aryl ring was positioned in between carbons at C-2/C-22 positions of 21-membered macrocyclic system. Other HMBCs from δ 2.94 (H-2) to δ 54.02 (C-3); δ 4.31 (H-9) to δ 39.86 (C-10); δ 2.34 (H-10) to δ 130.92 (C-11); δ 5.19 (H-12) to δ 130.92 (C-11); δ 2.42 (H-13) to δ 128.45 (C-12); δ 3.16 (H-15) to δ 24.76 (C-16) and δ 1.61 (H-21) to δ 25.05 (C-20) further confirmed the presence of 21-membered macrocyclic ring, 8-oxabicyclo[21.3.1]heptacosa-11,23,25,27-tetraene-7,18-dione. The 16-membered macrocyclic bislactone derivative was previously reported, which enclosed two ester linkages (δ 173.79, 172.30) (Chakraborty et al., 2019), whereas the present 21-membered macrocyclic compound enclosed one each of ester (δ 177.23) and keto (δ 213.34) functionalities. The 10/13/16-membered macrolide monoesters and diesters along with ether functionalities were explained in earlier literature (Chakraborty et al., 2019). The acetyl functionality was proposed through highly deshielded signal of carbon at δ 210.63, and its position at C-3 of the 21-membered macrocyclic ring was confirmed through the intense HMBCs from δ 2.75 (H-3) and 1.96 (H-3^2) to δ 210.63 (C-3^1). The shielded singlet methyl at δ 1.82 exhibiting HSQCs with δ 16.74 (C-11^1) was bonded at C-11 of macrocyclic ring through HMBCs from δ 1.82 (H-11^1) to δ 130.92 (C-11). The attachment of methyl group at C-11 in the macrocyclic ring was further corroborated by the HMBC correlation from δ 5.19 (H-12) to δ 16.74 (C-11^1). The HMBCs from δ 2.85 (H-14) to δ 154.98 (C-14^1, part of furan ring) confirmed the attachment of furan ring at C-14 position of macrocyclic ring. The coupling constants of these furan protons at H-14^2 (1H, d, 1.3 Hz), H-14^3 (1H, t, 2.9 Hz) and H-14^2 (1H, d, 1.6 Hz), which were <3, were found to be the characteristic features of furan protons (Abdelgaleil et al., 2006; Sadaka, 2017). The COSY correlations from δ 3.39 (H-15^1)/1.45 (H-15^2)/1.76 (H-15^3)/0.98 (H-15^4), 0.97 (H-15^5) along with HMBCs from δ 0.98 (H-15^4) to δ 23.63 (C-15^5), 40.69 (C-15^2); δ 0.97 (H-15^5) to δ 23.82 (C-15^4) proposed the presence of methylbutyloxy chain, and it was bonded at C-15 of a 21-membered macrocyclic ring through HMBCs from δ 3.16 (H-15) to 72.10 (C-15^1). These data suggested its degree of unsaturations as twelve corresponding to three ring systems and nine double bonds. The absolute stereochemistries of chiral centers in macrolides could not be determined by chemical or direct spectroscopic methods; thus we performed a rigorous conformational study supported by experimental distance derived from the NOESY spectrum.

The relative stereochemistries of the proton peaks at C-3, C-14 and C-15 were described unambiguously from the NOESY interactions (Figure 4.200 & 4.201). The proton at δ 2.85 (H-14) displayed NOESY cross-peak with that at δ 3.16 (H-15), which attributed that these might be disposed at the identical plane of symmetry, and therefore, assigned as β-oriented. The

orientation of H-14 and H-15 in the same plane in compound **13** was also corroborated by the NOESY cross-peaks between δ 2.34 (H-10)/ δ 5.19 (H-12); δ 5.19 (H-12)/ δ 2.42 (H-13); δ 3.39 (H-15^1)/ δ 1.80 (H-16); δ 2.42 (H-13)/ δ 2.85 (H-14); δ 3.16 (H-15)/ δ 1.80 (H-16). The chiral proton at δ 2.75 (H-3) displayed NOESY correlation with singlet methyl at δ 1.82 (H-11^1), which did not exhibit any NOE cross-peaks with the β-oriented proton signals, and hence, attributed as α-oriented.

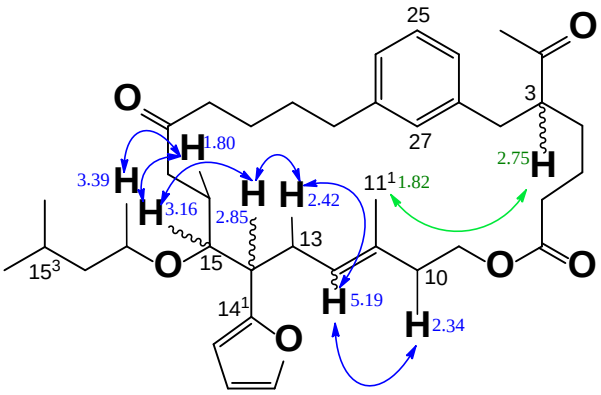

Figure 4.200.: NOE (double-barbed green coloured arrows for α-orientation and blue coloured arrows for β orientations) correlations of 3-acetyl-14-(furanyl)-11-methyl-15-(15^3-methylbutyloxy)-8-oxabicyclo-[21.3.1]heptacosa-11,23,25,27 tetraene-7,18-dione (**13**)

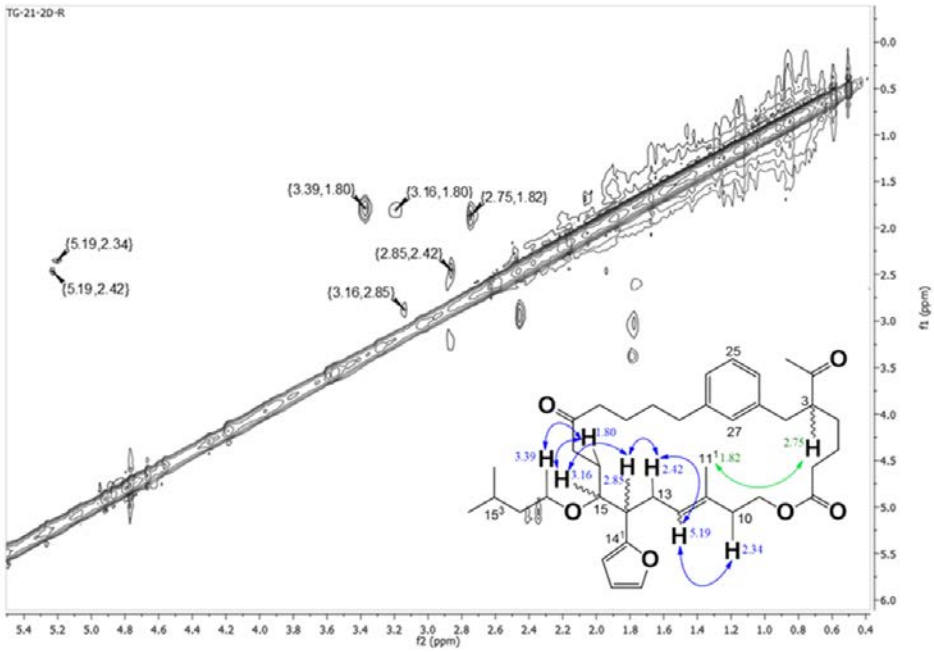

Figure 4.200.: NOESY spectrum of 3-acetyl-14-(furanyl)-11-methyl-15-(15^3-methylbutyloxy)-8-oxabicyclo-[21.3.1]heptacosa-11,23,25,27 tetraene-7,18-dione (**13**)

Table 4.20: NMR spectroscopic data of compound (**13),** 3-acetyl-14-(furanyl)-11-methyl-15-(15^3-methylbutyloxy)-8-oxabicyclo-[21.3.1]heptacosa-11,23,25,27 tetraene-7,18-dione (**13**) isolated from red seaweed *G. salicornia*

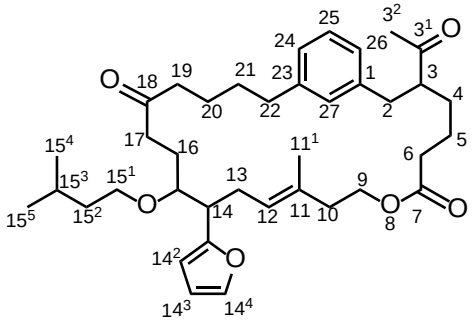

Compound **13** …….. 3-Acetyl-14-(furanyl)-11-methyl-15-(15^3-methylbutyloxy)-8-oxabicyclo-[21.3.1]heptacosa-11,23,25,27 tetraene-7,18-dione (**13**)

Type	**C. No.**	**^{13}C NMR**	**H. No. (int., mult., *J* in Hz)‡**	**^{1}H NMR**	**COSY**	**HMBC**
C	1	137.64	-	-	-	-
CH_2	2	35.80	1H,dd,11.1, 6.8 Hz	2.94	H-3	C-3,1
			1H,dd,11.0, 6.5 Hz	2.64	-	-
CH	3	54.02	1H,m	2.75	H-4	C-1,5,3^1
CH_2	4	27.30	1H,m	1.69	H-5	-
			1H,m	1.41	-	-
CH_2	5	24.11	1H,m	1.72	H-6	C-6,7
			1H,m	1.64	-	-
CH_2	6	32.87	2H,m	2.28	-	C-7
C	7	177.23	-	-	-	-
-	8		-	-	-	-
CH_2	9	65.58	2H,t,7.8 Hz	4.31	H-10	C-7,10,11
CH_2	10	39.86	2H,t,7.6 Hz	2.34	-	C-11,12
C	11	130.92	-	-	-	-
CH	12	128.45	1H,t, 6.2 Hz	5.19	H-13	C-11,14,11^1
CH_2	13	25.87	2H,m	2.42	H-14	C-12
CH	14	43.34	1H,m	2.85	H-15	C-14^1,15
CH	15	81.48	1H,m	3.16	H-16	C-16, 15^1
CH_2	16	24.76	2H,m	1.80	H-17	C-17
CH_2	17	34.76	2H,t,7.8 Hz	2.50	-	C-18
C	18	213.34	-	-	-	-
CH_2	19	40.16	2H, t,7.9 Hz	2.44	H-20	C-18,21
CH_2	20	25.05	2H,m	1.55	H-21	C-19
CH_2	21	29.69	2H,m	1.61	H-22	C-20,23
CH_2	22	34.38	2H,t,5.8 Hz	2.58	-	C-23
C	23	148.54	-	-	-	-
CH	24	126.80	1H,d,7.4 Hz	7.02	H-25	C-23,25
CH	25	128.85	1H,t,7.6 Hz	7.53	H-26	C-26
CH	26	126.13	1H,d,7.6 Hz	7.01	-	C-1
CH	27	133.80	1H,s	7.07	-	C-1,23

C	3^1	210.63	-	-	-	-
CH_3	3^2	30.56	3H,s	1.96	-	C-3^1
CH_3	11^1	16.74	3H,s	1.82	-	C-11
C	14^1	154.98	-	-	-	-
CH	14^2	109.31	1H,d,1.3Hz	6.08	H-14^3	C-14^1,14^3
CH	14^3	111.30	1H,t, 2.9 Hz	6.43	H-14^4	C-14^4
CH	14^4	140.57	1H,d,1.6 Hz	7.71	-	C-14^1
CH_2	15^1	72.10	2H,t,7.7 Hz	3.39	H-15^2	-
CH_2	15^2	40.69	2H,m	1.45	H-15^3	C-15^1,15^5
CH	15^3	24.09	1H,m	1.76	H-15^4, H-15^5	C-15^2
CH_3	15^4	23.82	3H,d,5.1 Hz	0.98		C-15^5,15^2
CH_3	15^5	23.63	3H,d,5.3 Hz	0.97		C-15^4

†NMR spectra were recorded using a Bruker AVANCE III 500 MHz (AV 500) spectrometer (Bruker, Karlsruhe, Germany) in $CDCl_3$ as aprotic solvent at ambient temperature with TMS as the internal standard (δ 0 ppm).

‡Values in ppm, multiplicity and coupling constants (*J* = Hz) were indicated in parentheses. Multiplicities were allocated by ^{135}DEPT NMR spectrum.

The assignments were made with the aid of the COSY, HSQC, HMBC and NOESY experiments.

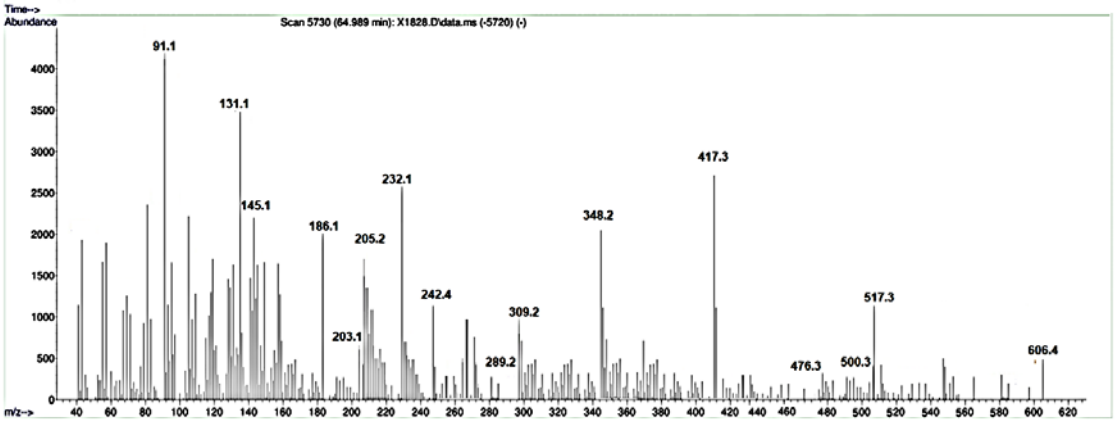

Figure 4.201.: EI-MS spectrum of 3-acetyl-14-(furanyl)-11-methyl-15-(15^3-methylbutyloxy)-8-oxabicyclo-[21.3.1]heptacosa-11,23,25,27 tetraene-7,18-dione (**13**)

The molecular ion peak at *m/z* 606 (**1**), with a molecular formula of $C_{38}H_{54}O_6$ appeared to undergo fragmentation by heterolytic cleavage followed by McLafferty rearrangement to yield a fragment at *m/z* 517 (**2**; $C_{33}H_{41}O_5^+$). The latter on further elimination of hydroxyl radical and acetylene formed the fragments, **3** and **4** with *m/z* 500 and 476,

respectively. The fragment at *m/z* 91 was found to be the base-peak that might correspond to $C_7H_7^+$ (Figure 4.201 & 4.202).

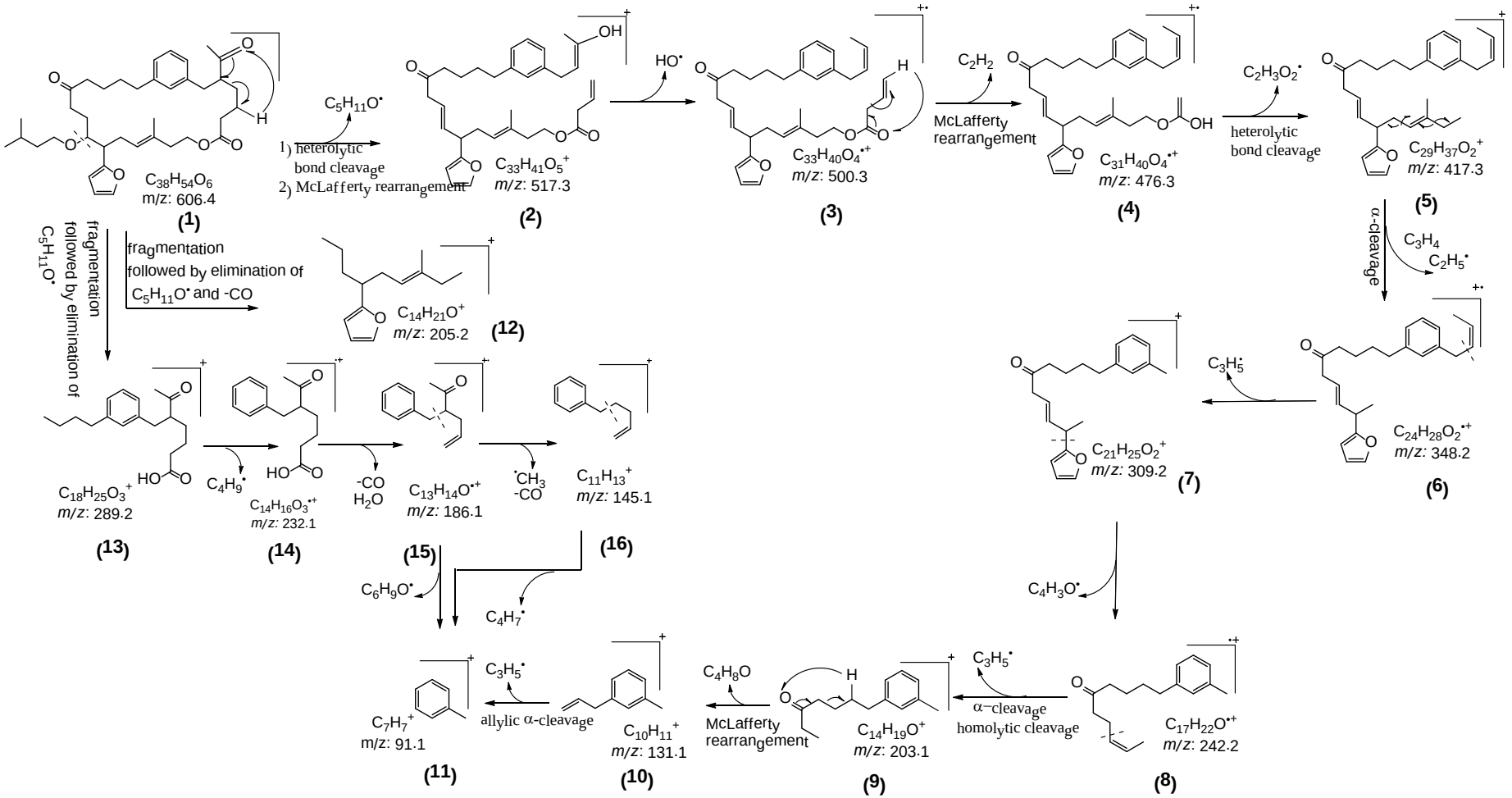

Figure 4.202.: Tentative mass fragmentation pattern of 3-acetyl-14-(furanyl)-11-methyl-15-(15^3-methylbutyloxy)-8-oxabicyclo-[21.3.1]heptacosa-11,23,25,27 tetraene-7,18-dione (**13**)

4.3.2.7b Structural characterization of Compound 14

(2E,12E,14E)-10-Acetyl-9-isopentyl-2-methyl-5,16,23[1]-trioxa-bicyclo[21.3.1]-heptacosa-2,12,14-triene-6,19-dione

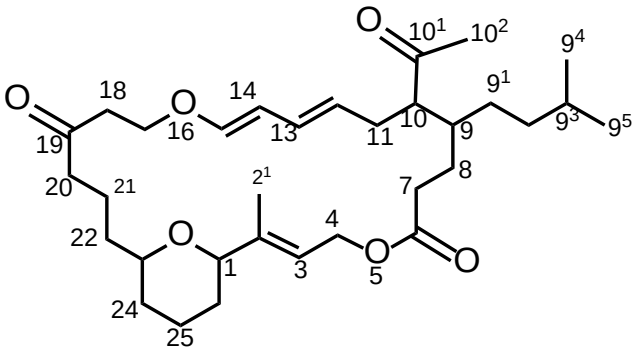

Sample yield	0.33% (> 99% purity, RP-C18 HPLC)
Physical description	Pale yellow oily
Molecular formula	$C_{32}H_{50}O_6$
Molecular mass	530.7358

The macrolide derivative, 3-acetyl-14-(furanyl)-11-methyl-15-(15[3]-methylbutyloxy)-8-oxabicyclo-[21.3.1]heptacosa-11,23,25,27 tetraene-7,18-dione was isolated as pale yellow oil. The compound (**13**) has exhibited UV absorbance (UV (MeOH) λ_{max}) at 237 nm (Figure 4.203). The homogeneity of the compound was ascertained by HPLC data on a bonded phase octadecylsilane (C_{18}) stationary phase (HPLC, MeCN/MeOH, 1:2 v/v) with R_t: 4.30 min (Figure 4.204).

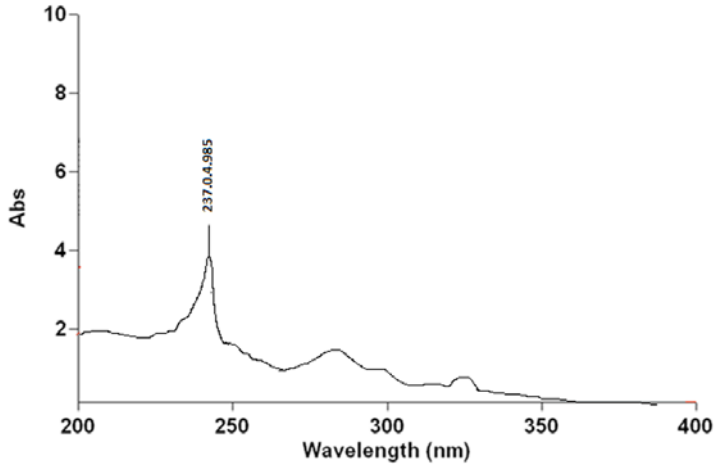

Figure 4.203.: UV spectrum of (2E,12E,14E)-10-acetyl-9-isopentyl-2-methyl-5,16,23[1]-trioxa-bicyclo[21.3.1]-heptacosa-2,12,14-triene-6,19-dione (**14**)

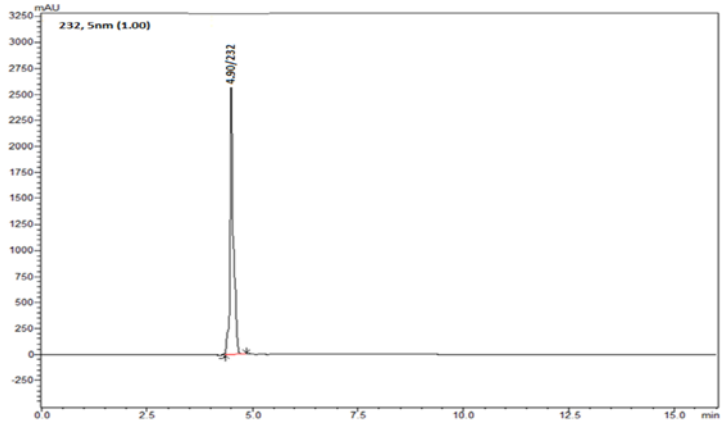

Figure 4.204.: HPLC chromatogram of (2E,12E,14E)-10-acetyl-9-isopentyl-2-methyl-5,16,23[1]-trioxa-bicyclo[21.3.1]-heptacosa-2,12,14-triene-6,19-dione (**14**)

The second compound in the series was characterised as (2*E*,12*E*,14*E*)-10-acetyl-9-isopentyl-2-methyl-5,16,23[1]-trioxa-bicyclo[21.3.1]heptacosa-2,12,14-triene-6,19-dione (**14**), and was acquired as a pale yellow oily substance with the elemental-composition of $C_{32}H_{50}O_6$. The molecular-ion peak was recorded at *m/z* 530.7 $[M]^+$ that along with HRESIMS data {*m/z* 531.3690 $[M+H]^+$} (Figure 4.205)were in agreement with one and two dimensional NMR data (Table 4.21)

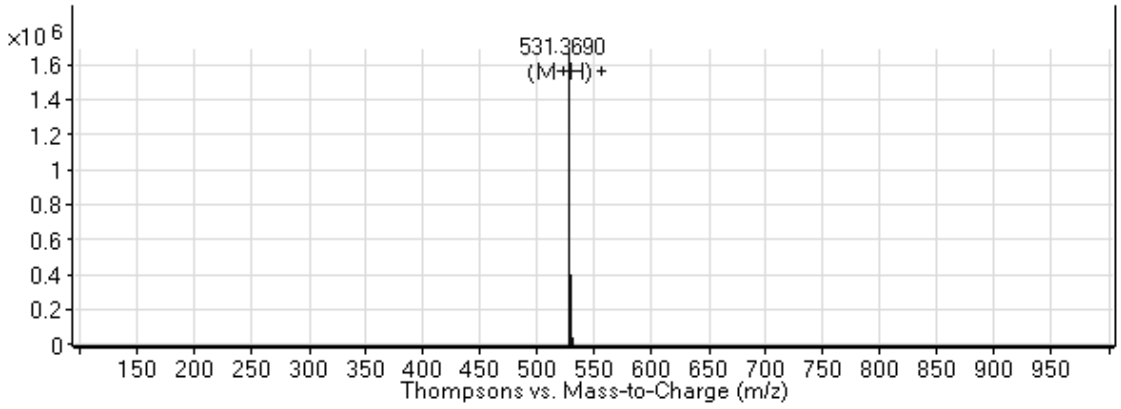

Figure 4.205.: HRESIMS spectrum of (2E,12E,14E)-10-acetyl-9-isopentyl-2-methyl-5,16,23[1]-trioxa-bicyclo[21.3.1]-heptacosa-2,12,14-triene-6,19-dione (**14**)

The FTIR spectrum exhibited stretching vibration peaks at 2923/2799, 1742 and 1717 cm^{-1}, which designated the occurrences of C-H, ester and ketone functional groups, respectively in compound **14** (Figure 4.206). The $^1H/^{13}C$ NMR and DEPT NMR established the possibilities of fourteen sp^3 methylenes, ten methines, four each of sp^3 methyls and quaternary carbons (two

carbonyl carbons, one ester carbon and one sp^2 carbon). The ^{13}C NMR along with DEPT displayed peaks at δ 177.30 for ester carbonyl and at δ 213.48 and 209.30 for carbonyl carbon functionalities. The greatly deshielded proton signals at δ 5.54, 5.81, 5.34, 5.05 and 6.37 bonded to the carbons at δ 125.14, 135.43, 133.64, 109.09 and 145.05, respectively (from HSQC) were deduced to correspond with olefinic functionalities in compound **14** (Figure 4.207-210).

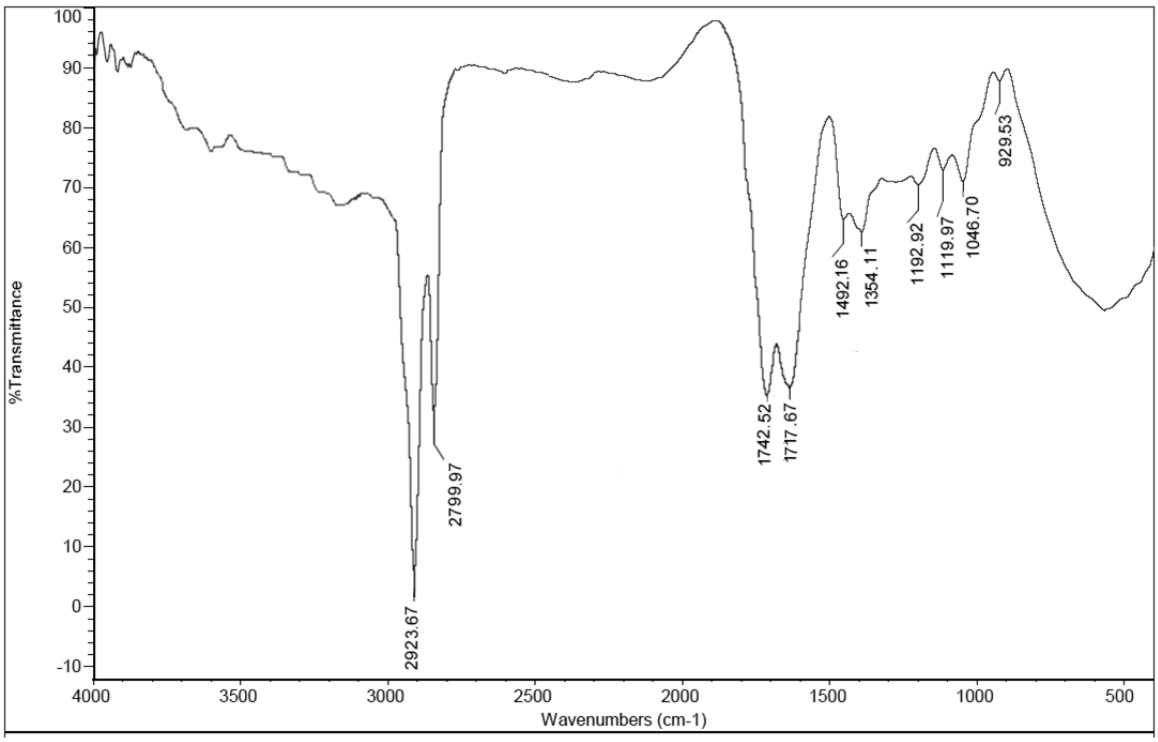

Figure 4.206.: FTIR spectrum of (2E,12E,14E)-10-acetyl-9-isopentyl-2-methyl-5,16,23[1]-trioxa-bicyclo[21.3.1]-heptacosa-2,12,14-triene-6,19-dione (**14**)

The COSY correlations suggested the spin systems, which were deduced as δ 4.78 (assigned at H-1)/1.80 (H-26); δ 1.72 (H-24)/3.65 (H-23)/1.53, 1.25 (H-22)/1.68, 1.56 (H-21)/2.49, 2.43 (H-20); δ 5.54 (H-3)/4.90 (H-4); δ 2.30 (H-7)/1.77 (H-8); δ 1.75 (H-9)/2.33 (H-10); δ 2.37 (H-11)/5.81 (H-12)/5.34 (H-13)/5.05 (H-14)/6.37 (H-15); δ 1.77 (H-24)/1.66 (H-25)/1.80 (H-26) (Figure 4.211 & 4.213). These spin systems might be the fragments of a 21-membered macrocyclic ring skeleton. The presence of an ester carbonyl functionality at δ 177.30 was proposed through the HMBCs from protons at δ 2.30 (H-7) and δ 4.90 (H-4) to δ 177.30 (C-6), which suggested that the ester carbonyl functionality was disposed in between C-7 and C-4 positions of the 21-membered macrocyclic ring. The carbonyl-carbon was found at δ 213.48 (C-19) through the intense HMBCs from δ 2.92 (H-18) and δ 2.49 (H-20) to δ 213.48 (C-19) (Figure 4.214).

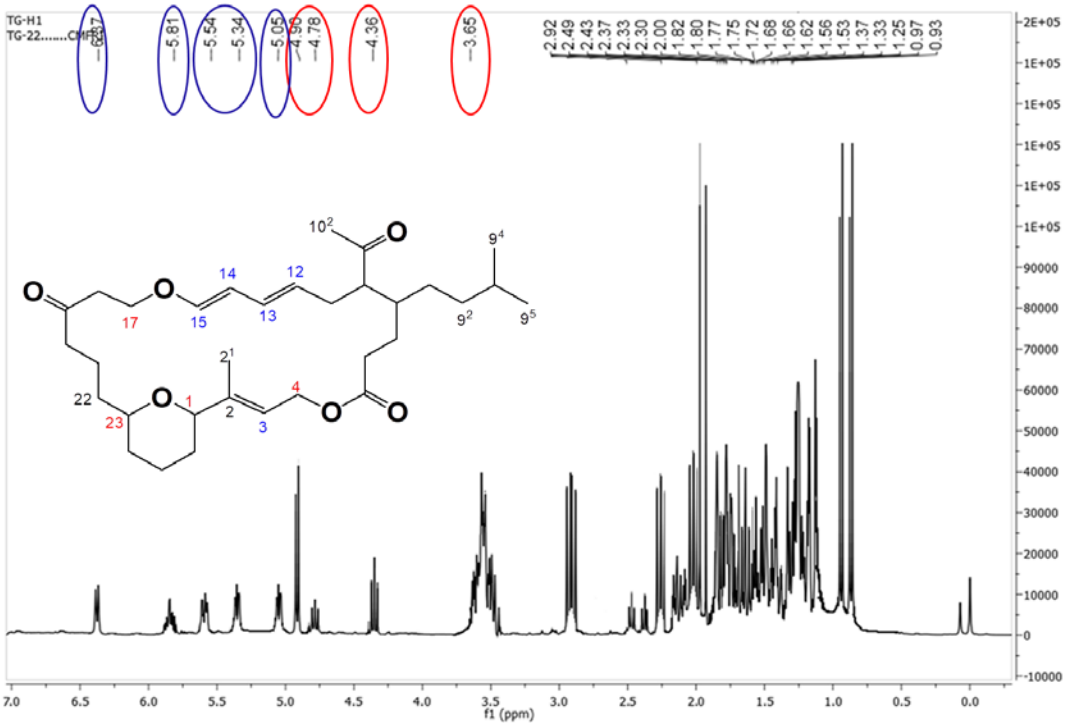

Figure 4.207.: ^{1}H NMR spectrum of (2E,12E,14E)-10-acetyl-9-isopentyl-2-methyl-5,16,23[1]-trioxa-bicyclo[21.3.1]-heptacosa-2,12,14-triene-6,19-dione (**14**)

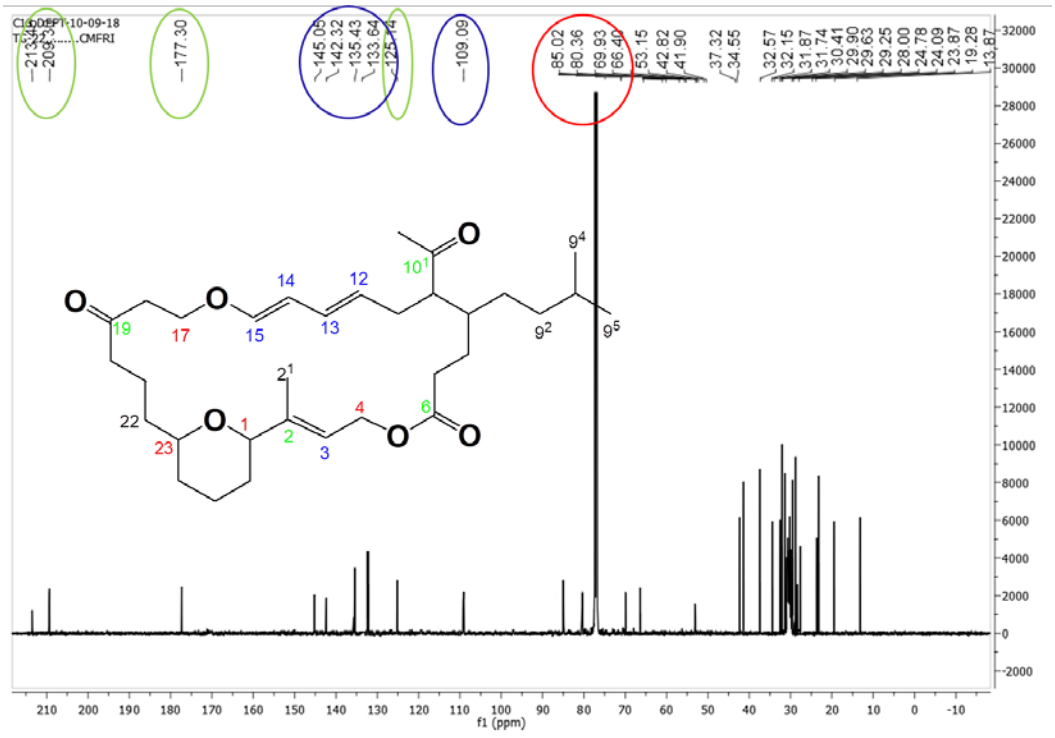

Figure 4.208.: ^{13}C NMR spectrum of (2E,12E,14E)-10-acetyl-9-isopentyl-2-methyl-5,16,23[1]-trioxa-bicyclo[21.3.1]-heptacosa-2,12,14-triene-6,19-dione (**14**)

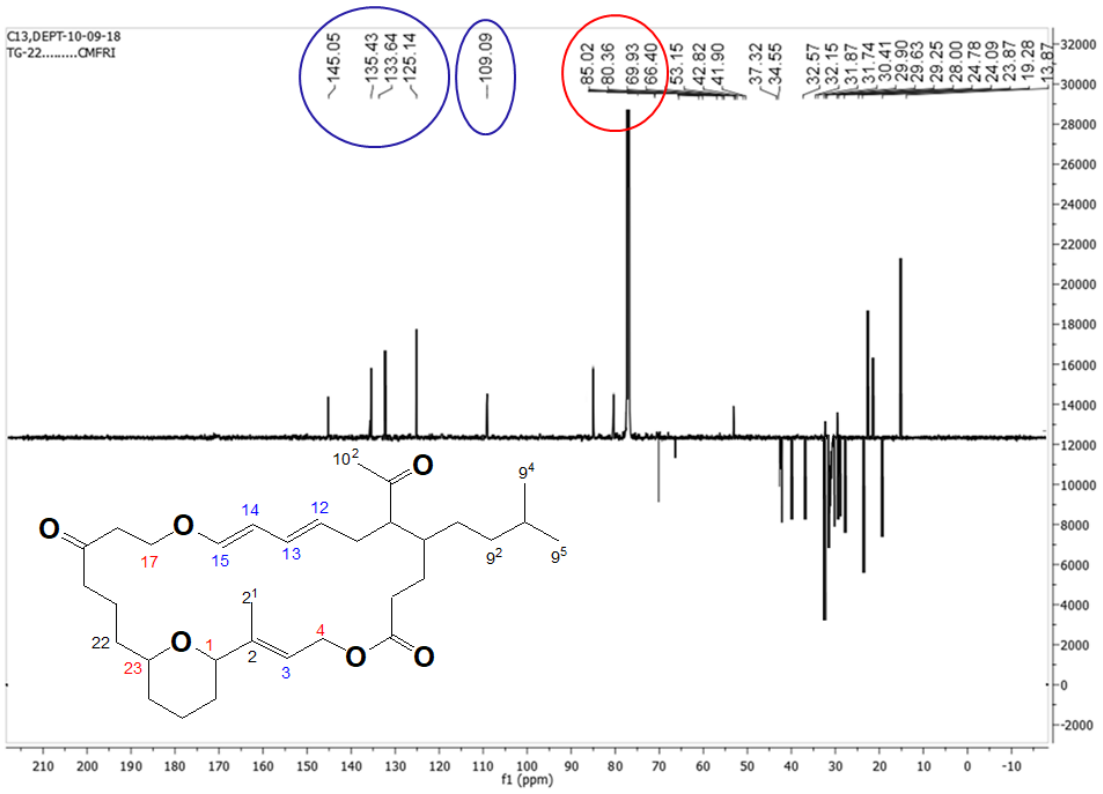

Figure 4.209.: ^{135}DEPT NMR spectrum of (2E,12E,14E)-10-acetyl-9-isopentyl-2-methyl-5,16,23[1]-trioxa-bicyclo[21.3.1]-heptacosa-2,12,14-triene-6,19-dione (**14**)

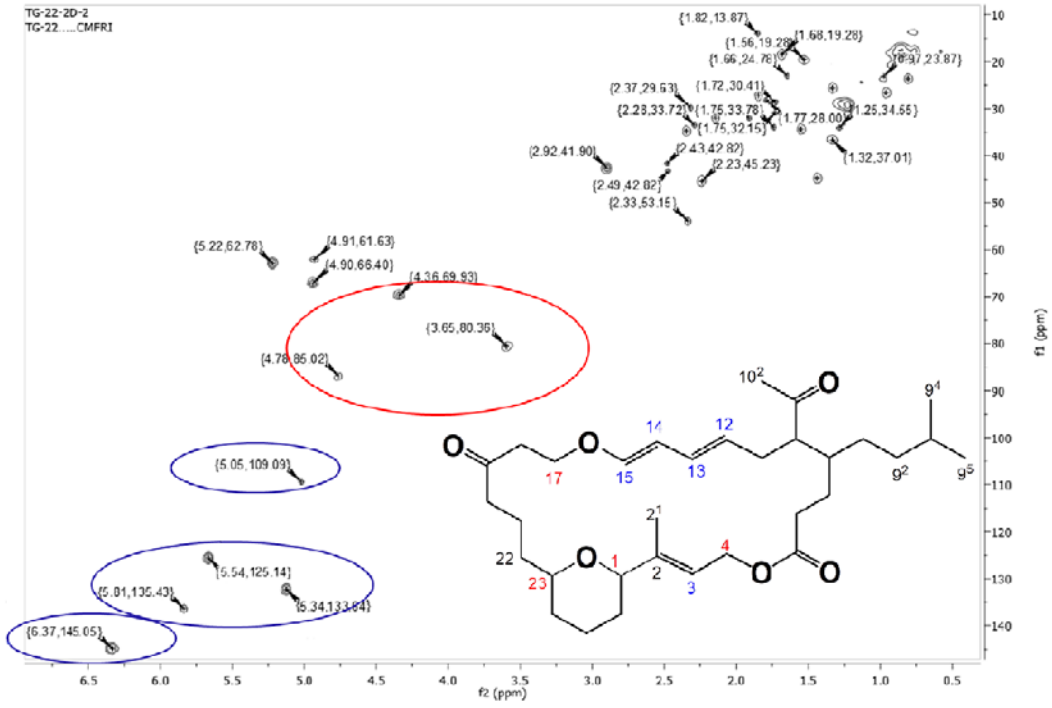

Figure 4.210.: HSQC spectrum of (2E,12E,14E)-10-acetyl-9-isopentyl-2-methyl-5,16,23[1]-trioxa-bicyclo[21.3.1]-heptacosa-2,12,14-triene-6,19-dione (**14**)

The previously reported 16-membered macrocyclic bislactone derivative enclosed two esters (δ 172-173) (Chakraborty et al., 2019), while the titled compound bound one each of ester (δ 177.30), ketone (δ 213.48) and ether functionalities. The HMBCs from δ 1.72 (H-24) to δ 80.36 (C-23), 34.55 (C-22); δ 1.66 (H-25) to δ 30.41 (C-24), and δ 1.80 (H-26) to δ 24.78 (C-25) assigned the presence of a pyran ring in a 21-membered macrocyclic ring. This pyran ring was located between C-2 and C-22 carbons through the HMBCs from δ 3.65 (H-23) to δ 34.55 (C-22), 85.02 (C-1) and δ 4.87 (H-1) to δ 24.78 (C-25) in the macrocyclic ring. The 14-membered macrocyclic derivative possessing a tetrahydropyran ring and 24-membered macrolactones enclosing tetrahydropyran moieties were previously reported from the marine organisms (Kito et al., 2008; Mondol et al., 2011).

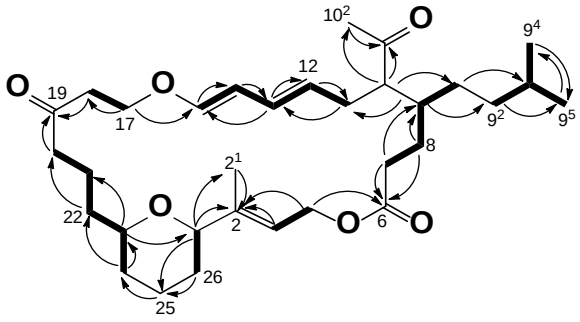

Figure 4.211.: ^{1}H-^{1}H COSY (bold face bonds) and HMBC (double-barbed arrows) correlations of (2E,12E,14E)-10-acetyl-9-isopentyl-2-methyl-5,16,23^{1}-trioxa-bicyclo[21.3.1]-heptacosa-2,12,14-triene-6,19-dione (**14**)

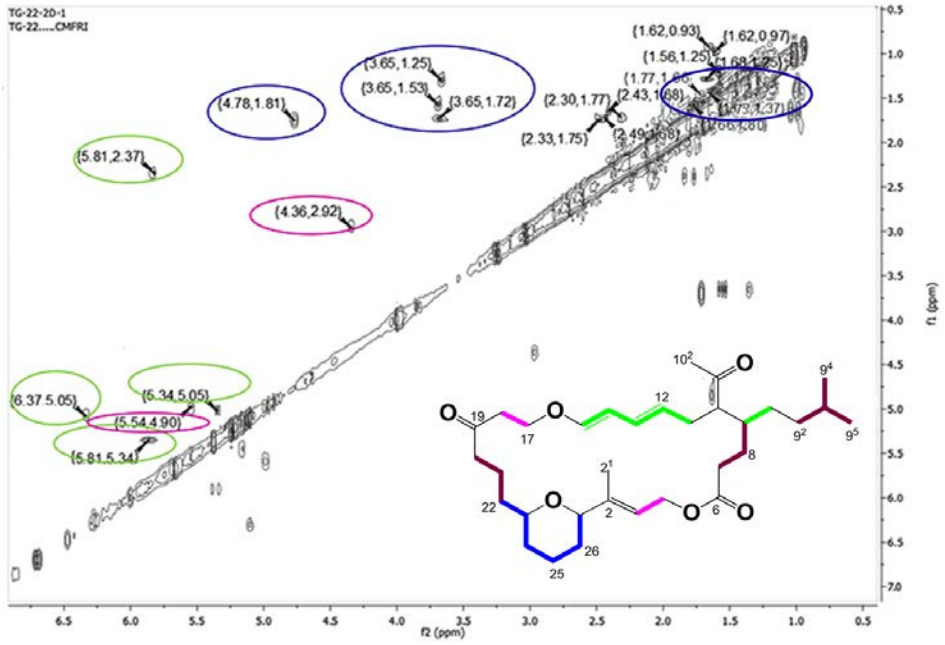

Figure 4.212.: ^{1}H-^{1}H COSY spectrum of (2E,12E,14E)-10-acetyl-9-isopentyl-2-methyl-5,16,23^{1}-trioxa-bicyclo[21.3.1]-heptacosa-2,12,14-triene-6,19-dione (**14**)

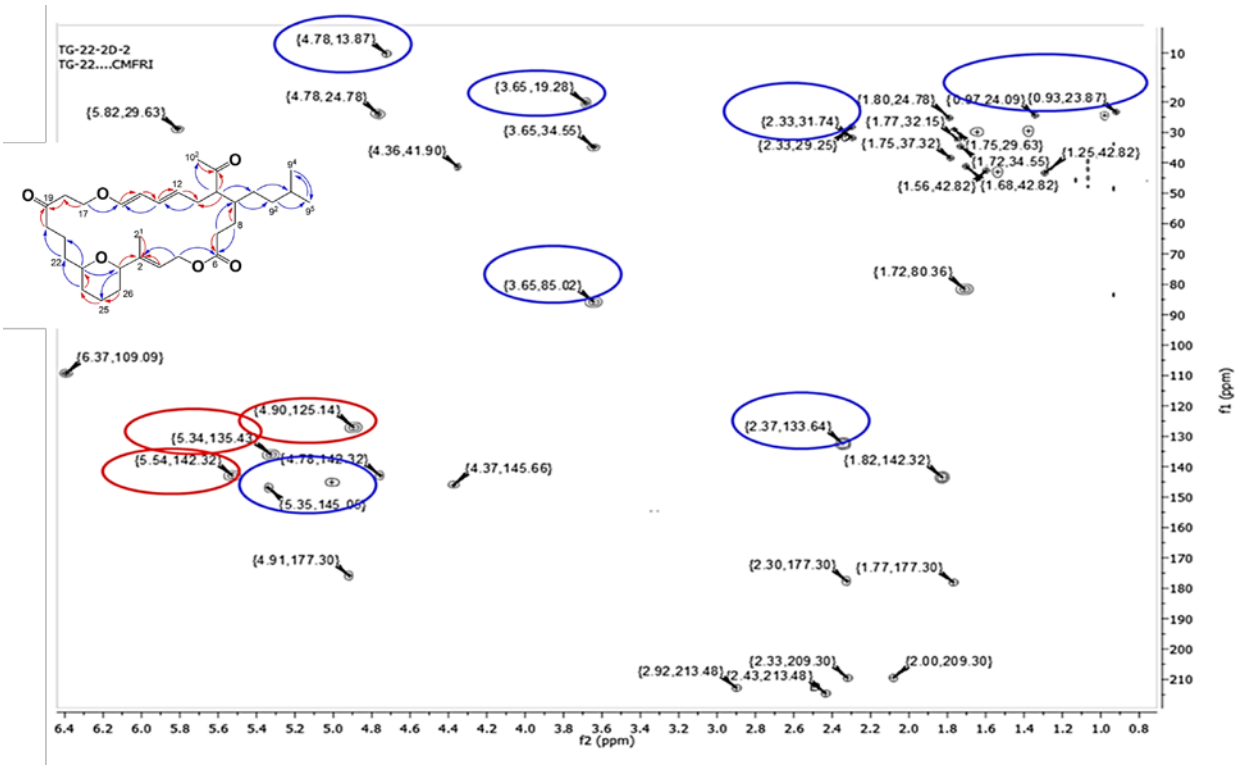

Figure 4.213.: HMBC spectrum of (2E,12E,14E)-10-acetyl-9-isopentyl-2-methyl-5,16,23[1]-trioxa-bicyclo[21.3.1]-heptacosa-2,12,14-triene-6,19-dione (**14**)

The 14-membered tetrahydropyran enclosed macrocyclic derivative exhibited chemical shifts at δ 4.23/74, 3.38/66, 1.95/21, 2.21/21, 4.21/71 corresponding to the hydroxyl attached tetrahydropyran ring along with disubstituted alkene at δ 5.79/132, 5.69/137 adjacent to the tetrahydropyran system (Kito et al., 2008; Mondol et al., 2011). These values were comparable with the pyran ring in compound **2**, except with the absence of hydroxyl and a trisubstituted alkene adjacent to the pyran ring instead of disubstituted alkene functionality, as described previously (Kito et al., 2008). Further, HMBCs were displayed from δ 5.54 (H-3) to δ 142.32 (C-2); δ 4.90 (H-4) to δ 125.14 (C-3); δ 1.77 (H-8) to δ 177.30 (C-6), 32.15 (C-9); δ 5.81 (H-12) to δ 29.63 (C-11); δ 5.05 (H-14) to δ 133.64 (C-13); δ 6.37 (H-15) to δ 109.09 (C-14); δ 4.36 (H-17) to δ 145.05 (C-15) and δ 1.53 (H-22) to δ 42.82 (C-20) that were coherent with the macrocyclic ring, 5,16,23[1]-trioxa-bicyclo[21.3.1] heptacosa-2,12,14-triene-6,19-dione. The shielded singlet methyl at δ 1.82/13.87 was bonded at C-2 position through the HMBCs obtained from δ 1.82 (H-2[1]) to δ 142.32 (C-2). The presence of methyl was further supported by the HMBC correlation from δ 4.78 (H-1) to δ 13.87 (C-2[1]). The acetyl group was supported by highly deshielded carbonyl carbon peak at δ 209.30 and the singlet methyl at δ 2.00/31.74. Its position was assigned at C-10 of the 21-memebered macrocyclic ring through the HMBCs from

δ 2.33 (H-10) to δ 209.30 (C-10^1), 31.74 (C-10^2) and δ 2.00 (H-10^2) to δ 209.30 (C-10^1). The COSYs from δ 1.75 (H-9)/1.37 (H-9^1)/1.33 (H-9^2)/1.62 (H-9^3)/0.97 (H-9^4), 0.93 (H-9^5) suggested the presence of isopentyl branching at C-9 of the 21-memebered macrocyclic ring. These were further supported through HMBCs from δ 1.75 (H-9) to 37.32 (C-9^2), δ 1.33 (H-9^2), 0.97 (H-94) to δ 24.09 (C-9^5) and δ 0.93 (H-9^5) to δ 23.87 (C-9^4). These data suggested its degree of unsaturations as eight, which were equivalent to two rings and six double bonded systems. The higher coupling constants of 11 to 12 Hz were found to correspond to the alkenic groups at C(12)=C(13) and C(14)=C(15) suggesting its trans (E) orientation in compound **14**.

Table 4.21: NMR spectroscopic data of compound (**14),** (2E,12E,14E)-10-acetyl-9-isopentyl-2-methyl-5,16,23[1]-trioxa-bicyclo[21.3.1]-heptacosa-2,12,14-triene-6,19-dione (**14**) isolated from red seaweed *G. salicornia*

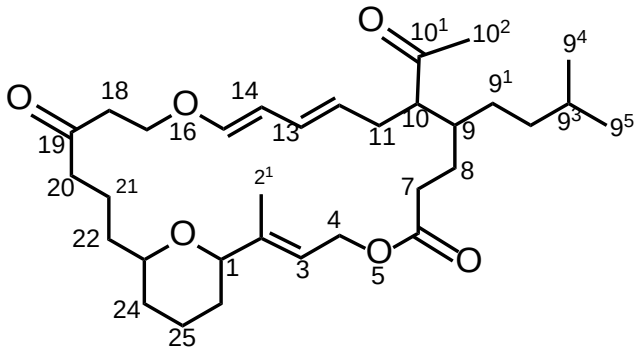

Compound **14** …….(2E,12E,14E)-10-acetyl-9-isopentyl-2-methyl-5,16,23[1]-trioxa-bicyclo[21.3.1]-heptacosa-2,12,14-triene-6,19-dione (**14**)

Type	**C. No.**	**^{13}C NMR**	**H. No. (int., mult., J in Hz)‡**	**^{1}H NMR**	**COSY**	**HMBC**
CH	1	85.02	1H,m	4.78	H-26	C-2,25, 2^1
C	2	142.32	-	-	-	-
CH	3	125.14	1H,t,6.4 Hz	5.54	H-4	C-2
CH_2	4	66.40	2H,d,10.1	4.90	-	C-3,6
-	5		-	-	-	-
C	6	177.30	-	-	-	-
CH_2	7	32.57	2H,t,7.5 Hz	2.30	H-8	C-6,9
CH_2	8	28.00	2H, m	1.77		C-6,9
CH	9	32.15	1H,m	1.75	H-10, H-9^1	C-9^2,11
CH	10	53.15	1H,m	2.33	H-11	C-9^1,10^1,10^2
CH_2	11	29.63	2H,m	2.37	H-12	C-13
CH	12	135.43	1H,m	5.81	H-13	C-11
CH	13	133.64	1H, t,12.1 Hz	5.34	H-14	C-12,15
CH	14	109.09	1H, t,11.0 Hz	5.05	H-15	C-13
CH	15	145.05	1H, d,11.1 Hz	6.37	-	C-14

-	16		-	-	-	-
CH_2	17	69.93	2H,m	4.36	H-18	C-15,18
CH_2	18	41.90	2H,t,4.8 Hz	2.92	-	C-19
C	19	213.48	-	-	-	-
CH_2	20	42.82	1H,m	2.49	H-21	C-19
			1H,m	2.43	-	-
CH_2	21	19.28	1H,m	1.68	H-22	C-20
			1H,m	1.56	-	-
CH_2	22	34.55	1H,m	1.53	H-23	C-20
			1H,m	1.25	-	-
CH	23	80.36	1H,m	3.65	H-24	C-22,1,21
-	23^1	-	-	-	-	-
CH_2	24	30.41	2H,m	1.72	H-25	C-23,22
CH_2	25	24.78	2H, m	1.66	H-26	C-24
CH_2	26	31.87	2H,m	1.80	-	C-25
CH_3	2^1	13.87	3H,s	1.82	-	C-2
CH_2	9^1	29.25	2H,m	1.37	-	C-9^3
CH_2	9^2	37.32	2H,m	1.33	H-9^3	C-9^5
CH	9^3	29.90	1H,m	1.62	H-9^4, H-9^5	-
CH_3	9^4	23.87	3H,d,6.3 Hz	0.97	-	C-9^5
CH_3	9^5	24.09	3H,d,5.2 Hz	0.93	-	C-9^4
C	10^1	209.30	-	-	-	-
CH_3	10^2	31.74	3H,s	2.00	-	C-10^1

†NMR spectra were recorded using a Bruker AVANCE III 500 MHz (AV 500) spectrometer (Bruker, Karlsruhe, Germany) in $CDCl_3$ as aprotic solvent at ambient temperature with TMS as the internal standard (δ 0 ppm).

‡Values in ppm, multiplicity and coupling constants (*J* = Hz) were indicated in parentheses. Multiplicities were allocated by ^{135}DEPT NMR spectrum.

The assignments were made with the aid of the COSY, HSQC, HMBC and NOESY experiments.

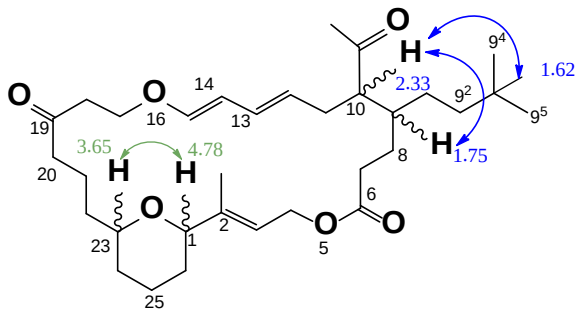

Figure 4.214.: NOESY (double-barbed green coloured arrows for α-orientation and blue coloured arrows for β orientations) correlations of (2E,12E,14E)-10-acetyl-9-isopentyl-2-methyl-5,16,23^1-trioxa-bicyclo[21.3.1]-heptacosa-2,12,14-triene-6,19-dione (**14**)

The relative stereochemistry of the protons at C-1, C-9, C-10 and C-23 were unambiguously inferred from the NOESY cross-peaks (Figure 4.215 & 4.215). The resonances of a proton at δ 4.78 (H-1) displayed NOESY correlation with the methine proton at δ 3.65 (H-23), which were located in the identical plane, and hence, arbitrarily assigned to be α-oriented. The proton at δ 2.33 (H-10) was found to be correlated with that at δ 1.75 (H-9), which were found as trans oriented to the α-protons, and hence, assigned to be β-oriented. This attribution was further supported by the NOE correlation between the protons at δ 2.33 (H-10)/δ 1.62 (H-9^3).

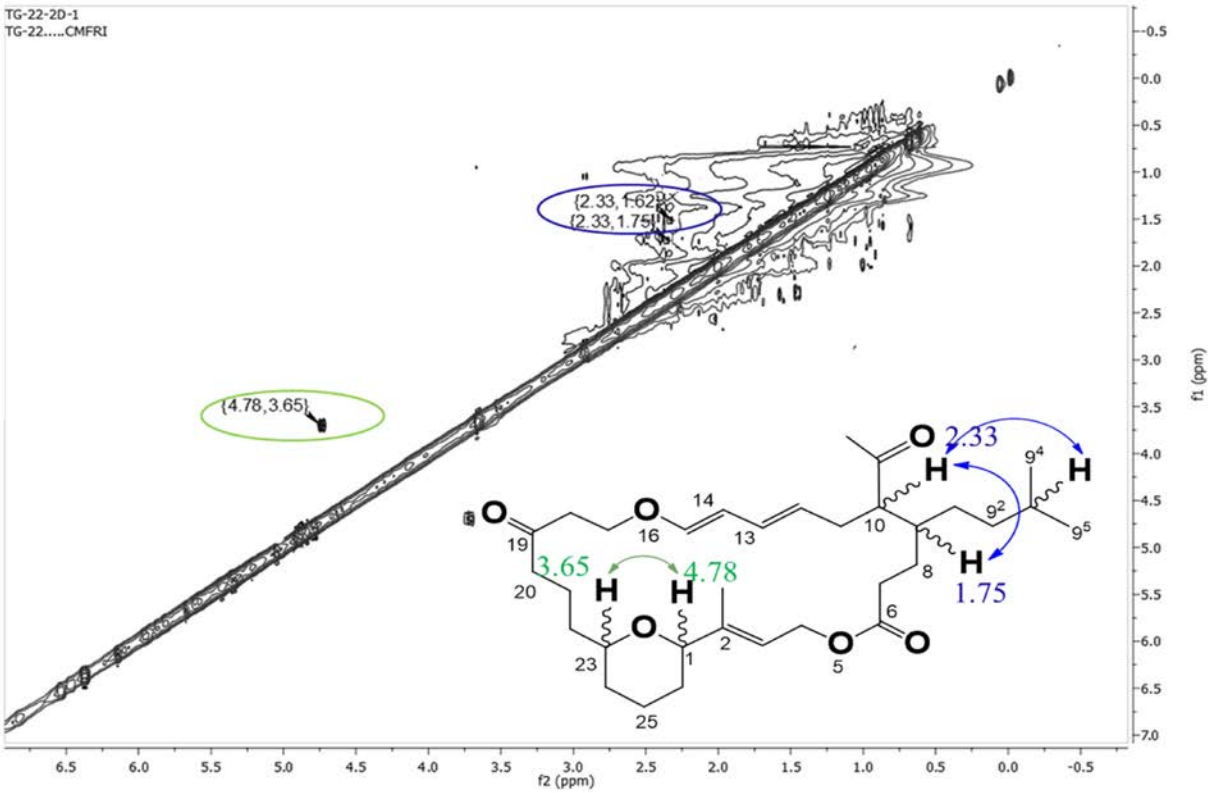

Figure 4.215.: NOE spectrum of (2E,12E,14E)-10-acetyl-9-isopentyl-2-methyl-5,16,23[1]-trioxa-bicyclo[21.3.1]-heptacosa-2,12,14-triene-6,19-dione (**14**)

The molecular ion peak at *m/z* 530 (**1**) with the chemical formula of $C_{32}H_{50}O_6$ underwent dehydration followed by McLafferty rearrangement to form a fragment, $C_{32}H_{48}O_5^{\bullet+}$ with *m/z* 512 (**2**). The fragment, **2** on elimination of $C_3H_5^{\bullet}$ radical by allylic cleavage could yield a fragment at **3** with *m/z* 473. The radical cation **3** on McLafferty rearrangement yielded **4** (*m/z* 318) and then to fragment **5** (*m/z* 293). The latter on further series of fragmentation by McLafferty rearrangement yielded **6** (*m/z* 165) and **7** (*m/z* 127). The ion peak at

m/z 165 on fragmentation yielded the base peak of $C_6H_{10}O^{\bullet+}$ (**8**) with *m/z* 98 (Figure 4.216-4.217).

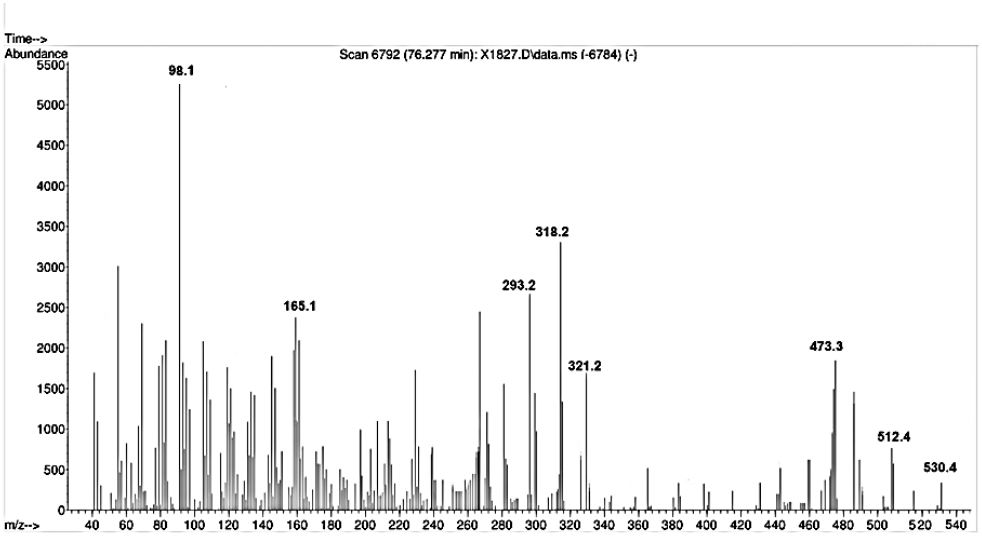

Figure 4.216.: EI-MS spectrum of (2E,12E,14E)-10-acetyl-9-isopentyl-2-methyl-5,16,23[1]-trioxa-bicyclo[21.3.1]-heptacosa-2,12,14-triene-6,19-dione (**14**)

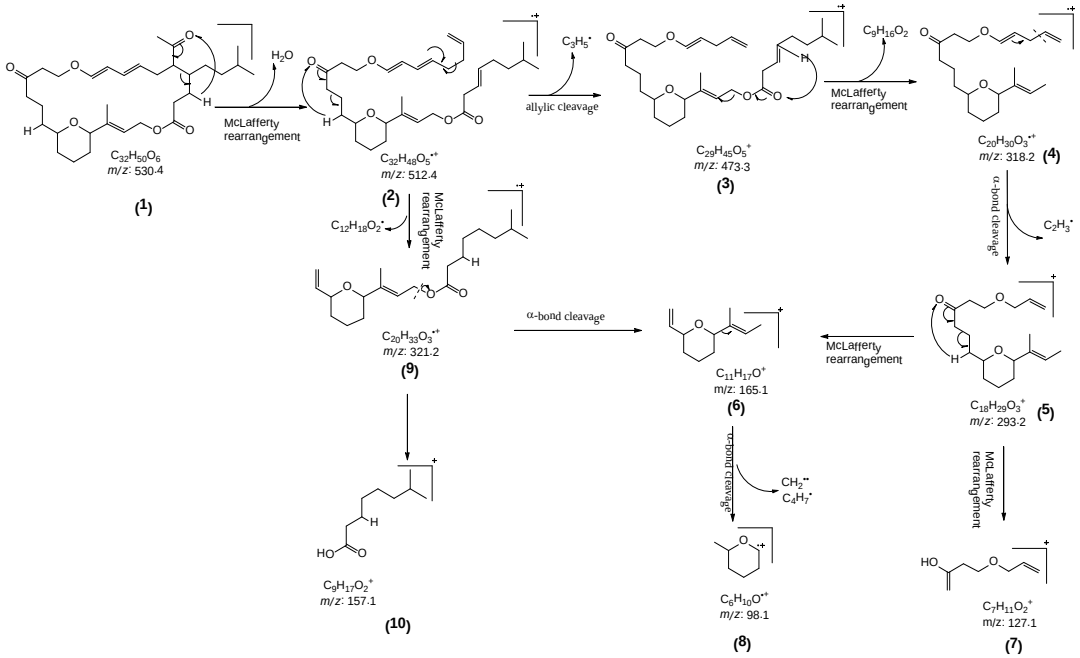

Figure 4.217.: Tentative mass fragmentation pattern of (2E,12E,14E)-10-acetyl-9-isopentyl-2-methyl-5,16,23[1]-trioxa-bicyclo[21.3.1]-heptacosa-2,12,14-triene-6,19-dione (**14**)

4.3.2.7c Structural characterization of Compound 15

(2Z,5E,16E)-8-Hydroxy-20-isobutyl-16-methyl-7,14-dioxa-bicyclo[19.3.1]-pentacosa-2,5,16-triene-10,23-dione

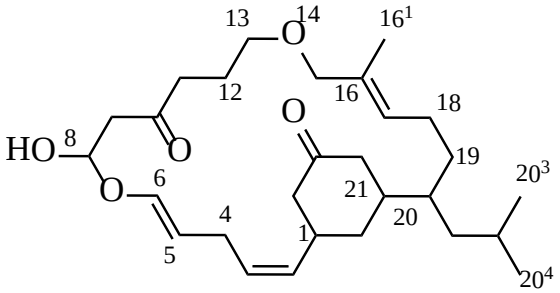

Sample yield	0.32% (> 99% purity, RP-C18 HPLC)
Physical description	Yellow oily
Molecular formula	$C_{28}H_{45}O_5$
Molecular mass	460.3189

The macrolide derivative, (2Z,5E,16E)-8-hydroxy-20-isobutyl-16-methyl-7,14-dioxa-bicyclo[19.3.1]-pentacosa-2,5,16-triene-10,23-dione was isolated as yellow oil. The compound (**15**) has exhibited UV absorbance (UV (MeOH) λ_{max}) at 234 nm (Figure 4.218). The homogeneity of the compound was ascertained by HPLC data on a bonded phase octadecylsilane (C_{18}) stationary phase (HPLC, MeCN/MeOH, 1:2 v/v) with R_t: 5.30 min (Figure 4.219).

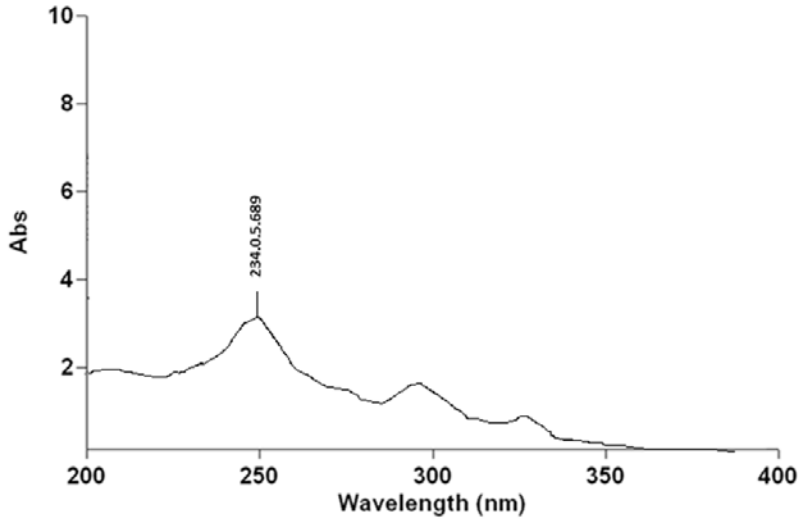

Figure 4.218.: UV spectrum of (2Z,5E,16E)-8-hydroxy-20-isobutyl-16-methyl-7,14-dioxa-bicyclo[19.3.1]-pentacosa-2,5,16-triene-10,23-dione (**15**)

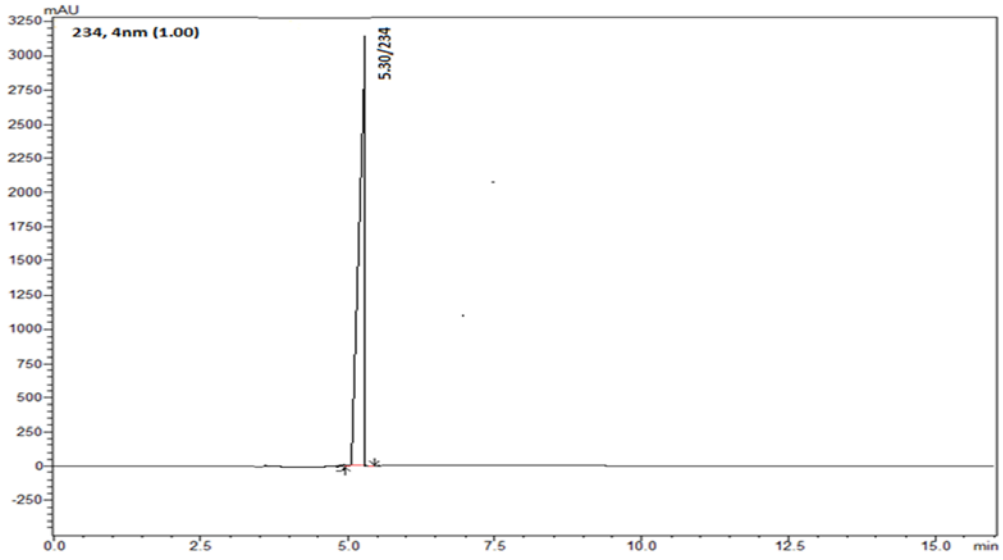

Figure 4.219.: HPLC chromatogram of (2Z,5E,16E)-8-hydroxy-20-isobutyl-16-methyl-7,14-dioxa-bicyclo[19.3.1]-pentacosa-2,5,16-triene-10,23-dione (**15**)

The compound, (2*Z*,5*E*,16*E*)-8-hydroxy-20-isobutyl-16-methyl-7,14-dioxa-bicyclo[19.3.1]pentacosa-2,5,16-triene-10,23-dione (**15**) was isolated as a yellow oily substance. The molecular formula was determined as $C_{28}H_{44}O_5$ from the integrated EIMS {*m/z* 460.3 $[M]^+$} and HR-ESI-MS data {*m/z* 461.3270 $[M+H]^+$} coupled with extensive one/two dimensional (1D/2D) NMR experiments (Table 4.22). The FTIR spectrum of compound **15** exhibited

absorption peaks at 3426, 2922/2856 and 1703 cm^{-1}, which could attribute the existence of alkane, hydroxyl and carbonyl moieties, in that order (Figure 4.220). The possibilities of twelve sp^3 methylenes, ten methines, three each of sp^3 methyls and quaternary carbons were confirmed through the combined $^1H/^{13}C$/DEPT NMR. The greatly deshielded carbon signals at δ 213.24 and 214.29 appeared to correspond to two carbonyl carbon functionalities. The highly deshielded signal at δ 5.62/96.11 was found to be sp^3 methine (-CH-), and this higher chemical shift might be due to the presence of highly electronegative groups like ketone and hydroxyl in its vicinity. Deshielded proton signals at δ 5.59, 5.82, 5.88, 5.98 and 5.43 were attached to the carbons at δ 136.44, 121.68, 126.81, 144.84 and 123.11, respectively, and were related to the non-conjugated olefinic functionalities (Figure 4.221-4.225).

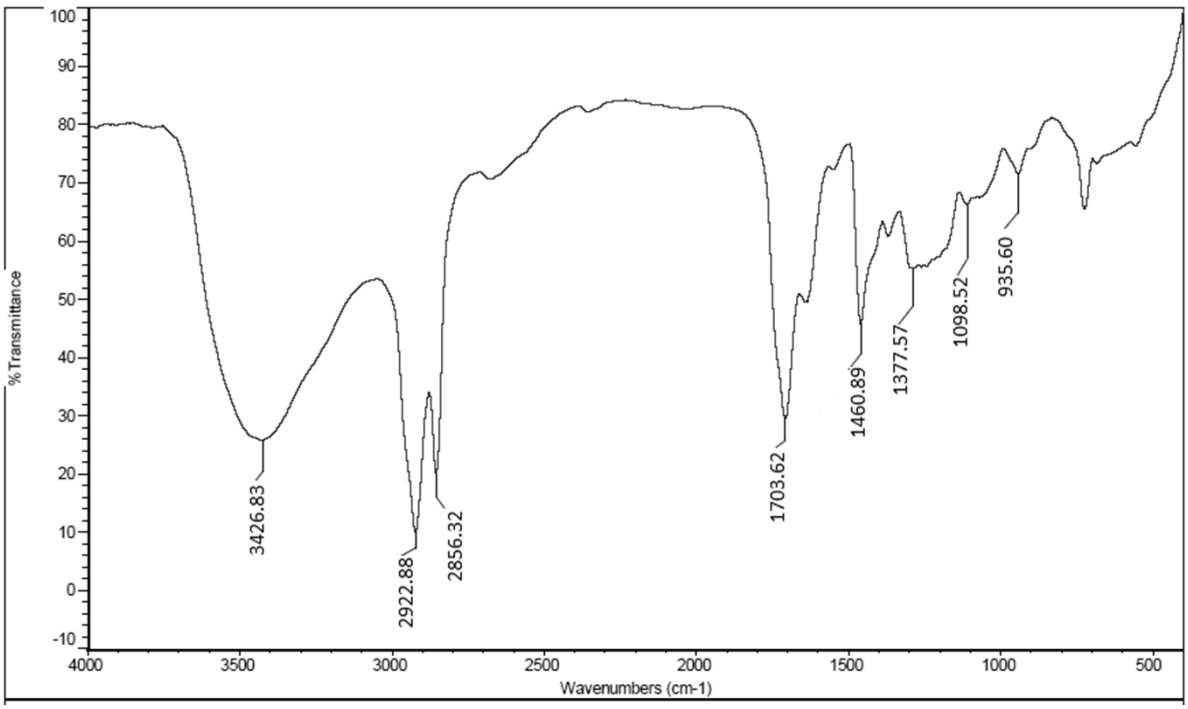

Figure 4.220.: FTIR spectrum of (2Z,5E,16E)-8-hydroxy-20-isobutyl-16-methyl-7,14-dioxa-bicyclo[19.3.1]-pentacosa-2,5,16-triene-10,23-dione (**15**)

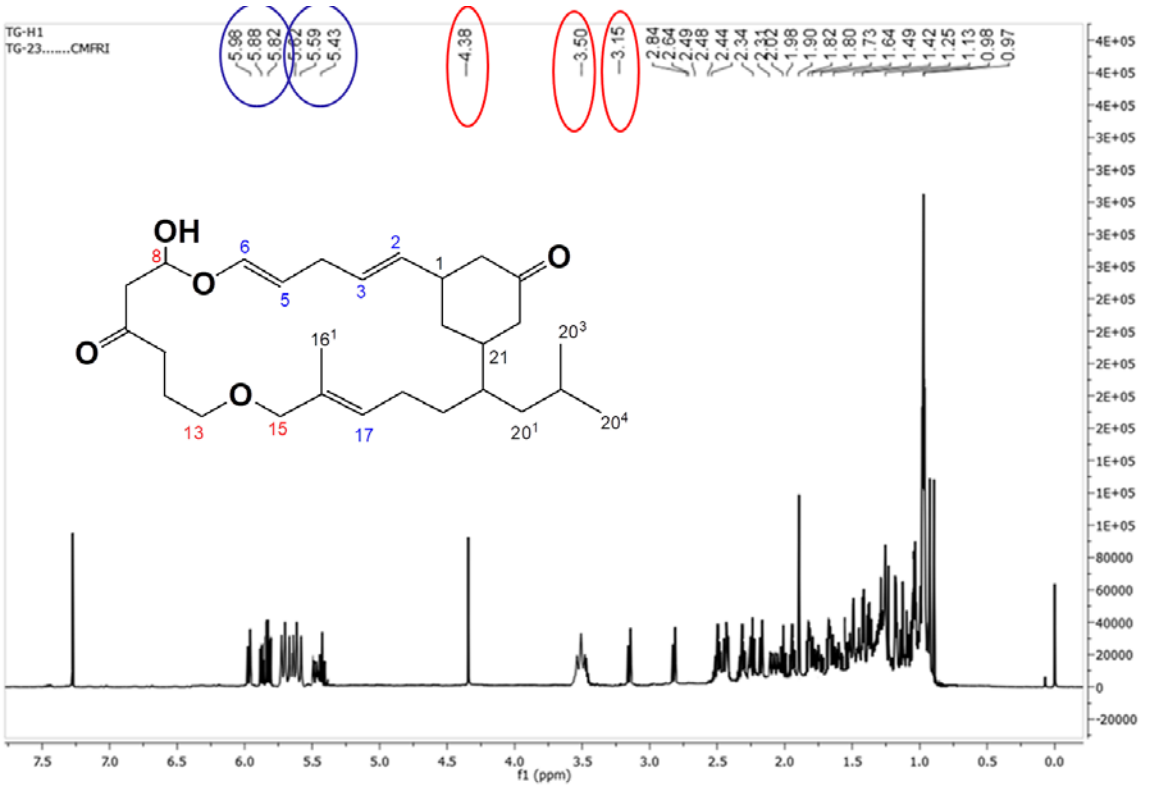

Figure 4.221.: ^{1}H NMR spectrum of (2Z,5E,16E)-8-hydroxy-20-isobutyl-16-methyl-7,14-dioxa-bicyclo[19.3.1]-pentacosa-2,5,16-triene-10,23-dione (**15**)

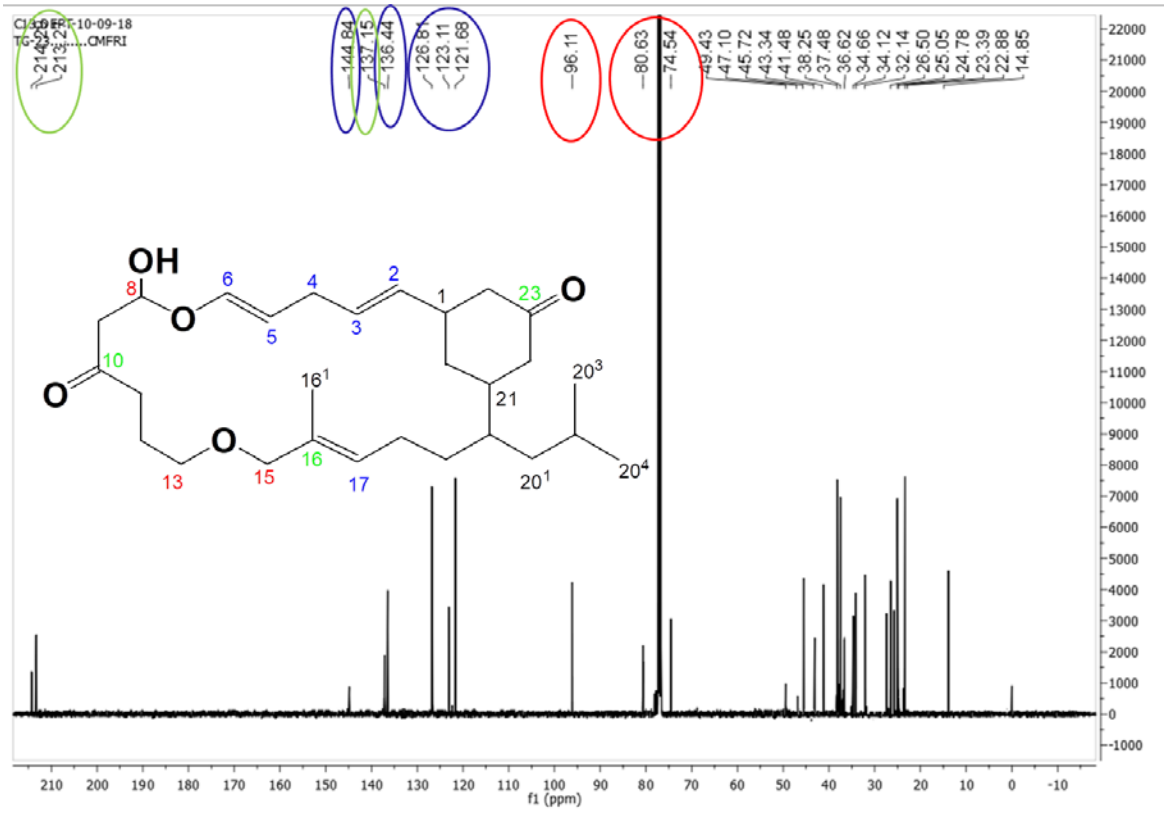

Figure 4.222.: ^{13}C NMR spectrum of (2Z,5E,16E)-8-hydroxy-20-isobutyl-16-methyl-7,14-dioxa-bicyclo[19.3.1]-pentacosa-2,5,16-triene-10,23-dione (**15**)

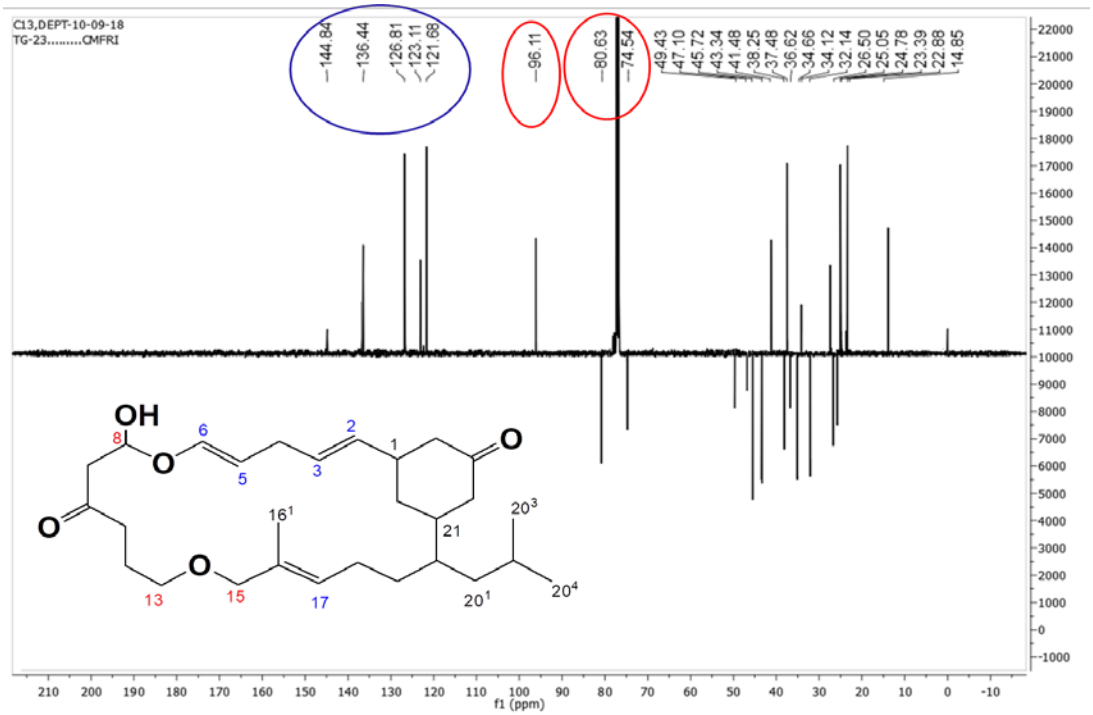

Figure 4.223.: ^{135}DEPT spectrum spectrum of (2Z,5E,16E)-8-hydroxy-20-isobutyl-16-methyl-7,14-dioxa-bicyclo[19.3.1]-pentacosa-2,5,16-triene-10,23-dione (**15**)

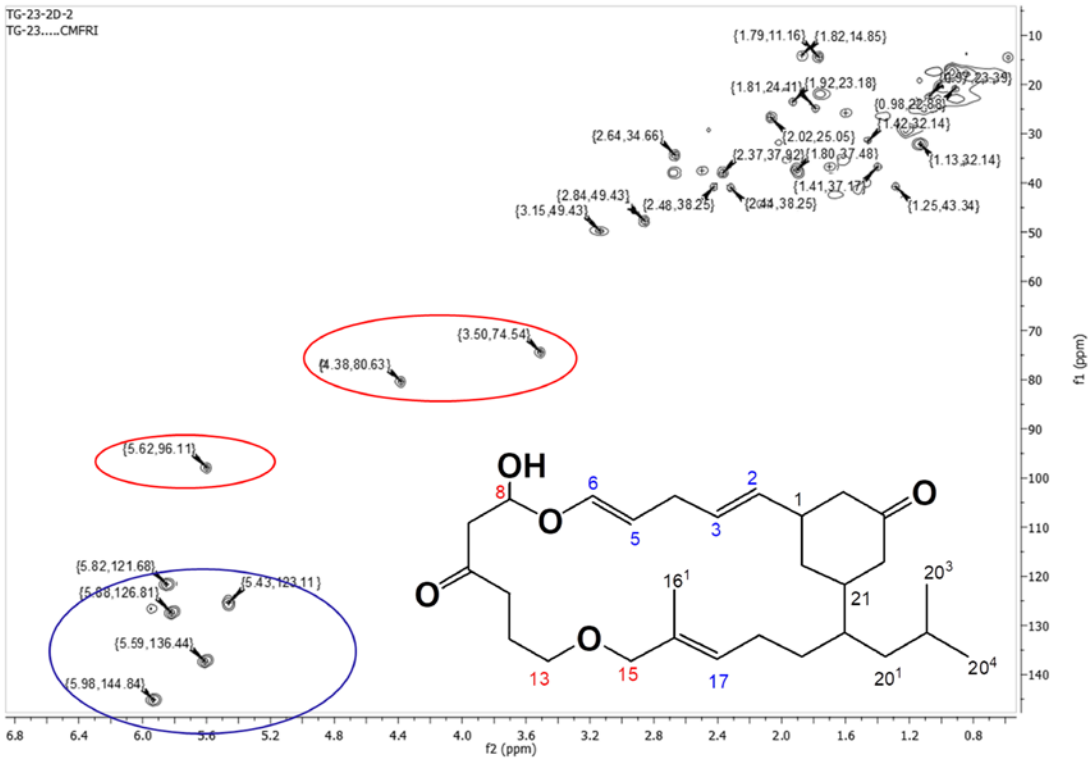

Figure 4.224.: HSQC spectrum of (2Z,5E,16E)-8-hydroxy-20-isobutyl-16-methyl-7,14-dioxa-bicyclo[19.3.1]-pentacosa-2,5,16-triene-10,23-dione (**15**)

The COSY correlations ascribed the continuous spin systems, which was displayed from δ 5.43 (assigned at H-17)/2.02, 1.98 (H-18)/1.42, 1.13 (H-19)/1.49 (H-20)/1.80 (H-21)/2.34 (H-22); δ 1.80 (H-21)/1.90 (H-25)/2.49 (H-1)/5.59 (H-2)/5.82 (H-3)/2.64 (H-4)/5.88 (H-5)/5.98 (H-6) and δ 2.49 (H-1)/2.31 (H-24) (Fig. 2). The HMBC correlations from δ 2.34 (H-22) and 2.31 (H-24) to δ 214.29 (C-23); δ 2.34 (H-22) to δ 37.48 (C-21) and δ 1.80 (H-21) to δ 41.48 (C-1) proposed the presence of cyclohexanone skeleton in compound **15** (Figure 4.225-4.227). The occurrence of another carbonyl carbon at δ 213.24 was proposed through the intense HMBCs from δ 2.48 (H-11) and δ 3.15 (H-9) to δ 213.24 (C-10) at the C-10 position. The previously reported 13-membered macrocyclic lactone derivative enclosed one ester (δ 172.55) along with ether substitution (Chakraborty et al., 2019), whereas the titled compound enclosed one ketone (δ 213.24) and ether functionalities in the macrocyclic-ring system. Spectral data of ^{13}C NMR showed one deshielded methine at δ 96.11 (δ 5.62, HSQC), which ascribed that it might be positioned between the hydroxyl and oxygen functionalities as compared to ^{13}C NMR spectrum of ten-membered cyclic lactone analogue with one deshielded quaternary carbon peak at δ 92.06 located between the oxygen and hydroxyl groups (Chakraborty et al., 2019). The lack of interchangeable hydroxyl moiety in the ^{1}H NMR by deuterium-exchange established the existence of hydroxyl at δ 96.11. The hydroxy methine at δ 5.62 was allocated at position C-8 through the HMBCs from δ 5.62 (H-8) to δ 144.84 (C-6) and δ 3.15 (H-9) to δ 96.11 (C-8). Further, HMBCs from δ 5.82 (H-3) to δ 34.66 (C-4); δ 1.73 (H-12) to δ 38.25 (C-11); δ 3.50 (H-13) to δ 24.78 (C-12); δ 4.38 (H-15) to δ 74.54 (C-13), 137.15 (C-16); δ 5.43 (H-17) to δ 137.15 (C-16) and δ 1.42 (H-19) to δ 25.05 (C-18), 34.12 (C-20) attributed the 19-memebered macrocyclic ring system of 8-hydroxy-7,14-dioxa-bicyclo[19.3.1] pentacosa-2,5,16-triene-10,23-dione .

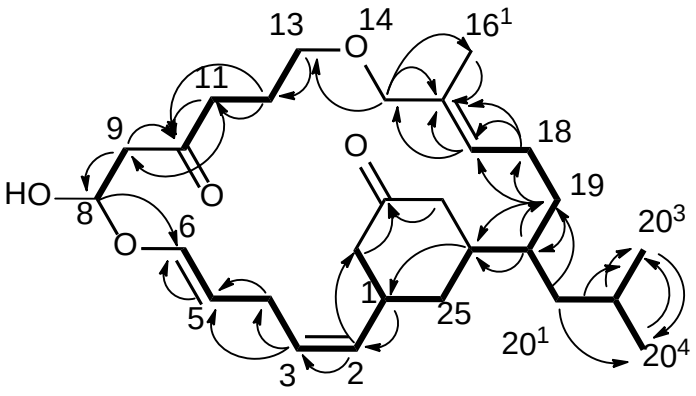

Figure 4.225.: ^{1}H-^{1}H COSY (bold-faced bonds) and HMBC (double-barbed arrows) correlations of (2Z,5E,16E)-8-hydroxy-20-isobutyl-16-methyl-7,14-dioxa-bicyclo[19.3.1]-pentacosa-2,5,16-triene-10,23-dione (**15**)

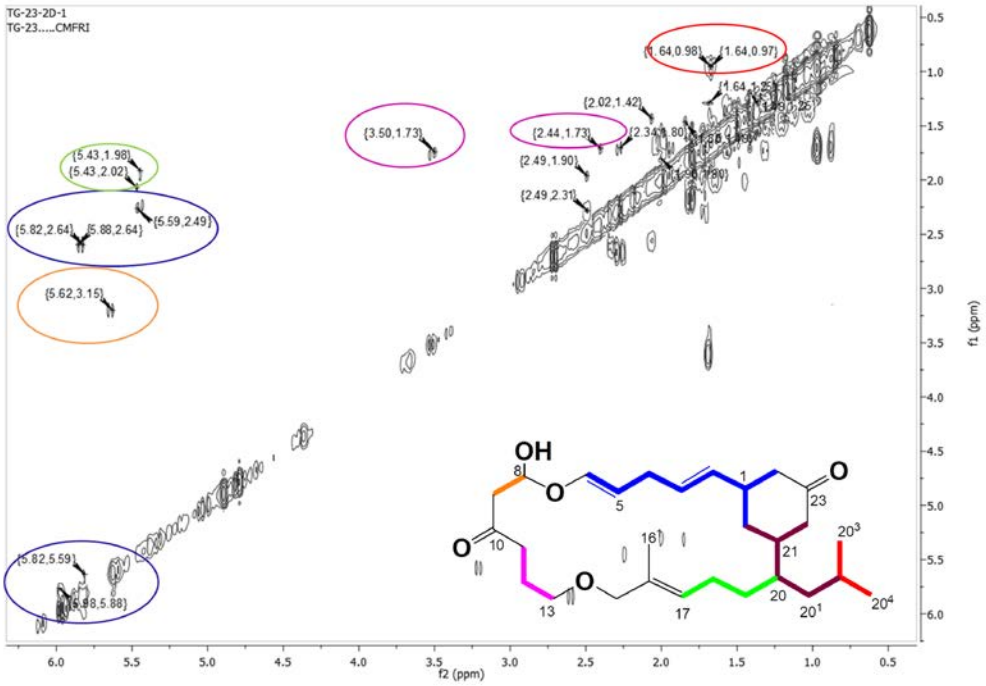

Figure 4.226.: HMBC spectrum of (2Z,5E,16E)-8-hydroxy-20-isobutyl-16-methyl-7,14-dioxa-bicyclo[19.3.1]-pentacosa-2,5,16-triene-10,23-dione (**15**)

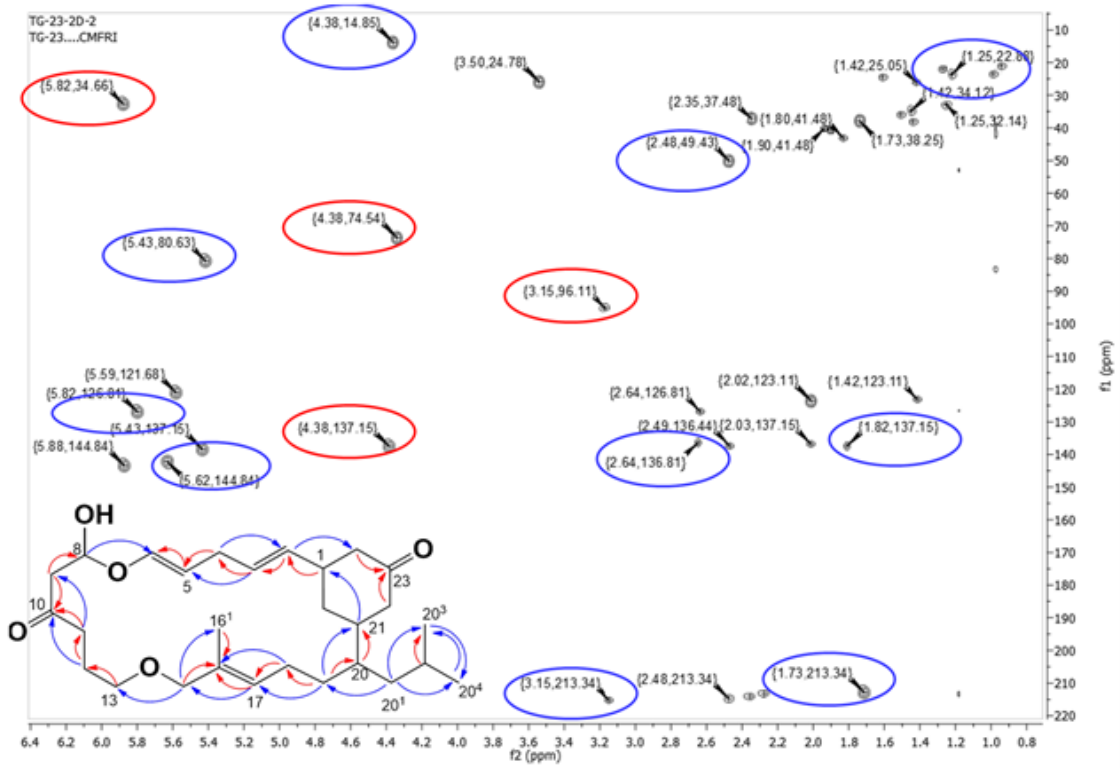

Figure 4.227.: HMBC spectrum of (2Z,5E,16E)-8-hydroxy-20-isobutyl-16-methyl-7,14-dioxa-bicyclo[19.3.1]-pentacosa-2,5,16-triene-10,23-dione (**15**)

The cyclohexanone ring was positioned between C-20 and C-2 positions through intense HMBCs from δ 1.49 (H-20) to δ 37.48 (C-21); δ 1.90 (H-25) to δ 41.48 (C-1) and δ 2.49 (H-1) to δ 136.44 (C-2) in the 19-membered macrocyclic ring. The shielded singlet methyl at δ 1.82/14.85 was positioned at C-16 position of the 19-membered macrocyclic ring through the HMBCs from δ 1.82 (H-16^1) to δ 137.15 (C-16). The COSYs from δ 1.49 (H-20)/1.25 (H-20^1)/1.64 (H-20^2)/0.97 (H-20^3), 0.98 (H-20^4) along with HMBCs from δ 1.25 (H-20^1) to δ 34.12 (C-20), 32.14 (C-19), 23.39 (C-20^3), 22.88 (C-20^4); δ 0.97 (H-20^3) to δ 22.88 (C-20^4) and δ 0.98 (H-20^4) to δ 23.39 (C-20^3) proposed the presence of isobutyl branching and its attachment at C-20 of the 19-membered macrocyclic ring. These combined data assigned its degree of unsaturations as seven corresponding to five double bonds and two ring systems. Notably, the multiplicity of the double bond at the position, C2=C3 (δ5.59) was a doublet of doublet possessing the coupling constant (J) of 6.9 Hz. The configuration of Δ2 was found to be Z, which was supported by the coupling constant (Table 1B, Fig. 1), and previous reports of literature. For example, the antibacterial macrolactins 2 and 3 were found to possess double bonds in between the carbon atoms C18 and C19 nearby to the cyclic rings (Mondol et al., 2011), which were similar to the double bonds located nearby to cyclohexane ring in compound **3.** The multiplicity

of CH proton attached to the double bonds was obtained as doublet of doublet, δ5.62 (dd) in macrolactin 2, and δ5.42 (dd) in macrolactin 3 (Mondol et al., 2011). Similarly, the cyclic ether-containing macrolactins, which were identified from marine *Bacillus sp.*, also possessed double bonds as found in compound **3**. The olefinic protons at δ5.64 (dd), 4.08 (dd) and 5.43 (dd) were reported from macrolactins also exhibited multiplicities as doublet of doublet (Mondol & Shin 2014), as found in the studied compound **3**. These results along with proton NMR data corroborated the assignment of multiplicity of H-2 (as doublet of doublet), configuration of double bond (as Z configuration), and coupling constant (J=6.9 Hz).

Table 4.22: NMR spectroscopic data of compound (**15**), (2Z,5E,16E)-8-hydroxy-20-isobutyl-16-methyl-7,14-dioxa-bicyclo[19.3.1]-pentacosa-2,5,16-triene-10,23-dione (**15**) isolated from red seaweed *G. salicornia*

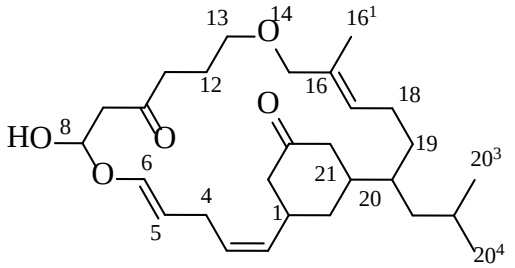

Compound **15**…… (2Z,5E,16E)-8-hydroxy-20-isobutyl-16-methyl-7,14-dioxa-bicyclo[19.3.1]-pentacosa-2,5,16-triene-10,23-dione (**15**)

Type	C. No.	^{13}C NMR	H. No. (int., mult., J in Hz)‡	^{1}H NMR	COSY	HMBC
CH	1	41.48	1H,m	2.49	H-2, H-25, H-24	C-2
CH	2	136.44	1H, dd,6.9, 6.9 Hz	5.59	H-3	C-3
CH	3	121.68	1H,m	5.82	H-4	C-4,5
CH_2	4	34.66	2H,t,7.1 Hz,	2.64	H-5	C-5
CH	5	126.81	1H,m	5.88	H-6	C-6
CH	6	144.84	1H,d,11.1 Hz	5.98	-	-
-	7	-	-	-	-	-
CH	8	96.11	1H,m	5.62	H-9	C-6
CH_2	9	49.43	1H,dd,5.6,12.3 Hz	3.15	-	C-8,10
			1H,dd,5.3,12.1 Hz	2.84	-	-
C	10	213.24	-	-	-	-
CH_2	11	38.25	1H,t,4.5 Hz	2.48	H-12	C-9,10
			1H,t,4.8 Hz	2.44	-	-
CH_2	12	24.78	2H,m	1.73	H-13	C-10,11
CH_2	13	74.54	2H,m	3.50	-	C-12
-	14	-	-	-	-	-
CH_2	15	80.63	1H,d,9.3 Hz	4.38	-	C-13,16,16¹
C	16	137.15	-	-	-	-

CH	17	123.11	1H,t, 5.8 Hz	5.43	H-18	C-15,16
CH_2	18	25.05	1H,m	2.02	H-19	C-16,17
			1H,m	1.98	-	-
		32.14	1H,m	1.42	H-20	C-17,18,20,21
CH_2	19					
			1H,m	1.13	-	-
CH	20	34.12	1H,m	1.49	H-21, H-20^1	C-21
CH	21	37.48	1H,m	1.80	H-22	C-1
CH_2	22	47.10	2H,d, 6.8 Hz	2.34	-	C-21,23
C	23	214.29	-	-	-	-
CH_2	24	45.72	2H,d,6.1 Hz	2.31	-	C-23
CH_2	25	36.62	2H,t,5.9 Hz	1.90	-	C-1
CH_3	16^1	14.85	3H,s	1.82	-	C-16
		43.34	2H,t,6.9 Hz	1.25	H-20^2	C-20,19,20^4, 20^3
CH_2	20^1					
CH	20^2	26.50	1H,m	1.64	H-20^3, H-20^4	C-20^3
CH_3	20^3	23.39	3H,d,5.9 Hz	0.97	-	C-20^4
CH_3	20^4	22.88	3H,d,6.2 Hz	0.98	-	C-20^3

†NMR spectra were recorded using a Bruker AVANCE III 500 MHz (AV 500) spectrometer (Bruker, Karlsruhe, Germany) in $CDCl_3$ as aprotic solvent at ambient temperature with TMS as the internal standard (δ 0 ppm).

‡Values in ppm, multiplicity and coupling constants (J= Hz) were indicated in parentheses. Multiplicities were allocated by ^{135}DEPT NMR spectrum.

The assignments were made with the aid of the COSY, HSQC, HMBC and NOESY experiments.

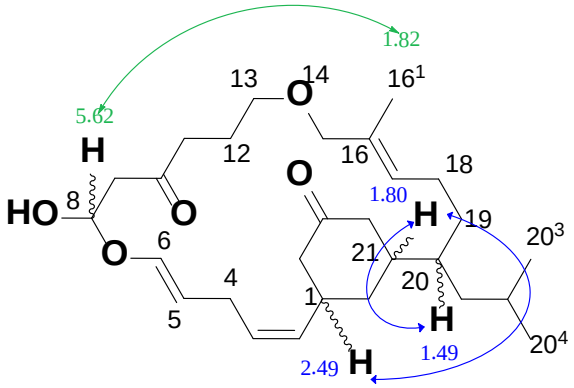

Figure 4.228.: NOESY (double-barbed green coloured arrows for α-orientation and blue coloured arrows for β orientations) correlations of (2Z,5E,16E)-8-hydroxy-20-isobutyl-16-methyl-7,14-dioxa-bicyclo[19.3.1]-pentacosa-2,5,16-triene-10,23-dione (**15**)

The relative stereochemistry of the protons at C-1, C-8, C-20 and C-21 were unambiguously deduced from the NOESY experiment (Figure 4.228-4.229).The proton resonances at δ 1.82 (H-16^1) displayed NOE cross-peaks with the methine proton at δ 5.62 (H-8), and those were distributed in an identical plane of symmetry, and hence, assigned to be α-oriented. The NOESY correlations from δ 2.49 (H-1)/1.80 (H-21)/1.49 (H-20) were found to be in the identical plane of symmetry and trans oriented to the α-protons, and therefore, arbitrarily assigned as β-oriented.

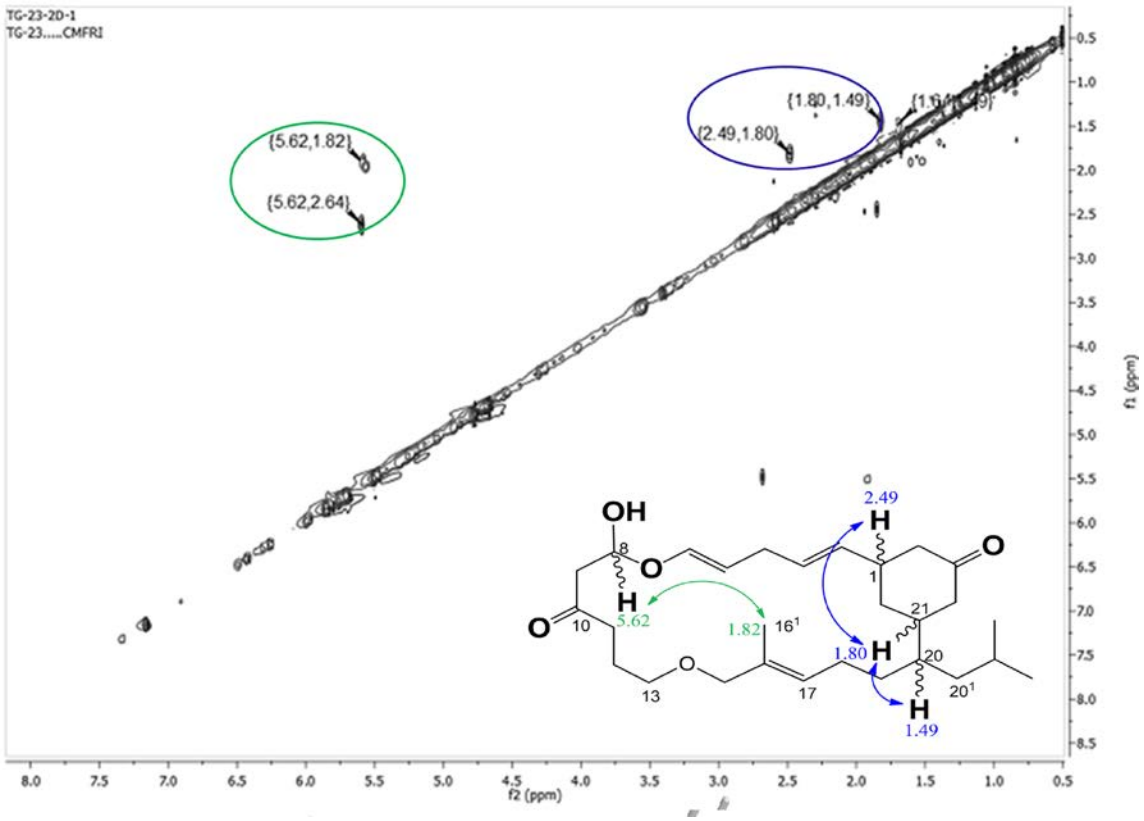

Figure 4.229.: NOESY spectrum of (2Z,5E,16E)-8-hydroxy-20-isobutyl-16-methyl-7,14-dioxa-bicyclo[19.3.1]-pentacosa-2,5,16-triene-10,23-dione (**15**)

The molecular ion peak at *m/z* 460 (**1**) with the molecular formula of $C_{28}H_{44}O_5$ appeared to eliminate a molecule of H_2O to form the fragment **2** (*m/z* 440), and participated in the McLafferty rearrangement to form **3** with *m/z* 441. The base-peak was acquired at *m/z* 96, which was deduced to correspond to $C_6H_8O^{\bullet+}$ (Figure 4.230-4.231)

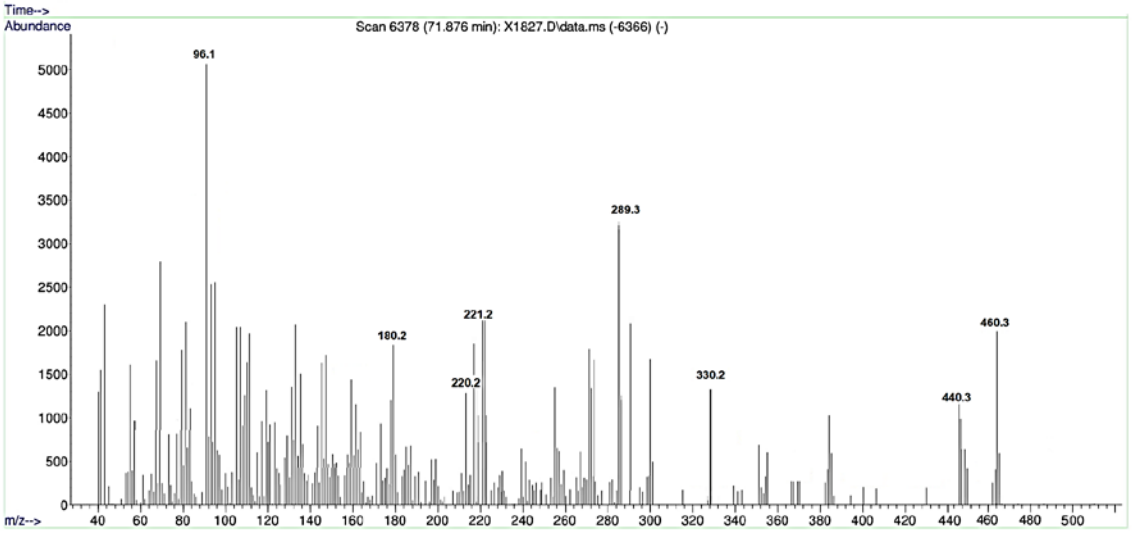

Figure 4.230.: NOESY spectrum of (2Z,5E,16E)-8-hydroxy-20-isobutyl-16-methyl-7,14-dioxa-bicyclo[19.3.1]-pentacosa-2,5,16-triene-10,23-dione (**15**)

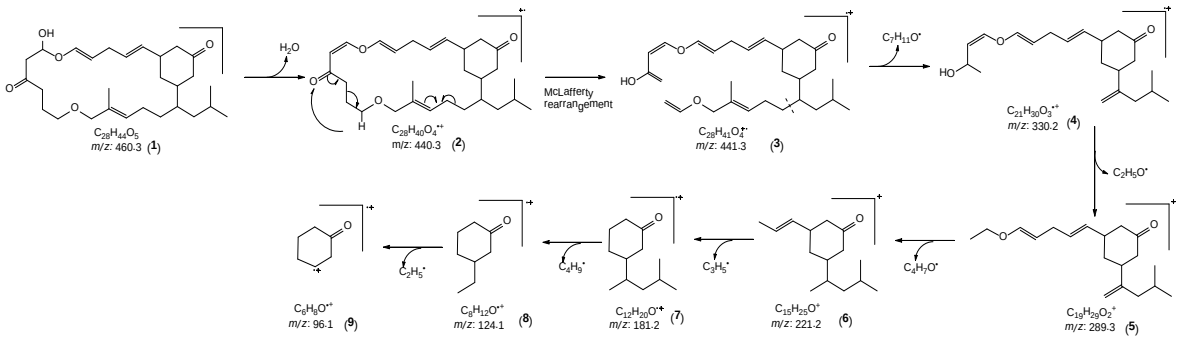

Figure 4.231.: Tentative mass spectrum of (2Z,5E,16E)-8-hydroxy-20-isobutyl-16-methyl-7,14-dioxa-bicyclo[19.3.1]-pentacosa-2,5,16-triene-10,23-dione (**15**)

This is the first report of the undescribed oxabicyclo[21.3.1]heptacosa-ene-diones (Compounds **13-14**) and oxabicyclo[19.3.1]pentacosa-ene-dione (compound **15**) bearing macrocyclic lactones from the red seaweed, *Gracilaria salicornia*. The unprecedented macrolides (**13-15**), namely 3-acetyl-14-(furanyl)-11-methyl-15-(15^{3}-methylbutyloxy)-8-oxabicyclo[21.3.1] heptacosa-11,23,25,27-tetraene-7,18-dione (**13**), (2*E*,12*E*,14*E*)-10-acetyl-9-isopentyl-2-methyl-5,16,23^{1}-trioxa-bicyclo[21.3.1]heptacosa-2,12,14-triene-6,19-dione (**14**) and

(2*Z*,5*E*,16*E*)-8-hydroxy-20-isobutyl-16-methyl-7,14-dioxa-bicyclo[19.3.1]pentacosa-2,5,16-triene-10,23-dione (**15**) were found to be possessed various oxygenated functionalities. In particular, the pyran enclosed macrocyclic lactone could be used as prospective natural therapeutic pharmacophore template.

4.3.3 Pharmacological potentials of secondary metabolites isolated from the organic extract of G. salicornia

4.3.3.1 Pharmacological potentials of abeo-labdane class of diterpenoid derivative (Compound 1)

Antioxidant activities of the methyl-16(13→14)-abeo-7-labdene-(12-oxo) carboxylate isolated from *G. salicornia* was investigated by *in vitro* radical quenching activities against DPPH and $ABTS^+$ radicals (Table 4.23). The studied compound exhibited comparable DPPH radical quenching activity (IC_{50} 1.97 mM) as standard antioxidant agent *α*-tocopherol (IC_{50} 1.49 mM). The studied abeo-labdane registered significantly higher bioactivities against pro-inflammatory 5-LOX (IC_{50} 2.33 mm) than that exhibited by non-steroidal anti-inflammatory agent ibuprofen (IC_{50} 4.51mM, $P<0.05$). The selectivity index of the titled compound was also found to be significantly higher (IC_{50}anti-COX-1/ IC_{50}anti-COX-2 ~ 1.40) than non-steroidal anti-inflammatory agent ibuprofen (0.43 mM) ($p < 0.05$). This appropriately recognized the greater selectivity of the studied abeo-labdane towards inducible pro-inflammatory cyclooxygenase-2 (COX-2) than its constitutive isoform cyclooxygenase-1 (COX-1). Earlier reports of literature also disclosed that the diterpenoids with decalin carbon system exhibited anti-inflammation potential (Chinou 2005;Tran et al. 2017). The isolated abeo-labdane registered significantly lesser bioactivities against carbolytic enzymes (α-amylase and α-glucosidase) (> IC_{50} 2.00 mM) than that exhibited by anti-diabetic agent acarbose (~IC_{50} 0.2 mM, $P>0.05$).

4.3.3.2 Pharmacological potentials of oleanane class of triterpenoid derivatives (Compounds 2-3)

The *in vitro* anti-diabetic potential of the studied abeo-oleanenes (**2** and **3**) were assessed by their inhibitory properties towards the carbolytics, α-glucosidase and α-amylase that were found to regulate the intestinal carbohydrate absorption, thereby reducing postprandial insulin level (Goldstein et al., 1998). Among the titled abeo-oleanenes, the one with 24(4→23)-abeo-oleanene framework (**3**) displayed significantly higher α-amylase and α-glucosidase inhibitory properties (IC_{50} 0.32 and 0.29 mM, respectively) over that bearing 24(4→23), 27(8→26), 30(20→29)-tris-abeo-oleanene moiety (**2**) (IC_{50} 0.40 and 0.34 mM, respectively)

(Table 4.23). The higher α-amylase and α-glucosidase inhibitory properties of 24(4→23)-abeo-oleanene framework (**3**) (IC_{50} 0.32 and 0.29 mM, respectively) exhibited close resemblance towards the reference carbolytic enzyme inhibitor acarbose (IC_{50} 0.22 and 0.19 mM, respectively mM). *In vitro* radical scavenging assays by $ABTS^+$ and DPPH radicals were employed to deduce the antioxidant properties of studied abeo-oleanenes. The studied compound, **3** exhibited greater radical scavenging activities (IC_{50} DPPH 1.33 mM; IC_{50} $ABTS^+$ 1.09 mM), when compared to those displayed by compound **2** (IC_{50} DPPH 1.56 mM; IC_{50} $ABTS^+$ 1.24 mM) and standard, *α*-tocopherol (IC_{50} DPPH 1.49 mM; IC_{50} $ABTS^+$ 1.69 mM). The isolated abeo-labdane registered significantly lesser potential against pro-inflammatory COX-2 and 5-LOX (> IC_{50} 3.00 mM).

4.3.3.3 Pharmacological potentials of drimane class of diterpenoid derivative (Compounds 4-6)

The *in vitro* radical scavenging assays by DPPH and $ABTS^+$ radicals were used to ascertain the antioxidant properties of the studied drimane sesquiterpene derivatives (Table 4.23). The studied compound, **4** bearing substituted 1*H*-benzo[a]xanthene-4,10,12-triol moiety exhibited greater radical scavenging activities (IC_{50} DPPH 1.33 mM; IC_{50} $ABTS^+$ 1.57 mM), when compared to the standard *α*-tocopherol (IC_{50} DPPH 1.49 mM; IC_{50} $ABTS^+$ 1.69 mM). There were previous reports on DPPH radical scavenging activities of drimane sesquiterpenoids (Perez-Garcia et al., 2005) that corroborated the antioxidant activity of terpenoids sketched in the current work. The aromatic, hydroxyls and ether functionalities in the studied compounds could be incorporated in the process of delocalization of electron in the radical scavenging mechanism of the DPPH radical, which might be one of the predominant reasons for potential antioxidant properties of the studied compounds (**4-6**). There were previous reports on the antioxidant properties of the metabolites with conjugated olefinic, aromatic, and hydroxyl functionalities (Rice-Evans et al., 1996). Among the isolated compounds, the one with substituted 1*H*-benzo[*a*]xanthene-4,10,12-triol (**4**) showed greater $ABTS^+$ and DPPH radical activities (IC_{50} 1.57 and 1.33 mM, respectively) over those exhibited by compounds **5** and **6** (IC_{50} 1.88-1.96 and 1.51-1.85 mM, respectively). The *in vitro* anti-inflammatory potential of the isolated compounds were evaluated by their inhibition potential towards pro-inflammatory COX-1, 2 and 5-LOX enzymes. Among the studied compounds, **4** showed greater COX-2 and 5-LOX inhibitory activities (IC_{50} 1.35 and 1.72 mM, respectively) over those displayed by **5-6** (COX-2 IC_{50} 1.56-1.91 mM and 5-LOX IC_{50} 1.90-2.55 mM, respectively). The drimane class of diterpenoids were displayed lower bioactivities against carbolytic enzymes (α-amylase and α-glucosidase) (> IC_{50} 2.00 mM).

4.3.3.4 Pharmacological potentials of 2H-chromenyl derivatives (Compounds 7-8)

Antioxidant potentials of the *2H*-chromenyl derivatives (**7**) and (**8**) isolated from *G. salicornia* was investigated by *in vitro* radical quenching activities against DPPH and $ABTS^+$ (Table 4.23). The compound **8** exhibited higher DPPH and $ABTS^+$ radical quenching activities (IC_{50} 1.17 and 1.33 mM, respectively) than those displayed by **7** and standard antioxidant agent α-tocopherol ($IC_{50} \geq 1.49$ mM). The compound **8** registered significantly higher activities against pro-inflammatory 5-LOX (IC_{50} 2.03 mM) than that displayed by **7** (IC_{50} 2.46 mM, $p < 0.05$). The selectivity index of the titled compound was also found to be higher (IC_{50} anti-COX-1/IC_{50} anti-COX-2 > 0.95) than non-steroidal anti-inflammatory agent ibuprofen (0.89) ($p < 0.05$). This appropriately suggested the greater selectivity of the studied chromenyls towards inducible pro-inflammatory cyclooxygenase-2 (COX-2) than its constitutive isoform cyclooxygenase-1 (COX-1). The bioactivities of *2H*-chromenyl derivatives (**7**) and (**8**) were found to be lower towards carbolytic enzymes (α-amylase and α-glucosidase) inhibition potentials (> IC_{50} 2.00 mM).

4.3.3.5 Pharmacological potentials of spiro-compound derivatives (Compounds 9-10)

Antioxidant potentials of the spiro-compounds (**9**) and (**10**) isolated from *G. salicornia* was investigated by *in vitro* radical quenching activities against DPPH and $ABTS^+$ (Table 4.23). The compound **9** exhibited higher DPPH and $ABTS^+$ radical quenching activities (IC_{50} 1.13 and 1.24 mM, respectively) than those displayed by **9** and standard antioxidant agent α-tocopherol ($IC_{50} \geq 1.49$ mM). The compound **10** registered significantly higher activities against pro-inflammatory 5-LOX (IC_{50} 1.91 mM) than that displayed by **9** (IC_{50} 2.78 mM, $p<0.05$). The selectivity index of the titled compound was also found to be higher (IC_{50} anti-COX-1/IC_{50} anti-COX-2 >1.05) than that exhibited by the non-steroidal anti-inflammatory agent ibuprofen (0.43) ($p<0.05$). This appropriately suggested the greater attenuating activities of the studied spiro-compounds against inducible pro-inflammatory cyclooxygenase-2 (COX-2) than cyclooxygenase-1 (COX-1). The bioactivities of spiro-compound derivatives (**9**) and (**10**) were considered to be lower towards carbolytic enzymes (α-amylase and α-glucosidase) inhibition potentials (> IC_{50} 2.00 mM).

4.3.3.6 Pharmacological potentials of polyether derivatives (Compounds 11-12)

The free radical quenching assays against DPPH and $ABTS^+$ ascertained the antioxidant potentials of the polyether derivatives. The isolated compound, **12** bearing furanyl-furo[3,2-b]pyran-2*H*-pyran registered potent radical quenching properties (IC_{50}DPPH 1.11 mM;

$IC_{50}ABTS^{+}$ 1.27 mM) when related to those displayed by compound, **11** bearing pyranyl-10-methylpyrano[3,2-b]pyran-methyleneoxepane moiety (IC_{50} > 1.6 mM) and standard α-tocopherol (IC_{50} > 1.49 mM) (Table 4.23). It was attributed that the furo[3,2-b]pyran and ester functionalities in compound **12** might play predominant roles for the greater electron delocalisations in the radical scavenging mechanism compared to compound **11**, which in turn, explained the greater radical scavenging properties of the former. The *in-vitro* anti-inflammatory potencies of the fractionated polyether triterpenoids, as determined by their attenuating properties against COX-1 and COX-2 were found to be considerably greater for compound **12** (IC_{50}COX-1 1.96 mM and IC_{50}COX-2 1.87 mM) ($p < 0.05$) than those exhibited by compound **11** (IC_{50}COX-1 2.67 mM and $IC_5COX\text{-}2_0$ 2.72 mM). Likewise, the polyether analogue bearing trimethyl-2*H*-pyran-3-yl butyrate moiety (**12**) registered greater attenuating properties against 5-LOX (IC_{50} 1.89 mM) enzyme when compared to those exhibited by compound **11** (IC_{50} 2.71 mM) and standard (ibuprofen IC_{50} 4.51 mM). Notably, the polyether derivative **12** was found to effectively attenuate 5-LOX/COX-2 enzymes while retaining COX-1/COX-2 ratio within the threshold limits (IC_{50} of anti-COX-1 to IC_{50} of anti-COX-2 > 1) for selective and target-oriented potencies against inflammatory response, compared to that displayed by **11** (0.98) attributing the greater attenuation property of the former against COX-2 over that in opposition to COX-1. It is of note that the selectivity index (IC_{50} of anti-COX-1 to IC_{50} of anti-COX-2) of the compound **12** was greater than 1.0 as compared to that displayed by the synthetic ibuprofen (0.43) (Table 4.23), and that in turn, signified the targeted attenuating property of the polyether analogue bearing trimethyl-2*H*-pyran-3-yl butyrate moiety against the inducible pro-inflammatory COX-2 and 5-LOX than that on COX-1, which has been recognized as a constitutive enzyme in the gastric and intestinal mucosal system.

The anti-inflammatory selectivity index of greater than **11** showed higher selectivity of the studied compounds towards the enzyme target site and lesser toxic side effects, such as inhibiting constitutive COX-1, and imparting side effects on the gastrointestinal mucosa. The COX-1 and 2 isoforms were found to exhibit differential properties, particularly, COX-1 produces prostaglandins (PGs) and mediate the basic functions, such as cytoprotection of gastric mucosa, regulation of renal blood flow and platelet aggregation (Kurumbail, 2001). In contrast, expression of COX-2 was found to rapidly induce by the inflammatory stimuli, such as pro-inflammatory cytokines, lipopolysaccharides, mitogens, etc. resulting in the increased production of PGs in inflamed tissues (Kurumbail, 2001). Thus, the inducible isozyme of COX-2 has been implicated in attenuating the pathological processes leading to inflammation.

Table 4.23.: *In vitro* antioxidant, anti-inflammatory and antidiabetic {radical scavenging, cyclooxygenase-1 & 2 (COX-1 & 2) and 5-lipoxygenase (5-LOX) and α-amylase/glucosidase} activities of the studied compounds (**1-15**) isolated from the EtOAc-MeOH extract of *G. salicornia* against commercial standard, tocopherol (T), ibuprofen (I) and acarbose (A)

Compounds	*Anti-oxidant activities in IC_{50} (mM)		*Anti-inflammatory properties IC_{50} (mM)				*Anti-diabetic activities in IC_{50} (mM)	
	DPPH quenching	ABTS quenching	COX-1 inhibition	COX-2 inhibition	5-LOX inhibition	Selectivity index†	α-amylase	α-glucosidase
1	^{a}1.97 ± 0.03	^{a}2.33 ± 0.04	^{a}2.39 ± 0.03	^{a}1.71 ± 0.02	^{a}2.33 ± 0.02	^{a}1.40 ± 0.02	^{a}2.88 ± 0.03	^{a}2.24 ± 0.04
2	^{b}1.56 ± 0.01	^{b}1.24 ± 0.02	^{b}3.04 ± 0.01	^{b}3.38 ± 0.01	^{b}3.98± 0.02	^{b}0.90± 0.02	^{b}0.40 ± 0.01	^{b}0.34 ± 0.01
3	**^{c}1.33 ± 0.01**	**^{c}1.09 ± 0.02**	**^{c}3.22 ± 0.02**	**^{c}3.29 ± 0.03**	**^{c}3.01± 0.02**	**^{c}0.98± 0.02**	**^{c}0.32 ± 0.02**	**^{b}0.29 ± 0.03**
4	**^{c}1.33 ± 0.01**	**^{d}1.57 ± 0.02**	**^{d}1.54 ± 0.02**	**^{d}1.35 ± 0.01**	**^{d}1.72 ± 0.01**	**^{dh}1.14 ± 0.02**	**^{d}2.42 ± 0.01**	**^{c}2.46 ± 0.02**
5	^{b}1.51 ± 0.01	^{e}1.88 ± 0.02	^{e}1.72 ± 0.03	^{e}1.56 ±0.01	^{e}1.90 ± 0.01	^{d}1.10 ± 0.01	^{e}2.62 ± 0.01	^{d}2.79 ± 0.02
6	^{d}1.85 ± 0.02	^{f}1.96 ± 0.01	^{f}2.09 ± 0.01	^{f}1.91 ± 0.02	^{f}2.55 ± 0.01	^{d}1.09 ± 0.02	^{f}2.96 ± 0.02	^{e}2.86 ± 0.01
7	^{e}1.40 ± 0.03	^{g}1.50 ± 0.04	^{g}2.34 ± 0.03	^{g}2.39 ± 0.01	^{g}2.46 ± 0.01	^{e}0.98 ± 0.01	^{g}2.51 ± 0.03	^{f}2.42 ± 0.04
8	**^{f}1.17 ± 0.01**	**^{h}1.33 ± 0.02**	**^{g}2.24 ± 0.01**	**^{j}2.12 ± 0.02**	**^{h}2.03 ± 0.02**	**^{d}1.06 ± 0.02**	**^{h}2.26 ± 0.01**	**^{g}2.23 ± 0.02**
9	^{g}1.61^{a} ± 0.03	^{i}1.72^{a} ± 0.04	^{h}2.70^{a} ± 0.03	^{i}2.75^{a} ± 0.01	^{i}2.78^{a} ± 0.01	^{e}0.98^{a} ± 0.01	^{h}2.72^{a} ± 0.03	^{h}2.63^{a} ± 0.04
10	**^{h}1.13^{b} ± 0.01**	**^{b}1.24^{a} ± 0.02**	**^{i}1.99^{b} ± 0.01**	**^{j}1.89^{a} ± 0.02**	**^{j}1.91^{b} ± 0.02**	**^{d}1.05^{b} ± 0.02**	**^{i}2.04^{b} ± 0.01**	**^{i}2.12^{a} ± 0.02**
11	^{g}1.62 ± 0.03	^{j}1.69 ± 0.04	^{j}2.67 ± 0.03	^{k}2.72 ± 0.01	^{k}2.71 ± 0.01	^{e}0.98 ± 0.01	^{g}2.53 ± 0.03	^{j}2.59 ± 0.04
12	**^{h}1.11 ± 0.01**	**^{b}1.27 ± 0.02**	**^{j}1.96 ± 0.01**	**^{j}1.87 ± 0.02**	**^{l}1.89 ± 0.02**	**^{d}1.05 ± 0.02**	**^{k}2.22 ± 0.01**	**^{k}2.16 ± 0.02**
13	^{e}1.40 ± 0.02	^{k}1.43 ± 0.02	^{d}1.58 ± 0.03	^{l}1.19 ± 0.03	^{m}1.43 ± 0.02	^{f}1.33 ± 0.01	^{g}2.51 ± 0.02	^{k}2.32 ± 0.02
14	**^{i}1.10 ± 0.03**	**^{k}1.21 ± 0.04**	**^{d}1.59 ± 0.03**	**^{m}1.13 ± 0.02**	**^{m}1.39 ± 0.02**	**^{g}1.41 ± 0.02**	**^{d}2.46 ± 0.03**	**^{k}2.31 ± 0.04**
15	^{e}1.42 ± 0.02	^{k}1.47 ± 0.03	^{k}1.42 ± 0.02	^{i}1.20 ± 0.03	^{m}1.47 ± 0.02	^{h}1.18 ± 0.02	^{h}2.33 ± 0.02	^{l}2.28 ± 0.03
Standards	^{bT}1.49 ± 0.04	^{jT}1.69 ± 0.05	^{ll}0.19 ± 0.00^{cl}	^{nl}0.44 ± 0.02^{cl}	^{nl}4.51 ± 0.11	^{il}0.43 ± 0.01	^{iA}0.22 ± 0.02	^{mA}0.19 ± 0.02

The samples were analyzed in triplicate (n = 3) and expressed as mean ± standard deviation. Means followed by different superscripts (a-n) within the same column indicated significant differences ($p < 0.05$). *The bioactivities were expressed as IC_{50} values (mM)

There were several reports available regarding the anti-inflammatory effects of the polyether triterpenoids and those partly bearing the skeleton of this class of compounds (Fernandez et al., 2000). Squalene derived triterpene lupeol was found to exhibit anti-inflammatory potential involving nuclear factor kappa B (NFκB) and phosphatidylinositol-3-kinase (PI3K) in a variety of cells (Saleem and Lupeol, 2009). In particular, the polyfunctionalized cyclic ether group of marine natural products were found to attract special interest, and among them, the natural products containing an oxepanyl moiety were found to possess interesting biological properties including anti-inflammation and other bioactivities Halogenated sesquiterpenoid, aplysistatin isolated from the marine macroalga *Laurencia snackeyi* was found to possess the oxepane moiety, and were reported to possess anti-inflammatory activities along with the ability to suppress the expressions of inducible nitric oxide synthase (iNOS) and COX-2 enzymes (Vairappan et al., 2013). Polyether triterpene-type metabolites, palisadins were found to contain oxepane moieties and fused rings, among which, 5β-hydroxipalisadin B showed effective anti-inflammatory properties in various *in vitro* models (Wijesinghe et al., 2014).

4.3.3.7 Pharmacological potentials of macrolide derivatives (Compounds 13-15)

In-vitro antioxidant assays were evaluated by the radical (radicals DPPH and $ABTS^+$) quenching abilities of compounds (**13-15**) against 1, 1-diphenyl-2-picryl-hydrazil (DPPH) and 2, 2'-azino-bis-3-ethylbenzothiozoline-6-sulfonic acid ($ABTS^+$), and the antioxidant activities were compared with the standard antioxidative agent, *α*-tocopherol (Table 4.23). Among the titled compounds, **14** showed higher radical scavenging potentials (IC_{50} DPPH 1.10 mM; IC_{50} $ABTS^+$ 1.21 mM) when compared to other studied compounds (**13-15**) (IC_{50} DPPH > 1.38 mM; IC_{50} $ABTS^+$ > 1.42 mM). It is of note that the free radical scavenging potential of the compound (**13-15**) were found to be significantly greater (IC_{50} < 1.50 mM) in comparison with the standard, α-tocopherol ($IC_{50} \geq 1.5$ mM; $P < 0.05$). The greater antioxidative properties against the free radicals were reported for the 12-membered macrocyclic lactone isolated from the seaweed, *S. wightii* (Maneesh and Chakraborty, 2017), a 16-membered macrocyclic bislactone and 10/13-membered macrocyclic lactones from the mollusk, *Amphioctopus neglectus* (Chakraborty et al., 2019). These results further substantiated the antioxidative potential of the studied compounds (**13-15**).

Compound **13** was found to contain two conjugated systems, such as 14-furanyl and 22-benzyl, which could easily transfer H-atoms (by hydrogen-atom transfer) located at C-14 and C-22 positions, respectively of oxabicyclo[21.3.1]heptacosa-11,23,25,27-tetraene-7,18-dione skeleton onto DPPH free radicals to form resonance stabilised 3-acetyl-14-(furan-2(5*H*)-ylidene)-15-(isopentyloxy)-11-methyl-8-oxa-bicyclo[21.3.1]heptacosa-26,11, 22,24-tetraene-

7,18-dione. These two positions (C-14 and C-22) could be considered as primary antioxidative reaction centers. Additionally, three more reaction centers related to the ester at C-7, 3-acetyl and 18-keto in the oxabicyclo[21.3.1]heptacosa-11,23,25,27-tetraene-7,18-dione framework, were found for compound **13**. The protons at C-6 (near to ester at C-7), C-3 (acetyl linked carbon) and C-19 (adjacent to keto at C-18) could participate in keto-enol resonance with the nearest >C(=O)< (keto) groups at C-7, C-3^1, and C-18, respectively leading to the generation of -CH=C(-OH)- (enol) functionality via repositioning the protons from C-6, C-3, and C-19, respectively to the DPPH free radical to form a resonance stabilized 14-(furanyl)-3-(1-hydroxyethylidene)-11-methyl-15-(153-methylbutyloxy)-8-oxabicyclo[21.3.1]heptacosa-hexaene-7,18-diol. These five sites of antioxidative reaction centers present in compound **13** could effectively participate in the resonance stabilization, which in turn, stabilize the DPPH radicals in the biological systems. Compound **14** exhibited four primary antioxidative reaction sites, which include three keto functionalities and one conjugated olefinic system. The conjugated olefinic groups (-C12=C13-C14=C15-) adjacent to the oxygenated functionality in Compound **14** could effectively involve in the electron delocalization to form -C11=C12-C13=C14-C15-O-, which in turn, transfer protons from C-11 to radicals through the hydrogen transfer via formation of resonance stabilized 10-acetyl-9-isopentyl-2-methyl-5,16,23^1-trioxa-bicyclo[21.3.1]heptacosa-2,11,13-triene-6,19-dione . The protons at C-7 (near to ester at C-6), C-10 (acetyl linked carbon) and C-20 (adjacent to keto at C-19) could involve in the keto-enol resonance with nearby >C(=O)< groups at C-6, C-10^1 and C-19, respectively resulting in the formation of -CH=C(-OH)- by replacing the protons from C-7, C-10, and C-20, respectively to DPPH radicals through the genesis of resonance stabilised 10-(1-hydroxyethylidene)-9-isopentyl-2-methyl-5,16,23^1-trioxa-bicyclo[21.3.1]heptacosa-2,6,10,12,14, 19-hexaene-6,19-diol. These four antioxidative reaction centres might be the predominant reasons for potential radical scavenging properties of Compound **14** through the neutralisation of DPPH radical. However, Compound **15** possessed only three reaction centres, which include two carbonyls and one hydroxyl functionalities. The free electron pair of -OH of -CHOH group located at C-8 of the macrolide might not efficiently contribute in resonance stabilization due to the weak acidic property of this proton, resulting in the formation of weakly stabilized DPPH radical. The protons at C-9 (near to keto at C-10) and C-22 (adjacent to keto at C-23 in the pyrone ring) could involve in the keto-enol resonance with the nearby >C(=O)< groups at C-10 and C-23, respectively leading to the formation of -CH=C(-OH)- by replacing the protons from C-9 and C-22, respectively to the DPPH radicals. These antioxidative reaction centers resulted in the resonance stabilized form of Compound **15**, 20-isobutyl-16-methyl-7,14-dioxa-bicyclo[19.3.1]pentacosa-2,5,9,16,22-pentaene-10,23-triol to neutralize the DPPH free radical . Notably, the compound **15** did not hold any extended conjugation as in **13** and **14**, and hence, it

could not effectively transfer H-atom to DPPH, and therefore, displayed weaker antioxidant activity (IC_{50} DPPH 1.42 mM; IC_{50} $ABTS^{+}$ 1.47 mM) than those displayed by Compounds **13** and **15** (IC_{50} DPPH 1.37-1.40 mM; IC_{50} $ABTS^{+}$ 1.41-1.43 mM).

In-vitro anti-inflammatory potential of the studied compounds was assessed by their attenuation potential against pro-inflammatory enzymes 5-lipoxygenase (5-LOX) and cyclooxygenase-1 and 2 (COX-1/2). Among the titled compounds, 21-membered pyran-enclosed Compound **14** displayed greater attenuation property against COX-2 (IC_{50} 1.13 mM) than those exhibited by the 21-membered aryl Compound **13** and 19-membered macrolide **C** (IC_{50} COX-2 ~ 1.2 mM). The attenuating potential of the studied compounds against 5-LOX was significantly greater (IC_{50} < 1.5 mM) than that displayed by ibuprofen (IC_{50} 4.5 mM), whereas the selectivity indices exhibited by macrolides against COX-2 were significantly higher (1.18-1.41, $P < 0.05$) when compared to ibuprofen (SI = 0.43) attributing the greater selectivity profile of the former towards inducible pro-inflammatory mediators than that exhibited by the latter. The polyether macrocyclic lactone isolated from the marine gastropod, *Babylonia spirata* was previously reported for its potential 5-LOX attenuation property (Salas and Chakraborty, 2018).

4.3.4 Structure-activity correlation analyses of bioactives isolated from EtOAc-MeOH extract of G. salicornia

4.3.4.1 Structure-activity correlation analyses of abeo-labdane class of diterpenoid derivative (Compound 1)

The target bioactivities of the studied compound **1** were assessed by different physico-chemical parameters, and these were utilised to correlate their structural attributes (Table 4.24). The electronic parameter of compound **1** was found to be obtained as tPSA, 43.37 and Pl ~38.25 x 10^{-24} cm^3, which could substantiate the greater inhibitory activities of compound towards oxidants and pro-inflammatory enzymes. The compound **1** was registered steric parameters as MR 97.78 cm^3 mol^{-1}, MV 341.5 cm^3 mol^{-1} and Pr 813.20 cm^3 mol^{-1} might efficiently bind with the enzyme active site, resulting in its higher inhibitory activity towards 5-LOX. It was also displayed that that an intermediate hydrophobicity (logarithmic value of octanol-water coefficient) (log P_{ow} 5.21) predominantly contributed towards its greater radical quenching and pro-inflammatory enzyme inhibitory activities. The hydrophobic values ~5 might interpret its hydrophobic-hydrophilic interactions (Lipinski 2004) and bonding with catalytic site of enzymes (Huuskonen et al., 2000) leading to its higher bioactive properties.

Table 4.24: Molecular descriptors (electronic, steric and hydrophobic)† of compound **1** from *G. salicornia*

Molecular descriptors

	Compound 1
Electronic	
tPSA	43.37
Pl ($X10^{-24}$ cm^3)	38.25
Steric	
MR (cm^3 mol^{-1})	97.78
MV (cm^3)	341.5
Pr (cm^3)	813.2
Hydrophobic	
Log P_{ow}	5.21

†Steric: MV, molar volume; Pr, parachor; MR, molar refractivity; Hydrophobic: Log P_{ow}, logarithmic scale of the octanol-water partition coefficient; Electronic: Pl, polarisability; tPSA, topological polar surface area.

The structure-activity relationship analyses were carried out by using different molecular descriptors of the purified compounds as described in the text.

4.3.4.2 Structure-activity correlation analyses of oleanane class of triterpenoid derivatives (Compounds 2-3)

The target bioactivities of the studied compounds (**2-3**) were assessed by different physico-chemical parameters, and these were utilized to correlate their structural attributes. It is consequential to record that the electronic parameter of 24(4→23)-abeo-oleanene (**3**) (Pl ~70 x 10^{-24} cm^3) was greater than that recorded with 24(4→23), 27(8→26), 30(20→29)-tris-abeo-oleanene (**2**) (polarisability, Pl ~65 x 10^{-24} cm^3), which could substantiate the greater inhibitory activities of former towards oxidants and carbolytic enzymes. It was apparent that the compound **3** was bulkier than **2**, as determined by the greater steric factors of the former. Comparatively lesser bulkiness of **2** and **3** (MR 163-178 cm^3 mol^{-1}, MV 541-575 cm^3 mol^{-1} and Pr 1320-1445 cm^3 mol^{-1}) might efficiently network with the enzyme active site remnants, resulting in its higher inhibitory activity towards starch digestive enzymes (Table 4.25). It was also likely that that a greater hydrophobicity (logarithmic value of octanol-water coefficient) of abeo-oleanenes, **2-3** (log P_{ow} 9.19-10.73) predominantly contributed towards its greater radical quenching and carbolytic enzyme inhibitory activities. The higher hydrophobic values might explain its requisite hydrophobic-hydrophilic interactions (Lipinski 2004) and bonding of receptor enzymes (Huuskonen et al., 2000) leading to its higher anti-hyperglycaemic and antioxidant properties.

Table 4.25: Molecular descriptors (electronic, steric and hydrophobic)† of compounds **2-3** from *G. salicornia*

Molecular descriptors

	Compound 2	Compound 3
Electronic		
tPSA	43.37	43.37
Pl ($X10^{-24}$ cm^3)	64.99	70.61
Steric		
MR (cm^3 mol^{-1})	163.95	178.13
MV (cm^3)	541.40	575.80
Pr (cm^3)	1320.60	1445.10
Hydrophobic		
Log P_{ow}	9.19	10.73

†Steric: MV, molar volume; Pr, parachor; MR, molar refractivity; Hydrophobic: Log P_{ow}, logarithmic scale of the octanol-water partition coefficient; Electronic: Pl, polarisability; tPSA, topological polar surface area.

The structure-activity relationship analyses were carried out by using different molecular descriptors of the purified compounds as described in the text.

4.3.4.3 Structure-activity correlation analyses of drimane class of diterpenoid derivative (Compounds 4-6)

The target bioactivities of the studied metabolites were corroborated by different physico-chemical parameters describing their structural features. It is pertinent to note that the electronic parameters of the drimane derivative bearing substituted 1*H*-benzo[*a*]xanthene-4,10,12-triol moiety (**4**) was higher (polarizability, Pl ~51.65 X 10^{-24} $cm^{3,}$ tPSA, topological polar surface area, 79.15) than those recorded by the compounds **5** and **6** (Pl 51.34-43.18 X 10^{-24} cm^3, tPSA, 38.69), which could be related with the greater pro-inflammatory inhibitory activities of the former (Table 4.26). It was apparent that the compound **5** was bulkier than **4**, as determined by the lower steric factors of the latter (molar refractivity, MR ~130.30 cm^3 mol^{-1}, molar volume, MV ~394.20 cm^3 mol^{-1}, and P ~1053.00 cm^3 mol^{-1}). The increased bulkiness of **5** might restrict the metabolite to efficiently interact with the active site of enzyme residues, resulting in its lesser inhibitory activity towards pro-inflammatory enzymes in comparison with compound **4.** It was also likely that that a medium hydrophobicity (logarithmic value of octanol-water coefficient, log P_{ow} 4.99) of compound (**4**) predominantly contributed towards the comparatively higher radical quenching and pro-inflammatory enzyme inhibitory activities than those displayed by its drimane quinol analogues (**5** & **6**). The compounds **5** and **6** were found to record higher (log P_{ow} 7.13 and 5.64, respectively) than the desired lipophilicity (log P_{ow} 2-5), which might explain

their lesser electronic interactions resulting in lower antioxidant and anti-inflammatory bioactivities (Shimizu et al., 2015).

The studied drimane sesquiterpene quinols, **4**-**6** were deduced to contain hydroxyphenyl functionality linked to the drimane framework. The hydroxyphenyl part of the studied compounds might be involved in the resonance stabilization through the transfer of proton from hydroxyl to DPPH radical via hydrogen atom transfer mechanism (HAT). The three titled compounds enclosed similar type of functionalities, even though the numbers of antioxidative reaction centres were found to differ. The greater number of electron rich reaction centres (three hydroxyls, one alkene, and phenyl) in **4** over those possessed by compounds **5**-**6** (one each of hydroxyl phenyl functionalities) in combination with the optimum hydrophobicity (log P_{ow} <5) factors, might occupy prominent roles in the greater bioactive potential of the former. The anti-inflammatory potentials of the drimane sesquiterpene quinols were reported in a previous report of literature (McNamara et al., 2005). A previous study on drimane based sesquiterpene quinol, dysiquinol D proposed that the compound bearing an ether linkage between C-8 and C-17 positions exhibited greater anti-inflammatory potential than dysiquinols A-C possessing ether bridge between C-1 and C-17 (Jiao et al., 2015). Herein, the compound **4** bearing substituted 1*H*-benzo[a]xanthene-4,10,12-triol moiety was structurally comparable with dysiquinol D and enclosed ether bridge in the identical position as in dysiquinol D attributing the greater bioactive potential of **4** than those exhibited by compounds **5** (no ether linkage) and **6** (comparable to dysiquinol A-C skeleton).

Table 4.26: Molecular descriptors (electronic, steric and hydrophobic)[†] of compounds **4**-**6** from *G. salicornia*

Molecular descriptors			
	Compound 4	**Compound 5**	**Compound 6**
Electronic			
tPSA	79.15	38.69	38.69
Pl ($X10^{-24}$ cm^3)	51.65	51.34	43.18
Steric			
MR (cm^3 mol^{-1})	130.30	129.50	108.93
MV (cm^3)	394.20	423.30	339.50
Pr (cm^3)	1053.00	1060.80	873.20
Hydrophobic			
Log P_{ow}	4.99	7.13	5.64

[†]Steric: MV, molar volume; Pr, parachor; MR, molar refractivity; Hydrophobic: Log P_{ow}, logarithmic scale of the octanol-water partition coefficient; Electronic: Pl, polarisability; tPSA, topological polar surface area.

The structure-activity relationship analyses were carried out by using different molecular descriptors of the purified compounds as described in the text.

4.3.4.4 Structure-activity correlation analyses of 2H-chromenyl derivatives (Compounds 7-8)

The molecular descriptor variables of studied *2H*-chromenyl derivatives correlated the structural parameters, which appeared to play predominant roles in attributing the target bioactivities. The antioxidative and anti-inflammatory activities were found to be directly proportional towards the electronic (topological polar surface area, tPSA and polarisability, Pl) and hydrophilic-lipophilic balance (log P_{ow}, logarithm of octanol/water partition-coefficient), and not by the molecular bulk. The tPSA of **8** was found to be greater (64.99) than that of **7** (55.76) and α-tocopherol (29.46). The total numbers of electron-rich centres were greater in **8** appeared to result in its higher polarisability and antioxidant potentials (Table 4.27). Therefore, the electronic factors appeared to play significant role to govern the bioactive potentials (Wang et al. 2007). The log P_{ow} of **8** was found to be within the desirable range (~ 6.1), which might cause a suitable lipophilic-hydrophobic relation (Lipinski 2007) and receptor binding (Huuskonen et al. 2000) leading to higher target bioactivities than other studied compounds.

Table 4.27: Molecular descriptors (electronic, steric and hydrophobic)[†] of compounds **7**-**8** from *G. salicornia*

Molecular descriptors		
	Compound 7	**Compound 8**
Electronic		
tPSA	55.76	64.99
Pl ($X10^{-24}$ cm^3)	47.82	50.02
Steric		
MR (cm^3 mol^{-1})	124.62	126.19
MV (cm^3)	398.00	395.00
Pr (cm^3)	979.80	1023.80
Hydrophobic		
Log P_{ow}	6.42	6.11

[†]Steric: MV, molar volume; Pr, parachor; MR, molar refractivity; Hydrophobic: Log P_{ow}, logarithmic scale of the octanol-water partition coefficient; Electronic: Pl, polarisability; tPSA, topological polar surface area.

The structure-activity relationship analyses were carried out by using different molecular descriptors of the purified compounds as described in the text.

4.3.4.5 Structure-activity correlation analyses of spiro- derivatives (Compounds 9-10)

The molecular descriptor variables of the studied spiro-compounds appeared to play predominant roles in attributing the target bioactivities. Antioxidative and anti-inflammatory activities were found to be directly proportional towards the electronic (topological polar surface area, tPSA and polarisability, Pl) and hydrophilic-lipophilic balance (log P_{ow}, logarithm of octanol/water partition-coefficient), and not the molecular bulk. The tPSA of **10** was found to be greater (111.52) than that of **9** (72.83) and α-tocopherol (29.46). The total numbers of electron-rich centres were greater in **10** appeared to result in its higher polarisability (48.07) and antioxidant potentials (Table 4.28). Therefore, the electronic factors appeared to play significant role to govern the bioactive potentials (Wang et al. 2007). The log P_{ow} of **10** was found to be within the desirable range (~2.2), which might cause a suitable lipophilic-hydrophobic relation (Lipinski 2007) and receptor binding (Huuskonen et al. 2000) leading to higher target bioactivities than other studied compounds.

Table 4.28: Molecular descriptors (electronic, steric and hydrophobic)[†] of compounds **9-10** from *G. salicornia*

Molecular descriptors		
	Compound 9	**Compound 10**
Electronic		
tPSA	72.83	11.52
Pl ($X10^{-24}$ cm^3)	39.75	48.07
Steric		
MR (cm^3 mol^{-1})	100.28	121.93
MV (cm^3)	336.10	387.50
Pr (cm^3)	852.30	1022.10
Hydrophobic		
Log P_{ow}	2.54	2.29

[†]Steric: MV, molar volume; Pr, parachor; MR, molar refractivity; Hydrophobic: Log P_{ow}, logarithmic scale of the octanol-water partition coefficient; Electronic: Pl, polarisability; tPSA, topological polar surface area.

The structure-activity relationship analyses were carried out by using different molecular descriptors of the purified compounds as described in the text.

4.3.4.6 Structure-activity correlation of polyether derivatives (Compounds 11-12)

The bio-potencies of polyether derivatives were established with their physico-chemical attributes to describe their structural characteristics, which might impart major roles in evaluating the target bioactive properties. Greater electronic properties were recorded for the titled polyether derivative, **12** bearing furanyl-furo[3,2-b]pyran-2*H*-pyran moiety based on their polarisability (Pl 64.05 x 10^{-24} cm^3) and topological polar surface area (94.45) than those recorded by **11** (Pl 56.09 x 10^{-24} cm^3; tPSA 66.38), ibuprofen (Pl 24.09 x 10^{-24} cm^3; tPSA 37.30) and α-tocopherol (Pl 53.54 x 10^{-24} cm^3; tPSA 29.46) (Table 4.29). These could be related to greater anti-inflammatory and radical scavenging potencies of polyether derivative **12** over those displayed by compound **11** bearing pyranyl-10-methylpyrano[3,2-b]pyran-methyleneoxepane moiety as well as standard agents. Further, steric factors of the studied polyether derivatives as determined by molar refractivity (121-141 cm^3 mol^{-1}), parachor (1367-1164 cm^3) and molar volume (458-538 cm^3 mol^{-1}) were found to be lesser than those exhibited by the antioxidant agent, α-tocopherol (MR 135 cm^3 mol^{-1}; MV 462 cm^3 mol^{-1}; P 1123 cm^3). The lesser steric bulkiness of the titled compounds might also explain efficient steric interaction with the pro-inflammatory enzymes and radical agents resulting in greater bioactivities. Moreover, the hydrophobic values (logarithmic value of octanol-water coefficient, log P_{ow1} 1.84; log P_{ow2} 4.58) of the polyether analogues were deduced to be within adequate ranges (log P_{ow} < 5) that might contribute towards its significantly greater radical quenching/anti-inflammatory potencies [35]. The highly electron-rich centres {with furo[3,2-b]pyran and ester functionalities} in **12** could effectively be involved in the proton transfer to free radicals via hydrogen-atom-transfer scheme than polyether **11** bearing pyrano[3,2-b]pyran and methyleneoxepane functionalities. The greater number of electron-rich reaction sites in **12** along with optimum hydrophobicity (log P_{OW2} < 5), lesser steric factor and greater electronic descriptors over **11** might play a prominent functional role in the greater bio-potential of the polyether derivative **12** bearing furanyl-furo[3,2-b]pyran-2*H*-pyran moiety.

Table 4.29: Molecular descriptors (electronic, steric and hydrophobic)† of compounds **11-12** from *G. salicornia*

Molecular descriptors		
	Compound 11	**Compound 12**
Electronic		
tPSA	66.38	94.45
Pl ($X10^{-24}$ cm^3)	56.09	64.05
Steric		
MR (cm^3 mol^{-1})	141.50	121.93
MV (cm^3)	458.40	538.10

Pr (cm^3)	1164.30	1367.30
Hydrophobic		
Log P_{ow}	1.84	4.58

[†]Steric: MV, molar volume; Pr, parachor; MR, molar refractivity; Hydrophobic: Log P_{ow}, logarithmic scale of the octanol-water partition coefficient; Electronic: Pl, polarisability; tPSA, topological polar surface area.

The structure-activity relationship analyses were carried out by using different molecular descriptors of the purified compounds as described in the text.

4.3.4.7 Structure-activity correlation analyses of macrolide derivatives (Compounds 13-15)

The bioactive potentials of the Compound **13-15** were substantiated with their physico-chemical-parameters. It is relevant to note that the electronic-parameters of 21-membered macrolide derivative (**13**) was higher (polarizability, Pl 59.35; topological polar surface area, tPSA 78.9) than that recorded with 19-membered macrolide derivative, **15** (Pl 52; tPSA, 72.8), and that could be correlated with the greater bioactivities of the former (Table 4.30). The higher electronic values recorded for Compound **14** further supported the possibilities of greater number of electron-rich centres, which in turn, resulted in its greater bioactive properties. Electronic or polar factors were reported to play important parts to govern the target pharmacological properties (Wang et al., 2007). Notably, the steric bulkiness of the 21-membered aryl macrolide, compound **13** (molar-volume, MV 565 cm^3 mol^{-1}; parachor, P 1455 cm^3) was significantly greater than the 21-membered pyran enclosed macrolide derivative, Compound **14** (MV 543 cm^3 mol^{-1}; P 1279 cm^3) and 19-membered cyclohexanone enclosed macrolide derivative, Compound **15** (MV 465 cm^3 mol^{-1}; P 1109 cm^3). The greater steric hindrance of Compound **13** due to its bulkier side chains of benzyl/furanyl ring systems could negatively affect its bioactivities, although its electronic parameters recorded higher values (Pl 69.4; tPSA, 78.9). The optimum hydrophobicity/lipophilicity (log P_{ow}) equilibrium of Compound **14** and **15** (5.6-6) appeared to contribute towards their greater bioactivities over Compound **13** that displayed greater

lipophilicity (log P_{ow} ~ 7.7). The balanced hydrophilic-lipophilic properties as determined by log P_{ow} was found to control the inter-membrane perviousness including requisite hydrophobic/lipophilic (Lipinski, 2004) relationship and binding of receptors (Huuskonen et al., 2000). Apparently, greater electronic parameters (electron-rich centres) along with optimum steric bulkiness and permissible hydrophobicity-lipophilicity equilibrium of Compound **14** could result in its greater antioxidative properties and effective interaction with the active site of inflammatory enzymes to impart anti-inflammatory properties compared to other studied compounds (Wang et al., 2007).

Table 4.30: Molecular descriptors (electronic, steric and hydrophobic)[†] of compounds **13-15** from *G. salicornia*

Molecular descriptors			
	Compound 13	**Compound 14**	**Compound 15**
Electronic			
tPSA	78.90	78.90	75.83
Pl ($X10^{-24}$ cm^3)	69.36	59.35	52.03
Steric			
MR (cm^3 mol^{-1})	174.98	149.71	174.98
MV (cm^3)	564.90	542.60	465.30
Pr (cm^3)	1455.00	1278.50	1109.70
Hydrophobic			
Log P_{ow}	7.70	6.00	5.60

[†]Steric: MV, molar volume; Pr, parachor; MR, molar refractivity; Hydrophobic: Log P_{ow}, logarithmic scale of the octanol-water partition coefficient; Electronic: Pl, polarisability; tPSA, topological polar surface area.

The structure-activity relationship analyses were carried out by using different molecular descriptors of the purified compounds as described in the text.

4.3.5. In silico molecular docking analysis of bioactivecompounds isolated from *G. salicornia*

4.3.5.1 In silico molecular docking analysis of *abeo-labdane class of diterpenoid derivative (Compound 1)*

The studied labdane analogue was subjected to molecular docking studies against proinflammatory enzymes, 5-LOX. The results were documented by their RMSD data. The molecular docking parameters, such as binding energy, intermolecular and torsional free energy, and inhibition constants of **1** were recorded (Table 4.31). *In silico* molecular docking analysis of the labdane with 5-LOX was initiated with grid box x=36.879, y=-20.280, z=28. (Figure 4.232). Compound **1** recorded least binding energy of -7.30 kcal mol^{-1} in interactions with 5-LOX enzyme target sites. Similarly, other parameters were obtained, such as inhibition constant (Ki) 1.03 nM, intermolecular energy was -7.34 kcal mol^{-1}. The molecular docking interaction of ligand (compound **1**) and 5-LOX showed two hydrogen bonds (displayed as red and blue-coloured lines) to amino acyl residues of Ser^{528} and Ser^{523} with the bond distances of 2.060 and 2.748 Å in the active binding site.

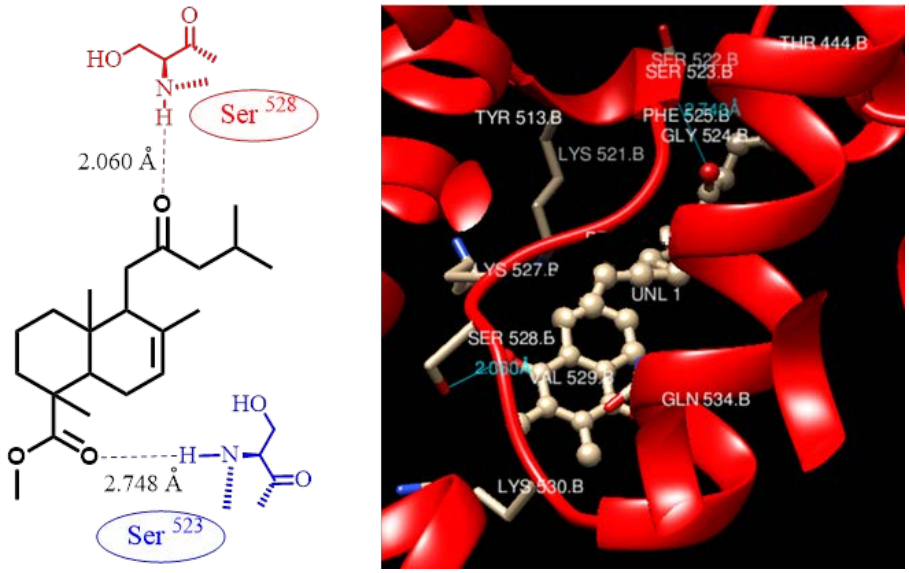

Figure 4.232.: Closer view of molecular binding interactions of compound **1** in the catalytic site of protein 5-LOX

Table 4.31: The binding energy, docking score, inhibition constant, intermolecular energy and torsional free energy between the ligands (compounds **1**) and the active sites of 5-lipoxygenase

Ligands	‡Binding energy (kcal mol^{-1})	‡Inhibition constant, Ki (nM)	‡Intermolecular energy (kcal mol^{-1})	‡ Torsional free energy (kcal mol^{-1})	Hydrogen bonded residues	Distance from hydrogen bonded residue (Å)
1	-7.30	1.03	-7.34	1.20	Ser^{528}, Ser^{523}	2.060 ,2.748

‡ Values were evaluated from the calculations based on the energy minimization.

4.3.5.2 In silico molecular docking analysis of *oleanane class of triterpenoid derivatives (Compounds 2-3)*

The inhibition of starch degrading enzymes, such as α-amylases and α-glucosidases is an effective methodology to monitoring the glucose level in blood. The commercially developed carbolytic enzyme inhibitors, such as acarbose and voglibose are widely used to control the blood glucose levels. The computation tools like structure based molecular docking simulations have been widely utilised to enrich a chemical library of active compounds with biomolecular structure and functions (Hyun et al., 2014). The studied oleanene analogues were subjected to molecular docking studies against starch digestive enzymes, α-glucosidase and α-amylase. The results were evaluated by their RMSD data. The molecular docking parameters, such as binding energy, intermolecular and torsional free energy, and inhibition constants of **2-3** were documented (Table 4.32). *In silico* molecular docking analysis of the abeo-oleanenes with α-glucosidase with grid box x=37.969, y=-19.190, z=29.008 and *α*-amylase with grid box x=-7.248 y=54.607, z=30.003 appropriately gave the impression that the ligands exhibited efficient interactions with the enzyme target sites (Figure 4.233). Among the studied compounds (**2-3**), compound **3** recorded least binding energy of -9.84 kcal mol^{-1} in interactions with α-glucosidase enzyme target sites subsequent to those exhibited by compound **2** (-9.42 kcal mol^{-1}). Likewise, the constant of enzyme inhibition (Ki) was lesser for **3** (61.61 nM) towards α-glucosidase enzyme than that exhibited by **2** (124.49 nM). Also, intermolecular energy was lesser for **3** (-11.44 kcal mol^{-1}). The molecular docking interaction of ligand (compound **3**) and α-glucosidase showed two hydrogen bonds (displayed as red-coloured lines) to amino acyl residues of THR^{83} and TRP^{36} with the bond distances of 3.148 and 3.044 Å in the active binding site, whereas **2**

showed one hydrogen-bonded interaction to amino acid residue of TRP^{36} with molecular distance of 2.766 Å.

Similarly, compound **3** exhibited least binding energy of -10.04 kcal mol^{-1} in *α*-amylase enzyme target site interactions than those exhibited by compound **2** (-5.52 kcal mol^{-1}). Additionally, two other parameters, such as intermolecular energy and inhibition constant (Ki) were also calculated. The compound **3** had lesser inhibition constant (38.15 nM) when compared to **2** (89.58 μM). Inhibition constant and binding energy were proportional to each other, and therefore, the inhibitory activity of α-amylase of **3** was substantiated by using intermolecular energy and inhibition constant. As mentioned in Table 4.32, the metabolite **3** exhibited intermolecular energy of -12.18 kcal mol^{-1}, which was lesser when compared to2 (-7.06 kcal mol^{-1}). These results further demonstrated greater α-amylase inhibition activity of oleanene **2** compared to **1**. The molecular docking analysis of oleanene **3** and α-amylase showed two hydrogen bonds with amino acyl residue of ARG^{346} with the bond distances of 2.954 and 2.878 Å in the active binding site, whereas compound **2** showed one hydrogen-bonded interaction with amino acyl residue of ASP^{381} with molecular distances of 2.467 Å. The comparison of molecular docking parameters on the basis of *in-vitro* experiment appropriately suggested that the abeo-oleanene derivative (**3**) exhibited closer molecular interactions with the starch digestive enzymes, which might explain its greater inhibitory potential against α-glucosidase and α-amylase (0.29-0.34 mM) when compared to those exhibited by **3** (0.32-0.40 mM). It was thus apparent that active inhibition of the pancreatic *α*-amylase enzyme could be an efficient approach to decrease the post-prandial hyperglycaemic levels via regulation of carbohydrate breakdown.

Table 4.32: The binding energy (B.E), inhibition constant (IC), intermolecular energy (I.E) and torsional free energy (T.E) between the ligands (compounds **2**-**3**) and the active sites of carbolytic enzymes *α*-glucosidase and *α*-amylase.

†Ligands	‡B.E	IC,	‡I.E	‡T.E	Amino acid residue	Molecular distances
	(kcal mol^{-1})	Ki (nM) (*μM)	(kcal mol^{-1})	(kcal mol^{-1})		
α-glucosidase						
2	-9.42	124.49	-11.14	1.79	Trp^{36}	2.766
3	-9.84	61.61	-11.44	2.39	Thr^{83}, Trp^{36}	3.148, 3.044
α-amylase						
2	-5.52	*89.58	-7.06	1.79	Asp^{381}	2.467
3	-10.04	38.15	-12.18	2.39	Arg^{346}	2.954, 2.878

† Molecular docking simulations were carried out using Autodock 4 software tool.

‡Values were evaluated from the calculations based on the energy minimization.

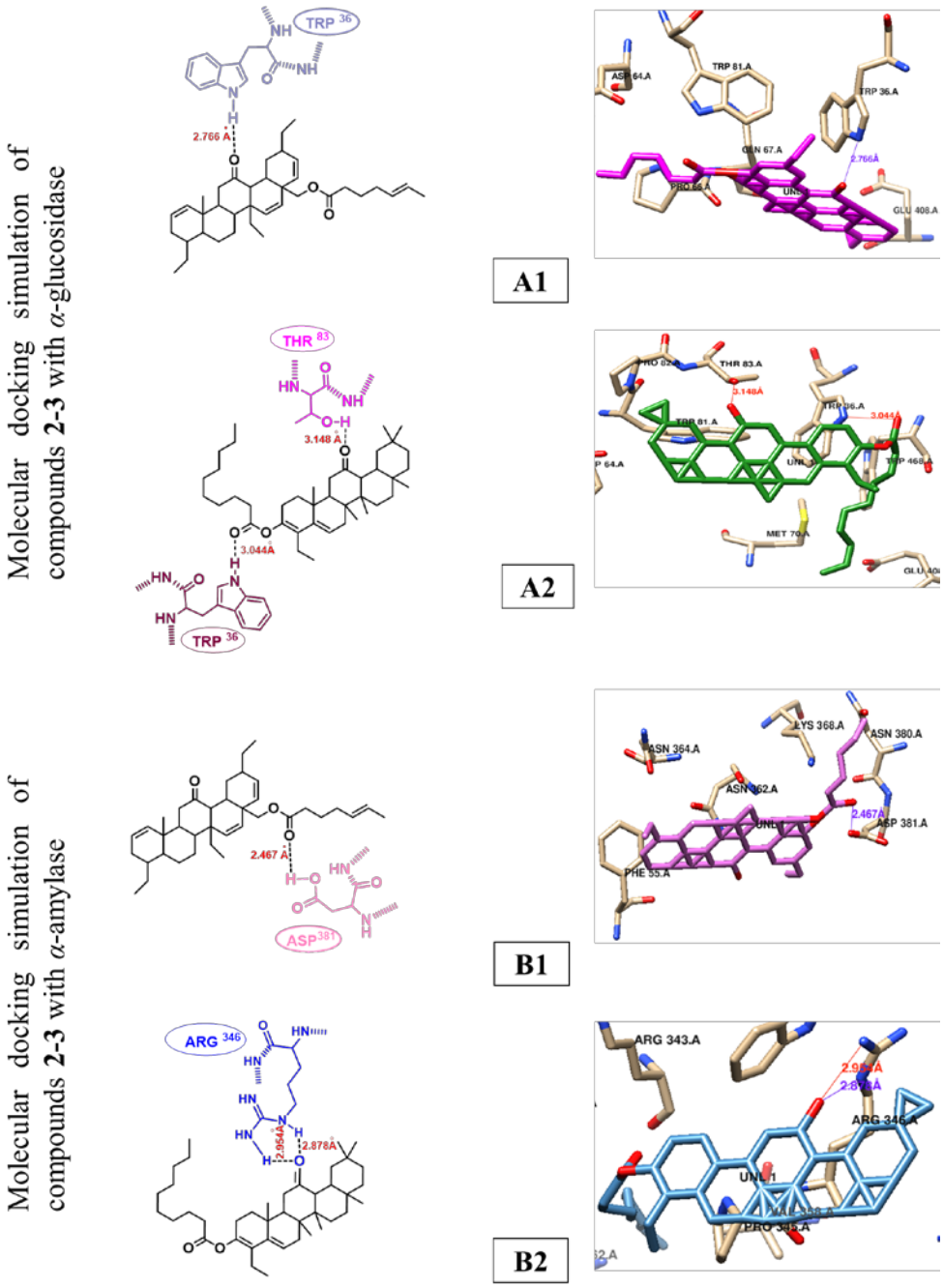

Figure 4.233.: Closer view of molecular binding interactions of (**A1**) 24(4→23), 27(8→26), 30(20→29)-tris-abeo-oleanene **2** and (**A2**) 24(4→23)-abeo-oleanene **3** derivatives in the catalytic site of protein *α*-glucosidase along with molecular binding interactions of (**B1**) 24(4→23), 27(8→26), 30(20→29)-tris-abeo-oleanene **2** and (**B2**) 24(4→23)-abeo-oleanene **3** derivatives in the catalytic site of *α*-amylase as deduced from its molecular modeling simulations.

4.3.5.2 In silico molecular docking analysis of *drimane class of diterpenoid derivative (Compounds 4-6)*

The studied compounds were subjected to *in silico* molecular docking analysis against pro-inflammatory 5-LOX and the results were evaluated by their RMSD data. The molecular docking parameters, such as binding energy, docking score, inhibition constant, hydrogen bonding interactions, torsional free energy and intermolecular energy between the active sites of 5-LOX and the ligands were documented in Table 4.33. The grid box of potential binding site was assigned as x=54.00 y=44, z=42. Among the studied compounds, substituted 1*H*-benzo[a]xanthene-4,10,12-triol (**4**), on molecular docking analysis with 5-LOX exhibited two hydrogen bond interaction with amino acyl residues Lys^{441} and Arg^{438} in the enzyme active site with molecular distances of 3.370 and 3.030 Å, respectively (Figure 4.234). Among the remaining drimane analogues, compounds **5** and **6** showed one hydrogen bonded interactions with the amino acyl residues Gly^{150} and Lys^{441} with molecular distances of 2.790 Å and 2.915 Å, respectively. The metabolite **4** exhibited greater number of hydrogen bond interactions with amino acyl residues than those recorded by compounds **5** and **6**. These results could be supported by the higher *in vitro* anti-inflammatory activity of **4** over those displayed by **5** and **6**. The comparison of molecular docking parameters appropriately suggested that compound **4** bearing substituted 1*H*-benzo[a]xanthene-4,10,12-triol moiety exhibited closer molecular interactions towards 5-LOX with least binding energy (-12.30 kcal mol^{-1}) and docking score (-12.96 kcal mol^{-1}), which were corroborated with their greater inhibition of 5-LOX than those exhibited by its drimane quinol analogues (compounds **5** and **6**).

Table 4.33: The binding energy, docking score, inhibition constant, intermolecular energy and torsional free energy between the ligands (compounds **4**-**6**) and the active sites of 5-lipoxygenase

Ligands	‡Binding energy (kcal mol^{-1})	‡Inhibition constant, Ki (nM)	‡Intermolecular energy (kcal mol^{-1})	‡ Torsional free energy (kcal mol^{-1})	Hydrogen bonded residues	Distance from hydrogen bonded residue (Å)
4	-12.30	1.23	-13.14	1.79	Lys^{441}, Arg^{438}	3.370, 3.030
5	-9.97	48.94	-11.10	1.19	Gln^{150}	2.790
6	-9.71	76.63	-10.75	1.19	Lys^{441}	2.915

‡ Values were evaluated from the calculations based on the energy minimization.

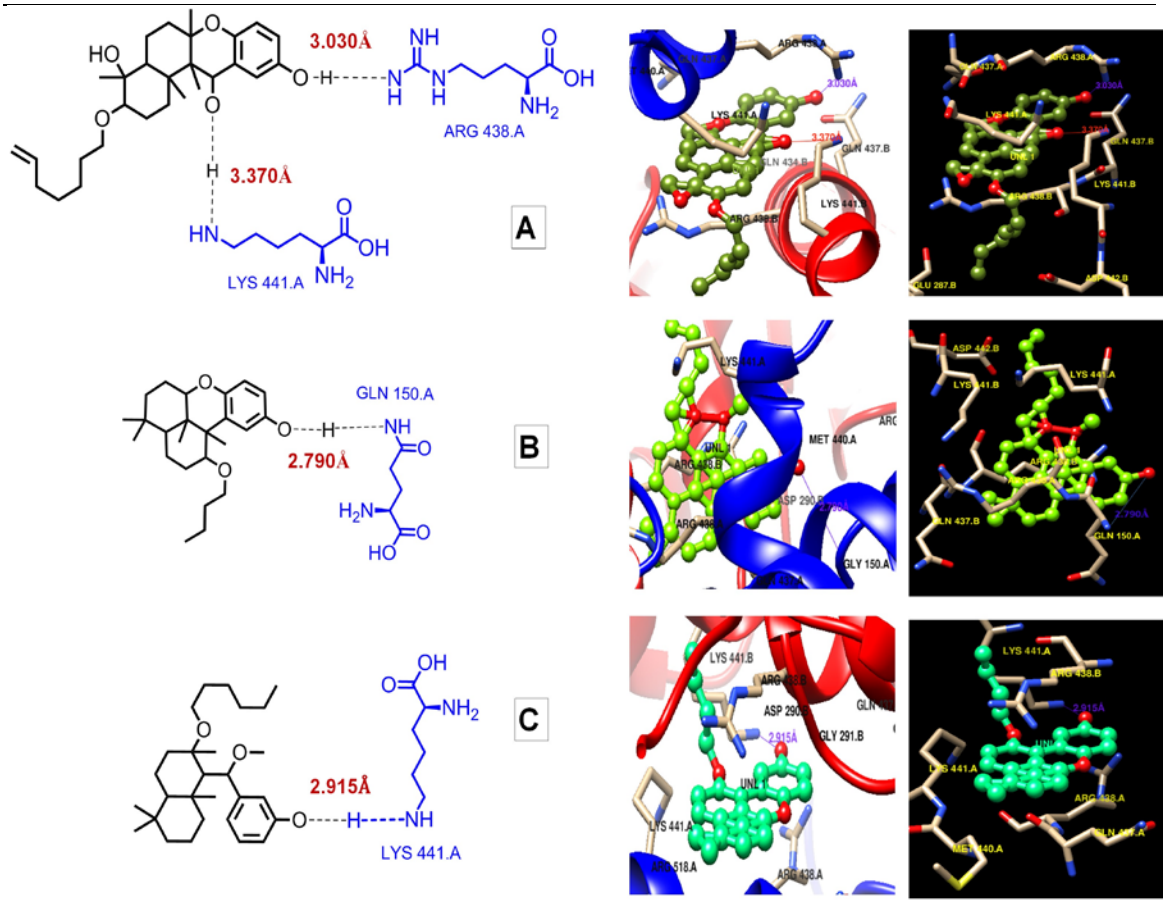

Figure 4.234.: Closer view of molecular binding interactions of the drimane sesquiterpene quinols in the catalytic site of (**A**-**C**) 5-lipoxygenase (5-LOX) as deduced from the molecular docking simulation experiment. The molecular docking analysis of ligands (studied sesquiterpene analogues **4**-**6**) and pro-inflammatory 5-LOX showed two hydrogen bonds (displayed as red and blue-coloured lines with amino acyl residues of Lys^{441} and Arg^{438} with bond distances of 3.370 and 3.030 Å, respectively) in the active binding site. The compounds **4** and **6** showed one hydrogen bonded interactions with amino acyl residues Gly^{150} and Lys^{441} with molecular distances of 2.790 Å and 2.915 Å, respectively.

4.3.5.4 In silico molecular docking analysis *of 2H-chromenyl derivatives (Compounds 7-8)*

The compounds **7-8** were subjected to *in silico* molecular docking analysis against pro-inflammatory 5-LOX and the results were evaluated by their root-mean-square deviation data. The molecular docking parameters between the active sites of 5-LOX and the ligands were documented in Table 4.34. The grid box of potential binding site was assigned as x=54.00 y=50, z=38. The molecular docking analysis of ligands (2*H*-chromenyl, **8**) and pro-inflammatory 5-LOX showed six hydrogen bonds (displayed as red and blue-coloured lines) with amino acyl residues of Ser^{522} and Ser^{628} with the bond distances of 2.743, 3.640, 3.117, 2.792, 2.668 and 3.075 Å in the active binding site, whereas compound **7** showed two hydrogen-bonded interactions with amino acid residues of Gln^{534} and Gln^{497} with molecular distances of 2.883, 3.046 Å, respectively. Therefore, the metabolite **8** exhibited greater number of hydrogen bonding interactions with amino acyl residues than those recorded by **7** (Figure 4.235). These results were supported by the higher *in vitro* anti-inflammatory activity of **2** over those displayed by **7**. The comparison of molecular docking parameters appropriately suggested that compound **8** exhibited close molecular interactions towards 5-LOX with least binding energy (-7.35 kcal mol^{-1}) which were corroborated with their greater potential of enzyme inhibition against 5-LOX (IC_{50} 2.03 mM) (Table 4.34) than those displayed by **7**.

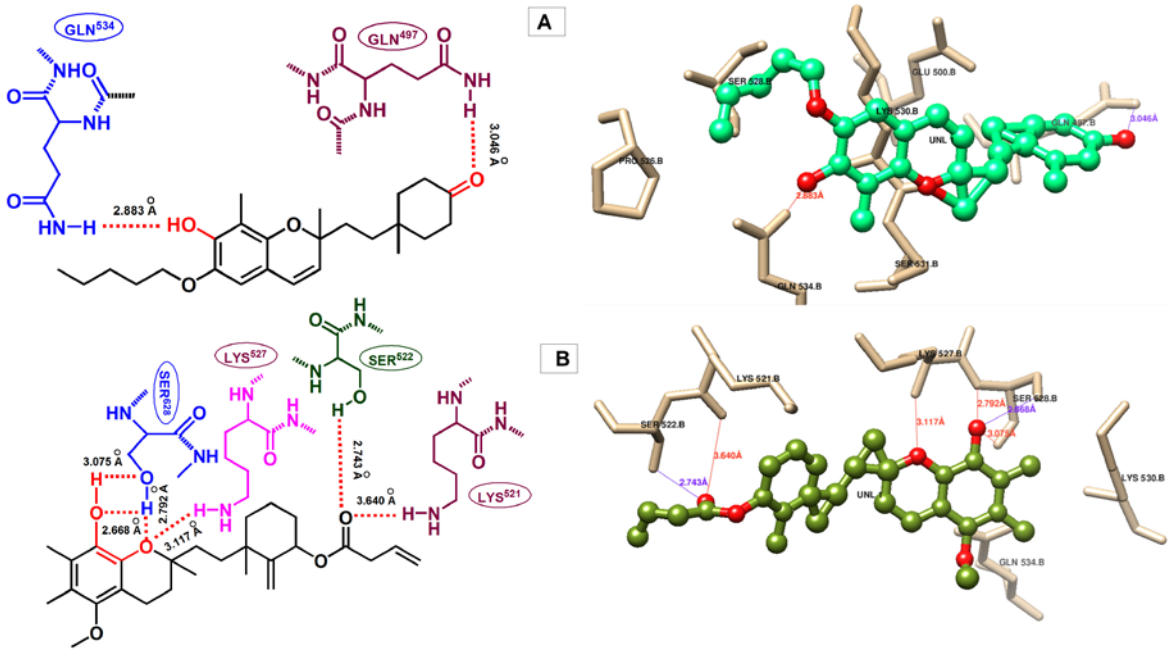

Figure 4.235.: Closer view of molecular binding interactions of the compounds **7-8** (**A** and **B**) in the catalytic site of 5-lipoxygenase (5-LOX) as deduced from the molecular docking simulation experiment. The molecular docking analysis of ligands (compound, **8**) and pro-inflammatory 5-LOX showed six hydrogen bonds (displayed as red and blue-coloured lines) with amino acyl

residues of Ser^{522}, Lys^{521}, Lys^{527} and Ser^{628} with bond distances of 2.743, 3.640, 3.117, 2.792, 2.668, and 3.075 Å in the active binding site. The compound **7** showed two hydrogen-bonded interactions with amino acid residues of Gln^{534} and Gln^{497} with molecular distances of 2.883, 3.046 Å, respectively.

Table 4.34: The binding energy, docking score, inhibition constant, intermolecular energy and torsional free energy between the ligands (compounds **7**-**8**) and the active sites of 5-lipoxygenase.

†Ligands	‡Binding energy (kcal mol^{-1})	‡Docking score (kcal mol^{-1})	‡Inhibition constant, Ki (nM)	‡Intermolecular energy (kcal mol^{-1})	‡Torsional free energy (kcal mol^{-1})	Hydrogen bonded residues	Distance from hydrogen bonded residue (Å)
7	-6.85	7.36	9.55	-7.44	1.49	Gln^{534}, Gln^{497},	2.883, 3.046
8	-7.35	8.74	4.09	-8.79	1.49	Ser^{522}, Lys^{521}, Lys^{527}, Ser^{628}	2.743, 3.640, 3.117, 2.792, 2.668, 3.075

† Molecular docking simulations were carried out using Autodock 4 software tool.

‡ Values were evaluated from the calculations based on the energy minimization.

4.3.5.5 In silico molecular docking analysis *of spiro- derivatives (Compounds 9-10)*

The attenuating potential of the studied spiro derivatives against the pro-inflammatory enzymes has been considered as one of the effective approaches to monitor the disturbances associated with inflammatory pathologies. The titled compounds were subjected to molecular docking analysis using pro-inflammatory enzyme 5-LOX (Figure 4.236), wherein the effective inhibition of compounds (**9**-**10**) was initially assessed by the RMSD reports in accordance with their decreasing order of binding energies (Table 4.35). Among the spiro-compounds, compound **2** recorded least binding energy of -10.13 kcal/mol subsequent to that exhibited by **9** (-10.00 kcal/mol). Likewise, the constant of enzyme inhibition (Ki) was lesser for **10** (37.80 nM) towards 5-LOX enzyme than that exhibited by **9** (46.89 nM). Also, intermolecular energy was lesser for **10** (-11.51 kcal/mol).

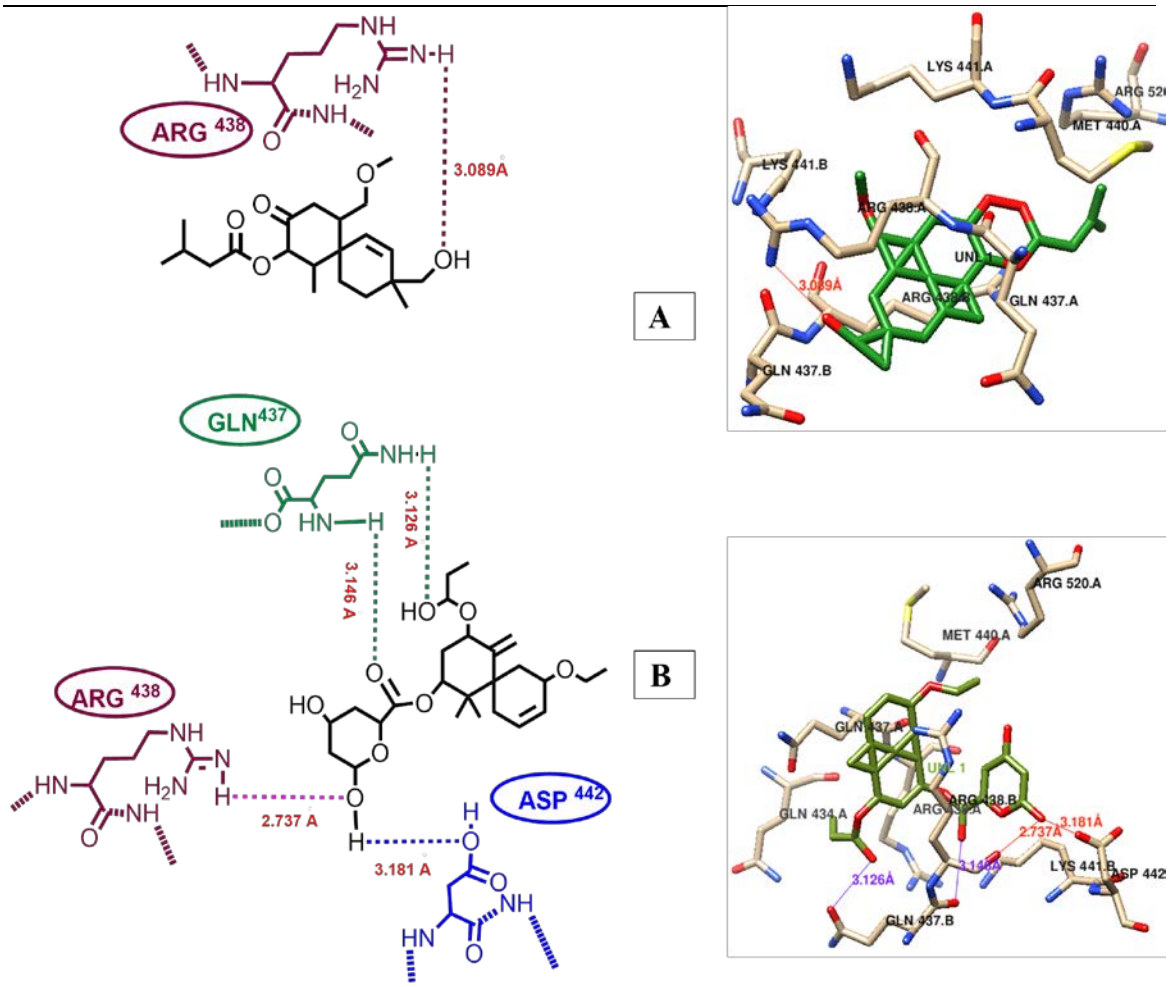

Figure 4.236.: Closer view of molecular binding interactions of the spiro[5.5]undecanes (A and B) in the catalytic site of 5-lipoxygenase (5-LOX) as deduced from the molecular docking simulation experiment. The molecular docking analysis of ligands (**10**) and pro-inflammatory 5-LOX showed four hydrogen bonds (displayed as red and blue-coloured lines) with amino acyl residues of GLN^{437} (2-hydrogen bonds), $ARG^{438}$and ASP^{442} with bond distances of 3.126, 3.146, 2.737 and 3.181 Å in the active binding site. The compound **9** showed two hydrogen-bonded interactions with amino acid residues of ARG^{438} with molecular distances of 3.089 Å.

Table 4.35: The binding energy, inhibition constant, intermolecular energy and torsional free energy between the ligands (compounds **9**-**10**) and the active sites of pro-inflammatory enzyme 5-LOX.

†Ligands	‡Binding energy (kcal mol^{-1})	‡Inhibition constant, Ki (nM)	‡Intermolecular energy (kcal mol^{-1})	‡Torsional free energy (kcal mol^{-1})	Amino acid residue	Molecular distances (Å)
9	-10.00	46.89	-10.75	0.60	ARG^{438}	3.089
10	-10.13	37.80	-11.51	2.09	GLN^{437} (2 hydrogen bonds), ARG^{438}, ASP^{442}	3.126, 3.146, 2.737, 3.181

†Molecular docking simulations were carried out using Autodock 4.0 software tool.
‡Values were evaluated from the calculations based on the energy minimization.

4.3.5.6 In silico molecular docking analysis *of polyether derivatives (Compounds 11-12)*

The titled polyether triterpenoids isolated from *G. salicornia* were taken into account for *in-silico* docking against 5-LOX, whereas the obtained results were analyzed through RMSD data. Molecular docking factors of 5-LOX active sites and ligands were represented in Table 4.34 (grid box for the potential binding site, x=28.855 y=14.080, z=65.462). Among the studied polyethers, the analogue **12** bearing furanyl-furo[3,2-b]pyran-2*H*-pyran moiety, on docking with 5-LOX displayed two hydrogen-bonding with amino-acyl parts of ARG^{246} and ASP^{442} in the active site of enzyme with molecular distances of 2.856 and 3.266 Å, respectively (Figure 4.236). Similarly, the compound **11** bearing pyrano[3,2-b]pyran and methyleneoxepane functionalities on docking with 5-LOX showed two hydrogen-bonded linkages with ARG^{246} and LYS^{441} (5.074 Å and 4.048 Å, respectively) amino acyl residues. Thus, the compound **12** revealed greater hydrogen-bond connections with the amino-acyl residues than those displayed by compound **11**, and the reports were corroborated through higher *in-vitro* anti-inflammatory potency of the former over those exhibited by the latter. The evaluation of molecular docking suitably apprehended that compound **12** bearing furanyl-furo[3,2-b]pyran-2*H*-pyran moiety exhibited closer molecular associations to 5-LOX with minimum binding energy (-10.96) and intermolecular energy (-12.23 kcal mol^{-1}), which appropriately corroborated with its greater attenuating potential against 5-LOX than those reported by polyether derivative **11** bearing pyranyl-10-methylpyrano[3,2-b]pyran-methyleneoxepane framework. These results signified the importance of compound **12** bearing furanyl-furo[3,2-b]pyran-2*H*-pyran moiety as a potential therapeutic lead against inflammation pathologies.

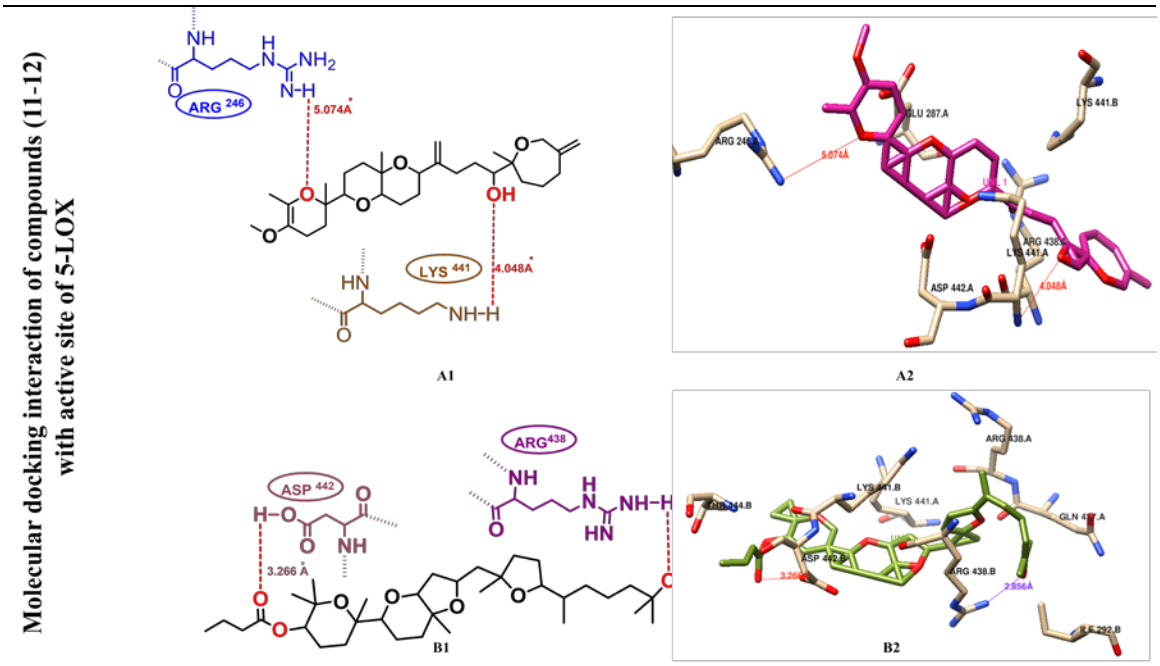

Figure 4.237.: Closer view of molecular binding interactions of compound (**11**) in the and 5-lipoxygenase (5-LOX) (**A**1-**A2**) catalytic site as obtained from molecular docking. Closer view of molecular binding interactions of the compound (**12**) in the 5-lipoxygenase (5-LOX) (**B**1-**B2**) catalytic sites as obtained from molecular docking.

Table 4.36: The binding energy, inhibition constant, intermolecular energy and torsional free energy between the ligands (compounds **11**-**12**) and the active sites of pro-inflammatory enzymes 5-LOX

†Ligands	‡Binding energy (kcal mol^{-1})	‡Inhibition constant, Ki (nM) µM*	‡Intermolecular energy (kcal mol^{-1})	‡Torsional free energy (kcal mol^{-1})	Amino acid residue	Molecular distances (Å)
1	-5.57	16.78*	-6.63	1.49	ARG^{246}, LYS^{441}	5.074, 4.048
2	-10.96	9.22	-12.23	2.68	ARG^{438}, ASP^{442}	2.856, 3.266

†Molecular docking simulations were carried out using Autodock 4.0 software tool.

‡Values were evaluated from the calculations based on the energy minimization

4.3.5.7 In silico molecular docking analysis *of macrolide derivatives (Compounds 13-15)*

The *in-silico* analyses of the titled compounds (**13-15**) attenuating pro-inflammatory enzyme 5-LOX were carried out and obtained reports were presented in Table 4.35. The docking parameters between the binding sites of 5-LOX and the ligands were recorded. The grid box was assigned as x = 4.591 y = -55.944, z = -30.599. Among the compounds, compound **14** exhibited five hydrogen-bonds with the amino-acyl residues of LYS^{254}, ASP^{290}, ARG^{438} and ARG^{520} in the 5-LOX enzyme binding site with 2.702, 2.914, 3.435, 3.049 and 2.393 Å molecular distances, respectively (Figure 4.237). Compound **13** exhibited three hydrogen-bonds with ASP^{442} and ARG^{246} with molecular distances of 4.077, 2.870 and 3.139 Å, respectively in the binding site of 5-LOX. However, compound **15** exhibited two hydrogen-bonds with ASP^{285} and LEU^{244} in the active site of 5-LOX, with molecular distances of 3.172 and 2.846 Å, respectively. Compound **14** displayed greater numbers of hydrogen-bonds with the amino acid residues than those documented by compounds **13** and **15**. The comparison of molecular docking parameters appropriately manifested that compound **14** showed minimally binding energy (-9.64 kcal mol^{-1}) and intermolecular energy (-10.51 kcal mol^{-1}), which were substantiated with their greater inhibition potentials of enzyme activity against 5-LOX than those exhibited by compounds **13** and **15** with higher binding (-9.15 and -8.74 kcal mol^{-1}, respectively) and intermolecular energies (-9.84 and -9.77 kcal mol^{-1}, respectively). The greater number of hydrogen bonding interactions and least binding/intermolecular energies of compound **14** were corroborated with its potential attenuation property against pro-inflammatory 5-LOX over those displayed by compounds **13** and **14**.

The enzyme binding affinities of compound **14** and pro-inflammatory initiator, arachidonic acid (a substrate of 5-lipoxygenase, 5-LOX) were compared through the *in-silico* molecular docking interactions (Table 4.35). The oxidative enzymes belonging to the class of lipoxygenase generates pro-inflammatory mediators, such as arachidonic acid-5-hydroperoxide (hydroperoxy eicosatetraenoic acids, HPETE) and leukotrienes from arachidonic acid through the cascade of peroxidation and epoxidation of allylic system at C5 of arachidonic acid via radical mechanism. These leukotrienes were found to be the signalling molecules responsible for different inflammation pathologies (Martel-Pelletier et al., 2013). Herein, arachidonic exhibited only two hydrogen-bonds with ARG^{438} and ARG^{520} with molecular distances of 2.785 and 2.820 Å, correspondingly in the active site of 5-LOX when compared to compound **14** with five hydrogen bonding interactions. Also, the higher binding energy (-5.80 kcal mol^{-1}) obtained for arachidonic acid in the active site of 5-LOX in comparison with compound **14** (-9.64 kcal mol^{-1}) attributed the greater 5-lipoxygenase interactions of the latter. The higher number of hydrogen bonding interactions along with least binding energy obtained from the *in-silico* studies suggested that compound **14** might effectively bind into the 5-LOX enzyme than arachidonic acid, and therefore, the latter could be protected from the peroxidation reactions catalysed by 5-

LOX. There were several conjugated olefinic positions available in arachidonic acid that could be easily epoxidised through 5-LOX (Funk, 2001), whereas compound **14** did not harbour any easily oxidisable positions. Furthermore, the electronegative functionalities, such as carbonyls and ester groups present in compound **15** were responsible for the inhibition of lipid peroxidation through the keto-enol resonance by replacing the acidic protons to the peroxide free radicals and inhibit the formation of free radicals in the biological systems. Therefore, the therapeutic anti-inflammatory potencies of macrocyclic lactones, particularly compound **14** might be due to its selective and competitive inhibition of pro-inflammatory 5-LOX enzyme at the arachidonic acid cascade and through the inhibition of lipid peroxidations of pro-inflammatory lipoxins.

Table 4.37: The binding energy, inhibition constant, intermolecular energy and torsional free energy between the ligands (compounds **13-15**) and the active sites of pro-inflammatory enzyme 5-LOX

†Ligands	‡Binding energy (kcal mol^{-1})	‡Inhibition constant, Ki (nM)	‡Intermolecular energy (kcal mol^{-1})	‡Torsional free energy (kcal mol^{-1})	Amino acid residue	Molecular distances (Å)
13	-9.15	194.90	-9.84	1.19	Asp^{442}, Arg^{438}	4.077, 2.870, 3.139
14	-9.64	85.15	-10.51	1.19	Lys^{254}, Asp^{290}, Arg^{438}, Arg^{520}	2.702, 2.914, 3.435, 3.049, 2.393
15	-8.74	391.76	-9.77	0.60	Asp^{285}, Leu^{244}	3.172, 2.846

†Molecular docking simulations were carried out using Autodock 4.0 software tool.

‡Values were evaluated from the calculations based on the energy minimization.

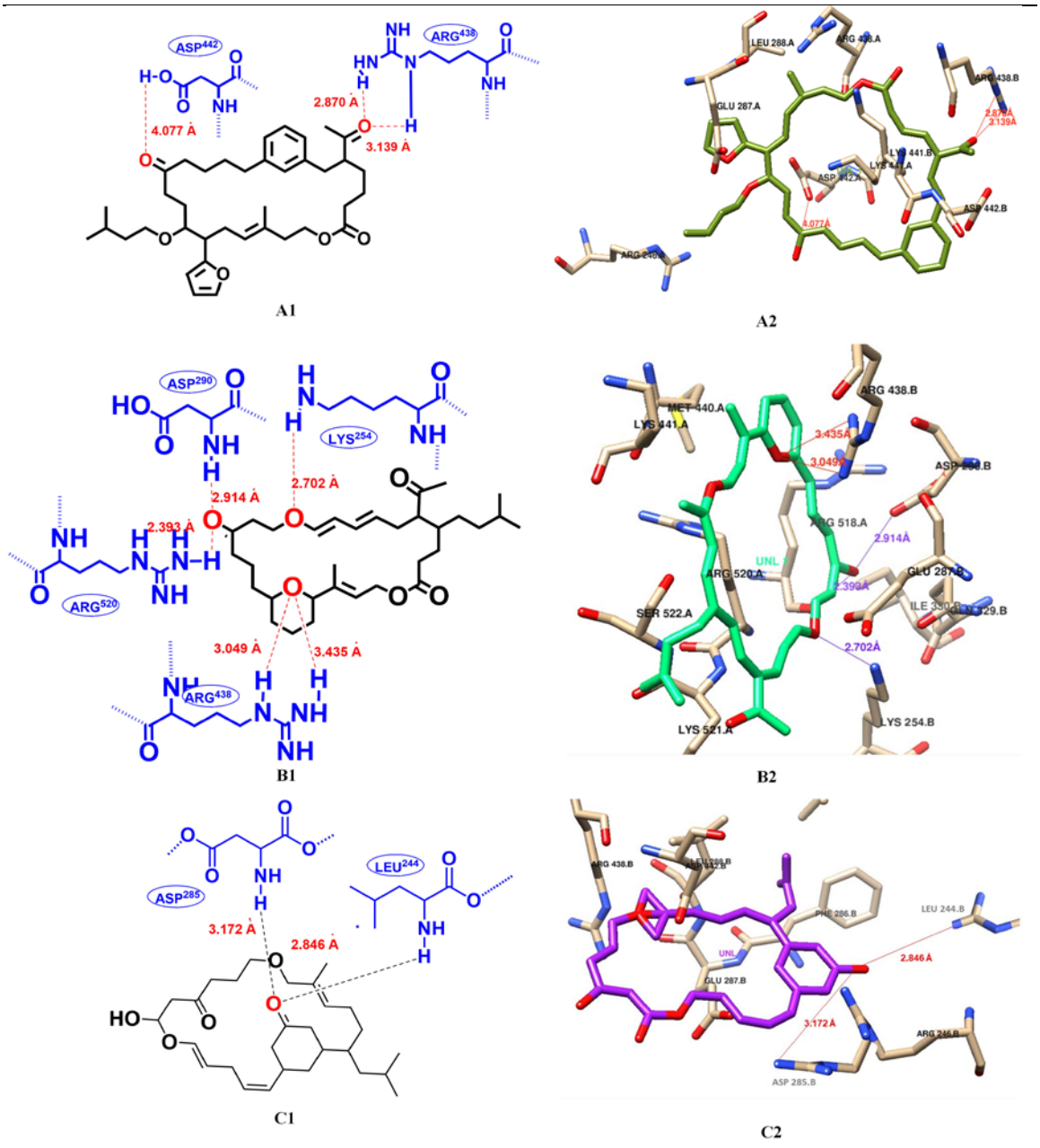

Figure 4.238.: Closer image of molecular docking interactions of compounds **13-15** (**A-C**) in the 5-LOX catalytic site as obtained by docking experiment. The docking analysis of compound **13** and pro-inflammatory 5-LOX showed three hydrogen-bonds (displayed as red and blue-coloured lines with amino-acyl residues of ASP^{442} And Arg^{438} with bond distances of 2.870, 3.139 and 4.077 Å) in binding site. Compound **14** displayed five hydrogen-bonds with amino acid residues of Lys^{254}, Asp^{290}, Arg^{438} and Arg^{520}, with molecular distances of 2.702, 2.914, 3.435, 3.049, and 2.393 Å. Compound **15** showed two hydrogen-bonds with amino acid residues of Asp^{285} and Leu^{244}, with molecular distances of 3.172 and 2.846 Å.

4.4. Conclusion

Bio-assay assisted chromatographical purification of the EtOAc-MeOH extract of *G. salicornia* yielded bioactive secondary metabolites, namely abeo-labdane class of diterpenoid (**1**), oleanene class of triterpenoids (**2-3**), drimane-associated quinols (**4-6**), 2*H*-chromenyl compounds (**7-8**), spiro-fused analogues (**9-10**), squalene polyether metabolites (**11-12**), and macrolides enclosing ether functionalities (**13-15**). The studied compounds exhibited comparable DPPH radical quenching activity as standard antioxidant agent *α*-tocopherol. The first class of compounds in this series abeo-labdene derivative registered significantly greater activities against pro-inflammatory 5-lipoxygenase than that displayed by non-steroidal anti-inflammatory drug ibuprofen. Its greater selectivity index as compared to that displayed by ibuprofen inferred the higher anti-inflammatory selectivity against pro-inflammatory cyclooxygenase-2.

In second class of metabolites among the isolated compounds, the one with 24(4→23) abeo-oleanene framework (**3**) exhibited higher carbolytic enzyme inhibitory activities (IC_{50} < 0.32 mM) over that bearing 24(4→23), 27(8→26), 30(20→29)-tris-abeo-oleanene moiety (**2**) (IC_{50} > 0.34 mM). The oleanene analogues isolated from *G. salicornia* registered greater radical scavenging potentials against $ABTS^{+}$ (IC_{50} < 1.10 mM) than that exhibited by α-tocopherol (IC_{50} > 1.69 mM). Structure-activity relationship analyses showed that higher polarisability and lesser steric bulk of abeo-oleanene (**3**) predominantly contributed towards the comparatively greater radical quenching and carbolytic enzyme inhibitory activities than those displayed by its tris-abeo-oleanene analogue (**2**). *In silico* molecular modelling studies were performed to designate the α-glucosidase and α-amylase inhibitory mechanism of the abeo-oleanene derivative (**2**) exhibiting binding energies of greater than 9.50 kcal mol^{-1}, which substantiated its potential inhibitory activity against the carbolytic enzymes responsible to cause hyperglycaemic disorders. An enzyme-assisted putative biosynthetic cascade leading to the formation of oleanene triterpenoid derivatives were proposed. In particular, the 24(4→23)-abeo-oleanene possessing (12-oxo)-3,5-diene-deconoate moiety (compound **2**) was found to be effective dual inhibitors of starch digestive enzymes along with potential antioxidative properties, and therefore, might be utilised as valuable medicinal lead against oxidant species and elevated postprandial glucose levels.

On third series of compounds, the compound (**4**) with benzo[*a*]xanthene-4,10,12-triol moiety showed greater pro-inflammatory enzyme inhibitory activities (IC_{50} 1.35-1.72 mM) over other studied drimane quinol chemotypes. Positive correlations between the antioxidant and anti-inflammatory activities were recorded, whereas the compound (**4**) displayed greater oxidant scavenging potentials (IC_{50} 1.33-1.57 mM) than that exhibited by α-tocopherol. Structure-

bioactivity correlation analysis showed that lesser hydrophobicity and steric bulk of the compound (**4**) predominantly contributed towards the comparatively greater radical quenching and pro-inflammatory enzyme inhibitory activities than those displayed by its drimane counterparts **5**-**6**. *In silico* molecular modelling studies were performed to designate the 5-lipoxygenase inhibitory mechanism of the compound (**4**) exhibiting binding energy of -12.30 kcal mol^{-1}, which substantiated its potential inhibitory activity against the inflammatory mediators. An enzyme-mediated biosynthetic cascade leading to the formation of drimane sesquiterpenoid quinol derivatives was proposed. The results illustrated the bioactive potential of the natural anti-inflammatory drimane sesquiterpenoid bearing benzo[*a*]xanthene-4,10,12-triol moiety attenuating pro-inflammatory 5-LOX from marine macroalga *G. salicornia.*

In chromenyl derivatives, which were characterised as 4'-[10'-[7-hydroxy-2,8-dimethyl-6-(pentyloxy)-2*H*-chromen-2-yl]ethyl]-3',4'-dimethyl-cyclohexanone (**7**) and 3'-[10'-(8-hydroxy-5-methoxy-2,6,7-trimethyl-2*H*-chromen-2-yl)ethyl]-3'-methyl-2'-methylene cyclohexyl butyrate (**8**) using comprehensive spectroscopic techniques. The compound **8** exhibited higher DPPH radical quenching activity than that displayed by compound **7** and standard antioxidant agent α-tocopherol. The chromenyl derivative registered significantly greater activities against pro-inflammatory 5-lipoxygenase than that displayed by non-steroidal anti-inflammatory drug ibuprofen. Its greater selectivity index as compared to that displayed by ibuprofen inferred the higher anti-inflammatory selectivity against pro-inflammatory cyclooxygenase-2. The newly described chromenyl analogue **8** characterised from the red seaweed *G. salicornia* has potential anti-inflammatory and antioxidant properties for utilisation in pharmaceutical and food formulations.

Among the isolated spiro-compounds, the one with spiro[5.5]undec-2-en framework (**10**) exhibited higher pro-inflammatory enzyme inhibitory activities (IC_{50} <1.91 mM) over that bearing oxospiro[5.5]undec-4-ene moiety (**9**) (IC_{50} > 2.78 mM). The spiro analogues isolated from *G. salicornia* registered greater radical scavenging potentials against $ABTS^{+}$ (IC_{50} < 1.75 mM) than that exhibited by α-tocopherol (IC_{50} > 1.75 mM). Structure-activity relationship analyses showed that higher polarisability, tPSA and lesser steric bulk of spiro[5.5]undec-2-en (**10**) predominantly contributed towards the comparatively radical quenching and proinflammatory enzyme inhibitory activities than those displayed by the oxospiro[5.5]undec-4-en analogue (**9**). Molecular docking analysis inferred that the spiro derivative (**2**) exhibited binding energy of -10.13 kcal/mol with efficient interactions of 5-LOX enzyme, which corroborated its greater inhibitory potential. In particular, spiro[5.5]undec-2-ene analogue was found to be an effective inhibitor of 5-LOX along with potential antioxidative properties, and therefore, might be utilised as valuable pharmacophore lead against oxidant species and inflammation pathology.

Among unreported polyether analogues, the compound **12** possessing furanyl-furo[3,2-b]pyran-2*H*-pyran skeleton displayed greater anti-inflammatory properties (IC_{50} < 2 mM) over that exhibited by **11** bearing pyranyl-10-methylpyrano[3,2-b]pyran-methyleneoxepane moiety (IC_{50} > 2.5 mM). Likewise, the potential anti-radical properties of **2** (IC_{50} 1.11-1.27 mM) in comparison with **11** (IC_{50} ~1.65 mM) and α-tocopherol (IC_{50} 1.49-1.69 mM) were reported. Structure-bioactivity-correlation studies displayed that the optimum hydrophobicity (log P_{OW2} < 5), lesser steric hindrance, which along with greater polarisability factors predominantly played significant roles in determining the greater bio-potential of polyether derivative, **12** over that of **11**. *In-silico* molecular modeling was analyzed to entitle 5-lipoxygenase inhibitory pathway of compound (2) exhibiting binding energy of -10.96 kcal mol^{-1}, that appropriately attributed its potent inhibitory properties against the inflammatory-mediators.

In the last series of compounds, the undescribed oxabicyclo[21.3.1]heptacosa-ene-diones (compounds **13**-**15**) and oxabicyclo[19.3.1]pentacosa-ene-dione (compound **15**) bearing macrocyclic lactones from the red seaweed, *G. salicornia*. The unprecedented compounds (**13**-**15**) displayed significantly higher antioxidative and pro-inflammatory 5-lipoxygense attenuating potential in comparison with the commercially existing antioxidative and anti-inflammation agents. The greater attenuation potential of the 21-membered pyran bearing compound **14** against 5-lipoxygense was correlated with its respective *in-silico* molecular docking simulations in the binding site of the pro-inflammatory enzyme through the least binding energy (-9.64 kcal mol^{-1}) and inhibitory constant (Ki 85.15 nm). The malonate-S-acyl carrier protein-mediated putative biosynthetic route appropriately corroborated the structural attributions of the studied salicornolides. In particular, the pyran enclosed macrocyclic lactone could be used as prospective natural therapeutic pharmacophore in attenuating the anti-inflammatory disorders and free radical-induced ailments.

CHAPTER 5

ISOLATION AND CHARACTERIZATION OF BIOACTIVE LEADS FROM BROWN SEAWEED (PHAEOPHYCEAE) *PADINA TETRASTROMATICA*

Contents

5.1 *Background*

5.2 *Materials and methods*

5.3 *Results and discussion*

5.4 *Conclusions*

5.1 Background

Seaweeds are prominent marine flora, which registered their existence in the marine ecology, as a promising natural resource possessing highly potent secondary metabolites. These bioactive potentials are associated with the diverse range of chemical constituents; in particular they varied from the low molecular weight bioactive-analogues to higher molecular weight phycocolloids. These might signify the utilities of seaweeds species to biosynthesize potentially useful therapeutic agents in pharmaceutical applications (Wijesinghe et al., 2011). Most of these bioactives were found to possess antioxidative activities, and thereby represent their role in the prevention of various chronic pathophysiologies related to the oxidative stress conditions (Garcia et al., 2012). Seaweeds are encompassed with enzymatic/non-enzymatic antioxidative compounds, and these could reduce or prevent the production of reactive-oxidants (RO_S). Hence, they are useful in the treatment of oxidative stress induced diseases through various cellular processess (Garcia et al., 2012). Among various seaweeds, brown seaweeds (Phaeophyta) were known to produce large number of antioxidant compounds representing the second largest position amongst marine macroalgal flora (Blunt et al. 2007). The major secondary metabolites found in the brown seaweeds belonged to the class of terpenoids and terpenoid-aromatic compounds (Blunt et al. 2007) beside polyphenols, acetogenins, phlorotannins, fucoidans, volatile compounds, fucoxanthins exhibiting prospective antioxidant, antidiabetic, antibiotic, anti-inflammatory, antifungal, antiviral, or anti-cancer activities (Folmer et al., 2010; Maneesh and Chakraborty, 2017a; Maneesh and Chakraborty, 2017b).

Previous reports of literature on brown seaweeds recorded that they were rich sources of terpenoid class of compounds (Paul et al., 2001). For example, new structures of diterpenes with acyclic skeleton have been reported from the Moroccan brown seaweed *Bifurcaria bifurcata* (Culioli et al., 2001). A novel diterpenoid of Stypolactone was reported from the *Stypopodium zonale* (Dorta et al., 2002). Dictyterpenoids A-B belonging to the class of diterpenoid with antifeedant activity has been identified from the Japanese seaweed *Dilophus okamurae* (Suzuki et al., 2002). A novel dictyotadimer A (bis-diterpene) was identified from *Dictyota Lamouroux* (Viano et al., 2011). The anti-viral diterpenes were identified from *Dictyota menstrualis* (Cavalcanti et al., 2011). From seaweed species of *Dictyota dichotoma,* a diterpene, amijiol acetate was reported (Ayyad et al., 2011). Novel diterpenes with 2,6-cyclo-xenicane entities have been documented from *Dilophus fasciola* and *Dilophus spiralis* (Ioannou et al., 2009). Furthermore, two diterpenes of dolastane skeletons with antiviral potentials have been identified from the brown seaweed *Canistrocarpus cervicornis* (Vallim et al., 2010). Sesquiterpenes with halogenation were reported from the brown seaweed species of *Padina antillarum* and *Dictyopteris divaricate* (Parameswaran et al., 1994, 1996; Ji et al., 2009). Moreover, two types of diterpenes, one with the prenylated-guaiane skeletons and the other with dolabellane and dolastane structures were reported from various brown seaweeds of the family Dictyotaceae, for instance, dichotomanes, xenianes, and xenicanes. Related compounds were reported from brown seaweed *Dictyota* spp, and xenianes were reported from *Padina* species of family Dictyotaceae (Paula et al., 2011).

Among various species of brown seaweeds, *Padina* spp belonging to family Dictyotaceae were considered as one of the predominant seaweeds with economic significance, and they were found to be rich in bioactive compounds with promising pharmaceutical potentials. Hence, they were found to be used in pharmaceutical, functional food and phycocolloid industries (De Almeida et al., 2011). The brown seaweed *Padina sp.* was found to constitute a foremost share in the family of Dictyotaceae, and about 50 taxa of this genus were reported in various parts of the globe. Among them, *Padina tetrastromatica* (Hauck) (family Dictyotaceae) has been predominant in the Indo-Pacific region (Guiry and Nic-dhonncha, 2003), and there were preliminary reports of their bioactive potentials (Chia et al., 2015; Mohsin et al., 2014). In the search for bioactive diterpenoids from this brown seaweed species, this work described the purification and characterizations of previously undescribed xenicane class of diterpenoids (**TP_1** through **TP_5**) and dolabellanes (**TP_6** through **TP_{10}**) from the ethyl acetate-methanol (EtOAc-MeOH) extract of the studied seaweed collected from the Gulf-of-Mannar of Peninsular India. The studied compounds were characterised by extensive spectroscopic experiments. The anti-inflammatory, antidiabetic and antioxidant potential of the studied compounds were analyzed by different *in vitro* assays, and various physicochemical descriptors

were utilized to substantiate the structure-activity correlations of the studied diterpenoids. *In silico* molecular modelling studies were performed to designate the 5-lipoxygenase inhibitory mechanism of the studied analogues.

5.2 Materials and methods

5.2.1 Chemicals and reagents

The chemicals and reagents utilized for the analysis were described under the section 4.2.1 of Chapter 4.

5.2.2 Chromatographic purification techniques and spectroscopic instrumentation analysis

5.2.2.1 Purification by column chromatography

The methodology for column chromatography was described under the section 4.2.2.1 of Chapter 4.

5.2.2.2 Purification by flash chromatography

The methodology of flash chromatography was described under the section 4.2.2.2 of Chapter 4.

5.2.2.3 Purification by high pressure liquid chromatography

The methodology of high pressure liquid chromatography was described under the section 4.2.2.3 of Chapter 4.

5.2.2.4 Purity assessment by thin layer chromatography and analytical HPLC

The methodology for purity assessment by thin layer chromatography and analytical HPLC was described under the section 4.2.2.4 of Chapter 4.

5.2.2.5 Spectrophotometric and spectroscopic analysis

The methodology for spectrophotometric and spectroscopic analysis was described under the section 4.2.2.4 of Chapter 4.

5.2.3 Preparation of solvent extracts from the brown seaweed P. tetrastromatica

The seaweed used in this study was *Padina tetrastromatica* (Hauck) (family Dictyotaceae). The seaweeds were freshly collected (CMFRI voucher specimen number AB.1.1.2.1) from the south east coast of India (Gulf of Mannar between 8º48′ N, 78º9′ E and 9º14′ N, 79º14′E) (Figure 5.1). The samples were identified by a marine algologist Dr. Chellaiah Periyasamy of Aquaculture Foundation of India, Madurai. Seaweeds were washed with seawater to exclude the externalities followed by washed with running tap water before being shade-dried (35±3 °C) for 72 h. Shade-dried samples were ground (1 kg dried), and were initially extracted with n-hexane {600 mL x 2, at room temperature (RT) for 24 h}, to remove pigmentous substances. The residues were extracted by reflux with solvents ethyl acetate/methanol (EtOAc-MeOH 1:1 v/v, 500 mL x 3, 60-70 ºC). The crude solvent extract collected after filtration (using Whatman No.1 filter paper) before being evaporated (50 °C) by a rotary vacuum evaporator to one-third of the initial volume, under reduced pressure, to yield a viscous mass of crude EtOAc-MeOH extract (38 g). The extract was utilized for various chromatographic fractionations to yield the bioactive metabolites.

Figure 5.1.: The brown seaweed *P. tetrastromatica* collected from the southeast coastline of the Indian sub-continent Gulf of Mannar region; between 8º48’ N, 78°9’ E and 9°14’ N, 79°14’ E)

5.2.4 Chromatographic fractionation of pure compounds and bioactive potentials of sub-column fractions from P. tetrastromatica

The EtOAc-MeOH extract (38 g) of *P. tetrastromatica* was made into slurry with silica gel (60-120 mesh, 5 g), and filled into a glass column (60 cm x 4 cm) loaded with adsorbent silica gel (60-120 mesh, 50 g) before being subjected to vacuum liquid chromatography. Initially the waxy material was removed by elution with *n*-hexane. The polarity of eluent was increased gradually by the addition of ethyl acetate (*n*-hexane:ethyl acetate 95:5 to 3:9, v/v) to obtain 20 column fractions (12 mL each), which were further pooled to 6 fractions (TP_1-TP_6) after TLC analysis (*n*-hexane/EtOAc, 9:1, v/v) after TLC (*n*-hexane:EtOAc, 9:1 v/v) along with RP-C_{18} HPLC (MeOH/MeCN, 2:1 v/v, isocratic). The pooled homogeneous fractions were assessed for their bioactive potential, and the fractions with greater bioactivities were subjected to further downstream purification.

The column fraction TP_2 was further fractionated by flash chromatography on a silica gel column (230-400 mesh, 12 g), and elution was carried out with EtOAc/*n*-hexane (0-100 %, by a step gradient mode) to yield a total of 30 column subfractions (15 mL each), which were combined to 8 column sub-fractions {$TP_{2(1-8)}$} after RP-C_8 HPLC {acetonitrile (MeCN)/H_2O, 85:15 v/v} and TLC (ethyl acetate/*n*-hexane, 3:1 v/v). Based on analytical TLC and HPLC, the homogeneous fractions were pooled, and were purified by using preparative RP-C_{18} HPLC with acetonitrile and methanol as mobile phase (MeOH/MeCN, 4:1 v/v). The fraction $TP_{2\text{-}4}$ was further purified by preparative HPLC with acetonitrile and methanol (MeOH/MeCN, 2:3 v/v) to to yield the pure compounds **TP_1** and **TP_2** (105 and 99 mg, respectively). Concentration of solvents followed by TLC (particle size 15 mm) using 30 % EtOAc/*n*-hexane supported the purity. The fractions $TP_{2\text{-}5}$ was further purified by preparative HPLC with acetonitrile and methanol (MeOH/ MeCN, 2:3 v/v) to afford the pure compounds **TP_3**, **TP_4** and **TP_5** (112, 122 and 103 mg, respectively).

the fractions, TP_3 and TP_4 were further fractionated over a glass column (45 cm x 3 cm) packed with fine silica (230-400 mesh) by using gradient elution with *n*-hexane/EtOAc (99:1 to 3:2, v/v) to yield 5 sub-fractions (32 mL each). The latter were pooled to 6 fractions on the basis of TLC (*n*-hexane: EtOAc, 9:1 v/v) and RP-C_{18} HPLC (3:2 MeOH/MeCN v/v, isocratic). The sub-fraction, $TP_{3\text{-}1\text{-}1}$ was subjected to preparatory HPLC purification (MeOH/MeCN, 2:1 v/v, isocratic) to yield the compounds **TP_6**, **TP_7** and **TP_8** (96, 98, and 102 mg, respectively). The bioactive sub-fraction, $TP_{4\text{-}2\text{-}2}$ was found to be a mixture, and consequently purified by HPLC using MeOH/MeCN (3:2 v/v, isocratic) to obtain **TP_9** and **TP_{10}** (65 and 80 mg, respectively). The purity of the compounds was monitored with TLC using EtOAc/*n*-hexane (3:17 v/v) and RP-C_{18} HPLC (MeOH: MeCN, 3:2 v/v, isocratic).

The repetitive bioassay-guided fractionation of EtOAc-MeOH extract of *P. tetrastromatica* along with yield and bioactive potentials of intermediate fractions were represented in Tables 5.1-5.3 in detail.

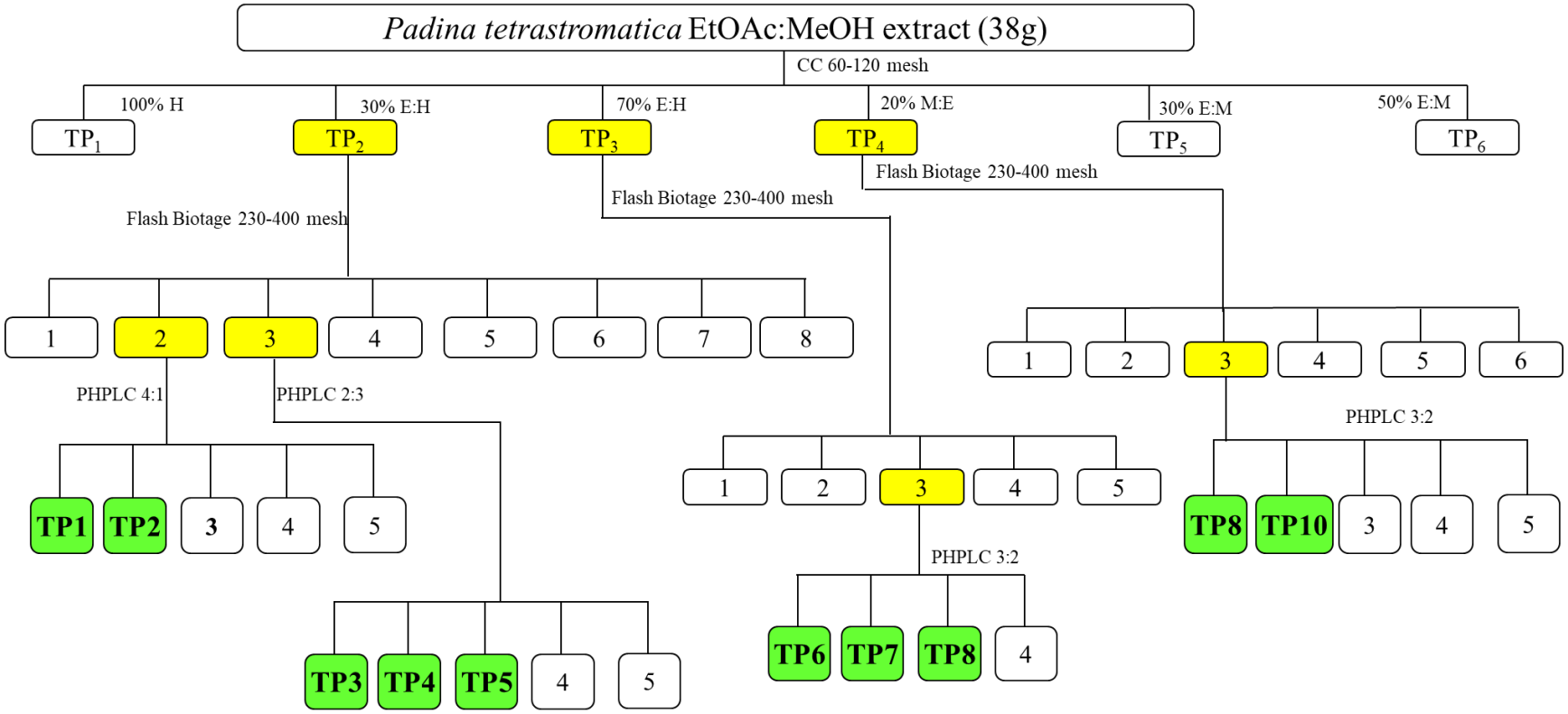

Figure 5.2.: Schematic representation of purification of fractions and compounds from the EtOAc-MeOH extract of *G. salicornia*.CC-column chromatography

5.2.5 Physicochemical description of the bioactive compounds isolated from the EtOAc-MeOH extract of P. tetrastromatica

5.2.5.1 Physicochemical description of compound-1 (TP_1)

12-Ethenyl-3a,6,9,10,11,12,12a,12b-octahydro-1-(1^2-hydroxy-1^2-methyl-propyl)-cyclonona[*d*]furo[2,3-*b*]pyran-6,10-diol; Colorless oil; [α]D^{22}–34 (c 0.96, $CHCl_3$); UV (MeOH) λ_{max} (log ε):249 (2.61) nm; TLC (Si gel GF_{254} 15 mm; 30 % EtOAc/*n*-hexane, v/v) R_f: 0.55; R_t (RP-C_8 HPLC, MeOH:MeCN, 4:1 v/v): 3.20 min; FTIR (ν_{max} cm^{-1}; bending δ, stretching ν, rocking ρ): 3472 (O-H_ν, br), 1112, 1076 (C-O_ν), 2923 (C-H_ν), 1621 (C=C_ν), 1510 (C=C_ν), 1459 (C-H_δ), 1182 (C-C_ν), 987 (=C-H_δ); ^{1}H NMR (500 MHz; $CDCl_3$; δ in ppm); 2.16 (1H, d, J=9.09 Hz), 1.91 (1H, d, J=8.47 Hz), 1.29 (3H, s), 1.29 (3H, s), 6.37 (1H, s), 6.06 (1H, d, J=10.74 Hz), 6.41 (1H, s), 3.69 (1H, d, J=14.70 Hz), 5.69 (1H, m), 5.51 (1H, m), 2.22 (1H, m), 1.97 (1H, m), 3.67 (1H, m), 1.33 (1H, m), 1.53 (1H, m), 2.03 (1H, dd, J= 12.35, 5.92), 5.72 (1H, m), 5.00 (1H, d, J=13.79 Hz), 4.99 (1H, d, J=12.91 Hz), 1.87 (1H, d, J=12.62), 2.17 (1H, dd, J=10.99, 8.86 Hz); ^{13}C-NMR (125 MHz; $CDCl_3$; δ in ppm); 115.2 (C), 39.9 (CH_2), 73.3 (C), 29.5(3) (CH_3), 29.5(4) (CH_3), 141.9 (CH), 104.2 (CH), 144.1 (CH), 115.3 (C), 70.2 (CH), 133.2 (CH), 125.4 (CH_3), 41.42 (CH), 70.2 (CH_3), 38.6 (CH_2), 48.9 (CH), 141.08 (CH), 116.4 (CH_2), 39.9 (CH), 49.8 (CH), DEPT, COSY, HSQC, and HMBC data were presented in Table 5.4. EI-MS *m/z*: calcd. for $C_{20}H_{28}O_5$ 348.2 $[M]^+$. HRESIMS (positive mode) *m/z*: found 349.2018 $[M+H]^+$, calcd. for $C_{20}H_{29}O_5$ 349.2014 $[M+H]^+$ (Δ 1.15 ppm).

5.2.5.2 Physicochemical description of compound-2 (TP_2)

1,2,5,5a,6,9,10,11,12,12a-Decahydro-11(11^2-hydroxypropyl)-2-[(*E*)-2^1-propenyl] cyclonona[*d*]-furo[2,3-*b*]pyran-9,12-diol; Yellow oil; [α]D^{22} –37 (c 1.80, $CHCl_3$) UV (MeOH) λ_{max} (log ε): 235 (3.1), 254 (3.7) nm; TLC (Si gel GF_{254} 15 mm; 30 % EtOAc/*n*-hexane) R_f: 0.54; R_t (RP-C_8 HPLC, MeOH: MeCN, 4:1 v/v): 3.24 min; FTIR (ν_{max} cm^{-1}): 3452 (O-H_ν, br), 1220 (C-O_ν), 2931 (C-H_ν), 1644 (C=C_ν), 1510 (C=C_ν), 1470 (C-H_δ), 1380 (C-H_ρ), 1169 (C-C_ν), 970 (=C-H_δ), 885, 746 (C-H_δ);^{1}H NMR (500 MHz; $CDCl_3$; δ in ppm); 2.68 (1H, dd, J=8.8, 7.69 Hz), 2.30 (1H, dd, J=13.01, 8.20 Hz), 4.88 (1H, dd, J=16.99, 8.06 Hz), 5.69 (1H, dd, J=14.47, 6.95 Hz), 5.87 (1H, m), 1.82 (3H, d, J= 6.75 Hz), 3.67 (1H, dd, J=12.77, 7.67 Hz), 3.70 (1H, dd, J=12.25, 7.66 Hz), 1.85 (1H, m), 2.01 (1H, m), 1.75 (H_β , m), 5.62 (1H, m), 5.67 (1H, dd, J=14.47, 6.95 Hz), 4.20 (1H, dd, J=15.60, 7.35 Hz), 1.29 (1H, m), 1.52 (H_β , m), 1.22 (1H, m), 1.35 (1H, t, J=5.70, 3.47 Hz), 4.07 (1H, m), 1.25 (3H, d, J=5.52 Hz), 3.33 (1H, dd, J=8.76, 1.86 Hz), 1.72 (1H, dd, J=11.46, 4.88 Hz), ^{13}C-NMR (125 MHz; $CDCl_3$; δ in ppm); 37.7 (CH_2), 83.1 (CH), 129.1(CH), 130.7 (CH), 17.6 (CH_3), 163.1 (C), 68.3 (CH_2), 36.1 (CH), 33.7 (CH), 132.0 (CH), 132.6 (CH), 72.1 (CH), 39.54(CH), 38.6 (CH), 43.9 (CH), 67.7 (CH), 23.9 (CH_3), 71.8 (CH), 41.3 (CH), 94.3 (C); DEPT, COSY, HSQC, and HMBC data were presented in Table 5.5. EI-MS *m/z*: calcd. for $C_{20}H_{30}O_5$

350.2098 $[M]^+$. HRESIMS (positive mode) *m/z*: found 351.2175 $[M+H]^+$, calcd. for $C_{20}H_{31}O_5$ 351.2171 $[M+H]^+$ (Δ 1.14 ppm).

5.2.5.3 Physicochemical description of compound-3 (TP_3)

4-(4^1,4^2-Dihydroxypropyl)-4,4a,5,6,7,8,11,11a-octahydro-8,11-dihydroxy-7-methyl-6-(6^1-methyl-6^2-propenyl)-cyclonona[*c*]pyran-3-(1*H*)-one; Pale yellow oil; $[\alpha]D^{22}$ +40 (c 0.16, $CHCl_3$); UV (MeOH) λ_{max} (log ε): 246.0 (2.90) nm; TLC (Si gel GF_{254} 15 mm; 30 % EtOAc/*n*-hexane) R_f: 0.40; R_t (RP-C_8 HPLC, MeOH:MeCN, 4:1 v/v): 4.20 min; FTIR (ν_{max} cm^{-1}): 3473 (O-H_ν, br), 3020 (C-H_ν), 1715 (C=O_ν), 1625 (C=C_ν), 1470 (C=C_ν), 1450 (C-H_δ), 1380 (C-H_ρ), 1283 (C=O_ν), 1166 (C-C_ν), 910 (=C-H_δ), 885 (C-H_δ); ^{1}H-NMR (500 MHz; $CDCl_3$; δ in ppm); 3.95 (1H, dd, J=10.1, 8.0 Hz), 4.22 (1H, dd, J=9.1, 7.86 Hz), 2.21 (1H, dd, J=9.8, 5.1 Hz), 1.62 (1H, m), 4.03 (1H, t, J=9.0 Hz), 3.42 (1H, m), 1.21 (3H, m), 1.26 (1H, m), 1.01 (1H, m), 1.15 (1H, m), 2.09 (1H, m), 1.22 (3H, m, 5.72 (1H, m), 5.01 (1H, dd, J=19.7, 17.1Hz), 4.99 (1H, dd, J=19.7, 9.7 Hz), 1.45 (1H, m), 0.90 (3H, d, J=3.2 Hz), 4.11 (1H, t, J=9.6 Hz), 5.91 (1H, d, J=11.7 Hz), 5.92 (1H, d, J=12.7 Hz), 4.10 (1H, t, J=9.5 Hz), 1.82 (1H, m); ^{13}C-NMR (125 MHz; $CDCl_3$; δ in ppm); 65.7 (CH_2), 172.35 (C), 48.8 (CH), 37.5 (CH), 73.4 (CH), 69.3 (CH), 19.3 (CH_3), 31.4 (CH_2), 43.9 (CH), 39.5 (CH), 18.3 (CH_3), 145.39 (CH), 114.8 (CH_2), 41.8 (CH), 13.3 (CH_3), 75.1 (CH), 137.4 (CH), 137.3 (CH), 73.4 (CH), 42.9 (CH);DEPT, COSY, HSQC, and HMBC data were presented in Table 5.6. EI-MS *m/z*: calcd. for $C_{20}H_{32}O_6$ 368.2199 $[M]^+$. HRESIMS (positive mode) *m/z*: found 369.2280 $[M+H]^+$, calcd. for $C_{20}H_{33}O_6$ 369.2277 $[M+H]^+$ (Δ 0.08 ppm)

5.2.5.4 Physicochemical description of compound-4 (TP_4)

4,4a,5,6,7,8,11,11a-Octahydro-7-hydroxy-6-(6^2-hydroxy-6^3-butenyl)-4-(4^1-hydroxypropyl)-11-methoxy-8-methyl-cyclonona[*c*]pyran-3-(1*H*)-one; Pale yellow oil; $[\alpha]D^{22}$ +43 (c 0.17, $CHCl_3$); UV (MeOH) λ_{max} (log ε): 209 (3.6), 249 (3.3) nm; TLC (Si gel GF_{254} 15 mm; 20 % EtOAc/*n*-hexane) R_f: 0.48; R_t (RP-C_8 HPLC, MeOH:CH_3CN, 2:3 v/v): 4.05 min; FTIR (ν_{max} cm^{-1}): 3451 (O-H_ν, br), 2963 (C-H_ν), 1737 (C=O_ν), 1702 (C=C_ν), 1511 (C=C_ν), 1447 (C-H_δ), 1370 (C-H_ρ), 1280 (C=O_ν), 1180 (C-C_ν), 966 (=C-H_δ), 906 (C-H_δ); ^{1}H-NMR (500 MHz; $CDCl_3$; δ in ppm); 3.96 (1H, dd, J=9.7, 9.2 Hz), 4.22 (1H, dd, J=8.20, 9.15 Hz), 2.21 (1H, m), 1.62 (1H, m), 4.05 (1H, m), 1.47 (1H, m), 1.49 (1H, m), 0.99 (3H, t, J=6.4 Hz), 1.02 (1H, m), 1.02 (1H, m), 1.26 (1H, m), 1.21 (1H, m), 1.42 (2H,dd, J=6.3, 4.0 Hz), 4.20 (1H, m), 5.92 (1H, m), 5.17 (1H, m), 5.20 (1H, m), 3.35 (1H, t, J=9.4 Hz), 2.20 (1H, m), 1.35 (3H, d, J=6.31 Hz), 5.70 (1H, m), 5.69 (1H, m), 3.80 (1H, dd, J=9.1, 4.6 Hz), 2.04 (1H, m), 3.30 (3H, s); ^{13}C-NMR (125 MHz; $CDCl_3$; δ in ppm); 65.0 (CH_2), 172.6 (C), 50.2 (CH), 36.1 (CH), 69.9 (CH), 27.2 (CH_2), 9.10 (CH_3), 31.3 (CH_2), 40.1 (CH), 38.6 (CH_2), 70.7 (CH), 142.3 (CH), 116.4 (CH_2), 77.02 (CH), 43.4 (CH), 16.1 (CH_3), 136.2

(CH), 134.6 (CH), 82.0 (CH), 40.4 (CH), 57.17 (CH_3); DEPT, COSY, HSQC, and HMBC data were presented in Table 5.7. EI-MS *m/z*: calcd. for $C_{21}H_{34}O_6$ 382.2355 $[M]^+$. HRESIMS (positive mode) *m/z*: found 383.2438 $[M+H]^+$, calcd. for $C_{21}H_{35}O_6$ 383.2434 $[M+H]^+$ (Δ 1.04 ppm).

5.2.5.5 Physicochemical description of compound-5 (TP_5)

4,4a,5,6,7,8,11,11a-Octahydro-1,7-dihydroxy-4-(4^1-hydroxy-4^2-methylpropyl)-6-(6^1-hydroxy-6^2-propenyl)-10-methyl-cyclonona[*c*]pyran-3(1*H*)-one; Yellow oil; $[\alpha]D^{22}$ +39 (c 0.13, $CHCl_3$); UV (MeOH) λ_{max} (log ε): 246.0 (2.90) nm; TLC (Si gel GF_{254} 15 mm; 30 % EtOAc/*n*-hexane) R_f: 0.40; R_t (RP-C_8 HPLC, MeOH:CH_3CN, 2:3 v/v): 3.23 min; FTIR (ν_{max} cm^{-1}): 3450 (O-H_v, br), 3020 (C-H_v), 1715 (C=O_v), 1614 (C=C_v), 1625 (C=C_v), 1470 (C-H_δ), 1380 (C-H_ρ), 1220 (C=O_v), 1140 (C-C_v), 955 (=C-H_δ), 885 (C-H_δ); ^{1}H-NMR (500 MHz; $CDCl_3$; δ in ppm); 6.26 (1H, d, J=9.6 Hz), 2.22 (1H, dd, J=9.6, 3..91 Hz), 1.62 (1H, m), 3.95 (1H, d, J=10.5 Hz), 2.07 (1H, m), 1.05 (3H, m), 1.05 (3H, d, J=6.52 Hz), 1.27 (1H, m), 1.01 (1H, m), 1.35 (1H, m), 4.10 (1H, dd, J=10.5, 6.5 Hz), 5.63 (1H, m), 5.11(1H,m),, 5.13 (1H, m), 1.53 (1H, m), 1.25 (1H, m), 4.20 (1H, dd, J=9.1, 7.6 Hz), 5.40 (1H, dd, J=15.68 Hz), 1.73 (3H, s), 2.02 (1H, dd, J=11.6, 8.5 Hz), 1.76 (1H, dd, J=12.2, 6.3 Hz), 1.84 (1H, m); ^{13}C-NMR (125 MHz; $CDCl_3$; δ in ppm); 96.1 (CH), 171.6 (C), 52.5 (CH), 40.2 (CH), 71.0 (CH), 31.5 (CH), 18.6(0) (CH_3), 18.6(1) (CH_3), 30.9 (CH_2), 40.7 (CH), 73.6 (CH), 140.9 (CH), 115.0(CH_2), 39.10 (CH_2), 66.8 (CH), 130.6 (CH), 132.3 (C), 17.7 (CH_3), 36.7 (CH_2), 41.57 (CH); DEPT, COSY, HSQC, and HMBC data were presented in Table 5.8. EI-MS *m/z*: calcd. for $C_{20}H_{32}O_6$ 368.2199. HRESIMS (positive mode) *m/z*: found 369.2280 $[M+H]^+$, calcd. for $C_{20}H_{33}O_6$ 369.2277 $[M+H]^+$ (Δ 0.08 ppm).

5.2.5.6 Physicochemical description of compound-6 (TP_6)

6-Methoxy-dolabella-8(17),12-diene-10β ,18-diol; Pale yellow oil; $[\alpha]^{22}{}_D$ -119.3° (*c* 0.22, $CHCl_3$) (polarimeter AP-300, ATAGO, Japan); UV (MeOH) λ_{max} (log ε) (Varian Cary 50, Palo Alto, CA): 242.6 (2.89) nm; TLC (Si-GF^{254} 15 mm; 30 % EtOAc:*n*-hexane, v/v) R_f: 0.38; R_t (HPLC RP-C_{18}, MeOH:MeCN 3:2, v/v, isocratic) (Luna, 250 x 4.6 mm, 5 µm, Phenomenex, Torrance, CA): 3.21 min; Infrared (cm^{-1}) (ν_{max}) (Perkin-Elmer Series 2000, Waltham, MA) 3434, 2978, 2927, 2871, 1639, 1629, 1457, 1404, 1364, 1272, 1112, 1076; ^{1}H-NMR (500 MHz; $CDCl_3$; δ in ppm); 1.25(1H,dd,11.1, 7.2Hz), 1.03(1H,dd,10.6, 5.7Hz), 1.26(1H,m),, 1.45(1H,m), 1.40(1H,m), 1.51(1H,t,10.6 Hz),, 1.27(1H,t, 9.9Hz), 3.23(1H,m), 3.35(1H,s), 2.20(1H,d,10.2 Hz), 1.95(1H,d, 9.8Hz), 2.22(1H,d,11.1 Hz), , 1.96(1H,d,9.6 Hz), 3.56(1H,m), 1.98(1H,d,10.2 Hz), 5.60(1H,t,9.8 Hz), 2.05(1H,d,9.3 Hz), 2.30(1H,d,9.7 Hz), 1.04(3H,s), 1.09(3H,d,6.4 Hz), 4.88(1H,s),, 4.65(1H,s), 1.41(3H,s), 1.42(1H, s); ^{13}C-NMR (125 MHz; $CDCl_3$; δ in ppm); 47.0 (C), 38.0 (CH_2), 37.3 (CH_2), 34.3 (CH), 47.3 (CH_2), 75.9 (CH), 56.5 (CH), 44.1 (CH_2), 137.3(C), 46.7 (CH_2), 65.62 (CH), 59.0 (CH), 153.4 (C), 121.5(CH), 47.3(CH_2), 23.3 (CH_3), 28.5 (CH_3), 118.7 (CH_2), 76.3 (C), 30.6 (CH_3),

30.6 (CH); DEPT, COSY, HSQC, and HMBC data were presented in Table 5.9; EI-MS *m/z*: calcd. for $C_{21}H_{36}O_3$ 336.27. HRESIMS (positive mode) *m/z*: found 337.2745 $[M+H]^+$, calcd. for $C_{21}H_{37}O_3$ 337.2742 $[M+H]^+$ (Δ 0.08 ppm).

5.2.5.6 Physicochemical description of compound-7 (TP_7)

3-Methoxy-dolabella-12(18)-ene-4β -ol; Yellow oil; $[\alpha]^{22}{}_D$ -116.9° (*c* 0.21, $CHCl_3$); UV (MeOH) λ_{max} (log ε): 246.0 (2.90) nm; TLC (Si-GF^{254} 15 mm; 30 % EtOAc:*n*-hexane, v/v) R_f: 0.40; R_t (HPLC RP-C_{18}, MeOH:MeCN 3:2, v/v, isocratic): 4.23 min; Infrared (cm^{-1}) 3520, 3020, 2923, 2855, 1625, 1470, 1450, 1380, 1220, 1140, 1065, 940, 885; ^{1}H-NMR (500 MHz; $CDCl_3$; δ in ppm); 1.15(1H,d,9.3Hz), 1.40(1H,d,10.2 Hz), 3.02(1H,t,10.6 Hz), 3.36(3H,s), 1.23(1H,dd,11.6, 6.9 Hz), 1.48(1H,dd,11.3, 6.6 Hz), 1.43(2H,m), 1.52(1H,m), 1.27(1H,m), 1.40(1H,m), 1.51(1H,m), 1.28(1H,m), 1.40(1H, m), 1.13(1H, m), 1.78(1H,t,5.7 Hz), 2.30(1H,m), 2.39(1Hα,m), 1.34(1H,dd, 10.9, 6.3 Hz), 1.08(1H,dd,10.7, 6.8 Hz),1.05(3H,s), 1.31(3H,s), 1.15(3H,s), 1.82(3H,s), 1.81(3H,s); ^{13}C-NMR (125 MHz; $CDCl_3$; δ in ppm); 45.5 (C), 39.2 (CH_2), 87.0 (CH), 57.7 (CH_3), 76.7 (C), 39.3 (CH_2), 19.8 (CH_2), 42.6 (CH_2), 35.0 (CH), 41.3 (CH_2), 24.8 (CH_2), 53.4 (CH), 132.3 (C), 31.1 (CH_2), 39.6 (CH_2), 23.5 (CH_3), 24.8 (CH_3), 27.6 (CH_3), 124.0(C), 20.4 (CH_3), 20.4 (CH_3); DEPT, COSY, HSQC, and HMBC data were presented in Table 5.10; EI-MS *m/z*: calcd. for $C_{21}H_{38}O_2$ 322.29 $[M^+]$. HRESIMS (positive mode) *m/z*: found 323.2953 $[M+H]^+$, calcd. for $C_{21}H_{39}O_2$ 323.2950 $[M^+]$ $[M+H]^+$ (Δ 0.09 ppm).

5.2.5.7 Physicochemical description of compound-8 (TP_8)

3-Methoxy-dolabella-10,18(19)-diene-5α,8β -diol ; Yellow oil; $[\alpha]^{22}{}_D$ -115.7° (c 0.22, $CHCl_3$); UV (MeOH) λ_{max} (log ε): 248 (3.1) nm; TLC (Si-GF^{254} 15 mm; 30 % EtOAc:*n*-hexane, v/v) R_f: 0.45; R_t (HPLC RP-C_{18}, MeOH:MeCN 3:2, v/v, isocratic): 4.02 min; Infrared (cm^{-1}) 3077, 2963, 2865, 1624, 1447, 1370, 1280, 1243, 1180, 966, 906; ^{1}H-NMR (500 MHz; $CDCl_3$; δ in ppm); 1.20 (1H,d,10.2 Hz), 1.46 (1H,d,9.8 Hz), 3.00(1H,m), 3.37(3H,s), 1.60(1H,m), 3.20(1H,m), 1.72(1H,m), 1.47(1H,m), 1.22(1H,t,2.5 Hz), 1.48(1H,t,2.7 Hz), 1.92(1H,d,12.6 Hz), 2.15(1H,d,12.4 Hz), 5.14(1H,t,11.3 Hz), 2.77(1H,t,9.6 Hz), 1.44(1H,m), 1.19(1H,m), 1.33(1H,dd,12.7 Hz), 1.08(1H,dd,6.8 Hz), 1.13(3H,s), 1.15(3H,d,6.8 Hz), 1.32(3H,s), 4.61(1H,m), 4.58(1H,m), 1.82(3H,s); ^{13}C-NMR (125 MHz; $CDCl_3$; δ in ppm); 45.3 (CH), 40.2 (CH_2), 83.9 (CH), 57.7 (CH_3), 41.0 (CH), 76.7 (CH), 27.3 (CH_2), 40.0 (CH_2), 74.3 (C), 46.8 (CH), 115.1 (CH_2), 154.8 (C), 48.9 (CH), 28.5 (CH_2), 39.1 (CH_2), 23.3 (CH_3), 17.9 (CH_3), 27.6 (CH_3), 146.8, (C) 113.0 (CH_2), 21.3 (CH_3); DEPT, COSY, HSQC, and HMBC data were presented in Table 5.11; EI-MS *m/z*: calcd. for $C_{21}H_{36}O_3$ 336.27 $[M^+]$. HRESIMS (positive mode) *m/z*: found 337.2745 $[M+H]^+$, calcd. for $C_{21}H_{37}O_3$ 337.2742 $[M+H]^+$ (Δ 0.08 ppm).

5.2.5.8 Physicochemical description of compound-9(TP_9)

2,7-Dimethoxy-14α-hydroxy-dolasta-1(15),9-diene; Colourless oil; $[\alpha]^{22}_D$ -89.1° (*c* 0.21, $CHCl_3$); UV (MeOH) λ_{max} (log ε): 246.0 (2.90) nm; TLC (Si-GF^{254} 15 mm; 30 % EtOAc:*n*-hexane, v/v) R_f: 0.40; R_t (HPLC RP-C_{18}, MeOH:MeCN 3:2, v/v, isocratic): 3.23 min; Infrared (cm^{-1}) 3520, 2923, 2855, 1625, 1470, 1410, 1380, 1220, 1140, 1090, 970, 910, 885; ^{1}H-NMR (500 MHz; $CDCl_3$; δ in ppm); 3.89 (1H,t,9.5 Hz), 3.33(3H,s), 1.74(1H,m), 2.06(1H,m), 1.02(1H,dd,11.7 Hz), 1.25(1H,dd,6.7 Hz), 1.40(1H,d, 12.5Hz), 1.14(1H,d, 12.6Hz), 1.14(1H,d, 12.6Hz), 4.30(1H,m), 3.35 (3H,s), 2.19(1H,d,10.9 Hz), 5.40(1H,t,11.3 Hz), 2.04(1H,d,12.2 Hz), 2.29 (1H,d,12.3 Hz), 1.34(1H,s), 1.24(1H,s), 5.09(1H,s), 4.84(1H,s), 1.13(3H,s), 3.40(1H,m), 1.16(3H,d,6.3 Hz), 1.15(3H,d,6.4 Hz), 1.08(3H,s); ^{13}C-NMR (125 MHz; $CDCl_3$; δ in ppm); 151.5 (C), 81.9 (CH), 56.9 (CH_3), 28.5 (CH_2), 31.7 (CH_2), 43.3 (C), 42.3 (CH_2), 77.4 (CH), 57.1 (CH_3), 53.3 (CH), 146.2 (C), 121.8 (CH), 49.4 (CH_2), 46.5 (C), 41.3 (CH_2), 83.6 (C), 111.5 (CH_2), 21.1(CH_3), 31.4 (CH), 22.3 (CH_3), 22.3 (CH_3), 25.5 (CH_3); DEPT, COSY, HSQC, and HMBC data were presented in Table 5.12; EI-MS *m/z*: calcd. for $C_{22}H_{36}O_3$ 348.27 [M^+]. HRESIMS (positive mode) *m/z*: found 349.2745 $[M+H]^+$, calcd. for $C_{22}H_{37}O_3$ 349.2742 $[M+H]^+$ (Δ 0.08 ppm).

5.2.5.9 Physicochemical description of compound-10 (TP_{10})

4,7-Dimethoxy-9β ,14α-dihydroxy-dolasta-1-ene; Colourless oil; $[\alpha]^{22}_D$ -92.3° (*c* 0.21, $CHCl_3$); UV (MeOH) λ_{max} (log ε): 245.0 (2.62) nm; TLC (Si-GF^{254} 15 mm; 30 % EtOAc:*n*-hexane, v/v) R_f: 0.42, R_t (HPLC RP-C_{18}, MeOH:MeCN, 3:2v/v, isocratic) 3.01 min; Infrared (cm^{-1}) 3570, 2922, 2845, 1640, 1455, 1250, 1175, 1115, 1085, 990, 910; ^{1}H-NMR (500 MHz; $CDCl_3$; δ in ppm); 5.49(1H,t,10.7 Hz), 2.21(1H,m), 1.96(1H,m), 3.26(1H,t,8.8 Hz), 3.39(3H,s), 1.40(1H,d,11.6 Hz), 1.16(1H,d,11.8Hz), 4.64(1H,m), 3.36(3H,s), 1.33(1H,d,9.1 Hz), 1.50(1H,m), 1.76(1H,m), 1.53(1H,t,6.6 Hz), 1.27(1H,t,6.7 Hz), 1.24(1H,s), 1.34(1H,s), 1.95(3H,s), 1.14(3H,s), 1.62(1H,m), 1.02(3H,d,7.6 Hz), 1.01(3H,d,7.7 Hz), 1.03(3H,s); ^{13}C-NMR (125 MHz; $CDCl_3$; δ in ppm); 142.9 (C), 124.3 (CH), 30.0 (CH_2), 83.3 (CH), 57.0 (CH_3), 42.1(C), 42.9(CH_2), 76.5 (CH), 57.8 (CH_3), 68.6 (CH), 87.3 (C), 34.5 (CH_2), 38.4 (CH_2), 42.3 (C), 44.2 (CH), 83.0 (C), 19.0 (CH_3), 18.3 (CH_3), 36.2 (CH), 17.8 (CH_3), 17.8 (CH_3), 25.6 (CH_3); DEPT, COSY, HSQC, and HMBC data were presented in Table 5.13; EI-MS *m/z*: calcd. for $C_{22}H_{38}O_4$ 366.28 [M^+]. HRESIMS (positive mode) *m/z*: found 367.2851$[M+H]^+$, calcd. for $C_{22}H_{39}O_4$ 367.2848 $[M+H]^+$ (Δ 0.08 ppm).

5.2.6 Evaluation of bioactive potencies

5.2.6.1 *In-vitro* antioxidative activities

5.2.6.1a 1, 1-Diphenyl-2-picryl-hydrazil radical/ DPPH$^{\bullet}$ scavenging activity

The estimation of antioxidant potencies of various fractions and pure compounds derived from the EtOAc-MeOH extracts of *G. salicornia* was carried out by *in vitro* DPPH$^{\bullet}$ scavenging assay. The details were described under the section 3.2.5.2a of Chapter 3.

5.2.6.1b 2,2′-Azino-bis-3-ethylbenzothiozoline-6-sulfonic acid diammonium salt/ ABTS$^{+\bullet}$ radical scavenging assay

The determination of antioxidant potencies of various fractions and pure compounds derived from the EtOAc-MeOH extracts of *G. salicornia* was carried out by *in vitro* ABTS$^{+\bullet}$ scavenging assay. The details were described under the section 3.2.5.2b of Chapter 3.

5.2.6.2 *In-vitro* anti-inflammation assays

452.6.2a Cyclooxygenases- (COX1/2) inhibition assay

The anti-inflammation bioactive potential of various fractions and pure compounds identified from the EtOAc-MeOH extracts of *G. salicornia* were evaluated by using the pro-inflammatory enzyme, cyclooxygenases (COX-1/2) inhibition assay. The methodology was detailed under the section 3.2.5.3a of Chapter 3.

5.2.6.2b 5-Lipoxygenase/5-LOX inhibition assay

The anti-inflammation bioactive potential of various fractions and pure compounds identified from the EtOAc-MeOH extracts of *G. salicornia* were evaluated by using the pro-inflammatory enzyme 5-lipoxygenase (5-LOX) inhibition assay. This was described under the section 3.2.5.3b of Chapter 3.

5.2.7 Structure-activity correlations of bioactive leads isolated from EtOAc-MeOH extract of P. tetrastromatica

The structure-bioactivity-correlation investigations were carried out by utilising different molecular factors, such as octanol-water partition-coefficient (log P_{ow}-hydrophobicity); electronic (Pl-polarisability; topological polar surface area-tPSA) and steric (MV-molar volume; P-parachor; MR-molar refractivity) (Lipinski 2000) through ACD-ChemSketch (Advanced Chemistry Development, Inc., Toronto, Canada; ver. 12.0) and ChemDraw-Ultra (Cambridge Soft Corporation, USA; ver. 12.0) softwares.

5.2.8 *Molecular modelling experiments*

In-silico molecular modeling analysis of the bioactive compounds derived from the seaweed *G. salicornia* was conducted by the software Auto-Dock-4 (ver. 1.5.6). The fractionated compounds were drawn using ACD/Chem-sketch, and were made into Molfiles before being converted to the PDB format (Open Babel, GUI 2.4.1). The X-ray crystal structures of 5-LOX (PDB 3V99, resolution 2.25 Å), α-glucosidase (PDB 3A4A, resolution 1.6 Å) and *α*-amylase (PDB 1HNY, resolution 1.8 Å) were acquired from the Protein Data Bank (www.pdb.org) and conformationally oriented (Swiss-Pdb Viewer, ver. 4.1.0) (Gilbert et al., 2012; Brayer et al., 1995; Yamamoto et al., 2010). The docking analyses were conducted by the molecular algorithm, which was run by Cygwin I-II. After auto docking, the RMSD data (root mean square deviation) was documented, and the conformations were oriented with the aid of docking parameters. Finally, molecular docking analyses were visualized using the Chimera software developed by University of California, San Francisco (USCF Chimera, ver. 1.11.2).

5.2.9 Statistical analysis

The entire sets of data were presented in triplicates along with their mean ± standard deviation. One-way analysis of variance (ANOVA; Statistical Program for Social Sciences, USA, ver. 13.0) was used to analyze the significant differences ($P \leq 0.05$) among the means of the results.

5.3 Results and discussion

5.3.1 Chromatographic fractionation of the pure compounds and bioactive potentials of the sub-column fractions from the organic extract of P. tetrastromatica

Chromatographic fractionation of the organic EtOAc-MeOH extract of seaweed, *P. tetrastromatica* on silica gel initially resulted in a total of 20 fractions, which upon pooling resulted in six major column-fractions (TP_1-TP_6), whereas percentage recovery of the sub-fractions, TP_2 (23 %) through TP_4 (28 %) were greater as compared to those displayed by TP_1 and TP_{5-6} (< 15 %, $P <$ 0.05). The fraction TP_2 on further purification by flash chromatography on a silica gel column (230-400 mesh, 12 g), with the solvent system of EtOAc/*n*-hexane (0-100 %, by a step gradient mode) yielded a total of 30 column subfractions (15 mL each), which were combined to 8 column sub-fractions. These fractions exhibited greater radical scavenging activities against DPPH (IC_{50} < 1 mg mL^{-1}) and $ABTS^{+}$ (IC_{50} 0.60-1.25 mg mL^{-1}) than other fractions (IC_{50} > 1.30 mg mL^{-1}). Potential anti-inflammatory bioactivities towards COX-2 and 5-LOX displayed the significance of the column sub-fractions, TP_{2-4} and TP_{2-5} (IC_{50} < 0.70 mg mL^{-1}) for further chromatographic sub-fractionation, whereas the inhibiting activities of the column fractions $TP_{2-(2-3)}$ and TP_{2-6}-TP_{2-8} towards COX-2 and

5-LOX were significantly lesser (IC_{50} > 1.5 mg mL^{-1}, P < 0.05). Consequently, repetitive chromatographic fractionation of TP_{2-4} and TP_{2-5} yielded two previously unreported xenicin class of diterpenoids with 2-oxabicyclo[7.4.0]tridecane ring system (**1-2**) along with three xeniolide-type diterpenoids (**3-5**) with unprecedented δ-lactone cyclononane skeleton bearing an oxabicyclo[7.4.0]tridecane framework. The structural characterizations of the studied compounds were carried out by extensive spectroscopic experiments.

The sub-fractions, TP_3 and TP_4 demonstrated greater antioxidative activities against 2,2'-azino-bis-3-ethylbenzothiozoline-6-sulfonic acid diammonium salt (IC_{50} 0.6-1.0 mg/mL) and 1,1-diphenyl-2-picrylhydrazyl (IC_{50} 0.60-0.80 mg/mL) than those displayed by other fractions (IC_{50} >1.20 mg/mL). Potential α-glucosidase and α-amylase attenuation activities were reported for the sub-fractions TP_3 and TP_4 (IC_{50} <0.25 mg/mL) compared to TP_1 and TP_{5-6} (IC_{50} >0.50 mg/mL). Therefore, the sub-fractions TP_3 and TP_4 were shortlisted for further repetitive fractionation by preparative HPLC yielding the diterpenoids of dolabellane (compounds **6-8**) and dolastane (compounds **9-10**) class of chemistries. The structures and relative stereochemistries of the titled compounds were interpreted by extensive spectroscopic experiments.

Table 5.1.: Yield and bioactivities (antioxidant, anti-inflammatory and antidiabetic) of the sub-fractions isolated from the EtOAc-MeOH extract of *P. tetrastromatica*

Fractions	***Yield (in %)**	**Bioactivity (IC_{50} in mg mL^{-1})**					
		Antioxidant		**Anti-inflammatory**		**Antidiabetic**	
		#DPPH	**#ABTS**	**#COX-2**	**#5-LOX**	**#α-amylase**	**#α-glucosidase**
TP_1	11.05	2.01^{a}±0.02	2.01^{a}±0.03	2.83^{a}±0.02	2.42^{a}±0.02	2.36^{a}±0.02	2.15^{a}±0.03
TP_2	**23.03**	**1.01^{b} ±0.02**	**1.05^{b}±0.04**	**1.02^{b}±0.02**	**0.99^{b}±0.03**	2.25^{b}±0.03	2.13^{a}±0.03
TP_3	**25.01**	1.03^{b}±0.03	1.06^{b}±0.05	2.13^{c}±0.03	2.36^{c}±0.04	**0.96^{c}±0.06**	**0.98^{b}±0.03**
TP_4	**28.00**	**1.02^{b}±0.03**	**1.03^{b}±0.07**	2.09^{c}±0.05	2.21^{d}±0.03	**1.01^{c}±0.03**	**0.97^{b}±0.06**
TP_5	5.34	2.31^{c}±0.06	2.69^{c}±0.03	2.53^{d}±0.03	2.32^{e}±0.05	2.26^{d}±0.06	2.39^{c}±0.01
TP_6	6.21	2.78^{d}±0.05	2.98^{d}±0.06	2.26^{e}±0.06	2.16^{f}±0.02	2.19^{e}±0.03	2.20^{d}±0.03

*The yield of major sub-column fractions calculated based on the crude EtOAc-MeOH extract (38.0 g of dry weight). The values were tabulated in triplicate (n=3) and indicated as mean±standard deviation. Significant differences were expressed as superscripts (a-f) within column (p < 0.05).

#The IC_{50} values were calculated in mg mL^{-1}

Table 5.2.: Yield and bioactivities (antioxidant, anti-inflammatory and antidiabetic) of sub-fractions from EtOAc-MeOH extract of *P. tetrastromatica*

Fractions	***Yield (in %)**	**Bioactivity (IC_{50} in mg mL^{-1})**					
		Antioxidant		**Anti-inflammatory**		**Antidiabetic**	
		#DPPH	**#ABTS**	**#COX-2**	**#5-LOX**	**#α-amylase**	**#α-glucosidase**
TP_{2-1}	2.15	1.18^{a}±0.02	1.20^{a}±0.03	1.72^{a}±0.02	1.61^{a}±0.02	2.71^{a}±0.02	2.34^{a}±0.03
TP_{2-2}	**13.18**	**0.98^{b} ±0.02**	**0.99^{b}±0.04**	**0.89^{b}±0.02**	**0.87^{b}±0.03**	**2.68^{a}±0.03**	**2.52^{b}±0.03**
TP_{2-3}	**11.26**	**0.96^{b}±0.03**	**0.98^{b}±0.05**	**0.91^{b}±0.03**	**0.90^{c}±0.04**	**2.56^{b}±0.06**	**2.42^{c}±0.03**
TP_{2-4}	0.82	1.12^{c}±0.03	1.11^{b}±0.07	1.83^{c}±0.05	1.75^{d}±0.03	2.02^{c}±0.03	2.09^{d}±0.06
TP_{2-5}	0.28	1.21^{a}±0.06	1.23^{c}±0.03	1.52^{d}±0.03	1.49^{e}±0.05	2.18^{d}±0.06	2.07^{d}±0.01
TP_{2-6}	0.74	1.29^{d}±0.05	1.31^{d}±0.06	1.27^{e}±0.06	1.23^{f}±0.02	2.37^{e}±0.03	2.18^{e}±0.03
TP_{2-7}	0.58	1.11^{c}±0.06	1.14^{b}±0.03	1.32^{f}±0.03	1.43^{e}±0.05	2.48^{f}±0.06	2.37^{a}±0.01
TP_{2-8}	0.82	1.17^{a}±0.05	1.19^{d}±0.06	1.28^{e}±0.06	1.21^{f}±0.02	2.47^{f}±0.03	2.31^{a}±0.03
TP_{2-2-1}	**0.28**	**0.79^{e}±0.02**	**0.81^{e}±0.03**	**0.71^{g}±0.02**	**0.73^{g}±0.02**	**2.82^{g}±0.02**	**2.32^{a}±0.03**
TP_{2-2-2}	**0.27**	**0.78^{e} ±0.02**	**0.80^{e}±0.04**	**0.70^{g}±0.02**	**0.71^{g}±0.03**	**2.87^{g}±0.03**	**2.33^{a}±0.03**
TP_{2-2-3}	25	1.13^{c}±0.03	1.14^{b}±0.05	1.11^{h}±0.03	1.10^{h}±0.04	2.66^{h}±0.06	2.29^{a}±0.03
TP_{2-2-4}	0.065	1.11^{c}±0.03	1.18^{d}±0.07	1.14^{h}±0.05	1.12^{i}±0.03	2.68^{h}±0.03	2.71^{f}±0.06
TP_{2-2-5}	0.052	1.09^{c}±0.06	1.17^{d}±0.03	1.13^{h}±0.03	1.11^{j}±0.05	2.67^{i}±0.06	2.73^{f}±0.01
TP_{3-2-1}	**0.31**	**0.71^{f}±0.02**	**0.75^{f}±0.03**	**0.69^{i}±0.02**	**0.68^{k}±0.02**	**2.31^{e}±0.02**	**2.35^{a}±0.03**
TP_{3-2-2}	**0.32**	**0.72^{f} ±0.02**	**0.73^{f}±0.04**	**0.73^{j}±0.02**	**0.74^{l}±0.03**	**2.38^{e}±0.03**	**2.39^{a}±0.03**
TP_{3-2-3}	**0.27**	**0.77^{e}±0.03**	**0.76^{f}±0.05**	**0.68^{i}±0.03**	**0.66^{k}±0.04**	**2.36^{e}±0.06**	**2.41^{c}±0.03**
TP_{3-2-4}	0.061	1.06^{c}±0.03	1.08^{b}±0.07	2.24^{k}±0.05	2.05^{m}±0.03	2.29^{f}±0.03	2.32^{a}±0.06
TP_{3-2-5}	0.063	1.02^{c}±0.06	1.07^{b}±0.03	2.41^{l}±0.03	2.59^{n}±0.05	2.28^{f}±0.06	2.34^{a}±0.01

*The yield of major sub-column fractions calculated based on the crude EtOAc-MeOH extract (38.0 g of dry weight). The values were tabulated in triplicate (n=3) and indicated as mean±standard deviation. Significant differences were expressed as superscripts (a-m) within column ($p < 0.05$).

#The IC_{50} values were calculated in mg mL^{-1}

Table 5.3.: Yield and bioactivities (antioxidant, anti-inflammatory and antidiabetic) of sub-fractions from EtOAc-MeOH extract of *P. tetrastromatica*

Fractions	***Yield (in %)**	**Bioactivity (IC_{50} in mg mL^{-1})**					
		Antioxidant		**Anti-inflammatory**		**Antidiabetic**	
		#DPPH	**#ABTS**	**#COX-2**	**#5-LOX**	**#α-amylase**	**#α-glucosidase**
TP_{3-1}	2.68	1.19^{a}±0.02	1.20^{a}±0.03	2.76^{a}±0.02	2.73^{a}±0.02	1.01^{a}±0.02	1.02^{a}±0.03
TP_{3-2}	2.71	1.17^{ac} ±0.02	1.19^{a}±0.04	2.73^{a}±0.02	2.70^{b}±0.03	1.03^{a}±0.03	1.04^{a}±0.03
TP_{3-3}	**22.0**	**0.98^{b}±0.03**	**0.99^{b}±0.05**	**1.90^{b}±0.03**	**1.87^{c}±0.04**	**0.86^{b}±0.06**	**0.88^{b}±0.03**
TP_{3-4}	1.04	1.12^{c}±0.03	1.14^{cg}±0.07	2.20^{c}±0.05	2.19^{d}±0.03	1.10^{c}±0.03	1.12^{c}±0.06
TP_{3-5}	2.73	1.09^{c}±0.06	1.10^{cg}±0.03	1.98^{c}±0.03	1.96^{e}±0.05	1.12^{c}±0.06	1.13^{c}±0.01
TP_{3-3-1}	**0.25**	**0.89^{d}±0.05**	**0.91^{d}±0.06**	**2.10^{d}±0.06**	**2.08^{f}±0.02**	**0.85^{b}±0.03**	**0.87^{d}±0.03**
TP_{3-3-2}	**0.26**	**0.87^{d}±0.02**	**0.89^{e}±0.03**	**2.09^{de}±0.02**	**2.04^{g}±0.02**	**0.84^{b}±0.02**	**0.85^{d}±0.03**
TP_{3-3-3}	**0.27**	**0.77^{e} ±0.02**	**0.79^{f}±0.04**	**2.03^{e}±0.02**	**2.01^{h}±0.03**	**0.78^{d}±0.03**	**0.79^{d}±0.03**
TP_{3-3-4}	0.05	1.10^{d}±0.03	1.12^{g}±0.05	2.41^{f}±0.03	2.38^{i}±0.04	1.06^{ac}±0.06	1.07^{a}±0.03
TP_{3-3-1}	0.06	1.06^{ad}±0.03	1.09^{g}±0.07	2.39^{f}±0.05	2.35^{i}±0.03	1.04^{a}±0.03	1.06^{a}±0.06
TP_{4-1}	0.07	1.13^{d}±0.06	1.14^{g}±0.03	2.43^{f}±0.03	2.41^{j}±0.05	1.12^{c}±0.06	1.14^{c}±0.01
TP_{4-2}	0.08	1.18^{a}±0.05	1.20^{h}±0.06	2.27^{g}±0.06	2.24^{k}±0.02	1.13^{c}±0.03	1.15^{c}±0.03
TP_{4-3}	**20.52**	**0.97^{b}±0.02**	**0.99^{d}±0.03**	**2.02^{e}±0.02**	**1.99^{e}±0.02**	**1.01^{a}±0.02**	**1.03^{a}±0.03**
TP_{4-4}	3.23	1.04^{d} ±0.02	1.07^{g}±0.04	2.36^{gh}±0.02	2.34^{i}±0.03	1.08^{c}±0.03	1.07^{a}±0.03
TP_{4-5}	4.31	1.10^{d}±0.03	1.13^{g}±0.05	2.34^{h}±0.03	2.31^{a}±0.04	1.14^{c}±0.06	1.15^{c}±0.03
TP_{4-6}	2.29	1.07^{d}±0.03	1.08^{g}±0.07	2.19^{c}±0.05	2.15^{d}±0.03	1.09^{c}±0.03	1.11^{c}±0.06
TP_{4-3-1}	**0.17**	**0.85^{d}±0.06**	**0.87^{h}±0.03**	**2.13^{d}±0.03**	**2.10^{f}±0.05**	**0.75^{d}±0.06**	**0.76^{d}±0.01**
TP_{4-3-2}	**0.21**	**0.76^{e}±0.05**	**0.78^{i}±0.06**	**2.21^{c}±0.06**	**2.19^{d}±0.02**	**0.73^{d}±0.03**	**0.74^{d}±0.03**
TP_{4-3-3}	29	1.08^{d}±0.02	1.09^{g}±0.03	2.35^{g}±0.02	2.33^{a}±0.02	1.07^{c}±0.02	1.08^{a}±0.03
TP_{4-3-4}	0.07	1.07^{d} ±0.02	1.15^{g}±0.04	2.37^{g}±0.02	2.34^{a}±0.03	1.11^{c}±0.03	1.12^{c}±0.03
TP_{4-3-5}	0.08	1.05^{d}±0.03	1.09^{g}±0.05	2.42^{f}±0.03	2.39^{i}±0.04	1.06^{ac}±0.06	1.09^{c}±0.03
TP_{4-3-6}	0.09	1.03^{d}±0.03	1.05^{g}±0.07	2.47^{if}±0.05	2.44^{j}±0.03	1.05^{ac}±0.03	1.03^{a}±0.06

*The yield of major sub-column fractions calculated based on the crude EtOAc-MeOH extract (38.0 g of dry weight). The values were tabulated in triplicate (n=3) and indicated as mean±standard deviation. Significant differences were expressed as superscripts (a-l) within column ($p < 0.05$).

#The IC_{50} values were calculated in mg mL^{-1}

5.*3.2* ***Spectroscopic characterization of the bioactive compounds derived from the EtOAc-MeOH extract of P. tetrastromatica***

The consecutive chromatographic purification of the EtOAc-MeOH crude extract of *P. tetrastromatica* led to the identification of bioactive secondary metabolic analogues. The structural elucidations of these lead molecules carried out using the nuclear magnetic resonance (NMR) analyses {^{1}H-proton-500 MHz; ^{13}C-carbon-125 MHz; DEPT; ^{1}H-^{1}H COSY; HSQC; HMBC; NOESY} using deuterated solvent along with mass spectrometric analyses (GC-EI-MS/HRESIMS), Fourier-transform infrared (FT-IR) (reported among 4000-400 cm^{-1}) and UV-spectrophotometric analyses. The isolated secondary metabolites were categorized under the different classes of chemistry, namely xenicane diterpene derivatives (**1-5**), and dolabellane diterpene derivatives (**6-10**) (Figure 5.3).

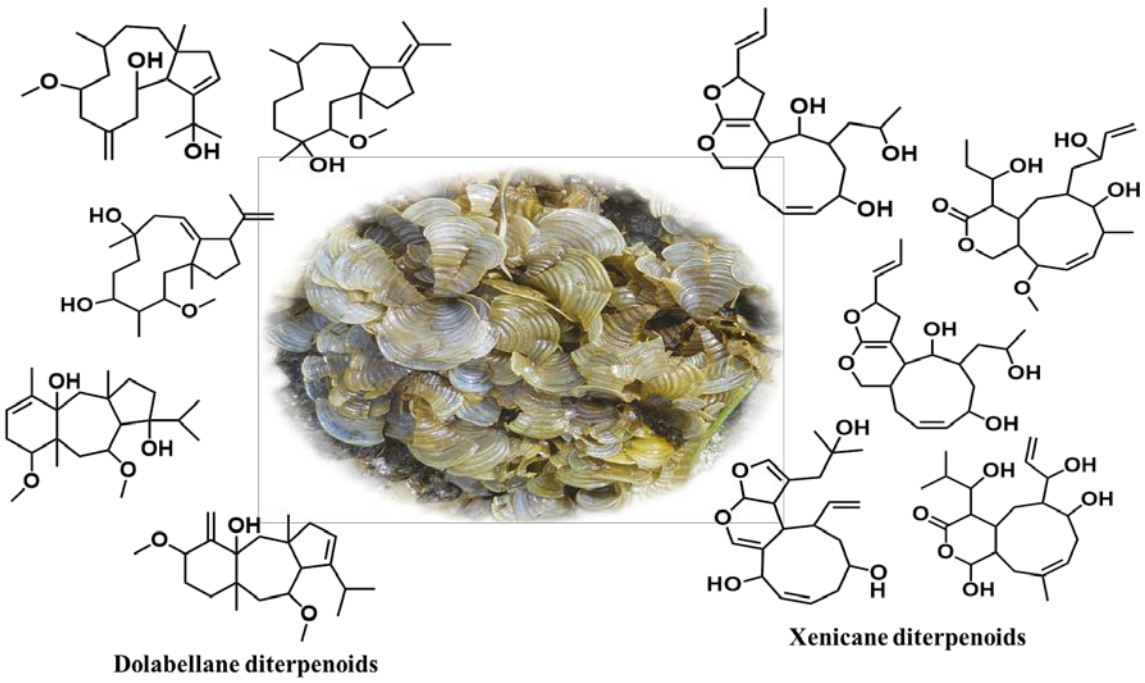

Figure 5.3.: Bioactive secondary metabolites isolated from the organic extract of *P. tetrastromatica* (family Dictyotaceae) and representative photograph of thalli of brown seaweed

5.3.2.1 ***Structural characterization of xenicane class of diterpenoid derivatives***

Seaweeds were viewed as promising sources of bioactive metabolites with functional food properties and pharmacological potentials (Plaza et al., 2008; Lann et al., 2016). Natural antioxidants in seaweeds were recognized to deter pathophysiological conditions leading to

oxidative stress conditions and increase the shelf life of food ingredients (Jimenez-Escrig et al., 2001). Among various seaweeds, those belonging to the class Phaeophyceae (brown seaweed) were found to be potential sources of antioxidants and bioactive pharmacophores (Kang et al., 2011; Kindleysides et al., 2012). The brown seaweeds belonging to the family Dictyotaceae were considered as one of the potential sources of biologically active diterpenoid metabolites (Blunt et al., 2009), and among which xenicanes were recognized to be an interesting class of bioactive leads, which were isolated as one of the largest class of diterpenoids in marine organisms, with potential bioactive properties (Faulkner 1998; Viano et al., 2009).

Earlier reports of literature revealed the isolation of xenicane natural products from brown seaweeds *Dilophus fasciola*, *Dilophus spiralis* (Ioannou et al., 2009), *Dictyota sp.* (Viano et al., 2009), and *Padina pavonia* (Awad et al., 2008). Xenicane from the soft coral *Xenia elongata* was the first member of xenicane diterpenoids, and there were reports on further discovery of various bioactive xenia metabolites from the brown seaweeds. The bicyclic framework of xenicanes containing *trans*-fused system of ring A and cyclononane carbocyclic ring B possessing a nine-membered ring were reported from the soft coral, *Xenia elongata* (Vanderah et al., 1997). This unique family of xenia diterpenoids was classified into three main subclasses; xenicanes or xenicins, xeniolides and xeniaphyllanes with bicycle [7.2.0] undecane ring (Groweiss et al., 1983) along with recently reported azamilide with nine-membered monocarbocyclic frame work acylated with $C_{16\text{-}20}$ fatty acids and an opened A ring. There were 53 main reports on xenia isoprenoids with several modifications in the ring and prenyl side chain (Blunt et al., 2009).

Seaweeds were recognized as invaluable marine resources in the Asian continent for use in food and pharmaceuticals (Barrento et al., 2016; Makkar and Chakraborty, 2018a-b). The brown seaweed *Padina sp.* was found to constitute a foremost share in the family Dictyotaceae and about 50 taxa of this genus were reported in various parts of the globe. Among them, *Padina tetrastromatica* (Hauck) (family Dictyotaceae) has been predominant in the Indo-Pacific region (Guiry and Nic-dhonncha, 2003), and there were preliminary reports of their bioactive potentials (Chia et al., 2015; Mohsin et al., 2014). In the search for bioactive diterpenoids from this brown seaweed species, this work described the purification and characterizations of previously undescribed five xenicane class of novaxenicin type diterpenoids (**1**-**2**) bearing cyclonona[*d*]furo[2,3-*b*]pyrandiol and three xeniolide-type diterpenes with octahydrocyclonona[*c*]pyran-3(1*H*)-one backbones (**3**-**5**) from the organic EtOAc/MeOH (ethyl acetate-methanol) extract of the studied seaweed (Figure 5.4) collected from the Gulf-of-Mannar of Peninsular India. The anti-inflammatory and antioxidant potential of the studied compounds were analyzed by different *in vitro* assays, and various physicochemical descriptors were utilized to substantiate the structure-activity correlations of the studied diterpenoids. *In silico* molecular

modelling studies were performed to designate the 5-lipoxygenase inhibitory mechanism of the studied xenicane analogues.

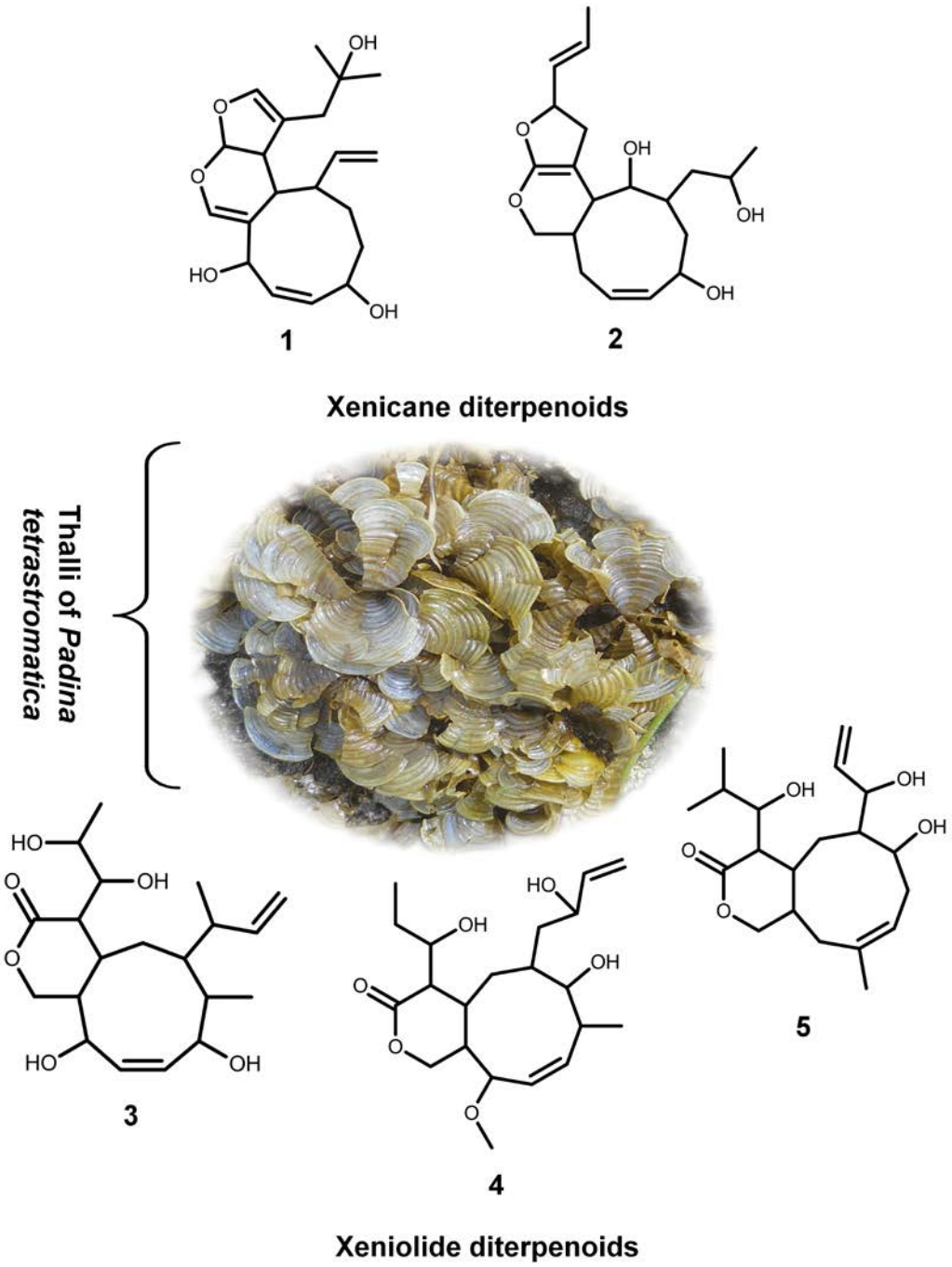

Figure 5.4.: Xenicane class of xenicins (**1-2**) bearing cyclonona[*d*]furo[2,3-*b*]pyrandiol and three xeniolide-type diterpenoids with octahydrocyclonona[*c*]pyran-3(1*H*)-one backbones (**3-5**) isolated from the seaweed *Padina tetrastromatica*.

5.3.2.1a Structural characterization of Compound 1(TP_1)

12-Ethenyl-3a,6,9,10,11,12,12a,12b-octahydro-1-(1^2-hydroxy-1^2-methyl-propyl)-cyclonona[*d*]furo[2,3-*b*]pyran-6,10-diol

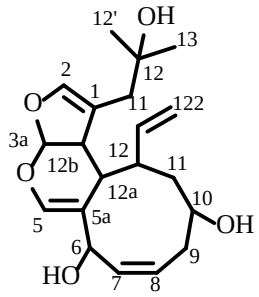

Sample yield	0.28% (> 99% purity, RP-C_{18} HPLC)
Physical description	Colourless oil
Molecular formula	$C_{20}H_{28}O_5$
Molecular mass	348.1937

The xenicane class of diterpenoid derivative, 12-ethenyl-3a,6,9,10,11,12,12a,12b-octahydro-1-(1^2-hydroxy-1^2-methyl-propyl)-cyclonona[*d*]furo[2,3-*b*]pyran-6,10-diol was isolated as colorless oil compound. The compound (**1**) has exhibited UV absorbance (UV (MeOH) λ_{max}) at 249 (2.61) nm (Figure 5.5). The homogeneity of the compound was ascertained by HPLC data on a bonded phase octadecylsilane (C_{18}) stationary phase (RP-C_8 HPLC, MeOH:MeCN, 4:1 v/v): 3.20 min (Figure 5.6).

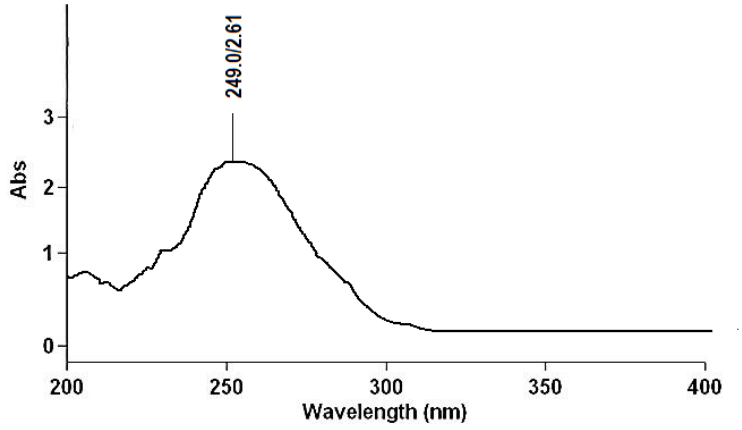

Figure 5.5.: UVspectrum of 12-ethenyl-3a,6,9,10,11,12,12a,12b-octahydro-1-(1^2-hydroxy-1^2-methyl-propyl)-cyclonona[*d*]furo[2,3-*b*]pyran-6,10-diol **(1)**

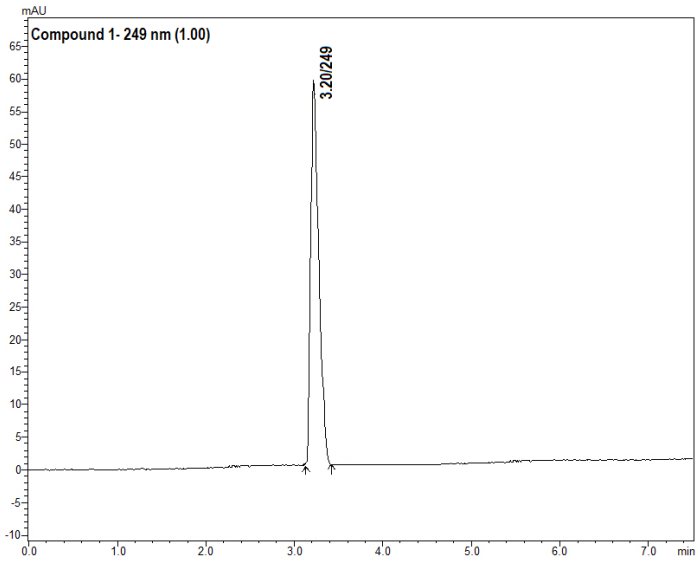

Figure 5.6.: HPLC chromatogram of 12-ethenyl-3a,6,9,10,11,12,12a,12b-octahydro-1-(1^2-hydroxy-1^2-methyl-propyl)-cyclonona[*d*]furo[2,3-*b*]pyran-6,10-diol **(1)**

Repeated chromatographic fractionation of *P. tetrastromatica* yielded compound **1** as a colorless oily substance. The molecular ion peak of **1** was appeared at *m/z* 348, whiles the molecular formula $C_{20}H_{28}O_5$ implying seven unsaturation degrees, and was associated with four olefinic bonds and three ring systems. The molecular ion peak by HRESIMS (positive mode) was found at *m/z* 349.2018 $[M+H]^+$ (Figure 5.6).

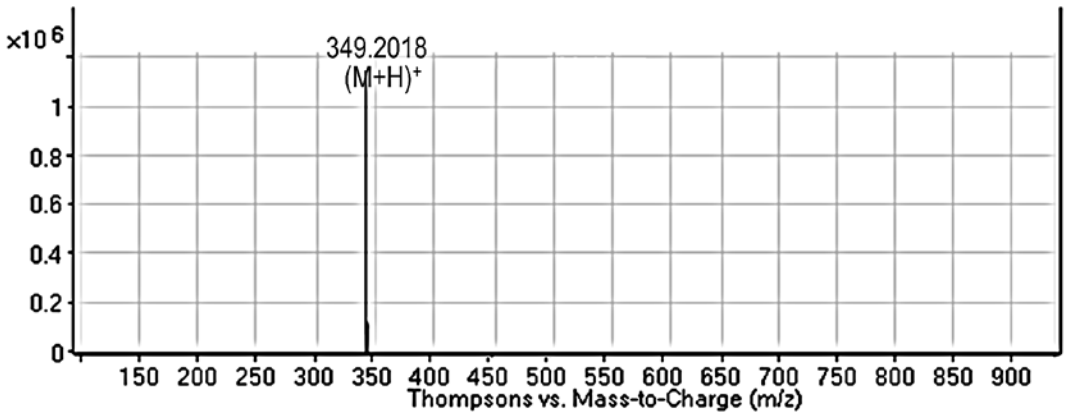

Figure 5.7.: HRESIMS of 12-ethenyl-3a,6,9,10,11,12,12a,12b-octahydro-1-(1^2-hydroxy-1^2-methyl-propyl)-cyclonona[*d*]furo[2,3-*b*]pyran-6,10-diol **(1)**

The ^{13}C-NMR and DEPT$_{135}$ experiments attributed the presence of 20 carbon signals, which included the presence of two methyls (δ29.53, 29.54), three sp^3 methylenes (δ 38.67, 41.42, 39.96), one sp^2 methylene (δ 116.46), six sp^3 methines (δ 104.24, 49.82, 39.94, 48.95, 70.27, 70.26), four sp^2 methines (δ 144.10, 133.29, 125.48, 141.92), along with one sp^3 (δ 73.30) and two sp^2 (δ 115.36, 115.25) quaternary carbons. The FTIR spectrum of **1** displayed absorption bands at 3472 cm^{-1} (-OH), 890 cm^{-1} (=CH$_2$) and 1112/1076 cm^{-1} (-C-O-C) (Figure 5.7), which were corroborated by ^{13}C-NMR resonances at δ 70.26, 70.27, 73.30, 29.53, 29.54, and 104.24.

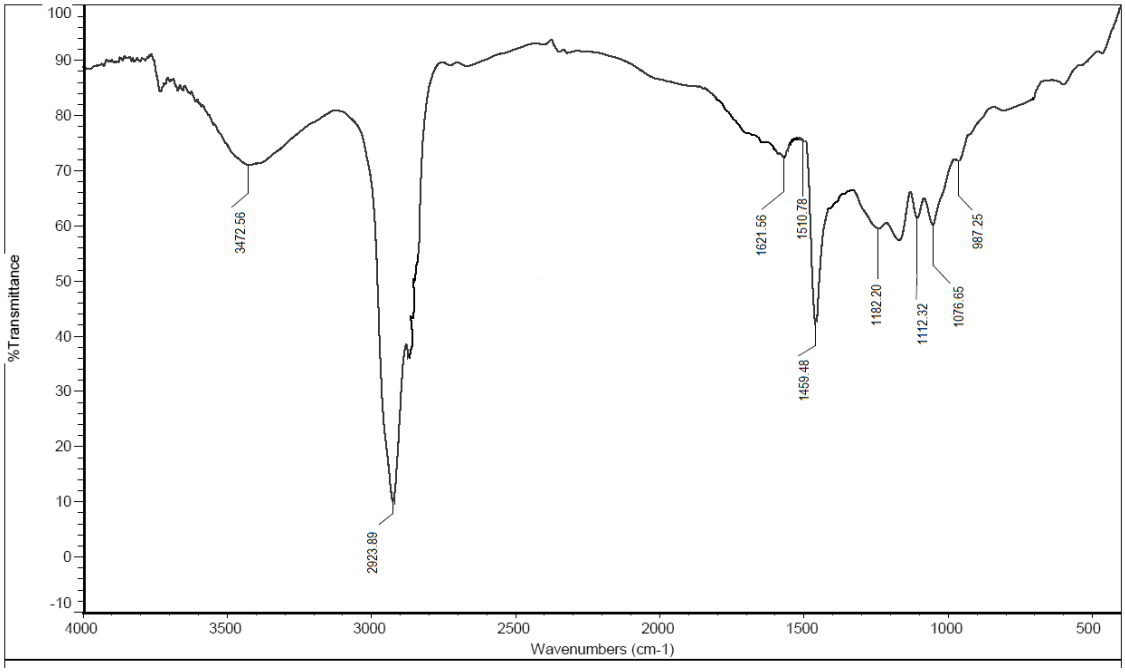

Figure 5.7.: FTIR of 12-ethenyl-3a,6,9,10,11,12,12a,12b-octahydro-1-(1^2-hydroxy-1^2-methyl-propyl)-cyclonona[*d*]furo[2,3-*b*]pyran-6,10-diol **(1)**

The lack of carbonyl absorption bands in the FTIR and the absence of signals above δ 150 in ^{13}C spectrum of **1** appropriately attributed that the all oxygen functionalities within the system might be in the form of ether or hydroxyl groups, which were also corroborated by an earlier report of literature (Bishara et al., 2006). The ^{13}C/^{1}H-NMR experiments indicated the presence of vinylic group due to the signals associated with δ 141.08/δ 5.72 (m) along with δ116.46/ 5.00, 4.99, which found resemblance with the values of exocyclic double bond of the novaxenicin framework (Bishara et al., 2006) (Figure 5.8-5.10; Table 5.4). The presence of two each of tri-substituted double bonds (δ115.36 and 115.25) and oxymethine (-O-CH<) groups (δ 141.92, 144.10 and δ 6.37, 6.41), along with one each of dioxymethine (-O-CH-O-) (δ 104.24/δ 6.06) and tert-alcohol functionality (δ 73.30) attributed the presence of novaxenicin framework (Bishara et al., 2006).

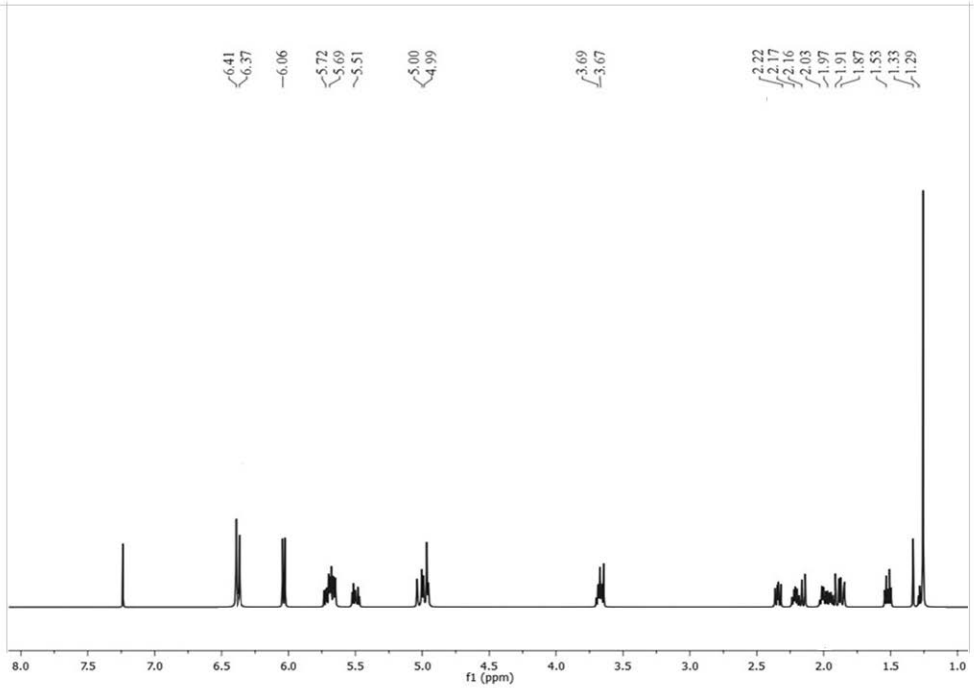

Figure 5.8.: ^{1}H NMR spectrum of 12-ethenyl-3a,6,9,10,11,12,12a,12b-octahydro-1-(1^{2}-hydroxy-1^{2}-methyl-propyl)-cyclonona[*d*]furo[2,3-*b*]pyran-6,10-diol **(1)**

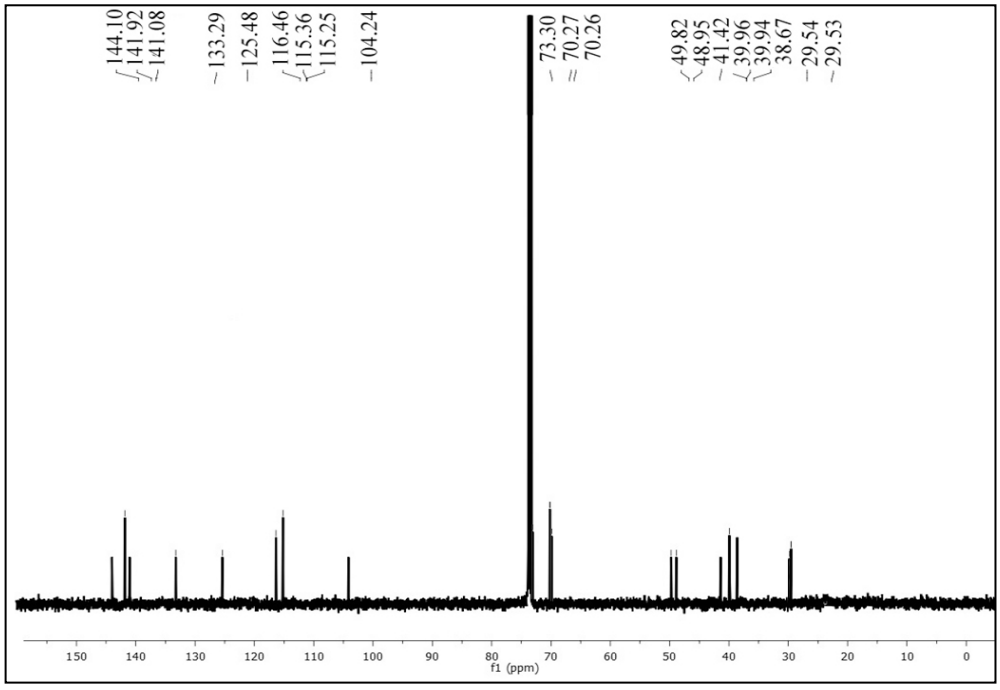

Figure 5.9.: ^{13} C NMR spectrum of 12-ethenyl-3a,6,9,10,11,12,12a,12b-octahydro-1-(1^{2}-hydroxy-1^{2}-methyl-propyl)-cyclonona[*d*]furo[2,3-*b*]pyran-6,10-diol **(1)**

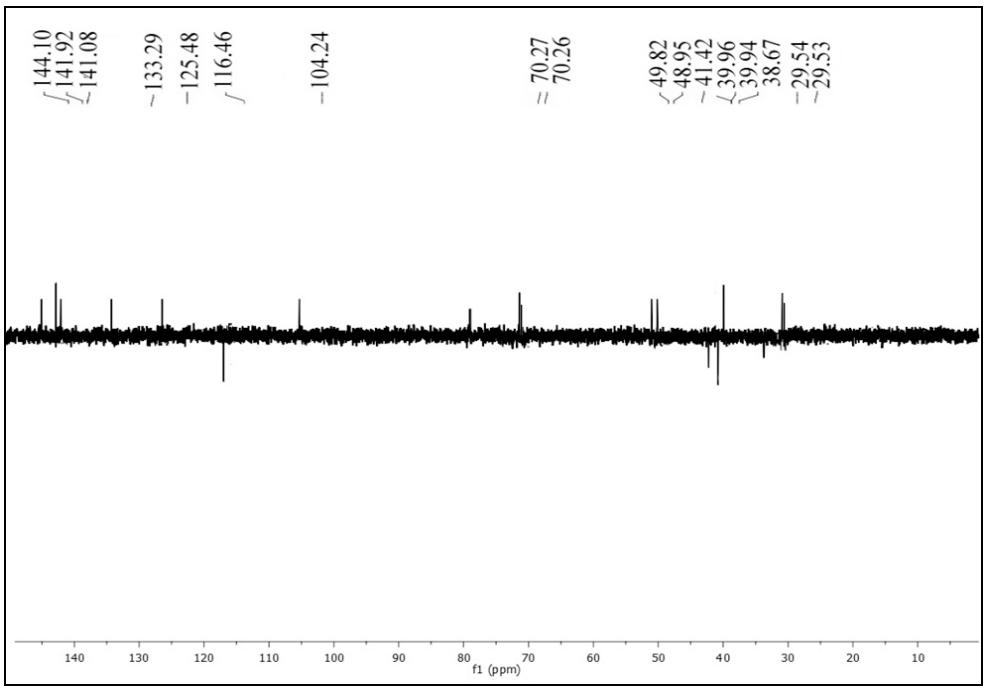

Figure 5.10.: [135] DEPT NMR spectrum of 12-ethenyl-3a,6,9,10,11,12,12a,12b-octahydro-1-(1^2-hydroxy-1^2-methyl-propyl)-cyclonona[*d*]furo[2,3-*b*]pyran-6,10-diol **(1)**

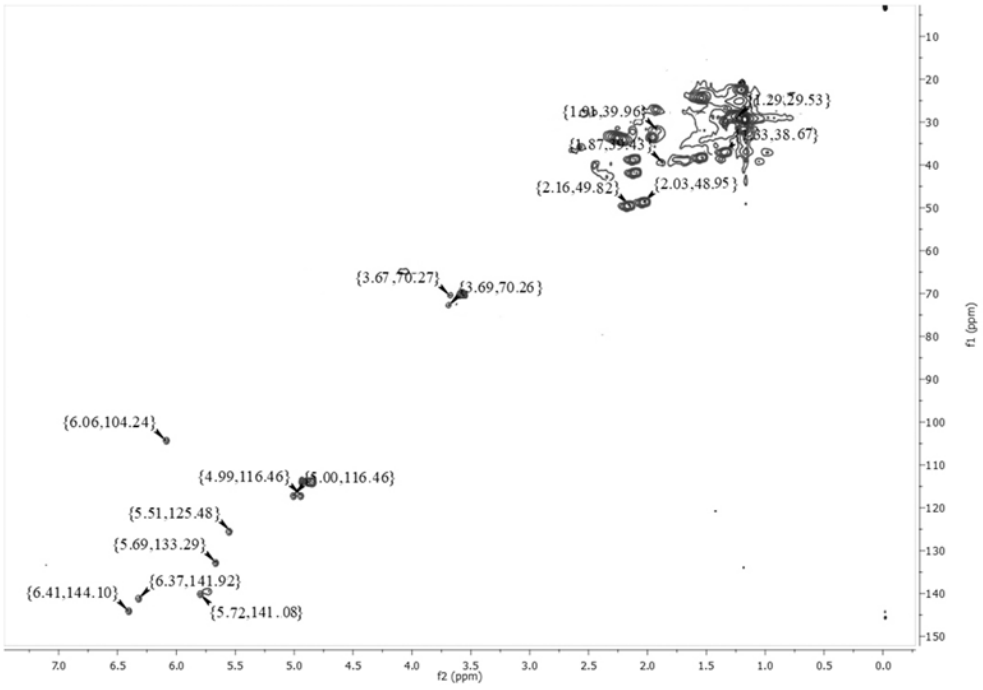

Figure 5.11.: HSQC spectrum of 12-ethenyl-3a,6,9,10,11,12,12a,12b-octahydro-1-(1^2-hydroxy-1^2-methyl-propyl)-cyclonona[*d*]furo[2,3-*b*]pyran-6,10-diol **(1)**

Carbon signals at δ 144.10, 141.92, 104.24, 70.27, 70.26, and 73.30 supported the presence of oxygen functionalities, and these might be due to the presence of oxymethine (-O-CH=, -O-CH<) or hydroxyl groups in **1.** The interchangeable hydroxyl protons at 70.27 (δ 3.67), 70.26 (δ 3.69) and 73.30 were ceased to exist upon interchange of D_2O asserting the existence of hydroxyl groups in its vicinity. The COSYs between the protons δ 6.06/2.17 in **1** along with HMBCs at δ 6.41/115.36; 1.87/115.36; 2.17/104.24; 6.06/39.94 and 6.06/144.10 proposed 6-membered ring system in **1**, which was identified as dihydro-*2H*-pyran ring system. Similarly, COSYs between the protons at δ 1.87/2.03/1.33 and 3.67/2.22/5.51 along with HMBCs δ 1.87/48.95; 1.33/70.27; 3.67/41.42/125.48; 2.22/125.48; 5.69/70.26; 3.69/125.48; 3.69/115.36, and 1.87/115.36 proposed a closed loop of 9-membered ring in **1** (Figure 5.12-5.13).

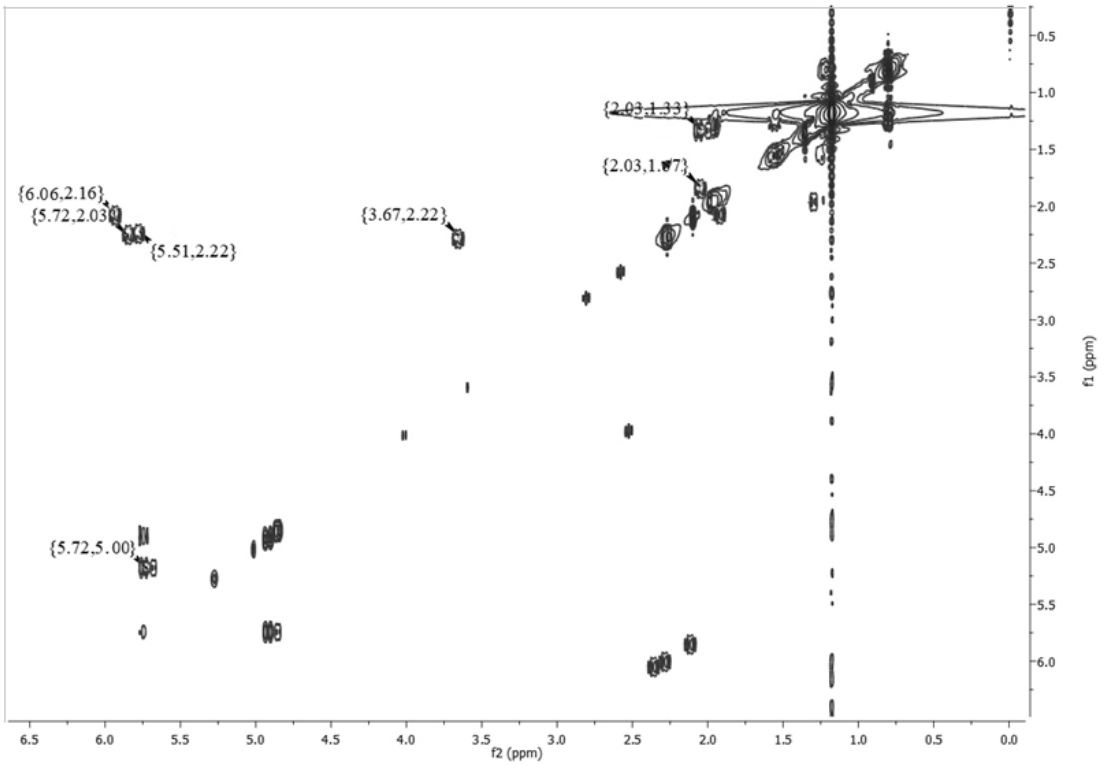

Figure 5.12.: ^{1}H-^{1}H COSY spectrum of 12-ethenyl-3a,6,9,10,11,12,12a,12b-octahydro-1-(1^2-hydroxy-1^2-methyl-propyl)-cyclonona[*d*]furo[2,3-*b*]pyran-6,10-diol **(1)**

Thus, the positions of carbons in dihydro-*2H*-pyran with cyclononane systems were assigned from C-5 to C-5a, continuously, on the basis of earlier literature (Ioannou et al., 2009; Bishara et al., 2006). The signals at C-12a (δ 39.94) and C-5a (δ 70.26) were identified as ring junctions based on earlier reports (Bishara et al., 2006). The COSYs of protons δ 6.06/2.17 including HMBCs at δ 6.06/141.92; 6.06/115.25; 6.37/141.92 and 2.16/115.25 proposed 5-membered ring in

1, designated as dihydrofuran. Deshielded signals at δ 104.24, 141.92 and 115.25 assigned the presence of oxymethine (-O-CH<, -O-CH=) and alkenic functionalities in **1** as the part of dihydrofuran skeleton. Thus, the positions of carbons in dihydrofuran were disposed as C-3a, 12b, 1 and 2 based on spectroscopic assignments and previous report of literature (Bishara et al., 2006). The carbons C-3a and C-12b were common to both dihydro-2H-pyran and dihydrofuran systems. Three cyclic systems, dihydrofuran, dihydro-2*H*-pyran and cyclononane in the tricyclic system were designated as **A, B** and **C**, respectively. Hence **A-B-C** tricyclic ring system was found to possess three spin systems, designated as **I-III** (H-3a/H-12b; H-12a/12/11, H-12/12^1/12^2; H-10/9/8) (depicted as bold in Figure 5.14).

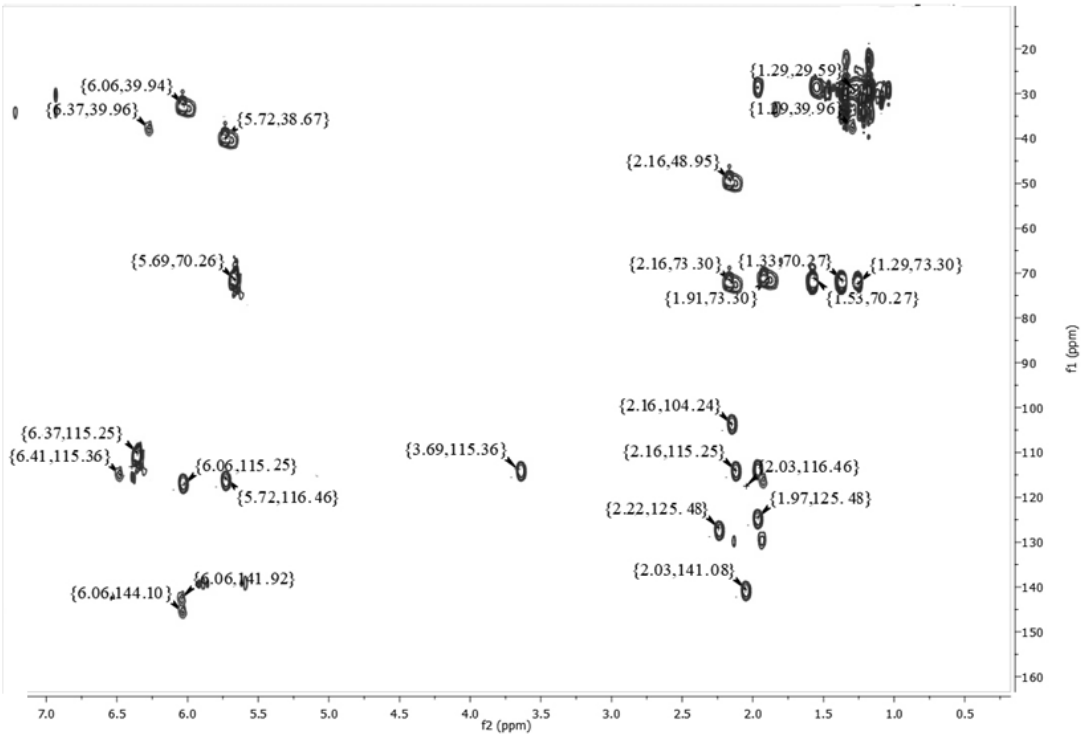

Figure 5.13.: HMBC spectrum of 12-ethenyl-3a,6,9,10,11,12,12a,12b-octahydro-1-(1^2-hydroxy-1^2-methyl-propyl)-cyclonona[*d*]furo[2,3-*b*]pyran-6,10-diol **(1)**

The moiety **I** included a carbinolic proton (δ 4.96, δ 70.26) connected with two double bond methines that was coupled with a relatively deshielded methylene at δ 2.22 and 1.97, which in turn were coupled with a sequence of protons due to carbinolic (δ 5.51, δ 125.48), methylene (δ 1.33, 1.53), allylic methine (δ 2.03), one double bond methine (δ 5.72) and double bond methylene (δ 5.00) groups. A series of $^{1,3}J_{H\text{-}C}$ correlations by HMBC were found to assemble the fragments, and to draw the planer structure of **1**.

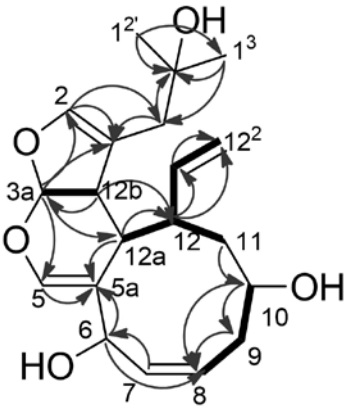

Figure 5.14.: Prominent ^{1}H-^{1}H COSY, and selected HMBC correlations of 12-ethenyl-3a,6,9,10,11,12,12a,12b-octahydro-1-(1^2-hydroxy-1^2-methyl-propyl)-cyclonona[*d*]furo[2,3-*b*]pyran-6,10-diol **(1)**. The key ^{1}H-^{1}H COSY couplings were represented in bold face bonds. The key HMBC couplings have been represented by double barbed arrows.

The COSYs between δ 6.06/2.17 (H-3a/H-12b) along with HMBCs from δ 6.06 (H-3a) to δ 144.10 (C-5), δ 39.94 (C-12a), δ 115.25 (C-1) and δ 141.92 (C-2) and methine proton H-12b linked (δ 2.17) to δ 104.24 (C-3a) and δ 48.95 (C-12) portrayed the spin systems of **I** and **II**. The HMBCs from oxymethine protons of dihydrofuran H-2 (δ 6.37) to C-5 (δ 115.25) and C-1^1 (96) allocated the occurrence of side chain 2-methylpropan-2-ol. The methylene protons H-1^1 (δ 2.16/1.91), methyl protons H-1$^{2'}$ (δ 1.29) and H-1^3 (δ 1.29) were associated with 2-methylpropan-2-ol displaying correlations to C-1 (δ 115.25), C-1^2 (δ 73.30), C-1^3 (δ 29.54), and C-1^1 (δ 39.96). With the aid of these HMBCs the occurrence of **A** ring was assigned, and among them carbons C-3a, and 12b were involved in cyclic system **B**. Two terminal methyls at C-1^2 resonating at δ 1.29 (C-1$^{2'}$) and δ 1.29 (C-1^3) were geminal, and were assigned by HMBCs of δ 1.29/δ 29.53 (H-1$^{2'}$/C-1^3), δ 1.29/δ 73.30 (H-1$^{2'}$/H-1^2), and between δ 1.29/ 73.30 (H-1^3/C-1^2). This spectral information was in good agreement with that of an earlier report (Bishara et al., 2006). The presence of COSYs between H-12a/H-12 (δ 1.87/δ 2.03), H-12/H-11 (δ 2.03/ 1.33), H-12/H-9 (δ 2.03/ 2.22) and H-12^1/H-12^2 (δ 5.72/5.00) depicted the presence of second spin **II**, which displayed HMBCs between the spins **II** and **III**. The connection of spin unit **II** and ring **B** was made by HMBCs between H-12b (δ 2.17)/ C-6 (δ 48.95) and H-12a (δ 1.87)/C-12 (δ 48.95), which constituted the part of cyclononane ring **C.** The correlation of exocyclic alkene to ring **C** was attributed by HMBCs between δ 2.01/δ 141.10 (H-12/C-12^1), δ 5.72/116.46 (H-12^1/C-12^2), δ 5.72/ δ 38.67 (H-12^1/C-11) and δ 2.03/116.46 (H-12/C-12^2). The COSYs of δ 3.67/2.22 (H-10/H-9), and δ 2.22/5.51 (H-9/H-8), suggested the third spin system **III**. The presence of olefinic bond in the ring **C** was in accordance with the terminal alkene in the previously reported xenia diterpenoids (Ioannou et al., 2009). The connection of COSY spin system **C** and ring **B** at C-12a and C-5a was allocated by strong HMBCs between dioxymethine proton at δ 6.41/δ 115.36 (H-5/C-5a) and δ 1.87/115.36 (H-12a/C-5a). These HMBCs designated the

occurrence of ring **B** among which C-12a and C-5a were also involved in ring **C**. The COSY spectrum exhibited the occurrence of three spin systems and HMBCs linked to the three spin systems together, allowing the assignment of the planar structure.

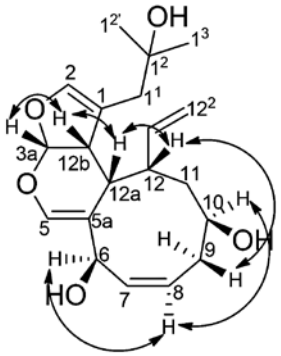

Figure 5.15.: Prominent NOE correlations of 12-ethenyl-3a,6,9,10,11,12,12a,12b-octahydro-1-(1^2-hydroxy-1^2-methyl-propyl)-cyclonona[*d*]furo[2,3-*b*]pyran-6,10-diol **(1)**. NOESY relations are represented by double-tailed arrows

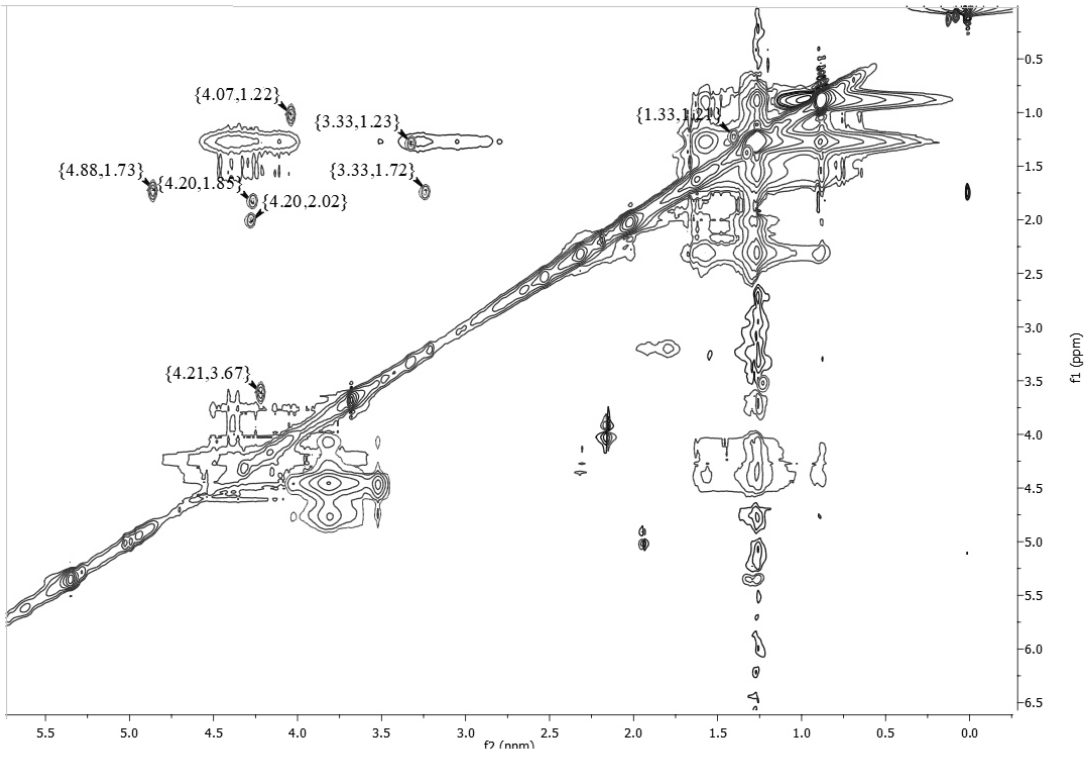

Figure 5.16.: NOE correlations of 12-ethenyl-3a,6,9,10,11,12,12a,12b-octahydro-1-(1^2-hydroxy-1^2-methyl-propyl)-cyclonona[*d*]furo[2,3-*b*]pyran-6,10-diol **(1)**.

The investigations on relative stereochemistry of the xenicin derivative were explained by NOESY experiments and coupling constants. A *trans* arrangement for the H-12a, H-5a was

assigned by comparison of coupling constants recorded in previous reports (Bishara et al., 2006). The proton at δ 6.06 (H-3a) was displayed NOE with protons at H-12b (δ 2.17). Similarly protons at H-12b (δ1.87), H-12a (δ1.87) and H-12 (δ 2.03) (Figure 5.15 & 5.16) exhibited NOEs with protons at H-12a (δ 1.87), H-12 (δ 2.03) and H-9 (δ 2.22), which were aligned in the β -plane of compound (**1**) (Tanaka et al., 1994). The assigned stereochemistry of hydroxyl group at C-10 and C-8 was in agreement with β -oriented protons. The chiral centers, mainly those of H-3a, 12b, 12a, 10 and H-6 were attributed by NOEs between H-3a/12b (δ 6.06/δ 2.17), H-12b/12a (δ 2.17/1.87), H-8/10 (δ 5.51/ 3.67) and H-8/6 (δ 5.51/3.69). Contrary to this β-orientation, the protons at H-8/10 (δ 5.51/δ 3.67) and H-8/6 (δ 5.51/3.69) were located at the α-side of the compound **1**.

Table 5.4.: NMR spectroscopic data[a] of 2-ethenyl-3a,6,9,10,11,12,12a,12b-octahydro-1-(1^2-hydroxy-1^2-methyl-propyl)-cyclonona[*d*]furo[2,3-*b*]pyran-6,10-diol (**1**) isolated from brown seaweed *P.tetrastromatica*

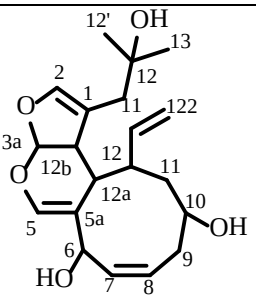

Compound **1**……..2-ethenyl-3a,6,9,10,11,12,12a,12b-octahydro-1-(1^2-hydroxy-1^2-methyl-propyl)-cyclonona[*d*]furo[2,3-*b*]pyran-6,10-diol (**1**)

C. No.	^{13}C NMR	^{1}H NMR (int., mult., J in Hz)[b]	COSY	HMB C
1	115.25	-	-	-
1^1	39.96	2.16 (1H, d, J=9.09 Hz) 1.91 (1H, d, J=8.47 Hz)	-	C-1,1^2
1^2	73.30	-	-	
$1^{2'}$	29.53	1.29 (3H, s)	-	C-1^3, 1^2
1^3	29.54	1.29 (3H, s)	-	C-1^2, 1^1
2	141.92	6.37 (1H, s)	-	C-1^1, 1
3	-	-	-	-
3a	104.24	6.06 (1H, d, J=10.74 Hz)	H-12b	C-12a,5,1,2
4	-	-	-	-
5	144.10	6.41 (1H, s)	-	C-5a
5a	115.36	-	-	-
6	70.26	3.69 (1H, d, J=14.70 Hz)	-	C-8, 5b
7	133.29	5.69 (1H, m)	H-6	C-6
8	125.48	5.51 (1H, m)	H-7	-
9	41.42	2.22 (1H, m), 1.97 (1H, m)	H-8	C-8
10	70.27	3.67 (1H, m)	H-9	C-9,8
11	38.67	1.33 (1H, m), 1.53 (1H, m)	-	C-10
12	48.95	2.03 (1H, dd, J= 12.35, 5.92)	H-11,12^1	C-12^1,12^2

12^1	141.08	5.72 (1H, m)	H-12^2	C-12^2, 11
12^2	116.46	5.00 (1H, d, J=13.79 Hz) 4.99 (1H, d, J=12.91 Hz)	-	-
12a	39.94	1.87 (1H, d, J=12.62)	H-6	C-12,5a
12b	49.82	2.17 (1H, dd, J=10.99, 8.86 Hz)	-	C-12,3a,1

[a]NMR spectra were recorded using a B ruker AVANCE III 500 MHz (AV 500) spectrometer (B ruker, Karlsruhe, Germany) in $CDCl_3$ as aprotic solvent at ambient temperature with TMS as the internal standard (δ 0 ppm).

[b]Values in ppm, multiplicity and coupling constants (J=Hz) were indicated in parentheses. Multiplicities were allocated by ^{135}DEPT NMR spectrum.

The assignments were made with the aid of the COSY, HSQC, HMB C and NOESY experiments.

The molecular ion peak of **1** was appeared at *m/z* 348 and base peak was ontained at *m/z* 41.0 (Figure 5.18 and 5.19).

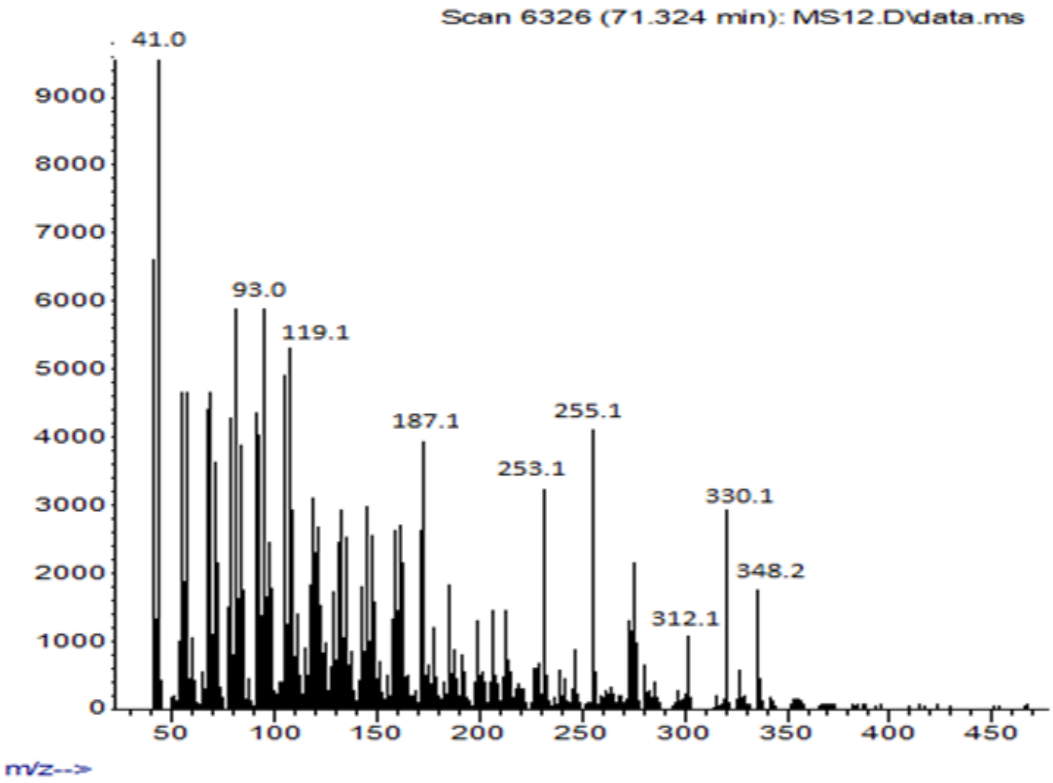

Figure 5.17.: EI-MS spectrum of 6-methoxy-dolabella-8(17),12-diene-10β ,18-diol (**1**)

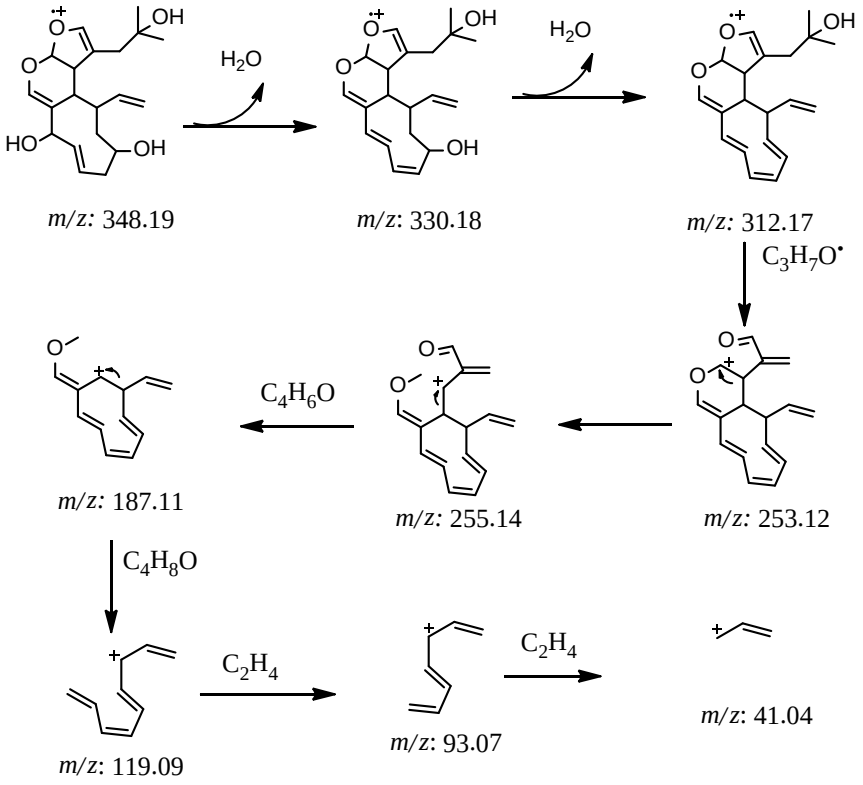

Figure 5.18.: Tentative mass fragmentation pattern of 6-methoxy-dolabella-8(17),12-diene-10β ,18-diol (**1**)

5.3.2.1b Structural characterization of Compound 2 (TP_2)

1,2,5,5a,6,9,10,11,12,12a-Decahydro-11(11^2-hydroxypropyl)-2-[(*E*)-2^1-propenyl] cyclonona[*d*]-furo[2,3-*b*]pyran-9,12-diol

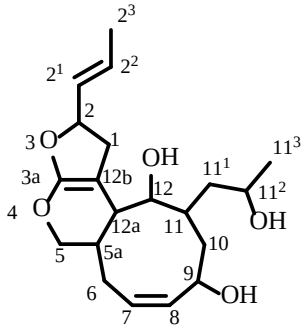

Sample yield	0.26% (> 99% purity, RP-C_{18} HPLC)
Physical description	Yellow oil
Molecular formula	$C_{20}H_{30}O_5$

Molecular mass	350.2093

The xenicane class of diterpenoid derivative, 1,2,5,5a,6,9,10,11,12,12a-Decahydro-11(11^2-hydroxypropyl)-2-[(*E*)-2^1-propenyl] cyclonona[*d*]-furo[2,3-*b*]pyran-9,12-diol was isolated as Colorless oil compound. The compound (**2**) has exhibited UV absorbance (UV (MeOH) λ_{max}) at 235 (3.1), 254 (3.7) nm (Figure 5.19). The homogeneity of the compound was ascertained by HPLC data on a bonded phase octadecylsilane (C_{18}) stationary phase (RP-C_8 HPLC, MeOH:MeCN, 4:1 v/v): 3.24 min (Figure 5.20).

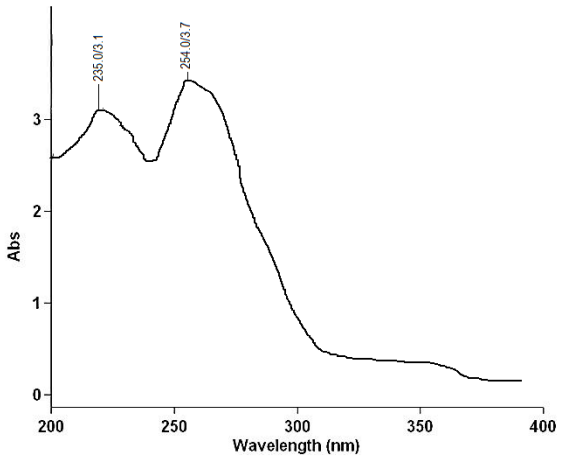

Figure 5.19.: UV spectrum of 1,2,5,5a,6,9,10,11,12,12a-decahydro-11(11^2-hydroxypropyl)-2-[(*E*)-2^1-propenyl] cyclonona[*d*]-furo[2,3-*b*]pyran-9,12-diol (**2**)

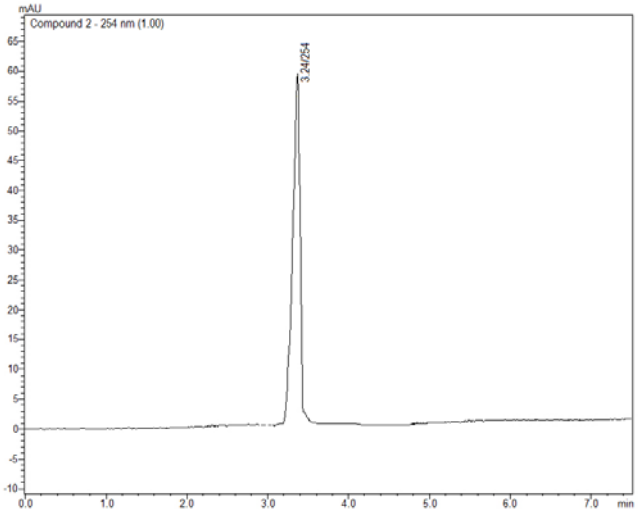

Figure 5.20.: HPLC chromatogram of 1,2,5,5a,6,9,10,11,12,12a-decahydro-11(11^2-hydroxypropyl)-2-[(*E*)-2^1-propenyl] cyclonona[*d*]-furo[2,3-*b*]pyran-9,12-diol (**2**)

The chromatographic separation of the solvent extract of *P. tetrastromatica* yielded **2** as a yellow oil. The molecular ion peak of **2** was appeared at *m/z* 350, while the molecular formula $C_{20}H_{30}O_5$, implying six unsaturation degrees, was associated with three olefinic bonds and three ring systems. The molecular ion peak by HRESIMS was observed at *m/z* 351.2175 $[M+H]^+$ (Figure 5.21). The FTIR spectrum of **2** displayed absorption bands at 3452 (O-H) and 1220 (C-O), (Figure 5.22)

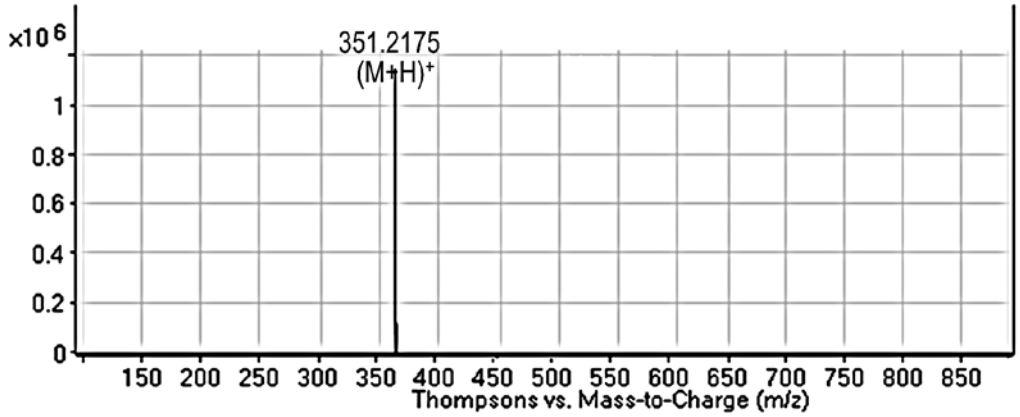

Figure 5.21.: HRESIMS of 1,2,5,5a,6,9,10,11,12,12a-decahydro-11(11^2-hydroxypropyl)-2-[(*E*)-2^1-propenyl] cyclonona[*d*]-furo[2,3-*b*]pyran-9,12-diol (**2**)

The ^{13}C-NMR of **2** along with $DEPT_{135}$ attributed the occurrence of 20 signals of carbons, which included two methyls (δ 17.65, 23.97), five sp^3 methylenes (δ 68.37, 39.54, 33.72, 37.74, 43.94), seven sp^3 methines (δ 41.36, 71.82, 38.69, 72.13, 36.15, 83.18, 67.75), four sp^2 methines (δ 132.60, 132.05, 129.17, 130.77), along with two sp^2 (δ 163.12, 94.31) quaternary carbons. The interchangeable hydroxyl protons at δ 71.82 (δ 3.33), δ 72.13 (δ 4.20) and δ 67.75 (δ 4.07) disappeared upon D_2O interchange, which ascribed the presence of hydroxyl groups in its vicinity (Figure 5.22-5.26). The HMBCs at δ 3.67/163.12; 1.72/163.12; 1.72/36.15; and 3.67/36.15 proposed the 6-membered ring in **2**, which was designated as dihydro-2*H*-pyran. The occurrence of deshielded signals at δ 94.31, 163.12 and 68.37 suggested the existence of alkenic functionalities and oxygenated carbons in **2** as the part dihydro-2*H*-pyran in **2**. Similarly, COSYs between protons at δ 1.72/3.33/1.22 and 5.62/2.01/1.85 along with HMBCs at δ1.72/33.72; 2.01/71.82; 1.29/71.82/72.13; 4.20/132.63; 5.67/132.05 and 2.01/132.05 assigned the 9-membered ring in **2**. The COSYs of protons δ 2.68/4.88 including HMBCs at δ 2.68/94.31/163.12; 4.88/37.74 reckoned the 5-membered ring in **2** (Figure 5.27-5.29). Deshielded signals at δ 163.12 and 94.31 attributed the alkenic and oxygenated carbons in **2** as the part of dihydrofuran (positions were assigned as C-3, 4, 12 and 13). The COSYs between H-2/H-2^1 (δ 4.88/5.69), H-2/H-1 (δ 4.88/2.30) and HMBCs at H-2/C-2^1 (δ 4.88/ δ 129.17), H-2/C-1 (δ 4.88/δ 37.74) depicted the presence of dioxymethine group in **2** (Bishara

et al., 2006). Particularly, compounds **1** and **2** exhibited similarities in their structures excluding the substitutions at C-2 and C-11. In **2**, a carbon side chain with modifications was attached to C-2.

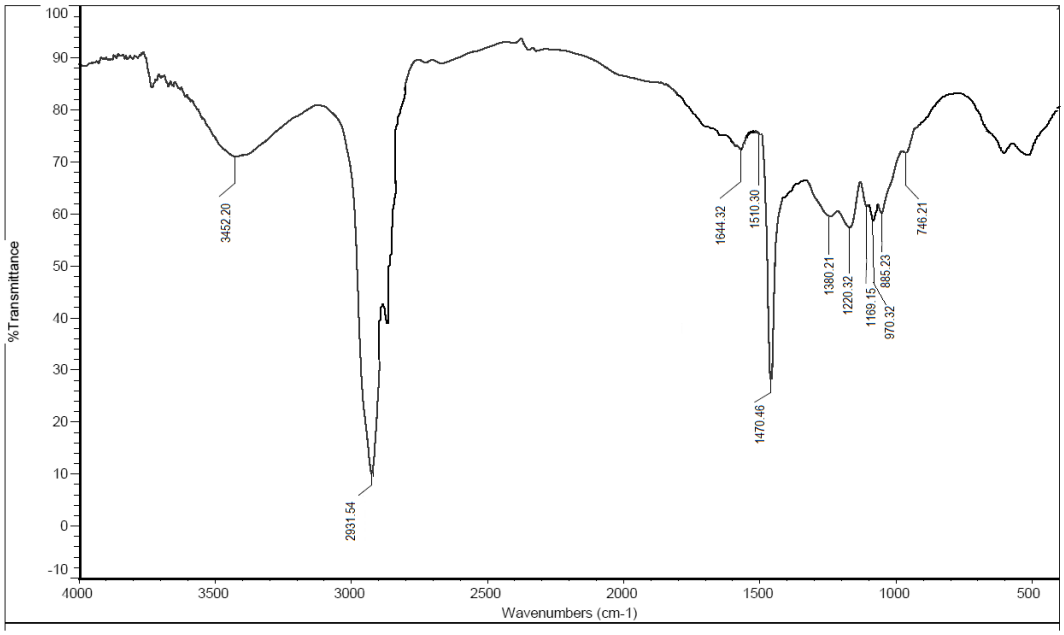

Figure 5.22.: FTIR spectrum of 1,2,5,5a,6,9,10,11,12,12a-decahydro-11(11^2-hydroxypropyl)-2-[(*E*)-2^1-propenyl] cyclonona[*d*]-furo[2,3-*b*]pyran-9,12-diol (**2**)

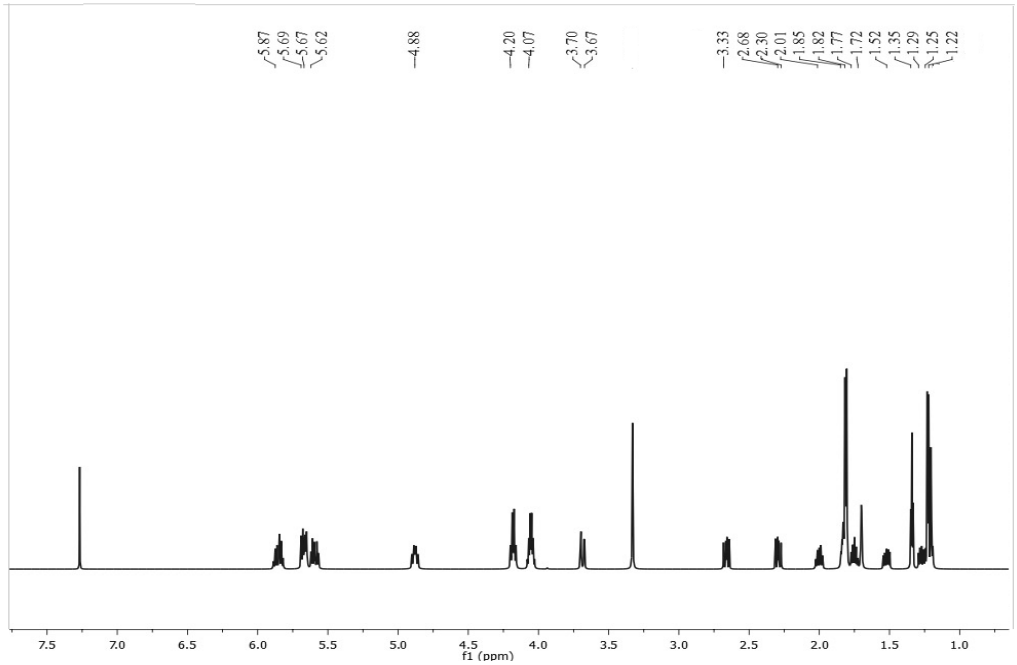

Figure 5.23.: ^{1}H NMR spectrum of 1,2,5,5a,6,9,10,11,12,12a-decahydro-11(11^2-hydroxypropyl)-2-[(*E*)-2^1-propenyl] cyclonona[*d*]-furo[2,3-*b*]pyran-9,12-diol (**2**)

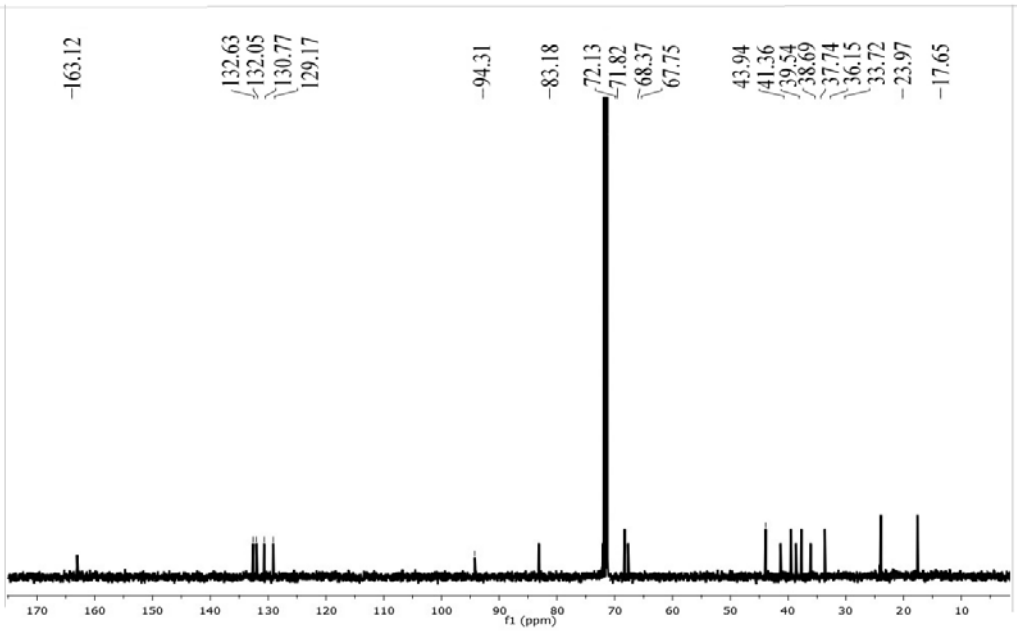

Figure 5.24.: ^{13}C NMR spectrum of 1,2,5,5a,6,9,10,11,12,12a-decahydro-11(11^{2}-hydroxypropyl)-2-[(*E*)-2^{1}-propenyl] cyclonona[*d*]-furo[2,3-*b*]pyran-9,12-diol (**2**)

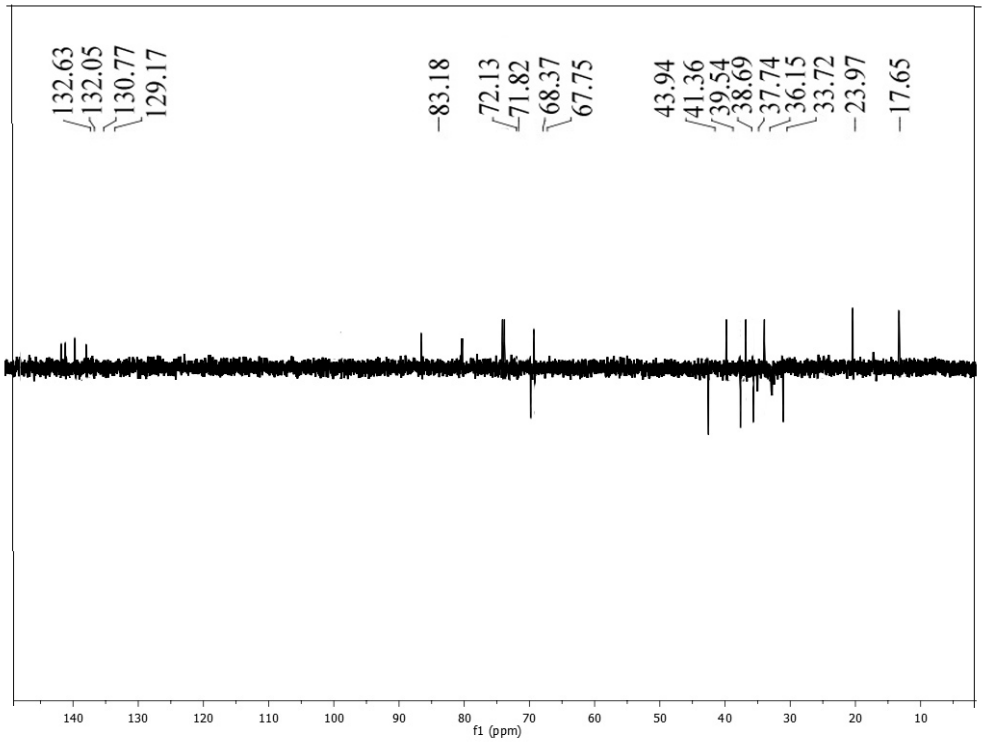

Figure 5.25.: ^{135}DEPT NMR spectrum of 1,2,5,5a,6,9,10,11,12,12a-decahydro-11(11^{2}-hydroxypropyl)-2-[(*E*)-2^{1}-propenyl] cyclonona[*d*]-furo[2,3-*b*]pyran-9,12-diol (**2**)

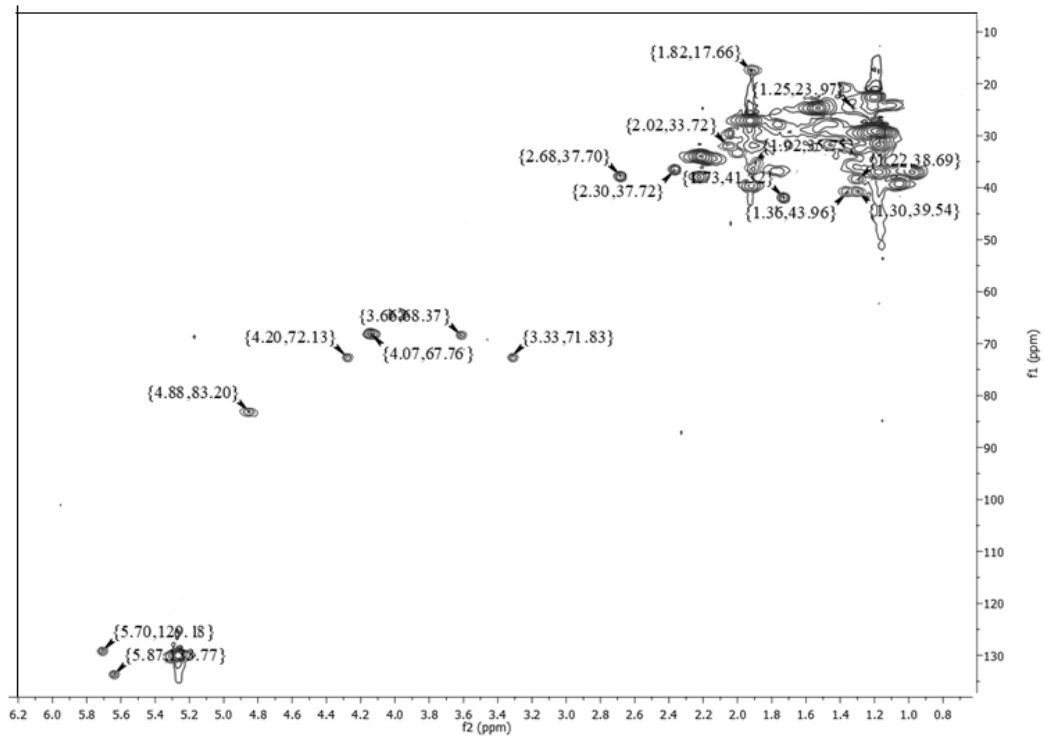

Figure 5.26.: HSQC spectrum of 1,2,5,5a,6,9,10,11,12,12a-decahydro-11(11^2-hydroxypropyl)-2-[(*E*)-2^1-propenyl] cyclonona[*d*]-furo[2,3-*b*]pyran-9,12-diol (**2**)

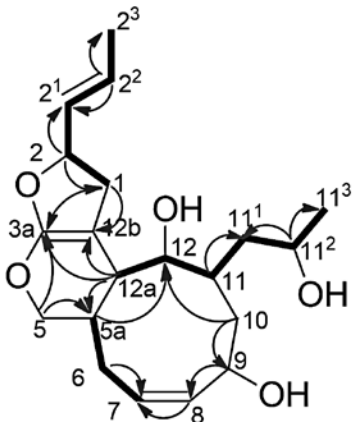

Figure 5.27.: Prominent ^{1}H-^{1}H COSY, and selected HMBC correlations of 1,2,5,5a,6,9,10,11,12,12a-decahydro-11(11^2-hydroxypropyl)-2-[(*E*)-2^1-propenyl] cyclonona[*d*]-furo[2,3-*b*]pyran-9,12-diol (**2**). The key ^{1}H-^{1}H COSY couplings were represented in bold face bonds. The key HMBC couplings have been represented by double barbed arrows.

The location of double bond was also shifted to C-3a/C-12b in **2**, wherein the extra substitution of propan-2-ol, and the arrangement of hydroxyls were different in **2** as compared to those found in **1**, and that these attributions were confirmed by three COSY spins (**I-III**) and

HMBCs. The COSY spectrum revealed the existence of three spin units (**I-III**) that were connected together by HMBCs in the tricyclic system, affirming the planer structure of **2**. The side chains prop-2-ene and propan-2-ol linked to the tricyclic ring system were supported by the spin systems **I** and **II**. The ^{1}H and ^{13}C-NMR experiments disclosed higher resemblance of **2** with **1**, in that former owned the similar tricyclic system, but varied in composition of the side chain.

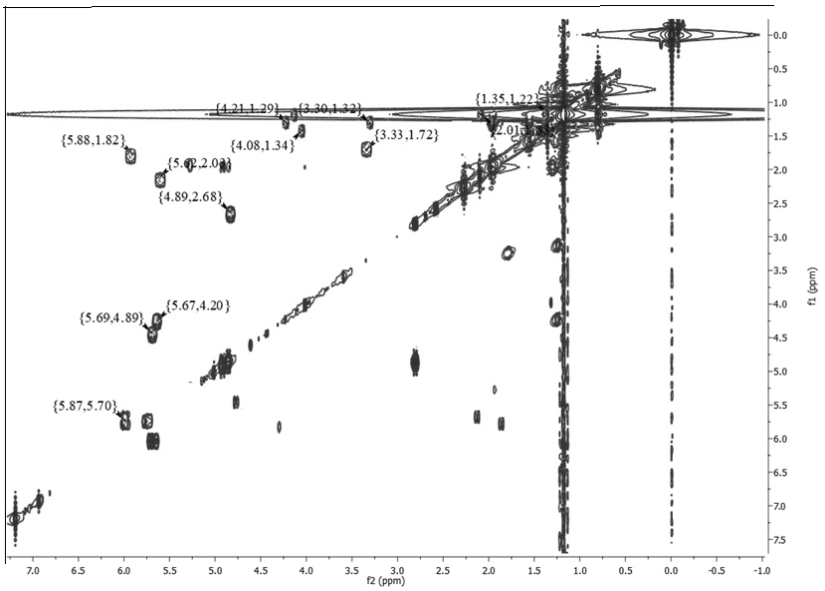

Figure 5.28.: ^{1}H-^{1}H COSY spectrum of 1,2,5,5a,6,9,10,11,12,12a-decahydro-11(11^{2}-hydroxypropyl)-2-[(*E*)-2^{1}-propenyl] cyclonona[*d*]-furo[2,3-*b*]pyran-9,12-diol (**2**)

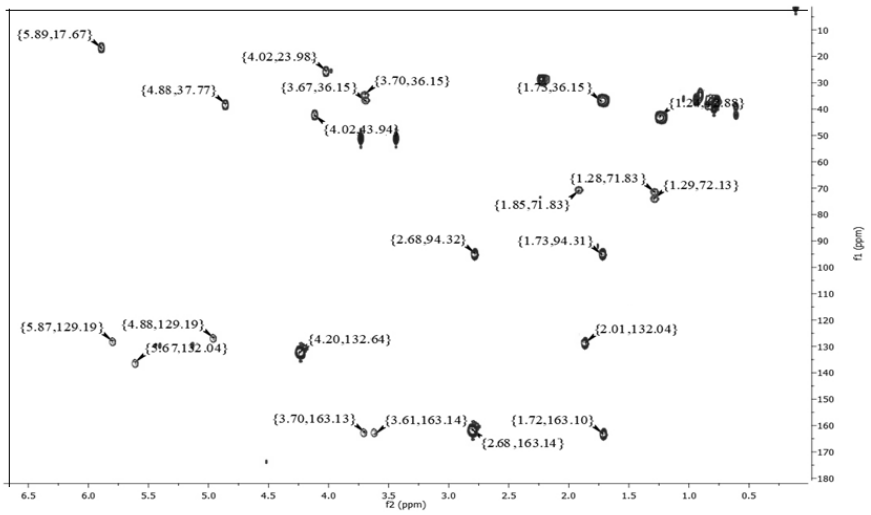

Figure 5.29.: HMBC spectrum of 1,2,5,5a,6,9,10,11,12,12a-decahydro-11(11^{2}-hydroxypropyl)-2-[(*E*)-2^{1}-propenyl] cyclonona[*d*]-furo[2,3-*b*]pyran-9,12-diol (**2**)

Relative stereochemistries of **2** were demonstrated with NOESY interactions, wherein the correlations between δ 4.88/1.72 (H-2/12a), δ 1.72/3.33 (H-12a/5), δ 3.33/1.22 (H-1/11), δ 1.22/1.35 (H-11/11^1) and δ 1.22/4.07 (H-11/11^2) revealed the presence of these protons on the similar face of the tricyclic system (arbitrarily assigned to β). NOEs between δ 1.85/4.20 (H-5a/H-9), δ 2.01/4.20 (H-6/H-9), and δ 3.67/4.20 (H-5/H-9) assigned the protons to be oriented towards the *α*-plane of the tricyclic system. NOESYs between H-2/H-12a, H-12a/H-12 and H-5a/H-9 established the *trans* orientation of the chiral carbons at C-12a and C-5a (Figure 5.30 & 5.31).

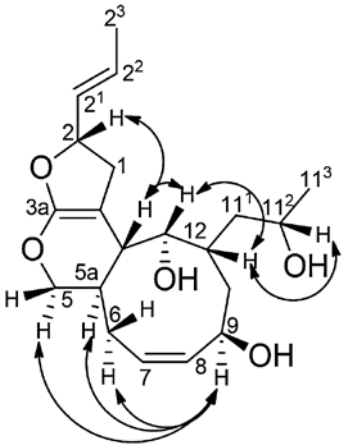

Figure 5.30.: HMBC spectrum of 1,2,5,5a,6,9,10,11,12,12a-decahydro-11(11^2-hydroxypropyl)-2-[(*E*)-2^1-propenyl] cyclonona[*d*]-furo[2,3-*b*]pyran-9,12-diol (**2**)

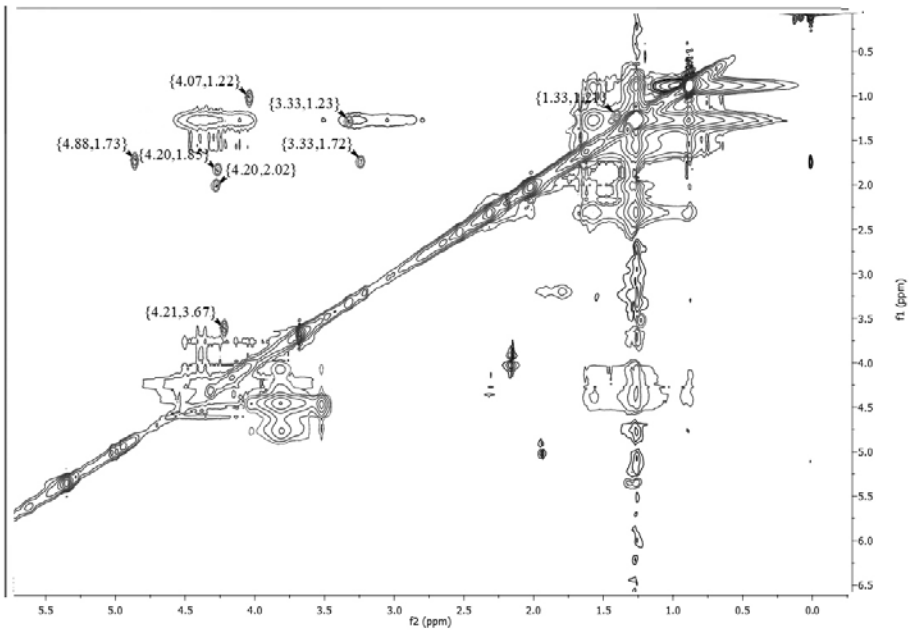

Figure 5.31.: NOESY spectrum of 1,2,5,5a,6,9,10,11,12,12a-decahydro-11(11^2-hydroxypropyl)-2-[(*E*)-2^1-propenyl] cyclonona[*d*]-furo[2,3-*b*]pyran-9,12-diol (**2**)

Table 5.5.: NMR spectroscopic data[a] of 1,2,5,5a,6,9,10,11,12,12a-decahydro-11(11^2-hydroxypropyl)-2-[(*E*)-2^1-propenyl] cyclonona[*d*]-furo[2,3-*b*]pyran-9,12-diol (**2**) isolated from brown seaweed *P.tetrastromatica*

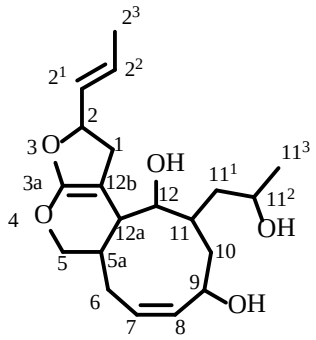

Compounds **2**…… 1,2,5,5a,6,9,10,11,12,12a-Decahydro-11(11^2-hydroxypropyl)-2-[(*E*)-2^1-propenyl] cyclonona[*d*]-furo[2,3-*b*]pyran-9,12-diol (**2**)

C. No.	**^{13}C NMR**	**^{1}H NMR (int., mult., J in Hz)[b]**	**COSY**	**HMBC**
1	37.74	2.68 (1H, dd, J=8.8, 7.69 Hz), 2.30 (1H, dd, J=13.01, 8.20 Hz)	H-2	C-12b, 3a
2	83.18	4.88 (1H, dd, J=16.99, 8.06 Hz)	H-2^1	C-1, 2^1
2^1	129.17	5.69 (1H, dd, J=14.47, 6.95 Hz)	H-2^2	-
2^2	130.77	5.87 (1H, m)	H-2^3	C-2^1, 2^3
2^3	17.65	1.82 (3H, d, J= 6.75 Hz)		-
3	-	-	-	-
3a	163.12	-	-	-
4	-	-	-	-
5	68.37	3.67 (1H, dd, J=12.77, 7.67 Hz) 3.70 (1H, dd, J=12.25, 7.66 Hz)	-	C-3a, 5a
5a	36.15	1.85 (1H, m)		C-12
6	33.72	2.01 (1H, m), 1.75 (H_β, m)	H-5a	C-7
7	132.05	5.62 (1H, m)	H-6	
8	132.63	5.67 (1H, dd, J=14.47, 6.95 Hz)	-	C-7
9	72.13	4.20 (1H, dd, J=15.60, 7.35 Hz)	H-8	C-8
10	39.54	1.29 (1H, m), 1.52 (H_β, m)	H-9	C-12, 9
11	38.69	1.22 (1H, m)	H-11^1	C-11^1
11^1	43.94	1.35 (1H, t, J=5.70, 3.47 Hz)	H-11^2	-
11^2	67.75	4.07 (1H, m)	H-11^3	C-11^1, 11^3
11^3	23.97	1.25 (3H, d, J=5.52 Hz)	-	-
12	71.82	3.33 (1H, dd, J=8.76, 1.86 Hz)	H-11	
12a	41.36	1.72 (1H, dd, J=11.46, 4.88 Hz)	H-12	C-5a, 3a ,12b
12b	94.31	-	-	-

[a]NMR spectra were recorded using a B ruker AVANCE III 500 MHz (AV 500) spectrometer (B ruker, Karlsruhe, Germany) in $CDCl_3$ as aprotic solvent at ambient temperature with TMS as the internal standard (δ 0 ppm).

[b]Values in ppm, multiplicity and coupling constants (J=Hz) were indicated in parentheses. Multiplicities were allocated by ^{135}DEPT NMR spectrum.

The assignments were made with the aid of the COSY, HSQC, HMBC and NOESY experiments.

The molecular ion peak of **2** was appeared at *m/z* 350 and base peak was ontained at *m/z* 40.0 (Figure 5.32 and 5.33).

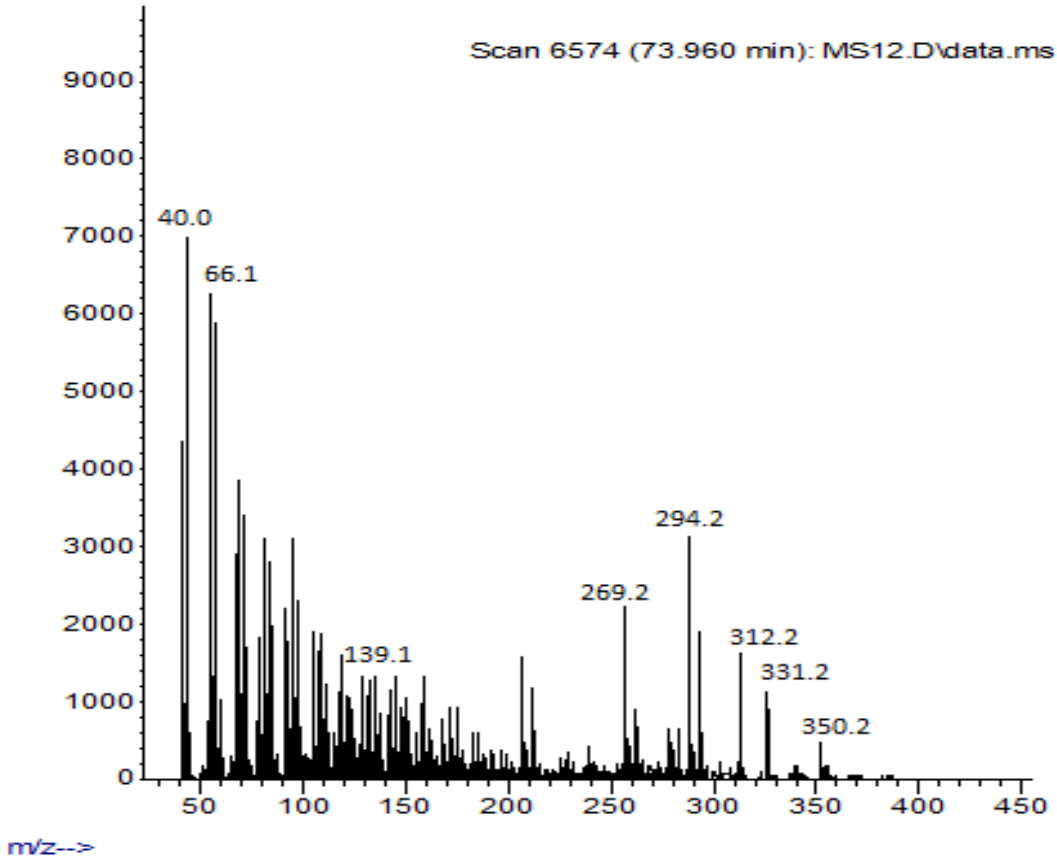

Figure 5.32.: EI-MS spectrum of 1,2,5,5a,6,9,10,11,12,12a-decahydro-11(11^2-hydroxypropyl)-2-[(*E*)-2^1-propenyl] cyclonona[*d*]-furo[2,3-*b*]pyran-9,12-diol (**2**)

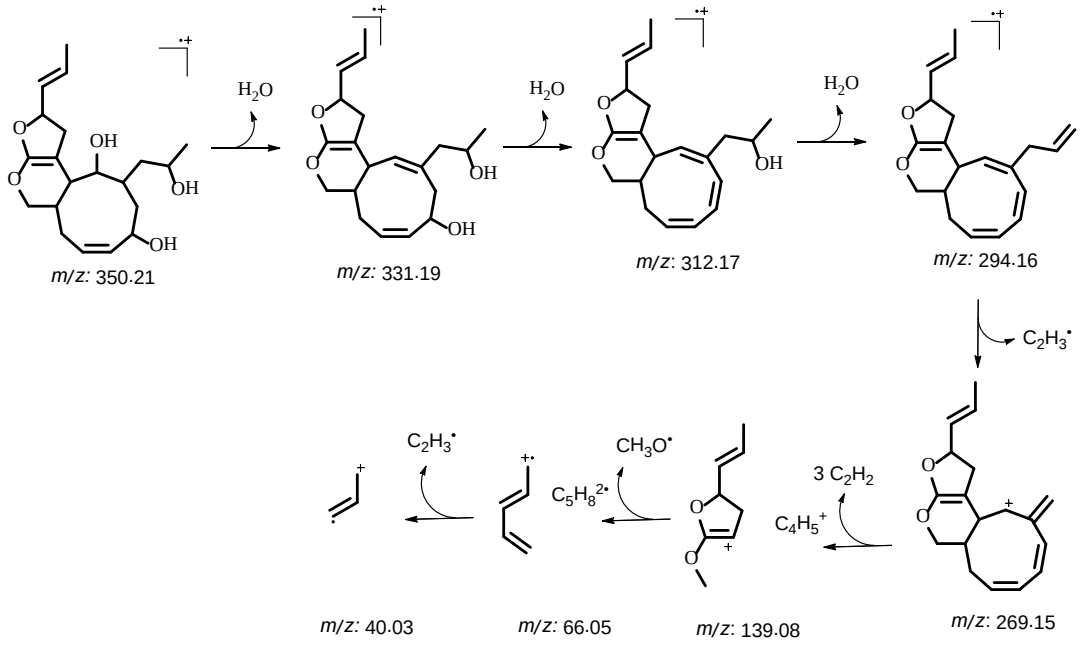

Figure 5.33.: Tentative mass fragmentation pattern of 1,2,5,5a,6,9,10,11,12,12a-decahydro-11(11^2-hydroxypropyl)-2-[(*E*)-2^1-propenyl] cyclonona[*d*]-furo[2,3-*b*]pyran-9,12-diol (**2**)

5.3.2.1c Structural characterization of Compound 3 (TP_3)

4-(4^1,4^2-Dihydroxypropyl)-4,4a,5,6,7,8,11,11a-octahydro-8,11-dihydroxy-7-methyl-6-(6^1-methyl-6^2-propenyl)-cyclonona[*c*]pyran-3-(1*H*)-one

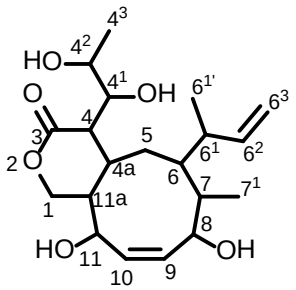

Sample yield	0.27% (> 99% purity, RP-C_{18} HPLC)
Physical description	Pale Yellow oil
Molecular formula	$C_{20}H_{32}O_6$
Molecular mass	368.2199

The xenicane class of diterpenoid derivative, 4-(4^1,4^2-Dihydroxypropyl)-4,4a,5,6,7,8,11,11a-octahydro-8,11-dihydroxy-7-methyl-6-(6^1-methyl-6^2-propenyl)-cyclonona[*c*]-pyran-3-(1*H*)-one was isolated as pale yellow oil compound. The compound (**3**) has exhibited UV absorbance (UV (MeOH) λ_{max}) at 246 (2.90) nm (Figure 5.34). The homogeneity of the compound was ascertained by HPLC data on a bonded phase octadecylsilane (C_{18}) stationary phase (RP-C_8 HPLC, MeOH: MeCN, 4:1 v/v): 4.20 min (Figure 5.35).

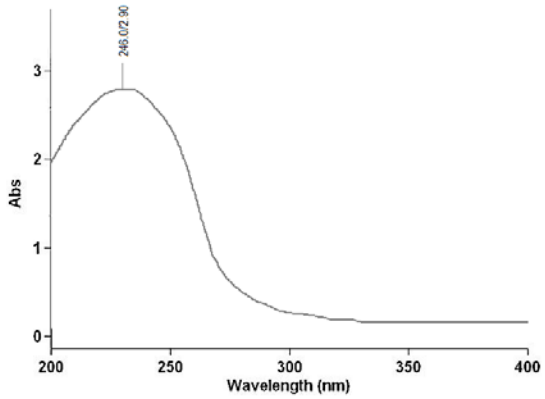

Figure 5.34.: UVspectrum of 4-(4^1,4^2-dihydroxypropyl)-4,4a,5,6,7,8,11,11a-octahydro-8,11-dihydroxy-7-methyl-6-(6^1-methyl-6^2-propenyl)-cyclonona[*c*]pyran-3-(1*H*)-one (**3**)

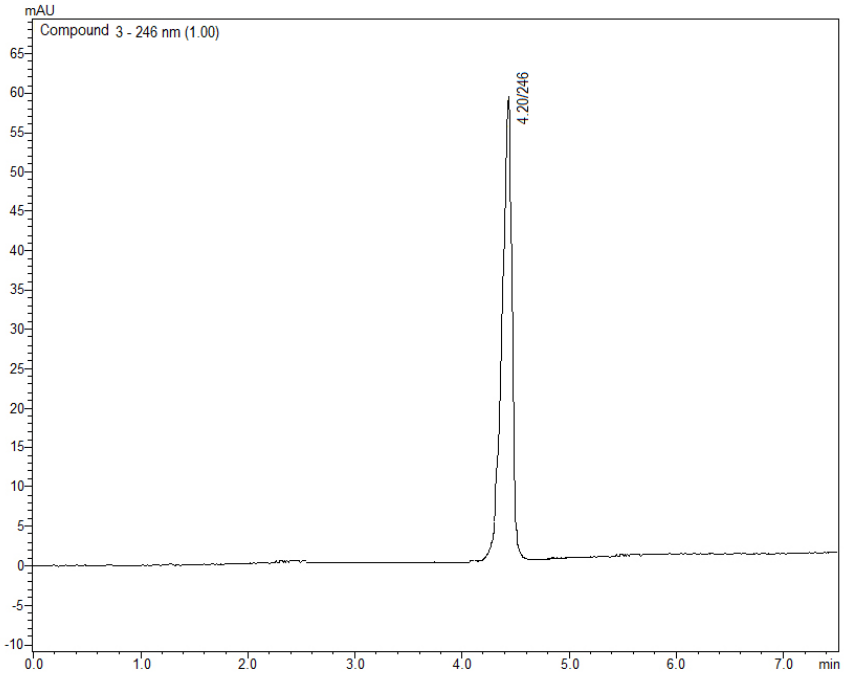

Figure 5.35.: HPLC chromatogram of 4-(4^1,4^2-dihydroxypropyl)-4,4a,5,6,7,8,11,11a-octahydro-8,11-dihydroxy-7-methyl-6-(6^1-methyl-6^2-propenyl)-cyclonona[*c*]pyran-3-(1*H*)-one (**3**)

The molecular ion peak by HRESIMS (positive mode) was observed at *m/z*: 369.2280 $[M+H]^+$ (Figure 5.36). The FTIR spectrum of **3** displayed absorption bands at, 3473 (O-H), and 1715 (C=O) (Figure 5.37).

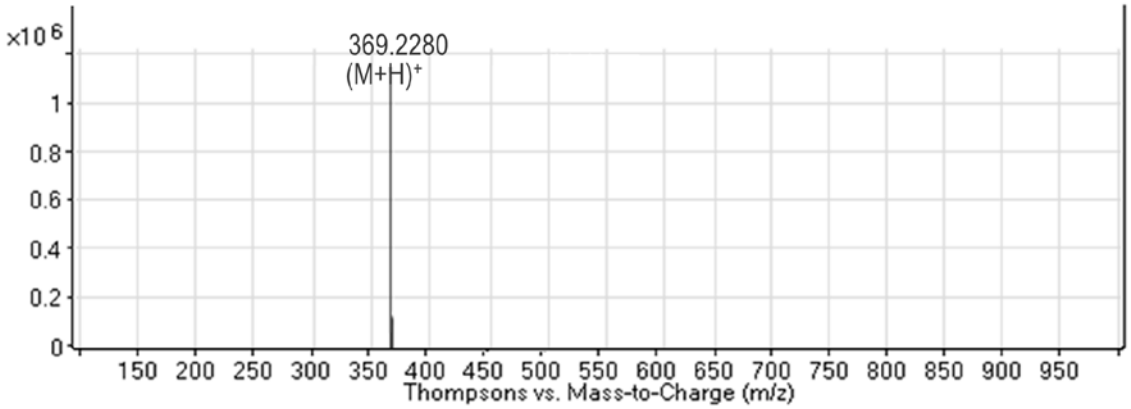

Figure 5.36.: HRESIMS of 4-(4^1,4^2-dihydroxypropyl)-4,4a,5,6,7,8,11,11a-octahydro-8,11-dihydroxy-7-methyl-6-(6^1-methyl-6^2-propenyl)-cyclonona[*c*]pyran-3-(1*H*)-one (**3**)

The chromatographic fraction of the crude extract of *P. tetrastromatica* yielded **3** as pale yellowish oil. The molecular ion peak of **3** was appeared at *m/z* 368, whereas the molecular formula $C_{20}H_{32}O_6$, implying five unsaturation degrees, was associated with three olefinic bonds and two ring systems. The spectroscopic data of **3** displayed, in conjunction with the similar substituted 9-membered cyclic system of diterpenoids **1-2** along with the δ-lactone signals at δ 65.75 (attributed to C-1), δ 3.95, 4.22; δ 172.35 (C-3), δ 48.80 (C-4); δ 2.21, δ 37.55 (C-4a), δ 1.62, and δ 42.93 (C-11a); δ 1.82 substituted with a 1,2-dihydroxypropyl functionality at δ 48.80 (C-4) (Figure 5.38-5.41).

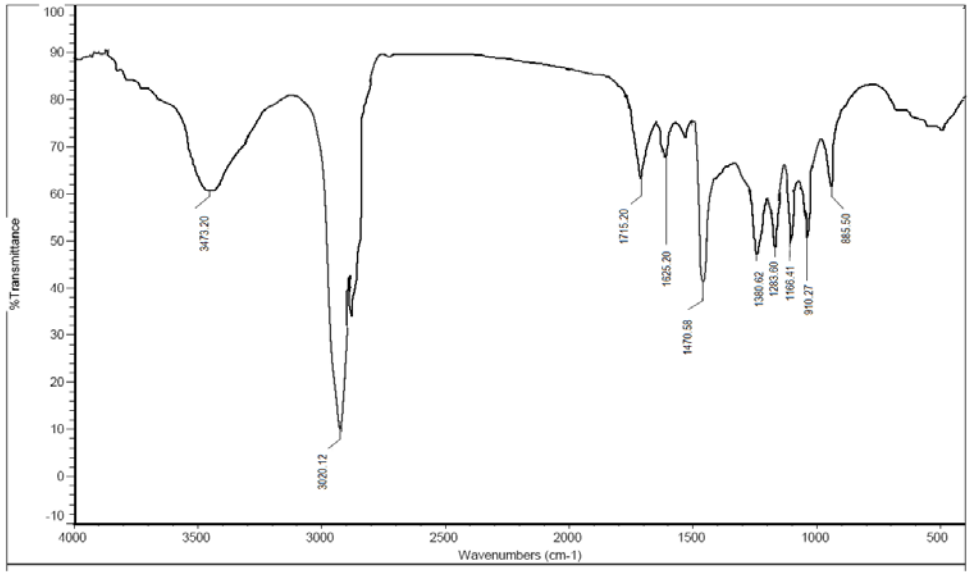

Figure 5.37.: FTIR spectrum of 4-(4^1,4^2-dihydroxypropyl)-4,4a,5,6,7,8,11,11a-octahydro-8,11-dihydroxy-7-methyl-6-(6^1-methyl-6^2-propenyl)-cyclonona[*c*]pyran-3-(1*H*)-one (**3**)

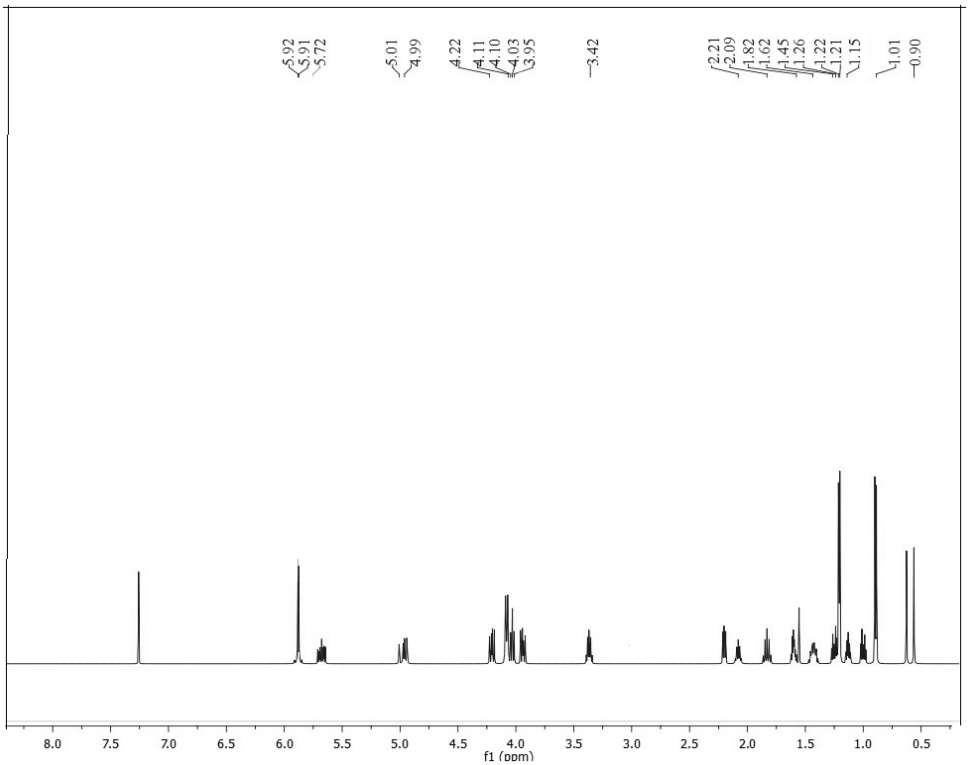

Figure 5.38.: ^{1}H NMR spectrum of -(4^1,4^2-dihydroxypropyl)-4,4a,5,6,7,8,11,11a-octahydro-8,11-dihydroxy-7-methyl-6-(6^1-methyl-6^2-propenyl)-cyclonona[*c*]pyran-3-(1*H*)-one (**3**)

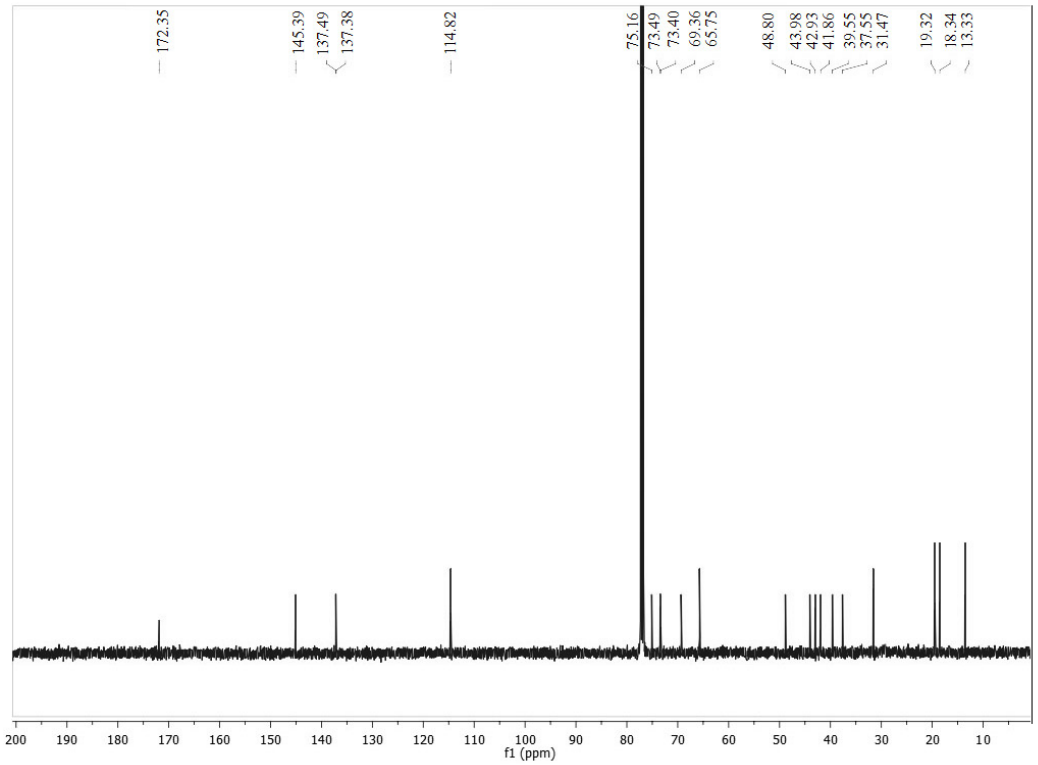

Figure 5.39.: ^{13}C NMR spectrum of 4-(4^{1},4^{2}-dihydroxypropyl)-4,4a,5,6,7,8,11,11a-octahydro-8,11-dihydroxy-7-methyl-6-(6^{1}-methyl-6^{2}-propenyl)-cyclonona[*c*]pyran-3-(1*H*)-one (**3**)

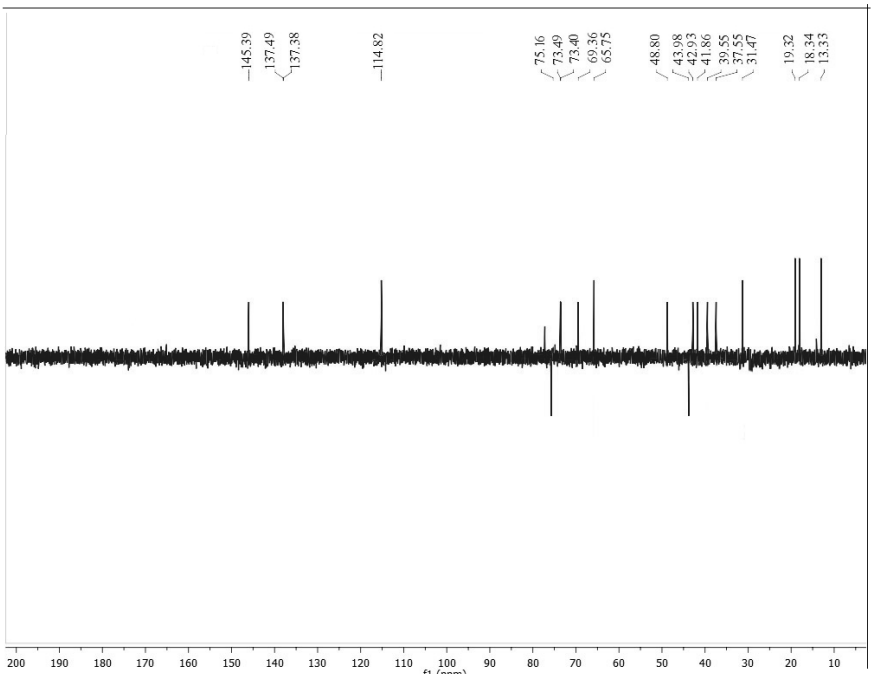

Figure 5.40.: ^{135}DEPT NMR spectrum of 4-(4^{1},4^{2}-dihydroxypropyl)-4,4a,5,6,7,8,11,11a-octahydro-8,11-dihydroxy-7-methyl-6-(6^{1}-methyl-6^{2}-propenyl)-cyclonona[*c*]pyran-3-(1*H*)-one (**3**)

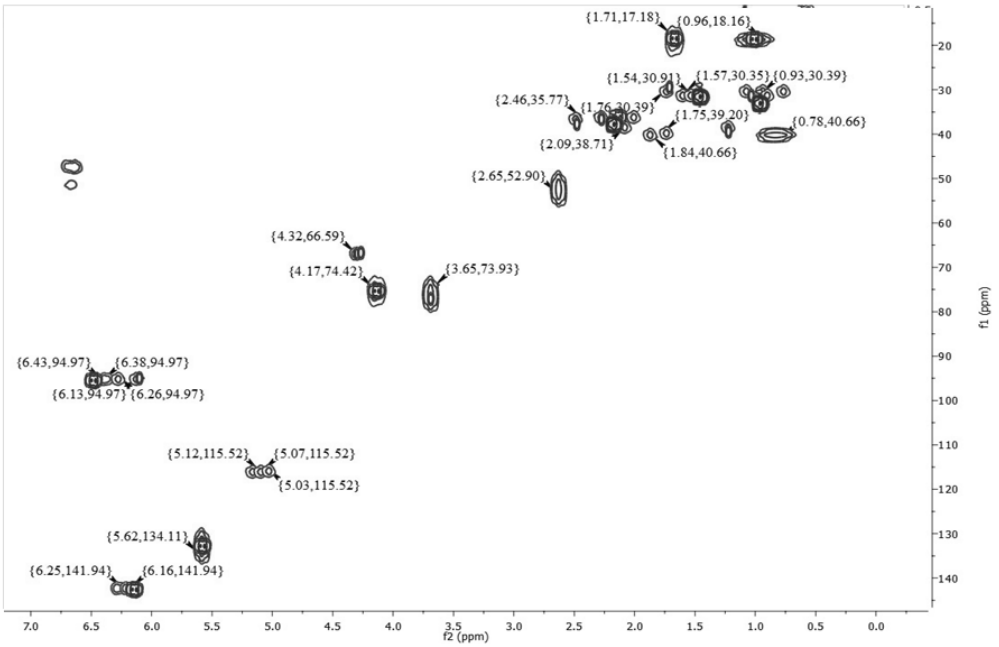

Figure 5.41.: HSQC spectrum of 4-(4[1],4[2]-dihydroxypropyl)-4,4a,5,6,7,8,11,11a-octahydro-8,11-dihydroxy-7-methyl-6-(6[1]-methyl-6[2]-propenyl)-cyclonona[*c*]pyran-3-(1*H*)-one (**3**)

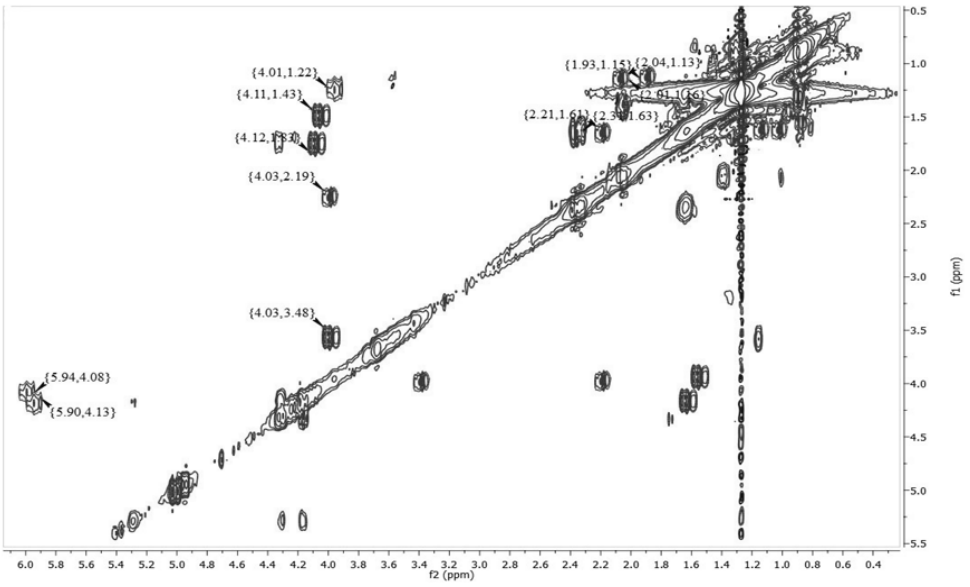

Figure 5.42.: [1]H-[1]H COSY of 4-(4[1],4[2]-dihydroxypropyl)-4,4a,5,6,7,8,11,11a-octahydro-8,11-dihydroxy-7-methyl-6-(6[1]-methyl-6[2]-propenyl)-cyclonona[*c*]pyran-3-(1*H*)-one (**3**)

The COSY spectrum revealed the existence of three spins (**I-III**) that were connected together by HMBCs, affirming its planer structure. An additional group of but-3-en-2-yl was

observed at δ 43.98 (C-6) associated with 9-membered cyclic ring, and the attribution was substantiated by the ^{13}C NMR bands at δ 43.98 (C-6), δ 39.55 (C-6^1), δ 145.39 (C-6^2), δ 114.82 (C-6^3), and δ 18.34 (C-6$^{1'}$). These connections were supported by COSYs between δ 1.01/1.15 (H-5/H-6), δ 1.15/1.45 (H-6/H-7), δ 1.15/2.09 (H-6/H-6^1), δ 2.09/5.72 (H-6^1/H-6^2), and δ 5.72/5.01 (H-6^2/H-6^3). The HMBCs between δ 1.15/31.47 (H-6/C-5), δ 2.09/43.98 (H-6^1/C-6), δ 2.09/145.39 (H-6^1/C-6^2), δ 1.22/39.55 (H-6$^{1'}$/C-6^1) and δ 5.01/39.55 (H-6^3/C-6^1) further substantiated the attributions (Figure 5.42-5.44).

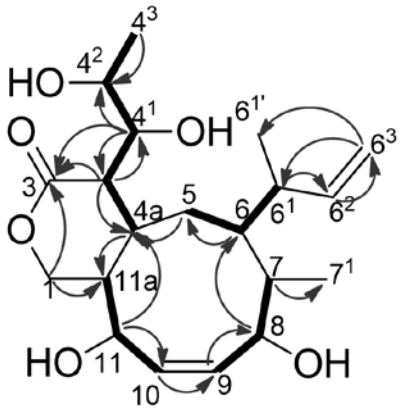

Figure 5.43.: Prominent ^{1}H-^{1}H COSY, and selected HMBC correlations of 4-(4^1,4^2-dihydroxypropyl)-4,4a,5,6,7,8,11,11a-octahydro-8,11-dihydroxy-7-methyl-6-(6^1-methyl-6^2-propenyl)-cyclonona-[*c*]-pyran-3-(1*H*)-one (**3**). The key ^{1}H-^{1}H COSY couplings were represented in bold face bonds. The key HMBC couplings have been represented by double barbed arrows.

The carbon signals of **3** showed a carbonyl carbon at δ 172.35 (C-3) and four olefinic ^{13}C signals (one methylene, three methines), which reckoned for five degrees of unsaturation. Three COSY spin systems (**I-III**) in **3** were supported by HMBCs between corresponding carbons and protons. The spin unit **I** was demonstrated by COSYs between δ 1.62/2.21 (H-4a/H-4), δ 2.21/4.03 (H-4/H-4^1), δ 4.03/δ 3.42 (H-4^1/H-4^2), which were connected to second and third spin system (**II** and **III**) by carbons C-4a and C-11a, respectively. The HMBCs at δ 1.01/37.55 (H-5/C-4a), δ 2.21/73.49 (H-4/C-4^1), δ 4.03/48.80 (H-4^1/C-4), δ 4.03/69.36 (H-4^1/C-4^2), and δ 1.21/69.36 (H-4^3/C-4^2) connected the different moieties in the spin system **I**. The HMBCs between δ 2.21/37.55 (H-4/C-4a), δ 4.03/172.35 (H-4^1/C-3) connected the spin system to δ-lactone and 9-membered cyclic ring. Similarly COSY spin systems **II**, **III** and **IV** were established between the protons δ 1.01/1.15 (H-5/H-6), δ 1.15/2.09 (H-6/H-6^1); δ 1.45/4.11 (H-7/H-8), δ 4.11/5.91 (H-8/H-9), δ 5.01/1.22 (H-6^3/H-6$^{1'}$); δ 5.92/4.10 (H-10/H-11), δ 4.10/1.82 (H-11/H-11a), which were connected each other by

HMBCs between δ 4.11/43.98 (H-8/C-6), δ 4.10/37.55 (H-11/C-4a), δ 1.62/42.93 (H-4a/C-11a), δ /δ 5.91/75.16 (H-9/C-8), δ /δ 5.92/137.49 (H-10/C-9), and δ 4.10/137.38 (H-11/C-10).

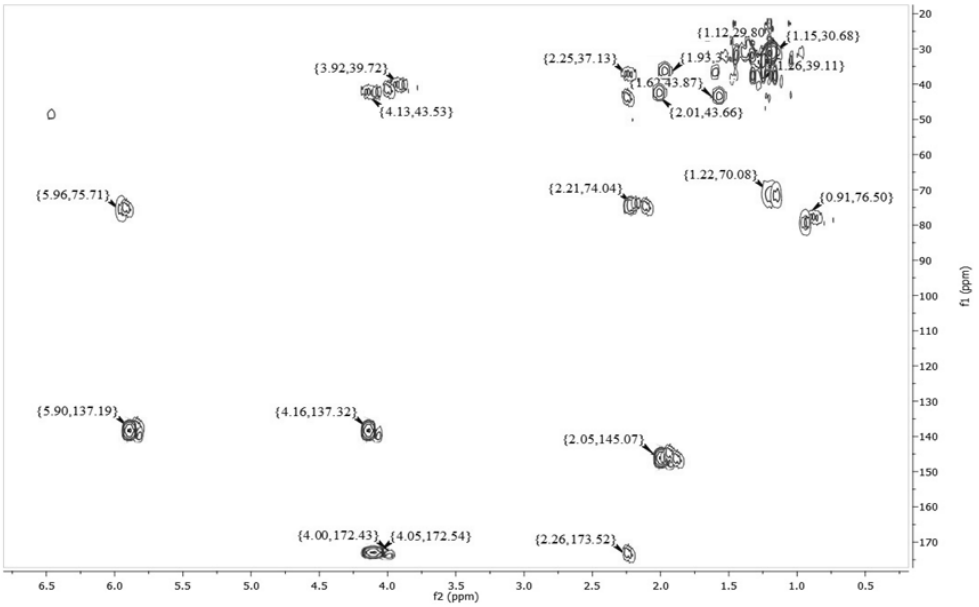

Figure 5.44.: HMBC spectrum of 4-(4^1,4^2-dihydroxypropyl)-4,4a,5,6,7,8,11,11a-octahydro-8,11-dihydroxy-7-methyl-6-(6^1-methyl-6^2-propenyl)-cyclonona[*c*]pyran-3-(1*H*)-one (**3**)

Relative stereochemistries of **3** was determined by NOESY experimental data, whereas the protons at δ 3.42 (H-4^2), δ 4.03 (H-12), δ 2.21 (H-4) and δ 1.62 (H-4a) showed strong NOEs, such as H-4^2/H-4^1, H-4^1/H-4, H-4/H-4a and H-4a/H-6^1, respectively. These were aligned towards the β -face of the reference plane of **3**. On the other hand, NOEs demonstrated the spatial proximity of the H-11a (δ 1.82) with the H-11 (δ 4.10); H-11 (δ 4.10) with H-7 (δ 1.45), and H-8 (δ 4.11) with H-7 (δ 1.45). These were aligned in the opposite plane of β -face of the reference plane of **3** (as *α*-protons (Figure 5.45 & 5.46)

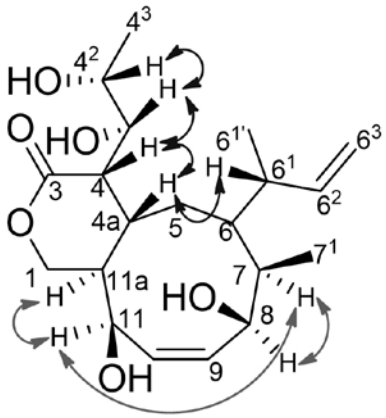

Figure 5.45.: Prominent NOE correlations of 4-(4[1],4[2]-dihydroxypropyl)-4,4a,5,6,7,8,11,11a-octahydro-8,11-dihydroxy-7-methyl-6-(6[1]-methyl-6[2]-propenyl)-cyclonona[*c*]pyran-3-(1*H*)-one (**3**). NOESY relations are represented by double-tailed arrows

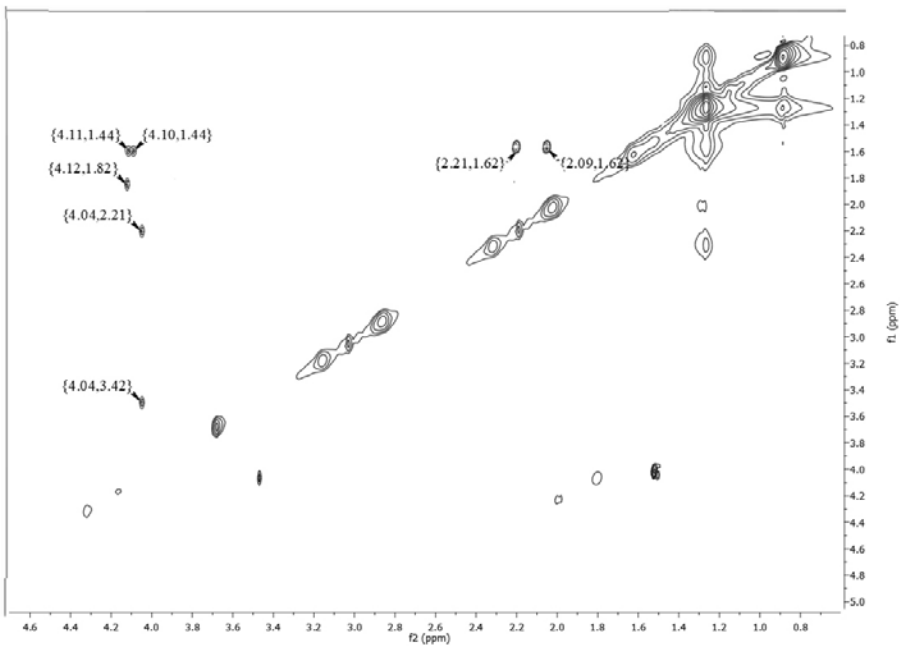

Figure 5.46.: NOESY spectrum of 4-(4[1],4[2]-dihydroxypropyl)-4,4a,5,6,7,8,11,11a-octahydro-8,11-dihydroxy-7-methyl-6-(6[1]-methyl-6[2]-propenyl)-cyclonona[*c*]pyran-3-(1*H*)-one (**3**)

Table 5.6.: NMR spectroscopic data[a] of 4-(4^1,4^2-Dihydroxypropyl)-4,4a,5,6,7,8,11,11a-octahydro-8,11-dihydroxy-7-methyl-6-(6^1-methyl-6^2-propenyl)-cyclonona[*c*]pyran-3-(1*H*)-one (**3**) isolated from brown seaweed *P.tetrastromatica*

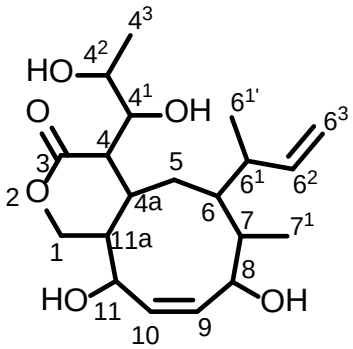

Compound **3**……4-(4^1,4^2-dihydroxypropyl)-4,4a,5,6,7,8,11,11a-octahydro-8,11-dihydroxy-7-methyl-6-(6^1-methyl-6^2-propenyl)-cyclonona[*c*]pyran-3-(1*H*)-one (**3**)

C. N.	^{13}C NMR	^{1}H NMR (int., mult., J in Hz)[b]	COSY	HMBC
		3.95 (1H, dd, J=10.1, 8.0 Hz)		
1	65.75	4.22 (1H, dd, J=9.1, 7.86 Hz)		C-3,11a
2	-	-	-	-
3	172.35	-	-	-
4	48.80	2.21 (1H, dd, J=9.8, 5.1 Hz)	H-4a, 4^1	C-3,4a,12
4a	37.55	1.62 (1H, m)	-	C-11a
4^1	73.49	4.03 (1H, t, J=9.0 Hz)	H-4^2	C-3,4,4^2
4^2	69.36	3.42 (1H, m)	-	
4^3	19.32	1.21 (3H, m)	-	C-4^2
		1.26 (1H, m),		
5	31.47	1.01 (1H, m)	H-6	H-4a
6	43.98	1.15 (1H, m)	H-6^1	C-5
6^1	39.55	2.09 (1H, m)	-	C-6, 6^2
$6^{1'}$	18.34	1.22 (3H, m)	-	C-6^1
6^2	145.39	5.72 (1H, m)		C-6^3
		5.01 (1H, dd, J=19.7, 17.1Hz),		
6^3	114.82	4.99 (1H, dd, J=19.7, 9.7 Hz)	-	C-6^1,$6^{1'}$
7	41.86	1.45 (1H, m)	H-8	C-7^1
7^1	13.33	0.90 (3H, d, J=3.2 Hz)	-	C-8
8	75.16	4.11 (1H, t, J=9.6 Hz)	H-9	C-6
9	137.49	5.91 (1H, d, J=11.7 Hz)	-	C-8
10	137.38	5.92 (1H, d, J=12.7 Hz)	H-11	C-9
11	73.40	4.10 (1H, t, J=9.5 Hz)	H-11a	C-10, 4a
11a	42.93	1.82 (1H, m)	-	-

[a]NMR spectra were recorded using a B ruker AVANCE III 500 MHz (AV 500) spectrometer (B ruker, Karlsruhe, Germany) in $CDCl_3$ as aprotic solvent at ambient temperature with TMS as the internal standard (δ 0 ppm).

[b]Values in ppm, multiplicity and coupling constants (J=Hz) were indicated in parentheses. Multiplicities were allocated by [135]DEPT NMR spectrum.

The assignments were made with the aid of the COSY, HSQC, HMB C and NOESY experiments.

The molecular ion peak of **3** was appeared at *m/z* 388 and base peak was ontained at *m/z* 40.0 (Figure 5.47 and 5.48).

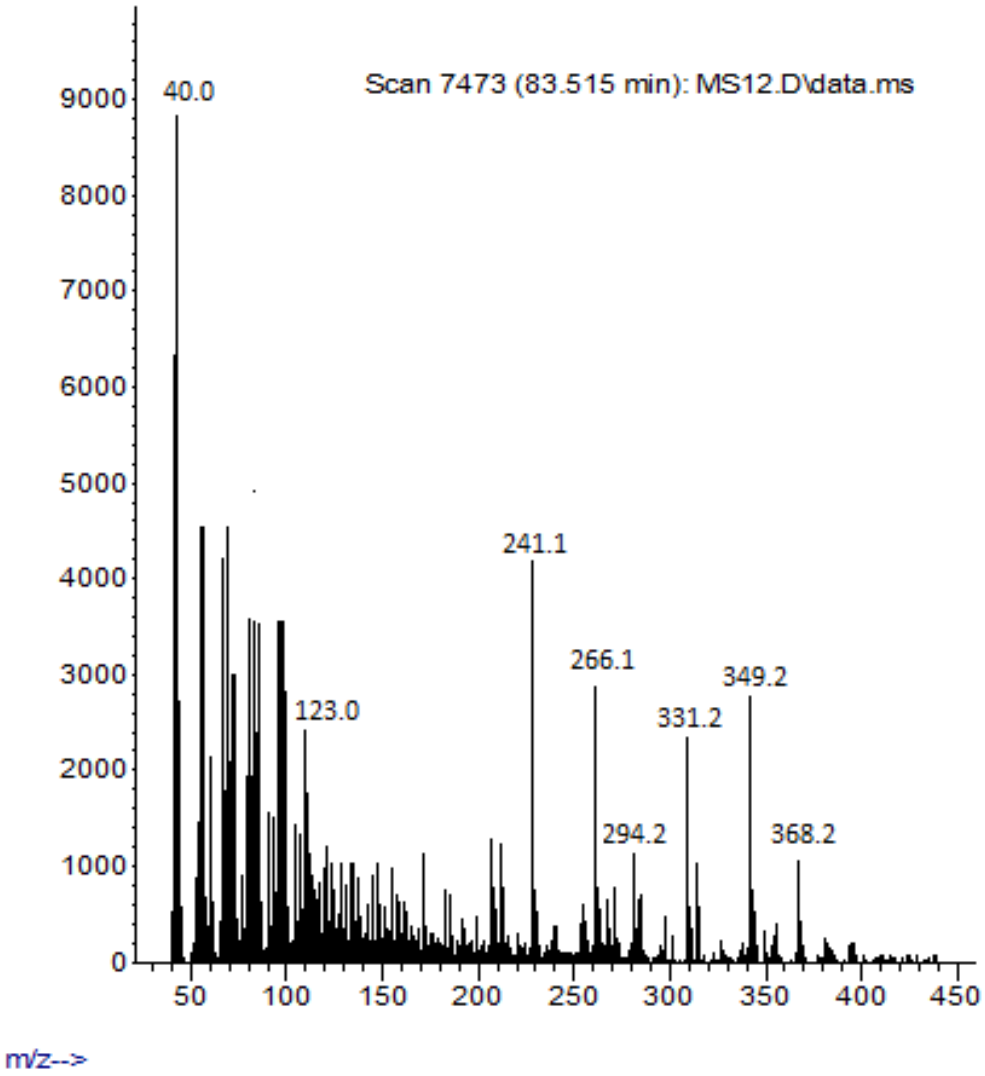

Figure 5.47.: EI-MS spectrum of 4-(4[1],4[2]-dihydroxypropyl)-4,4a,5,6,7,8,11,11a-octahydro-8,11-dihydroxy-7-methyl-6-(6[1]-methyl-6[2]-propenyl)-cyclononа[*c*]pyran-3-(1*H*)-one (**3**)

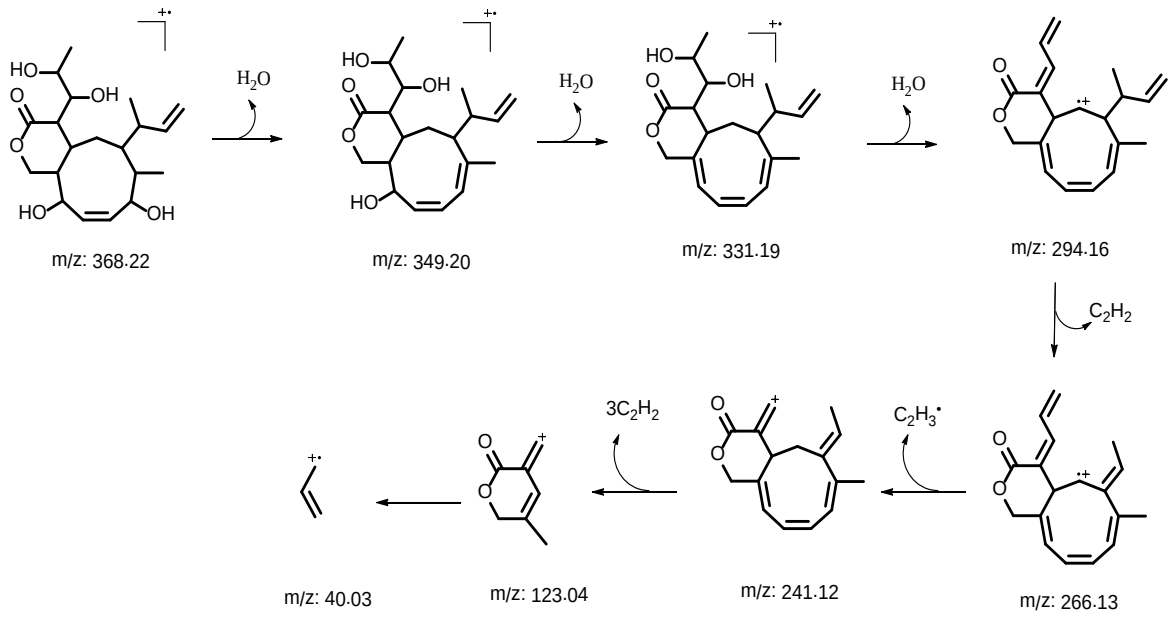

Figure 5.48.: Tentative mass fragmentation pattern of 4-(4[1],4[2]-dihydroxypropyl)-4,4a,5,6,7,8,11,11a-octahydro-8,11-dihydroxy-7-methyl-6-(6[1]-methyl-6[2]-propenyl)-cyclonona[*c*]-pyran-3-(1*H*)-one (**3**)

5.3.2.1d Structural characterization of Compound 4 (TP_4)

4,4a,5,6,7,8,11,11a-Octahydro-7-hydroxy-6-(6[2]-hydroxy-6[3]-butenyl)-4-(4[1]-hydroxypropyl)-11-methoxy-8-methyl-cyclonona[*c*]pyran-3-(1*H*)-one

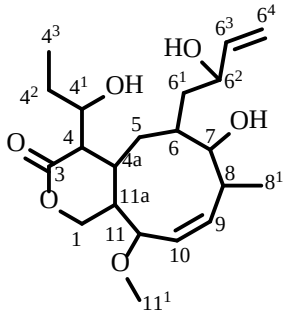

Sample yield	0.32% (> 99% purity, RP-C_{18} HPLC)
Physical description	Pale yellow oil
Molecular formula	$C_{21}H_{34}O_6$

Molecular mass	382.2355

The xenicane class of diterpenoid derivative, 4,4a,5,6,7,8,11,11a-octahydro-7-hydroxy-6-(6^2-hydroxy-6^3-butenyl)-4-(4^1-hydroxypropyl)-11-methoxy-8-methyl-cyclonona[*c*]pyran-3-(1*H*)-one was isolated as pale yellow oil compound. The compound (**4**) has exhibited UV absorbance (UV (MeOH) λ_{max}) at 209 (3.6), 249 (3.3) nm (Figure 5.49). The homogeneity of the compound was ascertained by HPLC data on a bonded phase octadecylsilane (C_{18}) stationary phase (RP-C_8 HPLC, MeOH: MeCN, 2:3 v/v): 4.05 min (Figure 5.50).

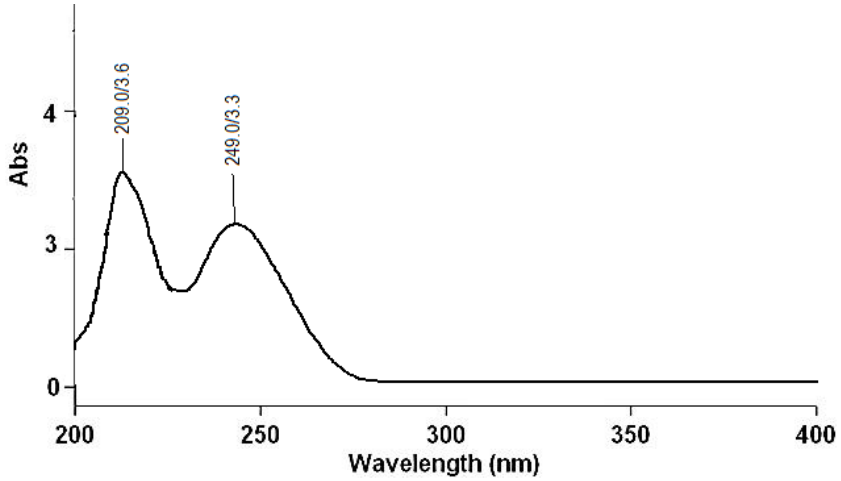

Figure 5.49.: UVspectrum of 4,4a,5,6,7,8,11,11a-octahydro-7-hydroxy-6-(6^2-hydroxy-6^3-butenyl)-4-(4^1-hydroxypropyl)-11-methoxy-8-methyl-cyclonona[*c*]pyran-3-(1*H*)-one (**4**)

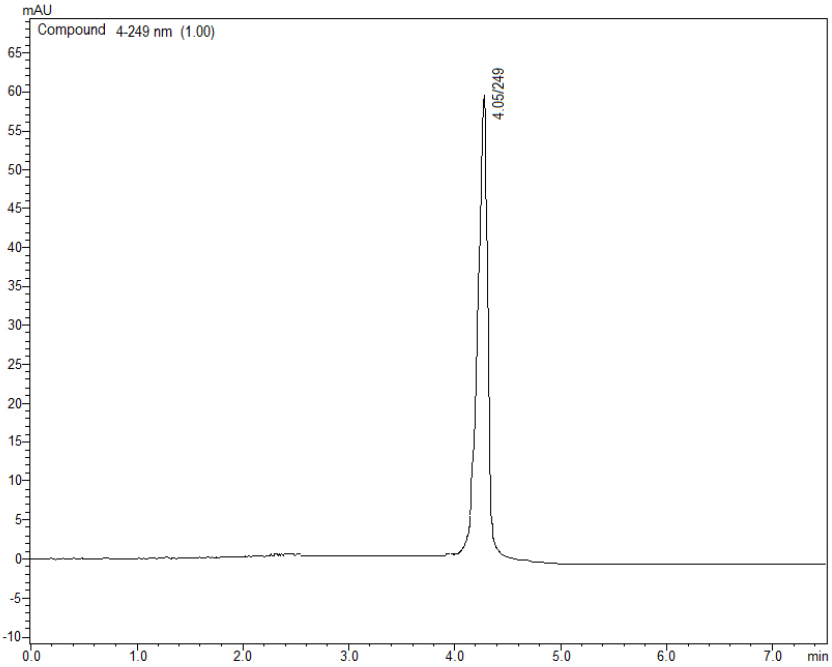

Figure 5.50.: HPLC chromatogram of 4,4a,5,6,7,8,11,11a-octahydro-7-hydroxy-6-(6^{2}-hydroxy-6^{3}-butenyl)-4-(4^{1}-hydroxypropyl)-11-methoxy-8-methyl-cyclonona[*c*]pyran-3-(1*H*)-one (**4**)

The molecular ion peak by HRESIMS (positive mode) was observed at *m/z* 383.2438 $[M+H]^{+}$ (Figure 5.51). The FTIR spectrum of **3** displayed absorption bands at 3451 (O-H) and 1737 (C=O) (Figure 5.52)

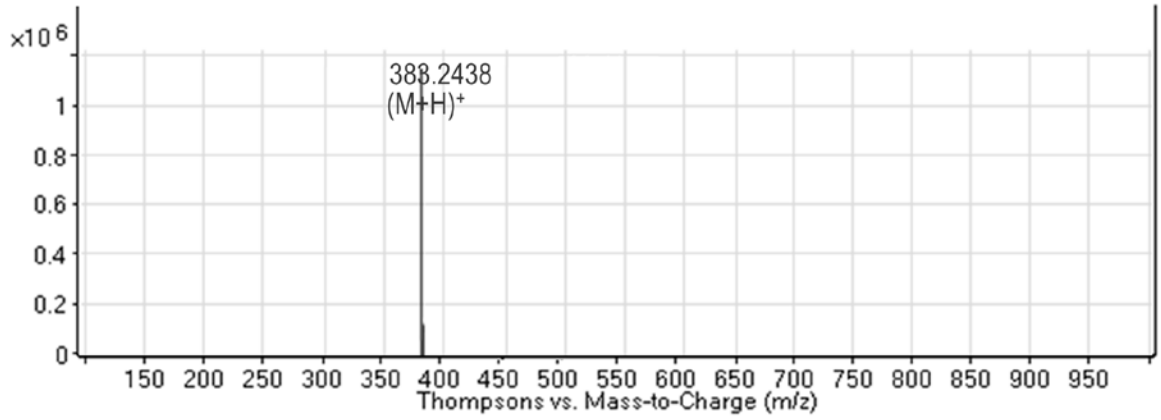

Figure 5.51.: HRESIMS of 4,4a,5,6,7,8,11,11a-octahydro-7-hydroxy-6-(6^{2}-hydroxy-6^{3}-butenyl)-4-(4^{1}-hydroxypropyl)-11-methoxy-8-methyl-cyclonona[*c*]pyran-3-(1*H*)-one (**4**)

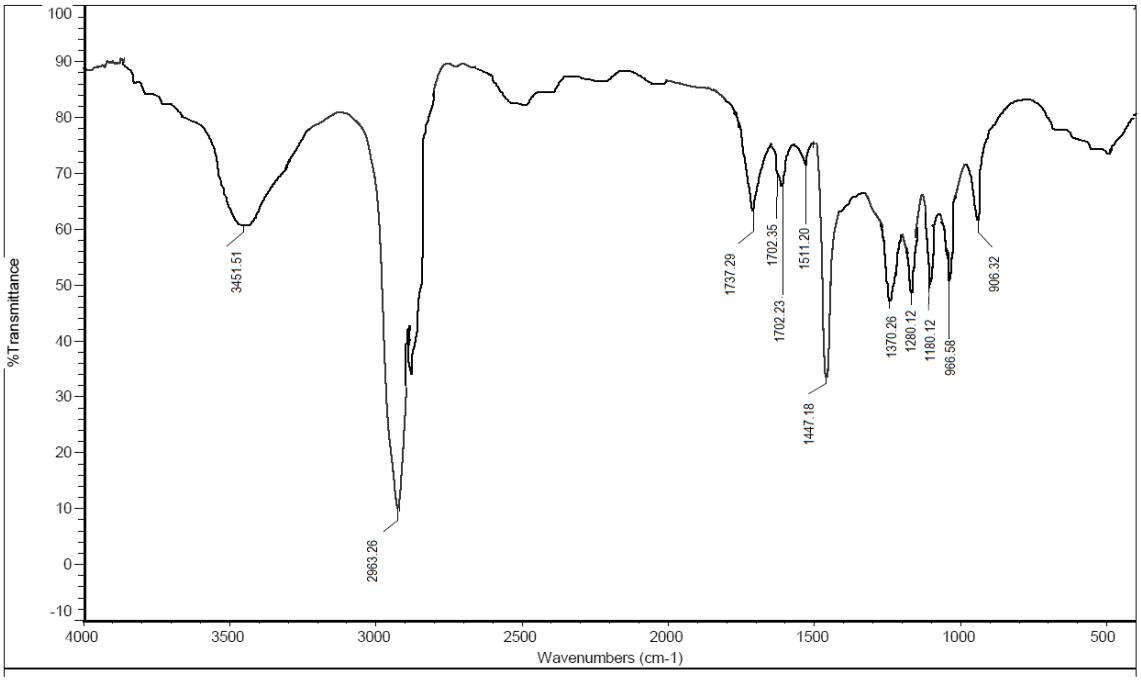

Figure 5.52.: FTIR of 4,4a,5,6,7,8,11,11a-octahydro-7-hydroxy-6-(6^2-hydroxy-6^3-butenyl)-4-(4^1-hydroxypropyl)-11-methoxy-8-methyl-cyclonona[*c*]pyran-3-(1*H*)-one (**4**)

Compound **4** was obtained as yellowish oil, whereas the molecular ion peak of **4** was appeared at *m/z* 382, and the molecular formula was determined as $C_{21}H_{34}O_6$. The spectroscopic characteristics of **4** were comparable to those of **3** with resonances exhibited by 9-membered cyclic ring bearing methoxy group at δ 82.04 (C-11) and substituted 2-hydroxybut-3-en-1-yl side chain at δ 40.16 (C-6) (Figure 5.46-). The ^{13}C-NMR and DEPT$_{135}$ spectra–displayed the occurrence of 21 signals of carbons incorporating twelve methine carbons (consisting of three olefinic methine carbons), five methylene carbons (including one olefinic methylene carbon signals and oxymethylene), three methyl carbons (including one methoxy carbon signal), suggesting five degrees of unsaturation, which proposed that **4** was a hydroxyl-substituted xeniolide diterpene (Figure 5.53-5.56). The proton NMR spectrum designated the existence of oxymethylene protons at δ 4.22, 3.96 and methoxy protons at 3.30 (H-11^1, 3H, *s*), which were attributed to the δ 65.02 (C-1) and δ 57.17 (C-11^1) (Table 2) of the xenicane diterpenoid skeleton (Bishara et al., 2006).

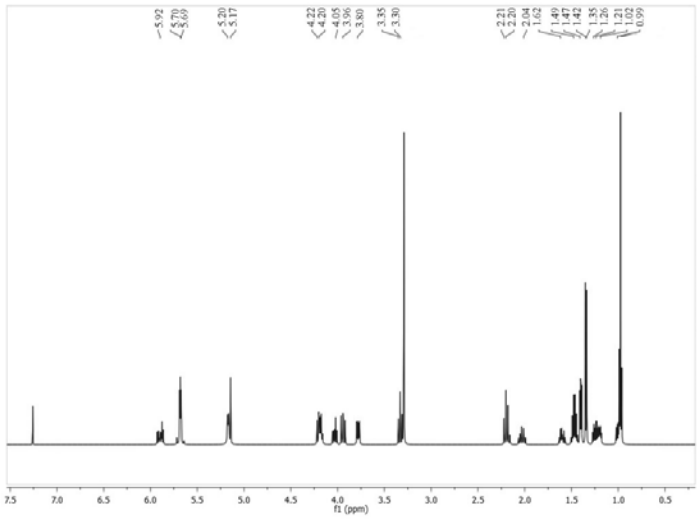

Figure 5.53.: ^{1}H-NMR of 4,4a,5,6,7,8,11,11a-octahydro-7-hydroxy-6-(6^{2}-hydroxy-6^{3}-butenyl)-4-(4^{1}-hydroxypropyl)-11-methoxy-8-methyl-cyclonona[*c*]pyran-3-(1*H*)-one (**4**)

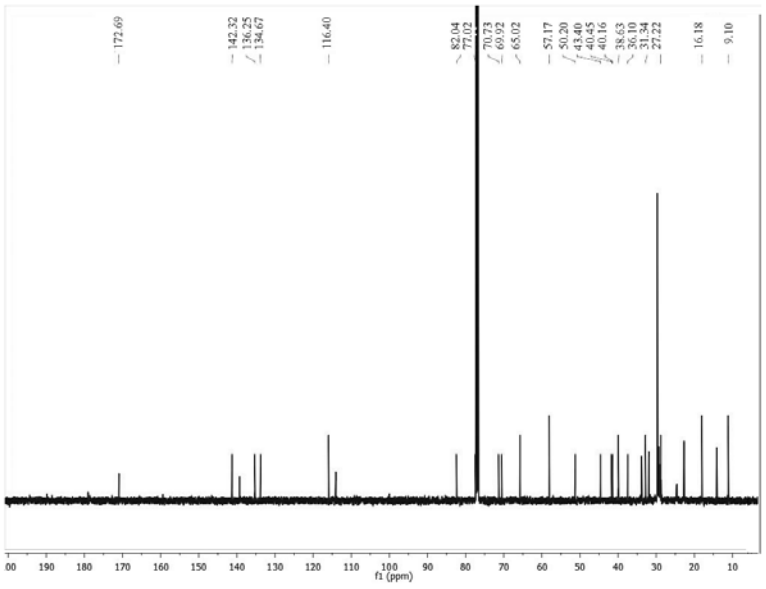

Figure 5.54.: ^{13}C-NMR of 4,4a,5,6,7,8,11,11a-octahydro-7-hydroxy-6-(6^{2}-hydroxy-6^{3}-butenyl)-4-(4^{1}-hydroxypropyl)-11-methoxy-8-methyl-cyclonona[*c*]pyran-3-(1*H*)-one (**4**)

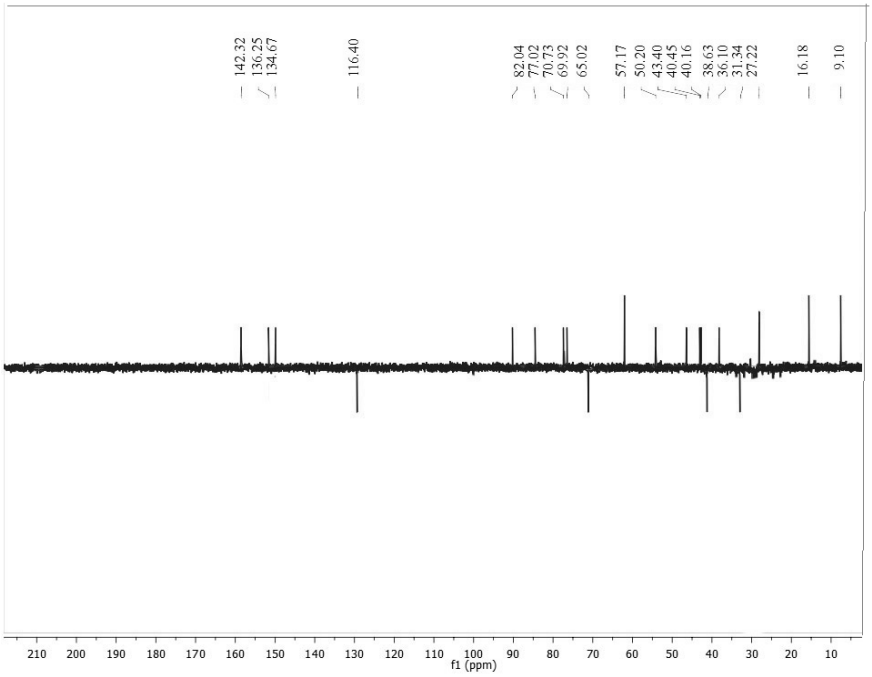

Figure 5.55.: DEPT spectrum of 4,4a,5,6,7,8,11,11a-octahydro-7-hydroxy-6-(6^2-hydroxy-6^3-butenyl)-4-(4^1-hydroxypropyl)-11-methoxy-8-methyl-cyclonona[*c*]pyran-3-(1*H*)-one (**4**)

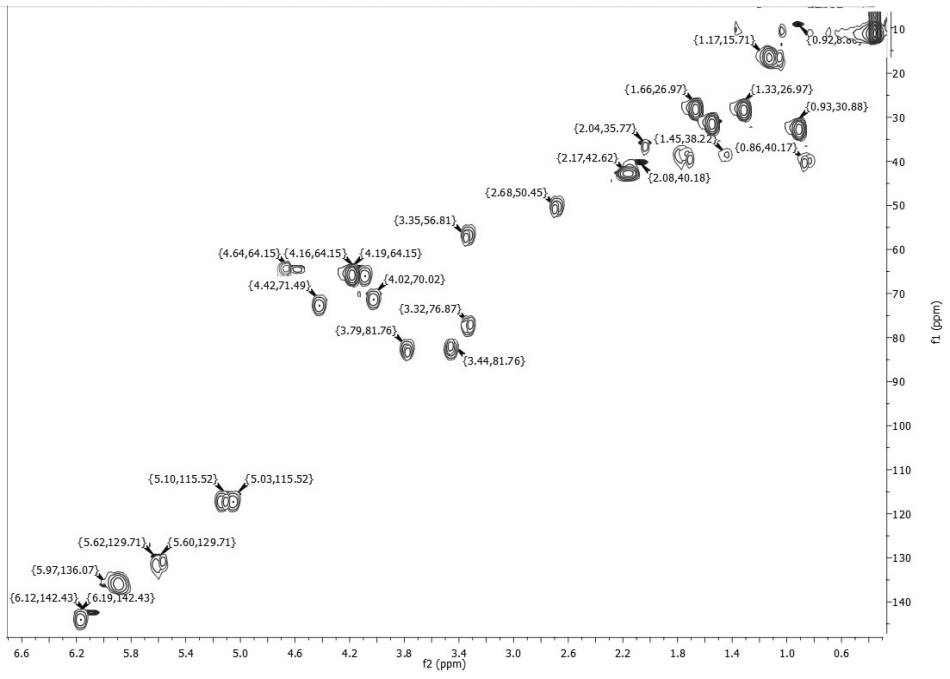

Figure 5.56.: HSQC spectrum of 4,4a,5,6,7,8,11,11a-octahydro-7-hydroxy-6-(6^2-hydroxy-6^3-butenyl)-4-(4^1-hydroxypropyl)-11-methoxy-8-methyl-cyclonona[*c*]pyran-3-(1*H*)-one (**4**)

The hydroxyl groups at C-7, C-4^1 and C-6^2 were fixed by ^{13}C-NMR signals at δ 77.02, 69.92, and 70.73, respectively. The location of hydroxyl group at the bicyclic system was designated by HMBCs between δ 3.35/δ 16.18 (H-7/C-8^1), δ 3.35/ δ 40.16 (H-7/C-6), δ 2.20/δ 77.02 (H-8/C-7), and also by COSYs between δ 1.21/3.35 (H-6/H-7). The methyl group at C-8, methoxy moiety at C-11 and alkenic bond at C-9 were associated with the fourth spin system between the protons δ 5.69/3.80 (H-10/H-11), δ 3.80/2.04 (H-11/H-11a), which were coupled with HMBCs between δ 5.69/δ 136.25 (H-10/C-9), δ 3.80/δ 134.67 (H-11/C-10), δ 3.80/δ 40.45 (H-11/C-11a), δ 2.04/δ 36.10 (H-11a/C-4a), δ 3.96/δ 40.45 (H-1/C-11a), and δ 3.80/δ 134.67 (H-11/C-10). In the spin system **I** (side chain 1-hydroxypropyl), the protons and carbons were connected by HMBCs, δ 2.21/δ 73.49 (H-4/C-4^1), δ 4.05/δ 172.69 (H-4^1/C-3), δ 4.05/δ 9.10 (H-4^1/C-4^3), δ 1.47/δ 69.92 (H-4^2/C-4^1), δ 1.47/δ 9.10 (H-4^2/C-4^3) along with COSYs δ 2.21/4.05 (H-4/H-4^1), δ 4.05/1.47 (H-4^1/H-4^2), δ 1.47/0.99 (H-4^2/H-4^3 that attributed that the spin unit **I** was linked to *δ*-lactone as well as fourth (**IV**) and second (**II**) spin system via HMBCs between δ 2.21/δ 36.10 (H-4/C-4a) and δ 2.04/δ 36.10 (H-11a/C-4a), respectively. Similarly, the second spin system (**II**) was explained by COSYs between δ 1.62/1.26 (H-4a/H-5) (Figure 5.57-5.59).

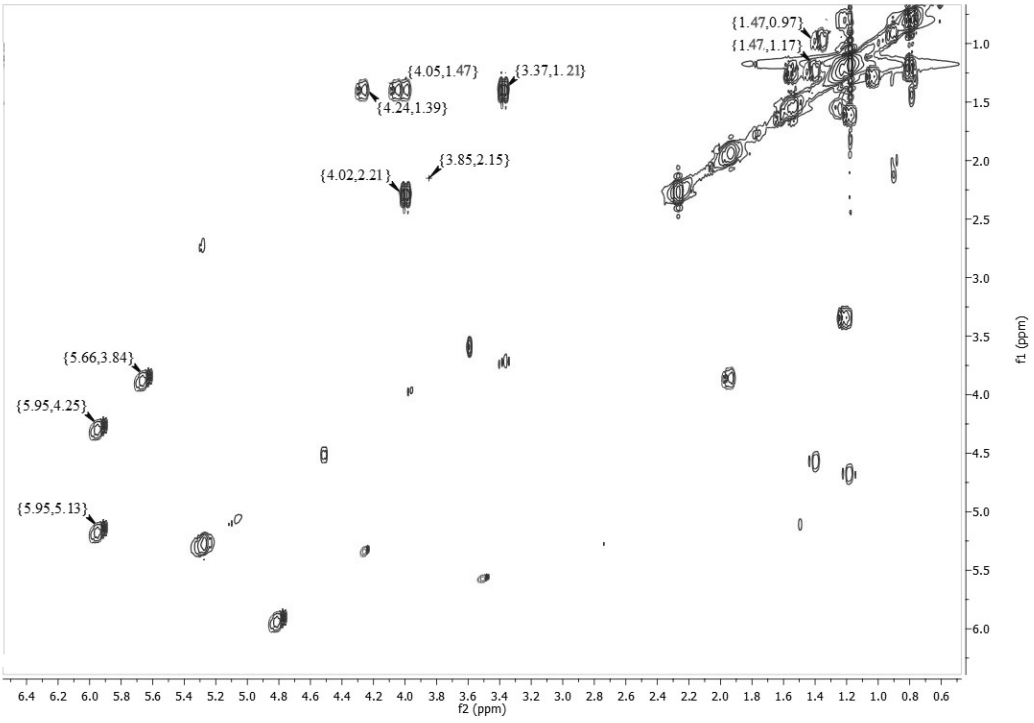

Figure 5.57.: COSY spectrum of 4,4a,5,6,7,8,11,11a-octahydro-7-hydroxy-6-(6^2-hydroxy-6^3-butenyl)-4-(4^1-hydroxypropyl)-11-methoxy-8-methyl-cyclonona[*c*]pyran-3-(1*H*)-one (**4**)

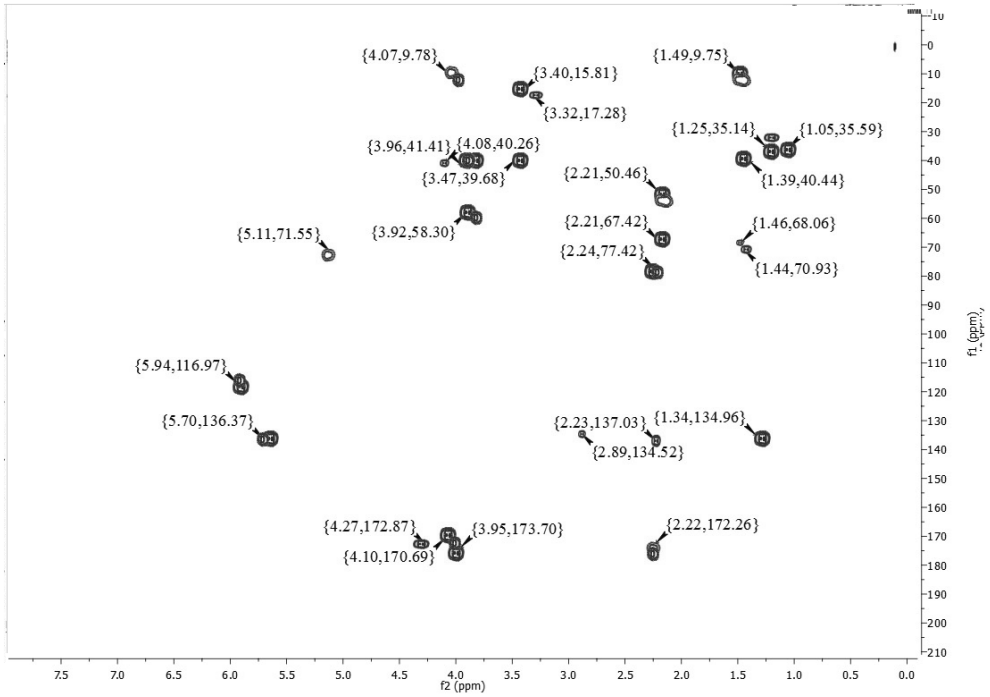

Figure 5.58.: HMBC spectrum of 4,4a,5,6,7,8,11,11a-octahydro-7-hydroxy-6-(6^2-hydroxy-6^3-butenyl)-4-(4^1-hydroxypropyl)-11-methoxy-8-methyl-cyclonona[*c*]pyran-3-(1*H*)-one (**4**)

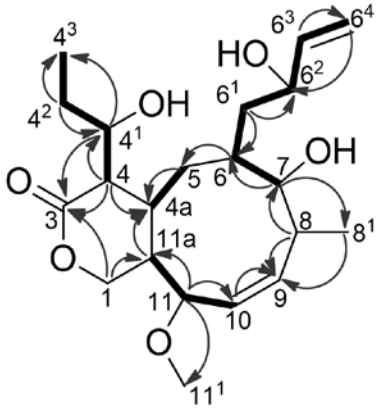

Figure 5.59.: Prominent ^{1}H-^{1}H COSY, and selected HMBC correlations of 4,4a,5,6,7,8,11,11a-Octahydro-7-hydroxy-6-(6^2-hydroxy-6^3-butenyl)-4-(4^1-hydroxypropyl)-11-methoxy-8-methyl-cyclonona[*c*]pyran-3-(1*H*)-one (**4**). The key ^{1}H-^{1}H COSY couplings were represented in bold face bonds. The key HMBC couplings have been represented by double barbed arrows.of

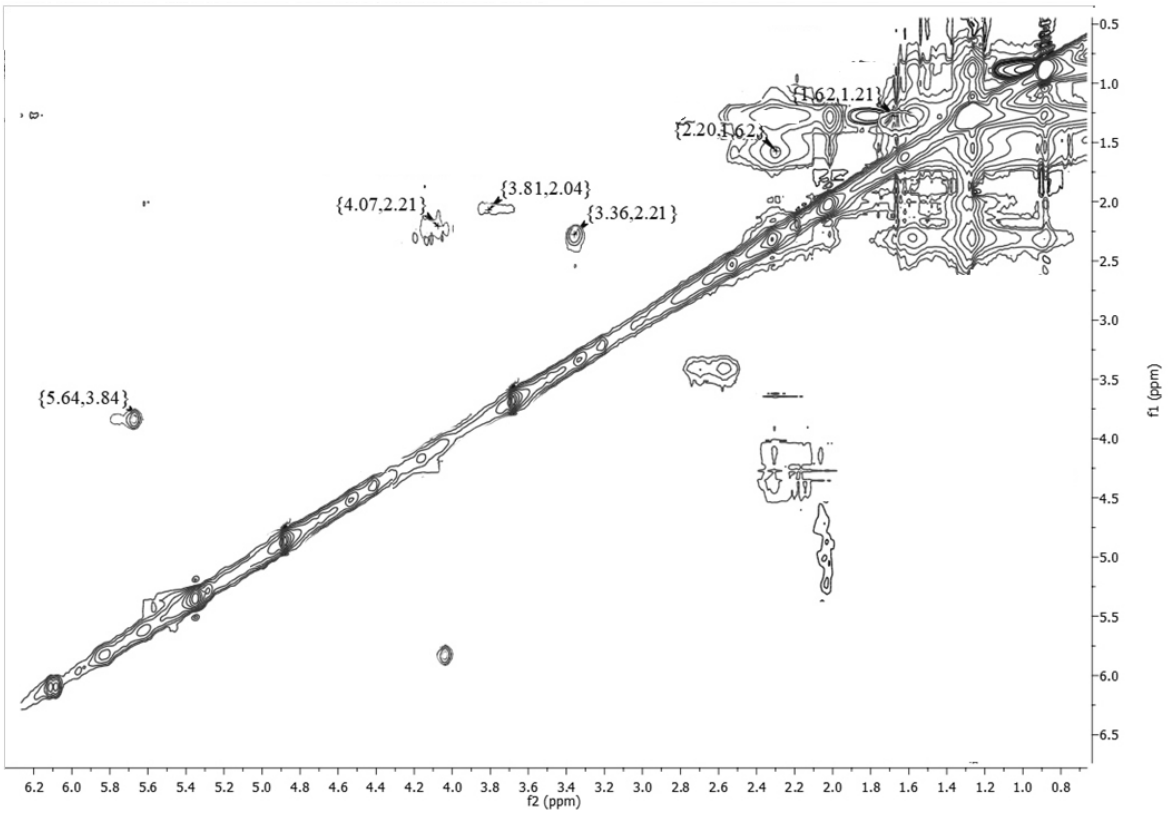

Figure 5.60.: NOESY spectrum of 4,4a,5,6,7,8,11,11a-octahydro-7-hydroxy-6-(6^2-hydroxy-6^3-butenyl)-4-(4^1-hydroxypropyl)-11-methoxy-8-methyl-cyclonona[*c*]pyran-3-(1*H*)-one (**4**)

Relative stereochemistries of **4** were resolved by NOEs, wherein proton signal showed NOEs, such as δ 4.05/2.21 (H-4^1/H-4); δ 1.62/2.21 (H-4/H-4a); δ 1.62/1.21 (H-4a/H-6), and δ 1.21/4.20 (H-6/H-6^2). These protons were arbitrarily assigned to align in the β-face of the diterpene tricyclic system. On the other hand, NOEs showed spatial proximity between protons δ 2.04/3.80 (H-11a/H-11) and δ 3.80/5.69 (H-11/H-10), which were attributed to be *α*-oriented (Figure 5.60-5.61).

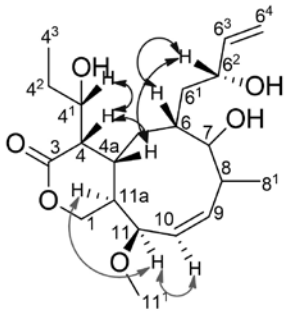

Figure 5.61.: Prominent NOE correlations of 4,4a,5,6,7,8,11,11a-octahydro-7-hydroxy-6-(6^2-hydroxy-6^3-butenyl)-4-(4^1-hydroxypropyl)-11-methoxy-8-methyl-cyclonona[*c*]pyran-3-(1*H*)-one (**4**). NOESY relations are represented by double-tailed arrows

Table 5.7.: NMR spectroscopic data[a] of ,4a,5,6,7,8,11,11a-octahydro-7-hydroxy-6-(6^2-hydroxy-6^3-butenyl)-4-(4^1-hydroxypropyl)-11-methoxy-8-methyl-cyclonona[*c*]pyran-3-(1*H*)-one (**4**) isolated from brown seaweed *P.tetrastromatica*

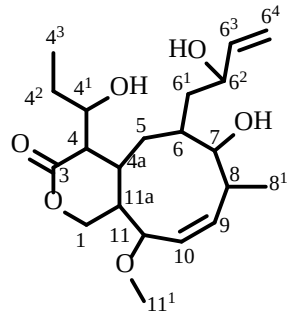

Compound **4** …….4,4a,5,6,7,8,11,11a-octahydro-7-hydroxy-6-(6^2-hydroxy-6^3-butenyl)-4-(4^1-hydroxypropyl)-11-methoxy-8-methyl-cyclonona[*c*]pyran-3-(1*H*)-one (**4)**

C. No.	^{13}C NMR	^{1}H NMR (int., mult., J in Hz)[b]	COSY	HMBC
1	65.02	3.96 (1H, dd, J=9.7, 9.2 Hz) 4.22 (1H, dd, J=8.20, 9.15 Hz)		C-3, 11a
2	-	-	-	-
3	172.69	-	-	-
4	50.20	2.21 (1H, m)	H-4^1	C-3, 4a, 4^1
4a	36.10	1.62 (1H, m)	-	-
4^1	69.92	4.05 (1H, m)	H-4^2	C-3, 4^3
4^2	27.22	1.47 (1H, m), 1.49 (1H, m)	H-4^3	C-4, 4^3
4^3	9.10	0.99 (3H, t, J=6.4 Hz)	-	-
5	31.34	1.02 (1H, m) 1.26 (1H, m)	-	C-4a
6	40.16	1.21 (1H, m)	H-7,6^1	C-5
6^1	38.63	1.42 (2H, dd, J=6.3, 4.0 Hz)	H-6^2	C-6, 6^2
6^2	70.73	4.20 (1H, m)	H-6^3	-
6^3	142.32	5.92 (1H, m)	H-6^4	C-6^4
6^4	116.40	5.17 (1H, m) 5.20 (1H, m)		C-6^2
7	77.02	3.35 (1H, t, J=9.4 Hz)	-	C-6, 8^1
8	43.40	2.20 (1H, m)	-	C-7, 9
8^1	16.18	1.35 (3H, d, J=6.31 Hz)	-	C-9
9	136.25	5.70 (1H, m)		
10	134.67	5.69 (1H, m)	H-11	C-9
11	82.04	3.80 (1H, dd, J=9.1, 4.6 Hz)	H-11a	C-10, 11^1
11a	40.45	2.04 (1H, m)	-	-
11^1	57.17	3.30 (3H, s)	-	-

[a]NMR spectra were recorded using a B ruker AVANCE III 500 MHz (AV 500) spectrometer (B ruker, Karlsruhe, Germany) in $CDCl_3$ as aprotic solvent at ambient temperature with TMS as the internal standard (δ 0 ppm).

[b]Values in ppm, multiplicity and coupling constants (J=Hz) were indicated in parentheses. Multiplicities were allocated by [135]DEPT NMR spectrum.

The assignments were made with the aid of the COSY, HSQC, HMB C and NOESY experiments.

The molecular ion peak of **4** was appeared at *m/z* 382 and base peak was ontained at *m/z* 27.0 (Figure 5.62 and 5.63).

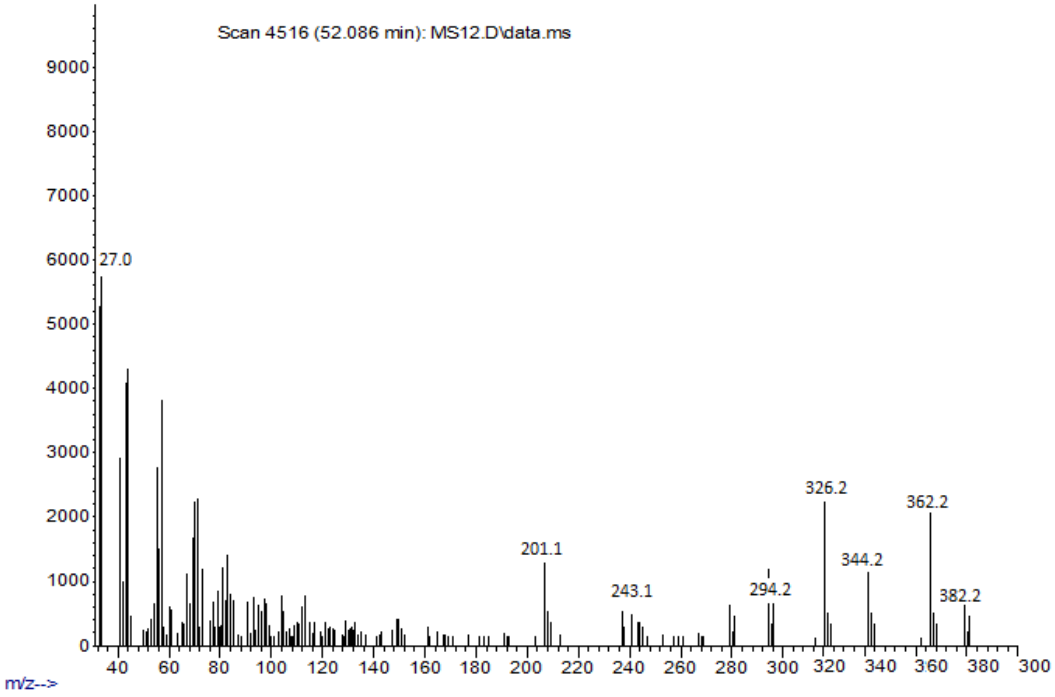

Figure 5.62.: EI-MS spectrum of 4,4a,5,6,7,8,11,11a-octahydro-7-hydroxy-6-(6[2]-hydroxy-6[3]-butenyl)-4-(4[1]-hydroxypropyl)-11-methoxy-8-methyl-cyclonona[*c*]pyran-3-(1*H*)-one (**4)**

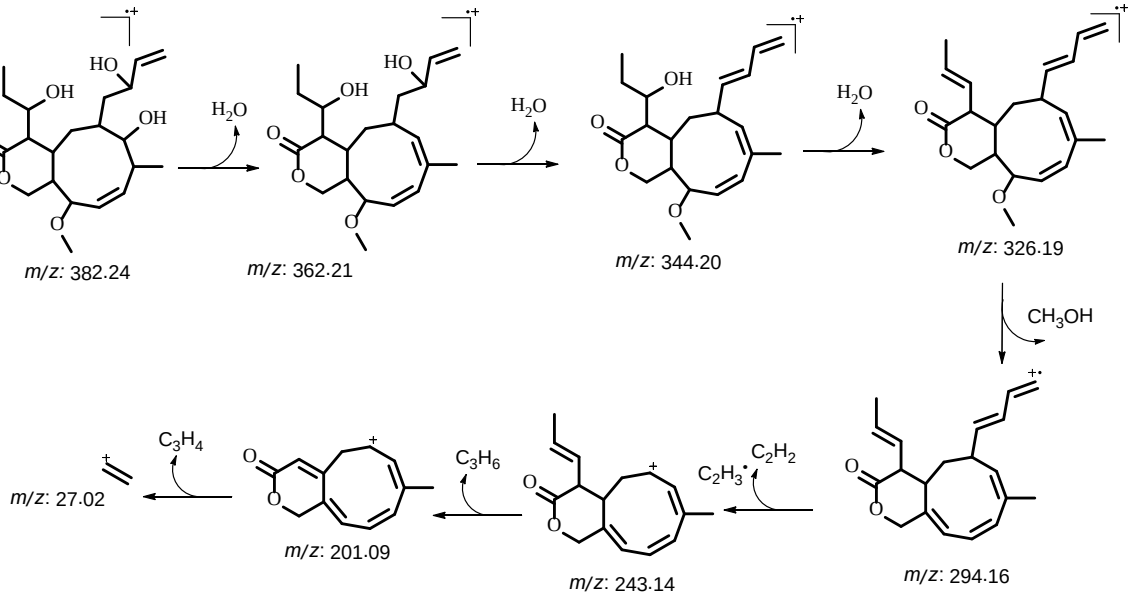

Figure 5.63.: Tentative mass fragmentation pattern of 4,4a,5,6,7,8,11,11a-octahydro-7-hydroxy-6-(6^2-hydroxy-6^3-butenyl)-4-(4^1-hydroxypropyl)-11-methoxy-8-methyl-cyclonona[*c*]pyran-3-(1*H*)-one (**4)**

Structural characterization of Compound 5 (TP_5)

4,4a,5,6,7,8,11,11a-Octahydro-1,7-dihydroxy-4-(4^1-hydroxy-4^2-methylpropyl)-6-(6^1-hydroxy-6^2-propenyl)-10-methyl-cyclonona[*c*]pyran-3(1*H*)-one

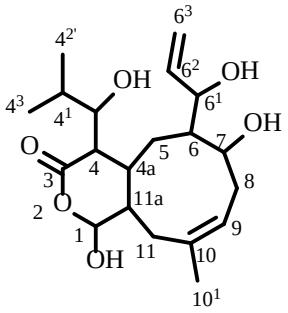

Sample yield	0.27% (> 99% purity, RP-C_{18} HPLC)
Physical description	Yellow oil
Molecular formula	$C_{20}H_{32}O_6$
Molecular mass	368.2199

The xenicane class of diterpenoid derivative, 4,4a,5,6,7,8,11,11a-octahydro-1,7-dihydroxy-4-(4^1-hydroxy-4^2-methylpropyl)-6-(6^1-hydroxy-6^2-propenyl)-10-methyl-cyclonona[*c*]-

pyran-3(1*H*)-one was isolated as yellow oil compound. The compound (**5**) has exhibited UV absorbance (UV (MeOH) λ_{max}) at 246.0 (2.90) nm (Figure 5.64). The homogeneity of the compound was ascertained by HPLC data on a bonded phase octadecylsilane (C_{18}) stationary phase (RP-C_8 HPLC, MeOH:MeCN, 2:3 v/v): 3.23 min (Figure 5.65).

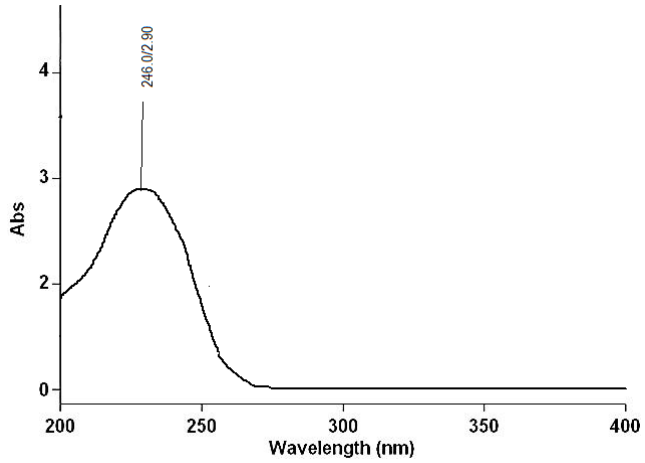

Figure 5.64.: UVspectrum of 4,4a,5,6,7,8,11,11a-octahydro-1,7-dihydroxy-4-(4^1-hydroxy-4^2-methylpropyl)-6-(6^1-hydroxy-6^2-propenyl)-10-methyl-cyclonona[*c*]pyran-3(1*H*)-one (**5**)

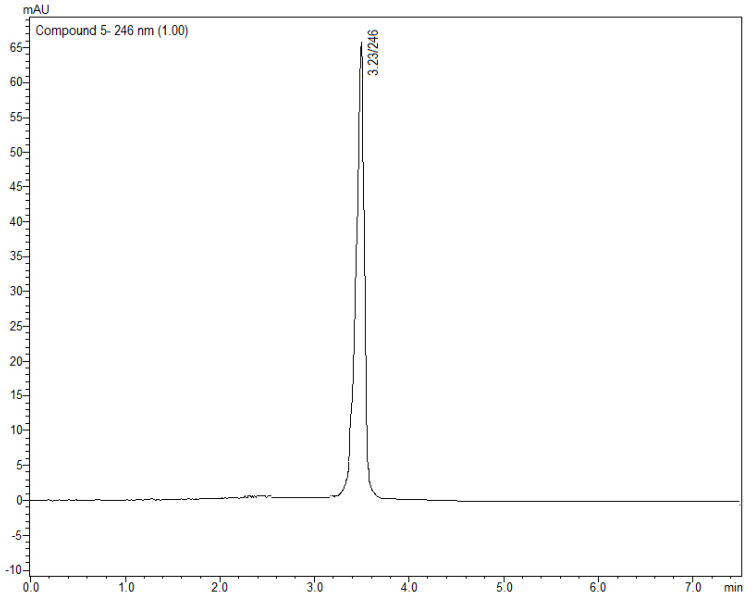

Figure 5.65.: HPLC chromatogram of 4,4a,5,6,7,8,11,11a-octahydro-1,7-dihydroxy-4-(4^1-hydroxy-4^2-methylpropyl)-6-(6^1-hydroxy-6^2-propenyl)-10-methyl-cyclonona[*c*]pyran-3(1*H*)-one (**5**)

The molecular ion peak by HRESIMS (positive mode) was observed at *m/z*: 369.2280 $[M+H]^+$, (Figure 5.66). The FTIR spectrum of **5** displayed absorption bands at, 3450 (O-H), 1715 (C=O) and 1140 (C-C) (Figure 5.67).

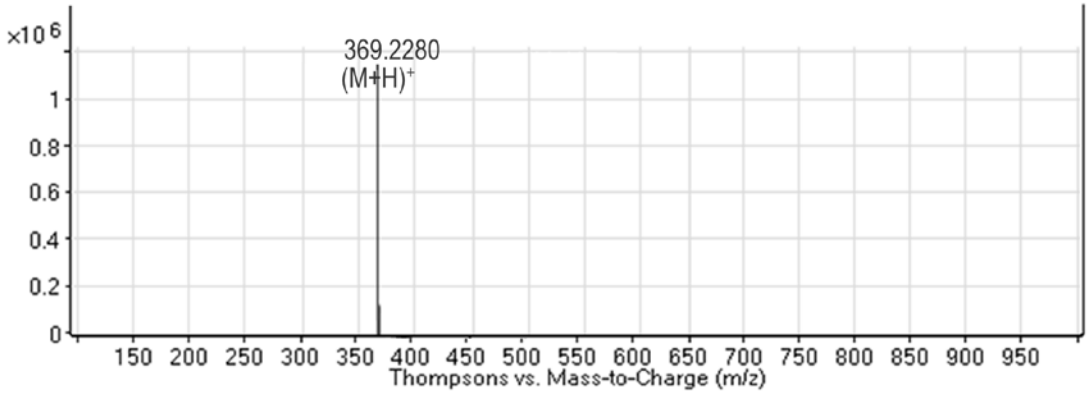

Figure 5.66.: HRESIMS of 4,4a,5,6,7,8,11,11a-octahydro-1,7-dihydroxy-4-(4[1]-hydroxy-4[2]-methylpropyl)-6-(6[1]-hydroxy-6[2]-propenyl)-10-methyl-cyclonona[*c*]pyran-3(1*H*)-one (**5**)

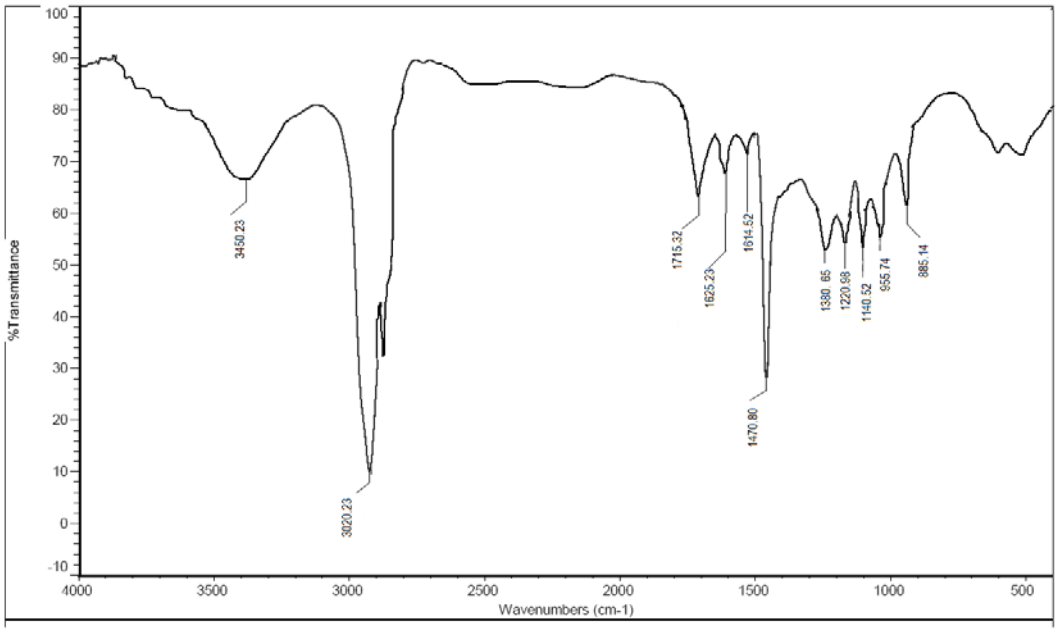

Figure 5.67.: FTIR spectrum of 4,4a,5,6,7,8,11,11a-octahydro-1,7-dihydroxy-4-(4[1]-hydroxy-4[2]-methylpropyl)-6-(6[1]-hydroxy-6[2]-propenyl)-10-methyl-cyclonona[*c*]pyran-3(1*H*)-one (**5**)

The xeniolide **5** was isolated as yellow oil, and the molecular ion peak was appeared at *m/z* 368, whereas the molecular formula $C_{20}H_{32}O_6$, implying five unsaturation degrees, was associated with three olefinic bonds and two ring systems. The compound **5** possessed substitutions on identical carbons (C-4 and C-6) of 9-membered ring, but differed in the substituted side chain patterns and occurrence of methyl moieties. The spectroscopic data of **5** were comparable with those obtained for **4** and **5**. The notable differences in the ^{13}C-NMR data of **5** from those of **4** and **5** were the substitutions at the C-1, C-4, C-6, C-7, and C-10, and corresponding variations were recorded in the ^{1}H NMR spectrum (Figure 5.68-5.71).

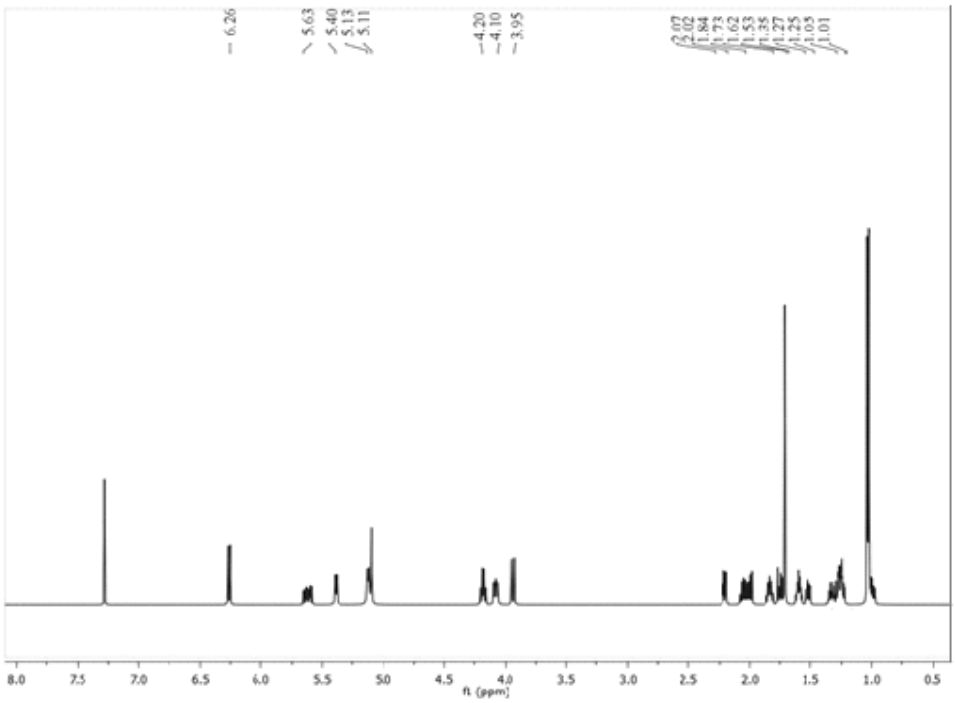

Figure 5.69.: ^{1}H NMR of 4,4a,5,6,7,8,11,11a-octahydro-1,7-dihydroxy-4-(4^{1}-hydroxy-4^{2}-methylpropyl)-6-(6^{1}-hydroxy-6^{2}-propenyl)-10-methyl-cyclonona[*c*]pyran-3(1*H*)-one (**5**)

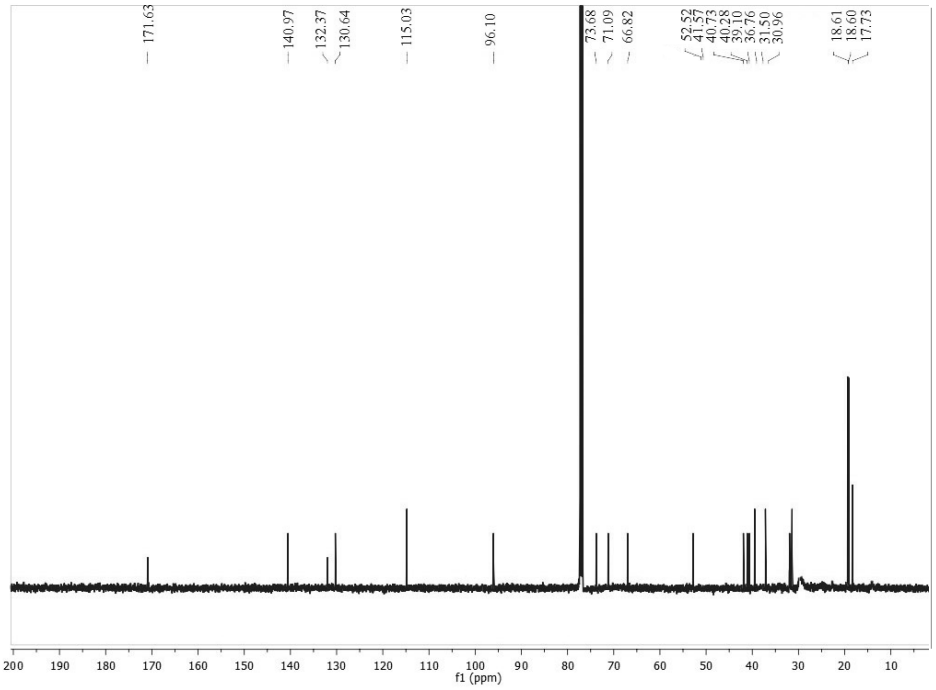

Figure 5.70.: ^{13}C-NMR of 4,4a,5,6,7,8,11,11a-octahydro-1,7-dihydroxy-4-(4^1-hydroxy-4^2-methylpropyl)-6-(6^1-hydroxy-6^2-propenyl)-10-methyl-cyclonona[*c*]pyran-3(1*H*)-one (**5**)

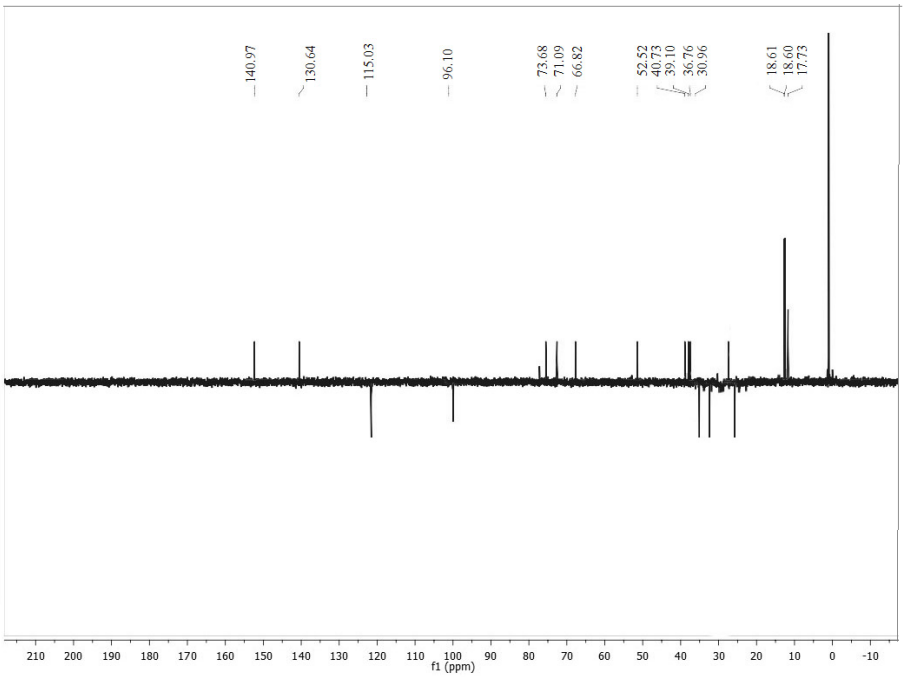

Figure 5.71.:DEPT spectrum of 4,4a,5,6,7,8,11,11a-octahydro-1,7-dihydroxy-4-(4^1-hydroxy-4^2-methylpropyl)-6-(6^1-hydroxy-6^2-propenyl)-10-methyl-cyclonona[*c*]pyran-3(1*H*)-one (**5**)

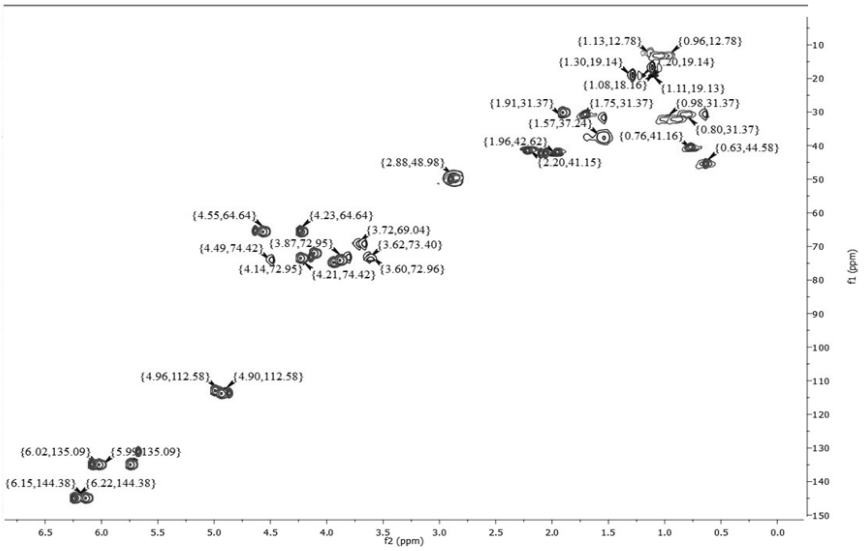

Figure 5.72.: HSQC of 4,4a,5,6,7,8,11,11a-octahydro-1,7-dihydroxy-4-(4^1-hydroxy-4^2-methylpropyl)-6-(6^1-hydroxy-6^2-propenyl)-10-methyl-cyclonona[*c*]pyran-3(1*H*)-one (**5**)

The compound **5** possessed an ester at δ 171.63 (C-3), methyl groups at δ 18.60 (C-4$^{2'}$), δ 18.61 (C-4^3) and δ 17.73 (C-10^1), four methylene groups at δ 36.76 (C-11), δ 66.82 (C-8), and δ 115.03 (C-6^3) (including olefinic methylene), ten methines at δ 96.10 (C-1), δ 52.52 (C-4), δ 40.28 (C-4a), δ 40.73 (C-6), δ 39.10 (C-7), δ 130.64 (C-9), δ 41.57 (C-11a), δ 71.09 (C-4^1), δ 18.60 (C-4$^{2'}$), δ 73.68 (C-6^1), and δ 140.97 (C-6^2) (including one oxymethine and three olefinic methines). The three COSY spin systems (**I, II** and **III**) included 1-hydroxy-2-methylpropyl, 1-hydroxyallyl, and bicyclic ring systems, respectively. The COSY spin system **I** represented correlations between the protons δ 2.07/1.05 (H-4^2/H-4$^{2'}$), δ 2.07/1.05 (H-4^2/H-4^3), which were connected to *δ*-lactone, nine membered ring and two other COSY spin systems (**II** and **III**) via two methine carbons {δ 52.52 (C-4), δ 40.28 (C-4a)}, and one quaternary carbon at δ 71.09 (C-4^1). The HMBCs between δ 1.05/δ 18.61 (H-4$^{2'}$/C-4^3) and δ 1.05/δ 18.60 (H-4^3/C-4$^{2'}$) supported COSY spin **I**, which was linked to *δ*-lactone by HMBC between δ 1.05/δ 71.09 (H-4^3 /C-4^1), δ 1.05/δ 71.09 (H-4$^{2'}$/C-4^1), δ 2.22/δ 171.63 (H-4/C-3), and δ 2.22/δ 71.09 (H-4/C-12). The HMBC at H-6/C-7 connected COSY spin system **I** to 9-membered cyclic system, and the spin system included the cross-peaks at δ 1.01/1.35 (H-5/H-6), δ 1.35/1.53 (H-6/H-7), δ 1.35/4.10 (H-6/H-6^1), and δ 4.10/5.63 (H-6^1/H-6^2). Similarly, COSY spin system **III** was accompanied by protons δ 1.76/1.84 (H-11/H-11a), δ 1.84/1.62 (H-11a/H-4a), δ 1.84/6.26 (H-11a/H-1), wherein the methyl group substituted at C-10 (δ 132.37) was correlated to the bicyclic ring system of xeniolide **5** by HMBCs at δ 1.73/δ 130.64 (H-10^1/C-9) and δ 1.73/δ 132.37 (H-10^1/C-10) (Figure 5.73-5.75).

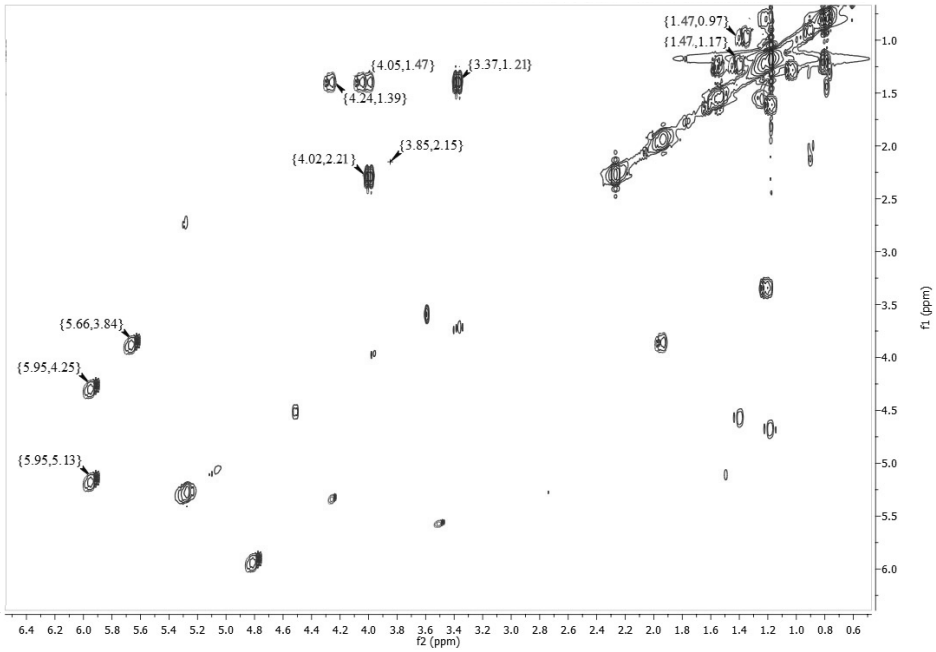

Figure 5.73.: ^{1}H-^{1}H COSY spectrum of 4,4a,5,6,7,8,11,11a-octahydro-1,7-dihydroxy-4-(4^{1}-hydroxy-4^{2}-methylpropyl)-6-(6^{1}-hydroxy-6^{2}-propenyl)-10-methyl-cyclonona[*c*]pyran-3(1*H*)-one (**5**)

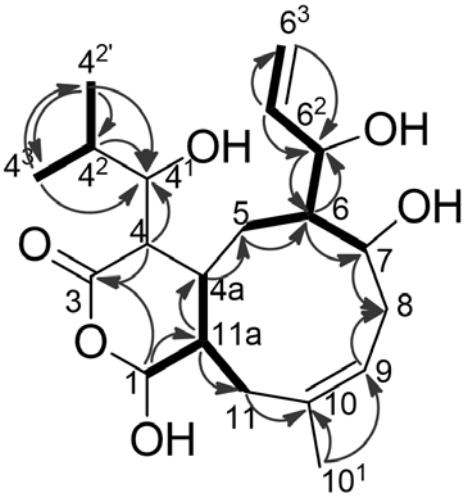

Figure 5.74.: Prominent ^{1}H-^{1}H COSY, and selected HMBC correlations of 4,4a,5,6,7,8,11,11a-octahydro-1,7-dihydroxy-4-(4^{1}-hydroxy-4^{2}-methylpropyl)-6-(6^{1}-hydroxy-6^{2}-propenyl)-10-methyl-cyclonona[*c*]pyran-3(1*H*)-one (**5**). The key ^{1}H-^{1}H COSY couplings were represented in bold face bonds. The key HMBC couplings have been represented by double barbed arrows.

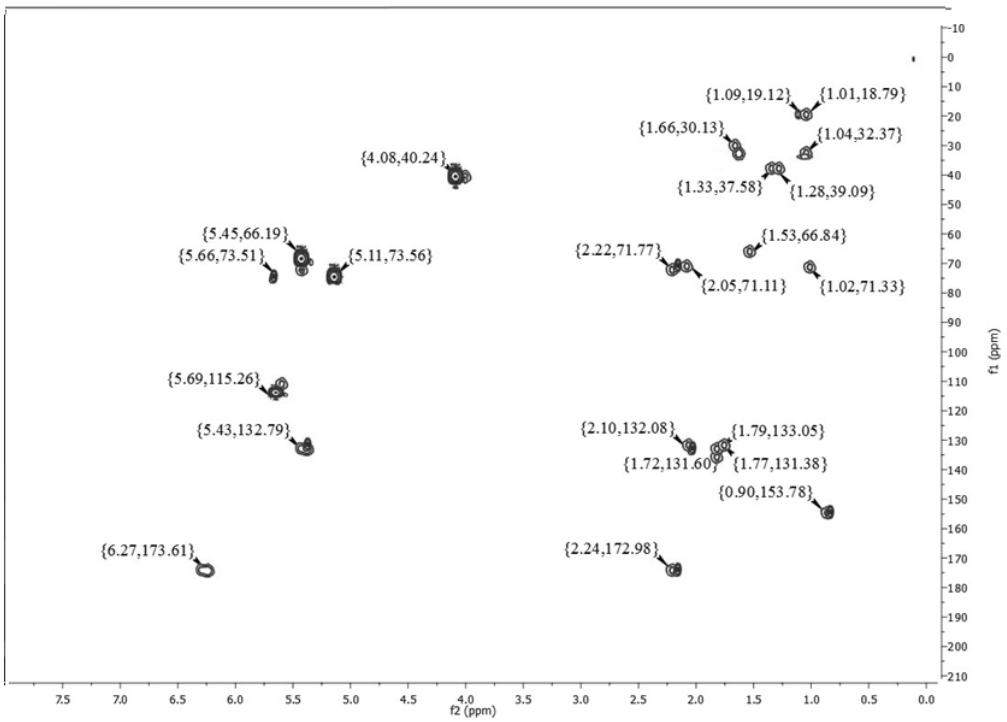

Figure 5.75.: HMBC spectrum of 4,4a,5,6,7,8,11,11a-octahydro-1,7-dihydroxy-4-(4^1-hydroxy-4^2-methylpropyl)-6-(6^1-hydroxy-6^2-propenyl)-10-methyl-cyclonona[*c*]pyran-3(1*H*)-one (**5**)

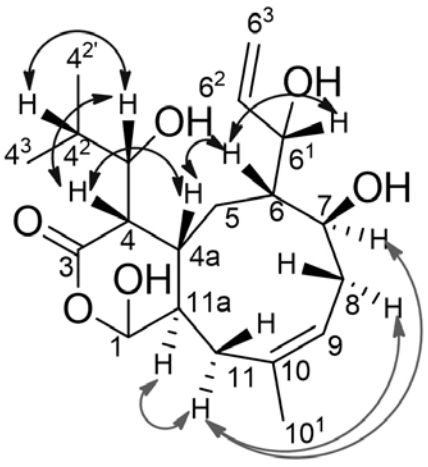

Figure 5.76.: Prominent NOE correlations of 4,4a,5,6,7,8,11,11a-octahydro-1,7-dihydroxy-4-(4^1-hydroxy-4^2-methylpropyl)-6-(6^1-hydroxy-6^2-propenyl)-10-methyl-cyclonona[*c*]pyran-3(1*H*)-one (**5**). NOESY relations are represented by double-tailed arrows

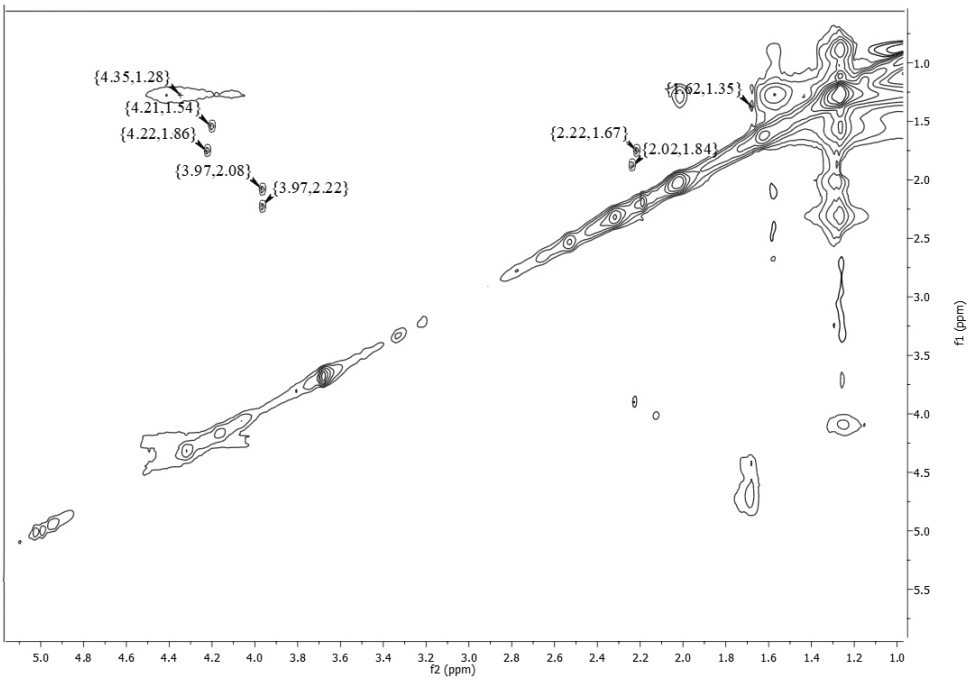

Figure 5.77.: NOESY spectrum of 4,4a,5,6,7,8,11,11a-octahydro-1,7-dihydroxy-4-(4^1-hydroxy-4^2-methylpropyl)-6-(6^1-hydroxy-6^2-propenyl)-10-methyl-cyclonona[*c*]pyran-3(1*H*)-one (**5**)

The NOE data established that the protons at H-4^2, H-4^1, H-4, H-4a and H-6 exhibited spatial correlations, such as H-4^2/H-4^1, H-4^1/H-4, H-4/H-4a, H-4a/H-6, and H-6/H-6^1, and thus, oriented in the similar reference plane of the molecule. These were arbitrarily attributed as β-aligned. Consequently, the protons at H-11a, H-11, H-8 and H-7 were aligned towards the *α*-face of the molecule. The protons at chiral centres C-4^1, C-4, C-4a, C-6 and C-6^1 were arranged in the β-face of the molecule, whereas those at chiral centres C-11a and C-7 were arranged towards the *α*-face (Figure 5.76-5.77).

Table 5.8.: NMR spectroscopic data[a] of 4,4a,5,6,7,8,11,11a-octahydro-1,7-dihydroxy-4-(4^1-hydroxy-4^2-methylpropyl)-6-(6^1-hydroxy-6^2-propenyl)-10-methyl-cyclonona[*c*]pyran-3(1*H*)-one (**5**) isolated from brown seaweed *P.tetrastromatica*

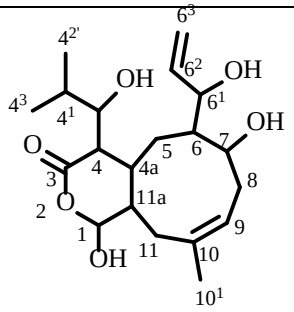

Compound **5**……. 4,4a,5,6,7,8,11,11a-octahydro-1,7-dihydroxy-4-(4^1-hydroxy-4^2-

methylpropyl)-6-(6^1-hydroxy-6^2-propenyl)-10-methyl-cyclonona[*c*]pyran-3(1*H*)-one (**5**)

C. N.	^{13}C NMR	^{1}H NMR (int., mult., J in Hz)[b]	COSY	HMBC
1	96.10	6.26 (1H, d, J=9.6 Hz)	H-11a	C-3
2	-	-	-	-
3	171.63	-		
4	52.52	2.22 (1H, dd, J=9.6, 3..91 Hz)	-	C-3, 4^1
4a	40.28	1.62 (1H, m)		C-5
4^1	71.09	3.95 (1H, d, J=10.5 Hz)	-	-
4^2	31.50	2.07 (1H, m)		C-4^1
$4^{2'}$	18.60	1.05 (3H, m)	H-4^1, 4^3	C-4^3, 4^1
4^3	18.61	1.05 (3H, d, J=6.52 Hz)	-	C-$4^{2'}$, 4^2, 4^1
5	30.96	1.27 (1H, m), 1.01 (1H, m)	H-6	C-6
6	40.73	1.35 (1H, m)	H-7, 6^1	C-7
6^1	73.68	4.10 (1H, dd, J=10.5, 6.5 Hz)	H-6^2	C-6
6^2	140.97	5.63 (1H, m)	H-6^3	C-6^1, 6^3
6^3	115.03	5.11(1H, m), 5.13 (1H, m)	-	C-6^1
7	39.10	1.53 (1H, m), 1.25 (1H, m)	-	C-8
8	66.82	4.20 (1H, dd, J=9.1, 7.6 Hz)		
9	130.64	5.40 (1H, dd, J=15.68 Hz)		C-8, 10
10	132.37	-		
10^1	17.73	1.73 (3H, s), 2.02 (1H, d d, J=11.6, 8.5 Hz)	-	C-10, 9
11	36.76	1.76 (1H, dd, J=12.2, 6.3 Hz)		C-10
11a	41.57	1.84 (1H, m)	H-4a, 11	C-11

[a]NMR spectra were recorded using a B ruker AVANCE III 500 MHz (AV 500) spectrometer (B ruker, Karlsruhe, Germany) in $CDCl_3$ as aprotic solvent at ambient temperature with TMS as the internal standard (δ 0 ppm).

[b]Values in ppm, multiplicity and coupling constants (J=Hz) were indicated in parentheses. Multiplicities were allocated by ^{135}DEPT NMR spectrum.

The assignments were made with the aid of the COSY, HSQC, HMB C and NOESY experiments.

The molecular ion peak of **5** was appeared at *m/z* 368 and base peak was ontained at *m/z* 27.0 (Figure 5.47 and 5.48).

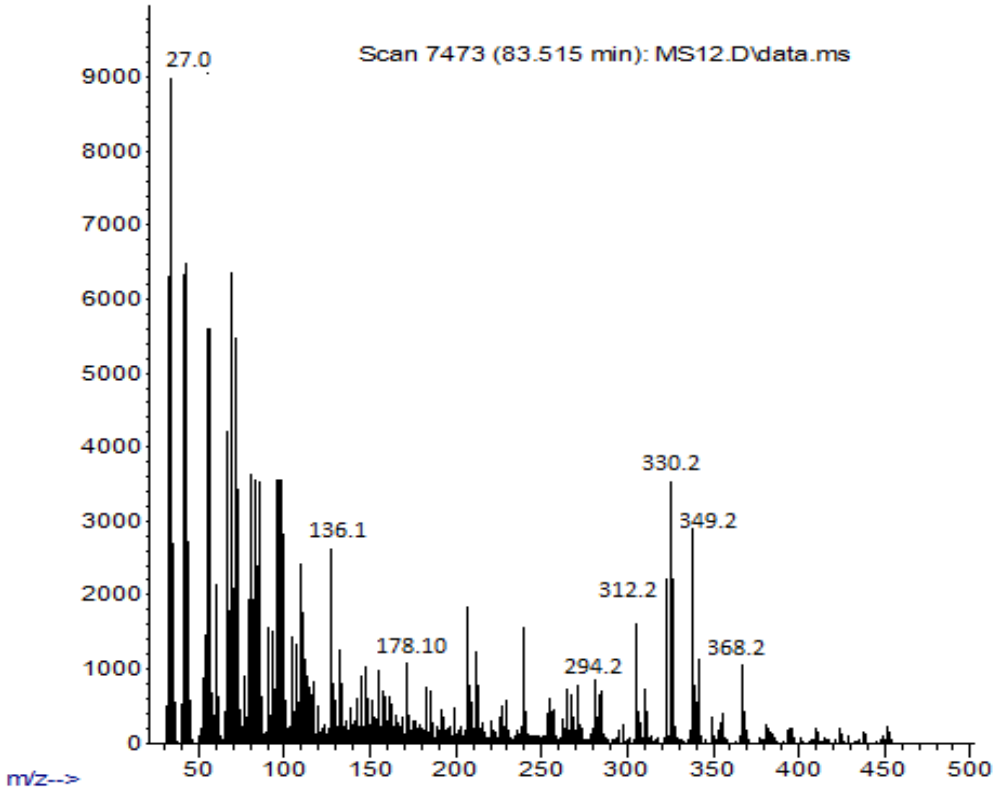

Figure 5.78.: EI-MS spectrum of 4,4a,5,6,7,8,11,11a-octahydro-1,7-dihydroxy-4-(4^1-hydroxy-4^2-methylpropyl)-6-(6^1-hydroxy-6^2-propenyl)-10-methyl-cyclonona[*c*]pyran-3(1*H*)-one (**5**)

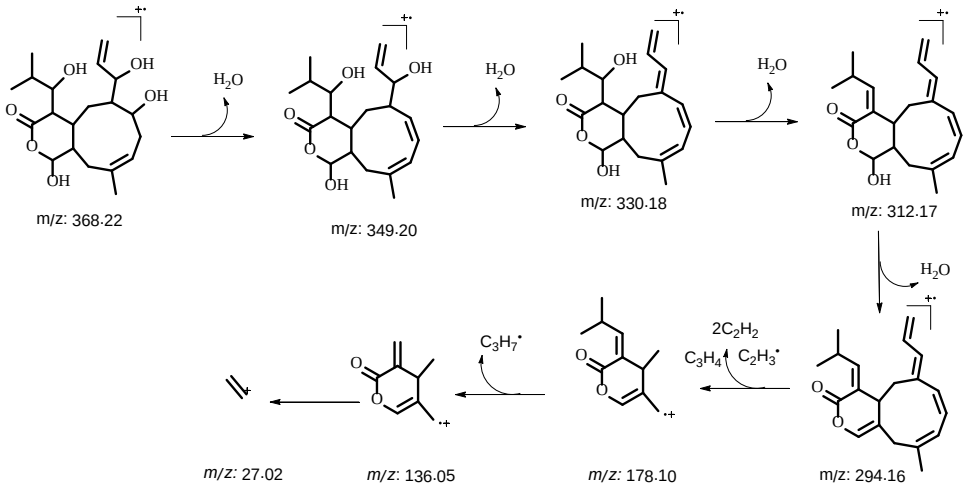

Figure 5.79.: Tentative mass fragmentation pattern of 4,4a,5,6,7,8,11,11a-octahydro-1,7-dihydroxy-4-(4^1-hydroxy-4^2-methylpropyl)-6-(6^1-hydroxy-6^2-propenyl)-10-methyl-cyclonona[*c*]-pyran-3(1*H*)-one (**5**)

5.3.2.2 Structural characterization of dolabellane class of diterpenoid derivatives (6-10)

Seaweeds of the family Dictyotaceae have emerged as a rich source of diterpenoids, and were characterised by mono-, bi- and tri-cyclic carbon skeletons of dolabellane, dolastane and seco-dolastane types, which exhibited wide range of bioactivities (Faulkner et al. 1996). The dolabellanes, which exhibited a regular [9.3.0] cyclotetradecane skeleton were found to constitute a significant chemistries of diterpenoid natural products (Ireland et al. 1976). The metabolites isolated from *Dolabella californica*, a sea hare, were first reported as dolabellanes by Ireland et al. (1976). Subsequent studies showed that dolabellanes were widely scattered among diverse species in marine habitats, especially in Dictyotaceae, and also constituted as secondary metabolites of fungi, liverwort and plants (Rodriguez et al. 1998). Dolabelladienols A-C, the new diterpenes were isolated from the Brazilian brown alga *Dictyota pfaffii* (Vargas et al. 2014). The dolastene variants 1,4-epoxy-17-dolastene, 1,4-dihydroxy-11-oxo-17-dolastene and hydroxy-11-oxo-1,17-dolastadiene were characterised from the brown alga *Dilophus spiralis* (Ioannou et al. 2008; Ioannou et al. 2013). Among various brown seaweeds of family Dictyotaceae, *Padina sp*. was found to constitute a predominant share, whereas about 50 taxa of this genus were distributed worldwide (Guiry and Dhonncha 2003). Among them, *Padina tetrastromatica* (Hauck) were found to be distributed in the coastal waters of the Indian peninsular (Guiry and Dhonncha 2003), and were explored for different bio-potential functionalities (Mohsin et al. 2014). Although most of the compounds belonging to dolabellanes and dolastanes were reported from the brown alga of Dictyotaceae family, there were no reports on detailed structural characterisation of bioactive leads *P. tetrastromatica* belonging to the same family. There were variants of this class of terpenoid compounds with previously unprecedented cabocyclic skeletons and functionalizations contributing towards their potential bioactivities, such as antioxidative and anti-diabetic pluralities. The present study described the isolation and characterisation of five previously unreported diterpenoids of dolabellane (**6-8**) and dolastane (**9-10**) class of chemistries from ethyl acetate: methanol (EtOAc:MeOH) extract of *P. tetrastromatica* collected from southeast coastal region of the Indian peninsular. The studied compounds were characterised by extensive spectroscopic experiments. The pharmacological activities were assessed by different *in vitro* antioxidant/anti-diabetic assays and physicochemical parameters were utilised to corroborate the structure-activity correlations with their bioactive potentials. The *in silico* mode of α-amylase inhibition by the studied compounds were assessed by the molecular docking models to correlate with their *in vitro* anti-hyperglycaemic potential.

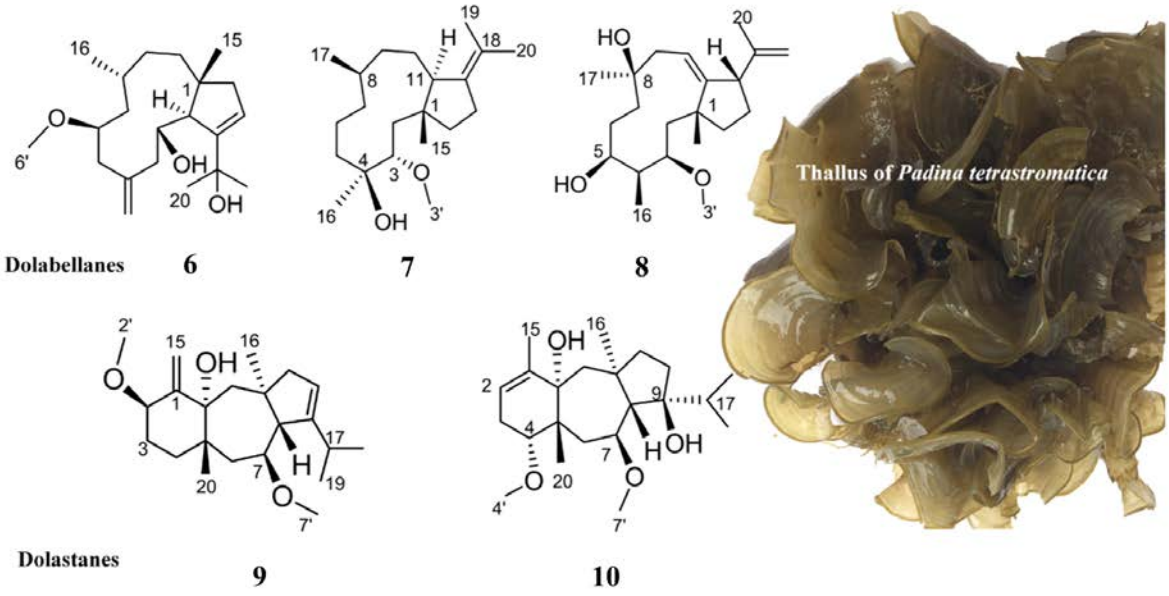

Figure 5.80.: The structures of 6-methoxy-dolabella-8(17),12-diene-10β,18-diol (**6**), 3-methoxy-dolabella-12(18)-ene-4β-ol (**7**), 3-methoxy-dolabella-10,18(19)-diene-5α,8β-diol (**8**), 2,7-dimethoxy-14*α*-hydroxy-dolasta-1(15),9-diene (**9**), and 4,7-dimethoxy-9β,14*α*-dihydroxy-dolasta-1-ene (**10**) isolated from *P. tetrastromatica*. Representative photograph of the thalli (leafy structures) of *P. tetrastromatica* was shown.

5.3.2.2a Structural characterization of Compound 5 (TP_6)

6-Methoxy-dolabella-8(17),12-diene-10β ,18-diol

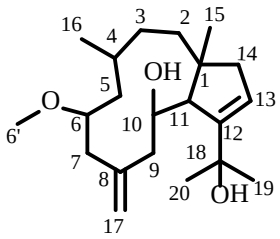

Sample yield	0.25% (> 99% purity, RP-C_{18} HPLC)
Physical description	pale yellow viscous oil
Molecular formula	$C_{21}H_{36}O_3$
Molecular mass	336.2664

The dolabellane class of diterpenoid derivative, 6-methoxy-dolabella-8(17),12-diene-10β ,18-diol was isolated as pale yellow viscous oil compound. The compound (**6**) has exhibited UV absorbance

(UV (MeOH) λ_{max}) at 242.6 (2.89) nm (Figure 5.81). The homogeneity of the compound was ascertained by HPLC data on a bonded phase octadecylsilane (C_{18}) stationary phase (RP-C_8 HPLC, MeOH: MeCN, 3:2 v/v): 3.21 min (Figure 5.82). The molecular ion peak by HRESIMS was observed at *m/z* 337.2742 $[M+H]^+$ (Figure 5.83) .

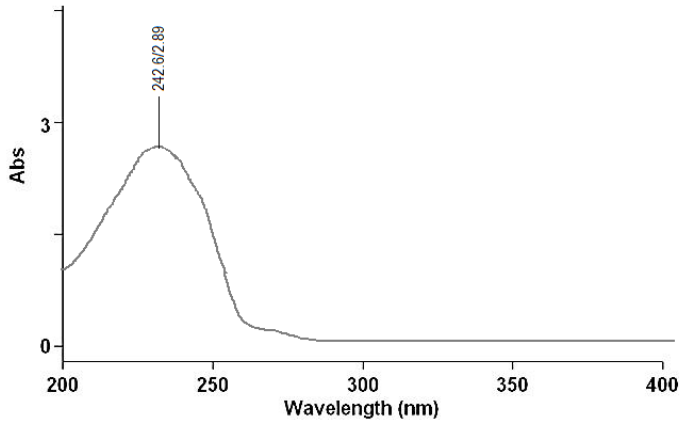

Figure 5.81.: UVspectrum of 6-methoxy-dolabella-8(17),12-diene-10β ,18-diol (**6**)

5.2.5.6 Physicochemical description of compound-6 (TP_6)

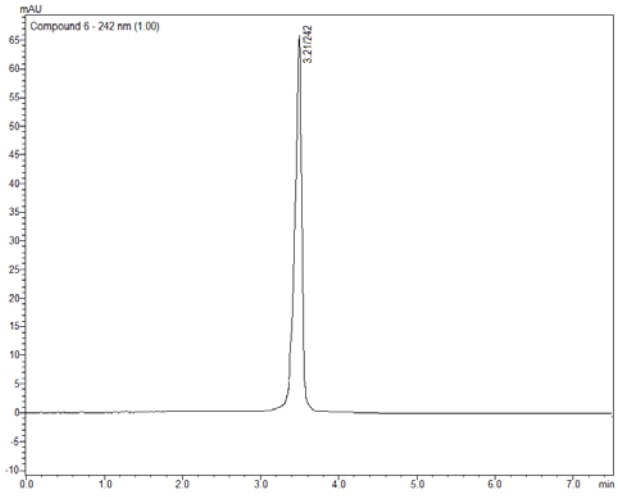

Figure 5.82.: HPLC chromatogram of 6-methoxy-dolabella-8(17),12-diene-10β ,18-diol (**6**)

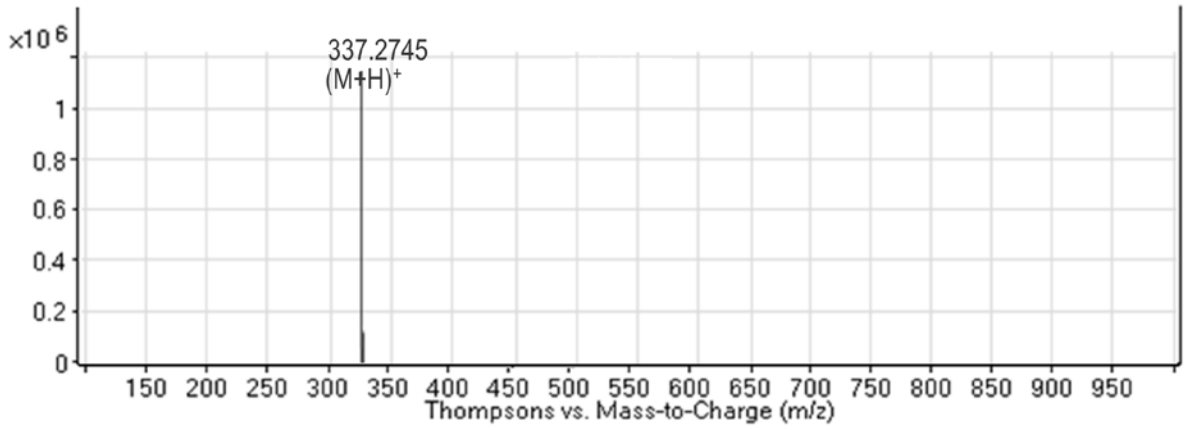

Figure 5.83.: HRESIMS of 6-methoxy-dolabella-8(17),12-diene-10β ,18-diol (**6**)

Repetitive purification of extract of *P. tetrastromatica* using preparatory RP-C_{18} HPLC yielded a dolabellane derivative (**6**) as pale yellow viscous oil. The elemental composition of **6** was deduced by detailed NMR/IR/mass analyses as $C_{21}H_{36}O_3$ with four degrees of unsaturation, which were related to two double bonds and ring systems (Figure 5.84-5.90, Table 5.8).

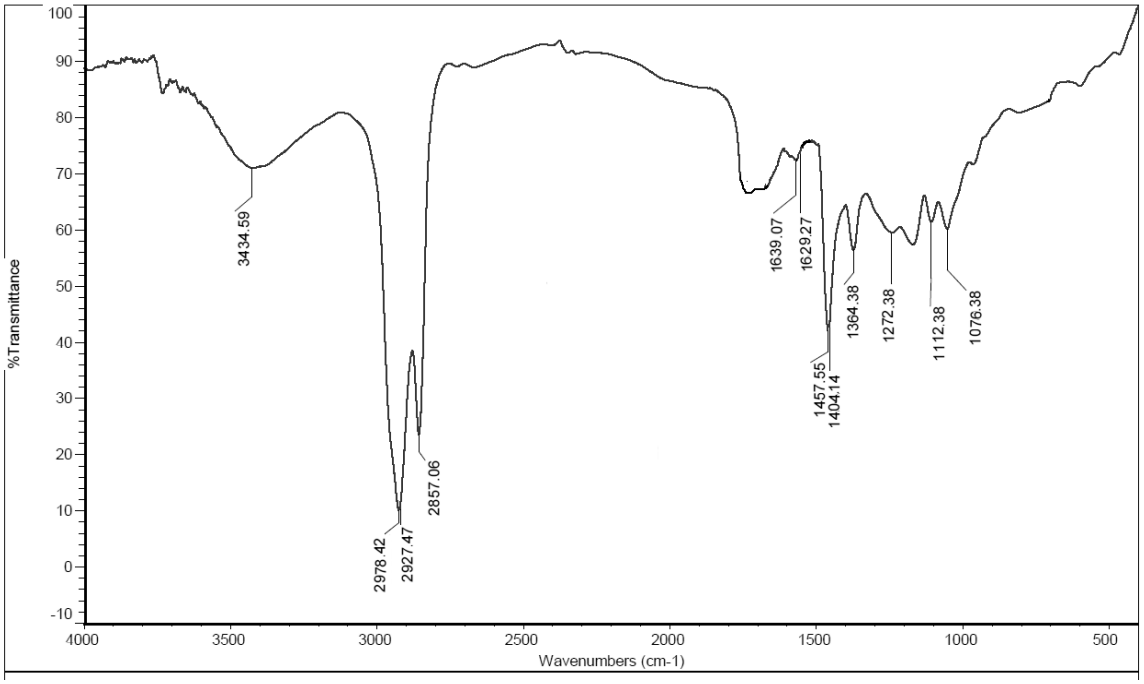

Figure 5.84.: FTIR spectrum of 6-methoxy-dolabella-8(17),12-diene-10β ,18-diol (**6**)

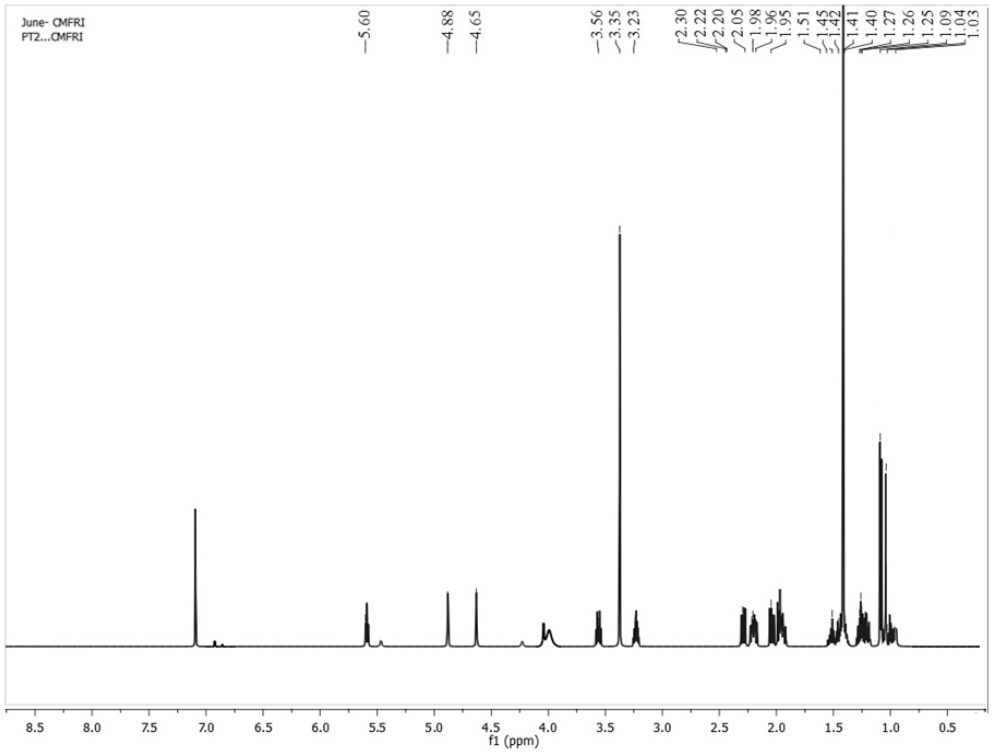

Figure 5.85.: ^{1}H NMR spectrum of 6-methoxy-dolabella-8(17),12-diene-10β ,18-diol (**6**)

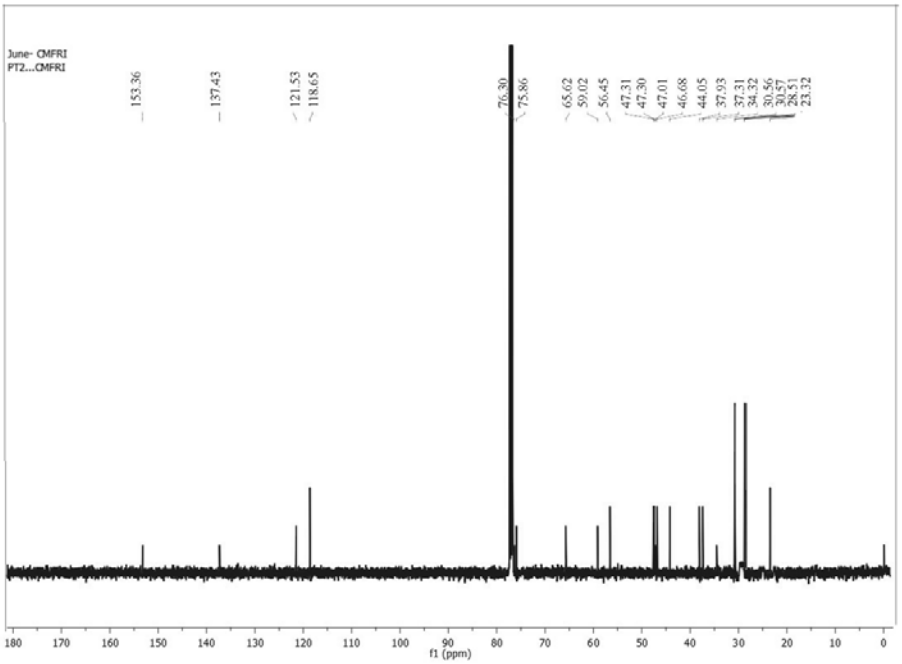

Figure 5.86.: ^{13}C NMR spectrum of 6-methoxy-dolabella-8(17),12-diene-10β ,18-diol (**6**)

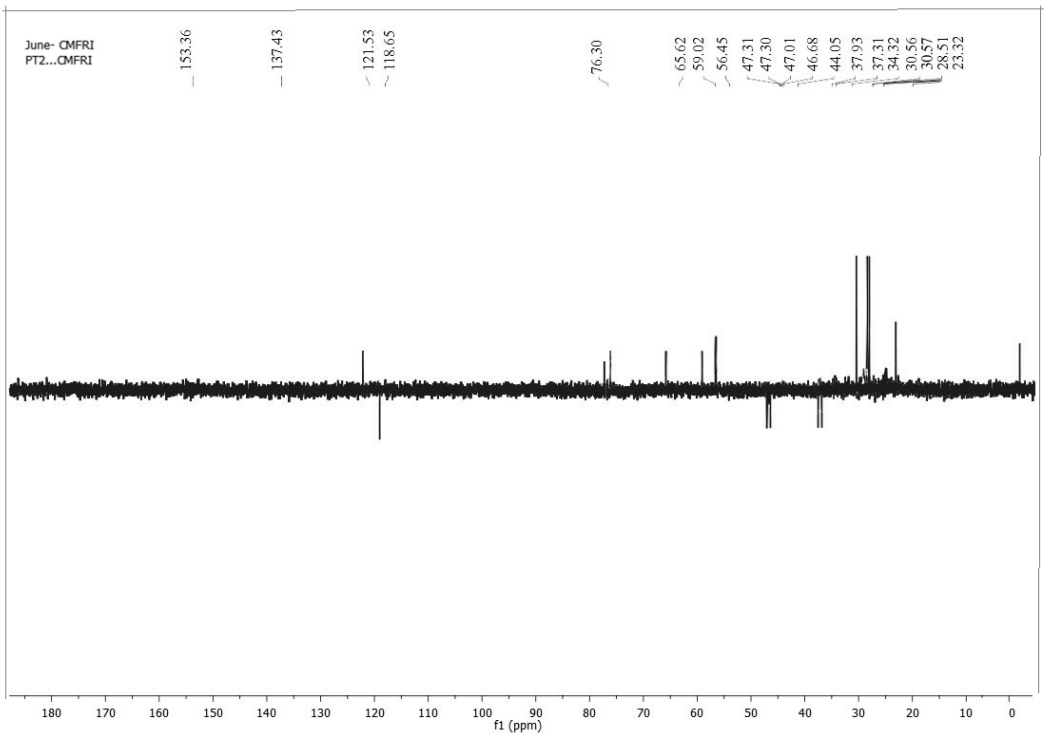

Figure 5.87.: DEPT spectrum of 6-methoxy-dolabella-8(17),12-diene-10β ,18-diol (**6**)

The molecular ion peak was found at *m/z* 336.27 [M^+]. Carbon signals at δ 75.9 (HSQC δ 3.23), 65.6 (HSQC δ 3.56) and 76.3 appropriately supported the presence of oxygen functionalities. The detailed NMR spectroscopic data of **6** was comparable with the basic chemical resonances of dolabellane type of diterpenes, such as 18-hydroxydolabella-4(16),7-dien-3-one and 3,4-epoxydolabella-7-en-18-ol (Cai et al. 2010). The ^{1}H-^{1}H COSYs between the protons δ 1.03 (H-2)/1.26 (H-3)/1.40 (H-4)/1.27 (H-5)/3.23 (H-6)/2.20 (H-7) and δ 2.22 (H-9)/3.56 (H-10) along with the HMBC cross-peaks at δ /δ 1.03 (H-2)/47.0 (C-1), δ /δ 1.51 (H-5)/44.0 (C-7) proposed a closed loop of 11-membered ring in **6** (Figure 5.91). Therefore, the positions of carbons in 11-membered ring were assigned from C-1 to C-11 continuously, which were in agreement with an earlier report (Cai et al. 2010). The HMBC correlations between δ /δ 1.98 (H-11)/153.4 (C-12), δ /δ 5.60 (H-13)/153.4 (C-12), δ /δ 2.05 (H-14)/59.02 (C-11), δ /δ 2.05 (H-14)/47.0 (C-1) in combination with the COSYs δ 5.60 (H-13)/2.05 (H-14) appropriately characterised the existence of 5-membered carbocyclic system, and also assigned the location of a double bond between C-12 and C-13 (Figure 5.91).

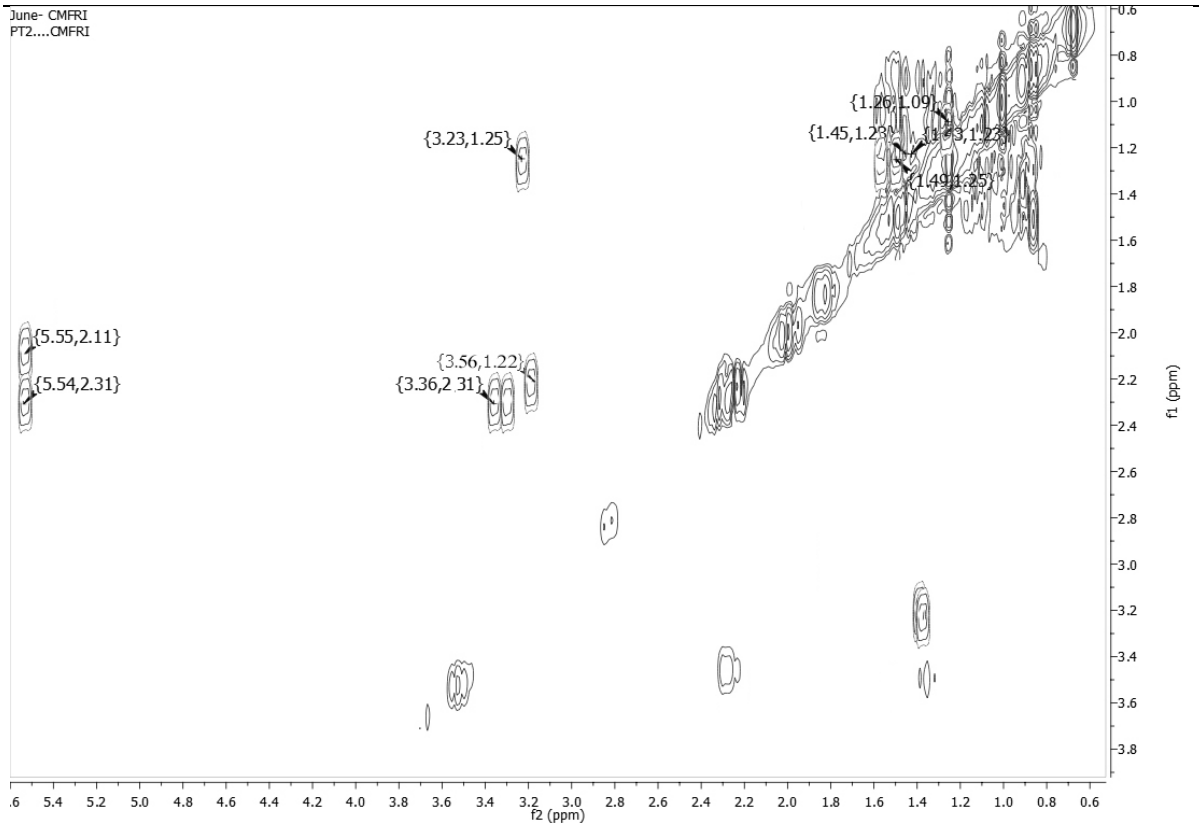

Figure 5.88.: ^{1}H-^{1}H COSY spectrum of 6-methoxy-dolabella-8(17),12-diene-10β ,18-diol (**6**)

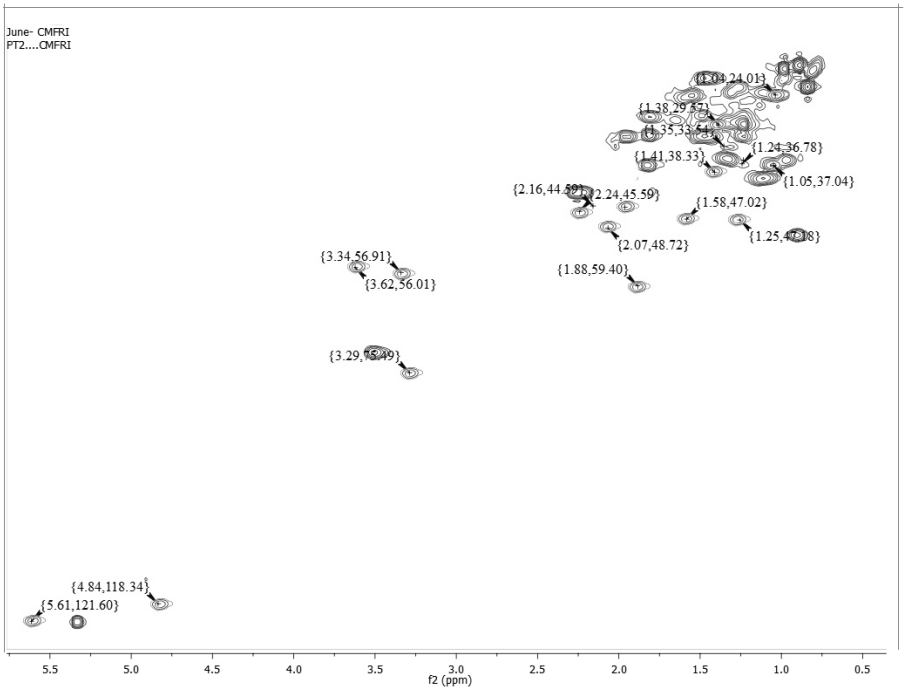

Figure 5.89.: HSQC spectrum of 6-methoxy-dolabella-8(17),12-diene-10β ,18-diol (**6**)

The presence of disubstituted exocyclic olefinic linkage at C-8 and C-17 positions were proposed by HMBCs, such as δ /δ 2.20 (H-7)/118.7 (C-17), δ /δ 1.96 (H-9)/118.7 (C-17) and δ /δ 4.88 (H-17)/137.4 (C-8). HMBC interactions of δ /δ 1.04 (H-15)/47.0 (C-1), 47.3 (C-14) appropriately explained the location of methyl group placed at C-15, (bonded to C-1). These spectroscopic data closely resembled to those of bicyclic dolabellane skeleton with fused 11- and 5-membered rings (Cai et al. 2010; Ioannou et al. 2012). The compound, dolabella-4(16),7-dien-3,18-diol, which was identified from the terrestrial plant, *Aglaia odorata* (Cai et al. 2010), enclosed the disubstituted exocyclic olefinic moiety at C-4, along with a tertiary hydroxyl at C-18 and trisubstituted olefinic group coupled with methyl at C7=C8 positions. Notably, the compound **6** enclosed disubstituted exocyclic olefinic moiety at C-8, tertiary hydroxyl at C-18, along with the trisubstituted alkene at C12=C13 and hydroxyl at C-10. The proton signals corresponding to the methyl groups attached to C-1 and C-4 were in agreement with the diterpenes isolated from the brown seaweed *Dictyota divaricata* (Konig et al. 1991). The compound, 18-hydroxy-2,7-dolabelladiene from *D. divaricata* comprised of endocyclic double bond coupled with methyl at C7=C8 (Konig et al. 1991), whereas the studied compound enclosed a disubstituted exocyclic olefinic moiety at C-8. It is of note that the studied dolabellane diterpenoid exhibited similarities with the dolabellane framework, even though, the carbocyclic skeleton with different olefinic and oxy functionalizations were present in the titled compound **6** accounting for its novelty.

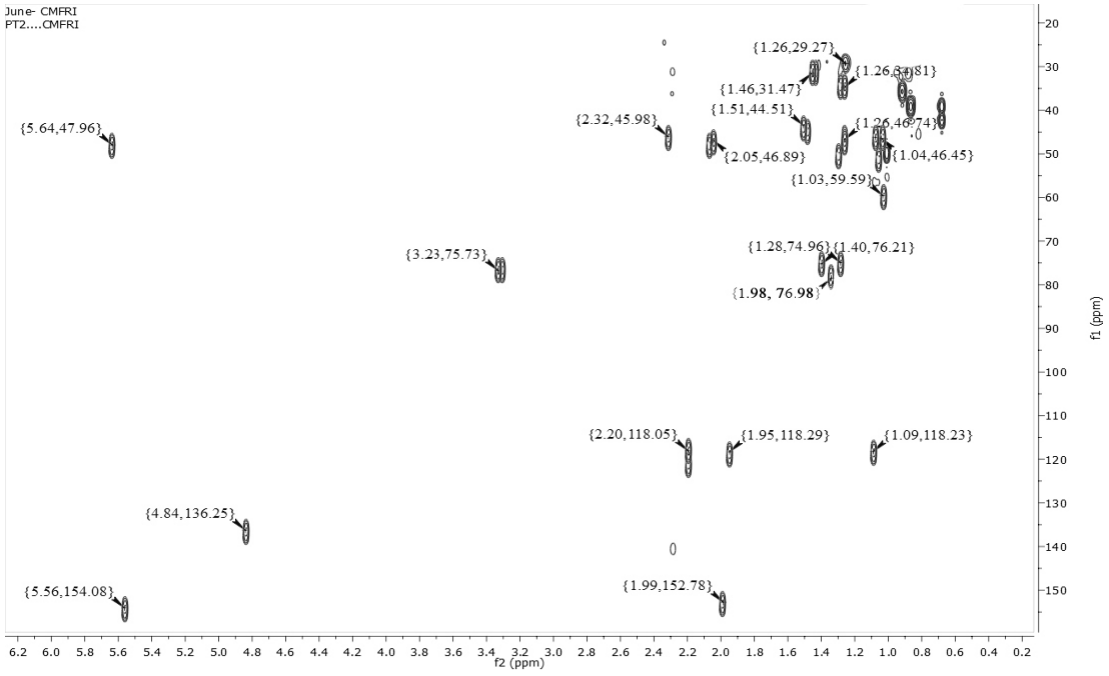

Figure 5.90.: HMBC spectrum of 6-methoxy-dolabella-8(17),12-diene-10β ,18-diol (**6**)

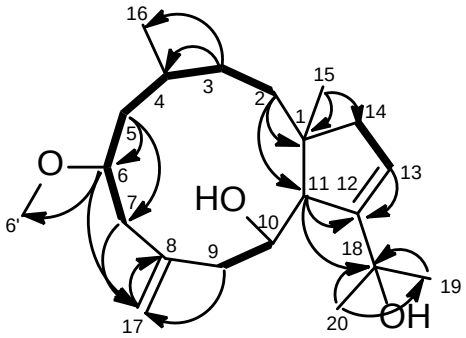

Figure 5.91.: Prominent ^{1}H-^{1}H COSY, and selected HMBC correlations of 6-methoxy-dolabella-8(17),12-diene-10β ,18-diol (**6**). The key ^{1}H-^{1}H COSY couplings were represented in bold face bonds. The key HMBC couplings have been represented by double barbed arrows.

Relative stereochemistries of the chiral centres at C-6, C-10 and C-11 in **6** were assigned by the NOESY experiments (Figure 5.92 & 5.93), and earlier reports (Konig et al. 1991). The NOESY correlations between δ 3.35 (H-6')/1.45 (Hβ-3)/1.05 (H-15), δ 1.40 (H-4)/2.20 (H-7)/4.65 (Hβ-17)/1.45 (Hβ-3) and δ 2.22 (H-9)/4.65 (Hβ-17) appropriately attributed that these protons were coordinated in the identical plane of reference, and hence were assigned as β-oriented.

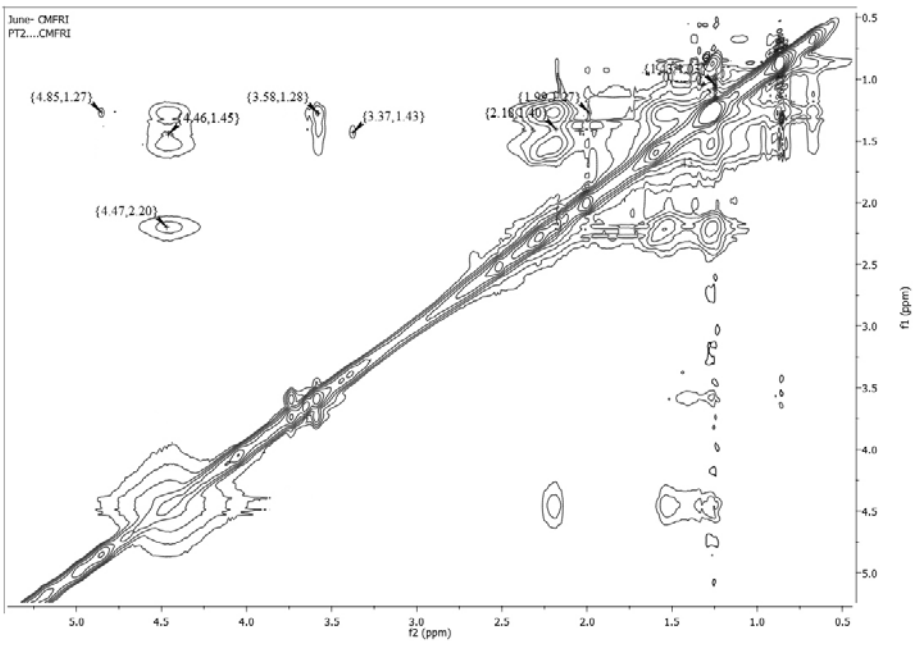

Figure 5.92.: NOESY spectrum of 6-methoxy-dolabella-8(17),12-diene-10β ,18-diol (**6**)

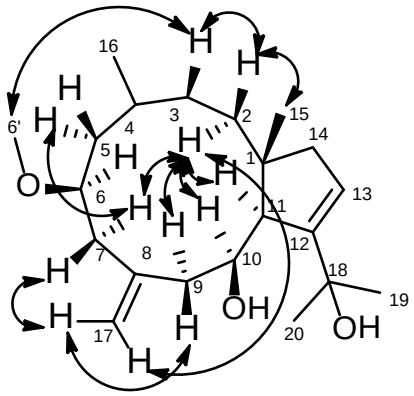

Figure 5.93.: Prominent NOE correlations of 1 6-methoxy-dolabella-8(17),12-diene-10β ,18-diol (**6**). NOESY relations are represented by double-tailed arrows

The molecular ion peak of **6** was appeared at *m/z* 336 and base peak was ontained at *m/z* 27.0 (Figure 5.94 and 5.95).

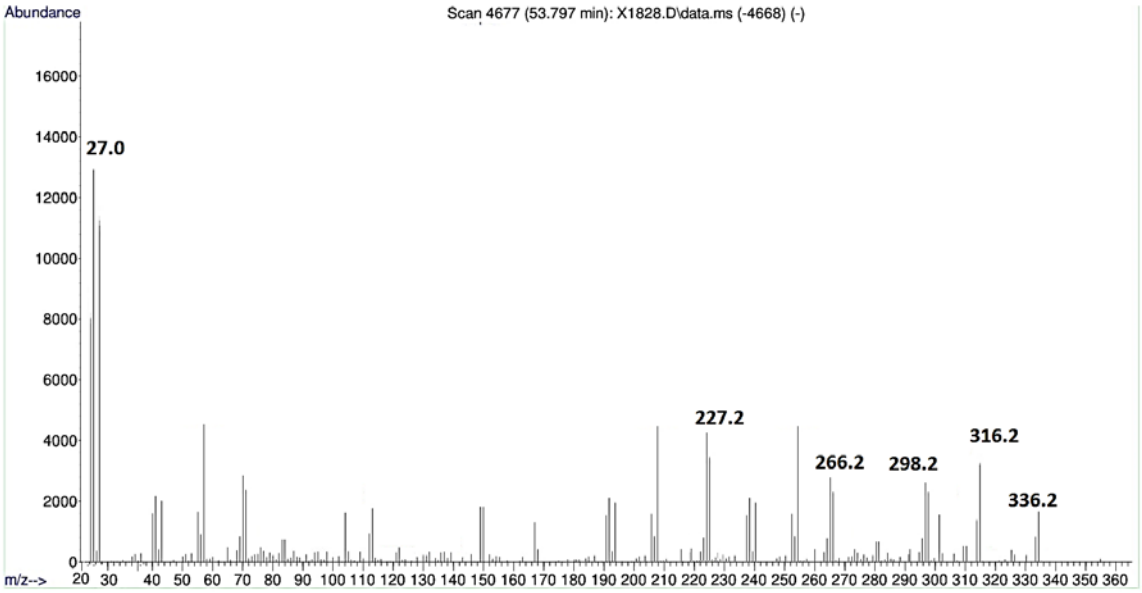

Figure 5.94.: EI-MS spectrum of 6-methoxy-dolabella-8(17),12-diene-10β ,18-diol (**6**)

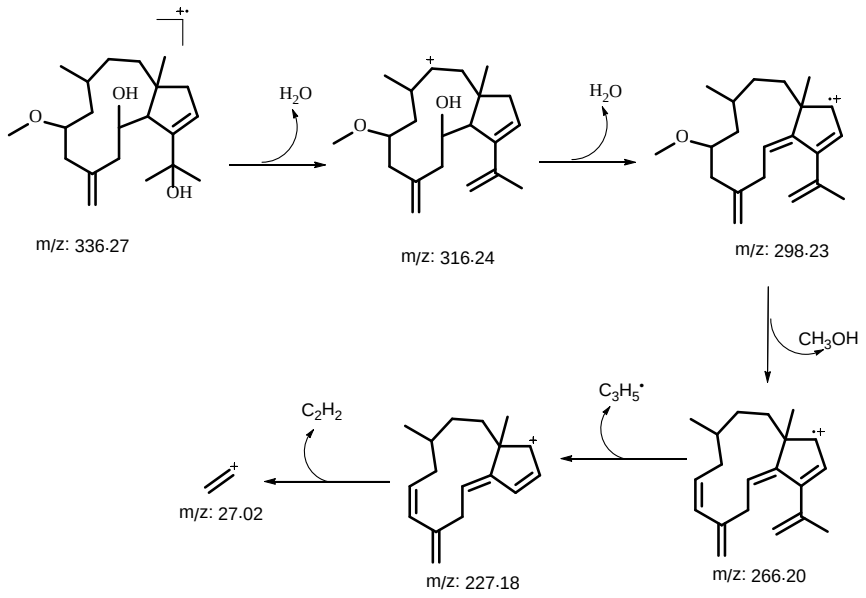

Figure 5.95.: Tentative mass fragmentation pattern of 6-methoxy-dolabella-8(17),12-diene-10β ,18-diol (**6**)

Table 5.9.: NMR spectroscopic data[a] of 3-methoxy-dolabella-12(18)-ene-4β-ol (**6**) isolated from brown seaweed *P.tetrastromatica*

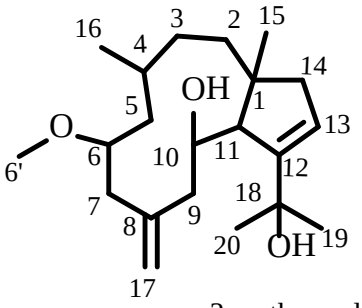

Compound **6**……3-methoxy-dolabella-12(18)-ene-4β-ol

C. No.	^{13}C NMR	^{1}H NMR (int.,mult., J in Hz)[b]	COSY	HMBC
1	47.0	-	-	-
2	38.0	1.25(1H,dd,11.1, 7.2Hz)	H-3	C-1
		1.03(1H,dd,10.6, 5.7Hz)	-	-
3	37.3	1.26(1H,m),	H-4	C-16, 4
		1.45(1H,m)	-	-
4	34.3	1.40(1H,m)	H-5	-
5	47.3	1.51(1H,t,10.6 Hz),	H-6	C-7
		1.27(1H,t, 9.9Hz)	-	C-6
6	75.9	3.23(1H,m)	H-7	C-17, 6’
6’	56.5	3.35(1H,s)	-	C-6
7	44.1	2.20(1H,d,10.2 Hz),	-	C-17

		1.95(1H,d, 9.8Hz)	-	-
8	137.3	-	-	-
9	46.7	2.22(1H,d,11.1 Hz),	H-10	C-17
		1.96(1H,d,9.6 Hz)		
10	65.62	3.56(1H,m)	-	-
11	59.0	1.98(1H,d,10.2 Hz)	-	C-12,18
12	153.4	-	-	-
13	121.5	5.60(1H,t,9.8 Hz)	H-14	C-14,12
14	47.3	2.05(1H,d,9.3 Hz)	-	C-1,11
		2.30(1H,d,9.7 Hz)	-	-
15	23.3	1.04(3H,s)	-	C-14,1
16	28.5	1.09(3H,d,6.4 Hz)	-	-
17	118.7	4.88(1H,s),	-	C-8
		4.65(1H,s)	-	-
18	76.3	-	-	-
19	30.6	1.41(3H,s)	-	C-18
20	30.6	1.42(1H, s)	-	C-19

[a]NMR spectra were recorded using a Bruker AVANCE III 500 MHz (AV 500) spectrometer (Bruker, Karlsruhe, Germany) in $CDCl_3$ as aprotic solvent at ambient temperature with TMS as the internal standard (δ 0 ppm).

[b]Values in ppm, multiplicity and coupling constants (*J*= Hz) were indicated in parentheses. Multiplicities were allocated by [135]DEPT NMR spectrum.

The assignments were made with the aid of the COSY, HSQC, HMBC and NOESY experiments.

5.3.2.2b Structural characterization of Compound 7 (TP_7)

3-Methoxy-dolabella-12(18)-ene-4β-ol

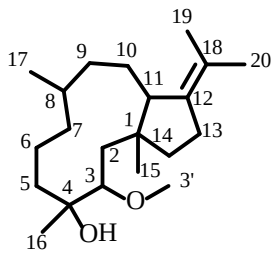

Sample yield	0.25% (> 99% purity, RP-C_{18} HPLC)
Physical description	Yellow oil
Molecular formula	$C_{21}H_{38}O_2$
Molecular mass	322.2872

The dolabellane class of diterpenoid derivative, 3-methoxy-dolabella-12(18)-ene-4β-ol was isolated as yellow oil compound. The compound (**7**) has exhibited UV absorbance (UV (MeOH)

λ_{max}) at 246.0 (2.90) nm (Figure 5.96). The homogeneity of the compound was ascertained by HPLC data on a bonded phase octadecylsilane (C_{18}) stationary phase (RP-C_8 HPLC, MeOH: MeCN, 3:2 v/v): 4.23 min (Figure 5.97). The molecular ion peak by HRESIMS was found to be observed at 323.2953 $[M+H]^+$,

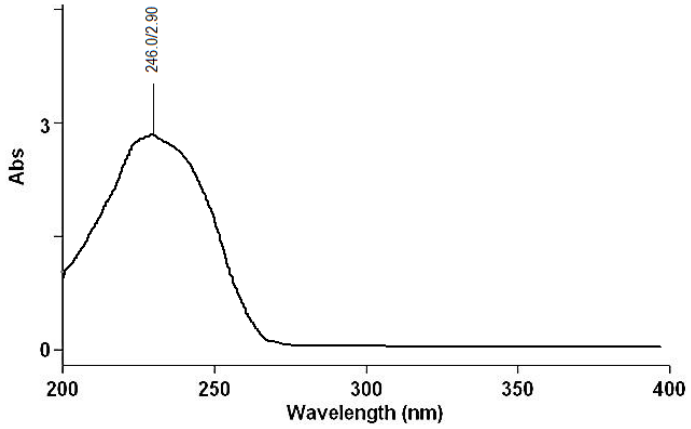

Figure 5.96.: UVspectrum of 3-methoxy-dolabella-12(18)-ene-4β-ol (**7**)

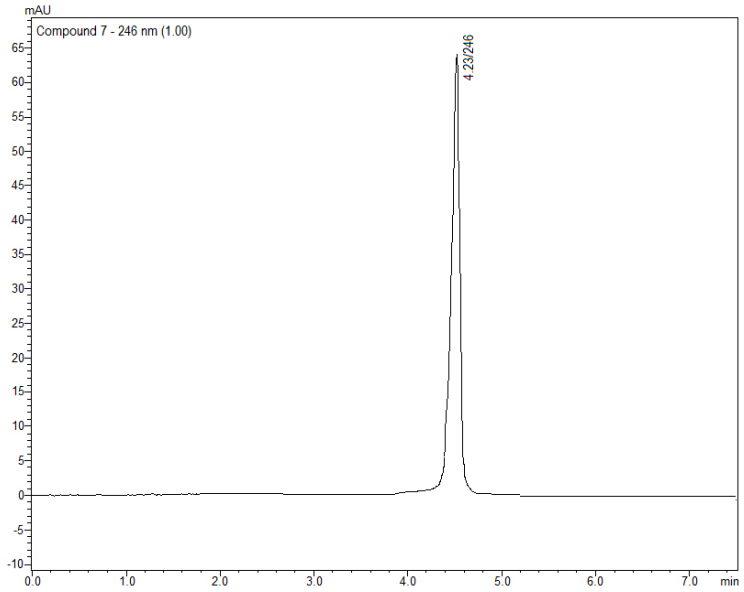

Figure 5.97.: HPLC chromatogram of 3-methoxy-dolabella-12(18)-ene-4β-ol (**7**)

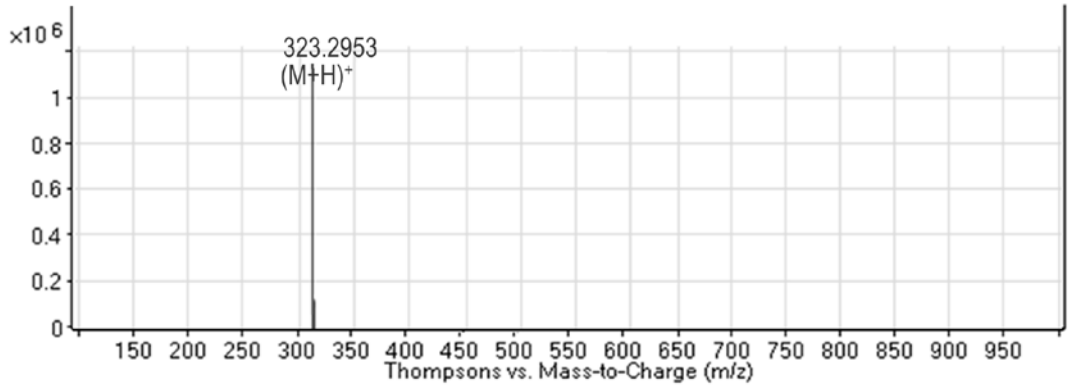

Figure 5.98.: HRESIMS of 3-methoxy-dolabella-12(18)-ene-4β-ol (**7**)

The crude extract of *P. tetrastromatica* on chromatographic separation yielded a compound (**7**), as pale yellowish oil. The mass spectroscopy-assisted NMR/IR/mass experiments established the elemental composition of **7** as $C_{21}H_{38}O_2$ bearing three degrees of unsaturation (one olefin and two ring systems) (Table 5.10; Figure 5.99-5.104).

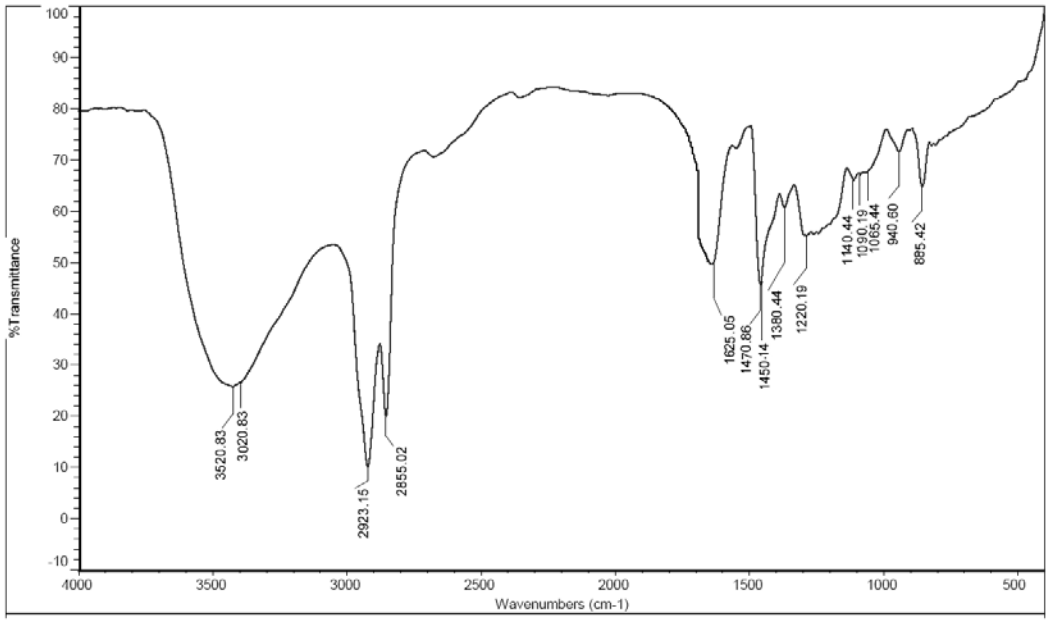

Figure 5.99.: FTIR of 3-methoxy-dolabella-12(18)-ene-4β-ol (**7**)

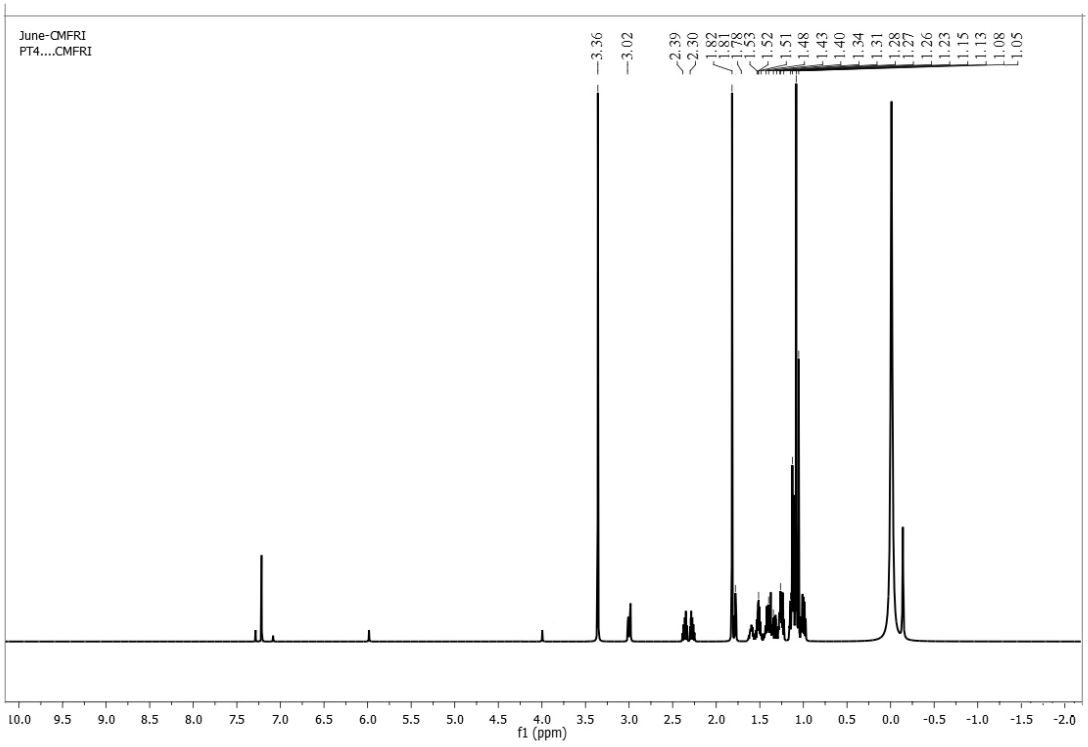

Figure 5.99.: ^{1}H NMR spectrum of 3-methoxy-dolabella-12(18)-ene-4β-ol (**7**)

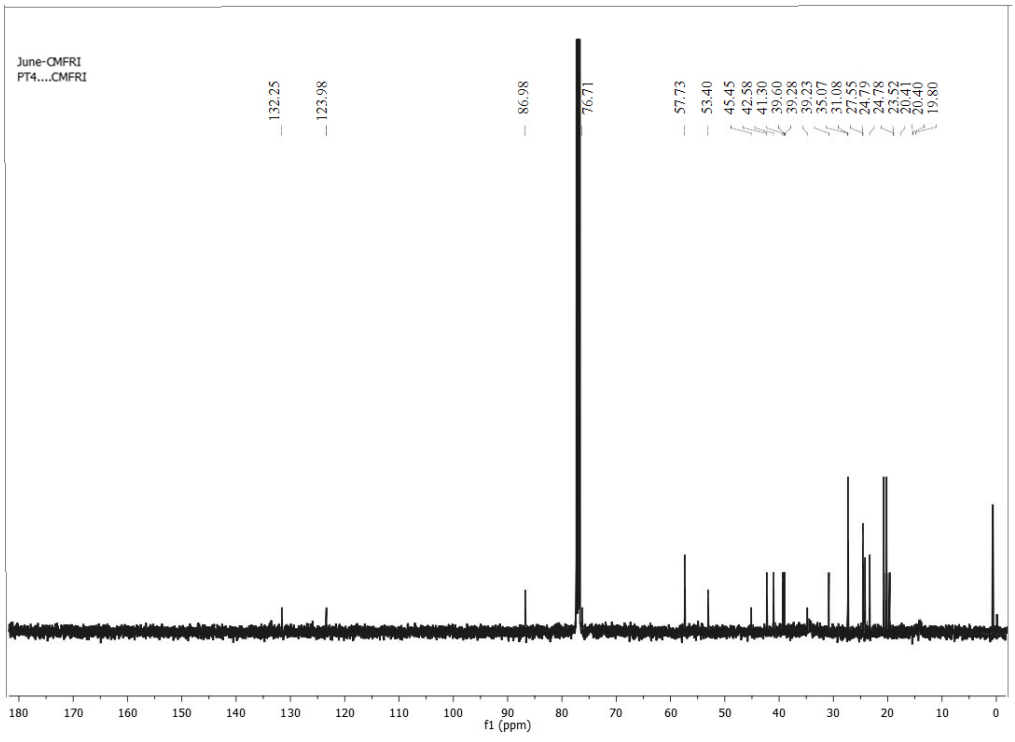

Figure 5.100.: ^{13}C NMR spectrum of 3-methoxy-dolabella-12(18)-ene-4β-ol (**7**)

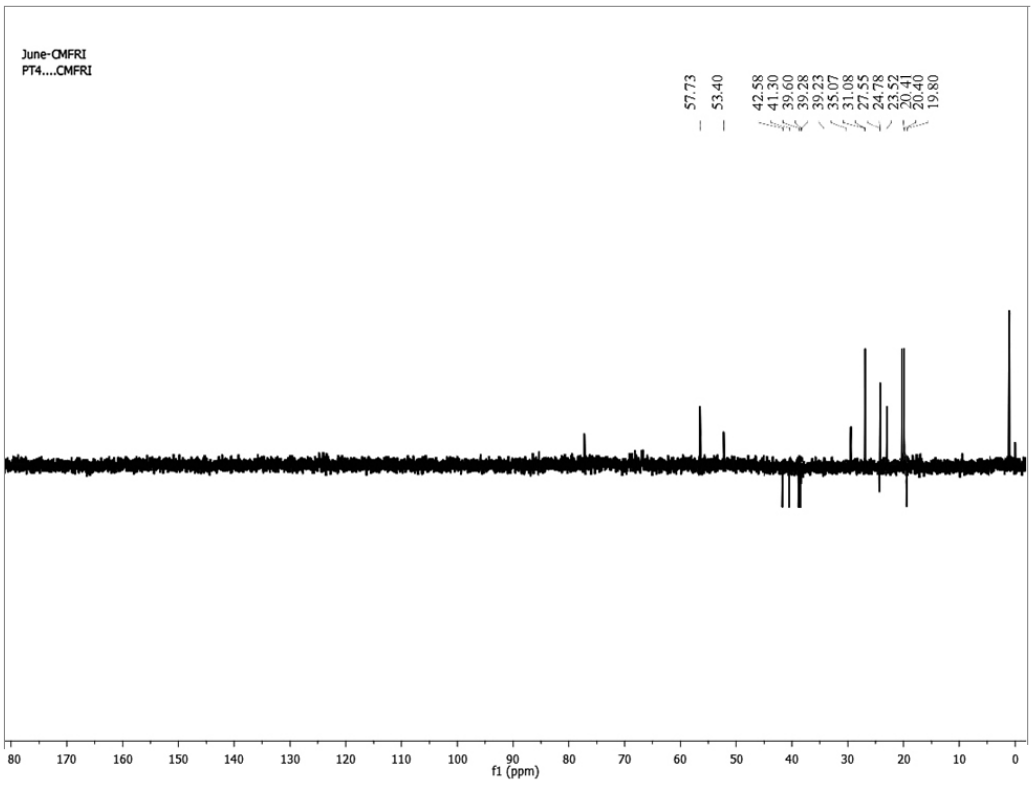

Figure 5.101.: DEPT spectrum of 3-methoxy-dolabella-12(18)-ene-4β-ol (**7**)

The molecular ion peak of **7** appeared at *m/z* 322.29 [M^+]. The COSYs between the protons δ 1.15 (H-2)/3.02 (H-3), δ 1.23 (H-5)/1.43 (H-6)/1.52 (H-7) and δ 1.51 (H-9)/1.13 (H-10) together with HMBCs δ /δ 1.40 (H-2)/45.6 (C-1), δ /δ 1.40 (H-2)/53.4 (C-11) and δ /δ 1.48 (H-5)/76.7 (C-4) explained the partial structure of **7**. The COSYs combined with HMBCs deduced a closed loop of 11-membered ring in **7** (Ioannou et al. 2012) (Figure 4.105). The fusion of 11-membered ring with 5-membered ring via carbons at C-1 and C-11 suggested the resemblance of the basic skeleton of **7** with that of compound **6**. Notably, the structural attributes of compound **6** was similar to those of **7** except the functionalities, such as methoxy at C-3, hydroxyl at C-4, methyl at C-8 and an additional isopropylidene group at C-12 (in **7**), which suggested their structural differences. The present compound was comprised of isopropylidenecyclopentane ring along with methoxy at C-3 and hydroxyl at C-4 unlike the previously reported dolabellane variant enclosing an isopropylidenecyclopentanone ring along with exocyclic olefinic moiety at C-4, acetoxy at C-3 and carbonyl at C6 positions, isolated from the coral *Eunicea sp.* (Wei et al. 2010). Therefore, the compound **7** represented the first description of dolabellane skeleton possessing an isopropylidenecyclopentane ring along with the oxy-functionalization from seaweed

P.tetrastromatica.

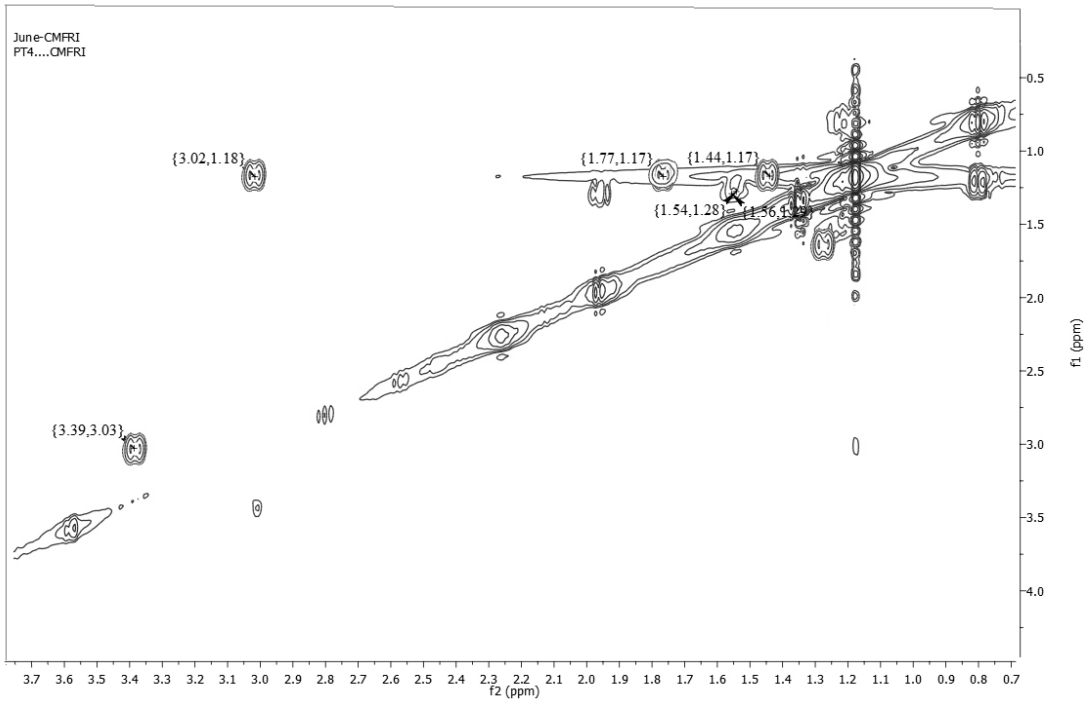

Figure 5.102.: ^{1}H-^{1}H COSY spectrum of 3-methoxy-dolabella-12(18)-ene-4β-ol (**7**)

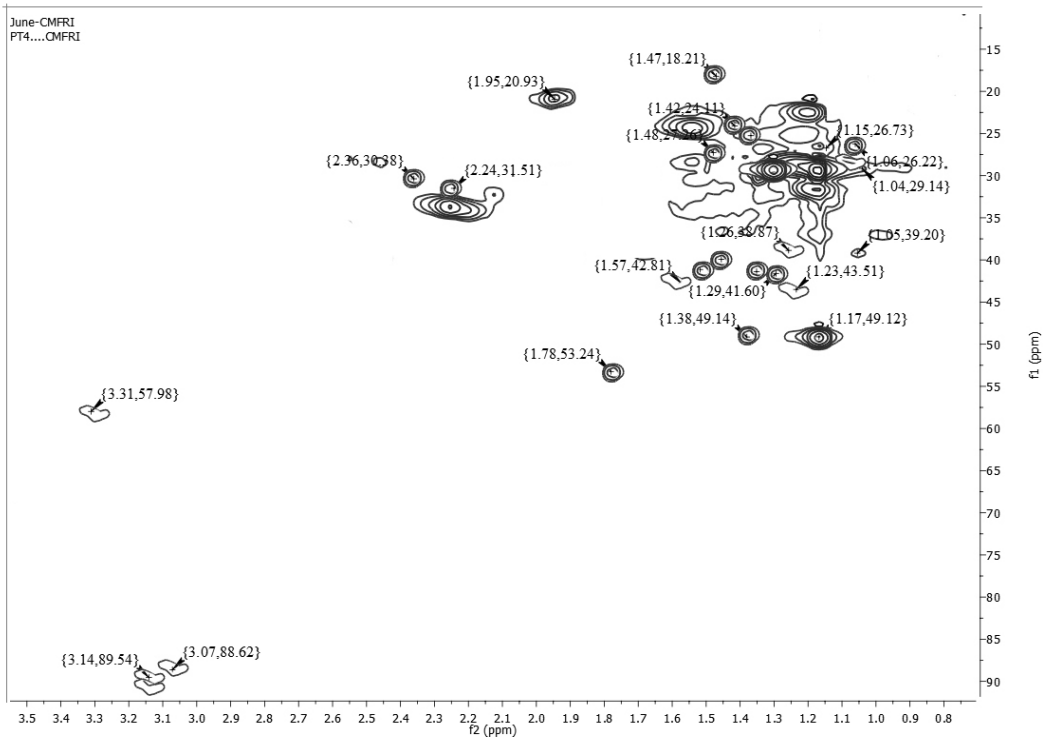

Figure 5.103.: HSQC spectrum of 3-methoxy-dolabella-12(18)-ene-4β-ol (**7**)

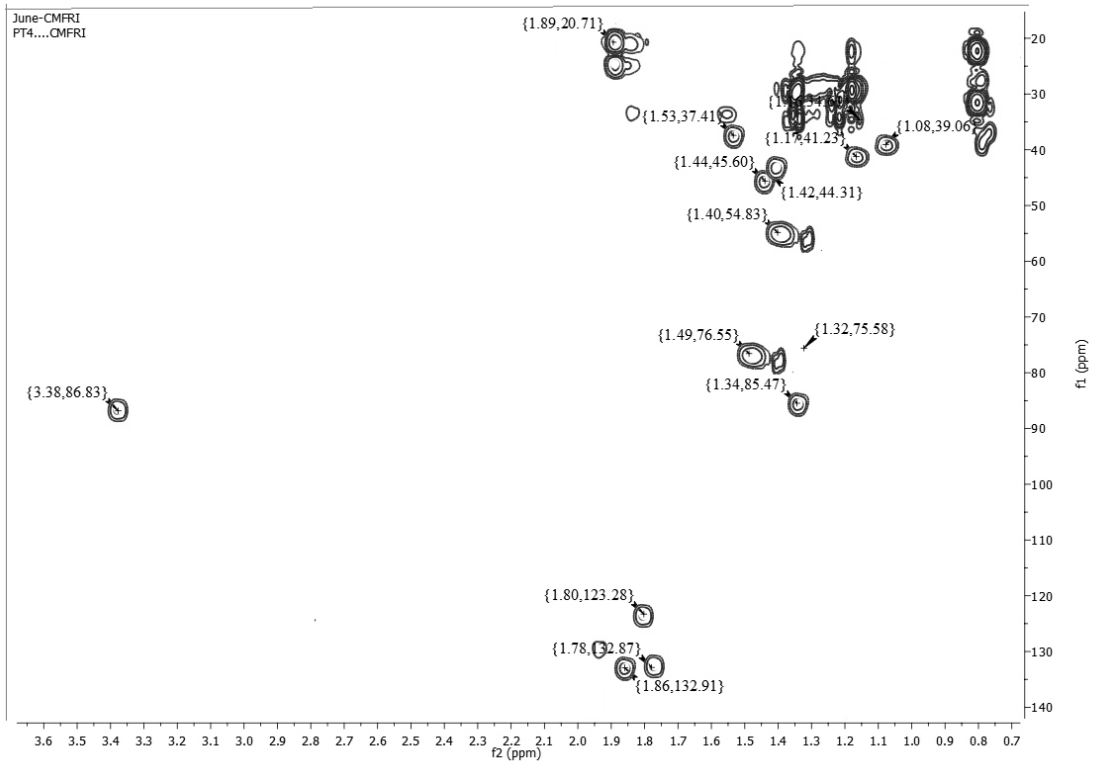

Figure 5.104.: HMBC spectrum of 3-methoxy-dolabella-12(18)-ene-4β-ol (**7**)

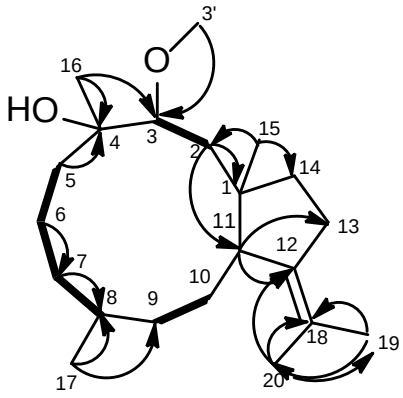

Figure 5.105.: Prominent ^{1}H-^{1}H COSY, and selected HMBC correlations of 3-methoxy-dolabella-12(18)-ene-4β-ol (**7**). The key ^{1}H-^{1}H COSY couplings were represented in bold face bonds. The key HMBC couplings have been represented by double barbed arrows.

NOESY spectrum demonstrated that the protons δ 1.05 (H-15)/1.28 (Hβ-9)/3.02 (H-3)/1.27 (Hβ-7)/2.30 (Hβ-13) and δ 1.27 (Hβ-7)/1.05 (H-15) displayed spatial correlations (Figure 5.106-5.107), and were located at the identical molecular reference plane, thus arbitrarily assigned as β-oriented. The protons at δ 3.36 (H-3') displayed NOESY correlations with the protons at δ 1.48 (H-5*α*), 1.31 (H-16), 1.40 (H-2*α*), 1.43 (H-6), 1.40 (H*α*-10), 1.40 (H*α*-8) and δ 1.48 (H*α*-5)/1.78 (H*α*-11), which were found to be *trans* oriented to the β-protons, and therefore, assigned as *α*-protons.

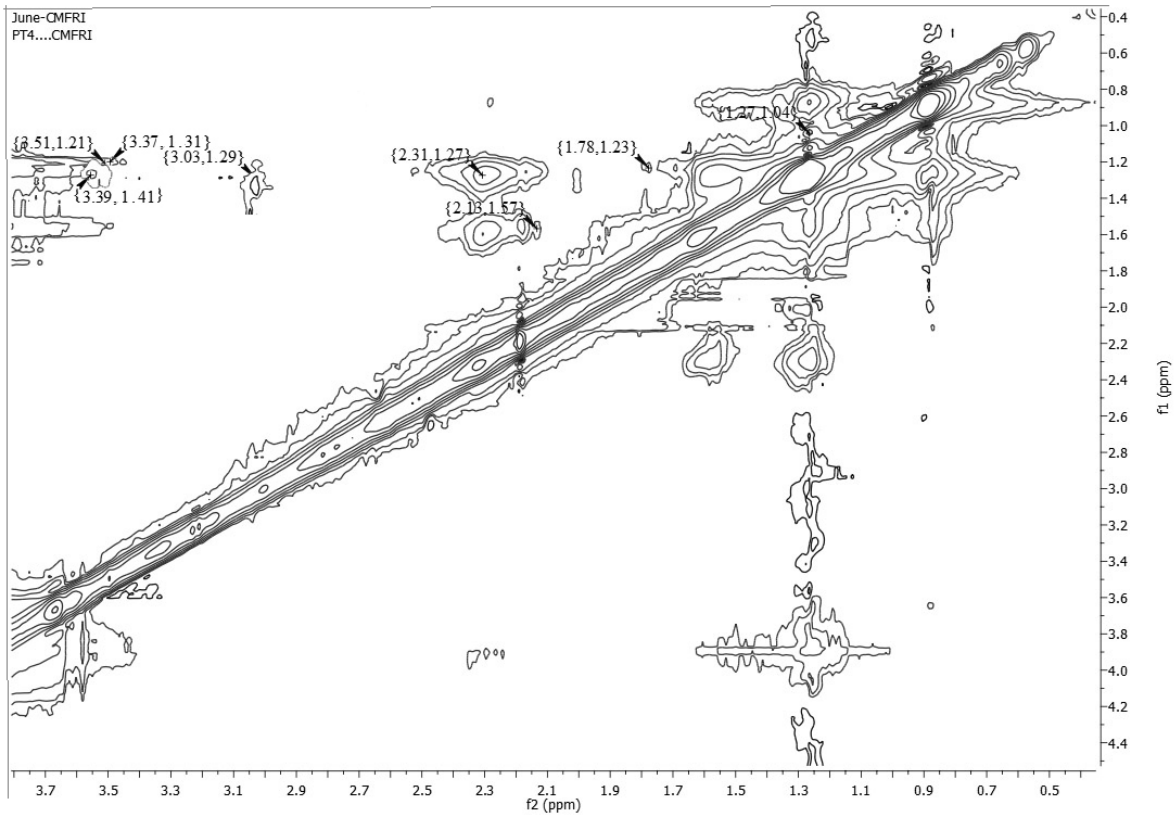

Figure 5.106.: NOESY of 3-methoxy-dolabella-12(18)-ene-4β-ol (**7**)

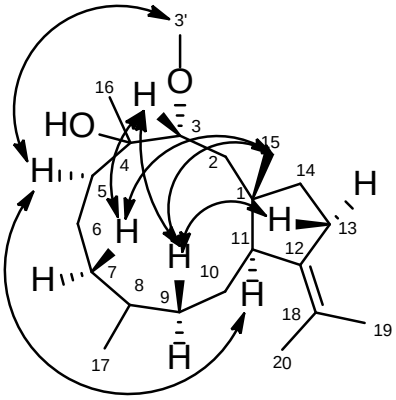

Figure 5.107.: Prominent NOE correlations of 3-methoxy-dolabella-12(18)-ene-4β-ol (**7**). NOESY relations are represented by double-tailed arrows

The molecular ion peak of **7** was appeared at *m/z* 322 and base peak was ontained at *m/z* 40.0 (Figure 5.108 and 5.109).

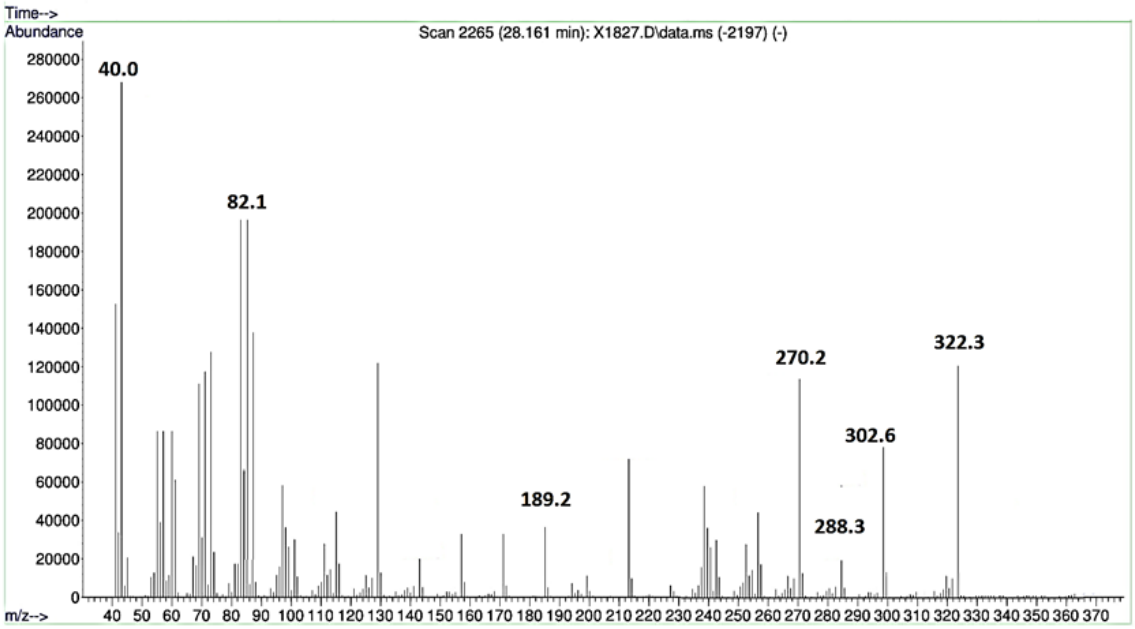

Figure 5.108.: EI-MS spectrum of 3-methoxy-dolabella-12(18)-ene-4β-ol (**7**)

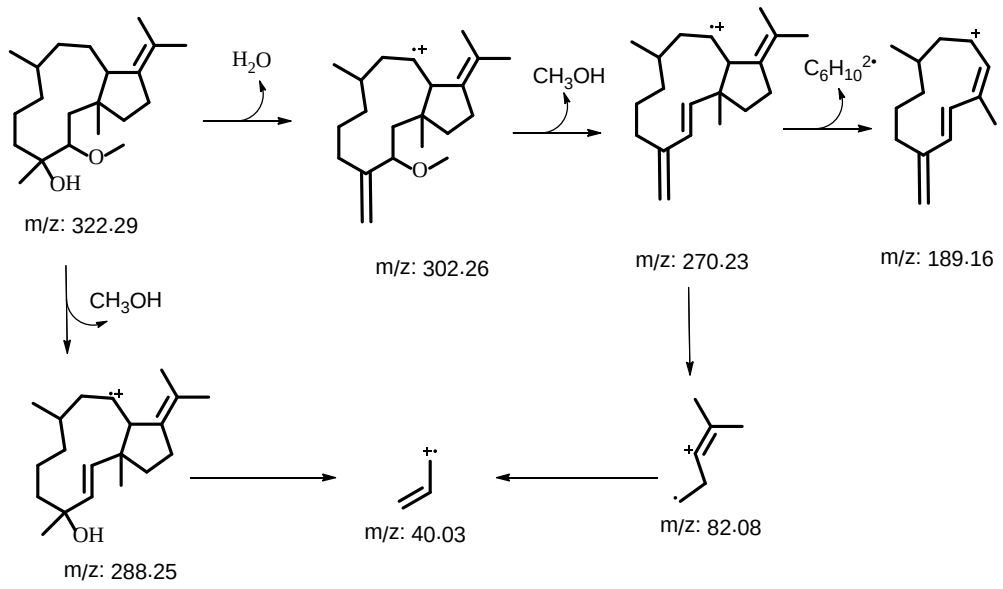

Figure 5.109.: EI-MS spectrum of 3-methoxy-dolabella-12(18)-ene-4β-ol (**7**)

Table 5.10.: NMR spectroscopic data[a] of 3-methoxy-dolabella-12(18)-ene-4β-ol (**7**) isolated from brown seaweed *P.tetrastromatica*

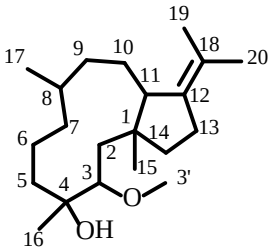

Compound **7**……3-methoxy-dolabella-12(18)-ene-4β-ol (**7**)

C. No.	^{13}C NMR	^{1}H NMR (int.,mult., J in Hz)[b]	COSY	HMBC
1	45.5	-	-	-
2	39.2	1.15(1H,d,9.3Hz)	H-3	C-1,11
		1.40(1H,d,10.2 Hz)	-	-
3	87.0	3.02(1H,t,10.6 Hz)	-	-
3’	57.7	3.36(3H,s)	-	C-3
4	76.7	-	-	-
5	39.3	1.23(1H,dd,11.6, 6.9 Hz)	H-6	C-4
		1.48(1H,dd,11.3, 6.6 Hz)	-	-
6	19.8	1.43(2H,m)	H-7	C-7
7	42.6	1.52(1H,m)	-	C-8
		1.27(1H,m)	-	-
8	35.0	1.40(1H,m)	-	-
9	41.3	1.51(1H,m)	H-10	-
		1.28(1H,m)	-	-
10	24.8	1.40(1H, m)	-	-
		1.13(1H, m)	-	-

11	53.4	1.78(1H,t,5.7 Hz)	-	C-12
12	132.3	-	-	-
13	31.1	2.30(1H,m)	-	-
		2.39(1H,m)	-	-
14	39.6	1.34(1H,dd, 10.9, 6.3 Hz)	-	-
		1.08(1H,dd,10.7, 6.8 Hz)		
15	23.5	1.05(3H,s)	-	C-14,2
16	24.8	1.31(3H,s)	-	C-4,3
17	27.6	1.15(3H,s)	-	C-8,9
18	124.0	-	-	-
19	20.4	1.82(3H,s)	-	C-18,20
				-
20	20.4	1.81(3H,s)	-	C-12,18

[a]NMR spectra were recorded using a Bruker AVANCE III 500 MHz (AV 500) spectrometer (Bruker, Karlsruhe, Germany) in $CDCl_3$ as aprotic solvent at ambient temperature with TMS as the internal standard (δ 0 ppm).

[b]Values in ppm, multiplicity and coupling constants (*J*= Hz) were indicated in parentheses. Multiplicities were allocated by ^{135}DEPT NMR spectrum.

The assignments were made with the aid of the COSY, HSQC, HMBC and NOESY experiments.

5.3.2.2c Structural characterization of Compound 8 (TP_8)

3-Methoxy-dolabella-10,18(19)-diene-5α,8β-diol

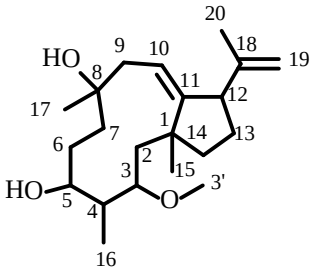

Sample yield	0.25% (> 99% purity, RP-C_{18} HPLC)
Physical description	Yellow oil
Molecular formula	$C_{21}H_{36}O_3$
Molecular mass	336.2664

The dolabellane class of diterpenoid derivative, 3-methoxy-dolabella-10,18(19)-diene-5α,8β -diol as yellow oil compound. The compound (**8**) has exhibited UV absorbance (UV (MeOH) λ_{max}) at 248 (3.1) nm (Figure 5.110). The homogeneity of the compound was ascertained by HPLC data on a bonded phase octadecylsilane (C_{18}) stationary phase (RP-C_8 HPLC, MeOH:MeCN, 3:2

v/v): 4.02 min (Figure 5.111). The molecular ion peak by HRESIMS was found to be observed at 337.2745 $[M+H]^+$ (Figure 5.112).

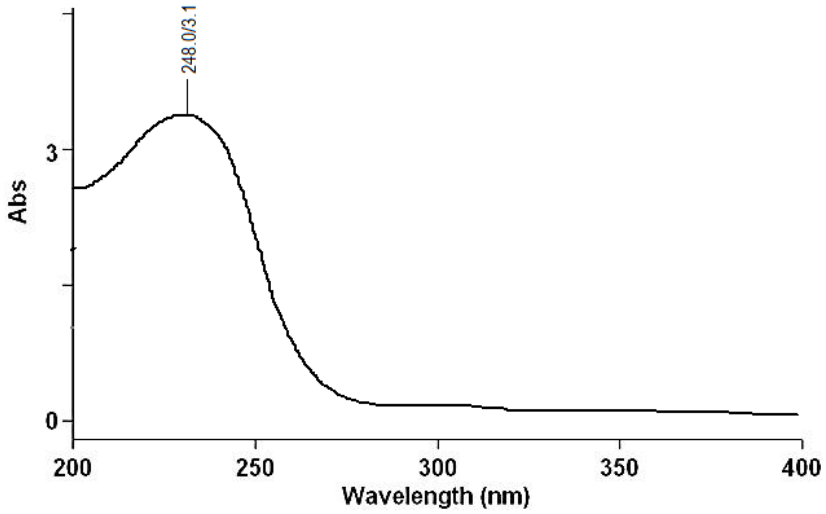

Figure 5.110.: UVspectrum of 3-methoxy-dolabella-10,18(19)-diene-5α,8β -diol (**8**)

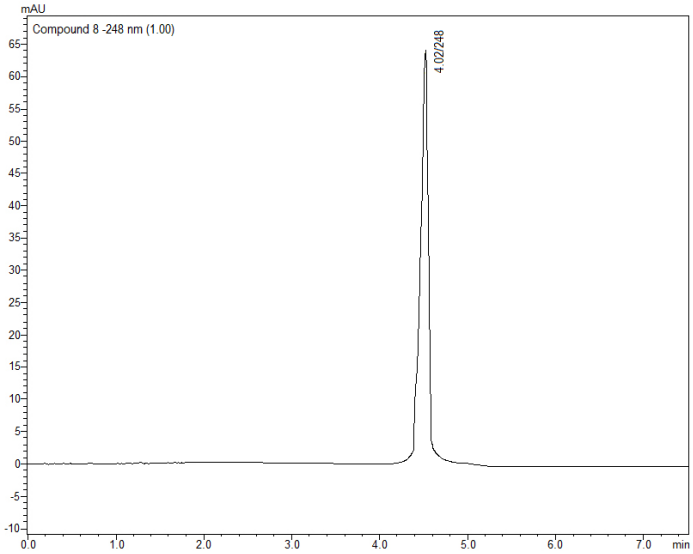

Figure 5.111.: HPLC chromatogram of 3-methoxy-dolabella-10,18(19)-diene-5α,8β -diol (**8**)

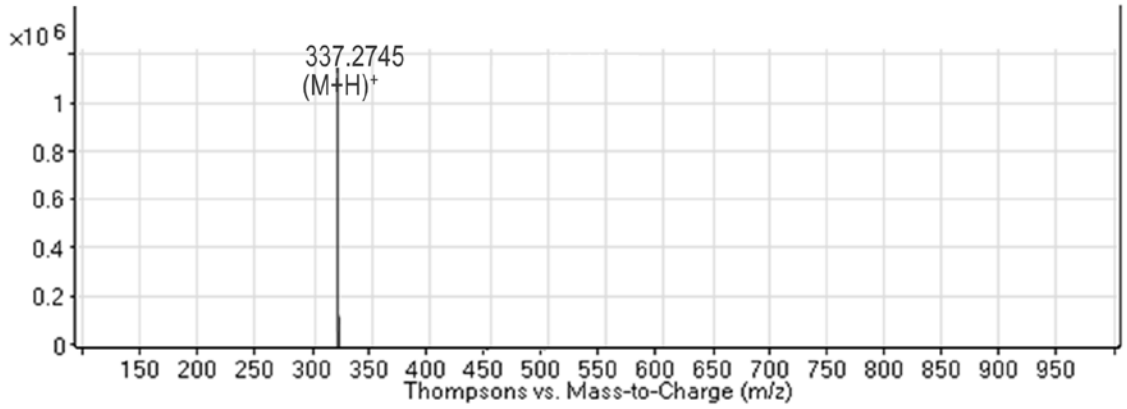

Figure 5.112.: HRESIMS of 3-methoxy-dolabella-10,18(19)-diene-5α,8β -diol (**8**)

The compound **8**, another dolabellane variant, was isolated as yellowish oil from the organic extract of *P. tetrastomatica* on column chromatographic separations. The molecular ion peak of **8** was found at *m/z* 336.27 [M^+], and the elemental composition was deduced as $C_{21}H_{36}O_3$, with detailed NMR/IR experiments (Table 5.11; Figure 5.113-5.118).

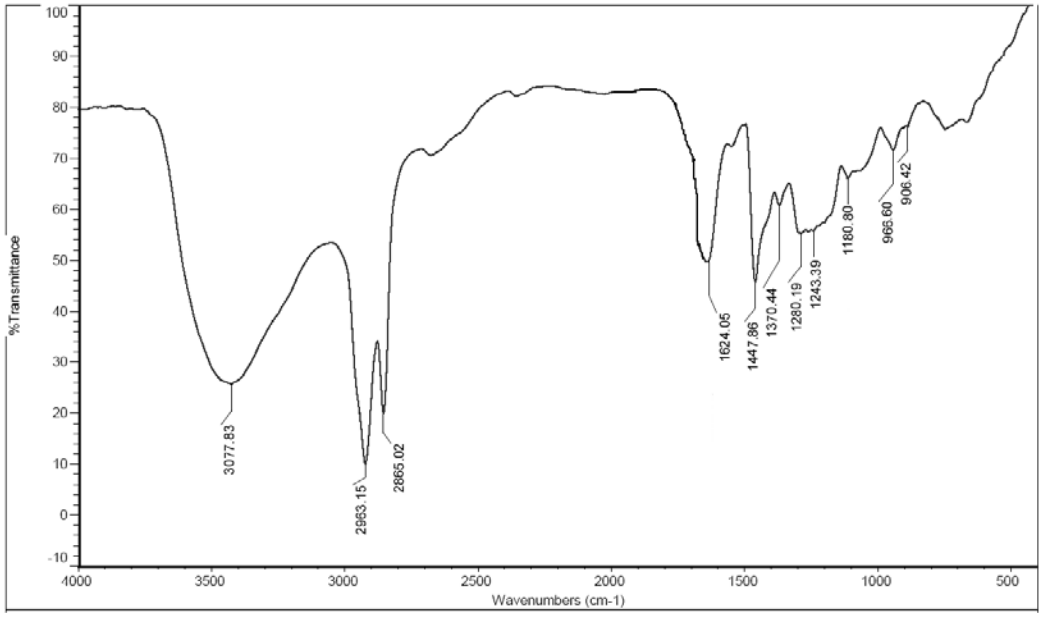

Figure 5.113.: FTIR spectrum of 3-methoxy-dolabella-10,18(19)-diene-5α,8β -diol (**8**)

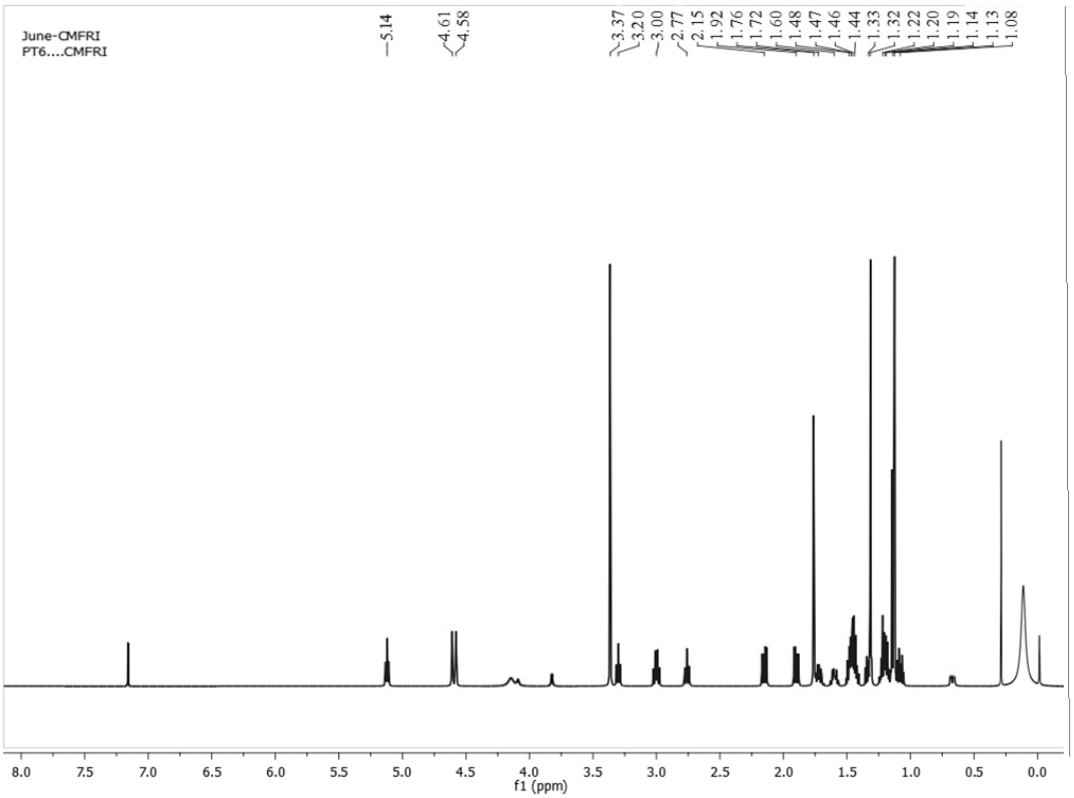

Figure 5.114.: ^{1}H NMR spectrum 3-methoxy-dolabella-10,18(19)-diene-5α,8β -diol (**8**)

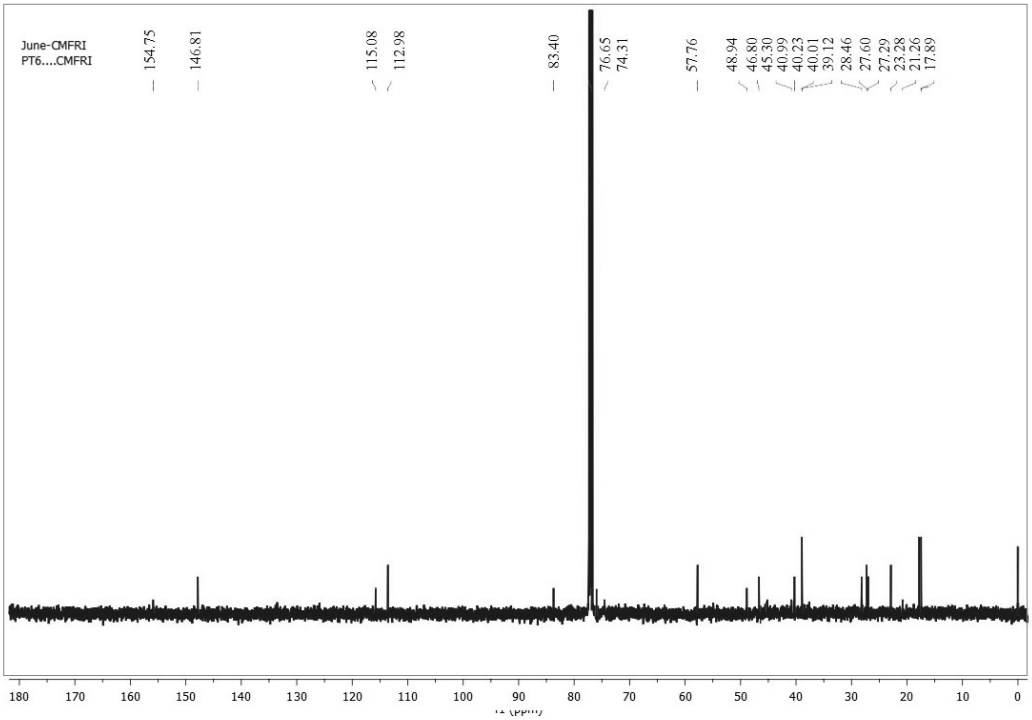

Figure 5.114.: ^{13}C NMR spectrum 3-methoxy-dolabella-10,18(19)-diene-5α,8β -diol (**8**)

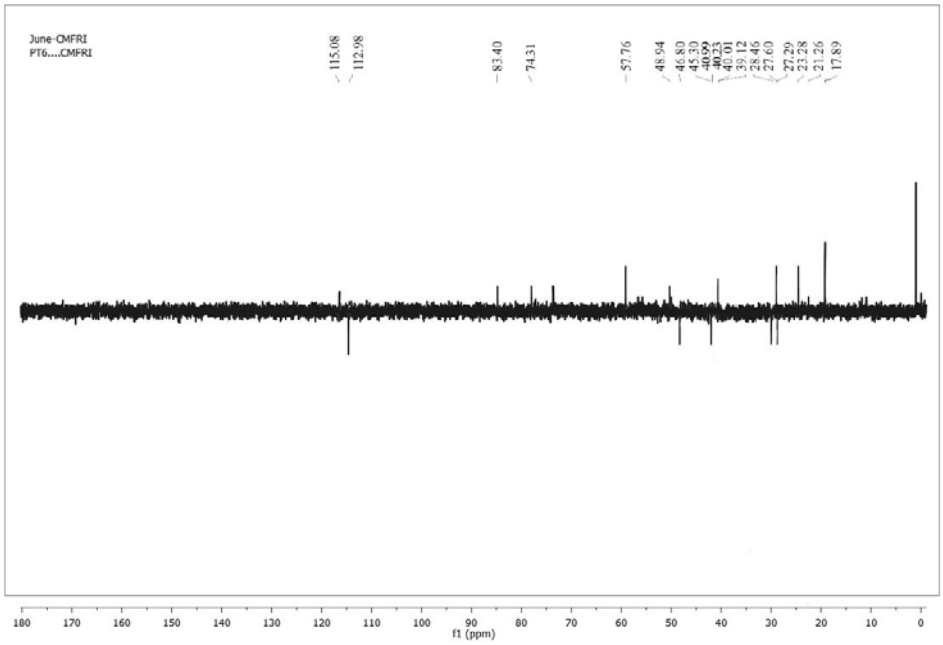

Figure 5.115.: DEPT spectrum spectrum 3-methoxy-dolabella-10,18(19)-diene-5α,8β -diol (**8**)

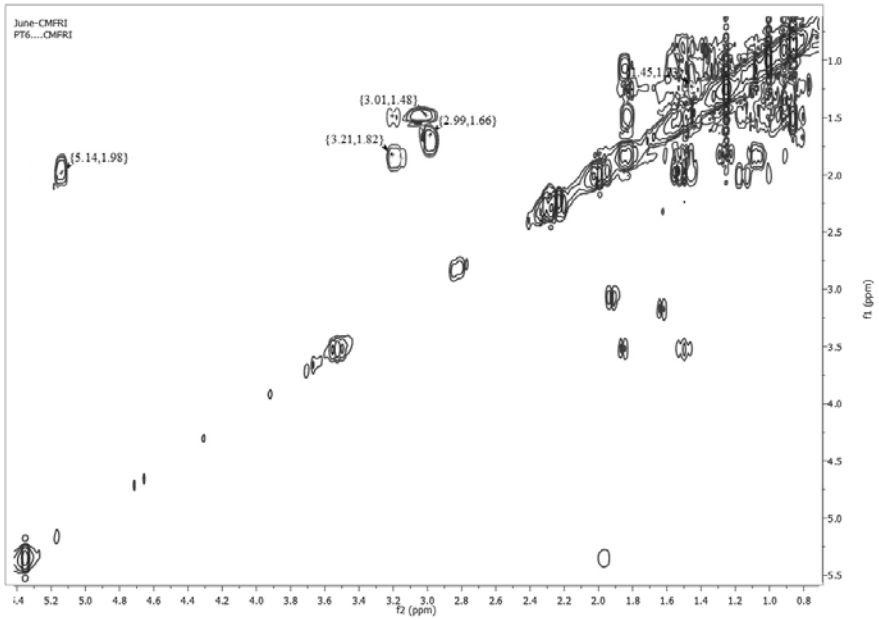

Figure 5.116.: ^{1}H-^{1}H COSY spectrum 3-methoxy-dolabella-10,18(19)-diene-5α,8β -diol (**8**)

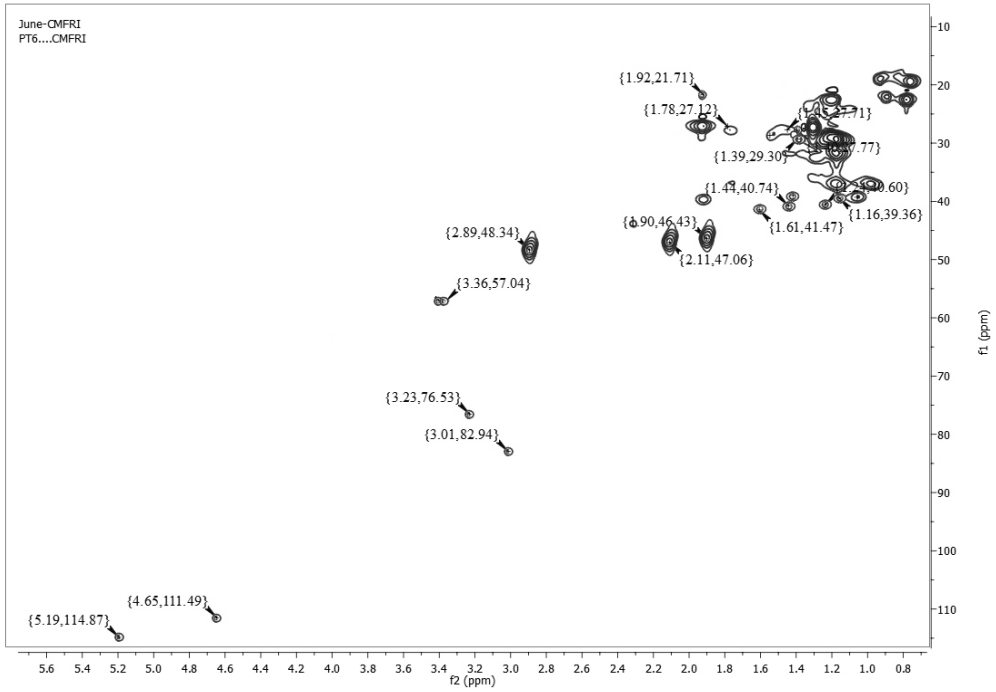

Figure 5.117.: HSQC spectrum 3-methoxy-dolabella-10,18(19)-diene-5α,8β -diol (**8**)

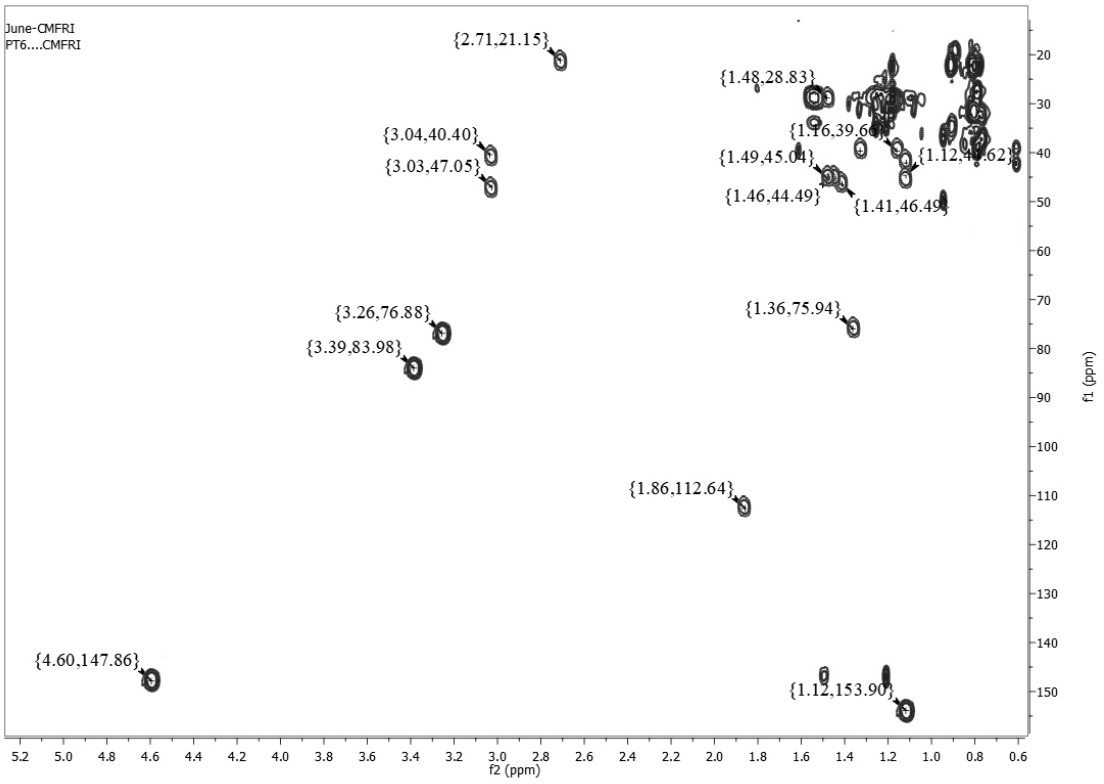

Figure 5.118.: HMBC spectrum 3-methoxy-dolabella-10,18(19)-diene-5α,8β -diol (**8**)

The molecular formula of **8** was assigned with four degrees of unsaturation, which was related to two each of double bond functionalities and ring systems. The HMBCs between δ /δ 1.46 (H-2)/45.3 (C-1), δ /δ 3.00 (H-3)/45.3 (C-1), 41.0(C-4), δ /δ 3.20 (H-5)/41.0 (C-4), δ /δ 1.48 (H-7)/46.8 (C-9), δ /δ 1.20 (H-2)/154.7 (C-11) explained the closed loop of 11-membered ring in **8** and the position of olefinic functional group. Compound **8** was similar to those of **7** except the functionalities of hydroxyls at C-5 and C-8, alkene at C10=C11 and an additional propenyl C-12 (in **8**). Notably, the compounds isolated from *D. spiralis* enclosed propenyl bonded dolabellane framework (Ioannou et al. 2012), which was comparable with the studied compound **8** except the presence in the greater number of oxygenated electronegative substituents at C-3, C-4 and C-8 in the latter (Figure 5.119).

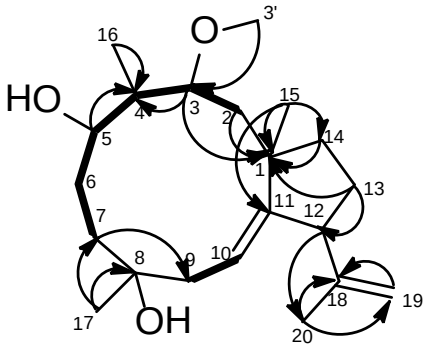

Figure 5.119.: Prominent ^{1}H-^{1}H COSY, and selected HMBC correlations of 3-methoxy-dolabella-10,18(19)-diene-5α,8β-diol (**8**). The key ^{1}H-^{1}H COSY couplings were represented in bold face bonds. The key HMBC couplings have been represented by double barbed arrows.

The relative stereochemistries of the chiral centres at C-3, C-4, C-8 and C-5 in **8** were designated through NOESY experiments (Figure 5.120-5.121). The NOESYs from both δ 1.20 (H-2) and δ 1.22 (H-7) to δ 3.20 (H-5)/2.77 (H-12)/1.82 (H-20)/1.13 (H-15) protons and δ 2.15 (H-9)/2.77 (H-12)/3.00 (H-3) were found to be at the same plane of symmetry, and therefore, attributed as β-faced protons. Similarly, NOEs were exhibited by the proton at δ 3.37 (H-3') with those at δ 1.32 (H-17), 1.48 (H*α*-7) and 1.60 (H-4). These protons were found to be situated at the opposite plane to the β-protons, and thus, *α*-disposed.

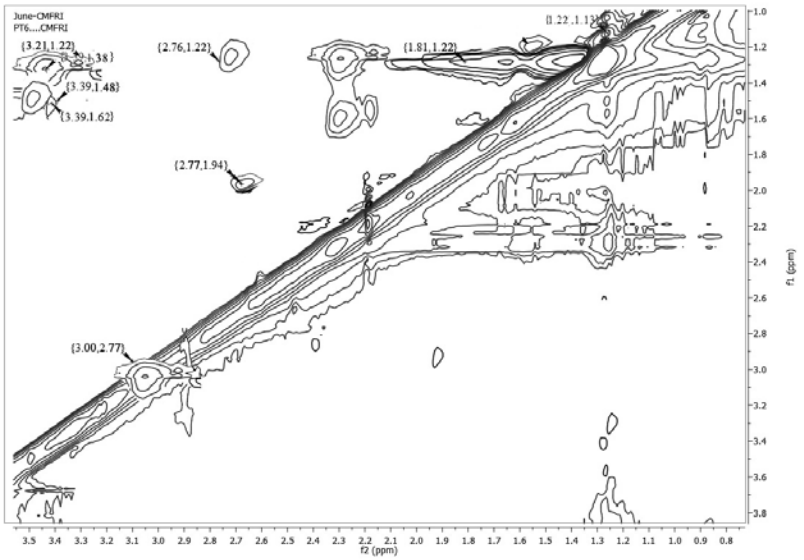

Figure 5.120.: NOESY spectrum 3-methoxy-dolabella-10,18(19)-diene-5α,8β -diol (**8**)

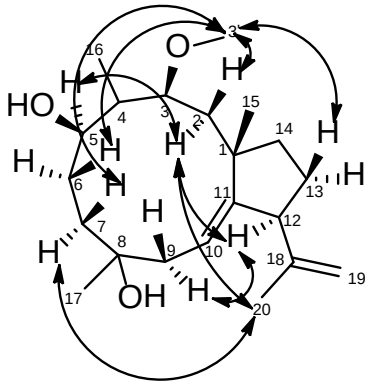

Figure 5.121.: Prominent NOE correlations of 3-methoxy-dolabella-10,18(19)-diene-5α,8β -diol (**8**). NOESY relations are represented by double-tailed arrows

The molecular ion peak of **8** was appeared at *m/z* 336 and base peak was ontained at *m/z* 27.0 (Figure 5.122 and 5.123).

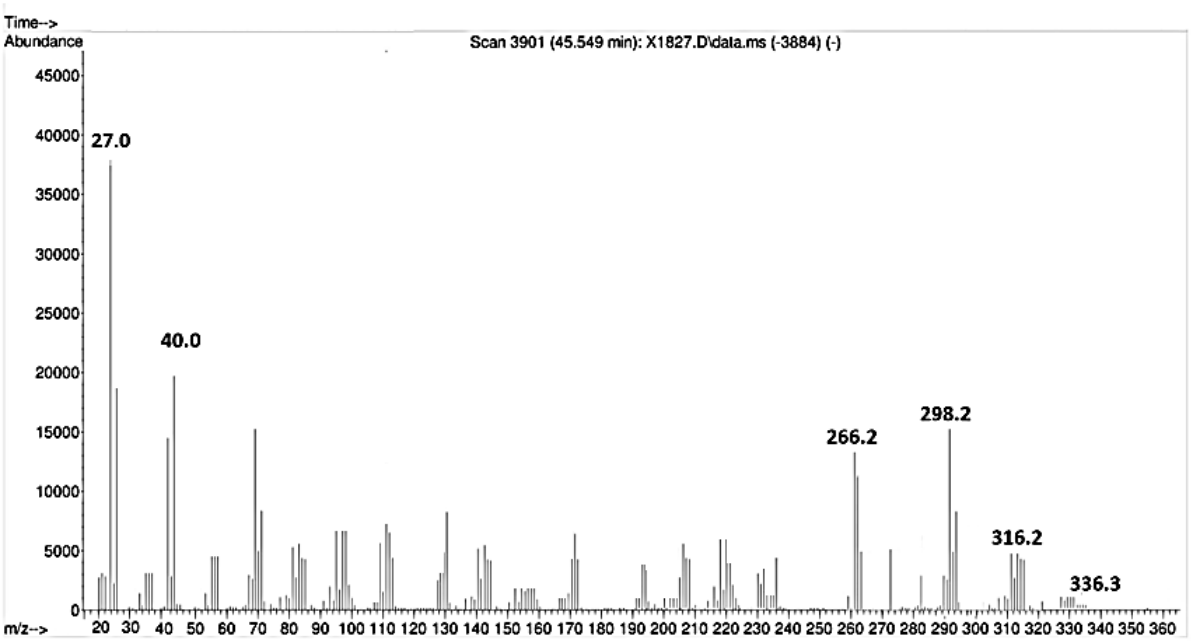

Figure 5.122.: EI-MS spectrum 3-methoxy-dolabella-10,18(19)-diene-5α,8β -diol (**8**)

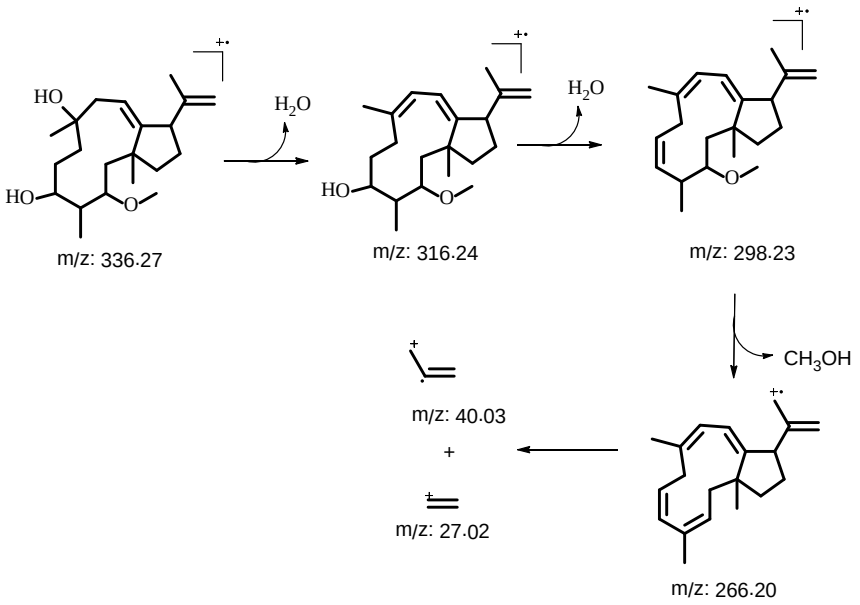

Figure 5.123.: Tentative mass fragmentation pattern of 3-methoxy-dolabella-10,18(19)-diene-5α,8β -diol (8)

Table 5.11.: NMR spectroscopic data[a] of 3-methoxy-dolabella-10,18(19)-diene-5α,8β -diol (**8**) isolated from brown seaweed *P.tetrastromatica*

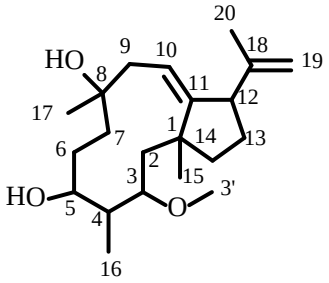

Compound **8**……..3-methoxy-dolabella-10,18(19)-diene-5α,8β -diol (**8**)

C. No.	^{13}C NMR	^{1}H NMR (int.,mult., J in Hz)[b]	COSY	HMBC
1	45.3	-	-	-
2	40.2	1.20(1H,d,10.2 Hz)	H-3	C-1,11
		1.46(1H,d,9.8 Hz)	-	-
3	83.9	3.00(1H,m)	H-4	C-1,4
3’	57.7	3.37(3H,s)	-	C-3
4	41.0	1.60(1H,m)	H-5	-
5	76.7	3.20(1H,m)	H-6	C-4
6	27.3	1.72(1H,m)	H-7	-
		1.47(1H,m)	-	-
7	40.0	1.22(1H,t,2.5 Hz)	-	C-9
		1.48(1H,t,2.7 Hz)	-	-
8	74.3	-	-	-
9	46.8	1.92(1H,d,12.6 Hz)	H-10	-
		2.15(1H,d,12.4 Hz)	-	-
10	115.1	5.14(1H,t,11.3 Hz)	-	-
11	154.8	-	-	-
12	48.9	2.77(1H,t,9.6 Hz)	-	C-20
13	28.5	1.44(1H,m)	-	C-12,1
		1.19(1H,m)	-	-
14	39.1	1.33(1H,dd,12.7 Hz)	-	C-1
		1.08(1H,dd,6.8 Hz)	-	-
15	23.3	1.13(3H,s)	-	C-14,11,1
16	17.9	1.15(3H,d,6.8 Hz)	-	C-4
17	27.6	1.32(3H,s)	-	C-8, 7
18	146.8	-	-	-
19	113.0	4.61(1H,m)	-	C-18
		4.58(1H,m)	-	-
20	21.3	1.82(3H,s)	-	C-18,19

[a]NMR spectra were recorded using a Bruker AVANCE III 500 MHz (AV 500) spectrometer (Bruker, Karlsruhe, Germany) in $CDCl_3$ as aprotic solvent at ambient temperature with TMS as the internal standard (δ 0 ppm).

[b]Values in ppm, multiplicity and coupling constants (J=Hz) were indicated in parentheses. Multiplicities were allocated by ^{135}DEPT NMR spectrum.

The assignments were made with the aid of the COSY, HSQC, HMBC and NOESY experiments.

5.3.2.2d Structural characterization of Compound 9 (TP_9)

2,7-Dimethoxy-14α-hydroxy-dolasta-1(15),9-diene

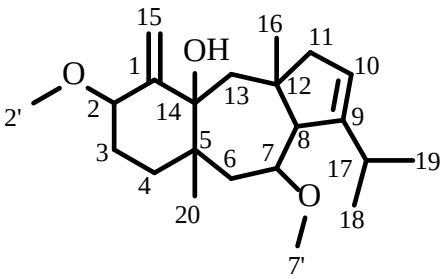

Sample yield	0.25% (> 99% purity, RP-C_{18} HPLC)
Physical description	Colourless oil
Molecular formula	$C_{22}H_{36}O_3$
Molecular mass	348.2664

The dolastane class of diterpenoid derivative, 2,7-dimethoxy-14α-hydroxy-dolasta-1(15),9-diene was isolated as Colorless oil compound. The compound (**9**) has exhibited UV absorbance (UV (MeOH) λ_{max}) at 246.0 (2.90) nm (Figure 5.124). The homogeneity of the compound was ascertained by HPLC data on a bonded phase octadecylsilane (C_{18}) stationary phase (RP-C_8 HPLC, MeOH:MeCN, 3:2 v/v): 3.23 min (Figure 5.125). The molecular ion peak by HRESIMS was found to be observed at 349.2745 $[M+H]^+$ (Figure 5.126).

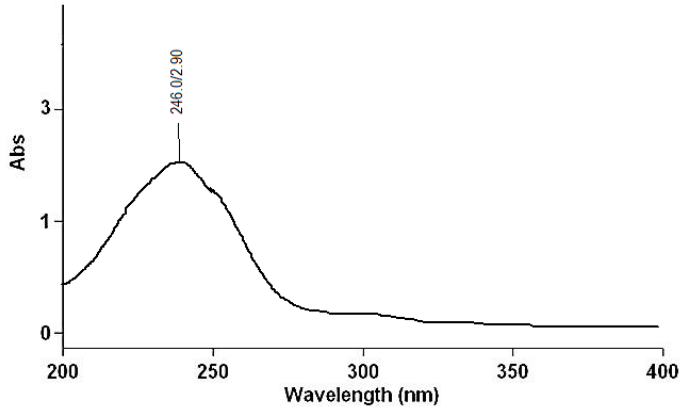

Figure 5.124.: UVspectrum of 2,7-dimethoxy-14α-hydroxy-dolasta-1(15),9-diene (**9**)

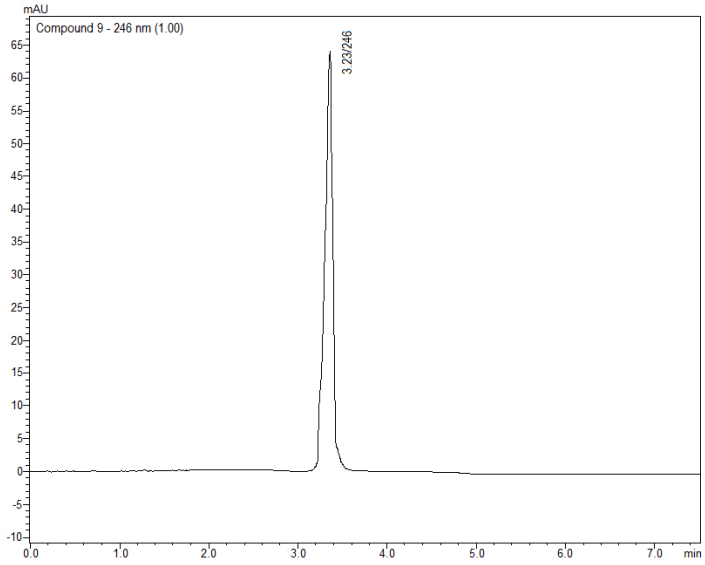

Figure 5.125.: HPLC chromatogram of 2,7-dimethoxy-14α-hydroxy-dolasta-1(15),9-diene (**9**)

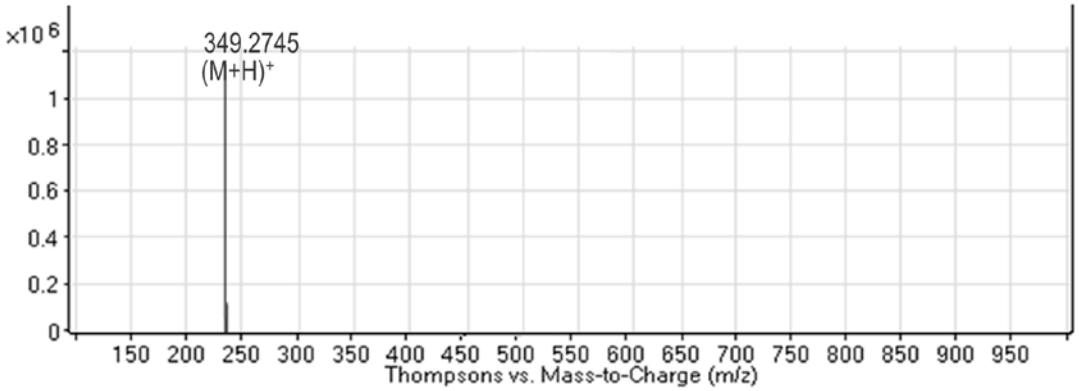

Figure 5.126.: HRESIMS of 2,7-dimethoxy-14α-hydroxy-dolasta-1(15),9-diene (**9**)

The dolastane diterpenoid, **9** was isolated as colourless oil from the EtOAc-MeOH extract of *P. tetrastromatica* on repeated column chromatographic separation. The molecular ion peak of **9** was recognized at *m/z* 348.27 [M^+] and elemental composition was deduced as $C_{22}H_{36}O_3$, with comprehensive NMR/IR spectroscopic experiments (Figure 5.127-5.133, Table 5.12).

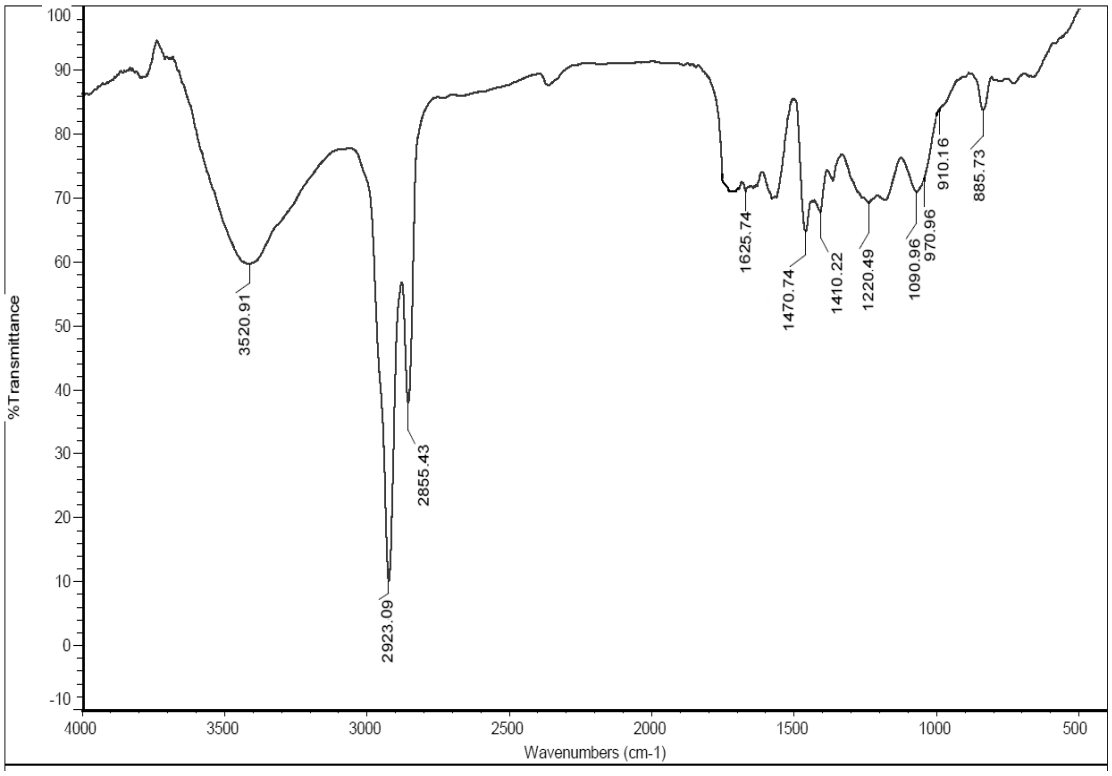

Figure 5.127.: FTIR spectrum of 2,7-dimethoxy-14α-hydroxy-dolasta-1(15),9-diene (**9**)

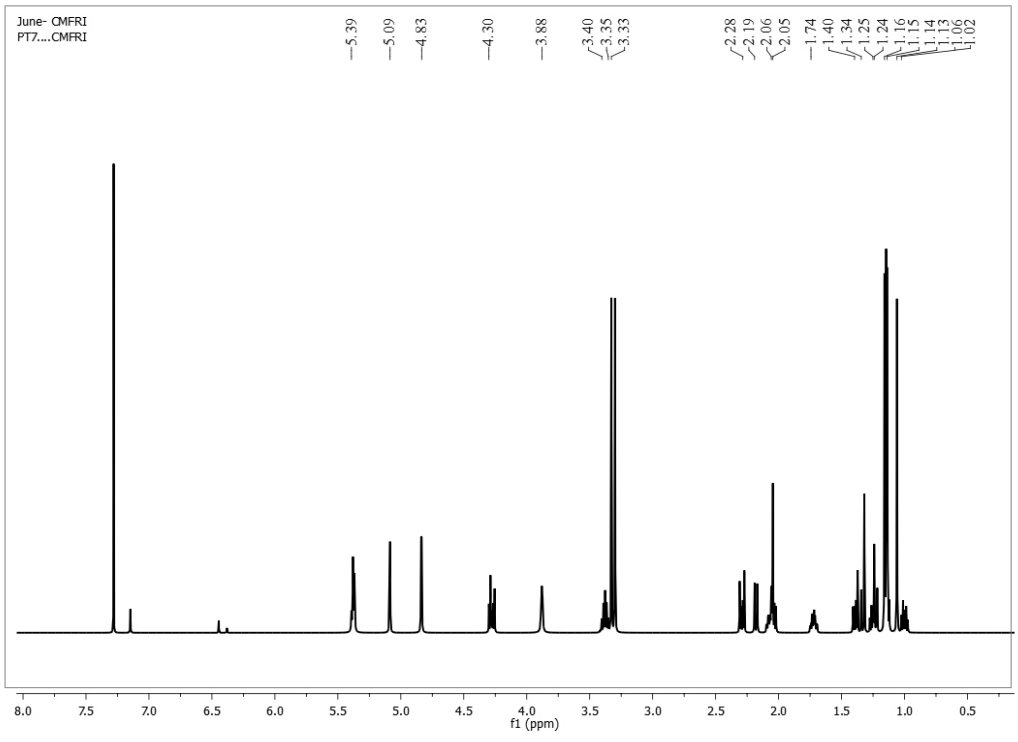

Figure 5.128.: ^{1}H NMR spectrum of 2,7-dimethoxy-14α-hydroxy-dolasta-1(15),9-diene (**9**)

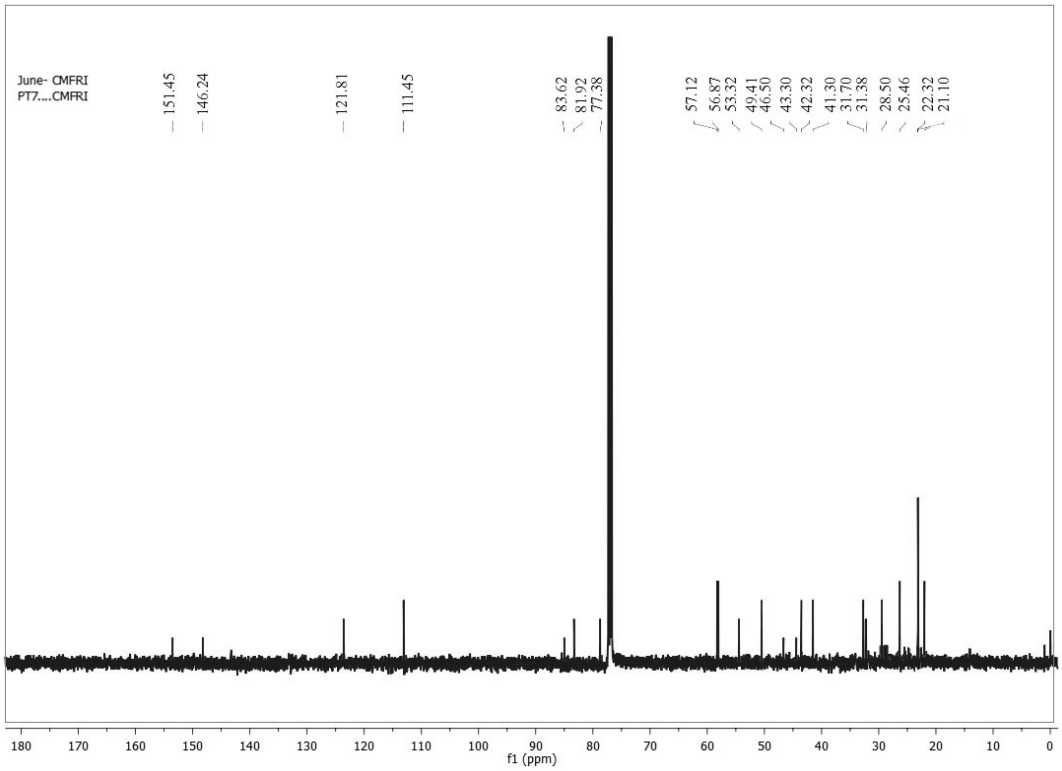

Figure 5.129.: ^{13}C NMR spectrum of 2,7-dimethoxy-14α-hydroxy-dolasta-1(15),9-diene (**9**)

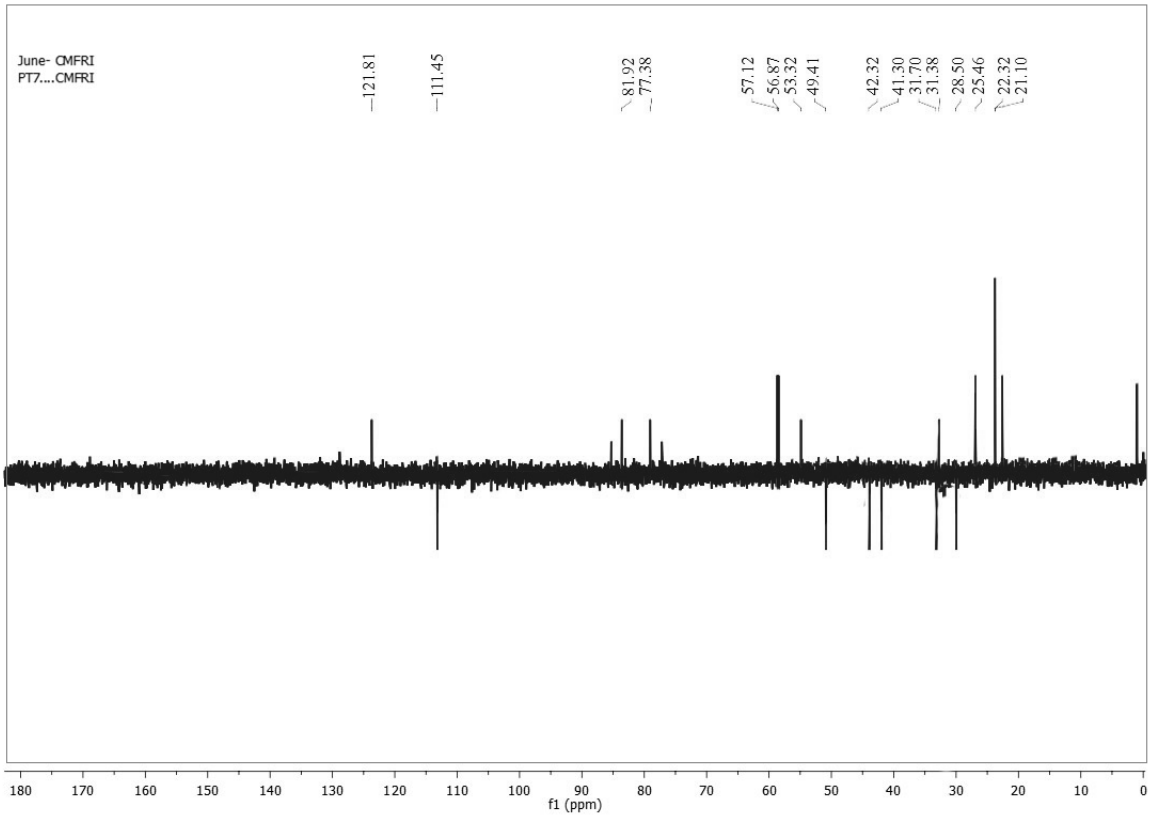

Figure 5.130.: DEPT spectrum of 2,7-dimethoxy-14α-hydroxy-dolasta-1(15),9-diene (**9**)

The detailed NMR spectroscopic data of **9** were comparable with the basic chemical resonances of dolastane type of diterpenes (Ioannou et al. 2013; Ioannou et al. 2008). The COSYs were recorded among the protons at δ 3.89 (H-2)/2.06 (H-3)/1.25 (H-4) along with HMBCs at δ /δ 3.89 (H-2)/151.5 (C-1), 83.6 (C-14), δ 1.25 (H-4)/43.3 (C-5), 83.6 (C-14), which proposed the closed loop of six-membered ring in **9** (Figure 5.134). Similarly, COSYs among the protons δ 1.40 (H-6)/4.30 (H-7)/2.19 (H-8) with HMBCs, such as δ /δ 1.40 (H-6)/43.3 (C-5), δ /δ 2.19 (H-8)/46.5 (C-12) and δ /δ 1.34 (H-13)/46.5 (C-12), 83.6 (C-14) constituted the cyclic structure of seven-membered ring. Correspondingly, the COSYs between the protons δ 5.40 (H-10)/2.04 (H-11) along with the HMBCs at δ /δ 5.40 (H-10)/146.2 (C-9), δ /δ 2.19 (H-8)/146.2 (C-9), δ /δ 2.19 (H-8)/46.5 (C-12) and δ /δ 5.40 (H-10)/46.5 (C-12) appropriately characterised the five-membered ring in **9** and its tricyclic frame work**.** The chemical resonances at C-5, C-8 and C-12 were apparent with the reported compounds 1,4-epoxy-17-dolastene and 1,4-dihydroxy-11-oxo-17-dolastene (Ioannou et al. 2013). The difference in chemical shift value of deshielded signal at C-14 was recorded by virtue of a hydroxyl attached to C-14. The deshielded signals at δ 151.5 (C-1) and 111.5 (C-15, HSQC δ 5.09, 4.84) were related to the terminal alkenes (>C=CH_2) along with δ 146.2 (C-9) and 121.8 (C-10, HSQC δ 5.40), which were related to trisubstituted alkenes in the cyclopentane ring (>C=CH-) (Ioannou et al. 2008).

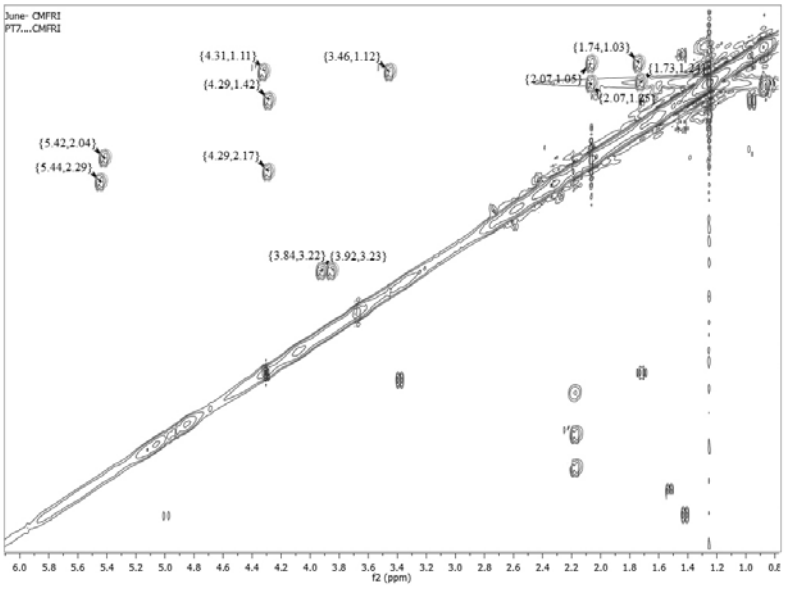

Figure 5.131.: ^{1}H-^{1}H COSY spectrum of 2,7-dimethoxy-14α-hydroxy-dolasta-1(15),9-diene (**9**)

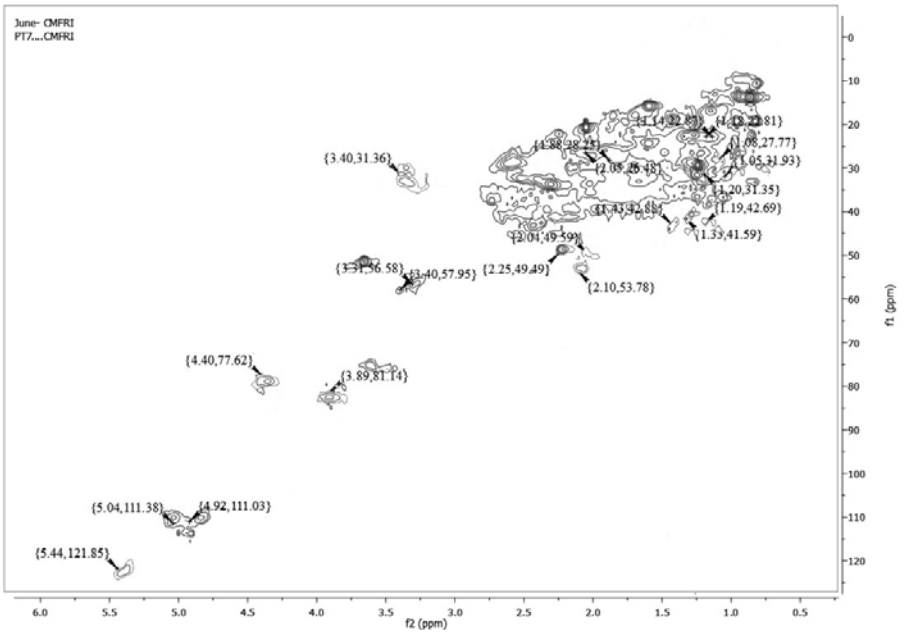

Figure 5.132.: HSQC spectrum of 2,7-dimethoxy-14α-hydroxy-dolasta-1(15),9-diene (**9**)

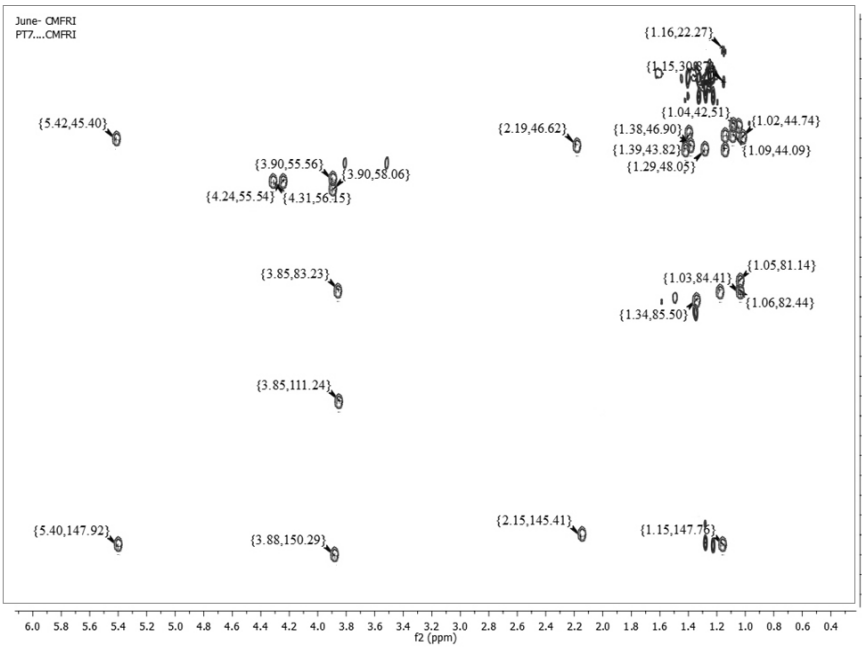

Figure 5.133.: HMBC spectrum of 2,7-dimethoxy-14α-hydroxy-dolasta-1(15),9-diene (**9**)

These attributions were appropriately supported by the HMBCs at δ 3.89 (H-2)/111.5 (C-15). The attachment of remaining four methyls in **9** at C-5, C-17, (C-19) and C-12 were apparent with those reported for a previously described dolastane analogue 4*α*-acetoxy-9β,14*α*-dihydroxydolast-1(15),7-diene (Garcia et al. 2009). It is of note that the dihydroxy-11-oxo-17-

dolastene and hydroxy-11-oxo-1,17-dolastadiene isolated from *D. spiralis* enclosed propenyl cyclopentanone moiety in dolastane skeleton (Ioannou et al. 2013), whereas, compound **9** exhibited some structural variations, such as isopropyl bonded cyclopentene, exocyclic double bond at C-1 and oxygenated functionalities at C-2, C-7, and C-14.

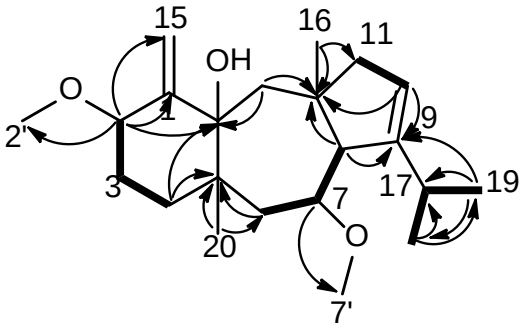

Figure 5.134.: Prominent ^{1}H-^{1}H COSY, and selected HMBC correlations of 2,7-dimethoxy-14α-hydroxy-dolasta-1(15),9-diene (**9**). The key ^{1}H-^{1}H COSY couplings were represented in bold face bonds. The key HMBC couplings have been represented by double barbed arrows.

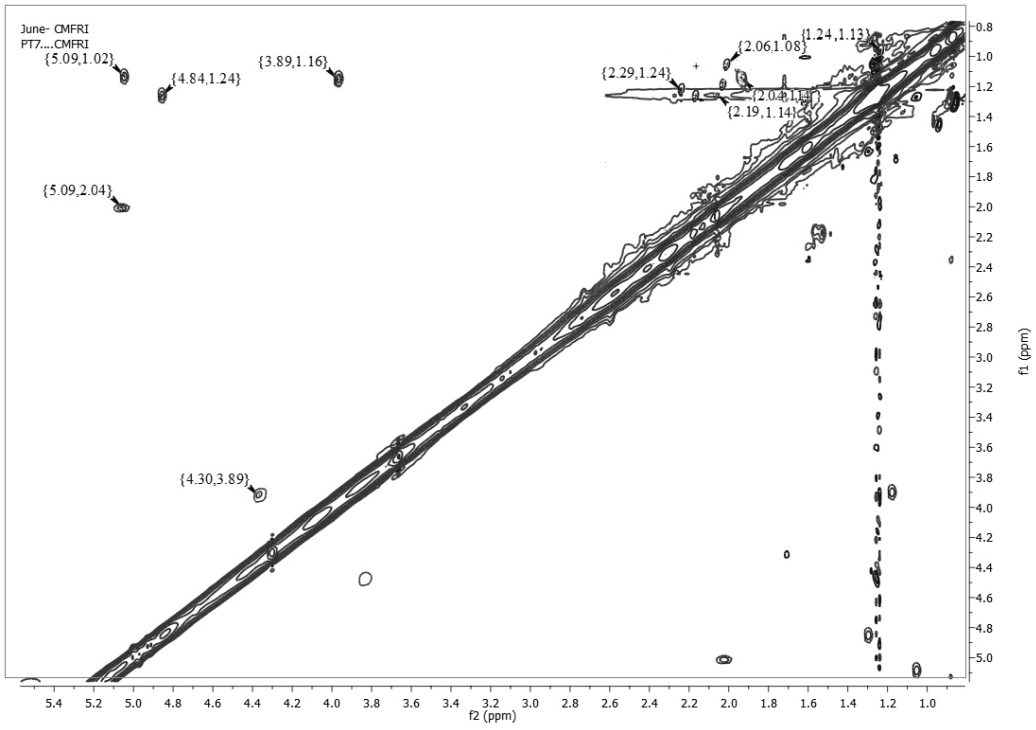

Figure 5.135.: NOESY spectrum of 2,7-dimethoxy-14α-hydroxy-dolasta-1(15),9-diene (**9**)

The NOESYs, such as δ 4.30 (H-7)/3.89 (H-2), δ 2.04 (Hβ-11)/5.09 (Hβ-15)/1.02 (Hβ-4) and δ 1.16 (H-18), 1.16 (H-19)/1.74 (Hβ-3)/1.08 (H-20), 1.14 (Hβ-6), 2.19 (H-8) were fixed at the same plane, and arbitrarily assigned as β-oriented. The NOESYs, such as δ 1.25 (H*α*-4)/2.29 (H*α*-11)/1.24 (H*α*-13) and δ 1.13 (H-16)/1.25 (H*α*-4)/4.84 (H*α*-15)/1.24 (H*α*-13) were aligned opposite to the β-protons, and thus, assigned as *α*-oriented (Figure 5.135-5.136). Thus, the relative stereochemistry of the hydroxyl at C-14 and Me-16 at C-12 were found to be *α*-oriented, which was found to be comparable with an earlier report of literature (Ioannou et al. 2013).

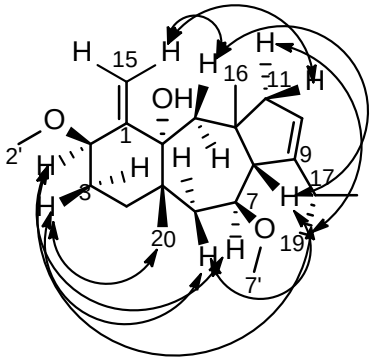

Figure 5.136.: Prominent NOE correlations of 2,7-Dimethoxy-14α-hydroxy-dolasta-1(15),9-diene (**9**). NOESY relations are represented by double-tailed arrows

The molecular ion peak of **9** was appeared at *m/z* 348 and base peak was ontained at *m/z* 27.0 (Figure 5.137 and 5.138).

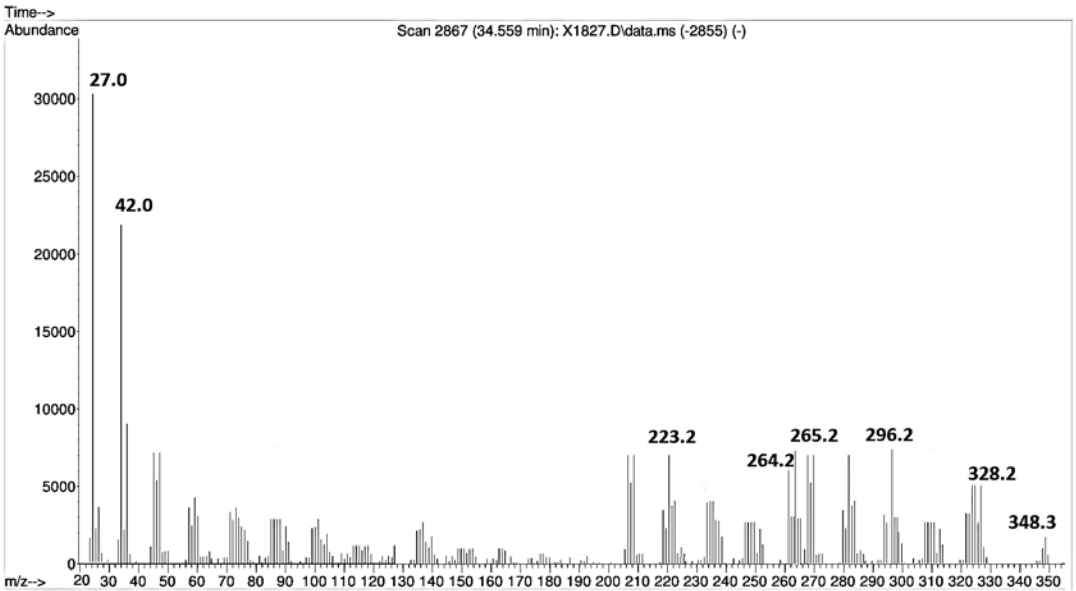

Figure 5.137.: EI-MS spectrum of 2,7-Dimethoxy-14α-hydroxy-dolasta-1(15),9-diene (**9**)

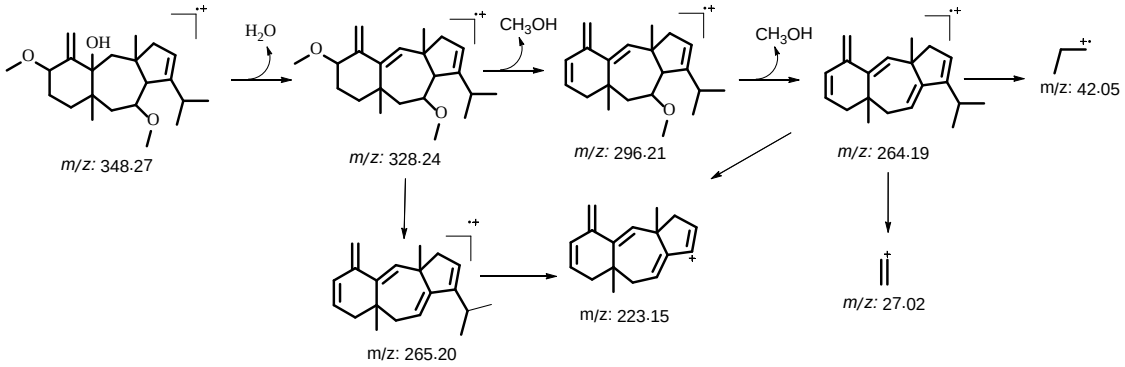

Figure 5.138.: Tentative mass fragmentation pattern of 2,7-dimethoxy-14α-hydroxy-dolasta-1(15),9-diene (**9**)

Table 5.12.: NMR spectroscopic data[a] of 2,7-dimethoxy-14α-hydroxy-dolasta-1(15),9-diene (**9**) isolated from brown seaweed *P.tetrastromatica*

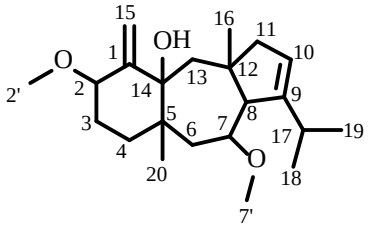

Compound **9**…….2,7-dimethoxy-14α-hydroxy-dolasta-1(15),9-diene (**9**)

C. No.	^{13}C	^{1}H NMR (int.,mult.,J in Hz)[b]	COSY	HMBC
1	151.5	-	-	-
2	81.9	3.89(1H,t,9.5 Hz)	H-3	C-15,2',14
2'	56.9	3.33(3H,s)	-	-
3	28.5	1.74(1H,m) 2.06(1H,m)	H-4	-
4	31.7	1.02(1H,dd,11.7 Hz) 1.25(1H,dd,6.7 Hz)	-	C-5,14
5	43.3	-	-	-
6	42.3	1.40(1H,d, 12.5Hz) 1.14(1H,d, 12.6Hz)	H-7	C-5
7	77.4	4.30(1H,m)	H-8	C-7'
7'	57.1	3.35 (3H,s)	-	-
8	53.3	2.19(1H,d,10.9 Hz)	-	C-9,12
9	146.2	-	-	-
10	121.8	5.40(1H,t,11.3 Hz)	H-11	C-12,9
11	49.4	2.04(1H,d,12.2 Hz)	-	-

		2.29 (1H,d,12.3 Hz)		
12	46.5	-	-	-
13	41.3	1.34(1H,s)	-	C-12,14
		1.24(1H,s)		
14	83.6	-	-	-
15	111.5	5.09(1H,s)	-	-
		4.84(1H,s)		
16	21.1	1.13(3H,s)	-	C-11,12
17	31.4	3.40(1H,m)	H-18,19	C-9
18	22.3	1.16(3H,d,6.3 Hz)	-	C-17,16
19	22.3	1.15(3H,d,6.4 Hz)	-	C-9,18, 17
20	25.5	1.08(3H,s)	-	C-5, 6

[a]NMR spectra were recorded using a Bruker AVANCE III 500 MHz (AV 500) spectrometer (Bruker, Karlsruhe, Germany) in $CDCl_3$ as aprotic solvent at ambient temperature with TMS as the internal standard (δ 0 ppm).

[b]Values in ppm, multiplicity and coupling constants (J=Hz) were indicated in parentheses. Multiplicities were allocated by ^{135}DEPT NMR spectrum.

The assignments were made with the aid of the COSY, HSQC, HMBC and NOESY experiments.

5.3.3.2d Structural characterization of Compound 10 (TP_{10})

4,7-Dimethoxy-9β,14α-dihydroxy-dolasta-1-ene

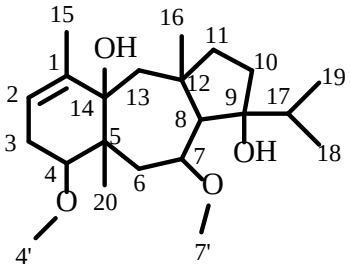

Sample yield	0.25% (> 99% purity, RP-C_{18} HPLC)
Physical description	Colourless oil
Molecular formula	$C_{22}H_{38}O_4$
Molecular mass	366.2770

The dolastane class of diterpenoid derivative, 1,2,5,5a,6,9,10,11,12,12a-Decahydro-11(11^2-hydroxypropyl)-2-[(*E*)-2^1-propenyl] cyclonona[*d*]-furo[2,3-*b*]pyran-9,12-diol was isolated as Colorless oil compound. The compound (**10**) has exhibited UV absorbance (UV (MeOH) λ_{max}) at 245.0 (2.62) nm (Figure 5.139). The homogeneity of the compound was ascertained by HPLC data on a bonded phase octadecylsilane (C_{18}) stationary phase (RP-C_8 HPLC, MeOH:MeCN, 3:2 v/v):

3.01 min (Figure 5.140). The molecular ion peak by HRESIMS was found to be observed at 367.2851$[M+H]^+$ (Figure 5.141).

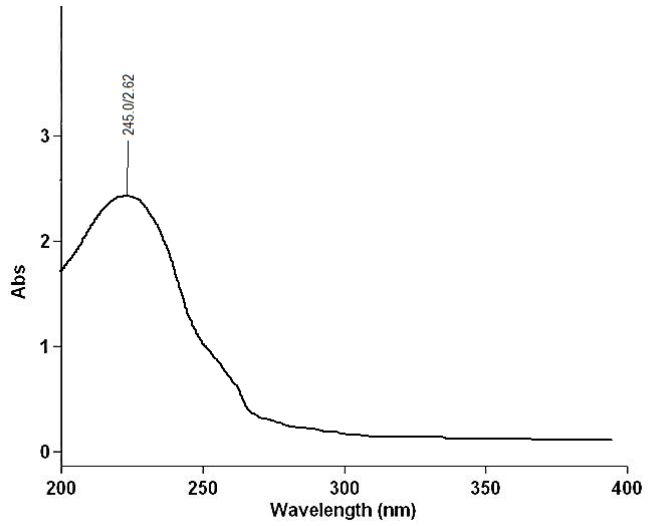

Figure 5.139.: UVspectrum of 4,7-dimethoxy-9β ,14α-dihydroxy-dolasta-1-ene (**10**)

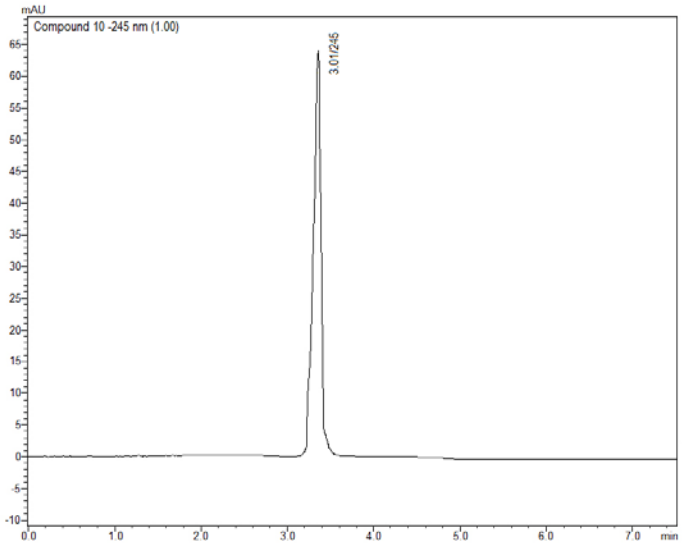

Figure 5.140.: HPLC chromatogram of 4,7-dimethoxy-9β ,14α-dihydroxy-dolasta-1-ene (**10**)

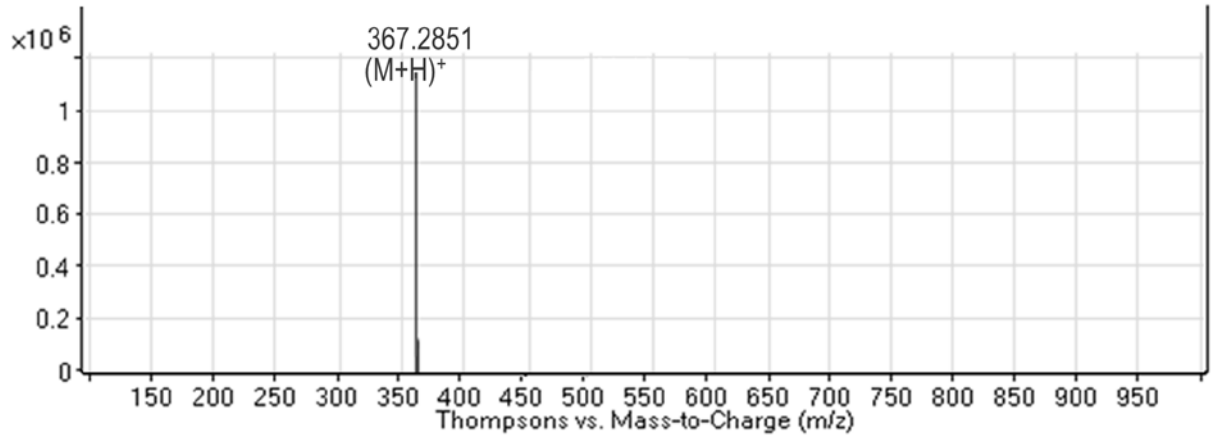

Figure 5.141.: HRESIMS of 4,7-dimethoxy-9β ,14α-dihydroxy-dolasta-1-ene (**10**)

The dolastane diterpenoid, **10** was isolated as colourless oil from *P. tetrastromatica* by repetitive chromatography. Compound **10** exhibited a molecular ion peak at *m/z* 366.28 [M^+], and the elemental composition was deduced as $C_{22}H_{38}O_4$, with comprehensive NMR/IR assignments (Figure 5.142-S47).

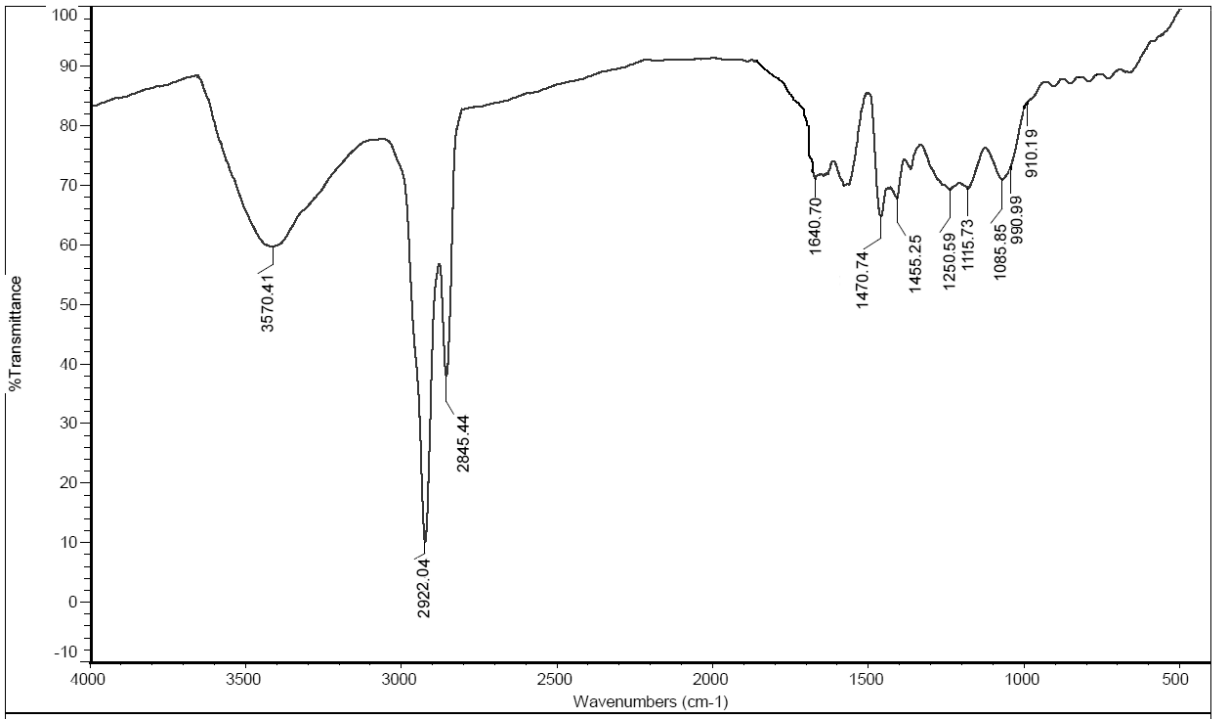

Figure 5.142.: FTIR spectrum of4,7-dimethoxy-9β ,14α-dihydroxy-dolasta-1-ene (**10**)

The molecular formula of **10** was assigned four degrees of unsaturation, which were related to one olefinic bond, and three ring systems. The detailed NMR spectroscopic data of **10**

were comparable with the basic chemical resonances of dolastane type of diterpenes and compound **9** (Ioannou et al. 2008; Ioannou et al. 2013). The COSYs at δ 5.49 (H-2)/1.96 (H-3) with HMBCs at δ /δ 5.49 (H-2)/142.9 (C-8), 83.0 (C-14), δ /δ 3.26 (H-4)/30.0 (C-3), 42.10 (C-5) proposed the six membered ring in **10** (Figure S2). The downfield signals at δ 142.9 (C-1) and 124.3 (C-2 HSQC δ 5.49) were related to the olefinic (>C=CH-) functionality (Ioannou et al. 2013), and their positions were corroborated through HMBCs, such as δ /δ 5.49 (H-2)/142.9 (C-1), 82.96 (C-14), 1.95 (H-15)/142.9 (C-1). The COSYs from δ 1.62 (H-17)/1.02 (H-18) and 1.02 (H-19) proposed the occurrence of isopropyl group in **10**, whereas its linkage was deduced with HMBCs from δ 1.62 (H-17) to δ 87.3 (C-9). The NOE correlations, such as δ 1.40 (Hβ-6), 1.76 (Hβ-10), 1.33 (H-8)/3.26 (H-4) and δ 1.33 (H-8)/1.03 (H-20) were found to be in the same plane of reference, and was arbitrarily assigned as β-oriented. The NOE couplings, such as δ 1.24 (H*α*-13), 1.53 (H*α*-11), 1.50 (H*α*-10)/4.64 (H-7), δ 1.53 (H*α*-11), 1.14 (H-16), 1.62 (H-17)/1.50 (H*α*-10) were aligned opposite to the β-protons, and therefore, assigned to be *α*-faced (Figure S2, S45).

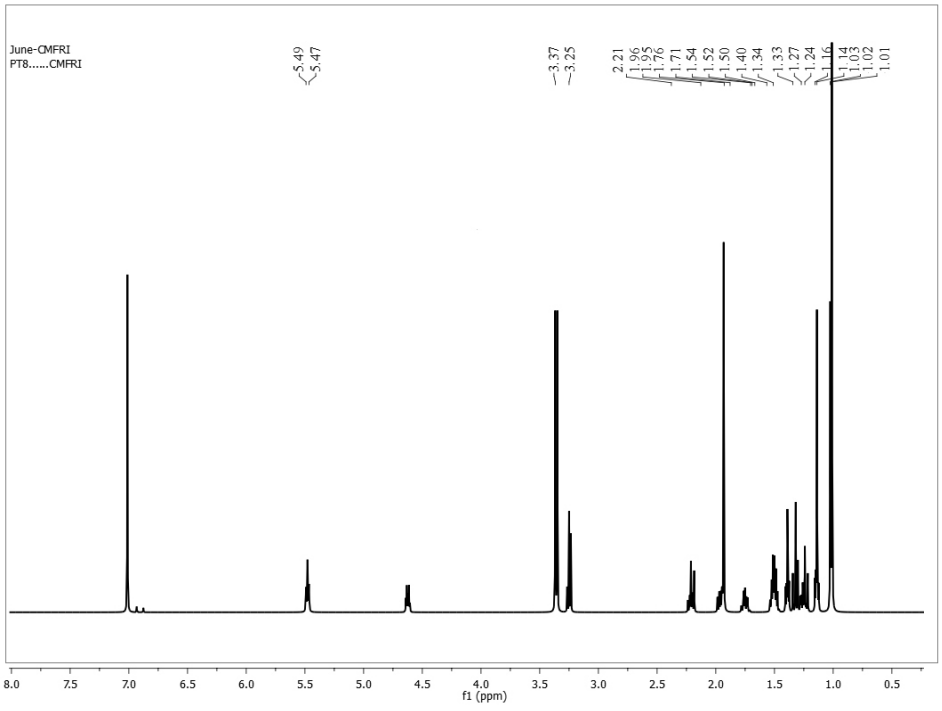

Figure 5.143.: ^{1}H NMR spectrum of4,7-dimethoxy-9β ,14α-dihydroxy-dolasta-1-ene (**10**)

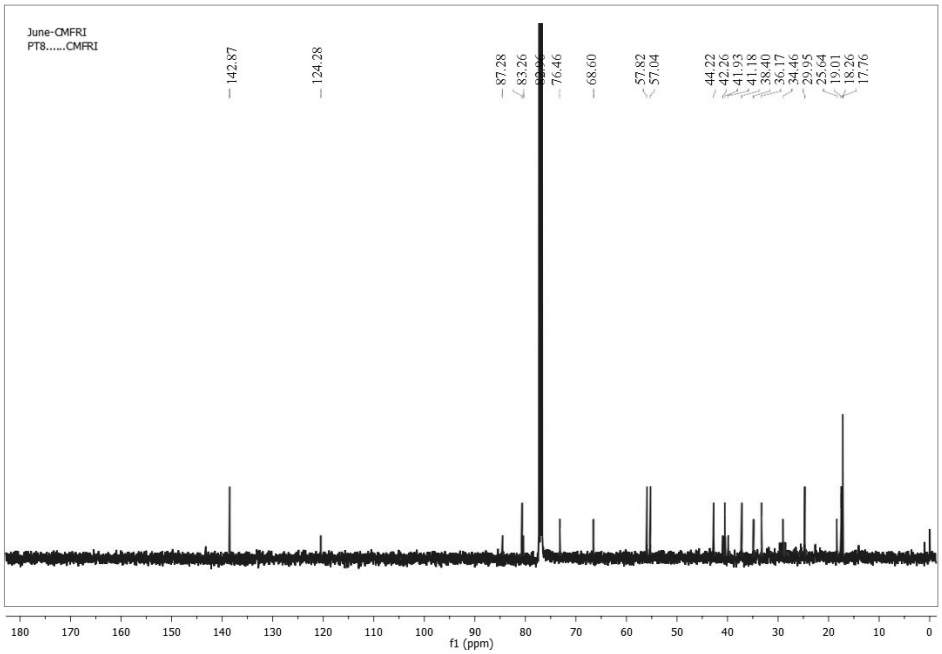

Figure 5.142.: ^{13}C NMR spectrum of4,7-dimethoxy-9β ,14α-dihydroxy-dolasta-1-ene (**10**)

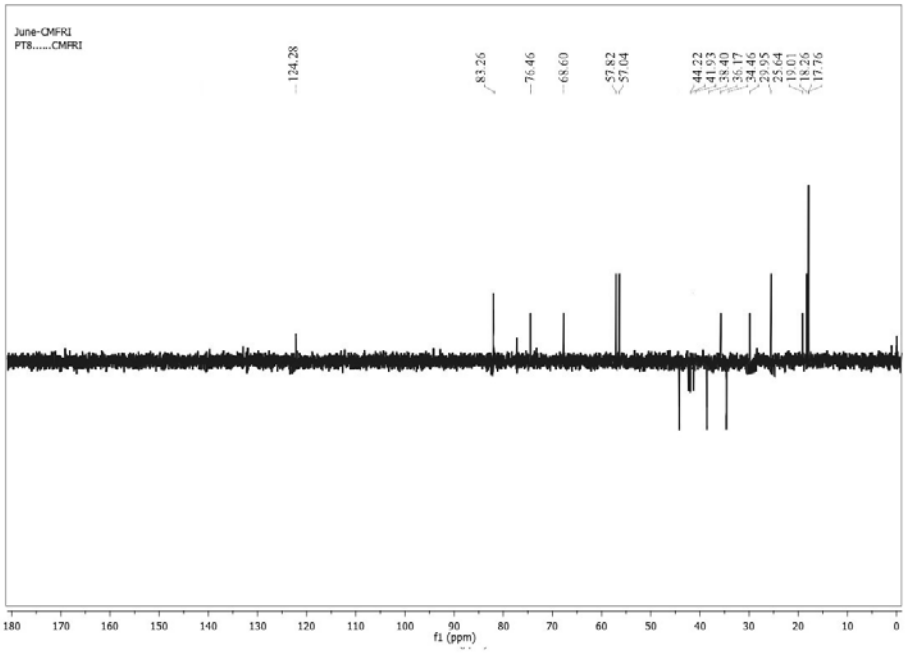

Figure 5.142.: DEPT spectrum of4,7-dimethoxy-9β ,14α-dihydroxy-dolasta-1-ene (**10**)

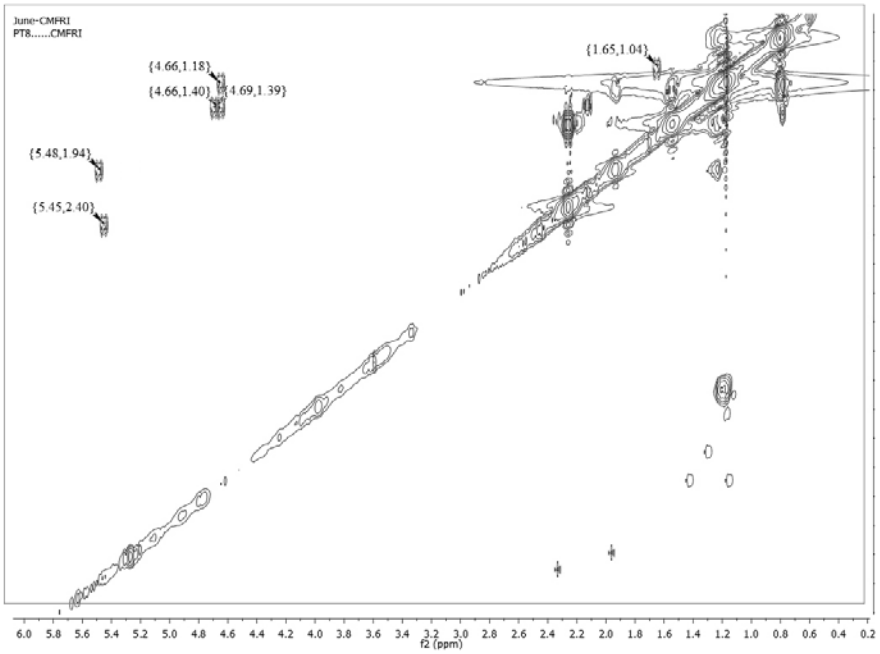

Figure 5.142.: ^{1}H-^{1}H COSY spectrum of4,7-dimethoxy-9β ,14α-dihydroxy-dolasta-1-ene (**10**)

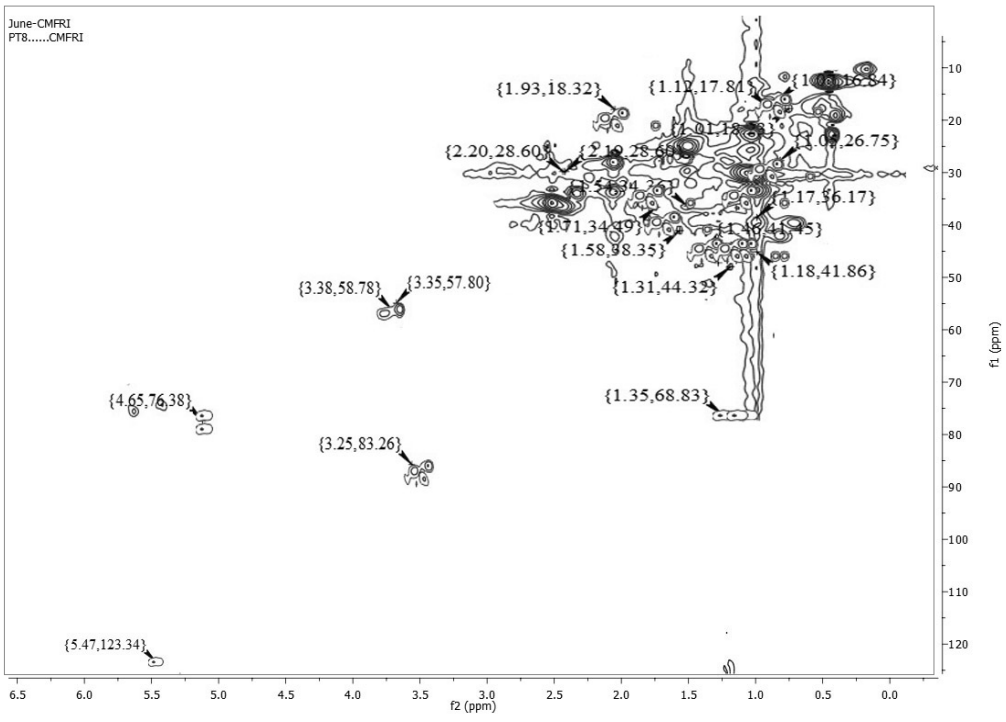

Figure 5.142.: HSQC spectrum of 4,7-dimethoxy-9β ,14α-dihydroxy-dolasta-1-ene (**10**)

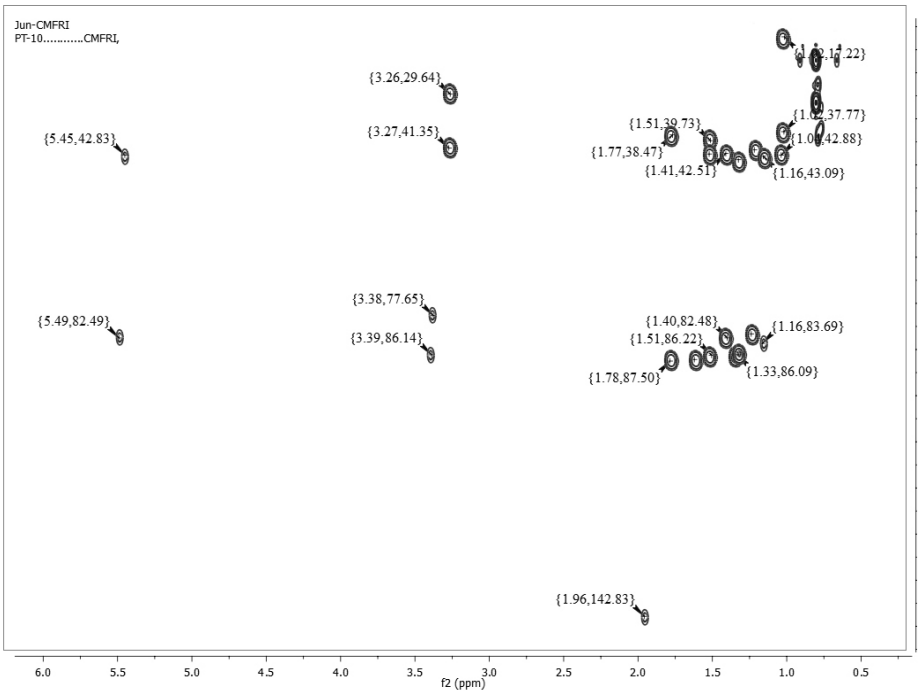

Figure 5.143.: HMBC spectrum of4,7-dimethoxy-9β ,14α-dihydroxy-dolasta-1-ene (**10**)

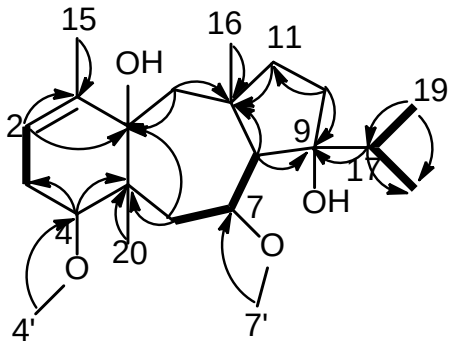

Figure 5.144.: Prominent ^{1}H-^{1}H COSY, and selected HMBC correlations of 4,7-dimethoxy-9β ,14α-dihydroxy-dolasta-1-ene (**10**). The key ^{1}H-^{1}H COSY couplings were represented in bold face bonds. The key HMBC couplings have been represented by double barbed arrows.

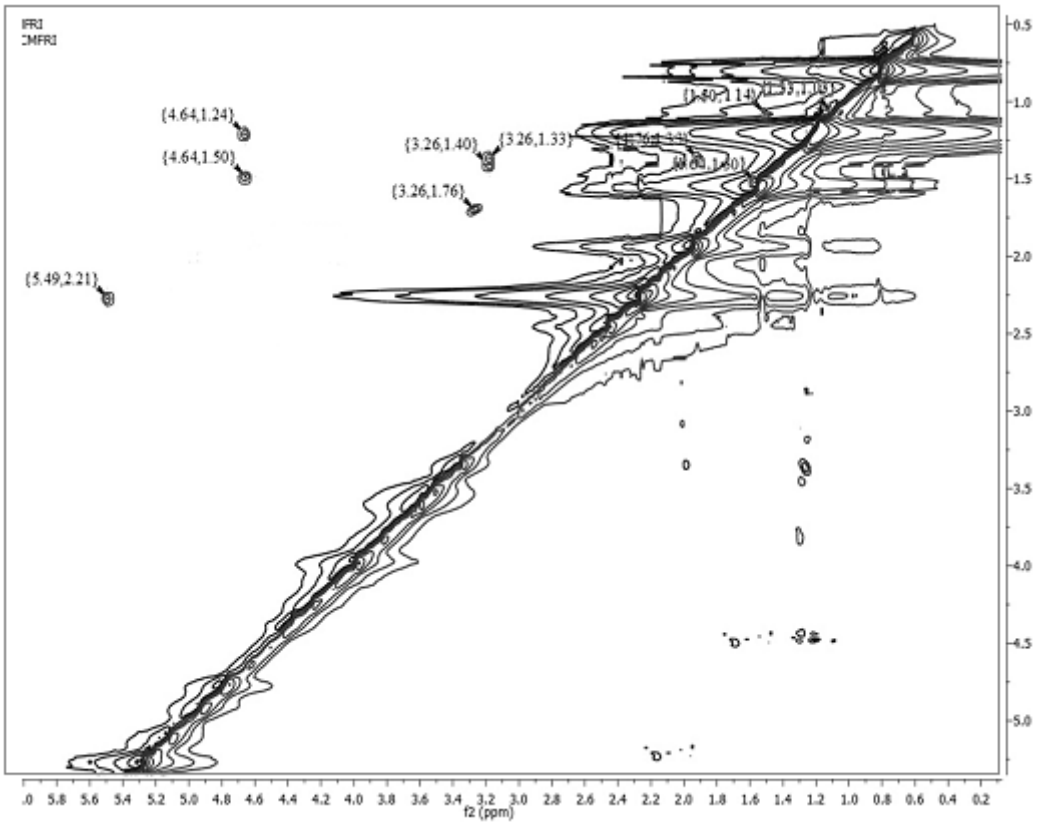

Figure 5.145.: NOESY spectrum of 4,7-dimethoxy-9β ,14α-dihydroxy-dolasta-1-ene (**10**)

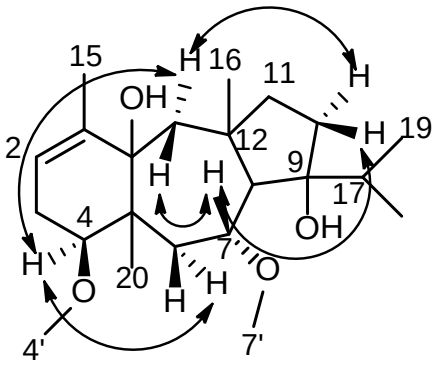

Figure 5.146.: Prominent NOE correlations of 2,7-dimethoxy-14α-hydroxy-dolasta-1(15),9-diene (**10**). NOESY relations are represented by double-tailed arrows

The molecular ion peak of **10** was appeared at *m/z* 366 and base peak was ontained at *m/z* 27.0 (Figure 5.147 and 5.148).

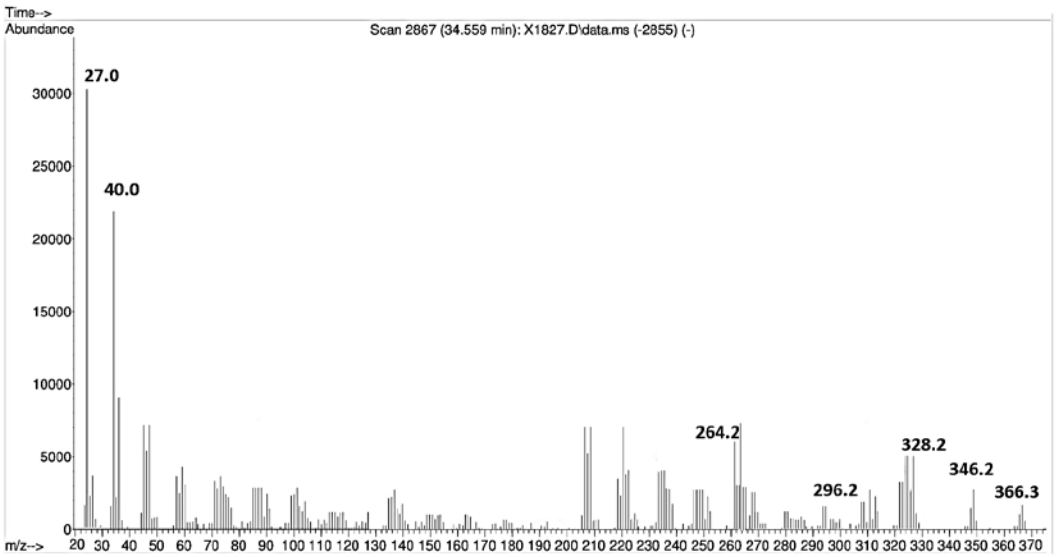

Figure 5.147.: EI-MS spectrum of 4,7-dimethoxy-9β ,14α-dihydroxy-dolasta-1-ene (**10**)

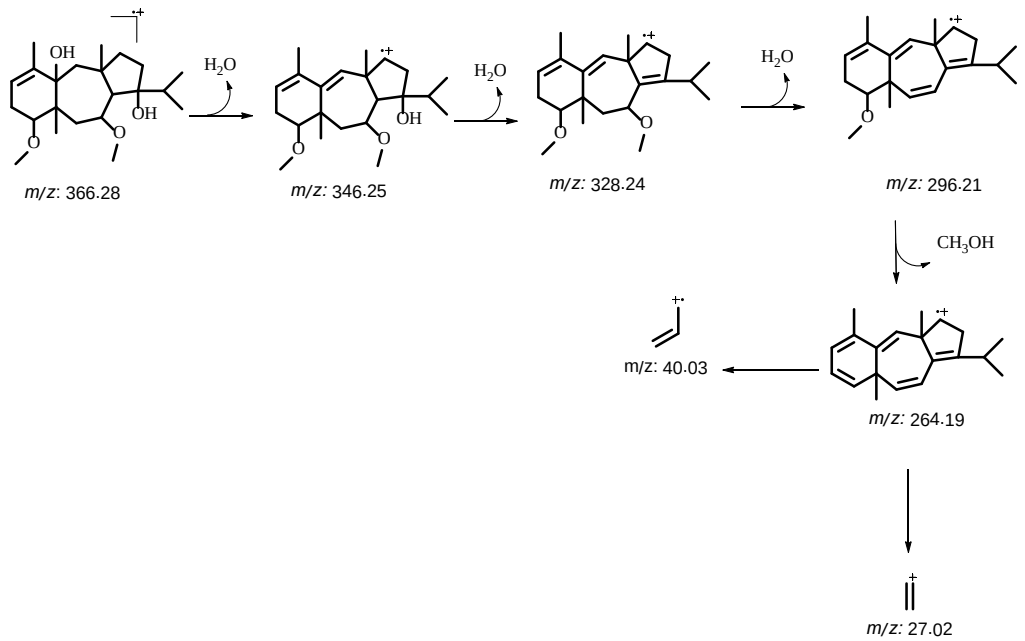

Figure 5.148.: Tentative mass fragmentation pattern of 4,7-dimethoxy-9β ,14α-dihydroxy-dolasta-1-ene (**10**)

Table 5.13.: NMR spectroscopic data[a] of 4,7-dimethoxy-9β ,14α-dihydroxy-dolasta-1-ene (**10**) isolated from brown seaweed *P.tetrastromatica*

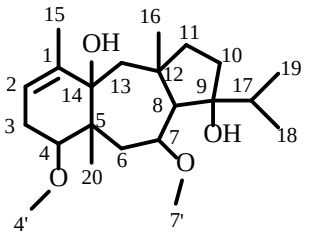

Compound **10**……4,7-dimethoxy-9β ,14α-dihydroxy-dolasta-1-ene (**10**)

C. No.	^{13}C	^{1}H NMR (int.,mult.,J in Hz)[b]	COSY	HMBC
1	142.9	-	-	-
2	124.3	5.49(1H,t,10.7 Hz)	H-3	C-14,1
3	30.0	2.21(1H,m) 1.96(1H,m)	-	-
4	83.3	3.26(1H,t,8.8 Hz)	-	C-3,5
4’	57.0	3.39(3H,s)	-	C-4
5	42.1	-	-	C-14
6	42.9	1.40(1H,d,11.6 Hz) 1.16(1H,d,11.8Hz)	H-7	C-5
7	76.5	4.64(1H,m)	H-8	C-6
7'	57.8	3.36(3H,s)	-	C-7
8	68.6	1.33(1H,d,9.1 Hz)	-	C-9,12
9	87.3	-	-	-
10	34.5	1.50(1H,m) 1.76(1H,m)	-	C-9,11
11	38.4	1.53(1H,t,6.6 Hz) 1.27(1H,t,6.7 Hz)	-	C-12
12	42.3	-	-	-
13	44.2	1.24(1H,s) 1.34(1H,s)	-	C-12,14
14	83.0	-	-	-
15	19.0	1.95(3H,s)	-	C-1
16	18.3	1.14(3H,s)	-	C-12
17	36.2	1.62(1H,m)	H-18, H-19	C-9,18
18	17.8	1.02(3H,d,7.6 Hz)	-	-
19	17.8	1.01(3H,d,7.7 Hz)	-	C-18,8
20	25.6	1.03(3H,s)	-	C-5

[a]NMR spectra were recorded using a Bruker AVANCE III 500 MHz (AV 500) spectrometer (Bruker, Karlsruhe, Germany) in $CDCl_3$ as aprotic solvent at ambient temperature with TMS as the internal standard (δ 0 ppm).

[b]Values in ppm, multiplicity and coupling constants (J= Hz) were indicated in parentheses. Multiplicities were allocated by ^{135}DEPT NMR spectrum.

The assignments were made with the aid of the COSY, HSQC, HMBC and NOESY experiments.

5.3.3 Pharmacological potentials of secondary metabolites isolated from the organic extract of P. tetrastromatica

5.3.3.1 Pharmacological potentials of xenicane class of diterpenoid derivative (1-5)

The organic extract of *P. tetrastromatica* derived five diterpene derivatives, which displayed potential anti-inflammatory and antioxidative activities in various *in vitro* systems (Table 5.14). Significant differences ($P < 0.05$) in radical scavenging properties were recorded amongst the xenicin (**1**-**2**) and α-tocopherol against $ABTS^+$ (IC_{50} ~ 1.91 mM; $P < 0.05$) and DPPH (IC_{50} ~ 1.64 mM) radicals. Significantly higher DPPH scavenging activity was observed for xeniolide **5** (IC_{50} 1.73 mM) followed by **4** and xenicins (**2**, **3**) (IC_{50} ~ 1.92 mM, $P < 0.05$), in declining order. In addition, the $ABTS^+$ scavenging efficacy was significantly higher for **5** and **4** (IC_{50} ~ 2.03 mM) as related to those revealed by the diterpene metabolites **1** through **3** (~2.30 mM, $P < 0.05$). Anti-inflammatory activities against 5-LOX and COX-2 were significantly higher for **5** (IC_{50} 1.88 and 1.41 mM, respectively) as compared to other homologues in this series ($IC_{50} < 2.26$ mM; $P < 0.05$). The compound **5** registered greater anti-5-LOX potential (IC_{50} 1.88 mM) than that exhibited by ibuprofen (IC_{50} 4.50 mM; $P < 0.05$). The greater selectivity indices of studied diterpenes (IC_{50}anti-COX-1/IC_{50}anti-COX-2 > 1) as compared to that displayed by ibuprofen (0.43) inferred higher anti-inflammatory selectivity against COX-2. Previous reports of literature inferred that oxidative stress directed the generation of free radicals, which in turn, caused inflammation and related pathophysiological conditions (D'Orazio et al., 2012; Joy and Chakraborty, 2017a). Thus, it is fitting to state that the higher antioxidative potentials of the studied compounds could be correlated to their anti-inflammation properties. Inflammation reactions were found to be concomitant with the formation of inflammatory prostaglandins or leukotrienes by enzymes, such as cyclooxygenases and lipoxygenase. The studied compounds from *P. tetrastromatica* were found to reduce the formation of inflammatory prostaglandins because of their potential inhibition of pro-inflammatory agents.

5.3.3.2 Pharmacological potentials of dolabellane class of diterpenoid derivative (6-10)

The antioxidant activities of compounds (**6**-**10**) were evaluated by their $ABTS^+$ and DPPH scavenging potentials, whereas their bioactivities were compared with standard antioxidant α-tocopherol (Table 5.15). The DPPH radical scavenging activities of **10** and **8** were greater (IC_{50} ~0.60 mg/mL) than other studied analogues and α-tocopherol (IC_{50} >0.6 mg/mL). The antioxidant potencial of **10** was further confirmed by the $ABTS^+$ scavenging activities (IC_{50} 0.71 mg/mL), which was greater than other studied analogues and α-tocopherol (IC_{50} >0.72 mg/mL). The attenuating activities of **10** against α-glucosidase (IC_{50} 0.11 mg/mL) and α-amylase (IC_{50} 0.13 mg/mL) were

comparable to the gold standard acarbose (IC_{50} 0.12 and 0.14 mg/mL, respectively) (Table 1). These results signified the potential anti-hyperglycaemic property of compound **10** over acarbose and other studied compounds.

5.3.4 Structure-activity correlation analyses of bioactive compounds isolated from EtOAc-MeOH extract of P. tetrastromatica

5.3.4.1 Structure-activity correlation analyses of xenicane class of diterpenoid derivative (1-5)

The physico-chemical parameters of studied xenicins (**1-2**) and xeniolides (**3-5**) corroborated the structural attributions that were accountable for targeted bioactive potentials (Joy and Chakraborty, 2017b). The bioactivities were essentially associated with electronic {polarizability (Pl) and topological polar surface area (tPSA)} and lipophilic parameters (log P_{ow} logarithmic value of octanol-water coefficient), and not by the steric factors. It is of note that the steric factor of **4** and **5** (P > 820 cm^3) were greater than xenicane class of diterpenoids (**1-2**, P < 780 cm^3) evidently due to the occurrence of the bulk bicyclic skeleton of the xeniolides (**3-5**) (Table 5.16). However, the electronic parameters were found to play illustrious role to govern the bioactive potentials (Wang et al., 2007; Chakraborty and Raola, 2018). The total numbers of electron-localized centres were lesser in **1** and **2** as designated by the assessment of electronic descriptors, thus resulting in their lower polarizability, than those documented with the xeniolides (**3-5**) (Table 3). The log P_{ow} of **5** was found to be within the desirable range (~1.95), which might cause a suitable lipophilic-hydrophobic relation (Lipinski 2004) and receptor binding (Huuskonen et al., 2000; McNally et al., 2007) leading to higher target bioactivities than other studied compounds.

5.3.4.2 Structure-activity correlation analyses of dolabellane class of diterpenoid derivative (6-8)

The structural attributions of the studied analogues were interpreted by their physico-chemical parameters. The previous reports demonstrated that the bioactive potentials were correlated with lipophilic (log P_{ow}, logarithmic value of octanol-water coefficient) and electronic parameters {polarisability (PI) and topological polar surface area (tPSA)} (Lipinski and Hopkins 2004; Antony and Chakraborty 2018). Notably, the steric bulk factors of **6-10** were of greater resemblance due to the presence of basic dolabellane framework, and therefore, did not constitute important functional role in determining their bioactive properties. The lesser steric bulk factors of **6-10** (molar refractivity, MR 97-105 cm^3/mol; molar volume, MV 328-337 cm^3; parachor, P 820-860 cm^3) might contributed towards its greater antioxidative properties than α-tocopherol with comparatively greater steric bulkiness (MR 135.06 cm^3/mol, MV 462.70 cm^3, P 1123.00 cm^3). The greater steric hindrance of acarbose (MR 141.21 cm^3/mol, MV 369.70 cm^3, P 1209.80 cm^3) over the titled compounds might

be corroborated with their greater attenuating activities against starch hydrolytic enzymes. The lesser steric bulkiness of the studied compounds might be responsible towards their effective interaction with the amino acyl residues of the enzyme catalytic site resulting in their potential anti-diabetic activities. Notably, the electronic and hydrophobicity factors of the studied compounds might also acquire prominent functional roles in determining bioactivities (Wang et al. 2007). The tPSA of **10** was found to be greater (58.92) than those exhibited by other studied analogues (tPSA <50) (Table 5.16), that might be corroborated with the greater reactivities towards free radicals. The greater tPSA of **8** (tPSA 49.69) and **10** (tPSA 58.92) over that of α-tocopherol (tPSA 29) might contribute towards its greater antioxidant properties than α-tocopherol. The log P_{ow} of the studied compounds were found to be within the acceptable limits of 2.69-4.82, when compared to that of α-tocopherol (log P_{ow} 9.98). The significantly lower value of log P_{ow} of -7.10 reported for acarbose might result in unfavourable hydrophobic-lipophilic interactions, whereas the log P_{ow} of the titled compounds were found to be within the favourable boundaries (log P_{ow} 2-5), which might result in potential anti-diabetic properties of the latter. The greater electronic descriptors of acarbose could effectively compensate for its effective anti-diabetic potentials, irrespective of its unfavourable log P_{ow} and greater steric bulkiness. The optimum log P_{ow} and electronic parameters along with lower steric values of the titled compounds could manifest towards its target bioactive properties. Generally, the compounds possessing lesser log P_{ow} values (<5) were recognised to be effective in keeping a steady balance of hydrophobic-lipophilic parameters (Lipinski and Hopkins 2004). Principle component analyses between log P_{ow} and bioactive potentials of the titled compounds appropriately showed that the bioactivities and log P_{ow} values were located in the similar quadrant. Therefore, an optimum hydrophobic-lipophilic balance appeared to constitute a predominant functional role in determining the target bioactive properties.

Table 5.14.: *In vitro* bioactive potentials (antioxidant and anti-inflammatory) of compounds **1-5** and commercially available references along with molecular descriptors (electronic, steric and hydrophobic) of the studied compounds isolated from *P. tetrastromatica.*

Compounds	**Anti-oxidant activities (IC_{50}, mM)**		**Anti-inflammatory activities (Inhibitory activities against pro-inflammatory enzymes, IC_{50}, mM)**			
	DPPH scavenging	**ABTS scavenging**	**COX-1 inhibitory**	**COX-2 inhibitory**	**5-LOX inhibitory**	**Selectivity index**
1	2.16 ± 0.03^{a}	2.41 ± 0.03^{a}	2.09 ± 0.03^{a}	1.98 ± 0.01^{a}	2.50 ± 0.01^{a}	1.05 ± 0.02^{a}
2	2.03 ± 0.02^{b}	2.23 ± 0.02^{b}	2.17 ± 0.03^{b}	1.80 ± 0.03^{a}	2.31 ± 0.02^{a}	1.20 ± 0.01^{b}
3	1.97 ± 0.02^{b}	2.26 ± 0.03^{b}	2.04 ± 0.02^{a}	1.77 ± 0.03^{a}	2.34 ± 0.02^{a}	1.15 ± 0.02^{b}
4	1.75 ± 0.03^{c}	2.04 ± 0.01^{c}	2.12 ± 0.02^{b}	1.43 ± 0.01^{b}	1.92 ± 0.03^{b}	1.48 ± 0.03^{c}
5	1.73 ± 0.03^{c}	2.01 ± 0.04^{c}	2.14 ± 0.03^{b}	1.41 ± 0.02^{b}	1.88 ± 0.02^{b}	1.52 ± 0.02^{c}
Standard	1.46 ± 0.04^{cT}	1.70 ± 0.05^{cT}	0.19 ± 0.00^{bI}	0.44 ± 0.02^{cI}	4.50 ± 0.11^{cI}	0.43 ± 0.01^{dI}

The anti-oxidant and anti-diabetic activities were expressed as IC_{50} values, mM).

$^{a-c}$ Column-wise values with different superscripts of this type indicate significant difference (P<0.05), which implied for the statistical evaluation of the results. Triplicate values were taken and the variance analyses (ANOVA) were carried out (using Statistical Program for Social Sciences 13.0) for means of all parameters to examine the significance level (P<0.05). The results were expressed as mean ± SD (n = 3).

^{T} Superscript of this type depicts α-tocopherol

^{I} Superscript of this type depicts ibuprofen

Table 5.15. *In vitro* bioactive potentials (antioxidant and anti-antidiabetic) of compounds **6-10** from *P. tetrastromatica* and commercially available references

	Bioactivities					
Antioxidant activity	**1**	**2**	**3**	**4**	**5**	***α*-tocopherol**
[p]DPPH scavenging activity	[a]0.65±0.02	[a]0.67±0.01	[b]0.60±0.02	[a]0.69±0.02	[b]0.59±0.01	[a]0.63±0.01[Q]
[p]$ABTS^+$ scavenging activity	[a]0.77±0.03	[b]0.83±0.02	[a]0.75±0.06	[b]0.81±0.03	[c]0.71±0.02	[a]0.74±0.03[Q]
Anti-diabetic activity	**1**	**2**	**3**	**4**	**5**	**Acarbose**
α-amylase inhibition activity	[a]0.18±0.01	[b]0.21±0.02	[a]0.16± 0.02	[b]0.22 ± 0.03	[c]0.13±0.02	[c]0.14 ± 0.02[R]
α-glucosidase inhibition activity	[a]0.15±0.01	[b]0.20±0.03	[a]0.14 ± 0.02	[b]0.21±0.02	[c]0.11±0.01	[c]0.12 ± 0.01[R]

The anti-oxidant and anti-diabetic activities were expressed as IC_{50} values (mM).

[a-c] Row-wise values with different superscripts of this type indicate significant difference (P<0.05), which implied for the statistical evaluation of the results. Triplicate values were taken and the variance analyses (ANOVA) were carried out (using Statistical Program for Social Sciences 13.0) for means of all parameters to examine the significance level (P<0.05).

Results were expressed as mean ± SD (n = 3).

Different superscripts (Q-R) indicate the standards used for different activities.

Table 5.16.: Molecular descriptors (electronic, steric and hydrophobic) of compounds **1-10** from *P. tetrastromatica.*

	Molecular descriptors[d]					
Compounds	**Electronic**		**Steric**			**Hydrophobic**
	PI ($x10^{-23}$ cm^3)	**tPSA**	**P (cm^3)**	**MV (cm^3)**	**MR (cm^3 mol^{-1})**	**Log P_{OW}**
1	37.87	79.15	762.9	284.5	95.53	1.17
2	37.95	79.15	775.5	289.4	95.73	1.52
3	38.74	107.22	822.1	317.6	97.73	1.29
4	40.78	96.22	867.5	331.4	102.87	1.61
5	38.74	107.22	826.4	315.6	97.73	1.93
6	39.30	49.69	820.3	328.6	99.15	3.18
7	38.80	29.46	816.2	335.4	97.87	4.82
8	39.30	49.69	820.3	328.6	99.15	3.16
9	40.41	38.69	830.5	335.1	101.95	3.42
10	41.21	58.92	858.4	337.7	103.96	2.69

MV, molar volume; P, parachor; MR, molar refractivity.

log P, logarithmic scale of the octanol-water partition coefficient.

Pl, polarizability; tPSA, topological polar surface area.

[d] The structure-activity relationship analysis was carried out by using different molecular descriptors of the purified compounds as described in the text.

5.3.5. *In silico* molecular docking analysis of bioactive compounds isolated from *P. tetrastromatica*

5.3.5.1 *In silico* molecular docking analysis of *xenicane class of diterpenoid derivative (1-5)*

The studied compounds were subjected to *in silico* molecular docking analysis against pro-inflammatory 5-lipoxygenase (LOX-5), and the results were evaluated by their RMSD data. The molecular docking parameters, such as binding energy, docking score, inhibition constant, hydrogen bonding interactions, intermolecular energy and torsional free energy between the ligands and the active sites of 5-lipoxygenase were documented in Table 5.18. The grid box of potential binding site was assigned as x=40.120, y=39.326, z=41.254. Among the studied compounds, xenicanes **1** and **2**, on molecular docking analysis with 5-lipoxygenase, exhibited one hydrogen bond interaction with amino residues Arg411 and Arg438 in the enzyme active site with molecular distances of 3.011 Å and 2.740 Å, respectively. Among the xeniolide analogues, compound **5** showed three hydrogen bonded interactions with amino acid residues, one hydrogen bonded with Lys441 (2.799 Å), and two with Gln434 (2.860 and 2.886 Å).

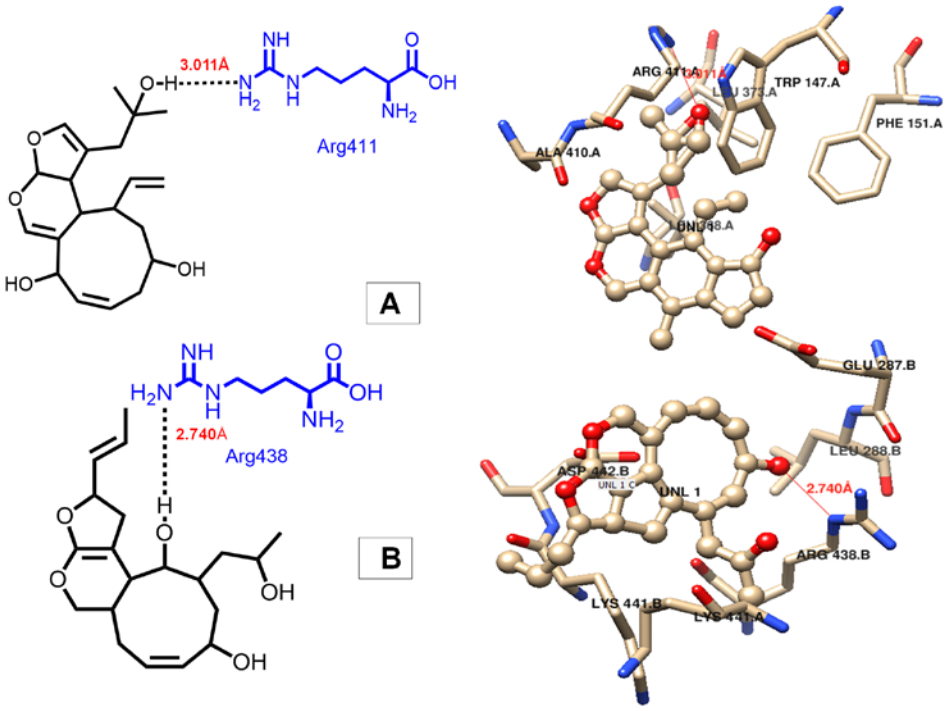

Fig. 5.149.: Closer view of molecular binding interactions of the xenicane derivatives **1** (**A**) and **2** (**B**) in the catalytic site of protein LOX-5 as deduced from its molecular modeling simulations. The xenicanes **1** and **2** exhibited one hydrogen bond interaction with amino residues Arg411 and Arg438 in the enzyme active site with molecular distances of 3.011 Å and 2.740 Å, respectively.

The compound **5** exhibited greater number of hydrogen bond interactions with amino acyl residues than those recorded by **3** (2.742 Å with Gln437) and **4** (2.935 Å with Asp290) (Fig. 5.149 & 5.150). The lesser distance of 2.740 Å in ligand-protien complex of compound **2** established its closer binding interaction towards protein than those displayed by xenicane **1** (3.011 Å). These results were supported by the higher *in vitro* anti-inflammatory activity of **2** over **1** against 5-LOX. The comparison of molecular docking parameters appropriately suggested that compound **5** exhibited close molecular interactions towards enzyme LOX-5 with least binding energy (-11.56 kcal mol^{-1}) and docking score (11.40 kcal mol^{-1}), which were corroborated with their greater potential of enzyme inhibition against LOX-5 (IC_{50} 1.88 mM) than those exhibited by **1**-**4**.

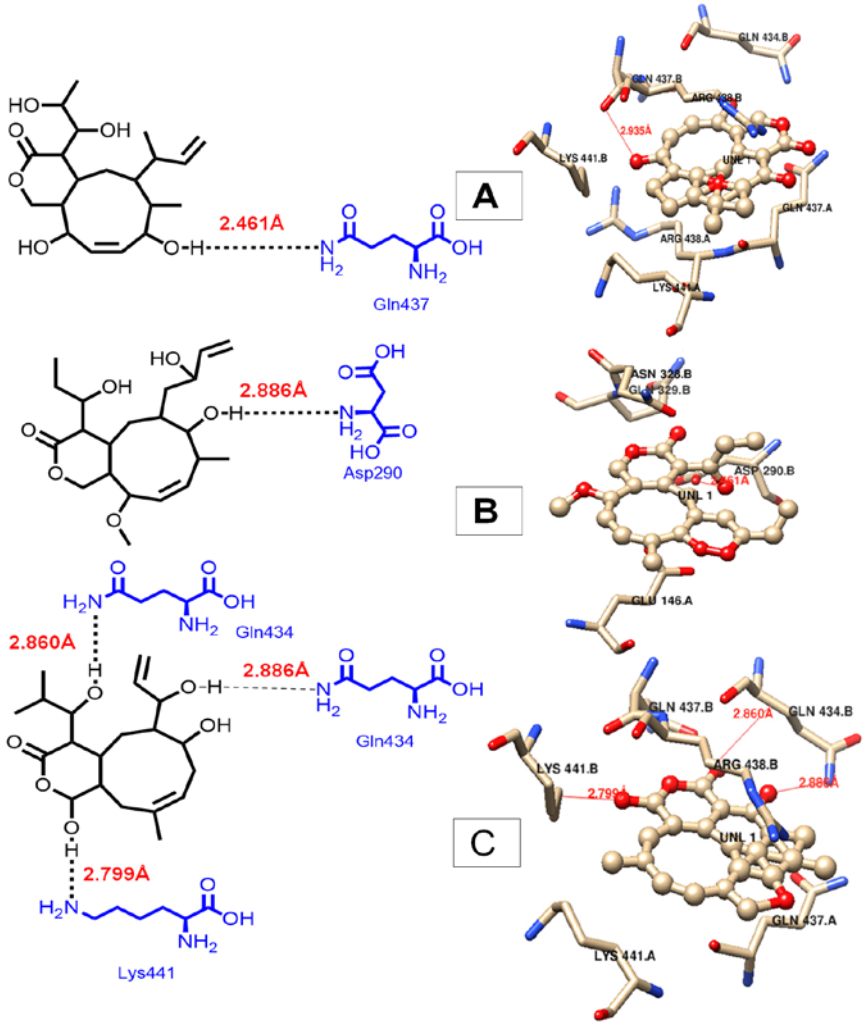

Figure 5.150.: Closer view of molecular binding interactions of the xeniolide derivatives **3** (**A**), **4** (**B**), and **5** (**C**) in the catalytic site of protein LOX-5 as deduced from its molecular modelling simulations. The xeniolide **5** showed three hydrogen bonded interactions with amino acid residues, one hydrogen bonded with Lys441 (2.799 Å), and two with Gln434 (2.860 and 2.886 Å). Compound

5 displayed greater number of hydrogen bond interactions with amino acyl residues than those recorded by **3** and **4**.

Table 5.17.: The *in silico* molecular docking parameters between the ligands (compounds **1**–**5**) and the active sites of 5-lipoxygenase

†Ligands	‡Binding energy (kcal mol^{-1})	‡Docking score (kcal mol^{-1})	‡Inhibition constant Ki (µM)	††Hydrogen bonding interactions	‡Intermolecular energy (kcal mol^{-1})	‡Torsional free energy (kcal mol^{-1})
1	-6.85	7.15	9.53	Arg411	-7.45	0.60
2	-7.39	8.44	3.83	Arg438	-8.58	1.19
3	-11.48	11.72	0.003	Gln437	-11.78	0.30
4	-8.66	9.43	0.449	Asp290	-9.71	1.19
5	-11.56	11.40	0.033	Lys441, Gln437	-11.56	0.00

† Molecular docking simulations were carried out using Autodock 4 software tool.

‡ Values were evaluated from the calculations based on the energy minimization.

††Hydrogen bonding interactions of ligands **1-5** with protein 5-lipoxygenase.

5.3.5.2 In silico molecular docking analysis of *dolabellane class of diterpenoids (6-8)*

The compounds (**6-10**) were subjected to molecular docking against the carbolytic enzyme *α*-amylase. The molecular docking parameters, such as docking score, binding energy, inhibition constant, intermolecular and torsional free energy were documented (Table 5.18). Among the dolabellanes, compound **8** recorded least binding energy (-9.71 kcal/mol) and docking score of -11.58 kcal/mol followed by those exhibited by **7** and **6** (-9.31 to -8.60 kcal/mol, and -10.60 to -11.20 kcal/mol, respectively). Likewise, among the dolastanes, compound **10** recorded least binding energy (-8.59 kcal/mol) and docking score of -10.64 kcal/mol followed by those exhibited by compound **9**. (Table 5.18). The comparison of lowest molecular docking parameters, such as constant of inhibition, binding energy, docking score, internal and torsional free energies appropriately suggested that the compounds **8** and **10** possessed close molecular interactions with the target carbolytic enzyme receptors, resulting in their greater potential of enzyme inhibition against *α*-amylase. The greater molecular docking interactions of compounds **8** and **10** in the active site of *α*-amylase were appropriately corroborated with their potent *in vitro α*-amylase inhibitory activities (IC_{50} <0.17 mg/mL). It was observed that the studied dolabellane and dolastane analogues efficiently interacted with the active site amino acyl residues in the binding site of *α*-amylase via

electrostatic interactions through the oxygen atom of the hydroxyl group (Liu et al. 2013). The interactions of compounds **8** and **10** with α-amylase receptors were described in Figure 5.151.

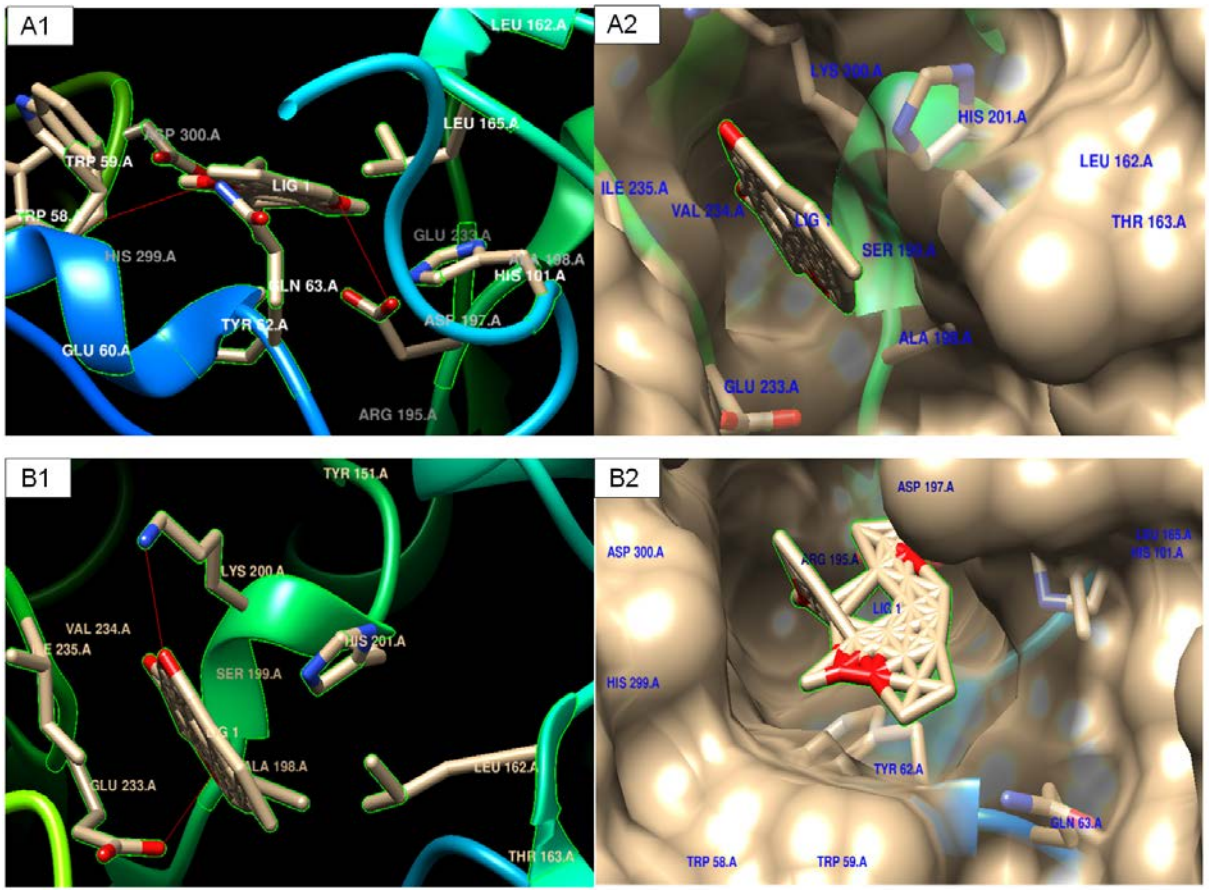

Figure 5.151. Closer view of molecular binding interactions of compounds **8** (**A1**-**A2**) and **10** (**B1**-**B2**) in the catalytic site of protein α-amylase deduced from molecular modeling simulations.

Table 5.18.: The binding energy, docking score, inhibition constant, intermolecular energy and torsional free energy between the ligands (compounds **6**–**10**) and the active sites of α-amylase

†Ligands	‡Binding energy (kcal/mol)	‡Docking score (kcal/mol)	‡Inhibition constant, Ki (µM)	‡Intermolecular energy (kcal/mol)	‡Torsional free energy (kcal/mol)
6	-8.60	-11.20	0.499	-11.20	2.98
7	-9.31	-10.60	0.149	-10.80	1.49
8	-9.71	-11.58	0.077	-11.58	1.48
9	-6.96	-9.63	0.790	-9.65	2.68
10	-8.59	-10.64	0.504	-10.68	2.09

† Molecular docking simulations were carried out using Autodock 4 software tool.

‡ Values were evaluated from the calculations based on the energy minimization.

5.4 Conclusion

Five previously unreported xenicanes were isolated from the ethyl acetate/methanol extract of *P. tetrastromatica* by extensive chromatographic fractionation, and were characterized by detailed spectroscopic experiments. The xeniolide derivative octahydro-1,7-dihydroxy-4-(4^1-hydroxy-4^2-methylpropyl)-6-(6^1-hydroxy-6^2-propenyl)-10-methyl-cyclonona[*c*]pyran-3(*1H*)-one (**5**) showed potential antioxidant and anti-inflammatory activities, with greater anti-inflammatory selectivity index against pro-inflammatory cyclooxygenase-2 than other studied xenicane derivatives and ibuprofen. Molecular docking analysis inferred that the xeniolide derivative **5** exhibited efficient interactions with 5-lipoxygenase, which validated its greater inhibitory potential against the pro-inflammatory enzyme. In particular, the xeniolide-type diterpenoids with octahydrocyclonona[*c*]pyran-3(1*H*)-one backbone could be potential functional food components for use against inflammatory diseases. The biologically active xeniolides isolated from brown seaweed *P. tetrastromatica* might constitute a promising potential natural alternative to the commercially available synthetic antioxidants and anti-inflammatory agents.

The EtOAc:MeOH extract of *P. tetrastromatica* was fractionated by repeated chromatographic techniques to obtain five unprecedented dolabellane and dolastane analogues, named 6-methoxy-dolabella-8(17),12-diene-10*β*,18-diol (**6**), 3-methoxy-dolabella-12(18)-ene-4*β*-ol (**7**), 3-methoxy-dolabella-10,18(19)-diene-5*α*,8*β*-diol (**8**) along with two previously unreported dolastanes 2,7-dimethoxy-14*α*-hydroxy-dolasta-1(15),9-diene (**9**) and 4,7-dimethoxy-9*β*,14*α*-dihydroxy-dolasta-1-ene (**10**). This is the first report of isolation of dolabellane and dolastane terpenoids from *P. tetrastomatica*. The structural features of the studied compounds were characterised using comprehensive spectroscopic techniques. The compounds **10** and **8** displayed greater inhibitory activities against starch digesting enzymes, and their activities were greater than those exhibited by acarbose. In particular, 4,7-dimethoxy-9,14-dihydroxy-dolasta-1-ene (**10**) was found to be an effective dual inhibitors of *α*-amylase and *α*-glucosidase along with potential antioxidative properties, and therefore, could be utilised as potential antioxidant/anti-diabetic pharmacophore in medicinal applications.

CHAPTER 6

ISOLATION AND CHARACTERIZATION OF POLYSACCHARIDES FROM RED SEAWEED *GRACILARIA SALICORNIA (RHODOPHYCEAE)*

Contents

6.1 *Background*

6.2 *Materials and methods*

6.3 *Results and discussion*

6.4 *Conclusions*

6.1 Background

Seaweeds are one of the richest marine resources to produce bioactive compounds, such as polysaccharides, polyphenols, proteins, lipids, mineral salts, and amino acids. Among various bioactive metabolites, polysaccharides registered an integral share in the globally booming phycocolloid industries. Polysaccharides are mainly associated with the structural component of the seaweed cell wall materials with varying range of concentrations of 1-76 % of dry weight, in different species. The composition of polysaccharides is found to be complex, which are existed as neutral/acidic, linear/mixtures of substituted forms.

Majority of red seaweeds (Rhodophyceae) were found to contain galactans, for example, agars and carrageenans, whereas brown seaweeds are known to be rich in alginates and fucoidans. The demand of various polysaccharides of seaweeds is increased in recent years due to their pharmaceutical, cosmeceutical and functional food applications. Polysaccharides from seaweeds are associated with their complex structural characteristics, such as glycosidic linkages, monosaccharide composition, ring size and ratio of sugar residues. These structural peculiarities are correlated with the bioactivities including anticoagulant, antioxidant, antidiabetic, and immunomodulatory effects.

Carbohydrate-polysaccharides are comprehensive and complex bio-polymeric carbohydrate skeletal structures. Their derivable reactive functionalities, physiological features, and structural composition were contributed towards the wide range of biological applications (Wang, Hu, Nie, Yu, & Xie, 2016). Moreover, the structure of polysaccharide is far more complicated based on the differences in composition of monosaccharide residues, glycosidic linkages, sequence of sugar units, degrees of

polymerization, and branching point. Due to all these characteristics, polysaccharides from different sources, especially from marine source are envisaged as promising substitutes of non-degradable polymers in many pharmaceutical combinations. There were many well-established reports on antioxidant, immunomodulation, antimicrobial and anti-lipidemic activities of polysaccharide from marine source. Though, they have less exploited for curing the most common prevalent diseases such as, diabetes and osteoporosis (Wang, Hu, Nie, Yu, & Xie, 2016). The prevalence of diabetes is increasing worldwide, and the number of cases is predicted to increase to approximately 592 million (1 in every 12 people) by 2035 (Guariguata et al., 2014). Diabetes is characterized by hyperglycemia, and is associated with an increased incidence of osteoporosis, possibly mediated by the effects of insulin deficiency and hyperglycemia on the bone (Yang, Zhao, Liang, Yu, & Qu, 2017). It was estimated that the number of patients worldwide with osteoporotic hip fractures has been more than 200 million (Cooper, Campion, & Melton, 1992). Currently, pharmacotherapy involving the synthetic agents, such as thiazolidinediones, α-glucosidase inhibitors, and dipeptidyl peptidase-IV inhibitors (DPP-IV) are available for hyperglycemic therapy. Especially, DPP-IV inhibitors administered from the early stage of hyperglycemia help to protect pancreatic β-cells and normalize glucagon secretion control, combining reliable hypoglycemic action and safety, inhibiting the progression of hyperglycemia and maintaining glycemic control (Kubota et al., 2012). Recently, DPP-IV have received attention for their potential use in the treatment of osteoporosis. It selectively cleaves alanine and proline from polypeptide substrates, resulting in the inactivation of these substrates, including glucagon-like peptide 1 (GLP-1) and gastric inhibitory polypeptide (GIP) (Kubota et al., 2012). Thus, the mechanism of DPP-IV inhibitors involves prolonging the half-life of these incretins (GLP-1 and GIP) and consequently promoting insulin secretion from β-pancreatic cells to improve glucose tolerance. DPP-IV inhibitors can affect bone metabolism through various mechanisms. Firstly, the DPP-IV inhibition may promote bone metabolism by lowering the glucose level. Secondly, DPP-IV substrates and DPP-IV-related energy metabolism may affect bone metabolism. Thirdly, DPP-IV inhibitors might affect bone metabolism through vitamin D-linked and other related signaling pathways (Yang, Zhao, Liang, Yu, & Qu, 2017). The reports revealed that DPP-IV inhibitors in combination with metformin significantly decreased the risk of developing bone fractures compared to metformin monotherapy (Dombrowski et al., 2017). Similar results were reported by Choi et al. (2016), which showed the efficacy of DPP-IV inhibitors in reducing bone fracture risks, thus implying their therapeutic potential in osteoporosis. The reports also showed that DPP-IV inhibitor, sitagliptin treatment was reported to improve the vertebral volumetric bone mineral density (BMD) and significantly improved cortical bone volume, trabecular architecture, and bone strength (Kyle et al., 2011; Glorie et al., 2014). The reports also showed the possibility that the DPP-IV inhibitors might be effective in treating

osteoporosis and reducing the risk of fractures by improving BMD and bone quality. Moreover, the previous studies revealed that DPP-IV inhibitors could decrease parathyroid hormone level, and thus inhibit the release of calcium from the bone to blood and reduce bone destruction (Yang, Zhao, Liang, Yu, & Qu, 2017). DPP-IV inhibitors could significantly increase the serum concentration of 25-hydroxy vitamin D3 (25(OH)-D), which has been reported to regulate the concentration of calcium and phosphate in the bloodstream, thereby promoting the growth and remodeling of the bone. The level of 25(OH)-D was also associated with the duration of DPP-IV inhibitor treatment and strength of DPP-IV inhibitory activity (Yang, Zhao, Liang, Yu, & Qu, 2017). A cross-sectional study showed that serum DPP-IV inhibitors was positively associated with the bone formation markers, bone-specific alkaline phosphatase (ALP) and osteocalcin. Moreover, DPP-IV inhibitor, sitagliptin was found to significantly reduce alkaline phosphatase (ALP) level. A non-significant decline in serum osteocalcin was also reported. In diabetic patients, insulin deficiency and hyperglycemia appeared to play a prominent role in reducing bone formation. Advanced glycation end product (AGE) accumulation or AGE/RAGE (receptors for AGE) axis imbalance were deduced to directly influence the osteoblast activity by decreasing their number and function (Yang, Zhao, Liang, Yu, & Qu, 2017). Notably, various natural polysaccharides were found to possess potential anti-diabetic activity, and use of these polysaccharides as adjuncts to conventional therapies is increasing. There were many reports on osteoporotic and hyperglycemic activity of polysaccharide compounds. Polysaccharides derived from the leaves of *L. barbarum* enhanced the splenocyte proliferation to demonstrate immuno-stimulating potential (Liu et al., 2017); Anti-osteoporotic potentials were discovered from of polysaccharides of dioscoreae, and tamarind (Ma et al., 2016; Sanyasi, Kumar, Goswami, Bandyopadhyay, & Goswami, 2014). Likewise, polysaccharides from seaweeds *G. opuntia, K. alvarezii, S. duplicatum* and *T. decurens* showed anti-hyperglycemic activity (Hardoko, Siratantri, Eveline, Yogabuana, & Olivia, 2014; Makkar & Chakraborty, 2016). Sulfated polysaccharides incorporated scaffolds of carrageenans and agar were reported to improve the osteogenic differentiation capacity (Li et al., 2014). Therefore, polysaccharides from the natural sources, especially from marine origin might be good candidates as anti-hyperglycemic and anti-osteoporotic agents (Makkar & Chakraborty, 2016). However, higher-molecular-weight bioactive molecules have limitations due to their instability in delivery both *in vitro* and *in vivo* as well as their immunogenicity and shorter half-lives (Iki et al., 2017). Therefore, there is a great need to design the nano-based polysaccharide scaffolds with enhanced half-lives and reduced immunogenicity for use in pharmaceuticals (Iki et al., 2017). Hence, like polysaccharides, polysaccharide based nanoparticles also have drawn therapeutic potential against various diseases. Polysaccharide-based nanoparticles greatly enrich versatility of nanoparticle carriers in terms of function and category (Balan et al, 2016). Among different

nanoparticles, biopolymers and metallic silver based nano composites were found to exhibit several applications, which were better than that of native polysaccharides (Elsupikhe, Shameli, Ahmad, Ibrahim, & Zainudin, 2015; Elsupikhe, Ahmad, Shameli, Ibrahim, & Zainuddin, 2016). On metal nanoparticles, silver-nano-particles have received considerable attention owing to their interesting physicochemical properties, and their interesting bioactive potential with respect to antioxidant, anti-inflammatory and anti-diabetic potential (Sankar, 2015, Deepak et al, 2018; Govindappa, Hemashekhar, Arthikala, Rai, & Ramachandra, 2018). In light of these, the present study focused on the extraction and characterization of polysaccharide from bioactive red seaweed *Gracilaria salicornia* (C.Agardh) E.Y.Dawson (Gracilariaceae, Phylum Rhodophyta). There were many reports on water and ethanol/methanol extractions of *Gracilaria* genus, and most of them revealed their bioactive constituents and health promoting effects such as hyperglycemia, anti-inflammatory, anti-hypercholesterolemia, antioxidative, and antimicrobial properties (Vijaya Sankar, 2015, Deepak et al, 2018; Govindappa, Hemashekhar, Arthikala, Ravishankar Rai, & Ramachandra, 2018). Sulfated galactans extracted from *Gracilaria sp.* have been previously reported as a hybrid of various carrageenan moieties on the basis of ^{1}H and ^{13}C NMR data (De Almeida et al., 2011).

In this view, the polysaccharides isolated from the marine macroalgae *P. tetrastromatica* and *G. salicornia* were evaluated for various pharmacological properties, and among these two species the latter was found to display prospective bioactivities. Therefore, *G. salicornia* was shortlisted to isolate the polysaccharide compound, which was characterized as (1⋯→3)-*O*-6-sulfonato-β-D-galactopyranosyl-(1→⋯4)-3,6-anhydro-α-D-galactopyranose-(1⋯→) with exhaustive spectroscopic experiments and chemical derivatisations, such as methylation, reduction, and acetylation. The chemical constituents and bioactivities of polysaccharide derived from the water extract of *G. salicornia* were carried out by different analytical methods and bioassays with respect to hyperglycemia and osteopathy. This study also attempted to develop the polysaccharide based bioactive-silver-nano-composite (AgNPC), which was found to improve the bioactive potential of the native polysaccharide. The characterization of polyglactan based P-AgNPC were performed by various spectroscopic and physical analysis, such as fourier transform infrared (FTIR) spectroscopy, scanning electron microscopy (SEM) with energy-dispersive X-ray spectroscopy (EDX), and X-ray diffraction (XRD) technique, particle size analysis, zeta potential, along with atomic force microscopy (AFM). The pharmacological properties of polysaccharide and polysaccharide-based AgNPC with regard to antioxidant, anti-hyperglycemic and anti-osteoporotic activities were evaluated by using different *in vitro* models. The catalytic binding effect of polysaccharide was evaluated with the aid of *in silico* molecular docking studies with proteins such as DPP-IV, α-amylase, α-glucosidase and ALP.

6.2 Materials and methods

6.2.1 Chemicals and reagents

The chemicals and reagents utilized for the analysis were described under the section 4.2.1 of Chapter 4.

6.2.2 Chromatographic purification techniques and spectroscopic instrumentation analysis

6.2.2.1 Collection and processing of seaweed materials

Fresh samples of seaweed, *P. tetrastromatica* and *G. salicornia* were harvested from the Mandapam region (Gulf of Mannar, 8º48' N, 78°9' E and 9°14' N, 79°14' E) on the southeast Indian Peninsular (Figure 6.1 & 6.2). The samples were identified by a marine algologist Dr. Chellaiah Periyasamy of the Aquaculture Foundation of India, Madurai, and were deposited in the project repository under the accession number of AB.1.1.2.1. The samples were washed thoroughly, shade-dried, and powdered to homogeneity before being utilized for further laboratory experiments.

6.2.2.2 Spectrophotometric, spectroscopic analysis and morphological analysis

The documentation of FTIR (Fourier transform infrared) was carried out in between 4000-400 cm^{-1} using FTIR Perkin-Elmer Series 2000 spectrometer (Waltham, MA). The UV analysis was performed by UV-VIS Varian Cary 50 spectrophotometer (Palo Alto, CA). The one and two-dimensional NMR including ^{1}H-NMR-500 MHz, ^{13}C-NMR-125 MHz, DEPT, COSY, HSQC, HMBC, NOESY) were recorded with a Bruker Avance DPX 500 MHz NMR spectrometer (Bruker Co., Billerica, MA) (Maneesh & Chakraborty, 2018). A gas chromatograph/mass spectrometer (GC/MS) operating with the electron-impact (EI) mode (Varian GC model, CP-3800 housed in a mass spectrometer model Varian 1200L) was used for the mass spectral analysis. High resolution mass spectrometric detection was performed on a Bruker Daltonic (GmbH, Germany) micro-TOF series mass spectrometer with negative ion mode (ESI-MS). The reverse-phase high pressure liquid chromatography (RP-HPLC) analyses were carried out by Shimadzu LC-20AD pump device (Shimadzu Corporation, Nakagyo-ku, Japan), fitted with RID 10A

refractive index detector (Kyoto, Japan) connected to an LC-20AD pump with an amino column (Luna 250 × 4.6 mm, 5 μm) (Phenomenex, USA).

The synthesized polysaccharide-silver nanocomposite (AgNPC) was characterized using a Varian-Cary 50 UV/VIS spectrophotometer (Varian Cary 50, Palo Alto, CA) recorded at 200-800 nm. The morphology with regard to the size, distribution and the shape of AgNPC were visualized using a field emission-scanning electron microscope (SEM) (JEOL Model JSM - 6390LV). EDX characterization was performed with an Oxford XMX-N instrument by drop coating P-AgNPCs on the tungsten film. The particle size, dispersion, aggregation along with atomic scale in aqueous environment with a high spatial resolution (<1.0 nm) were provided by transmission electron microscopy (TEM). A zeta potential measurement of P-AgNPC was carried out by using a Malvern Zetasizer Instrument (Zetasizer Ver. 7.12). The dispersion and aggregation of P-AgNPC were also measured using an atomic force microscopy (AFM - APE research nanotechnology model - A 100-AFM) coupled with silicon nitride tip (with resolution of 256x256 pixels) in non-contact mode. The quantitative identification of the molecular crystal structure was analyzed by X-ray diffraction (XRD) analysis using Bruker AXS D8 Advance coupled with X-ray source Cu of wavelength 1.5406 Å and detector Si (Li) PSD.

6.2.3 Preparation of crude extracts of seaweeds

6.2.3.1 Preparation of crude extracts from brown seaweed P. tetrastromatica

The dried seaweed powder of *P. tetrastromatica* was extracted by the previously described method (Yang et al. 2008). Initially, the 500 g of ground seaweed was treated with 85 % ethanol and stirred continuously (1 L, room temperature for 12 h) to eliminate pigments and proteins, before being washed with acetone, centrifuged (10,000×g for 20 min, 4 °C (Sorvell Biofuge Stratos, Thermo Scientific, USA), and dried. The dried seaweed powder was then extracted with distilled water (1 L, 60-70 °C for 3 h × 2) and filtered to yield the crude aqueous extract. The crude aqueous extract (2.5 L) was precipitated with $CaCl_2$ (1 % w/v ~ 25 g) and kept at 4 °C (for 5 h) before being clarified by centrifugation (8000×g for 20 min, 4 °C) to separate the calcium salt of residues. Thereafter, the supernatant (1000 mL) was reduced to $1/10^{th}$ of the original volume (100 mL) via concentration by using a rotational vacuum concentrator (Martin Christ RVC 2-33 IR, Germany) and allowed to cool. Three volumes of ethanol (500 mL 3:1, v/v) was used to precipitate the supernatant and kept overnight at 4 °C for the complete precipitation of crude polysaccharide (PF) (27 g; yield based on powdered seaweed, 5.4 %).

Figure 6.1.: The brown seaweed *P. tetrastromatica* collected from the southeast coastline of the Indian sub-continent of Gulf of Mannar region (8º48' N, 78°9' E and 9°14' N, 79°14' E)

6.2.3.2 Preparation of crude extracts from red seaweed G. salicornia

The ground seaweed material was pre-treated with organic solvent acetone to remove the pigments. The pigmentous materials were removed by filtration followed by concentration at 45 °C with the help of a rotary vacuum concentrator (Heidolph, Instruments GmbH & Co., Schwabach, Germany). The acetone-free seaweed residue was soaked in a solution of 200 g of KOH (1 M) at 85° C for 4 h according to the modified method by Pereira et al. (Pereira, Amado, Critchley, van de Velde, & Ribeiro-Claro, 2009), and neutralized to pH 6-8 with HCl (0.3 M) before being kept for drying. The dried seaweed residue (200 g) was extracted with hot water at 80 °C for 4 h to yield the aqueous crude extract (Makkar & Chakraborty, 2016), which was allowed to cool and clarified by centrifugation at 8500 rpm for 15 min, at 4°C (Sorvell Biofuge Stratos, Thermo Scientific, USA). The residual mass of seaweeds were re-extracted and centrifuged two times with water to remove the solid residues. The obtained supernatant (1000 mL) was then concentrated to $1/10^{th}$ of the original volume (100 mL) by utilizing a rotational vacuum concentrator (Martin Christ RVC 2-33 IR, Martin Christ, Germany). The decreased volume of the supernatant was cooled and then precipitated with three volumes of 96 % ethanol (300 mL,

3:1, v/v). The obtained solution was kept overnight at 4 °C for the complete precipitation of the polysaccharide. The precipitated polysaccharide material was subjected for lyophilization with the aid of a laboratory-scale lyophilizer (Martin Christ alpha 1-4 LD plus, Martin Christ, Germany) to obtain the crude polysaccharide (8.78 g, yield based on powdered seaweed, 4.39 %).

Figure 6.1.: The red seaweed *G. salicornia* collected from the southeast coastline of the Indian sub-continent of Gulf of Mannar region (8º48’ N, 78°9’ E and 9°14’ N, 79°14’ E)

6.2.4 Purification of crude polysaccharide by anion exchange column chromatography

The crude polysaccharide extracted was sequentially purified by the aid of anion exchange chromatography of DEAE-cellulose according to the previously reported method (Maneesh & Chakraborty, 2018) with required modifications. Initially, the polysaccharide was dissolved in the distilled H_2O and passed through a packed column of resin, before being eluted with water, 0.1, 0.5, 1.0, 1.5 and 2.0 M NaCl solutions, in order, to yield various column subfractions. Each fraction was collected and monitored by the phenol-sulfuric acid method (absorbance of the reaction mixture was recorded at 490 nm) by using a spectrophotometer. The column fractions were subjected to phenol-sulfuric acid assay for the positive chemical reaction of polysaccharide (Dubois, Gilles, Hamilton, Rebers, & Smith, 1956). The eluted column fractions were freeze dried to obtain the powdered pure polysaccharide fractions.

These were further subjected to HPLC analysis to deduce the monosaccharide composition and the purity by using the evaporative light scattering detector (ELSD 10A) connected to an LC-20-AD pump by employing an amino column (Luna 250 × 4.6 mm, 5 μm).

6.2.4 Monosaccharide composition analysis

The monosaccharide composition analysis was carried out using the hydrolysates of polysaccharide (Maneesh & Chakraborty, 2018). In brief, the pure and dried fraction of polysaccharide was subjected for hydrolysis with 1 M trifluoroacetic acid (TFA) for 8 h. The solution was allowed to cool to room temperature. The traces of TFA were removed from the solution under a stream of N_2 and dissolved in double distilled water (DDW; 6 mL). The hydrolysates of polysaccharide (20 μL; 1 mg/mL) along with commercial monosaccharaide standards (20 μL; 1 mg/mL) were injected into an analytical HPLC connected with the evaporative-light-scattering (ELS) detector. The composition of monosaccharaides was monitored by HPLC and the obtained results were compared with the commercial monosaccharaide standards. The acetonitrile-water (80:20, v/v) was used as the HPLC mobile phase.

6.2.5. Structural characterization of the polysaccharide motifs by hydrolysis

The hydrolysates of polysaccharide were prepared by trifluoroacetic acid (TFA) method (as mentioned above) (Maneesh & Chakraborty, 2018). Briefly, the dried hydrolysates (oligosaccharides) of polysaccharide were subjected to 1D/2D-NMR spectroscopic analysis (Bruker Avance DPX 500 MHz NMR spectrometer Bruker Co., Billerica, MA). The hydrolysates were dissolved in D_2O (2-3 mg/500 μL) prior to the NMR analysis. The molecular weight of hydrolysates was determined by high resolution mass spectrometric detection by using micro-TOF series mass spectrometer (Bruker Daltonic (GmbH, Germany) with positive mode (ESI-MS, $M+H^+$).

6.2.6 Structural characterization of the polysaccharide motif by methylation analysis

The structural composition of the pure polysaccharide fraction, GSP-2 was performed with the aid of a modified method of methylation (Ciucanu & Kerek, 1984), and NMR spectroscopic analysis. Initially, the pure polysaccharide fraction (3 mg) was made completely soluble in dimethylsulfoxide (DMSO, 1 mL) in the presence of powdered alkali (NaOH ~0.1 g) under constant stirring in an inert atmosphere. The reagent, methyl iodide (MeI, 200 μL) was added to the reaction mixture for methylation with constant stirring for 45 min. The methylation of reaction mixture was then quenched with deionized water (~1 mL) and partitioned with chloroform and water. The methylated polysaccharide was collected with chloroform layer and under-methylated contents were discarded with water layer. The organic layer

was then concentrated under vacuum to remove the traces of solvents. The methylated residue of the polysaccharide was hydrolysed, and the methylated hydrolysates were subjected to 1D and 2D-NMR spectroscopic analysis with the aid of a Bruker Avance DPX 500 MHz NMR spectrometer (Bruker Co., Billerica, MA).

6.2.7 Linkage pattern and structural analysis of the polysaccharide motifs by reductive cleavage method

The linkage pattern and structure of pure polysaccharide, GSP-2 was further analysed by modified method of reductive cleavage (of the glycosidic linkage) (Ciucanu & Kerek, 1984). Initially, the homogenous polysaccharide (3 mg) was undergone methylation analysis as discussed in the previous section. The residue obtained in chloroform layer after methylation was then reduced with sodium borohydride ($NaBH_4$), and was acetylated with acetic anhydride (Ac_2O) and pyridine. The linkage and sulfation of polysaccharide was acquired from the position of acetylation, and was characterized using GC-MS experiment (Bjorndal, Hellerqvist, Lindberg, & Svensson, 1970). The structural characterization of the acetylated polysaccharide was carried out by extensive 1D and 2D-NMR spectroscopic analysis.

6.2.7. Component analysis of polysaccharide by analytical methods

6.2.7.1 Determination of total carbohydrate content

Determination of total carbohydrate content was determined by the dinitrosalicylic acid method using D-glucose as the standard (Miller 1959). Briefly, 3,5-dinitrosalicylic acid (1 g) was dissolved in an aqueous alkaline solution (2M NaOH, 50 mL) at the room temperature and added with the Rochelle salt (Na-K-tartrate, 30 g). The contents were made up the volume to 100 mL with distilled water. The purified polysaccharide solution (0.2 % w/v) was added to the reaction mixture and was heated for 10 min using a water bath (100 °C) and cooled at room temperature. The absorbance was measured at 540 nm, and the standard curve was plotted against glucose solutions at different concentrations (2.5, 1, 0.5, 0.25 mg mL^{-1}). The total carbohydrate content (% w/w) was estimated by the following equation: Total carbohydrate content (% w/w) = {(X) × V/W}, where X = concentration of the polysaccharide fraction obtained from the slope of the graph, V = total volume of solution taken (= 3 mL), and W = weight of the polysaccharide (in mg) (Miller 1959).

6.2.7.2 Determination of uronic acid content

Uronic acid content was estimated by modified carbazole method applying D-glucuronic acid as the standard (Bitter and Muir 1962). Briefly, glucuronic acid at different concentrations (1, 0.5, 0.25, 0.1 mg mL^{-1}) was prepared, and each of these solutions (0.1 mL) were added with concentrated H_2SO_4 (6 mL) under ice-cold condition. The sample solutions (0.1 mL) at different concentrations were added with concentrated H_2SO_4 (6 mL) and the alcoholic solution of carbazole (0.2 mL, 0.1% in ethanol) under an ice-cold condition; the mixture was heated (at 55 °C) for 30 min, and the absorbance was measured at 530 nm. Uronic acid content (% w/w) in the sample was estimated using the following equation:

Uronic acid (% w/w) = {(X) × V/W}, where X = concentration of the polysaccharide fraction obtained from the slope of the graph, V = total volume of solution taken (= 6.3 mL), and W= weight of the polysaccharide in milligram.

6.2.7.3 Determination of protein content

The protein content was determined by the method of Lowry et al. (1951). The absorbance of the protein aliquot was measured at 660 nm within 15 min against the reagent blank. The protein content of the sample was calculated from the standard curve of bovine serum albumin and expressed as % w/w of the polysaccharide fraction.

6.2.7.4 Determination of sulfate content

The sulfate content was estimated by the turbidimetric method (Dodgson and Price 1962). Briefly, the polysaccharide fraction (2-4 mg) was hydrolyzed with HCl (2 N, 1 mL), and the aliquot (0.2 mL) was added with trichloroacetic acid (3.8 mL of 3 % w/v) and barium chloride-gelatin solution (1 mL) before being incubated at room temperature for 20 min. The absorbance of the test solution was recorded at 360 nm on a spectrophotometer against a reagent blank. A standard curve was developed with potassium sulfate solution, and the concentration of sulfate content (% w/w) in the polysaccharide fraction was calculated from the slope and Y-intercept of the graph.

6.2.8 Synthesis of polysaccharide-silver nanoparticle composite (P-AgNPC) from G. salicornia

The synthesis of polysaccharide-silver nano-composite (P-AgNPC) was found to be a promising application in the pharmaceutical industry. Therefore, the synthesis of P-AgNPC was performed by reduction, according to the modified method of Elsupikhe et al. (2015). In brief, different solutions of polysaccharides of 40 mL were prepared with 0.1, 0.15, 0.20, 0.25, and 0.3 wt %, respectively. The solutions were stirred for 2 h for complete dissolution. About 10 mL of 0.1 M $AgNO_3$ solutions were added into the each of the 40 mL solutions of polysaccharides. The reaction mixtures were

stirred for 1 h for complete precipitation of nano particle in the suspension. The resultant suspensions were exposed to high-intensity ultrasound irradiation for 90 min with ultrasonic liquid processors (750 Watt ultrasonic processor, Sonics, Newtown, CT 06470 USA, and 50/60 Hz) immersed directly into the reaction solution under 50 % amplitude at the room temperature. Nano particles in suspensions were centrifuged for 30 min and repeatedly washed with double distilled water (DDW) water to eliminate the silver ion residues. The formation of P-AgNPC was then monitored by using a UV-Vis spectrophotometer and the particles were collected by centrifugation. The quantification of P-AgNPC was carried out by the particle size analyzer (PSA). Based on the yield, 3 % solution of P-AgNPC was subjected to ultra-sonic irradiation for 60 min and then to 120 min for furthermore reducing the particle size. The reduction in size, polydispersity index (PDI) and zeta potential of the P-AgNPC were analyzed by PSA with the diluent water. The PDI measurement of polysaccharide was aimed to determine the uniform particle size distribution of P-AgNP in suspension. The further morphological characterization of P-AgNPC (with 0.3 % solution) was performed using SEM, TEM and AFM analyses. The quantitative measurement of particle size of P-AgNPC was carried out using XRD analysis. FTIR was used to detect the formation of nanoparticle in suspension.

6.2.9 In vitro bioactive potentials polysaccharide solutions

6.2.9.1 Determination of free radical scavenging activity of **polysaccharide** *solutions*

The polysaccharide samples GSP, GSP-2 and P-AgNPC were subjected to free radical scavenging assays and the activity was measured with the stable radicals, such as 1, 1-diphenyl-2-picryl-hydrazil (DPPH) and 2, 2'-azino-bis-3-ethylbenzothiozoline-6-sulfonic acid ($ABTS^{+}$) (Wojdyło, Oszmianski, & Czemerys, 2007).

6.2.9.2 Determination of carbolytic and proteolytic enzyme inhibition activities of polysaccharide

The *in vitro* carbolytic and proteolytic enzyme inhibition potentials of the polysaccharide solutions (0.25-2.00 mg mL^{-1}) were analysed by α-amylase, α-glucosidase and DPP-IV (dipeptidyl peptidase-IV) enzyme attenuation assays (Hamdan & Afifi 2004). The inhibitory concentration, 50 % (IC_{50}) was calculated from the graph plotted with concentrations of sample versus percentage inhibition. The results were expressed as IC_{50} (50% of its activity). The determination of percentage inhibition (%) was carried out using the equation: $(A_C–A_S)/A_C) \times 100$, where A_C and A_S represented the absorbance of control and sample, respectively.

6.2.9.3 Determination cytotoxicity of pure polysaccharide and P-AgNPC on osteoblastic human mesenchymal Stem (MSC) cell lines

The cytotoxicity of polysaccharide (GSP) and P-AgNPC was measured by the 3-[4,5-dimethylthiazol]-2, 5-diphenylterazolium bromide assay (MTT assay) (Liu, Xu, Ma, Cheng, Hua, & Huang G, 2017). In brief, the osteoblastic cell line (MSCS) (200 µL cell suspension) was plated in the 96-well plates at a density of 20 x 10^3 cells per well without the test reagent. The cells were allowed to grow for 24 h. Thereafter, the cells in various wells were treated with each compound at the concentrations of 150, 250, 500, 750 and 1000 µG. After incubation, the plates were taken out from the incubator, and removed spent media. MTT reagent was added to each well of final concentration of 0.5 mg mL^{-1} of total volume and incubated for 24, 48, 72 h at 37 °C in a 5 % CO_2 atmosphere. The plates were wrapped with the aluminium foil to avoid contact to the light, and these were again incubated for 3 h. The MTT reagent was removed and then added 100 µL of dimethylsulfoxide (DMSO) solution to dissolve the formazan salts. Then, the plates were read at 570 and 630 nm by an ELISA reader (Bio-Rad, model 550). The IC_{50} values were determined by using linear-regression-equation.

6.2.9.4 Determination of alkaline phosphatase activity of polysaccharide and P-AgNPC on osteoblastic human mesenchymal stem (MSC) cell line

ALP is found as one of the important bio-markers of osteoblastic cell differentiation. ALP secretion in higher amount represents strong cell-differentiation potential (Liu, et al., 2017). Primary osteoblasts were seeded (500 µL cell suspension) at a density of 250 x 10^3 cells/well in the 96-well plates without the test reagent. The cells were allowed to grow for about 24-48 h. After incubation, the cells in various wells were treated with polysaccharide and P-AgNPC at concentration of 500 µg mL^{-1}. The plates were incubated for 21 days at 37 °C in a 5 % CO_2 atmosphere by maintaining the cells regularly 2 times per week. After the incubation period, taken out the plates from incubator, and removed spent media. The cells were fixed with suitable fixative solution (2 % para-formaldehyde, Thermo) for 5 min and rinsed in deionized water for 45 sec. Alkaline phosphatase dye mixture of 100 µL was added and incubated the cells for 30 min at 37 ºC. the immersed slides were protected from the direct light, and after 30 min, the slides were removed and rinsed thoroughly with deionized water for 2 min. The cells were subjected to counterstain with fast violet B salt in water for 2 min. Resultant blue nuclear stain was evaluated microscopically and measured the absorbance at 405 nm using an ELISA Reader.

6.2.10 In silico analysis of polysaccharide

In silico analysis of polysaccharide motif in the present study was carried out using Autodock 4 (ver-1.5.6) docking software, which analysed the conformation of enzyme and ligand-composite. The 2D and 3D structural conformations of the polysaccharide analogues were drawn by the software, such as Chemsketch 3.5 and OpenBabel 2.4.1 versions. The X-ray crystal structures of α-amylase (PDB 1HNY; 1.8 Å), α-glucosidase (PDB 3A4A; 1.6 Å), DPP-IV (PDB 2ONC; 2.5 Å) and ALP (PDB 1ZED; 1.57 Å) were retrieved from the Protein Data Bank (Brayer, Luo, & Withers, 1995; Yamamoto, Miyake, Kusunoki, & Osaki, 2010; Llinas, Stura, Ménez, Kiss, Stigbrand, Millan, & Le Du, 2005) and conformationally arranged (Swiss-Pdb Viewer, ver-4.1.0). USCF Chimera (University of California, San Francisco, ver-1.11.2) was used for the visualization of the molecular docking analyses. The *in silico* analysis was carried out using Lamarckian algorithm methods and it was run by Cygwin I-II. The preferred docked conformations were examined with RMSD (root-mean-square deviation) data.

6.2.11 Statistical analysis

All experimental results were expressed as the mean of triplicate ± standard deviation and were examined for significant variations by one-way analysis of variance (ANOVA) using the SPSS 13.0. The significant differences were considered as $P < 0.05$.

6.3 Result and discussion

6.3.1 Extraction, purification, yield, and chemical composition of polysaccharide derived from G. salicornia

The crude polysaccharide fraction from red seaweed *G. salicornia* was obtained by hot water extraction method, and the gelling polysaccharide fraction was obtained with yield of 4.39 % of the seaweed dry weight. The resulting aqueous extract was sequentially fractionated with the aid of anion exchange chromatographic column filled with an anion exchange resin (DEAE-cellulose) according to the previously reported method (Maneesh & Chakraborty, 2018) with modifications to obtain the crude polysaccharide fraction (GSP). The latter (8.78 g) was initially dissolved in double distilled water (5 mL) and passed through packed anion exchange resin, before being eluted with water, 0.1, 0.2, 1.3, 0.4 and 0.5 M NaCl solutions to yield the subfractions GSP-1 (1.19 g), GSP-2 (1.03 g), GSP-3 (0.51 g), GSP-4 (0.22 g) and GSP-5 (0.22 g). The presence of carbohydrate in each fraction was monitored by the phenol-sulfuric acid method at 490 nm with the aid of a spectrophotometer and the elution curve of polysaccharide fractions was plotted and shown in Figure 6.4. The polysaccharide fractions obtained after fractionation were subjected to chemical composition analysis and the carbohydrate, uronic acid, protein,

sulfate content, and monosaccharide compositions were summarized in Table 6.1. The GSP exhibited the percentage yield of total carbohydrate as 63.89 %. Similarly, it has displayed the percentage yield uronic acid content as 9.81 %, protein content as 4.10 %, and sulfate content as 14.88 %. The percentage yield of total carbohydrate content in different polysaccharide fractions GSP-1 (18.26 %), GSP-2 (54.62 %), GSP-3 (16.98 %), GSP-4 (16.21 %) and GSP-5(15.23 %) were compared with the standard. The fraction GSP-2 (54.62 %, ≥ 50 %) exhibited higher percentage yield of total carbohydrate, and which was comparable with the crude polysaccharide (63.89 %). This data revealed that the GSP-2 was rich in polysaccharide content than that of other fractions (≤ 50%). The percentage of uronic acid content in different polysaccharide fractions were compared with each other, and which followed the decreasing order of GSP-1 (3.98 %) > GSP-3 (2.28 %) > GSP-4 (2.20 %) > GSP-2 (2.01%) > GSP-5 (1.63 %). The fraction GSP-1 (3.98 %) displayed higher percentage of uronic acid than that of other fractions (≤ 2.3 %). The percentage yield of protein in different polysaccharide fractions were also compared with each other, and which followed the order of GSP-1 (2.01 %) > GSP-3 (1.02 %) > GSP-2 (0.89 %) > GSP-4 (0.86 %) > GSP-5 (0.12 %). The sulfate content of different polysaccharide fractions were found out, and which followed the order of GSP-2 (13.52 %) > GSP-1 (11.28 %) > GSP-3 (9.13 %) > GSP-4 (7.58%) > GSP-5 (2.12 %). The amount of sulfate was found to be more in GSP-2 (13.52 %), and which was comparable with the crude polysaccharide (14.88 %). From the chemical composition analysis, the fraction GSP-2 was found to be rich in polysaccharide and sulfate content, which was comparable with the crude polysaccharide, GSP. The sulfate content of GSP from *G. salicornia* was higher than that reported for other *Gracilaria sp*.; 6.4% for *Gracilaria birdiae*, 11.7% for *Gracilaria corticata*, and 4.8% for *Gracilaria cornea* (Mazumder, Ghosal, Pujol, Carlucci, Damonte, & Ray, 2002; Maciel, Chaves, Souza, Teixeira, Freitas, Feitosa, 2008). The previous reports recorded that the biological activity of polysaccharides were influenced by the charge density arose from sulfate groups and glycosidic linkage {either (1→3) or (1→4)} of the neighboring sulfate groups (Chaidedgumjorn et al., 2002; Pereira, Melo, & Mourão, 2002). The crude polysaccharide fraction of GSP was found to contain different monosaccharides, such as galactose (67.2 %), xylose (3.2 %), glucose (2.6 %) and mannose (1.1 %) in different concentrations. This data indicated that the studied polysaccharide was found to be rich in galactose, and which might be associated with (1→3) and (1→4) galactose and galactose analogs.

The fractionated polysaccharides GSP-1, GSP-2, GSP-3, GSP-4 and GSP-5 were found to possess galactose in 9.2, 61.4, 3.3, 2.1, and 1.3 % respectively. On comparison, GSP-2 was was found to possess higher percentage of galactose units than other eluted fractions (< 60%) (Figure 6.5). The presence of other monosaccharides was also found in the polysaccharide fractions in trace quantities (xylose contents were 1.5, 1.2, 0.9, and 0.21 % in GSP-1, GSP-3, GSP-4, and GSP-5, respectively). The

fractions, GSP-1 and GSP-2 were also found to contain monosaccharides glucose and mannose in 0.8-0.6 % and 0.08-0.06 %, respectively. The chemical composition results showed that the major part of polysaccharide was eluted by the 0.5 M NaOH than that of other concentrations of NaOH. Therefore, the pure polysaccharide fraction of GSP-2 was selected for further analysis of bioactive potentials, and was subjected to chemical degradation process, such as methylation, reduction and acetylation for their structural interpretation by NMR spectroscopy, as well as gas chromatography-mass spectrometry (GC-MS). The bioactive polysaccharide was further made into nano composite by the implantation of $AgNO_3$ in different concentration, and which were further subjected for structural and morphological analysis. The pharmacological activities of the polysaccharide (GSP-2) and P-AgNPC composite were analyzed with ALP, proteolytic, and carbolytic enzyme models and *in vitro* antioxidant assays.

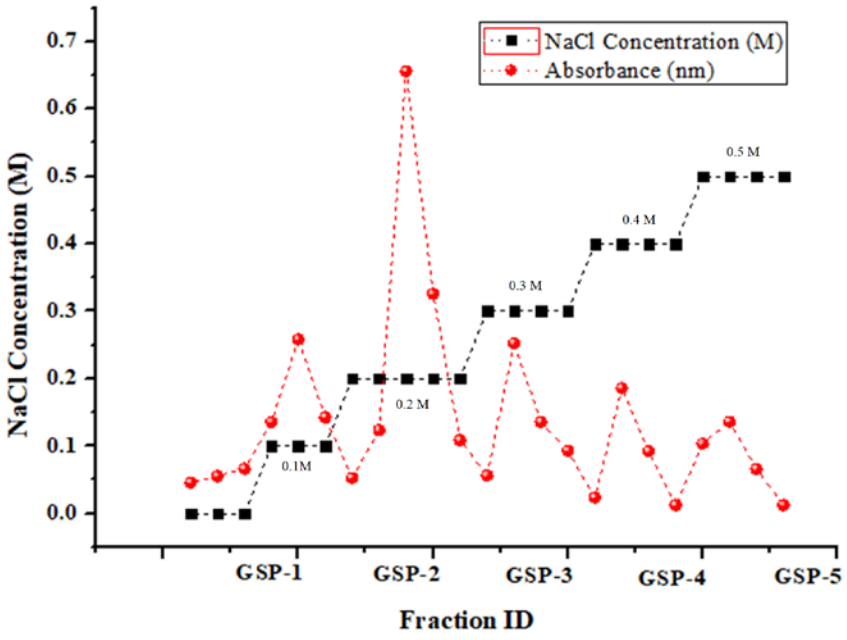

Figure 6.4.: Elution profile of polysaccharide solutions isolated from *G. salicornia* through DEAE Cellulose

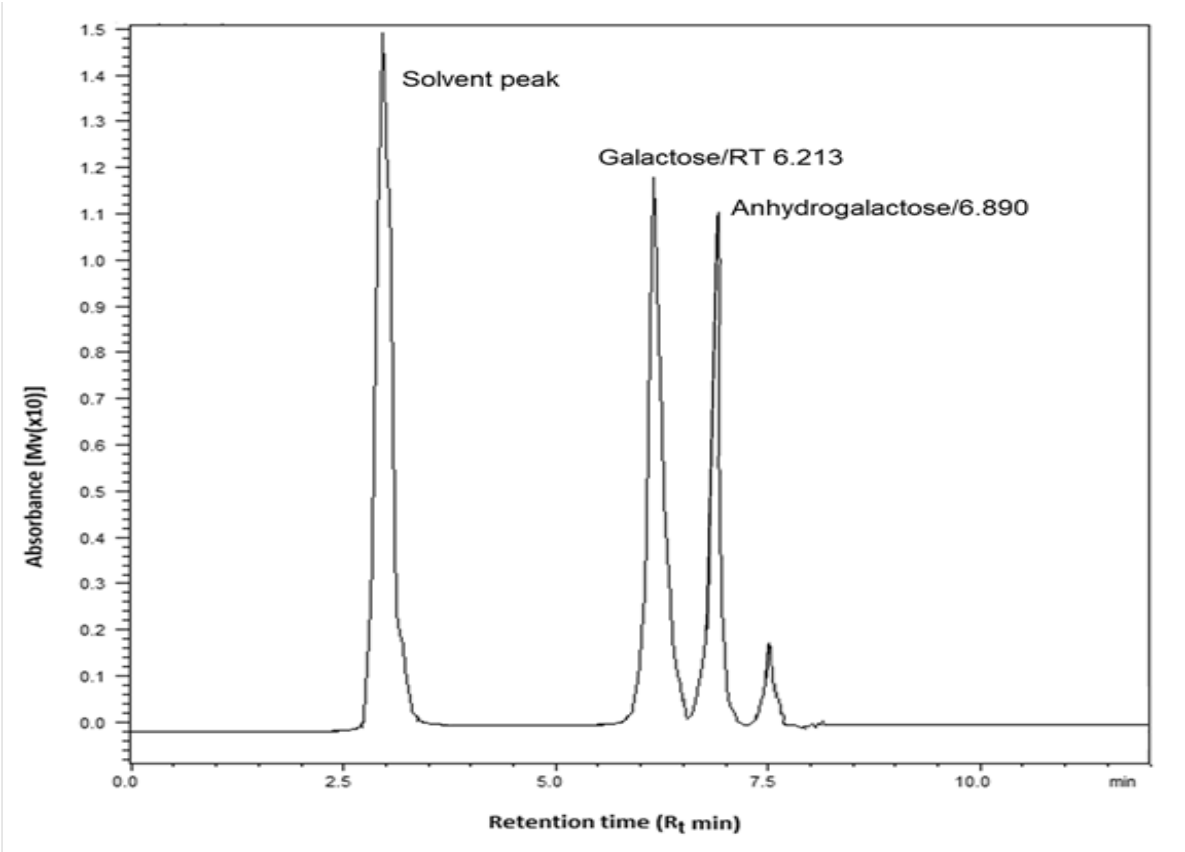

Figure 6.5.: Monosaccharide composition analysis of polysaccharide analogue

Table 6.1: Yield, protein content, sulfate content, and monosaccharide composition of crude polysaccharide fractions from *G. salicornia*.

	Crude polysaccharide	**Subfractions of polysaccharide**				
Compositions[#] (%)	GSP	GSP-1 (0.1 M NaCl)	GSP-2 (0.2 M NaCl)	GSP-3 (0.3 M NaCl)	GSP-4 (0.4 M NaCl)	GSP-5 (0.5 M NaCl)
Yield	4.39^{a}	14.31^{b}	24.31^{c}	20.28^{d}	18.10^{e}	11.65^{f}
Total carbohydrate	$63.89^{a} \pm 0.30$	$18.26^{b} \pm 0.31$	$54.62^{c} \pm 0.23$	$16.98^{d} \pm 0.02$	$16.21^{d} \pm 0.02$	$15.23^{e} \pm 0.05$
Uronic acid	$9.81^{a} \pm 0.11$	$3.98^{b} \pm 0.13$	$2.01^{c} \pm 0.07$	$2.28^{d} \pm 0.01$	$2.20^{d} \pm 0.07$	$1.63^{e} \pm 0.11$
Protein	$4.10^{a} \pm 0.03$	$3.21^{b} \pm 0.04$	$0.89^{c} \pm 0.01$	$1.02^{d} \pm 0.01$	$0.86^{d} \pm 0.03$	$0.12^{e} \pm 0.01$
Sulfate	$14.88^{a} \pm 0.06$	$11.28^{b} \pm 0.07$	$13.52^{c} \pm 0.41$	$9.13^{d} \pm 0.05$	$7.58^{e} \pm 0.12$	$2.12^{f} \pm 0.01$
Monosaccharide composition*						
Galactose	67.20	19.20	61.40	3.30	2.10	1.30
Xylose	3.20	1.50	0.03	1.20	0.90	0.21
Glucose	2.60	0.80	0.08	-	-	-
Mannose	1.10	0.60	0.02	-	-	-

[#]The composition of polysaccharide was expressed in %.

*Monosaccharide composition was expressed in %

6.3.1 Extraction, purification, yield, and chemical composition of polysaccharide derived from P. tetrastromatica

The crude polysaccharide from the brown seaweed *P. tetrastromatica* was extracted using hot water by the method reported earlier (Maneesh and Chakraborty, 2018). The yield obtained for crude the polysaccharide derived from *P. tetrastromatica* was 5.4 %. The purification of the crude polysaccharide of *P. tetrastromatica* was carried out using anion exchange chromatography by the aid of DEAE cellulose. Separation of the polysaccharides from other impurities of the crude polysaccharide involves careful selection of chromatographic parameters by using their physico-chemical properties and distribution of surface charges that in turn affects their degree of interaction on DEAE-cellulose resin. The fractions were eluted with increasing gradient of NaCl solution (0.1, 0.5, 0.75, and 1 M), and were labeled as PF-1, PF-2, PF-3 and PF-4, respectively. In the present study, the percentage yields obtained for four different fractions PF-1, PF-2, PF-3 and PF-4 were 13.05, 20.35, 19.81 and 17.12 %, respectively. Chemical composition analysis exhibited by crude polysaccharide (PF) showed a total carbohydrate content of 69.01 % by the phenol-sulfuric acid method and sulfate content of 13.01 % (Table 6.2). Among other studied fractions derived from the crude polysaccharide, the fraction PF-2 displayed significantly greater percentage yield of 56.32 % (Figure 6.6) and sulfate content of 12.31 % than those exhibited by other fractions. The fraction PF-2 also exhibited lesser protein content of 0.99 % and uronic acid content of 2.98 % than those exhibited by other fractions {~ 10.9 % (PF-1-3-4) and 5.6 % (PF-1-3-4), respectively}. The fraction PF-2 derived from the crude polysaccharide fractions of *P. tetrastromatica* displayed significantly greater DPPH and $ABTS^{+}$ radical scavenging activities (IC_{50} 0.59 mg mL^{-1} and 0.62 mg mL^{-1}, respectively, $p<0.05$). Additionally, the fraction PF-2 displayed significantly greater antidiabetic (IC_{50} α-amylase 0.98 mg mL^{-1} and α-glucosidase 0.87 mg mL^{-1}) properties. The monosaccharide composition analysis of the crude polysaccharide showed the presence of fucose (69.8 %) as the major constituent followed by fucose and galactose (~13 %), and a lesser percentage of glucose, mannose and xylose residues (0.21, 0.61 and 0.01 %, respectively) (Table 6.2). The column fraction designated as PF-2 recorded greater percentage of monosaccharide of fucose (61.4 %) and galactose (10.01 %) units as constituent sugar residues than other fractions (Figure 6.7).

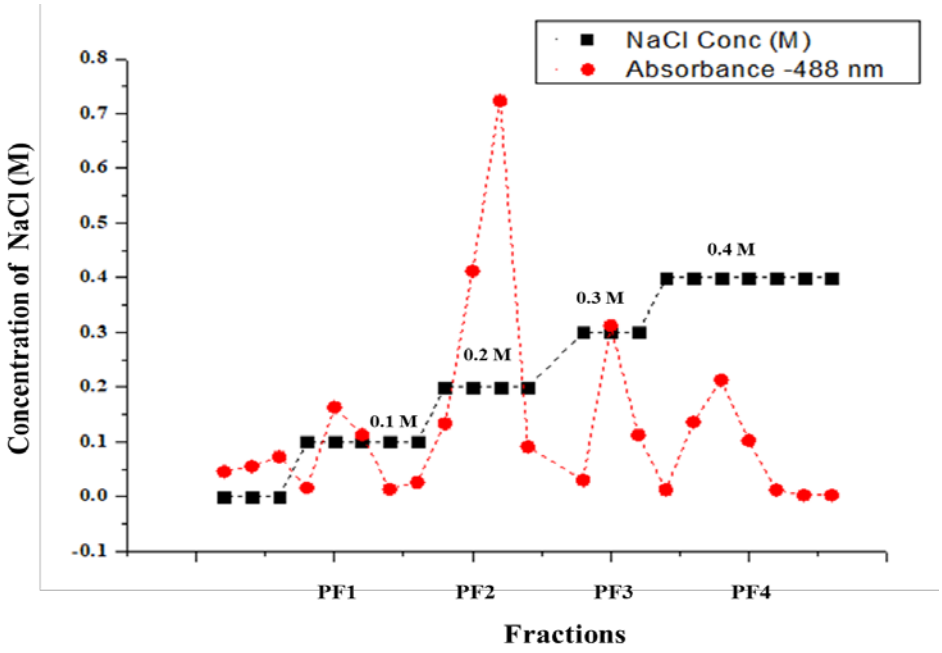

Figure 6.6.: Elution profile of polysaccharide fractions derived from the brown seaweed *P. tetrastromatica*

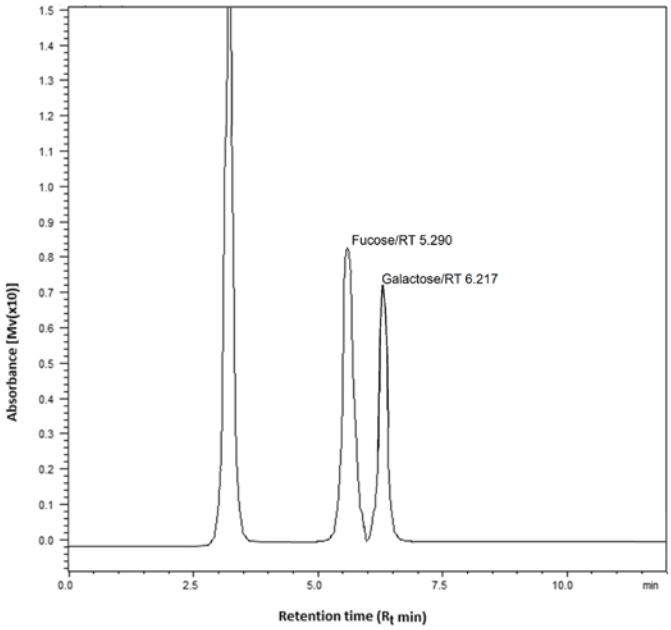

Figure 6.7.: Monosaccharide composition of polysaccharide derived from the brown seaweed *P. tetrastromatica*

Table 6.2.: Yield and chemical composition of crude polysaccharide (PF) and eluted fractions of polysaccharides from the brown seaweed *P. tetrastromatica*

Fractions	**Yield (%)**	**Total carbohydrate (%)**	**Uronic acid (%)**	**Protein (%)**	**Sulfate (%)**
*PF	4.01	69.01 ± 0.22	7.28 ± 0.07	3.83 ± 0.03	13.01 ±0.07
PF-1 (0.1 M NaCl)	13.05	17.02 ± 0.19	5.62 ± 0.11	2.99 ± 0.09	10.95 ± 0.05
PF-2 (0.2 M NaCl)	16.35	56.32 ± 0.20	2.98 ± 0.09	0.99 ± 0.07	12.31 ± 0.42
PF-3 (0.3 M NaCl)	19.81	15.96 ± 0.07	2.30 ± 0.02	0.79 ± 0.03	9.10 ± 0.01
PF-4 (0.4M NaCl)	17.12	15.62 ± 0.05	2.15 ± 0.06	0.73 ± 0.02	7.82 ± 0.10
Monosaccharide composition (%)					
Fucose	69.8	39.2	61.4	3.2	2.1
Galactose	13.01	9.02	10.01	0.98	0.98
Glucose	0.21	0.11	0.20	-	-
Mannose	0.61	0.32	0.21	-	-
Xylose	0.01	0.02	0.05	0.01	0.09

The yield and chemical composition of the fractions were expressed as % w/w. The chemical composition analyses were carried out in triplicate (n=3) and are expressed as mean ± standard deviation.

* Crude polysaccharide fraction. #PF-1, PF-2, PF-3, PF-4 were indicated subfractions

6.3.2. Bioactive potentials and yield of column sub-fractions from G. salicornia and P. tetrastromatica

The results on antioxidant and antidiabetic potentials of crude sulfated polysaccharides and polysaccharide fractions from the seaweeds *G. salicornia* and *P. tetrastromatica* were represented in Table 6.3. The IC_{50} values of GSP against the free radicals DPPH and $ABTS^+$ were recorded as 1.28 and 1.32 mg mL^{-1}, respectively. The IC_{50} values of polysaccharide fractions GSP-1, GSP-2, GSP-3, GSP-4 and GSP-5 were assessed against the free radical DPPH, and which were documented IC_{50} values of 1.08, 0.35, 1.21, 0.36 and 0.41 mg mL^{-1}, respectively. They exhibited antioxidant activities against the radical cation $ABTS^+$, and which were expressed as IC_{50} values of 1.11, 0.48, 1.39, 0.56 and 0.57 mg mL^{-1}, respectively. Among the different polysaccharide fractions, the fraction GSP-2 displayed higher antioxidant activity than that exhibited by other fractions (>0.37 mg mL^{-1}). The result indicated that the DPPH and $ABTS^+$ radical scavenging activities of GSP-2 were higher than that of standard antioxidant agent ascorbic acid (DPPH 0.37 and $ABTS^+$ 0.51 mg mL^{-1}) and other fractions (> 0.29 mg mL^{-1}).

Similarly, α-amylase and α-glucosidase inhibition activities of GSP were evaluated, and which were recorded as IC_{50} values of 1.17 and 1.19 mg mL^{-1}, respectively. The antidiabetic activity of GSP was further evaluated with DPP-IV inhibition capacity and was recorded as IC_{50} value of 1.17 mg mL^{-1}. These data on comparison with commercial standard designated that the α-amylase (IC_{50} 1.38 mg mL^{-1}), α-glucosidase (IC_{50} 1.47 mg mL^{-1}) and DPP-IV inhibition activities of polysaccharide GSP was lesser than the standard drug acarbose (IC_{50} 0.13 mg mL^{-1}). Furthermore, α-amylase and α-glucosidase inhibition activities of polysaccharide fractions followed the decreasing order of activities, GSP-2 (IC_{50} 0.98 and 0.87 mg mL^{-1}) > GSP-1 (IC_{50} 1.06 and 1.05 mg mL^{-1}) >GSP-3 (IC_{50} 1.61 and 1.69 mg mL^{-1}) >GSP-4 (IC_{50} 1.65 and 1.67 mg mL^{-1}) >GSP-5 (IC_{50} 1.82 and 1.86 mg mL^{-1}) >. The fraction GSP-2 represented prospective inhibition against the starch digestive enzymes α-amylase (IC_{50} 0.98 mg mL^{-1}) and α-glucosidase (IC_{50} 0.87 mg mL^{-1}). The antidiabetic activity of polysaccharide fractions were further evaluated with DPP-IV inhibition capacity, and which followed the order of GSP-2 (IC_{50} 0.32 mg mL^{-1}) >GSP-3(IC_{50} 0.98 mg mL^{-1}) >GSP-4 (IC_{50} 1.01 mg mL^{-1})> GSP-5 (IC_{50} 1.25 mg mL^{-1})>GSP-1(IC_{50} 1.98 mg mL^{-1}). These data on comparison with the commercial standard designated that the DPP-IV inhibition activities of GSP-2 (IC_{50} 0.63 mg mL^{-1}) was higher than the standard drug acarbose (IC_{50} 0.13 mg mL^{-1}).

The IC_{50} values of PF against the free radicals DPPH and $ABTS^+$ were recorded as 2.12 and 2.19 mg mL^{-1}, respectively. The IC_{50} values of polysaccharide fractions PF-1, PF-2, PF-3, and PF-4 were assessed against the free radical DPPH, and which were documented as 1.26, 0.89, 1.83, and 1.88 mg mL^{-1}, respectively. They exhibited potential antioxidant activity against the radical cation $ABTS^+$ and which were expressed as IC_{50} values of 1.24, 0.91, 1.92, and 1.82 mg mL^{-1}, respectively. Among the different

polysaccharide fractions, the fraction PF-2 displayed higher antioxidant activity than that of other fractions (IC_{50} <1 mg mL^{-1}). The results indicated that the DPPH and $ABTS^{+}$ radical scavenging activities of PF-2 were higher than that of standard drug ascorbic acid (IC_{50} DPPH 0.37 and $ABTS^{+}$ 0.51 mg mL^{-1}) and other fractions (IC_{50} > 1 mg mL^{-1}).

Similarly, α-amylase and α-glucosidase inhibition activities of PF were evaluated and which were IC_{50} of 2.33 and 2.49 mg mL^{-1}, respectively. The antidiabetic activity of PF was further evaluated with DPP-IV inhibition capacity (IC_{50} 2.26 mg mL^{-1}). These data on comparison with commercial standard designated that the α-amylase (IC_{50} 1.38 mg mL^{-1}), and α-glucosidase (IC_{50} 1.47 mg mL^{-1}) inhibition activities of polysaccharide PF was lower than the standard drug acarbose (IC_{50} 0.13 mg mL^{-1}). Furthermore, the α-amylase and α-glucosidase inhibition activities of polysaccharide fractions followed the decreasing order of activities, PF-2 (IC_{50} 1.58 and 1.54 mg mL^{-1}) > PF-4 (IC_{50} 1.75 and 1.37mg mL^{-1}) >PF-3 (IC_{50} 1.85 and 1.89 mg mL^{-1}) > >PF-1 (IC_{50} 1.98 and 1.88 mg mL^{-1}). The fraction PF-2 represented higher inhibition against starch digestive enzymes α-amylase (IC_{50} 1.58 mg mL^{-1}) and α-glucosidase (IC_{50} 1.54 mg mL^{-1}). The antidiabetic activity of polysaccharide fractions were further evaluated with DPP-IV inhibition capacity, and which followed the order, PF-2 (IC_{50} 0.98 mg mL^{-1}) > PF-4 (IC_{50} 1.01 mg mL^{-1})> PF-1 (IC_{50} 1.93 mg mL^{-1})> PF-3 (IC_{50} 1.98 mg mL^{-1}). Among the different polysaccharide fractions considered from the red seaweed G. *salicornia* and brown seaweed *P. tetrastromatica,* the fraction GSP-2 was found to exhibit higher antioxidant and anti-diabetic potentials than that of other fractions. Therefore, on the basis of yield and bioactivities, the fraction GSP-2 was selected for further structural characterization and bioactivity analysis.

Table 6.3.: Yield and bioactive potentials (anti-oxidant and antidiabetic activities) of crude polysaccharides and sub-fractions derived from *G. salicornia* and *P. tetrastromatica*

Antioxidant activities (in mg mL^{-1})			**Antidiabetic activities (in mg mL^{-1})**			**Yield**
Sl. No.	DPPH radical scavenging	ABTS^{+} radical scavenging	α-amylase inhibition	α-glucosidase inhibition	DPP-IV inhibition	(in %)
GSP	1.28±0.03^{a}	1.32±0.07^{a}	1.17±0.03^{a}	1.19±0.04^{a}	1.17±0.03^{a}	4.39
GSP-1	1.08±0.01^{b}	1.11±0.02^{b}	1.06±0.04^{b}	1.05±0.02^{b}	1.02±0.03^{b}	14.31
GSP-2	**0.35±0.02^{c}**	**0.48±0.02^{c}**	**0.98±0.03^{c}**	**0.87±0.03^{c}**	**0.32±0.04^{c}**	**24.31**
GSP-3	1.21±0.01^{d}	1.39±0.03^{d}	1.61±0.03^{d}	1.69±0.04^{d}	0.98±0.03^{d}	20.28
GSP-4	0.36±0.02^{e}	0.56±0.04^{e}	1.65±0.04^{e}	1.67±0.03^{e}	1.01±0.02^{e}	18.10
GSP-5	0.41±0.03^{f}	0.57±0.05^{f}	1.82±0.04^{f}	1.86±0.02^{f}	1.25±0.02^{f}	11.65
PF	2.12^{a} ±0.03	2.19^{a} ±0.07	2.33^{a} ±0.03	2.49^{a} ±0.04	2.26^{a} ±0.03	4.01
PF-1	1.26^{b} ±0.01	1.24^{b} ±0.02	1.98^{b} ±0.04	1.88^{b} ±0.02	1.93^{b} ±0.03	13.05
PF-2	**0.89^{c} ±0.02**	**0.91^{c} ±0.02**	**1.58^{c} ±0.03**	**1.54^{c} ±0.03**	**0.98^{c} ±0.04**	**16.35**
PF-3	1.83^{d} ±0.01	1.92^{d} ±0.03	1.85^{d} ±0.03	1.89^{d} ±0.04	1.98^{d} ±0.03	19.8
PF-4	1.88^{e} ±0.02	1.82^{e} ±0.04	1.75^{e} ±0.04	1.37^{e} ±0.03	1.01^{e} ±0.02	17.12
Standards	0.37±0.05^{hp}	0.51±0.04^{hp}	1.38 ± 0.06^{hR}	1.47 ± 0.05^{hR}	0.13 ± 0.07^{hR}	-

[#]The bioactivities were expressed as IC_{50} values (mg/mL) and [¥]The yield and chemical composition of the fractions are expressed as % w/w. The samples were analyzed in triplicate (n=3) and expressed as mean±standard deviation. Means followed by different superscripts (a-h) within the same row indicated significant differences (p<0.05).

P and R indicate the standards used for different activities: P-ascorbic acid and R- acarbose.

6.3.3 Structural interpretation of hydrolyzed polysaccharide

6.3.3.1 Structural interpretation of hydrolyzed polysaccharide by Fourier transforms infrared spectrum analysis (FTIR)

The preliminary spectral characterization of polysaccharide, GSP-2 was carried out by FTIR spectrum analysis. The characteristic peak at 1242 cm^{-1} indicated the presence of sulfate ester functionality in GSP-2. The spectrum possessed two intense absorption bands at 934 cm^{-1} and at 848 cm^{-1} corresponding to the anhydro galactopyranosyl and axial sulfate ester at *O*-6 of D-galactopyranosyl, respectively. These results were corroborated by the absorptions bands observed for commercial carrageenan at 1220 cm^{-1}(ester sulfate) and 928 cm^{-1} (3,6-anhydrogalactose) (Volery, Besson, & Schaffer-Lequart, 2004). Similarly, the absorption at 844 cm^{-1} was corroborated by the presence of galactans in GSP-2. The existence of stretching vibration of hydroxyl group (OH) was confirmed with the absorption band located at 3437 cm^{-1}. Absorption band at 2923 cm^{-1} was observed due to the stretching vibration of C-H bonds. Moreover, the absorption peak at 1639 cm^{-1} was due to asymmetric stretching vibration of O-C-O functionality (Figure 6.7).

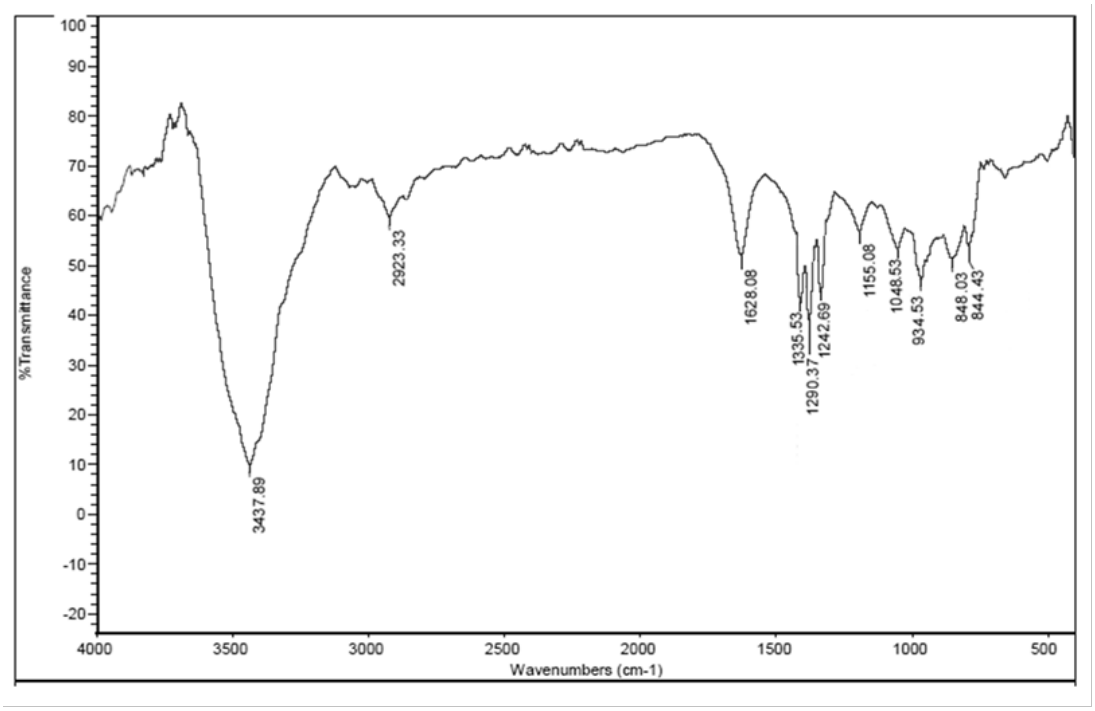

Figure 6.8.: FTIR of polysaccharide derived from the brown seaweed *P. tetrastromatica*

The FT-IR peaks at 1290 cm^{-1} and 1048 cm^{-1} were due to the stretching vibration of C-O of the attached sulfate esters and hydroxyl functionalities, respectively. In addition, the absorption bands at 1335 cm^{-1} represented the wagging mode of the CH_2 group. The peak at 1155 cm^{-1} could indicate the coupling of the C-O and C-C stretches. The characteristic absorption bands at 1258, 1075, 930 and 891 cm^{-1} of polysaccharide isolated from *G. caudata* were corroborated by the functional group observed in the polysaccharide GSP-2 (Barros, da Silva, Sombra, Maciel, Feitosa, Freitas, & de Paula, 2013; Knutsen et al., 1994; Usov et al., 2011). All these attributions together contributed the presence of the sulfate bearing galactose and anhydrogalactose in the studied polysaccharide, GSP-2.

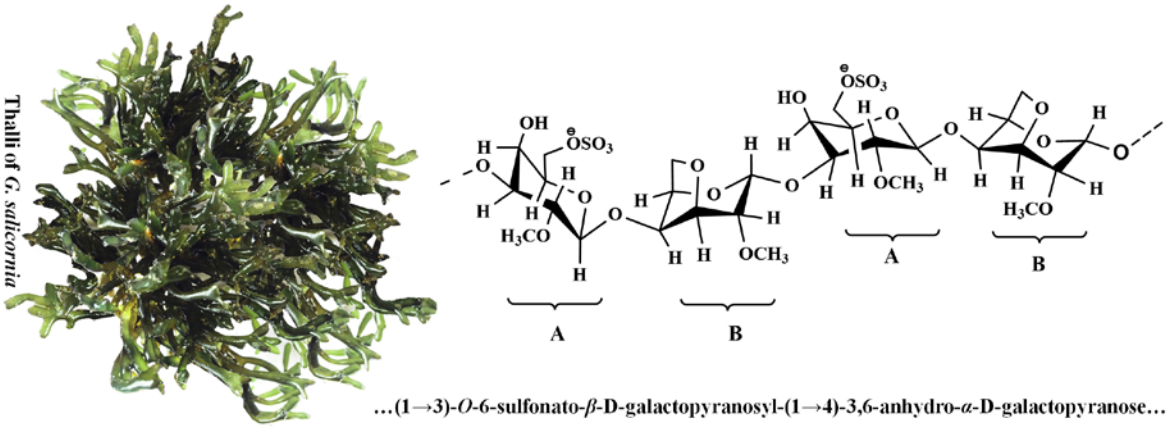

Figure 6.9.: Structural representations of polysaccharide, (1⋯→3)-*O*-6-sulfonato-β-Dgalactopyranosyl-(1→⋯4)-3,6-anhydro-α-D-galactopyranose-(1⋯→) derived from the aqueous extract of *G. salicornia*.

6.3.3.2 Structural interpretation of hydrolyzed polysaccharide by NMR spectroscopic analysis

NMR spectroscopy (1D and 2D) was found to be a significant tool for the structural interpretation of seaweed polysaccharides, which could provide various structural attributions, such as the monosaccharide composition, linkage pattern, configurations of anomeric protons/carbons, branching and positions of different functionalities (Figure 6.10-6.117, Table 6.4). The ^{1}H-NMR of oligosaccharide obtained after the hydrolysis of GSP-2 exhibited highly deshielded protons at δ4.90 and 5.32 along with other protons in the range of δ3.40-4.74. These protons were further supported by ^{13}C NMR and DEPT^{135} along with HSQC spectrum. Based on these, assigned the carbons associated with protons in the oligosaccharide, such as δ4.90 (δ106.33; CH), δ5.32 (δ115.17; CH), δ4.74 (δ86.34; CH), δ4.66 (δ69.66; CH_2), δ4.56 (δ63.38; CH_2), δ3.90 (δ74.15; CH), δ3.82 (δ69.34; CH), δ3.80 (δ63.38; CH_2), δ3.76 (δ69.66; CH_2), δ3.75 (δ780.68; CH), δ3.69 (δ89.68; CH), δ3.65 (δ92.10; CH), δ3.61 (δ85.45; CH), δ3.42 (δ60.76; CH) and δ3.40 (δ60.61; CH).

Table 6.4.: NMR spectroscopic data[a] of polysaccharide …(1→3)-*O*-6-sulfonato-*β*-D-galactopyranosyl-(1→4)-3,6-anhydro-*α*-D-galactopyranose…from red seaweed *G. salicornia*

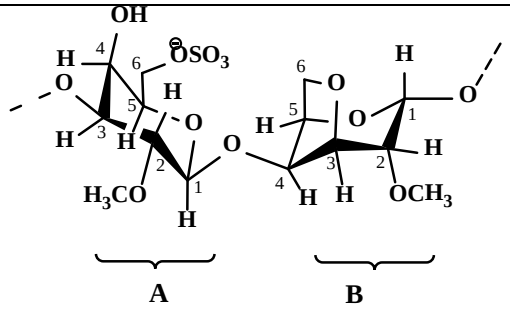

Type of C	C. No.	^{13}C NMR	^{1}H NMR	COSY	HMBC
CH	A1	106.33	4.90	H-A2	C-A2, A3,A5
CH	A2	80.68	3.75	-	C-A3, A7
CH	A3	89.68	3.69	-	C-A4
CH	A4	69.34	3.82	-	C-A5,A6
CH	A5	74.15	3.76	H-A6	C-A6
CH_2	A6	69.66	3.76, 4.66	-	
CH_3	A7	60.76	3.42	-	
Unit B					
CH	B1	115.17	5.32	H-B2	C-B2
CH	B2	85.51	3.73	H-B3	C-B3,B4,B7
CH	B3	86.34	4.74	H-B4	C-B5, B6
CH	B4	85.45	3.61	-	C-B5, A1
CH	B5	92.10	3.65	H-B6	C-B1,B6
CH_2	B6	63.38	3.80, 4.56	-	
CH_3	B7	60.61	3.40	-	

[a]NMR spectra were recorded using a Bruker AVANCE III 500 MHz (AV 500) spectrometer (Bruker, Karlsruhe, Germany) in MeOH as aprotic solvent at ambient temperature with TMS as the internal standard (δ 0 ppm).

[b]Values in ppm, multiplicity and coupling constants (*J*= Hz) were indicated in parentheses. Multiplicities were allocated by ^{135}DEPT NMR spectrum. The assignments were made with the aid of the COSY, HSQC, HMBC and NOESY experiments.

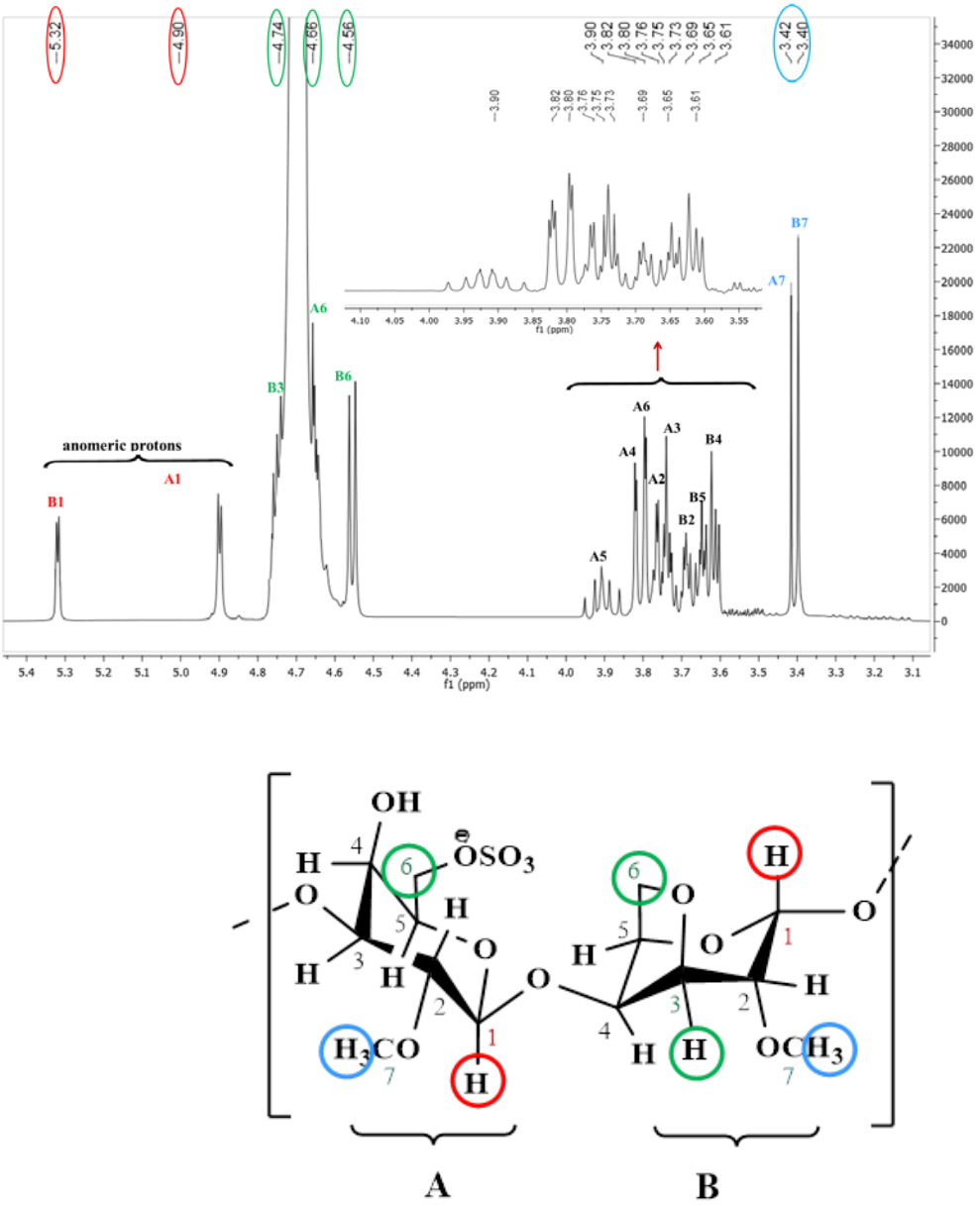

Figure 6.10.: ^{1}H NMR spectrum of the hydrolyzed polysaccharide analogue

The CH protons, δ4.90 (δ106.33; CH) and δ5.32 (δ115.17; CH) appeared as two intense signals, whereas these protons and carbons were found to be related to the anomeric region, which indicated that the polysaccharide on purification yielded two residues of sugar units. These major signals were assigned for C_1 positions of oligosaccharides formed after sequential purification. The two sugar units were named as (**A**) and (**B**) based on their increasing values of chemical shifts in the anomeric region. The literature values also indicated the chemical shift values in the range of δ4.60-5.00 corresponding to the β-linked galactose (Gal*p*) units; and the region between δ5.00-5.60

was related to the α-linked anhydrogalactose (AnGal*p*) units (Stortz, Bacon, Cherniak, & Cerezo, 1994).

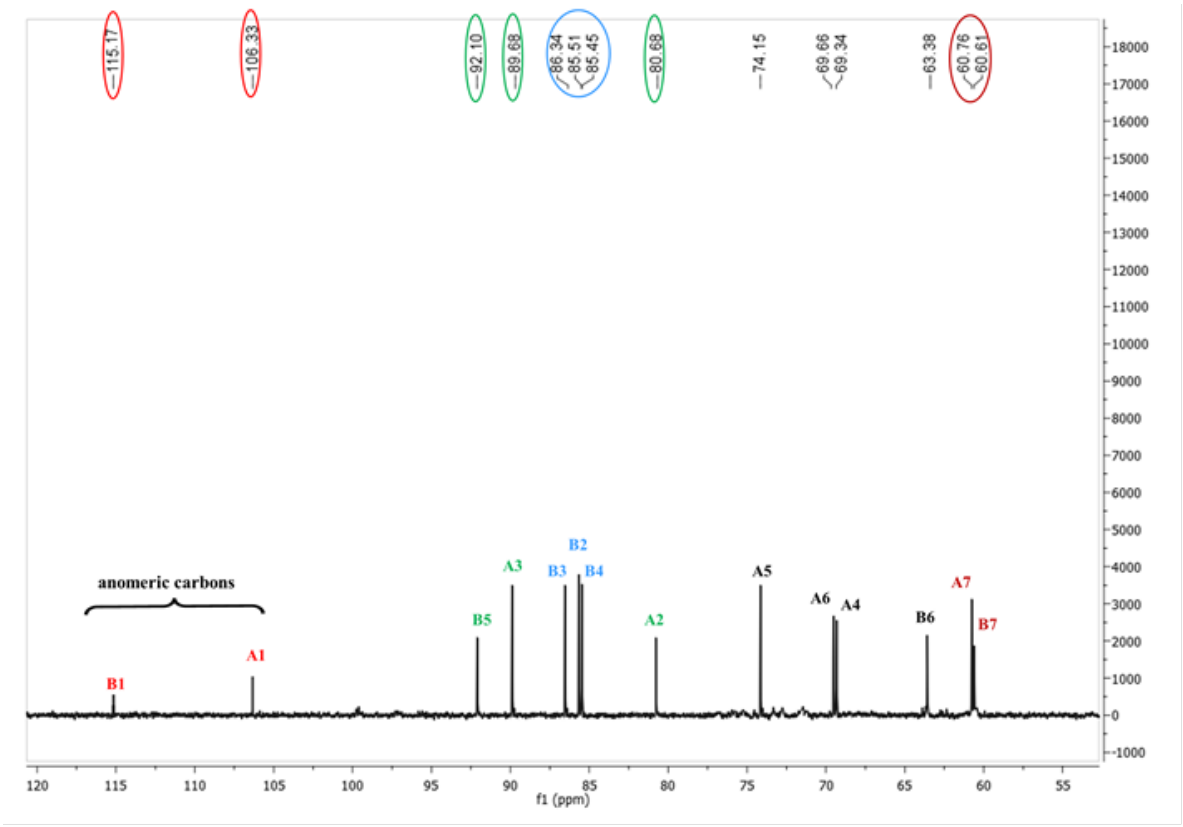

Figure 6.11.: ^{13}C NMR spectrum of the hydrolyzed polysaccharide analogue

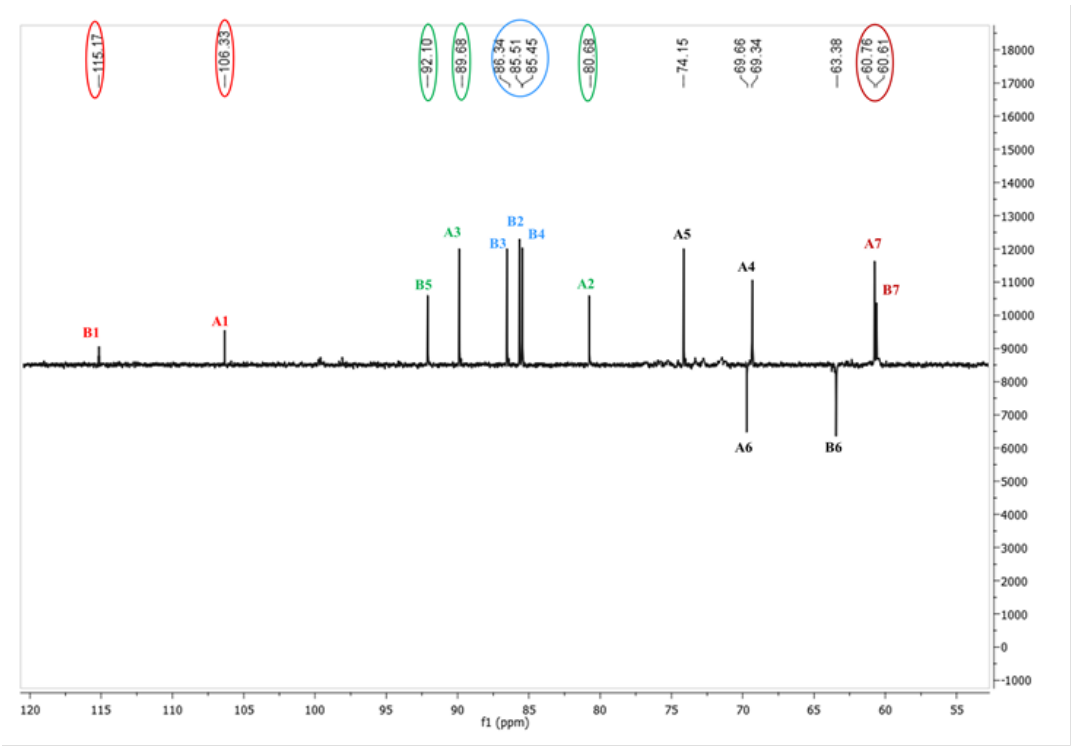

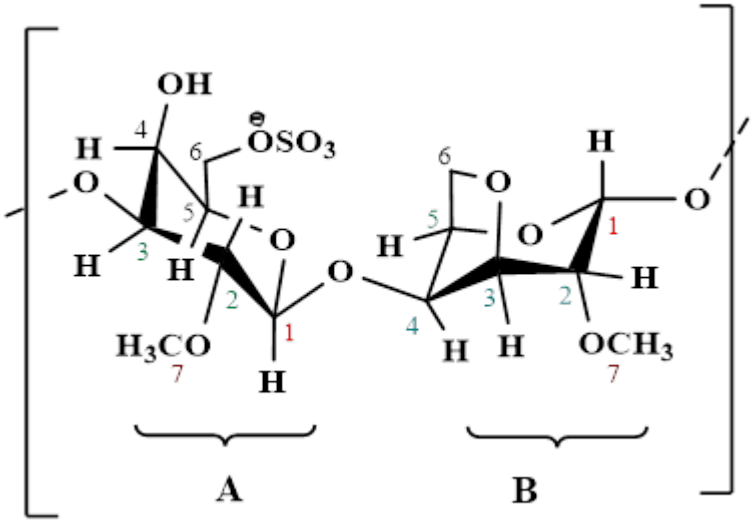

Figure 6.12.: DEPT^{135} spectrum of the hydrolyzed polysaccharide analogue

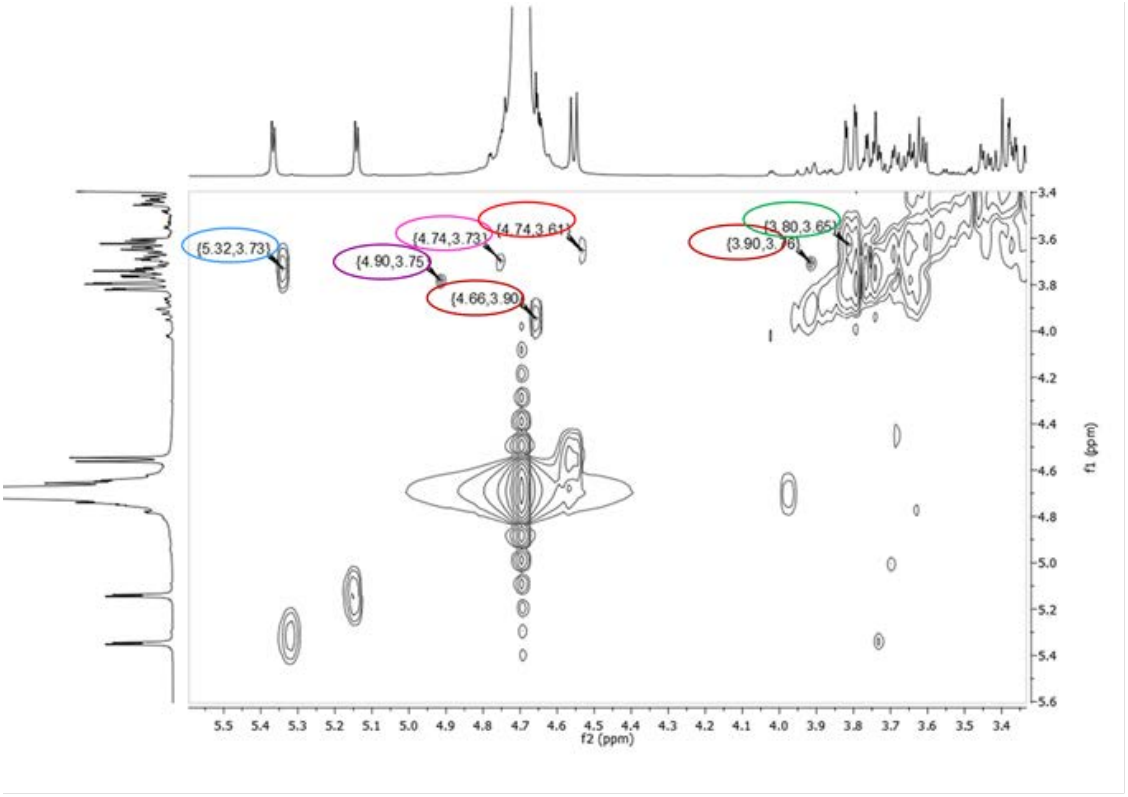

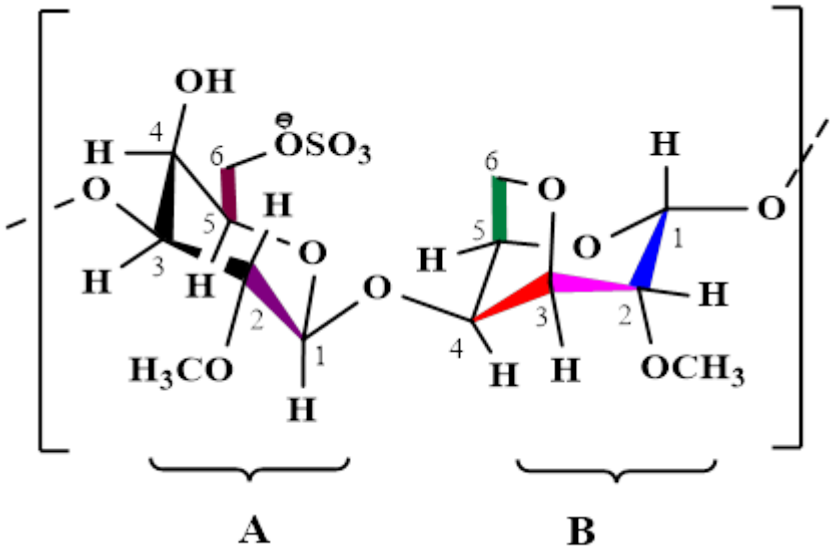

Figure 6.13.: ^{1}H-^{1}H COSY NMR spectrum of the hydrolyzed polysaccharide analogue

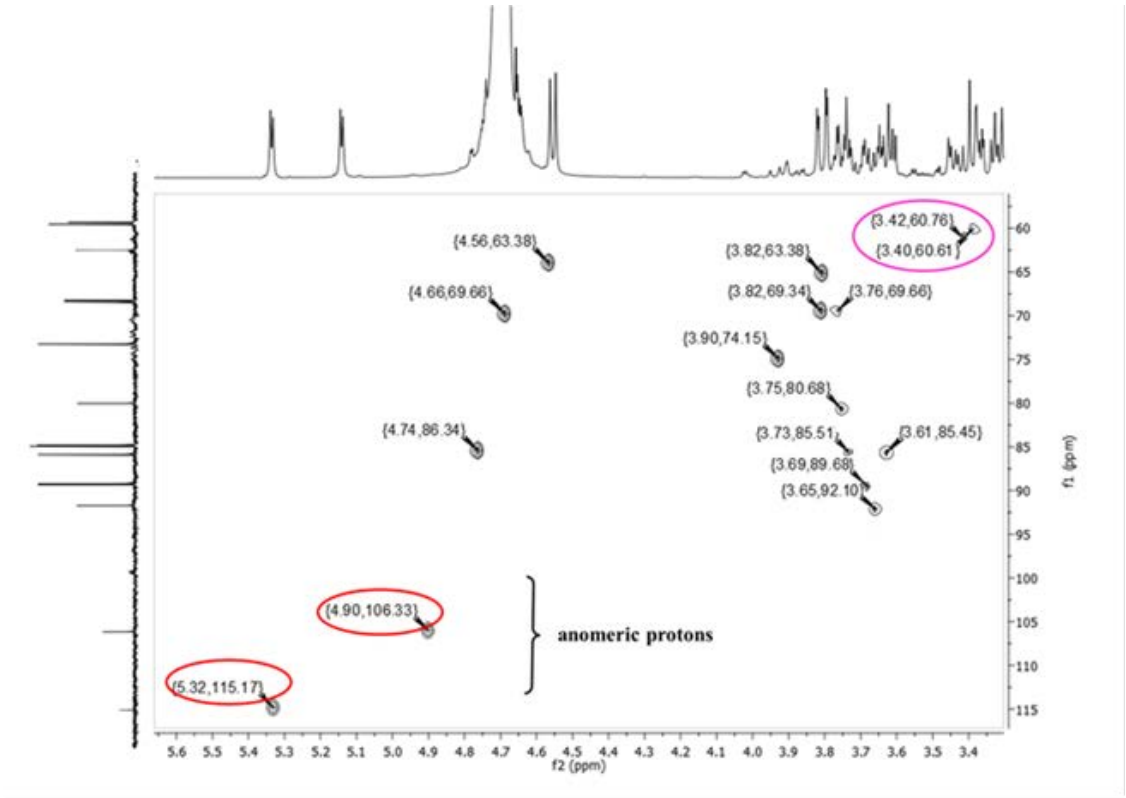

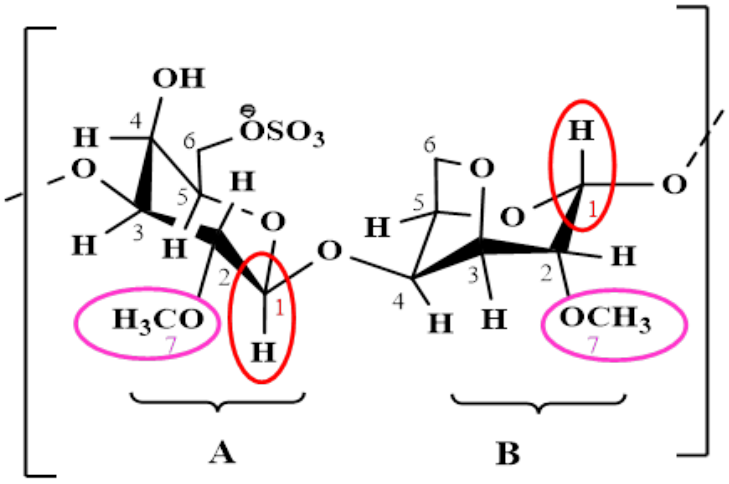

Figure 6.14.: HSQC spectrum of the hydrolyzed polysaccharide analogue

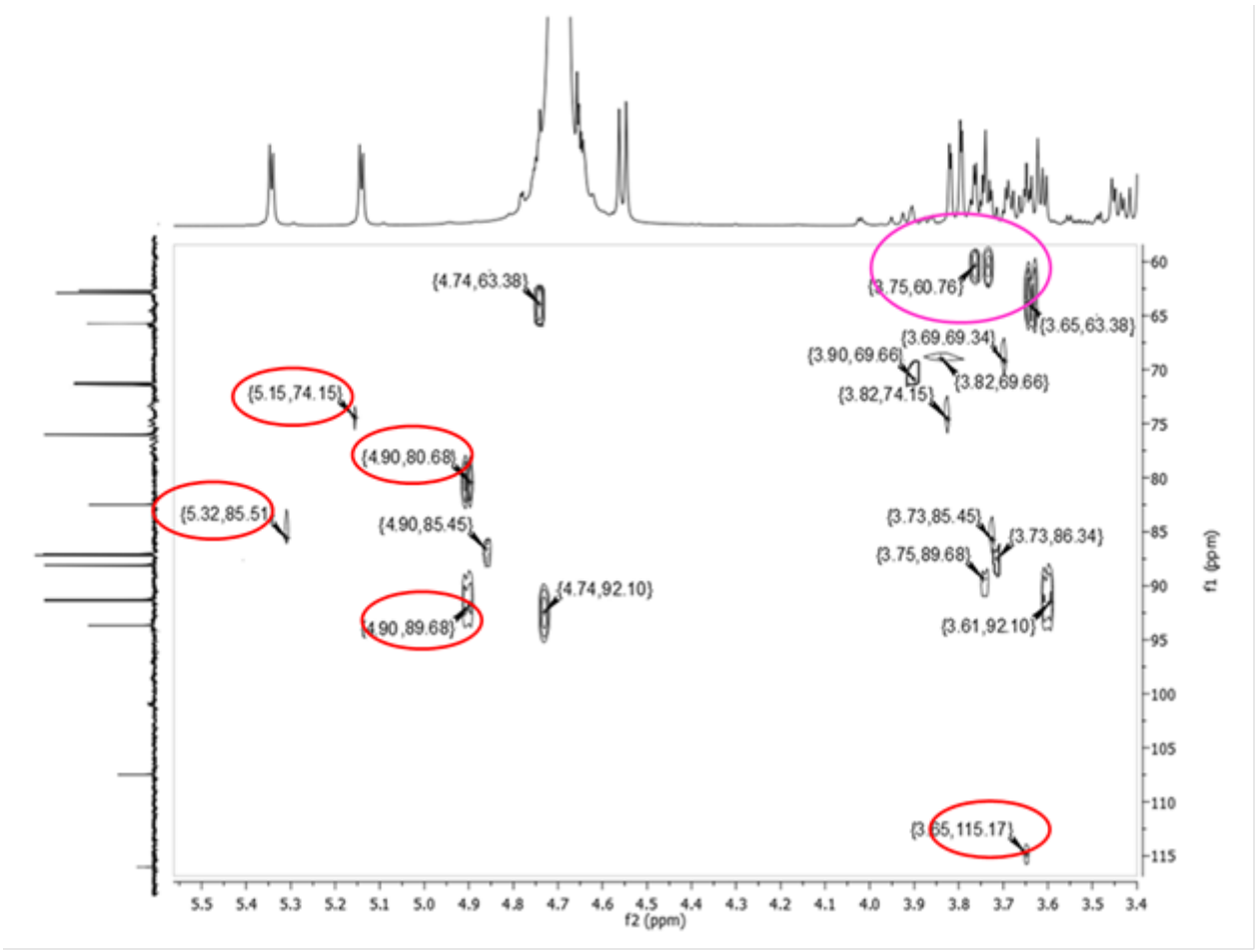

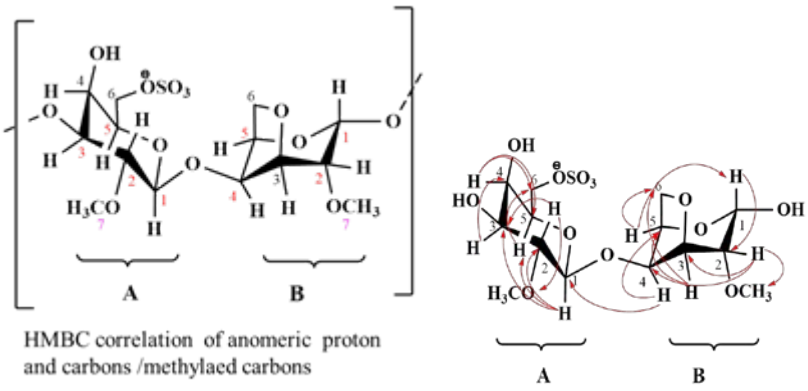

HMBC correlation of anomeric proton and carbons /methylaed carbons

Figure 6.15.: HMBC spectrum of the hydrolyzed polysaccharide analogue

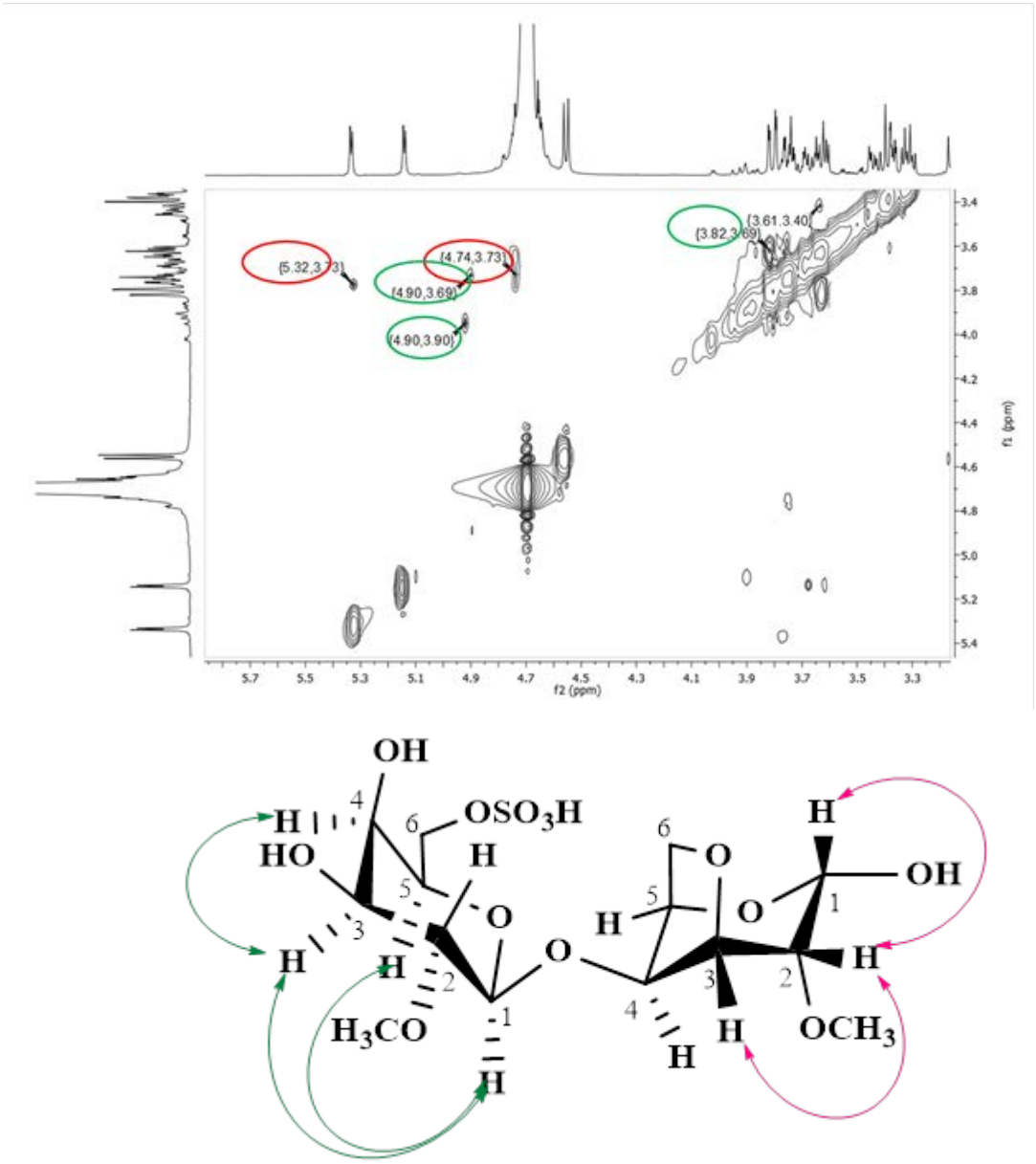

Figure 6.16.: NOESY spectrum of the hydrolyzed polysaccharide analogue

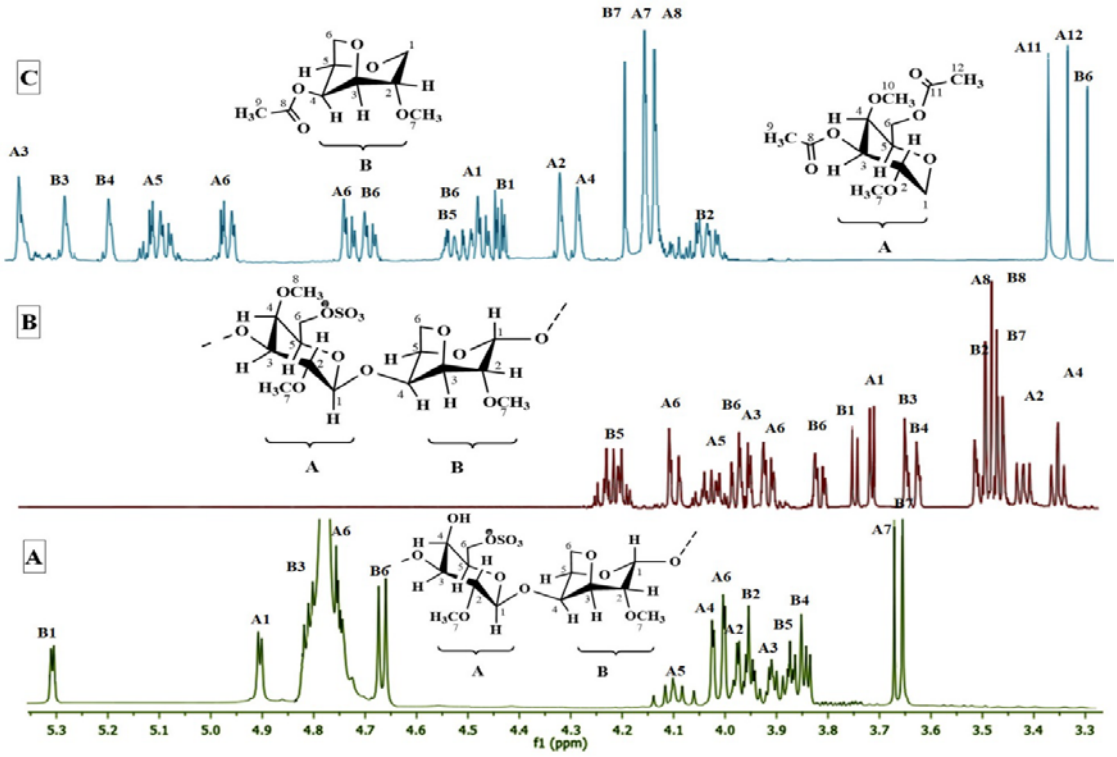

Figure 6.17.: ^{1}H NMR spectra of the polysaccharide, (1⋯→3)-*O*-6-sulfonato-β-D-galactopyranosyl-(1→⋯4)-3,6-anhydro-α-D-galactopyranose-(1⋯→) obtained after the process of (**A**) hydrolysis (**B**) methylation and (C) acetylation

In light of these data, δ4.90 (δ106.33; CH) was assigned to the monosaccharide unit, (**A**), which might ascribe the presence of Gal*p* ring. The position of this anomeric proton in unit (**A**) and other fragments associated with them was further confirmed by detailed COSY and HMBC correlation spectra. The proton at δ4.90 (d, 3.8 Hz) displayed COSY correlation with proton at δ3.75. These correlations were directed towards the oxygenated functionality bearing neighboring CH group in unit (**A**). Moreover, the intense HMBC correlation from proton δ3.75 (δ80.68; CH) to carbon δ60.76 (δ3.42) confirmed the neighboring -OCH_3 group linked to CH (δ3.75; δ80.68), which was assigned as C_2. Therefore, it was seemed that anomeric functionality -CH(O-) was directly attached to the fragment CH(O-CH_3)-. These attributions were further corroborated by the occurrence of methyl ether at C-6 position in agars extracted from different *Gracilaria* species, with the degree of substitution varying among species (Barros et al., 2013). Furthermore, the HMBC correlations from the protons at δ4.90 (δ106.33; CH) to carbons at δ80.68 (δ3.75, t), 89.68 (δ3.69, t) and δ74.15 (δ3.90, m); from δ3.75 (δ780.68; CH) to δ89.68 (δ3.69; t); from δ3.69 (δ89.68; CH) to δ69.34 (δ3.82; t) and from δ3.82 (δ69.34; CH) to δ74.15 (δ3.90; m) suggested the partial ring structure -CH(O-)-CH(OCH_3)-CH(OH)-CH(OH)-CH< in unit (**A**), positions assigned to

the positions of C_1-C_5. The interchangeable hydroxyl protons at δ3.69 (δ89.68; CH) and δ3.82 (δ69.34; CH) were found to be ceased to locate upon exchange of D_2O thereby assigning the presence of (-OH) groups in its close proximity. The COSY correlation between the protons δ3.90/δ3.76/δ4.66 assigned the linkage between the CH proton at δ3.90 and CH_2 protons at δ3.76/4.66. Similarly, the HMBC correlations from the protons at δ3.82 and δ3.90 to the carbon δ69.66 assigned the fragment -CH(O-)-CH_2(O-), namely C_5-C_6. The HMBC correlation between δ4.90 and δ74.15 suggested the closure of ring protons, and which furthermore confirmed the presence of galactopyranose (Gal*p*) ring in the oligosaccharide with two substitutions, -OCH_3 and -CH_2O- at C_2 and C_5 positions, respectively. The deshielded doublet of doublet signal observed at δ3.76 and δ4.66 assigned the presence of CH_2 bearing sulfonato (-OSO_3^-) group in unit (**A**). Therefore, glycoside residue (**A**) was characterised as *O*-6-sulfonato-2-methyl-β-D-Gal*p* (*O*-6-sulfonato-2-Me-β-D-Gal*p*).

Similarly, the proton at δ5.32 (δ115.17; CH) was assigned to C_1 position of the monosaccharide unit, (**B**), which might be the part of anhydrogalactopyranose (AnGal*p*) ring related to the monosaccharide unit, (**B**). The position of this anomeric proton in unit, (**B**) and other related fragments were further confirmed by COSY and HMBC correlations. The proton at δ5.35 (d) displayed COSY correlation with proton at δ3.73. This correlation appropriately suggested the presence of oxygenated functionality bearing neighboring CH group in unit (**B**). Furthermore, the strong HMBC correlation from proton δ3.73 (δ85.51; CH) to carbon δ60.61 (δ3.40) suggested the presence of -OCH_3 group linked to CH (δ3.73, δ85.51), corresponding to the position C_2 in (**B**). Therefore, anomeric -CH(O-) functionality was directly attached to the CH(O-CH_3)- group in (**B**), assigned as C_1-C_2. Besides, the COSY correlations in between the protons δ3.73/δ4.74/δ3.61 suggested the presence of the fragment -CH(OCH_3)-CH(O-)-CH(O-)-, corresponding to C_2-C_4 in (**B**). These COSY cross peaks were further supported by the HMBC correlations from the protons at δ3.73 (δ85.51; CH) to carbons at δ86.34 (δ4.74, t), and δ85.45 (δ3.61, m); from δ4.74 (δ86.34; CH) to δ92.10 (δ3.65; t); and from δ3.61 (δ85.45; CH) to δ92.10 (δ3.65; t), which attributed the fragment -CH(OCH_3)-CH(O-)-CH(O-)-CH(O-), at the positions of C_2-C_5. Moreover, the COSY correlations between the protons δ3.65/δ3.80/δ4.56 assigned the connection of the fragment -CH(O-)-CH_2(O-)-, for the positions of C_5-C_6 . The HMBC correlation from δ4.74 (δ86.34) to δ92.10 (δ3.65) suggested the presence of five membered ring fragment -CH(O-)-CH(O-)-CH(O-)-CH_2(O-), corresponding to the closed furanose ring C_3-C_6. At the same time, the proton at δ3.65 (δ92.10) displayed HMBC correlation with the anomeric carbon δ115.17 (δ5.32), which attributed the closure of the second ring in (**B**). The second monosaccharide unit was found to exist as the combinations of 5 and 6 membered rings, and which was considered as 2-methyl-α-D-3,6-AnGal*p* (2-Me-α-D-3,6-AnGal*p*) moiety in oligosaccharide.

The HMBC correlation from the proton δ3.61 (C_4 in **B**) to carbon δ106.33 (C_1 in **A**) was directed towards the assumption of the linkage pattern. From this correlation, it has seen that, C_1 of the *O*-6-sulfonato-2-Me-β-D-Gal*p* was connected to the C_4 of 2-Me-α-D-3,6-AnGal*p*. Therefore, the glycoside residue in GSP-2 might possess an alternate (····1→4) (····1→3) or (····1→3) (····1→4) in between *O*-6-sulfonato-2-methyl-β-D-Gal*p* and 2-methyl-α-D-3,6-AnGal*p*. The further connections of glycoside residues in GSP-2 were confirmed by the methylation and linkage pattern analyses.

The relative stereochemistries of protons attached to the chiral carbons at C_1, C_2, C_3, C_4 and C_5 in unit (**A**) and C_1, C_2, C_3 and C_4 in unit (**B**) were explained with the aid of nuclear overhauser effect spectroscopic (NOESY) experiments. In unit (**A**), the signal of proton at chiral centre, wherein H_1 exhibited NOEs with methine protons H_5 and H_3; H_3 exhibited NOE with H_4, which were oriented in the α-side of unit (**A**) in the oligosaccharide. Conversely, the other protons were in β-face of the unit (**A**) in oligosaccharide. Likewise, in unit (**B**), the signal of proton at the chiral centre, H-1 showed NOE with the methine proton H_2; H_2 showed NOE with H_3, which were oriented in the β-side of the oligosaccharide. Conversely, the other protons were in the α-face of the unit (**B**) in the oligosaccharide of GSP-2.

These data proposed that the sequence of linkage pattern of residues of monosaccharides in GSP-2 as (····→3)-*O*-6-sulfonato-2-methyl-β-D-Galactopyranose-(1→4)-2-methyl-α-D-3,6-Anhydrogalactopyranose-(1→····) or (····→3)-*O*-6S-2-Me-β-D-Gal*p*-(1→4)-2-Me-α-D-3,6-AnGal*p*(1→····) or [2-Me-G6S-2-MeAnG]. The structural composition of the skeletal chain of the galactopyran was reinforced with the repetitive units of the sulfated galactopyranosyl-anhydroglactopyranose.

6.3.3.4 Molecular weight of polysaccharide by ESI-MS Analysis

The elution curve obtained for GSP-2 (Figure 6.3) was found to show an intense single peak, which confirmed the purity of the fraction GSP-2. The ESI-MS analysis of oligosaccharide, which was obtained by hydrolysis, was performed in negative-ion mode due to the presence of sulfate groups. The polysaccharide sample on sequential purification was found to comprise of the disaccharide units. The intense molecular ion peak occurred at *m/z* 431.3, which corresponds to the single-charged anion $[2\text{-Me-G6S-2-MeAnG}]^-$ of the disaccharide parts, and it encompassed with glycosidic residues of *O*-6-sulfonato-2-Me-β-D-Gal*p* and 2-Me-α-D-3,6-AnGal*p*. The spectrum was consisted of two peaks at *m/z* 273.2 and *m/z* 176.2, which correspond to the fragments $[2\text{-Me-G6S}]^-$ and $[2\text{-MeAnG}]^-$, respectively (Figure 6.18).

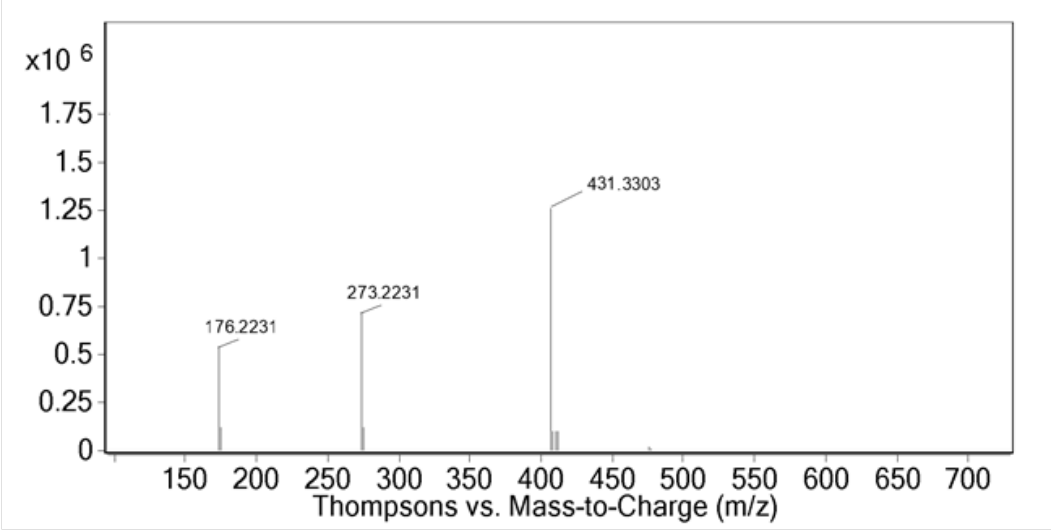

Figure 6.18.: ESI-MS spectrum of the oligosaccharide analogue

6.3.3.5 Structural interpretation of polysaccharide by methylation analysis

The linkage pattern and functionalities in polysaccharide were further confirmed by methylation followed by hydrolysis. On methylation, all hydroxyl groups present in the polysaccharide were found to be substituted by methoxyl groups and further hydrolysis of polysaccharide could lead to the breakdown of glycosidic linkage. The free glycosidic linkages were ensured by the presence of hydroxyl groups, which have clearly depicted the pattern of linkages in between the monosaccharide residues. The structural characterization of the methylated polysaccharide was carried out with the aid of 1D and 2D NMR spectroscopic methods (Figure 6.19- 6.25, Table 6.6). The proton NMR spectrum of the methylated GSP-2 was depicted in Figure 6.17. Two sugar residues (characterized in the previous section) in polysaccharide was designated as (MeA or MeGal*p*) and (MeB or MeAnGal*p*). Three major singlets appeared in the proton NMR in between the δ3.30-3.50, which attributed the presence of methylated moieties in the polysaccharide GSP-2. At the same time two intense signals were seen in the region of δ3.60-3.70, which might be due to the cleaved glycosidic bonds in between the sugar residues. These signals were further ensured by the 1D-NMR along with HSQC spectrum. On the basis of these spectra, the individual protons attached to the carbon in the methylated polysaccharide were assigned. The lack of two intense signals in the anomeric region depicted the cleavage of glycosidic linkage in methylated GSP-2. At the same time, two intense peaks at δ3.67 (d; δ69.76; CH_2) and δ3.65 (d; δ69.56; CH_2) were found in the spectrum with same integral and multiplicities, indicating the proton substituted C_1 positions in MeGal*p* and MeAnGal*p*, respectively. The deshielded signals at δ3.67 (δ69.76; CH_2) and δ3.65 (δ69.56; CH_2) were appeared as doublet, indicating the oxygen

bearing CH functionality in the nearby position of C_1. The HMBCs from δ3.67 and δ3.65 to the δ93.94 (δ3.24) and δ88.75 (δ3.36) were directed towards the presence of neighboring CH groups, assigned as C_2 in MeGal*p* and MeAnGal*p*, respectively. The signals at δ3.24 (C_2 in MeA) and δ3.36 (C_2 in MeB) exhibited HMBCs with δ59.04 (δ3.33) and δ59.78 (δ3.30), respectively. These results indicated the presence of methoxyl (-OCH_3) substitutions at the C_2 position of two sugar residues (MeA) and (MeB). Thus, the presence of methoxyl functionalities at positions C_2 attached to the anomeric C_1 positions in MeGal*p* and MeAnGal*p* (described in section 3.3.2) were confirmed. These correlations together resulted in the -CH_2-(CH-OCH_3); (C_1-C_2) fragments in MeGal*p* and MeAnGal*p*, respectively.

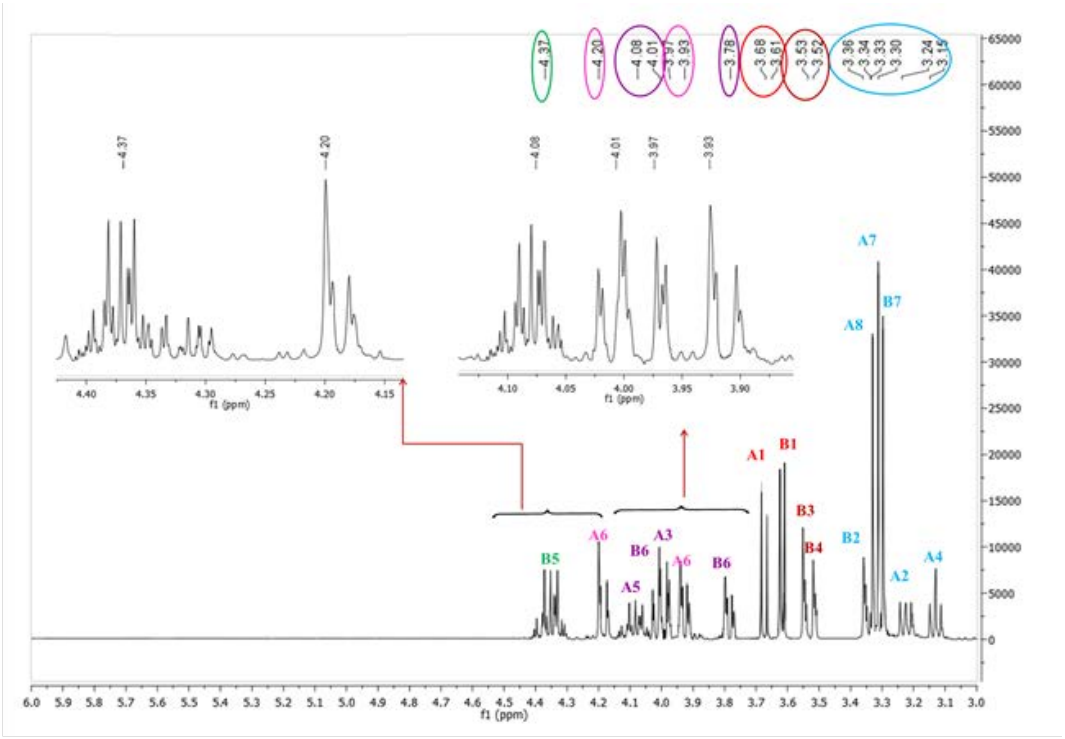

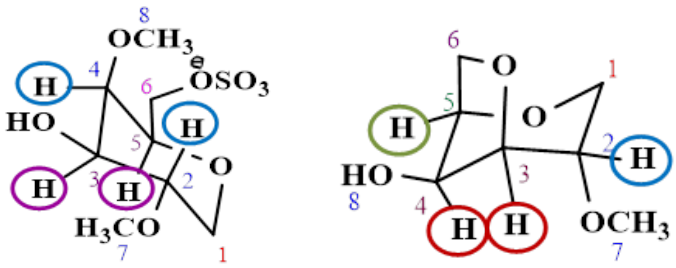

Monomer unit A **Monomer unit B**

Figure 6.19.: ^{1}H NMR spectrum of methylated polysaccharide analogue after hydrolysis

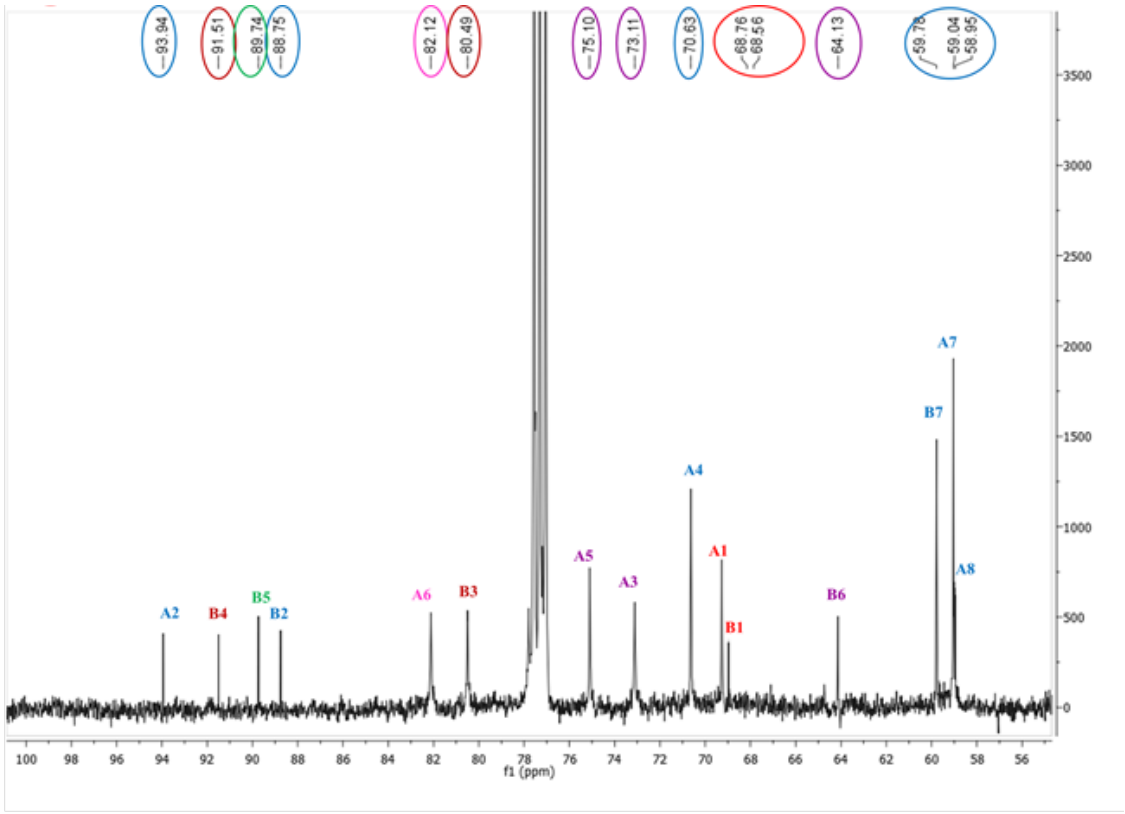

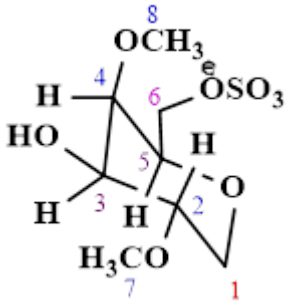

Monomer unit A

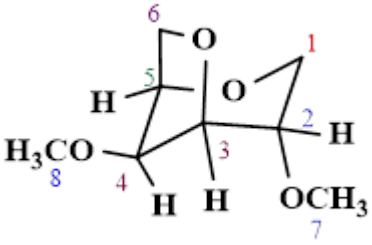

Monomer unit B

Figure 6.20.: ^{13}C NMR spectrum of methylated polysaccharide analogue after hydrolysis

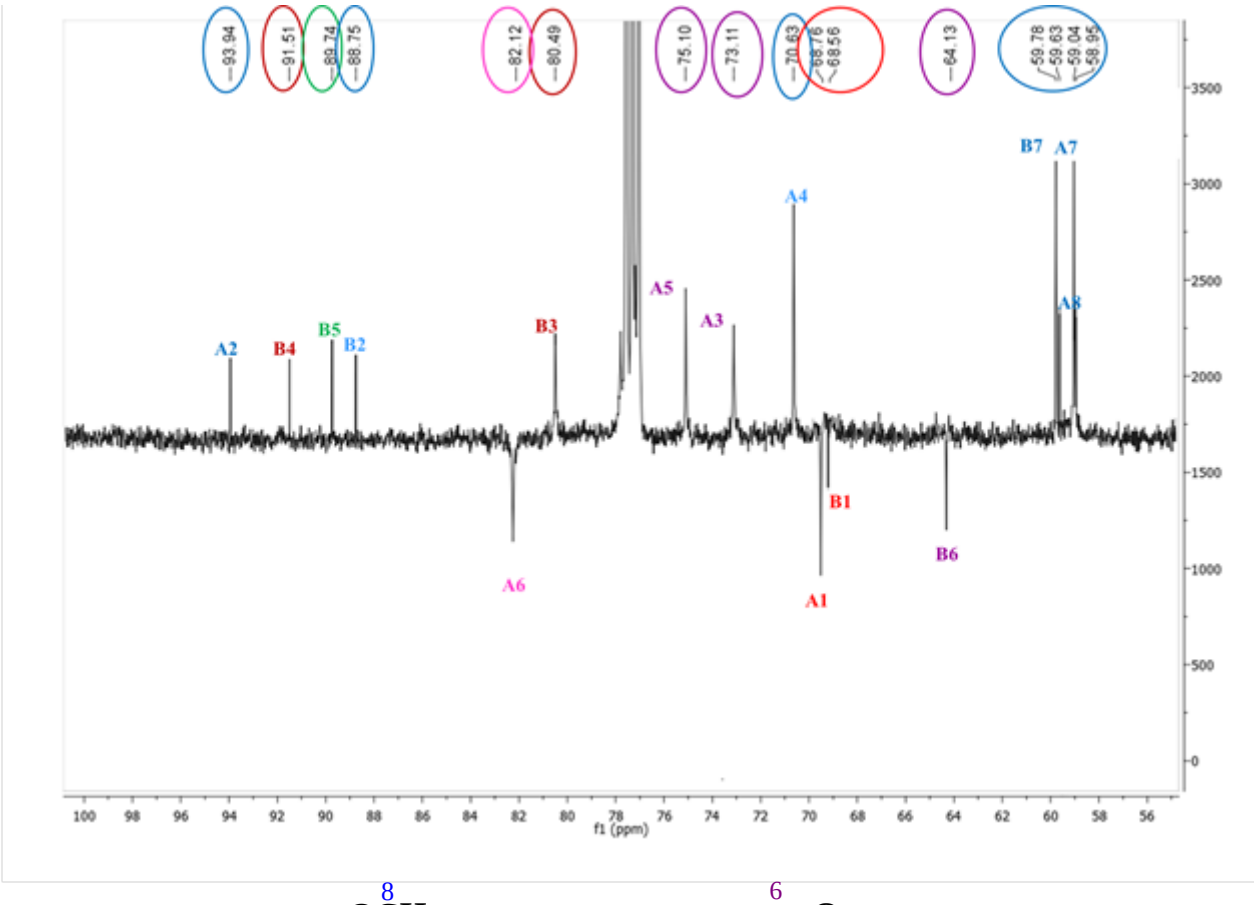

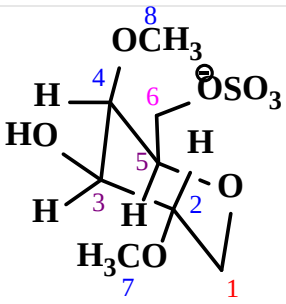

Monomer unit A

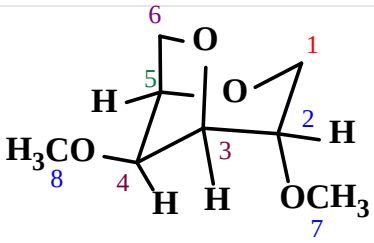

Monomer unit B

Figure 6.21.: DEPT[135] spectrum of methylated polysaccharide analogue after hydrolysis

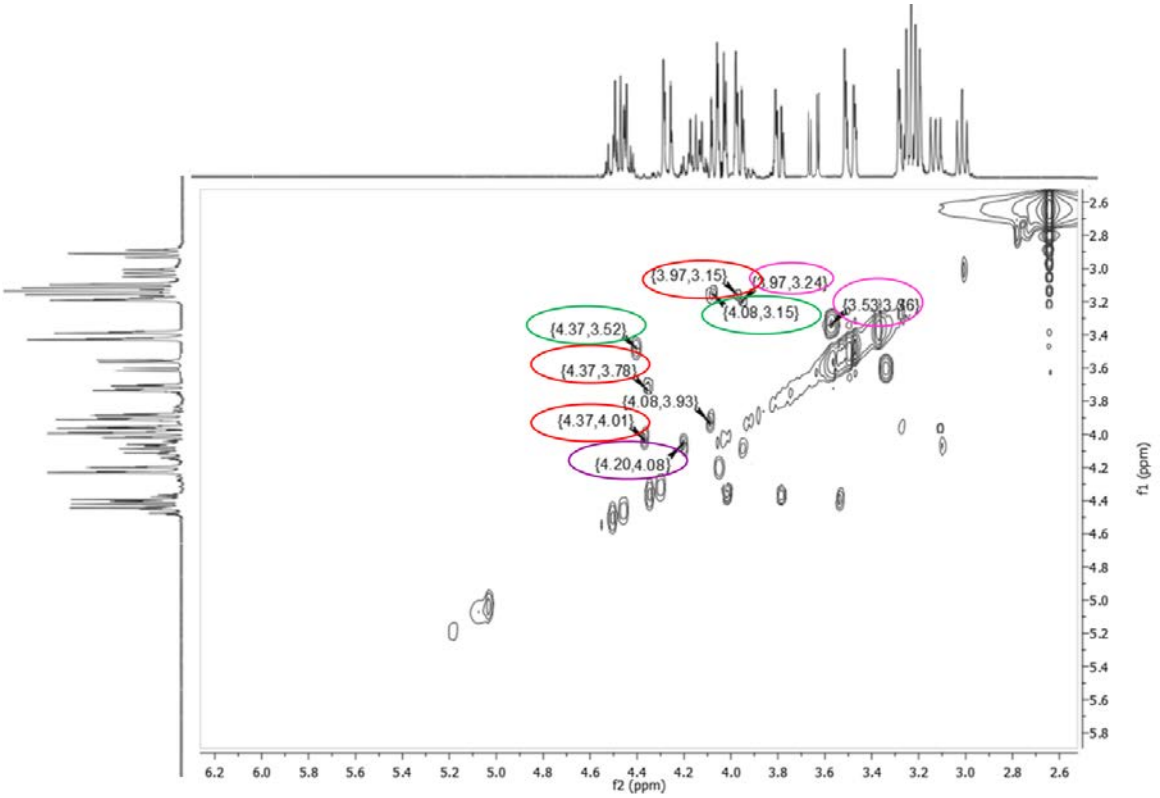

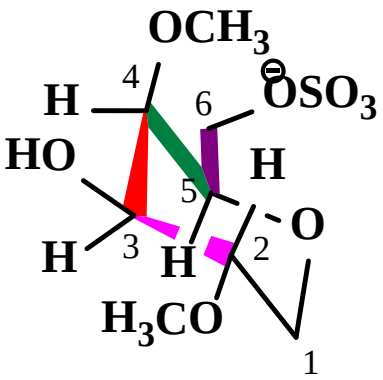

Monomer unit A

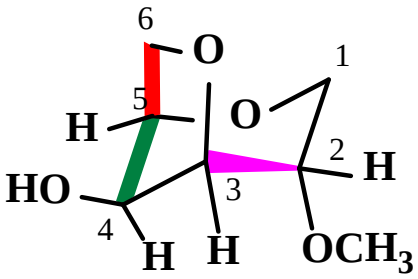

Monomer unit B

Figure 6.22.: ^{1}H-^{1}H COSY NMR spectrum of methylated polysaccharide analogue after hydrolysis

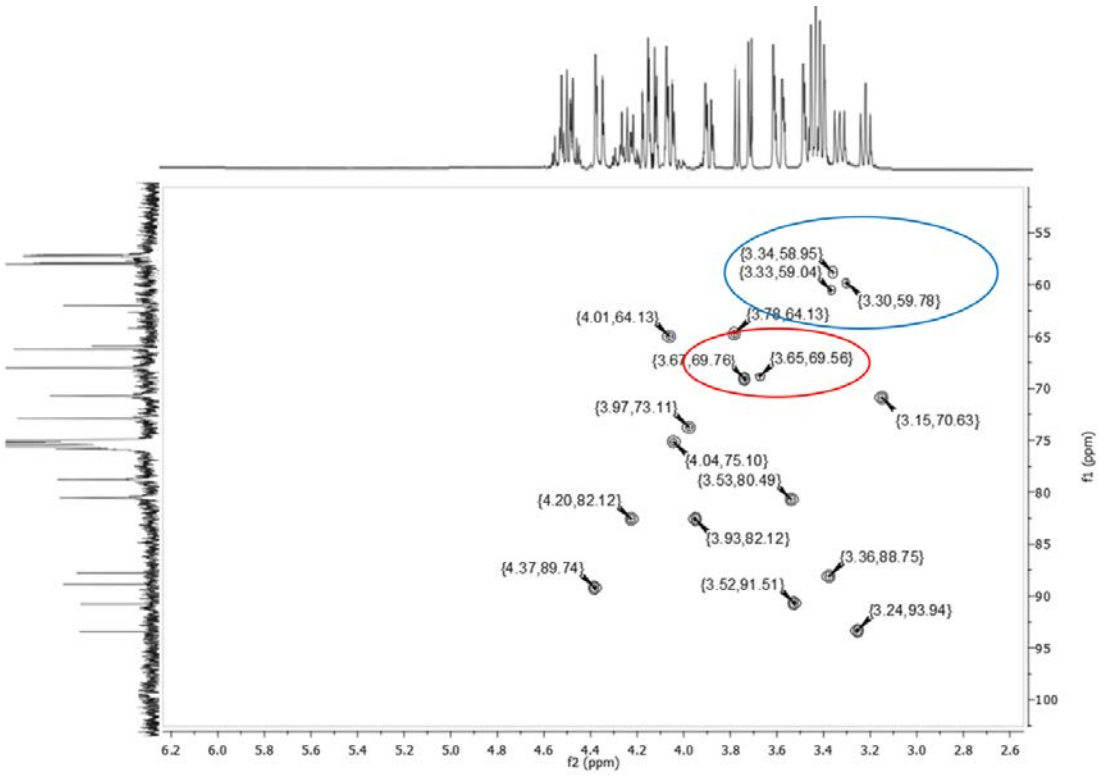

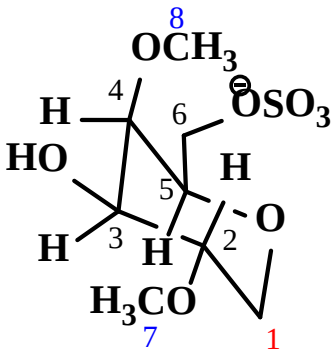

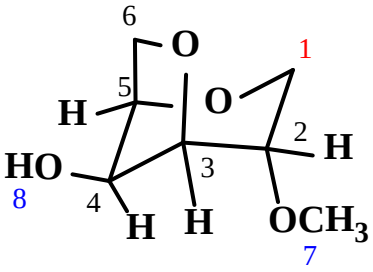

Monomer unit A **Monomer unit B**

Figure 6.23.: HSQC spectrum of methylated polysaccharide analogue after hydrolysis

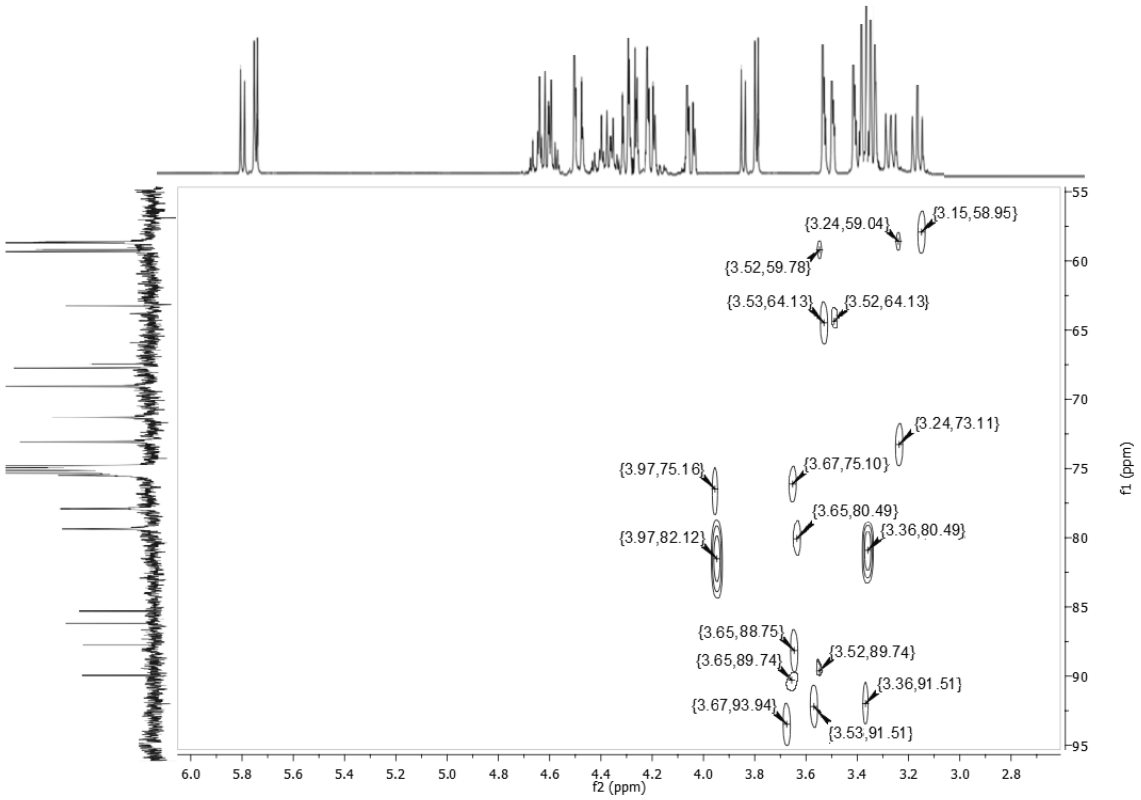

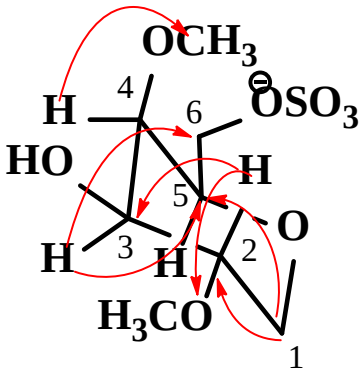

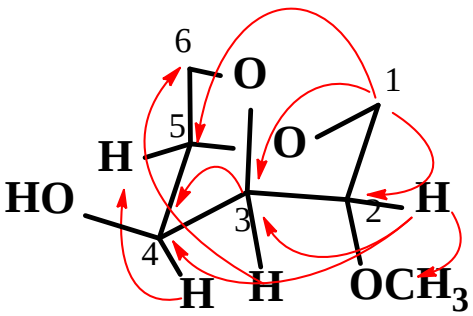

Monomer unit A **Monomer unit B**

Figure 6.24.: HMBC spectrum of methylated polysaccharide analogue after hydrolysis

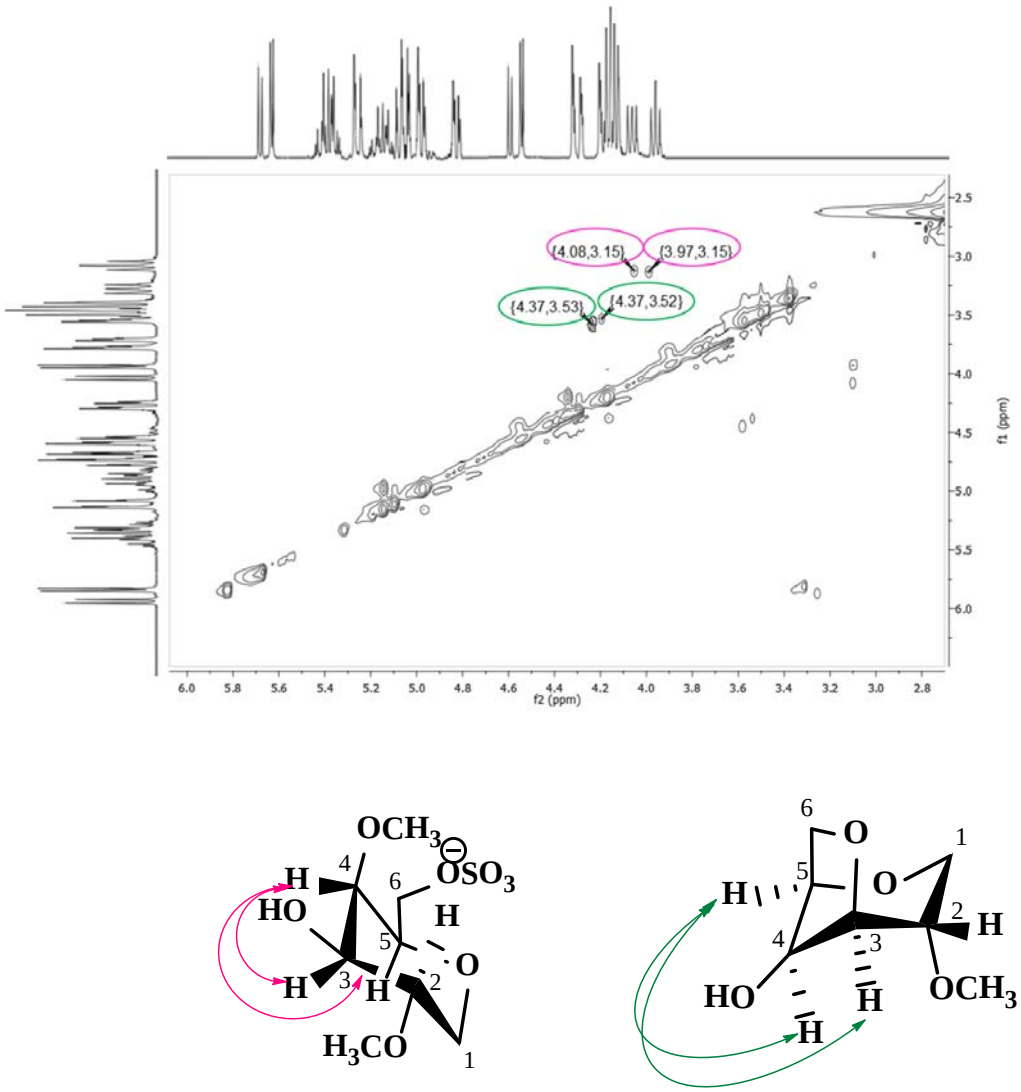

Figure 6.25.: NOESY spectrum of methylated polysaccharide analogue after hydrolysis

Table 6.6.: NMR spectroscopic data[a] of polysaccharide …(1→3)-*O*-6-sulfonato-β-D-galactopyranosyl-(1→4)-3,6-anhydro-α-D-galactopyranose…isolated from the red seaweed *G. salicornia*

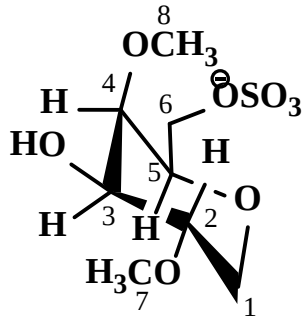

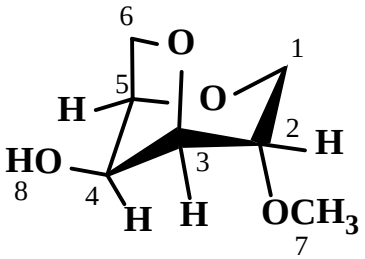

Type of C	C. No.	^{13}C NMR	^{1}H NMR	COSY	HMBC	Type of C	C. No.	^{13}C NMR	^{1}H NMR	COSY	HMBC
Unit A						**Unit B**					
CH_2	A1	69.76	3.67	-	C-A2,A5	CH_2	B1	69.56	3.65	-	C-B2,B3,B5
CH	A2	93.94	3.24	H-A3	C-A7,A3	CH	B2	88.75	3.36	H-B3	C-B3,B7
CH	A3	73.11	3.97	H-A4	C-A5,A6	CH	B3	80.49	3.53	-	C-B6
CH	A4	70.63	3.15	H-A5	C-A8	CH	B4	91.51	3.52	H-B5	C-B5,B6
CH	A5	75.10	4.08	H-A6	-	CH	B5	89.74	4.37	H-B6	-
CH_2	A6	82.12	4.20,3.93	-	-	CH_2	B6	64.13	4.01,3.78	-	-
CH_3	A7	59.04	3.33	-	-	CH_3	B7	59.78	3.30	-	-
CH_3	A8	58.95	3.34	-	-	-	-	-	-	-	-

[a]NMR spectra were recorded using a Bruker AVANCE III 500 MHz (AV 500) spectrometer (Bruker, Karlsruhe, Germany) in MeOH as aprotic solvent at ambient temperature with TMS as the internal standard (δ 0 ppm).

[b]Values in ppm, multiplicity were indicated in parentheses. Multiplicities were allocated by ^{135}DEPT NMR spectrum. The assignments were made with the aid of the COSY, HSQC, HMBC and NOESY experiments.

Furthermore, the COSY correlations H_2 (δ3.24)/H_3 (δ3.97)/H_4 (δ3.15)/H_5 (δ4.08)/H_6 (δ4.20/3.93) framed the fragment as the extension of C_1-C_2; -CH_2-CH-(OCH_3)-CH(O-)-CH(O-)-CH(O-)-CH_2- in (MeA). These fragments were further confirmed by the HMBCs correlations from δ3.24 to δ73.11; δ3.97 to δ75.10 and δ82.12. Moreover, the deshielded signal δ3.97 (H_3) was appeared as triplet at C_3, and which did not show any branching like C_2. Therefore, it was assigned as -CH(OH), while deshielded signal was apparent at δ3.15 (H_4) exhibited an intense HMBC with δ58.95, indicating the presence of methoxyl substitution, CH(-OCH_3). Similarly, the signal at δ4.08 (H_5) was appeared as multiplet, which has connected to a CH_2 functionality via a COSY; H_5 (δ4.08)/H_6(δ4.20/3.93), and they exhibited higher chemical shift due to the presence of oxygen functionality as the part of ring. Finally, the signals at δ4.20 and δ3.93 indicated the presence of sulfated functionality, and these intense deshielded signals were attached to CH_2 group. These results were corroborated by the deshielded signals beyond δ4.00 observed for CH_2 functionalities attached sulfate group in the carrageenan-type of polysaccharides, which were isolated from the red algae (Stortz, et al., 1994). From these results, in MeGal*p*, the positions C_1 was found to be protonated, and C_3 was attached with OH group, thus indicating the presence of (1⋯→3) linkage. Therefore, the methylated Gal*p* was characterized as *O*-6-sulfonato-2,4-dimethyl-β-D-Gal*p* or *O*-6S-2,4-Me_2-β-D-Gal*p* with linkage pattern(1⋯→3).

Similarly, the COSY correlations H_2(δ3.36)/H_3(δ3.53) and H_4(δ3.52)/H_5(δ4.37)/H_6(δ4.01/3.78) framed the fragment as the extension of C_1-C_2; -CH_2-CH-(OCH_3)-CH(O-)-CH(O-)-CH(O-)-CH_2- in (MeB). These fragments were further confirmed by HMBCs correlations from δ3.36 to δ80.49; δ3.52 to δ89.64 and δ64.13. Furthermore, the HMBC signals from δ3.53 to δ91.51 and δ3.52 to δ64.13 along with COSYs at H_4(δ3.52)/H_5(δ4.37)/H_6(δ4.01/3.78) appropriately deduced the presence of furanose ring in MeAnGal*p*. Besides, the deshielded signal δ3.53 (H_3) was appeared as triplet, and did not show any substitution, whereas their higher chemical shift values was due to the presence of directly attached oxygen of furanose ring in MeAnGal*p*. The deshielded signal at δ3.52 (H_4) was connected to C_3 and C_5 via the HMBC correlation H_3 (δ3.53)/C_4(δ91.51) and COSY correlation H_4(δ3.52)/H_5(δ4.37). The signals δ4.37 (H_5), and 4.01/3.78 (H_6) appeared with high chemical shift value due to the connection with oxygen moiety as the part of ring. Thus, in MeAnGal*p*, the positions C_1 and C_4 appeared with lack of methoxy substitutions and C_4 was found to be consisted of OH group, indicating the presence of (1⋯→4) linkage. The methylated AnGal*p* was characterized as 2-methyl-α-D-AnGal*p* or *O*-6S-2-Me-α-D-AnGal*p*. The relative configurations obtained for methylated polysaccharide was depicted in Figure 6.25.

These data confirmed that the sequence of linkage pattern (1⋯→3) and (1→⋯4) in between the alternatively repeating monosaccharides of MeGal*p* and MeAnGal*p*. Therefore, the

polysaccharide was named as (1⋯→3)-*O*-6S-2-Me-β-D-Gal*p*-(1→4)-2-Me-α-D-3,6-AnGal*p*(1→⋯).

6.3.3.5 Structural interpretation of the polysaccharide by acetylation

The reductive cleavage (acetylation) is found as one of the important methods to characterize the linkage pattern and functionalities of the polysaccharide. This includes a series of chemical reactions, such as methylation, reduction and acetylation. Thus, the linkage pattern in polysaccharide was ensured by the incidence of acetyl group on the cleaved glycosidic end of polysaccharide. Like earlier method, initially the polysaccharide was subjected for methylation followed by reduction yielded two methylated sugar residues after the cleavage of polysaccharide. Finally, the free glycosidic ends were substituted with acetyl functionalities. This partially methylated and acetylated polysaccharide were characterized by extensive 1D and 2D NMR spectroscopic analysis (Figure 6.26-6.32, Table 6.7). The proton NMR spectrum of acetylated GSP-2 was depicted in Figure 6.17. As described in the previous section, the acetylated sugar residues were designated as (AcA or AcGal*p*) and (AcB or AcAnGal*p*).

Table 6.7.: NMR spectroscopic data[a] of polygalactan …(1→3)-*O*-6-sulfonato-β-D-galactopyranosyl-(1→4)-3,6-anhydro-α-D-galactopyranose…from the red seaweed *G. salicornia*

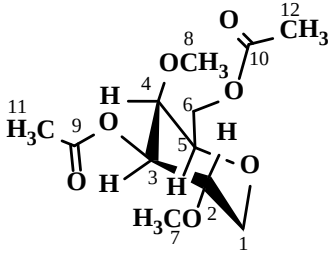

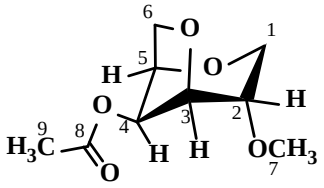

Type of C	C. No.	^{13}C NMR	^{1}H NMR	COSY	HMBC	Type of C	C. No.	^{13}C NMR	^{1}H NMR	COSY	HMBC
Unit A						**Unit B**					
CH_2	A1	69.80	3.72	-	-	CH_2	B1	67.27	3.71	H-2B	-
CH	A2	81.60	3.53	H-3A	C-1A,7A,3A	CH	B2	82.34	3.24	H-3B	C-7B,4B
CH	A3	72.40	4.90	H-4A	C-8A,4A	CH	B3	91.40	4.78	-	C-4B,6B
CH	A4	62.43	3.52	H-5A	C-10A, 6A	CH	B4	82.24	4.67	H-5B	C-8B,6B
CH	A5	81.58	4.54	H-6A	C-1A	CH	B5	88.40	3.78	H-6B	C-1B
CH_2	A6	86.24	4.37,4.08	-	C-10A	CH_2	B6	62.56	4.05,3.75	-	-
O-CH_3	A7	59.76	3.36	-	-	O-CH_3	B7	59.07	3.41	-	-
O-CH3	A8	59.55	3.34	-	-	C	B8	174.27	-	-	-
C	A9	175.24	-	-	-	CH_3	B9	20.90	2.27	-	C-8B
C	A10	174.49	-	-	-	-	-	-	-	-	-
(CO)CH3	A11	22.64	2.37	-	C-9A	-	-	-	-	-	-
(CO)CH3	A12	22.18	2.31	-	C-10A	-	-	-	-	-	-

[a]NMR spectra were recorded using a Bruker AVANCE III 500 MHz (AV 500) spectrometer (Bruker, Karlsruhe, Germany) in MeOH as aprotic solvent at ambient temperature with TMS as the internal standard (δ 0 ppm).

[b]Values in ppm, multiplicity and coupling constants (*J*= Hz) were indicated in parentheses. Multiplicities were allocated by [135]DEPT NMR spectrum. The assignments were made with the aid of the COSY, HSQC, HMBC and NOESY experiments.

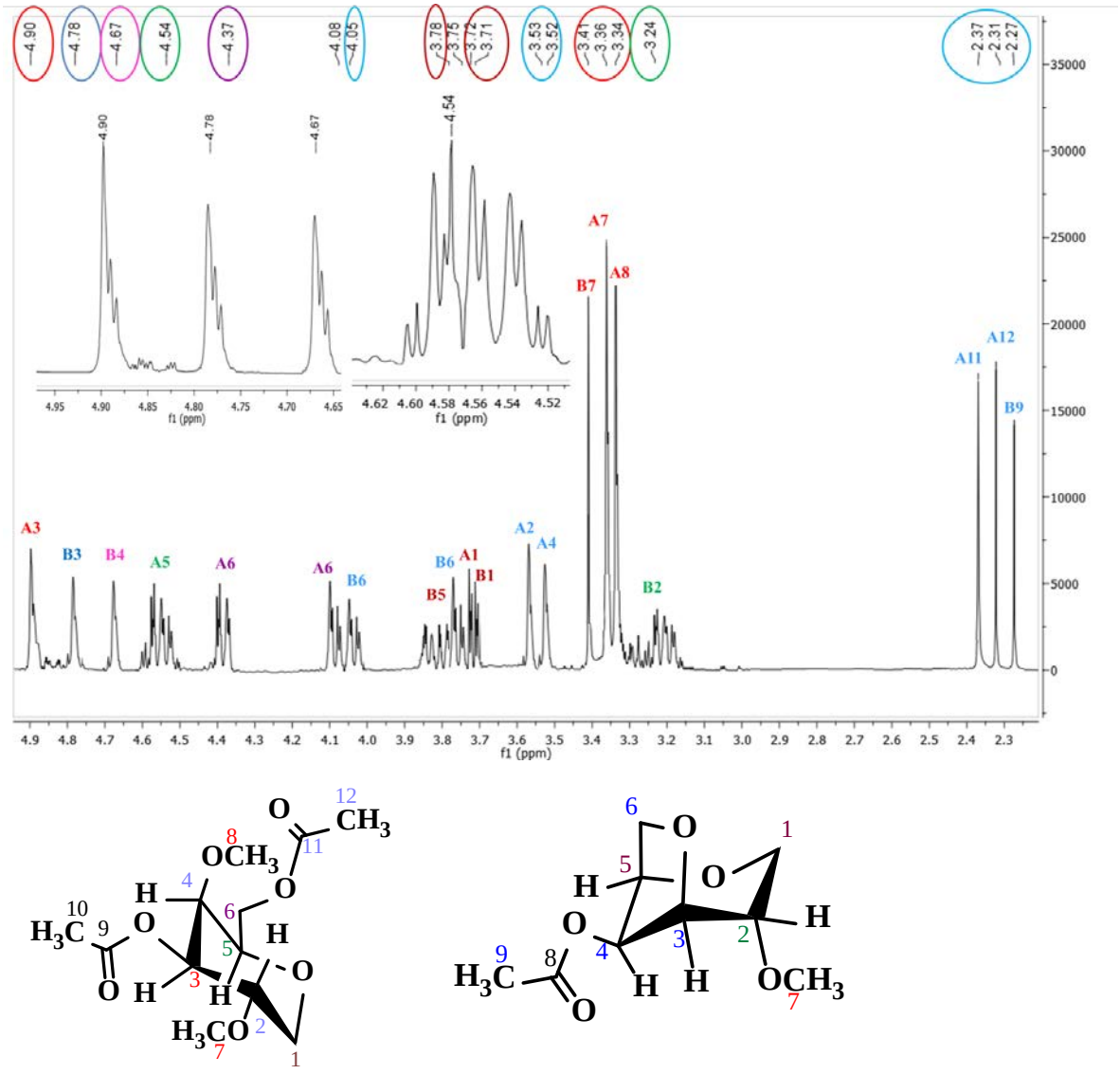

Figure 6.26.: ^{1}H NMR spectrum of the acetylated polysaccharide analogue

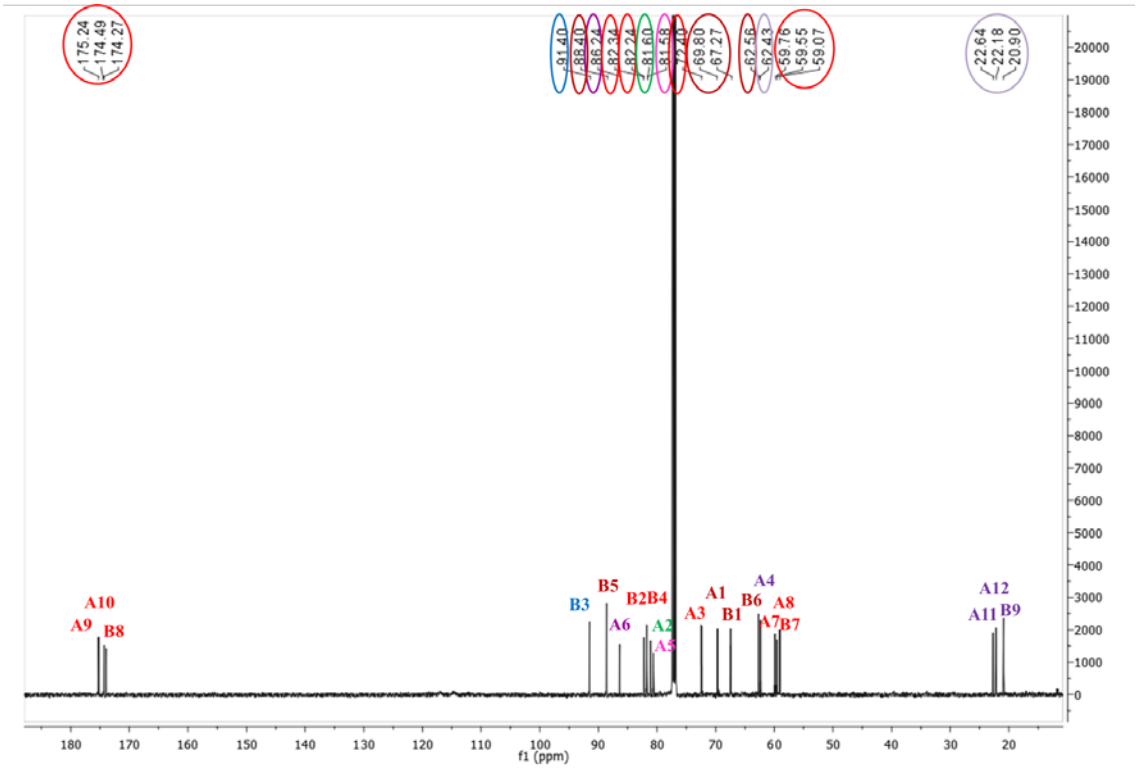

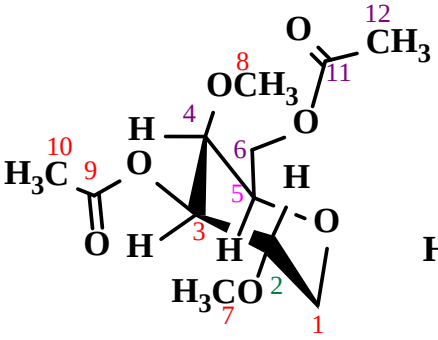

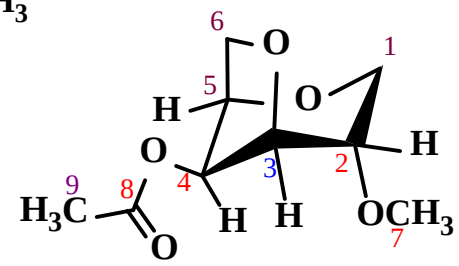

Monomer unit A **Monomer unit B**

Figure 6.27.: ^{13}C NMR spectrum of the acetylated polysaccharide analogue

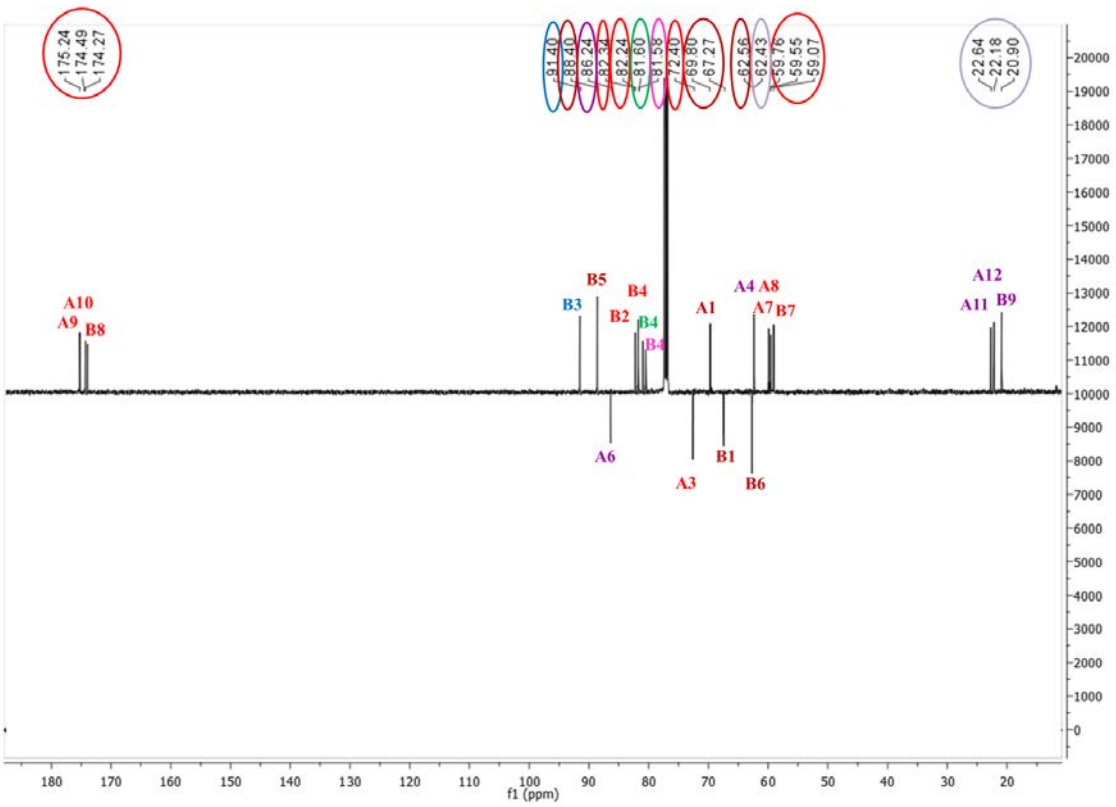

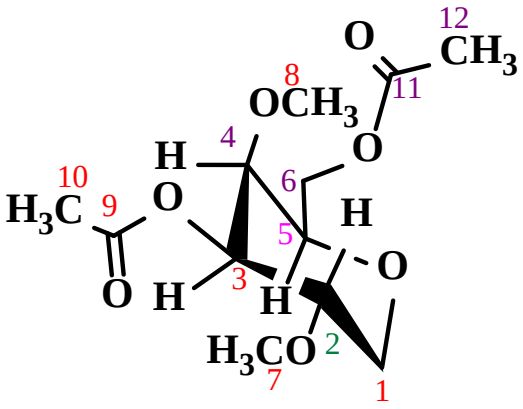

Monomer unit A

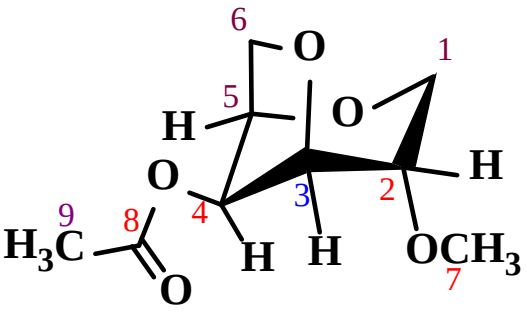

Monomer unit B

Figure 6.28. DEPT[135] spectrum of the acetylated polysaccharide analogue

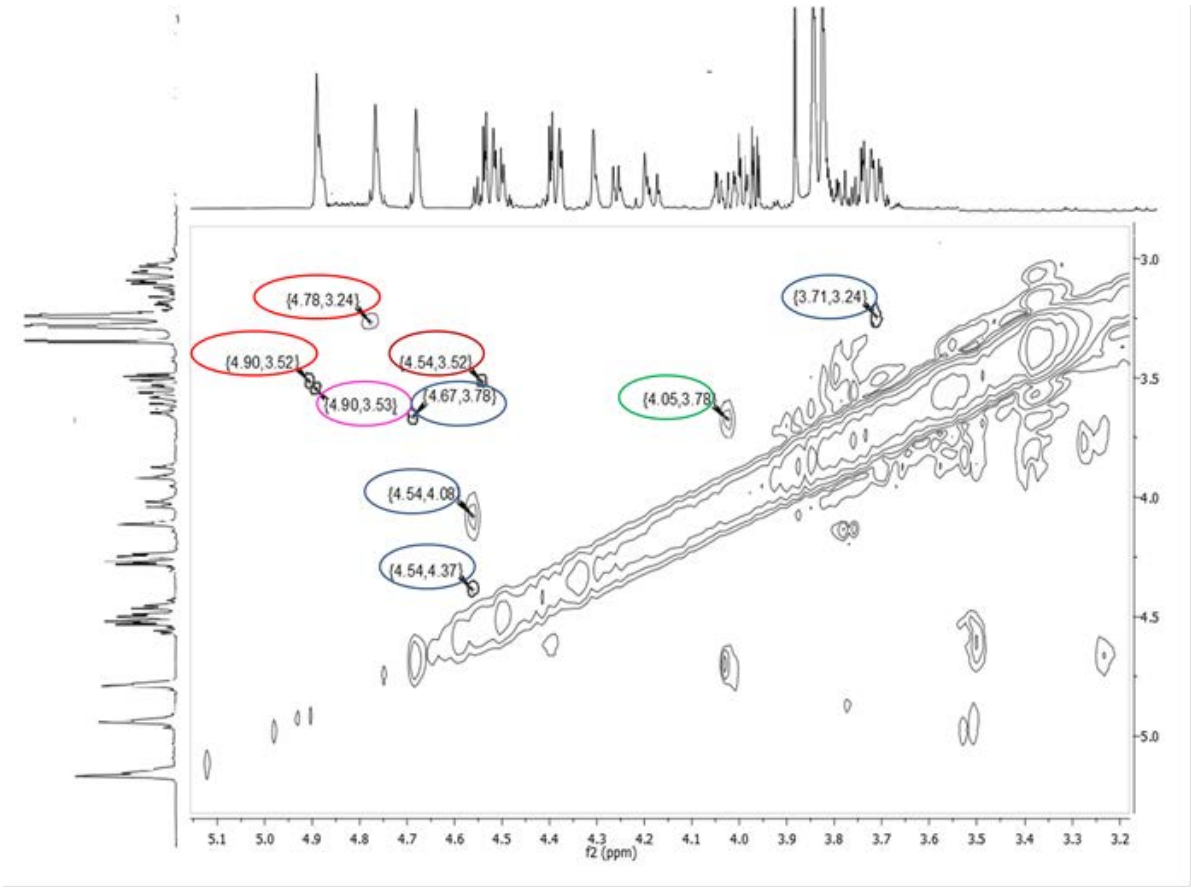

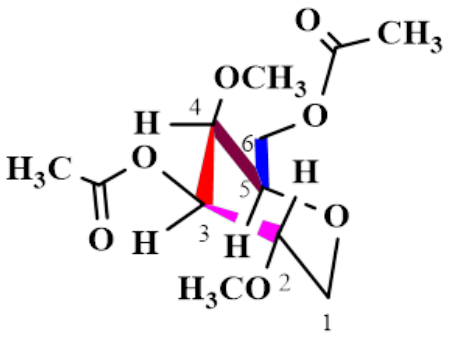

Monomer unit A

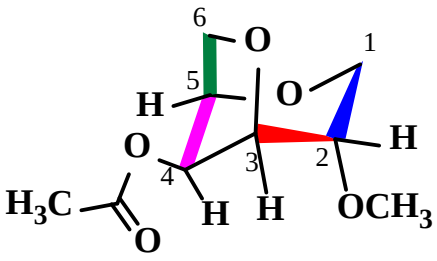

Monomer unit B

Figure 6.29.: COSY spectrum of the methylated polysaccharide analogue

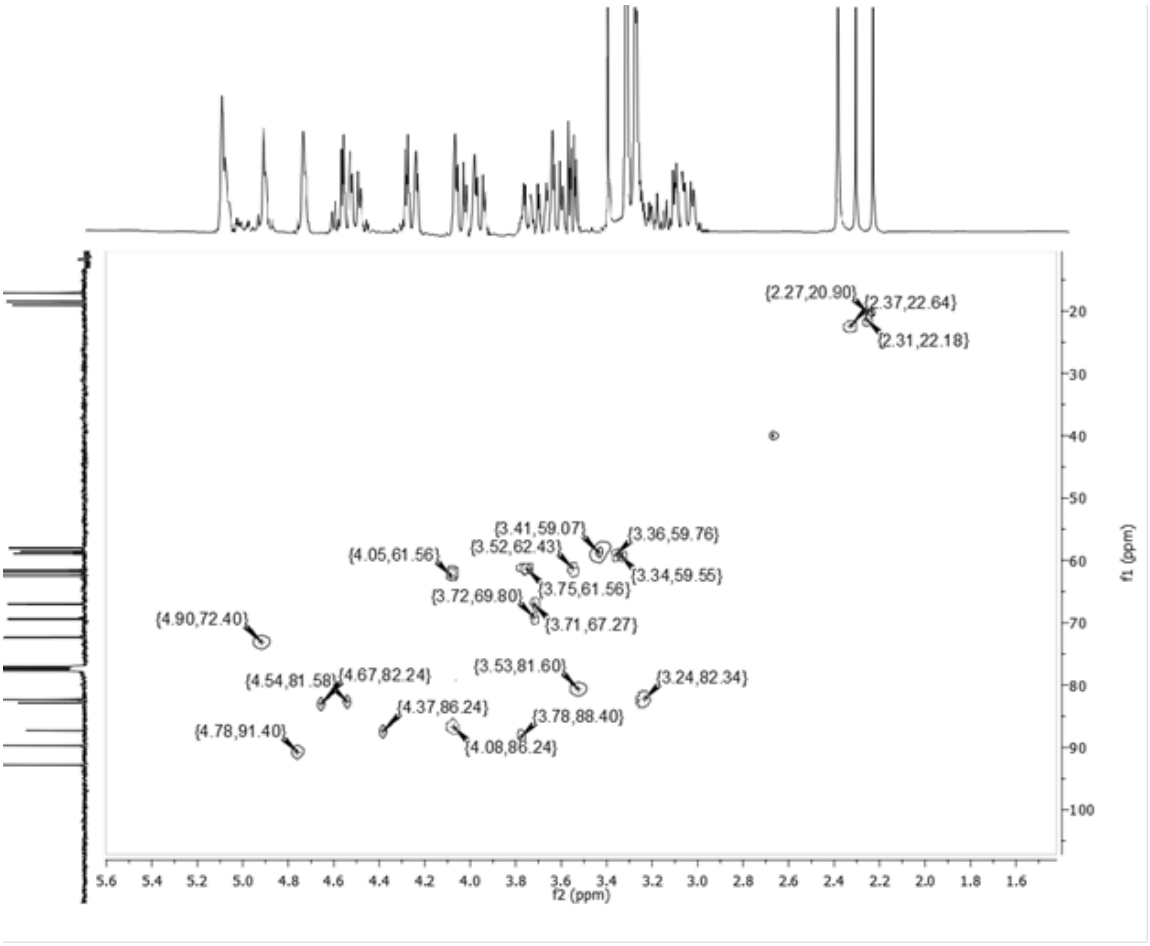

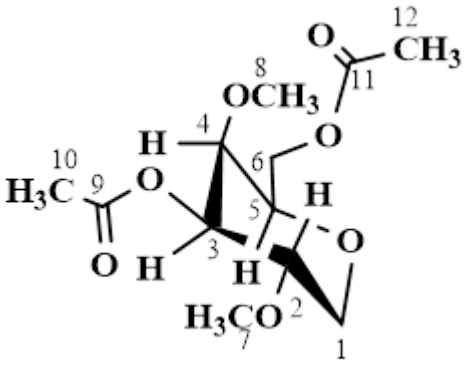

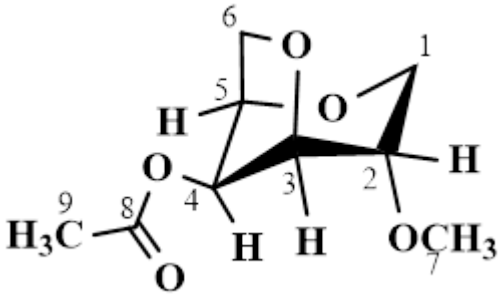

Monomer unit A **Monomer unit B**

Figure 6.30.: HSQC spectrum of the methylated polysaccharide analogue

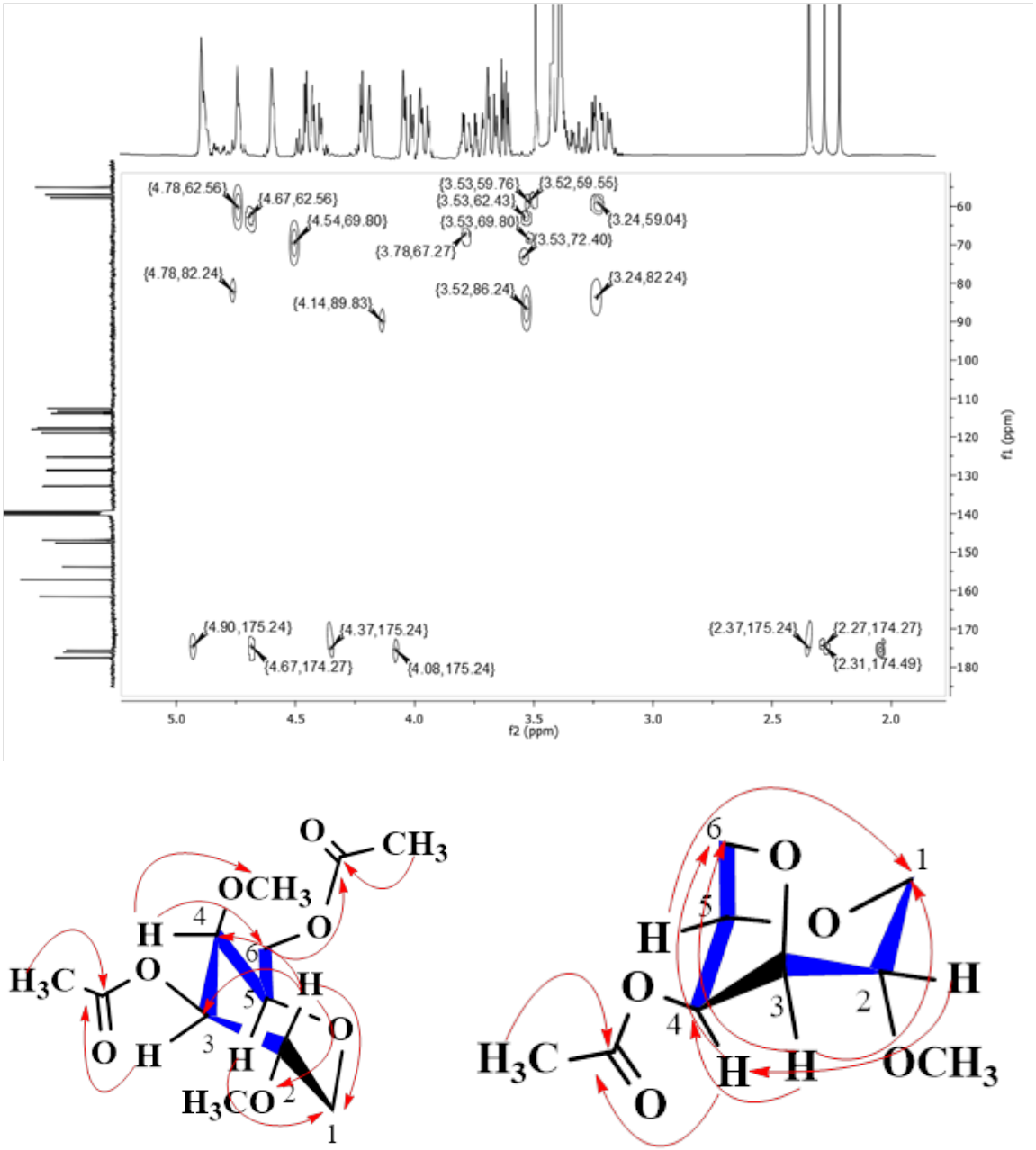

Figure 6.31.: HMBC spectrum of the methylated polysaccharide analogue

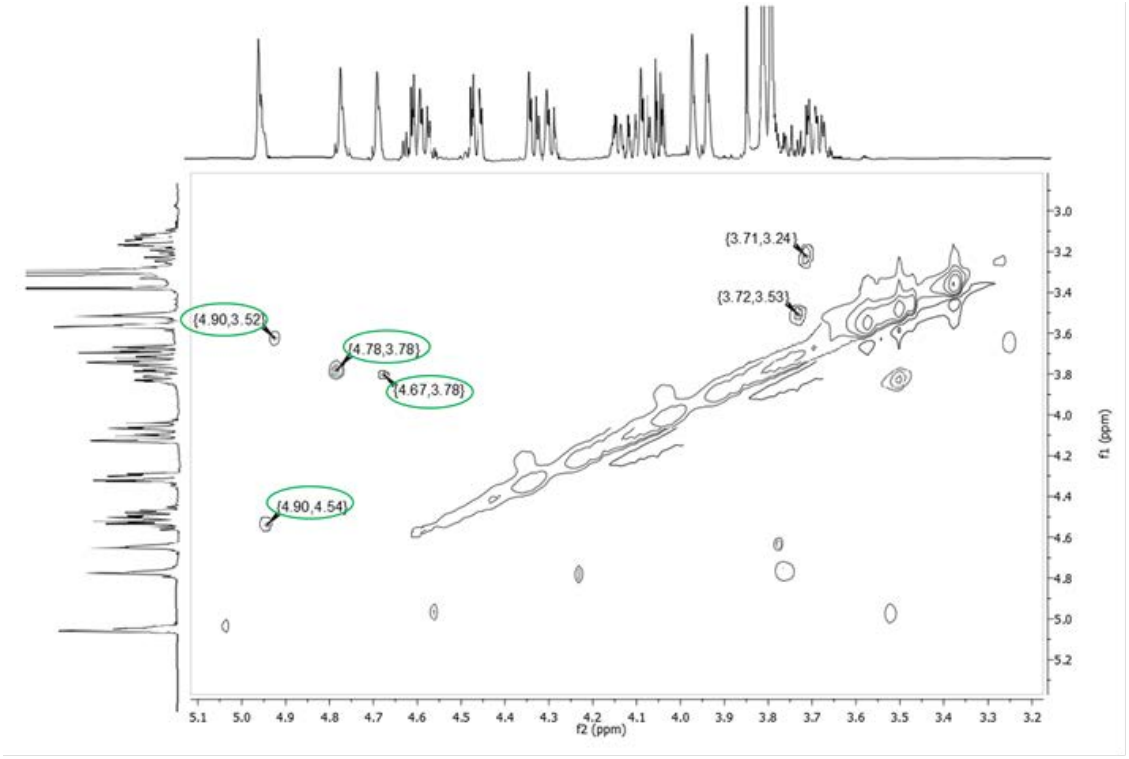

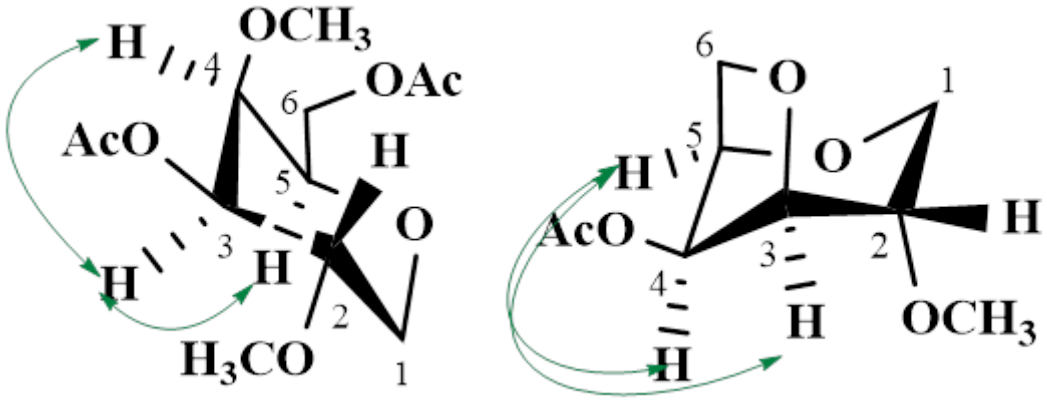

Monomer unit A **Monomer unit B**

Figure 6.32.: NOESY spectrum of the methylated polysaccharide analogue

Three major signals were discernable in the proton NMR in between the region of δ2.0-2.5 and δ3.3-3.5, representing the partially methylated and acetylated sugar residues in the studied polysaccharide, GSP-2. The doublet appeared at δ3.72 and δ3.71 (with same integral) depicted the protonated anomeric region in polysaccharide after cleavage of the glycosidic linkage. The 1D NMR along with HSQC characterized the proton and carbon signals in the acetylated polysaccharide, and the absence of anomeric region in the proton NMR ensured the acetylation of glycosidic residues in GSP-2. Thus, the signals at δ3.72 (δ69.80; CH_2) and δ3.71 (δ67.27; CH_2)

were assigned as C_1 positions of AcGal*p* and AcAnGal*p*, respectively. The signal at δ3.72 (δ69.80; CH_2) was found to exhibit HMBC correlation with δ81.60 (δ3.53), which framed the fragment of -CH_2-CH-(O-); C_1-C_2. The proton signal at δ3.53 displayed HMBC correlation with the carbon at δ59.76 (δ3.36), representing the methoxyl group attached to the C_2 position; -CH-(O-CH_3). The further fragments in the AcGal*p* were framed by the COSY correlation, such as H_2(δ3.53)/H_3(δ4.90)/H_4(δ3.52)/H_5(δ4.54)/H_6(δ4.37/4.08), assigning the fragment of -CH_2-CH-(OCH_3)-CH(O-)-CH(O-)-CH(O-)-CH_2-; C_1-C_6. These fragments were further confirmed by the HMBC correlations, H_2 (δ3.53) to C_3 (δ72.40); H_3 (δ4.90) to C_4 (δ62.43); H_4 (δ3.52) to C_6 (δ86.24), H_5 (δ4.54) to C_1 (δ69.80). The -CH- at δ4.90 (H_3) displayed HMBC correlation with δ175.24, demonstrated the (-C=O) substitution at C_3. At the same time, the HMBC correlation in between δ2.37 and δ175.24 assigned the connection of methyl (-CH_3) to (-C=O) functionality. These correlations represented the substitution of acetyl functionality at C_3; -CH-((-C=O)-CH_3). The -CH- functionality at δ3.52 (H_4) showed the HMBC with δ59.55, indicating the presence of methoxyl functionality at C_4; -CH-(OCH_3). The highly deshielded proton signal at δ4.54 proximal to the oxygen moiety of the pyranose ring with multiplet was found to be correlated with -CH_2- functionality at C_6 via the COSY correlation, H_5(δ4.54)/H_6(δ4.37/4.08). Finally, the HMBC correlations from the signals at δ4.37, δ4.08 and δ2.31 to the δ174.49, revealed the acetyl substitution at C_6. The observations from the acetylation along the methylation (in section 3.3.3) apparently revealed that the sulfated functionality at C_6 was replaced by an acetyl group. Thus, in AcGal*p*, C_2 and C_4 positions were substituted with methyl entities and C_3 and C_6 positions were substituted with the acetyl moieties. Therefore, in AcGal*p*, the positions at C_1 and C_3 confirmed the linkage pattern of (1⋯→3). The partially methylated and acetylated AcGal*p* were characterized as 3,6-diacetyl-2,4-dimethyl-β-D-Gal*p* and 3,6-Ac_2-2,4-Me_2-β-D-Gal*p*, respectively.

Further, the signal at δ3.71 (δ67.27; CH_2) was found to exhibit COSY correlation with δ3.24 (δ82.34), which framed the fragment of -CH_2-CH-(O-); C_1-C_2. The signal at δ3.24 displayed HMBC correlation with δ59.07 (δ3.41), indicating the methoxyl group attached at the C_2 position; -CH-(O-CH_3). Additional fragments in the AcAnGal*p* was framed by the COSY correlations, at H_2(δ3.24)/H_3(δ4.78) and H_4(δ4.67)/H_5(δ3.78)/H_6(δ4.05/3.75) along with HMBC correlations, H_2 (δ3.24) to C_3 (δ82.34); H_3 (δ4.78) to C_4 (δ82.24); H_4 (δ4.67) to C_6 (δ62.56), H_5 (δ3.78) to C_1 (δ67.27), indicating the presence of the fragment -CH_2-CH-(OCH_3)-CH(O-)-CH(O-)-CH(O-)-CH_2-; C_1-C_6. The functionality at δ4.67 (H_4) showed HMBC correlation with δ174.27, indicating the attachment of (-C=O) group at C_4. At the same time, the proton signal at δ2.27 displayed the HMBC with δ174.27. These HMBC correlations together demonstrated the presence of the acetyl functionality at C_4; -CH-((-C=O)-CH_3). The relative configurations obtained for partially methylated and acetylated polysaccharide were depicted in Figure 6.32.

Thus, in AcAnGal*p*, C_2 and C_4 positions were substituted with methyl and acetyl entities, respectively. The C_1 was found to be protonated like AcGal*p*. Therefore, the linkage pattern was confirmed as (1⁻⁻→4). The partially methylated and acetylated AcAnGal*p* was characterized as 4-acetyl-2-methyl-α-D-AnGal*p* or 4-Ac-2-Me-α-D-AnGal*p*. These results together confirmed that the following sequel of linkage pattern of monosaccharide residues were apparent in GSP-2 derived from *G. salicornia*, and were interpreted as (1⁻⁻→3)-*O*-6-sulfonato-2-methyl-β-D-Galactopyranose-(1→4)-2-methyl-α-D-3,6-Anhydrogalactopyranose-(1→⁻⁻) and (1⁻⁻→3)-*O*-6S-2-Me-β-D-Gal*p*-(1→4)-2-Me-α-D-3,6-AnGal*p*(1→⁻⁻) or [2-Me-G6S-2-MeAnG].

6.3.3.6 Linkage pattern analysis of polysaccharide by reductive cleavage method

The modern technique of reductive cleavage was introduced for the determination of linkage pattern and position of rings in polysaccharide. This method forms the basis of a series of chemical reactions, such as methylation, reduction and acetylation analysis; wherein the polysaccharides on partial methylation followed by reduction and acetylation formed partially methylated and acetylated (PMA) sugar residues. These resultant PMA derivatives were further characterized by GC-MS. The PMA-D-hexitols and PMA-3,6-anhydro-D-hexitols having galactose configuration, namely, 3,6-diacetyl-2,4-dimethyl-β-D-Gal*p* and 4-acetyl-2-methyl-α-D-AnGal*p*, respectively, were deduced. The spectrum was found to exhibit signals corresponding to these PMA-D-hexitols and PMA-3,6-anhydro-D-hexitols at *m/z* 274.1 and 200.1, respectively, thereby indicating the molecular weight of these components. Appearance of the peaks in the spectrum revealed differences in the positional-isomers in terms of the presence of some ions, such as $CH_3C{\equiv}O^+$ (*m/z* 43) and their intensity related to the base peak. The signals of some ions, such as *m/z* 243.1, 211.1, 152.0 were detected in the spectrum due to the eliminations of methanol/O-methyl and acetic acid/O-acetyl, wherein those peaks were arosed due to the cleavage of C_2, C_3, C_4 and C_6 from D-hexitols. Similarly, the signals of certain ions, like *m/z* 169.1and 109.0, were ascertained in the spectrum due to the eliminations of methanol/O-methyl and acetic acid/O-acetyl, wherein those peaks arosed due to the cleavage of C_2 and C_3 from anhydro-D-hexitols. The base peak was appeared at *m/z* 94.0.

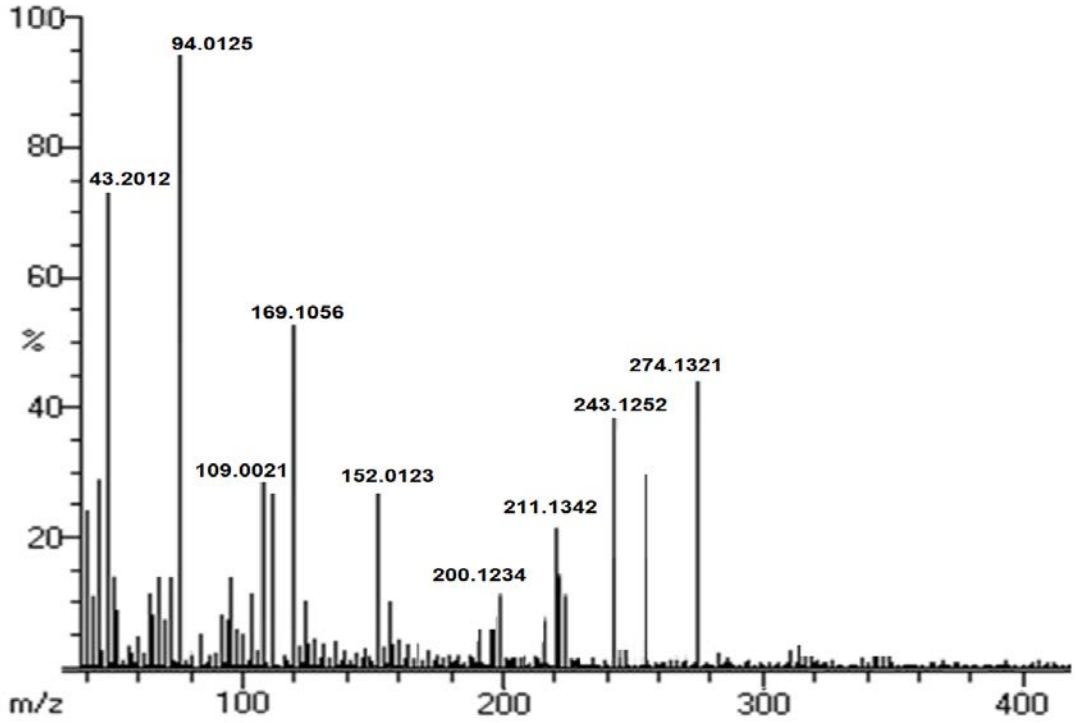

Figure 6.33.: GCMS spectrum of the polysaccharide analogue

6.3.3.6 Structural interpretation of polysaccharide-nano composite (P-AgNPs)

The different concentrations of polysaccharide solutions (0.1, 0.15, 0.2, 0.25, and 0.3 % in a, b, c, d, and e, respectively) were agitated with $AgNO_3$ for the nanoparticle formation. The yields obtained for different concentrations were found to be 0.042 g, 0.063 g, 0.85 g, 0.120 g and 0.158 g, respectively. These were further confirmed by the surface plasmon resonance (SPR) bands observed from the UV chromatogram. These results revealed that the formation of numbers of AgNPs increased with the increasing concentration of polysaccharide. Therefore, the solution of 0.3 % with higher yield was selected for the further analysis and characterization of silver nano composite (P-AgNPC) of polysaccharide.

6.3.3.7 Structural interpretation of polysaccharide-nano composite (P-AgNPCs) by UV

UV-visible spectroscopic data was used to determine the formation of silver nanocomposite (AgNPC) by observing the SPR bands. The absorption spectrum of nano particles (NP_S) depends on their shape, size, and distribution. However, characteristic SPR bands of Ag-NPs were identified around in the region of 402 to 420 nm (Fig. S27), which indicates the formation of Ag-NPs. As shown in Figure 6.34, when the concentrations of polysaccharide in solution increased (0.1, 0.15, 0.2, 0.25, and 0.3 % in a, b, c, d, and e, respectively), the intensity of the SPR peak also regularly increased. The increase in the absorbance was indicative the increasing concentration of

Ag-NPC. Furthermore, with an increase in the concentrations of polysaccharide, the absorbance also increased and shifted to the lower wavelength at 402 nm to blue-shift, which was referred to a decrease in the particle size. Based on Mie's theory (Elsupikhe et al, 2015, 2016), the nanoparticles with different sizes should demonstrate different optical properties due to the difference in the SPR bands. It was observed that the 0.3 % polysaccharide solution had a larger absorbance compared to other samples, indicating the increased concentration of Ag-NPC in 0.3 % polysaccharide solution (Elsupikhe et al, 2015, 2016).

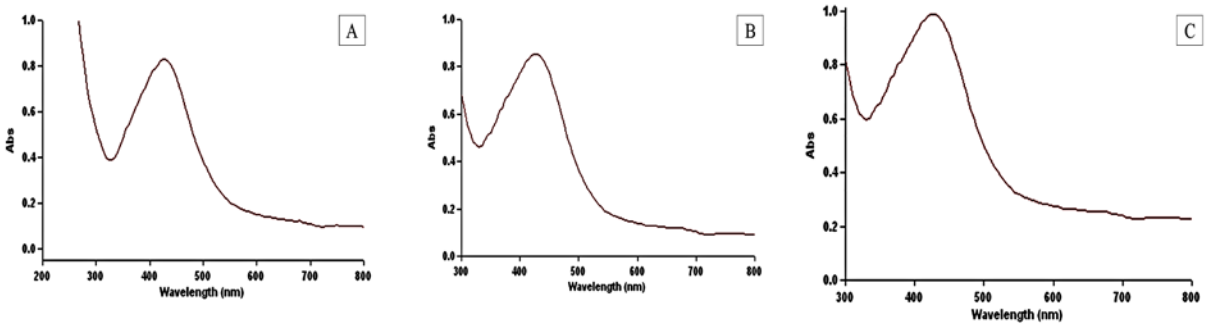

Figure 6.34.: UV chromatogram of polysaccharide-silver nano composite (AgNPC) at different time intervals, (A) 30, (B) 60 and (C) 120 minutes

6.3.3.7 Structural interpretation of polysaccharide-nano composite (P-Ag-NPC) by FTIR

FT-IR spectrum of the polysaccharide silver nanocomposite (P-Ag-NPC) showed absorption bands at 3,385 cm^{-1} and 2,912 cm^{-1} that were characteristics of the O-H stretching and interlayer C-H stretching, respectively. The absorption band at 1,446 cm^{-1} was corresponding to sulfate stretch and absorption at 1,238 cm^{-1} was due to the ester sulfate group. Additionally, the absorption peak at 1,048 cm^{-1} was assigned to the glycosidic linkage and absorption band at 924 cm^{-1} for 3,6-anhydro-D-galactose. The absorption at 847 cm^{-1} assigned the presence of C-O-S axial secondary sulfate on the C-4 group of the galactose (Barros et al., 2013; Knutsen et al., 1994; Usov et al., 2011). However, after adding $AgNO_3$ followed by ultrasonic irradiation resulted a new peak at 1,757 cm^{-1}, which was due to the formation of the carbonyl group (Figure 6.35). This result was reinforced by the carbonyl group resulted from the oxidation of carbohydrate radicals generated inside the polysaccharide (Elsupikhe et al, 2015, 2016). The peaks of polysaccharide after reaction with $AgNO_3$ were narrowed down at 3385 cm^{-1}, indicating the polymeric O-H functional groups of polysaccharide got involved in capping silver nanoparticles. The broad peak in the range 100 to 500 cm^{-1} was related to the Ag-NPs bonding with oxygen from of the hydroxyl groups of the polysaccharide chains (Elsupikhe et al, 2015, 2016). This is according to the presence of van der

Waals forces between the positively charged groups that surround the surface of the inert Ag-NPCs, and negatively charged groups presenting in the molecular structure of the polysaccharide (Figure 6.35). Moreover, the change in the wavenumber in the P-Ag-NPC samples that shifted to the lower wave numbers indicated an interaction between the polysaccharide and Ag-NPC (Elsupikhe et al, 2015, 2016). These FTIR spectral attributions confirmed the interactions of Ag-NPCs with the studied polysaccharide.

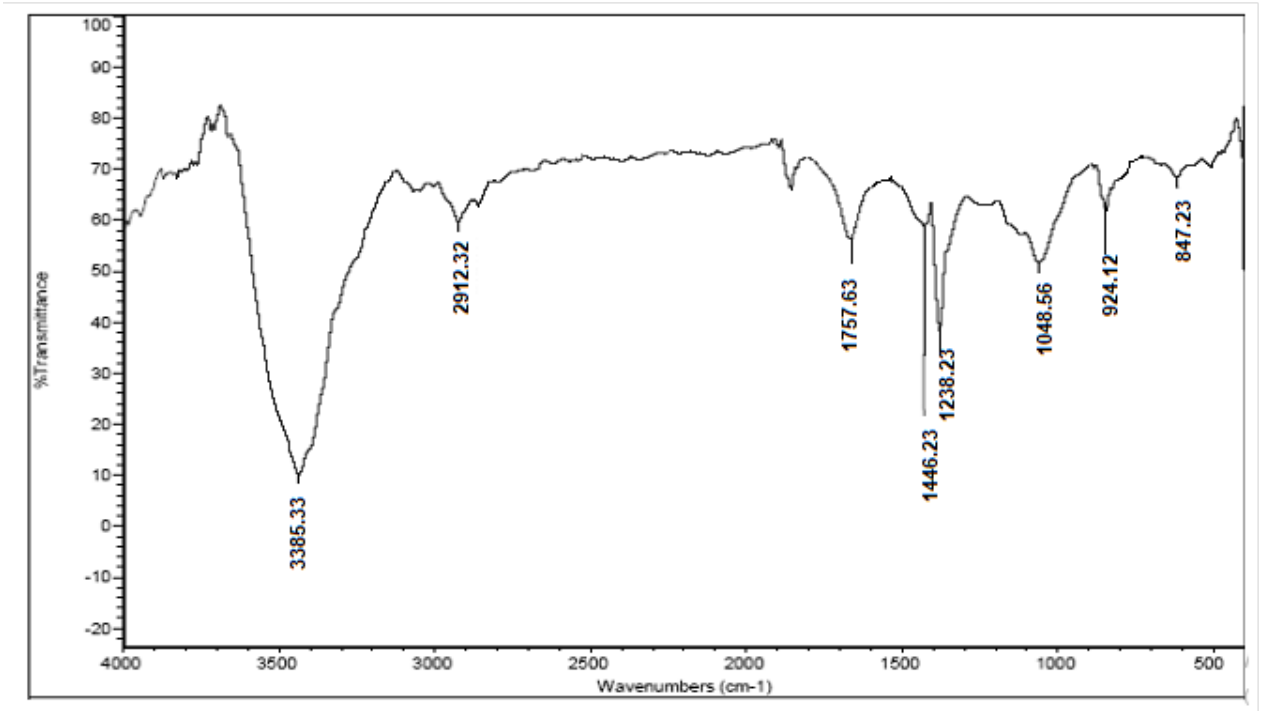

Figure 6.35.: FTIR spectrum of the polysaccharide-silver nano composite (Ag-NPC)

6.3.3.7 Morphological analysis of polysaccharide and polysaccharide-silver nanocomposite (P-Ag-NPCs) by SEM analysis

The polysaccharide (GSP-2) and polysaccharide-silver nanocomposite (P-Ag-NPC) have unique physical and chemical properties owing to their size and shape-dependent effects. Therefore, the morphological features of GSP-2 and P-Ag-NPCs were studied by using SEM experiment (Figure 6.36). The GSP-2 was found to be comprised of spindle-shaped fibrous polymer units. They were of ~1.40 µm length and ~2.50 nm thickness. The appearance and formation of Ag-NPs in 0.3 % polysaccharide solution were analyzed by SEM and EDX experiments (Figure 6.36). The higher percentage of silver along with other elements, such as C, O and S were indicative of their presence in P-Ag-NPC. Higher percentage of silver signals implied the formation of P-Ag-NPCs. The peak of sulfur substantiating the role of polysaccharide sulfate groups in capping P-Ag-

NPs. The P-Ag-NPs were found to appear in spherical shape with the size range of 451 to 551 nm. This solution of 0.3 % was further irradiated with ultrasonicator (750 Watt ultrasonic processor, Sonics, Newtown, CT 06470 USA, and 50/60 Hz) to reduce the size of the particles. Therefore, the 0.3 % solution was subjected to subsequent irradiations with time intervals of 30, 60 and 120 min. The P-Ag-NPC was formed after 30 min interval, and wasappeared as spherical in shape, with the particle size being 110-225 nm.

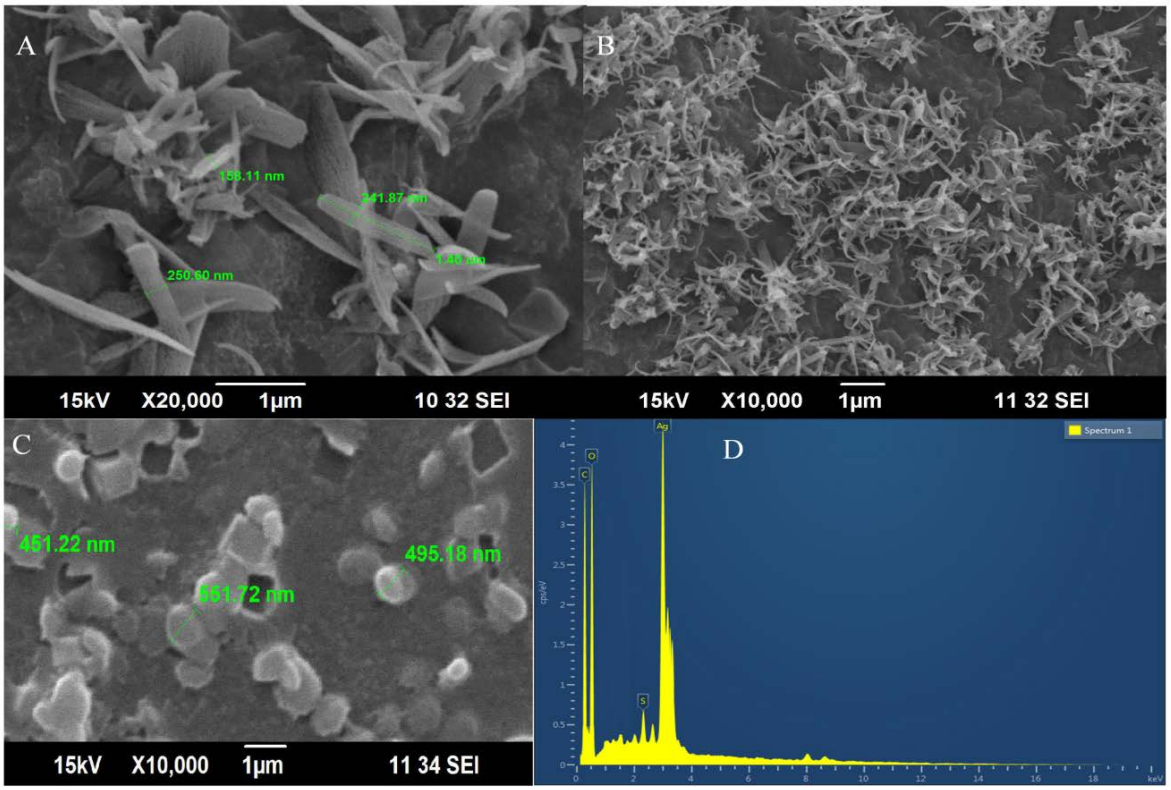

Figure 6.36.: Scanning electron microscopic (SEM) image of the studied polysaccharide, (1⋯→3)-*O*-6-sulfonato-β-D-galactopyranosyl-(1→⋯4)-3,6-anhydro-α-D-galactopyranose-(1⋯→).

Similarly, the uniform distribution of spherical P-Ag-NPC was observed after 60 and 120 min, and which were found to carry the particles of size of 45 nm and 18 nm, respectively (Figure 6.37). SEM micrograph depicted that polysaccharide has a structure filled with intrusions, while a smooth surface was observed for polysaccharide. Therefore, it can be said that the addition of Ag-NPs smoothens the surface of P-Ag-NPC. SEM images of P-Ag-NPC also indicated the change in the surface of Ag-NPC when the concentration of polysaccharide was found to be increased. However, the size of Ag-NPCs became smaller with an increasing concentration of polysaccharide. Moreover, Figure 6.37 exhibited the smallest size and increasing numbers of Ag-

NPsthereby referring that the yields of Ag-NPs (with smaller spherical size) were proportionally increased with the increasing concentration of polysaccharide (Elsupikhe et al, 2015, 2016).

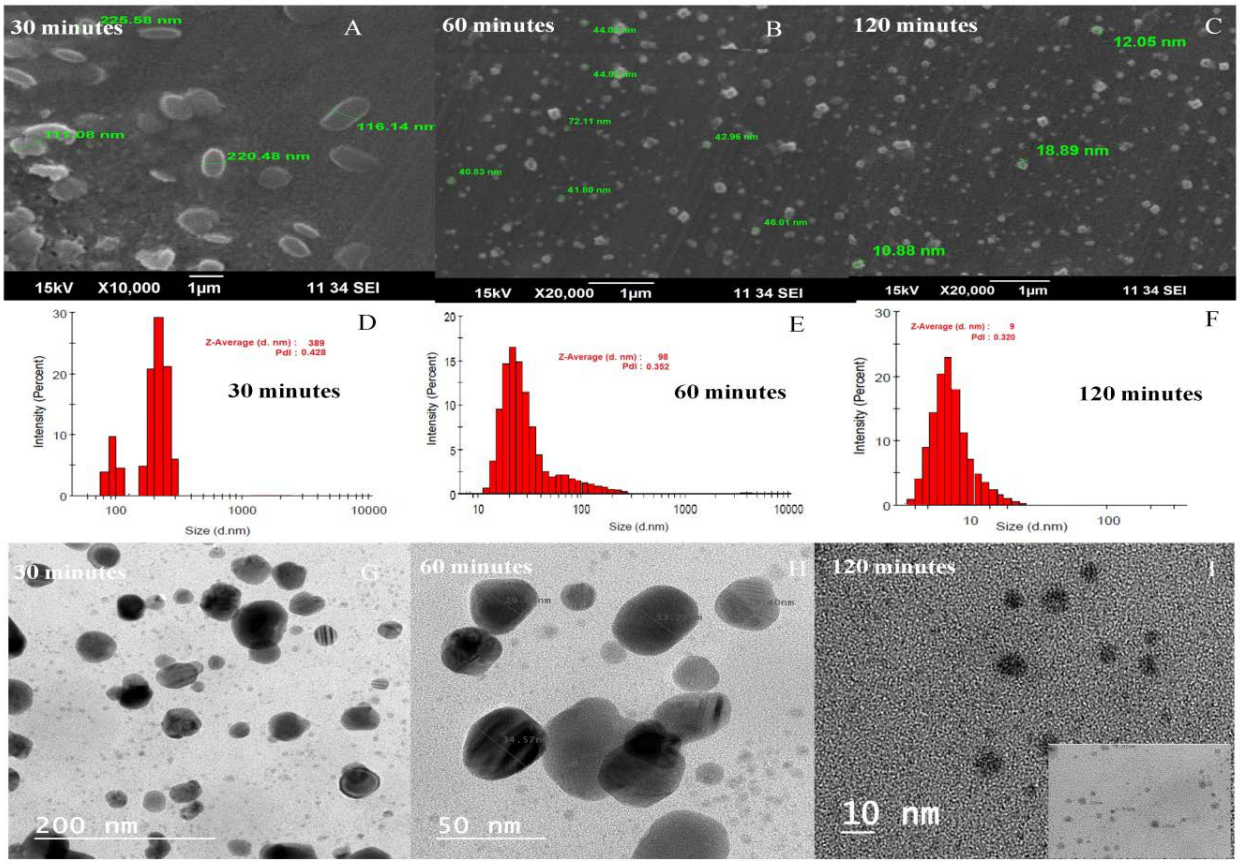

Figure 6.37.: Scanning electron microscopic (SEM) image of polysaccharide-silver nano composite (P-Ag-NPC) after (**A**) 30, (**B**) 60 and (**C**) 120 min of ultra-sonication. Particle size distribution curves of polysaccharide-silver nano composite (P-Ag-NPC) by DLS methods after (**D**) 30, (**E**) 60 and (**F**) 120 min of ultra-sonication. Transmission electron microscopic images of polysaccharide-silver nano composite (P-Ag-NPC) after (**G**) 30, (**H**) 60 and (**I**) 120 min of ultra-sonication.

6.3.3.8 Structural interpretation of polysaccharide-nano composite by XRD analysis

From Figure 6.38, it could be clearly seen that no diffraction peak was observed for the pure polysaccharide, while the Ag^0 polysaccharide-nano composite (P-Ag-NPCs) showed a diffraction peak at = 29.743 and 34.483, of the face centered cubic structure of Ag^0. This faced-centered cubic (fcc) structure indicated that Ag^0 nanoparticles were dispersed in the polysaccharide-nano composite (P-Ag-NPCs), which was confirmed with the SEM image shown in Figure 6.36 & 6.37. These results were mainly due to the strong interaction between the Ag^0 nanoparticles and polysaccharide-nano composite (P-Ag-NPCs).

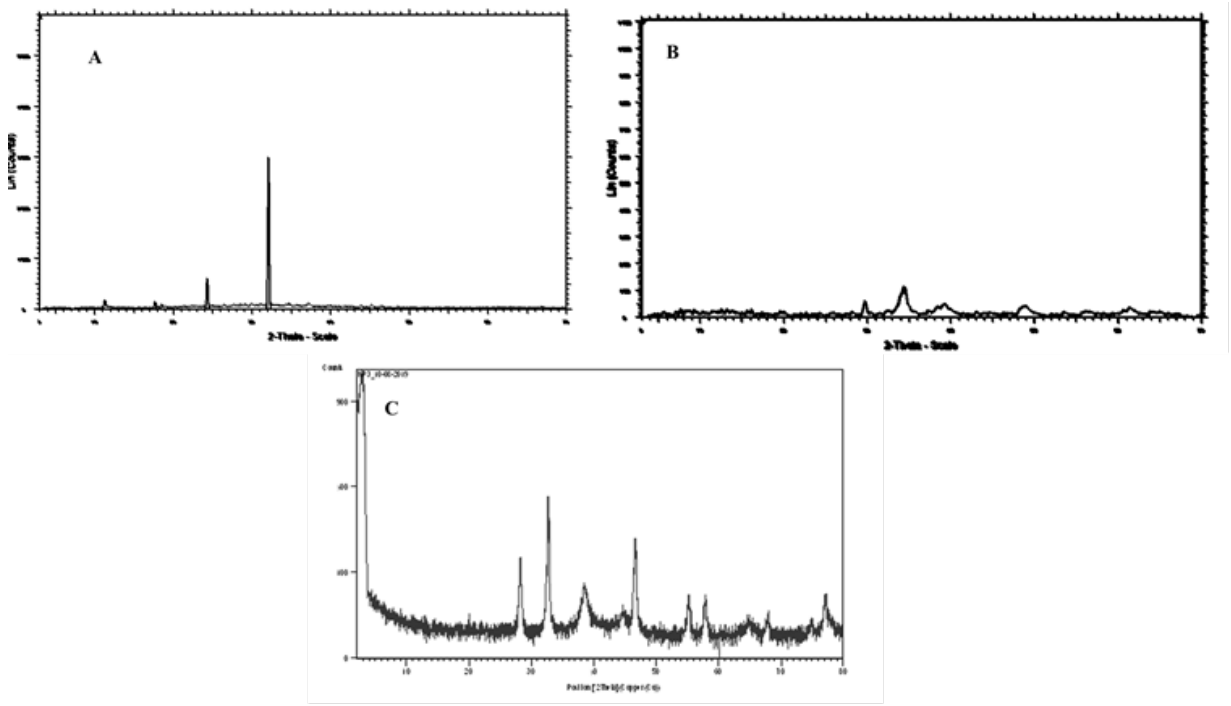

Figure 6.38.: XRD of polysaccharide-silver nano composite (AgNPC) at different time intervals, (**A**) 30, (**B**) 60 and 120 min (**C**)

6.3.3.9 Structural interpretation of polysaccharide-nano composite by TEM analysis

The TEM images of Ag-NPC 0.3 % solution of polysaccharide with different time intervals (30, 60 and 120 min, respectively) were depicted in Figure 6.37. TEM images and their size distributions indicated that the mean diameters and standard deviation of Ag-NPC were about 96.36 ± 24.33, 34.08 ± 3.33, and 4.21 ± 3.91 nm for 30, 60 and 120 min, respectively. The TEM results were in agreement with the UV-vis spectral data, which indicated that when the concentrations of polysaccharide were increased, the size of Ag-NPs decreased with increasing distribution. These results were also corroborated by the SEM images of Ag-NPC formed after time intervals (30, 60 and 120 min, respectively) (Figure 6.37).

6.3.3.10 Structural interpretation of polysaccharide-nano composite by AFM analysis

The P-Ag-NPC was further characterized by atomic force microscopic (AFM) analysis (Fig. 6). AFM provides a three-dimensional surface profile for nanoparticles. The area of polysaccharide analyzed was 1 µm × 1 µm. Although the lateral dimensions were influenced by the shape of the probe, the height measurements could provide the height of nanoparticles with a high degree of accuracy and precision. As shown in the histogram of AFM (Figure 6.39), the size distribution of the P-Ag-NPs was found to be in the range of ~56 nm after 60 min of time interval. The 3D-profile of P-Ag-NPs displayed uniform distribution of the nanoparticles throughout the

surface of the polymer. The white patches observed in the 2D-histogram revealed the spherical shape of P-Ag-NPs.

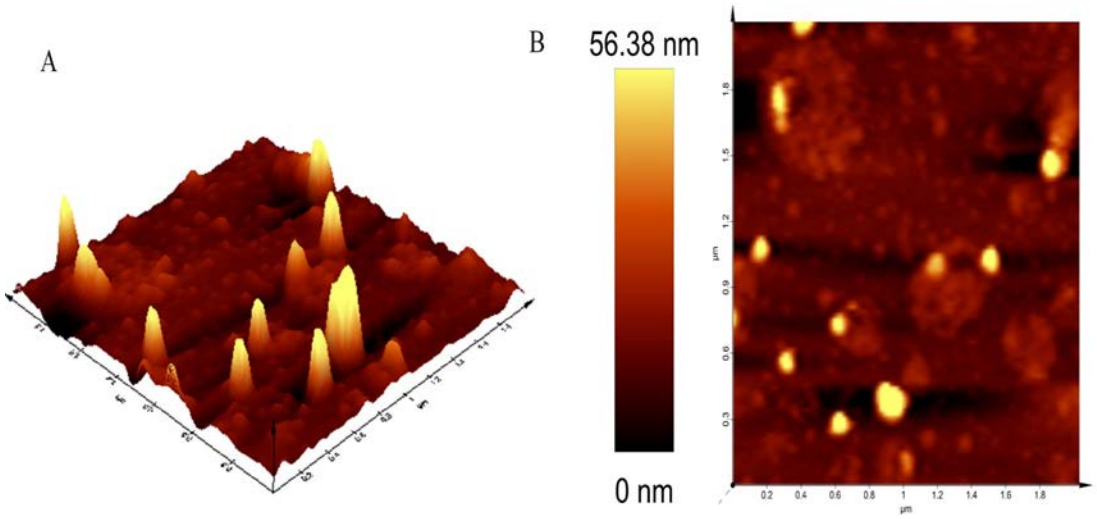

Figure 6.39.: AFM data of polysaccharide-silver nano particle (P-Ag-NPC) composite 2D and 3D images after 60 min (**A**) 2D AFM image of P-AgNPC nanoparticles (**B**) 3D image AFM image of P-Ag-NPC nanoparticles

6.3.3.11 Structural interpretation of polysaccharide-nano composite by Particle size analysis and zeta potential

The particle size analysis has been found as the primary characteristic in the synthesis of nanoparticles and in general, the nanoparticle size ranges of 1-100 nm. The particle size of Ag-NPC was determined by the particle size analyzer (PSA) with the diluent water by using dynamic light scattering (DLS) method. The average particle size of Ag-NPC at different time intervals was depicted in Figure 6.40. The P-Ag-NPC on 30 min of ultrasonic irradiation resulted in the particles with average size in the range of 100-500 nm. After 60 min interval, the size of the Ag-NPs was reduced to ~100 nm. Similarly, the size of the particles was reduced to ~10 nm after 120 min of ultrasonic irradiation. Measurement of the particles using PSA was also obtained by polydispersity index (PDI) value. Measurement of the value of PDI aimed to determine the particle size distribution, which indicated the level of uniformity of the size of the nanoparticles produced. The PDI of P-Ag-NPC composite after 30 min of ultrasonic irradiation resulted in the particles with PDI, 0.428. This was shifted to 0.352, and then 0.320 after 60 min and 120 min of ultrasonic irradiation, respectively. The PDI value below 0.5 indicated the homogeneous dispersion of the particles in the solution, and they were considered as monodispersed system. The monodispersed

systems were found to start from 0.01 up to the value of 0.5-0.7. While the value of PDI of more than 0.7 showed a very wide size distribution, and might contain largeer particles or aggregates. Smaller values of PDI showed narrower particle size distribution and more homogeneous particle size diameter.

Zeta potential is one of the most important nanoparticle characterization tools, which was used to determine the surface charge and give an idea repulsive force among particles of the resulting nanoparticle dispersion system. The interaction between the particles had a prominent role in the stability of the colloidal solution. In general, a dispersion system declared stable if the value of the zeta potential was more positive than +30 mV, or more negative than -30 mV, and were determined based on the electrostatic repulsion. The formula containing polysaccharide nano-composite was found to possess a zeta potential value of -0.23, -0.25 and -0.28, at 30, 60 and 120 min time intervals, respectively. This was influenced by the presence of a sulfate group that could cause increased surface charge and zeta potential value generated.

6.3.4 Molecular docking analysis of the studied polysaccharide from G. salicornia

The attenuation potential of starch degrading enzymes, α-glucosidases and α-amylases inhibition by the studied polysaccharide is an effective procedure to attribute the prospective anti-diabetic properties of the studied compound. The commercially standards acarbose and voglibose have been extensively used to regulate the glucose levels in blood. The derived sulfated polysaccharide analogue was subjected to *in silico* analysis against these carbolytic enzymes (α-amylases and α-glucosidase). The RMSD data were used to evaluate their results. The *in silico* analysis parameters, such as binding energy, intermolecular and torsional free energy, and inhibition constants of polysaccharide were documented (Figure 6.41, Table 6.8). *In silico* molecular docking analysis of the polysaccharide with α-glucosidase with grid box x = 37.224, y = -18.821, z = 28.301, α-amylase with grid box x = -9.251, y = 53.269, z = 29.658 and DPP-IV with grid box x = 28.493, y = -19.821, z = 25.004 displayed the efficient interactions of ligand polysaccharide with the enzyme target sites (Fig. 9). The polysaccharide recorded least binding energy of -5.24 kcal mol^{-1} in interactions with α-glucosidase enzyme target sites. Likewise, the constant of enzyme inhibition (Ki) was 144.49 nM towards α-glucosidase enzyme. Also, intermolecular energy of polysaccharide was -6.43 kcal mol^{-1}. The molecular docking interaction of ligand polysaccharide and α-glucosidase showed four hydrogen bonds (displayed as red and blue coloured lines) to the amino acyl residues of THR^{83}, LYS^{40}, ASP^{34} and ASN^{32} with the bond distances of 2.772, 3.288, 3.054 and 2.806 Å in the active binding site. The polysaccharide recorded least binding energy of -2.44 kcal mol^{-1} in interactions with α-amylases enzyme target sites. Likewise, the constant of enzyme inhibition (Ki) was 16.22 nM towards α-glucosidase enzyme. Also, intermolecular energy of polysaccharide was -3.71 kcal mol^{-1}. The molecular docking

interaction of ligand polysaccharide and α-amylases showed one hydrogen bond (displayed as red and blue coloured lines) to amino acyl residues of HIS^{299} with the bond distances of 3.620Å in the active binding site. The polysaccharide recorded least binding energy of -11.13 kcal mol^{-1} in interactions with DPP-IV enzyme target sites. Likewise, the constant of enzyme inhibition (Ki) was 6.94 nM. Also, intermolecular energy of polysaccharide was -12.40 kcal mol^{-1}. The molecular docking interaction of ligand polysaccharide and DPP-IV showed ten hydrogen bonds (displayed as red and blue coloured lines) to amino acyl residues of THR^{156}, THR^{216}, SER^{106}, ILE^{107}, ARG^{61} with the bond distances of 2.546, 1.603,2.536, 3.198, 2.008, 2.198, 2.350, 2.496, 2.438, 2.666 Å in the active binding site. Likewise, the polysaccharide recorded least binding energy of -6.98 kcal mol^{-1} in interactions with ALP enzyme target sites. The constant of enzyme inhibition (Ki) was 7.68 nM towards the ALP enzyme. Also, intermolecular energy of polysaccharide was -8.22 kcal mol^{-1}. The molecular docking interaction of ligand polysaccharide and DPP-IV showed ten hydrogen bonds (displayed as red and blue coloured lines) to amino acyl residues of ILE^{374}, SER^{373}, PHE^{375}, GLU^{411}, SER^{414} with the bond distances of 3.343, 2.446, (3.266, 3.204), (3.027, 3.196, 2.750), 3.367 Å in the active binding site.

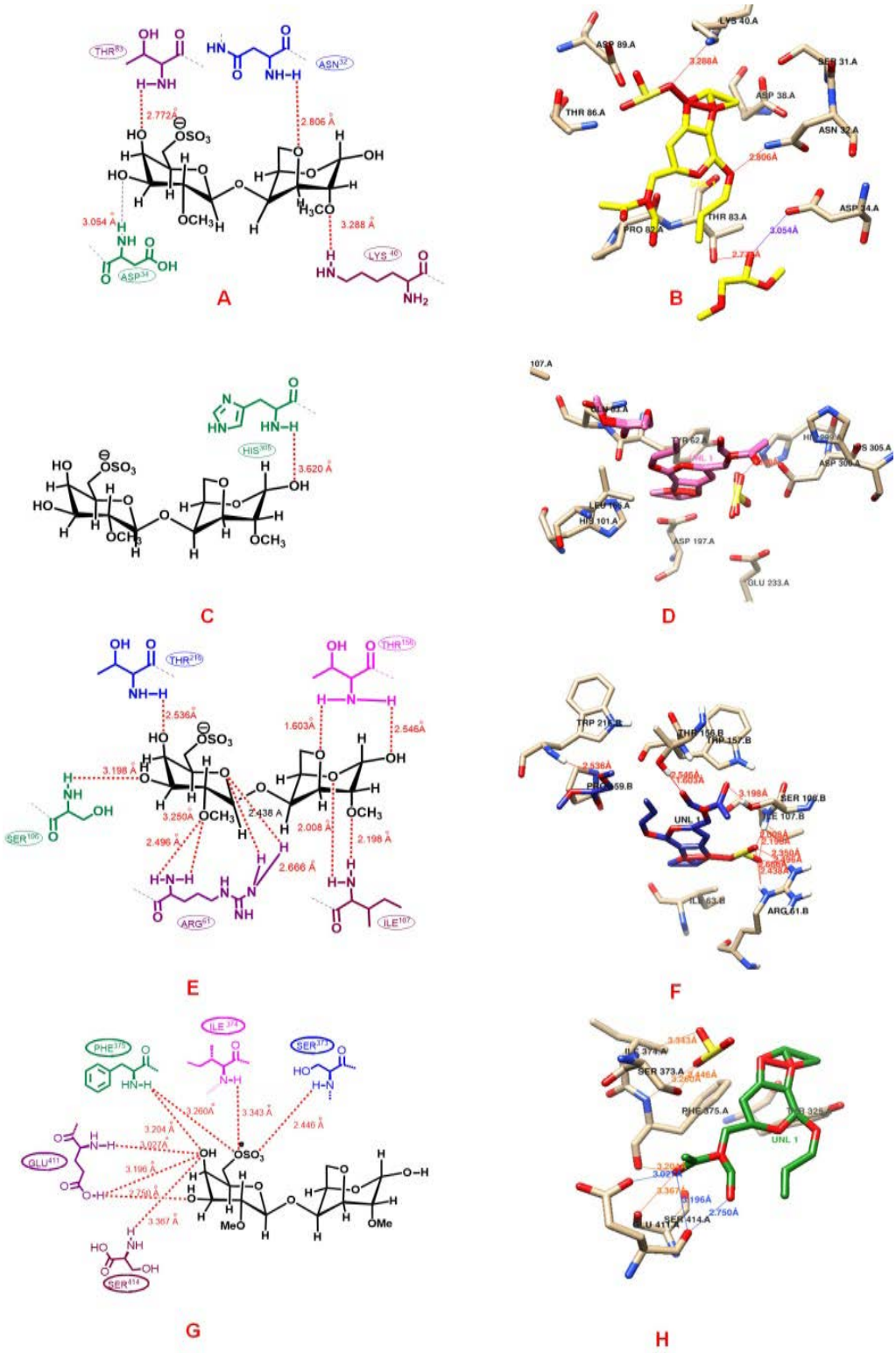

Figure 6.41.: Closer image of molecular docking interactions of polysaccharide in the catalytic site of α-amylase, α-glucosidase, proteolytic DPP-IV and alkaline phosphate (ALP), as obtained by docking experiment. The molecular docking interaction of ligand polysaccharide and α-amylases showed one hydrogen bond (displayed as red and blue coloured lines) to amino acyl residues of

HIS^{299} with the bond distances of 3.620Å in the active binding site. The molecular docking interaction of ligand polysaccharide and α-glucosidase showed four hydrogen bonds (displayed as red and blue coloured lines) to amino acyl residues of THR^{83}, LYS^{40}, ASP^{34} and ASN^{32} with the bond distances of 2.772, 3.288, 3.054 and 2.806 Å in the active binding site. The molecular docking interaction of ligand polysaccharide and DPP-IV showed ten hydrogen bonds (displayed as red and blue coloured lines) to amino acyl residues of THR^{156}, THR^{216}, SER^{106}, ILE^{107}, ARG^{61} with the bond distances of 2.546, 1.603,2.536, 3.198, 2.008, 2.198, 2.350, 2.496, 2.438, 2.666 Å in the active binding site. The molecular docking interaction of ligand polysaccharide and DPP-IV showed ten hydrogen bonds (displayed as red and blue coloured lines) to amino acyl residues of ILE^{374}, SER^{373}, PHE^{375}, GLU^{411}, SER^{414} with the bond distances of 3.343, 2.446, (3.266, 3.204), (3.027, 3.196, 2.750), 3.367 Å in the active binding site.

6.4. Conclusion

The present study demonstrated that the marine-derived polysaccharide and its nano composite (P-Ag-NPs) with the silver particles derivative constituted promising candidates to combat the hyperglycemic conditions. The titled polysaccharide derivatives were found to be effective in attenuating DPP-IV enzyme and carbolytic enzymes such as α-amylases and α-glucosidases. A novel (DPP)-IV inhibiting polysaccharide, A (1⋯→3)-*O*-6-sulfonato-β-D-galactopyranosyl-(1→⋯4)-3,6-anhydro-α-D-galactopyranose-(1⋯→) from red seaweed *Gracilaria salicornia,* was isolated and structurally characterized. The seaweed derived polysaccharide registered greater reduction potentials against proteolytic DPP-IV (IC_{50} 0.63 mg mL^{-1}) and carbolytic enzymes α-amylase and α-glucosidase (IC_{50} 1.48-1.51 mg mL^{-1}), whereas the activities were comparable with those displayed by acarbose (IC_{50} DPP-IV 0.13 mg mL^{-1}, carbolytics IC_{50} 1.38-1.47 mg mL^{-1}). Likewise, the antioxidative potential of the polysaccharide was higher (IC_{50} 0.35-0.48 mg mL^{-1}) than that of commercial standard ascorbic acid (IC_{50} 0.37-0.51 mg mL^{-1}). The presence of chemical constituents in polysaccharide was assessed by the analytical methods, which were corroborated with the bioactivity of polyglactan. The polysaccharides exhibited lower binding energy conformation (-11.13 kcal mol^{-1}) towards the catalytic binding site of DPP-IV, and this was also reinforced with the bioactivity of polysaccharide. Based on the bioactivity, silver-nano-composite of polysaccharide was synthesized for prospective activities against hyperglycemia. The polysaccharide-silver-nano-composite (P-Ag-NP-composite) demonstrated greater inhibition potential against proteolytic (DPP-IV IC_{50} 0.52 mg mL^{-1}) and carbolytic enzyme (α-amylase and α-glucosidase IC_{50} 0.22-0.70 mg mL^{-1}, respectively) than that of the native polysaccharide (≥ 1.0 mg mL^{-1} and ≥ 0.6 mg mL^{-1}, respectively). The nano particle synthesized from polysaccharide was found to be of 4-400 nm size, at different time intervals of 30, 60 and 120 min, and their shape was found to be spherical. The inhibition potential of polysaccharide and its silver nano composite

against DPP-IV along with antioxidant potential suggested the formulation of bioactive leads to reduce the risk of hyperglycemic pathologies.

CHAPTER 7

SUMMARY

Seaweeds have developed an adaptive strategy for their survival in their competitive surroundings by the production of large array of metabolites, and they act as chemically and biologically active defense systems against several life style diseases. Studies on natural product chemistry and chemical defense systems of seaweeds recognized the presence of bioactive leads with prominent pharmacological activities. Phlorotannins and polyphenols from seaweeds have revealed their activities against proliferation of cancer cells and produce some effects on anti-inflammatory and anti-diabetic responses. Bioactive components in seaweeds were recognized to modulate glucose-induced oxidative stress and their ability to control the presence of starch-digestive enzymes. Potential side effects attributed to the synthetic drugs, demanded naturally obtained potential bioactive components for curing of persistent metabolic syndromes. Therefore, consumption and addition of these seaweeds might be increased their food and pharmaceutical applications.

Bioactive constituents of seaweeds also revealed their nutritional and bioactive properties against various life style diseases, which include hypertension, diabetes mellitus and inflammation. Bioactive components of seaweeds also act as the inhibitor of angiotensin-I converting enzyme (ACE), which secrete the angiotensin-II vasoconstrictor. The potential side effects produced by the commercial ACE-inhibitors upsurges the demand of naturally occurring homologues. Specific constituents of seaweeds were found to function as chemical intermediaries, which control the stimulations associated with mammalian defense mechanism and produces inflammatory deregulators.

A total of ten different seaweeds belonging to the subclasses Dictyotophycidae, Rhodymeniophycidae and Corallinophycidae collected from the Gulf of Mannar of Peninsular India were screened for *in vitro* antioxidant, anti-diabetic, anti-inflammatory and anti-hypertensive activities. Among various seaweeds considered in the present study, those belonging to the subclasses Dictyotophycidae and Rhodymeniophycidae displayed considerably greater pharmacological potentials. In particular, the organic extracts of *G. salicornia* and *P. tetrastromatica* registered significantly greater pharmacological properties than those derived from other studied seaweeds. This study also disclosed that the spectral fingerprinting could quickly deduce the signal pattern of the resonances, and conclusions could be drawn as to the likely structural classes involved in the organic extracts of the studied seaweeds. The present study recognized that the seaweeds *G. salicornia* and *P. tetrastromatica* might be promising

candidates to isolate high value compounds for pharmacological use and their application as functional foods.

Bio-assay assisted chromatographical purification of the EtOAc-MeOH extract of *G. salicornia* yielded bioactive secondary metabolites, namely abeo-labdane class of diterpenoid (**TG$_1$**), oleanene class of triterpenoids (**TG$_2$**- **TG$_3$**), drimane-associated quinols (**TG$_4$**- **TG$_6$**), 2*H*-chromenyl compounds (**TG$_7$**- **TG$_8$**), spiro-fused analogues (**TG$_9$**- **TG$_{10}$**), squalene polyether metabolites (**TG$_{11}$**- **TG$_{12}$**), and macrolides enclosing ether functionalities (**TG$_{13}$**-**TG$_{15}$**). The studied compounds exhibited comparable DPPH radical quenching activity as standard antioxidant agent *α*-tocopherol. The first class of compounds in this series abeo-labdene derivative (**TG$_1$**) registered significantly greater activities against pro-inflammatory 5-lipoxygenase than that displayed by non-steroidal anti-inflammatory drug ibuprofen. Its greater selectivity index as compared to that displayed by ibuprofen inferred the higher anti-inflammatory selectivity against pro-inflammatory cyclooxygenase-2.

In second class of metabolites among the isolated compounds, the one with 24(4→23) abeo-oleanene framework (**TG$_3$**) exhibited higher carbolytic enzyme inhibitory activities ($IC_{50} \leq 0.32$ mM) over that bearing 24(4→23), 27(8→26), 30(20→29)-tris-abeo-oleanene moiety (**TG$_2$**) ($IC_{50} \geq 0.34$ mM). The oleanene analogues isolated from *G. salicornia* registered greater radical scavenging potentials against $ABTS^+$ ($IC_{50} < 1.10$ mM) than that exhibited by α-tocopherol ($IC_{50} > 1.69$ mM). Structure-activity relationship analyses showed that higher polarisability and lesser steric bulk of abeo-oleanene (**TG$_3$**) predominantly contributed towards the comparatively greater radical quenching and carbolytic enzyme inhibitory activities than those displayed by its tris-abeo-oleanene analogue (**TG$_2$**). *In silico* molecular modelling studies were performed to designate the α-glucosidase and α-amylase inhibitory mechanism of the abeo-oleanene derivative (**TG$_2$**) exhibiting binding energies of greater than 9.50 kcal mol^{-1}, which substantiated its potential inhibitory activity against the carbolytic enzymes responsible to cause hyperglycaemic disorders. An enzyme-assisted putative biosynthetic cascade leading to the formation of oleanene triterpenoid derivatives were proposed. In particular, the 24(4→23)-abeo-oleanene possessing (12-oxo)-3,5-diene-deconoate moiety (compound **TG$_2$**) was found to be effective dual inhibitors of starch digestive enzymes along with potential antioxidative properties, and therefore, might be utilised as valuable medicinal lead against oxidant species and elevated postprandial glucose levels.

On third series of compounds, the compound (**TG$_4$**) with benzo[*a*]xanthene-4,10,12-triol moiety showed greater pro-inflammatory enzyme inhibitory activities (IC_{50} 1.35-1.72 mM) over other studied drimane quinol chemotypes. Positive correlations between the antioxidant and anti-inflammatory activities were recorded, whereas the compound (**TG$_4$**) displayed greater

oxidant scavenging potentials (IC_{50} 1.33-1.57 mM) than that exhibited by α-tocopherol. Structure-bioactivity correlation analysis showed that lesser hydrophobicity and steric bulk of the compound (**TG_4**) predominantly contributed towards the comparatively greater radical quenching and pro-inflammatory enzyme inhibitory activities than those displayed by its drimane counterparts **TG_5**-**TG_6**. *In silico* molecular modelling studies were performed to designate the 5-lipoxygenase inhibitory mechanism of the compound (**TG_4**) exhibiting binding energy of -12.30 kcal mol^{-1}, which substantiated its potential inhibitory activity against the inflammatory mediators. An enzyme-mediated biosynthetic cascade leading to the formation of drimane sesquiterpenoid quinol derivatives was proposed. The results illustrated the bioactive potential of the natural anti-inflammatory drimane sesquiterpenoid bearing benzo[*a*]xanthene-4,10,12-triol moiety attenuating pro-inflammatory 5-LOX from marine macroalga *G. salicornia.*

In chromenyl derivatives, which were characterised as 4'-[10'-[7-hydroxy-2,8-dimethyl-6-(pentyloxy)-2*H*-chromen-2-yl]ethyl]-3',4'-dimethyl-cyclohexanone (**7**) and 3'-[10'-(8-hydroxy-5-methoxy-2,6,7-trimethyl-2*H*-chromen-2-yl)ethyl]-3'-methyl-2'-methylene cyclohexyl butyrate (**TG_8**) using comprehensive spectroscopic techniques. The compound **TG_8** exhibited higher DPPH radical quenching activity than that displayed by compound **TG_7** and standard antioxidant agent α-tocopherol. The chromenyl derivative registered significantly greater activities against pro-inflammatory 5-lipoxygenase than that displayed by non-steroidal anti-inflammatory drug ibuprofen. Its greater selectivity index as compared to that displayed by ibuprofen inferred the higher anti-inflammatory selectivity against pro-inflammatory cyclooxygenase-2. The newly described chromenyl analogue **TG_8** characterised from the red seaweed *G. salicornia* has potential anti-inflammatory and antioxidant properties for utilisation in pharmaceutical and food formulations.

Among the isolated spiro-compounds, the one with spiro[5.5]undec-2-en framework (**TG_{10}**) exhibited higher pro-inflammatory enzyme inhibitory activities ($IC_{50} \leq 1.91$ mM) over that bearing oxospiro[5.5]undec-4-ene moiety (**TG_9**) ($IC_{50} \geq 2.78$ mM). The spiro analogues isolated from *G. salicornia* registered greater radical scavenging potentials against $ABTS^+$ ($IC_{50} < 1.75$ mM) than that exhibited by α-tocopherol ($IC_{50} > 1.75$ mM). Structure-activity relationship analyses showed that higher polarisability, tPSA and lesser steric bulk of spiro[5.5]undec-2-en (**TG_{10}**) predominantly contributed towards the comparatively radical quenching and proinflammatory enzyme inhibitory activities than those displayed by the oxospiro[5.5]undec-4-en analogue (**TG_9**). Molecular docking analysis inferred that the spiro derivative (**TG_2**) exhibited binding energy of -10.13 kcal/mol with efficient interactions of 5-LOX enzyme, which corroborated its greater inhibitory potential. In particular, spiro[5.5]undec-

2-ene analogue was found to be an effective inhibitor of 5-LOX along with potential antioxidative properties, and therefore, might be utilised as valuable pharmacophore lead against oxidant species and inflammation pathology.

Among unreported polyether analogues, the compound **TG$_{12}$** possessing furanyl-furo[3,2-b]pyran-2*H*-pyran skeleton displayed greater anti-inflammatory properties (IC_{50} < 2 mM) over that exhibited by **TG$_{11}$** bearing pyranyl-10-methylpyrano[3,2-b]pyran-methyleneoxepane moiety (IC_{50} > 2.5 mM). Likewise, the potential anti-radical properties of **TG$_{12}$** (IC_{50} 1.11-1.27 mM) in comparison with **TG$_{11}$** (IC_{50} ~1.65 mM) and α-tocopherol (IC_{50} 1.49-1.69 mM) were reported. Structure-bioactivity-correlation studies displayed that the optimum hydrophobicity (log P_{OW2} < 5), lesser steric hindrance, which along with greater polarisability factors predominantly played significant roles in determining the greater bio-potential of polyether derivative, **TG$_{12}$** over that of **TG$_{11}$**. *In-silico* molecular modeling was analyzed to entitle 5-lipoxygenase inhibitory pathway of compound (**TG$_{12}$**) exhibiting binding energy of -10.96 kcal mol^{-1}, that appropriately attributed its potent inhibitory properties against the inflammatory-mediators.

In the last series of compounds, the undescribed oxabicyclo[21.3.1]heptacosa-ene-diones (compounds **TG$_{13}$**- **TG$_{15}$**) and oxabicyclo[19.3.1]pentacosa-ene-dione (compound **TG$_{15}$**) bearing macrocyclic lactones from the red seaweed, *G. salicornia*. The unprecedented compounds (**TG$_{13}$**- **TG$_{15}$**) displayed significantly higher antioxidative and pro-inflammatory 5-lipoxygense attenuating potential in comparison with the commercially existing antioxidative and anti-inflammation agents. The greater attenuation potential of the 21-membered pyran bearing compound **TG$_{14}$** against 5-lipoxygense was correlated with its respective *in-silico* molecular docking simulations in the binding site of the pro-inflammatory enzyme through the least binding energy (-9.64 kcal mol^{-1}) and inhibitory constant (Ki 85.15 nm). The malonate-S-acyl carrier protein-mediated putative biosynthetic route appropriately corroborated the structural attributions of the studied salicornolides. In particular, the pyran enclosed macrocyclic lactone could be used as prospective natural therapeutic pharmacophore in attenuating the anti-inflammatory disorders and free radical-induced ailments.

Among seven classes of compounds derived from *G. salicornia*, **TG$_{14}$** belonging to macrolide class of chemistries was registered significantly higher anti-inflammatory activity. *In-vitro* antioxidant assays were evaluated by the radical (radicals DPPH and $ABTS^{+}$) quenching abilities of compounds (**TG$_{13}$**- **TG$_{15}$**) against 1, 1-diphenyl-2-picryl-hydrazil (DPPH) and 2, 2'-azino-bis-3-ethylbenzothiozoline-6-sulfonic acid ($ABTS^{+}$), and the antioxidant activities were compared with the standard antioxidative agent, *α*-tocopherol.

Among the titled compounds, **14** showed higher radical scavenging potentials (IC_{50} DPPH 1.10 mM; IC_{50} $ABTS^+$ 1.21 mM) when compared to other studied compounds (**13-15**) (IC_{50} DPPH > 1.38 mM; IC_{50} $ABTS^+$ > 1.42 mM). It is of note that the free radical scavenging potential of the compound (**13-15**) were found to be significantly greater (IC_{50} < 1.50 mM) in comparison with the standard, α-tocopherol ($IC_{50} \geq 1.5$ mM; $P < 0.05$). The greater antioxidative properties against the free radicals were reported for the 12-membered macrocyclic lactone isolated from the seaweed, *S. wightii* (Maneesh and Chakraborty, 2017), a 16-membered macrocyclic bislactone and 10/13-membered macrocyclic lactones from the mollusk, *Amphioctopus neglectus* (Chakraborty et al., 2019). These results further substantiated the antioxidative potential of the studied compounds (**13-15**).

Compound **13** was found to contain two conjugated systems, such as 14-furanyl and 22-benzyl, which could easily transfer H-atoms (by hydrogen-atom transfer) located at C-14 and C-22 positions, respectively of oxabicyclo[21.3.1]heptacosa-11,23,25,27-tetraene-7,18-dione skeleton onto DPPH free radicals to form resonance stabilised 3-acetyl-14-(furan-2(5*H*)-ylidene)-15-(isopentyloxy)-11-methyl-8-oxa-bicyclo[21.3.1]heptacosa-26,11, 22,24-tetraene-7,18-dione. These two positions (C-14 and C-22) could be considered as primary antioxidative reaction centers. Additionally, three more reaction centers related to the ester at C-7, 3-acetyl and 18-keto in the oxabicyclo[21.3.1]heptacosa-11,23,25,27-tetraene-7,18-dione framework, were found for compound **13**. The protons at C-6 (near to ester at C-7), C-3 (acetyl linked carbon) and C-19 (adjacent to keto at C-18) could participate in keto-enol resonance with the nearest >C(=O)< (keto) groups at C-7, C-3^1, and C-18, respectively leading to the generation of -CH=C(-OH)- (enol) functionality via repositioning the protons from C-6, C-3, and C-19, respectively to the DPPH free radical to form a resonance stabilized 14-(furanyl)-3-(1-hydroxyethylidene)-11-methyl-15-(153-methylbutyloxy)-8-oxabicyclo[21.3.1]heptacosa-hexaene-7,18-diol. These five sites of antioxidative reaction centers present in compound $\mathbf{TG_{13}}$ could effectively participate in the resonance stabilization, which in turn, stabilize the DPPH radicals in the biological systems. Compound $\mathbf{TG_{14}}$ exhibited four primary antioxidative reaction sites, which include three keto functionalities and one conjugated olefinic system. The conjugated olefinic groups (-C12=C13-C14=C15-) adjacent to the oxygenated functionality in Compound $\mathbf{TG_{14}}$ could effectively involve in the electron delocalization to form -C11=C12-C13=C14-C15-O-, which in turn, transfer protons from C-11 to radicals through the hydrogen transfer via formation of resonance stabilized 10-acetyl-9-isopentyl-2-methyl-5,16,23^1-trioxa-bicyclo[21.3.1]heptacosa-2,11,13-triene-6,19-dione . The protons at C-7 (near to ester at C-6), C-10 (acetyl linked carbon) and C-20 (adjacent to keto at C-19) could involve in the keto-enol resonance with nearby >C(=O)< groups at C-6, C-10^1 and C-19, respectively resulting in the

formation of -CH=C(-OH)- by replacing the protons from C-7, C-10, and C-20, respectively to DPPH radicals through the genesis of resonance stabilised 10-(1-hydroxyethylidene)-9-isopentyl-2-methyl-5,16,23[1]-trioxa-bicyclo[21.3.1]heptacosa-2,6,10,12,14, 19-hexaene-6,19-diol. These four antioxidative reaction centres might be the predominant reasons for potential radical scavenging properties of Compound **TG_{14}** through the neutralisation of DPPH radical. However, Compound **TG_{15}** possessed only three reaction centres, which include two carbonyls and one hydroxyl functionalities. The free electron pair of -OH of -CHOH group located at C-8 of the macrolide might not efficiently contribute in resonance stabilization due to the weak acidic property of this proton, resulting in the formation of weakly stabilized DPPH radical. The protons at C-9 (near to keto at C-10) and C-22 (adjacent to keto at C-23 in the pyrone ring) could involve in the keto-enol resonance with the nearby >C(=O)< groups at C-10 and C-23, respectively leading to the formation of -CH=C(-OH)- by replacing the protons from C-9 and C-22, respectively to the DPPH radicals. These antioxidative reaction centers resulted in the resonance stabilized form of Compound **TG_{15}**, 20-isobutyl-16-methyl-7,14-dioxa-bicyclo[19.3.1]pentacosa-2,5,9,16,22-pentaene-10,23-triol to neutralize the DPPH free radical . Notably, the compound **TG_{15}** did not hold any extended conjugation as in **TG_{13}** and **TG_{14}**, and hence, it could not effectively transfer H-atom to DPPH, and therefore, displayed weaker antioxidant activity (IC_{50} DPPH 1.42 mM; IC_{50} $ABTS^{+}$ 1.47 mM) than those displayed by Compounds **TG_{13}** and **TG_{15}** (IC_{50} DPPH 1.37-1.40 mM; IC_{50} $ABTS^{+}$ 1.41-1.43 mM).*In-vitro* anti-inflammatory potential of the studied compounds was assessed by their attenuation potential against pro-inflammatory enzymes 5-lipoxygenase (5-LOX) and cyclooxygenase-1 and 2 (COX-1/2). Among the titled compounds, 21-membered pyran-enclosed Compound **TG_{14}** displayed greater attenuation property against COX-2 (IC_{50} 1.13 mM) than those exhibited by the 21-membered aryl Compound **TG_{13}** and 19-membered macrolide **C** (IC_{50} COX-2 ~ 1.2 mM). The attenuating potential of the studied compounds against 5-LOX was significantly greater (IC_{50} < 1.5 mM) than that displayed by ibuprofen (IC_{50} 4.5 mM), whereas the selectivity indices exhibited by macrolides against COX-2 were significantly higher (1.18-1.41, $P < 0.05$) when compared to ibuprofen (SI = 0.43) attributing the greater selectivity profile of the former towards inducible pro-inflammatory mediators than that exhibited by the latter.

The bioactive potentials of the Compound **TG_{13}- TG_{15}** were substantiated with their physico-chemical-parameters. It is relevant to note that the electronic-parameters of 21-membered macrolide derivative (**TG_{13}**) was higher (polarizability, Pl 59.35; topological polar surface area, tPSA 78.9) than that recorded with 19-membered macrolide derivative, **TG_{15}** (Pl 52; tPSA, 72.8), and that could be correlated with the greater bioactivities of the former (Table 4.30). The higher electronic values recorded for Compound **TG_{14}** further supported the possibilities of

greater number of electron-rich centres, which in turn, resulted in its greater bioactive properties. Electronic or polar factors were reported to play important parts to govern the target pharmacological properties (Wang et al., 2007). Notably, the steric bulkiness of the 21-membered aryl macrolide, compound **TG$_{13}$** (molar-volume, MV 565 cm^3 mol^{-1}; parachor, P 1455 cm^3) was significantly greater than the 21-membered pyran enclosed macrolide derivative, Compound **TG$_{14}$** (MV 543 cm^3 mol^{-1}; P 1279 cm^3) and 19-membered cyclohexanone enclosed macrolide derivative, Compound **TG$_{15}$** (MV 465 cm^3 mol^{-1}; P 1109 cm^3). The greater steric hindrance of Compound **TG$_{13}$** due to its bulkier side chains of benzyl/furanyl ring systems could negatively affect its bioactivities, although its electronic parameters recorded higher values (Pl 69.4; tPSA, 78.9). The optimum hydrophobicity/lipophilicity (log P_{ow}) equilibrium of Compound **TG$_{14}$** and **TG$_{15}$** (5.6-6) appeared to contribute towards their greater bioactivities over Compound **TG$_{13}$** that displayed greater lipophilicity (log P_{ow} ~ 7.7). The balanced hydrophilic-lipophilic properties as determined by log P_{ow} was found to control the inter-membrane perviousness including requisite hydrophobic/lipophilic (Lipinski, 2004) relationship and binding of receptors (Huuskonen et al., 2000). Apparently, greater electronic parameters (electron-rich centres) along with optimum steric bulkiness and permissible hydrophobicity-lipophilicity equilibrium of Compound **TG$_{14}$** could result in its greater antioxidative properties and effective interaction with the active site of inflammatory enzymes to impart anti-inflammatory properties compared to other studied compounds (Wang et al., 2007).

At the same time, the abeo-oleanane class of compounds from *G. salicornia* was registered higher anti-diabetic potential. the *in vitro* anti-diabetic potential of the studied abeo-oleanenes (**TG$_2$** and **TG$_3$**) were assessed by their inhibitory properties towards the carbolytics, α-glucosidase and α-amylase that were found to regulate the intestinal carbohydrate absorption, thereby reducing postprandial insulin level (Goldstein et al., 1998). Among the titled abeo-oleanenes, the one with 24(4→23)-abeo-oleanene framework (**TG$_3$**) displayed significantly higher α-amylase and α-glucosidase inhibitory properties (IC_{50} 0.32 and 0.29 mM, respectively) over that bearing 24(4→23), 27(8→26), 30(20→29)-tris-abeo-oleanene moiety (**TG$_2$**) (IC_{50} 0.40 and 0.34 mM, respectively). The higher α-amylase and α-glucosidase inhibitory properties of 24(4→23)-abeo-oleanene framework (**TG$_3$**) (IC_{50} 0.32 and 0.29 mM, respectively) exhibited close resemblance towards the reference carbolytic enzyme inhibitor acarbose (IC_{50} 0.22 and 0.19 mM, respectively mM). *In vitro* radical scavenging assays by $ABTS^+$ and DPPH radicals were employed to deduce the antioxidant properties of studied abeo-oleanenes. The studied compound, **TG$_3$** exhibited greater radical scavenging activities (IC_{50} DPPH 1.33 mM; IC_{50} $ABTS^+$ 1.09 mM), when compared to those displayed by compound **TG$_2$** (IC_{50} DPPH 1.56 mM; IC_{50} $ABTS^+$ 1.24 mM) and standard, *α*-tocopherol (IC_{50} DPPH 1.49 mM; IC_{50} $ABTS^+$

1.69 mM). The isolated abeo-labdane registered significantly lesser potential against pro-inflammatory COX-2 and 5-LOX (> IC_{50} 3.00 mM).

Five previously unreported xenicanes were isolated from the ethyl acetate/methanol extract of *P. tetrastromatica* by extensive chromatographic fractionation, and were characterized by detailed spectroscopic experiments. The xeniolide derivative octahydro-1,7-dihydroxy-4-(4^1-hydroxy-4^2-methylpropyl)-6-(6^1-hydroxy-6^2-propenyl)-10-methyl-cyclonona[*c*]pyran-3(*1H*)-one (**TP_5**) showed potential antioxidant and anti-inflammatory activities, with greater selectivity index pro-inflammatory cyclooxygenase-2 than other studied xenicane derivatives and ibuprofen. Molecular docking analysis inferred that the xeniolide derivative **TP_5** exhibited efficient interactions with 5-lipoxygenase, which validated its greater inhibitory potential against the pro-inflammatory enzyme. In particular, the xeniolide-type diterpenoids with octahydrocyclonona[*c*]pyran-3(1*H*)-one backbone could be potential functional food components for use against inflammatory diseases. The biologically active xeniolides isolated from brown seaweed *P. tetrastromatica* might constitute a promising potential natural alternative to the commercially available synthetic antioxidants and anti-inflammatory agents.

The EtOAc-MeOH extract of *P. tetrastromatica* was fractionated by repeated chromatographic techniques to obtain five unprecedented dolabellane and dolastane analogues, named 6-methoxy-dolabella-8(17),12-diene-10*β*,18-diol (**TP_6**), 3-methoxy-dolabella-12(18)-ene-4*β*-ol **TP_7**), 3-methoxy-dolabella-10,18(19)-diene-5*α*,8*β*-diol (**TP_8**) along with two previously unreported dolastanes 2,7-dimethoxy-14*α*-hydroxy-dolasta-1(15),9-diene (**TP_9**) and 4,7-dimethoxy-9*β*,14*α*-dihydroxy-dolasta-1-ene (**TP_{10}**). This is the first report of isolation of dolabellane and dolastane terpenoids from *P. tetrastomatica*. The structural features of the studied compounds were characterised using comprehensive spectroscopic techniques. The compounds **TP_6** and **TP_{10}** displayed greater inhibitory activities against starch digesting enzymes, and their activities were greater than those exhibited by acarbose. In particular, 4,7-dimethoxy-9,14-dihydroxy-dolasta-1-ene (**TP_{10}**) was found to be an effective dual inhibitors of *α*-amylase and *α*-glucosidase along with potential antioxidative properties, and therefore, could be utilised as potential antioxidant/anti-diabetic pharmacophore in medicinal applications.

Among two classes of diterpene compounds derived from *G. salicornia*, **TG_{14}** belonging to macrolide class of chemistries was registered significantly higher anti-inflammatory activity.

The present study demonstrated that the marine-derived polysaccharide and its nano composite (P-Ag-NPs) with the silver particles derivative constituted promising candidates to

combat the hyperglycemic conditions. The titled polysaccharide derivatives were found to be effective in attenuating DPP-IV enzyme and carbolytic enzymes such as α-amylases and α-glucosidases. Here we have extracted the novel (DPP)-IV inhibiting polysaccharide, A (1⋯→3)-*O*-6-sulfonato-β-D-galactopyranosyl-(1→⋯4)-3,6-anhydro-α-D-galactopyranose-(1⋯→) from red seaweed *Gracilaria salicornia.* The seaweed derived polysaccharide registered greater reduction potentials against proteolytic DPP-IV (IC_{50} 0.63 mg mL^{-1}) and carbolytic α-amylase and α-glucosidase (IC_{50} 0.98-0.87 mg mL^{-1}) were comparable with those displayed by acarbose (IC_{50} DPP-IV 0.13 mg mL^{-1}, carbolytics IC_{50} 1.38-1.47 mg mL^{-1}) whereas the antioxidative potential of polysaccharide was higher (IC_{50} 0.35-0.48 mg mL^{-1}) than that of commercial standard ascorbic acid (IC_{50} 0.37-0.51 mg mL^{-1}). The presence of chemical constituents in polysaccharide was assessed by analytical methods which were corroborated with the bioactivity of polysaccharide. The polysaccharides were exhibited lower binding energy conformation (-11.13 kcal mol^{-1}) towards catalytic binding site of DPP-IV and this was also reinforced with the bioactivity of polysaccharide. Based on the bioactivity, silver-nano-composite of polysaccharide was synthesized to reduce the risk of hyperglycemia. The polysaccharide-silver-nano-composite (P-Ag-NP-composite) was demonstrated greater inhibition potential against proteolytic (DPP-IV IC_{50} 0.22 mg mL^{-1}) and carbolytic enzyme (α-amylase and α-glucosidase IC_{50} 0.52-0.70 mg mL^{-1}, respectively) than that of polysaccharide motif (≥ 1.0 mg mL^{-1} and ≥ 0.6 mg mL^{-1}, respectively) whereas they have exhibited greater antioxidant potentials (IC_{50} 0.32-0.41 mg mL^{-1}) than those displayed by polysaccharide motif. The nano particle synthesized from polysaccharide was found to be covered the range of 4-400 nm in different time intervals of 30, 60 and 120 min, by the X-ray diffraction analysis and their shape was assigned as spherical by SEM-EDX, TEM and AFM morphological analysis. The average size, distribution and the stability of nano particle were assigned by particle size analysis; the average size and zeta potential distribution of nano particle at different time intervals 30, 60 and 120 min were assigned as 389, 98 and 9 nm and -23, -25 and 0.28 respectively. The inhibition potential of polysaccharide and its silver nano composite against DPP-IV along with antioxidant potential suggested the formulation of bioactive leads to reduce the risk of hyperglycemic pathologies.

REFERENCES

A. Maneesh, K. Chakraborty, Previously undescribed fridooleanenes and oxygenated labdanes from the brown seaweed *Sargassum wightii* and their protein tyrosine phosphatase-1B inhibitory activity. Phytochemistry. 144 (2017) 19–32.

A. Wojdylo, J. Oszmianski, R. Czemerys, Antioxidant activity and phenolic compounds in 32 selected herbs. Food Chem. 105 (2007) 940–949.

A. Wojdylo, J. Oszmianski, R. Czemerys, Antioxidant activity and phenolic compounds in 32 selected herbs, Food Chem. 105 (2007) 940–949.

A.G. Gonzalez, J.M. Arteaga, J.J. Fernandez, J.D. Martin, M. Norte, J.Z. Ruano, Terpenoids of the red alga *Laurencia pinnatifida*, Tetrahedron. 40(14) (1984) 2751–2755.

A.L. Lane, L. Mular, E.J. Drenkard, T.L. Shearer, S. Engel, S. Fredericq, C.R. Fairchild, J. Prudhomme, K. Le Roch, M.E. Hay, W. Aalbersberg, J. Kubanek, Ecological leads for natural product discovery: Novel sesquiterpene hydroquinones from the red macroalga *Peyssonnelia sp*. Tetrahedron. 66 (2010) 455–461.

Abad, M.J., Bedoya, L.M., Bermejo, P., 2008. Natural marine anti-inflammatory products. Mini Rev. Med. Chem. 8(8), 740–754.

Abdelgaleil, S., Doe, M., Morimoto, Y., and Nakatani, M., 2006. Rings B, D-seco limonoids from the leaves of *Swietenia mahogani*. Phytochemistry. 67(5), 452–458.

Ahmad Z, Mehmood S, Fatima I, Malik A, Ifzal R, Afza N, Iqbal L, Latif M, Nizami TA (2008) Structural determination of salsolins A and B, new antioxidant polyoxygenated triterpenes from *Salsola baryosma* by 1D and 2D NMR spectroscopy. Magn Reson Chem 46:94-98.

Antony T, Chakraborty K (2018) First report of antioxidant abeo-labdane type diterpenoid from intertidal red seaweed *Gracilaria salicornia* with 5-lipoxygenase inhibitory potential. Nat Prod Res doi:10.1080/14786419.2018.1508150. Online published.

Antony T, Chakraborty K. 2018. First report of antioxidant abeo-labdane type diterpenoid from intertidal red seaweed *Gracilaria salicornia* with 5-lipoxygenase inhibitory potential. Nat Prod Res. Epub ahead of print, doi: 10.1080/14786419.2018.1508150.

Antony T, Chakraborty K. 2018. First report of antioxidant abeo-labdane type diterpenoid from intertidal red seaweed *Gracilaria salicornia* with 5-lipoxygenase inhibitory potential. Nat Prod Res. Epub ahead of print, doi:10.1080/14786419.2018.1508150.

Antony T, Chakraborty K. 2018. First report of antioxidant abeo-labdane type diterpenoid from intertidal red seaweed *Gracilaria salicornia* with 5-lipoxygenase inhibitory potential. Nat Prod Res. Epub ahead of print, doi:10.1080/14786419.2018.1508150.

Antony, T., and Chakraborty, K. 2019. Xenicanes attenuate pro-inflammatory 5-lipoxygenase: Prospective natural anti-inflammatory leads from intertidal brown seaweed *Padina tetrastromatica*. Med. Chem. Res. 28(4): 591-607.

Antony, T., Chakraborty, K., 2018. First report of antioxidant abeo-labdane type diterpenoid from intertidal red seaweed *Gracilaria salicornia* with 5-lipoxygenase inhibitory potential. Nat. Prod. Res. Epub ahead of print, doi: 10.1080/14786419.2018.1508150.

Antony, T., Chakraborty, K., 2019. Pharmacological properties of seaweeds against progressive lifestyle diseases. J. Aquat. Food Prod. T. Epub ahead of print, doi: 10.1080/10498850.2019.1684407.

Atkinson, A.B., and Rovertson, J. 1979. Captopril in the treatment of clinical hypertension and cardiac failure. Lancet. 2: 836–839.

Awad NE, Selim, MA, Metawe HM, Matloub AA (2008) Cytotoxic xenicane diterpenes from the brown alga *Padina pavonia* (L.). Gaill. Phytother Res 22: 1610-1613.

Ayala A, Muñoz MF, Argüelles S (2014). Lipid peroxidation: production, metabolism, and signaling mechanisms of malondialdehyde and 4-hydroxy-2-nonenal. Oxidative medicine and cellular longevity. Article ID 360438, 31 pages.

B.J.M. Jansen, A. de Groot, Occurrence, biological activity and synthesis of drimane sesquiterpenoids. Nat. Prod. Rep. 21 (2004) 449–477.

B.K. Carte, Biomedical potential of marine natural products: Marine organisms are yielding novel molecules for use in basic research and medical applications, Bioscience. 46 (1996) 271–286.

Bansemir A, Blume M, Schroder S, Lindequist U. 2006. Screening of cultivated seaweeds for antibacterial activity against fish pathogenic bacteria. Aquaculture. 252(1):79-84.

Barrento S, Camus C, Sousa-Pinto I, Buschmann AH (2016) Germplasm banking of the giant kelp: Our biological insurance in a changing environment. Algal Res 13: 134-140.

Bartoli A, Rodier F, Commeiras L, Parrain J.L, Chouraqui G. 2011. Construction of spirolactones with concomitant formation of the fused quaternary centre -application to the synthesis of natural products. Nat Prod Rep. 28:763-782.

Baylac S, Racine P (2003) Inhibition of 5-lipoxygenase by essential oils and other natural fragment extracts. Int J Aromather 13:138-142.

Baylac S, Racine P (2003). Inhibition of 5-lipoxygenase by essential oils and other natural fragment extracts, Int J Aromather. 13 138-142.

Baylac S, Racine P. 2003. Inhibition of 5-lipoxygenase by essential oils and other natural fragment extracts. Int J Aromather. 13(2-3):138-142.

Baylac S, Racine P. 2003. Inhibition of 5-lipoxygenase by essential oils and other natural fragment extracts. Int J Aromather. 13(2-3):138-142.

Baylac S, Racine P. 2003. Inhibition of 5-lipoxygenase by essential oils and other natural fragment extracts. Int J Aromather. 13(2-3):138-142.

Baylac, S., and Racine, P. 2003. Inhibition of 5-lipoxygenase by essential oils and other natural fragrant extracts. Int. J. Aromather. 13: 138–142.

Baylac, S., Racine, P., 2003. Inhibition of 5-lipoxygenase by essential oils and other natural fragment extracts. Int. J. Aromather. 13(2-3), 138-142.

Birringer M, Siems K, Maxones A, Frank J, Lorkowski S. 2018. Natural 6-hydroxy-chromanols and chromenols: Structural diversity, biosynthetic pathways and health implications. RSC Adv. 8(9):4803-4841.

Bishara A, Rudi A, Goldberg I, Benayahu Y, Kashman Y (2006) Novaxenicins A–D and xeniolides I–K, seven new diterpenes from the soft coral *Xenia novaebrittanniae.* Tetrahedron 62: 12092-12097.

Blunt JW, Carroll AR, Copp BR, Davis RA, Keyzers RA, Prinsep MR (2018). Marine natural products. Nat Prod Rep 35, 8-53.

Blunt JW, Copp BR, Hu W, Munro MHG, Northcote PT, Prinsep M (2008). Marine natural products. Nat Prod Rep 25, 35-94.

Blunt JW, Copp BR, Hu WP, Munro MHG, Northcotec PT, Prinsep MR (2009) Marine natural products. Nat Prod Rep 26(2): 170-244.

Blunt JW, Copp BR, Keyzers RA, Munro MH, Prinsep MR (2012). Marine natural products. Nat Prod Rep 29 (2), 144.

Blunt JW, Copp BR, Keyzers RA, Munro MH, Prinsep MR (2013). Marine natural products. Nat Prod Rep 30 (2), 237-323.

Blunt JW, Copp BR, Keyzers RA, Munro MH, Prinsep MR (2014). Marine natural products. Nat Prod Rep 31 (2), 160-258.

Blunt JW, Copp BR, Keyzers RA, Munro MHG, Prinsep MR (2017). Marine natural products. Nat Prod Rep 34, 235-294.

Blunt JW, Copp BR, Munro MHG, Northcote PT, Prinsep MR. 2006. Marine natural products. Nat Prod Rep. 23:26-78.

Blunt, J.W., Copp, B.R., Keyzers, R.A., Munro, M.H., Prinsep, M.R., 2013. Marine natural products. Nat. Prod. Rep. 30(2), 237–323.

Brayer GD, Luo Y, Withers SG (1995) The structure of human pancreatic alpha-amylase at 1.8 A resolution and comparisons with related enzymes. Protein Sci 4:1730-1742.

C. Rice-Evans, D. Leake, K.R. Bruckdorfer, A.T. Diplock, Practical approaches to low density lipoprotein oxidation: Whys, wherefores and pitfalls. Free Radic. Res. 25 (1996) 285–311.

C.A. Lipinski, Lead and drug-like compounds: The rule-of-five revolution. Drug. Discov. Today Technol. 1, (2004) 337–341.

C.A. Lipinski, Lead and drug-like compounds: The rule-of-five revolution, Drug Discov. Today Technol. 1(4) (2004) 337–341.

C.E. McNamara, L. Larsen, N.B. Perry, J.L. Harper, M.V. Berridge, E.W. Chia, M. Kelly, V.L. Webb, Anti-inflammatory sesquiterpene-quinones from the New Zealand sponge *Dysidea cf. Cristagalli*. J. Nat. Prod. 68 (2005) 1431–1433.

C.N. Serhan, J. Savill, Resolution of inflammation: The beginning programs the end. Nat. Immunol. 6 (2005) 1191–1197.

C.N. Serhan, J. Savill, Resolution of inflammation: The beginning programs the end, Nat. Immunol. 6 (2005) 1191–1197.

C.S. Vairappan, T. Kamada, W.-W. Lee, Y.-J. Jeon, Anti-inflammatory activity of halogenated secondary metabolites of *Laurencia snackeyi* (Weber-van Bosse) Masuda in LPS-stimulated RAW 264.7 macrophages, J. Appl. Phycol. 25 (2013) 1805–1813.

Cai X-H, Wang Y-Y, Zhao P-J, Li Y, Luo X-D. 2010. Dolabellane diterpenoids from *Aglaia odorata*. Phytochemistry. 71:1020–1024.

Calder PC, (2009). Polyunsaturated fatty acids and inflammatory processes: New twists in an old tale. Biochimie. 91, 791-795.

Cardozo, K.H.M., Guaratini, T., Barros, M.P., Falcao, V.R., Tonon, A.P., Lopes, N.P., Campos, S., Torres, M.A., Souza, A.O., and Colepicolo, P. 2007. Review: Metabolites from algae with economical impact. Comp. Biochem. Physiol. C: Toxicol. Pharmacol. 146: 60–78.

Carroll AR, Copp BR, Davis RA, Keyzers RA, Prinsep MR (2019). Marine natural products. Nat Prod Rep 36, 122-173.

Cen-Pacheco F, Nordstrom L, Souto ML, Martin MN, Fernandez JJ, Daranas AH (2010) Review: Studies on polyethers produced by red algae. Mar Drugs 8:1178-1188.

Chakraborty K (2010a). A process to prepare antioxidant and anti-inflammatory concentrates from brown and red seaweeds and a product thereof. Patent Grant number 294451 (2064/CHE/2010-Indian patent).

Chakraborty K (2010b). A process to prepare antioxidant and anti-inflammatory concentrates from brown and red seaweeds and a product thereof. Patent Grant number 294451 (2064/CHE/2010-Indian patent).

Chakraborty K (2010b). A product containing anti-inflammatory principles from brown seaweeds (Indian patent Appl. no. 5199/CHE/2012-Grant order under Section 43 due).

Chakraborty K (2010c). A product containing anti-inflammatory principles from brown seaweeds (Indian patent Appl. no. 5199/CHE/2012-Grant order under Section 43 due).

Chakraborty K (2010d). A process to concentrate anti-inflammatory principles from green mussel *Perna viridis L*. and a product incorporating these ingredients. Patent Grant number 302803 (2065/CHE/2010-Indian patent).

Chakraborty K and Joseph D (2016). Anti-inflammatory concentrate enriched with substituted oligofucans derived from brown seaweed *Turbinaria conoides* (J. Agardh) Kützing and its safety assessment on wistar rats. J. Aquat. Food Prod. Technol. 25(8), 1323-1338.

Chakraborty K et al (2010a). A product containing anti-inflammatory principles from green mussel *Perna viridis L*. and a process thereof. Patent Grant number 303813 (2066/CHE/2010-Indian patent)

Chakraborty K et al (2015b) A process to prepare antidiabetic concentrates from seaweeds and a product thereof (Indian Patent Appl. no. 3366/DEL/2015)

Chakraborty K et al (2015c). Anti-inflammatory principles in a preparation of brown seaweeds (Indian Patent Appl. no. 4254/DEL/2015)

Chakraborty K et al (2017d). A process to prepare anti-dyslipidemic concentrate from seaweed and a product therof (Indian Patent Appl. no. 201711018741)

Chakraborty K, Antony T (2019a). First report of spiro-compounds from marine macroalga *Gracilaria salicornia*: Prospective natural anti-inflammatory agents attenuate 5-lipoxygenase and cyclooxygenase-2. Nat Prod Res.1608545, 1-12

Chakraborty K, Antony T, Joy M (2019). Prospective natural anti-inflammatory drimanes attenuating pro-inflammatory 5-lipoxygenase from marine macroalga *Gracilaria salicornia*. Algal Res, 39, 101472.

Chakraborty K, Antony T, Joy M (2019b). Prospective natural anti-inflammatory drimanes attenuating pro-inflammatory 5-lipoxygenase from marine macroalga *Gracilaria salicornia*. Algal Res. 39, 101472.

Chakraborty K, Chakkalakal SJ, Joseph D (2014). Response of pro-inflammatory prostaglandin contents in anti-inflammatory supplements from green mussel *Perna viridis L*. in a time-dependent accelerated shelf-life study. J. Funct Foods. 7, 527-540.

Chakraborty K, Dhara S (2019). First report of substituted 2*H*-pyranoids from brown seaweed *Turbinaria conoides* with antioxidant and anti-inflammatory activities. Nat Prod Res.DOI: 10.1080/14786419.1578761

Chakraborty K, Joseph D, Praveen NK (2015a). Antioxidant activities and phenolic contents of three red seaweeds (Division: Rhodophyta) harvested from the Gulf of Mannar of Peninsular India. J Food Sci Technol 52(4), 1924-1935.

Chakraborty K, Joseph D, Vamshi KR (2016). Anti-inflammatory concentrate enriched with substituted oligofucans derived from brown seaweed Turbinaria conoides (J. Agardh) Kützing and its safety assessment on wistar rats. J Aquat Food Prod. T 25 (8), 1323-1338.

Chakraborty K, Joseph D, Vamshi KR (2016.) Anti-inflammatory concentrate enriched with substituted oligofucans derived from brown seaweed *Turbinaria conoides* (J. Agardh) Kützing and its safety assessment on wistar rats. J Aquat Food Prod T 25 (8), 1323-1338.

Chakraborty K, Lipton AP, Paulraj R, Vijayan KK. 2010. Antibacterial labdane diterpenoids of *Ulva fasciata* Delile from southwestern coast of the Indian Peninsula. Food Chem.119:1399-1408.

Chakraborty K, Raola V K (2018) Oxygenated heterocyclic metabolites with dual cyclooxygenase-2 and 5-lipoxygenase inhibitory potentials from *Rhizophora annamalayana*. Med Chem Res 27: 1679-1689.

Chakraborty, K., Antony, T., and Joy, M. 2019. Prospective natural anti-inflammatory drimanes attenuating pro-inflammatory 5-lipoxygenase from marine macroalga *Gracilaria salicornia.* Algal Res. 39: 101472.

Chakraborty, K., Krishnan, S., Joy, M., 2019. Macrocyclic lactones from seafood *Amphioctopus neglectus*: Newly described natural leads to attenuate angiotensin-II induced cardiac hypertrophy. Biomed. Pharmacother. 110, 155–167.

Chakraborty, K., Thilakan, B., Chakraborty, R.D., Raola, V.K., Joy, M., 2017. *O*-heterocyclic derivatives with antibacterial properties from marine bacterium *Bacillus subtilis* associated with seaweed, *Sargassum myriocystum*. Appl. Microbiol. Biotechnol. 101, 569–583.

Chakraborty, K., Thilakan, B., Raola, V.K., 2014. Polyketide family of novel antibacterial 7-*O*-methyl-5′-hydroxy-3'-heptenoate-macrolactin from seaweed-associated *Bacillus subtilis* MTCC 10403. J. Agric. Food. Chem. 62(50), 12194–12208.

Chia YY, Kanthimathi MS, Khoo KS, Rajarajeswaran J, Cheng HM, Yap WS (2015) Antioxidant and cytotoxic activities of three species of tropical seaweeds. BMC Complement Altern Med 15: 339.

Chinou I, 2005. Labdanes of natural origin-biological activities. Curr Med Chem. 12(11):1295-1317.

Cho, M.L., Lee, H.S., Kang, I.J., Won, M.H., and You, S.G. 2011. Antioxidant properties of extract and fractions from *Enteromorpha prolifera*, a type of green seaweed. Food Chem. 127: 999–1006.

Cismas C, Terec A, Mager S, Grosu I. 2005. Six-membered ring spiranes: Carbocycles and heterocycles with oxygen. Curr Org Chem. 9(14):1287-1314.

Costa, P., Gonçalves, S., Andrade, P.B., Valentao, P., and Romano, A. 2011. Inhibitory effect of *Lavandula viridis* on Fe^{2+}-induced lipid peroxidation, antioxidant and anti-cholinesterase properties. Food Chem. 126: 1779–1786.

Cui Y, Luo D (2008). Fucoidan: Advances in the study of its anti-inflammatory and antioxidative effects. Yao Xue Xue Bao [Acta Pharmaceutica Sinica]. 43(12):1186-1189

Curtiss, C., Chon, J.N., Vrobel, T., and Francious, J.A. 1978. Role of the rennin-angiotensin system in the systemic vasoconstriction of chronic congestive heart failure. Circulation. 58: 763–770.

D.J. Faulkner, Marine natural products, Nat. Prod. Rep. 19 (2002) 1–48.

D'Orazio N, Gammone MA, Gemello E, De Girolamo M, Cusenza S, Riccioni G (2012) Marine bioactives: Pharmacological properties and potential applications against inflammatory diseases. Mar Drugs 10: 812-833.

Da Rocha CQ, Vilela FC, Santa-Cecilia FV, Cavalcante GP, Vilegas W, Giusti-Paiva A, Dos Santos MH (2015) Oleanane-type triterpenoid: An anti-inflammatory compound of the roots *Arrabidaea brachypoda.* Rev Bras Farmacogn 25:228-232.

Davyt D, Enz W, Manta E, Navarro G, Norte M. 1997. New Chromenols from the brown alga *Desmarestia menziesii*. Nat Prod Lett. 9(4):305-312.

Davyt D, Fernandez R, Suescun L, Mombru AW, Saldana J, Dominguez L, Coll J, Fujii MT, Manta E. 2001. New sesquiterpene derivatives from the red alga *Laurencia scoparia*. Isolation, structure determination, and anthelmintic activity. J Nat Prod. 64(12):1552-1555.

De Almeida CLF, Falcao HDF, Lima GRDM, Montenegro CDA, Lira NS, de Athayde-Filho PF, Rodrigues LC, de Souza MDFV, Barbosa-Filho JM, Batista LM (2011) Bioactivities from marine algae of the genus *Gracilaria.* Int J Mol Sci 12:4550-4573.

Demetzos C, Dimas, KS. 2001. Labdane-type diterpenes: Chemistry and biological activity. Stud Nat Prod Chem. 25:235-292.

Dewi, M. K., Arsianti, A., Zagloel, C. R. Z., Aziza, Y. A. N., Kurniasari, K.D., Mandasaril, B.K.D., Masita, R., Zulfa, F. R., Azizah,N.N., and Putrianingsih, R. 2018. *In vitro* evaluation of seaweed *Gracilaria verrucosa* for cytotoxic activity against Cervical HeLa Cells. Pharmacogn. J. 10: 1007-1011.

Driggers, E.M., Hale, S.P., Lee, J., Terrett, N.K., 2008. The exploration of macrocycles for drug discovery an underexploited structural class. Nat. Rev. Drug. Discov. 7(7), 608–624.

E. Ibanez, M. Herrero, J. Mendiola, M. Castro-Puyana, Extraction and characterization of bioactive compounds with health benefits from marine resources: Macro and micro algae, cyanobacteria, and invertebrates. In: M. Hayes, (Eds.), Marine bioactive compounds: Sources, characterization and applications (Chapter 2), Springer US, New York, USA, 2012, pp. 55–98.

E. Perez-Garcia, E. Zubia, M.J. Ortega, J.L. Carballo, Merosesquiterpenes from two sponges of the genus *Dysidea*. J. Nat. Prod. 68 (2005) 653–658.

E.S. Silverman, J.M. Drazen, The biology of 5-lipoxygenase: Function, structure and regulatory mechanisms. Proc. Assoc. Am. Physicians. 111 (1999) 525–536.

El-Beih AA, Kato H, Ohta T, Tsukamoto S. 2007. (3R,4aR,5S,6R)-6-hydroxy-5-methylramulosin: A new ramulosin derivative from a marine-derived sterile mycelium. Chem Pharm Bull. 55:953-954.

Esterbauer, H., Pubi, H., and Dieber-Rothender, M. 1991. Effect of antioxidants on oxidative modification of LDL. Ann. Med. 23: 573–81.

F. Makkar, K. Chakraborty, Antioxidant and anti-inflammatory oxygenated meroterpenoids from the thalli of red seaweed *Kappaphycus alvarezii*, Med. Chem. Res. 27 (2018) 2016–2026.

F. Makkar, K. Chakraborty, Highly oxygenated antioxidative 2*H*-chromen derivative from the red seaweed *Gracilaria opuntia* with pro-inflammatory cyclooxygenase and lipoxygenase inhibitory properties. Nat. Prod. Res. (2017) Epub ahead of print. doi:10.1080/14786419.2017.1378209.

F. Makkar, K. Chakraborty, Highly oxygenated antioxidative 2*H*-chromen derivative from the red seaweed *Gracilaria opuntia* with pro-inflammatory cyclooxygenase and lipoxygenase inhibitory properties, Nat. Prod. Res. 32 (2019) 2756–2765.

F. Makkar, K. Chakraborty, Novel furanyl derivatives from the red seaweed *Gracilaria opuntia* with pharmacological activities using different *in vitro* models. Med. Chem. Res. 27 (2018) 1245–1259.

F. Makkar, K. Chakraborty, Novel furanyl derivatives from the red seaweed *Gracilaria opuntia* with pharmacological activities using different *in vitro* models, Med. Chem. Res. 27 (2018) 1245–1259.

F.C. Pacheco, J.A. Villa-Pulgarin, F. Mollinedo, M.N. Martin, J.J. Fernandez, A.H. Daranas, New polyether triterpenoids from *Laurencia viridis* and their biological evaluation, Mar. Drugs. 9(11) (2011) 2220–2235.

F.C. Pacheco, L. Nordstrom, M.L. Souto, M.N. Martin, J.J. Fernandez, A.H. Daranas, Studies on polyethers produced by red algae, Mar. Drugs. 8 (2010) 1178–1188.

Faulkner DJ. 1996. Marine natural products. Nat Prod Rep. 13:75–125.

Faulkner DJ. Marine natural products (1998) Nat Prod Rep 15: 113-158.

Faulkner, D.J. 2002. Marine natural products. Nat. Prod. Rep. 19: 1–49.

Fazeela MBS, Hemalatha S (2017). Characterisation, in silico and in vitro determination of antidiabetic and anti-inflammatory potential of ethanolic extract of *Sargassum wightii*. Asian J. Pharm. Clin. Res.10, 297-301.

Fernandes E, Costa D, Toste SA, Lima JLFC, Reis S (2004). In vitro scavenging activity for reactive oxygen and nitrogen species by nonsteroidal anti-inflammatory indole, pyrrole, and oxazole derivative drugs. Free RadicBiol Med. 37, 1895-1905.

Fernando IPS, Nah JW, Jeon YJ (2016). Potential anti-inflammatory natural products from marine algae. Environ. Toxicol. Pharmacol. 48, 22-30.

Francavilla M, Franchi M, Monteleone M, Caroppo C (2013) The red seaweed *Gracilaria gracilis* as a multi products source. Mar Drugs 11:3754-3776.

Funk, C.D., 2001. Prostaglandins and leukotrienes: Advances in eicosanoid biology. Science 294, 1871–1875.

G. Genta-Jouve, O.P. Thomas, Sponge chemical diversity: From biosynthetic pathways to ecological roles. Adv. Mar. Biol. 62 (2012) 183–230.

G.M. Cragg, D.J. Newman, Natural products as sources of new drugs over the last 25 years, J. Nat. Prod. 70 (2007) 461–477.

G.M. Cragg, P.G. Grothaus, D.J. Newman, Impact of natural products on developing new anti-cancer agents, Chem. Rev. 109 (2009) 3012–3043.

Ganesan P, Chandini SK, Bhaskar N (2008). Antioxidant properties of methanol extract and its solvent fractions obtained from selected Indian red seaweeds. Bioresour Technol 99, 2717-2723.

Garcia DG, Bianco EM, Santos MCB, Pereira RC, Faria MVD, Teixeira VL, Burth P. 2009. Inhibition of mammal Na^+/K^+-ATPase by diterpenes extracted from the Brazilian brown alga *Dictyota cervicornis*. Phytother Res. 23:943–947.

Gaven KMC, Percot A (2010). Alkaloids in marine algae. Mar Drugs. 8(2):269-284

Gilbert NC, Rui Z, Neau DB, Waight MT, Bartlett SG, Boeglin WE, Brash AR, Newcomer ME. 2012. Conversion of human 5-lipoxygenase to a 15-lipoxygenase by a point mutation to mimic phosphorylation at Serine-663. Faseb J. 26:3222-3229.

Gilbert NC, Rui Z, Neau DB, Waight MT, Bartlett SG, Boeglin WE, Brash AR, Newcomer ME. 2012. Conversion of human 5-lipoxygenase to a 15-lipoxygenase by a point mutation to mimic phosphorylation at Serine-663. Faseb J. 26:3222-3229.

Gilbert, N.C., Rui, Z., Neau, D.B., Waight, M.T., Bartlett, S.G., Boeglin, W.E., Brash, A.R., Newcomer, M.E., 2012. Conversion of human 5-lipoxygenase to a 15-lipoxygenase by a point mutation to mimic phosphorylation at serine-663. FASEB. J. 26, 3222–3229.

Goldstein BJ, Ahmad F, Ding, W, Li PM, Zhang WR (1998) Regulation of the insulin signaling pathway by cellular protein-tyrosine phosphatases. Mol Cell Biol 182:91-99.

Groweiss A, Shmueli U, Kashman Y (1983) Marine toxins of *Latrunculia magnifica*. J Org Chem 48: 3512-3516.

Guiry MD, Dhonncha EN. 2003. http://www.algaebase.org.

Guiry MD, Nic-dhonncha E (2003) Algaebase. J Phycol 39: 19-20.

Gulcin, I., Oktay, M., Kirecci, E., and Kufrevioglu, O.I. 2003. Screening of antioxidant and antimicrobial activities of anise (*Pimpinella anisum* L.) seed extracts. Food Chem. 83: 371–382.

H. Andriamanatoanina, G. Chambat, M. Rinaudo, Fractionation of extracted Madagascan *Gracilaria corticata* polysaccharides: Structure and properties. Carbohydr. Polym. 68 (2007) 77–88.

H. Mitome, T. Nagasawa, H. Miyaoka, Y. Yamada, R.W.M. van Soest, A new sesquiterpenoid quinone and other related compounds from the Okinawan marine sponge *Dactylospongia elegans*. J. Nat. Prod. 66 (2003) 46–50.

H. Qi, T. Zhao, Q. Zhang, Z. Li, Z. Zhao, Antioxidant activity of different molecular weight sulfated polysaccharides from *Ulva pertusa* Kjellm (Chlorophyta), J. Appl. Phycol. 17 (2005) 527–534.

H. Shimizu, T. Koyama, S. Yamada, S.A. Lipton, T. Satoh, Zonarol, a sesquiterpene from the brown algae *Dictyopteris undulata*, provides neuroprotection by activating the Nrf2/ARE pathway. Biochem. Biophys. Res. Commun. 457 (2015) 718–722.

Hamdan II, Afifi FU (2004) Studies on the *in vitro* and *in vivo* hypoglycemic activities of some medicinal plants used in treatment of diabetes in Jordanian traditional medicine. J Ethanopharmacol 93:117-121.

Hamdan, I.I., and Afifi, F.U. 2004. Studies on the *in vitro* and *in vivo* hypoglycemic activities of some medicinal plants used in treatment of diabetes in Jordanian traditional medicine. J. Ethnopharmacol. 93: 117–121.

Hanson JR. 2000. Diterpenoids. Nat Prod Rep. 17(2):165-174.

Hanson JR. 2001. Diterpenoids. Nat Prod Rep. 18(1):88-94.

Hanson JR. 2002. Diterpenoids. Nat Prod Rep. 9(2):125-132.

Hara, Y., and Honda, M., 1990. The inhibition of α–amylase by tea polyphenols. Agric. Biol. Chem. 54: 1939–1945.

Hassan EM, Mohammed MMD, Mohamed SM (2012). Two new phorbol-type diterpene esters from *Synadenium grantii* Hook F. leaves. Rec Nat Prod 6:255-262.

Henriksen EJ, Diamond-Stanic MK, Marchionne EM (2011) Oxidative stress and the etiology of insulin resistance and type-2 diabetes. Free Radic Biol Med 51:993-999.

Heo SJ, Yoon WJ (2010). Evaluation of anti-inflammatory effect of fucoxanthin isolated from brown algae in lipopolysaccharide-stimulated RAW 264.7 macrophages. Food Chem Toxicol. 48(8):2045-2051

Hill RA, Connolly JD (2012). Triterpenoids. Nat Prod Rep 29:780-818.

Hu JF, Geng MY, Zhang JT, Jiang HD (2001). An in vitro study of the structure-activity relationships of sulfated polysaccharide from brown algae to its antioxidant effect. J Asian Nat Prod Res 3, 353-358.

Huang R, Zhou X (2010). Diketopiperazines from marine organisms. Chem Biodivers. 7(12):2809-2829

Huang YL, Sachi N, Tanaka T, Matsuo Y, Saito Y, Kouno I (2013) Two new oleanane-type triterpenes isolated from Japanese post-fermented tea produced by anaerobic microbial fermentation. Molecules 18:4868-4875.

Huuskonen JJ, Livingstone DJ, Tetko IV (2000) Neural network modeling for estimation of partition coefficient based on atom-type electrotopological state indices. J Chem Inf Model 40: 947-955.

Huuskonen JJ, Livingstone DJ, Tetko IV (2000). Neural network modelling for estimation of partition coefficient based on atom-type electrotopological state indices. J Chem Inf Comput Sci 40:947-955.

Huuskonen JJ, Livingstone DJ, Tetko IV. 2000. Neural network modelling for estimation of partition coefficient based on atom-type electrotopological state indices. J Chem Inf Model. 40:947-955.

Huuskonen JJ, Livingstone DJ, Tetko IV. 2000. Neural network modelling for estimation of partition coefficient based on atom-type electrotopological state indices. J Chem Inf Model. 40:947-955.

Huuskonen, J.J., Livingstone, D.J., Tetko, I.V., 2000. Neural network modeling for estimation of partition coefficient based on atom-type electrotopological state indices. J. Chem. Inf. Comput. Sci. 40, 947–955.

Hwa JK, Lee BH, Wook CB, Lee H, Shin J. 2005. Chromenes from the brown alga *Sargassum siliquastrum*. J Nat Prod. 68:716-723.

Hyun TK, Eom SH, Kim J-S (2014) Molecular docking studies for discovery of plant-derived α-glucosidase inhibitors. POJ 7:166-170.

I.S. Marcos, A. Conde, R.F. Moro, P. Basabe, D. Diez, J.G. Urones, Quinone/hydroquinone sesquiterpenes. Mini Rev. Org. Chem. 7 (2010) 230–254.

Ioannou E, Quesada A, Rahman MM, Gibbons S, Vagias C, Roussis V. 2012. Structures and antibacterial activities of minor dolabellanes from the brown alga *Dilophus spiralis*. Eur J Org Chem. 2012(27):5177–5186.

Ioannou E, Quesada A, Vagias C, Roussis V. 2008. Dolastanes from the brown alga *Dilophus spiralis*: Absolute stereochemistry and evaluation of cytotoxicity. Tetrahedron. 64:3975–3979.

Ioannou E, Vagias C, Roussis V. 2013. Isolation and structure elucidation of three new dolastanes from the brown alga *Dilophus spiralis*. Mar Drugs. 11:1104–1112.

Ioannou E, Zervoub M, Ismailc A, Ktaric L, Vagiasa C, Roussisa V (2009) 2, 6-Cyclo-xenicanes from the brown algae *Dilophus fasciola* and *Dilophus spiralis.* Tetrahedron 65: 10565-10572.

Ireland C, Faulkner DJ, Finer J, Clardy J. 1976. A novel diterpene from *Dollabella californica*. J Am Chem Soc. 98(15):4664–4665.

Iwashima M, Mori J, Ting X, Matsunaga T, Hayashi K, Shinoda D, Saito H, Sankawa U, Hayashi T. 2005. Antioxidant and antiviral activities of plastoquinones from the brown alga *Sargassum micracanthum*, and a new chromene derivative converted from the plastoquinones. Biol Pharm Bull. 28(2):374-377.

J. Martel-Pelletier, D. Lajeunesse, P. Reboul, J.P. Pelletier, Therapeutic role of dual inhibitors of 5-LOX and COX, selective and non-selective non-steroidal anti-inflammatory drugs. Ann. Rheum. Dis. 62 (2003) 501–509.

J. Martel-Pelletier, D. Lajeunesse, P. Reboul, J.P. Pelletier, Therapeutic role of dual inhibitors of 5-LOX and COX, selective and non-selective non-steroidal anti-inflammatory drugs, Ann. Rheum. Dis. 62 (2003) 501–509.

J.J. Fernandez, M.L. Souto, M. Norte, Marine polyether triterpenes, Nat. Prod. Rep. 17(3) (2000) 235–246.

J.W. Blunt, B.R. Copp, M.H.G. Munro, P.T. Northcote, M.R. Prinsep, Marine natural products, Nat. Prod. Rep. 28 (2011) 196–268.

Jaggi R, Wurgler U, Grandjean F, Weiser M, (2004). Dual inhibition of 5-lipoxygenase/cyclooxygenase by a reconstituted homeopathic remedy; possible explanation for clinical efficacy and favourable gastrointestinal tolerability. J.Inflamm. Res, 53, 150-157.

Jang KH, Lee BH, Choi BW, Lee H-S, Shin J. 2005. Chromenes from the brown alga *Sargassum siliquastrum*. J Nat Prod. 68:716-723.

Ji N-Y, Li X-M, Li K, Ding, L-P, Gloer JB, Wang B-G. 2007. Diterpenes, sesquiterpenes, and a C_{15}-acetogenin from the marine red alga *Laurencia mariannensis*. J Nat Prod. 70(12):1901-1905.

Jimenez-Escrig A, Jimenez-Jimenez I, Pulido R, Saura-Calixto F (2001) Antioxidant activity of fresh and processed edible seaweeds. J Sci Food Agric 81: 530-534.

Joshipura, K.J., Hu, F.B., and Manson, J.E. 2001. The effect of fruit and vegetable intake on risk for coronary heart disease. Ann. Intern. Med. 134: 1106–1114.

Joy M, Chakraborty K (2017a) Nutritional qualities of the low-value bivalve mollusks *Paphia malabarica* and *Villorita cyprinoides* at the estuarine waters of the southwestern coast of India. J Aquat Food Prod T 26(1): 54-70.

Joy M, Chakraborty K (2018). Antioxidative and anti-inflammatory pyranoids and isochromenyl analogues from Corbiculid bivalve clam, *Villorita cyprinoides*. Food Chem. 251, 125-134.

Joy M, Chakraborty K (2018). Specialized oxygenated heterocyclics from *Villorita cyprinoides* with cyclooxygenase-2 and 5-lipoxygenase inhibitory properties. Food Res Int. 106, 164-172

Joy M, Chakraborty K. 2017a. Previously undescribed antioxidative and anti-inflammatory chromenyls bearing 3*H*-isochromenone and furanyl-2*H*-chromenyl skeletons from the venerid clam, *Paphia malabarica* . Med Chem Res. 26(8):1708-1722.

Joy M, Chakraborty K. 2017b. First report of two new antioxidative meroterpeno 2Hpyranoids from short-necked yellow-foot clam Paphia malabarica (family: Veneridae) with bioactivity against pro-inflammatory cyclooxygenases and lipoxygenase. Nat Prod Res. 31(6):615−625.

Joy M, Chakraborty K. 2018. Antioxidative and anti-inflammatory pyranoids and isochromenyl analogues from Corbiculid bivalve clam, *Villorita cyprinoides*. Food Chem. 251:125-134.

Joy M, Chakraborty, K (2017b) Previously undescribed antioxidative and anti-inflammatory chromenyls bearing 3*H*-isochromenone and furanyl-2*H*-chromenyl skeletons from the venerid clam, *Paphia malabarica*. Med Chem Res 26: 1708-1722.

Joy, M., Chakraborty, K., 2017. Previously undescribed antioxidative and anti-inflammatory chromenyls bearing 3*H*-isochromenone and furanyl-2*H*-chromenyl skeletons from the venerid clam, *Paphia malabarica*. Med. Chem. Res. 26(8), 1708–1722.

K. Chakraborty, S.J. Chakkalakal, D. Joseph, Response of pro-inflammatory prostaglandin contents in anti-inflammatory supplements from green mussel *Perna viridis* L. in a time-dependent accelerated shelf-life study, J. Funct. Foods. 7 (2014) 527–540.

K. Chakraborty, T. Antony, M. Joy, Prospective natural anti-inflammatory drimanes attenuating pro-inflammatory 5-lipoxygenase from marine macroalga *Gracilaria salicornia*, Algal Res. 39 (2019) 101472.

K. Hagiwara, J.E.G. Hernandez, M.K. Harper, A. Carroll, C.A. Motti, J. Awaya, H.Y. Nguyen, A.D. Wright, Puupehenol, a potent antioxidant antimicrobial meroterpenoid from a Hawaiian deep-water *Dactylospongia sp*. Sponge. J. Nat. Prod. 78 (2015) 325–329.

K. Seibert, J.L. Masferrer, Role of inducible cyclooxygenase (COX-2) in inflammation, Receptor Spring. 4(1) (1994) 17–23.

K.R.R. Rengasamy, M.G. Kulkarni, W.A. Stirk, J. Van Staden, Advances in algal drug research with emphasis on enzyme inhibitors. Biotechnol. Adv. 32 (2014) 1364–1381.

Kang SM, Lee SH, Heo SJ, Kim KN, Jeon YJ (2011) Evaluation of antioxidant properties of a new compound, pyrogallol-phloroglucinol-6, 6'-bieckol isolated from brown algae, *Ecklonia cava*. Nutr Res Pract 5: 495-502.

Karawita, R., Siriwardhana, N., Lee, K.W., Heo, M.S., Yeo, I.K., and Lee, Y.D. 2005. Reactive oxygen species scavenging, metal chelating, reducing power and lipid peroxidation inhibition properties of different solvent fractions from *Hizikia fusiformis*. Eur. Food Res. Technol. 220: 363–371.

Kaza-owska K, Hsu T, (2010). Anti-inflammatory properties of phenolic compounds and crude extract from Porphyra dentata. J. Ethnopharmacol. 128(1):123-130

Kazlauskas, R., Murphy, P.T., Wells, R.J., Blackman, A.J., 1982. Macrocyclic enolethers containing an acetylenic group from the red alga *Phacelocarpus labillardieri*. Aust. J. Chem. 35, 113–120.

Kim M, Kim K, Park S, Choi H, Park S, Kim J, Jang M, Im M, Ahn D, (2017). Anti-Inflammatory effect of Sargassum patens C. Agardh ethanol extract in LPS-induced RAW264.7 cells and mouse ear edema. Korean J. Microbiol. Biotechnol. 45, 110-117.

Kim SK, Wijesekara I (2010). Development and biological activities of marine-derived bioactives: A review. J Funct Foods 2, 1-9.

Kim, A.R., Shin, T.S., Lee, M.S., Park, J.Y., Park, K.E., Yoon, N.Y. Kim, J.S., Choi, J.S., Jang, B.C., Byun, D.S., Park, N.K., and Kim, H.R. 2009. Isolation and identification of phlorotannins from *Ecklonia stolonifera* with antioxidant and anti-inflammatory properties. J. Agric. Food Chem. 57: 3483–3489.

Kindleysides S, Quek SY, Miller MR (2012) Inhibition of fish oil oxidation and the radical scavenging activity of New Zealand seaweed extracts. Food Chem 133: 1624-1631.

Kindleysides S, Quek SY, Miller MR. 2012. Inhibition of fish oil oxidation and the radical scavenging activity of New Zealand seaweed extracts. Food Chem. 133:1624-1631.

Kito, K., Ookura, R., Yoshida, S., Namikoshi, M., Ooi, T., Kusumi, T., 2008. New cytotoxic 14-membered macrolides from marine-derived fungus *Aspergillus ostianus*. Org. Lett. 10, 225–228.

Koay YC, Wong KC, Osman H, Eldeen I, Asmawi MZ (2013) Chemical constituents and biological activities of *Strobilanthes crispus* L. Rec Nat Prod 7:59-64.

Konig GM, Wright AD, Sticher O. 1991. Diterpenes from the brown alga *Dictyota divaricata*. Phytochemistry. 30:3679–3682.

Koutsaviti A, Daskalaki MG, Agusti S, Kampranis SC, Tsatsanis C, Duarte CM, Roussis V, Loannou E (2019). Thuwalallenes A–E and Thuwalenynes A–C: New C15 acetogenins with anti-inflammatory activity from a Saudi Arabian red sea *Laurencia sp*. Mar Drugs.17, 644

Kuda, T., and Ikemori, T. 2009. Minerals, polysaccharides and antioxidant properties of aqueous solutions obtained from macroalgal beach-casts in the Noto Peninsula, Ishikawa, Japan. Food Chem. 12: 575–581.

Kuda, T., Tsunekawaa, M., Goto, H., and Araki, Y. 2005. Antioxidant properties of four edible algae harvested in the Noto Peninsular, Japan. J. Food Compos. Anal. 18: 625–633.

Kulisic, T., Radonic, A., Katalinic, V., and Milos, M. 2004. Use of different methods for testing antioxidative activity of oregano essential oil. Food Chem. 85: 633–640.

Kumar S, Narwal S, Kumar V, Prakash O (2011) α-Glucosidase inhibitor from plants: A natural approach to treat diabetes. Phcog Rev 5:19-29.

Kumar V, Gill KD (2018). Estimation of urea in serum and urine. In: Basic concepts in clinical Biochemistry: A Practical Guide. Springer, Singapore.

Kwon YI, Apostolidis E, Kim YC, Shetty K (2007) Health benefits of traditional corn, beans and pumpkin: *In vitro* studies for hyperglycemia and hypertension management. J Med Food 10:266-275.

Kwon, Y.I., Apostolidis, E., Kim, Y.C., and Shetty, K. 2007. Health benefits of traditional corn beans and pumpkin *in vitro* studies for hyperglycemia and hypertension management. J. Med. Food. 10: 266–275.

L. Hui, X-M. Li, Y. Liu, P. Zhang, J-N. Wang, B-G. Wang, Chermesins A-D: Meroterpenoids with a drimane-type spirosesquiterpene skeleton from the marine algal-derived endophytic fungus *Penicillium chermesinum* EN-480. J. Nat. Prod. 79 (2015) 806-811.

L. Minale, R. Riccio, G. Sodano, Avarol, a novel sesquiterpenoid hydroquinone with a rearranged drimane skeleton from the sponge *Dysidea avara*. Tetrahedron Lett. 15 (1974) 3401–3404.

L.N. Larsen, E. Dahl, J. Bremer, Peroxidative oxidation of leuco dichloroluorescein by prostaglandin H synthase in prostaglandin biosynthesis from polyunsaturated fatty acids. Biochim. Biophys. Acta. 1299 (1996) 47–53.

L.N. Larsen, E. Dahl, J. Bremer, Peroxidative oxidation of leuco-dichloroluorescein by prostaglandin H synthase in prostaglandin biosynthesis from polyunsaturated fatty acids, Biochim. Biophys. Acta. 1299 (1996) 47–53.

Lanhers MC, Joyeux M, Soulimani R, Fleurentin J, Sayag M, Mortier F, Younos C, Pelt JM (1991). Hepatoprotective and anti-inflammatory effects of a traditional medicinal plant of Chile, Peumus boldus. Planta Med, 57(2):110-5.

Lann KL, Surget G, Couteau C, Coiffard L, Cérantola S, Gaillard F, Larnicol M, Zubia M, Guérard F, Poupart N, Valérie SP (2016) Sunscreen, antioxidant, and bactericide capacities of phlorotannins from the brown macroalga *Halidrys siliquosa*. J Appl Phycol 28: 3547-3559.

Larsen LN, Dahl E, Bremer J (1996) Peroxidative oxidation of leuco dichloroluorescein by prostaglandin H synthase in prostaglandin biosynthesis from polyunsaturated fatty acids. BBA 1299: 47-53.

Larsen LN, Dahl E, Bremer J (1996). Peroxidative oxidation of leuco-dichloroluorescein by prostaglandin H synthase in prostaglandin biosynthesis from polyunsaturated fatty acids, Biochim. Biophys. Acta. 1299 47-53.

Larsen LN, Dahl E, Bremer J. 1996. Peroxidative oxidation of leuco-dichloroluorescein by prostaglandin-H synthase in prostaglandin biosynthesis from polyunsaturated fatty acids. BBA: Lipid Lipid Met. 1299(1):47-53.

Larsen LN, Dahl E, Bremer J. 1996. Peroxidative oxidation of leuco-dichloroluorescein by prostaglandin-H synthase in prostaglandin biosynthesis from polyunsaturated fatty acids. BBA: Lipid Lipid Met. 1299(1):47-53.

Larsen LN, Dahl E, Bremer J. 1996. Peroxidative oxidation of leuco-dichloroluorescein by prostaglandin-H synthase in prostaglandin biosynthesis from polyunsaturated fatty acids. BBA: Lipid Lipid Met. 1299(1):47-53.

Larsen, L.N., Dahl, E., and Bremer, J. 1996. Peroxidative oxidation of leucodichlorofluorescein by prostaglandin H synthase in prostaglandin biosynthesis from polyunsaturated fatty acids. Biochim. Biophys. Acta. 1: 47–53.

Larsen, L.N., Dahl, E., Bremer J., 1996. Peroxidative oxidation of leuco-dichloroluorescein by prostaglandin-H synthase in prostaglandin biosynthesis from polyunsaturated fatty acids. BBA: Lipid Lipid Met. 1299(1), 47–53.

Laszczyk MN (2009) Pentacyclic triterpenes of the lupane, oleanane and ursane group as tools in cancer therapy. Planta Med 75:1549-1560.

Le Cesne A, Blay JY, Bui BN, Bouche O, Adenis A, Domont J(2010). Phase II study of oral masitinib mesilate in imatinib-naive patients with locally advanced or metastatic gastro-intestinal stromal tumour (GIST). Eur J Cancer 46, 1344-1351.

Leal MC, Munro MHG, Blunt JW, Puga J, Jesus B, Calado R (2013). Biogeography and biodiscovery hotspots of macroalgal marine natural products. Nat Prod Rep 30, 1380-1390.

Ledesma, B.H., Alvarez, P.J.M., and Pueyo, E. 2003. Assessment of the spectrophotometric method for determination of angiotensin-converting-enzyme activity: Influence of the inhibition type. J. Agric. Food Chem. 51: 4175–4179.

Lee DY, Yang H, Kim HW, Sung SH (2017) New polyhydroxy triterpenoid derivatives from fruits of *Terminalia chebula* Retz and their α-glucosidase and α-amylase inhibitory activity. Bioorg Med Chem Lett 27:34-39.

Lee, J.C., Hou, M.F., Huang, H.W., Chang, F.R., Yeh, C.C., Tang, J.Y., Chang, H.W., 2013. Marine algal natural products with anti-oxidative, anti-inflammatory, and anti-cancer properties. Cancer Cell Int. 13, 55.

Lee, S.H., Li, Y., Karadeniz, F., Kim, M.M., and Kim, S.K. 2008. α-Glucosidase and α-amylase inhibitory activities of phloroglucinol derivatives from edible marine brown alga, *Ecklonia cava*. J. Sci. Food Agric. 89: 1552–1558.

Leonid GV, Svetlana K, Tatiana NB, Alexandr BE, Valery ST. Sergey VT, Victor NK, Alexey VV. 2012. Novel synthetic route toward benzofuran-pyridine based spirans. Synth Commun. 42(22):3337-3343.

Lipinski C, Hopkins A. 2004. Navigating chemical space for biology and medicine. Nature. 432:855–861.

Lipinski CA (2004) Lead and drug-like compounds: the rule-of-five revolution. Drug Discov Today Technol 1:337-341.

Lipinski CA (2004) Lead and drug-like compounds: The rule-of-five revolution. Drug Discov Today Technol 1(4): 337-341.

Lipinski CA. 2004. Lead and drug-like compounds: The rule-of-five revolution. Drug Discov Today Technol. 1(4):337-341.

Lipinski CA. 2004. Lead and drug-like compounds: The rule-of-five revolution. Drug Discov Today Technol. 1(4):337-341.

Lipinski, C.A., 2004. Lead and drug-like compounds: the rule-of-five revolution. Drug. Discov. Today Technol. 1(4), 337–341.

Liu T, Yip YM, Song L, Feng S, Liud Y, Laid F, Zhang D, Huanga D. 2013. Inhibiting enzymatic starch digestion by the phenolic compound diboside-A: A mechanistic and in silico study. Food Res Int. 54:595–600.

Liu WK, Ling YH, Cheung FWK, Che CT, Stellettin A (2012). Endoplasmic reticulum stress in murine B16 melanoma cells. J Nat Prod 75, 586-590.

Lordan S, Ross RP, Stanton C (2011). Marine bioactives as functional food ingredients: potential to reduce the incidence of chronic diseases. Mar Drugs 9, 1056-1100.

Lorenzo-Morales J, Díaz-Marrero AR, Cen-Pacheco F, Sifaoui I, Reyes-Batlle M, Souto ML, Daranas AH, Piñero JE, Fernández JJ (2019). Evaluation of oxasqualenoids from the red alga *Laurencia viridis* against Acanthamoeba Mar Drugs.17, 420

Lowry OH, Roseborouch NI, Farrand AL, Randal RJ (1951). Protein measurement with the folin-phenol reagent. J Biol Chem, 263-275.

M. Abe, D. Inoue, K. Matsunaga, Y. Ohizumi, H. Ueda, T. Asano, M. Murakami, Y. Sato, Goniodomin A, an antifungal polyether macrolide, exhibits antiangiogenic activities via inhibition of actin reorganization in endothelial cells, J. Cell Physiol. 190 (2002) 109–116.

M. Francavilla, M. Franchi, M. Monteleone, C. Caroppo, The red seaweed *Gracilaria gracilis* as a multi products source. Mar Drugs. 11 (2013) 3754–3776.

M. Murakami, K. Makabe, S. Yamaguchi, S. Konosu, R. Walchi, A novel polyether macrolide from the dinoflagellate *Goniodoma pseudogoniaulax*, Tetrahedron Lett. 29 (1988) 1149–1152.

M. Norte, J. Fernandez, M.L. Souto, New polyether squalene derivatives from *Laurencia*, Tetrahedron. 53(13) (1997) 4649–4654.

M. Saleem, Lupeol, a novel anti-inflammatory and anti-cancer dietary triterpene, Cancer Lett. 285 (2009) 109–115.

M.B. Quin, C.M. Flynn, C. Schmidt-Dannert, Traversing the fungal terpenome. Nat. Prod. Rep. 31 (2014) 1449–1473.

Makkar F, Chakraborty K (2017). Antidiabetic and anti-inflammatory potential of sulphated polygalactans from red seaweeds *Kappaphycus alverizii* and *Gracilaria opuntia.* Int. J. Food Prop. 20(6), 1326-1337.

Makkar F, Chakraborty K (2018a) Novel furanyl derivatives from the red seaweed *Gracilaria opuntia* with pharmacological activities using different *in vitro* models. Med Chem Res 27: 1245-1259.

Makkar F, Chakraborty K (2018a). Previously undescribed antioxidative azocinyl morpholinone alkaloid from red seaweed *Gracilaria opuntia* with anti-cyclooxygenase and lipoxygenase properties. Nat Prod. Res. 32(10), 1150-1160.

Makkar F, Chakraborty K (2018b) Antioxidant and anti-inflammatory oxygenated meroterpenoids from the thalli of red seaweed *Kappaphycus alvarezii*. Med Chem Res 27: 2016-2026.

Makkar F, Chakraborty K (2019). Highly oxygenated antioxidative 2*H*-chromen derivative from the red seaweed *Gracilaria opuntia* with pro-inflammatory cyclooxygenase and lipoxygenase inhibitory properties. Nat Prod Res. 32(23), 2756-2765.

Makkar F, Chakraborty K. 2017. Unprecedented antioxidative cyclic ether from the red seaweed *Kappaphycus alvarezii* with anti-cyclooxygenase and lipoxidase activities. Nat Prod Res. 31(10):1131-1141.

Makkar F, Chakraborty K. 2017a. Unprecedented antioxidative cyclic ether from the red seaweed *Kappaphycus alvarezii* with anti-cyclooxygenase and lipoxidase activities. Nat Prod Res. 31(10):1131-1141.

Makkar F, Chakraborty K. 2017b. Highly oxygenated antioxidative 2*H*-chromen derivative from the red seaweed *Gracilaria opuntia* with pro-inflammatory cyclooxygenase and lipoxygenase inhibitory properties. Nat Prod Res. Epub ahead of print. doi:10.1080/14786419.2017.1378209.

Makkar F, Chakraborty K. 2018a. Antioxidative sulphated polygalactans from marine macroalgae as angiotensin-I converting enzyme inhibitors. Nat Prod Res. 32 (17):2100-2106.

Makkar F, Chakraborty K. 2018a. Highly oxygenated antioxidative 2*H*-chromen derivative from the red seaweed *Gracilaria opuntia* with pro-inflammatory cyclooxygenase and lipoxygenase inhibitory properties. Nat Prod Res. 32 (23):2756-2765.

Makkar F, Chakraborty K. 2018b. Antioxidative sulphated polygalactans from marine macroalgae as angiotensin-I converting enzyme inhibitors. Nat Prod Res. 32 (17):2100-2106.

Makkar F, Chakraborty K. 2018b. Previously undescribed antioxidative azocinyl morpholinone alkaloid from red seaweed *Gracilaria opuntia* with anti-cyclooxygenase and lipoxygenase properties. Nat Prod Res. 32(10):1150-1160.

Makkar F, Chakraborty K. 2018c. Previously undescribed antioxidative azocinyl morpholinone alkaloid from red seaweed *Gracilaria opuntia* with anti-cyclooxygenase and lipoxygenase properties. Nat Prod Res. 32(10):1150-1160.

Makkar F, Chakraborty K (2018b). Antioxidant and anti-inflammatory oxygenated meroterpenoids from the thalli of red seaweed *Kappaphycus alvarezii*. Med Chem. Res. 27(8), 2016-2026.

Makkar F, Chakraborty K (2019a). Highly oxygenated antioxidative 2*H*-chromen derivative from the red seaweed *Gracilaria opuntia* with pro-inflammatory cyclooxygenase and lipoxygenase inhibitory properties. Nat Prod. Res. 32(23), 2756-2765.

Makkar F. Chakraborty K (2018c). First report of dual cyclooxygenase-2 and 5-lipoxygenase inhibitory halogen derivatives from the thallus of intertidal seaweed *Kappaphycus alvarezii*. Med Chem. Res. 27, 2331-2340.

Makkar, F., Chakraborty, K., 2017. Unprecedented antioxidative cyclic ether from the red seaweed *Kappaphycus alvarezii* with anti-cyclooxygenase and lipoxidase activities. Nat Prod Res. 31(10):1131-1141.

Makkar, F., Chakraborty, K., 2018a. Antioxidative sulphated polygalactans from marine macroalgae as angiotensin-I converting enzyme inhibitors. Nat Prod Res. Epub ahead of print, doi: 10.1080/14786419.2017.1363756, 2017, 1-7

Makkar, F., Chakraborty, K., 2018b. Previously undescribed antioxidative azocinyl morpholinone alkaloid from red seaweed *Gracilaria opuntia* with anti-cyclooxygenase and lipoxygenase properties. Nat Prod Res. 32(10):1150-1160.

Makkar, F., Chakraborty, K., 2018c. Highly oxygenated antioxidative 2*H*-chromen derivative from the red seaweed *Gracilaria opuntia* with pro-inflammatory cyclooxygenase and lipoxygenase inhibitory properties. Nat Prod Res. Epub ahead of print, doi: 10.1080/14786419.2017.1378209.

Maneesh A, Chakraborty K (2017b). Unprecedented antioxidative and anti-inflammatory aryl polyketides from the brown seaweed *Sargassum wightii*. Food Research International, 100, 640–649.

Maneesh A, Chakraborty K, Makkar F (2017a). Pharmacological activities of brown seaweed *Sargassum wightii* (Family Sargassaceae) using different *in vitro* models. Int. J. Food Prop. 20, 931-945.

Maneesh A, Chakraborty K (2017) Previously undescribed fridooleanenes and oxygenated labdanes from the brown seaweed *Sargassum wightii* and their protein tyrosine phosphatase-1B inhibitory activity. Phytochem 144:19-32.

Maneesh A, Chakraborty K (2018). Pharmacological potential of sulfated polygalactopyranosyl-fucopyranan from the brown seaweed *Sargassum wightii*. J. Appl. Phycol. 30, 1971-1988.

Maneesh A, Chakraborty K. 2017. Previously undescribed fridooleanenes and oxygenated labdanes from the brown seaweed *Sargassum wightii* and their protein tyrosine phosphatase-1B inhibitory activity. Phytochem. 144: 19-32.

Maneesh A, Chakraborty K. 2017. Previously undescribed fridooleanenes and oxygenated labdanes from the brown seaweed *Sargassum wightii* and their protein tyrosine phosphatase-1B inhibitory activity. Phytochemistry. 144:19-32.

Maneesh, A., and Chakraborty, K. 2017. Previously undescribed fridooleanenes and oxygenated labdanes from the brown seaweed *Sargassum wightii* and their protein tyrosine phosphatase-1B inhibitory activity. Phytochemistry. 144: 19-32.

Maneesh, A., and Chakraborty, K. 2018. Pharmacological potential of sulfated polygalactopyranosyl-fucopyranan from the brown seaweed *Sargassum wightii*. J. Appl. Phycol. 30(3): 1971–1988.

Maneesh, A., Chakraborty, K., 2017. Unprecedented antioxidative and anti-inflammatory aryl polyketides from the brown seaweed *Sargassum wightii*. Food Res. Int. 100, 640–649.

Marsault, E., Peterson, M.L., 2011. Macrocycles are great cycles: Applications, opportunities, and challenges of synthetic macrocycles in drug discovery. J. Med. Chem. 54(7), 1961–2004.

Martel-Pelletier, J., Lajeunesse, D., Reboul, P., Pelletier, J.P., 2003. Therapeutic role of dual inhibitors of 5-LOX and COX, selective and non-selective non-steroidal anti-inflammatory drugs. Ann. Rheum. Dis. 62, 501–509.

Matsukawa, R., Dubinsky, Z., Kishimoto, E., Masaki, K., Masuda, Y., Takeuchi, T., Chihara, M., Yamamoto, Y., Niki, E., and Karube, I.A. 1997. Comparison of screening methods for antioxidant activity in seaweeds. J. Appl. Phycol. 9: 29–35.

Mayer AMS, Lehmann VKB (2000). Marine Pharmacology in 1998: Marine compounds with antibacterial, anticoagulant, anti-inflammatory, anthelmintic, antiplatelet, antiprotozoan, and antiviral activities; with actions on the cardiovascular, endocrine, immune, and nervous systems; and other miscellaneous mechanisms of action, The Pharmacologist, 42 (2), 62-69.

McNally VA, Rajabi M, Gbaj A, Stratford IJ, Edwards PN, Douglas KT, Bryce RA, Jaffar, M, Freeman S (2007) Design, synthesis and enzymatic evaluation of 6-bridged imidazolyluracil derivatives as inhibitors of human thymidine phosphorylase. J Pharm Pharmacol 59(4): 537-547.

McPhee S, Hodges LD, Wright PF, Wynne PM, Kalafatis N, Harney DW, Macrides TA (2007). Anti-cyclooxygenase effects of lipid extracts from the New Zealand green lipped mussel, *Perna canaliculus*. Comparative Biochemistry and Physiology. Part B, Biochemistry & Molecular Biology, 146, 3, 346-356.

Medeiros V, Queiroz K (2008). Sulfated galactofucan from *Lobophora variegata*: Anticoagulant and anti-inflammatory properties. Biochem (Mosc). 73(9): 1018-1024

Meenakshi S, Manicka Gnanambigai D, Tamilmozhi S, Arumugam M, Balasubramanian T (2009). Total flavanoid and in vitro antioxidant activity of two seaweeds from Rameshwaram Coast. Global J Pharmacol 3, 59-62.

Meirer, K., Steinhilber, D., Proschak, E., 2014. Inhibitors of the arachidonic acid cascade: Interfering with multiple pathways. Basic Clin. Pharmacol. Toxicol. 114, 83–91.

Milan M, Mirjana M, Desanka B, Sanja M, Neda N, Vladimir M, Vukovic N, Sukdolak S, Solujic S. 2011. *In vitro* antioxidant of selected 4-hydroxy-chromene-2-one derivatives-SAR, QSAR and DFT studies. Int J Mol Sci. 12(5):2822-2841.

Mishra, B.B., Tiwari, V.K., 2011. Natural products: An evolving role in future drug discovery. Eur. J. Med. Chem. 46(10), 4769–807.

Mohsin S, Mahadevan R, Kurup GM (2014) Free-radical-scavenging activity and antioxidant effect of ascophyllan from marine brown algae *Padina tetrastromatica.* Biomed Preventive Nutr 4: 75-79.

Mohsin S, Mahadevan R, Kurup GM. 2014. Free-radical scavenging activity and antioxidant effect of ascophyllan from marine brown algae *Padina tetrastromatica*. Biomed Prev Nutr. 4:75–79.

Molinski, T.F., Dalisay, D.S., Lievens, S.L., Saludes, J.P., 2009. Drug development from marine natural products. Nat. Rev. Drug Discov. 8(1), 69–85.

Mondol, M. A. M., Tareq, F. S., Kim, J. H., Lee, Ma, Lee, H.-S., Lee, Y.-J., Lee, J.-S., Shin, H. J. (2011). Cyclic ether-containing macrolactins, antimicrobial 24-membered isomeric macrolactones from a marine *Bacillus* sp. J. Nat. Prod. 74(12): 2582–2587.

Mondol, M., & Shin, H. (2014). Anti-bacterial and anti-yeast compounds from marine-derived bacteria. Mar. Drugs. 12(5): 2913–2921.

Mondol, M.A., Tareq, F.S., Kim, J.H., Lee, Ma, Lee, H.S., Lee, Y.J., Lee, J.S., Shin, H.J., 2011. Cyclic ether-containing macrolactins, antimicrobial 24-membered isomeric macrolactones from a marine *Bacillus sp*. J. Nat. Prod. 74(12), 2582–2587.

Monk JM, Jia Q, Callaway E, Weeks B, Alaniz RC, McMurray DN, Chapkin RS (2012). Th17 cell accumulation is decreased during chronic experimental colitis by (*n*-3) PUFA in Fat-1 mice. J Nutr 142, 117-124.

Mullane KM, Kraemer R, Smith B (1985). Myeloperoxidase activity as a quantitative assessment of neutrophil infiltration into ischemic myocardium. J. Pharmacol. Methods, 4(3),157-67.

Murakami, M., Matsuda, H., Makabe, K., Yamaguchi, K., 1991. Oscillariolide, a novel macrolide from a blue-green alga *Oscillatoria sp*. Tetrahedron Lett. 32, 2391–2394.

N. Fuestani, T. Sugawara, S. Matsunago, Potent antitumor metabolites from a marine sponge, J. Org. Chem. 57 (1992) 3828–3832.

Na M, Cui L, Min BS, Bae K, Yoo JK, Kim BY (2006) Protein tyrosine phosphatase-1B inhibitory activity of triterpenes isolated from *Astilbe koreana*. Bioorg Med Chem Lett 16:3273-3276.

Narasimhan M.K., Pavithra, S.K., Krishnan, V., and Chandrasekaran M. 2013. *In vitro* analysis of antioxidant, antimicrobial and antiproliferative activity of *Enteromorpha antenna*, *Enteromorpha linza* and *Gracilaria corticata* extracts. J. Nat. Pharm. Prod. 8: 151-159.

Nastrucci C, Cesario A and Russo P (2012). Recent Patents on Anti-Cancer Drug Discovery 7, 218-232.

Nazaruk J, Borzym-Kluczyk M (2015) The role of triterpenes in the management of diabetes mellitus and its complications. Phytochem Rev 14:675-690.

Newman DJ, Cragg GM (2012). Natural products as sources of new drugs over the 30 years from 1981 to 2010. J Nat Prod 75(3), 311-335.

Ngatu NR, Okajima MK (2012). Anti-inflammatory effects of sacran, a novel polysaccharide from *Aphanothece sacrum*, on 2,4,6-trinitrochlorobenzene-induced allergic dermatitis in vivo. Ann. Allergy Asthma Immunol.108(2):117-122. e2.

Nickavar, B., and Yousefian, N. 2011. Evaluation of α-amylase inhibitory activities of selected antidiabetic medicinal plants. J. Verbr. Lebensm. 6: 191–195.

Nitin K, Sushil K, Himanshu G, Sharma PK. 2012. 3-hydroxy-2(substituted phenyl)-4*H*-chromen-4-one derivatives-synthesis, spectral characterisation and pharmacological screening. World Res J Biochem. 1(1):1-5.

Novoa, A.V., Andrade-Wartha, E.R.S., Linares, A.F., Silva, A.M.O., Genovese, M.I., Gonzalez, A.E.B., Vuorela, P., Costa, A., and Mancini-Filho, J. 2011. Antioxidant activity and possible bioactive components in hydrophilic and lipophilic fractions from the seaweed *Halimeda incrassata*. Rev. Bras. Farmacogn. 21: 53–57.

Oramas-Royo SM, Chavez H, Martin-Rodriguez P, Fernandez-Perez L, Ravelo AG, Estevez-Braun A (2010) Cytotoxic triterpenoids from *Maytenus retusa*. J Nat Prod 73:2029-2034.

Ovenden SPB, Nielson JL, Liptrot CH, Willis RH, Tapiolas DM, Wright AD, Motti CA. 2011. Metachromins U-W: Cytotoxic merosesquiterpenoids from an Australian specimen of the sponge *Thorecta reticulata*. J Nat Prod. 74(5):1335-1338.

P. Cohen, C. Holmes, Y. Tsukitani, Okadaic acid: A new probe for the study of cellular regulation, Trends Biochem. Sci. 15 (1990) 98–102.

P. Torres, J.P. Santos, F. Chow, D.Y.A.C. dos Santos, A comprehensive review of traditional uses, bioactivity potential, and chemical diversity of the genus *Gracilaria* (Gracilariales, Rhodophyta), Algal Res. 37 (2019) 288–306.

Pacienza N, Lee RH, Bae EH, Kim DK, Liu Q, Prockop DJ, Yannarelli G (2018). *In vitro* macrophage assay predicts the *in vivo* anti-inflammatory potential of exosomes from human mesenchymal stromal cells. Mol Ther Methods Clin Dev. 13, 67-76.

Park HY, Han MH (2011). Anti-inflammatory effects of fucoidan through inhibition of NF-IB, MAPK and Akt activation in lipopolysaccharide-induced BV2 microglia cells. Food Chem. Toxicol. 49(8):1745-1752.

Pati MP, Sharma SD, Nayak L, Panda CR (2016). Uses of seaweed and its application to human welfare: a review. Int J Pharm Pharm Sci. 8(10), 12-20.

Peake M, Whiting M (2006). Measurement of serum creatinine-current status and future goals. Clin Biochem Rev. 27(4), 173-184.

Perera PRD, Ekanayake S, Ranaweera KKDS (2013) *In vitro* study on antiglycation activity, antioxidant activity and phenolic content of *Osbeckia octandra* L. leaf decoction. J Pharmacogn Phytochem 2:198-201.

Peters RJ. 2010. Two rings in them all: The labdane-related diterpenoids. Nat Prod Rep. 27(11):1521-1530.

Plaza M, Cifuentes A, Ibanez E (2008) In the search of new functional food ingredients from algae. Trends Food Sci Technol 19(1): 31-39.

R. Kurumbail, Cyclooxygenase enzymes: catalysis and inhibition, Curr. Opin. Struct. Biol. 11 (2001) 752–760.

R.M. McMillan, E.R.H. Walker, Designing therapeutically effective 5-lipoxygenase inhibitors. Trends Pharmacol. Sci. 13 (1992) 323–330.

Reitman S, Frankel S (1957). A colorimetric method for the determination of serum glutamic oxalacetic and glutamic pyruvic transaminases. Am. J. Clin Pathol, 28(1), 56-63.

Ren Q, Siau, W-Y, Du Z, Zhang K, Wang J. 2011. Expeditious assembly of a 2-amino-4*H*-chromene skeleton by using an enantioselective mannich intramolecular ring cyclization-tautomerization cascade sequence. Chem Eur J. 17(28):7781-7785.

Rocha, D.H.A., Seca, A.M.L., and Pinto, D.C.G.A. 2018. Seaweed secondary metabolites *in vitro* and *in vivo* anticancer activity. Mar. Drugs. 16(11): 410-437.

Rodriguez AD, Gonzalez E, Ramirez C. 1998. The structural chemistry, reactivity, and total synthesis of dolabellane diterpenes. Tetrahedron. 54:11683–11729.

Roth BL, Baner K, Westkaemper R, Siebert D, Rice KC, Steinberg S, Ernsberger P, Rothman RB (2002) Salvinorin A: A potent naturally occurring non nitrogenous kappa opioid selective agonist. Proc Natl Acad Sci USA 99:11934-11939.

Ruzicka L (1963) Perspectives of the biogenesis and chemistry of terpenes. Pure Appl Chem 6:493-522.

S. Baylac, P. Racine, Inhibition of 5-lipoxygenase by essential oils and other natural fragment extracts. Int. J. Aromather. 13 (2003)138–142.

S. Baylac, P. Racine, Inhibition of 5-lipoxygenase by essential oils and other natural fragment extracts, Int. J. Aromather. 13 (2003)138–142.

S. Cao, Z. Gao, S.J. Thomas, S.M. Hecht, J.S. Lazo, D.G.I. Kingston, Marine sesquiterpenoids that inhibit the lyase activity of DNA polymerase-β. J. Nat. Prod. 67 (2004) 1716–1718.

Sadaka, M. W. M., 2017. A New Neo-clerodane diterpenoid from *Teucrium polium* Linn. Int. J. Pharmacogn. 4(9): 287–293.

Salas, S., Chakraborty, K., 2018. An unreported polyether macrocyclic lactone with antioxidative and anti-lipoxygenase activities from the Babylonidae gastropod mollusc *Babylonia spirata*. Med. Chem. Res. 27(11-12), 2446–2453.

Saraswati, Giriwono PE, Iskandriati D, Tan CP, Andarwulan N (2019). *Sargassum* seaweed as a source of anti-inflammatory substances and the potential insight of the tropical species: A review, Mar. Drugs. 17, 590

Sasaki T, Li W, Morimura H, Li S, Li Q, Asada Y, Koike K (2011) Chemical constituents from *Sambucus adnata* and their protein-tyrosine phosphatase-1B inhibitory activities. Chem Pharm Bull 59:1396-1399.

Sedlak J, Lindsay RH (1968). Estimation of total, protein-bound, and nonprotein sulfhydryl groups in tissue with Ellman's reagent. Anal. Biochem, 25, 192-205.

Sekar S, Viswanathan KP, Kishnan B, Ganesan KK (2015) Evaluation of anti-hyperglycemic effect of *Gracilaria corticata* extract in normal and streptozotocin-induced diabetic rats. Chem Biol Lett 2:6-11.

Shreadah MA, Abd NM, Moneam E (2018). Phytochemical and pharmacological screening of *Sargassium vulgare* from Suez Canal, Egypt. Food Sci. Biotechnol. 27, 963-979.

Sindhu RK, Sood N, Puri V, Arora S (2017). Various animal models for preclinical testing of anti-inflammatory agents. Int J Pharm Sci Res 8(4), 1550-1557.

Singh M, Pal M, Sharma RP. 1999. Biological activity of the labdane diterpenes. Planta Med. 65(1):2-8.

Stout, E.P., Hasemeyer, A.P., Lane, A.L., Davenport, T.M., Engel, S., Hay, M.E., Fairchild, C.R., Prudhomme, J., Roch K.L., Aalbersberg, W., Kubanek, J., 2009. Antibacterial neurymenolides from the Fijian red alga *Neurymenia fraxinifolia*. Org. Lett. 11(1), 225–228.

Suleria HAR, Gobe G, Masci P, Osborne SA (2016). Marine bioactive compounds and health promoting perspectives; innovation pathways for drug discovery. Trends Food Sci Technol. 50: 44-55.

Suzuki M, Daitoh M, Vairappan CS, Abe T, Masuda M. 2001. Novel halogenated metabolites from the Malaysian *Laurencia pannosa*. J Nat Prod. 64(5):597-602.

Suzuki M, Kurosawa E, Kurata K.1988. Venustanol, a brominated labdane diterpene from the red alga *Laurencia venusta.* Phytochem. 27(4):1209-1210.

Suzuki M, Nakano S, Takahashi Y, Abe T, Masuda M, Takahashi H, Kobayashi K. 2002. Brominated labdane-type diterpenoids from an Okinawan *Laurencia sp*. J Nat Prod. 65(6):801-804.

T. Antony, K. Chakraborty, First report of antioxidant abeo-labdane type diterpenoid from intertidal red seaweed *Gracilaria salicornia* with 5-lipoxygenase inhibitory potential, Nat. Prod. Res. (2018) 1-8. doi: 10.1080/14786419.2018.1508150. Epub ahead of print.

Tahrani AA, Bailey CJ, Del Prato S, Barnett AH (2011) Management of type 2 diabetes: New and future developments in treatment. Lancet 378:182-197.

Tanaka J, Ogawa N, Liang J, Higa T, deNys R, Bowden BF, Carroll R, Coll J, Bernardinelli G, Jefford CW (1994) Helioxenicins A-C: Diterpenes from the blue coral *Heliopora coerulea*, Tetrahedron 50: 9989-9996.

Thanh-Sang, V., Dai-Hung, N., and Se-Kwon, K. 2012. Phospholipase A2: Function and pharmacological regulation. Inflamm. Allergy Drug Targets. 11: 90–101.

Thomas, N.V., and Kim, S.K. 2011. Potential pharmacological applications of polyphenolic derivates from marine brown algae. Environ. Toxicol. Pharmacol. 32: 325–335.

Tran QTN, Wong WSF, Chai CLL. 2017. Labdane diterpenoids as potential anti-inflammatory agents. Pharmacol Res. 124:43-63.

Udenigwe, C.C., Lin, Y., Hou, W., and Aluko, R.E. 2009. Kinetic of the inhibition of renin angiotensin I-converting enzyme by flaxseed protein hydrolysate functions. J. Funct. Foods. 1: 199–207.

Uemura, D., Takahashi, K., Yamamoto, T., Katayama, C., Tanaka, J., Okumura, Y., Yoshimasa, H., 1985. Norhalichondrin A: An antitumor polyether macrolide from a marine sponge. J. Am. Chem. Soc. 107, 4796–4798.

V.K. Sali, R. Malarvizhi, V.M. Manikandamathavan, H.R. Vasanthi, Isolation and evaluation of phytoconstituents from red alga *Acanthophora spicifera* as potential apoptotic agents towards A549 and HeLa cancer cells lines. Algal Res. 32 (2018) 172–181.

Vanderah DJ, Steudler PA, Ciereszko LS, Schmitz FJ, Ekstrand JD, Van der Helm D (1977) Marine natural products. Xenicin: A diterpenoid possessing a nine-membered ring from the soft coral, *Xenia elongata*. J Am Chem Soc 99: 5780-5784.

Vargas P, Oliveira IDB, Stephens PRS, Santos CCC, Paixao CNDP, Ramos FA, Jimenez C, Resende JALC, Teixeira VL, Castellanos L. 2014. Dolabelladienols A-C, new diterpenes isolated from Brazilian brown alga *Dictyota pfaffii*. Mar Drugs. 12:4247–4259.

Veena CK, Josephine A, Preetha SP, Varalakshmi P (2007). Beneficial role of sulfated polysaccharides from edible seaweed *Fucus vesiculosus* in experimental hyperoxaluria. Food Chem 100(4), 1552-1559.

Viano Y, Bonhomme D, Camps M, Briand JF, Ortalo-Magne A, Blache Y, Piovetti L, Culioli G (2009) Diterpenoids from the Mediterranean brown alga *Dictyota sp*. evaluated as antifouling substances against a marine bacterial biofilm. J Nat Prod 72:1299-1304.

Vijayabaskar P, Shiyamala V (2012). Antioxidant properties of seaweed polyphenol from *Turbinaria ornata* (Turner) J. Agardh, 1848. Asian Pac J Trop Biomed 2, S90-S98.

W.A. Wijesinghe, E.A. Kim, M.C. Kang, W.W. Lee, H.S. Lee, C.S. Vairappan, Y.J. Jeon, Assessment of anti-inflammatory effect of 5β-hydroxypalisadin B isolated from red seaweed *Laurencia snackeyi* in zebrafish embryo in vivo model, Environ. Toxicol. Pharmacol. 37 (2014) 110–117.

Wang J, Xie XQ, Hou T, Xu X (2007) Fast approaches for molecular polarizability calculations. J Phys Chem A 111: 4443-4448.

Wang J, Xie X-Q, Hou T, Xu X (2007) Fast approaches for molecular polarisability calculations. J Phys Chem A 111:4443-4448.

Wang J, Xie X-Q, Hou T, Xu X. 2007. Fast Approaches for molecular polarisability calculations. J Phys Chem A. 111(20):4443–4448.

Wang J, Xie X-Q, Hou T, Xu X. 2007. Fast Approaches for molecular polarisability calculations. J Phys Chem A. 111(20):4443-4448.

Wang J, Xu QL, Zheng M-F, Ren H, Lei T, Wu P, Zhou ZY, Wei XY, Tan JW (2014) Bioactive 30-noroleanane triterpenes from the pericarps of *Akebia trifoliata*. Molecules 19:4301-4312.

Wang T, Jónsdóttir R, Liu H, Gu L, Kristinsson HG, Raghavan S (2012). Antioxidant capacities of phlorotannins extracted from the brown algae *Fucus vesiculosus*. J Agr Food Chem, 60(23), 5874-5883.

Wang, J, Xie, X-Q, Hou T, Xu, X. 2007. Fast Approaches for molecular polarisability calculations. J Phys Chem A. 111(20):4443-4448.

Wang, J., Xie, X.Q., Hou, T., Xu, X., 2007. Fast approaches for molecular polarizability calculations. J. Phys. Chem. A 111, 4443–4448.

Wang, T., Jonsdottir, R., Liu, H., Gu, L., Kristinsson, H.G., Raghavan, S., and Olafsdóttir, G. 2012. Antioxidant capacities of phlorotannins extracted from the brown algae *Fucus vesiculosus*. J. Agric. Food Chem. 60: 5874–5883.

Wei X, Rodríguez AD, Baran P, Raptis RG. 2010. Dolabellane-type diterpenoids with antiprotozoan activity from a southwestern Caribbean gorgonian octocoral of the genus *Eunicea*. J Nat Prod. 73(5):925–934.

Wessjohann, L.A., Ruijter, E., Garcia-Rivera, D., Brandt, W., 2005. What can a chemist learn from nature's macrocycles?-A brief, conceptual view. Mol. Divers. 9, 171–186.

W-H. Jiao, T-T. Xu, B-B. Gu, G-H. Shi, Y. Zhu, F. Yang, B-N. Han, S-P. Wang, Y-S. Li, W. Zhang, J. Li, H-W. Lin, Bioactive sesquiterpene quinols and quinones from the marine sponge *Dysidea avara*. RSC Adv. 5 (2015) 87730–87738.

Wijesinghe, W.A.J.P., Athukorala, Y., and Jeon, Y.J. 2011. Effect of anticoagulative sulfated polysaccharide purified from enzyme-assistant extract of a brown seaweed *Ecklonia cava* on Wistar rats. Carbohydr. Polym. 86: 917–921.

Winter JM, Chiou G, Bothwell IR, Xu W, Garg NK, Luo M, Tang Y (2016). Expanding the structural diversity of polyketides by exploring the cofactor tolerance of an inline methyltransferase domain. Org Lett 15, 3774-7.

Wojdylo A, Oszmianski J, Czemerys R (2007) Antioxidant activity and phenolic compounds in 32 selected herbs. Food Chem 105:940-949.

Wojdylo A, Oszmianski J, Czemerys R (2007) Antioxidant activity and phenolic compounds in 32 selected herbs. Food Chem 105: 940-949.

Wojdylo A, Oszmianski J, Czemerys R. 2007. Antioxidant activity and phenolic compounds in 32 selected herbs. Food Chem. 105:940-949.

Wojdylo A, Oszmianski J, Czemerys R. 2007. Antioxidant activity and phenolic compounds in 32 selected herbs. Food Chem. 105(3):940-949.

Wojdylo A, Oszmianski J, Czemerys R. 2007. Antioxidant activity and phenolic compounds in 32 selected herbs. Food Chem. 105(3):940-949.

Wojdylo, A., Oszmianski, J., and Czemerys, R. 2007. Antioxidant activity and phenolic compounds in 32 selected herbs. Food Chem. 105: 940–949.

Wojdylo, A., Oszmianski, J., Czemerys, R., 2007. Antioxidant activity and phenolic compounds in 32 selected herbs. Food Chem. 105(3), 940–949.

Wu C, Huang S, Yen GC (2011) Silymarin: A novel antioxidant with antiglycation and antiinflammatory properties *in vitro* and *in vivo*. Antioxid Redox Signal 14:353-366.

Xie J, Zhang AH, Sun H, Yan GL and Wang XJ (2018). Recent advances and effective strategies in the discovery and applications of natural products. RSC Adv 8, 812-824.

Y.V. Yuan, M.F. Carringto, N.A. Walsh, Extracts from dulse (*Palmaria palmata*) are effective antioxidants and inhibitors of cell proliferation *in vitro*, Food Chem. Toxicol. 43 (2005) 1073–1081.

Yamamoto K, Miyake H, Kusunoki M, Osaki S (2010) Crystal structures of isomaltase from *Saccharomyces cerevisiae* and in complex with its competitive inhibitor maltose. FEBS J 277:4205-4214.

Yan X, Nagata T, Fan X (1998). Antioxidative activities in some common seaweeds. Plant Foods for Human Nutrition, 52, 253-262.

Yan XJ, Fang GM, Lou QX (1999). Studies on free radical scavenging activity in Chinese seaweeds. Part I. Screening results. Chinese Journal of Oceanology and Limnology 17, 240-246.

Yan XJ, Li XC, Zhou CX, Fan X (1996). Prevention of fish oil rancidity by phlorotannins from *Sargassum kjellmanianum*. J. Appl. Psychol, 8, 201-203.

Yang L, Zhang LM (2009). Chemical structural and chain conformational characterization of some bioactive polysaccharides isolated from natural sources. Carbohydr Polym. 76(3):349-361

Yang Z, Yin J, Wang Y, Wang J, Xia B, Li T, Yang X, Hu S, Ji C Guo S (2019). The fucoidan A3 from the seaweed *Ascophyllum nodosum* enhances RCT-related genes expression in hyperlipidemic C57BL/6J mice. Int. J. Biol. Macromol.134, 759.

Yeh, C.-C., Yang, J.-I., Lee, J.-C., Tseng, C.-N., Chan, Y.-C., Hseu, Y.-C., Tang, J-.Y. Chuang, L.-Y., Huang, H-.W, Chang, F.-R. Chang, H.-W. 2012. Anti-proliferative effect of methanolic extract of *Gracilaria tenuistipitata* on oral cancer cells involves apoptosis, DNA damage, and oxidative stress. BMC Complement. Altern. Med. 12: 142.

Yin J, Wang J, Li F, Yang Z, Yang X, Sun W, Xia B, Li T, Song W, Guo S (2019). The fucoidan from the brown seaweed *Ascophyllum nodosum ameliorates* atherosclerosis in apolipoprotein E-deficient mice *Food Funct.* 10, 5124.

Younus H (2018). Therapeutic potentials of superoxide dismutase. IJHS, 12(3), 88-93.

Yu X-Q, Jiang C-S, Zhang Y, Sun P, Kurtan T, Mandi, A, Li X-L, Yao L-G, Liu A-H, Wang B, Guo Y-W, Mao, S-C. 2017. Compositacins A-K: Bioactive chamigrane-type

halosesquiterpenoids from the red alga *Laurencia composita* Yamada. Phytochemistry. 136:81-93.

Zedler S, Faist E (2006). The impact of endogenous triggers on trauma-associated inflammation. Current Opinion in Critical Care.12(6):595-601

Zhang W, Okimura T, Xu L, Zhang LJ, Oda T, Kwak M, Yu Q, Jin JO (2016). Ascophyllan functions as an adju-vant to promote anti-cancer effect by dendritic cell activation. Oncotarget, *7*, 19284-19298.

1. **Tima Antony** & Kajal Chakraborty (2019). Pharmacological Properties of Seaweeds against Progressive Lifestyle Diseases. Journal of Aquatic Food Product Technology, 28(10):1-13. DOI:10.1080/10498850.2019.1684407.
2. **Tima Antony** & Kajal Chakraborty (2019). Xenicanes attenuate pro-inflammatory 5-lipoxygenase: Prospective natural anti-inflammatory leads from intertidal brown seaweed *Padina tetrastromatica*. Medicinal Chemistry Research, 28 (4), 591-607. DOI:10.1007/s00044-019-02322-8
3. **Tima Antony** & Kajal Chakraborty & Minju Joy (2019). Antioxidative dolabellanes and dolastanes from brown seaweed *Padina tetrastromatica* as dual inhibitors of starch digestive enzymes. Natural Product Research, 1-13. E-publication ahead of print; DOI: 10.1080/14786419.2019.1591402
4. **Tima Antony** & Kajal Chakraborty (2018). First report of antioxidant abeo-labdane type diterpenoid from intertidal red seaweed *Gracilaria salicornia* with 5-lipoxygenase inhibitory potential. Natural Product Research, 1-8. E-publication ahead of print; DOI: 10.1080/14786419.2018.1508150.
5. **Tima Antony** & Kajal Chakraborty (2019). First report of antioxidative 2H-chromenyl derivatives from the intertidal red seaweed *Gracilaria salicornia* as potential anti-inflammatory agents. Natural Product Research, 1–13. E-publication ahead of print; DOI: 10.1080/14786419.2019.1579807.
6. Kajal Chakraborty, **Tima Antony** & Minju Joy (2019). Prospective natural anti-inflammatory drimanes attenuating pro-inflammatory 5-lipoxygenase from marine macroalga *Gracilaria salicornia*. Algal Research, 40, 101472. DOI:10.1016/j.algal.2019.101472.
7. Kajal Chakraborty & **Tima Antony** (2019). First report of spiro-compounds from marine macroalga *Gracilaria salicornia*: prospective natural anti-inflammatory agents attenuate 5-lipoxygenase and cyclooxygenase-2. Natural Product Research, 1-12. E-publication ahead of print; DOI: 10.1080/14786419.2019.1608545.
8. Kajal Chakraborty & **Tima Antony** (2019). First report of antioxidative abeo-oleanenes from red seaweed *Gracilaria salicornia* as dual inhibitors of starch digestive enzymes. Medicinal Chemistry Research, 28 (5), 696-710. DOI:10.1007/s00044-019-02328-2
9. Kajal Chakraborty & **Tima Antony** (2020). Salicornolides A-C from Gracilaria salicornia attenuates pro-inflammatory 5-lipoxygense: Prospective natural anti-

inflammatory leads. Phytochemistry, 172, 112259. E-publication ahead of print; DOI: 10.1016/j.phytochem.2020.112259.

10. **Tima Antony** & Kajal Chakraborty (2020). Anti-inflammatory polyether triterpenoids from the marine macroalga Gracilaria salicornia: Newly described natural leads attenuate proinflammatory 5-lipoxygenase and cyclooxygenase-2, Algal Research 46,101791. E-publication ahead of print; DOI: 10.1016/j.phytochem.2020.112259

PAPERS IN CONFERENCES

1. **Tima Antony** & Kajal Chakraborty (2017). Pharmacological properties of seaweeds against lifestyle diseases. Presented a poster in 11th IFAF, November 21-24, 2017, Book of Abstracts. 438-439. Asian Fisheries Society Indian Branch, ICAR- Central Institute of Fisheries Technology. Kochi, Kerala, India
2. **Tima Antony** (2019). First report of anti-oxidative 2*H*-chromenyl derivatives from red seaweed *Gracilaria salicornia* as potential anti-inflammatory agents. Presented a poster in MATCON 2019, March 14-16, 2019. International conference on materials for the millennium. Department of applied chemistry Cochin University of Science and Technology. Kochi, Kerala, India.
3. **Tima Antony** & Kajal Chakraborty (2019). Natural anti-Inflammatory drimanes to attenuate pro-Inflammatory 5-Lipoxygenase from marine macroalga *Gracilaria Salicornia* participated in ICCM-2019, October 17-19, Book of Abstracts. 86-87. International Conference on Advances in Chemical & Materials Sciences (ICCM-2019), Department of Studies in Chemistry Mangalore University, Mangalagangothri - 574 199 Karnataka, India.
4. **Tima Antony** & Kajal Chakraborty (2020). Natural anti-inflammatory compounds isolated from *Gracilaria salicornia*: Attenuate 5-lipoxygenase activity, January 8-10, Book of Abstracts. 440-441. International Symposium Marine Ecosystems Challenges & Opportunities (MECOS 3), Marine Biological Association of India (MBAI), CMFRI, Kochi, Kerala, India

Isolation of Small Molecular Weight Bioactive Compounds and Polysaccharides from Seaweeds (Phaeophyceae and Rhodophyceae)

Thesis submitted in partial fulfillment of the requirement for the degree of

DOCTOR OF PHILOSOPHY

in

CHEMISTRY

Submitted to

MANGALORE UNIVERSITY

By

Ms. TIMA ANTONY

(Ref. No. MU/EXB/Ph.D./CR.84/Chem./2017-18/E.13, dated 07-07-2017)

Guided By

Dr. KAJAL CHAKRABORTY

Senior Scientist (Organic Chemistry),

Marine Biotechnology Division, Central Marine Fisheries Research Institute (CMFRI)

Under the Faculty of Science and Technology

MANGALORE UNIVERSITY

MANGALAGANGOTHRI – 574 199

Dakshina Kannada Dist. Karnataka, India

भारतीय कृषि अनुसंधान परिषद

केन्द्रीय समुद्री मात्स्यिकी अनुसंधान संस्थान

[कृषि अनुसंधान एवं शिक्षा विभाग, कृषि मंत्रालय,भारत सरकार]

Indian Council of Agricultural Research

Central Marine Fisheries Research Institute

[Department of Agricultural Research and Education, Ministry of Agriculture, Govt. of India]

पोस्ट बोक्स सं.1603, एरणाकुलम नोर्त पी.ओ.,कोच्ची–682018, केरल, भारत

Post Box No.1603, Ernakulam North P.O., Kochi - 682018, Kerala, India

JANUARY 2020

भारतीय कृषि अनुसंधान परिषद
Indian Council of Agricultural Research
केन्द्रीय समुद्री मात्स्यिकी अनुसंधान संस्थान
Central Marine Fisheries Research Institute
(कृषि अनुसंधान एवं शिक्षा विभाग, केन्द्र कृषि एवं किसान कल्याण मंत्रालय, भारत सरकार)
(Department of Agricultural Research and Education, Ministry of Agriculture and Farmers' Welfare, Govt. of India)
पोस्ट बोक्स सं. 1603, एरणाकुलम नोर्थ पी.ओ., कोच्ची - 682 018, केरल, भारत
Post Box No. 1603, Ernakulam North P.O., Kochi - 682 018, Kerala, India
Phone: 91 484 2394867/2391407, Fax: 91 484 2394909/2396685, Email: director@cmfri.org.in, Web: www.cmfri.org.in
CMFRI Platinum Jubilee - Celebrating 70 years of Excellence in Research

Dr. Kajal Chakraborty

Senior Scientist (Organic Chemistry)

Certificate

*This is to certify that this thesis entitled "**Isolation of Small Molecular Weight Bioactive Compounds and Polysaccharides from Seaweeds (Phaeophyceae and Rhodophyceae)**" submitted by **Ms. TIMA ANTONY**, Research Fellow of Marine Biotechnology Division of Central Marine Fisheries Research Institute, for the award of the degree of Doctor of Philosophy in Chemistry is the result of bonafide research work carried out by her in the Marine Biotechnology Division of Central Marine Fisheries Research Institute in Chemistry, Kochi-682018, under my guidance and direct supervision. I further certify that this thesis or part thereof has not previously formed the basis for the award of any degree, diploma and associateship of any other University or Institution.*

Kajal Chakraborty

Place: Kochi

Date:

Declaration

*I do hereby declare that the thesis entitled "**Isolation of Small Molecular Weight Bioactive Compounds and Polysaccharides from Seaweeds (Phaeophyceae and Rhodophyceae**" is an authentic record of research work carried out by me under the guidance and supervision of Dr. Kajal Chakraborty, Senior Scientist (Organic Chemistry), Marine Biotechnology Division, Central Marine Fisheries Research Institute, Kochi-682018 and the same has not previously formed the basis for the award of any degree or diploma.*

Whenever the work described is based on the findings of other researchers, due acknowledgement is made in keeping with the general practice of reporting scientific observations. However, errors and unintentional oversights, if any are regretted.

TIMA ANTONY

Place: Kochi

Date:

Acknowledgements

First and foremost, all praise, honour and glory to my Lord Jesus Christ for His richest grace and mercy for the accomplishment of this research work successfully. You have given me the power to believe in myself and pursue my dreams. You have given me the strength and confidence to face all my difficult situations and hardships throughout my journey. I express my sincere gratitude and thanks to God for giving me strength, wisdom, health and luck to accomplish this endeavor. I could never have done this without the faith I have in you, the Almighty.

I would like to express my special appreciation and thanks to my Research supervisor and Guide Dr. Kajal Chakraborty, Senior Scientist (Organic Chemistry), Central Marine Fisheries Research Institute, you have been a tremendous mentor for me. I would like to thank you for giving me the proper guidance and the priceless support. I will always be obliged to you for your valuable advices and suggestions at times when I needed them the most. Thank you sir for enhancing my interest and widening my research path. I still remember the efforts he has put in for providing me all the facilities in lab for carrying out the experiments and above all, for the valuable time he has invested on me to clarify my doubts and the moral support granted for the fulfillment of my thesis. I will always be debted to you for the fanatical concern you have shown during the intricate situations.

I wish to place in record, my deep sense of respect and gratitude to Dr. A. Gopalakrishnan, Director, Central Marine Fisheries Research Institute for providing all the necessary facilities and support required to carry out my research work. I am extremely grateful to him for equipping me with a peaceful and positive atmosphere throughout my research period.

I express my sincere thanks to Dr. Vijayagopal Pananghat, Head of the Department, Marine Biotechnology Division, Central Marine Fisheries Research Institute for his constant encouragement and the support granted to complete my research activities in his prestigious

department. I take this opportunity to show my courtesy towards Dr. Bobby Ignatius, Principal Scientist and Head of HRD Cell of CMFRI for extending me all the necessary support regarding the doctoral work. I have great pleasure in expressing my gratitude and obligations to the scientists of Marine Biotechnology Division, Dr. N. K. Sanil, Dr. Sandhya Sukumaran and Dr. M. A. Pradeep. I will be indebted to Late. Mr. Nandakumar Rao, Mrs. G. Shylaja (Technical Officers, CMFRI) , Dr. M.P. Paulton (Senior Technical Officer), Mrs. P. Vineetha, SIC librarian, library support staff, staff members of the HRD Cell, the canteen, security personnel and all the employees of CMFRI, Kochi, for their kindhearted service and support bestowed on me throughout my research life.

I am grateful to the staffs of Sophisticated Analytical Instrument Facility (SAIF), Indian Institute of Technology (IIT), Chennai, Tamil Nadu especially, Dr. S.S.Bhattacharya, Head of SAIF, Dr. C. Baby (Technical officer), Mr. V. Srinivasan, Mr and. R. Sathiyamoorthi and the staffs of Sophisticated Test and Instrumentation Centre (STIC), Cochin University of Science and Technology (CUSAT) for their honest support and help in providing the spectroscopic and analytical experimental results.

I thank my intimate colleagues Vinaya K.K, Soumya Salas, Soumya Krishnan, Minju Joy, Fasina Makkar, Anusree Maneesh, Vamshi Krishna Raola, Dexy Joseph, Anjaly Thambi, Archana M K, Prima Francis, Shubhajit Dhara, Silpa KK, Vishnupriya and Suji Chandru, for the stimulating discussions, valuable feedbacks, co-operation and for all the fun we have had in the last four years. I wish to thank all other research scholars of CMFRI for a mesmerizing research life.

I would like to acknowledge the people who mean world to me, my parents and siblings for the selfless efforts, sacrifices and their endless prayers. Thank you appacha and amma for showing faith in me and giving me the opportunity to nurture my wings to fly behind my dreams. I would like to pay my special concern and love to my elder sister, brother-in -law and her family, for their creative criticisms, moral support and everlasting inspiration throughout the entire course of work.

Words fail to express my deep sense of gratitude towards my loving Chettayi, Mr.Nikhil Jose, for his understanding, patience, and the support he has given for me to accomplish this endeavor. I value his concern, support and encouragement at all times, good and bad.

I feel extremely privileged to show my appreciation to my family, and all those who put selfless efforts.

Finally I wish to thank all

Tima Antony

Place: Cochin

Date:02/01/2020

Dedicated to my. . . .

Lord Jesus Christ

Beloved parents &Family

ABSTRACT

Seaweeds were consumed as staple food items of the cuisines in many Asian countries, and are considered as essential components of a healthy diet. The pharmacological potential of ethyl acetate-methanol (EtOAc-MeOH) extract of ten species of seaweeds belonging to the subclasses Dictyotophycidae, Rhodymeniophycidae, and Corallinophycidae against progressive lifestyle diseases was determined by various *in vitro* models. Among the studied species, the organic extracts of *Gracilaria salicornia* and *Padina tetrastromatica* exhibited potential dipeptidyl-peptidase-4 inhibiting activity (IC_{50} ~ 0.03 mg mL^{-1}) and angiotensin converting enzyme-I inhibitory property (ACE-I) (IC_{50} 0.12 mg mL^{-1}) compared to those displayed by other studied species. The organic extracts of *G. salicornia* and *P. tetrastromatica* also displayed significantly greater attenuation properties against pro-inflammatory cyclooxygenase-2 and 5-lipoxygenase (IC_{50} 0.98-1.34 mg mL^{-1}, $P < 0.05$) compared to those derived from other species (IC_{50} 1.99-5.02 mg mL^{-1}). The nuclear magnetic resonance-guided dereplication of organic extracts of the studied seaweed species recognized the co-linearity between the bioactive potential and downfield electronegative functionalities. These results recognized the significance of the organic extracts of *G. salicornia* and *P. tetrastromatica* to isolate compounds for functional food applications against oxidative stress and induced diseases, such as diabetes, hypertension, and inflammation.

Phytochemical investigation on the biologically active compounds of seaweed *G. salicornia* (family Gracilariaceae) guided to the separation of a previously unreported abeo-labdane class of diterpenoid. The compound was characterized as methyl-16(13→14)-abeo-7-labdene-(12-oxo) carboxylate (**1**) by extensive spectroscopic experiments, and comparison with the related compounds. The studied compound registered significantly greater activities against pro-inflammatory 5-lipoxygenase (IC_{50} 2.33 mM) than that exhibited by non-steroidal anti-inflammatory agent ibuprofen (IC_{50} 4.51 mM, $P<0.05$). Likewise, this compound exhibited comparable radical quenching (1, 1-diphenyl-2-picryl-hydrazil) activity (IC_{50} 1.97 mM) as standard antioxidant agent α-tocopherol (IC_{50} 1.49 mM).

Carbolytic enzyme-associated cascades have been considered as potential curative target in attenuating diabetic mellitus pathogenesis. Two oleanene class of triterpenoids characterised as 24(4→23), 27(8→26), 30(20→29)-tris-abeo-olean-(12-oxo)-1,15,22-triene-methyl hept-5-enoate (**2**) and 24(4→23)-abeo-olean-(12-oxo)-3,5-diene-deconoate (**3**) with potential inhibitory activities against the starch digestive enzymes α-glucosidase and α-amylase,

were purified from the organic extract of intertidal red seaweed *G. salicornia* (family Gracilariaceae). Structural interpretation of compounds was carried out by detailed spectroscopic analysis, and their antioxidant/anti-diabetic potentials were assessed. Inhibitory potential of abeo-oleanene derivative (**3**) towards the starch digestive enzymes, α-glucosidase (IC_{50} 0.29 mM) and α-amylase (IC_{50} 0.32 mM) were greater than those displayed by its abeo-oleanene chemotype **2** (IC_{50} 0.34-0.40 mM). The molecular modelling studies were performed to designate the α-amylase and α-glucosidase inhibitory mechanism of oleanene analogues, and the comparison of docking parameters suggested that compound **3** exhibited least binding energy of -10.04 and -9.84 kcal mol^{-1} towards α-amylase and α-glucosidase respectively, and those results were corroborated with its greater inhibition potential against carbolytic enzymes. These results demonstrated that abeo-oleanene derivative (**3**) might constitute prospective anti-hyperglycaemic pharmaceutical candidate to moderate the likelihood of type-II diabetes.

The 5-lipoxygenase-associated cascade has appeared as potential therapeutic target in attenuating inflammatory pathologies. Progression and pathophysiology of inflammation have also shown potential involvement of oxidative stress and inflammatory pathways. Three drimane sesquiterpene quinols, characterised as 3-(hept-3^6-enyloxy)- decahydro-4,6a,12a,12b-tetramethyl-1*H*-benzo[*a*]xanthene-4,10,12-triol (**4**), 13-[[2-(hexyloxy)-2,5,5,8a-tetramethyldecahydro-1-naphthalenyl](methoxy)methyl]benzenol (**5**), and 1-butoxy-4,4,11b,11c-tetramethyl-decahydrobenzo[*kl*]xanthen-10-ol (**6**) were purified from the organic solvent extract of intertidal marine macroalga *Gracilaria salicornia*, obtained from the southeast coastal region of Indian peninsular. The 1*H*-benzo[a]xanthene-triol derivative (**4**) registered potential activities against pro-inflammatory 5-lipoxygenase (IC_{50} 1.7 mM) and free radicals (IC_{50} 1.3-1.5 mM). The *in silico* molecular modelling studies to designate 5-lipoxygenase inhibitory mechanism of the studied analogues and the comparison of docking parameters attributed that the drimane sesquiterpene **4** exhibited least binding energy of -12.30 kcal mol^{-1}, and showed effective hydrogen bonding interactions with the catalytic site of the enzyme. The higher electronic parameters and permissible hydrophobic-hydrophilic balance of the drimane sesquiterpene bearing 1*H*-benzo[*a*]xanthene-triol moiety (**4**) appeared to constitute significant roles towards the attenuation of pro-inflammatory 5-lipoxygenase. Putative biosynthetic pathway of the studied compounds involving cyclisation of farnesyl diphosphate and carbocationic rearrangement through a battery of enzyme-mediated cascade validated their structural attributions. These results demonstrated that the drimane-type sesquiterpenoids with 1*H*-benzo[*a*]xanthene-triol framework could be used as a potential therapeutic agent for the treatment of 5-lipoxygenase-mediated inflammatory pathologies.

Phytochemical investigation on biologically active compounds of an intertidal red seaweed *G. salicornia* (family Gracilariaceae) guided to the separation of two previously undisclosed *2H*-chromenyl derivatives. The compounds were characterised as 4'-[10'-[7-hydroxy-2,8-dimethyl-6-(pentyloxy)-2*H*-chromen-2-yl]ethyl]-3',4'-dimethyl-cyclohexanone (**7**) and 3'-[10'-(8-hydroxy-5-methoxy-2,6,7-trimethyl-2*H*-chromen-2-yl)ethyl]-3'-methyl-2'-methylene cyclohexyl butyrate (**8**) by extensive spectroscopic experiments. The studied metabolites recorded prospective bioactivities against 5-lipoxygenase (IC_{50} < 2.50 mM), whereas their selectivity indices were significantly greater (~ 1) than ibuprofen (0.89) (p < 0.05), which attributed higher anti-inflammatory selectivity of 2*H*-chromenyl compounds against inducible cyclooxygenase-2 than its constitutive pro-inflammatory isoform of cyclooxygenase-1. The radical scavenging potential of **8** against oxidants, 2,2-diphenyl-1-picrylhydrazyl and 2,2'-azino-bis-3 ethylbenzothiozoline-6-sulfonic acid were higher (IC_{50} < 1.35 mM) than standard antioxidant, α-tocopherol (IC_{50} 1.42-1.79 mM). The greater hydrogen bond interactions and binding affinity of **8** (-7.35 kcal mol^{-1}) bearing *2H*-chromenyl ethyl-3'-methyl-4'-methylenecyclohexyl butyrate moiety with 5-lipoxygenase, along with higher electronic properties and permissible hydrophobic-hydrophilic balance, manifested towards its greater anti-inflammatory activity than **7**.

The inflammation pathology is an orchestrated biological process and the dual inhibition of pro-inflammatory enzymes 5-lipoxygenase and cyclooxygenase-2 has been found to be an effective approach against inflammation. This study involves the characterisation of two previously undescribed spiro[5.5]undecanes, 3-(hydroxymethyl)-7-(methoxymethyl)-3,11-dimethyl-9-oxospiro[5.5]undec-4-en-10-methylbutanoate (**9**) and 4-ethoxy-11,11-dimethyl-7-methylene-8-(propionyloxy)spiro[5.5]undec-2-en-10^3,10^5-dihydroxytetrahydro-2*H*-pyran-10-carboxylate (**10**) with potential anti-inflammatory properties, from seaweed *Gracilaria salicornia* by extensive-spectroscopic-experiments. These metabolites recorded prospective bioactivities against 5-lipoxygenase (IC_{50} < 2.80 mM), whereas their selectivity indices were significantly greater (~1) than ibuprofen (0.89) (p<0.05), which attributed selective anti-inflammatory potencies of the studied spiro[5.5]undecane derivatives against inducible cyclooxygenase-2 than constitutive cyclooxygenase-1. Radical scavenging potential of spiro[5.5]undec-2-en-10^3,10^5-dihydroxytetrahydro-2*H*-pyran-10-carboxylate analogue (**10**) against oxidants, 2,2-diphenyl-1-picrylhydrazyl and 2,2'-azino-bis-3 ethylbenzothiozoline-6-sulfonic acid were found to be greater (IC_{50} < 1.25 mM) than commercial standard, α-tocopherol (IC_{50} 1.42-1.79 mM). The greater hydrogen-bonding interactions and binding affinity of **10** (-10.13 kcal/mol) with 5-LOX appropriately corroborated its prospective anti-inflammatory activity.

5-Lipoxygenase (5-LOX)/cyclooxygenase-2 (COX-2) were found to be the two major inducible pro-inflammatory enzymes catalysing the rate-limiting stage in the development of pro-inflammatory prostaglandins/thromboxanes by COX-2 pathway and leukotrienes by 5-LOX pathway. Instantaneous quenching of COX-2/5-LOX-associated cascade is an important therapeutic objective in the attenuation of inflammatory pathologies. Two polyether triterpenoids, characterised as 15-(octahydro-7-(4,5-dihydro-3-methoxy-2,6-dimethyl-2*H*-pyran-6-yl)-10-methylpyrano[3,2-b]pyran-14-yl)-18-(19-methyl-23-methyleneoxepan-19-yl)pent-15-en-18-ol (**11**) and tetrahydro-6-(hexahydro-13-((tetrahydro-18-(23-hydroxy-23-methylheptan-19-yl)-15-methylfuran-15-yl)methyl)-10-methyl-2*H*-furo[3,2-b]pyran-7-yl)-2,2,6-trimethyl-2*H*-pyran-3-yl butyrate (**12**) were isolated from the organic extract of the marine macroalga, *Gracilaria salicornia* harvested from southeast-coastal zones of Indian peninsular. Polyether analogue bearing trimethyl-2*H*-pyran-3-yl butyrate moiety (**12**) disclosed potent attenuation properties against 5-LOX (IC_{50} 1.89 mM) and COX-2 (IC_{50} 1.87 mM) enzymes. *In-silico* molecular docking methods designated the anti-inflammatory mechanisms of isolated compounds and their comparison of docking factors assigned that the polyether **2** displayed the smallest binding energy of -10.29 and -10.96 kcal mol^{-1} in COX-2 and 5-LOX active sites, respectively and designated competent hydrogen-bonding associations with the enzymatic catalytic regions. Greater electronic factors along with lesser steric bulk of the polyether **12** bearing furanyl-furo[3,2-b]pyran-2*H*-pyran moiety was found to have noteworthy functional roles to attenuate the inflammatory enzymes. Proposed bio-synthetic origin leading to the polyether analogues comprising the cyclization of squalene epoxides through the sequences of enzyme-catalysed cascade corroborated their structural attributions. These reports designated that polyether triterpenoid enclosing furanyl-furo[3,2-b]pyran-2*H*-pyran skeleton might be considered as a prospective anti-inflammatory therapeutic source to alleviate COX-2 and 5-LOX-mediated inflammatory pathologies.

Three macrolides bearing the carbon framework of oxabicyclo[21.3.1]heptacosa-ene-diones (**13** and **14**) and oxabicyclo[19.3.1]pentacosa-ene-dione (**15**) were isolated and characterised from the organic extract of the intertidal red seaweed *G. salicornia* (family Gracilariaceae), which were named as compounds **13**-**15**. These natural macrolides were conformationally pre-organised ring structure providing diverse functionalities, and their potential bioactive properties led to the development of pharmacophores with anti-inflammatory properties. The 21-membered pyran-enclosed compound **14** displayed greater cyclooxygenase-2 (IC_{50} COX-2 1.13 mM) inhibitory activity than those exhibited by the 21-membered aryl compound **13** and 19-membered compound **15** (IC_{50} COX-2 ~1.2 mM). The attenuating potential of the studied compounds against pro-inflammatory enzyme, 5-lipoxygenase (IC_{50}

LOX < 1.5 mM) was significantly greater than that displayed by the non-steroidal anti-inflammatory ibuprofen (IC_{50} 4.5 mM), whereas the selectivity indices exhibited by salicornolides against cyclooxygenase-2 was significantly higher (1.18-1.41, $P < 0.05$) when compared to that of ibuprofen (SI 0.43) attributing the greater selectivity profile of the former towards inducible pro-inflammatory mediators than the latter. The minimal binding energy of compound **14** (-9.64 kcal mol^{-1}), a greater number of hydrogen-bonds and lesser inhibitory constant (Ki 85.15 nM) might be responsible for effective binding towards 5-lipoxygenase, and that could attribute its greater anti-inflammation potential than those displayed by other compounds. The putative biosynthetic cascade initiated by malonate-acyl carrier protein unambiguously confirmed the structural attributions of the titled macrocyclic lactones. The undescribed compounds **13**-**15** from seaweed *Gracilaria salicornia* attenuating pro-inflammatory 5-lipoxygense might be considered as prospective natural anti-inflammatory leads for pharmaceutical applications.

Two previously unreported xenicane class of novaxenicin-type xenicin diterpenoids (**1**-**2**) bearing cyclonona[*d*]furo [2,3-*b*]pyrandiol and three xeniolide-type diterpenoids with unprecedented octahydrocyclonona[*c*]pyran-3(1*H*)-one backbones (**3**-**5**) were separated from the organic extract of the intertidal seaweed *Padina tetrastomatica* (family Dictyotaceae), collected from southern India. The compounds were deduced to bear a xenicane moiety with a 2-oxabicyclo[7.4.0]tridecane cyclic system. The structures of these specialized metabolites were attributed based on the extensive nuclear magnetic resonance spectral analyses, and comparison of related compounds. Xeniolide type diterpenes (**3**-**5**) registered significantly greater attenuation potential against pro-inflammatory 5-lipoxygenase (IC_{50} ~ 2.04 mM) than that exhibited by non-steroidal anti-inflammatory drug ibuprofen (IC_{50} 4.50 mM, $P < 0.05$). The xeniolide derivative octahydro-1,7-dihydroxy-4-(4^1-hydroxy-4^2-methylpropyl)-6-(6^1-hydroxy-6^2-propenyl)-10-methyl-cyclonona[*c*]pyran-3(*1H*)-one (**5**) exhibited comparable antioxidant activity (DPPH IC_{50} 1.73 mM) along with standard antioxidative agent α-tocopherol (IC_{50} < 2 mM). *In silico* molecular modelling studies were performed to designate the 5-lipoxygenase inhibitory mechanism of the xenicanes, and the comparison of docking parameters suggested that the xeniolide derivative **5** exhibited least binding energy of −11.56 kcal mol^{-1}, and that was corroborated with its greater inhibition potential against the pro-inflammatory enzyme. These results demonstrated that the xeniolide-type diterpenoids with previously unreported *δ*-lactone cyclononane framework might constitute promising anti-inflammatory leads with pro-inflammatory 5-lipoxygenase enzyme inhibitory activities.

New dolabellanes {6-methoxy-dolabella-8(17),12-diene-10*β*,18-diol (**6**), 3-methoxy-dolabella-12(18)-ene-4*β*-ol (**7**), 3-methoxy-dolabella-10,18(19)-diene-5α,8*β*-diol (**8**)} and

dolastanes {2,7-dimethoxy-14α-hydroxy-dolasta-1(15),9-diene (**9**) and 4,7-dimethoxy-9*β*,14α-dihydroxy-dolasta-1-ene (**10**)} were identified from brown seaweed *Padina tetrastomatica* (family Dictyotaceae), collected from the southeast coast of India. Compounds **6**-**8** were found to possess dolabellane skeleton with [9.3.0] cyclotetradecane framework whereas, **9**-**10** were composed of tricyclic diterpenes with linear arrangement of six-seven-five fused alicyclic rings. Compounds **8** and **10** registered greater antioxidative activities (IC_{50} ≤0.63 mg/mL) than other analogues (IC_{50} ≥0.65 mg/mL), whereas their attenuating potentials against carbolytics α-amylase and α-glucosidase (IC_{50} ~0.12-0.14 mg/mL) were comparable with those displayed by acarbose (IC_{50} 0.14-0.12 mg/mL). Bioactive potentials of titled compounds were assessed by electronic and lipophilic parameters. The lesser binding energies of **8** (-9.71 kcal/mol) and **10** (-8.59 kcal/mol) through molecular docking demonstrated their effective hydrogen bonding interactions with α-amylase. Thus, dolabellanes and dolastanes might be used as anti-diabetic and antioxidant leads to reduce the risk of hyperglycaemia.

ABBREVIATIONS

^{1}D NMR	-	One Dimensional NMR
^{1}H NMR	-	Proton Nuclear Magnetic Resonance
$^1O_2$	-	Singlet Oxygen
2D NMR	-	Two Dimensional NMR
5-LOX	-	5-Lipoxygenase
AA	-	Arachidonic Acid
$ABTS^+$	-	2, 2-Azino-Bis-3ethylbenzothiozoline-6-Sulfonic Acid
Ac_2O	-	Acetic anhydride
ACE	-	Angiotensin Converting Enzyme
AI	-	Atherogenicity Index
AIP	-	Atherogenic Index of Plasma
ALP	-	Alkaline Phosphatase
ALT	-	Alanine aminotransferase
ANOVA	-	Analysis of Variance
AST	-	Aspartate aminotransferase
BSA	-	Bovine Serum Albumin
CC	-	Column Chromatography
COSY	-	Correlation Spectroscopy
COX	-	Cyclooxygenase
DCM	-	Dichloromethane
DDT	-	Dithiothreitol
DEAE	-	Diethylaminoethyl
DEPT	-	Distortionless Enhancement by Polarization Transfer
DHA	-	Docosahexaenoic acid
DMSO	-	Dimethyl Sulfoxide
DPPH	-	1,1-Diphenyl-2-Picrylhydrazyl
EDTA	-	Ethylenediaminetetra Acetic Acid

EI-MS	-	Electron Ionisation Mass Spectra
EtOAc	-	Ethyl Acetate
FAPGG	-	*N*-(3-[2-furyl] acryloyl)-Phe-Gly-Gly
FC	-	Flash Chromatography
FFA	-	Free Fatty Acid
FT-IR	-	Fourier Transform Infra Red
GAE	-	Gallic Acid Equivalence
GC-MS	-	Gas Chromatography-Mass Spectrometry
GPPN	-	Gly-Pro-p-Nitroanilide
GPx	-	Glutathione Peroxidase
GSH	-	Glucocorticoid Suppressible Hyperaldosteronism
GSH	-	Reduced Glutathione
H_2O_2	-	Hydrogen Peroxide
HAT	-	Hydrogen Atom Transfer
HMBC	-	Heteronuclear Multiple Bond Correlation
HPLC	-	High-Performance Liquid Chromatography
HRESIMS	-	High Resolution Electro Spray Mass Spectroscopy
HSQC	-	Heteronuclear Single Quantum Coherence
IC_{50}	-	Inhibition Concentration at 50 %
m/z	-	Mass-to-Charge Ratio
MDA	-	Malondialdehyde/Malonaldehyde
MDAEQ	-	Malondialdehyde Equivalent
MeI	-	Methyl Iodide
MeOH	-	Methanol
MNP	-	Marine Natural Products
NaOH	-	Sodium Hydroxide
NMR	-	Nuclear Magnetic Resonance
NOESY	-	Nuclear Overhauser Effect Spectroscopy
NSAIDs	-	Non-Steroidal Anti-inflammatory Drugs
O_2^-	-	Superoxide Anion
OH·	-	Hydroxyl Radical

PBS	-	Phosphatase Buffered Saline
PCA	-	Principal Component Analysis
PDA	-	Photodiode Array
PGs	-	Prostaglandins
PMAAs	-	Partially Methylated Alditol Acetates
ppm	-	Parts Per Million
PTLC	-	Preparative Thin Layer Chromatography
PUFA	-	Poly Unsaturated Fatty Acid
QSAR	-	Quantitative Structure Activity Relationship
R_f	-	Retardation Factor
RID	-	Refractive Index Detector
RMSD	-	Root Mean Square Deviation
ROS	-	Reactive Oxygen Species
RP-HPLC	-	Reverse Phase High-Performance Liquid Chromatography
R_t	-	Retention Time
RT	-	Room Temperature
SD	-	Standard Deviation
SEM	-	Scaning Electron Microscope
SOD	-	Superoxide Dismutase
SPSS	-	Statistical Program for Social Sciences
TBA	-	Thiobarbituric Acid
TBARS	-	Thiobarbituric Acid Reactive Species
TLC	-	Thin Layer Chromatography
TPC	-	Total Phenolic Content
UV-VIS	-	Ultra Violet-Visible

LIST OF CONTENTS

SL. NO. **TITLE**

CHAPTER 1: INTRODUCTION

1.1 Background
1.2 Marine environment as a potential source of bioactive compounds……...
1.3 Bioactive potentials of seaweeds and their secondary metabolites……
1.3.1 Major classification of seaweeds……..
1.3.2 Distribution and diversity of seaweeds in Indian coastline……
1.3.3 Pharmacological importance of seaweeds …….
1.4 Free radicals in the defense mechanism……..
1.4.1 Impact of free radicals in the defense mechanism
1.4.2 Free radicals induced various chronic disorders…….
1.5 Seaweeds and their metabolites combat oxidative stress induced life style disorders……..
1.5.1 Seaweeds and their metabolites as natural alternative to combat various oxidative stress induced life style disorders……
1.5.2 Role of seaweeds belonging to the class of Phaeophyceae and Rhodophyceae in the oxidative stress defense mechanism…….
1.6 Objectives……
1.7 Thesis outline……..

CHAPTER 2: REVIEW OF LITERATURE

2.1 Background…….....
2.2 Marine ecosystem as a source of bioactives……
2.3 Seaweeds as a source of bioactives…….
2.3.1 Secondary metabolites derived from seaweeds.…….
2.3.1.1 Terpenoids……...
2.3.1.2 Phenolic compounds…….....
2.3.1.3 Steroids…….
2.3.1.4 Alkaloids…….
2.3.1.5 Lipids and Fatty acid derivatives……
2.3.1.6 Protein and peptides……
2.3.1.7 Polysaccharides……...
2.4 An outline of bioactive secondary metabolites derived from seaweeds belonging to Rhodophyceae and Phaeophyceae …….
2.4.1 Bioactive secondary metabolites derived from seaweeds belonging to the class Rhodophyceae…….
2.4.2 Bioactivities secondary metabolites derived from seaweeds belonging to the class Phaeophyceae…….
2.5 Over all morphological features of the seaweeds belonging to Rhodophyceae and Phaeophyceae ……
2.5.1 Morphology and distribution of *Gracilaria* species …….....

2.5.3 Morphology and distribution of *Padina* species …….....
2.6 Conclusions…….

CHAPTER 3: SCREENING OF BIOACTIVE POTENTIALS OF CRUDE SOLVENT EXTRACTS FROM RED AND BROWN SEAWEEDS (RHODOPHYCEAE AND PHAEOPHYCEAE)

3.1 Background.……
3.2 Materials and methods……
3.2.1 Chemicals, reagents and solvents…..……..
3.2.2 Materials of seaweed and depiction of work area……..
3.2.3 Preparation of organic extracts from seaweeds……..
3.2.4 Instrumentation……...
3.2.5 Analysis of pharmacological activities of EtOAc:MeOH crude solvent extracts……
3.2.5.1 Determination of total phenolic content…….
3.2.5.2 *In vitro* antioxidant activities……...
3.2.5.2a 1,1-Diphenyl-2-picryl hydrazil (DPPH) radical scavenging activitity……
3.2.5.2b 2,2'-Azino-bis-3-ethylbenzothiozoline-6-sulfonic Acid ($ABTS^{+}$) radical scavenging activitity……...
3.2.5.2c Hydrogen peroxide (H_2O_2) scavenging activities……...
3.2.5.2d Ferrous ion chelating (Fe^{2+} ion) activity……..
3.2.5.2e Thiobarbituric acid-reactive species (TBARS) formation inhibitory activity……
3.2.5.3 *In vitro* anti-inflammatory activities……...
3.2.5.3a Cyclooxygenases (COX) inhibition assay……...
3.2.5.3b 5-Lipoxygenase (5-LOX) inhibition assay……..
3.2.5.4 *In vitro* antidiabetic activities…….....
3.2.5.4a α -Amylase inhibition assay……
3.2.5.4b α-Glucosidase inhibition assay……
3.2.5.4c Dipeptidyl peptidase-4 (DPP-4) inhibition assay……
3.2.5.5 *In vitro* antihypertensive activities…….....
3.2.5.5a Angiotensin converting enzyme-I (ACE-I) inhibitory activity... …….
3.2.6 Statistical analysis……...
3.3 Results and discussion……
3.3.1 Bioactive potentials and correlation analysis of the organic extracts of seaweeds
3.3.1.1 Total phenolic content and antioxidant activities……
3.3.1.2 Antioxidant activities……..
3.3.1.3 Anti-diabetic activities……
3.3.1.4 Antihypertensive and anti-inflammatory activities…….....
3.3.2 Spectroscopic characterization of solvent extracts …….
3.4 Conclusions…….

CHAPTER 4: ISOLATION AND CHARACTERIZATION OF BIOACTIVE LEADS FROM RED SEAWEED (RHODOPHYCEAE) *GRACILARIA SALICORNIA*

4.1 Background.……
4.2 Materials and methods……

4.2.1 Instrumentation, chemicals and reagents……
4.2.2 Chromatographic purification techniques …….....
4.2.2.1 Purification by column chromatography ……
4.2.2.2 Purification by flash chromatography…….
4.2.2.3 Purification by High pressure liquid chromatography (HPLC) ……
4.2.2.4 Percentage of purity assessment by thin layer chromatography and analytical HPLC……..
4.2.3 Spectrophotometric and spectroscopic analysis……
4.2.4 Chromatographic purification of pure compounds and bioactive potentials of sub-column fractions from *G. salicornia* …….
4.2.5 Physicochemical description of bioactive-leads isolated from EtOAc-MeOH extract of *G. salicornia*
4.2.5.1 Physicochemical description of compound **1** ...…….
4.2.5.2 Physicochemical description of compound **2**…….
4.2.5.3 Physicochemical description of compound **3**…….
4.2.5.4 Physicochemical description of compound **4**…….
4.2.5.5 Physicochemical description of compound **5**…….
4.2.5.6 Physicochemical description of compound **6** ……
4.2.5.7 Physicochemical description of compound **7**…….
4.2.5.8 Physicochemical description of compound **8**…….
4.2.5.9 Physicochemical description of compound **9**…….
4.2.5.10 Physicochemical description of compound **10**……
4.2.5.11 Physicochemical description of compound **11**……
4.2.5.12 Physicochemical description of compound **12**……
4.2.5.13 Physicochemical description of compound **13**……
4.2.5.14 Physicochemical description of compound **14**……
4.2.5.15 Physicochemical description of compound **15**……
4.2.6 Assessment *in vitro* of bioactive potentials……
4.2.6.1 *In vitro* antioxidant assays……..
4.2.6.2 1,1-Diphenyl-2-picryl hydrazil (DPPH) radical scavenging activities……..
4.2.6.3 2,2'-Azino-bis-3-ethylbenzothiozoline-6-sulfonic Acid ($ABTS^{+}$) radical scavenging activities……...
4.2.7 *In vitro* anti-inflammatory assays
4.2.7.1 Cyclooxygenases (COX) inhibition properties……...
4.2.7.2 5-Lipoxygenase (5-LOX) inhibition properties……..
4.2.8 *In vitro* anti-diabetic activities…….....
4.2.8.1 α-Amylase inhibition assay…….
4.2.8.2 α-Glucosidase inhibition assay……
4.2.8.3 Dipeptidyl peptidase-4 (DPP-4) inhibition assay……
4.2.9 Structure-activity correlations of bioactive leads isolated from EtOAc-MeOH extract of *G. salicornia* ……...
4.2.10 Molecular modelling experiments ……..
4.2.11 Statistical analyses……..
4.3 Results and discussion…….
4.3.1 Chromatographic fractionation, bioactive potentials and spectroscopic analyses
4.3.1.1 Chromatographic fractionation, bioactive potentials and spectroscopic analyses

of intermediate fractions from EtOAc:MeOH extract of *G. salicornia* ……
4.3.2 Spectroscopic characterization of bioactive compounds derived from EtOAc-MeOH extract of *G. salicornia*……
4.3.3 Isolation of bioactive secondary metabolites from EtOAc:MeOH extract of *G. salicornia*…….
4.3.4 Spectroscopic analyses of bioactive secondary metabolites isolated from EtOAc:MeOH extract of *G. salicornia*……...
4.3.4.1 Structural characterization of labdane diterpene derivatives (**1**) ……
4.3.4.2 Structural characterization of oleanane triterpene derivatives (**2-3**) ……
4.3.4.2a Structural characterization of compound **2**…….
4.3.4.2b Structural characterization of compound **3**…….
4.3.4.3 Structural characterization of drimane diterpene derivatives (**4-6**) ……
4.3.4.3a Structural characterization of compound **4**……..
4.3.4.3b Structural characterization of compound **5**……..
4.3.4.3c Structural characterization of compound **6**……..
4.3.4.3 Structural characterization of 2*H*-chromenyl derivatives (**7-8**) …….
4.3.4.3a Structural characterization of compound **7**…….
4.3.4.3b Structural characterization of compound **8**…….
4.3.4.4 Structural characterization of spiro compounds (**9-10**) …….
4.3.4.4a Structural characterization of compound **9**…….
4.3.4.4b Structural characterization of compound **10**……...
4.3.4.5 Structural characterization of polyether derivatives (**11-12**) …….
4.3.4.5a Structural characterization of compound **11**……...
4.3.4.5b Structural characterization of compound **12**……...
4.3.4.6 Structural characterization of macrolide derivatives (**13-15**) ……
4.3.4.7 Structural characterization of compound **13** …….
4.3.4.7a Structural characterization of compound **14**……..
4.3.4.7b Structural characterization of compound **15**……...
4.3.5 Pharmacological potentials of secondary metabolites isolated from EtOAc-MeOH extract of *G. salicornia;* antioxidant, anti-inflammatory and antidiabetic properties…….
4.3.6 Structure-activity correlation analyses of bioactives isolated from EtOAc-MeOH extract of *G. salicornia*……...
4.3.7 *In silico* molecular docking analysis of bioactives isolated from *G. salicornia*
4.4 Conclusions…….

CHAPTER 5: ISOLATION AND CHARACTERIZATION OF BIOACTIVE LEADS FROM BROWN SEAWEED *PADINA TETRASTROMATICA*

5.1 Background.……
5.2 Materials and methods……
5.2.1 Instrumentation, chemicals and reagents……
5.2.2 Chromatographic purification techniques …….....
5.2.2.1 Purification by column chromatography…….
5.2.2.2 Purification by flash chromatography…….
5.2.2.3 Purification by High pressure liquid chromatography (HPLC) …….

5.2.2.4 Percentage of purity assessment by thin layer chromatography and analytical HPLC……...
5.2.3 Spectrophotometric and spectroscopic analysis……..
5.2.3.1 UV-Visible spectrophotometric analysis……
5.2.3.2 Fourier transform infrared (FTIR) spectroscopy……
5.2.3.3 Mass spectroscopic (MS) analysis…….
5.2.3.4 Nuclear magnetic resonance (NMR) spectroscopic analysis…….
5.2.4 Chromatographic purification of pure compounds from *P. tetrastromatica*……
5.2.5 Analysis of physicochemical parameters of pure bioactive compounds from EtOAc:MeOH extract of *P. tetrastromatica*…….....
5.2.5.1 Analysis of physicochemical parameters of compound **1** …….
5.2.5.2 Analysis of physicochemical parameters of compound **2**…….
5.2.5.3 Analysis of physicochemical parameters of compound **3**…….
5.2.5.4 Analysis of physicochemical parameters of compound **4**…….
5.2.5.5 Analysis of physicochemical parameters of compound **5**…….
5.2.5.6 Analysis of physicochemical parameters of compound **6**…….
5.2.5.7 Analysis of physicochemical parameters of compound **7**…….
5.2.5.8 Analysis of physicochemical parameters of compound **8**…….
5.2.5.9 Analysis of physicochemical parameters of compound **9**…….
5.2.5.10 Analysis of physicochemical parameters of compound **10**……
5.2.6 Assessment of *in vitro* of bioactive potentials……
5.2.6.1 *In vitro* antioxidant assays……...
5.2.6.2 1,1-Diphenyl-2-picryl hydrazil (DPPH) radical scavenging activities……...
5.2.6.3 2,2'-Azino-bis-3-ethylbenzothiozoline-6-sulfonic Acid ($ABTS^{+}$) radical scavenging activities……...
5.2.7 *In vitro* anti-inflammatory assays……
5.2.7.1 Cyclooxygenases (COX) inhibition properties……...
5.2.7.2 5-Lipoxygenase (5-LOX) inhibition properties …….
5.2.8 *In vitro* anti-diabetic activities…….....
5.2.8.1 α-Amylase inhibition assay…….
5.2.8.2 α-Glucosidase inhibition assay……
5.2.8.3 Dipeptidyl peptidase-4 (DPP-4) inhibition assay……
5.2.9 The structure-activity relationship analyses of secondary metabolites isolated from EtOAc:MeOH extract of *P. tetrastromatica*……..
5.2.10 *In silico* molecular modeling……..
5.2.11 Statistical analyses……..
5.3 Results and discussion……
5.3.1 Chromatographic fractionation, bioactive potentials and spectroscopic analyses
5.3.1.1 Chromatographic fractionation, bioactive potentials and spectroscopic analyses of intermediate fractions from EtOAc:MeOH extract of *P. tetrastromatica* ……
5.3.2 Spectroscopic analyses of intermediate fractions from EtOAc:MeOH extract of *P. tetrastromatica* ……
5.3.3 Isolation of bioactive secondary metabolites from EtOAc:MeOH extract of *P. tetrastromatica* …….
5.3.4 Spectroscopic analyses of bioactive secondary metabolites isolated from

EtOAc:MeOH extract of *P. tetrastromatica* ……..
5.3.4.1 Structural characterization of xenicane diterpene derivatives (**1**-**5**) ……
5.3.4.1a Structural characterization of compound **1**……
5.3.4.1b Structural characterization of compound **2**……
5.3.4.1c Structural characterization of compound **3**……
5.3.4.1d Structural characterization of compound **4**……
5.3.4.1e Structural characterization of compound **5**……
5.3.4.2 Structural characterization of dolabellane and dolastane diterpene derivatives (**6**-**10**) …….
5.3.4.2a Structural characterization of compound **6**……
5.3.4.2b Structural characterization of compound **7**……
5.3.4.2c Structural characterization of compound **8**……
5.3.4.2d Structural characterization of compound **9**……
5.3.4.2e Structural characterization of compound **10**……..
5.3.5 Pharmacological potentials of secondary metabolites isolated from EtOAc-MeOH extract of *P. tetrastromatica;* antioxidant, anti-inflammatory and antidiabetic properties……
5.3.5.1 Antioxidative properties of bioactives isolated from EtOAc:MeOH extract of *P. tetrastromatica*……
5.3.5.2 Anti-inflammatory properties of bioactives isolated from EtOAc:MeOH extract of *P. tetrastromatica*……..
5.3.5.3 Anti-diabetic properties of bioactives isolated from EtOAc:MeOH extract of *P. tetrastromatica*……
5.3.6 Structure-activity correlation analyses of bioactives isolated from EtOAc:MeOH extract of *P. tetrastromatica*……
5.3.7 *In silico* molecular docking analysis of bioactives isolated from *P. tetrastromatica*……
5.4 Conclusions…….

CHAPTER 6: EXTRACTION, PURIFICATION AND STRUCTURAL CHARACTERIZATION OF POLYSACCHARIDES FROM SEAWEEDS (PHAEOPHYCEAE AND RHODOPHYCEAE)AND PHARMACOLOGICAL APPLICATIONS

6.1 Background……
6.2 Materials and methods……
6.2.1 Collection and processing of seaweed materials……....
6.2.2 Chemicals, reagents and instrumentation……
6.2.3 Extraction, isolation and purification of sulfated polysaccharide from red seaweed *G. salicornia*……
6.2.4 Composition analysis of polysaccharide fractions……..
6.2.4.1 Determination of total carbohydrate content……...
6.2.4.2 Determination of uronic acid content……..
6.2.4.3 Determination of sulfate content…….
6.2.4.4 Determination of protein content……
6.2.5 Analysis of monosaccharide composition……...

6.2.6 Preparation of sulfated polysaccharide based silver nano composite
6.2.7 Pharmacological activities of polysaccharide fractions, pure polysaccharide and polysaccharide based nano composite…….
6.2.7.1 *In vitro* antioxidant activities……...
6.2.7.1.1 1,1-Diphenyl-2-picryl hydrazil (DPPH) and 2,2-azino-bis-3-ethylbenzothiozoline-6- sulfonic acid ($ABTS^{+}$) radical scavenging activities…...
6.2.7.2 *In vitro* antidiabetic activities……..
6.2.7.2.1 α-Amylase inhibition assay……
6.2.8.2.2 α-Glucosidase inhibition assay……
6.2.8.2.3 Dipeptidyl peptidase-4 (DPP-4) inhibition assay……
6.2.7.3 *In vitro* anti-osteoporotic activities…….
6.2.7.3.1 Alkaline phosphatase inhibitory activity…….
6.2.7.3.2 Cytotoxicity analysis by MTT assay on mesenchymal cells……..
6.2.8 Spectroscopic analysis of sulfated polysaccharide derived from *G. salicornia*…
6.2.9 Glycosidic linkage pattern analysis of sulfated polysaccharide derived from *G. salicornia*…….
6.2.10 Statistical analysis……...
6.3 Results and discussion…….
6.3.1 Extraction, purification, yield and chemical composition analysis of the seaweed derived sulfated polysaccharide……..
6.3.2 Structural characterization of sulfated polysaccharide……
6.3.3 Fourier transform infrared spectral (FT-IR) analysis of ……
6.3.4 NMR spectroscopic analysis……...
6.3.5 Pharmacological properties of sulfated polysaccharide…….
6.3.5.1 *In vitro* antioxidant activities……...
6.3.5.2 *In vitro* antidiabetic activities……..
6.3.5.3 *In vitro* anti-osteoporotic activities…….
6.3.6 Structural characterization of sulfated polysaccharide by methylation analysis……
6.3.7 Structural elucidation and Glycosidic linkage analysis reductive cleavage method using mass, NMR and FT-IR spectroscopic methods……
6.4 Conclusions…….

CHAPTER 8: SUMMARY…….
REFERENCES ……..…….
PUBLICATIONS ……...……..

TABLE CAPTIONS

Table 1. Percentage yield, phenolic contents and pharmacological activities of the organic extracts of seaweeds belonging to Dictyotophycidae, Rhodymeniophycidae and Corallinophycidae

Table 2. Type and integral values of protons obtained from the 1H-NMR of the organic extracts of seaweeds belonging to the subclasses Dictyotophycidae (phylum Ochrophyta), Rhodymeniophycidae and Corallinophycidae (phylum Rhodophyta).

Table 4.1.: Yield and bioactivities (antioxidant, anti-inflammatory and antidiabetic) of sub-fractions from EtOAc-MeOH extract of *G. salicornia*

Table 4.10: NMR spectroscopic data[a] of 24(4→23)-abeo-olean-(12-oxo)-3,5-diene-deconoate (**3**) isolated from red seaweed *G. salicornia*

Table 4.13: NMR spectroscopic data of compound (**6**), 1-butoxy-4,4,11b,11c-tetramethyl-1,2,3,3a,4,5,6,6a,11b,11c-decahydrobenzo[kl]-xanthen-10-ol (**6**)isolated from red seaweed *G. salicornia*

Table 4.14: NMR spectroscopic data of compound (**7**), 4'-[10'-[7-Hydroxy-2,8-dimethyl-6-(pentyloxy)-*2H*-chromen-2-yl]ethyl]-3',4'-dimethyl-cyclohexanone (**7**) isolated from red seaweed *G. salicornia*

Table 4.15: NMR spectroscopic data of compound (**8**), 3'-[10'-(8-Hydroxy-5-methoxy-2,6,7-trimethyl-*2H*-chromen-2-yl)ethyl]-3'-methyl-2'-methylene cyclohexyl butyrate (**8**) isolated from red seaweed *G. salicornia***Table 4.16:** NMR spectroscopic data of compound (**9**), 3-(hydroxymethyl)-7-(methoxymethyl)-3,11-dimethyl-9-oxospiro[5.5]undec-4-en-10-methylbutanoate (**9**) isolated from red seaweed *G. salicornia*

Table 4.17: NMR spectroscopic data of compound (**10),** 4-ethoxy-11,11-dimethyl-7-methylene-8-(propionyloxy)spiro[5.5]undec-2-en-10^3,10^5-dihydroxytetrahydro-*2H*-pyran-10-carboxylate (**10**) isolated from red seaweed *G. salicornia*

Table 4.18: NMR spectroscopic data of compound (**11),** 15-(Octahydro-7-(4,5-dihydro-3-methoxy-2,6-dimethyl-*2H*-pyran-6-yl)-10-methylpyrano[3,2-b]pyran-14-yl)-18-(19-methyl-23-methyleneoxepan-19-yl)pent-15-en-18-ol (**11**) isolated from red seaweed *G. salicornia*

Table 4.19: NMR spectroscopic data of compound (**12),** tetrahydro-6-(hexahydro-13-((tetrahydro-18-(23-hydroxy-23-methylheptan-19-yl)-15-methylfuran-15-yl)methyl)-10-methyl-*2H*-furo[3,*2-b*]pyran-7-yl)-2,2,6-trimethyl-*2H*-pyran-3-yl (**12**) isolated from red seaweed *G. salicornia*

Table 4.2.: Yield and bioactivities of (antioxidant, anti-inflammatory and antidiabetic) sub-column fractions derived from EtOAc-MeOH extract of *G. salicornia*

Table 4.20: NMR spectroscopic data of compound (**13),** 3-acetyl-14-(furanyl)-11-methyl-15-(15^3-methylbutyloxy)-8-oxabicyclo-[21.3.1]heptacosa-11,23,25,27 tetraene-7,18-dione (**13**) isolated from red seaweed *G. salicornia*

Table 4.21: NMR spectroscopic data of compound (**14),** (2E,12E,14E)-10-acetyl-9-isopentyl-2-methyl-5,16,23^1-trioxa-bicyclo[21.3.1]-heptacosa-2,12,14-triene-6,19-dione (**14**) isolated from red seaweed *G. salicornia*

Table 4.22: NMR spectroscopic data of compound (**15),** (2Z,5E,16E)-8-hydroxy-20-isobutyl-16-methyl-7,14-dioxa-bicyclo[19.3.1]-pentacosa-2,5,16-triene-10,23-dione (**15**) isolated from red seaweed *G. salicornia*

Table 4.23.: *In vitro* antioxidant, anti-inflammatory and antidiabetic {radical scavenging, cyclooxygenase-1 & 2 (COX-1 & 2) and 5-lipoxygenase (5-LOX)) and α-amylase/glucosidase} activities of compounds (**1-15**) isolated from EtOAc-MeOH extract of *G. salicornia* against commercial standard, tocopherol (T), ibuprofen (I) and acarbose (A)

Table 4.24: Molecular descriptors (electronic, steric and hydrophobic)[†] of compound **1** from *G. salicornia*

Table 4.25: Molecular descriptors (electronic, steric and hydrophobic)[†] of compounds **2**-**3** from *G. salicornia*
Table 4.26: Molecular descriptors (electronic, steric and hydrophobic)[†] of compounds **4**-**6** from *G. salicornia*
Table 4.27: Molecular descriptors (electronic, steric and hydrophobic)[†] of compounds **7**-**8** from *G. salicornia*
Table 4.28: Molecular descriptors (electronic, steric and hydrophobic)[†] of compounds **9**-**10** from *G. salicornia*
Table 4.29: Molecular descriptors (electronic, steric and hydrophobic)[†] of compounds **11**-**12** from *G. salicornia*
Table 4.3.: Yield and bioactivities of (antioxidant, anti-inflammatory and antidiabetic) sub-column fractions derived from EtOAc-MeOH extract of *G. salicornia*
Table 4.30: Molecular descriptors (electronic, steric and hydrophobic)[†] of compounds **13**-**15** from *G. salicornia*
Table 4.31: The binding energy, docking score, inhibition constant, intermolecular energy and torsional free energy between the ligands (compounds **1**) and the active sites of 5-lipoxygenase
Table 4.32: The binding energy (B.E), inhibition constant (IC), intermolecular energy (I.E) and torsional free energy (T.E) between the ligands (compounds **2**-**3**) and the active sites of carbolytic enzymes α-glucosidase and α-amylase.
Table 4.33: The binding energy, docking score, inhibition constant, intermolecular energy and torsional free energy between the ligands (compounds **4**-**6**) and the active sites of 5-lipoxygenase
Table 4.34: The binding energy, docking score, inhibition constant, intermolecular energy and torsional free energy between the ligands (compounds **7**-**8**) and the active sites of 5-lipoxygenase.
Table 4.35: The binding energy, inhibition constant, intermolecular energy and torsional free energy between the ligands (compounds **9**-**10**) and the active sites of pro-inflammatory enzyme 5-LOX
Table 4.36: The binding energy, inhibition constant, intermolecular energy and torsional free energy between the ligands (compounds **11**-1**2**) and the active sites of pro-inflammatory enzymes 5-LOX
Table 4.37: The binding energy, inhibition constant, intermolecular energy and torsional free energy between the ligands (compounds **13**-**15**) and the active sites of pro-inflammatory enzyme 5-LOX
Table 4.4.: Yield and bioactivities (antioxidant, anti-inflammatory and antidiabetic) of sub-fractions from EtOAc-MeOH extract of *G. salicornia*
Table 4.5.: Yield and bioactivities (antioxidant, anti-inflammatory and antidiabetic) of sub-fractions from EtOAc-MeOH extract of *G. salicornia*
Table 4.6.: Yield and bioactivities (antioxidant, anti-inflammatory and antidiabetic) of sub-fractions from EtOAc-MeOH extract of *G. salicornia*
Table 4.7.: Yield and bioactivities (antioxidant, anti-inflammatory and antidiabetic) of sub-fractions from EtOAc-MeOH extract of *G. salicornia*
Table 4.8: NMR spectroscopic data[a] of methyl-16(13→14)-abeo-7-labdene-(12-oxo) carboxylate (**1**) isolated from red seaweed *G. salicornia*
Table 4.9: NMR spectroscopic data[a] of 24(4→23), 27(8→26), 30(20→29)-tris-abeo-olean-(12-oxo)-1,15,22-triene-methyl-hept-5-enoate (**2**) isolated from red seaweed *G. salicornia*

FIGURE CAPTIONS

Figure 1.1.: The percentage share of seaweeds along with different classes of marine organisms
Figure 1.2.: The percentage share of different seaweeds in the classification
Figure 1.3.: The major collection spots in Indian coastline
Figure 1.4.: The distribution of seaweeds in coastal region of India
Figure 1.5.: ROS induce oxidative damage to proteins, lipids and DNA
Figure 1.6.: Enzymatic and non-enzymatic antioxidants in seaweeds.
Figure 2.1.: Number of marine bioactive compounds isolated in the periods of 1965-2016 (Alves et al., 2018)
Figure 2.2.: The distribution of different marine living forms by phylum (Blunt *et al*., 2002)
Figure 2.3.: The Distribution of marine living forms between the various phyla isolated over the period of 1971-2015 (Blunt *et al*., 2017)
Figure 2.4.: Distribution of the seaweed secondary metabolites isolated per year (Blunt et al., 2009) and coupled with data from the same authors (Blunt et al., 2010, 2011, 2017 & 2018)
Figure 2.5.: Percentage diversity of the seaweeds and approximate proportion of secondary metabolites identified from seaweeds belonging to three major classes, Rhodophyceae, Phaeophyceae and Chlorophyceae over the period of 2000 - 2018 (approximate proportions of secondary metabolites assembled from Faulkner (2000 - 2002) and Blunt et al. (2003 - 2018).
Figure 2.6.: Thallus of *Gracilaria species* belonging to the family Gracilariaceae (Rhodophyta, Gracilariales)
Figure 2.7.: Thallus of *Padina species* is belonging to the family Dictyotaceae (Phaeophyta, Dictyotales)
Figure 3.1.: Representative photograph of sample collection site located between 8º48′ N, 78º9′ E and 9º14′ N, 79º14′ E at Gulf of Mannar of Mandapam region
Figure 3.10.: ^{1}H NMR spectrum of EtOAc-MeOH extract of *G. salicornia*
Figure 3.11.: ^{1}H NMR spectrum of EtOAc-MeOH extract of *P. tetrastromatica*
Figure 3.12.: ^{1}H NMR spectrum of EtOAc-MeOH extract of *G. canaliculata*
Figure 3.13.: ^{1}H NMR spectrum of EtOAc-MeOH extract of *G. corticata*
Figure 3.14.: ^{1}H NMR spectrum of EtOAc-MeOH extract of *H. edulis*
Figure 3.15.: ^{1}H NMR spectrum of EtOAc-MeOH extract of *A. fragilissima*
Figure 3.16.: ^{1}H NMR spectrum of EtOAc-MeOH extract of *P. pedrochei*
Figure 3.17.: ^{1}H NMR spectrum of EtOAc-MeOH extract of *S. filamentosa*
Figure 3.18.: ^{1}H NMR spectrum of EtOAc-MeOH extract of *H. dilatata*
Figure 3.19.: ^{1}H NMR spectrum of EtOAc-MeOH extract of *P. hornemannii*
Figure 3.2.: Representative photograph of four seaweeds, *P. tetrastromatica, G. salicornia, G. canaliculata and G. corticata* selected for the pharmacological screening
Figure 3.20.: ^{13}C NMR spectrum of EtOAc-MeOH extract of *G. salicornia*
Figure 3.21.: ^{13}C NMR spectrum of EtOAc-MeOH extract of *P. tetrastromatica*
Figure 3.22.: ^{13}C NMR spectrum of EtOAc-MeOH extract of *G. canaliculata*
Figure 3.23.: ^{13}C NMR spectrum of EtOAc-MeOH extract of *G. corticata*
Figure 3.24.: ^{13}C NMR spectrum of EtOAc-MeOH extract of *H. edulis*
Figure 3.25.: ^{13}C NMR spectrum of EtOAc-MeOH extract of *A. fragilissima*
Figure 3.26.: ^{13}C NMR spectrum of EtOAc-MeOH extract of *P. pedrochei*
Figure 3.27.: ^{13}C NMR spectrum of EtOAc-MeOH extract of *S. filamentosa*
Figure 3.28.: ^{13}C NMR spectrum of EtOAc-MeOH extract of *H. dilatata*
Figure 3.29.: ^{13}C NMR spectrum of EtOAc-MeOH extract of *P. hornemannii*
Figure 3.3.: Representative photograph of six seaweeds, *G. corticata, P. pedrochei, H. dilatata, S. filamentosa, P. hornemannii and A. fragilissima* selected for the pharmacological screening
Figure 3.30.: FTIR spectrum of EtOAc-MeOH extract of *G. salicornia*
Figure 3.31.: FTIR spectrum of EtOAc-MeOH extract of *P. tetrastromatica*

Figure 3.32.: FTIR spectrum of EtOAc-MeOH extract of *G. canaliculata*
Figure 3.33.: FTIR spectrum of EtOAc-MeOH extract of *G. corticata*
Figure 3.34.: FTIR spectrum of EtOAc-MeOH extract of *H. edulis*
Figure 3.35.: FTIR spectrum of EtOAc-MeOH extract of *A. fragilissima*
Figure 3.36.: FTIR spectrum of EtOAc-MeOH extract of *P. pedrochei*
Figure 3.37.: FTIR spectrum of EtOAc-MeOH extract of *S. filamentosa*
Figure 3.38.: FTIR spectrum of EtOAc-MeOH extract of *H. dilatata*
Figure 3.39.: FTIR spectrum of EtOAc-MeOH extract of *P. hornemannii*
Figure 3.4.: FTIR spectra of the organic extracts of *G. salicornia*-TA1, *P. tetrastromatica*-TA2, *G. canaliculata*-TA3, *G. corticata*-TA4, *H. edulis*-TA5, *A. fragilissima*-TA6, *P. pedrochei*-TA7, *S. filamentosa*-TA8, *H. dilatata*-TA9, and *P. hornemannii*-TA10.
Figure 3.5.: ^{1}H-NMR spectra of the organic extracts of (A) *G. salicornia*, (B) *P. tetrastromatica*, (C) *G. canaliculata*, (D) *G. corticata*, and (E) *H. edulis*. The spectra were vertically stacked according to their decreasing order of activities.
Figure 3.6.: ^{1}H-NMR spectra of the organic extracts of (F) *A. fragilissima*, (G) *P. pedrochei*, (H) *S. filamentosa*, (I) *H. dilatata*, and (J) *P. hornemannii*. The spectra were vertically stacked according to their decreasing order of activities
Figure 3.7.: ^{13}C-NMR spectra of the organic extracts of (A) *G. salicornia*, (B) *P. tetrastromatica*, (C) *G. canaliculata*, (D) *G. corticata*, and (E) *H. edulis*. The spectra were vertically stacked according to their decreasing order of activities.
Figure 3.8.: ^{13}C-NMR spectra of the organic extracts of (F) *A. fragilissima*, (G) *P. pedrochei*, (H) *S. filamentosa*, (I) *H. dilatata*, and (J) *P. hornemannii*. The spectra were vertically stacked according to their decreasing order of activities.
Figure 3.9.: Loading plot diagram (various components, PC1 and PC2 in the rotated space) of antioxidant activities vs anti-inflammatory, anti-diabetic and anti-hypertensive activities of the organic extracts of the studied seaweeds.
Figure 4.1.: The red seaweed *G. salicornia* of collected from the southeast coastline of the Indian sub-continent Gulf of Mannar region; between 8º48' N, 78°9' E and 9°14' N, 79°14' E)
Figure 4.10.: Key ^{1}H-^{1}H COSY (bold face bonds), selected HMBC (black coloured double barbed arrows) correlations of methyl-16(13→14)-abeo-7-labdene-(12-oxo) carboxylate
Figure 4.10.: ^{13}C-NMR spectrum of methyl-16(13→14)-abeo-7-labdene-(12-oxo) carboxylate (**1**)
Figure 4.100.: FTIR spectrum of 4'-[10'-[7-Hydroxy-2,8-dimethyl-6-(pentyloxy)-*2H*-chromen-2-yl]ethyl]-3',4'-dimethyl-cyclohexanone (7)
Figure 4.101.: ^{1}H NMR spectrum of 4'-[10'-[7-hydroxy-2,8-dimethyl-6-(pentyloxy)-*2H*-chromen-2-yl]ethyl]-3',4'-dimethyl-cyclohexanone (7)
Figure 4.102.: ^{13}C NMR spectrum of 4'-[10'-[7-hydroxy-2,8-dimethyl-6-(pentyloxy)-*2H*-chromen-2-yl]ethyl]-3',4'-dimethyl-cyclohexanone (7)
Figure 4.103.: ^{135}DEPT spectrum of 4'-[10'-[7-hydroxy-2,8-dimethyl-6-(pentyloxy)-*2H*-chromen-2-yl]ethyl]-3',4'-dimethyl-cyclohexanone (7)
Figure 4.104.: HSQC spectrum of 4'-[10'-[7-hydroxy-2,8-dimethyl-6-(pentyloxy)-*2H*-chromen-2-yl]ethyl]-3',4'-dimethyl-cyclohexanone (7)
Figure 4.105.: ^{1}H-^{1}H COSY (bold face bonds), and selected HMBCs (double-barbed arrows), correlations of 4'-[10'-[7-Hydroxy-2,8-dimethyl-6-(pentyloxy)-*2H*-chromen-2-yl]ethyl]-3',4'-dimethyl-cyclohexanone (**7**)
Figure 4.106.: ^{1}H-^{1}H COSY spectrum of 4'-[10'-[7-Hydroxy-2,8-dimethyl-6-(pentyloxy)-*2H*-chromen-2-yl]ethyl]-3',4'-dimethyl-cyclohexanone (7)
Figure 4.107.: HMBC spectrum of 4'-[10'-[7-hydroxy-2,8-dimethyl-6-(pentyloxy)-*2H*-chromen-2-yl]ethyl]-3',4'-dimethyl-cyclohexanone (7)
Figure 4.108.: NOESY (double-barbed arrows), correlations of 4'-[10'-[7-hydroxy-2,8-dimethyl-6-(pentyloxy)-*2H*-chromen-2-yl]ethyl]-3',4'-dimethyl-cyclohexanone (7)

Figure 4.109.: NOESY (double-barbed arrows), correlations of 4'-[10'-[7-hydroxy-2,8-dimethyl-6-(pentyloxy)-*2H*-chromen-2-yl]ethyl]-3',4'-dimethyl-cyclohexanone (7)
Figure 4.11.: ^{1}H-^{1}H COSY correlation spectrum of methyl-16(13→14)-abeo-7-labdene-(12-oxo) carboxylate (**1**)
Figure 4.110.: EI-MS spectrum of 4'-[10'-[7-hydroxy-2,8-dimethyl-6-(pentyloxy)-*2H*-chromen-2-yl]ethyl]-3',4'-dimethyl-cyclohexanone (7)
Figure 4.111.: Tentative mass fragmentation pattern of 4'-[10'-[7-hydroxy-2,8-dimethyl-6-(pentyloxy)-*2H*-chromen-2-yl]ethyl]-3',4'-dimethyl-cyclohexanone (7)
Figure 4.112.: UV spectrum of 3'-[10'-(8-hydroxy-5-methoxy-2,6,7-trimethyl-*2H*-chromen-2-yl)ethyl]-3'-methyl-2'-methylene cyclohexyl butyrate (**8**)
Figure 4.113.: HPLC chromatogram of 3'-[10'-(8-Hydroxy-5-methoxy-2,6,7-trimethyl-*2H*-chromen-2-yl)ethyl]-3'-methyl-2'-methylene cyclohexyl butyrate (**8**)
Figure 4.114.: HRESIMS of 3'-[10'-(8-hydroxy-5-methoxy-2,6,7-trimethyl-*2H*-chromen-2-yl)ethyl]-3'-methyl-2'-methylene cyclohexyl butyrate (**8**)
Figure 4.115.: FTIR spectrum of 3'-[10'-(8-hydroxy-5-methoxy-2,6,7-trimethyl-*2H*-chromen-2-yl)ethyl]-3'-methyl-2'-methylene cyclohexyl butyrate (**8**)
Figure 4.116.: ^{1}H NMR spectrum of 3'-[10'-(8-hydroxy-5-methoxy-2,6,7-trimethyl-*2H*-chromen-2-yl)ethyl]-3'-methyl-2'-methylene cyclohexyl butyrate (**8**)
Figure 4.117.: ^{13}C NMR spectrum of 3'-[10'-(8-hydroxy-5-methoxy-2,6,7-trimethyl-*2H*-chromen-2-yl)ethyl]-3'-methyl-2'-methylene cyclohexyl butyrate (**8**)
Figure 4.118.: ^{135}DEPT NMR spectrum of 3'-[10'-(8-hydroxy-5-methoxy-2,6,7-trimethyl-*2H*-chromen-2-yl)ethyl]-3'-methyl-2'-methylene cyclohexyl butyrate (**8**)
Figure 4.119.: HSQC spectrum of 3'-[10'-(8-hydroxy-5-methoxy-2,6,7-trimethyl-*2H*-chromen-2-yl)ethyl]-3'-methyl-2'-methylene cyclohexyl butyrate (**8**)
Figure 4.12.: HMBC correlation spectrum methyl-16(13→14)-abeo-7-labdene-(12-oxo) carboxylate (**1**)
Figure 4.120.: ^{1}H-^{1}H COSY (bold face bonds), and selected HMBCs (double-barbed arrows), correlations of 3'-[10'-(8-hydroxy-5-methoxy-2,6,7-trimethyl-*2H*-chromen-2-yl)ethyl]-3'-methyl-2'-methylene cyclohexyl butyrate (**8**)
Figure 4.121.: ^{1}H-^{1}H COSY spectrum of 3'-[10'-(8-hydroxy-5-methoxy-2,6,7-trimethyl-*2H*-chromen-2-yl)ethyl]-3'-methyl-2'-methylene cyclohexyl butyrate (**8**)
Figure 4.122.: HMBC spectrum of 3'-[10'-(8-hydroxy-5-methoxy-2,6,7-trimethyl-*2H*-chromen-2-yl)ethyl]-3'-methyl-2'-methylene cyclohexyl butyrate (**8**)
Figure 4.123.: NOESY (double-barbed arrows), correlations of 3'-[10'-(8-hydroxy-5-methoxy-2,6,7-trimethyl-*2H*-chromen-2-yl)ethyl]-3'-methyl-2'-methylene cyclohexyl butyrate (**8**)
Figure 4.124.: ^{1}H NMR spectrum of 3'-[10'-(8-hydroxy-5-methoxy-2,6,7-trimethyl-*2H*-chromen-2-yl)ethyl]-3'-methyl-2'-methylene cyclohexyl butyrate (**8**)
Figure 4.125.: EI-MS spectrum of 3'-[10'-(8-hydroxy-5-methoxy-2,6,7-trimethyl-*2H*-chromen-2-yl)ethyl]-3'-methyl-2'-methylene cyclohexyl butyrate (**8**)
Figure 4.126.: Tentative mass fragmentation pattern of 3'-[10'-(8-hydroxy-5-methoxy-2,6,7-trimethyl-*2H*-chromen-2-yl)ethyl]-3'-methyl-2'-methylene cyclohexyl butyrate (**8**)
Figure 4.127.: Structures of spiro[5.5]undecane compounds (**9**-**10**) isolated from the seaweed *G. salicornia*. The representative image of the thalli of *G. salicornia* was shown.
Figure 4.128.: UV spectrum of 3-(hydroxymethyl)-7-(methoxymethyl)-3,11-dimethyl-9-oxospiro[5.5]undec-4-en-10-methylbutanoate (**9**)
Figure 4.129.: HPLC chromatogram of 3-(hydroxymethyl)-7-(methoxymethyl)-3,11-dimethyl-9-oxospiro[5.5]undec-4-en-10-methylbutanoate (**9**)
Figure 4.13.: HSQC spectrum methyl-16(13→14)-abeo-7-labdene-(12-oxo) carboxylate (**1**)
Figure 4.130.: ESIMS spectrum of 3-(hydroxymethyl)-7-(methoxymethyl)-3,11-dimethyl-9-oxospiro[5.5]undec-4-en-10-methylbutanoate (**9**)

Figure 4.131.: FTIR spectrum of 3-(hydroxymethyl)-7-(methoxymethyl)-3,11-dimethyl-9-oxospiro[5.5]undec-4-en-10-methylbutanoate (**9**)
Figure 4.132.: ^{1}H-NMR spectrum of 3-(hydroxymethyl)-7-(methoxymethyl)-3,11-dimethyl-9-oxospiro[5.5]undec-4-en-10-methylbutanoate (**9**)
Figure 4.133.: ^{13}C-NMR spectrum of 3-(hydroxymethyl)-7-(methoxymethyl)-3,11-dimethyl-9-oxospiro[5.5]undec-4-en-10-methylbutanoate (**9**)
Figure 4.134.: ^{135}DEPT spectrum of 3-(hydroxymethyl)-7-(methoxymethyl)-3,11-dimethyl-9-oxospiro[5.5]undec-4-en-10-methylbutanoate (**9**)
Figure 4.135.: HSQC spectrum of 3-(hydroxymethyl)-7-(methoxymethyl)-3,11-dimethyl-9-oxospiro[5.5]undec-4-en-10-methylbutanoate (**9**)
Figure 4.136.: ^{1}H-^{1}H COSY (bold face bonds), and selected HMBCs (double-barbed arrows), correlations of 3-(hydroxymethyl)-7-(methoxymethyl)-3,11-dimethyl-9-oxospiro[5.5]undec-4-en-10-methylbutanoate (**9**)
Figure 4.137.: ^{1}H-^{1}H COSY spectrum of 3-(hydroxymethyl)-7-(methoxymethyl)-3,11-dimethyl-9-oxospiro[5.5]undec-4-en-10-methylbutanoate (**9**)
Figure 4.138.: HMBC spectrum of 3-(hydroxymethyl)-7-(methoxymethyl)-3,11-dimethyl-9-oxospiro[5.5]undec-4-en-10-methylbutanoate (**9**)
Figure 4.139.: NOESY (double barbed arrows) correlations of 3-(hydroxymethyl)-7-(methoxymethyl)-3,11-dimethyl-9-oxospiro[5.5]undec-4-en-10-methylbutanoate (**9**)
Figure 4.14.: Key NOESY correlations (double headed arrows) of methyl-16(13→14)-abeo-7-labdene-(12-oxo) carboxylate.
Figure 4.140.: NOESY spectrum of 3-(hydroxymethyl)-7-(methoxymethyl)-3,11-dimethyl-9-oxospiro[5.5]undec-4-en-10-methylbutanoate (**9**)
Figure 4.141.: EI-MS spectrum of 3-(hydroxymethyl)-7-(methoxymethyl)-3,11-dimethyl-9-oxospiro[5.5]undec-4-en-10-methylbutanoate (**9**)
Figure 4.142.: Tentative mass fragmentation pattern of 3-(hydroxymethyl)-7-(methoxymethyl)-3,11-dimethyl-9-oxospiro[5.5]undec-4-en-10-methylbutanoate (**9**)
Figure 4.143.: UV spectrum of 4-ethoxy-11,11-dimethyl-7-methylene-8-(propionyloxy)spiro[5.5]undec-2-en-10^{3},10^{5}-dihydroxytetrahydro-*2H*-pyran-10-carboxylate (**10**)
Figure 4.144.: HPLC chromatogram of 4-ethoxy-11,11-dimethyl-7-methylene-8-(propionyloxy)spiro[5.5]undec-2-en-10^{3},10^{5}-dihydroxytetrahydro-*2H*-pyran-10-carboxylate (**10**)
Figure 4.145.: HRESIMS spectrum of 4-ethoxy-11,11-dimethyl-7-methylene-8-(propionyloxy)spiro[5.5]undec-2-en-10^{3},10^{5}-dihydroxytetrahydro-*2H*-pyran-10-carboxylate (**10**)
Figure 4.146.: FTIR spectrum of 4-ethoxy-11,11-dimethyl-7-methylene-8-(propionyloxy)spiro[5.5]undec-2-en-10^{3},10^{5}-dihydroxytetrahydro-*2H*-pyran-10-carboxylate (**10**)
Figure 4.147.: ^{1}H-NMR spectrum of 4-ethoxy-11,11-dimethyl-7-methylene-8-(propionyloxy)spiro[5.5]undec-2-en-10^{3},10^{5}-dihydroxytetrahydro-*2H*-pyran-10-carboxylate (**10**)
Figure 4.148.: ^{13}C-NMR spectrum of 4-ethoxy-11,11-dimethyl-7-methylene-8-(propionyloxy)spiro[5.5]undec-2-en-10^{3},10^{5}-dihydroxytetrahydro-*2H*-pyran-10-carboxylate (**10**)
Figure 4.149.: ^{135}DEPT spectrum of 4-ethoxy-11,11-dimethyl-7-methylene-8-(propionyloxy)spiro[5.5]undec-2-en-10^{3},10^{5}-dihydroxytetrahydro-*2H*-pyran-10-carboxylate (**10**)
Figure 4.15.: NOESY spectrum of methyl-16(13→14)-abeo-7-labdene-(12-oxo) carboxylate (**1**).
Figure 4.150.: HSQC spectrum of 4-ethoxy-11,11-dimethyl-7-methylene-8-(propionyloxy)spiro[5.5]undec-2-en-10^{3},10^{5}-dihydroxytetrahydro-*2H*-pyran-10-carboxylate (**10**)
Figure 4.151.: ^{1}H-^{1}H COSY spectrum of 4-ethoxy-11,11-dimethyl-7-methylene-8-(propionyloxy)spiro[5.5]undec-2-en-10^{3},10^{5}-dihydroxytetrahydro-*2H*-pyran-10-carboxylate (**10**)
Figure 4.152.: ^{1}H-^{1}H COSY (bold face bonds), and selected HMBCs (double-barbed arrows), correlations of 4-ethoxy-11,11-dimethyl-7-methylene-8-(propionyloxy)spiro[5.5]undec-2-en-10^{3},10^{5}-dihydroxytetrahydro-*2H*-pyran-10-carboxylate (**10**)
Figure 4.153.: HMBC spectrum of 4-ethoxy-11,11-dimethyl-7-methylene-8-(propionyloxy)spiro[5.5]undec-2-en-10^{3},10^{5}-dihydroxytetrahydro-*2H*-pyran-10-carboxylate (**10**)

Figure 4.154.: NOESY correlations (double barbed arrows) of 4-ethoxy-11,11-dimethyl-7-methylene-8-(propionyloxy)spiro[5.5]undec-2-en-10^3,10^5-dihydroxytetrahydro-*2H*-pyran-10-carboxylate (**10**)

Figure 4.155.: EI-MS spectrum of 4-ethoxy-11,11-dimethyl-7-methylene-8-(propionyloxy)spiro[5.5]undec-2-en-10^3,10^5-dihydroxytetrahydro-*2H*-pyran-10-carboxylate (**10**)

Figure 4.156.: Tentative mass fragmentation pattern of 4-ethoxy-11,11-dimethyl-7-methylene-8-(propionyloxy)spiro[5.5]undec-2-en-10^3,10^5-dihydroxytetrahydro-*2H*-pyran-10-carboxylate (**10**)

Figure 4.157.: Structural representations of (**A**) 3-methoxy-2,6-dimethyl-3,4-dihydro-2*H*-pyranyl-(6-(7-(10-methyl-octahydropyrano[3,2-*b*]pyranyl)-14-((19-methyl-23-methyleneoxepan)-(15-pentene-18-ol)) (**11**) and (**B**) 14-(15-methyltetrahydrofuranyl)-(18-(23-(hydroxy-23-methylheptanyl)-10-methylhexahydro-2*H*-furo-[3,2-*b*]pyranyl))-2,2,6-trimethyltetrahydro-2*H*-pyran-3- butyrate (**12**) purified from *G. salicornia*. (**D**) The characteristic of thalli (leaf-like structures) of *G. salicornia* was presented.

Figure 4.158.: UV spectrum of 15-(octahydro-7-(4,5-dihydro-3-methoxy-2,6-dimethyl-*2H*-pyran-6-yl)-10-methylpyrano[3,2-b]pyran-14-yl)-18-(19-methyl-23-methyleneoxepan-19-yl)pent-15-en-18-ol (**11**)

Figure 4.159.: HPLC chromatogram of 15-(octahydro-7-(4,5-dihydro-3-methoxy-2,6-dimethyl-*2H*-pyran-6-yl)-10-methylpyrano[3,2-b]pyran-14-yl)-18-(19-methyl-23-methyleneoxepan-19-yl)pent-15-en-18-ol (**11**)

Figure 4.16.: EI-MS spectrum of methyl-16(13→14)-abeo-7-labdene-(12-oxo) carboxylate (**1**)

Figure 4.160.: HRESIMS spectrum of 15-(octahydro-7-(4,5-dihydro-3-methoxy-2,6-dimethyl-*2H*-pyran-6-yl)-10-methylpyrano[3,2-b]pyran-14-yl)-18-(19-methyl-23-methyleneoxepan-19-yl)pent-15-en-18-ol (**11**)

Figure 4.161.: FTIR spectrum of 15-(octahydro-7-(4,5-dihydro-3-methoxy-2,6-dimethyl-*2H*-pyran-6-yl)-10-methylpyrano[3,2-b]pyran-14-yl)-18-(19-methyl-23-methyleneoxepan-19-yl)pent-15-en-18-ol (**11**)

Figure 4.162.: ^{1}H NMR spectrum of 15-(octahydro-7-(4,5-dihydro-3-methoxy-2,6-dimethyl-*2H*-pyran-6-yl)-10-methylpyrano[3,2-b]pyran-14-yl)-18-(19-methyl-23-methyleneoxepan-19-yl)pent-15-en-18-ol (**11**)

Figure 4.163.: ^{13}C NMR spectrum of 15-(octahydro-7-(4,5-dihydro-3-methoxy-2,6-dimethyl-*2H*-pyran-6-yl)-10-methylpyrano[3,2-b]pyran-14-yl)-18-(19-methyl-23-methyleneoxepan-19-yl)pent-15-en-18-ol (**11**)

Figure 4.164.: ^{135}DEPT spectrum of 15-(octahydro-7-(4,5-dihydro-3-methoxy-2,6-dimethyl-*2H*-pyran-6-yl)-10-methylpyrano[3,2-b]pyran-14-yl)-18-(19-methyl-23-methyleneoxepan-19-yl)pent-15-en-18-ol (**11**)

Figure 4.165.: HSQC spectrum of 15-(octahydro-7-(4,5-dihydro-3-methoxy-2,6-dimethyl-*2H*-pyran-6-yl)-10-methylpyrano[3,2-b]pyran-14-yl)-18-(19-methyl-23-methyleneoxepan-19-yl)pent-15-en-18-ol (**11**)

Figure 4.166.: ^{1}H-^{1}H COSY (bold face bonds) and selected HMBCs (double-barbed arrows) correlations of 15-(Octahydro-7-(4,5-dihydro-3-methoxy-2,6-dimethyl-*2H*-pyran-6-yl)-10-methylpyrano[3,2-b]pyran-14-yl)-18-(19-methyl-23-methyleneoxepan-19-yl)pent-15-en-18-ol (**11**)

Figure 4.167.: ^{1}H-^{1}H COSY spectrum of 15-(octahydro-7-(4,5-dihydro-3-methoxy-2,6-dimethyl-*2H*-pyran-6-yl)-10-methylpyrano[3,2-b]pyran-14-yl)-18-(19-methyl-23-methyleneoxepan-19-yl)pent-15-en-18-ol (**11**)

Figure 4.168.: HMBC spectrum of 15-(octahydro-7-(4,5-dihydro-3-methoxy-2,6-dimethyl-*2H*-pyran-6-yl)-10-methylpyrano[3,2-b]pyran-14-yl)-18-(19-methyl-23-methyleneoxepan-19-yl)pent-15-en-18-ol (**11**)

Figure 4.169.: NOESY correlations (double headed arrows) of 15-(octahydro-7-(4,5-dihydro-3-methoxy-2,6-dimethyl-*2H*-pyran-6-yl)-10-methylpyrano[3,2-b]pyran-14-yl)-18-(19-methyl-23-methyleneoxepan-19-yl)pent-15-en-18-ol (**11**)

Figure 4.17.: Tentative mass fragmentation pattern of methyl-16(13→14)-abeo-7-labdene-(12-oxo) carboxylate (**1**)

Figure 4.170.: NOESY spectrum of 15-(octahydro-7-(4,5-dihydro-3-methoxy-2,6-dimethyl-*2H*-pyran-6-yl)-10-methylpyrano[3,2-b]pyran-14-yl)-18-(19-methyl-23-methyleneoxepan-19-yl)pent-15-en-18-ol (**11**)

Figure 4.171.: EI-MS spectrum of 15-(octahydro-7-(4,5-dihydro-3-methoxy-2,6-dimethyl-*2H*-pyran-6-yl)-10-methylpyrano[3,2-b]pyran-14-yl)-18-(19-methyl-23-methyleneoxepan-19-yl)pent-15-en-18-ol (**11**)

Figure 4.172.: Mass fragmentation pattern of 15-(octahydro-7-(4,5-dihydro-3-methoxy-2,6-dimethyl-*2H*-pyran-6-yl)-10-methylpyrano[3,2-b]pyran-14-yl)-18-(19-methyl-23-methyleneoxepan-19-yl)pent-15-en-18-ol (**11**)

Figure 4.173.: UV spectrum of tetrahydro-6-(hexahydro-13-((tetrahydro-18-(23-hydroxy-23-methylheptan-19-yl)-15-methylfuran-15-yl)methyl)-10-methyl-*2H*-furo[3,2-b]pyran-7-yl)-2,2,6-trimethyl-*2H*-pyran-3-yl (**12**)

Figure 4.174.: HPLC chromatogram of tetrahydro-6-(hexahydro-13-((tetrahydro-18-(23-hydroxy-23-methylheptan-19-yl)-15-methylfuran-15-yl)methyl)-10-methyl-*2H*-furo[3,2-b]pyran-7-yl)-2,2,6-trimethyl-*2H*-pyran-3-yl (**12**)

Figure 4.175.: HRESIMS spectrum of tetrahydro-6-(hexahydro-13-((tetrahydro-18-(23-hydroxy-23-methylheptan-19-yl)-15-methylfuran-15-yl)methyl)-10-methyl-*2H*-furo[3,2-b]pyran-7-yl)-2,2,6-trimethyl-*2H*-pyran-3-yl (**12**)

Figure 4.176.: FTIR spectrum of tetrahydro-6-(hexahydro-13-((tetrahydro-18-(23-hydroxy-23-methylheptan-19-yl)-15-methylfuran-15-yl)methyl)-10-methyl-*2H*-furo[3,*2-b*]pyran-7-yl)-2,2,6-trimethyl-*2H*-pyran-3-yl (**12**)

Figure 4.177.: ^{1}H NMR spectrum of tetrahydro-6-(hexahydro-13-((tetrahydro-18-(23-hydroxy-23-methylheptan-19-yl)-15-methylfuran-15-yl)methyl)-10-methyl-*2H*-furo[3,*2-b*]pyran-7-yl)-2,2,6-trimethyl-*2H*-pyran-3-yl (**12**)

Figure 4.178.: ^{13}C NMR spectrum of tetrahydro-6-(hexahydro-13-((tetrahydro-18-(23-hydroxy-23-methylheptan-19-yl)-15-methylfuran-15-yl)methyl)-10-methyl-*2H*-furo[3,*2-b*]pyran-7-yl)-2,2,6-trimethyl-*2H*-pyran-3-yl (**12**)

Figure 4.179.: ^{135}DEPT spectrum of tetrahydro-6-(hexahydro-13-((tetrahydro-18-(23-hydroxy-23-methylheptan-19-yl)-15-methylfuran-15-yl)methyl)-10-methyl-*2H*-furo[3,*2-b*]pyran-7-yl)-2,2,6-trimethyl-*2H*-pyran-3-yl (**12**)

Figure 4.18.: Structural representations of (**A1**) 24(4→23), 27(8→26), 30(20→29)-tris-abeo-olean-(12-oxo)-1,15,22-triene-methyl hept-5-enoate (**1**) and (**A2**) 24(4→23)-abeo-olean-(12-oxo)-3,5-diene-deconoate (**2**) isolated from *G. salicornia*. (**A3**) Representative photograph of thalli of the red seaweed *G. salicornia*.

Figure 4.180.: HSQC spectrum of tetrahydro-6-(hexahydro-13-((tetrahydro-18-(23-hydroxy-23-methylheptan-19-yl)-15-methylfuran-15-yl)methyl)-10-methyl-*2H*-furo[3,*2-b*]pyran-7-yl)-2,2,6-trimethyl-*2H*-pyran-3-yl (**12**)

Figure 4.181.: ^{1}H-^{1}H COSY (bold face bonds) and selected HMBCs (double-barbed arrows), correlations of tetrahydro-6-(hexahydro-13-((tetrahydro-18-(23-hydroxy-23-methylheptan-19-yl)-15-methylfuran-15-yl)methyl)-10-methyl-*2H*-furo[3,*2-b*]pyran-7-yl)-2,2,6-trimethyl-*2H*-pyran-3-yl (**12**)

Figure 4.182.: ^{1}H-^{1}H COSY spectrum of tetrahydro-6-(hexahydro-13-((tetrahydro-18-(23-hydroxy-23-methylheptan-19-yl)-15-methylfuran-15-yl)methyl)-10-methyl-*2H*-furo[3,*2-b*]pyran-7-yl)-2,2,6-trimethyl-*2H*-pyran-3-yl (**12**)

Figure 4.183.: HMBC spectrum of tetrahydro-6-(hexahydro-13-((tetrahydro-18-(23-hydroxy-23-methylheptan-19-yl)-15-methylfuran-15-yl)methyl)-10-methyl-*2H*-furo[3,*2-b*]pyran-7-yl)-2,2,6-trimethyl-*2H*-pyran-3-yl (**12**)

Figure 4.184.: HMBC spectrum of tetrahydro-6-(hexahydro-13-((tetrahydro-18-(23-hydroxy-23-methylheptan-19-yl)-15-methylfuran-15-yl)methyl)-10-methyl-*2H*-furo[3,2-b]pyran-7-yl)-2,2,6-trimethyl-*2H*-pyran-3-yl (**12**)

Figure 4.185.: NOE spectrum of tetrahydro-6-(hexahydro-13-((tetrahydro-18-(23-hydroxy-23-methylheptan-19-yl)-15-methylfuran-15-yl)methyl)-10-methyl-*2H*-furo[3,2-b]pyran-7-yl)-2,2,6-trimethyl-*2H*-pyran-3-yl (**12**)

Figure 4.186.: EI-MS spectrum of tetrahydro-6-(hexahydro-13-((tetrahydro-18-(23-hydroxy-23-methylheptan-19-yl)-15-methylfuran-15-yl)methyl)-10-methyl-*2H*-furo[3,2-b]pyran-7-yl)-2,2,6-trimethyl-*2H*-pyran-3-yl (**12**)

Figure 4.187.: Mass fragmentation pattern m of tetrahydro-6-(hexahydro-13-((tetrahydro-18-(23-hydroxy-23-methylheptan-19-yl)-15-methylfuran-15-yl)methyl)-10-methyl-*2H*-furo[3,2-b]pyran-7-yl)-2,2,6-trimethyl-*2H*-pyran-3-yl (**12**)

Figure 4.188.: Structural representations of 3 macrolides (**13-15**) along with the characteristic of thalli (leaf-like structures) of *G. salicornia* were presented.

Figure 4.189.: UV spectrum of 3-acetyl-14-(furanyl)-11-methyl-15-(15^3-methylbutyloxy)-8-oxabicyclo-[21.3.1]heptacosa-11,23,25,27 tetraene-7,18-dione (**13**)

Figure 4.19.: UVspectrum of 24(4→23), 27(8→26), 30(20→29)-tris-abeo-olean-(12-oxo)-1,15,22-triene-methyl hept-5-enoate **(2)**

Figure 4.190.: HPLC chromatogram of 3-acetyl-14-(furanyl)-11-methyl-15-(15^3-methylbutyloxy)-8-oxabicyclo-[21.3.1]heptacosa-11,23,25,27 tetraene-7,18-dione (**13**)

Figure 4.191.: HRESIMS spectrum of 3-acetyl-14-(furanyl)-11-methyl-15-(15^3-methylbutyloxy)-8-oxabicyclo-[21.3.1]heptacosa-11,23,25,27 tetraene-7,18-dione (**13**)

Figure 4.192.: FTIR spectrum of 3-acetyl-14-(furanyl)-11-methyl-15-(15^3-methylbutyloxy)-8-oxabicyclo-[21.3.1]heptacosa-11,23,25,27 tetraene-7,18-dione (**13**)

Figure 4.193.: ^{1}H NMR spectrum of 3-acetyl-14-(furanyl)-11-methyl-15-(15^3-methylbutyloxy)-8-oxabicyclo-[21.3.1]heptacosa-11,23,25,27 tetraene-7,18-dione

Figure 4.194.: ^{13}C NMR spectrum of 3-acetyl-14-(furanyl)-11-methyl-15-(15^3-methylbutyloxy)-8-oxabicyclo-[21.3.1]heptacosa-11,23,25,27 tetraene-7,18-dione (**13**)

Figure 4.195.: ^{135}DEPT NMR spectrum of 3-acetyl-14-(furanyl)-11-methyl-15-(15^3-methylbutyloxy)-8-oxabicyclo-[21.3.1]heptacosa-11,23,25,27 tetraene-7,18-dione (**13**)

Figure 4.196.: HSQC spectrum of 3-acetyl-14-(furanyl)-11-methyl-15-(15^3-methylbutyloxy)-8-oxabicyclo-[21.3.1]heptacosa-11,23,25,27 tetraene-7,18-dione (**13**)

Figure 4.197.: ^{1}H-^{1}H COSY (bold face bonds) and HMBC (double-barbed arrows) correlations of 3-acetyl-14-(furanyl)-11-methyl-15-(15^3-methylbutyloxy)-8-oxabicyclo-[21.3.1]heptacosa-11,23,25,27 tetraene-7,18-dione (**13**)

Figure 4.198.: ^{1}H-^{1}H COSY spectrum of 3-acetyl-14-(furanyl)-11-methyl-15-(15^3-methylbutyloxy)-8-oxabicyclo-[21.3.1]heptacosa-11,23,25,27 tetraene-7,18-dione (**13**)

Figure 4.199.: ^{1}H-^{1}H COSY (bold face bonds) and HMBC (double-barbed arrows) correlations of 3-acetyl-14-(furanyl)-11-methyl-15-(15^3-methylbutyloxy)-8-oxabicyclo-[21.3.1]heptacosa-11,23,25,27 tetraene-7,18-dione (**13**)

Figure 4.2.: Schematic representation of purification of fractions and compounds from the EtOAc-MeOH extract of *G. salicornia*. CC- column chromatograph

Figure 4.20.: HPLC chromatogram of 24(4→23), 27(8→26), 30(20→29)-tris-abeo-olean-(12-oxo)-1,15,22-triene-methyl hept-5-enoate (**2**)

Figure 4.200.: NOE (double-barbed green coloured arrows for α-orientation and blue coloured arrows for β orientations) correlations of 3-acetyl-14-(furanyl)-11-methyl-15-(15^3-methylbutyloxy)-8-oxabicyclo-[21.3.1]heptacosa-11,23,25,27 tetraene-7,18-dione (**13**)

Figure 4.200.: NOESY spectrum of 3-acetyl-14-(furanyl)-11-methyl-15-(15^3-methylbutyloxy)-8-oxabicyclo-[21.3.1]heptacosa-11,23,25,27 tetraene-7,18-dione (**13**)

Figure 4.201.: EI-MS spectrum of 3-acetyl-14-(furanyl)-11-methyl-15-(15^3-methylbutyloxy)-8-oxabicyclo-[21.3.1]heptacosa-11,23,25,27 tetraene-7,18-dione (**13**)

Figure 4.202.: Tentative mass fragmentation pattern of 3-acetyl-14-(furanyl)-11-methyl-15-(15^3-methylbutyloxy)-8-oxabicyclo-[21.3.1]heptacosa-11,23,25,27 tetraene-7,18-dione (**13**)

Figure 4.203.: UV spectrum of (2E,12E,14E)-10-acetyl-9-isopentyl-2-methyl-5,16,23[1]-trioxa-bicyclo[21.3.1]-heptacosa-2,12,14-triene-6,19-dione (**14**)
Figure 4.204.: HPLC chromatogram of (2E,12E,14E)-10-acetyl-9-isopentyl-2-methyl-5,16,23[1]-trioxa-bicyclo[21.3.1]-heptacosa-2,12,14-triene-6,19-dione (**14**)
Figure 4.205.: HRESIMS spectrum of (2E,12E,14E)-10-acetyl-9-isopentyl-2-methyl-5,16,23[1]-trioxa-bicyclo[21.3.1]-heptacosa-2,12,14-triene-6,19-dione (**14**)
Figure 4.206.: FTIR spectrum of (2E,12E,14E)-10-acetyl-9-isopentyl-2-methyl-5,16,23[1]-trioxa-bicyclo[21.3.1]-heptacosa-2,12,14-triene-6,19-dione (**14**)
Figure 4.207.: ^{1}H NMR spectrum of (2E,12E,14E)-10-acetyl-9-isopentyl-2-methyl-5,16,23[1]-trioxa-bicyclo[21.3.1]-heptacosa-2,12,14-triene-6,19-dione (**14**)
Figure 4.208.: ^{13}C NMR spectrum of (2E,12E,14E)-10-acetyl-9-isopentyl-2-methyl-5,16,23[1]-trioxa-bicyclo[21.3.1]-heptacosa-2,12,14-triene-6,19-dione (**14**)
Figure 4.209.: ^{135}DEPT NMR spectrum of (2E,12E,14E)-10-acetyl-9-isopentyl-2-methyl-5,16,23[1]-trioxa-bicyclo[21.3.1]-heptacosa-2,12,14-triene-6,19-dione (**14**)
Figure 4.21.: HRESIMS of 24(4→23), 27(8→26), 30(20→29)-tris-abeo-olean-(12-oxo)-1,15,22-triene-methyl hept-5-enoate **(2)**
Figure 4.210.: HSQC spectrum of (2E,12E,14E)-10-acetyl-9-isopentyl-2-methyl-5,16,23[1]-trioxa-bicyclo[21.3.1]-heptacosa-2,12,14-triene-6,19-dione (**14**)
Figure 4.211.: ^{1}H-^{1}H COSY (bold face bonds) and HMBC (double-barbed arrows) correlations of (2E,12E,14E)-10-acetyl-9-isopentyl-2-methyl-5,16,23[1]-trioxa-bicyclo[21.3.1]-heptacosa-2,12,14-triene-6,19-dione (**14**)
Figure 4.212.: ^{1}H-^{1}H COSY spectrum of (2E,12E,14E)-10-acetyl-9-isopentyl-2-methyl-5,16,23[1]-trioxa-bicyclo[21.3.1]-heptacosa-2,12,14-triene-6,19-dione (**14**)
Figure 4.213.: HMBC spectrum of (2E,12E,14E)-10-acetyl-9-isopentyl-2-methyl-5,16,23[1]-trioxa-bicyclo[21.3.1]-heptacosa-2,12,14-triene-6,19-dione (**14**)
Figure 4.214.: NOESY (double-barbed green coloured arrows for α-orientation and blue coloured arrows for β orientations) correlations of (2E,12E,14E)-10-acetyl-9-isopentyl-2-methyl-5,16,23[1]-trioxa-bicyclo[21.3.1]-heptacosa-2,12,14-triene-6,19-dione (**14**)
Figure 4.215.: NOE spectrum of (2E,12E,14E)-10-acetyl-9-isopentyl-2-methyl-5,16,23[1]-trioxa-bicyclo[21.3.1]-heptacosa-2,12,14-triene-6,19-dione (**14**)
Figure 4.216.: EI-MS spectrum of (2E,12E,14E)-10-acetyl-9-isopentyl-2-methyl-5,16,23[1]-trioxa-bicyclo[21.3.1]-heptacosa-2,12,14-triene-6,19-dione (**14**)
Figure 4.217.: Tentative mass fragmentation pattern of (2E,12E,14E)-10-acetyl-9-isopentyl-2-methyl-5,16,23[1]-trioxa-bicyclo[21.3.1]-heptacosa-2,12,14-triene-6,19-dione (**14**)
Figure 4.218.: UV spectrum of (2Z,5E,16E)-8-hydroxy-20-isobutyl-16-methyl-7,14-dioxa-bicyclo[19.3.1]-pentacosa-2,5,16-triene-10,23-dione (**15**)
Figure 4.219.: HPLC chromatogram of (2Z,5E,16E)-8-hydroxy-20-isobutyl-16-methyl-7,14-dioxa-bicyclo[19.3.1]-pentacosa-2,5,16-triene-10,23-dione (**15**)
Figure 4.22.: FT-IR of 24(4→23), 27(8→26), 30(20→29)-tris-abeo-olean-(12-oxo)-1,15,22-triene-methyl hept-5-enoate **(2)**
Figure 4.220.: FTIR spectrum of (2Z,5E,16E)-8-hydroxy-20-isobutyl-16-methyl-7,14-dioxa-bicyclo[19.3.1]-pentacosa-2,5,16-triene-10,23-dione (**15**)
Figure 4.221.: ^{1}H NMR spectrum of (2Z,5E,16E)-8-hydroxy-20-isobutyl-16-methyl-7,14-dioxa-bicyclo[19.3.1]-pentacosa-2,5,16-triene-10,23-dione (**15**)
Figure 4.222.: ^{13}C NMR spectrum of (2Z,5E,16E)-8-hydroxy-20-isobutyl-16-methyl-7,14-dioxa-bicyclo[19.3.1]-pentacosa-2,5,16-triene-10,23-dione (**15**)
Figure 4.223.: ^{135}DEPT spectrum spectrum of (2Z,5E,16E)-8-hydroxy-20-isobutyl-16-methyl-7,14-dioxa-bicyclo[19.3.1]-pentacosa-2,5,16-triene-10,23-dione (**15**)
Figure 4.224.: HSQC spectrum of (2Z,5E,16E)-8-hydroxy-20-isobutyl-16-methyl-7,14-dioxa-bicyclo[19.3.1]-pentacosa-2,5,16-triene-10,23-dione (**15**)

Figure 4.225.: ^{1}H-^{1}H COSY (bold-faced bonds) and HMBC (double-barbed arrows) correlations of (2Z,5E,16E)-8-hydroxy-20-isobutyl-16-methyl-7,14-dioxa-bicyclo[19.3.1]-pentacosa-2,5,16-triene-10,23-dione (**15**)

Figure 4.226.: HMBC spectrum of (2Z,5E,16E)-8-hydroxy-20-isobutyl-16-methyl-7,14-dioxa-bicyclo[19.3.1]-pentacosa-2,5,16-triene-10,23-dione (**15**)

Figure 4.227.: HMBC spectrum of (2Z,5E,16E)-8-hydroxy-20-isobutyl-16-methyl-7,14-dioxa-bicyclo[19.3.1]-pentacosa-2,5,16-triene-10,23-dione (**15**)

Figure 4.228.: NOESY (double-barbed green coloured arrows for α-orientation and blue coloured arrows for β orientations) correlations of (2Z,5E,16E)-8-hydroxy-20-isobutyl-16-methyl-7,14-dioxa-bicyclo[19.3.1]-pentacosa-2,5,16-triene-10,23-dione (**15**)

Figure 4.229.: NOESY spectrum of (2Z,5E,16E)-8-hydroxy-20-isobutyl-16-methyl-7,14-dioxa-bicyclo[19.3.1]-pentacosa-2,5,16-triene-10,23-dione (**15**)

Figure 4.23.: ^{1}H-NMR of 24(4→23), 27(8→26), 30(20→29)-tris-abeo-olean-(12-oxo)-1,15,22-triene-methyl hept-5-enoate **(2)**

Figure 4.230.: NOESY spectrum of (2Z,5E,16E)-8-hydroxy-20-isobutyl-16-methyl-7,14-dioxa-bicyclo[19.3.1]-pentacosa-2,5,16-triene-10,23-dione (**15**)

Figure 4.231.: Tentative mass spectrum of (2Z,5E,16E)-8-hydroxy-20-isobutyl-16-methyl-7,14-dioxa-bicyclo[19.3.1]-pentacosa-2,5,16-triene-10,23-dione (**15**)

Figure 4.232.: Closer view of molecular binding interactions of compound **1** in the catalytic site of protein 5-LOX

Figure 4.233.: Closer view of molecular binding interactions of (**A1**) 24(4→23), 27(8→26), 30(20→29)-tris-abeo-oleanene **2** and (**A2**) 24(4→23)-abeo-oleanene **3** derivatives in the catalytic site of protein *α*-glucosidase along with molecular binding interactions of (**B1**) 24(4→23), 27(8→26), 30(20→29)-tris-abeo-oleanene **2** and (**B2**) 24(4→23)-abeo-oleanene **3** derivatives in the catalytic site of *α*-amylase as deduced from its molecular modeling simulations.

Figure 4.234.: Closer view of molecular binding interactions of the drimane sesquiterpene quinols in the catalytic site of (**A-C**) 5-lipoxygenase (5-LOX) as deduced from the molecular docking simulation experiment. The molecular docking analysis of ligands (studied sesquiterpene analogues **4-6**) and pro-inflammatory 5-LOX showed two hydrogen bonds (displayed as red and blue-coloured lines with amino acyl residues of Lys^{441} and Arg^{438} with bond distances of 3.370 and 3.030 Å, respectively) in the active binding site. The compounds **4** and **6** showed one hydrogen bonded interactions with amino acyl residues Gly^{150} and Lys^{441} with molecular distances of 2.790 Å and 2.915 Å, respectively.

Figure 4.235.: Closer view of molecular binding interactions of the compounds **7**-**8** (**A** and **B**) in the catalytic site of 5-lipoxygenase (5-LOX) as deduced from the molecular docking simulation experiment. The molecular docking analysis of ligands (compound, **8**) and pro-inflammatory 5-LOX showed six hydrogen bonds (displayed as red and blue-coloured lines) with amino acyl residues of Ser^{522}, Lys^{521}, Lys^{527} and Ser^{628} with bond distances of 2.743, 3.640, 3.117, 2.792, 2.668, and 3.075 Å in the active binding site. The compound **7** showed two hydrogen-bonded interactions with amino acid residues of Gln^{534} and Gln^{497} with molecular distances of 2.883, 3.046 Å, respectively**Figure 4.236.:** Closer view of molecular binding interactions of the spiro[5.5]undecanes (A and B) in the catalytic site of 5-lipoxygenase (5-LOX) as deduced from the molecular docking simulation experiment. The molecular docking analysis of ligands (**10**) and pro-inflammatory 5-LOX showed four hydrogen bonds (displayed as red and blue-coloured lines) with amino acyl residues of GLN^{437} (2-hydrogen bonds), $ARG^{438}$and ASP^{442} with bond distances of 3.126, 3.146, 2.737 and 3.181 Å in the active binding site. The compound **9** showed two hydrogen-bonded interactions with amino acid residues of ARG^{438} with molecular distances of 3.089 Å.

Figure 4.237.: Closer view of molecular binding interactions of compound (**11**) in the and 5-lipoxygenase (5-LOX) (**A**1-**A2**) catalytic site as obtained from molecular docking. Closer view of molecular

binding interactions of the compound (**12**) in the 5-lipoxygenase (5-LOX) (**B**1-**B2**) catalytic sites as obtained from molecular docking.

Figure 4.238.: Closer image of molecular docking interactions of compounds **13**-**15** (**A**-**C**) in the 5-LOX catalytic site as obtained by docking experiment. The docking analysis of compound **13** and pro-inflammatory 5-LOX showed three hydrogen-bonds (displayed as red and blue-coloured lines with amino-acyl residues of ASP^{442} And Arg^{438} with bond distances of 2.870, 3.139 and 4.077 Å) in binding site. Compound **14** displayed five hydrogen-bonds with amino acid residues of Lys^{254}, Asp^{290}, Arg^{438} and Arg^{520}, with molecular distances of 2.702, 2.914, 3.435, 3.049, and 2.393 Å. Compound **15** showed two hydrogen-bonds with amino acid residues of Asp^{285} and Leu^{244}, with molecular distances of 3.172 and 2.846 Å.

Figure 4.24.: ^{13}C NMR of 24(4→23), 27(8→26), 30(20→29)-tris-abeo-olean-(12-oxo)-1,15,22-triene-methyl hept-5-enoate **(2)**

Figure 4.25.: ^{135}DEPT spectrum of 24(4→23), 27(8→26), 30(20→29)-tris-abeo-olean-(12-oxo)-1,15,22-triene-methyl hept-5-enoate **(2)**

Figure 4.26.: HSQC spectrum of 24(4→23), 27(8→26), 30(20→29)-tris-abeo-olean-(12-oxo)-1,15,22-triene-methyl hept-5-enoate **(2)**

Figure 4.27.: ^{1}H-^{1}H COSY (bold-face bonds), and selected HMBC (double-barbed arrows) correlations of 24(4→23), 27(8→26), 30(20→29)-tris-abeo-olean-(12-oxo)-1,15,22-triene-methyl hept-5-enoate (**2**) isolated from *G. salicornia*.

Figure 4.28.: ^{1}H-^{1}H COSY spectrum of 24(4→23), 27(8→26), 30(20→29)-tris-abeo-olean-(12-oxo)-1,15,22-triene-methyl hept-5-enoate **(2)**

Figure 4.29.: HMBC spectrum of 24(4→23), 27(8→26), 30(20→29)-tris-abeo-olean-(12-oxo)-1,15,22-triene-methyl hept-5-enoate **(2)**

Figure 4.3.: Structure of methyl-16(13→14)-abeo-7-labdene-(12-oxo) carboxylate isolated from *G. salicornia* (family Gracilariaceae), (B) representative photograph of thalli of red seaweed *G. salicornia*

Figure 4.30.: NOESY spectrum of 24(4→23), 27(8→26), 30(20→29)-tris-abeo-olean-(12-oxo)-1,15,22-triene-methyl hept-5-enoate (**2**)

Figure 4.31.: NOE correlations of 24(4→23), 27(8→26), 30(20→29)-tris-abeo-olean-(12-oxo)-1,15,22-triene-methyl-hept-5-enoate (**2**) isolated from *G. salicornia*.

Figure 4.32.: EI-MS spectrum of 24(4→23), 27(8→26), 30(20→29)-tris-abeo-olean-(12-oxo)-1,15,22-triene-methyl-hept-5-enoate (**2**) isolated from *G. salicornia*.

Figure 4.32.: EI-MS spectrum of 24(4→23), 27(8→26), 30(20→29)-tris-abeo-olean-(12-oxo)-1,15,22-triene-methyl-hept-5-enoate (**2**)

Figure 4.34.: UVspectrum of 24(4→23)-abeo-olean-(12-oxo)-3,5-diene-deconoate (**3**)

Figure 4.35.: HPLC chromatogram of 24(4→23)-abeo-olean-(12-oxo)-3,5-diene-deconoate (**3**)

Figure 4.36.: HRESIMS spectrum of 24(4→23)-abeo-olean-(12-oxo)-3,5-diene-deconoate (**3**

Figure 4.37.: FT-IR spectrum of 24(4→23)-abeo-olean-(12-oxo)-3,5-diene-deconoate (**3**)

Figure 4.38.: ^{1}HNMR spectrum of 24(4→23)-abeo-olean-(12-oxo)-3,5-diene-deconoate (**3**)

Figure 4.39.: ^{13}C NMR spectrum of 24(4→23)-abeo-olean-(12-oxo)-3,5-diene-deconoate (**3**)

Figure 4.4.: UV spectrum of methyl-16(13→14)-abeo-7-labdene-(12-oxo) carboxylate (**1**)

Figure 4.40.: ^{135}DEPT spectrum of 24(4→23)-abeo-olean-(12-oxo)-3,5-diene-deconoate (**3**)

Figure 4.41.: HSQC spectrum of 24(4→23)-abeo-olean-(12-oxo)-3,5-diene-deconoate (**3**

Figure 4.42.: ^{1}H-^{1}H COSY (bold-face bonds), selected HMBC (double-barbed arrows) correlations of 24(4→23)-abeo-olean-(12-oxo)-3,5-diene-deconoate (**3**)

Figure 4.43.: ^{1}H-^{1}H COSY spectrum of 24(4→23)-abeo-olean-(12-oxo)-3,5-diene-deconoate (**3**)

Figure 4.44.: HMBC spectrum of 24(4→23)-abeo-olean-(12-oxo)-3,5-diene-deconoate (**3**)

Figure 4.45.: NOE (single headed arrows) correlations of 24(4→23)-abeo-olean-(12-oxo)-3,5-diene-deconoate (**3**)

Figure 4.46.: NOE spectrum of 24(4→23)-abeo-olean-(12-oxo)-3,5-diene-deconoate (**3**)

Figure 4.47.: EI-MS spectrum of 24(4→23)-abeo-olean-(12-oxo)-3,5-diene-deconoate (**3**)

Figure 4.48.: Tentative mass fragmentation pattern of 24(4→23)-abeo-olean-(12-oxo)-3,5-diene-deconoate (**3**)
Figure 4.49.: Structural representations of (**A**) 3-(hept-3^6-enyloxy)-decahydro-4,6a,12a,12b-tetramethyl-1*H*-benzo[*a*]xanthene-4,10,12-triol (compound **4**), (**B**) 13-[[2-(hexyloxy)-2,5,5,8a-tetramethyldecahydro-1-naphthalenyl](methoxy)methyl]benzenol (compound **5**), and (**C**) 1-butoxy-4,4,11b,11c-tetramethyl-decahydrobenzo[*kl*]xanthen-10-ol (compound **6**) isolated from red seaweed *G. salicornia*. (**D**) The representative photograph of thalli (leaf-like structures) of *G. salicornia*.
Figure 4.5.: HPLC chromatogram of methyl-16(13→14)-abeo-7-labdene-(12-oxo) carboxylate (**1**)
Figure 4.50.: UV spectrum of 3-(Hept-3^6-enyloxy)-2,3,4,4a,5,6,6a,12,12a,12b-decahydro-4,6a,12a,12b-tetramethyl-*1H*-benzo[a]xanthene-4,10,12-triol (**4**)
Figure 4.51.: HPLC chromatogram of 3-(Hept-3^6-enyloxy)-2,3,4,4a,5,6,6a,12,12a,12b-decahydro-4,6a,12a,12b-tetramethyl-*1H*-benzo[a]xanthene-4,10,12-triol (**4**)
Figure 4.52.: HRESIMS spectrum of 3-(Hept-3^6-enyloxy)-2,3,4,4a,5,6,6a,12,12a,12b-decahydro-4,6a,12a,12b-tetramethyl-*1H*-benzo[a]xanthene-4,10,12-triol (**4**)
Figure 4.53.: FTIR spectrum of 3-(Hept-3^6-enyloxy)-2,3,4,4a,5,6,6a,12,12a,12b-decahydro-4,6a,12a,12b-tetramethyl-*1H*-benzo[a]xanthene-4,10,12-triol
Figure 4.54.: FTIR spectrum of 3-(Hept-3^6-enyloxy)-2,3,4,4a,5,6,6a,12,12a,12b-decahydro-4,6a,12a,12b-tetramethyl-*1H*-benzo[a]xanthene-4,10,12-triol
Figure 4.55.: ^{13}C-NMR spectrum of 3-(Hept-3^6-enyloxy)-2,3,4,4a,5,6,6a,12,12a,12b-decahydro-4,6a,12a,12b-tetramethyl-*1H*-benzo[a]xanthene-4,10,12-triol (**4**)
Figure 4.56.: DEPT spectrum of 3-(Hept-3^6-enyloxy)-2,3,4,4a,5,6,6a,12,12a,12b-decahydro-4,6a,12a,12b-tetramethyl-*1H*-benzo[a]xanthene-4,10,12-triol (**4**)
Figure 4.57.: HSQC spectrum of 3-(Hept-3^6-enyloxy)-2,3,4,4a,5,6,6a,12,12a,12b-decahydro-4,6a,12a,12b-tetramethyl-*1H*-benzo[a]xanthene-4,10,12-triol (**4**
Figure 4.58.: ^{1}H-^{1}H COSY (bold face bonds), and selected HMBCs (double-barbed arrows), correlations of 3-(Hept-3^6-enyloxy)-2,3,4,4a,5,6,6a,12,12a,12b-decahydro-4,6a,12a,12b-tetramethyl-*1H*-benzo[a]xanthene-4,10,12-triol (**4**)
Figure 4.59.: ^{1}H-^{1}H COSY spectrum of 3-(Hept-3^6-enyloxy)-2,3,4,4a,5,6,6a,12,12a,12b-decahydro-4,6a,12a,12b-tetramethyl-*1H*-benzo[a]xanthene-4,10,12-triol (**4**)
Figure 4.6.: HRESIMS spectrum of methyl-16(13→14)-abeo-7-labdene-(12-oxo) carboxylate (**1**)
Figure 4.60.: NOE spectrum of 3-(Hept-3^6-enyloxy)-2,3,4,4a,5,6,6a,12,12a,12b-decahydro-4,6a,12a,12b-tetramethyl-*1H*-benzo[a]xanthene-4,10,12-triol (**4**)
Figure 4.61.: DEPT spectrum of 3-(Hept-3^6-enyloxy)-2,3,4,4a,5,6,6a,12,12a,12b-decahydro-4,6a,12a,12b-tetramethyl-*1H*-benzo[a]xanthene-4,10,12-triol (**4**)
Figure 4.62.: NOE correlations of 3-(hept-3^6-enyloxy)-2,3,4,4a,5,6,6a,12,12a,12b-decahydro-4,6a,12a,12b-tetramethyl-1*H*-benzo[a]xanthene-4,10,12-triol (**4**)
Figure 4.63.: EI-MS spectrum of 3-(Hept-3^6-enyloxy)-2,3,4,4a,5,6,6a,12,12a,12b-decahydro-4,6a,12a,12b-tetramethyl-*1H*-benzo[a]xanthene-4,10,12-triol (**4**)
Figure 4.64.: Mass fragmentation pattern of 3-(Hept-3^6-enyloxy)-2,3,4,4a,5,6,6a,12,12a,12b-decahydro-4,6a,12a,12b-tetramethyl-*1H*-benzo[a]xanthene-4,10,12-triol (**4**)
Figure 4.66.: UV spectrum of 13-[[2-(Hexyloxy)-2,5,5,8a-tetramethyldecahydro-1-naphthalenyl](methoxy-)-methyl]-benzenol (**5**)
Figure 4.67.: HPLC chromatogram of 13-[[2-(Hexyloxy)-2,5,5,8a-tetramethyldecahydro-1-naphthalenyl](methoxy-)-methyl]-benzenol (**5**)
Figure 4.68.: HRESIMS spectrum of 13-[[2-(Hexyloxy)-2,5,5,8a-tetramethyldecahydro-1-naphthalenyl](methoxy-)-methyl]-benzenol (**5**)
Figure 4.69.: FTIR spectrum of 13-[[2-(Hexyloxy)-2,5,5,8a-tetramethyldecahydro-1-naphthalenyl](methoxy-)-methyl]-benzenol (**5**)
Figure 4.7.: FT-IR spectrum of methyl-16(13→14)-abeo-7-labdene-(12-oxo) carboxylate (**1**)

Figure 4.70.: ^{1}H-NMR spectrum of 13-[[2-(Hexyloxy)-2,5,5,8a-tetramethyldecahydro-1-naphthalenyl](methoxy-)-methyl]-benzenol (**5**)
Figure 4.71.: ^{13}C-NMR spectrum of 13-[[2-(Hexyloxy)-2,5,5,8a-tetramethyldecahydro-1-naphthalenyl](methoxy-)-methyl]-benzenol (**5**)
Figure 4.72.: ^{135}DEPT spectrum of 13-[[2-(Hexyloxy)-2,5,5,8a-tetramethyldecahydro-1-naphthalenyl](methoxy-)-methyl]-benzenol (**5**)
Figure 4.73.: HSQC spectrum of 13-[[2-(Hexyloxy)-2,5,5,8a-tetramethyldecahydro-1-naphthalenyl](methoxy-)-methyl]-benzenol (**5**)
Figure 4.74.: ^{1}H-^{1}H COSY spectrum of 13-[[2-(Hexyloxy)-2,5,5,8a-tetramethyldecahydro-1-naphthalenyl](methoxy-)-methyl]-benzenol (**5**)
Figure 4.75.: ^{1}H-^{1}H COSY (bold face bonds), and selected HMBCs (double-barbed arrows), correlations of 13-[[2-(Hexyloxy)-2,5,5,8a-tetramethyldecahydro-1-naphthalenyl](methoxy-)-methyl]-benzenol (**5**)
Figure 4.76.: HMBC spectrum of 13-[[2-(Hexyloxy)-2,5,5,8a-tetramethyldecahydro-1-naphthalenyl](methoxy-)-methyl]-benzenol (**5**)
Figure 4.77.: NOE correlations of 13-[[2-(Hexyloxy)-2,5,5,8a-tetramethyldecahydro-1-naphthalenyl](methoxy-)-methyl]-benzenol (**5**)
Figure 4.77.: NOE spectrum of 13-[[2-(Hexyloxy)-2,5,5,8a-tetramethyldecahydro-1-naphthalenyl](methoxy-)-methyl]-benzenol (**5**)
Figure 4.78.: EI-MS spectrum of 3-(Hept-3^{6}-enyloxy)-2,3,4,4a,5,6,6a,12,12a,12b-decahydro-4,6a,12a,12b-tetramethyl-*1H*-benzo[a]xanthene-4,10,12-triol (**5**)
Figure 4.8.: ^{1}H-NMR spectrum of methyl-16(13→14)-abeo-7-labdene-(12-oxo) carboxylate (**1**)
Figure 4.80.: Mass fragmentation pattern of 3-(Hept-3^{6}-enyloxy)-2,3,4,4a,5,6,6a,12,12a,12b-decahydro-4,6a,12a,12b-tetramethyl-*1H*-benzo[a]xanthene-4,10,12-triol (**5**)
Figure 4.81.: UV spectrum of 1-butoxy-4,4,11b,11c-tetramethyl-1,2,3,3a,4,5,6,6a,11b,11c-decahydrobenzo[kl]-xanthen-10-ol (**6**)
Figure 4.82.: HPLC chromatogram of 1-butoxy-4,4,11b,11c-tetramethyl-1,2,3,3a,4,5,6,6a,11b,11c-decahydrobenzo[kl]-xanthen-10-ol (**6**)
Figure 4.83.: HRESIMS spectrum of 1-butoxy-4,4,11b,11c-tetramethyl-1,2,3,3a,4,5,6,6a,11b,11c-decahydrobenzo[kl]-xanthen-10-ol (**6**)
Figure 4.84.: FTIR spectrum of 1-butoxy-4,4,11b,11c-tetramethyl-1,2,3,3a,4,5,6,6a,11b,11c-decahydrobenzo[kl]-xanthen-10-ol (**6**)
Figure 4.85.: ^{1}H-NMR spectrum of 1-butoxy-4,4,11b,11c-tetramethyl-1,2,3,3a,4,5,6,6a,11b,11c-decahydrobenzo[kl]-xanthen-10-ol (**6**)
Figure 4.86.: ^{13}C-NMR spectrum of 1-butoxy-4,4,11b,11c-tetramethyl-1,2,3,3a,4,5,6,6a,11b,11c-decahydrobenzo[kl]-xanthen-10-ol (**6**)
Figure 4.87.: ^{135}DEPT spectrum of 1-butoxy-4,4,11b,11c-tetramethyl-1,2,3,3a,4,5,6,6a,11b,11c-decahydrobenzo[kl]-xanthen-10-ol (**6**)
Figure 4.88.: HSQC spectrum of 1-butoxy-4,4,11b,11c-tetramethyl-1,2,3,3a,4,5,6,6a,11b,11c-decahydrobenzo[kl]-xanthen-10-ol (**6**)
Figure 4.89.: ^{1}H-^{1}H COSY (bold face bonds), and selected HMBCs (double-barbed arrows) of 1-butoxy-4,4,11b,11c-tetramethyl-1,2,3,3a,4,5,6,6a,11b,11c-decahydrobenzo[kl]-xanthen-10-ol (**6**)
Figure 4.9.: ^{13}C-NMR spectrum of methyl-16(13→14)-abeo-7-labdene-(12-oxo) carboxylate (**1**)
Figure 4.90.: ^{1}H-^{1}H COSY spectrum of 1-butoxy-4,4,11b,11c-tetramethyl-1,2,3,3a,4,5,6,6a,11b,11c-decahydrobenzo-[kl]-xanthen-10-ol (**6**)
Figure 4.91.: HMBC spectrum of 1-butoxy-4,4,11b,11c-tetramethyl-1,2,3,3a,4,5,6,6a,11b,11c-decahydrobenzo[kl]-xanthen-10-ol (**6**)
Figure 4.92.: NOE (double barbed arrows) correlations of 1-butoxy-4,4,11b,11c-tetramethyl-1,2,3,3a,4,5,6,6a,11b,11c-decahydrobenzo[kl]-xanthen-10-ol (**6**)
Figure 4.93.: NOESY spectrum of 1-butoxy-4,4,11b,11c-tetramethyl-1,2,3,3a,4,5,6,6a,11b,11c-decahydrobenzo[kl]-xanthen-10-ol (**6**)

Figure 4.94.: EI-MS spectrum of 1-butoxy-4,4,11b,11c-tetramethyl-1,2,3,3a,4,5,6,6a,11b,11c-decahydrobenzo[kl]-xanthen-10-ol (**6**)
Figure 4.95.: Mass fragmentation pattern of 1-butoxy-4,4,11b,11c-tetramethyl-1,2,3,3a,4,5,6,6a,11b,11c-decahydrobenzo[kl]-xanthen-10-ol (**6**)
Figure 4.96.: Structures of 2*H*-chromenyl derivatives (**7**-**8**) isolated from the seaweed *Gracilaria salicornia*. The representative photograph of the thalli of *G. salicornia* was shown
Figure 4.97.: UV spectrum of 4'-[10'-[7-Hydroxy-2,8-dimethyl-6-(pentyloxy)-*2H*-chromen-2-yl]ethyl]-3',4'-dimethyl-cyclohexanone (7)
Figure 4.98.: HPLC chromatogram of 4'-[10'-[7-hydroxy-2,8-dimethyl-6-(pentyloxy)-*2H*-chromen-2-yl]ethyl]-3',4'-dimethyl-cyclohexanone (7)
Figure 4.99.: HRESIMS spectrum of 4'-[10'-[7-Hydroxy-2,8-dimethyl-6-(pentyloxy)-*2H*-chromen-2-yl]ethyl]-3',4'-dimethyl-cyclohexanone (7)
Figure 5.1.: The brown seaweed *P. tetrastromatica* of collected from the southeast coastline of the Indian sub-continent Gulf of Mannar region; between 8º48' N, 78°9' E and 9°14' N, 79°14' E)
Figure 5.10.: ^{135} DEPT NMR spectrum of 12-ethenyl-3a,6,9,10,11,12,12a,12b-octahydro-1-(1^2-hydroxy-1^2-methyl-propyl)-cyclonona[*d*]furo[2,3-*b*]pyran-6,10-diol **(1)**
Figure 5.101.: DEPT spectrum of 3-methoxy-dolabella-12(18)-ene-4β-ol (**7**)
Figure 5.102.: ^{1}H-^{1}H COSY spectrum of 3-methoxy-dolabella-12(18)-ene-4β-ol (**7**)
Figure 5.103.: HSQC spectrum of 3-methoxy-dolabella-12(18)-ene-4β-ol (**7**)
Figure 5.104.: HMBC spectrum of 3-methoxy-dolabella-12(18)-ene-4β-ol (**7**)
Figure 5.105.: Prominent ^{1}H-^{1}H COSY, and selected HMBC correlations of 3-methoxy-dolabella-12(18)-ene-4β-ol (**7**). The key ^{1}H-^{1}H COSY couplings were represented in bold face bonds. The key HMBC couplings have been represented by double barbed arrows.
Figure 5.106.: NOESY of 3-methoxy-dolabella-12(18)-ene-4β-ol (**7**)
Figure 5.107.: Prominent NOE correlations of 3-methoxy-dolabella-12(18)-ene-4β-ol (**7**). NOESY relations are represented by double-tailed arrows**Figure 5.108.:** EI-MS spectrum of 3-methoxy-dolabella-12(18)-ene-4β-ol (**7**)
Figure 5.109.: EI-MS spectrum of 3-methoxy-dolabella-12(18)-ene-4β-ol (**7**)
Figure 5.11.: HSQC spectrum of 12-ethenyl-3a,6,9,10,11,12,12a,12b-octahydro-1-(1^2-hydroxy-1^2-methyl-propyl)-cyclonona[*d*]furo[2,3-*b*]pyran-6,10-diol **(1)**
Figure 5.110.: UVspectrum of 3-methoxy-dolabella-10,18(19)-diene-5α,8β -diol (**8**)
Figure 5.111.: HPLC chromatogram of 3-methoxy-dolabella-10,18(19)-diene-5α,8β -diol (**8**)
Figure 5.112.: HRESIMS of 3-methoxy-dolabella-10,18(19)-diene-5α,8β -diol (**8**)
Figure 5.113.: FTIR spectrum of 3-methoxy-dolabella-10,18(19)-diene-5α,8β -diol (**8**)
Figure 5.114.: ^{13}C NMR spectrum 3-methoxy-dolabella-10,18(19)-diene-5α,8β -diol (**8**)
Figure 5.114.: ^{1}H NMR spectrum 3-methoxy-dolabella-10,18(19)-diene-5α,8β -diol (**8**)
Figure 5.115.: DEPT spectrum spectrum 3-methoxy-dolabella-10,18(19)-diene-5α,8β -diol (**8**)
Figure 5.116.: ^{1}H-^{1}H COSY spectrum 3-methoxy-dolabella-10,18(19)-diene-5α,8β -diol (**8**)
Figure 5.117.: HSQC spectrum 3-methoxy-dolabella-10,18(19)-diene-5α,8β -diol (**8**)
Figure 5.118.: HMBC spectrum 3-methoxy-dolabella-10,18(19)-diene-5α,8β -diol (**8**)
Figure 5.119.: Prominent ^{1}H-^{1}H COSY, and selected HMBC correlations of 3-methoxy-dolabella-10,18(19)-diene-5α,8β-diol (**8**). The key ^{1}H-^{1}H COSY couplings were represented in bold face bonds. The key HMBC couplings have been represented by double barbed arrows.
Figure 5.12.: ^{1}H-^{1}H COSY spectrum of 12-ethenyl-3a,6,9,10,11,12,12a,12b-octahydro-1-(1^2-hydroxy-1^2-methyl-propyl)-cyclonona[*d*]furo[2,3-*b*]pyran-6,10-diol **(1)**
Figure 5.120.: NOESY spectrum 3-methoxy-dolabella-10,18(19)-diene-5α,8β -diol (**8**)
Figure 5.121.: Prominent NOE correlations of 3-methoxy-dolabella-10,18(19)-diene-5α,8β -diol (**8**). NOESY relations are represented by double-tailed arrows
Figure 5.122.: EI-MS spectrum 3-methoxy-dolabella-10,18(19)-diene-5α,8β -diol (**8**)
Figure 5.123.: Tentative mass fragmentation pattern of 3-methoxy-dolabella-10,18(19)-diene-5α,8β -diol (8)

Figure 5.124.: UVspectrum of 2,7-dimethoxy-14α-hydroxy-dolasta-1(15),9-diene (**9**)
Figure 5.125.: HPLC chromatogram of 2,7-dimethoxy-14α-hydroxy-dolasta-1(15),9-diene (**9**)
Figure 5.126.: HRESIMS of 2,7-dimethoxy-14α-hydroxy-dolasta-1(15),9-diene (**9**)
Figure 5.127.: FTIR spectrum of 2,7-dimethoxy-14α-hydroxy-dolasta-1(15),9-diene (**9**)
Figure 5.128.: ^{1}H NMR spectrum of 2,7-dimethoxy-14α-hydroxy-dolasta-1(15),9-diene (**9**)
Figure 5.129.: ^{13}C NMR spectrum of 2,7-dimethoxy-14α-hydroxy-dolasta-1(15),9-diene (**9**)
Figure 5.13.: HMBC spectrum of 12-ethenyl-3a,6,9,10,11,12,12a,12b-octahydro-1-(1^{2}-hydroxy-1^{2}-methyl-propyl)-cyclonona[*d*]furo[2,3-*b*]pyran-6,10-diol **(1)**
Figure 5.130.: DEPT spectrum of 2,7-dimethoxy-14α-hydroxy-dolasta-1(15),9-diene (**9**)
Figure 5.131.: ^{1}H-^{1}H COSY spectrum of 2,7-dimethoxy-14α-hydroxy-dolasta-1(15),9-diene (**9**)
Figure 5.132.: HSQC spectrum of 2,7-dimethoxy-14α-hydroxy-dolasta-1(15),9-diene (**9**)
Figure 5.133.: HMBC spectrum of 2,7-dimethoxy-14α-hydroxy-dolasta-1(15),9-diene (**9**)
Figure 5.134.: Prominent ^{1}H-^{1}H COSY, and selected HMBC correlations of 2,7-dimethoxy-14α-hydroxy-dolasta-1(15),9-diene (**9**). The key ^{1}H-^{1}H COSY couplings were represented in bold face bonds. The key HMBC couplings have been represented by double barbed
Figure 5.135.: NOESY spectrum of 2,7-dimethoxy-14α-hydroxy-dolasta-1(15),9-diene (**9**)
Figure 5.136.: Prominent NOE correlations of 2,7-Dimethoxy-14α-hydroxy-dolasta-1(15),9-diene (**9**). NOESY relations are represented by double-tailed arrows
Figure 5.137.: EI-MS spectrum of 2,7-Dimethoxy-14α-hydroxy-dolasta-1(15),9-diene**Figure 5.138.:** Tentative mass fragmentation pattern of 2,7-dimethoxy-14α-hydroxy-dolasta-1(15),9-diene (**9**)
Figure 5.138.: Tentative mass fragmentation pattern of 2,7-dimethoxy-14α-hydroxy-dolasta-1(15),9-diene (**9**)
Figure 5.139.: UVspectrum of 4,7-dimethoxy-9β ,14α-dihydroxy-dolasta-1-ene (**10**)
Figure 5.14.: Prominent ^{1}H-^{1}H COSY, and selected HMBC correlations of 12-ethenyl-3a,6,9,10,11,12,12a,12b-octahydro-1-(1^{2}-hydroxy-1^{2}-methyl-propyl)-cyclonona[*d*]furo[2,3-*b*]pyran-6,10-diol **(1)**. The key ^{1}H-^{1}H COSY couplings were represented in bold face bonds. The key HMBC couplings have been represented by double barbed arrows.
Figure 5.140.: HPLC chromatogram of 4,7-dimethoxy-9β ,14α-dihydroxy-dolasta-1-ene (**10**)
Figure 5.141.: HRESIMS of 4,7-dimethoxy-9β ,14α-dihydroxy-dolasta-1-ene (**10**)
Figure 5.142.: ^{13}C NMR spectrum of4,7-dimethoxy-9β ,14α-dihydroxy-dolasta-1-ene (**10**) **Figure 5.142.:** HSQC spectrum of 4,7-dimethoxy-9β ,14α-dihydroxy-dolasta-1-ene (**10**)
Figure 5.142.: ^{1}H-^{1}H COSY spectrum of4,7-dimethoxy-9β ,14α-dihydroxy-dolasta-1-ene (**10**)
Figure 5.142.: DEPT spectrum of4,7-dimethoxy-9β ,14α-dihydroxy-dolasta-1-ene (**10**)
Figure 5.142.: FTIR spectrum of4,7-dimethoxy-9β ,14α-dihydroxy-dolasta-1-ene (**10**)
Figure 5.143.: ^{1}H NMR spectrum of4,7-dimethoxy-9β ,14α-dihydroxy-dolasta-1-ene (**10**)
Figure 5.143.: HMBC spectrum of4,7-dimethoxy-9β ,14α-dihydroxy-dolasta-1-ene (**10**)
Figure 5.144.: Prominent ^{1}H-^{1}H COSY, and selected HMBC correlations of 4,7-dimethoxy-9β ,14α-dihydroxy-dolasta-1-ene (**10**). The key ^{1}H-^{1}H COSY couplings were represented in bold face bonds. The key HMBC couplings have been represented by double barbed arrows.
Figure 5.145.: NOESY spectrum of 4,7-dimethoxy-9β ,14α-dihydroxy-dolasta-1-ene (**10**)
Figure 5.146.: Prominent NOE correlations of 2,7-dimethoxy-14α-hydroxy-dolasta-1(15),9-diene (**10**). NOESY relations are represented by double-tailed arrows
Figure 5.147.: EI-MS spectrum of 4,7-dimethoxy-9β ,14α-dihydroxy-dolasta-1-ene (**10**)
Figure 5.148.: Tentative mass fragmentation pattern of 4,7-dimethoxy-9β ,14α-dihydroxy-dolasta-1-ene (**10**)
Fig. 5.149.: Closer view of molecular binding interactions of the xenicane derivatives **1** (**A**) and **2** (**B**) in the catalytic site of protein LOX-5 as deduced from its molecular modeling simulations. The xenicanes **1** and **2** exhibited one hydrogen bond interaction with amino residues Arg411 and Arg438 in the enzyme active site with molecular distances of 3.011 Å and 2.740 Å, respectivel

Figure 5.152.: Prominent NOE correlations of 12-ethenyl-3a,6,9,10,11,12,12a,12b-octahydro-1-(1^2-hydroxy-1^2-methyl-propyl)-cyclonona[*d*]furo[2,3-*b*]pyran-6,10-diol **(1)**. NOESY relations are represented by double-tailed arrows

Figure 5.150.: Closer view of molecular binding interactions of the xeniolide derivatives **3** (**A**), **4** (**B**), and **5** (**C**) in the catalytic site of protein LOX-5 as deduced from its molecular modelling simulations. The xeniolide **5** showed three hydrogen bonded interactions with amino acid residues, one hydrogen bonded with Lys441 (2.799 Å), and two with Gln434 (2.860 and 2.886 Å). Compound **5** displayed greater number of hydrogen bond interactions with amino acyl residues than those recorded by **3** and **4**.

Figure 5.151. Closer view of molecular binding interactions of compounds **8** (**A1**-**A2**) and **10** (**B1**-**B2**) in the catalytic site of protein *α*-amylase deduced from molecular modeling simulations.

Figure 5.16.: NOE correlations of 12-ethenyl-3a,6,9,10,11,12,12a,12b-octahydro-1-(1^2-hydroxy-1^2-methyl-propyl)-cyclonona[*d*]furo[2,3-*b*]pyran-6,10-diol **(1)**.

Figure 5.17.: EI-MS spectrum of 6-methoxy-dolabella-8(17),12-diene-10β ,18-diol (**1**)

Figure 5.18.: Tentative mass fragmentation pattern of 6-methoxy-dolabella-8(17),12-diene-10β ,18-diol (**1**)

Figure 5.19.: UVspectrum of 1,2,5,5a,6,9,10,11,12,12a-decahydro-11(11^2-hydroxypropyl)-2-[(*E*)-2^1-propenyl] cyclonona[*d*]-furo[2,3-*b*]pyran-9,12-diol (**2**)

Figure 5.2.: Schematic representation of purification of fractions and compounds from the EtOAc-MeOH extract of *G. salicornia*.CC-column chromatography

Figure 5.20.: HPLC chromatogram of 1,2,5,5a,6,9,10,11,12,12a-decahydro-11(11^2-hydroxypropyl)-2-[(*E*)-2^1-propenyl] cyclonona[*d*]-furo[2,3-*b*]pyran-9,12-diol (**2**)

Figure 5.21.: HRESIMS of 1,2,5,5a,6,9,10,11,12,12a-decahydro-11(11^2-hydroxypropyl)-2-[(*E*)-2^1-propenyl] cyclonona[*d*]-furo[2,3-*b*]pyran-9,12-diol (**2**)

Figure 5.22.: FTIR spectrum of 1,2,5,5a,6,9,10,11,12,12a-decahydro-11(11^2-hydroxypropyl)-2-[(*E*)-2^1-propenyl] cyclonona[*d*]-furo[2,3-*b*]pyran-9,12-diol (**2**)

Figure 5.23.: ^{1}H NMR spectrum of 1,2,5,5a,6,9,10,11,12,12a-decahydro-11(11^2-hydroxypropyl)-2-[(*E*)-2^1-propenyl] cyclonona[*d*]-furo[2,3-*b*]pyran-9,12-diol (**2**)

Figure 5.24.: ^{13}C NMR spectrum of 1,2,5,5a,6,9,10,11,12,12a-decahydro-11(11^2-hydroxypropyl)-2-[(*E*)-2^1-propenyl] cyclonona[*d*]-furo[2,3-*b*]pyran-9,12-diol (**2**)

Figure 5.25.: ^{135}DEPT NMR spectrum of 1,2,5,5a,6,9,10,11,12,12a-decahydro-11(11^2-hydroxypropyl)-2-[(*E*)-2^1-propenyl] cyclonona[*d*]-furo[2,3-*b*]pyran-9,12-diol (**2**)

Figure 5.26.: HSQC spectrum of 1,2,5,5a,6,9,10,11,12,12a-decahydro-11(11^2-hydroxypropyl)-2-[(*E*)-2^1-propenyl] cyclonona[*d*]-furo[2,3-*b*]pyran-9,12-diol (**2**)

Figure 5.27.: Prominent ^{1}H-^{1}H COSY, and selected HMBC correlations of 1,2,5,5a,6,9,10,11,12,12a-decahydro-11(11^2-hydroxypropyl)-2-[(*E*)-2^1-propenyl] cyclonona[*d*]-furo[2,3-*b*]pyran-9,12-diol (**2**). The key ^{1}H-^{1}H COSY couplings were represented in bold face bonds. The key HMBC couplings have been represented by double barbed arrows.

Figure 5.28.: ^{1}H-^{1}H COSY spectrum of 1,2,5,5a,6,9,10,11,12,12a-decahydro-11(11^2-hydroxypropyl)-2-[(*E*)-2^1-propenyl] cyclonona[*d*]-furo[2,3-*b*]pyran-9,12-diol (**2**)

Figure 5.29.: HMBC spectrum of 1,2,5,5a,6,9,10,11,12,12a-decahydro-11(11^2-hydroxypropyl)-2-[(*E*)-2^1-propenyl] cyclonona[*d*]-furo[2,3-*b*]pyran-9,12-diol (**2**)

Figure 5.3.: Bioactive secondary metabolites isolated from *P. tetrastromatica* (family Dictyotaceae) and representative photograph of thalli of brown seaweed *P. tetrastromatica*

Figure 5.30.: HMBC spectrum of 1,2,5,5a,6,9,10,11,12,12a-decahydro-11(11^2-hydroxypropyl)-2-[(*E*)-2^1-propenyl] cyclonona[*d*]-furo[2,3-*b*]pyran-9,12-diol (**2**)

Figure 5.31.: NOESY spectrum of 1,2,5,5a,6,9,10,11,12,12a-decahydro-11(11^2-hydroxypropyl)-2-[(*E*)-2^1-propenyl] cyclonona[*d*]-furo[2,3-*b*]pyran-9,12-diol (**2**)

Figure 5.32.: EI-MS spectrum of 1,2,5,5a,6,9,10,11,12,12a-decahydro-11(11^2-hydroxypropyl)-2-[(*E*)-2^1-propenyl] cyclonona[*d*]-furo[2,3-*b*]pyran-9,12-diol (**2**)

Figure 5.33.: Tentative mass fragmentation pattern of 1,2,5,5a,6,9,10,11,12,12a-decahydro-11(11^2-hydroxypropyl)-2-[(*E*)-2^1-propenyl] cyclonona[*d*]-furo[2,3-*b*]pyran-9,12-diol (**2**)

Figure 5.34.: UVspectrum of 4-(4^1,4^2-dihydroxypropyl)-4,4a,5,6,7,8,11,11a-octahydro-8,11-dihydroxy-7-methyl-6-(6^1-methyl-6^2-propenyl)-cyclonona[*c*]pyran-3-(1*H*)-one (**3**)

Figure 5.35.: HPLC chromatogram of 4-(4^1,4^2-dihydroxypropyl)-4,4a,5,6,7,8,11,11a-octahydro-8,11-dihydroxy-7-methyl-6-(6^1-methyl-6^2-propenyl)-cyclonona[*c*]pyran-3-(1*H*)-one (**3**)

Figure 5.36.: HRESIMS of 4-(4^1,4^2-dihydroxypropyl)-4,4a,5,6,7,8,11,11a-octahydro-8,11-dihydroxy-7-methyl-6-(6^1-methyl-6^2-propenyl)-cyclonona[*c*]pyran-3-(1*H*)-one (**3**)

Figure 5.37.: FTIR spectrum of 4-(4^1,4^2-dihydroxypropyl)-4,4a,5,6,7,8,11,11a-octahydro-8,11-dihydroxy-7-methyl-6-(6^1-methyl-6^2-propenyl)-cyclonona[*c*]pyran-3-(1*H*)-one (**3**)

Figure 5.38.: ^{1}H NMR spectrum of -(4^1,4^2-dihydroxypropyl)-4,4a,5,6,7,8,11,11a-octahydro-8,11-dihydroxy-7-methyl-6-(6^1-methyl-6^2-propenyl)-cyclonona[*c*]pyran-3-(1*H*)-one (**3**)

Figure 5.39.: ^{13}C NMR spectrum of 4-(4^1,4^2-dihydroxypropyl)-4,4a,5,6,7,8,11,11a-octahydro-8,11-dihydroxy-7-methyl-6-(6^1-methyl-6^2-propenyl)-cyclonona[*c*]pyran-3-(1*H*)-one (**3**)

Figure 5.4.: Xenicane class of xenicins (**1**-**2**) bearing cyclonona[*d*]furo[2,3-*b*]pyrandiol and three xeniolide-type diterpenoids with octahydrocyclonona[*c*]pyran-3(1*H*)-one backbones (**3**-**5**) isolated from the seaweed *Padina tetrastromatica*.

Figure 5.40.: ^{135}DEPT NMR spectrum of 4-(4^1,4^2-dihydroxypropyl)-4,4a,5,6,7,8,11,11a-octahydro-8,11-dihydroxy-7-methyl-6-(6^1-methyl-6^2-propenyl)-cyclonona[*c*]pyran-3-(1*H*)-one (**3**)

Figure 5.41.: HSQC spectrum of 4-(4^1,4^2-dihydroxypropyl)-4,4a,5,6,7,8,11,11a-octahydro-8,11-dihydroxy-7-methyl-6-(6^1-methyl-6^2-propenyl)-cyclonona[*c*]pyran-3-(1*H*)-one (**3**)

Figure 5.42.: ^{1}H-^{1}H COSY of 4-(4^1,4^2-dihydroxypropyl)-4,4a,5,6,7,8,11,11a-octahydro-8,11-dihydroxy-7-methyl-6-(6^1-methyl-6^2-propenyl)-cyclonona[*c*]pyran-3-(1*H*)-one (**3**)

Figure 5.43.: Prominent ^{1}H-^{1}H COSY, and selected HMBC correlations of 4-(4^1,4^2-dihydroxypropyl)-4,4a,5,6,7,8,11,11a-octahydro-8,11-dihydroxy-7-methyl-6-(6^1-methyl-6^2-propenyl)-cyclonona-[*c*]-pyran-3-(1*H*)-one (**3**). The key ^{1}H-^{1}H COSY couplings were represented in bold face bonds. The key HMBC couplings have been represented by double barbed arrows

Figure 5.44.: HMBC spectrum of 4-(4^1,4^2-dihydroxypropyl)-4,4a,5,6,7,8,11,11a-octahydro-8,11-dihydroxy-7-methyl-6-(6^1-methyl-6^2-propenyl)-cyclonona[*c*]pyran-3-(1*H*)-one (**3**)

Figure 5.45.: Prominent NOE correlations of 4-(4^1,4^2-dihydroxypropyl)-4,4a,5,6,7,8,11,11a-octahydro-8,11-dihydroxy-7-methyl-6-(6^1-methyl-6^2-propenyl)-cyclonona[*c*]pyran-3-(1*H*)-one (**3**). NOESY relations are represented by double-tailed arrows

Figure 5.46.: NOESY spectrum of 4-(4^1,4^2-dihydroxypropyl)-4,4a,5,6,7,8,11,11a-octahydro-8,11-dihydroxy-7-methyl-6-(6^1-methyl-6^2-propenyl)-cyclonona[*c*]pyran-3-(1*H*)-one (**3**)

Figure 5.47.: EI-MS spectrum of 4-(4^1,4^2-dihydroxypropyl)-4,4a,5,6,7,8,11,11a-octahydro-8,11-dihydroxy-7-methyl-6-(6^1-methyl-6^2-propenyl)-cyclonona[*c*]pyran-3-(1*H*)-one (**3**)

Figure 5.48.: Tentative mass fragmentation pattern of 4-(4^1,4^2-dihydroxypropyl)-4,4a,5,6,7,8,11,11a-octahydro-8,11-dihydroxy-7-methyl-6-(6^1-methyl-6^2-propenyl)-cyclonona[*c*]-pyran-3-(1*H*)-one (**3**)

Figure 5.49.: UVspectrum of 4,4a,5,6,7,8,11,11a-octahydro-7-hydroxy-6-(6^2-hydroxy-6^3-butenyl)-4-(4^1-hydroxypropyl)-11-methoxy-8-methyl-cyclonona[*c*]pyran-3-(1*H*)-one (**4**)

Figure 5.5.: UVspectrum of 12-ethenyl-3a,6,9,10,11,12,12a,12b-octahydro-1-(1^2-hydroxy-1^2-methyl-propyl)-cyclonona[*d*]furo[2,3-*b*]pyran-6,10-diol **(1)**

Figure 5.50.: HPLC chromatogram of 4,4a,5,6,7,8,11,11a-octahydro-7-hydroxy-6-(6^2-hydroxy-6^3-butenyl)-4-(4^1-hydroxypropyl)-11-methoxy-8-methyl-cyclonona[*c*]pyran-3-(1*H*)-one (**4**)

Figure 5.51.: HRESIMS of 4,4a,5,6,7,8,11,11a-octahydro-7-hydroxy-6-(6^2-hydroxy-6^3-butenyl)-4-(4^1-hydroxypropyl)-11-methoxy-8-methyl-cyclonona[*c*]pyran-3-(1*H*)-one (**4**)

Figure 5.52.: FTIR of 4,4a,5,6,7,8,11,11a-octahydro-7-hydroxy-6-(6^2-hydroxy-6^3-butenyl)-4-(4^1-hydroxypropyl)-11-methoxy-8-methyl-cyclonona[*c*]pyran-3-(1*H*)-one (**4**)

Figure 5.53.: ^{1}H-NMR of 4,4a,5,6,7,8,11,11a-octahydro-7-hydroxy-6-(6^2-hydroxy-6^3-butenyl)-4-(4^1-hydroxypropyl)-11-methoxy-8-methyl-cyclonona[*c*]pyran-3-(1*H*)-one (**4**)

Figure 5.54.: ^{13}C-NMR of 4,4a,5,6,7,8,11,11a-octahydro-7-hydroxy-6-(6^2-hydroxy-6^3-butenyl)-4-(4^1-hydroxypropyl)-11-methoxy-8-methyl-cyclonona[*c*]pyran-3-(1*H*)-one (**4**)
Figure 5.55.: DEPT spectrum of 4,4a,5,6,7,8,11,11a-octahydro-7-hydroxy-6-(6^2-hydroxy-6^3-butenyl)-4-(4^1-hydroxypropyl)-11-methoxy-8-methyl-cyclonona[*c*]pyran-3-(1*H*)-one (**4**)
Figure 5.56.: HSQC spectrum of 4,4a,5,6,7,8,11,11a-octahydro-7-hydroxy-6-(6^2-hydroxy-6^3-butenyl)-4-(4^1-hydroxypropyl)-11-methoxy-8-methyl-cyclonona[*c*]pyran-3-(1*H*)-one (**4**)
Figure 5.57.: COSY spectrum of 4,4a,5,6,7,8,11,11a-octahydro-7-hydroxy-6-(6^2-hydroxy-6^3-butenyl)-4-(4^1-hydroxypropyl)-11-methoxy-8-methyl-cyclonona[*c*]pyran-3-(1*H*)-one (**4**)
Figure 5.58.: HMBC spectrum of 4,4a,5,6,7,8,11,11a-octahydro-7-hydroxy-6-(6^2-hydroxy-6^3-butenyl)-4-(4^1-hydroxypropyl)-11-methoxy-8-methyl-cyclonona[*c*]pyran-3-(1*H*)-one (**4**)
Figure 5.59.: Prominent ^{1}H-^{1}H COSY, and selected HMBC correlations of 4,4a,5,6,7,8,11,11a-Octahydro-7-hydroxy-6-(6^2-hydroxy-6^3-butenyl)-4-(4^1-hydroxypropyl)-11-methoxy-8-methyl-cyclonona[*c*]pyran-3-(1*H*)-one (**4**). The key ^{1}H-^{1}H COSY couplings were represented in bold face bonds. The key HMBC couplings have been represented by double barbed arrows.of
Figure 5.6.: HPLC chromatogram of 12-ethenyl-3a,6,9,10,11,12,12a,12b-octahydro-1-(1^2-hydroxy-1^2-methyl-propyl)-cyclonona[*d*]furo[2,3-*b*]pyran-6,10-diol **(1)**
Figure 5.60.: NOESY spectrum of 4,4a,5,6,7,8,11,11a-octahydro-7-hydroxy-6-(6^2-hydroxy-6^3-butenyl)-4-(4^1-hydroxypropyl)-11-methoxy-8-methyl-cyclonona[*c*]pyran-3-(1*H*)-one (**4**) **Figure 5.61.:** Prominent NOE correlations of 4,4a,5,6,7,8,11,11a-octahydro-7-hydroxy-6-(6^2-hydroxy-6^3-butenyl)-4-(4^1-hydroxypropyl)-11-methoxy-8-methyl-cyclonona[*c*]pyran-3-(1*H*)-one (**4**). NOESY relations are represented by double-tailed arrows
Figure 5.62.: EI-MS spectrum of 4,4a,5,6,7,8,11,11a-octahydro-7-hydroxy-6-(6^2-hydroxy-6^3-butenyl)-4-(4^1-hydroxypropyl)-11-methoxy-8-methyl-cyclonona[*c*]pyran-3-(1*H*)-one (**4)**
Figure 5.63.: Tentative mass fragmentation pattern of 4,4a,5,6,7,8,11,11a-octahydro-7-hydroxy-6-(6^2-hydroxy-6^3-butenyl)-4-(4^1-hydroxypropyl)-11-methoxy-8-methyl-cyclonona[*c*]pyran-3-(1*H*)-one (**4)**
Figure 5.64.: UVspectrum of 4,4a,5,6,7,8,11,11a-octahydro-1,7-dihydroxy-4-(4^1-hydroxy-4^2-methylpropyl)-6-(6^1-hydroxy-6^2-propenyl)-10-methyl-cyclonona[*c*]pyran-3(1*H*)-one (**5**)
Figure 5.65.: HPLC chromatogram of 4,4a,5,6,7,8,11,11a-octahydro-1,7-dihydroxy-4-(4^1-hydroxy-4^2-methylpropyl)-6-(6^1-hydroxy-6^2-propenyl)-10-methyl-cyclonona[*c*]pyran-3(1*H*)-one (**5**)
Figure 5.66.: HRESIMS of 4,4a,5,6,7,8,11,11a-octahydro-1,7-dihydroxy-4-(4^1-hydroxy-4^2-methylpropyl)-6-(6^1-hydroxy-6^2-propenyl)-10-methyl-cyclonona[*c*]pyran-3(1*H*)-one (**5**)
Figure 5.67.: FTIR spectrum of 4,4a,5,6,7,8,11,11a-octahydro-1,7-dihydroxy-4-(4^1-hydroxy-4^2-methylpropyl)-6-(6^1-hydroxy-6^2-propenyl)-10-methyl-cyclonona[*c*]pyran-3(1*H*)-one (**5**)
Figure 5.69.: ^{1}H NMR of 4,4a,5,6,7,8,11,11a-octahydro-1,7-dihydroxy-4-(4^1-hydroxy-4^2-methylpropyl)-6-(6^1-hydroxy-6^2-propenyl)-10-methyl-cyclonona[*c*]pyran-3(1*H*)-one (**5**)
Figure 5.7.: FTIR of 12-ethenyl-3a,6,9,10,11,12,12a,12b-octahydro-1-(1^2-hydroxy-1^2-methyl-propyl)-cyclonona[*d*]furo[2,3-*b*]pyran-6,10-diol **(1)**
Figure 5.7.: HRESIMS of 12-ethenyl-3a,6,9,10,11,12,12a,12b-octahydro-1-(1^2-hydroxy-1^2-methyl-propyl)-cyclonona[*d*]furo[2,3-*b*]pyran-6,10-diol **(1)**
Figure 5.70.: ^{13}C-NMR of 4,4a,5,6,7,8,11,11a-octahydro-1,7-dihydroxy-4-(4^1-hydroxy-4^2-methylpropyl)-6-(6^1-hydroxy-6^2-propenyl)-10-methyl-cyclonona[*c*]pyran-3(1*H*)-one (**5**)
Figure 5.71.:DEPT spectrum of 4,4a,5,6,7,8,11,11a-octahydro-1,7-dihydroxy-4-(4^1-hydroxy-4^2-methylpropyl)-6-(6^1-hydroxy-6^2-propenyl)-10-methyl-cyclonona[*c*]pyran-3(1*H*)-one (**5**)
Figure 5.72.: HSQC of 4,4a,5,6,7,8,11,11a-octahydro-1,7-dihydroxy-4-(4^1-hydroxy-4^2-methylpropyl)-6-(6^1-hydroxy-6^2-propenyl)-10-methyl-cyclonona[*c*]pyran-3(1*H*)-one (**5**)
Figure 5.73.: ^{1}H-^{1}H COSY spectrum of 4,4a,5,6,7,8,11,11a-octahydro-1,7-dihydroxy-4-(4^1-hydroxy-4^2-methylpropyl)-6-(6^1-hydroxy-6^2-propenyl)-10-methyl-cyclonona[*c*]pyran-3(1*H*)-one (**5**)
Figure 5.74.: Prominent ^{1}H-^{1}H COSY, and selected HMBC correlations of 4,4a,5,6,7,8,11,11a-octahydro-1,7-dihydroxy-4-(4^1-hydroxy-4^2-methylpropyl)-6-(6^1-hydroxy-6^2-propenyl)-10-

methyl-cyclonona[*c*]pyran-3(1*H*)-one (**5**). The key ^{1}H-^{1}H COSY couplings were represented in bold face bonds. The key HMBC couplings have been represented by double barbed arrows.

Figure 5.75.: HMBC spectrum of 4,4a,5,6,7,8,11,11a-octahydro-1,7-dihydroxy-4-(4^{1}-hydroxy-4^{2}-methylpropyl)-6-(6^{1}-hydroxy-6^{2}-propenyl)-10-methyl-cyclonona[*c*]pyran-3(1*H*)-one (**5**)

Figure 5.76.: Prominent NOE correlations of 4,4a,5,6,7,8,11,11a-octahydro-1,7-dihydroxy-4-(4^{1}-hydroxy-4^{2}-methylpropyl)-6-(6^{1}-hydroxy-6^{2}-propenyl)-10-methyl-cyclonona[*c*]pyran-3(1*H*)-one (**5**). NOESY relations are represented by double-tailed arrows

Figure 5.77.: NOESY spectrum of 4,4a,5,6,7,8,11,11a-octahydro-1,7-dihydroxy-4-(4^{1}-hydroxy-4^{2}-methylpropyl)-6-(6^{1}-hydroxy-6^{2}-propenyl)-10-methyl-cyclonona[*c*]pyran-3(1*H*)-one (**5**)

Figure 5.78.: EI-MS spectrum of 4,4a,5,6,7,8,11,11a-octahydro-1,7-dihydroxy-4-(4^{1}-hydroxy-4^{2}-methylpropyl)-6-(6^{1}-hydroxy-6^{2}-propenyl)-10-methyl-cyclonona[*c*]pyran-3(1*H*)-one (**5**)

Figure 5.79.: Tentative mass fragmentation pattern of 4,4a,5,6,7,8,11,11a-octahydro-1,7-dihydroxy-4-(4^{1}-hydroxy-4^{2}-methylpropyl)-6-(6^{1}-hydroxy-6^{2}-propenyl)-10-methyl-cyclonona[*c*]-pyran-3(1*H*)-one (**5**)

Figure 5.8.: ^{1}H NMR spectrum of 12-ethenyl-3a,6,9,10,11,12,12a,12b-octahydro-1-(1^{2}-hydroxy-1^{2}-methyl-propyl)-cyclonona[*d*]furo[2,3-*b*]pyran-6,10-diol **(1)**

Figure 5.80.: The structures of 6-methoxy-dolabella-8(17),12-diene-10β,18-diol (**6**), 3-methoxy-dolabella-12(18)-ene-4β-ol (**7**), 3-methoxy-dolabella-10,18(19)-diene-5α,8β-diol (**8**), 2,7-dimethoxy-14*α*-hydroxy-dolasta-1(15),9-diene (**9**), and 4,7-dimethoxy-9β,14*α*-dihydroxy-dolasta-1-ene (**10**) isolated from *P. tetrastromatica*. Representative photograph of the thalli (leafy structures) of *P. tetrastromatica* was shown**Figure 5.81.:** UVspectrum of 6-methoxy-dolabella-8(17),12-diene-10β ,18-diol (**6**)

Figure 5.82.: HPLC chromatogram of 6-methoxy-dolabella-8(17),12-diene-10β ,18-diol (**6**)

Figure 5.83.: HRESIMS of 6-methoxy-dolabella-8(17),12-diene-10β ,18-diol (**6**)

Figure 5.84.: FTIR spectrum of 6-methoxy-dolabella-8(17),12-diene-10β ,18-diol (**6**)

Figure 5.85.: ^{1}H NMR spectrum of 6-methoxy-dolabella-8(17),12-diene-10β ,18-diol (**6**)

Figure 5.86.: ^{13}C NMR spectrum of 6-methoxy-dolabella-8(17),12-diene-10β ,18-diol (**6**)

Figure 5.87.: DEPT spectrum of 6-methoxy-dolabella-8(17),12-diene-10β ,18-diol (**6**)

Figure 5.88.: ^{1}H-^{1}H COSY spectrum of 6-methoxy-dolabella-8(17),12-diene-10β ,18-diol (**6**)

Figure 5.89.: HSQC spectrum of 6-methoxy-dolabella-8(17),12-diene-10β ,18-diol (**6**)

Figure 5.9.: ^{13} C NMR spectrum of 12-ethenyl-3a,6,9,10,11,12,12a,12b-octahydro-1-(1^{2}-hydroxy-1^{2}-methyl-propyl)-cyclonona[*d*]furo[2,3-*b*]pyran-6,10-diol **(1)**

Figure 5.90.: HMBC spectrum of 6-methoxy-dolabella-8(17),12-diene-10β ,18-diol (**6**)

Figure 5.91.: Prominent ^{1}H-^{1}H COSY, and selected HMBC correlations of 6-methoxy-dolabella-8(17),12-diene-10β ,18-diol (**6**). The key ^{1}H-^{1}H COSY couplings were represented in bold face bonds. The key HMBC couplings have been represented by double barbed arrows**Figure 5.92.:** NOESY spectrum of 6-methoxy-dolabella-8(17),12-diene-10β ,18-diol (**6**)

Figure 5.93.: Prominent NOE correlations of 1 6-methoxy-dolabella-8(17),12-diene-10β ,18-diol (**6**). NOESY relations are represented by double-tailed arrows

Figure 5.94.: EI-MS spectrum of 6-methoxy-dolabella-8(17),12-diene-10β ,18-diol (**6**) **Figure 5.95.:** Tentative mass fragmentation pattern of 6-methoxy-dolabella-8(17),12-diene-10β ,18-diol (**6**)

Figure 5.96.: UVspectrum of 3-methoxy-dolabella-12(18)-ene-4β-ol (**7**)

Figure 5.97.: HPLC chromatogram of 3-methoxy-dolabella-12(18)-ene-4β-ol (**7**)

Figure 5.98.: HRESIMS of 3-methoxy-dolabella-12(18)-ene-4β-ol (**7**)

Figure 5.99.: ^{1}H NMR spectrum of 3-methoxy-dolabella-12(18)-ene-4β-ol (**7**) **Figure 5.100.:** ^{13}C NMR spectrum of 3-methoxy-dolabella-12(18)-ene-4β-ol (**7**)

Figure 5.99.: FTIR of 3-methoxy-dolabella-12(18)-ene-4β-ol (**7**)

Figure 6.1.: The brown seaweed *P. tetrastromatica* collected from the southeast coastline of the Indian sub-continent Gulf of Mannar region; between 8º48’ N, 78°9’ E and 9°14’ N, 79°14’ E)

Figure 6.1.: The red seaweed *G. salicornia* collected from the southeast coastline of the Indian sub-continent Gulf of Mannar region; between 8º48’ N, 78°9’ E and 9°14’ N, 79°14’ E)

Figure 6.10.: NOESY spectrum of hydrolyzed polysaccharide analogue
Figure 6.11.: ESI-MS Spectrum of polysaccharide analogue
Figure 6.12.: ^{1}H NMR spectrum of methylated polysaccharide analogue after hydrolysis
Figure 6.13.: ^{13}C NMR spectrum of methylated polysaccharide analogue after hydrolysis
Figure 6.14.: DEPT^{135} spectrum of methylated polysaccharide analogue after hydrolysis
Figure 6.15.: ^{1}H-^{1}H COSY NMR spectrum of methylated polysaccharide analogue after hydrolysis
Figure 6.16.: HSQC spectrum of methylated polysaccharide analogue after hydrolysis
Figure 6.17.: HMBC spectrum of methylated polysaccharide analogue after hydrolysis
Figure 6.18.: NOESY spectrum of methylated polysaccharide analogue after hydrolysis
Figure 6.19.: ^{1}H NMR spectrum of acetylated polysaccharide analogue
Figure 6.20.: ^{13}C NMR spectrum of acetylated polysaccharide analogue
Figure 6.21.: DEPT^{135} spectrum of acetylated polysaccharide analogue
Figure 6.22.: COSY spectrum of methylated polysaccharide analogue
Figure 6.23.: HSQC spectrum of methylated polysaccharide analogue**Figure S24.** HMBC spectrum of methylated polysaccharide analogue**Figure S25**. NOESY spectrum of methylated polysaccharide analogue
Figure 6.27.: UV chromatogram of polysaccharide-silver nano composite (AgNPC) at different time intervals, 30, 60 and 120 minutes
Figure 6.28.: FTIR spectrum of polysaccharide-silver nano composite (Ag-NPC)
Figure 6.29.: XRD of polysaccharide-silver nano composite (AgNPC) at different time intervals, 30, 60 and 120 minuteS
Figure 6.3.: FTIR spectrum of hydrolyzed polysaccharide analogue
Figure 6.4.: ^{1}H NMR spectrum of hydrolyzed polysaccharide analogue
Figure 6.4.: Elution profile of polysaccharide solutions isolated from *G. salicornia* through DEAE Cellulose
Figure 6.5.: ^{13}C NMR spectrum of hydrolyzed polysaccharide analogue
Figure 6.5.: Monosaccharide composition analysis of polysaccharide analogue
Figure 6.6.: DEPT^{135} spectrum of hydrolyzed polysaccharide analogue
Figure 6.7.: ^{1}H-^{1}H COSY NMR spectrum of hydrolyzed polysaccharide analogue
Figure 6.8.: HSQC spectrum of hydrolyzed polysaccharide analogue
Figure 6.9.: HMBC spectrum of hydrolyzed polysaccharide analogue

CHAPTER 1
INTRODUCTION

Contents

1.1 Background
1.2 Marine environment as a potential source of bioactive compounds
1.3 Bioactive potentials of seaweeds and their secondary metabolites
1.4. Impact of free radicals in the defense mechanism
1.5 Seaweeds and their metabolites as natural alternative to combat various oxidative stress induced life style disorders
1.6 Objectives
1.7 Thesis outline

1.1. Background

In recent years, marine organisms have been attracted much attention to the natural product chemists due to their phenomenal biodiversity, and were considered to be prolific natural resources of structurally diverse pharmacologically active lead molecules. The bioactives derived from the marine organisms were found to represent useful leads in the production of pharmaceutical and functional food agents. Numerous novel compounds with interesting bioactivities and chemical organizations were developed from the marine organisms during the last decades (El Gamal, 2010). Since then, the recognition on untapped potential of the marine biodiversity, the mining of potential bioactive compounds, research and commercialization of high value compounds were exponentially increased during the later part of the 20th century. These led to the surge in investments on marine bio-source based research, ultimately boosted the number of publications, patents and marketing the products derived from marine source (Ypsita & Archana 2009). A unique set of bioactive compounds were found to be derived from marine based resources, such as marine plants, animals, microalgae, and seaweeds (otherwise termed as marine macroalgae).

The most interesting phyla with respect to pharmacologically active marine compounds include the abundantly available seaweed species, among which the brown and red seaweeds (belonging to the classes Phaeophyceae and Rhodophyceae, respectively) are potential sources of bioactive substances (Blunt et al., 2018; Blunt et al., 2017). Seaweeds are valuable sources of

bioactive compounds and could be introduced for the preparation of novel functional ingredients in food and also a good approach for the treatment or prevention of chronic inflammatory diseases (Carroll et al., 2019). Approximately, 271 genera and 1153 species of marine algae, including forms and varieties have been enumerated till date from the Indian waters. Seaweeds are macroscopic algae (non-flowering stem less water plant) found attached to the solid bottom substrate of rocks, dead corals, pebbles, shells and other plant materials. The seaweeds spread along the Indian coastline and its nine maritime states and islands {Gujarat-1700, Maharashtra-572, Goa-104, Karnataka-280, Kerala-560, Tamil Nadu-980, Andhra Pradesh-960, Orissa-432, West Bengal-280, Andaman and Nicobar Islands-1500 (approx.), Lakshadweep Islands-120 (approx.) in km} (Pati et al., 2016).

Seaweeds are among the most inexhaustible sources with varied chemical moieties of pharmacological potentials. They exist in each marine environmental zone, from the region of intertidal to abyssal, yielding a larger range of structures of chemical entities than any other group of marine algae. Other sources of marine bioactive entities with therapeutic activities are ascidians, bryozoans, cnidarians, molluscs and sponges (Figure 1.1.). Seaweeds are also considered as the valuable source with particular interest and gradually become the focus of area of natural products research (Lordan, Ross, & Stanton 2011). On seaweeds, especially seaweeds belonging to the class of Rhodophyceae and Phaeophyceae were found to contribute significantly, and have been extensively distributed in the marine habitats.

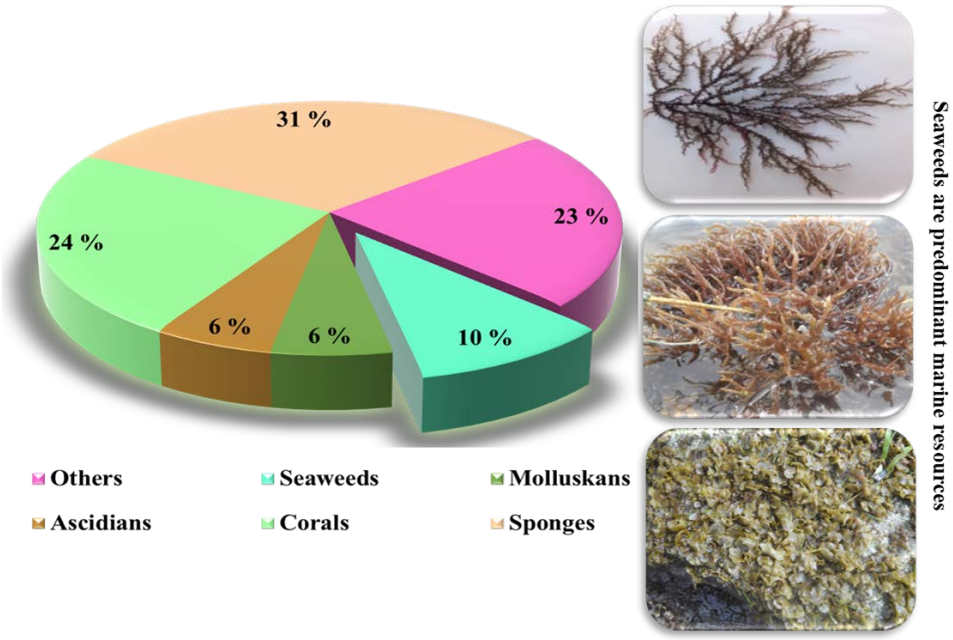

Figure 1.1.: The percentage share of seaweeds along with different classes of marine organisms

Seaweeds play an essential biological and ecological role in the marine environment. They provide a substantial contribution in primary production and make habitat for benthic communities in marine ecosystem (Mann, 1973; Williams & Smith, 2007). Seaweeds were utilized as food source in earlier times. Even though, their wide ranging nutritional status greatly contributes to industries due to its richness in micronutrients and vitamins. Therefore, around 220 species of seaweeds exhibited their commercial value. Around 200 species of seaweeds upsurge the international economy by the production of phycocolloids and food products (Bixler and Porse 2011; FAO 2013). Since the richness in nutrients, polyphenols, polysaccharides and small molecular weight bioactive compounds, the estimates from 2005 revealed that the production of seaweeds was increased to 1.3 and 14.8 million tonnes by capture and aquaculture, respectively. The production of seaweeds have doubled to 30.4 million tonnes with 29.4 and 1.1 million tonnes by culture and capture sectors as per the reports on 2015. It was estimated that the global demand of seaweeds has been increasing with rises in usage beyond traditional applications (Rebours et al., 2014; Hafting et al., 2015). The reports revealed that around 45000 species were widely distributed round the world (Bequette &France 1997). The presence of highly diverse bioactive phytochemical constituents in seaweeds registered their biomedical application from 17th century, these bioactivities including antioxidant, anti-inflammatory, anti-diabetic and hypocholesterolemic activity (Frestedt et al. 2009; Ravikumar and Kathiresan 1993). The seaweeds are unlike plants, not possessed roots, stems and real leaves, are grouped mainly into three on the basis of their content of pigments and structural characteristics, namely Rhodophyceae (Red seaweeds), Phaeophyceae (brown seaweeds), and Chlorophyceae (green seaweeds) (Mouritsen, 2013).

The seaweeds contain a large assemblage of species that predominate in the coastal shelf areas of Indian subcontinent

Seaweeds exhibited high biodiversity with more than 10,000 species (Philips 2001; Ang et al 2013). It was assessed that around 1800 of different brown species, 6200 of red species and 1800 of green species were found in the marine ecosystem. Among which, red seaweed species were found to be more diverse. The brown seaweed species were found as the largest group among them. In seaweeds, most of them are possessed soft tissues along with greater or lesser degree of calcification. The calcium layer formation in these seaweeds was found to be controlled by the presence of polysaccharide in their cell walls. The distribution of seaweeds in marine environment is varied for different group of seaweeds. The red species of seaweeds are grown at extreme depth, normally 30 meters down. The green seaweed species are bloomed in water surface and brown species are found to be in between, according to the optimal conditions such as temperature, light and content of nutrients. The combined effect of seaweed species is massive in global ecosystem. Seaweeds along with phytoplankton produce 90 % of oxygen and 80 % of the organic material on Earth (Mouritsen, 2013).

The seaweeds contain minerals ten times greater than that of terrestrial plants, whereas, they were found to be endowed with different types of trace elements and vitamins along with about 45-75 % carbohydrates and fibers, 7-35 % proteins, < 5 % fats, and a large number of different vitamins (Mouritsen, 2013). The carbohydrates and monosaccharide combinations in seaweeds are varied among the red, green, and brown species (Mouritsen, 2013). They were also found to contain essential amino acids. In general, these seaweed species have been widely utilized for polysaccharides and low molecular weight bioactive compounds by the pharmaceutical and functional food industries. However, most of the species belonging to the class of Rhodophyceae and Phaeophyceae were not broadly explored for their biochemical and pharmacological potentials. The significance of these species belonging to the class of Rhodophyceae and Phaeophyceae as potential bioactive source has been known in recent times, and their pharmaceutical potential started to attract substantial attention.

1.2 Marine environment as a potential source of bioactive compounds

The marine ecosystem consisted of almost 2,00,000 species of invertebrates and algae, representing an unexploited diverse resource of novel bioactive chemicals with pharmaceutical potential, which could use in the treatment of various prevalent disorders. In last few decades, the bioactive potentials of marine natural products (MNP) have captivated by research field. The importance of marine environment began to reveal by the isolation of spongothymidine and spongouridine from the marine sponge *Tethya crypta* and led to the development Cytarabine (an antileukemia agent) and Vidarabine (an antiviral agent), respectively. The pharmacological

approaches associated with MNPs included various novel chemical entities targeted to specific diseases and molecular targets, which were accelerated with sustained progresses in technology to isolate and characterize skeletal structures of MNP components (Hemant & Kritarth, 2018).

Marine derived bioactive compounds have the potencies to serve as prospective alternatives against deadly diseases. These compounds varied structurally and biologically, and around 30,000 compounds with distinctive structures and diverse pharmacological potentials were identified from the marine source. The seaweeds extracts from *Hypnea muciformis*, low molecular weight fucoidans from *Laminaria japonica* were found to be exhibited antioxidative, anti-inflammatory, anti-apoptotic effects and hepatoprotective activities (Nair, Weiskirchen, & Al-Musharafi, 2014). Several steroid entities such as polyoxygenated steroid contignasterol with anti-inflammatory properties isolated from marine organisms *Petrosia contignata, Xestospongia bergquisicta and Clathria lissosclera,* which hinders aggregation of platelets (Nair, Weiskirchen, & Al-Musharafi, 2014). The reports revealed that peptides identified from different marine protein hydrolysates could act as potential antioxidants (Nair, Weiskirchen, & Al-Musharafi, 2014). They were isolated from the marine organisms, such as squid, tuna, and sea cucumber, and exhibited higher antioxidative potentials than α-tocopherol. Similarly, oligosaccharides from *Apostichopus japonicus* found to be showed *in vitro* radical scavenging properties. These bioactive compounds from marine organisms were used in nutraceutical and pharmaceuticals, or substituted as synthetic antioxidants (Nair, Weiskirchen, & Al-Musharafi, 2014). Marine derived polysaccharides possessed various pharmaceutical, medical, and biotechnical applications, which were used in the fabrication of biomaterials for wound dressings and scaffolds. Marine-based chitosan from shrimp and crab shells used in the production of gels for the drug delivery of insulin and growth factors. These microgels used in the reduction of glucose level in blood thereby used in the treatment of type-1 diabetes. The fish oil rich in polyunsaturated fatty acids showed anti-oxidative effect. The novel components in fish oil supplements beneficial in liver pathophysiology (Nair, Weiskirchen, & Al-Musharafi, 2014).

Seaweeds were reported to be rich in bioactive entities, such as fibers, peptides, proteins, sulfated polysaccharides, phlorotannins, sulfolipids, carotenoids, vitamins, minerals, fatty acids and antioxidants (Khalid et al., 2018). They are used in gelling and thickening agents in the pharmaceutical and food industries. The potential effect of seaweeds is recently utilized in complementary medicine also (Khalid et al., 2018). Seaweed derived bioactive components and the functional food ingredients with potential health benefits are an emerging area of research. Various nutraceutical or functional food supplements and biomedical products from seaweeds provide a myriad of benefits for human health and multiple life threatening diseases, and

therefore, are the attractive options for the pharmaceutical and healthcare industry. The seaweeds of red, brown and green displayed prominent therapeutic activities for the management of degenerative-metabolic diseases, such as antiobesity, anticancer, antidiabetic, antihypertensive, antihyperlipidemic, anticoagulant, antioxidant, anti-inflammatory, thyroid stimulating, immunomodulatory, tissue healing properties, antiviral, antibacterial, neuroprotective, antifungal, and antiestrogenic potencies (Khalid et al., 2018). The various seaweed species belonging to marine origin represent potentially unexploited sources of bioactives with pharmacological and medicinal properties.

1.3 Bioactive potentials of seaweeds and their secondary metabolites

Novel secondary bioactive metabolites from these ocean herbs are attracting attention because of the growing demand for new compounds of 'marine natural' origin, having potential applications in pharmaceutical fields, and concerns about the toxic effects by synthetic drugs and their derivatives. The rich diversity of seaweeds belonging to the classes Phaeophyceae and Florideophyceae represents an untapped reservoir of bioactive compounds with valuable pharmaceutical and biomedical use. Seaweed derived functional food ingredients have potential pharmaceutical advantages, and is endowed with pluralities of bioactivities against different diseases (Carroll et al., 2019; Blunt et al., 2018; Blunt et al., 2017).

1.3.1 Major classification of seaweeds

In marine world, the divisions of algae include four groups, namely, Plantae, Bacteria, Protozoa and Chromista. They exhibited distinct size and morphology, which lead to the formation of unicellular organisms to micro algae. Their colony was found to be consisted of large groups of macrophytes and seaweeds. On the basis of size seaweeds are divided into two: microalgae (phytoplankton) and macroalgae (seaweed) with 5000 and 6000 species, respectively (Ravikumar et., 1993). Seaweeds are located in littoral habitats or rocks. They propagate in surface of coastal waters and in depth of sea regions up to the distance of 180 m. The most common classification of seaweeds was on the basis of the content of their characteristic pigments. These macroscopic algae are classified in to three groups, namely, brown (Phaeophyceae), red (Rhodophyceae) and green (Chlorophyceae) seaweeds, respectively.

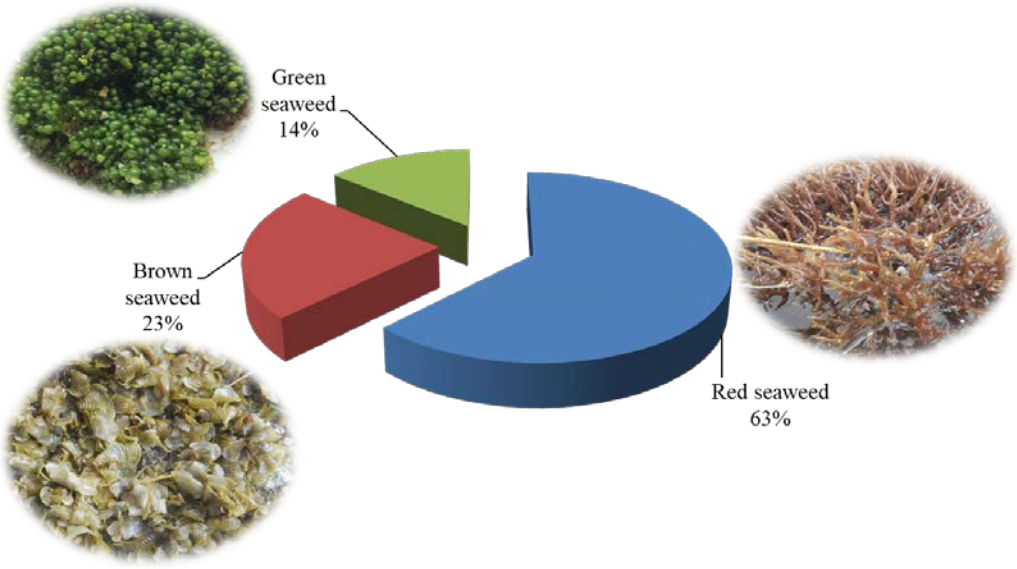

Figure 1.2..: Major classification of seaweeds

The presence of natural pigment fucoxanthin was found to be responsible for brown coloration of brown (Phaeophyceae) seaweeds. The dominance of pigments phycocyanin and phycoerythrin on other pigments chlorophyll, xanthophylls and carotene provides red color to the red (Rhodophyceae) seaweeds (Figure 1.2). The concentration of chlorophyll and related components in green (Chlorophyceae) seaweeds provide green color as in the plants (Khalid et al., 2018).

1.3.2 Distribution and diversity of seaweeds in Indian coastline

The Indian coastline is distributed up to 7000 km, which harbors a great diversity of seaweed species (Sahoo et al., 2003). The flora of seaweeds is greatly diversified in India and includes tropical seaweed species along with subtropical species. Among the various marine algal species, 1153 taxa of algae are reported, among which 271 genera have been estimated from the India. Most of these seaweed species are located in the rocky areas, coral reefs mudflats, lagoons and estuaries, Indian coastal region deliver ideal habitations for these seaweeds (Rao & Mantri, 2006). Indian coastline consisted of a total of 42 coastal stations along with 14 Gulf of Mannar islands. These regions include a total of 282 species of seaweeds. Among which, species of 80 seaweeds belong to Chlorophyta, 56 belong to Phaeophyceae and a total of 146 seaweeds belong to Rhodophyta (Ganesan, 2019). The seaweed-rich beds are located in the southern coastal regions, which are Gulf of Mannar, Mahabalipuram, Tuticorin, Tiruchendur, Kanyakumari and Kerala, along with the eastern coast of Visakhapatnam. The western coast incudes the region Veraval and Gulf of Kutch. Seaweeds are also found to be rich

in Lakshadweep Andaman and Nicobar Islands (Domettila et al., 2013). India is considered as the 12 mega-biodiversity realms in the world. The stocks of seaweed as 97,400 tonnes wet wt. were recorded from Tamil Nadu coast, 7500 tonnes wet wt. at the region of Andhra Pradesh coast, and 19,345 tonnes wet wt. throughout the islands of Lakshadweep (Kaliaperumal and Kalimuthu 1997). The diversity of seaweeds in these regions were further updated by Oza and Zaidi (2001) and documented as 434, 216, and 194 species of red, green, and brown seaweeds, respectively from a total of 844 species of total seaweeds (Figure 1.3-1.4). The Gujarat and Tamil Nadu coasts (Jha et al. 2009) were known as two large maritime states, where 366 species of seaweed were estimated, which nearly half is of total seaweed diversity in India.

Figure 1.3.: The major collection spots in Indian coastline

According to Domettila et al., in south-west coast of Indian waters, especially in Muttom coastal zone, a total of 38 species were reported due to the occurrences of intertidal rocky reefs, among which 19 species reported from the class of Florideophyceae (50 % of the total), 11 species reported from Phaeophyceae (28.9 %), while the remaining species were reported from Bryopsidophyceae (10 %) and Ulvophyceae (11 %) (Domettila et al., 2013). At the west coast of India, in particular in Maharashtra coast, the species diversity was found maximum during pre- and post- monsoon periods. Of 19 species of seaweeds, 15 families and 13 orders were documented from the Uran coast, among which, 7 species were found to belong to Rhodophyta and Chlorophyta. Varied diversity of seaweeds was recorded from three sites. Among these seaweeds, 36.8 % belonged to Rhodophyta and Chlorophyta, whereas 10.5 % were reported from Cyanobacteria and Ochrophyta, and remaining 5.2 % were reported from

Charophyta (Pawar, 2017). The coastline of Gujarat, particularly the Gulf of Kachchh extended up to 1000 km (includes 42 islands) was reported to harbor about 198 species, and among them a total of 109 belonged to Rhodophyta species, 54 belongs to Chlorophyta species, and 35 belong to Phaeophyceae species. Seaweeds of 130 species were reported from Gulf of Kachchh, whereas a total of 93 and 14 species were reported from Kalubhar Island and Narara Island, respectively (Ganesan et al., 2019).

A photo of seaweed harvest

In the southeast coastal region of Indian peninsular, the coastline of Tamil Nadu is extended to 1076 km long including 13 districts and 15 ports. It covers the region of the Bay of Bengal, Arabian Sea, and the Indian Ocean. Species of different seaweed genera were found in these regions, such as *Chaetomorpha, Ulva, Grateloupia* and *Bryopsis.* The central Tamil Nadu coast includes Palk Bay, which is in deltaic region. Several species of *Gracilaria* are dominant in this region. The Gulf of Mannar situated in the southern region of Tamil Nadu is extended up to 1 m, and support the growing of species, such as *Sargassum, Hypnea*, *Ulva* and *Acanthophora.* All these coastal regions together support the diversity of seaweeds in the Indian coastline with great economic value.

Figure 1.4.: Distribution of seaweeds as large assemblage of species predominating in the coastal shelf areas of Indian subcontinent

1.3.3 Pharmacological importance of seaweeds

Edible seaweeds have become a good source of food and alternative medicine in the Asian countries, and in the western countries they are used for many industrial applications in food (Suleria et al., 2016), cosmetics and pharmaceuticals. Traditionally, indigenous people, notably in Japan and throughout the South Pacific use seaweed supplements as a remedy for arthritis. Pluralities of studies on bioactive compounds from seaweeds exhibiting antitumor, antileukaemic, antibacterial and antiviral activities have been reported worldwide (Lorenzo-Morales et al., 2019; Yang et al., 2019).

The demand of seaweeds has been increased from the previous periods towards the nutrition, medical and healthy diet, and is the leading target in the formulation of foods and pharmaceuticals. Seaweeds from the natural origin are capable to provide bioactives for the production of novel substances with pharmaceutical and medicinal applications. Seaweed derived bioactive components and the functional food ingredients with potential health benefits are an emerging area of research. Various nutraceutical or functional food supplements and biomedical products from seaweeds provide a myriad of benefits for human health and multiple life threatening diseases, and therefore, are the attractive options for the pharmaceutical and healthcare industry. Novel secondary bioactive metabolites from these ocean herbs are attracting attention because of the growing demand for new compounds of 'marine natural' origin, having potential applications in pharmaceutical fields, and concerns about the toxic effects by synthetic drugs and their derivatives.

Since seaweeds are widely utilized as functional foods, they are highly exploited for their nutritional potentials. The significance of seaweeds as an essential source of functional ingredients in the marine ecosystem is increased because of their diverse origin, richness and universal obtainability. These are regarded as the reservoir of various bioactives and sulfated polysaccharides with pharmaceutical and bio-medical applications (Frestedt et al., 2009). The biomedical application of components in seaweeds includes antioxidant properties, anti-inflammatory activities, anticoagulant activities, antimicrobial activities, antiviral activities, anti-tumour activities and hypocholesterolemic activities (Frestedt et al., 2009). The bioactivities of seaweeds were due to the presence of numerous secondary metabolites. These bioactivities were broadly approved due to their potential health benefits. Most of these biological components include natural pigments (NPs), polyunsaturated fatty acids (PUFAs), lipids, proteins and polysaccharides. The content of bioactive compounds in the seaweeds are influenced by nutrients, CO_2 availability, light, pH, contaminants, temperature, salinity, and biotic relations (Stengel et al., 2011).

Seaweeds are considered as one of the abundant resources of naturally occurring antioxidants amongst the various marine organisms. These antioxidants protect the living cells

from the damage caused by attack of reactive oxygen species (ROS) on macromolecules, such as DNA, lipids and proteins leading to the development of prevalent disorders of cancer, diabetes, aging, and neurodegenerative diseases (Khalid et al., 2018). These can be prevented by various classes of natural and potent antioxidants, such as fucoxanthin, phycoerythrobilin, chlorophyll-a and their derivatives present in the seaweeds. The seaweed *Enteromorpha prolifera* was found to display strong antioxidant potentials due to the content of chlorophyll-a and related compounds, pheophorbidea, and phenolics (Khalid et al., 2018). Fucoxantin and their derivatives from seaweed *Undaria pinnatifida* were found to be the alternative for synthetic antioxidatives in various nutraceuticals and pharmaceutical formulations (Khalid et al., 2018). The presence of two hydroxyls in the ring structure of fucoxanthin were found to be attenuate the formation of ROS, which could also exhibit cytoprotective effect induced by H_2O_2 thereby effecting the suppression of ROS (Heo et a, 2008). The isolated phycoerythrobilin from *Porphyra* sp. also demonstrated potential antioxidant activity. Seaweeds could be used as a rich source of natural antioxidants with potential application in the food industry as well as cosmetic and pharmaceutical areas (Pangestuti & Kim, 2011).

The brown seaweed-derived polysaccharides were considered to be used as an alternate source for the production of anticoagulants than red and green seaweeds (Matsubara, 2004). There were various reports on the anticoagulant activities of the sulfated polysaccharides (SPs) (Mestechkina & Shcherbukhin, 2010). The sulfated galactan from red seaweeds and sulfated fucoidans from brown seaweeds were recognized with greater anticoagulant activities, which were due to presence of sulfate content, the sulfation position, and nature of the monosaccharide moieties. The SPs, xyloarabinogalactans, sulfated galactan, from the species of *Codium fragile*, *Codium cylindricum*, and *Monostroma nitidum* yielded higher anticoagulant activity than heparin (Khalid et al., 2018).

The large number of metabolites from the seaweeds also exhibited activities against inflammation along with and antioxidant properties (Khalid et al., 2018). Mainly, seaweeds derived fatty acids and marine terpenes, with structural entities ranged from the aliphatic groups of linear chains to complex polycyclic functionalities exhibiting potential activity against inflammation. A polysaccharide from *Aphanothece sacrum* produce an epicutaneous effect on 2,4,6-picryl chloride induced allergies by decreasing the production of pro-inflammatory cytokine (Ngatu et al., 2012). Phlorotannins from seaweeds also showed anti-inflammation effect (Khalid et al., 2018). The extract of red edible seaweed, *Porphyria dentate* has been used in the treatment of inflammatory diseases from previous decades due to their rich content of phenolics, such as catechol, rutin and hesperidin. Cyclic dipeptides, diketopiperazine, terpenes and steroids are the classes of anti-inflammatory compounds, which were found ubiquitously in

the seaweeds. Alkaloids isolated from the seaweeds showed to possess prospective anti-inflammatory properties (Khalid et al., 2018). The genus *Padina* belonging to the class, Phaeophyceae (brown seaweeds) are recognized active against some pathogen microbes, antioxidant and inflammation (Marques et al., 2012). Due to their different and unique living condition, the brown seaweed *Padina* sp., was found to be considered as a source of new chemical structures from seaweeds. Among the seaweeds belonging to class of Rhodophyceae (red seaweeds), genus *Gracilaria* was found to be a prospective candidate due to their capability to get high yields of the commercially valuable extracts. These were found to be a rich source of phycocolloids, such as agar and galactans. The prospective seaweeds for commercial phycocolloid extractions were reported as *G. confervoides*, *G. dura*, *G. chilensi*, and *G. secundata* (De Almeida et al., 2011). These seaweeds were also used in the production of bioactive metabolites, such as eicosanoids and prostanoids, which are derived through oxidative pathways of arachidonic acid and eicosapentaenoic acids from C_{20} polyunsaturated fatty acid (PUFA) metabolism (De Almeida et al., 2011). The pharmacophores, such as lipids, steroids, variety of compounds like alpha linolenic acid, gamma linolenic acid, glycolipids, 5-dehydro avenasterol, fucosterol, myristic acid, desmosterol, and 5-alpha-24(S)-ethyl-cholestane-3-beta-6-beta-diol are also abundant in this genus (De Almeida et al., 2011). Seaweeds are valued resources of bioactive metabolites, and could be used for the production of novel functional constituents in food and prevention of chronic disorders.

1.4 Free radicals in the defense mechanism

The exposure of regular and common biochemical reactions from the dietary-xenobiotics to the environment lead to the development of reactive oxygen species (ROS). These were found to be responsible for the oxidative stress in different pathophysiological states. As a consequence of these oxidative stress inductions, the cellular composition appeared to undergo alterations, which could result in chronic disease conditions (Nimse & Pal, 2015). The free radicals, such as hydroxyl radical ($^{\bullet}OH$), superoxide anion ($O_2^{\bullet-}$), non-free-radical entities like hydrogen peroxide (H_2O_2), singlet oxygen ($^1O_2$) are classified examples of ROS. The biological reactions, such as phosphorylation of protein, stimulation of several transcriptional factors, immunity, apoptosis, and differentiation, are reliant on the production of low level of ROS. When production of ROS increases, they show detrimental effects on the biomolecules (Pizzino et al., 2017). The production of ROS takes place in the mitochondria, during the pathophysiological condition, whereas $O_2^{\bullet-}$ can be generated by the cellular respiration, by pro-inflammatory cyclooxygenases (COX) and lipoxygenases (LOX), through the pathway of arachidonic acid and by inflammatory. The cells organize an antioxidant

defensive system on the basis of enzymatic constituents like superoxide dismutase-SOD, catalase-CAT, and glutathione peroxidase-GPx, to defend themselves from the cellular damage caused by the ROS (Figure 1.5) (Pizzino et al., 2017). ROS are produced by enzyme reactions those involved in the respiration, phagocytosis, synthesis of prostaglandin, and cytochrome P_{450} system. The free radical superoxide ($O_2^{\bullet-}$) is produced by the action of enzymes, such as xanthine oxidase, NADPH oxidase, and peroxidases (Pizzino et al., 2017). These superoxide radicals then lead to the generation of more free radicals, such as hydroxyl radical ($OH^{\bullet}$), hydrogen peroxide, hypochlorous acid (HOCl) and peroxynitrite ($ONOO^-$). The non-radical H_2O_2 is produced by the action of enzyme amino acid oxidase and enzyme xanthine oxidase. The most reactive hydroxyl radicals (OH•), are formed by the action of $O_2^{\bullet-}/H_2O_2$ with Fe^{2+}/Cu^{+}. Nitric oxide radicals (NO•), are synthesized by the oxidation of arginine to citrulline through enzyme nitric oxide synthase (NOS) (Pizzino et al., 2017).

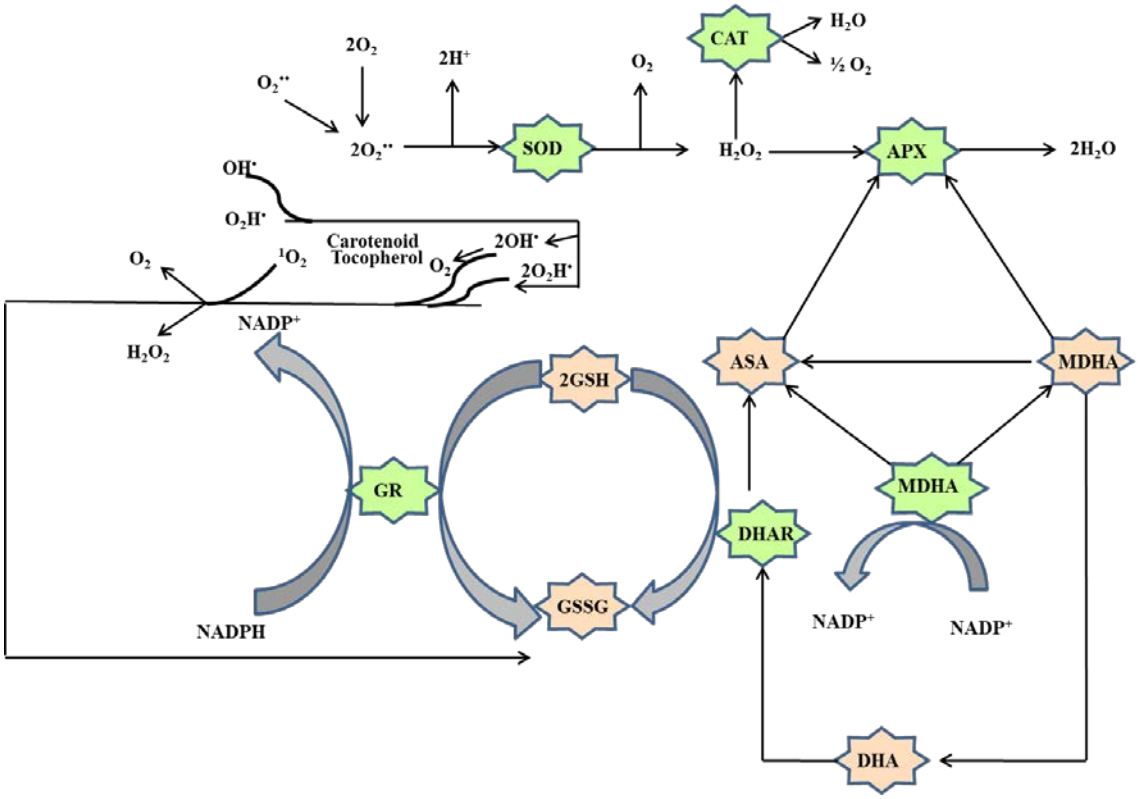

Figure 1.5.: Enzymatic and non-enzymatic antioxidants in seaweeds.

The electron transfer or higher energy exposure to molecular oxygen (O_2) were found to propagate the generation of reactive ROS (Nimse & Pal, 2015). The excess level of these ROS species in the defense mechanisms could cause peroxidation effect on lipids, oxidation of normal proteins and nucleic acids, inhibition of enzymes, finally leading to the death of the

unstressed cells. The oxidative stress could be efficiently neutralized by increasing the level of cellular defense with the aid of antioxidants (Lobo et al., 2010). The disproportionate equilibrium among the free radicals (FR), reactive oxygen species (ROS) and the defense mechanisms were deduced to lead to the state of oxidative stress. The normal metabolism of the body requires oxidant and antioxidant functionalities in the same proportion to maintain the transduction and the regulation of signals for the cellular functions (Sharma, 2014).

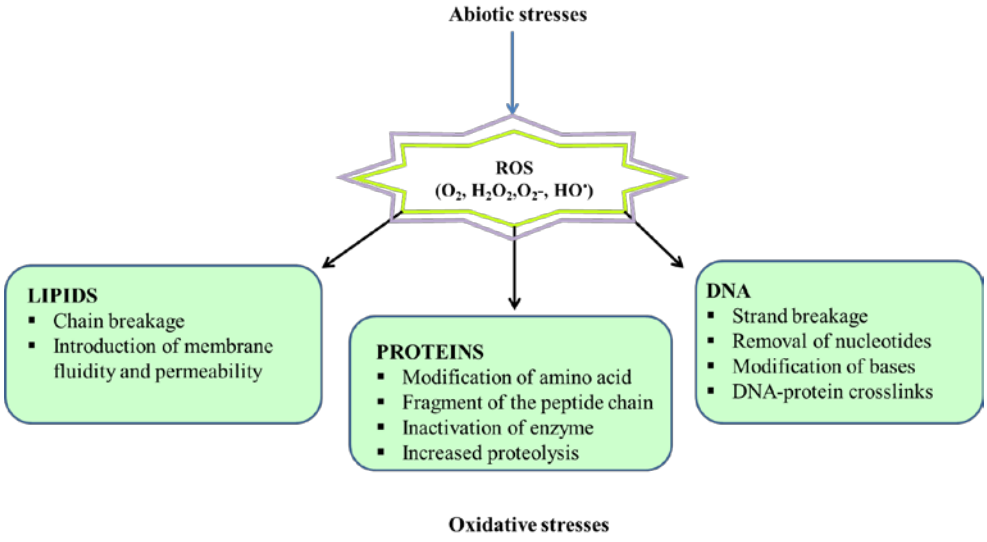

Figure 1.6.: ROS induce oxidative damage to proteins, lipids and DNA

Free radicals react with various biomolecules, especially they attack the polyunsaturated fatty acids (PUFA) in the cell wall membrane (Figure 1.6). The oxidative damage occuring in PUFA moieties could lead to the peroxidation of lipids through the intermediate free radical species, such as fatty acid peroxyl radical, lipid hydroperoxides etc. In particular, they propagate the chain reaction, which in turn lead to the formation of more free radicals and then towards the destruction of cellular system (Nimse & Pal, 2015). The action on free radicals, such as hydroxyls (•OH) on carbohydrates functionalities could lead to the abstraction of hydrogen atom from the molecule, and which in turn forms carbon centered free radicals. This destructs the molecular chain in carbohydrate molecules and finally produces the oxiradicals as a result of neutrophil activation, thus leading to inflammation of synovial fluid in the joints and cause rheumatoid arthritis (Sharma, 2014). The free radical actions on the cellular constituents generate the numerous pathological conditions, such as cancer, cardiovascular disorders, neurological diseases, diabetes conditions, ischemia, other chronic diseases and ageing (Sharma, 2014). These diseases can be categorized by the mitochondrial oxidative stress-induced disorders and inflammatory oxidative stress induced diseases, respectively. The shifting of the

thiol or disulphide redox state by pro-oxidants, damaging glucose regulation and mitochondrial oxidative stress were found to result in the pathophysiological situations leading to cancer and diabetes mellitus (Sharma, 2014). In inflammatory oxidative conditions, the greater action of either NAD(P)H oxidase or xanthine oxidase-induced the generation of ROS and finally leading to atherosclerosis and chronic inflammation, ischemia and reperfusion injury (Sharma, 2014).

1.4.2 Free radicals induced various chronic disorders

Oxidative stress destructs the critical balance between the free radical generation and antioxidant defense mechanisms. This imbalance damages the biological molecular species including nucleic acids, lipids, and proteins (Sharma, 2014). The occurrence of oxidative stress on infected tissues produce activation of radical generating enzymes, such as lipogenase, xanthine oxidase, cyclooxygenase, and lead to the initiation of phagocytes, release of Fe^{2+}, Cu^{2+}, or a disturbance in the electron transport chains of oxidative phosphorylation, making excess ROS. The ROS involved in the complications of age-related disease, diabetes mellitus, and neurodegenerative disorders (Sharma, 2014).

The DNA damage by oxidative stress is one of the reasons of cancer development. The activation of oncogene during the process of oxidative stress led to chromosomal abnormalities and then to cancer. Chemical carcinogenesis was reported to occurr by the oxidation of DNA by products, such as hydrolyzed DNA bases (Valko et al., 2004, 2006, 2007). The development of these kinds of adducts causing mutation of genes and hinders the cell growth by altering the physiological characteristics. Oxidative stress causes alteration in the structure of DNA, for instance, modification of lesions of sugar and base, cross-linkages in DNA-protein, breaking of DNA strands, and modification of base-free sites. The peroxidation of lipids due to oxidative stress also could play an important role in different types of cancer (Valko et al., 2004, 2006, 2007).

Oxidative stress was considered to be one of the preliminary causes of multifactorial etiologies associated with the cardiovascular disease risk factors (CVDs), such as hypertension, hypercholesterolaemia, unbalanced diet, diabetes, and stress (Bahorun ey al., 2006; Chatterjee et al., 2007; Ceriello et al., 2008). Oxidative stress also triggers atherosclerosis, and also was found to cause oxidation of LDL leading to the accumulation of lipid. Oxidative stress also leading to the diseased conditions such as ischemia, hypertension cardiomyopathy, congestive heart failure, and cardiac hypertrophy (Bahorun et al., 2006; Chatterjee et al., 2007; Ceriello et al., 2008). Oxidative stressed conditions were also associated with the neurological disorders and oxidative damage leading to neuron loss to progression of amyotrophic lateral sclerosis (ALS), Alzheimer's disease (AD), Parkinson's disease, depression, memory loss, and multiple

sclerosis (Pizzino et al., 2017). Oxidants were found to enhance the inflammation pathologies and activating several kinases pathways/NF-kappa β transcription, which in turn was found to lead to asthma, chronic obstructive pulmonary disease, and local chronic inflammation (Pizzino et al., 2017).

1.5 Seaweeds and their metabolites combat oxidative stress induced life style disorders

Seaweed-derived bioactive components with potential health benefits are an emerging area of research. Seaweeds have a long tradition as a food source in Asian countries, being part of the Western diet only to a limited extent. In 2014, production of seaweeds through mariculture (44% of all aquaculture) was estimated at about 27 million tons wet weight, registering annual growth rate of 8% and valued at 7 billion US$ (FAO 2016).

1.5.1 Seaweeds and their metabolites as natural alternative to combat various oxidative stress induced life style disorders

Seaweeds constitute a major share of marine flora, and they were reported to possess structurally diverse compounds of various bioactivities endowed with antihypertensive, anti-inflammatory, and anti-carcinogenic activities. These species grows in extremely hostile saline habitats, and evolved a number of specialized biochemical mechanisms to withstand salt-triggered oxidative stress conditions, which is governed by multiple biochemical mechanisms facilitating cell homeostasis and retention of water ability. However, the absence of oxidative damage in the structural components, deterrence of predation, and the ability to reproduce successfully suggest that their cells are the storehouse of bioactive metabolites with potential pharmacological properties. Therefore, these marine floras are considered as valuable sources of bioactive compounds with potential pharmacological significance.

Seaweeds are considered as a rich source of antioxidant components and bioactives. They were found to produce highly bioactive compounds as a part of their survival of harsh and stressful surroundings (Pinteus et al., 2017). There were several reports on oxidative-stress inhibiting effect of seaweeds, especially *in vitro* and in human issues. For instance, the seaweed species *Acanthophora spicifera*, *Padina tetrastromatica* and *Ulva lactuca* collected from the Gulf of Mannar exhibited effective antioxidant activities than standard drug alpha-tocopherol. The reports also revealed the greater antioxidant effect of methanolic extract of *Gracilaria* sp. than that of tocopherol by H_2O_2 scavenging assay method (Athiperumalsami et al. 2010).

Similar reports were documented on seaweeds, *Saccharina japonica* and *Sargassum horneri* oils by Sivagnanam et al. (2015).

The inhibitory effect on oxidative stress induced diseases and antioxidant potencies of phenolic components from seaweeds have been previously recorded (Kadam et al., 2016; Nakai et al., 2006). The polyphenol rich seaweed *Sargassum muticum* exhibited antioxidant effect along with anti-proliferative and anti-angiogenic properties Namvar et al. (2013). This species has been introduced for prevention of cancer Namvar et al. (2013). The seaweeds polyphenol were found to enhanced activities of different enzymes, such as glutathione peroxidase, catalase, and superoxide dismutase (Sanchez et al., 2018).

In recent days, development of value-added products, functional food candidates, nutraceuticals, and pharmaceutical leads from these underutilized seaweed species for commercial utilization has gained significance. Seaweeds are the natural bounty of the great Ocean, and these invaluable marine herbs are gifted with extraordinary medicinal properties (Pangestuti et., 2011; Ahn et al., 2012; Jin et al., 2006). Studies on seaweeds revealed that they are prospective source of micro/macro bioactive molecules along with large number of antioxidants, such as heterogeneous diverse group of polyphenols. Owing to the presence of rich content of polyphenolic compounds and phlorotannins in the seaweeds, inclusion of seaweeds and their metabolites in the daily diet has been linked with a reduced risk of different chronic diseases, including cancer, metabolic and neurodegenerative disorders and CVDs. The bromophenols, phenolic acids, and flavonoids were found to be rich in green and red seaweeds while phlorotannins were deduced to be the dominant polyphenolic compounds present in brown seaweeds as good antioxidants (Lee & Kim, 2013).

The seaweeds, *Undaria pinnatifida*, *Palmaria palmate*, *Porphyra columbina* and *Porphyra yezoensis* reported antioxidant effects, thereby exhibiting the positive impact on hypertension, cholesterol and diabetes mellitus. In addition, seaweed *Ishige okamurae Yendo* showed defense mechanism against the UV-radiation (Lee & Kim, 2013). Antioxidant components isolated and identified from this species was reported to enhance its antioxidant activity along with anti-inflammation/antidiabetic potential (Lee & Kim, 2013). Seaweeds *Ecklonia cava*, *Polysiphonia morrowii*, *Dictyopteris undulata*, *Sargassm micracanthum*, and *Sargassum macrocarpum* exhibited free radical-quenching activity. Electron donors from the seaweeds were found to react with the free radicals to form more stable products, which in turn could terminate the radical chain reactions (Lee & Kim, 2013). The seaweeds were found to neutralize the toxicity of the ROS generated from activated phagocytes, thereby reducing the formation of superoxide anions and maintained the redox homeostasis in the cellular metabolic system (Lee & Kim, 2013).

1.5.2 Role of seaweeds belonging to the class of Phaeophyceae and Rhodophyceae in the oxidative stress defense mechanism

Oxidative stress has considered being involved in pathophysiological states of many prevalent disorders. Seaweeds provided two defensive approaches for survival of effect on ROS before the impairment on cellular biological constituents. The seaweeds and seaweed derived extracts were reported to possess various pharmacological activities as a promising source of bioactive secondary metabolites with greater pharmaceutical potentials (Smith et al., 2004). Seaweeds are found to be rich in anti-oxidative metabolites, like various pigments, carotenoids, polyphenolic compounds and complex structural polysaccharides. Majority of these compounds were registered greater bioactive potentials like antioxidants. For instance, secondary metabolite phylopheophytin derived from *Eisenia bicyclis* (Cahyana et al., 1992), phlorotannin derived *Sargassum kjellamanianum* (Yan et al., 1996), fucoxanthin reported from *Hijikia fusiformis* (Yan et al., 1999), sulfated polysaccharide isolated from seaweed *Laminaria japonica* (Wang et al., 2008) and mycosporin-amino acids derived from red seaweeds (Nakayama et al., 1999). These metabolites were revealed their inhibition potential against peroxide chain initiation and decomposition, inhibition of proton abstraction, scavenging of free radicals, binding and reduction of metal ions. Therefore, seaweeds are considered as the alternative resource for natural antioxidants. Moreover, seaweed polyphenols are capable to inhibit peroxidation of lipids and chelation of metal ions. Polyphenolic metabolites including glycosylated flavanols, flavanols, and gallocatechin bearing chromenyl ring, catechin, and their derivatives have reported from seaweeds (Yoshie et al., 2003). Phenolic compounds greater antioxidant activities were identified from *Petalonia binghamiae* (Murakami et al., 2002). Potent antioxidants like phlorotannins have been reported seaweed *Ecklonia stolonifera* and E. (Kang et al., 2003). Bioactive metabolites isolated from *Turbinaria sp* were also possessed potential antioxidant a agents (Chakraborty et al., 2013; Zubia et al., 2009).

Antioxidant potential has been isolated from different species of seaweeds belonging to the class of Rhodophyceae, Phaeophyceae, and Chlorophyceae. Especially, extracts from seaweed species belong to Rhodophyceae and Phaeophyceae, and their bioactive metabolites exhibit significant role in oxidative stress defense mechanism (Lee et al., 2013).

1.6 Objectives

Based on this, the objectives of the Thesis are as follows:

1. To screen the extracts/fractions from the seaweeds belonging to the classes Phaeophyceae and Rhodophyceae from the marine and coastal ecosystems for antihypertensive, anti-inflammatory, antidiabetic and antioxidant activities.
2. To isolate the small molecular weight lead molecules and substituted polysaccharides from the extracts/fractions of the seaweeds *Padina tetrastromatica* and *Gracilaria salicornia* belonging to the classes Phaeophyceae and Rhodophyceae, respectively by various physical/chromatographic techniques, coupled with evaluation of biological activities using selective antidiabetic, anti-inflammatory, antihypertensive and antioxidant assays against different pharmacological models.
3. To characterize the purified compounds by exhaustive spectroscopic experiments.
4. To predict the biological properties by chemiinformatic tools, structure-activity relationship analyses and generation of database of potential lead molecules.

1.7 Thesis outline

On the basis of the above objectives, the current Thesis is classified into a total of seven chapters. The importance of this study on the bioactive potentials of the selected seaweeds, along with objectives was discussed in the introductory chapter (Chapter **1**). The detailed review of the studies was based on the significance of seaweeds as antioxidative, antidiabetic, antihypertensive and anti-inflammatory bioactive sources along with the characterized bioactive compounds and their medicinal values were envisaged in the Chapter **2**. Chapter **3** described the *in vitro* evaluation of the antioxidant, anti-diabetic and anti-inflammatory potentials of the organic extracts of seaweeds *Padina tetrastromatica* and *Gracilaria salicornia* belonging to the classes Phaeophyceae and Rhodophyceae, respectively. The isolation and characterization of secondary metabolites responsible for antioxidant, antidiabetic and anti-inflammatory activities from *Padina tetrastromatica* and *Gracilaria salicornia* were described in Chapter **4** and Chapter **5**, respectively. The isolation and characterization of the polysaccharides responsible for antidiabetic and anti-inflammatory activities from *Padina tetrastromatica* and *Gracilaria salicornia* were described in Chapter **6**. The summary and conclusion of the work and major research findings from the current study were detailed in Chapter **7**.

CHAPTER 2

REVIEW OF LITERATURE

Contents

2.1 *Background*

2.2 *Marine ecosystem as a source of bioactives*

2.3 *Seaweeds belonging to the class Rhodophyceae and Phaeophyceae: Specialized morphological features*

2.4 *Seaweeds as prolific source of bioactive metabolites*

2.5 *Specialized bioactive secondary metabolites of seaweeds belonging to Rhodophyceae and Phaeophyceae*

2.6 *Conclusions*

2.1. Background

The extensive extraction on marine biomes for identification and characterization of potential candidates of the therapeutics has significantly increased since past few decades. Consequently, diverse classes of compounds, which have substantial pharmaceutical potencial were developed as novel types of drug targets (Chojnacka, 2012; Pinto et al., 2012). Marine bioactive components and the functional food ingredients having potential applications in pharmaceutical fields with potential health benefits demonstrated to possess advantageous as functional food with added health benefits, and are attracting attention because of the growing demand for new compounds of 'marine natural' origin. The most interesting phyla with respect to pharmacologically active marine compounds include the abundantly available seaweed species occuring in te rocky layer of tidal/intertidal region of coastal waters, wherein the brown and red seaweeds (belonging to the classes Phaeophyceae and Rhodophyceae, respectively) are potential sources of bioactive substances (Carroll et al., 2019; Blunt et al., 2018; Blunt et al., 2017). Seaweeds are valuable sources of bioactive compounds and could be introduced for the preparation of novel functional ingredients in food and also a good approach for the treatment or prevention of chronic inflammatory diseases. Seaweeds have drawn relevant attention in recent years in the search for beneficial health properties, and showed great potential as anti-inflammatory, antimicrobial, antiviral and anti-tumor drugs (Chojnacka, 2012; Pinto et al., 2012). Due to these significant bioactive potentials, pharmaceutical industries are more

interestingly focused towards the seaweeds for the exploration of new drug targets. The value of extraction of seaweeds is also utilized by biochemical and medicinal fields of research.

In earlier 1950s, the application of seaweeds was constrained to the folk and traditional medications (Lincoln et al., 1991). Seaweed has long been part of the traditional diet of coastal communities. It is widely consumed in East Asia, particularly in Japan, China and Korea. Studies demonstrated that in Japan, the rate of mortality is less and hence their life expectancies are very high. It is reasonable to evaluate this result, because Japanese are regular consumers of seaweeds. After 1980s, bioactives with pharmacological potencies were discovered from seaweeds (Mayer & Lehmann, 2000). There were about 3200 new bioactive compounds reported from seaweeds. According to the estimation by 1977-1987, seaweeds occupied about 35 % of the newly discovered phytochemical constituents, followed by 29 % of sponges and 22 % of cnidarians (Kelecom, 2002).

Recently, much attention has been paid by the consumers toward natural bioactive compounds as functional ingredients in foods, and hence, seaweeds could be alternative sources for synthetic ingredients that can contribute to consumer's well-being, by being a part of new functional foods and pharmaceuticals. Majority of secondary metabolites isolated from seaweeds' structures have identified as the class of chemistries of fatty acid derivatives, hydroxyl unsaturated fatty acid derivatives, glycolipids, polysaccharides, steroid skeletal structures, phenolics and terpenes (Plaza et al. 2010; Karthikryan et al., 2010). Previous reports also suggested that the antioxidant, antibiotic or antifungal properties of bioactive metabolites isolated from seaweeds belonged to the class of halogenated diterpenoid and triterpenoids with bromine, chlorine and iodine substitutions (Bhagavathy et al. 2011). Recently, about 15 million mg of seaweeds products has been produce around the world. Among which, a small portion of about 250,000 mg of extracts were reported to be manufactured from seaweeds (Bhagavathy et al., 2011). However, utilization of seaweed extracts was increased globally because those can be easily made into the bioactive products (Bhagavathy et al., 2011). Besides the bioactive small molecular weight compounds, seaweeds were found to possess hydrocolloids, such as agar, carrageenan, and algin, which have exponentially increased the industrial value of seaweeds (Omar et al., 2017). Several studies have been carried out on extracts and pure bioactive leads acquired from red, brown and green seaweeds for evaluating the bioactive potencies against various disease targets (Omar et al., 2017).

2.2. Marine ecosystem as a source of bioactives

The oceans cover about 70% of the planet surface and holds high biodiversity; even though very few species have been explored or used for pharmaceutical purposes. The bioactive

metabolites of marine origin have attracted the attention of medical practitioners and scientists for the past few decades, because several of these chemicals exhibit pronounced pharmacological activities. The exploration on marine environment has been began at the period of 1970, and exhibited a dynamic increase during the 1980s, whereas during the past two decades it has reached to the optimum level of utilization according to estimation between the periods 2000-2018 (Alves et al., 2018). It was revealed that the bioactive natural metabolites with marine origin have effectively contributed towards the production of functional foods, nutraceuticals, medicinal, hydrocolloids and cosmetic industries (Alves et al., 2018). The distinct and unique chemistries of marine natural products (MNPs) include small molecular weight bioactives, such as terpenes, steroids, polyphenolic compounds, fatty acid derivatives and high molecular weight polysaccharides and oligosaccharides along with marine biotoxins. The number of bioactive compounds isolated from marine ecology in the periods of 1965-2016 was represented by the Figure 2.1 (Alves et al., 2018).

Seaweeds are one of the predominant oceanic flora, and these invaluable marine herbs are considered as a prolific source of bioactive compounds as they are able to produce a great variety of secondary metabolites characterized by a broad spectrum of extraordinary medicinal properties. These species grows in extremely hostile saline habitats, and evolved a number of specialized biochemical mechanisms to withstand salt-triggered oxidative stress conditions, which is governed by multiple biochemical mechanisms facilitating cell homeostasis and retention of water ability. However, the absence of oxidative damage in the structural components, deterrence of predation, and the ability to reproduce successfully suggest that their cells are the storehouse of bioactive metabolites with potential pharmacological properties. Therefore, these marine floras are considered as valuable sources of bioactive compounds with potential pharmacological significance.

Fig. 2.1. A photo of seaweed harvest

The marine environment included more than 2 lakhs of species of seaweeds and invertebrates from the 15 representative phyla of marine organisms (Figure 2.2) (Blunt *et al*., 2017). This estimation was found to be represented a minor percentage from the total estimated species that have yet to be exposed. The marine habitat represents an essentially untapped source of organisms for identification of new drug targets with pharmacological potencies (Blunt *et al*., 2002; Blunt *et al*., 2015; Blunt *et al*., 2016; Blunt *et al*., 2017; Blunt *et al*., 2018). The distribution of marine living forms between the various phyla isolated over the period of 1971-2016 was represented by the Figure 2.3 (Blunt *et al*., 2017). The secondary metabolites produced from different marine organisms displayed potencies like pharmaceutical leads, these were supposed to form as a part of evolutionary change. Because majority of these marine organisms are believed to be located in complex habitats, and these immobile living forms only possessed simple defensive mechanisms, they have produced biochemical components as a part of defensive strategies to hinder other entities settling on them. The identification of novel bioactive components with marine origin has established greater prospective to utilize them against various disease targets (Blunt *et al*., 2002; Blunt *et al*., 2015; Blunt *et al*., 2016; Blunt *et al*., 2017; Blunt *et al*., 2018). Exploration on the basis these unique habitats from the marine environments provided underexplored sources for detection of unique chemicals with therapeutic properties. Marine organisms are particularly attracted attention since they correlated with the traditional therapeutical schemes of a natural drug resource, and therefore, they found their utilization for development of pharmacolophore and drug candidates over the past few decades, and were considered as an untapped reservoir of novel bioactive leads for future.

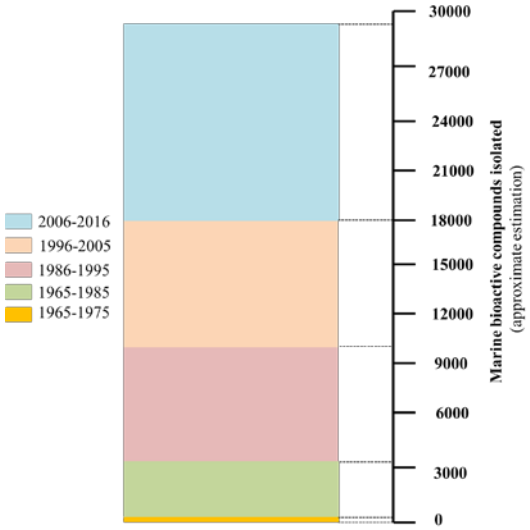

Figure 2.2.: Number of marine bioactive compounds isolated in the periods of 1965-2016 (Alves et al., 2018)

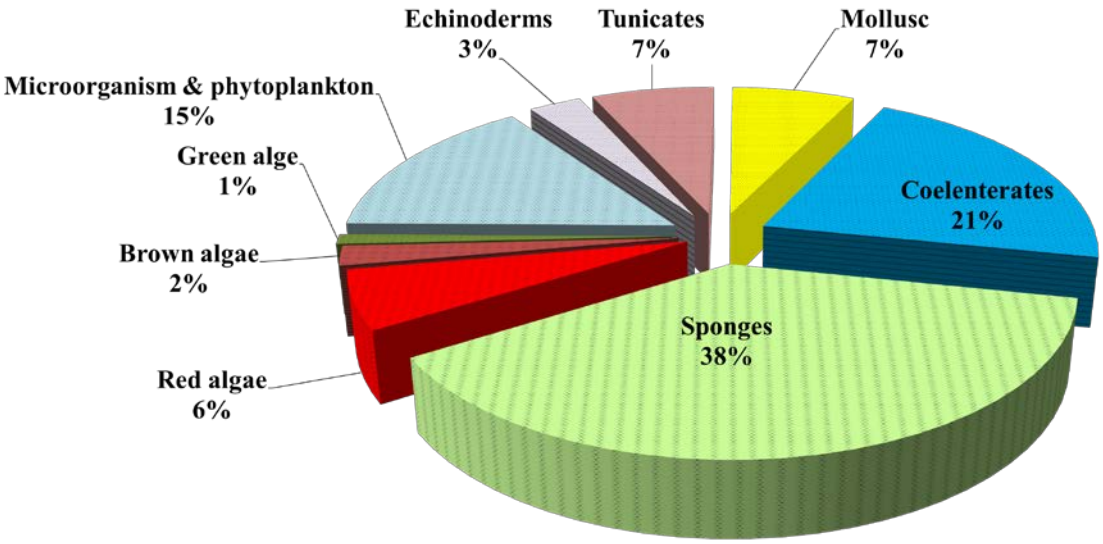

Figure 2.2.: The distribution of different marine living forms by phylum (Blunt *et al*., 2002)

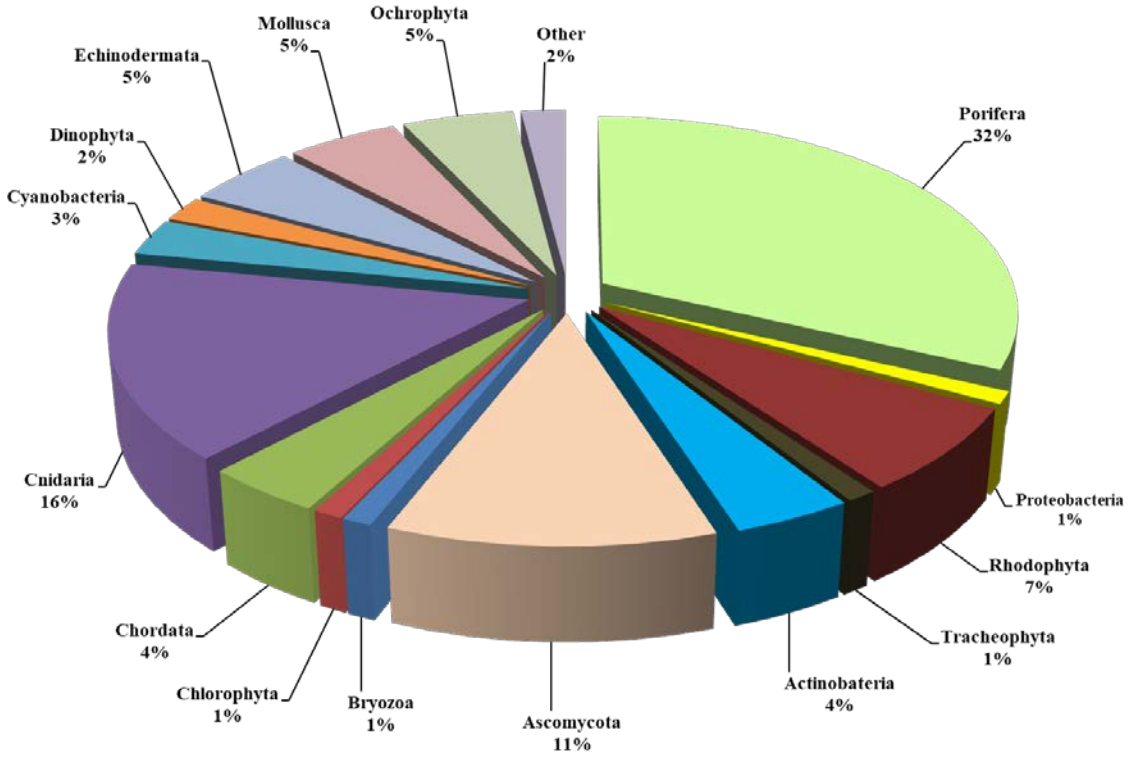

Figure 2.3.: The Distribution of marine living forms between the various phyla isolated over the period of 1971-2015 (Blunt *et al*., 2017)

2.3. Seaweeds as prolific source of bioactive metabolites

Seaweeds are considered as one of the leading producers of bioactive compounds among the various marine living forms (Bhadury et al., 2004). They can lead to the formation of broad array of secondary metabolites with prominent bioactive potentials. Seaweeds contain a large assemblage of species that predominate in the coastal shelf areas of Indian subcontinent. Seaweeds are rich source of secondary metabolites like halogenated compounds, alcohols, aldehydes, steroids, alkaloids, polysaccharides, fatty acid derivatives and terpenoids, and have therapeutic and functional food applications (Smit, 2004). Seaweeds and their extracts are estimated as the treasure-trove of potentially active components. Their utilities in nutrition and medicines were recognized during the past decades, and are valued now-a-days, for the production of novel biogenic products, functional food, fertilizer, fodder, and as source of medicaments (Kolanjinathan et al., 2014). They have found their usefor the industrial productions of hydrocolloids, and have been continuously explored by the Asian countries for food and pharmaceuticals. They are not possessed any true leaves, stem, and root. Seaweeds produce a diverse array of secondary metabolites, which play pivotal roles as therapeutic agents to alleviate undesirable pathophysiological conditions due to inflammation, diabetes, and other oxidative stress-induced diseases. The different groups of seaweeds belonging to the classes Rhodophyceae (red seaweeds), Phaeophyceae (brown seaweeds) and Chlorophyceae (green seaweeds) were contributed to bioactive marine natural products as primary producers and therefore, seaweeds were constituted as highly productive and dynamic groups among the various phyla in the marine ecosystem (Kolanjinathan et al., 2014). Bioactive compounds generated from the seaweeds were varied according to the environmental characteristics, such as competition for habitat, growing surfaces, and protection from predators. Therefore, different types of biologically active compounds derived from same species possessed varying bioactivities due to their geographical zone, habitat and climatic parameters. According to the reports obtained from 1977-2002 by D. J Faulkner, seaweeds are rich renewable resources of various secondary biogenic compounds (Faulkner, 1977). Estimation by Faulkner revealed that seaweeds consisted of more than 440 bioactives, along with the approximate number of 250 and 30 compounds were identified from the red and green seaweeds, respectively (Faulkner, 2002). Afterwards, Blunt et al. picked up these sequences and published updated data on MNP every year (up to 2018). The Figure 2.4 represented number MNP identified by the last 11 years showing that the number compounds isolated from seaweeds nearly reached to twice than the first 40 years (Brodie et al., 2007). From the reports, red and brown seaweeds have attracted by scientific research field because of their higher abundance of highly bioactive compounds from these groups. Majority of these bioactive compounds belonging to the classes of terpenes,

sterols, polyphenolics, lipids, macrolides and cytotoxic compounds, isolated from seaweeds have been reported to possess various pharmacological potencies, such as antimicrobial, antioxidant, anti-inflammatory, anticoagulant, antidiabetic, anti-proliferative, and anti-angiogenesis properties (Blunt et al., 2009; Blunt et al., 2010; Blunt et al., 2011; Blunt et al., 2017 ; Blunt et al., 2018).

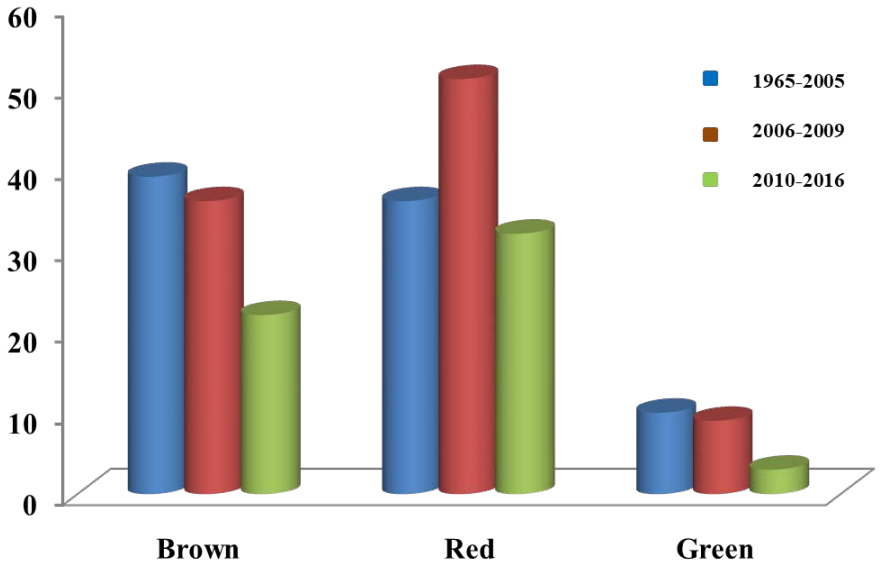

Figure 2.4.: Distribution of the seaweed secondary metabolites isolated per year (Blunt et al., 2009) and coupled with data from the same authors (Blunt et al., 2010, 2011, 2017 & 2018)

Recently, seaweeds are widely extracted for various polysaccharides due to their higher commercial values. The polysaccharides like alginate and agar extensively extracted from brown and red seaweeds, respectively, by the phycocolloid industry (Kolanjinathan et al., 2014). Seaweed polysaccharides, agar and carrageenan from the red seaweeds are utilized as gelling and thickening agents by the food industry, and are also used for preparing medium for growth of microorganisms (Kolanjinathan et al., 2014). Additionally, cell wall polysaccharides, such as fucoidans, ulvans and xylans isolated from the classes of Phaeophyceae, Chlorophyceae, and Rhodophyceae, respectively, were used as the functional food ingredients. Moreover, storage polysaccharides like laminarin, floridean starch from brown and red seaweeds are used as dietary fibers. Many of these soluble polysaccharides have documented to exhibit hypoglycemic and hypocholesterolemic activities (Kolanjinathan et al., 2014). The sulfated fucoidans from brown seaweeds found to display bioactive properties, such as anticancer, anti-proliferative, anti-thrombotic, anti-coagulant, anti-viral, anti-complementary, and anti-inflammatory agent. Furthermore, seaweeds were found to be rich reservoir of minerals, macro and micro elements,

and vitamins (Kolanjinathan et al., 2014). Hence, vitamin B rich brown seaweeds have been used as tradition remedy for thyroid goiters. The seaweeds were also found to contain proteins, fatty acids and lipids; whereas higher protein content was obtained from green and red seaweeds. The omega 3 and omega 6 polyunsaturated fatty acids obtained from seaweeds were found as effective therapy for cardiovascular diseases, diabetes, and osteoarthritis. The higher level of α-linolenic acid found in green seaweeds and fatty acids like eicosapentaenoic acid and arachidonic acid in red and brown seaweeds also raised the value of seaweeds and seaweed extracts (Kolanjinathan et al., 2014).

2.3.1 Secondary metabolites derived from seaweeds

In recent years, studies of marine natural product have yielded a considerable number of drug candidates (Yin et al., 2019; Xie et al., 2018; Koutsaviti et al., 2019; Lorenzo-Morales et al., 2019; Yang et al., 2019; Carroll et al., 2019; Blunt et al., 2018; Blunt et al., 2017). Marine bioactive components and the functional food ingredients with potential health benefits demonstrated to possess advantageous as functional food with added health benefits. Novel secondary bioactive metabolites from the red and brown seaweeds are attracting attention because of the growing demand for new compounds of 'marine natural' origin, having potential applications in pharmaceutical fields. The bioactive secondary metabolites identified from the seaweed included broad array of biochemical compounds, which were found to possess different classes of chemistries, including terpenes, sterols, polyphenols, acetogenins and others. The overview on seaweeds reveled that nine thousand species of seaweeds have been widely distributed into three classes according to their concentration of pigments, namely Rhodophyta, Phaeophyta, and Chlorophyta (or the red, brown, and green seaweeds, respectively) (Blunt et al., 2009; Blunt et al., 2010; Blunt et al., 2011; Blunt et al., 2017; Blunt et al., 2018). Percentage diversity of the seaweeds and approximate proportion of secondary metabolites identified from the seaweeds belonging to three major classes, Rhodophyceae, Phaeophyceae and Chlorophyceae, over the period of 2000 to 2018, was represented by the Figure 2.5 {approximate proportions of secondary metabolites assembled from Faulkner (2000 - 2002) and Blunt et al. (2003 - 2018)}. The diversity of various secondary metabolites have showed that several bioactivities along with potential therapeutic benefits like antidiabetic, antihypertensive, antihyperlipidemic, antioxidant, anti-inflammatory, antibacterial, and immunomodulatory properties. The red seaweed species are constituted as one of the dynamic source of halogenated secondary metabolites including terpenenoids, C_{15}-acetogenins, polyketide derivatives, alkaloids, phenolic compounds and peptide derivatives. Moreover, red seaweeds are found as major resources of hydrocolloids, such as agar, sulfated cell wall polysaccharides,

nucleic and shikimic acid analogues. With wide range of bioactive compounds, red seaweeds were associated with various pharmacological properties (Blunt et al. 2018). The halogenated terpene derivatives obtained from Rhodophyta were synthesized as a part of chemical defensive mechanisms against herbivores. The brown seaweeds are producers of structurally different compounds derived from isoprene-entities. Besides the terpenoids class of chemistries, they were found to produce cell wall polysaccharides, polyphenolic compounds, pigments, with numerous biological potentials (Pinto et al., 2012). Additionally, by the enzymatic modifications of fatty acid long chains, synthesized cyclic/acyclic volatile hydrocarbon analogues with number of carbons ranging from C_8 to C_{11}. The secondary metabolites derived from the green seaweed species are the least representative groups in marine natural metabolites. The representative classes of these compounds are the derivatives of isoprenoid entities. Like other seaweed species, amino acid-analogues, phycocolloids and shikimate-analogues were reported from these species. The cyclic peptides were examples of the most prominent class of compounds isolated from the green seaweed species (Pinto et al., 2012).

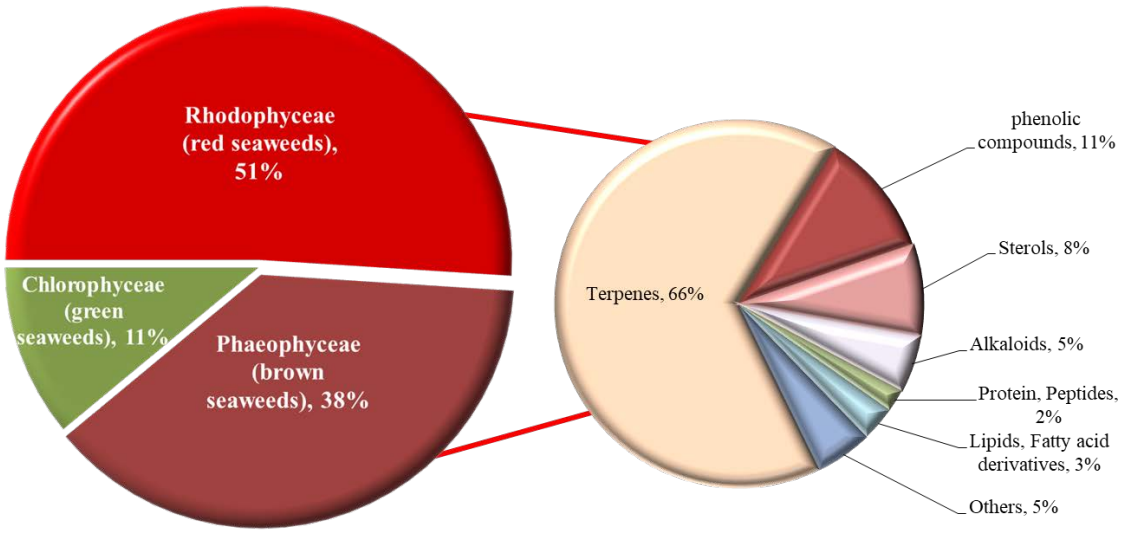

Figure 2.5.: Percentage diversity of the seaweeds and approximate proportion of secondary metabolites identified from seaweeds belonging to three major classes, Rhodophyceae, Phaeophyceae and Chlorophyceae over the period of 2000 - 2018 (approximate proportions of secondary metabolites assembled from Faulkner (2000 - 2002) and Blunt et al. (2003 - 2018).

2.3.1.1 Terpenoids

Terpenoids constitute one of the domineering classes of secondary metabolites; which are derived from the isoprene entity with five numbers of carbons oriented in a head to tail/tail

to tail fashion, with various functionalities at different positions. Structural modifications and assemblage of isoprene entities leads to the development of diverse and novel compounds with unique chemistries and bioactivities. These bioactive compounds varied structurally from ten-membered volatile hydrocarbons to forty-membered polyenes (Soltani, 2016). Their diversification includes monoterpenes, sesquiterpenes, diterpenes, sesterpenes and triterpenes with two, three, four, five and six isoprene entities, respectively. Terpenoids are synthesized from the mevalonic (MV) acid pathway through the two isomers of five carbon building blocks, namely, dimethylallyl diphosphate (DMAPP) and isopentenyl diphosphate (IPP) by the assemblage of precursors of ten, fifteen and twenty carbons, such as geranyl diphosphate (5C, GPP), neryl diphosphate (10C, NPP), farnesyl diphosphate (15C, FPP), geranylgeranyl diphosphate (20C, GGPP), and nerylneryl diphosphate (20C, NNPP) along with prenyltransferases. These ten, fifteen and twenty carbon substrates, on reaction with terpene synthases, produce cyclic/acyclic terpene class of olefins/alcohols through the series of regio/stereo selective reactions. The natural bio-synthesis of interesting chemistries of terpenoid structures were found to occur through the different combinations of terpene synthases with various enzymes, such as P450 enzymes through different chemical reactions, namely glycosylation, methylations, acylations, oxidations or peroxidation (Soltani, 2016). The pharmaceutical significance of these economically and traditionally dominant terpenoids started from the primitive times, and due to their wide range of medical applications, they were used to alleviate numerous disorders. These metabolites also possessed wide range of industrial applications and chemoecological functions (Gross and Konig, 2006). Marine organisms harvest a wide variety of unique class of terpenoids, differentiated by structural characteristic features. Some of the predominant marine taxa, such as algae and invertebrates are produced interesting structures with various functionalities (Gross and Konig, 2006; Blunt et al., 2005).

Three cytotoxic sesquiterpenes **1**-**3** with halogenated functionality has been reported from *Laurencia* species, which were found to exhibit cytotoxic property towards tumour cell line (Faulkner, 1996). A sesquiterpene class of cytotoxic peroxide majapolene **4** was reported from the red seaweed *Laurencia majuscula* from the Philippine. The derivative of this sesquiterpene, majapolone **5** and majapolols **6**-**10** were reported as diastereomers (Faulkner, 1996).

1 $R^1=R^2=H$
2 $R^1=Br$; $R^2=H$
3 $R^1=H$; $R^2=Br$

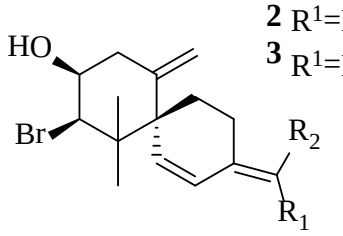

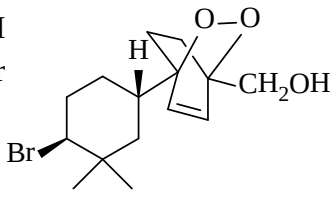

4

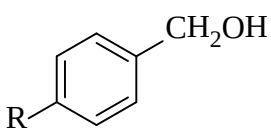

5
R=a

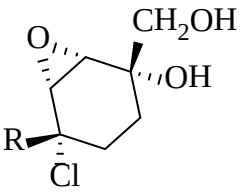

8 R=a

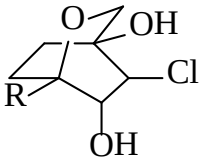

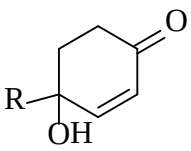

6

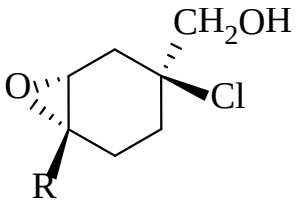

9 R=a

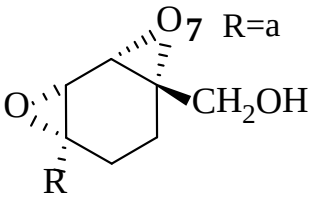

7 R=a

10 R=a

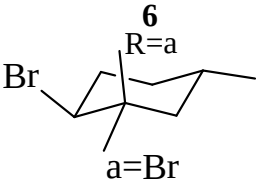

The meroditerpenoids, namely, a series of nahocols and isonahocols **11-13** and **14-15**, were isolated from *Sargassum autumnale* from Japan, and were endothelin antagonists. The meronorsesquiterpenes, cystomexicones **16** and **17** along with 4-(5-hydroxy-2-methoxy-3-methylphenyl)-butan-2-one **18** were identified from the brown species *Cystoseira abies marina* (from Tenerife) (Faulkner, 2000). Halogenated terpenes, pantopyranoids **19-21**, pantoisofuranoids **22-24**, pantoneurotriols **25-26** along with monoterpenes with linear structures, such as compounds **27-28** and pantoneurines **29-30** were recorded from the red seaweed species of *Pantoneura plocamioides (*from Antarctica) (Faulkner, 2000). Four moncyclic diterpenes **31-34** were reported from *Caulerpa trifaria* (from Tasmania) (Faulkner, 2002). A new brown seaweed derived meroterpenoid schimperiol **35** was separated from *Stypopodium schimperi*. The sesquiterpenes, such as zonarol **36** and isozonarol **37** were derived from seaweed *Dictyopteris zonaroides* (Faulkner, 2002).

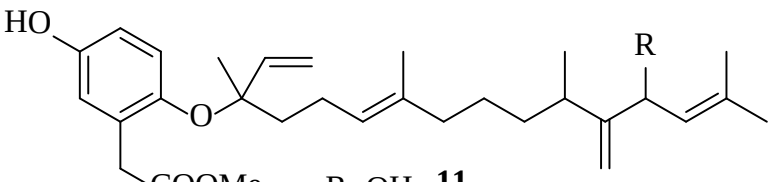

R=OH **11**
R=H **12**

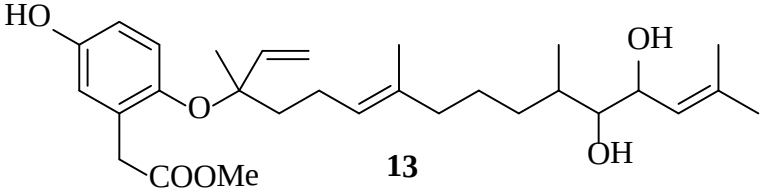

13

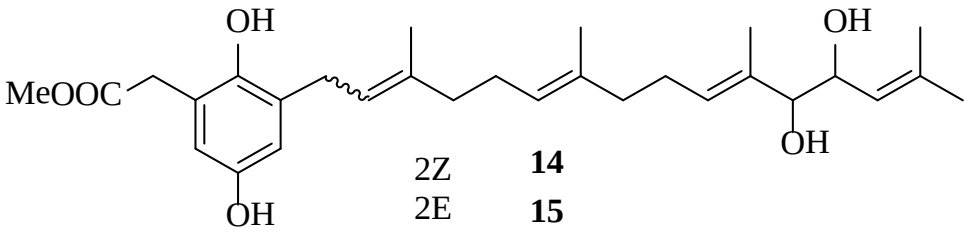

2Z **14**
2E **15**

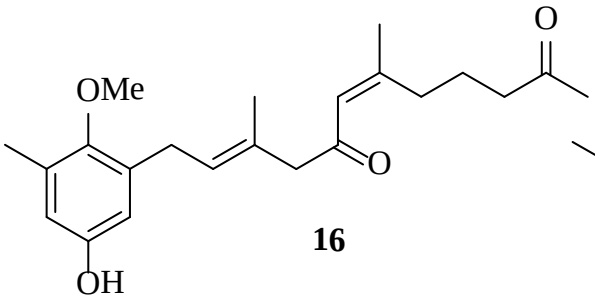

16

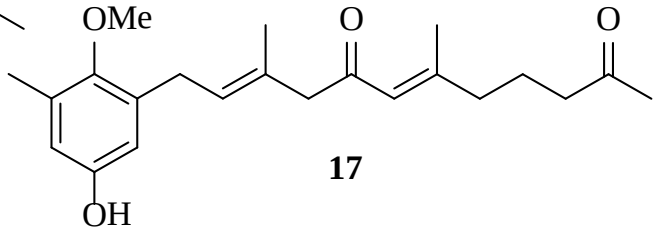

17

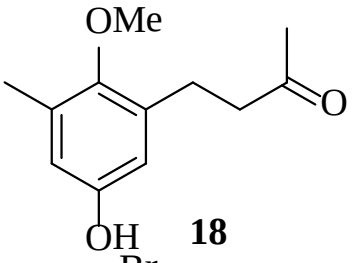

18

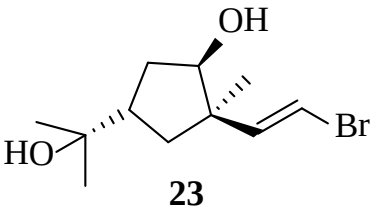

23

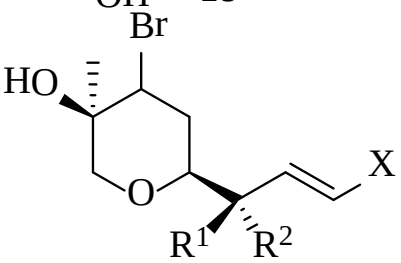

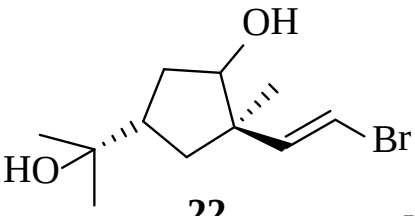

22

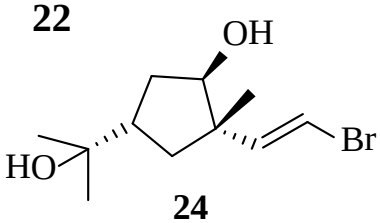

24

19 R^1=OH; R^2=Me; X=Br
20 R^1=Me; R^2=OH; X=Cl
21 R^1=OH ; R^2=Me; X=Cl

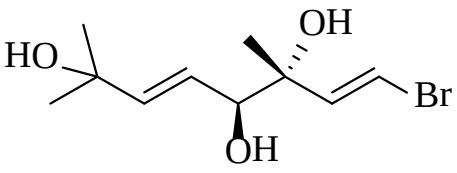

25

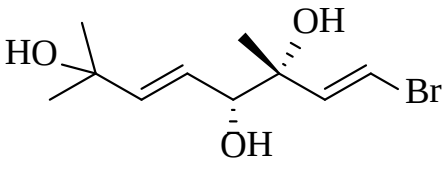

26

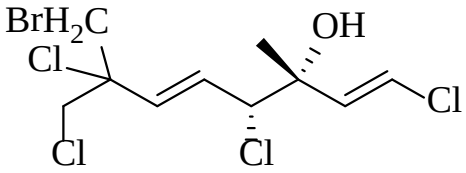

28

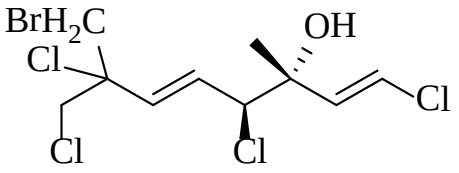

27

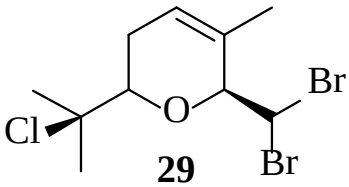

29

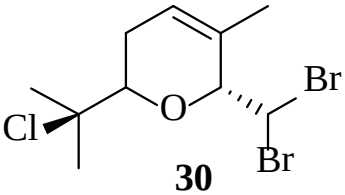

30

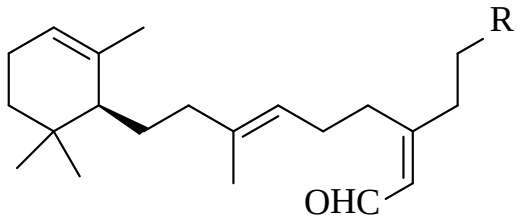

32 R=CHO

33 R=CH_2OAc

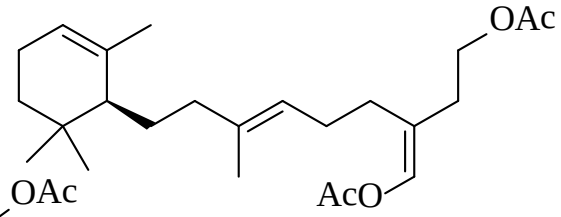

31

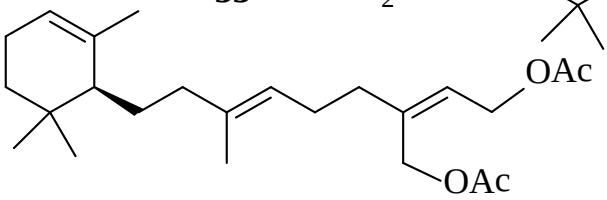

34

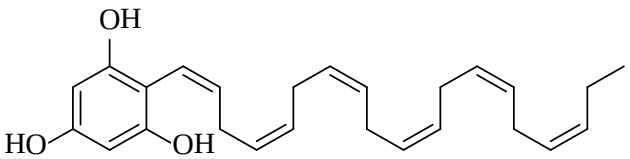

35

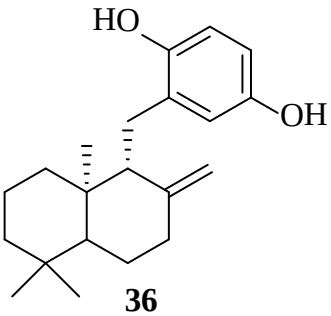

36

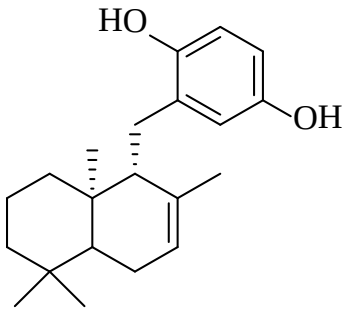

37

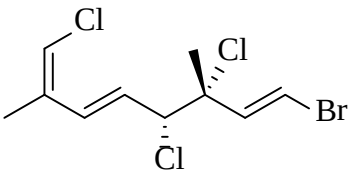

38

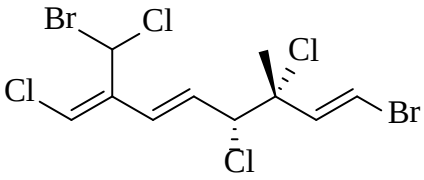

39

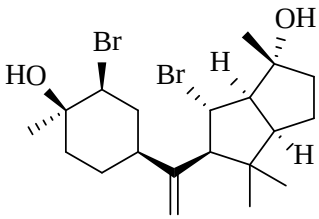

40

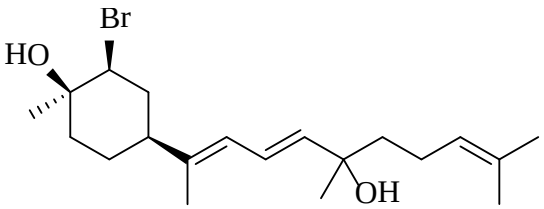

41

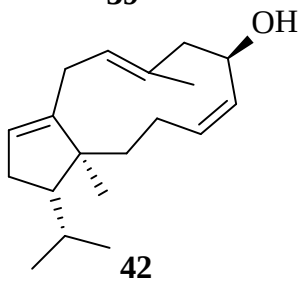

42

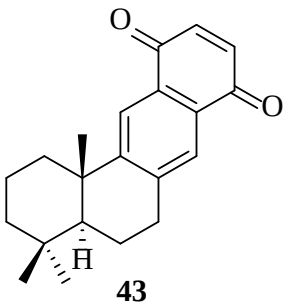

43

The polyhalogenated monoterpenes **37** and **38** were reported from an Eastern Tasmanian red seaweed *Plocamium cartilagineum*. The diterpenes neorogioldiol **39**, rogioldiol D **40** and $O^{11},^{15}$-cyclo-14-bromo-14,15-dihydrorogiol-3,11-diol **41**, were identified from *Laurencia microcladia* (Faulkner, 2002). A hydroclathrol **42**, dolabellane diterpene and enantio specific sesquiterpene benzoquinone (+)-cyclozonarone **43** were identified from the brown seaweeds *Hydroclathrus tenuis* and *Dictyopteris undulata*, respectively. New acyclic diterpenes **44-47** was documented from the seaweed *Bifurcaria bifurcata* (from the Atlantic coast of Morocco). The sesquiterpene 8-bromochamigren-1-en **48** was isolated from the red seaweed *Laurencia majuscula* (from the South China Sea) (Blunt et al., 2003). Novel antibacterial halogenated sesquiterpenes analogues, pannosanol **49** and pannosane **50** were isolated from red seaweed *Laurencia pannosa* (from Malaysia) (Blunt et al., 2003).

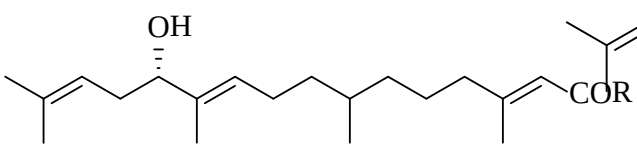

44 R=OMe
45 R=H

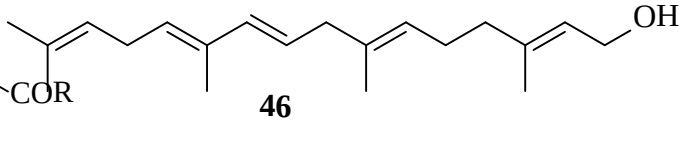

46

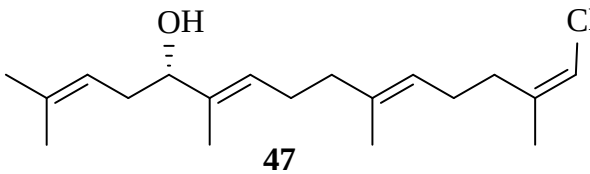

47

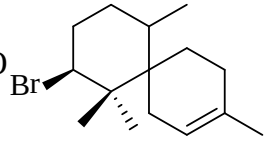

48

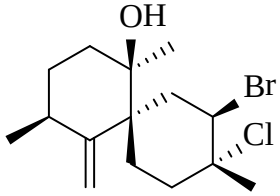

49

Five brominated sesquiterpenes isopalisol **51**, luzonensol **52**, luzonensol acetate **53**, luzonensin **54** and (3*Z*,6*E*)-1-bromo-2-hydroxy-3,7,11-trimethyldodeca-3,6,10-triene **55**, and a bromoditerpene 3-bromobarekoxide **56** were isolated from the seaweed species *Laurencia. luzonensis* (from Okinawan waters) (Blunt et al., 2003). Sesquiterpenes, such as scopariol **57** with reorganized chamigrane skeletal structure, isorigidol **58**, is a β-chamigrene, which were isolated from *L. scoparia* (collected from Brazilian waters). Squalene-derived four triterpenes pseudodehydrothyrsiferol **59**, martiriol **60**, dioxepandehydrothyrsiferol **61** as well as 16-epihydroxydehydrothyrsiferol **62** were isolated from *L. viridis* (Canary Islands) (Blunt et al., 2003). Another sesquiterpene, Calenzanol **63**, with novel ring system was obtained from of *L. microcladia* (Elba Island in the Mediterranean). The sesquiterpene with halogenation (6R,9R,10S)-10-bromo-9-hydroxychamigra-2,7(14)-diene **64** was derived from the Okinawan red seaweed *L. majuscula*. These compounds were found to exhibit prospective antibacterial activity (Blunt et al., 2003). Brominated diterpenes, Prevezols A **65** and B **66** were isolated from *L. obtusa* that was collected from the Greek waters. Bomotriterpene polyether analogues, armatols A-F **67-72** were identified from *Chondria armata* collected from the Indian Ocean. The homosesquiterpenic acids **73-76**, are polyhalogenated terpenes, which were isolated from *P. cartilagineum* (from the Mediterranean). Similarly, bromoditerpenes, sphaerolabdiene-3,14-diol **77** and bromosphaerone **78**, were isolated from a collection of *Sphaerococcus coronopifolius* from the Atlantic coast of Morocco (Blunt et al., 2003).

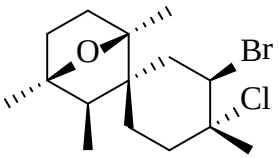

50

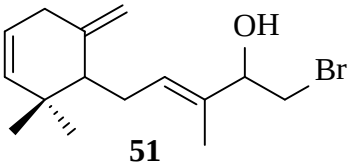

51

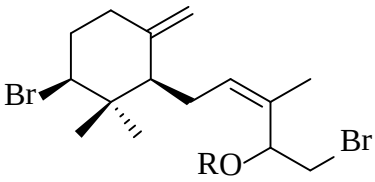

52 R=H
53 R=Ac

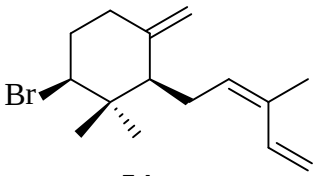

54

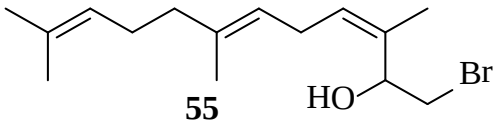

55

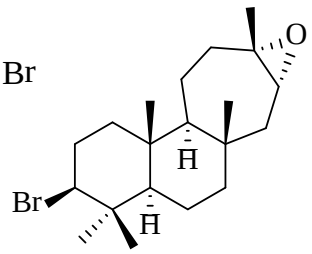

56

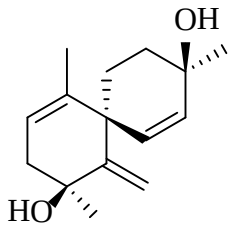

57

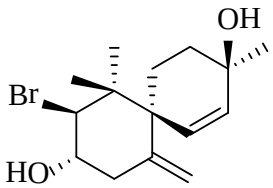

58

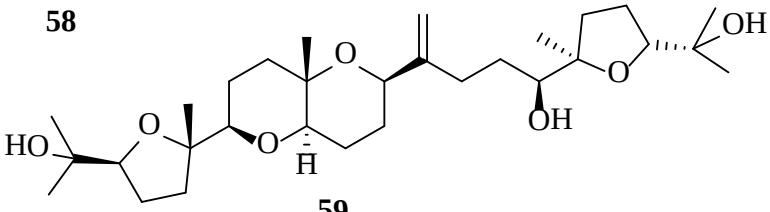

59

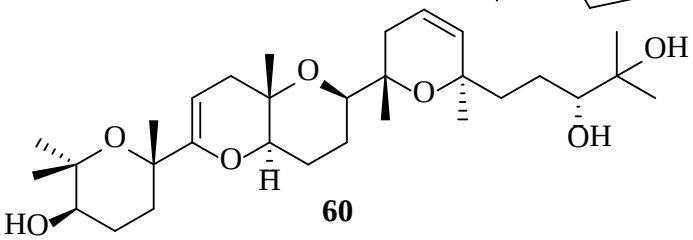

60

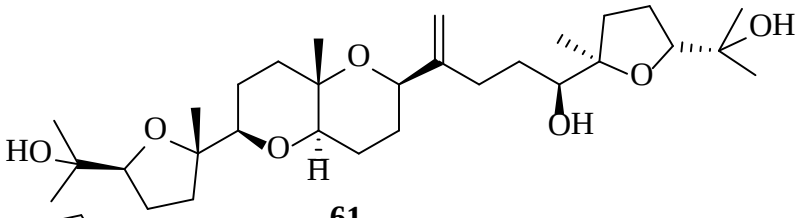

61

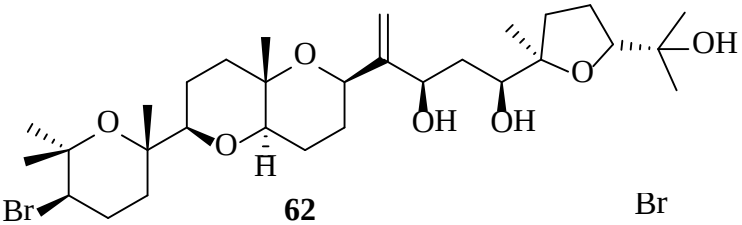

62

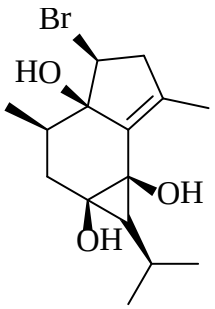

63

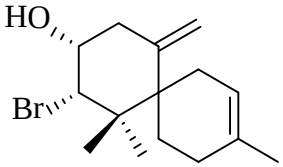

64

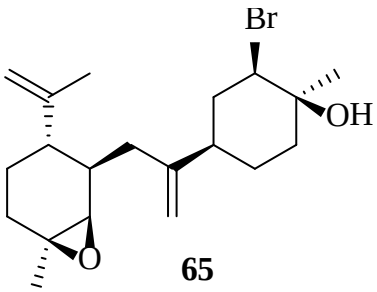

65

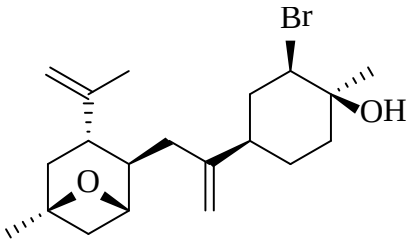

66

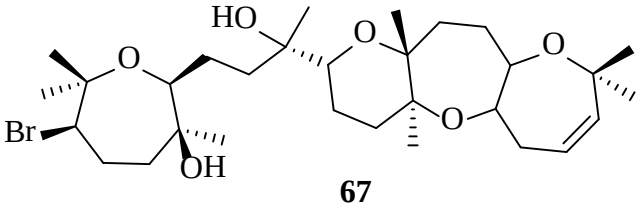

67

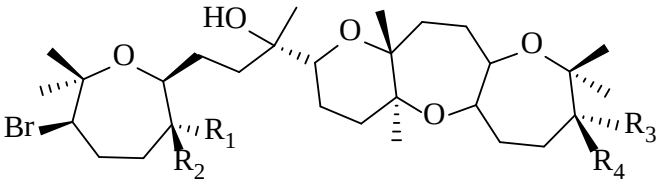

68 R_1=Me, R_2=OH, R_3=Br, R_4=H
69 R_1=OH, R_2=Me, R_3=Br, R_4=H
70 R_1=Me, R_2=OH, R_3=H, R_4=H
71 R_1=OH, R_2=Me, R_3=H, R_4=Br

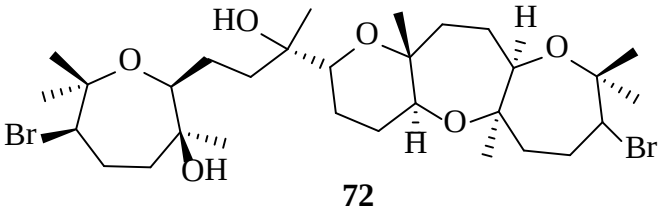

72

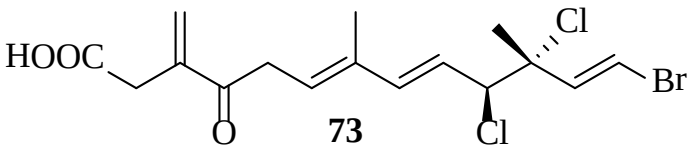

73

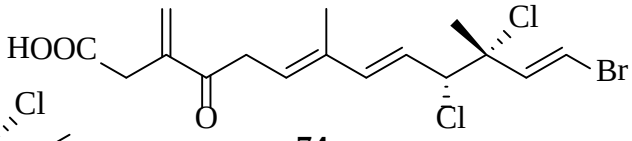

74

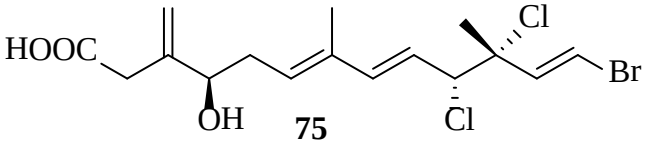

75

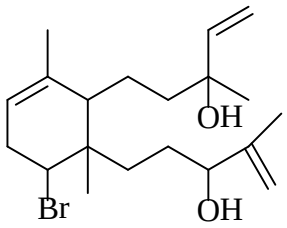

77

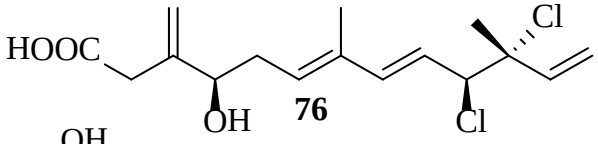

76

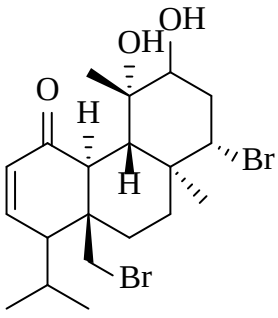

78

A diterpenoid, Stypolactone **79**, with weak *in vitro* cytotoxicity against the A-549 and H-116 cell lines, was identified from the brown seaweed *Stypopodium zonale* (Blunt et al., 2004). Novel diterpenoids, namely, dictyterpenoids A-B **80-81** have been derived from the seaweed *Dilophus okamurae*, which was harvested from the Coast of Japan Sea, and exhibited antifeedant activity (Blunt et al., 2004). Chilean red seaweed of *Plocamium cartilagineum* yielded a monoterpene, Prefuroplocamioid **82,** which is a linear polyhalohydroxylated monoterpenes, **83** and halogenated monoterpenes **84** and **85-88**. The species *L. obtusa* obtained from Coco, Cayo Cuba yielded oxachamigrene sesquiterpene **89** and 5-acetoxyoxachamigrene

90 (Blunt et al., 2004). The diterpenoids, such as seco-dolastane dichotone **91**, dichotodione **92**, dichototetraol **93** and dichopentaol **94**, and the related enone dolastane dichotenones A **95** and B **96** were reported from *D. dichotoma* collected from the Coast of Arabian Sea (Blunt et al., 2005). Novel diterpene dictyocrenulol **97** was yielded from the brown seaweed *Dictyota crenulata* obtained from the Easter Island. Other sets of terpenes like calenzanane sesquiterpene, debromoisocalenzanol **98**, indene-type sesquiterpene **99** were reported from *L. microcladia* collected from the coast of Elba Island (Blunt et al., 2005). The red seaweed *L. obtusa* collected from Bademli, Turkey was found to containsesquiterpenes, **100-103** along with the snyderol derivatives **104** and **105** (Blunt et al., 2005). *Laurencia perforata*, harvested from the Australian coast, was considered as the source of the sesquiterpenes 4-hydroxy-1,8-epi-isotenerone **106** and two 3-epi-perforenone A derivatives, **107** and **108**. Red seaweed *L. obtusa* harvested from the Greece yielded brominated diterpenes **109** and **110**. The red seaweed, *Portieria hornemanni*, was reported to yield monoterpenes **111-115** with potential bioactive properties (Blunt et al., 2005).

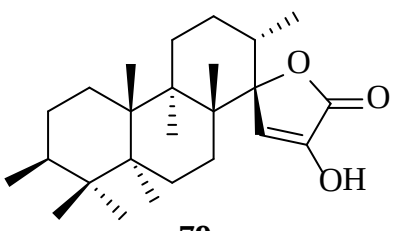

79

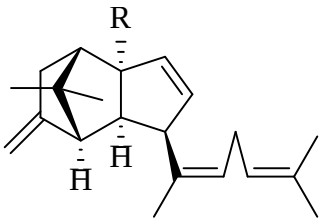

80 R=CHO
81 R=CH_2OH

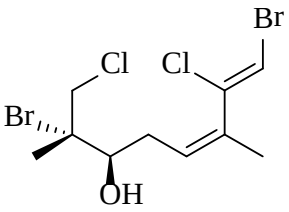

82

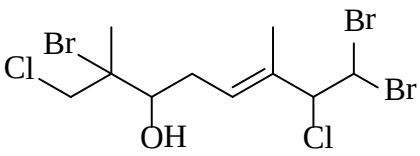

83

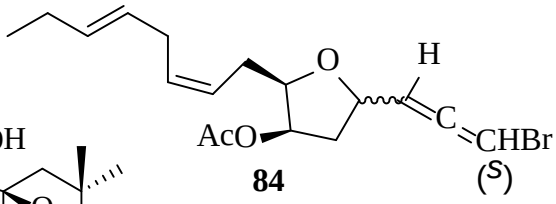

84 (S)

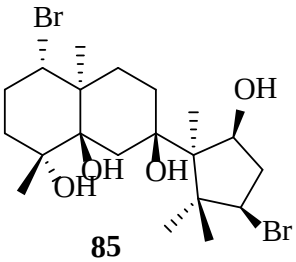

85

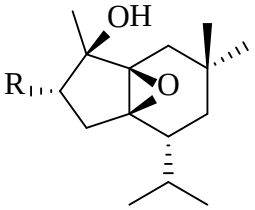

86 R=Cl
87 R=Br

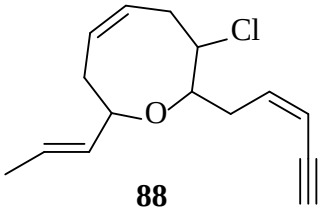

88

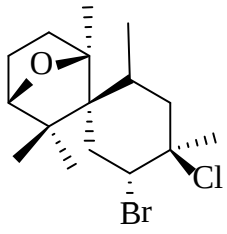

90

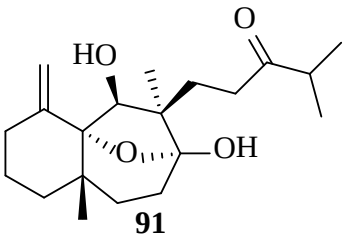

91

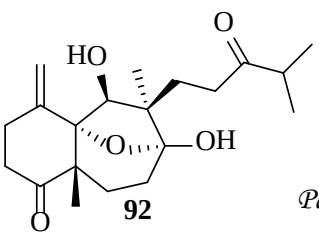

92

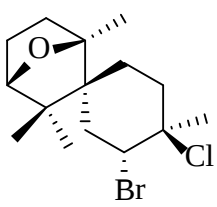

89

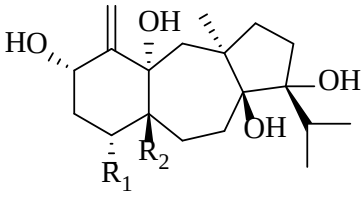

93 R=Me
94 R=CH_2OH

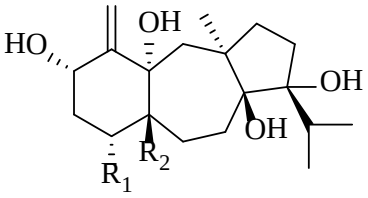

95

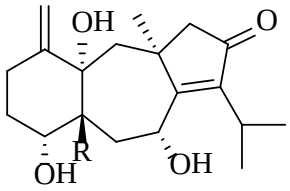

96 R=Me
97 R=OAc

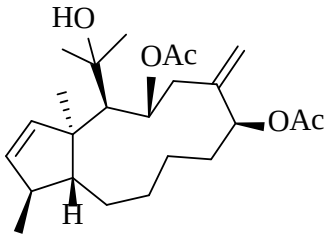

98 R=Me
99 R=OAc

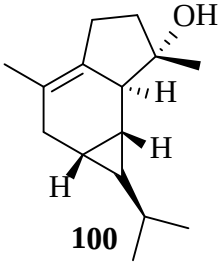

100

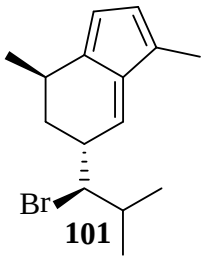

101

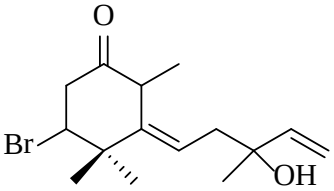

102

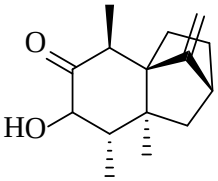

103

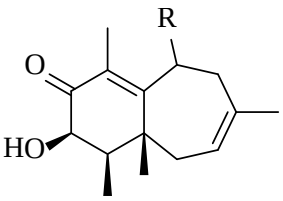

104 R=OH
105 R=H

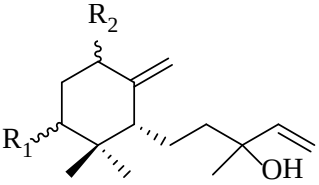

106 R_1=αBr, R_2=βBr
107 R_1=βBr, R_2=αBr

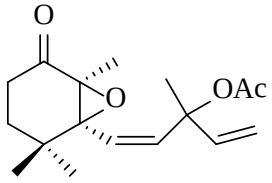

108

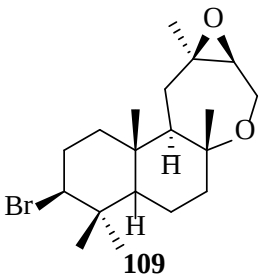

109

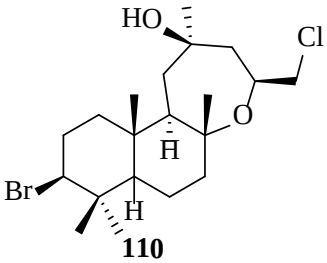

110

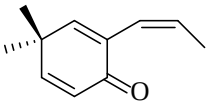

114 R=Br
115 R=Cl

The organic extract of the species *Bifurcaria bifurcate*, collected from the Atlantic coast of Morocco, yielded two trihydroxylated diterpenes **116** and **117**. The diterpenes, isopachydictyolal **118**, 4a-acetyldictyodial **119**, dichotenols A-C **120-122**, and dolabelladiene derivative **123** were reported from *Dictyota dichotoma* and *Dictyota linearis*, respectively

(Blunt et al., 2006). The brown seaweed *Stypopodium flabelliforme* collected from Papua New Guinea, yielded bioactive meroditerpenoids, such as 2β,3α-epitaondiol **124**, flabellinol **125**, flabellinone **126**, stypotriolaldehyde **127** stypohydroperoxide **128**, which displayed cytotoxic activity along with regulation of calcium concentrations in the cells (Blunt et al., 2007). Red seaweed *L. microcladia* collected from North Aegean Sea was found to be contain cuparene sesquiterpenes **129-131**. These were found as cytotoxic against the cancer cell lines. Other set of cuparene sesquiterpenes Laureperoxide **132**, 10-bromoisoaplysin **133**, isodebromolaurinterol **134** and 10-hydroxyisolaurene **135** were identified from the Chinese red seaweed *L. okamurai* (Blunt et al., 2007). A perhydroazulene diterpene, dictyol J **136** was identified from *D. dichotoma*. These compounds displayed algicidal activity to the bloom formation. Monoterpenes with halogenation **137-139** has been derived from *P. hornemannii* collected from Madagascar. These were found as moderate inhibitors of DNA methyl transferase-1 (Blunt et al., 2008). The bromine bearing diterpenes, 10-hydroxykahukuene B **140**, sesquiterpenes, such as 9-deoxyelatol **141** and isodactyloxene A **142** and halogenated sesquiterpenes **143** and **144** were afforded from Chinese *L. mariannensis.* The aromatic-sesquiterpene analogues **145**, **146** and **147**, cyclolaurane sesquiterpene **148** and sesquiterpene alcohol **149** were reported from *L. okamurai* obtained from China (Blunt et al., 2009). Selinane terpenes **150** and **151**, the brominated sesquiterpenoids were obtained from Chinese *Dictyopteris divaricate*. A brominated neorogioltriol **152**, exhibited analgesic property, was afforded from *L. glandulifera* (Greece) (Blunt et al., 2010). Diterpenoids, xenicanes **153** and **154** were obtained from the seaweed *Dictyota ciliolata* (Morocco). A special category of sesquiterpene hydroquinones peyssonoic acid A **155** and B **156** were characterized from *Peyssonnelia* species (Fiji). The compounds were found to inhibit the growth of the marine algal bacterial-pathogen (Blunt et al., 2012). From *Dictyota sp.* (France), dictyotadimer A **157** was isolated**,** which was an unusual diterpenoid dimer (Blunt et al., 2013). Chamigranes laurecomin sesquiterpene A-D **158-162** were obtained from *L. composita* (China), and among which, Laurecomin B was found to exhibit antifungal activity (Blunt et al., 2014). Meroditerpenoids with antioxidant activities, namely cystodione A-F **163-168** were identified from *Cystoseira usneoides* (Gibraltar Strait). The sesquiterpenes belonging to chamigrane class; yicterpene A **169** and B **170** were identified from *L. composita* (China) (Blunt et al., 2015).

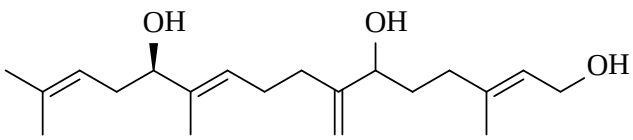

116

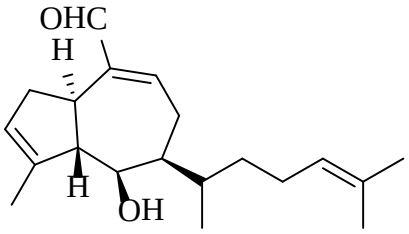

118

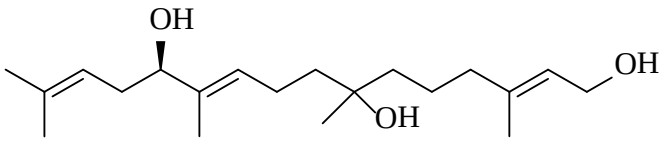

117

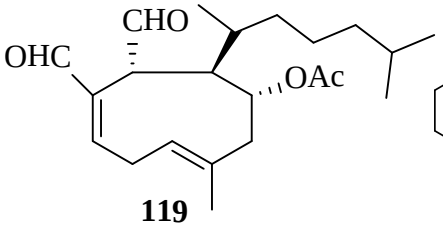

119

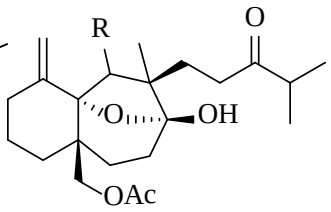

120 R=H
121 R=OH

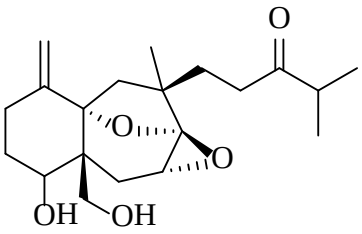

122

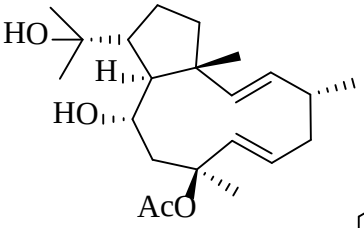

123

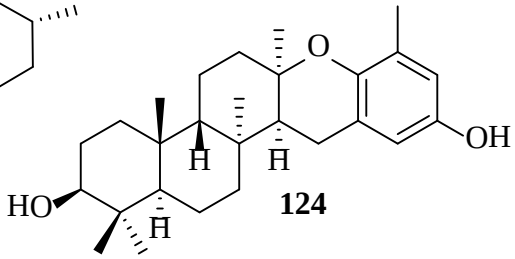

124

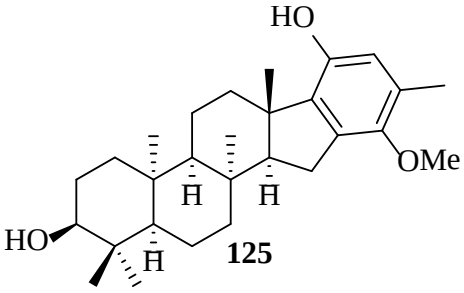

125

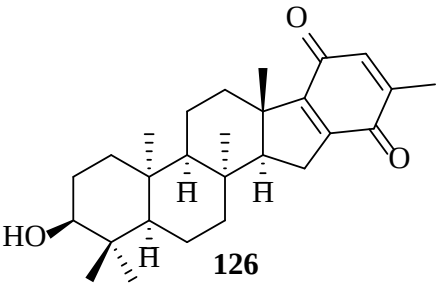

126

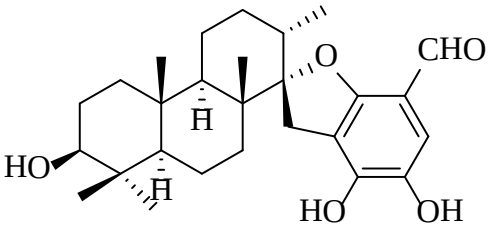

127

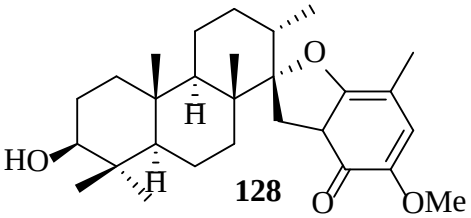

128

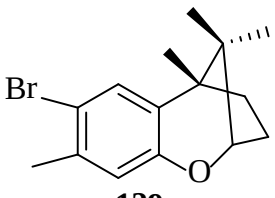

129

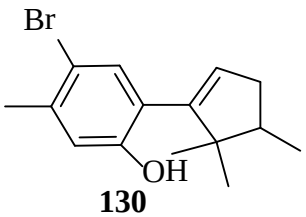

130

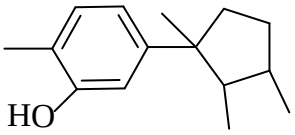

131

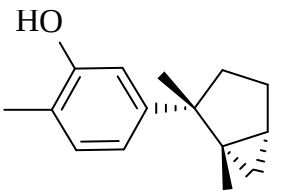

134

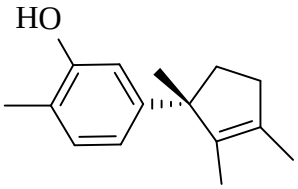

135

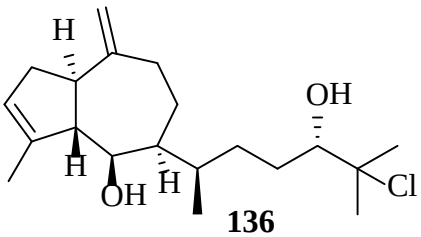

136

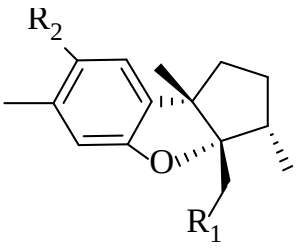

132 $R_{1=}OOH$, R_2=Br
133 R_1=R_2=Br

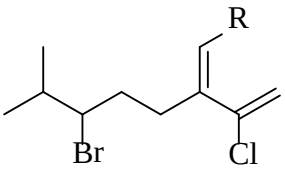

137 R=Br
138 R=Cl

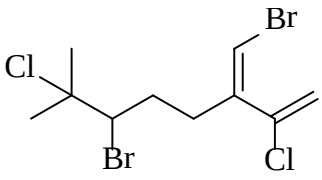

139

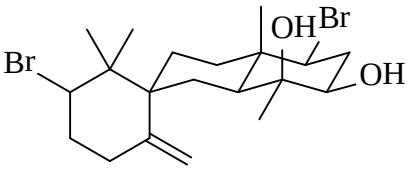

140

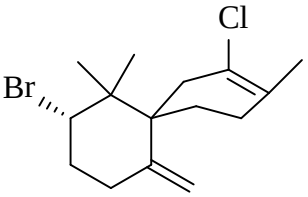

141

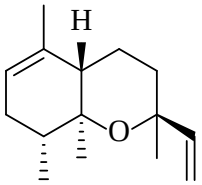

142

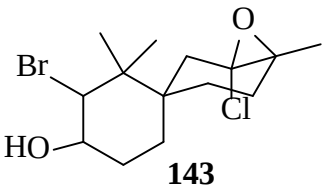

143

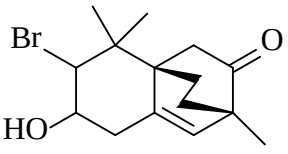

144

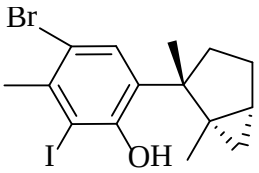

145

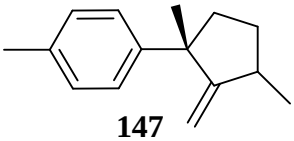

147

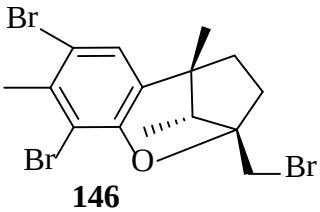

146

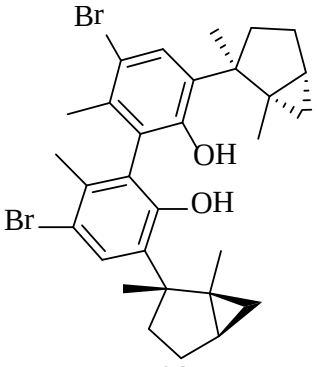

148

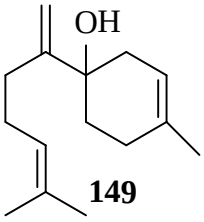

149

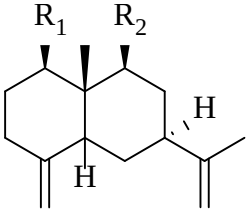

150 R_1=Br, R_2=H
151 R_1=H, R_2=Br

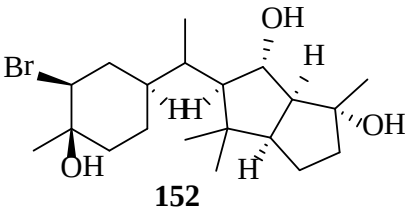

152

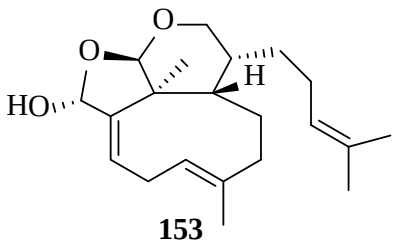

153

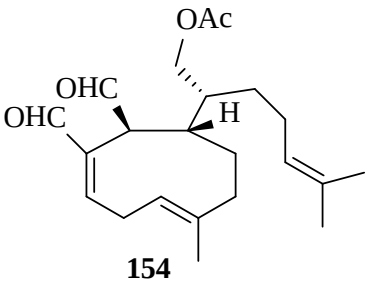

154

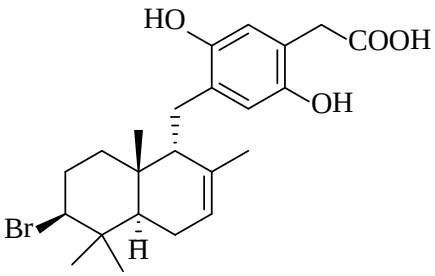

155

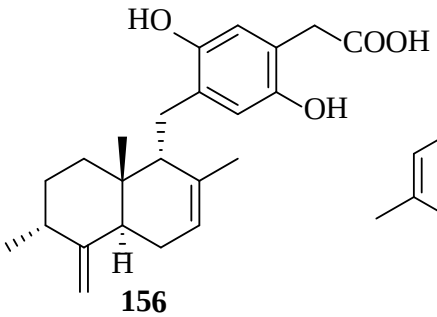

156

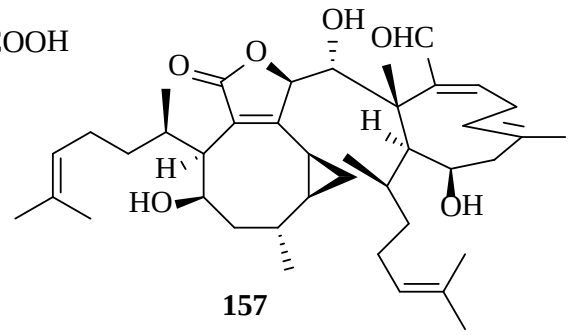

157

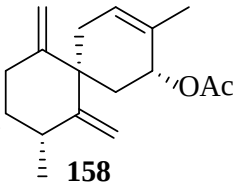

158

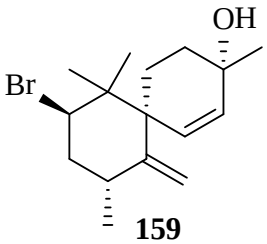

159

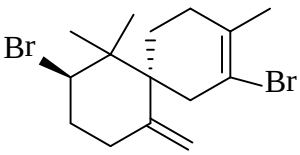

160

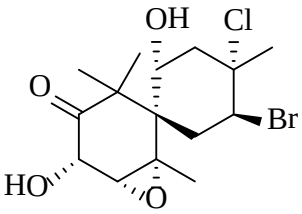

161

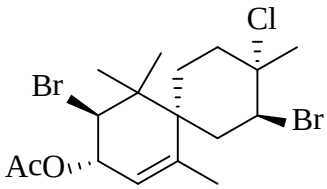

162

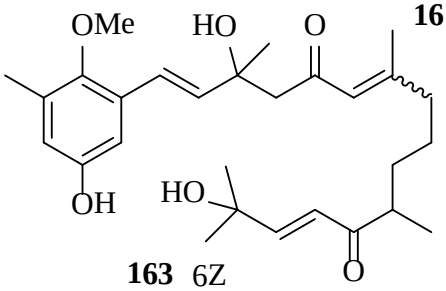

163 6Z
164 6E

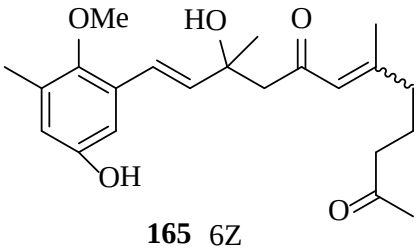

165 6Z
166 6E

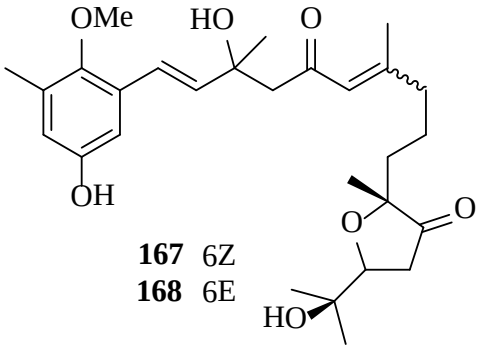

167 6Z
168 6E

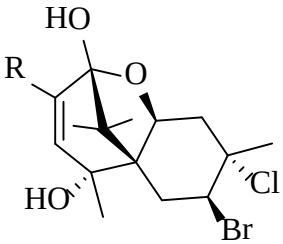

169 R=Cl
170 R=Br

2.3.1.2 Phenolic compounds

Polyphenolic compounds are considered as secondary metabolites derived by the combinations of aromatic benzene ring with more than one hydroxyl entities linked directly to the aromatic rings along with other functional moieties (Generali et al., 2019). A wide range of bioactive phenolic compounds have been identified from different marine living sources with varying structural peculiarities and bioactivities, including small molecular weight compounds to high molecular weight polymers. Phenolic compounds are used against various diseased targets due to their antioxidant potentials (Freile-Pelegrín and Robledo, 2013). Around 8000 phenolic secondary metabolites are presently known, and most of them were found to belong to the marine resources, especiallybof seaweed origin (Freile-Pelegrín and Robledo, 2013). These promising bioactive leads were biosynthesized in seaweeds by two major primary synthetic pathways, such as the acetate and shikimate pathways, and were found to produce phenolic acids to complex phlorotannins analogues (PHT). The polymerization of phloroglucinol (PG) units via the acetate-malonate/polyketide pathway leads to the formation of phlorotannins and these analogues restricted to the brown seaweeds. PHT metabolites are found to be detected in the cytoplasm, and these act as primarily constituents of the cell wall and thereby, found to act in early developmental stages to adult plants. On the basis of linkage pattern of the PG units, along with the number and the orientation of hydroxyl moieties, PHT metabolites were classified as phlorethols and fuhalols, fucols, fucophlorethols, and eckols. Among the various secondary metabolites, phenolics were considered as good free radical scavengers and reducing agents, which could interact actively with the living systems (Generali et al., 2019). They were found to exhibit potential pharmaceutical and nutraceutical application. The high concentration of polyphenolic analogues in seaweed species contributes towards the antioxidant potencies, which can reduce oxidative stress induced damages to health (Generali et al., 2019). During oxidative stress circumstances, destruction of biomolecules due to lipid peroxidation were found to be inhibited by polyphenolic metabolites and thereby, reduce the risk associated with cardiovascular diseases (CVDs) and cancers, and neurodegenerative diseases and diabetes (Freile-Pelegrín and Robledo, 2013). Phenolic terpenoids secondary metabolites have been identified from red and brown seaweeds. Phenolic compounds of meroditerpenoids including plastoquinones, chromanols, and chromenes are present in brown seaweeds. Diterpenes and sesquiterpenes obtained from the red seaweeds are examples of polyphenolic compounds. The presence of diterpene-benzoate macrolides from seaweeds also contributed towards the large number of polyphenolic compounds (Freile-Pelegrín and Robledo, 2013).

Bromophenols (BPs) are one of the phenolic compounds derived from red seaweeds with potential antioxidant activity. For example, BPs **171-175**, which were identified from the

species of red seaweeds *Symphyocladia latiuscula* displayed DPPH radical scavenging potencies. BPs identified from the brown seaweed *Leathesia nana*, **176-180,** exhibited cytotoxic properties against various cell lines of human cancer (Liu et al., 2011). Phlorotannins of eckol-type, **181-182**, **183-187** and **188** were identified from the brown seaweeds *Eisenia bicyclis* and *E. arbores*, respectively. Among which, **181** and **182** exhibited substantial inhibitory potential against the carbolytic enzymes. Compound **189** displayed inhibitory action on histamine discharge (Peng et al., 2015). Fuhalol-type phlorotannins, **190** and **191**, were isolated by the ethanolic extraction of the brown seaweed *Carpophyllum angustifolium*. The fucophlorethols **192-196** were derived from the seaweeds *Sargassum spinuligerum* and *Cystophora torulosa* (Peng et al., 2015). Three phlorethols **197-200** were isolated from *Sargassum spinuligerum.* A novel bromophenol **201** was identified from *Vertebrata lanosa* collected from Norway. These were found to exhibit prospective antioxidant potencies (Blunt et al., 2015). The brown seaweed *Ishige foliacea* obtained from the Jeju Island, yielded a phlorotannin octaphlorethol A **202**. This was known to exhibit antidiabetic potential by the regulation of glucose uptake. The seaweed *Ecklonia cava* also from Jeju Island yielded a new antioxidant 2,7″-phloroglucinol-6,60-bieckol **203** (Blunt et al., 2013). From the Korean species, *S. siliquastrum* (collected from Jeju Island), three sargachromanols **204-206** were isolated. These compounds displayed inhibition against radical-oxygen entities and up-regulate the level of glutathione. The Korean species, such as *Sargassum yezoense*, yielded a novel meroterphenol A-D **207-210** with potential bioactive properties. These were known to regulate energy metabolism via the activation peroxisome proliferator-activated-receptor-gamma (PPARg) (Blunt et al., 2013). The antioxidant phlorotannin, diphlorethohydroxycarmalol **211** was derived from the Japanese seaweed *Ishige okamurae.* This compound also acted as potential inhibitor of carbolytic enzymes, and thereby used to treat diabetes. The bromophenol **212** was isolated from the Chinese *Polysiphonia urceolata.* Novel nitrogen containing bromophenolic compound, colensolide A **213** was identified from *Osmundaria colensoi* (New Zealand) (Blunt et al., 2010). A new chromene, sargothunbergol A **214** with free radical scavenging activity was reported from *Sargassum thunbergii* (Youngdo Is., Busan, Korea). Bromophenols **215-217,** with C–N coupled with nucleoside base analogues were reported from the seaweed *Rhodomela confervoides* (China). Brominated tyrosine analogue **218**, bromophenols **219-221** were isolated from *Polysiphonia urceolata* (China). Brominated bis-phenols **221-223** with potent free radical scavenging potential were derived from the seaweed *Symphyocladia latiuscula* (China). Compounds **224** and **225**, bis(2,3,6-tribromo-4,5-dihydroxyphenyl)methane ether and 2,3,6-tribromo-4,5-dihydroxybenzyl methyl were identified from *Symphyocladia latiuscula* (China), as potential radical scavengers. Novel callophycoic acids A-H **226-233**, diterpene-phenols,

callophycols A and B **234** and **235**, were identified from the seaweed species *Callophycus serratus* (Fiji), whereas some of them exhibited antimalarial, antibacterial, antifungal and antitumour activity.

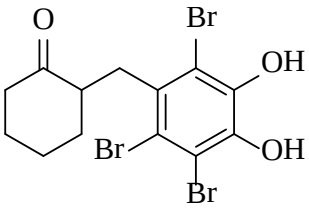

171

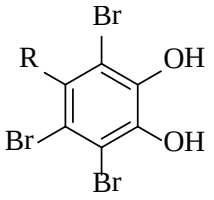

172 R=CH_2OH
173 R=CH_2OCH_3
174 R=CH_3
175 R=CHO

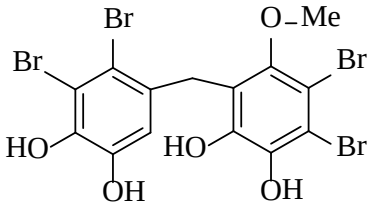

176

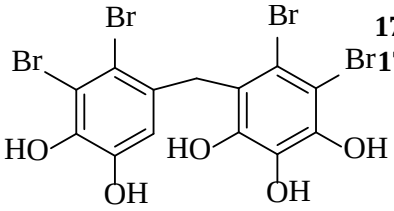

177

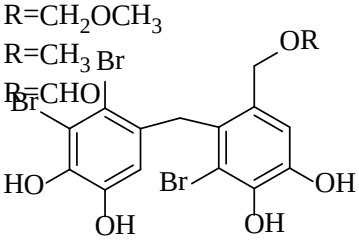

178 R=Et
179 R=Me

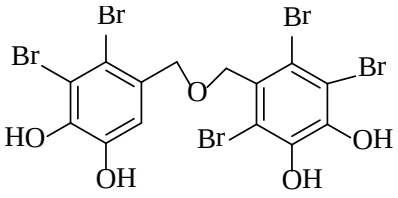

180

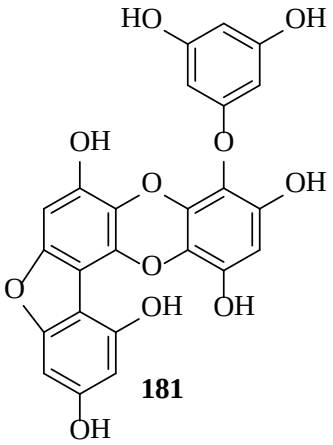

181

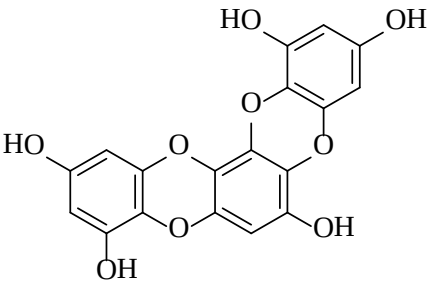

182

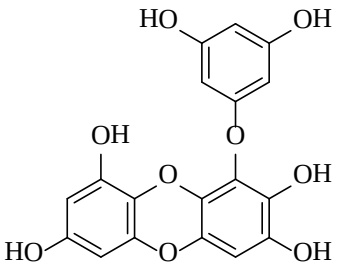

183

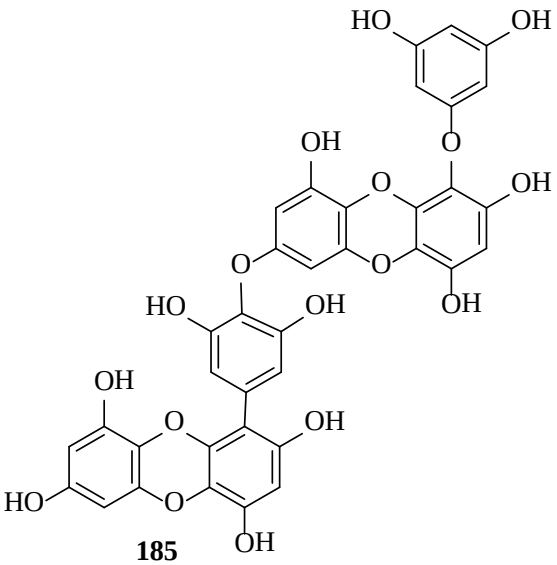

185

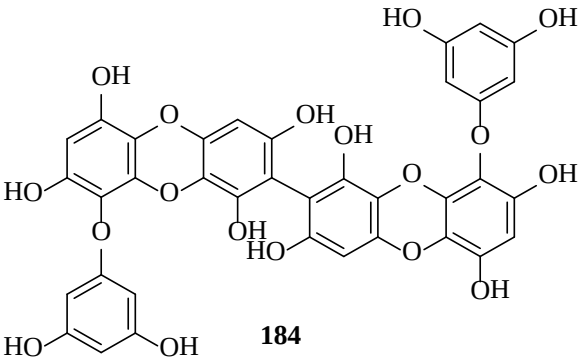

184

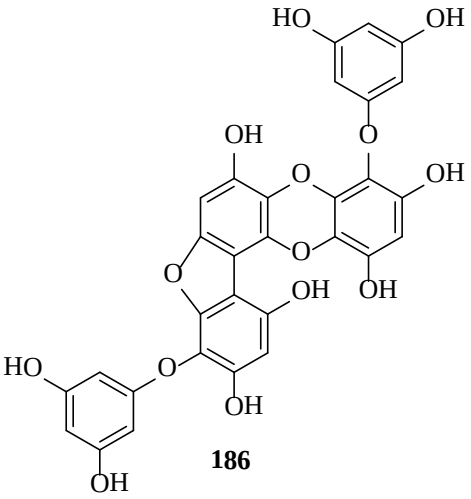

186

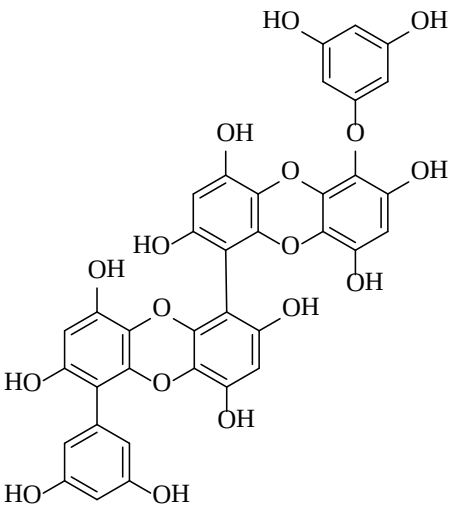

187

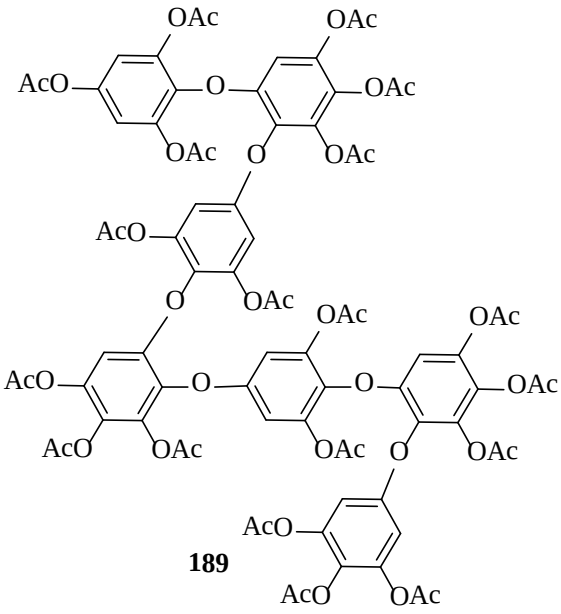

189

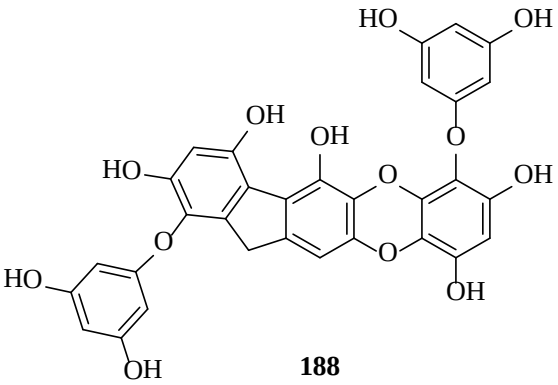

188

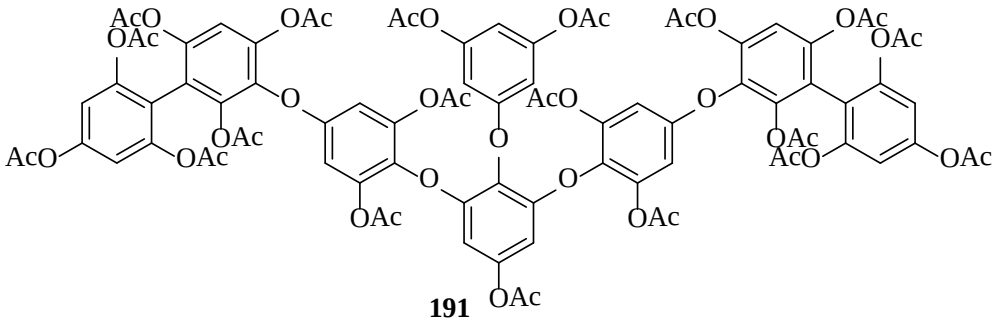

191

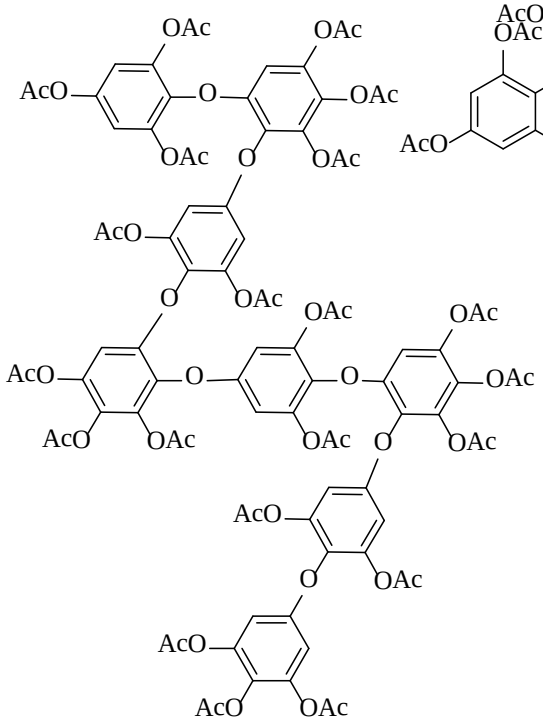

190

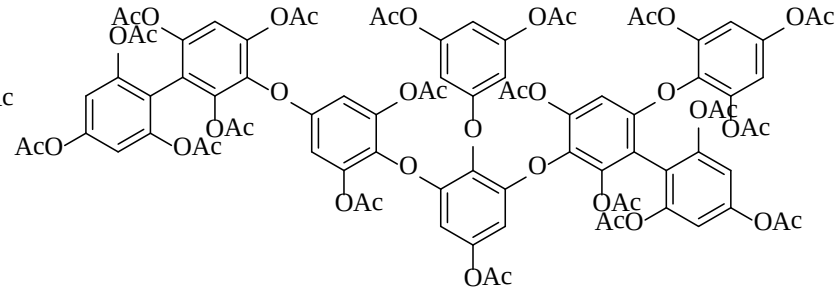

192

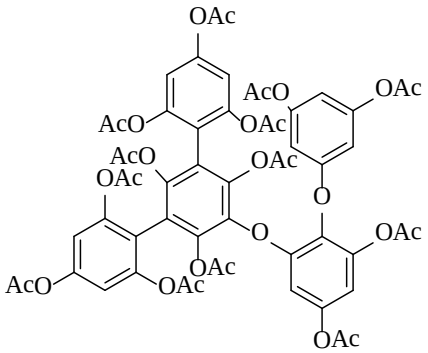

194

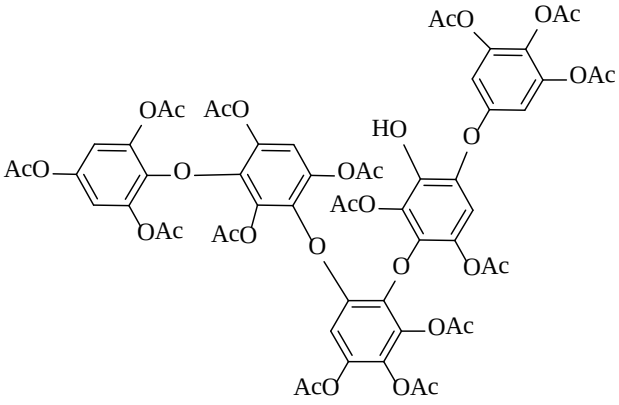

193

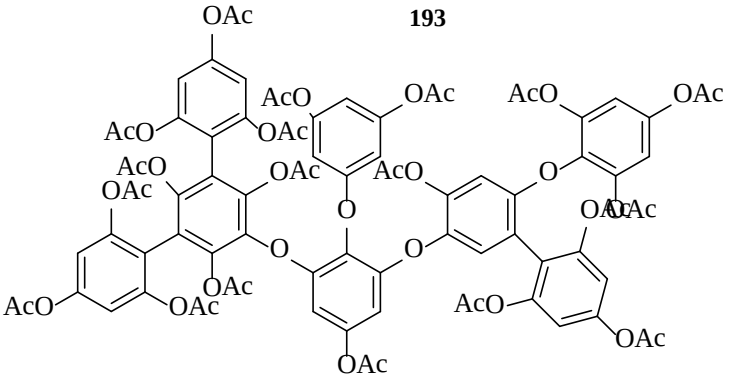

195

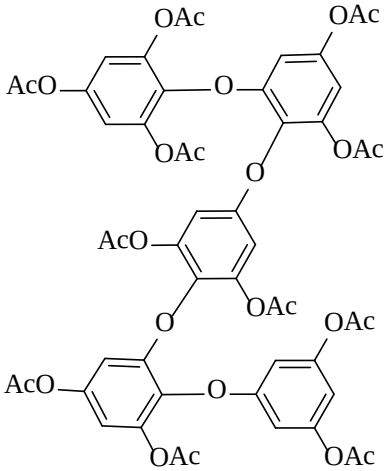

196

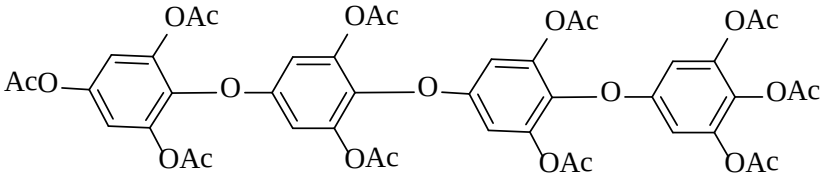

197

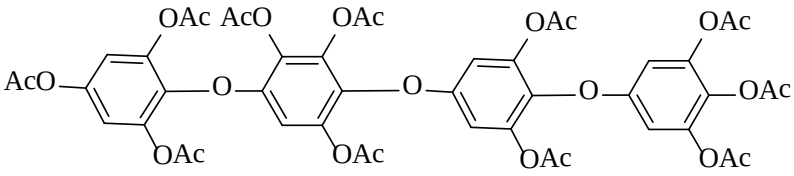

198

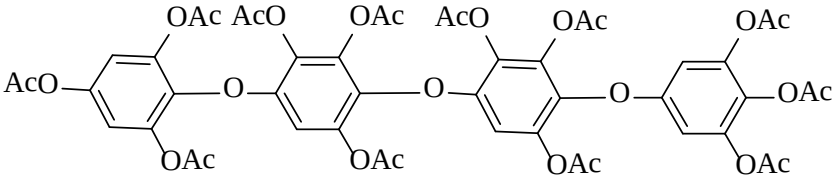

199

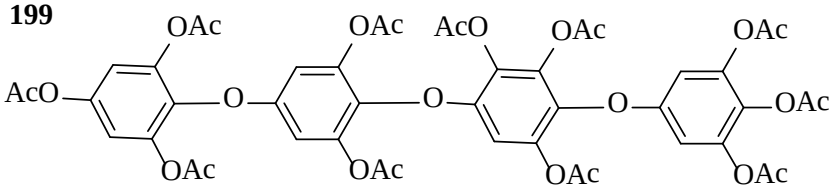

200

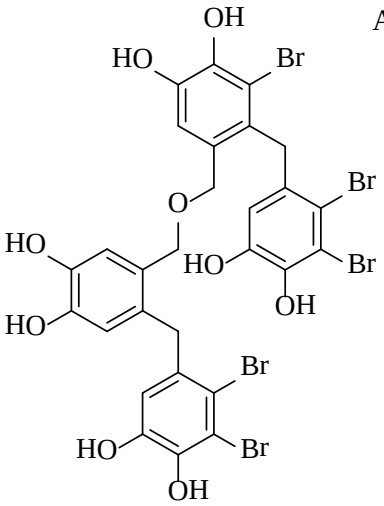

201

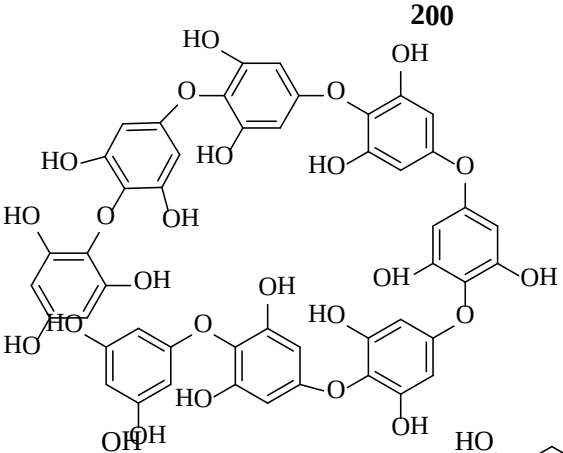

202

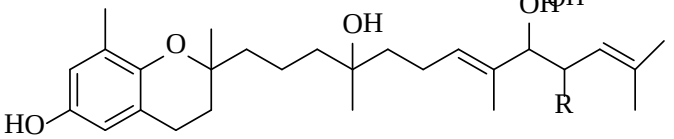

204 R=

205 R=

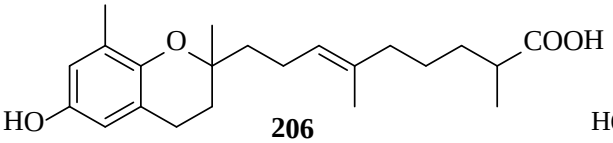

206

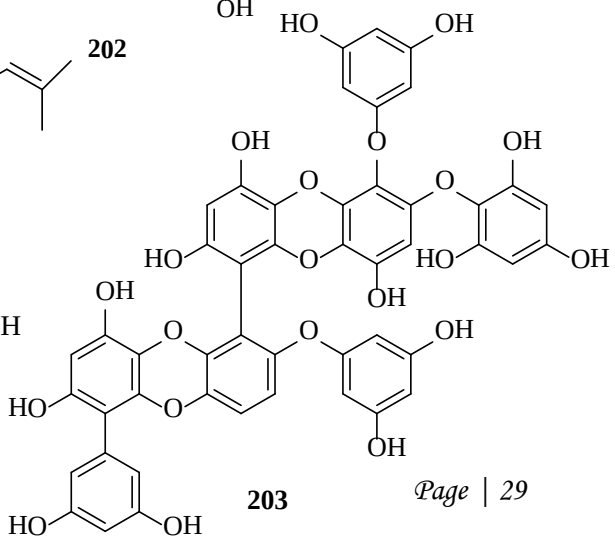

203

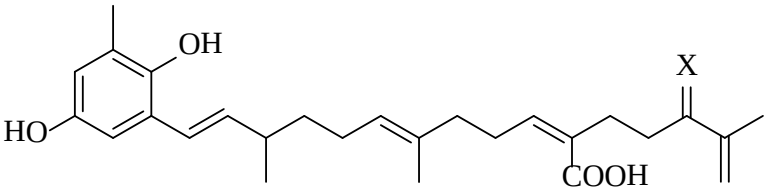

207 X= H, OH
208 X=O

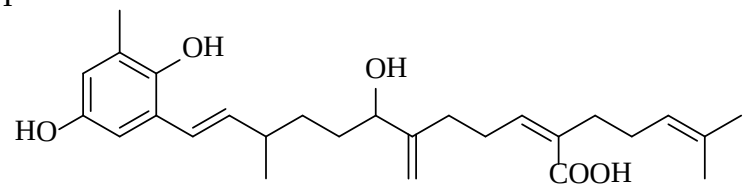

209

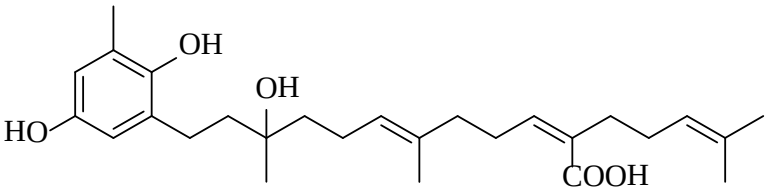

210

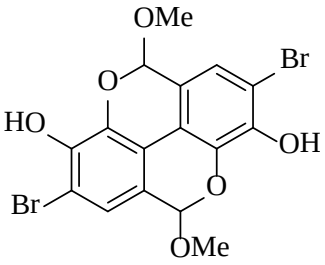

212

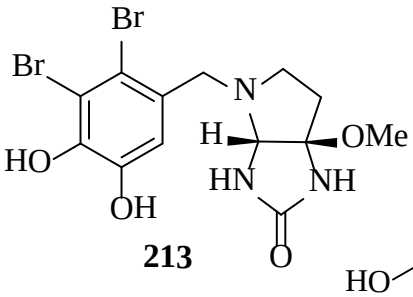

213

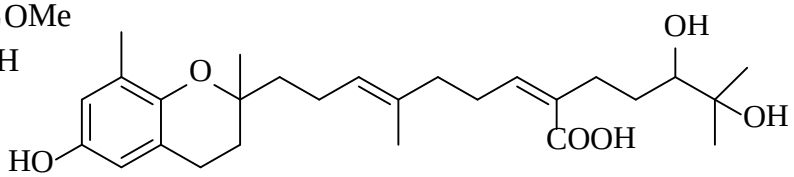

214

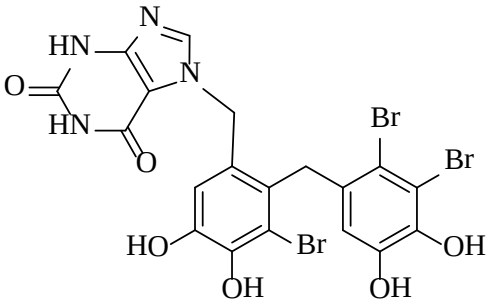

215

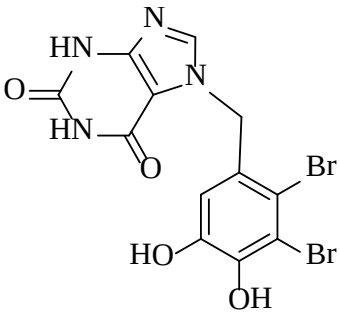

216

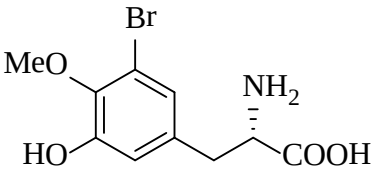

218

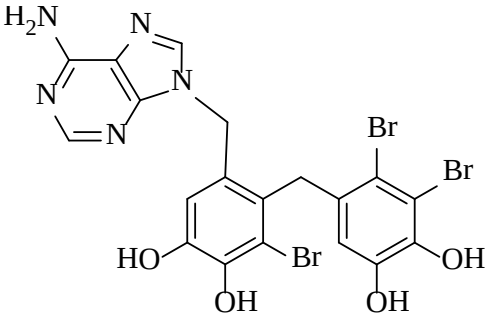

217

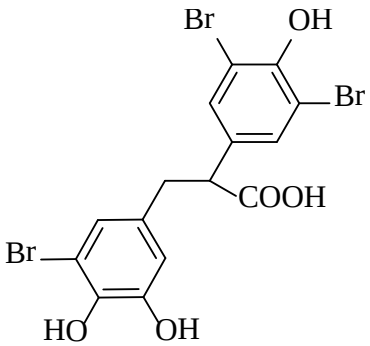

219

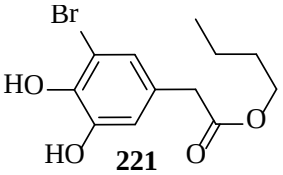

221

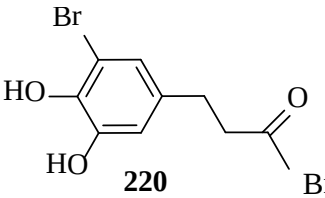

220

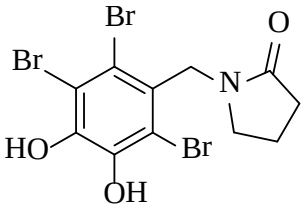

222

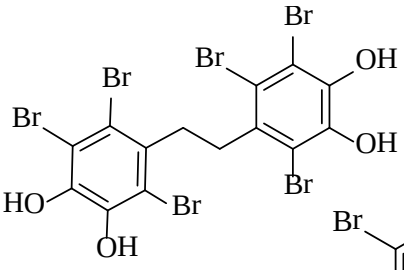

223

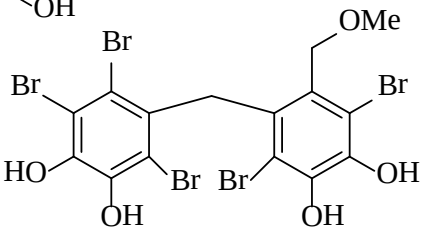

224

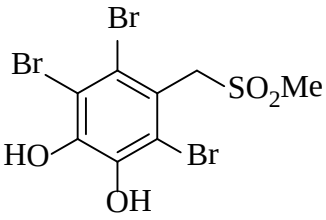

225

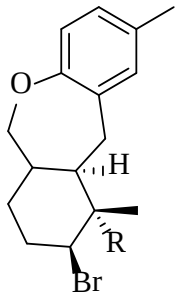

226 R= a
227 R=b

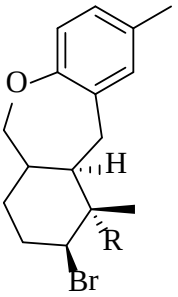

228 R= a
229 R=b

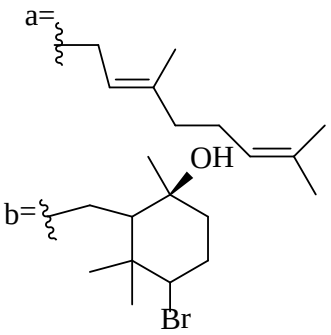

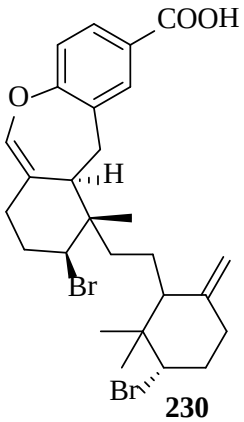

230

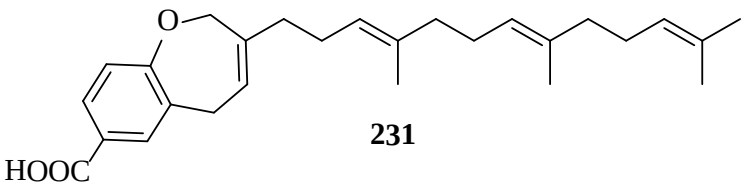

231

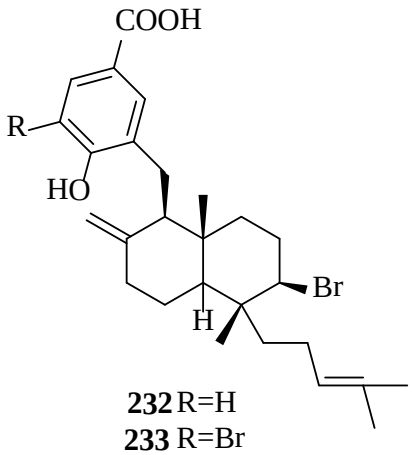

232 R=H
233 R=Br

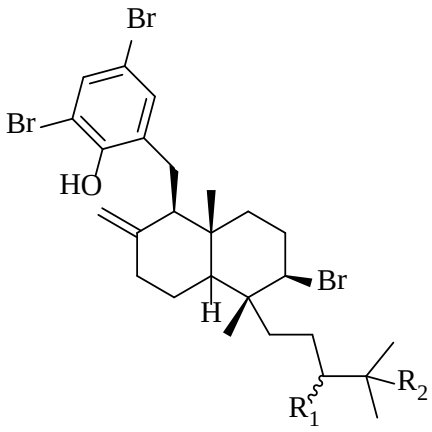

234 R_1=Br, R_2=Cl
235 R_1=Cl, R_2=Br

2.3.1.3 Steroids

Steroids are characteristic triterpene compounds with peculiar orientation of four rings of cyclo alkanes linked to each other. These were found to be derived by the cyclization of bio-precursor squalene along with a series of rearrangements including unsaturation, and substitution. Hundreds of steroidal skeletons were found to be identified from distinct marine living forms. Among which, the seaweed-derived steroids were considered to possess four different carbon skeletons, such as C26, C27, C28, and C29. The majority of red seaweeds were found to possess the carbon skeletons of C27 and C28 steroids, with small percentage of C29 steroids. Brown seaweeds were predominantly comprised of C29 steroids in higher percentage (Peng et al., 2015). These classes of terpenes were found to interact with various metabolic and physiological functions by binding with the steroid receptors (Sultan et al., 2015). Seaweeds have been considered as one of the major sources characteristic sterols with variations in the attached side chains and core skeleton (Peng et al., 2015).

The bioactive oxygenated cholesterols, such as clerosterols **235-237** were reported from green seaweed *Codium arabicum* (Faulkner, 1996). Two novel steroids, namely (20*S*)-3β,20-dihydroxyergosta-5,24(28)-dien-16-one **238** and 3β-hydroxyergosta-5,24(28)-dien-16-one **239** were obtained from the brown seaweed *Cystophora brownie*, originally harvested from the coastal location of South Australia . A cytotoxic steroid, 16β-hydroxy-5α-cholestane-3,6-dione **240** was reported from the red seaweed *Jania rubens* (collected from Tunisia) (Faulkner, 2002). A derivative of stigmastadiendiol **241** has been derived from *Laurencia majuscula* (from the South China Sea) (Blunt et al., 2003). A novel steroid, iyengadione **242** and two steroidal glycosides, iyengarosides A **243** and B **244** with moderate antibacterial activity were derived from the green seaweed *Codium iyengarii* from the coast of the Arabian Sea. A novel sterol 24-norchola-5,22-dien-3β-ol **245** has been isolated from the *Cystoseira crinite*, a brown seaweed collected from the Mediterranean region of Turkey (Blunt et al., 2004). Two new

pharmacologically active sterols **246** and **247** were separated from the seaweed *S. carpophyllum* harvested from the South China Sea. the sterol **112** isolated from seaweed exhibited cytotoxic activity against cancer cell lines. A sterol, stigmast-5,23,25-triene **248** was isolated from the seaweed *S. polycystum* harvested from North China Sea (Blunt et al., 2004). Red seaweed *Porphyridium cruentum* was found to yield inseparable mixture of steroids **249** and **250** from their sulfoglycolipidic fraction (Blunt et al., 2004).

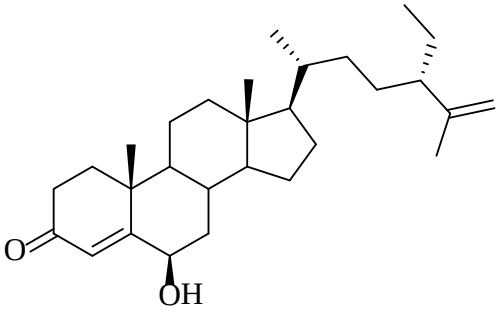

235

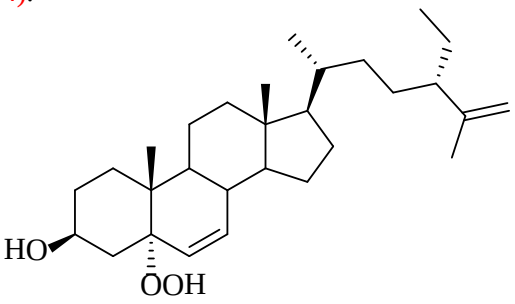

236

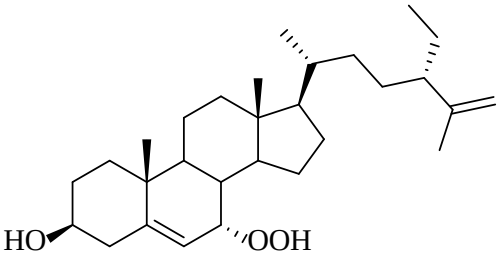

237

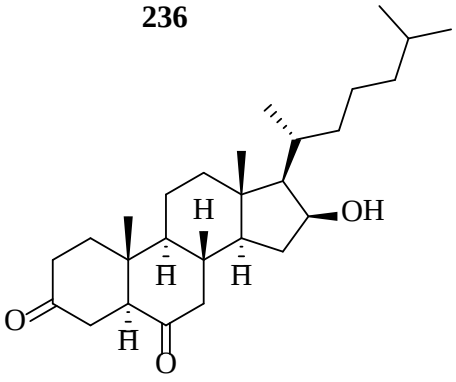

238

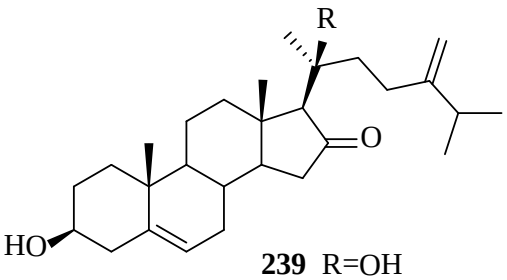

239 R=OH
240 R=H

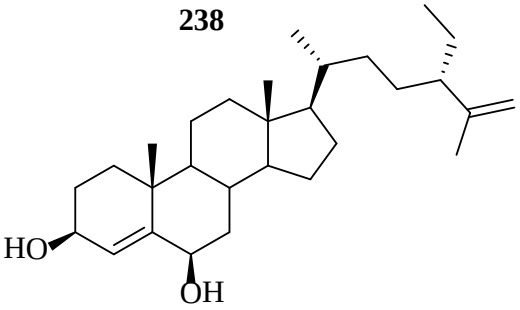

241

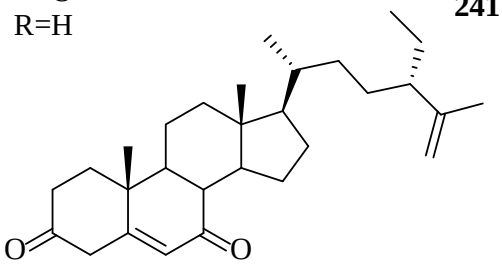

242

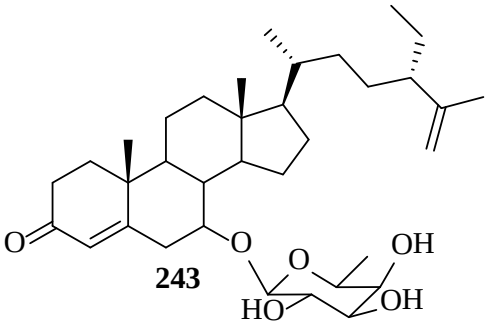

243

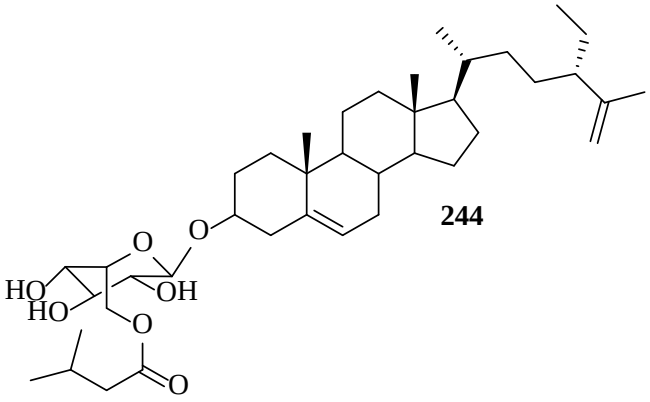

244

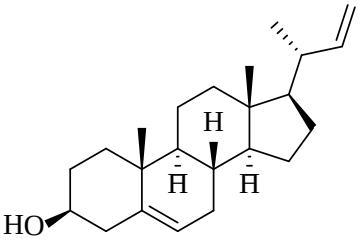

245

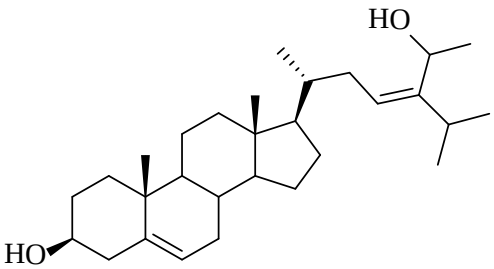

246

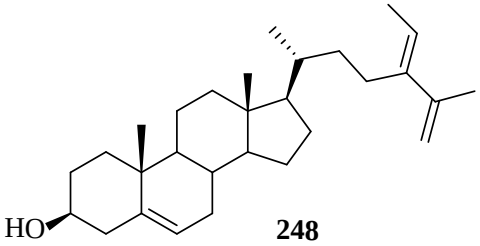

248

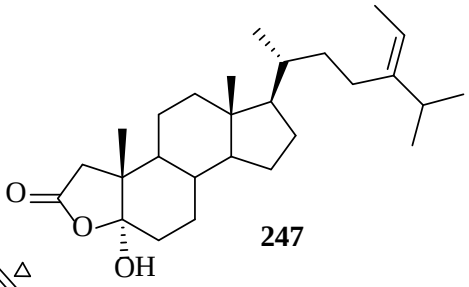

247

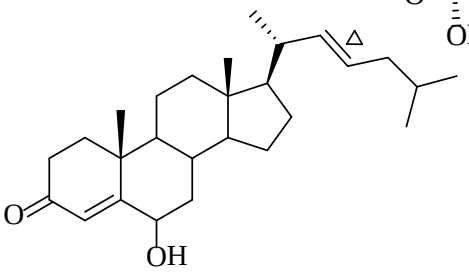

249 △ Saturated
250

2.3.1.4 Alkaloids

Alkaloids are cyclic, nitrogen containing secondary metabolites along with halogenation at different positions, and were reported to form as the part of their defensive mechanism. The presence of alkaloids in seaweeds is considered as relatively rare when compared with other terrestrial sources. However, these characteristic structural skeletons identified from the seaweeds mainly belonged to the halogenated alkaloids, indole and phenyl ethylamine groups. Among the different types of seaweeds, red seaweeds are considered as the most prominent source of alkaloids than green seaweeds, whereas least percentage of alkaloids are found in the brown seaweeds (Güven et al., 2013). .

The indole alkaloidal structures of chondriamide **251** and 3-indoleacrylamide **252** were identified with anthelmintic sactivitie, from the seaweed species, *Chondria atropurpurea* (Faulkner, 2000). Bromoindole alkaloids **253** and **254** were identified from the red seaweed *Laurencia similis* collected from China (Blunt et al., 2010). The indole alkaloid, jolynamine **255** was identified from *Jolyna laminaroides* collected from the coast of Karachi (Blunt et al., 2013). The new antifungal chloro-bisindole **256** metabolite was isolated from green seaweed *Caulerpa racemosa* (China) (Blunt et al., 2014). Halogenated alkaloids **257** was derived from the red seaweed *Laurencia brongniartii* harvested from the Caribbean and Okinawan sea (Güven et al., 2013). The alkaloid compounds **258** and **259** were identified from a red alga *Laurencia decumbens* collected from the Weizhou Island (China). The alkaloids **260**-**267** were identified from a red seaweed *Laurencia similis* harvested from Malaysia and China, respectively (Güven et al., 2013). Polyhalogenated bis-indole alkaloids **268** and **269** were identified from the green seaweeds *Chaetomorpha basiretorsa* and *Laurencia similis* harvested in China (Güven et al., 2013).

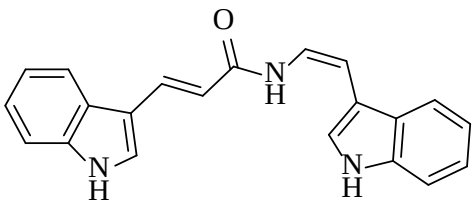

251

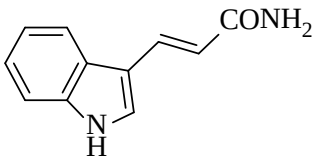

252

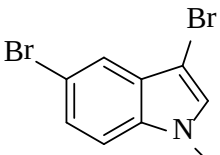

253

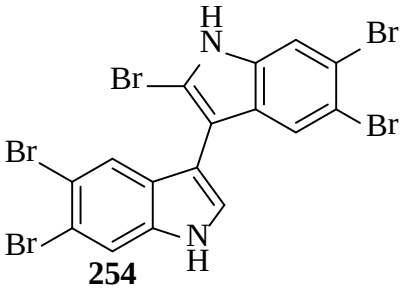

254

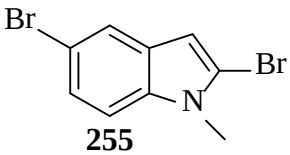

255

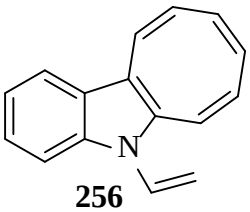

256

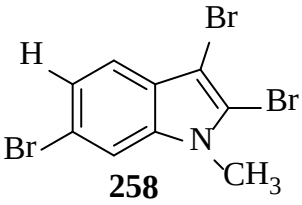

258

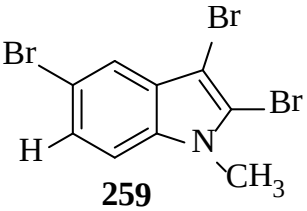

259

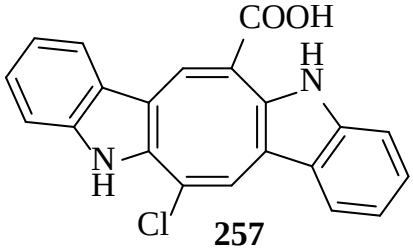

257

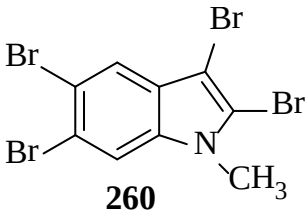

260

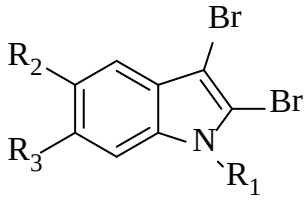

261 R_1=H; R_2=Br; R_3=Br
262 R_1=CH_3; R_2=Br; R_3=Br

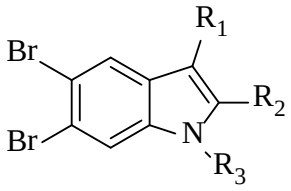

263 R_1=H; R_2=Br; R_3=H
264 R_1=Br; R_2=Br; R_3=H

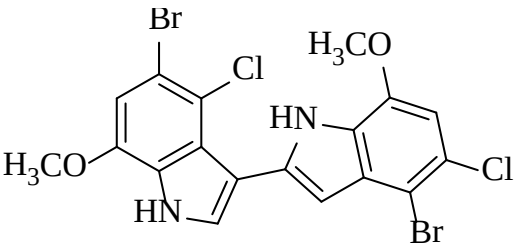

268

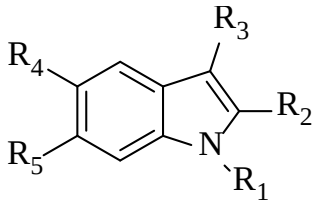

265 R_1=H; R_2=H; R_3, R_4, R_5=Br
266 R_1=CH_3; R_2=H; R_3, R_4, R_5=Br
267 R_1=CH_3; R_4=H; R_2 R_3, R_5=Br

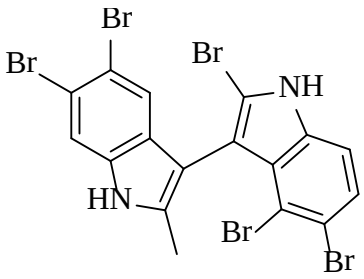

269

2.3.1.5 Lipids and fatty acids

Seaweeds are comprised of lower percentage of lipids (~5%), and thereby, they can be utilized for health benefits, such as source of food and nutrition due to the less content of energy (Peng et al., 2015). However, polyunsaturated fatty acids (PUFAs), such as eicosapentaenoic acid (EPA) and arachidonic acid (AA) were found to occupy the half of the portion of the lipids (Peng et al., 2015). The PUFAs were found to comprise greater than 18 carbons, which are essential to the nutritional benefits in human (Stengel et al., 2011). Glycoglycerolipids are significant class of membrane proteins with one or more sugar entities, which are attached to the glycerol-lipids via glycosidic bonds. These glycerol-lipids were considered to inhibit tumour cell generation (Stengel et al., 2011). Furthermore, they were found to be capable to normalize blood pressure and decrease the risk of various disorders, such as diabetes, cardiovascular diseases, and osteoporosis. Seaweed lipids and their constituents, such as phospho- and glycolipids have received greater attention owing to their prospective applications in food,

pharmaceutical, and cosmetic industries. Lipid levels and their composition in seaweeds were reported to vary according to their habitat and growth conditions (Stengel et al., 2011).

A novel polyunsaturated fatty acid, (42,72, 9E, 11E, l3 Z,16 Z,19Z)-docosaheptaenoic acid **270**, was reported from the seaweed species, *Anadyomene stellata* harvested from Florida (Faulkner, 1996). The fatty acids with methoxyl functionality, and named as 9-methoxypentadecenoic acid **271**, 9-methoxyheptadecenoic acid **272**, 13-methoxyheneicosanoic acid **273** and 15-methoxytricosanoic acid **274**, were reported from the Sicilian red seaweed species of *Schizymenia dubyi* (Faulkner, 2000). Four fatty acid derived oxylipins, named as (5R,6S,7E,9E,11Z,14Z)-5,6-dihydroxyicosa-7,9,11,14-tetraenoic acid **275**, (5R,6S,7E,9E,11Z,14Z,17Z)-5,6-dihydroxyicosa-7,9,11,14,17-pentaenoic acid **276**, (6E,8Z,11Z,14Z)-5-hydroxyicosa-6,8,11,14-tetraenoic acid **277**, and (6E,8Z,11Z,14Z,17Z)-5-hydroxyicosa-6,8,11,14,17-pentaenoic acid **278** were characterized from the red seaweed, *Rhodymenia pertusa* (Faulkner, 2002). A mixture of nitrogenous glycerolipids **279-281** was identified from the green seaweed *Ulva fasciata* from the Coast of India.

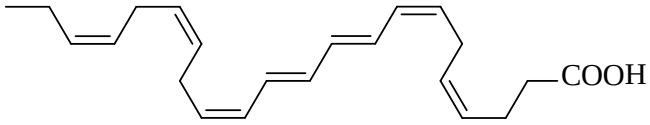

270

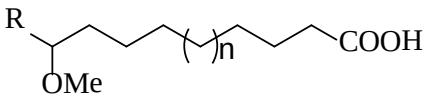

271 R=C_6H_{13}; n=1
272 R=C_8H_{17}; n=1
273 R=C_8H_{17}; n=5
274 R=C_8H_{17}; n=7

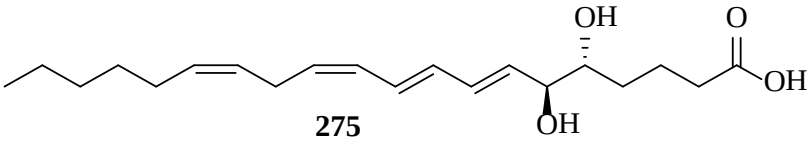

275

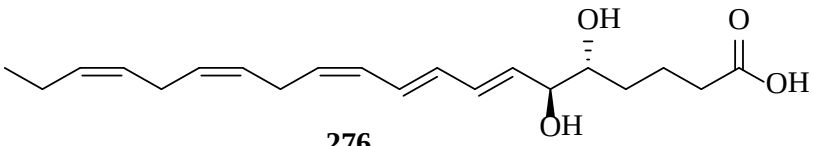

276

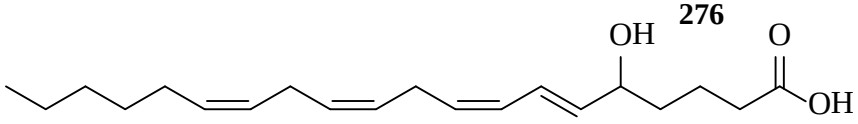

277

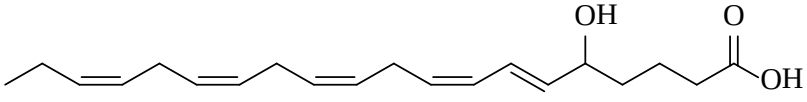

278

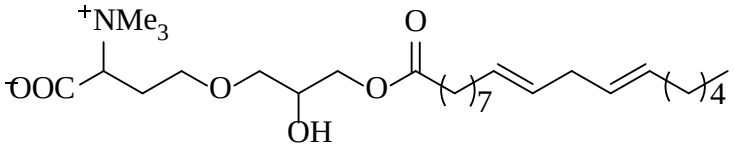

279

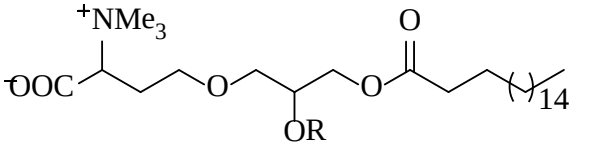

280 R=H
281 R=CO$(CH_2)_{14}CH_3$

2.1.3.6 Protein and peptides

Proteins extracted from the seaweeds were known to play prominent roles in cellular level, and they occurred in different range of forms at various locations of cells, like cell wall constituent, as enzymes, and linked to carbohydrates and pigments (Stengel et al., 2011). The distribution of proteins in seaweeds was varied by fluctuations induced by surroundings. The proteins identified from seaweed exhibited multiple bioactivities, such as the pepsin isolated from *Porphyra yezoensis* species were reported to have blood sugar reducing effect, cholesterol lowering, antioxidative activity, ACE-inhibitory potential, anti-mutagenic, inhibition effect on calcium precipitation, and activate hepatic functions (Stengel et al., 2011). In free existing form, they were found to bind with carbohydrates entities, glycoproteins, pigments, and proteoglycans; and further activating the formation of wide array of proteinaceous analogues in seaweeds. Seaweed proteins were considered as the richest source of dietary-proteins, amino acids, enzymes, peptides and bioactive lectins. The percentage of protein in seaweeds was found as almost in the range of 10-47 % of their dry weight (Stengel et al., 2011). Among the seaweeds, red seaweeds were consisted of protein around ~ 47 % dry weight; green and brown seaweeds ~26 % and ~15 % dry weight, respectively. Proteins isolated from the seaweeds possessed higher degree of digestibility. The seaweeds proteins, such as phycobiliproteins and lectins displayed several bioactivities including, anti-inflammatory, antibiotic, anti-HIV, cytotoxic, lowering pain sensitivity, anti-hypertensive activities and inhibition of platelet aggregation (Stengel et al., 2011). The depsipeptide, namely kahalalide O **282**, was isolated from the green seaweed *Bryopsis sp* (Faulkner, 2002). Two cyclic peptides such as lipopeptides mebamamide A **283** and B **284** were isolated from *Derbesia marina* (Blunt et al., 2017).

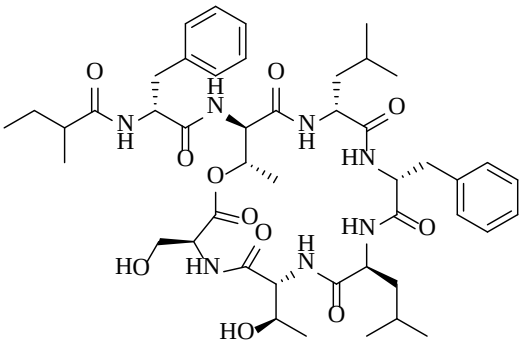

282

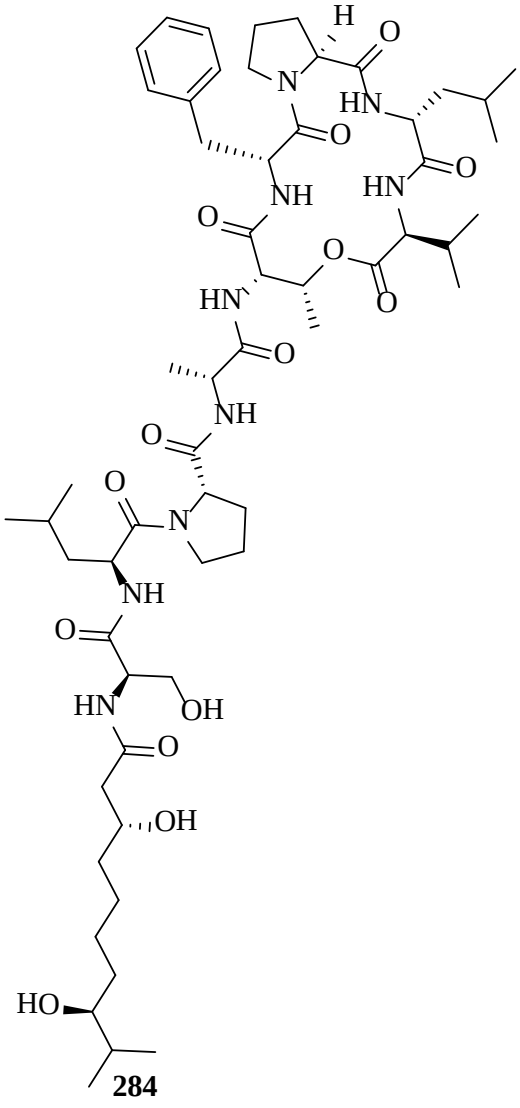

284

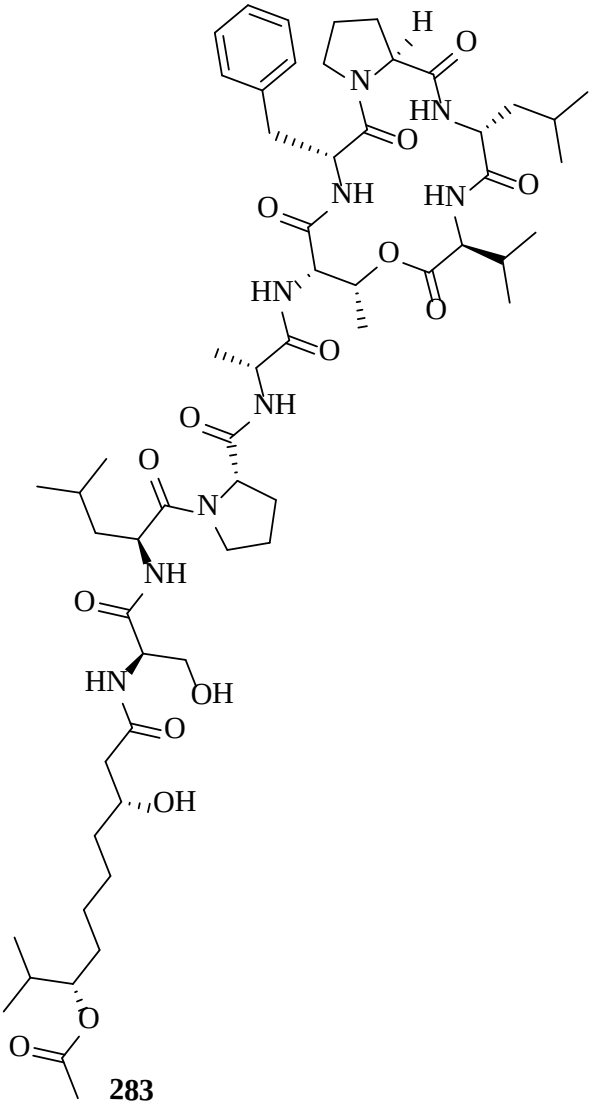

283

2.1.3.6 Polysaccharides

The polysaccharides derived from seaweeds are composed of comparatively few in numbers, even though they were found to be linked in infinite number of combination by different possible linkages with monosaccharide entities, resulting in the wide array of oligosaccharide building-blocks with structural complexities. The structural-diversity of polysaccharide analogues could be further improved by the series of chemical reactions, such as sulfation, methylation and acetylation (Wijesekara et al., 2011). Moreover, the polysaccharides derived from seaweeds were encompassed with various metabolic activities; for example, they could act as either a cell wall constituent or a storage lead molecule, and were found to be endured with several structural modifications during their formation cycle (Craigie, 1990). Because of these complex and unique structural features with multiple bioactive functionalities, seaweed polysaccharides were comprehensively exploited by food, nutraceutical, and pharmaceutical industries (Rinaudo, 2007). The physical properties of polysaccharides like solubility (Lahaye and Kaeffer, 1997), colloidal properties and gelling strength were found to be varied depending on their chemical structures. For example, the commercially relevant red seaweed phycocolloids, such as agar-agar and carrageenan **285-287** exhibited linear structures; linear galactose and anhygrogalactose repeating units of α(1→3)-(D-galactose) found in carrageenan along with sulfation at various positions and α(1→3) β (1→4)-(L-galactose) found in agars with partially methylated structures (Michel et al., 2006). Agar hydrocolloids with greater gel strength were observed in red seaweed of *Gelidium sp* (Rinaudo, 2007). Other commercially important polysaccharide alginate **288**, obtained from the brown seaweeds, also displayed particular variations in gelling strength depending on their percentage of monosaccharide units, D-mannuronic acid (M) to L-guluronic acid (G) and anionic properties (Rinaudo, 2007). Physical properties along with binding peculiarities in polysaccharides resulted in potential bioactivities, for instance, ulvan polysaccharide from green seaweeds were bound to bile acids and produce anti-hyperlipidemic effect (Yu et al., 2003).

Sulfated polysaccharides obtained from various species of seaweeds were reported to possess antioxidant potency. For instance, sulfated fucan **289** that was identified from *Fucus vesiculosus* displayed higher ferric reducing and superoxide radical scavenging properties (Jiao et al., 2011). Fucan obtained from *L. japonica* exhibited hydroxyl and superoxide radical scavenging potentials (Jiao et al., 2011). This polysaccharide also found to reduce LDL-cholesterol/triglycerides and increase HDL-cholesterol in rat model of hyperlipidemia (Jiao et al., 2011). Sulfated polysaccharide isolated from the seaweed *S. wightii* decreased hyperlipidemia in plasma (Jiao et al., 2011). The fucans reported from *S. polycystum* showed to inhibit the biosynthesis of cholesterol and triglycerides in serum (Raghavendran et al., 2005).

Sulfated galactoporphyrin from *Porphyra sp.* was reported to possess antitumor, hypotensive and anti-cholesterol activity (Raposo et al., 2015). The polysaccharide derived from *Gelidium crinale* displayed prospective anticoagulant activity (Pereira et al., 2005). The hydrocolloids, such as sulfated-agarans and hybrid DL-galactans, which were reported from *Pterocladia capillacea*, exhibited antiviral potential (Pujol et al., 1996). Sulfated-agarans and galactans extracted from the seaweed *Aghardiella tenera* showed antiviral potential (Raposo et al., 2015). The sulfated polysaccharide from *Gracilaria caudate* was found to exhibit potential antioxidant activity (Costa et al., 2010), whereas the sulfated agar and galactan isolated from *G. corticata* showed antiviral potential (Mazumder et al., 2002).

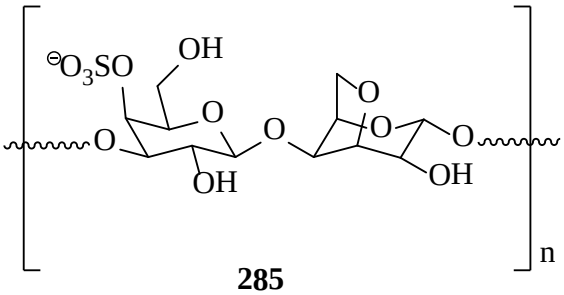

285

κ-carrageenam

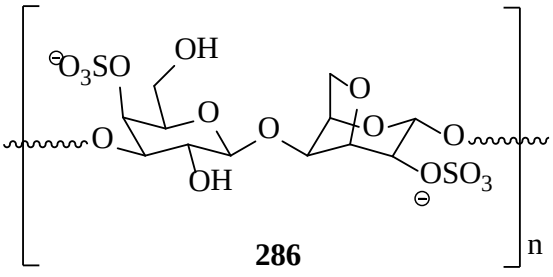

286

ι-carrageenam

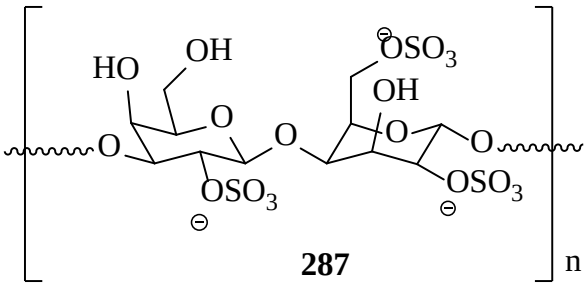

287

λ-carrageenam

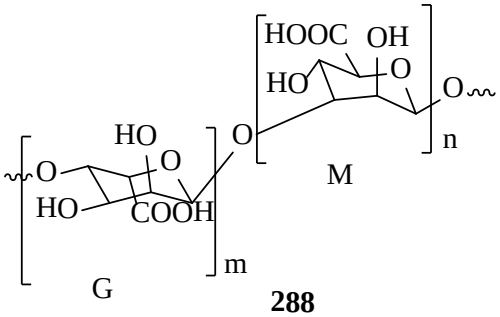

M

G

288

Repeating monosaccharide units of alginate

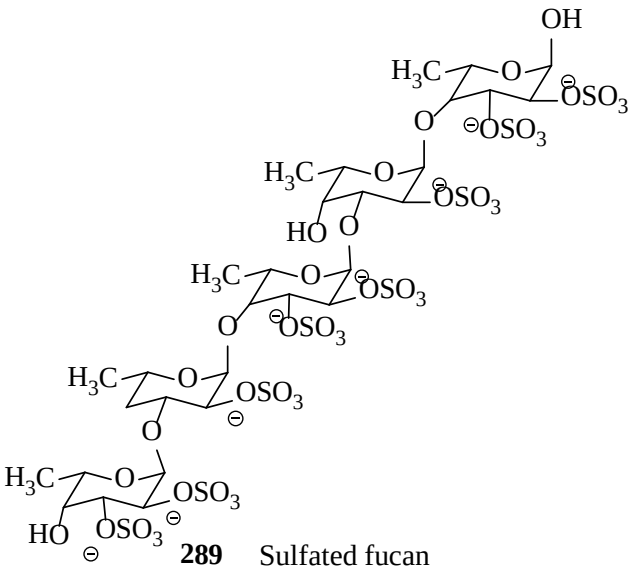

289 Sulfated fucan

2.4 Specialized bioactive secondary metabolites of seaweeds belonging to Rhodophyceae and Phaeophyceae

2.4.1 Bioactive secondary metabolites derived from seaweeds belonging to the class Rhodophyceae

Seaweeds belonging to the class of Rhodophyceae (red seaweeds, 98 %) are dynamic source of halogenated secondary metabolites, extending from terpenes, indoles, peptides, acetogenins phenolic compounds, and polyketides to volatile hydrocarbons with halogenation (Cabrita et al., 2010; Fujii et al., 2011). Furthermore, the red seaweeds produce large number of sulfated hydrocolloids (as cell wall material), and acid derivatives of nucleic and shikimate entities (Wijesekara et al., 2011; Güven et al., 2010). A wide range of pharmacological potencies were known to be related with red seaweed metabolites, such as anti-inflammatory, cytotoxic, antibacterial, antiproliferative, antifungal, antifouling, antiviral, insecticidal ichthyotoxic and antifeedant properties.

Related to applications of red seaweeds, the extracts acquired from the seaweed species *Digenea simplex* (Rhodomelaceae, Ceramiales) were utilized as a vermifuge for last dedades as the traditional medicament of Eastern region of the Asian countries (Pei-Gen & Shan-Lin, 1986). Further phytochemical analysis directed towards the separation of Kainic (KA) amino acid, recognized as the potentially active analogue in this seaweed extract, was performed. The later studies led to the re-discovery of anthelmintic KA amino acid **290**, which was found to be potential neuro-active and neuronal-glutamate-receptors (Hopkins et al., 2000; Sakai et al., 2005). The structural characteristics of KA were found to be associated with other neuronal amino acids, like domoic amino acid, separated from the extract of red seaweed *Chondria armata*, as an anthelmintic analogue (Sakai et al., 2005). Presently, kainoid derivatives have been utilized in neuro-biological study as a standardized reagent, and were found to play significant role in the treatment of neuro-physiological syndromes, such as Parkinson, Alzheimer and epilepsy (Higa & Kuniyoshi, 2000; Smit, 2004). In spite of pharmaceutical usages, the earlier studies on seaweed natural products were concentrated on halogenated secondary-metabolites, like the monoterpene analogue halomon **291**, which was identified from the species of red seaweed *Portieria hornemanni* (Clardy & Walsh, 2004; Fuller et al., 1992). This terpene displayed specific cytotoxic activity towards the tumor cells of renal, brain, and colon, and was used for the development of preclinical drug of cancer. Furthermore, halomon **291** analogue has been recognized as one of the promising secondary metabolites of seaweeds. Bicyclic diterpene, laurenditerpenol **292** was constituted as one of the potential halogenated

analogues from red seaweed. The isolation of laurenditerpenol **292** was carried out by the bioassay-assisted separation of the lipidic extract obtained from the red seaweed *Laurencia intricata*, and was found to be the first seaweed natural product that prevented the transcription factor induced by hypoxia; and as a tumor cell line-specific molecular drug target towards the development of cancer drug candidate (Chittiboyina et al., 2007; Jung & Im, 2008; Nagle & Zhou, 2009). Moreover, *Laurencia*, belonging to the family, Rhodomelaceae is the comprehensively extracted genus in the Rhodophyta phylum, and has been extensively studied over the last few years. This extensive exploration led towards the characterization of diverse array of bioactive lead molecules, such as the cytotoxic diterpene brasilenol **293**, calicladol (triterpene) **294**, antibacterial C-15 acetogenine analogues, and laurencin **295**. Additionally, with reference to red seaweed analogues, there are extensive researches related to the sulfated polysaccharides with antiviral properties (Luescher-Mattli, 2003; Campo et al., 2009). The carrageenans **285-287** were found to be the prominent sulfated-polygalactans from the red seaweeds. These polysaccharide analogues displayed potential immunomodulatory properties (Luescher-Mattli, 2003). In addition, carrageenan derived from the other families, such as *Tichocarpacea* and *Gigartinaceae*, also showed anticoagulant, antioxidant, and antithrombic properties (Sokolova et al., 2011).

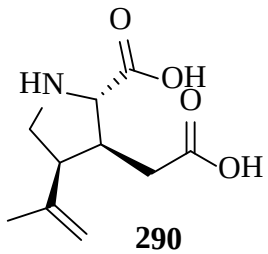

290

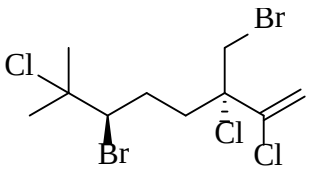

291

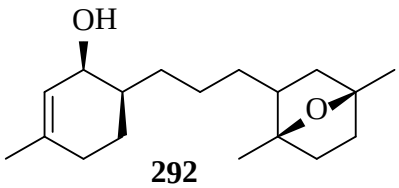

292

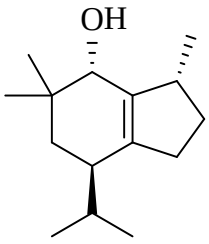

293

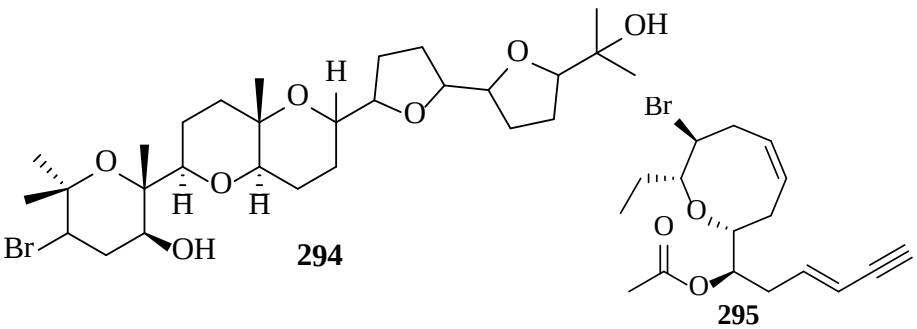

294 **295**

2.4.2 Bioactive secondary metabolites derived from seaweeds belonging to the class Phaeophyceae

The phylum Phaeophyta (brown seaweeds), which are known to be prolific producers of bioactive metabolites, was reported to produce derivatives of isoprene entities, as one of the

predominant bioactive metabolites (McClintock & Baker, 2001). Besides the large number of unique structures of terpenoids biosynthesized by the brown seaweeds, the volatile hydrocarbons, fucan polysaccharides, phlorotannins and fucoxanthins along with bioactivities, such as antioxidant, antibiotic, antifungal, antiviral, and anti-cancer activities, were also reported (Folmer et al., 2010). The major volatile metabolites derived from the brown seaweeds were recognized as cyclic or acyclic, which arose from the modification of long chain fatty acids. These compounds and their decomposition products were involved in chemical defense mechanism. For example, dictyotene **296**, which is an algal pheromone, was isolated from *Dictyota sp*., , and was used in the chemical defensive system (McClintock & Baker, 2001; Rui & Boland, 2010).

Bioactive phenolic compounds were recognized as one of the significant bioactive leads from brown seaweeds. For instance, phlorotannins isolated from brown seaweeds of family Laminariaceae, and these tannin derivatives were resulted by the polymerization of phloroglucinol moieties (Thomas & Kim, 2011; Wijesinghe & Jeon, 2011). Most of these compounds are used in the formulation of pharmacophores due to their bioactive potencies including antioxidant, anti-inflammatory, antihypertensive, antitumor, antidiabetic, and anti-allergic activities (Thomas & Kim, 2011). Currently, alginate **288** and some of the phlorotannin metabolites, such as, dieckol **297** and fucoxanthins **298** were used as the promising potentials for anti-aging and whitening formulations due their photo-oxidative stress and tyrosinase inhibitory properties (Heo et al., 2009; Li et al., 2009; Wijesinghe & Jeon, 2011). Recently, the antiviral diterpene **299** and antioxidant diterpene amijiol acetate **300** were reported from the brown seaweeds *Dictyota menstrualis* and *Dictyota dichotoma*, respectively (Cavalcanti et al., 2011; Ayyad et al. 2011). Antioxidative diterpene with 2,6-cycloxenicane moiety **301**, was reported from *Dilophus fasciola* and *Dilophus spiralis* (Ioannou et al., 2009). The cytotoxic bisprenylated quinol **302**, antiviral dolastane diterpenes, and anti-diabetic phlorotannins were reported from *Sporochnus comosus*, *Canistrocarpus cervicornis* and *Ecklonia stolonifera*, respectively (Oveden et al. 2011; Vallim et al., 2010; Moon et al., 2011). Polysaccharide fucoidans with antiviral activity were isolated from the brown seaweed *Cladosiphon okamuranus* (Phaeophyceae) (Hidari et al. 2008).

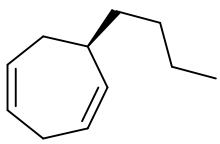

296

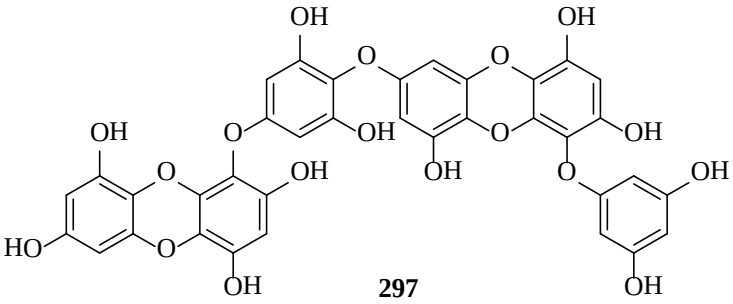

297

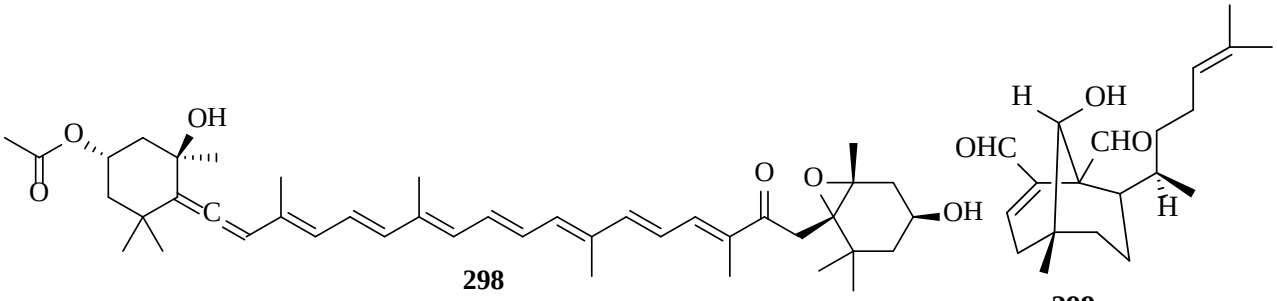

298 **299**

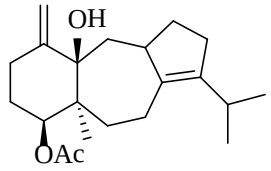

300

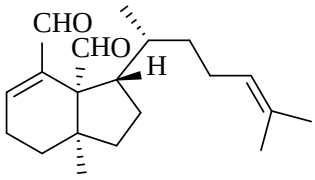

301

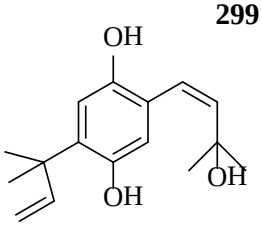

302

2.5 *Seaweeds belonging to the class Rhodophyceae and Phaeophyceae: Specialized morphological features*

Seaweeds were found to exhibit distinct morphological and physiological characteristics. Certain species of larger seaweeds possess complex structural features with specialized tissues that offer assistance to transport photosynthetic products and nutrients (Mouritsen, 2013). These largest seaweeds are found to appear ~50 meters long, while other category of smallest seaweeds appeared in few millimeters in size. The cells present in seaweeds also found in different size; in some of the species of seaweeds they can be measured more than one centimeter. The different organelles present in these large cells are responsible for the development of proteins, and to provide assistance for the cell functioning and their growth. Among the three major groups of seaweeds, all of them were found to contain pigments along with chlorophyll; whereas the characteristic colors of seaweeds are resulted from the percentage of extra pigments (Mouritsen, 2013).

The red seaweeds belong to the class of Rhodophyceae, which is a morphologically diverse class of photosynthetic-protists. Most of the red seaweed species were found as marine, excluding some of the fresh water species, for example, Batrachospermum (Yoon et al., 2017). Their morphology diverges from unicellular to complex multicellular species along with filamentous, pseudoparenchymatous, parenchymatous sheets, ribbons and lace-like features. These distinct eukaryotic seaweeds were found to appear in red colour due to the presence of pigments phycocyanin and phycoerythrin along with chlorophyll A. These well-established seaweeds possess uni/multiseriate filaments, and could also appeared in branched or unbranched forms with foliose thalli (blade-like). Some of the red seaweed species are found in erect and

crustose forms, and calcified. The red seaweeds have non-stacked thylakoids in their plastids, and they lack centrioles and flagella (Yoon et al., 2017).

Seaweeds belonging to the class Phaeophyceae (brown seaweeds) are much like plants, and generally appeared with three distinguishable parts. These seaweeds are found as exclusively marine, and characterized with brown colour due to the presence of dominant pigment fucoxanthin. They have layered cell wall with cellulose in the inner layer algin, and fucoidans is found in outer layer. The holdfast, which is a root-like structural part, is found in the bottom providing support to sustain in their habitat. Along with the root-like holdfast, seaweeds have stipe (or stem) and the leaf-like blades. The stipe makes the connection between the holdfast and blades (Mouritsen, 2013). The shape and number of blades are varied in different species. The blades have distinctive midribs in certain types of seaweeds. The long stipe in brown seaweeds provides assistance for blades to stand on the surface of the water, to absorb sufficient light, and consequently to perform photosynthesis. Some of the brown seaweeds have air containing bladders, which support them to stand on the surface of water to access light. Most of these bladders are in fifteen centimeter of height (Mouritsen, 2013).

2.5.1 Morphology and distribution of Gracilaria species

Gracilaria sp. belongs to the family of Gracilariaceae (Rhodophyta, Gracilariales) (Figure 2.6). This species consisted of solitary entities linked to the substratum, and was connected by holdfast; which appeared as decumbent and branched. The holdfast of *Gracilaria sp.*is found to appear as crust or disc, and which developed more than one erect axis. The thalli are found as segmented. Thalli are observed as erect- to prostrate structure or from terete- to widely flatten, which may be found as cylindrical and irregularly branched. These thalli are appeared in green, olive, and red to purple with some of the species possessed soft, smooth, and dentate structure. The thalli of *Gracilaria sp.* have divided into three kinds of tissues, such as epidermis, cortex, and medulla (Guiry & Guiry 2011). The irregularly branched thalli possessed robust arrangement and restricted throughout body, whereas the stipe of this species is cylindrical.

*Gracilaria sp.*was recognized in 1830 by Greville, and it was constituted as the third biggest genus in Rhodophyceae group along with more than 150 species around the world. Almost twenty eight species of *Gracilaria* have been derived from Indian coastline (Sahoo et al., 2001). These species of seaweeds can grow in saline water in the depth of 5-34 ppt. *Gracilaria sp.* is mostly harvested for the production of phycocolloid, agar, which provide > 50 % supply of agar in the total production of the world.

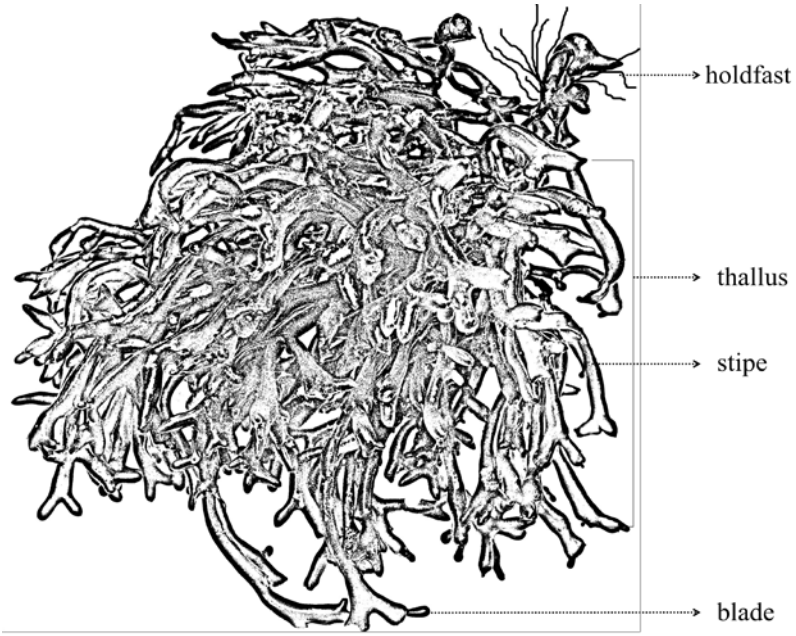

Figure 2.6.: Thallus of *Gracilaria sp.*belonging to the family Gracilariaceae (Rhodophyta, Gracilariales)

2.5.2 Morphology and distribution of *Padina* species

The *Padina sp.* belongs to the family Dictyotaceae (Phaeophyta, Dictyotales) (Figure 2.7), which is structurally featured by calcareous and flatten-fan-shaped thalli. They have possessed 2-3 or more than 3 stacked layers of parenchymatous-cells (Okazaki et al. 1986, van den Hoek, Mann and Johns 1995). The deposition of calcium carbonate/lime stone on the surface of flatten and fan-shaped thalli is considered as one of the distinctive characteristics of this species. The deposition of calcium is varied from species, and may occur either in a single surface or both surfaces. Certain species of *Padina* is lacked with calcium deposition, for instance, *P. arboresens* (Okazaki et al. 1986) and *P. glabra* (Wynne and De Clerck, 1999). The circinately coiled shape of distal margin is other notable peculiarity of *Padina sp.*, which can protect the apical cells (Bold and Wynne 1978). The division of the apical cells in this species led to the growth and their life cycle, which found as isomorphic and diplohaplontic (van den Hoek, Mann and Johns 1995). *Padina sp.* are found in pale brown/yellowish brown colour in appearance. They are smooth in bottom and relatively brittle on the top, which are grown in cluster or twisted shape. They have 5-6 stacked cell-layers, linked with stupose and holdfast, which is measured 2-4 mm in diameter. The margin of thallus is simple or irregularly divided.

Padina sp. is widely distributed in the world and around thirty two species were distributed throughout the tropical and temperate region of the sea (Guiry 2005). Among which, a total of 18 species are distributed in the Asiatic water bodies. These economically relevant

seaweeds are widely used as the source of polysaccharides, such as algin, which can be used as the functional food ingredient (Zaneveld, 1955) and fertilizer (Trono 2002, Soe-Htun 2005).

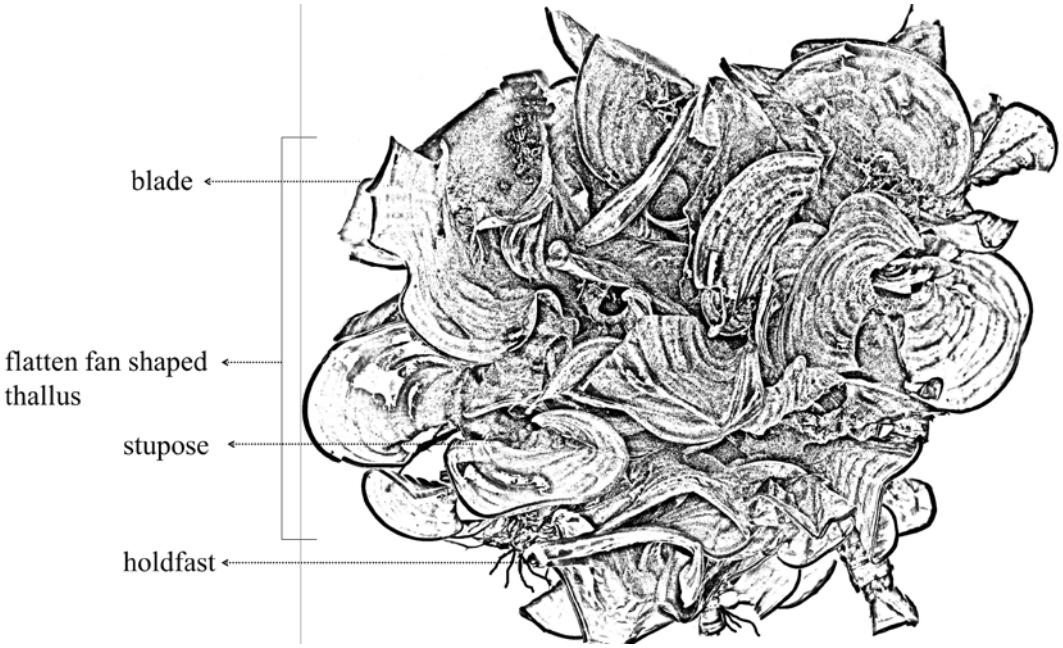

Figure 2.7.: Thallus of *Padina sp.* belonging to the family Dictyotaceae (Phaeophyta, Dictyotales)

2.6 Conclusion

The bioactive potencies of seaweeds, especially belonging to the classes of Rhodophyceae and Phaeophyceae directed towards the isolation of lead molecule with wide array of applications in food, medicinal, nutraceutical and pharmaceutical fields is extremely large, and has been directed towards the comprehensive extraction of novel bioactive compounds. In light of this, the present review properly corroborated those seaweeds, particularly of Rhodophyta and Phaeophyta as dynamic and promising candidates for identification, structural interpretation and bioactivity analysis of the seaweed-derived secondary metabolites, so as to reveal new natural entities with antioxidative, anti-inflammatory, and anti-diabetic potential.

CHAPTER 3

SCREENING OF BIOACTIVE POTENTIALS OF CRUDE SOLVENT EXTRACTS FROM RED AND BROWN SEAWEEDS (RHODOPHYCEAE AND PHAEOPHYCEAE

Contents

3.1 Background
3.2 Materials and methods
3.3 Results and discussion
3.4 Conclusions

3.1 Background

Seaweeds have established an adaptive stratagem for their endurance in the competitive surrounds by the development of enormous array of secondary metabolic analogues, and they can act as biologically as well as chemically dynamic defensive schemes against numerous life style disorders (Cardozo et al., 2007). Researches on natural-product-chemistry and chemical defensive systems of seaweeds documented the presence of bioactive lead molecules with prominent pharmacological activities (Faulkner, 2002). Phlorotannins and polyphenols from seaweeds have revealed their activities against proliferation of cancer cells (Kwon et al., 2007) and produce some effects on anti-inflammatory and anti-diabetic responses (Kim et al., 2009). Bioactive components in seaweeds were recognized to modulate glucose-induced oxidative stress and their ability to control the presence of starch-digestive enzymes (Lee et al., 2008). Potential side effects attributed to the synthetic drugs, demanded naturally obtained potential bioactive components for curing of persistent metabolic syndromes. Therefore, consumption and addition of these seaweeds might be increased their food and pharmaceutical applications**.**

Bioactive constituents of seaweeds also revealed their nutritional and bioactive properties against various life style diseases, which include hypertension, diabetes mellitus and inflammation (Joshipura et al., 2001; Maneesh and Chakraborty, 2017; Maneesh and Chakraborty, 2018; Antony and Chakraborty, 2019; Chakraborty et al., 2019). Bioactive

components of seaweeds also act as the inhibitor of angiotensin-I converting enzyme (ACE), which secrete the angiotensin-II vasoconstrictor (Curtiss et al., 1978). The potential side effects produced by the commercial ACE-inhibitors upsurges the demand of naturally occurring homologues (Atkinson and Robertson, 1979). Specific constituents of seaweeds were found to function as chemical intermediaries, which control the stimulations associated with mammalian defense mechanism and produces inflammatory deregulators (Thanh-Sang et al., 2012).

The present study evaluated the pharmacological potentials of ten different seaweeds belonging to the subclasses Dictyotophycidae (phylum Ochrophyta), Rhodymeniophycidae and Corallinophycidae (phylum Rhodophyta) collected from the southeast coastal areas of Indian Peninsular, using different *in vitro* models. The ethyl acetate-methanol (EtOAc-MeOH) extracts of various seaweeds were analyzed for various pharmacological potentials, such as anti-oxidant, anti-diabetic, anti-hypertension, and anti-inflammatory properties. The current study also described the nuclear magnetic resonance-guided spectroscopic de-replication of the prominent functional group fingerprints in the EtOAc-MeOH extracts of different seaweeds, and to correlate their presence with the bioactivities.

3.2 Materials and Methods

3.2.2 Chemicals, reagents and solvents

The chemicals used in this study include regents, solvents and solutions, which were acquired from Sigma-Aldrich Chemicals Co. Inc. (St. Louis, MO) and E-Merck (Darmstadt, Germany). Different buffers and solutions for screening studies were freshly made as and when required. All essential enzymes for biological assays were obtained from Sigma-Aldrich Chemicals Co. Inc. (St. Louis, MO). In detail, the chemicals include bases, acids for this such as Folin-Ciocalteu (F-C) reagent, Sodium carbonate/Na_2CO_3, potassium persulfate/$K_2S_2O_8$ ferrous sulphate/$FeSO_4$, sodium hydroxide/NaOH, ferrozine, diacetate of leuco-2,7-dichlorofluoresce, hematin, phenol, Gly-Pro-p-nitroanilide, N-(3-[2-furyl]acryloyl)-Phe-Gly-Gly/FAPGG, acids such as arachidonic acid, acetic acid, linoleic acid, 3,5-dinitrosalicylic acid were obtained from Sigma-Aldrich (St. Louis, MO). Furthermore, commercial standards, free radicals and non-free radicals for the *in vitro* anti-oxidative analysis such as 1,1-diphenyl-2-picryl-hydrazil/DPPH, 2,2'-azino-bis-3-ethylbenzothiozoline-6-sulfonic acid diammonium salt/$ABTS^+$, malondialdehyde, thiobarbituric acid/TBA, gallic acid, hydrogen peroxide/H_2O_2 were acquitted from Sigma-Aldrich (St. Louis, MO). The reagents for buffer preparations such as potassium phosphate buffer, sodium phosphate buffer, tris-buffer, were acquired from E-Merck (Darmstadt, Germany)/HiMedia (Pennsylvania, USA). Enzymes for biological assays such as

dipeptidyl peptidase-4/DPP-4 (from porcine-kidney), angiotensin converting enzyme-1/ACE-1 (from rabbit-lung), cyclooxygenase-1/COX-1 (from sheep), cyclooxygenase-2/COX-2 (human recombinant), 5-lipoxygenase/5-LOX (from soybean) were procured from Sigma-Aldrich (St. Louis, MO). The other enzymes, α-amylase (from porcine-pancreas) and α-glucosidase (from yeast) were procured from Sisco Research Laboratories (Mumbai, India). All glass wares were procured from Borosil (India).

3.2.2 Materials of seaweed and depiction of work area

The seaweeds used in this study were obtained from the southeast coastal areas of Peninsular India. The seaweeds belonging to the subclasses Dictyotophycidae (*Padina tetrastromatica* Hauck) (Figure 3.1), Rhodymeniophycidae {*Gracilaria salicornia* (C. Agardh) E. Y. Dawson (Figure 3.2), *Gracilaria canaliculata* Sonder, *Hydropuntia edulis* (S.G.Gmelin) Gurgel & Fredericq, *Gracilaria corticata* (J. Agardh) J. Agardh, *Palisada pedrochei* J.N.Norris, *Halymenia dilatata* Zanardini, *Spyridia filamentosa* (Wulfen) Harvey and *Portieria hornemannii* (Lyngbye) P.C. Silva} and Corallinophycidae {*Amphiroa fragilissima* (Linnaeus) J.V. Lamouroux} were collected. The collection site was located between 8º48′ N, 78º9′ E and 9º14′ N, 79º14′ E at Gulf of Mannar of Mandapam region (Figure 3.3). The seaweeds were initially washed with tap water to eliminate sand and unwanted constituents, and thoroughly washed with distilled water. The wet seaweeds were dried at room temperature, and stored in airtight containers for further experiments.

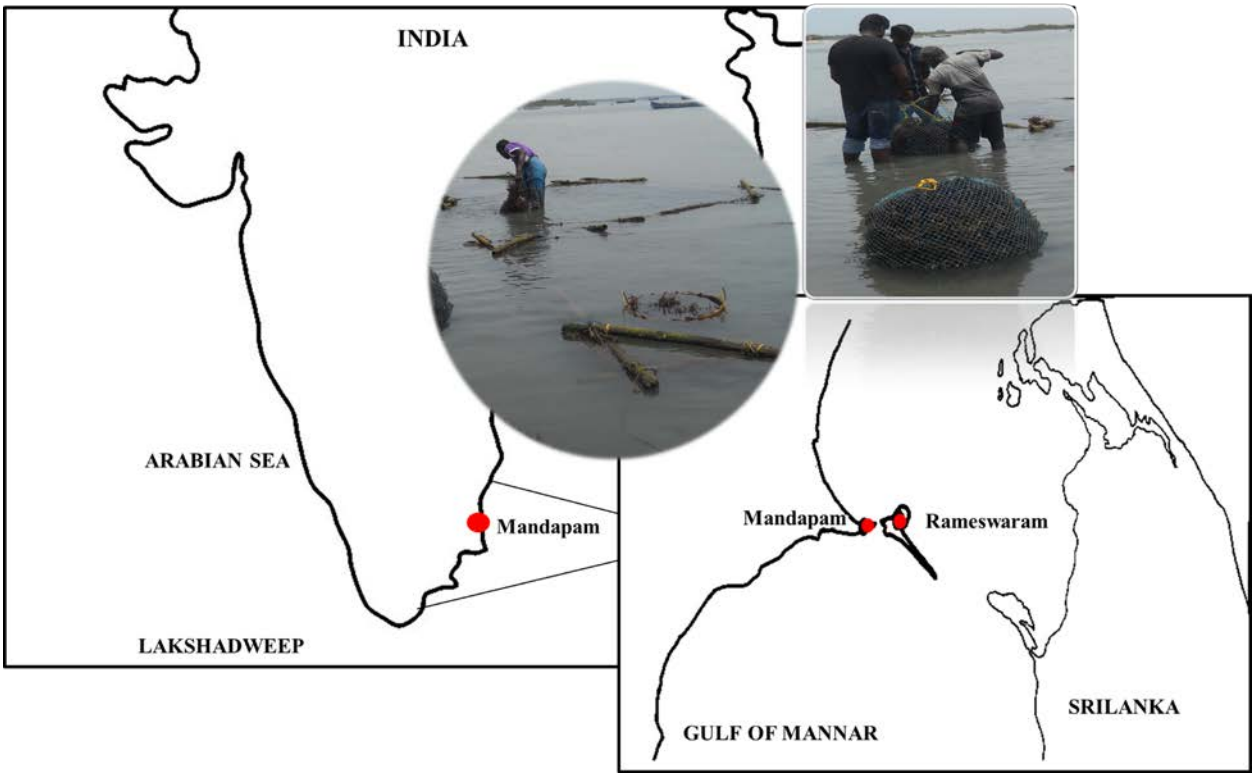

Figure 3.1.: Representative photograph of sample collection site located between 8º48′ N, 78º9′ E and 9º14′ N, 79º14′ E at Gulf of Mannar of Mandapam region

Figure 3.2.: Representative photograph of four seaweeds, *P. tetrastromatica, G. salicornia, G. canaliculata and G. corticata* selected for the pharmacological screening

Gracilaria corticata
Subclass Rhodymeniophycidae
Order Gracilariales
Family Gracilariaceae
Genus *Gracilaria*

Palisada pedrochei
Subclass Rhodymeniophycidae
Order Ceramiales
Family Rhodomelaceae
Genus *Palisada*

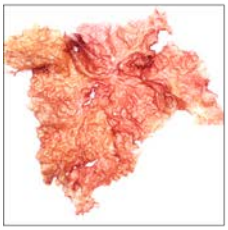

Halymenia dilatata
Subclass Rhodymeniophycidae
Order Halymeniales
Family Halymeniaceae
Genus *Halymenia*

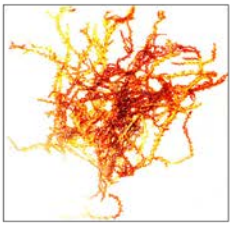

Spyridia filamentosa
Subclass Rhodymeniophycidae
Order Ceramiales
Family Callithamniaceae
Genus *Spyridia*

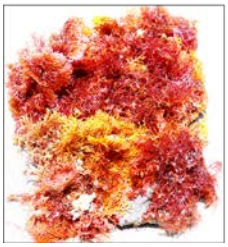

Portieria hornemannii
Subclass Rhodymeniophycidae
Order Gigartinales
Family Rhizophyllidaceae
Genus *Portieria*

Amphiroa fragilissima
Subclass Corallinophycidae
Order Corallinales
Family Lithophyllaceae
Genus *Amphiroa*

Figure 3.3.: Representative photograph of six seaweeds, *G. corticata, P. pedrochei, H. dilatata, S. filamentosa, P. hornemannii and A. fragilissima* selected for the pharmacological screening

3.2.3 Preparation of organic extracts from seaweeds

The dried seaweeds (1 kg) were powdered and were extracted with solvent *n*-hexane (700 mL) at 45 °C to remove pigments. Likewise, the second extraction of seaweed residues were carried out with acidified ethyl acetate-methanol (EtOAc-MeOH, 1:1 v/v) (700 mL x 3) mixture at 70 °C. The extracts obtained were pooled together, and filtered by Whatman No-1 filter paper. Filtrates were collected and evaporated by rotary vacuum concentrator to get the crude organic extracts. The EtOAc-MeOH extracts derived from seaweeds belonging to the subclass Dictyotophycidae was found to possess higher yield (~8.1 g) followed by subclasses Rhodymeniophycidae and Corallinophycidae (~6.5-7.8 g), in descending order. The extracts of seaweeds were stored in refrigerator (4-6 °C) until further use.

3.2.4 Instrumentation

Varian Cary 50 ultra-violet-visible (UV-VIS) spectrophotometer (Varian Cary, USA) was used for spectrophotometric analysis of samples. The Fourier transform infrared spectral (FTIR) analysis was carried out by Perkin-Elmer Series 400 FTIR spectrophotometer with an air-cooled deuterated triglycine sulfate (DTGS) detector within the scan range of 4000 and 400 cm^{-1}

by using KBR pellets, and the spectra were acquired with 32 scans with the spectral resolution of 4 cm (Figure 3.4). Bruker AVANCE III 500 MHz (AV 500) nuclear magnetic resonance (NMR) spectrometer (Bruker, Karlsruhe, Germany) used for the spectroscopic characterization of organic extracts. Appropriate dilutions of EtOAc-MeOH extracts prepared in NMR tubes (Norell, 5 mm OD and 7 inches length) with deuterated solvent ($CDCl_3$). Tetramethylsilane (TMS; Cortec, Paris, France) was used as the reference standard (δ 0 ppm). Each NMR spectra was referenced with TMS signal and residual solvent signal of $CDCl_3$. The chemical shift values were expressed in ppm, and were examined for specific regions, such as δ_H 1.0-2.0 (corresponding to saturated hydrocarbons, RCH_3, R_2CH_2 and R_3CH), δ_H 2-2.5 {representing acetyl ($RC(=O)CH_3$)/alkanoates of alkyl functionality (R_1O (O=)C-CH_2R)/alkyl amine substitutions (CH_3NR_2)}, δ_H 2.8-3.5 (signifying methoxyl moieties (CH_3-O-)/halides of alkyl groups (X-CH_2R)/substituted alkanol (CH_2OHR)}, δ_H 4-6 {indicating olefinic ($RCH=CHR_1$)/alkanoates of aryl functionalities ($CH_3O(O=)CCH_2R$)}, those at δ_H 6.5-8.5 {specifying aromatic protons (Ar-H)} (Figure 3.5 & 3.6).

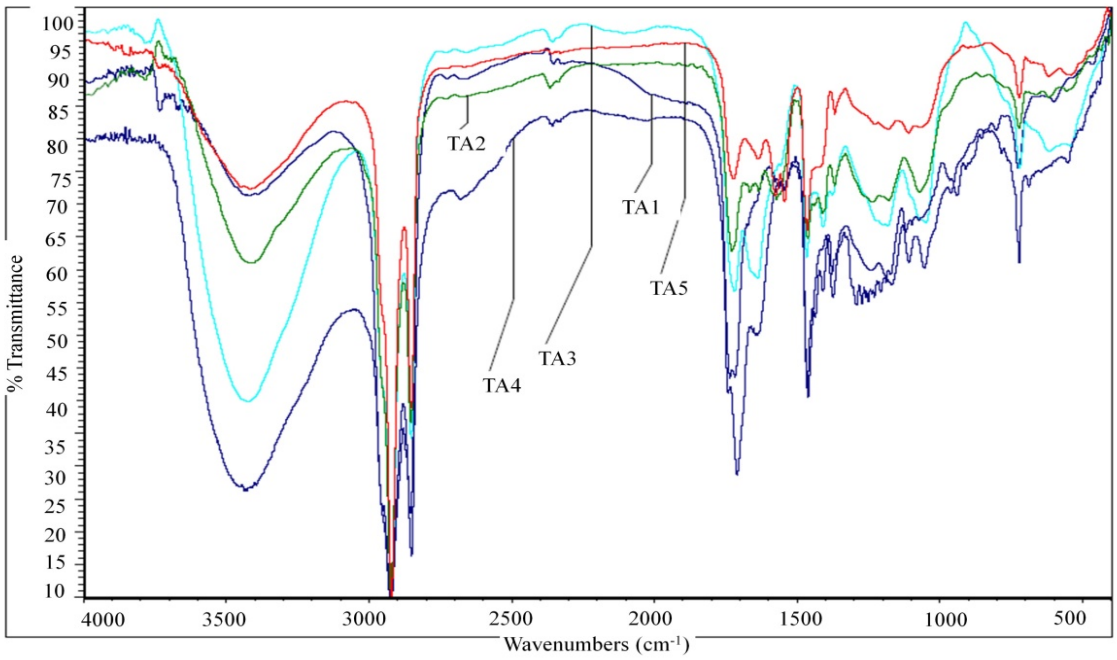

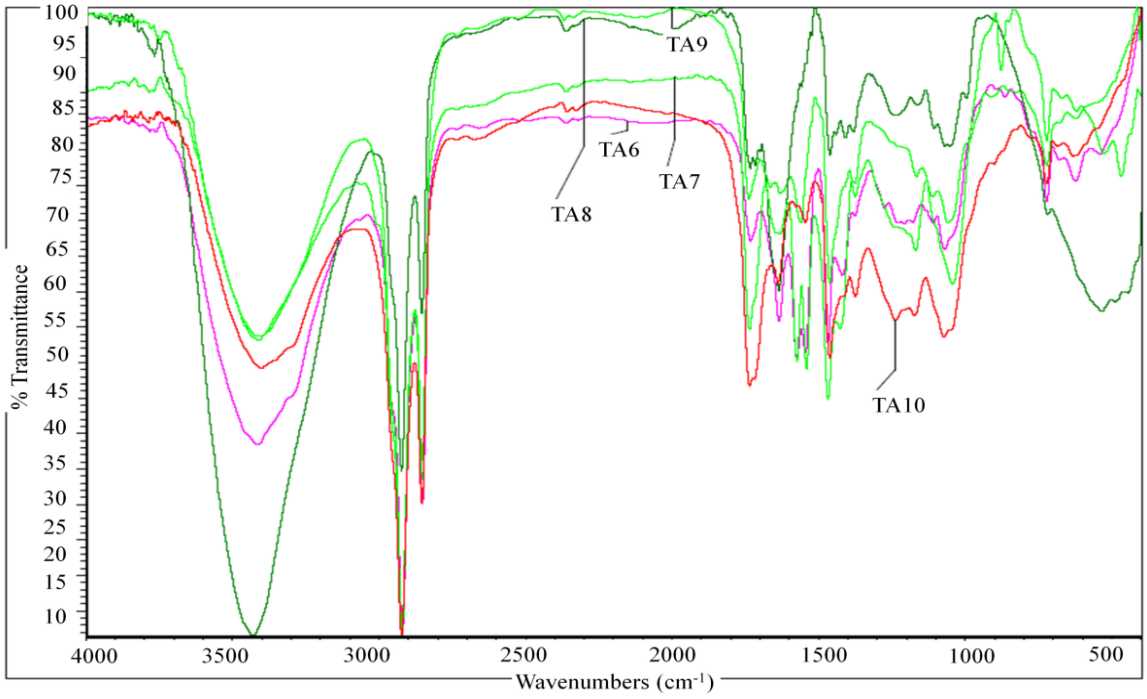

Figure 3.4.: FTIR spectra of the organic extracts of *G. salicornia*-TA1, *P. tetrastromatica*-TA2, *G. canaliculata*-TA3, *G. corticata*-TA4, *H. edulis*-TA5, *A. fragilissima*-TA6, *P. pedrochei*-TA7, *S. filamentosa*-TA8, *H. dilatata*-TA9, and *P. hornemannii*-TA10.

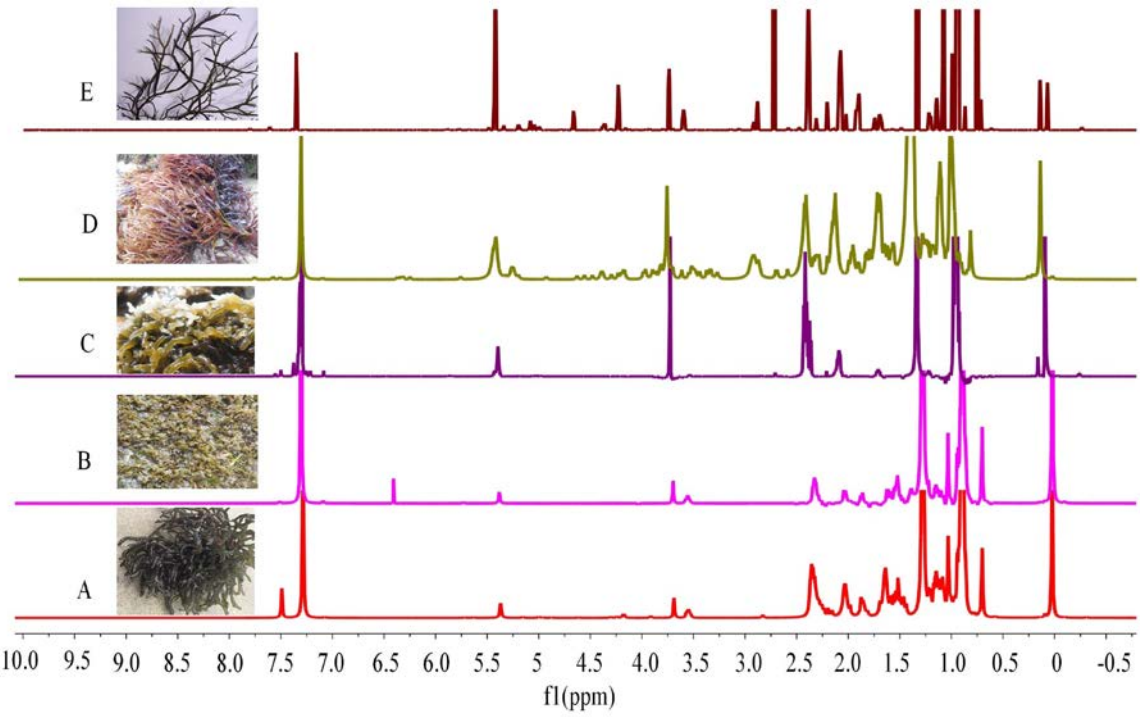

Figure 3.5.: ^{1}H-NMR spectra of the organic extracts of (A) *G. salicornia*, (B) *P. tetrastromatica*, (C) *G. canaliculata*, (D) *G. corticata*, and (E) *H. edulis*. The spectra were vertically stacked according to their decreasing order of activities.

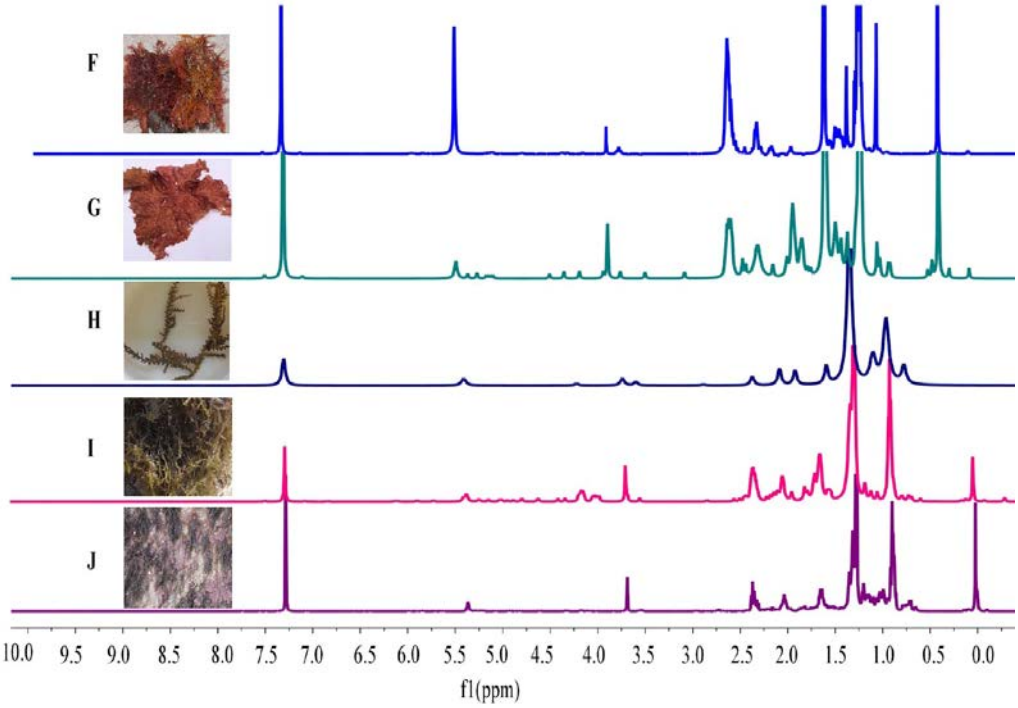

Figure 3.6.: ^{1}H-NMR spectra of the organic extracts of (F) *A. fragilissima*, (G) *P. pedrochei*, (H) *S. filamentosa*, (I) *H. dilatata*, and (J) *P. hornemannii*. The spectra were vertically stacked according to their decreasing order of activities

The chemical shift values at δ_H 9-10 represented the presence of the aldehyde proton in the proton NMR spectra. Integration of these distinct regions displayed the number of protons corresponding to these regions. Likewise, carbon signals in ^{13}C-NMR spectra were investigated. The different regions at δ_C 10-40 (aliphatic), δ_C 45-70 (alkoxy carbon; RCH_2OR_1), δ_C 70-80 {alkanoates of alkyl functionality ($R_1O(O=)CCH_2R$)}, δ_C 110-140 (functionalities of olefins), δ_C 140-160 (aromatic), δ_C 160-180 {ester alkanoate carbon atoms, $R_1O(O=)CR$}, and δ_C 180-210 (carbonyl carbon) were considered from the ^{13}C-NMR spectra (Figure 3.7 & 3.8).

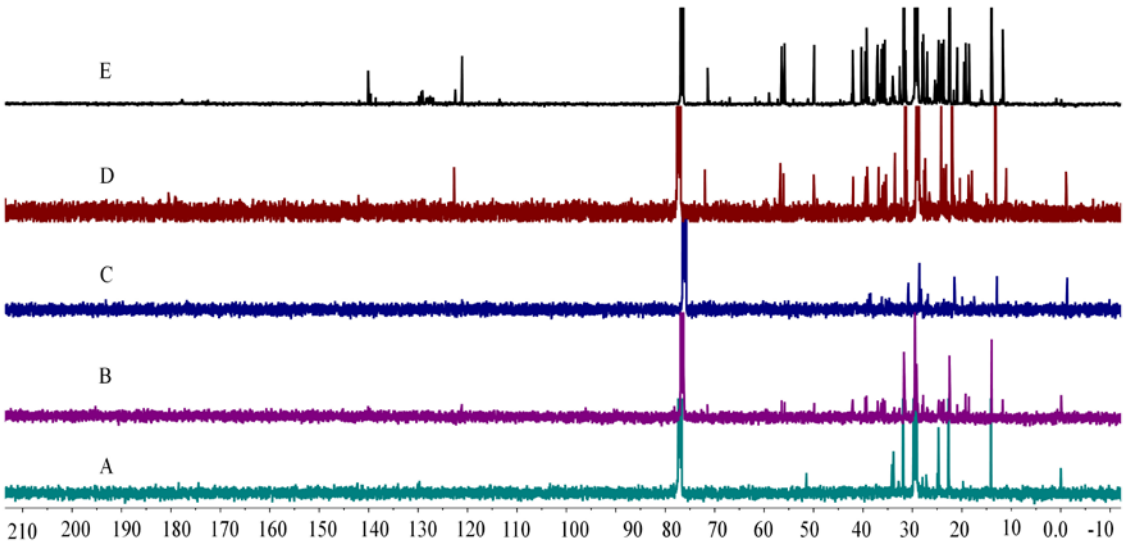

Figure 3.7.: ^{13}C-NMR spectra of the organic extracts of (A) *G. salicornia*, (B) *P. tetrastromatica*, (C) *G. canaliculata*, (D) *G. corticata*, and (E) *H. edulis*. The spectra were vertically stacked according to their decreasing order of activities.

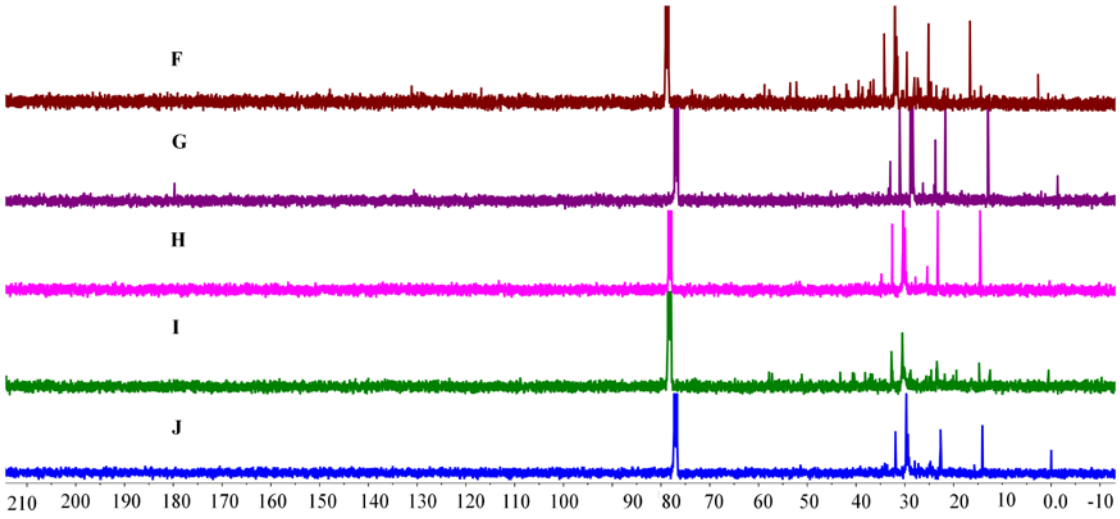

Figure 3.8.: ^{13}C-NMR spectra of the organic extracts of (F) *A. fragilissima*, (G) *P. pedrochei*, (H) *S. filamentosa*, (I) *H. dilatata*, and (J) *P. hornemannii*. The spectra were vertically stacked according to their decreasing order of activities.

3.2.5 Analysis of pharmacological activities of EtOAc:MeOH crude solvent extracts

3.2.5.1 Determination of total phenolic content

The Folin-Ciocalteu colorimetric method (Wojdylo et al., 2007) with suitable modification was used for the determination of total phenolic content (TPC) of the EtOAc-MeOH organic extracts of the seaweed samples (10 mg mL^{-1}) (nine red seaweeds and one brown seaweed) by using a UV-VIS spectrophotometer (Varian Cary 50, Palo Alto, CA, USA). In

detail, the EtOAc-MeOH organic extracts of the seaweed samples (10 mg) in methanol (1 mL) were added into the vial containing Folin-Ciocalteu (F-C) reagent of 5 mL. The mixture obtained was mixed with 4 mL sodium carbonate (0.7 M) solution, and allowed for incubation for 120 min (at 25 °C). The absorbance of the mixture was measured at 760 nm along with blank solution, methanol. The results obtained were evaluated with aid of standard curve procured from different concentrations of commercial standard gallic acid (0.2 to 0.005 mg mL^{-1}) with the equation y=mx+c. Finally, the TPC in EtOAc-MeOH organic extracts of the seaweed samples was estimated as milligram of gallic acid equivalents (mg GAE)/g of the organic extracts.

TPC was estimated with the equation: (mg GAE)/g = (x*w)/v

Where, 'x' is the concentration of mg/g gallic acid equivalent, 'w' is the weight of sample in gram, and 'v' is the volume of the extract.

3.2.5.2 In vitro antioxidant activities

3.2.5.2a 1,1-Diphenyl-2-picrylhydrazil (DPPH) radical scavenging activity

Radical scavenging activities of the organic extracts of the seaweeds against active free radical DPPH was evaluated according to an established method (Wojdylo et al., 2007) by using a UV-VIS spectrophotometer (Varian Cary 50, Palo Alto, CA, USA). Initially, the various concentrations (0.1-1.0 mg mL^{-1}) of organic extracts of the seaweeds were prepared by serial dilution of stock solutions. The equal volumes of various concentration of the organic extracts and DPPH (0.1 mM) in methanol (1.0 mL) were mixed with each other. The mixture was agitated properly, and kept for incubation at room temperature for 30 min in dark. The absorbance of coloured mixture formed was recorded at 517 nm along with blank solution (methanol) and control (1.0 mL of DPPH solution-methanol) after 20 min. The experiment was repeated to obtain triplicate results. The estimation of percentage inhibition along with the IC_{50} values were carried out for different concentrations of DPPH-extract reaction mixtures.

Percentage of radical (DPPH) scavenging activity (%) was calculated by the following equation, (%) = $(A_0-A_1)/A_0$ x 100, wherein, A_0 is the absorbance of control and A_1 is the absorbance of the sample. From the plot of scavenging activity of free radicals, IC_{50} values of (mg mL^{-1}) the organic extracts were calculated. IC_{50} is the concentration, at which the samples inhibits 50 % of radical scavenging activities.

3.2.5.2b 2,2[1]-Azino-bis-3-ethylbenzothiozoline-6-sulfonic acid ($ABTS^+$) radical scavenging activity

Radical scavenging activity of the EtOAc-MeOH organic extracts of the seaweeds against active free radical $ABTS^+$ was evaluated according to an established method (Wojdylo et al., 2007). In brief, the stock solution of $ABTS^+$ radical was prepared by the addition of 7 mM of $ABTS^+$ into the 2.45 mM of potassium persulfate solution. The mixture was allowed to stand for 16 h at room temperature in dark. The methanol was added to the concentrated $ABTS^+$ stock solution to get the absorbance of diluted solution as ~0.70 at 734 nm. The organic extracts of the seaweeds (0.1 mL) of various concentrations (0.1-1.0 mg mL^{-1}) was mixed with 5 mL of diluted $ABTS^+$. The absorbance of resulted coloured mixtures was measured at 734 nm along with the blank solution (methanol) by using a UV-VIS spectrophotometer (Varian Cary 50, Palo Alto, CA, USA). The estimation of percentage inhibition along with the IC_{50} values was carried out for different concentration of $ABTS^+$-extract reaction mixtures.

Percentage of radical ($ABTS^+$) scavenging activity (%) was calculated by following equation, (%) = $(A_0\text{-}A_1)/A_0$ x 100, wherein, A_0 is the absorbance of control and A_1 is the absorbance of the sample. From the plot of scavenging activity of free radicals, IC_{50} values of (mg mL^{-1}) the organic extracts were calculated. IC_{50} is the concentration at which samples inhibits 50 % of radical scavenging activities.

3.2.5.2c Hydrogen peroxide scavenging activities

Hydrogen peroxide (H_2O_2) scavenging abilities of the EtOAc-MeOH organic extracts of seaweeds were assayed by the established method with appropriate modifications (Gulcin et al., 2003). Initially, the various concentrations (0.1-1.0 mg mL^{-1}) of organic extracts of seaweeds were prepared in methanol by serial dilution of stock solutions (1 mg mL^{-1}). Thereafter, the H_2O_2 (40 mM) solution was made in phosphate (pH 7.4) buffer. Various concentrations of 3.0 mL of seaweed extracts were measured out into a vial containing 3.0 mL of H_2O_2 solution. The mixture was agitated thoroughly and allowed to stand for incubation for 10 min. The absorbances of different concentrations of seaweed extracts, blank (phosphate buffer), and control (H_2O_2-methanol mixture were measured at 230 nm after 10 min with UV-VIS spectrophotometer. The experiment was repeatedly carried out to obtain triplicate results and IC_{50} (mg mL^{-1}) values were recorded for various concentrations of H_2O_2-organic extract reaction mixtures from the calculation of percentage inhibition.

The percentage of H_2O_2 scavenging activity was determined and recorded as IC_{50} values. The percentage H_2O_2 scavenging activity (%) was found to be, $(A_0\text{-}A_1)/A_0$ x 100, where, A_0 = absorbance of control and A_1 = the absorbance of the sample.

3.2.5.2d Ferrous ion chelating activity

The ferrous ion chelating abilities of the organic extracts of seaweed samples were estimated according to the established method (Gulcin et al., 2003). The different concentrations (0.1 to 1.0 mg mL^{-1}) of organic seaweed extracts of 1 mL was mixed with equal volumes of 0.313 mM ferrozine reagent (1.0 mL) and 0.125 mM of $FeSO_4$ (1 mL). The solutions were mixed properly and kept for 10 min for the equilibration. The absorbances of solutions, such as organic extracts of seaweeds, blank solution (methanol) and control ($FeSO_4$-ferrozine mixture) were measured at 562 nm after 10 min of incubation, using a UV-VIS-spectrophotometer. The experiments were carried out repeatedly to obtain the triplicate values of results. The percentage inhibition and IC_{50} (mg mL^{-1}) values were recorded for various concentrations of reaction mixtures.

The percentage of chelation (%) was determined as, $(A_0-A_1)/A_0$ x 100, whereas A_0 = Absorbance of control, A_1 = Absorbance of sample.

3.2.5.2e Thiobarbituric acid-reactive species formation inhibitory activity

The lipid peroxidation inhibiting activity of the EtOAc-MeOH organic extracts was assessed by thiobarbituric acid reactive species (TBARS) assay (Kulisic et al., 2004). The lyophilized powder of *Perna viridis* L. (green mussel) was used as the lipid source (model system) in this assay. The organic extracts of seaweed samples (2 mg mL^{-1}) were incubated with 10 mg of lyophilized powder of green mussel meat. A total of 2 mL of ice cold acetic acid (pH 3.6, 20 % v/v) solution was added into the incubation mixture to terminate the reaction. Thiobarbituric acid (TBA) (2 mL, 0.78 % w/v in acetic acid solution) was added to the above reaction mixture and incubated at 95 ºC for 45 min. The reaction mixture was allowed to cool to room temperature and kept for centrifugation at 8000 rpm for 10 min. The formation of malondialdehyde was monitored spectrophotometrically by measuring the absorbance at 532 nm, and the results were expressed as mM of malondialdehyde equivalent compounds formed per kg sample (MDAEQ/kg sample).

3.2.5.3 In vitro anti-inflammatory activities

3.2.5.3a Cyclooxygenases (COX) inhibition assay

Bioactive assays using pro-inflammatory enzymes cyclooxygenases (COX-1/2) were used to recognize the anti-inflammatory activities of the EtOAc-MeOH organic extracts of seaweeds (Larsen et al., 1996). The leuco-2,7-dichlorofluorescein diacetate (5 mg) was incubated with NaOH solution (1 M, 50 µL) at room temperature for 10 min, for the formation of the hydrolysates. The hydrolysed reaction mixture was mixed with HCl (1 M, 30 µL) for the

production of 1-dichlorofluorescein (1-DCF). The excess NaOH present in the reaction mixture was neutralized with HCl, and the resulting 1-DCF was diluted with 0.1 M tris-HCl buffer (pH 8). The cyclooxygenase isoforms (COX-1/2) were made into soluble in 0.1 M tris-HCl buffer. The different concentrations of organic extracts of seaweed samples (0.1-1.0 mg mL^{-1}) were incubated with the pro-inflammatory enzymes in the presence hematin for 5 min at room temperature. The premixed solutions of 1-DCF, arachidonic acid and phenol were poured into the prepared enzyme-seaweed organic extract mixture for the initialization of the reaction, which led to formation of final reaction mixture (with volume 1 mL of 0.1 M tris-HCl buffer). The absorbances were measured at 502 nm for different concentrations of the reaction mixtures by using a spectrophotometer. The experiments were repeated to get triplicate values of results. The percentage inhibition was calculated for different concentrations of reactions mixture and which were recorded to obtain the final IC_{50} (mg mL^{-1}) values.

The results were expressed as percentage (%) inhibition of the enzymes, $(Ab_0-Ab_1)/Ab_0$ x 100, whereas Ab_0=Absorbance of control, Ab_1=Absorbance of sample, and the results were calculated as IC_{50} (mg mL^{-1}), the concentration at which samples inhibits 50 % of enzyme activities.

3.2.5.3b 5-Lipoxygenase (5-LOX) inhibition assay

The 5-lipoxygenase (5-LOX) inhibitory potential of the EtOAc-MeOH organic extracts of seaweeds was evaluated by the established method (Baylac and Racine 2003). The different concentrations of organic extracts of seaweed samples were prepared (0.1-1.0 mg mL^{-1}) in the mixture of DMSO and Tween 20 (29:1, w/w, 50 µL). The pre-heated 0.1 M, potassium phosphate buffer (2.95 mL; pH 6.3) and linoleic acid (48 µL) were added into the reaction mixture and mixed properly. Ice-cold potassium phosphate buffer (12 µL) was poured into the mixture after the addition of pro-inflammatory 5-LOX enzyme of 100 U. The absorbances of the reaction mixtures, control (DMSO-Tween 20), and blank solution (potassium phosphate buffer) were measured at 234 nm by a UV-Visible spectrophotometer, for different concentrations of the reaction mixtures. The experiments were repeated to get triplicate values of results. The percentage inhibition was calculated for different concentrations of reactions mixtures and which were recorded to obtain the final IC_{50} (mg mL^{-1}) values.

The results were expressed as percentage (%) inhibition of the enzymes, $(Ab_0-Ab_1)/Ab_0$ x 100, whereas Ab_0=Absorbance of control, Ab_1=Absorbance of sample, and the results were calculated as IC_{50} (mg mL^{-1}), the concentration at which samples inhibits 50 % of enzyme activities.

3.2.5.4 In vitro antidiabetic activities

3.2.5.4a α -Amylase inhibition assay

Inhibitory activities of the organic extracts against *α*-amylase were used for assessing their anti-diabetic properties (Hamdan and Afifi, 2004). The test solutions of organic extracts of seaweed samples with different concentrations (0.1-1.0 mg mL^{-1}) were prepared by serial dilution. The test solutions of equal volumes were added into the 0.20 mM, phosphate buffer (pH 6.9) containing enzyme, *α*-amylase (0.5 mg mL^{-1}). The reaction mixtures were subjected for incubation at 25 °C for 10 min. Furthermore, pre-incubated reaction mixture was mixed with 0.02 M phosphate buffer (pH 6.9) containing 1 % starch solution, and allowed to stand for 10 min at 25°C. The reaction mixture was warmed with 3, 5 dinitrosalicylic acid (1.0 mL) under boiling the water bath for 5 min to terminate the reaction, and allowed to cool to room temperature. The absorbances of various concentrations of reaction mixtures were measured out at 540 nm after the dilution with double distilled water. The experiments were repeated to get triplicate values of results. The percentage inhibition was calculated for different concentrations of reactions mixture, and were recorded to obtain the final IC_{50} (mg mL^{-1}) values.

The results were expressed as percentage (%) inhibition of the enzymes, $(Ab_0-Ab_1)/Ab_0$ x 100, Ab_0=Absorbance of control, Ab_1=Absorbance of sample, and the results were calculated as IC_{50} (mg mL^{-1}), the concentration at which samples inhibits 50 % of enzyme activities.

3.2.5.4b α-Glucosidase inhibition assay

Inhibitory potentials of the EtOAc-MeOH organic extracts of seaweeds against *α*-glucosidase enzyme were used for analyzing their anti-diabetic properties (Hamdan and Afifi, 2004). The organic extracts of various concentrations (0.1-1.0 mg mL^{-1}) were prepared in 0.2 M, tris-HCl buffer (500 µL, pH 8). The test solutions were pre-incubated with 500 µL of starch solution (2 % w/v) at 37 °C for 5 min, and then incubated with enzyme (1 U/mL) prepared in 0.2 M tris-HCl (pH 8.0) at 37 °C for 10 min. The reaction mixture was warmed with 3,5 dinitrosalicylic acid (1.0 mL) under the boiling water bath for 2 min to terminate the reaction and allowed to cool to room temperature. The absorbances of various concentrations of reaction mixtures were measured at 540 nm after dilution with double distilled water. The experiments were repeated to get triplicate values of readings. The percentage inhibition was calculated for different concentrations of reactions mixtures, and were recorded to obtain the IC_{50} (mg mL^{-1}) values.

The results were expressed as percentage (%) inhibition of the enzymes, $(Ab_0-Ab_1)/Ab_0$ x 100, whereas Ab_0=Absorbance of control, Ab_1=Absorbance of sample, and the results were calculated as IC_{50} (mg mL^{-1}), the concentration at which samples inhibits 50 % of enzyme activities.

3.2.5.4c Dipeptidyl peptidase-4 (DPP-4) inhibition assay

The dipeptidyl peptidase-4 (DPP-4) inhibitory potencies of EtOAc-MeOH organic extracts of seaweed samples were carried out by established method (Kojima *et al*., 1980). The organic extracts of samples with various concentrations (0.1-1.0 mg mL^{-1}) in 50 mM tris-HCl buffer (pH 7.5) was mixed with 15 µL of DPP-4 enzyme (0.05 U/mL) in 100 mM tris-HCl buffer (pH 8). The mixture was subjected for incubation at 37°C for 30 min. The Gly-Pro-p-nitroanilide (50 µL, 1.4 mM) in tris-HCl buffer (0.2 M) was added and incubated for 30 min at 37°C. The absorbances of various concentrations of reaction mixtures were measured at 405 nm by using a UV-VIS spectrophotometer (Varian Cary 50, Palo Alto, CA, USA). The experiments were repeated to get triplicate values of readings. The percentage inhibition was calculated for different concentrations of reactions mixture and which were recorded to obtain the IC_{50} (mg mL^{-1}) values.

The results were expressed as percentage (%) inhibition of the enzymes, $(Ab_0-Ab_1)/Ab_0$ x 100, whereas Ab_0=Absorbance of control, Ab_1=Absorbance of sample, and the results were calculated as IC_{50} (mg mL^{-1}), the concentration at which samples inhibits 50% of enzyme activities.

3.2.5.5 In vitro antihypertensive activities

3.2.5.5a Angiotensin converting enzyme-I (ACE-I) inhibitory activity

Determination of anti-hypertensive potentials of the EtOAc-MeOH organic extracts of the studied seaweeds was conducted with ACE-I inhibiting activity (ACE-I from rabbit lung, 20 µL, 20 mu) (Udenigwe et al., 2009). The organic extracts of seaweed samples (0.2-0.5 mg) were mixed with 20 mU of ACE-1 (1 U/mL, 20 µL) enzyme. The 50 mM tris-HCl buffer (pH 7.5) containing 0.5 mM FAPGG (1 mL) and 0.3 M sodium chloride were added to the enzyme-sample mixtures and the decrease in absorbances were found at 345 nm against the reagent blank (distilled water) by using a UV-VIS spectrophotometer (Varian Cary 50, Palo Alto, CA, USA).

The results were expressed as percentage (%) inhibition of the enzymes, $(Ab_0-Ab_1)/Ab_0$ x 100, where Ab_0=Absorbance of control, Ab_1=Absorbance of sample, and the results

were calculated as IC_{50} (mg mL^{-1}), the concentration at which samples inhibits 50% of enzyme activities.

3.2.6 Statistical analysis

The variances (ANOVA) between various results were analyzed by Statistical Program for Social Science (SPSS, ver. 13.0, SPSS Inc., Quarry Bay, HK), and was used for assessing the significant differences between the means. The significant differences were represented as $P < 0.05$, and the readings were presented as mean of triplicates ± standard deviation. Principal component analysis (PCA) was used to recognize the mean variances in the data set.

3.3 Results and Discussion

3.3.1 Bioactive potentials of the organic extracts of seaweeds

Pharmacological properties, such as antioxidant, anti-diabetic, anti-inflammatory and anti-hypertensive potentials of the organic extracts of the studied seaweeds were assessed with various *in vitro* bio-assays (Table 3.1), and the activities were statistically correlated.

3.3.1.1 Total phenolic content (TPC)

The TPC contents were found to vary from 0.06 to 2.02 mg GAE g^{-1} of extract (Table 3.1), and that the seaweeds of subclass Dictyotophycidae possessed higher amount of polyphenols than seaweeds of subclasses Rhodymeniophycidae and Corallinophycidae. Amongst the selected seaweeds, the TPC was significantly greater for the organic extracts of *P. tetrastromatica* (Dictyotophycidae) (2.02 mg GAE g^{-1}) and *G. salicornia* (Rhodymeniophycidae) (1.57 mg GAE g^{-1}) than those displayed by other studied seaweeds (1.2-0.06 mg GAE g^{-1}). Previous reports of literature deduced that the phenolic compounds could possess important bioactivities, such as antioxidant, anti-inflammatory, anti-tumour, and anti-viral properties (Novoa et al., 2011; Thomas and Kim, 2011; Wijesinghe and Jeon, 2012).

3.3.1.2 Antioxidant activities

The organic extracts acquired from different seaweeds belonging to the subclasses Dictyotophycidae, Rhodymeniophycidae and Corallinophycidae were evaluated for their antioxidant properties using scavenging activity of free radicals ($ABTS^{+}$, DPPH and H_2O_2). Among various organic extracts, that of *P. tetrastromatica* displayed greater scavenging ability on DPPH radicals (IC_{50} 0.39 mg mL^{-1}) followed by those obtained from *G. salicornia* (IC_{50} 0.42

mg mL^{-1}), *G. canaliculata* (0.53 mg mL^{-1}), and *G. corticata* (0.55 mg mL^{-1}), in descending order. The $ABTS^+$ free radical scavenging activities of the organic extract of the studied seaweeds varied considerably (IC_{50} 0.66-0.98 mg mL^{-1}) (Table 3.1). Notably, the organic extract of seaweed *P. tetrastromatica* exhibited higher $ABTS^+$ radical scavenging activity (IC_{50} 0.66 mg mL^{-1}), whereas among seaweeds belonging to Rhodymeniophycidae, *G. salicornia* (IC_{50} 0.78 mg mL^{-1}) showed potential $ABTS^+$ radical scavenging activity (Table 3.1). The organic extract of the seaweed, *P. tetrastromatica* (IC_{50} 0.18 mg mL^{-1}) displayed greater hydrogen peroxide radical scavenging activity followed by those obtained from the seaweeds belonging to the subclasses Rhodymeniophycidae and Corallinophycidae (Table 3.1). The organic extracts of seaweeds, *G. salicornia* (IC_{50} 0.19 mg mL^{-1}), *G. corticata* (IC_{50} 0.24 mg mL^{-1}), *G. canaliculata* (IC_{50} 0.20 mg mL^{-1}), and *H. edulis* (IC_{50} 0.22 mg mL^{-1}) displayed greater peroxyl radical scavenging potential than those obtained from other studied species of seaweeds (IC_{50} > 0.25 mg mL^{-1}) (Table 3.1).

The antioxidant activities of the EtOAc-MeOH extracts of seaweeds were analyzed by principal component analysis (PCA), whereas PC1 and PC2 contributed 45.21 and 39.65 % towards the studied bioactivities (Figure 3.9). The DPPH and $ABTS^+$ radical scavenging activities of the organic extracts appeared in the same quadrant in the PCA diagram. High loading of DPPH as well as $ABTS^+$ scavenging activities on PC1 revealed that EtOAc-MeOH extracts of seaweeds belonging to the subclasses Dictyotophycidae and Rhodymeniophycidae were potential antioxidants.

The inhibitions of lipid peroxide formation of the organic extracts of the studied seaweeds were displayed in Table 3.1. The TBARS formation inhibitory effects of EtOAc-MeOH extract of *P. tetrastromatica* was 58.86 mM MDAEQ/kg, whereas that of *G. salicornia* was 51.96 mM MDAEQ kg^{-1}. Besides *G. salicornia*, the organic extracts of seaweeds *G. corticata* (49.64 mM MDAEQ kg^{-1}), *G. canaliculata* (46.45 mM MDAEQ kg^{-1}), and *H. edulis* (48.23 mM MDAEQ kg^{-1}) exhibited significantly higher inhibition of TBARS formation than those derived from the seaweeds belonging to the subclasses Rhodymeniophycidae and Corallinophycidae.

The metal binding property of the seaweeds could be identified from their ferrous ion chelating activities (Table 3.1). Amongst the studied seaweeds, the ferrous ion chelating efficiency was significantly greater for the organic extract of *P. tetrastromatica* (IC_{50} 0.13 mg mL^{-1}) and decreased in the order, *G. salicornia* (IC_{50} 0.15 mg mL^{-1}) > *H. edulis* (IC_{50} 0.24 mg mL^{-1}) > *G. canaliculata* (IC_{50} 0.25 mg mL^{-1}).

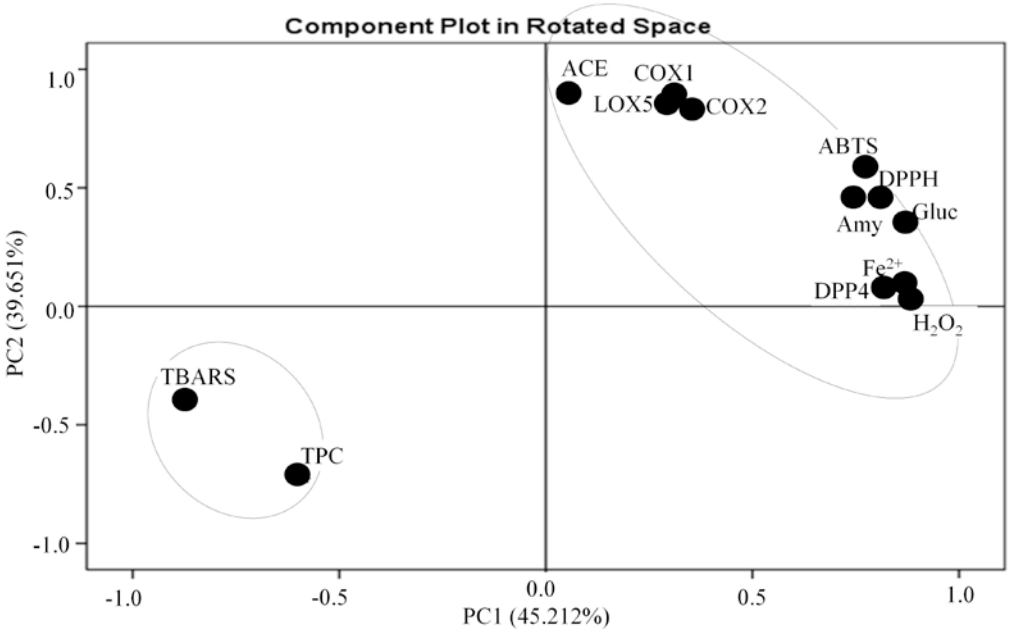

Figure 3.9.: Loading plot diagram (various components, PC1 and PC2 in the rotated space) of antioxidant activities vs anti-inflammatory, anti-diabetic and anti-hypertensive activities of the organic extracts of the studied seaweeds.

DPPH is a highly potent free radical that is used to find out the reducing power due to the presence of phenolic components, and hydrogen atom donating ability of antioxidants (Cho et al., 2011). The higher DPPH scavenging ability of seaweeds *P. tetrastromatica* (IC_{50} 0.39 mg mL^{-1}) and *G. salicornia* (IC_{50} 0.42 mg mL^{-1}) might be correlated with their greater TPC contents in the organic extracts. Earlier reports suggested that seaweeds of the subclass Dictyotophycidae showed greater DPPH radical scavenging activity than that exhibited by seaweeds of subclasses Rhodymeniophycidae and Corallinophycidae (Matsukawa et al., 1997). The antioxidant activity of the EtOAc-MeOH extracts of the studied seaweeds were also investigated by the non-radical species of hydrogen peroxide and that the scavenging activity of H_2O_2 recognized the reducing power of antioxidants against active radicals formed by the H_2O_2 during its reaction. The peroxyls were found to be potentially reactive oxidizing radicals that could act with the bioactive molecules resulting in the development of other radical species, such as alkoxy radicals. As the peroxyl radicals are the conveyors of the chain reaction, they oxidize polyunsaturated fatty acid (PUFA) molecules and begin new chains, inducing lipid peroxides that could be, fragmented to yet more radicals (Esterbauer and Porter, 1990). In this direction, the TBARS assay was used to deduce the inhibitory activity of antioxidants against free radical generation leading to lipid peroxidation. This assay indicated the formation of malondialdehyde as stable end product from oxidative degradation of unsaturated fatty acids. It has been

postulated that the presence of polyphenolic components might be responsible to hinder lipid peroxidation resulting in termination of free radical chain reactions (Karawita et al., 2005).

The metal binding property of the seaweeds could be identified from the ferrous ion chelating activity (Table 3.1). The iron in reduced form (Fe^{2+}) appeared to decompose the lipid hydroperoxides into radicals, such as peroxyls and alkoxyls, which make peroxidation of lipids, and could abstract hydrogen and extend the lipid peroxidation reaction (Costa et al., 2011). Therefore, the chelators of Fe^{2+} ion could be recommended as active lipid peroxidation inhibitors. The Fe^{2+} ion chelating activity of brown seaweed *Scytosiphon lomentaria* was previously reported (Kuda et al., 2005), and the studies revealed that the phenolic components in the polar solvent extracts of seaweeds of subclass Dictyotophycidae might be potential chelators of heavy metals (Wang et al., 2012). The Fe^{2+} chelating capabilities of the organic extracts of the seaweeds were also demonstrated by the existence of different kinds of non-phenolic compounds (Kuda et al., 2009). The negative correlation between TPC and Fe^{2+} chelating abilities might appropriately demonstrate the functional role of non-phenolic antioxidant components in the studied seaweeds.

The content of phenolic compounds in the seaweeds was varied from 2.02 mg GAE g^{-1}(*P. tetrastromatica*) to 0.06 mg GAE g^{-1} (*H. dilatata*) mg GAE g^{-1}. The phenolic contents in the organic extracts of *P. tetrastromatica* and *G. salicornia* extract (> 1.5 mg GAE g^{-1}) were significantly greater ($p < 0.05$) compared with those of the other species (< 1.25 mg GAE g^{-1}). The presence of phenolic group of compounds could be attributed to be one of the predominant reasons of antioxidant potential in the studied seaweed species (Rocha et al., 2018). Previous reports of literature demonstrated the functional roles of polyphenols and antioxidants as anticancer metabolites and growth suppressors of the cancer cells (Rocha et al., 2018). Among various brown seaweeds *Ecklonia cava* Kjellman and *Ecklonia stolonifera* Okamura displayed moderate antiproliferative activity against breast cancer cell lines, MCF-7 and MDA-MB-231 (Rocha et al., 2018). The red seaweeds belonging to the species of *Gracilaria* including *G. tenuistipitata*, *G. corticata* and *G. verrucosa* were found to exhibit cytotoxic potential against oral squamous carcinoma cells, HepG2, MCF7 and HeLa cancer cells (Yeh et al., 2012; Narasimhan et al., 2013; Dewi et al., 2018).

Table 1. Percentage yield, phenolic contents and pharmacological activities of the organic extracts of seaweeds belonging to Dictyotophycidae, Rhodymeniophycidae and Corallinophycidae

	A. fragillissima	*H. edulis*	*G. salicornia*	*G. corticata*	*P. pedrochei*	*S. filamentosa*	*P. hornemannii*	*H. dilatata*	*P. tetrastromatica*	*G. canaliculata*
Yield (%)	0.63±0.01^{a}	0.74±0.02^{b}	0.75±0.02^{b}	0.70±0.01^{c}	0.65±0.01^{a}	0.71±0.02^{c}	0.67±0.02^{a}	0.60±0.02^{d}	0.81±0.01^{e}	0.71±0.02^{c}
Total phenolics†	0.09±0.01^{a}	1.23±0.01^{b}	1.57±0.01^{c}	0.98±0.02^{d}	0.06±0.01^{a}	0.76±0.02^{e}	1.03±0.01^{f}	0.100±0.01^{a}	2.02±0.01^{g}	1.00±0.01^{dfh}
Antioxidant activities‡										
DPPH radical scavenging	0.72±0.01^{a}	0.62±0.01^{b}	0.42±0.01^{c}	0.55±0.01^{d}	0.59±0.01^{bde}	0.64±0.01^{bf}	0.78±0.01^{g}	0.75±0.01^{ag}	0.39±0.01^{ch}	0.53±0.01^{di}
$ABTS^{+}$ radical scavenging	0.98±0.01^{a}	0.93±0.01^{b}	0.78±0.01^{c}	0.81±0.01^{cd}	1.02±0.01^{a}	0.97±0.01^{ab}	0.89±0.01^{be}	0.98±0.01^{ab}	0.66±0.01^{f}	0.87±0.01^{eg}
Fe^{2+} ion chelating	0.33±0.02^{a}	0.24±0.01^{b}	0.15±0.01^{c}	0.33±0.02^{a}	0.45±0.02^{d}	0.90±0.02^{e}	0.43±0.02^{df}	0.89±0.01^{eg}	0.13±0.02^{ch}	0.25±0.01^{bi}
H_2O_2 scavenging	0.21±0.02^{a}	0.22±0.01^{a}	0.19±0.01^{a}	0.24±0.02^{abc}	0.29±0.02^{b}	0.30±0.02^{bc}	0.31±0.02^{bd}	0.28±0.01^{be}	0.18±0.02^{a}	0.20±0.01^{a}
Lipid peroxidation‡ inhibition	38.52±0.01^{a}	48.23±0.01^{b}	51.96±0.01^{c}	49.64±0.01^{d}	35.6±0.01^{e}	36.9±0.01^{f}	31.61±0.01^{g}	32.87±0.01^{h}	58.86±0.01^{i}	46.45±0.01^{j}
Anti-inflammatory activities‡										
COX-1 inhibition	4.99±0.01^{a}	2.91±0.01^{b}	1.01±0.01^{c}	2.99±0.01^{d}	4.04±0.01^{e}	3.01±0.01^{df}	2.01±0.01^{g}	3.04±0.01^{dh}	1.23±0.01^{i}	2.92±0.01^{bj}
COX-2 inhibition	5.01±0.01^{a}	3.01±0.01^{b}	1.02±0.01^{c}	3.01±0.01^{bd}	4.03±0.01^{e}	2.98±0.01^{bf}	1.99±0.01^{g}	3.00±0.01^{bh}	1.34±0.01^{i}	2.00±0.01^{bj}
5-LOX inhibition	5.02±0.01^{a}	2.98±0.01^{b}	0.98±0.01^{c}	3.02±0.02^{bd}	4.01±0.01^{e}	3.04±0.02^{df}	2.03±0.01^{g}	3.02±0.01^{bfh}	1.28±0.01^{i}	2.01±0.01^{gj}
Anti-diabetic activities‡										
α-Amylase inhibition	0.87±0.02^{a}	0.79±0.01^{b}	0.50±0.01^{c}	0.54±0.02^{cd}	0.61±0.02^{e}	0.77±0.02^{bf}	0.81±0.02^{bg}	0.95±0.02^{h}	0.45±0.02^{ci}	0.70±0.01^{j}
α-Glucosidase inhibition	0.73±0.02^{a}	0.63±0.02^{b}	0.45±0.02^{c}	0.53±0.0^{2d}	0.64±0.02^{b}	0.73±0.02^{a}	0.83±0.02^{f}	0.82±0.02^{fg}	0.40±0.02^{ch}	0.65±0.02^{bc}
DPP-IV inhibition	0.05±0.01^{a}	0.06±0.01^{a}	0.03±0.01^{a}	0.06±0.01^{a}	0.08±0.01^{ab}	0.05±0.01^{a}	0.08±0.01^{a}	0.17±0.01^{c}	0.02±0.01^{ad}	0.07±0.01^{a}
Anti-hypertensive activities‡										
ACE-I inhibition	0.62±0.02^{a}	0.18±0.01^{b}	0.09±0.01^{c}	0.20±0.02bd	0.21±0.02^{be}	0.24±0.02^{bf}	0.22±0.02^{bg}	0.23±0.02^{bh}	0.12±0.02^{ci}	0.19±0.01^{bj}

†Total phenolic contents were determined at 5 mg mL^{-1}, and presented as mg of gallic acid equivalence (GAE) g^{-1}.

‡The IC_{50} values were expressed as mg mL-1. Lipid peroxidation inhibitory (TBARS assay) was expressed as mM MDAEQ kg^{-1}.

The samples were analyzed in triplicate (n = 3) and expressed as mean ± standard deviation. Means followed by the different superscripts (a-j) within the same row indicate significant difference ($P < 0.05$).

3.3.1.3 Anti-diabetic activities

The organic extracts of seaweeds belonging to subclasses Dictyotophycidae, Rhodymeniophycidae and Corallinophycidae were evaluated for their attenuating properties against carbolytic enzymes *α*-amylase and *α*-glucosidase. The EtOAc-MeOH extracts of seaweed *P. tetrastromatica* exhibited greater attenuating properties against *α*-amylase (IC_{50} 0.45 mg mL^{-1}) than those obtained from other studied seaweed species (Table 3.1). Likewise, the organic extracts of *P. tetrastromatica* and *G. salicornia* exhibited significantly higher *α*-glucosidase inhibiting activity (IC_{50} ~0.4 mg mL^{-1}) than other studied seaweeds. The DPP-IV inhibitory potentials of the organic extracts of *P. tetrastromatica* (IC_{50} 0.02 mg mL^{-1}) and *G. salicornia* (IC_{50} 0.03 mg mL^{-1}) were considerably higher than those exhibited by other seaweed species (Table 3.1).

Diabetic mellitus is a chronic metabolic disease, and was found to occur because of insufficiency of insulin secretion or resistance (Nickavar and Yousefian, 2011). The complex starch degrading enzyme *α*-amylase was reported to perform major functional role in the hydrolysis of 1, 4-glycosidic linkages of various simple oligosaccharides, and the enzyme *α*-glucosidase additionally decomposes the disaccharides into smaller moieties for the intestinal absorption. The inhibitions of these enzyme activities were considered to be effective to reduce absorption of glucose to the blood (Hara et al., 1990).

3.3.1.4 Anti-hypertensive and anti-inflammatory activities

The organic extract of *G. salicornia* and *P. tetrastromatica* exhibited considerably greater anti-hypertensive activities as displayed by the higher ACE-I (IC_{50} 0.09 and 0.12 mg mL^{-1}, respectively; $P < 0.05$) inhibiting potential than those exhibited by other seaweeds (Table 3.1). The organic extracts *P. tetrastromatica* and *G. salicornia* exhibited greater attenuation properties against 5-LOX (IC_{50} 1.28 and 0.98 mg mL^{-1}, respectively) compared to the other studied seaweed species belonging to Rhodymeniophycidae (*H. edulis, G. canaliculata, G. corticata, P. hornemannii, P. pedrochei, S. filamentosa, H. dilatata*) and Corallinophycidae (*A. fragilissima*) (IC_{50} > 2 mg mL^{-1}) (Table 3.1). The organic extracts of seaweeds exhibited a positive correlation on PCA analyses, and was demonstrated by the co-linearity between antioxidative properties and ACE-I inhibitory activities. Notably, the organic extracts of *P. tetrastromatica* and *G. salicornia* exhibited higher duel COX-2 and 5-LOX inhibiting activity compared to the other studied seaweed species belonging to Rhodymeniophycidae and Corallinophycidae.

3.3.2 Spectroscopic fingerprinting of functional groups

The EtOAc-MeOH extracts obtained from the seaweeds displayed characteristic chemical shift values and corresponding integrals in the spectra (Figure 3.10-3.19, Table 3.2). The characterization of the signature peaks from the ^{1}H-NMR spectra was performed in an effective manner by a deconvolution method of the whole range of the ^{1}H-NMR spectra, whereas the algorithm of peak analysis and global spectral deconvolution untangled the transitions in ^{1}H-NMR spectra of the constitutive components. The ^{1}H-NMR spectra of the organic extracts of *P. tetrastromatica* and *G. salicornia* documented the occurrence of higher proton integrals at δ_H 4-6, which might be due to the occurrence of protons connected with the olefinic and the parent hydride group of alkyl alkanoates {$RCH_2C(=O)OCH_3$}. The signals at the region δ_C 125-135 might be assigned to the olefinic carbon atoms. Furthermore, the intense signals at δ_C160-180 in the ^{13}C-NMR spectra were assigned owing to the existence of alkanoate carbon atom of esters {$RC(=O)OR_1$} in the organic extracts of *P. tetrastromatica* and *G. salicornia*. The EtOAc-MeOH extracts of *P. tetrastromatica* and *G. salicornia* displayed prominent ^{13}C-NMR signals at δ_C 173, which could be attributed to the carbonyl groups. The ^{1}H-NMR spectra of the organic extracts of *G. salicornia* and *A. fragilissima* displayed common peaks in the range of δ_H 6.0-8.5, which could be associated with the aromatic traces. The characteristic peaks at δ_H 2.2-3 and δ_H 3.3-4.0 in the ^{1}H-NMR spectra of the organic extract of seaweeds might be attributed to the presence of benzylic groups (Ar-CH_3) and ether (R-O-CH_3) functional groups. The characteristic proton signals in the region δ_H 2.74-2.92 might be attributed to superimposed >CH_2 bis-allylic protons, which was deduced to be more important in the organic extracts of *P. tetrastromatica* and *G. salicornia,* belonging to the subclasses Dictyotophycidae and Rhodymeniophycidae, respectively. The signals owing to bis-allylic groups might also demonstrate the ubiquity of the unsaturated fatty acids in these seaweed extracts. The ^{1}H-NMR spectra obtained from the organic extracts of *P. tetrastromatica* and *G. salicornia* also earned well resolved, deshielded signals at about δ_H 5.0-5.3, which presumably explained the existence of oligosaccharide units. These assignments were furthermore evaluated by the ^{13}C-NMR spectra (Figure 3.20-3.29), which were acquired from the EtOAc-MeOH extracts of the seaweed species contemplated in this study. The organic extracts of *P. tetrastromatica* and *G. salicornia* exhibited very intense signals at δ_H 2.8-3.5, which might be associated with the electronegative groups, such as alkoxy/alkyl halide/functionalized hydride of the substituted alkanols. The signals at δ_C 45-70 and δ_C 70-80 in the ^{13}C-NMR spectra, might be due to the alkoxy carbon (RCH_2OR_1), and the carbons connected to the parent hydride group of alkyl alkanoates {$RCH_2C(=O)OCH_3$}, respectively. The organic extracts of the seaweeds did not show the occurrence of the intense aromatic carbon residues (at δ_C 142), with the exclusion of those obtained from *P. tetrastromatica* and *G. salicornia*.

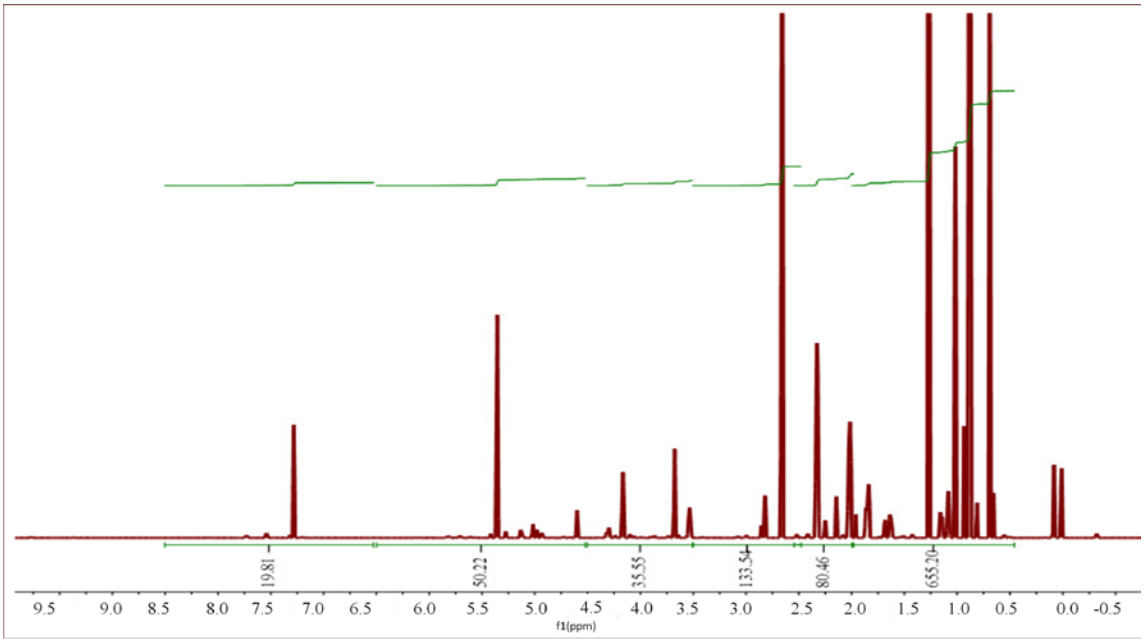

Figure 3.10.: ^{1}H NMR spectrum of EtOAc-MeOH extract of *G. salicornia*

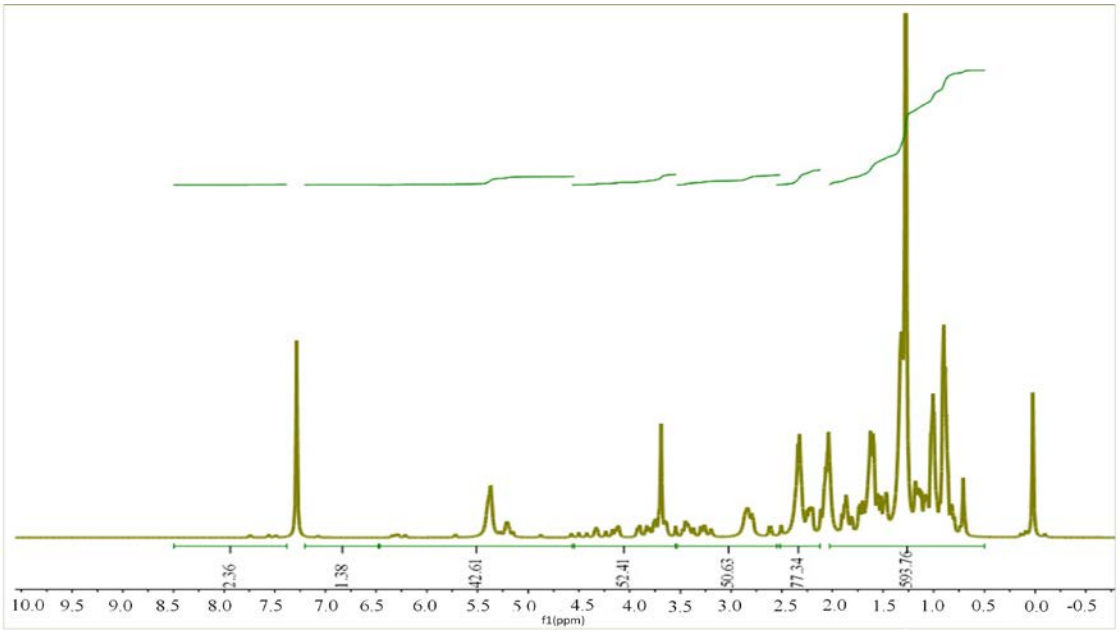

Figure 3.11.: ^{1}H NMR spectrum of EtOAc-MeOH extract of *P. tetrastromatica*

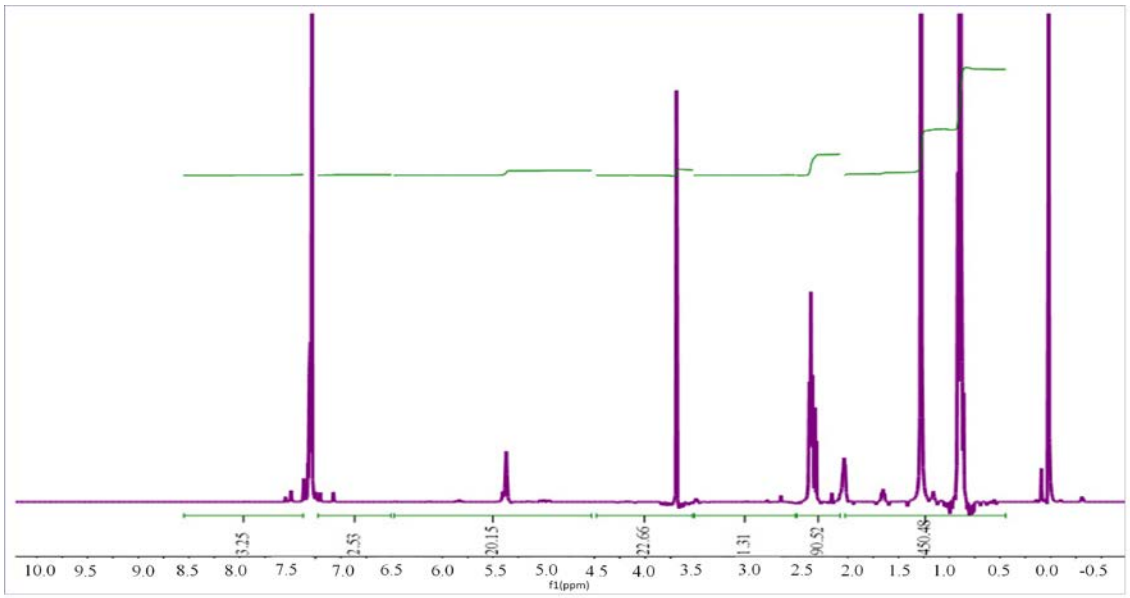

Figure 3.12.: ^{1}H NMR spectrum of EtOAc-MeOH extract of *G. canaliculata*

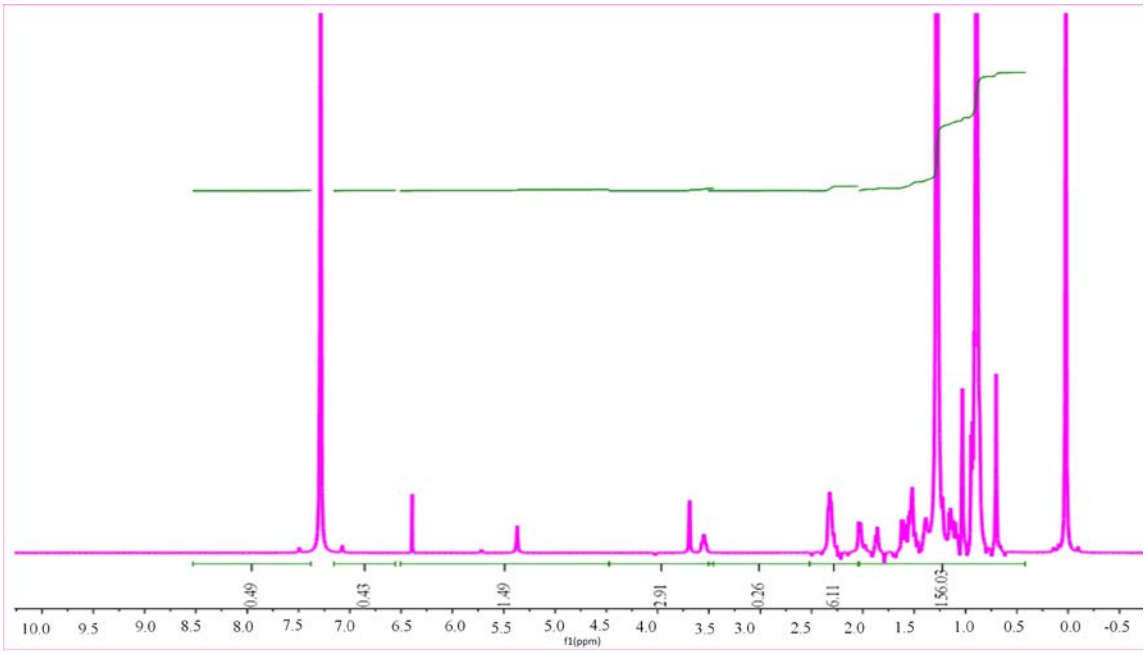

Figure 3.13.: ^{1}H NMR spectrum of EtOAc-MeOH extract of *G. corticata*

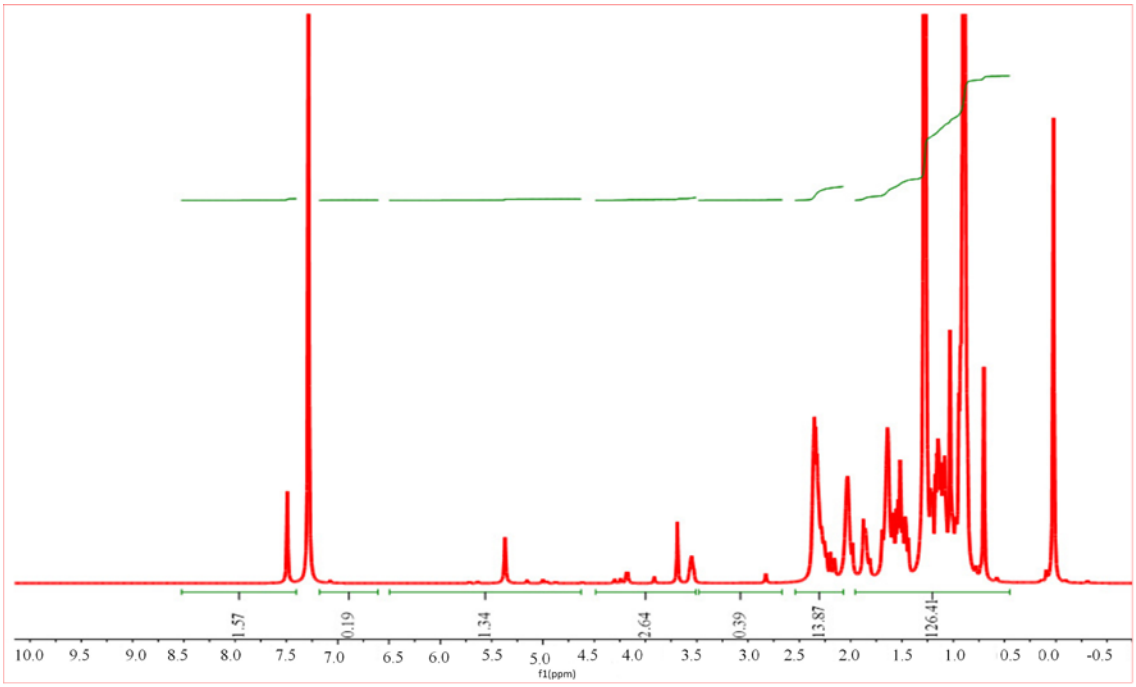

Figure 3.14.: ^{1}H NMR spectrum of EtOAc-MeOH extract of *H. edulis*

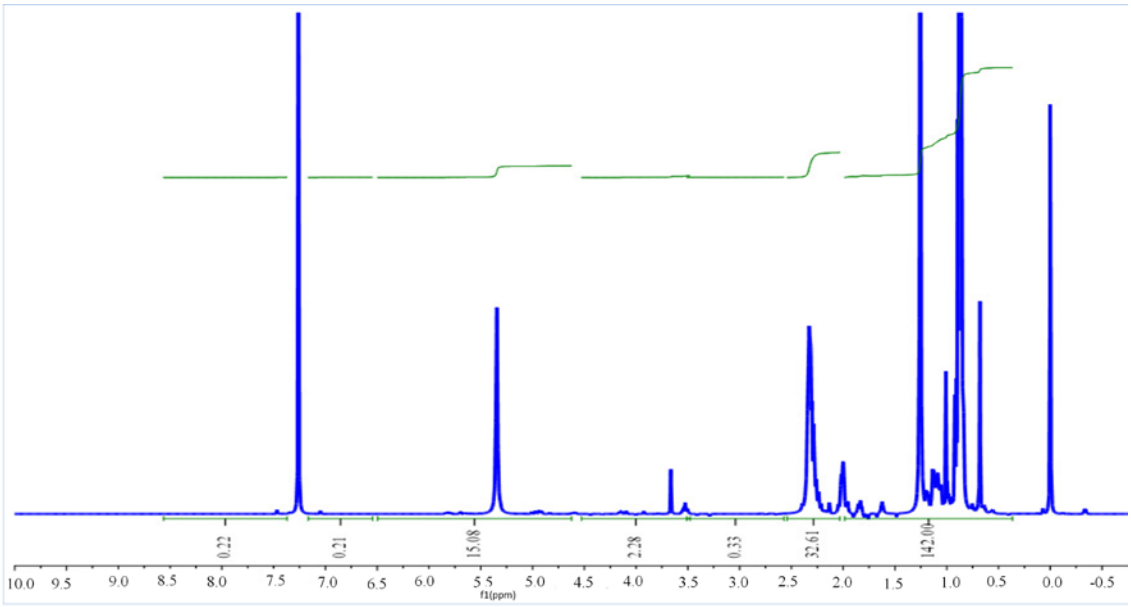

Figure 3.15.: ^{1}H NMR spectrum of EtOAc-MeOH extract of *A. fragilissima*

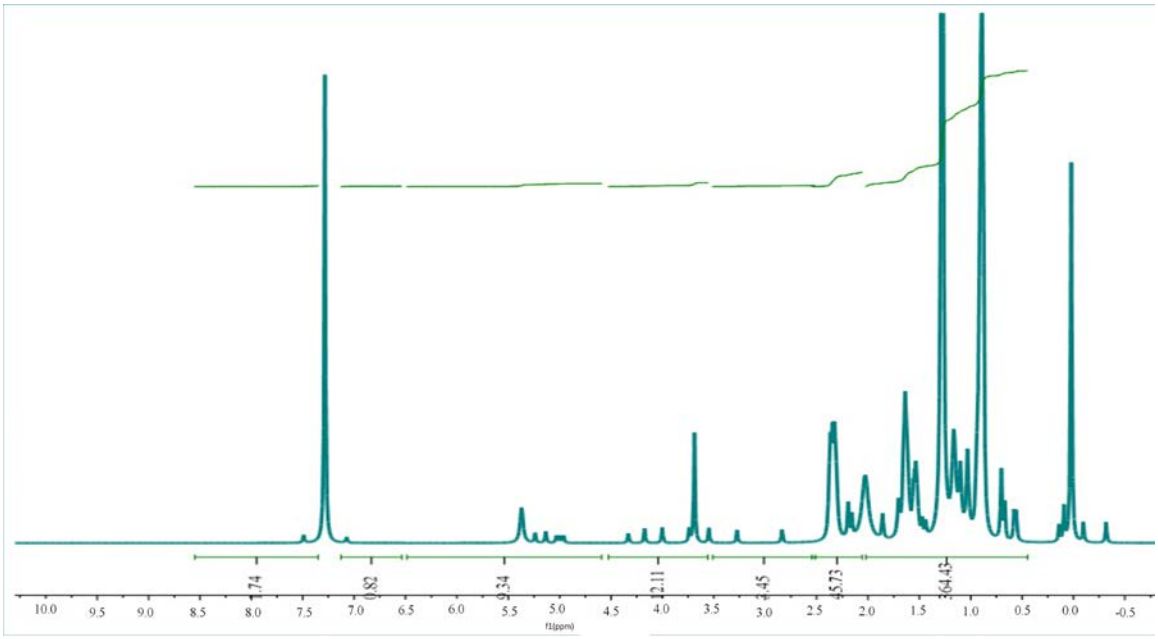

Figure 3.16.: ^{1}H NMR spectrum of EtOAc-MeOH extract of *P. pedrochei*

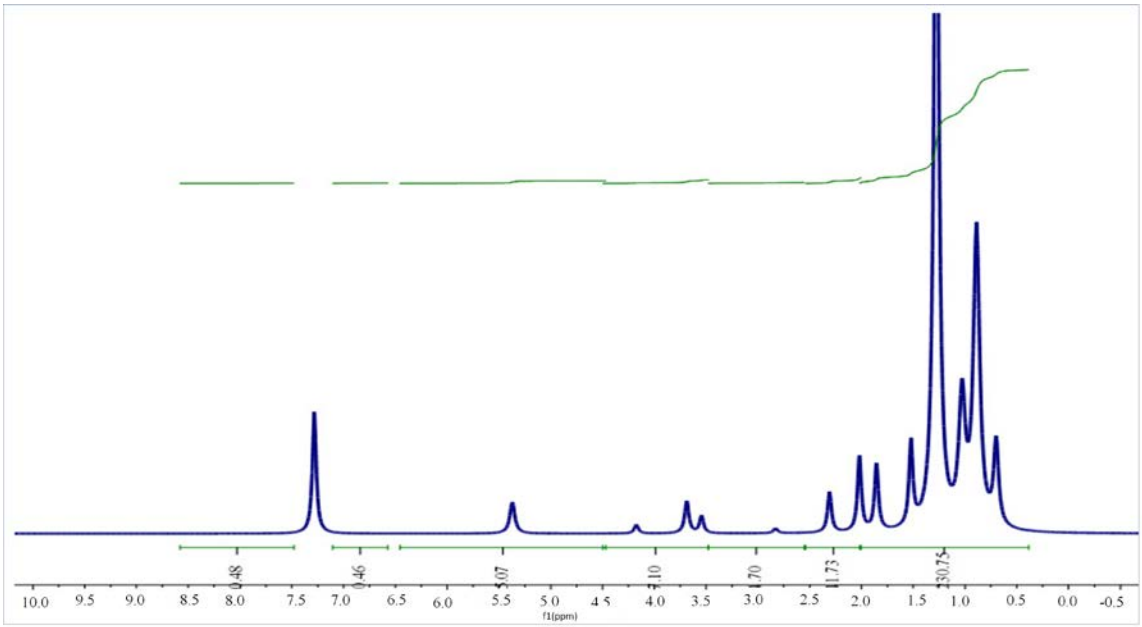

Figure 3.17.: ^{1}H NMR spectrum of EtOAc-MeOH extract of *S. filamentosa*

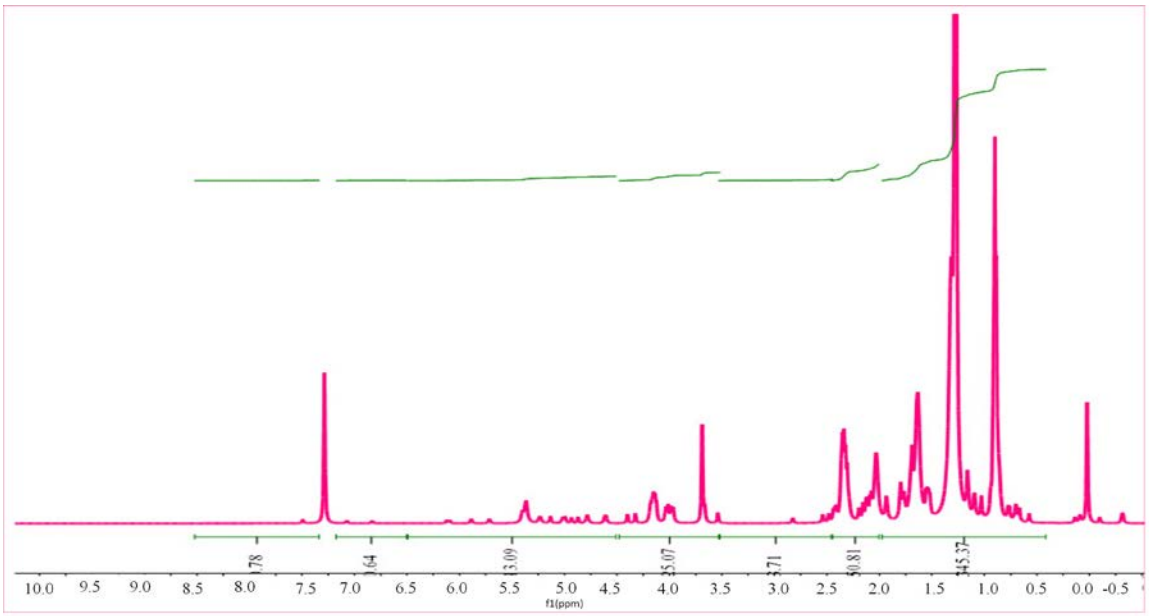

Figure 3.18.: ^{1}H NMR spectrum of EtOAc-MeOH extract of *H. dilatata*

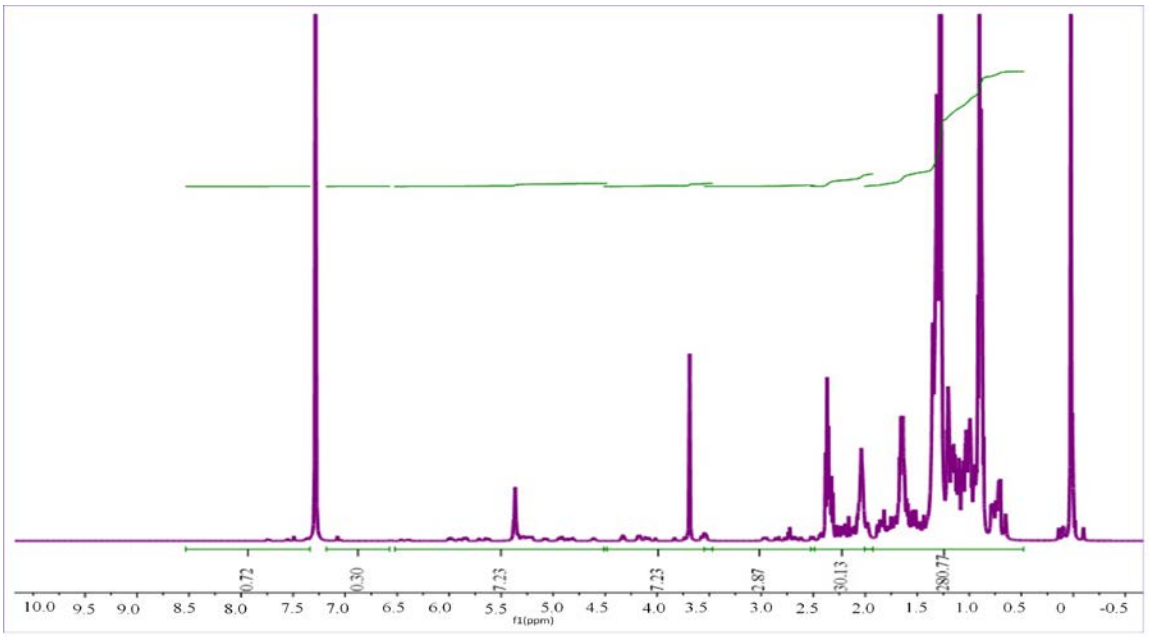

Figure 3.19.: ^{1}H NMR spectrum of EtOAc-MeOH extract of *P. hornemannii*

Table 2. Type and integral values of protons obtained from the 1H-NMR of the organic extracts of seaweeds belonging to the subclasses Dictyotophycidae (phylum Ochrophyta), Rhodymeniophycidae and Corallinophycidae (phylum Rhodophyta).

Seaweeds	**Integral values of protons (∑H) at the specified region (δ_H) of ^{1}H NMR spectra***					
	δ_H 0.5-2.0[a]	**2.0-2.5**[b]	**2.5-3.5**[c]	**3.5-4.5**[d]	**4.5-6.0**[e]	**6.5-8.5**[f]
G. salicornia	665.2	80.46	133.54	35.55	50.22	19.81
P. tetrastromatica	593.76	77.34	50.63	52.41	42.61	3.74
G. canaliculata	450.48	90.52	1.31	22.66	20.15	5.78
G. corticata	364.43	45.73	3.45	12.11	9.34	2.56
H. edulis	345.37	50.81	3.71	25.07	13.09	1.42
A. fragilissima	280.77	30.13	2.87	7.23	7.23	1.08
P. pedrochei	230.75	11.73	1.70	7.10	5.07	0.94
S. filamentosa	156.03	6.11	0.26	2.91	1.49	0.92
H. dilatata	142.00	32.61	0.39	2.28	15.08	0.43
P. hornemannii	126.41	13.87	0.33	2.64	1.34	1.76

[*]The protons signals appeared in the ^{1}H-NMR spectra of seaweeds were integrated to acquire the ratio of number of protons in selected regions.

[a] Saturated hydrocarbons

[b] CH_2=CH-CH_3/RC(=O)CH_3/RCH_2C(=O)OR_1/Ar-CH_3

[c] OCH_3/R-CH_2-X/R-CH_2-OH

[d] Anomeric (due to polysaccharides)

[e] RCH=CHR_1/RCH_2C(=O)OCH_3

[f]Ar-H

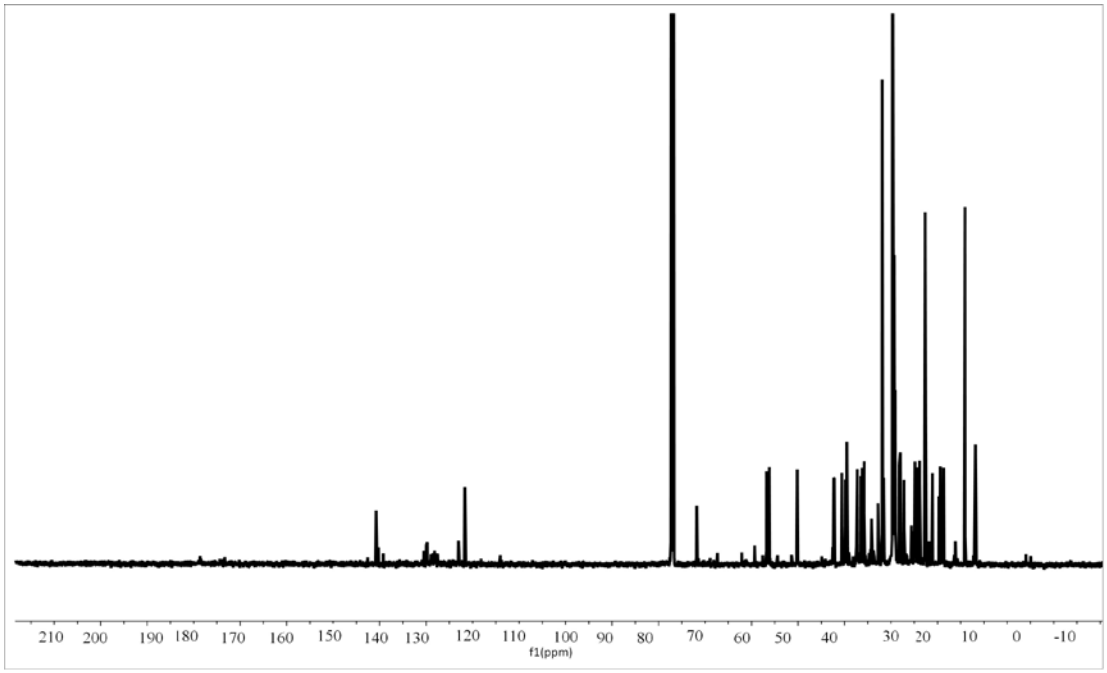

Figure 3.20.: ^{13}C NMR spectrum of EtOAc-MeOH extract of *G. salicornia*

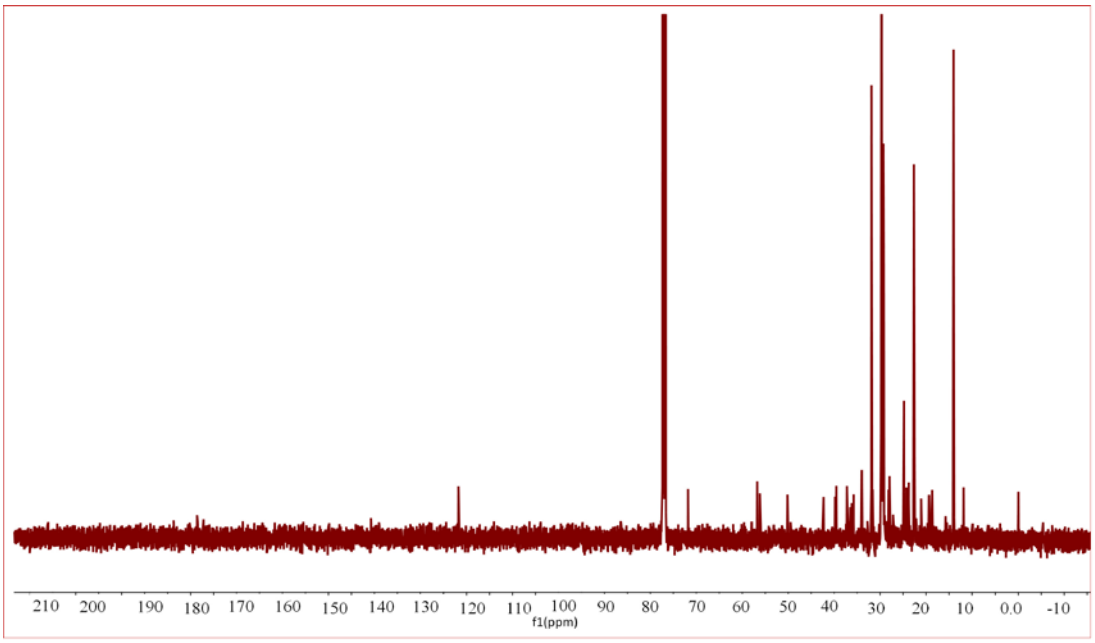

Figure 3.21.: ^{13}C NMR spectrum of EtOAc-MeOH extract of *P. tetrastromatica*

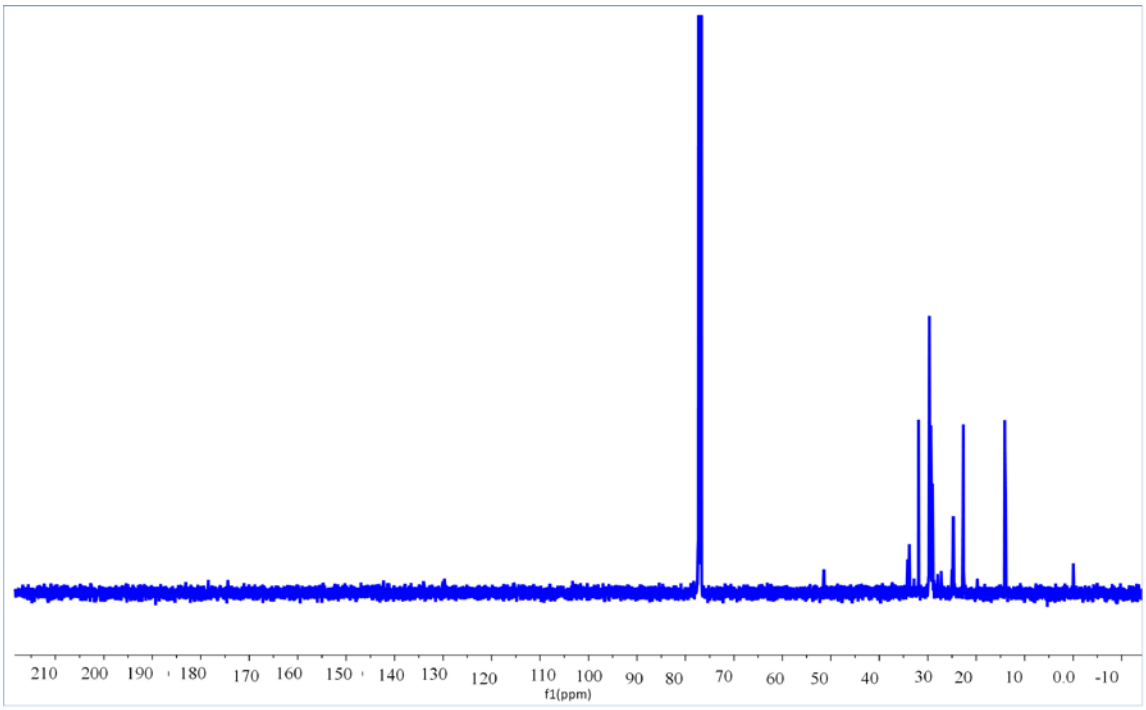

Figure 3.22.: ^{13}C NMR spectrum of EtOAc-MeOH extract of *G. canaliculata*

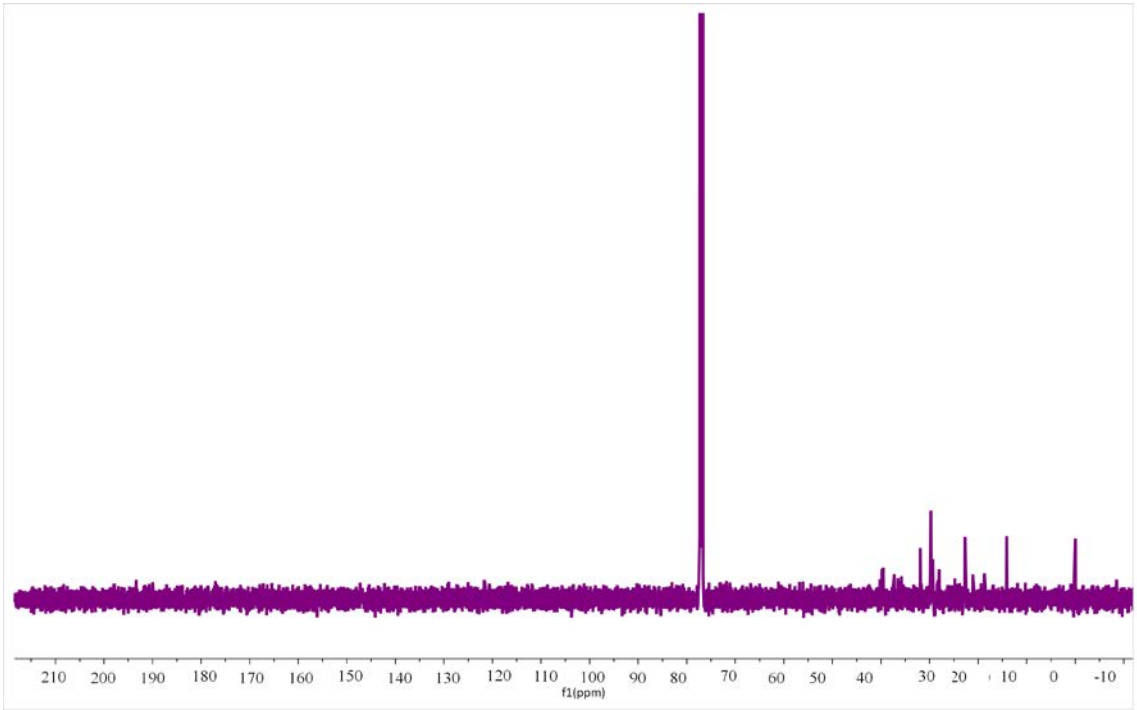

Figure 3.23.: ^{13}C NMR spectrum of EtOAc-MeOH extract of *G. corticata*

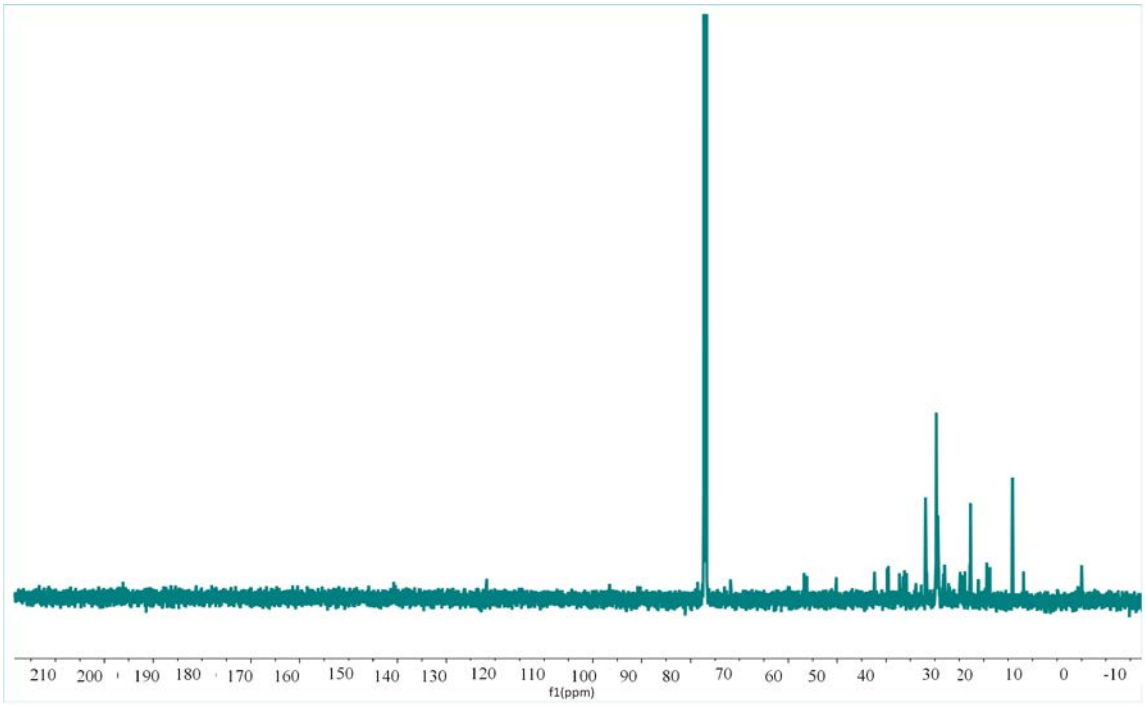

Figure 3.24.: ^{13}C NMR spectrum of EtOAc-MeOH extract of *H. edulis*

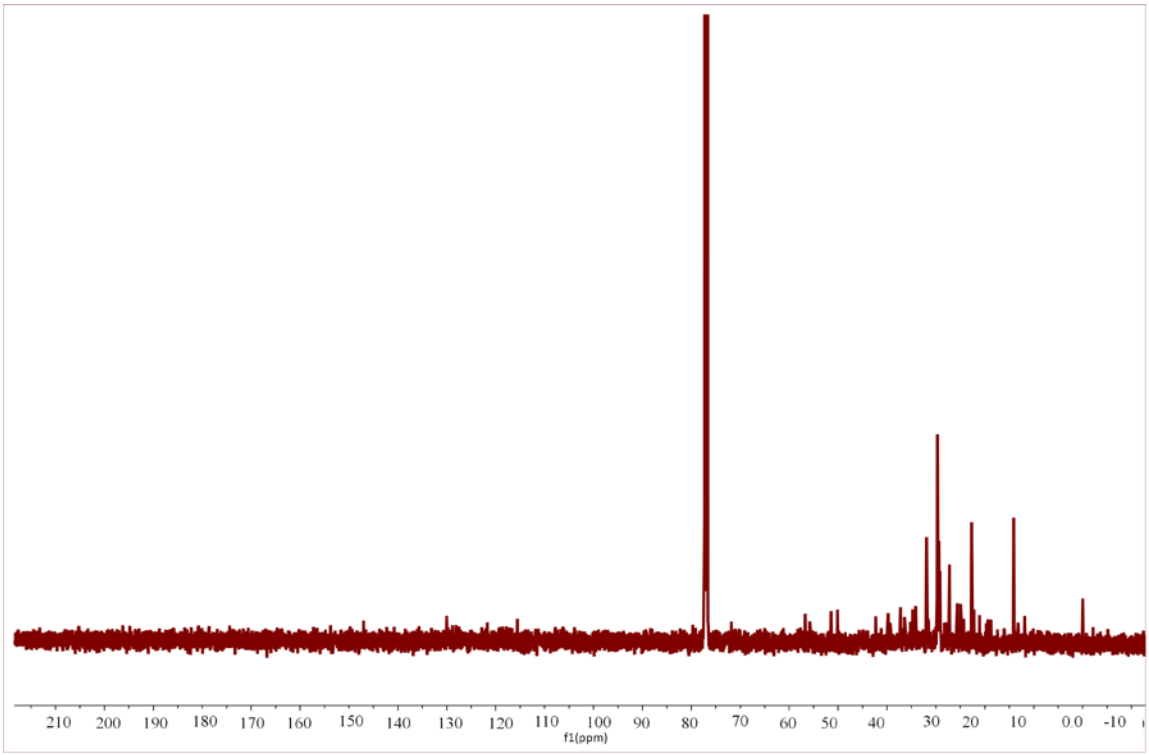

Figure 3.25.: ^{13}C NMR spectrum of EtOAc-MeOH extract of *A. fragilissima*

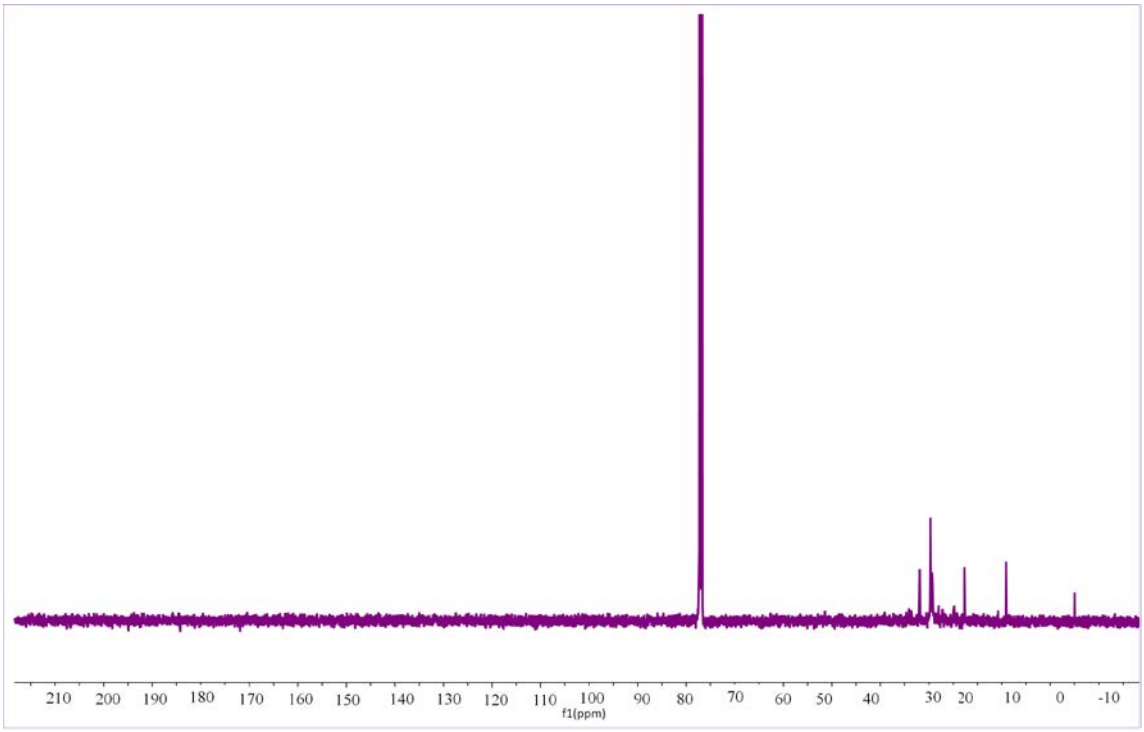

Figure 3.26.: ^{13}C NMR spectrum of EtOAc-MeOH extract of *P. pedrochei*

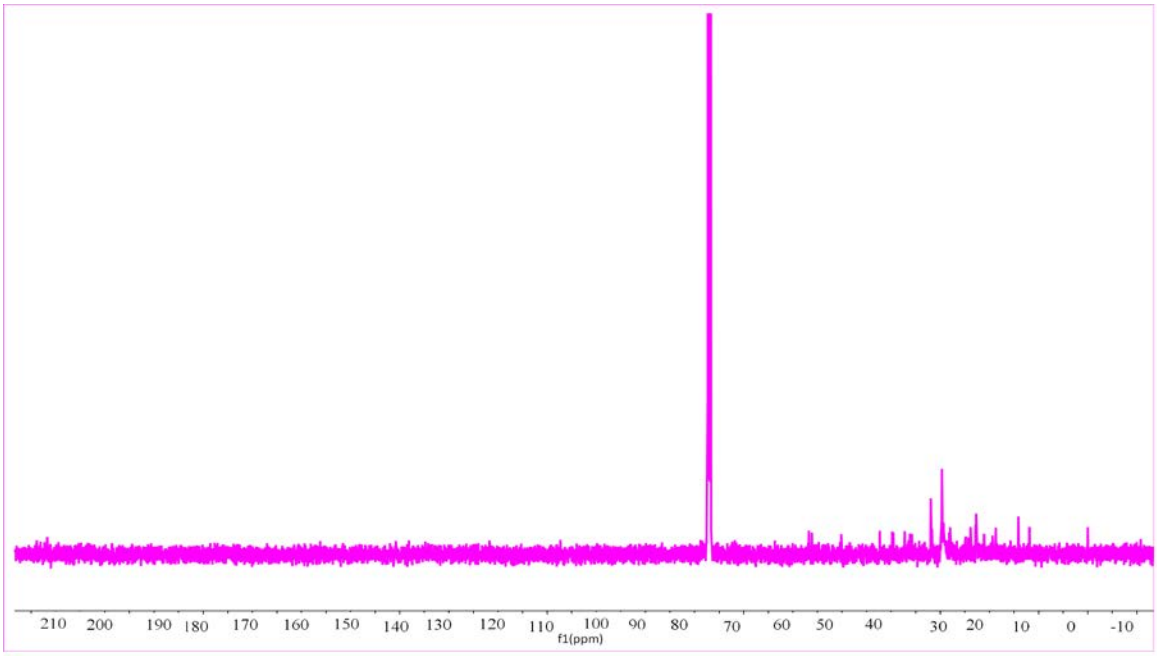

Figure 3.27.: ^{13}C NMR spectrum of EtOAc-MeOH extract of *S. filamentosa*

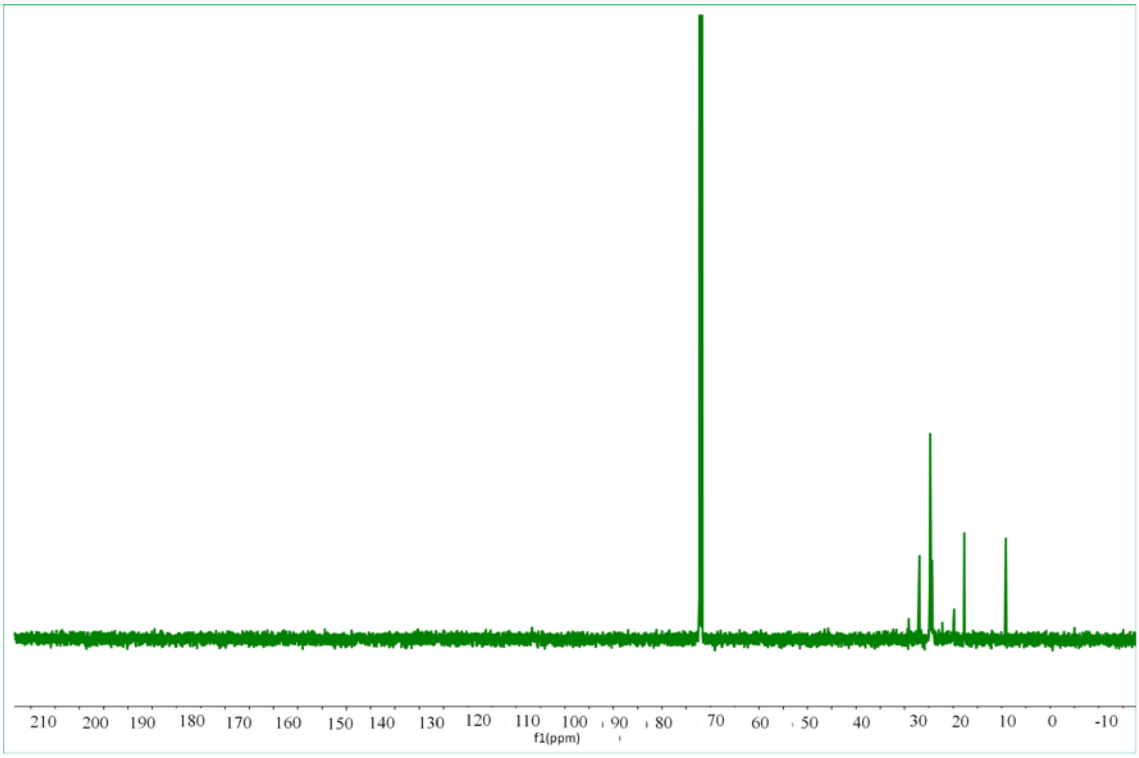

Figure 3.28.: ^{13}C NMR spectrum of EtOAc-MeOH extract of *H. dilatata*

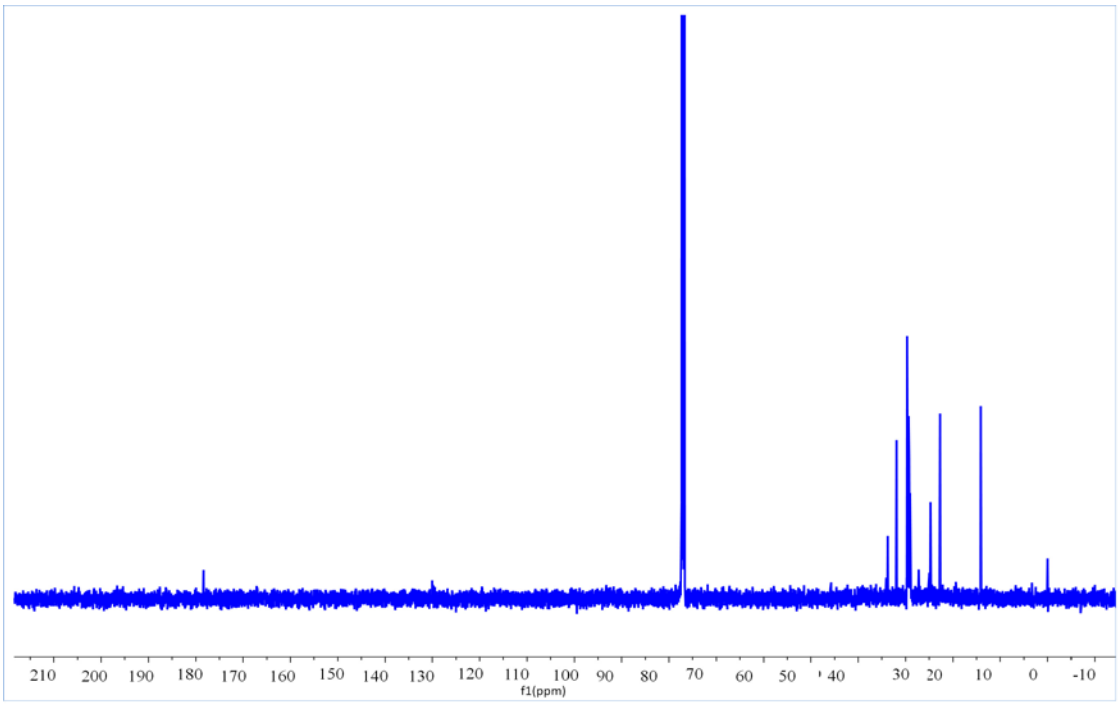

Figure 3.29.: ^{13}C NMR spectrum of EtOAc-MeOH extract of *P. hornemannii*

The proton integrals in the downfield section of the ^{1}H-NMR spectra at about δ_H 2-2.5 and 4.5-6.5 were feeble for *H. edulis* (ΣH 80.46 and 50.22, respectively) and *P. hornemannii* (ΣH 13.87 and 1.34, respectively), and comparatively lesser bioactivities of the organic extracts of these seaweeds described that these functional groups could be responsible for the studied pharmacological properties. Conversely, the organic extracts of *P. tetrastromatica* and *G. salicornia* showed greater proton integrals in the low-field region of the ^{1}H-NMR spectra, which might be attributed to the higher bioactivities of these seaweeds. A substantial co-linearity was observed to prevail among the electronegative groups in the downfield position of ^{1}H-NMR spectra *vis-a-vis* anti-diabetic and anti-inflammatory activities of the organic extracts of the seaweeds *P. tetrastromatica* and *G. salicornia*.

The NMR fingerprinting analyses were appropriately corroborated with those of infra-red (IR) spectral data. Characteristic IR traces at 1732 and 1724 cm^{-1} could be attributed to the C=O stretching frequencies of aldehydes or saturated aliphatic groups (Figure 3.30-3.39). Strong band appeared at 1540 cm^{-1} in the organic extract of *G. salicornia* might represent the occurrence of carbonyl functionalities, whereas the band at 1373 cm^{-1} have shown coupled C-O and O-H stretching frequencies.

The ^{1}H-NMR approach of de-replication could quickly lead to a conclusion of the types and number of protons that might be associated with the bioactive components present in the extracts. The presence of electronegative functionalities in the organic extracts of *G. salicornia, G. canaliculata* and *P. tetrastromatica* might be attributed to potential pharmacological activities as also corroborated by the *in vitro* bioactivity assays. Integrative spectroscopic analyses of the organic extracts of the seaweed species assessed the pattern of the resonances to differentiate the constitution of signals and intensities of moieties of the likely structural classes involved. In general, the organic extracts of *P. tetrastromatica* and *G. salicornia* displayed significantly greater proton integrals than other studied seaweeds in the downfield region of the spectra. It is apparent that the electronegative groups harbored by the organic extracts of these species, and those present in the downfield space of the ^{1}H-NMR and ^{13}C-NMR spectra, might structure strong electrostatic linkage with the Zn^{2+} ion present in the ACE-I enzyme active site that might explain the potential ACE-I activity (Ledesma et al., 2003). Positive correlation between the ACE-I inhibitory and Fe^{2+}chelation activities of the organic extracts of *P. tetrastromatica* and *G. salicornia* might also explain the functional role of Fe^{2+} ion chelating components to induce the anti-hypertensive properties.

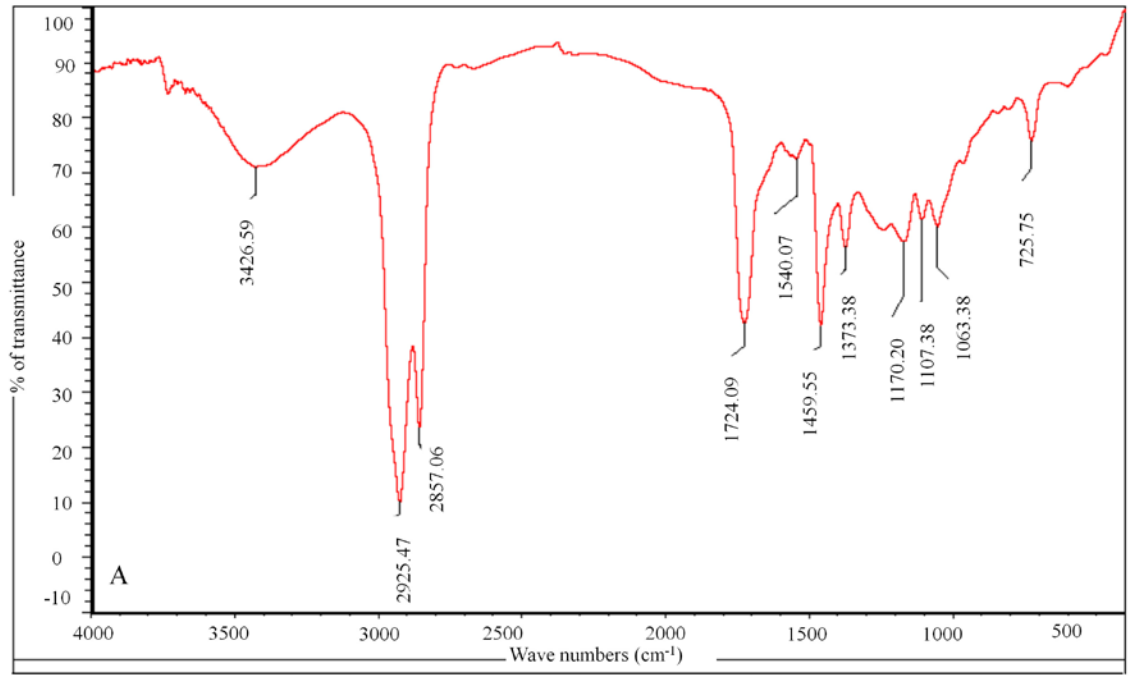

Figure 3.30.: FTIR spectrum of EtOAc-MeOH extract of *G. salicornia*

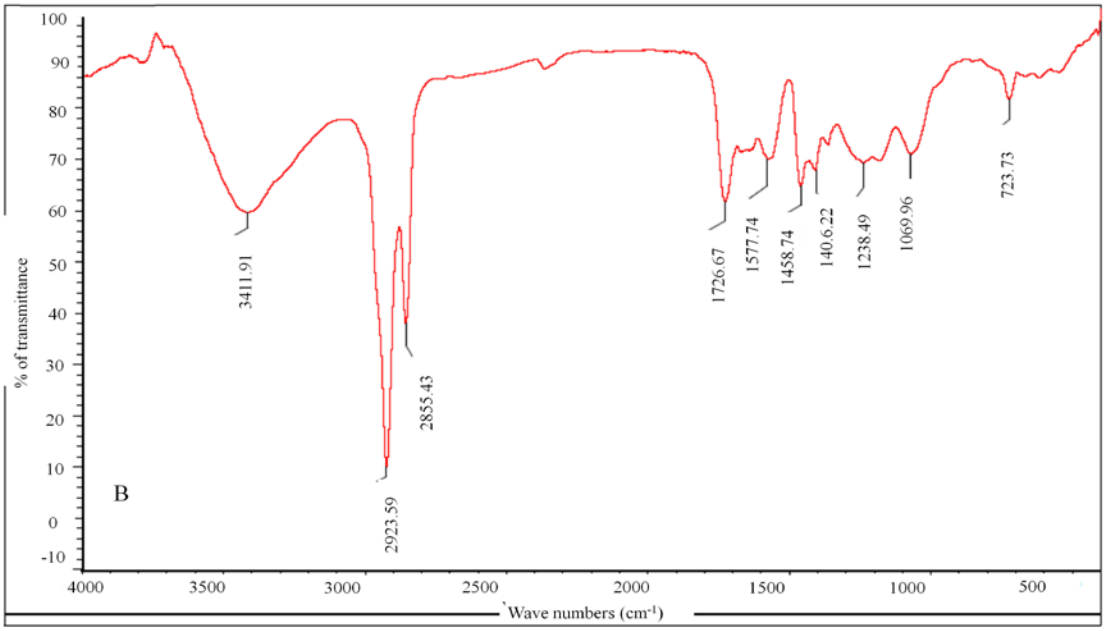

Figure 3.31.: FTIR spectrum of EtOAc-MeOH extract of *P. tetrastromatica*

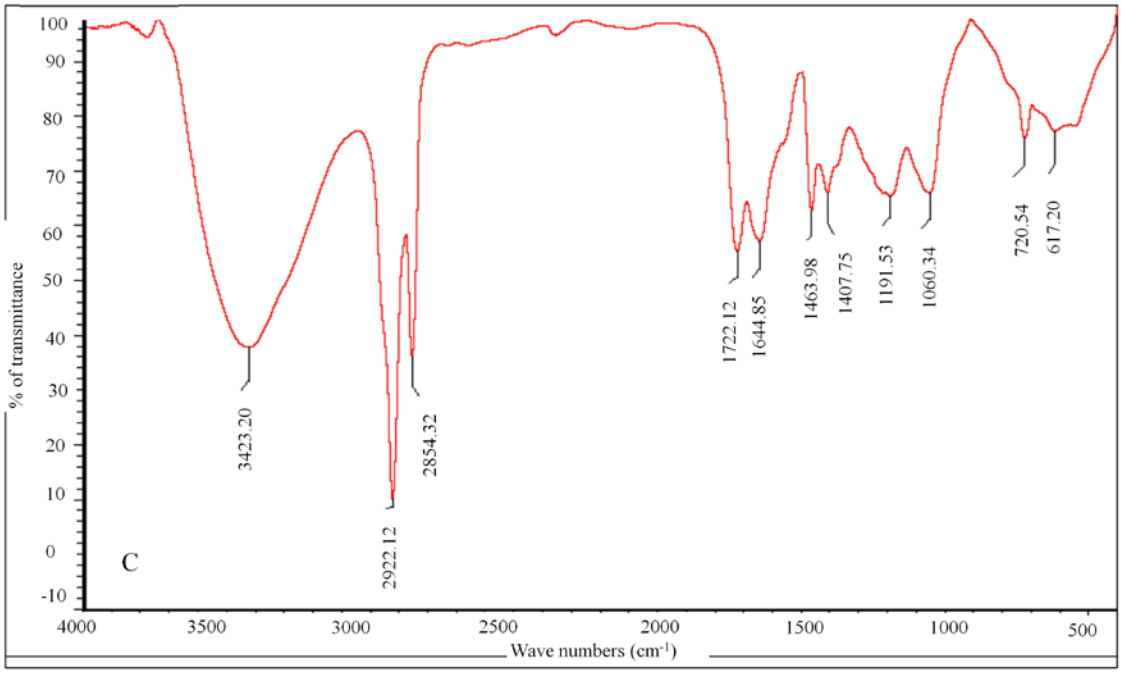

Figure 3.32.: FTIR spectrum of EtOAc-MeOH extract of *G. canaliculata*

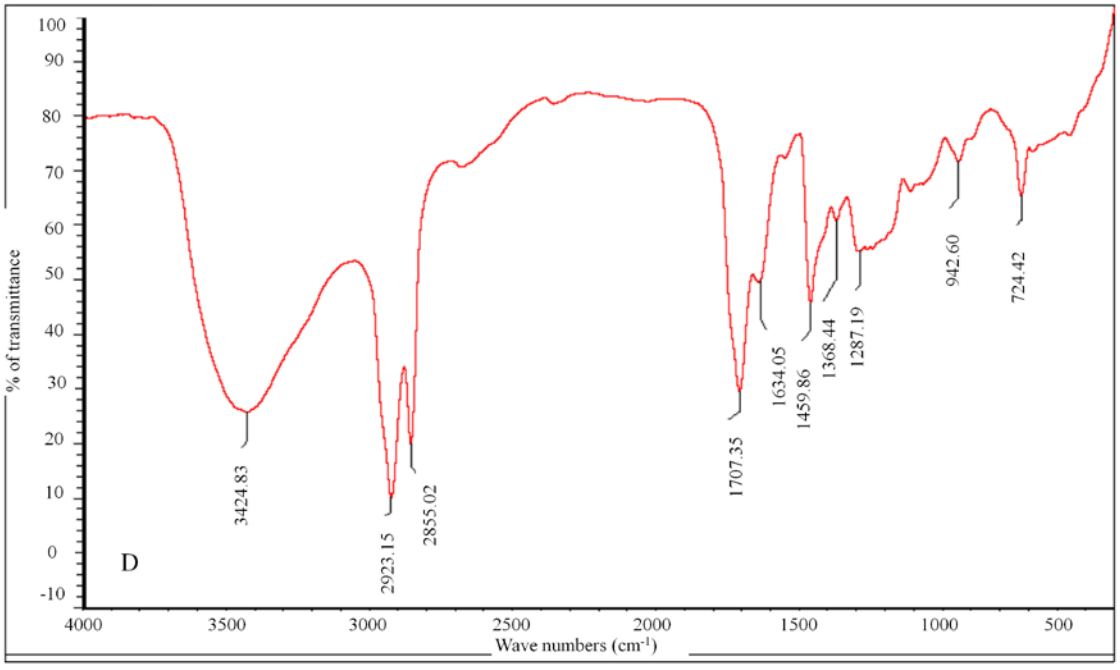

Figure 3.33.: FTIR spectrum of EtOAc-MeOH extract of *G. corticata*

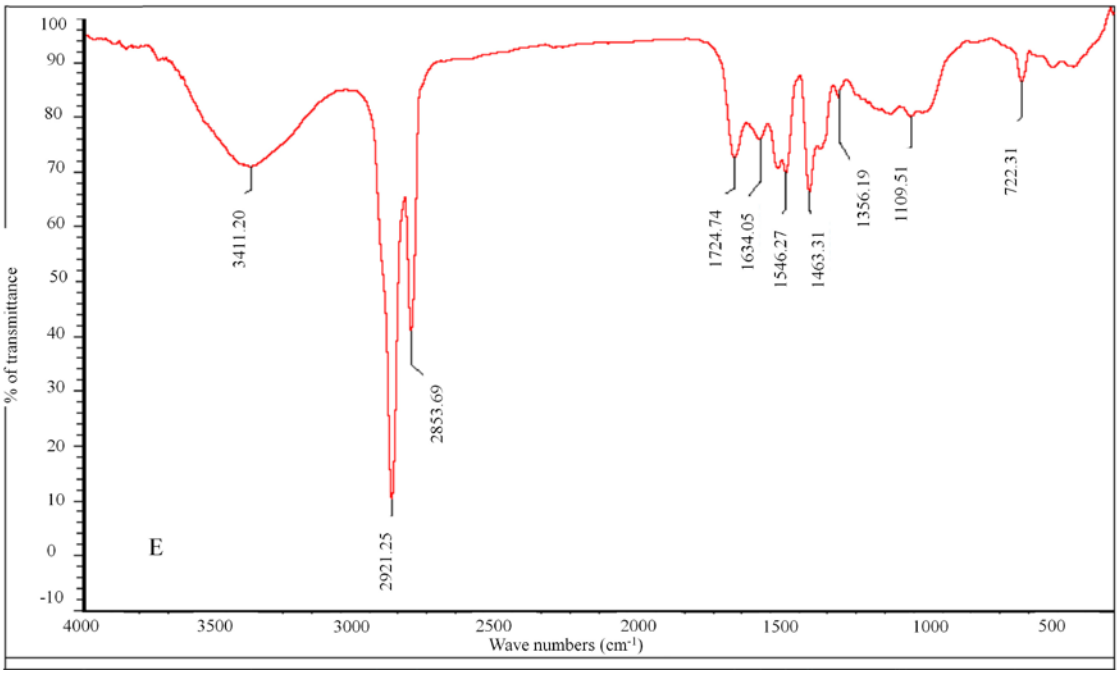

Figure 3.34.: FTIR spectrum of EtOAc-MeOH extract of *H. edulis*

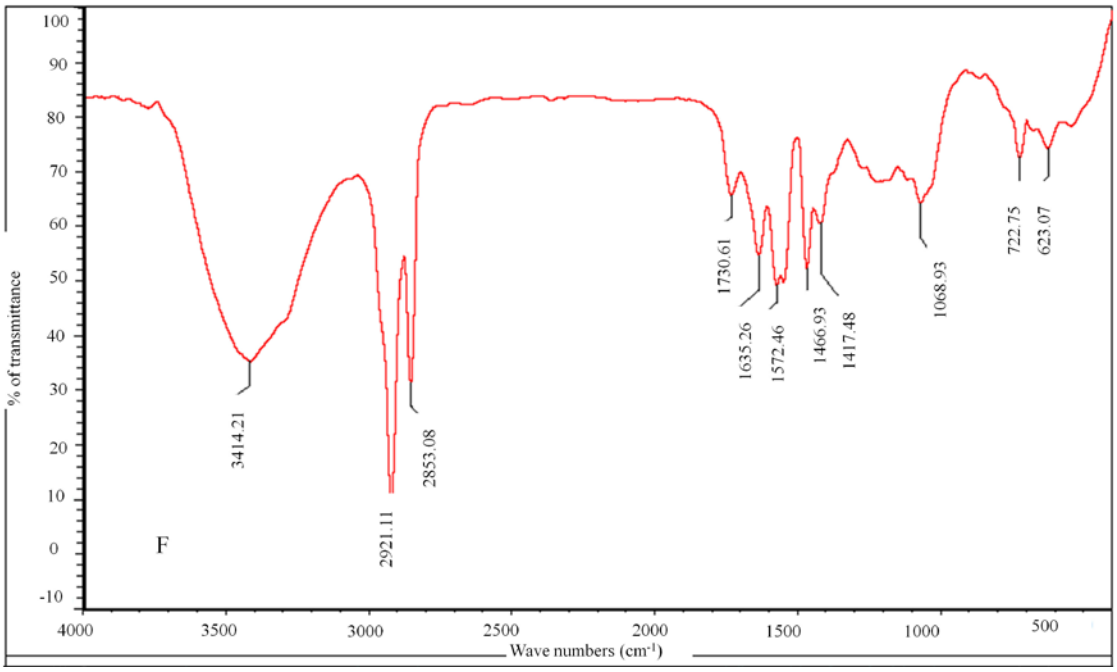

Figure 3.35.: FTIR spectrum of EtOAc-MeOH extract of *A. fragilissima*

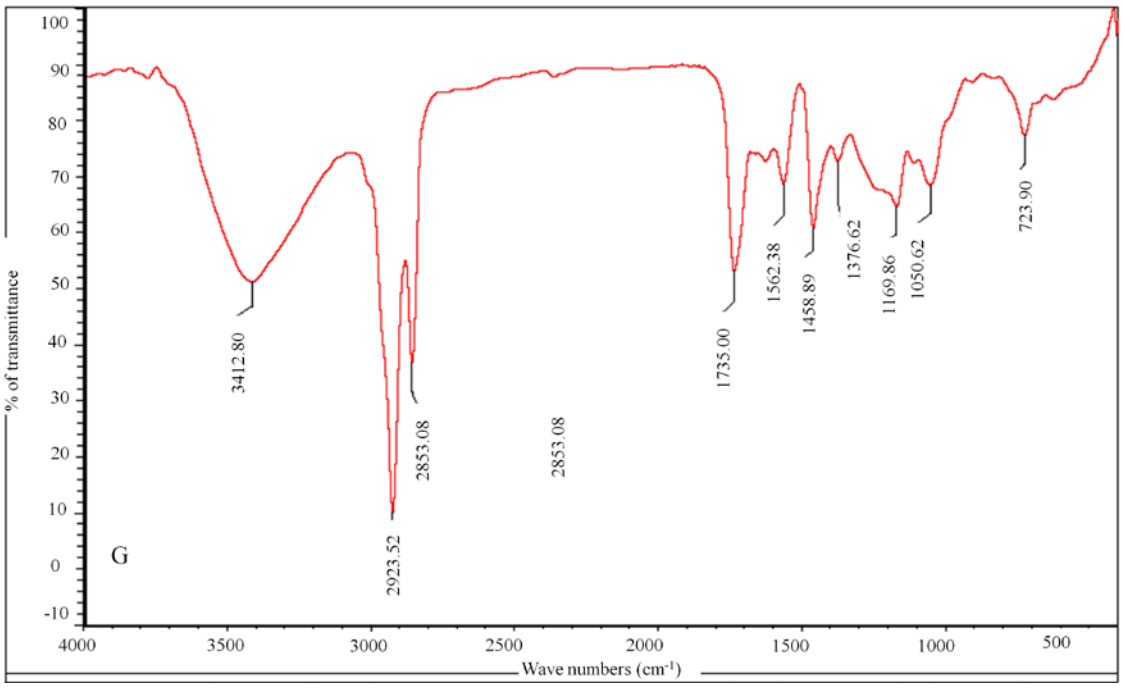

Figure 3.36.: FTIR spectrum of EtOAc-MeOH extract of *P. pedrochei*

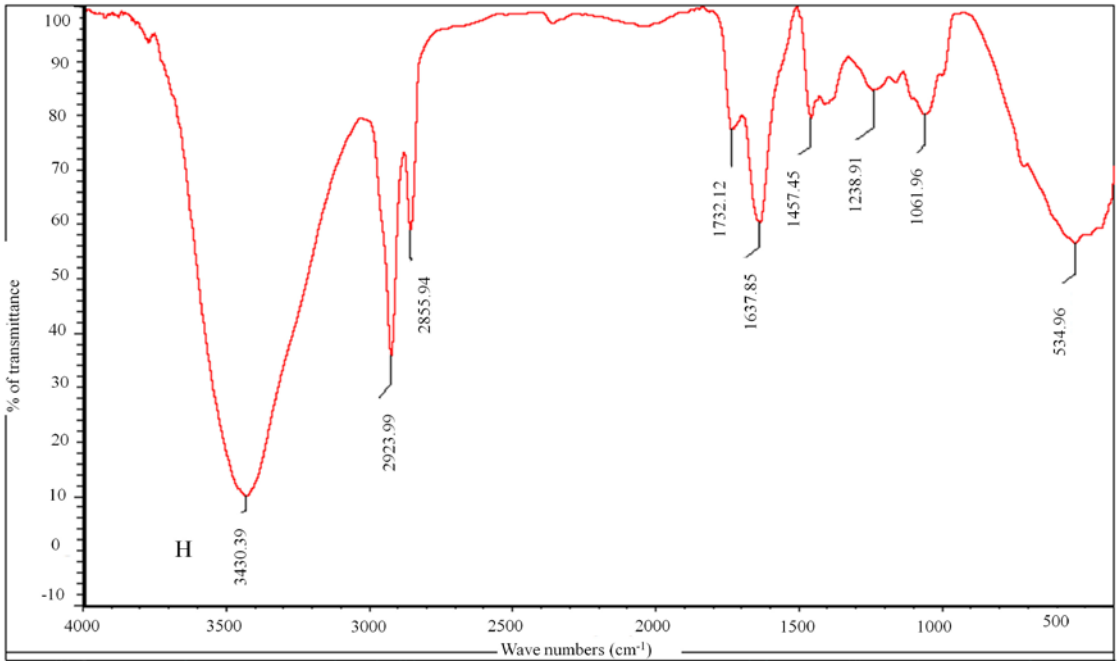

Figure 3.37.: FTIR spectrum of EtOAc-MeOH extract of *S. filamentosa*

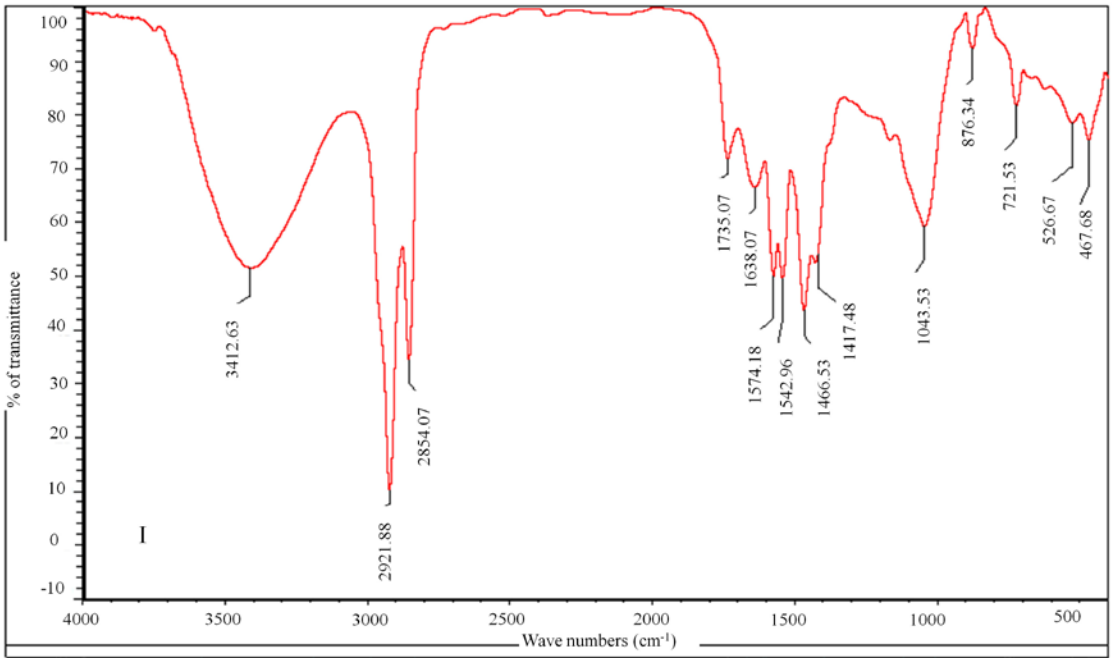

Figure 3.38.: FTIR spectrum of EtOAc-MeOH extract of *H. dilatata*

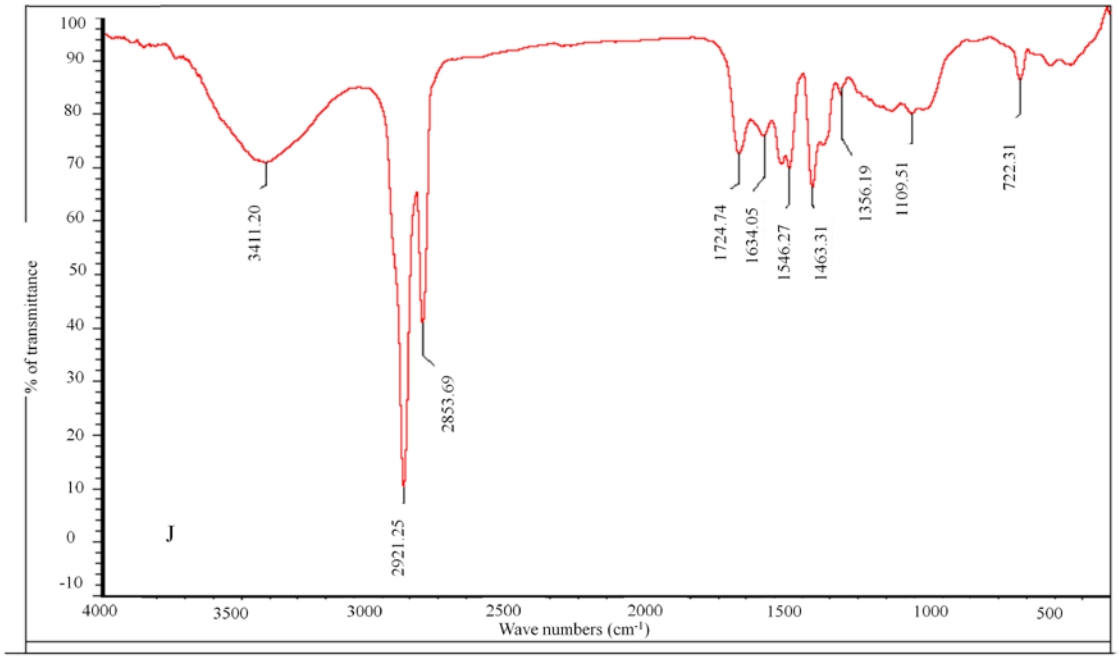

Figure 3.39.: FTIR spectrum of EtOAc-MeOH extract of *P. hornemannii*

3.4 Conclusions

A total of ten different seaweeds belonging to the subclasses Dictyotophycidae, Rhodymeniophycidae and Corallinophycidae collected from the Gulf of Mannar of Peninsular India were screened for *in vitro* antioxidant, anti-diabetic, anti-inflammatory and anti-hypertensive activities. Among various seaweeds considered in the present study, those belonging to the subclasses Dictyotophycidae and Rhodymeniophycidae displayed considerably greater pharmacological potentials. In particular, the organic extracts of *G. salicornia* and *P. tetrastromatica* registered significantly greater pharmacological properties than those derived from other studied seaweeds. This study also disclosed that the spectral fingerprinting could quickly deduce the signal pattern of the resonances, and conclusions could be drawn as to the likely structural classes involved in the organic extracts of the studied seaweeds. The present study recognized that the seaweeds *G. salicornia* and *P. tetrastromatica* might be promising candidates to isolate high value compounds for pharmacological use and their application as functional foods.

CHAPTER 4

ISOLATION AND CHARACTERIZATION OF BIOACTIVE LEADS FROM RED SEAWEED (RHODOPHYCEAE) *GRACILARIA SALICORNIA*

Contents

4.1 Background
4.2 Materials and methods
4.3 Results and discussion
4.4 Conclusions

4.1 Background

Seaweeds are prospective marine bioresources to isolate secondary metabolites with varied structural patterns and bio-activities, particularly, and have been considered as promising sources of new antioxidants (Ito and Hori, 1989). Antioxidants are found to be played significant role in the inhibition or scavenging of free radicals, and thus they can protect the organs from degenerative disorders and infections (Garcia et al., 2012). Generally, the formation of reactive oxygen species (ROS) surpasses the anti-oxidative defensive mechanism of the cells, and thereby, they can attack the structure and functions of biological molecules, such as lipids, carbohydrates, and proteins. These metabolic dysfunctions lead to the biological and physiological abnormalities in the cells, leading to the pathogenesis of type-2 diabetes, inflammation, cancer, cardiovascular disorders, and aging (Garcia et al., 2012). Antioxidants are able to donate electrons to the reactive radical species and convert them to harmless functionalities, and therefore, are endowed with potential applications in pharmaceutical and functional food. Notably, the bioavailability of natural antioxidants was found to be substantially greater related to the synthetic antioxidant molecules (Chioma, 2016; Athukorala et al., 2006). The chemical constituents present in seaweeds, such as terpenoids, amino acid derivatives, halogenated compounds, oxygenated cyclic/non-cyclic compounds and alkanes could potentially make them more attractive source of structurally and biologically novel potential metabolites than other marine living forms (Mtolera et al., 2010). Among various seaweeds, red seaweeds

were comprised large number of terpenoids, polyphenols, polysaccharides, proteins and peptides with bioactive potentials. The whole seaweeds of Rhodophyta have been used as traditional food, while polysaccharides and high value bioactive compounds were extracted for various properties including functional food, pharmaceutical and biotechnological applications.

Previous records on bioactive metabolites from seaweeds revealed the presence of various classes of secondary metabolites, namely macrocyclic compounds, diterpenoids, polyethers, triterpenoids, heterocyclic compounds, spiro compounds and polyketides, with bioactive potencies (Blunt et al., 2015). The α-pyrone macrolides, neurymenolides A and B were isolated from seaweed, *Neurymenia fraxinifolia* (Stout et al., 2009) and 2,6-disubstituted pyran-4-one along with 6-substituted pyran-2-one macrolides were documented from *Phacelocarpus labillardieri* (Kazlauskas et al., 1982). The macrolide, methyl-2-(12-oxo-7-phenyl-8-vinyl-1-oxa-4,9-cyclododecadien-3-yl)-acetate was reported from seaweed, *Sargassum wightii* (Maneesh and Chakraborty, 2017) with potent antioxidant and anti-inflammatory pluralities. An antibacterial macrolide, 7-*O*-methyl-5′-hydroxy-3’-heptenoate-macrolactin was reported from seaweed-associated bacteria, *Bacillus subtilis* (Chakraborty et al., 2014). Structurally diverse skeletons of drimane sesquiterpenes, such as sesquiterpene hydroquinones have been isolated from red seaweed *Peyssonnelia sp*. (Lane et al., 2010). The cytotoxic squalene-derived polyethers were identified from the red seaweed belonging to the genera of *Chondria* and *Laurencia* (family Rhodomelaceae) (Pacheco et al., 2011; Pacheco et al., 2010). Polyether compound, thyrsiferol was isolated from *Laurencia thyrsifera*, and further examples of polyether metabolites were reported from green seaweed *Botryococcus brauniis* (Faulkner, 2002; Blunt et al., 2011). Dehydrothyrsiferol was found to be another example of this polyether series, identified from *Laurencia pinnatifida* in the Canary Islands of Spain. Fatty acyl polyether okadaic acid with protein phosphatase inhibitory property was characterised from *Prorocentrum sp*. (Cohen et al., 1990). The non-halogenated rearranged spiro-compound, 1,4,9-trimethyl-5-methylidenespiro[5.5]undec-1,7-diene-4,9-diol and halogenated spiro-fused compounds, such as 2-bromo-1,1,9-trimethyl-5-methylidenespiro[5.5]undec-7-ene-3,9-diol and 2-bromo-9-bromomethylidene-1,1-dimethyl-5-methylene spiro [5.5]undec-7-ene were previously reported from a red seaweed, *Laurencia scoparia* with bio-potentials (Davyt et al. 2001). The halogenated and nonhalogenated spiro-compounds, which were classified as compositacins, were reported from the red seaweed, *Laurencia composita* (Yu et al., 2017). Chromenols have been derived from the seaweed *Desmarestia menziesii* (Davyt et al., 1997). Chromenyl metabolites, such as benzopyrans or benzopyrones were reported from the seaweeds *Sargassum micracanthum* and *Sargassum siliquastrum* (Iwashima et al., 2005; Jang et al., 2005). Labdane bicyclic diterpenoids were reported from seaweeds with broad range of biological activities

(Singh 1999; Demetzos & Dimas 2001; Hanson 2000; Hanson 2001; Hanson 2002; Blunt et al., 2006). Oleanane triterpenoids with anti-diabetic properties were characterised from *Sambucus adnata* (Sasaki et al., 2011) and *Astilbe koreana* (Na et al., 2006). The inhibitory potencies of fridooleanene triterpenoids against α-amylase and α-glucosidase were previously reported from the seaweed *Sargassum wightii* (Maneesh and Chakraborty, 2017). Although these classes of secondary metabolites deserve special consideration because of their targeted therapeutic potentials, very few studies were reported with the anti-diabetic activities of naturally-derived triterpenoids (Nazaruk and Borzym-Kluczyk, 2015).

Among the red seaweeds, the genus *Gracilaria* was found as the most promising candidate due to their ability to provide high yields and biosynthesizing commercially significant bioactive compounds and extracts (De Almeida et al., 2011). The species *G. asiatica* documented the presence of terpene *cis* and *trans*-phytol (Sims et al., 1976). Various types of lactone compounds were derived from *G. confervoides* (Nagai et al., 1997; Nagai et al., 1996). The compounds, such as polycavernoside B-B2, and polycavernoside A2-A3 have been identified from *G. crassa* (Yotsu-yamashita et al., 1993; Yotsu-yamashita et al., 1995). The protein, R-phycoerythrin were reported from two species, namely *G. salicornia* (D'agnolo et al., 1994) and *G. longa* (Talarico et al., 1978). The steroids and prostaglandins were isolated from red seaweeds *G. coronopifolia* and *G. crassa*, respectively (De Almeida et al., 2011). Commercially important agar, carrageenan and esterified polysaccharides were reported from seaweeds, *G. confervoides*, *G. dura*, *G. chilensi*, and *G. secundata* (De Almeida et al., 2011).

The significant and attractive phyla in terms of their pharmacologically active MNPs comprise the abundantly available seaweed species, among which the red seaweeds are potential sources of bioactive substances (Makkar and Chakraborty, 2019; Makkar and Chakraborty, 2018). Pluralities of investigations on bio-active components from seaweed demonstrating antiviral, antibacterial, antitumor and antileukaemic properties were reported worldwide. The rich diversity of red seaweeds particularly belonging to *Gracilaria sp.* along the coastline of South Indian subcontinent represents an unexploited source of bio-compounds with valuable biomedical as well as pharmaceutical use, although these species was not comprehensively studied to identify/characterize the bio-active leads (Makkar and Chakraborty, 2018). The seaweed of genus *Gracilaria sp*. are abundantly available in the coastal peninsular India with more than 300 reported species, and were recognized in industrial seaweed biotechnology due to the commercial product phycocolloid widely used in food, pharmaceutical and cosmetic industries (Makkar and Chakraborty, 2017; Andriamanatoanina et al., 2007; Francavilla et al., 2013). It has been documented that the organic extracts of *Gracilaria* sp. (family Gracilariaceae) comprised bioactive secondary metabolites along with anti-inflammatory, antioxidant,

antidiabetic and antimicrobial potentials (Bansemir et al. 2006, Makkar & Chakraborty 2018b, Makkar and Chakraborty 2018c). Among different species of the genus *Gracilaria*, *Gracilaria salicornia* (C. Agardh) E.Y. Dawson was found to be ubiquitous in the coastal waters of Indian peninsular, although the species was not extensively studied to characterize the bioactive leads. Since initial studies carried out in our laboratory provided us with promising leads, the current study is envisaged the isolation followed by characterization of bioactive secondary metabolites from the ethyl acetate/methanol (1:1 v/v) extract of *Gracilaria salicornia* by repeated chromatographic separation methods. The bioactive secondary metabolites characterized were grouped under different classes of chemistries, namely abeo-labdane class of diterpenoid (**1**), oleanene class of triterpenoids (**2**-**3**), drimane-associated quinols (**4**-**6**), 2*H*-chromenyl compounds (**7**-**8**), spiro-fused analogues (**9**-**10**), squalene polyether metabolites (**11**-**12**), and macrolides enclosing ether functionalities (**13**-**15**). These compounds were characterized through comprehensive spectroscopic techniques. Pharmacological properties were analyzed by various *in-vitro* antioxidant/anti-inflammatory/antidiabetic methods. The physico-chemical factors of the studied analogues were used to substantiate the chemistries of structures with their respective biological properties. Various physicochemical parameters were used to validate the structure-activity relationships of the titled compounds, and *in-silico* mode of attenuating potential against various enzymes was conducted by molecular docking analysis to corroborate the anti-inflammatory/antidiabetic potentials of the studied metabolites (**1**-**15)**.

4.2 Materials and methods

4.2.1 Chemicals and reagents

The chemicals used in this study include regents, solvents and solutions, which were acquired from Sigma-Aldrich Chemicals Co. Inc. (St. Louis, MO) and E-Merck (Darmstadt, Germany). Different buffers and solutions for screening studies were freshly made as and when required. All essential enzymes for biological assays were obtained from Sigma-Aldrich Chemicals Co. Inc. (St. Louis, MO). All analytical and spectroscopic graded reagents/solvents were purchased from E-Merck (Darmstadt, Germany) and Sigma-Aldrich Chemical Company, Inc. (Missouri, USA).

4.2.2 Chromatographic purification techniques and spectroscopic instrumentation analysis

4.2.2.1 Purification by column chromatography

Initially, the adsorbent dry silica gel of various mesh size, namely 60-120, 100-200, and 230-400 mesh (E-Merck, Germany) were packed with non-polar mobile phase (*n*-hexane) in vertically placed glass columns of different length and diameter (100 cm x 8 cm; 50 cm x 4 cm; 20 cm x 1.5 cm, Borosil, India), as found appropriate. The organic extracts of seaweed samples was made into slurry with silica (60-120 mesh size, 5 g) and loaded into the glass column. The components in the extracts were eluted by using different solvents with increasing order of polarity (*n*-hexane; dichloromethane; ethyl acetate and methanol). The sequential fractions were separately collected for further analysis.

4.2.2.2 Purification by flash chromatography

The organic extracts/fractions obtained from seaweed samples were separated by flash (Biotage AB SP1-B1A, Sweden) chromatographic technique using a silica column of 230-400 mesh size (Biotage Ref. No. 12 + M. Si). The organic extracts/fractions were loaded into the column in the form of slurry with silica gel. The sequential elution of components with desired wave length in the organic extracts/fractions was carried out using the non-polar mobile phase. The separation of fractions was monitored by the chromatograph, and they were collected separately.

4.2.2.3 Purification by high pressure liquid chromatography

The preparatory high pressure liquid chromatograph (PHPLC) system (Shimadzu Corporation, Nakagyo-ku, Japan) connected with a bonded reverse phase C_{18} (RP C_{18}) column (Shimadzu; Luna 250 mm X 14.0 mm, 5 μm) fitted with binary gradient pump (Shimadzu LC-20AP), column oven (CTO-20AC, Shimadzu), photodiode array detector (SPD-M20A, Kyoto, Japan) and a controller (CBM-20A, Shimadzu) were used for fine purification of the compounds. The injection volume was 2 mL and the column temperature retained at 40 °C. The various percentages of MeOH and acetonitrile were utilized as mobile phases with 6-8 mL/min flow rate. The absorbance was recorded between the range of 200-800 nm wavelengths and the mobile phase was comprised of various proportions of MeOH and acetonitrile with 1 mL/min flow rate.

The samples were filtered through the solid phase extraction cartridges (SPE; 55 mm, 70 Å, Strata C_{18}-E; Phenomenex, California, USA) and PTFE syringe filter (0.20 μm, Sartorius, Germany) prior to the injection to the analytical HPLC (AHPLC) and preparatory HPLC (PHPLC) systems, as and when deemed appropriate.

4.2.2.4 Purity assessment by thin layer chromatography and analytical HPLC

The purity of fractions was monitored by thin layer chromatography (TLC) and analytical high pressure liquid chromatography (AHPLC). The pure isolated fractions were spotted on the thin layer aluminium sheets (silica GF_{254}; E-Merck, Germany) by using capillary tubes after dissolved in small volume of desired solvents to analyse the presence of various components in the isolated fractions based on their R_f, retention factors (ratio of distance moved by component spot and solvent front). The various solvents with increasing polarity were used as the mobile phase (*n*-hexane; dichloromethane; ethyl acetate and methanol). The spots of the individual components were visualised in the 254 and 366 nm wavelengths by the UV lamp (Cole-Parmer, India).

An analytical HPLC system (Shimadzu Corporation, Nakagyo-ku, Japan) bonded with the reverse phase C_{18} (RP-C_{18}) column (Phenomenex, Torrance, California, USA; Luna 250 mm X 4.6 mm, 5 μm) fitted to binary gradient pump (Shimadzu LC-20AD), column oven (CTO-20A, Shimadzu), photodiode array detector (SPD-M20A, Kyoto, Japan) and a controller (CBM-20A, Shimadzu) were used to analyze the purity of isolated compounds. The injection-volume was 20 μL, and the column temperature was maintained at 40 °C. The fractions were eluted with mobile phases, such as methanol and acetonitrile in different proportions with a flow rate 1 mL/min in between the wavelengths 200-800 nm.

The samples were filtered through the solid phase extraction cartridges (SPE; 55 mm, 70 Å, Strata C_{18}-E; Phenomenex, California, USA) and PTFE syringe filter (0.20 μm, Sartorius, Germany) prior to the injection to the AHPLC/PHPLC system(s).

4.2.2.5 Spectrophotometric and spectroscopic analysis

The UV-spectrophotometric analyses were carried out using a Varian-Cary 50 UV/VIS spectrophotometer (Varian Cary 50, Palo Alto, CA) as well as micro-plate reader (Thermo Scientific™ Multiskan™ GO, USA). The quartz cuvettes (dimension 1:1:4.5 cm) and 96-well plates (Thermo Fisher Scientific; China) were used for measuring the absorbances of the samples. The infrared spectrum of the studied compounds was reported among 4000-400 cm^{-1} using KBR pellets through Perkin-Elmer Series 2000 FT-IR (Fourier-transform-infrared) spectrometer (Waltham, MA). The samples were mixed with KBr pellets, and the pressure was applied on them to make it transparent. The readings were recorded as % transmittance. Optical rotation was analysed in methanol by using a Perkin-Elmer 341 polarimeter.

The nuclear magnetic resonance (NMR) analyses {^{1}H-proton-500 MHz; ^{13}C-carbon-125 MHz; DEPT; ^{1}H-^{1}H COSY-; HSQC; HMBC; NOESY} were carried out through Bruker Avance DPX 500 MHz spectrometer (Rheinstetten, Germany) using deuterated chloroform

($CDCl_3$). The NMR data were attained by BrukerTopSpin™ 2 software and MestReNova-7.1.1-9649 (Mestrelab Research S.L.) was used for data processing. The mass spectrometric analyses were documented through Perkin-Elmer Clarus 680 gas chromatograph-mass spectrometer (GC-MS) functioning with the electron-impact (EI) method (Waltham, MA). A Bruker Daltonic micro-TOF series high-resolution-mass-spectrometer (HRMS) (GmbH; Germany) operating in positive mode electrospray ionisation {ESI-MS, $[M+H]^+$} has been used for high-resolution-mass-spectroscopy. The organic solvents extracts were concentrated using rotary vacuum evaporating instrument (IKA Werke GmbH & Co., Germany). All analytical and spectroscopic graded reagents/solvents were purchased from E-Merck (Darmstadt, Germany) and Sigma-Aldrich Chemical Company, Inc. (Missouri, USA).

4.2.3 Preparation of crude solvent extracts from red seaweed G. salicornia

The leaves (thalli) of red seaweed *G. salicornia* (voucher specimen number AC.3.1.1.4) was harvested during the low spring tides in the inter-monsoon wet period of March, 2017 from Mandapam (Gulf of Mannar region; between 8º48’ N, 78°9’ E and 9°14’ N, 79°14’ E) on the southeast coastline of the Indian sub-continent. The samples were identified by a marine algologist Dr. Chellaiah Periyasamy of Aquaculture Foundation of India, Madurai, and were deposited in the project repository under the accession number of GS. 1.4.2.1. The samples were subjected to repetitive washing with tap water and dehydrated at room temperature for 4 days. Dried leaves of seaweed were powdered (~1000 g) before being extracted with the solvent ethyl acetate (EtOAc) and methanol (MeOH) (1:1, v/v, 750 mL) at 50 °C for 3 h under reflux. The extracts were filtered over Whatman No. 1 filter paper using sodium sulfate (~ 115 g) and evaporated using a rotary vacuum evaporator (IKA Werke GmbH & Co., Germany) below 55 °C to obtain the crude extract (35 g) of *G. salicornia*. The extract was utilized for various chromatographic fractionations to yield the bioactive metabolites.

Figure 4.1.: The red seaweed *G. salicornia* of collected from the southeast coastline of the Indian sub-continent Gulf of Mannar region; between 8º48' N, 78°9' E and 9°14' N, 79°14' E)

4.2.4 Chromatographic purification of pure compounds and bioactive potentials of sub-column fractions from G. salicornia

The EtOAc-MeOH fraction (33.0 g) of *G. salicornia* was subjected for vacuum liquid chromatography (over silica gel, 60-120 mesh) and eluted primarily with 100% *n*-hexane to remove pigmentous and waxy type materials. The polarity of the mobile phase was gradually increased from, *n*-hexane (*n*-hex) to ethyl acetate (EtOAc) and then to methanol (MeOH) {*n*-hex: EtOAc (8:2 to 1: 9; v/v) and EtOAc: MeOH (9:1 to 3:7; v/v)} to obtain a total of 20 column fractions, such as GS_1-GS_{20}, respectively (Figure 4.2). The crude extract was mixed with silica (5 g, 60-120 mesh) to make a slurry before being packed into the glass column of dimension, 100 cm x 8 cm, which was enclosed with adsorbent silica gel (60-120 mesh). The bioactivities of the fractions were checked, and based on the results seven fractions (GS_2, GS_4, GS_7, GS_8, GS_{12}, GS_{13} and GS_{15}) were selected for further purifications. The column fractions were subjected for the analysis of antioxidant, anti-inflammatory and antidiabetic activities. The fraction GS_2 obtained by eluting with 30 % EtOAc was fractionated using *n*-hexane/EtOAc/MeOH on 230-400 mesh sized silica to afford 3 fractions ($GS_{2\text{-}1}$ – $GS_{2\text{-}3}$). The fraction $GS_{2\text{-}1}$ (30 % EtOAc:*n*-hexane) was found to be pure, which was further purified to homogeneity by preparative HPLC on octadecylsilane (C_{18}) bonded column using the solvent system of MeOH (methanol) / (water) H_2O (3:2, v/v) to yield the compound **TG_1** (0.86 mg), which was found to be homogeneous on

TLC plate (*n*-hexane:EA, 9:1 v/v) and reverse phase HPLC (MeOH/H_2O, 2:1 v/v), with 100% purity. The fraction GS_4 obtained by eluting with 50 % EtOAc:*n*-hexane was sub-fractionated on a preparatory RP-C_{18} HPLC system {using solvent system of (methanol) MeOH/ acetonitrile (MeCN, 2:1 v/v)} to yield the compounds, **TG_2** (0.83 mg) and **TG_3** (0.88 mg), which were homogeneous after TLC (EtOAc:*n*-hexane, 1:19 v/v) and RP-C_{18} HPLC (MeCN/MeOH, 1:2 v/v). The fraction GS_7 obtained with 5 % MeOH elution was subjected to the silica gel chromatography using *n*-hexane/EtOAc/MeOH solent system to afford six pooled fractions (GS_{7-1} - GS_{7-6}) on the basis of TLC (*n*-hexane:EtOAc, 8:2 v/v) as well as RP-C_{18} HPLC (3:2 MeOH/MeCN v/v) analyses. The fraction GS_{7-2-2} on repeated chromatographic/PHPLC purification techniques (by using the solvent gradient of MeOH/MeCN, 2:1 v/v) on a RP-C_{18} bonded-phase adsorbent yielded the compound **TG_4** (112 mg). The fraction GS_{7-2-3} on repeated HPLC purification techniques yielded compound **TG_5** (115 mg) and **TG_6** (108 mg), which were homogeneous after TLC (EtOAc/*n*-hexane, 1:19 v/v) and RP-C_{18} HPLC (MeCN/MeOH, 1:2 v/v). The fraction GS_8 on repeated chromatographic/HPLC purifications over octadecylsilane (C_{18}) bonded column with MeOH/MeCN (3:2, v/v) yielded compound **TG_7** (102 mg) and **TG_8** (98 mg), respectively, which were found to be homogeneous after TLC (*n*-hexane:EtOAc, 8:2 v/v) and RP-HPLC (MeOH/CH_3CN, 3:2 v/v).

The fraction GS_{12} obtained by eluting with 15 % MeOH, was subjected to further purification using *n*-hexane/EtOAc/MeOH on flash Biotage 230-400 mesh sized silica (25+M) to afford a total of 5-fractions (GS_{3-1} - GS_{3-5}). The fraction GS_{3-4} was further fractionated by flash chromatographic purification with *n*-hexane/EtOAc/MeOH as eluting solvent system to yield five sub-fractions, such as, GS_{3-4-1} - GS_{3-4-5}. The potentially active column sub-fraction $GS_{3-4-3,}$ was then fractionated with MeOH/MeCN solvent system (3:7, v/v) by reverse phase preparative HPLC over octadecylsilane (C_{18}) bonded column yielding **TG_9** (96 mg) and **TG_{10}** (103 mg), which were homogeneous after TLC (*n*-hexane:EtOAc, 8:2 v/v) and RP-HPLC (MeOH/MeCN, 3:7 v/v). The fraction GS_{13} obtained by eluting with 20 % MeOH on further purification using *n*-hexane/EtOAc/MeOH on flash Biotage 230-400 mesh sized silica (25+M) afforded a total of 4 fractions (GS_{13-1} - GS_{13-4}). The fraction GS_{13-4} was further fractionated by flash chromatographic purification with *n*-hexane/EtOAc/MeOH as eluting solvent system to yield five sub-fractions, named as GS_{13-4-1} - GS_{13-4-5}. The fraction, GS_{13-4-3} was found to contain two major compounds, which were purified by PHPLC (MeOH/MeCN, 1:1 v/v) fractionations on reverse phase C_{18} stationary phase to obtain two pure compounds **TG_{11}** (94 mg) and **TG_{12}** (128 mg), whereas their purities were checked through TLC (EtOAc/*n*-hexane, 1:9 v/v)/ RP-C_{18} HPLC (MeCN/MeOH, 1:1 v/v). Another active fraction GS_{15} was chromatographically fractionated by *n*-hexane/EtOAc/MeOH to yield three sub-fractions designated as, GS_{15-6-1} - GS_{15-6-3}. The

fractions, $GS_{15\text{-}6\text{-}1}$ and $GS_{15\text{-}6\text{-}2}$ were purified by repetitive RP-C_{18} bonded-phase column of HPLC by using binary gradient elution of MeOH and MeCN (3:2 v/v) to afford compounds **TG_{13}** (123 mg), **TG_{14}** (120 mg) and **TG_{15}** (107 mg), respectively, and were homogenous in TLC/RP-HPLC. The purities of the studied compounds were checked through TLC (EtOAc/n-hexane, 1:19 v/v) experiment and RP-C_{18} HPLC using binary gradient elution of MeCN/MeOH (1:2 v/v).

The repetitive bioassay guided fractionation of EtOAc-MeOH extract of *G. salicornia* along with the yield and bioactive potentials of the intermediate fractions were represented in Tables 4.1-4.7.

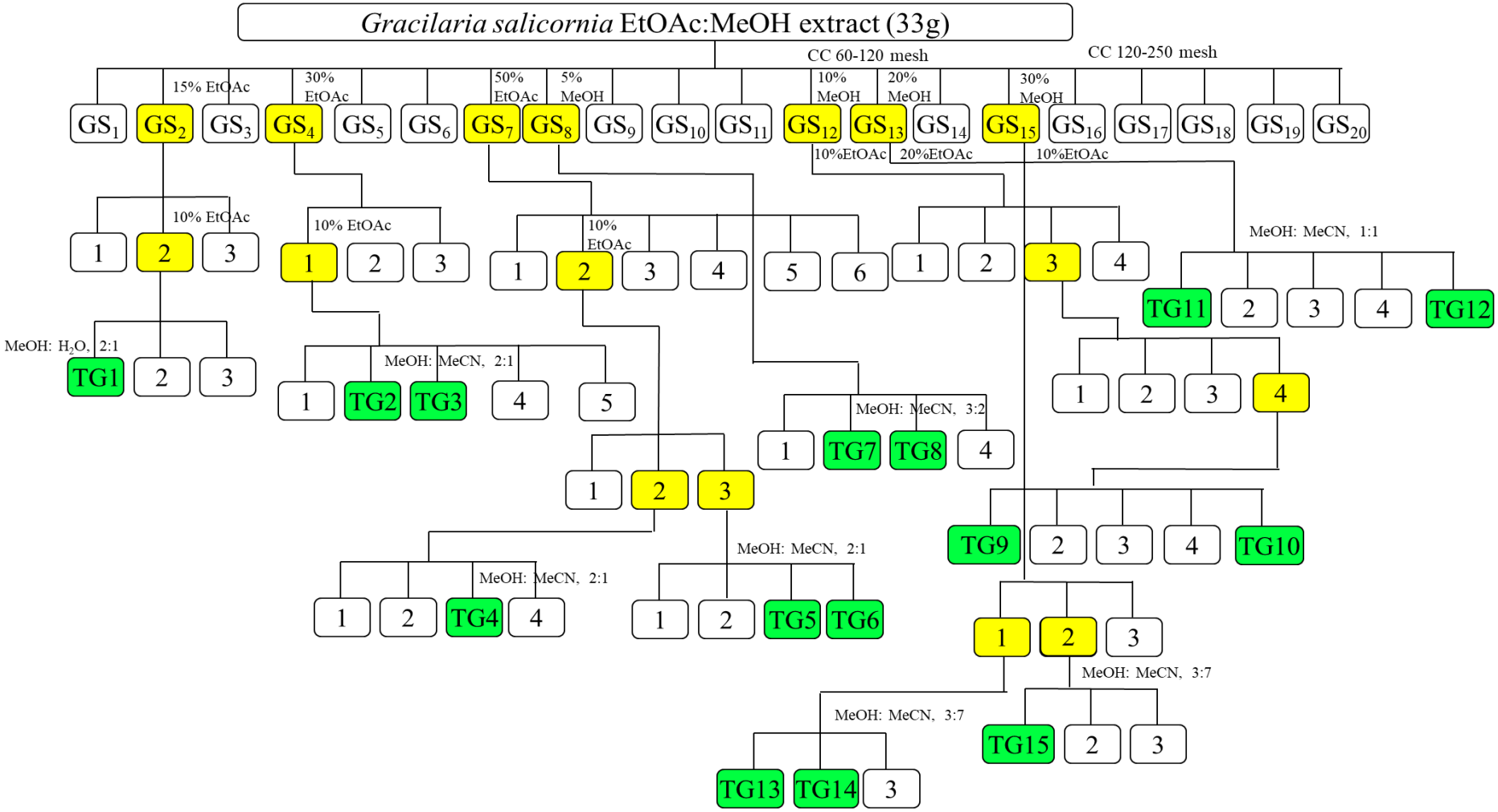

Figure 4.2.: Schematic representation of purification of fractions and compounds from the EtOAc-MeOH extract of *G. salicornia*. CC- column chromatograph

4.2.5 Physicochemical description of bioactive-leads isolated from EtOAc-MeOH extract of G. salicornia

4.2.5.1 Physicochemical description of compound-1 (TG_1)

Methyl-16(13→14)-abeo-7-labdene-(12-oxo)carboxylate; Yellowish-white amorphous powder; UV (MeOH) λ_{max}, log ε: 242 (2.35) nm; R_f: 0.81 (*n*-hexane:EtOAc, 9:1 v/v); R_t (HPLC, MeOH/H_2O, 2:1 v/v): 3.4 min; FTIR (KBr, cm^{-1}) υ_{max}: 840.76, 892.05 (=C-H_δ), 1172.96 (C-O_υ), 1377.46 (C-H_ρ), 1463.15 (CH_δ), 1644.13 (C-C_υ), 1725.25 (C-O_υ), 1736.25 (C=O_υ) 2854.11, 2925.88 (C-H_υ); ^{1}H NMR (500 MHz, MeOH; δ in ppm): δ_H 1.54 (1H, t, J=5.5 Hz), 1.30 (1H, t, J=4.2 Hz), 1.54 (1H, m), 1.42 (1H, m), 2.19 (1H, t, J=5.0 Hz), 1.88 (1H, t, J=4.2 Hz), 1.98 (1H, t, J=3.54 Hz), 1.79 (1H, t, J=5.1 Hz), 1.98 (1H,t, J=5.7.1 Hz), 5.55 (1H, t, J=6.6 Hz), 2.21 (1H, t, J=5.5 Hz), 2.37 (1H, dd, J=10.9, 6.5 Hz), 2.28 (1H, dd, J=12.7, 5.4 Hz), 2.30 (2H, d, J=6.5 Hz), 1.99 (1H,m), 0.79 (3H, d, J=6.0 Hz), 0.87 (3H, d, J=6.1 Hz), 1.14 (3H, s), 1.38 (3H, s), 0.63 (3H, s), 3.46 (3H,s); ^{13}C NMR (125 MHz, MeOH; δ in ppm): δ_C ^{13}C NMR (125 MHz, MeOH δ in ppm): δ_C 38.6 (CH_2), 20.8 (CH_2), 38.2 (CH_2), 42.9 (C), 44.6 (CH), 23.5 (CH_2), 124.8 (CH), 135.9 (C), 45.1 (CH), 39.2 (C), 41.3 (CH_2), 203.2 (C), 54.8 (CH_2), 24.1 (CH), 16.2 (CH_3), 17.9 (CH_3), 19.6 (CH_3), 17.9 (CH_2) 167.6 (C), 10.9 (CH_3), 69.7 (CH_3); ^{1}H-^{1}H COSY, and HMBC data were presented in Table 4.8; EI-MS *m/z*: calcd. for $C_{21}H_{34}O_3$ 334.2508; HRESIMS *m/z* found 335.2589 $[M+H]^+$, calcd for $C_{21}H_{35}O_3$ 335.2586 (Δ 0.08 ppm).

4.2.5.2 Physicochemical description of compound-2 (TG_2)

24(4→23), 27(8→26), 30(20→29)-tris-abeo-olean-(12-oxo)-1,15,22-triene-methyl hept-5-enoate; Pale yellow oily; UV_{MeOH} λ_{max} (log ε): 244 (2.91) nm; TLC {silica-GF(254); EtOAc/*n*-hexane, 1:19 v/v} R_f: 0.38; R_t (RP-C_{18} HPLC, MeOH/MeCN 2:1, v/v): 3.41 min; FTIR thin film (KBr) ν_{max} (bending *δ*, stretching *v*, rocking *ρ*): 2930 (C-H_v), 1730 {(-C(=O)-O-)$_v$}, 1726 (C=O_v), 1458 (C=C_v), 1406 (C-H_δ), 1238 (C-H_ρ), 1069 (C-C_v), 723 (C-H_δ) cm^{-1}; ^{1}H NMR (500 MHz, MeOH; δ in ppm): δ_H 5.32 (1H, d, J = 10.3 Hz), 5.28 (1H, dt, J = 8.9, 7.6 Hz), 1.77 (1H, t, J = 4.9 Hz), 2.01(1H, t, J = 4.9 Hz), 1.62 (1H, m), 1.30 (1H, m), 1.51 (1H, m), 1.28 (1H, m), 1.55 (1H, m), 1.26 (1H, m), 1.33 (1H, td, J = 6.8, 5.2 Hz), 1.66 (1H, td, J = 5.8, 5.5 Hz), 2.22 (1H, d, J = 8.6 Hz), 2.27 (1H, d, J = 8.0 Hz), 2.75 (1H, d, J = 6.7 Hz), 5.34 (1H, d, J = 12.1 Hz), 5.30 (1H, d, J = 13.0 Hz), 2.77 (1H, m), 1.65 (1H, m), 1.56 (1H, m), 1.93 (1H, m), 5.29 (1H, t, J = 14.0 Hz), 5.33 (1H, d, J = 12.7 Hz), 1.53 (2H, m), 0.80 (3H, t, J = 4.2 Hz), 1.32 (3H, s), 1.25 (2H, d, J = 3.7 Hz), 0.78 (3H, t, J = 4.9 Hz), 3.60 (2H, s), 1.52 (2H, m), 0.82 (3H, t, J = 5.0 Hz), 1.63 (2H, t, J = 4.7 Hz), 1.58 (2H, m), 2.20 (2H, m), 5.26 (1H, dt, J = 11.7 Hz), 5.25 (1H, m),

2.05 (3H, d, J = 9.2 Hz); ^{13}C NMR (125 MHz, MeOH; δ in ppm): δ_C 130.2 (CH), 127.8 (CH), 31.8 (CH_2), 33.9 (CH), 52.3 (CH), 29.0 (CH_2), 28.9 (CH_2), 29.7 (CH), 47.9 (CH), 46.8 (C), 39.3 (CH_2), 193.7 (C), 56.7 (CH), 34.4 (C), 130.5 (CH), 127.7 (CH), 43.5 (C), 31.9 (CH), 31.7 (CH_2), 37.2 (CH), 132.0 (CH), 127.5 (CH), 24.7 (CH_2), 12.2 (CH_3), 19.7 (CH_3), 29.8 (CH_2), 11.8 (CH_3), 65.7 (CH), 29.1 (CH_2), 13.1 (CH_3), 179.4 (C), 25.6 (CH_2), 26.9 (CH_2), 33.2 (CH_2), 129.7 (CH), 128.0 (CH), 14.2(CH_3) [135]DEPT, COSY, HSQC, and HMBC data data were presented in Table 4.9; EI-MS *m/z*: calcd. for $C_{37}H_{54}O_3$ 546.4073. HRESIMS *m/z* found 547.4155 $[M+H]^+$, calcd for $C_{37}H_{55}O_3$ 547.4151 (Δ 0.07 ppm)

4.2.5.3 Physicochemical description of compound-3 (TG$_3$)

24(4→23)-Abeo-olean-(12-oxo)-3,5-diene-deconoate; Yellowish oily; UV_{MeOH} λ_{max} (log ε): 247.24 (2.92) nm; TLC {silica-GF(254); EtOAc /*n*-hexane, 1:19 v/v} R_f: 0.40; R_t (RP-C_{18} HPLC, MeOH:MeCN 2:1, v/v): 2.91 min; FTIR thin film (KBr) ν_{max}: 2924 (C-H_v), 1734 {(-C(=O)-O-)$_v$}, 1634 (C-O_v), 1546 (C=C_v), 1463, 1356 (C-H_δ), 1109 (C-C_v), 722 (C-H_δ); ^{1}H NMR (500 MHz, MeOH; δ in ppm): δ_H 1.42 (1H, dt, J = 13.9, 5.9 Hz) , 1.15 (1H, dt, J = 11.8, 7.8 Hz), 2.03 (1H, dt, J = 11.2, 6.2 Hz), 1.72, 5.82(1H, t, J = 11.7 Hz), 2.00 (1H, d, J = 8.2 Hz), 1.75 (1H, d, J = 5.0 Hz), 1.70 (1H, t, J = 7.2 Hz), 2.33 (1H, dd, J = 10.8, 3.2 Hz), 2.07 (1H, dd, J = 9.9, 2.6 Hz), 2.30 (1H, d, J = 12.9 Hz), 1.59 (1H, dt, J = 10.9, 6.3 Hz), 1.35 (1H, dt, J = 11.9, 5.9 Hz), 1.60 (1H, dt, J = 10.9, 5.9 Hz), 1.38 (1H, dt, J = 11.2, 4.9 Hz), 1.62 (1H, m), 1.20 (1H, t, J = 4.9 Hz), 1.43 (1H, t, J = 4.0 Hz), 1.61 (1H, dt, J = 11.0, 4.8 Hz), 1.34 (1H, dt, J = 10.0, 4.0 Hz), 1.56 (1H, dt, J = 10.9, 4.7 Hz), 1.36 (1H, dt, J = 10.5, 4.0 Hz), 2.13 (2H, q, J = 5.7 Hz), 1.06 (3H, t, J = 6.9 Hz), 1.33 (3H, s), 1.04 (3H, s), 1.08 (3H, s), 1.10 (3H, s), 0.88 (3H, s), 0.96 (3H, s), 1.62 (2H, t, J = 10.9 Hz), 1.20 (2H, m), 1.43 (2H, m), 1.61 (2H, m), 1.34 (2H, m), 1.56 (2H, m), 1.36 (2H, m), 2.13(2H, m), 1.06 (2H, m), 1.33 (2H, m), 1.04 (2H, m), 1.08 (2H, m), 1.10 (2H, m), 0.88 (2H, m), 0.96 (2H, m), 2.34 (2H, m), 1.63 (2H, m), 1.29 (2H, m), 1.23 (2H, m), 1.28 (2H, m), 1.32 (2H, m), 1.30 (2H, m), 1.31 (2H, m), 0.84 (3H, t, J = 7.3 Hz); ^{13}C NMR (125 MHz, MeOH; δ in ppm): δ_C 30.5 (CH_2), 24.7 (CH_2), 132.2 (C), 128.8 (C), 139.2 (C), 130.9 (CH), 34.0 (CH_2), 42.7 (C), 43.4 (CH), 31.4 (C), 36.9 (CH_2), 213.1(C), 51.9 (CH), 38.8 (C), 29.4 (CH_2), 37.0 (CH_2), 33.4 (C), 41.4 (CH), 37.7 (CH_2), 28.0 (C), 33.9 (CH_2), 34.3 (CH_2), 19.1 (CH_2), 19.9 (CH_3), 20.8 (CH_3), 19.7 (CH_3), 19.4 (CH_3), 22.8 (CH_3), 30.2 (CH_3), 30.1 (CH_3), 176.1 (C), 26.7 (CH_2), 26.4 (CH_2), 29.2 (CH_2), 29.5 (CH_2), 29.6 (CH_2) , 29.3 (CH_2), 31.8 (CH_2), 22.6 (CH_2), 14.0 (CH_3); [135]DEPT, COSY, HSQC, and HMBC data were presented in Table 4.10; EI-MS *m/z*: calcd. for $C_{40}H_{64}O_3$ 592.2485. HRESIMS *m/z* found 593.4938 $[M+H]^+$, calcd for $C_{40}H_{65}O_3$ 593.4934 (Δ 0.06 ppm).

4.2.5.4 Physicochemical description of compound-4 (TG_4)

3-(Hept-3^6-enyloxy)-2,3,4,4a,5,6,6a,12,12a,12b-decahydro-4,6a,12a,12b-tetramethyl-*1H*-benzo[a] xanthene-4,10,12-triol; Pale yellow oil; $[\alpha]^{25}_D$ +58.9 (*c* 0.1, CH_3OH); UV_{MeOH} λ_{max} (log ε): 278 (3.44) nm; TLC (Si-GF_{254} 15 mm; EtOAc/*n*-hexane, 1:19 v/v) R_f: 0.38; R_t (HPLC-RP-C_{18}, MeCN/MeOH, 1:2 v/v): 3.241 min; FTIR thin film (ν_{max} in cm^{-1}; bending δ, stretching ν, rocking ρ): 3420 (O-H_ν), 3029 (C-$H_{\nu\ (aromatic)}$), 2855 (C-H_ν), 1625 (C=C_ν),1559 (C=$C_{\delta\ (aromatic)}$), 1460 (C-H_δ), 1373 ca(C-H_ρ), 1112, 1076 (-C-O-C_ν), 856 (C-$H_{\delta\ (aromatic)}$), 724 (C-H_δ); ^{1}H-NMR (500 MHz, MeOH; δ in ppm): δ_H 1.43 (1H, t, J = 12.0 Hz), 1.23 (1H, t, J = 12.1 Hz), 1.96 (1H, m), 1.56 (1H, m), 2.80 (1H, t, J = 9.8 Hz), 1.53 (1H, dd, J = 1.5, 12.1 Hz), 1.73 (1H, m), 1.45 (1H, m), 1.70 (1H, td, J = 12.5, 3.4 Hz), 1.37 (1H, td, J = 12.5, 3.0 Hz), 6.81 (1H, d, J = 13.4 Hz), 6.61 (1H, d, J = 13.8 Hz), 6.51 (1H, s), 4.68 (1H, s), 1.15 (3H, s), 1.42 (3H, s), 0.88 (3H, s), 0.83 (3H, s), 3.69 (2H, t, J = 8.6 Hz), 1.55 (2H, m), 1.21 (2H, m), 1.33 (2H, m), 2.04 (2H, m), 5.82 (1H, m), 5.01 (1H, dd, J = 3.4, 16.7 Hz), 4.94 (1H, dd, J = 3.4, 12.2 Hz); ^{13}C-NMR (125 MHz, MeOH; δ in ppm): δ_C 37.0 (CH_2), 24.7 (CH_2), 84.6 (CH), 73.9 (C), 68.7 (CH), 21.7 (CH_2), 33.4 (CH_2), 81.6 (C), 146.5 (C), 119.0 (CH), 119.1 (C), 140.9 (C), 115.2 (CH), 126.3 (C), 65.5 (CH), 61.0 (C), 42.8 (C), 22.6 (CH_3), 23.9 (CH_3), 14.1 (CH_3), 19.6 (CH_3), 71.1 (CH_2), 31.9 (CH_2), 26.7 (CH_2), 29.6 (CH_2), 33.8 (CH_2), 139.2 (CH), 114.0 (CH_2), DEPT, COSY, HSQC and HMBC were presented in Table 4.11; EI-MS *m/z* calcd. for $C_{28}H_{42}O_5$ 458.3032. HRESIMS *m/z* found 459.3114 $[M+H]^+$, calcd for $C_{28}H_{43}O_5$ 459.3110 (Δ 0.08 ppm)

4.2.5.5 Physicochemical description of compound-5 (TG_5)

13-[[2-(Hexyloxy)-2,5,5,8a-tetramethyldecahydro-1-naphthalenyl](methoxy-)-methyl]-benzenol; Yellowish oil; $[\alpha]^{25}_D$ +53.2 (*c* 0.1, CH_3OH); UV_{MeOH} λ_{max} (log ε): 281 (3.82) nm; TLC (Si-GF_{254} 15 mm; EtOAc/*n*-hexane, 1:19 v/v) R_f: 0.40; R_t (HPLC-RP-C_{18}, MeCN/MeOH, 1:2 v/v): 3.811 min; FTIR thin film (ν_{max}, cm^{-1}): 3402 (O-H_ν), 3028 (C-$H_{\nu\ (aromatic)}$), 2923, 2855 (C-H_ν), 1634 (C=C_ν), 1550 (C=$C_{\delta\ (aromatic)}$), 1540 (C=C_ν), 1459, 1372 (C-H_δ), 1239, 1070 (C-C_ν), 1120, 1070 (-C-O-C_ν), 850 (C-$H_{\delta\ (aromatic)}$), 723 (=C-H_δ); ^{1}H-NMR (500 MHz, MeOH; δ in ppm): δ_H 1.92 (1H, d, J = 8.0 Hz), 1.77 (1H, m), 1.56 (1H, m), 1.62 (1H, m), 1.42 (1H, m), 0.88 (1H, dd, J = 1.8, 12.2 Hz), 1.50 (1H, td, J = 13.5, 4.1 Hz), 1.17 (1H, td, J = 12.9, 4.2 Hz), 1.75 (1H, m), 1.07 (1H, m), 1.51 (1H, t, J = 12.0 Hz), 1.12 (1H, t, J = 12.0 Hz), 1.22 (3H, s), 1.03 (3H, s), 1.00 (3H, s), 1.02 (3H, s), 4.39 (1H, d, J = 8.2 Hz), 3.37 (3H, s), 6.28 (1H, s), 6.35 (1H, d, J = 12.1 Hz), 7.08 (1H, t, J = 13.2 Hz), 6.23 (1H, d, J = 13.1 Hz), 3.69 (2H, m), 1.53 (2H, m), 1.31 (2H, m), 1.34 (2H, m), 1.33 (2H, m), 0.94 (3H, t, J = 6.7 Hz); ^{13}C-NMR (125 MHz, MeOH; δ in ppm): δ_C 65.7 (CH), 72.4 (C), 39.3 (CH_2), 19.6 (CH_2), 55.0 (CH), 32.7 (C), 45.0 (CH_2), 19.3 (CH_2), 39.4 (CH_2), 37.2 (C), 22.5 (CH_3), 29.7 (CH_3), 29.3 (CH_3), 16.3

(CH_3), 82.7 (CH), 58.9 (CH_3), 154.3 (C), 113.0 (CH), 144.0 (C), 123.7 (CH), 128.4 (CH), 113.1 (CH), 65.0 (CH_2), 31.9 (CH_2), 25.6 (CH_2), 33.7 (CH_2), 22.7 (CH_2), 14.1 (CH_3); DEPT, COSY, HSQC, and HMBC were presented in Table 4.12; EI-MS *m/z* calcd. for $C_{28}H_{46}O_3$ 430.3447. HRESIMS *m/z* found 431.3528 $[M+H]^+$, calcd for $C_{28}H_{47}O_3$ 431.3525 (Δ 0.06 ppm)

4.2.5.6 Physicochemical description of compound-6 (TG_6)

1-Butoxy-4,4,11b,11c-tetramethyl-1,2,3,3a,4,5,6,6a,11b,11c-decahydrobenzo[kl]-xanthen-10-ol; Yellowish oil; $[\alpha]^{25}_D$ +55.6 (*c* 0.1, CH_3OH); UV_{MeOH} λ_{max} (log ε): 283 (4.97) nm; TLC (Si-GF_{254} 15 mm; EtOAc/*n*-hexane, 1:19 v/v) R_f: 0.43; R_t (HPLC-RP-C_{18}, MeCN/MeOH, 1:2 v/v): 4.204 min; FTIR thin film (ν_{max}, cm^{-1}): 3412 (O-H_ν), 3026 (C-$H_{\nu\,(aromatic)}$), 2921, 2854 (C-H_ν), 1638 (C=C_ν), 1560 (C=$C_{\delta\,(aromatic)}$), 1574, 1542 (C=C_ν), 1466, 1417 (C-H_δ), 1115, 1043 (-C-O-C_ν), 876, 854 (C-$H_{\delta\,(aromatic)}$), 721 (=C-H_δ); ^{1}H-NMR (500 MHz, MeOH; δ in ppm): δ_H 3.88 (1H, t, J = 9.2 Hz), 1.81 (1H, m), 1.60 (1H, m), 1.57 (1H, m), 1.31 (1H, m), 1.21 (1H, dd, J = 1.9, 12.1 Hz), 1.20 (1H, td, J = 13.2, 4.1 Hz), 1.51 (1H, td, J = 13.2, 4.3 Hz), 1.84 (1H, t, J = 12.7 Hz), 1.70 (1H, t, J = 12.9, 4.2 Hz), 3.20 (1H, t, J = 9.2 Hz), 6.26 (1H, d, J = 13.1 Hz), 6.20 (1H, d, J = 13.2 Hz), 6.31 (1H, s), 1.00 (3H, s), 0.98 (3H, s), 1.37 (3H, s), 1.15 (3H, s), 3.44 (2H, t, J = 9.8 Hz), 1.50 (2H, m), 1.43 (2H, m), 0.88 (3H, t, J = 6.8 Hz); ^{13}C-NMR (125 MHz, MeOH; δ in ppm): δ_C 78.1 (CH), 29.6 (CH_2), 22.7 (CH_2), 52.3 (CH), 37.2 (C), 42.2 (CH_2), 24.4 (CH_2), 81.0 (CH), 139.9 (C), 118.1 (CH), 121.7 (CH), 155.9 (C), 115.1 (CH), 128.7 (C), 45.4 (C), 39.3 (C), 28.8 (CH_3), 29.3 (CH_3), 22.6 (CH_3), 12.8 (CH_3), 74.6 (CH), 31.9 (CH_2), 18.7 (CH_2), 14.1 (CH_3); DEPT, COSY, HSQC, and HMBC were presented in Table 4.13; EI-MS *m/z* calcd. for $C_{24}H_{36}O_3$ 372.2664. HRESIMS *m/z* found 373.3746 $[M+H]^+$, calcd for $C_{24}H_{37}O_3$ 373.3742 (Δ 1.0 ppm)

4.2.5.7 Physicochemical description of compound-7 (TG_7)

4'-[10'-[7-Hydroxy-2,8-dimethyl-6-(pentyloxy)-*2H*-chromen-2-yl]ethyl]-3',4'-dimethyl-cyclohexanone; Yellowish-oil; UV $\lambda_{max\ MeOH}$ (log ε 2.91): 270 nm; $[\alpha]^{26}_D$ -20.4° ($CHCl_3$, c0.016); TLC (silica GF_{254}; *n*-hexane:EtOAc, 8:2 v/v) R_f: 0.65; R_t (HPLC, MeOH/CH_3CN, 3:2 v/v): 2.93 min; FTIR (KBr, cm^{-1}) υ_{max}: 840, 858 (C-$H_{(aromatic)}$), 892 (=C-H_δ), 1114, 1078 (-C-O-C-), 1377 (C-H_p),1457 (C-H_δ), 1562 (C=$C_{(aromatic)}$), 1637 (C=C), 1644 (C-C_υ), 1727 (C-O_υ), 1732 (C=O_υ), 2855, 2923 (C-H_υ), 3027 (C-$H_{(aromatic)}$), 3430 (O-H);^{1}H NMR (500 MHz, $CDCl_3$; δ in ppm): δ_H 6.07 (1H, d, J = 13.2 Hz), 6.33 (1H, d, J = 7.8 Hz), 6.21 (1H, s), 1.54 (3H, s), 2.35 (3H, s), 2.10 (1H, dd, J = 7.2, 5.8 Hz), 1.95 (1H, dd, J = 7.1, 5.9 Hz), 1.64 (1H, m), 1.82 (1H, dt, J = 7.3, 6.2 Hz), 1.68 (1H, dt, J = 7.1, 6.0 Hz), 2.49 (1H, dt, J = 6.8, 6.0 Hz), 2.43 (1H, dt, J = 7.1, 6.0 Hz), 1.14 (3H, d, J = 7.1 Hz), 1.20 (3H, s), 1.34 (1H, dt, J = 6.8, 5.9

Hz), 1.23 (1H, dt, J = 6.9, 5.7 Hz), 1.73 (2H, dd, J = 7.1, 6.3 Hz), 4.09 (2H, t, J = 9.8 Hz), 1.71(2H, m), 1.36 (2H, m), 1.39 (2H, m), 1.04 (3H, t, J = 5.4 Hz); ^{13}C NMR (125 MHz; $CDCl_3$; δ in ppm): δ_C 75.0 (C), 130.1 (CH), 128.4 (CH), 113.1 (C), 110.5 (CH), 142.8 (C), 148.6 (C), 114.8 (C), 148.6 (C), 24.8 (CH_3), 14.1 (CH_3), 213.9 (C), 39.4 (CH_2), 37.4 (CH), 32.9 (C), 36.8 (CH_2), 37.2 (CH_2), 22.6 (CH_3), 22.7 (CH_3), 32.8 (CH_2), 36.8 (CH_2), 65.5 (CH_2), 27.9 (CH_2), 29.7 (CH_2), 24.4 (CH_2), 19.7 (CH_3).^{1}H-^{1}H COSY, HSQC and HMBC data were presented in Table 4.14; EI-MS *m/z* calcd for $C_{26}H_{38}O_4$ 414.2770. HRESIMS *m/z* found 415.2852 $[M+H]^+$, calcd for $C_{26}H_{39}O_4$ 415.2848 (Δ 0.09 ppm).

4.2.5.8 Physicochemical description of compound-8 (TG$_8$) **3'-[10'-(8-Hydroxy-5-methoxy-2,6,7-trimethyl-*2H*-chromen-2-yl)ethyl]-3'-methyl-2'-methylene cyclohexyl butyrate**

Pale yellowish oil; UV $\lambda_{max\ MeOH}$ (log ε 2.43): 264 nm; $[\alpha]^{26}_D$ -21.6° ($CHCl_3$, c0.014); TLC (silica GF_{254}; *n*-hexane:EtOAc, 8:2 v/v) R_f: 0.35; R_t (HPLC, MeOH/CH_3CN, 3:2 v/v): 3.70 min; FTIR (KBr, cm^{-1}) υ_{max}: 857 (C-$H_{(aromatic)}$), 876, 893 (=C-H_δ), 1077, 1113 (O-C-O_υ), 1377 (C-H_p), 1466 (C-H_δ), 1574 (C=$C_{(aromatic)}$), 1638 (C=C_υ), 1728 (C-O_υ), 1735 (C=O_υ), 2854, 2921 (C-H_υ), 3027 (C-$H_{(aromatic)}$), 3412 (O-H); ^{1}H NMR (500 MHz; $CDCl_3$; δ in ppm); δ_H 6.20 (1H, d, J = 12.8 Hz), 6.79 (1H, d, J = 11.8 Hz), 3.73 (3H, s), 1.60 (3H, s), 2.39 (3H, s), 2.31(3H, s), 4.14 (1H, d, J = 7.2 Hz), 1.46 (2H, dt, J = 6.9, 4.3 Hz), 1.39 (2H, m), 1.94 (2H, dt, J = 5.2, 4.0 Hz), 5.19 (2H, s), 1.10 (3H, s), 1.33 (1H, dt, J = 9.3, 5.6 Hz), 1.28 (1H, dt, J = 9.8, 5.1 Hz), 1.74 (2H, dd, J = 7.8, 5.9 Hz), 2.17 (2H, d, J = 7.9 Hz), 1.72 (2H, m), 0.91 (3H, t, J = 6.9 Hz); ^{13}C NMR (125 MHz; $CDCl_3$; δ in ppm); δ_C 83.17 (C), 127.8 (CH), 120.9 (CH), 111.5 (C), 148.7 (C), 56.8 (CH_3), 114.1 (C), 123.3 (C), 143.5 (C), 142.8 (C), 24.2 (CH_3), 13.8 (CH_3), 12.5 (CH_3), 71.4 (CH), 154.3 (C), 42.2 (C), 42.0 (CH_2), 18.7 (CH_2), 31.8 (CH_2), 104.2 (CH_2), 22.5 (CH_3), 39.5 (CH_2), 35.8 (CH_2), 175.4 (C), 34.9 (CH_2), 18.7 (CH_2), 14.2 (CH_3); ^{1}H-^{1}H COSY, HSQC and HMBC data were presented in Table 4.15; EI-MS *m/z* calcd for $C_{27}H_{38}O_5$ 442.2719. HRESIMS *m/z* found 443.2800 $[M+H]^+$, calcd for $C_{27}H_{39}O_5$ 443.2797 (Δ 0.06 ppm)

4.2.5.9 Physicochemical description of compound-9 (TG$_9$)

3-(Hydroxymethyl)-7-(methoxymethyl)-3,11-dimethyl-9-oxospiro[5.5]undec-4-en-10-methylbutanoate; Colourless oily; $[\alpha]^{20}_D$ -52.0° (*c*0.04, $CHCl_3$); UV_{MeOH} λ_{max} (log ε): 247 (4.02) nm (Figure S21); TLC {silica-GF(254); EtOAc/*n*-hexane, 2:18 v/v} R_f: 0.45; R_t (HPLC-RP-C_{18}, MeOH:MeCN 1:2, v/v): 4.42 min; FTIR thin film (KBr) ν_{max} (bending *δ*, stretching *ν*, rocking *ρ*): 722 (=C-H_δ), 1068 (C-O_υ), 3114 (=C-H_ν), 1471, 1466 (C-H_υ), 1078 (-C-O-C), 2853, 2921 (C-H_δ), 1572, 1635 (C=C), 1716, 1736 (C=O_υ), 3414 (O-H); ^{1}H NMR (500

MHz; $CDCl_3$; δ in ppm); δ_H 1.70 (2H, t, 3.5 Hz), 1.77 (2H ,t, 3.8 Hz), 4.52 (1H, d, 7.6 Hz), 2.16 (1H, t, 4.2 Hz), 2.09 (2H, d, 9.6 Hz), 4.41(1H, d, 10.5 Hz), 2.82 (1H, d, 7.5 Hz), 0.88 (3H, d, 8.2 Hz), 3.69 (2H, d, 3.5 Hz), 1.33 (3H, d, 11.3 Hz), 3.37 (2H, s), 2.00 (2H, d, 8.1 Hz), 2.37 (1H, t, 3.5 Hz), 0.81 (3H, t, 3.5 Hz), 0.86 (3H, t, 3.5 Hz), 3.20 (3H, s);^{13}C NMR (125 MHz; $CDCl_3$; δ in ppm); δ_C 29.6 (CH_2), 31.9 (CH_2), 37.2 (C), 128.4 (CH), 133.0 (CH), 41.2 (C), 31.6 (CH), 36.6 (CH_2), 203.5 (C), 94.9 (CH), 32.6 (CH), 22.4 (CH_3), 50.0 (CH_2), 24.7 (CH_3), 72.4 (CH_2), 179.6 (C), 39.3 (CH_2), 33.7 (CH), 19.3 (CH_3), 19.6 (CH_3), 55.03 (CH_3). DEPT, COSY, HSQC, and HMBC data were presented in Table 4.16. EI-MS *m/z*: calcd. for $C_{21}H_{34}O_5$ 366.2406. HRESIMS (positive mode) *m/z*: found 367.4999 $[M+H]^+$, calcd. for $C_{21}H_{35}O_5$ 367.4996 $[M+H]^+$ (Δ 0.08 ppm).

4.2.5.10 Physicochemical description of compound-10 (TG_{10})

4-Ethoxy-11,11-dimethyl-7-methylene-8-(propionyloxy)spiro[5.5]undec-2-en-10^3,10^5-dihydroxytetrahydro-*2H*-pyran-10-carboxylate: Colourless oily; $[\alpha]^{20}_D$ -53.0° (*c*1.13, $CHCl_3$); UV_{MeOH} λ_{max} (log ε): 270 (3.32) nm; TLC {silica-GF(254); EtOAc/*n*-hexane, 1:19 v/v} R_f: 0.48; R_t (HPLC-RP-C_{18}, MeOH:MeCN 1:2, v/v): 3.35 min; FTIR thin film (KBr) ν_{max} (bending *δ*, stretching *ν*, rocking *ρ*): 722 (=C-H_δ), 3111 (=C-H_υ), 1109, 1156 (C-O_δ), 1356, 1463 (C-H_δ), 1463 (C-H_δ), 1546, 1634 (C=C_υ), 1724, 1746 (C=O_υ)$_{ester,}$ 2853, 2921 (C-H_υ), 3411 (O-H); ^{1}H NMR (500 MHz; $CDCl_3$; δ in ppm); δ_H 2.03 (1H, d, 4.8 Hz), 1.79 (1H, d, 4.8 Hz), 5.36 (1H, t, 7.1 Hz), 5.13 (1H, t ,8.3 Hz), 3.98 (1H, m), 1.62 (2H, d, 6.3 Hz), 4.00 (1H, t, 8.3 Hz), 1.93 (2H, m), 4.15 (1H, t, 5.3 Hz), 0.88 (3H, s), 0.87 (3H, s), 4.35 (1H, t, 12.6 Hz), 4.33(1H, t, 12.5 Hz), 4.18 (1H, t, 5.8Hz), 2.12 (2H, t, 6.8 Hz), 3.68 (1H, m), 2.10 (2H, t), 5.23 (1H, t, 5.5 Hz), 2.30 (2H ,m), 0.99 (3H, t, 4.1 Hz), 3.30 (2H, m), 0.89 (3H, t, 4.3 Hz); ^{13}C NMR (125 MHz; $CDCl_3$; δ in ppm); δ_C 31.92 (CH_2), 126.07 (CH), 132.97 (CH), 75.27 (CH), 39.61 (CH_2), 32.35 (C), 141.81 (C), 68.38 (CH), 33.65 (CH_2), 72.67 (CH), 36.90 (C), 16.49 (CH_3), 16.03 (CH_3), 119.45 (CH_2), 162.75 (C), 72.50 (CH), 39.66 (CH_2), 70.72 (CH), 37.66 (CH_2), 101.64 (CH), 172.15 (C), 27.99 (CH_2), 14.13 (CH_3), 65.64 (CH_2), 15.77 (CH_3). DEPT, COSY, HSQC, HMBC data were presented in Table 4.17; EI-MS *m/z*: calcd. for $C_{25}H_{38}O_8$ 466.2567. HRESIMS (positive mode) *m/z*: found 467.2648 $[M]^+$, calcd. for $C_{25}H_{39}O_8$ 467.2645 $[M+H]^+$ (Δ 0.06 ppm).

4.2.5.11 Physicochemical description of compound-11 (TG_{11})

15-(Octahydro-7-(4,5-dihydro-3-methoxy-2,6-dimethyl-*2H*-pyran-6-yl)-10-methylpyrano[3,2-b]pyran-14-yl)-18-(19-methyl-23-methyleneoxepan-19-yl)pent-15-en-18-ol; Colourless oil; $[\alpha]^{25}_D$ +9.8 (*c*0.18, CH_3OH); UV_{MeOH} λ_{max} (log ε): 240 (3.30) nm; TLC {Si-GF_{254} 15 mm; EtOAc/*n*-hexane, 1/9, v/v} R_f: 0.41; R_t (HPLC RP-C_{18}, MeOH:MeCN, 1:1, v/v):

3.28 min; FTIR thin film (KBr) ν_{max} (cm^{-1}) (bending δ, stretching υ, rocking ρ): 581 (=C-H_{δ}), 1044 (C-O-C_{υ}), 1372, 1455 (C-H_{υ}), 2854, 2925 (C-H_{δ}), 3390 (O-Hυ); ^{1}H NMR (500 MHz; $CDCl_3$; δ in ppm); δ_H 2.28 (3H,s), 1.97 (1H,t,4.2 Hz), 1.87 (1H ,t, 4.2 Hz), 1.76 (1H, t, 4.2 Hz), 1.96 (1H, t, 4.2 Hz), 3.61 (1H, t, 4.3 Hz), 1.72 (1H, m), 1.60 (1H, m), 1.82 (1H, t, 5.0 Hz), 1.52 (1H, t, 4.9 Hz), 3.05 (1H, t, 4.3 Hz), 1.91 (1H, m), 1.62 (1H, m), 1.74 (2H, m), 4.14 (1H, t, 4.3 Hz), 1.99 (2H, t, 4.2 Hz), 1.42 (2H, m), 3.78 (1H, t, 4.7 Hz), 1.54 (2H, t, 4.3 Hz), 1.38 (2H, m), 1.95 (2H, t, 6.2), 4.01 (1H, d, 8.2 Hz), 3.93 (1H, d, 8.3 Hz), 1.41 (3H, s), 1.33 (3H, s), 5.33 (1H, d, 10.0 Hz), 5.18 (1H, d, 9.3 Hz), 1.28 (3H, s), 5.36 (1H, d, 9.3 Hz), 5.17 (1H, d, 9.3 Hz), 3.68 (3H, s).^{13}C NMR (125 MHz; $CDCl_3$; δ in ppm); δ_C 20.3 (CH_3), 129.4 (C), 137.1 (C), 21.5 (CH_2), 24.6 (CH_2), 81.4 (C), 80.9 (CH), 22.3 (CH_2), 39.1 (CH_2), 77.1 (C), 78.8 (CH), 24.48 (CH_2), 25.7 (CH_2), 75.3 (CH), 147.0 (C), 29.3 (CH_2), 31.6 (CH_2), 74.1 (CH), 81.4 (C), 35.0 (CH_2), 21.8 (CH_2), 31.0 (CH_2), 143.2 (C), 72.4 (CH_2), 24.3 (CH_3), 19.3 (CH_3), 114.5 (CH_2), 18.82 (CH_3), 114.0 (CH_2), 60.0 (CH_3). [135]DEPT, COSY, HSQC, and HMBC data were presented in Table 4.18; EI-MS *m/z*: calcd. for $C_{30}H_{48}O_6$ 504.3451. HRESIMS (positive mode) *m/z*: found 505.3533 $[M+H]^+$, calcd. for $C_{30}H_{49}O_6$ 505.3529 (Δ 0.07 ppm)

4.2.5.12 Physicochemical description of compound-12 (TG_{12})

Tetrahydro-6-(hexahydro-13-((tetrahydro-18-(23-hydroxy-23-methylheptan-19-yl)-15-methylfuran-15-yl)methyl-10-methyl-*2H*-furo[3,2-b]pyran-7-yl)-2,2,6-trimethyl-*2H*-pyran-3-yl; Colourless oil; $[\alpha]^{25}_{D}$ +10.3 (*c*0.18, CH_3OH); UV_{MeOH} λ_{max} (log ε): 242 (3.23) nm; TLC {Si-GF_{254} 15 mm; EtOAc/*n*-hexane, 1/9, v/v} R_f: 0.45; R_t (HPLC RP-C_{18}, MeOH:MeCN 1:1, v/v): 3.18 min; FTIR ν_{max} (cm^{-1}): 720 (=C-H_{δ}), 1043 (C-O-C_{υ}), 1239, 1376 (C-H_{δ}), 2852, 2922 (C-H_{υ}), 3383 (O-Hυ); ^{1}H NMR (500 MHz; $CDCl_3$; δ in ppm); δ_H 1.24 (3H, s), 4.10 (1H, t, 4.2 Hz), 1.73 (1H, m), 1.99 (1H, m), 1.62 (1H, t, 4.3 Hz), 1.40 (1H, t, 4.3 Hz), 3.69 (1H, t, 6.2 Hz), 1.72 (1H, m), 1.44 (1H, m), 1.83 (1H, t, 5.2 Hz), 1.58 (1H, t, 5.2 Hz), 3.33 (1H, t, 9.2 Hz), 2.05 (1H, t, 6.4 Hz), 1.87 (1H, t, 6.5 Hz), 3.56 (1H, m), 1.50 (2H, d, 6.8 Hz), 2.01 (2H, t, 4.2 Hz), 1.75 (2H, m), 3.67 (1H, m), 1.92 (1H, m), 1.34 (2H, m), 1.30 (2H, m), 1.47 (2H, m), 1.19 (3H, s), 1.26 (3H,s), 1.29 (3H, s), 1.28 (3H, s), 1.31 (3H, s), 0.99 (3H, d, 7.2 Hz), 1.17 (3H, s), 2.33 (2H, t, 6.8 Hz), 1.77 (2H, m), 0.92 (3H, t, 4.1 Hz); ^{13}C NMR (125 MHz; $CDCl_3$; δ in ppm); δ_C 27.5 (CH_3), 83.9 (C), 71.5 (CH), 21.3 (CH_2), 30.3 (CH_2), 32.6 (C), 90.4 (CH), 22.3 (CH_2), 39.6 (CH_2), 81.4 (C), 80.5 (CH), 38.6 (CH_2), 65.2 (CH), 46.3 (CH_2), 79.5 (C), 36.0 (CH_2), 29.3 (CH_2), 79.1 (CH), 36.7 (CH), 33.9 (CH_2), 22.0 (CH_2), 42.6 (CH_2), 78.9 (C), 28.8 (CH_3), 26.3 (CH_3), 21.1 (CH_3), 17.3 (CH_3), 26.9 (CH_3), 18.1 (CH_3), 28.5 (CH_3), 167.9 (C), 36.6 (CH_2), 18.8 (CH_2), 13.9 (CH_3).[135]DEPT, COSY, HSQC, and HMBC data were presented in Table 4.19; EI-

MS *m/z*: calcd. for $C_{34}H_{60}O_7$ 580.4339. HRESIMS (positive mode) *m/z*: found 581.4420 $[M+H]^+$, calcd. for $C_{21}H_{61}O_3$ 581.4417 (Δ 0.05 ppm).

4.2.5.13 Physicochemical description of compound-13 (TG_{13})

3-acetyl-14-(furanyl)-11-methyl-15-(15[3]-methylbutyloxy)-8-oxabicyclo-[21.3.1]heptacosa-11,23,25,27 tetraene-7,18-dione. Pale yellow oily; $[\alpha]^{22}_D$ -118.6° (*c* 0.25, $CHCl_3$); UV (EtOAc) λ_{max} (log ε): 232 (4.315) nm; TLC (Si-GF254; EtOAc:*n*-hexane, 1/19 v/v) R_f: 0.42; RP-C_{18} HPLC R_t: 4.90 min (232 nm) (MeCN/MeOH, 1:2 v/v); FTIR (KBr, cm^{-1}) ν_{max}: 925/974 (alkene C-H_δ), 1085 (C-O-C_ν), 1220 (C-H_ρ), 1440 (C-H_δ), 1715 (C-CO-C_ν), 1735 (-C(=O)-O-), 2939/3009 (C-H_ν); ^{1}H NMR (500 MHz, $CDCl_3$; δ in ppm) δ_H 2.94 (1H, dd, 11.1, 6.8 Hz), 2.64 (1H, dd, 11.0, 6.5 Hz), 2.75 (1H, m), 2.69 (1H, m), 1.41 (1H, m), 1.72 (1H, m), 1.64 (1H, m), 2.28 (2H, m), 4.31 (2H, t, 7.8 Hz), 2.34 (2H, t, 7.6 Hz), 5.19 (1H, t, 6.2 Hz), 2.42 (2H, m), 2.85 (1H, m), 3.16 (1H, m), 1.80 (2H, m), 2.50 (2H, t, 7.8 Hz), 2.44 (2H, t, 7.9 Hz), 1.55 (2H, m), 1.61 (2H, m), 2.58 (2H, t, 5.8 Hz), 7.02 (1H, d, 7.4 Hz), 7.53 (1H, t, 7.6 Hz), 7.01 (1H, d, 7.6 Hz), 7.07 (1H,s), 1.96 (3H, s), 1.82 (3H, s), 6.08 (1H, d, 1.3Hz), 6.43 (1H, t, 2.9 Hz), 7.71 (1H, d, 1.6 Hz), 3.39 (2H, t, 7.9 Hz), 1.45 (2H, m), 1.76 (1H, m), 0.98 (3H, d, 5.1 Hz), 0.97 (3H, d, 5.3 Hz); ^{13}C NMR (125 MHz, $CDCl_3$; δ in ppm) δ_C 137.6 (C), 35.8 (CH_2), 54.0 (CH), 27.3 (CH_2), 24.1 (CH_2), 32.8 (CH_2), 177.2 (C), 65.5 (CH_2), 39.8 (CH_2), 130.9 (C), 128.4 (CH), 25.8 (CH_2), 43.3 (CH), 81.4 (CH), 24.7 (CH_2), 34.7 (CH_2), 213.3 (C), 40.1 (CH_2), 25.30 (CH_2), 29.6 (CH_2), 34.3 (CH_2), 148.5 (C), 126.8 (CH), 128.8 (CH), 126.1 (CH), 133.8 (CH), 210.6 (C), 30.5 (CH_3), 16.7 (CH_3), 154.9 (C), 109.3 (CH), 111.3 (CH), 140.5 (CH), 72.1 (CH_2), 40.6 (CH_2), 24.0 (CH), 23.8 (CH_3), 23.6 (CH_3) ^{1}H-^{1}H COSY, HSQC, and HMBC data were presented in Table 4.20; EI-MS *m/z* found 606.4 $[M]^+$. HRESIMS *m/z* calcd. for $C_{38}H_{55}O_6$ 607.3999, found 607.4003 $[M+H]^+$ (Δ = 0.6 ppm).

4.2.5.14 Physicochemical description of compound-14 (TG_{14})

(2E,12E,14E)-10-acetyl-9-isopentyl-2-methyl-5,16,23[1]-trioxa-bicyclo[21.3.1]-heptacosa-2,12,14-triene-6,19-dione. Pale yellow oily; $[\alpha]^{22}_D$ -125.5° (*c* 0.18, $CHCl_3$); UV (EtOAc) λ_{max} (log ε): 237 (4.985) nm; TLC (Si-GF254; EtOAc:*n*-hexane, 1/19 v/v) R_f: 0.38; RP-C_{18} HPLC R_t: 4.30 min (237 nm) (MeCN/MeOH, 1:2 v/v); FTIR (KBr, cm^{-1}) ν_{max}: 929 (alkene C-H_δ), 1046/1119/1192 (C-O-C_ν), 1354 (C-H_ρ), 1492 (C-H_δ), 1717 (C-CO-C_ν), 1742 (-C(=O)-O-), 2923/2799 (C-H_ν)**:** ^{1}H NMR (500 MHz, $CDCl_3$; δ in ppm), δ_H 4.78 (1H, m), 5.54 (1H, t, 6.4 Hz), 4.90 (2H, d,10.1 Hz), 2.30 (2H, t, 7.5 Hz), 1.77 (2H, m), 1.75 (1H, m), 2.33 (1H, m), 2.37 (2H, m), 5.81 (1H, m), 5.34 (1H, t,12.1 Hz), 5.05 (1H, t,11.0 Hz), 6.37 (1H, d,11.1 Hz), 4.36

(2H, m), 2.92 (2H, t, 4.8 Hz), 2.49 (1H, m), 2.43 (1H, m), 1.68 (1H, m), 1.56 (1H, m), 1.53 (1H, m), 1.25 (1H, m), 3.65 (1H, m), 1.72 (2H, m), 1.66 (2H, m), 1.80 (2H, m), 1.82 (3H, s), 1.37 (2H, m), 1.33 (2H, m), 1.62 (1H, m), 0.97 (3H, d, 6.3 Hz), 0.93 (3H, d, 5.2 Hz), 2.00 (3H, s); ^{13}C NMR (125 MHz, $CDCl_3$; δ in ppm), δ_C 85.0 (CH), 142.3 (C), 125.1 (CH), 66.4 (CH), 177.3 (C), 32.5 (CH_2), 28.0 (CH_2), 32.1 (CH), 53.1 (CH), 29.6 (CH_2), 135.4 (CH), 133.6 (CH), 109.0(CH), 145.0 (CH), 69.9 (CH_2), 41.9 (CH_2), 213.4 (C), 42.8 (CH_2), 19.2 (CH_2), 34.5 (CH_2), 80.3 (CH), 30.4 (CH_2), 24.7 (CH_2), 31.8 (CH_2), 13.8 (CH_3), 29.2 (CH_2), 37.3 (CH_2), 29.9 (CH), 23.8 (CH_3), 24.0 (CH_3), 209.3 (C), 31.7 (CH_3); ^{1}H-^{1}H COSY, HSQC and HMBC data were presented in Table 4.21; EIMS *m/z* found 530.7 $[M]^+$;HRESIMS *m/z* calcd. for $C_{32}H_{51}O_6$ 531.3686, found 531.3690 $[M+H]^+$ (Δ = 0.7 ppm).

4.2.5.15 Physicochemical description of compound-15 (TG_{15})

(2Z,5E,16E)-8-hydroxy-20-isobutyl-16-methyl-7,14-dioxa-bicyclo[19.3.1]-pentacosa-2,5,16-triene-10,23-dione. Yellow oily; $[\alpha]^{22}_D$ -124.2° (*c* 0.18, $CHCl_3$); UV (EtOAc) λ_{max} (log ε): 234 (4.985) nm; TLC (Si-GF254; EtOAc:*n*-hexane, 1/19 v/v) R_f: 0.42; RP-C_{18} HPLC R_t: 5.30 min (234 nm) (MeCN/MeOH, 1:2 v/v); FTIR (KBr, cm^{-1}) ν_{max}: 935 (alkene C-H_δ), 1098 (C-O-C_ν), 1377 (C-H_ρ), 1460 (C-H_δ), 1703 (C-CO-C_ν), 2856, 2922 (C-H_ν) 3426 (O-H_ν); ^{1}H NMR (500 MHz, $CDCl_3$; δ in ppm), δ_H 2.49 (1H, m), 5.59 (1H, dd, 6.9, 6.9 Hz), 5.82 (1H, m), 2.64 (2H, t, 7.1 Hz), 5.88 (1H, m), 5.98 (1H, d, 11.1 Hz), 5.62 (1H, m), 3.15 (1H, dd, 5.6,12.3 Hz), 2.84 (1H, dd, 5.3,12.1 Hz), 2.48 (1H, t, 4.5 Hz), 2.44 (1H, t, 4.8 Hz), 1.73 (2H, m), 3.50 (2H, m), 4.38 (1H, d, 9.3 Hz), 5.43 (1H, t, 5.8 Hz), 2.02 (1H, m), 1.98 (1H, m), 1.42 (1H, m), 1.13 (1H, m), 1.49 (1H, m), 1.80 (1H, m), 2.34 (2H, d, 6.8 Hz), 2.31 (2H, d, 6.1 Hz), 1.90 (2H, t, 5.9 Hz), 1.82 (3H, s), 1.25 (2H, t, 6.9 Hz), 1.64 (1H, m), 1.97 (3H, d, 5.9 Hz), 0.98 (3H, d, 6.2 Hz); ^{13}C NMR (125 MHz, $CDCl_3$; δ in ppm), δ_C 41.4 (CH), 136.4 (CH), 121.6 (CH), 34.6 (CH_2), 126.8 (CH), 144.8 (CH), 96.1 (CH), 49.4 (CH_2), 213.2 (C), 38.2 (CH_2), 24.7 (CH_2), 74.5 (CH_2), 80.6 (CH_2), 137.1 (C), 123.1 (CH), 25.0 (CH_2), 32.1 (CH_2), 34.1 (CH), 37.4 (CH), 47.1 (CH_2), 214.2 (C), 45.7 (CH_2), 36.6 (CH_2), 14.8 (CH_3), 43.3 (CH_2), 26.5 (CH), 23.3 (CH_3), 22.8 (CH_3). ^{1}H-^{1}H COSY, HSQC, and HMBC were presented in Table 4.22; EIMS *m/z* found 460.3 $[M]^+$; HRESIMS *m/z* calcd. for $C_{28}H_{45}O_5$ 461.3267, found 461.3270 $[M+H]^+$ (Δ = 0.6 ppm).

4.2.6 Evaluation of bioactive potencies

4.2.6.1 *In-vitro* antioxidative activities

4.2.6.1a 1, 1-Diphenyl-2-picryl-hydrazil radical/ $DPPH^{\bullet}$ scavenging activity

The estimation of antioxidant potencies of various fractions and pure compounds derived from the EtOAc-MeOH extracts of *G. salicornia* was carried out by *in vitro* $DPPH^{\bullet}$ scavenging assay. The details were described under the section 3.2.5.2a of Chapter 3.

4.2.6.1b 2,2′-Azino-bis-3-ethylbenzothiozoline-6-sulfonic acid diammonium salt/ $ABTS^{+\bullet}$ radical scavenging assay

The determination of antioxidant potencies of various fractions and pure compounds derived from the EtOAc-MeOH extracts of *G. salicornia* was carried out by *in vitro* $ABTS^{+\bullet}$ scavenging assay. The details were described under the section 3.2.5.2b of Chapter 3.

4.2.6.2 *In-vitro* anti-inflammation assays

4.2.6.2a Cyclooxygenases- (COX1/2) inhibition assay

The anti-inflammation bioactive potential of various fractions and pure compounds identified from the EtOAc-MeOH extracts of *G. salicornia* were evaluated by using the pro-inflammatory enzyme, cyclooxygenases (COX-1/2) inhibition assay. The methodology was detailed under the section 3.2.5.3a of Chapter 3.

4.2.6.2b 5-Lipoxygenase/5-LOX inhibition assay

The anti-inflammation bioactive potential of various fractions and pure compounds identified from the EtOAc-MeOH extracts of *G. salicornia* were evaluated by using the pro-inflammatory enzyme 5-lipoxygenase (5-LOX) inhibition assay. This was described under the section 3.2.5.3b of Chapter 3.

4.2.7 Structure-activity correlations of bioactive leads isolated from EtOAc-MeOH extract of G. salicornia

The structure-bioactivity-correlation investigations were carried out by utilising different molecular factors like octanol-water partition-coefficient (log P_{ow}-hydrophobicity); electronic (Pl-polarisability; topological polar surface area-tPSA) and steric (MV-molar volume; P-parachor; MR-molar refractivity) (Lipinski 2000) through ACD-ChemSketch (Advanced Chemistry Development, Inc., Toronto, Canada; ver. 12.0) and ChemDraw-Ultra (Cambridge Soft Corporation, USA; ver. 12.0) softwares.

4.2.8 *Molecular modelling experiments*

In-silico molecular modeling analysis of the bioactive compounds derived from seaweed *G. salicornia* was conducted by the software Auto-Dock-4 (ver. 1.5.6). The fractionated

compounds were drawn using ACD/Chem-sketch and were made into Molfiles before being converted to the PDB format (Open Babel, GUI 2.4.1). The X-ray crystal structures of 5-LOX (PDB 3V99, resolution 2.25 Å), α-glucosidase (PDB 3A4A, resolution 1.6 Å) and α-amylase (PDB 1HNY, resolution 1.8 Å) were acquired from the Protein Data Bank (www.pdb.org) and conformationally oriented (Swiss-Pdb Viewer, ver. 4.1.0) (Gilbert et al., 2012; Brayer et al., 1995; Yamamoto et al., 2010). The docking analyses were conducted by the molecular algorithm, which was run by Cygwin I-II. After auto docking, the RMSD data (root mean square deviation) was documented, and the conformations were oriented with the aid of docking parameters. Finally, molecular docking analyses were visualized using the Chimera software developed by University of California, San Francisco (USCF Chimera, ver. 1.11.2).

4.2.9 Statistical analysis

The entire sets of data were presented in triplicates along with their mean ± standard deviation. One-way analysis of variance (ANOVA; Statistical Program for Social Sciences, USA, ver. 13.0) was used to analyze the significant differences ($P \leq 0.05$) among the means of results.

4.3. Results and discussion

4.3.1. Chromatographic purification of pure compounds and bioactive potentials of sub-column fractions from G. salicornia

The organic extract of *G. salicornia* (33 g) was fractionated by extensive chromatographic fractionation. Initially, the slurry of the crude extract was made with the silica gel of mesh size 60-120 mesh (5 g), and it was packed into a glass column (100 cm x 4 cm) for chromatographic purification. The separation of compounds was carried out with solvents of increasing polarity (*n*-hexane; EtOAc and MeOH) to collect a total of 20 fractions. These fractions were subjected for subsequent chromatographic purification after TLC (*n*-hexane: EtOAc) along with RP C_{18}-HPLC experiments. The fractions that were reported higher percentage yield (> 9 %) on the basis of the dry weight of EtOAc-MeOH extract of *G. salicornia*, were subjected to repeated purification. The pooled homogeneous column fractions were assessed for their bioactive potencies to analyze their inhibition potentials against the carbolytic enzymes (α-amylase and α-glucosidase), pro-inflammatory cyclooxygenases (COX-1/COX-2) and lipoxygenases (5-LOX) along with free-stable-radicals ($DPPH^{\bullet}$ and $ABTS^{+\bullet}$). The fractions with greater bioactive potential were subjected to further downstream-purification. Further bioassay-guided chromatographic separation of major intermediate column fractions

were resulted in seven classes of previously undescribed bioactive compounds (a total of fifteen compounds). The fractionation, yield and bioactive potentials (antioxidative, ant-inflammatory and anti-diabetic) of the secondary metabolites isolated from the EtOAc-MeOH extract of *G. salicornia* was represented in Tables 4.1-4.7 in detail.

Table 4.1.: Yield and bioactivities (antioxidant, anti-inflammatory and antidiabetic) of sub-fractions from EtOAc-MeOH extract of *G. salicornia*

Fractions	***Yield (in %)**	**Bioactivity (IC_{50} in mg mL^{-1})**					
		Antioxidant		**Anti-inflammatory**		**Antidiabetic**	
		#DPPH	**#ABTS**	**#COX-2**	**#5-LOX**	**#α-amylase**	**#α-glucosidase**
GS_1	0.70	1.98^{a}±0.02	2.01^{a}±0.03	2.71^{a}±0.02	2.51^{a}±0.02	2.81^{a}±0.02	2.33^{a}±0.03
GS_2	**9.79**	**1.03^{b} ±0.02**	**1.05^{b}±0.04**	**1.02^{b}±0.02**	**1.01^{b}±0.03**	2.78^{b}±0.03	2.01^{b}±0.03
GS_3	0.97	2.10^{c}±0.03	2.22^{c}±0.05	2.11^{c}±0.03	2.54^{a}±0.04	2.56^{c}±0.06	2.21^{c}±0.03
GS_4	**11.79**	**1.05^{b}±0.03**	**1.08^{b}±0.07**	2.24^{d}±0.05	2.05^{c}±0.03	**0.92^{d}±0.03**	**0.94^{d}±0.06**
GS_5	0.58	2.21^{d}±0.06	2.87^{c}±0.03	2.41^{e}±0.03	2.59^{d}±0.05	2.68^{e}±0.06	2.48^{e}±0.01
GS_6	0.70	2.77^{e}±0.05	3.01^{d}±0.06	2.19^{f}±0.06	2.22^{e}±0.02	2.57^{c}±0.03	2.36^{f}±0.03
GS_7	**11.15**	**0.87^{f}±0.02**	**0.98^{e}±0.06**	**1.01^{b}±0.06**	**1.04^{b}±0.06**	2.87^{f}±0.06	3.01^{g}±0.02
GS_8	**11.79**	**1.03^{b}±0.04**	**0.99^{e}±0.03**	**1.03^{b}±0.04**	**1.02^{b}±0.04**	2.67^{e}±0.06	3.12^{h}±0.06
GS_9	1.70	3.01^{g}±0.02	3.21^{f}±0.03	2.34^{g}±0.06	2.88^{f}±0.03	2.79^{b}±0.03	3.08^{i}±0.07
GS_{10}	3.12	3.33^{h}±0.03	3.48^{g}±0.05	2.26^{h}±0.07	2.93^{g}±0.01	3.12^{g}±0.06	3.14^{h}±0.03
GS_{11}	3.06	3.51^{i}±0.04	3.65^{h}±0.06	2.47^{i}±0.03	2.49^{h}±0.02	3.02^{h}±0.03	2.87^{j}±0.02
GS_{12}	**11.79**	**0.96^{j}±0.02**	**1.06^{b}±0.05**	**1.04^{b}±0.05**	**1.05^{b}±0.03**	2.88^{f}±0.06	2.03^{b}±0.03
GS_{13}	**12.06**	**0.91^{k}±0.03**	**0.97^{e}±0.06**	**0.97^{j}±0.03**	**0.95^{i}±0.02**	2.63^{j}±0.05	2.04^{b}±0.02
GS_{14}	0.79	2.17^{k}±0.08	2.25^{i}±0.07	2.68^{k}±0.06	2.80^{j}±0.08	2.82^{a}±0.06	2.50^{e}±0.06
GS_{15}	**12.15**	**0.82^{l}±0.03**	**0.85^{j}±0.01**	**0.86^{l}±0.04**	**0.88^{k}±0.04**	2.69^{e}±0.06	2.09^{bk}±0.06
GS_{16}	1.45	2.89^{m}±0.06	2.98^{j}±0.03	2.72^{a}±0.01	2.79^{l}±0.01	3.89^{k}±0.02	2.20^{c}±0.07
GS_{17}	0.79	3.02^{g}±0.07	3.12^{k}±0.05	2.69^{a}±0.02	2.53^{a}±0.05	3.76^{l}±0.03	2.23^{c}±0.05
GS_{18}	1.00	2.27^{n}±0.05	2.58^{l}±0.04	2.73^{a}±0.03	2.56^{a}±0.04	3.65^{m}±0.06	2.41^{k}±0.02
GS_{19}	0.70	2.63^{o}±0.02	2.78^{m}±0.03	2.75^{a}±0.01	2.63^{d}±0.07	3.25^{n}±0.07	2.30^{a}±0.04
GS_{20}	0.67	2.84^{p}±0.03	2.86^{c}±0.06	2.86^{m}±0.06	2.71^{m}±0.02	3.13^{g}±0.06	2.99^{l}±0.05

*The yield of major sub-column fractions calculated based on the crude EtOAc-MeOH extract (33.0 g of dry weight). The values were tabulated in triplicate (n=3) and indicated as

mean±standard deviation. Significant differences were expressed as superscripts (a-p) within column ($p < 0.05$).

[#]The IC_{50} values were calculated in mg mL^{-1}

Table 4.2.: Yield and bioactivities of (antioxidant, anti-inflammatory and antidiabetic) sub-column fractions derived from EtOAc-MeOH extract of *G. salicornia*

Fractions	Bioactivity (IC_{50} in mg mL^{-1})						*Yield
	Antioxidant		Anti-inflammatory		Antidiabetic		
	#DPPH•	#$ABTS^{•+}$	#COX-2	#5-LOX	#α-amylase	#α-glucosidase	in %
GS_{2-1}	1.09^{a} ±0.02	1.12^{a}±0.02	1.02^{a}±0.02	1.01^{a}±0.03	2.08^{a}±0.03	2.02^{a}±0.03	7.66
GS_{2-2}	**0.97^{b}±0.03**	**0.98^{b}±0.03**	**0.92^{b}±0.03**	**0.94^{b}±0.04**	**2.06^{a}±0.06**	**2.11^{b}±0.03**	**1.60**
GS_{2-3}	1.04^{b} ±0.02	1.05^{c} ±0.02	1.06^{c}±0.02	1.03^{a}±0.03	2.04^{a}±0.03	2.13^{b}±0.03	1.42
GS_{2-2-1}	**0.87^{c}±0.06**	**0.89^{d}±0.06**	**0.78^{e}±0.03**	**0.73^{c}±0.05**	**2.32^{b}±0.06**	**2.18^{c}±0.1**	**0.31**
GS_{2-2-2}	1.08^{a}±0.05	1.01^{c}±0.05	1.09^{c}±0.06	1.02^{a}±0.02	2.17^{c}±0.03	2.16^{c}±0.03	0.06
GS_{2-2-3}	1.01^{b}±0.02	1.04^{c}±0.02	1.07^{c}±0.06	1.04^{a}±0.06	2.12^{c}±0.06	2.93^{d}±0.02	0.04

*The yield of sub-column fractions calculated based on the crude EtOAc-MeOH extract (33.0 g of dry weight). The values were tabulated in triplicate (n=3) and indicated as mean±standard deviation. Significant differences were expressed as superscripts (a-d) within column ($p < 0.05$). #The IC_{50} values were calculated in mg mL^{-1}

Table 4.3.: Yield and bioactivities of (antioxidant, anti-inflammatory and antidiabetic) sub-column fractions derived from EtOAc-MeOH extract of *G. salicornia*

Fractions	Bioactivity (IC_{50} in mg mL^{-1})						*Yield
	Antioxidant		Anti-inflammatory		Antidiabetic		
	#DPPH$^{\bullet}$	#ABTS$^{\bullet+}$	#COX-2	#5-LOX	#α-amylase	#α-glucosidase	in %
GS_{4-1}	**$1.03^{a}\pm0.03$**	**$1.02^{a}\pm0.03$**	**$1.18^{a}\pm0.03$**	**$1.17^{a}\pm0.04$**	**$1.03^{a}\pm0.06$**	**$1.01^{a}\pm0.03$**	**8.55**
GS_{4-2}	$1.05^{a}\pm0.03$	$1.07^{b}\pm0.03$	$1.21^{a}\pm0.05$	$1.25^{b}\pm0.03$	$1.11^{b}\pm0.03$	$1.09^{b}\pm0.06$	1.10
GS_{4-3}	$1.10^{b}\pm0.03$	$1.11^{b}\pm0.03$	$1.12^{b}\pm0.05$	$1.27^{b}\pm0.03$	$1.12^{b}\pm0.03$	$1.10^{a}\pm0.06$	0.99
GS_{4-1-1}	$1.05^{ab}\pm0.06$	$1.06^{a}\pm0.06$	$2.22^{c}\pm0.03$	$2.39^{c}\pm0.05$	$1.05^{a}\pm0.06$	$1.04^{a}\pm0.01$	0.07
GS_{4-1-2}	**$0.87^{c}\pm0.05$**	**$0.89^{b}\pm0.05$**	**$2.18^{c}\pm0.06$**	**$2.23^{d}\pm0.02$**	**$0.68^{c}\pm0.03$**	**$0.65^{c}\pm0.03$**	**0.36**
GS_{4-1-3}	**$0.84^{c}\pm0.02$**	**$0.85^{b}\pm0.02$**	**$2.11^{d}\pm0.06$**	**$2.15^{e}\pm0.06$**	**$0.69^{c}\pm0.06$**	**$0.63^{c}\pm0.02$**	**0.35**
GS_{4-1-4}	$1.04^{a}\pm0.05$	$1.10^{b}\pm0.05$	$2.12^{d}\pm0.06$	$2.14^{e}\pm0.02$	$2.62^{d}\pm0.03$	$2.59^{d}\pm0.03$	0.06
GS_{4-1-5}	$1.09^{bd}\pm0.05$	$1.08^{b}\pm0.05$	$2.20^{c}\pm0.06$	$2.25^{d}\pm0.02$	$2.52^{e}\pm0.03$	$2.48^{e}\pm0.03$	0.05

*The yield of sub-column fractions calculated based on the crude EtOAc-MeOH extract (33.0 g of dry weight). The values were tabulated in triplicate (n=3) and indicated as mean±standard deviation. Significant differences were expressed as superscripts (a-e) within column ($p < 0.05$). #The IC_{50} values were calculated in mg mL^{-1}

Table 4.4.: Yield and bioactivities (antioxidant, anti-inflammatory and antidiabetic) of sub-fractions from EtOAc-MeOH extract of *G. salicornia*

Fractions	Bioactivity (IC_{50} in mg mL^{-1})						*Yield
	Antioxidant		Anti-inflammatory		Antidiabetic		
	#DPPH•	#ABTS•+	#COX-2	#5-LOX	#α-amylase	#α-glucosidase	in %
GS_{7-1}	1.04^{a} ±0.02	1.10^{a} ±0.02	1.02^{a}±0.02	1.03^{a}±0.03	2.37^{a}±0.03	2.51^{a}±0.03	0.99
GS_{7-2}	**1.02^{a}±0.03**	**1.03^{b}±0.03**	**0.99^{b}±0.03**	**0.96^{b}±0.04**	**2.59^{b}±0.06**	**2.63^{b}±0.03**	**8.27**
GS_{7-3}	1.10^{b}±0.03	1.11^{a}±0.03	1.05^{a}±0.05	1.05^{a}±0.03	2.23^{c}±0.03	2.31^{c}±0.06	0.82
GS_{7-4}	1.08^{b}±0.06	1.09^{a}±0.06	1.04^{a}±0.03	1.06^{ac}±0.05	2.48^{d}±0.06	2.54^{a}±0.01	0.57
GS_{7-5}	1.11^{b}±0.05	1.08^{a}±0.05	1.03^{a}±0.06	1.01^{a}±0.02	2.67^{e}±0.03	2.68^{b}±0.03	0.98
GS_{7-6}	1.12^{b}±0.02	1.13^{a}±0.02	1.01^{a}±0.06	1.02^{a}±0.06	2.83^{f}±0.06	2.85^{c}±0.02	1.11
GS_{7-2-1}	1.02^{a}±0.06	1.07^{a}±0.03	1.05^{ac}±0.03	1.09^{c}±0.05	2.08^{g}±0.06	2.04^{d}±0.01	1.01
GS_{7-2-2}	**0.98^{c}±0.05**	**1.04^{b}±0.06**	**0.97^{b}±0.06**	**0.92^{b}±0.02**	**2.17^{h}±0.03**	**2.03^{d}±0.03**	**1.29**
GS_{7-2-3}	**0.97^{c}±0.02**	**1.02^{b}±0.06**	**0.96^{b}±0.06**	**0.93^{b}±0.06**	**2.18^{h}±0.06**	**2.16^{e}±0.02**	**1.56**
$GS_{7-2-2-1}$	1.05^{a}±0.02	1.12^{a}±0.06	1.02^{a}±0.06	1.07^{c}±0.06	2.13^{h}±0.06	2.21^{f}±0.02	0.08
$GS_{7-2-2-2}$	1.06^{a}±0.05	1.10^{a}±0.06	1.06^{a}±0.06	1.02^{a}±0.02	2.07^{i}±0.03	2.20^{f}±0.03	0.06
$GS_{7-2-2-3}$	**0.72^{d} ±0.02**	**0.81^{c}±0.02**	**0.73^{c}±0.02**	**0.72^{d}±0.03**	**2.06^{hi}±0.03**	**2.19^{f}±0.03**	**0.38**
$GS_{7-2-2-4}$	1.11^{b}±0.03	1.06^{b}±0.03	1.08^{c}±0.03	1.04^{a}±0.04	2.10^{i}±0.06	2.18^{f}±0.03	0.08
$GS_{7-2-3-1}$	1.09^{b}±0.03	1.05^{b}±0.05	1.05^{a}±0.05	1.05^{a}±0.03	1.98^{j}±0.03	2.07^{d}±0.06	0.05
$GS_{7-2-3-2}$	1.07^{b}±0.06	1.01^{b}±0.03	1.07^{c}±0.03	1.08^{c}±0.05	1.99^{j}±0.06	2.09^{d}±0.01	0.04
$GS_{7-2-3-3}$	**0.76^{d}±0.05**	**0.83^{c}±0.06**	**0.74^{d}±0.06**	**0.73^{d}±0.02**	**2.01^{k}±0.03**	**2.06^{d}±0.03**	**0.39**
$GS_{7-2-3-4}$	**0.75^{d}±0.02**	**0.86^{c}±0.06**	**0.76^{d}±0.06**	**0.75^{d}±0.06**	**2.03^{k}±0.06**	**2.01^{d}±0.02**	**0.38**

*The yield of sub-column fractions calculated based on the crude EtOAc-MeOH extract (33.0 g of dry weight). The values were tabulated in triplicate (n=3) and indicated as mean±standard deviation. Significant differences were expressed as superscripts (a-k) within column ($p < 0.05$). #The IC_{50} values were calculated in mg mL^{-1}

Table 4.5.: Yield and bioactivities (antioxidant, anti-inflammatory and antidiabetic) of sub-fractions from EtOAc-MeOH extract of *G. salicornia*

Fractions	Bioactivity (IC_{50} in mg mL^{-1})						*Yield
	Antioxidant		Anti-inflammatory		Antidiabetic		
	#DPPH$^{\bullet}$	#ABTS$^{\bullet+}$	#COX-2	#5-LOX	#α-amylase	#α-glucosidase	in %
GS_{8-1}	1.03^{a}±0.06	1.04^{a}±0.03	1.01^{a}±0.04	1.02^{a}±0.05	2.26^{a}±0.06	2.18^{a}±0.01	1.15
GS_{8-2}	**0.89^{b}±0.05**	**0.93^{b}±0.06**	**0.87^{b}±0.07**	**0.85^{b}±0.07**	**2.57^{b}±0.03**	**2.16^{a}±0.03**	**0.31**
GS_{8-3}	**0.88^{b}±0.02**	**0.91^{b}±0.06**	**0.86^{b}±0.03**	**0.83^{b}±0.02**	**2.53^{b}±0.06**	**2.49^{b}±0.02**	**0.38**
GS_{8-4}	1.08^{c}±0.02	1.06^{cd}±0.06	1.02^{a}±0.05	1.03^{a}±0.07	2.63^{c}±0.06	2.51^{b}±0.02	1.36
GS_{12-1}	1.07^{c}±0.05	1.10^{d}±0.06	1.11^{c}±0.05	1.09^{c}±0.04	2.51^{b}±0.03	2.63^{c}±0.03	1.5
$GS_{12.-2}$	1.06^{c} ±0.02	1.12^{d}±0.02	1.10^{c}±0.01	1.08^{c}±0.02	2.23^{a}±0.03	2.20^{a}±0.03	3.68
$GS_{12.-3}$	**1.12^{d}±0.03**	**1.05^{c}±0.03**	**1.04^{a}±0.03**	**1.06^{ac}±0.01**	**2.25^{a}±0.06**	**2.28^{d}±0.03**	**5.51**
$GS_{12-.4}$	1.16^{d}±0.03	1.14^{d}±0.05	1.06^{ac}±0.07	1.04^{a}±0.06	2.01^{d}±0.03	2.14^{a}±0.06	2.60
$GS_{12-.3-1}$	1.15^{d}±0.06	1.16^{d}±0.03	1.05^{a}±0.03	1.07^{ac}±0.01	2.32^{e}±0.06	2.33^{d}±0.01	1.92
$GS_{12-.3-2}$	1.10^{d}±0.05	1.18^{de}±0.06	1.08^{ac}±0.06	1.10^{c}±0.02	2.07^{f}±0.03	2.09^{e}±0.03	2.08
GS_{12-3-3}	1.09^{c}±0.02	1.08^{a}±0.06	1.09^{c}±0.08	1.11^{c}±0.06	2.12^{g}±0.06	2.13^{a}±0.02	2.18
GS_{12-3-4}	**1.01^{a}±0.06**	**1.02^{a}±0.03**	**0.99^{e}±0.03**	**1.01^{a}±0.03**	**2.03^{d}±0.06**	**2.08^{e}±0.01**	**1.78**
$GS_{12-3-4-1}$	**0.87^{b}±0.05**	**0.89^{f}±0.06**	**0.78^{f}±0.02**	**0.76^{e}±0.02**	**2.58^{b}±0.07**	**2.47^{b}±0.02**	**0.37**
$GS_{12-3-4-2}$	1.01^{a}±0.06	1.07^{a}±0.04	1.03^{a}±0.03	1.04^{a}±0.01	2.61^{c}±0.07	2.59^{f}±0.02	0.08
$GS_{12-3-4-3}$	1.02^{a}±0.02	1.01^{a}±0.02	1.05^{a}±0.04	1.03^{a}±0.01	2.52^{b}±0.04	2.48^{b}±0.05	0.04
$GS_{12-3-4-4}$	1.04^{a}±0.02	1.06^{a}±0.05	1.07^{a}±0.05	1.01^{a}±0.04	2.73^{h}±0.04	2.70^{g}±0.04	0.06
$GS_{12-3-4-5}$	**0.86^{b}±0.01**	**0.87^{f}±0.07**	**0.75^{f}±0.06**	**0.73^{e}±0.07**	**2.67^{i}±0.04**	**2.68^{h}±0.07**	**0.35**

*The yield of sub-column fractions calculated based on the crude EtOAc-MeOH extract (33.0 g of dry weight). The values were tabulated in triplicate (n=3) and indicated as mean±standard deviation. Significant differences were expressed as superscripts (a-i) within column ($p < 0.05$). #The IC_{50} values were calculated in mg mL^{-1}

Table 4.6.: Yield and bioactivities (antioxidant, anti-inflammatory and antidiabetic) of sub-fractions from EtOAc-MeOH extract of *G. salicornia*

Fractions	Bioactivity (IC_{50} in mg mL^{-1})						*Yield
	Antioxidant		Anti-inflammatory		Antidiabetic		
	#DPPH$^{\bullet}$	#$ABTS^{\bullet+}$	#COX-2	#5-LOX	#α-amylase	#α-glucosidase	in %
$GS_{13\text{-}1}$	**$0.82^{a}\pm0.05$**	**$0.84^{a}\pm0.05$**	**$0.72^{a}\pm0.05$**	**$0.70^{a}\pm0.04$**	**$2.53^{a}\pm0.05$**	**$2.50^{a}\pm0.06$**	**0.36**
$GS_{13\text{-}2}$	$1.03^{b}\pm0.08$	$1.05^{b}\pm0.03$	$1.04^{b}\pm0.02$	$0.99^{b}\pm0.02$	$2.54^{a}\pm0.05$	$2.51^{a}\pm0.02$	1.50
$GS_{13\text{-}3}$	$1.05^{b}\pm0.03$	$1.07^{b}\pm0.02$	$1.06^{b}\pm0.06$	$1.02^{a}\pm0.01$	$2.57^{a}\pm0.05$	$2.49^{a}\pm0.02$	0.80
$GS_{13\text{-}4}$	$1.06^{b}\pm0.04$	$1.08^{b}\pm0.06$	$1.07^{b}\pm0.05$	$1.05^{c}\pm0.05$	$2.28^{b}\pm0.03$	$2.26^{b}\pm0.07$	0.02
$GS_{13\text{-}5}$	**$0.80^{a}\pm0.04$**	**$0.81^{a}\pm0.02$**	**$0.71^{a}\pm0.04$**	**$0.70^{a}\pm0.03$**	**$2.31^{b}\pm0.04$**	**$2.30^{b}\pm0.07$**	**0.34**

*The yield of sub-column fractions calculated based on the crude EtOAc-MeOH extract (33.0 g of dry weight). The values were tabulated in triplicate (n=3) and indicated as mean±standard deviation. Significant differences were expressed as superscripts (a-b) within column ($p < 0.05$). #The IC_{50} values were calculated in mg mL^{-1}

Table 4.7.: Yield and bioactivities (antioxidant, anti-inflammatory and antidiabetic) of sub-fractions from EtOAc-MeOH extract of *G. salicornia*

Fractions	Bioactivity (IC_{50} in mg mL^{-1})						*Yield
	Antioxidant		Anti-inflammatory		Antidiabetic		
	#DPPH$^{\bullet}$	#ABTS$^{\bullet+}$	#COX-2	#5-LOX	#α-amylase	#α-glucosidase	in %
$GS_{15.-1}$	**1.05^{a}±0.04**	**1.09^{bd}±0.03**	**1.05^{a}±0.05**	**1.04^{a}±0.01**	**2.37^{a}±0.03**	**2.32^{a}±0.07**	**6.43**
$GS_{15.-2}$	**1.07^{a}±0.02**	**1.10^{d}±0.06**	**1.03^{a}±0.05**	**1.01^{a}±0.01**	**2.27^{b}±0.06**	**2.22^{b}±0.04**	**8.56**
$GS_{15.-3}$	1.11^{b}±0.06	1.12^{d}±0.03	1.01^{a}±0.03	1.00^{a}±0.05	2.18^{c}±0.06	2.08^{c}±0.04	3.27
$GS_{15.-1-1}$	**0.70^{c}±0.05**	**0.72^{f}±0.06**	**0.62^{b}±0.06**	**0.60^{b}±0.02**	**2.28^{b}±0.03**	**2.21^{b}±0.03**	**0.36**
$GS_{15.-1-2}$	**0.69^{c} ±0.02**	**0.71^{b}±0.02**	**0.60^{b}±0.02**	**0.59^{b}±0.03**	**2.31^{a}±0.03**	**2.18^{b}±0.03**	**0.34**
$GS_{15.-1-3}$	1.12^{b}±0.03	1.14^{c}±0.03	1.02^{a}±0.03	0.99^{a}±0.04	2.36^{a}±0.06	2.33^{c}±0.03	0.21
$GS_{15.-2-1}$	**0.71^{c}±0.03**	**0.72^{d}±0.05**	**0.65^{b}±0.05**	**0.63^{b}±0.03**	**2.41^{a}±0.03**	**2.38^{c}±0.06**	**0.33**
$GS_{15.-2-2}$	1.09^{b}±0.06	1.11^{e}±0.03	1.04^{a}±0.03	1.02^{a}±0.05	2.38^{a}±0.06	2.26^{b}±0.01	0.18
$GS_{15.-2-3}$	1.10^{b}±0.05	1.13^{f}±0.06	1.03^{a}±0.06	1.04^{a}±0.02	2.35^{a}±0.03	2.31^{a}±0.03	0.10

*The yield of sub-column fractions calculated based on the crude EtOAc-MeOH extract (33.0 g of dry weight). The values were tabulated in triplicate (n=3) and indicated as mean±standard deviation. Significant differences were expressed as superscripts (a-f) within column ($p < 0.05$). #The IC_{50} values were calculated in mg mL^{-1}

4.3.2 *Spectroscopic characterization of bioactive compounds derived from EtOAc-MeOH extract of G. salicornia*

The sequential chromatographic purification of EtOAc-MeOH crude extract of *G. salicornia* was led to the identification of bioactive secondary metabolic analogues. The structural interpretation of these lead molecules carried out using the nuclear magnetic resonance (NMR) analyses {^{1}H-proton-500 MHz; ^{13}C-carbon-125 MHz; DEPT; ^{1}H-^{1}H COSY; HSQC; HMBC; NOESY} using deuterated solvents along with mass spectrometric analyses (GC-EI-MS/HRESIMS), infrared spectrum analysis (FT-IR) (reported among 4000-400 cm^{-1}) and UV-spectrophotometric analyses. The isolated secondary metabolic analogues were categorized under the different classes of chemistries, namely abeo-labdane class of diterpenoid (**1**), oleanene class of triterpenoids (**2-3**), drimane-associated quinols (**4-6**), 2*H*-chromenyl compounds (**7-8**), spiro-fused analogues (**9-10**), squalene polyether metabolites (**11-12**), and macrolides enclosing ether functionalities (**13-15**).

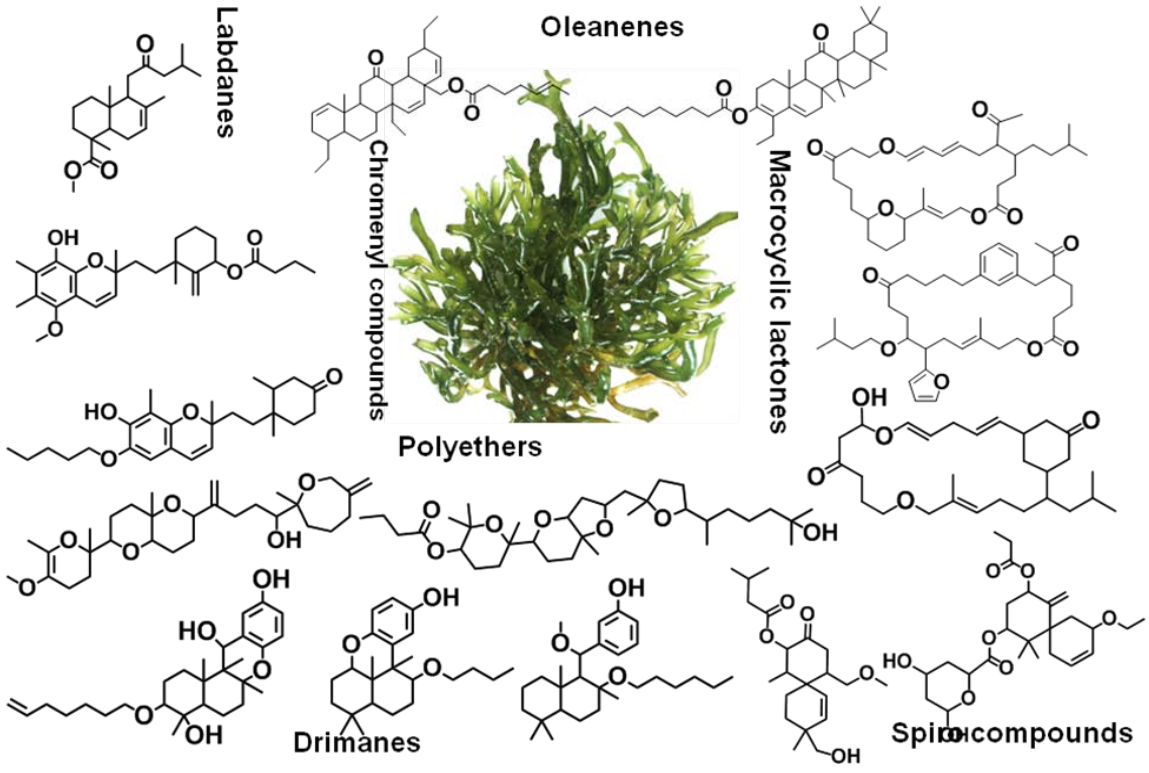

4.3.2.1 *Structural characterization of abeo-labdane class of diterpenoid derivative (Compound 1)*

Diterpenoids are large classes of bioactive leads assembled by isoprene moieties, with prominent functional and structural diversity (Hanson 2002). Labdanes are one of the predominant bicyclic diterpenoids in seaweeds with broad range of biological activities (Singh

1999, Demetzos & Dimas 2001, Hanson 2000, Hanson 2001, Hanson 2002, Blunt et al. 2006). The basic carbon frame work of labdane could be oriented into a decalin fused system C(1)-C(10) and a six-carbon branched side chain at C(9) {(C(11)-C(16), with C(16) connected to C(13)}. The remaining four methyl carbons from C(17)-C(20) were attached at C(8), C(40) {with C(18) and C(19) being attached}, and C(10) of the decalin system, respectively. The majority of labdanes were present in *trans* configuration at the C(5):C(10) junction of the ring, whereas labdanes with a *cis* orientation of C(5):C(10) ring junction were identified to a much lesser extent. On the basis of the ring junction stereochemistry, labdanes were further categorized by their orientations stereochemistries at C(9) and C(10). Subsequently, the classifications of labdane framework were defined as 'normal-', 'ent-', 'syn-', and 'syn–ent-', based on the configuration of the ring junctions and the substituents at C(9) and C(10) (Peters 2010, Demetzos & Dimas 2001, Tran et al. 2017).

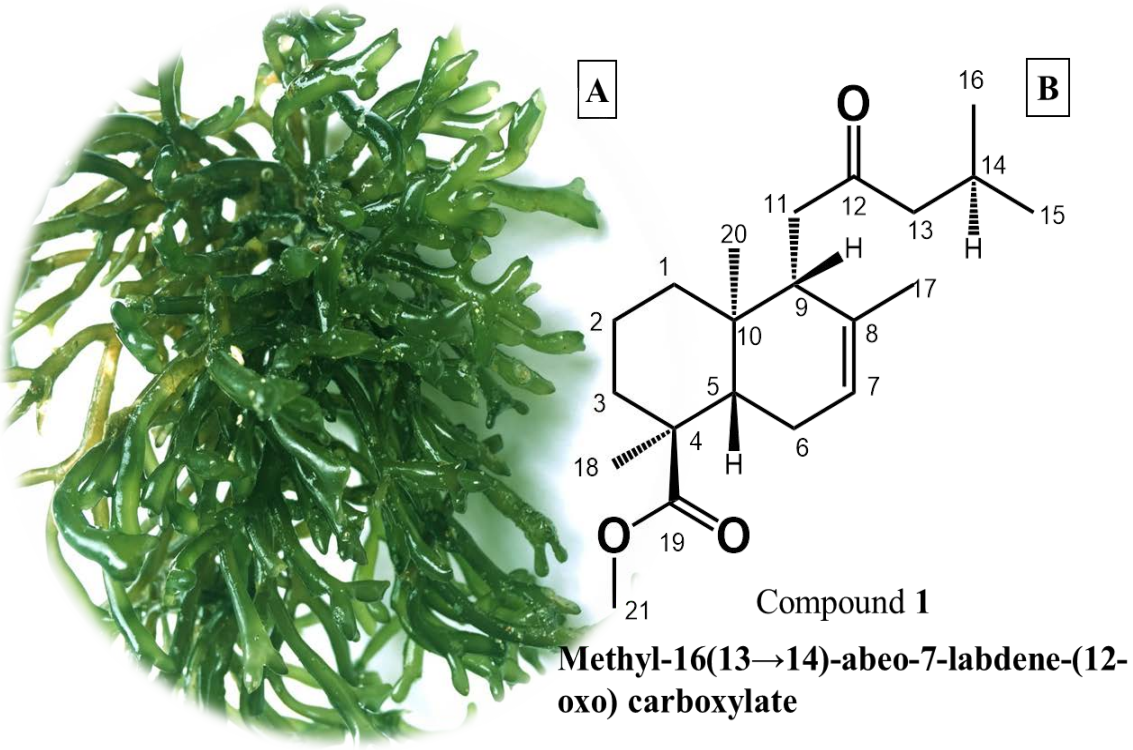

Compound **1**

Methyl-16(13→14)-abeo-7-labdene-(12-oxo) carboxylate

Figure 4.3.: Structure of methyl-16(13→14)-abeo-7-labdene-(12-oxo) carboxylate isolated from *G. salicornia* (family Gracilariaceae), (B) representative photograph of thalli of red seaweed *G. salicornia*

It has been documented that the organic extracts of *Gracilaria* sp. (family Gracilariaceae) comprised bioactive secondary metabolites along with anti-inflammatory, antioxidant, and antimicrobial potentials (Bansemir et al. 2006, Makkar and Chakraborty 2018b, Makkar and Chakraborty 2018c). The labdanes, 2α-hydroxy-8(17), 12 E, 14-labdatriene and 3β, 6β, 13α-trihydroxy 8(17), 12E, 14-labdatriene were isolated from brown seaweed *Sargassum wightii* (Maneesh et al., 2017) along with Venustanol from red seaweed *Laurencia venusta* (Suzuki et al. 1988; Suzuki et al. 2002). Here, we have characterized a 16(13→14)-abeo-labdene class of diterpenoid, namely methyl-16(13→14)-abeo-7-labdene-(12-oxo) carboxylate from the EtOAc-MeOH (ethyl acetate-methanol) extract of *G. salicornia* collected from the southern coast of Indian peninsular (Figure 4.3). The pharmacological activities were evaluated by various *in vitro* anti-inflammatory and antioxidant assays.

4.3.2.1a Structural characterization of Compound 1(TG_1)

Methyl-16(13→14)-abeo-7-labdene-(12-oxo) carboxylate

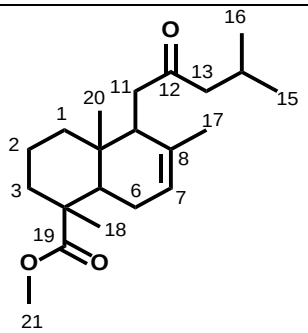

Sample yield	0.31% (> 99% purity, RP-C18 HPLC)
Physical description	Yellowish-white amorphous
Molecular formula	$C_{21}H_{34}O_3$
Molecular mass	334.2508

The abeo-labdane class of diterpenoid derivative, methyl-16(13→14)-abeo-7-labdene-(12-oxo) carboxylate was isolated as yellowish-white amorphous compound. The compound (**1**) has exhibited UV absorbance (UV (MeOH) λ_{max}) at 242 nm (Figure 4.4). The homogeneity of the compound was ascertained by HPLC data on a bonded phase octadecylsilane (C_{18}) stationary phase (HPLC, MeOH/H_2O, 2:1 v/v) with R_t: 3.4 min (Figure 4.5).

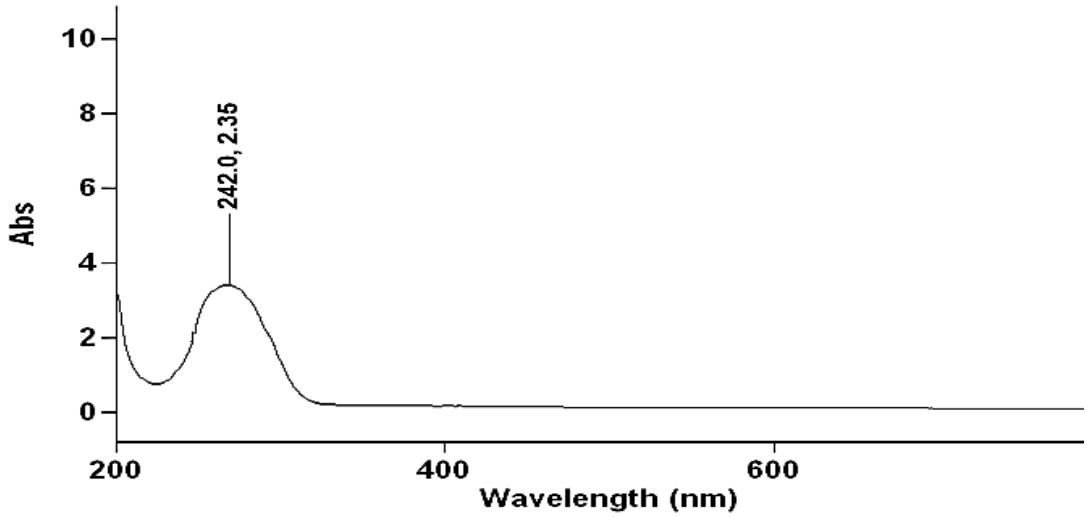

Figure 4.4.: UV spectrum of methyl-16(13→14)-abeo-7-labdene-(12-oxo) carboxylate (**1**)

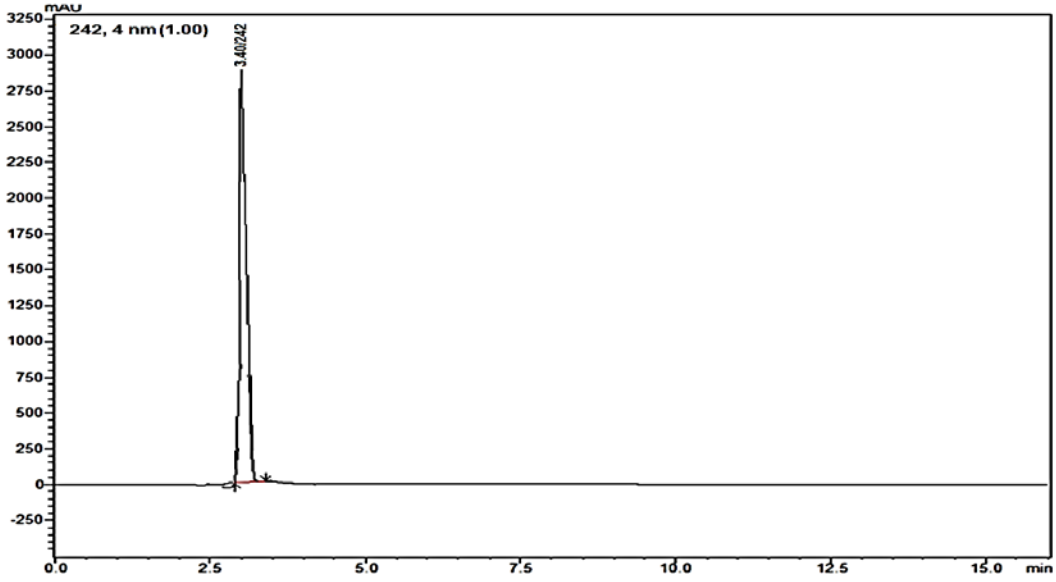

Figure 4.5.: HPLC chromatogram of methyl-16(13→14)-abeo-7-labdene-(12-oxo) carboxylate (**1**)

The chromatography-based fractionation of EtOAc-MeOH organic extract of *G. salicornia* afforded methyl-16(13→14)-abeo-7-labdene-(12-oxo) carboxylate as a homogeneous compound with greater than 99% purity. The ESI-MS (positive) experiment displayed a pseudo-molecular ion peak at m/z 335.2589 (HRESIMS *m/z* calcd 335.2586 [$M+H^+$]) (Figure 4.6), while the molecular formula $C_{21}H_{34}O_3$, implying five unsaturation degrees, was associated with one olefinic bond and two each of cyclic systems and carbonyl moieties based on integrative ^{13}C NMR-MS spectroscopic experiments.

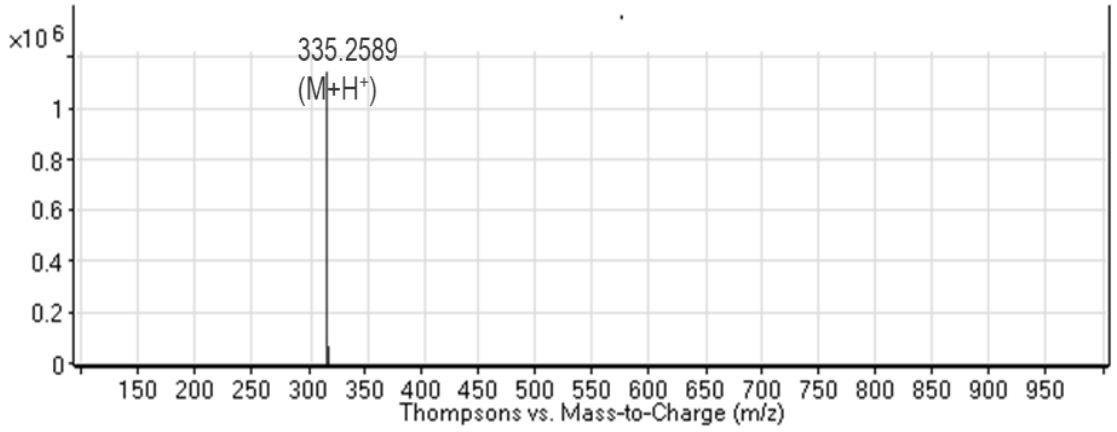

Figure 4.6.: HRESIMS spectrum of methyl-16(13→14)-abeo-7-labdene-(12-oxo) carboxylate (**1**)

The FTIR absorption bands at 1735 and 1725cm^{-1} indicated the presence of carbonyl and ester moieties, respectively (Figure 4.7). The ^{13}C NMR spectrum along with $DEPT_{135}$ analysis deduced 21 carbon signals in the studied compound (Table 4.8) including the signals due to five quaternary carbons (δ 42.41, δ 135.93, δ 39.27, δ 203.27, and δ 167.73), three sp^3 methines (δ 44.70, δ 124.87, δ 45.18, and δ 24.16), and one sp^2 methine (δ 124.87) other than six sp^3 methylene signals (δ 38.65, δ_C 20.85, δ 38.26, δ 23.54, δ 41.32 and δ 54.80) suggesting the structural features of labdane diterpene skeleton (Tran et al., 2017).

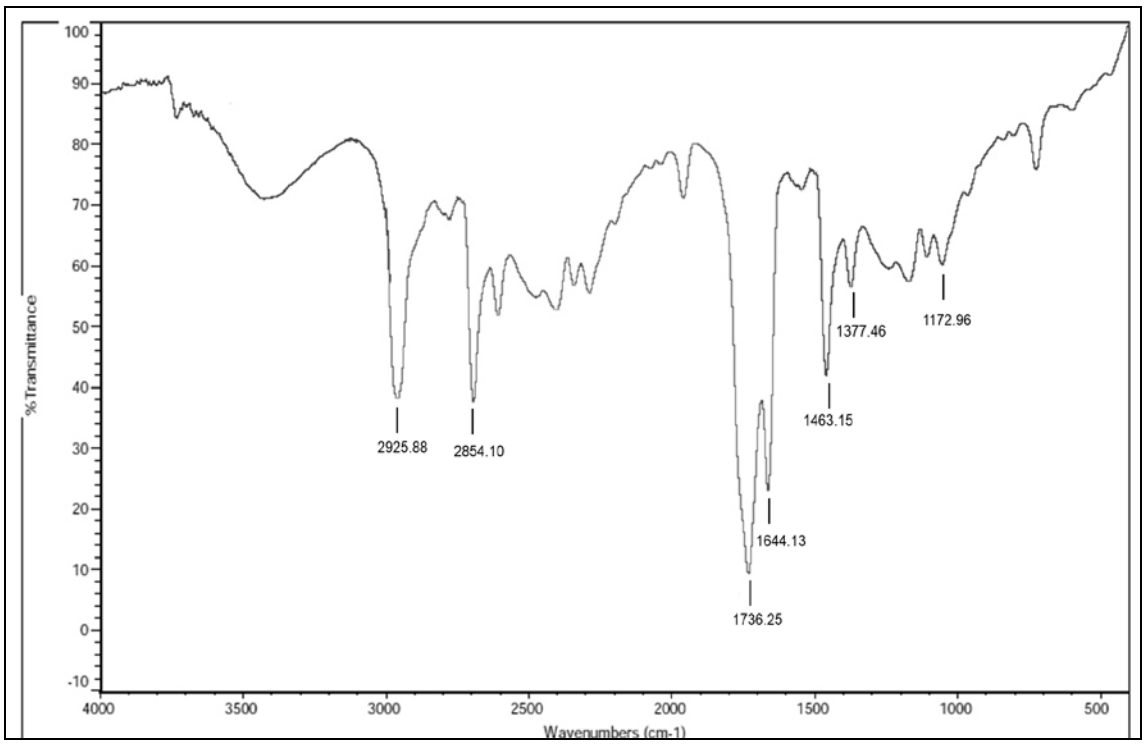

Figure 4.7.: FT-IR spectrum of methyl-16(13→14)-abeo-7-labdene-(12-oxo) carboxylate (**1**)

In addition, the analyses of the ^{13}C NMR spectrum designated the occurrence of one each of ketone group and ester functionality at δ 124.87 and 167.63, respectively. The ^{1}H NMR spectrum demonstrated five methyl groups at δ 0.79 (3H, d, J=6.0 Hz); δ 0.87 (3H, d, J=6.1 Hz); δ 1.14 (3H, s); δ 1.38 (3H, s), δ 0.63 (3H, s) (one angular methyl moiety), and δ 3.46 (3H, s) which were similar to labdane-type diterpenoid skelton (Suzuki et al., 1988; Chakraborty et al., 2010; Suzuki et al., 2002; Tran., 2017; Maneesh et al., 2017) (Figure 4.8-4.10).

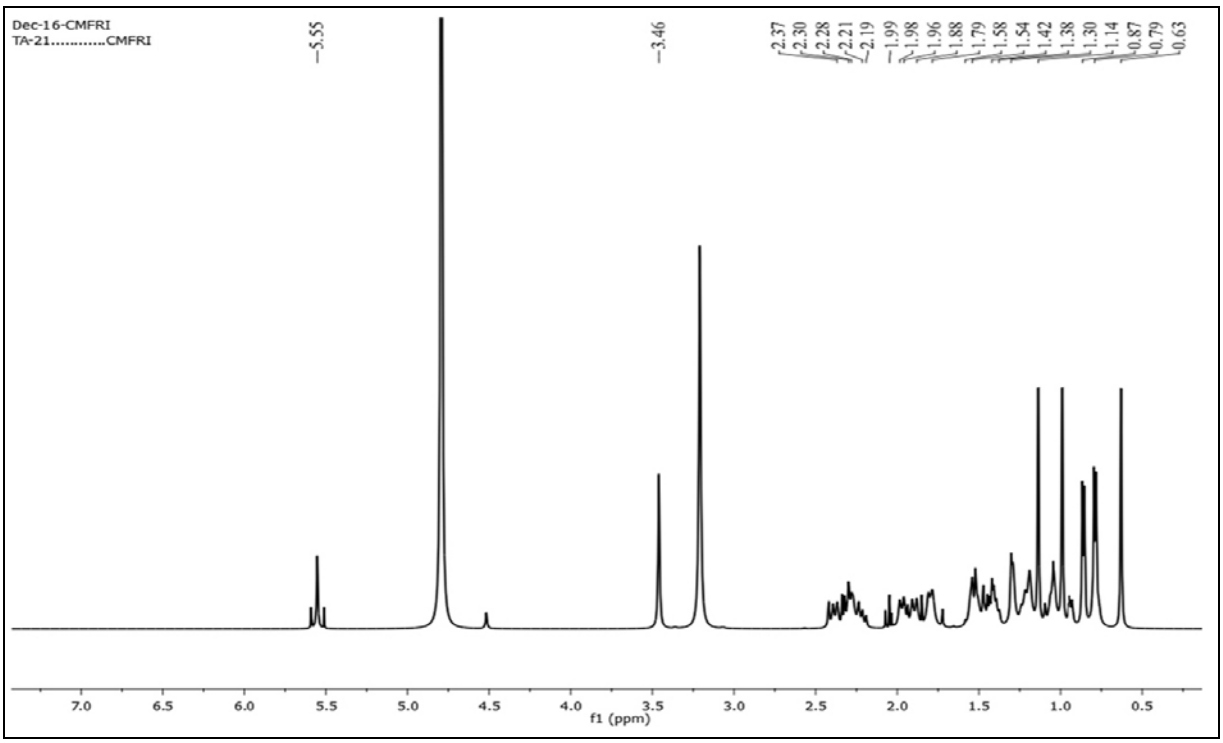

Figure 4.8.: ^{1}H-NMR spectrum of methyl-16(13→14)-abeo-7-labdene-(12-oxo) carboxylate (**1**)

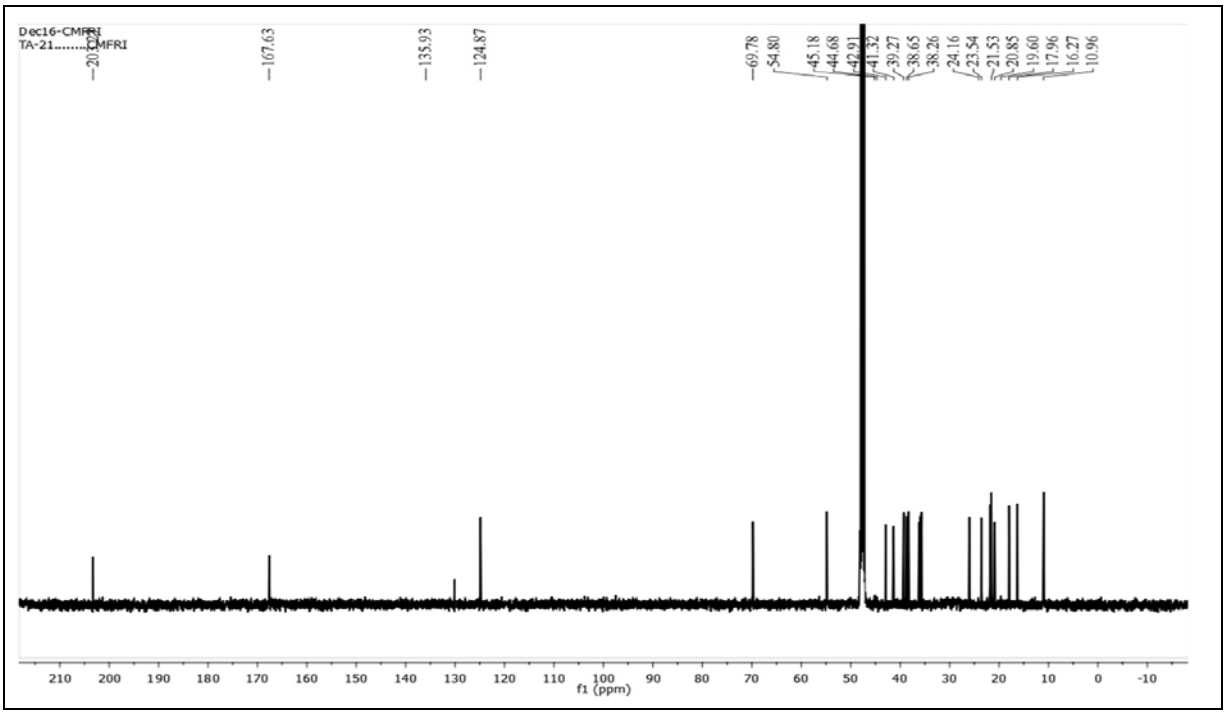

Figure 4.9.: ^{13}C-NMR spectrum of methyl-16(13→14)-abeo-7-labdene-(12-oxo) carboxylate (**1**)

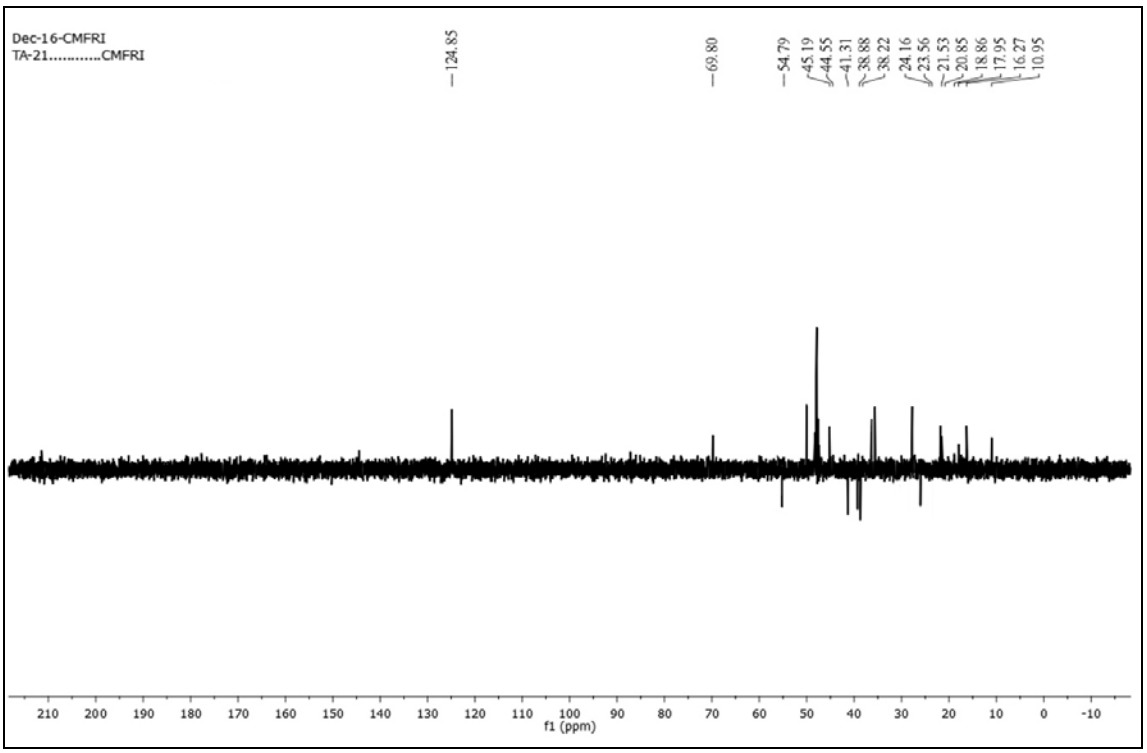

Figure 4.10.: ^{13}C-NMR spectrum of methyl-16(13→14)-abeo-7-labdene-(12-oxo) carboxylate (**1**)

A methyl singlet was apparent at δ 0.79, and this was confirmed by the ^{1}H-^{1}H COSY correlations between δ 0.79/1.96. The ^{1}H-^{1}H COSYs between the δ 1.54/1.42/2.18 along with HMBCs between δ1.54/20.85; 1.42/20.85; 1.54/39.27; 2.18/42.91; 1.98/39.27 revealed the occurrence of C_6-ring in the studied compound. Similarly, ^{1}H-^{1}H COSYs between δ 1.98/1.78/5.55 along with HMBCs between δ 1.98/23.54; 5.55/13.5.93; 2.18/135.93/39.27 demonstrated the second C_6-ring (Figure 4.10). The assembly of these ^{1}H-^{1}H COSYs and HMBCs led to the formation bicyclic decalin system in 16(13→14)-abeo-labdene. Hence, the positions of carbons in this decalin system were disposed from C-1 to C-10 continuously. The ^{1}H NMR data demonstrated the occurrence of an alkenic proton at δ 5.55(1H, t, J=6.6 Hz), exhibiting HSQC with the carbon at δ 124.87, and HMBCs with δ 135.93 and 44.68 (Figure 4.11-4.13). These assignments explained the occurrence of olefinic bond in decalin system between C(7)-C(8). The NMR spectrum of ^{13}C in combination with DEPT$_{135}$ exhibited six more carbon resonances, and which were attached at C-9 of the decalin system as corroborated by their 2D NMR spectral data. The ^{1}H-^{1}H COSYs from H-9/11(δ 2.21/2.37), H-13/14/15and H-14/16 and HMBCs between H-9/C-11, H-11/C-12, H-13/C-12 and H-14/C-12 appropriately explained the substitution of side chain 5-methyl-3-hexanone at C-9. The carbonyl functionality

(C=O) was attached to decalin system by long range correlation between H-9/C-12. The HMBCs from H-3 to C-19 described the occurrence of ester functionality at C-4. The HMBCs between H-9/C-8 and H-17/C-8 confirmed the presence of methyl functionality at C-8. Similarly, the substitution of methyl protons (H-20) was explained by the HMBCs between H-20/C-10. These attributions were specific features of labdanes (Suzuki et al. 1988; Chakraborty et al. 2010; Suzuki et al. 2002; Tran 2017; Maneesh et al. 2017).

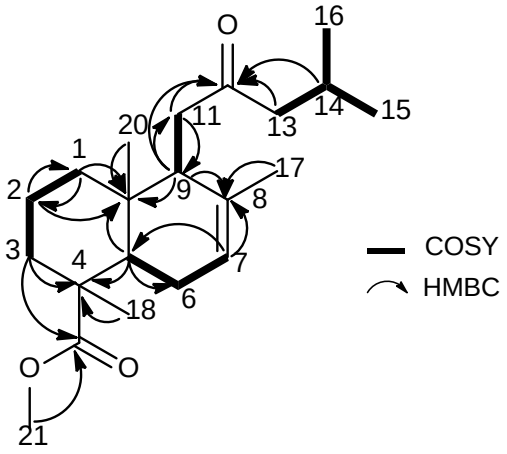

Figure 4.10.: Key ^{1}H-^{1}H COSY (bold face bonds), selected HMBC (black coloured double barbed arrows) correlations of methyl-16(13→14)-abeo-7-labdene-(12-oxo) carboxylate

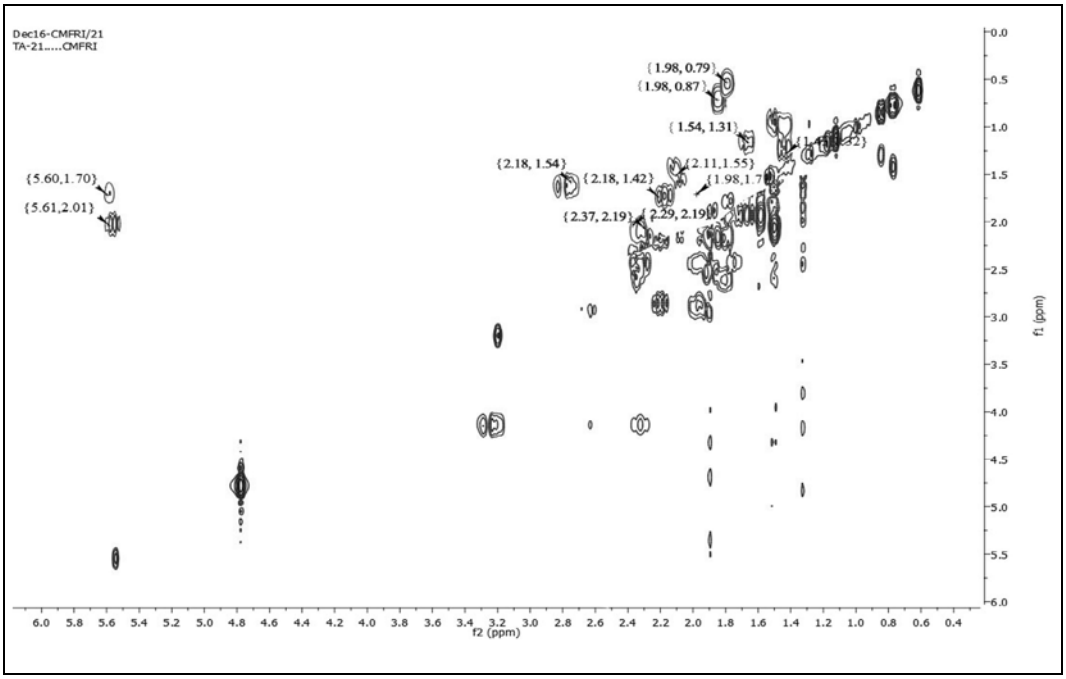

Figure 4.11.: ^{1}H-^{1}H COSY correlation spectrum of methyl-16(13→14)-abeo-7-labdene-(12-oxo) carboxylate (**1**)

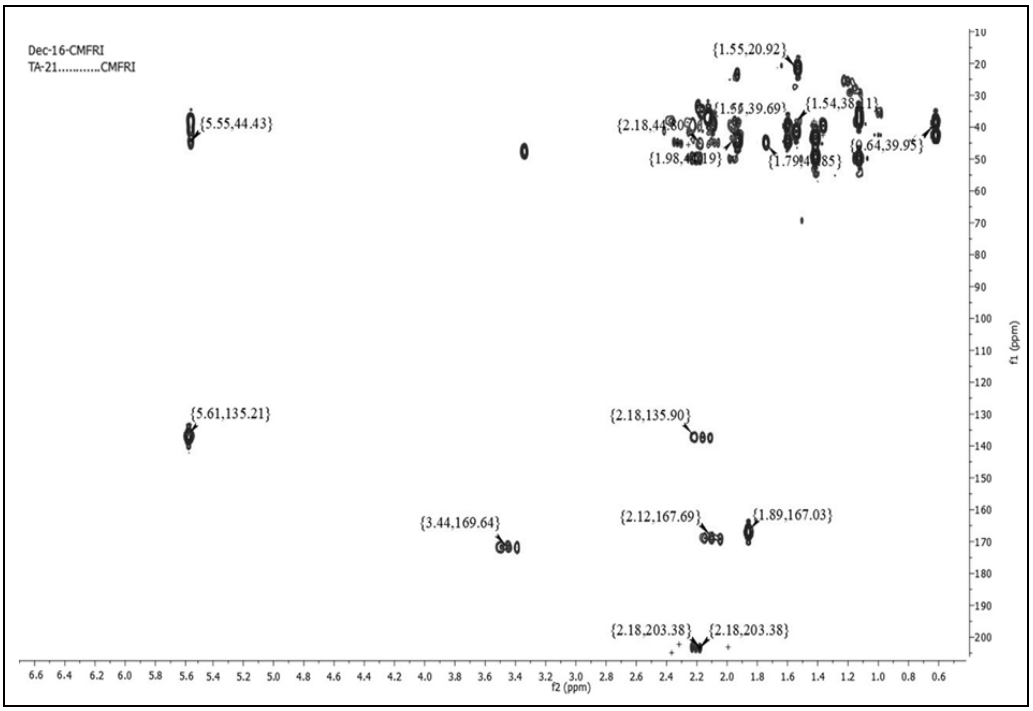

Figure 4.12.: HMBC correlation spectrum methyl-16(13→14)-abeo-7-labdene-(12-oxo) carboxylate (**1**)

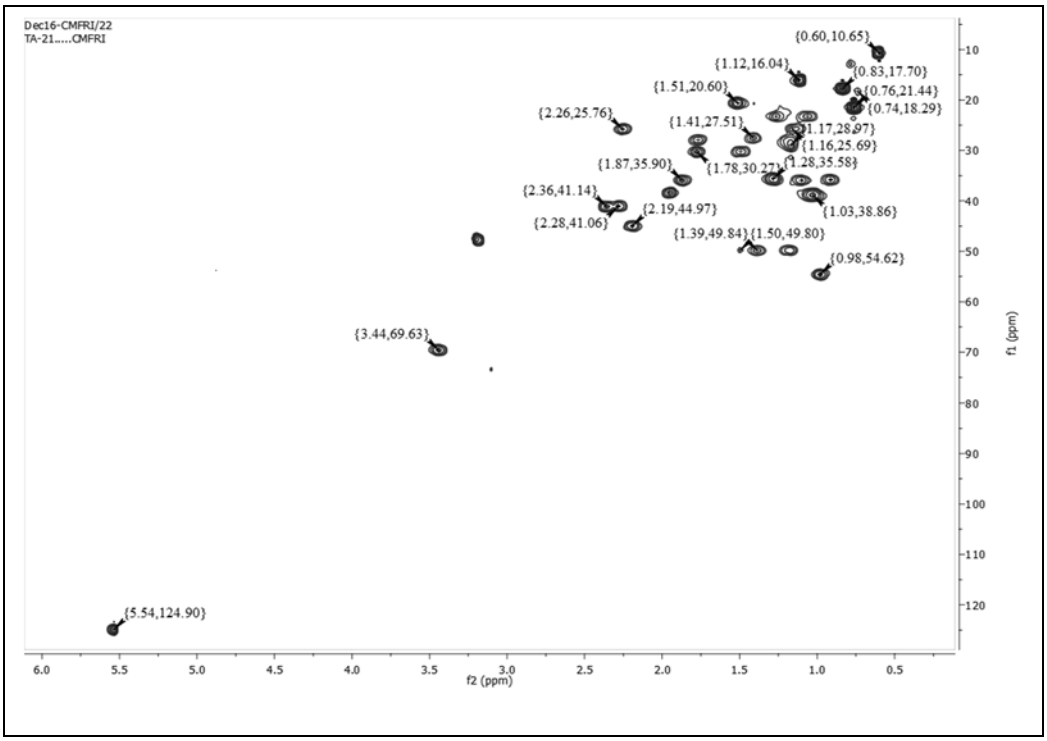

Figure 4.13.: HSQC spectrum methyl-16(13→14)-abeo-7-labdene-(12-oxo) carboxylate (**1**)

Table 4.8: NMR spectroscopic data[a] of methyl-16(13→14)-abeo-7-labdene-(12-oxo) carboxylate (**1**) isolated from red seaweed *G. salicornia*

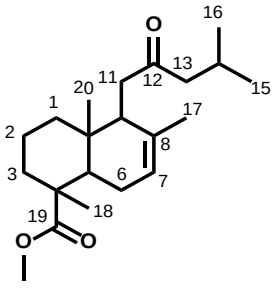

Compound **1**. Methyl-16(13→14)-abeo-7-labdene-(12-oxo)-carboxylate

Type of C	C. No.	^{13}C NMR	^{1}H NMR	int., mult., J in Hz[b]	COSY	HMBC
CH_2	1	38.65	1.54	t, J=5.5Hz	H-2	C-2, 10
			1.30	t, J=4.2Hz	-	-
CH_2	2	20.85	1.54	m	H-3	C-1, 10
			1.42	m	-	-
CH_2	3	38.26	2.19	t, J=5.0Hz	-	C-4, 19
			1.88	t, J=5.0Hz	-	-
C	4	42.91	-	-	-	-
CH	5	44.68	1.98	t, J=3.54Hz	H-6	C-4, 6, 10
CH_2	6	23.54	1.79	t, J=5.1Hz	H-7	-
			1.98	t, J=5.7.1Hz	-	-
CH	7	124.87	5.55	t, J=6.6Hz	-	C-5, 8
C	8	135.93	-	-	-	-
CH	9	45.18	2.21	t, J=5.5Hz	H-11	C-8, 10, 11, 12
C	10	39.27	-	-	-	-
CH_2	11	41.32	2.37	dd, J=10.9, 6.5 Hz	-	C-9, 12
			2.28	dd, J=12.7, 5.4Hz	-	-
C	12	203.27	-	-	-	-
CH_2	13	54.80	2.30	d, J=6.5Hz	H-14	C-12
CH	14	24.16	1.99	m	H-15, 16	C-12
CH_3	15	16.27	0.79	d, J=6.0Hz	-	-
CH_3	16	17.96	0.87	d, J=6.1 Hz	-	-
CH_3	17	19.60	1.14	s	-	C-8
CH_3	18	17.96	1.38	s	-	C-4
C	19	167.63	-	-	-	-
CH_3	20	10.96	0.63	s	-	C-10
CH_3	21	69.78	3.46	s	-	C-19

[a]NMR spectra were recorded using a Bruker AVANCE III 500 MHz (AV 500) spectrometer (Bruker, Karlsruhe, Germany) in MeOH as aprotic solvent at ambient temperature with TMS as the internal standard (δ 0 ppm). [b]Values in ppm, multiplicity and coupling constants (*J*= Hz) were indicated in parentheses. Multiplicities were allocated by [135]DEPT NMR spectrum. The assignments were made with the aid of the COSY, HSQC, HMBC and NOESY experiments.

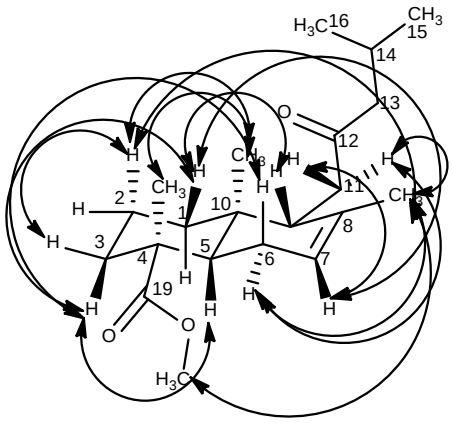

Figure 4.14.: Key NOESY correlations (double headed arrows) of methyl-16(13→14)-abeo-7-labdene-(12-oxo) carboxylate.

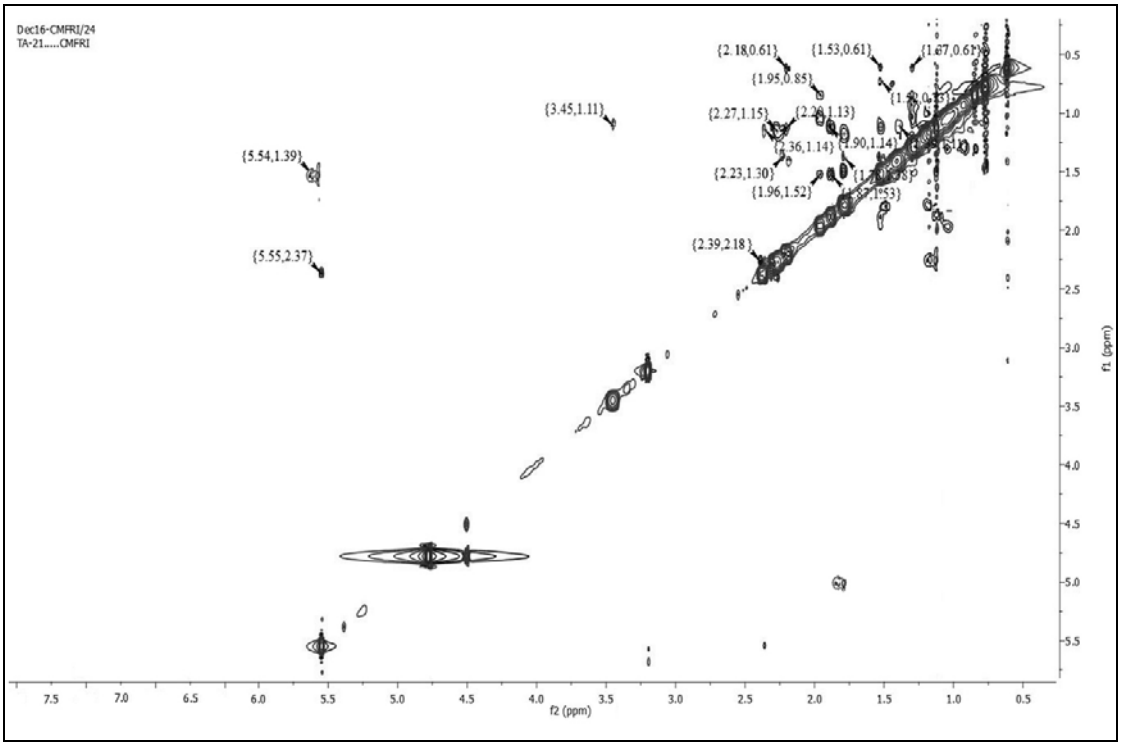

Figure 4.15.: NOESY spectrum of methyl-16(13→14)-abeo-7-labdene-(12-oxo) carboxylate (**1**).

The relative stereochemistries over the rigid bicyclic system of labdane was explained by NOESY experiment (Figure 4.14 & 4.15), whereas NOEs of H-2 (δ 1.54) with H-18 (δ 1.38) and H-20 (δ 0.63) recognized the axial arrangement of the β-face of the decalin frame work, as also supported by previous report of literature (Maneesh et al. 2017). The

spatial arrangement of protons at H-20/H-18 (δ 0.63/1.37), H-17/H-6 (δ 1.53/1.87), H-2/H-3 (δ 1.54/1.88), H-2/H-20 (δ 1.54/0.63), H-17/ H-3 (δ 1.14/1.88), H-6/H-11 (δ 1.79/2.27), H-2/H-17 (δ 1.54/1.79), H-17/H-11 (δ 1.14/2.28) and H-7/H-2 (δ 1.14/3.46) corroborated the β-alignment of these groups in decalin system. NOEs were exhibited between H-6/H-3 (δ 1.79/2.19), H-5/H-3 (δ 1.98/2.19), H-1/H-9 (δ 1.30/2.21), H-1/H-3 (δ 1.30/2.19), H-11/H-7 (δ 2.37/5.55) and H-1/H-7 (δ 1.30/5.55) suggesting that the protons were oriented at the α-face of the compound. These assignments were corroborated the occurrence of *trans*-decalin system with ester and ketone functionalities at C-4 and C-12.

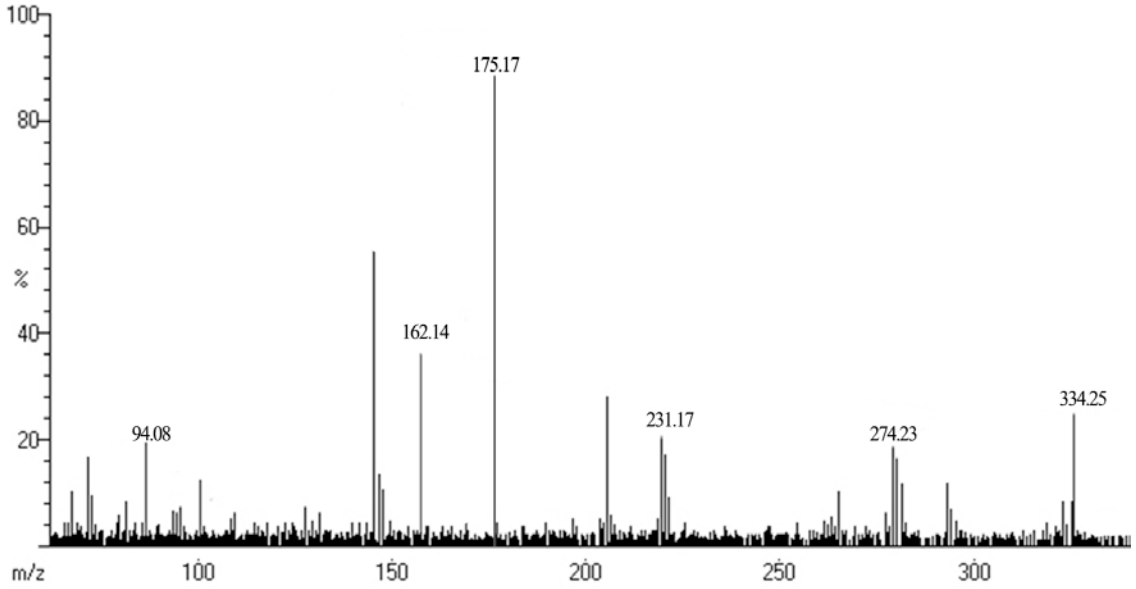

Figure 4.16.: EI-MS spectrum of methyl-16(13→14)-abeo-7-labdene-(12-oxo) carboxylate (**1**)

The FTIR spectrum displayed absorption signals corresponding to these functionalities. The molecular ion peak at m/z 335 (**a**) ($[M+H]^+$) performed an elimination of the side chain by the cleavage of bond, C4-C19 and the reorganization of bonds led to the formation of olefinic bond between C4 and C5 resulting in the fragment peak at *m/z* 274 (**b**). Exclusion of $C_6H_{11}O^+$ ion and radical methyl led to the formation of mass fragments **d** and **e** (*m/z* 175 and 162, respectively). The radical cation **d** also performed a rearrangement mechanism specific to labdane-type diterpenoid to form **f** with the *m/z* 94. The molecular ion peak at *m/z* 175 was found to be the base peak (Figure 4.16 & 4.17). On the basis of these detailed spectral data, the structure of compound was interpreted as 16(13→14)-abeo-7-labdene.

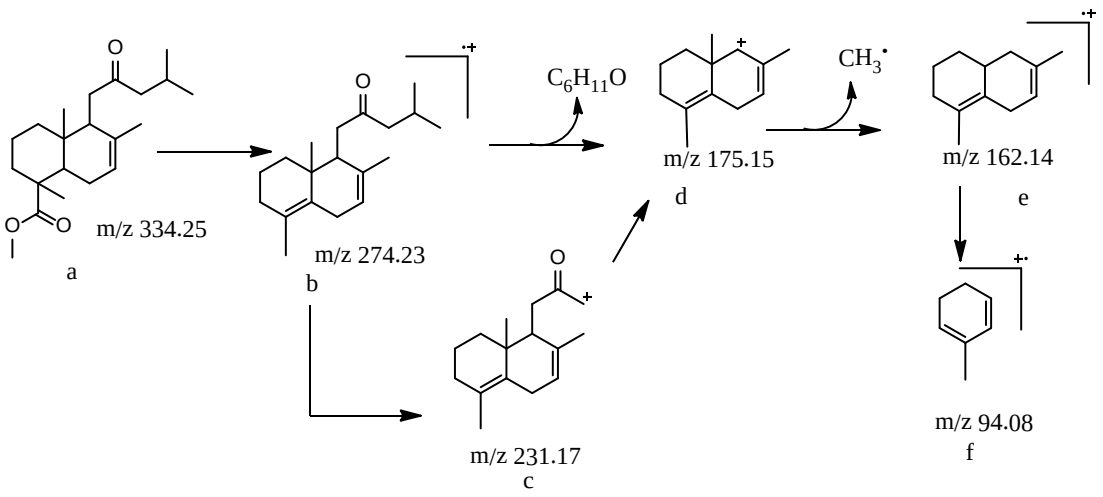

Figure 4.17.: Tentative mass fragmentation pattern of methyl-16(13→14)-abeo-7-labdene-(12-oxo) carboxylate (**1**)

Bio-assay assisted chromatographical purification of the EtOAc-MeOH extract of *G. salicornia* yielded a labdane diterpenoid, characterized as methyl-16(13→14)-abeo-7-labdene-(12-oxo) carboxylate. This ester and ketone functionalities enclosed these type of compounds can be used to develop as targeted bioactive templates.

4.3.2.2 Structural characterization of oleanane class of triterpenoid derivatives (Compounds 2-3)

Triterpenoids, which constitute a wide range of biogenetically derived structurally divergent class of natural compounds resulting from thirty-carbon squalene or analogues precursors, were found to possess potential anti-hyperglycaemic properties (Nazaruk and Borzym-Kluczyk, 2015; Hill and Connolly, 2012). Most of these compounds are tetracycles (6-6-6-5), pentacycles {6-6-6-6-5(6)}, although mono-, bi-, tri-, hexacyclic and acyclic class of triterpenoids were identified from naturally occurring resources (Ruzicka, 1963). Triterpenoids are ubiquitous in marine organisms, such as in seaweeds (Cen-Pacheco et al., 2010), and more than 20,000 triterpenoid metabolites and their variants belonging to oleanane, ursane, lanostane, dammarane, lupane, hopane, along with their pharmacological potential, were characterised (Hill and Connolly, 2012; Laszczyk 2009). Pentacyclic oleanene triterpenoids derived from natural sources were found to be pharmacologically active compounds that were found to lessen the likelihood of postprandial hyperglycaemia by obstructing the functionalities of starch digestive

enzymes (Lee et al., 2017). Oleanane triterpenoids with anti-diabetic properties were characterised from *Sambucus adnata* (Sasaki et al., 2011) and *Astilbe koreana* (Na et al., 2006). The inhibitory potencies of fridooleanene triterpenoids against α-amylase and α-glucosidase were previously reported from the seaweed *Sargassum wightii* (Maneesh and Chakraborty, 2017). Although these classes of secondary metabolites deserve special consideration because of their targeted therapeutic potentials, very few studies were reported with the anti-diabetic activities of naturally-derived triterpenoids (Nazaruk and Borzym-Kluczyk, 2015).

Here, characterized two previously unreported triterpenoids of oleanane class of chemistries from the ethyl acetate-methanol (EtOAc-MeOH) extract of *G. salicornia* collected from the southeast coastal region of Indian peninsular. The studied compounds were designated as 24(4→23), 27(8→26), 30(20→29)-tris-abeo-olean-(12-oxo)-1,15,22-triene-methyl hept-5-enoate (**2**) and 24(4→23)-abeo-olean-(12-oxo)-3,5-diene-deconoate (**3**) by extensive spectroscopic experiments (Figure 4.18).

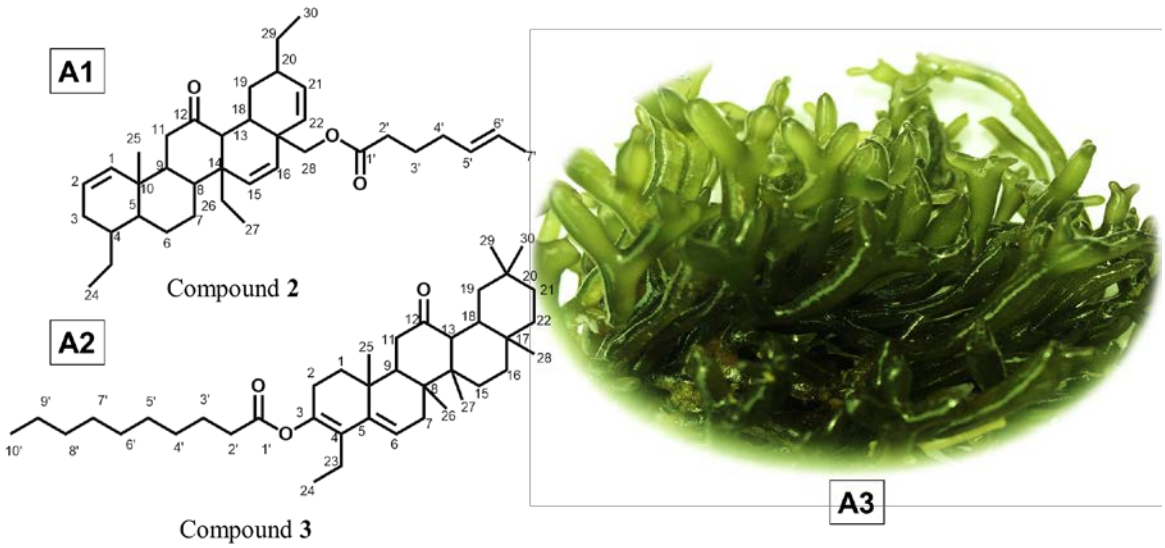

Figure 4.18.: Structural representations of (**A1**) 24(4→23), 27(8→26), 30(20→29)-tris-abeo-olean-(12-oxo)-1,15,22-triene-methyl hept-5-enoate (**1**) and (**A2**) 24(4→23)-abeo-olean-(12-oxo)-3,5-diene-deconoate (**2**) isolated from *G. salicornia*. (**A3**) Representative photograph of thalli of the red seaweed *G. salicornia*.

4.3.2.2a Structural characterization of Compound 2

24(4→23), 27(8→26), 30(20→29)-tris-abeo-olean-(12-oxo)-1,15,22-triene-methyl hept-5-enoate (2)

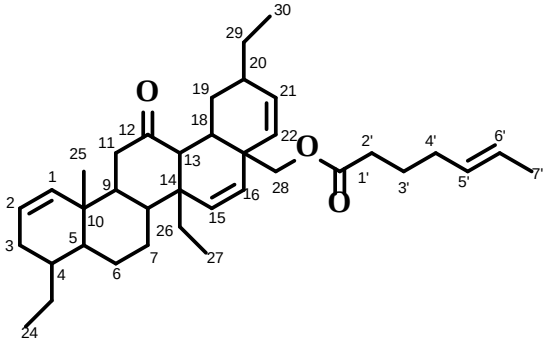

Sample yield	0.29% (> 99% purity, RP-C18 HPLC)
Physical description	Pale yellow oily
Molecular formula	$C_{37}H_{54}O_3$
Molecular mass	546.4073

The abeo-labdane class of diterpenoid derivative, 24(4→23), 27(8→26), 30(20→29)-tris-abeo-olean-(12-oxo)-1,15,22-triene-methyl hept-5-enoate (**2**) was isolated as yellowish-white amorphous compound. The compound (**2**) has exhibited UV absorbance (UV (MeOH) λ_{max}) at 244 nm (Figure 4.19.). The homogeneity of the compound was ascertained by HPLC data on a bonded phase octadecylsilane (C_{18}) stationary phase (HPLC, MeOH/MeCN, 2:1 v/v) with R_t: 3.41 min (Figure 4.20.).

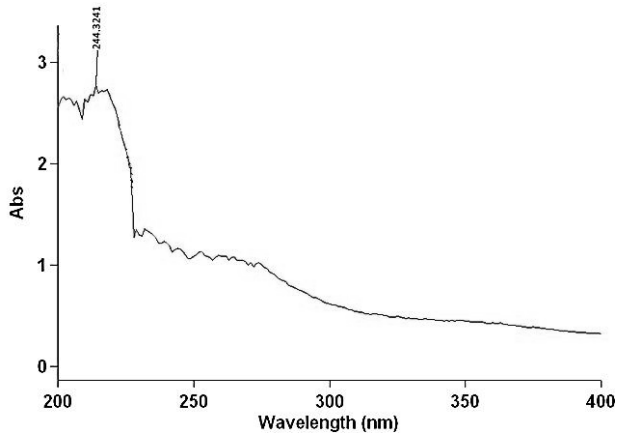

Figure 4.19.: UVspectrum of 24(4→23), 27(8→26), 30(20→29)-tris-abeo-olean-(12-oxo)-1,15,22-triene-methyl hept-5-enoate **(2)**

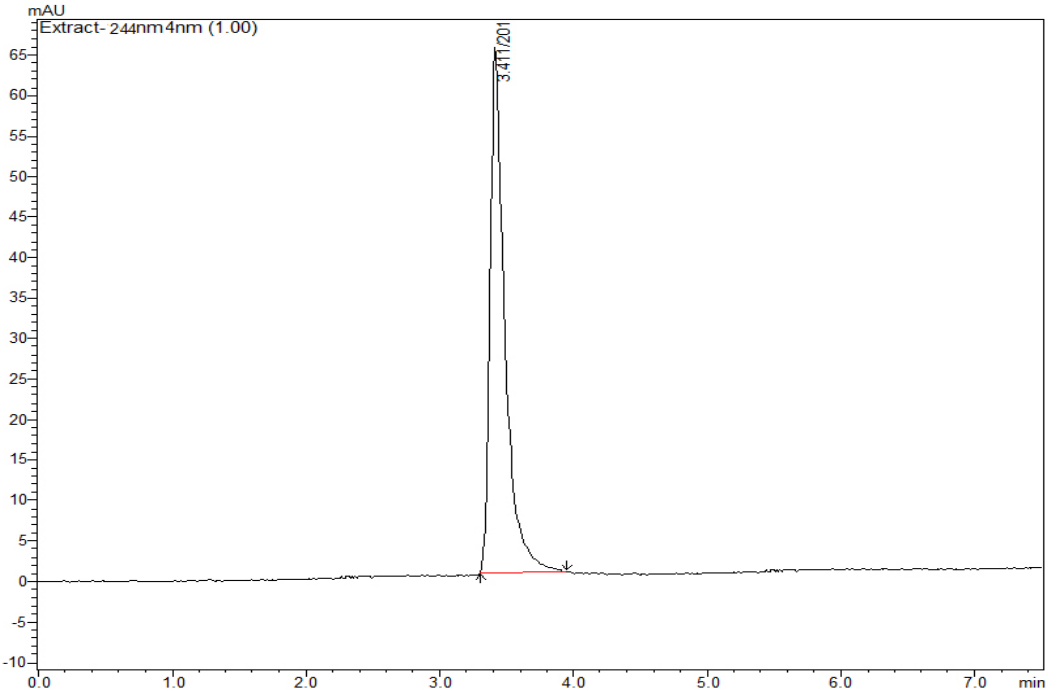

Figure 4.20.: HPLC chromatogram of 24(4→23), 27(8→26), 30(20→29)-tris-abeo-olean-(12-oxo)-1,15,22-triene-methyl hept-5-enoate (**2**)

Repeated column chromatographic fractionation of *G. salicornia* yielded compound (**2**) as an yellow oily substance, which was characterised as 24(4→23), 27(8→26), 30(20→29)-tris-abeo-olean-(12-oxo)-1,15,22-triene-methyl hept-5-enoate (**2**). The HRESIMS experiment displayed the molecular ion peak at *m/z* 547.4155 $[M+H]^+$, (Figure 4.21), which along with NMR-IR spectroscopic analyses deduced its molecular formula as $C_{37}H_{55}O_3$ (Table 4.8).

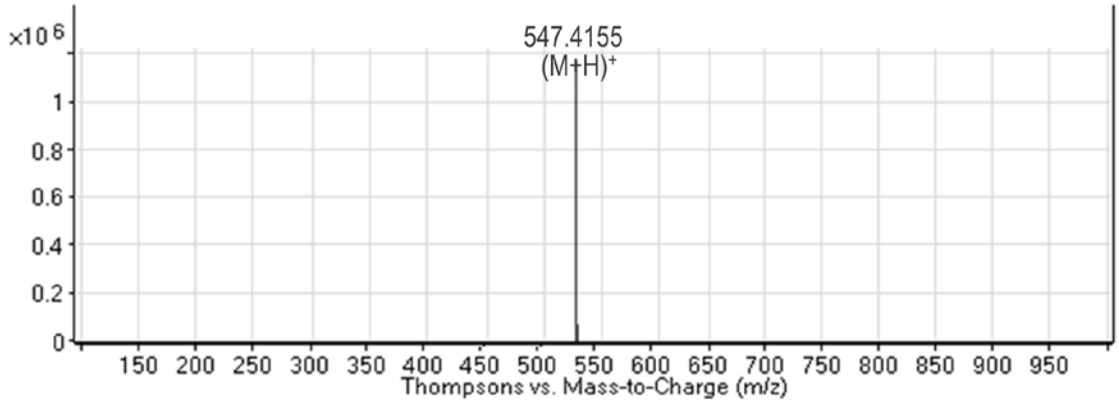

Figure 4.21.: HRESIMS of 24(4→23), 27(8→26), 30(20→29)-tris-abeo-olean-(12-oxo)-1,15,22-triene-methyl hept-5-enoate **(2)**

The FTIR signals at 1730 and 1726 cm^{-1} attributed the probable existence of ester and carbonyl functionalities, respectively (Figure 4.22). The ^{1}H NMR spectrum illustrated the occurrence of six deshielded olefinic hydrogens at δ 5.32, 5.28, 5.34, 5.30, 5.29, 5.33, 5.26, and 5.25. In addition, the shielded methyls (appeared as triplets) at δ 0.80, 0.78 and 0.82 suggested the presence of methyl substitutions on triterpenoid system (Figure 4.23). The ^{13}C NMR, ^{135}DEPT along with HSQC spectrum with of **(2)** disclosed 37 carbon traces, encompassing five methyls (δ 12.2, 11.8, 19.7, 13.1, 14.2), twelve sp^3 methylenes (δ 31.8, 29.0, 28.9, 39.3, 31.7, 4.7, 29.8, 65.7, 29.1, 25.6, 26.9, 33.2), eight sp^2 methines (δ 130.2, 127.8, 130.5, 127.7, 132.0, 127.5, 129.7, 128.0), seven sp^3 methines (δ 33.9, 52.3, 29.7, 47.9, 56.7, 31.9, 37.2), and five quaternary carbons (δ 46.8, 34.4, 43.5), including two carbonyls (δ 193.7, 179.4) (Figure 4.24-4.26).

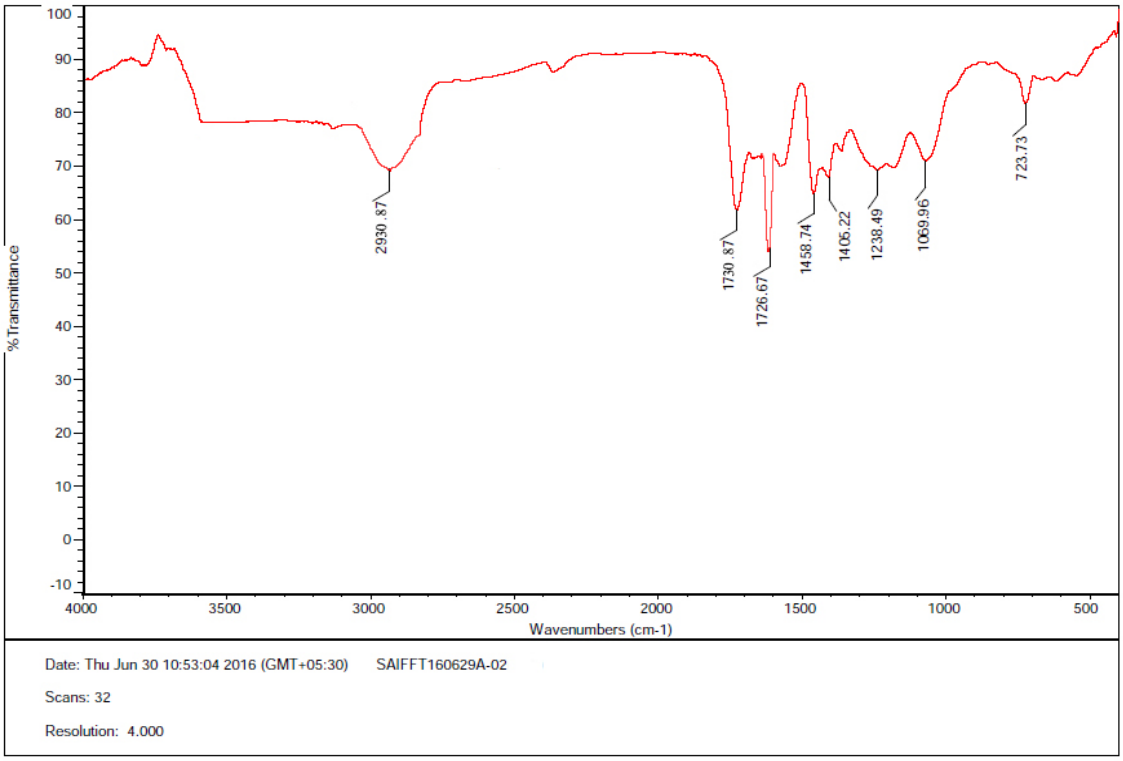

Figure 4.22.: FT-IR of 24(4→23), 27(8→26), 30(20→29)-tris-abeo-olean-(12-oxo)-1,15,22-triene-methyl hept-5-enoate **(2)**

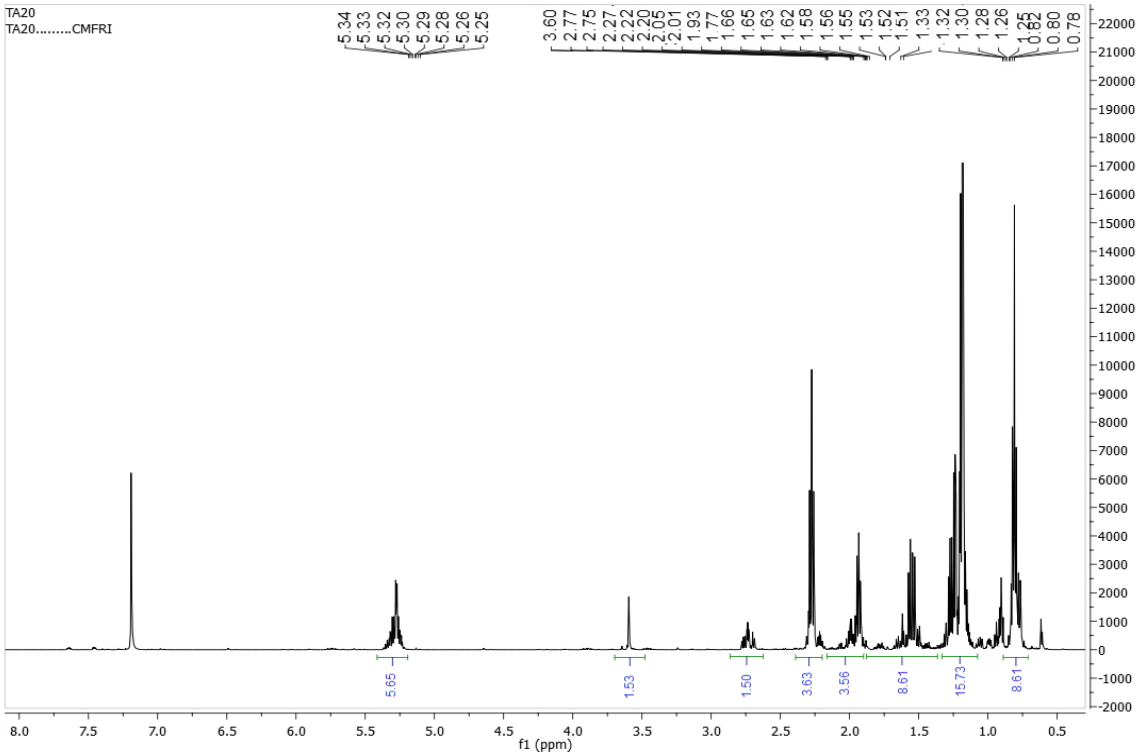

Figure 4.23.: ^{1}H-NMR of 24(4→23), 27(8→26), 30(20→29)-tris-abeo-olean-(12-oxo)-1,15,22-triene-methyl hept-5-enoate **(2)**

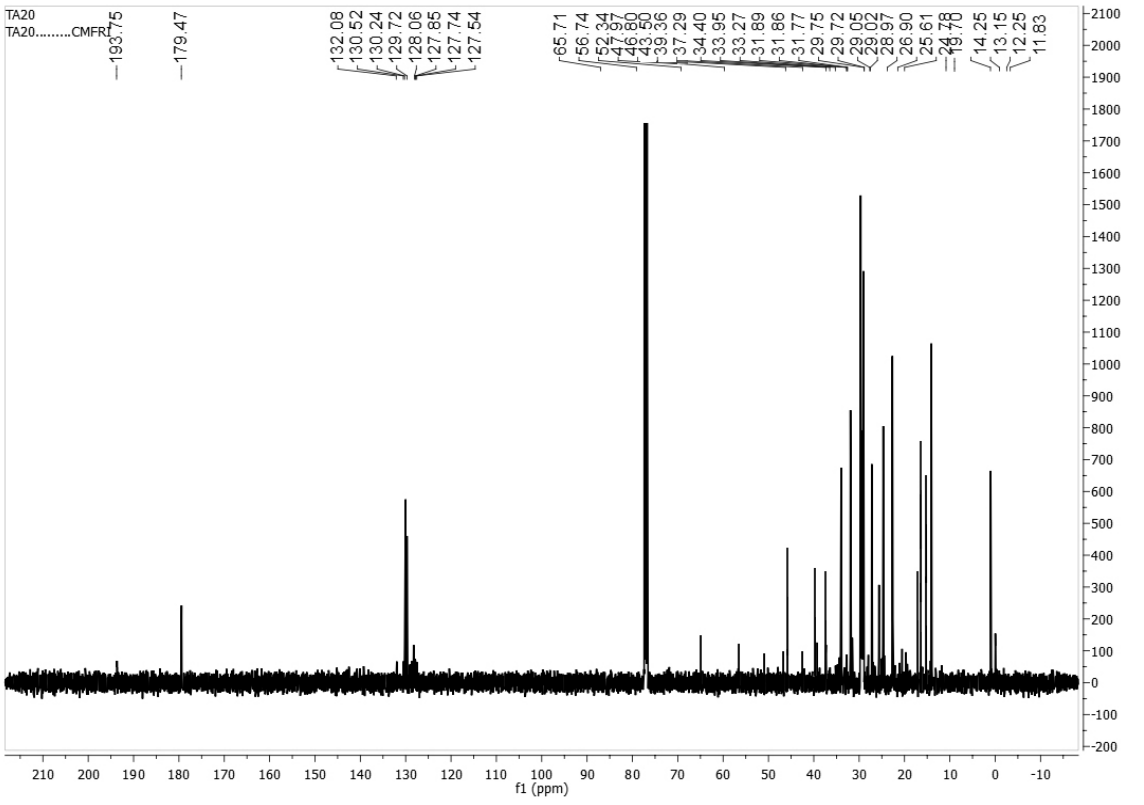

Figure 4.24.: ^{13}C NMR of 24(4→23), 27(8→26), 30(20→29)-tris-abeo-olean-(12-oxo)-1,15,22-triene-methyl hept-5-enoate **(2)**

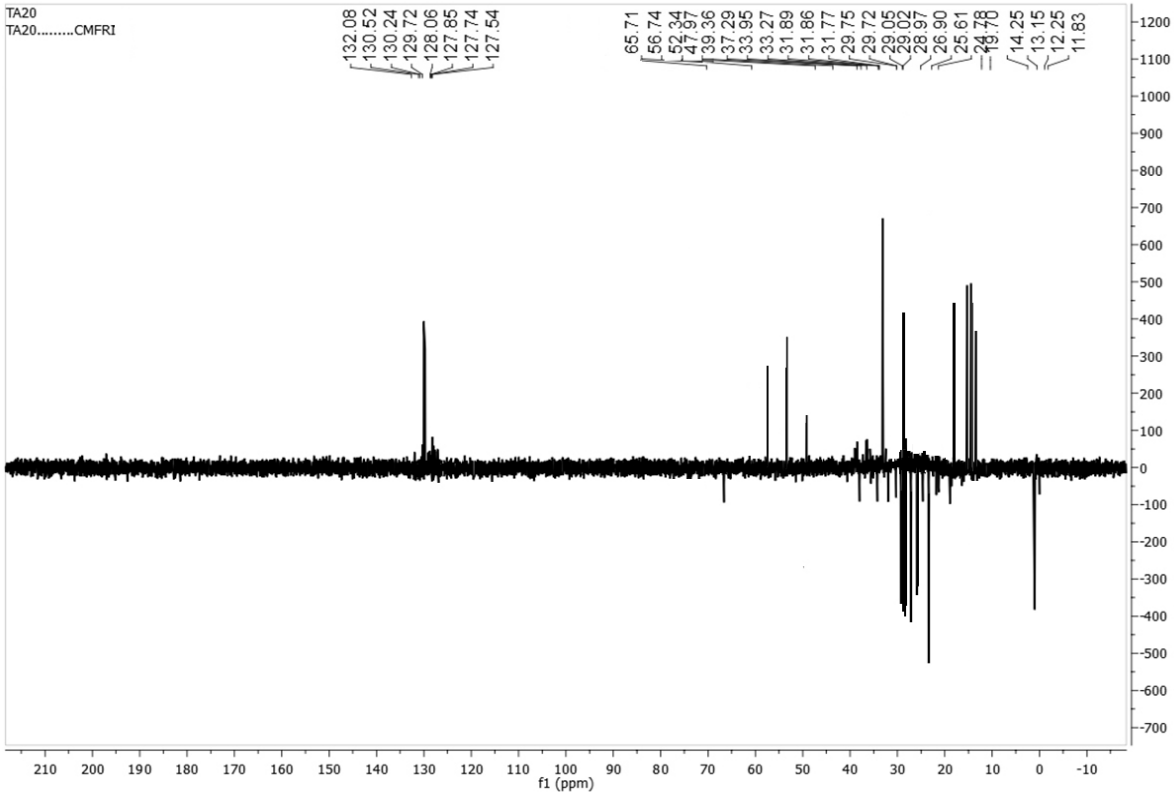

Figure 4.25.: ^{135}DEPT spectrum of 24(4→23), 27(8→26), 30(20→29)-tris-abeo-olean-(12-oxo)-1,15,22-triene-methyl hept-5-enoate **(2)**

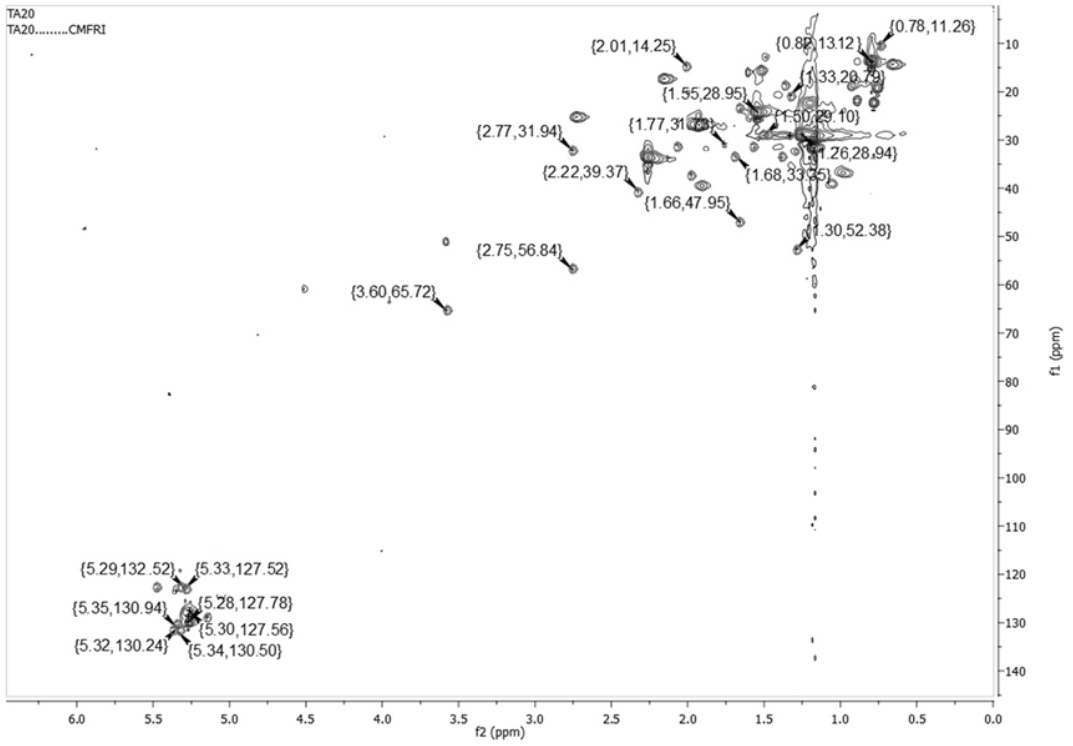

Figure 4.26.: HSQC spectrum of 24(4→23), 27(8→26), 30(20→29)-tris-abeo-olean-(12-oxo)-1,15,22-triene-methyl hept-5-enoate **(2)**

The intense ^{1}H-^{1}H COSY spectrum of compound **2** demonstrated the occurrence of spin networks between (CH-δ5.28) (arbitrarily assigned as H-2)-(CH_2-δ 1.77) (H-3)-(CH-δ1.62) (H-4)-(CH-δ1.30) (H-5)-(CH_2-δ1.51) (H-6)-(CH_2-δ1.26) (H-7)-(CH-δ1.33) (H-8)-(CH-δ1.66) (H-9)-(CH_2-δ2.22) (H-11) and (CH_2-δ1.65) (H-19)-(CH-δ 1.93) (H-20)-(CH-δ5.29) (H-21), which supported the partial skeleton of pentacyclic ring in the triterpenoid (Figure 4.27 & 4.28). The HMBC interactions from CH-1 (δ 5.32) to CH-2 (δ 127.8) and C-10 (δ 46.8) determined the occurrence of olefinic bond at C-1 (δ 5.32/δ 130.2) and C-2 (δ 5.28/δ 127.8) (Figure 4.29). The HMBC interactions between CH-15 (δ 5.34) to C-14 (δ 34.4) and those from CH-16 (δ 5.30) to C-15 (δ 130.5), C-17 (δ 43.5) assigned an olefinic bond at C-15 (δ 5.34/130.5) and C-16 (δ 5.30/δ 127.7). Likewise, HMBCs from CH-20 (δ 1.93) and CH-21 (δ 5.29) to C-22 (δ 127.5) and from CH-22 (δ 5.33) to C-17 (δ 43.5) ascribed the occurrence of an olefinic bond between CH-21 (δ 5.29/δ132.0) and CH-22 (δ 5.33/δ 127.5). This attribution was in agreement with the presence of olefinic bond in the E-ring system (Maneesh and Chakraborty, 2017). Other HMBC correlations from CH-5 (δ 1.30) to C-10 (δ 46.8), C-9 (δ 47.9); from CH_2-6 (δ 1.51) to C-5 (δ 52.3); from CH-8 (δ 1.33) to C-13 (δ 56.7); CH-13 (δ 2.75) to C-18 (δ 31.9), C-14 (δ 34.4) and from CH-18 (δ 2.77) to C-19 (δ 31.7), C-17 (δ 43.5) were persistent with the pentacyclic

skeleton of triterpenoid, (**2**). The long range couplings from CH-9 (δ 1.66), CH-13 (δ 2.75) and CH_2-11 (δ 2.22) to C-12 (δ 193.7) revealed the C-12 keto functionality in (**2**). This was comparable with the previously reported compound, dihydroxyolean-12-one, in which the chemical shift of C-12 was found to be δ 208 due to the presence of neighbouring hydroxyl group at C-11 (δ 71.8) (Da Rocha et al., 2015). No electronegative functionalities were apparent adjacent to keto group at C-12, hence it recorded lower chemical shift value in the present compound.

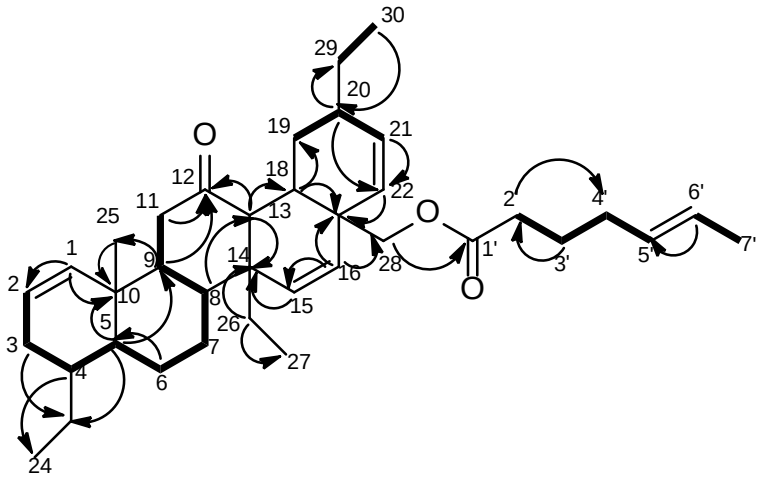

Figure 4.27.: ^{1}H-^{1}H COSY (bold-face bonds), and selected HMBC (double-barbed arrows) correlations of 24(4→23), 27(8→26), 30(20→29)-tris-abeo-olean-(12-oxo)-1,15,22-triene-methyl hept-5-enoate (**2**) isolated from *G. salicornia*.

These NMR assignments together with earlier reported values (Da Rocha et al., 2015; Huang et al., 2013; Maneesh and Chakraborty, 2017) substantiated the presence of pentacyclic triterpenoid bearing olean-(12-oxo)-1,15,22-triene framework. The typical oleanene skeleton enclosed seven tertiary methyls in the range of δ 0.7 to δ 1.25 at C-4, C-10, C-8, C-14, C-17 and C-20 positions (Da Rocha et al., 2015; Maneesh and Chakraborty, 2017), whereas the titled compound comprised of only one tertiary methyl at C-10. The position of tertiary methyl (CH_3-25) at C-10 was ascertained through the HMBCs from CH-9 (δ 1.66) to CH_3-25 (δ 19.7) and CH_3-25 (δ 19.7) to C-10 (δ 46.8), which was comparable with the earlier reports (Da Rocha et al., 2015).

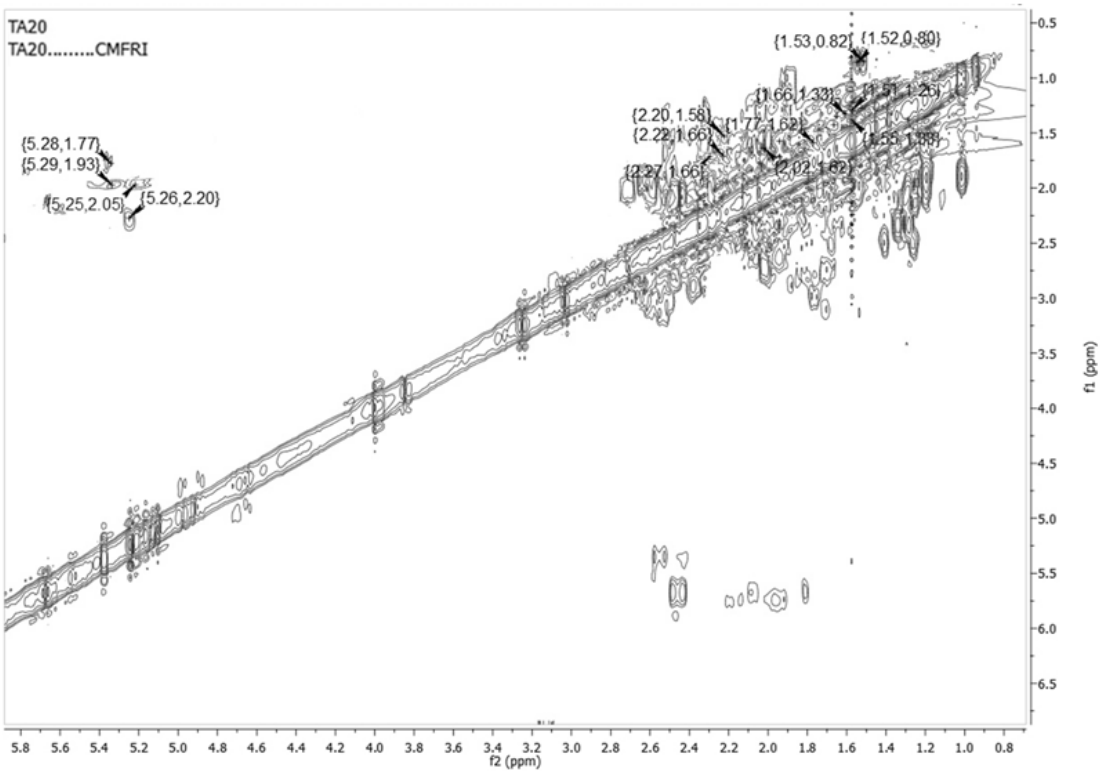

Figure 4.28.: ^{1}H-^{1}H COSY spectrum of 24(4→23), 27(8→26), 30(20→29)-tris-abeo-olean-(12-oxo)-1,15,22-triene-methyl hept-5-enoate **(2)**

The angular methyl at C-4 (CH_3-24) in the basic oleanene framework was shifted to C-23, which was affirmed by the HMBC connections from CH_2-3 (δ 1.77) to CH_2-23 (δ 24.7); CH-4 (δ 1.62) to CH_3-24 (δ 12.2) and CH-5 (δ 1.30) to CH_2-23 (δ 24.7). The methyl at C-8 (CH_3-27) was shifted to C-26, which was corroborated by the HMBCs from CH_2-26 (δ 1.25) to CH_3-27 (δ 11.8), C-14 (δ 34.4) (Fig. 2). Similarly, one of the gem dimethyl groups at C-20 (CH_3-30) was shifted to C-29, and was confirmed through the HMBC couplings from CH_3-30 (δ 0.82) to CH-20 (δ 37.2) and COSY couplings from (CH_2-δ 1.52) (H-29)-(CH_3-δ 0.82) (H-30). Therefore, the titled compound was classified as tris-abeo-oleanene triterpenoid, (**2**) which was named as 24(4→23), 27(8→26), 30(20→29)-tris-abeo-olean-(12-oxo)-triene. The typical angular methyl at C-17 (CH_3-28) was found to be deshielded in the present compound when compared to the previously reported chemical shift values (CH_3-28, δ 28.43/0.84) (Da Rocha et al., 2015), which was found to be δ 65.7/3.60 (CH_2-28). This higher chemical shift was typical for the oxygenated protons, and its HMBC coupling to δ179.4 (C-1') along with HMBC from CH-16 (δ 5.30) to CH_2-28 (δ 65.7) suggested the presence of an ester linkage in which oxygen was directly bonded to the sp^3 methylene at δ 3.60. The spin systems from (CH_2-δ 1.63)

(arbitrarily assigned as H-2')-(CH_2-δ 1.58) (H-3')-(CH_2-δ 2.20) (H-4')-(CH-δ 5.26) (H-5') and (CH-δ 5.25) (H-6')-(CH_3-δ 2.05) (H-7') along with HMBCs from CH_2-2' (δ 1.63) to CH_2-4' (δ 33.2); CH_2-3' (δ 1.58) to CH_2-2' (δ 25.6) and CH-6' (δ 5.25) to CH-5' (δ 129.7) appropriately supported the presence of methyl hept-5-enoate chain at C-17. The titled compound was structurally related to previously reported oleanenes (Da Rocha et al., 2015; Huang et al., 2013; Maneesh and Chakraborty, 2017; Oramas-Royo et al., 2010) besides the dissimilarities recognized in the positions of alkenes, tertiary methyls, ester linkages along with absence of hydroxyl functionalities.

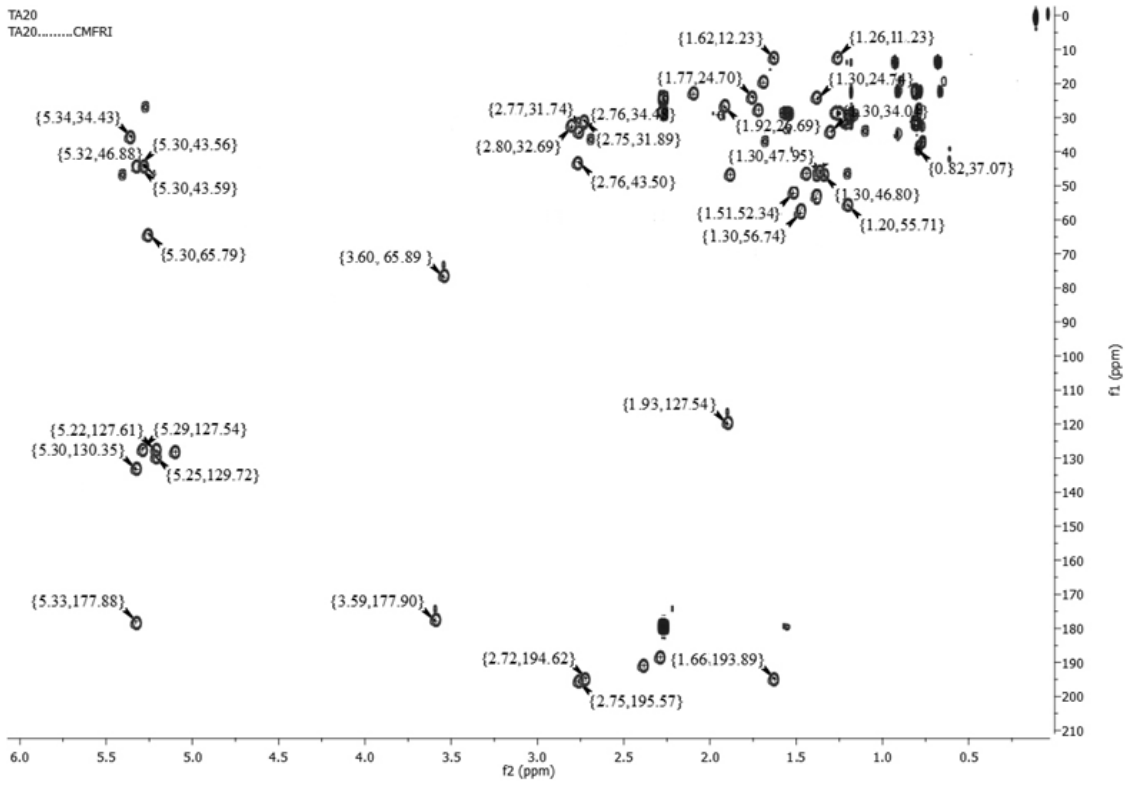

Figure 4.29.: HMBC spectrum of 24(4→23), 27(8→26), 30(20→29)-tris-abeo-olean-(12-oxo)-1,15,22-triene-methyl hept-5-enoate **(2)**

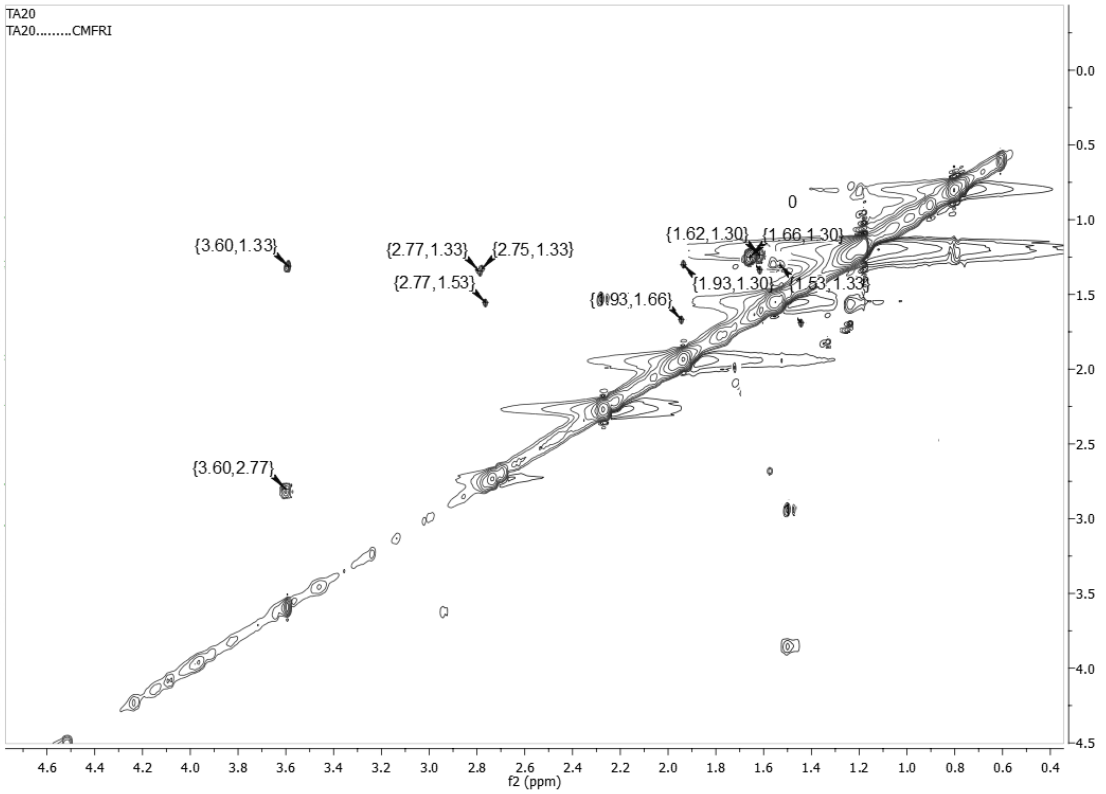

Figure 4.30.: NOESY spectrum of 24(4→23), 27(8→26), 30(20→29)-tris-abeo-olean-(12-oxo)-1,15,22-triene-methyl hept-5-enoate (**2**)

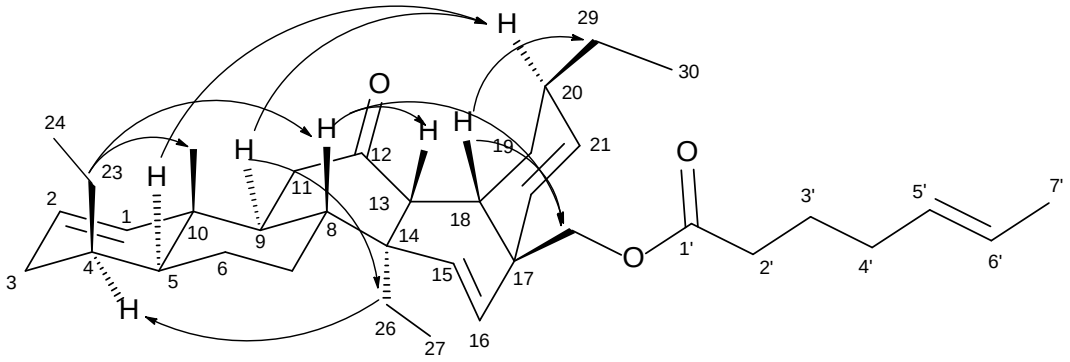

Figure 4.31.: NOE correlations of 24(4→23), 27(8→26), 30(20→29)-tris-abeo-olean-(12-oxo)-1,15,22-triene-methyl-hept-5-enoate (**2**) isolated from *G. salicornia*.

The relative stereochemistry of the chiral centres at δ 33.9 (C-4), 52.3 (C-5), 29.7 (C-8), 47.9 (C-9), 56.7 (C-13), 31.9 (C-18) and 37.2 (C-20) were deduced from nuclear overhauser

effect spectroscopy (NOESY) (Figure 4.30 and 4.31). The proton at chiral centre, δ 1.62 (assigned as CH-4) exhibited NOE with the proton (angular methyl) at δ 1.30 (H-5) that were α-aligned (Wang et al., 2014). The α-disposition of protons at H-4, H-5, H-9 and H-20 were inferred by the NOE correlations between H-5 (δ 1.30)/H-9 (δ 1.66) and H-9 (δ 1.66)/H-20 (δ 1.93). On the contrary, the protons at δ 1.32 (H-25), δ 2.75 (H-13), δ 1.33 (H-8), and δ 2.77 (H-18) were positioned at the β-surface of reference plane, which were inferred by NOE correlations between H-25 (δ 1.32)/H-13 (δ 2.75), H-8 (δ 1.33)/H-18 (δ 2.77) and H-8 (δ 1.33)/H-13 (δ 2.75), The trans- and cis-intersection of ABCD and DE parts were reinforced by their stereochemical attributions (Koay et al., 2013).

Table 4.9: NMR spectroscopic data[a] of 24(4→23), 27(8→26), 30(20→29)-tris-abeo-olean-(12-oxo)-1,15,22-triene-methyl-hept-5-enoate (**2**) isolated from red seaweed *G. salicornia*

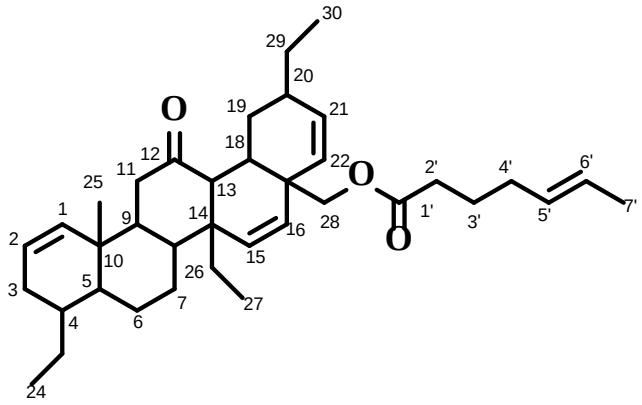

Compound 2……24(4→23), 27(8→26), 30(20→29)-tris-abeo-olean-(12-oxo)-1,15,22-triene-methyl-hept-5-enoate (**2**)

Type	C. No.	^{13}C NMR	^{1}H. No. (int., mult., J in Hz)[b]	^{1}H NMR	COSY	HMBC
CH	1	130.2	1H, d, J = 10.3 Hz	5.32	-	C-2,10
CH	2	127.8	1H, dt, J = 8.9, 7.6 Hz	5.28	H-3	-
CH_2	3	31.8	1H, t, J = 4.9 Hz	1.77	H-4	C-23
			1H, t, J = 4.9 Hz	2.01	-	-
CH	4	33.9	1H, m	1.62	H-5	C-24
CH	5	52.3	1H, m	1.30	H-6	C-23,9,10
CH_2	6	29.0	1H, m	1.51	H-7	C-5
			1H, m	1.28	-	-
CH_2	7	28.9	1H, m	1.55	H-8	-
			1H, m	1.26	-	-
CH	8	29.7	1H, td, J = 6.8, 5.2 Hz	1.33	H-9	C-13
CH	9	47.9	1H, td, J = 5.8, 5.5 Hz	1.66	H-11	C-12,25
C	10	46.8	-	-	-	-
CH_2	11	39.3	1H, d, J = 8.6 Hz	2.22	-	C-12
			1H, d, J = 8.0 Hz	2.27	-	-

C	12	193.7	-	-	-	-
CH	13	56.7	1H, d, J = 6.7 Hz	2.75	-	C-12,14,18
C	14	34.4	-	-	-	-
CH	15	130.5	1H, d, J = 12.1 Hz	5.34	-	C-14
CH	16	127.7	1H, d, J = 13.0 Hz	5.30	-	C-15,17,28
C	17	43.5	-	-	-	-
CH	18	31.9	1H, m	2.77	-	C-19,17
CH_2	19	31.7	1H, m	1.65	H-20	-
			1H, m	1.56	-	-
CH	20	37.2	1H, m	1.93	H-21	C-29,22
CH	21	132.0	1H, t, J = 14.0 Hz	5.29	-	C-22
CH	22	127.5	1H, d, J = 12.7 Hz	5.33	-	C-17
CH_2	23	24.7	2H, m	1.53	-	-
CH_3	24	12.2	3H, t, J = 4.2 Hz	0.80	-	-
CH_3	25	19.7	3H, s	1.32	-	C-10
CH_2	26	29.8	2H, d, J = 3.7 Hz	1.25	-	C-14,27
CH_3	27	11.8	3H, t, J = 4.9 Hz	0.78	-	-
CH_2	28	65.7	2H, s	3.60	-	C-1'
CH_2	29	29.1	2H, m	1.52	H-30	-
CH_3	30	13.1	3H, t, J = 5.0 Hz	0.82	-	C-20
C	1'	179.4	-	-	-	-
CH_2	2'	25.6	2H, t, J = 4.7 Hz	1.63	H-3'	C-4'
CH_2	3'	26.9	2H, m	1.58	H-4'	C-2'
CH_2	4'	33.2	2H, m	2.20	H-5'	-
CH	5'	129.7	1H, dt, J = 11.7 Hz	5.26	-	-
CH	6'	128.0	1H, m	5.25	H-7'	C-5'
CH_3	7'	14.2	3H, d, J = 9.2 Hz	2.05	-	-

[a]NMR spectra were recorded using a Bruker AVANCE III 500 MHz (AV 500) spectrometer (Bruker, Karlsruhe, Germany) in $CDCl_3$ as aprotic solvent at ambient temperature with TMS as the internal standard (δ 0 ppm).

[b]Values in ppm, multiplicity and coupling constants (J = Hz) were indicated in parentheses. Multiplicities were allocated by ^{135}DEPT NMR spectrum.

The assignments were made with the aid of the COSY, HSQC, HMBC and NOESY experiments.

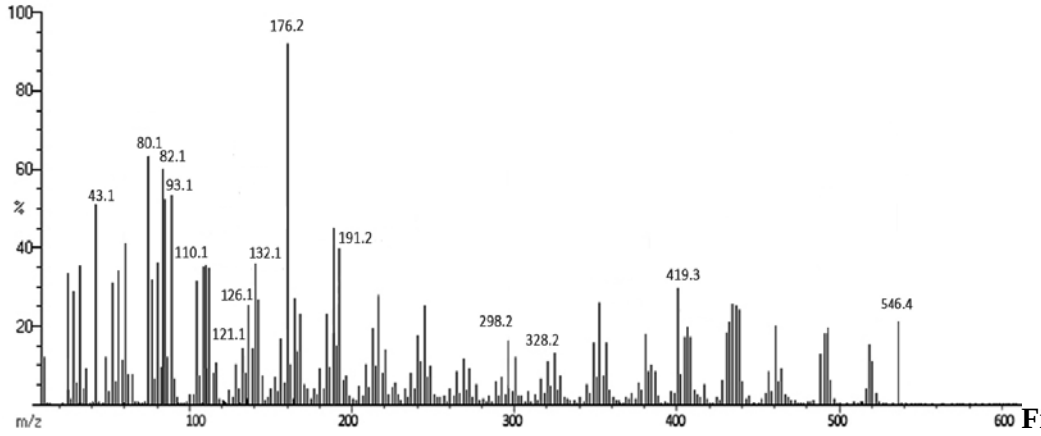

Figure 4.32.: EI-MS spectrum of 24(4→23), 27(8→26), 30(20→29)-tris-abeo-olean-(12-oxo)-1,15,22-triene-methyl-hept-5-enoate (**2**) isolated from *G. salicornia*.

The structural elucidation of **2** was corroborated by the mass spectral experiment wherein the molecular ion at 546.4 (1a) experienced the exclusion of methyl-hept-5-enoate to result 24(4→23), 27(8→26), 30(20→29)-tris-abeo-olean-(12-oxo)-1,15,22-triene (1b, m/z 419.3). The latter along with 1a underwent retro-Diels-Alder (rDA) rearrangement yielding the fragments m/z 126.1 (1c), 176.2 (1g), and 328.2 (1k). The spectroscopic experiments along with previous reports of literature unambiguously constructed of complete framework of oleanene triterpenoid, 24(4→23), 27(8→26), 30(20→29)-tris-abeo-olean-(12-oxo)-1,15,22-triene-methyl hept-5-enoate (1). The ion peak at 176.2 (1g) was considered as the base peak (Fig. S12). These analyses suggested its molecular formula as $C_{37}H_{54}O_3$ enclosing eleven indices of hydrogen deficiencies associated with six olefinic bonds (comprising four alkenes and two carbonyls) and five ring systems. The spectroscopic experiments along with previous reports of literature unambiguously constructed of complete framework of oleanene triterpenoid, 24(4→23), 27(8→26), 30(20→29)-tris-abeo-olean-(12-oxo)-1,15,22-triene-methyl hept-5-enoate (**2**) (Figure 4.32 & 4.33).

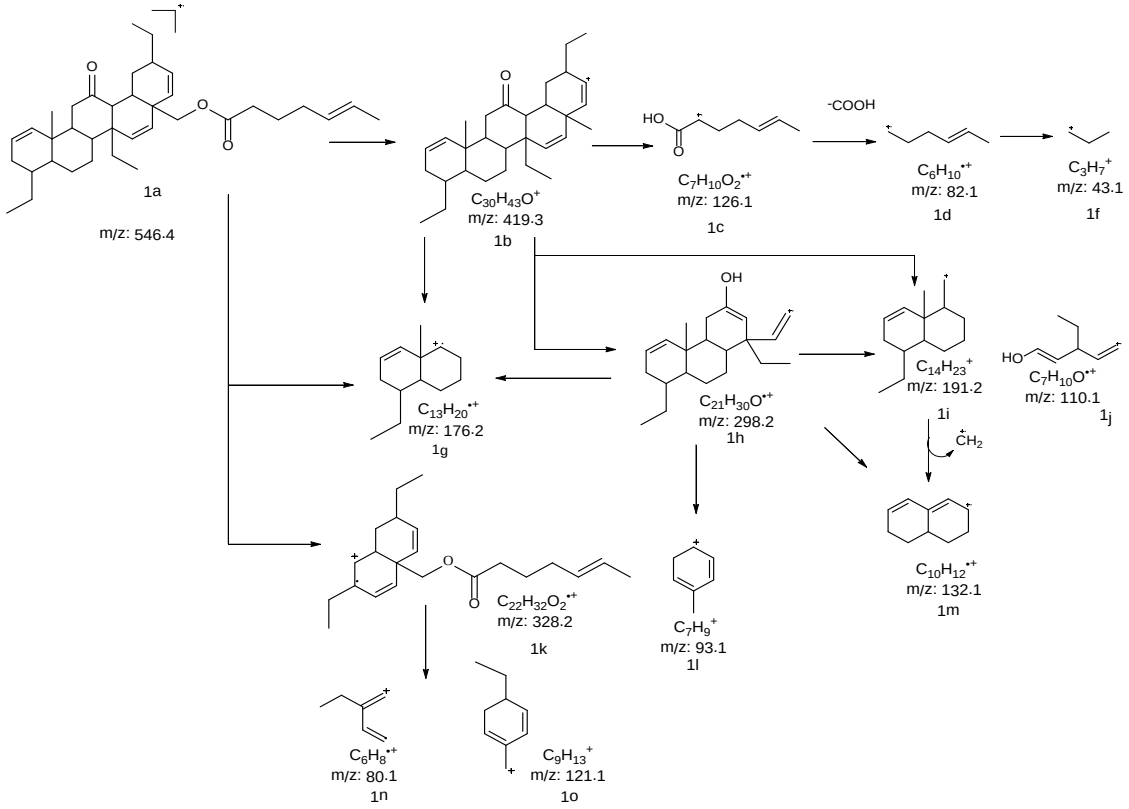

Figure 4.32.: EI-MS spectrum of 24(4→23), 27(8→26), 30(20→29)-tris-abeo-olean-(12-oxo)-1,15,22-triene-methyl-hept-5-enoate (**2**)

4.3.2.2b Structural characterization of Compound 3

24(4→23)-Abeo-olean-(12-oxo)-3,5-diene-deconoate	
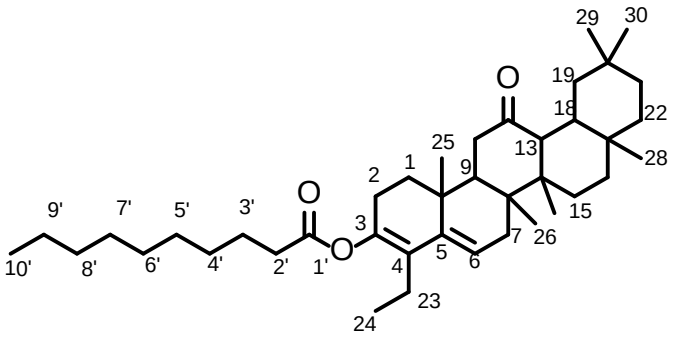	
Sample yield	0.30% (> 99% purity, RP-C18 HPLC)
Physical description	Yellowish oily
Molecular formula	$C_{40}H_{64}O_3$
Molecular mass	592.2485

The abeo-oleanane class of triterpenoid derivative, 24(4→23)-abeo-olean-(12-oxo)-3,5-diene-deconoate (**3**) was isolated as yellowish oily compound. The compound (**3**) has exhibited UV absorbance (UV (MeOH) λ_{max} at 247 nm (Figure 4.34.). The homogeneity of the compound was ascertained by HPLC data on a bonded phase octadecylsilane (C_{18}) stationary phase (HPLC, MeOH/MeCN, 2:1 v/v) with R_t: 2.91 min (Figure 4.35.).

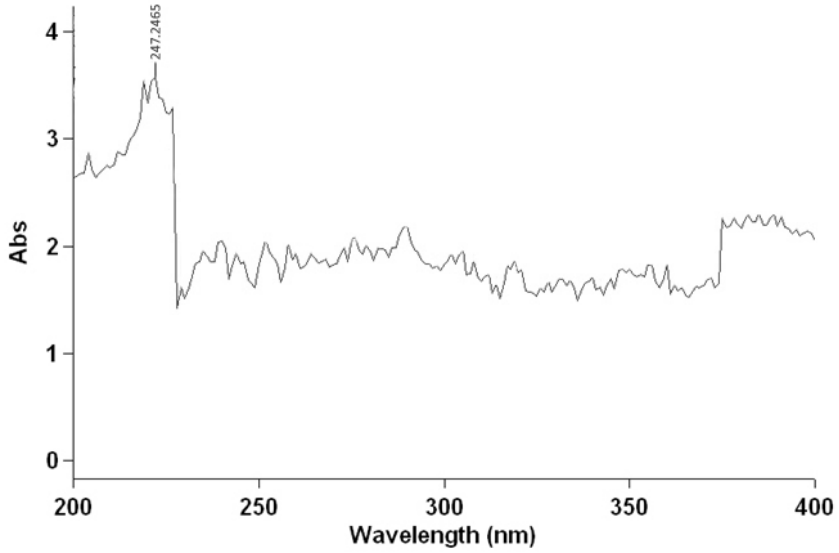

Figure 4.34.: UVspectrum of 24(4→23)-abeo-olean-(12-oxo)-3,5-diene-deconoate (**3**)

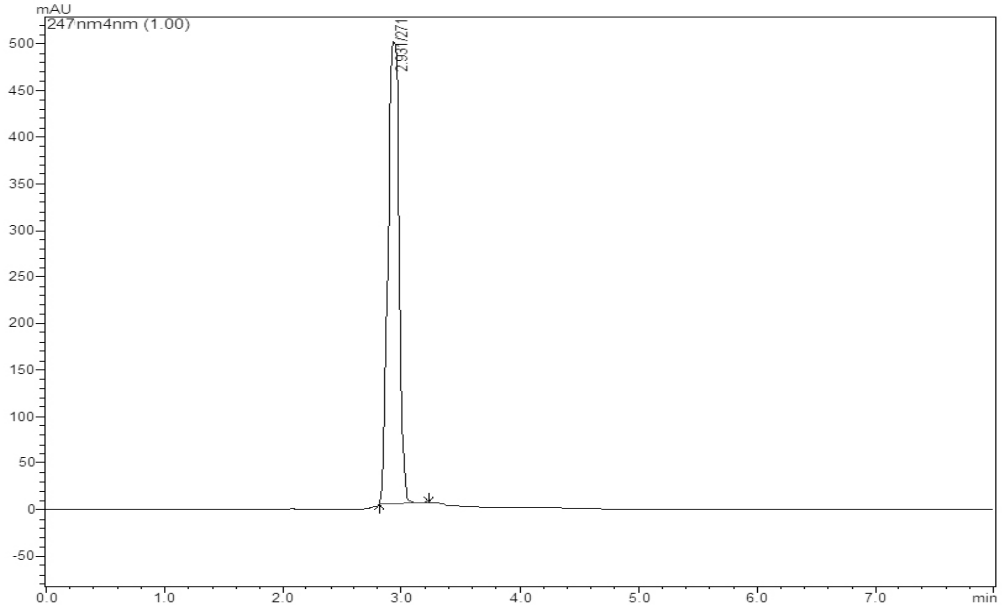

Figure 4.35.: HPLC chromatogram of 24(4→23)-abeo-olean-(12-oxo)-3,5-diene-deconoate (**3**)

Repeated column chromatographic purification of the crude of *G. salicornia*, yielded compound **3** as yellowish oily, which was characterised as 24(4→23)-abeo-olean-(12-oxo)-3,5-diene-deconoate (**3**). The HRESIMS experiment displayed the molecular ion peak at *m/z* 593.4938 $[M+H]^+$, (Figure 4.36) which along with NMR-IR spectroscopic analyses deduced its molecular formula as $C_{40}H_{65}O_3$ (Table 4.10).

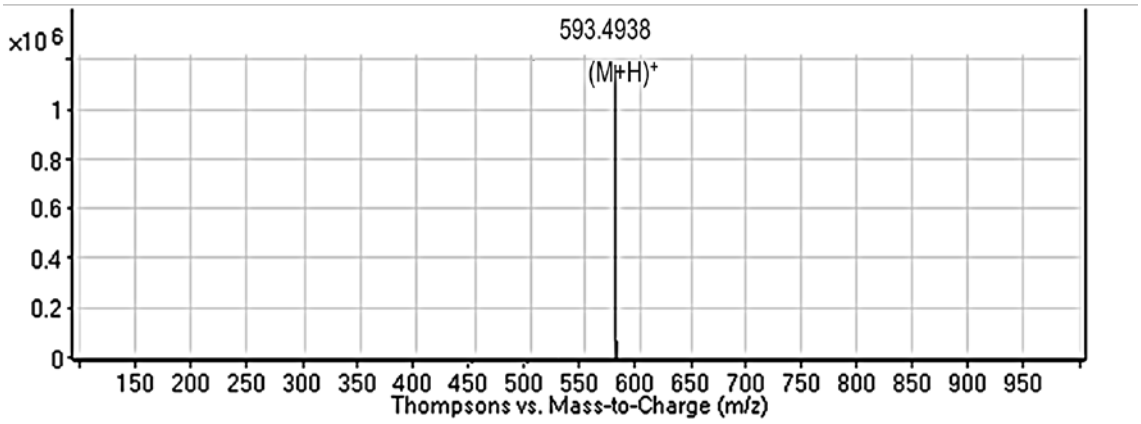

Figure 4.36.: HRESIMS spectrum of 24(4→23)-abeo-olean-(12-oxo)-3,5-diene-deconoate (**3**)

The FTIR vibrations at 1734 and 1634 cm^{-1} recognised the existence of ester and carbonyl functionalities, respectively (Figure 4.37). The ^{13}C along with ^{135}DEPT spectrum of **3** displayed the presence of forty carbon signals, including eight methyl groups (δ 19.9, δ 20.8, δ 19.7, δ 19.4, δ 22.8, δ 30.2, δ 14.0), eighteen sp^3 methylenes (δ 30.5, δ 24.7, δ 34.0, δ 36.9, δ 29.4, δ 37.0, δ 37.7, δ 33.9, δ 34.3, δ 19.1, δ 26.7, δ 26.4, δ 29.2, δ 29.5, δ 29.6, δ 29.3, δ31.8, δ 22.6), one sp^2 methine (δ 130.9), three sp^3 methines (δ 43.4, δ 51.9, δ 41.4), and ten quaternary carbons (δ 128.8, δ 132.2, δ 139.2, δ 42.7, δ 31.4, δ 38.8, δ 33.4, δ 28.0) including two carbonyl carbons (δ 213.1, δ 176.1). The presence of one olefinic hydrogen was apparent at δ 5.82, which exhibited HSQC correlation with δ 130.9 (Figure 4.38 - 4.41).

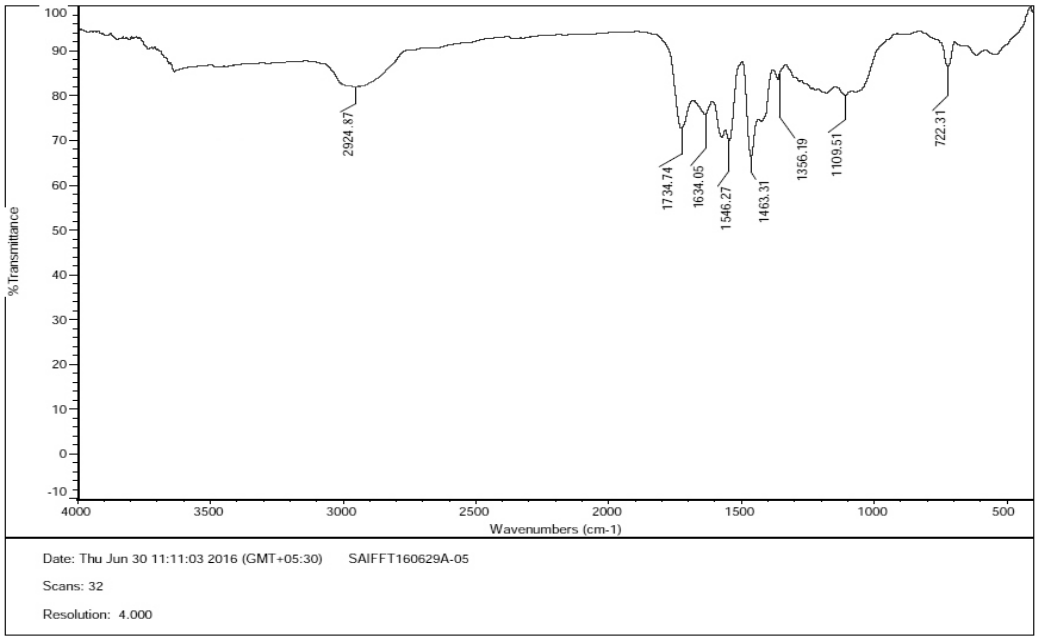

Figure 4.37.: FT-IR spectrum of 24(4→23)-abeo-olean-(12-oxo)-3,5-diene-deconoate (**3**)

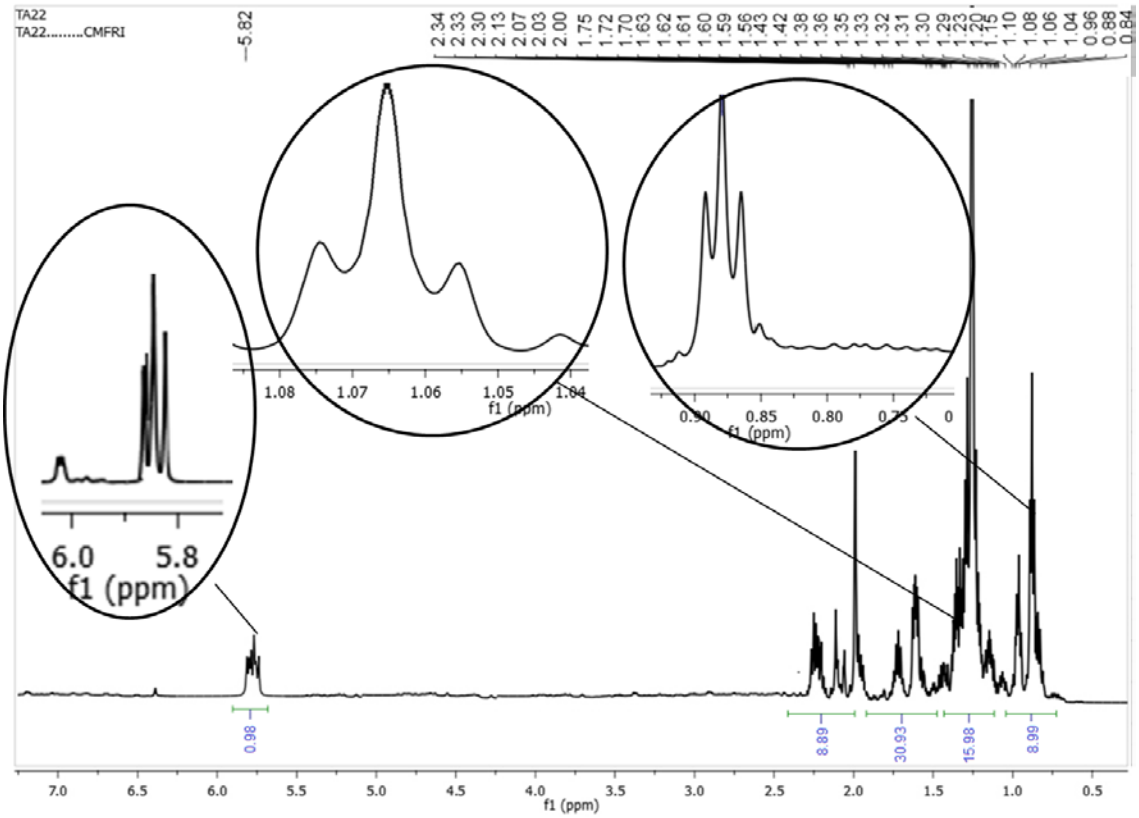

Figure 4.38.: [1]HNMR spectrum of 24(4→23)-abeo-olean-(12-oxo)-3,5-diene-deconoate (**3**)

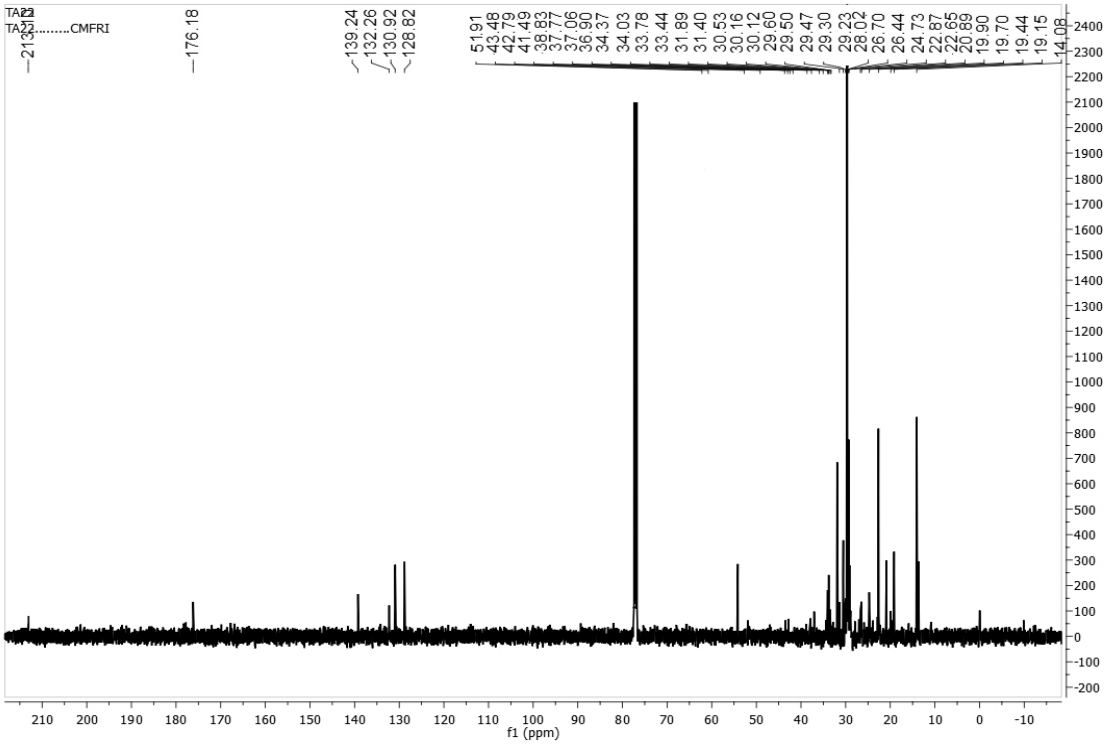

Figure 4.39.: ^{13}C NMR spectrum of 24(4→23)-abeo-olean-(12-oxo)-3,5-diene-deconoate (**3**)

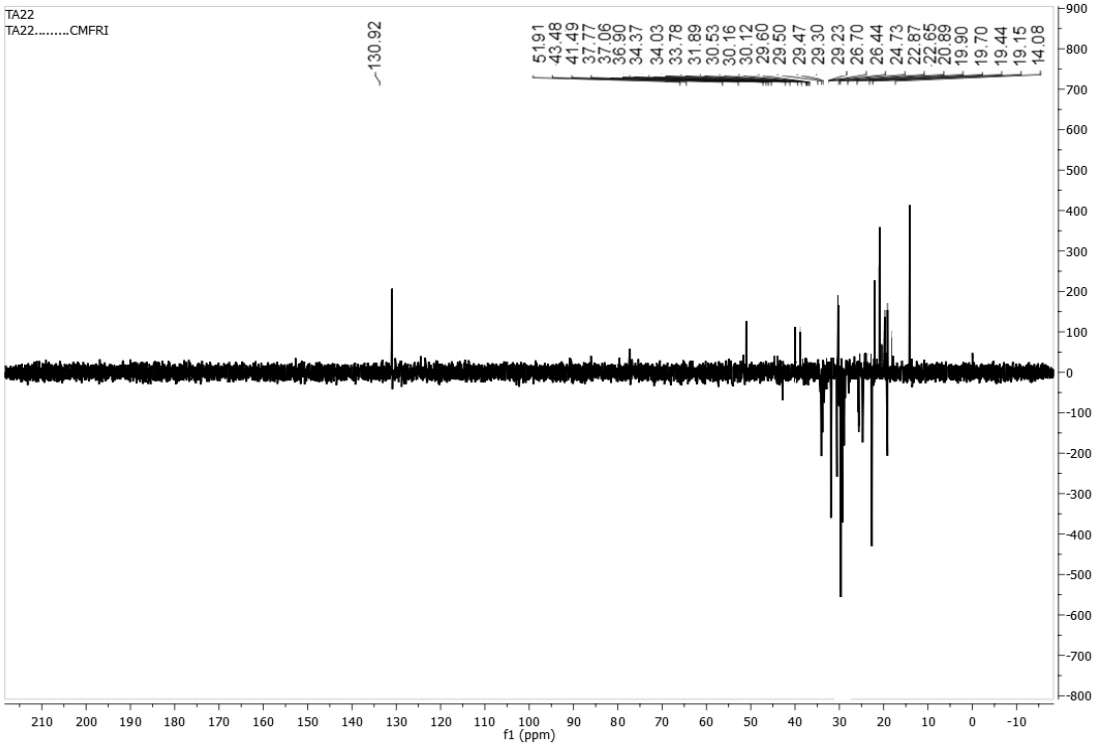

Figure 4.40.: ^{135}DEPT spectrum of 24(4→23)-abeo-olean-(12-oxo)-3,5-diene-deconoate (**3**)

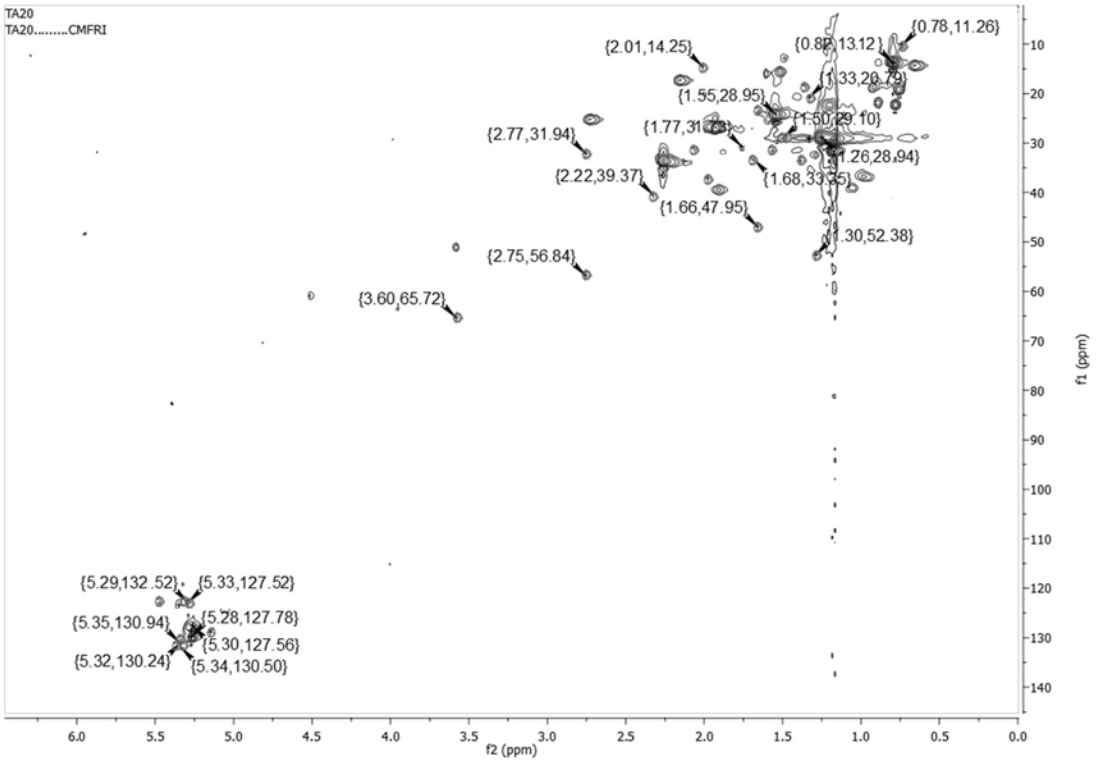

Figure 4.41.: HSQC spectrum of 24(4→23)-abeo-olean-(12-oxo)-3,5-diene-deconoate (**3**)

The ^{1}H-^{1}H COSY experiment put forward the occurrence of three spin networks, which were found to be (CH_2-δ 1.42) (arbitrarily assigned as H-1)-(CH_2-δ 2.03) (H-2); (CH-δ 1.70) (H-9)-(CH_2-δ 2.33) (H-11) and (CH-δ 2.30) (H-13)-(CH-δ 1.62) (H-18)-(CH_2-δ 1.20) (H-19) suggesting the partial fragments of pentacyclic ring in the triterpenoid (Figure 4.42 & 4.43). The HMBC interactions from CH_2-2 (δ 2.03) to C-4 (δ 128.8), C-3 (δ 132.2) determined the occurrence of tetrasubstituted olefinic bond at C-3 (δ 132.2) and C-4 (δ 128.8) and HMBCs from CH-6 (δ 5.82) to C-5 (δ 139.2), C-7 (δ 34.0) attributed a trisubstituted olefinic bond at C-5 (δ 139.2) and C-6 (δ 5.82/130.9) (Figure 4.44). Other HMBC correlations from CH_2-1 (δ 1.42) to C-10 (δ 31.4), C-5 (139.2); CH_2-2 (δ 2.03) to C-1 (δ 30.5); CH_2-7 (δ 2.00) to C-8 (δ 42.7); CH-9 (δ 1.70) to C-8 (δ 42.7), C-10 (δ 31.4), C-11 (δ 36.9); CH-13 (δ 2.30) to C-8 (δ 42.7) and C-14 (δ 38.8); CH_2-15 (δ 1.59) to C-14 (δ_C38.8) and C-16 (δ_C37.0); CH_2-16 (δ_H1.60) to C-17 (δ_C33.4); CH-18 (δ_H1.62) to C-17 (δ 33.4); CH_2-19 (δ 1.20) to C-17 (δ 33.4); CH_2-21 (δ 1.61) to C-20 (δ 28.0) and CH_2-22 (δ_H1.56) to C-21 (δ_C33.9) appropriately supported the complete structure of pentacyclic triterpenoid, **3**. The long range couplings from both CH_2-11 (δ 2.33) and CH-13 (δ 2.30) to C-12 (δ 213.1) deduced the C-12 keto functionality in **3**, whereas the attributions were comparable with the previously reported compound, trihydroxyolean-12-one in which the chemical shift of C-12 was found to be δ 212 (Da Rocha et al., 2015). These NMR

assignments in comparison with earlier reported chemical shift values (Da Rocha et al., 2015; Maneesh and Chakraborty, 2017) substantiated the presence of pentacyclic triterpenoid bearing olean-(12-oxo)-3,5-diene skeleton.

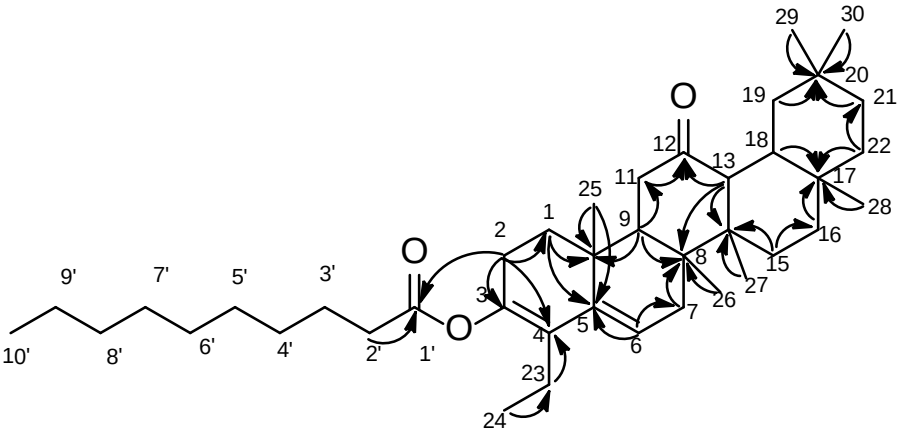

Figure 4.42.: ^{1}H-^{1}H COSY (bold-face bonds), selected HMBC (double-barbed arrows) correlations of 24(4→23)-abeo-olean-(12-oxo)-3,5-diene-deconoate (**3**)

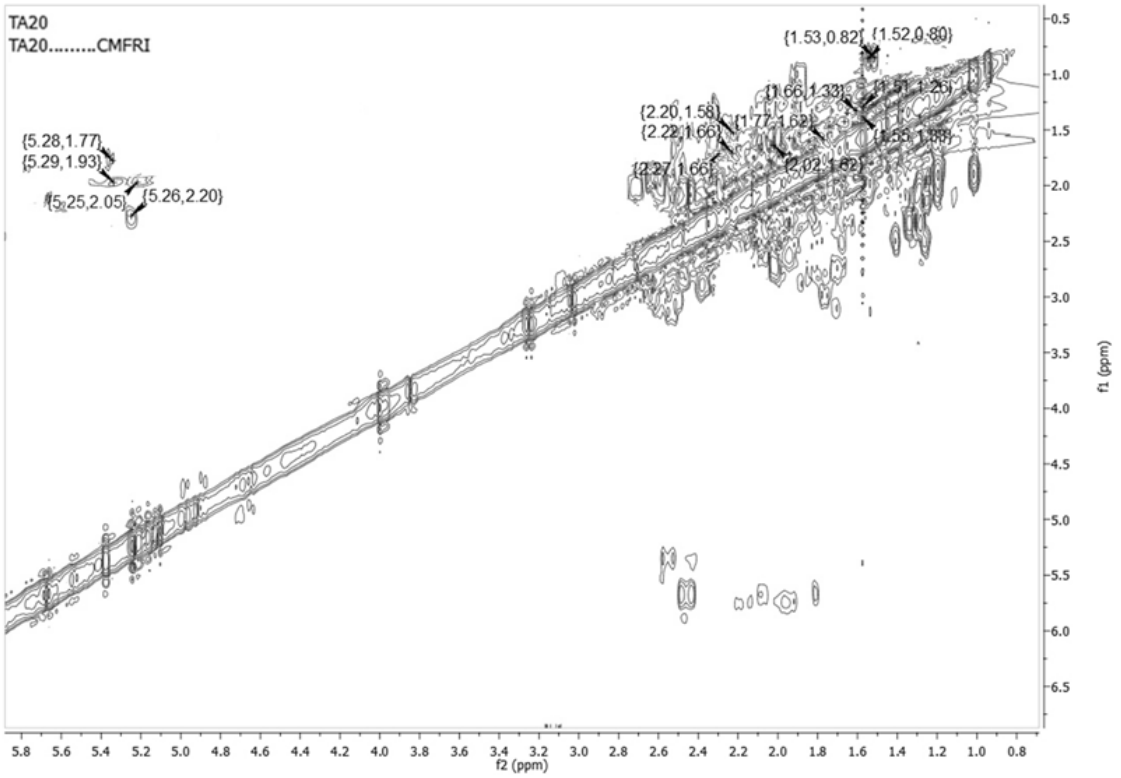

Figure 4.43.: ^{1}H-^{1}H COSY spectrum of 24(4→23)-abeo-olean-(12-oxo)-3,5-diene-deconoate (**3**)

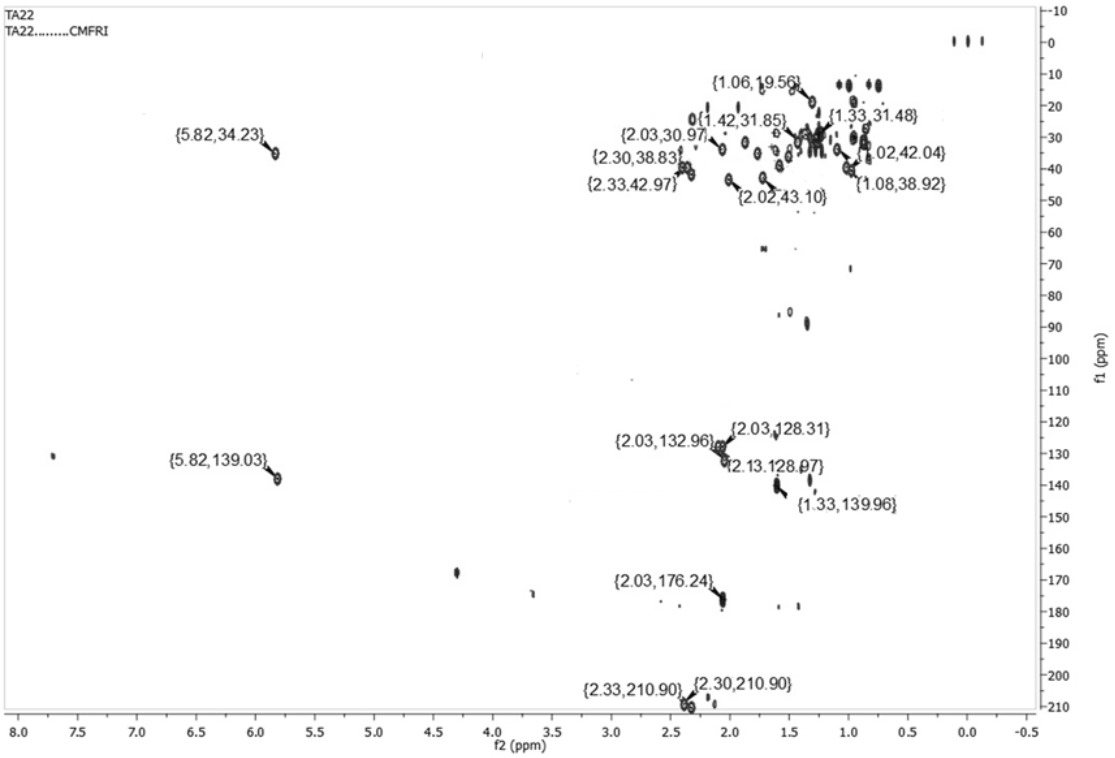

Figure 4.44.: HMBC spectrum of 24(4→23)-abeo-olean-(12-oxo)-3,5-diene-deconoate (**3**)

The distinctive oleanene framework comprised of seven angular methyls in the δ 0.7 to δ 1.25 range at C-4 (CH_3-23, CH_3-24), C-10 (CH_3-25), C-8 (CH_3-26), C-14 (CH_3-27), C-17 (CH_3-28) and C-20 (CH_3-29, CH_3-30) positions (Da Rocha et al., 2015; Maneesh and Chakraborty, 2017), whereas the titled compound comprised of six tertiary methyls at δ 1.33 (s), δ 1.04(s), δ 1.08 (s), δ 1.10 (s), δ 0.88 (s) and δ 0.96 (s). The position of tertiary methyl, δ 1.33 (s) (CH_3-25) at C-10 was ascertained through HMBCs from δ 1.33 to δ 31.4 (C-10), δ 139.2(C-5) and the HMBC correlations between δ 1.04 to δ 42.7 (C-8) suggested the position of tertiary methyl, δ 1.04 (s) (CH_3-26) at C-8. Similary, the HMBC couplings from δ 1.08 to δ 38.8 (C-14) and that from δ 1.10 (CH_3-28) to δ 33.4 (C-17) confirmed the presence of angular methyl substitutions of CH_3-27 at C-14 and CH_3-28 at C-17, respectively. The gem dimethyls (CH_3-29, CH_3-30) at C-20 were confirmed by the long range relations of δ 0.88 and 0.96 to δ 28.0 (C-20). These six typical angular methyls were comparable with earlier reported chemical shifts of basic oleanene skelton (Da Rocha et al., 2015; Hassan et al., 2012). One of the gem dimethyl groups at C-4 (CH_3-24) was shifted to C-23, and this assignment was corroborated through the HMBC couplings from CH_2-23 (δ 2.13) to C-4 (δ 128.8) and CH_3-24 (δ 1.06) to C-23 (δ 19.1). Due to the methyl shift at C-4, the titled compound was classified as abeo oleanene triterpenoid, **3** which was named as 24(4→23)-abeo-olean-(12-oxo)-3,5-diene. The COSY spin systems (CH_2-δ 2.34)

(H-2')-(CH_2-δ 1.63) (H-3')-(CH_2-δ 1.29) (H-4')-(CH_2-δ 1.23) (H-5')-(CH-δ 1.28) (H-6')-(CH_2-δ 1.32) (H-7')-(CH_2-δ 1.30) (H-8')-(CH_2-δ 1.31) (H-9')-(CH_3-δ 0.84) (H-10') attributed the presence of a linear side chain with nine carbon atoms. The HMBCs from CH_2-2 (δ 2.03) to C-1' (δ 176.1) and CH_2-2' (δ 2.34) to C-1' (δ 176.1) supported the presence of a ester linkage attached to the nine alkyl membered linear chain, which was classified as deconoate. The previous reports of 3-(stearyloxy)olean-12-ene enclosed 18-membered alkyl ester group in which the chemical shift at CH-3 was found to be δ 80.51/4.52, and the chemical shift of ester carbonyl at C-1' was found to be δ 173.55 (Da Rocha et al., 2015). Herein, the chemical shift of ester carbonyl at C-1' was found to be δ 176.1 and this increase in the chemical shift was due to the direct attachment of oxygen end of the ester carbonyl to an alkenic quarternary carbon at C-3. The compound, **3** was structurally correlated to previously reported oleanenes (Da Rocha et al., 2015; Huang et al., 2013; Maneesh and Chakraborty, 2017) beside the differences recorded in the dispositions of alkenes, ester linkages and presence of abeo tertiary methyls along with absence of hydroxyl functionalities.

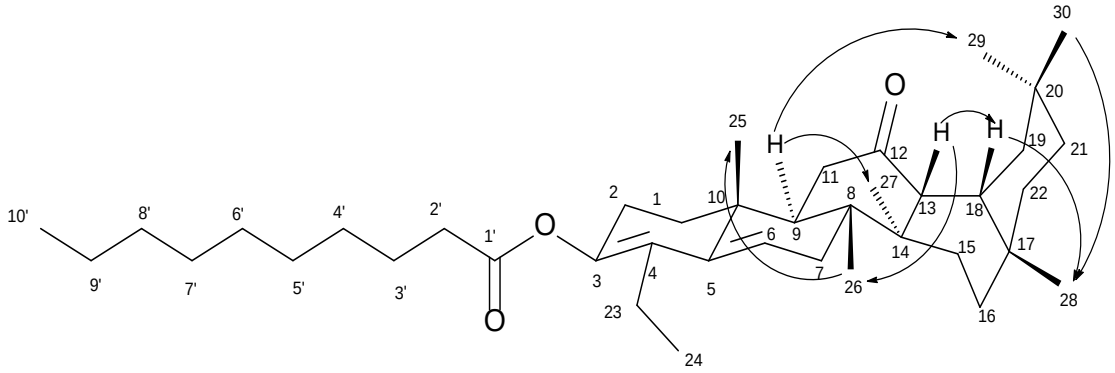

Figure 4.45.: NOE (single headed arrows) correlations of 24(4→23)-abeo-olean-(12-oxo)-3,5-diene-deconoate (**3**)

The relative stereochemistry of chiral centres at δ 43.4 (C-9), 51.9 (C-13) and 41.4 (C-18) were worked out by nuclear overhauser effect spectroscopic (NOESY) experiments. The proton at δ 2.30 (assigned to CH-13) exhibited NOE correlation with the angular methyl proton at δ 1.04 (H-26) and δ 1.62 (H-18) (Figure 4.45 & 4.46) that was positioned in the β-plane (Wang et al., 2014). In addition, the β-disposition of chiral protons H-18, H-25, H-26, H-28 and H-30 were inferred by the NOE association between H-25 (δ 1.33)/H-26 (δ 1.04), H-26 (δ 1.04)/H-13(δ 2.30), H-13 (δ 2.30)/H-18 (δ 1.62), H-18 (δ 1.62)/H-28 (δ 1.10) and H-28 (δ 1.10)/H-30 (δ 0.96). These assessments were in agreement with the alignments of methyl

functionalities at C-10, C-8 and C-20, as described in the previous reports of literature (Wang et al., 2014).

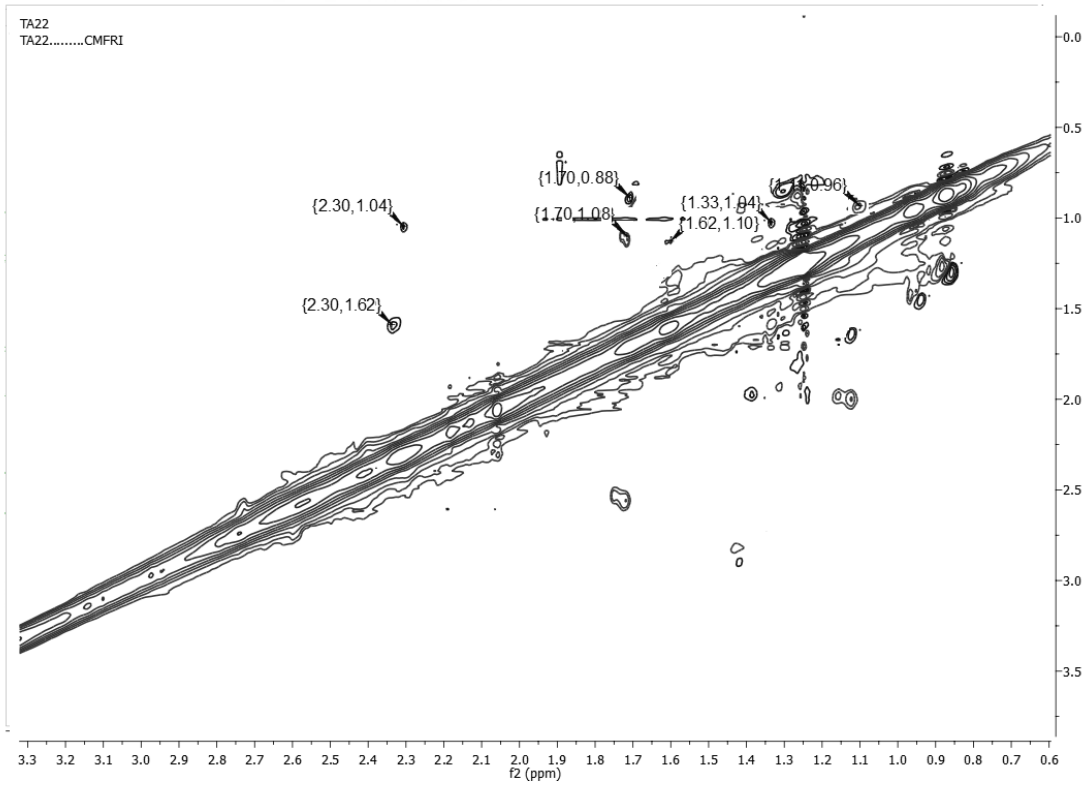

Figure 4.46.: NOE spectrum of 24(4→23)-abeo-olean-(12-oxo)-3,5-diene-deconoate (**3**)

Conversely, the proton at the chiral centre, δ 1.70 (assigned as CH-9) exhibited NOE correlation with the proton at δ 0.88 (H-29) that was disposed in the α-face. The other proton at δ_H1.08 (H-27) was found to be α-aligned. The trans-, cis-coincidence of ABCD and DE skeletons were substantiated by stereochemical attributions (Koay et al., 2013).

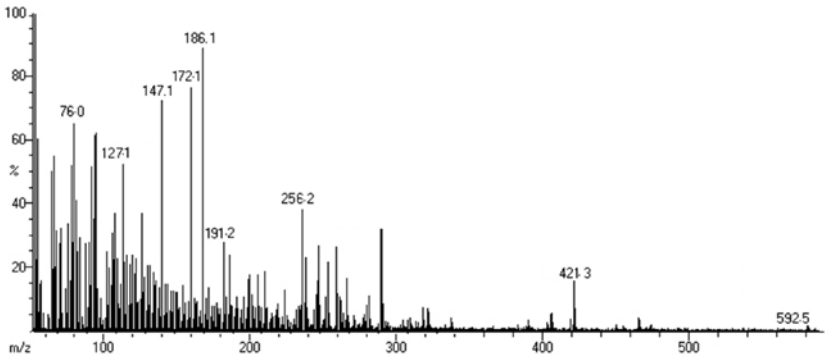

Figure 4.47.: EI-MS spectrum of 24(4→23)-abeo-olean-(12-oxo)-3,5-diene-deconoate (**3**)

Table 4.10: NMR spectroscopic data[a] of 24(4→23)-abeo-olean-(12-oxo)-3,5-diene-deconoate (**3**) isolated from red seaweed *G. salicornia*

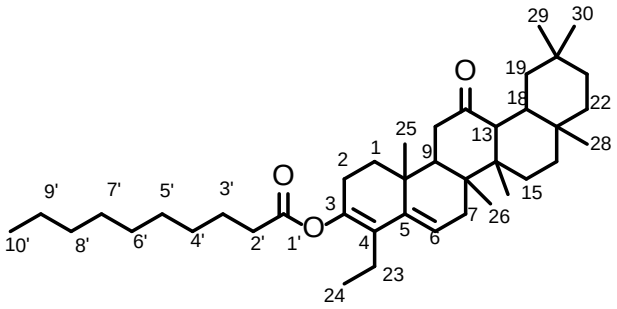

Compound **3**……...24(4→23)-abeo-olean-(12-oxo)-3,5-diene-deconoate (**3**)

Type	C. No.	^{13}C NMR	^{1}H. No. (int., mult., *J* in Hz)[b]	^{1}H NMR	COSY	HMBC
CH_2	1	30.5	1H, dt, J = 13.0, 6.5 Hz	1.42	H-2	C-10, 5
			1H, dt, J = 13.9, 5.9 Hz	1.15	-	-
CH_2	2	24.7	1H, dt, J = 11.8, 7.8 Hz	2.03	-	C-1,3,4,1'
			1H, dt, J = 11.2, 6.2 Hz	1.72	-	-
C	3	132.2	-	-	-	-
C	4	128.8	-	-	-	-
C	5	139.2	-	-	-	-
CH	6	130.9	1H, t, J = 11.7 Hz	5.82	-	C-5,7
CH_2	7	34.0	1H, d, J = 8.2 Hz	2.00	-	C-8
			1H, d, J = 5.0 Hz	1.75	-	-
C	8	42.7	-	-	-	-
CH	9	43.4	1H, t, J = 7.2 Hz	1.70	H-11	C-8,10,11
C	10	31.4	-	-	-	-
CH_2	11	36.9	1H, dd, J = 10.8, 3.2 Hz	2.33	-	C-12
			1H, dd, J = 9.9, 2.6 Hz	2.07	-	-
C	12	213.1	-	-	-	-
CH	13	51.9	1H, d, J = 12.9 Hz	2.30	H-18	C-12,8,14
C	14	38.8	-	-	-	-
CH_2	15	29.4	1H, dt, J = 10.9, 6.3 Hz	1.59	-	C-14,16
			1H, dt, J = 11.9, 5.9 Hz	1.35	-	-
CH_2	16	37.0	1H, dt, J = 10.9, 5.9 Hz	1.60	-	C-17
			1H, dt, J = 11.2, 4.9 Hz	1.38	-	-
C	17	33.4	-	-	-	-
CH	18	41.4	1H, m	1.62	H-19	C-17
CH_2	19	37.7	1H, t, J = 4.9 Hz	1.20	-	C-20
			1H, t, J = 4.0 Hz	1.43	-	-
C	20	28.0	-	-	-	-
CH_2	21	33.9	1H, dt, J = 11.0, 4.8 Hz	1.61	-	C-20
			1H, dt, J = 10.0, 4.0 Hz	1.34	-	-
CH_2	22	34.3	1H, dt, J = 10.9, 4.7 Hz	1.56	-	C-21,17
			1H, dt, J = 10.5, 4.0 Hz	1.36	-	-
CH_2	23	19.1	2H, q, J = 5.7 Hz	2.13	-	C-4
CH_3	24	19.9	3H, t, J = 6.9 Hz	1.06	-	C-23
CH_3	25	20.8	3H, s	1.33	-	C-10,5

CH_3	26	19.7	3H, s	1.04	-	C-8
CH_3	27	19.4	3H, s	1.08	-	C-14
CH_3	28	22.8	3H, s	1.10	-	C-17
CH_3	29	30.2	3H, s	0.88	-	C-20
CH_3	30	30.1	3H, s	0.96	-	C-20
C	1'	176.1	-	-	-	-
CH_2	2'	26.7	2H, t, J = 10.9 Hz	2.34	H-3'	C-1'
CH_2	3'	26.4	2H, m	1.63	H-4'	-
CH_2	4'	29.2	2H, m	1.29	H-5'	-
CH_2	5'	29.5	2H, m	1.23	H-6'	-
CH_2	6'	29.6	2H, m	1.28	H-7'	-
CH_2	7'	29.3	2H, m	1.32	H-8'	-
CH_2	8'	31.8	2H, m	1.30	H-9'	-
CH_2	9'	22.6	2H, m	1.31	H-10'	-
CH_3	10'	14.0	3H, t, J = 7.3 Hz	0.84	-	-

[a]NMR spectra were recorded using a Bruker AVANCE III 500 MHz (AV 500) spectrometer (Bruker, Karlsruhe, Germany) in $CDCl_3$ as aprotic solvent at ambient temperature with TMS as the internal standard (δ 0 ppm).

[b]Values in ppm, multiplicity and coupling constants (J = Hz) were indicated in parentheses. Multiplicities were allocated by ^{135}DEPT NMR spectrum.

The assignments were made with the aid of the COSY, HSQC, HMBC and NOESY experiments.

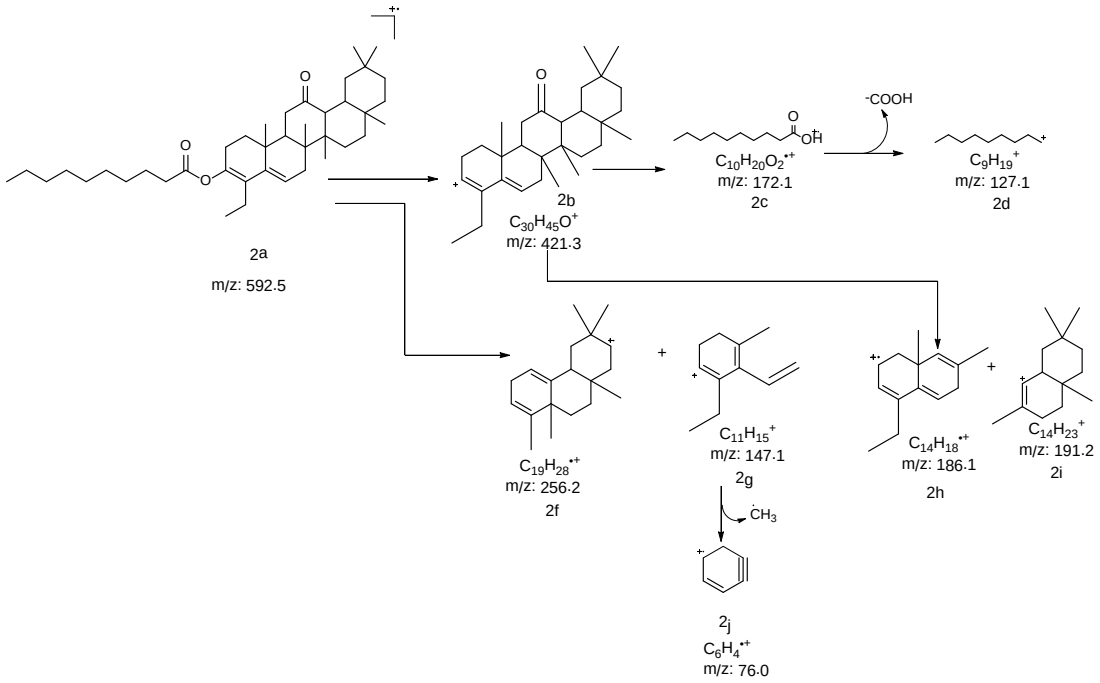

Figure 4.48.: Tentative mass fragmentation pattern of 24(4→23)-abeo-olean-(12-oxo)-3,5-diene-deconoate (**3**)

The structural elucidation of **3** was corroborated by the mass spectral data wherein the molecular ion (*m/z* 592.5, 2a) experienced the exclusion of 2c to yield abeo-24(4→23)-olean-(12-oxo)-3,5-diene (2b) with *m/z* 421.3. The fragment, 1a underwent retro-Diels-Alder (rDA) rearrangement to afford the mass fragments 2h and 2i (*m/z* 186.1 and 191.2, respectively). The ion peak at 186.1 (2h) was considered as the base peak) (Figure 4.47 & 4.48). These analyses deduced its molecular formula as $C_{40}H_{64}O_3$ enclosing nine indices of hydrogen deficiencies, which were associated with five ring systems and four olefinic bonds (comprising two carbonyls and two alkenes). The spectroscopic experiments along with previous reports of literature unambiguously characterised the oleanene triterpenoid as 24(4→23)-abeo-olean-(12-oxo)-3,5-diene-deconoate (**3**).

The organic extract of *G. salicornia* was fractionated by repeated chromatographic techniques to obtain two unprecedented abeo-oleanene analogues. The isolated compounds, 24(4→23), 27(8→26), 30(20→29)-tris-abeo-oleanene moiety (**2**) and 24(4→23) abeo-oleanene framework (**3**) bearing ester and keto- carbonyl functionalities along with olefinic bonds. These functional groups present in the studied analogues contributed towards the various bioactivities of these compounds (**2-3**)**.**

4.3.2.3 Structural characterization of drimane class of diterpenoid derivative (Compounds 4-6)

Red seaweeds (phylum Rhodophyta) were found to be the important sources of pharmacologically active sesquiterpenes, and these algae received greater attention due to their capability to biosynthesise structurally diverse skeletons of sesquiterpenes, such as sesquiterpenoid quinols (Lane et al., 2010; Sali et al., 2018).

The present work described the purification and characterisation of three previously unreported drimane-associated quinols from the organic solvent extract of *G. salicornia* collected from the southeast coastal region of Indian peninsular. The studied compounds, which were designated as 3-(hept-3^6-enyloxy)-decahydro-4,6a,12a,12b-tetramethyl-1*H*-benzo[*a*]xanthene-4,10,12-triol (**4**), 13-[[2-(hexyloxy)-2,5,5,8a-tetramethyldecahydro-1-naphthalenyl](methoxy)methyl]benzenol (**5**), and 1-butoxy-4,4,11b,11c-tetramethyl-decahydrobenzo[*kl*]xanthen-10-ol (**6**) (Figure. 4.4.) were characterised by extensive spectroscopic experiments. The pharmacological activities were assessed by different selective *in vitro* assays. The physicochemical parameters of these compounds were utilised to corroborate their structural features with their bioactive potentials.

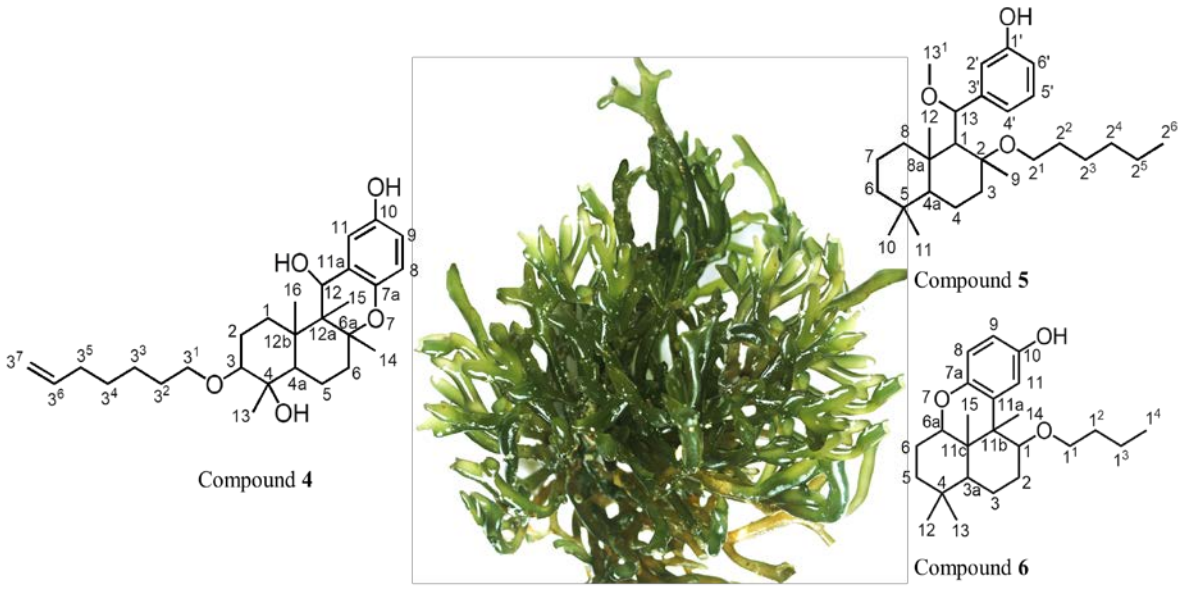

Figure 4.49.: Structural representations of (**A**) 3-(hept-3^6-enyloxy)-decahydro-4,6a,12a,12b-tetramethyl-1*H*-benzo[*a*]xanthene-4,10,12-triol (compound **4**), (**B**) 13-[[2-(hexyloxy)-2,5,5,8a-tetramethyldecahydro-1-naphthalenyl](methoxy)methyl]benzenol (compound **5**), and (**C**) 1-butoxy-4,4,11b,11c-tetramethyl-decahydrobenzo[*kl*]xanthen-10-ol (compound **6**) isolated from red seaweed *G. salicornia*. (**D**) The representative photograph of thalli (leaf-like structures) of *G. salicornia*.

4.3.2.3a Structural characterization of Compound 4

3-(hept-3^6-enyloxy)-decahydro-4,6a,12a,12b-tetramethyl-1*H*-benzo[*a*]xanthene-4,10,12-triol

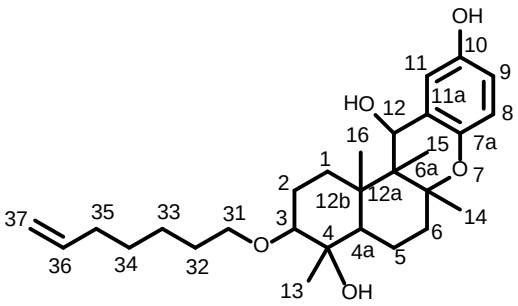

Sample yield	0.33% (> 99% purity, RP-C18 HPLC)
Physical description	Pale yellow oil
Molecular formula	$C_{28}H_{42}O_5$
Molecular mass	458.3032

The drimane class of diterpenoid derivative, 3-(Hept-3^6-enyloxy)-2,3,4,4a,5,6,6a,12,12a,12b-decahydro-4,6a,12a,12b-tetramethyl-*1H*-benzo[a]-xanthene-4,10,12-triol was isolated as yellowish-white amorphous compound. The compound (**4**) has exhibited UV absorbance (UV (MeOH) λ_{max}) at 278 nm (Figure 4.50.). The homogeneity of the compound was ascertained by HPLC data on a bonded phase octadecylsilane (C_{18}) stationary phase (HPLC, MeCN/MeOH, 1:2 v/v) with R_t: 3.24 min (Figure 4.51.).

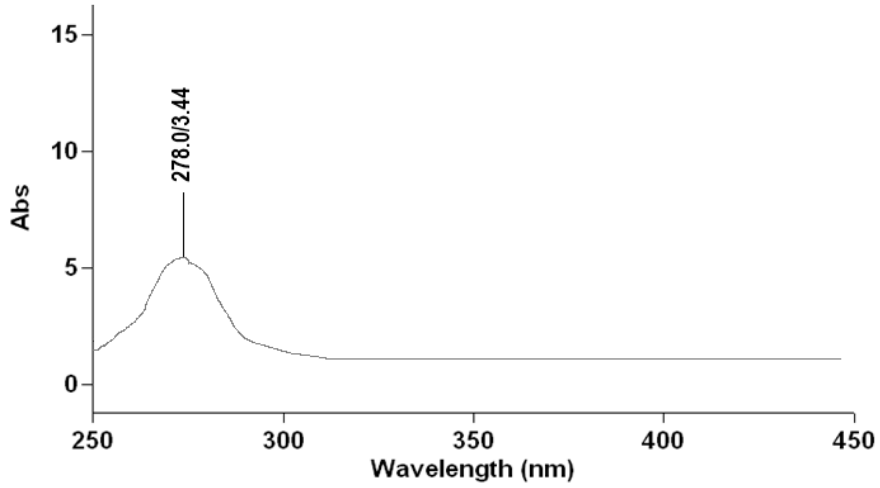

Figure 4.50.: UV spectrum of 3-(Hept-3^6-enyloxy)-2,3,4,4a,5,6,6a,12,12a,12b-decahydro-4,6a,12a,12b-tetramethyl-*1H*-benzo[a]xanthene-4,10,12-triol (**4**)

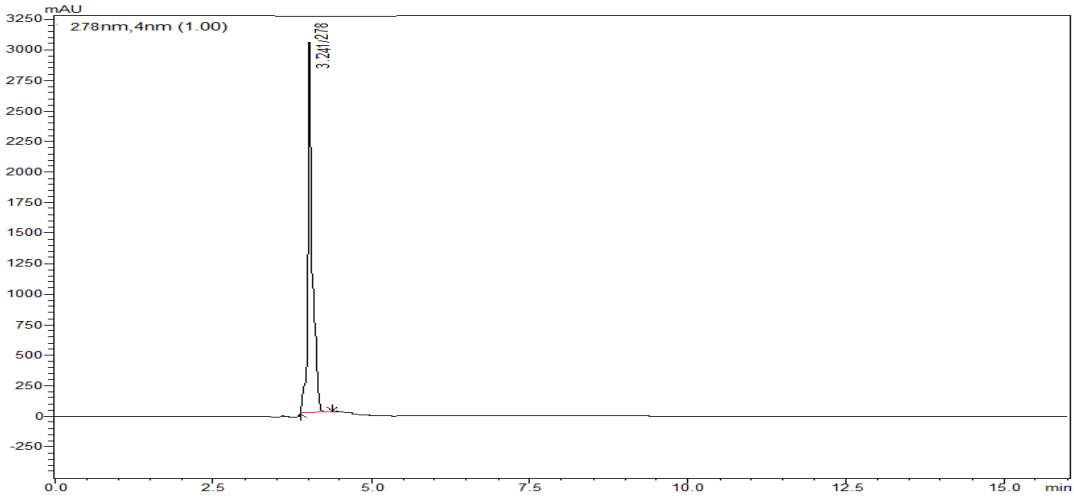

Figure 4.51.: HPLC chromatogram of 3-(Hept-3^6-enyloxy)-2,3,4,4a,5,6,6a,12,12a,12b-decahydro-4,6a,12a,12b-tetramethyl-*1H*-benzo[a]xanthene-4,10,12-triol (**4**)

Repeated column chromatographic fractionation of *G. salicornia* yielded drimane sesquiterpene quinol class of compound, **4** that was characterised as 3-(hept-3^6-enyloxy)-2,3,4,4a,5,6,6a,12,12a,12b-decahydro-4,6a,12a,12b-tetramethyl-1*H*-benzo[*a*]xanthene-4,10,12-triol. The mass spectroscopic experiment displayed its molecular ion peak at *m/z* 458 $[M]^+$, which corroborated its molecular formula of $C_{28}H_{42}O_5$. It showed eight indices of hydrogen deficiencies associated with one each of olefinic bond and benzene along with three rings. The HRESIMS experiment displayed the molecular ion peak at *m/z* 459.3114 $[M+H]^+$, (Figure 4.52.) which along with NMR-IR spectroscopic analyses deduced its molecular formula as $C_{28}H_{43}O_5$ $[M+H]^+$ (Table 4.11).

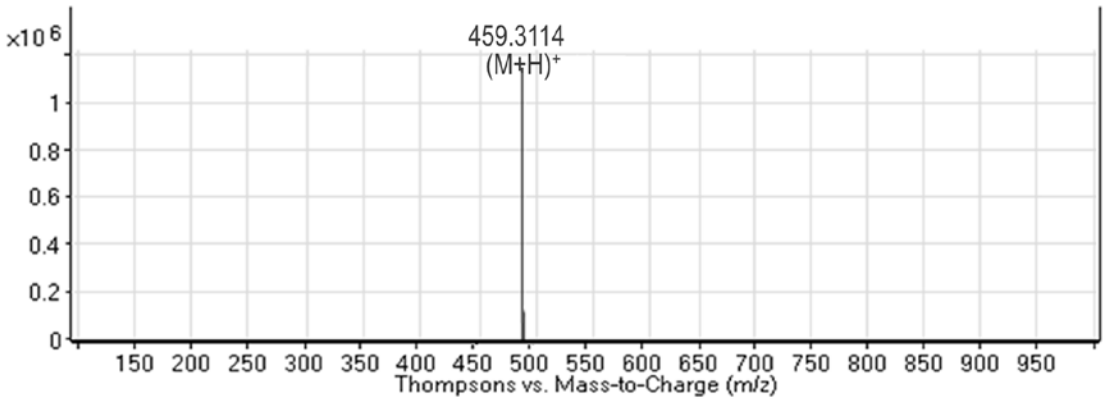

Figure 4.52.: HRESIMS spectrum of 3-(Hept-3^6-enyloxy)-2,3,4,4a,5,6,6a,12,12a,12b-decahydro-4,6a,12a,12b-tetramethyl-*1H*-benzo[a]xanthene-4,10,12-triol (**4**)

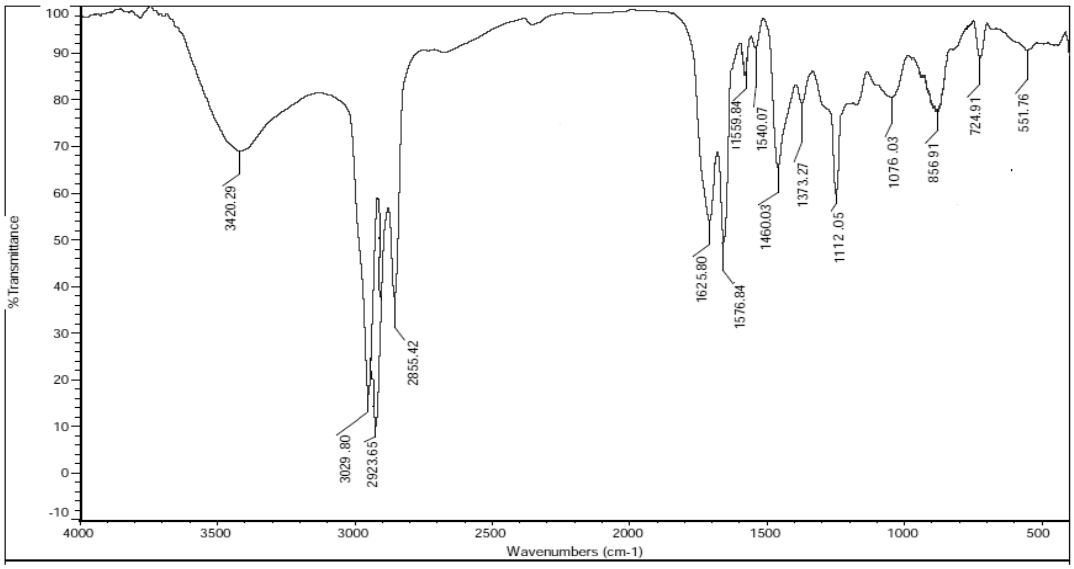

Figure 4.53.: FTIR spectrum of 3-(Hept-3^6-enyloxy)-2,3,4,4a,5,6,6a,12,12a,12b-decahydro-4,6a,12a,12b-tetramethyl-*1H*-benzo[a]xanthene-4,10,12-triol

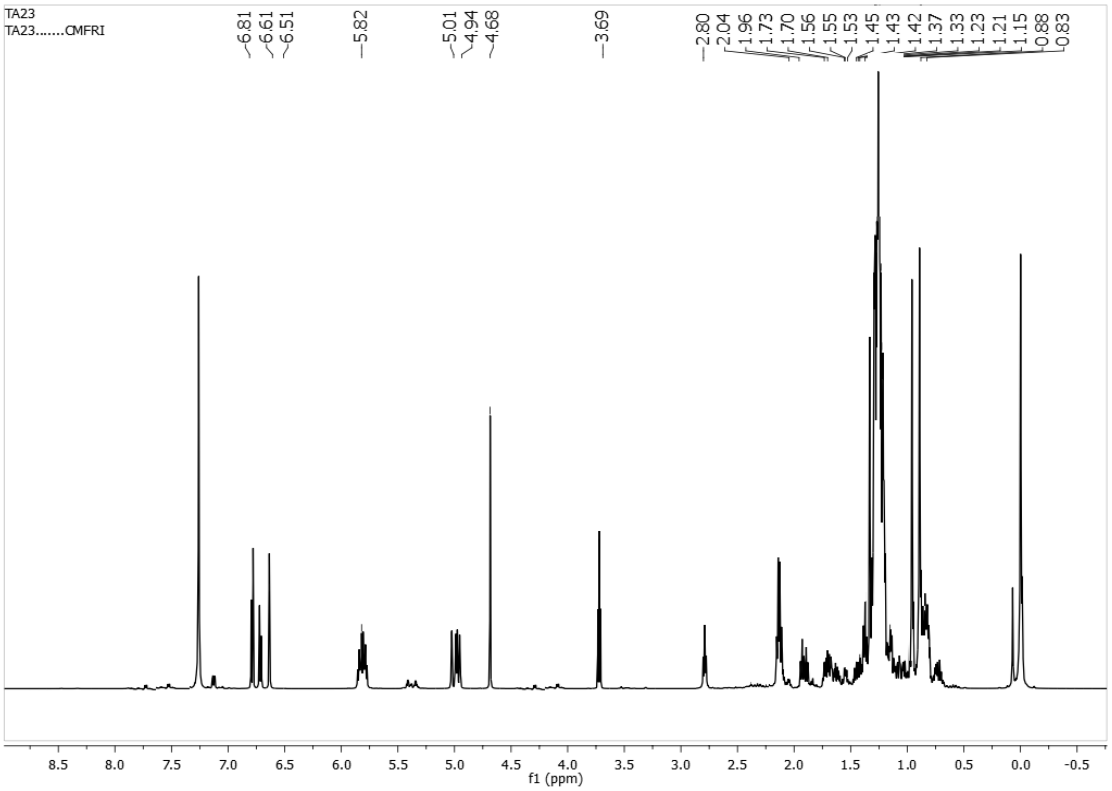

Figure 4.54.: FTIR spectrum of 3-(Hept-3[6]-enyloxy)-2,3,4,4a,5,6,6a,12,12a,12b-decahydro-4,6a,12a,12b-tetramethyl-*1H*-benzo[a]xanthene-4,10,12-triol

The FTIR absorption peaks of **4** at 3420, 856, 1559 and 1112-1076 cm^{-1} indicated the occurrences of hydroxyl, C-H aromatic, C=C aromatic and ether functionalities, respectively (Figure 4.53). The ^{1}H-NMR spectrum of **1** showed singlet signals for tertiary methyls at δ 1.42, 1.15, 0.88 and 0.83, which suggested the tetra-methyl substitution in **4**. The ^{1}H-NMR spectrum indicated the presence of six deshielded protons at δ 5.82, 5.01, 4.94, 6.81, 6.61 and 6.51, which might be associated with the olefinic and aromatic groups (Figure 4.54).

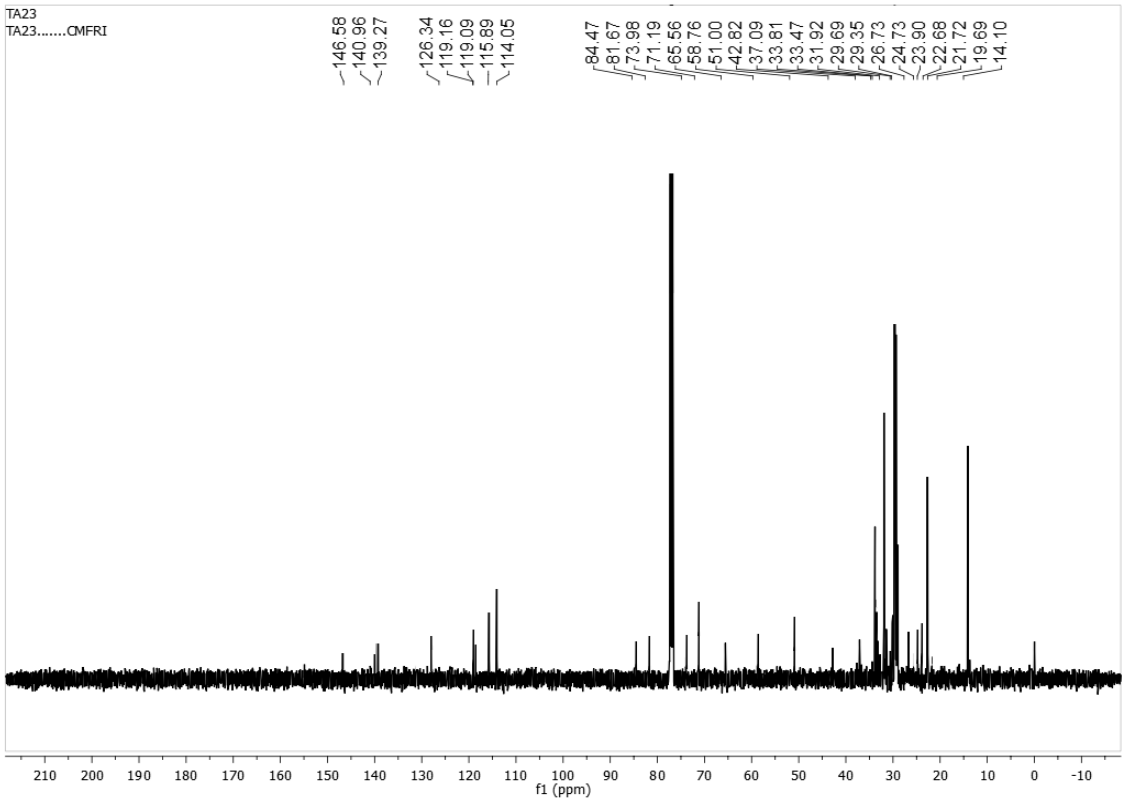

Figure 4.55.: ^{13}C-NMR spectrum of 3-(Hept-3^{6}-enyloxy)-2,3,4,4a,5,6,6a,12,12a,12b-decahydro-4,6a,12a,12b-tetramethyl-*1H*-benzo[a]xanthene-4,10,12-triol (**4**)

The ^{13}C-NMR, DEPT$_{135}$ along with HSQC spectra displayed 28 signals comprised of four methyls (δ 23.9, 22.6, 14.1, 19.6), nine sp^3 methylenes (δ 37.0, 24.7, 21.7, 33.4, 71.1, 31.9, 26.7, 29.6, 33.8), one sp^2 methylene (δ 114.0), four sp^2 methine (δ 139.2, 119.0, 119.1, 115.2), three sp^3 methines (δ 84.6, 58.7, 65.5) and seven non-protonated carbons (δ 73.9, 81.6, 51.0, 42.8, 126.3, 146.5, 140.9) (Figure 4.55-4.57). The COSY spectrum of **4** represented the occurrence of two individual spin systems: I δ (1.23)-(1.56)-(2.80) and II δ (1.53)-(1.73)-(1.37), which was assigned from H-1 to H-3 and H-4 to H-6, respectively (Figure 4.58 & 4.59). These spin systems were further connected by HMBC correlations from CH_2-1 (δ 1.23) to C-12b (δ 42.8); CH-3 (δ 2.80) to C-4 (δ 73.9); CH-4a (δ 1.53) to C-4 (δ 73.9) and CH_2-6 (δ 1.70) to C-6a (δ 81.6), C-12a (δ 51.0), which supported the bicyclic framework of **4** (Figure 4.60).

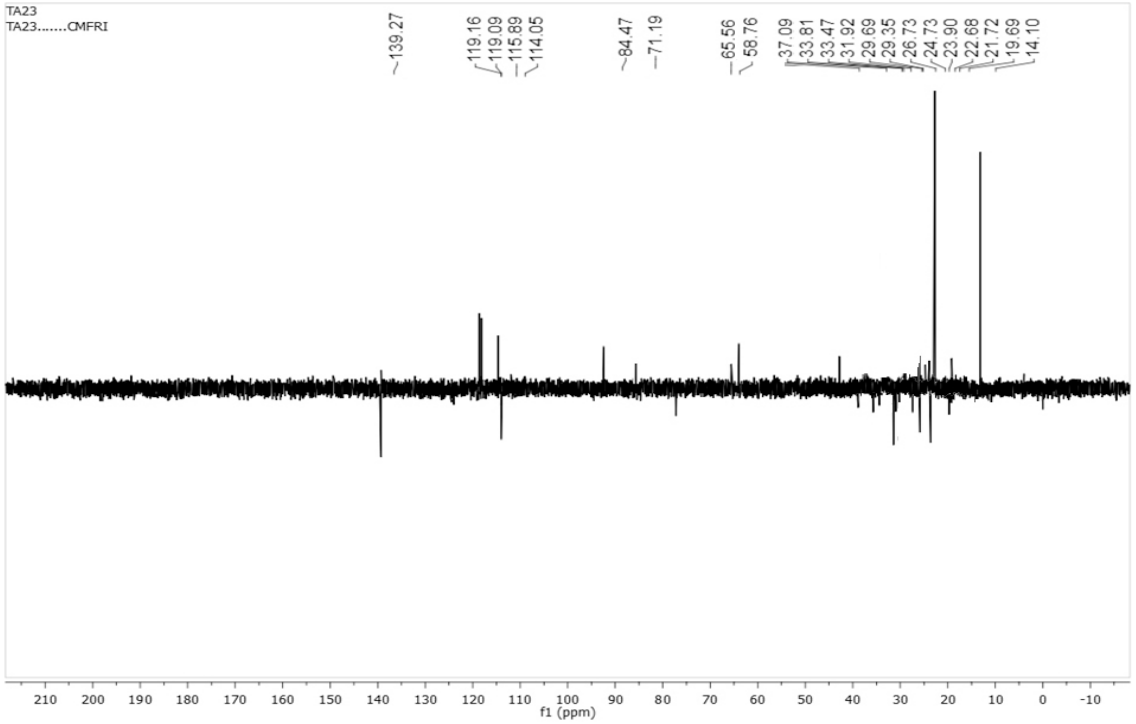

Figure 4.56.: DEPT spectrum of 3-(Hept-3[6]-enyloxy)-2,3,4,4a,5,6,6a,12,12a,12b-decahydro-4,6a,12a,12b-tetramethyl-*1H*-benzo[a]xanthene-4,10,12-triol (**4**)

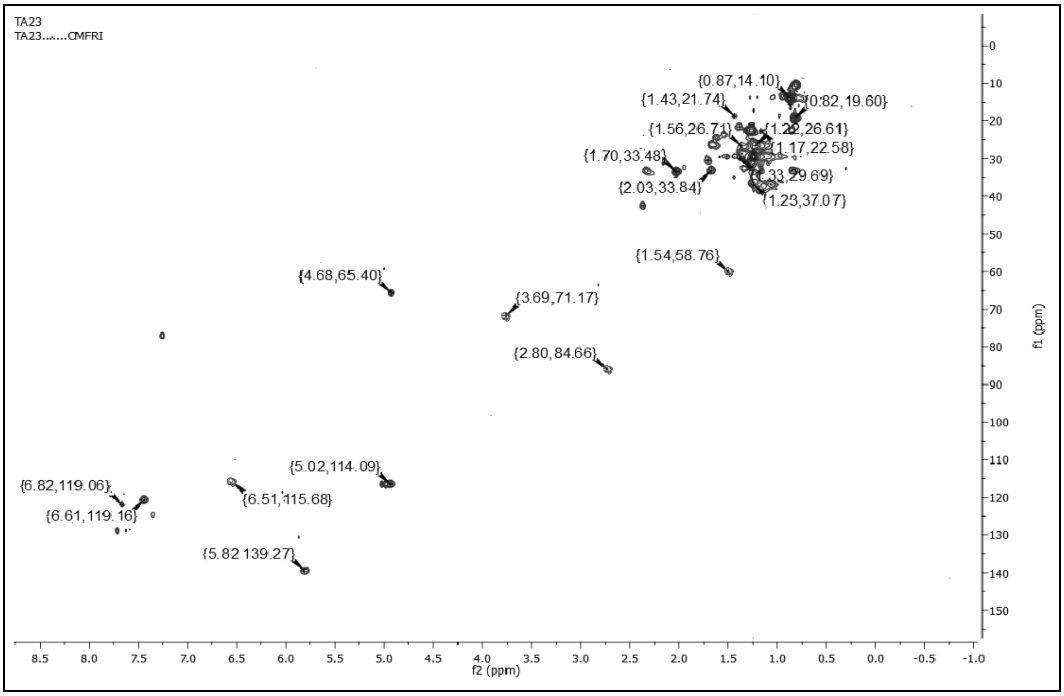

Figure 4.57.: HSQC spectrum of 3-(Hept-3[6]-enyloxy)-2,3,4,4a,5,6,6a,12,12a,12b-decahydro-4,6a,12a,12b-tetramethyl-*1H*-benzo[a]xanthene-4,10,12-triol (**4**)

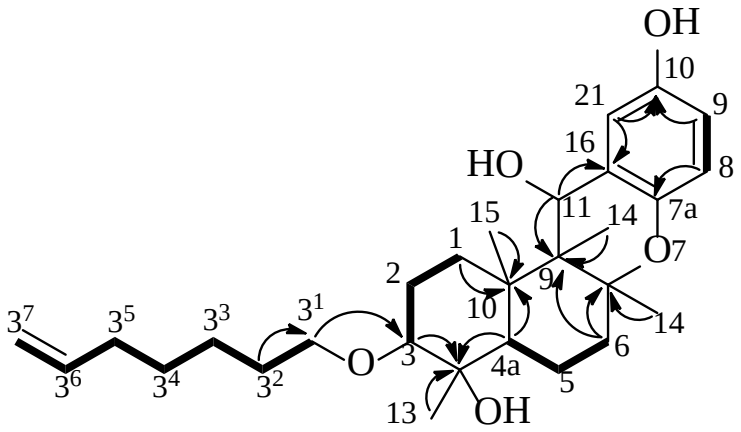

Figure 4.58.: ^{1}H-^{1}H COSY (bold face bonds), and selected HMBCs (double-barbed arrows), correlations of 3-(Hept-3^6-enyloxy)-2,3,4,4a,5,6,6a,12,12a,12b-decahydro-4,6a,12a,12b-tetramethyl-*1H*-benzo[a]xanthene-4,10,12-triol (**4**)

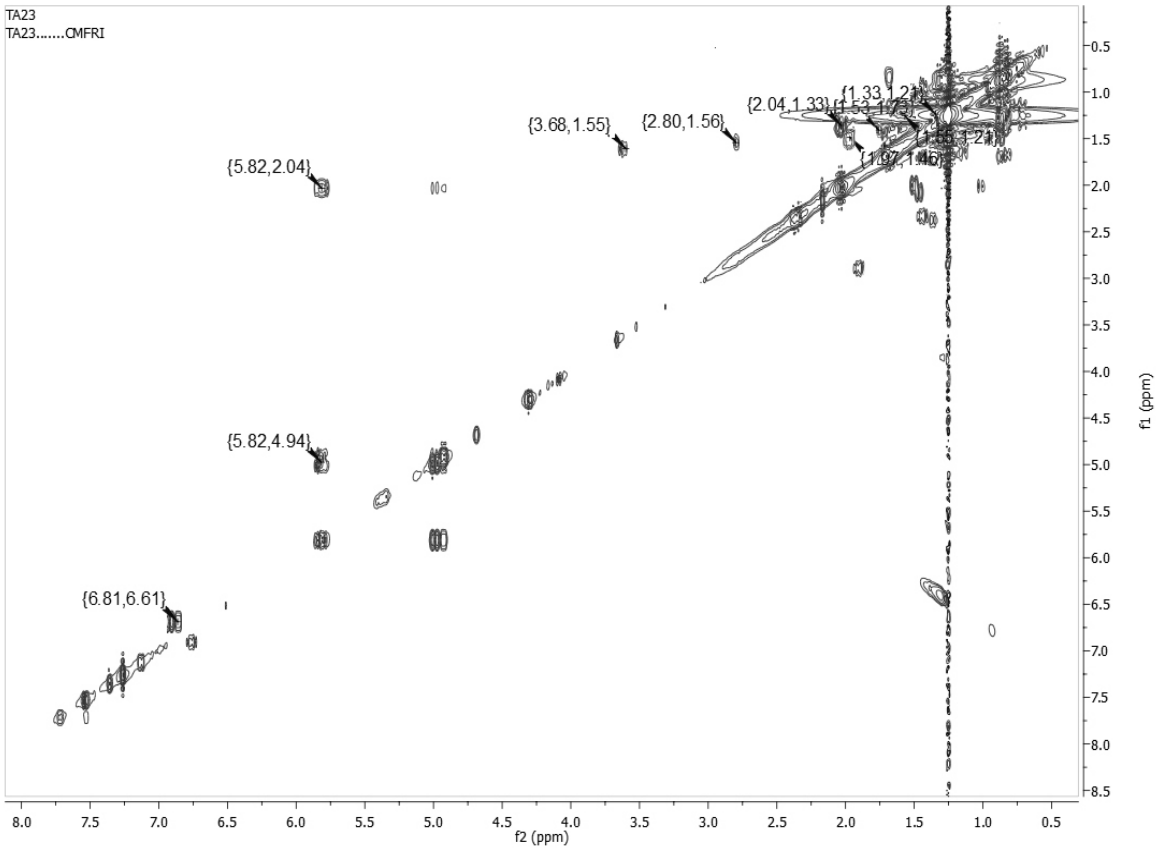

Figure 4.59.: ^{1}H-^{1}H COSY spectrum of 3-(Hept-3^6-enyloxy)-2,3,4,4a,5,6,6a,12,12a,12b-decahydro-4,6a,12a,12b-tetramethyl-*1H*-benzo[a]xanthene-4,10,12-triol (**4**)

Other HMBCs from CH_3-14 (δ 1.42) to C-6a (δ 81.6); CH_3-13 (δ 1.15) to C-4 (δ_C 73.9); CH_3-15 (δ 0.88) to C-12 (δ 51.0) and CH_3-16 (δ 0.83) to C-12b (δ 42.8) confirmed the attachment of four singlet methyl carbons at C-6a, C-4, C-12a, and C-12b, respectively, which appropriately corroborated the presence of bicyclic framework of drimane sesquiterpenoid. The three protons at δ 6.5-6.8 of **4** showed that aromatic ring might be trisubstituted and the COSY correlations from δ (6.81)-(6.61) (H-8 to H-9) along with singlet aromatic signal at δ 6.51 suggested that it might be in the meta-para fused relationship with the basic framework of **4**. The greatly deshielded quaternary carbon at δ 146.5 was related to the hydroxyl attached to the benzene ring.

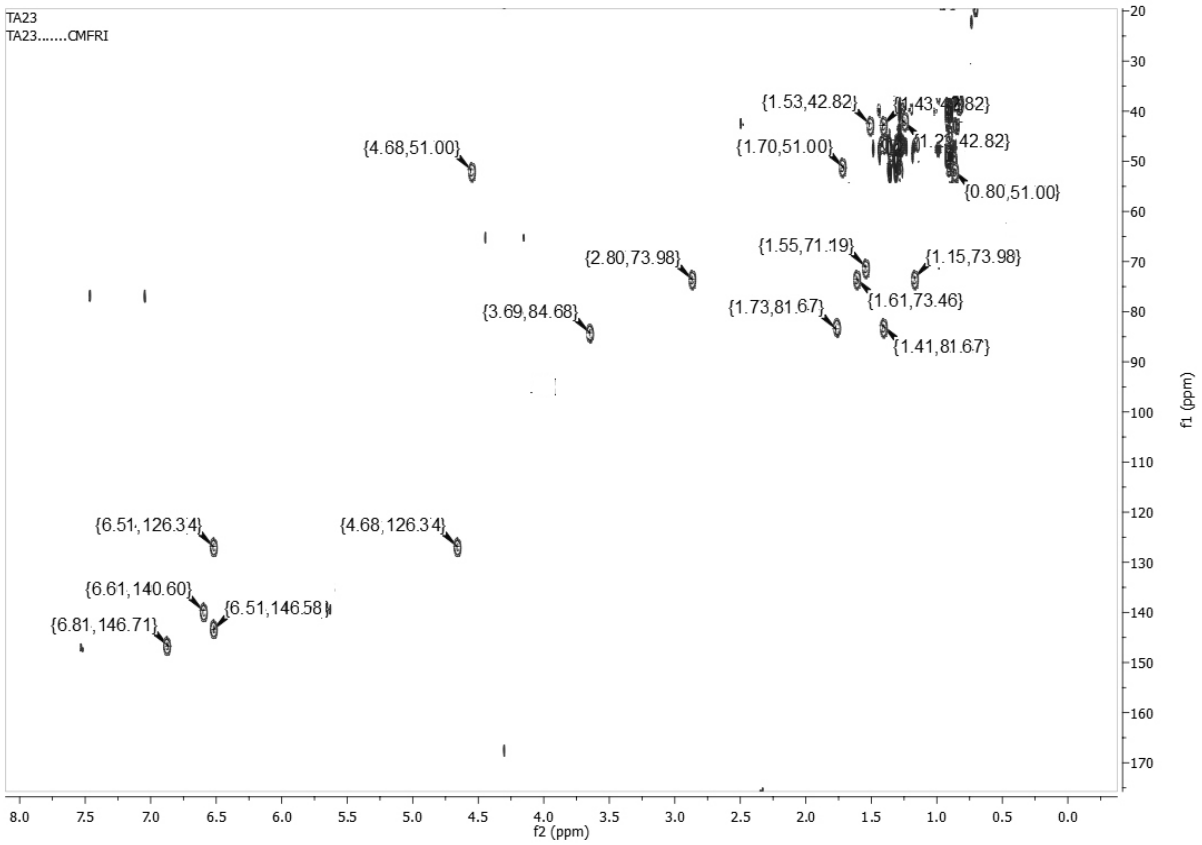

Figure 4.60.: NOE spectrum of 3-(Hept-3^6-enyloxy)-2,3,4,4a,5,6,6a,12,12a,12b-decahydro-4,6a,12a,12b-tetramethyl-*1H*-benzo[a]xanthene-4,10,12-triol (**4**)

The highly deshielded singlet proton at δ 4.68 exhibited HMBCs to C-12a (δ 51.0) of the drimane sesquiterpenoid and to C-11a (δ 126.3) of the aromatic ring. The deshielded signals at C-3 (δ 84.6), C-4 (δ 73.9), C-6a (δ 81.6), C-10 (δ 140.9) and C-12 (δ 65.5) in the ^{13}C-NMR spectrum and absence of any carbonyl absorbances in IR spectrum of **1** were accounted for

oxygenated functional groups, such as hydroxyl or ether. The greatly deshielded oxygenated quaternary carbon at δ 146.5 revealed that one of the oxygen atoms might form an ether bridge from drimane sesquiterpenoid to the aromatic ring system. These attributions recognized the occurrence of a quinol moiety in **4**, and suggested the association of drimane-quinol framework (benzo-xanthene) of sesquiterpene **4**. These spectroscopic assignments suggested the resemblance of compound **4** with the previously reported drimane sesquiterpene quinols and quinons (Mitome et al., 2003; Jiao et al., 2015; Hagiwara et al., 2015; Perez-Garcia et al., 2005; Hui et al., 2015; Cao et al., 2004). The greatly deshielded olefinic groups at δ 5.01, 4.94/δ 114.0 and δ 5.82/δ 139.2 with higher coupling constants (J=12.2-16.7) suggested the possibilities of a terminal monosubstituted vinylic group at -CH(3^6)=CH_2(3^7). The spin system from δ (3.69)-(1.55)-(1.21)-(1.33)-(2.04)-(5.82)-(4.94) suggested the linear arrangement of protons from H-3^1 to H-3^7, which was identified as hept-3^6-enyloxy chain. The strong HMBC coupling from CH_2-3^1 (δ 3.69) to C-3 (δ 84.6) appropriately delineated the attachment of hept-3^6-enyloxy at C-3 (δ 84.6) of the substituted drimane framework as an ether linkage.

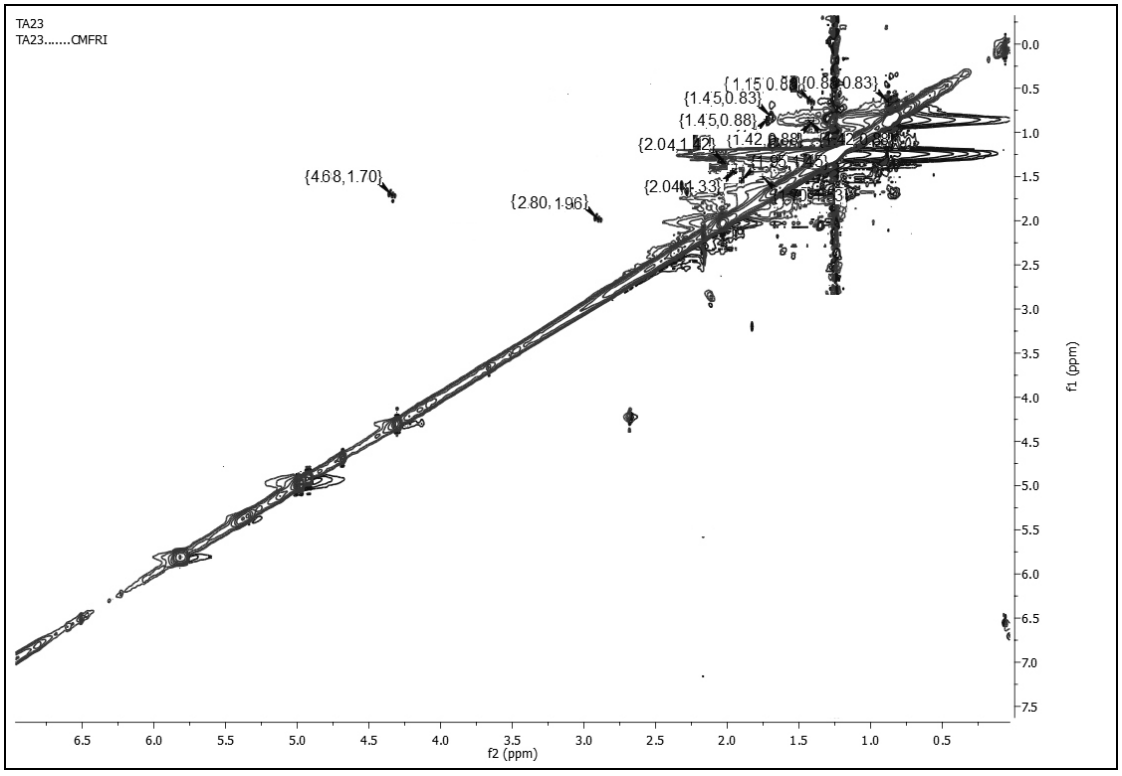

Figure 4.61.: DEPT spectrum of 3-(Hept-3^6-enyloxy)-2,3,4,4a,5,6,6a,12,12a,12b-decahydro-4,6a,12a,12b-tetramethyl-*1H*-benzo[a]xanthene-4,10,12-triol (**4**)

Relative stereochemistries of chiral centers at C-3, C-4, C-4a, C-6a, C-12a, C-12, and C-12b in **4** were assigned by NOESY experiments (Figure 4.61 & 4.62). The NOESY correlations between δ 1.96 (Hβ-2)/2.80 (H-3)/1.45 (Hβ-5); δ 1.15 (H-13)/0.83 (H-16)/1.45 (Hβ-5)/0.88 (H-15)/1.42 (H-14) attributed that these protons were coordinated in the same plane of reference, and hence, were arbitrarily assigned as β-oriented. Deshielded proton signals at δ 4.68 (H-12)/1.70 (Hα-6)/1.53 (H-4a) were found to be opposite to the β-oriented protons, and thus were arbitrarily attributed as α-aligned.

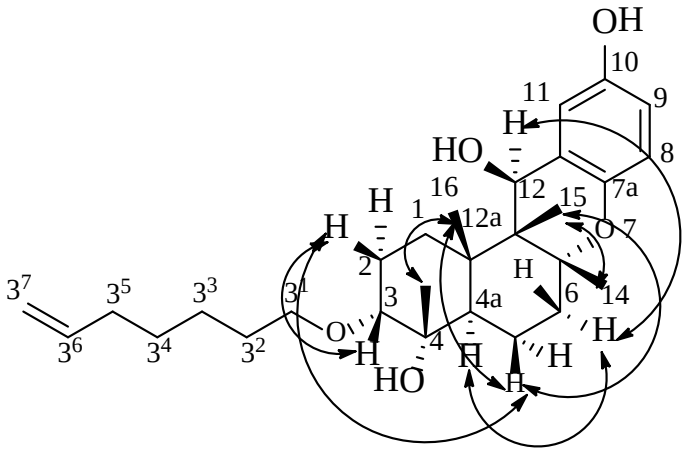

Figure 4.62.: NOE correlations of 3-(hept-3^6-enyloxy)-2,3,4,4a,5,6,6a,12,12a,12b-decahydro-4,6a,12a,12b-tetramethyl-1*H*-benzo[a]xanthene-4,10,12-triol (**4**)

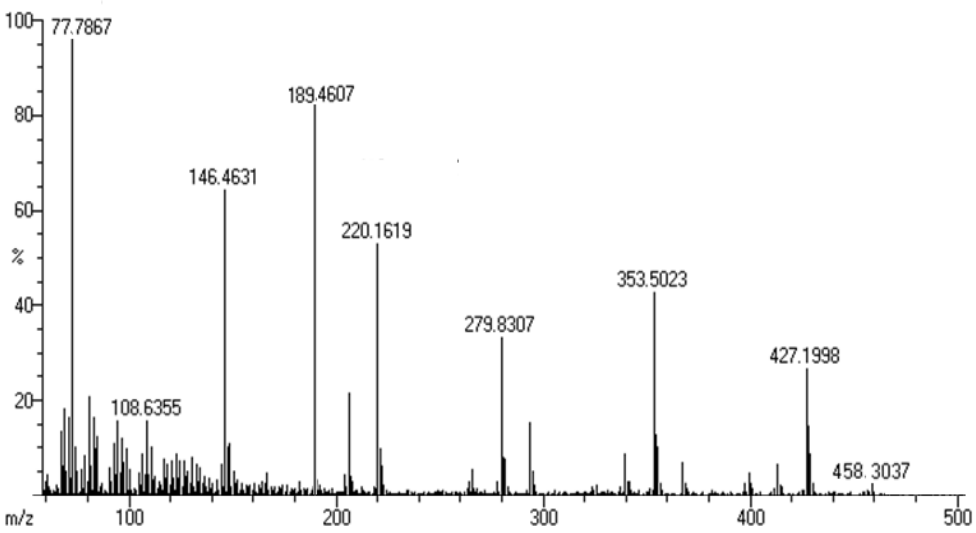

Figure 4.63.: EI-MS spectrum of 3-(Hept-3^6-enyloxy)-2,3,4,4a,5,6,6a,12,12a,12b-decahydro-4,6a,12a,12b-tetramethyl-*1H*-benzo[a]xanthene-4,10,12-triol (**4**)

Table 4.11: NMR spectroscopic data of compound (**4),** 3-(Hept-3^6-enyloxy)-2,3,4,4a,5,6,6a,12,12a,12b-decahydro-4,6a,12a,12b-tetramethyl-*1H*-benzo[a]-xanthene-4,10,12-triol (**4**)

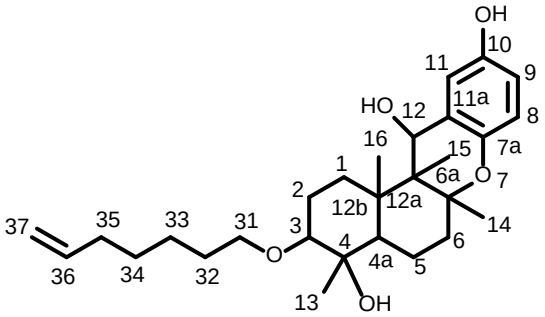

Compound **4**……3-(Hept-3^6-enyloxy)-2,3,4,4a,5,6,6a,12,12a,12b-decahydro-4,6a,12a,12b-tetramethyl-*1H*-benzo[a]-xanthene-4,10,12-triol (**4**)

C. No.	^{13}C-NMR	H. int., mult., J in Hz‡	^{1}H-NMR	COSY	HMBC
1	37.0	1H, t, J = 12.0 Hz	1.43	H-2	C-12b
		1H, t, J = 12.1 Hz	1.23	-	-
2	24.7	1H, m	1.96	H-3	-
		1H, m	1.56	-	-
3	84.6	1H, t, J = 9.8 Hz	2.80	-	C-4
		-	-	-	-
4	73.9	-	-	-	-
4a	58.7	1H, dd, J = 1.5, 12.1 Hz	1.53	H-5	C-4
5	21.7	1H, m	1.73	H-6	-
		1H, m	1.45	-	-
6	33.4	1H, td, J = 12.5, 3.4 Hz	1.70	-	C-6a,12a
		1H, td, J = 12.5, 3.0 Hz	1.37	-	-
6a	81.6	-	-	-	-
7a	146.5	-	-	-	-
8	119.0	1H, d, J = 13.4 Hz	6.81	H-9	C-7a
9	119.1	1H, d, J = 13.8 Hz	6.61	-	C-10
10	140.9	-	-	-	-
11	115.2	1H, s	6.51	-	C-11a,10
11a	126.3	-	-	-	-
12	65.5	1H, s	4.68	-	C-12a,11a
12a	51.0	-	-	-	-
12b	42.8	-	-	-	-
13	22.6	3H, s	1.15	-	C-4
14	23.9	3H, s	1.42	-	C-6a
15	14.1	3H, s	0.88	-	C-12a
16	19.6	3H, s	0.83	-	C-12b
3^1	71.1	2H, t, J = 8.6 Hz	3.69	H-3^2	C-3
3^2	31.9	2H, m	1.55	H-3^3	C-3^1
3^3	26.7	2H, m	1.21	H-3^4	-
3^4	29.6	2H, m	1.33	H-3^5	-

3^5	33.8	2H, m	2.04	H-3^6	-
3^6	139.2	1H, m	5.82	H-3^7	-
3^7	114.0	1H, dd, J = 3.4, 16.7 Hz	5.01	-	-
		1H, dd, J = 3.4, 12.2 Hz	4.94	-	-

‡ Values in ppm, multiplicity and coupling constants (J= Hz) were indicated in parentheses. Multiplicities were allocated by ^{135}DEPT NMR spectrum.

The assignments were made with the aid of the COSY, HSQC, HMBC and NOESY experiments.

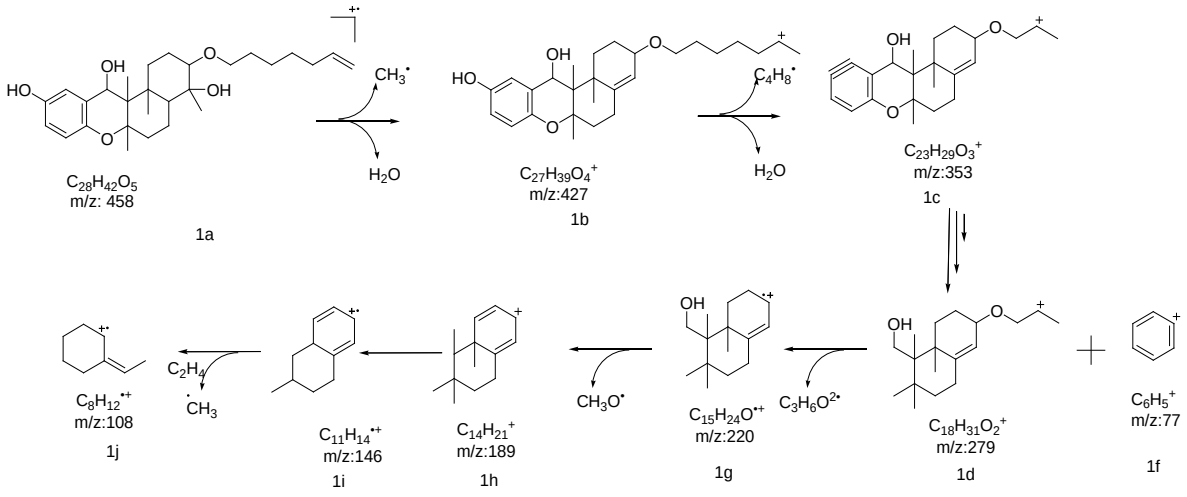

Figure 4.64.: Mass fragmentation pattern of 3-(Hept-3^6-enyloxy)-2,3,4,4a,5,6,6a,12,12a,12b-decahydro-4,6a,12a,12b-tetramethyl-*1H*-benzo[a]xanthene-4,10,12-triol (**4**)

The structural assignments of **4** were corroborated by mass spectral experiment, wherein the molecular ion peak at *m/z* 458 (1a) experienced the removal of a methyl-radical and H_2O to result $C_{27}H_{39}O_4^{\bullet+}$ (1b) with *m/z* 427. The elimination of $C_4H_8^{\bullet}$ and H_2O from 1b could result in the formation of $C_{23}H_{29}O_3^+$ with *m/z* 353 (1c). The fragment, 1c appeared to undergo further series of fragmentation to yield the mass fragments at *m/z* 77, 220, 189, 146, and 108. The base peak of the compound **4** was found at *m/z* 77, which was found to correspond to the phenyl cation ($C_6H_5^+$) (Figure 4.63 & 4.64). The 1D and 2D NMR assignments along with mass spectroscopic data unambiguously constructed the structure of the drimane sesquiterpene with substituted 1*H*-benzo[*a*]xanthene-4,10,12-triol moiety (**4**).

4.3.2.3b Structural characterization of Compound 5

13-[[2-(Hexyloxy)-2,5,5,8a-tetramethyldecahydro-1-naphthalenyl](methoxy-)-methyl]-benzenol

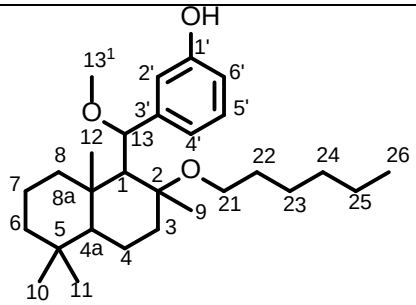

Sample yield	0.35 % (> 99% purity, RP-C18 HPLC)
Physical description	Yellowish oil
Molecular formula	$C_{28}H_{46}O_3$
Molecular mass	430.3447

The drimane class of diterpenoid derivative, 13-[[2-(Hexyloxy)-2,5,5,8a-tetramethyldecahydro-1-naphthalenyl](methoxy-)-methyl]-benzenol was isolated as yellowish-white amorphous compound. The compound (**5**) has exhibited UV absorbance (UV (MeOH) λ_{max}) at 281 nm (Figure 4.65). The homogeneity of the compound was ascertained by HPLC data on a bonded phase octadecylsilane (C_{18}) stationary phase (HPLC, MeCN/MeOH, 1:2 v/v) with R_t: 3.81 min (Figure 4.66).

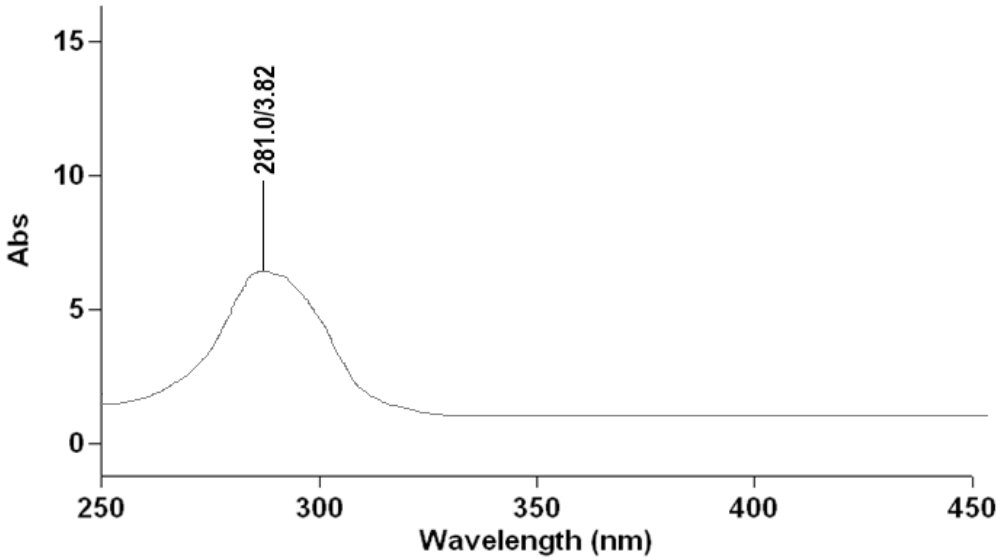

Figure 4.66.: UV spectrum of 13-[[2-(Hexyloxy)-2,5,5,8a-tetramethyldecahydro-1-naphthalenyl](methoxy-)-methyl]-benzenol (**5**)

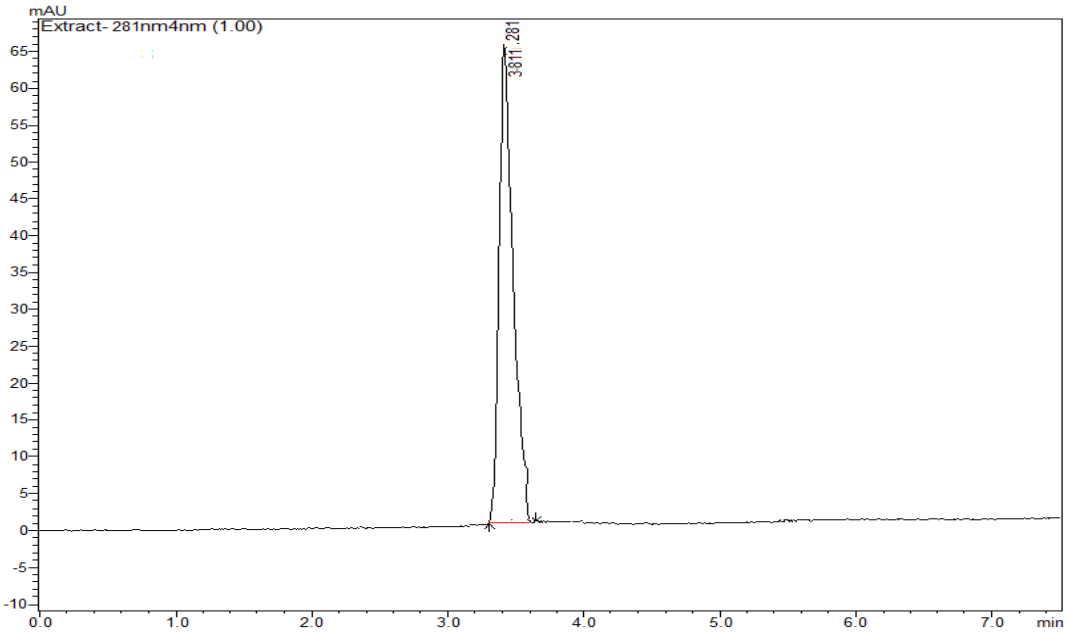

Figure 4.67.: HPLC chromatogram of 13-[[2-(Hexyloxy)-2,5,5,8a-tetramethyldecahydro-1-naphthalenyl](methoxy-)-methyl]-benzenol (**5**)

Repeated silica-gel column fractionation of the solvent extract of *G. salicornia* yielded substituted drimane derivative, **5** that was characterised as 13-[[2-(hexyloxy)-2,5,5,8a-tetramethyldecahydro-1-naphthalenyl](methoxy)methyl]benzenol. The molecular formula of **2** was inferred as $C_{28}H_{46}O_3$, using integrated mass (*m/z* 430) and comprehensive NMR data (Table 1, S1). Its six degrees of unsaturation was corroborated for two cyclic rings and aromatic ring. The HRESIMS experiment displayed the molecular ion peak at *m/z* 431.3528 $[M+H]^+$, (Figure 4.68) which along with NMR-IR spectroscopic analyses deduced its molecular formula as $C_{28}H_{47}O_3$ $[M+H]^+$ (Table 4.12).

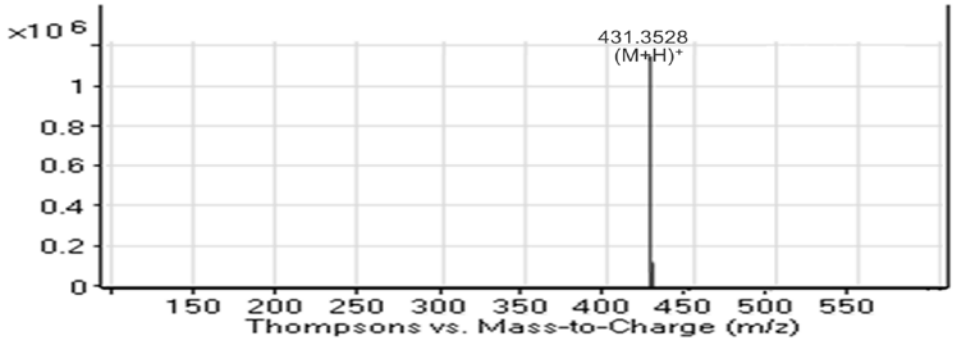

Figure 4.68.: HRESIMS spectrum of 13-[[2-(Hexyloxy)-2,5,5,8a-tetramethyldecahydro-1-naphthalenyl](methoxy-)-methyl]-benzenol (**5**)

The FTIR absorption peaks at 3402, 3028, 850, 1550 and 1120-1070 cm^{-1} suggested the probable presence of hydroxyl, aromatic and ether functionalities in the compound **5** (Figure 4.69). The ^{1}H-NMR spectrum of the studied compound showed singlet signals for four tertiary methyls at δ 1.22, 1.03, 1.00 and 1.02, which suggested the presence of tetramethyl groups (Figure 4.70).

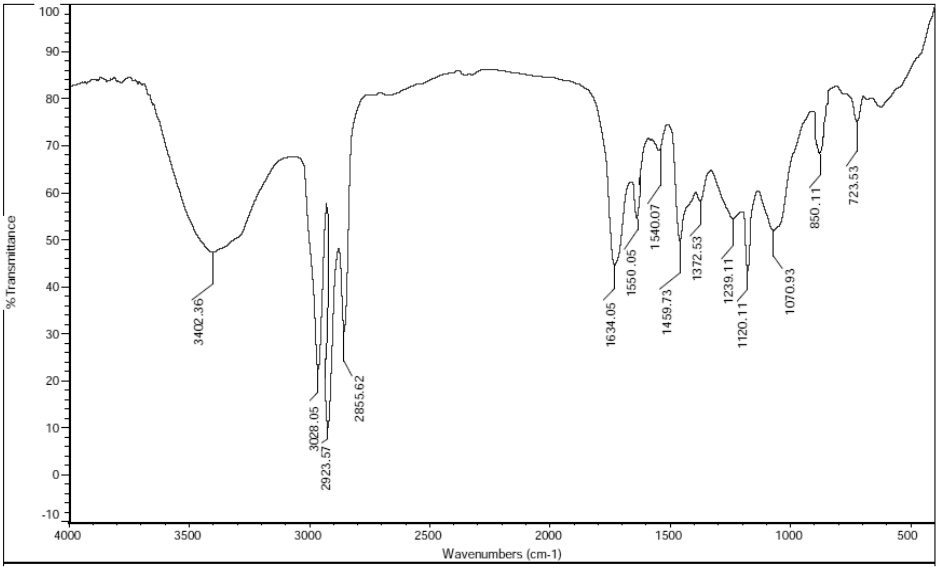

Figure 4.69.: FTIR spectrum of 13-[[2-(Hexyloxy)-2,5,5,8a-tetramethyldecahydro-1-naphthalenyl](methoxy-)-methyl]-benzenol (**5**)

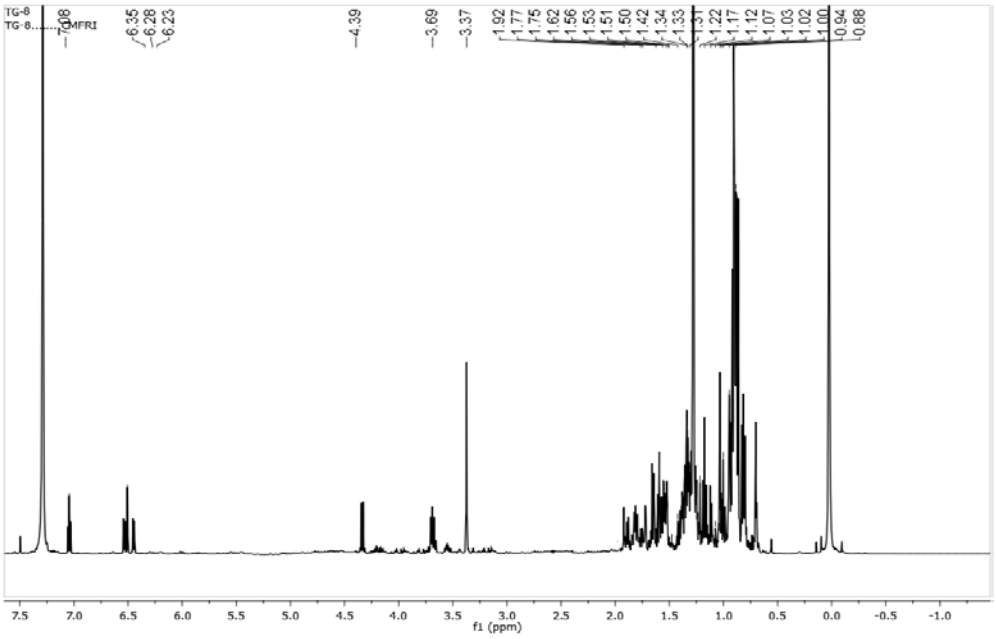

Figure 4.70.: ^{1}H-NMR spectrum of 13-[[2-(Hexyloxy)-2,5,5,8a-tetramethyldecahydro-1-naphthalenyl](methoxy-)-methyl]-benzenol (**5**)

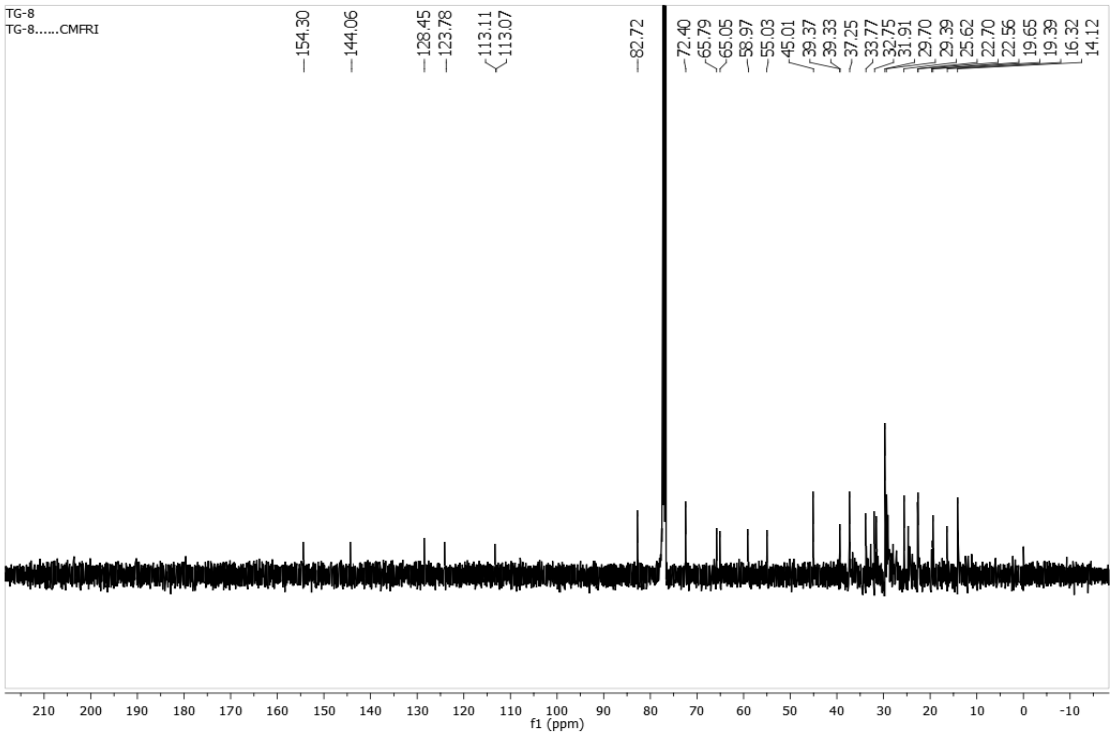

Figure 4.71.: ^{13}C-NMR spectrum of 13-[[2-(Hexyloxy)-2,5,5,8a-tetramethyldecahydro-1-naphthalenyl](methoxy-)-methyl]-benzenol (**5**)

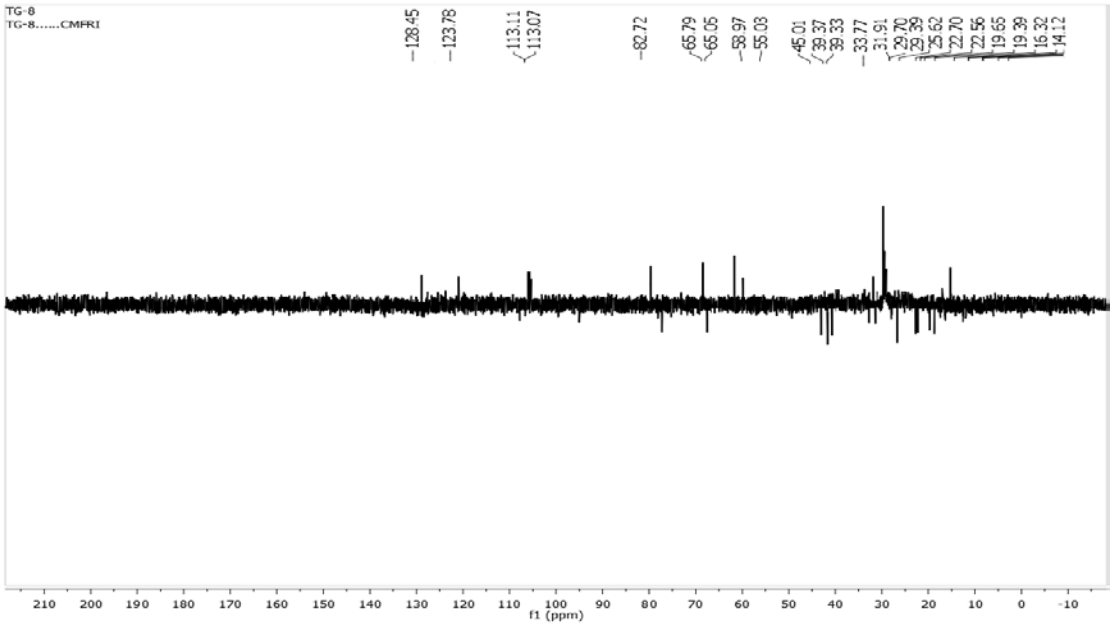

Figure 4.72.: ^{135}DEPT spectrum of 13-[[2-(Hexyloxy)-2,5,5,8a-tetramethyldecahydro-1-naphthalenyl](methoxy-)-methyl]-benzenol (**5**)

The spectrum also indicated the presence of four aromatic hydrogens at δ 6.35, 7.08, 6.23 and 6.28. The deshielded protons at δ 3.69 and 3.37 might be associated with an oxygenated functionality, such as ether linkage. The ^{13}C-NMR along with DEPT$_{135}$ spectra of **5** displayed the presence of 28 carbon signals, including six methyls (δ 22.5, 29.7, 29.3, 16.3, 14.1, 58.9), ten sp^3 methylenes (δ 39.3, 19.3, 45.0, 19.6, 39.4, 65.0, 31.9, 25.6, 33.7, 22.7), three sp^3 methines (δ 55.0, 65.7, 82.7), four sp^2 methines (δ 123.7, 128.4, 113.1, 113.0), and five quaternary carbons (δ 32.7, 72.4, 37.2, 144.0, 154.3) (Figure 4.71 & 4.72). These data was further supported by HSQC spectrum analysis (Figure 4.73).

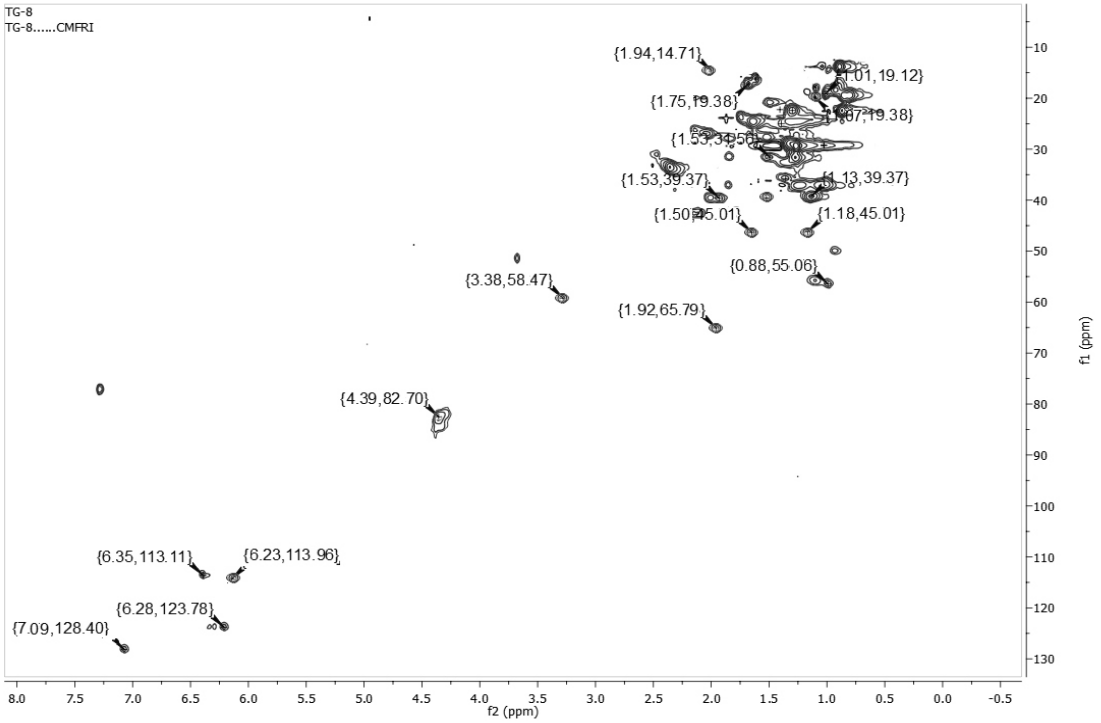

Figure 4.73.: HSQC spectrum of 13-[[2-(Hexyloxy)-2,5,5,8a-tetramethyldecahydro-1-naphthalenyl](methoxy-)-methyl]-benzenol (**5**)

The COSY spectrum of **5** suggested the presence of spin systems, such as δ (1.51)-(1.75)-(1.50) and δ (0.88)-(1.42)-(1.77), which corresponds to the partial structure of bicyclic ring from H-8/H-7/H-6 and H-4a/H-4/H-3, respectively (Figure 4.74 & 4.75). The HMBCs from CH_3-9 (δ 1.22) to C-2 (δ_C 72.4); CH_3-10 (δ 1.03) and CH_3-11 (δ1.00) to C-5 (δ 32.7); and from CH_3-12 (δ 1.02) to C-8a (δ 37.2) demonstrated the methyl substitutions at C-2, C-5 and C-8a (Figure 4.76).

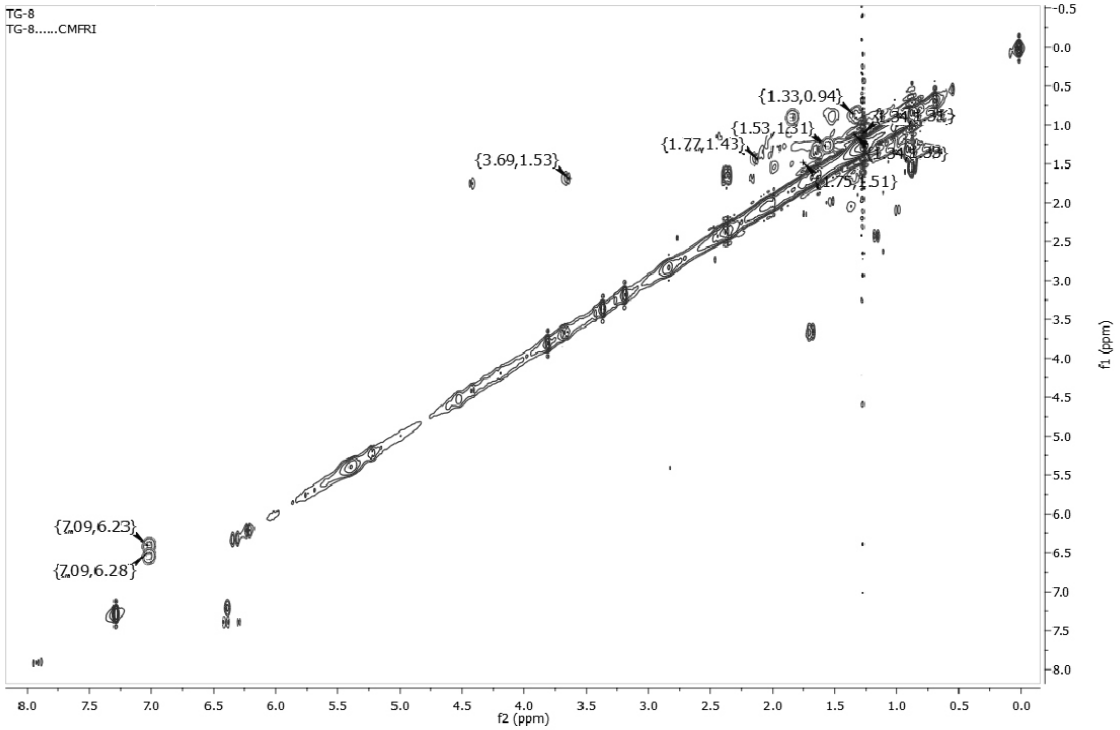

Figure 4.74.: ^{1}H-^{1}H COSY spectrum of 13-[[2-(Hexyloxy)-2,5,5,8a-tetramethyldecahydro-1-naphthalenyl](methoxy-)-methyl]-benzenol (**5**)

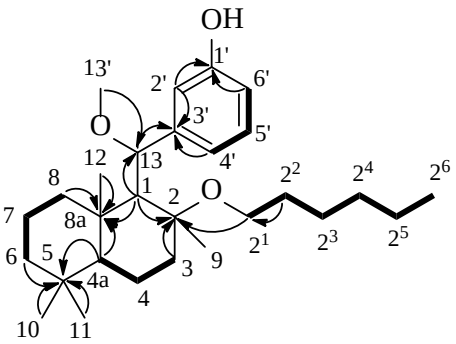

Figure 4.75.: ^{1}H-^{1}H COSY (bold face bonds), and selected HMBCs (double-barbed arrows), correlations of 13-[[2-(Hexyloxy)-2,5,5,8a-tetramethyldecahydro-1-naphthalenyl](methoxy-)-methyl]-benzenol (**5**)

The NMR spectroscopic investigations along with previous studies suggested the basic skeleton of **5** as a drimane sesquiterpenoid (Hui et al., 2015; Cao et al., 2004). The aromatic region of the proton spectrum exhibited an integral four in which one singlet, two doublets and one triplet were accounted. The greatly deshielded carbon signal at δ 154.3 (assigned as C-1') supported the presence of hydroxylated functionality at that position. The spin systems among the aromatic protons from δ (6.35)-(7.08)-(6.23) {H-4'/H-5'H-6'} suggested the

occurrence of 1,3-disubstituted aromatic ring. The HMBC correlations from CH-4' (δ 6.35) to C-3' (δ 144.0); from CH-6' (δ 6.23) to C-1' (δ 154.3) and CH-2' (δ 6.28) to C-3' (δ 144.0), C-1' (δ 154.3) attributed the possibilities of hydroxylated aromatic ring system. The strong HMBCs from δ 4.39 (H-13) to δ 144.0 (C-3') of benzene ring supported the attachment of hydroxybenzene to methine of the driamane skeleton located at C-13 position. Other spin systems from δ (3.69)-(1.53)-(1.31)-(1.34)-(1.33)-(0.94) assigned the continuous linear chain of hexane from H-2^1 to H-2^6 in which H-2^1 was found to be oxygenated, hence named as hexyloxy chain, the latter was linked at C-2 of the basic drimane skeleton as it recorded strong HMBCs from CH-2^1 (δ 3.69) to C-2 (δ 72.4). On the basis of 1D and 2D experimental data, the basic core of compound **5** strongly resembled to the quinol associated drimane sesquiterpene system (Perez-Garcia et al., 2005).

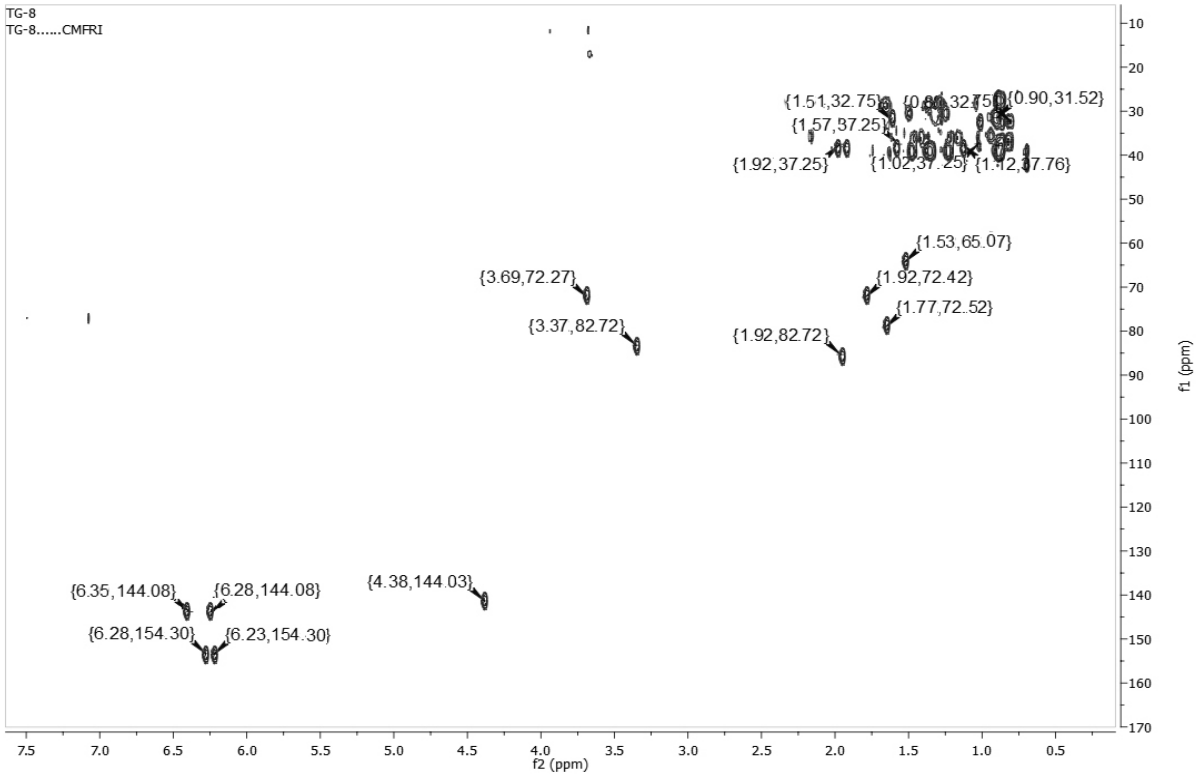

Figure 4.76.: HMBC spectrum of 13-[[2-(Hexyloxy)-2,5,5,8a-tetramethyldecahydro-1-naphthalenyl](methoxy-)-methyl]-benzenol (**5**)

Relative stereochemistries of the chiral centers at C-1, C-2, C-4a, C-5, C-8a and C-13 in **2** were assigned by NOESY experiments (Figure 4.77 & 4.78). The NOESY spectrum demonstrated that the protons δ 1.02 (H-12)/1.42 (Hβ-4)/1.22 (H-9) and δ 1.42 (Hβ-4)/1.03 (H-

10) displayed similar spatial correlations, and these protons were located in identical molecular reference plane, thus arbitrarily assigned as β-oriented. The NOESY correlations at δ 4.39 (H-13)/1.00 (H-11)/0.88 (H-4a), 1.17 (Hα-6), 1.92 (H-1) were found to be trans oriented to the β-protons, and therefore, assigned as α-protons.

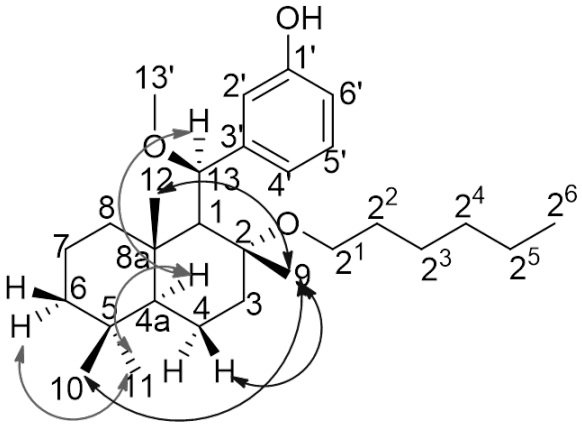

Figure 4.77.: NOE correlations of 13-[[2-(Hexyloxy)-2,5,5,8a-tetramethyldecahydro-1-naphthalenyl](methoxy-)-methyl]-benzenol (**5**)

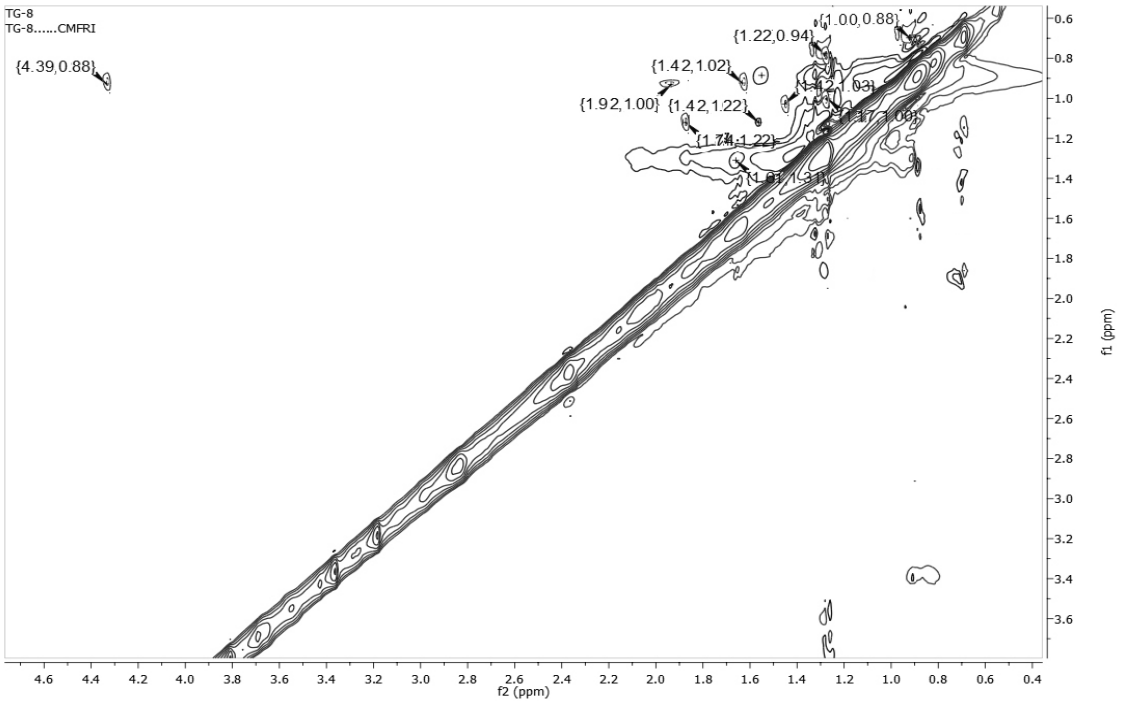

Figure 4.77.: NOE spectrum of 13-[[2-(Hexyloxy)-2,5,5,8a-tetramethyldecahydro-1-naphthalenyl](methoxy-)-methyl]-benzenol (**5**)

Table 4.12: NMR spectroscopic data of 13-[[2-(Hexyloxy)-2,5,5,8a-tetramethyldecahydro-1-naphthalenyl](methoxy-)-methyl]-benzenol (**5**)

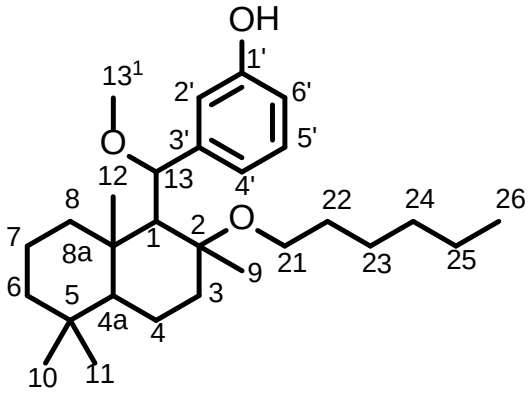

Compound **5**…….13-[[2-(Hexyloxy)-2,5,5,8a-tetramethyldecahydro-1-naphthalenyl](methoxy-)-methyl]-benzenol (**5**)

C. No.	^{13}C -NMR	H. int., mult., J in Hz‡	^{1}H-NMR	COSY	HMBC
1	65.7	1H, d, J = 8.0 Hz	1.92	-	C-2,8a,13
2	72.4	-	-	-	-
3	39.3	1H, m	1.77	H-4	C-2
		1H, m	1.56	-	-
4	19.6	1H, m	1.62	H-4a	-
		1H, m	1.42	-	-
4a	55.0	1H, dd, J = 1.8, 12.2 Hz	0.88	-	C-5,8a
5	32.7	-	-	-	-
6	45.0	1H, td, J = 13.5, 4.1 Hz	1.50	H-7	C-5
		1H, td, J = 12.9, 4.2 Hz	1.17	-	-
7	19.3	1H, m	1.75	H-8	-
		1H, m	1.07	-	-
8	39.4	1H, t, J = 12.0 Hz	1.51	-	-
		1H, t, J = 12.0 Hz	1.12	-	C-8a
8a	37.2	-	-	-	
9	22.5	3H, s	1.22	-	C-2
10	29.7	3H, s	1.03	-	C-5
11	29.3	3H, s	1.00	-	C-5
12	16.3	3H, s	1.02	-	C-8a
13	82.7	1H, d, J = 8.2 Hz	4.39	-	C-3’
13^1	58.9	3H, s	3.37	-	C-13
1’	154.3	-	-	-	-
2’	113.0	1H, s	6.28	-	C-1’,3’
3’	144.0	-	-	-	-
4’	123.7	1H, d, J = 12.1 Hz	6.35	H-5’	C-3’
5’	128.4	1H, t, J = 13.2 Hz	7.08	H-6’	-
6’	113.1	1H, d, J = 13.1 Hz	6.23	-	C-1’
2^1	65.0	2H, m	3.69	H-2^2	C-2
2^2	31.9	2H, m	1.53	H-2^3	-
2^3	25.6	2H, m	1.31	H-2^4	-

2^4	33.7	2H, m	1.34	H-2^5	-
2^5	22.7	2H, m	1.33	H-2^6	-
2^6	14.1	3H, t, J = 6.7 Hz	0.94	-	-

‡ Values in ppm, multiplicity and coupling constants (J= Hz) were indicated in parentheses. Multiplicities were allocated by ^{135}DEPT NMR spectrum.

The assignments were made with the aid of the COSY, HSQC, HMBC and NOESY experiments.

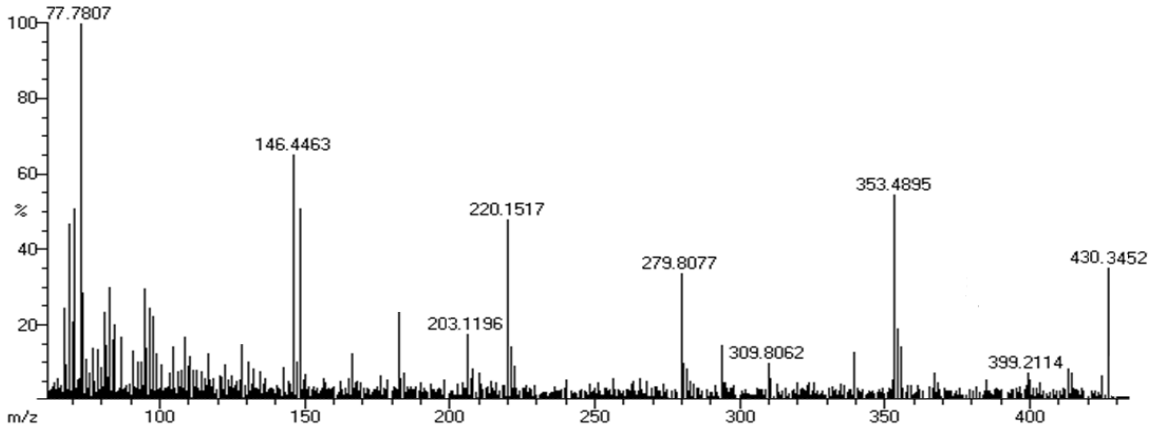

Figure 4.78.: EI-MS spectrum of 3-(Hept-3^6-enyloxy)-2,3,4,4a,5,6,6a,12,12a,12b-decahydro-4,6a,12a,12b-tetramethyl-*1H*-benzo[a]xanthene-4,10,12-triol (**5**)

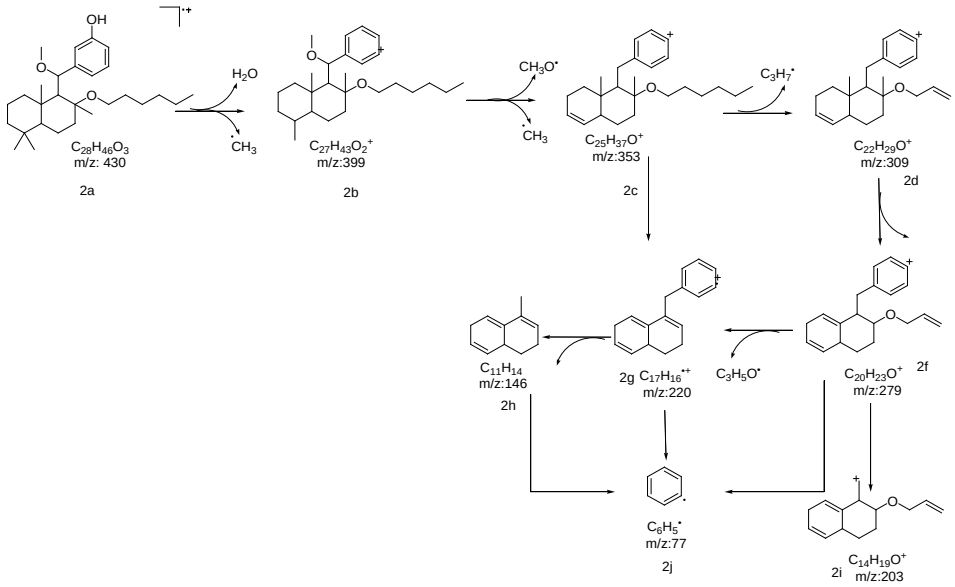

Figure 4.80.: Mass fragmentation pattern of 3-(Hept-3^6-enyloxy)-2,3,4,4a,5,6,6a,12,12a,12b-decahydro- 4,6a,12a,12b-tetramethyl-*1H*-benzo[a]xanthene-4,10,12-triol (**5**)

The structure elucidation of **5** was corroborated by the mass spectral experiment, wherein the molecular ion peak at *m/z* 430 (2a) experienced the removal of a methyl-radical and H_2O to yield $C_{27}H_{43}O_2^{\bullet+}$ (2b) with *m/z* 399. The elimination of $CH_3O^{\bullet}$ and $^{\bullet}CH_3$ from 2b resulted in the formation of $C_{25}H_{37}O^{\bullet+}$ with *m/z* 353 (2c). The fragment at *m/z* 309 (2d) underwent further series of fragmentation to result *m/z* 77 (2j) as the base peak, which was found to correspond the phenyl radical ($C_6H_5^{\bullet}$) (Figure 4.79 & 4.80). The NMR assignments along with mass spectroscopic data unambiguously constructed the structure of drimane sesquiterpene with substituted [(naphthalenyl)(methoxy)methyl]benzenol framework of the studied compound (**5**).

4.3.2.3c Structural characterization of Compound 6

1-Butoxy-4,4,11b,11c-tetramethyl-1,2,3,3a,4,5,6,6a,11b,11c-decahydrobenzo[kl]-xanthen-10-ol

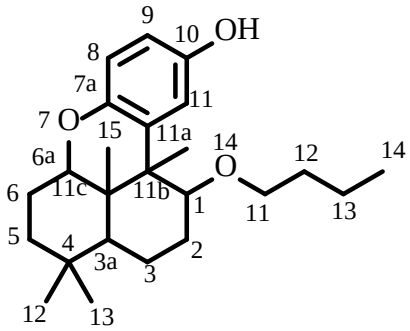

Sample yield	0.32 % (> 99% purity, RP-C18 HPLC)
Physical description	Yellowish oil
Molecular formula	$C_{24}H_{36}O_3$
Molecular mass	372.2664

The drimane class of diterpenoid derivative, 1-butoxy-4,4,11b,11c-tetramethyl-1,2,3,3a,4,5,6,6a,11b,11c-decahydrobenzo[kl]-xanthen-10-ol (**6**) was isolated as yellowish-white amorphous compound. The compound (**6**) has exhibited UV absorbance (UV (MeOH) λ_{max}) at 283 nm (Figure 4.81.). The homogeneity of the compound was ascertained by HPLC data on a bonded phase octadecylsilane (C_{18}) stationary phase (HPLC, MeCN/MeOH, 1:2 v/v) with R_t: 4.20 min (Figure 4.82.).

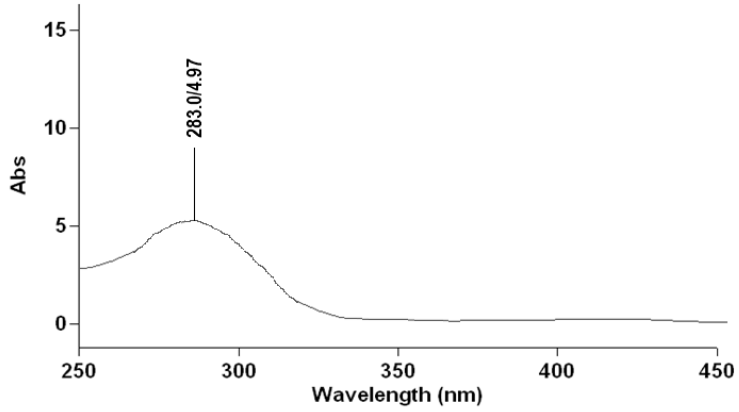

Figure 4.81.: UV spectrum of 1-butoxy-4,4,11b,11c-tetramethyl-1,2,3,3a,4,5,6,6a,11b,11c-decahydrobenzo[kl]-xanthen-10-ol (**6**)

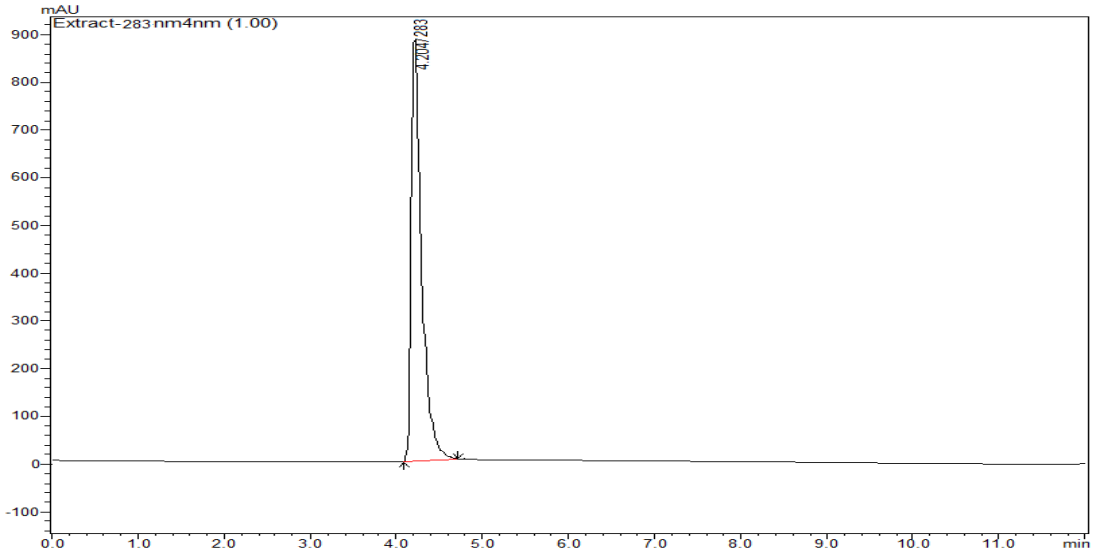

Figure 4.82.: HPLC chromatogram of 1-butoxy-4,4,11b,11c-tetramethyl-1,2,3,3a,4,5,6,6a,11b,11c-decahydrobenzo[kl]-xanthen-10-ol (**6**)

Repeated chromatographic fractionation of the organic solvent extract of *G. salicornia* resulted to substituted drimane derivative, **6** that was characterised as 1-butoxy-4,4,11b,11c-tetramethyl-1,2,3,3a,4,5,6,6a,11b,11c-decahydrobenzo[*kl*]xanthen-10-ol. The molecular formula of **5** was inferred as $C_{24}H_{36}O_3$, using integrated mass (*m/z* 372) and NMR experiments (Table 4.13). Its seven degrees of unsaturations were corroborated to three ring systems and one aromatic ring. The HRESIMS experiment displayed the molecular ion peak at *m/z* 373.3746 $[M+H]^+$, (Figure 4.83).

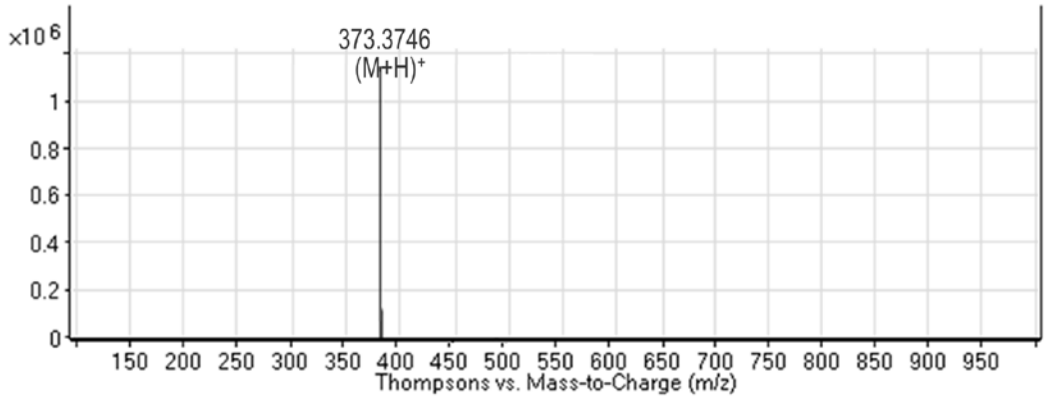

Figure 4.83.: HRESIMS spectrum of 1-butoxy-4,4,11b,11c-tetramethyl-1,2,3,3a,4,5,6,6a,11b,11c-decahydrobenzo[kl]-xanthen-10-ol (**6**)

The FTIR absorption peaks at 3412, 3026, 854, 1560 and 1115-1043 cm^{-1} assigned the occurrences of hydroxyl, aromatic and ether functionalities (Figure 4.84). The ^{1}H-NMR showed signals of four tertiary methyls at δ 1.37, 1.00, 0.98 and 1.15, which were typical of the drimane sesquiterpene framework (Hagiwara et al., 2015) (Figure 4.85).

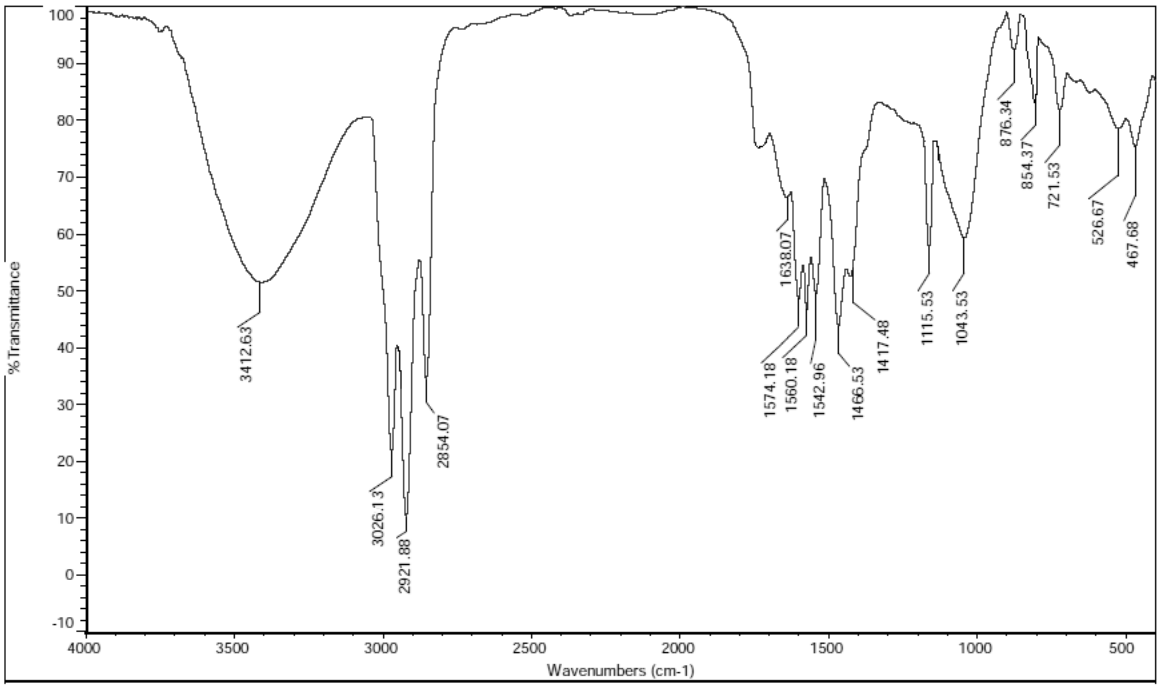

Figure 4.84.: FTIR spectrum of 1-butoxy-4,4,11b,11c-tetramethyl-1,2,3,3a,4,5,6,6a,11b,11c-decahydrobenzo[kl]-xanthen-10-ol (**6**)

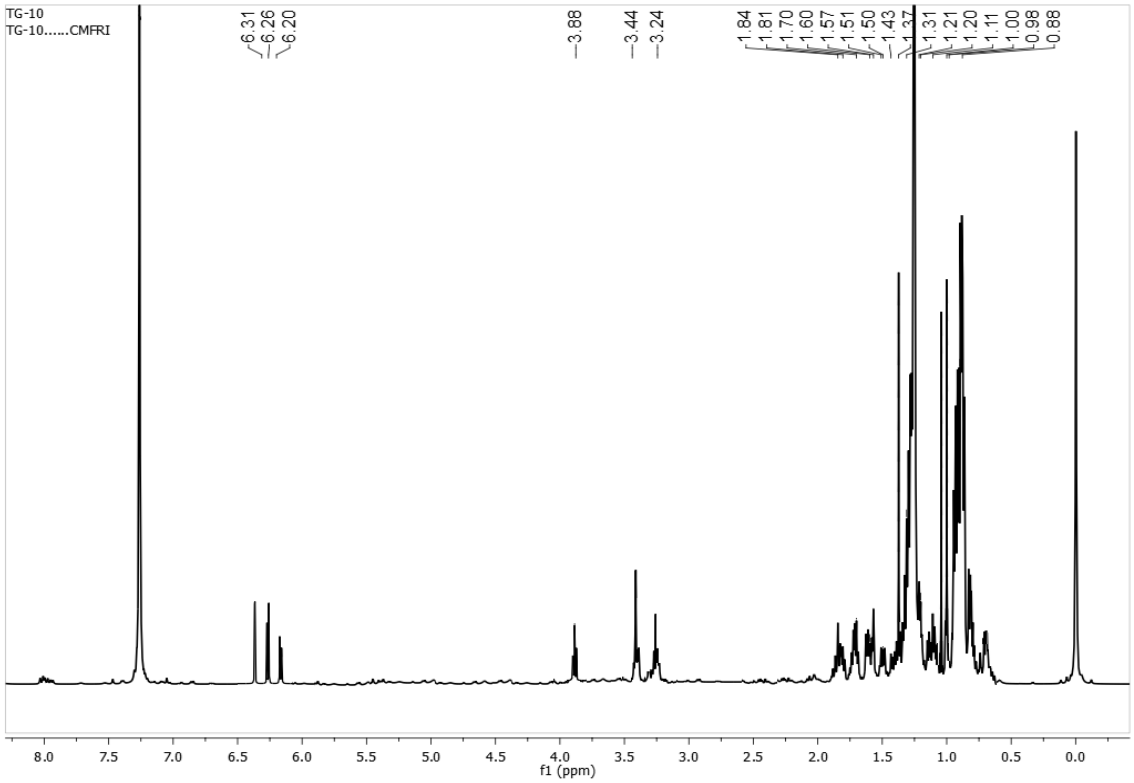

Figure 4.85.: ^{1}H-NMR spectrum of 1-butoxy-4,4,11b,11c-tetramethyl-1,2,3,3a,4,5,6,6a,11b,11c-decahydrobenzo[kl]-xanthen-10-ol (**6**)

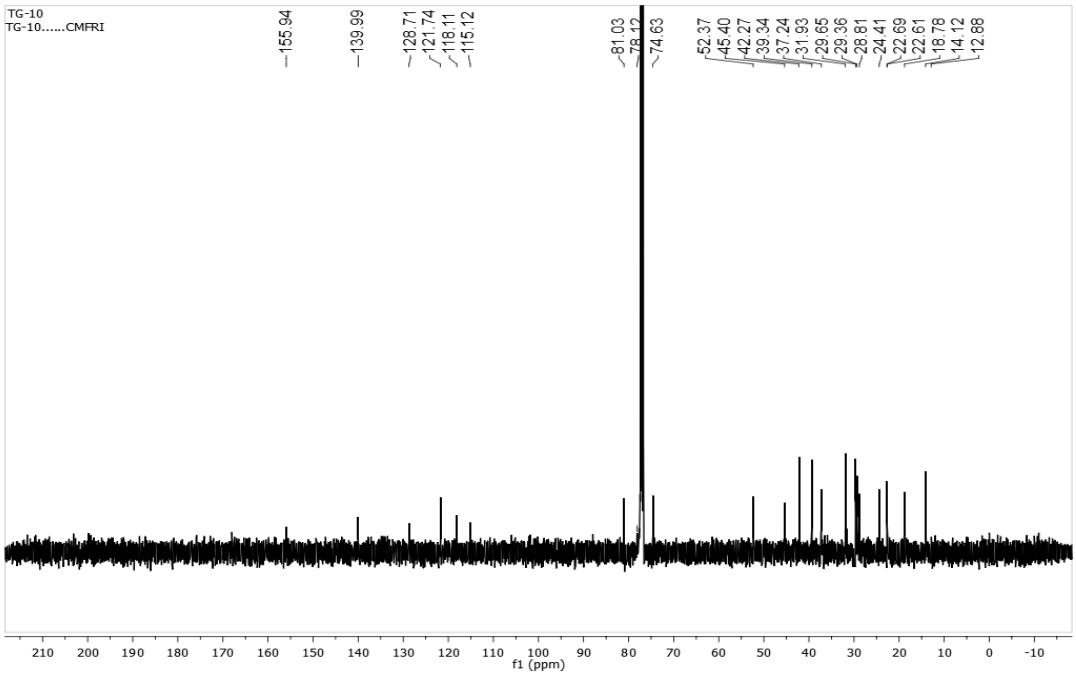

Figure 4.86.: ^{13}C-NMR spectrum of 1-butoxy-4,4,11b,11c-tetramethyl-1,2,3,3a,4,5,6,6a,11b,11c-decahydrobenzo[kl]-xanthen-10-ol (**6**)

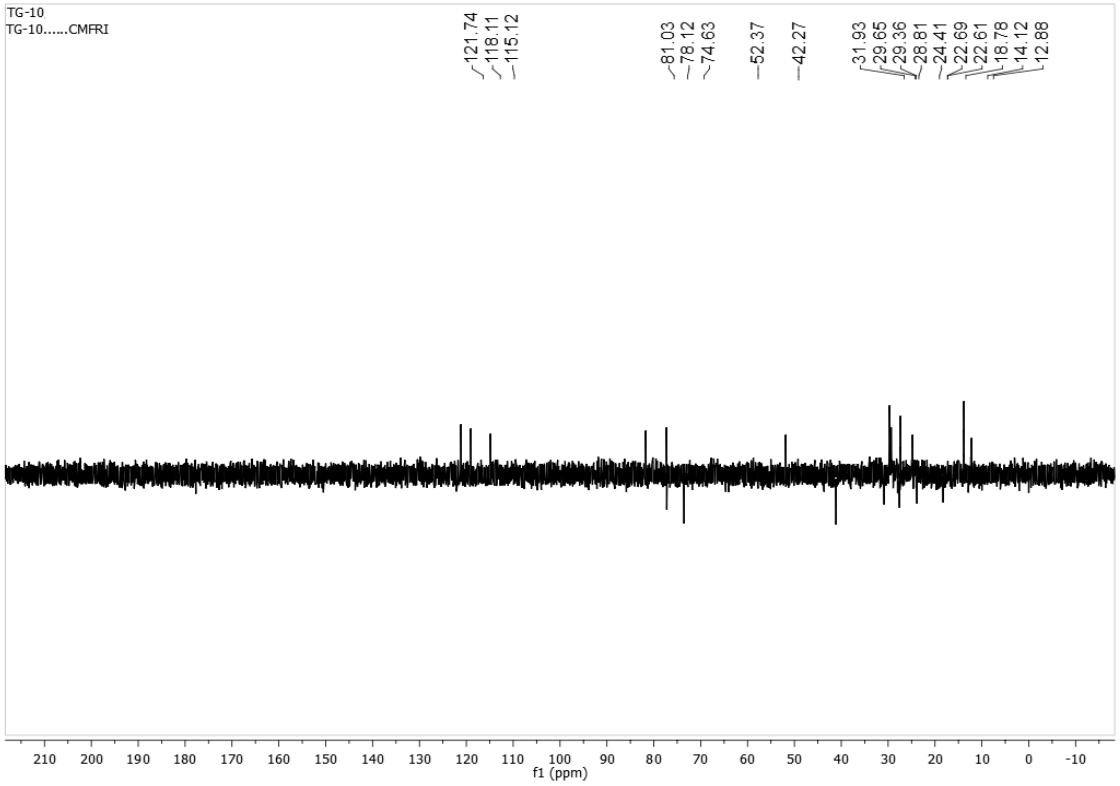

Figure 4.87.: ^{135}DEPT spectrum of 1-butoxy-4,4,11b,11c-tetramethyl-1,2,3,3a,4,5,6,6a,11b,11c-decahydrobenzo[kl]-xanthen-10-ol (**6**)

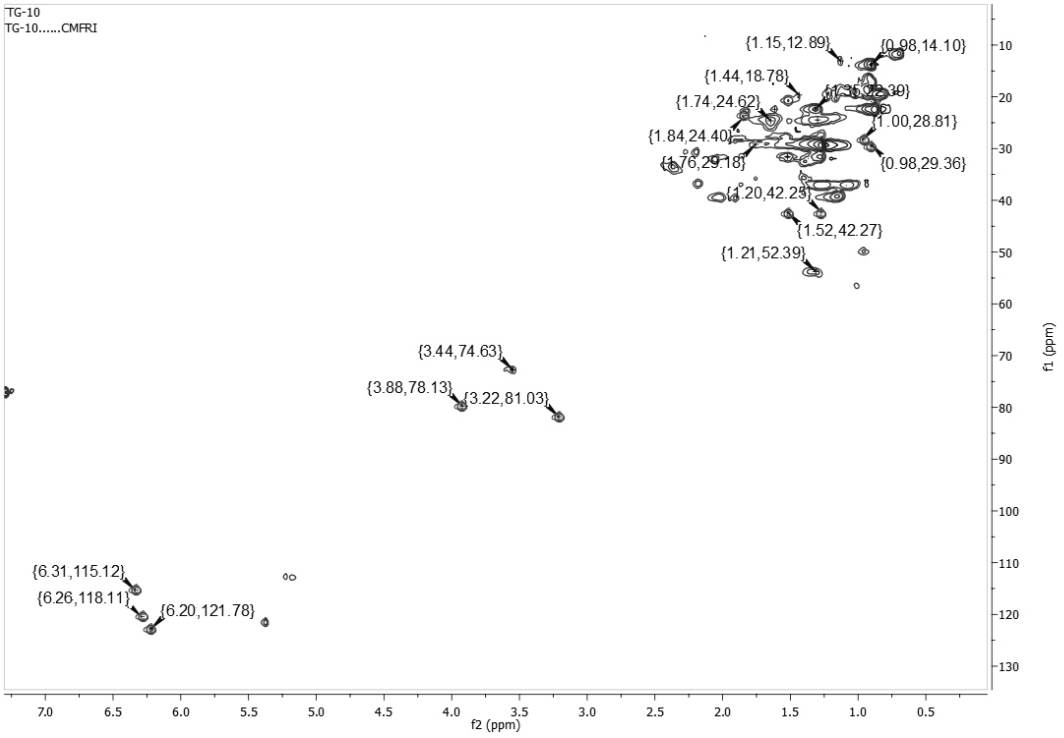

Figure 4.88.: HSQC spectrum of 1-butoxy-4,4,11b,11c-tetramethyl-1,2,3,3a,4,5,6,6a,11b,11c-decahydrobenzo[kl]-xanthen-10-ol (**6**)

The spectrum also indicated the presence of three aromatic hydrogens at δ 6.31, 6.26, and 6.20. In addition, a methyl triplet at δ 0.88 suggested the occurrence of terminal methyl substitution. The ^{13}C-NMR along with DEPT$_{135}$ spectra of **6** displayed the presence of 24 carbon signals, including five methyls (δ 22.6, 28.8, 29.3, 12.8, 14.1), seven sp^3 methylenes (δ 24.4, 42.2, 22.7, 29.6, 74.6, 31.9, 18.7), three each of sp^3 methines (δ 81.0, 78.1, 52.3) and sp^2 methines (δ 115.1, 118.1, 121.7) along with six quaternary carbons (δ 37.2, 45.4, 39.3, 128.7, 139.9, 155.9) (Figure 4.86 & 4.87). These data were further corroborated by HSQC spectral information (Figure 4.88).

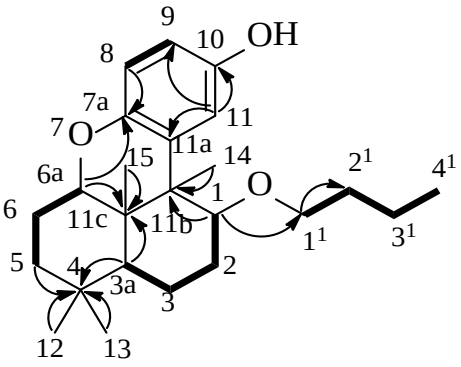

Figure 4.89.: ^{1}H-^{1}H COSY (bold face bonds), and selected HMBCs (double-barbed arrows) of 1-butoxy-4,4,11b,11c-tetramethyl-1,2,3,3a,4,5,6,6a,11b,11c-decahydrobenzo[kl]-xanthen-10-ol (**6**)

The COSY spectrum of **6** assigned the occurrences of four individual spin units, I: δ (3.20)-(1.84)-(1.51) and II: δ (1.21)-(1.57)-(1.81)-(3.88), which were accounted for the partial structure of the bicyclic ring; III: δ (6.26)-(6.20) corresponding to the aromatic ring part, and IV: δ (3.44)-(1.50)-(1.43)-(0.88) was accounted for the presence of butoxy chain (Figure 4.89 & 4.90). The HMBC correlations from CH-6a (δ 3.20) to C-11c (δ 39.3); from CH_2-5 (δ 1.20) and CH-3a (δ 1.21) to C-4 (δ 37.2); from CH-3a (δ 1.21) to C-11c (δ 39.3) and from CH-1 (δ 3.88) to C-11b (δ 45.4) appropriately suggested the complete structure of bicyclic drimane skeleton (Figure 4.91). Other key HMBCs were assigned from CH_3-12 (δ 1.00) and CH_3-13 (δ 0.98) to C-4 (δ 37.2); from CH_3-15 (δ 1.15) to C-11c (δ 39.3) and from CH_3-14 (δ 1.37) to C-11b (δ 45.4), which attributed the methyl substitutions at C-4, C-11c and C-11b. The greater deshielded signal at δ 155.9 was found to be due to the aromatic hydroxyl, whereas the aromatic proton integral of three suggested the possibility of trisubstituted aromatic ring in **6**. Other HMBCs from CH-11 (δ 6.31) to C-11a (δ 128.7), C-9 (δ 121.7), C-10 (δ 155.9) and from CH-8 (δ 6.26) to C-7a (δ 139.9) attributed to the occurrence of hydroxybenzene ring functionality.

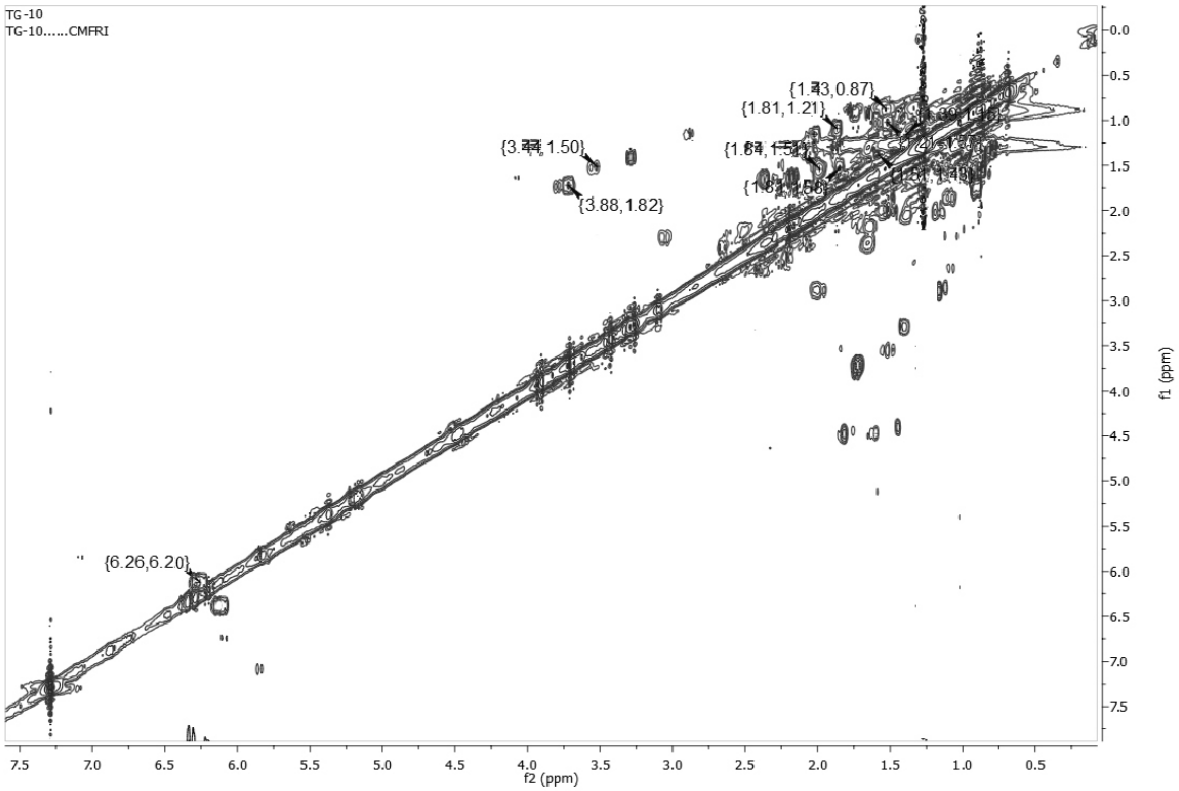

Figure 4.90.: ^{1}H-^{1}H COSY spectrum of 1-butoxy-4,4,11b,11c-tetramethyl-1,2,3,3a,4,5,6,6a,11b,11c-decahydrobenzo-[kl]-xanthen-10-ol (**6**)

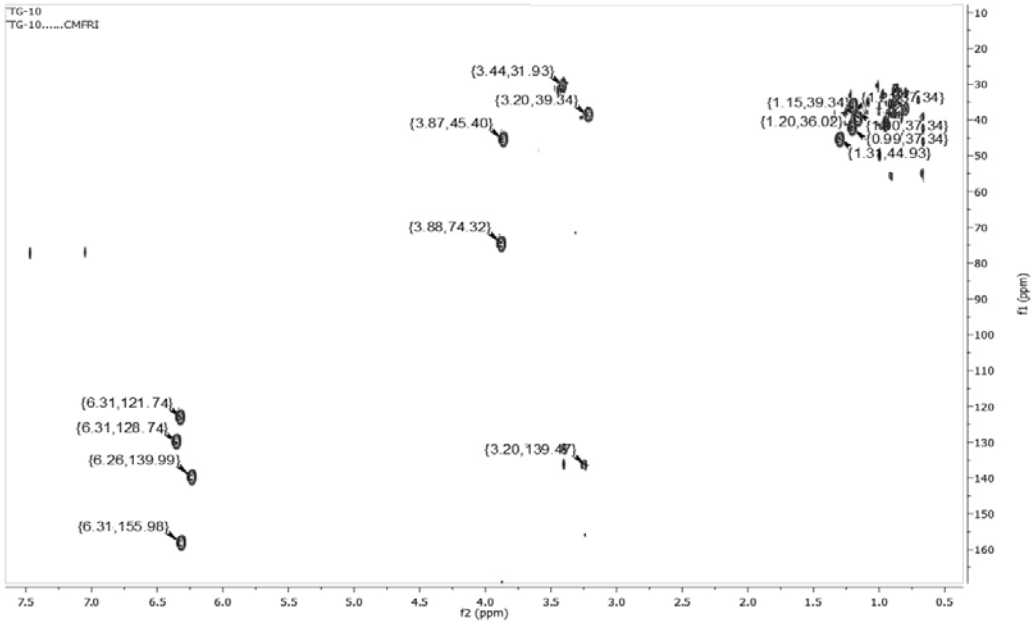

Figure 4.91.: HMBC spectrum of 1-butoxy-4,4,11b,11c-tetramethyl-1,2,3,3a,4,5,6,6a,11b,11c-decahydrobenzo[kl]-xanthen-10-ol (**6**)

The strong HMBC correlation from CH-6a (δ 3.20) to C-7a (δ 139.9) supported the attachment of drimane skeleton to the aromatic ring through an ether linkage. The butoxy side chain was attached at C-1 of the quinol associated drimane sesquiterpene, and this attribution was confirmed through strong HMBCs from CH-1 (δ 3.88) to C-1^1 (δ 74.6). The compound **6** was structurally related to the previously reported quinol fused drimane sesquiterpenes (Mitome et al., 2003; Hagiwara et al., 2015) and compound **4** except the dissimilarities perceived in the NMR signals due to the ether substitutions of the tetracyclic core, and also in the position and number of the methyl functionalities.

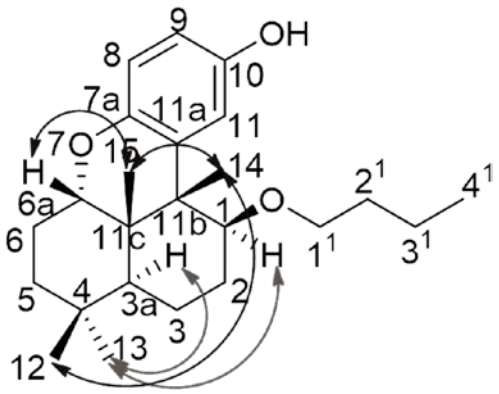

Figure 4.92.: NOE (double barbed arrows) correlations of 1-butoxy-4,4,11b,11c-tetramethyl-1,2,3,3a,4,5,6,6a,11b,11c-decahydrobenzo[kl]-xanthen-10-ol (**6**)

The relative stereochemistries of the chiral centers at C-1, C-3a, C-4, C-6a, C-11b, and C-11c in **6** were designated through NOESY experiments (Figure 4.92 & 4.93). The NOESY correlations between δ 3.20 (H-6a)/1.15 (H-15)/1.37 (H-14)/1.00 (H-12) were found to be in the identical plane of symmetry, and therefore, were arbitrarily attributed as β-faced protons. Similarly, NOE correlations were exhibited by the proton at δ 0.98 (H-13) with those at δ 3.88 (H-1) and 1.21 (H-3a). These were found to be situated at the opposite plane of the β-protons, and thus, were assigned as α-disposed.

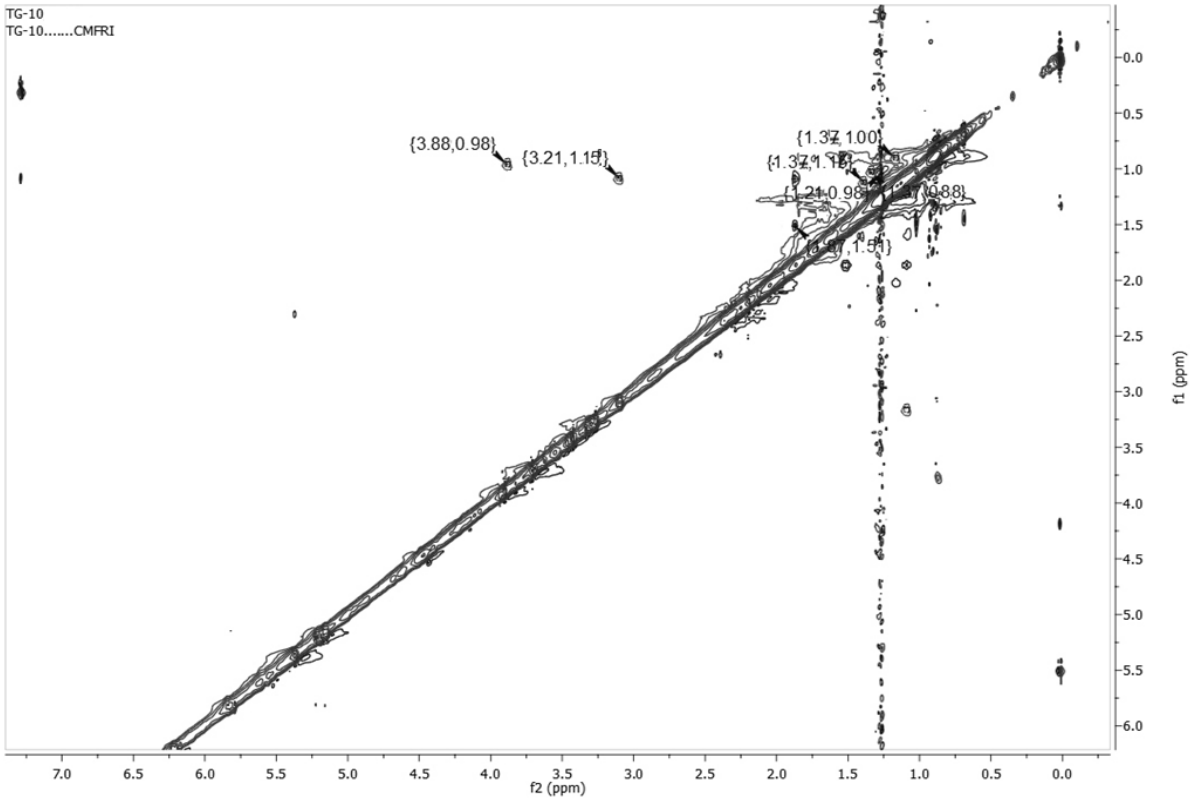

Figure 4.93.: NOESY spectrum of 1-butoxy-4,4,11b,11c-tetramethyl-1,2,3,3a,4,5,6,6a,11b,11c-decahydrobenzo[kl]-xanthen-10-ol (**6**)

Table 4.13: NMR spectroscopic data of compound (**6**), 1-butoxy-4,4,11b,11c-tetramethyl-1,2,3,3a,4,5,6,6a,11b,11c-decahydrobenzo[kl]-xanthen-10-ol (**6**)isolated from red seaweed *G. salicornia*

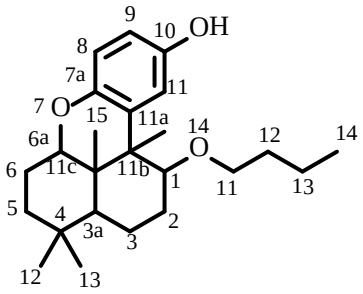

Compound **6** …….1-Butoxy-4,4,11b,11c-tetramethyl-1,2,3,3a,4,5,6,6a,11b,11c-decahydrobenzo[kl]-xanthen-10-ol (**6**)

C. No.	^{13}C-NMR	H. int., mult., J in Hz‡	^{1}H -NMR	COSY	HMBC
1	78.1	1H, t, J = 9.2 Hz	3.88	H-1	C-11b,1[1]
2	29.6	1H, m	1.81	H-3	-
		1H, m	1.60	-	-
3	22.7	1H, m	1.57	H-3a	-
		1H, m	1.31	-	-

3a	52.3	1H, dd, J = 1.9, 12.1 Hz	1.21	-	C-4,11c
4	37.2	-	-	-	-
5	42.2	1H, td, J = 13.2, 4.1 Hz	1.20	H-6	C-4
		1H, td, J = 13.2, 4.3 Hz	1.51	-	-
6	24.4	1H, t, J = 12.7, Hz	1.84	H-6a	-
		1H, t, J = 12.9, 4.2 Hz	1.70	-	-
6a	81.0	1H, t, J = 9.2 Hz	3.20	-	C-11c,7a
7a	139.9	-	-	-	-
8	118.1	1H, d, J = 13.1H	6.26	H-9	C-7a
9	121.7	1H, d, J = 13.2Hz	6.20	-	-
10	155.9	-	-	-	-
11	115.1	1H, s	6.31	-	C-11a,9,10
11a	128.7	-	-	-	-
11b	45.4	-	-	-	-
11c	39.3	-	-	-	-
12	28.8	3H, s	1.00	-	C-4
13	29.3	3H, s	0.98	-	C-4
14	22.6	3H, s	1.37	-	C11b
15	12.8	3H, s	1.15	-	C-11c
1^1	74.6	2H, t, J = 9.8 Hz	3.44	-	
1^2	31.9	2H, m	1.50	-	
1^3	18.7	2H, m	1.43	-	
1^4	14.1	3H, t, J = 6.8 Hz	0.88	-	

‡ Values in ppm, multiplicity and coupling constants (J= Hz) were indicated in parentheses. Multiplicities were allocated by ^{135}DEPT NMR spectrum.

The assignments were made with the aid of the COSY, HSQC, HMBC and NOESY experiments.

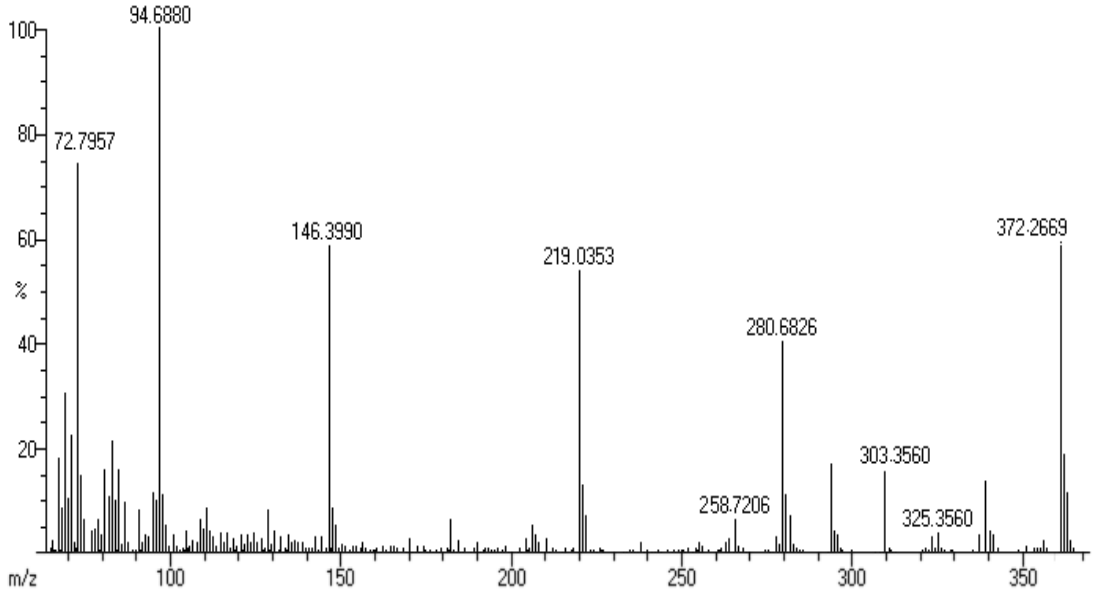

Figure 4.94.: EI-MS spectrum of 1-butoxy-4,4,11b,11c-tetramethyl-1,2,3,3a,4,5,6,6a,11b,11c-decahydrobenzo[kl]-xanthen-10-ol (**6**)

The structure elucidation of **3** was corroborated by the mass spectral experiment, wherein the molecular ion peak at *m/z* 372 (3a) experienced the elimination of a $C_2H_5^{\bullet}$ radical and H_2O to result the mass fragment $C_{22}H_{29}O_2^{+}$ (3b) with *m/z* 325. The removal of $C_2H_5O^{\bullet}$ from the latter could result in the formation of $C_{20}H_{24}O^{\bullet+}$ with *m/z* 280 (3c). The fragment (3d) with *m/z* 258 appeared to undergo further series of fragmentation to yield *m/z* 94, which was considered as the base peak (Figure 4.94 & 4.95).

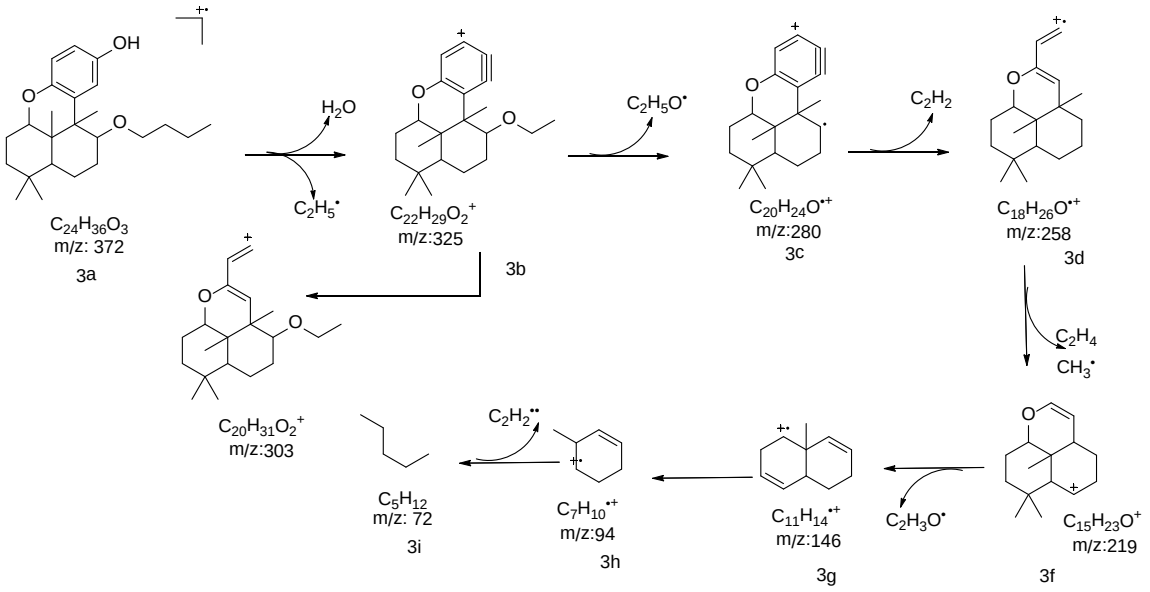

Figure 4.95.: Mass fragmentation pattern of 1-butoxy-4,4,11b,11c-tetramethyl-1,2,3,3a,4,5,6,6a,11b,11c-decahydrobenzo[kl]-xanthen-10-ol (**6**)

The organic solvent extract of the intertidal red saeweed, *G. salicornia* was fractionated by repeated techniques of chromatography to obtain three unprecedented drimane sesquiterpene quinol analogues. The isolated compounds, (**4**-**6**) were found to be bearing hydroxyl, benzene, ether and olefinic functionalities. Therefore, these metabolites can be used for the further analysis of biological activities.

4.3.2.4 Structural characterization of 2H-chromenyl derivative (Compounds 7-8)

Chromene analogues with natural and synthetic origin were identified as valuable pharmacophores exhibiting potential antioxidant (Milan et al. 2011) and anti-inflammatory (Nitin et al. 2012) activities. These oxygen heterocycles recognized greater attention due to their wide occurrence and broad pharmaceutical significance. Chromene analogues were found to constitute the basic backbone of bioactive polyphenols, alkaloids, tocopherols, flavonoids, and anthocyanins (Ren et al., 2011). Anti-inflammatory and antioxidative chromenyls with furanyl-2*H*-chromenyl and isochromenone derivatives were isolated and characterized from the marine organisms (Joy and Chakraborty, 2017a; Joy and Chakraborty, 2018). Bioactive secondary metabolites bearing oxygen heterocyclic analogues and sargachromanol A-P were recorded from the marine organisms (Jang et al. 2005, Joy & Chakraborty, 2017b). There were reports on the occurrences of chromenyl metabolites or chromenone-based skeletons, such as benzopyrans or benzopyrones from seaweeds (Davyt et al. 1997; El-Beih et al. 2007; Hwa et al. 2005; Iwashima et al. 2005). The natural chromene derivative (benzopyran), α-tocopherol possessing the 6-hydroxychromenol motif is a commonly used antioxidant agent with lipid peroxidation properties (Kindleysides et al. 2012, Birringer et al. 2018).

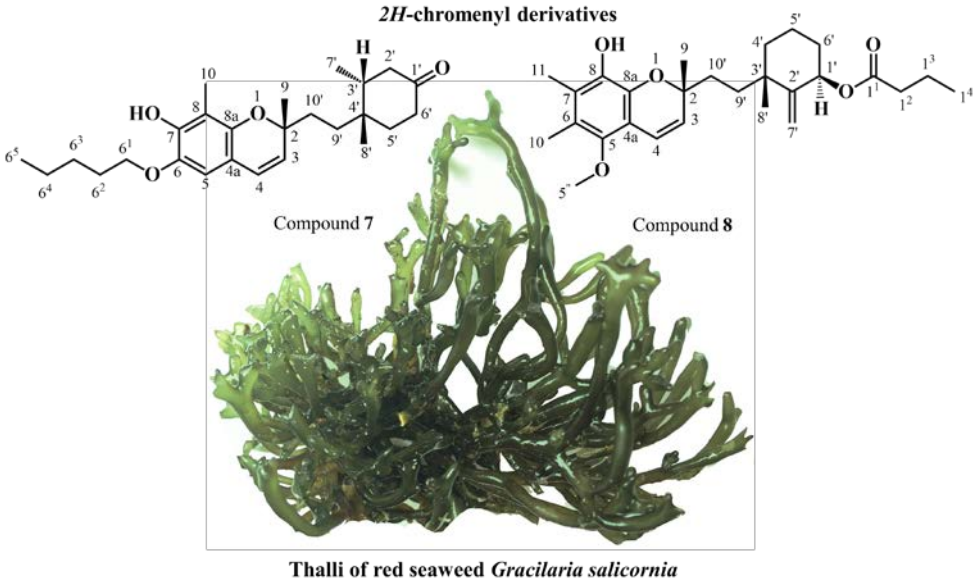

Figure 4.96.: Structures of 2*H*-chromenyl derivatives (**7**-**8**) isolated from the seaweed *Gracilaria salicornia*. The representative photograph of the thalli of *G. salicornia* was shown

Phytochemical investigation on red seaweeds reported different biological activities (Makkar and Chakraborty 2017a; Makkar and Chakraborty 2017b). It has been documented that the organic extracts of *Gracilaria* sp. (family Gracilariaceae) comprised bioactive secondary metabolites along with anti-inflammatory and antioxidant potentials (Antony and Chakraborty 2018; Makkar and Chakraborty 2018a; Makkar and Chakraborty 2018b. The current work described the separation and characterisation of chromene class of compounds, 4'-[10'-[7-hydroxy-2,8-dimethyl-6-(pentyloxy)-*2H*-chromen-2-yl]ethyl]-3',4'-dimethyl-cyclohexanone (**7**) and 3'-[10'-(8-hydroxy-5-methoxy-2,6,7-trimethyl-*2H*-chromen-2-yl)ethyl]-3'-methyl-2'-methylene cyclohexyl butyrate (**8**) from the EtOAc-MeOH (ethyl acetate-methanol) extract of *G. salicornia* collected from the southern coast of Indian peninsular (Figure 4.96).

4.3.2.4a Structural characterization of Compound 7

4'-[10'-[7-Hydroxy-2,8-dimethyl-6-(pentyloxy)-*2H*-chromen-2-yl]ethyl]-3',4'-dimethyl-cyclohexanone

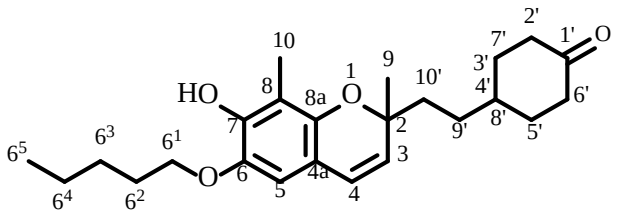

Sample yield	0.30% (> 99% purity, RP-C18 HPLC)
Physical description	Yellowish oil
Molecular formula	$C_{26}H_{38}O_4$
Molecular mass	414.2775

The *2H*-chromenyl derivative, 4'-[10'-[7-hydroxy-2,8-dimethyl-6-(pentyloxy)-*2H*-chromen-2-yl]ethyl]-3',4'-dimethyl-cyclohexanone was isolated as yellowish oil. The compound (**7**) has exhibited UV absorbance (UV (MeOH) λ_{max}) at 270 nm (Figure 4.97). The homogeneity of the compound was ascertained by HPLC data on a bonded phase octadecylsilane (C_{18}) stationary phase (HPLC, MeCN/MeOH, 3:2 v/v) with R_t: 2.93 min (Figure 4.98).

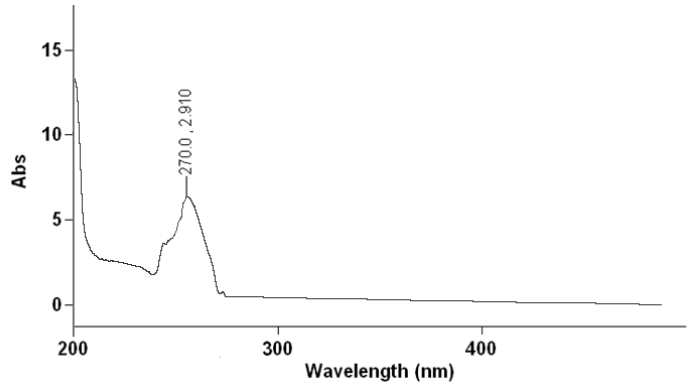

Figure 4.97.: UV spectrum of 4'-[10'-[7-Hydroxy-2,8-dimethyl-6-(pentyloxy)-*2H*-chromen-2-yl]ethyl]-3',4'-dimethyl-cyclohexanone (7)

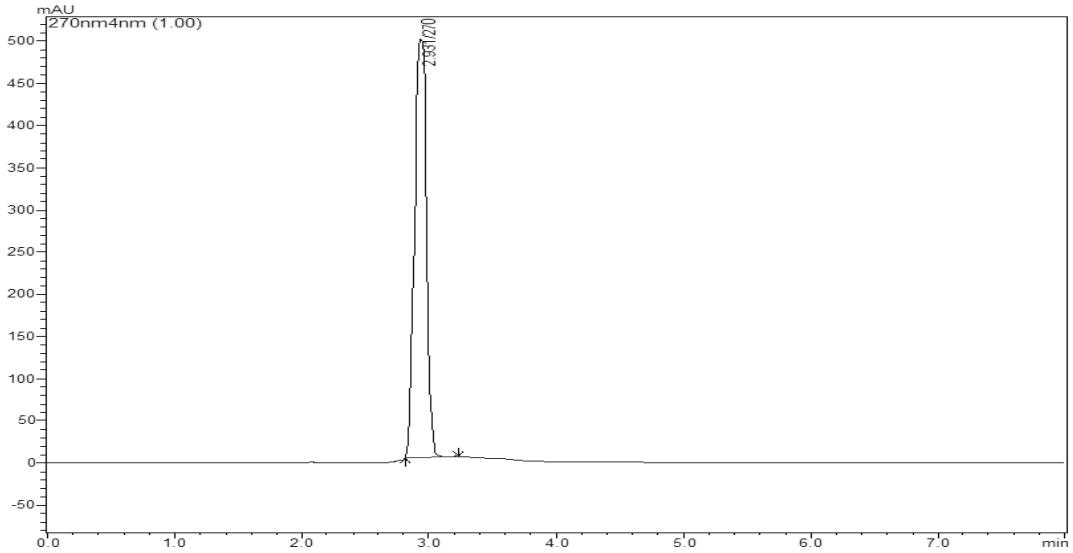

Figure 4.98.: HPLC chromatogram of 4'-[10'-[7-hydroxy-2,8-dimethyl-6-(pentyloxy)-*2H*-chromen-2-yl]ethyl]-3',4'-dimethyl-cyclohexanone (7)

Bioassay-assisted chromatographic fractionation of organic extract of *G. salicornia* yielded 4'-[10'-[7-hydroxy-2,8-dimethyl-6-(pentyloxy)-2*H*-chromen-2-yl]ethyl]-3',4'-dimethyl-cyclohexanone (**7**) as a yellowish oily substance, with about 99 % purity. The mass spectroscopic experiment displayed the molecular ion peak at *m/z* 414, which along with integrative NMR-IR spectroscopic experiments deduced its molecular formula as $C_{26}H_{38}O_4$ (Table 4.14). The HRESIMS experiment displayed the molecular ion peak at *m/z* 415.2852 $[M+H]^+$, (Figure 4.99).

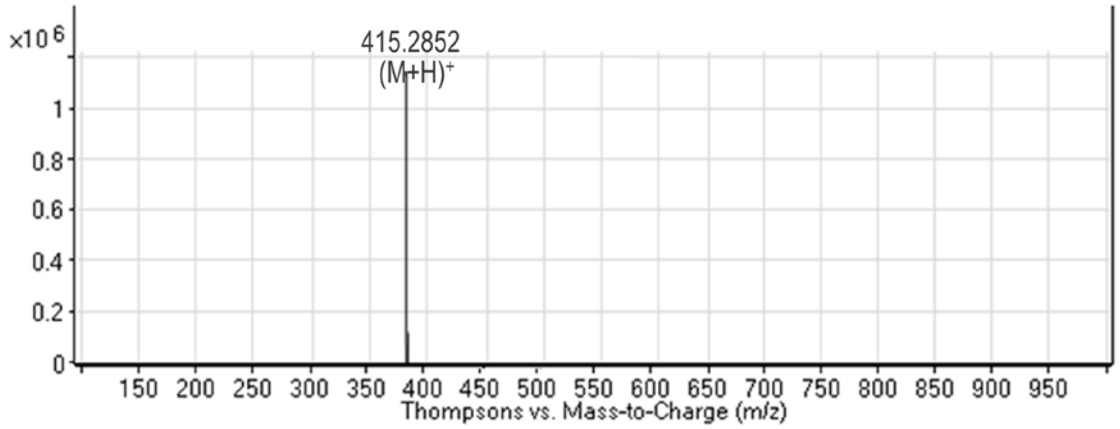

Figure 4.99.: HRESIMS spectrum of 4'-[10'-[7-Hydroxy-2,8-dimethyl-6-(pentyloxy)-*2H*-chromen-2-yl]ethyl]-3',4'-dimethyl-cyclohexanone (7)

The FTIR absorption peaks at 3430, 1727, 1732 and 1562 indicated the occurrences of hydroxyl, ether, carbonyl and aromatic ($C=C_{(aromatic)}$) functionalities, respectively (Figure 4.100). The ^{1}H-NMR experiments showed signals corresponding to methyl groups at δ 1.54 (3H, s), δ 2.35 (3H, s), δ 1.20 (3H, s) and δ 1.14 (3H, d, J=7.1Hz). The spectrum indicated the presence of greatly deshielded hydrogens at δ 6.07 (1H, d, J = 13.2 Hz), δ 6.33 (1H, d, J = 7.8 Hz) and δ 6.21 (1H, s), which might be related to alkene or aromatic protons (Figure 4.101).

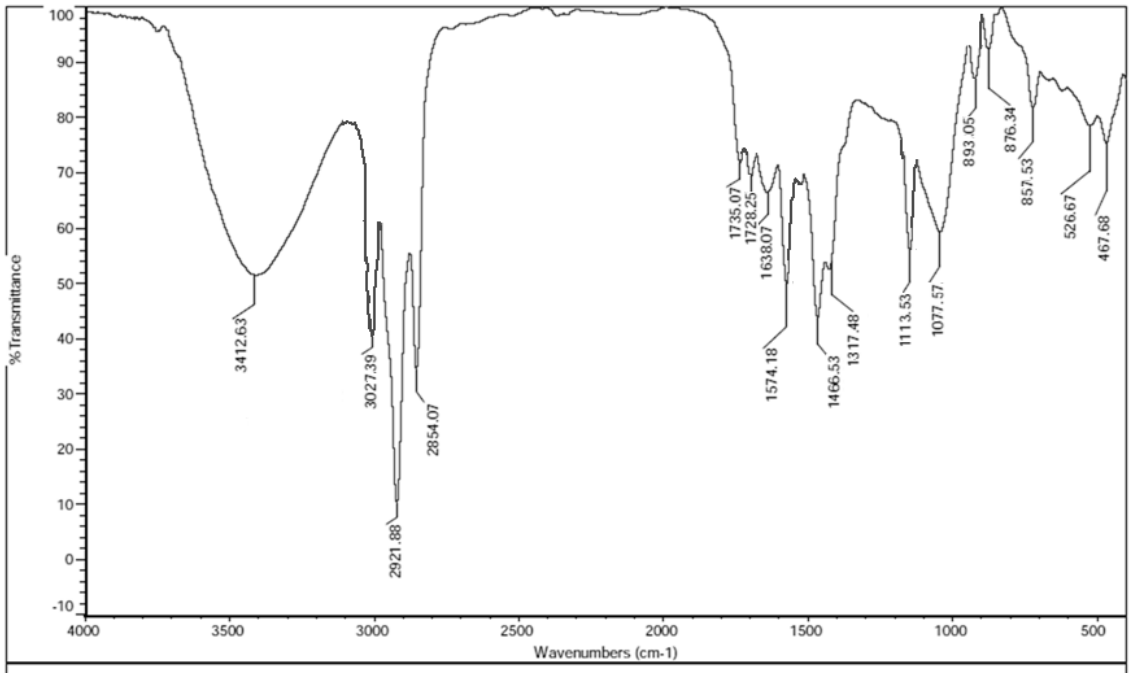

Figure 4.100.: FTIR spectrum of 4'-[10'-[7-Hydroxy-2,8-dimethyl-6-(pentyloxy)-*2H*-chromen-2-yl]ethyl]-3',4'-dimethyl-cyclohexanone (7)

The ^{13}C NMR spectrum along with $DEPT_{135}$ analysis deduced 26 carbon signals in the studied compound including the signals due to eight quaternary carbons (δ 75.00, δ 113.13, δ 142.82, δ 148.65, δ 148.67, δ 114.85, δ 32.99 and δ 213.90), one sp^3 methine (δ 37.43), and three sp^2 methine (δ 130.14, δ 128.46 and δ 110.56) other than nine sp^3 methylene signals (δ 36.81, δ 32.80, δ 36.84, δ 37.29, δ 39.37, δ 65.54, δ 27.99, δ 29.71 and δ 24.48) and five methyl groups (δ 24.81, δ 14.14, δ 22.64, δ 22.74 and δ 19.76) (Figure 4.102 & 4.103). In addition, the analyses of the ^{13}C NMR spectrum designated the occurrence of one each of ketone (δ 213.90) and two oxygenated functionalities (δ 75.00, δ 148.67, δ 142.82 and δ 65.54). These data were corroborated by HSQC spectral assignments (Figure 4.104).

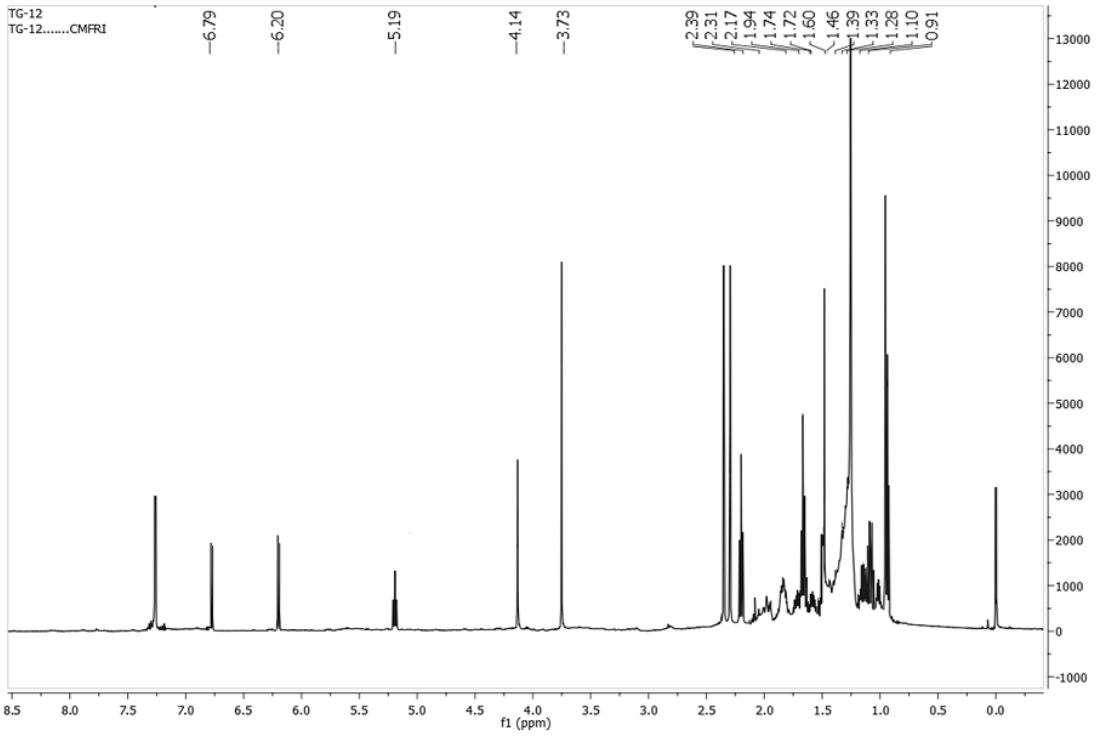

Figure 4.101.: ^1H NMR spectrum of 4'-[10'-[7-hydroxy-2,8-dimethyl-6-(pentyloxy)-*2H*-chromen-2-yl]ethyl]-3',4'-dimethyl-cyclohexanone (7)

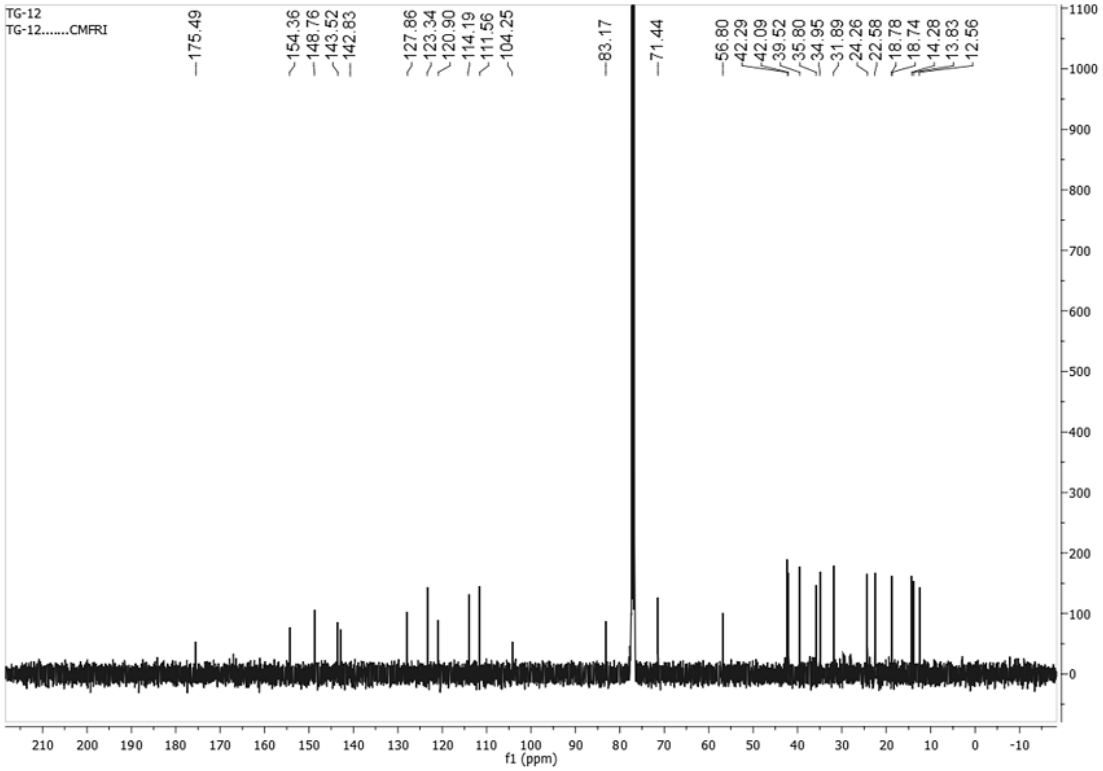

Figure 4.102.: ^{13}C NMR spectrum of 4'-[10'-[7-hydroxy-2,8-dimethyl-6-(pentyloxy)-*2H*-chromen-2-yl]ethyl]-3',4'-dimethyl-cyclohexanone (7)

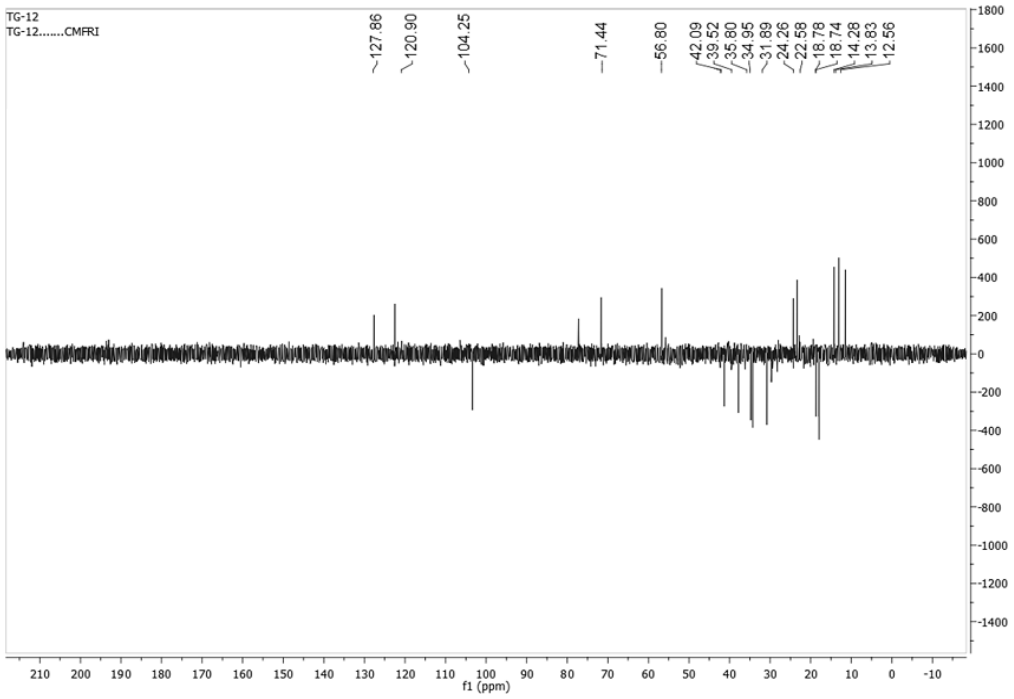

Figure 4.103.: ^{135}DEPT spectrum of 4'-[10'-[7-hydroxy-2,8-dimethyl-6-(pentyloxy)-*2H*-chromen-2-yl]ethyl]-3',4'-dimethyl-cyclohexanone (7)

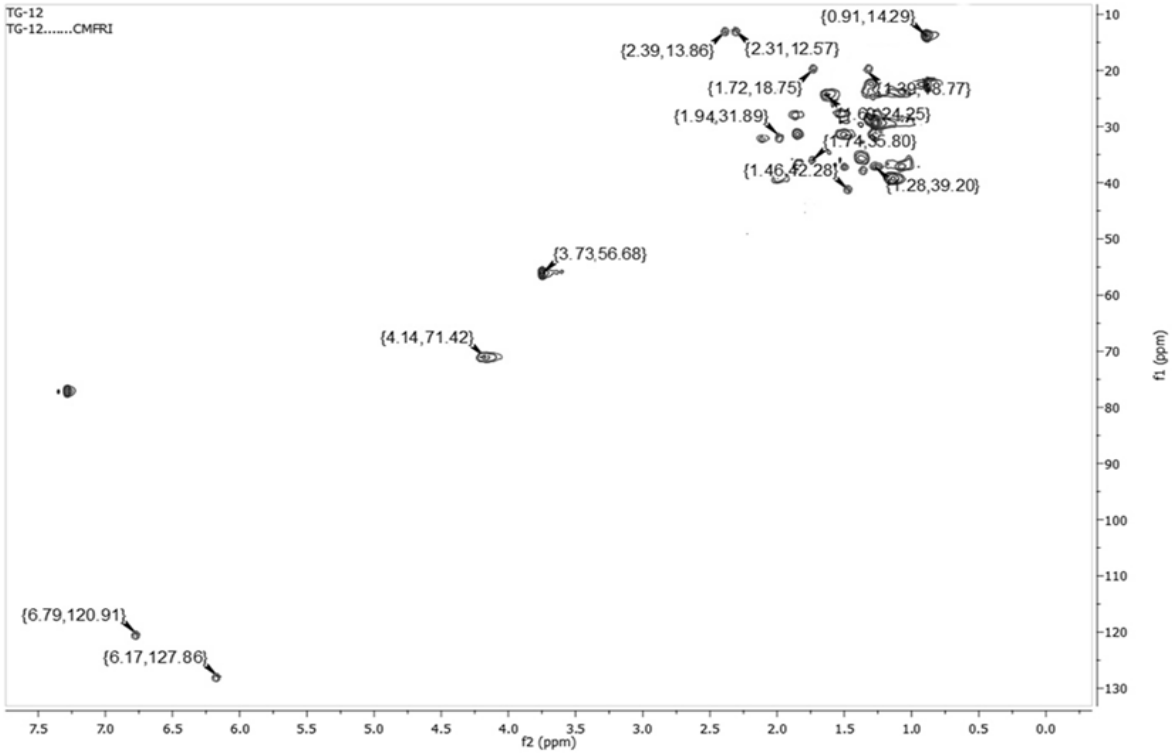

Figure 4.104.: HSQC spectrum of 4'-[10'-[7-hydroxy-2,8-dimethyl-6-(pentyloxy)-*2H*-chromen-2-yl]ethyl]-3',4'-dimethyl-cyclohexanone (7)

The partial structure of the studied compound was constructed with help of ^{1}H-^{1}H COSY correlations along with previous literature reports (Davyt et al. 1997; Ovenden et al. 2011). The ^{1}H-^{1}H COSY spectrum of **7** represented the occurrence of five individual spin systems: I (CH_3-δ 1.04)-(CH_2-δ 1.39)-(CH_2-δ 1.36)-(CH_2-δ 1.71)-(CH_2-δ 4.09); II (CH-δ 6.33)-(CH-δ 6.07); III (CH_2-δ 1.73)-(CH_2-δ 1.34); IV (CH_2-δ 2.49)-(CH_2-δ 1.82) and V (CH_2-δ 2.10)-(CH-δ 1.64)-(CH_3-δ 1.14). The positions of nine carbon signals in the studied compound were assigned from C-2 to C-10, which resembled the typical chromene bicyclic system (Hwa et al. 2005) (Figure 4.105 & 4.106). The remaining positions were assigned from 1' to 10' and 6^1 to 6^5, which represented substitutions on chromenyl merosesquiterpenoid framework. The HMBC correlations from CH_2-6^2-(δ 1.71) to C-6^1-(δ 65.54); CH_2-6^1-(δ 4.09) to C-6-(δ 142.82); CH-5-(δ 6.21) to C-6-(δ 142.82)/C-7-(δ 148.65)/C-4a (δ 113.13), and CH-4-(δ 6.33) to C-4a-(δ 113.13)/C-8a-(δ 148.67)/C-3-(δ 130.14) supported the bicyclic ring of chromene framework (Figure 4.107).

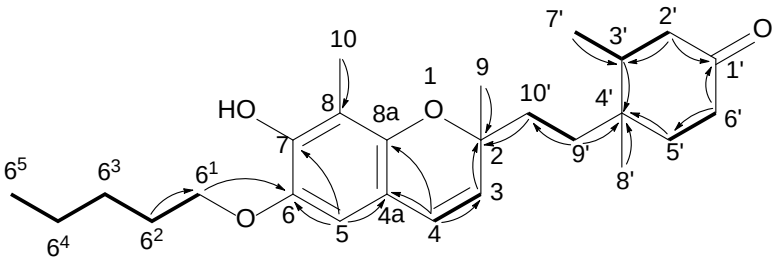

Figure 4.105.: ^{1}H-^{1}H COSY (bold face bonds), and selected HMBCs (double-barbed arrows), correlations of 4'-[10'-[7-Hydroxy-2,8-dimethyl-6-(pentyloxy)-*2H*-chromen-2-yl]ethyl]-3',4'-dimethyl-cyclohexanone (**7**)

This spectroscopic information appropriately explained the chromenyl system, and confirmed the attachment of oxygenated substitution, 6-pentyloxy at C-6-(δ 148.82). Other key HMBCs were apparent from CH-3-(δ 6.07) to C-2-(δ 75.00); CH_2-10'-(δ 1.73) to C-2-(δ 75.00); CH_2-9'-(δ 1.34) to C-10'-(δ 36.81)/C-4'-(δ 32.99); CH_2-5'-(δ 1.82) to C-4'-(δ 32.99); CH_2-6'-(δ 2.49.) to C-5'-(δ 36.84)/C-1'-(δ 213.90); and CH_2-2'-(δ 2.10) to C-1'-(δ 213.90)/C-3'-(δ 37.43), which suggested the presence of spin units-II, III, IV, and V. These spectroscopic assignments appropriately explained the fusion of bicyclic chromene system, and the connectivity between the carbons from C-1 to C-10 in **7**. The remaining HMBCs from CH_3-10-(δ 2.35) to C-8-(δ 114.85), CH_3-9-(δ 1.54) to C-2 (δ 75.00), CH_3-8'-(δ 1.20) to C-4'-(δ 32.99) and CH_3-7'-(δ1.14) to C-3'-(δ 37.43) confirmed the attachment of methyl carbons at C-8, C-2, C-4' and C-3', respectively.

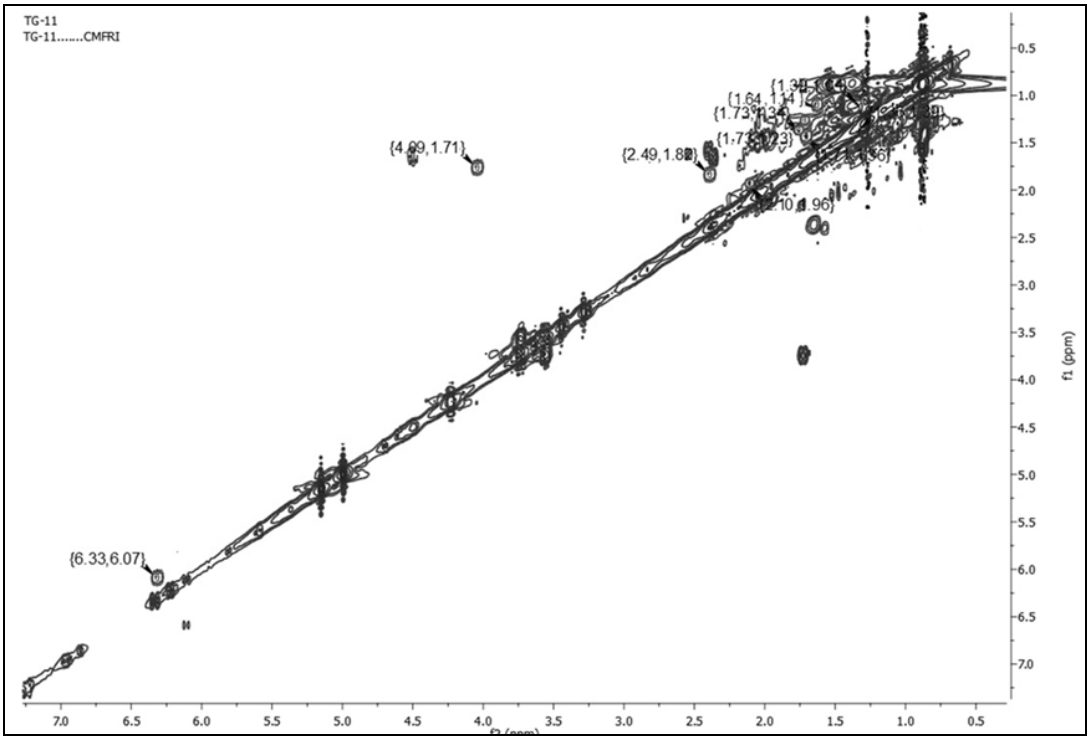

Figure 4.106.: ^{1}H-^{1}H COSY spectrum of 4'-[10'-[7-Hydroxy-2,8-dimethyl-6-(pentyloxy)-*2H*-chromen-2-yl]ethyl]-3',4'-dimethyl-cyclohexanone (7)

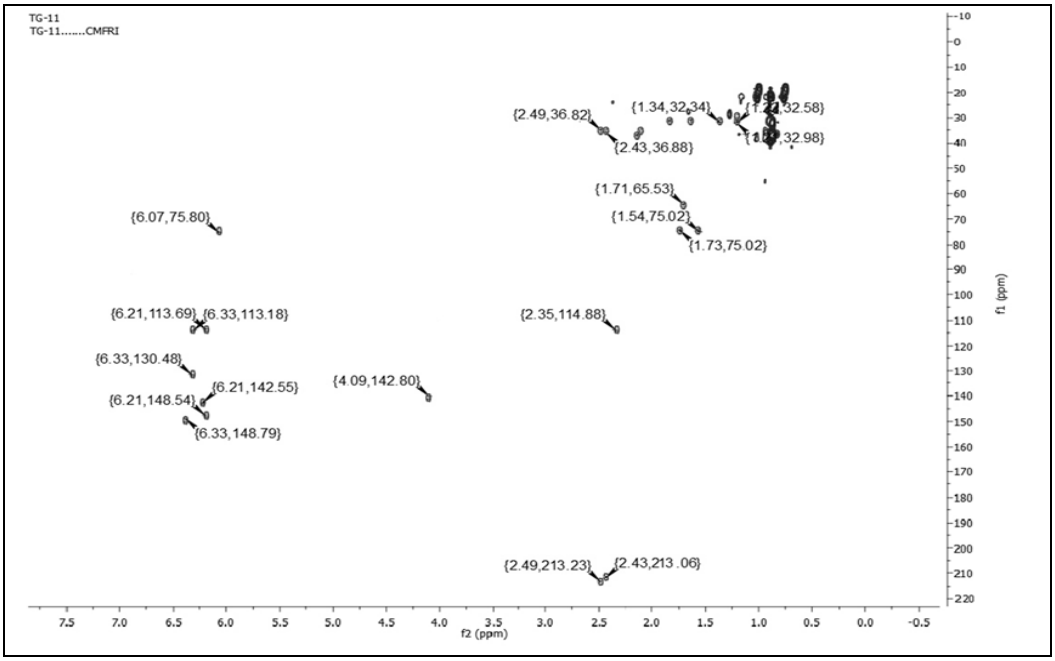

Figure 4.107.: HMBC spectrum of 4'-[10'-[7-hydroxy-2,8-dimethyl-6-(pentyloxy)-*2H*-chromen-2-yl]ethyl]-3',4'-dimethyl-cyclohexanone (7)

Table 4.14: NMR spectroscopic data of compound (**7**), 4'-[10'-[7-hydroxy-2,8-dimethyl-6-(pentyloxy)-*2H*-chromen-2-yl]ethyl]-3',4'-dimethyl-cyclohexanone (**7**) isolated from red seaweed *G. salicornia*

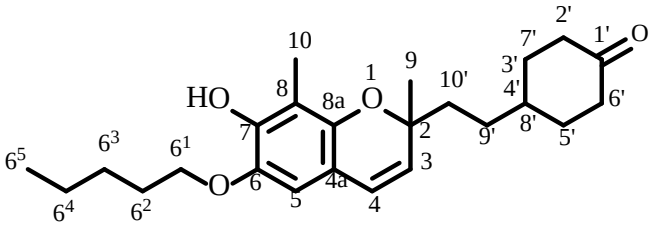

Compound **7** ……. 4'-[10'-[7-hydroxy-2,8-dimethyl-6-(pentyloxy)-*2H*-chromen-2-yl]ethyl]-3',4'-dimethyl-cyclohexanone (**7**)

Type	**C. No.**	**^{13}C NMR**	**H. No. (int., mult., J in Hz)[b]**	**^{1}H NMR**	**COSY**	**HMBC**
-	-	-	-	-	-	-
C	2	75.00	-	-	-	-
CH	3	130.14	1H, d, J = 13.2 Hz	6.07	H-4	C-2
CH	4	128.46	1H, d, J = 7.8 Hz	6.33	-	C-3,4a,8a
C	4a	113.13	-	-	-	
CH	5	110.56	1H, s	6.21	-	C-4a,7,6
C	6	142.82	-		-	
C	7	148.65	-	-	-	
C	8	114.85	-	-	-	
C	8a	148.67	-	-	-	
CH_3	9	24.81	3H, s	1.54	-	C-2
CH_3	10	14.14	3H, s	2.35	-	C-8
C	1'	213.90	-	-	-	-
CH_2	2'	39.37	1H, dd, J = 7.2, 5.8 Hz	2.10	H-3'	C-1',3'
	-	-	1H, dd, J = 7.1, 5.9 Hz	1.95	-	
CH	3'	37.43	1H, m	1.64	H-7'	C-4'
C	4'	32.99	-	-	-	
CH_2	5'	36.84	1H, dt, J = 7.3, 6.2 Hz	1.82	H-6'	C-4'
			1H, dt, J = 7.1, 6.0 Hz	1.68	-	
CH_2	6'	37.29	1H, dt, J = 6.8, 6.0 Hz	2.49	-	C-5',1'
	-	-	1H, dt, J = 7.1, 6.0 Hz	2.43	-	
CH_3	7'	22.64	3H, d, J = 7.1 Hz	1.14	-	C-3'
CH_3	8'	22.74	3H, s	1.20	-	C-4'
CH_2	9'	32.80	1H, dt, J = 6.8, 5.9 Hz	1.34	-	C-10',4'
	-	-	1H, dt, J = 6.9, 5.7 Hz	1.23	-	
CH_2	10'	36.81	2H, dd, J = 7.1, 6.3 Hz	1.73	H-9'	C-2
CH_2	6^1	65.54	2H, t, J = 9.8 Hz	4.09	H-6^2	C-6
CH_2	6^2	27.99	2H, m	1.71	H-6^3	C-6^1
CH_2	6^3	29.71	2H, m	1.36	H-6^4	-
CH_2	6^4	24.48	2H, m	1.39	H-6^5	-
CH_3	6^5	19.76	3H, t, J = 5.4 Hz	1.04	-	-

[a]NMR spectra were recorded using a Bruker AVANCE III 500 MHz (AV 500) spectrometer (Bruker, Karlsruhe, Germany) in $CDCl_3$ as aprotic solvent at ambient temperature with TMS as the internal standard (δ 0 ppm).

[b]Values in ppm, multiplicity and coupling constants (J = Hz) were indicated in parentheses.
Multiplicities were allocated by [135]DEPT NMR spectrum.
The assignments were made with the aid of the COSY, HSQC, HMBC and NOESY experiments.

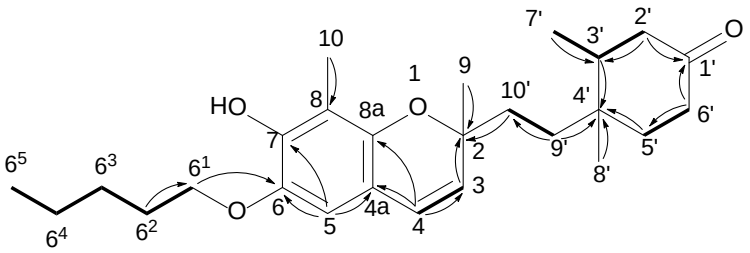

Figure 4.108.: NOESY (double-barbed arrows), correlations of 4'-[10'-[7-hydroxy-2,8-dimethyl-6-(pentyloxy)-*2H*-chromen-2-yl]ethyl]-3',4'-dimethyl-cyclohexanone (7)

The relative stereochemistries of protons attached to chiral carbon at C-3' (δ 37.43) and other methyl protons at C-10 (14.14), C-9 (24.81) and C-8' (22.74) were explained with nuclear overhauser effect spectroscopic (NOESY) experiments (Figure 4.108 & 4.109). The methyl proton at δ 1.14 (assigned to H-7' on C-3) exhibited NOEs with proton at δ 1.23 (H-9'α), which were oriented in α-side of **7**. Conversely, other protons in β-face of the molecule, particularly those of H-9, H-10, H-3', H-8', and H-9'β were deduced by NOE relationships between H-10 (δ 2.35)/H-9 (δ 1.54), H-9 (δ 1.54)/H-9'β (δ 1.34), H-9 (δ 1.54)/H-8' (δ 1.20) and H-3' (δ 1.64)/H-8' (δ 1.20).

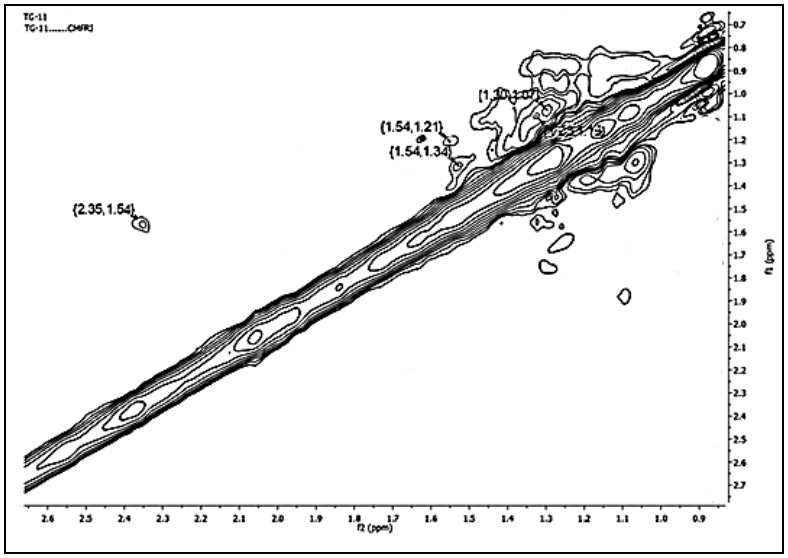

Figure 4.109.: NOESY (double-barbed arrows), correlations of 4'-[10'-[7-hydroxy-2,8-dimethyl-6-(pentyloxy)-*2H*-chromen-2-yl]ethyl]-3',4'-dimethyl-cyclohexanone (7)

The molecular ion peak at *m/z* 414 (**a**) $[M]^+$ underwent an elimination of $C_5H_{12}O$ moiety and the reorganization of bonds led to a fragment peak at *m/z* 327 (**b**). Further fragmentation of the latter led to the formation of mass fragments, **c** and **d** (*m/z* 174 and 152, respectively). The radical cation, **c** also performed a rearrangement mechanism to form **f** and **g** with the *m/z* 131 and 77, respectively. The mass fragment at *m/z* 77 ($C_6H_6^+$) was found to be the base peak. These detailed spectral data unambiguously interpreted the structure of the isolated compound as 4'-[10'-[7-hydroxy-2,8-dimethyl-6-(pentyloxy)-2*H*-chromen-2-yl]ethyl]-3',4'-dimethyl-cyclohexanone (**7**) (Figure 4.110 & 4.111).

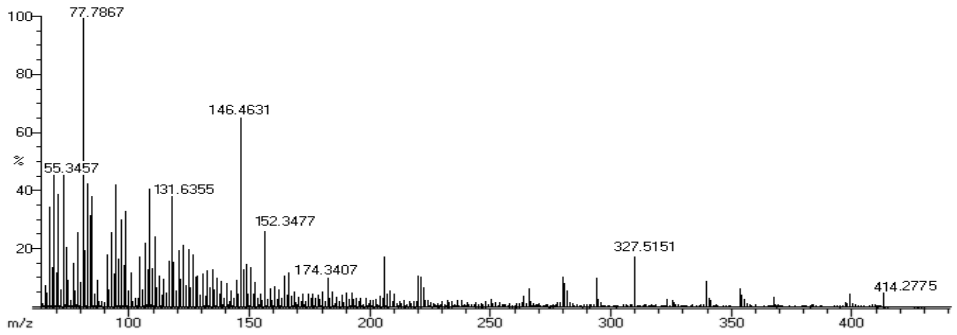

Figure 4.110.: EI-MS spectrum of 4'-[10'-[7-hydroxy-2,8-dimethyl-6-(pentyloxy)-*2H*-chromen-2-yl]ethyl]-3',4'-dimethyl-cyclohexanone (7)

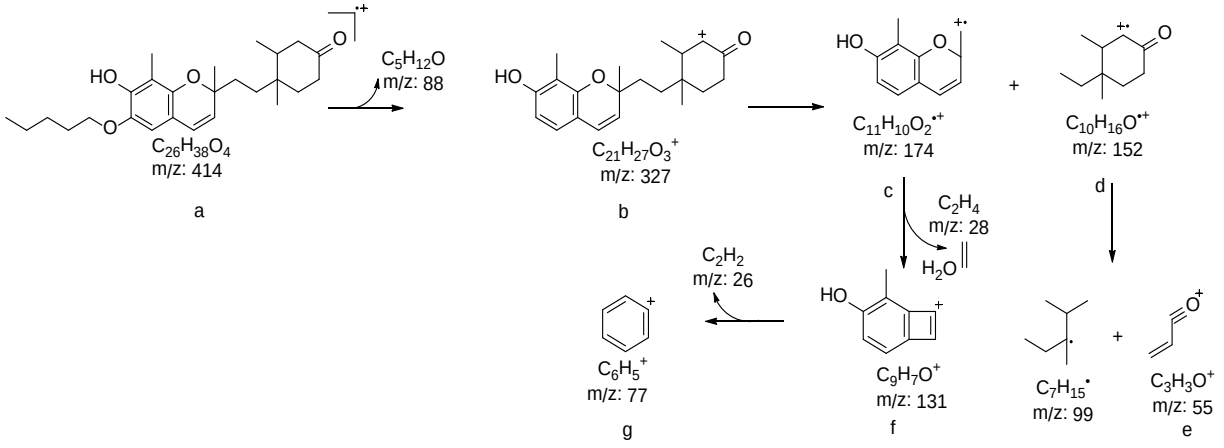

Figure 4.111.: Tentative mass fragmentation pattern of 4'-[10'-[7-hydroxy-2,8-dimethyl-6-(pentyloxy)-*2H*-chromen-2-yl]ethyl]-3',4'-dimethyl-cyclohexanone (7)

4.3.2.4b Structural characterization of Compound 8

3'-[10'-(8-Hydroxy-5-methoxy-2,6,7-trimethyl-*2H*-chromen-2-yl)ethyl]-3'-methyl-2'-methylene cyclohexyl butyrate

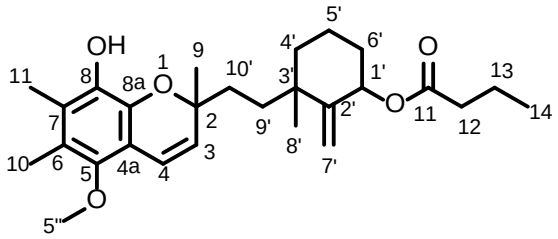

Sample yield	0.37% (> 99% purity, RP-C18 HPLC)
Physical description	Pale yellowish oil
Molecular formula	$C_{27}H_{38}O_5$
Molecular mass	442.2724

The *2H*-chromenyl derivative, 3'-[10'-(8-Hydroxy-5-methoxy-2,6,7-trimethyl-*2H*-chromen-2-yl)ethyl]-3'-methyl-2'-methylene cyclohexyl butyrate was isolated as yellowish oil. The compound (**8**) has exhibited UV absorbance (UV (MeOH) λ_{max}) at 264 nm (Figure 4.112). The homogeneity of the compound was ascertained by HPLC data on a bonded phase octadecylsilane (C_{18}) stationary phase (HPLC, MeCN/MeOH, 3:2 v/v) with R_t: 3.70 min (Figure 4.113).

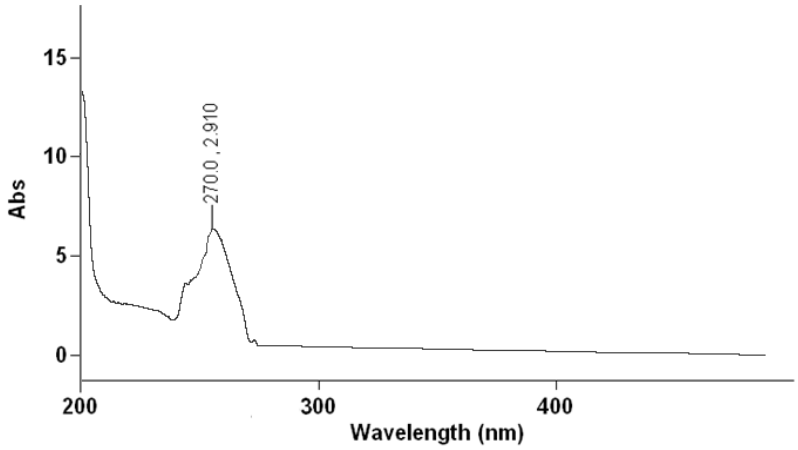

Figure 4.112.: UV spectrum of 3'-[10'-(8-hydroxy-5-methoxy-2,6,7-trimethyl-*2H*-chromen-2-yl)ethyl]-3'-methyl-2'-methylene cyclohexyl butyrate (**8**)

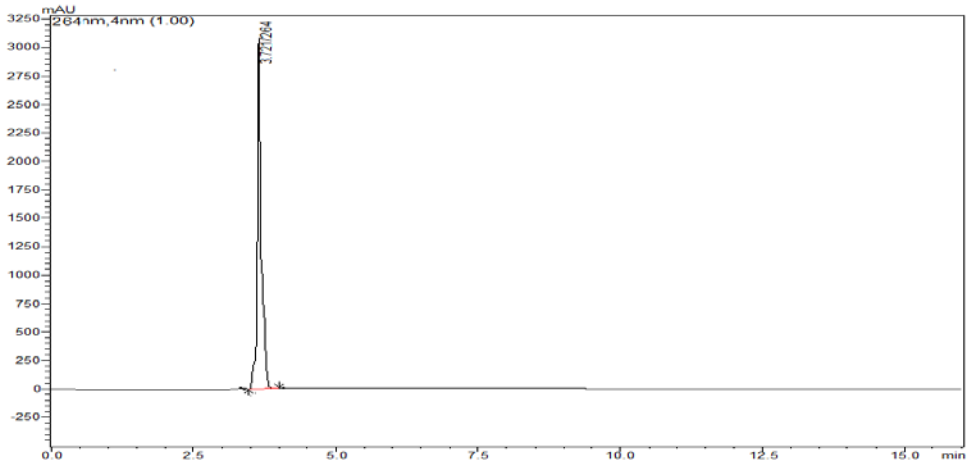

Figure 4.113.: HPLC chromatogram of 3'-[10'-(8-Hydroxy-5-methoxy-2,6,7-trimethyl-*2H*-chromen-2-yl)ethyl]-3'-methyl-2'-methylene cyclohexyl butyrate (**8**)

The chromatography-based fractionation of EtOAc-MeOH extract of *G. salicornia* afforded the titled compound as a pale yellowish oily substance. The EI-MS experiment displayed the molecular ion peak at *m/z* 442 along with integrative NMR-IR spectroscopic experiments were deduced its molecular formula as $C_{27}H_{38}O_5$ (Table 4.15). The HRESIMS experiment displayed the molecular ion peak at *m/z* 443.2797 $[M+H]^+$, (Figure 4.114).

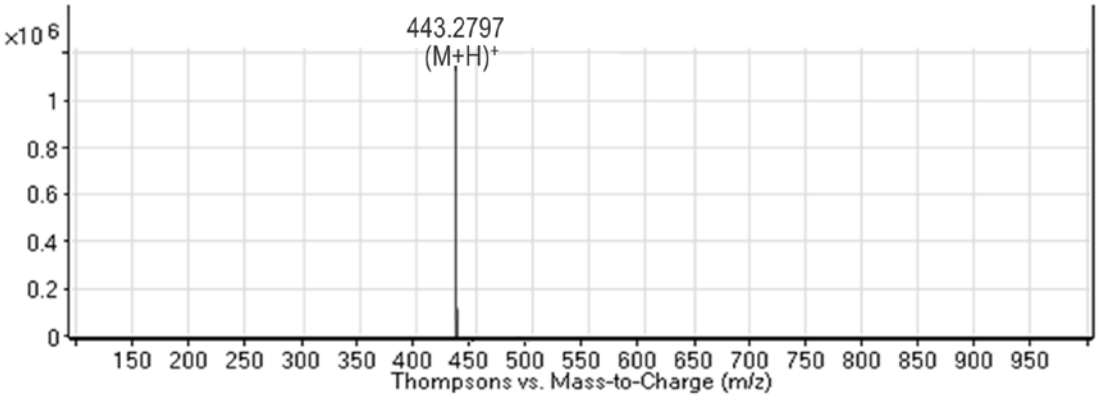

Figure 4.114.: HRESIMS of 3'-[10'-(8-hydroxy-5-methoxy-2,6,7-trimethyl-*2H*-chromen-2-yl)ethyl]-3'-methyl-2'-methylene cyclohexyl butyrate (**8**)

The FTIR absorption peaks at 3412, 1728, 1735 and 1574 assigned the occurrences of hydroxyl, ether, carbonyl and aromatic ($C=C_{(aromatic)}$) moieties, respectively (Figure 4.115). The ^{1}H-NMR experiments showed signals corresponding to methyl groups at δ 3.73 (3H, s), δ 2.39 (3H, s), δ 2.31 (3H, s), δ 1.60 (3H, s), and δ 0.91 (3H, t, J = 6.9 Hz). The spectrum also indicated the presence of three olefinic hydrogens at δ 6.20 (1H, d, J = 12.8 Hz), δ 6.79 (1H, d, J

= 11.8 Hz) and δ 5.19 (2H, s) (Figure 4.116). The ^{13}C NMR spectrum along with $DEPT_{135}$ analysis deduced 27 carbon signals in compound **8** including the signals due to ten quaternary carbons (δ 83.17, δ 111.56, δ 148.76, δ 114.19, δ 123.34, δ 143.52, δ 142.83, δ 42.29, δ 154.36 and δ 175.49), one sp^3 methine (δ 71.44) and two sp^2 methine (δ 127.86 and δ 120.90) other than seven sp^3 methylene signals (δ 35.80, δ 39.52, δ 31.89, δ 18.78, δ 42.09, δ 34.95 and δ 18.74), one sp^2 methylene (δ 104.25) signal and six methyl groups (δ 24.26, δ 13.83, δ 12.56, δ 56.80, δ 22.58 and δ 14.28) (Figure 4.117 and 4.118). In addition, the analyses of ^{13}C NMR spectrum designated the occurrence of one each of ester (δ 175.49) and two oxygenated functionalities (δ 83.17, δ 142.83, and δ 148.76). These spectral data were further supported by HSQC data (Figure 4.119).

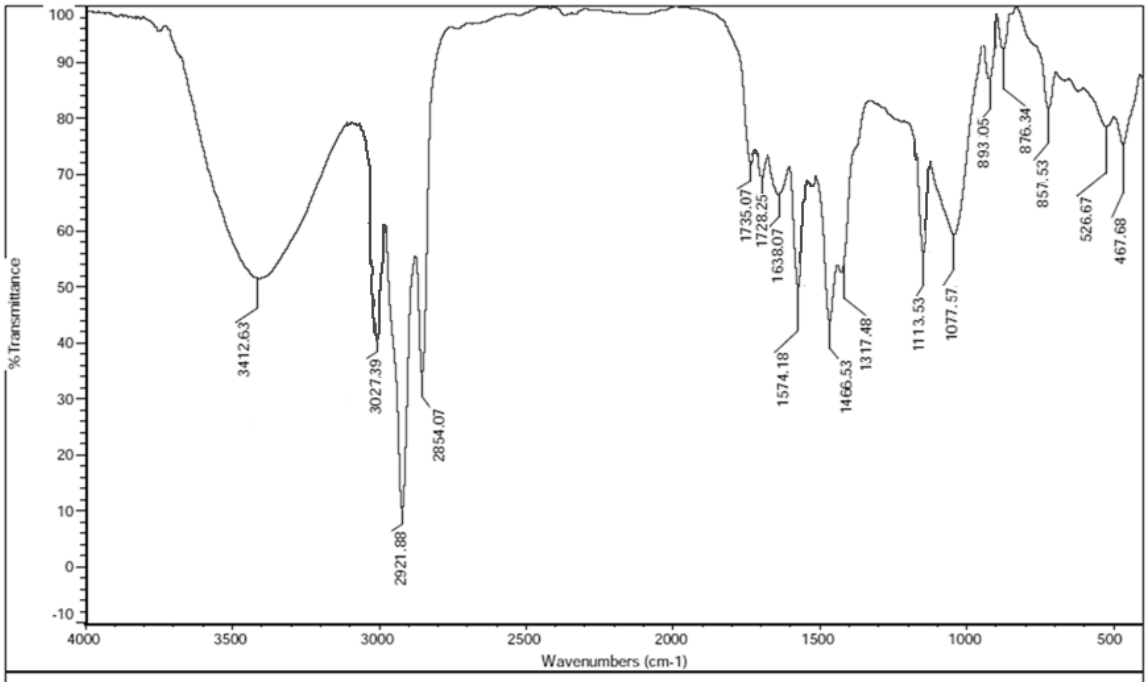

Figure 4.115.: FTIR spectrum of 3'-[10'-(8-hydroxy-5-methoxy-2,6,7-trimethyl-*2H*-chromen-2-yl)ethyl]-3'-methyl-2'-methylene cyclohexyl butyrate (**8**)

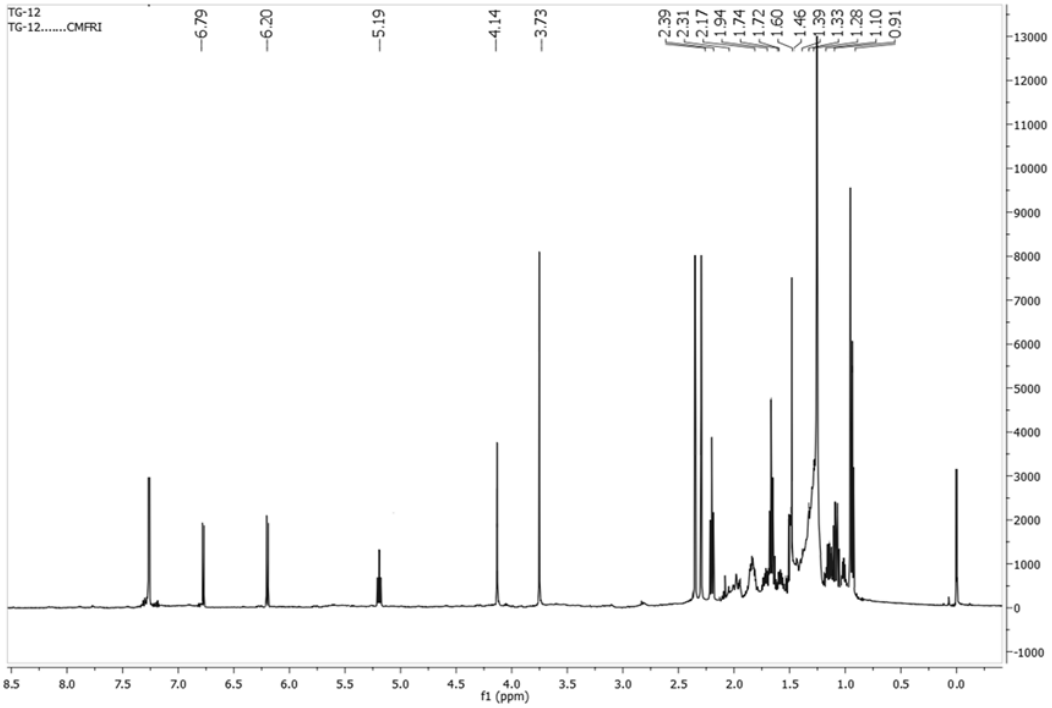

Figure 4.116.: ^{1}H NMR spectrum of 3'-[10'-(8-hydroxy-5-methoxy-2,6,7-trimethyl-*2H*-chromen-2-yl)ethyl]-3'-methyl-2'-methylene cyclohexyl butyrate (**8**)

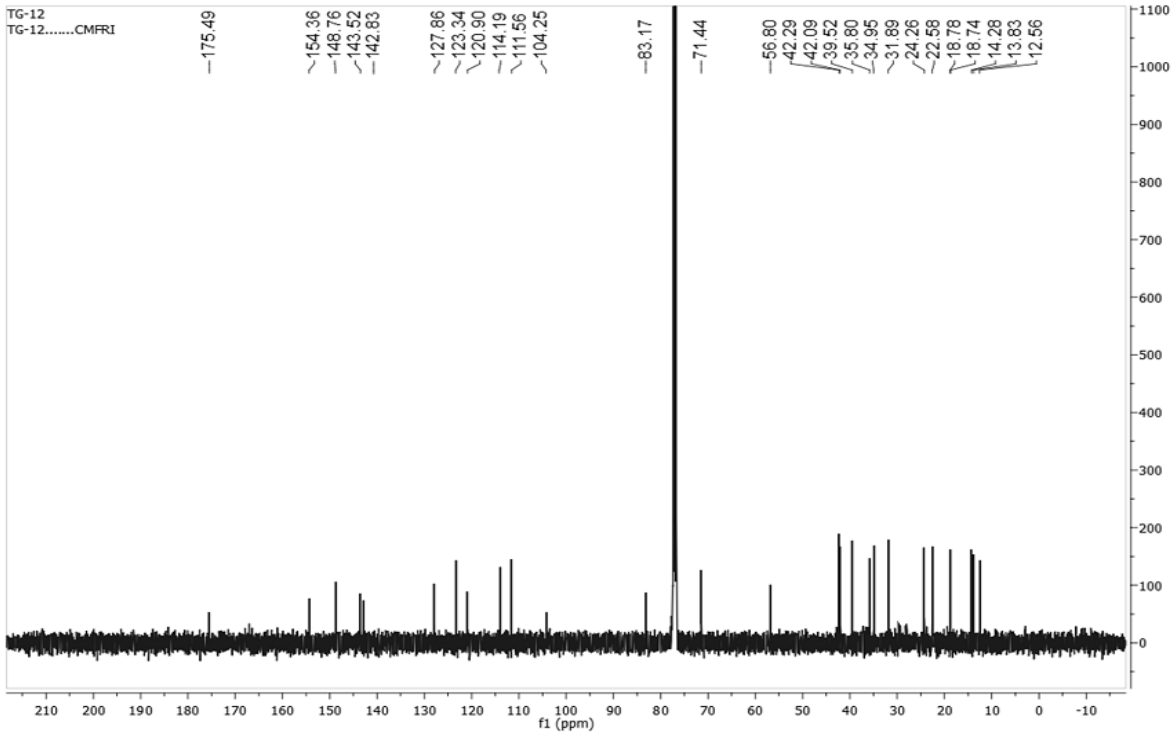

Figure 4.117.: ^{13}C NMR spectrum of 3'-[10'-(8-hydroxy-5-methoxy-2,6,7-trimethyl-*2H*-chromen-2-yl)ethyl]-3'-methyl-2'-methylene cyclohexyl butyrate (**8**)

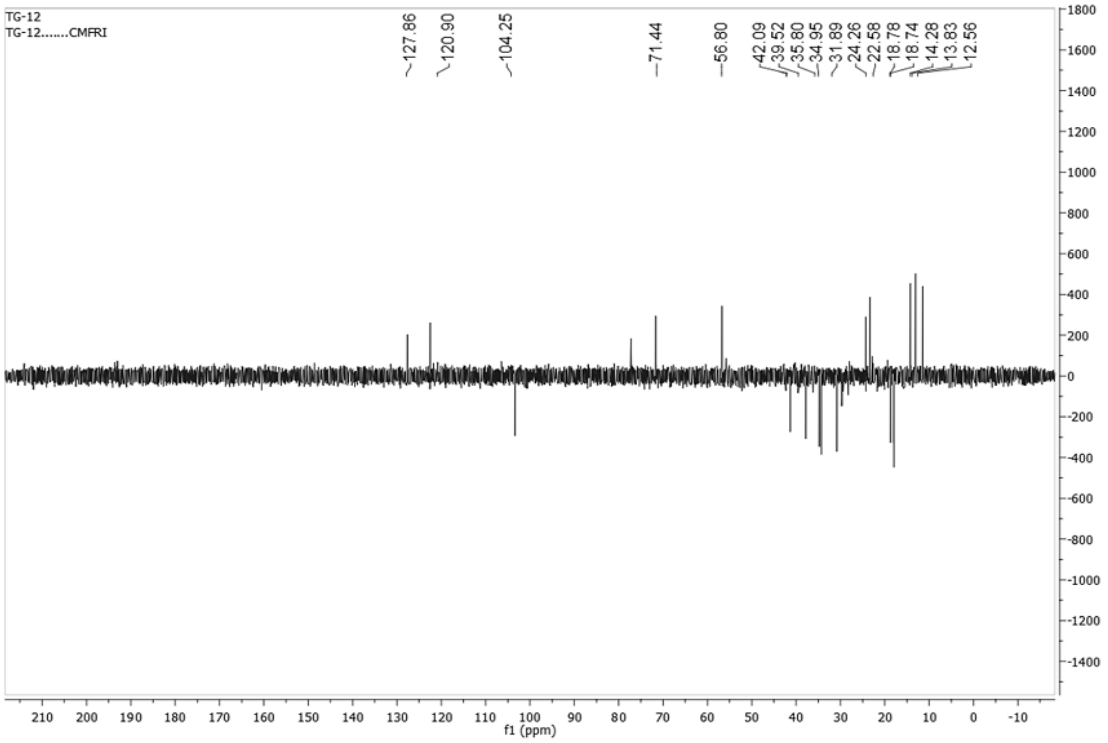

Figure 4.118.: [135]DEPT NMR spectrum of 3'-[10'-(8-hydroxy-5-methoxy-2,6,7-trimethyl-*2H*-chromen-2-yl)ethyl]-3'-methyl-2'-methylene cyclohexyl butyrate (**8**)

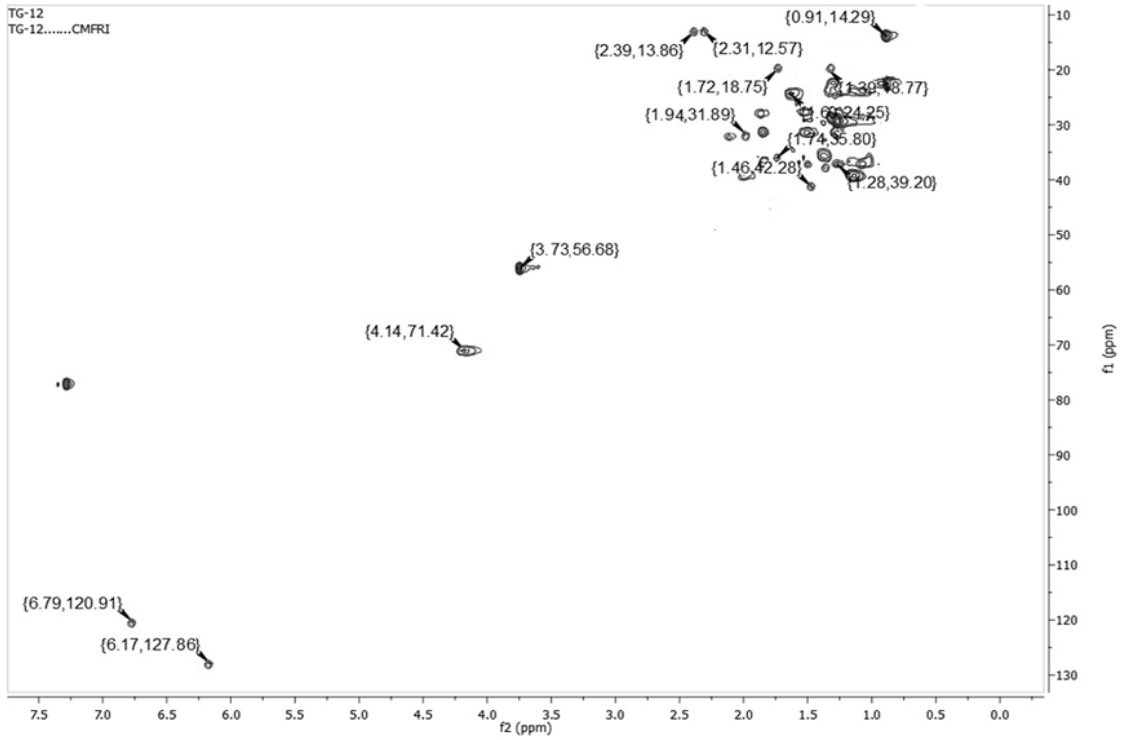

Figure 4.119.: HSQC spectrum of 3'-[10'-(8-hydroxy-5-methoxy-2,6,7-trimethyl-*2H*-chromen-2-yl)ethyl]-3'-methyl-2'-methylene cyclohexyl butyrate (**8**)

The partial structures of the studied compound were constructed with help of 1D NMR and ^{1}H-^{1}H COSY correlations along with previously reports of literature (Davyt et al. 1997; Iwashima et al. 2005; Ovenden et al. 2011). ^{1}H-^{1}H COSY spectrum of **8** assigned the occurrence of four individual spin systems: I (CH-δ 6.20)-(CH-δ 6.79); II (CH_2-δ 1.74)-(CH_2-1.33); III (CH_2-δ 1.46)-(CH_2-δ 1.39)-(CH_2-δ 1.94)-(CH-δ 4.14); and IV (CH_2-δ 2.17)-(CH_2-δ 1.72)-(CH-δ 0.91). The positions of nine carbon signals in the studied compound were assigned from C-2 to C-10, which resembled the typical chromene bicyclic system with methyl substitutions (Figure 4.120 & 4.121). The remaining positions were assigned from 1' to 10' and 1^{1} to 1^{4}, which represented the substitutions on chromenyl framework of **8**. HMBC correlations from CH-4-(δ 6.79) to C-4a-(δ 111.56)/C-5-(δ 148.76)/C-8a-(δ 142.83) and CH-3-(δ 6.20) to C-2-(δ 83.17) assigned the position of highly deshielded alkenic protons in the bicyclic ring of chromene framework (Figure 4.122). Other key HMBCs were apparent from CH_2-10'-(δ 1.74) to C-2-(δ 83.17); CH_2-9'-(δ 1.33) to C-10'-(δ 35.80)/C-3'-(δ 42.29); CH_2-4'-(δ 1.46) to C-3'-(δ 42.29)/C-2'-(δ 154.36); CH-1'-(δ 4.14) to C-2'-(δ 154.36); CH_2-6'-(δ 1.94) to C-5'-(δ 18.78); CH_2-1^{3}-(δ 1.72) to C-1^{2}-(δ 34.95), which suggested the presence of spin units-II, III, and IV. These spectroscopic assignments appropriately explained the fusion of the bicyclic chromene system, and the connectivity between the carbons from C-1 to C-8 in chromene ring system. The remaining HMBCs from CH_3-11-(δ 2.31) to C-7-(δ 123.34), CH_3-10-(δ 2.39) to C-6 (δ 114.19), CH_3-5"-(δ 3.73) to C-5-(δ 148.76), CH_3-9-(δ 1.60) to C-2-(δ 83.17), CH_3-8'-(δ 1.10) to C-3'-(δ 42.29) and CH_3-7'-(δ 5.19) to C-2'-(δ 154.36) confirmed the attachment of methyl carbons at C-7, C-6, C-5 (-O-CH_3), C-2, C-3' and C-2', respectively.

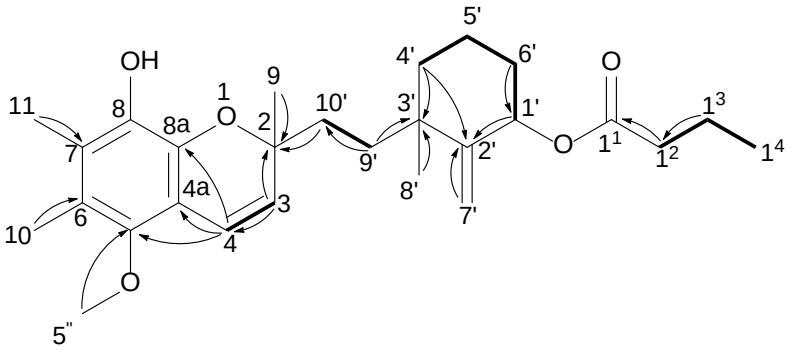

Figure 4.120.: ^{1}H-^{1}H COSY (bold face bonds), and selected HMBCs (double-barbed arrows), correlations of 3'-[10'-(8-hydroxy-5-methoxy-2,6,7-trimethyl-*2H*-chromen-2-yl)ethyl]-3'-methyl-2'-methylene cyclohexyl butyrate (**8**)

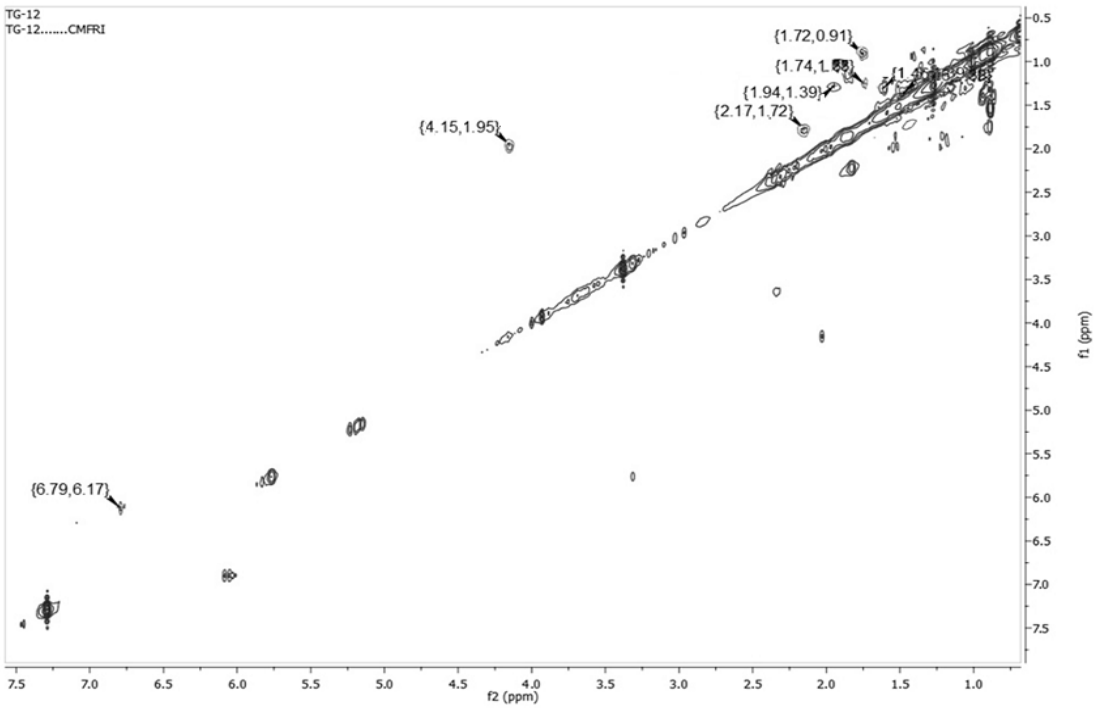

Figure 4.121.: ^{1}H-^{1}H COSY spectrum of 3'-[10'-(8-hydroxy-5-methoxy-2,6,7-trimethyl-*2H*-chromen-2-yl)ethyl]-3'-methyl-2'-methylene cyclohexyl butyrate (**8**)

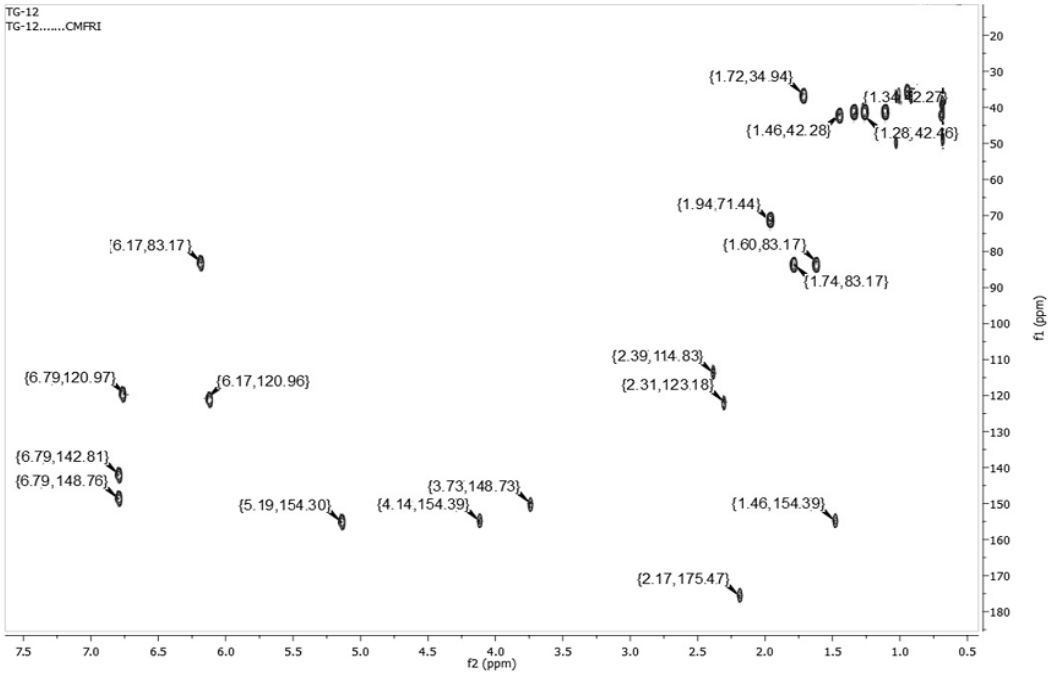

Figure 4.122.: HMBC spectrum of 3'-[10'-(8-hydroxy-5-methoxy-2,6,7-trimethyl-*2H*-chromen-2-yl)ethyl]-3'-methyl-2'-methylene cyclohexyl butyrate (**8**)

Table 4.15: NMR spectroscopic data of compound (**8**), 3'-[10'-(8-hydroxy-5-methoxy-2,6,7-trimethyl-*2H*-chromen-2-yl)ethyl]-3'-methyl-2'-methylene cyclohexyl butyrate (**8**) isolated from red seaweed *G. salicornia*

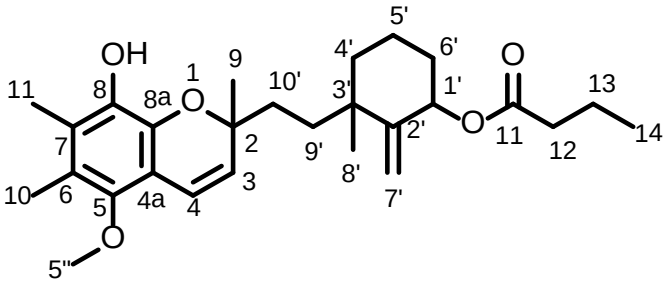

Compound **8** ……3'-[10'-(8-hydroxy-5-methoxy-2,6,7-trimethyl-*2H*-chromen-2-yl)ethyl]-3'-methyl-2'-methylene cyclohexyl butyrate (**8**)

Type	**C. No.**	**^{13}C NMR**	**H. No. (int., mult., J in Hz)[b]**	**^{1}H NMR**	**COSY**	**HMBC**
-	-	-	-	-	-	-
C	2	83.17	-	-		
CH	3	127.86	1H, d, J = 12.8 Hz	6.20	H-4	C-2,4
CH	4	120.90	1H, d, J = 11.8 Hz	6.79	-	C-4a, 8a,5
C	4a	111.56	-	-	-	-
C	5	148.76	-	-	-	-
CH_3	5''	56.80	3H, s	3.73	-	C-5
C	6	114.19	-	-	-	-
C	7	123.34	-	-	-	-
C	8	143.52	-	-	-	-
C	8a	142.83	-	-	-	-
CH_3	9	24.26	3H, s	1.60	-	C-2
CH_3	10	13.83	3H, s	2.39	-	C-6
CH_3	11	12.56	3H, s	2.31	-	C-7
CH	1'	71.44	1H, d, J = 7.2 Hz	4.14	H-6'	C-2'
C	2'	154.36	-	-	-	-
C	3'	42.29	-	-	-	-
CH_2	4'	42.09	2H, dt, J = 6.9, 4.3 Hz	1.46	-	C-2',3'
CH_2	5'	18.78	2H, m	1.39	H-4'	-
CH_2	6'	31.89	2H, dt, J = 5.2, 4.0 Hz	1.94	H-5'	C-1'
CH_2	7'	104.25	2H, s	5.19	-	C-2'
CH_3	8'	22.58	3H, s	1.10	-	C-3'
CH_2	9'	39.52	1H, dt, J = 9.3, 5.6 Hz	1.33	-	C-10',3'
			1H, dt, J = 9.8, 5.1 Hz	1.28	-	-
CH_2	10'	35.80	2H, dd, J = 7.8, 5.9 Hz	1.74	H-9'	C-2
C	1^1	175.49	-	-	-	-
CH_2	1^2	34.95	2H, d, J = 7.9 Hz	2.17	H-1^3	C-1^1
CH_2	1^3	18.74	2H, m	1.72	H-1^4	C-1^2
CH_3	1^4	14.28	3H, t, J = 6.9 Hz	0.91	-	-

[a]NMR spectra were recorded using a Bruker AVANCE III 500 MHz (AV 500) spectrometer (Bruker, Karlsruhe, Germany) in $CDCl_3$ as aprotic solvent at ambient temperature with TMS as the internal standard (δ 0 ppm).

[b]Values in ppm, multiplicity and coupling constants (*J* = Hz) were indicated in parentheses. Multiplicities were allocated by [135]DEPT NMR spectrum.

The assignments were made with the aid of the COSY, HSQC, HMBC and NOESY experiments.

The relative stereochemistries of protons attached to chiral carbon at C-1' (δ 71.44) and other methyl protons at C-9, C-8', C-10 and C-11 were explained with nuclear overhauser effect spectroscopic (NOESY) experiments (Figure 4.123 & 4.124). The signal of proton at chiral centre, δ 1.28 (assigned to H-9'α) exhibited NOEs with methylene proton at δ 4.14 (H-1'), which were oriented in the α-side of the compound. Conversely, the other protons in β-face of the molecule, particularly those of H-9, H-8', H-11, H-10 and H-9' were deduced by NOE relationships between H-11 (δ 2.31)/H-9 (δ 1.60), H-10 (δ 2.39)/H-9 (δ 1.60), H-9 (δ 1.60)/H-8' (δ 1.10) and H-9'β (δ 1.33)/H-8' (δ 1.10).

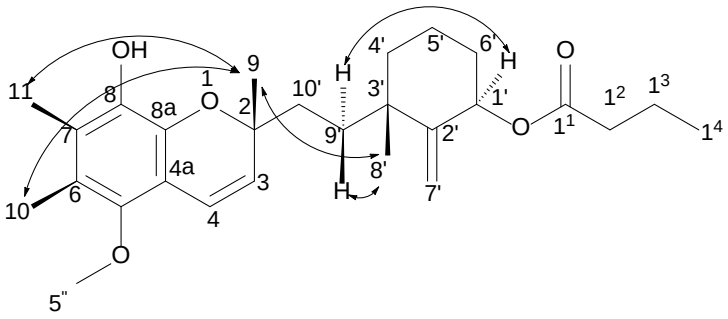

Figure 4.123.: NOESY (double-barbed arrows), correlations of 3'-[10'-(8-hydroxy-5-methoxy-2,6,7-trimethyl-*2H*-chromen-2-yl)ethyl]-3'-methyl-2'-methylene cyclohexyl butyrate (**8**)

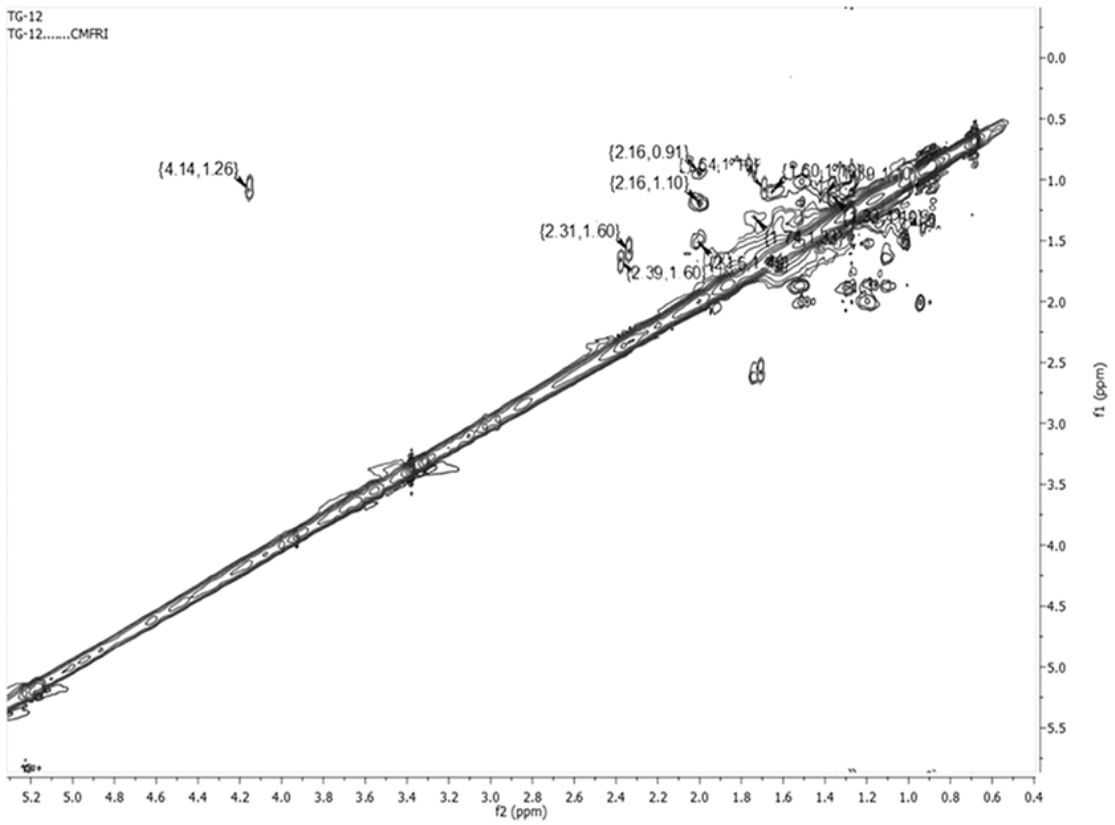

Figure 4.124.: ^{1}H NMR spectrum of 3'-[10'-(8-hydroxy-5-methoxy-2,6,7-trimethyl-*2H*-chromen-2-yl)ethyl]-3'-methyl-2'-methylene cyclohexyl butyrate (**8**)

The molecular ion peak at *m/z* 442 (**a**) $[M]^+$ underwent elimination of $C_4H_8O_2$ moiety and further rearrangement led to a fragment peak at *m/z* 370 (**b**). Further fragmentation of (**b**) led to the formation of radical cation **c** (*m/z* 352). The fragment ion **c** performed a rearrangement to form **d** and **g** (with *m/z* 218 and 135, respectively), whereas the latter led to the formation of **e** (with *m/z* 175) upon further fragmentation. The base peak at *m/z* 77 (**f**) ($C_6H_6^+$) appeared to form upon fragmentation of the mass fragment at *m/z* 175 (Figure 4.125 & 4.126). These detailed spectroscopic data unambiguously attributed the structure of isolated compound was as 3'-[10'-(8-hydroxy-5-methoxy-2,6,7-trimethyl-2*H*-chromen-2-yl)ethyl]-3'-methyl-2'-methylene cyclohexyl butyrate (**8**).

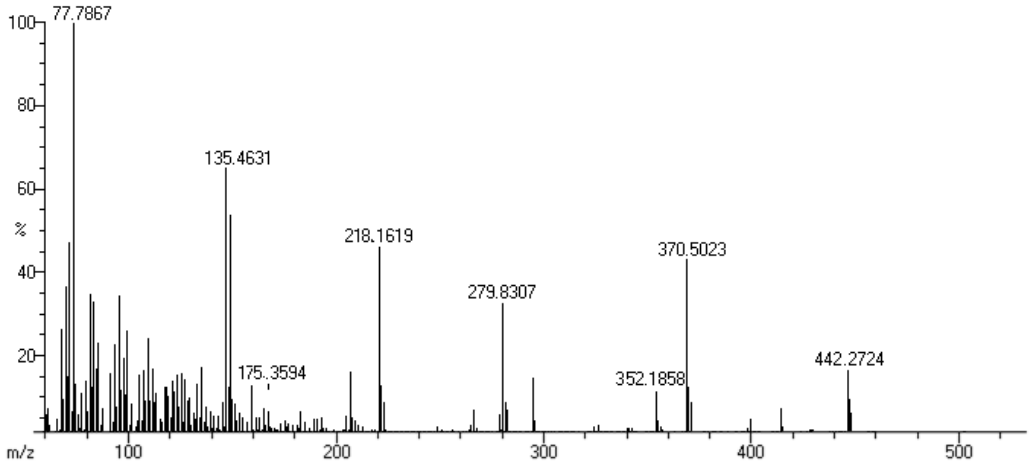

Figure 4.125.: EI-MS spectrum of 3'-[10'-(8-hydroxy-5-methoxy-2,6,7-trimethyl-*2H*-chromen-2-yl)ethyl]-3'-methyl-2'-methylene cyclohexyl butyrate (**8**)

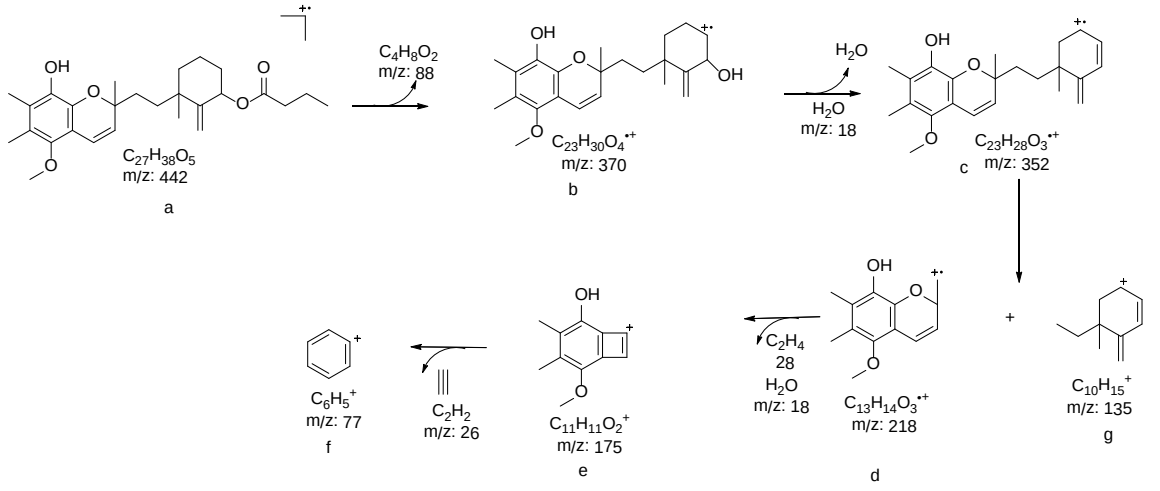

Figure 4.126.: Tentative mass fragmentation pattern of 3'-[10'-(8-hydroxy-5-methoxy-2,6,7-trimethyl-*2H*-chromen-2-yl)ethyl]-3'-methyl-2'-methylene cyclohexyl butyrate (**8**)

Bioassay-assisted repeated chromatographic fractionation of the organic extract of red seaweed, *G. salicornia* yielded two chromenyl derivatives, which were characterised as 4'-[10'-[7-hydroxy-2,8-dimethyl-6-(pentyloxy)-2*H*-chromen-2-yl]ethyl]-3',4'-dimethyl-cyclohexanone (**7**) and 3'-[10'-(8-hydroxy-5-methoxy-2,6,7-trimethyl-2*H*-chromen-2-yl)ethyl]-3'-methyl-2'-methylene cyclohexyl butyrate (**8**) using comprehensive spectroscopic techniques. This is considered as the first report of *2H*-chromenyl derivatives from *G. salicornia*.

4.3.2.5 Structural characterization of spiro-compound derivative (Compounds 9-10)

Spiro frameworks were represented as a significant class of naturally occurring compounds characterised with highly potent bioactive properties and has been known to be present in various phytochemicals with their wide range of pharmacological applications (Leonid et al. 2012). These spirocyclic compounds are of recent interest due to their remarkable conformational features and their structural implications on biological systems and were largely found in various biologically active natural products and pharmaceuticals (Bartoli et al. 2011). The stereochemistries of spiranes with six-membered rings have been extensively studied (Cismas et al. 2005). The non-halogenated rearranged spiro-compound, 1,4,9-trimethyl-5-methylidenespiro[5.5]undec-1,7-diene-4,9-diol and halogenated spiro-fused compounds, such as 2-bromo-1,1,9-trimethyl-5-methylidenespiro[5.5]undec-7-ene-3,9-diol and 2-bromo-9-bromomethylidene-1,1-dimethyl-5-methylene spiro [5.5]undec-7-ene were previously reported from a red seaweed, *Laurencia scoparia* with bio-potentials (Davyt et al. 2001). Also, the halogenated and nonhalogenated spiro-compounds, which were classified as compositacins, were reported from red seaweed, *Laurencia composita* (Yu et al. 2017). In order to access the versatile motifs of spiro-compounds with unique structural features, it has become one of the prominent research areas to the natural product chemists.

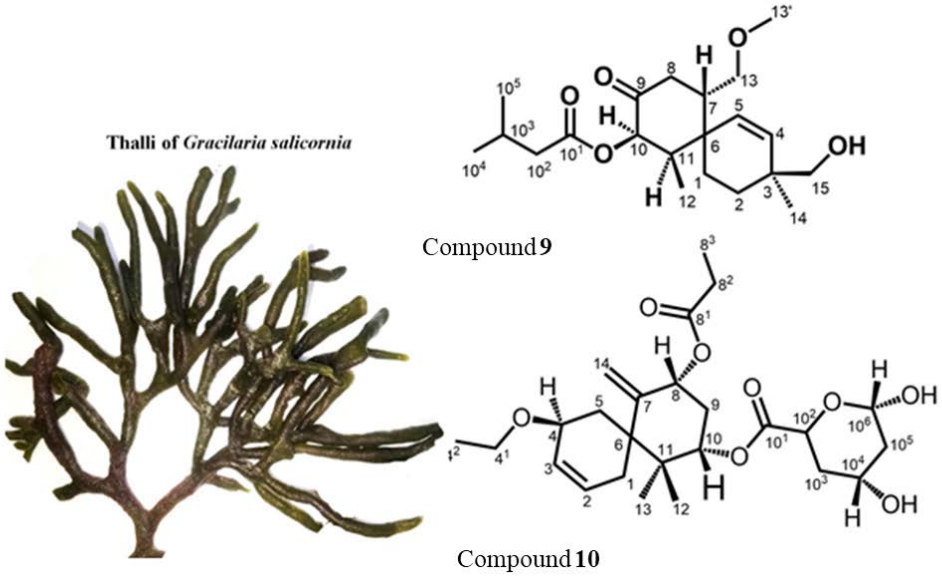

Figure 4.127.: Structures of spiro[5.5]undecane compounds (**9**-**10**) isolated from the seaweed *G. salicornia*. The representative image of the thalli of *G. salicornia* was shown.

In the present study, the organic ethyl acetate-methanol (EtOAc-MeOH) extract of *G. salicornia* collected from southern coastline of Indian peninsular was fractionated by repeated chromatographic techniques, which resulted in the identification of two unprecedented spiro-fused analogues, 3-(hydroxymethyl)-7-(methoxymethyl)-3,11-dimethyl-9-oxospiro[5.5]undec-4-

en-10-methylbutanoate (**9**) and 4-ethoxy-11,11-dimethyl-7-methylene-8-(propionyloxy)spiro[5.5]undec-2-en-10^3,10^5-dihydroxytetrahydro-*2H*-pyran-10-carboxylate (**10**) through the extensive spectroscopic experiments (Figure 4.127).

4.3.2.5a Structural characterization of Compound 9

3-(Hydroxymethyl)-7-(methoxymethyl)-3,11-dimethyl-9-oxospiro[5.5]undec-4-en-10-methylbutanoate

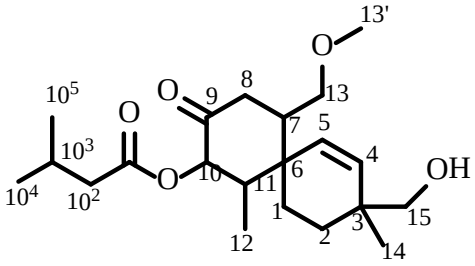

Sample yield	0.36 % (> 99% purity, RP-C18 HPLC)
Physical description	Colourless oily
Molecular formula	$C_{21}H_{34}O_5$
Molecular mass	366.2406

The spiro-compound, 3-(hydroxymethyl)-7-(methoxymethyl)-3,11-dimethyl-9-oxospiro[5.5]undec-4-en-10-methylbutanoate was isolated as colourless oil. The compound (**9**) has exhibited UV absorbance (UV (MeOH) λ_{max}) at 247 nm (Figure 4.128). The homogeneity of the compound was ascertained by HPLC data on a bonded phase octadecylsilane (C_{18}) stationary phase (HPLC, MeOH/ MeCN , 1:2 v/v) with R_t: 4.42 min (Figure 4.129).

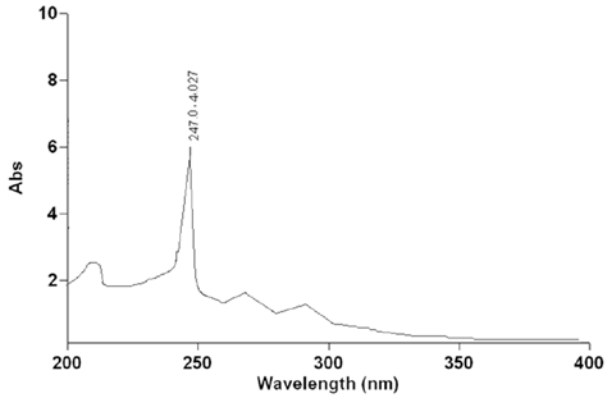

Figure 4.128.: UV spectrum of 3-(hydroxymethyl)-7-(methoxymethyl)-3,11-dimethyl-9-oxospiro[5.5]undec-4-en-10-methylbutanoate (**9**)

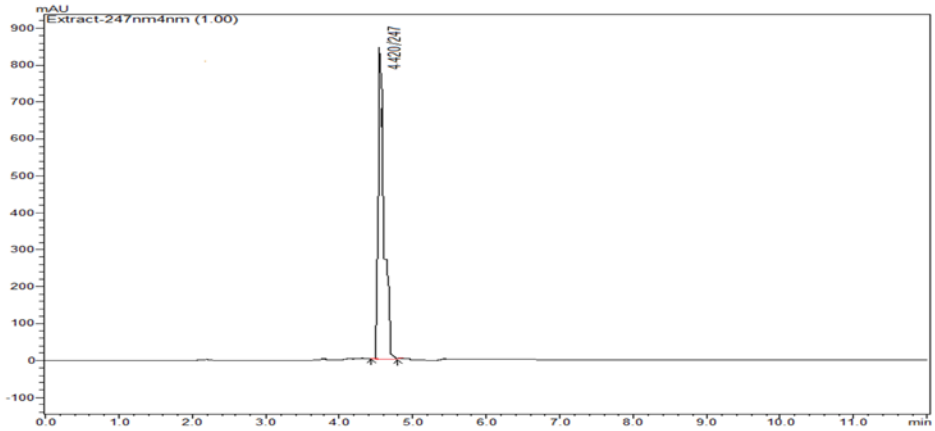

Figure 4.129.: HPLC chromatogram of 3-(hydroxymethyl)-7-(methoxymethyl)-3,11-dimethyl-9-oxospiro[5.5]undec-4-en-10-methylbutanoate (**9**)

Bioactivity-guided chromatographic purification using reverse phase preparative HPLC of the organic extract of *G. salicornia* yielded 3-(hydroxymethyl)-7-(methoxymethyl)-3,11-dimethyl-9-oxospiro[5.5]undec-4-en-10-methylbutanoate (**9**) as a colourless oily substance. The molecular ion peak was analyzed by mass spectroscopic (electrosparay ionization method; Bruker Daltonic, GmbH, Germany) experiment and its molecular ion peak was observed at *m/z* 367.4996 $[M+H]^+$ (Figure 4.130). The mass spectroscopy along with integrative NMR-IR experiments deduced the molecular formula of **9** as $C_{21}H_{34}O_5$ (Table 4.16), which was indicative of five sites of unsaturation.

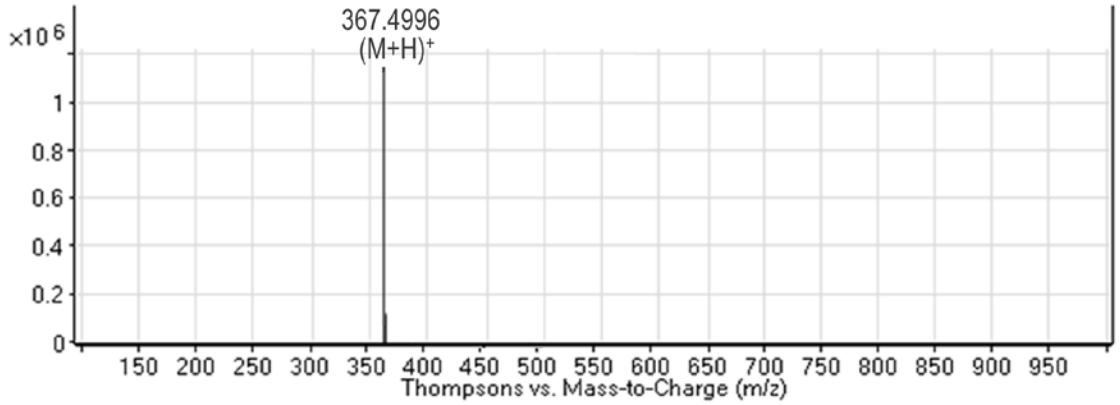

Figure 4.130.: ESIMS spectrum of 3-(hydroxymethyl)-7-(methoxymethyl)-3,11-dimethyl-9-oxospiro[5.5]undec-4-en-10-methylbutanoate (**9**)

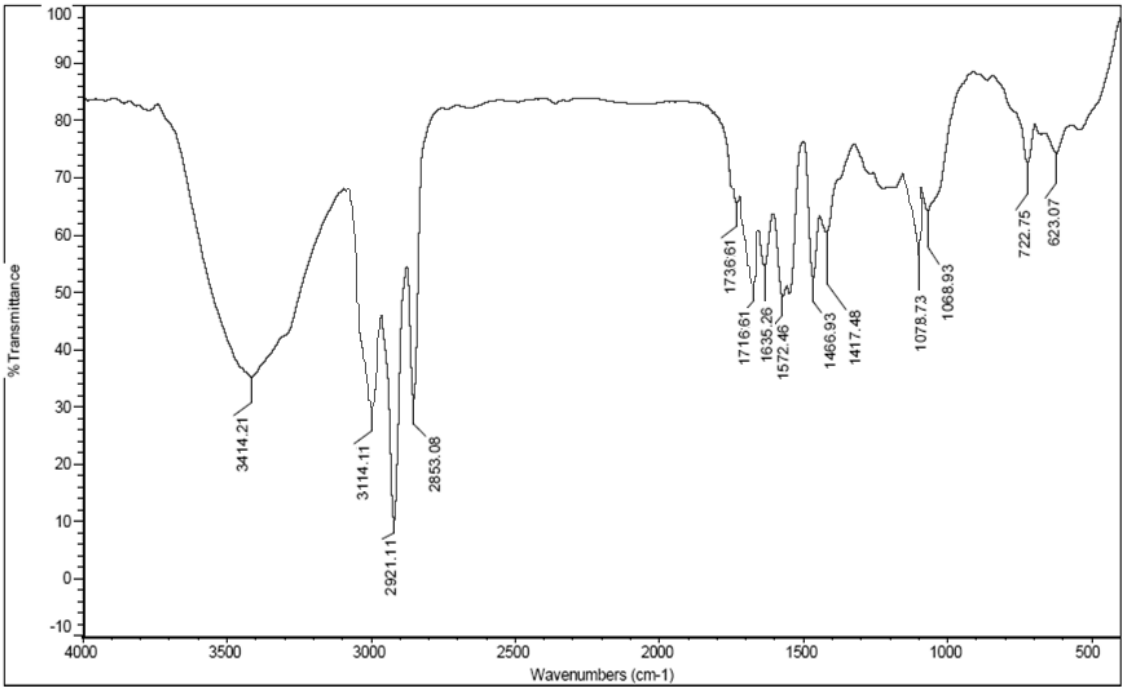

Figure 4.131.: FTIR spectrum of 3-(hydroxymethyl)-7-(methoxymethyl)-3,11-dimethyl-9-oxospiro[5.5]undec-4-en-10-methylbutanoate (**9**)

The FTIR spectrum of **9** exhibited absorption peaks at 3414, 1068, 1716 and 1736 cm^{-1} that might correspond to hydroxyl (-OH), ether (-C-O-C), carbonyl (-C=O) and ester {-O-(C=O)-} functionalities, respectively (Figure 4.131). The ^{13}C-NMR spectrum of **9** showed the signals for 21 carbons. The types of the carbon signals determined from DEPT spectrum were five methyls, six each of methylenes and methines (two olefinic), along with four non-protonated carbons (one each of carbonyl and carbonyl ester groups). The ^{1}H spectrum of **9** displayed signals at δ 5.24 and 4.52 due to the olefinic protons. Doublets at δ 4.41, 3.69 and singlets at δ 3.37 and 3.20 were assigned to protons, which were geminal to the oxygen atom, whereas nine well-resolved signals, each attributed to one of the remaining aliphatic protons, were recorded at δ 1.70-2.82. Four shielded protons at δ 0.81, 0.86, 0.88 and 1.33 were accounted for the methyl protons in **9**. In compound **9**, the chemical shifts for five methyls, four sp^3 methines, two sp^2 methines, six sp^3 methylenes and four quaternary carbons were identified by exhaustive ^{1}H/^{13}C/DEPT experiments(Figure 4.132-1.134). The ^{13}C exhibited highly deshielded resonances for four protonated carbons at δ 94.97, 50.09, 55.03 and 72.40, which might be directly attached to oxygen. The sp^2 protons with highly deshielded resonance at δ 4.52

and 5.24 with doublets were bonded to the carbons at δ 128.45 and 133.09, respectively, as inferred from the HSQC spectrum (Figure 4.135).

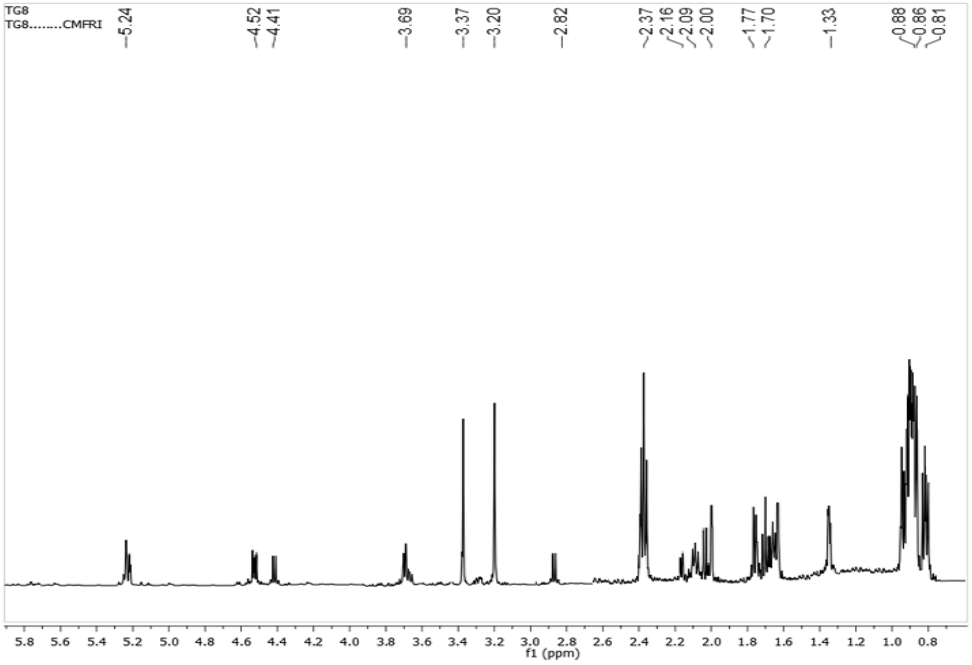

Figure 4.132.: ^{1}H-NMR spectrum of 3-(hydroxymethyl)-7-(methoxymethyl)-3,11-dimethyl-9-oxospiro[5.5]undec-4-en-10-methylbutanoate (**9**)

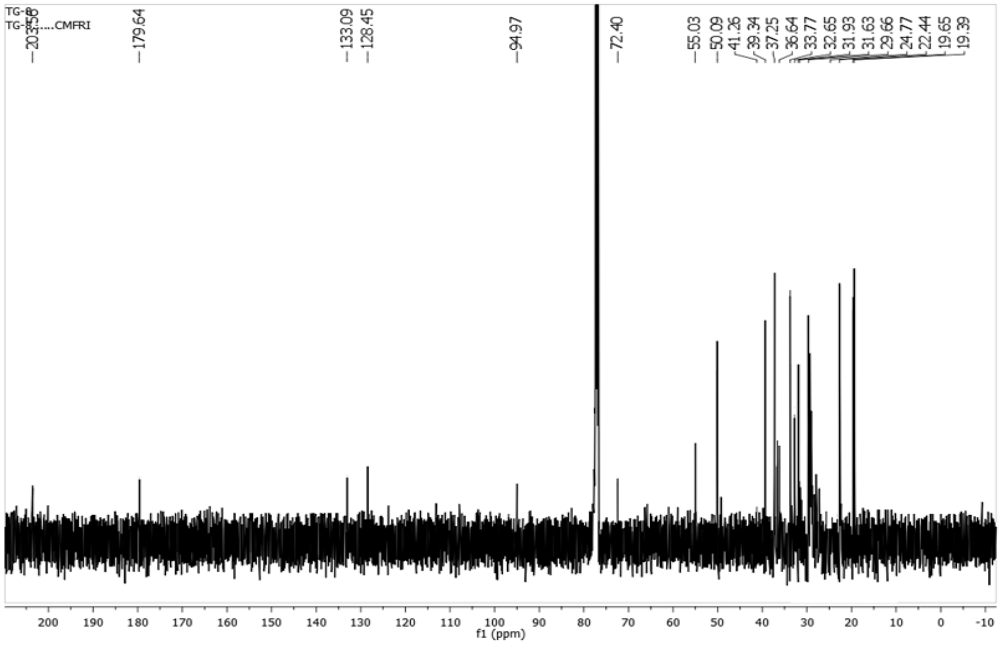

Figure 4.133.: ^{13}C-NMR spectrum of 3-(hydroxymethyl)-7-(methoxymethyl)-3,11-dimethyl-9-oxospiro[5.5]undec-4-en-10-methylbutanoate (**9**)

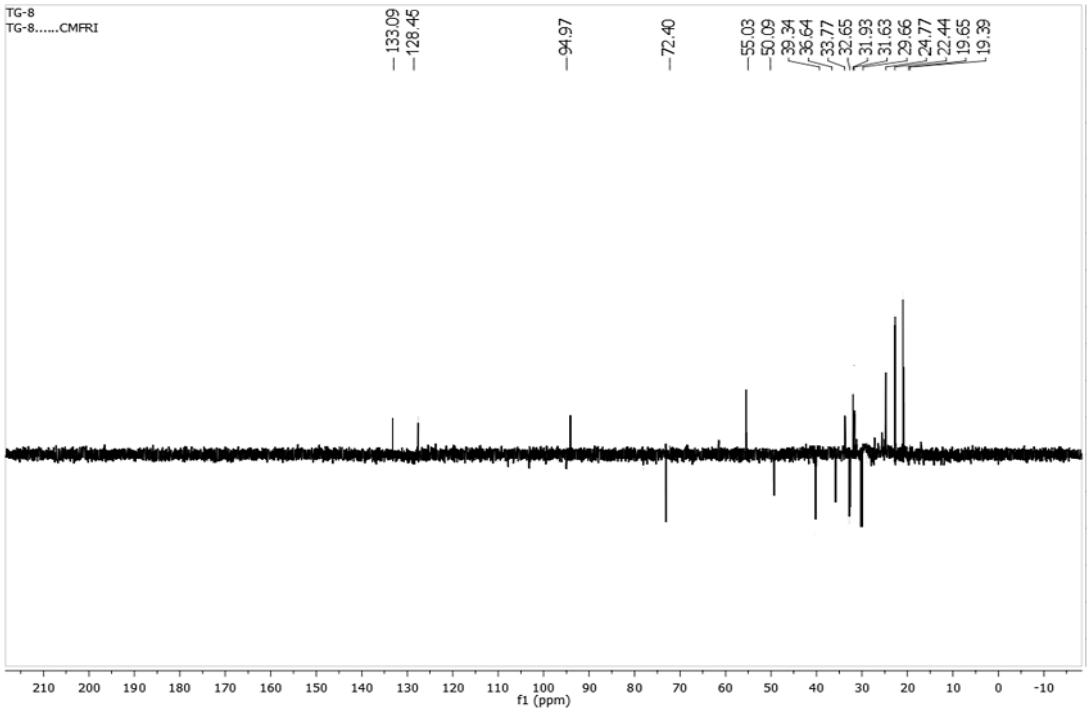

Figure 4.134.: [135]DEPT spectrum of 3-(hydroxymethyl)-7-(methoxymethyl)-3,11-dimethyl-9-oxospiro[5.5]undec-4-en-10-methylbutanoate (**9**)

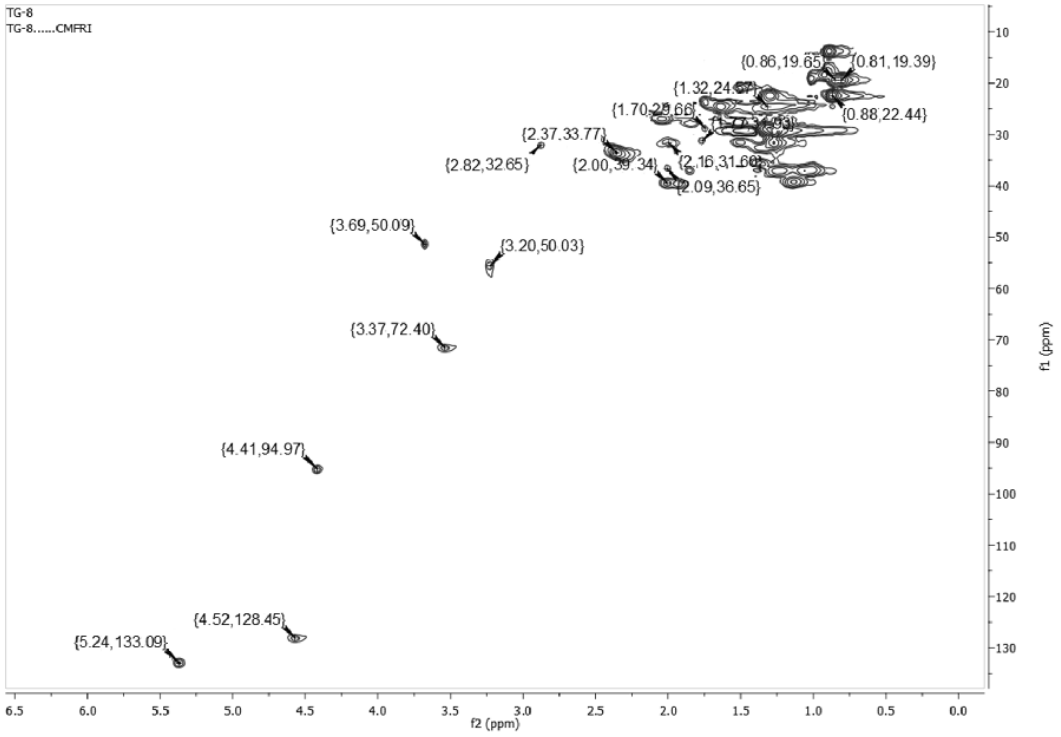

Figure 4.135.: HSQC spectrum of 3-(hydroxymethyl)-7-(methoxymethyl)-3,11-dimethyl-9-oxospiro[5.5]undec-4-en-10-methylbutanoate (**9**)

Besides these, COSYs from δ 4.52 (assigned at H-4) to δ 5.24 (H-5) and HMBCs from δ 4.52 (H-4) to δ 37.25 (C-3) and δ 5.24 (H-5) to δ 128.45 (C-4) confirmed the presence of olefinic carbons at C-4 and C-5, and quaternary carbon at C-3 (Figure 4.136-4.138). These were further attributed by HMBC correlations between H-2 and C-3 {δ 1.77 (H-2)/37.25 (C-3); -CH_2-C} and H-1 and C-2 {δ 1.70 (H-1)/31.93 (C-2)}. The HMBCs from the methyl proton at H-14 (δ 1.33) and methylene proton at H-15 (δ 3.37) to the shielded non-protonated carbon at C-3 (δ 37.25) confirmed the linkage of methyl and hydroxymethyl at C-3 of cyclohexene ring. These attributions established the partial structure of 3-hydroxymethyl-3-methyl cyclohexene ring in the compound. Similarly, HMBCs from H-7 (δ 2.16) to δ 36.64 (C-8), H-8 (2.09) to highly deshielded carbon, C-9 (δ 203.56) along with the HMBC linkages of H-10 (δ 4.41) to carbons at C-9 (δ 203.56), C-11 (δ 32.65) confirmed the presence of carbonyl group in the bicyclic frame work in the nearby position of C-8 (-CH_2). The previously reported spiro-compound, compositacin C enclosed carbonyl at C-10 with carbon signal of about δ 205, and this carbon shift was comparable with the present compounds with carbonyl at C-9 (δ 203.56) (Yu et al. 2017). Moreover, the COSY correlations from δ 2.09 (H-8)/2.06 (H-7)/3.69 (H-13) {H-8/H-7/H-13} and from δ 4.41 (H-10)/2.82 (H-10)/0.88 {H-12/H-10/H-12} together with the HMBCs from δ 0.88 (H-12) to δ 32.65 (C-11); δ 3.69 (H-13) to δ 2.16 (C-7), 55.03 (C-13') attributed to the partial structure of methoxymethyl-12-methylcyclohexanone ring system in **9**. The partial structure of 3-hydroxymethyl-3-methyl cyclohexene and 7-methoxymethyl-11-methyl cyclohexanone rings were spiro fused at C-6, which was confirmed through the HMBCs from H-5 to C-6 {δ 5.24 (H-5)/41.26 (C-6); =CH(5)-C(6)<}, H-1 to C-6{1.70 (H-1)/41.26 (C-6); -CH_2-CH_2-C-}, H-7 to H-11 {δ 2.16 (H-7)/41.26 (C-6)} and from H-11 to C-6 {2.82 (H-11)/41.26 (C-6); -CH-C-CH-}.

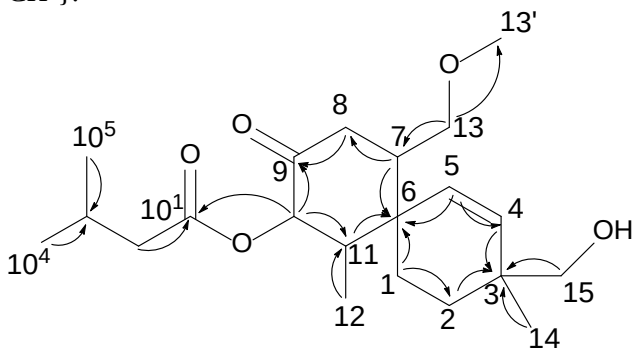

Figure 4.136.: ^{1}H-^{1}H COSY (bold face bonds), and selected HMBCs (double-barbed arrows), correlations of 3-(hydroxymethyl)-7-(methoxymethyl)-3,11-dimethyl-9-oxospiro[5.5]undec-4-en-10-methylbutanoate (**9**)

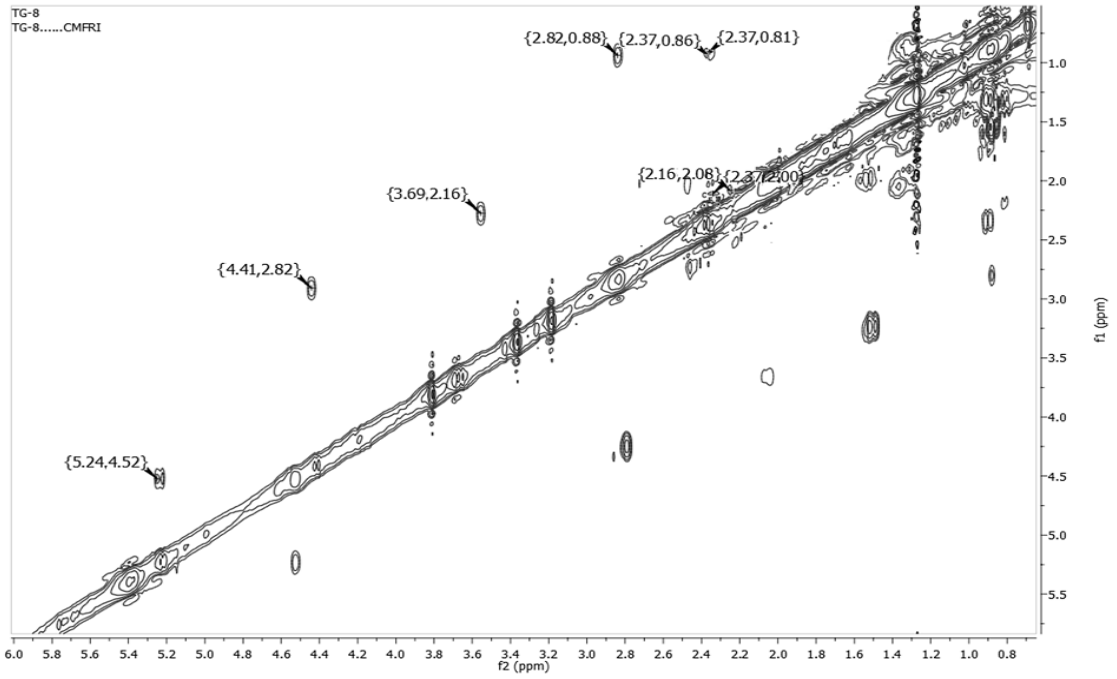

Figure 4.137.: ^{1}H-^{1}H COSY spectrum of 3-(hydroxymethyl)-7-(methoxymethyl)-3,11-dimethyl-9-oxospiro[5.5]undec-4-en-10-methylbutanoate (**9**)

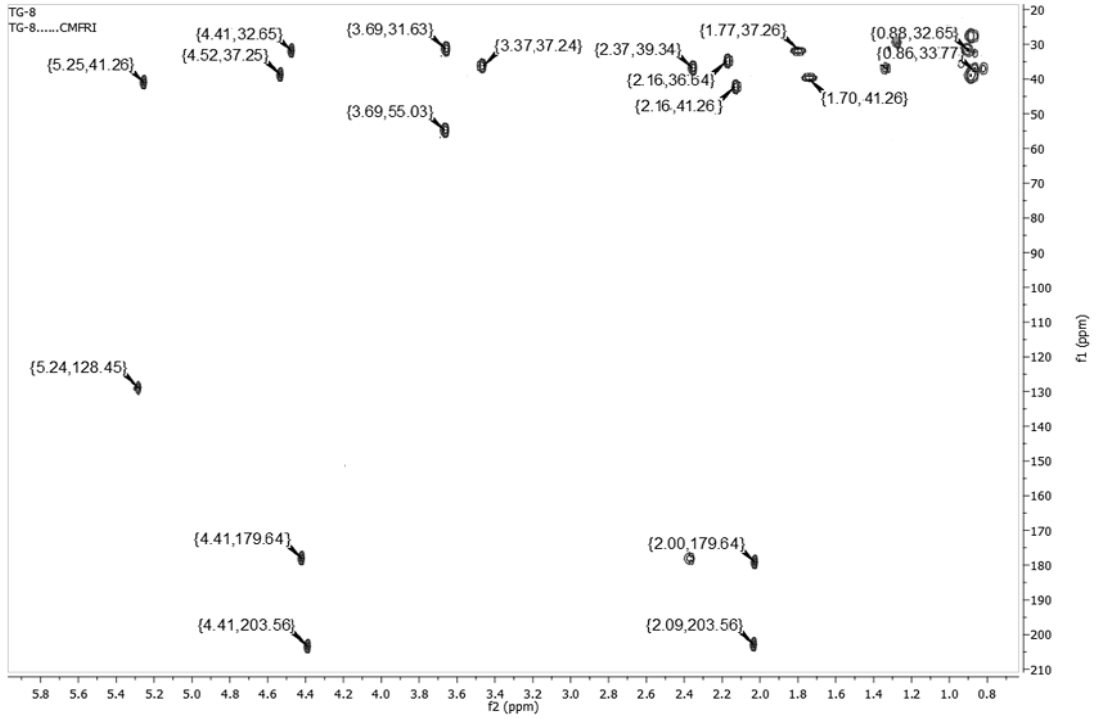

Figure 4.138.: HMBC spectrum of 3-(hydroxymethyl)-7-(methoxymethyl)-3,11-dimethyl-9-oxospiro[5.5]undec-4-en-10-methylbutanoate (**9**)

The titled compound **9** was supported by the previous reports of spiro[5.5]undecane derivatives (Davyt et al. 2001; Ji et al. 2007; Suzuki et al. 2001). The COSY couplings from δ 2.00 (H-10^2)/2.37 (H-10^3)/0.81 (H-10^4), 0.86 (H-10^5) along with ^{1}H-^{13}C HMBCs, such as δ 2.00 (H-10^2) to δ 179.64 (C-10^1); δ 2.37 (H-10^3) to δ 39.34 (C-10^2); δ 0.81 (H-10^4) to δ 33.77 (C-10^3) and δ 0.86 (H-10^5) to δ 33.77 (C-10^3) confirmed the ester side chain assignment. The long bond ^{1}H-^{13}C HMBCs from H-10 to C-10^1 of ester carbonyl {δ 4.41 (H-10)/179.64 (C-10^1)} suggested the attachment of ester carbonyl part of 3-methylbutanoate at C-10 of cyclohexanone ring. Notably, the olefinic group at δ 4.52 (H-4), 5.24 (H-5) recorded lesser coupling constants (J) of 7.6 and 5.5 Hz, respectively, and therefore, the configuration of these olefinic groups in oxospiro[5.5]undecen-4-ene was ascertained as cis oriented in the cyclohexene ring. Thus, the compound **9** was deduced to possess a rearranged bicyclic skeleton of cyclohexanone ring spiro-fused to substituted cyclohexene framework, and was found to possess a spiro[5.5]undecane skeleton.

Table 4.16: NMR spectroscopic data of compound (**9**), 3-(hydroxymethyl)-7-(methoxymethyl)-3,11-dimethyl-9-oxospiro[5.5]undec-4-en-10-methylbutanoate (**9**) isolated from red seaweed *G. salicornia*

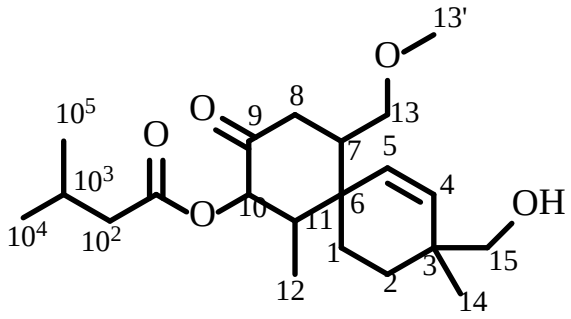

Compound **9…….**3-(Hydroxymethyl)-7-(methoxymethyl)-3,11-dimethyl-9-oxospiro[5.5]undec-4-en-10-methylbutanoate (**9**)

C. No.	^{13}C	^{1}H(int.,mult.,J in Hz)[b]	^{1}H-^{1}H COSY	HMBC
1	29.66	1.70(2H,t,3.5 Hz)	-	C-2,6
2	31.93	1.77(2H,t,3.8 Hz)	-	C-3
3	37.25	-	-	-
4	128.45	4.52(1H,d,7.6 Hz)	H-5	C-3
5	133.09	5.24(1H,t,8.5 Hz)	-	C-4,6
6	41.26	-	-	-
7	31.63	2.16(1H,t,4.2 Hz)	H-8, H-13	C-6, 8
8	36.64	2.09(2H,d,9.6Hz)	-	C-9
9	203.56	-	-	-

10	94.97	4.41(1H,d,10.5 Hz)	H-11	C-9,11,10^1
11	32.65	2.82(1H,d,7.5 Hz)	H-12	C-6
12	22.44	0.88(3H,d,8.2 Hz)	-	C-11
13	50.09	3.69(2H,d,3.5 Hz)	-	C-7,13'
14	24.77	1.33(3H,d,11.3 Hz)	-	C-3
15	72.40	3.37(2H,s)	-	C-3
10^1	179.64	-	-	-
10^2	39.34	2.00(2H,d,8.1 Hz)	H-10^3	C-10^1
10^3	33.77	2.37(1H,t,3.5 Hz)	H-10^4, H-10^5	C-10^2
10^4	19.39	0.81(3H,t,3.5 Hz)	-	C-10^3
10^5	19.65	0.86(3H,t,3.5 Hz)	-	C-10^3
13'	55.03	3.20(3H,s)	-	-

[a] NMR spectra recorded using Bruker AVANCE III 500 MHz (AV 500) spectrometers.

[b] Values in ppm, multiplicity and coupling constants (J = Hz) are indicated in parentheses.

Assignments were made with the aid of the ^{1}H-^{1}H COSY, HSQC, HMBC and NOESY experiments.

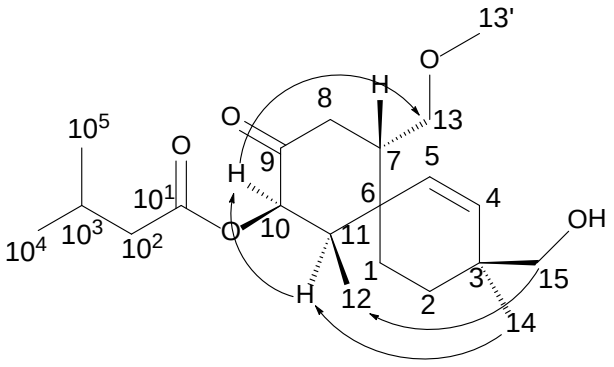

Figure 4.139.: NOESY (double barbed arrows) correlations of 3-(hydroxymethyl)-7-(methoxymethyl)-3,11-dimethyl-9-oxospiro[5.5]undec-4-en-10-methylbutanoate (**9**)

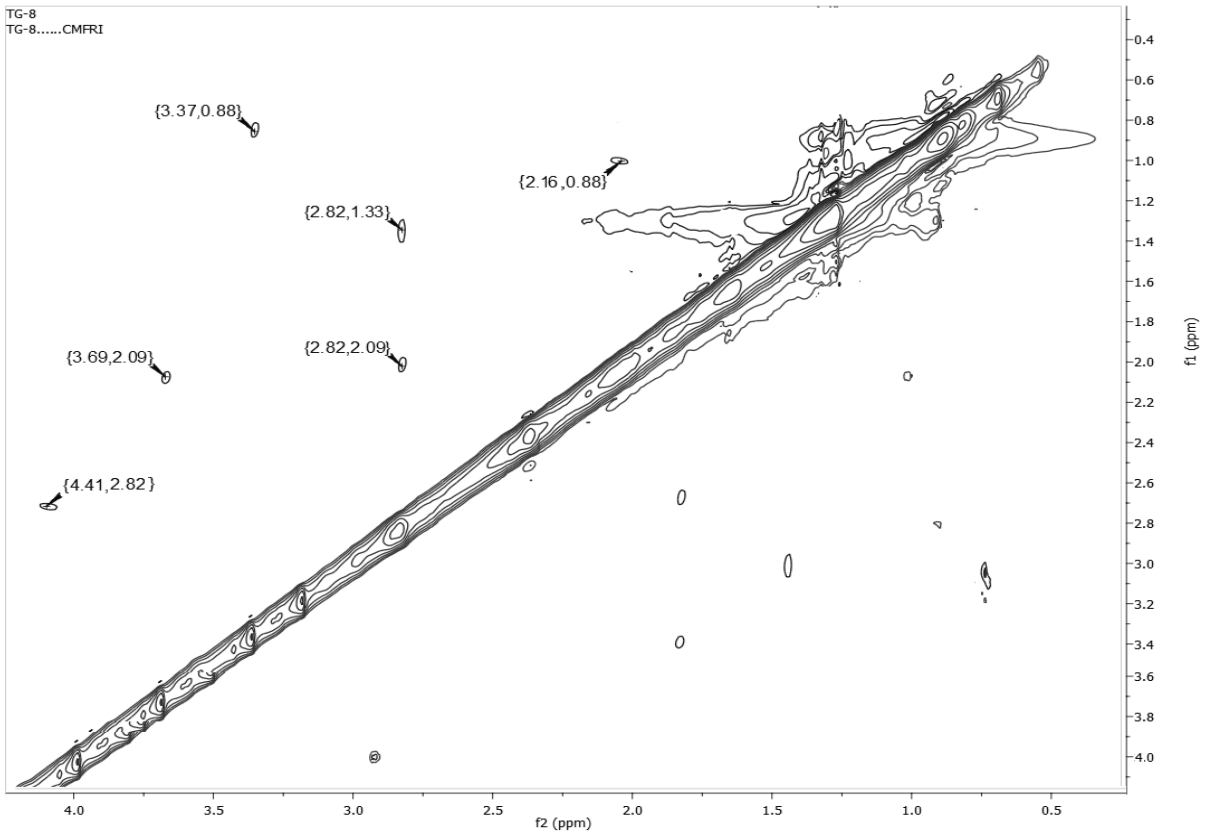

Figure 4.140.: NOESY spectrum of 3-(hydroxymethyl)-7-(methoxymethyl)-3,11-dimethyl-9-oxospiro[5.5]undec-4-en-10-methylbutanoate (**9**)

Relative stereochemistries of the protons chiral centers, mainly at C-3, C-7, C-10 and C-11 were deduced by extensive NOESY experiments (Figure 4.139-4.140). The NOE correlations from δ 1.33 (H-14)/2.82 (H-11)/4.41 (H-10) confirmed the equiplaner alignment of these protons in their close proximity, and these were arbitrarily allocated in the α-direction with reference to its molecular plane of symmetry. The NOE correlation from δ 2.16 (H-7)/0.88 (H-12) attributed that these protons were aligned opposite to α-protons, and therefore, assigned as β-oriented. Therefore, the 7-methoxymethyl at C-7 was α-directed being trans to the β-proton at C-7, whereas the hydroxymethyl was β-oriented being trans to the α-proton at C-3.

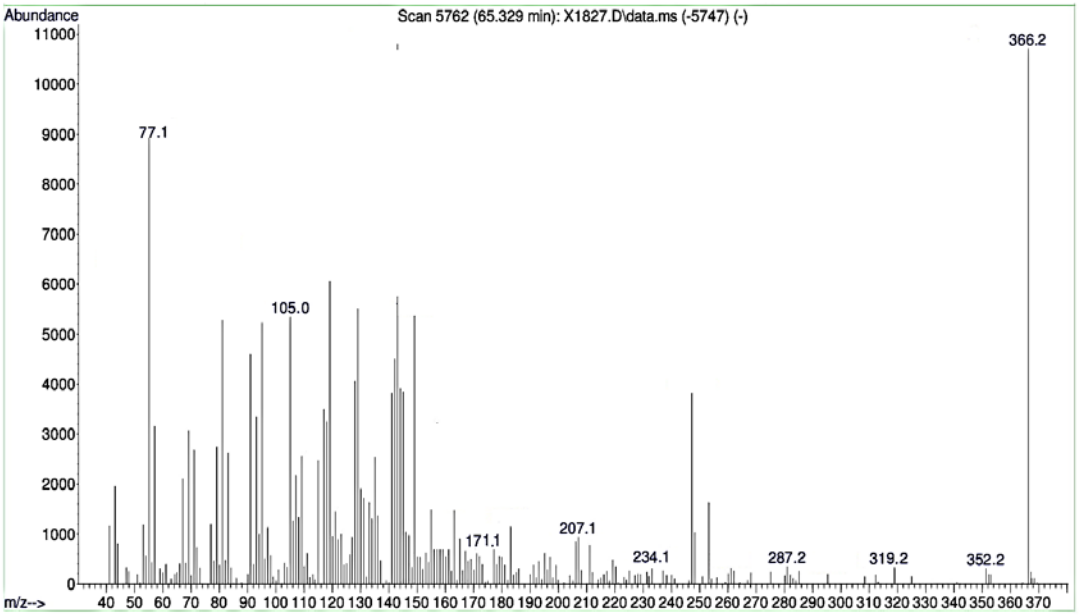

Figure 4.141.: EI-MS spectrum of 3-(hydroxymethyl)-7-(methoxymethyl)-3,11-dimethyl-9-oxospiro[5.5]undec-4-en-10-methylbutanoate (**9**)

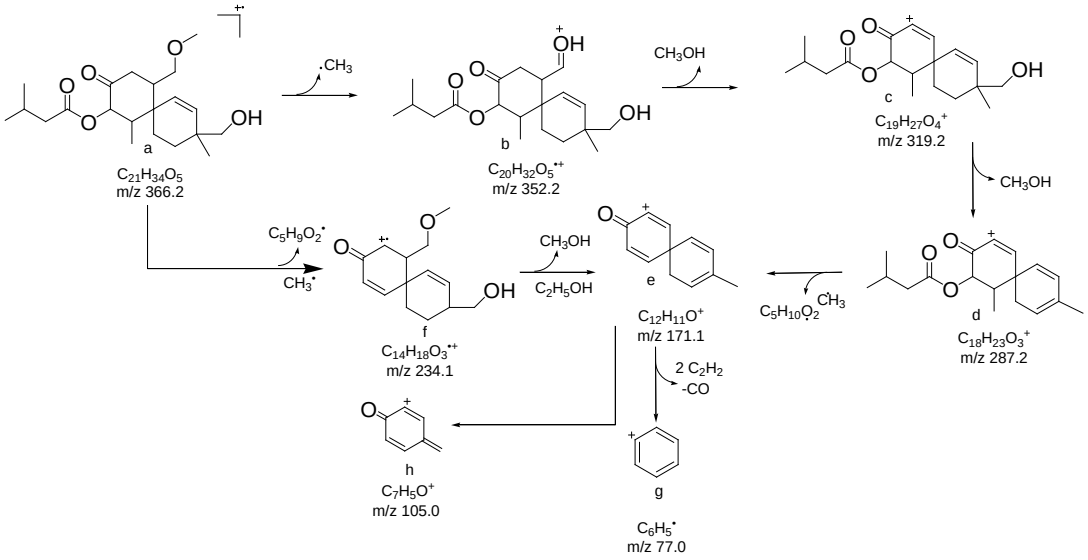

Figure 4.142.: Tentative mass fragmentation pattern of 3-(hydroxymethyl)-7-(methoxymethyl)-3,11-dimethyl-9-oxospiro[5.5]undec-4-en-10-methylbutanoate (**9**)

The molecular ion peak at *m/z* 366 (**a**) $[M]^+$ underwent an elimination of methyl and $C_5H_9O_2^{\bullet}$ along with reorganization of bonds leading to the fragment peaks at *m/z* 352 (**b**) and 234 (**f**). Further fragmentation of (**b**) led to the formation of mass fragment, **c** at *m/z* 319. The radical cation, **c** also performed an elimination of methanol radical ion leading to a rearrangement mechanism to yield **d**. The mass fragment (**f**) at *m/z* 234 was also led to the

formation of **e** and then to **h** (*m/z* 105). The fragment at *m/z* 77 was found to be the base peak (Figure 4.141-4.142).

4.3.2.5b Structural characterization of Compound 10

4-Ethoxy-11,11-dimethyl-7-methylene-8-(propionyloxy)spiro[5.5]undec-2-en-10^3,10^5-dihydroxytetrahydro-*2H*-pyran-10-carboxylate

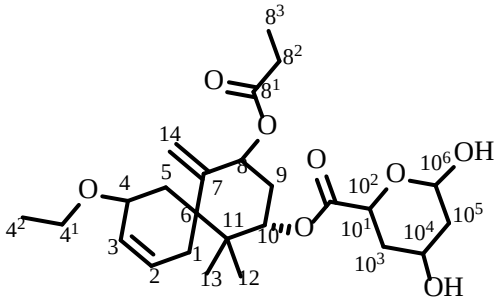

Sample yield	0.34% (> 99% purity, RP-C18 HPLC)
Physical description	Colourless oily
Molecular formula	$C_{25}H_{38}O_8$
Molecular mass	466.2567

The spiro-compound derivative, 4-ethoxy-11,11-dimethyl-7-methylene-8-(propionyloxy)spiro[5.5]undec-2-en-10^3,10^5-dihydroxytetrahydro-*2H*-pyran-10-carboxylate was isolated as colourless oil. The compound (**10**) has exhibited UV absorbance (UV (MeOH) λ_{max}) at 270 nm (Figure 4.143). The homogeneity of the compound was ascertained by HPLC data on a bonded phase octadecylsilane (C_{18}) stationary phase (HPLC, MeOH/MeCN , 1:2 v/v) with R_t: 3.35 min (Figure 4.144).

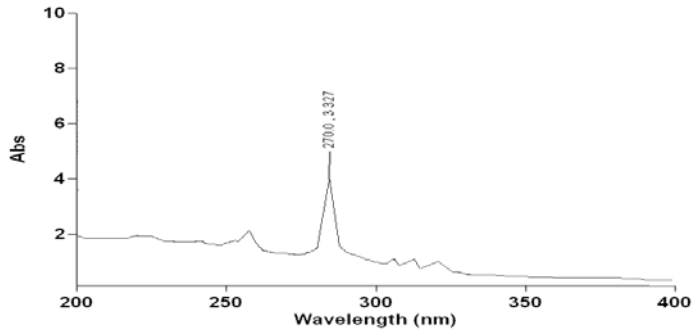

Figure 4.143.: UV spectrum of 4-ethoxy-11,11-dimethyl-7-methylene-8-(propionyloxy)spiro[5.5]undec-2-en-10^3,10^5-dihydroxytetrahydro-*2H*-pyran-10-carboxylate (**10**)

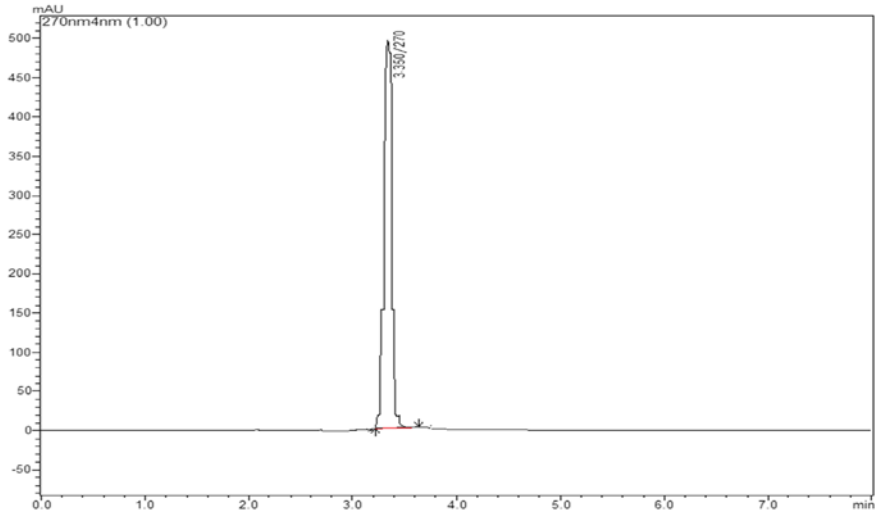

Figure 4.144.: HPLC chromatogram of 4-ethoxy-11,11-dimethyl-7-methylene-8-(propionyloxy)spiro[5.5]undec-2-en-10^3,10^5-dihydroxytetrahydro-*2H*-pyran-10-carboxylate (**10**)

The chromatographic fractionation of the organic extract of *G. salicornia* yielded 4-ethoxy-11,11-dimethyl-7-methylene-8-(propionyloxy)spiro[5.5]undec-2-en-10^3,10^5-dihydroxytetrahydro-2*H*-pyran-10-carboxylate (**10**) as a colourless oily substance. The molecular ion peak was observed at *m/z* 467.2645 $[M+H]^+$ (Figure 4.145). The mass spectroscopy along with integrative NMR-IR experiments deduced the molecular formula of **10** as $C_{25}H_{38}O_8$ (Table 4.17), which was indicative of six sites of unsaturation.

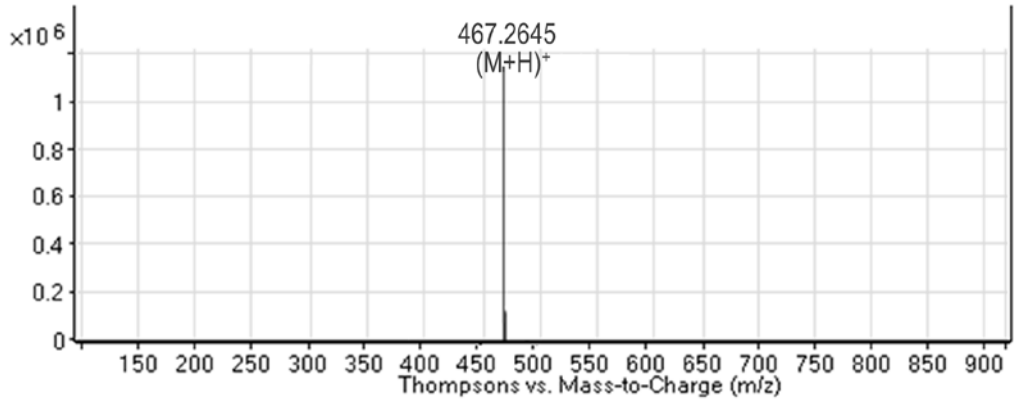

Figure 4.145.: HRESIMS spectrum of 4-ethoxy-11,11-dimethyl-7-methylene-8-(propionyloxy)spiro[5.5]undec-2-en-10^3,10^5-dihydroxytetrahydro-*2H*-pyran-10-carboxylate (**10**)

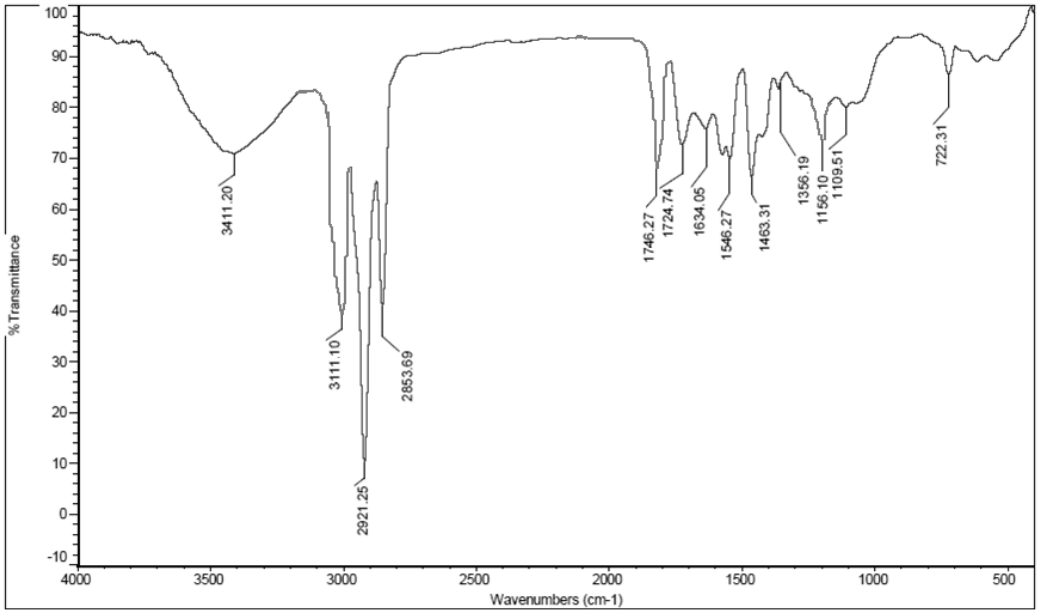

Figure 4.146.: FTIR spectrum of 4-ethoxy-11,11-dimethyl-7-methylene-8-(propionyloxy)spiro[5.5]undec-2-en-10^3,10^5-dihydroxytetrahydro-*2H*-pyran-10-carboxylate (**10**)

The FTIR spectrum of **10** exhibited the presence of absorption peaks at 3411, 1109 and 1746 cm^{-1} that might correspond to the hydroxyl (-OH), ether (-C-O-C) and ester {-O-(C=O)-} functionalities, respectively (Figure 4.146). The ^{13}C-NMR spectrum of **10** showed signals for 25 carbons. The type of carbon signals determined from DEPT spectrum were of four methyls, seven sp^3 methylene, one sp^2 methylene (exocyclic), six sp^3 methine, two sp^2 methines (one olefinic) and five non-protonated carbons (two ester groups).

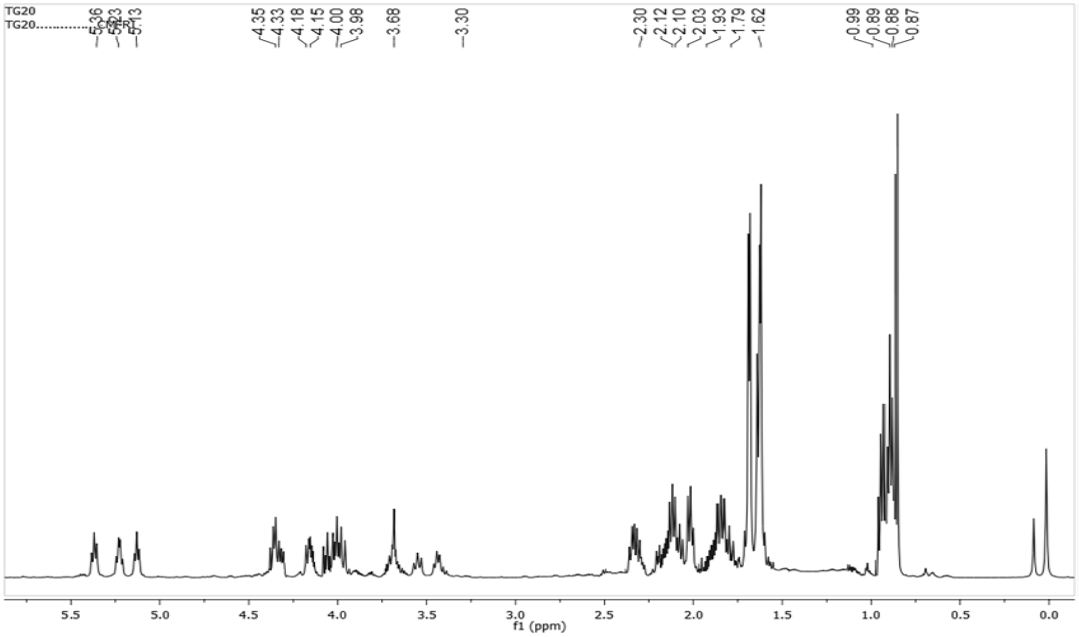

Figure 4.147.: ^{1}H-NMR spectrum of 4-ethoxy-11,11-dimethyl-7-methylene-8-(propionyloxy)spiro[5.5]undec-2-en-10^{3},10^{5}-dihydroxytetrahydro-*2H*-pyran-10-carboxylate (**10**)

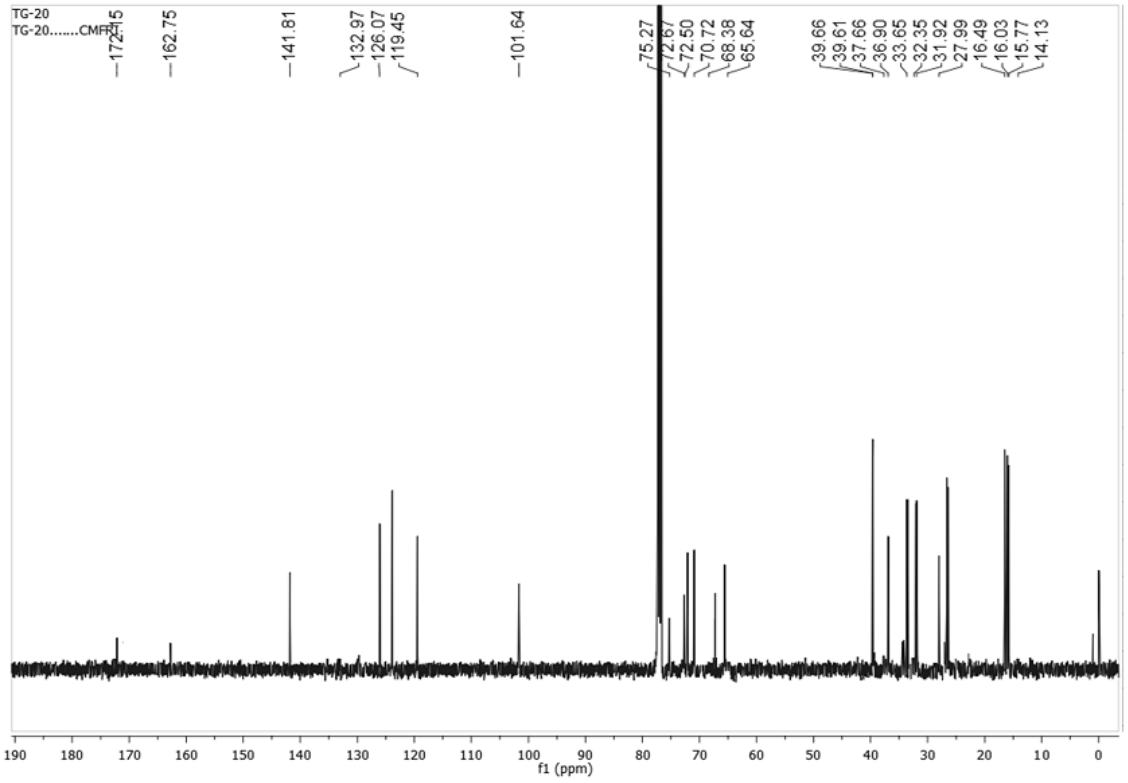

Figure 4.148.: ^{13}C-NMR spectrum of 4-ethoxy-11,11-dimethyl-7-methylene-8-(propionyloxy)spiro[5.5]undec-2-en-10^{3},10^{5}-dihydroxytetrahydro-*2H*-pyran-10-carboxylate (**10**)

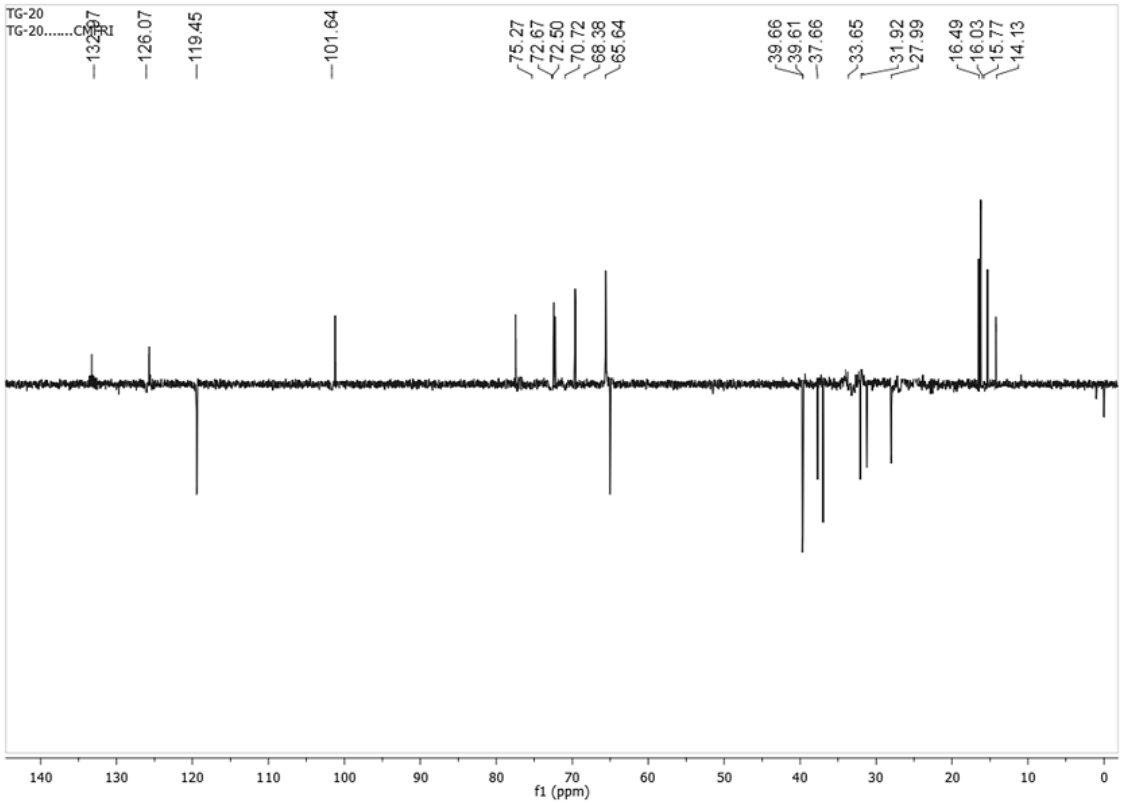

Figure 4.149.: ^{135}DEPT spectrum of 4-ethoxy-11,11-dimethyl-7-methylene-8-(propionyloxy)spiro[5.5]undec-2-en-10^{3},10^{5}-dihydroxytetrahydro-*2H*-pyran-10-carboxylate (**10**)

The ^{1}H-NMR spectrum of **10** displayed signals at δ 5.36 and 5.13 due to olefinic protons. Triplets at δ 4.00, 4.15, 4.18, 5.23 and multiplets at δ 3.30, 3.98 were assigned to protons geminal to the oxygen atom, whereas seven well-resolved signals, each attributed to one of the remaining aliphatic protons, appeared at δ 1.62-2.30. The chemical shift values at δ 0.87, 0.88, 0.89 and 0.99 were assigned to methyls in **10**. The ^{13}C-NMR of **10** displayed highly deshielded resonances for four protonated carbons at δ 75.27, 65.64, 72.50 and 101.64, which were directly attached to oxygen (Figure 4.147-4.149). The sp^{2} protons with highly deshielded resonance at δ 5.36 and 5.13 with triplets were bonded to the carbons at δ 126.07 and 132.97, respectively as inferred from the HSQC spectrum (Figure 4.150). Besides these, COSY correlations from H-1 to H-2; H-2 to H-3; H-3 to H-4 and H-4 to H-5 attributed to the presence of olefinic carbons (C-2 and C-3), and therefore, ascertained the partial portion of cyclohexene ring in **10** {δ 1.79 (assigned at H-1)/5.36 (H-2)/5.13 (H-3)/3.98 (H-4)/1.62 (H-5); -CH_2-CH=CH-CH-CH_2} (Figure 4.151 & 4.152). These attributions were further supported by the HMBC correlations between the H-1 and C-2 {δ 1.79 (H-1)/126.07 (C-2); CH_2-CH=}, H-3 and

C-2/C-4 {δ 5.13 (H-3)/126.07 (C-2)/75.27 (C-4); >CH=CH-CH<} and H-5 to C-4 {δ 1.62 (H-5)/75.27 (C-4); CH_2-CH<}.

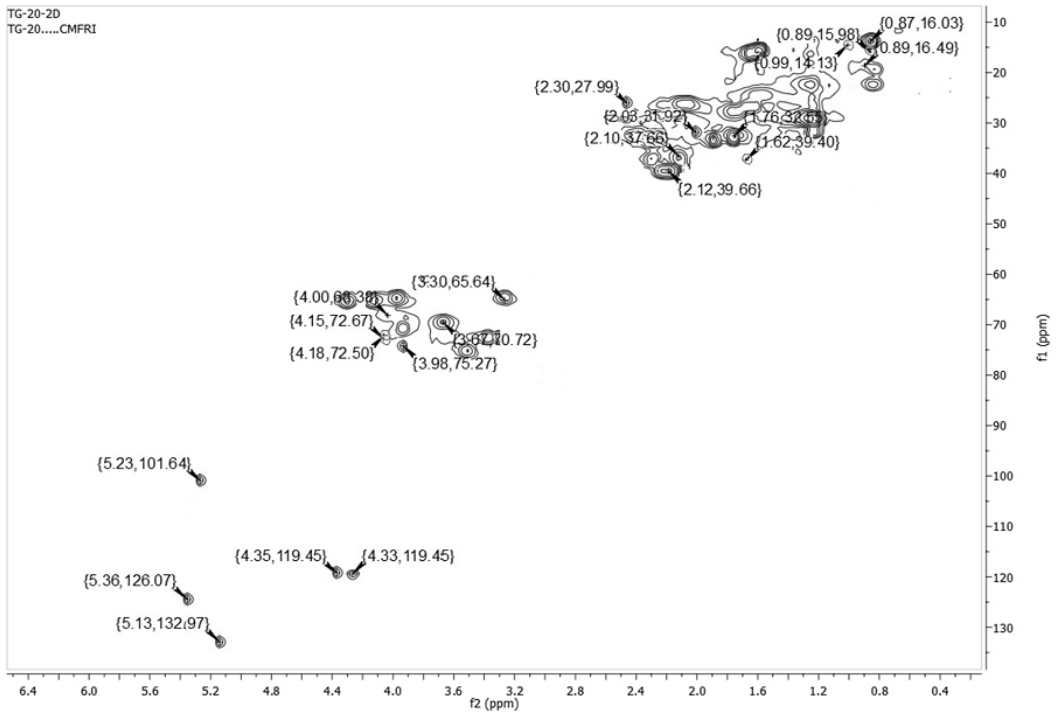

Figure 4.150.: HSQC spectrum of 4-ethoxy-11,11-dimethyl-7-methylene-8-(propionyloxy)spiro[5.5]undec-2-en-10^3,10^5-dihydroxytetrahydro-*2H*-pyran-10-carboxylate (**10**)

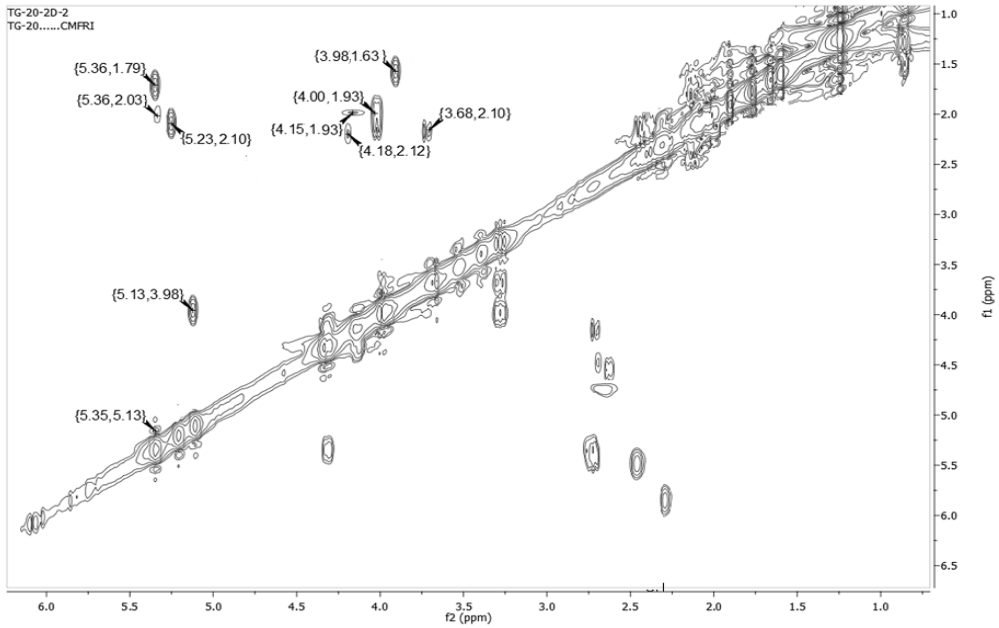

Figure 4.151.: ^{1}H-^{1}H COSY spectrum of 4-ethoxy-11,11-dimethyl-7-methylene-8-(propionyloxy)spiro[5.5]undec-2-en-10^3,10^5-dihydroxytetrahydro-*2H*-pyran-10-carboxylate (**10**)

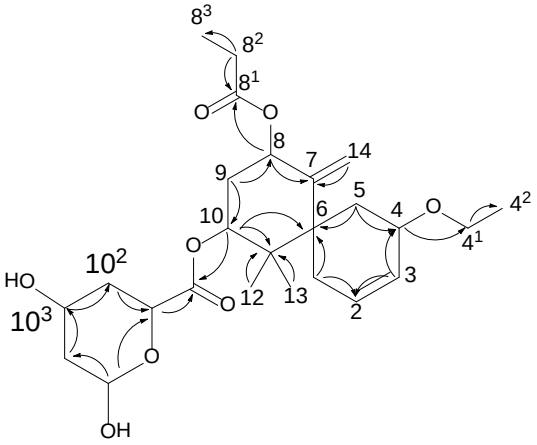

Figure 4.152.: ^{1}H-^{1}H COSY (bold face bonds), and selected HMBCs (double-barbed arrows), correlations of 4-ethoxy-11,11-dimethyl-7-methylene-8-(propionyloxy)spiro[5.5]undec-2-en-10^{3},10^{5}-dihydroxytetrahydro-*2H*-pyran-10-carboxylate (**10**)

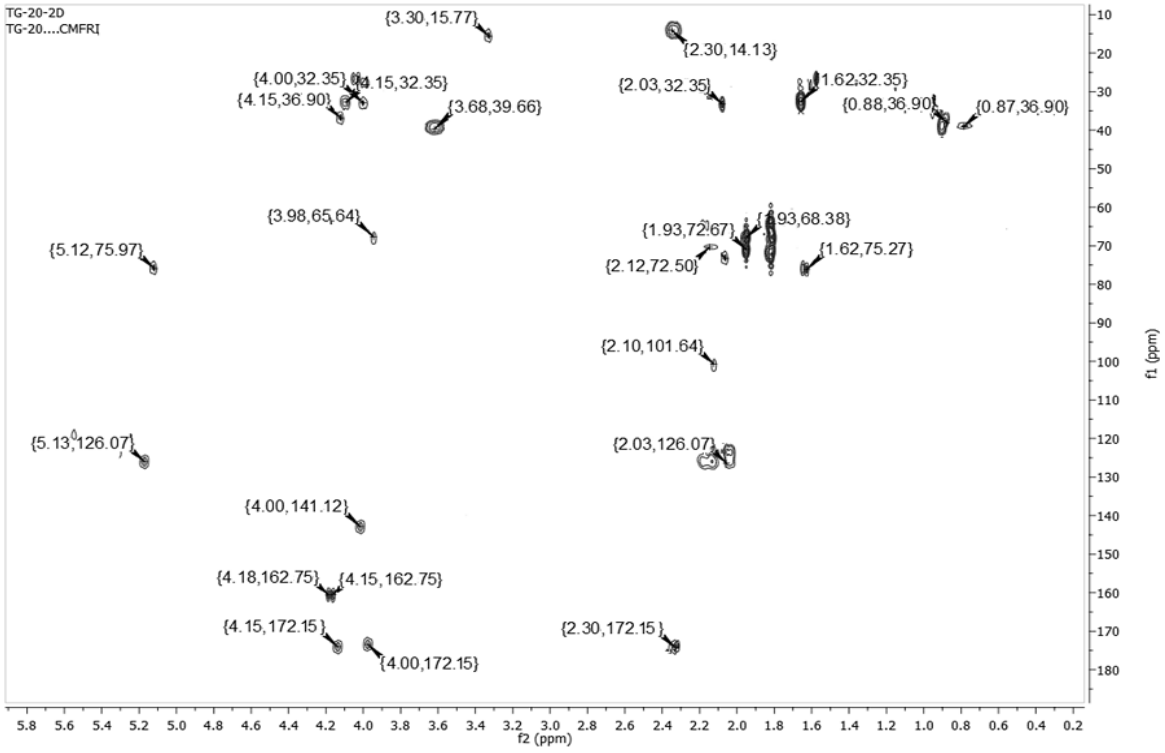

Figure 4.153.: HMBC spectrum of 4-ethoxy-11,11-dimethyl-7-methylene-8-(propionyloxy)spiro[5.5]undec-2-en-10^{3},10^{5}-dihydroxytetrahydro-*2H*-pyran-10-carboxylate (**10**)

The signals at δ 3.98 (H-4) and 3.30 (H-4^{1}) displaying HSQC correlation with δ 75.27 and 65.64, respectively were geminal to oxygen atom in the ether linkage {-CH(O)CH_2}. The proton signal at δ 4.18 (H-10^{2}) and 5.23 (H-10^{6}) displayed HSQC correlation with the

carbon traces at δ 72.50 and 101.64, respectively that were geminal to oxygen atom in pyran ring {-CH(O)CH-}. The previously reported spiro-compound, 1,4,9-trimethyl-5-methylidenespiro[5.5]undec-1,7-diene-4,9-diol bearing the exocyclic double bond between C-7 and C-14 with a chemical shift of δ 154.6 (C-7) and δ 110.2 (C-14) along with hydroxylated non-protonated carbon at δ 72.5 were comparable with the chemical shifts of **10** {δ 141.81 (C-7); δ 119.45 (C-14); δ 68.38 (C-8)} (Davyt et al. 2001). The lower chemical shift of δ 68.38 at C-8 in the titled compound might be due to the presence of protonated carbon and the derivatisation of hydroxyl group at C-8, whereas in the reported 1,4,9-trimethyl-5-methylidenespiro[5.5]undec-1,7-diene-4,9-diol (**10**), the C-8 position was found as non-protonated carbon with a hydroxyl group (Davyt et al. 2001). COSY spin systems between H-10^2/H-10^3/H-10^4/H-10^5/H-10^6 {δ 4.18 (H-10^2)/2.12 (H-10^3)/3.68 (H-10^4)/2.10 (H-10^5)/5.23 (H-10^6); -CH-CH_2-CH-CH_2-CH-} along with HMBCs from H-10^2 to C-10^1 {δ 4.18 (H-10^2)/162.75 (C-10^1)}, H-10^3 to C-10^2 {δ 2.12 (H-10^3)/72.50 (C-10^2)}, H-10^4 to C-10^3 {δ 3.68 (H-10^4)/39.66 (C-10^3)}, H-10^5 to C-10^4 {δ 2.10 (H-10^5)/70.72 (C-10^4)}, H-10^6 to C-10^5/C-10^1 {δ 5.23 (H-10^6)/37.66 (C-10^5)/162.75 (C-10^1)} attributed to the ester-linked side chain of 10^4,10^6-dihydroxytetrahydro-2H-pyran-10^2-carboxylate.

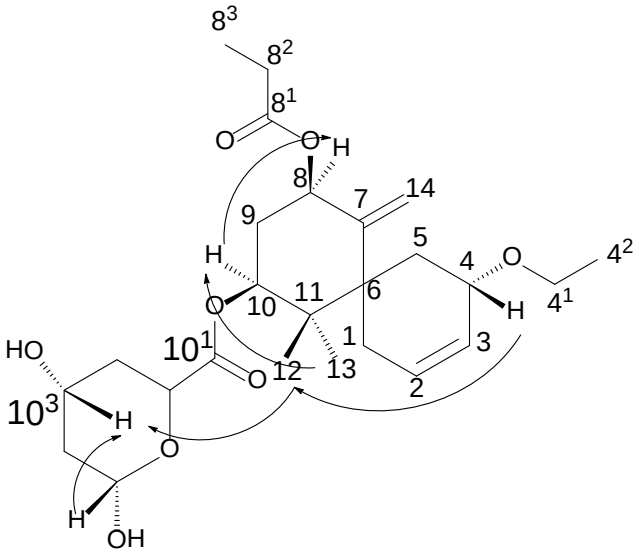

Figure 4.154.: NOESY correlations (double barbed arrows) of 4-ethoxy-11,11-dimethyl-7-methylene-8-(propionyloxy)spiro[5.5]undec-2-en-10^3,10^5-dihydroxytetrahydro-*2H*-pyran-10-carboxylate (**10**)

The attachment of 10^4,10^6-dihydroxytetrahydro-2H-pyran-10^2-carboxylate side chain at C-10 of cyclohexane ring was confirmed by the strong HMBCs from H-10 to C-10^1 {δ 4.15

(H-10)/162.75 (C-10^1); -CH-O-(C=O)}. The partial structure of 4-ethoxy cyclohexene and 10^3,10^5-dihydroxytetrahydro-*2H*-pyran-10-carboxylate attached 11,11-dimethyl-7-methylene-8-(propionyloxy) cyclohexane were spiro-fused at C-6, which confirmed through the HMBCs from H-1 to C-6 {δ 1.79 (H-1)/32.35 (C-6)}, H-5 to C-6 {δ 1.62 (H-5)/32.35 (C-6)}, H-8 to C-6 {δ 4.00 (H-8)/32.35 (C-6)} and H-10 to C-6 {4.15 (H-10)/32.35 (C-6)} (Figure 4.153). The assignment of spiro moiety in **10** was explained on the basis of previous literatures of spiro[5.5]undecane derivatives (Davyt et al. 2001; Ji et al. 2007; Yu et al. 2017). Notably, the olefinic group at δ 5.36 (H-2) and 5.13 (H-3) recorded higher coupling constants (J) of 7.1 and 8.3 Hz, respectively, and therefore, the configuration of these olefinic group in oxospiro[5.5]undecen-2-ene was ascertained as cis oriented. The relative stereochemistries of the chiral centers, mainly at C-4, C-8, C-10, C-11, C-10^4 and C-10^6 were deduced by extensive NOESY experiments. NOE correlations between δ 0.87 (H-13) (methyl proton)/4.15 (H-10)/4.00 (H-8) appropriately confirmed the equiplaner alignment of these protons in their close proximity and these were arbitrarily allocated in α-direction with reference to its molecular plane of symmetry. The NOE correlation between δ 3.98 (H-4)/0.88 (H-12)/3.68 (H-10^4)/5.23 (H-10^6) attributed that these protons were aligned opposite to α-protons, and therefore, assigned as β-oriented.

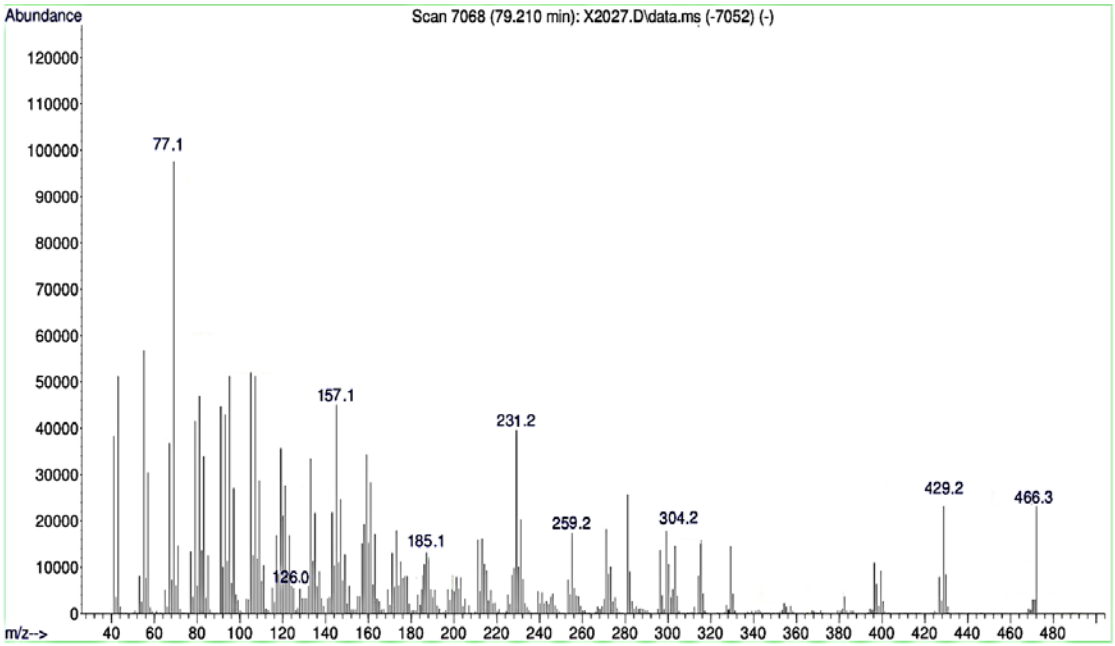

Figure 4.155.: EI-MS spectrum of 4-ethoxy-11,11-dimethyl-7-methylene-8-(propionyloxy)spiro[5.5]undec-2-en-10^3,10^5-dihydroxytetrahydro-*2H*-pyran-10-carboxylate (**10**)

Table 4.17: NMR spectroscopic data of compound (**10),** 4-ethoxy-11,11-dimethyl-7-methylene-8-(propionyloxy)spiro[5.5]undec-2-en-10^3,10^5-dihydroxytetrahydro-*2H*-pyran-10-carboxylate (**10**) isolated from red seaweed *G. salicornia*

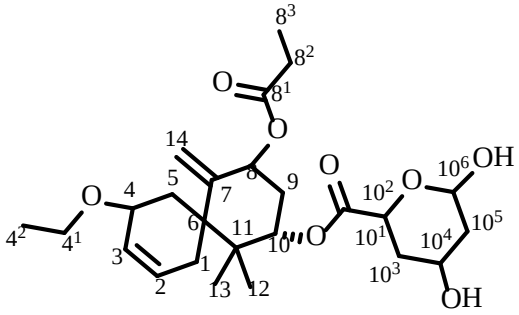

Compound **10**……4-Ethoxy-11,11-dimethyl-7-methylene-8-(propionyloxy)spiro[5.5]undec-2-en-10^3,10^5-dihydroxytetrahydro-*2H*-pyran-10-carboxylate (**10**)

C. No.	**^{13}C**	**^{1}H(int.,mult.,*J* in Hz)[b]**	**^{1}H-^{1}H COSY**	**HMBC**
		2.03(1H,*d*,4.8 Hz)		
1	31.92	1.79(1H,*d*,4.8 Hz)	H-2	C-2,6
2	126.07	5.36(1H,*t*,7.1 Hz)	H-3	-
3	132.97	5.13(1H,*t*,8.3 Hz)	H-4	C-2,4
4	75.27	3.98(1H,*m*)	H-5	C-4^1
5	39.61	1.62(2H,*d*,6.3 Hz)	-	C-4,6
6	32.35	-	-	-
7	141.81	-	-	-
8	68.38	4.00(1H,*t*,8.3 Hz)	H-9	C-7, 6,8^1
9	33.65	1.93(2H,*m*)	H-10	C-8,10
10	72.67	4.15(1H,*t*,5.3 Hz)	-	C-11,6,10^1,8^1
11	36.90	-	-	-
12	16.49	0.88(3H,*s*)	-	C-11
13	16.03	0.87(3H,*s*)	-	C-11
14	119.45	4.35(1H,*t*,12.6 Hz)	-	-
		4.33(1H,*t*,12.5 Hz)	-	-
10^1	162.75	-	-	-
10^2	72.50	4.18(1H,*t*,5.8Hz)	H-10^3	C-10^1
10^3	39.66	2.12(2H,*t*,6.8 Hz)	H-10^4	C-10^2
10^4	70.72	3.68(1H,*m*)	H-10^5	C-10^3
10^5	37.66	2.10(2H,*t*)	H-10^6	C-10^6, 10^2
10^6	101.64	5.23(1H,*t*,5.5 Hz)	-	-
8^1	172.15	-	-	-
8^2	27.99	2.30(2H,*m*)	-	C-8^3, 8^1
8^3	14.13	0.99(3H,*t*,4.1 Hz)	-	-
4^1	65.64	3.30(2H,*m*)	-	-
4^2	15.77	0.89(3H,*t*,4.3 Hz)	-	-

[a] NMR spectra recorded using Bruker AVANCE III 500 MHz (AV 500) spectrometers.

[b] Values in ppm, multiplicity and coupling constants (J = Hz) are indicated in parentheses. Assignments were made with the aid of the ^{1}H-^{1}H COSY, HSQC, HMBC and NOESY experiments.

The molecular ion peak at *m/z* 466 (**a**) $[M]^{+}$ underwent elimination of water molecule and reorganization of bonds leading to a fragment at *m/z* 429 (**b**). Further elimination radical cation at *m/z* 126 led to the formation of fragment, **c** (*m/z* 304). The radical cation, **c** also performed an elimination of neutral molecule $C_3H_6O_2$ and led to the formation of **d** at *m/z* 231. The further fragmentation of **d**, and fragment **f** at *m/z* 259 was formed from (**a**) leading to the formation of **e** at *m/z* 185. The latter on further mass fragmentation led to the formation of **g** at *m/z* 157 and then to **h** at *m/z* 77, which was deduced to be the base peak (Figure 4.156).

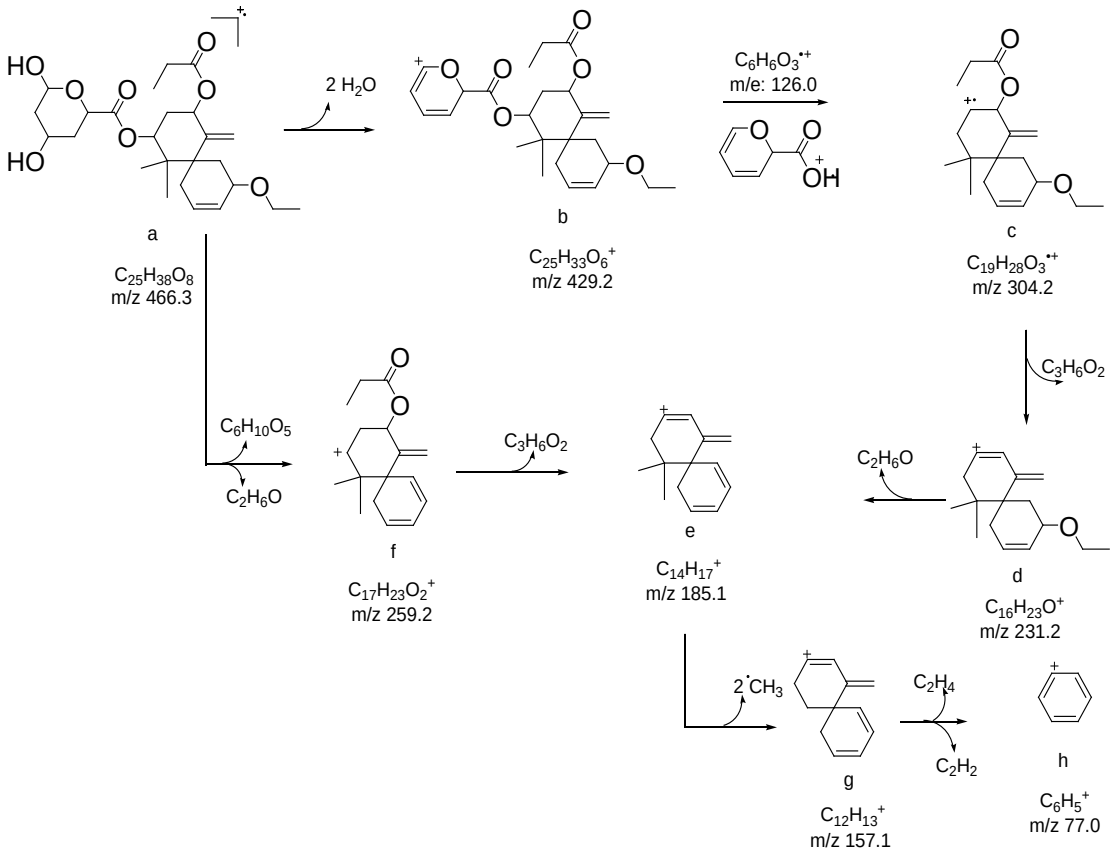

Figure 4.156.: Tentative mass fragmentation pattern of 4-ethoxy-11,11-dimethyl-7-methylene-8-(propionyloxy)spiro[5.5]undec-2-en-10^{3},10^{5}-dihydroxytetrahydro-*2H*-pyran-10-carboxylate (**10**)

4.3.2.6 Structural characterization of polyether derivatives (Compounds 11-12)

Seaweeds comprise an abundant and heterogeneous group of marine organisms, and obtained greater attention in the exploration of bioactive components to formulate newer pharmacophores as well as healthy diets (Qi et al., 2005; Ibanez et al., 2012). They were found to produce specialised secondary metabolites characterised by broad spectra of biological activities (Yuan et al., 2005). In particular, the seaweeds belonging to the *Gracilaria* genus, which has been ubiquitous on the coast of peninsular India, was considered to be one of the extensively studied for various pharmacological properties among those belonging to the family of Rhodophyceae (Cragg et al., 2009; Faulkner, 2002). Among the bioactive metabolites derived from the seaweed, the polyether components comprehended the distinctive group disclosing wide-diversity of chemistries and pharmacological properties, like ion-channel stoppers, stimulating neurotransmitter release, enzyme quenchers, and effective cytotoxicities (Faulkner, 2002; Blunt et al., 2011). The most valuable class of marine natural products (MNPs) includes polyether components that are structurally spiro or *trans*-fused systems of rings of diverse frameworks with potential bioactivities against various pharmaceutical targets. Their bio-genetic formations were found to be originated in the fatty acids or terpenoid derivatives (Fernandez et al., 2000). Polyether group of macrolides were ubiquitous in the marine organisms, for example, Halichondrin-B, isolated from the sponge *Halichondria okadai* and another polyether macrolide, theopederins isolated from the marine sponge *Theonella spp*., were found to possess anti-carcinogenic properties (Carte, 1996; Fuestani et al., 1992). The cytotoxic squalene-derived polyethers were identified from the red seaweeds belonging to the genera of *Chondria* and *Laurencia* (family Rhodomelaceae) (Pacheco, 2011; Pacheco et al., 2010). Historically, the explorations of these components have been initiated with the identification of thyrsiferol isolated from *Laurencia thyrsifera*, and further examples of polyether metabolites were reported from various marine organisms including green alga *Botryococcus brauniis*, sponges belonging to the family *Axinellidae* and mollusk *Dolabella auricularia* (Faulkner, 2002; Blunt et al., 2011; Pacheco et al., 2010). Thyrsiferol consisted of a middle *trans* fused pyrano-pyran fragment, attached bromo-ether ring and aliphatic side-chain bonding the middle part to the *trans* tetrahydrofuran unit (Fernandez et al., 2000). Dehydrothyrsiferol was found to be another example of this polyether series, identified from *Laurencia pinnatifida* in the Canary Islands of Spain. Its skeleton was formed by the chemical modification of thyrsiferolm and that differed by a double bond between C15-C28 position (end vinylic) in dehydrothyrsiferol, whereas thyrsiferol enclosed methyl and hydroxyl in the similar position (C15) (Gonzalez et al., 1984). Fatty acyl polyether Okadaic acid with protein phosphatase inhibitory property was characterised

from *Prorocentrum spp*. (Cohen et al., 1990). An anti-microbial polyether macrolide, Goniodomin-A, which was identified and characterised from the dinoflagellate *Goniodoma pseudogoniaulax* (Murakami et al., 1988), was found to exhibit anti-angiogenic activities via inhibition of actin reorganization in endothelial cells (Abe et al., 2002).

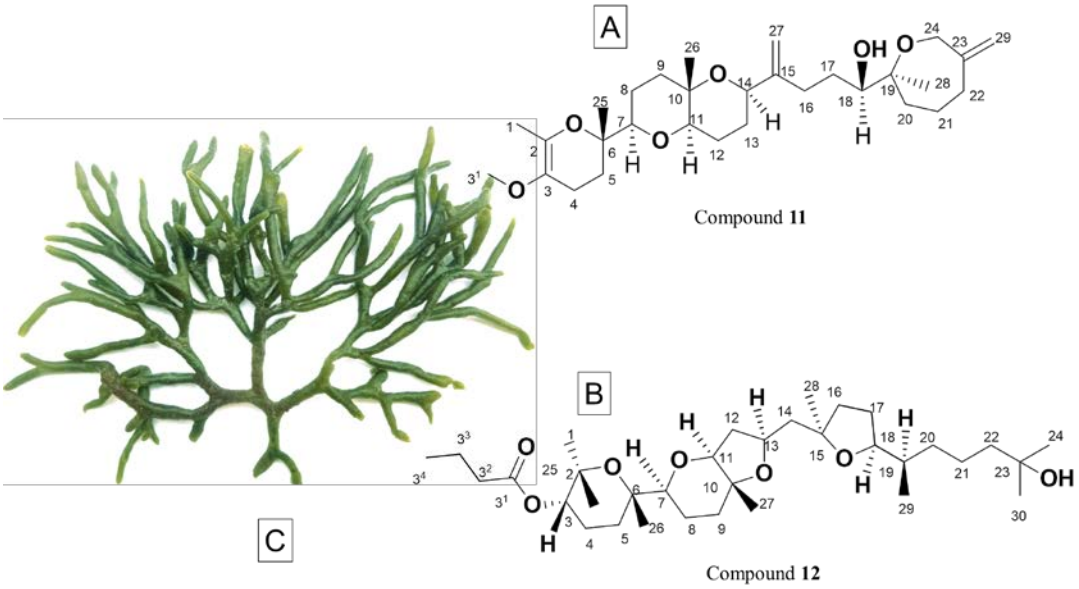

Figure 4.157.: Structural representations of (**A**) 3-methoxy-2,6-dimethyl-3,4-dihydro-2*H*-pyranyl-(6-(7-(10-methyl-octahydropyrano[3,2-*b*]pyranyl)-14-((19-methyl-23-methyleneoxepan)-(15-pentene-18-ol)) (**11**) and (**B**) 14-(15-methyltetrahydrofuranyl)-(18-(23-(hydroxy-23-methylheptanyl)-10-methylhexahydro-2*H*-furo-[3,2-*b*]pyranyl))-2,2,6-trimethyltetrahydro-2*H*-pyran-3- butyrate (**12**) purified from *G. salicornia*. (**D**) The characteristic of thalli (leaf-like structures) of *G. salicornia* was presented.

The significant and attractive phyla in terms of their pharmacologically active MNPs comprise the abundantly available seaweed species, among which the red seaweed are potential sources of bioactive substances (Makkar and Chakraborty, 2019; Makkar and Chakraborty, 2018) Pluralities of investigations on bio-active components from these seaweed demonstrating antiviral, antibacterial, antitumor, and antileukaemic properties were reported world-wide. Traditionally, natives of Japan and South-Pacific utilise seaweed supplements as arthritic remedies. The rich diversity of red seaweeds particularly belonging to *G. salicornia* along the coastline of South Indian subcontinent represents an unexploited source of bio-compounds with valuable biomedical as well as pharmaceutical use, although this species was not comprehensively studied to identify/characterise the bio-active leads (Makkar and Chakraborty,

2018; Since the initial studies carried out in our laboratory provided us with promising ideas; the current study has envisaged the isolation followed by characterisation of two formerly unreported squalene polyether metabolites from the ethyl acetate-methanol (EtOAc-MeOH) extract of *G. salicornia*. The studied compounds were designated as 15-(octahydro-7-(4,5-dihydro-3-methoxy-2,6-dimethyl-2*H*-pyran-6-yl)-10-methylpyrano[3,2-b]pyran-14-yl)-18-(19-methyl-23-methyleneoxepan-19-yl)pent-15-en-18-ol (**11**) and tetrahydro-6-(hexahydro-13-((tetrahydro-18-(23-hydroxy-23-methylheptan-19-yl)-15-methylfuran-15-yl)methyl)-10-methyl-2*H*-furo[3,2-b]pyran-7-yl)-2,2,6-trimethyl-2*H*-pyran-3-yl butyrate (**12**) (Figure 4.157) by comprehensive spectroscopic experiments.

4.3.2.6a Structural characterization of Compound 11

15-(Octahydro-7-(4,5-dihydro-3-methoxy-2,6-dimethyl-*2H*-pyran-6-yl)-10-methylpyrano[3,2-b]pyran-14-yl)-18-(19-methyl-23-methyleneoxepan-19-yl)pent-15-en-18-ol

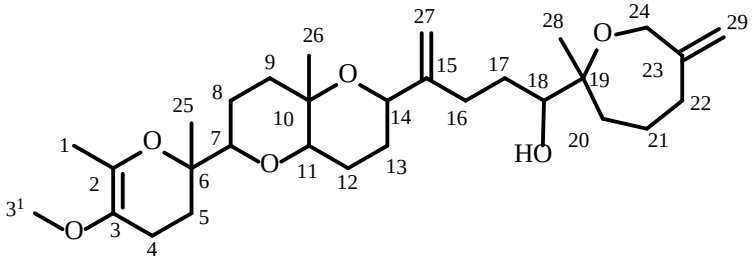

Sample yield	0.35% (> 99% purity, RP-C18 HPLC)
Physical description	Colourless oil
Molecular formula	$C_{30}H_{48}O_6$
Molecular mass	504.3451

The polyether derivative, 15-(octahydro-7-(4,5-dihydro-3-methoxy-2,6-dimethyl-*2H*-pyran-6-yl)-10-methylpyrano[3,2-b]pyran-14-yl)-18-(19-methyl-23-methyleneoxepan-19-yl)pent-15-en-18-ol was isolated as Colourless oil. The compound (**11**) has exhibited UV absorbance (UV (MeOH) λ_{max}) at 240 nm (Figure 4.158). The homogeneity of the compound was ascertained by HPLC data on a bonded phase octadecylsilane (C_{18}) stationary phase (HPLC, MeOH/MeCN, 1:2 v/v) with R_t: 3.28 min (Figure 4.159).

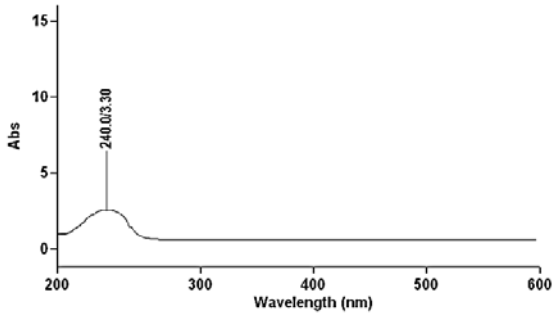

Figure 4.158.: UV spectrum of 15-(octahydro-7-(4,5-dihydro-3-methoxy-2,6-dimethyl-*2H*-pyran-6-yl)-10-methylpyrano[3,2-b]pyran-14-yl)-18-(19-methyl-23-methyleneoxepan-19-yl)pent-15-en-18-ol (**11**)

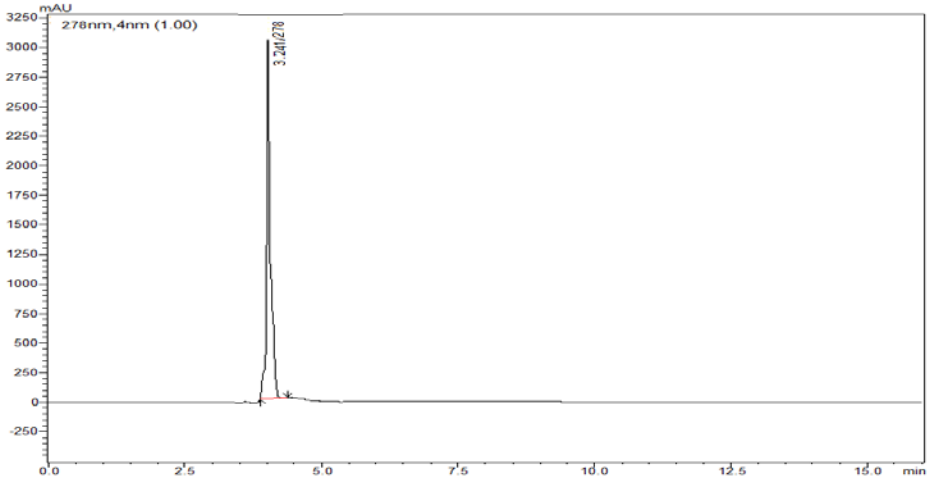

Figure 4.159.: HPLC chromatogram of 15-(octahydro-7-(4,5-dihydro-3-methoxy-2,6-dimethyl-*2H*-pyran-6-yl)-10-methylpyrano[3,2-b]pyran-14-yl)-18-(19-methyl-23-methyleneoxepan-19-yl)pent-15-en-18-ol (**11**)

Bioactive potential-assisted chromatographic purification of the organic extract of *G. salicornia* afforded a previously undisclosed polyether derivative, **11**, which was identified as 15-(octahydro-7-(4,5-dihydro-3-methoxy-2,6-dimethyl-2*H*-pyran-6-yl)-10-methylpyrano[3,2-b]pyran-14-yl)-18-(19-methyl-23-methyleneoxepan-19-yl)pent-15-en-18-ol. The molecular ion peak was analysed by HRESIMS (positive mode) registered $[M+H]^+$ at *m/z*: found 505.3533 (Figure 4.160).

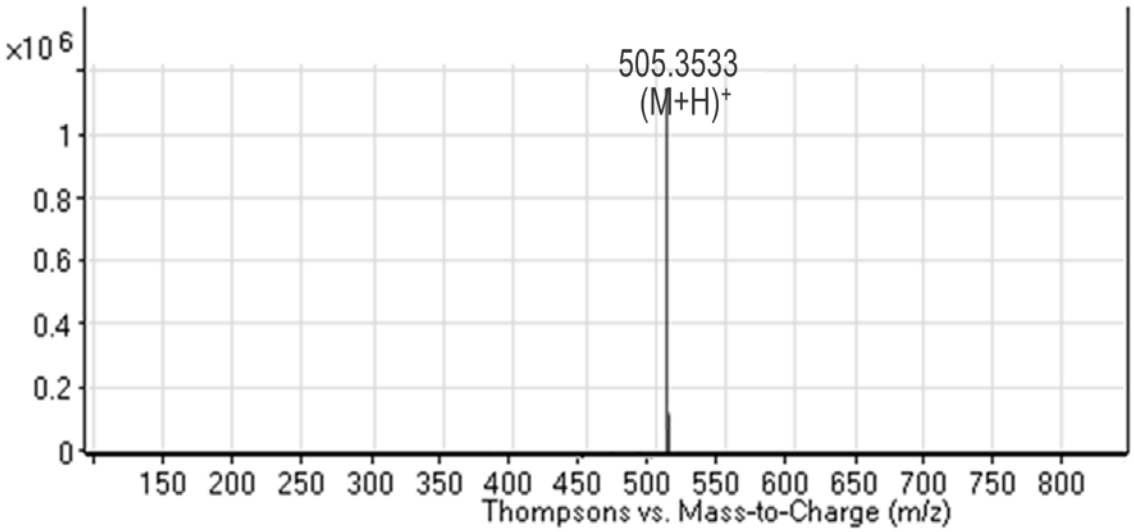

Figure 4.160.: HRESIMS spectrum of 15-(octahydro-7-(4,5-dihydro-3-methoxy-2,6-dimethyl-*2H*-pyran-6-yl)-10-methylpyrano[3,2-b]pyran-14-yl)-18-(19-methyl-23-methyleneoxepan-19-yl)pent-15-en-18-ol (**11**)

The FTIR of **11** reported the occurrence of absorption peaks at 3390 cm^{-1} and 1044 cm^{-1}, which specified the possibilities of hydroxyl (-OH) and ether (-C-O-C) groups, respectively (Figure 4.161). The combined mass-NMR-IR techniques deduced the molecular formula of **11** as $C_{30}H_{48}O_6$, which indicated its seven sites of unsaturations (Table 4.18). The ^{13}C NMR spectrum of **11** showed signal for 30 carbon atoms and the types of the carbon signals were determined from its ^{135}DEPT spectrum, which were found to be five methyls (δ 20.33, 24.37, 19.38, 18.82, 60.01), twelve sp^3 methylenes (δ 21.57, 24.63, 22.33, 39.13, 24.48, 25.74, 29.35, 31.66, 35.08, 21.82, 37.08, 72.42), two sp^2 methylenes (δ 114.50, 114.01), four sp^3 methines (δ 80.93, 78.80, 75.32, 74.15) and seven non-protonated carbons (δ 129.48, 137.14, 81.49, 77.13, 147.00, 81.44, 143.29). The highly deshielded ^{13}C NMR resonances observed at δ 81.49 (assigned at C-6), 80.93 (C-7), 77.13 (C-10), 78.80 (C-11), 75.32 (C-14), 74.15 (C-18), 81.44 (C-19), 72.42 (C-24) and 60.01 (C-3^1) were found to be related to the oxygen attached protonated carbons. ^1H NMR of **11** revealed the proton chemical shifts at δ 5.33/5.18 and δ 5.36/5.17 due to the olefinic protons; triplet signals at δ 3.61, 3.05, 4.14, 3.78; doublets at δ 4.01/3.93 and singlets at δ 3.68 (which might be adjacent to the oxygen atom), 1.41, 1.33, 1.28, and 2.28. The three shielded singlet protons at δ 1.41, 1.33 and 1.28 were accounted for the methyl protons directly attached to quaternary carbons in compound **11** and the slightly deshielded singlet proton at δ 2.28 was accounted for the methyl attached to non-protonated deshielded carbon atom (Figure 4.162-4.164).

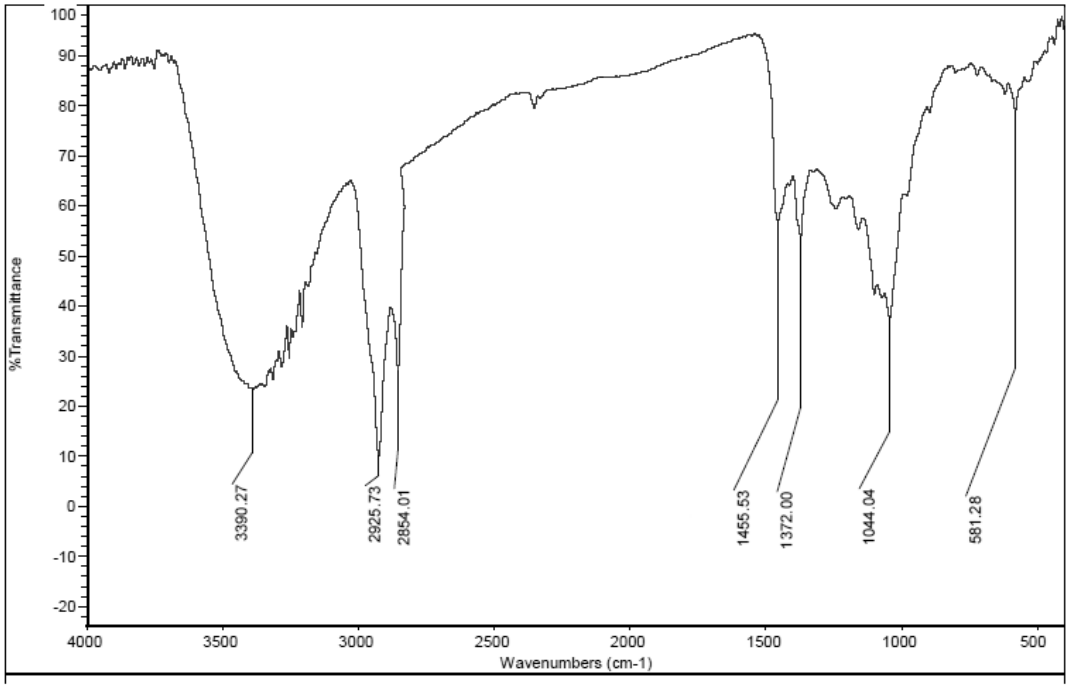

Figure 4.161.: FTIR spectrum of 15-(octahydro-7-(4,5-dihydro-3-methoxy-2,6-dimethyl-*2H*-pyran-6-yl)-10-methylpyrano[3,2-b]pyran-14-yl)-18-(19-methyl-23-methyleneoxepan-19-yl)pent-15-en-18-ol (**11**)

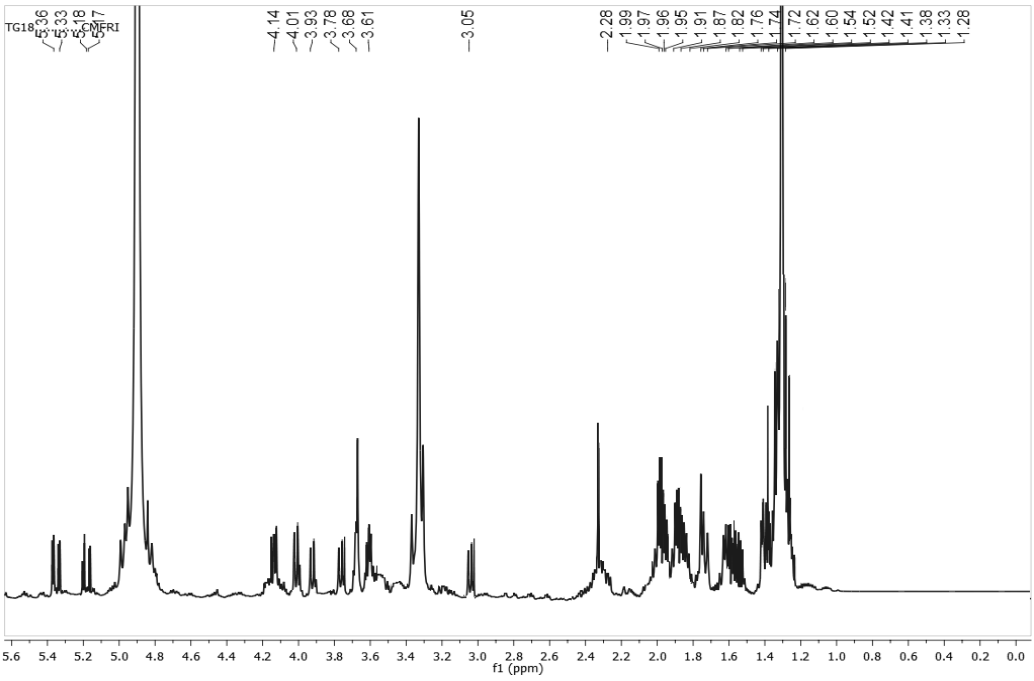

Figure 4.162.: ^{1}H NMR spectrum of 15-(octahydro-7-(4,5-dihydro-3-methoxy-2,6-dimethyl-*2H*-pyran-6-yl)-10-methylpyrano[3,2-b]pyran-14-yl)-18-(19-methyl-23-methyleneoxepan-19-yl)pent-15-en-18-ol (**11**)

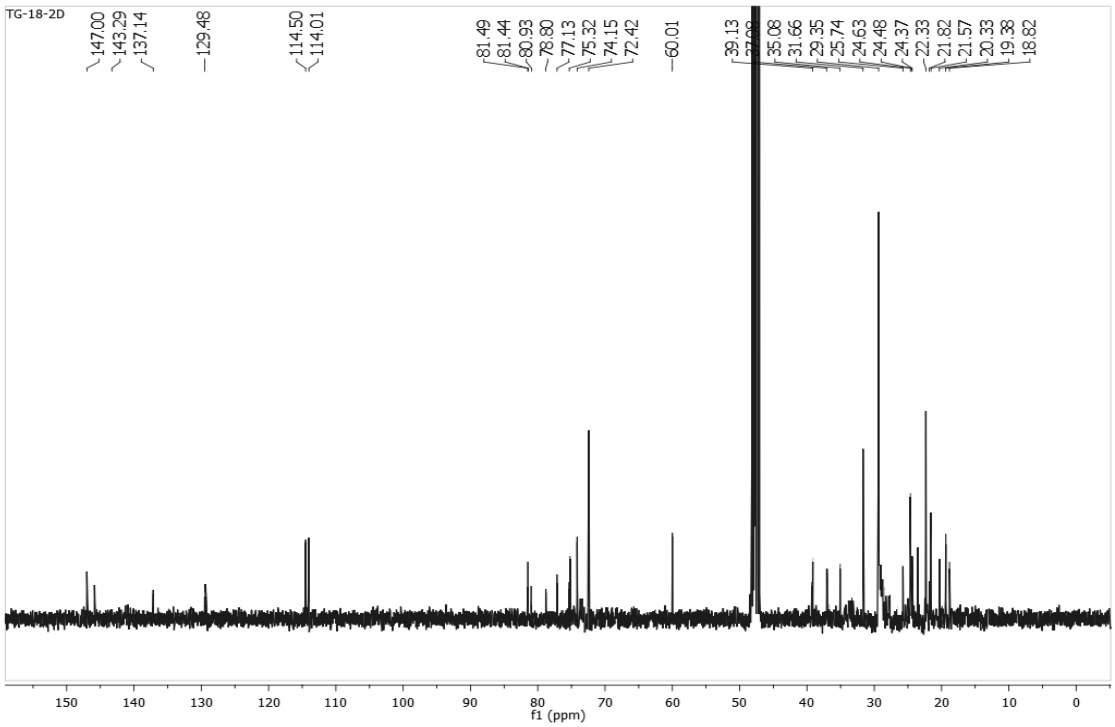

Figure 4.163.: ^{13}C NMR spectrum of 15-(octahydro-7-(4,5-dihydro-3-methoxy-2,6-dimethyl-*2H*-pyran-6-yl)-10-methylpyrano[3,2-b]pyran-14-yl)-18-(19-methyl-23-methyleneoxepan-19-yl)pent-15-en-18-ol (**11**)

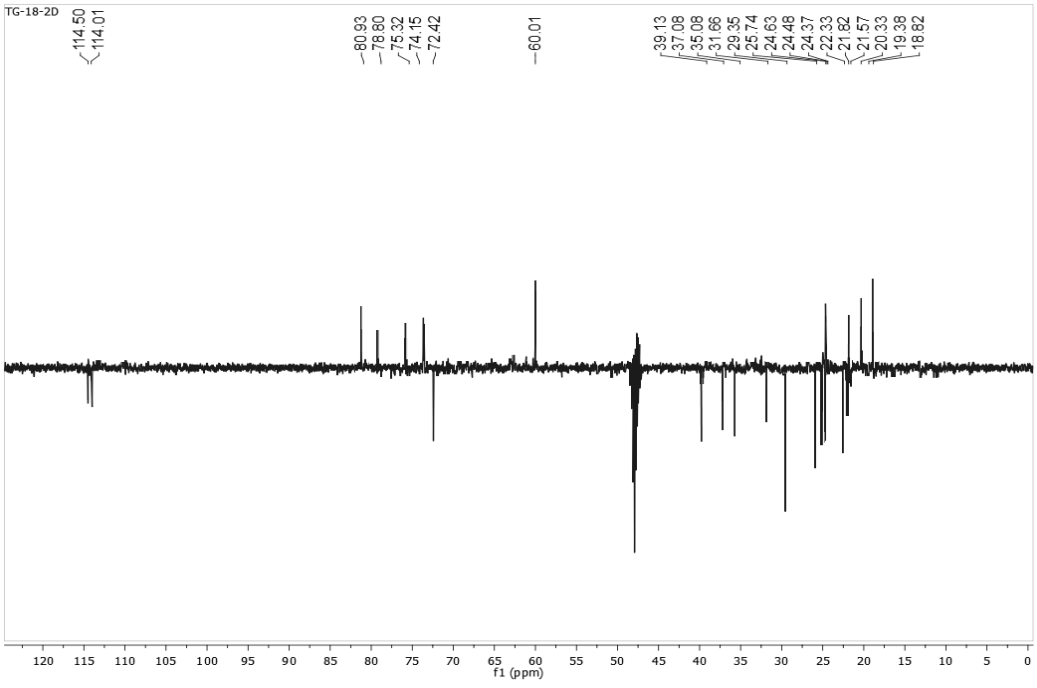

Figure 4.164.: ^{135}DEPT spectrum of 15-(octahydro-7-(4,5-dihydro-3-methoxy-2,6-dimethyl-*2H*-pyran-6-yl)-10-methylpyrano[3,2-b]pyran-14-yl)-18-(19-methyl-23-methyleneoxepan-19-yl)pent-15-en-18-ol (**11**)

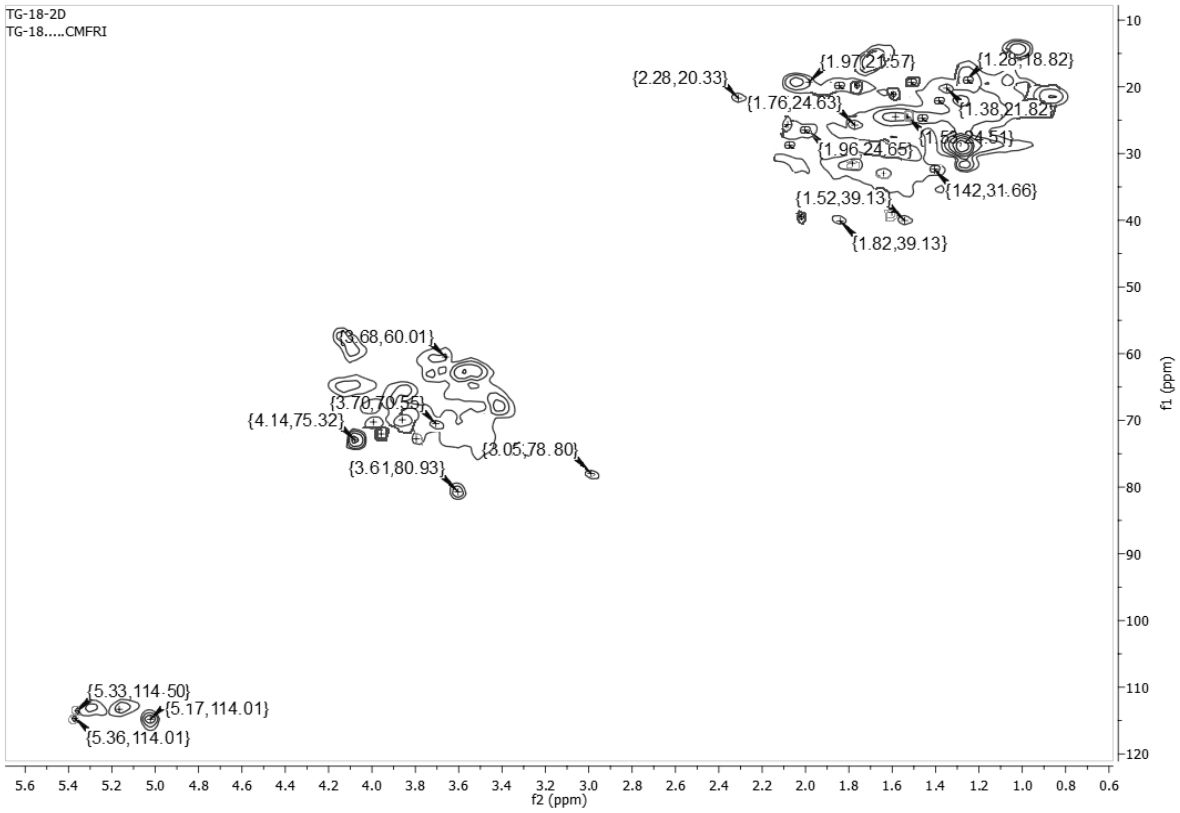

Figure 4.165.: HSQC spectrum of 15-(octahydro-7-(4,5-dihydro-3-methoxy-2,6-dimethyl-*2H*-pyran-6-yl)-10-methylpyrano[3,2-b]pyran-14-yl)-18-(19-methyl-23-methyleneoxepan-19-yl)pent-15-en-18-ol (**11**)

All these attributions established the ether substitutions in the titled compound and the chemical shift values were comparable with squalene-derived halogenated polyethers, such as dehydrothyrsiferol, 22-hydroxy-15(28)-dehydrovenustatriol and iuboli isolated from red seaweed, *Laurencia viridis*. The sp^2 protons with greatly deshielded resonance at δ 5.33/5.18 and δ 5.36/5.17 having doublet splitting were bonded to the carbons at δ 114.50 (H-27) and δ 114.01 (H-29), respectively, as inferred from the HSQC spectrum (Figure 4.165). Highly deshielded non-protonated carbons at δ 129.48 and 81.49 attributed the presence of oxygen between C-2 and C-6 carbon atoms.

The COSY conjunctions between δ 1.97 (H-4)/1.76 (H-5) and HMBC correlations from δ 1.97 (H-4) to δ 24.36 (C-5), 137.14 (C-3); δ 1.76 (H-5) to δ 81.49 (C-6); δ 2.28 (H-1) to δ 129.48 (C-5), 137.14 (C-3); δ 1.41 (H-25) to δ 81.49 (C-6) and δ 3.68 (H-3^1) to δ 137.14 (C-3) appropriately assigned the partial structure of **11** as 4,5-dihydro-3-methoxy-2,6-dimethyl-2H-pyran. Similarly, compound **11** exhibited COSY correlations δ 3.61 (H-7)/1.72 (H-8)/1.82 (H-9) and from δ 3.05 (H-11)/1.91 (H-12)/1.74 (H-13)/4.14 (H-14) (Figure 4.166 & 4.167). These COSY fragments were further connected by the HMBC correlations from δ 1.72 (H-8) to δ 80.93

(C-7); δ 1.82 (H-9) to δ 22.33 (C-8), 77.13 (C-10); δ 3.05 (H-11) to δ 77.13 (C-10), 24.48 (C-12), 80.93 (C-7); δ 1.74 (H-13) to δ 75.32 (C-14).

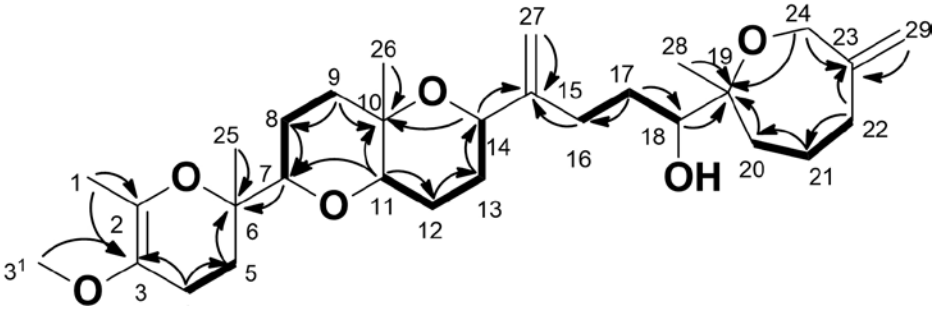

Figure 4.166.: ^{1}H-^{1}H COSY (bold face bonds) and selected HMBCs (double-barbed arrows) correlations of 15-(Octahydro-7-(4,5-dihydro-3-methoxy-2,6-dimethyl-*2H*-pyran-6-yl)-10-methylpyrano[3,2-b]pyran-14-yl)-18-(19-methyl-23-methyleneoxepan-19-yl)pent-15-en-18-ol (**11**)

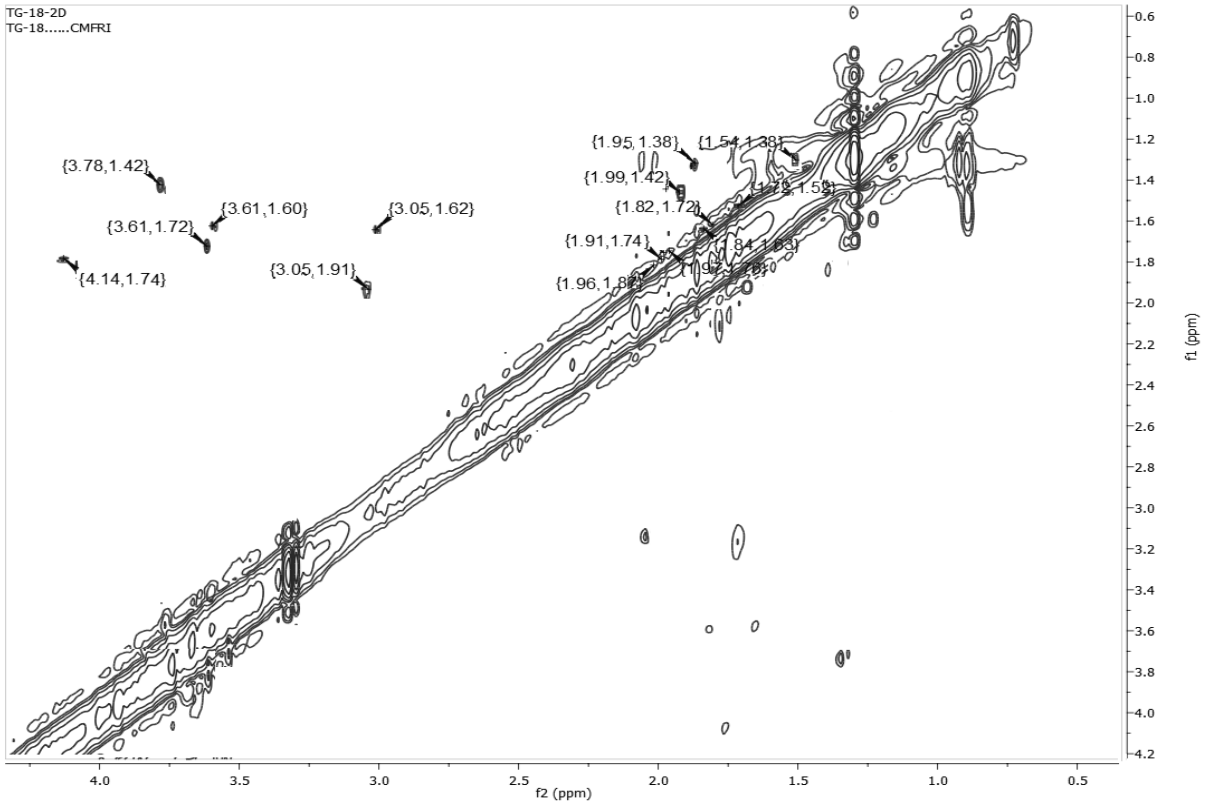

Figure 4.167.: ^{1}H-^{1}H COSY spectrum of 15-(octahydro-7-(4,5-dihydro-3-methoxy-2,6-dimethyl-*2H*-pyran-6-yl)-10-methylpyrano[3,2-b]pyran-14-yl)-18-(19-methyl-23-methyleneoxepan-19-yl)pent-15-en-18-ol (**11**)

These attributed the presence of octahydro-10-methylpyrano[3,2-b]pyran part in compound **11**. The attachment of octahydro-10-methylpyrano[3,2-b]pyran at C-6 of 4,5-dihydro-3-methoxy-2,6-dimethyl-2*H*-pyran was assigned through HMBC from δ 3.61 (H-7) to δ 81.49 (C-6) (Figure 4.168). Besides these, another COSY spin system from δ 1.54 (H-20)/1.38 (H-21)/1.95 (H-22) along with HMBC correlations from δ 1.54 (H-20) to δ 81.44 (C-19); δ 1.38 (H-21) to δ 35.08 (C-20); δ 1.95 (H-22) to δ 21.82 (C-21), 143.29 (C-23); δ 1.28 (H-28) to δ 81.44 (C-19); δ 4.01 (H-24) to δ 143.29 (C-23), 81.44 (C-19) and from exocyclic alkenic proton at δ 5.36 (H-29) to δ 143.29 (C-23) ascribed the seven-membered ring named as 19-methyl-23-methyleneoxepane. The characteristic signals at δ 74.9 (C-6) in the brominated pyran ring, δ 3.08 (H-7)/86.7 (C-7), 72.9 (C-10), 3.43 (H-11)/78.9 (C-11), 4.28 (H-14)/72.5 (C-14) in pyrano[3,2-b]pyran ring and δ 3.52 (H-18)/76.2 (C-18) for the hydroxylated methine of pentenol chain reported for dehydrothyrsiferol and iuboli (Pacheco, 2011) were comparable with the studied compound. The titled compound recorded characteristic signals at δ 81.49 (C-6) in the brominated pyran ring (unsaturated pyran), δ 3.61 (H-7)/80.93 (C-7), 77.13 (C-10), 3.05 (H-11)/78.80 (C-11), 4.14 (H-14)/75.32 (C-14) in pyrano[*3,2-b*]pyran ring and δ 3.78 (H-18)/74.15 (C-18) for the hydroxylated methine of pentenol chain. An exocyclic vinylic linkage at C-27 was directly bonded to non-protonated carbons at δ 147.00 (C-15) as obtained through HMBC correlations from δ 5.33 (H-27) to δ 147.00 (C-15), which was comparable with the exocyclic alkene assigned at >C(15)=CH_2(28) in a previously reported compound, dehydrothyrsiferol with chemical shifts of δ 151 (C-15) and δC 109/δ 4.88, 5.05 (C-28) (Pacheco, 2011). Also, other HMBCs from δ 1.42 (H-17) to δ 29.35 (C-16), δ 74.15 (C-18) and from δ 1.99 (H-16) to δ 147.00 (C-15) along with COSY spin system from H-16/H-17/H-18 {δ 1.99 (H-16)/1.42 (H-17)/3.78 (H-18)} ascribed the presence of a linear chain named as pent-15-en-18-ol. The octahydro-10-methylpyrano[*3,2-b*]pyran and 19-methyl-23-methyleneoxepane fragments were connected through the pent-15-en-18-ol chain, and the assignment was established through strong HMBCs from δ 4.41 (H-14 of pyrano[3,2-b]pyran) to δ 147.00 (C-15 of pentenol) and from δ 3.78 (H-18 of pentenol) to δ 81.44 (C-19 of methyleneoxepane). The compound dehydrothyrsiferol enclosed octahydro-methylpyrano[3,2-b]pyran, bromo-tetrahydro trimethyl-2*H*-pyran, connecting linkage pentenol and tetrahydro-hydroxypropanyl enclosed methylfuranyl at C-18 and the compound, iuboli was found to be similar to dehydrothyrsiferol except the presence of tetrahydro-trimethyl-2*H*-pyranol at C-18 (Pacheco et al., 2010). In short, these previously reported halogenated polyether derivatives enclosed seven-membered and five-membered rings at the C-18 position of the pent-15-en-18-ol chain (Pacheco, 2011; Pacheco et al., 2010), whereas the present compound enclosed a seven-membered ring. The titled compound was similar to the previously reported thyrsiferol except for the presence of methyl and hydroxyl

functionalities at C-15 and the tetrahydro-hydroxypropanyl methylfuranyl part at C-18 in thyrsiferol (Pacheco et al., 2010), whereas the studied compound **11** enclosed terminal vinylic moiety at C-15 and methyl-23-methyleneoxepan-19-yl ring at C-18

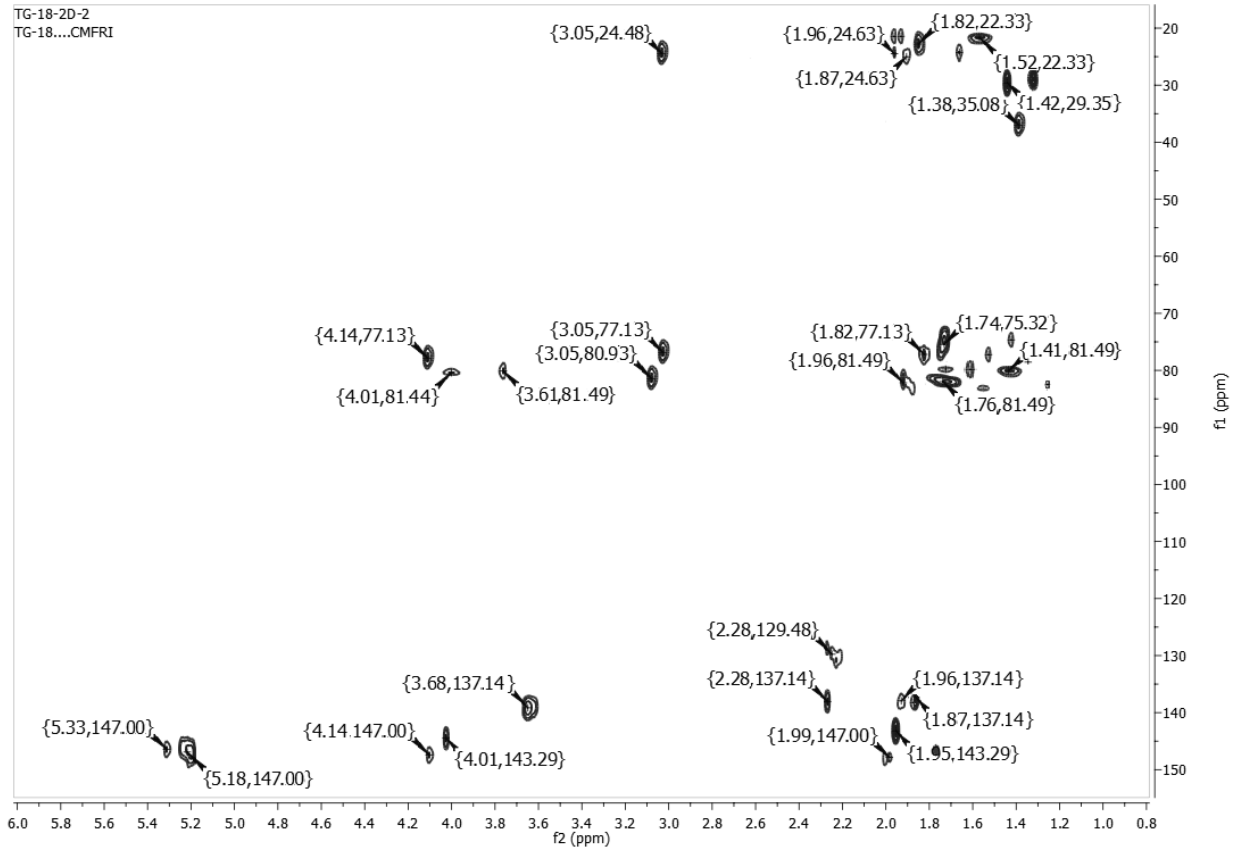

Figure 4.168.: HMBC spectrum of 15-(octahydro-7-(4,5-dihydro-3-methoxy-2,6-dimethyl-*2H*-pyran-6-yl)-10-methylpyrano[3,2-b]pyran-14-yl)-18-(19-methyl-23-methyleneoxepan-19-yl)pent-15-en-18-ol (**11**)

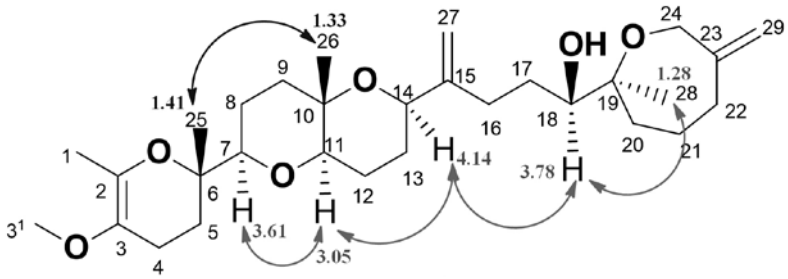

Figure 4.169.: NOESY correlations (double headed arrows) of 15-(octahydro-7-(4,5-dihydro-3-methoxy-2,6-dimethyl-*2H*-pyran-6-yl)-10-methylpyrano[3,2-b]pyran-14-yl)-18-(19-methyl-23-methyleneoxepan-19-yl)pent-15-en-18-ol (**11**)

Table 4.18: NMR spectroscopic data of compound (**11),** 15-(octahydro-7-(4,5-dihydro-3-methoxy-2,6-dimethyl-*2H*-pyran-6-yl)-10-methylpyrano[3,2-b]pyran-14-yl)-18-(19-methyl-23-methyleneoxepan-19-yl)pent-15-en-18-ol (**11**) isolated from red seaweed *G. salicornia*

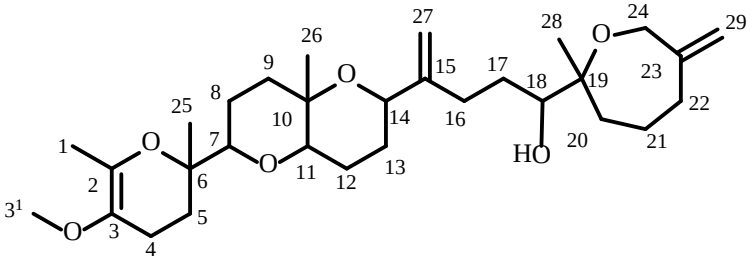

Compound **11** ……..15-(Octahydro-7-(4,5-dihydro-3-methoxy-2,6-dimethyl-*2H*-pyran-6-yl)-10-methylpyrano[3,2-b]pyran-14-yl)-18-(19-methyl-23-methyleneoxepan-19-yl)pent-15-en-18-ol (**11**)

C. No.	**^{13}C**	**^{1}H (int.,mult., *J* in Hz)[b]**	**^{1}H-^{1}H COSY**	**HMBC**
1	20.33	2.28 (3H,s)	-	C-2,3
2	129.48	-	-	-
3	137.14	-	-	-
4	21.57	1.97 (1H,t,4.2 Hz)	H-5	C-3,5
		1.87 (1H,t,4.2 Hz)	-	C-3,5
5	24.63	1.76 (1H,t,4.2 Hz)	-	C-6
		1.96 (1H,t,4.2 Hz)	-	C-6
6	81.49	-	-	-
7	80.93	3.61 (1H,t,4.3 Hz)	H-8	C-6
8	22.33	1.72 (1H,m)	H-9	C-7
		1.60 (1H,m)	-	-
9	39.13	1.82 (1H,t,5.0 Hz)	-	C-8,10
		1.52 (1H,t,4.9 Hz)	-	C-8
10	77.13	-	-	-
11	78.80	3.05 (1H,t,4.3 Hz)	H-12	C-10,12,7
12	24.48	1.91 (1H,m)	H-13	-
		1.62 (1H,m)	-	C-13
13	25.74	1.74 (2H,m)	H-14	C-14
14	75.32	4.14 (1H,t,4.3 Hz)	-	C-15,10
15	147.00	-	-	-
16	29.35	1.99 (2H,t,4.2 Hz)	H-17	C-15
17	31.66	1.42 (2H,m)	H-18	C-16,18
18	74.15	3.78 (1H,t,4.7 Hz)	-	C-19
19	81.44	-	-	-
20	35.08	1.54 (2H,t,4.3 Hz)	H-21	C-19
21	21.82	1.38 (2H,m)	H-22	C-20
22	37.08	1.95 (2H,t)	-	C-21,23
23	143.29	-	-	-
24	72.42	4.01 (1H,d,8.2 Hz)	-	C-23,19
		3.93 (1H,d,8.3 Hz)	-	-
25	24.37	1.41 (3H,s)	-	C-6

26	19.38	1.33 (3H,s)	-	C-10
27	114.50	5.33 (1H,d,10.0 Hz)	-	C-15
		5.18 (1H,d,9.3 Hz)	-	C-15
28	18.82	1.28 (3H,s)	-	C-19
29	114.01	5.36 (1H,d,9.3 Hz)	-	C-23
		5.17 (1H,d,9.3 Hz)	-	-
3^1	60.01	3.68 (3H,s)	-	C-3

[a]NMR spectra recorded using Bruker AVANCE III 500 MHz (AV 500) spectrometers.

[b]Values in ppm, multiplicity and coupling constants (J = Hz) are indicated in parentheses.

Assignments were made with the aid of the ^{1}H-^{1}H COSY, HSQC, HMBC and NOESY experiments. The stereo-chemical orientations in the structures were represented by wedge-faced and dash-faced bonds based on NOESY spectra.

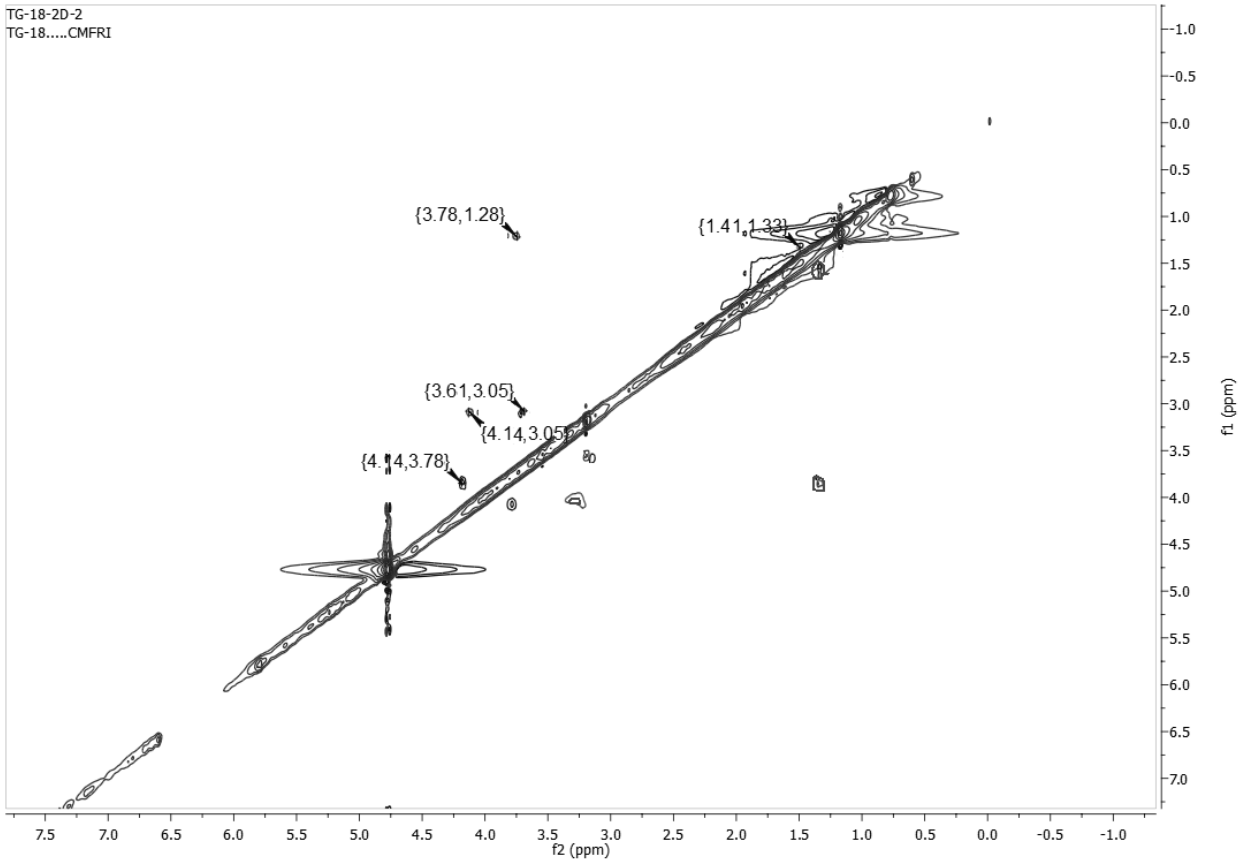

Figure 4.170.: NOESY spectrum of 15-(octahydro-7-(4,5-dihydro-3-methoxy-2,6-dimethyl-*2H*-pyran-6-yl)-10-methylpyrano[3,2-b]pyran-14-yl)-18-(19-methyl-23-methyleneoxepan-19-yl)pent-15-en-18-ol (**11**)

The relative stereo-chemical alignments of protons in the chiral centers, mainly at C-6, C-10, C-11, C-14, C-18, and C-19 were assigned through comprehensive NOESY experimentations (Figure 4.169 & 4.170). The NOE correlations from δ 3.61 (H-7)/3.05 (H-11)/4.14 (H-14)/3.78 (H-18)/1.28 (H-28) confirmed the equiplaner alignment of these protons in their close proximity and these were arbitrarily allocated in the α-direction with regard to its molecular plane of symmetry. The methyl protons δ 1.41 (H-25) and 1.33 (H-26) were positioned opposite to the α-protons, and therefore, allocated as β-oriented. The squalene-derived polyethers from L. viridis registered β-orientations for methyls at C-26, C-27, and 18-OH and α-orientations for the protons at H-7, H-11, H-14 and Me-29 (Pacheco, 2011; Pacheco et al., 2010), which were comparable to the present compound.

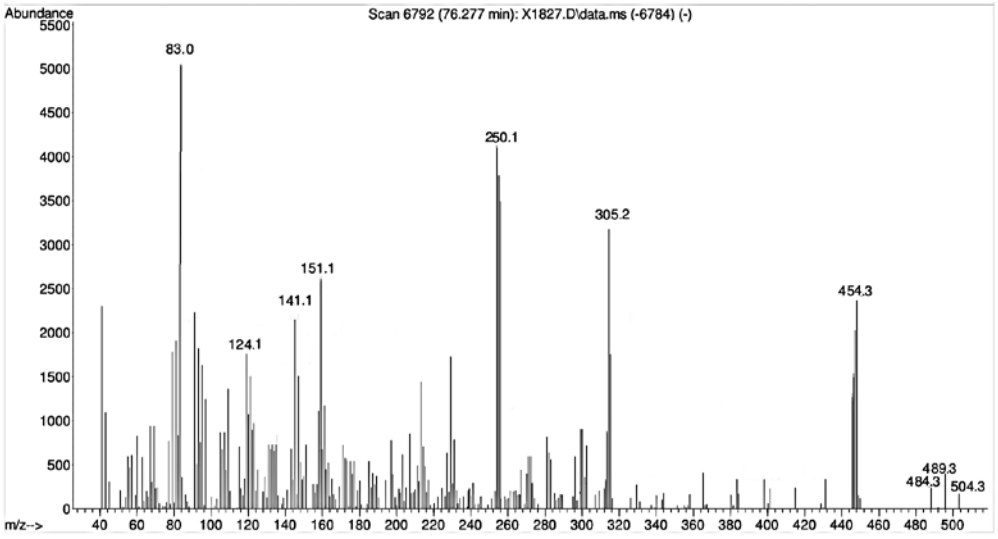

Figure 4.171.: EI-MS spectrum of 15-(octahydro-7-(4,5-dihydro-3-methoxy-2,6-dimethyl-*2H*-pyran-6-yl)-10-methylpyrano[3,2-b]pyran-14-yl)-18-(19-methyl-23-methyleneoxepan-19-yl)pent-15-en-18-ol (**11**)

The complete structural characterisation of **11** were further substantiated by mass spectral experiments, wherein the ion peak at *m/z* 504 (a) experienced methyl-radical removal and H_2O removal to form fragments $C_{29}H_{45}O_6^+$ (b) with *m/z* 489 and $C_{30}H_{44}O_5^{\bullet+}$ with *m/z* 484 (c), respectively. The elimination of CH_3OH and H_2O from (a) resulted in the formation of $C_{29}H_{42}O_4^{\bullet+}$ with *m/z* 454 (d). The fragment (d) underwent a further sequence of fragmentations to obtain the fragments at *m/z* 305 (e), which on further fragmentation resulted in the fragment $C_{15}H_{22}O_3^{\bullet+}$ with *m/z* 250 (h). The fragment (h) then directed to fragmented peaks at *m/z* 141 (g) and *m/z* 83 (i). The base peak of **11** was obtained at *m/z* 83 corresponding to $C_5H_7O^+$ (Figure 4.171-4.172).

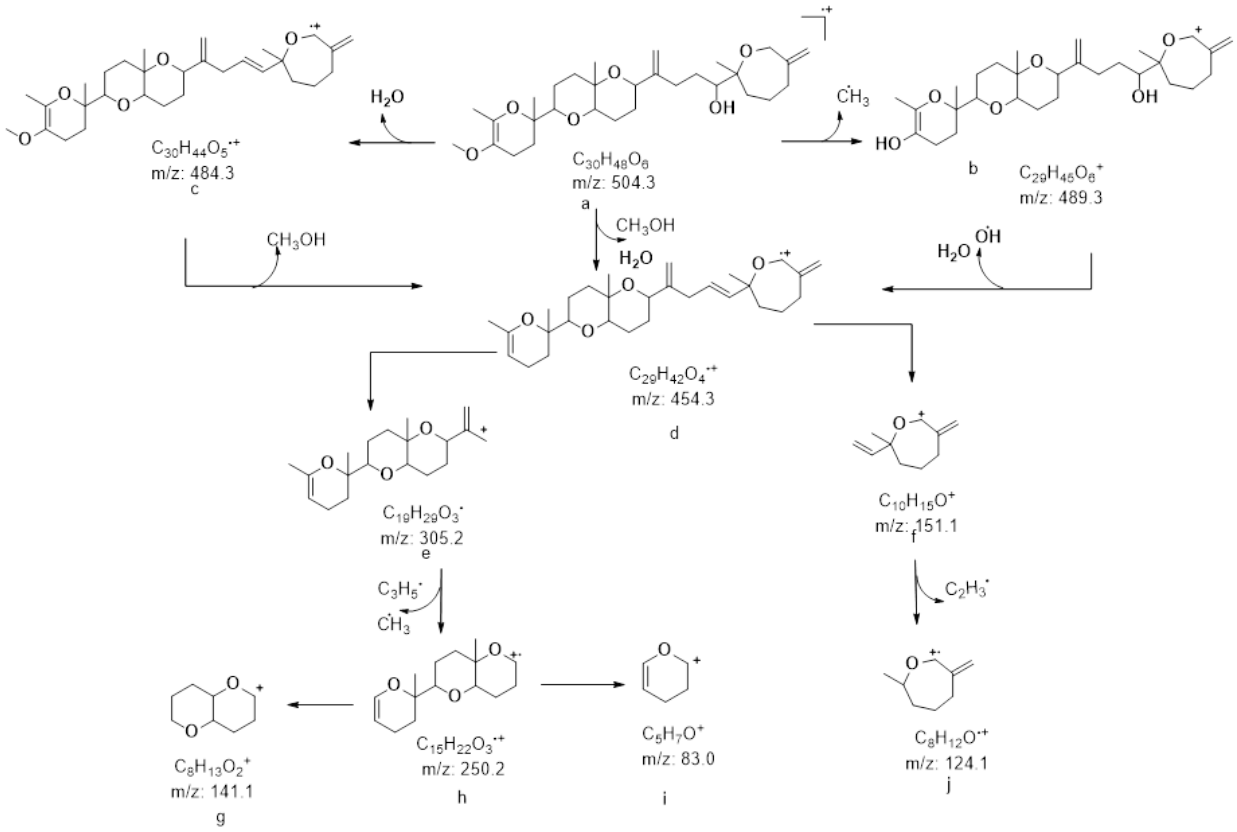

Figure 4.172.: Mass fragmentation pattern of 15-(octahydro-7-(4,5-dihydro-3-methoxy-2,6-dimethyl-*2H*-pyran-6-yl)-10-methylpyrano[3,2-b]pyran-14-yl)-18-(19-methyl-23-methyleneoxepan-19-yl)pent-15-en-18-ol (**11**)

4.3.2.6b Structural characterization of Compound 12

Tetrahydro-6-(hexahydro-13-((tetrahydro-18-(23-hydroxy-23-methylheptan-19-yl)-15-methylfuran-15-yl)methyl)-10-methyl-*2H*-furo[3,2-b]pyran-7-yl)-2,2,6-trimethyl-*2H*-pyran-3-yl

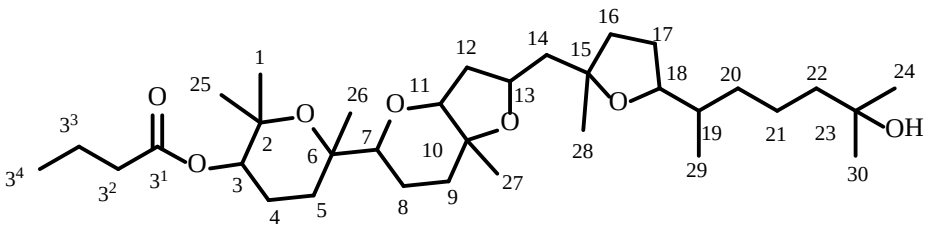

Sample yield	0.33% (> 99% purity, RP-C18 HPLC)
Physical description	Colourless oily
Molecular formula	$C_{34}H_{60}O_7$
Molecular mass	580.4339

The polyether derivative, tetrahydro-6-(hexahydro-13-((tetrahydro-18-(23-hydroxy-23-methylheptan-19-yl)-15-methylfuran-15-yl)methyl)-10-methyl-*2H*-furo[3,2-b]pyran-7-yl)-2,2,6-trimethyl-*2H*-pyran-3-yl was isolated as Colourless oil. The compound (**12**) has exhibited UV absorbance (UV (MeOH) λ_{max}) at 242 nm (Figure 4.173). The homogeneity of the compound was ascertained by HPLC data on a bonded phase octadecylsilane (C_{18}) stationary phase (HPLC, MeOH/MeCN, 1:1 v/v) with R_t: 3.18 min (Figure 4.174).

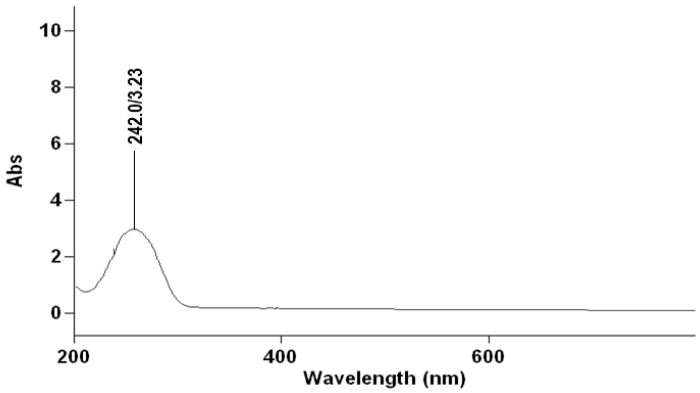

Figure 4.173.: UV spectrum of tetrahydro-6-(hexahydro-13-((tetrahydro-18-(23-hydroxy-23-methylheptan-19-yl)-15-methylfuran-15-yl)methyl)-10-methyl-*2H*-furo[3,2-b]pyran-7-yl)-2,2,6-trimethyl-*2H*-pyran-3-yl (**12**)

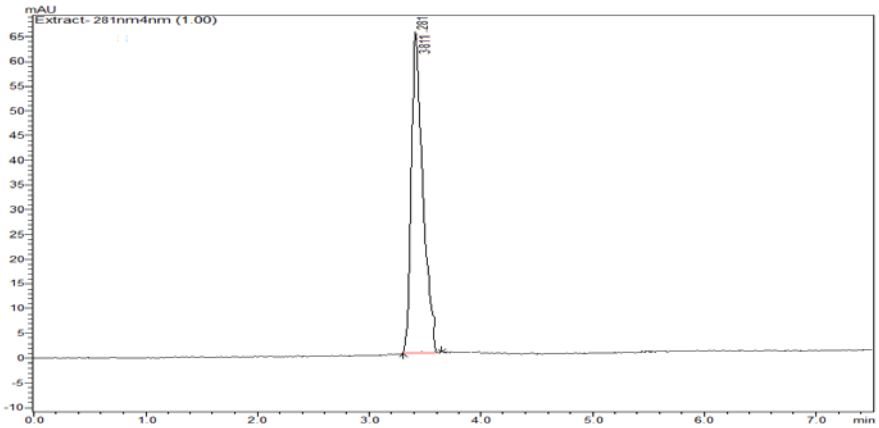

Figure 4.174.: HPLC chromatogram of tetrahydro-6-(hexahydro-13-((tetrahydro-18-(23-hydroxy-23-methylheptan-19-yl)-15-methylfuran-15-yl)methyl)-10-methyl-*2H*-furo[3,2-b]pyran-7-yl)-2,2,6-trimethyl-*2H*-pyran-3-yl (**12**)

Bioactivity-based chromatographic purification of the organic extract of *G. salicornia* afforded a previously undisclosed polyether derivative, characterised as tetrahydro-6-(hexahydro-13-((tetrahydro-18-(23-hydroxy-23-methylheptan-2-yl)-15-methylfuran-15-yl)methyl)-10-methyl-2*H*-furo[3,2-b]pyran-7-yl)-2,2,6-trimethyl-2*H*-pyran-3-yl butyrate (1**2**). The molecular ion peak has been analysed by HRESIMS (positive mode) spectroscopic experiment, and its molecular $[M+H]^+$ ion peak has been recorded at *m/z* 581.4420 (Figure 4.175). The integrative EIMS-NMR-IR techniques deduced the molecular formula of **12** as $C_{34}H_{60}O_7$, indicative of five sites of unsaturation (Table 4.19).

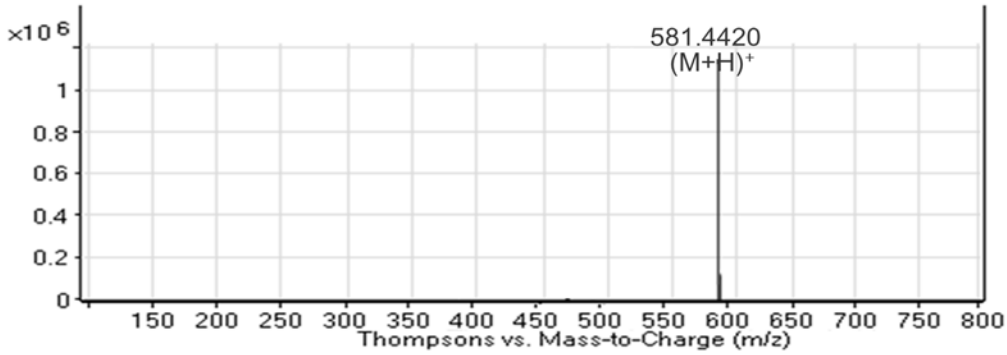

Figure 4.175.: HRESIMS spectrum of tetrahydro-6-(hexahydro-13-((tetrahydro-18-(23-hydroxy-23-methylheptan-19-yl)-15-methylfuran-15-yl)methyl)-10-methyl-*2H*-furo[3,2-b]pyran-7-yl)-2,2,6-trimethyl-*2H*-pyran-3-yl (**12**)

The FTIR spectrum of **12** registered absorption peaks at 3383 and 1043 cm^{-1}, which represented hydroxyl (-OH) and ether (-C-O-C) groups, correspondingly (Figure 4.176). The ^{13}C NMR of **12** registered 34 carbon atoms and the types of the carbon signals were determined from the ^{135}DEPT spectrum. It was deduced to include nine methyls (δ 27.58, 28.88, 26.39, 21.11, 17.31, 26.94, 18.13, 28.53, 13.99), thirteen sp^3 methylenes (δ 21.38, 30.32, 22.32, 39.67, 38.65, 46.37, 36.06, 29.34, 33.97, 22.04, 42.61, 36.61, 18.85), six sp^3 methines (δ 71.52, 90.49, 80.50, 65.26, 79.17, 36.72), and six non-protonated carbons (δ 83.98, 82.62, 81.42, 79.53, 78.93, 167.92). The ^{13}C NMR exhibited highly deshielded resonances for eight carbons observed at δ 71.52 (assigned at C-3), 82.62 (C-6), 90.49 (C-7), 81.42 (C-10), 80.50 (C-11), 65.26 (C-13), 79.17 (C-18) and 78.93 (C-23), which might be attributed to hydroxyl, ether and ester substitutions in the studied compound **12**, and these values were further corroborated by previous literature (Pacheco, 2011). ^1H NMR spectrum of **12** displayed deshielded proton signals at δ 4.10, 3.69, 3.33, 3.56 and 3.67 that were assigned to protons adjacent to the oxygen atoms. Seven shielded singlet protons at δ 1.19, 1.24, 1.26, 1.28, 1.29 and 1.31 were accounted for the methyls

in compound **12** (Figure 4.177-4.179). These attributions were corroborated by HSQC spectral analysis (Figure 4.180).

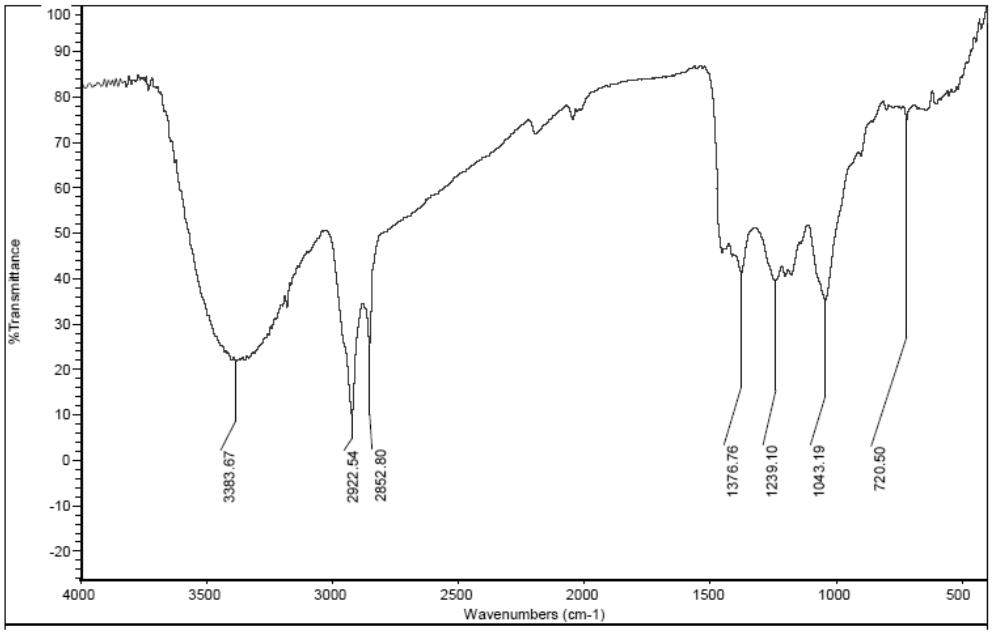

Figure 4.176.: FTIR spectrum of tetrahydro-6-(hexahydro-13-((tetrahydro-18-(23-hydroxy-23-methylheptan-19-yl)-15-methylfuran-15-yl)methyl)-10-methyl-*2H*-furo[3,*2-b*]pyran-7-yl)-2,2,6-trimethyl-*2H*-pyran-3-yl (**12**)

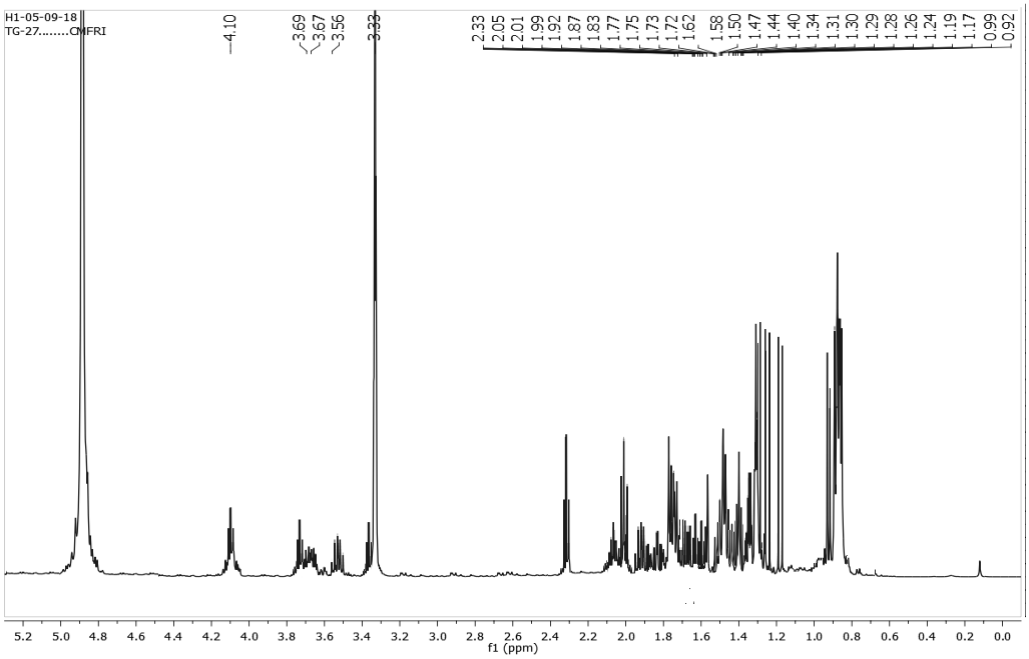

Figure 4.177.: ^{1}H NMR spectrum of tetrahydro-6-(hexahydro-13-((tetrahydro-18-(23-hydroxy-23-methylheptan-19-yl)-15-methylfuran-15-yl)methyl)-10-methyl-*2H*-furo[3,*2-b*]pyran-7-yl)-2,2,6-trimethyl-*2H*-pyran-3-yl (**12**)

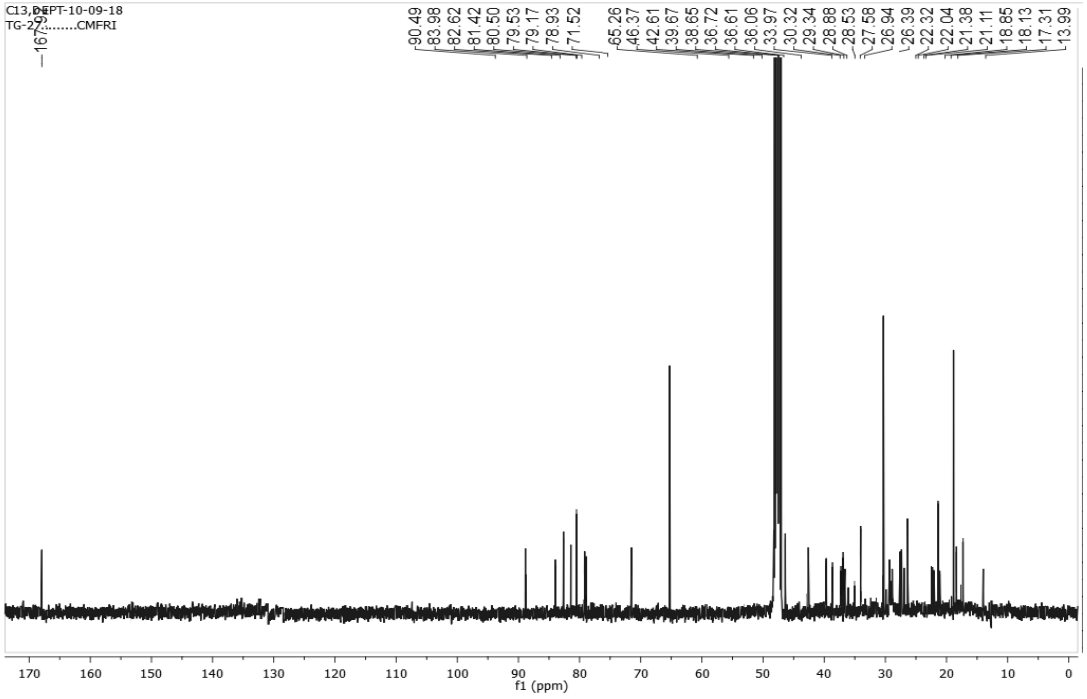

Figure 4.178.: ^{13}C NMR spectrum of tetrahydro-6-(hexahydro-13-((tetrahydro-18-(23-hydroxy-23-methylheptan-19-yl)-15-methylfuran-15-yl)methyl)-10-methyl-*2H*-furo[3,*2-b*]pyran-7-yl)-2,2,6-trimethyl-*2H*-pyran-3-yl (**12**)

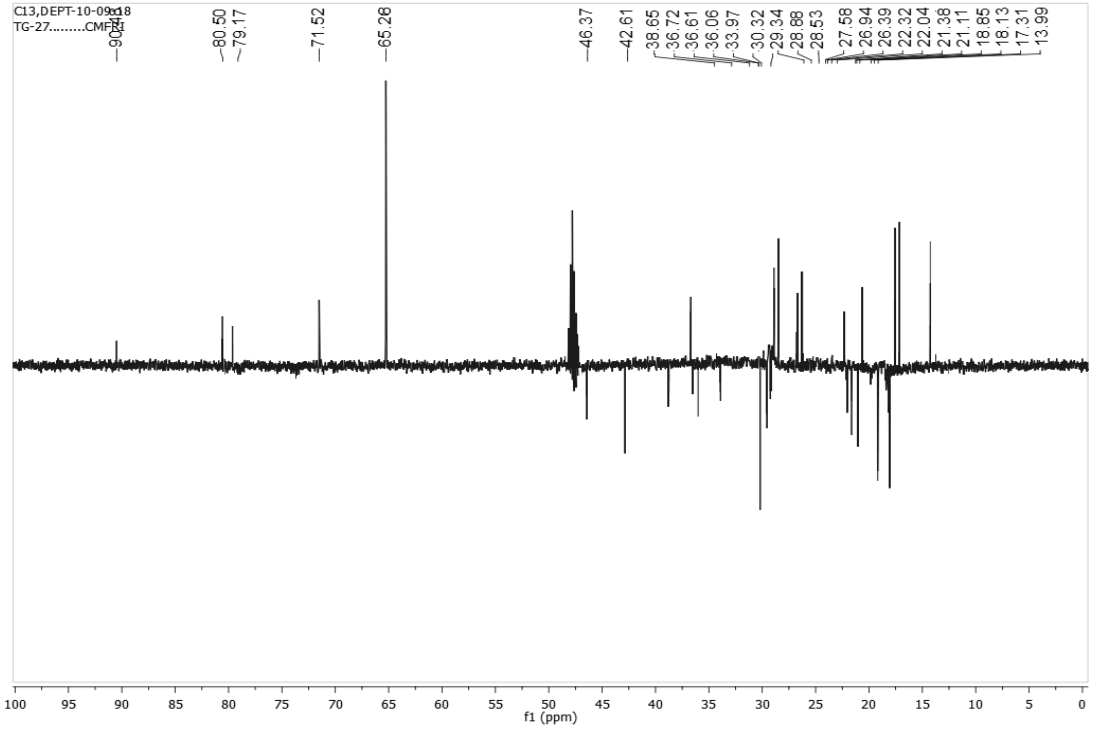

Figure 4.179.: ^{135}DEPT spectrum of tetrahydro-6-(hexahydro-13-((tetrahydro-18-(23-hydroxy-23-methylheptan-19-yl)-15-methylfuran-15-yl)methyl)-10-methyl-*2H*-furo[3,*2-b*]pyran-7-yl)-2,2,6-trimethyl-*2H*-pyran-3-yl (**12**)

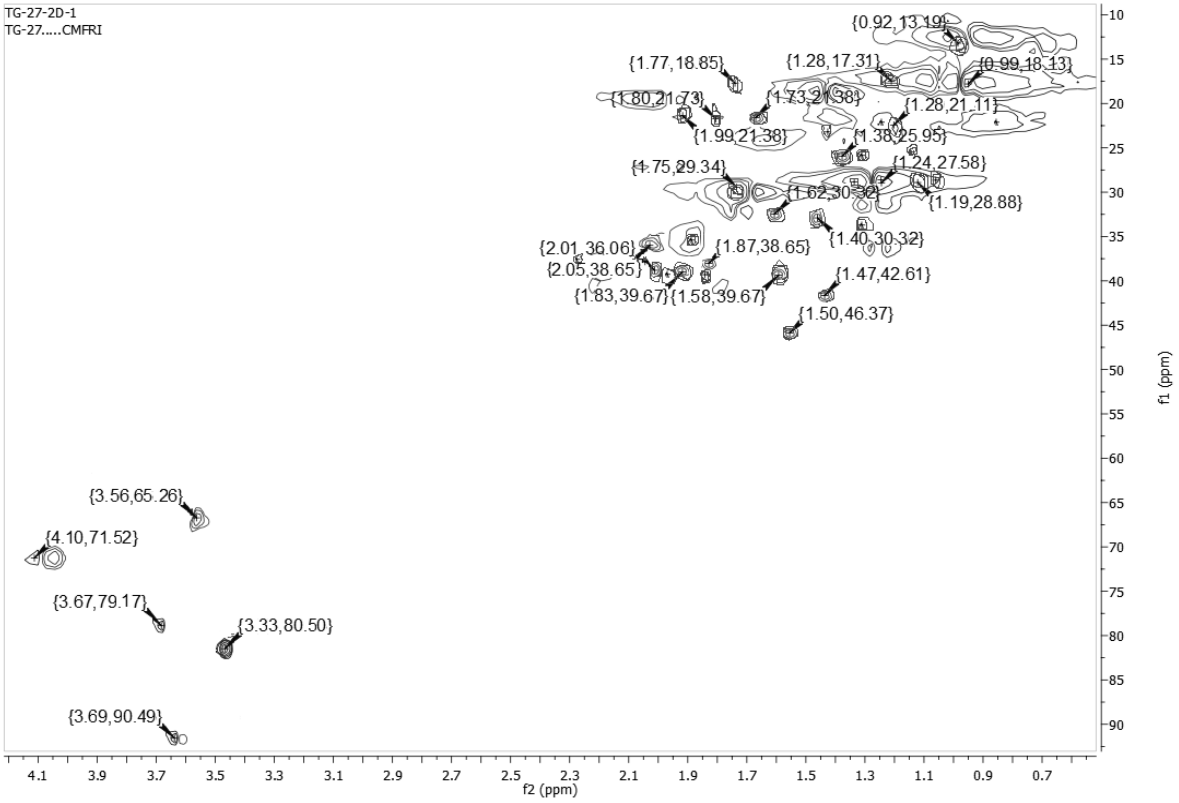

Figure 4.180.: HSQC spectrum of tetrahydro-6-(hexahydro-13-((tetrahydro-18-(23-hydroxy-23-methylheptan-19-yl)-15-methylfuran-15-yl)methyl)-10-methyl-*2H*-furo[3,*2-b*]pyran-7-yl)-2,2,6-trimethyl-*2H*-pyran-3-yl (**12**)

The COSY spin unit from δ 4.10 (H-3)/1.73 (H-4)/1.40 (H-5) and HMBC correlations from δ 4.10 (H-3) to δ 83.98 (C-2); δ 1.62 (H-5) to δ 82.62 (C-6); δ 1.24 (H-3) to δ 83.98 (C-2); δ 1.26 (H-25) to δ 83.98 (C-2) and δ 1.29 (H-6) to δ 82.62 (C-6) ascribed the presence of tetrahydro-2,2,6-trimethyl-*2H*-pyran moiety in the studied compound (Figure 4.181-4.183). The ^{1}H-^{1}H COSYs among δ 2.33 (H-3^{1})/1.77 (H-3^{2})/0.92 (H-3^{3}) along with HMBCs from δ 2.33 (H-3^{2}) to δ 167.92 (C-3^{1}) supported the occurrence of the butyrate side chain, which was directly attached at C-3 of tetrahydro-2,2,6-trimethyl-*2H*-pyran through the HMBCs from δ 4.10 (H-3) to ester carbonyl at δ 167.92 (C-3^{1}). Similarly, compound **12** exhibited COSYs like δ 3.69 (H-7)/1.72 (H-8)/1.58 (H-9) and δ 3.33 (H-11)/2.05 (H-12)/3.56 (H-13). These COSY fragments were further connected by the HMBC correlations from δ 1.72 (H-8) to δ 90.49 (C-7); H-9 to both C-8/C-10 {δ 1.83 (H-9) to δ 22.32 (C-8)/81.42 (C-10)}; H-11 to both C-10/C-7 {δ 3.33 (H-11) to δ 81.42 (C-10)/90.49 (C-7)}; H-12 to both C-11/C-13 {δ 2.05 (H-12) to δ 80.50 (C-11)/65.26 (C-13)} and from δ 3.56 (H-13) to δ 81.42 (C-10), which attributed the presence of 10-methyl-2*H*-furo[3,2-b]pyran. The attachment of furo[3,2-b]pyran at C-6 of tetrahydro-2,2,6-trimethyl-2*H*-pyran was ascribed through HMBCs from δ 3.69 (H-7) to δ 82.62 (C-6). Another

tetrahydro-furanyl ring was formed through COSYs from δ 2.01 (H-16)/1.75 (H-17)/3.67 (H-18), and which was extended with a seven-membered linear side chain at C-18 through the COSYs from δ 3.67 (H-18)/1.92 (H-19)/1.34 (H-20)/1.30 (H-21)/1.47 (H-22) along with δ 1.92 (H-19)/0.99 (H-29).

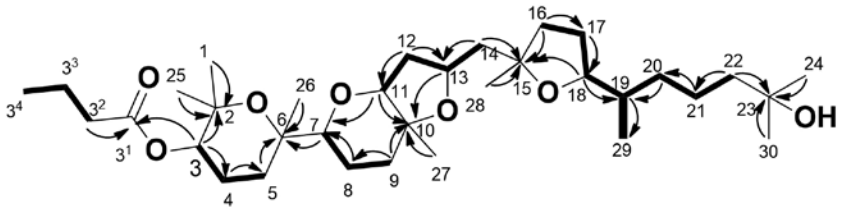

Figure 4.181.: ^{1}H-^{1}H COSY (bold face bonds) and selected HMBCs (double-barbed arrows), correlations of tetrahydro-6-(hexahydro-13-((tetrahydro-18-(23-hydroxy-23-methylheptan-19-yl)-15-methylfuran-15-yl)methyl)-10-methyl-*2H*-furo[3,*2-b*]pyran-7-yl)-2,2,6-trimethyl-*2H*-pyran-3-yl (**12**)

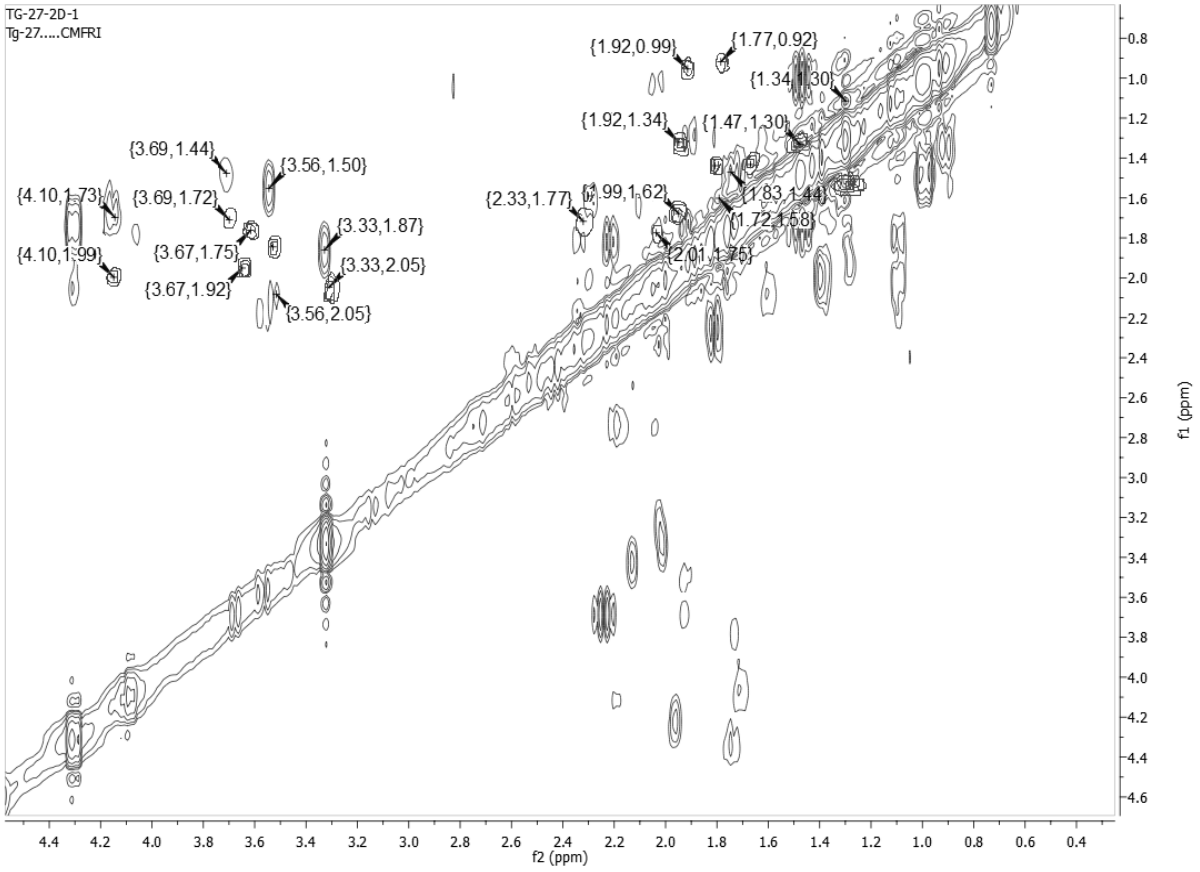

Figure 4.182.: ^{1}H-^{1}H COSY spectrum of tetrahydro-6-(hexahydro-13-((tetrahydro-18-(23-hydroxy-23-methylheptan-19-yl)-15-methylfuran-15-yl)methyl)-10-methyl-*2H*-furo[3,*2-b*]pyran-7-yl)-2,2,6-trimethyl-*2H*-pyran-3-yl (**12**)

Further, the HMBCs from δ 2.01 (H-16) to δ 79.53 (C-15); δ 3.67 (H-18) to δ 79.53 (C-15); H-12 to both δ 1.92 (H-19) to δ 18.13 (C-29); δ 1.47 (H-22) to δ 78.93 (C-23); δ 1.19 (H-24) to δ 78.93 (C-23), and from δ 1.31 (H-28) to δ 79.53 (C-15) appropriately established the partial structure of tetrahydro-18-(23-hydroxy-23-methylheptan-19-yl)-15-methylfuran group. The tetrahydro-furanyl ring with linear side chain enclosing 22-hydroxy-15(28)-dehydrovenustatriol was previously reported (Pacheco, 2011), and the chemical shifts were comparable with the titled compound. The 10-methyl-2*H*-furo[3,2-b]pyran ring and tetrahydro-18-(23-hydroxy-23-methylheptan-19-yl)-15-methylfuran group were connected through a methylene linkage, which was assigned by the strong HMBCs from the methylene proton at δ 1.50 located at H-14 to methine carbon at δ 65.26 (C-13 of furo[3,2-b]pyran) and to the non-protonated carbon at δ 79.53 (C-15 of furan enclosed side chain).

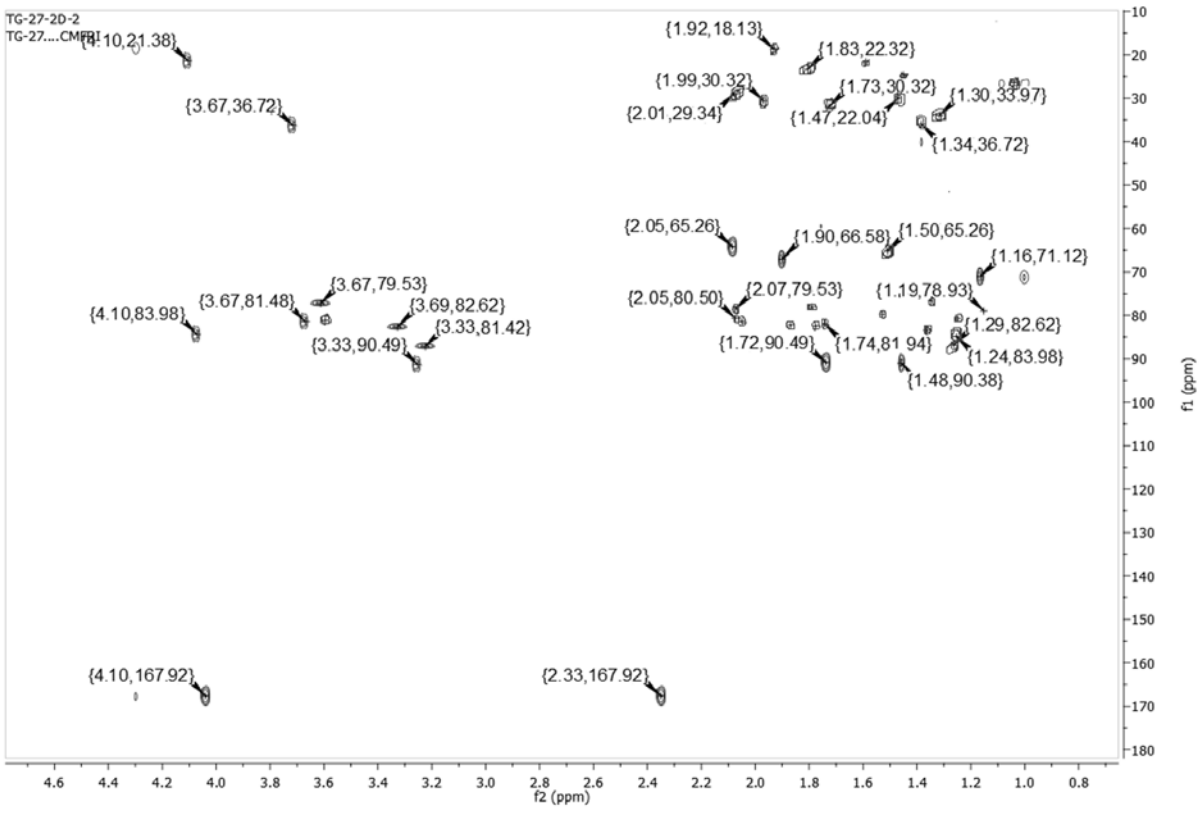

Figure 4.183.: HMBC spectrum of tetrahydro-6-(hexahydro-13-((tetrahydro-18-(23-hydroxy-23-methylheptan-19-yl)-15-methylfuran-15-yl)methyl)-10-methyl-*2H*-furo[3,*2-b*]pyran-7-yl)-2,2,6-trimethyl-*2H*-pyran-3-yl (**12**)

The spiro-dehydrovenustatriol enclosed trimethyl pyran with bromine at C-3 with chemical shifts of δ 1.28 (H-1)/29.7 (C-1), 74.9 (C-2), 3.90 (H-3)/59.1 (C-3), 74.8 (C-6); spiro-fused tetrahydro-furano-tetrahydro-pyran at C-11 with chemical shift signals at δ 72.9 (C-10), 109.9 (C-11); methyl tetrahydro-furan with chemical shifts at δ 84.6 (C-19), 1.60-2.01 (H-20)/35.0 (C-20), 1.77 (H-21)/24.7 (C-21), 3.76 (H-22)/86.7 (C-22) and a propan-2-ol end with chemical shift signals at δ 70.6 (C-23), 1.11 (H-24)/25.4 (C-24), 1.20 (H-30)/28.2 (C-30) (Pacheco et al., 2010) were apparent. Similarly, the present compound enclosed trimethyl pyran with ester linkage at C-3 with chemical shifts of δ 1.24 (H-1)/27.58 (C-1), 83.98 (C-2), 4.10 (H-3)/71.52 (C-3), 82.62 (C-6), and the greater chemical shifts at C-3 was due to the presence of highly electronegative groups like ester. It enclosed fused tetrahydro-furano-tetrahydro-pyran at C-10 and C-11 positions, and therefore, the chemical shift at C-11 was appeared to be lower (δ 80.50) when compared to spiro-fused compound spiro-dehydrovenustatriol (Pacheco et al., 2010). The chemical shifts of methyl tetrahydro-furan were found at δ 79.53 (C-15), 2.01 (H-16)/36.06 (C-16), 1.75 (H-17)/29.34 (C-17), 3.67 (H-18)/79.17 (C-18) and propan-2-ol end were found at δ 78.93 (C-23), 1.19 (H-24)/28.88 (C-24), 1.17 (H-30)/28.53 (C-30), which were comparable to the previously reported spiro-dehydrovenustatriol (Pacheco, 2011; Pacheco et al., 2010).

Table 4.19: NMR spectroscopic data of compound (**12),** tetrahydro-6-(hexahydro-13-((tetrahydro-18-(23-hydroxy-23-methylheptan-19-yl)-15-methylfuran-15-yl)methyl)-10-methyl-*2H*-furo[3,*2-b*]pyran-7-yl)-2,2,6-trimethyl-*2H*-pyran-3-yl (**12**) isolated from red seaweed *G. salicornia*

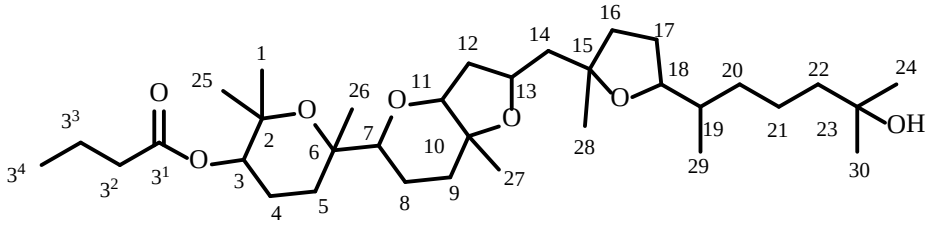

Compound **12**……. tetrahydro-6-(hexahydro-13-((tetrahydro-18-(23-hydroxy-23-methylheptan-19-yl)-15-methylfuran-15-yl)methyl)-10-methyl-*2H*-furo[3,*2-b*]pyran-7-yl)-2,2,6-trimethyl-*2H*-pyran-3-yl (**12**)

C. No.	**^{13}C**	**^{1}H (int.,mult., J in Hz)^{b}**	**^{1}H-^{1}H COSY**	**HMBC**
1	27.58	1.24 (3H,s)	-	C-2

2	83.98	-	-	-
3	71.52	4.10 (1H,t,4.2 Hz)	H-4	C-2,4,3[1]
4	21.38	1.73 (1H,m)	H-5	C-5
		1.99 (1H,m)	-	-
5	30.32	1.62 (1H,t,4.3 Hz)	-	C-6
		1.40 (1H,t,4.3 Hz)	-	-
6	82.62	-	-	-
7	90.49	3.69 (1H,t,6.2 Hz)	H-8	C-6
8	22.32	1.72 (1H,m)	H-9	C-7
		1.44 (1H,m)	-	-
9	39.67	1.83 (1H,t,5.2 Hz)	-	C-8,10
		1.58 (1H,t,5.2 Hz)	-	-
10	81.42	-	-	-
11	80.50	3.33 (1H,t,9.2 Hz)	H-12	C-7,10
12	38.65	2.05 (1H,t,6.4 Hz)	H-13	C-11,13
		1.87 (1H,t,6.5 Hz)	-	-
13	65.26	3.56 (1H,m)	H-14	C-10
14	46.37	1.50 (2H,d,6.8 Hz)	-	C-13,15
15	79.53	-	-	-
16	36.06	2.01 (2H,t,4.2 Hz)	H-17	C-15,17
17	29.34	1.75 (2H,m)	H-18	C-18
18	79.17	3.67 (1H,m)	H-19	C-19,15
19	36.72	1.92 (1H,m)	H-20, H-29	C-29
20	33.97	1.34 (2H,m)	H-21	C19
21	22.04	1.30 (2H,m)	H-22	C-20
22	42.61	1.47 (2H,m)	-	C-21,23
23	78.93	-	-	-
24	28.88	1.19 (3H,s)	-	C-23
25	26.39	1.26 (3H,s)	-	C-2
26	21.11	1.29 (3H,s)	-	C-6
27	17.31	1.28 (3H,s)	-	C-10
			-	-
28	26.94	1.31 (3H,s)	-	C-15
29	18.13	0.99 (3H,d,7.2 Hz)	-	-
			-	-
30	28.53	1.17 (3H,s)	-	C-23
3^1	167.92	-	-	-
3^2	36.61	2.33 (2H,t,6.8 Hz)	H-3^3	C-3^1
3^3	18.85	1.77 (2H,m)	H-3^4	-
3^4	13.99	0.92 (3H,t,4.1 Hz)	-	-

[a]NMR spectra recorded using Bruker AVANCE III 500 MHz (AV 500) spectrometers.

[b]Values in ppm, multiplicity and coupling constants (J = Hz) are indicated in parentheses.

Assignments were made with the aid of the ^{1}H-^{1}H COSY, HSQC, HMBC and NOESY experiments. The stereo-chemical orientations in the structures were represented by wedge-faced and dash-faced bonds based on NOESY spectra.

Relative stereo-chemical representations of the protons at the chiral points, mainly at C-2, C-3, C-6, C-7, C-10, C-11, C-13, C-15, C-18, and C-19 were corroborated via NOESYs

(Figure 4.184-4.185). The NOE correlations between δ 1.24 (H-1)/3.69 (H-7)/3.33 (H-11)/3.56 (H-13)/1.31 (H-28)/3.67 (H-18) and δ 1.31 (H-28)/1.92 (H-19) attributed the equi-planer arrangement of protons, and that these protons were arbitrarily aligned towards the α-direction with respect to its molecular plane of symmetry. The proton at δ 4.10 (H-3) and methyl protons at 1.26 (H-25), 1.29 (H-26) and 1.28 (H-27) were aligned opposite to the α-protons, and hence, allocated as β-oriented.

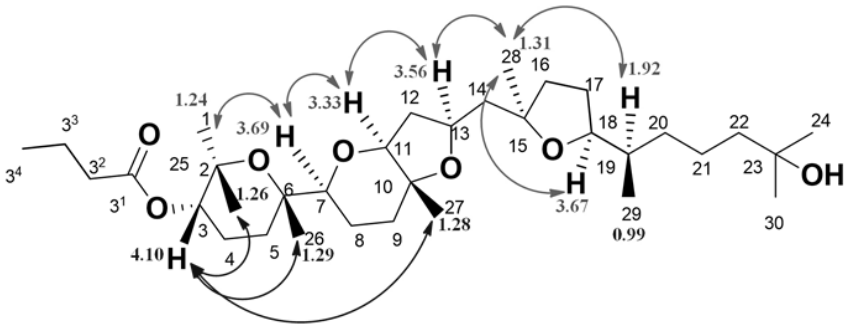

Figure 4.184.: HMBC spectrum of tetrahydro-6-(hexahydro-13-((tetrahydro-18-(23-hydroxy-23-methylheptan-19-yl)-15-methylfuran-15-yl)methyl)-10-methyl-*2H*-furo[3,2-b]pyran-7-yl)-2,2,6-trimethyl-*2H*-pyran-3-yl (**12**)

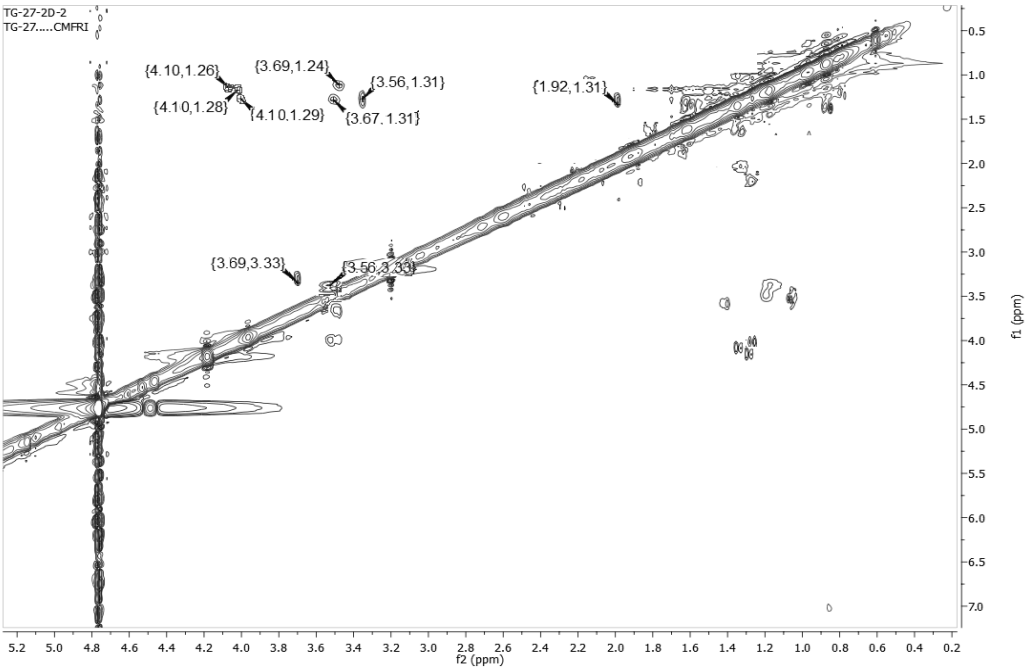

Figure 4.185.: NOE spectrum of tetrahydro-6-(hexahydro-13-((tetrahydro-18-(23-hydroxy-23-methylheptan-19-yl)-15-methylfuran-15-yl)methyl)-10-methyl-*2H*-furo[3,2-b]pyran-7-yl)-2,2,6-trimethyl-*2H*-pyran-3-yl (**12**)

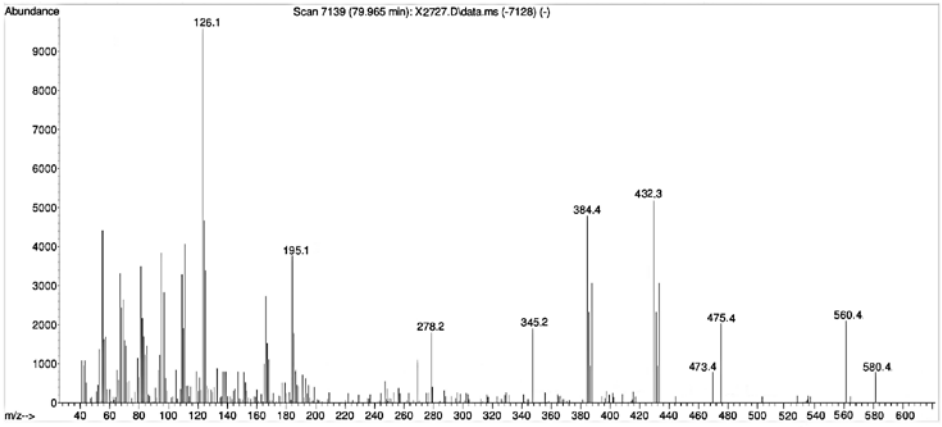

Figure 4.186.: EI-MS spectrum of tetrahydro-6-(hexahydro-13-((tetrahydro-18-(23-hydroxy-23-methylheptan-19-yl)-15-methylfuran-15-yl)methyl)-10-methyl-*2H*-furo[3,2-b]pyran-7-yl)-2,2,6-trimethyl-*2H*-pyran-3-yl (**12**)

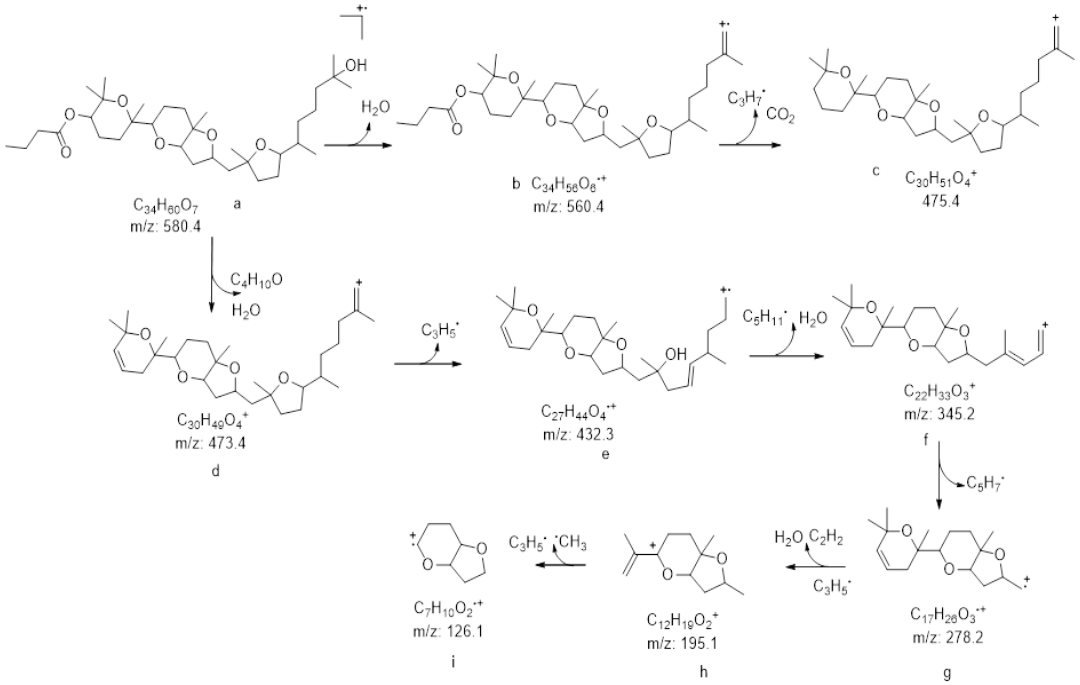

Figure 4.187.: Mass fragmentation pattern m of tetrahydro-6-(hexahydro-13-((tetrahydro-18-(23-hydroxy-23-methylheptan-19-yl)-15-methylfuran-15-yl)methyl)-10-methyl-*2H*-furo[3,2-b]pyran-7-yl)-2,2,6-trimethyl-*2H*-pyran-3-yl (**12**)

The structural assignments of **12** recorded molecular ion peak at *m/z* 580 (a) that could undergo elimination of water to result in the fragment of $C_{34}H_{56}O_6^{\bullet+}$ with *m/z* 560 (b). The elimination of $C_4H_{10}O$ and water from (a) might result in a fragment at $C_{30}H_{49}O_4^+$ with *m/z* 473 (d), whereas the elimination of $C_3H_7^+$ and CO_2 from (b) led to $C_{30}H_{51}O_4^+$ formation with *m/z* 475 (c). The fragment (d) underwent further series of fragmentation to yield the mass fragments at *m/z* 432 (e), 345 (f), 278 (g), 195 (h), and 126 (i). The base peak of **12** was reported at *m/z* 126 corresponding to $C_7H_{10}O_2^{+\cdot}$ (Figure 4.186-4.187).

The sequential chromatographic fractionation of EtOAc-MeOH extract of the seaweed, *G. salicornia* led to the identification of two previously unreported polyether analogues, 3-methoxy-2,6-dimethyl-3,4-dihydro-2*H*-pyranyl-(6-(7-(10-methyl-octahydropyrano[3,2-*b*]pyranyl)-14-((19-methyl-23-methyleneoxepan)-(15-pentene-18-ol)) (**11**) and 14-(15-methyltetrahydrofuranyl)-(18-(23-(hydroxy-23-methylheptanyl)-10-methylhexahydro-2*H*-furo-[3,2-*b*]pyranyl))-2,2,6-trimethyltetrahydro-2*H*-pyran-3- butyrate (**12**). The polyether triterpenoid possessing furanyl, pyranyl along with other oxygenated functionalities can be used to design as potential pharmacophore leads for use against various pathophysiologies.

4.3.2.7 Structural characterization of macrolide derivatives (Compounds 13-15)

Macrolides were recognized as a class of polyketide or polyene macrocyclic chemistries, which were identified as important sources of pharmacophores (Mishra and Tiwari, 2011; Blunt et al., 2013). Almost 100,000 natural derived secondary metabolites were identified previously, and among those, approximately 3 % were found to be macrocyclic compounds (Driggers et al., 2008). A significant number of marine polyketide or ether enclosed macrolides were isolated from various marine organisms, such as sponges (Uemura et al., 1985), mollusks (Chakraborty et al., 2019), seaweeds (Murakami et al., 1991) and seaweed-associated microorganisms (Chakraborty et al., 2014). Most of the naturally occurring macrocyclic metabolites were found to contain only carbon atoms in their ring skeletons like isoprenoids with or without unsaturations (Wessjohann et al., 2005). However, the macrocyclic lactones or ethers with more than ten-membered ring systems containing alkene, ester, ether or hydroxyl moieties were identified as significant pharmacophores (Molinski, 2009). These exhibited higher molecular weights (in the range of 450-850 g mol^{-1}), even though the greater numbers of proton-bond donors, higher polarizabilities along with their lesser number of rotatable bonds than their respective acyclic metabolites could enhance their bio-potencies and bio-availabilities through the effective interactions in the active binding sites of the targeted proteins (Driggers et al., 2008; Marsault and Peterson, 2011). The macrolides could be classified as polyketide derivatives that

typically enclosed multiple carbonyl functionalities, which might be responsible for its various bio-potencies like anti-inflammatory, antioxidant, anti-bacterial etc. (Chakraborty et al., 2017; Maneesh and Chakraborty, 2018). Therefore, macrocyclic lactone scaffolds were used as therapeutics due to its structural features than that of typical small-molecular therapeutics (Driggers et al., 2008). The α-pyrone macrolides, neurymenolides A and B were isolated from the seaweed, *Neurymenia fraxinifolia* (Stout et al., 2009). The 2,6-disubstituted pyran-4-one along with 6-substituted pyran-2-one macrolides were characterised from *Phacelocarpus labillardieri* (Kazlauskas et al., 1982). The macrolide, methyl-2-(12-oxo-7-phenyl-8-vinyl-1-oxa-4,9-cyclododecadien-3-yl)-acetate was reported from the brown seaweed, *Sargassum wightii* (Maneesh and Chakraborty, 2017) with potential antioxidant and anti-inflammatory activities. An antibacterial macrolide, 7-*O*-methyl-5′-hydroxy-3'-heptenoate-macrolactin was reported from seaweed-associated bacterium, *Bacillus subtilis* (Chakraborty et al., 2014).

Among various marine organisms, seaweeds were considered as one of the significant sources of specialised bioactive metabolites (Stout et al., 2009). The search for pharmacophores with active anti-inflammatory/antioxidant potentials from *G. salicornia* obtained from the south-east-coastline areas of Indian peninsular resulted in the isolation of three macrolides enclosing ether functionalities, (Figure. 4.188). The studied compounds were classified as 3-acetyl-14-(furanyl)-11-methyl-15-(15^3-methylbutyloxy)-8-oxabicyclo[21.3.1] heptacosa-11,23,25,27-tetraene-7,18-dione (**13**), (2*E*,12*E*,14*E*)-10-acetyl-9-isopentyl-2-methyl-5,16,23^1-trioxa-bicyclo[21.3.1]heptacosa-2,12,14-triene-6,19-dione (**14**) and (2*Z*,5*E*,16*E*)-8-hydroxy-20-isobutyl-16-methyl-7,14-dioxa-bicyclo[19.3.1]pentacosa-2,5,16-triene-10,23-dione (**15**) through comprehensive spectroscopic techniques.

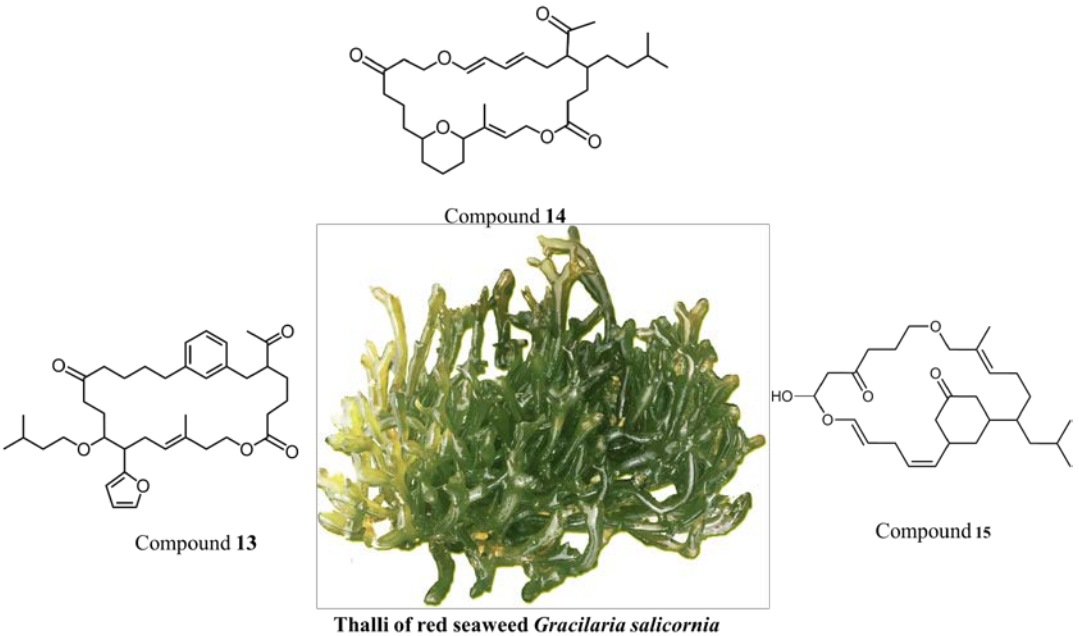

Figure 4.188.: Structural representations of 3 macrolides (**13-15**) along with the characteristic of thalli (leaf-like structures) of *G. salicornia* were presented.

4.3.2.7a Structural characterization of Compound 13

3-Acetyl-14-(furanyl)-11-methyl-15-(15^3-methylbutyloxy)-8-oxabicyclo-[21.3.1]heptacosa-11,23,25,27 tetraene-7,18-dione

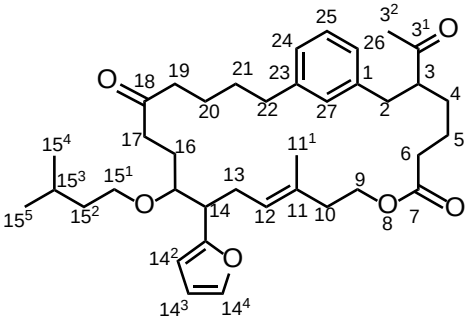

Sample yield	0.37% (> 99% purity, RP-C18 HPLC)
Physical description	Pale yellow oily
Molecular formula	$C_{38}H_{55}O_6$
Molecular mass	606.3920

The macrolide derivative, 3-acetyl-14-(furanyl)-11-methyl-15-(15^3-methylbutyloxy)-8-oxabicyclo-[21.3.1]heptacosa-11,23,25,27 tetraene-7,18-dione was isolated as pale yellow oil. The compound (**13**) has exhibited UV absorbance (UV (MeOH) λ_{max}) at 232 nm (Figure 4.189). The homogeneity of the compound was ascertained by HPLC data on a bonded phase octadecylsilane (C_{18}) stationary phase (HPLC, MeCN/MeOH, 1:2 v/v) with R_t: 4.90 min (Figure 4.190).

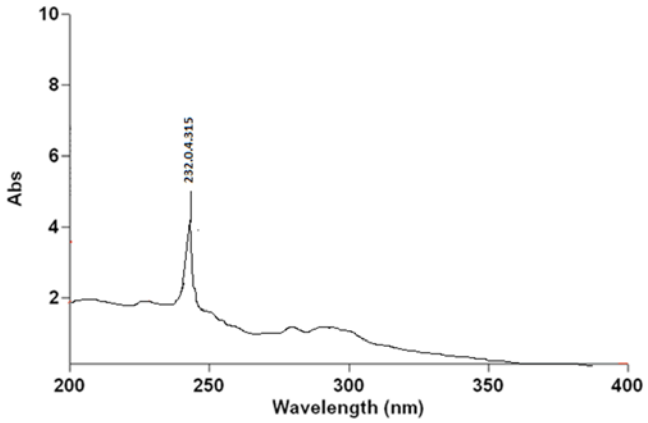

Figure 4.189.: UV spectrum of 3-acetyl-14-(furanyl)-11-methyl-15-(15[3]-methylbutyloxy)-8-oxabicyclo-[21.3.1]heptacosa-11,23,25,27 tetraene-7,18-dione (**13**)

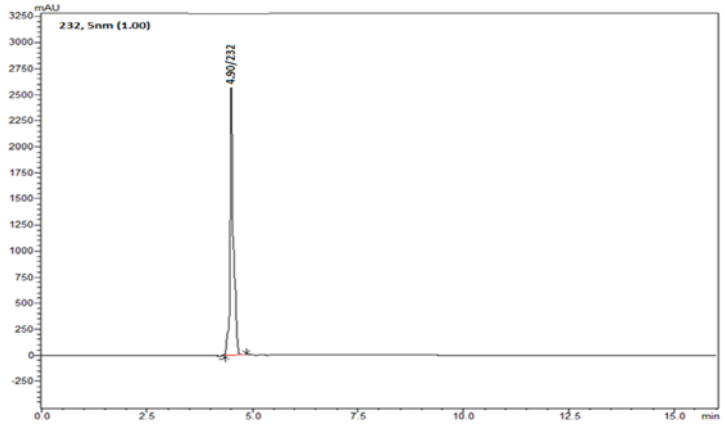

Figure 4.190.: HPLC chromatogram of 3-acetyl-14-(furanyl)-11-methyl-15-(15[3]-methylbutyloxy)-8-oxabicyclo-[21.3.1]heptacosa-11,23,25,27 tetraene-7,18-dione (**13**)

The first in the series of macrolides, 3-acetyl-14-(furanyl)-11-methyl-15-(15[3]-methylbutyloxy)-8-oxabicyclo[21.3.1] heptacosa-11,23,25,27-tetraene-7,18-dione (**13**) was acquired as a pale yellow oily substance with the molecular formula of $C_{38}H_{54}O_6$. This was ascertained by its molecular ion peak at *m/z* 606.4 $[M]^+$ along with HRESIMS data {*m/z* 607.4003 $[M+H]^+$} (Figure 4.191) that were in agreement with one/two dimensional NMR data (Table 4.20). The FTIR spectrum of compound **13** exhibited peaks at 3009/2939, 1735 and 1715 cm^{-1}, which confirmed the occurrences of C-H stretching, ester stretching (-C(=O)-O-) and C=O stretching (carbonyl), respectively (Figure 4.192).

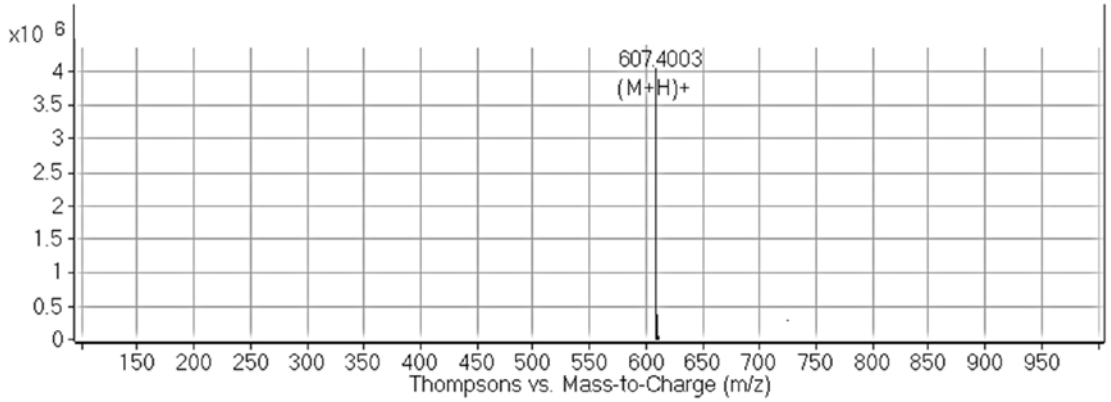

Figure 4.191.: HRESIMS spectrum of 3-acetyl-14-(furanyl)-11-methyl-15-(15^3-methylbutyloxy)-8-oxabicyclo-[21.3.1]heptacosa-11,23,25,27 tetraene-7,18-dione (**13**)

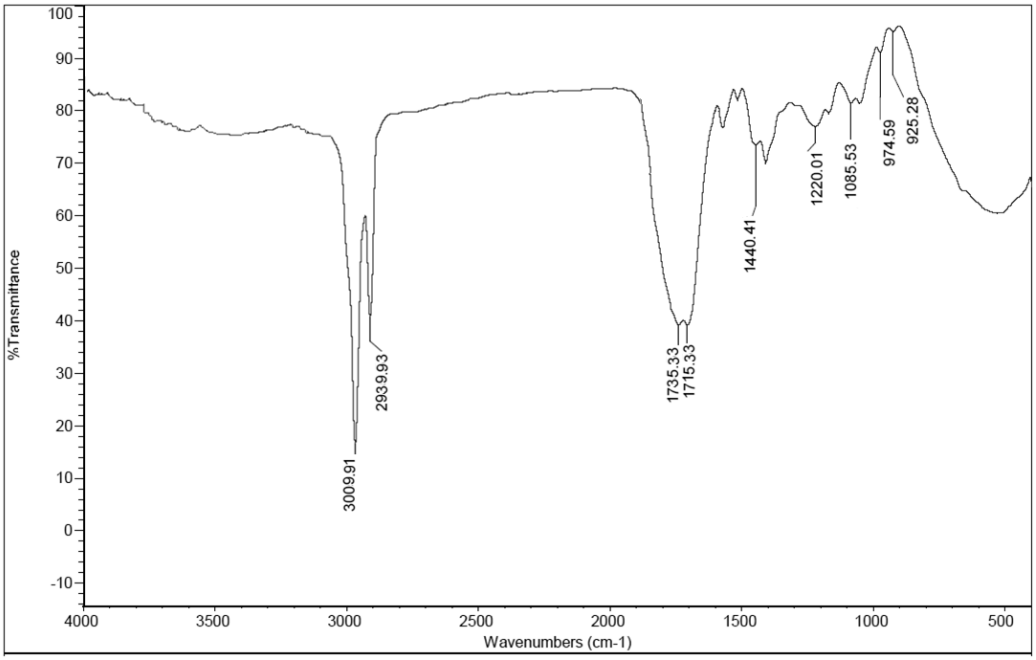

Figure 4.192.: FTIR spectrum of 3-acetyl-14-(furanyl)-11-methyl-15-(15^3-methylbutyloxy)-8-oxabicyclo-[21.3.1]heptacosa-11,23,25,27 tetraene-7,18-dione (**13**)

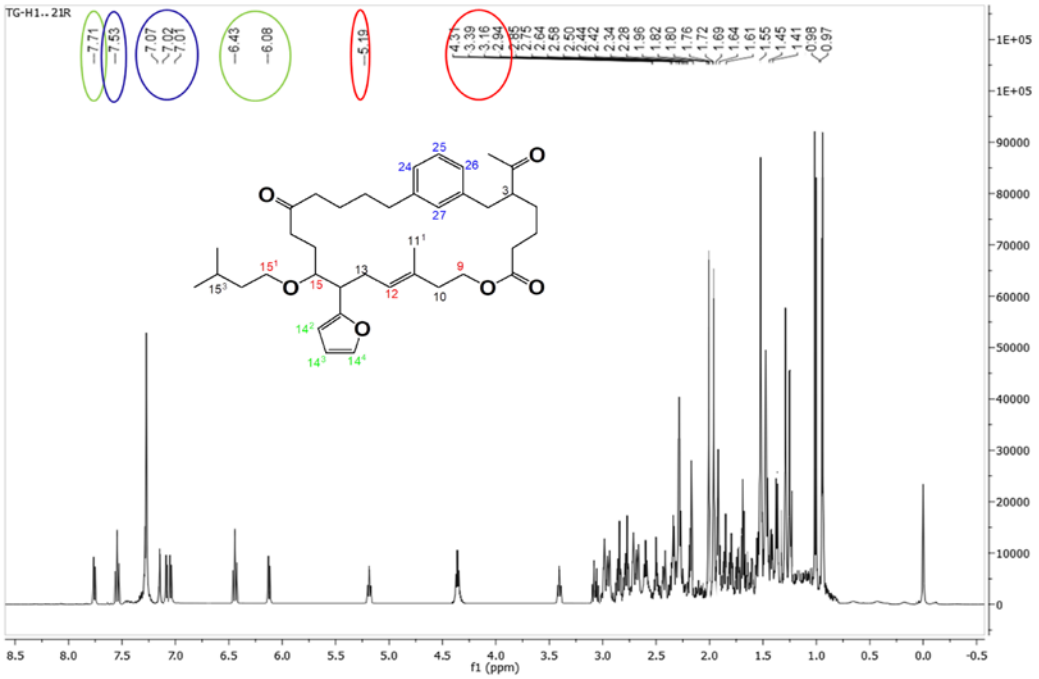

Figure 4.193.: ^{1}H NMR spectrum of 3-acetyl-14-(furanyl)-11-methyl-15-(15^{3}-methylbutyloxy)-8-oxabicyclo-[21.3.1]heptacosa-11,23,25,27 tetraene-7,18-dione

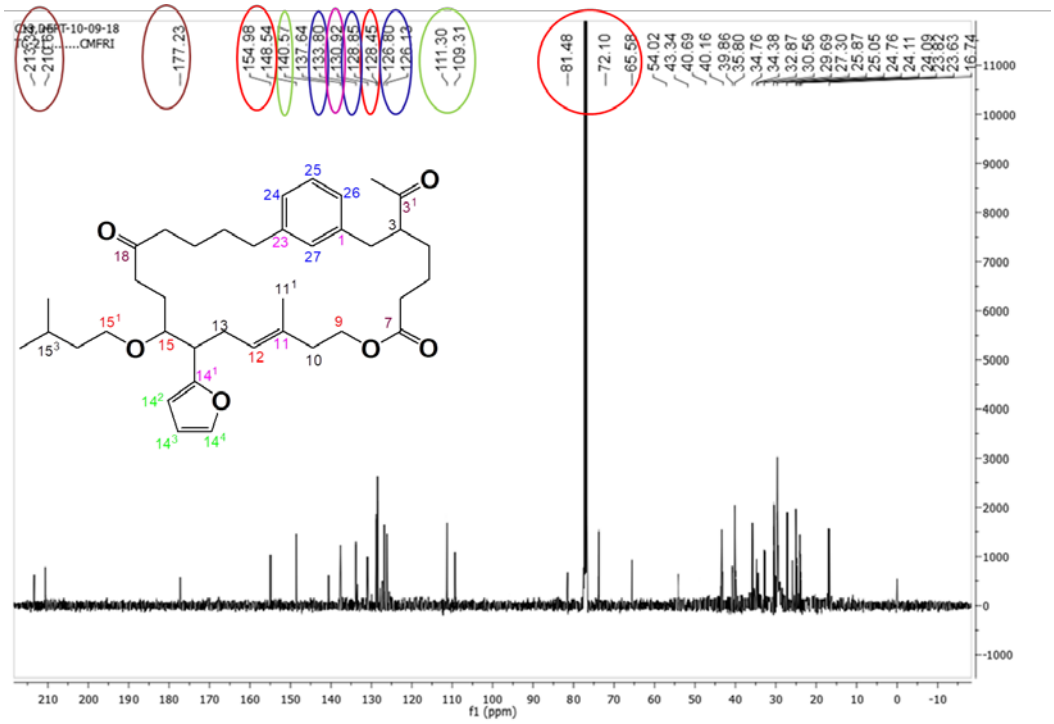

Figure 4.194.: ^{13}C NMR spectrum of 3-acetyl-14-(furanyl)-11-methyl-15-(15^{3}-methylbutyloxy)-8-oxabicyclo-[21.3.1]heptacosa-11,23,25,27 tetraene-7,18-dione (**13**)

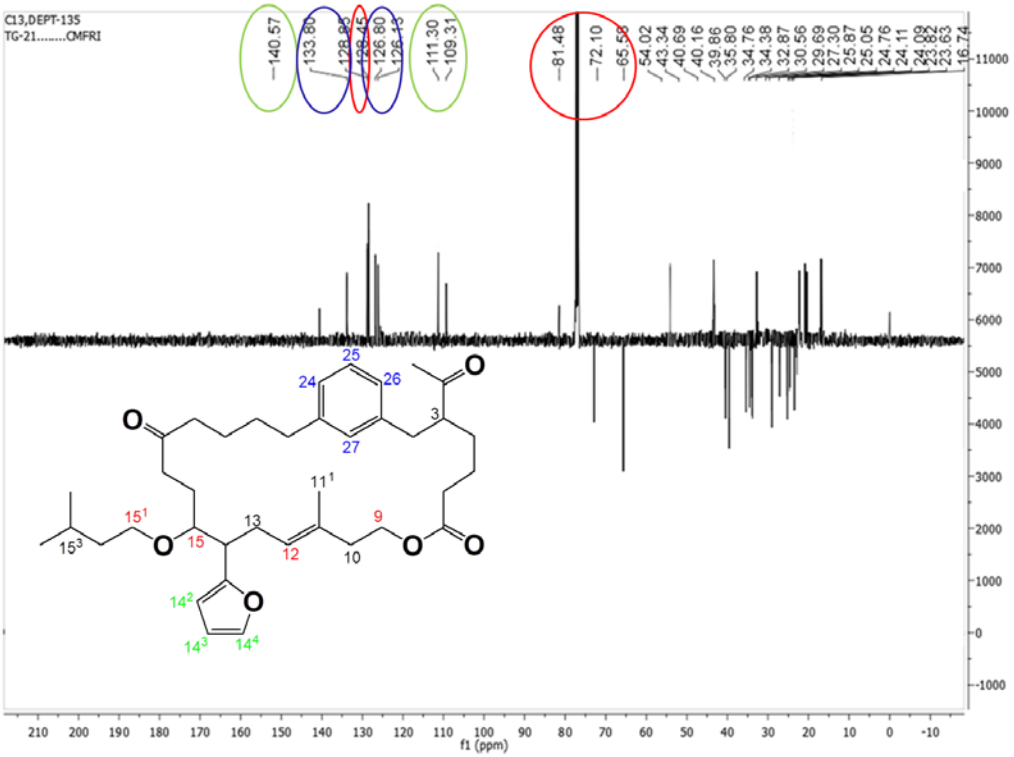

Figure 4.195.: ^{135}DEPT NMR spectrum of 3-acetyl-14-(furanyl)-11-methyl-15-(15^{3}-methylbutyloxy)-8-oxabicyclo-[21.3.1]heptacosa-11,23,25,27 tetraene-7,18-dione (**13**)

The proton (^{1}H NMR) and carbon NMR (^{13}C NMR) with DEPT spectra documented fifteen sp^{3} methylenes, twelve methines, four sp^{3} methyls along with seven quaternary carbons (two carbonyl carbons, one ester carbon and four sp^{2} carbons) (Figure 4.193). The ^{13}C NMR along with DEPT data recorded peaks at δ 177.23 corresponding to ester carbonyl {-C=O)-O-} and signals at δ 213.34 and 210.63 attributed to keto (-C=O) functionality. The sp^{2} methine groups at δ 7.02/126.80, 7.53/128.85, 7.01/126.13, 7.07/133.80, 6.08/109.31, 6.43/111.30 and 7.71/140.57 along with sp^{2} quaternary carbons at δ 137.64, 148.54 and 154.98 attributed the presence of two aromatic functionalities in compound **13** (Figure 4.194 & 4.195). These were also supported by the HSQC spectral data (Figure 4.196).

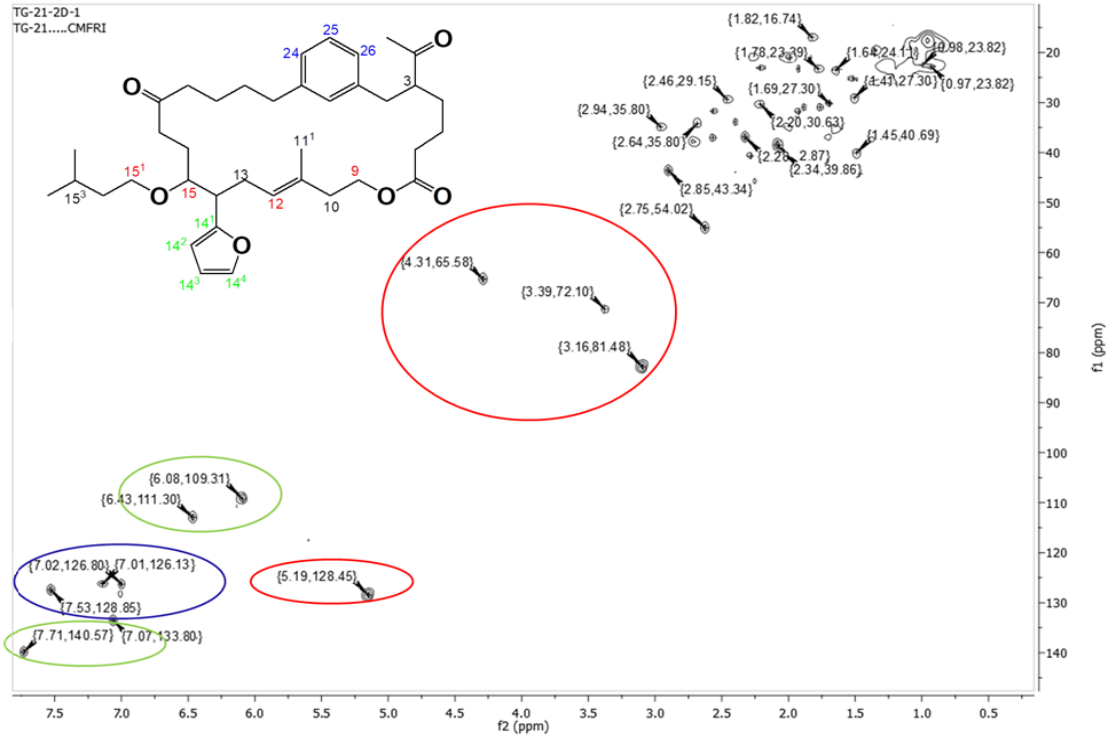

Figure 4.196.: HSQC spectrum of 3-acetyl-14-(furanyl)-11-methyl-15-(15^3-methylbutyloxy)-8-oxabicyclo-[21.3.1]heptacosa-11,23,25,27 tetraene-7,18-dione (**13**)

One of the aromatic ring skeletons were found to be benzene through the COSY (^{1}H-^{1}H) spin unit from δ 7.02/7.53/7.01 along with long-range-HMBCs observed from δ 7.02 to δ 148.54; δ 7.53 to δ 126.13 and δ 7.07, δ 7.01 to δ 148.54, which suggested the presence of a disubstituted aryl ring. The previously reported macrolactone bearing monosubstituted aryl ring as an attachment exhibited ^{13}C NMR peaks in the region of δ 129-132 (^{1}H NMR in the region of δ 7.0-7.8) with one aryl quaternary carbon at δ 132.29 (Maneesh and Chakraborty, 2017). Herein, two aryl quaternary carbons were recorded (δ 148.54, 137.64), and four proton integrals including one singlet (δ 7.0-7.5) appropriately confirmed the presence of disubstituted aryl functionality in compound **13**. Another aromatic ring skeleton was proposed as furan through COSY relations from δ 6.08/6.43/7.71 along with long-range HMBCs from δ 6.08 to δ 154.98, 111.30; δ 6.43 to δ 140.57 and δ 7.71 to δ 154.98 (Figure 4.197-4.199). Previously reported monosubstituted furan enclosed chromene recorded the quaternary carbon at δ 152.12 (Joy and Chakraborty, 2017), which was comparable to the quaternary carbon of furan ring system at δ 154.98 in present compound.

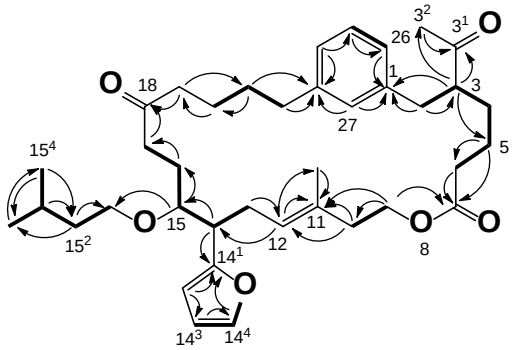

Figure 4.197.: ^{1}H-^{1}H COSY (bold face bonds) and HMBC (double-barbed arrows) correlations of 3-acetyl-14-(furanyl)-11-methyl-15-(15^{3}-methylbutyloxy)-8-oxabicyclo-[21.3.1]heptacosa-11,23,25,27 tetraene-7,18-dione (**13**)

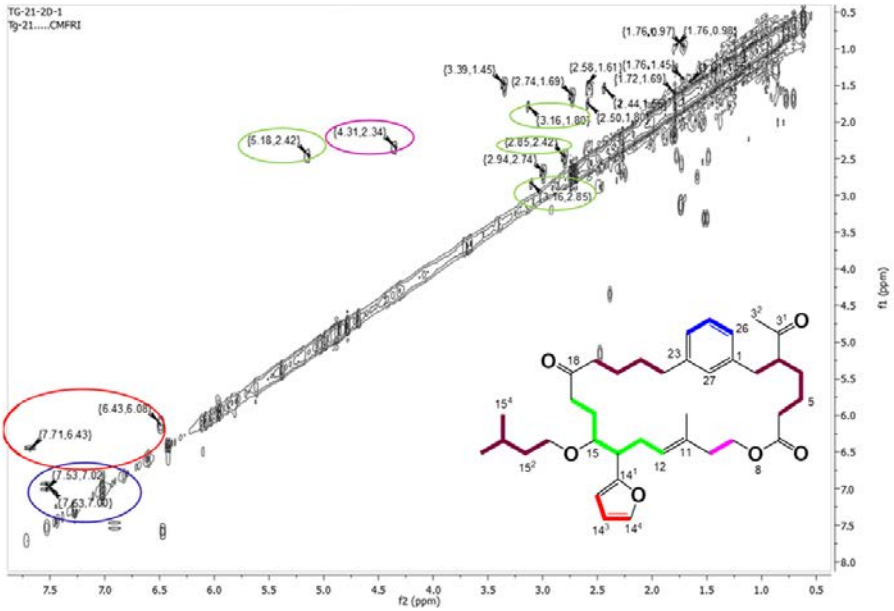

Figure 4.198.: ^{1}H-^{1}H COSY spectrum of 3-acetyl-14-(furanyl)-11-methyl-15-(15^{3}-methylbutyloxy)-8-oxabicyclo-[21.3.1]heptacosa-11,23,25,27 tetraene-7,18-dione (**13**)

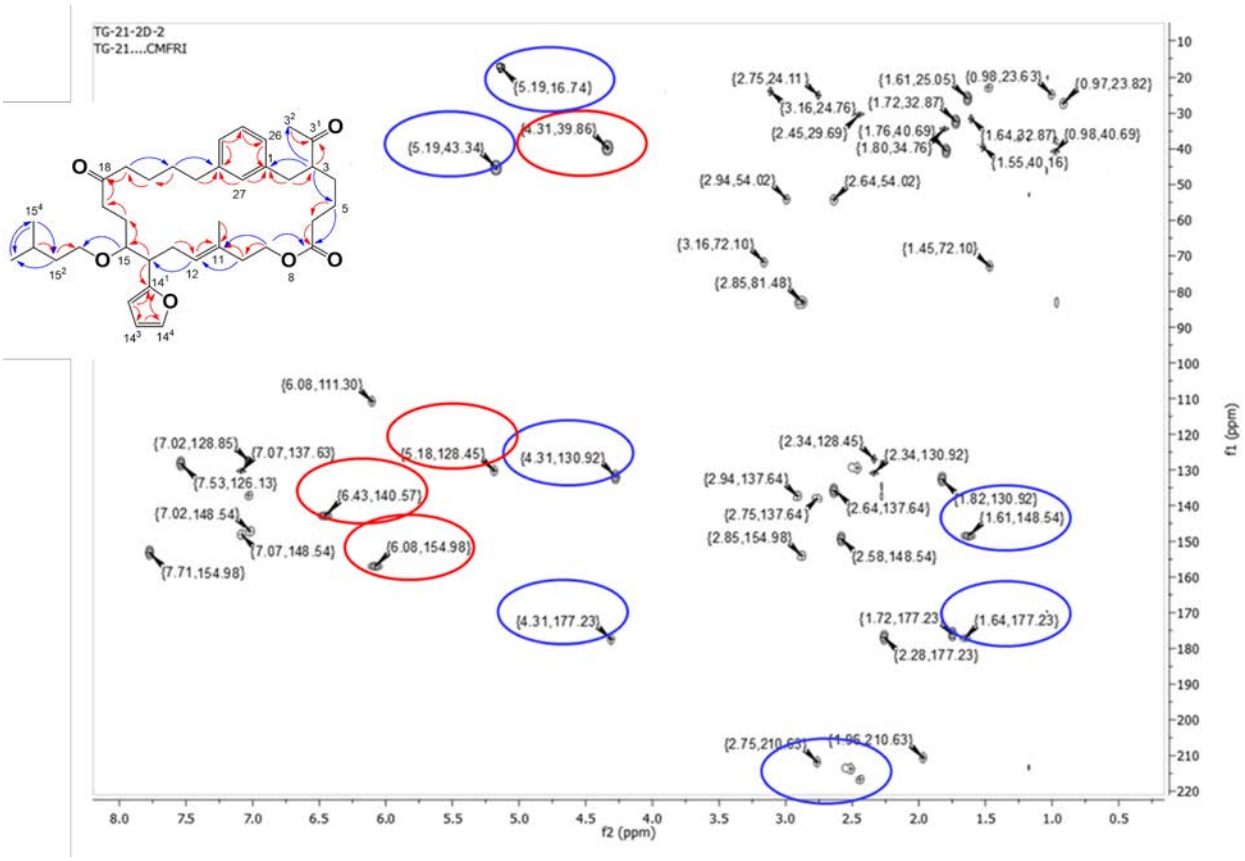

Figure 4.199.: ^{1}H-^{1}H COSY (bold face bonds) and HMBC (double-barbed arrows) correlations of 3-acetyl-14-(furanyl)-11-methyl-15-(15^{3}-methylbutyloxy)-8-oxabicyclo-[21.3.1]heptacosa-11,23,25,27 tetraene-7,18-dione (**13**)

The COSY correlations from δ 2.94, 2.64 (assigned at H-2)/2.75 (H-3)/1.69, 1.41 (H-4)/1.72, 1.64 (H-5)/2.28 (H-6); δ 4.31 (H-9)/2.34 (H-10); δ 5.19 (H-12)/2.42 (H-13)/2.85 (H-14)/3.16 (H-15)/1.80 (H-16)/2.50 (H-17) and δ 2.44 (H-19)/1.55 (H-20)/1.61 (H-21)/2.58 (H-22) were found to be the fragments of 21-membered macrocyclic ring skeleton. The relatively deshielded chemical shifts of methylene proton at δ 4.31 (at δ 65.58, HSQC) were found to reside near to an oxygen functionality of ester moiety (δ 177.23). This attribution was furthermore confirmed with the chemical shifts documented for methylenes (δC 65.58/δH 4.22-4.31) near to ester carbonyl moiety present in the aryl enclosed macrocyclic compound (Maneesh and Chakraborty, 2017). Further, the position of ester carbonyl functionality at δ 177.23 (C-7) was supported by HMBCs from δ 2.28 (H-6) and 4.31 (H-9) to δ 177.23, which designated the presence of respective ester carbonyl between C-6 and C-9 positions in the 21-membered macrocyclic ring. Similarly, the carbonyl carbon at δ 213.34 was positioned between C-17 and C-19 position of the macrocyclic ring through HMBCs from δ 2.44 (H-19) and 2.50 (H-17) to δ

213.34. The HMBC cross-peaks from δ 2.94 (H-2), 7.01 (H-26), 7.07 (H-27) to δ 137.64 (C-1) and from δ 2.58 (H-22) to δ 148.54 (C-23) appropriately assigned that the aryl ring was positioned in between carbons at C-2/C-22 positions of 21-membered macrocyclic system. Other HMBCs from δ 2.94 (H-2) to δ 54.02 (C-3); δ 4.31 (H-9) to δ 39.86 (C-10); δ 2.34 (H-10) to δ 130.92 (C-11); δ 5.19 (H-12) to δ 130.92 (C-11); δ 2.42 (H-13) to δ 128.45 (C-12); δ 3.16 (H-15) to δ 24.76 (C-16) and δ 1.61 (H-21) to δ 25.05 (C-20) further confirmed the presence of 21-membered macrocyclic ring, 8-oxabicyclo[21.3.1]heptacosa-11,23,25,27-tetraene-7,18-dione. The 16-membered macrocyclic bislactone derivative was previously reported, which enclosed two ester linkages (δ 173.79, 172.30) (Chakraborty et al., 2019), whereas the present 21-membered macrocyclic compound enclosed one each of ester (δ 177.23) and keto (δ 213.34) functionalities. The 10/13/16-membered macrolide monoesters and diesters along with ether functionalities were explained in earlier literature (Chakraborty et al., 2019). The acetyl functionality was proposed through highly deshielded signal of carbon at δ 210.63, and its position at C-3 of the 21-membered macrocyclic ring was confirmed through the intense HMBCs from δ 2.75 (H-3) and 1.96 (H-3^2) to δ 210.63 (C-3^1). The shielded singlet methyl at δ 1.82 exhibiting HSQCs with δ 16.74 (C-11^1) was bonded at C-11 of macrocyclic ring through HMBCs from δ 1.82 (H-11^1) to δ 130.92 (C-11). The attachment of methyl group at C-11 in the macrocyclic ring was further corroborated by the HMBC correlation from δ 5.19 (H-12) to δ 16.74 (C-11^1). The HMBCs from δ 2.85 (H-14) to δ 154.98 (C-14^1, part of furan ring) confirmed the attachment of furan ring at C-14 position of macrocyclic ring. The coupling constants of these furan protons at H-14^2 (1H, d, 1.3 Hz), H-14^3 (1H, t, 2.9 Hz) and H-14^2 (1H, d, 1.6 Hz), which were <3, were found to be the characteristic features of furan protons (Abdelgaleil et al., 2006; Sadaka, 2017). The COSY correlations from δ 3.39 (H-15^1)/1.45 (H-15^2)/1.76 (H-15^3)/0.98 (H-15^4), 0.97 (H-15^5) along with HMBCs from δ 0.98 (H-15^4) to δ 23.63 (C-15^5), 40.69 (C-15^2); δ 0.97 (H-15^5) to δ 23.82 (C-15^4) proposed the presence of methylbutyloxy chain, and it was bonded at C-15 of a 21-membered macrocyclic ring through HMBCs from δ 3.16 (H-15) to 72.10 (C-15^1). These data suggested its degree of unsaturations as twelve corresponding to three ring systems and nine double bonds. The absolute stereochemistries of chiral centers in macrolides could not be determined by chemical or direct spectroscopic methods; thus we performed a rigorous conformational study supported by experimental distance derived from the NOESY spectrum.

The relative stereochemistries of the proton peaks at C-3, C-14 and C-15 were described unambiguously from the NOESY interactions (Figure 4.200 & 4.201). The proton at δ 2.85 (H-14) displayed NOESY cross-peak with that at δ 3.16 (H-15), which attributed that these might be disposed at the identical plane of symmetry, and therefore, assigned as β-oriented. The

orientation of H-14 and H-15 in the same plane in compound **13** was also corroborated by the NOESY cross-peaks between δ 2.34 (H-10)/ δ 5.19 (H-12); δ 5.19 (H-12)/ δ 2.42 (H-13); δ 3.39 (H-15^1)/ δ 1.80 (H-16); δ 2.42 (H-13)/ δ 2.85 (H-14); δ 3.16 (H-15)/ δ 1.80 (H-16). The chiral proton at δ 2.75 (H-3) displayed NOESY correlation with singlet methyl at δ 1.82 (H-11^1), which did not exhibit any NOE cross-peaks with the β-oriented proton signals, and hence, attributed as α-oriented.

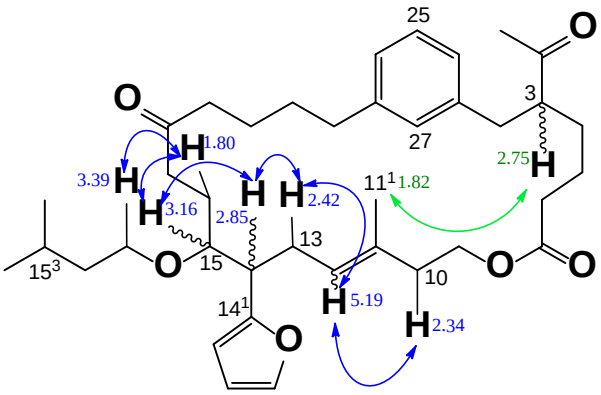

Figure 4.200.: NOE (double-barbed green coloured arrows for α-orientation and blue coloured arrows for β orientations) correlations of 3-acetyl-14-(furanyl)-11-methyl-15-(15^3-methylbutyloxy)-8-oxabicyclo-[21.3.1]heptacosa-11,23,25,27 tetraene-7,18-dione (**13**)

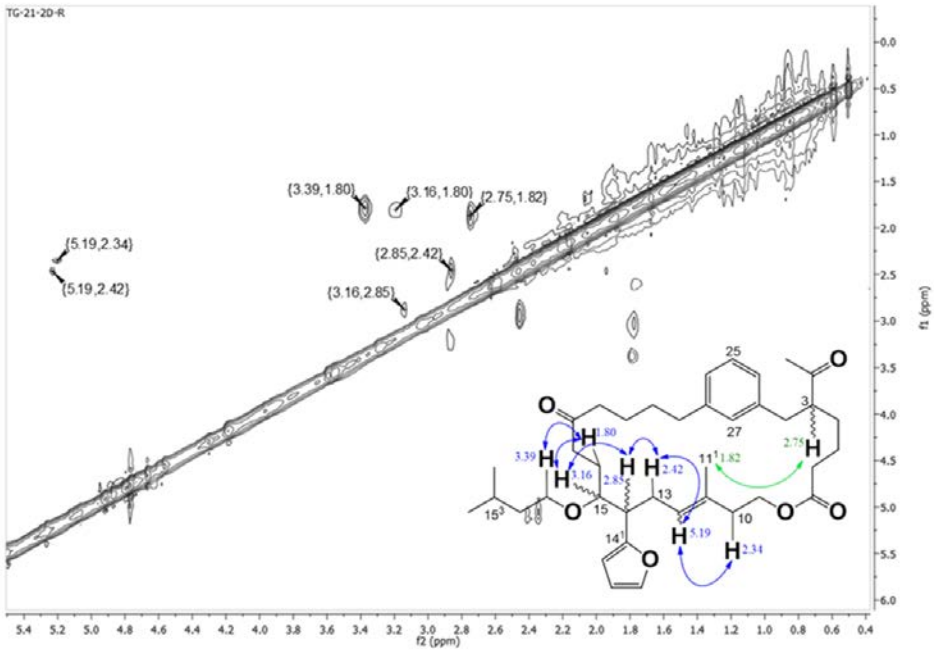

Figure 4.200.: NOESY spectrum of 3-acetyl-14-(furanyl)-11-methyl-15-(15^3-methylbutyloxy)-8-oxabicyclo-[21.3.1]heptacosa-11,23,25,27 tetraene-7,18-dione (**13**)

Table 4.20: NMR spectroscopic data of compound (**13),** 3-acetyl-14-(furanyl)-11-methyl-15-(15^3-methylbutyloxy)-8-oxabicyclo-[21.3.1]heptacosa-11,23,25,27 tetraene-7,18-dione (**13**) isolated from red seaweed *G. salicornia*

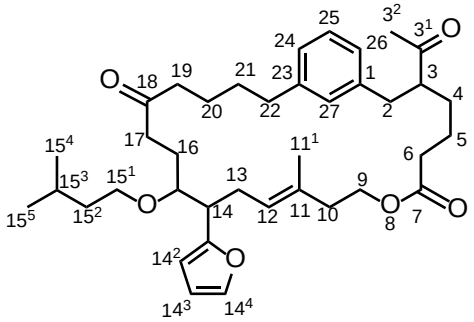

Compound **13** …….. 3-Acetyl-14-(furanyl)-11-methyl-15-(15^3-methylbutyloxy)-8-oxabicyclo-[21.3.1]heptacosa-11,23,25,27 tetraene-7,18-dione (**13**)

Type	**C. No.**	**^{13}C NMR**	**H. No. (int., mult., *J* in Hz)‡**	**^{1}H NMR**	**COSY**	**HMBC**
C	1	137.64	-	-	-	-
CH_2	2	35.80	1H,dd,11.1, 6.8 Hz	2.94	H-3	C-3,1
			1H,dd,11.0, 6.5 Hz	2.64	-	-
CH	3	54.02	1H,m	2.75	H-4	C-1,5,3^1
CH_2	4	27.30	1H,m	1.69	H-5	-
			1H,m	1.41	-	-
CH_2	5	24.11	1H,m	1.72	H-6	C-6,7
			1H,m	1.64	-	-
CH_2	6	32.87	2H,m	2.28	-	C-7
C	7	177.23	-	-	-	-
-	8		-	-	-	-
CH_2	9	65.58	2H,t,7.8 Hz	4.31	H-10	C-7,10,11
CH_2	10	39.86	2H,t,7.6 Hz	2.34	-	C-11,12
C	11	130.92	-	-	-	-
CH	12	128.45	1H,t, 6.2 Hz	5.19	H-13	C-11,14,11^1
CH_2	13	25.87	2H,m	2.42	H-14	C-12
CH	14	43.34	1H,m	2.85	H-15	C-14^1,15
CH	15	81.48	1H,m	3.16	H-16	C-16, 15^1
CH_2	16	24.76	2H,m	1.80	H-17	C-17
CH_2	17	34.76	2H,t,7.8 Hz	2.50	-	C-18
C	18	213.34	-	-	-	-
CH_2	19	40.16	2H, t,7.9 Hz	2.44	H-20	C-18,21
CH_2	20	25.05	2H,m	1.55	H-21	C-19
CH_2	21	29.69	2H,m	1.61	H-22	C-20,23
CH_2	22	34.38	2H,t,5.8 Hz	2.58	-	C-23
C	23	148.54	-	-	-	-
CH	24	126.80	1H,d,7.4 Hz	7.02	H-25	C-23,25
CH	25	128.85	1H,t,7.6 Hz	7.53	H-26	C-26
CH	26	126.13	1H,d,7.6 Hz	7.01	-	C-1
CH	27	133.80	1H,s	7.07	-	C-1,23

C	3^1	210.63	-	-	-	-
CH_3	3^2	30.56	3H,s	1.96	-	C-3^1
CH_3	11^1	16.74	3H,s	1.82	-	C-11
C	14^1	154.98	-	-	-	-
CH	14^2	109.31	1H,d,1.3Hz	6.08	H-14^3	C-14^1,14^3
CH	14^3	111.30	1H,t, 2.9 Hz	6.43	H-14^4	C-14^4
CH	14^4	140.57	1H,d,1.6 Hz	7.71	-	C-14^1
CH_2	15^1	72.10	2H,t,7.7 Hz	3.39	H-15^2	-
CH_2	15^2	40.69	2H,m	1.45	H-15^3	C-15^1,15^5
CH	15^3	24.09	1H,m	1.76	H-15^4, H-15^5	C-15^2
CH_3	15^4	23.82	3H,d,5.1 Hz	0.98		C-15^5,15^2
CH_3	15^5	23.63	3H,d,5.3 Hz	0.97		C-15^4

†NMR spectra were recorded using a Bruker AVANCE III 500 MHz (AV 500) spectrometer (Bruker, Karlsruhe, Germany) in $CDCl_3$ as aprotic solvent at ambient temperature with TMS as the internal standard (δ 0 ppm).

‡Values in ppm, multiplicity and coupling constants (*J* = Hz) were indicated in parentheses. Multiplicities were allocated by ^{135}DEPT NMR spectrum.

The assignments were made with the aid of the COSY, HSQC, HMBC and NOESY experiments.

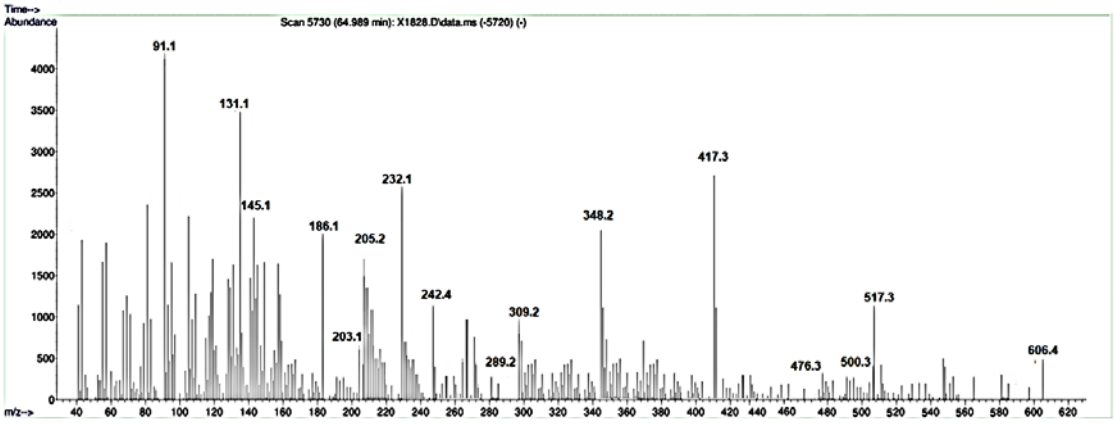

Figure 4.201.: EI-MS spectrum of 3-acetyl-14-(furanyl)-11-methyl-15-(15^3-methylbutyloxy)-8-oxabicyclo-[21.3.1]heptacosa-11,23,25,27 tetraene-7,18-dione (**13**)

The molecular ion peak at *m/z* 606 (**1**), with a molecular formula of $C_{38}H_{54}O_6$ appeared to undergo fragmentation by heterolytic cleavage followed by McLafferty rearrangement to yield a fragment at *m/z* 517 (**2**; $C_{33}H_{41}O_5^+$). The latter on further elimination of hydroxyl radical and acetylene formed the fragments, **3** and **4** with *m/z* 500 and 476,

respectively. The fragment at *m/z* 91 was found to be the base-peak that might correspond to $C_7H_7^+$ (Figure 4.201 & 4.202).

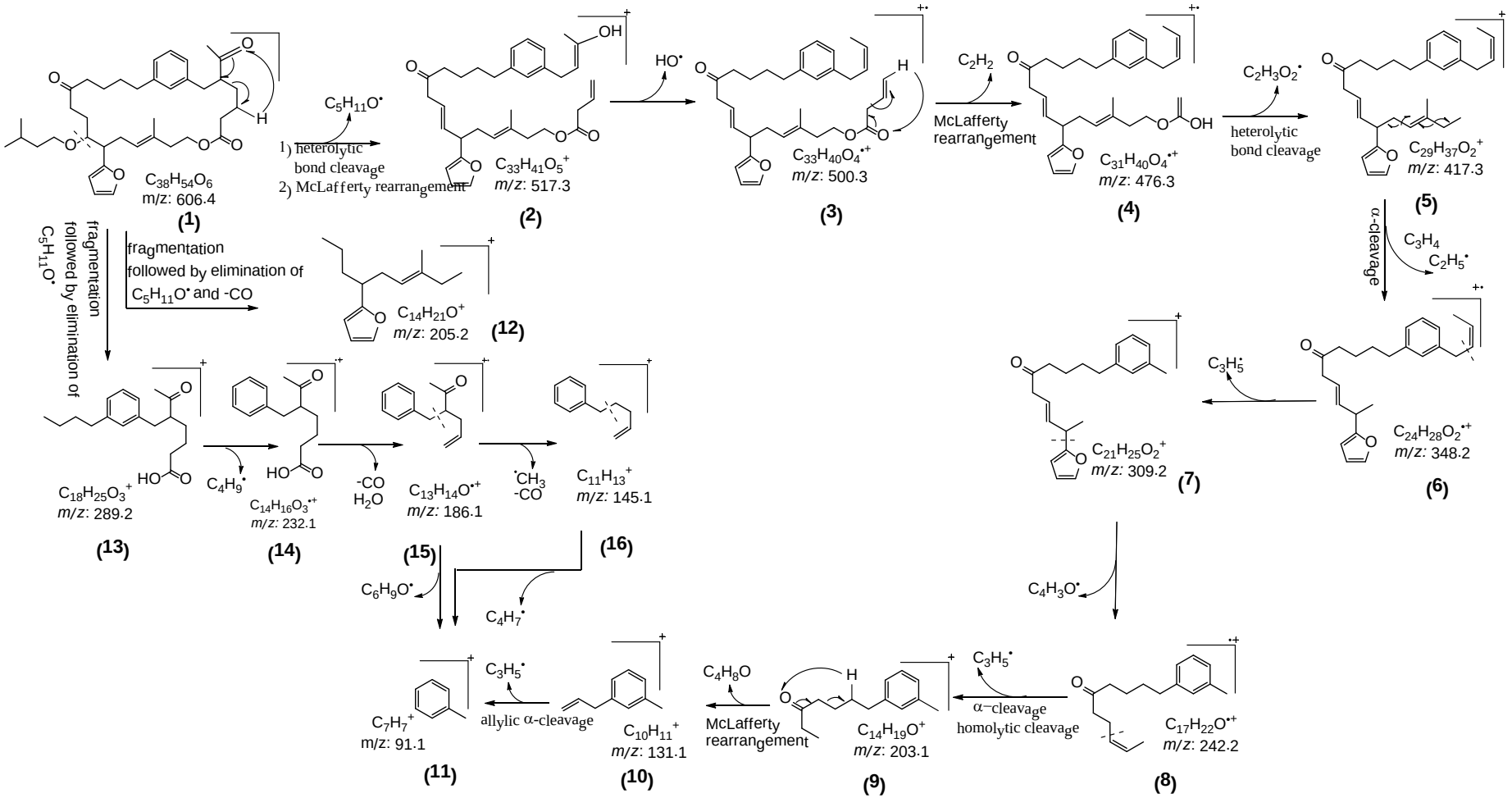

Figure 4.202.: Tentative mass fragmentation pattern of 3-acetyl-14-(furanyl)-11-methyl-15-(15^3-methylbutyloxy)-8-oxabicyclo-[21.3.1]heptacosa-11,23,25,27 tetraene-7,18-dione (**13**)

4.3.2.7b Structural characterization of Compound 14

(2E,12E,14E)-10-Acetyl-9-isopentyl-2-methyl-5,16,23[1]-trioxa-bicyclo[21.3.1]-heptacosa-2,12,14-triene-6,19-dione

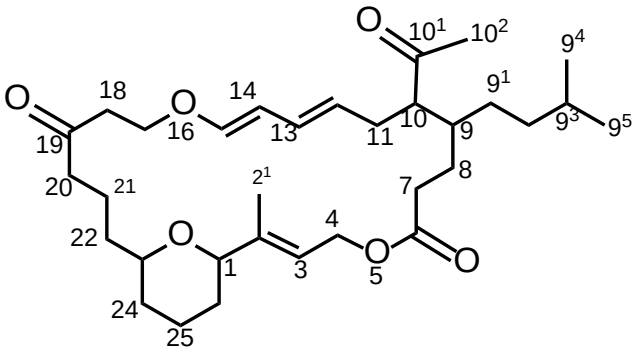

Sample yield	0.33% (> 99% purity, RP-C18 HPLC)
Physical description	Pale yellow oily
Molecular formula	$C_{32}H_{50}O_6$
Molecular mass	530.7358

The macrolide derivative, 3-acetyl-14-(furanyl)-11-methyl-15-(15[3]-methylbutyloxy)-8-oxabicyclo-[21.3.1]heptacosa-11,23,25,27 tetraene-7,18-dione was isolated as pale yellow oil. The compound (**13**) has exhibited UV absorbance (UV (MeOH) λ_{max}) at 237 nm (Figure 4.203). The homogeneity of the compound was ascertained by HPLC data on a bonded phase octadecylsilane (C_{18}) stationary phase (HPLC, MeCN/MeOH, 1:2 v/v) with R_t: 4.30 min (Figure 4.204).

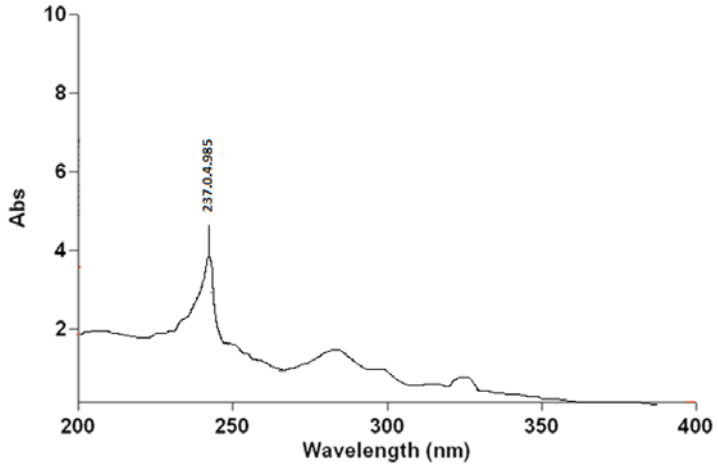

Figure 4.203.: UV spectrum of (2E,12E,14E)-10-acetyl-9-isopentyl-2-methyl-5,16,23[1]-trioxa-bicyclo[21.3.1]-heptacosa-2,12,14-triene-6,19-dione (**14**)

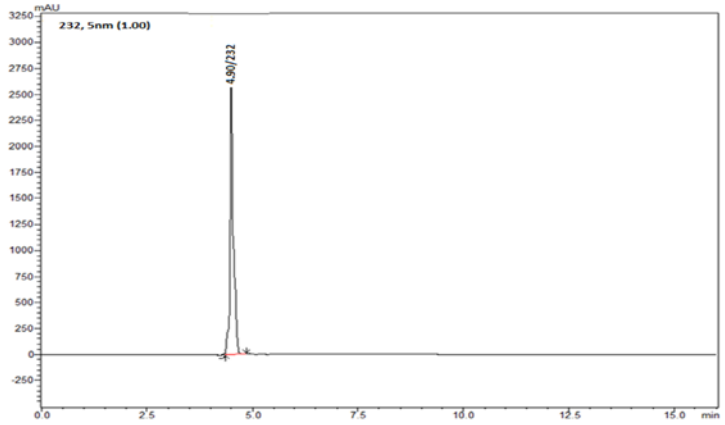

Figure 4.204.: HPLC chromatogram of (2E,12E,14E)-10-acetyl-9-isopentyl-2-methyl-5,16,23[1]-trioxa-bicyclo[21.3.1]-heptacosa-2,12,14-triene-6,19-dione (**14**)

The second compound in the series was characterised as (2*E*,12*E*,14*E*)-10-acetyl-9-isopentyl-2-methyl-5,16,23[1]-trioxa-bicyclo[21.3.1]heptacosa-2,12,14-triene-6,19-dione (**14**), and was acquired as a pale yellow oily substance with the elemental-composition of $C_{32}H_{50}O_6$. The molecular-ion peak was recorded at *m/z* 530.7 $[M]^+$ that along with HRESIMS data {*m/z* 531.3690 $[M+H]^+$} (Figure 4.205)were in agreement with one and two dimensional NMR data (Table 4.21)

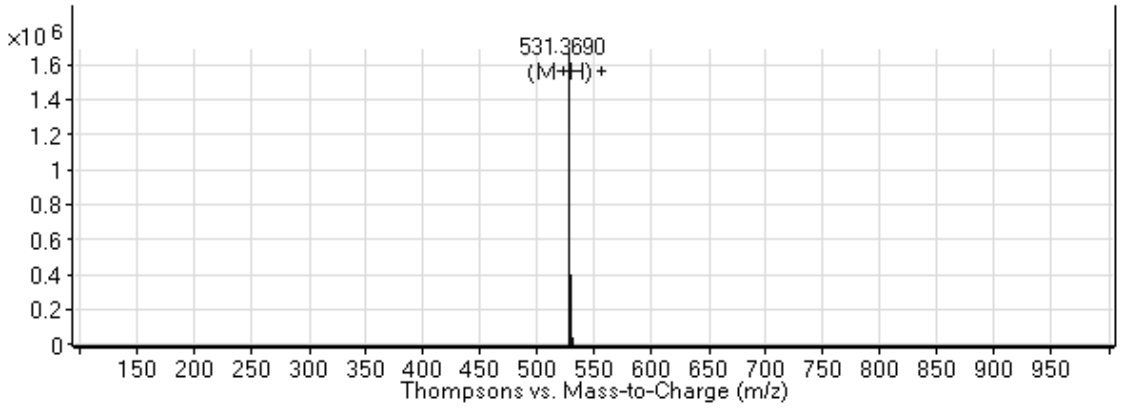

Figure 4.205.: HRESIMS spectrum of (2E,12E,14E)-10-acetyl-9-isopentyl-2-methyl-5,16,23[1]-trioxa-bicyclo[21.3.1]-heptacosa-2,12,14-triene-6,19-dione (**14**)

The FTIR spectrum exhibited stretching vibration peaks at 2923/2799, 1742 and 1717 cm^{-1}, which designated the occurrences of C-H, ester and ketone functional groups, respectively in compound **14** (Figure 4.206). The $^1H/^{13}C$ NMR and DEPT NMR established the possibilities of fourteen sp^3 methylenes, ten methines, four each of sp^3 methyls and quaternary carbons (two

carbonyl carbons, one ester carbon and one sp^2 carbon). The ^{13}C NMR along with DEPT displayed peaks at δ 177.30 for ester carbonyl and at δ 213.48 and 209.30 for carbonyl carbon functionalities. The greatly deshielded proton signals at δ 5.54, 5.81, 5.34, 5.05 and 6.37 bonded to the carbons at δ 125.14, 135.43, 133.64, 109.09 and 145.05, respectively (from HSQC) were deduced to correspond with olefinic functionalities in compound **14** (Figure 4.207-210).

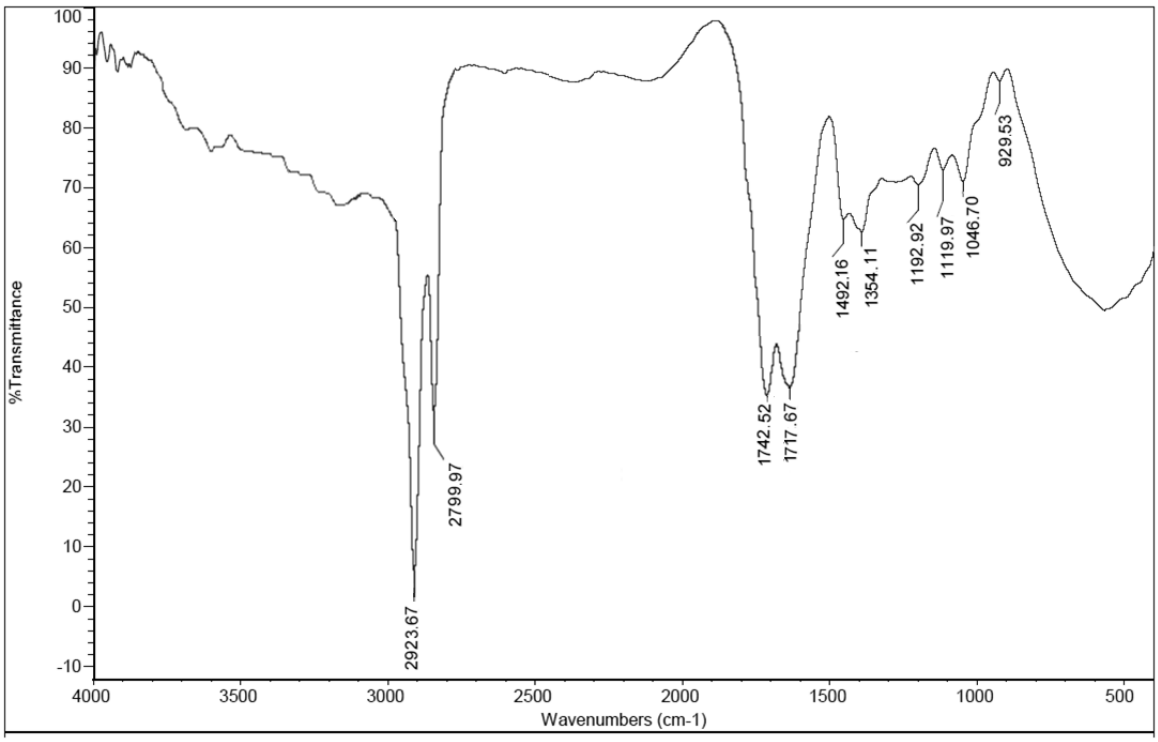

Figure 4.206.: FTIR spectrum of (2E,12E,14E)-10-acetyl-9-isopentyl-2-methyl-5,16,23[1]-trioxa-bicyclo[21.3.1]-heptacosa-2,12,14-triene-6,19-dione (**14**)

The COSY correlations suggested the spin systems, which were deduced as δ 4.78 (assigned at H-1)/1.80 (H-26); δ 1.72 (H-24)/3.65 (H-23)/1.53, 1.25 (H-22)/1.68, 1.56 (H-21)/2.49, 2.43 (H-20); δ 5.54 (H-3)/4.90 (H-4); δ 2.30 (H-7)/1.77 (H-8); δ 1.75 (H-9)/2.33 (H-10); δ 2.37 (H-11)/5.81 (H-12)/5.34 (H-13)/5.05 (H-14)/6.37 (H-15); δ 1.77 (H-24)/1.66 (H-25)/1.80 (H-26) (Figure 4.211 & 4.213). These spin systems might be the fragments of a 21-membered macrocyclic ring skeleton. The presence of an ester carbonyl functionality at δ 177.30 was proposed through the HMBCs from protons at δ 2.30 (H-7) and δ 4.90 (H-4) to δ 177.30 (C-6), which suggested that the ester carbonyl functionality was disposed in between C-7 and C-4 positions of the 21-membered macrocyclic ring. The carbonyl-carbon was found at δ 213.48 (C-19) through the intense HMBCs from δ 2.92 (H-18) and δ 2.49 (H-20) to δ 213.48 (C-19) (Figure 4.214).

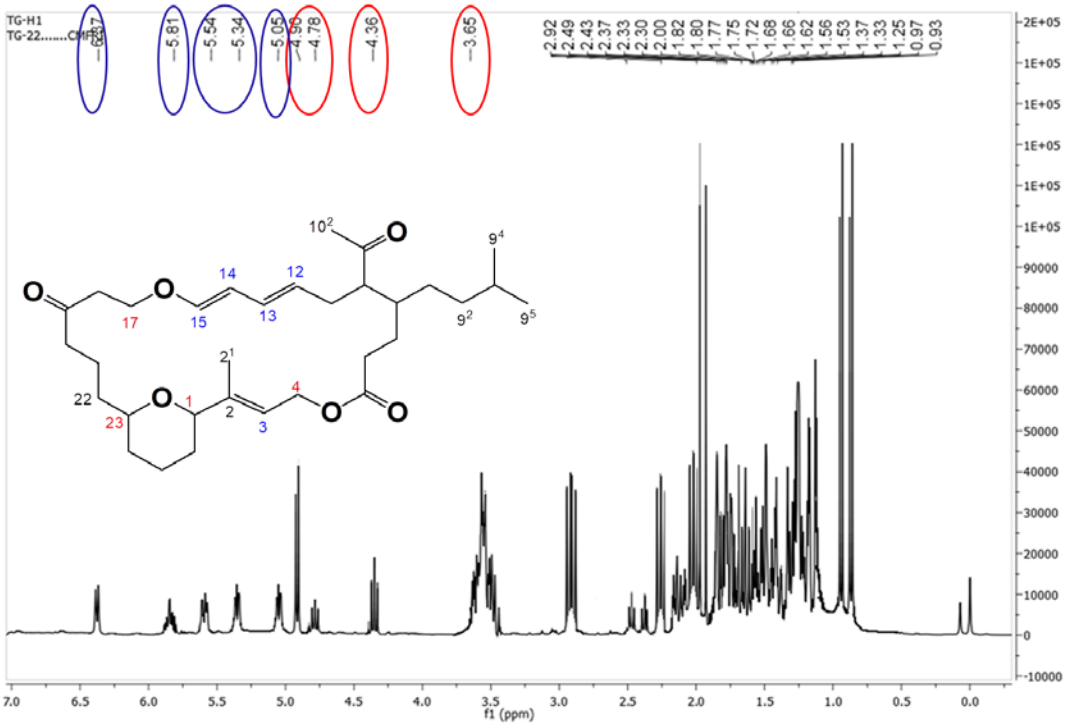

Figure 4.207.: ^{1}H NMR spectrum of (2E,12E,14E)-10-acetyl-9-isopentyl-2-methyl-5,16,23[1]-trioxa-bicyclo[21.3.1]-heptacosa-2,12,14-triene-6,19-dione (**14**)

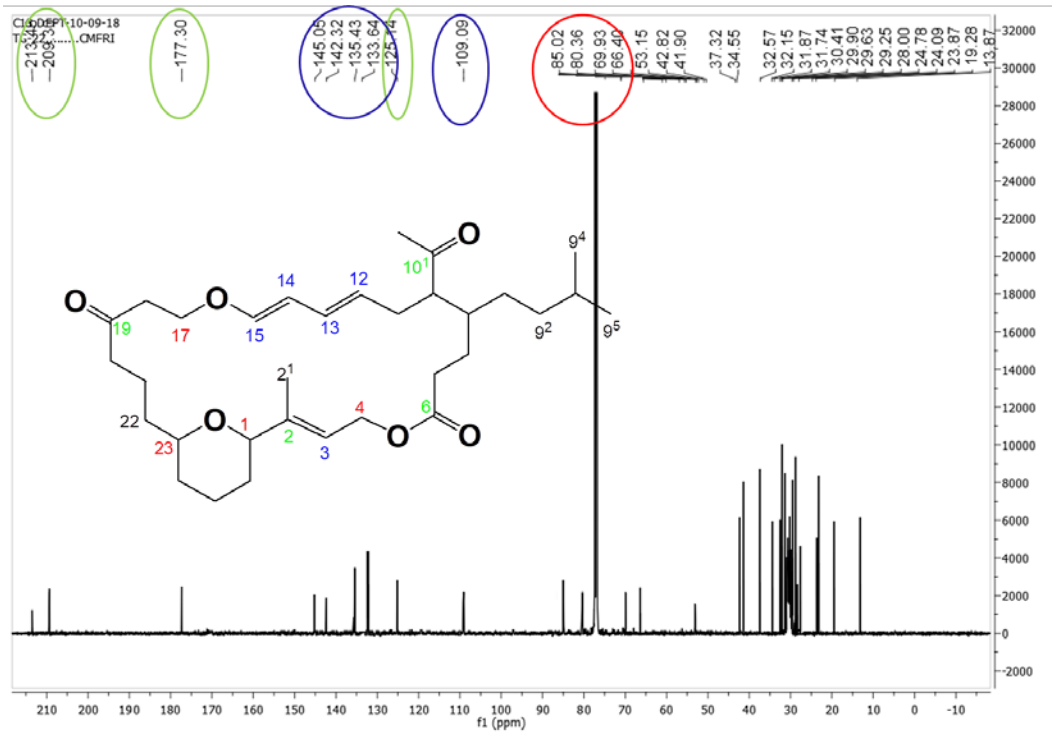

Figure 4.208.: ^{13}C NMR spectrum of (2E,12E,14E)-10-acetyl-9-isopentyl-2-methyl-5,16,23[1]-trioxa-bicyclo[21.3.1]-heptacosa-2,12,14-triene-6,19-dione (**14**)

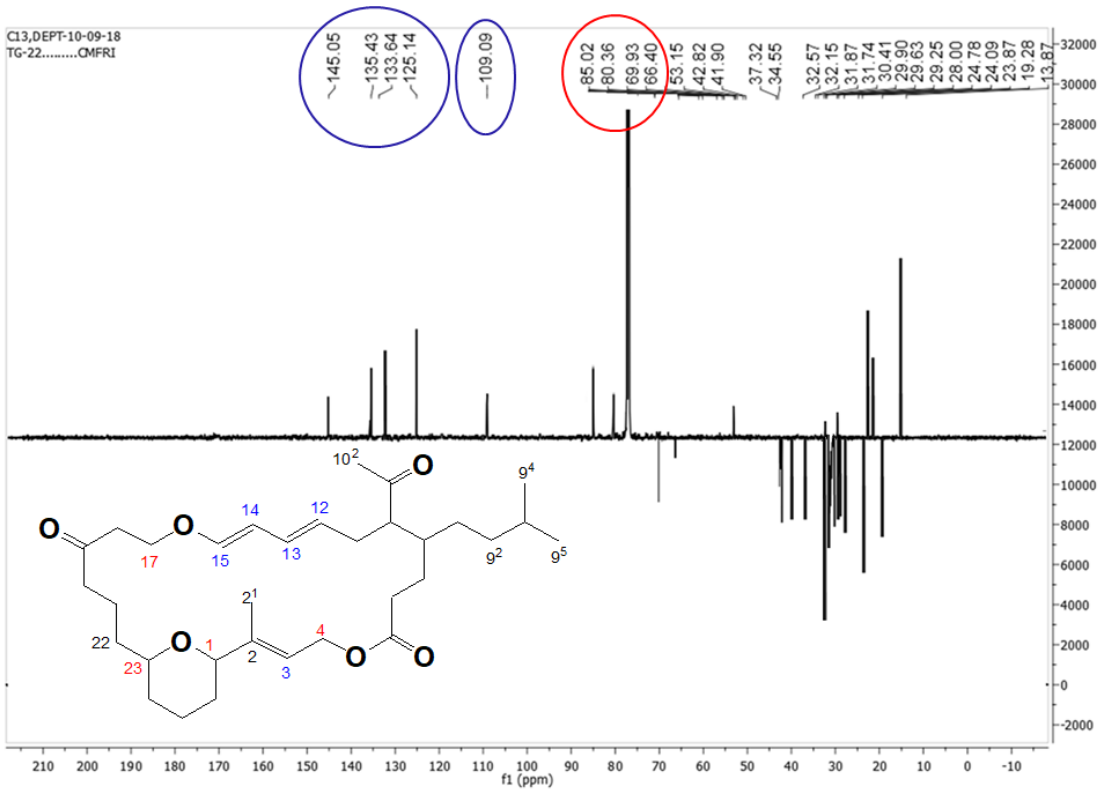

Figure 4.209.: ^{135}DEPT NMR spectrum of (2E,12E,14E)-10-acetyl-9-isopentyl-2-methyl-5,16,23[1]-trioxa-bicyclo[21.3.1]-heptacosa-2,12,14-triene-6,19-dione (**14**)

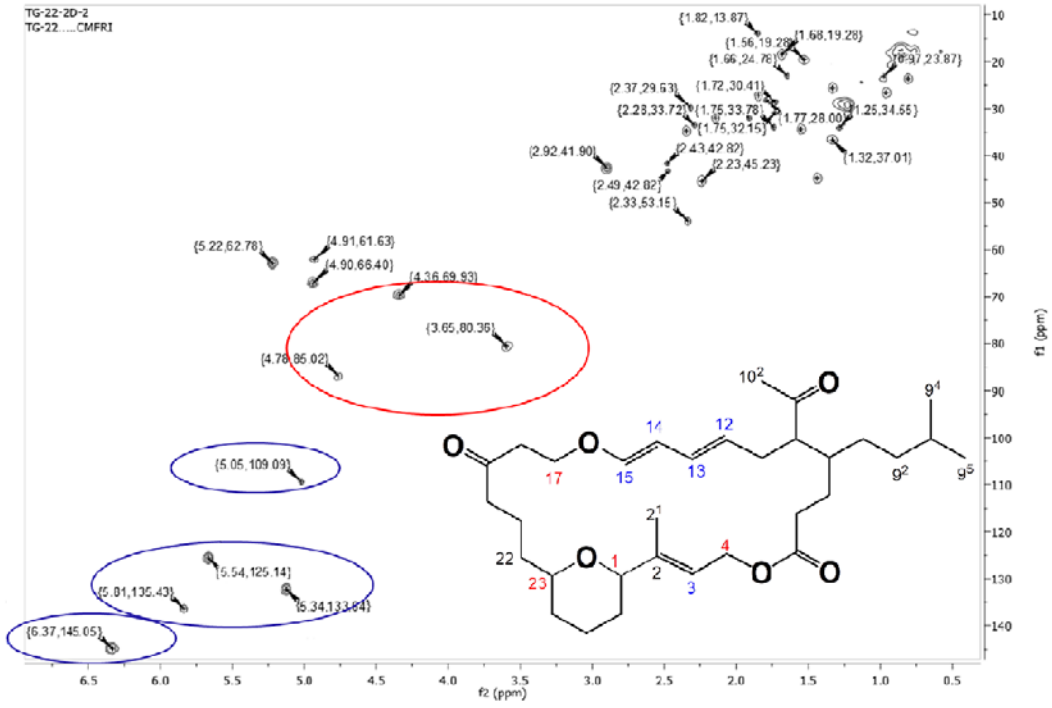

Figure 4.210.: HSQC spectrum of (2E,12E,14E)-10-acetyl-9-isopentyl-2-methyl-5,16,23[1]-trioxa-bicyclo[21.3.1]-heptacosa-2,12,14-triene-6,19-dione (**14**)

The previously reported 16-membered macrocyclic bislactone derivative enclosed two esters (δ 172-173) (Chakraborty et al., 2019), while the titled compound bound one each of ester (δ 177.30), ketone (δ 213.48) and ether functionalities. The HMBCs from δ 1.72 (H-24) to δ 80.36 (C-23), 34.55 (C-22); δ 1.66 (H-25) to δ 30.41 (C-24), and δ 1.80 (H-26) to δ 24.78 (C-25) assigned the presence of a pyran ring in a 21-membered macrocyclic ring. This pyran ring was located between C-2 and C-22 carbons through the HMBCs from δ 3.65 (H-23) to δ 34.55 (C-22), 85.02 (C-1) and δ 4.87 (H-1) to δ 24.78 (C-25) in the macrocyclic ring. The 14-membered macrocyclic derivative possessing a tetrahydropyran ring and 24-membered macrolactones enclosing tetrahydropyran moieties were previously reported from the marine organisms (Kito et al., 2008; Mondol et al., 2011).

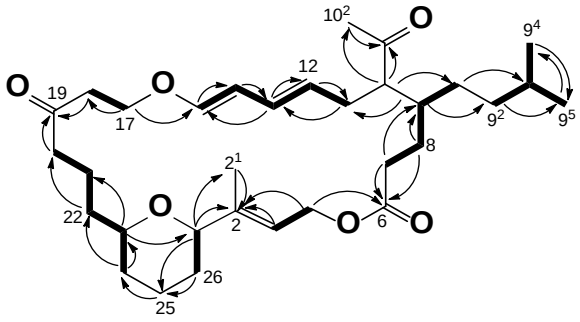

Figure 4.211.: ^{1}H-^{1}H COSY (bold face bonds) and HMBC (double-barbed arrows) correlations of (2E,12E,14E)-10-acetyl-9-isopentyl-2-methyl-5,16,23^{1}-trioxa-bicyclo[21.3.1]-heptacosa-2,12,14-triene-6,19-dione (**14**)

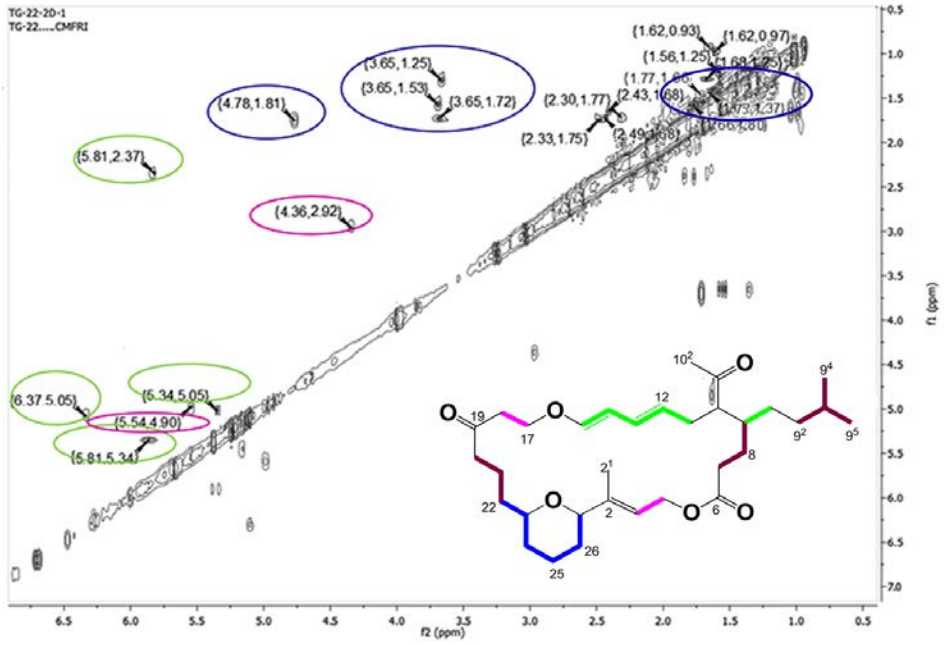

Figure 4.212.: ^{1}H-^{1}H COSY spectrum of (2E,12E,14E)-10-acetyl-9-isopentyl-2-methyl-5,16,23^{1}-trioxa-bicyclo[21.3.1]-heptacosa-2,12,14-triene-6,19-dione (**14**)

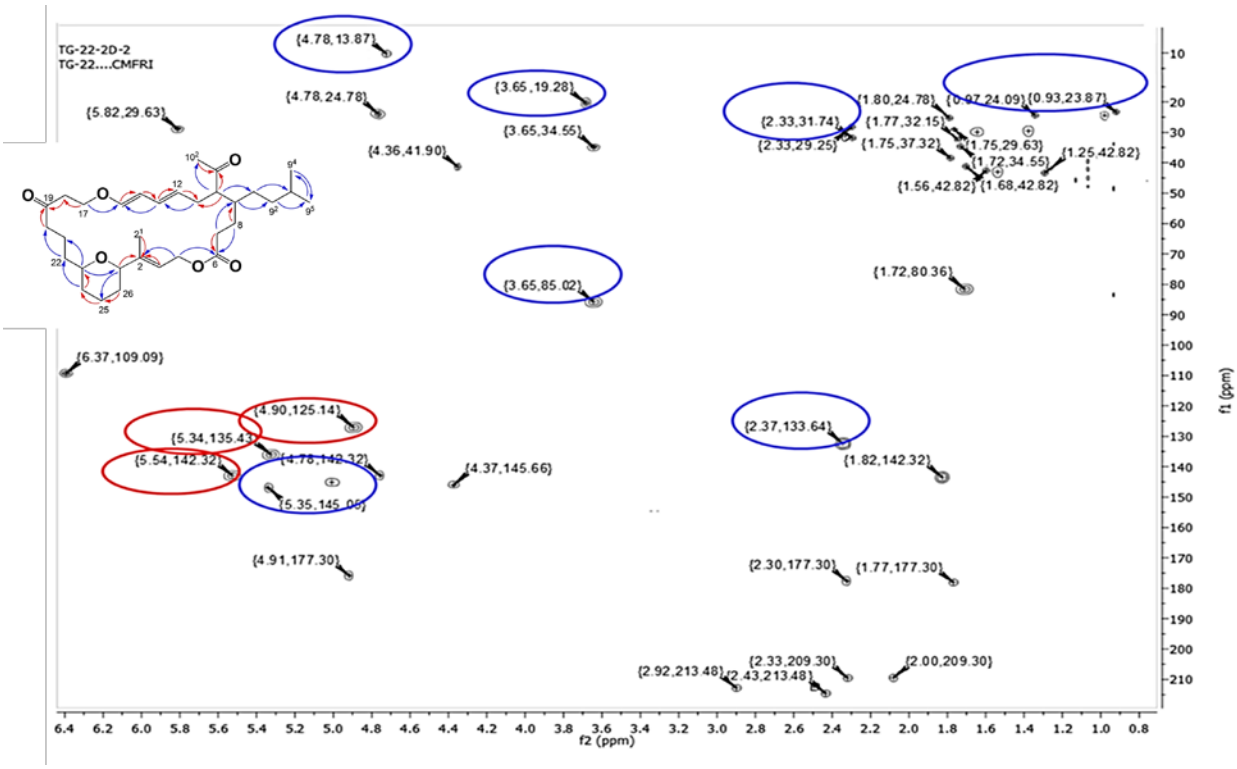

Figure 4.213.: HMBC spectrum of (2E,12E,14E)-10-acetyl-9-isopentyl-2-methyl-5,16,23[1]-trioxa-bicyclo[21.3.1]-heptacosa-2,12,14-triene-6,19-dione (**14**)

The 14-membered tetrahydropyran enclosed macrocyclic derivative exhibited chemical shifts at δ 4.23/74, 3.38/66, 1.95/21, 2.21/21, 4.21/71 corresponding to the hydroxyl attached tetrahydropyran ring along with disubstituted alkene at δ 5.79/132, 5.69/137 adjacent to the tetrahydropyran system (Kito et al., 2008; Mondol et al., 2011). These values were comparable with the pyran ring in compound **2**, except with the absence of hydroxyl and a trisubstituted alkene adjacent to the pyran ring instead of disubstituted alkene functionality, as described previously (Kito et al., 2008). Further, HMBCs were displayed from δ 5.54 (H-3) to δ 142.32 (C-2); δ 4.90 (H-4) to δ 125.14 (C-3); δ 1.77 (H-8) to δ 177.30 (C-6), 32.15 (C-9); δ 5.81 (H-12) to δ 29.63 (C-11); δ 5.05 (H-14) to δ 133.64 (C-13); δ 6.37 (H-15) to δ 109.09 (C-14); δ 4.36 (H-17) to δ 145.05 (C-15) and δ 1.53 (H-22) to δ 42.82 (C-20) that were coherent with the macrocyclic ring, 5,16,23[1]-trioxa-bicyclo[21.3.1] heptacosa-2,12,14-triene-6,19-dione. The shielded singlet methyl at δ 1.82/13.87 was bonded at C-2 position through the HMBCs obtained from δ 1.82 (H-2[1]) to δ 142.32 (C-2). The presence of methyl was further supported by the HMBC correlation from δ 4.78 (H-1) to δ 13.87 (C-2[1]). The acetyl group was supported by highly deshielded carbonyl carbon peak at δ 209.30 and the singlet methyl at δ 2.00/31.74. Its position was assigned at C-10 of the 21-memebered macrocyclic ring through the HMBCs from

δ 2.33 (H-10) to δ 209.30 (C-10^1), 31.74 (C-10^2) and δ 2.00 (H-10^2) to δ 209.30 (C-10^1). The COSYs from δ 1.75 (H-9)/1.37 (H-9^1)/1.33 (H-9^2)/1.62 (H-9^3)/0.97 (H-9^4), 0.93 (H-9^5) suggested the presence of isopentyl branching at C-9 of the 21-memebered macrocyclic ring. These were further supported through HMBCs from δ 1.75 (H-9) to 37.32 (C-9^2), δ 1.33 (H-9^2), 0.97 (H-94) to δ 24.09 (C-9^5) and δ 0.93 (H-9^5) to δ 23.87 (C-9^4). These data suggested its degree of unsaturations as eight, which were equivalent to two rings and six double bonded systems. The higher coupling constants of 11 to 12 Hz were found to correspond to the alkenic groups at C(12)=C(13) and C(14)=C(15) suggesting its trans (E) orientation in compound **14**.

Table 4.21: NMR spectroscopic data of compound (**14),** (2E,12E,14E)-10-acetyl-9-isopentyl-2-methyl-5,16,23[1]-trioxa-bicyclo[21.3.1]-heptacosa-2,12,14-triene-6,19-dione (**14**) isolated from red seaweed *G. salicornia*

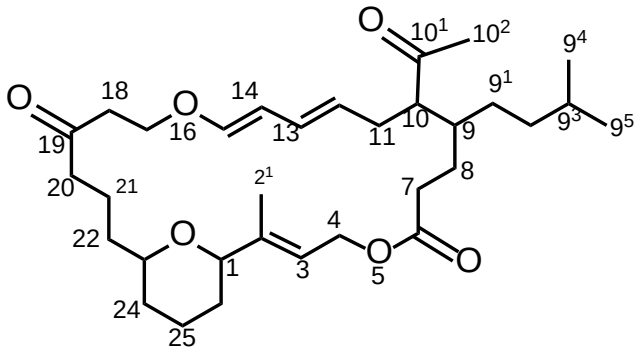

Compound **14** …….(2E,12E,14E)-10-acetyl-9-isopentyl-2-methyl-5,16,23[1]-trioxa-bicyclo[21.3.1]-heptacosa-2,12,14-triene-6,19-dione (**14**)

Type	**C. No.**	**^{13}C NMR**	**H. No. (int., mult., J in Hz)‡**	**^{1}H NMR**	**COSY**	**HMBC**
CH	1	85.02	1H,m	4.78	H-26	C-2,25, 2^1
C	2	142.32	-	-	-	-
CH	3	125.14	1H,t,6.4 Hz	5.54	H-4	C-2
CH_2	4	66.40	2H,d,10.1	4.90	-	C-3,6
-	5		-	-	-	-
C	6	177.30	-	-	-	-
CH_2	7	32.57	2H,t,7.5 Hz	2.30	H-8	C-6,9
CH_2	8	28.00	2H, m	1.77		C-6,9
CH	9	32.15	1H,m	1.75	H-10, H-9^1	C-9^2,11
CH	10	53.15	1H,m	2.33	H-11	C-9^1,10^1,10^2
CH_2	11	29.63	2H,m	2.37	H-12	C-13
CH	12	135.43	1H,m	5.81	H-13	C-11
CH	13	133.64	1H, t,12.1 Hz	5.34	H-14	C-12,15
CH	14	109.09	1H, t,11.0 Hz	5.05	H-15	C-13
CH	15	145.05	1H, d,11.1 Hz	6.37	-	C-14

-	16		-	-	-	-
CH_2	17	69.93	2H,m	4.36	H-18	C-15,18
CH_2	18	41.90	2H,t,4.8 Hz	2.92	-	C-19
C	19	213.48	-	-	-	-
CH_2	20	42.82	1H,m	2.49	H-21	C-19
			1H,m	2.43	-	-
CH_2	21	19.28	1H,m	1.68	H-22	C-20
			1H,m	1.56	-	-
CH_2	22	34.55	1H,m	1.53	H-23	C-20
			1H,m	1.25	-	-
CH	23	80.36	1H,m	3.65	H-24	C-22,1,21
-	23^1	-	-	-	-	-
CH_2	24	30.41	2H,m	1.72	H-25	C-23,22
CH_2	25	24.78	2H, m	1.66	H-26	C-24
CH_2	26	31.87	2H,m	1.80	-	C-25
CH_3	2^1	13.87	3H,s	1.82	-	C-2
CH_2	9^1	29.25	2H,m	1.37	-	C-9^3
CH_2	9^2	37.32	2H,m	1.33	H-9^3	C-9^5
CH	9^3	29.90	1H,m	1.62	H-9^4, H-9^5	-
CH_3	9^4	23.87	3H,d,6.3 Hz	0.97	-	C-9^5
CH_3	9^5	24.09	3H,d,5.2 Hz	0.93	-	C-9^4
C	10^1	209.30	-	-	-	-
CH_3	10^2	31.74	3H,s	2.00	-	C-10^1

†NMR spectra were recorded using a Bruker AVANCE III 500 MHz (AV 500) spectrometer (Bruker, Karlsruhe, Germany) in $CDCl_3$ as aprotic solvent at ambient temperature with TMS as the internal standard (δ 0 ppm).

‡Values in ppm, multiplicity and coupling constants (*J* = Hz) were indicated in parentheses. Multiplicities were allocated by ^{135}DEPT NMR spectrum.

The assignments were made with the aid of the COSY, HSQC, HMBC and NOESY experiments.

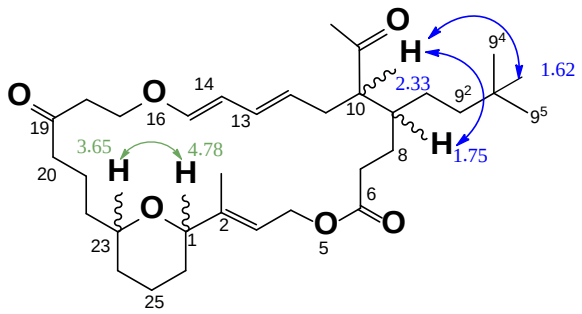

Figure 4.214.: NOESY (double-barbed green coloured arrows for α-orientation and blue coloured arrows for β orientations) correlations of (2E,12E,14E)-10-acetyl-9-isopentyl-2-methyl-5,16,23^1-trioxa-bicyclo[21.3.1]-heptacosa-2,12,14-triene-6,19-dione (**14**)

The relative stereochemistry of the protons at C-1, C-9, C-10 and C-23 were unambiguously inferred from the NOESY cross-peaks (Figure 4.215 & 4.215). The resonances of a proton at δ 4.78 (H-1) displayed NOESY correlation with the methine proton at δ 3.65 (H-23), which were located in the identical plane, and hence, arbitrarily assigned to be α-oriented. The proton at δ 2.33 (H-10) was found to be correlated with that at δ 1.75 (H-9), which were found as trans oriented to the α-protons, and hence, assigned to be β-oriented. This attribution was further supported by the NOE correlation between the protons at δ 2.33 (H-10)/δ 1.62 (H-9^3).

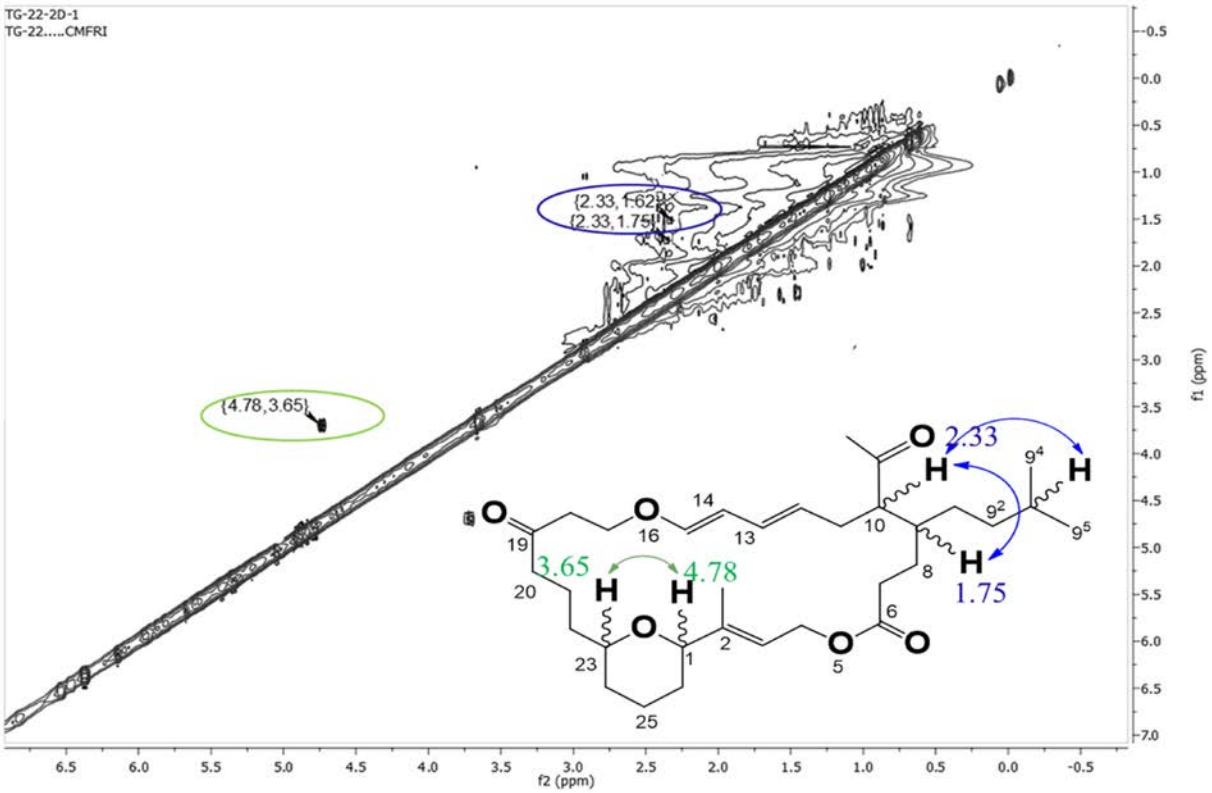

Figure 4.215.: NOE spectrum of (2E,12E,14E)-10-acetyl-9-isopentyl-2-methyl-5,16,23[1]-trioxa-bicyclo[21.3.1]-heptacosa-2,12,14-triene-6,19-dione (**14**)

The molecular ion peak at *m/z* 530 (**1**) with the chemical formula of $C_{32}H_{50}O_6$ underwent dehydration followed by McLafferty rearrangement to form a fragment, $C_{32}H_{48}O_5^{\bullet+}$ with *m/z* 512 (**2**). The fragment, **2** on elimination of $C_3H_5^{\bullet}$ radical by allylic cleavage could yield a fragment at **3** with *m/z* 473. The radical cation **3** on McLafferty rearrangement yielded **4** (*m/z* 318) and then to fragment **5** (*m/z* 293). The latter on further series of fragmentation by McLafferty rearrangement yielded **6** (*m/z* 165) and **7** (*m/z* 127). The ion peak at

m/z 165 on fragmentation yielded the base peak of $C_6H_{10}O^{\bullet+}$ (**8**) with *m/z* 98 (Figure 4.216-4.217).

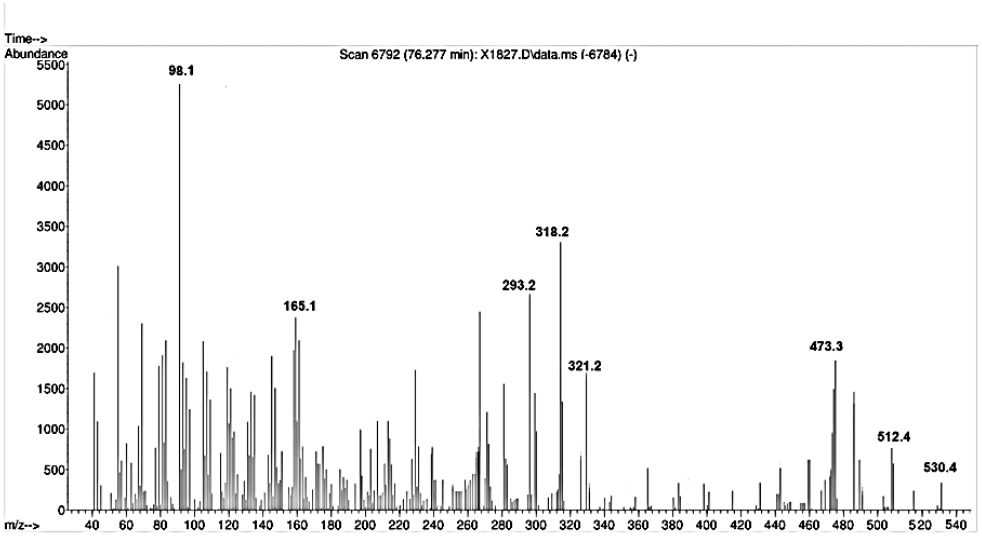

Figure 4.216.: EI-MS spectrum of (2E,12E,14E)-10-acetyl-9-isopentyl-2-methyl-5,16,23[1]-trioxa-bicyclo[21.3.1]-heptacosa-2,12,14-triene-6,19-dione (**14**)

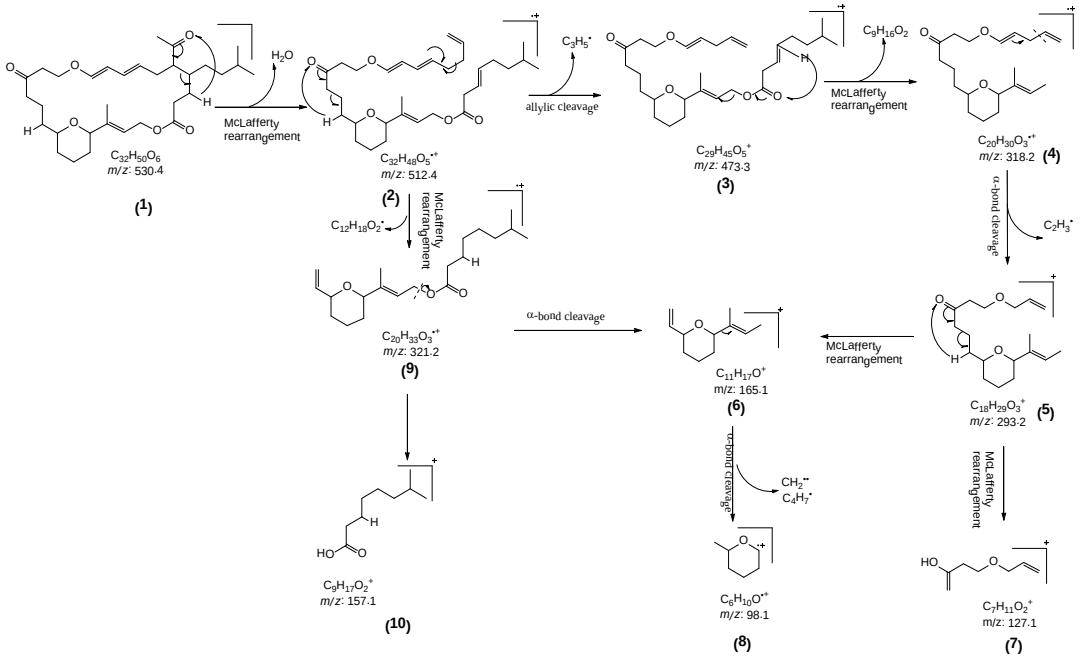

Figure 4.217.: Tentative mass fragmentation pattern of (2E,12E,14E)-10-acetyl-9-isopentyl-2-methyl-5,16,23[1]-trioxa-bicyclo[21.3.1]-heptacosa-2,12,14-triene-6,19-dione (**14**)

4.3.2.7c Structural characterization of Compound 15

(2Z,5E,16E)-8-Hydroxy-20-isobutyl-16-methyl-7,14-dioxa-bicyclo[19.3.1]-pentacosa-2,5,16-triene-10,23-dione

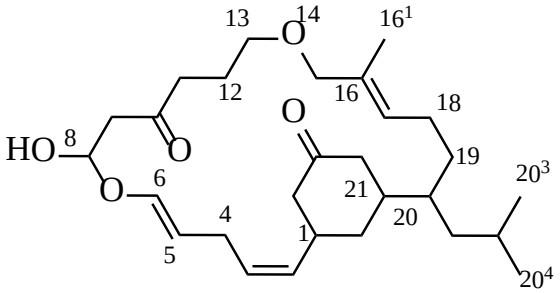

Sample yield	0.32% (> 99% purity, RP-C18 HPLC)
Physical description	Yellow oily
Molecular formula	$C_{28}H_{45}O_5$
Molecular mass	460.3189

The macrolide derivative, (2Z,5E,16E)-8-hydroxy-20-isobutyl-16-methyl-7,14-dioxa-bicyclo[19.3.1]-pentacosa-2,5,16-triene-10,23-dione was isolated as yellow oil. The compound (**15**) has exhibited UV absorbance (UV (MeOH) λ_{max}) at 234 nm (Figure 4.218). The homogeneity of the compound was ascertained by HPLC data on a bonded phase octadecylsilane (C_{18}) stationary phase (HPLC, MeCN/MeOH, 1:2 v/v) with R_t: 5.30 min (Figure 4.219).

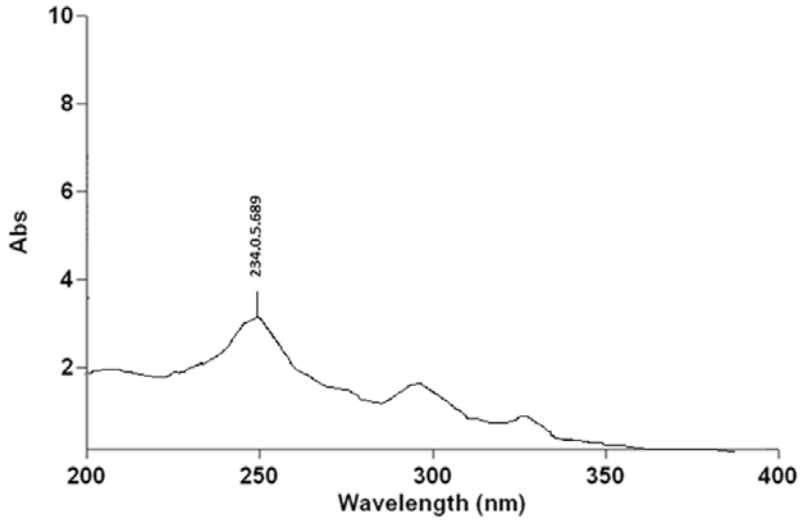

Figure 4.218.: UV spectrum of (2Z,5E,16E)-8-hydroxy-20-isobutyl-16-methyl-7,14-dioxa-bicyclo[19.3.1]-pentacosa-2,5,16-triene-10,23-dione (**15**)

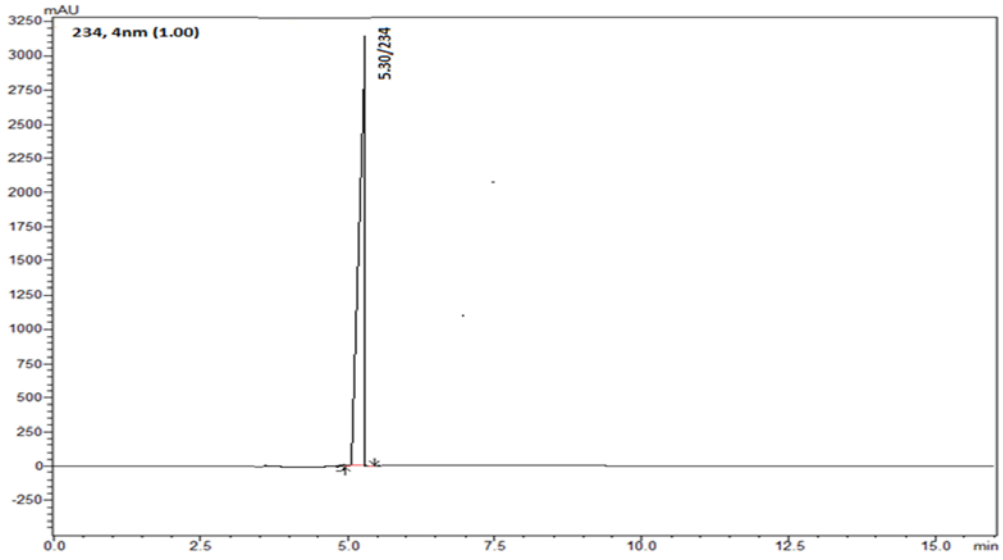

Figure 4.219.: HPLC chromatogram of (2Z,5E,16E)-8-hydroxy-20-isobutyl-16-methyl-7,14-dioxa-bicyclo[19.3.1]-pentacosa-2,5,16-triene-10,23-dione (**15**)

The compound, (2*Z*,5*E*,16*E*)-8-hydroxy-20-isobutyl-16-methyl-7,14-dioxa-bicyclo[19.3.1]pentacosa-2,5,16-triene-10,23-dione (**15**) was isolated as a yellow oily substance. The molecular formula was determined as $C_{28}H_{44}O_5$ from the integrated EIMS {*m/z* 460.3 $[M]^+$} and HR-ESI-MS data {*m/z* 461.3270 $[M+H]^+$} coupled with extensive one/two dimensional (1D/2D) NMR experiments (Table 4.22). The FTIR spectrum of compound **15** exhibited

absorption peaks at 3426, 2922/2856 and 1703 cm^{-1}, which could attribute the existence of alkane, hydroxyl and carbonyl moieties, in that order (Figure 4.220). The possibilities of twelve sp^3 methylenes, ten methines, three each of sp^3 methyls and quaternary carbons were confirmed through the combined $^1H/^{13}C$/DEPT NMR. The greatly deshielded carbon signals at δ 213.24 and 214.29 appeared to correspond to two carbonyl carbon functionalities. The highly deshielded signal at δ 5.62/96.11 was found to be sp^3 methine (-CH-), and this higher chemical shift might be due to the presence of highly electronegative groups like ketone and hydroxyl in its vicinity. Deshielded proton signals at δ 5.59, 5.82, 5.88, 5.98 and 5.43 were attached to the carbons at δ 136.44, 121.68, 126.81, 144.84 and 123.11, respectively, and were related to the non-conjugated olefinic functionalities (Figure 4.221-4.225).

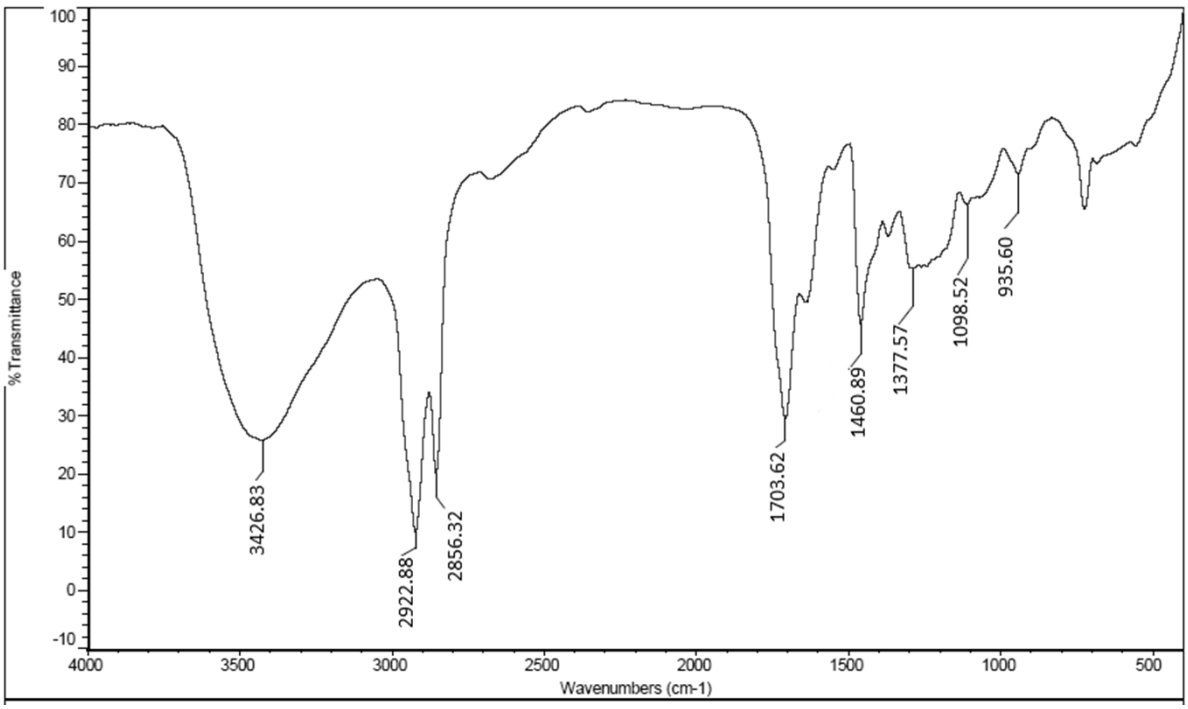

Figure 4.220.: FTIR spectrum of (2Z,5E,16E)-8-hydroxy-20-isobutyl-16-methyl-7,14-dioxa-bicyclo[19.3.1]-pentacosa-2,5,16-triene-10,23-dione (**15**)

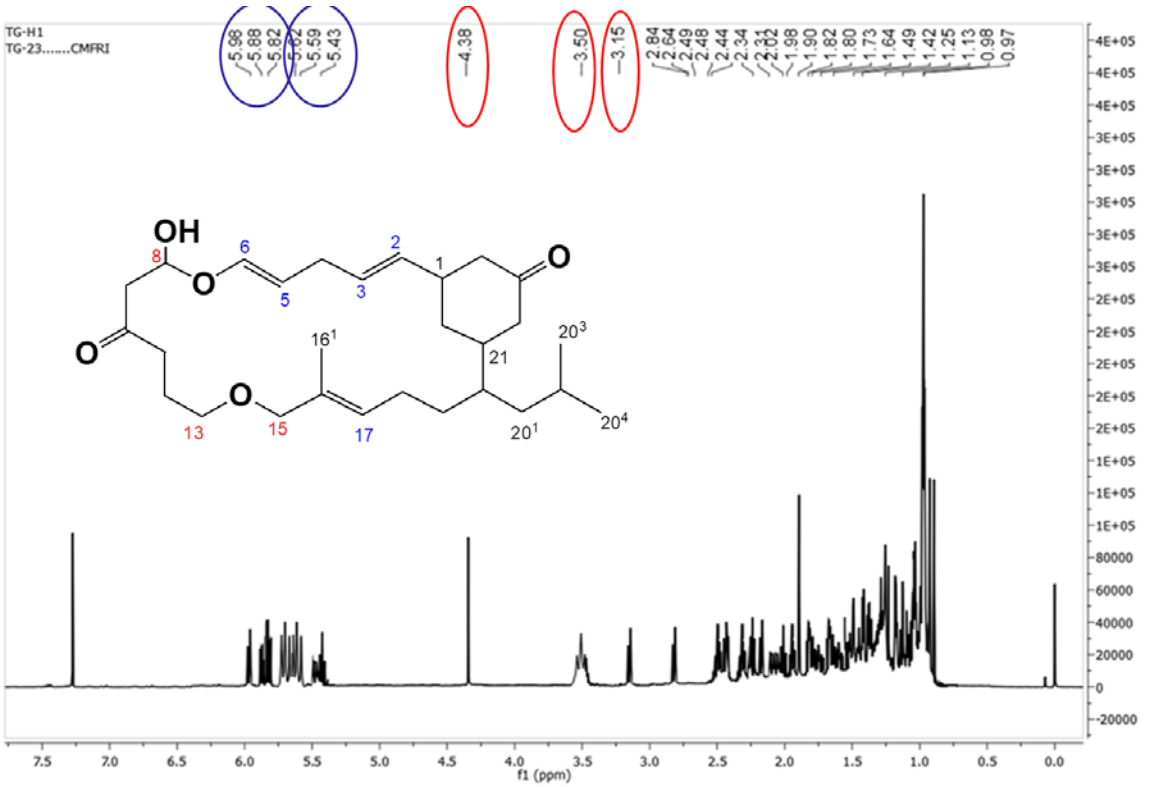

Figure 4.221.: ^{1}H NMR spectrum of (2Z,5E,16E)-8-hydroxy-20-isobutyl-16-methyl-7,14-dioxa-bicyclo[19.3.1]-pentacosa-2,5,16-triene-10,23-dione (**15**)

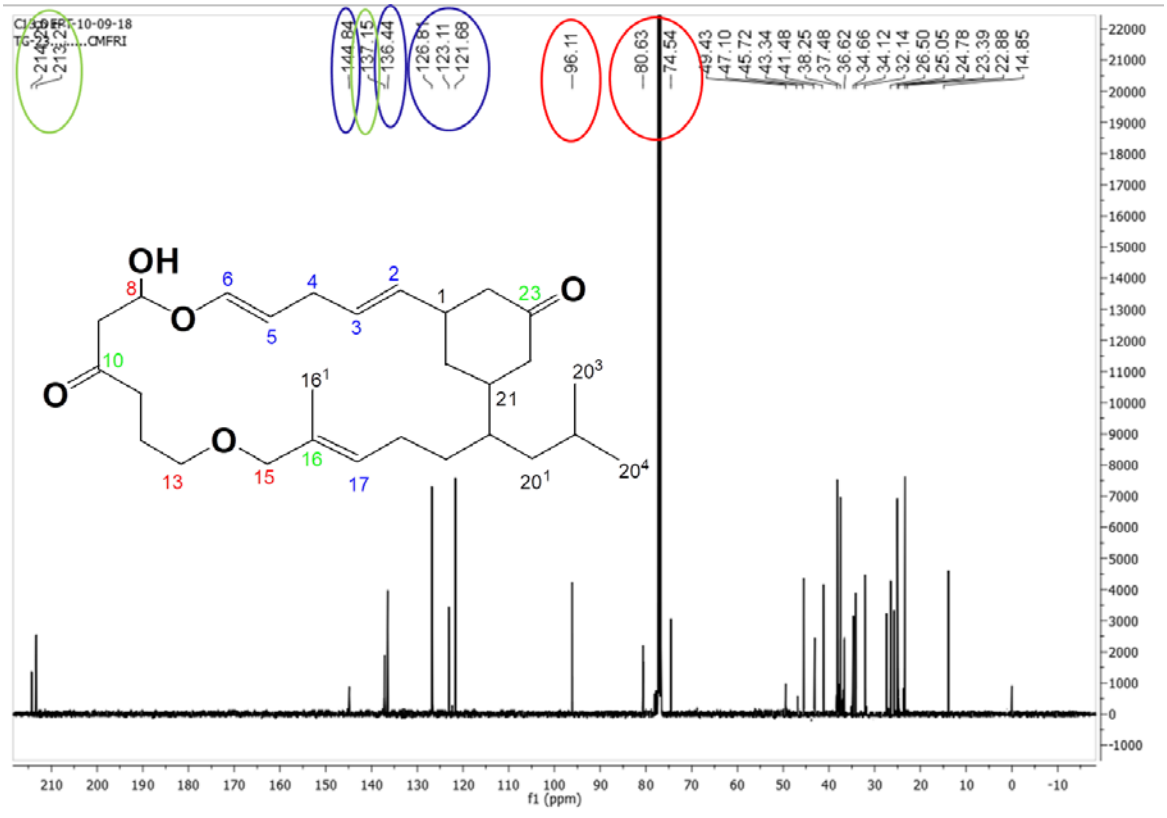

Figure 4.222.: ^{13}C NMR spectrum of (2Z,5E,16E)-8-hydroxy-20-isobutyl-16-methyl-7,14-dioxa-bicyclo[19.3.1]-pentacosa-2,5,16-triene-10,23-dione (**15**)

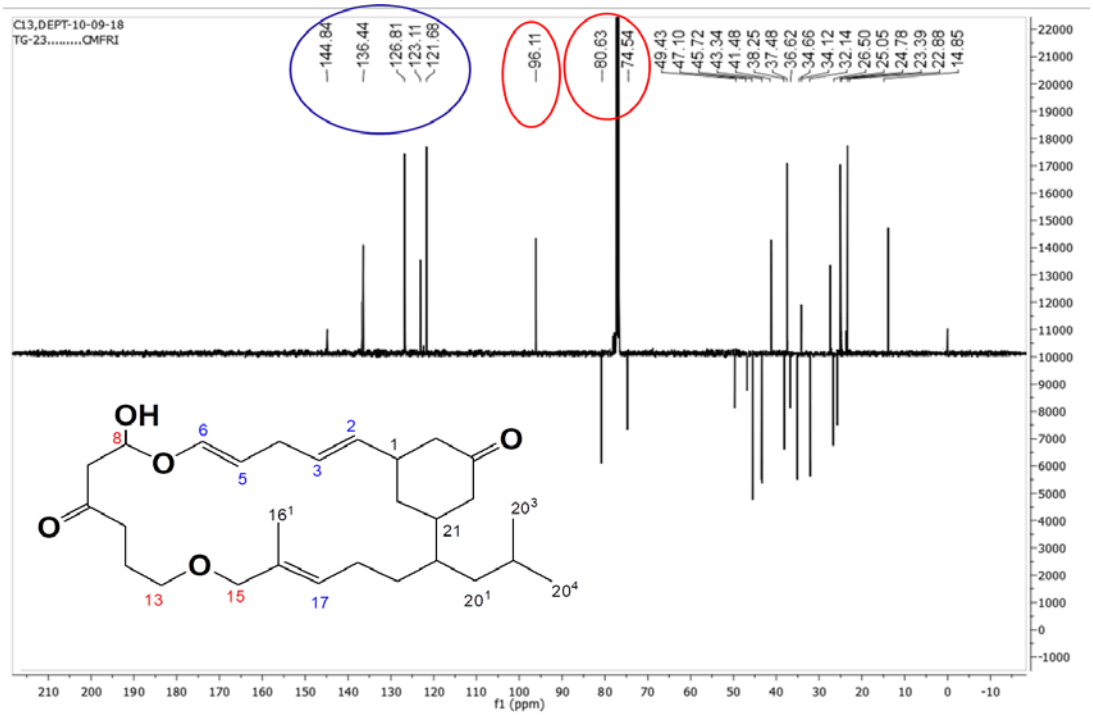

Figure 4.223.: ^{135}DEPT spectrum spectrum of (2Z,5E,16E)-8-hydroxy-20-isobutyl-16-methyl-7,14-dioxa-bicyclo[19.3.1]-pentacosa-2,5,16-triene-10,23-dione (**15**)

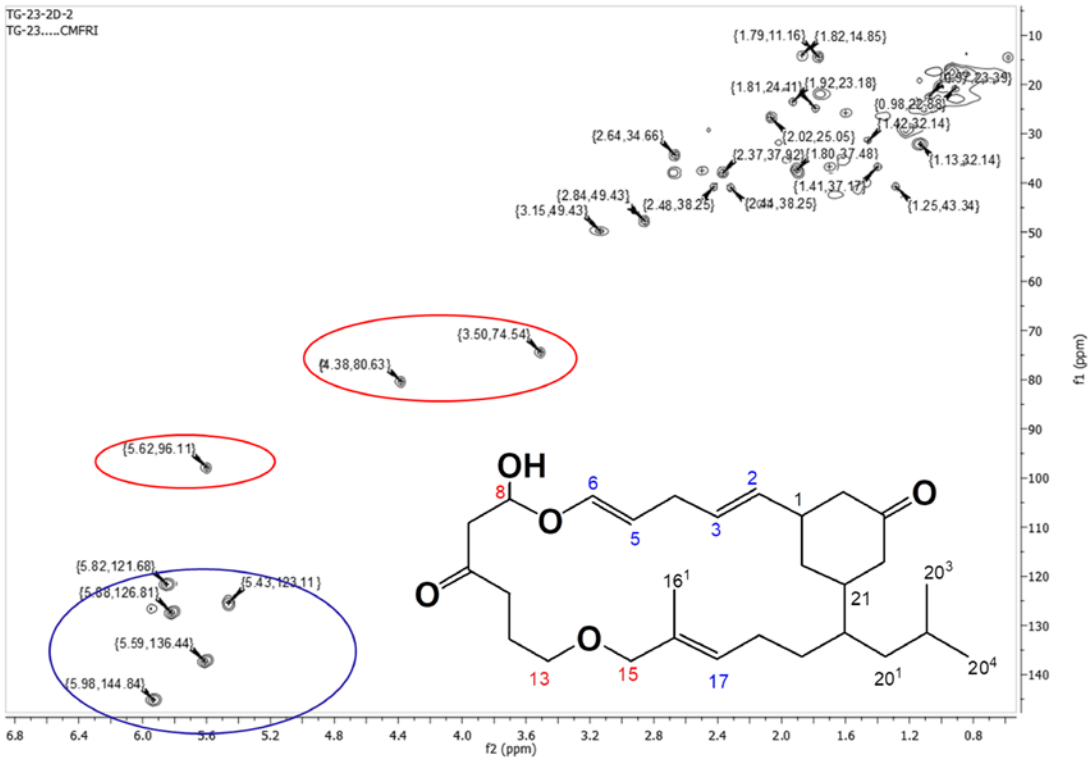

Figure 4.224.: HSQC spectrum of (2Z,5E,16E)-8-hydroxy-20-isobutyl-16-methyl-7,14-dioxa-bicyclo[19.3.1]-pentacosa-2,5,16-triene-10,23-dione (**15**)

The COSY correlations ascribed the continuous spin systems, which was displayed from δ 5.43 (assigned at H-17)/2.02, 1.98 (H-18)/1.42, 1.13 (H-19)/1.49 (H-20)/1.80 (H-21)/2.34 (H-22); δ 1.80 (H-21)/1.90 (H-25)/2.49 (H-1)/5.59 (H-2)/5.82 (H-3)/2.64 (H-4)/5.88 (H-5)/5.98 (H-6) and δ 2.49 (H-1)/2.31 (H-24) (Fig. 2). The HMBC correlations from δ 2.34 (H-22) and 2.31 (H-24) to δ 214.29 (C-23); δ 2.34 (H-22) to δ 37.48 (C-21) and δ 1.80 (H-21) to δ 41.48 (C-1) proposed the presence of cyclohexanone skeleton in compound **15** (Figure 4.225-4.227). The occurrence of another carbonyl carbon at δ 213.24 was proposed through the intense HMBCs from δ 2.48 (H-11) and δ 3.15 (H-9) to δ 213.24 (C-10) at the C-10 position. The previously reported 13-membered macrocyclic lactone derivative enclosed one ester (δ 172.55) along with ether substitution (Chakraborty et al., 2019), whereas the titled compound enclosed one ketone (δ 213.24) and ether functionalities in the macrocyclic-ring system. Spectral data of ^{13}C NMR showed one deshielded methine at δ 96.11 (δ 5.62, HSQC), which ascribed that it might be positioned between the hydroxyl and oxygen functionalities as compared to ^{13}C NMR spectrum of ten-membered cyclic lactone analogue with one deshielded quaternary carbon peak at δ 92.06 located between the oxygen and hydroxyl groups (Chakraborty et al., 2019). The lack of interchangeable hydroxyl moiety in the ^{1}H NMR by deuterium-exchange established the existence of hydroxyl at δ 96.11. The hydroxy methine at δ 5.62 was allocated at position C-8 through the HMBCs from δ 5.62 (H-8) to δ 144.84 (C-6) and δ 3.15 (H-9) to δ 96.11 (C-8). Further, HMBCs from δ 5.82 (H-3) to δ 34.66 (C-4); δ 1.73 (H-12) to δ 38.25 (C-11); δ 3.50 (H-13) to δ 24.78 (C-12); δ 4.38 (H-15) to δ 74.54 (C-13), 137.15 (C-16); δ 5.43 (H-17) to δ 137.15 (C-16) and δ 1.42 (H-19) to δ 25.05 (C-18), 34.12 (C-20) attributed the 19-memebered macrocyclic ring system of 8-hydroxy-7,14-dioxa-bicyclo[19.3.1] pentacosa-2,5,16-triene-10,23-dione .

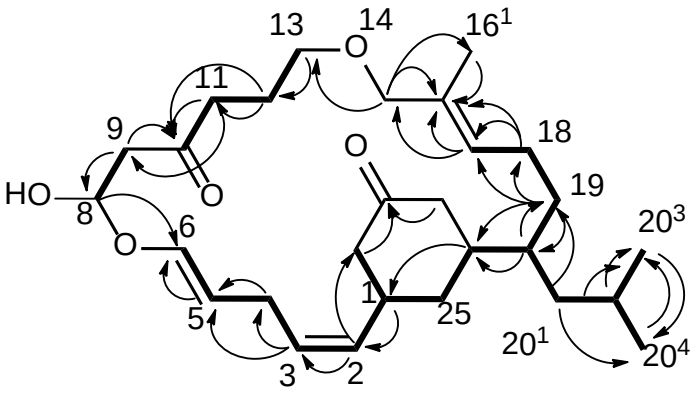

Figure 4.225.: ^{1}H-^{1}H COSY (bold-faced bonds) and HMBC (double-barbed arrows) correlations of (2Z,5E,16E)-8-hydroxy-20-isobutyl-16-methyl-7,14-dioxa-bicyclo[19.3.1]-pentacosa-2,5,16-triene-10,23-dione (**15**)

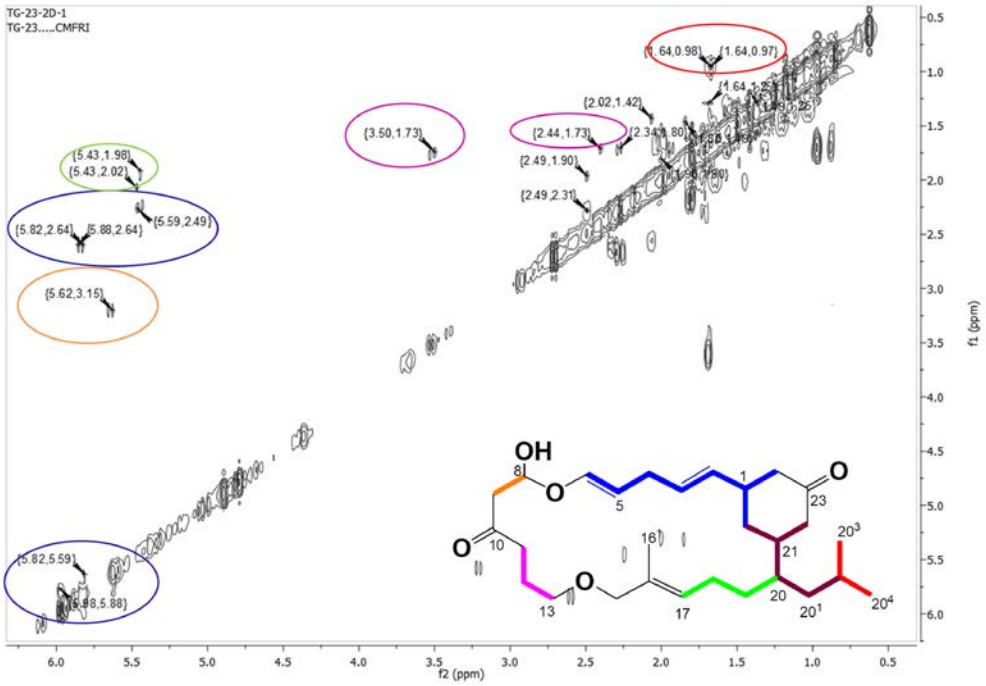

Figure 4.226.: HMBC spectrum of (2Z,5E,16E)-8-hydroxy-20-isobutyl-16-methyl-7,14-dioxa-bicyclo[19.3.1]-pentacosa-2,5,16-triene-10,23-dione (**15**)

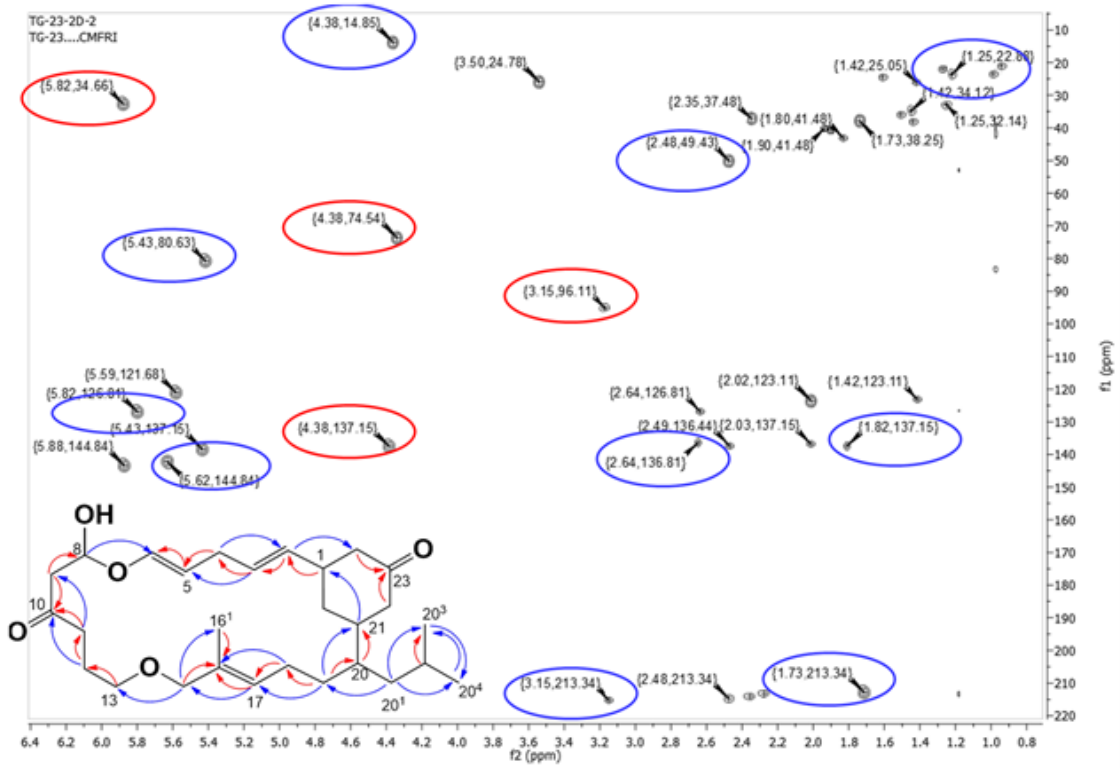

Figure 4.227.: HMBC spectrum of (2Z,5E,16E)-8-hydroxy-20-isobutyl-16-methyl-7,14-dioxa-bicyclo[19.3.1]-pentacosa-2,5,16-triene-10,23-dione (**15**)

The cyclohexanone ring was positioned between C-20 and C-2 positions through intense HMBCs from δ 1.49 (H-20) to δ 37.48 (C-21); δ 1.90 (H-25) to δ 41.48 (C-1) and δ 2.49 (H-1) to δ 136.44 (C-2) in the 19-membered macrocyclic ring. The shielded singlet methyl at δ 1.82/14.85 was positioned at C-16 position of the 19-membered macrocyclic ring through the HMBCs from δ 1.82 (H-16^1) to δ 137.15 (C-16). The COSYs from δ 1.49 (H-20)/1.25 (H-20^1)/1.64 (H-20^2)/0.97 (H-20^3), 0.98 (H-20^4) along with HMBCs from δ 1.25 (H-20^1) to δ 34.12 (C-20), 32.14 (C-19), 23.39 (C-20^3), 22.88 (C-20^4); δ 0.97 (H-20^3) to δ 22.88 (C-20^4) and δ 0.98 (H-20^4) to δ 23.39 (C-20^3) proposed the presence of isobutyl branching and its attachment at C-20 of the 19-membered macrocyclic ring. These combined data assigned its degree of unsaturations as seven corresponding to five double bonds and two ring systems. Notably, the multiplicity of the double bond at the position, C2=C3 (δ5.59) was a doublet of doublet possessing the coupling constant (J) of 6.9 Hz. The configuration of Δ2 was found to be Z, which was supported by the coupling constant (Table 1B, Fig. 1), and previous reports of literature. For example, the antibacterial macrolactins 2 and 3 were found to possess double bonds in between the carbon atoms C18 and C19 nearby to the cyclic rings (Mondol et al., 2011), which were similar to the double bonds located nearby to cyclohexane ring in compound **3.** The multiplicity

of CH proton attached to the double bonds was obtained as doublet of doublet, δ5.62 (dd) in macrolactin 2, and δ5.42 (dd) in macrolactin 3 (Mondol et al., 2011). Similarly, the cyclic ether-containing macrolactins, which were identified from marine *Bacillus sp.*, also possessed double bonds as found in compound **3**. The olefinic protons at δ5.64 (dd), 4.08 (dd) and 5.43 (dd) were reported from macrolactins also exhibited multiplicities as doublet of doublet (Mondol & Shin 2014), as found in the studied compound **3**. These results along with proton NMR data corroborated the assignment of multiplicity of H-2 (as doublet of doublet), configuration of double bond (as Z configuration), and coupling constant (J=6.9 Hz).

Table 4.22: NMR spectroscopic data of compound (**15**), (2Z,5E,16E)-8-hydroxy-20-isobutyl-16-methyl-7,14-dioxa-bicyclo[19.3.1]-pentacosa-2,5,16-triene-10,23-dione (**15**) isolated from red seaweed *G. salicornia*

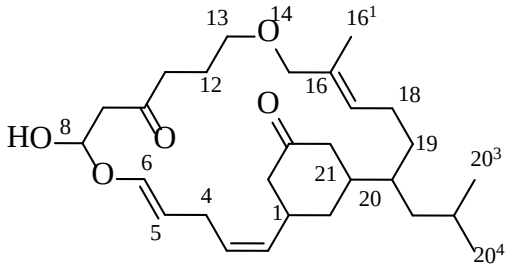

Compound **15**…… (2Z,5E,16E)-8-hydroxy-20-isobutyl-16-methyl-7,14-dioxa-bicyclo[19.3.1]-pentacosa-2,5,16-triene-10,23-dione (**15**)

Type	C. No.	^{13}C NMR	H. No. (int., mult., J in Hz)‡	^{1}H NMR	COSY	HMBC
CH	1	41.48	1H,m	2.49	H-2, H-25, H-24	C-2
CH	2	136.44	1H, dd,6.9, 6.9 Hz	5.59	H-3	C-3
CH	3	121.68	1H,m	5.82	H-4	C-4,5
CH_2	4	34.66	2H,t,7.1 Hz,	2.64	H-5	C-5
CH	5	126.81	1H,m	5.88	H-6	C-6
CH	6	144.84	1H,d,11.1 Hz	5.98	-	-
-	7	-	-	-	-	-
CH	8	96.11	1H,m	5.62	H-9	C-6
CH_2	9	49.43	1H,dd,5.6,12.3 Hz	3.15	-	C-8,10
			1H,dd,5.3,12.1 Hz	2.84	-	-
C	10	213.24	-	-	-	-
CH_2	11	38.25	1H,t,4.5 Hz	2.48	H-12	C-9,10
			1H,t,4.8 Hz	2.44	-	-
CH_2	12	24.78	2H,m	1.73	H-13	C-10,11
CH_2	13	74.54	2H,m	3.50	-	C-12
-	14	-	-	-	-	-
CH_2	15	80.63	1H,d,9.3 Hz	4.38	-	C-13,16,16¹
C	16	137.15	-	-	-	-

CH	17	123.11	1H,t, 5.8 Hz	5.43	H-18	C-15,16
CH_2	18	25.05	1H,m	2.02	H-19	C-16,17
			1H,m	1.98	-	-
		32.14	1H,m	1.42	H-20	C-17,18,20,21
CH_2	19					
			1H,m	1.13	-	-
CH	20	34.12	1H,m	1.49	H-21, H-20^1	C-21
CH	21	37.48	1H,m	1.80	H-22	C-1
CH_2	22	47.10	2H,d, 6.8 Hz	2.34	-	C-21,23
C	23	214.29	-	-	-	-
CH_2	24	45.72	2H,d,6.1 Hz	2.31	-	C-23
CH_2	25	36.62	2H,t,5.9 Hz	1.90	-	C-1
CH_3	16^1	14.85	3H,s	1.82	-	C-16
		43.34	2H,t,6.9 Hz	1.25	H-20^2	C-20,19,20^4, 20^3
CH_2	20^1					
CH	20^2	26.50	1H,m	1.64	H-20^3, H-20^4	C-20^3
CH_3	20^3	23.39	3H,d,5.9 Hz	0.97	-	C-20^4
CH_3	20^4	22.88	3H,d,6.2 Hz	0.98	-	C-20^3

†NMR spectra were recorded using a Bruker AVANCE III 500 MHz (AV 500) spectrometer (Bruker, Karlsruhe, Germany) in $CDCl_3$ as aprotic solvent at ambient temperature with TMS as the internal standard (δ 0 ppm).

‡Values in ppm, multiplicity and coupling constants (J= Hz) were indicated in parentheses. Multiplicities were allocated by ^{135}DEPT NMR spectrum.

The assignments were made with the aid of the COSY, HSQC, HMBC and NOESY experiments.

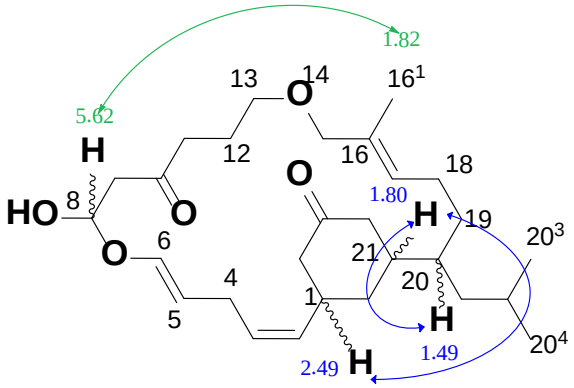

Figure 4.228.: NOESY (double-barbed green coloured arrows for α-orientation and blue coloured arrows for β orientations) correlations of (2Z,5E,16E)-8-hydroxy-20-isobutyl-16-methyl-7,14-dioxa-bicyclo[19.3.1]-pentacosa-2,5,16-triene-10,23-dione (**15**)

The relative stereochemistry of the protons at C-1, C-8, C-20 and C-21 were unambiguously deduced from the NOESY experiment (Figure 4.228-4.229).The proton resonances at δ 1.82 (H-16^1) displayed NOE cross-peaks with the methine proton at δ 5.62 (H-8), and those were distributed in an identical plane of symmetry, and hence, assigned to be α-oriented. The NOESY correlations from δ 2.49 (H-1)/1.80 (H-21)/1.49 (H-20) were found to be in the identical plane of symmetry and trans oriented to the α-protons, and therefore, arbitrarily assigned as β-oriented.

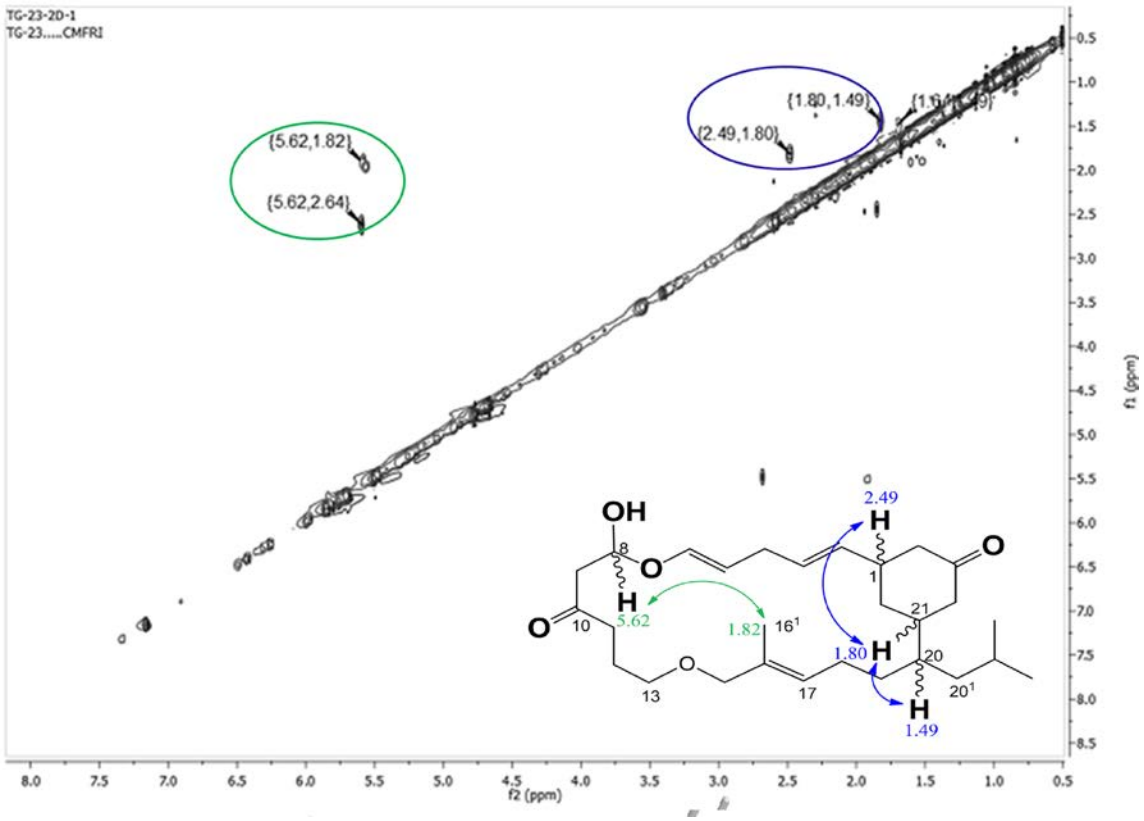

Figure 4.229.: NOESY spectrum of (2Z,5E,16E)-8-hydroxy-20-isobutyl-16-methyl-7,14-dioxa-bicyclo[19.3.1]-pentacosa-2,5,16-triene-10,23-dione (**15**)

The molecular ion peak at *m/z* 460 (**1**) with the molecular formula of $C_{28}H_{44}O_5$ appeared to eliminate a molecule of H_2O to form the fragment **2** (*m/z* 440), and participated in the McLafferty rearrangement to form **3** with *m/z* 441. The base-peak was acquired at *m/z* 96, which was deduced to correspond to $C_6H_8O^{\bullet+}$ (Figure 4.230-4.231)

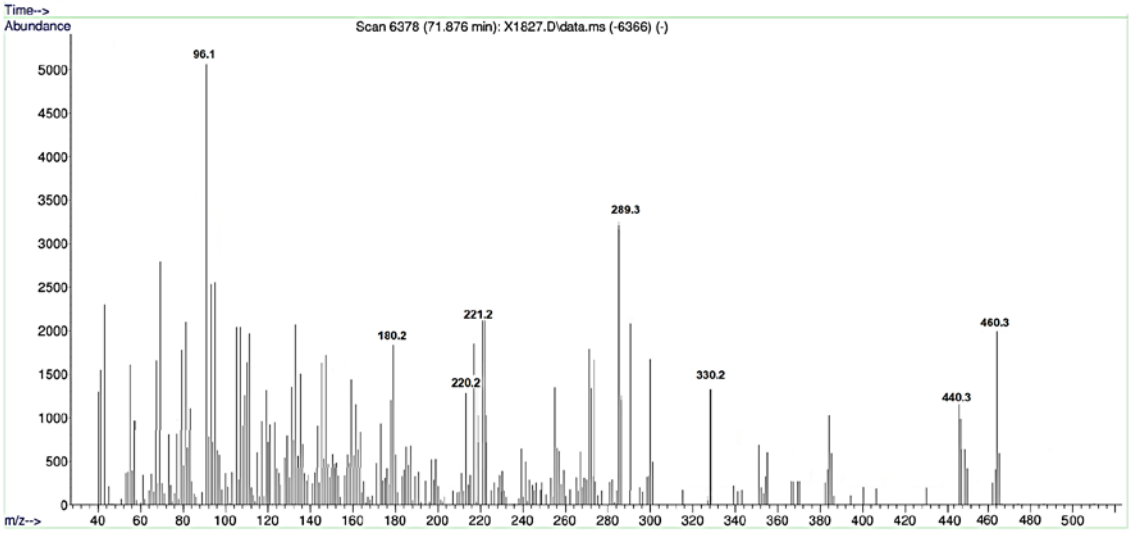

Figure 4.230.: NOESY spectrum of (2Z,5E,16E)-8-hydroxy-20-isobutyl-16-methyl-7,14-dioxa-bicyclo[19.3.1]-pentacosa-2,5,16-triene-10,23-dione (**15**)

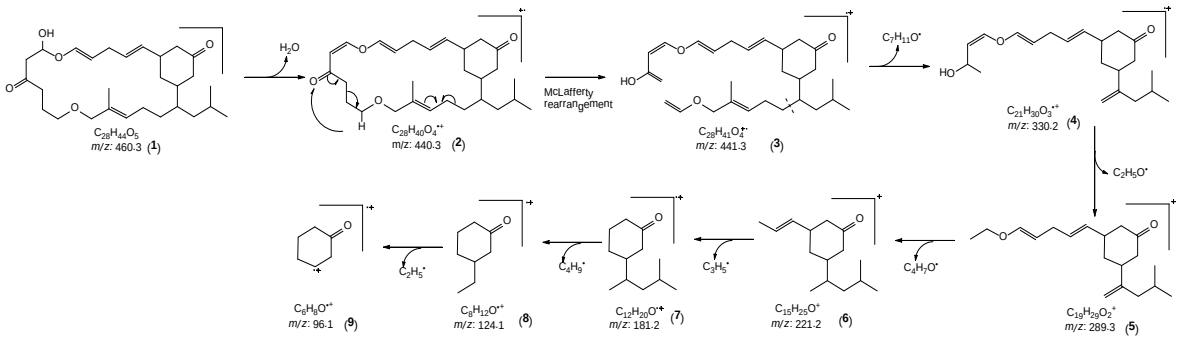

Figure 4.231.: Tentative mass spectrum of (2Z,5E,16E)-8-hydroxy-20-isobutyl-16-methyl-7,14-dioxa-bicyclo[19.3.1]-pentacosa-2,5,16-triene-10,23-dione (**15**)

This is the first report of the undescribed oxabicyclo[21.3.1]heptacosa-ene-diones (Compounds **13-14**) and oxabicyclo[19.3.1]pentacosa-ene-dione (compound **15**) bearing macrocyclic lactones from the red seaweed, *Gracilaria salicornia*. The unprecedented macrolides (**13-15**), namely 3-acetyl-14-(furanyl)-11-methyl-15-(15^{3}-methylbutyloxy)-8-oxabicyclo[21.3.1] heptacosa-11,23,25,27-tetraene-7,18-dione (**13**), (2*E*,12*E*,14*E*)-10-acetyl-9-isopentyl-2-methyl-5,16,23^{1}-trioxa-bicyclo[21.3.1]heptacosa-2,12,14-triene-6,19-dione (**14**) and

(2*Z*,5*E*,16*E*)-8-hydroxy-20-isobutyl-16-methyl-7,14-dioxa-bicyclo[19.3.1]pentacosa-2,5,16-triene-10,23-dione (**15**) were found to be possessed various oxygenated functionalities. In particular, the pyran enclosed macrocyclic lactone could be used as prospective natural therapeutic pharmacophore template.

4.3.3 Pharmacological potentials of secondary metabolites isolated from the organic extract of G. salicornia

4.3.3.1 Pharmacological potentials of abeo-labdane class of diterpenoid derivative (Compound 1)

Antioxidant activities of the methyl-16(13→14)-abeo-7-labdene-(12-oxo) carboxylate isolated from *G. salicornia* was investigated by *in vitro* radical quenching activities against DPPH and $ABTS^+$ radicals (Table 4.23). The studied compound exhibited comparable DPPH radical quenching activity (IC_{50} 1.97 mM) as standard antioxidant agent *α*-tocopherol (IC_{50} 1.49 mM). The studied abeo-labdane registered significantly higher bioactivities against pro-inflammatory 5-LOX (IC_{50} 2.33 mm) than that exhibited by non-steroidal anti-inflammatory agent ibuprofen (IC_{50} 4.51mM, $P<0.05$). The selectivity index of the titled compound was also found to be significantly higher (IC_{50}anti-COX-1/ IC_{50}anti-COX-2 ~ 1.40) than non-steroidal anti-inflammatory agent ibuprofen (0.43 mM) ($p < 0.05$). This appropriately recognized the greater selectivity of the studied abeo-labdane towards inducible pro-inflammatory cyclooxygenase-2 (COX-2) than its constitutive isoform cyclooxygenase-1 (COX-1). Earlier reports of literature also disclosed that the diterpenoids with decalin carbon system exhibited anti-inflammation potential (Chinou 2005;Tran et al. 2017). The isolated abeo-labdane registered significantly lesser bioactivities against carbolytic enzymes (α-amylase and α-glucosidase) (> IC_{50} 2.00 mM) than that exhibited by anti-diabetic agent acarbose (~IC_{50} 0.2 mM, $P>0.05$).

4.3.3.2 Pharmacological potentials of oleanane class of triterpenoid derivatives (Compounds 2-3)

The *in vitro* anti-diabetic potential of the studied abeo-oleanenes (**2** and **3**) were assessed by their inhibitory properties towards the carbolytics, α-glucosidase and α-amylase that were found to regulate the intestinal carbohydrate absorption, thereby reducing postprandial insulin level (Goldstein et al., 1998). Among the titled abeo-oleanenes, the one with 24(4→23)-abeo-oleanene framework (**3**) displayed significantly higher α-amylase and α-glucosidase inhibitory properties (IC_{50} 0.32 and 0.29 mM, respectively) over that bearing 24(4→23), 27(8→26), 30(20→29)-tris-abeo-oleanene moiety (**2**) (IC_{50} 0.40 and 0.34 mM, respectively)

(Table 4.23). The higher α-amylase and α-glucosidase inhibitory properties of 24(4→23)-abeo-oleanene framework (**3**) (IC_{50} 0.32 and 0.29 mM, respectively) exhibited close resemblance towards the reference carbolytic enzyme inhibitor acarbose (IC_{50} 0.22 and 0.19 mM, respectively mM). *In vitro* radical scavenging assays by $ABTS^+$ and DPPH radicals were employed to deduce the antioxidant properties of studied abeo-oleanenes. The studied compound, **3** exhibited greater radical scavenging activities (IC_{50} DPPH 1.33 mM; IC_{50} $ABTS^+$ 1.09 mM), when compared to those displayed by compound **2** (IC_{50} DPPH 1.56 mM; IC_{50} $ABTS^+$ 1.24 mM) and standard, *α*-tocopherol (IC_{50} DPPH 1.49 mM; IC_{50} $ABTS^+$ 1.69 mM). The isolated abeo-labdane registered significantly lesser potential against pro-inflammatory COX-2 and 5-LOX (> IC_{50} 3.00 mM).

4.3.3.3 Pharmacological potentials of drimane class of diterpenoid derivative (Compounds 4-6)

The *in vitro* radical scavenging assays by DPPH and $ABTS^+$ radicals were used to ascertain the antioxidant properties of the studied drimane sesquiterpene derivatives (Table 4.23). The studied compound, **4** bearing substituted 1*H*-benzo[a]xanthene-4,10,12-triol moiety exhibited greater radical scavenging activities (IC_{50} DPPH 1.33 mM; IC_{50} $ABTS^+$ 1.57 mM), when compared to the standard *α*-tocopherol (IC_{50} DPPH 1.49 mM; IC_{50} $ABTS^+$ 1.69 mM). There were previous reports on DPPH radical scavenging activities of drimane sesquiterpenoids (Perez-Garcia et al., 2005) that corroborated the antioxidant activity of terpenoids sketched in the current work. The aromatic, hydroxyls and ether functionalities in the studied compounds could be incorporated in the process of delocalization of electron in the radical scavenging mechanism of the DPPH radical, which might be one of the predominant reasons for potential antioxidant properties of the studied compounds (**4-6**). There were previous reports on the antioxidant properties of the metabolites with conjugated olefinic, aromatic, and hydroxyl functionalities (Rice-Evans et al., 1996). Among the isolated compounds, the one with substituted 1*H*-benzo[*a*]xanthene-4,10,12-triol (**4**) showed greater $ABTS^+$ and DPPH radical activities (IC_{50} 1.57 and 1.33 mM, respectively) over those exhibited by compounds **5** and **6** (IC_{50} 1.88-1.96 and 1.51-1.85 mM, respectively). The *in vitro* anti-inflammatory potential of the isolated compounds were evaluated by their inhibition potential towards pro-inflammatory COX-1, 2 and 5-LOX enzymes. Among the studied compounds, **4** showed greater COX-2 and 5-LOX inhibitory activities (IC_{50} 1.35 and 1.72 mM, respectively) over those displayed by **5-6** (COX-2 IC_{50} 1.56-1.91 mM and 5-LOX IC_{50} 1.90-2.55 mM, respectively). The drimane class of diterpenoids were displayed lower bioactivities against carbolytic enzymes (α-amylase and α-glucosidase) (> IC_{50} 2.00 mM).

4.3.3.4 Pharmacological potentials of 2H-chromenyl derivatives (Compounds 7-8)

Antioxidant potentials of the *2H*-chromenyl derivatives (**7**) and (**8**) isolated from *G. salicornia* was investigated by *in vitro* radical quenching activities against DPPH and $ABTS^+$ (Table 4.23). The compound **8** exhibited higher DPPH and $ABTS^+$ radical quenching activities (IC_{50} 1.17 and 1.33 mM, respectively) than those displayed by **7** and standard antioxidant agent α-tocopherol ($IC_{50} \geq 1.49$ mM). The compound **8** registered significantly higher activities against pro-inflammatory 5-LOX (IC_{50} 2.03 mM) than that displayed by **7** (IC_{50} 2.46 mM, $p < 0.05$). The selectivity index of the titled compound was also found to be higher (IC_{50} anti-COX-1/IC_{50} anti-COX-2 > 0.95) than non-steroidal anti-inflammatory agent ibuprofen (0.89) ($p < 0.05$). This appropriately suggested the greater selectivity of the studied chromenyls towards inducible pro-inflammatory cyclooxygenase-2 (COX-2) than its constitutive isoform cyclooxygenase-1 (COX-1). The bioactivities of *2H*-chromenyl derivatives (**7**) and (**8**) were found to be lower towards carbolytic enzymes (α-amylase and α-glucosidase) inhibition potentials (> IC_{50} 2.00 mM).

4.3.3.5 Pharmacological potentials of spiro-compound derivatives (Compounds 9-10)

Antioxidant potentials of the spiro-compounds (**9**) and (**10**) isolated from *G. salicornia* was investigated by *in vitro* radical quenching activities against DPPH and $ABTS^+$ (Table 4.23). The compound **9** exhibited higher DPPH and $ABTS^+$ radical quenching activities (IC_{50} 1.13 and 1.24 mM, respectively) than those displayed by **9** and standard antioxidant agent α-tocopherol ($IC_{50} \geq 1.49$ mM). The compound **10** registered significantly higher activities against pro-inflammatory 5-LOX (IC_{50} 1.91 mM) than that displayed by **9** (IC_{50} 2.78 mM, $p<0.05$). The selectivity index of the titled compound was also found to be higher (IC_{50} anti-COX-1/IC_{50} anti-COX-2 >1.05) than that exhibited by the non-steroidal anti-inflammatory agent ibuprofen (0.43) ($p<0.05$). This appropriately suggested the greater attenuating activities of the studied spiro-compounds against inducible pro-inflammatory cyclooxygenase-2 (COX-2) than cyclooxygenase-1 (COX-1). The bioactivities of spiro-compound derivatives (**9**) and (**10**) were considered to be lower towards carbolytic enzymes (α-amylase and α-glucosidase) inhibition potentials (> IC_{50} 2.00 mM).

4.3.3.6 Pharmacological potentials of polyether derivatives (Compounds 11-12)

The free radical quenching assays against DPPH and $ABTS^+$ ascertained the antioxidant potentials of the polyether derivatives. The isolated compound, **12** bearing furanyl-furo[3,2-b]pyran-2*H*-pyran registered potent radical quenching properties (IC_{50}DPPH 1.11 mM;

$IC_{50}ABTS^{+}$ 1.27 mM) when related to those displayed by compound, **11** bearing pyranyl-10-methylpyrano[3,2-b]pyran-methyleneoxepane moiety (IC_{50} > 1.6 mM) and standard α-tocopherol (IC_{50} > 1.49 mM) (Table 4.23). It was attributed that the furo[3,2-b]pyran and ester functionalities in compound **12** might play predominant roles for the greater electron delocalisations in the radical scavenging mechanism compared to compound **11**, which in turn, explained the greater radical scavenging properties of the former. The *in-vitro* anti-inflammatory potencies of the fractionated polyether triterpenoids, as determined by their attenuating properties against COX-1 and COX-2 were found to be considerably greater for compound **12** (IC_{50}COX-1 1.96 mM and IC_{50}COX-2 1.87 mM) ($p < 0.05$) than those exhibited by compound **11** (IC_{50}COX-1 2.67 mM and $IC_5COX\text{-}2_0$ 2.72 mM). Likewise, the polyether analogue bearing trimethyl-2*H*-pyran-3-yl butyrate moiety (**12**) registered greater attenuating properties against 5-LOX (IC_{50} 1.89 mM) enzyme when compared to those exhibited by compound **11** (IC_{50} 2.71 mM) and standard (ibuprofen IC_{50} 4.51 mM). Notably, the polyether derivative **12** was found to effectively attenuate 5-LOX/COX-2 enzymes while retaining COX-1/COX-2 ratio within the threshold limits (IC_{50} of anti-COX-1 to IC_{50} of anti-COX-2 > 1) for selective and target-oriented potencies against inflammatory response, compared to that displayed by **11** (0.98) attributing the greater attenuation property of the former against COX-2 over that in opposition to COX-1. It is of note that the selectivity index (IC_{50} of anti-COX-1 to IC_{50} of anti-COX-2) of the compound **12** was greater than 1.0 as compared to that displayed by the synthetic ibuprofen (0.43) (Table 4.23), and that in turn, signified the targeted attenuating property of the polyether analogue bearing trimethyl-2*H*-pyran-3-yl butyrate moiety against the inducible pro-inflammatory COX-2 and 5-LOX than that on COX-1, which has been recognized as a constitutive enzyme in the gastric and intestinal mucosal system.

The anti-inflammatory selectivity index of greater than **11** showed higher selectivity of the studied compounds towards the enzyme target site and lesser toxic side effects, such as inhibiting constitutive COX-1, and imparting side effects on the gastrointestinal mucosa. The COX-1 and 2 isoforms were found to exhibit differential properties, particularly, COX-1 produces prostaglandins (PGs) and mediate the basic functions, such as cytoprotection of gastric mucosa, regulation of renal blood flow and platelet aggregation (Kurumbail, 2001). In contrast, expression of COX-2 was found to rapidly induce by the inflammatory stimuli, such as pro-inflammatory cytokines, lipopolysaccharides, mitogens, etc. resulting in the increased production of PGs in inflamed tissues (Kurumbail, 2001). Thus, the inducible isozyme of COX-2 has been implicated in attenuating the pathological processes leading to inflammation.

Table 4.23.: *In vitro* antioxidant, anti-inflammatory and antidiabetic {radical scavenging, cyclooxygenase-1 & 2 (COX-1 & 2) and 5-lipoxygenase (5-LOX) and α-amylase/glucosidase} activities of the studied compounds (**1-15**) isolated from the EtOAc-MeOH extract of *G. salicornia* against commercial standard, tocopherol (T), ibuprofen (I) and acarbose (A)

Compounds	*Anti-oxidant activities in IC_{50} (mM)		*Anti-inflammatory properties IC_{50} (mM)				*Anti-diabetic activities in IC_{50} (mM)	
	DPPH quenching	ABTS quenching	COX-1 inhibition	COX-2 inhibition	5-LOX inhibition	Selectivity index†	α-amylase	α-glucosidase
1	^{a}1.97 ± 0.03	^{a}2.33 ± 0.04	^{a}2.39 ± 0.03	^{a}1.71 ± 0.02	^{a}2.33 ± 0.02	^{a}1.40 ± 0.02	^{a}2.88 ± 0.03	^{a}2.24 ± 0.04
2	^{b}1.56 ± 0.01	^{b}1.24 ± 0.02	^{b}3.04 ± 0.01	^{b}3.38 ± 0.01	^{b}3.98± 0.02	^{b}0.90± 0.02	^{b}0.40 ± 0.01	^{b}0.34 ± 0.01
3	**^{c}1.33 ± 0.01**	**^{c}1.09 ± 0.02**	**^{c}3.22 ± 0.02**	**^{c}3.29 ± 0.03**	**^{c}3.01± 0.02**	**^{c}0.98± 0.02**	**^{c}0.32 ± 0.02**	**^{b}0.29 ± 0.03**
4	**^{c}1.33 ± 0.01**	**^{d}1.57 ± 0.02**	**^{d}1.54 ± 0.02**	**^{d}1.35 ± 0.01**	**^{d}1.72 ± 0.01**	**^{dh}1.14 ± 0.02**	**^{d}2.42 ± 0.01**	**^{c}2.46 ± 0.02**
5	^{b}1.51 ± 0.01	^{e}1.88 ± 0.02	^{e}1.72 ± 0.03	^{e}1.56 ±0.01	^{e}1.90 ± 0.01	^{d}1.10 ± 0.01	^{e}2.62 ± 0.01	^{d}2.79 ± 0.02
6	^{d}1.85 ± 0.02	^{f}1.96 ± 0.01	^{f}2.09 ± 0.01	^{f}1.91 ± 0.02	^{f}2.55 ± 0.01	^{d}1.09 ± 0.02	^{f}2.96 ± 0.02	^{e}2.86 ± 0.01
7	^{e}1.40 ± 0.03	^{g}1.50 ± 0.04	^{g}2.34 ± 0.03	^{g}2.39 ± 0.01	^{g}2.46 ± 0.01	^{e}0.98 ± 0.01	^{g}2.51 ± 0.03	^{f}2.42 ± 0.04
8	**^{f}1.17 ± 0.01**	**^{h}1.33 ± 0.02**	**^{g}2.24 ± 0.01**	**^{j}2.12 ± 0.02**	**^{h}2.03 ± 0.02**	**^{d}1.06 ± 0.02**	**^{h}2.26 ± 0.01**	**^{g}2.23 ± 0.02**
9	^{g}1.61^{a} ± 0.03	^{i}1.72^{a} ± 0.04	^{h}2.70^{a} ± 0.03	^{i}2.75^{a} ± 0.01	^{i}2.78^{a} ± 0.01	^{e}0.98^{a} ± 0.01	^{h}2.72^{a} ± 0.03	^{h}2.63^{a} ± 0.04
10	**^{h}1.13^{b} ± 0.01**	**^{b}1.24^{a} ± 0.02**	**^{i}1.99^{b} ± 0.01**	**^{j}1.89^{a} ± 0.02**	**^{j}1.91^{b} ± 0.02**	**^{d}1.05^{b} ± 0.02**	**^{i}2.04^{b} ± 0.01**	**^{i}2.12^{a} ± 0.02**
11	^{g}1.62 ± 0.03	^{j}1.69 ± 0.04	^{j}2.67 ± 0.03	^{k}2.72 ± 0.01	^{k}2.71 ± 0.01	^{e}0.98 ± 0.01	^{g}2.53 ± 0.03	^{j}2.59 ± 0.04
12	**^{h}1.11 ± 0.01**	**^{b}1.27 ± 0.02**	**^{j}1.96 ± 0.01**	**^{j}1.87 ± 0.02**	**^{l}1.89 ± 0.02**	**^{d}1.05 ± 0.02**	**^{k}2.22 ± 0.01**	**^{k}2.16 ± 0.02**
13	^{e}1.40 ± 0.02	^{k}1.43 ± 0.02	^{d}1.58 ± 0.03	^{l}1.19 ± 0.03	^{m}1.43 ± 0.02	^{f}1.33 ± 0.01	^{g}2.51 ± 0.02	^{k}2.32 ± 0.02
14	**^{i}1.10 ± 0.03**	**^{k}1.21 ± 0.04**	**^{d}1.59 ± 0.03**	**^{m}1.13 ± 0.02**	**^{m}1.39 ± 0.02**	**^{g}1.41 ± 0.02**	**^{d}2.46 ± 0.03**	**^{k}2.31 ± 0.04**
15	^{e}1.42 ± 0.02	^{k}1.47 ± 0.03	^{k}1.42 ± 0.02	^{i}1.20 ± 0.03	^{m}1.47 ± 0.02	^{h}1.18 ± 0.02	^{h}2.33 ± 0.02	^{l}2.28 ± 0.03
Standards	^{bT}1.49 ± 0.04	^{jT}1.69 ± 0.05	^{ll}0.19 ± 0.00^{cl}	^{nl}0.44 ± 0.02^{cl}	^{nl}4.51 ± 0.11	^{il}0.43 ± 0.01	^{iA}0.22 ± 0.02	^{mA}0.19 ± 0.02

The samples were analyzed in triplicate (n = 3) and expressed as mean ± standard deviation. Means followed by different superscripts (a-n) within the same column indicated significant differences ($p < 0.05$). *The bioactivities were expressed as IC_{50} values (mM)

There were several reports available regarding the anti-inflammatory effects of the polyether triterpenoids and those partly bearing the skeleton of this class of compounds (Fernandez et al., 2000). Squalene derived triterpene lupeol was found to exhibit anti-inflammatory potential involving nuclear factor kappa B (NFκB) and phosphatidylinositol-3-kinase (PI3K) in a variety of cells (Saleem and Lupeol, 2009). In particular, the polyfunctionalized cyclic ether group of marine natural products were found to attract special interest, and among them, the natural products containing an oxepanyl moiety were found to possess interesting biological properties including anti-inflammation and other bioactivities Halogenated sesquiterpenoid, aplysistatin isolated from the marine macroalga *Laurencia snackeyi* was found to possess the oxepane moiety, and were reported to possess anti-inflammatory activities along with the ability to suppress the expressions of inducible nitric oxide synthase (iNOS) and COX-2 enzymes (Vairappan et al., 2013). Polyether triterpene-type metabolites, palisadins were found to contain oxepane moieties and fused rings, among which, 5β-hydroxipalisadin B showed effective anti-inflammatory properties in various *in vitro* models (Wijesinghe et al., 2014).

4.3.3.7 Pharmacological potentials of macrolide derivatives (Compounds 13-15)

In-vitro antioxidant assays were evaluated by the radical (radicals DPPH and $ABTS^+$) quenching abilities of compounds (**13-15**) against 1, 1-diphenyl-2-picryl-hydrazil (DPPH) and 2, 2'-azino-bis-3-ethylbenzothiozoline-6-sulfonic acid ($ABTS^+$), and the antioxidant activities were compared with the standard antioxidative agent, *α*-tocopherol (Table 4.23). Among the titled compounds, **14** showed higher radical scavenging potentials (IC_{50} DPPH 1.10 mM; IC_{50} $ABTS^+$ 1.21 mM) when compared to other studied compounds (**13-15**) (IC_{50} DPPH > 1.38 mM; IC_{50} $ABTS^+$ > 1.42 mM). It is of note that the free radical scavenging potential of the compound (**13-15**) were found to be significantly greater (IC_{50} < 1.50 mM) in comparison with the standard, α-tocopherol ($IC_{50} \geq 1.5$ mM; $P < 0.05$). The greater antioxidative properties against the free radicals were reported for the 12-membered macrocyclic lactone isolated from the seaweed, *S. wightii* (Maneesh and Chakraborty, 2017), a 16-membered macrocyclic bislactone and 10/13-membered macrocyclic lactones from the mollusk, *Amphioctopus neglectus* (Chakraborty et al., 2019). These results further substantiated the antioxidative potential of the studied compounds (**13-15**).

Compound **13** was found to contain two conjugated systems, such as 14-furanyl and 22-benzyl, which could easily transfer H-atoms (by hydrogen-atom transfer) located at C-14 and C-22 positions, respectively of oxabicyclo[21.3.1]heptacosa-11,23,25,27-tetraene-7,18-dione skeleton onto DPPH free radicals to form resonance stabilised 3-acetyl-14-(furan-2(5*H*)-ylidene)-15-(isopentyloxy)-11-methyl-8-oxa-bicyclo[21.3.1]heptacosa-26,11, 22,24-tetraene-

7,18-dione. These two positions (C-14 and C-22) could be considered as primary antioxidative reaction centers. Additionally, three more reaction centers related to the ester at C-7, 3-acetyl and 18-keto in the oxabicyclo[21.3.1]heptacosa-11,23,25,27-tetraene-7,18-dione framework, were found for compound **13**. The protons at C-6 (near to ester at C-7), C-3 (acetyl linked carbon) and C-19 (adjacent to keto at C-18) could participate in keto-enol resonance with the nearest >C(=O)< (keto) groups at C-7, C-3^1, and C-18, respectively leading to the generation of -CH=C(-OH)- (enol) functionality via repositioning the protons from C-6, C-3, and C-19, respectively to the DPPH free radical to form a resonance stabilized 14-(furanyl)-3-(1-hydroxyethylidene)-11-methyl-15-(153-methylbutyloxy)-8-oxabicyclo[21.3.1]heptacosa-hexaene-7,18-diol. These five sites of antioxidative reaction centers present in compound **13** could effectively participate in the resonance stabilization, which in turn, stabilize the DPPH radicals in the biological systems. Compound **14** exhibited four primary antioxidative reaction sites, which include three keto functionalities and one conjugated olefinic system. The conjugated olefinic groups (-C12=C13-C14=C15-) adjacent to the oxygenated functionality in Compound **14** could effectively involve in the electron delocalization to form -C11=C12-C13=C14-C15-O-, which in turn, transfer protons from C-11 to radicals through the hydrogen transfer via formation of resonance stabilized 10-acetyl-9-isopentyl-2-methyl-5,16,23^1-trioxa-bicyclo[21.3.1]heptacosa-2,11,13-triene-6,19-dione . The protons at C-7 (near to ester at C-6), C-10 (acetyl linked carbon) and C-20 (adjacent to keto at C-19) could involve in the keto-enol resonance with nearby >C(=O)< groups at C-6, C-10^1 and C-19, respectively resulting in the formation of -CH=C(-OH)- by replacing the protons from C-7, C-10, and C-20, respectively to DPPH radicals through the genesis of resonance stabilised 10-(1-hydroxyethylidene)-9-isopentyl-2-methyl-5,16,23^1-trioxa-bicyclo[21.3.1]heptacosa-2,6,10,12,14, 19-hexaene-6,19-diol. These four antioxidative reaction centres might be the predominant reasons for potential radical scavenging properties of Compound **14** through the neutralisation of DPPH radical. However, Compound **15** possessed only three reaction centres, which include two carbonyls and one hydroxyl functionalities. The free electron pair of -OH of -CHOH group located at C-8 of the macrolide might not efficiently contribute in resonance stabilization due to the weak acidic property of this proton, resulting in the formation of weakly stabilized DPPH radical. The protons at C-9 (near to keto at C-10) and C-22 (adjacent to keto at C-23 in the pyrone ring) could involve in the keto-enol resonance with the nearby >C(=O)< groups at C-10 and C-23, respectively leading to the formation of -CH=C(-OH)- by replacing the protons from C-9 and C-22, respectively to the DPPH radicals. These antioxidative reaction centers resulted in the resonance stabilized form of Compound **15**, 20-isobutyl-16-methyl-7,14-dioxa-bicyclo[19.3.1]pentacosa-2,5,9,16,22-pentaene-10,23-triol to neutralize the DPPH free radical . Notably, the compound **15** did not hold any extended conjugation as in **13** and **14**, and hence, it

could not effectively transfer H-atom to DPPH, and therefore, displayed weaker antioxidant activity (IC_{50} DPPH 1.42 mM; IC_{50} $ABTS^{+}$ 1.47 mM) than those displayed by Compounds **13** and **15** (IC_{50} DPPH 1.37-1.40 mM; IC_{50} $ABTS^{+}$ 1.41-1.43 mM).

In-vitro anti-inflammatory potential of the studied compounds was assessed by their attenuation potential against pro-inflammatory enzymes 5-lipoxygenase (5-LOX) and cyclooxygenase-1 and 2 (COX-1/2). Among the titled compounds, 21-membered pyran-enclosed Compound **14** displayed greater attenuation property against COX-2 (IC_{50} 1.13 mM) than those exhibited by the 21-membered aryl Compound **13** and 19-membered macrolide **C** (IC_{50} COX-2 ~ 1.2 mM). The attenuating potential of the studied compounds against 5-LOX was significantly greater (IC_{50} < 1.5 mM) than that displayed by ibuprofen (IC_{50} 4.5 mM), whereas the selectivity indices exhibited by macrolides against COX-2 were significantly higher (1.18-1.41, $P < 0.05$) when compared to ibuprofen (SI = 0.43) attributing the greater selectivity profile of the former towards inducible pro-inflammatory mediators than that exhibited by the latter. The polyether macrocyclic lactone isolated from the marine gastropod, *Babylonia spirata* was previously reported for its potential 5-LOX attenuation property (Salas and Chakraborty, 2018).

4.3.4 Structure-activity correlation analyses of bioactives isolated from EtOAc-MeOH extract of G. salicornia

4.3.4.1 Structure-activity correlation analyses of abeo-labdane class of diterpenoid derivative (Compound 1)

The target bioactivities of the studied compound **1** were assessed by different physico-chemical parameters, and these were utilised to correlate their structural attributes (Table 4.24). The electronic parameter of compound **1** was found to be obtained as tPSA, 43.37 and Pl ~38.25 x 10^{-24} cm^3, which could substantiate the greater inhibitory activities of compound towards oxidants and pro-inflammatory enzymes. The compound **1** was registered steric parameters as MR 97.78 cm^3 mol^{-1}, MV 341.5 cm^3 mol^{-1} and Pr 813.20 cm^3 mol^{-1} might efficiently bind with the enzyme active site, resulting in its higher inhibitory activity towards 5-LOX. It was also displayed that that an intermediate hydrophobicity (logarithmic value of octanol-water coefficient) (log P_{ow} 5.21) predominantly contributed towards its greater radical quenching and pro-inflammatory enzyme inhibitory activities. The hydrophobic values ~5 might interpret its hydrophobic-hydrophilic interactions (Lipinski 2004) and bonding with catalytic site of enzymes (Huuskonen et al., 2000) leading to its higher bioactive properties.

Table 4.24: Molecular descriptors (electronic, steric and hydrophobic)† of compound **1** from *G. salicornia*

Molecular descriptors

	Compound 1
Electronic	
tPSA	43.37
Pl ($X10^{-24}$ cm^3)	38.25
Steric	
MR (cm^3 mol^{-1})	97.78
MV (cm^3)	341.5
Pr (cm^3)	813.2
Hydrophobic	
Log P_{ow}	5.21

†Steric: MV, molar volume; Pr, parachor; MR, molar refractivity; Hydrophobic: Log P_{ow}, logarithmic scale of the octanol-water partition coefficient; Electronic: Pl, polarisability; tPSA, topological polar surface area.

The structure-activity relationship analyses were carried out by using different molecular descriptors of the purified compounds as described in the text.

4.3.4.2 Structure-activity correlation analyses of oleanane class of triterpenoid derivatives (Compounds 2-3)

The target bioactivities of the studied compounds (**2-3**) were assessed by different physico-chemical parameters, and these were utilized to correlate their structural attributes. It is consequential to record that the electronic parameter of 24(4→23)-abeo-oleanene (**3**) (Pl ~70 x 10^{-24} cm^3) was greater than that recorded with 24(4→23), 27(8→26), 30(20→29)-tris-abeo-oleanene (**2**) (polarisability, Pl ~65 x 10^{-24} cm^3), which could substantiate the greater inhibitory activities of former towards oxidants and carbolytic enzymes. It was apparent that the compound **3** was bulkier than **2**, as determined by the greater steric factors of the former. Comparatively lesser bulkiness of **2** and **3** (MR 163-178 cm^3 mol^{-1}, MV 541-575 cm^3 mol^{-1} and Pr 1320-1445 cm^3 mol^{-1}) might efficiently network with the enzyme active site remnants, resulting in its higher inhibitory activity towards starch digestive enzymes (Table 4.25). It was also likely that that a greater hydrophobicity (logarithmic value of octanol-water coefficient) of abeo-oleanenes, **2-3** (log P_{ow} 9.19-10.73) predominantly contributed towards its greater radical quenching and carbolytic enzyme inhibitory activities. The higher hydrophobic values might explain its requisite hydrophobic-hydrophilic interactions (Lipinski 2004) and bonding of receptor enzymes (Huuskonen et al., 2000) leading to its higher anti-hyperglycaemic and antioxidant properties.

Table 4.25: Molecular descriptors (electronic, steric and hydrophobic)† of compounds **2-3** from *G. salicornia*

Molecular descriptors

	Compound 2	Compound 3
Electronic		
tPSA	43.37	43.37
Pl ($X10^{-24}$ cm^3)	64.99	70.61
Steric		
MR (cm^3 mol^{-1})	163.95	178.13
MV (cm^3)	541.40	575.80
Pr (cm^3)	1320.60	1445.10
Hydrophobic		
Log P_{ow}	9.19	10.73

†Steric: MV, molar volume; Pr, parachor; MR, molar refractivity; Hydrophobic: Log P_{ow}, logarithmic scale of the octanol-water partition coefficient; Electronic: Pl, polarisability; tPSA, topological polar surface area.

The structure-activity relationship analyses were carried out by using different molecular descriptors of the purified compounds as described in the text.

4.3.4.3 Structure-activity correlation analyses of drimane class of diterpenoid derivative (Compounds 4-6)

The target bioactivities of the studied metabolites were corroborated by different physico-chemical parameters describing their structural features. It is pertinent to note that the electronic parameters of the drimane derivative bearing substituted 1*H*-benzo[*a*]xanthene-4,10,12-triol moiety (**4**) was higher (polarizability, Pl ~51.65 X 10^{-24} $cm^{3,}$ tPSA, topological polar surface area, 79.15) than those recorded by the compounds **5** and **6** (Pl 51.34-43.18 X 10^{-24} cm^3, tPSA, 38.69), which could be related with the greater pro-inflammatory inhibitory activities of the former (Table 4.26). It was apparent that the compound **5** was bulkier than **4**, as determined by the lower steric factors of the latter (molar refractivity, MR ~130.30 cm^3 mol^{-1}, molar volume, MV ~394.20 cm^3 mol^{-1}, and P ~1053.00 cm^3 mol^{-1}). The increased bulkiness of **5** might restrict the metabolite to efficiently interact with the active site of enzyme residues, resulting in its lesser inhibitory activity towards pro-inflammatory enzymes in comparison with compound **4.** It was also likely that that a medium hydrophobicity (logarithmic value of octanol-water coefficient, log P_{ow} 4.99) of compound (**4**) predominantly contributed towards the comparatively higher radical quenching and pro-inflammatory enzyme inhibitory activities than those displayed by its drimane quinol analogues (**5** & **6**). The compounds **5** and **6** were found to record higher (log P_{ow} 7.13 and 5.64, respectively) than the desired lipophilicity (log P_{ow} 2-5), which might explain

their lesser electronic interactions resulting in lower antioxidant and anti-inflammatory bioactivities (Shimizu et al., 2015).

The studied drimane sesquiterpene quinols, **4**-**6** were deduced to contain hydroxyphenyl functionality linked to the drimane framework. The hydroxyphenyl part of the studied compounds might be involved in the resonance stabilization through the transfer of proton from hydroxyl to DPPH radical via hydrogen atom transfer mechanism (HAT). The three titled compounds enclosed similar type of functionalities, even though the numbers of antioxidative reaction centres were found to differ. The greater number of electron rich reaction centres (three hydroxyls, one alkene, and phenyl) in **4** over those possessed by compounds **5**-**6** (one each of hydroxyl phenyl functionalities) in combination with the optimum hydrophobicity (log P_{ow} <5) factors, might occupy prominent roles in the greater bioactive potential of the former. The anti-inflammatory potentials of the drimane sesquiterpene quinols were reported in a previous report of literature (McNamara et al., 2005). A previous study on drimane based sesquiterpene quinol, dysiquinol D proposed that the compound bearing an ether linkage between C-8 and C-17 positions exhibited greater anti-inflammatory potential than dysiquinols A-C possessing ether bridge between C-1 and C-17 (Jiao et al., 2015). Herein, the compound **4** bearing substituted 1*H*-benzo[a]xanthene-4,10,12-triol moiety was structurally comparable with dysiquinol D and enclosed ether bridge in the identical position as in dysiquinol D attributing the greater bioactive potential of **4** than those exhibited by compounds **5** (no ether linkage) and **6** (comparable to dysiquinol A-C skeleton).

Table 4.26: Molecular descriptors (electronic, steric and hydrophobic)[†] of compounds **4**-**6** from *G. salicornia*

Molecular descriptors			
	Compound 4	**Compound 5**	**Compound 6**
Electronic			
tPSA	79.15	38.69	38.69
Pl ($X10^{-24}$ cm^3)	51.65	51.34	43.18
Steric			
MR (cm^3 mol^{-1})	130.30	129.50	108.93
MV (cm^3)	394.20	423.30	339.50
Pr (cm^3)	1053.00	1060.80	873.20
Hydrophobic			
Log P_{ow}	4.99	7.13	5.64

[†]Steric: MV, molar volume; Pr, parachor; MR, molar refractivity; Hydrophobic: Log P_{ow}, logarithmic scale of the octanol-water partition coefficient; Electronic: Pl, polarisability; tPSA, topological polar surface area.

The structure-activity relationship analyses were carried out by using different molecular descriptors of the purified compounds as described in the text.

4.3.4.4 Structure-activity correlation analyses of 2H-chromenyl derivatives (Compounds 7-8)

The molecular descriptor variables of studied *2H*-chromenyl derivatives correlated the structural parameters, which appeared to play predominant roles in attributing the target bioactivities. The antioxidative and anti-inflammatory activities were found to be directly proportional towards the electronic (topological polar surface area, tPSA and polarisability, Pl) and hydrophilic-lipophilic balance (log P_{ow}, logarithm of octanol/water partition-coefficient), and not by the molecular bulk. The tPSA of **8** was found to be greater (64.99) than that of **7** (55.76) and α-tocopherol (29.46). The total numbers of electron-rich centres were greater in **8** appeared to result in its higher polarisability and antioxidant potentials (Table 4.27). Therefore, the electronic factors appeared to play significant role to govern the bioactive potentials (Wang et al. 2007). The log P_{ow} of **8** was found to be within the desirable range (~ 6.1), which might cause a suitable lipophilic-hydrophobic relation (Lipinski 2007) and receptor binding (Huuskonen et al. 2000) leading to higher target bioactivities than other studied compounds.

Table 4.27: Molecular descriptors (electronic, steric and hydrophobic)[†] of compounds **7**-**8** from *G. salicornia*

Molecular descriptors		
	Compound 7	**Compound 8**
Electronic		
tPSA	55.76	64.99
Pl ($X10^{-24}$ cm^3)	47.82	50.02
Steric		
MR (cm^3 mol^{-1})	124.62	126.19
MV (cm^3)	398.00	395.00
Pr (cm^3)	979.80	1023.80
Hydrophobic		
Log P_{ow}	6.42	6.11

[†]Steric: MV, molar volume; Pr, parachor; MR, molar refractivity; Hydrophobic: Log P_{ow}, logarithmic scale of the octanol-water partition coefficient; Electronic: Pl, polarisability; tPSA, topological polar surface area.

The structure-activity relationship analyses were carried out by using different molecular descriptors of the purified compounds as described in the text.

4.3.4.5 Structure-activity correlation analyses of spiro- derivatives (Compounds 9-10)

The molecular descriptor variables of the studied spiro-compounds appeared to play predominant roles in attributing the target bioactivities. Antioxidative and anti-inflammatory activities were found to be directly proportional towards the electronic (topological polar surface area, tPSA and polarisability, Pl) and hydrophilic-lipophilic balance (log P_{ow}, logarithm of octanol/water partition-coefficient), and not the molecular bulk. The tPSA of **10** was found to be greater (111.52) than that of **9** (72.83) and α-tocopherol (29.46). The total numbers of electron-rich centres were greater in **10** appeared to result in its higher polarisability (48.07) and antioxidant potentials (Table 4.28). Therefore, the electronic factors appeared to play significant role to govern the bioactive potentials (Wang et al. 2007). The log P_{ow} of **10** was found to be within the desirable range (~2.2), which might cause a suitable lipophilic-hydrophobic relation (Lipinski 2007) and receptor binding (Huuskonen et al. 2000) leading to higher target bioactivities than other studied compounds.

Table 4.28: Molecular descriptors (electronic, steric and hydrophobic)[†] of compounds **9-10** from *G. salicornia*

Molecular descriptors		
	Compound 9	**Compound 10**
Electronic		
tPSA	72.83	11.52
Pl ($X10^{-24}$ cm^3)	39.75	48.07
Steric		
MR (cm^3 mol^{-1})	100.28	121.93
MV (cm^3)	336.10	387.50
Pr (cm^3)	852.30	1022.10
Hydrophobic		
Log P_{ow}	2.54	2.29

[†]Steric: MV, molar volume; Pr, parachor; MR, molar refractivity; Hydrophobic: Log P_{ow}, logarithmic scale of the octanol-water partition coefficient; Electronic: Pl, polarisability; tPSA, topological polar surface area.

The structure-activity relationship analyses were carried out by using different molecular descriptors of the purified compounds as described in the text.

4.3.4.6 Structure-activity correlation of polyether derivatives (Compounds 11-12)

The bio-potencies of polyether derivatives were established with their physico-chemical attributes to describe their structural characteristics, which might impart major roles in evaluating the target bioactive properties. Greater electronic properties were recorded for the titled polyether derivative, **12** bearing furanyl-furo[3,2-b]pyran-2*H*-pyran moiety based on their polarisability (Pl 64.05 x 10^{-24} cm^3) and topological polar surface area (94.45) than those recorded by **11** (Pl 56.09 x 10^{-24} cm^3; tPSA 66.38), ibuprofen (Pl 24.09 x 10^{-24} cm^3; tPSA 37.30) and α-tocopherol (Pl 53.54 x 10^{-24} cm^3; tPSA 29.46) (Table 4.29). These could be related to greater anti-inflammatory and radical scavenging potencies of polyether derivative **12** over those displayed by compound **11** bearing pyranyl-10-methylpyrano[3,2-b]pyran-methyleneoxepane moiety as well as standard agents. Further, steric factors of the studied polyether derivatives as determined by molar refractivity (121-141 cm^3 mol^{-1}), parachor (1367-1164 cm^3) and molar volume (458-538 cm^3 mol^{-1}) were found to be lesser than those exhibited by the antioxidant agent, α-tocopherol (MR 135 cm^3 mol^{-1}; MV 462 cm^3 mol^{-1}; P 1123 cm^3). The lesser steric bulkiness of the titled compounds might also explain efficient steric interaction with the pro-inflammatory enzymes and radical agents resulting in greater bioactivities. Moreover, the hydrophobic values (logarithmic value of octanol-water coefficient, log P_{ow1} 1.84; log P_{ow2} 4.58) of the polyether analogues were deduced to be within adequate ranges (log P_{ow} < 5) that might contribute towards its significantly greater radical quenching/anti-inflammatory potencies [35]. The highly electron-rich centres {with furo[3,2-b]pyran and ester functionalities} in **12** could effectively be involved in the proton transfer to free radicals via hydrogen-atom-transfer scheme than polyether **11** bearing pyrano[3,2-b]pyran and methyleneoxepane functionalities. The greater number of electron-rich reaction sites in **12** along with optimum hydrophobicity (log P_{OW2} < 5), lesser steric factor and greater electronic descriptors over **11** might play a prominent functional role in the greater bio-potential of the polyether derivative **12** bearing furanyl-furo[3,2-b]pyran-2*H*-pyran moiety.

Table 4.29: Molecular descriptors (electronic, steric and hydrophobic)† of compounds **11-12** from *G. salicornia*

Molecular descriptors		
	Compound 11	**Compound 12**
Electronic		
tPSA	66.38	94.45
Pl ($X10^{-24}$ cm^3)	56.09	64.05
Steric		
MR (cm^3 mol^{-1})	141.50	121.93
MV (cm^3)	458.40	538.10

Pr (cm^3)	1164.30	1367.30
Hydrophobic		
Log P_{ow}	1.84	4.58

[†]Steric: MV, molar volume; Pr, parachor; MR, molar refractivity; Hydrophobic: Log P_{ow}, logarithmic scale of the octanol-water partition coefficient; Electronic: Pl, polarisability; tPSA, topological polar surface area.

The structure-activity relationship analyses were carried out by using different molecular descriptors of the purified compounds as described in the text.

4.3.4.7 Structure-activity correlation analyses of macrolide derivatives (Compounds 13-15)

The bioactive potentials of the Compound **13-15** were substantiated with their physico-chemical-parameters. It is relevant to note that the electronic-parameters of 21-membered macrolide derivative (**13**) was higher (polarizability, Pl 59.35; topological polar surface area, tPSA 78.9) than that recorded with 19-membered macrolide derivative, **15** (Pl 52; tPSA, 72.8), and that could be correlated with the greater bioactivities of the former (Table 4.30). The higher electronic values recorded for Compound **14** further supported the possibilities of greater number of electron-rich centres, which in turn, resulted in its greater bioactive properties. Electronic or polar factors were reported to play important parts to govern the target pharmacological properties (Wang et al., 2007). Notably, the steric bulkiness of the 21-membered aryl macrolide, compound **13** (molar-volume, MV 565 cm^3 mol^{-1}; parachor, P 1455 cm^3) was significantly greater than the 21-membered pyran enclosed macrolide derivative, Compound **14** (MV 543 cm^3 mol^{-1}; P 1279 cm^3) and 19-membered cyclohexanone enclosed macrolide derivative, Compound **15** (MV 465 cm^3 mol^{-1}; P 1109 cm^3). The greater steric hindrance of Compound **13** due to its bulkier side chains of benzyl/furanyl ring systems could negatively affect its bioactivities, although its electronic parameters recorded higher values (Pl 69.4; tPSA, 78.9). The optimum hydrophobicity/lipophilicity (log P_{ow}) equilibrium of Compound **14** and **15** (5.6-6) appeared to contribute towards their greater bioactivities over Compound **13** that displayed greater

lipophilicity (log P_{ow} ~ 7.7). The balanced hydrophilic-lipophilic properties as determined by log P_{ow} was found to control the inter-membrane perviousness including requisite hydrophobic/lipophilic (Lipinski, 2004) relationship and binding of receptors (Huuskonen et al., 2000). Apparently, greater electronic parameters (electron-rich centres) along with optimum steric bulkiness and permissible hydrophobicity-lipophilicity equilibrium of Compound **14** could result in its greater antioxidative properties and effective interaction with the active site of inflammatory enzymes to impart anti-inflammatory properties compared to other studied compounds (Wang et al., 2007).

Table 4.30: Molecular descriptors (electronic, steric and hydrophobic)[†] of compounds **13-15** from *G. salicornia*

Molecular descriptors			
	Compound 13	**Compound 14**	**Compound 15**
Electronic			
tPSA	78.90	78.90	75.83
Pl ($X10^{-24}$ cm^3)	69.36	59.35	52.03
Steric			
MR (cm^3 mol^{-1})	174.98	149.71	174.98
MV (cm^3)	564.90	542.60	465.30
Pr (cm^3)	1455.00	1278.50	1109.70
Hydrophobic			
Log P_{ow}	7.70	6.00	5.60

[†]Steric: MV, molar volume; Pr, parachor; MR, molar refractivity; Hydrophobic: Log P_{ow}, logarithmic scale of the octanol-water partition coefficient; Electronic: Pl, polarisability; tPSA, topological polar surface area.

The structure-activity relationship analyses were carried out by using different molecular descriptors of the purified compounds as described in the text.

4.3.5. In silico molecular docking analysis of bioactivecompounds isolated from *G. salicornia*

4.3.5.1 In silico molecular docking analysis of *abeo-labdane class of diterpenoid derivative (Compound 1)*

The studied labdane analogue was subjected to molecular docking studies against proinflammatory enzymes, 5-LOX. The results were documented by their RMSD data. The molecular docking parameters, such as binding energy, intermolecular and torsional free energy, and inhibition constants of **1** were recorded (Table 4.31). *In silico* molecular docking analysis of the labdane with 5-LOX was initiated with grid box x=36.879, y=-20.280, z=28. (Figure 4.232). Compound **1** recorded least binding energy of -7.30 kcal mol^{-1} in interactions with 5-LOX enzyme target sites. Similarly, other parameters were obtained, such as inhibition constant (Ki) 1.03 nM, intermolecular energy was -7.34 kcal mol^{-1}. The molecular docking interaction of ligand (compound **1**) and 5-LOX showed two hydrogen bonds (displayed as red and blue-coloured lines) to amino acyl residues of Ser^{528} and Ser^{523} with the bond distances of 2.060 and 2.748 Å in the active binding site.

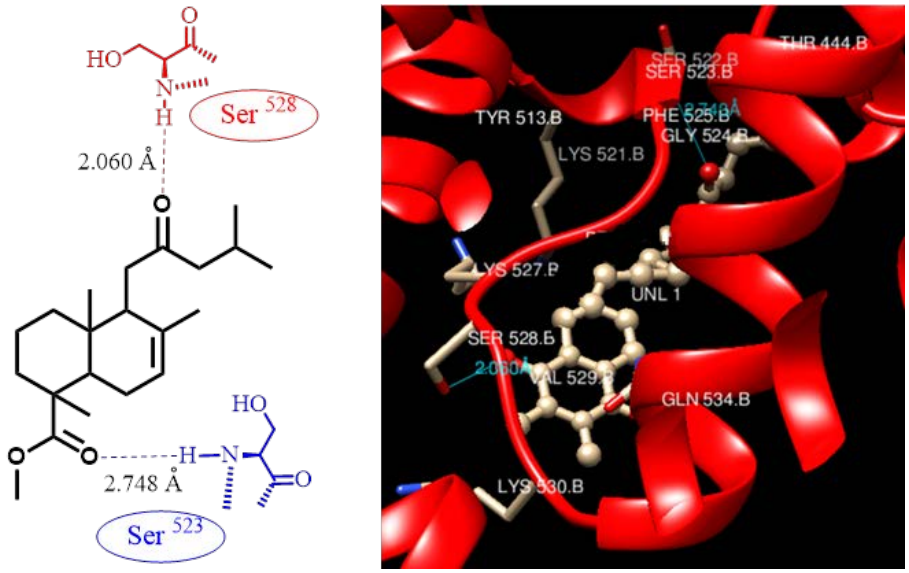

Figure 4.232.: Closer view of molecular binding interactions of compound **1** in the catalytic site of protein 5-LOX

Table 4.31: The binding energy, docking score, inhibition constant, intermolecular energy and torsional free energy between the ligands (compounds **1**) and the active sites of 5-lipoxygenase

Ligands	‡Binding energy (kcal mol^{-1})	‡Inhibition constant, Ki (nM)	‡Intermolecular energy (kcal mol^{-1})	‡ Torsional free energy (kcal mol^{-1})	Hydrogen bonded residues	Distance from hydrogen bonded residue (Å)
1	-7.30	1.03	-7.34	1.20	Ser^{528}, Ser^{523}	2.060 ,2.748

‡ Values were evaluated from the calculations based on the energy minimization.

4.3.5.2 In silico molecular docking analysis of *oleanane class of triterpenoid derivatives (Compounds 2-3)*

The inhibition of starch degrading enzymes, such as α-amylases and α-glucosidases is an effective methodology to monitoring the glucose level in blood. The commercially developed carbolytic enzyme inhibitors, such as acarbose and voglibose are widely used to control the blood glucose levels. The computation tools like structure based molecular docking simulations have been widely utilised to enrich a chemical library of active compounds with biomolecular structure and functions (Hyun et al., 2014). The studied oleanene analogues were subjected to molecular docking studies against starch digestive enzymes, α-glucosidase and α-amylase. The results were evaluated by their RMSD data. The molecular docking parameters, such as binding energy, intermolecular and torsional free energy, and inhibition constants of **2-3** were documented (Table 4.32). *In silico* molecular docking analysis of the abeo-oleanenes with α-glucosidase with grid box x=37.969, y=-19.190, z=29.008 and *α*-amylase with grid box x=-7.248 y=54.607, z=30.003 appropriately gave the impression that the ligands exhibited efficient interactions with the enzyme target sites (Figure 4.233). Among the studied compounds (**2-3**), compound **3** recorded least binding energy of -9.84 kcal mol^{-1} in interactions with α-glucosidase enzyme target sites subsequent to those exhibited by compound **2** (-9.42 kcal mol^{-1}). Likewise, the constant of enzyme inhibition (Ki) was lesser for **3** (61.61 nM) towards α-glucosidase enzyme than that exhibited by **2** (124.49 nM). Also, intermolecular energy was lesser for **3** (-11.44 kcal mol^{-1}). The molecular docking interaction of ligand (compound **3**) and α-glucosidase showed two hydrogen bonds (displayed as red-coloured lines) to amino acyl residues of THR^{83} and TRP^{36} with the bond distances of 3.148 and 3.044 Å in the active binding site, whereas **2**

showed one hydrogen-bonded interaction to amino acid residue of TRP^{36} with molecular distance of 2.766 Å.

Similarly, compound **3** exhibited least binding energy of -10.04 kcal mol^{-1} in *α*-amylase enzyme target site interactions than those exhibited by compound **2** (-5.52 kcal mol^{-1}). Additionally, two other parameters, such as intermolecular energy and inhibition constant (Ki) were also calculated. The compound **3** had lesser inhibition constant (38.15 nM) when compared to **2** (89.58 μM). Inhibition constant and binding energy were proportional to each other, and therefore, the inhibitory activity of α-amylase of **3** was substantiated by using intermolecular energy and inhibition constant. As mentioned in Table 4.32, the metabolite **3** exhibited intermolecular energy of -12.18 kcal mol^{-1}, which was lesser when compared to2 (-7.06 kcal mol^{-1}). These results further demonstrated greater α-amylase inhibition activity of oleanene **2** compared to **1**. The molecular docking analysis of oleanene **3** and α-amylase showed two hydrogen bonds with amino acyl residue of ARG^{346} with the bond distances of 2.954 and 2.878 Å in the active binding site, whereas compound **2** showed one hydrogen-bonded interaction with amino acyl residue of ASP^{381} with molecular distances of 2.467 Å. The comparison of molecular docking parameters on the basis of *in-vitro* experiment appropriately suggested that the abeo-oleanene derivative (**3**) exhibited closer molecular interactions with the starch digestive enzymes, which might explain its greater inhibitory potential against α-glucosidase and α-amylase (0.29-0.34 mM) when compared to those exhibited by **3** (0.32-0.40 mM). It was thus apparent that active inhibition of the pancreatic *α*-amylase enzyme could be an efficient approach to decrease the post-prandial hyperglycaemic levels via regulation of carbohydrate breakdown.

Table 4.32: The binding energy (B.E), inhibition constant (IC), intermolecular energy (I.E) and torsional free energy (T.E) between the ligands (compounds **2**-**3**) and the active sites of carbolytic enzymes *α*-glucosidase and *α*-amylase.

†Ligands	‡B.E	IC,	‡I.E	‡T.E	Amino acid residue	Molecular distances
	(kcal mol^{-1})	Ki (nM) (*μM)	(kcal mol^{-1})	(kcal mol^{-1})		
α-glucosidase						
2	-9.42	124.49	-11.14	1.79	Trp^{36}	2.766
3	-9.84	61.61	-11.44	2.39	Thr^{83}, Trp^{36}	3.148, 3.044
α-amylase						
2	-5.52	*89.58	-7.06	1.79	Asp^{381}	2.467
3	-10.04	38.15	-12.18	2.39	Arg^{346}	2.954, 2.878

† Molecular docking simulations were carried out using Autodock 4 software tool.

‡Values were evaluated from the calculations based on the energy minimization.

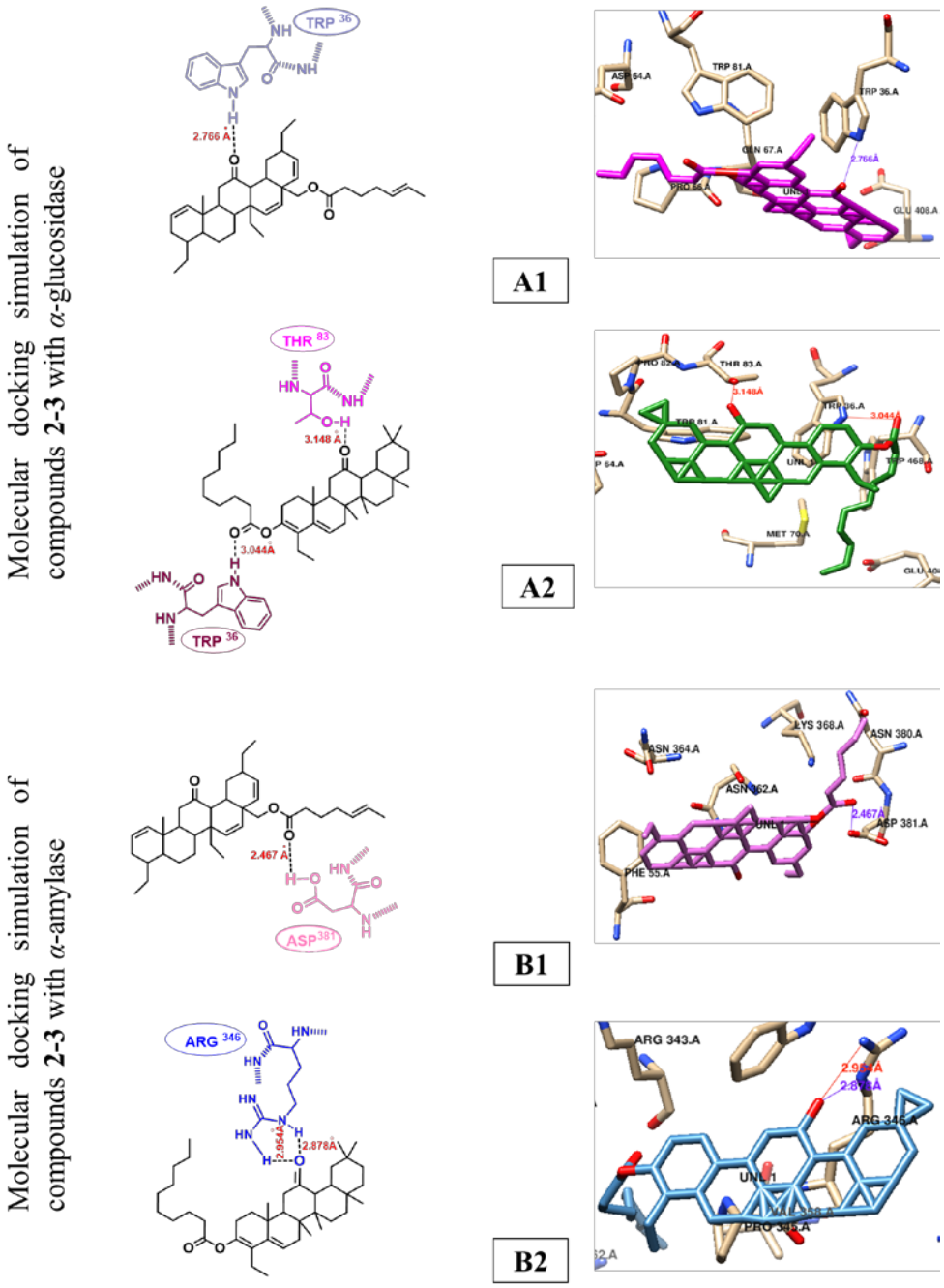

Figure 4.233.: Closer view of molecular binding interactions of (**A1**) 24(4→23), 27(8→26), 30(20→29)-tris-abeo-oleanene **2** and (**A2**) 24(4→23)-abeo-oleanene **3** derivatives in the catalytic site of protein *α*-glucosidase along with molecular binding interactions of (**B1**) 24(4→23), 27(8→26), 30(20→29)-tris-abeo-oleanene **2** and (**B2**) 24(4→23)-abeo-oleanene **3** derivatives in the catalytic site of *α*-amylase as deduced from its molecular modeling simulations.

4.3.5.2 In silico molecular docking analysis of *drimane class of diterpenoid derivative (Compounds 4-6)*

The studied compounds were subjected to *in silico* molecular docking analysis against pro-inflammatory 5-LOX and the results were evaluated by their RMSD data. The molecular docking parameters, such as binding energy, docking score, inhibition constant, hydrogen bonding interactions, torsional free energy and intermolecular energy between the active sites of 5-LOX and the ligands were documented in Table 4.33. The grid box of potential binding site was assigned as x=54.00 y=44, z=42. Among the studied compounds, substituted 1*H*-benzo[a]xanthene-4,10,12-triol (**4**), on molecular docking analysis with 5-LOX exhibited two hydrogen bond interaction with amino acyl residues Lys^{441} and Arg^{438} in the enzyme active site with molecular distances of 3.370 and 3.030 Å, respectively (Figure 4.234). Among the remaining drimane analogues, compounds **5** and **6** showed one hydrogen bonded interactions with the amino acyl residues Gly^{150} and Lys^{441} with molecular distances of 2.790 Å and 2.915 Å, respectively. The metabolite **4** exhibited greater number of hydrogen bond interactions with amino acyl residues than those recorded by compounds **5** and **6**. These results could be supported by the higher *in vitro* anti-inflammatory activity of **4** over those displayed by **5** and **6**. The comparison of molecular docking parameters appropriately suggested that compound **4** bearing substituted 1*H*-benzo[a]xanthene-4,10,12-triol moiety exhibited closer molecular interactions towards 5-LOX with least binding energy (-12.30 kcal mol^{-1}) and docking score (-12.96 kcal mol^{-1}), which were corroborated with their greater inhibition of 5-LOX than those exhibited by its drimane quinol analogues (compounds **5** and **6**).

Table 4.33: The binding energy, docking score, inhibition constant, intermolecular energy and torsional free energy between the ligands (compounds **4**-**6**) and the active sites of 5-lipoxygenase

Ligands	‡Binding energy (kcal mol^{-1})	‡Inhibition constant, Ki (nM)	‡Intermolecular energy (kcal mol^{-1})	‡ Torsional free energy (kcal mol^{-1})	Hydrogen bonded residues	Distance from hydrogen bonded residue (Å)
4	-12.30	1.23	-13.14	1.79	Lys^{441}, Arg^{438}	3.370, 3.030
5	-9.97	48.94	-11.10	1.19	Gln^{150}	2.790
6	-9.71	76.63	-10.75	1.19	Lys^{441}	2.915

‡ Values were evaluated from the calculations based on the energy minimization.

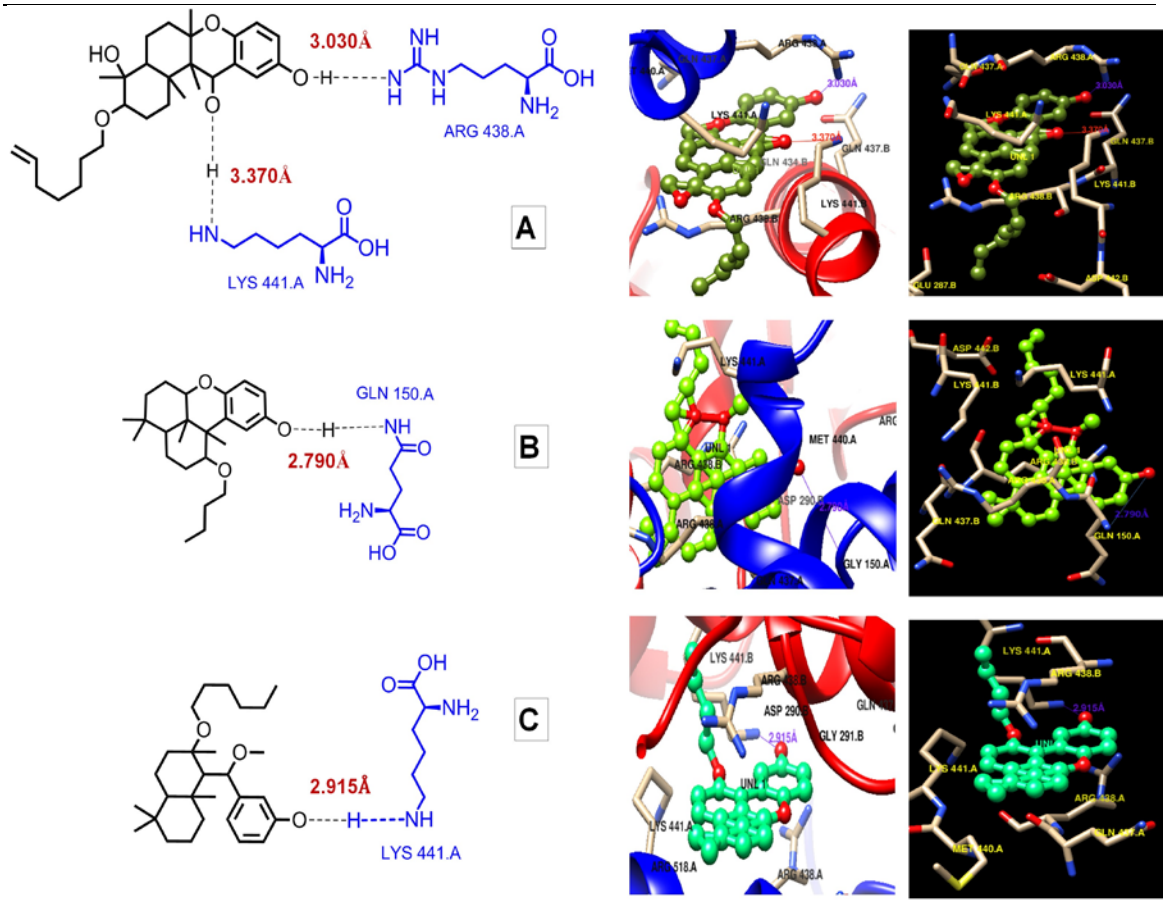

Figure 4.234.: Closer view of molecular binding interactions of the drimane sesquiterpene quinols in the catalytic site of (**A**-**C**) 5-lipoxygenase (5-LOX) as deduced from the molecular docking simulation experiment. The molecular docking analysis of ligands (studied sesquiterpene analogues **4**-**6**) and pro-inflammatory 5-LOX showed two hydrogen bonds (displayed as red and blue-coloured lines with amino acyl residues of Lys^{441} and Arg^{438} with bond distances of 3.370 and 3.030 Å, respectively) in the active binding site. The compounds **4** and **6** showed one hydrogen bonded interactions with amino acyl residues Gly^{150} and Lys^{441} with molecular distances of 2.790 Å and 2.915 Å, respectively.

4.3.5.4 In silico molecular docking analysis *of 2H-chromenyl derivatives (Compounds 7-8)*

The compounds **7-8** were subjected to *in silico* molecular docking analysis against pro-inflammatory 5-LOX and the results were evaluated by their root-mean-square deviation data. The molecular docking parameters between the active sites of 5-LOX and the ligands were documented in Table 4.34. The grid box of potential binding site was assigned as x=54.00 y=50, z=38. The molecular docking analysis of ligands (2*H*-chromenyl, **8**) and pro-inflammatory 5-LOX showed six hydrogen bonds (displayed as red and blue-coloured lines) with amino acyl residues of Ser^{522} and Ser^{628} with the bond distances of 2.743, 3.640, 3.117, 2.792, 2.668 and 3.075 Å in the active binding site, whereas compound **7** showed two hydrogen-bonded interactions with amino acid residues of Gln^{534} and Gln^{497} with molecular distances of 2.883, 3.046 Å, respectively. Therefore, the metabolite **8** exhibited greater number of hydrogen bonding interactions with amino acyl residues than those recorded by **7** (Figure 4.235). These results were supported by the higher *in vitro* anti-inflammatory activity of **2** over those displayed by **7**. The comparison of molecular docking parameters appropriately suggested that compound **8** exhibited close molecular interactions towards 5-LOX with least binding energy (-7.35 kcal mol^{-1}) which were corroborated with their greater potential of enzyme inhibition against 5-LOX (IC_{50} 2.03 mM) (Table 4.34) than those displayed by **7**.

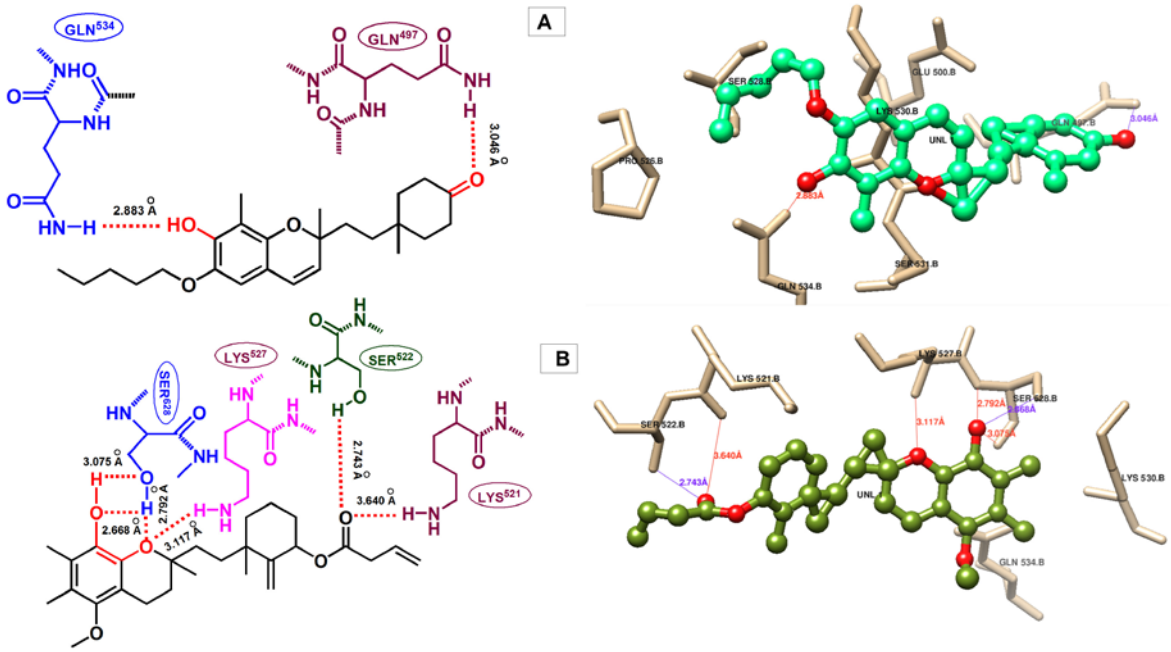

Figure 4.235.: Closer view of molecular binding interactions of the compounds **7-8** (**A** and **B**) in the catalytic site of 5-lipoxygenase (5-LOX) as deduced from the molecular docking simulation experiment. The molecular docking analysis of ligands (compound, **8**) and pro-inflammatory 5-LOX showed six hydrogen bonds (displayed as red and blue-coloured lines) with amino acyl

residues of Ser^{522}, Lys^{521}, Lys^{527} and Ser^{628} with bond distances of 2.743, 3.640, 3.117, 2.792, 2.668, and 3.075 Å in the active binding site. The compound **7** showed two hydrogen-bonded interactions with amino acid residues of Gln^{534} and Gln^{497} with molecular distances of 2.883, 3.046 Å, respectively.

Table 4.34: The binding energy, docking score, inhibition constant, intermolecular energy and torsional free energy between the ligands (compounds **7**-**8**) and the active sites of 5-lipoxygenase.

†Ligands	‡Binding energy (kcal mol^{-1})	‡Docking score (kcal mol^{-1})	‡Inhibition constant, Ki (nM)	‡Intermolecular energy (kcal mol^{-1})	‡Torsional free energy (kcal mol^{-1})	Hydrogen bonded residues	Distance from hydrogen bonded residue (Å)
7	-6.85	7.36	9.55	-7.44	1.49	Gln^{534}, Gln^{497},	2.883, 3.046
8	-7.35	8.74	4.09	-8.79	1.49	Ser^{522}, Lys^{521}, Lys^{527}, Ser^{628}	2.743, 3.640, 3.117, 2.792, 2.668, 3.075

† Molecular docking simulations were carried out using Autodock 4 software tool.

‡ Values were evaluated from the calculations based on the energy minimization.

4.3.5.5 In silico molecular docking analysis *of spiro- derivatives (Compounds 9-10)*

The attenuating potential of the studied spiro derivatives against the pro-inflammatory enzymes has been considered as one of the effective approaches to monitor the disturbances associated with inflammatory pathologies. The titled compounds were subjected to molecular docking analysis using pro-inflammatory enzyme 5-LOX (Figure 4.236), wherein the effective inhibition of compounds (**9**-**10**) was initially assessed by the RMSD reports in accordance with their decreasing order of binding energies (Table 4.35). Among the spiro-compounds, compound **2** recorded least binding energy of -10.13 kcal/mol subsequent to that exhibited by **9** (-10.00 kcal/mol). Likewise, the constant of enzyme inhibition (Ki) was lesser for **10** (37.80 nM) towards 5-LOX enzyme than that exhibited by **9** (46.89 nM). Also, intermolecular energy was lesser for **10** (-11.51 kcal/mol).

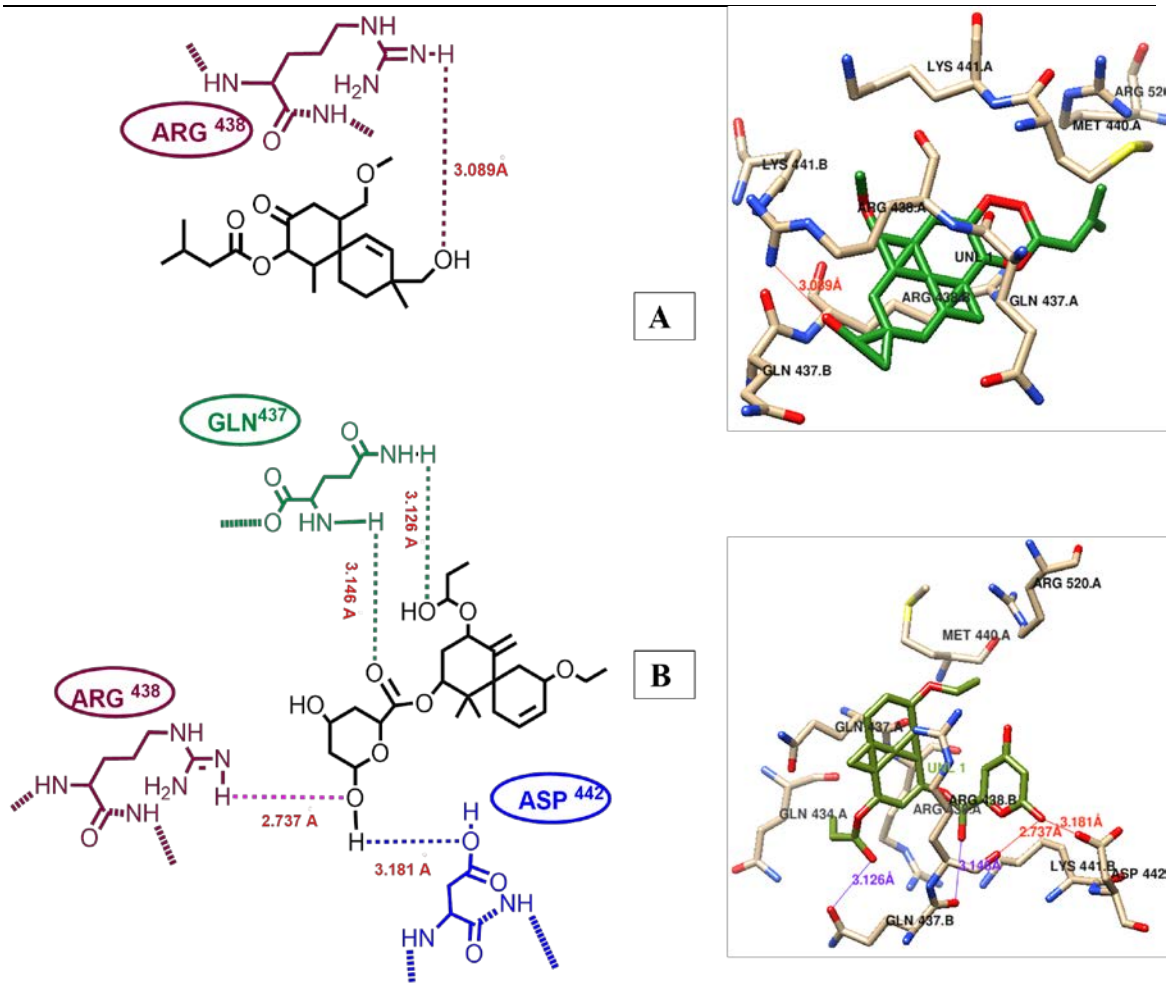

Figure 4.236.: Closer view of molecular binding interactions of the spiro[5.5]undecanes (A and B) in the catalytic site of 5-lipoxygenase (5-LOX) as deduced from the molecular docking simulation experiment. The molecular docking analysis of ligands (**10**) and pro-inflammatory 5-LOX showed four hydrogen bonds (displayed as red and blue-coloured lines) with amino acyl residues of GLN^{437} (2-hydrogen bonds), $ARG^{438}$and ASP^{442} with bond distances of 3.126, 3.146, 2.737 and 3.181 Å in the active binding site. The compound **9** showed two hydrogen-bonded interactions with amino acid residues of ARG^{438} with molecular distances of 3.089 Å.

Table 4.35: The binding energy, inhibition constant, intermolecular energy and torsional free energy between the ligands (compounds **9**-**10**) and the active sites of pro-inflammatory enzyme 5-LOX.

†Ligands	‡Binding energy (kcal mol^{-1})	‡Inhibition constant, Ki (nM)	‡Intermolecular energy (kcal mol^{-1})	‡Torsional free energy (kcal mol^{-1})	Amino acid residue	Molecular distances (Å)
9	-10.00	46.89	-10.75	0.60	ARG^{438}	3.089
10	-10.13	37.80	-11.51	2.09	GLN^{437} (2 hydrogen bonds), ARG^{438}, ASP^{442}	3.126, 3.146, 2.737, 3.181

†Molecular docking simulations were carried out using Autodock 4.0 software tool.
‡Values were evaluated from the calculations based on the energy minimization.

4.3.5.6 In silico molecular docking analysis *of polyether derivatives (Compounds 11-12)*

The titled polyether triterpenoids isolated from *G. salicornia* were taken into account for *in-silico* docking against 5-LOX, whereas the obtained results were analyzed through RMSD data. Molecular docking factors of 5-LOX active sites and ligands were represented in Table 4.34 (grid box for the potential binding site, x=28.855 y=14.080, z=65.462). Among the studied polyethers, the analogue **12** bearing furanyl-furo[3,2-b]pyran-2*H*-pyran moiety, on docking with 5-LOX displayed two hydrogen-bonding with amino-acyl parts of ARG^{246} and ASP^{442} in the active site of enzyme with molecular distances of 2.856 and 3.266 Å, respectively (Figure 4.236). Similarly, the compound **11** bearing pyrano[3,2-b]pyran and methyleneoxepane functionalities on docking with 5-LOX showed two hydrogen-bonded linkages with ARG^{246} and LYS^{441} (5.074 Å and 4.048 Å, respectively) amino acyl residues. Thus, the compound **12** revealed greater hydrogen-bond connections with the amino-acyl residues than those displayed by compound **11**, and the reports were corroborated through higher *in-vitro* anti-inflammatory potency of the former over those exhibited by the latter. The evaluation of molecular docking suitably apprehended that compound **12** bearing furanyl-furo[3,2-b]pyran-2*H*-pyran moiety exhibited closer molecular associations to 5-LOX with minimum binding energy (-10.96) and intermolecular energy (-12.23 kcal mol^{-1}), which appropriately corroborated with its greater attenuating potential against 5-LOX than those reported by polyether derivative **11** bearing pyranyl-10-methylpyrano[3,2-b]pyran-methyleneoxepane framework. These results signified the importance of compound **12** bearing furanyl-furo[3,2-b]pyran-2*H*-pyran moiety as a potential therapeutic lead against inflammation pathologies.

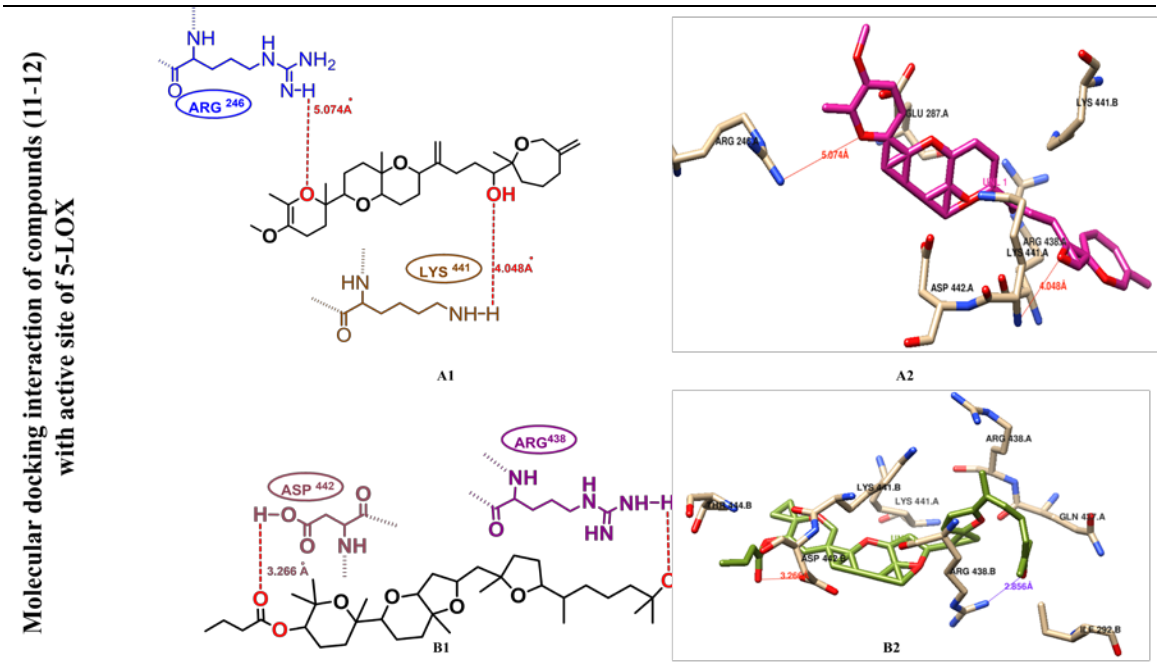

Figure 4.237.: Closer view of molecular binding interactions of compound (**11**) in the and 5-lipoxygenase (5-LOX) (**A**1-**A2**) catalytic site as obtained from molecular docking. Closer view of molecular binding interactions of the compound (**12**) in the 5-lipoxygenase (5-LOX) (**B**1-**B2**) catalytic sites as obtained from molecular docking.

Table 4.36: The binding energy, inhibition constant, intermolecular energy and torsional free energy between the ligands (compounds **11**-**12**) and the active sites of pro-inflammatory enzymes 5-LOX

†Ligands	‡Binding energy (kcal mol^{-1})	‡Inhibition constant, Ki (nM) µM*	‡Intermolecular energy (kcal mol^{-1})	‡Torsional free energy (kcal mol^{-1})	Amino acid residue	Molecular distances (Å)
1	-5.57	16.78*	-6.63	1.49	ARG^{246}, LYS^{441}	5.074, 4.048
2	-10.96	9.22	-12.23	2.68	ARG^{438}, ASP^{442}	2.856, 3.266

†Molecular docking simulations were carried out using Autodock 4.0 software tool.

‡Values were evaluated from the calculations based on the energy minimization

4.3.5.7 In silico molecular docking analysis *of macrolide derivatives (Compounds 13-15)*

The *in-silico* analyses of the titled compounds (**13-15**) attenuating pro-inflammatory enzyme 5-LOX were carried out and obtained reports were presented in Table 4.35. The docking parameters between the binding sites of 5-LOX and the ligands were recorded. The grid box was assigned as x = 4.591 y = -55.944, z = -30.599. Among the compounds, compound **14** exhibited five hydrogen-bonds with the amino-acyl residues of LYS^{254}, ASP^{290}, ARG^{438} and ARG^{520} in the 5-LOX enzyme binding site with 2.702, 2.914, 3.435, 3.049 and 2.393 Å molecular distances, respectively (Figure 4.237). Compound **13** exhibited three hydrogen-bonds with ASP^{442} and ARG^{246} with molecular distances of 4.077, 2.870 and 3.139 Å, respectively in the binding site of 5-LOX. However, compound **15** exhibited two hydrogen-bonds with ASP^{285} and LEU^{244} in the active site of 5-LOX, with molecular distances of 3.172 and 2.846 Å, respectively. Compound **14** displayed greater numbers of hydrogen-bonds with the amino acid residues than those documented by compounds **13** and **15**. The comparison of molecular docking parameters appropriately manifested that compound **14** showed minimally binding energy (-9.64 kcal mol^{-1}) and intermolecular energy (-10.51 kcal mol^{-1}), which were substantiated with their greater inhibition potentials of enzyme activity against 5-LOX than those exhibited by compounds **13** and **15** with higher binding (-9.15 and -8.74 kcal mol^{-1}, respectively) and intermolecular energies (-9.84 and -9.77 kcal mol^{-1}, respectively). The greater number of hydrogen bonding interactions and least binding/intermolecular energies of compound **14** were corroborated with its potential attenuation property against pro-inflammatory 5-LOX over those displayed by compounds **13** and **14**.

The enzyme binding affinities of compound **14** and pro-inflammatory initiator, arachidonic acid (a substrate of 5-lipoxygenase, 5-LOX) were compared through the *in-silico* molecular docking interactions (Table 4.35). The oxidative enzymes belonging to the class of lipoxygenase generates pro-inflammatory mediators, such as arachidonic acid-5-hydroperoxide (hydroperoxy eicosatetraenoic acids, HPETE) and leukotrienes from arachidonic acid through the cascade of peroxidation and epoxidation of allylic system at C5 of arachidonic acid via radical mechanism. These leukotrienes were found to be the signalling molecules responsible for different inflammation pathologies (Martel-Pelletier et al., 2013). Herein, arachidonic exhibited only two hydrogen-bonds with ARG^{438} and ARG^{520} with molecular distances of 2.785 and 2.820 Å, correspondingly in the active site of 5-LOX when compared to compound **14** with five hydrogen bonding interactions. Also, the higher binding energy (-5.80 kcal mol^{-1}) obtained for arachidonic acid in the active site of 5-LOX in comparison with compound **14** (-9.64 kcal mol^{-1}) attributed the greater 5-lipoxygenase interactions of the latter. The higher number of hydrogen bonding interactions along with least binding energy obtained from the *in-silico* studies suggested that compound **14** might effectively bind into the 5-LOX enzyme than arachidonic acid, and therefore, the latter could be protected from the peroxidation reactions catalysed by 5-

LOX. There were several conjugated olefinic positions available in arachidonic acid that could be easily epoxidised through 5-LOX (Funk, 2001), whereas compound **14** did not harbour any easily oxidisable positions. Furthermore, the electronegative functionalities, such as carbonyls and ester groups present in compound **15** were responsible for the inhibition of lipid peroxidation through the keto-enol resonance by replacing the acidic protons to the peroxide free radicals and inhibit the formation of free radicals in the biological systems. Therefore, the therapeutic anti-inflammatory potencies of macrocyclic lactones, particularly compound **14** might be due to its selective and competitive inhibition of pro-inflammatory 5-LOX enzyme at the arachidonic acid cascade and through the inhibition of lipid peroxidations of pro-inflammatory lipoxins.

Table 4.37: The binding energy, inhibition constant, intermolecular energy and torsional free energy between the ligands (compounds **13-15**) and the active sites of pro-inflammatory enzyme 5-LOX

†Ligands	‡Binding energy (kcal mol^{-1})	‡Inhibition constant, Ki (nM)	‡Intermolecular energy (kcal mol^{-1})	‡Torsional free energy (kcal mol^{-1})	Amino acid residue	Molecular distances (Å)
13	-9.15	194.90	-9.84	1.19	Asp^{442}, Arg^{438}	4.077, 2.870, 3.139
14	-9.64	85.15	-10.51	1.19	Lys^{254}, Asp^{290}, Arg^{438}, Arg^{520}	2.702, 2.914, 3.435, 3.049, 2.393
15	-8.74	391.76	-9.77	0.60	Asp^{285}, Leu^{244}	3.172, 2.846

†Molecular docking simulations were carried out using Autodock 4.0 software tool.

‡Values were evaluated from the calculations based on the energy minimization.

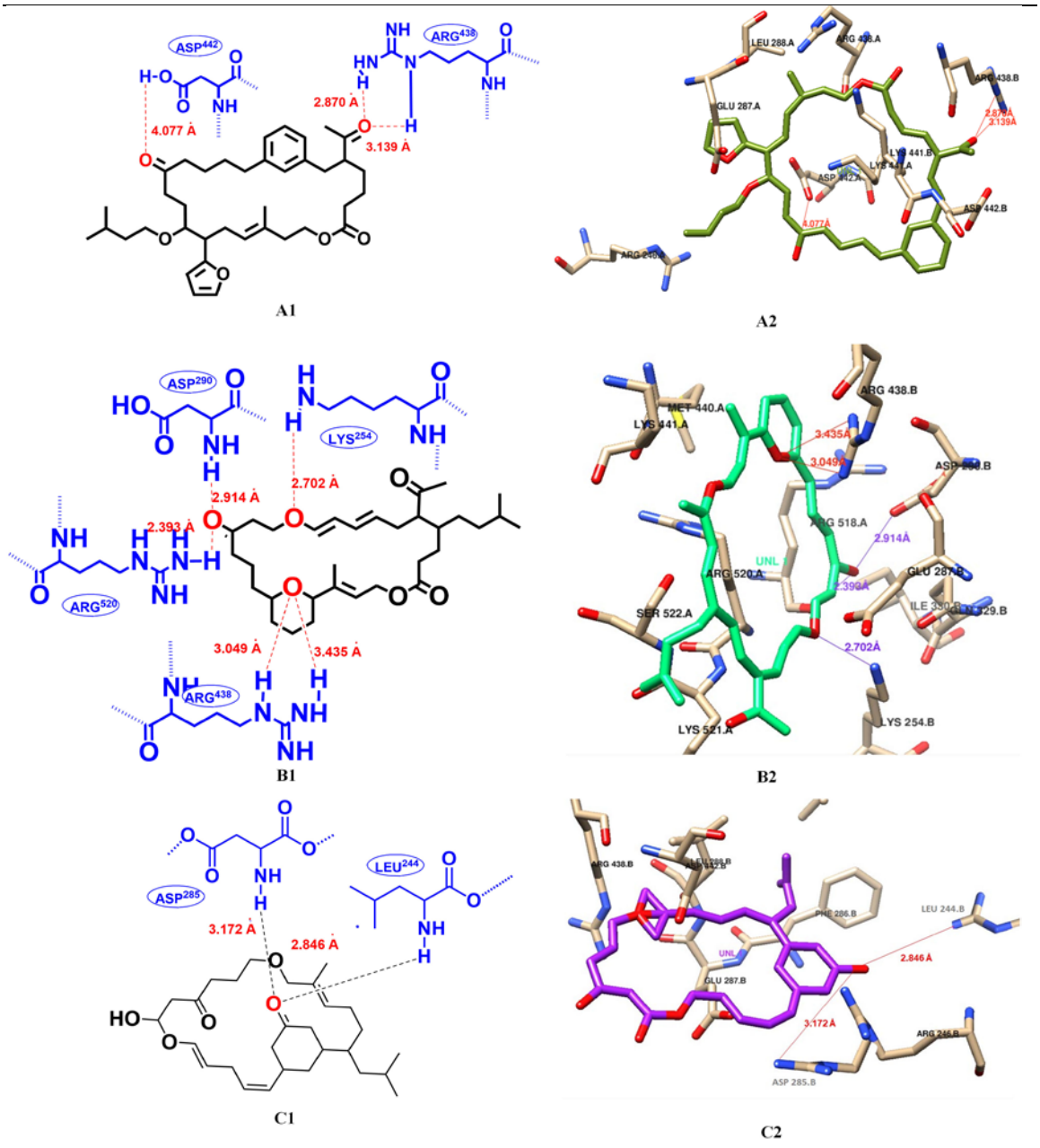

Figure 4.238.: Closer image of molecular docking interactions of compounds **13-15** (**A-C**) in the 5-LOX catalytic site as obtained by docking experiment. The docking analysis of compound **13** and pro-inflammatory 5-LOX showed three hydrogen-bonds (displayed as red and blue-coloured lines with amino-acyl residues of ASP^{442} And Arg^{438} with bond distances of 2.870, 3.139 and 4.077 Å) in binding site. Compound **14** displayed five hydrogen-bonds with amino acid residues of Lys^{254}, Asp^{290}, Arg^{438} and Arg^{520}, with molecular distances of 2.702, 2.914, 3.435, 3.049, and 2.393 Å. Compound **15** showed two hydrogen-bonds with amino acid residues of Asp^{285} and Leu^{244}, with molecular distances of 3.172 and 2.846 Å.

4.4. Conclusion

Bio-assay assisted chromatographical purification of the EtOAc-MeOH extract of *G. salicornia* yielded bioactive secondary metabolites, namely abeo-labdane class of diterpenoid (**1**), oleanene class of triterpenoids (**2-3**), drimane-associated quinols (**4-6**), 2*H*-chromenyl compounds (**7-8**), spiro-fused analogues (**9-10**), squalene polyether metabolites (**11-12**), and macrolides enclosing ether functionalities (**13-15**). The studied compounds exhibited comparable DPPH radical quenching activity as standard antioxidant agent *α*-tocopherol. The first class of compounds in this series abeo-labdene derivative registered significantly greater activities against pro-inflammatory 5-lipoxygenase than that displayed by non-steroidal anti-inflammatory drug ibuprofen. Its greater selectivity index as compared to that displayed by ibuprofen inferred the higher anti-inflammatory selectivity against pro-inflammatory cyclooxygenase-2.

In second class of metabolites among the isolated compounds, the one with 24(4→23) abeo-oleanene framework (**3**) exhibited higher carbolytic enzyme inhibitory activities (IC_{50} < 0.32 mM) over that bearing 24(4→23), 27(8→26), 30(20→29)-tris-abeo-oleanene moiety (**2**) (IC_{50} > 0.34 mM). The oleanene analogues isolated from *G. salicornia* registered greater radical scavenging potentials against $ABTS^{+}$ (IC_{50} < 1.10 mM) than that exhibited by α-tocopherol (IC_{50} > 1.69 mM). Structure-activity relationship analyses showed that higher polarisability and lesser steric bulk of abeo-oleanene (**3**) predominantly contributed towards the comparatively greater radical quenching and carbolytic enzyme inhibitory activities than those displayed by its tris-abeo-oleanene analogue (**2**). *In silico* molecular modelling studies were performed to designate the α-glucosidase and α-amylase inhibitory mechanism of the abeo-oleanene derivative (**2**) exhibiting binding energies of greater than 9.50 kcal mol^{-1}, which substantiated its potential inhibitory activity against the carbolytic enzymes responsible to cause hyperglycaemic disorders. An enzyme-assisted putative biosynthetic cascade leading to the formation of oleanene triterpenoid derivatives were proposed. In particular, the 24(4→23)-abeo-oleanene possessing (12-oxo)-3,5-diene-deconoate moiety (compound **2**) was found to be effective dual inhibitors of starch digestive enzymes along with potential antioxidative properties, and therefore, might be utilised as valuable medicinal lead against oxidant species and elevated postprandial glucose levels.

On third series of compounds, the compound (**4**) with benzo[*a*]xanthene-4,10,12-triol moiety showed greater pro-inflammatory enzyme inhibitory activities (IC_{50} 1.35-1.72 mM) over other studied drimane quinol chemotypes. Positive correlations between the antioxidant and anti-inflammatory activities were recorded, whereas the compound (**4**) displayed greater oxidant scavenging potentials (IC_{50} 1.33-1.57 mM) than that exhibited by α-tocopherol. Structure-

bioactivity correlation analysis showed that lesser hydrophobicity and steric bulk of the compound (**4**) predominantly contributed towards the comparatively greater radical quenching and pro-inflammatory enzyme inhibitory activities than those displayed by its drimane counterparts **5**-**6**. *In silico* molecular modelling studies were performed to designate the 5-lipoxygenase inhibitory mechanism of the compound (**4**) exhibiting binding energy of -12.30 kcal mol^{-1}, which substantiated its potential inhibitory activity against the inflammatory mediators. An enzyme-mediated biosynthetic cascade leading to the formation of drimane sesquiterpenoid quinol derivatives was proposed. The results illustrated the bioactive potential of the natural anti-inflammatory drimane sesquiterpenoid bearing benzo[*a*]xanthene-4,10,12-triol moiety attenuating pro-inflammatory 5-LOX from marine macroalga *G. salicornia.*

In chromenyl derivatives, which were characterised as 4'-[10'-[7-hydroxy-2,8-dimethyl-6-(pentyloxy)-2*H*-chromen-2-yl]ethyl]-3',4'-dimethyl-cyclohexanone (**7**) and 3'-[10'-(8-hydroxy-5-methoxy-2,6,7-trimethyl-2*H*-chromen-2-yl)ethyl]-3'-methyl-2'-methylene cyclohexyl butyrate (**8**) using comprehensive spectroscopic techniques. The compound **8** exhibited higher DPPH radical quenching activity than that displayed by compound **7** and standard antioxidant agent α-tocopherol. The chromenyl derivative registered significantly greater activities against pro-inflammatory 5-lipoxygenase than that displayed by non-steroidal anti-inflammatory drug ibuprofen. Its greater selectivity index as compared to that displayed by ibuprofen inferred the higher anti-inflammatory selectivity against pro-inflammatory cyclooxygenase-2. The newly described chromenyl analogue **8** characterised from the red seaweed *G. salicornia* has potential anti-inflammatory and antioxidant properties for utilisation in pharmaceutical and food formulations.

Among the isolated spiro-compounds, the one with spiro[5.5]undec-2-en framework (**10**) exhibited higher pro-inflammatory enzyme inhibitory activities (IC_{50} <1.91 mM) over that bearing oxospiro[5.5]undec-4-ene moiety (**9**) (IC_{50} > 2.78 mM). The spiro analogues isolated from *G. salicornia* registered greater radical scavenging potentials against $ABTS^{+}$ (IC_{50} < 1.75 mM) than that exhibited by α-tocopherol (IC_{50} > 1.75 mM). Structure-activity relationship analyses showed that higher polarisability, tPSA and lesser steric bulk of spiro[5.5]undec-2-en (**10**) predominantly contributed towards the comparatively radical quenching and proinflammatory enzyme inhibitory activities than those displayed by the oxospiro[5.5]undec-4-en analogue (**9**). Molecular docking analysis inferred that the spiro derivative (**2**) exhibited binding energy of -10.13 kcal/mol with efficient interactions of 5-LOX enzyme, which corroborated its greater inhibitory potential. In particular, spiro[5.5]undec-2-ene analogue was found to be an effective inhibitor of 5-LOX along with potential antioxidative properties, and therefore, might be utilised as valuable pharmacophore lead against oxidant species and inflammation pathology.

Among unreported polyether analogues, the compound **12** possessing furanyl-furo[3,2-b]pyran-2*H*-pyran skeleton displayed greater anti-inflammatory properties (IC_{50} < 2 mM) over that exhibited by **11** bearing pyranyl-10-methylpyrano[3,2-b]pyran-methyleneoxepane moiety (IC_{50} > 2.5 mM). Likewise, the potential anti-radical properties of **2** (IC_{50} 1.11-1.27 mM) in comparison with **11** (IC_{50} ~1.65 mM) and α-tocopherol (IC_{50} 1.49-1.69 mM) were reported. Structure-bioactivity-correlation studies displayed that the optimum hydrophobicity (log P_{OW2} < 5), lesser steric hindrance, which along with greater polarisability factors predominantly played significant roles in determining the greater bio-potential of polyether derivative, **12** over that of **11**. *In-silico* molecular modeling was analyzed to entitle 5-lipoxygenase inhibitory pathway of compound (2) exhibiting binding energy of -10.96 kcal mol^{-1}, that appropriately attributed its potent inhibitory properties against the inflammatory-mediators.

In the last series of compounds, the undescribed oxabicyclo[21.3.1]heptacosa-ene-diones (compounds **13**-**15**) and oxabicyclo[19.3.1]pentacosa-ene-dione (compound **15**) bearing macrocyclic lactones from the red seaweed, *G. salicornia*. The unprecedented compounds (**13**-**15**) displayed significantly higher antioxidative and pro-inflammatory 5-lipoxygense attenuating potential in comparison with the commercially existing antioxidative and anti-inflammation agents. The greater attenuation potential of the 21-membered pyran bearing compound **14** against 5-lipoxygense was correlated with its respective *in-silico* molecular docking simulations in the binding site of the pro-inflammatory enzyme through the least binding energy (-9.64 kcal mol^{-1}) and inhibitory constant (Ki 85.15 nm). The malonate-S-acyl carrier protein-mediated putative biosynthetic route appropriately corroborated the structural attributions of the studied salicornolides. In particular, the pyran enclosed macrocyclic lactone could be used as prospective natural therapeutic pharmacophore in attenuating the anti-inflammatory disorders and free radical-induced ailments.

CHAPTER 5

ISOLATION AND CHARACTERIZATION OF BIOACTIVE LEADS FROM BROWN SEAWEED (PHAEOPHYCEAE) *PADINA TETRASTROMATICA*

Contents

5.1 *Background*

5.2 *Materials and methods*

5.3 *Results and discussion*

5.4 *Conclusions*

5.1 Background

Seaweeds are prominent marine flora, which registered their existence in the marine ecology, as a promising natural resource possessing highly potent secondary metabolites. These bioactive potentials are associated with the diverse range of chemical constituents; in particular they varied from the low molecular weight bioactive-analogues to higher molecular weight phycocolloids. These might signify the utilities of seaweeds species to biosynthesize potentially useful therapeutic agents in pharmaceutical applications (Wijesinghe et al., 2011). Most of these bioactives were found to possess antioxidative activities, and thereby represent their role in the prevention of various chronic pathophysiologies related to the oxidative stress conditions (Garcia et al., 2012). Seaweeds are encompassed with enzymatic/non-enzymatic antioxidative compounds, and these could reduce or prevent the production of reactive-oxidants (RO_S). Hence, they are useful in the treatment of oxidative stress induced diseases through various cellular processess (Garcia et al., 2012). Among various seaweeds, brown seaweeds (Phaeophyta) were known to produce large number of antioxidant compounds representing the second largest position amongst marine macroalgal flora (Blunt et al. 2007). The major secondary metabolites found in the brown seaweeds belonged to the class of terpenoids and terpenoid-aromatic compounds (Blunt et al. 2007) beside polyphenols, acetogenins, phlorotannins, fucoidans, volatile compounds, fucoxanthins exhibiting prospective antioxidant, antidiabetic, antibiotic, anti-inflammatory, antifungal, antiviral, or anti-cancer activities (Folmer et al., 2010; Maneesh and Chakraborty, 2017a; Maneesh and Chakraborty, 2017b).

Previous reports of literature on brown seaweeds recorded that they were rich sources of terpenoid class of compounds (Paul et al., 2001). For example, new structures of diterpenes with acyclic skeleton have been reported from the Moroccan brown seaweed *Bifurcaria bifurcata* (Culioli et al., 2001). A novel diterpenoid of Stypolactone was reported from the *Stypopodium zonale* (Dorta et al., 2002). Dictyterpenoids A-B belonging to the class of diterpenoid with antifeedant activity has been identified from the Japanese seaweed *Dilophus okamurae* (Suzuki et al., 2002). A novel dictyotadimer A (bis-diterpene) was identified from *Dictyota Lamouroux* (Viano et al., 2011). The anti-viral diterpenes were identified from *Dictyota menstrualis* (Cavalcanti et al., 2011). From seaweed species of *Dictyota dichotoma,* a diterpene, amijiol acetate was reported (Ayyad et al., 2011). Novel diterpenes with 2,6-cyclo-xenicane entities have been documented from *Dilophus fasciola* and *Dilophus spiralis* (Ioannou et al., 2009). Furthermore, two diterpenes of dolastane skeletons with antiviral potentials have been identified from the brown seaweed *Canistrocarpus cervicornis* (Vallim et al., 2010). Sesquiterpenes with halogenation were reported from the brown seaweed species of *Padina antillarum* and *Dictyopteris divaricate* (Parameswaran et al., 1994, 1996; Ji et al., 2009). Moreover, two types of diterpenes, one with the prenylated-guaiane skeletons and the other with dolabellane and dolastane structures were reported from various brown seaweeds of the family Dictyotaceae, for instance, dichotomanes, xenianes, and xenicanes. Related compounds were reported from brown seaweed *Dictyota* spp, and xenianes were reported from *Padina* species of family Dictyotaceae (Paula et al., 2011).

Among various species of brown seaweeds, *Padina* spp belonging to family Dictyotaceae were considered as one of the predominant seaweeds with economic significance, and they were found to be rich in bioactive compounds with promising pharmaceutical potentials. Hence, they were found to be used in pharmaceutical, functional food and phycocolloid industries (De Almeida et al., 2011). The brown seaweed *Padina sp.* was found to constitute a foremost share in the family of Dictyotaceae, and about 50 taxa of this genus were reported in various parts of the globe. Among them, *Padina tetrastromatica* (Hauck) (family Dictyotaceae) has been predominant in the Indo-Pacific region (Guiry and Nic-dhonncha, 2003), and there were preliminary reports of their bioactive potentials (Chia et al., 2015; Mohsin et al., 2014). In the search for bioactive diterpenoids from this brown seaweed species, this work described the purification and characterizations of previously undescribed xenicane class of diterpenoids (**TP_1** through **TP_5**) and dolabellanes (**TP_6** through **TP_{10}**) from the ethyl acetate-methanol (EtOAc-MeOH) extract of the studied seaweed collected from the Gulf-of-Mannar of Peninsular India. The studied compounds were characterised by extensive spectroscopic experiments. The anti-inflammatory, antidiabetic and antioxidant potential of the studied compounds were analyzed by different *in vitro* assays, and various physicochemical descriptors

were utilized to substantiate the structure-activity correlations of the studied diterpenoids. *In silico* molecular modelling studies were performed to designate the 5-lipoxygenase inhibitory mechanism of the studied analogues.

5.2 Materials and methods

5.2.1 Chemicals and reagents

The chemicals and reagents utilized for the analysis were described under the section 4.2.1 of Chapter 4.

5.2.2 Chromatographic purification techniques and spectroscopic instrumentation analysis

5.2.2.1 Purification by column chromatography

The methodology for column chromatography was described under the section 4.2.2.1 of Chapter 4.

5.2.2.2 Purification by flash chromatography

The methodology of flash chromatography was described under the section 4.2.2.2 of Chapter 4.

5.2.2.3 Purification by high pressure liquid chromatography

The methodology of high pressure liquid chromatography was described under the section 4.2.2.3 of Chapter 4.

5.2.2.4 Purity assessment by thin layer chromatography and analytical HPLC

The methodology for purity assessment by thin layer chromatography and analytical HPLC was described under the section 4.2.2.4 of Chapter 4.

5.2.2.5 Spectrophotometric and spectroscopic analysis

The methodology for spectrophotometric and spectroscopic analysis was described under the section 4.2.2.4 of Chapter 4.

5.2.3 Preparation of solvent extracts from the brown seaweed P. tetrastromatica

The seaweed used in this study was *Padina tetrastromatica* (Hauck) (family Dictyotaceae). The seaweeds were freshly collected (CMFRI voucher specimen number AB.1.1.2.1) from the south east coast of India (Gulf of Mannar between 8º48′ N, 78º9′ E and 9º14′ N, 79º14′E) (Figure 5.1). The samples were identified by a marine algologist Dr. Chellaiah Periyasamy of Aquaculture Foundation of India, Madurai. Seaweeds were washed with seawater to exclude the externalities followed by washed with running tap water before being shade-dried (35±3 °C) for 72 h. Shade-dried samples were ground (1 kg dried), and were initially extracted with n-hexane {600 mL x 2, at room temperature (RT) for 24 h}, to remove pigmentous substances. The residues were extracted by reflux with solvents ethyl acetate/methanol (EtOAc-MeOH 1:1 v/v, 500 mL x 3, 60-70 ºC). The crude solvent extract collected after filtration (using Whatman No.1 filter paper) before being evaporated (50 °C) by a rotary vacuum evaporator to one-third of the initial volume, under reduced pressure, to yield a viscous mass of crude EtOAc-MeOH extract (38 g). The extract was utilized for various chromatographic fractionations to yield the bioactive metabolites.

Figure 5.1.: The brown seaweed *P. tetrastromatica* collected from the southeast coastline of the Indian sub-continent Gulf of Mannar region; between 8º48’ N, 78°9’ E and 9°14’ N, 79°14’ E)

5.2.4 Chromatographic fractionation of pure compounds and bioactive potentials of sub-column fractions from P. tetrastromatica

The EtOAc-MeOH extract (38 g) of *P. tetrastromatica* was made into slurry with silica gel (60-120 mesh, 5 g), and filled into a glass column (60 cm x 4 cm) loaded with adsorbent silica gel (60-120 mesh, 50 g) before being subjected to vacuum liquid chromatography. Initially the waxy material was removed by elution with *n*-hexane. The polarity of eluent was increased gradually by the addition of ethyl acetate (*n*-hexane:ethyl acetate 95:5 to 3:9, v/v) to obtain 20 column fractions (12 mL each), which were further pooled to 6 fractions (TP_1-TP_6) after TLC analysis (*n*-hexane/EtOAc, 9:1, v/v) after TLC (*n*-hexane:EtOAc, 9:1 v/v) along with RP-C_{18} HPLC (MeOH/MeCN, 2:1 v/v, isocratic). The pooled homogeneous fractions were assessed for their bioactive potential, and the fractions with greater bioactivities were subjected to further downstream purification.

The column fraction TP_2 was further fractionated by flash chromatography on a silica gel column (230-400 mesh, 12 g), and elution was carried out with EtOAc/*n*-hexane (0-100 %, by a step gradient mode) to yield a total of 30 column subfractions (15 mL each), which were combined to 8 column sub-fractions {$TP_{2(1-8)}$} after RP-C_8 HPLC {acetonitrile (MeCN)/H_2O, 85:15 v/v} and TLC (ethyl acetate/*n*-hexane, 3:1 v/v). Based on analytical TLC and HPLC, the homogeneous fractions were pooled, and were purified by using preparative RP-C_{18} HPLC with acetonitrile and methanol as mobile phase (MeOH/MeCN, 4:1 v/v). The fraction $TP_{2\text{-}4}$ was further purified by preparative HPLC with acetonitrile and methanol (MeOH/MeCN, 2:3 v/v) to to yield the pure compounds **TP_1** and **TP_2** (105 and 99 mg, respectively). Concentration of solvents followed by TLC (particle size 15 mm) using 30 % EtOAc/*n*-hexane supported the purity. The fractions $TP_{2\text{-}5}$ was further purified by preparative HPLC with acetonitrile and methanol (MeOH/ MeCN, 2:3 v/v) to afford the pure compounds **TP_3**, **TP_4** and **TP_5** (112, 122 and 103 mg, respectively).

the fractions, TP_3 and TP_4 were further fractionated over a glass column (45 cm x 3 cm) packed with fine silica (230-400 mesh) by using gradient elution with *n*-hexane/EtOAc (99:1 to 3:2, v/v) to yield 5 sub-fractions (32 mL each). The latter were pooled to 6 fractions on the basis of TLC (*n*-hexane: EtOAc, 9:1 v/v) and RP-C_{18} HPLC (3:2 MeOH/MeCN v/v, isocratic). The sub-fraction, $TP_{3\text{-}1\text{-}1}$ was subjected to preparatory HPLC purification (MeOH/MeCN, 2:1 v/v, isocratic) to yield the compounds **TP_6**, **TP_7** and **TP_8** (96, 98, and 102 mg, respectively). The bioactive sub-fraction, $TP_{4\text{-}2\text{-}2}$ was found to be a mixture, and consequently purified by HPLC using MeOH/MeCN (3:2 v/v, isocratic) to obtain **TP_9** and **TP_{10}** (65 and 80 mg, respectively). The purity of the compounds was monitored with TLC using EtOAc/*n*-hexane (3:17 v/v) and RP-C_{18} HPLC (MeOH: MeCN, 3:2 v/v, isocratic).

The repetitive bioassay-guided fractionation of EtOAc-MeOH extract of *P. tetrastromatica* along with yield and bioactive potentials of intermediate fractions were represented in Tables 5.1-5.3 in detail.

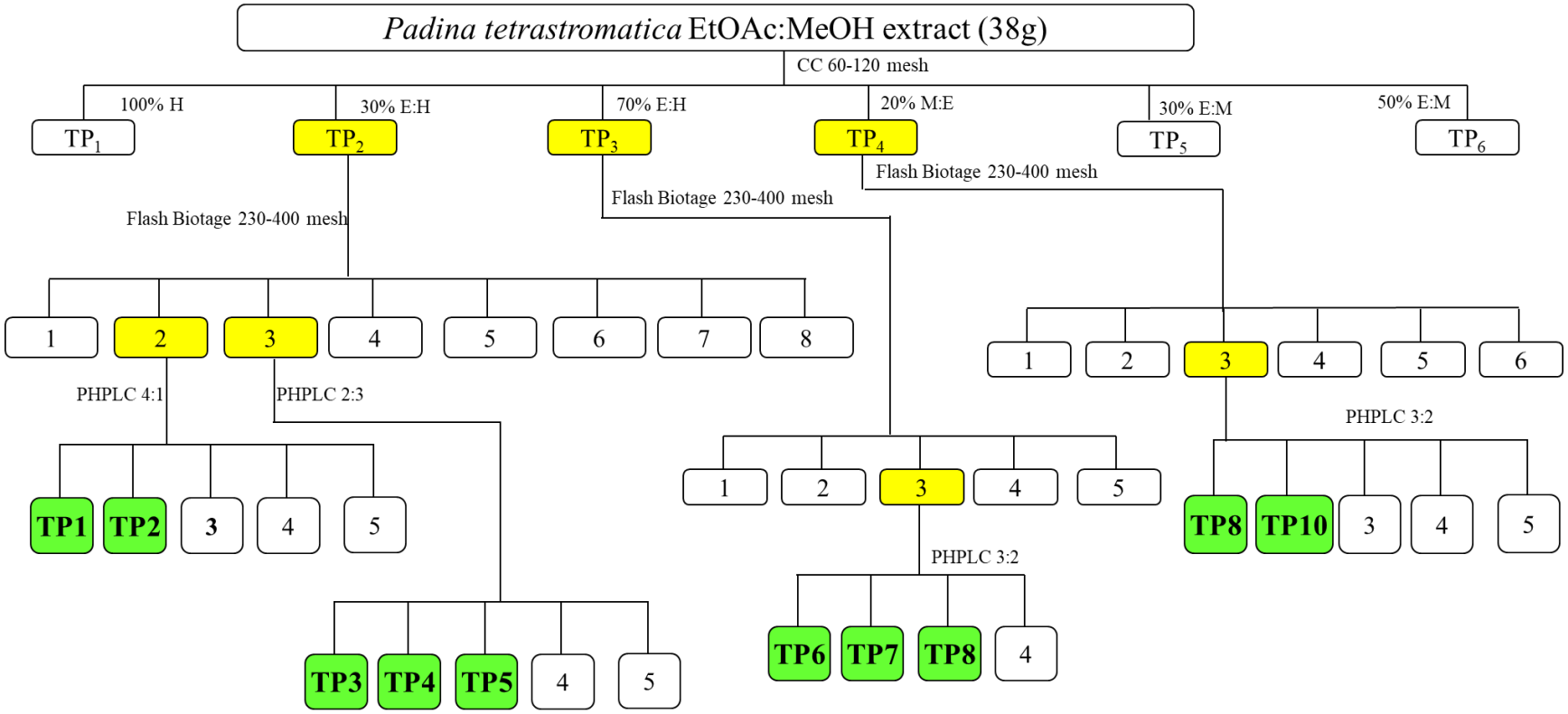

Figure 5.2.: Schematic representation of purification of fractions and compounds from the EtOAc-MeOH extract of *G. salicornia*.CC-column chromatography

5.2.5 Physicochemical description of the bioactive compounds isolated from the EtOAc-MeOH extract of P. tetrastromatica

5.2.5.1 Physicochemical description of compound-1 (TP_1)

12-Ethenyl-3a,6,9,10,11,12,12a,12b-octahydro-1-(1^2-hydroxy-1^2-methyl-propyl)-cyclonona[*d*]furo[2,3-*b*]pyran-6,10-diol; Colorless oil; [α]D^{22}–34 (c 0.96, $CHCl_3$); UV (MeOH) λ_{max} (log ε):249 (2.61) nm; TLC (Si gel GF_{254} 15 mm; 30 % EtOAc/*n*-hexane, v/v) R_f: 0.55; R_t (RP-C_8 HPLC, MeOH:MeCN, 4:1 v/v): 3.20 min; FTIR (ν_{max} cm^{-1}; bending δ, stretching ν, rocking ρ): 3472 (O-H_ν, br), 1112, 1076 (C-O_ν), 2923 (C-H_ν), 1621 (C=C_ν), 1510 (C=C_ν), 1459 (C-H_δ), 1182 (C-C_ν), 987 (=C-H_δ); ^{1}H NMR (500 MHz; $CDCl_3$; δ in ppm); 2.16 (1H, d, J=9.09 Hz), 1.91 (1H, d, J=8.47 Hz), 1.29 (3H, s), 1.29 (3H, s), 6.37 (1H, s), 6.06 (1H, d, J=10.74 Hz), 6.41 (1H, s), 3.69 (1H, d, J=14.70 Hz), 5.69 (1H, m), 5.51 (1H, m), 2.22 (1H, m), 1.97 (1H, m), 3.67 (1H, m), 1.33 (1H, m), 1.53 (1H, m), 2.03 (1H, dd, J= 12.35, 5.92), 5.72 (1H, m), 5.00 (1H, d, J=13.79 Hz), 4.99 (1H, d, J=12.91 Hz), 1.87 (1H, d, J=12.62), 2.17 (1H, dd, J=10.99, 8.86 Hz); ^{13}C-NMR (125 MHz; $CDCl_3$; δ in ppm); 115.2 (C), 39.9 (CH_2), 73.3 (C), 29.5(3) (CH_3), 29.5(4) (CH_3), 141.9 (CH), 104.2 (CH), 144.1 (CH), 115.3 (C), 70.2 (CH), 133.2 (CH), 125.4 (CH_3), 41.42 (CH), 70.2 (CH_3), 38.6 (CH_2), 48.9 (CH), 141.08 (CH), 116.4 (CH_2), 39.9 (CH), 49.8 (CH), DEPT, COSY, HSQC, and HMBC data were presented in Table 5.4. EI-MS *m/z*: calcd. for $C_{20}H_{28}O_5$ 348.2 $[M]^+$. HRESIMS (positive mode) *m/z*: found 349.2018 $[M+H]^+$, calcd. for $C_{20}H_{29}O_5$ 349.2014 $[M+H]^+$ (Δ 1.15 ppm).

5.2.5.2 Physicochemical description of compound-2 (TP_2)

1,2,5,5a,6,9,10,11,12,12a-Decahydro-11(11^2-hydroxypropyl)-2-[(*E*)-2^1-propenyl] cyclonona[*d*]-furo[2,3-*b*]pyran-9,12-diol; Yellow oil; [α]D^{22} –37 (c 1.80, $CHCl_3$) UV (MeOH) λ_{max} (log ε): 235 (3.1), 254 (3.7) nm; TLC (Si gel GF_{254} 15 mm; 30 % EtOAc/*n*-hexane) R_f: 0.54; R_t (RP-C_8 HPLC, MeOH: MeCN, 4:1 v/v): 3.24 min; FTIR (ν_{max} cm^{-1}): 3452 (O-H_ν, br), 1220 (C-O_ν), 2931 (C-H_ν), 1644 (C=C_ν), 1510 (C=C_ν), 1470 (C-H_δ), 1380 (C-H_ρ), 1169 (C-C_ν), 970 (=C-H_δ), 885, 746 (C-H_δ);^{1}H NMR (500 MHz; $CDCl_3$; δ in ppm); 2.68 (1H, dd, J=8.8, 7.69 Hz), 2.30 (1H, dd, J=13.01, 8.20 Hz), 4.88 (1H, dd, J=16.99, 8.06 Hz), 5.69 (1H, dd, J=14.47, 6.95 Hz), 5.87 (1H, m), 1.82 (3H, d, J= 6.75 Hz), 3.67 (1H, dd, J=12.77, 7.67 Hz), 3.70 (1H, dd, J=12.25, 7.66 Hz), 1.85 (1H, m), 2.01 (1H, m), 1.75 (H_β , m), 5.62 (1H, m), 5.67 (1H, dd, J=14.47, 6.95 Hz), 4.20 (1H, dd, J=15.60, 7.35 Hz), 1.29 (1H, m), 1.52 (H_β , m), 1.22 (1H, m), 1.35 (1H, t, J=5.70, 3.47 Hz), 4.07 (1H, m), 1.25 (3H, d, J=5.52 Hz), 3.33 (1H, dd, J=8.76, 1.86 Hz), 1.72 (1H, dd, J=11.46, 4.88 Hz), ^{13}C-NMR (125 MHz; $CDCl_3$; δ in ppm); 37.7 (CH_2), 83.1 (CH), 129.1(CH), 130.7 (CH), 17.6 (CH_3), 163.1 (C), 68.3 (CH_2), 36.1 (CH), 33.7 (CH), 132.0 (CH), 132.6 (CH), 72.1 (CH), 39.54(CH), 38.6 (CH), 43.9 (CH), 67.7 (CH), 23.9 (CH_3), 71.8 (CH), 41.3 (CH), 94.3 (C); DEPT, COSY, HSQC, and HMBC data were presented in Table 5.5. EI-MS *m/z*: calcd. for $C_{20}H_{30}O_5$

350.2098 $[M]^+$. HRESIMS (positive mode) *m/z*: found 351.2175 $[M+H]^+$, calcd. for $C_{20}H_{31}O_5$ 351.2171 $[M+H]^+$ (Δ 1.14 ppm).

5.2.5.3 Physicochemical description of compound-3 (TP_3)

4-(4^1,4^2-Dihydroxypropyl)-4,4a,5,6,7,8,11,11a-octahydro-8,11-dihydroxy-7-methyl-6-(6^1-methyl-6^2-propenyl)-cyclonona[*c*]pyran-3-(1*H*)-one; Pale yellow oil; $[\alpha]D^{22}$ +40 (c 0.16, $CHCl_3$); UV (MeOH) λ_{max} (log ε): 246.0 (2.90) nm; TLC (Si gel GF_{254} 15 mm; 30 % EtOAc/*n*-hexane) R_f: 0.40; R_t (RP-C_8 HPLC, MeOH:MeCN, 4:1 v/v): 4.20 min; FTIR (ν_{max} cm^{-1}): 3473 (O-H_ν, br), 3020 (C-H_ν), 1715 (C=O_ν), 1625 (C=C_ν), 1470 (C=C_ν), 1450 (C-H_δ), 1380 (C-H_ρ), 1283 (C=O_ν), 1166 (C-C_ν), 910 (=C-H_δ), 885 (C-H_δ); ^{1}H-NMR (500 MHz; $CDCl_3$; δ in ppm); 3.95 (1H, dd, J=10.1, 8.0 Hz), 4.22 (1H, dd, J=9.1, 7.86 Hz), 2.21 (1H, dd, J=9.8, 5.1 Hz), 1.62 (1H, m), 4.03 (1H, t, J=9.0 Hz), 3.42 (1H, m), 1.21 (3H, m), 1.26 (1H, m), 1.01 (1H, m), 1.15 (1H, m), 2.09 (1H, m), 1.22 (3H, m, 5.72 (1H, m), 5.01 (1H, dd, J=19.7, 17.1Hz), 4.99 (1H, dd, J=19.7, 9.7 Hz), 1.45 (1H, m), 0.90 (3H, d, J=3.2 Hz), 4.11 (1H, t, J=9.6 Hz), 5.91 (1H, d, J=11.7 Hz), 5.92 (1H, d, J=12.7 Hz), 4.10 (1H, t, J=9.5 Hz), 1.82 (1H, m); ^{13}C-NMR (125 MHz; $CDCl_3$; δ in ppm); 65.7 (CH_2), 172.35 (C), 48.8 (CH), 37.5 (CH), 73.4 (CH), 69.3 (CH), 19.3 (CH_3), 31.4 (CH_2), 43.9 (CH), 39.5 (CH), 18.3 (CH_3), 145.39 (CH), 114.8 (CH_2), 41.8 (CH), 13.3 (CH_3), 75.1 (CH), 137.4 (CH), 137.3 (CH), 73.4 (CH), 42.9 (CH);DEPT, COSY, HSQC, and HMBC data were presented in Table 5.6. EI-MS *m/z*: calcd. for $C_{20}H_{32}O_6$ 368.2199 $[M]^+$. HRESIMS (positive mode) *m/z*: found 369.2280 $[M+H]^+$, calcd. for $C_{20}H_{33}O_6$ 369.2277 $[M+H]^+$ (Δ 0.08 ppm)

5.2.5.4 Physicochemical description of compound-4 (TP_4)

4,4a,5,6,7,8,11,11a-Octahydro-7-hydroxy-6-(6^2-hydroxy-6^3-butenyl)-4-(4^1-hydroxypropyl)-11-methoxy-8-methyl-cyclonona[*c*]pyran-3-(1*H*)-one; Pale yellow oil; $[\alpha]D^{22}$ +43 (c 0.17, $CHCl_3$); UV (MeOH) λ_{max} (log ε): 209 (3.6), 249 (3.3) nm; TLC (Si gel GF_{254} 15 mm; 20 % EtOAc/*n*-hexane) R_f: 0.48; R_t (RP-C_8 HPLC, MeOH:CH_3CN, 2:3 v/v): 4.05 min; FTIR (ν_{max} cm^{-1}): 3451 (O-H_ν, br), 2963 (C-H_ν), 1737 (C=O_ν), 1702 (C=C_ν), 1511 (C=C_ν), 1447 (C-H_δ), 1370 (C-H_ρ), 1280 (C=O_ν), 1180 (C-C_ν), 966 (=C-H_δ), 906 (C-H_δ); ^{1}H-NMR (500 MHz; $CDCl_3$; δ in ppm); 3.96 (1H, dd, J=9.7, 9.2 Hz), 4.22 (1H, dd, J=8.20, 9.15 Hz), 2.21 (1H, m), 1.62 (1H, m), 4.05 (1H, m), 1.47 (1H, m), 1.49 (1H, m), 0.99 (3H, t, J=6.4 Hz), 1.02 (1H, m), 1.02 (1H, m), 1.26 (1H, m), 1.21 (1H, m), 1.42 (2H,dd, J=6.3, 4.0 Hz), 4.20 (1H, m), 5.92 (1H, m), 5.17 (1H, m), 5.20 (1H, m), 3.35 (1H, t, J=9.4 Hz), 2.20 (1H, m), 1.35 (3H, d, J=6.31 Hz), 5.70 (1H, m), 5.69 (1H, m), 3.80 (1H, dd, J=9.1, 4.6 Hz), 2.04 (1H, m), 3.30 (3H, s); ^{13}C-NMR (125 MHz; $CDCl_3$; δ in ppm); 65.0 (CH_2), 172.6 (C), 50.2 (CH), 36.1 (CH), 69.9 (CH), 27.2 (CH_2), 9.10 (CH_3), 31.3 (CH_2), 40.1 (CH), 38.6 (CH_2), 70.7 (CH), 142.3 (CH), 116.4 (CH_2), 77.02 (CH), 43.4 (CH), 16.1 (CH_3), 136.2

(CH), 134.6 (CH), 82.0 (CH), 40.4 (CH), 57.17 (CH_3); DEPT, COSY, HSQC, and HMBC data were presented in Table 5.7. EI-MS *m/z*: calcd. for $C_{21}H_{34}O_6$ 382.2355 $[M]^+$. HRESIMS (positive mode) *m/z*: found 383.2438 $[M+H]^+$, calcd. for $C_{21}H_{35}O_6$ 383.2434 $[M+H]^+$ (Δ 1.04 ppm).

5.2.5.5 Physicochemical description of compound-5 (TP_5)

4,4a,5,6,7,8,11,11a-Octahydro-1,7-dihydroxy-4-(4^1-hydroxy-4^2-methylpropyl)-6-(6^1-hydroxy-6^2-propenyl)-10-methyl-cyclonona[*c*]pyran-3(1*H*)-one; Yellow oil; $[\alpha]D^{22}$ +39 (c 0.13, $CHCl_3$); UV (MeOH) λ_{max} (log ε): 246.0 (2.90) nm; TLC (Si gel GF_{254} 15 mm; 30 % EtOAc/*n*-hexane) R_f: 0.40; R_t (RP-C_8 HPLC, MeOH:CH_3CN, 2:3 v/v): 3.23 min; FTIR (ν_{max} cm^{-1}): 3450 (O-H_v, br), 3020 (C-H_v), 1715 (C=O_v), 1614 (C=C_v), 1625 (C=C_v), 1470 (C-H_δ), 1380 (C-H_ρ), 1220 (C=O_v), 1140 (C-C_v), 955 (=C-H_δ), 885 (C-H_δ); ^{1}H-NMR (500 MHz; $CDCl_3$; δ in ppm); 6.26 (1H, d, J=9.6 Hz), 2.22 (1H, dd, J=9.6, 3..91 Hz), 1.62 (1H, m), 3.95 (1H, d, J=10.5 Hz), 2.07 (1H, m), 1.05 (3H, m), 1.05 (3H, d, J=6.52 Hz), 1.27 (1H, m), 1.01 (1H, m), 1.35 (1H, m), 4.10 (1H, dd, J=10.5, 6.5 Hz), 5.63 (1H, m), 5.11(1H,m),, 5.13 (1H, m), 1.53 (1H, m), 1.25 (1H, m), 4.20 (1H, dd, J=9.1, 7.6 Hz), 5.40 (1H, dd, J=15.68 Hz), 1.73 (3H, s), 2.02 (1H, dd, J=11.6, 8.5 Hz), 1.76 (1H, dd, J=12.2, 6.3 Hz), 1.84 (1H, m); ^{13}C-NMR (125 MHz; $CDCl_3$; δ in ppm); 96.1 (CH), 171.6 (C), 52.5 (CH), 40.2 (CH), 71.0 (CH), 31.5 (CH), 18.6(0) (CH_3), 18.6(1) (CH_3), 30.9 (CH_2), 40.7 (CH), 73.6 (CH), 140.9 (CH), 115.0(CH_2), 39.10 (CH_2), 66.8 (CH), 130.6 (CH), 132.3 (C), 17.7 (CH_3), 36.7 (CH_2), 41.57 (CH); DEPT, COSY, HSQC, and HMBC data were presented in Table 5.8. EI-MS *m/z*: calcd. for $C_{20}H_{32}O_6$ 368.2199. HRESIMS (positive mode) *m/z*: found 369.2280 $[M+H]^+$, calcd. for $C_{20}H_{33}O_6$ 369.2277 $[M+H]^+$ (Δ 0.08 ppm).

5.2.5.6 Physicochemical description of compound-6 (TP_6)

6-Methoxy-dolabella-8(17),12-diene-10β ,18-diol; Pale yellow oil; $[\alpha]^{22}{}_D$ -119.3° (*c* 0.22, $CHCl_3$) (polarimeter AP-300, ATAGO, Japan); UV (MeOH) λ_{max} (log ε) (Varian Cary 50, Palo Alto, CA): 242.6 (2.89) nm; TLC (Si-GF^{254} 15 mm; 30 % EtOAc:*n*-hexane, v/v) R_f: 0.38; R_t (HPLC RP-C_{18}, MeOH:MeCN 3:2, v/v, isocratic) (Luna, 250 x 4.6 mm, 5 µm, Phenomenex, Torrance, CA): 3.21 min; Infrared (cm^{-1}) (ν_{max}) (Perkin-Elmer Series 2000, Waltham, MA) 3434, 2978, 2927, 2871, 1639, 1629, 1457, 1404, 1364, 1272, 1112, 1076; ^{1}H-NMR (500 MHz; $CDCl_3$; δ in ppm); 1.25(1H,dd,11.1, 7.2Hz), 1.03(1H,dd,10.6, 5.7Hz), 1.26(1H,m),, 1.45(1H,m), 1.40(1H,m), 1.51(1H,t,10.6 Hz),, 1.27(1H,t, 9.9Hz), 3.23(1H,m), 3.35(1H,s), 2.20(1H,d,10.2 Hz), 1.95(1H,d, 9.8Hz), 2.22(1H,d,11.1 Hz), , 1.96(1H,d,9.6 Hz), 3.56(1H,m), 1.98(1H,d,10.2 Hz), 5.60(1H,t,9.8 Hz), 2.05(1H,d,9.3 Hz), 2.30(1H,d,9.7 Hz), 1.04(3H,s), 1.09(3H,d,6.4 Hz), 4.88(1H,s),, 4.65(1H,s), 1.41(3H,s), 1.42(1H, s); ^{13}C-NMR (125 MHz; $CDCl_3$; δ in ppm); 47.0 (C), 38.0 (CH_2), 37.3 (CH_2), 34.3 (CH), 47.3 (CH_2), 75.9 (CH), 56.5 (CH), 44.1 (CH_2), 137.3(C), 46.7 (CH_2), 65.62 (CH), 59.0 (CH), 153.4 (C), 121.5(CH), 47.3(CH_2), 23.3 (CH_3), 28.5 (CH_3), 118.7 (CH_2), 76.3 (C), 30.6 (CH_3),

30.6 (CH); DEPT, COSY, HSQC, and HMBC data were presented in Table 5.9; EI-MS *m/z*: calcd. for $C_{21}H_{36}O_3$ 336.27. HRESIMS (positive mode) *m/z*: found 337.2745 $[M+H]^+$, calcd. for $C_{21}H_{37}O_3$ 337.2742 $[M+H]^+$ (Δ 0.08 ppm).

5.2.5.6 Physicochemical description of compound-7 (TP_7)

3-Methoxy-dolabella-12(18)-ene-4β -ol; Yellow oil; $[\alpha]^{22}{}_D$ -116.9° (*c* 0.21, $CHCl_3$); UV (MeOH) λ_{max} (log ε): 246.0 (2.90) nm; TLC (Si-GF^{254} 15 mm; 30 % EtOAc:*n*-hexane, v/v) R_f: 0.40; R_t (HPLC RP-C_{18}, MeOH:MeCN 3:2, v/v, isocratic): 4.23 min; Infrared (cm^{-1}) 3520, 3020, 2923, 2855, 1625, 1470, 1450, 1380, 1220, 1140, 1065, 940, 885; ^{1}H-NMR (500 MHz; $CDCl_3$; δ in ppm); 1.15(1H,d,9.3Hz), 1.40(1H,d,10.2 Hz), 3.02(1H,t,10.6 Hz), 3.36(3H,s), 1.23(1H,dd,11.6, 6.9 Hz), 1.48(1H,dd,11.3, 6.6 Hz), 1.43(2H,m), 1.52(1H,m), 1.27(1H,m), 1.40(1H,m), 1.51(1H,m), 1.28(1H,m), 1.40(1H, m), 1.13(1H, m), 1.78(1H,t,5.7 Hz), 2.30(1H,m), 2.39(1Hα,m), 1.34(1H,dd, 10.9, 6.3 Hz), 1.08(1H,dd,10.7, 6.8 Hz),1.05(3H,s), 1.31(3H,s), 1.15(3H,s), 1.82(3H,s), 1.81(3H,s); ^{13}C-NMR (125 MHz; $CDCl_3$; δ in ppm); 45.5 (C), 39.2 (CH_2), 87.0 (CH), 57.7 (CH_3), 76.7 (C), 39.3 (CH_2), 19.8 (CH_2), 42.6 (CH_2), 35.0 (CH), 41.3 (CH_2), 24.8 (CH_2), 53.4 (CH), 132.3 (C), 31.1 (CH_2), 39.6 (CH_2), 23.5 (CH_3), 24.8 (CH_3), 27.6 (CH_3), 124.0(C), 20.4 (CH_3), 20.4 (CH_3); DEPT, COSY, HSQC, and HMBC data were presented in Table 5.10; EI-MS *m/z*: calcd. for $C_{21}H_{38}O_2$ 322.29 $[M^+]$. HRESIMS (positive mode) *m/z*: found 323.2953 $[M+H]^+$, calcd. for $C_{21}H_{39}O_2$ 323.2950 $[M^+]$ $[M+H]^+$ (Δ 0.09 ppm).

5.2.5.7 Physicochemical description of compound-8 (TP_8)

3-Methoxy-dolabella-10,18(19)-diene-5α,8β -diol ; Yellow oil; $[\alpha]^{22}{}_D$ -115.7° (c 0.22, $CHCl_3$); UV (MeOH) λ_{max} (log ε): 248 (3.1) nm; TLC (Si-GF^{254} 15 mm; 30 % EtOAc:*n*-hexane, v/v) R_f: 0.45; R_t (HPLC RP-C_{18}, MeOH:MeCN 3:2, v/v, isocratic): 4.02 min; Infrared (cm^{-1}) 3077, 2963, 2865, 1624, 1447, 1370, 1280, 1243, 1180, 966, 906; ^{1}H-NMR (500 MHz; $CDCl_3$; δ in ppm); 1.20 (1H,d,10.2 Hz), 1.46 (1H,d,9.8 Hz), 3.00(1H,m), 3.37(3H,s), 1.60(1H,m), 3.20(1H,m), 1.72(1H,m), 1.47(1H,m), 1.22(1H,t,2.5 Hz), 1.48(1H,t,2.7 Hz), 1.92(1H,d,12.6 Hz), 2.15(1H,d,12.4 Hz), 5.14(1H,t,11.3 Hz), 2.77(1H,t,9.6 Hz), 1.44(1H,m), 1.19(1H,m), 1.33(1H,dd,12.7 Hz), 1.08(1H,dd,6.8 Hz), 1.13(3H,s), 1.15(3H,d,6.8 Hz), 1.32(3H,s), 4.61(1H,m), 4.58(1H,m), 1.82(3H,s); ^{13}C-NMR (125 MHz; $CDCl_3$; δ in ppm); 45.3 (CH), 40.2 (CH_2), 83.9 (CH), 57.7 (CH_3), 41.0 (CH), 76.7 (CH), 27.3 (CH_2), 40.0 (CH_2), 74.3 (C), 46.8 (CH), 115.1 (CH_2), 154.8 (C), 48.9 (CH), 28.5 (CH_2), 39.1 (CH_2), 23.3 (CH_3), 17.9 (CH_3), 27.6 (CH_3), 146.8, (C) 113.0 (CH_2), 21.3 (CH_3); DEPT, COSY, HSQC, and HMBC data were presented in Table 5.11; EI-MS *m/z*: calcd. for $C_{21}H_{36}O_3$ 336.27 $[M^+]$. HRESIMS (positive mode) *m/z*: found 337.2745 $[M+H]^+$, calcd. for $C_{21}H_{37}O_3$ 337.2742 $[M+H]^+$ (Δ 0.08 ppm).

5.2.5.8 Physicochemical description of compound-9(TP_9)

2,7-Dimethoxy-14α-hydroxy-dolasta-1(15),9-diene; Colourless oil; $[\alpha]^{22}_D$ -89.1° (*c* 0.21, $CHCl_3$); UV (MeOH) λ_{max} (log ε): 246.0 (2.90) nm; TLC (Si-GF^{254} 15 mm; 30 % EtOAc:*n*-hexane, v/v) R_f: 0.40; R_t (HPLC RP-C_{18}, MeOH:MeCN 3:2, v/v, isocratic): 3.23 min; Infrared (cm^{-1}) 3520, 2923, 2855, 1625, 1470, 1410, 1380, 1220, 1140, 1090, 970, 910, 885; ^{1}H-NMR (500 MHz; $CDCl_3$; δ in ppm); 3.89 (1H,t,9.5 Hz), 3.33(3H,s), 1.74(1H,m), 2.06(1H,m), 1.02(1H,dd,11.7 Hz), 1.25(1H,dd,6.7 Hz), 1.40(1H,d, 12.5Hz), 1.14(1H,d, 12.6Hz), 1.14(1H,d, 12.6Hz), 4.30(1H,m), 3.35 (3H,s), 2.19(1H,d,10.9 Hz), 5.40(1H,t,11.3 Hz), 2.04(1H,d,12.2 Hz), 2.29 (1H,d,12.3 Hz), 1.34(1H,s), 1.24(1H,s), 5.09(1H,s), 4.84(1H,s), 1.13(3H,s), 3.40(1H,m), 1.16(3H,d,6.3 Hz), 1.15(3H,d,6.4 Hz), 1.08(3H,s); ^{13}C-NMR (125 MHz; $CDCl_3$; δ in ppm); 151.5 (C), 81.9 (CH), 56.9 (CH_3), 28.5 (CH_2), 31.7 (CH_2), 43.3 (C), 42.3 (CH_2), 77.4 (CH), 57.1 (CH_3), 53.3 (CH), 146.2 (C), 121.8 (CH), 49.4 (CH_2), 46.5 (C), 41.3 (CH_2), 83.6 (C), 111.5 (CH_2), 21.1(CH_3), 31.4 (CH), 22.3 (CH_3), 22.3 (CH_3), 25.5 (CH_3); DEPT, COSY, HSQC, and HMBC data were presented in Table 5.12; EI-MS *m/z*: calcd. for $C_{22}H_{36}O_3$ 348.27 [M^+]. HRESIMS (positive mode) *m/z*: found 349.2745 $[M+H]^+$, calcd. for $C_{22}H_{37}O_3$ 349.2742 $[M+H]^+$ (Δ 0.08 ppm).

5.2.5.9 Physicochemical description of compound-10 (TP_{10})

4,7-Dimethoxy-9β ,14α-dihydroxy-dolasta-1-ene; Colourless oil; $[\alpha]^{22}_D$ -92.3° (*c* 0.21, $CHCl_3$); UV (MeOH) λ_{max} (log ε): 245.0 (2.62) nm; TLC (Si-GF^{254} 15 mm; 30 % EtOAc:*n*-hexane, v/v) R_f: 0.42, R_t (HPLC RP-C_{18}, MeOH:MeCN, 3:2v/v, isocratic) 3.01 min; Infrared (cm^{-1}) 3570, 2922, 2845, 1640, 1455, 1250, 1175, 1115, 1085, 990, 910; ^{1}H-NMR (500 MHz; $CDCl_3$; δ in ppm); 5.49(1H,t,10.7 Hz), 2.21(1H,m), 1.96(1H,m), 3.26(1H,t,8.8 Hz), 3.39(3H,s), 1.40(1H,d,11.6 Hz), 1.16(1H,d,11.8Hz), 4.64(1H,m), 3.36(3H,s), 1.33(1H,d,9.1 Hz), 1.50(1H,m), 1.76(1H,m), 1.53(1H,t,6.6 Hz), 1.27(1H,t,6.7 Hz), 1.24(1H,s), 1.34(1H,s), 1.95(3H,s), 1.14(3H,s), 1.62(1H,m), 1.02(3H,d,7.6 Hz), 1.01(3H,d,7.7 Hz), 1.03(3H,s); ^{13}C-NMR (125 MHz; $CDCl_3$; δ in ppm); 142.9 (C), 124.3 (CH), 30.0 (CH_2), 83.3 (CH), 57.0 (CH_3), 42.1(C), 42.9(CH_2), 76.5 (CH), 57.8 (CH_3), 68.6 (CH), 87.3 (C), 34.5 (CH_2), 38.4 (CH_2), 42.3 (C), 44.2 (CH), 83.0 (C), 19.0 (CH_3), 18.3 (CH_3), 36.2 (CH), 17.8 (CH_3), 17.8 (CH_3), 25.6 (CH_3); DEPT, COSY, HSQC, and HMBC data were presented in Table 5.13; EI-MS *m/z*: calcd. for $C_{22}H_{38}O_4$ 366.28 [M^+]. HRESIMS (positive mode) *m/z*: found 367.2851$[M+H]^+$, calcd. for $C_{22}H_{39}O_4$ 367.2848 $[M+H]^+$ (Δ 0.08 ppm).

5.2.6 Evaluation of bioactive potencies

5.2.6.1 *In-vitro* antioxidative activities

5.2.6.1a 1, 1-Diphenyl-2-picryl-hydrazil radical/ DPPH$^{\bullet}$ scavenging activity

The estimation of antioxidant potencies of various fractions and pure compounds derived from the EtOAc-MeOH extracts of *G. salicornia* was carried out by *in vitro* DPPH$^{\bullet}$ scavenging assay. The details were described under the section 3.2.5.2a of Chapter 3.

5.2.6.1b 2,2′-Azino-bis-3-ethylbenzothiozoline-6-sulfonic acid diammonium salt/ ABTS$^{+\bullet}$ radical scavenging assay

The determination of antioxidant potencies of various fractions and pure compounds derived from the EtOAc-MeOH extracts of *G. salicornia* was carried out by *in vitro* ABTS$^{+\bullet}$ scavenging assay. The details were described under the section 3.2.5.2b of Chapter 3.

5.2.6.2 *In-vitro* anti-inflammation assays

452.6.2a Cyclooxygenases- (COX1/2) inhibition assay

The anti-inflammation bioactive potential of various fractions and pure compounds identified from the EtOAc-MeOH extracts of *G. salicornia* were evaluated by using the pro-inflammatory enzyme, cyclooxygenases (COX-1/2) inhibition assay. The methodology was detailed under the section 3.2.5.3a of Chapter 3.

5.2.6.2b 5-Lipoxygenase/5-LOX inhibition assay

The anti-inflammation bioactive potential of various fractions and pure compounds identified from the EtOAc-MeOH extracts of *G. salicornia* were evaluated by using the pro-inflammatory enzyme 5-lipoxygenase (5-LOX) inhibition assay. This was described under the section 3.2.5.3b of Chapter 3.

5.2.7 Structure-activity correlations of bioactive leads isolated from EtOAc-MeOH extract of P. tetrastromatica

The structure-bioactivity-correlation investigations were carried out by utilising different molecular factors, such as octanol-water partition-coefficient (log P_{ow}-hydrophobicity); electronic (Pl-polarisability; topological polar surface area-tPSA) and steric (MV-molar volume; P-parachor; MR-molar refractivity) (Lipinski 2000) through ACD-ChemSketch (Advanced Chemistry Development, Inc., Toronto, Canada; ver. 12.0) and ChemDraw-Ultra (Cambridge Soft Corporation, USA; ver. 12.0) softwares.

5.2.8 *Molecular modelling experiments*

In-silico molecular modeling analysis of the bioactive compounds derived from the seaweed *G. salicornia* was conducted by the software Auto-Dock-4 (ver. 1.5.6). The fractionated compounds were drawn using ACD/Chem-sketch, and were made into Molfiles before being converted to the PDB format (Open Babel, GUI 2.4.1). The X-ray crystal structures of 5-LOX (PDB 3V99, resolution 2.25 Å), α-glucosidase (PDB 3A4A, resolution 1.6 Å) and *α*-amylase (PDB 1HNY, resolution 1.8 Å) were acquired from the Protein Data Bank (www.pdb.org) and conformationally oriented (Swiss-Pdb Viewer, ver. 4.1.0) (Gilbert et al., 2012; Brayer et al., 1995; Yamamoto et al., 2010). The docking analyses were conducted by the molecular algorithm, which was run by Cygwin I-II. After auto docking, the RMSD data (root mean square deviation) was documented, and the conformations were oriented with the aid of docking parameters. Finally, molecular docking analyses were visualized using the Chimera software developed by University of California, San Francisco (USCF Chimera, ver. 1.11.2).

5.2.9 Statistical analysis

The entire sets of data were presented in triplicates along with their mean ± standard deviation. One-way analysis of variance (ANOVA; Statistical Program for Social Sciences, USA, ver. 13.0) was used to analyze the significant differences ($P \leq 0.05$) among the means of the results.

5.3 Results and discussion

5.3.1 Chromatographic fractionation of the pure compounds and bioactive potentials of the sub-column fractions from the organic extract of P. tetrastromatica

Chromatographic fractionation of the organic EtOAc-MeOH extract of seaweed, *P. tetrastromatica* on silica gel initially resulted in a total of 20 fractions, which upon pooling resulted in six major column-fractions (TP_1-TP_6), whereas percentage recovery of the sub-fractions, TP_2 (23 %) through TP_4 (28 %) were greater as compared to those displayed by TP_1 and TP_{5-6} (< 15 %, $P <$ 0.05). The fraction TP_2 on further purification by flash chromatography on a silica gel column (230-400 mesh, 12 g), with the solvent system of EtOAc/*n*-hexane (0-100 %, by a step gradient mode) yielded a total of 30 column subfractions (15 mL each), which were combined to 8 column sub-fractions. These fractions exhibited greater radical scavenging activities against DPPH (IC_{50} < 1 mg mL^{-1}) and $ABTS^{+}$ (IC_{50} 0.60-1.25 mg mL^{-1}) than other fractions (IC_{50} > 1.30 mg mL^{-1}). Potential anti-inflammatory bioactivities towards COX-2 and 5-LOX displayed the significance of the column sub-fractions, TP_{2-4} and TP_{2-5} (IC_{50} < 0.70 mg mL^{-1}) for further chromatographic sub-fractionation, whereas the inhibiting activities of the column fractions $TP_{2-(2-3)}$ and TP_{2-6}-TP_{2-8} towards COX-2 and

5-LOX were significantly lesser (IC_{50} > 1.5 mg mL^{-1}, P < 0.05). Consequently, repetitive chromatographic fractionation of TP_{2-4} and TP_{2-5} yielded two previously unreported xenicin class of diterpenoids with 2-oxabicyclo[7.4.0]tridecane ring system (**1-2**) along with three xeniolide-type diterpenoids (**3-5**) with unprecedented δ-lactone cyclononane skeleton bearing an oxabicyclo[7.4.0]tridecane framework. The structural characterizations of the studied compounds were carried out by extensive spectroscopic experiments.

The sub-fractions, TP_3 and TP_4 demonstrated greater antioxidative activities against 2,2'-azino-bis-3-ethylbenzothiozoline-6-sulfonic acid diammonium salt (IC_{50} 0.6-1.0 mg/mL) and 1,1-diphenyl-2-picrylhydrazyl (IC_{50} 0.60-0.80 mg/mL) than those displayed by other fractions (IC_{50} >1.20 mg/mL). Potential α-glucosidase and α-amylase attenuation activities were reported for the sub-fractions TP_3 and TP_4 (IC_{50} <0.25 mg/mL) compared to TP_1 and TP_{5-6} (IC_{50} >0.50 mg/mL). Therefore, the sub-fractions TP_3 and TP_4 were shortlisted for further repetitive fractionation by preparative HPLC yielding the diterpenoids of dolabellane (compounds **6-8**) and dolastane (compounds **9-10**) class of chemistries. The structures and relative stereochemistries of the titled compounds were interpreted by extensive spectroscopic experiments.

Table 5.1.: Yield and bioactivities (antioxidant, anti-inflammatory and antidiabetic) of the sub-fractions isolated from the EtOAc-MeOH extract of *P. tetrastromatica*

Fractions	***Yield (in %)**	**Bioactivity (IC_{50} in mg mL^{-1})**					
		Antioxidant		**Anti-inflammatory**		**Antidiabetic**	
		#DPPH	**#ABTS**	**#COX-2**	**#5-LOX**	**#α-amylase**	**#α-glucosidase**
TP_1	11.05	2.01^{a}±0.02	2.01^{a}±0.03	2.83^{a}±0.02	2.42^{a}±0.02	2.36^{a}±0.02	2.15^{a}±0.03
TP_2	**23.03**	**1.01^{b} ±0.02**	**1.05^{b}±0.04**	**1.02^{b}±0.02**	**0.99^{b}±0.03**	2.25^{b}±0.03	2.13^{a}±0.03
TP_3	**25.01**	1.03^{b}±0.03	1.06^{b}±0.05	2.13^{c}±0.03	2.36^{c}±0.04	**0.96^{c}±0.06**	**0.98^{b}±0.03**
TP_4	**28.00**	**1.02^{b}±0.03**	**1.03^{b}±0.07**	2.09^{c}±0.05	2.21^{d}±0.03	**1.01^{c}±0.03**	**0.97^{b}±0.06**
TP_5	5.34	2.31^{c}±0.06	2.69^{c}±0.03	2.53^{d}±0.03	2.32^{e}±0.05	2.26^{d}±0.06	2.39^{c}±0.01
TP_6	6.21	2.78^{d}±0.05	2.98^{d}±0.06	2.26^{e}±0.06	2.16^{f}±0.02	2.19^{e}±0.03	2.20^{d}±0.03

*The yield of major sub-column fractions calculated based on the crude EtOAc-MeOH extract (38.0 g of dry weight). The values were tabulated in triplicate (n=3) and indicated as mean±standard deviation. Significant differences were expressed as superscripts (a-f) within column (p < 0.05).

#The IC_{50} values were calculated in mg mL^{-1}

Table 5.2.: Yield and bioactivities (antioxidant, anti-inflammatory and antidiabetic) of sub-fractions from EtOAc-MeOH extract of *P. tetrastromatica*

Fractions	***Yield (in %)**	**Bioactivity (IC_{50} in mg mL^{-1})**					
		Antioxidant		**Anti-inflammatory**		**Antidiabetic**	
		#DPPH	**#ABTS**	**#COX-2**	**#5-LOX**	**#α-amylase**	**#α-glucosidase**
TP_{2-1}	2.15	1.18^{a}±0.02	1.20^{a}±0.03	1.72^{a}±0.02	1.61^{a}±0.02	2.71^{a}±0.02	2.34^{a}±0.03
TP_{2-2}	**13.18**	**0.98^{b} ±0.02**	**0.99^{b}±0.04**	**0.89^{b}±0.02**	**0.87^{b}±0.03**	**2.68^{a}±0.03**	**2.52^{b}±0.03**
TP_{2-3}	**11.26**	**0.96^{b}±0.03**	**0.98^{b}±0.05**	**0.91^{b}±0.03**	**0.90^{c}±0.04**	**2.56^{b}±0.06**	**2.42^{c}±0.03**
TP_{2-4}	0.82	1.12^{c}±0.03	1.11^{b}±0.07	1.83^{c}±0.05	1.75^{d}±0.03	2.02^{c}±0.03	2.09^{d}±0.06
TP_{2-5}	0.28	1.21^{a}±0.06	1.23^{c}±0.03	1.52^{d}±0.03	1.49^{e}±0.05	2.18^{d}±0.06	2.07^{d}±0.01
TP_{2-6}	0.74	1.29^{d}±0.05	1.31^{d}±0.06	1.27^{e}±0.06	1.23^{f}±0.02	2.37^{e}±0.03	2.18^{e}±0.03
TP_{2-7}	0.58	1.11^{c}±0.06	1.14^{b}±0.03	1.32^{f}±0.03	1.43^{e}±0.05	2.48^{f}±0.06	2.37^{a}±0.01
TP_{2-8}	0.82	1.17^{a}±0.05	1.19^{d}±0.06	1.28^{e}±0.06	1.21^{f}±0.02	2.47^{f}±0.03	2.31^{a}±0.03
TP_{2-2-1}	**0.28**	**0.79^{e}±0.02**	**0.81^{e}±0.03**	**0.71^{g}±0.02**	**0.73^{g}±0.02**	**2.82^{g}±0.02**	**2.32^{a}±0.03**
TP_{2-2-2}	**0.27**	**0.78^{e} ±0.02**	**0.80^{e}±0.04**	**0.70^{g}±0.02**	**0.71^{g}±0.03**	**2.87^{g}±0.03**	**2.33^{a}±0.03**
TP_{2-2-3}	25	1.13^{c}±0.03	1.14^{b}±0.05	1.11^{h}±0.03	1.10^{h}±0.04	2.66^{h}±0.06	2.29^{a}±0.03
TP_{2-2-4}	0.065	1.11^{c}±0.03	1.18^{d}±0.07	1.14^{h}±0.05	1.12^{i}±0.03	2.68^{h}±0.03	2.71^{f}±0.06
TP_{2-2-5}	0.052	1.09^{c}±0.06	1.17^{d}±0.03	1.13^{h}±0.03	1.11^{j}±0.05	2.67^{i}±0.06	2.73^{f}±0.01
TP_{3-2-1}	**0.31**	**0.71^{f}±0.02**	**0.75^{f}±0.03**	**0.69^{i}±0.02**	**0.68^{k}±0.02**	**2.31^{e}±0.02**	**2.35^{a}±0.03**
TP_{3-2-2}	**0.32**	**0.72^{f} ±0.02**	**0.73^{f}±0.04**	**0.73^{j}±0.02**	**0.74^{l}±0.03**	**2.38^{e}±0.03**	**2.39^{a}±0.03**
TP_{3-2-3}	**0.27**	**0.77^{e}±0.03**	**0.76^{f}±0.05**	**0.68^{i}±0.03**	**0.66^{k}±0.04**	**2.36^{e}±0.06**	**2.41^{c}±0.03**
TP_{3-2-4}	0.061	1.06^{c}±0.03	1.08^{b}±0.07	2.24^{k}±0.05	2.05^{m}±0.03	2.29^{f}±0.03	2.32^{a}±0.06
TP_{3-2-5}	0.063	1.02^{c}±0.06	1.07^{b}±0.03	2.41^{l}±0.03	2.59^{n}±0.05	2.28^{f}±0.06	2.34^{a}±0.01

*The yield of major sub-column fractions calculated based on the crude EtOAc-MeOH extract (38.0 g of dry weight). The values were tabulated in triplicate (n=3) and indicated as mean±standard deviation. Significant differences were expressed as superscripts (a-m) within column ($p < 0.05$).

#The IC_{50} values were calculated in mg mL^{-1}

Table 5.3.: Yield and bioactivities (antioxidant, anti-inflammatory and antidiabetic) of sub-fractions from EtOAc-MeOH extract of *P. tetrastromatica*

Fractions	***Yield (in %)**	**Bioactivity (IC_{50} in mg mL^{-1})**					
		Antioxidant		**Anti-inflammatory**		**Antidiabetic**	
		#DPPH	**#ABTS**	**#COX-2**	**#5-LOX**	**#α-amylase**	**#α-glucosidase**
TP_{3-1}	2.68	1.19^{a}±0.02	1.20^{a}±0.03	2.76^{a}±0.02	2.73^{a}±0.02	1.01^{a}±0.02	1.02^{a}±0.03
TP_{3-2}	2.71	1.17^{ac} ±0.02	1.19^{a}±0.04	2.73^{a}±0.02	2.70^{b}±0.03	1.03^{a}±0.03	1.04^{a}±0.03
TP_{3-3}	**22.0**	**0.98^{b}±0.03**	**0.99^{b}±0.05**	**1.90^{b}±0.03**	**1.87^{c}±0.04**	**0.86^{b}±0.06**	**0.88^{b}±0.03**
TP_{3-4}	1.04	1.12^{c}±0.03	1.14^{cg}±0.07	2.20^{c}±0.05	2.19^{d}±0.03	1.10^{c}±0.03	1.12^{c}±0.06
TP_{3-5}	2.73	1.09^{c}±0.06	1.10^{cg}±0.03	1.98^{c}±0.03	1.96^{e}±0.05	1.12^{c}±0.06	1.13^{c}±0.01
TP_{3-3-1}	**0.25**	**0.89^{d}±0.05**	**0.91^{d}±0.06**	**2.10^{d}±0.06**	**2.08^{f}±0.02**	**0.85^{b}±0.03**	**0.87^{d}±0.03**
TP_{3-3-2}	**0.26**	**0.87^{d}±0.02**	**0.89^{e}±0.03**	**2.09^{de}±0.02**	**2.04^{g}±0.02**	**0.84^{b}±0.02**	**0.85^{d}±0.03**
TP_{3-3-3}	**0.27**	**0.77^{e} ±0.02**	**0.79^{f}±0.04**	**2.03^{e}±0.02**	**2.01^{h}±0.03**	**0.78^{d}±0.03**	**0.79^{d}±0.03**
TP_{3-3-4}	0.05	1.10^{d}±0.03	1.12^{g}±0.05	2.41^{f}±0.03	2.38^{i}±0.04	1.06^{ac}±0.06	1.07^{a}±0.03
TP_{3-3-1}	0.06	1.06^{ad}±0.03	1.09^{g}±0.07	2.39^{f}±0.05	2.35^{i}±0.03	1.04^{a}±0.03	1.06^{a}±0.06
TP_{4-1}	0.07	1.13^{d}±0.06	1.14^{g}±0.03	2.43^{f}±0.03	2.41^{j}±0.05	1.12^{c}±0.06	1.14^{c}±0.01
TP_{4-2}	0.08	1.18^{a}±0.05	1.20^{h}±0.06	2.27^{g}±0.06	2.24^{k}±0.02	1.13^{c}±0.03	1.15^{c}±0.03
TP_{4-3}	**20.52**	**0.97^{b}±0.02**	**0.99^{d}±0.03**	**2.02^{e}±0.02**	**1.99^{e}±0.02**	**1.01^{a}±0.02**	**1.03^{a}±0.03**
TP_{4-4}	3.23	1.04^{d} ±0.02	1.07^{g}±0.04	2.36^{gh}±0.02	2.34^{i}±0.03	1.08^{c}±0.03	1.07^{a}±0.03
TP_{4-5}	4.31	1.10^{d}±0.03	1.13^{g}±0.05	2.34^{h}±0.03	2.31^{a}±0.04	1.14^{c}±0.06	1.15^{c}±0.03
TP_{4-6}	2.29	1.07^{d}±0.03	1.08^{g}±0.07	2.19^{c}±0.05	2.15^{d}±0.03	1.09^{c}±0.03	1.11^{c}±0.06
TP_{4-3-1}	**0.17**	**0.85^{d}±0.06**	**0.87^{h}±0.03**	**2.13^{d}±0.03**	**2.10^{f}±0.05**	**0.75^{d}±0.06**	**0.76^{d}±0.01**
TP_{4-3-2}	**0.21**	**0.76^{e}±0.05**	**0.78^{i}±0.06**	**2.21^{c}±0.06**	**2.19^{d}±0.02**	**0.73^{d}±0.03**	**0.74^{d}±0.03**
TP_{4-3-3}	29	1.08^{d}±0.02	1.09^{g}±0.03	2.35^{g}±0.02	2.33^{a}±0.02	1.07^{c}±0.02	1.08^{a}±0.03
TP_{4-3-4}	0.07	1.07^{d} ±0.02	1.15^{g}±0.04	2.37^{g}±0.02	2.34^{a}±0.03	1.11^{c}±0.03	1.12^{c}±0.03
TP_{4-3-5}	0.08	1.05^{d}±0.03	1.09^{g}±0.05	2.42^{f}±0.03	2.39^{i}±0.04	1.06^{ac}±0.06	1.09^{c}±0.03
TP_{4-3-6}	0.09	1.03^{d}±0.03	1.05^{g}±0.07	2.47^{if}±0.05	2.44^{j}±0.03	1.05^{ac}±0.03	1.03^{a}±0.06

*The yield of major sub-column fractions calculated based on the crude EtOAc-MeOH extract (38.0 g of dry weight). The values were tabulated in triplicate (n=3) and indicated as mean±standard deviation. Significant differences were expressed as superscripts (a-l) within column ($p < 0.05$).

#The IC_{50} values were calculated in mg mL^{-1}

5.*3.2* ***Spectroscopic characterization of the bioactive compounds derived from the EtOAc-MeOH extract of P. tetrastromatica***

The consecutive chromatographic purification of the EtOAc-MeOH crude extract of *P. tetrastromatica* led to the identification of bioactive secondary metabolic analogues. The structural elucidations of these lead molecules carried out using the nuclear magnetic resonance (NMR) analyses {^{1}H-proton-500 MHz; ^{13}C-carbon-125 MHz; DEPT; ^{1}H-^{1}H COSY; HSQC; HMBC; NOESY} using deuterated solvent along with mass spectrometric analyses (GC-EI-MS/HRESIMS), Fourier-transform infrared (FT-IR) (reported among 4000-400 cm^{-1}) and UV-spectrophotometric analyses. The isolated secondary metabolites were categorized under the different classes of chemistry, namely xenicane diterpene derivatives (**1-5**), and dolabellane diterpene derivatives (**6-10**) (Figure 5.3).

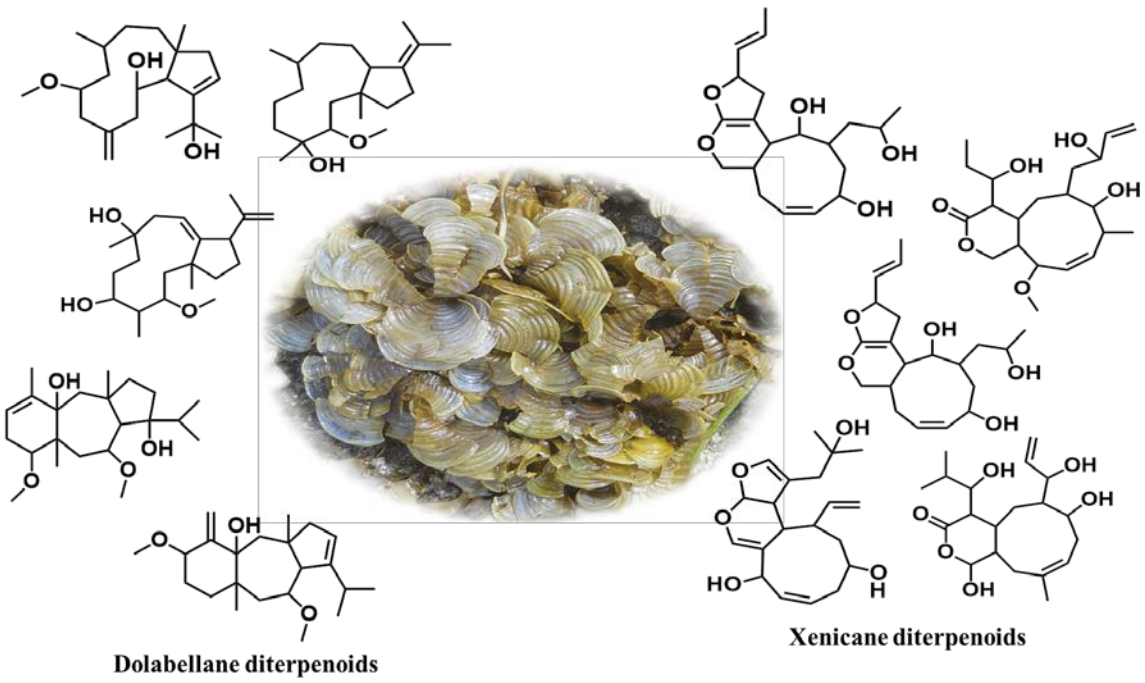

Figure 5.3.: Bioactive secondary metabolites isolated from the organic extract of *P. tetrastromatica* (family Dictyotaceae) and representative photograph of thalli of brown seaweed

5.3.2.1 ***Structural characterization of xenicane class of diterpenoid derivatives***

Seaweeds were viewed as promising sources of bioactive metabolites with functional food properties and pharmacological potentials (Plaza et al., 2008; Lann et al., 2016). Natural antioxidants in seaweeds were recognized to deter pathophysiological conditions leading to

oxidative stress conditions and increase the shelf life of food ingredients (Jimenez-Escrig et al., 2001). Among various seaweeds, those belonging to the class Phaeophyceae (brown seaweed) were found to be potential sources of antioxidants and bioactive pharmacophores (Kang et al., 2011; Kindleysides et al., 2012). The brown seaweeds belonging to the family Dictyotaceae were considered as one of the potential sources of biologically active diterpenoid metabolites (Blunt et al., 2009), and among which xenicanes were recognized to be an interesting class of bioactive leads, which were isolated as one of the largest class of diterpenoids in marine organisms, with potential bioactive properties (Faulkner 1998; Viano et al., 2009).

Earlier reports of literature revealed the isolation of xenicane natural products from brown seaweeds *Dilophus fasciola*, *Dilophus spiralis* (Ioannou et al., 2009), *Dictyota sp.* (Viano et al., 2009), and *Padina pavonia* (Awad et al., 2008). Xenicane from the soft coral *Xenia elongata* was the first member of xenicane diterpenoids, and there were reports on further discovery of various bioactive xenia metabolites from the brown seaweeds. The bicyclic framework of xenicanes containing *trans*-fused system of ring A and cyclononane carbocyclic ring B possessing a nine-membered ring were reported from the soft coral, *Xenia elongata* (Vanderah et al., 1997). This unique family of xenia diterpenoids was classified into three main subclasses; xenicanes or xenicins, xeniolides and xeniaphyllanes with bicycle [7.2.0] undecane ring (Groweiss et al., 1983) along with recently reported azamilide with nine-membered monocarbocyclic frame work acylated with $C_{16\text{-}20}$ fatty acids and an opened A ring. There were 53 main reports on xenia isoprenoids with several modifications in the ring and prenyl side chain (Blunt et al., 2009).

Seaweeds were recognized as invaluable marine resources in the Asian continent for use in food and pharmaceuticals (Barrento et al., 2016; Makkar and Chakraborty, 2018a-b). The brown seaweed *Padina sp.* was found to constitute a foremost share in the family Dictyotaceae and about 50 taxa of this genus were reported in various parts of the globe. Among them, *Padina tetrastromatica* (Hauck) (family Dictyotaceae) has been predominant in the Indo-Pacific region (Guiry and Nic-dhonncha, 2003), and there were preliminary reports of their bioactive potentials (Chia et al., 2015; Mohsin et al., 2014). In the search for bioactive diterpenoids from this brown seaweed species, this work described the purification and characterizations of previously undescribed five xenicane class of novaxenicin type diterpenoids (**1**-**2**) bearing cyclonona[*d*]furo[2,3-*b*]pyrandiol and three xeniolide-type diterpenes with octahydrocyclonona[*c*]pyran-3(1*H*)-one backbones (**3**-**5**) from the organic EtOAc/MeOH (ethyl acetate-methanol) extract of the studied seaweed (Figure 5.4) collected from the Gulf-of-Mannar of Peninsular India. The anti-inflammatory and antioxidant potential of the studied compounds were analyzed by different *in vitro* assays, and various physicochemical descriptors were utilized to substantiate the structure-activity correlations of the studied diterpenoids. *In silico* molecular

modelling studies were performed to designate the 5-lipoxygenase inhibitory mechanism of the studied xenicane analogues.

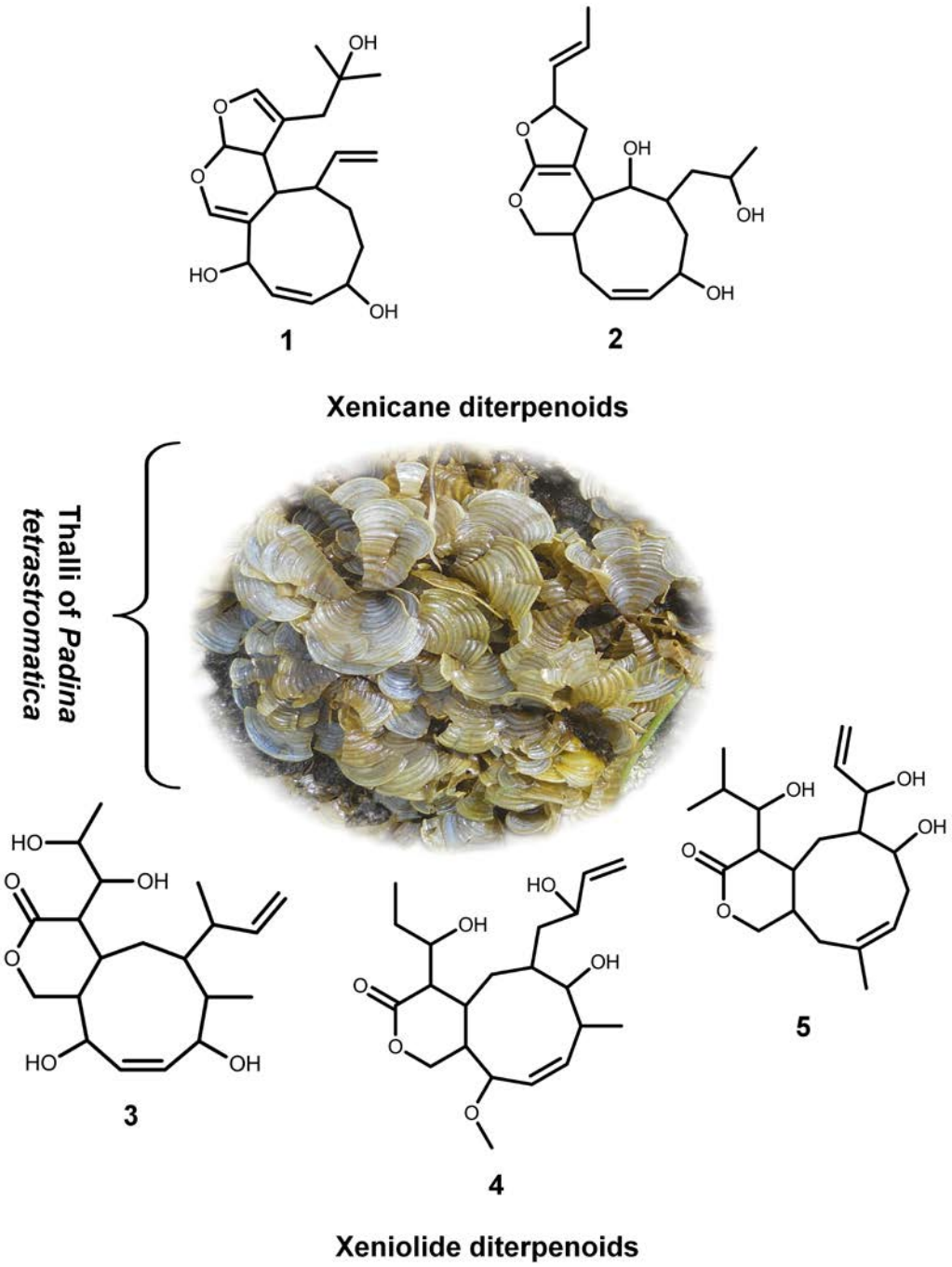

Figure 5.4.: Xenicane class of xenicins (**1-2**) bearing cyclonona[*d*]furo[2,3-*b*]pyrandiol and three xeniolide-type diterpenoids with octahydrocyclonona[*c*]pyran-3(1*H*)-one backbones (**3-5**) isolated from the seaweed *Padina tetrastromatica*.

5.3.2.1a Structural characterization of Compound 1(TP_1)

12-Ethenyl-3a,6,9,10,11,12,12a,12b-octahydro-1-(1^2-hydroxy-1^2-methyl-propyl)-cyclonona[*d*]furo[2,3-*b*]pyran-6,10-diol

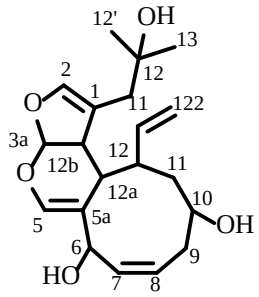

Sample yield	0.28% (> 99% purity, RP-C_{18} HPLC)
Physical description	Colourless oil
Molecular formula	$C_{20}H_{28}O_5$
Molecular mass	348.1937

The xenicane class of diterpenoid derivative, 12-ethenyl-3a,6,9,10,11,12,12a,12b-octahydro-1-(1^2-hydroxy-1^2-methyl-propyl)-cyclonona[*d*]furo[2,3-*b*]pyran-6,10-diol was isolated as colorless oil compound. The compound (**1**) has exhibited UV absorbance (UV (MeOH) λ_{max}) at 249 (2.61) nm (Figure 5.5). The homogeneity of the compound was ascertained by HPLC data on a bonded phase octadecylsilane (C_{18}) stationary phase (RP-C_8 HPLC, MeOH:MeCN, 4:1 v/v): 3.20 min (Figure 5.6).

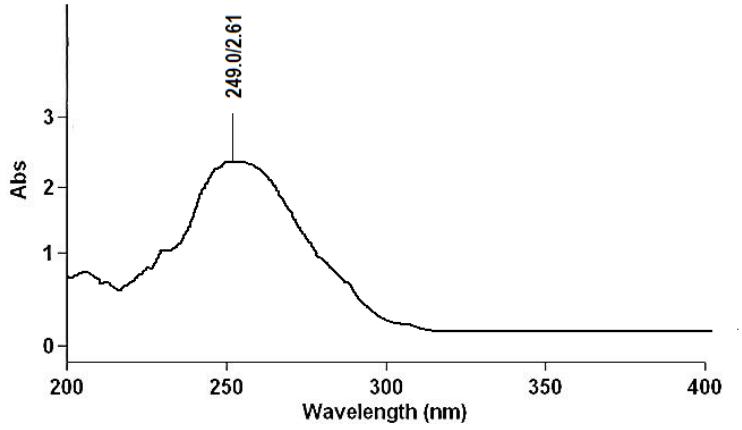

Figure 5.5.: UVspectrum of 12-ethenyl-3a,6,9,10,11,12,12a,12b-octahydro-1-(1^2-hydroxy-1^2-methyl-propyl)-cyclonona[*d*]furo[2,3-*b*]pyran-6,10-diol **(1)**

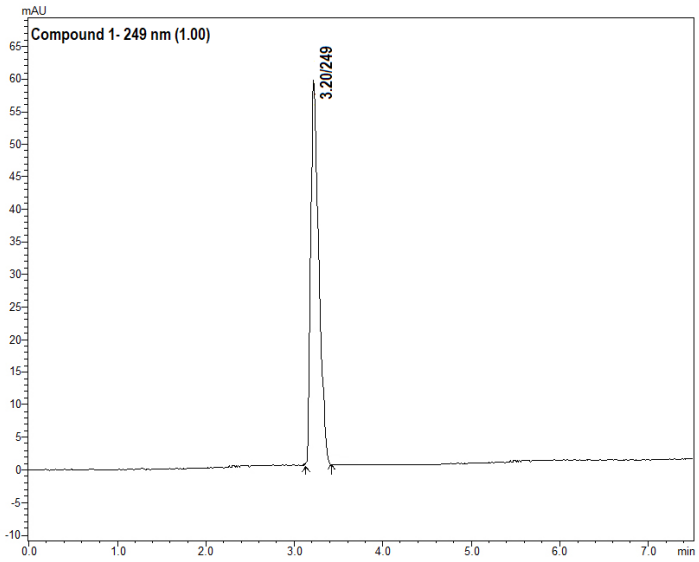

Figure 5.6.: HPLC chromatogram of 12-ethenyl-3a,6,9,10,11,12,12a,12b-octahydro-1-(1^2-hydroxy-1^2-methyl-propyl)-cyclonona[*d*]furo[2,3-*b*]pyran-6,10-diol **(1)**

Repeated chromatographic fractionation of *P. tetrastromatica* yielded compound **1** as a colorless oily substance. The molecular ion peak of **1** was appeared at *m/z* 348, whiles the molecular formula $C_{20}H_{28}O_5$ implying seven unsaturation degrees, and was associated with four olefinic bonds and three ring systems. The molecular ion peak by HRESIMS (positive mode) was found at *m/z* 349.2018 $[M+H]^+$ (Figure 5.6).

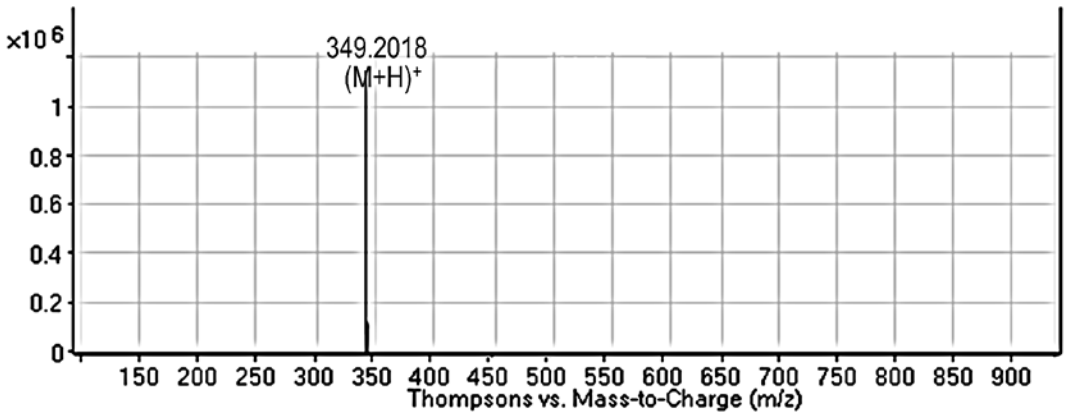

Figure 5.7.: HRESIMS of 12-ethenyl-3a,6,9,10,11,12,12a,12b-octahydro-1-(1^2-hydroxy-1^2-methyl-propyl)-cyclonona[*d*]furo[2,3-*b*]pyran-6,10-diol **(1)**

The ^{13}C-NMR and DEPT$_{135}$ experiments attributed the presence of 20 carbon signals, which included the presence of two methyls (δ29.53, 29.54), three sp^3 methylenes (δ 38.67, 41.42, 39.96), one sp^2 methylene (δ 116.46), six sp^3 methines (δ 104.24, 49.82, 39.94, 48.95, 70.27, 70.26), four sp^2 methines (δ 144.10, 133.29, 125.48, 141.92), along with one sp^3 (δ 73.30) and two sp^2 (δ 115.36, 115.25) quaternary carbons. The FTIR spectrum of **1** displayed absorption bands at 3472 cm^{-1} (-OH), 890 cm^{-1} (=CH$_2$) and 1112/1076 cm^{-1} (-C-O-C) (Figure 5.7), which were corroborated by ^{13}C-NMR resonances at δ 70.26, 70.27, 73.30, 29.53, 29.54, and 104.24.

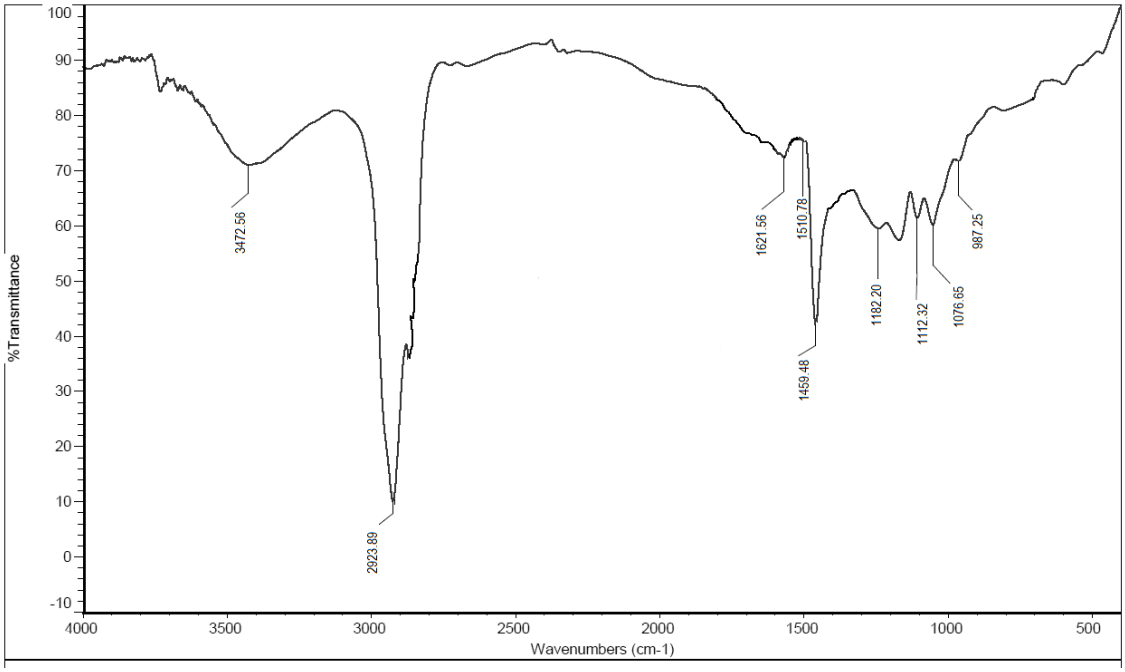

Figure 5.7.: FTIR of 12-ethenyl-3a,6,9,10,11,12,12a,12b-octahydro-1-(1^2-hydroxy-1^2-methyl-propyl)-cyclonona[*d*]furo[2,3-*b*]pyran-6,10-diol **(1)**

The lack of carbonyl absorption bands in the FTIR and the absence of signals above δ 150 in ^{13}C spectrum of **1** appropriately attributed that the all oxygen functionalities within the system might be in the form of ether or hydroxyl groups, which were also corroborated by an earlier report of literature (Bishara et al., 2006). The ^{13}C/^{1}H-NMR experiments indicated the presence of vinylic group due to the signals associated with δ 141.08/δ 5.72 (m) along with δ116.46/ 5.00, 4.99, which found resemblance with the values of exocyclic double bond of the novaxenicin framework (Bishara et al., 2006) (Figure 5.8-5.10; Table 5.4). The presence of two each of tri-substituted double bonds (δ115.36 and 115.25) and oxymethine (-O-CH<) groups (δ 141.92, 144.10 and δ 6.37, 6.41), along with one each of dioxymethine (-O-CH-O-) (δ 104.24/δ 6.06) and tert-alcohol functionality (δ 73.30) attributed the presence of novaxenicin framework (Bishara et al., 2006).

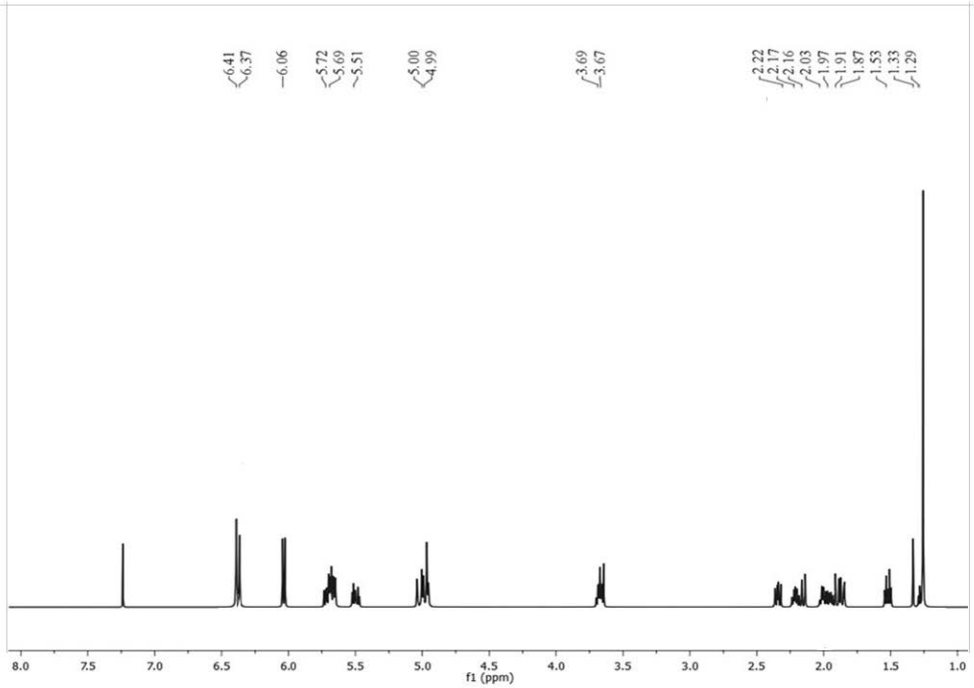

Figure 5.8.: ^{1}H NMR spectrum of 12-ethenyl-3a,6,9,10,11,12,12a,12b-octahydro-1-(1^{2}-hydroxy-1^{2}-methyl-propyl)-cyclonona[*d*]furo[2,3-*b*]pyran-6,10-diol **(1)**

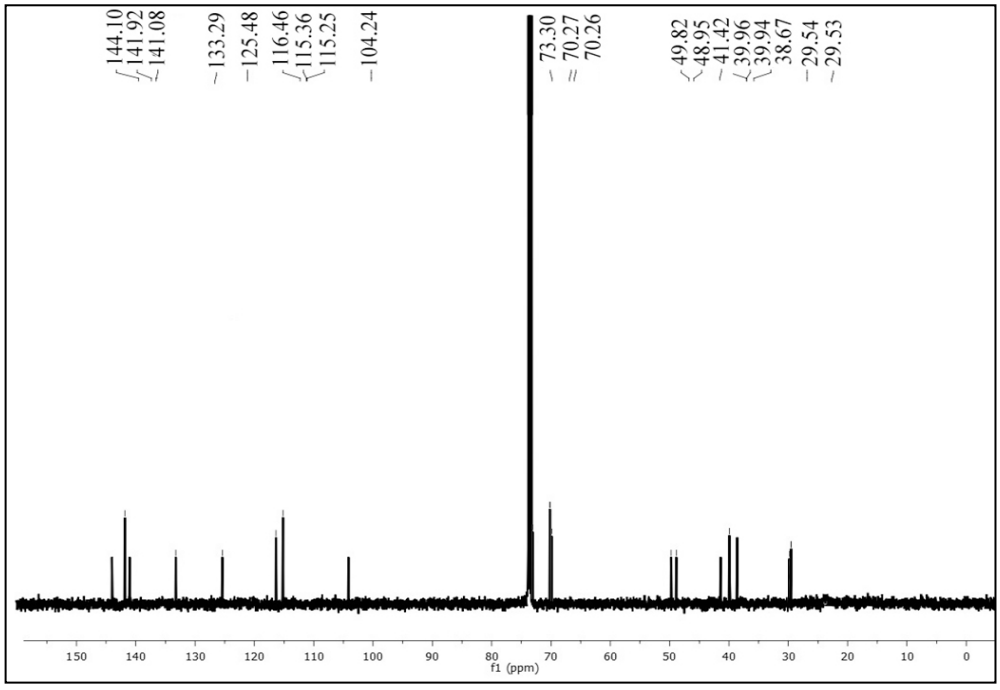

Figure 5.9.: ^{13} C NMR spectrum of 12-ethenyl-3a,6,9,10,11,12,12a,12b-octahydro-1-(1^{2}-hydroxy-1^{2}-methyl-propyl)-cyclonona[*d*]furo[2,3-*b*]pyran-6,10-diol **(1)**

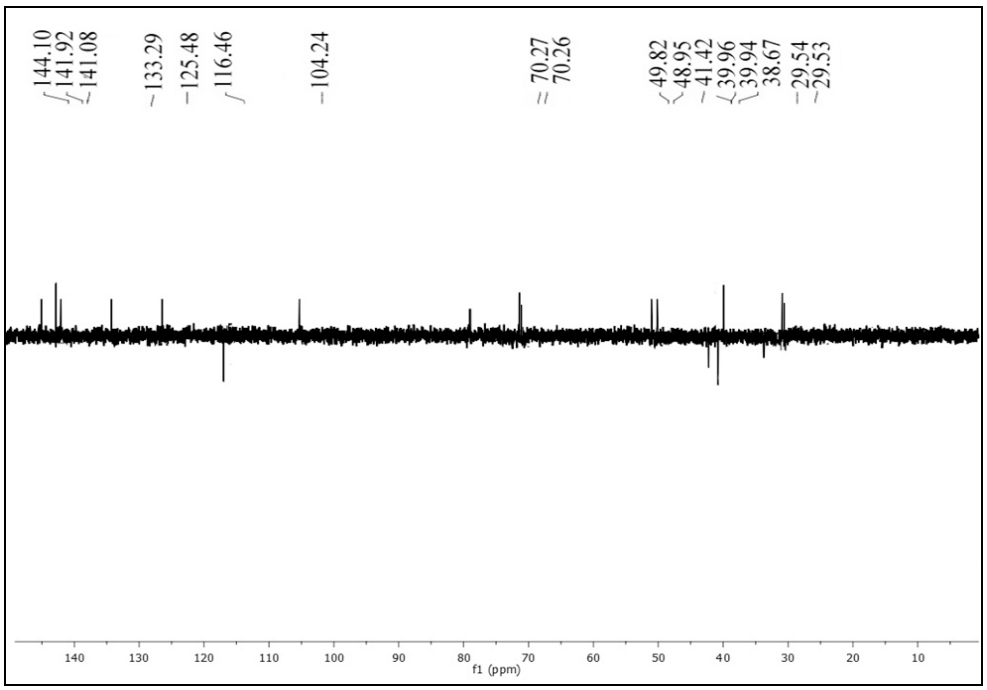

Figure 5.10.: [135] DEPT NMR spectrum of 12-ethenyl-3a,6,9,10,11,12,12a,12b-octahydro-1-(1^2-hydroxy-1^2-methyl-propyl)-cyclonona[*d*]furo[2,3-*b*]pyran-6,10-diol **(1)**

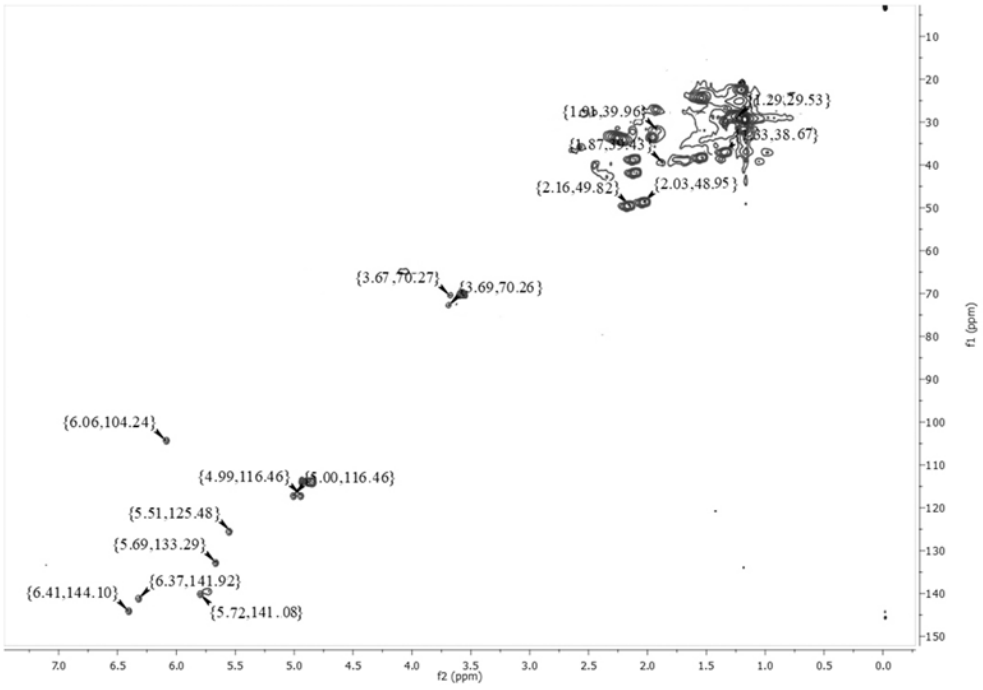

Figure 5.11.: HSQC spectrum of 12-ethenyl-3a,6,9,10,11,12,12a,12b-octahydro-1-(1^2-hydroxy-1^2-methyl-propyl)-cyclonona[*d*]furo[2,3-*b*]pyran-6,10-diol **(1)**

Carbon signals at δ 144.10, 141.92, 104.24, 70.27, 70.26, and 73.30 supported the presence of oxygen functionalities, and these might be due to the presence of oxymethine (-O-CH=, -O-CH<) or hydroxyl groups in **1.** The interchangeable hydroxyl protons at 70.27 (δ 3.67), 70.26 (δ 3.69) and 73.30 were ceased to exist upon interchange of D_2O asserting the existence of hydroxyl groups in its vicinity. The COSYs between the protons δ 6.06/2.17 in **1** along with HMBCs at δ 6.41/115.36; 1.87/115.36; 2.17/104.24; 6.06/39.94 and 6.06/144.10 proposed 6-membered ring system in **1**, which was identified as dihydro-*2H*-pyran ring system. Similarly, COSYs between the protons at δ 1.87/2.03/1.33 and 3.67/2.22/5.51 along with HMBCs δ 1.87/48.95; 1.33/70.27; 3.67/41.42/125.48; 2.22/125.48; 5.69/70.26; 3.69/125.48; 3.69/115.36, and 1.87/115.36 proposed a closed loop of 9-membered ring in **1** (Figure 5.12-5.13).

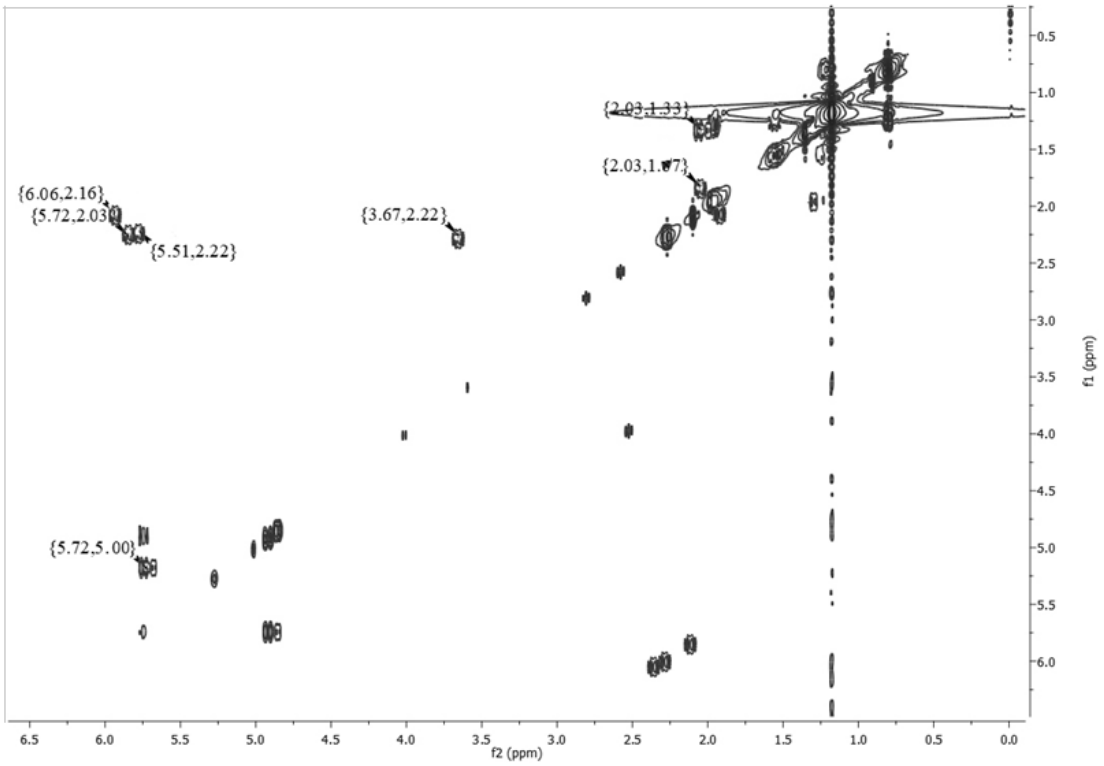

Figure 5.12.: ^{1}H-^{1}H COSY spectrum of 12-ethenyl-3a,6,9,10,11,12,12a,12b-octahydro-1-(1^2-hydroxy-1^2-methyl-propyl)-cyclonona[*d*]furo[2,3-*b*]pyran-6,10-diol **(1)**

Thus, the positions of carbons in dihydro-*2H*-pyran with cyclononane systems were assigned from C-5 to C-5a, continuously, on the basis of earlier literature (Ioannou et al., 2009; Bishara et al., 2006). The signals at C-12a (δ 39.94) and C-5a (δ 70.26) were identified as ring junctions based on earlier reports (Bishara et al., 2006). The COSYs of protons δ 6.06/2.17 including HMBCs at δ 6.06/141.92; 6.06/115.25; 6.37/141.92 and 2.16/115.25 proposed 5-membered ring in

1, designated as dihydrofuran. Deshielded signals at δ 104.24, 141.92 and 115.25 assigned the presence of oxymethine (-O-CH<, -O-CH=) and alkenic functionalities in **1** as the part of dihydrofuran skeleton. Thus, the positions of carbons in dihydrofuran were disposed as C-3a, 12b, 1 and 2 based on spectroscopic assignments and previous report of literature (Bishara et al., 2006). The carbons C-3a and C-12b were common to both dihydro-2H-pyran and dihydrofuran systems. Three cyclic systems, dihydrofuran, dihydro-2*H*-pyran and cyclononane in the tricyclic system were designated as **A, B** and **C**, respectively. Hence **A-B-C** tricyclic ring system was found to possess three spin systems, designated as **I-III** (H-3a/H-12b; H-12a/12/11, H-12/12^1/12^2; H-10/9/8) (depicted as bold in Figure 5.14).

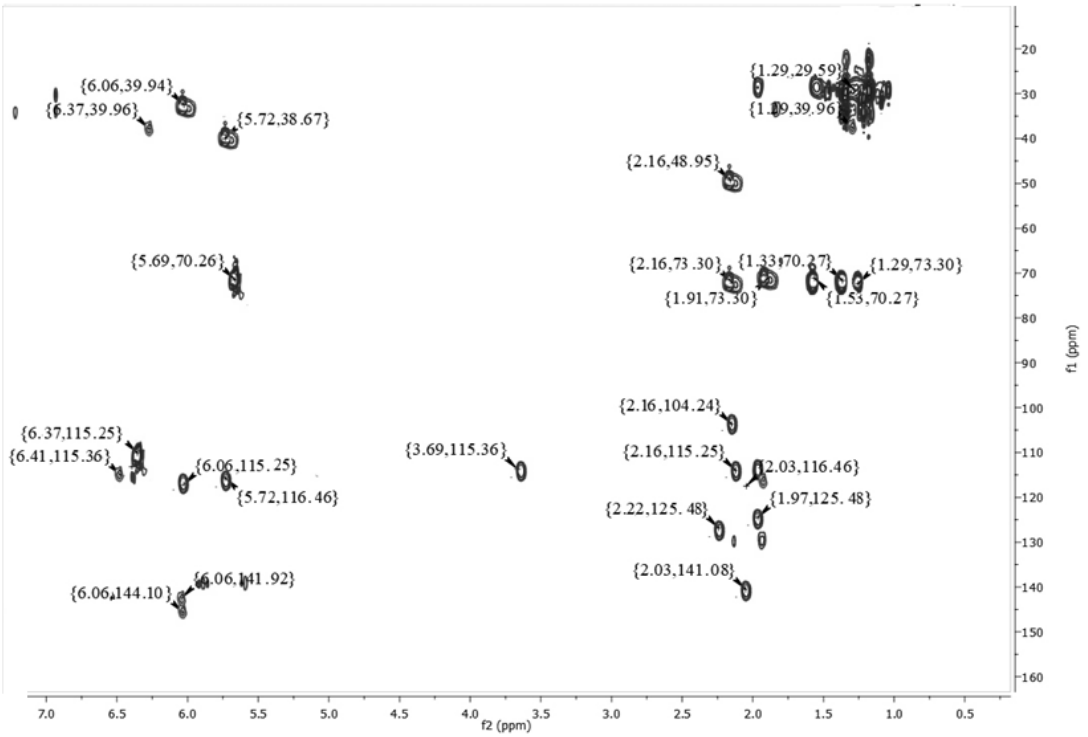

Figure 5.13.: HMBC spectrum of 12-ethenyl-3a,6,9,10,11,12,12a,12b-octahydro-1-(1^2-hydroxy-1^2-methyl-propyl)-cyclonona[*d*]furo[2,3-*b*]pyran-6,10-diol **(1)**

The moiety **I** included a carbinolic proton (δ 4.96, δ 70.26) connected with two double bond methines that was coupled with a relatively deshielded methylene at δ 2.22 and 1.97, which in turn were coupled with a sequence of protons due to carbinolic (δ 5.51, δ 125.48), methylene (δ 1.33, 1.53), allylic methine (δ 2.03), one double bond methine (δ 5.72) and double bond methylene (δ 5.00) groups. A series of $^{1,3}J_{H\text{-}C}$ correlations by HMBC were found to assemble the fragments, and to draw the planer structure of **1**.

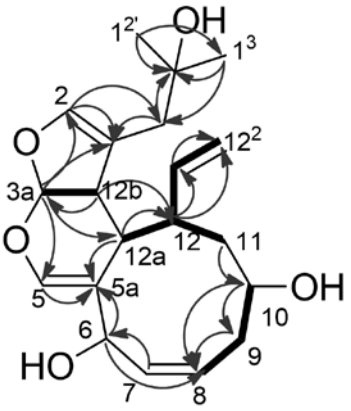

Figure 5.14.: Prominent ^{1}H-^{1}H COSY, and selected HMBC correlations of 12-ethenyl-3a,6,9,10,11,12,12a,12b-octahydro-1-(1^2-hydroxy-1^2-methyl-propyl)-cyclonona[*d*]furo[2,3-*b*]pyran-6,10-diol **(1)**. The key ^{1}H-^{1}H COSY couplings were represented in bold face bonds. The key HMBC couplings have been represented by double barbed arrows.

The COSYs between δ 6.06/2.17 (H-3a/H-12b) along with HMBCs from δ 6.06 (H-3a) to δ 144.10 (C-5), δ 39.94 (C-12a), δ 115.25 (C-1) and δ 141.92 (C-2) and methine proton H-12b linked (δ 2.17) to δ 104.24 (C-3a) and δ 48.95 (C-12) portrayed the spin systems of **I** and **II**. The HMBCs from oxymethine protons of dihydrofuran H-2 (δ 6.37) to C-5 (δ 115.25) and C-1^1 (96) allocated the occurrence of side chain 2-methylpropan-2-ol. The methylene protons H-1^1 (δ 2.16/1.91), methyl protons H-1$^{2'}$ (δ 1.29) and H-1^3 (δ 1.29) were associated with 2-methylpropan-2-ol displaying correlations to C-1 (δ 115.25), C-1^2 (δ 73.30), C-1^3 (δ 29.54), and C-1^1 (δ 39.96). With the aid of these HMBCs the occurrence of **A** ring was assigned, and among them carbons C-3a, and 12b were involved in cyclic system **B**. Two terminal methyls at C-1^2 resonating at δ 1.29 (C-1$^{2'}$) and δ 1.29 (C-1^3) were geminal, and were assigned by HMBCs of δ 1.29/δ 29.53 (H-1$^{2'}$/C-1^3), δ 1.29/δ 73.30 (H-1$^{2'}$/H-1^2), and between δ 1.29/ 73.30 (H-1^3/C-1^2). This spectral information was in good agreement with that of an earlier report (Bishara et al., 2006). The presence of COSYs between H-12a/H-12 (δ 1.87/δ 2.03), H-12/H-11 (δ 2.03/ 1.33), H-12/H-9 (δ 2.03/ 2.22) and H-12^1/H-12^2 (δ 5.72/5.00) depicted the presence of second spin **II**, which displayed HMBCs between the spins **II** and **III**. The connection of spin unit **II** and ring **B** was made by HMBCs between H-12b (δ 2.17)/ C-6 (δ 48.95) and H-12a (δ 1.87)/C-12 (δ 48.95), which constituted the part of cyclononane ring **C.** The correlation of exocyclic alkene to ring **C** was attributed by HMBCs between δ 2.01/δ 141.10 (H-12/C-12^1), δ 5.72/116.46 (H-12^1/C-12^2), δ 5.72/ δ 38.67 (H-12^1/C-11) and δ 2.03/116.46 (H-12/C-12^2). The COSYs of δ 3.67/2.22 (H-10/H-9), and δ 2.22/5.51 (H-9/H-8), suggested the third spin system **III**. The presence of olefinic bond in the ring **C** was in accordance with the terminal alkene in the previously reported xenia diterpenoids (Ioannou et al., 2009). The connection of COSY spin system **C** and ring **B** at C-12a and C-5a was allocated by strong HMBCs between dioxymethine proton at δ 6.41/δ 115.36 (H-5/C-5a) and δ 1.87/115.36 (H-12a/C-5a). These HMBCs designated the

occurrence of ring **B** among which C-12a and C-5a were also involved in ring **C**. The COSY spectrum exhibited the occurrence of three spin systems and HMBCs linked to the three spin systems together, allowing the assignment of the planar structure.

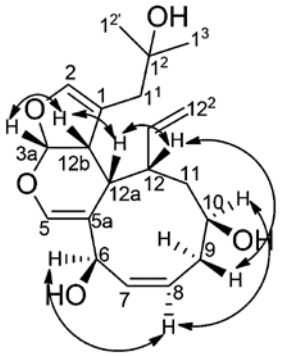

Figure 5.15.: Prominent NOE correlations of 12-ethenyl-3a,6,9,10,11,12,12a,12b-octahydro-1-(1^2-hydroxy-1^2-methyl-propyl)-cyclonona[*d*]furo[2,3-*b*]pyran-6,10-diol **(1)**. NOESY relations are represented by double-tailed arrows

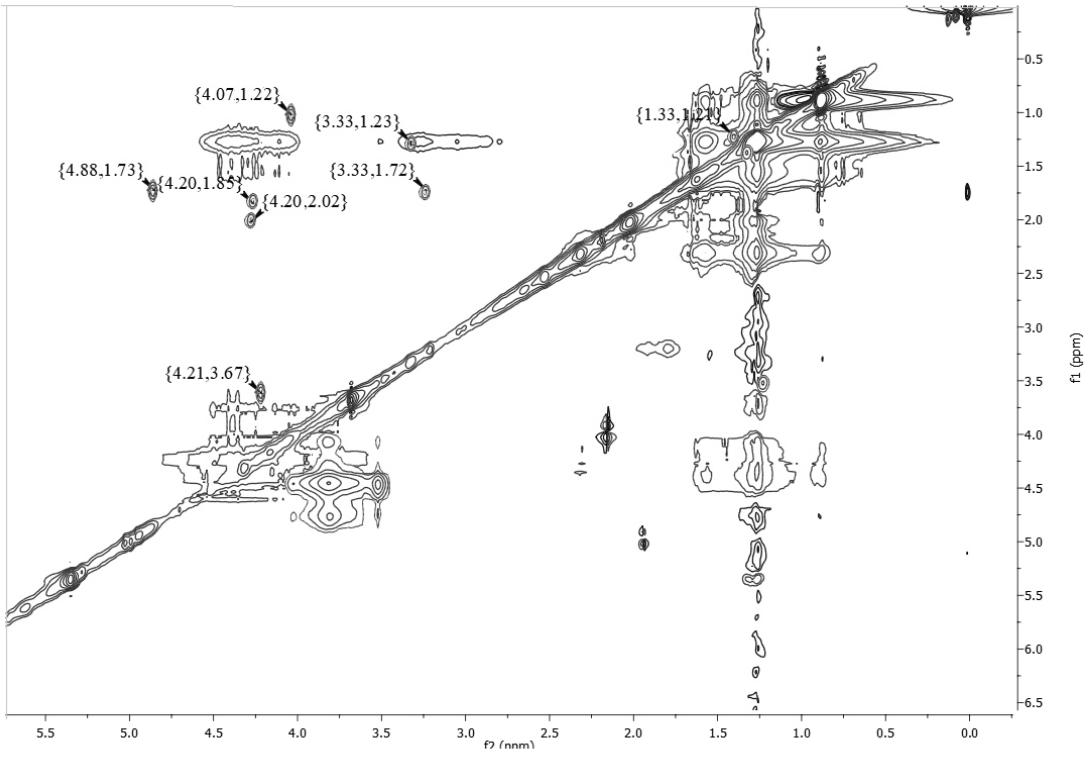

Figure 5.16.: NOE correlations of 12-ethenyl-3a,6,9,10,11,12,12a,12b-octahydro-1-(1^2-hydroxy-1^2-methyl-propyl)-cyclonona[*d*]furo[2,3-*b*]pyran-6,10-diol **(1)**.

The investigations on relative stereochemistry of the xenicin derivative were explained by NOESY experiments and coupling constants. A *trans* arrangement for the H-12a, H-5a was

assigned by comparison of coupling constants recorded in previous reports (Bishara et al., 2006). The proton at δ 6.06 (H-3a) was displayed NOE with protons at H-12b (δ 2.17). Similarly protons at H-12b (δ1.87), H-12a (δ1.87) and H-12 (δ 2.03) (Figure 5.15 & 5.16) exhibited NOEs with protons at H-12a (δ 1.87), H-12 (δ 2.03) and H-9 (δ 2.22), which were aligned in the β -plane of compound (**1**) (Tanaka et al., 1994). The assigned stereochemistry of hydroxyl group at C-10 and C-8 was in agreement with β -oriented protons. The chiral centers, mainly those of H-3a, 12b, 12a, 10 and H-6 were attributed by NOEs between H-3a/12b (δ 6.06/δ 2.17), H-12b/12a (δ 2.17/1.87), H-8/10 (δ 5.51/ 3.67) and H-8/6 (δ 5.51/3.69). Contrary to this β-orientation, the protons at H-8/10 (δ 5.51/δ 3.67) and H-8/6 (δ 5.51/3.69) were located at the α-side of the compound **1**.

Table 5.4.: NMR spectroscopic data[a] of 2-ethenyl-3a,6,9,10,11,12,12a,12b-octahydro-1-(1^2-hydroxy-1^2-methyl-propyl)-cyclonona[*d*]furo[2,3-*b*]pyran-6,10-diol (**1**) isolated from brown seaweed *P.tetrastromatica*

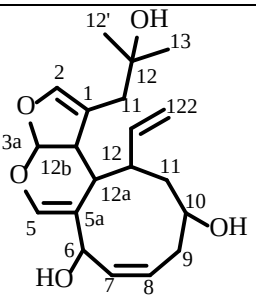

Compound **1**……..2-ethenyl-3a,6,9,10,11,12,12a,12b-octahydro-1-(1^2-hydroxy-1^2-methyl-propyl)-cyclonona[*d*]furo[2,3-*b*]pyran-6,10-diol (**1**)

C. No.	^{13}C NMR	^{1}H NMR (int., mult., J in Hz)[b]	COSY	HMB C
1	115.25	-	-	-
1^1	39.96	2.16 (1H, d, J=9.09 Hz) 1.91 (1H, d, J=8.47 Hz)	-	C-1,1^2
1^2	73.30	-	-	
$1^{2'}$	29.53	1.29 (3H, s)	-	C-1^3, 1^2
1^3	29.54	1.29 (3H, s)	-	C-1^2, 1^1
2	141.92	6.37 (1H, s)	-	C-1^1, 1
3	-	-	-	-
3a	104.24	6.06 (1H, d, J=10.74 Hz)	H-12b	C-12a,5,1,2
4	-	-	-	-
5	144.10	6.41 (1H, s)	-	C-5a
5a	115.36	-	-	-
6	70.26	3.69 (1H, d, J=14.70 Hz)	-	C-8, 5b
7	133.29	5.69 (1H, m)	H-6	C-6
8	125.48	5.51 (1H, m)	H-7	-
9	41.42	2.22 (1H, m), 1.97 (1H, m)	H-8	C-8
10	70.27	3.67 (1H, m)	H-9	C-9,8
11	38.67	1.33 (1H, m), 1.53 (1H, m)	-	C-10
12	48.95	2.03 (1H, dd, J= 12.35, 5.92)	H-11,12^1	C-12^1,12^2

12^1	141.08	5.72 (1H, m)	H-12^2	C-12^2, 11
12^2	116.46	5.00 (1H, d, J=13.79 Hz) 4.99 (1H, d, J=12.91 Hz)	-	-
12a	39.94	1.87 (1H, d, J=12.62)	H-6	C-12,5a
12b	49.82	2.17 (1H, dd, J=10.99, 8.86 Hz)	-	C-12,3a,1

[a]NMR spectra were recorded using a B ruker AVANCE III 500 MHz (AV 500) spectrometer (B ruker, Karlsruhe, Germany) in $CDCl_3$ as aprotic solvent at ambient temperature with TMS as the internal standard (δ 0 ppm).

[b]Values in ppm, multiplicity and coupling constants (J=Hz) were indicated in parentheses. Multiplicities were allocated by ^{135}DEPT NMR spectrum.

The assignments were made with the aid of the COSY, HSQC, HMB C and NOESY experiments.

The molecular ion peak of **1** was appeared at *m/z* 348 and base peak was ontained at *m/z* 41.0 (Figure 5.18 and 5.19).

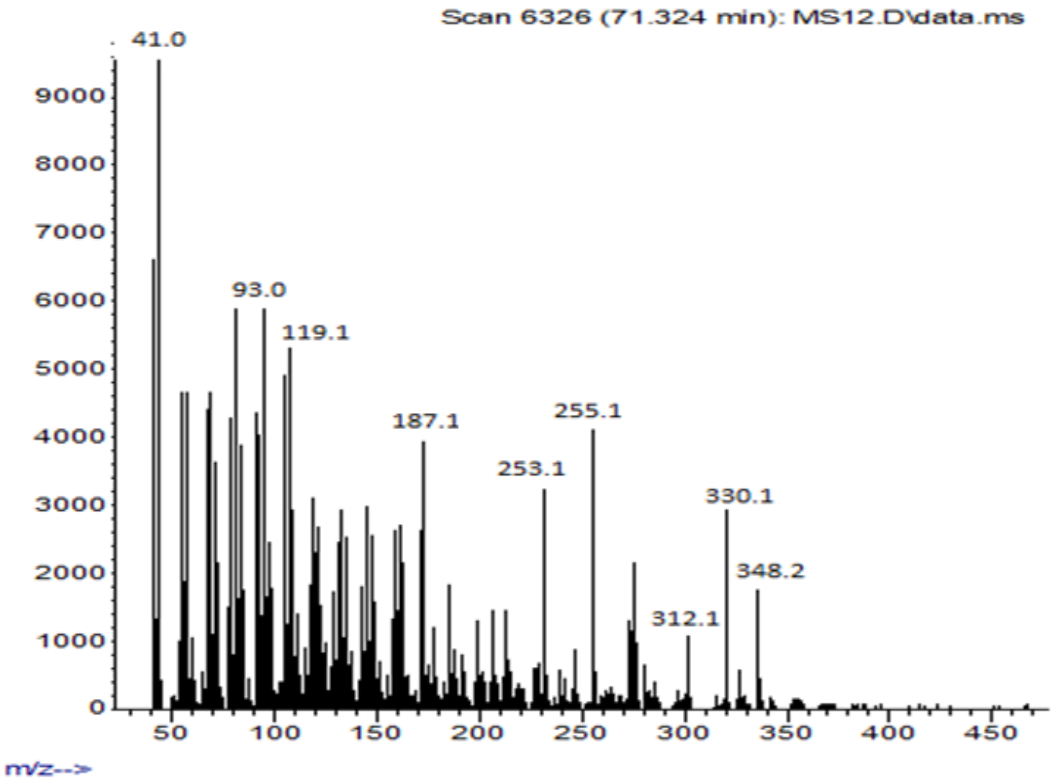

Figure 5.17.: EI-MS spectrum of 6-methoxy-dolabella-8(17),12-diene-10β ,18-diol (**1**)

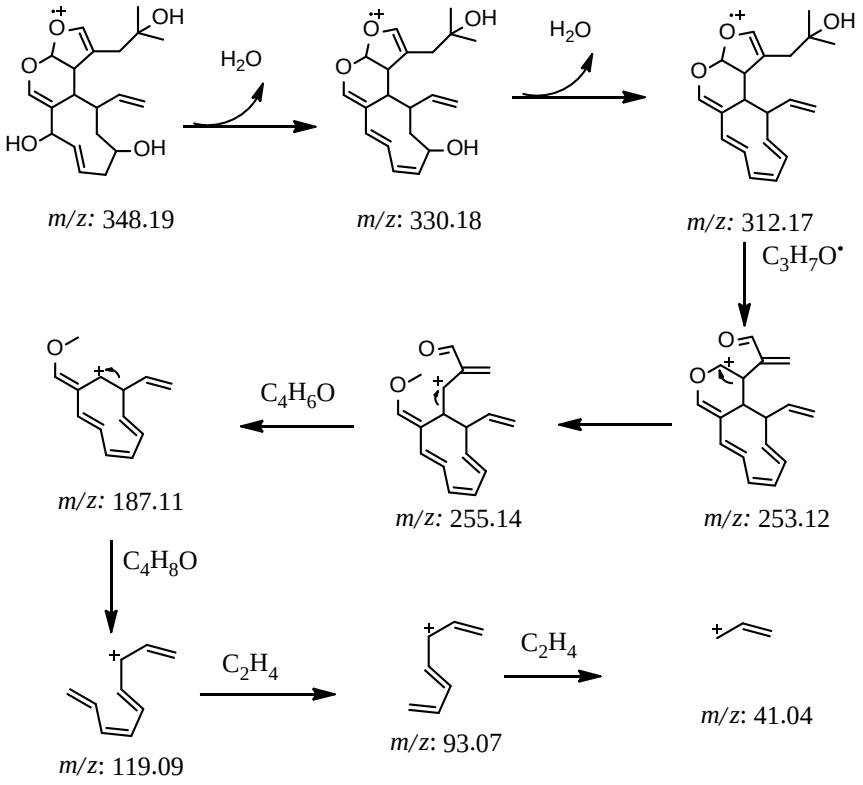

Figure 5.18.: Tentative mass fragmentation pattern of 6-methoxy-dolabella-8(17),12-diene-10β ,18-diol (**1**)

5.3.2.1b Structural characterization of Compound 2 (TP_2)

1,2,5,5a,6,9,10,11,12,12a-Decahydro-11(11^2-hydroxypropyl)-2-[(*E*)-2^1-propenyl] cyclonona[*d*]-furo[2,3-*b*]pyran-9,12-diol

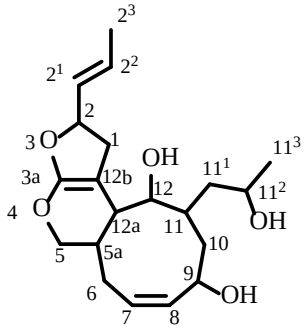

Sample yield	0.26% (> 99% purity, RP-C_{18} HPLC)
Physical description	Yellow oil
Molecular formula	$C_{20}H_{30}O_5$

Molecular mass	350.2093

The xenicane class of diterpenoid derivative, 1,2,5,5a,6,9,10,11,12,12a-Decahydro-11(11^2-hydroxypropyl)-2-[(*E*)-2^1-propenyl] cyclonona[*d*]-furo[2,3-*b*]pyran-9,12-diol was isolated as Colorless oil compound. The compound (**2**) has exhibited UV absorbance (UV (MeOH) λ_{max}) at 235 (3.1), 254 (3.7) nm (Figure 5.19). The homogeneity of the compound was ascertained by HPLC data on a bonded phase octadecylsilane (C_{18}) stationary phase (RP-C_8 HPLC, MeOH:MeCN, 4:1 v/v): 3.24 min (Figure 5.20).

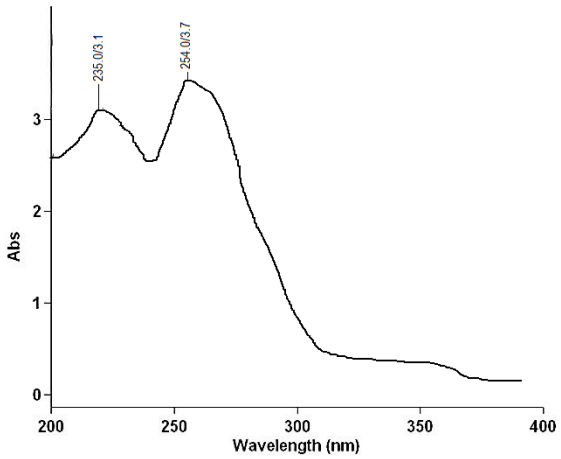

Figure 5.19.: UV spectrum of 1,2,5,5a,6,9,10,11,12,12a-decahydro-11(11^2-hydroxypropyl)-2-[(*E*)-2^1-propenyl] cyclonona[*d*]-furo[2,3-*b*]pyran-9,12-diol (**2**)

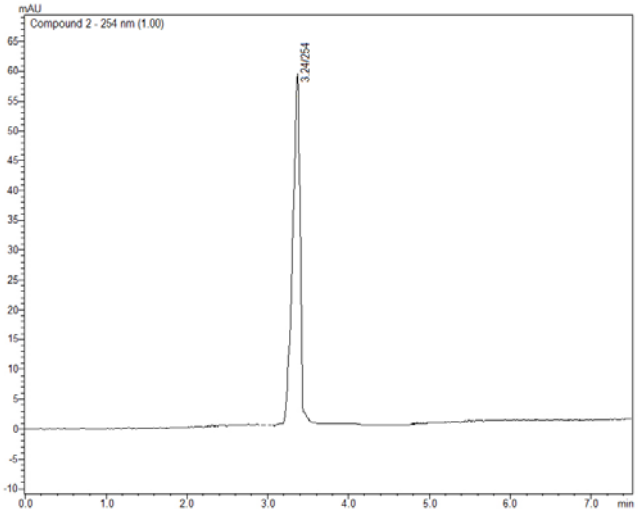

Figure 5.20.: HPLC chromatogram of 1,2,5,5a,6,9,10,11,12,12a-decahydro-11(11^2-hydroxypropyl)-2-[(*E*)-2^1-propenyl] cyclonona[*d*]-furo[2,3-*b*]pyran-9,12-diol (**2**)

The chromatographic separation of the solvent extract of *P. tetrastromatica* yielded **2** as a yellow oil. The molecular ion peak of **2** was appeared at *m/z* 350, while the molecular formula $C_{20}H_{30}O_5$, implying six unsaturation degrees, was associated with three olefinic bonds and three ring systems. The molecular ion peak by HRESIMS was observed at *m/z* 351.2175 $[M+H]^+$ (Figure 5.21). The FTIR spectrum of **2** displayed absorption bands at 3452 (O-H) and 1220 (C-O), (Figure 5.22)

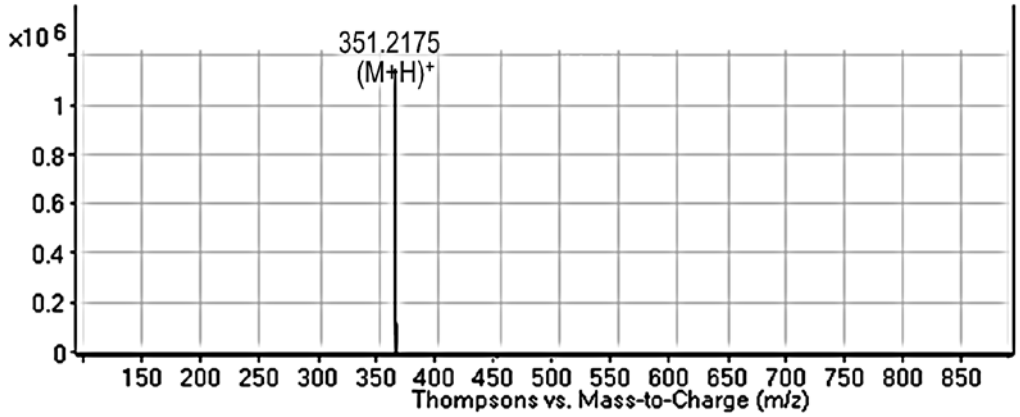

Figure 5.21.: HRESIMS of 1,2,5,5a,6,9,10,11,12,12a-decahydro-11(11^2-hydroxypropyl)-2-[(*E*)-2^1-propenyl] cyclonona[*d*]-furo[2,3-*b*]pyran-9,12-diol (**2**)

The ^{13}C-NMR of **2** along with $DEPT_{135}$ attributed the occurrence of 20 signals of carbons, which included two methyls (δ 17.65, 23.97), five sp^3 methylenes (δ 68.37, 39.54, 33.72, 37.74, 43.94), seven sp^3 methines (δ 41.36, 71.82, 38.69, 72.13, 36.15, 83.18, 67.75), four sp^2 methines (δ 132.60, 132.05, 129.17, 130.77), along with two sp^2 (δ 163.12, 94.31) quaternary carbons. The interchangeable hydroxyl protons at δ 71.82 (δ 3.33), δ 72.13 (δ 4.20) and δ 67.75 (δ 4.07) disappeared upon D_2O interchange, which ascribed the presence of hydroxyl groups in its vicinity (Figure 5.22-5.26). The HMBCs at δ 3.67/163.12; 1.72/163.12; 1.72/36.15; and 3.67/36.15 proposed the 6-membered ring in **2**, which was designated as dihydro-2*H*-pyran. The occurrence of deshielded signals at δ 94.31, 163.12 and 68.37 suggested the existence of alkenic functionalities and oxygenated carbons in **2** as the part dihydro-2*H*-pyran in **2**. Similarly, COSYs between protons at δ 1.72/3.33/1.22 and 5.62/2.01/1.85 along with HMBCs at δ1.72/33.72; 2.01/71.82; 1.29/71.82/72.13; 4.20/132.63; 5.67/132.05 and 2.01/132.05 assigned the 9-membered ring in **2**. The COSYs of protons δ 2.68/4.88 including HMBCs at δ 2.68/94.31/163.12; 4.88/37.74 reckoned the 5-membered ring in **2** (Figure 5.27-5.29). Deshielded signals at δ 163.12 and 94.31 attributed the alkenic and oxygenated carbons in **2** as the part of dihydrofuran (positions were assigned as C-3, 4, 12 and 13). The COSYs between H-2/H-2^1 (δ 4.88/5.69), H-2/H-1 (δ 4.88/2.30) and HMBCs at H-2/C-2^1 (δ 4.88/ δ 129.17), H-2/C-1 (δ 4.88/δ 37.74) depicted the presence of dioxymethine group in **2** (Bishara

et al., 2006). Particularly, compounds **1** and **2** exhibited similarities in their structures excluding the substitutions at C-2 and C-11. In **2**, a carbon side chain with modifications was attached to C-2.

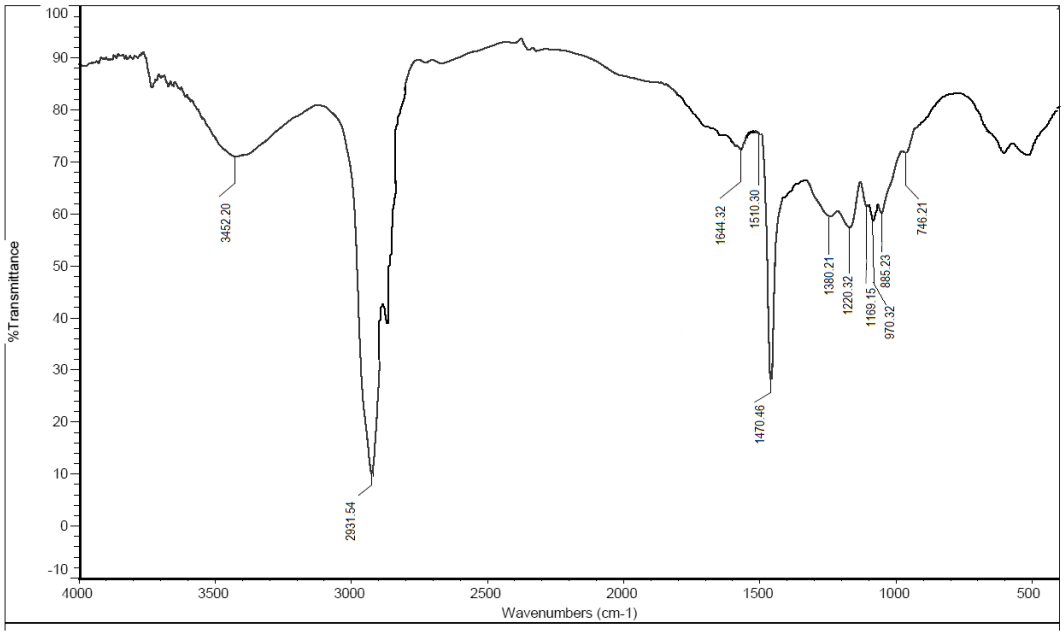

Figure 5.22.: FTIR spectrum of 1,2,5,5a,6,9,10,11,12,12a-decahydro-11(11^2-hydroxypropyl)-2-[(*E*)-2^1-propenyl] cyclonona[*d*]-furo[2,3-*b*]pyran-9,12-diol (**2**)

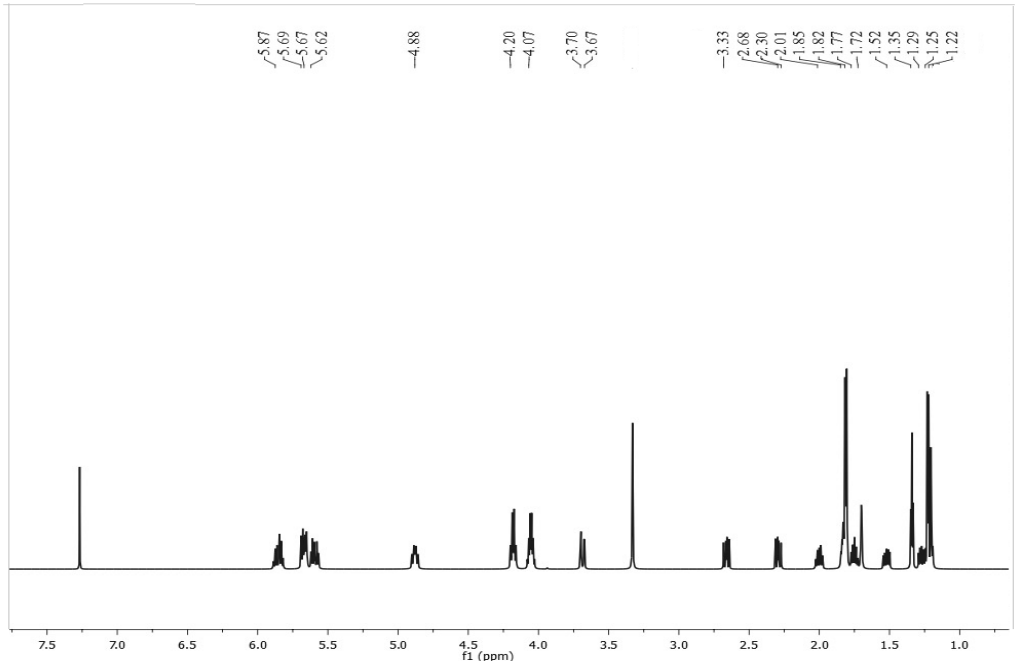

Figure 5.23.: ^{1}H NMR spectrum of 1,2,5,5a,6,9,10,11,12,12a-decahydro-11(11^2-hydroxypropyl)-2-[(*E*)-2^1-propenyl] cyclonona[*d*]-furo[2,3-*b*]pyran-9,12-diol (**2**)

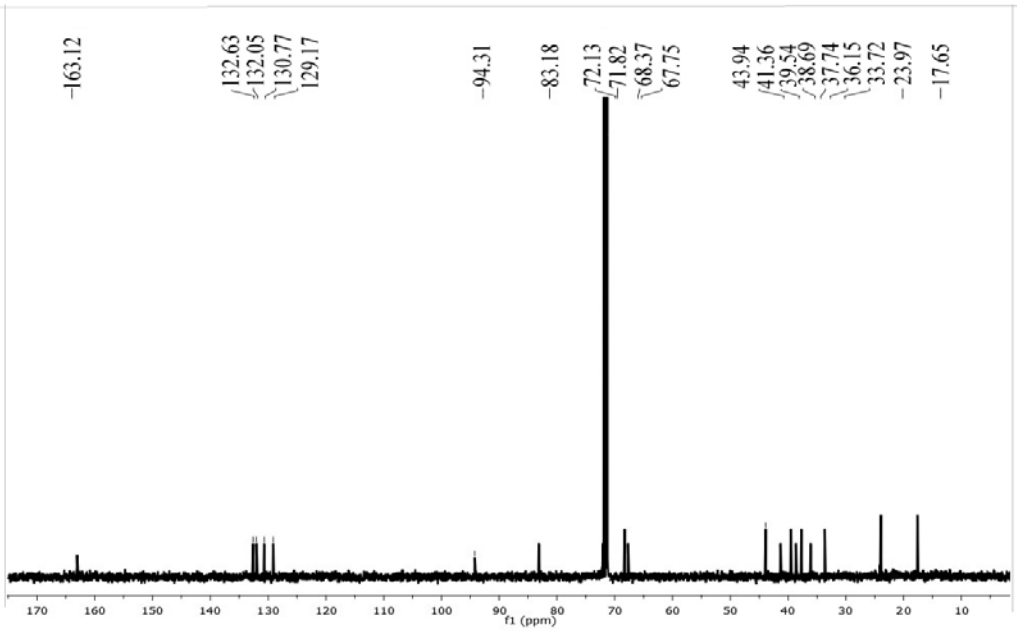

Figure 5.24.: ^{13}C NMR spectrum of 1,2,5,5a,6,9,10,11,12,12a-decahydro-11(11^{2}-hydroxypropyl)-2-[(*E*)-2^{1}-propenyl] cyclonona[*d*]-furo[2,3-*b*]pyran-9,12-diol (**2**)

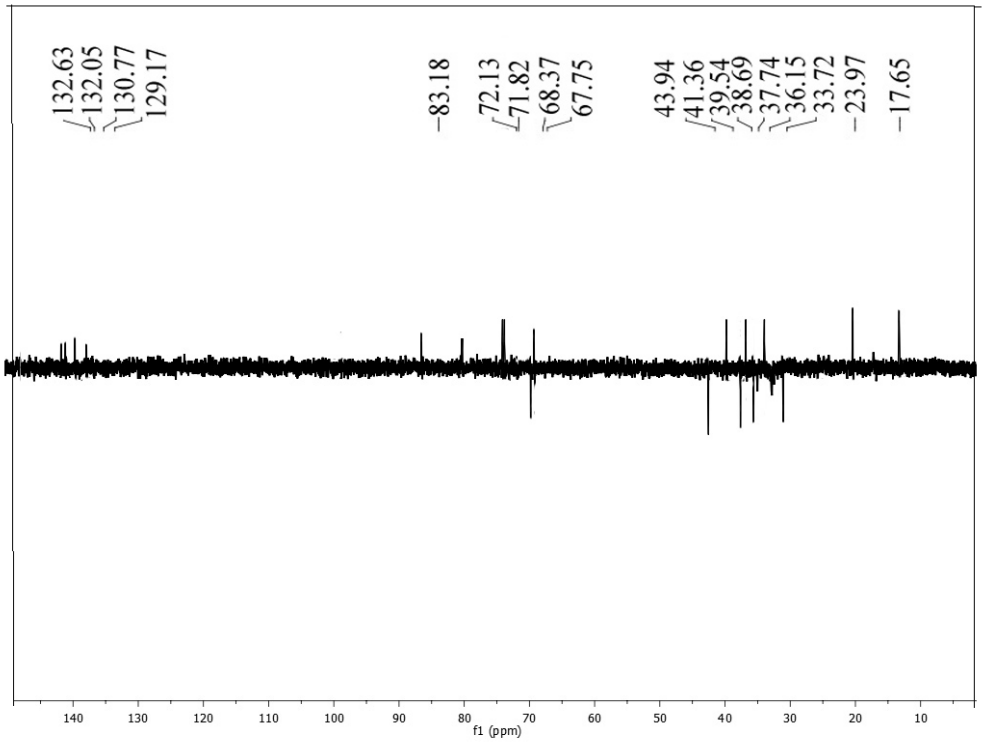

Figure 5.25.: ^{135}DEPT NMR spectrum of 1,2,5,5a,6,9,10,11,12,12a-decahydro-11(11^{2}-hydroxypropyl)-2-[(*E*)-2^{1}-propenyl] cyclonona[*d*]-furo[2,3-*b*]pyran-9,12-diol (**2**)

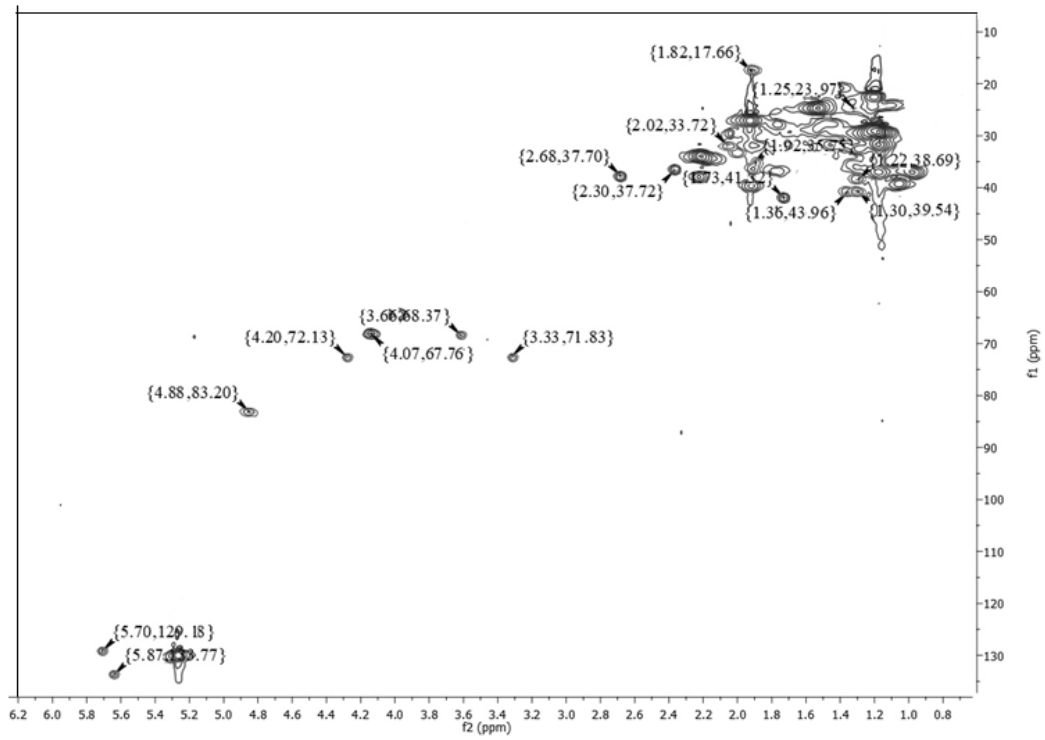

Figure 5.26.: HSQC spectrum of 1,2,5,5a,6,9,10,11,12,12a-decahydro-11(11^2-hydroxypropyl)-2-[(*E*)-2^1-propenyl] cyclonona[*d*]-furo[2,3-*b*]pyran-9,12-diol (**2**)

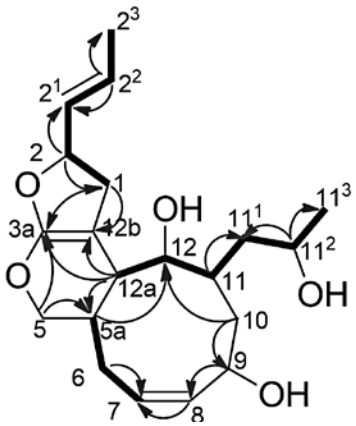

Figure 5.27.: Prominent ^{1}H-^{1}H COSY, and selected HMBC correlations of 1,2,5,5a,6,9,10,11,12,12a-decahydro-11(11^2-hydroxypropyl)-2-[(*E*)-2^1-propenyl] cyclonona[*d*]-furo[2,3-*b*]pyran-9,12-diol (**2**). The key ^{1}H-^{1}H COSY couplings were represented in bold face bonds. The key HMBC couplings have been represented by double barbed arrows.

The location of double bond was also shifted to C-3a/C-12b in **2**, wherein the extra substitution of propan-2-ol, and the arrangement of hydroxyls were different in **2** as compared to those found in **1**, and that these attributions were confirmed by three COSY spins (**I-III**) and

HMBCs. The COSY spectrum revealed the existence of three spin units (**I-III**) that were connected together by HMBCs in the tricyclic system, affirming the planer structure of **2**. The side chains prop-2-ene and propan-2-ol linked to the tricyclic ring system were supported by the spin systems **I** and **II**. The ^{1}H and ^{13}C-NMR experiments disclosed higher resemblance of **2** with **1**, in that former owned the similar tricyclic system, but varied in composition of the side chain.

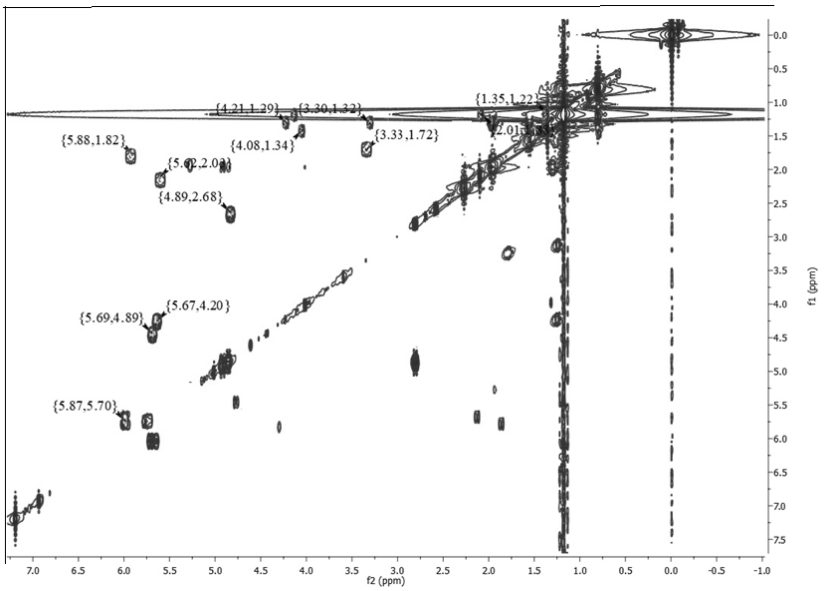

Figure 5.28.: ^{1}H-^{1}H COSY spectrum of 1,2,5,5a,6,9,10,11,12,12a-decahydro-11(11^{2}-hydroxypropyl)-2-[(*E*)-2^{1}-propenyl] cyclonona[*d*]-furo[2,3-*b*]pyran-9,12-diol (**2**)

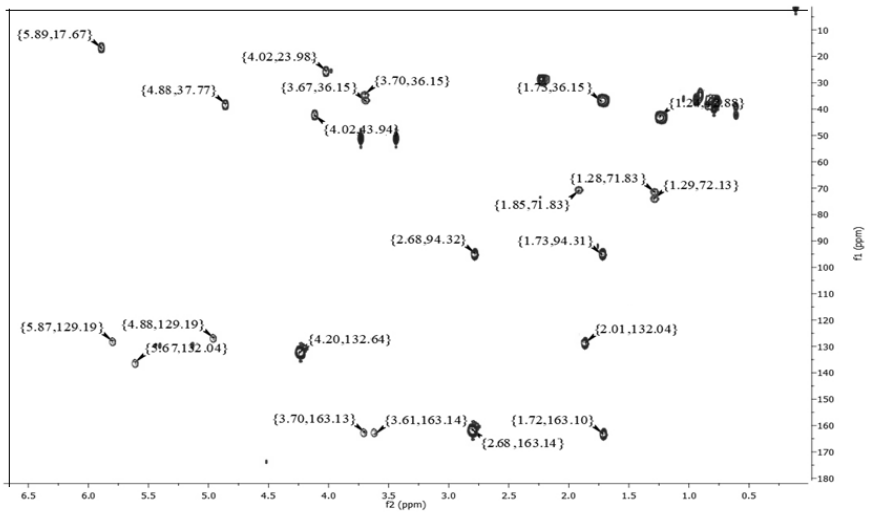

Figure 5.29.: HMBC spectrum of 1,2,5,5a,6,9,10,11,12,12a-decahydro-11(11^{2}-hydroxypropyl)-2-[(*E*)-2^{1}-propenyl] cyclonona[*d*]-furo[2,3-*b*]pyran-9,12-diol (**2**)

Relative stereochemistries of **2** were demonstrated with NOESY interactions, wherein the correlations between δ 4.88/1.72 (H-2/12a), δ 1.72/3.33 (H-12a/5), δ 3.33/1.22 (H-1/11), δ 1.22/1.35 (H-11/11^1) and δ 1.22/4.07 (H-11/11^2) revealed the presence of these protons on the similar face of the tricyclic system (arbitrarily assigned to β). NOEs between δ 1.85/4.20 (H-5a/H-9), δ 2.01/4.20 (H-6/H-9), and δ 3.67/4.20 (H-5/H-9) assigned the protons to be oriented towards the *α*-plane of the tricyclic system. NOESYs between H-2/H-12a, H-12a/H-12 and H-5a/H-9 established the *trans* orientation of the chiral carbons at C-12a and C-5a (Figure 5.30 & 5.31).

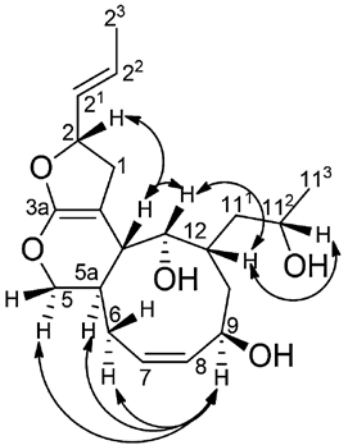

Figure 5.30.: HMBC spectrum of 1,2,5,5a,6,9,10,11,12,12a-decahydro-11(11^2-hydroxypropyl)-2-[(*E*)-2^1-propenyl] cyclonona[*d*]-furo[2,3-*b*]pyran-9,12-diol (**2**)

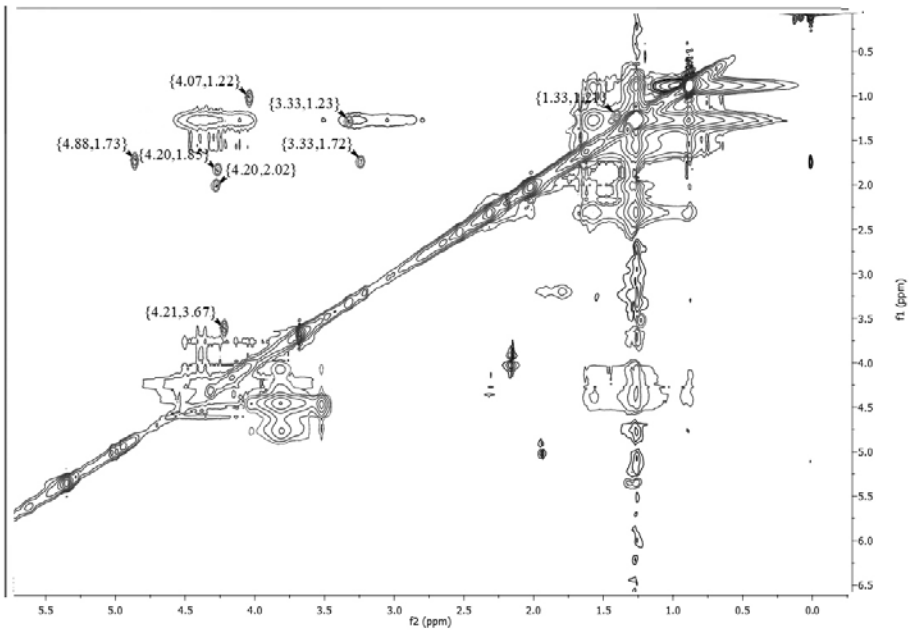

Figure 5.31.: NOESY spectrum of 1,2,5,5a,6,9,10,11,12,12a-decahydro-11(11^2-hydroxypropyl)-2-[(*E*)-2^1-propenyl] cyclonona[*d*]-furo[2,3-*b*]pyran-9,12-diol (**2**)

Table 5.5.: NMR spectroscopic data[a] of 1,2,5,5a,6,9,10,11,12,12a-decahydro-11(11^2-hydroxypropyl)-2-[(*E*)-2^1-propenyl] cyclonona[*d*]-furo[2,3-*b*]pyran-9,12-diol (**2**) isolated from brown seaweed *P.tetrastromatica*

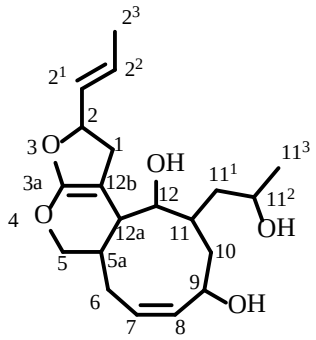

Compounds **2**…… 1,2,5,5a,6,9,10,11,12,12a-Decahydro-11(11^2-hydroxypropyl)-2-[(*E*)-2^1-propenyl] cyclonona[*d*]-furo[2,3-*b*]pyran-9,12-diol (**2**)

C. No.	**^{13}C NMR**	**^{1}H NMR (int., mult., J in Hz)[b]**	**COSY**	**HMBC**
1	37.74	2.68 (1H, dd, J=8.8, 7.69 Hz), 2.30 (1H, dd, J=13.01, 8.20 Hz)	H-2	C-12b, 3a
2	83.18	4.88 (1H, dd, J=16.99, 8.06 Hz)	H-2^1	C-1, 2^1
2^1	129.17	5.69 (1H, dd, J=14.47, 6.95 Hz)	H-2^2	-
2^2	130.77	5.87 (1H, m)	H-2^3	C-2^1, 2^3
2^3	17.65	1.82 (3H, d, J= 6.75 Hz)		-
3	-	-	-	-
3a	163.12	-	-	-
4	-	-	-	-
5	68.37	3.67 (1H, dd, J=12.77, 7.67 Hz) 3.70 (1H, dd, J=12.25, 7.66 Hz)	-	C-3a, 5a
5a	36.15	1.85 (1H, m)		C-12
6	33.72	2.01 (1H, m), 1.75 (H_β, m)	H-5a	C-7
7	132.05	5.62 (1H, m)	H-6	
8	132.63	5.67 (1H, dd, J=14.47, 6.95 Hz)	-	C-7
9	72.13	4.20 (1H, dd, J=15.60, 7.35 Hz)	H-8	C-8
10	39.54	1.29 (1H, m), 1.52 (H_β, m)	H-9	C-12, 9
11	38.69	1.22 (1H, m)	H-11^1	C-11^1
11^1	43.94	1.35 (1H, t, J=5.70, 3.47 Hz)	H-11^2	-
11^2	67.75	4.07 (1H, m)	H-11^3	C-11^1, 11^3
11^3	23.97	1.25 (3H, d, J=5.52 Hz)	-	-
12	71.82	3.33 (1H, dd, J=8.76, 1.86 Hz)	H-11	
12a	41.36	1.72 (1H, dd, J=11.46, 4.88 Hz)	H-12	C-5a, 3a ,12b
12b	94.31	-	-	-

[a]NMR spectra were recorded using a B ruker AVANCE III 500 MHz (AV 500) spectrometer (B ruker, Karlsruhe, Germany) in $CDCl_3$ as aprotic solvent at ambient temperature with TMS as the internal standard (δ 0 ppm).

[b]Values in ppm, multiplicity and coupling constants (J=Hz) were indicated in parentheses. Multiplicities were allocated by ^{135}DEPT NMR spectrum.

The assignments were made with the aid of the COSY, HSQC, HMBC and NOESY experiments.

The molecular ion peak of **2** was appeared at *m/z* 350 and base peak was ontained at *m/z* 40.0 (Figure 5.32 and 5.33).

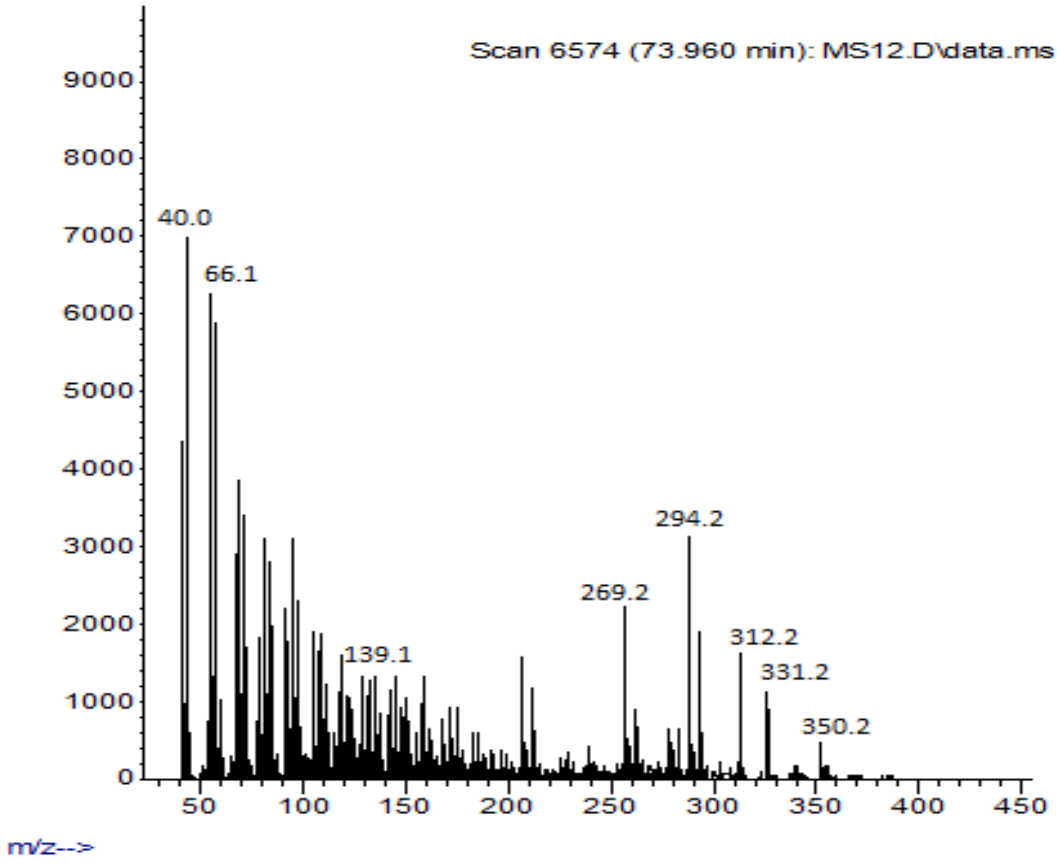

Figure 5.32.: EI-MS spectrum of 1,2,5,5a,6,9,10,11,12,12a-decahydro-11(11^2-hydroxypropyl)-2-[(*E*)-2^1-propenyl] cyclonona[*d*]-furo[2,3-*b*]pyran-9,12-diol (**2**)

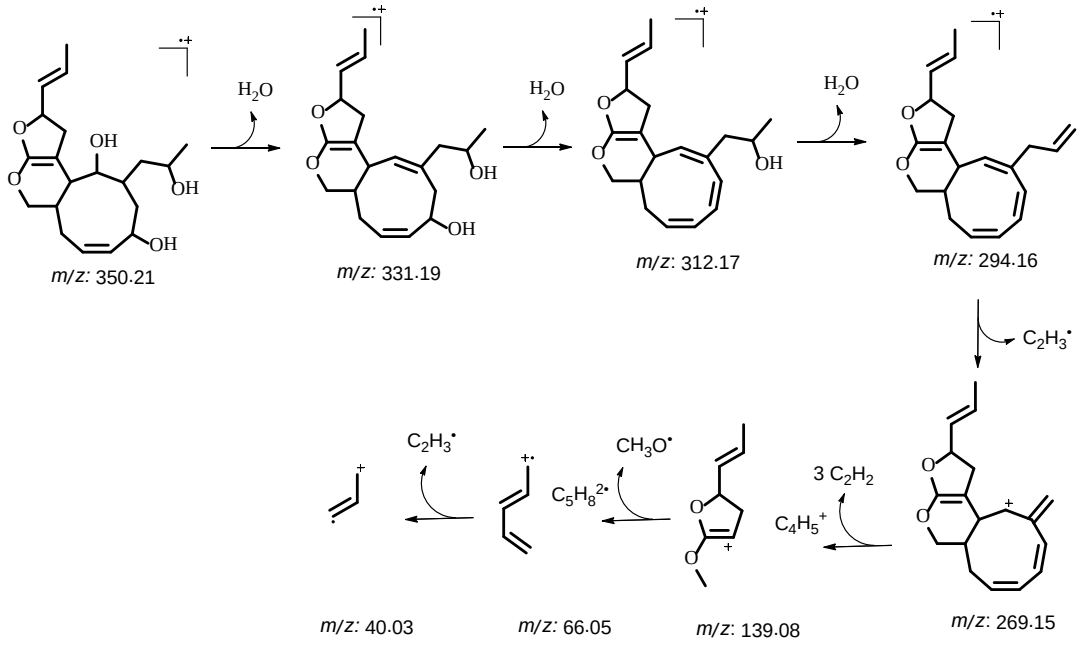

Figure 5.33.: Tentative mass fragmentation pattern of 1,2,5,5a,6,9,10,11,12,12a-decahydro-11(11^2-hydroxypropyl)-2-[(*E*)-2^1-propenyl] cyclonona[*d*]-furo[2,3-*b*]pyran-9,12-diol (**2**)

5.3.2.1c Structural characterization of Compound 3 (TP_3)

4-(4^1,4^2-Dihydroxypropyl)-4,4a,5,6,7,8,11,11a-octahydro-8,11-dihydroxy-7-methyl-6-(6^1-methyl-6^2-propenyl)-cyclonona[*c*]pyran-3-(1*H*)-one

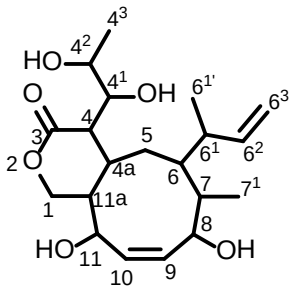

Sample yield	0.27% (> 99% purity, RP-C_{18} HPLC)
Physical description	Pale Yellow oil
Molecular formula	$C_{20}H_{32}O_6$
Molecular mass	368.2199

The xenicane class of diterpenoid derivative, 4-(4^1,4^2-Dihydroxypropyl)-4,4a,5,6,7,8,11,11a-octahydro-8,11-dihydroxy-7-methyl-6-(6^1-methyl-6^2-propenyl)-cyclonona[*c*]-pyran-3-(1*H*)-one was isolated as pale yellow oil compound. The compound (**3**) has exhibited UV absorbance (UV (MeOH) λ_{max}) at 246 (2.90) nm (Figure 5.34). The homogeneity of the compound was ascertained by HPLC data on a bonded phase octadecylsilane (C_{18}) stationary phase (RP-C_8 HPLC, MeOH: MeCN, 4:1 v/v): 4.20 min (Figure 5.35).

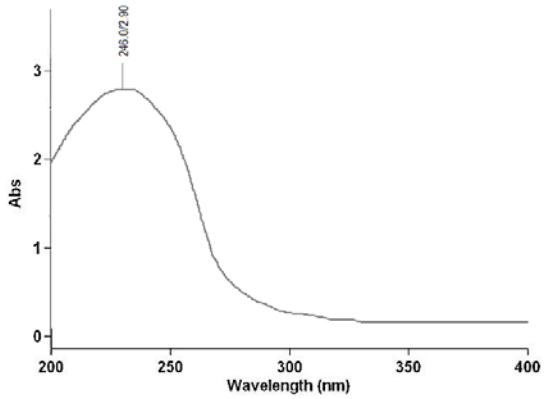

Figure 5.34.: UVspectrum of 4-(4^1,4^2-dihydroxypropyl)-4,4a,5,6,7,8,11,11a-octahydro-8,11-dihydroxy-7-methyl-6-(6^1-methyl-6^2-propenyl)-cyclonona[*c*]pyran-3-(1*H*)-one (**3**)

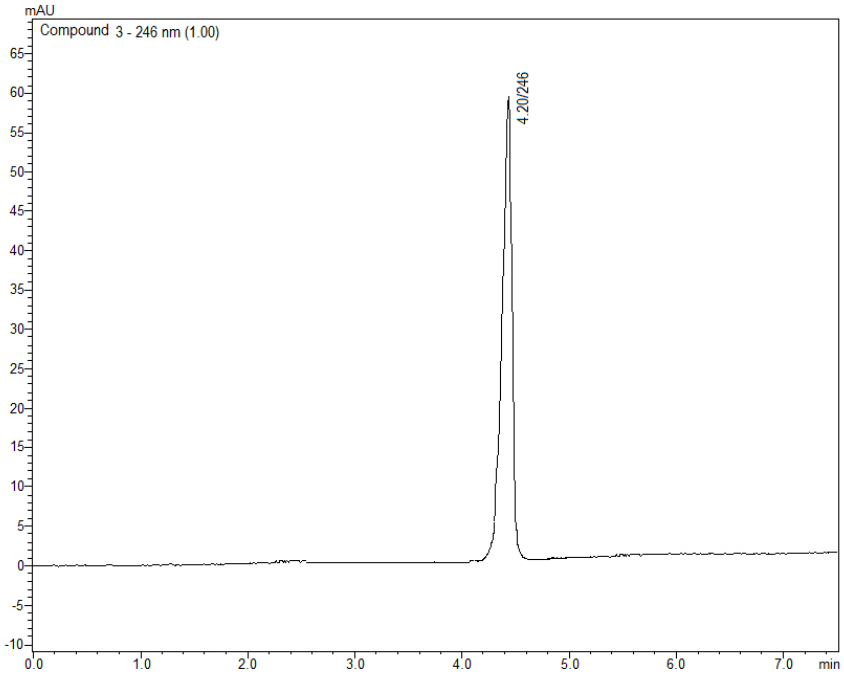

Figure 5.35.: HPLC chromatogram of 4-(4^1,4^2-dihydroxypropyl)-4,4a,5,6,7,8,11,11a-octahydro-8,11-dihydroxy-7-methyl-6-(6^1-methyl-6^2-propenyl)-cyclonona[*c*]pyran-3-(1*H*)-one (**3**)

The molecular ion peak by HRESIMS (positive mode) was observed at *m/z*: 369.2280 $[M+H]^+$ (Figure 5.36). The FTIR spectrum of **3** displayed absorption bands at, 3473 (O-H), and 1715 (C=O) (Figure 5.37).

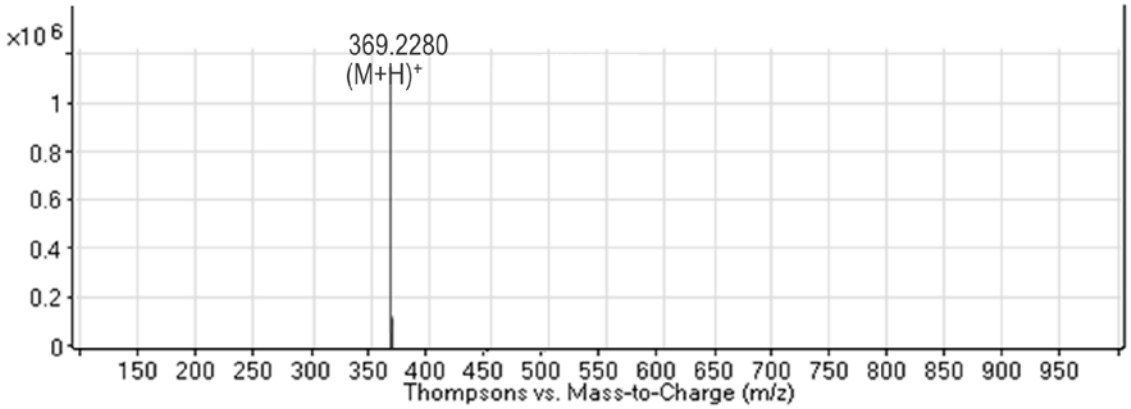

Figure 5.36.: HRESIMS of 4-(4^1,4^2-dihydroxypropyl)-4,4a,5,6,7,8,11,11a-octahydro-8,11-dihydroxy-7-methyl-6-(6^1-methyl-6^2-propenyl)-cyclonona[*c*]pyran-3-(1*H*)-one (**3**)

The chromatographic fraction of the crude extract of *P. tetrastromatica* yielded **3** as pale yellowish oil. The molecular ion peak of **3** was appeared at *m/z* 368, whereas the molecular formula $C_{20}H_{32}O_6$, implying five unsaturation degrees, was associated with three olefinic bonds and two ring systems. The spectroscopic data of **3** displayed, in conjunction with the similar substituted 9-membered cyclic system of diterpenoids **1-2** along with the δ-lactone signals at δ 65.75 (attributed to C-1), δ 3.95, 4.22; δ 172.35 (C-3), δ 48.80 (C-4); δ 2.21, δ 37.55 (C-4a), δ 1.62, and δ 42.93 (C-11a); δ 1.82 substituted with a 1,2-dihydroxypropyl functionality at δ 48.80 (C-4) (Figure 5.38-5.41).

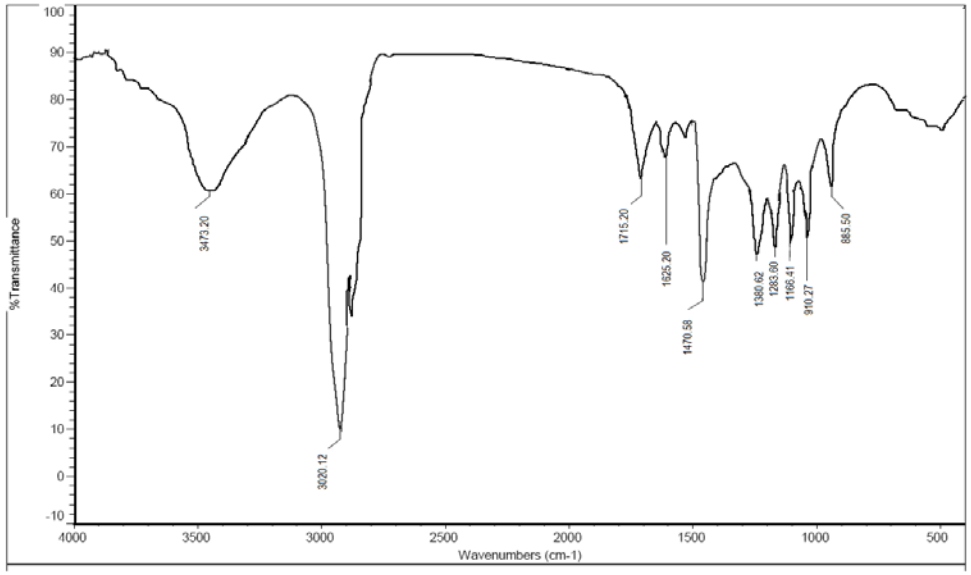

Figure 5.37.: FTIR spectrum of 4-(4^1,4^2-dihydroxypropyl)-4,4a,5,6,7,8,11,11a-octahydro-8,11-dihydroxy-7-methyl-6-(6^1-methyl-6^2-propenyl)-cyclonona[*c*]pyran-3-(1*H*)-one (**3**)

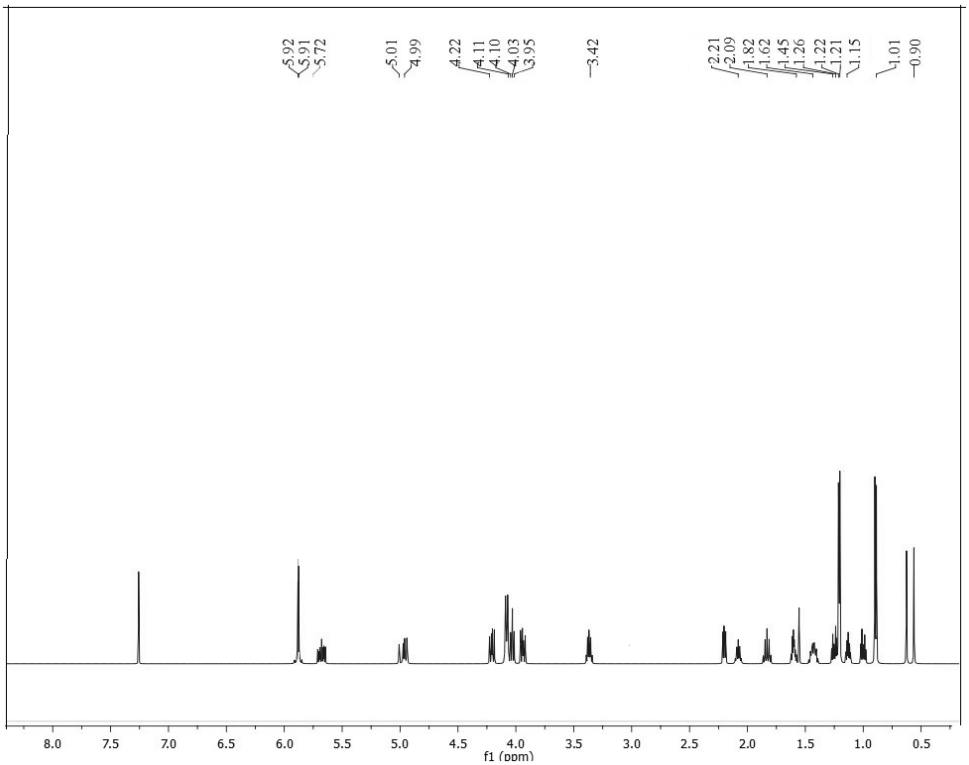

Figure 5.38.: ^{1}H NMR spectrum of -(4^1,4^2-dihydroxypropyl)-4,4a,5,6,7,8,11,11a-octahydro-8,11-dihydroxy-7-methyl-6-(6^1-methyl-6^2-propenyl)-cyclonona[*c*]pyran-3-(1*H*)-one (**3**)

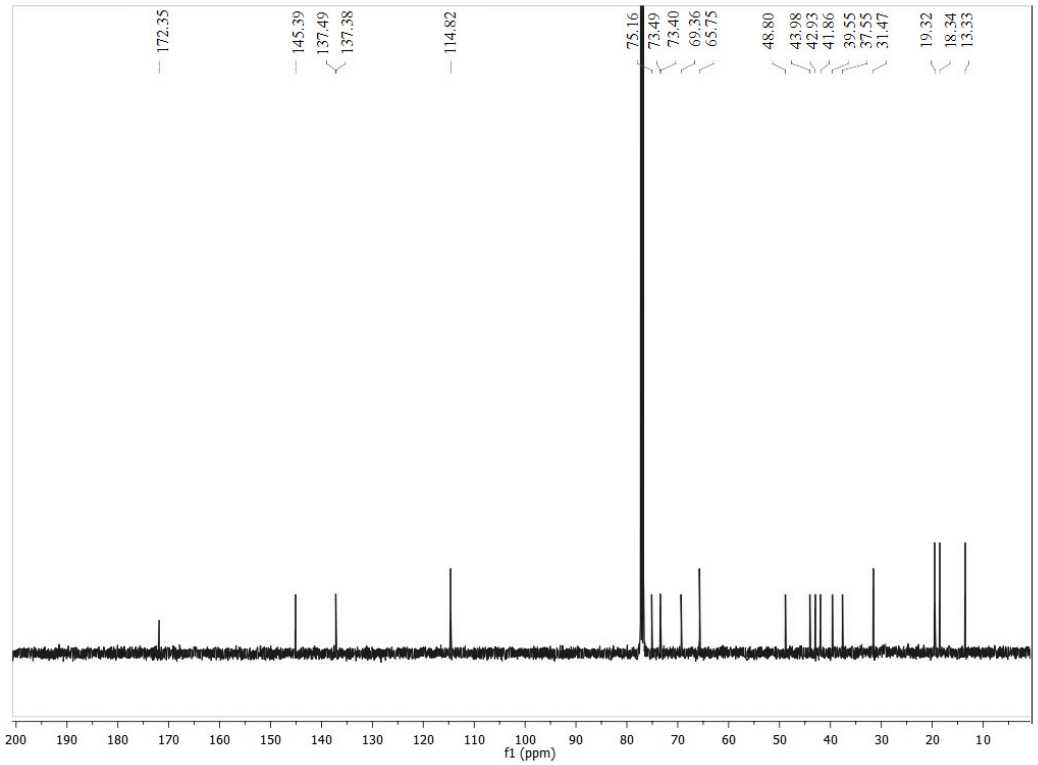

Figure 5.39.: ^{13}C NMR spectrum of 4-(4^{1},4^{2}-dihydroxypropyl)-4,4a,5,6,7,8,11,11a-octahydro-8,11-dihydroxy-7-methyl-6-(6^{1}-methyl-6^{2}-propenyl)-cyclonona[*c*]pyran-3-(1*H*)-one (**3**)

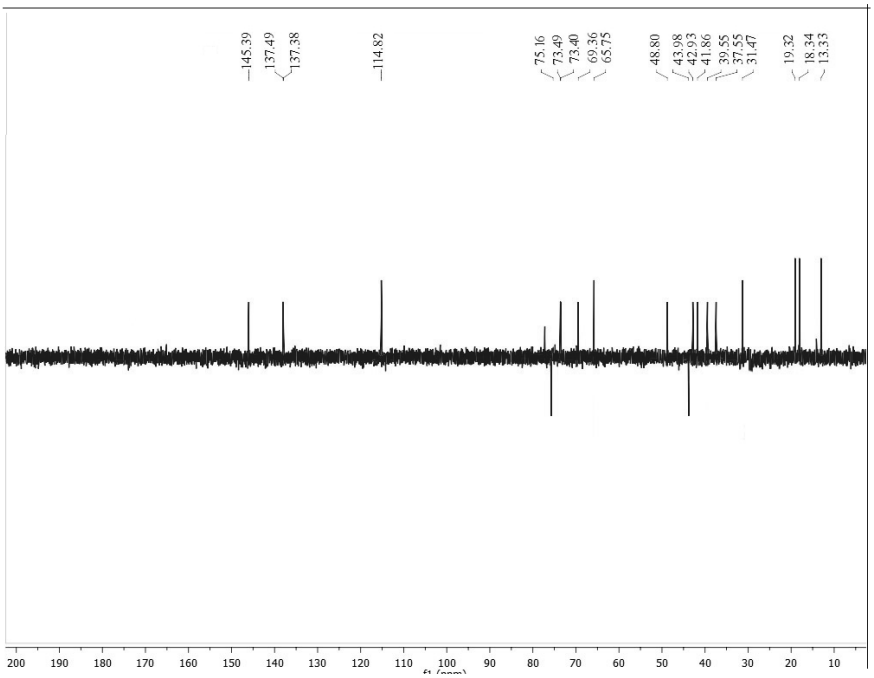

Figure 5.40.: ^{135}DEPT NMR spectrum of 4-(4^{1},4^{2}-dihydroxypropyl)-4,4a,5,6,7,8,11,11a-octahydro-8,11-dihydroxy-7-methyl-6-(6^{1}-methyl-6^{2}-propenyl)-cyclonona[*c*]pyran-3-(1*H*)-one (**3**)

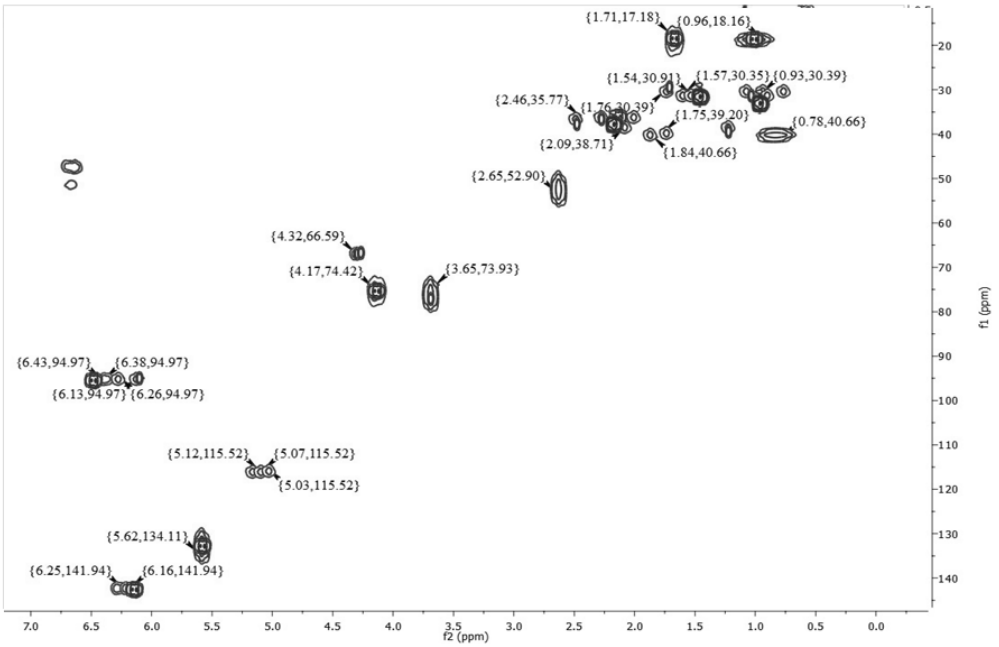

Figure 5.41.: HSQC spectrum of 4-(4[1],4[2]-dihydroxypropyl)-4,4a,5,6,7,8,11,11a-octahydro-8,11-dihydroxy-7-methyl-6-(6[1]-methyl-6[2]-propenyl)-cyclonona[*c*]pyran-3-(1*H*)-one (**3**)

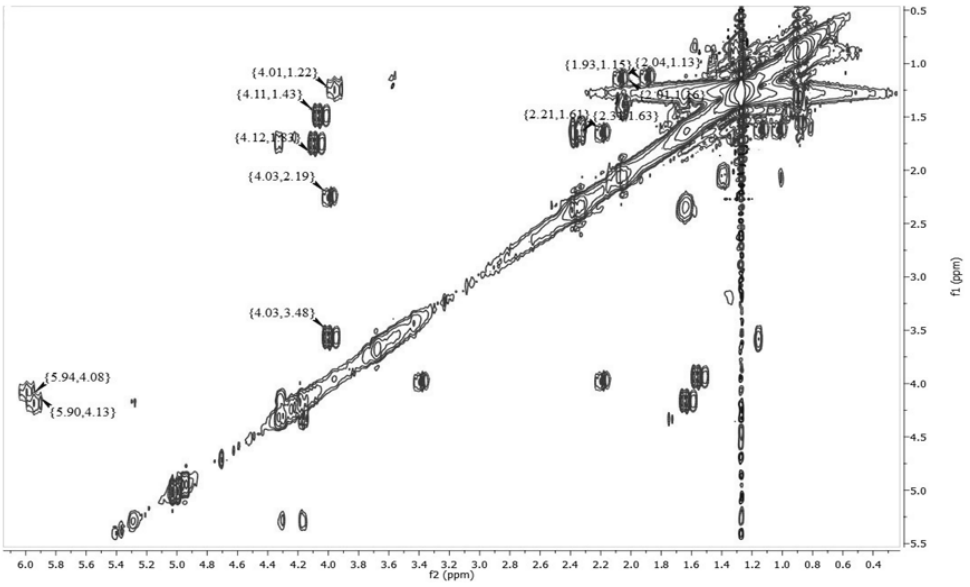

Figure 5.42.: [1]H-[1]H COSY of 4-(4[1],4[2]-dihydroxypropyl)-4,4a,5,6,7,8,11,11a-octahydro-8,11-dihydroxy-7-methyl-6-(6[1]-methyl-6[2]-propenyl)-cyclonona[*c*]pyran-3-(1*H*)-one (**3**)

The COSY spectrum revealed the existence of three spins (**I-III**) that were connected together by HMBCs, affirming its planer structure. An additional group of but-3-en-2-yl was

observed at δ 43.98 (C-6) associated with 9-membered cyclic ring, and the attribution was substantiated by the ^{13}C NMR bands at δ 43.98 (C-6), δ 39.55 (C-6^1), δ 145.39 (C-6^2), δ 114.82 (C-6^3), and δ 18.34 (C-6$^{1'}$). These connections were supported by COSYs between δ 1.01/1.15 (H-5/H-6), δ 1.15/1.45 (H-6/H-7), δ 1.15/2.09 (H-6/H-6^1), δ 2.09/5.72 (H-6^1/H-6^2), and δ 5.72/5.01 (H-6^2/H-6^3). The HMBCs between δ 1.15/31.47 (H-6/C-5), δ 2.09/43.98 (H-6^1/C-6), δ 2.09/145.39 (H-6^1/C-6^2), δ 1.22/39.55 (H-6$^{1'}$/C-6^1) and δ 5.01/39.55 (H-6^3/C-6^1) further substantiated the attributions (Figure 5.42-5.44).

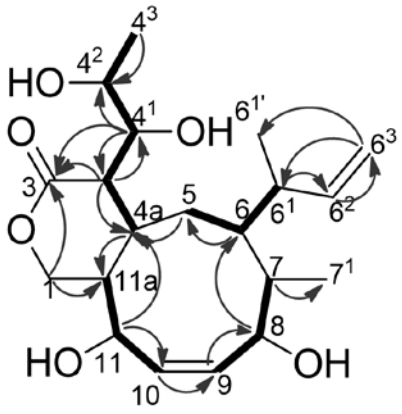

Figure 5.43.: Prominent ^{1}H-^{1}H COSY, and selected HMBC correlations of 4-(4^1,4^2-dihydroxypropyl)-4,4a,5,6,7,8,11,11a-octahydro-8,11-dihydroxy-7-methyl-6-(6^1-methyl-6^2-propenyl)-cyclonona-[*c*]-pyran-3-(1*H*)-one (**3**). The key ^{1}H-^{1}H COSY couplings were represented in bold face bonds. The key HMBC couplings have been represented by double barbed arrows.

The carbon signals of **3** showed a carbonyl carbon at δ 172.35 (C-3) and four olefinic ^{13}C signals (one methylene, three methines), which reckoned for five degrees of unsaturation. Three COSY spin systems (**I-III**) in **3** were supported by HMBCs between corresponding carbons and protons. The spin unit **I** was demonstrated by COSYs between δ 1.62/2.21 (H-4a/H-4), δ 2.21/4.03 (H-4/H-4^1), δ 4.03/δ 3.42 (H-4^1/H-4^2), which were connected to second and third spin system (**II** and **III**) by carbons C-4a and C-11a, respectively. The HMBCs at δ 1.01/37.55 (H-5/C-4a), δ 2.21/73.49 (H-4/C-4^1), δ 4.03/48.80 (H-4^1/C-4), δ 4.03/69.36 (H-4^1/C-4^2), and δ 1.21/69.36 (H-4^3/C-4^2) connected the different moieties in the spin system **I**. The HMBCs between δ 2.21/37.55 (H-4/C-4a), δ 4.03/172.35 (H-4^1/C-3) connected the spin system to δ-lactone and 9-membered cyclic ring. Similarly COSY spin systems **II**, **III** and **IV** were established between the protons δ 1.01/1.15 (H-5/H-6), δ 1.15/2.09 (H-6/H-6^1); δ 1.45/4.11 (H-7/H-8), δ 4.11/5.91 (H-8/H-9), δ 5.01/1.22 (H-6^3/H-6$^{1'}$); δ 5.92/4.10 (H-10/H-11), δ 4.10/1.82 (H-11/H-11a), which were connected each other by

HMBCs between δ 4.11/43.98 (H-8/C-6), δ 4.10/37.55 (H-11/C-4a), δ 1.62/42.93 (H-4a/C-11a), δ /δ 5.91/75.16 (H-9/C-8), δ /δ 5.92/137.49 (H-10/C-9), and δ 4.10/137.38 (H-11/C-10).

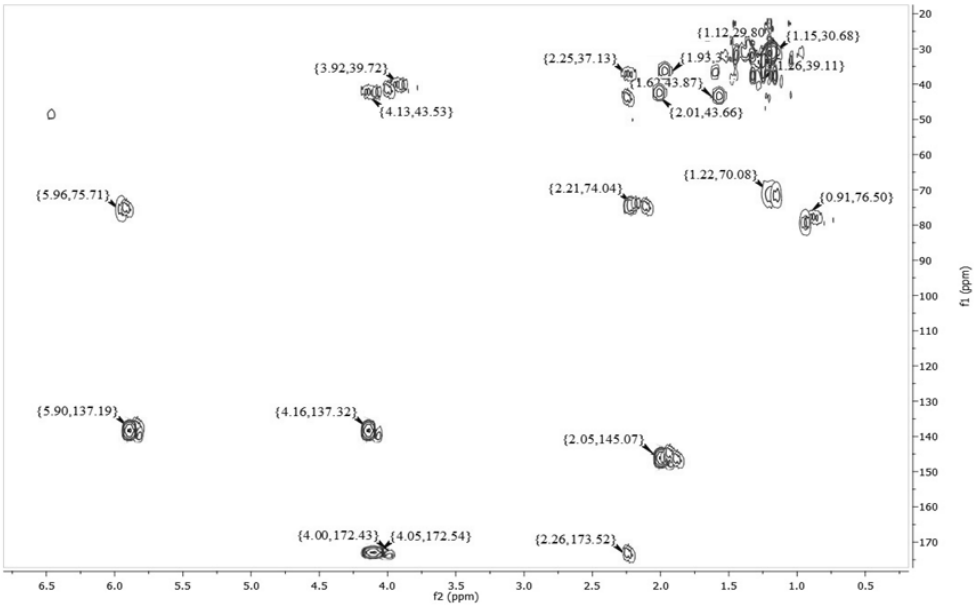

Figure 5.44.: HMBC spectrum of 4-(4^1,4^2-dihydroxypropyl)-4,4a,5,6,7,8,11,11a-octahydro-8,11-dihydroxy-7-methyl-6-(6^1-methyl-6^2-propenyl)-cyclonona[*c*]pyran-3-(1*H*)-one (**3**)

Relative stereochemistries of **3** was determined by NOESY experimental data, whereas the protons at δ 3.42 (H-4^2), δ 4.03 (H-12), δ 2.21 (H-4) and δ 1.62 (H-4a) showed strong NOEs, such as H-4^2/H-4^1, H-4^1/H-4, H-4/H-4a and H-4a/H-6^1, respectively. These were aligned towards the β -face of the reference plane of **3**. On the other hand, NOEs demonstrated the spatial proximity of the H-11a (δ 1.82) with the H-11 (δ 4.10); H-11 (δ 4.10) with H-7 (δ 1.45), and H-8 (δ 4.11) with H-7 (δ 1.45). These were aligned in the opposite plane of β -face of the reference plane of **3** (as *α*-protons (Figure 5.45 & 5.46)

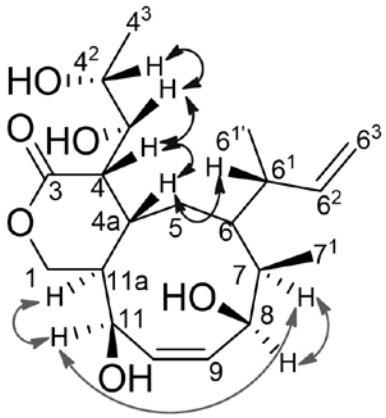

Figure 5.45.: Prominent NOE correlations of 4-(4[1],4[2]-dihydroxypropyl)-4,4a,5,6,7,8,11,11a-octahydro-8,11-dihydroxy-7-methyl-6-(6[1]-methyl-6[2]-propenyl)-cyclonona[*c*]pyran-3-(1*H*)-one (**3**). NOESY relations are represented by double-tailed arrows

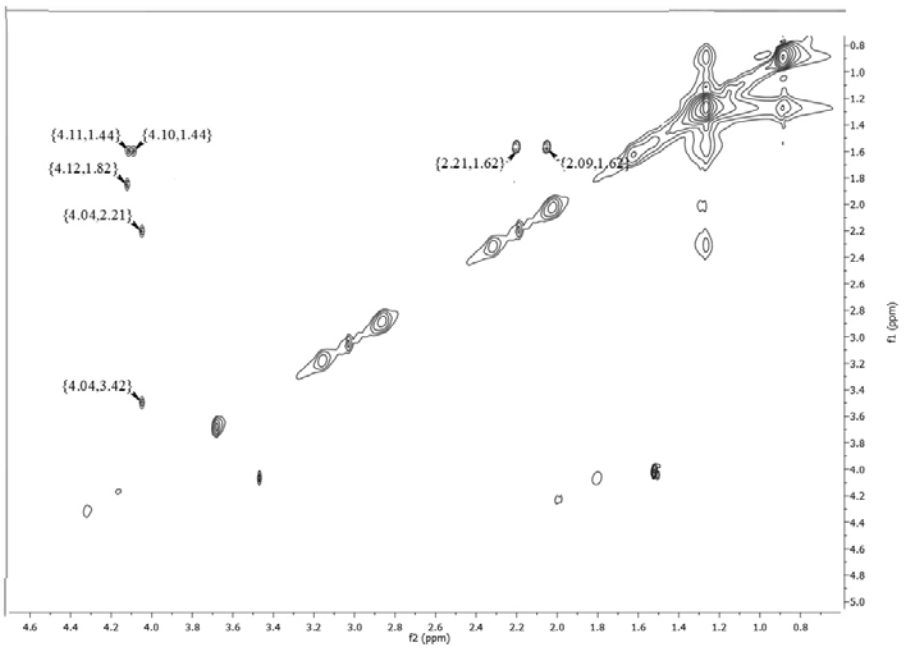

Figure 5.46.: NOESY spectrum of 4-(4[1],4[2]-dihydroxypropyl)-4,4a,5,6,7,8,11,11a-octahydro-8,11-dihydroxy-7-methyl-6-(6[1]-methyl-6[2]-propenyl)-cyclonona[*c*]pyran-3-(1*H*)-one (**3**)

Table 5.6.: NMR spectroscopic data[a] of 4-(4^1,4^2-Dihydroxypropyl)-4,4a,5,6,7,8,11,11a-octahydro-8,11-dihydroxy-7-methyl-6-(6^1-methyl-6^2-propenyl)-cyclonona[*c*]pyran-3-(1*H*)-one (**3**) isolated from brown seaweed *P.tetrastromatica*

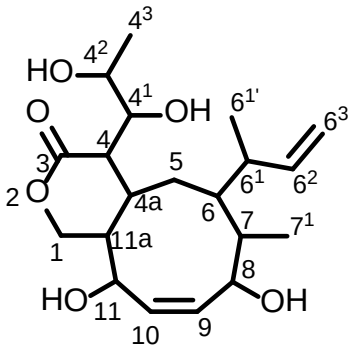

Compound **3**……4-(4^1,4^2-dihydroxypropyl)-4,4a,5,6,7,8,11,11a-octahydro-8,11-dihydroxy-7-methyl-6-(6^1-methyl-6^2-propenyl)-cyclonona[*c*]pyran-3-(1*H*)-one (**3**)

C. N.	^{13}C NMR	^{1}H NMR (int., mult., J in Hz)[b]	COSY	HMBC
		3.95 (1H, dd, J=10.1, 8.0 Hz)		
1	65.75	4.22 (1H, dd, J=9.1, 7.86 Hz)		C-3,11a
2	-	-	-	-
3	172.35	-	-	-
4	48.80	2.21 (1H, dd, J=9.8, 5.1 Hz)	H-4a, 4^1	C-3,4a,12
4a	37.55	1.62 (1H, m)	-	C-11a
4^1	73.49	4.03 (1H, t, J=9.0 Hz)	H-4^2	C-3,4,4^2
4^2	69.36	3.42 (1H, m)	-	
4^3	19.32	1.21 (3H, m)	-	C-4^2
		1.26 (1H, m),		
5	31.47	1.01 (1H, m)	H-6	H-4a
6	43.98	1.15 (1H, m)	H-6^1	C-5
6^1	39.55	2.09 (1H, m)	-	C-6, 6^2
$6^{1'}$	18.34	1.22 (3H, m)	-	C-6^1
6^2	145.39	5.72 (1H, m)		C-6^3
		5.01 (1H, dd, J=19.7, 17.1Hz),		
6^3	114.82	4.99 (1H, dd, J=19.7, 9.7 Hz)	-	C-6^1,$6^{1'}$
7	41.86	1.45 (1H, m)	H-8	C-7^1
7^1	13.33	0.90 (3H, d, J=3.2 Hz)	-	C-8
8	75.16	4.11 (1H, t, J=9.6 Hz)	H-9	C-6
9	137.49	5.91 (1H, d, J=11.7 Hz)	-	C-8
10	137.38	5.92 (1H, d, J=12.7 Hz)	H-11	C-9
11	73.40	4.10 (1H, t, J=9.5 Hz)	H-11a	C-10, 4a
11a	42.93	1.82 (1H, m)	-	-

[a]NMR spectra were recorded using a B ruker AVANCE III 500 MHz (AV 500) spectrometer (B ruker, Karlsruhe, Germany) in $CDCl_3$ as aprotic solvent at ambient temperature with TMS as the internal standard (δ 0 ppm).

[b]Values in ppm, multiplicity and coupling constants (J=Hz) were indicated in parentheses. Multiplicities were allocated by [135]DEPT NMR spectrum.

The assignments were made with the aid of the COSY, HSQC, HMB C and NOESY experiments.

The molecular ion peak of **3** was appeared at *m/z* 388 and base peak was ontained at *m/z* 40.0 (Figure 5.47 and 5.48).

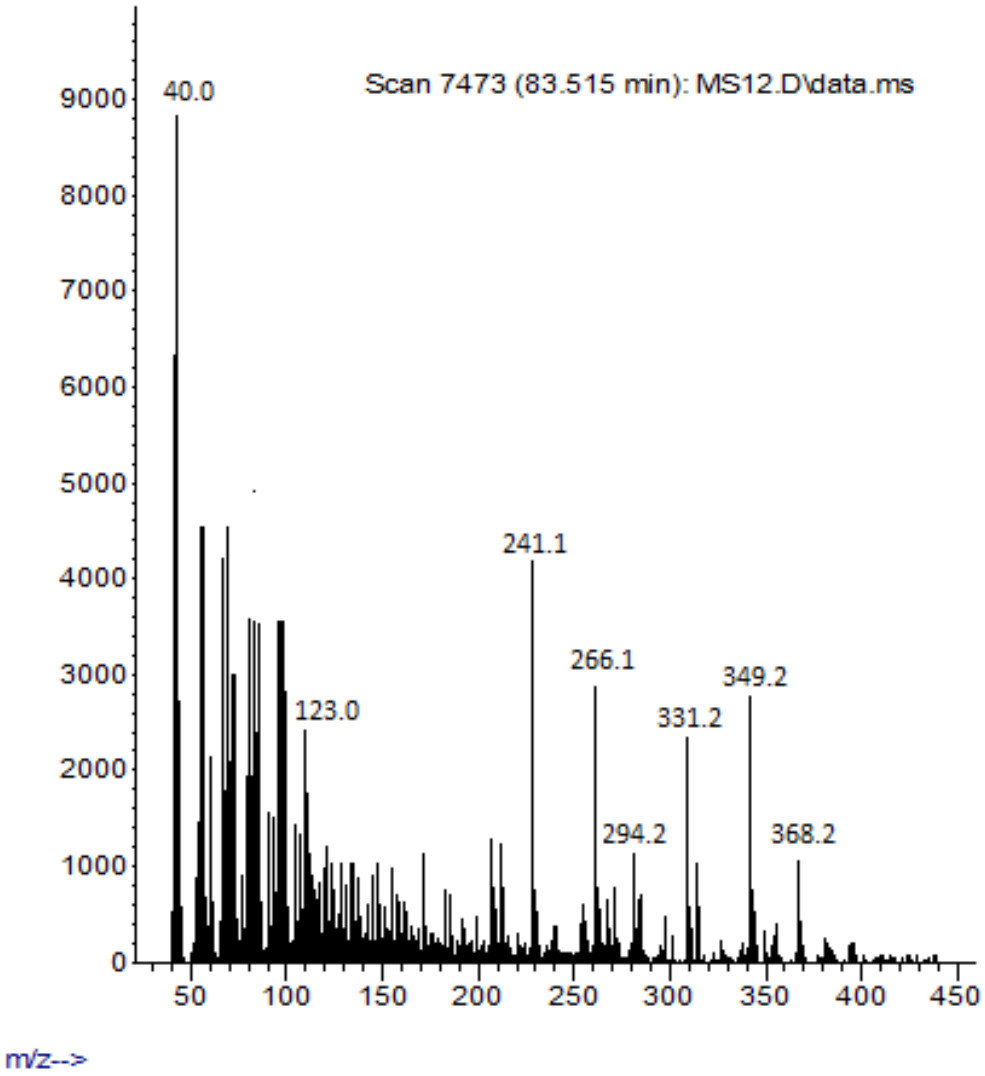

Figure 5.47.: EI-MS spectrum of 4-(4[1],4[2]-dihydroxypropyl)-4,4a,5,6,7,8,11,11a-octahydro-8,11-dihydroxy-7-methyl-6-(6[1]-methyl-6[2]-propenyl)-cyclononа[*c*]pyran-3-(1*H*)-one (**3**)

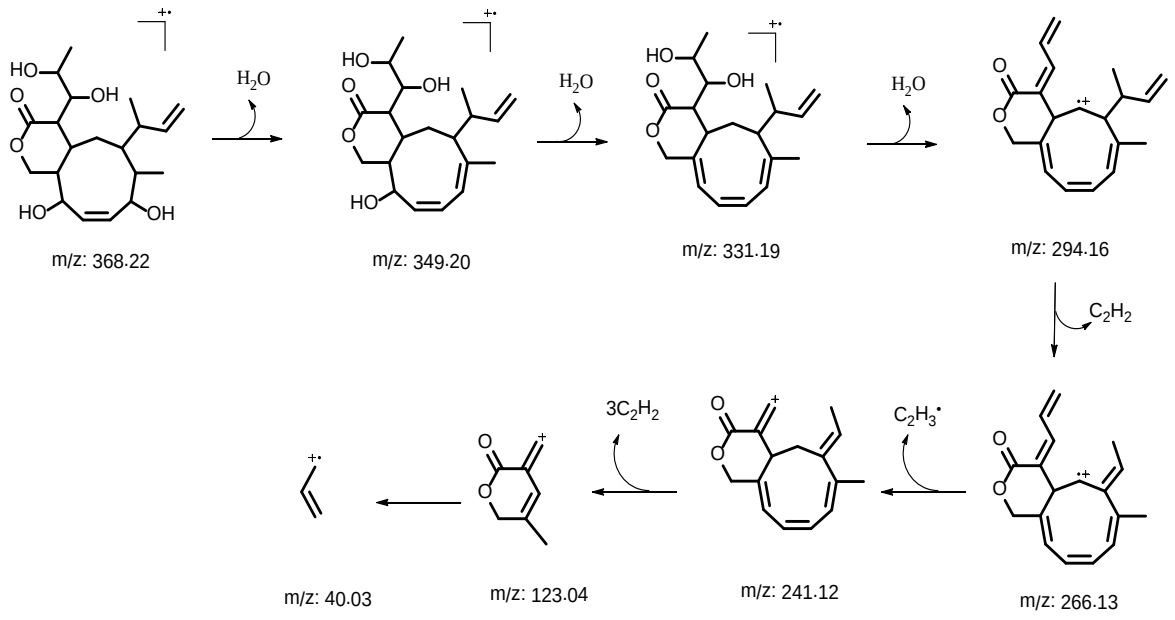

Figure 5.48.: Tentative mass fragmentation pattern of 4-(4[1],4[2]-dihydroxypropyl)-4,4a,5,6,7,8,11,11a-octahydro-8,11-dihydroxy-7-methyl-6-(6[1]-methyl-6[2]-propenyl)-cyclonona[*c*]-pyran-3-(1*H*)-one (**3**)

5.3.2.1d Structural characterization of Compound 4 (TP_4)

4,4a,5,6,7,8,11,11a-Octahydro-7-hydroxy-6-(6[2]-hydroxy-6[3]-butenyl)-4-(4[1]-hydroxypropyl)-11-methoxy-8-methyl-cyclonona[*c*]pyran-3-(1*H*)-one

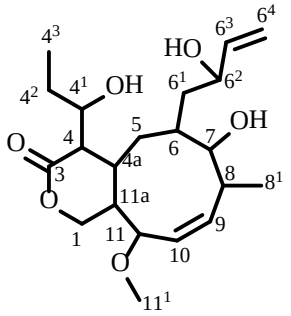

Sample yield	0.32% (> 99% purity, RP-C_{18} HPLC)
Physical description	Pale yellow oil
Molecular formula	$C_{21}H_{34}O_6$

Molecular mass	382.2355

The xenicane class of diterpenoid derivative, 4,4a,5,6,7,8,11,11a-octahydro-7-hydroxy-6-(6^2-hydroxy-6^3-butenyl)-4-(4^1-hydroxypropyl)-11-methoxy-8-methyl-cyclonona[*c*]pyran-3-(1*H*)-one was isolated as pale yellow oil compound. The compound (**4**) has exhibited UV absorbance (UV (MeOH) λ_{max}) at 209 (3.6), 249 (3.3) nm (Figure 5.49). The homogeneity of the compound was ascertained by HPLC data on a bonded phase octadecylsilane (C_{18}) stationary phase (RP-C_8 HPLC, MeOH: MeCN, 2:3 v/v): 4.05 min (Figure 5.50).

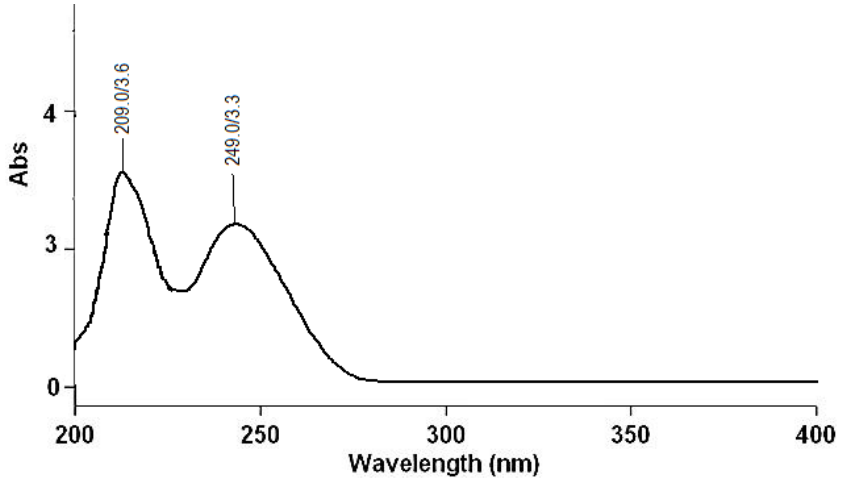

Figure 5.49.: UVspectrum of 4,4a,5,6,7,8,11,11a-octahydro-7-hydroxy-6-(6^2-hydroxy-6^3-butenyl)-4-(4^1-hydroxypropyl)-11-methoxy-8-methyl-cyclonona[*c*]pyran-3-(1*H*)-one (**4**)

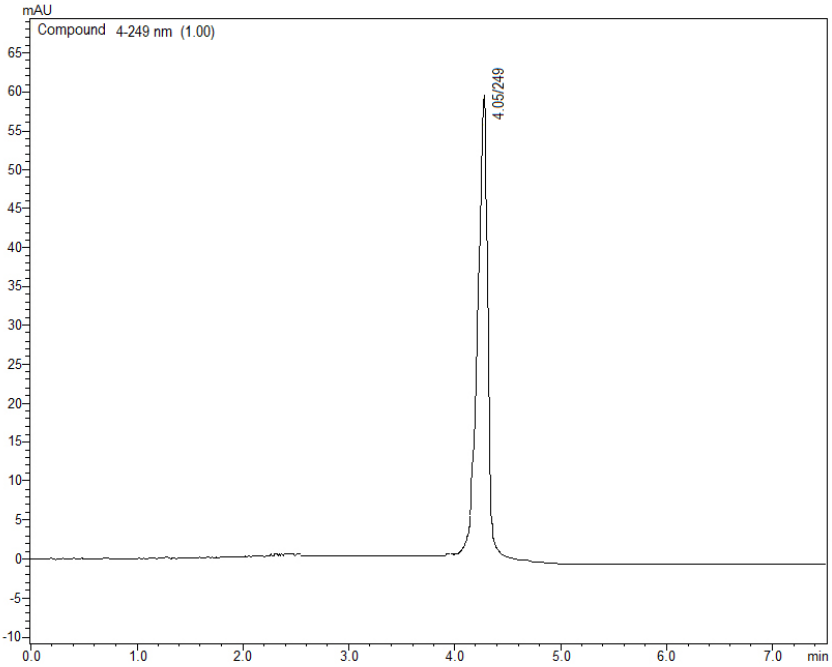

Figure 5.50.: HPLC chromatogram of 4,4a,5,6,7,8,11,11a-octahydro-7-hydroxy-6-(6^{2}-hydroxy-6^{3}-butenyl)-4-(4^{1}-hydroxypropyl)-11-methoxy-8-methyl-cyclonona[*c*]pyran-3-(1*H*)-one (**4**)

The molecular ion peak by HRESIMS (positive mode) was observed at *m/z* 383.2438 $[M+H]^{+}$ (Figure 5.51). The FTIR spectrum of **3** displayed absorption bands at 3451 (O-H) and 1737 (C=O) (Figure 5.52)

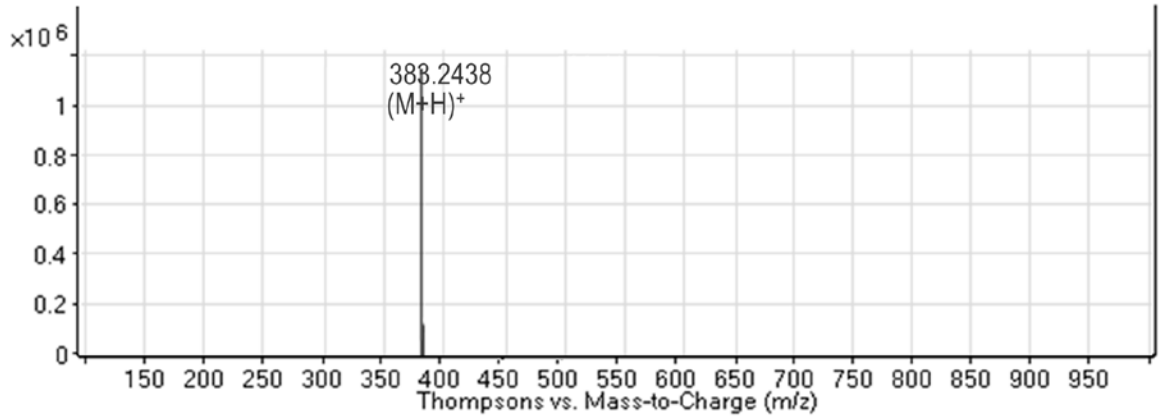

Figure 5.51.: HRESIMS of 4,4a,5,6,7,8,11,11a-octahydro-7-hydroxy-6-(6^{2}-hydroxy-6^{3}-butenyl)-4-(4^{1}-hydroxypropyl)-11-methoxy-8-methyl-cyclonona[*c*]pyran-3-(1*H*)-one (**4**)

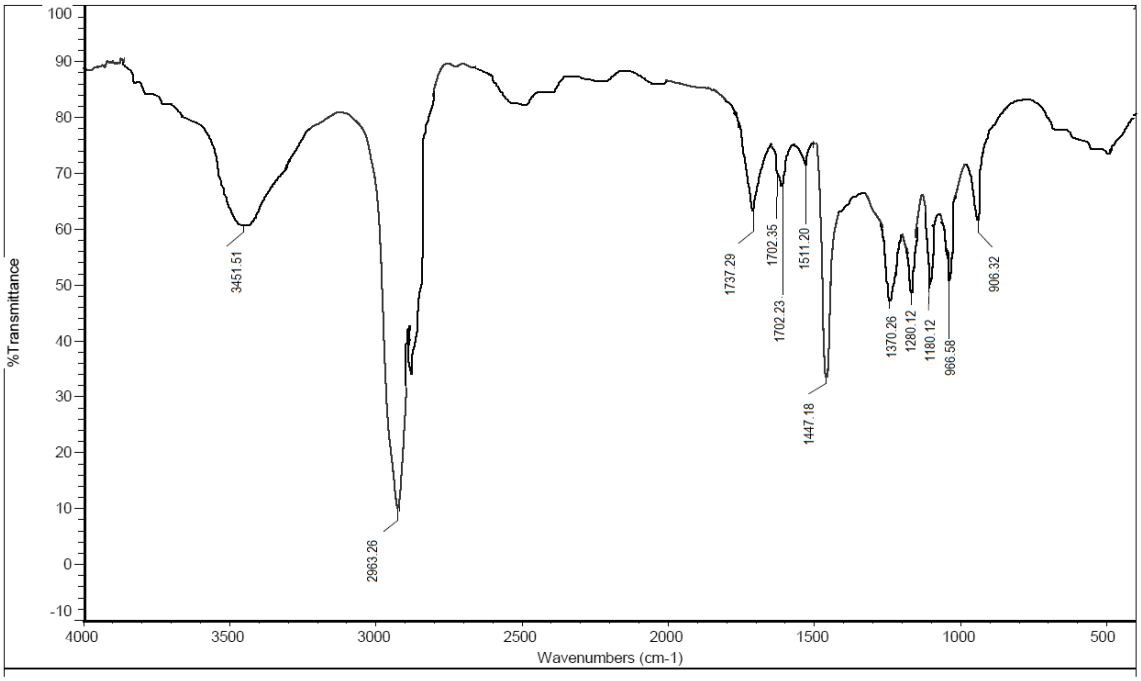

Figure 5.52.: FTIR of 4,4a,5,6,7,8,11,11a-octahydro-7-hydroxy-6-(6^2-hydroxy-6^3-butenyl)-4-(4^1-hydroxypropyl)-11-methoxy-8-methyl-cyclonona[*c*]pyran-3-(1*H*)-one (**4**)

Compound **4** was obtained as yellowish oil, whereas the molecular ion peak of **4** was appeared at *m/z* 382, and the molecular formula was determined as $C_{21}H_{34}O_6$. The spectroscopic characteristics of **4** were comparable to those of **3** with resonances exhibited by 9-membered cyclic ring bearing methoxy group at δ 82.04 (C-11) and substituted 2-hydroxybut-3-en-1-yl side chain at δ 40.16 (C-6) (Figure 5.46-). The ^{13}C-NMR and DEPT$_{135}$ spectra–displayed the occurrence of 21 signals of carbons incorporating twelve methine carbons (consisting of three olefinic methine carbons), five methylene carbons (including one olefinic methylene carbon signals and oxymethylene), three methyl carbons (including one methoxy carbon signal), suggesting five degrees of unsaturation, which proposed that **4** was a hydroxyl-substituted xeniolide diterpene (Figure 5.53-5.56). The proton NMR spectrum designated the existence of oxymethylene protons at δ 4.22, 3.96 and methoxy protons at 3.30 (H-11^1, 3H, *s*), which were attributed to the δ 65.02 (C-1) and δ 57.17 (C-11^1) (Table 2) of the xenicane diterpenoid skeleton (Bishara et al., 2006).

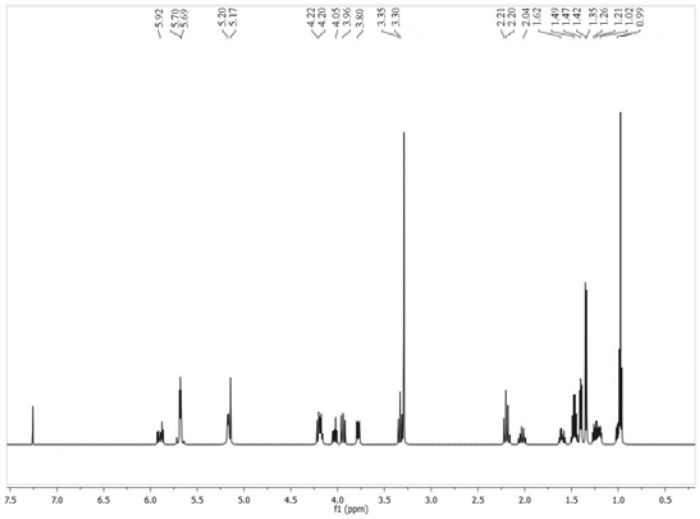

Figure 5.53.: ^{1}H-NMR of 4,4a,5,6,7,8,11,11a-octahydro-7-hydroxy-6-(6^{2}-hydroxy-6^{3}-butenyl)-4-(4^{1}-hydroxypropyl)-11-methoxy-8-methyl-cyclonona[*c*]pyran-3-(1*H*)-one (**4**)

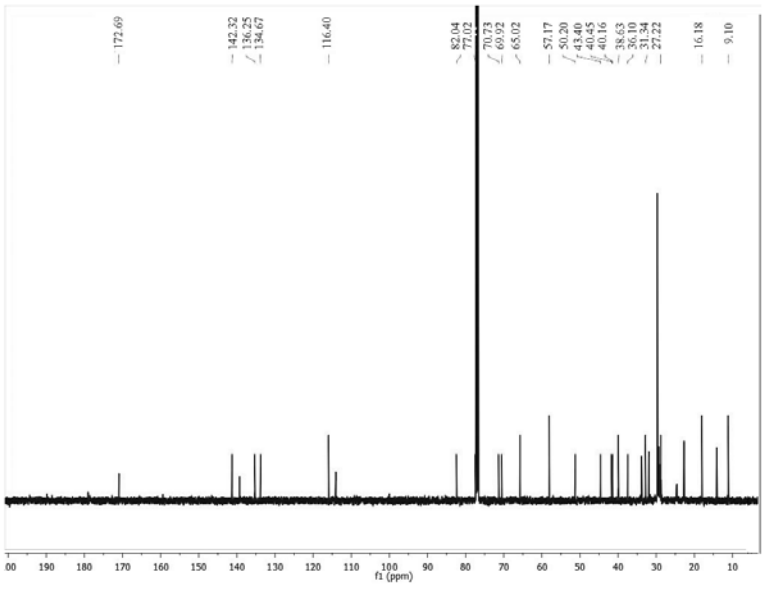

Figure 5.54.: ^{13}C-NMR of 4,4a,5,6,7,8,11,11a-octahydro-7-hydroxy-6-(6^{2}-hydroxy-6^{3}-butenyl)-4-(4^{1}-hydroxypropyl)-11-methoxy-8-methyl-cyclonona[*c*]pyran-3-(1*H*)-one (**4**)

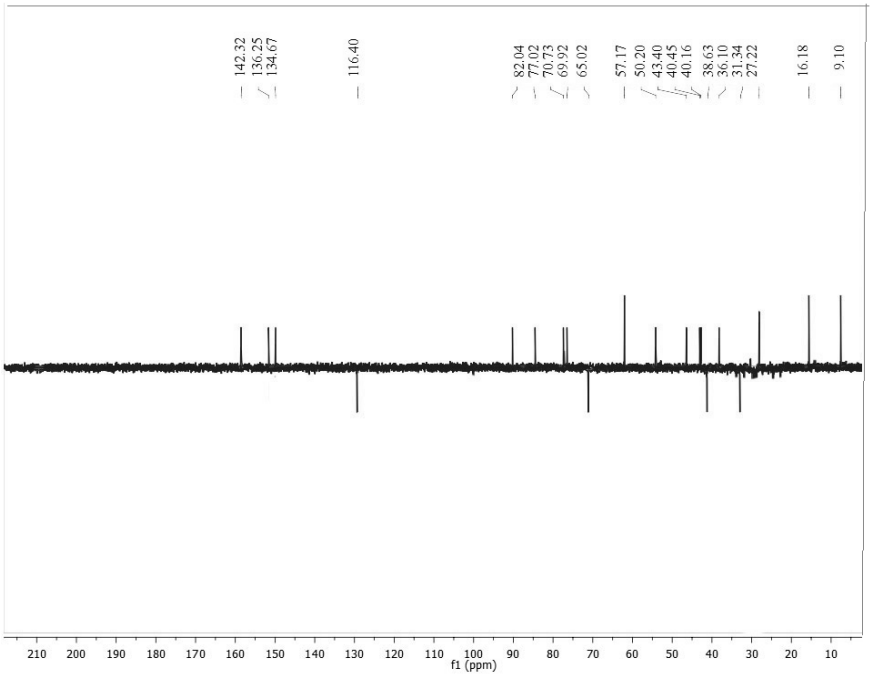

Figure 5.55.: DEPT spectrum of 4,4a,5,6,7,8,11,11a-octahydro-7-hydroxy-6-(6^2-hydroxy-6^3-butenyl)-4-(4^1-hydroxypropyl)-11-methoxy-8-methyl-cyclonona[*c*]pyran-3-(1*H*)-one (**4**)

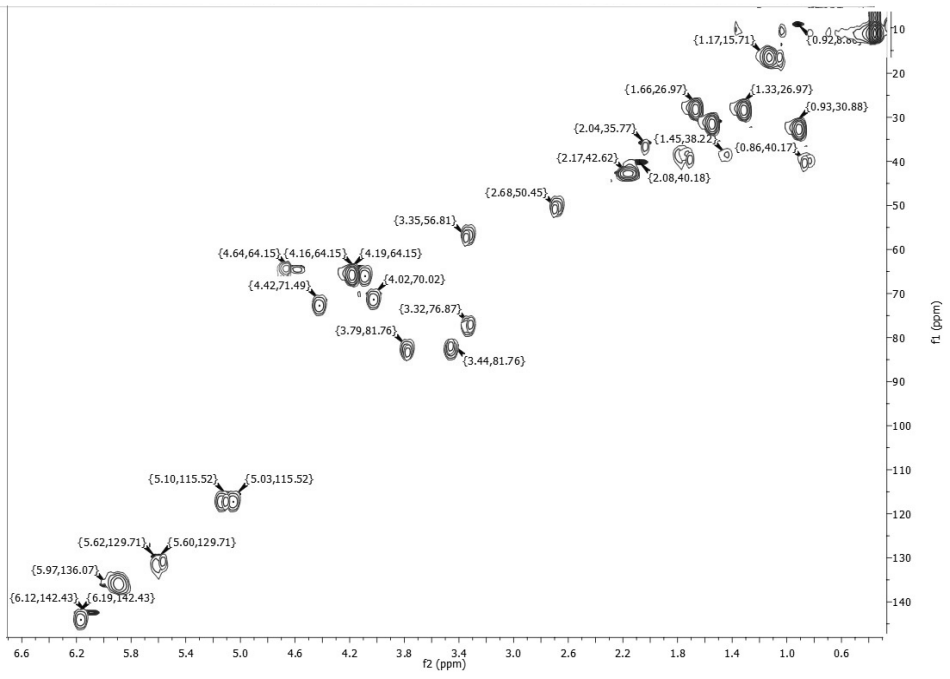

Figure 5.56.: HSQC spectrum of 4,4a,5,6,7,8,11,11a-octahydro-7-hydroxy-6-(6^2-hydroxy-6^3-butenyl)-4-(4^1-hydroxypropyl)-11-methoxy-8-methyl-cyclonona[*c*]pyran-3-(1*H*)-one (**4**)

The hydroxyl groups at C-7, C-4^1 and C-6^2 were fixed by ^{13}C-NMR signals at δ 77.02, 69.92, and 70.73, respectively. The location of hydroxyl group at the bicyclic system was designated by HMBCs between δ 3.35/δ 16.18 (H-7/C-8^1), δ 3.35/ δ 40.16 (H-7/C-6), δ 2.20/δ 77.02 (H-8/C-7), and also by COSYs between δ 1.21/3.35 (H-6/H-7). The methyl group at C-8, methoxy moiety at C-11 and alkenic bond at C-9 were associated with the fourth spin system between the protons δ 5.69/3.80 (H-10/H-11), δ 3.80/2.04 (H-11/H-11a), which were coupled with HMBCs between δ 5.69/δ 136.25 (H-10/C-9), δ 3.80/δ 134.67 (H-11/C-10), δ 3.80/δ 40.45 (H-11/C-11a), δ 2.04/δ 36.10 (H-11a/C-4a), δ 3.96/δ 40.45 (H-1/C-11a), and δ 3.80/δ 134.67 (H-11/C-10). In the spin system **I** (side chain 1-hydroxypropyl), the protons and carbons were connected by HMBCs, δ 2.21/δ 73.49 (H-4/C-4^1), δ 4.05/δ 172.69 (H-4^1/C-3), δ 4.05/δ 9.10 (H-4^1/C-4^3), δ 1.47/δ 69.92 (H-4^2/C-4^1), δ 1.47/δ 9.10 (H-4^2/C-4^3) along with COSYs δ 2.21/4.05 (H-4/H-4^1), δ 4.05/1.47 (H-4^1/H-4^2), δ 1.47/0.99 (H-4^2/H-4^3 that attributed that the spin unit **I** was linked to *δ*-lactone as well as fourth (**IV**) and second (**II**) spin system via HMBCs between δ 2.21/δ 36.10 (H-4/C-4a) and δ 2.04/δ 36.10 (H-11a/C-4a), respectively. Similarly, the second spin system (**II**) was explained by COSYs between δ 1.62/1.26 (H-4a/H-5) (Figure 5.57-5.59).

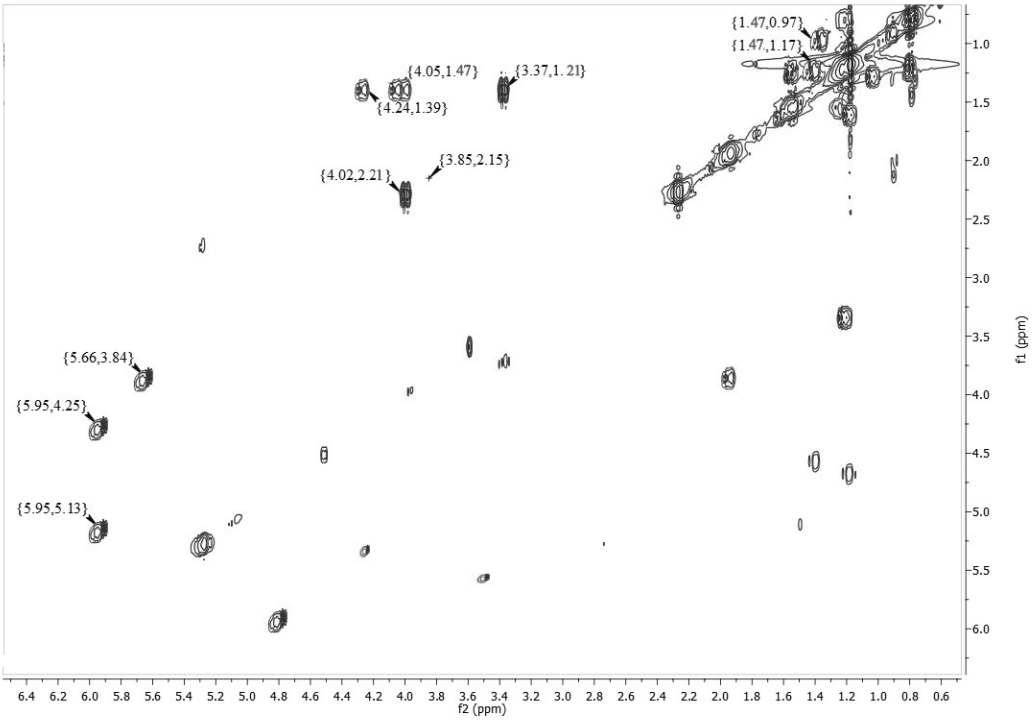

Figure 5.57.: COSY spectrum of 4,4a,5,6,7,8,11,11a-octahydro-7-hydroxy-6-(6^2-hydroxy-6^3-butenyl)-4-(4^1-hydroxypropyl)-11-methoxy-8-methyl-cyclonona[*c*]pyran-3-(1*H*)-one (**4**)

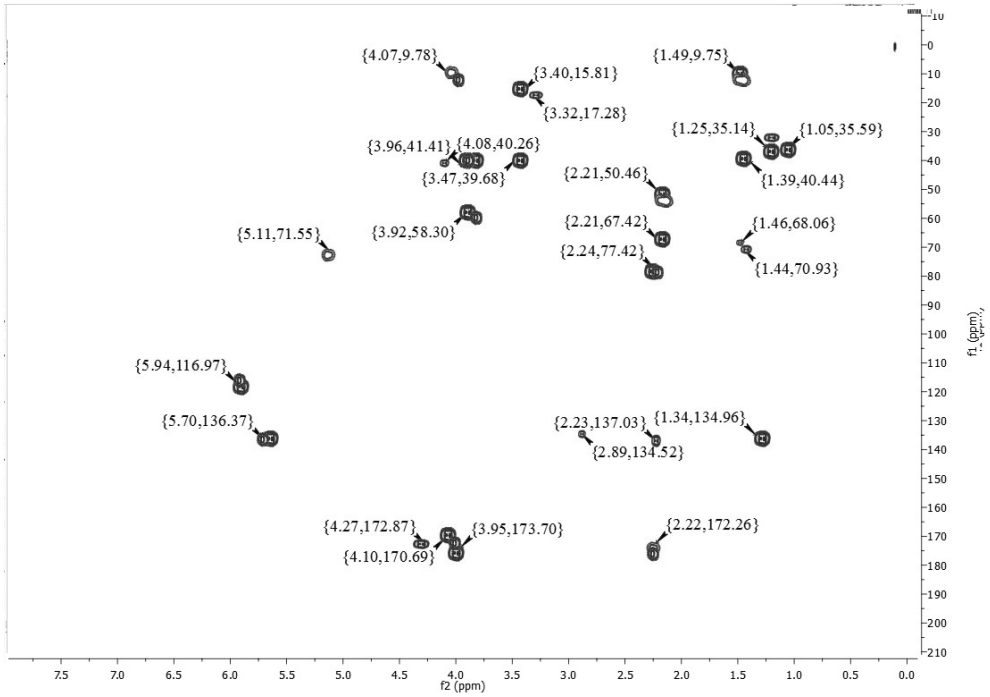

Figure 5.58.: HMBC spectrum of 4,4a,5,6,7,8,11,11a-octahydro-7-hydroxy-6-(6^2-hydroxy-6^3-butenyl)-4-(4^1-hydroxypropyl)-11-methoxy-8-methyl-cyclonona[*c*]pyran-3-(1*H*)-one (**4**)

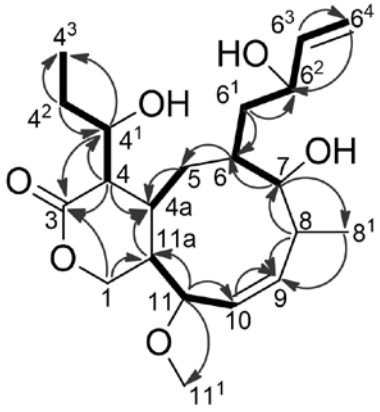

Figure 5.59.: Prominent ^{1}H-^{1}H COSY, and selected HMBC correlations of 4,4a,5,6,7,8,11,11a-Octahydro-7-hydroxy-6-(6^2-hydroxy-6^3-butenyl)-4-(4^1-hydroxypropyl)-11-methoxy-8-methyl-cyclonona[*c*]pyran-3-(1*H*)-one (**4**). The key ^{1}H-^{1}H COSY couplings were represented in bold face bonds. The key HMBC couplings have been represented by double barbed arrows.of

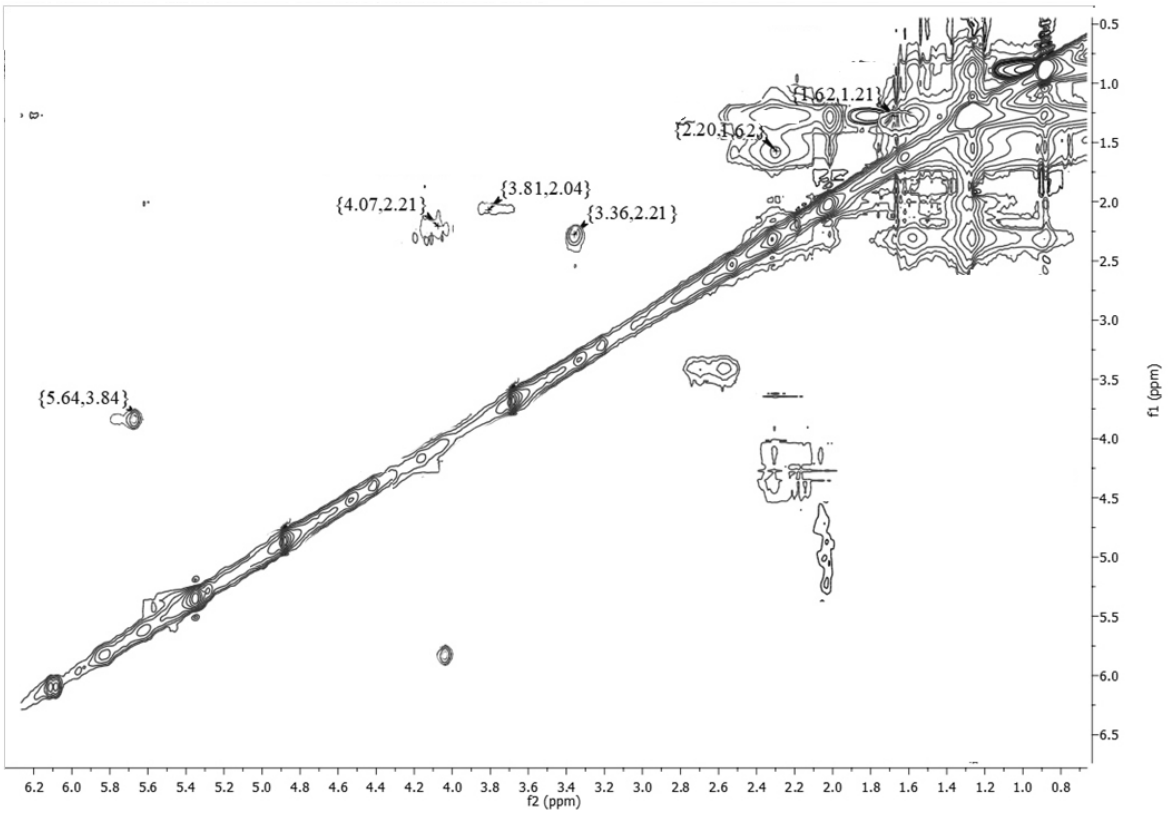

Figure 5.60.: NOESY spectrum of 4,4a,5,6,7,8,11,11a-octahydro-7-hydroxy-6-(6^2-hydroxy-6^3-butenyl)-4-(4^1-hydroxypropyl)-11-methoxy-8-methyl-cyclonona[*c*]pyran-3-(1*H*)-one (**4**)

Relative stereochemistries of **4** were resolved by NOEs, wherein proton signal showed NOEs, such as δ 4.05/2.21 (H-4^1/H-4); δ 1.62/2.21 (H-4/H-4a); δ 1.62/1.21 (H-4a/H-6), and δ 1.21/4.20 (H-6/H-6^2). These protons were arbitrarily assigned to align in the β-face of the diterpene tricyclic system. On the other hand, NOEs showed spatial proximity between protons δ 2.04/3.80 (H-11a/H-11) and δ 3.80/5.69 (H-11/H-10), which were attributed to be *α*-oriented (Figure 5.60-5.61).

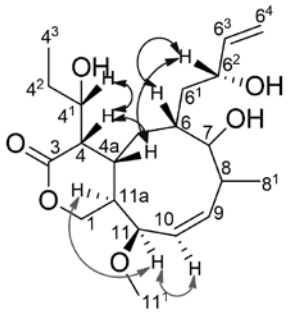

Figure 5.61.: Prominent NOE correlations of 4,4a,5,6,7,8,11,11a-octahydro-7-hydroxy-6-(6^2-hydroxy-6^3-butenyl)-4-(4^1-hydroxypropyl)-11-methoxy-8-methyl-cyclonona[*c*]pyran-3-(1*H*)-one (**4**). NOESY relations are represented by double-tailed arrows

Table 5.7.: NMR spectroscopic data[a] of ,4a,5,6,7,8,11,11a-octahydro-7-hydroxy-6-(6^2-hydroxy-6^3-butenyl)-4-(4^1-hydroxypropyl)-11-methoxy-8-methyl-cyclonona[*c*]pyran-3-(1*H*)-one (**4**) isolated from brown seaweed *P.tetrastromatica*

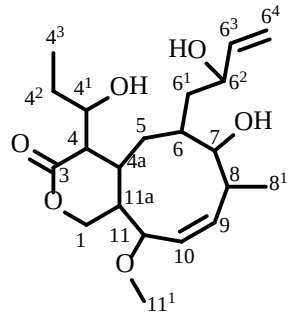

Compound **4** …….4,4a,5,6,7,8,11,11a-octahydro-7-hydroxy-6-(6^2-hydroxy-6^3-butenyl)-4-(4^1-hydroxypropyl)-11-methoxy-8-methyl-cyclonona[*c*]pyran-3-(1*H*)-one (**4)**

C. No.	^{13}C NMR	^{1}H NMR (int., mult., J in Hz)[b]	COSY	HMBC
1	65.02	3.96 (1H, dd, J=9.7, 9.2 Hz) 4.22 (1H, dd, J=8.20, 9.15 Hz)		C-3, 11a
2	-	-	-	-
3	172.69	-	-	-
4	50.20	2.21 (1H, m)	H-4^1	C-3, 4a, 4^1
4a	36.10	1.62 (1H, m)	-	-
4^1	69.92	4.05 (1H, m)	H-4^2	C-3, 4^3
4^2	27.22	1.47 (1H, m), 1.49 (1H, m)	H-4^3	C-4, 4^3
4^3	9.10	0.99 (3H, t, J=6.4 Hz)	-	-
5	31.34	1.02 (1H, m) 1.26 (1H, m)	-	C-4a
6	40.16	1.21 (1H, m)	H-7,6^1	C-5
6^1	38.63	1.42 (2H, dd, J=6.3, 4.0 Hz)	H-6^2	C-6, 6^2
6^2	70.73	4.20 (1H, m)	H-6^3	-
6^3	142.32	5.92 (1H, m)	H-6^4	C-6^4
6^4	116.40	5.17 (1H, m) 5.20 (1H, m)		C-6^2
7	77.02	3.35 (1H, t, J=9.4 Hz)	-	C-6, 8^1
8	43.40	2.20 (1H, m)	-	C-7, 9
8^1	16.18	1.35 (3H, d, J=6.31 Hz)	-	C-9
9	136.25	5.70 (1H, m)		
10	134.67	5.69 (1H, m)	H-11	C-9
11	82.04	3.80 (1H, dd, J=9.1, 4.6 Hz)	H-11a	C-10, 11^1
11a	40.45	2.04 (1H, m)	-	-
11^1	57.17	3.30 (3H, s)	-	-

[a]NMR spectra were recorded using a B ruker AVANCE III 500 MHz (AV 500) spectrometer (B ruker, Karlsruhe, Germany) in $CDCl_3$ as aprotic solvent at ambient temperature with TMS as the internal standard (δ 0 ppm).

[b]Values in ppm, multiplicity and coupling constants (J=Hz) were indicated in parentheses. Multiplicities were allocated by [135]DEPT NMR spectrum.

The assignments were made with the aid of the COSY, HSQC, HMB C and NOESY experiments.

The molecular ion peak of **4** was appeared at *m/z* 382 and base peak was ontained at *m/z* 27.0 (Figure 5.62 and 5.63).

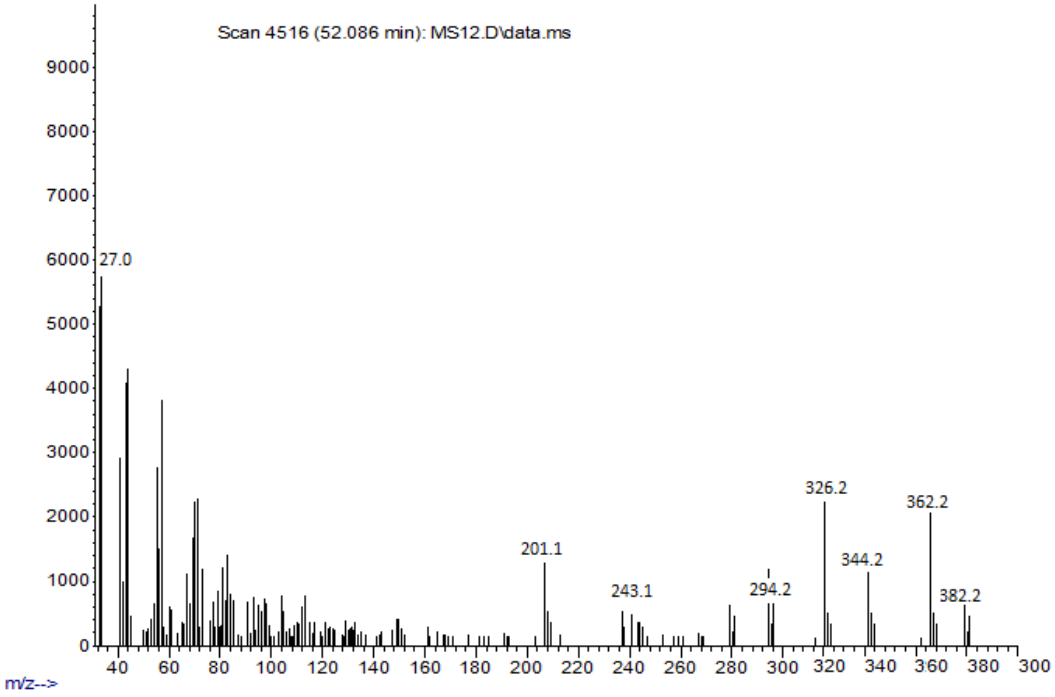

Figure 5.62.: EI-MS spectrum of 4,4a,5,6,7,8,11,11a-octahydro-7-hydroxy-6-(6[2]-hydroxy-6[3]-butenyl)-4-(4[1]-hydroxypropyl)-11-methoxy-8-methyl-cyclonona[*c*]pyran-3-(1*H*)-one (**4)**

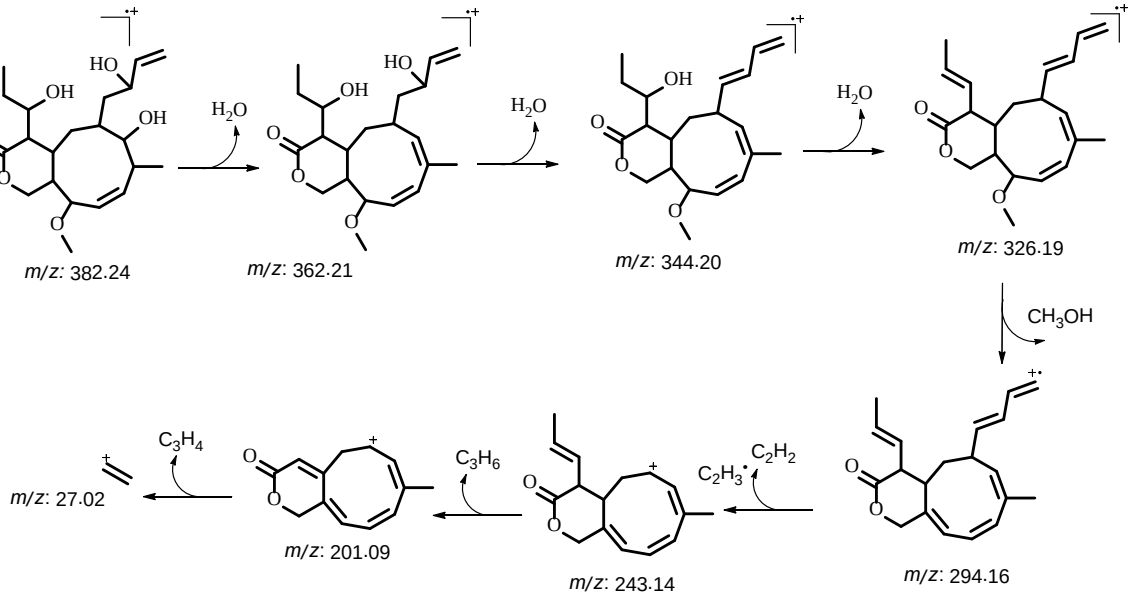

Figure 5.63.: Tentative mass fragmentation pattern of 4,4a,5,6,7,8,11,11a-octahydro-7-hydroxy-6-(6^2-hydroxy-6^3-butenyl)-4-(4^1-hydroxypropyl)-11-methoxy-8-methyl-cyclonona[*c*]pyran-3-(1*H*)-one (**4)**

Structural characterization of Compound 5 (TP_5)

4,4a,5,6,7,8,11,11a-Octahydro-1,7-dihydroxy-4-(4^1-hydroxy-4^2-methylpropyl)-6-(6^1-hydroxy-6^2-propenyl)-10-methyl-cyclonona[*c*]pyran-3(1*H*)-one

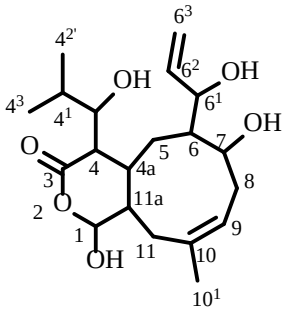

Sample yield	0.27% (> 99% purity, RP-C_{18} HPLC)
Physical description	Yellow oil
Molecular formula	$C_{20}H_{32}O_6$
Molecular mass	368.2199

The xenicane class of diterpenoid derivative, 4,4a,5,6,7,8,11,11a-octahydro-1,7-dihydroxy-4-(4^1-hydroxy-4^2-methylpropyl)-6-(6^1-hydroxy-6^2-propenyl)-10-methyl-cyclonona[*c*]-

pyran-3(1*H*)-one was isolated as yellow oil compound. The compound (**5**) has exhibited UV absorbance (UV (MeOH) λ_{max}) at 246.0 (2.90) nm (Figure 5.64). The homogeneity of the compound was ascertained by HPLC data on a bonded phase octadecylsilane (C_{18}) stationary phase (RP-C_8 HPLC, MeOH:MeCN, 2:3 v/v): 3.23 min (Figure 5.65).

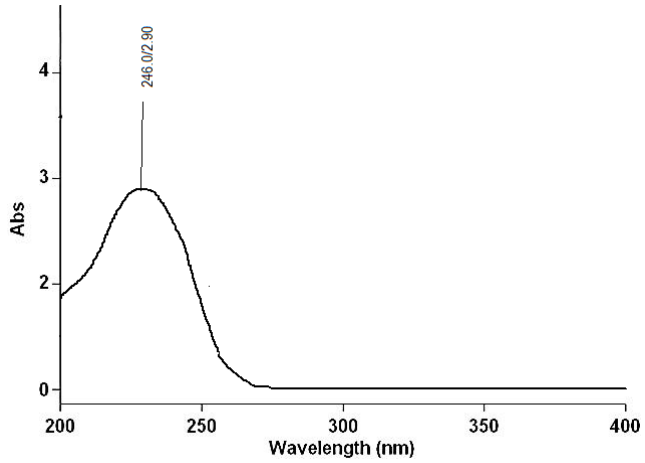

Figure 5.64.: UVspectrum of 4,4a,5,6,7,8,11,11a-octahydro-1,7-dihydroxy-4-(4^1-hydroxy-4^2-methylpropyl)-6-(6^1-hydroxy-6^2-propenyl)-10-methyl-cyclonona[*c*]pyran-3(1*H*)-one (**5**)

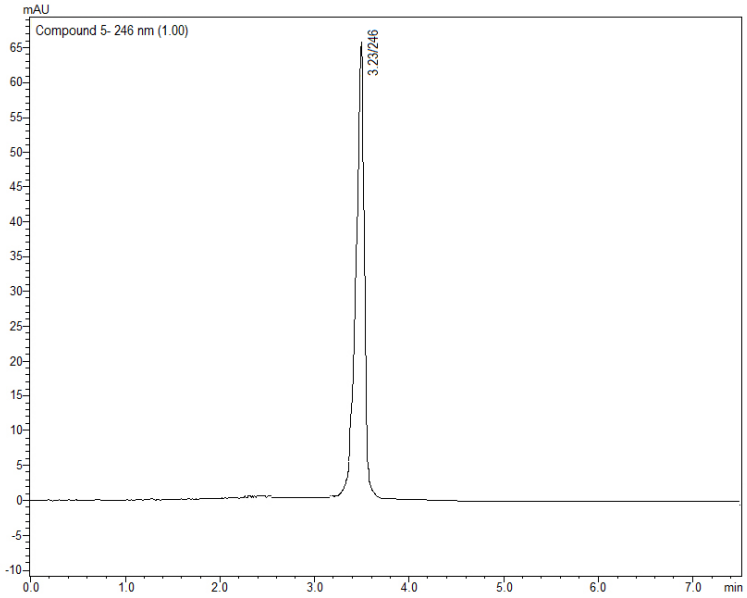

Figure 5.65.: HPLC chromatogram of 4,4a,5,6,7,8,11,11a-octahydro-1,7-dihydroxy-4-(4^1-hydroxy-4^2-methylpropyl)-6-(6^1-hydroxy-6^2-propenyl)-10-methyl-cyclonona[*c*]pyran-3(1*H*)-one (**5**)

The molecular ion peak by HRESIMS (positive mode) was observed at *m/z*: 369.2280 $[M+H]^+$, (Figure 5.66). The FTIR spectrum of **5** displayed absorption bands at, 3450 (O-H), 1715 (C=O) and 1140 (C-C) (Figure 5.67).

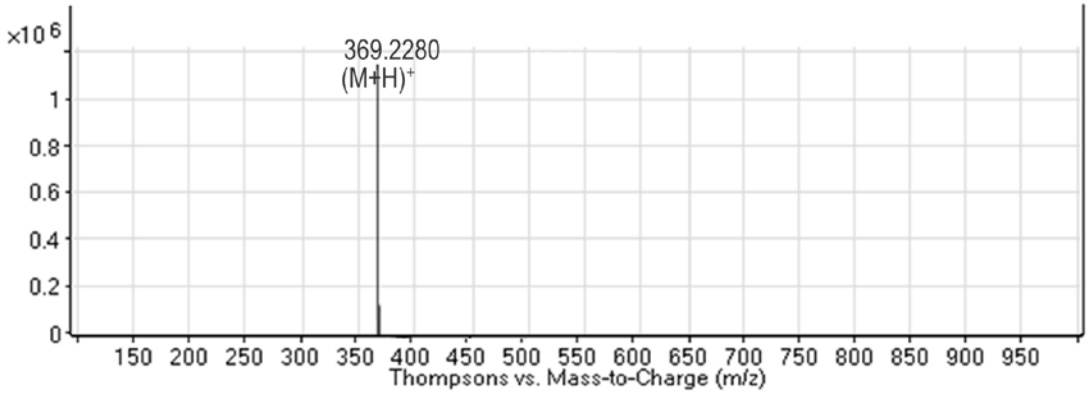

Figure 5.66.: HRESIMS of 4,4a,5,6,7,8,11,11a-octahydro-1,7-dihydroxy-4-(4[1]-hydroxy-4[2]-methylpropyl)-6-(6[1]-hydroxy-6[2]-propenyl)-10-methyl-cyclonona[*c*]pyran-3(1*H*)-one (**5**)

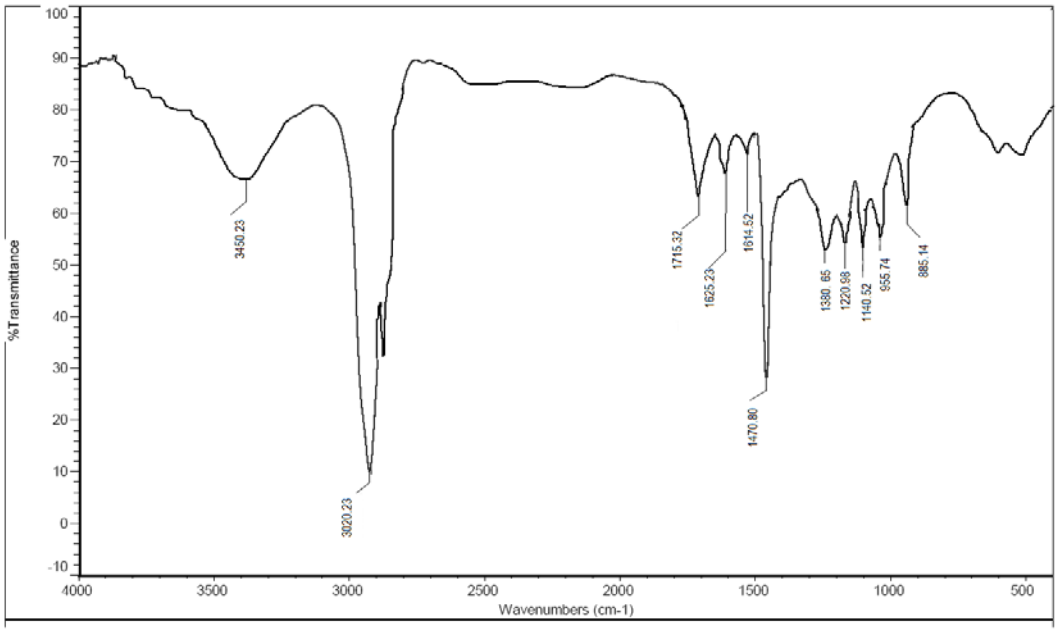

Figure 5.67.: FTIR spectrum of 4,4a,5,6,7,8,11,11a-octahydro-1,7-dihydroxy-4-(4[1]-hydroxy-4[2]-methylpropyl)-6-(6[1]-hydroxy-6[2]-propenyl)-10-methyl-cyclonona[*c*]pyran-3(1*H*)-one (**5**)

The xeniolide **5** was isolated as yellow oil, and the molecular ion peak was appeared at *m/z* 368, whereas the molecular formula $C_{20}H_{32}O_6$, implying five unsaturation degrees, was associated with three olefinic bonds and two ring systems. The compound **5** possessed substitutions on identical carbons (C-4 and C-6) of 9-membered ring, but differed in the substituted side chain patterns and occurrence of methyl moieties. The spectroscopic data of **5** were comparable with those obtained for **4** and **5**. The notable differences in the ^{13}C-NMR data of **5** from those of **4** and **5** were the substitutions at the C-1, C-4, C-6, C-7, and C-10, and corresponding variations were recorded in the ^{1}H NMR spectrum (Figure 5.68-5.71).

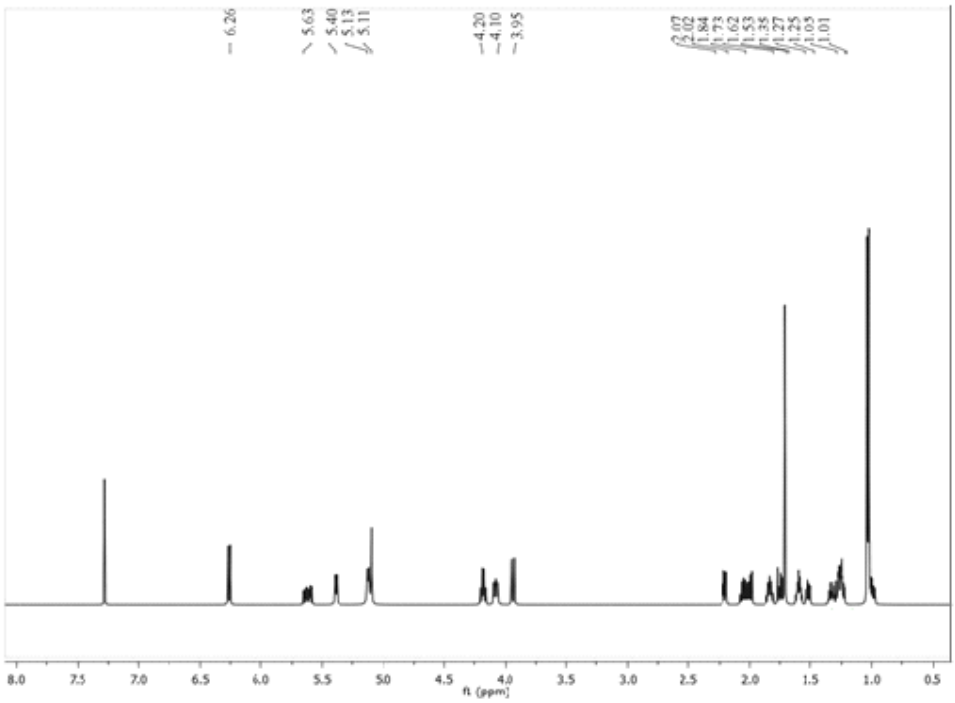

Figure 5.69.: ^{1}H NMR of 4,4a,5,6,7,8,11,11a-octahydro-1,7-dihydroxy-4-(4^{1}-hydroxy-4^{2}-methylpropyl)-6-(6^{1}-hydroxy-6^{2}-propenyl)-10-methyl-cyclonona[*c*]pyran-3(1*H*)-one (**5**)

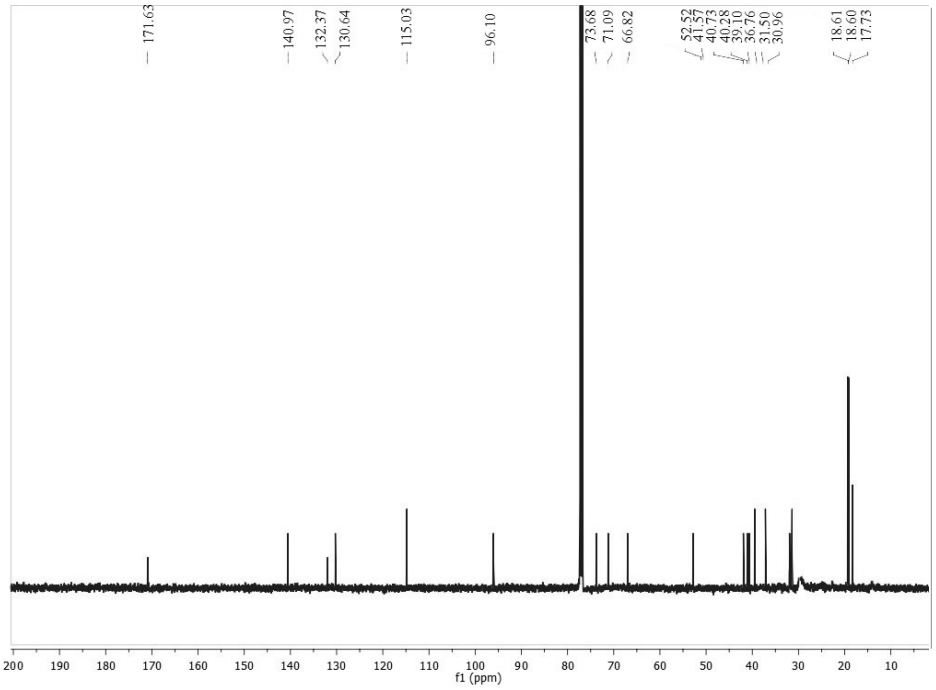

Figure 5.70.: ^{13}C-NMR of 4,4a,5,6,7,8,11,11a-octahydro-1,7-dihydroxy-4-(4^1-hydroxy-4^2-methylpropyl)-6-(6^1-hydroxy-6^2-propenyl)-10-methyl-cyclonona[*c*]pyran-3(1*H*)-one (**5**)

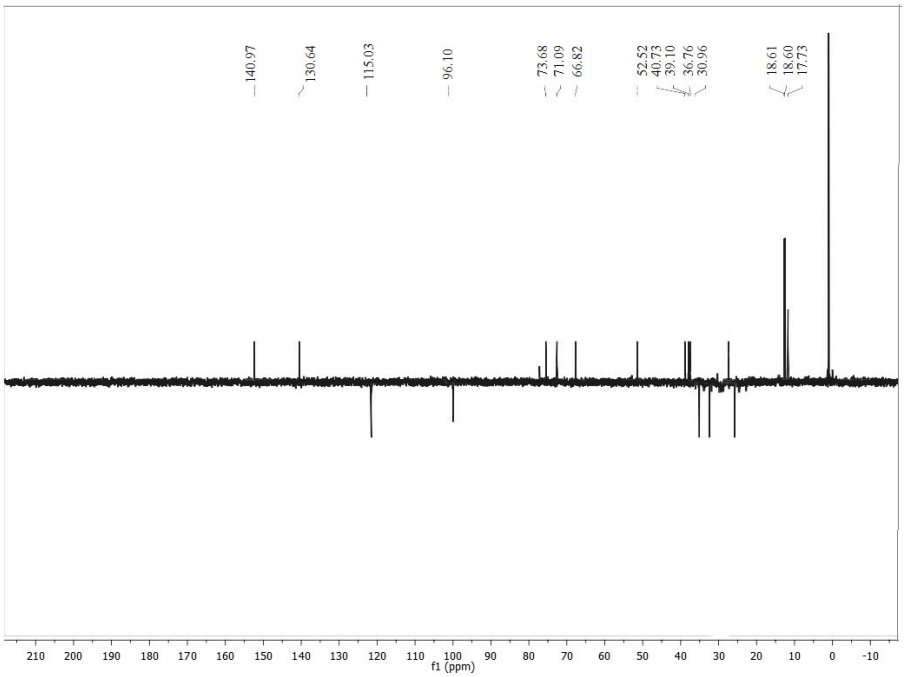

Figure 5.71.:DEPT spectrum of 4,4a,5,6,7,8,11,11a-octahydro-1,7-dihydroxy-4-(4^1-hydroxy-4^2-methylpropyl)-6-(6^1-hydroxy-6^2-propenyl)-10-methyl-cyclonona[*c*]pyran-3(1*H*)-one (**5**)

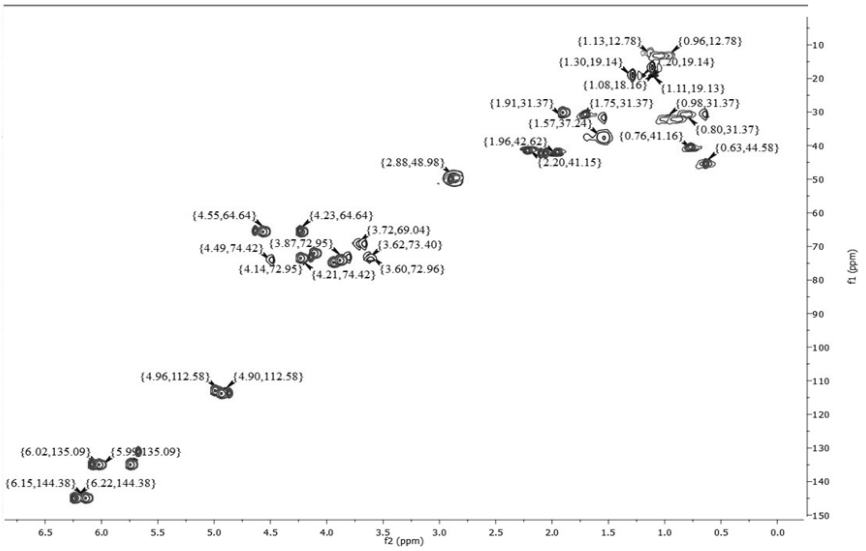

Figure 5.72.: HSQC of 4,4a,5,6,7,8,11,11a-octahydro-1,7-dihydroxy-4-(4^1-hydroxy-4^2-methylpropyl)-6-(6^1-hydroxy-6^2-propenyl)-10-methyl-cyclonona[*c*]pyran-3(1*H*)-one (**5**)

The compound **5** possessed an ester at δ 171.63 (C-3), methyl groups at δ 18.60 (C-4$^{2'}$), δ 18.61 (C-4^3) and δ 17.73 (C-10^1), four methylene groups at δ 36.76 (C-11), δ 66.82 (C-8), and δ 115.03 (C-6^3) (including olefinic methylene), ten methines at δ 96.10 (C-1), δ 52.52 (C-4), δ 40.28 (C-4a), δ 40.73 (C-6), δ 39.10 (C-7), δ 130.64 (C-9), δ 41.57 (C-11a), δ 71.09 (C-4^1), δ 18.60 (C-4$^{2'}$), δ 73.68 (C-6^1), and δ 140.97 (C-6^2) (including one oxymethine and three olefinic methines). The three COSY spin systems (**I, II** and **III**) included 1-hydroxy-2-methylpropyl, 1-hydroxyallyl, and bicyclic ring systems, respectively. The COSY spin system **I** represented correlations between the protons δ 2.07/1.05 (H-4^2/H-4$^{2'}$), δ 2.07/1.05 (H-4^2/H-4^3), which were connected to *δ*-lactone, nine membered ring and two other COSY spin systems (**II** and **III**) via two methine carbons {δ 52.52 (C-4), δ 40.28 (C-4a)}, and one quaternary carbon at δ 71.09 (C-4^1). The HMBCs between δ 1.05/δ 18.61 (H-4$^{2'}$/C-4^3) and δ 1.05/δ 18.60 (H-4^3/C-4$^{2'}$) supported COSY spin **I**, which was linked to *δ*-lactone by HMBC between δ 1.05/δ 71.09 (H-4^3 /C-4^1), δ 1.05/δ 71.09 (H-4$^{2'}$/C-4^1), δ 2.22/δ 171.63 (H-4/C-3), and δ 2.22/δ 71.09 (H-4/C-12). The HMBC at H-6/C-7 connected COSY spin system **I** to 9-membered cyclic system, and the spin system included the cross-peaks at δ 1.01/1.35 (H-5/H-6), δ 1.35/1.53 (H-6/H-7), δ 1.35/4.10 (H-6/H-6^1), and δ 4.10/5.63 (H-6^1/H-6^2). Similarly, COSY spin system **III** was accompanied by protons δ 1.76/1.84 (H-11/H-11a), δ 1.84/1.62 (H-11a/H-4a), δ 1.84/6.26 (H-11a/H-1), wherein the methyl group substituted at C-10 (δ 132.37) was correlated to the bicyclic ring system of xeniolide **5** by HMBCs at δ 1.73/δ 130.64 (H-10^1/C-9) and δ 1.73/δ 132.37 (H-10^1/C-10) (Figure 5.73-5.75).

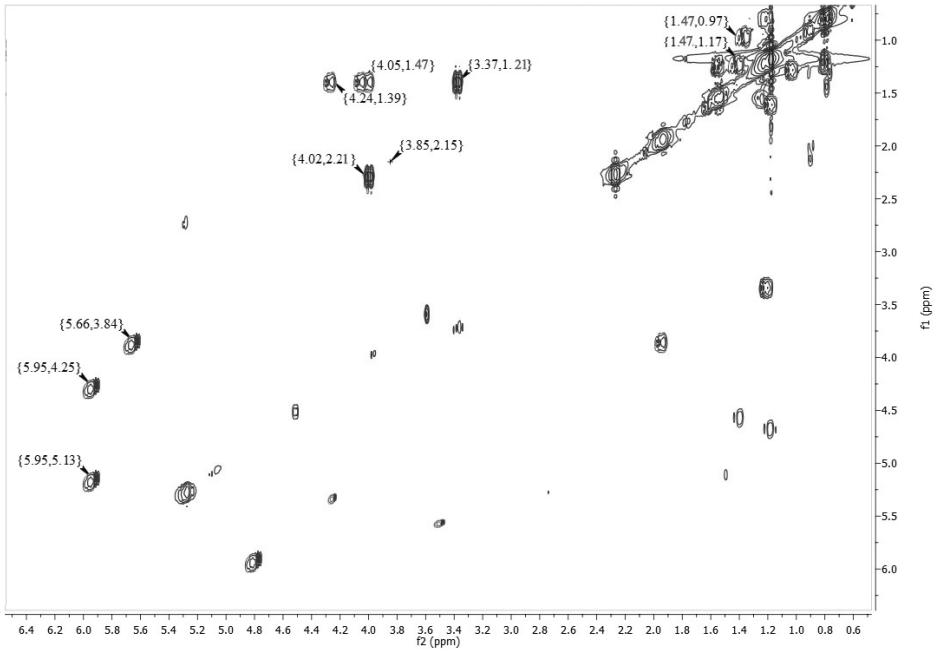

Figure 5.73.: ^{1}H-^{1}H COSY spectrum of 4,4a,5,6,7,8,11,11a-octahydro-1,7-dihydroxy-4-(4^{1}-hydroxy-4^{2}-methylpropyl)-6-(6^{1}-hydroxy-6^{2}-propenyl)-10-methyl-cyclonona[*c*]pyran-3(1*H*)-one (**5**)

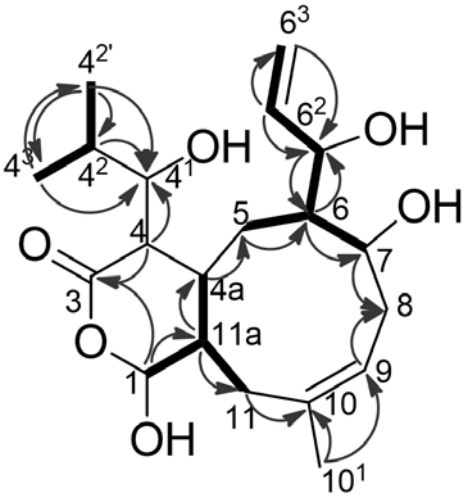

Figure 5.74.: Prominent ^{1}H-^{1}H COSY, and selected HMBC correlations of 4,4a,5,6,7,8,11,11a-octahydro-1,7-dihydroxy-4-(4^{1}-hydroxy-4^{2}-methylpropyl)-6-(6^{1}-hydroxy-6^{2}-propenyl)-10-methyl-cyclonona[*c*]pyran-3(1*H*)-one (**5**). The key ^{1}H-^{1}H COSY couplings were represented in bold face bonds. The key HMBC couplings have been represented by double barbed arrows.

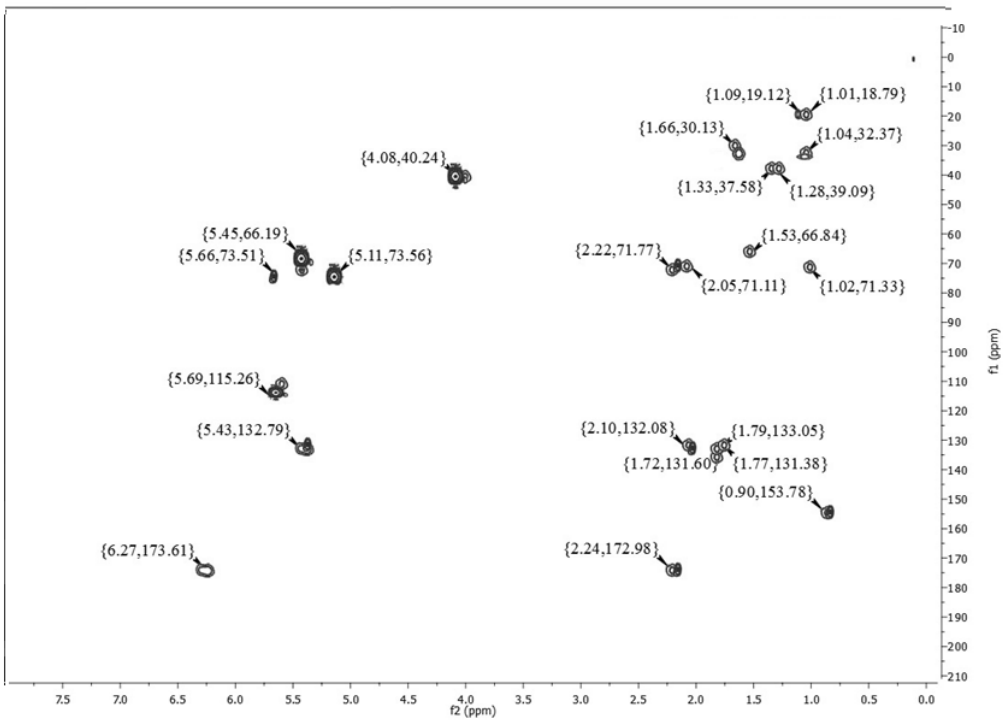

Figure 5.75.: HMBC spectrum of 4,4a,5,6,7,8,11,11a-octahydro-1,7-dihydroxy-4-(4^1-hydroxy-4^2-methylpropyl)-6-(6^1-hydroxy-6^2-propenyl)-10-methyl-cyclonona[*c*]pyran-3(1*H*)-one (**5**)

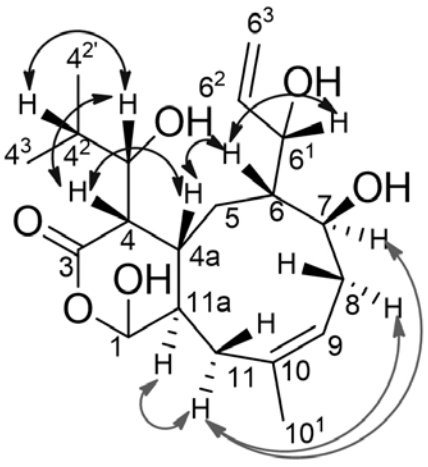

Figure 5.76.: Prominent NOE correlations of 4,4a,5,6,7,8,11,11a-octahydro-1,7-dihydroxy-4-(4^1-hydroxy-4^2-methylpropyl)-6-(6^1-hydroxy-6^2-propenyl)-10-methyl-cyclonona[*c*]pyran-3(1*H*)-one (**5**). NOESY relations are represented by double-tailed arrows

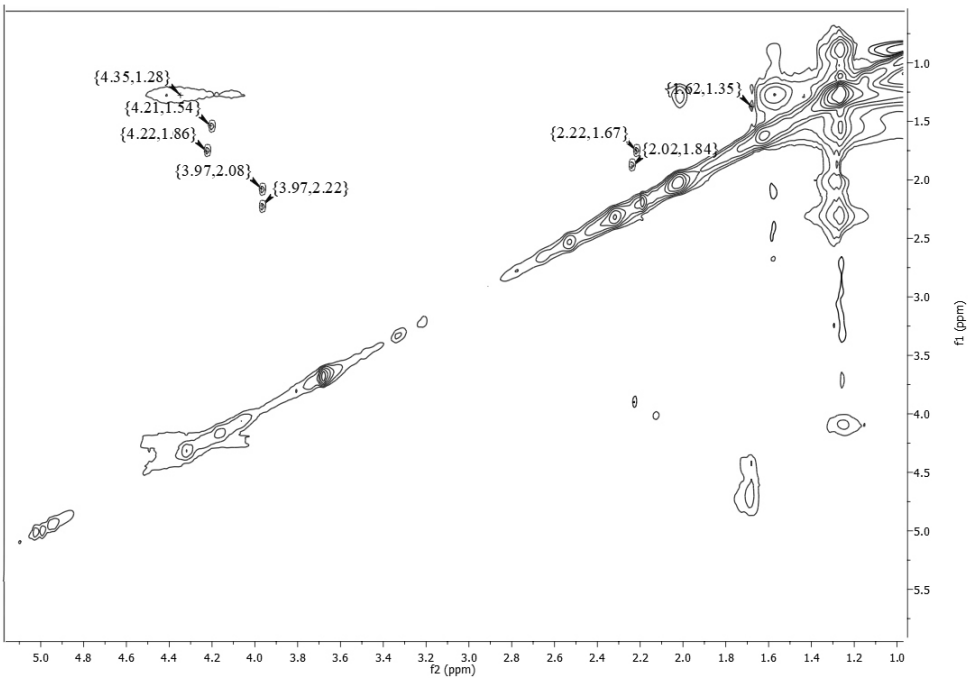

Figure 5.77.: NOESY spectrum of 4,4a,5,6,7,8,11,11a-octahydro-1,7-dihydroxy-4-(4^1-hydroxy-4^2-methylpropyl)-6-(6^1-hydroxy-6^2-propenyl)-10-methyl-cyclonona[*c*]pyran-3(1*H*)-one (**5**)

The NOE data established that the protons at H-4^2, H-4^1, H-4, H-4a and H-6 exhibited spatial correlations, such as H-4^2/H-4^1, H-4^1/H-4, H-4/H-4a, H-4a/H-6, and H-6/H-6^1, and thus, oriented in the similar reference plane of the molecule. These were arbitrarily attributed as β-aligned. Consequently, the protons at H-11a, H-11, H-8 and H-7 were aligned towards the *α*-face of the molecule. The protons at chiral centres C-4^1, C-4, C-4a, C-6 and C-6^1 were arranged in the β-face of the molecule, whereas those at chiral centres C-11a and C-7 were arranged towards the *α*-face (Figure 5.76-5.77).

Table 5.8.: NMR spectroscopic data[a] of 4,4a,5,6,7,8,11,11a-octahydro-1,7-dihydroxy-4-(4^1-hydroxy-4^2-methylpropyl)-6-(6^1-hydroxy-6^2-propenyl)-10-methyl-cyclonona[*c*]pyran-3(1*H*)-one (**5**) isolated from brown seaweed *P.tetrastromatica*

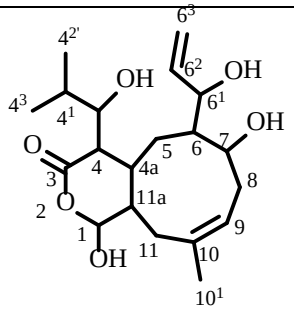

Compound **5**……. 4,4a,5,6,7,8,11,11a-octahydro-1,7-dihydroxy-4-(4^1-hydroxy-4^2-

methylpropyl)-6-(6^1-hydroxy-6^2-propenyl)-10-methyl-cyclonona[*c*]pyran-3(1*H*)-one (**5**)

C. N.	^{13}C NMR	^{1}H NMR (int., mult., J in Hz)[b]	COSY	HMBC
1	96.10	6.26 (1H, d, J=9.6 Hz)	H-11a	C-3
2	-	-	-	-
3	171.63	-		
4	52.52	2.22 (1H, dd, J=9.6, 3..91 Hz)	-	C-3, 4^1
4a	40.28	1.62 (1H, m)		C-5
4^1	71.09	3.95 (1H, d, J=10.5 Hz)	-	-
4^2	31.50	2.07 (1H, m)		C-4^1
$4^{2'}$	18.60	1.05 (3H, m)	H-4^1, 4^3	C-4^3, 4^1
4^3	18.61	1.05 (3H, d, J=6.52 Hz)	-	C-$4^{2'}$, 4^2, 4^1
5	30.96	1.27 (1H, m), 1.01 (1H, m)	H-6	C-6
6	40.73	1.35 (1H, m)	H-7, 6^1	C-7
6^1	73.68	4.10 (1H, dd, J=10.5, 6.5 Hz)	H-6^2	C-6
6^2	140.97	5.63 (1H, m)	H-6^3	C-6^1, 6^3
6^3	115.03	5.11(1H, m), 5.13 (1H, m)	-	C-6^1
7	39.10	1.53 (1H, m), 1.25 (1H, m)	-	C-8
8	66.82	4.20 (1H, dd, J=9.1, 7.6 Hz)		
9	130.64	5.40 (1H, dd, J=15.68 Hz)		C-8, 10
10	132.37	-		
10^1	17.73	1.73 (3H, s), 2.02 (1H, d d, J=11.6, 8.5 Hz)	-	C-10, 9
11	36.76	1.76 (1H, dd, J=12.2, 6.3 Hz)		C-10
11a	41.57	1.84 (1H, m)	H-4a, 11	C-11

[a]NMR spectra were recorded using a B ruker AVANCE III 500 MHz (AV 500) spectrometer (B ruker, Karlsruhe, Germany) in $CDCl_3$ as aprotic solvent at ambient temperature with TMS as the internal standard (δ 0 ppm).

[b]Values in ppm, multiplicity and coupling constants (J=Hz) were indicated in parentheses. Multiplicities were allocated by ^{135}DEPT NMR spectrum.

The assignments were made with the aid of the COSY, HSQC, HMB C and NOESY experiments.

The molecular ion peak of **5** was appeared at *m/z* 368 and base peak was ontained at *m/z* 27.0 (Figure 5.47 and 5.48).

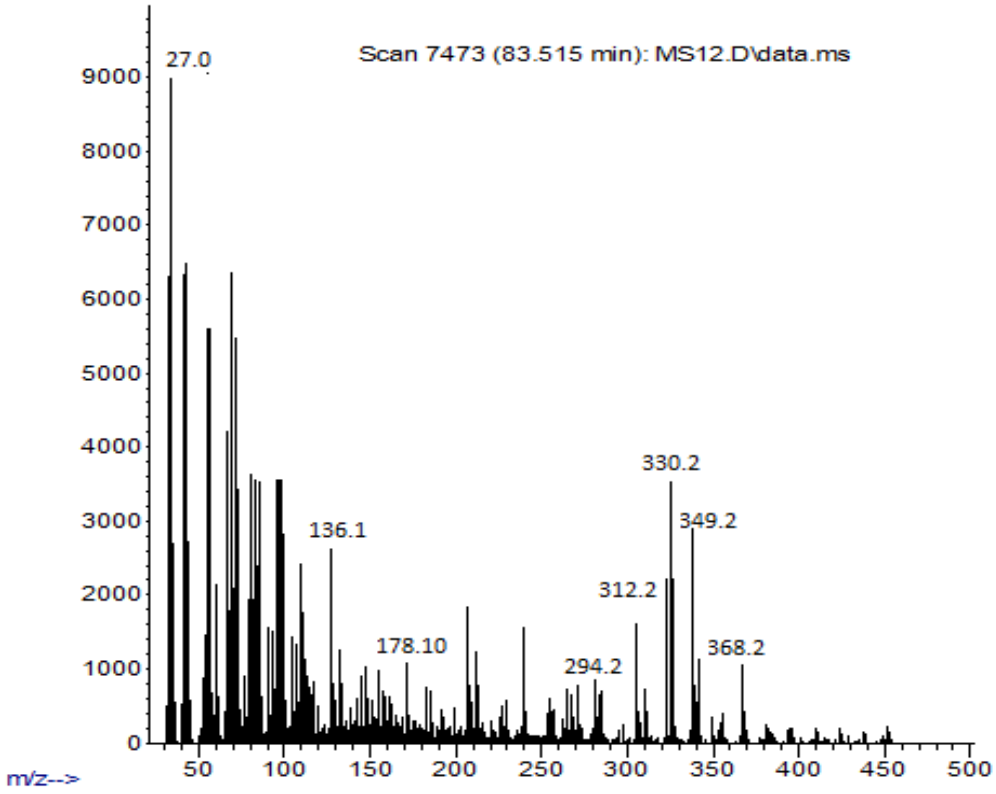

Figure 5.78.: EI-MS spectrum of 4,4a,5,6,7,8,11,11a-octahydro-1,7-dihydroxy-4-(4^1-hydroxy-4^2-methylpropyl)-6-(6^1-hydroxy-6^2-propenyl)-10-methyl-cyclonona[*c*]pyran-3(1*H*)-one (**5**)

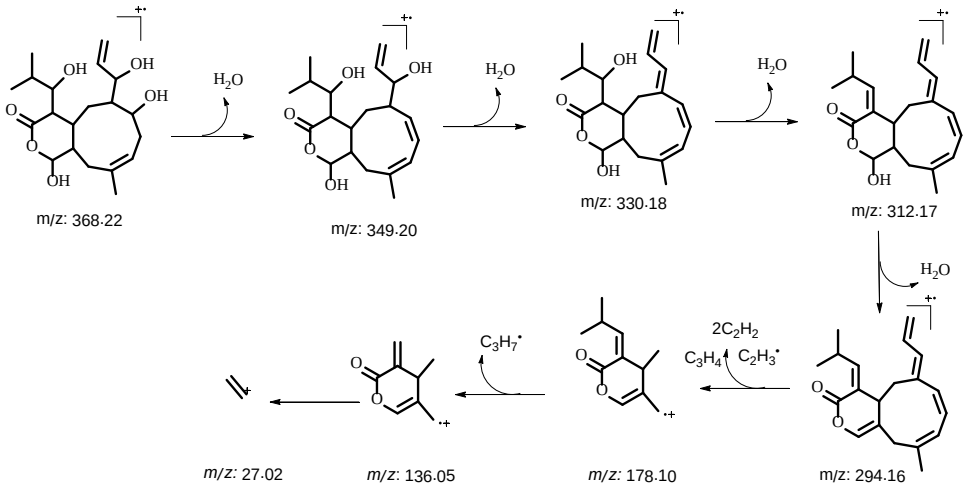

Figure 5.79.: Tentative mass fragmentation pattern of 4,4a,5,6,7,8,11,11a-octahydro-1,7-dihydroxy-4-(4^1-hydroxy-4^2-methylpropyl)-6-(6^1-hydroxy-6^2-propenyl)-10-methyl-cyclonona[*c*]-pyran-3(1*H*)-one (**5**)

5.3.2.2 Structural characterization of dolabellane class of diterpenoid derivatives (6-10)

Seaweeds of the family Dictyotaceae have emerged as a rich source of diterpenoids, and were characterised by mono-, bi- and tri-cyclic carbon skeletons of dolabellane, dolastane and seco-dolastane types, which exhibited wide range of bioactivities (Faulkner et al. 1996). The dolabellanes, which exhibited a regular [9.3.0] cyclotetradecane skeleton were found to constitute a significant chemistries of diterpenoid natural products (Ireland et al. 1976). The metabolites isolated from *Dolabella californica*, a sea hare, were first reported as dolabellanes by Ireland et al. (1976). Subsequent studies showed that dolabellanes were widely scattered among diverse species in marine habitats, especially in Dictyotaceae, and also constituted as secondary metabolites of fungi, liverwort and plants (Rodriguez et al. 1998). Dolabelladienols A-C, the new diterpenes were isolated from the Brazilian brown alga *Dictyota pfaffii* (Vargas et al. 2014). The dolastene variants 1,4-epoxy-17-dolastene, 1,4-dihydroxy-11-oxo-17-dolastene and hydroxy-11-oxo-1,17-dolastadiene were characterised from the brown alga *Dilophus spiralis* (Ioannou et al. 2008; Ioannou et al. 2013). Among various brown seaweeds of family Dictyotaceae, *Padina sp*. was found to constitute a predominant share, whereas about 50 taxa of this genus were distributed worldwide (Guiry and Dhonncha 2003). Among them, *Padina tetrastromatica* (Hauck) were found to be distributed in the coastal waters of the Indian peninsular (Guiry and Dhonncha 2003), and were explored for different bio-potential functionalities (Mohsin et al. 2014). Although most of the compounds belonging to dolabellanes and dolastanes were reported from the brown alga of Dictyotaceae family, there were no reports on detailed structural characterisation of bioactive leads *P. tetrastromatica* belonging to the same family. There were variants of this class of terpenoid compounds with previously unprecedented cabocyclic skeletons and functionalizations contributing towards their potential bioactivities, such as antioxidative and anti-diabetic pluralities. The present study described the isolation and characterisation of five previously unreported diterpenoids of dolabellane (**6-8**) and dolastane (**9-10**) class of chemistries from ethyl acetate: methanol (EtOAc:MeOH) extract of *P. tetrastromatica* collected from southeast coastal region of the Indian peninsular. The studied compounds were characterised by extensive spectroscopic experiments. The pharmacological activities were assessed by different *in vitro* antioxidant/anti-diabetic assays and physicochemical parameters were utilised to corroborate the structure-activity correlations with their bioactive potentials. The *in silico* mode of α-amylase inhibition by the studied compounds were assessed by the molecular docking models to correlate with their *in vitro* anti-hyperglycaemic potential.

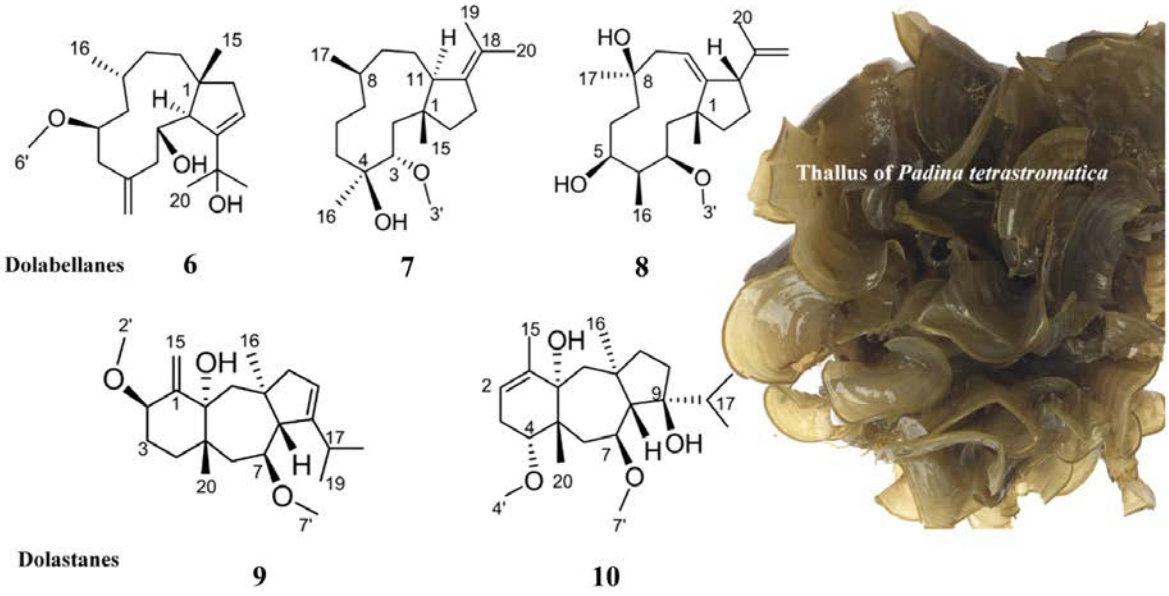

Figure 5.80.: The structures of 6-methoxy-dolabella-8(17),12-diene-10β,18-diol (**6**), 3-methoxy-dolabella-12(18)-ene-4β-ol (**7**), 3-methoxy-dolabella-10,18(19)-diene-5α,8β-diol (**8**), 2,7-dimethoxy-14*α*-hydroxy-dolasta-1(15),9-diene (**9**), and 4,7-dimethoxy-9β,14*α*-dihydroxy-dolasta-1-ene (**10**) isolated from *P. tetrastromatica*. Representative photograph of the thalli (leafy structures) of *P. tetrastromatica* was shown.

5.3.2.2a Structural characterization of Compound 5 (TP_6)

6-Methoxy-dolabella-8(17),12-diene-10β ,18-diol

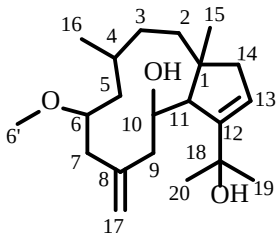

Sample yield	0.25% (> 99% purity, RP-C_{18} HPLC)
Physical description	pale yellow viscous oil
Molecular formula	$C_{21}H_{36}O_3$
Molecular mass	336.2664

The dolabellane class of diterpenoid derivative, 6-methoxy-dolabella-8(17),12-diene-10β ,18-diol was isolated as pale yellow viscous oil compound. The compound (**6**) has exhibited UV absorbance

(UV (MeOH) λ_{max}) at 242.6 (2.89) nm (Figure 5.81). The homogeneity of the compound was ascertained by HPLC data on a bonded phase octadecylsilane (C_{18}) stationary phase (RP-C_8 HPLC, MeOH: MeCN, 3:2 v/v): 3.21 min (Figure 5.82). The molecular ion peak by HRESIMS was observed at *m/z* 337.2742 $[M+H]^+$ (Figure 5.83) .

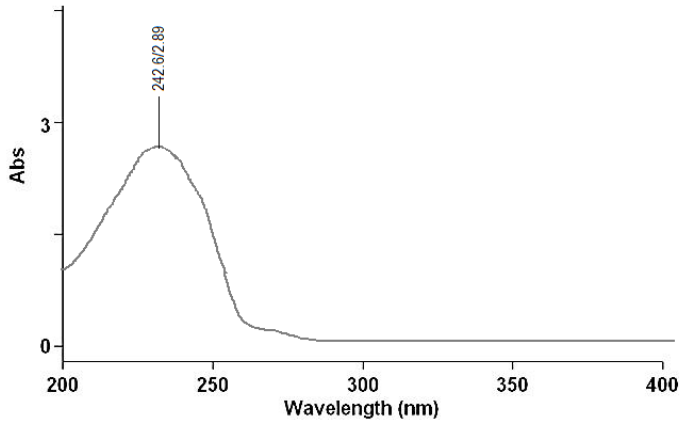

Figure 5.81.: UVspectrum of 6-methoxy-dolabella-8(17),12-diene-10β ,18-diol (**6**)

5.2.5.6 Physicochemical description of compound-6 (TP_6)

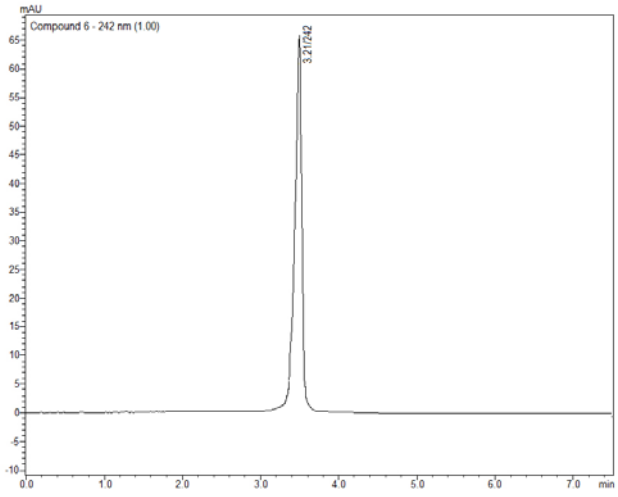

Figure 5.82.: HPLC chromatogram of 6-methoxy-dolabella-8(17),12-diene-10β ,18-diol (**6**)

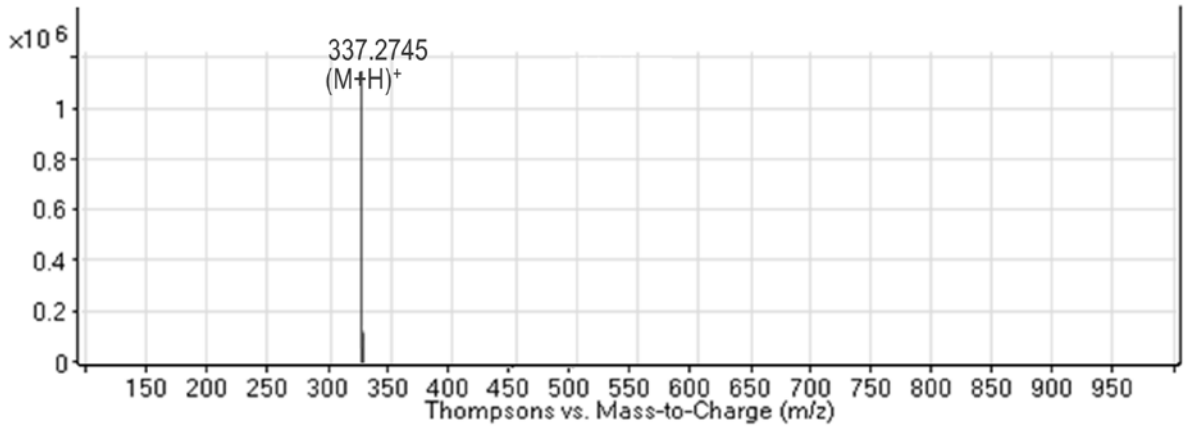

Figure 5.83.: HRESIMS of 6-methoxy-dolabella-8(17),12-diene-10β ,18-diol (**6**)

Repetitive purification of extract of *P. tetrastromatica* using preparatory RP-C_{18} HPLC yielded a dolabellane derivative (**6**) as pale yellow viscous oil. The elemental composition of **6** was deduced by detailed NMR/IR/mass analyses as $C_{21}H_{36}O_3$ with four degrees of unsaturation, which were related to two double bonds and ring systems (Figure 5.84-5.90, Table 5.8).

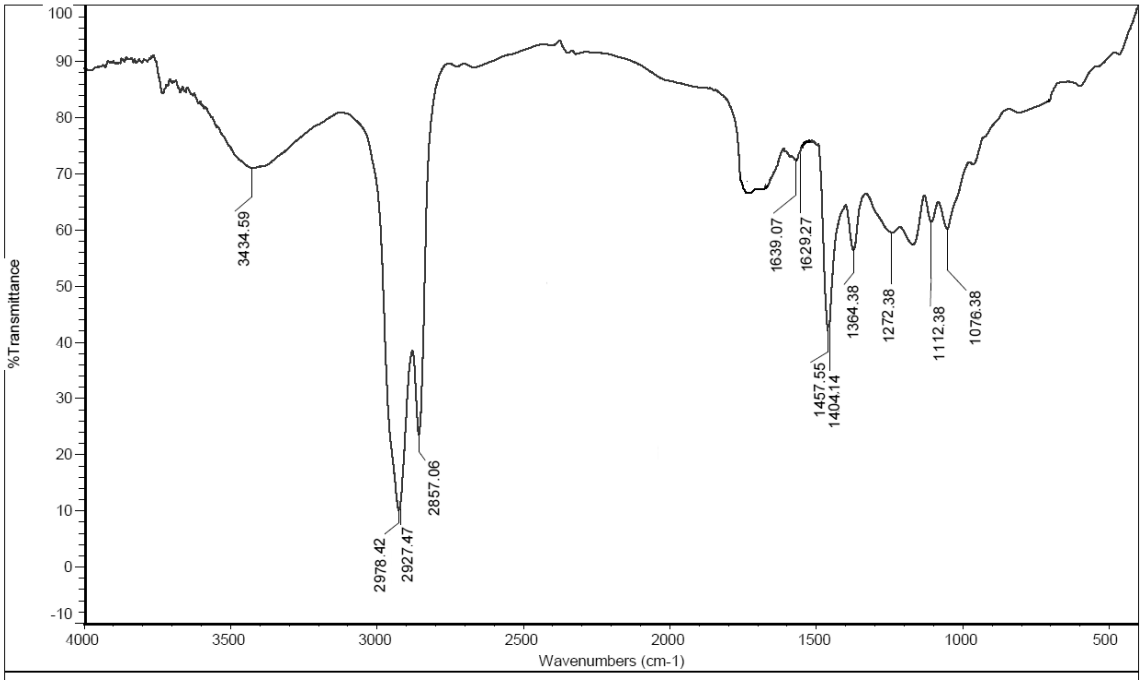

Figure 5.84.: FTIR spectrum of 6-methoxy-dolabella-8(17),12-diene-10β ,18-diol (**6**)

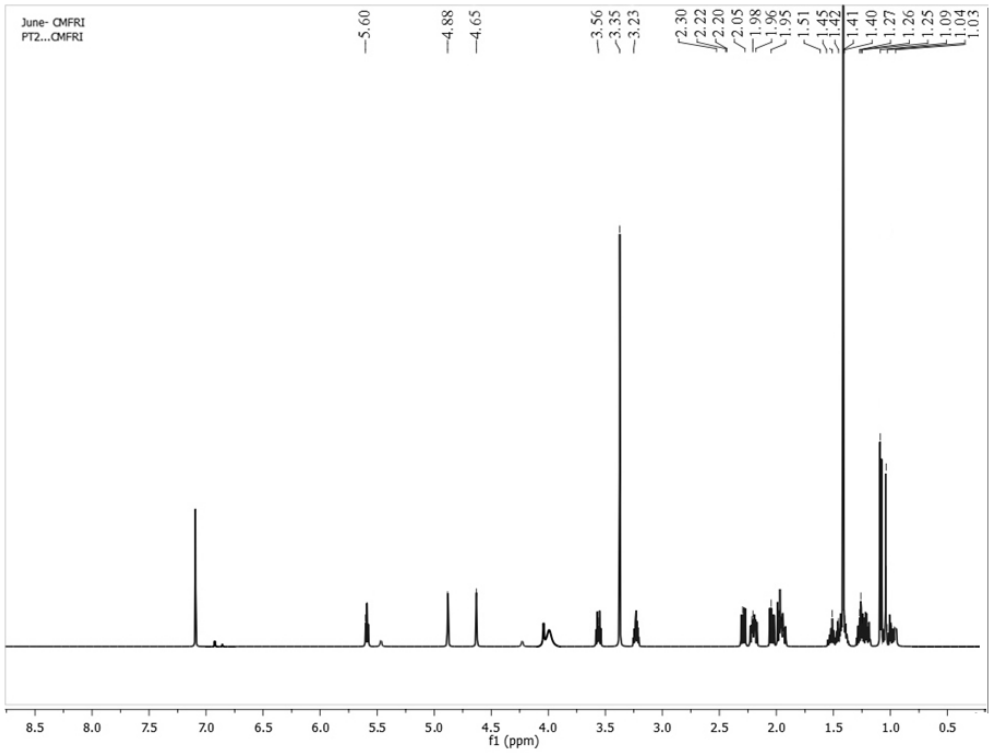

Figure 5.85.: ^{1}H NMR spectrum of 6-methoxy-dolabella-8(17),12-diene-10β ,18-diol (**6**)

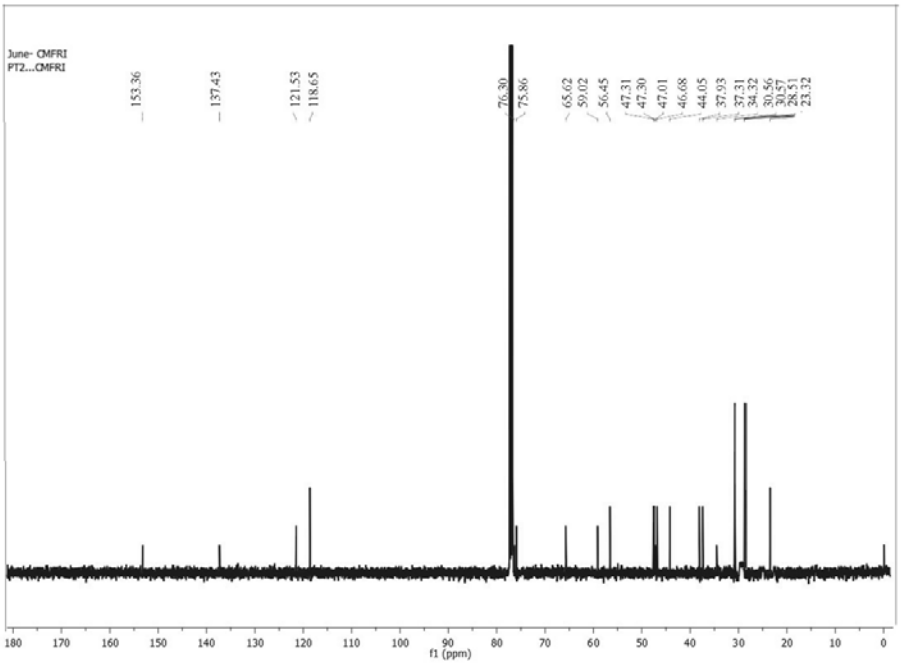

Figure 5.86.: ^{13}C NMR spectrum of 6-methoxy-dolabella-8(17),12-diene-10β ,18-diol (**6**)

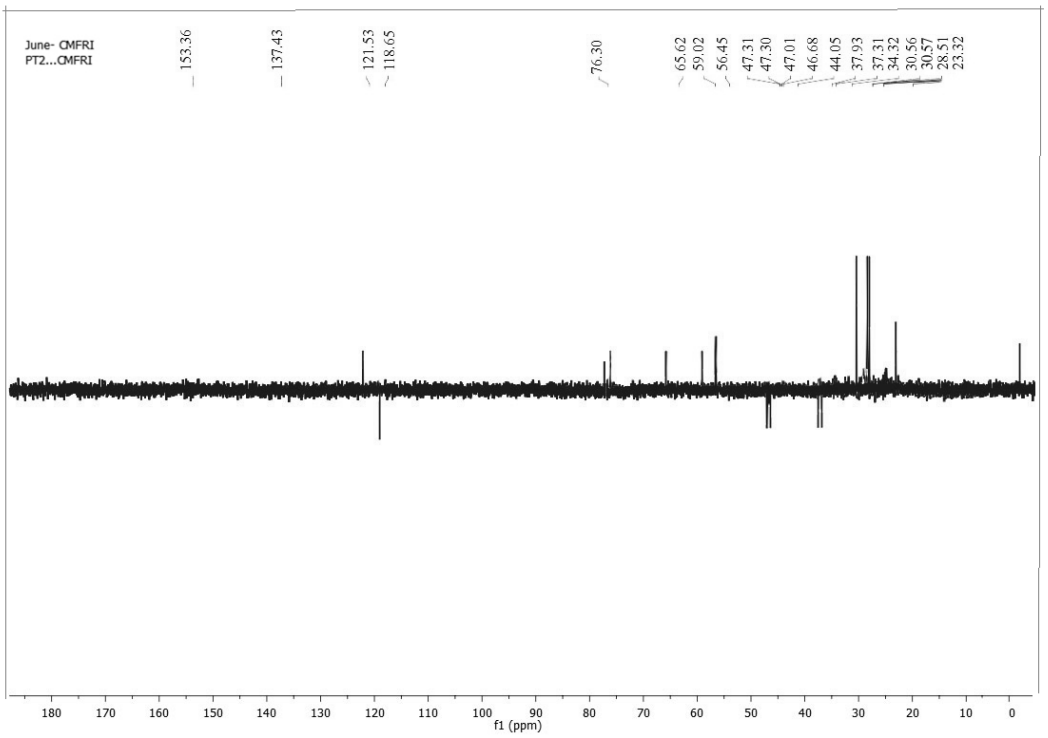

Figure 5.87.: DEPT spectrum of 6-methoxy-dolabella-8(17),12-diene-10β ,18-diol (**6**)

The molecular ion peak was found at *m/z* 336.27 [M^+]. Carbon signals at δ 75.9 (HSQC δ 3.23), 65.6 (HSQC δ 3.56) and 76.3 appropriately supported the presence of oxygen functionalities. The detailed NMR spectroscopic data of **6** was comparable with the basic chemical resonances of dolabellane type of diterpenes, such as 18-hydroxydolabella-4(16),7-dien-3-one and 3,4-epoxydolabella-7-en-18-ol (Cai et al. 2010). The ^{1}H-^{1}H COSYs between the protons δ 1.03 (H-2)/1.26 (H-3)/1.40 (H-4)/1.27 (H-5)/3.23 (H-6)/2.20 (H-7) and δ 2.22 (H-9)/3.56 (H-10) along with the HMBC cross-peaks at δ /δ 1.03 (H-2)/47.0 (C-1), δ /δ 1.51 (H-5)/44.0 (C-7) proposed a closed loop of 11-membered ring in **6** (Figure 5.91). Therefore, the positions of carbons in 11-membered ring were assigned from C-1 to C-11 continuously, which were in agreement with an earlier report (Cai et al. 2010). The HMBC correlations between δ /δ 1.98 (H-11)/153.4 (C-12), δ /δ 5.60 (H-13)/153.4 (C-12), δ /δ 2.05 (H-14)/59.02 (C-11), δ /δ 2.05 (H-14)/47.0 (C-1) in combination with the COSYs δ 5.60 (H-13)/2.05 (H-14) appropriately characterised the existence of 5-membered carbocyclic system, and also assigned the location of a double bond between C-12 and C-13 (Figure 5.91).

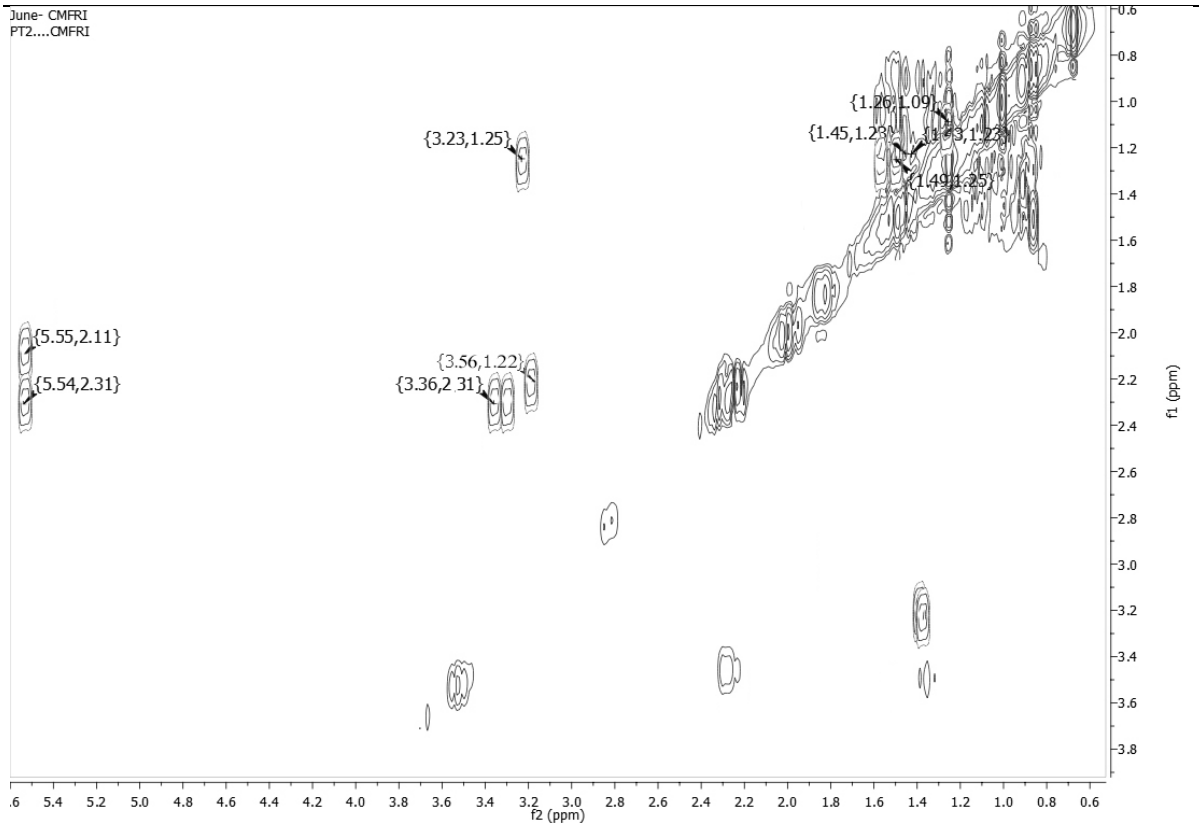

Figure 5.88.: ^{1}H-^{1}H COSY spectrum of 6-methoxy-dolabella-8(17),12-diene-10β ,18-diol (**6**)

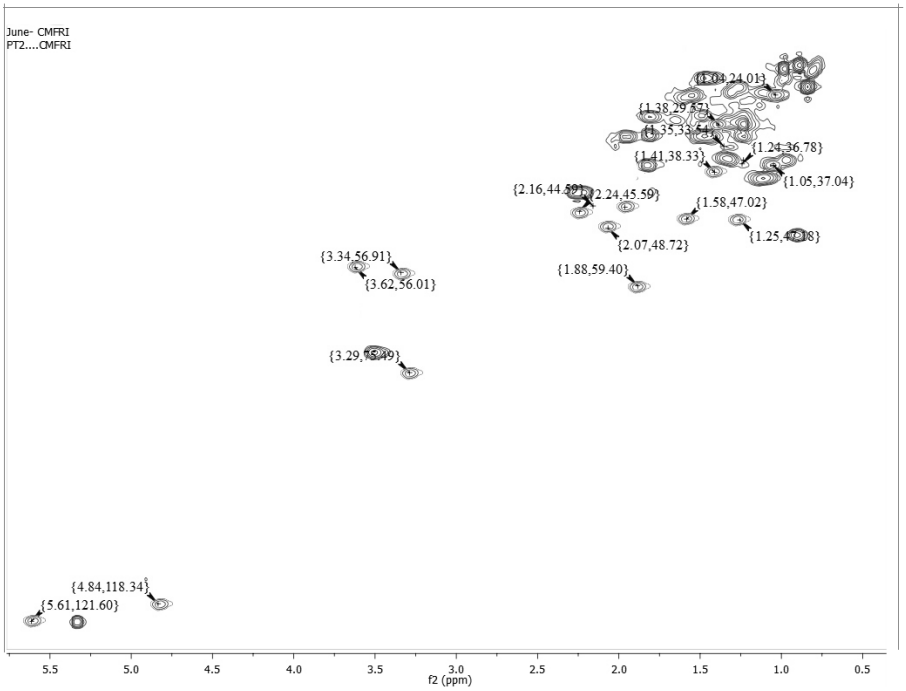

Figure 5.89.: HSQC spectrum of 6-methoxy-dolabella-8(17),12-diene-10β ,18-diol (**6**)

The presence of disubstituted exocyclic olefinic linkage at C-8 and C-17 positions were proposed by HMBCs, such as δ /δ 2.20 (H-7)/118.7 (C-17), δ /δ 1.96 (H-9)/118.7 (C-17) and δ /δ 4.88 (H-17)/137.4 (C-8). HMBC interactions of δ /δ 1.04 (H-15)/47.0 (C-1), 47.3 (C-14) appropriately explained the location of methyl group placed at C-15, (bonded to C-1). These spectroscopic data closely resembled to those of bicyclic dolabellane skeleton with fused 11- and 5-membered rings (Cai et al. 2010; Ioannou et al. 2012). The compound, dolabella-4(16),7-dien-3,18-diol, which was identified from the terrestrial plant, *Aglaia odorata* (Cai et al. 2010), enclosed the disubstituted exocyclic olefinic moiety at C-4, along with a tertiary hydroxyl at C-18 and trisubstituted olefinic group coupled with methyl at C7=C8 positions. Notably, the compound **6** enclosed disubstituted exocyclic olefinic moiety at C-8, tertiary hydroxyl at C-18, along with the trisubstituted alkene at C12=C13 and hydroxyl at C-10. The proton signals corresponding to the methyl groups attached to C-1 and C-4 were in agreement with the diterpenes isolated from the brown seaweed *Dictyota divaricata* (Konig et al. 1991). The compound, 18-hydroxy-2,7-dolabelladiene from *D. divaricata* comprised of endocyclic double bond coupled with methyl at C7=C8 (Konig et al. 1991), whereas the studied compound enclosed a disubstituted exocyclic olefinic moiety at C-8. It is of note that the studied dolabellane diterpenoid exhibited similarities with the dolabellane framework, even though, the carbocyclic skeleton with different olefinic and oxy functionalizations were present in the titled compound **6** accounting for its novelty.

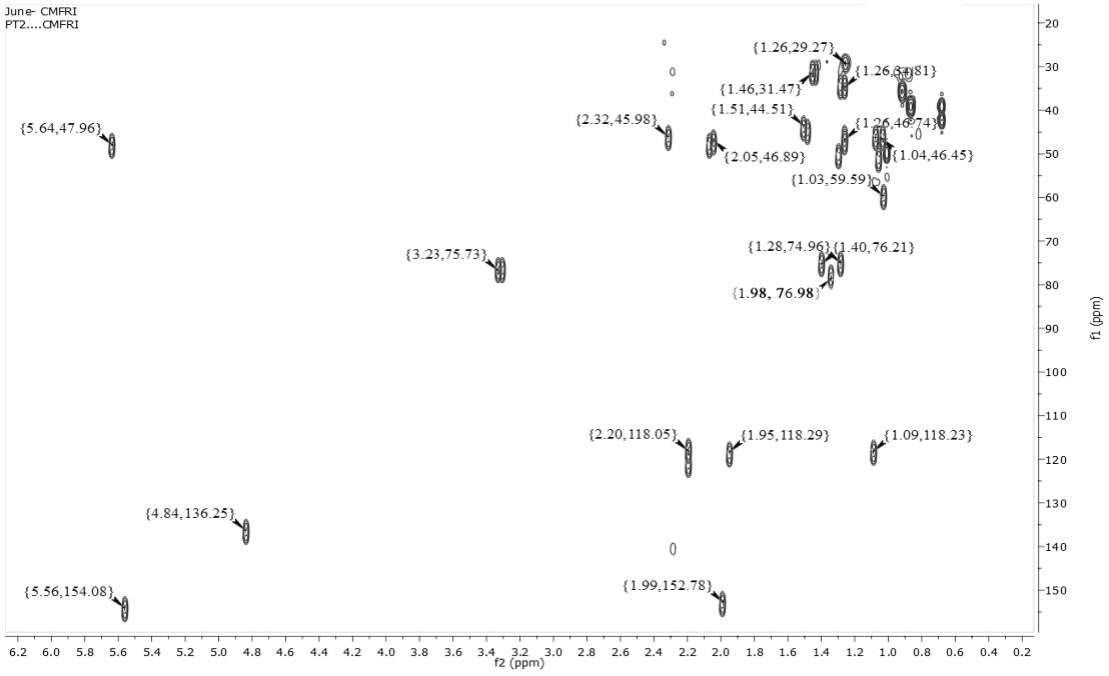

Figure 5.90.: HMBC spectrum of 6-methoxy-dolabella-8(17),12-diene-10β ,18-diol (**6**)

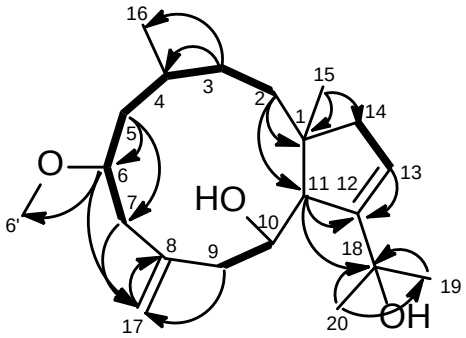

Figure 5.91.: Prominent ^{1}H-^{1}H COSY, and selected HMBC correlations of 6-methoxy-dolabella-8(17),12-diene-10β ,18-diol (**6**). The key ^{1}H-^{1}H COSY couplings were represented in bold face bonds. The key HMBC couplings have been represented by double barbed arrows.

Relative stereochemistries of the chiral centres at C-6, C-10 and C-11 in **6** were assigned by the NOESY experiments (Figure 5.92 & 5.93), and earlier reports (Konig et al. 1991). The NOESY correlations between δ 3.35 (H-6')/1.45 (Hβ-3)/1.05 (H-15), δ 1.40 (H-4)/2.20 (H-7)/4.65 (Hβ-17)/1.45 (Hβ-3) and δ 2.22 (H-9)/4.65 (Hβ-17) appropriately attributed that these protons were coordinated in the identical plane of reference, and hence were assigned as β-oriented.

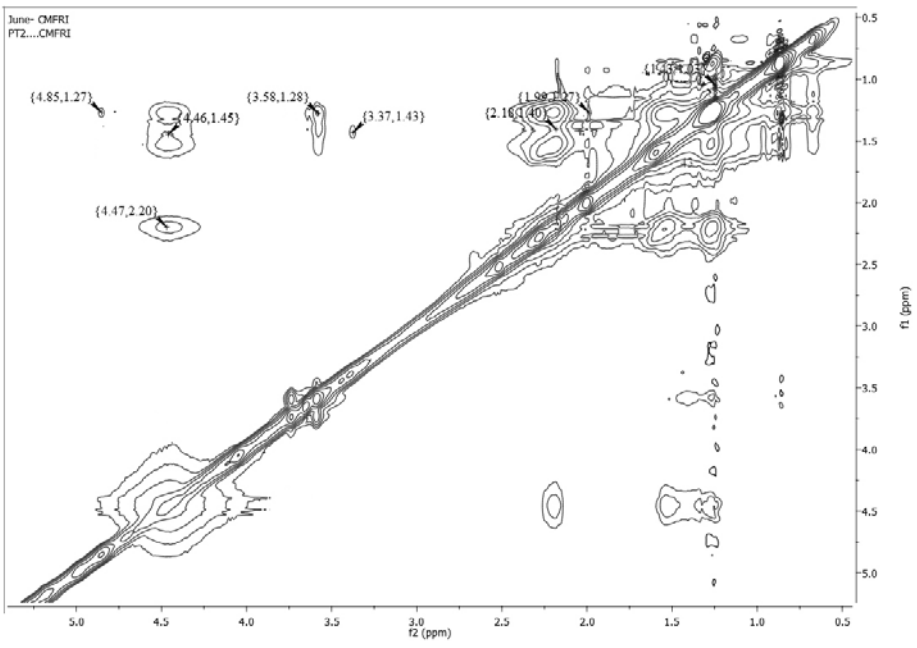

Figure 5.92.: NOESY spectrum of 6-methoxy-dolabella-8(17),12-diene-10β ,18-diol (**6**)

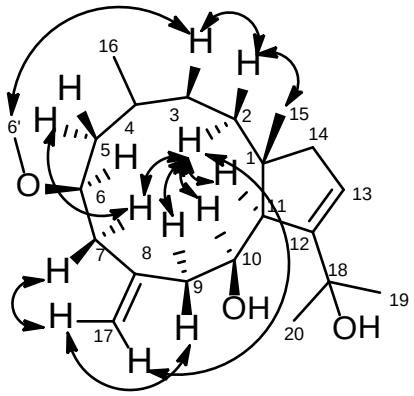

Figure 5.93.: Prominent NOE correlations of 1 6-methoxy-dolabella-8(17),12-diene-10β ,18-diol (**6**). NOESY relations are represented by double-tailed arrows

The molecular ion peak of **6** was appeared at *m/z* 336 and base peak was ontained at *m/z* 27.0 (Figure 5.94 and 5.95).

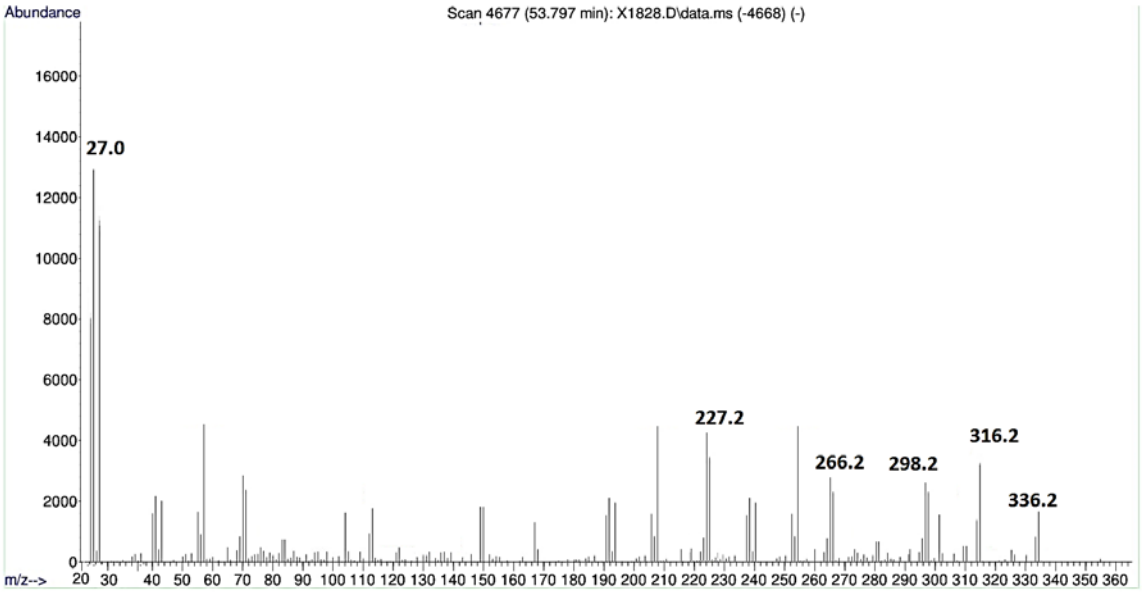

Figure 5.94.: EI-MS spectrum of 6-methoxy-dolabella-8(17),12-diene-10β ,18-diol (**6**)

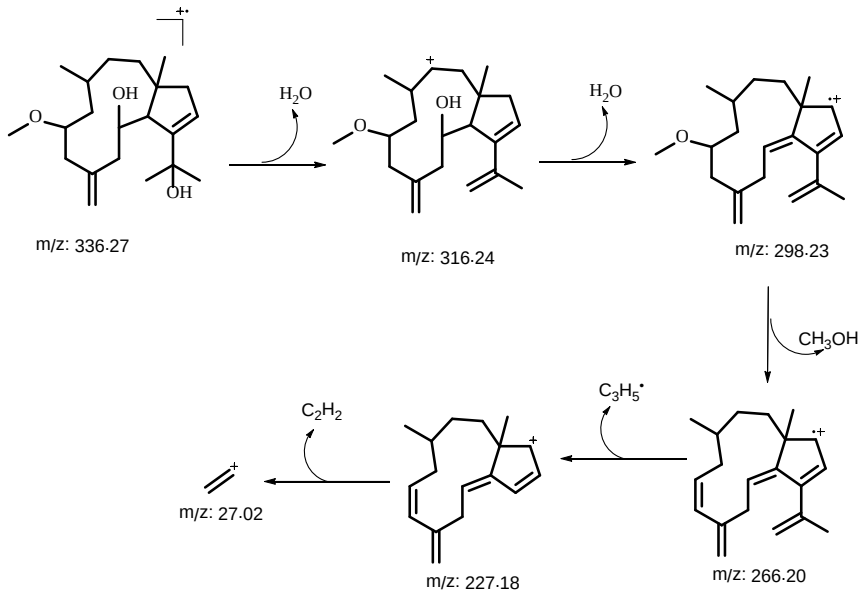

Figure 5.95.: Tentative mass fragmentation pattern of 6-methoxy-dolabella-8(17),12-diene-10β ,18-diol (**6**)

Table 5.9.: NMR spectroscopic data[a] of 3-methoxy-dolabella-12(18)-ene-4β-ol (**6**) isolated from brown seaweed *P.tetrastromatica*

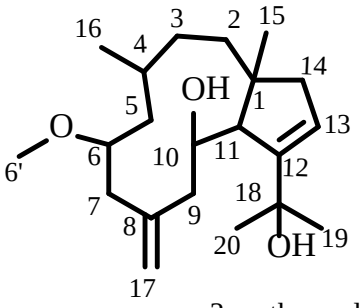

Compound **6**……3-methoxy-dolabella-12(18)-ene-4β-ol

C. No.	^{13}C NMR	^{1}H NMR (int.,mult., J in Hz)[b]	COSY	HMBC
1	47.0	-	-	-
2	38.0	1.25(1H,dd,11.1, 7.2Hz)	H-3	C-1
		1.03(1H,dd,10.6, 5.7Hz)	-	-
3	37.3	1.26(1H,m),	H-4	C-16, 4
		1.45(1H,m)	-	-
4	34.3	1.40(1H,m)	H-5	-
5	47.3	1.51(1H,t,10.6 Hz),	H-6	C-7
		1.27(1H,t, 9.9Hz)	-	C-6
6	75.9	3.23(1H,m)	H-7	C-17, 6’
6’	56.5	3.35(1H,s)	-	C-6
7	44.1	2.20(1H,d,10.2 Hz),	-	C-17

		1.95(1H,d, 9.8Hz)	-	-
8	137.3	-	-	-
9	46.7	2.22(1H,d,11.1 Hz),	H-10	C-17
		1.96(1H,d,9.6 Hz)		
10	65.62	3.56(1H,m)	-	-
11	59.0	1.98(1H,d,10.2 Hz)	-	C-12,18
12	153.4	-	-	-
13	121.5	5.60(1H,t,9.8 Hz)	H-14	C-14,12
14	47.3	2.05(1H,d,9.3 Hz)	-	C-1,11
		2.30(1H,d,9.7 Hz)	-	-
15	23.3	1.04(3H,s)	-	C-14,1
16	28.5	1.09(3H,d,6.4 Hz)	-	-
17	118.7	4.88(1H,s),	-	C-8
		4.65(1H,s)	-	-
18	76.3	-	-	-
19	30.6	1.41(3H,s)	-	C-18
20	30.6	1.42(1H, s)	-	C-19

[a]NMR spectra were recorded using a Bruker AVANCE III 500 MHz (AV 500) spectrometer (Bruker, Karlsruhe, Germany) in $CDCl_3$ as aprotic solvent at ambient temperature with TMS as the internal standard (δ 0 ppm).

[b]Values in ppm, multiplicity and coupling constants (*J*= Hz) were indicated in parentheses. Multiplicities were allocated by [135]DEPT NMR spectrum.

The assignments were made with the aid of the COSY, HSQC, HMBC and NOESY experiments.

5.3.2.2b Structural characterization of Compound 7 (TP_7)

3-Methoxy-dolabella-12(18)-ene-4β-ol

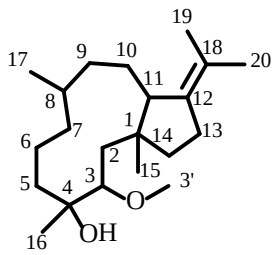

Sample yield	0.25% (> 99% purity, RP-C_{18} HPLC)
Physical description	Yellow oil
Molecular formula	$C_{21}H_{38}O_2$
Molecular mass	322.2872

The dolabellane class of diterpenoid derivative, 3-methoxy-dolabella-12(18)-ene-4β-ol was isolated as yellow oil compound. The compound (**7**) has exhibited UV absorbance (UV (MeOH)

λ_{max}) at 246.0 (2.90) nm (Figure 5.96). The homogeneity of the compound was ascertained by HPLC data on a bonded phase octadecylsilane (C_{18}) stationary phase (RP-C_8 HPLC, MeOH: MeCN, 3:2 v/v): 4.23 min (Figure 5.97). The molecular ion peak by HRESIMS was found to be observed at 323.2953 $[M+H]^+$,

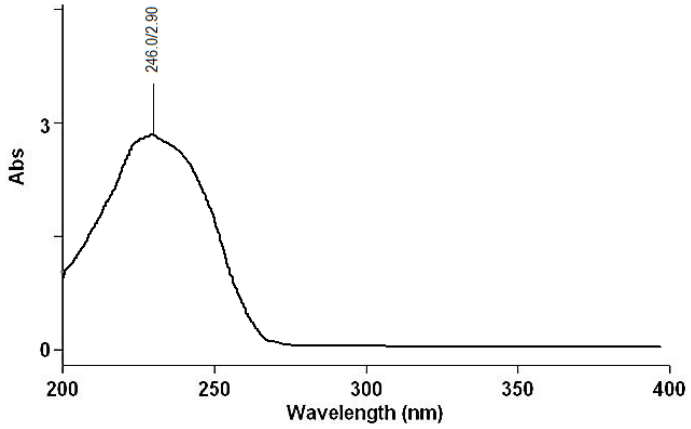

Figure 5.96.: UVspectrum of 3-methoxy-dolabella-12(18)-ene-4β-ol (**7**)

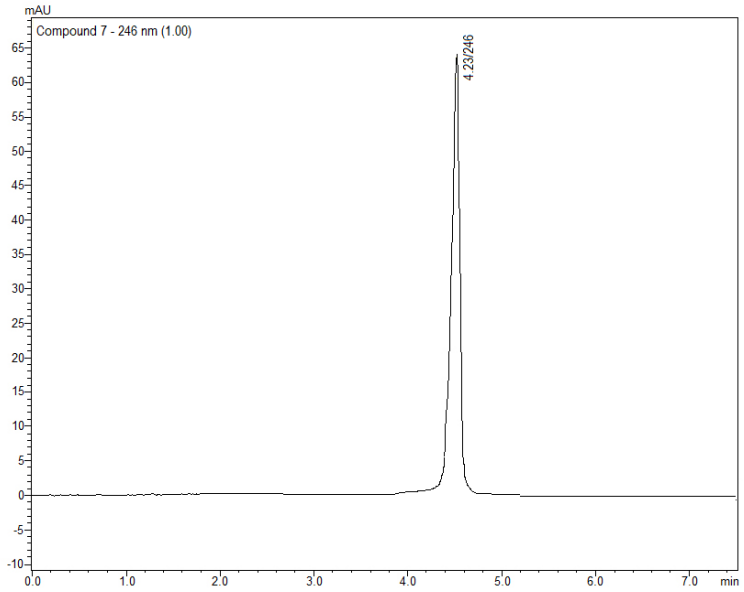

Figure 5.97.: HPLC chromatogram of 3-methoxy-dolabella-12(18)-ene-4β-ol (**7**)

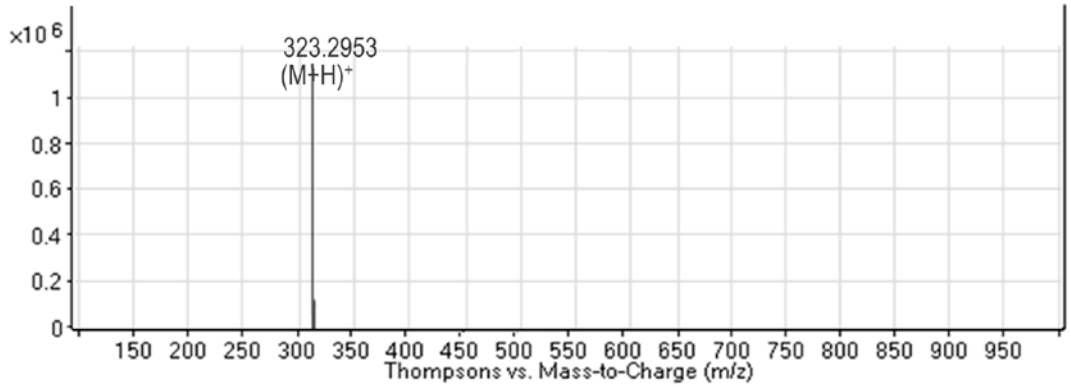

Figure 5.98.: HRESIMS of 3-methoxy-dolabella-12(18)-ene-4β-ol (**7**)

The crude extract of *P. tetrastromatica* on chromatographic separation yielded a compound (**7**), as pale yellowish oil. The mass spectroscopy-assisted NMR/IR/mass experiments established the elemental composition of **7** as $C_{21}H_{38}O_2$ bearing three degrees of unsaturation (one olefin and two ring systems) (Table 5.10; Figure 5.99-5.104).

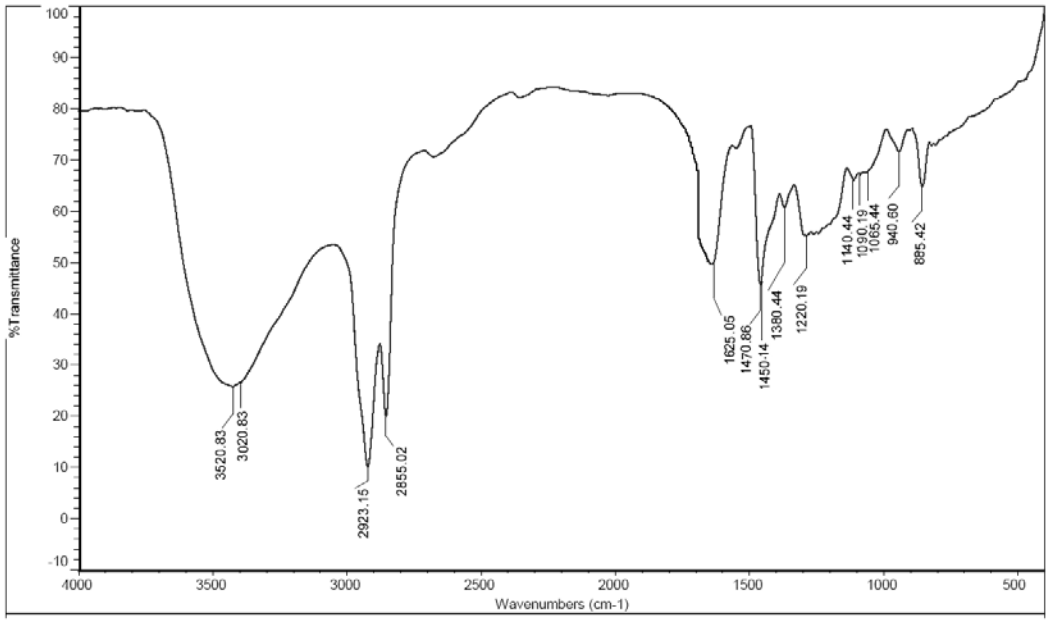

Figure 5.99.: FTIR of 3-methoxy-dolabella-12(18)-ene-4β-ol (**7**)

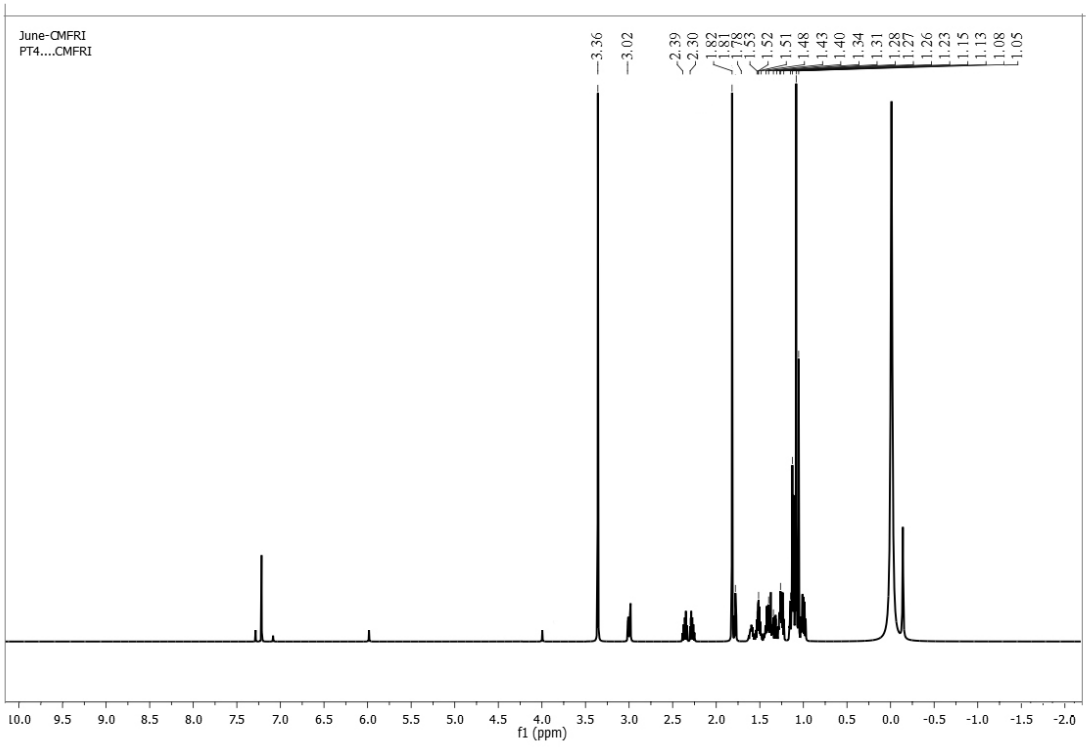

Figure 5.99.: ^{1}H NMR spectrum of 3-methoxy-dolabella-12(18)-ene-4β-ol (**7**)

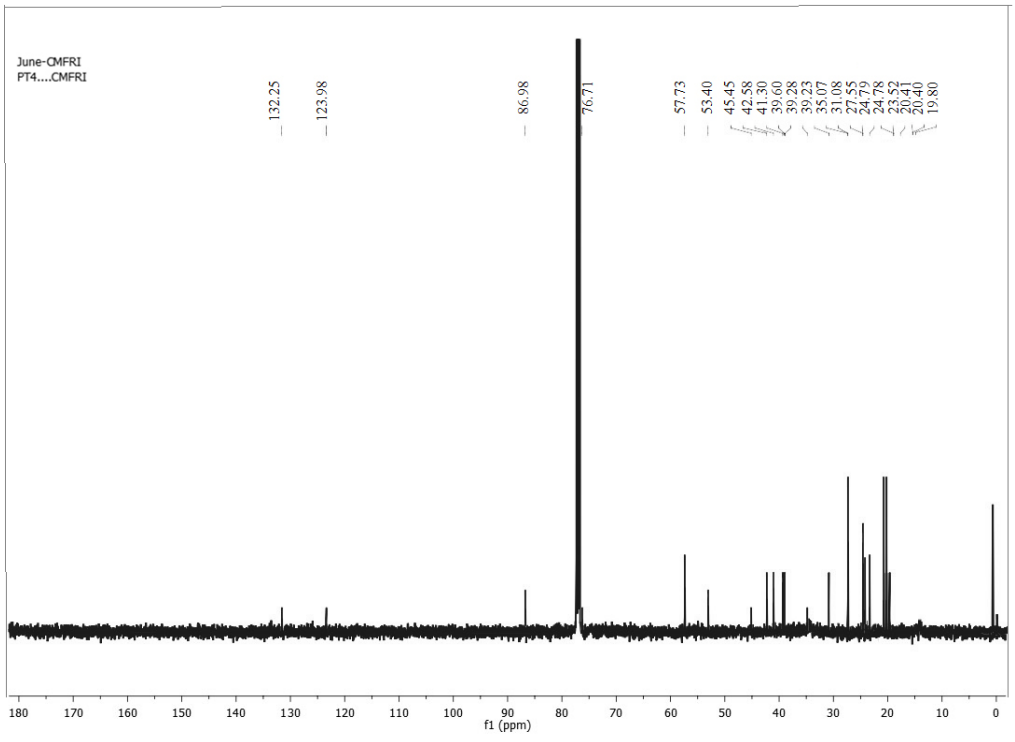

Figure 5.100.: ^{13}C NMR spectrum of 3-methoxy-dolabella-12(18)-ene-4β-ol (**7**)

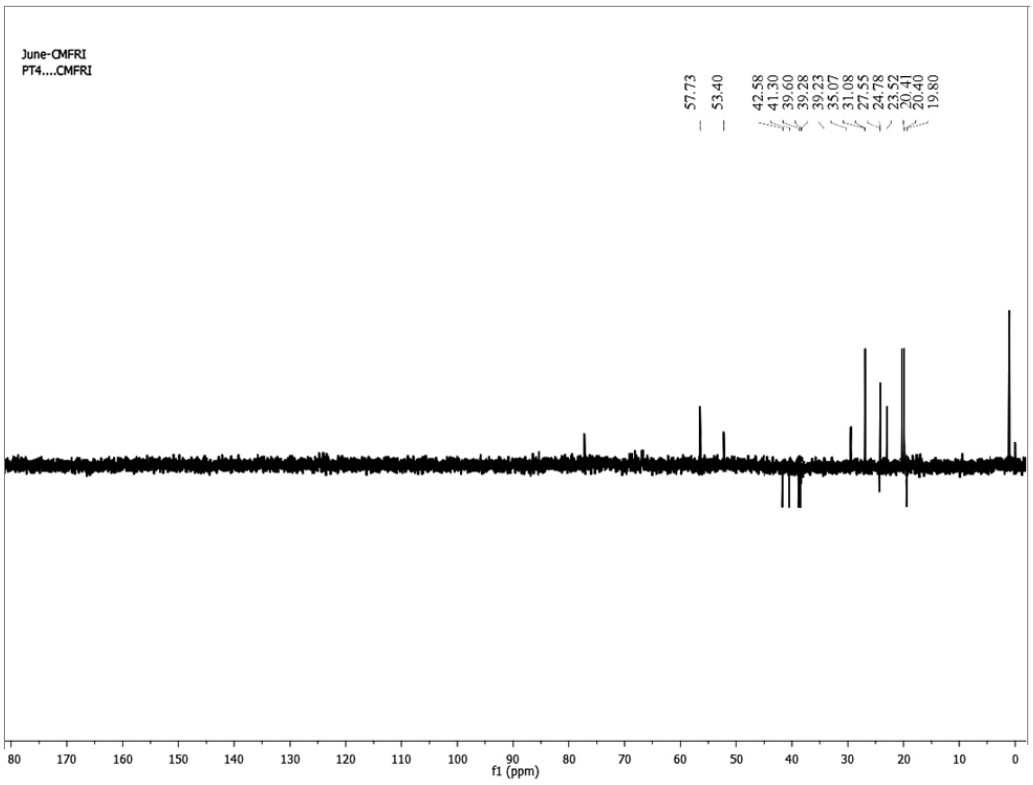

Figure 5.101.: DEPT spectrum of 3-methoxy-dolabella-12(18)-ene-4β-ol (**7**)

The molecular ion peak of **7** appeared at *m/z* 322.29 [M^+]. The COSYs between the protons δ 1.15 (H-2)/3.02 (H-3), δ 1.23 (H-5)/1.43 (H-6)/1.52 (H-7) and δ 1.51 (H-9)/1.13 (H-10) together with HMBCs δ /δ 1.40 (H-2)/45.6 (C-1), δ /δ 1.40 (H-2)/53.4 (C-11) and δ /δ 1.48 (H-5)/76.7 (C-4) explained the partial structure of **7**. The COSYs combined with HMBCs deduced a closed loop of 11-membered ring in **7** (Ioannou et al. 2012) (Figure 4.105). The fusion of 11-membered ring with 5-membered ring via carbons at C-1 and C-11 suggested the resemblance of the basic skeleton of **7** with that of compound **6**. Notably, the structural attributes of compound **6** was similar to those of **7** except the functionalities, such as methoxy at C-3, hydroxyl at C-4, methyl at C-8 and an additional isopropylidene group at C-12 (in **7**), which suggested their structural differences. The present compound was comprised of isopropylidenecyclopentane ring along with methoxy at C-3 and hydroxyl at C-4 unlike the previously reported dolabellane variant enclosing an isopropylidenecyclopentanone ring along with exocyclic olefinic moiety at C-4, acetoxy at C-3 and carbonyl at C6 positions, isolated from the coral *Eunicea sp.* (Wei et al. 2010). Therefore, the compound **7** represented the first description of dolabellane skeleton possessing an isopropylidenecyclopentane ring along with the oxy-functionalization from seaweed

P.tetrastromatica.

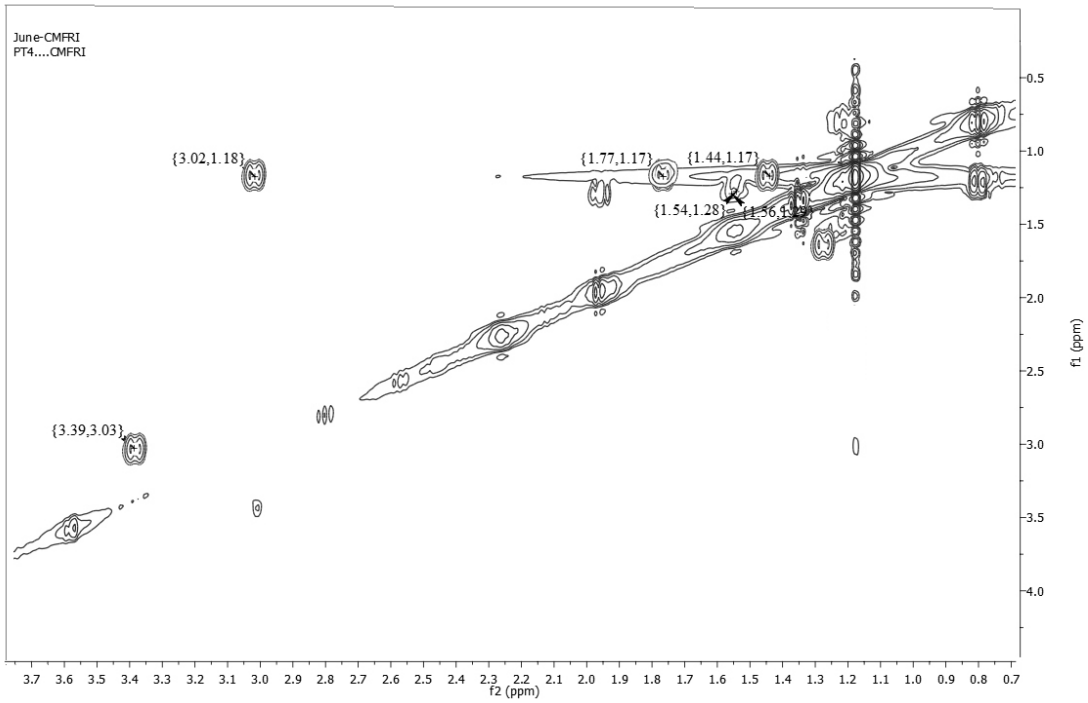

Figure 5.102.: ^{1}H-^{1}H COSY spectrum of 3-methoxy-dolabella-12(18)-ene-4β-ol (**7**)

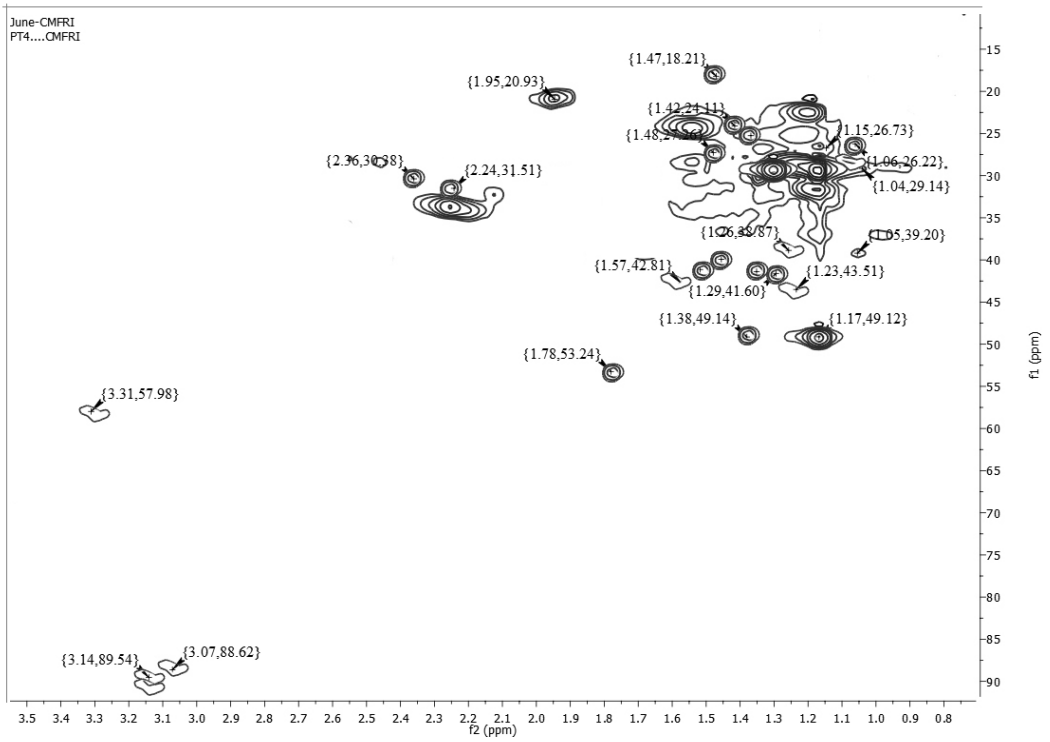

Figure 5.103.: HSQC spectrum of 3-methoxy-dolabella-12(18)-ene-4β-ol (**7**)

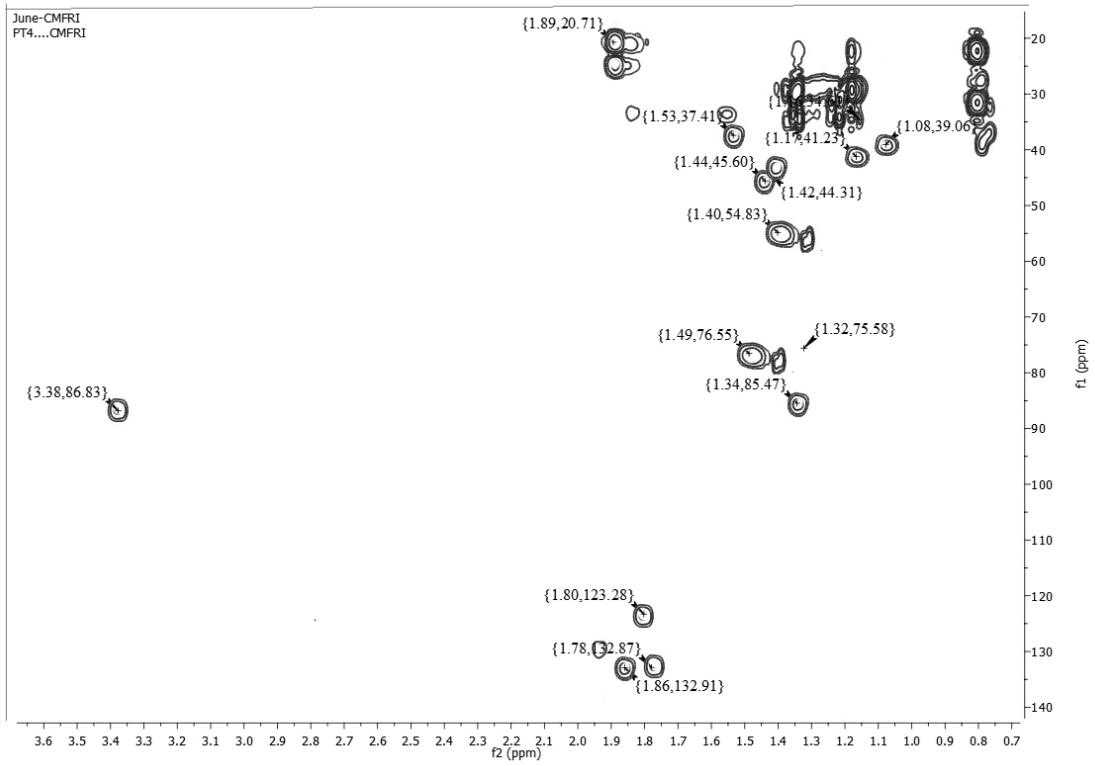

Figure 5.104.: HMBC spectrum of 3-methoxy-dolabella-12(18)-ene-4β-ol (**7**)

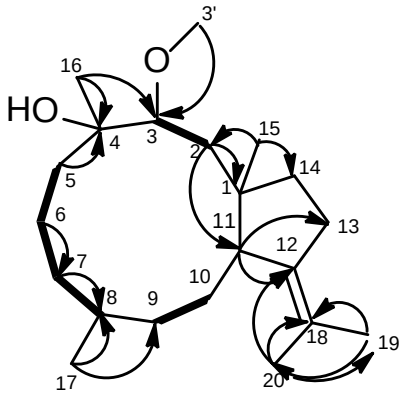

Figure 5.105.: Prominent ^{1}H-^{1}H COSY, and selected HMBC correlations of 3-methoxy-dolabella-12(18)-ene-4β-ol (**7**). The key ^{1}H-^{1}H COSY couplings were represented in bold face bonds. The key HMBC couplings have been represented by double barbed arrows.

NOESY spectrum demonstrated that the protons δ 1.05 (H-15)/1.28 (Hβ-9)/3.02 (H-3)/1.27 (Hβ-7)/2.30 (Hβ-13) and δ 1.27 (Hβ-7)/1.05 (H-15) displayed spatial correlations (Figure 5.106-5.107), and were located at the identical molecular reference plane, thus arbitrarily assigned as β-oriented. The protons at δ 3.36 (H-3') displayed NOESY correlations with the protons at δ 1.48 (H-5*α*), 1.31 (H-16), 1.40 (H-2*α*), 1.43 (H-6), 1.40 (H*α*-10), 1.40 (H*α*-8) and δ 1.48 (H*α*-5)/1.78 (H*α*-11), which were found to be *trans* oriented to the β-protons, and therefore, assigned as *α*-protons.

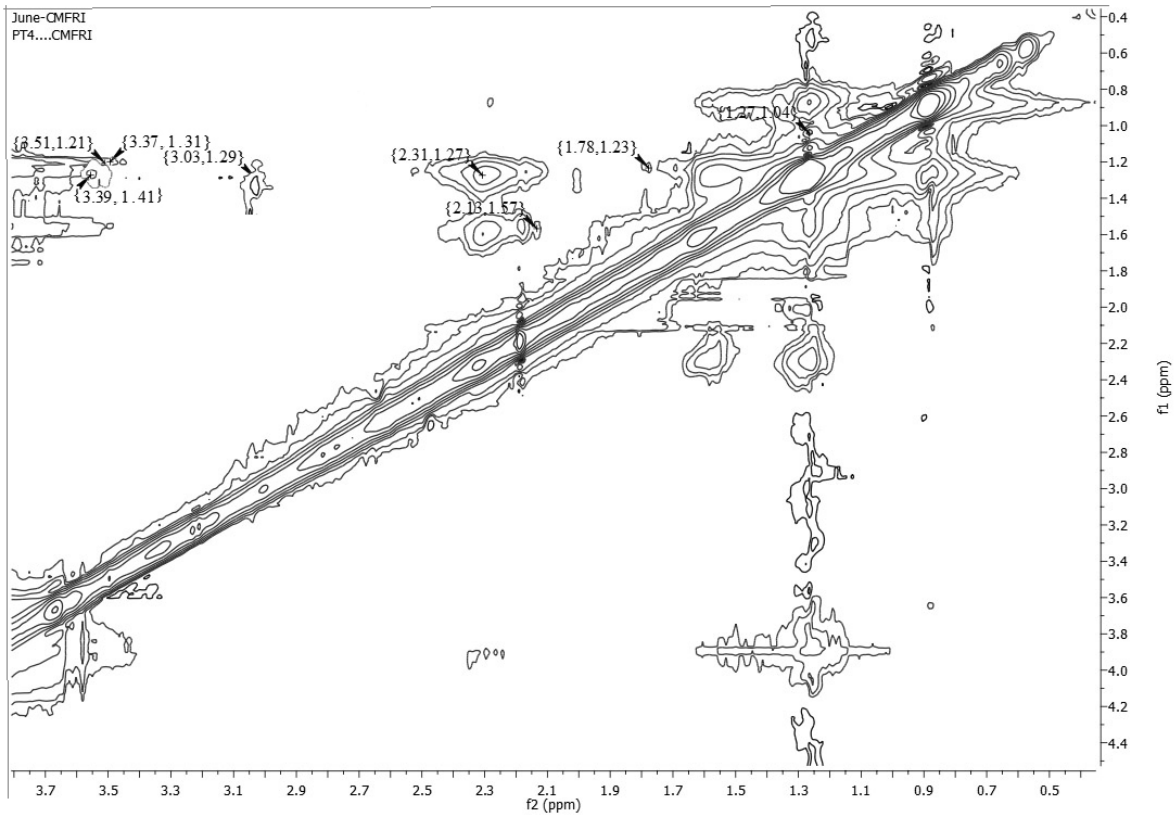

Figure 5.106.: NOESY of 3-methoxy-dolabella-12(18)-ene-4β-ol (**7**)

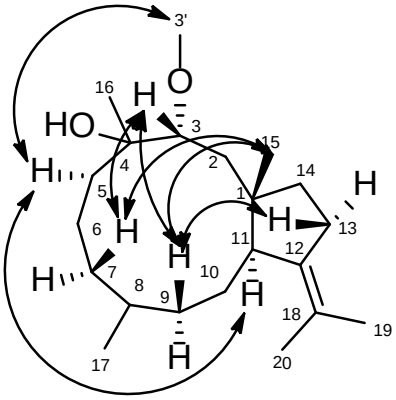

Figure 5.107.: Prominent NOE correlations of 3-methoxy-dolabella-12(18)-ene-4β-ol (**7**). NOESY relations are represented by double-tailed arrows

The molecular ion peak of **7** was appeared at *m/z* 322 and base peak was ontained at *m/z* 40.0 (Figure 5.108 and 5.109).

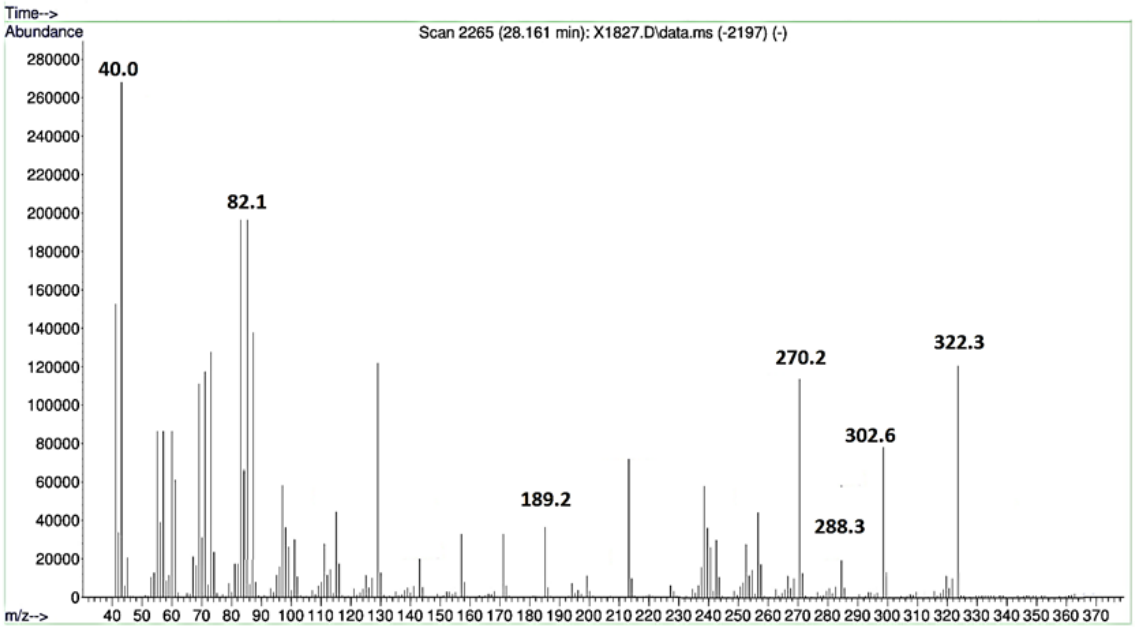

Figure 5.108.: EI-MS spectrum of 3-methoxy-dolabella-12(18)-ene-4β-ol (**7**)

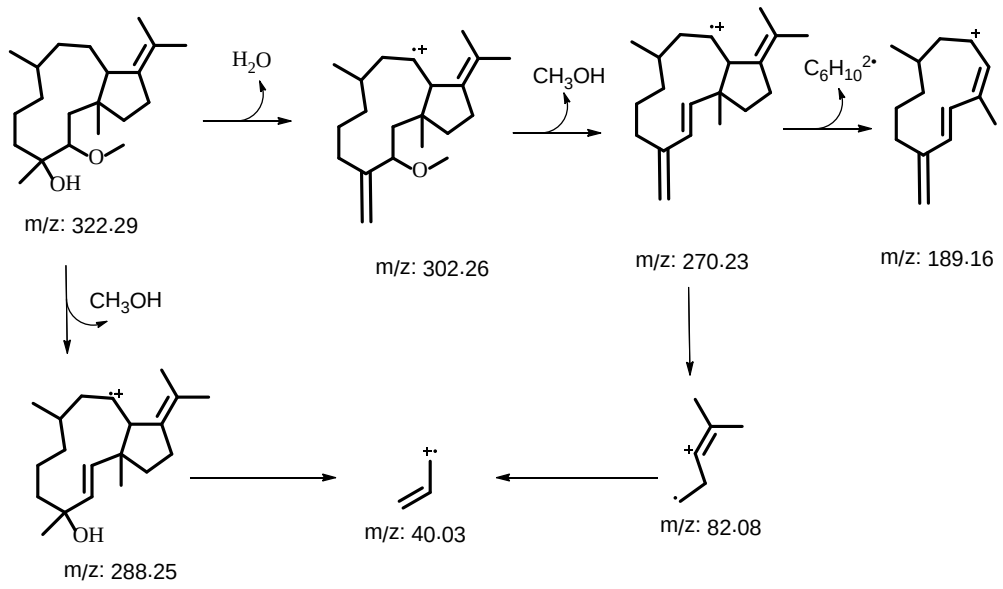

Figure 5.109.: EI-MS spectrum of 3-methoxy-dolabella-12(18)-ene-4β-ol (**7**)

Table 5.10.: NMR spectroscopic data[a] of 3-methoxy-dolabella-12(18)-ene-4β-ol (**7**) isolated from brown seaweed *P.tetrastromatica*

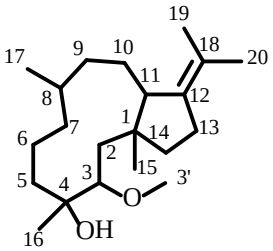

Compound **7**……3-methoxy-dolabella-12(18)-ene-4β-ol (**7**)

C. No.	^{13}C NMR	^{1}H NMR (int.,mult., J in Hz)[b]	COSY	HMBC
1	45.5	-	-	-
2	39.2	1.15(1H,d,9.3Hz)	H-3	C-1,11
		1.40(1H,d,10.2 Hz)	-	-
3	87.0	3.02(1H,t,10.6 Hz)	-	-
3’	57.7	3.36(3H,s)	-	C-3
4	76.7	-	-	-
5	39.3	1.23(1H,dd,11.6, 6.9 Hz)	H-6	C-4
		1.48(1H,dd,11.3, 6.6 Hz)	-	-
6	19.8	1.43(2H,m)	H-7	C-7
7	42.6	1.52(1H,m)	-	C-8
		1.27(1H,m)	-	-
8	35.0	1.40(1H,m)	-	-
9	41.3	1.51(1H,m)	H-10	-
		1.28(1H,m)	-	-
10	24.8	1.40(1H, m)	-	-
		1.13(1H, m)	-	-

11	53.4	1.78(1H,t,5.7 Hz)	-	C-12
12	132.3	-	-	-
13	31.1	2.30(1H,m)	-	-
		2.39(1H,m)	-	-
14	39.6	1.34(1H,dd, 10.9, 6.3 Hz)	-	-
		1.08(1H,dd,10.7, 6.8 Hz)		
15	23.5	1.05(3H,s)	-	C-14,2
16	24.8	1.31(3H,s)	-	C-4,3
17	27.6	1.15(3H,s)	-	C-8,9
18	124.0	-	-	-
19	20.4	1.82(3H,s)	-	C-18,20
				-
20	20.4	1.81(3H,s)	-	C-12,18

[a]NMR spectra were recorded using a Bruker AVANCE III 500 MHz (AV 500) spectrometer (Bruker, Karlsruhe, Germany) in $CDCl_3$ as aprotic solvent at ambient temperature with TMS as the internal standard (δ 0 ppm).

[b]Values in ppm, multiplicity and coupling constants (*J*= Hz) were indicated in parentheses. Multiplicities were allocated by ^{135}DEPT NMR spectrum.

The assignments were made with the aid of the COSY, HSQC, HMBC and NOESY experiments.

5.3.2.2c Structural characterization of Compound 8 (TP_8)

3-Methoxy-dolabella-10,18(19)-diene-5α,8β-diol

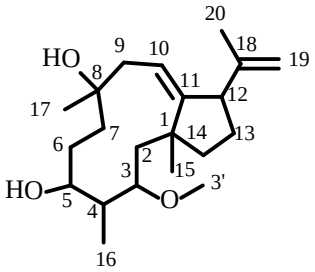

Sample yield	0.25% (> 99% purity, RP-C_{18} HPLC)
Physical description	Yellow oil
Molecular formula	$C_{21}H_{36}O_3$
Molecular mass	336.2664

The dolabellane class of diterpenoid derivative, 3-methoxy-dolabella-10,18(19)-diene-5α,8β -diol as yellow oil compound. The compound (**8**) has exhibited UV absorbance (UV (MeOH) λ_{max}) at 248 (3.1) nm (Figure 5.110). The homogeneity of the compound was ascertained by HPLC data on a bonded phase octadecylsilane (C_{18}) stationary phase (RP-C_8 HPLC, MeOH:MeCN, 3:2

v/v): 4.02 min (Figure 5.111). The molecular ion peak by HRESIMS was found to be observed at 337.2745 $[M+H]^+$ (Figure 5.112).

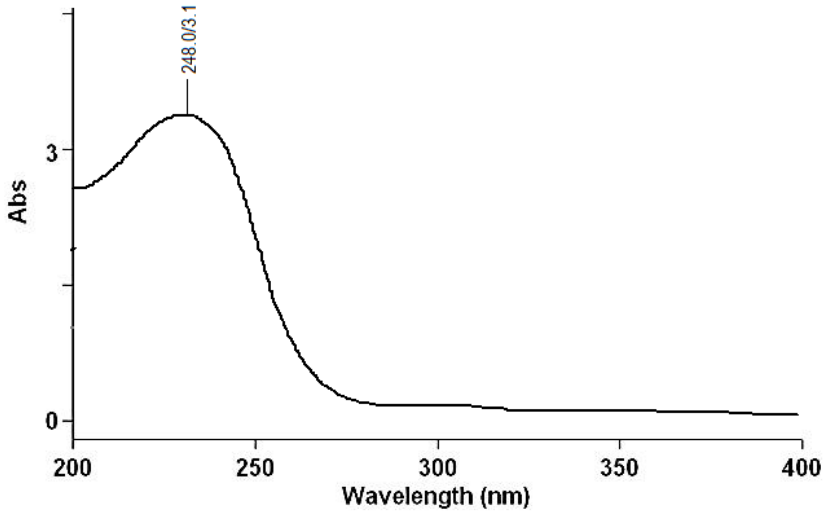

Figure 5.110.: UVspectrum of 3-methoxy-dolabella-10,18(19)-diene-5α,8β -diol (**8**)

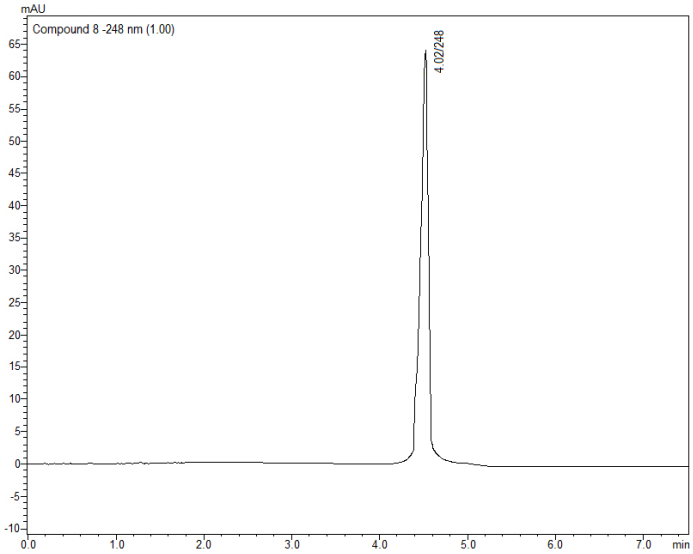

Figure 5.111.: HPLC chromatogram of 3-methoxy-dolabella-10,18(19)-diene-5α,8β -diol (**8**)

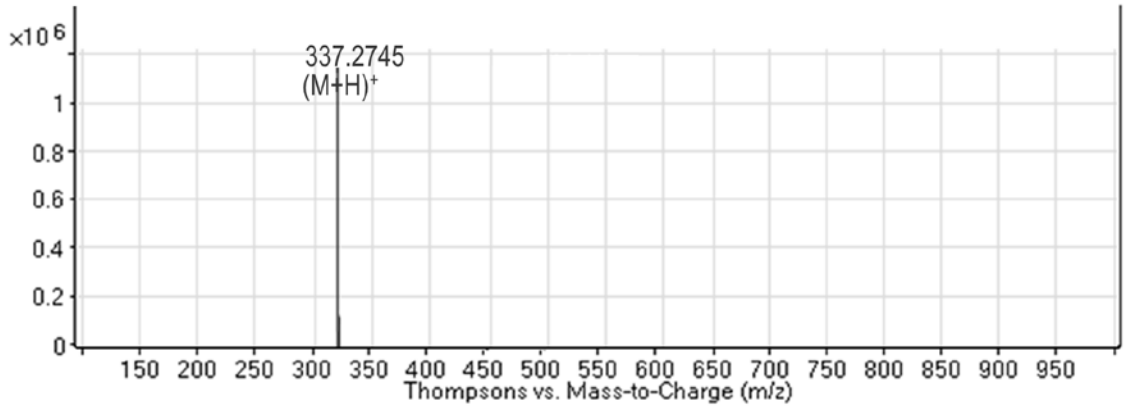

Figure 5.112.: HRESIMS of 3-methoxy-dolabella-10,18(19)-diene-5α,8β -diol (**8**)

The compound **8**, another dolabellane variant, was isolated as yellowish oil from the organic extract of *P. tetrastomatica* on column chromatographic separations. The molecular ion peak of **8** was found at *m/z* 336.27 [M^+], and the elemental composition was deduced as $C_{21}H_{36}O_3$, with detailed NMR/IR experiments (Table 5.11; Figure 5.113-5.118).

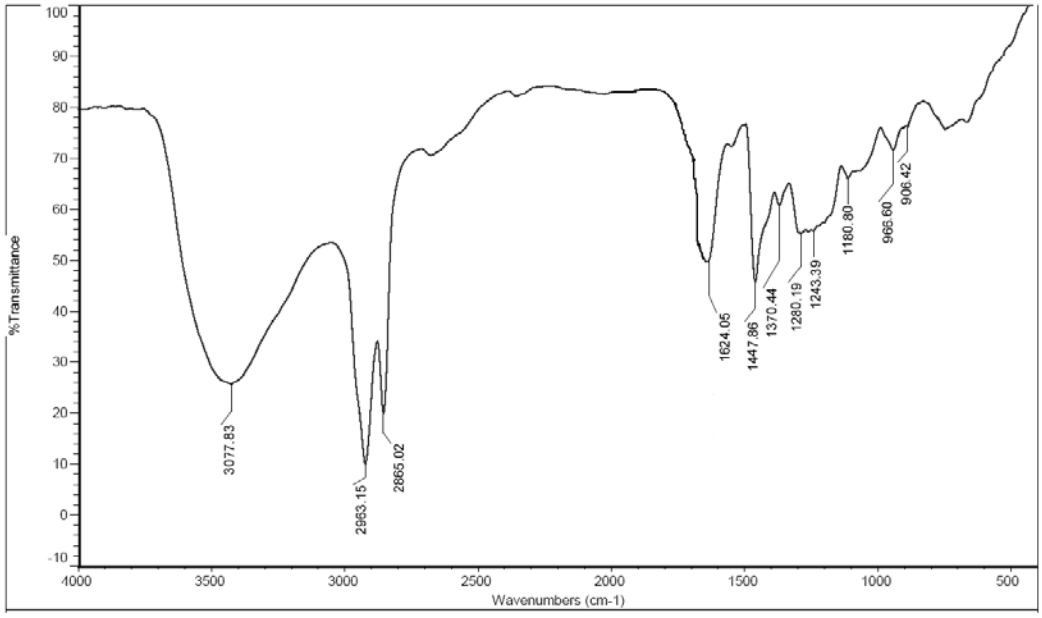

Figure 5.113.: FTIR spectrum of 3-methoxy-dolabella-10,18(19)-diene-5α,8β -diol (**8**)

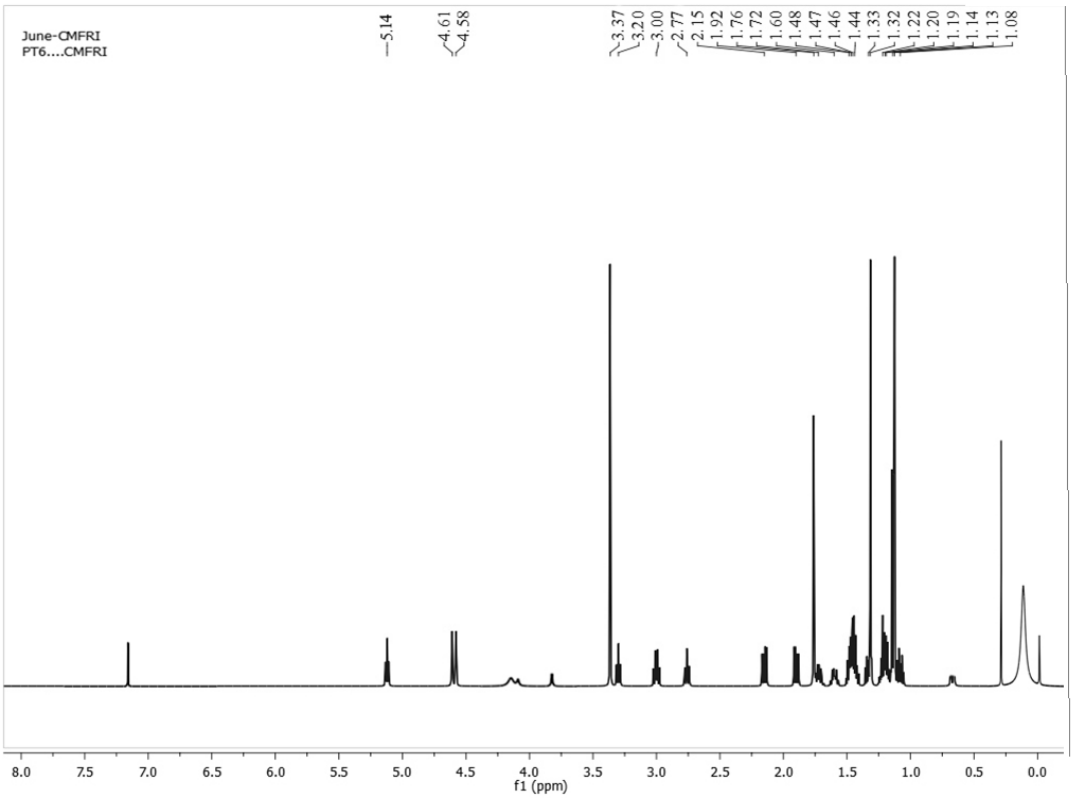

Figure 5.114.: ^{1}H NMR spectrum 3-methoxy-dolabella-10,18(19)-diene-5α,8β -diol (**8**)

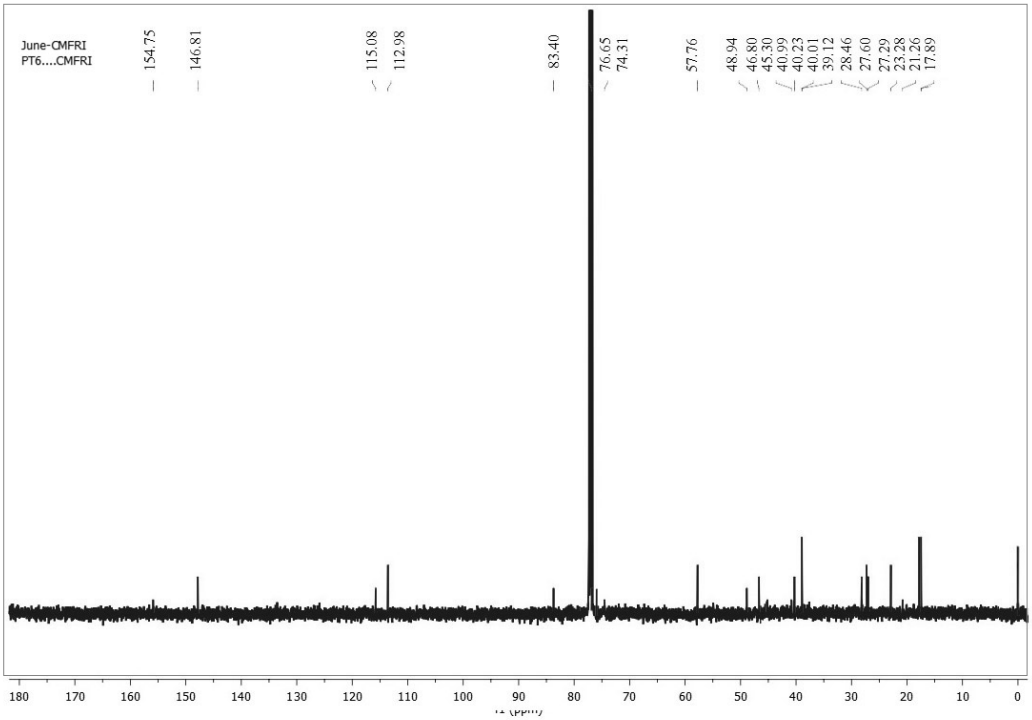

Figure 5.114.: ^{13}C NMR spectrum 3-methoxy-dolabella-10,18(19)-diene-5α,8β -diol (**8**)

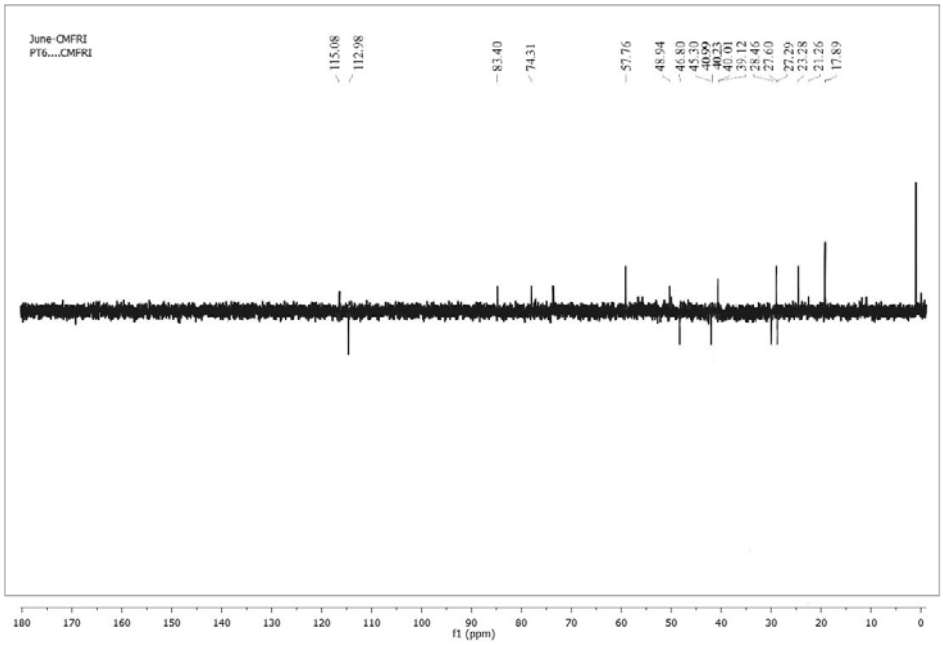

Figure 5.115.: DEPT spectrum spectrum 3-methoxy-dolabella-10,18(19)-diene-5α,8β -diol (**8**)

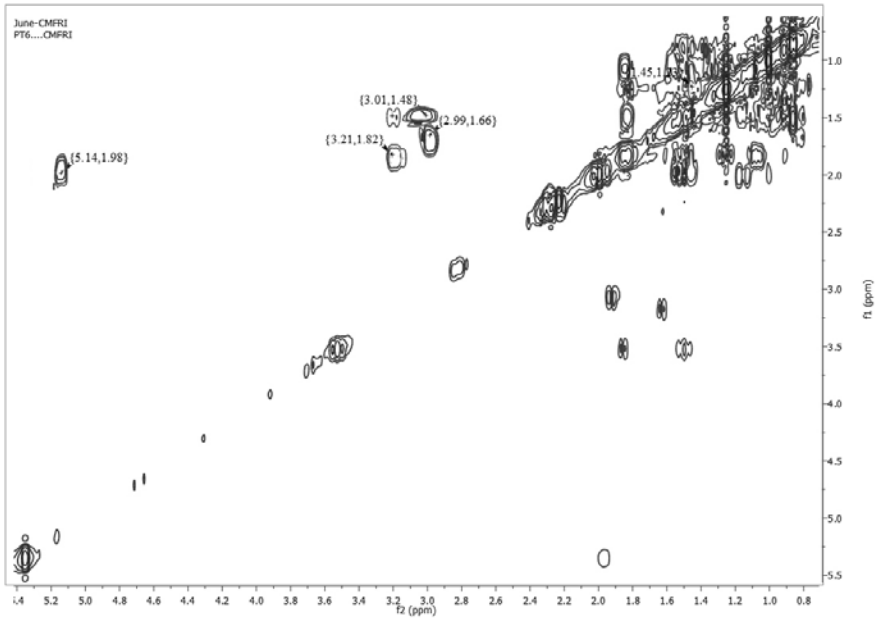

Figure 5.116.: ^{1}H-^{1}H COSY spectrum 3-methoxy-dolabella-10,18(19)-diene-5α,8β -diol (**8**)

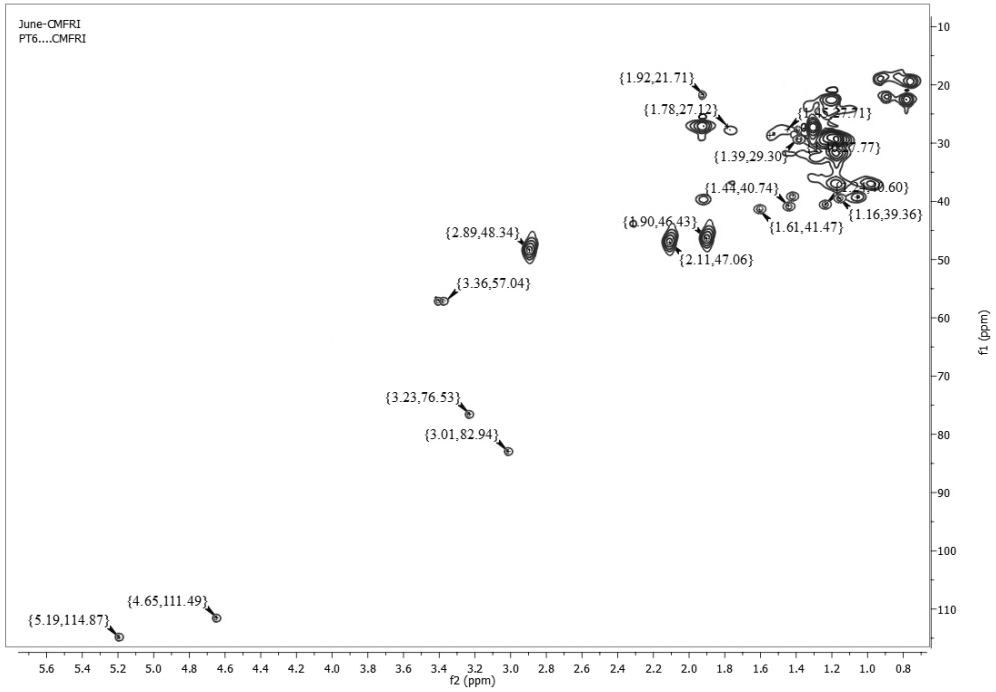

Figure 5.117.: HSQC spectrum 3-methoxy-dolabella-10,18(19)-diene-5α,8β -diol (**8**)

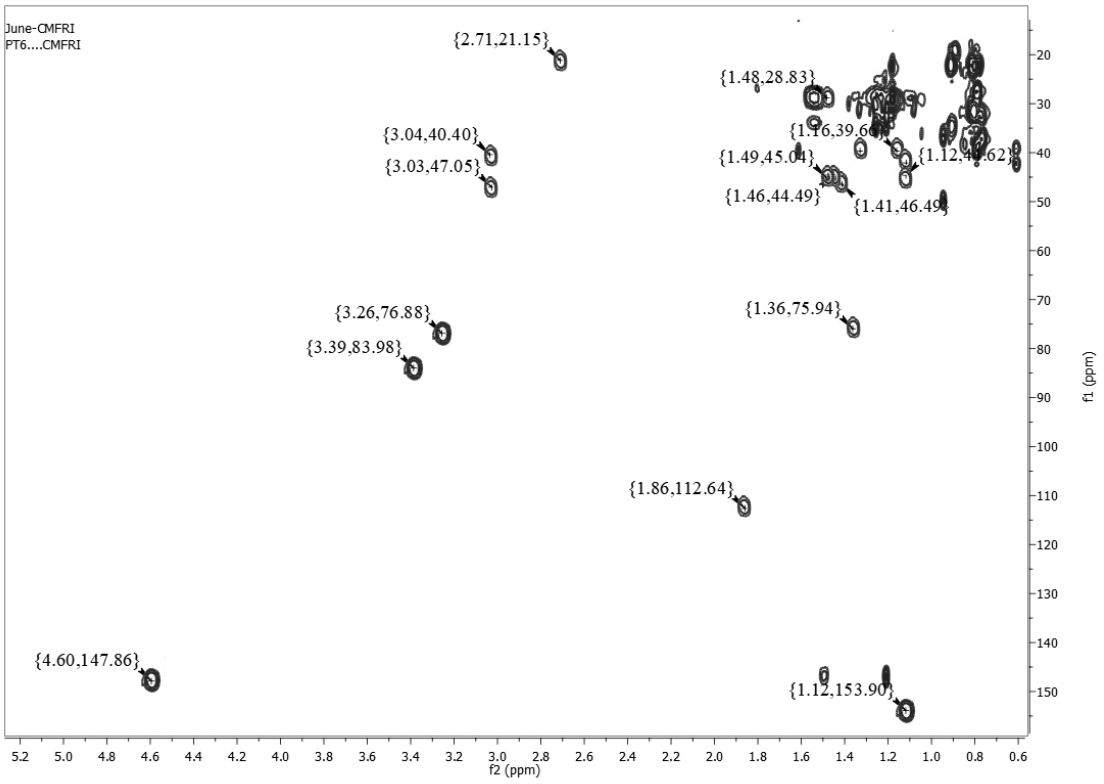

Figure 5.118.: HMBC spectrum 3-methoxy-dolabella-10,18(19)-diene-5α,8β -diol (**8**)

The molecular formula of **8** was assigned with four degrees of unsaturation, which was related to two each of double bond functionalities and ring systems. The HMBCs between δ /δ 1.46 (H-2)/45.3 (C-1), δ /δ 3.00 (H-3)/45.3 (C-1), 41.0(C-4), δ /δ 3.20 (H-5)/41.0 (C-4), δ /δ 1.48 (H-7)/46.8 (C-9), δ /δ 1.20 (H-2)/154.7 (C-11) explained the closed loop of 11-membered ring in **8** and the position of olefinic functional group. Compound **8** was similar to those of **7** except the functionalities of hydroxyls at C-5 and C-8, alkene at C10=C11 and an additional propenyl C-12 (in **8**). Notably, the compounds isolated from *D. spiralis* enclosed propenyl bonded dolabellane framework (Ioannou et al. 2012), which was comparable with the studied compound **8** except the presence in the greater number of oxygenated electronegative substituents at C-3, C-4 and C-8 in the latter (Figure 5.119).

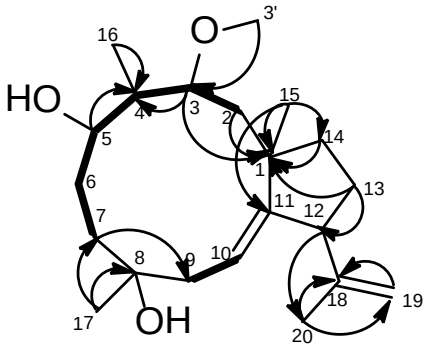

Figure 5.119.: Prominent ^{1}H-^{1}H COSY, and selected HMBC correlations of 3-methoxy-dolabella-10,18(19)-diene-5α,8β-diol (**8**). The key ^{1}H-^{1}H COSY couplings were represented in bold face bonds. The key HMBC couplings have been represented by double barbed arrows.

The relative stereochemistries of the chiral centres at C-3, C-4, C-8 and C-5 in **8** were designated through NOESY experiments (Figure 5.120-5.121). The NOESYs from both δ 1.20 (H-2) and δ 1.22 (H-7) to δ 3.20 (H-5)/2.77 (H-12)/1.82 (H-20)/1.13 (H-15) protons and δ 2.15 (H-9)/2.77 (H-12)/3.00 (H-3) were found to be at the same plane of symmetry, and therefore, attributed as β-faced protons. Similarly, NOEs were exhibited by the proton at δ 3.37 (H-3') with those at δ 1.32 (H-17), 1.48 (H*α*-7) and 1.60 (H-4). These protons were found to be situated at the opposite plane to the β-protons, and thus, *α*-disposed.

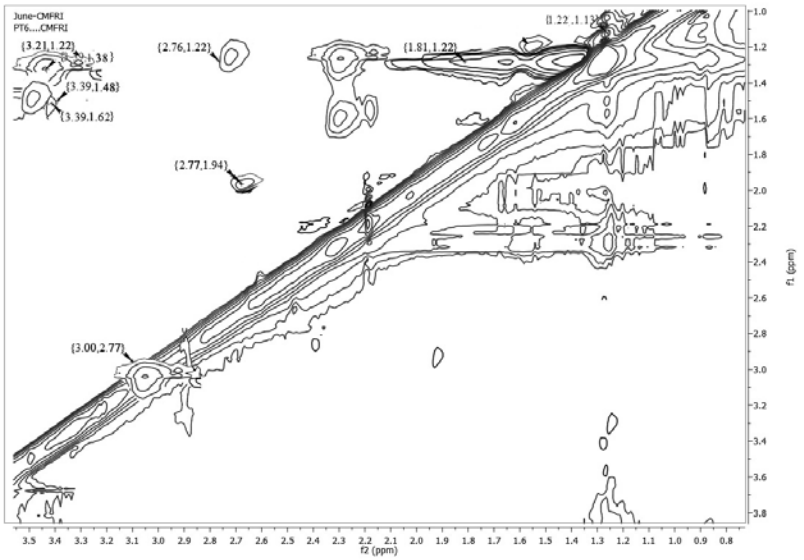

Figure 5.120.: NOESY spectrum 3-methoxy-dolabella-10,18(19)-diene-5α,8β -diol (**8**)

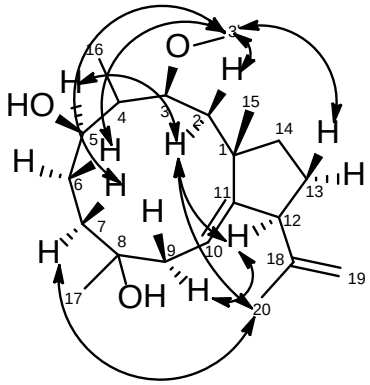

Figure 5.121.: Prominent NOE correlations of 3-methoxy-dolabella-10,18(19)-diene-5α,8β -diol (**8**). NOESY relations are represented by double-tailed arrows

The molecular ion peak of **8** was appeared at *m/z* 336 and base peak was ontained at *m/z* 27.0 (Figure 5.122 and 5.123).

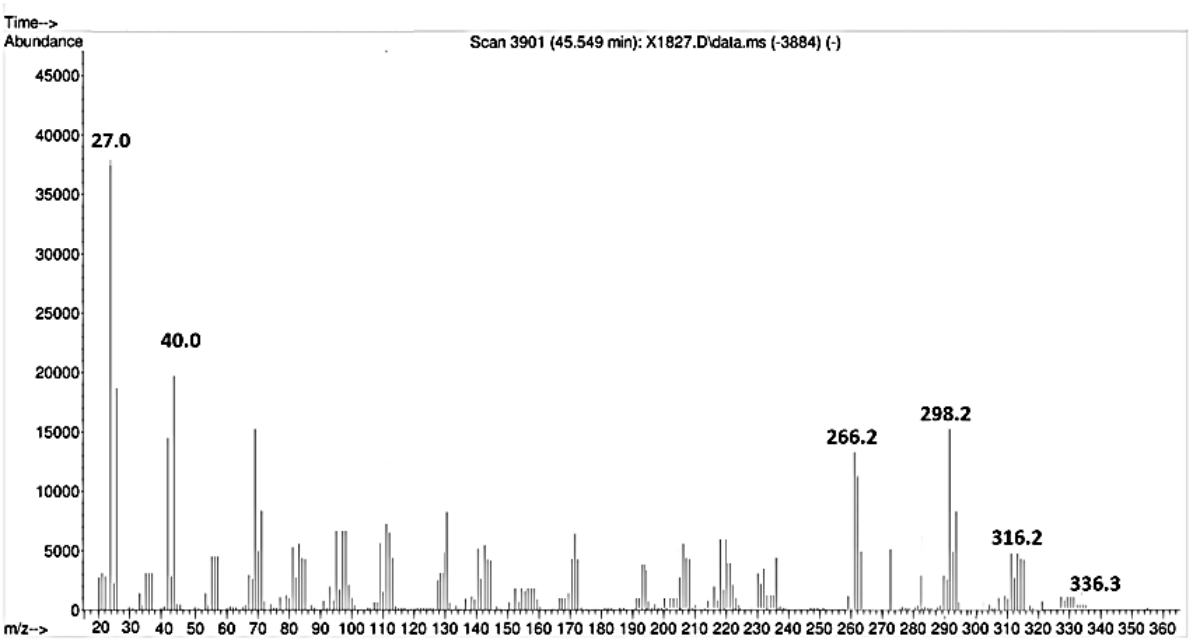

Figure 5.122.: EI-MS spectrum 3-methoxy-dolabella-10,18(19)-diene-5α,8β -diol (**8**)

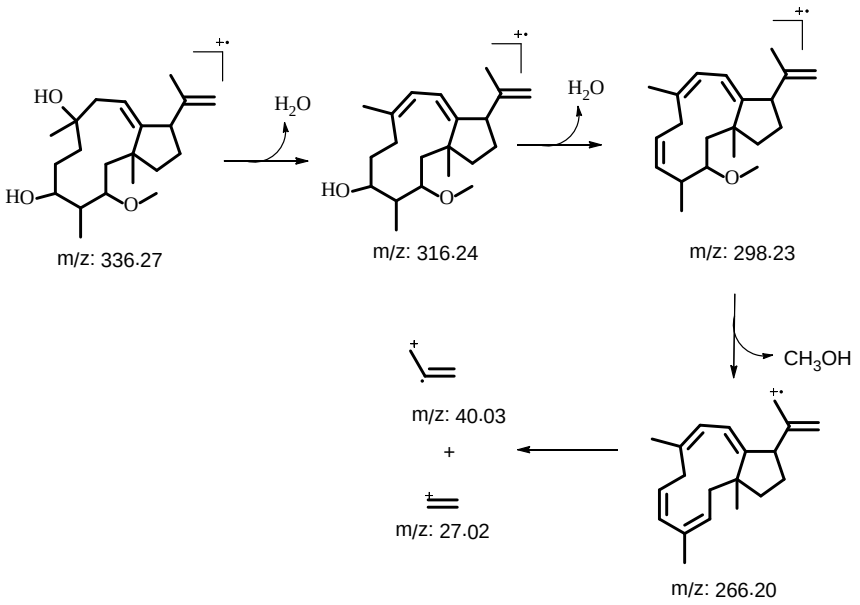

Figure 5.123.: Tentative mass fragmentation pattern of 3-methoxy-dolabella-10,18(19)-diene-5α,8β -diol (8)

Table 5.11.: NMR spectroscopic data[a] of 3-methoxy-dolabella-10,18(19)-diene-5α,8β -diol (**8**) isolated from brown seaweed *P.tetrastromatica*

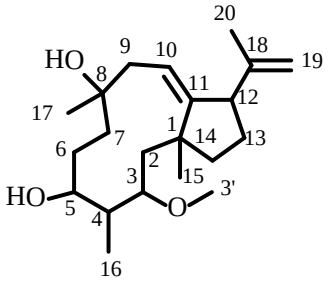

Compound **8**……..3-methoxy-dolabella-10,18(19)-diene-5α,8β -diol (**8**)

C. No.	^{13}C NMR	^{1}H NMR (int.,mult., J in Hz)[b]	COSY	HMBC
1	45.3	-	-	-
2	40.2	1.20(1H,d,10.2 Hz)	H-3	C-1,11
		1.46(1H,d,9.8 Hz)	-	-
3	83.9	3.00(1H,m)	H-4	C-1,4
3’	57.7	3.37(3H,s)	-	C-3
4	41.0	1.60(1H,m)	H-5	-
5	76.7	3.20(1H,m)	H-6	C-4
6	27.3	1.72(1H,m)	H-7	-
		1.47(1H,m)	-	-
7	40.0	1.22(1H,t,2.5 Hz)	-	C-9
		1.48(1H,t,2.7 Hz)	-	-
8	74.3	-	-	-
9	46.8	1.92(1H,d,12.6 Hz)	H-10	-
		2.15(1H,d,12.4 Hz)	-	-
10	115.1	5.14(1H,t,11.3 Hz)	-	-
11	154.8	-	-	-
12	48.9	2.77(1H,t,9.6 Hz)	-	C-20
13	28.5	1.44(1H,m)	-	C-12,1
		1.19(1H,m)	-	-
14	39.1	1.33(1H,dd,12.7 Hz)	-	C-1
		1.08(1H,dd,6.8 Hz)	-	-
15	23.3	1.13(3H,s)	-	C-14,11,1
16	17.9	1.15(3H,d,6.8 Hz)	-	C-4
17	27.6	1.32(3H,s)	-	C-8, 7
18	146.8	-	-	-
19	113.0	4.61(1H,m)	-	C-18
		4.58(1H,m)	-	-
20	21.3	1.82(3H,s)	-	C-18,19

[a]NMR spectra were recorded using a Bruker AVANCE III 500 MHz (AV 500) spectrometer (Bruker, Karlsruhe, Germany) in $CDCl_3$ as aprotic solvent at ambient temperature with TMS as the internal standard (δ 0 ppm).

[b]Values in ppm, multiplicity and coupling constants (J=Hz) were indicated in parentheses. Multiplicities were allocated by ^{135}DEPT NMR spectrum.

The assignments were made with the aid of the COSY, HSQC, HMBC and NOESY experiments.

5.3.2.2d Structural characterization of Compound 9 (TP_9)

2,7-Dimethoxy-14α-hydroxy-dolasta-1(15),9-diene

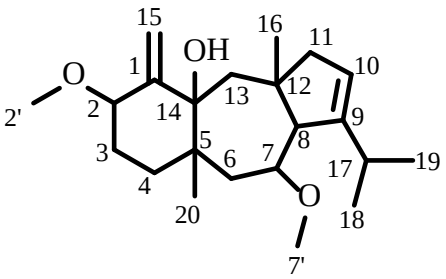

Sample yield	0.25% (> 99% purity, RP-C_{18} HPLC)
Physical description	Colourless oil
Molecular formula	$C_{22}H_{36}O_3$
Molecular mass	348.2664

The dolastane class of diterpenoid derivative, 2,7-dimethoxy-14α-hydroxy-dolasta-1(15),9-diene was isolated as Colorless oil compound. The compound (**9**) has exhibited UV absorbance (UV (MeOH) λ_{max}) at 246.0 (2.90) nm (Figure 5.124). The homogeneity of the compound was ascertained by HPLC data on a bonded phase octadecylsilane (C_{18}) stationary phase (RP-C_8 HPLC, MeOH:MeCN, 3:2 v/v): 3.23 min (Figure 5.125). The molecular ion peak by HRESIMS was found to be observed at 349.2745 $[M+H]^+$ (Figure 5.126).

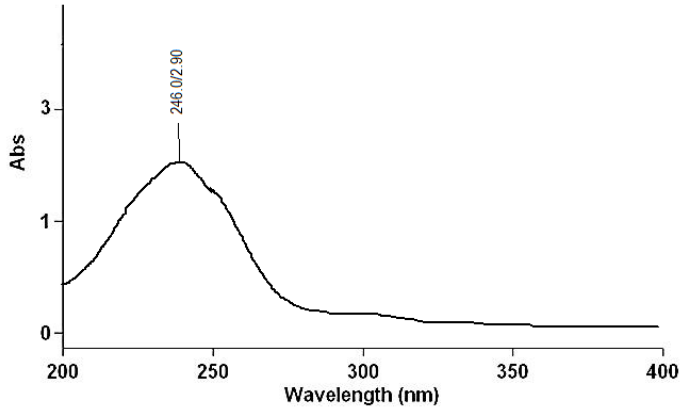

Figure 5.124.: UVspectrum of 2,7-dimethoxy-14α-hydroxy-dolasta-1(15),9-diene (**9**)

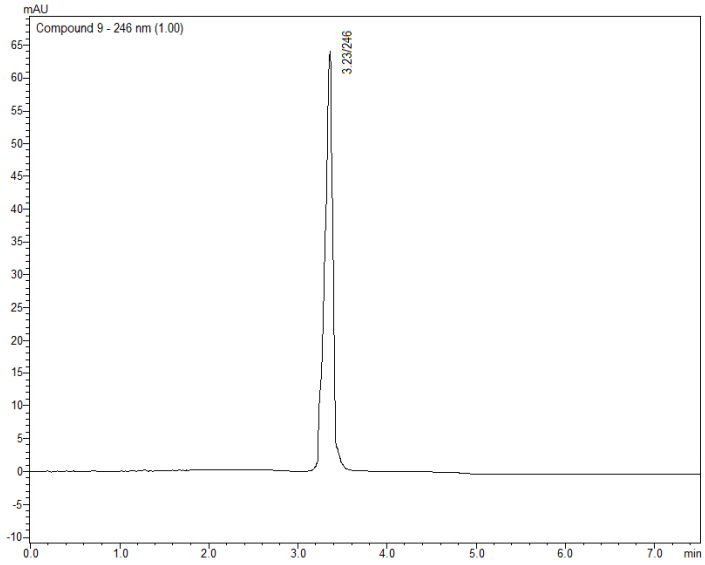

Figure 5.125.: HPLC chromatogram of 2,7-dimethoxy-14α-hydroxy-dolasta-1(15),9-diene (**9**)

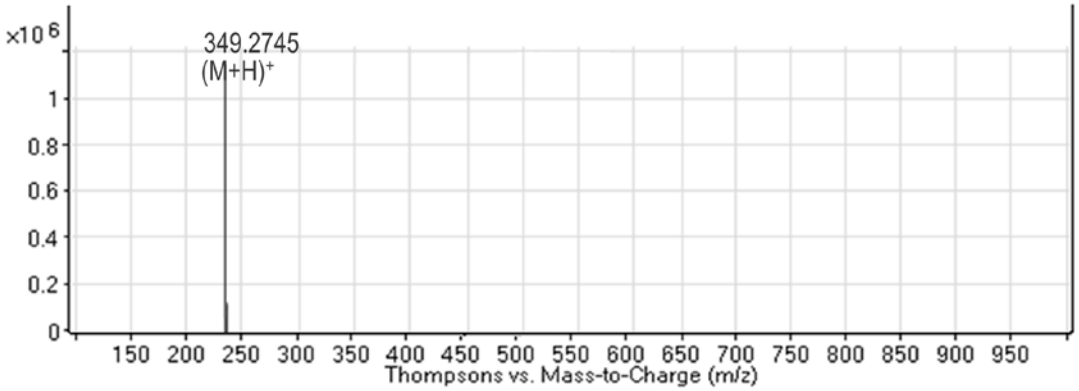

Figure 5.126.: HRESIMS of 2,7-dimethoxy-14α-hydroxy-dolasta-1(15),9-diene (**9**)

The dolastane diterpenoid, **9** was isolated as colourless oil from the EtOAc-MeOH extract of *P. tetrastromatica* on repeated column chromatographic separation. The molecular ion peak of **9** was recognized at *m/z* 348.27 [M^+] and elemental composition was deduced as $C_{22}H_{36}O_3$, with comprehensive NMR/IR spectroscopic experiments (Figure 5.127-5.133, Table 5.12).

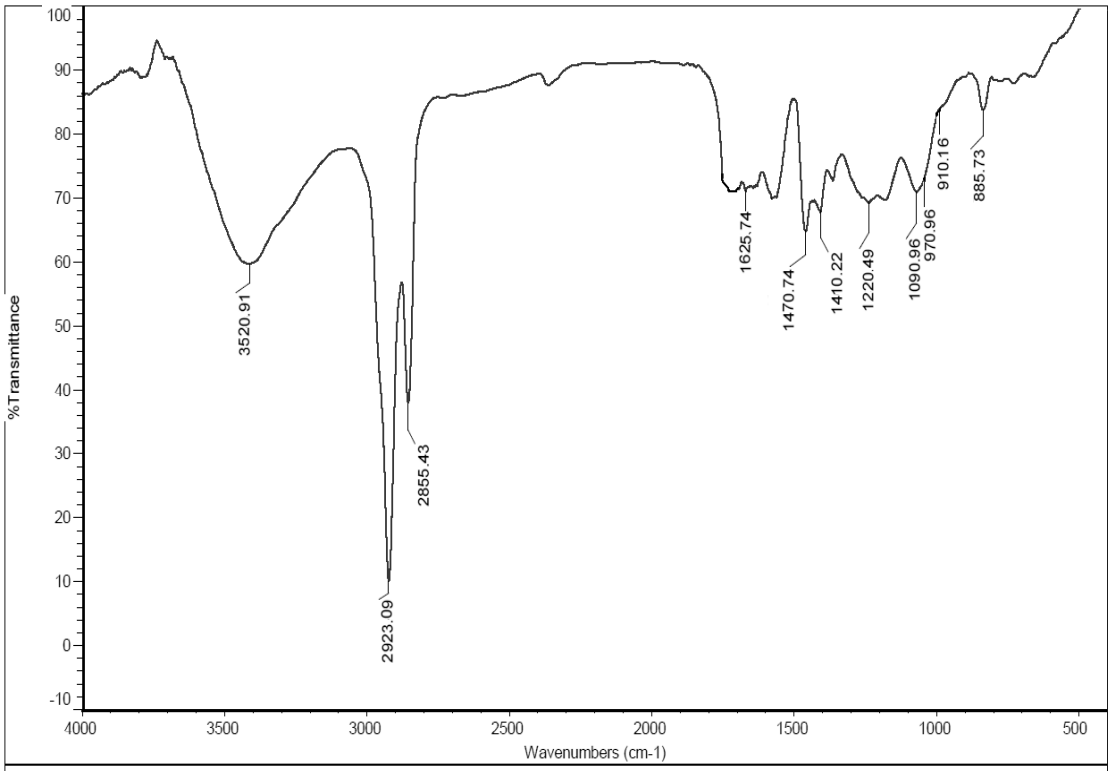

Figure 5.127.: FTIR spectrum of 2,7-dimethoxy-14α-hydroxy-dolasta-1(15),9-diene (**9**)

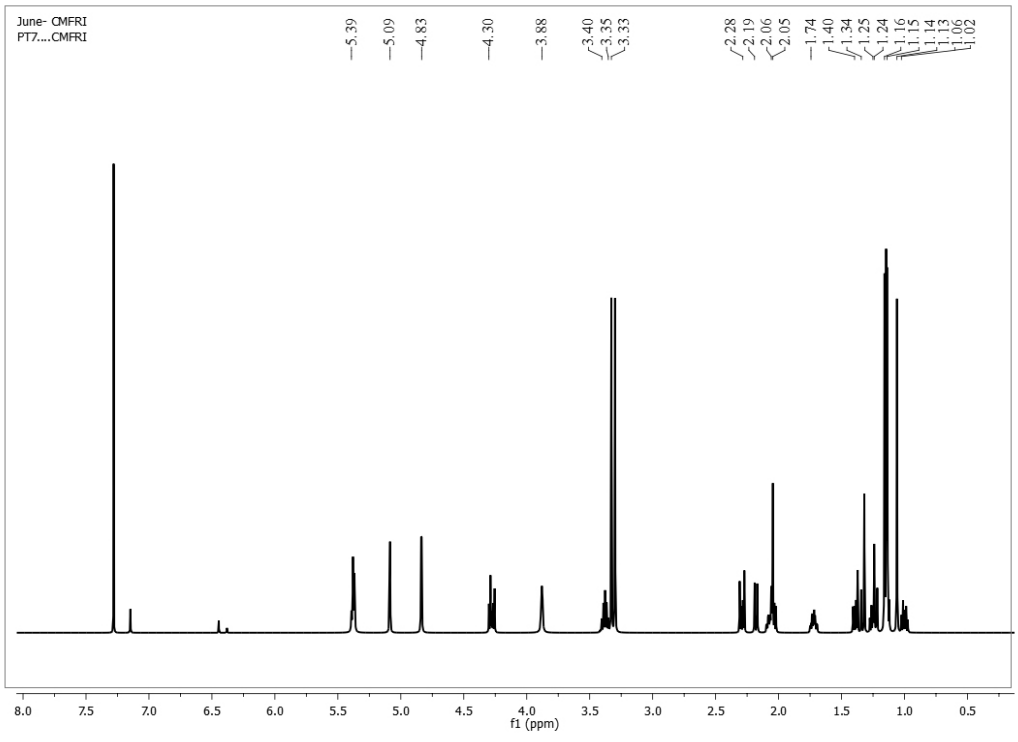

Figure 5.128.: ^{1}H NMR spectrum of 2,7-dimethoxy-14α-hydroxy-dolasta-1(15),9-diene (**9**)

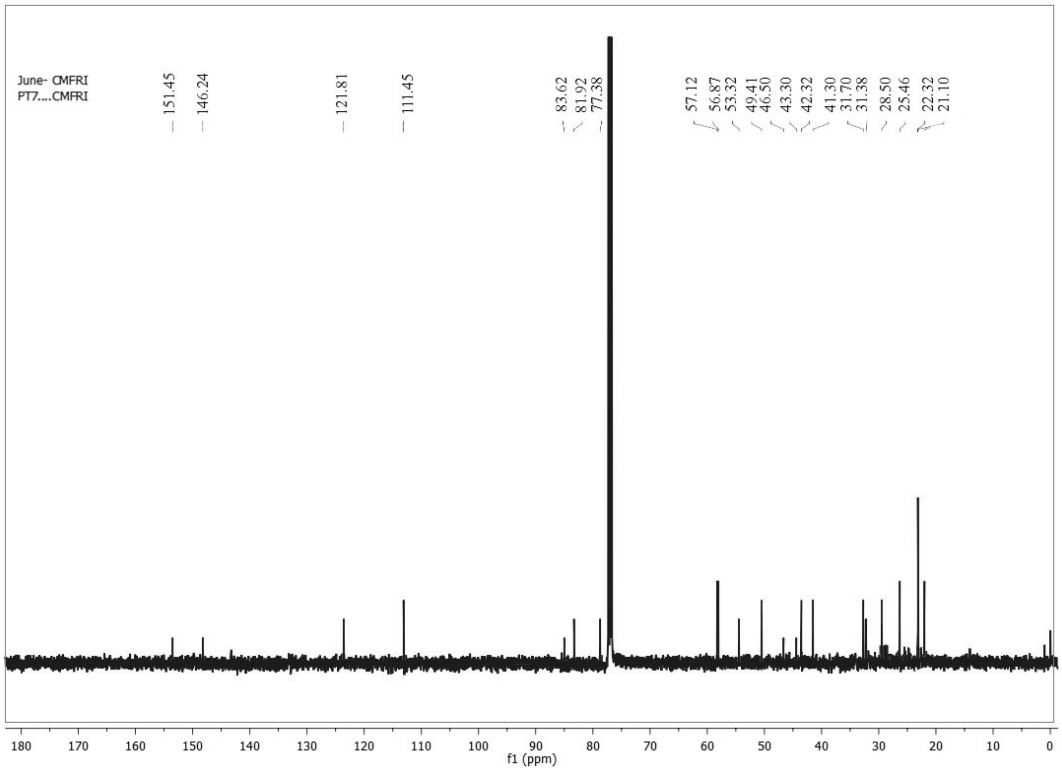

Figure 5.129.: ^{13}C NMR spectrum of 2,7-dimethoxy-14α-hydroxy-dolasta-1(15),9-diene (**9**)

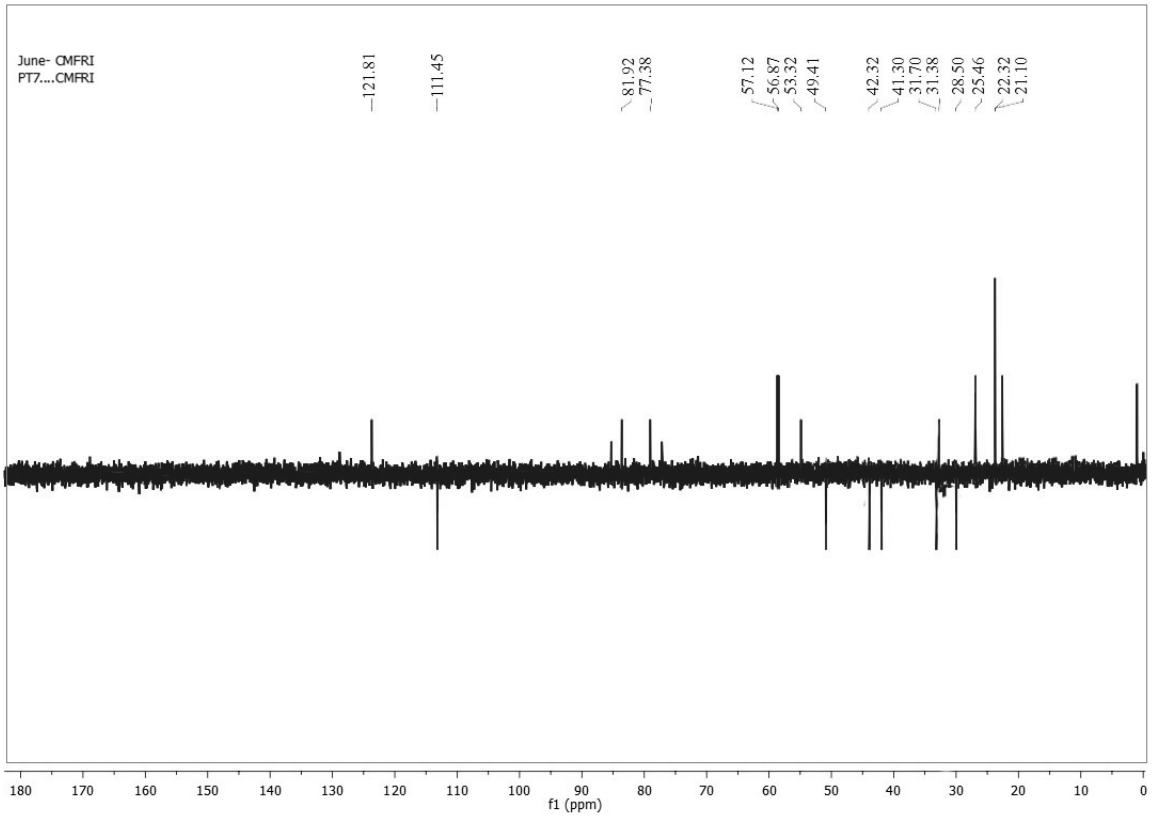

Figure 5.130.: DEPT spectrum of 2,7-dimethoxy-14α-hydroxy-dolasta-1(15),9-diene (**9**)

The detailed NMR spectroscopic data of **9** were comparable with the basic chemical resonances of dolastane type of diterpenes (Ioannou et al. 2013; Ioannou et al. 2008). The COSYs were recorded among the protons at δ 3.89 (H-2)/2.06 (H-3)/1.25 (H-4) along with HMBCs at δ /δ 3.89 (H-2)/151.5 (C-1), 83.6 (C-14), δ 1.25 (H-4)/43.3 (C-5), 83.6 (C-14), which proposed the closed loop of six-membered ring in **9** (Figure 5.134). Similarly, COSYs among the protons δ 1.40 (H-6)/4.30 (H-7)/2.19 (H-8) with HMBCs, such as δ /δ 1.40 (H-6)/43.3 (C-5), δ /δ 2.19 (H-8)/46.5 (C-12) and δ /δ 1.34 (H-13)/46.5 (C-12), 83.6 (C-14) constituted the cyclic structure of seven-membered ring. Correspondingly, the COSYs between the protons δ 5.40 (H-10)/2.04 (H-11) along with the HMBCs at δ /δ 5.40 (H-10)/146.2 (C-9), δ /δ 2.19 (H-8)/146.2 (C-9), δ /δ 2.19 (H-8)/46.5 (C-12) and δ /δ 5.40 (H-10)/46.5 (C-12) appropriately characterised the five-membered ring in **9** and its tricyclic frame work**.** The chemical resonances at C-5, C-8 and C-12 were apparent with the reported compounds 1,4-epoxy-17-dolastene and 1,4-dihydroxy-11-oxo-17-dolastene (Ioannou et al. 2013). The difference in chemical shift value of deshielded signal at C-14 was recorded by virtue of a hydroxyl attached to C-14. The deshielded signals at δ 151.5 (C-1) and 111.5 (C-15, HSQC δ 5.09, 4.84) were related to the terminal alkenes (>C=CH_2) along with δ 146.2 (C-9) and 121.8 (C-10, HSQC δ 5.40), which were related to trisubstituted alkenes in the cyclopentane ring (>C=CH-) (Ioannou et al. 2008).

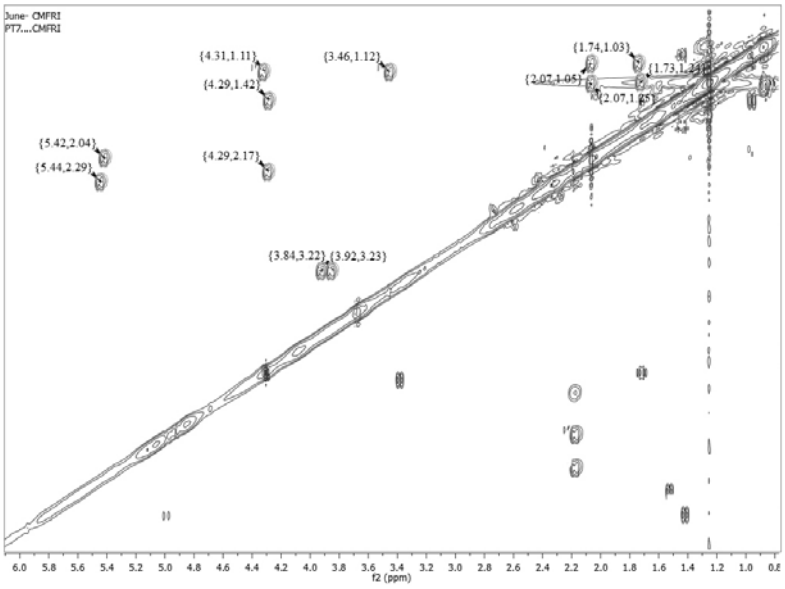

Figure 5.131.: ^{1}H-^{1}H COSY spectrum of 2,7-dimethoxy-14α-hydroxy-dolasta-1(15),9-diene (**9**)

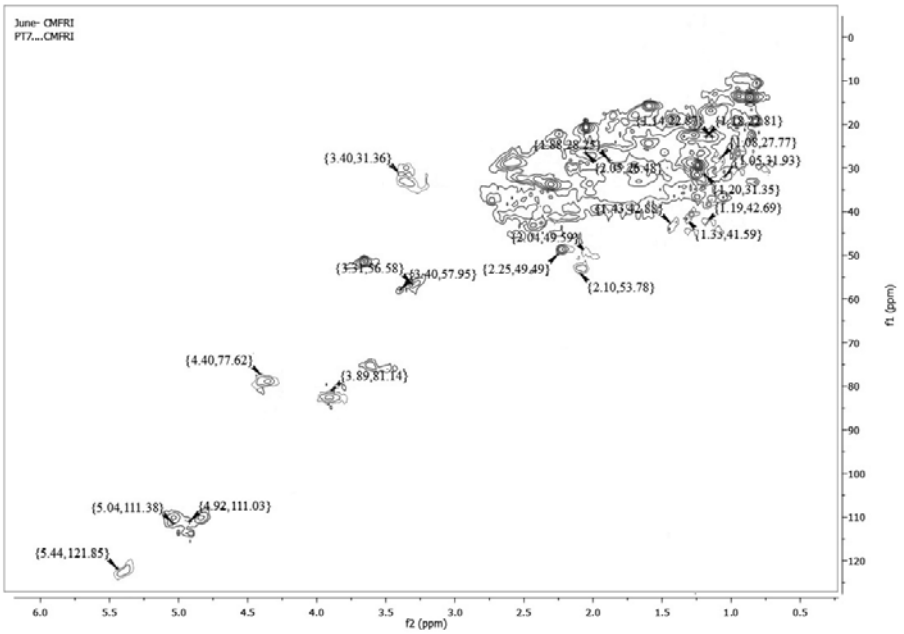

Figure 5.132.: HSQC spectrum of 2,7-dimethoxy-14α-hydroxy-dolasta-1(15),9-diene (**9**)

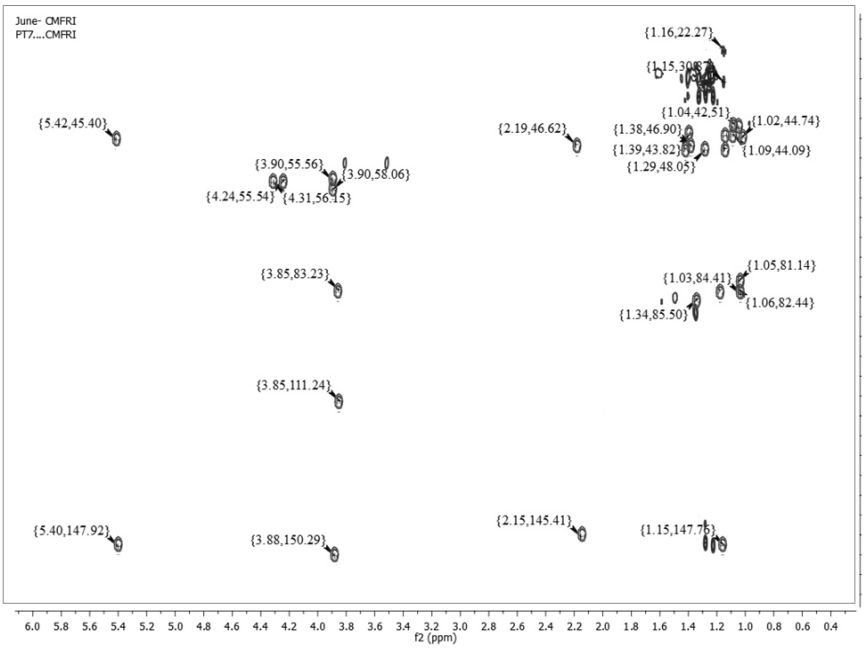

Figure 5.133.: HMBC spectrum of 2,7-dimethoxy-14α-hydroxy-dolasta-1(15),9-diene (**9**)

These attributions were appropriately supported by the HMBCs at δ 3.89 (H-2)/111.5 (C-15). The attachment of remaining four methyls in **9** at C-5, C-17, (C-19) and C-12 were apparent with those reported for a previously described dolastane analogue 4*α*-acetoxy-9β,14*α*-dihydroxydolast-1(15),7-diene (Garcia et al. 2009). It is of note that the dihydroxy-11-oxo-17-

dolastene and hydroxy-11-oxo-1,17-dolastadiene isolated from *D. spiralis* enclosed propenyl cyclopentanone moiety in dolastane skeleton (Ioannou et al. 2013), whereas, compound **9** exhibited some structural variations, such as isopropyl bonded cyclopentene, exocyclic double bond at C-1 and oxygenated functionalities at C-2, C-7, and C-14.

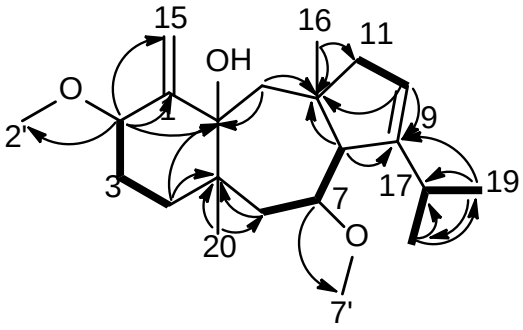

Figure 5.134.: Prominent ^{1}H-^{1}H COSY, and selected HMBC correlations of 2,7-dimethoxy-14α-hydroxy-dolasta-1(15),9-diene (**9**). The key ^{1}H-^{1}H COSY couplings were represented in bold face bonds. The key HMBC couplings have been represented by double barbed arrows.

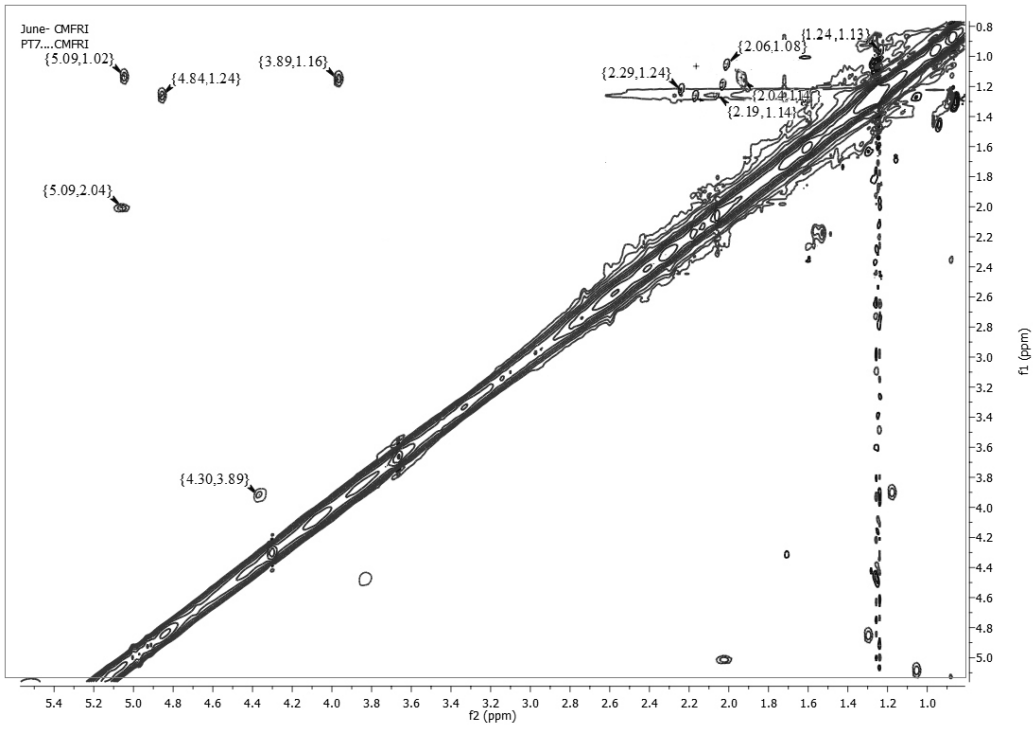

Figure 5.135.: NOESY spectrum of 2,7-dimethoxy-14α-hydroxy-dolasta-1(15),9-diene (**9**)

The NOESYs, such as δ 4.30 (H-7)/3.89 (H-2), δ 2.04 (Hβ-11)/5.09 (Hβ-15)/1.02 (Hβ-4) and δ 1.16 (H-18), 1.16 (H-19)/1.74 (Hβ-3)/1.08 (H-20), 1.14 (Hβ-6), 2.19 (H-8) were fixed at the same plane, and arbitrarily assigned as β-oriented. The NOESYs, such as δ 1.25 (H*α*-4)/2.29 (H*α*-11)/1.24 (H*α*-13) and δ 1.13 (H-16)/1.25 (H*α*-4)/4.84 (H*α*-15)/1.24 (H*α*-13) were aligned opposite to the β-protons, and thus, assigned as *α*-oriented (Figure 5.135-5.136). Thus, the relative stereochemistry of the hydroxyl at C-14 and Me-16 at C-12 were found to be *α*-oriented, which was found to be comparable with an earlier report of literature (Ioannou et al. 2013).

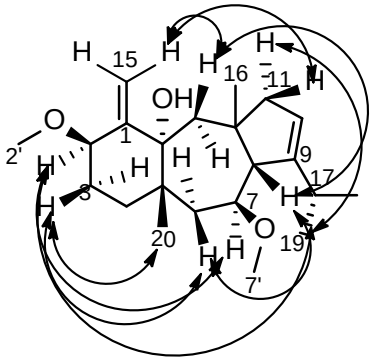

Figure 5.136.: Prominent NOE correlations of 2,7-Dimethoxy-14α-hydroxy-dolasta-1(15),9-diene (**9**). NOESY relations are represented by double-tailed arrows

The molecular ion peak of **9** was appeared at *m/z* 348 and base peak was ontained at *m/z* 27.0 (Figure 5.137 and 5.138).

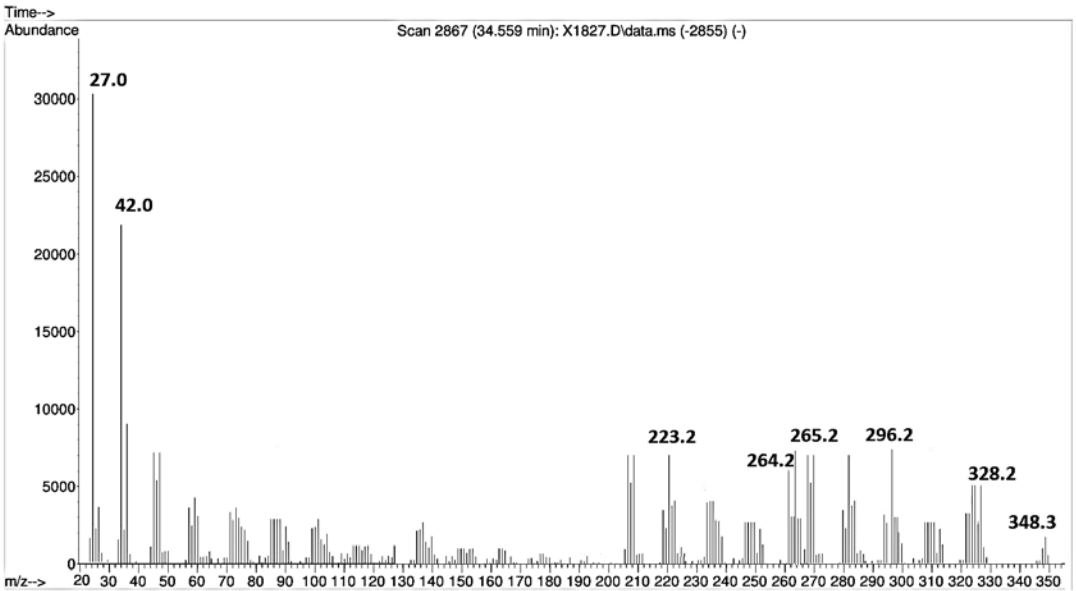

Figure 5.137.: EI-MS spectrum of 2,7-Dimethoxy-14α-hydroxy-dolasta-1(15),9-diene (**9**)

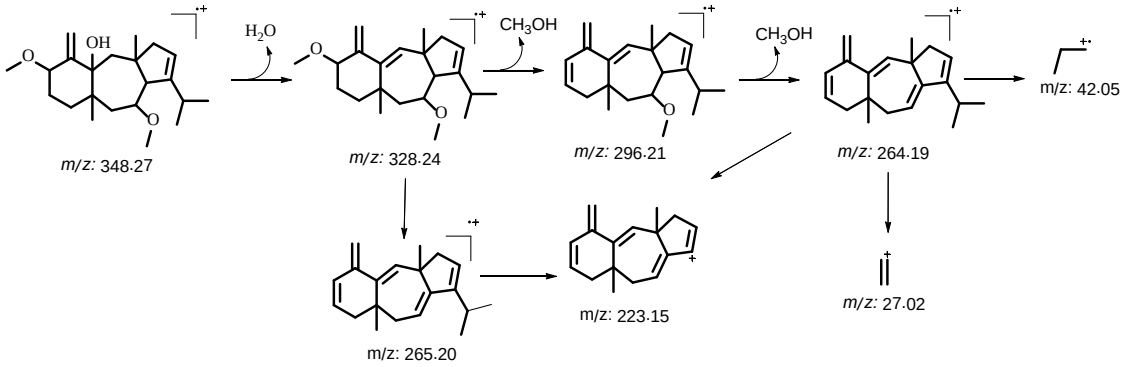

Figure 5.138.: Tentative mass fragmentation pattern of 2,7-dimethoxy-14α-hydroxy-dolasta-1(15),9-diene (**9**)

Table 5.12.: NMR spectroscopic data[a] of 2,7-dimethoxy-14α-hydroxy-dolasta-1(15),9-diene (**9**) isolated from brown seaweed *P.tetrastromatica*

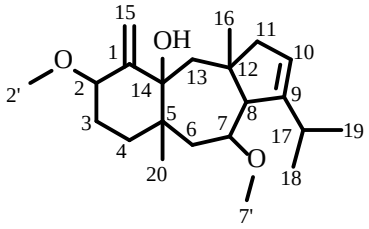

Compound **9**…….2,7-dimethoxy-14α-hydroxy-dolasta-1(15),9-diene (**9**)

C. No.	^{13}C	^{1}H NMR (int.,mult.,J in Hz)[b]	COSY	HMBC
1	151.5	-	-	-
2	81.9	3.89(1H,t,9.5 Hz)	H-3	C-15,2',14
2'	56.9	3.33(3H,s)	-	-
3	28.5	1.74(1H,m) 2.06(1H,m)	H-4	-
4	31.7	1.02(1H,dd,11.7 Hz) 1.25(1H,dd,6.7 Hz)	-	C-5,14
5	43.3	-	-	-
6	42.3	1.40(1H,d, 12.5Hz) 1.14(1H,d, 12.6Hz)	H-7	C-5
7	77.4	4.30(1H,m)	H-8	C-7'
7'	57.1	3.35 (3H,s)	-	-
8	53.3	2.19(1H,d,10.9 Hz)	-	C-9,12
9	146.2	-	-	-
10	121.8	5.40(1H,t,11.3 Hz)	H-11	C-12,9
11	49.4	2.04(1H,d,12.2 Hz)	-	-

		2.29 (1H,d,12.3 Hz)		
12	46.5	-	-	-
13	41.3	1.34(1H,s)	-	C-12,14
		1.24(1H,s)		
14	83.6	-	-	-
15	111.5	5.09(1H,s)	-	-
		4.84(1H,s)		
16	21.1	1.13(3H,s)	-	C-11,12
17	31.4	3.40(1H,m)	H-18,19	C-9
18	22.3	1.16(3H,d,6.3 Hz)	-	C-17,16
19	22.3	1.15(3H,d,6.4 Hz)	-	C-9,18, 17
20	25.5	1.08(3H,s)	-	C-5, 6

[a]NMR spectra were recorded using a Bruker AVANCE III 500 MHz (AV 500) spectrometer (Bruker, Karlsruhe, Germany) in $CDCl_3$ as aprotic solvent at ambient temperature with TMS as the internal standard (δ 0 ppm).

[b]Values in ppm, multiplicity and coupling constants (J=Hz) were indicated in parentheses. Multiplicities were allocated by ^{135}DEPT NMR spectrum.

The assignments were made with the aid of the COSY, HSQC, HMBC and NOESY experiments.

5.3.3.2d Structural characterization of Compound 10 (TP_{10})

4,7-Dimethoxy-9β,14α-dihydroxy-dolasta-1-ene

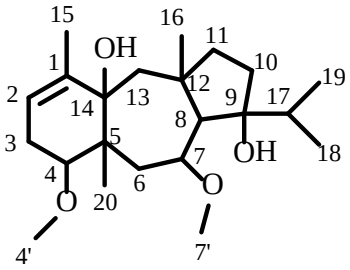

Sample yield	0.25% (> 99% purity, RP-C_{18} HPLC)
Physical description	Colourless oil
Molecular formula	$C_{22}H_{38}O_4$
Molecular mass	366.2770

The dolastane class of diterpenoid derivative, 1,2,5,5a,6,9,10,11,12,12a-Decahydro-11(11^2-hydroxypropyl)-2-[(*E*)-2^1-propenyl] cyclonona[*d*]-furo[2,3-*b*]pyran-9,12-diol was isolated as Colorless oil compound. The compound (**10**) has exhibited UV absorbance (UV (MeOH) λ_{max}) at 245.0 (2.62) nm (Figure 5.139). The homogeneity of the compound was ascertained by HPLC data on a bonded phase octadecylsilane (C_{18}) stationary phase (RP-C_8 HPLC, MeOH:MeCN, 3:2 v/v):

3.01 min (Figure 5.140). The molecular ion peak by HRESIMS was found to be observed at 367.2851$[M+H]^+$ (Figure 5.141).

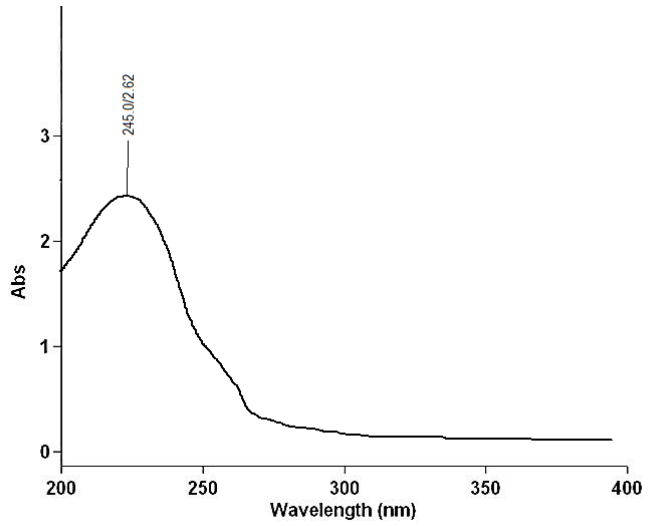

Figure 5.139.: UVspectrum of 4,7-dimethoxy-9β ,14α-dihydroxy-dolasta-1-ene (**10**)

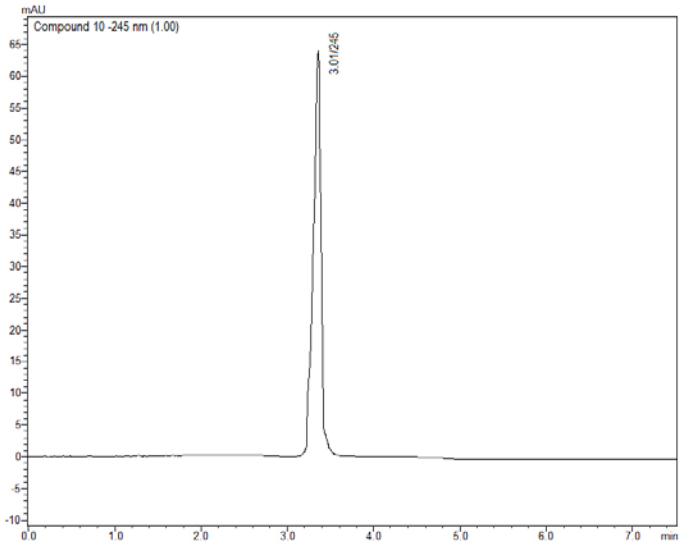

Figure 5.140.: HPLC chromatogram of 4,7-dimethoxy-9β ,14α-dihydroxy-dolasta-1-ene (**10**)

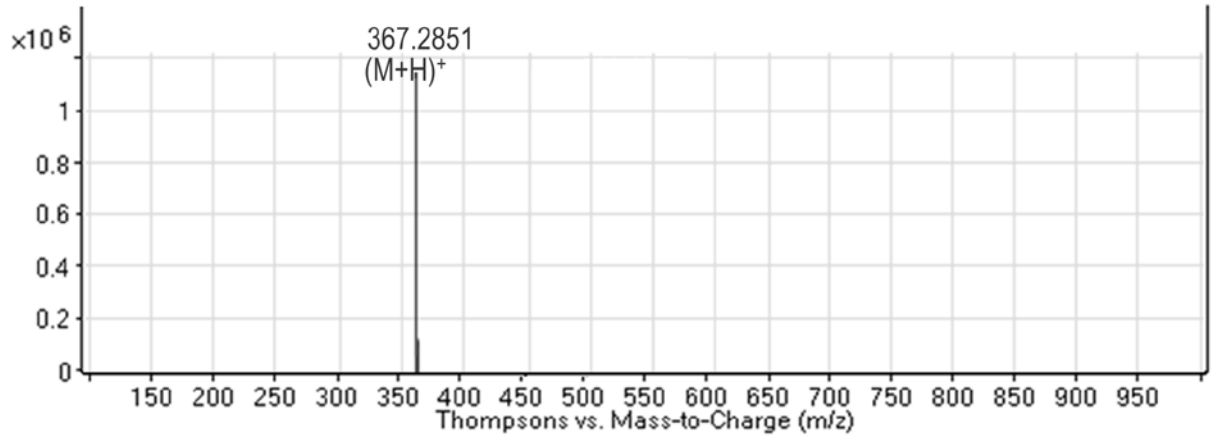

Figure 5.141.: HRESIMS of 4,7-dimethoxy-9β ,14α-dihydroxy-dolasta-1-ene (**10**)

The dolastane diterpenoid, **10** was isolated as colourless oil from *P. tetrastromatica* by repetitive chromatography. Compound **10** exhibited a molecular ion peak at *m/z* 366.28 [M^+], and the elemental composition was deduced as $C_{22}H_{38}O_4$, with comprehensive NMR/IR assignments (Figure 5.142-S47).

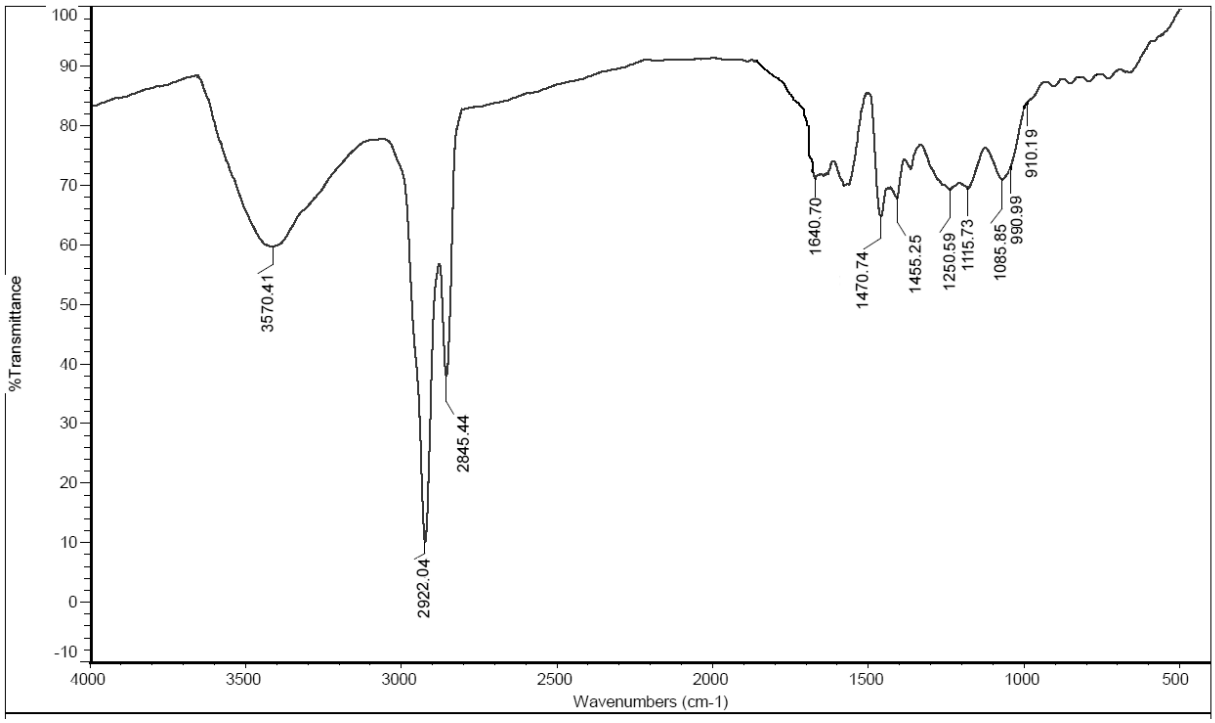

Figure 5.142.: FTIR spectrum of4,7-dimethoxy-9β ,14α-dihydroxy-dolasta-1-ene (**10**)

The molecular formula of **10** was assigned four degrees of unsaturation, which were related to one olefinic bond, and three ring systems. The detailed NMR spectroscopic data of **10**

were comparable with the basic chemical resonances of dolastane type of diterpenes and compound **9** (Ioannou et al. 2008; Ioannou et al. 2013). The COSYs at δ 5.49 (H-2)/1.96 (H-3) with HMBCs at δ /δ 5.49 (H-2)/142.9 (C-8), 83.0 (C-14), δ /δ 3.26 (H-4)/30.0 (C-3), 42.10 (C-5) proposed the six membered ring in **10** (Figure S2). The downfield signals at δ 142.9 (C-1) and 124.3 (C-2 HSQC δ 5.49) were related to the olefinic (>C=CH-) functionality (Ioannou et al. 2013), and their positions were corroborated through HMBCs, such as δ /δ 5.49 (H-2)/142.9 (C-1), 82.96 (C-14), 1.95 (H-15)/142.9 (C-1). The COSYs from δ 1.62 (H-17)/1.02 (H-18) and 1.02 (H-19) proposed the occurrence of isopropyl group in **10**, whereas its linkage was deduced with HMBCs from δ 1.62 (H-17) to δ 87.3 (C-9). The NOE correlations, such as δ 1.40 (Hβ-6), 1.76 (Hβ-10), 1.33 (H-8)/3.26 (H-4) and δ 1.33 (H-8)/1.03 (H-20) were found to be in the same plane of reference, and was arbitrarily assigned as β-oriented. The NOE couplings, such as δ 1.24 (H*α*-13), 1.53 (H*α*-11), 1.50 (H*α*-10)/4.64 (H-7), δ 1.53 (H*α*-11), 1.14 (H-16), 1.62 (H-17)/1.50 (H*α*-10) were aligned opposite to the β-protons, and therefore, assigned to be *α*-faced (Figure S2, S45).

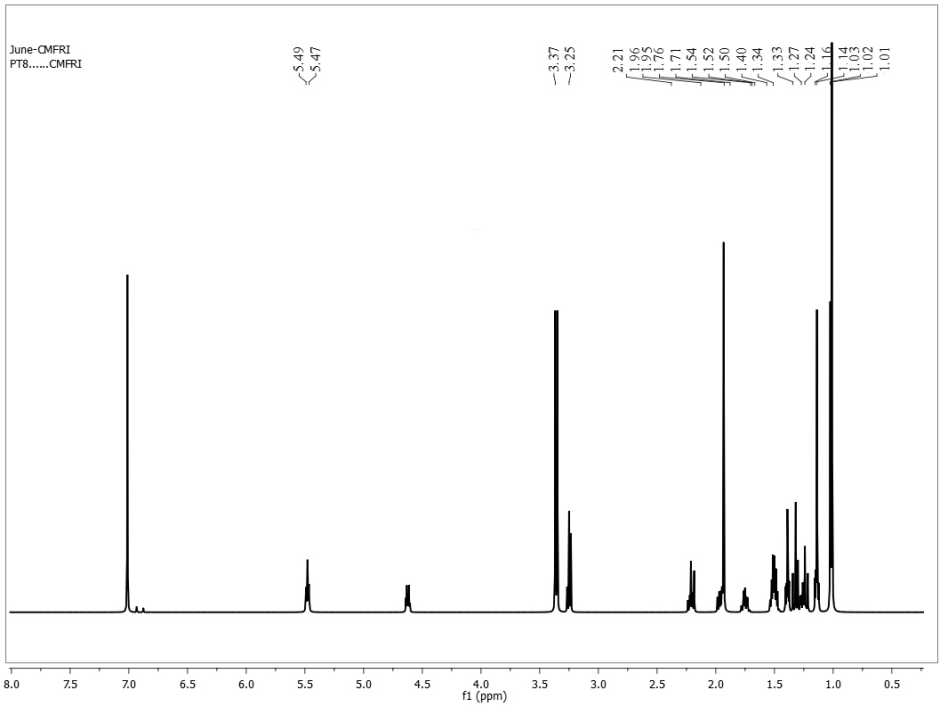

Figure 5.143.: ^{1}H NMR spectrum of4,7-dimethoxy-9β ,14α-dihydroxy-dolasta-1-ene (**10**)

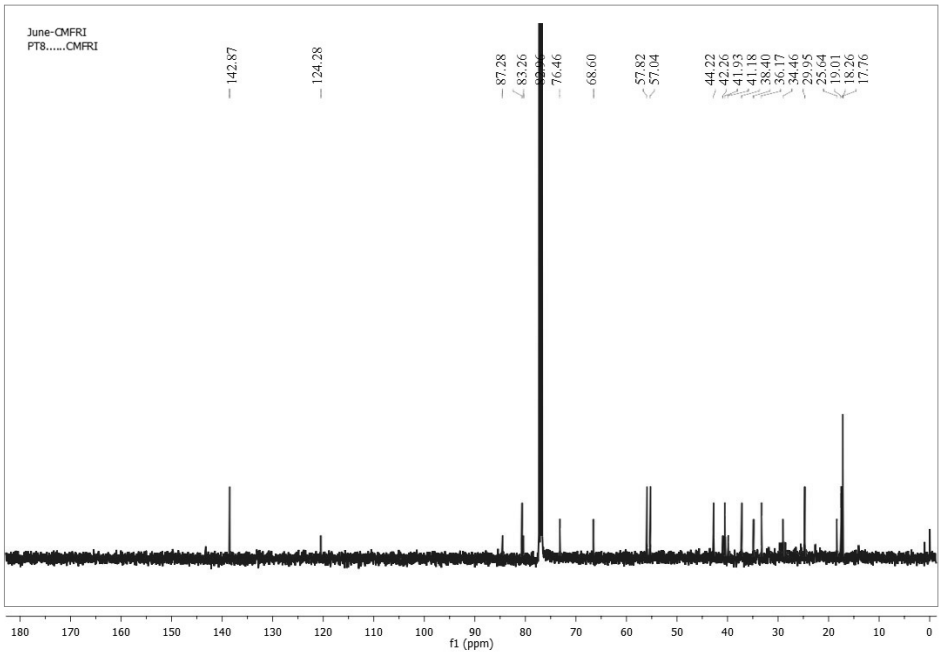

Figure 5.142.: ^{13}C NMR spectrum of4,7-dimethoxy-9β ,14α-dihydroxy-dolasta-1-ene (**10**)

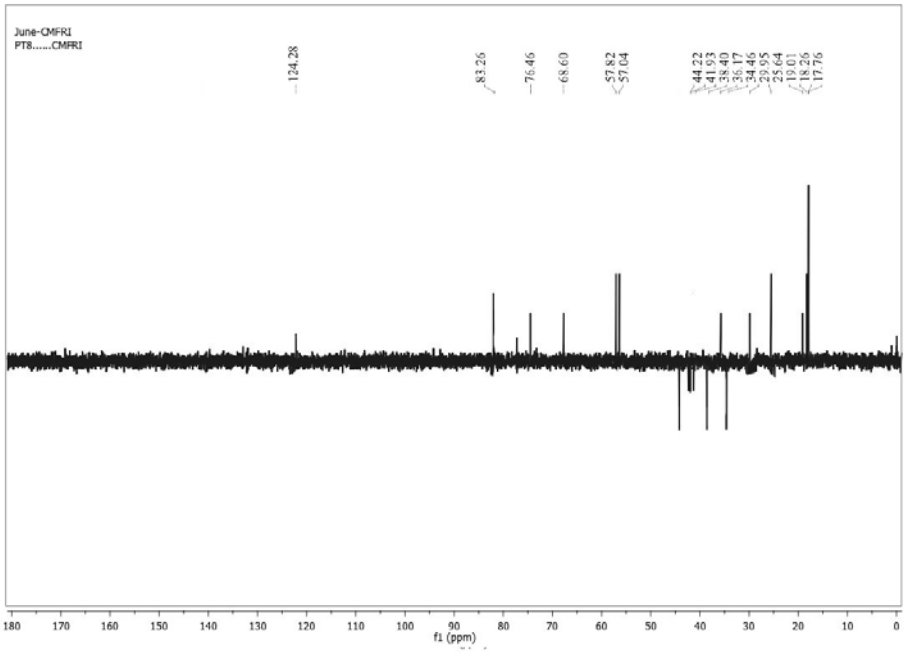

Figure 5.142.: DEPT spectrum of4,7-dimethoxy-9β ,14α-dihydroxy-dolasta-1-ene (**10**)

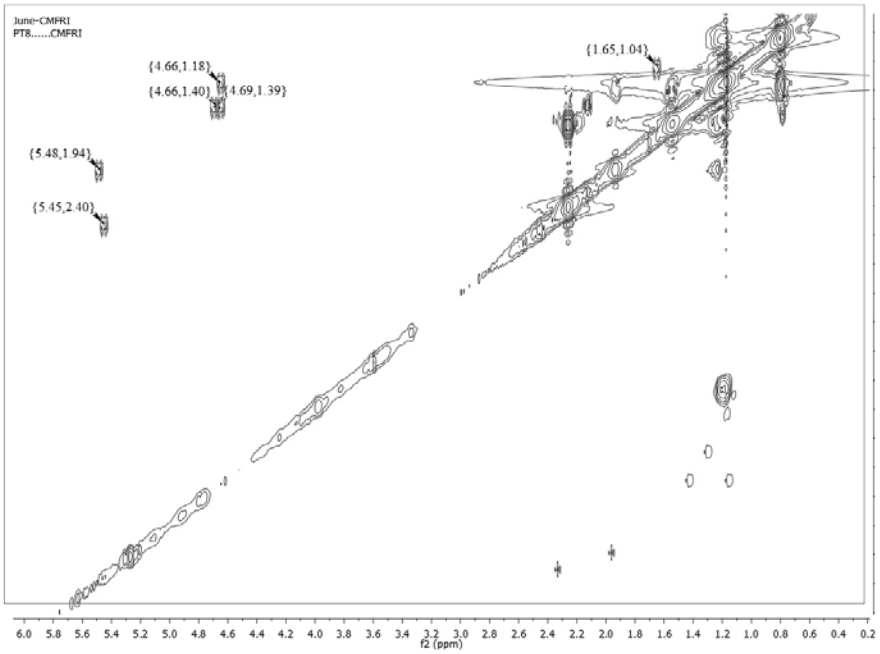

Figure 5.142.: ^{1}H-^{1}H COSY spectrum of4,7-dimethoxy-9β ,14α-dihydroxy-dolasta-1-ene (**10**)

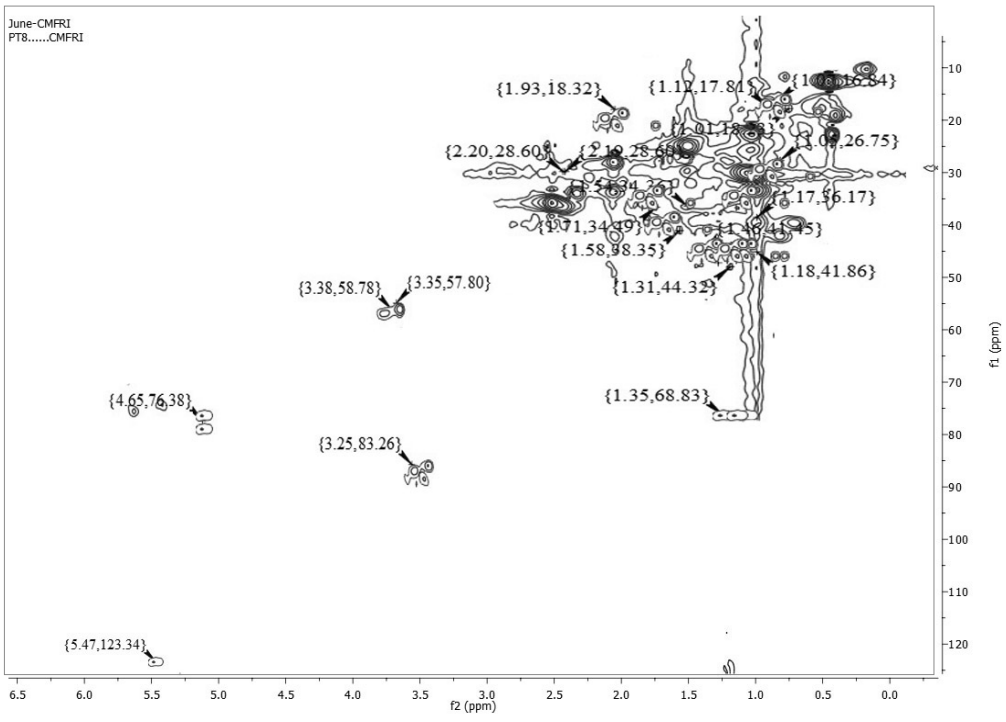

Figure 5.142.: HSQC spectrum of 4,7-dimethoxy-9β ,14α-dihydroxy-dolasta-1-ene (**10**)

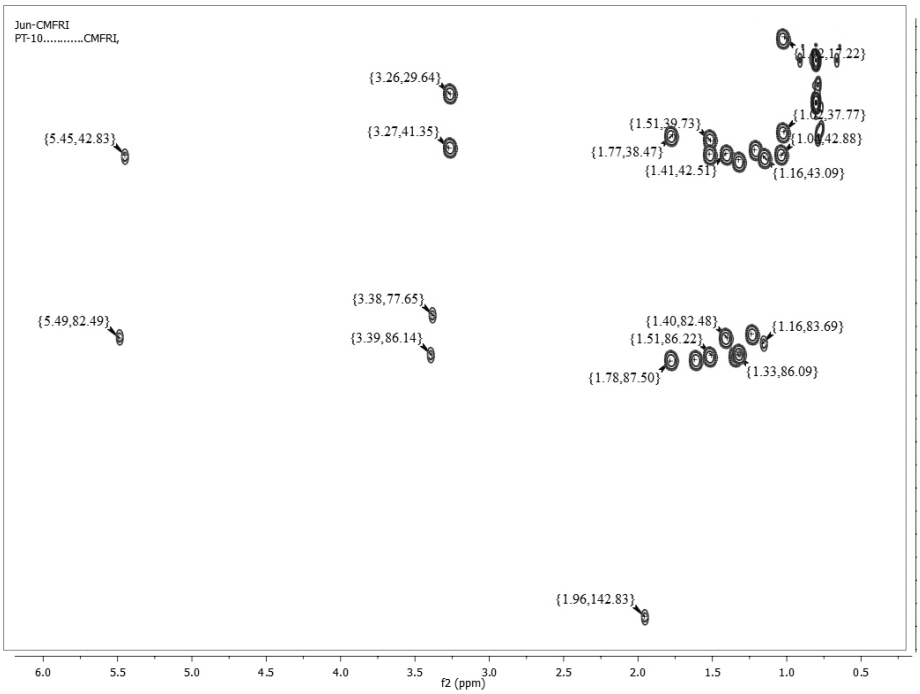

Figure 5.143.: HMBC spectrum of4,7-dimethoxy-9β ,14α-dihydroxy-dolasta-1-ene (**10**)

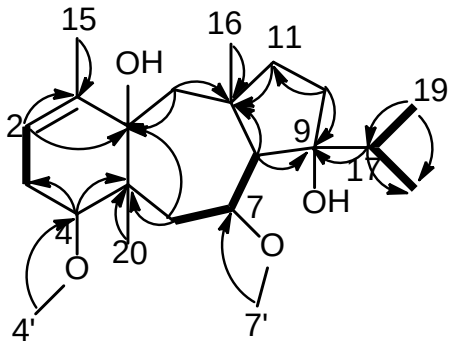

Figure 5.144.: Prominent ^{1}H-^{1}H COSY, and selected HMBC correlations of 4,7-dimethoxy-9β ,14α-dihydroxy-dolasta-1-ene (**10**). The key ^{1}H-^{1}H COSY couplings were represented in bold face bonds. The key HMBC couplings have been represented by double barbed arrows.

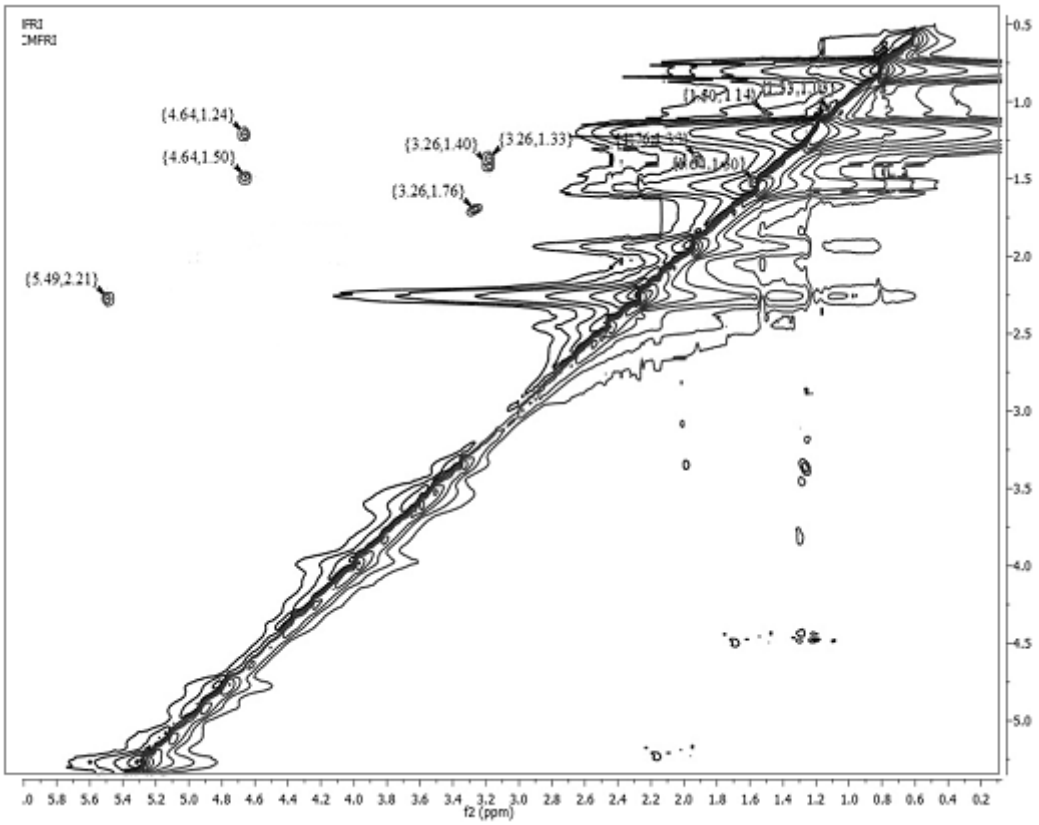

Figure 5.145.: NOESY spectrum of 4,7-dimethoxy-9β ,14α-dihydroxy-dolasta-1-ene (**10**)

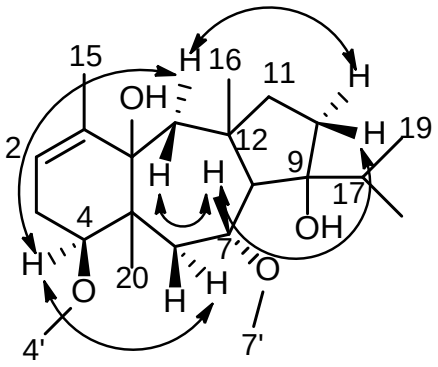

Figure 5.146.: Prominent NOE correlations of 2,7-dimethoxy-14α-hydroxy-dolasta-1(15),9-diene (**10**). NOESY relations are represented by double-tailed arrows

The molecular ion peak of **10** was appeared at *m/z* 366 and base peak was ontained at *m/z* 27.0 (Figure 5.147 and 5.148).

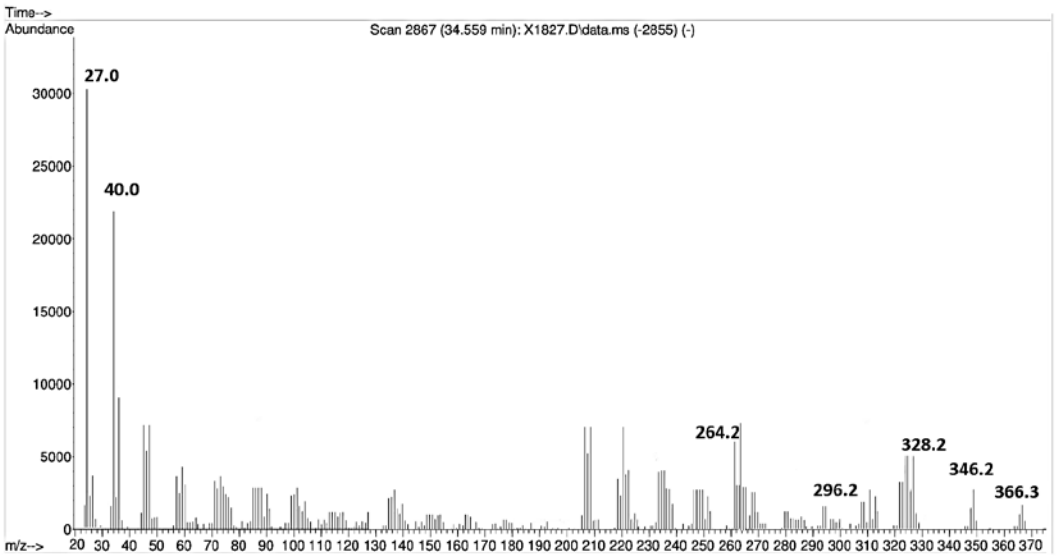

Figure 5.147.: EI-MS spectrum of 4,7-dimethoxy-9β ,14α-dihydroxy-dolasta-1-ene (**10**)

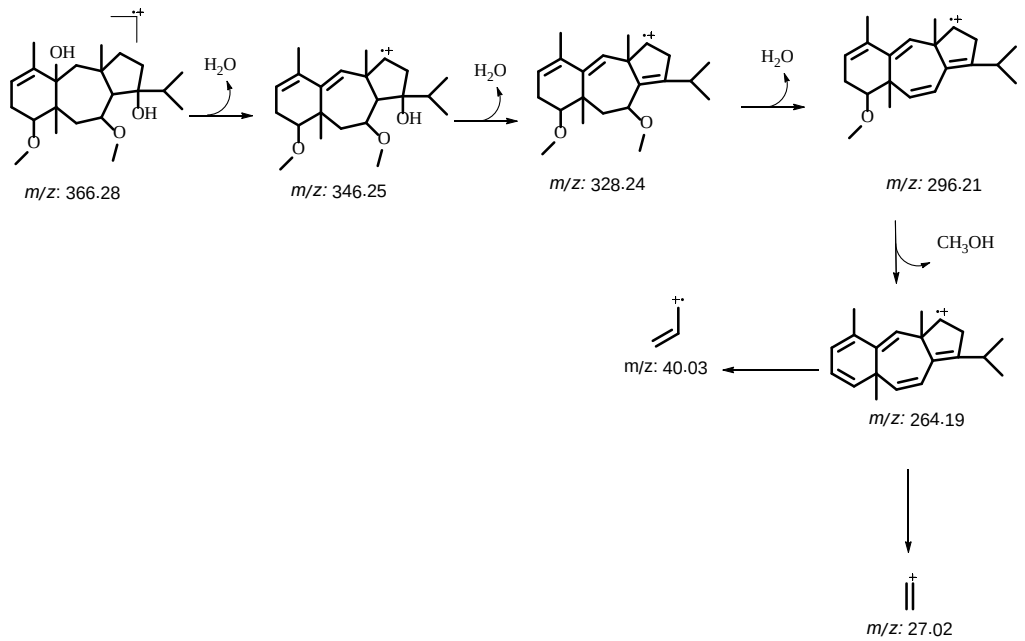

Figure 5.148.: Tentative mass fragmentation pattern of 4,7-dimethoxy-9β ,14α-dihydroxy-dolasta-1-ene (**10**)

Table 5.13.: NMR spectroscopic data[a] of 4,7-dimethoxy-9β ,14α-dihydroxy-dolasta-1-ene (**10**) isolated from brown seaweed *P.tetrastromatica*

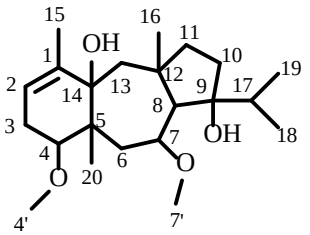

Compound **10**……4,7-dimethoxy-9β ,14α-dihydroxy-dolasta-1-ene (**10**)

C. No.	^{13}C	^{1}H NMR (int.,mult.,J in Hz)[b]	COSY	HMBC
1	142.9	-	-	-
2	124.3	5.49(1H,t,10.7 Hz)	H-3	C-14,1
3	30.0	2.21(1H,m) 1.96(1H,m)	-	-
4	83.3	3.26(1H,t,8.8 Hz)	-	C-3,5
4’	57.0	3.39(3H,s)	-	C-4
5	42.1	-	-	C-14
6	42.9	1.40(1H,d,11.6 Hz) 1.16(1H,d,11.8Hz)	H-7	C-5
7	76.5	4.64(1H,m)	H-8	C-6
7'	57.8	3.36(3H,s)	-	C-7
8	68.6	1.33(1H,d,9.1 Hz)	-	C-9,12
9	87.3	-	-	-
10	34.5	1.50(1H,m) 1.76(1H,m)	-	C-9,11
11	38.4	1.53(1H,t,6.6 Hz) 1.27(1H,t,6.7 Hz)	-	C-12
12	42.3	-	-	-
13	44.2	1.24(1H,s) 1.34(1H,s)	-	C-12,14
14	83.0	-	-	-
15	19.0	1.95(3H,s)	-	C-1
16	18.3	1.14(3H,s)	-	C-12
17	36.2	1.62(1H,m)	H-18, H-19	C-9,18
18	17.8	1.02(3H,d,7.6 Hz)	-	-
19	17.8	1.01(3H,d,7.7 Hz)	-	C-18,8
20	25.6	1.03(3H,s)	-	C-5

[a]NMR spectra were recorded using a Bruker AVANCE III 500 MHz (AV 500) spectrometer (Bruker, Karlsruhe, Germany) in $CDCl_3$ as aprotic solvent at ambient temperature with TMS as the internal standard (δ 0 ppm).

[b]Values in ppm, multiplicity and coupling constants (J= Hz) were indicated in parentheses. Multiplicities were allocated by ^{135}DEPT NMR spectrum.

The assignments were made with the aid of the COSY, HSQC, HMBC and NOESY experiments.

5.3.3 Pharmacological potentials of secondary metabolites isolated from the organic extract of P. tetrastromatica

5.3.3.1 Pharmacological potentials of xenicane class of diterpenoid derivative (1-5)

The organic extract of *P. tetrastromatica* derived five diterpene derivatives, which displayed potential anti-inflammatory and antioxidative activities in various *in vitro* systems (Table 5.14). Significant differences ($P < 0.05$) in radical scavenging properties were recorded amongst the xenicin (**1**-**2**) and α-tocopherol against $ABTS^+$ (IC_{50} ~ 1.91 mM; $P < 0.05$) and DPPH (IC_{50} ~ 1.64 mM) radicals. Significantly higher DPPH scavenging activity was observed for xeniolide **5** (IC_{50} 1.73 mM) followed by **4** and xenicins (**2**, **3**) (IC_{50} ~ 1.92 mM, $P < 0.05$), in declining order. In addition, the $ABTS^+$ scavenging efficacy was significantly higher for **5** and **4** (IC_{50} ~ 2.03 mM) as related to those revealed by the diterpene metabolites **1** through **3** (~2.30 mM, $P < 0.05$). Anti-inflammatory activities against 5-LOX and COX-2 were significantly higher for **5** (IC_{50} 1.88 and 1.41 mM, respectively) as compared to other homologues in this series ($IC_{50} < 2.26$ mM; $P < 0.05$). The compound **5** registered greater anti-5-LOX potential (IC_{50} 1.88 mM) than that exhibited by ibuprofen (IC_{50} 4.50 mM; $P < 0.05$). The greater selectivity indices of studied diterpenes (IC_{50}anti-COX-1/IC_{50}anti-COX-2 > 1) as compared to that displayed by ibuprofen (0.43) inferred higher anti-inflammatory selectivity against COX-2. Previous reports of literature inferred that oxidative stress directed the generation of free radicals, which in turn, caused inflammation and related pathophysiological conditions (D'Orazio et al., 2012; Joy and Chakraborty, 2017a). Thus, it is fitting to state that the higher antioxidative potentials of the studied compounds could be correlated to their anti-inflammation properties. Inflammation reactions were found to be concomitant with the formation of inflammatory prostaglandins or leukotrienes by enzymes, such as cyclooxygenases and lipoxygenase. The studied compounds from *P. tetrastromatica* were found to reduce the formation of inflammatory prostaglandins because of their potential inhibition of pro-inflammatory agents.

5.3.3.2 Pharmacological potentials of dolabellane class of diterpenoid derivative (6-10)

The antioxidant activities of compounds (**6**-**10**) were evaluated by their $ABTS^+$ and DPPH scavenging potentials, whereas their bioactivities were compared with standard antioxidant α-tocopherol (Table 5.15). The DPPH radical scavenging activities of **10** and **8** were greater (IC_{50} ~0.60 mg/mL) than other studied analogues and α-tocopherol (IC_{50} >0.6 mg/mL). The antioxidant potencial of **10** was further confirmed by the $ABTS^+$ scavenging activities (IC_{50} 0.71 mg/mL), which was greater than other studied analogues and α-tocopherol (IC_{50} >0.72 mg/mL). The attenuating activities of **10** against α-glucosidase (IC_{50} 0.11 mg/mL) and α-amylase (IC_{50} 0.13 mg/mL) were

comparable to the gold standard acarbose (IC_{50} 0.12 and 0.14 mg/mL, respectively) (Table 1). These results signified the potential anti-hyperglycaemic property of compound **10** over acarbose and other studied compounds.

5.3.4 Structure-activity correlation analyses of bioactive compounds isolated from EtOAc-MeOH extract of P. tetrastromatica

5.3.4.1 Structure-activity correlation analyses of xenicane class of diterpenoid derivative (1-5)

The physico-chemical parameters of studied xenicins (**1-2**) and xeniolides (**3-5**) corroborated the structural attributions that were accountable for targeted bioactive potentials (Joy and Chakraborty, 2017b). The bioactivities were essentially associated with electronic {polarizability (Pl) and topological polar surface area (tPSA)} and lipophilic parameters (log P_{ow} logarithmic value of octanol-water coefficient), and not by the steric factors. It is of note that the steric factor of **4** and **5** (P > 820 cm^3) were greater than xenicane class of diterpenoids (**1-2**, P < 780 cm^3) evidently due to the occurrence of the bulk bicyclic skeleton of the xeniolides (**3-5**) (Table 5.16). However, the electronic parameters were found to play illustrious role to govern the bioactive potentials (Wang et al., 2007; Chakraborty and Raola, 2018). The total numbers of electron-localized centres were lesser in **1** and **2** as designated by the assessment of electronic descriptors, thus resulting in their lower polarizability, than those documented with the xeniolides (**3-5**) (Table 3). The log P_{ow} of **5** was found to be within the desirable range (~1.95), which might cause a suitable lipophilic-hydrophobic relation (Lipinski 2004) and receptor binding (Huuskonen et al., 2000; McNally et al., 2007) leading to higher target bioactivities than other studied compounds.

5.3.4.2 Structure-activity correlation analyses of dolabellane class of diterpenoid derivative (6-8)

The structural attributions of the studied analogues were interpreted by their physico-chemical parameters. The previous reports demonstrated that the bioactive potentials were correlated with lipophilic (log P_{ow}, logarithmic value of octanol-water coefficient) and electronic parameters {polarisability (PI) and topological polar surface area (tPSA)} (Lipinski and Hopkins 2004; Antony and Chakraborty 2018). Notably, the steric bulk factors of **6-10** were of greater resemblance due to the presence of basic dolabellane framework, and therefore, did not constitute important functional role in determining their bioactive properties. The lesser steric bulk factors of **6-10** (molar refractivity, MR 97-105 cm^3/mol; molar volume, MV 328-337 cm^3; parachor, P 820-860 cm^3) might contributed towards its greater antioxidative properties than α-tocopherol with comparatively greater steric bulkiness (MR 135.06 cm^3/mol, MV 462.70 cm^3, P 1123.00 cm^3). The greater steric hindrance of acarbose (MR 141.21 cm^3/mol, MV 369.70 cm^3, P 1209.80 cm^3) over the titled compounds might

be corroborated with their greater attenuating activities against starch hydrolytic enzymes. The lesser steric bulkiness of the studied compounds might be responsible towards their effective interaction with the amino acyl residues of the enzyme catalytic site resulting in their potential anti-diabetic activities. Notably, the electronic and hydrophobicity factors of the studied compounds might also acquire prominent functional roles in determining bioactivities (Wang et al. 2007). The tPSA of **10** was found to be greater (58.92) than those exhibited by other studied analogues (tPSA <50) (Table 5.16), that might be corroborated with the greater reactivities towards free radicals. The greater tPSA of **8** (tPSA 49.69) and **10** (tPSA 58.92) over that of α-tocopherol (tPSA 29) might contribute towards its greater antioxidant properties than α-tocopherol. The log P_{ow} of the studied compounds were found to be within the acceptable limits of 2.69-4.82, when compared to that of α-tocopherol (log P_{ow} 9.98). The significantly lower value of log P_{ow} of -7.10 reported for acarbose might result in unfavourable hydrophobic-lipophilic interactions, whereas the log P_{ow} of the titled compounds were found to be within the favourable boundaries (log P_{ow} 2-5), which might result in potential anti-diabetic properties of the latter. The greater electronic descriptors of acarbose could effectively compensate for its effective anti-diabetic potentials, irrespective of its unfavourable log P_{ow} and greater steric bulkiness. The optimum log P_{ow} and electronic parameters along with lower steric values of the titled compounds could manifest towards its target bioactive properties. Generally, the compounds possessing lesser log P_{ow} values (<5) were recognised to be effective in keeping a steady balance of hydrophobic-lipophilic parameters (Lipinski and Hopkins 2004). Principle component analyses between log P_{ow} and bioactive potentials of the titled compounds appropriately showed that the bioactivities and log P_{ow} values were located in the similar quadrant. Therefore, an optimum hydrophobic-lipophilic balance appeared to constitute a predominant functional role in determining the target bioactive properties.

Table 5.14.: *In vitro* bioactive potentials (antioxidant and anti-inflammatory) of compounds **1-5** and commercially available references along with molecular descriptors (electronic, steric and hydrophobic) of the studied compounds isolated from *P. tetrastromatica.*

Compounds	**Anti-oxidant activities (IC_{50}, mM)**		**Anti-inflammatory activities (Inhibitory activities against pro-inflammatory enzymes, IC_{50}, mM)**			
	DPPH scavenging	**ABTS scavenging**	**COX-1 inhibitory**	**COX-2 inhibitory**	**5-LOX inhibitory**	**Selectivity index**
1	2.16 ± 0.03^{a}	2.41 ± 0.03^{a}	2.09 ± 0.03^{a}	1.98 ± 0.01^{a}	2.50 ± 0.01^{a}	1.05 ± 0.02^{a}
2	2.03 ± 0.02^{b}	2.23 ± 0.02^{b}	2.17 ± 0.03^{b}	1.80 ± 0.03^{a}	2.31 ± 0.02^{a}	1.20 ± 0.01^{b}
3	1.97 ± 0.02^{b}	2.26 ± 0.03^{b}	2.04 ± 0.02^{a}	1.77 ± 0.03^{a}	2.34 ± 0.02^{a}	1.15 ± 0.02^{b}
4	1.75 ± 0.03^{c}	2.04 ± 0.01^{c}	2.12 ± 0.02^{b}	1.43 ± 0.01^{b}	1.92 ± 0.03^{b}	1.48 ± 0.03^{c}
5	1.73 ± 0.03^{c}	2.01 ± 0.04^{c}	2.14 ± 0.03^{b}	1.41 ± 0.02^{b}	1.88 ± 0.02^{b}	1.52 ± 0.02^{c}
Standard	1.46 ± 0.04^{cT}	1.70 ± 0.05^{cT}	0.19 ± 0.00^{bI}	0.44 ± 0.02^{cI}	4.50 ± 0.11^{cI}	0.43 ± 0.01^{dI}

The anti-oxidant and anti-diabetic activities were expressed as IC_{50} values, mM).

$^{a-c}$ Column-wise values with different superscripts of this type indicate significant difference (P<0.05), which implied for the statistical evaluation of the results. Triplicate values were taken and the variance analyses (ANOVA) were carried out (using Statistical Program for Social Sciences 13.0) for means of all parameters to examine the significance level (P<0.05). The results were expressed as mean ± SD (n = 3).

^{T} Superscript of this type depicts α-tocopherol

^{I} Superscript of this type depicts ibuprofen

Table 5.15. *In vitro* bioactive potentials (antioxidant and anti-antidiabetic) of compounds **6-10** from *P. tetrastromatica* and commercially available references

	Bioactivities					
Antioxidant activity	**1**	**2**	**3**	**4**	**5**	***α*-tocopherol**
[p]DPPH scavenging activity	[a]0.65±0.02	[a]0.67±0.01	[b]0.60±0.02	[a]0.69±0.02	[b]0.59±0.01	[a]0.63±0.01[Q]
[p]$ABTS^+$ scavenging activity	[a]0.77±0.03	[b]0.83±0.02	[a]0.75±0.06	[b]0.81±0.03	[c]0.71±0.02	[a]0.74±0.03[Q]
Anti-diabetic activity	**1**	**2**	**3**	**4**	**5**	**Acarbose**
α-amylase inhibition activity	[a]0.18±0.01	[b]0.21±0.02	[a]0.16± 0.02	[b]0.22 ± 0.03	[c]0.13±0.02	[c]0.14 ± 0.02[R]
α-glucosidase inhibition activity	[a]0.15±0.01	[b]0.20±0.03	[a]0.14 ± 0.02	[b]0.21±0.02	[c]0.11±0.01	[c]0.12 ± 0.01[R]

The anti-oxidant and anti-diabetic activities were expressed as IC_{50} values (mM).

[a-c] Row-wise values with different superscripts of this type indicate significant difference (P<0.05), which implied for the statistical evaluation of the results. Triplicate values were taken and the variance analyses (ANOVA) were carried out (using Statistical Program for Social Sciences 13.0) for means of all parameters to examine the significance level (P<0.05).

Results were expressed as mean ± SD (n = 3).

Different superscripts (Q-R) indicate the standards used for different activities.

Table 5.16.: Molecular descriptors (electronic, steric and hydrophobic) of compounds **1-10** from *P. tetrastromatica.*

	Molecular descriptors[d]					
Compounds	**Electronic**		**Steric**			**Hydrophobic**
	PI ($x10^{-23}$ cm^3)	**tPSA**	**P (cm^3)**	**MV (cm^3)**	**MR (cm^3 mol^{-1})**	**Log P_{OW}**
1	37.87	79.15	762.9	284.5	95.53	1.17
2	37.95	79.15	775.5	289.4	95.73	1.52
3	38.74	107.22	822.1	317.6	97.73	1.29
4	40.78	96.22	867.5	331.4	102.87	1.61
5	38.74	107.22	826.4	315.6	97.73	1.93
6	39.30	49.69	820.3	328.6	99.15	3.18
7	38.80	29.46	816.2	335.4	97.87	4.82
8	39.30	49.69	820.3	328.6	99.15	3.16
9	40.41	38.69	830.5	335.1	101.95	3.42
10	41.21	58.92	858.4	337.7	103.96	2.69

MV, molar volume; P, parachor; MR, molar refractivity.

log P, logarithmic scale of the octanol-water partition coefficient.

Pl, polarizability; tPSA, topological polar surface area.

[d] The structure-activity relationship analysis was carried out by using different molecular descriptors of the purified compounds as described in the text.

5.3.5. *In silico* molecular docking analysis of bioactive compounds isolated from *P. tetrastromatica*

5.3.5.1 *In silico* molecular docking analysis of *xenicane class of diterpenoid derivative (1-5)*

The studied compounds were subjected to *in silico* molecular docking analysis against pro-inflammatory 5-lipoxygenase (LOX-5), and the results were evaluated by their RMSD data. The molecular docking parameters, such as binding energy, docking score, inhibition constant, hydrogen bonding interactions, intermolecular energy and torsional free energy between the ligands and the active sites of 5-lipoxygenase were documented in Table 5.18. The grid box of potential binding site was assigned as x=40.120, y=39.326, z=41.254. Among the studied compounds, xenicanes **1** and **2**, on molecular docking analysis with 5-lipoxygenase, exhibited one hydrogen bond interaction with amino residues Arg411 and Arg438 in the enzyme active site with molecular distances of 3.011 Å and 2.740 Å, respectively. Among the xeniolide analogues, compound **5** showed three hydrogen bonded interactions with amino acid residues, one hydrogen bonded with Lys441 (2.799 Å), and two with Gln434 (2.860 and 2.886 Å).

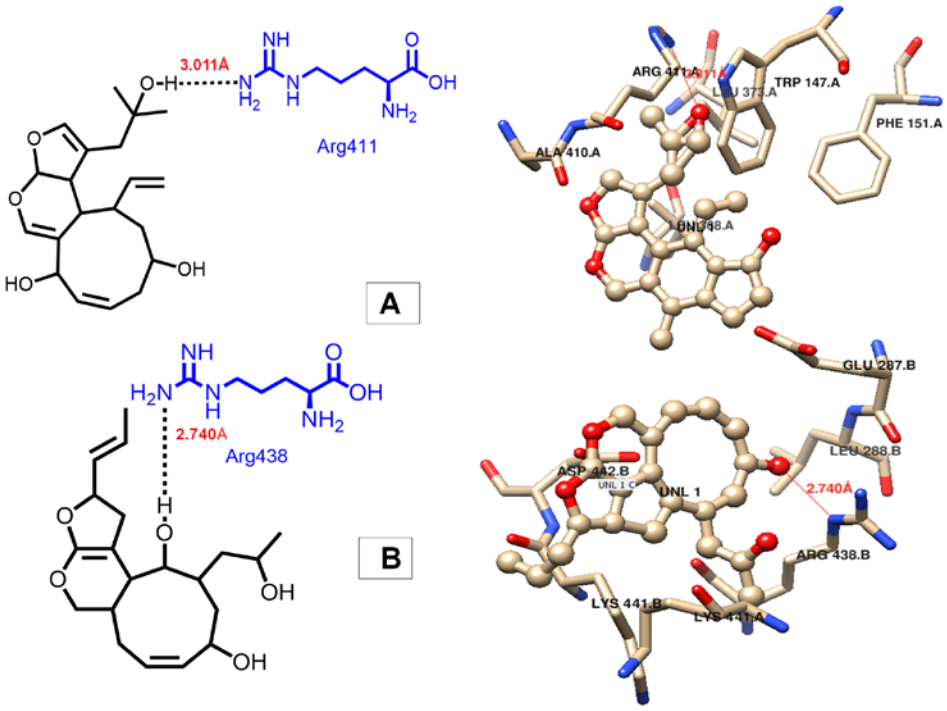

Fig. 5.149.: Closer view of molecular binding interactions of the xenicane derivatives **1** (**A**) and **2** (**B**) in the catalytic site of protein LOX-5 as deduced from its molecular modeling simulations. The xenicanes **1** and **2** exhibited one hydrogen bond interaction with amino residues Arg411 and Arg438 in the enzyme active site with molecular distances of 3.011 Å and 2.740 Å, respectively.

The compound **5** exhibited greater number of hydrogen bond interactions with amino acyl residues than those recorded by **3** (2.742 Å with Gln437) and **4** (2.935 Å with Asp290) (Fig. 5.149 & 5.150). The lesser distance of 2.740 Å in ligand-protien complex of compound **2** established its closer binding interaction towards protein than those displayed by xenicane **1** (3.011 Å). These results were supported by the higher *in vitro* anti-inflammatory activity of **2** over **1** against 5-LOX. The comparison of molecular docking parameters appropriately suggested that compound **5** exhibited close molecular interactions towards enzyme LOX-5 with least binding energy (-11.56 kcal mol^{-1}) and docking score (11.40 kcal mol^{-1}), which were corroborated with their greater potential of enzyme inhibition against LOX-5 (IC_{50} 1.88 mM) than those exhibited by **1**-**4**.

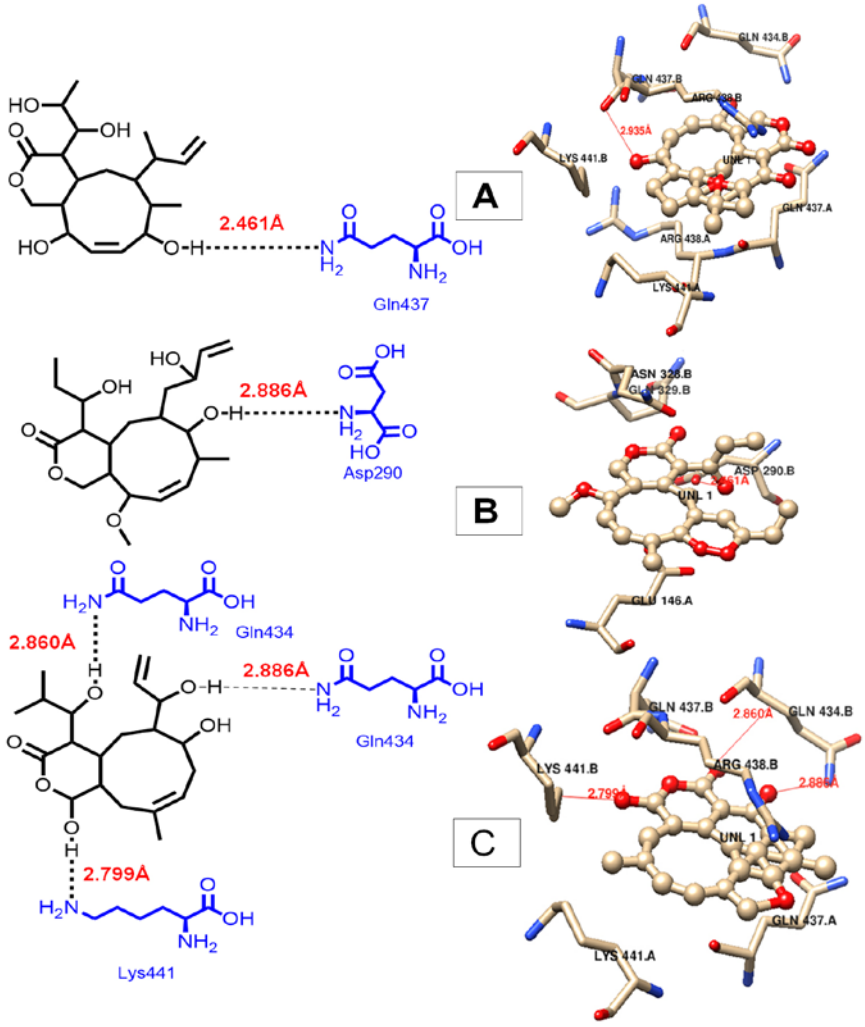

Figure 5.150.: Closer view of molecular binding interactions of the xeniolide derivatives **3** (**A**), **4** (**B**), and **5** (**C**) in the catalytic site of protein LOX-5 as deduced from its molecular modelling simulations. The xeniolide **5** showed three hydrogen bonded interactions with amino acid residues, one hydrogen bonded with Lys441 (2.799 Å), and two with Gln434 (2.860 and 2.886 Å). Compound

5 displayed greater number of hydrogen bond interactions with amino acyl residues than those recorded by **3** and **4**.

Table 5.17.: The *in silico* molecular docking parameters between the ligands (compounds **1**–**5**) and the active sites of 5-lipoxygenase

†Ligands	‡Binding energy (kcal mol^{-1})	‡Docking score (kcal mol^{-1})	‡Inhibition constant Ki (µM)	††Hydrogen bonding interactions	‡Intermolecular energy (kcal mol^{-1})	‡Torsional free energy (kcal mol^{-1})
1	-6.85	7.15	9.53	Arg411	-7.45	0.60
2	-7.39	8.44	3.83	Arg438	-8.58	1.19
3	-11.48	11.72	0.003	Gln437	-11.78	0.30
4	-8.66	9.43	0.449	Asp290	-9.71	1.19
5	-11.56	11.40	0.033	Lys441, Gln437	-11.56	0.00

† Molecular docking simulations were carried out using Autodock 4 software tool.

‡ Values were evaluated from the calculations based on the energy minimization.

††Hydrogen bonding interactions of ligands **1-5** with protein 5-lipoxygenase.

5.3.5.2 In silico molecular docking analysis of *dolabellane class of diterpenoids (6-8)*

The compounds (**6-10**) were subjected to molecular docking against the carbolytic enzyme *α*-amylase. The molecular docking parameters, such as docking score, binding energy, inhibition constant, intermolecular and torsional free energy were documented (Table 5.18). Among the dolabellanes, compound **8** recorded least binding energy (-9.71 kcal/mol) and docking score of -11.58 kcal/mol followed by those exhibited by **7** and **6** (-9.31 to -8.60 kcal/mol, and -10.60 to -11.20 kcal/mol, respectively). Likewise, among the dolastanes, compound **10** recorded least binding energy (-8.59 kcal/mol) and docking score of -10.64 kcal/mol followed by those exhibited by compound **9**. (Table 5.18). The comparison of lowest molecular docking parameters, such as constant of inhibition, binding energy, docking score, internal and torsional free energies appropriately suggested that the compounds **8** and **10** possessed close molecular interactions with the target carbolytic enzyme receptors, resulting in their greater potential of enzyme inhibition against *α*-amylase. The greater molecular docking interactions of compounds **8** and **10** in the active site of *α*-amylase were appropriately corroborated with their potent *in vitro α*-amylase inhibitory activities (IC_{50} <0.17 mg/mL). It was observed that the studied dolabellane and dolastane analogues efficiently interacted with the active site amino acyl residues in the binding site of *α*-amylase via

electrostatic interactions through the oxygen atom of the hydroxyl group (Liu et al. 2013). The interactions of compounds **8** and **10** with α-amylase receptors were described in Figure 5.151.

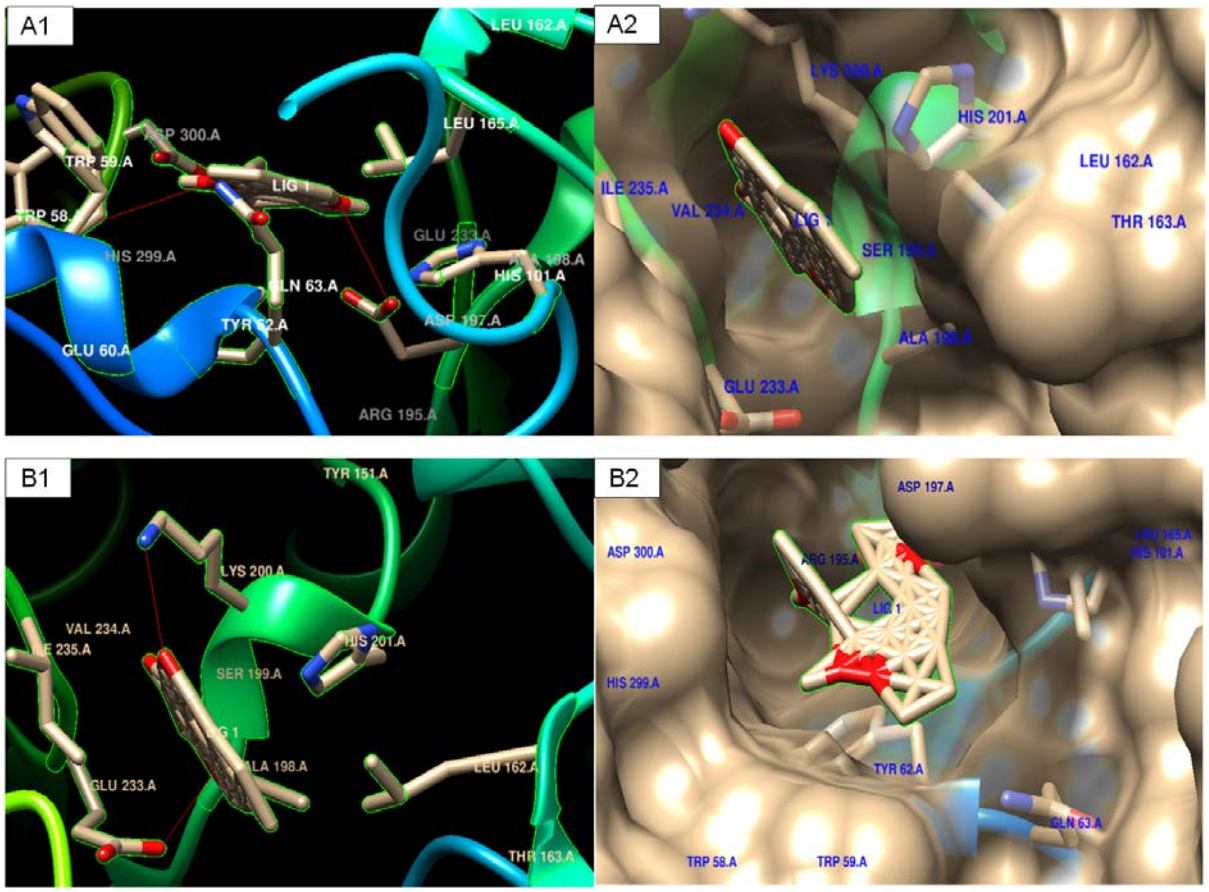

Figure 5.151. Closer view of molecular binding interactions of compounds **8** (**A1**-**A2**) and **10** (**B1**-**B2**) in the catalytic site of protein α-amylase deduced from molecular modeling simulations.

Table 5.18.: The binding energy, docking score, inhibition constant, intermolecular energy and torsional free energy between the ligands (compounds **6**–**10**) and the active sites of α-amylase

†Ligands	‡Binding energy (kcal/mol)	‡Docking score (kcal/mol)	‡Inhibition constant, Ki (µM)	‡Intermolecular energy (kcal/mol)	‡Torsional free energy (kcal/mol)
6	-8.60	-11.20	0.499	-11.20	2.98
7	-9.31	-10.60	0.149	-10.80	1.49
8	-9.71	-11.58	0.077	-11.58	1.48
9	-6.96	-9.63	0.790	-9.65	2.68
10	-8.59	-10.64	0.504	-10.68	2.09

† Molecular docking simulations were carried out using Autodock 4 software tool.

‡ Values were evaluated from the calculations based on the energy minimization.

5.4 Conclusion

Five previously unreported xenicanes were isolated from the ethyl acetate/methanol extract of *P. tetrastromatica* by extensive chromatographic fractionation, and were characterized by detailed spectroscopic experiments. The xeniolide derivative octahydro-1,7-dihydroxy-4-(4^1-hydroxy-4^2-methylpropyl)-6-(6^1-hydroxy-6^2-propenyl)-10-methyl-cyclonona[*c*]pyran-3(*1H*)-one (**5**) showed potential antioxidant and anti-inflammatory activities, with greater anti-inflammatory selectivity index against pro-inflammatory cyclooxygenase-2 than other studied xenicane derivatives and ibuprofen. Molecular docking analysis inferred that the xeniolide derivative **5** exhibited efficient interactions with 5-lipoxygenase, which validated its greater inhibitory potential against the pro-inflammatory enzyme. In particular, the xeniolide-type diterpenoids with octahydrocyclonona[*c*]pyran-3(1*H*)-one backbone could be potential functional food components for use against inflammatory diseases. The biologically active xeniolides isolated from brown seaweed *P. tetrastromatica* might constitute a promising potential natural alternative to the commercially available synthetic antioxidants and anti-inflammatory agents.

The EtOAc:MeOH extract of *P. tetrastromatica* was fractionated by repeated chromatographic techniques to obtain five unprecedented dolabellane and dolastane analogues, named 6-methoxy-dolabella-8(17),12-diene-10*β*,18-diol (**6**), 3-methoxy-dolabella-12(18)-ene-4*β*-ol (**7**), 3-methoxy-dolabella-10,18(19)-diene-5*α*,8*β*-diol (**8**) along with two previously unreported dolastanes 2,7-dimethoxy-14*α*-hydroxy-dolasta-1(15),9-diene (**9**) and 4,7-dimethoxy-9*β*,14*α*-dihydroxy-dolasta-1-ene (**10**). This is the first report of isolation of dolabellane and dolastane terpenoids from *P. tetrastomatica*. The structural features of the studied compounds were characterised using comprehensive spectroscopic techniques. The compounds **10** and **8** displayed greater inhibitory activities against starch digesting enzymes, and their activities were greater than those exhibited by acarbose. In particular, 4,7-dimethoxy-9,14-dihydroxy-dolasta-1-ene (**10**) was found to be an effective dual inhibitors of *α*-amylase and *α*-glucosidase along with potential antioxidative properties, and therefore, could be utilised as potential antioxidant/anti-diabetic pharmacophore in medicinal applications.

CHAPTER 6

ISOLATION AND CHARACTERIZATION OF POLYSACCHARIDES FROM RED SEAWEED *GRACILARIA SALICORNIA (RHODOPHYCEAE)*

Contents

6.1 *Background*

6.2 *Materials and methods*

6.3 *Results and discussion*

6.4 *Conclusions*

6.1 Background

Seaweeds are one of the richest marine resources to produce bioactive compounds, such as polysaccharides, polyphenols, proteins, lipids, mineral salts, and amino acids. Among various bioactive metabolites, polysaccharides registered an integral share in the globally booming phycocolloid industries. Polysaccharides are mainly associated with the structural component of the seaweed cell wall materials with varying range of concentrations of 1-76 % of dry weight, in different species. The composition of polysaccharides is found to be complex, which are existed as neutral/acidic, linear/mixtures of substituted forms.

Majority of red seaweeds (Rhodophyceae) were found to contain galactans, for example, agars and carrageenans, whereas brown seaweeds are known to be rich in alginates and fucoidans. The demand of various polysaccharides of seaweeds is increased in recent years due to their pharmaceutical, cosmeceutical and functional food applications. Polysaccharides from seaweeds are associated with their complex structural characteristics, such as glycosidic linkages, monosaccharide composition, ring size and ratio of sugar residues. These structural peculiarities are correlated with the bioactivities including anticoagulant, antioxidant, antidiabetic, and immunomodulatory effects.

Carbohydrate-polysaccharides are comprehensive and complex bio-polymeric carbohydrate skeletal structures. Their derivable reactive functionalities, physiological features, and structural composition were contributed towards the wide range of biological applications (Wang, Hu, Nie, Yu, & Xie, 2016). Moreover, the structure of polysaccharide is far more complicated based on the differences in composition of monosaccharide residues, glycosidic linkages, sequence of sugar units, degrees of

polymerization, and branching point. Due to all these characteristics, polysaccharides from different sources, especially from marine source are envisaged as promising substitutes of non-degradable polymers in many pharmaceutical combinations. There were many well-established reports on antioxidant, immunomodulation, antimicrobial and anti-lipidemic activities of polysaccharide from marine source. Though, they have less exploited for curing the most common prevalent diseases such as, diabetes and osteoporosis (Wang, Hu, Nie, Yu, & Xie, 2016). The prevalence of diabetes is increasing worldwide, and the number of cases is predicted to increase to approximately 592 million (1 in every 12 people) by 2035 (Guariguata et al., 2014). Diabetes is characterized by hyperglycemia, and is associated with an increased incidence of osteoporosis, possibly mediated by the effects of insulin deficiency and hyperglycemia on the bone (Yang, Zhao, Liang, Yu, & Qu, 2017). It was estimated that the number of patients worldwide with osteoporotic hip fractures has been more than 200 million (Cooper, Campion, & Melton, 1992). Currently, pharmacotherapy involving the synthetic agents, such as thiazolidinediones, α-glucosidase inhibitors, and dipeptidyl peptidase-IV inhibitors (DPP-IV) are available for hyperglycemic therapy. Especially, DPP-IV inhibitors administered from the early stage of hyperglycemia help to protect pancreatic β-cells and normalize glucagon secretion control, combining reliable hypoglycemic action and safety, inhibiting the progression of hyperglycemia and maintaining glycemic control (Kubota et al., 2012). Recently, DPP-IV have received attention for their potential use in the treatment of osteoporosis. It selectively cleaves alanine and proline from polypeptide substrates, resulting in the inactivation of these substrates, including glucagon-like peptide 1 (GLP-1) and gastric inhibitory polypeptide (GIP) (Kubota et al., 2012). Thus, the mechanism of DPP-IV inhibitors involves prolonging the half-life of these incretins (GLP-1 and GIP) and consequently promoting insulin secretion from β-pancreatic cells to improve glucose tolerance. DPP-IV inhibitors can affect bone metabolism through various mechanisms. Firstly, the DPP-IV inhibition may promote bone metabolism by lowering the glucose level. Secondly, DPP-IV substrates and DPP-IV-related energy metabolism may affect bone metabolism. Thirdly, DPP-IV inhibitors might affect bone metabolism through vitamin D-linked and other related signaling pathways (Yang, Zhao, Liang, Yu, & Qu, 2017). The reports revealed that DPP-IV inhibitors in combination with metformin significantly decreased the risk of developing bone fractures compared to metformin monotherapy (Dombrowski et al., 2017). Similar results were reported by Choi et al. (2016), which showed the efficacy of DPP-IV inhibitors in reducing bone fracture risks, thus implying their therapeutic potential in osteoporosis. The reports also showed that DPP-IV inhibitor, sitagliptin treatment was reported to improve the vertebral volumetric bone mineral density (BMD) and significantly improved cortical bone volume, trabecular architecture, and bone strength (Kyle et al., 2011; Glorie et al., 2014). The reports also showed the possibility that the DPP-IV inhibitors might be effective in treating

osteoporosis and reducing the risk of fractures by improving BMD and bone quality. Moreover, the previous studies revealed that DPP-IV inhibitors could decrease parathyroid hormone level, and thus inhibit the release of calcium from the bone to blood and reduce bone destruction (Yang, Zhao, Liang, Yu, & Qu, 2017). DPP-IV inhibitors could significantly increase the serum concentration of 25-hydroxy vitamin D3 (25(OH)-D), which has been reported to regulate the concentration of calcium and phosphate in the bloodstream, thereby promoting the growth and remodeling of the bone. The level of 25(OH)-D was also associated with the duration of DPP-IV inhibitor treatment and strength of DPP-IV inhibitory activity (Yang, Zhao, Liang, Yu, & Qu, 2017). A cross-sectional study showed that serum DPP-IV inhibitors was positively associated with the bone formation markers, bone-specific alkaline phosphatase (ALP) and osteocalcin. Moreover, DPP-IV inhibitor, sitagliptin was found to significantly reduce alkaline phosphatase (ALP) level. A non-significant decline in serum osteocalcin was also reported. In diabetic patients, insulin deficiency and hyperglycemia appeared to play a prominent role in reducing bone formation. Advanced glycation end product (AGE) accumulation or AGE/RAGE (receptors for AGE) axis imbalance were deduced to directly influence the osteoblast activity by decreasing their number and function (Yang, Zhao, Liang, Yu, & Qu, 2017). Notably, various natural polysaccharides were found to possess potential anti-diabetic activity, and use of these polysaccharides as adjuncts to conventional therapies is increasing. There were many reports on osteoporotic and hyperglycemic activity of polysaccharide compounds. Polysaccharides derived from the leaves of *L. barbarum* enhanced the splenocyte proliferation to demonstrate immuno-stimulating potential (Liu et al., 2017); Anti-osteoporotic potentials were discovered from of polysaccharides of dioscoreae, and tamarind (Ma et al., 2016; Sanyasi, Kumar, Goswami, Bandyopadhyay, & Goswami, 2014). Likewise, polysaccharides from seaweeds *G. opuntia, K. alvarezii, S. duplicatum* and *T. decurens* showed anti-hyperglycemic activity (Hardoko, Siratantri, Eveline, Yogabuana, & Olivia, 2014; Makkar & Chakraborty, 2016). Sulfated polysaccharides incorporated scaffolds of carrageenans and agar were reported to improve the osteogenic differentiation capacity (Li et al., 2014). Therefore, polysaccharides from the natural sources, especially from marine origin might be good candidates as anti-hyperglycemic and anti-osteoporotic agents (Makkar & Chakraborty, 2016). However, higher-molecular-weight bioactive molecules have limitations due to their instability in delivery both *in vitro* and *in vivo* as well as their immunogenicity and shorter half-lives (Iki et al., 2017). Therefore, there is a great need to design the nano-based polysaccharide scaffolds with enhanced half-lives and reduced immunogenicity for use in pharmaceuticals (Iki et al., 2017). Hence, like polysaccharides, polysaccharide based nanoparticles also have drawn therapeutic potential against various diseases. Polysaccharide-based nanoparticles greatly enrich versatility of nanoparticle carriers in terms of function and category (Balan et al, 2016). Among different

nanoparticles, biopolymers and metallic silver based nano composites were found to exhibit several applications, which were better than that of native polysaccharides (Elsupikhe, Shameli, Ahmad, Ibrahim, & Zainudin, 2015; Elsupikhe, Ahmad, Shameli, Ibrahim, & Zainuddin, 2016). On metal nanoparticles, silver-nano-particles have received considerable attention owing to their interesting physicochemical properties, and their interesting bioactive potential with respect to antioxidant, anti-inflammatory and anti-diabetic potential (Sankar, 2015, Deepak et al, 2018; Govindappa, Hemashekhar, Arthikala, Rai, & Ramachandra, 2018). In light of these, the present study focused on the extraction and characterization of polysaccharide from bioactive red seaweed *Gracilaria salicornia* (C.Agardh) E.Y.Dawson (Gracilariaceae, Phylum Rhodophyta). There were many reports on water and ethanol/methanol extractions of *Gracilaria* genus, and most of them revealed their bioactive constituents and health promoting effects such as hyperglycemia, anti-inflammatory, anti-hypercholesterolemia, antioxidative, and antimicrobial properties (Vijaya Sankar, 2015, Deepak et al, 2018; Govindappa, Hemashekhar, Arthikala, Ravishankar Rai, & Ramachandra, 2018). Sulfated galactans extracted from *Gracilaria sp.* have been previously reported as a hybrid of various carrageenan moieties on the basis of ^{1}H and ^{13}C NMR data (De Almeida et al., 2011).

In this view, the polysaccharides isolated from the marine macroalgae *P. tetrastromatica* and *G. salicornia* were evaluated for various pharmacological properties, and among these two species the latter was found to display prospective bioactivities. Therefore, *G. salicornia* was shortlisted to isolate the polysaccharide compound, which was characterized as (1⋯→3)-*O*-6-sulfonato-β-D-galactopyranosyl-(1→⋯4)-3,6-anhydro-α-D-galactopyranose-(1⋯→) with exhaustive spectroscopic experiments and chemical derivatisations, such as methylation, reduction, and acetylation. The chemical constituents and bioactivities of polysaccharide derived from the water extract of *G. salicornia* were carried out by different analytical methods and bioassays with respect to hyperglycemia and osteopathy. This study also attempted to develop the polysaccharide based bioactive-silver-nano-composite (AgNPC), which was found to improve the bioactive potential of the native polysaccharide. The characterization of polyglactan based P-AgNPC were performed by various spectroscopic and physical analysis, such as fourier transform infrared (FTIR) spectroscopy, scanning electron microscopy (SEM) with energy-dispersive X-ray spectroscopy (EDX), and X-ray diffraction (XRD) technique, particle size analysis, zeta potential, along with atomic force microscopy (AFM). The pharmacological properties of polysaccharide and polysaccharide-based AgNPC with regard to antioxidant, anti-hyperglycemic and anti-osteoporotic activities were evaluated by using different *in vitro* models. The catalytic binding effect of polysaccharide was evaluated with the aid of *in silico* molecular docking studies with proteins such as DPP-IV, α-amylase, α-glucosidase and ALP.

6.2 Materials and methods

6.2.1 Chemicals and reagents

The chemicals and reagents utilized for the analysis were described under the section 4.2.1 of Chapter 4.

6.2.2 Chromatographic purification techniques and spectroscopic instrumentation analysis

6.2.2.1 Collection and processing of seaweed materials

Fresh samples of seaweed, *P. tetrastromatica* and *G. salicornia* were harvested from the Mandapam region (Gulf of Mannar, 8º48' N, 78°9' E and 9°14' N, 79°14' E) on the southeast Indian Peninsular (Figure 6.1 & 6.2). The samples were identified by a marine algologist Dr. Chellaiah Periyasamy of the Aquaculture Foundation of India, Madurai, and were deposited in the project repository under the accession number of AB.1.1.2.1. The samples were washed thoroughly, shade-dried, and powdered to homogeneity before being utilized for further laboratory experiments.

6.2.2.2 Spectrophotometric, spectroscopic analysis and morphological analysis

The documentation of FTIR (Fourier transform infrared) was carried out in between 4000-400 cm^{-1} using FTIR Perkin-Elmer Series 2000 spectrometer (Waltham, MA). The UV analysis was performed by UV-VIS Varian Cary 50 spectrophotometer (Palo Alto, CA). The one and two-dimensional NMR including ^{1}H-NMR-500 MHz, ^{13}C-NMR-125 MHz, DEPT, COSY, HSQC, HMBC, NOESY) were recorded with a Bruker Avance DPX 500 MHz NMR spectrometer (Bruker Co., Billerica, MA) (Maneesh & Chakraborty, 2018). A gas chromatograph/mass spectrometer (GC/MS) operating with the electron-impact (EI) mode (Varian GC model, CP-3800 housed in a mass spectrometer model Varian 1200L) was used for the mass spectral analysis. High resolution mass spectrometric detection was performed on a Bruker Daltonic (GmbH, Germany) micro-TOF series mass spectrometer with negative ion mode (ESI-MS). The reverse-phase high pressure liquid chromatography (RP-HPLC) analyses were carried out by Shimadzu LC-20AD pump device (Shimadzu Corporation, Nakagyo-ku, Japan), fitted with RID 10A

refractive index detector (Kyoto, Japan) connected to an LC-20AD pump with an amino column (Luna 250 × 4.6 mm, 5 μm) (Phenomenex, USA).

The synthesized polysaccharide-silver nanocomposite (AgNPC) was characterized using a Varian-Cary 50 UV/VIS spectrophotometer (Varian Cary 50, Palo Alto, CA) recorded at 200-800 nm. The morphology with regard to the size, distribution and the shape of AgNPC were visualized using a field emission-scanning electron microscope (SEM) (JEOL Model JSM - 6390LV). EDX characterization was performed with an Oxford XMX-N instrument by drop coating P-AgNPCs on the tungsten film. The particle size, dispersion, aggregation along with atomic scale in aqueous environment with a high spatial resolution (<1.0 nm) were provided by transmission electron microscopy (TEM). A zeta potential measurement of P-AgNPC was carried out by using a Malvern Zetasizer Instrument (Zetasizer Ver. 7.12). The dispersion and aggregation of P-AgNPC were also measured using an atomic force microscopy (AFM - APE research nanotechnology model - A 100-AFM) coupled with silicon nitride tip (with resolution of 256x256 pixels) in non-contact mode. The quantitative identification of the molecular crystal structure was analyzed by X-ray diffraction (XRD) analysis using Bruker AXS D8 Advance coupled with X-ray source Cu of wavelength 1.5406 Å and detector Si (Li) PSD.

6.2.3 Preparation of crude extracts of seaweeds

6.2.3.1 Preparation of crude extracts from brown seaweed P. tetrastromatica

The dried seaweed powder of *P. tetrastromatica* was extracted by the previously described method (Yang et al. 2008). Initially, the 500 g of ground seaweed was treated with 85 % ethanol and stirred continuously (1 L, room temperature for 12 h) to eliminate pigments and proteins, before being washed with acetone, centrifuged (10,000×g for 20 min, 4 °C (Sorvell Biofuge Stratos, Thermo Scientific, USA), and dried. The dried seaweed powder was then extracted with distilled water (1 L, 60-70 °C for 3 h × 2) and filtered to yield the crude aqueous extract. The crude aqueous extract (2.5 L) was precipitated with $CaCl_2$ (1 % w/v ~ 25 g) and kept at 4 °C (for 5 h) before being clarified by centrifugation (8000×g for 20 min, 4 °C) to separate the calcium salt of residues. Thereafter, the supernatant (1000 mL) was reduced to $1/10^{th}$ of the original volume (100 mL) via concentration by using a rotational vacuum concentrator (Martin Christ RVC 2-33 IR, Germany) and allowed to cool. Three volumes of ethanol (500 mL 3:1, v/v) was used to precipitate the supernatant and kept overnight at 4 °C for the complete precipitation of crude polysaccharide (PF) (27 g; yield based on powdered seaweed, 5.4 %).

Figure 6.1.: The brown seaweed *P. tetrastromatica* collected from the southeast coastline of the Indian sub-continent of Gulf of Mannar region (8º48' N, 78°9' E and 9°14' N, 79°14' E)

6.2.3.2 Preparation of crude extracts from red seaweed G. salicornia

The ground seaweed material was pre-treated with organic solvent acetone to remove the pigments. The pigmentous materials were removed by filtration followed by concentration at 45 °C with the help of a rotary vacuum concentrator (Heidolph, Instruments GmbH & Co., Schwabach, Germany). The acetone-free seaweed residue was soaked in a solution of 200 g of KOH (1 M) at 85° C for 4 h according to the modified method by Pereira et al. (Pereira, Amado, Critchley, van de Velde, & Ribeiro-Claro, 2009), and neutralized to pH 6-8 with HCl (0.3 M) before being kept for drying. The dried seaweed residue (200 g) was extracted with hot water at 80 °C for 4 h to yield the aqueous crude extract (Makkar & Chakraborty, 2016), which was allowed to cool and clarified by centrifugation at 8500 rpm for 15 min, at 4°C (Sorvell Biofuge Stratos, Thermo Scientific, USA). The residual mass of seaweeds were re-extracted and centrifuged two times with water to remove the solid residues. The obtained supernatant (1000 mL) was then concentrated to $1/10^{th}$ of the original volume (100 mL) by utilizing a rotational vacuum concentrator (Martin Christ RVC 2-33 IR, Martin Christ, Germany). The decreased volume of the supernatant was cooled and then precipitated with three volumes of 96 % ethanol (300 mL,

3:1, v/v). The obtained solution was kept overnight at 4 °C for the complete precipitation of the polysaccharide. The precipitated polysaccharide material was subjected for lyophilization with the aid of a laboratory-scale lyophilizer (Martin Christ alpha 1-4 LD plus, Martin Christ, Germany) to obtain the crude polysaccharide (8.78 g, yield based on powdered seaweed, 4.39 %).

Figure 6.1.: The red seaweed *G. salicornia* collected from the southeast coastline of the Indian sub-continent of Gulf of Mannar region (8º48’ N, 78°9’ E and 9°14’ N, 79°14’ E)

6.2.4 Purification of crude polysaccharide by anion exchange column chromatography

The crude polysaccharide extracted was sequentially purified by the aid of anion exchange chromatography of DEAE-cellulose according to the previously reported method (Maneesh & Chakraborty, 2018) with required modifications. Initially, the polysaccharide was dissolved in the distilled H_2O and passed through a packed column of resin, before being eluted with water, 0.1, 0.5, 1.0, 1.5 and 2.0 M NaCl solutions, in order, to yield various column subfractions. Each fraction was collected and monitored by the phenol-sulfuric acid method (absorbance of the reaction mixture was recorded at 490 nm) by using a spectrophotometer. The column fractions were subjected to phenol-sulfuric acid assay for the positive chemical reaction of polysaccharide (Dubois, Gilles, Hamilton, Rebers, & Smith, 1956). The eluted column fractions were freeze dried to obtain the powdered pure polysaccharide fractions.

These were further subjected to HPLC analysis to deduce the monosaccharide composition and the purity by using the evaporative light scattering detector (ELSD 10A) connected to an LC-20-AD pump by employing an amino column (Luna 250 × 4.6 mm, 5 μm).

6.2.4 Monosaccharide composition analysis

The monosaccharide composition analysis was carried out using the hydrolysates of polysaccharide (Maneesh & Chakraborty, 2018). In brief, the pure and dried fraction of polysaccharide was subjected for hydrolysis with 1 M trifluoroacetic acid (TFA) for 8 h. The solution was allowed to cool to room temperature. The traces of TFA were removed from the solution under a stream of N_2 and dissolved in double distilled water (DDW; 6 mL). The hydrolysates of polysaccharide (20 μL; 1 mg/mL) along with commercial monosaccharaide standards (20 μL; 1 mg/mL) were injected into an analytical HPLC connected with the evaporative-light-scattering (ELS) detector. The composition of monosaccharaides was monitored by HPLC and the obtained results were compared with the commercial monosaccharaide standards. The acetonitrile-water (80:20, v/v) was used as the HPLC mobile phase.

6.2.5. Structural characterization of the polysaccharide motifs by hydrolysis

The hydrolysates of polysaccharide were prepared by trifluoroacetic acid (TFA) method (as mentioned above) (Maneesh & Chakraborty, 2018). Briefly, the dried hydrolysates (oligosaccharides) of polysaccharide were subjected to 1D/2D-NMR spectroscopic analysis (Bruker Avance DPX 500 MHz NMR spectrometer Bruker Co., Billerica, MA). The hydrolysates were dissolved in D_2O (2-3 mg/500 μL) prior to the NMR analysis. The molecular weight of hydrolysates was determined by high resolution mass spectrometric detection by using micro-TOF series mass spectrometer (Bruker Daltonic (GmbH, Germany) with positive mode (ESI-MS, $M+H^+$).

6.2.6 Structural characterization of the polysaccharide motif by methylation analysis

The structural composition of the pure polysaccharide fraction, GSP-2 was performed with the aid of a modified method of methylation (Ciucanu & Kerek, 1984), and NMR spectroscopic analysis. Initially, the pure polysaccharide fraction (3 mg) was made completely soluble in dimethylsulfoxide (DMSO, 1 mL) in the presence of powdered alkali (NaOH ~0.1 g) under constant stirring in an inert atmosphere. The reagent, methyl iodide (MeI, 200 μL) was added to the reaction mixture for methylation with constant stirring for 45 min. The methylation of reaction mixture was then quenched with deionized water (~1 mL) and partitioned with chloroform and water. The methylated polysaccharide was collected with chloroform layer and under-methylated contents were discarded with water layer. The organic layer

was then concentrated under vacuum to remove the traces of solvents. The methylated residue of the polysaccharide was hydrolysed, and the methylated hydrolysates were subjected to 1D and 2D-NMR spectroscopic analysis with the aid of a Bruker Avance DPX 500 MHz NMR spectrometer (Bruker Co., Billerica, MA).

6.2.7 Linkage pattern and structural analysis of the polysaccharide motifs by reductive cleavage method

The linkage pattern and structure of pure polysaccharide, GSP-2 was further analysed by modified method of reductive cleavage (of the glycosidic linkage) (Ciucanu & Kerek, 1984). Initially, the homogenous polysaccharide (3 mg) was undergone methylation analysis as discussed in the previous section. The residue obtained in chloroform layer after methylation was then reduced with sodium borohydride ($NaBH_4$), and was acetylated with acetic anhydride (Ac_2O) and pyridine. The linkage and sulfation of polysaccharide was acquired from the position of acetylation, and was characterized using GC-MS experiment (Bjorndal, Hellerqvist, Lindberg, & Svensson, 1970). The structural characterization of the acetylated polysaccharide was carried out by extensive 1D and 2D-NMR spectroscopic analysis.

6.2.7. Component analysis of polysaccharide by analytical methods

6.2.7.1 Determination of total carbohydrate content

Determination of total carbohydrate content was determined by the dinitrosalicylic acid method using D-glucose as the standard (Miller 1959). Briefly, 3,5-dinitrosalicylic acid (1 g) was dissolved in an aqueous alkaline solution (2M NaOH, 50 mL) at the room temperature and added with the Rochelle salt (Na-K-tartrate, 30 g). The contents were made up the volume to 100 mL with distilled water. The purified polysaccharide solution (0.2 % w/v) was added to the reaction mixture and was heated for 10 min using a water bath (100 °C) and cooled at room temperature. The absorbance was measured at 540 nm, and the standard curve was plotted against glucose solutions at different concentrations (2.5, 1, 0.5, 0.25 mg mL^{-1}). The total carbohydrate content (% w/w) was estimated by the following equation: Total carbohydrate content (% w/w) = {(X) × V/W}, where X = concentration of the polysaccharide fraction obtained from the slope of the graph, V = total volume of solution taken (= 3 mL), and W = weight of the polysaccharide (in mg) (Miller 1959).

6.2.7.2 Determination of uronic acid content

Uronic acid content was estimated by modified carbazole method applying D-glucuronic acid as the standard (Bitter and Muir 1962). Briefly, glucuronic acid at different concentrations (1, 0.5, 0.25, 0.1 mg mL^{-1}) was prepared, and each of these solutions (0.1 mL) were added with concentrated H_2SO_4 (6 mL) under ice-cold condition. The sample solutions (0.1 mL) at different concentrations were added with concentrated H_2SO_4 (6 mL) and the alcoholic solution of carbazole (0.2 mL, 0.1% in ethanol) under an ice-cold condition; the mixture was heated (at 55 °C) for 30 min, and the absorbance was measured at 530 nm. Uronic acid content (% w/w) in the sample was estimated using the following equation:

Uronic acid (% w/w) = {(X) × V/W}, where X = concentration of the polysaccharide fraction obtained from the slope of the graph, V = total volume of solution taken (= 6.3 mL), and W= weight of the polysaccharide in milligram.

6.2.7.3 Determination of protein content

The protein content was determined by the method of Lowry et al. (1951). The absorbance of the protein aliquot was measured at 660 nm within 15 min against the reagent blank. The protein content of the sample was calculated from the standard curve of bovine serum albumin and expressed as % w/w of the polysaccharide fraction.

6.2.7.4 Determination of sulfate content

The sulfate content was estimated by the turbidimetric method (Dodgson and Price 1962). Briefly, the polysaccharide fraction (2-4 mg) was hydrolyzed with HCl (2 N, 1 mL), and the aliquot (0.2 mL) was added with trichloroacetic acid (3.8 mL of 3 % w/v) and barium chloride-gelatin solution (1 mL) before being incubated at room temperature for 20 min. The absorbance of the test solution was recorded at 360 nm on a spectrophotometer against a reagent blank. A standard curve was developed with potassium sulfate solution, and the concentration of sulfate content (% w/w) in the polysaccharide fraction was calculated from the slope and Y-intercept of the graph.

6.2.8 Synthesis of polysaccharide-silver nanoparticle composite (P-AgNPC) from G. salicornia

The synthesis of polysaccharide-silver nano-composite (P-AgNPC) was found to be a promising application in the pharmaceutical industry. Therefore, the synthesis of P-AgNPC was performed by reduction, according to the modified method of Elsupikhe et al. (2015). In brief, different solutions of polysaccharides of 40 mL were prepared with 0.1, 0.15, 0.20, 0.25, and 0.3 wt %, respectively. The solutions were stirred for 2 h for complete dissolution. About 10 mL of 0.1 M $AgNO_3$ solutions were added into the each of the 40 mL solutions of polysaccharides. The reaction mixtures were

stirred for 1 h for complete precipitation of nano particle in the suspension. The resultant suspensions were exposed to high-intensity ultrasound irradiation for 90 min with ultrasonic liquid processors (750 Watt ultrasonic processor, Sonics, Newtown, CT 06470 USA, and 50/60 Hz) immersed directly into the reaction solution under 50 % amplitude at the room temperature. Nano particles in suspensions were centrifuged for 30 min and repeatedly washed with double distilled water (DDW) water to eliminate the silver ion residues. The formation of P-AgNPC was then monitored by using a UV-Vis spectrophotometer and the particles were collected by centrifugation. The quantification of P-AgNPC was carried out by the particle size analyzer (PSA). Based on the yield, 3 % solution of P-AgNPC was subjected to ultra-sonic irradiation for 60 min and then to 120 min for furthermore reducing the particle size. The reduction in size, polydispersity index (PDI) and zeta potential of the P-AgNPC were analyzed by PSA with the diluent water. The PDI measurement of polysaccharide was aimed to determine the uniform particle size distribution of P-AgNP in suspension. The further morphological characterization of P-AgNPC (with 0.3 % solution) was performed using SEM, TEM and AFM analyses. The quantitative measurement of particle size of P-AgNPC was carried out using XRD analysis. FTIR was used to detect the formation of nanoparticle in suspension.

6.2.9 In vitro bioactive potentials polysaccharide solutions

6.2.9.1 Determination of free radical scavenging activity of **polysaccharide** *solutions*

The polysaccharide samples GSP, GSP-2 and P-AgNPC were subjected to free radical scavenging assays and the activity was measured with the stable radicals, such as 1, 1-diphenyl-2-picryl-hydrazil (DPPH) and 2, 2'-azino-bis-3-ethylbenzothiozoline-6-sulfonic acid ($ABTS^{+}$) (Wojdyło, Oszmianski, & Czemerys, 2007).

6.2.9.2 Determination of carbolytic and proteolytic enzyme inhibition activities of polysaccharide

The *in vitro* carbolytic and proteolytic enzyme inhibition potentials of the polysaccharide solutions (0.25-2.00 mg mL^{-1}) were analysed by α-amylase, α-glucosidase and DPP-IV (dipeptidyl peptidase-IV) enzyme attenuation assays (Hamdan & Afifi 2004). The inhibitory concentration, 50 % (IC_{50}) was calculated from the graph plotted with concentrations of sample versus percentage inhibition. The results were expressed as IC_{50} (50% of its activity). The determination of percentage inhibition (%) was carried out using the equation: $(A_C–A_S)/A_C) \times 100$, where A_C and A_S represented the absorbance of control and sample, respectively.

6.2.9.3 Determination cytotoxicity of pure polysaccharide and P-AgNPC on osteoblastic human mesenchymal Stem (MSC) cell lines

The cytotoxicity of polysaccharide (GSP) and P-AgNPC was measured by the 3-[4,5-dimethylthiazol]-2, 5-diphenylterazolium bromide assay (MTT assay) (Liu, Xu, Ma, Cheng, Hua, & Huang G, 2017). In brief, the osteoblastic cell line (MSCS) (200 µL cell suspension) was plated in the 96-well plates at a density of 20 x 10^3 cells per well without the test reagent. The cells were allowed to grow for 24 h. Thereafter, the cells in various wells were treated with each compound at the concentrations of 150, 250, 500, 750 and 1000 µG. After incubation, the plates were taken out from the incubator, and removed spent media. MTT reagent was added to each well of final concentration of 0.5 mg mL^{-1} of total volume and incubated for 24, 48, 72 h at 37 °C in a 5 % CO_2 atmosphere. The plates were wrapped with the aluminium foil to avoid contact to the light, and these were again incubated for 3 h. The MTT reagent was removed and then added 100 µL of dimethylsulfoxide (DMSO) solution to dissolve the formazan salts. Then, the plates were read at 570 and 630 nm by an ELISA reader (Bio-Rad, model 550). The IC_{50} values were determined by using linear-regression-equation.

6.2.9.4 Determination of alkaline phosphatase activity of polysaccharide and P-AgNPC on osteoblastic human mesenchymal stem (MSC) cell line

ALP is found as one of the important bio-markers of osteoblastic cell differentiation. ALP secretion in higher amount represents strong cell-differentiation potential (Liu, et al., 2017). Primary osteoblasts were seeded (500 µL cell suspension) at a density of 250 x 10^3 cells/well in the 96-well plates without the test reagent. The cells were allowed to grow for about 24-48 h. After incubation, the cells in various wells were treated with polysaccharide and P-AgNPC at concentration of 500 µg mL^{-1}. The plates were incubated for 21 days at 37 °C in a 5 % CO_2 atmosphere by maintaining the cells regularly 2 times per week. After the incubation period, taken out the plates from incubator, and removed spent media. The cells were fixed with suitable fixative solution (2 % para-formaldehyde, Thermo) for 5 min and rinsed in deionized water for 45 sec. Alkaline phosphatase dye mixture of 100 µL was added and incubated the cells for 30 min at 37 ºC. the immersed slides were protected from the direct light, and after 30 min, the slides were removed and rinsed thoroughly with deionized water for 2 min. The cells were subjected to counterstain with fast violet B salt in water for 2 min. Resultant blue nuclear stain was evaluated microscopically and measured the absorbance at 405 nm using an ELISA Reader.

6.2.10 In silico analysis of polysaccharide

In silico analysis of polysaccharide motif in the present study was carried out using Autodock 4 (ver-1.5.6) docking software, which analysed the conformation of enzyme and ligand-composite. The 2D and 3D structural conformations of the polysaccharide analogues were drawn by the software, such as Chemsketch 3.5 and OpenBabel 2.4.1 versions. The X-ray crystal structures of α-amylase (PDB 1HNY; 1.8 Å), α-glucosidase (PDB 3A4A; 1.6 Å), DPP-IV (PDB 2ONC; 2.5 Å) and ALP (PDB 1ZED; 1.57 Å) were retrieved from the Protein Data Bank (Brayer, Luo, & Withers, 1995; Yamamoto, Miyake, Kusunoki, & Osaki, 2010; Llinas, Stura, Ménez, Kiss, Stigbrand, Millan, & Le Du, 2005) and conformationally arranged (Swiss-Pdb Viewer, ver-4.1.0). USCF Chimera (University of California, San Francisco, ver-1.11.2) was used for the visualization of the molecular docking analyses. The *in silico* analysis was carried out using Lamarckian algorithm methods and it was run by Cygwin I-II. The preferred docked conformations were examined with RMSD (root-mean-square deviation) data.

6.2.11 Statistical analysis

All experimental results were expressed as the mean of triplicate ± standard deviation and were examined for significant variations by one-way analysis of variance (ANOVA) using the SPSS 13.0. The significant differences were considered as $P < 0.05$.

6.3 Result and discussion

6.3.1 Extraction, purification, yield, and chemical composition of polysaccharide derived from G. salicornia

The crude polysaccharide fraction from red seaweed *G. salicornia* was obtained by hot water extraction method, and the gelling polysaccharide fraction was obtained with yield of 4.39 % of the seaweed dry weight. The resulting aqueous extract was sequentially fractionated with the aid of anion exchange chromatographic column filled with an anion exchange resin (DEAE-cellulose) according to the previously reported method (Maneesh & Chakraborty, 2018) with modifications to obtain the crude polysaccharide fraction (GSP). The latter (8.78 g) was initially dissolved in double distilled water (5 mL) and passed through packed anion exchange resin, before being eluted with water, 0.1, 0.2, 1.3, 0.4 and 0.5 M NaCl solutions to yield the subfractions GSP-1 (1.19 g), GSP-2 (1.03 g), GSP-3 (0.51 g), GSP-4 (0.22 g) and GSP-5 (0.22 g). The presence of carbohydrate in each fraction was monitored by the phenol-sulfuric acid method at 490 nm with the aid of a spectrophotometer and the elution curve of polysaccharide fractions was plotted and shown in Figure 6.4. The polysaccharide fractions obtained after fractionation were subjected to chemical composition analysis and the carbohydrate, uronic acid, protein,

sulfate content, and monosaccharide compositions were summarized in Table 6.1. The GSP exhibited the percentage yield of total carbohydrate as 63.89 %. Similarly, it has displayed the percentage yield uronic acid content as 9.81 %, protein content as 4.10 %, and sulfate content as 14.88 %. The percentage yield of total carbohydrate content in different polysaccharide fractions GSP-1 (18.26 %), GSP-2 (54.62 %), GSP-3 (16.98 %), GSP-4 (16.21 %) and GSP-5(15.23 %) were compared with the standard. The fraction GSP-2 (54.62 %, ≥ 50 %) exhibited higher percentage yield of total carbohydrate, and which was comparable with the crude polysaccharide (63.89 %). This data revealed that the GSP-2 was rich in polysaccharide content than that of other fractions (≤ 50%). The percentage of uronic acid content in different polysaccharide fractions were compared with each other, and which followed the decreasing order of GSP-1 (3.98 %) > GSP-3 (2.28 %) > GSP-4 (2.20 %) > GSP-2 (2.01%) > GSP-5 (1.63 %). The fraction GSP-1 (3.98 %) displayed higher percentage of uronic acid than that of other fractions (≤ 2.3 %). The percentage yield of protein in different polysaccharide fractions were also compared with each other, and which followed the order of GSP-1 (2.01 %) > GSP-3 (1.02 %) > GSP-2 (0.89 %) > GSP-4 (0.86 %) > GSP-5 (0.12 %). The sulfate content of different polysaccharide fractions were found out, and which followed the order of GSP-2 (13.52 %) > GSP-1 (11.28 %) > GSP-3 (9.13 %) > GSP-4 (7.58%) > GSP-5 (2.12 %). The amount of sulfate was found to be more in GSP-2 (13.52 %), and which was comparable with the crude polysaccharide (14.88 %). From the chemical composition analysis, the fraction GSP-2 was found to be rich in polysaccharide and sulfate content, which was comparable with the crude polysaccharide, GSP. The sulfate content of GSP from *G. salicornia* was higher than that reported for other *Gracilaria sp*.; 6.4% for *Gracilaria birdiae*, 11.7% for *Gracilaria corticata*, and 4.8% for *Gracilaria cornea* (Mazumder, Ghosal, Pujol, Carlucci, Damonte, & Ray, 2002; Maciel, Chaves, Souza, Teixeira, Freitas, Feitosa, 2008). The previous reports recorded that the biological activity of polysaccharides were influenced by the charge density arose from sulfate groups and glycosidic linkage {either (1→3) or (1→4)} of the neighboring sulfate groups (Chaidedgumjorn et al., 2002; Pereira, Melo, & Mourão, 2002). The crude polysaccharide fraction of GSP was found to contain different monosaccharides, such as galactose (67.2 %), xylose (3.2 %), glucose (2.6 %) and mannose (1.1 %) in different concentrations. This data indicated that the studied polysaccharide was found to be rich in galactose, and which might be associated with (1→3) and (1→4) galactose and galactose analogs.

The fractionated polysaccharides GSP-1, GSP-2, GSP-3, GSP-4 and GSP-5 were found to possess galactose in 9.2, 61.4, 3.3, 2.1, and 1.3 % respectively. On comparison, GSP-2 was was found to possess higher percentage of galactose units than other eluted fractions (< 60%) (Figure 6.5). The presence of other monosaccharides was also found in the polysaccharide fractions in trace quantities (xylose contents were 1.5, 1.2, 0.9, and 0.21 % in GSP-1, GSP-3, GSP-4, and GSP-5, respectively). The

fractions, GSP-1 and GSP-2 were also found to contain monosaccharides glucose and mannose in 0.8-0.6 % and 0.08-0.06 %, respectively. The chemical composition results showed that the major part of polysaccharide was eluted by the 0.5 M NaOH than that of other concentrations of NaOH. Therefore, the pure polysaccharide fraction of GSP-2 was selected for further analysis of bioactive potentials, and was subjected to chemical degradation process, such as methylation, reduction and acetylation for their structural interpretation by NMR spectroscopy, as well as gas chromatography-mass spectrometry (GC-MS). The bioactive polysaccharide was further made into nano composite by the implantation of $AgNO_3$ in different concentration, and which were further subjected for structural and morphological analysis. The pharmacological activities of the polysaccharide (GSP-2) and P-AgNPC composite were analyzed with ALP, proteolytic, and carbolytic enzyme models and *in vitro* antioxidant assays.

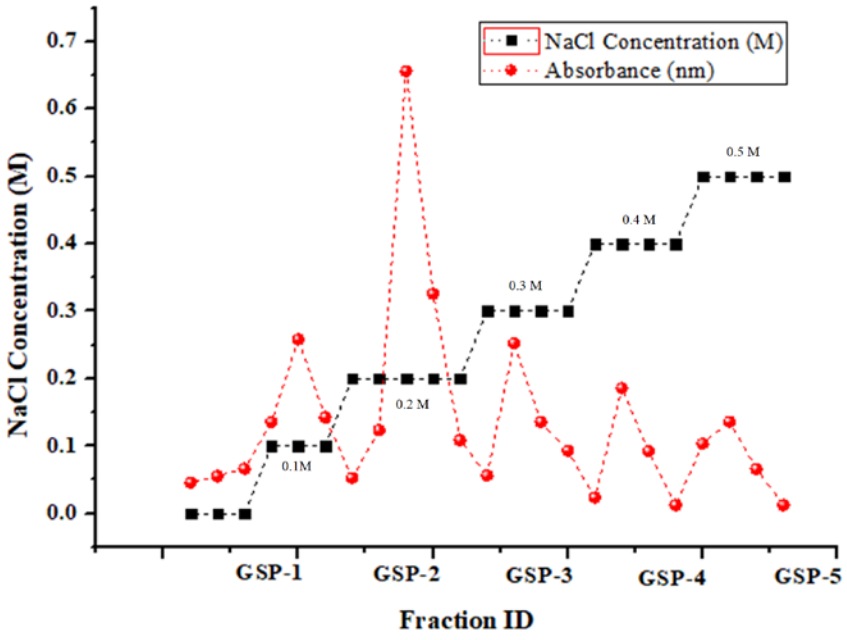

Figure 6.4.: Elution profile of polysaccharide solutions isolated from *G. salicornia* through DEAE Cellulose

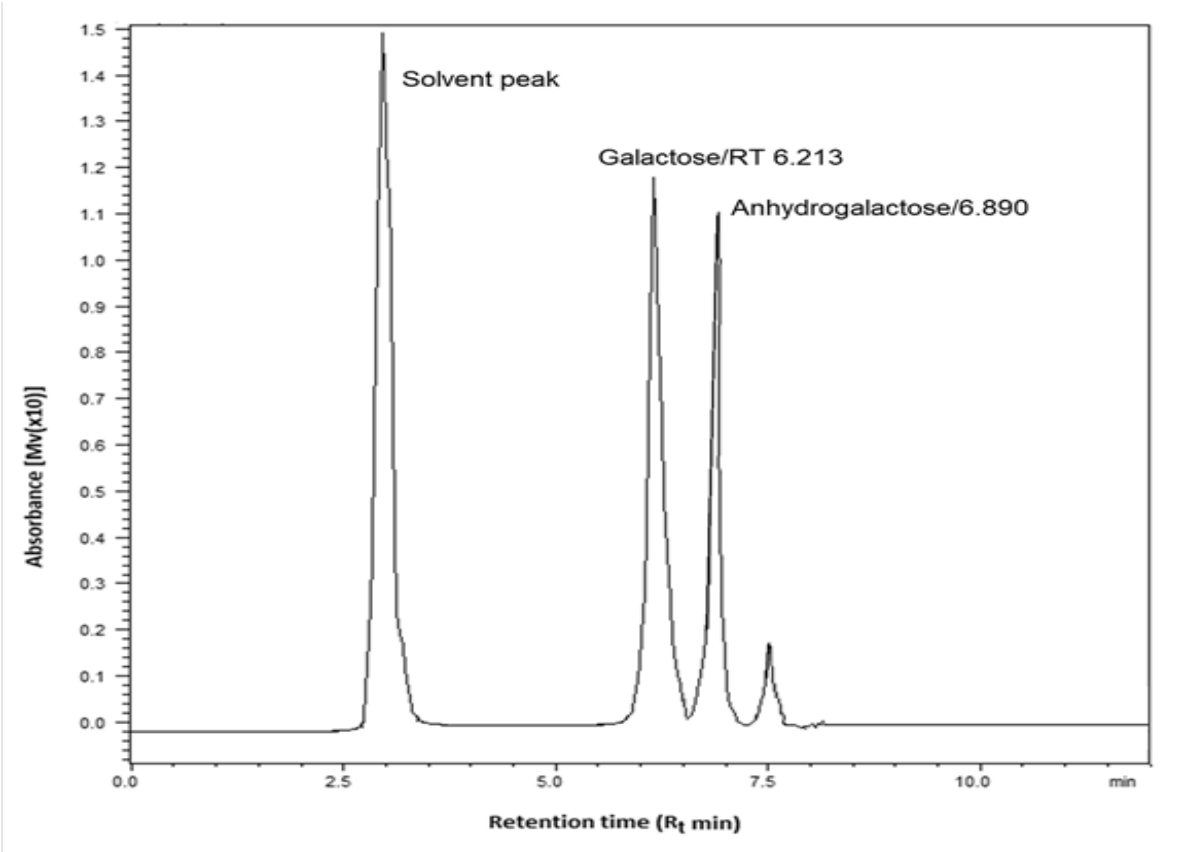

Figure 6.5.: Monosaccharide composition analysis of polysaccharide analogue

Table 6.1: Yield, protein content, sulfate content, and monosaccharide composition of crude polysaccharide fractions from *G. salicornia*.

	Crude polysaccharide	**Subfractions of polysaccharide**				
Compositions[#] (%)	GSP	GSP-1 (0.1 M NaCl)	GSP-2 (0.2 M NaCl)	GSP-3 (0.3 M NaCl)	GSP-4 (0.4 M NaCl)	GSP-5 (0.5 M NaCl)
Yield	4.39^{a}	14.31^{b}	24.31^{c}	20.28^{d}	18.10^{e}	11.65^{f}
Total carbohydrate	$63.89^{a} \pm 0.30$	$18.26^{b} \pm 0.31$	$54.62^{c} \pm 0.23$	$16.98^{d} \pm 0.02$	$16.21^{d} \pm 0.02$	$15.23^{e} \pm 0.05$
Uronic acid	$9.81^{a} \pm 0.11$	$3.98^{b} \pm 0.13$	$2.01^{c} \pm 0.07$	$2.28^{d} \pm 0.01$	$2.20^{d} \pm 0.07$	$1.63^{e} \pm 0.11$
Protein	$4.10^{a} \pm 0.03$	$3.21^{b} \pm 0.04$	$0.89^{c} \pm 0.01$	$1.02^{d} \pm 0.01$	$0.86^{d} \pm 0.03$	$0.12^{e} \pm 0.01$
Sulfate	$14.88^{a} \pm 0.06$	$11.28^{b} \pm 0.07$	$13.52^{c} \pm 0.41$	$9.13^{d} \pm 0.05$	$7.58^{e} \pm 0.12$	$2.12^{f} \pm 0.01$
Monosaccharide composition*						
Galactose	67.20	19.20	61.40	3.30	2.10	1.30
Xylose	3.20	1.50	0.03	1.20	0.90	0.21
Glucose	2.60	0.80	0.08	-	-	-
Mannose	1.10	0.60	0.02	-	-	-

[#]The composition of polysaccharide was expressed in %.

*Monosaccharide composition was expressed in %

6.3.1 Extraction, purification, yield, and chemical composition of polysaccharide derived from P. tetrastromatica

The crude polysaccharide from the brown seaweed *P. tetrastromatica* was extracted using hot water by the method reported earlier (Maneesh and Chakraborty, 2018). The yield obtained for crude the polysaccharide derived from *P. tetrastromatica* was 5.4 %. The purification of the crude polysaccharide of *P. tetrastromatica* was carried out using anion exchange chromatography by the aid of DEAE cellulose. Separation of the polysaccharides from other impurities of the crude polysaccharide involves careful selection of chromatographic parameters by using their physico-chemical properties and distribution of surface charges that in turn affects their degree of interaction on DEAE-cellulose resin. The fractions were eluted with increasing gradient of NaCl solution (0.1, 0.5, 0.75, and 1 M), and were labeled as PF-1, PF-2, PF-3 and PF-4, respectively. In the present study, the percentage yields obtained for four different fractions PF-1, PF-2, PF-3 and PF-4 were 13.05, 20.35, 19.81 and 17.12 %, respectively. Chemical composition analysis exhibited by crude polysaccharide (PF) showed a total carbohydrate content of 69.01 % by the phenol-sulfuric acid method and sulfate content of 13.01 % (Table 6.2). Among other studied fractions derived from the crude polysaccharide, the fraction PF-2 displayed significantly greater percentage yield of 56.32 % (Figure 6.6) and sulfate content of 12.31 % than those exhibited by other fractions. The fraction PF-2 also exhibited lesser protein content of 0.99 % and uronic acid content of 2.98 % than those exhibited by other fractions {~ 10.9 % (PF-1-3-4) and 5.6 % (PF-1-3-4), respectively}. The fraction PF-2 derived from the crude polysaccharide fractions of *P. tetrastromatica* displayed significantly greater DPPH and $ABTS^{+}$ radical scavenging activities (IC_{50} 0.59 mg mL^{-1} and 0.62 mg mL^{-1}, respectively, $p<0.05$). Additionally, the fraction PF-2 displayed significantly greater antidiabetic (IC_{50} α-amylase 0.98 mg mL^{-1} and α-glucosidase 0.87 mg mL^{-1}) properties. The monosaccharide composition analysis of the crude polysaccharide showed the presence of fucose (69.8 %) as the major constituent followed by fucose and galactose (~13 %), and a lesser percentage of glucose, mannose and xylose residues (0.21, 0.61 and 0.01 %, respectively) (Table 6.2). The column fraction designated as PF-2 recorded greater percentage of monosaccharide of fucose (61.4 %) and galactose (10.01 %) units as constituent sugar residues than other fractions (Figure 6.7).

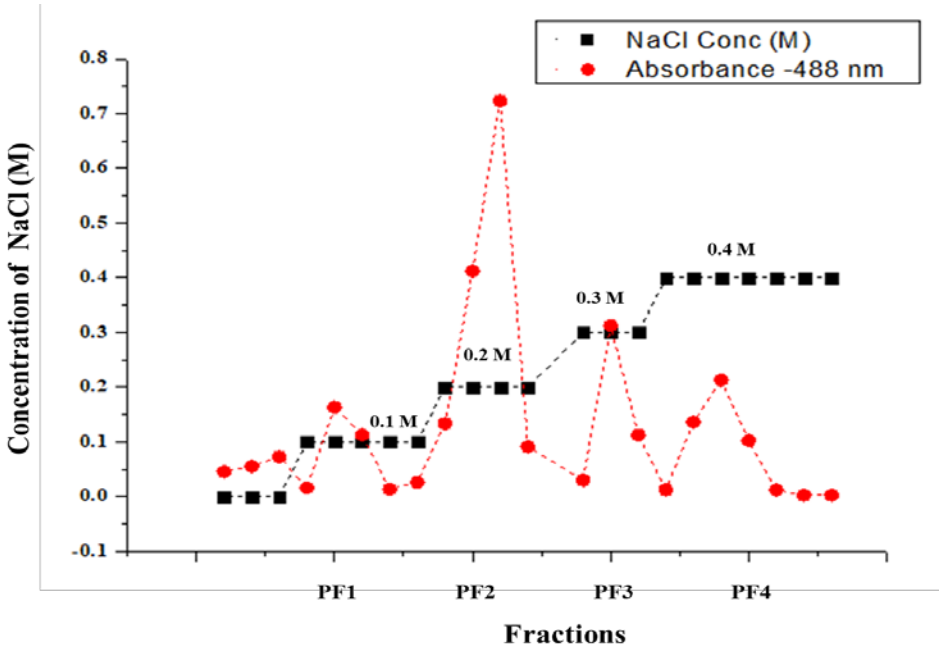

Figure 6.6.: Elution profile of polysaccharide fractions derived from the brown seaweed *P. tetrastromatica*

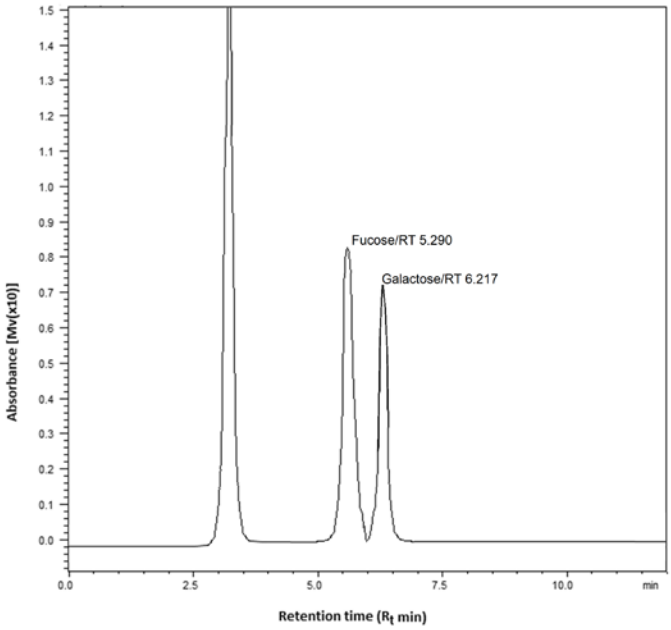

Figure 6.7.: Monosaccharide composition of polysaccharide derived from the brown seaweed *P. tetrastromatica*

Table 6.2.: Yield and chemical composition of crude polysaccharide (PF) and eluted fractions of polysaccharides from the brown seaweed *P. tetrastromatica*

Fractions	**Yield (%)**	**Total carbohydrate (%)**	**Uronic acid (%)**	**Protein (%)**	**Sulfate (%)**
*PF	4.01	69.01 ± 0.22	7.28 ± 0.07	3.83 ± 0.03	13.01 ±0.07
PF-1 (0.1 M NaCl)	13.05	17.02 ± 0.19	5.62 ± 0.11	2.99 ± 0.09	10.95 ± 0.05
PF-2 (0.2 M NaCl)	16.35	56.32 ± 0.20	2.98 ± 0.09	0.99 ± 0.07	12.31 ± 0.42
PF-3 (0.3 M NaCl)	19.81	15.96 ± 0.07	2.30 ± 0.02	0.79 ± 0.03	9.10 ± 0.01
PF-4 (0.4M NaCl)	17.12	15.62 ± 0.05	2.15 ± 0.06	0.73 ± 0.02	7.82 ± 0.10
Monosaccharide composition (%)					
Fucose	69.8	39.2	61.4	3.2	2.1
Galactose	13.01	9.02	10.01	0.98	0.98
Glucose	0.21	0.11	0.20	-	-
Mannose	0.61	0.32	0.21	-	-
Xylose	0.01	0.02	0.05	0.01	0.09

The yield and chemical composition of the fractions were expressed as % w/w. The chemical composition analyses were carried out in triplicate (n=3) and are expressed as mean ± standard deviation.

* Crude polysaccharide fraction. #PF-1, PF-2, PF-3, PF-4 were indicated subfractions

6.3.2. Bioactive potentials and yield of column sub-fractions from G. salicornia and P. tetrastromatica

The results on antioxidant and antidiabetic potentials of crude sulfated polysaccharides and polysaccharide fractions from the seaweeds *G. salicornia* and *P. tetrastromatica* were represented in Table 6.3. The IC_{50} values of GSP against the free radicals DPPH and $ABTS^+$ were recorded as 1.28 and 1.32 mg mL^{-1}, respectively. The IC_{50} values of polysaccharide fractions GSP-1, GSP-2, GSP-3, GSP-4 and GSP-5 were assessed against the free radical DPPH, and which were documented IC_{50} values of 1.08, 0.35, 1.21, 0.36 and 0.41 mg mL^{-1}, respectively. They exhibited antioxidant activities against the radical cation $ABTS^+$, and which were expressed as IC_{50} values of 1.11, 0.48, 1.39, 0.56 and 0.57 mg mL^{-1}, respectively. Among the different polysaccharide fractions, the fraction GSP-2 displayed higher antioxidant activity than that exhibited by other fractions (>0.37 mg mL^{-1}). The result indicated that the DPPH and $ABTS^+$ radical scavenging activities of GSP-2 were higher than that of standard antioxidant agent ascorbic acid (DPPH 0.37 and $ABTS^+$ 0.51 mg mL^{-1}) and other fractions (> 0.29 mg mL^{-1}).

Similarly, α-amylase and α-glucosidase inhibition activities of GSP were evaluated, and which were recorded as IC_{50} values of 1.17 and 1.19 mg mL^{-1}, respectively. The antidiabetic activity of GSP was further evaluated with DPP-IV inhibition capacity and was recorded as IC_{50} value of 1.17 mg mL^{-1}. These data on comparison with commercial standard designated that the α-amylase (IC_{50} 1.38 mg mL^{-1}), α-glucosidase (IC_{50} 1.47 mg mL^{-1}) and DPP-IV inhibition activities of polysaccharide GSP was lesser than the standard drug acarbose (IC_{50} 0.13 mg mL^{-1}). Furthermore, α-amylase and α-glucosidase inhibition activities of polysaccharide fractions followed the decreasing order of activities, GSP-2 (IC_{50} 0.98 and 0.87 mg mL^{-1}) > GSP-1 (IC_{50} 1.06 and 1.05 mg mL^{-1}) >GSP-3 (IC_{50} 1.61 and 1.69 mg mL^{-1}) >GSP-4 (IC_{50} 1.65 and 1.67 mg mL^{-1}) >GSP-5 (IC_{50} 1.82 and 1.86 mg mL^{-1}) >. The fraction GSP-2 represented prospective inhibition against the starch digestive enzymes α-amylase (IC_{50} 0.98 mg mL^{-1}) and α-glucosidase (IC_{50} 0.87 mg mL^{-1}). The antidiabetic activity of polysaccharide fractions were further evaluated with DPP-IV inhibition capacity, and which followed the order of GSP-2 (IC_{50} 0.32 mg mL^{-1}) >GSP-3(IC_{50} 0.98 mg mL^{-1}) >GSP-4 (IC_{50} 1.01 mg mL^{-1})> GSP-5 (IC_{50} 1.25 mg mL^{-1})>GSP-1(IC_{50} 1.98 mg mL^{-1}). These data on comparison with the commercial standard designated that the DPP-IV inhibition activities of GSP-2 (IC_{50} 0.63 mg mL^{-1}) was higher than the standard drug acarbose (IC_{50} 0.13 mg mL^{-1}).

The IC_{50} values of PF against the free radicals DPPH and $ABTS^+$ were recorded as 2.12 and 2.19 mg mL^{-1}, respectively. The IC_{50} values of polysaccharide fractions PF-1, PF-2, PF-3, and PF-4 were assessed against the free radical DPPH, and which were documented as 1.26, 0.89, 1.83, and 1.88 mg mL^{-1}, respectively. They exhibited potential antioxidant activity against the radical cation $ABTS^+$ and which were expressed as IC_{50} values of 1.24, 0.91, 1.92, and 1.82 mg mL^{-1}, respectively. Among the different

polysaccharide fractions, the fraction PF-2 displayed higher antioxidant activity than that of other fractions (IC_{50} <1 mg mL^{-1}). The results indicated that the DPPH and $ABTS^{+}$ radical scavenging activities of PF-2 were higher than that of standard drug ascorbic acid (IC_{50} DPPH 0.37 and $ABTS^{+}$ 0.51 mg mL^{-1}) and other fractions (IC_{50} > 1 mg mL^{-1}).

Similarly, α-amylase and α-glucosidase inhibition activities of PF were evaluated and which were IC_{50} of 2.33 and 2.49 mg mL^{-1}, respectively. The antidiabetic activity of PF was further evaluated with DPP-IV inhibition capacity (IC_{50} 2.26 mg mL^{-1}). These data on comparison with commercial standard designated that the α-amylase (IC_{50} 1.38 mg mL^{-1}), and α-glucosidase (IC_{50} 1.47 mg mL^{-1}) inhibition activities of polysaccharide PF was lower than the standard drug acarbose (IC_{50} 0.13 mg mL^{-1}). Furthermore, the α-amylase and α-glucosidase inhibition activities of polysaccharide fractions followed the decreasing order of activities, PF-2 (IC_{50} 1.58 and 1.54 mg mL^{-1}) > PF-4 (IC_{50} 1.75 and 1.37mg mL^{-1}) >PF-3 (IC_{50} 1.85 and 1.89 mg mL^{-1}) > >PF-1 (IC_{50} 1.98 and 1.88 mg mL^{-1}). The fraction PF-2 represented higher inhibition against starch digestive enzymes α-amylase (IC_{50} 1.58 mg mL^{-1}) and α-glucosidase (IC_{50} 1.54 mg mL^{-1}). The antidiabetic activity of polysaccharide fractions were further evaluated with DPP-IV inhibition capacity, and which followed the order, PF-2 (IC_{50} 0.98 mg mL^{-1}) > PF-4 (IC_{50} 1.01 mg mL^{-1})> PF-1 (IC_{50} 1.93 mg mL^{-1})> PF-3 (IC_{50} 1.98 mg mL^{-1}). Among the different polysaccharide fractions considered from the red seaweed G. *salicornia* and brown seaweed *P. tetrastromatica,* the fraction GSP-2 was found to exhibit higher antioxidant and anti-diabetic potentials than that of other fractions. Therefore, on the basis of yield and bioactivities, the fraction GSP-2 was selected for further structural characterization and bioactivity analysis.

Table 6.3.: Yield and bioactive potentials (anti-oxidant and antidiabetic activities) of crude polysaccharides and sub-fractions derived from *G. salicornia* and *P. tetrastromatica*

Antioxidant activities (in mg mL^{-1})			**Antidiabetic activities (in mg mL^{-1})**			**Yield**
Sl. No.	DPPH radical scavenging	ABTS^{+} radical scavenging	α-amylase inhibition	α-glucosidase inhibition	DPP-IV inhibition	(in %)
GSP	1.28±0.03^{a}	1.32±0.07^{a}	1.17±0.03^{a}	1.19±0.04^{a}	1.17±0.03^{a}	4.39
GSP-1	1.08±0.01^{b}	1.11±0.02^{b}	1.06±0.04^{b}	1.05±0.02^{b}	1.02±0.03^{b}	14.31
GSP-2	**0.35±0.02^{c}**	**0.48±0.02^{c}**	**0.98±0.03^{c}**	**0.87±0.03^{c}**	**0.32±0.04^{c}**	**24.31**
GSP-3	1.21±0.01^{d}	1.39±0.03^{d}	1.61±0.03^{d}	1.69±0.04^{d}	0.98±0.03^{d}	20.28
GSP-4	0.36±0.02^{e}	0.56±0.04^{e}	1.65±0.04^{e}	1.67±0.03^{e}	1.01±0.02^{e}	18.10
GSP-5	0.41±0.03^{f}	0.57±0.05^{f}	1.82±0.04^{f}	1.86±0.02^{f}	1.25±0.02^{f}	11.65
PF	2.12^{a} ±0.03	2.19^{a} ±0.07	2.33^{a} ±0.03	2.49^{a} ±0.04	2.26^{a} ±0.03	4.01
PF-1	1.26^{b} ±0.01	1.24^{b} ±0.02	1.98^{b} ±0.04	1.88^{b} ±0.02	1.93^{b} ±0.03	13.05
PF-2	**0.89^{c} ±0.02**	**0.91^{c} ±0.02**	**1.58^{c} ±0.03**	**1.54^{c} ±0.03**	**0.98^{c} ±0.04**	**16.35**
PF-3	1.83^{d} ±0.01	1.92^{d} ±0.03	1.85^{d} ±0.03	1.89^{d} ±0.04	1.98^{d} ±0.03	19.8
PF-4	1.88^{e} ±0.02	1.82^{e} ±0.04	1.75^{e} ±0.04	1.37^{e} ±0.03	1.01^{e} ±0.02	17.12
Standards	0.37±0.05^{hp}	0.51±0.04^{hp}	1.38 ± 0.06^{hR}	1.47 ± 0.05^{hR}	0.13 ± 0.07^{hR}	-

[#]The bioactivities were expressed as IC_{50} values (mg/mL) and [¥]The yield and chemical composition of the fractions are expressed as % w/w. The samples were analyzed in triplicate (n=3) and expressed as mean±standard deviation. Means followed by different superscripts (a-h) within the same row indicated significant differences (p<0.05).

P and R indicate the standards used for different activities: P-ascorbic acid and R- acarbose.

6.3.3 Structural interpretation of hydrolyzed polysaccharide

6.3.3.1 Structural interpretation of hydrolyzed polysaccharide by Fourier transforms infrared spectrum analysis (FTIR)

The preliminary spectral characterization of polysaccharide, GSP-2 was carried out by FTIR spectrum analysis. The characteristic peak at 1242 cm^{-1} indicated the presence of sulfate ester functionality in GSP-2. The spectrum possessed two intense absorption bands at 934 cm^{-1} and at 848 cm^{-1} corresponding to the anhydro galactopyranosyl and axial sulfate ester at *O*-6 of D-galactopyranosyl, respectively. These results were corroborated by the absorptions bands observed for commercial carrageenan at 1220 cm^{-1}(ester sulfate) and 928 cm^{-1} (3,6-anhydrogalactose) (Volery, Besson, & Schaffer-Lequart, 2004). Similarly, the absorption at 844 cm^{-1} was corroborated by the presence of galactans in GSP-2. The existence of stretching vibration of hydroxyl group (OH) was confirmed with the absorption band located at 3437 cm^{-1}. Absorption band at 2923 cm^{-1} was observed due to the stretching vibration of C-H bonds. Moreover, the absorption peak at 1639 cm^{-1} was due to asymmetric stretching vibration of O-C-O functionality (Figure 6.7).

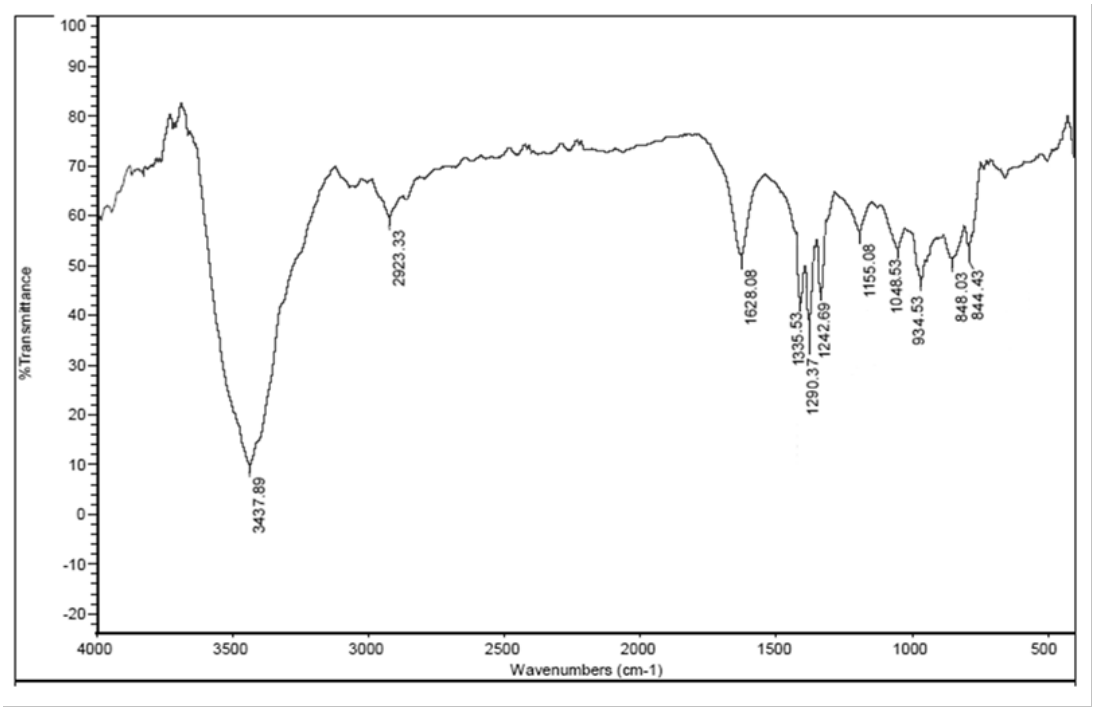

Figure 6.8.: FTIR of polysaccharide derived from the brown seaweed *P. tetrastromatica*

The FT-IR peaks at 1290 cm^{-1} and 1048 cm^{-1} were due to the stretching vibration of C-O of the attached sulfate esters and hydroxyl functionalities, respectively. In addition, the absorption bands at 1335 cm^{-1} represented the wagging mode of the CH_2 group. The peak at 1155 cm^{-1} could indicate the coupling of the C-O and C-C stretches. The characteristic absorption bands at 1258, 1075, 930 and 891 cm^{-1} of polysaccharide isolated from *G. caudata* were corroborated by the functional group observed in the polysaccharide GSP-2 (Barros, da Silva, Sombra, Maciel, Feitosa, Freitas, & de Paula, 2013; Knutsen et al., 1994; Usov et al., 2011). All these attributions together contributed the presence of the sulfate bearing galactose and anhydrogalactose in the studied polysaccharide, GSP-2.

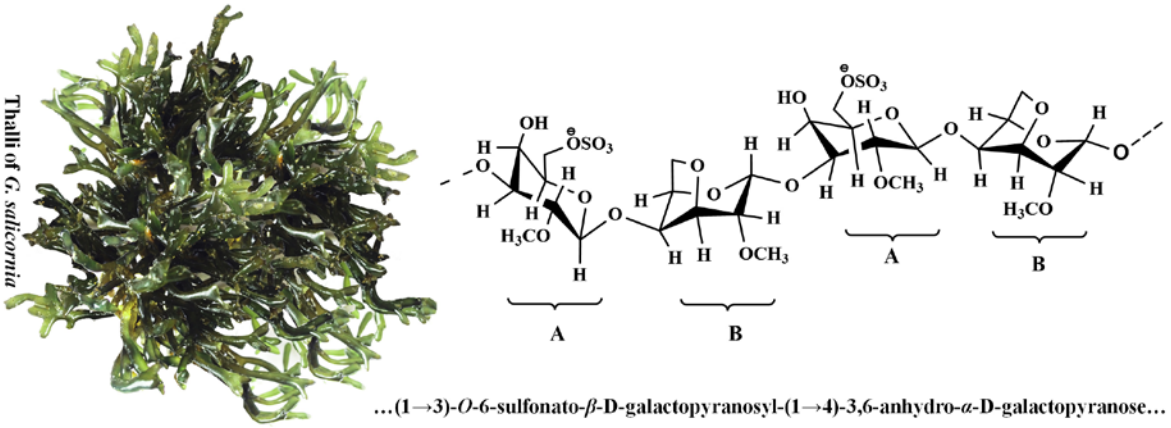

Figure 6.9.: Structural representations of polysaccharide, (1⋯→3)-*O*-6-sulfonato-β-Dgalactopyranosyl-(1→⋯4)-3,6-anhydro-α-D-galactopyranose-(1⋯→) derived from the aqueous extract of *G. salicornia*.

6.3.3.2 Structural interpretation of hydrolyzed polysaccharide by NMR spectroscopic analysis

NMR spectroscopy (1D and 2D) was found to be a significant tool for the structural interpretation of seaweed polysaccharides, which could provide various structural attributions, such as the monosaccharide composition, linkage pattern, configurations of anomeric protons/carbons, branching and positions of different functionalities (Figure 6.10-6.117, Table 6.4). The ^{1}H-NMR of oligosaccharide obtained after the hydrolysis of GSP-2 exhibited highly deshielded protons at δ4.90 and 5.32 along with other protons in the range of δ3.40-4.74. These protons were further supported by ^{13}C NMR and DEPT^{135} along with HSQC spectrum. Based on these, assigned the carbons associated with protons in the oligosaccharide, such as δ4.90 (δ106.33; CH), δ5.32 (δ115.17; CH), δ4.74 (δ86.34; CH), δ4.66 (δ69.66; CH_2), δ4.56 (δ63.38; CH_2), δ3.90 (δ74.15; CH), δ3.82 (δ69.34; CH), δ3.80 (δ63.38; CH_2), δ3.76 (δ69.66; CH_2), δ3.75 (δ780.68; CH), δ3.69 (δ89.68; CH), δ3.65 (δ92.10; CH), δ3.61 (δ85.45; CH), δ3.42 (δ60.76; CH) and δ3.40 (δ60.61; CH).

Table 6.4.: NMR spectroscopic data[a] of polysaccharide …(1→3)-*O*-6-sulfonato-*β*-D-galactopyranosyl-(1→4)-3,6-anhydro-*α*-D-galactopyranose…from red seaweed *G. salicornia*

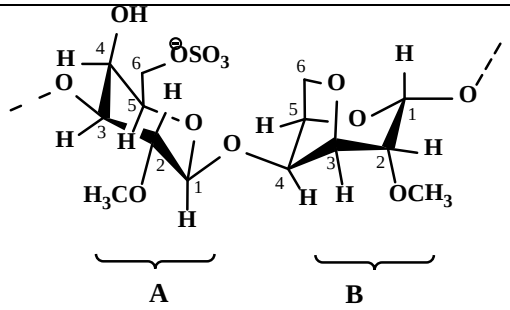

Type of C	C. No.	^{13}C NMR	^{1}H NMR	COSY	HMBC
CH	A1	106.33	4.90	H-A2	C-A2, A3,A5
CH	A2	80.68	3.75	-	C-A3, A7
CH	A3	89.68	3.69	-	C-A4
CH	A4	69.34	3.82	-	C-A5,A6
CH	A5	74.15	3.76	H-A6	C-A6
CH_2	A6	69.66	3.76, 4.66	-	
CH_3	A7	60.76	3.42	-	
Unit B					
CH	B1	115.17	5.32	H-B2	C-B2
CH	B2	85.51	3.73	H-B3	C-B3,B4,B7
CH	B3	86.34	4.74	H-B4	C-B5, B6
CH	B4	85.45	3.61	-	C-B5, A1
CH	B5	92.10	3.65	H-B6	C-B1,B6
CH_2	B6	63.38	3.80, 4.56	-	
CH_3	B7	60.61	3.40	-	

[a]NMR spectra were recorded using a Bruker AVANCE III 500 MHz (AV 500) spectrometer (Bruker, Karlsruhe, Germany) in MeOH as aprotic solvent at ambient temperature with TMS as the internal standard (δ 0 ppm).

[b]Values in ppm, multiplicity and coupling constants (*J*= Hz) were indicated in parentheses. Multiplicities were allocated by ^{135}DEPT NMR spectrum. The assignments were made with the aid of the COSY, HSQC, HMBC and NOESY experiments.

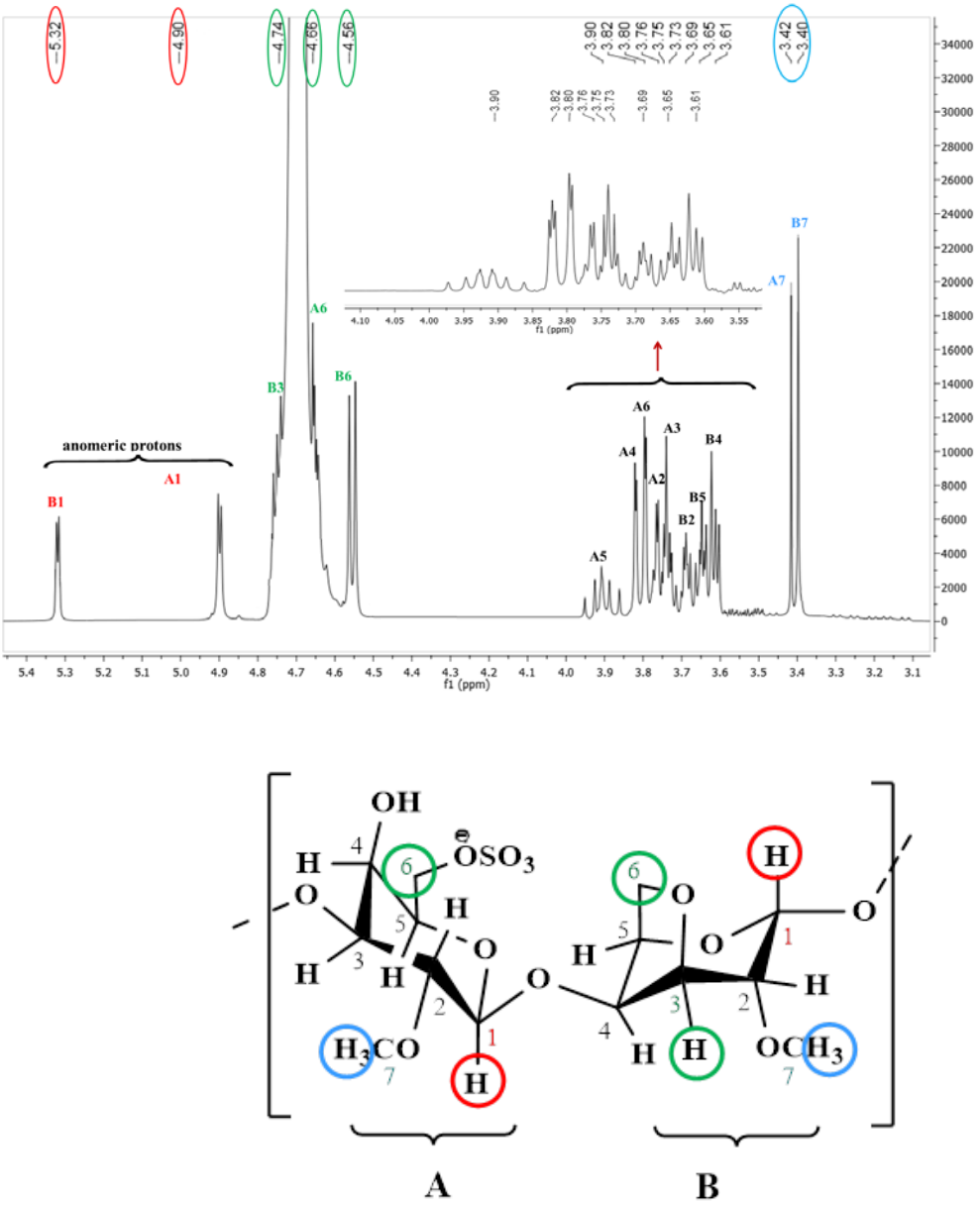

Figure 6.10.: ^{1}H NMR spectrum of the hydrolyzed polysaccharide analogue

The CH protons, δ4.90 (δ106.33; CH) and δ5.32 (δ115.17; CH) appeared as two intense signals, whereas these protons and carbons were found to be related to the anomeric region, which indicated that the polysaccharide on purification yielded two residues of sugar units. These major signals were assigned for C_1 positions of oligosaccharides formed after sequential purification. The two sugar units were named as (**A**) and (**B**) based on their increasing values of chemical shifts in the anomeric region. The literature values also indicated the chemical shift values in the range of δ4.60-5.00 corresponding to the β-linked galactose (Gal*p*) units; and the region between δ5.00-5.60

was related to the α-linked anhydrogalactose (AnGal*p*) units (Stortz, Bacon, Cherniak, & Cerezo, 1994).

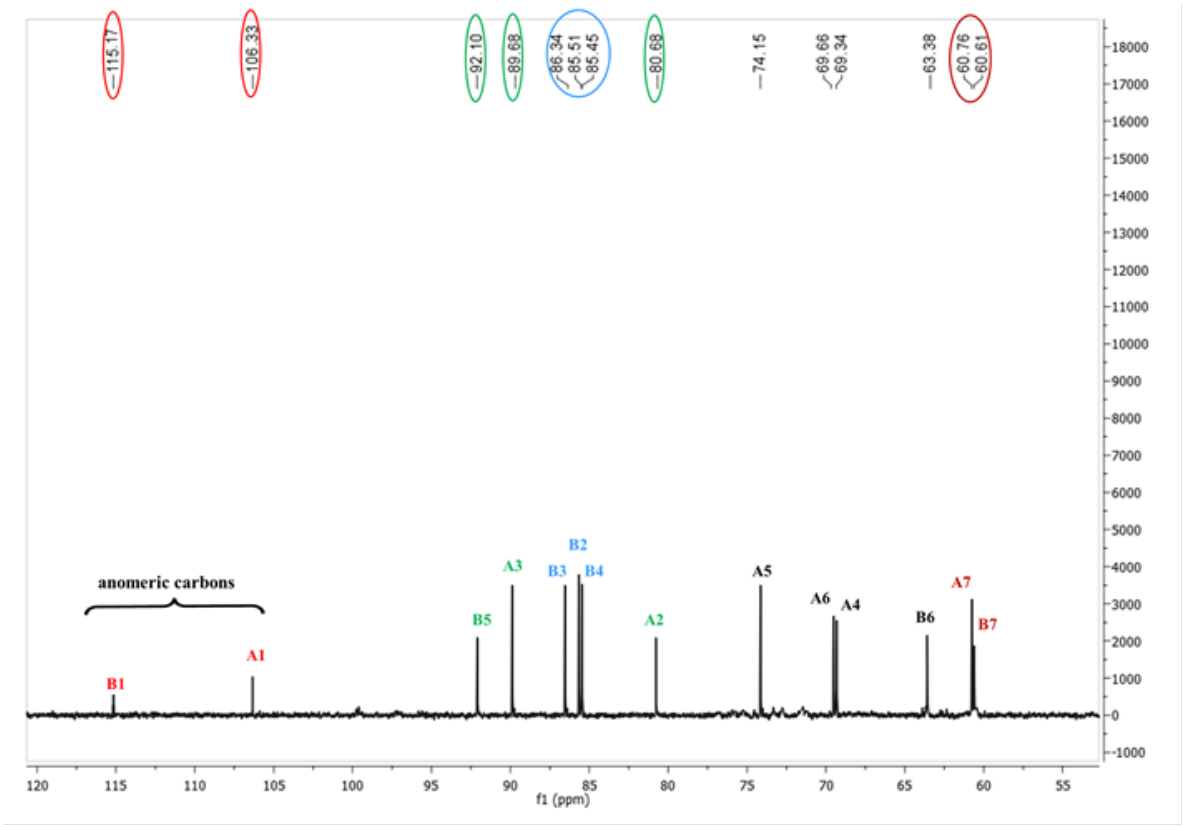

Figure 6.11.: ^{13}C NMR spectrum of the hydrolyzed polysaccharide analogue

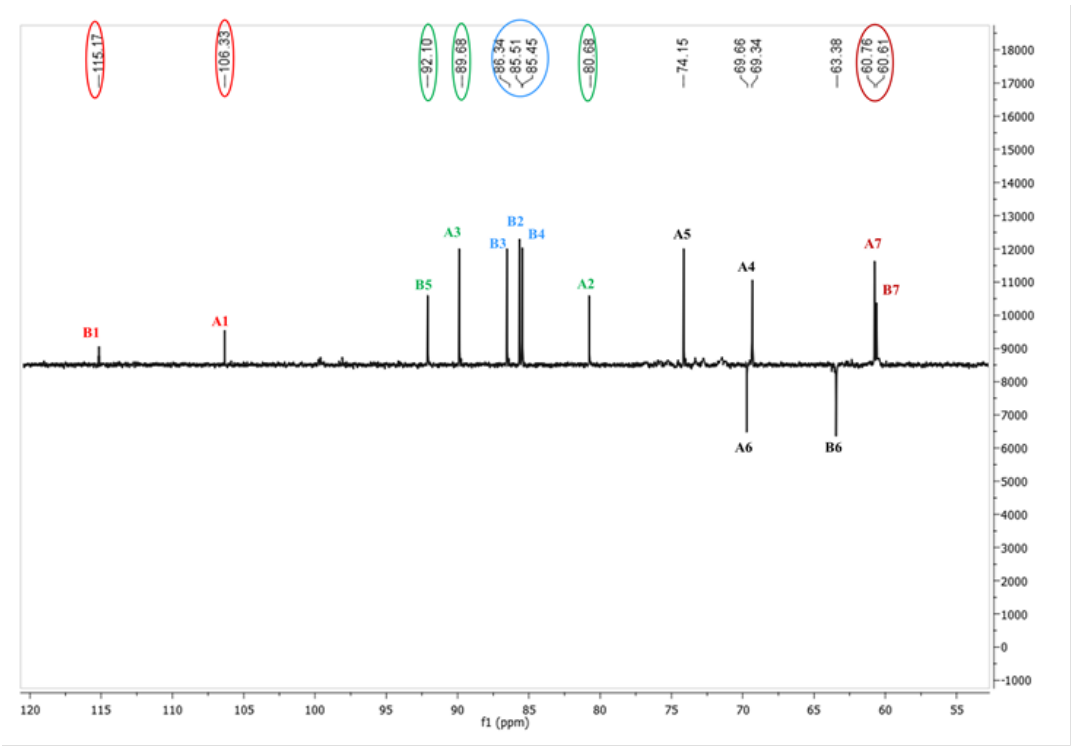

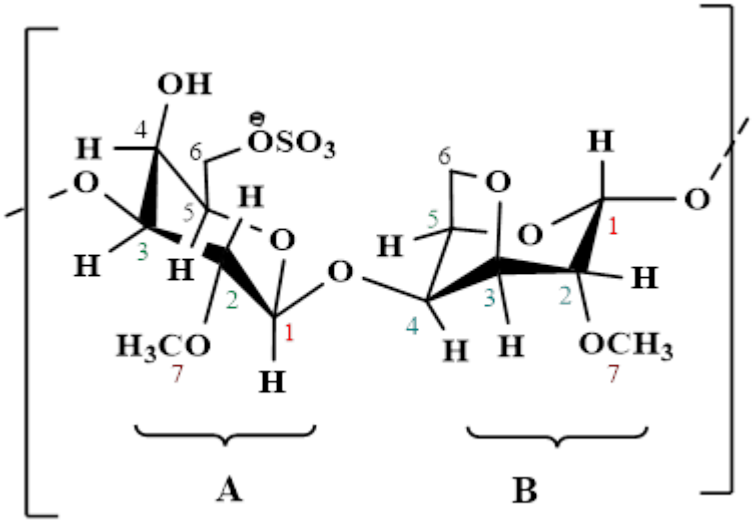

Figure 6.12.: DEPT^{135} spectrum of the hydrolyzed polysaccharide analogue

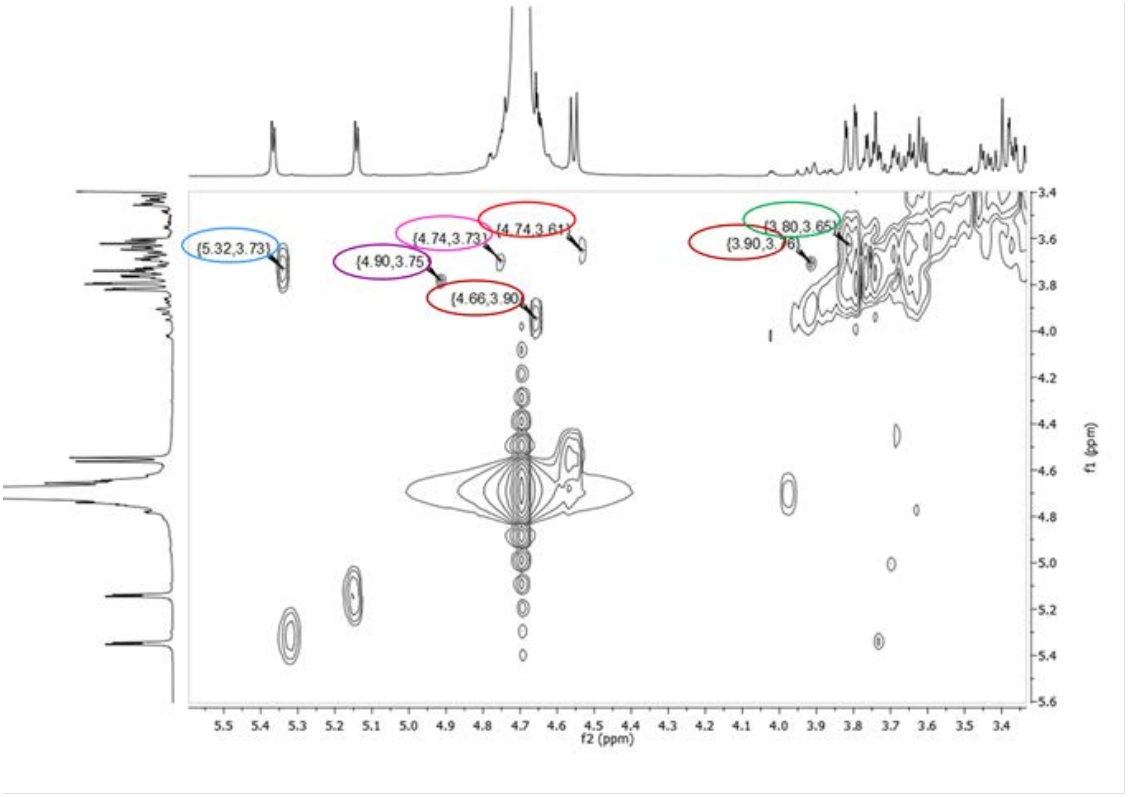

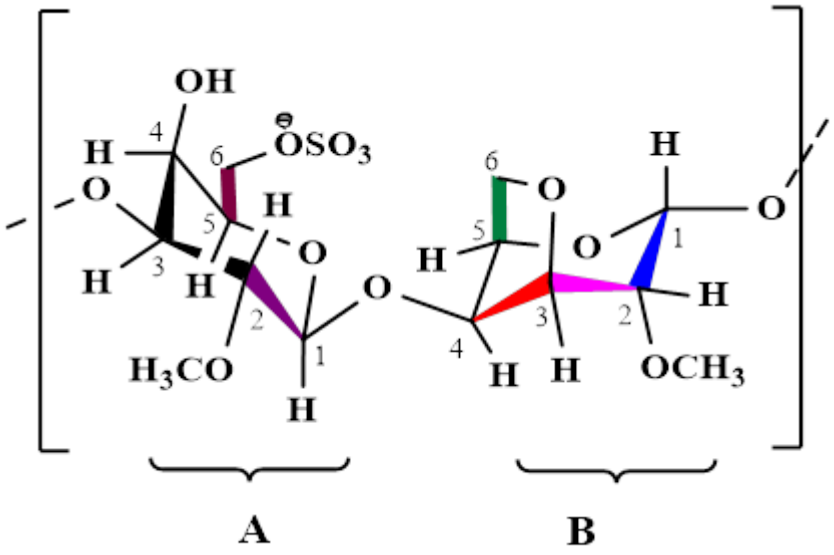

Figure 6.13.: ^{1}H-^{1}H COSY NMR spectrum of the hydrolyzed polysaccharide analogue

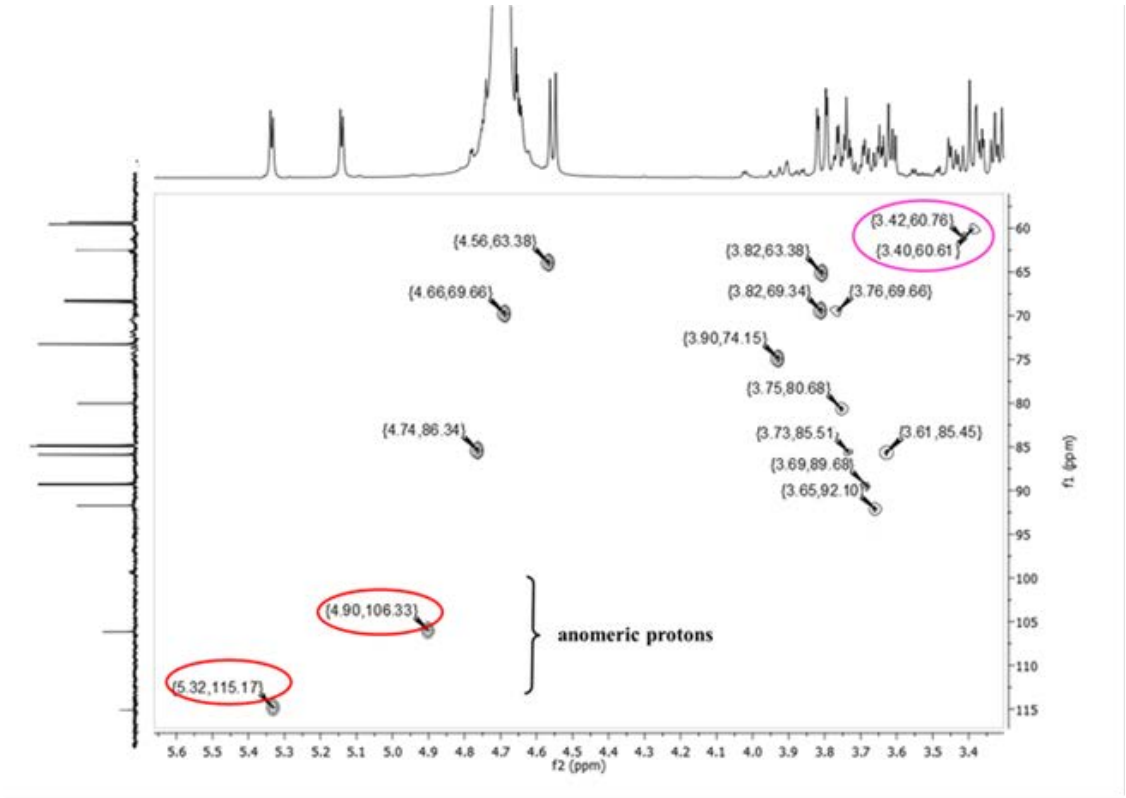

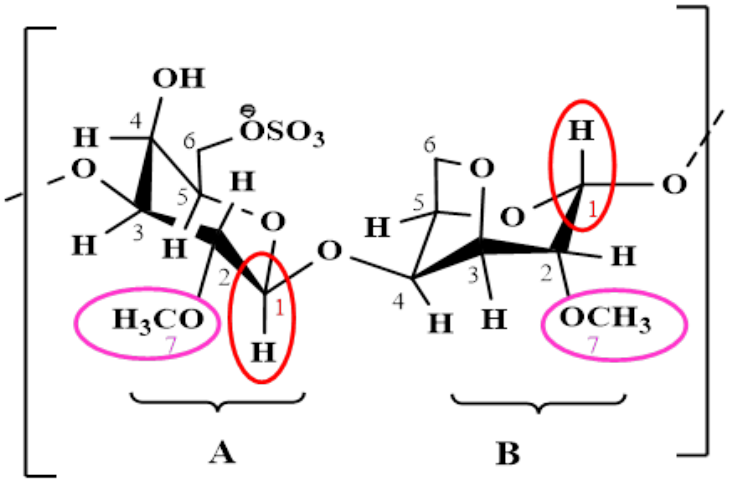

Figure 6.14.: HSQC spectrum of the hydrolyzed polysaccharide analogue

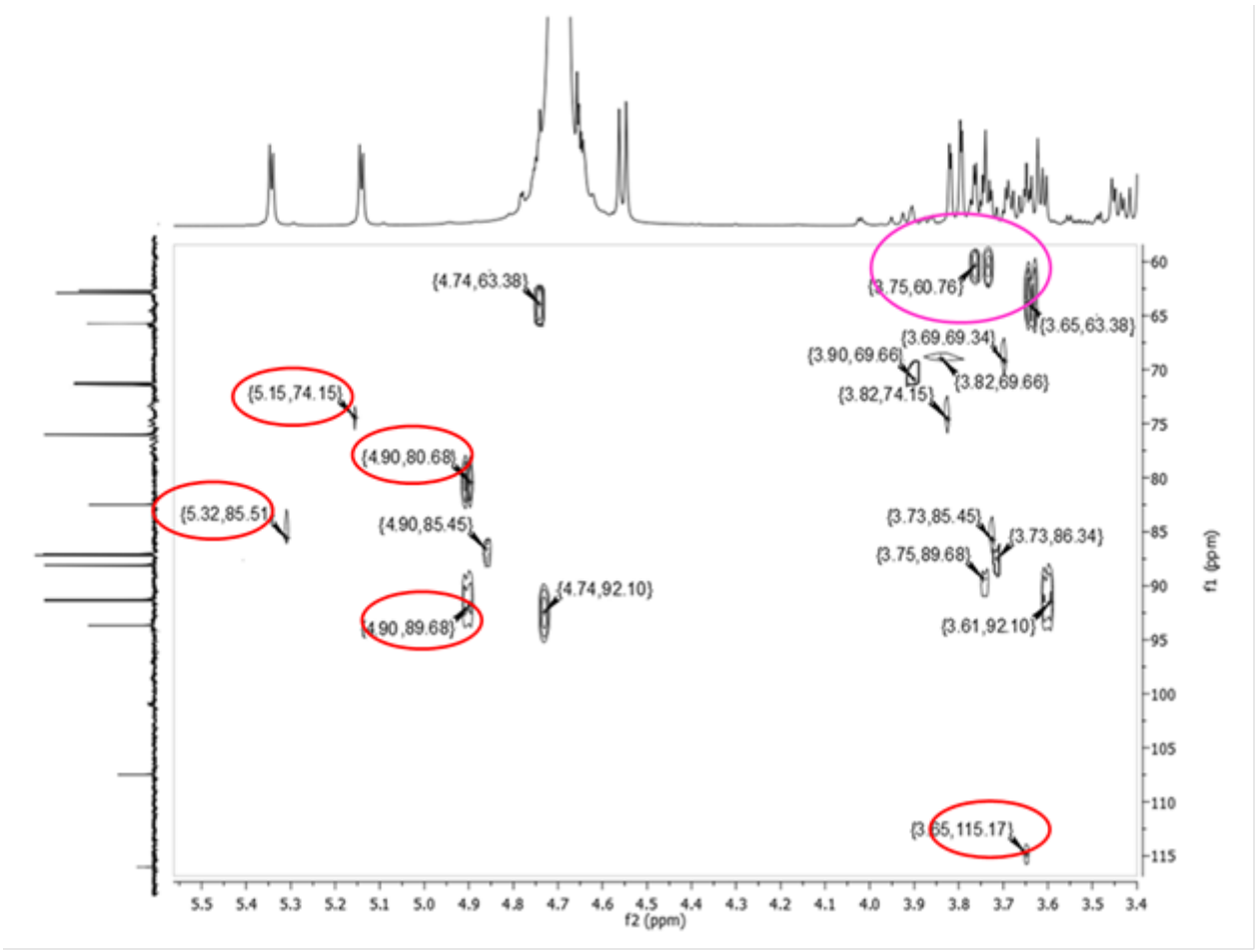

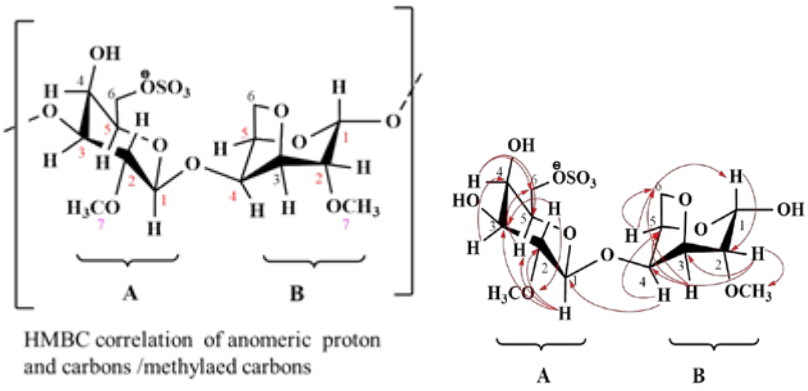

HMBC correlation of anomeric proton and carbons /methylaed carbons

Figure 6.15.: HMBC spectrum of the hydrolyzed polysaccharide analogue

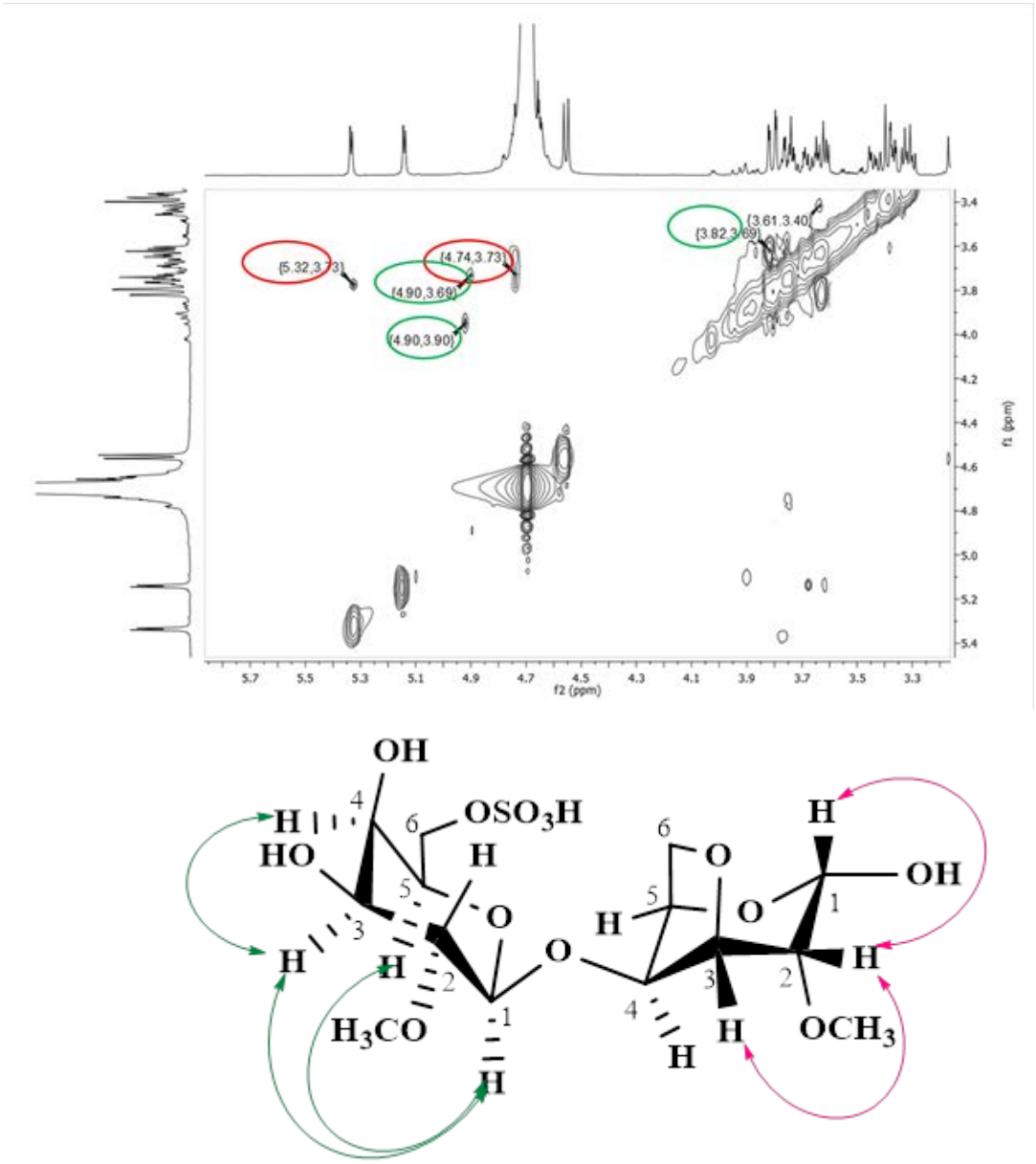

Figure 6.16.: NOESY spectrum of the hydrolyzed polysaccharide analogue

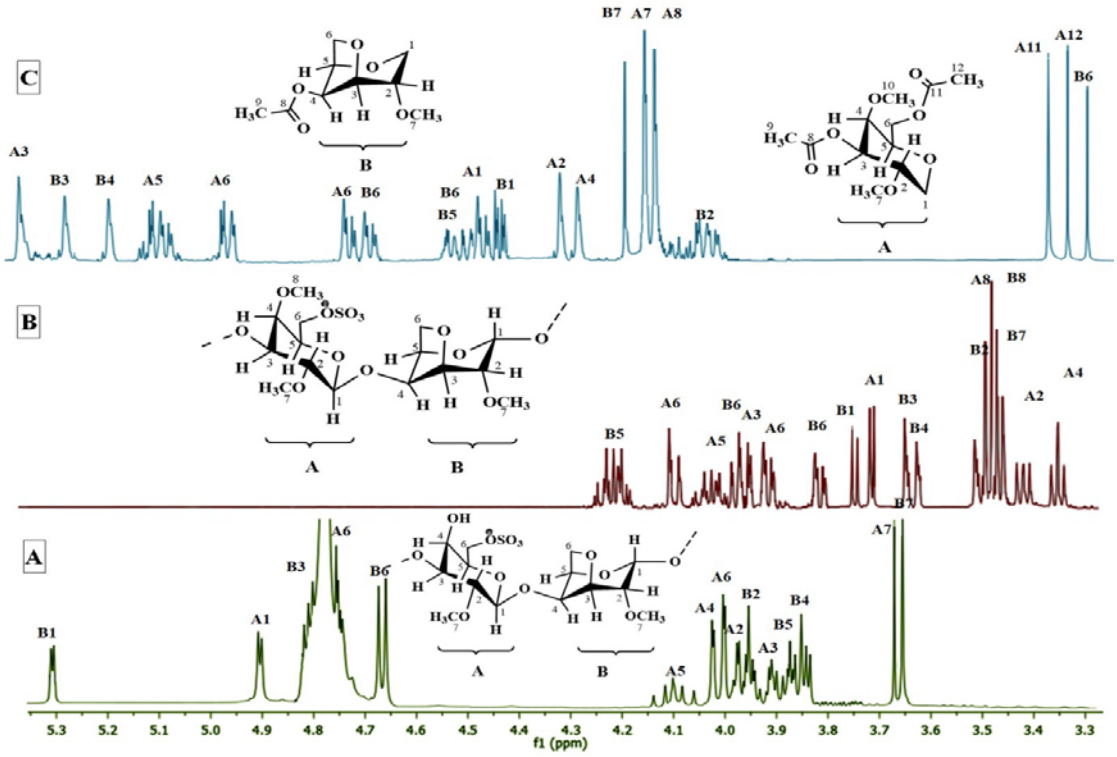

Figure 6.17.: ^{1}H NMR spectra of the polysaccharide, (1⋯→3)-*O*-6-sulfonato-β-D-galactopyranosyl-(1→⋯4)-3,6-anhydro-α-D-galactopyranose-(1⋯→) obtained after the process of (**A**) hydrolysis (**B**) methylation and (C) acetylation

In light of these data, δ4.90 (δ106.33; CH) was assigned to the monosaccharide unit, (**A**), which might ascribe the presence of Gal*p* ring. The position of this anomeric proton in unit (**A**) and other fragments associated with them was further confirmed by detailed COSY and HMBC correlation spectra. The proton at δ4.90 (d, 3.8 Hz) displayed COSY correlation with proton at δ3.75. These correlations were directed towards the oxygenated functionality bearing neighboring CH group in unit (**A**). Moreover, the intense HMBC correlation from proton δ3.75 (δ80.68; CH) to carbon δ60.76 (δ3.42) confirmed the neighboring -OCH_3 group linked to CH (δ3.75; δ80.68), which was assigned as C_2. Therefore, it was seemed that anomeric functionality -CH(O-) was directly attached to the fragment CH(O-CH_3)-. These attributions were further corroborated by the occurrence of methyl ether at C-6 position in agars extracted from different *Gracilaria* species, with the degree of substitution varying among species (Barros et al., 2013). Furthermore, the HMBC correlations from the protons at δ4.90 (δ106.33; CH) to carbons at δ80.68 (δ3.75, t), 89.68 (δ3.69, t) and δ74.15 (δ3.90, m); from δ3.75 (δ780.68; CH) to δ89.68 (δ3.69; t); from δ3.69 (δ89.68; CH) to δ69.34 (δ3.82; t) and from δ3.82 (δ69.34; CH) to δ74.15 (δ3.90; m) suggested the partial ring structure -CH(O-)-CH(OCH_3)-CH(OH)-CH(OH)-CH< in unit (**A**), positions assigned to

the positions of C_1-C_5. The interchangeable hydroxyl protons at δ3.69 (δ89.68; CH) and δ3.82 (δ69.34; CH) were found to be ceased to locate upon exchange of D_2O thereby assigning the presence of (-OH) groups in its close proximity. The COSY correlation between the protons δ3.90/δ3.76/δ4.66 assigned the linkage between the CH proton at δ3.90 and CH_2 protons at δ3.76/4.66. Similarly, the HMBC correlations from the protons at δ3.82 and δ3.90 to the carbon δ69.66 assigned the fragment -CH(O-)-CH_2(O-), namely C_5-C_6. The HMBC correlation between δ4.90 and δ74.15 suggested the closure of ring protons, and which furthermore confirmed the presence of galactopyranose (Gal*p*) ring in the oligosaccharide with two substitutions, -OCH_3 and -CH_2O- at C_2 and C_5 positions, respectively. The deshielded doublet of doublet signal observed at δ3.76 and δ4.66 assigned the presence of CH_2 bearing sulfonato (-OSO_3^-) group in unit (**A**). Therefore, glycoside residue (**A**) was characterised as *O*-6-sulfonato-2-methyl-β-D-Gal*p* (*O*-6-sulfonato-2-Me-β-D-Gal*p*).

Similarly, the proton at δ5.32 (δ115.17; CH) was assigned to C_1 position of the monosaccharide unit, (**B**), which might be the part of anhydrogalactopyranose (AnGal*p*) ring related to the monosaccharide unit, (**B**). The position of this anomeric proton in unit, (**B**) and other related fragments were further confirmed by COSY and HMBC correlations. The proton at δ5.35 (d) displayed COSY correlation with proton at δ3.73. This correlation appropriately suggested the presence of oxygenated functionality bearing neighboring CH group in unit (**B**). Furthermore, the strong HMBC correlation from proton δ3.73 (δ85.51; CH) to carbon δ60.61 (δ3.40) suggested the presence of -OCH_3 group linked to CH (δ3.73, δ85.51), corresponding to the position C_2 in (**B**). Therefore, anomeric -CH(O-) functionality was directly attached to the CH(O-CH_3)- group in (**B**), assigned as C_1-C_2. Besides, the COSY correlations in between the protons δ3.73/δ4.74/δ3.61 suggested the presence of the fragment -CH(OCH_3)-CH(O-)-CH(O-)-, corresponding to C_2-C_4 in (**B**). These COSY cross peaks were further supported by the HMBC correlations from the protons at δ3.73 (δ85.51; CH) to carbons at δ86.34 (δ4.74, t), and δ85.45 (δ3.61, m); from δ4.74 (δ86.34; CH) to δ92.10 (δ3.65; t); and from δ3.61 (δ85.45; CH) to δ92.10 (δ3.65; t), which attributed the fragment -CH(OCH_3)-CH(O-)-CH(O-)-CH(O-), at the positions of C_2-C_5. Moreover, the COSY correlations between the protons δ3.65/δ3.80/δ4.56 assigned the connection of the fragment -CH(O-)-CH_2(O-)-, for the positions of C_5-C_6 . The HMBC correlation from δ4.74 (δ86.34) to δ92.10 (δ3.65) suggested the presence of five membered ring fragment -CH(O-)-CH(O-)-CH(O-)-CH_2(O-), corresponding to the closed furanose ring C_3-C_6. At the same time, the proton at δ3.65 (δ92.10) displayed HMBC correlation with the anomeric carbon δ115.17 (δ5.32), which attributed the closure of the second ring in (**B**). The second monosaccharide unit was found to exist as the combinations of 5 and 6 membered rings, and which was considered as 2-methyl-α-D-3,6-AnGal*p* (2-Me-α-D-3,6-AnGal*p*) moiety in oligosaccharide.

The HMBC correlation from the proton δ3.61 (C_4 in **B**) to carbon δ106.33 (C_1 in **A**) was directed towards the assumption of the linkage pattern. From this correlation, it has seen that, C_1 of the *O*-6-sulfonato-2-Me-β-D-Gal*p* was connected to the C_4 of 2-Me-α-D-3,6-AnGal*p*. Therefore, the glycoside residue in GSP-2 might possess an alternate (····1→4) (····1→3) or (····1→3) (····1→4) in between *O*-6-sulfonato-2-methyl-β-D-Gal*p* and 2-methyl-α-D-3,6-AnGal*p*. The further connections of glycoside residues in GSP-2 were confirmed by the methylation and linkage pattern analyses.

The relative stereochemistries of protons attached to the chiral carbons at C_1, C_2, C_3, C_4 and C_5 in unit (**A**) and C_1, C_2, C_3 and C_4 in unit (**B**) were explained with the aid of nuclear overhauser effect spectroscopic (NOESY) experiments. In unit (**A**), the signal of proton at chiral centre, wherein H_1 exhibited NOEs with methine protons H_5 and H_3; H_3 exhibited NOE with H_4, which were oriented in the α-side of unit (**A**) in the oligosaccharide. Conversely, the other protons were in β-face of the unit (**A**) in oligosaccharide. Likewise, in unit (**B**), the signal of proton at the chiral centre, H-1 showed NOE with the methine proton H_2; H_2 showed NOE with H_3, which were oriented in the β-side of the oligosaccharide. Conversely, the other protons were in the α-face of the unit (**B**) in the oligosaccharide of GSP-2.

These data proposed that the sequence of linkage pattern of residues of monosaccharides in GSP-2 as (····→3)-*O*-6-sulfonato-2-methyl-β-D-Galactopyranose-(1→4)-2-methyl-α-D-3,6-Anhydrogalactopyranose-(1→····) or (····→3)-*O*-6S-2-Me-β-D-Gal*p*-(1→4)-2-Me-α-D-3,6-AnGal*p*(1→····) or [2-Me-G6S-2-MeAnG]. The structural composition of the skeletal chain of the galactopyran was reinforced with the repetitive units of the sulfated galactopyranosyl-anhydroglactopyranose.

6.3.3.4 Molecular weight of polysaccharide by ESI-MS Analysis

The elution curve obtained for GSP-2 (Figure 6.3) was found to show an intense single peak, which confirmed the purity of the fraction GSP-2. The ESI-MS analysis of oligosaccharide, which was obtained by hydrolysis, was performed in negative-ion mode due to the presence of sulfate groups. The polysaccharide sample on sequential purification was found to comprise of the disaccharide units. The intense molecular ion peak occurred at *m/z* 431.3, which corresponds to the single-charged anion $[2\text{-Me-G6S-2-MeAnG}]^-$ of the disaccharide parts, and it encompassed with glycosidic residues of *O*-6-sulfonato-2-Me-β-D-Gal*p* and 2-Me-α-D-3,6-AnGal*p*. The spectrum was consisted of two peaks at *m/z* 273.2 and *m/z* 176.2, which correspond to the fragments $[2\text{-Me-G6S}]^-$ and $[2\text{-MeAnG}]^-$, respectively (Figure 6.18).

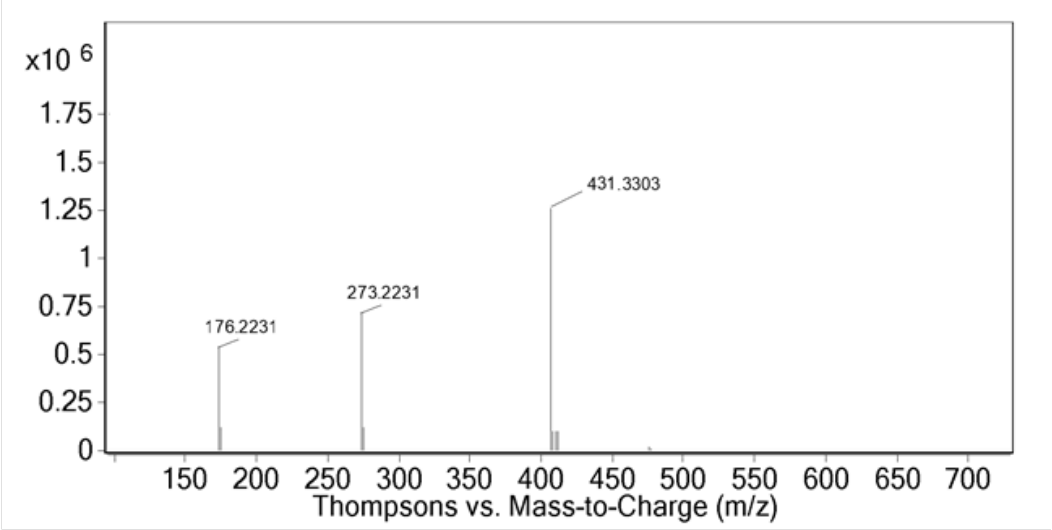

Figure 6.18.: ESI-MS spectrum of the oligosaccharide analogue

6.3.3.5 Structural interpretation of polysaccharide by methylation analysis

The linkage pattern and functionalities in polysaccharide were further confirmed by methylation followed by hydrolysis. On methylation, all hydroxyl groups present in the polysaccharide were found to be substituted by methoxyl groups and further hydrolysis of polysaccharide could lead to the breakdown of glycosidic linkage. The free glycosidic linkages were ensured by the presence of hydroxyl groups, which have clearly depicted the pattern of linkages in between the monosaccharide residues. The structural characterization of the methylated polysaccharide was carried out with the aid of 1D and 2D NMR spectroscopic methods (Figure 6.19- 6.25, Table 6.6). The proton NMR spectrum of the methylated GSP-2 was depicted in Figure 6.17. Two sugar residues (characterized in the previous section) in polysaccharide was designated as (MeA or MeGal*p*) and (MeB or MeAnGal*p*). Three major singlets appeared in the proton NMR in between the δ3.30-3.50, which attributed the presence of methylated moieties in the polysaccharide GSP-2. At the same time two intense signals were seen in the region of δ3.60-3.70, which might be due to the cleaved glycosidic bonds in between the sugar residues. These signals were further ensured by the 1D-NMR along with HSQC spectrum. On the basis of these spectra, the individual protons attached to the carbon in the methylated polysaccharide were assigned. The lack of two intense signals in the anomeric region depicted the cleavage of glycosidic linkage in methylated GSP-2. At the same time, two intense peaks at δ3.67 (d; δ69.76; CH_2) and δ3.65 (d; δ69.56; CH_2) were found in the spectrum with same integral and multiplicities, indicating the proton substituted C_1 positions in MeGal*p* and MeAnGal*p*, respectively. The deshielded signals at δ3.67 (δ69.76; CH_2) and δ3.65 (δ69.56; CH_2) were appeared as doublet, indicating the oxygen

bearing CH functionality in the nearby position of C_1. The HMBCs from δ3.67 and δ3.65 to the δ93.94 (δ3.24) and δ88.75 (δ3.36) were directed towards the presence of neighboring CH groups, assigned as C_2 in MeGal*p* and MeAnGal*p*, respectively. The signals at δ3.24 (C_2 in MeA) and δ3.36 (C_2 in MeB) exhibited HMBCs with δ59.04 (δ3.33) and δ59.78 (δ3.30), respectively. These results indicated the presence of methoxyl (-OCH_3) substitutions at the C_2 position of two sugar residues (MeA) and (MeB). Thus, the presence of methoxyl functionalities at positions C_2 attached to the anomeric C_1 positions in MeGal*p* and MeAnGal*p* (described in section 3.3.2) were confirmed. These correlations together resulted in the -CH_2-(CH-OCH_3); (C_1-C_2) fragments in MeGal*p* and MeAnGal*p*, respectively.

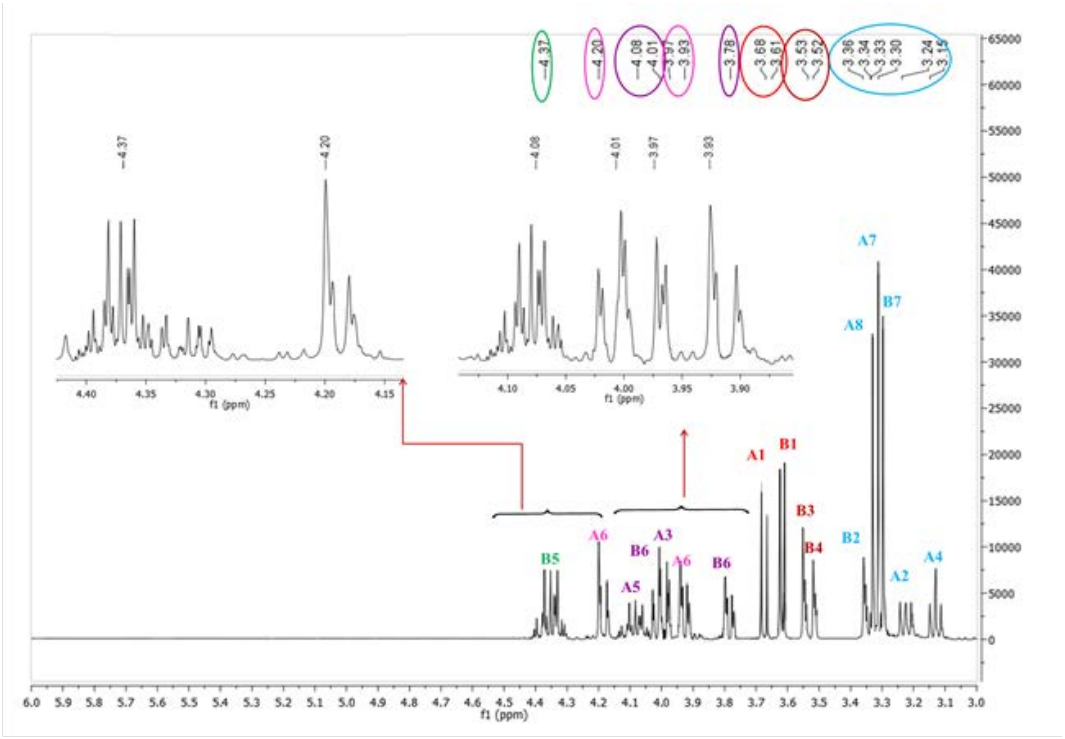

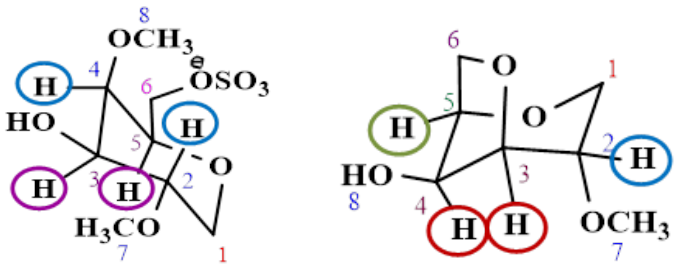

Monomer unit A **Monomer unit B**

Figure 6.19.: ^{1}H NMR spectrum of methylated polysaccharide analogue after hydrolysis

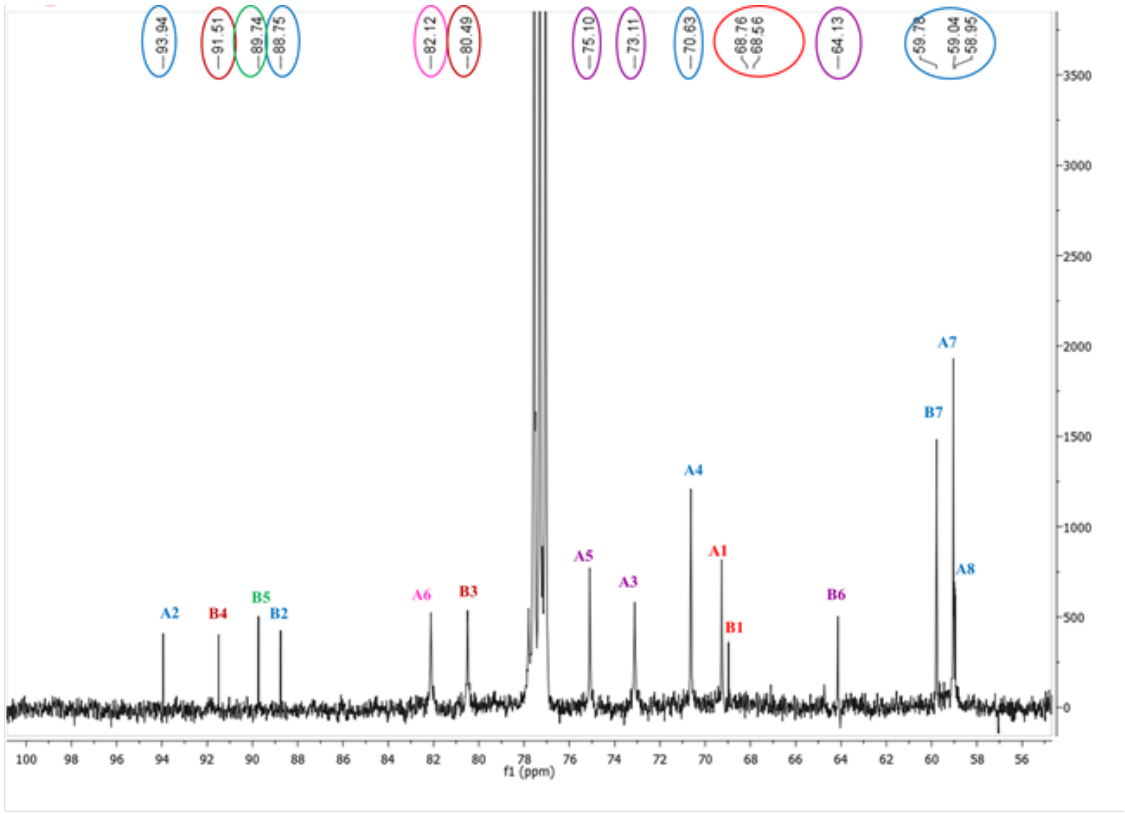

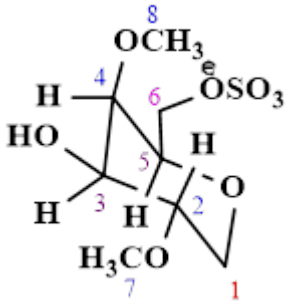

Monomer unit A

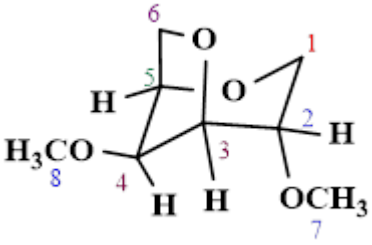

Monomer unit B

Figure 6.20.: ^{13}C NMR spectrum of methylated polysaccharide analogue after hydrolysis

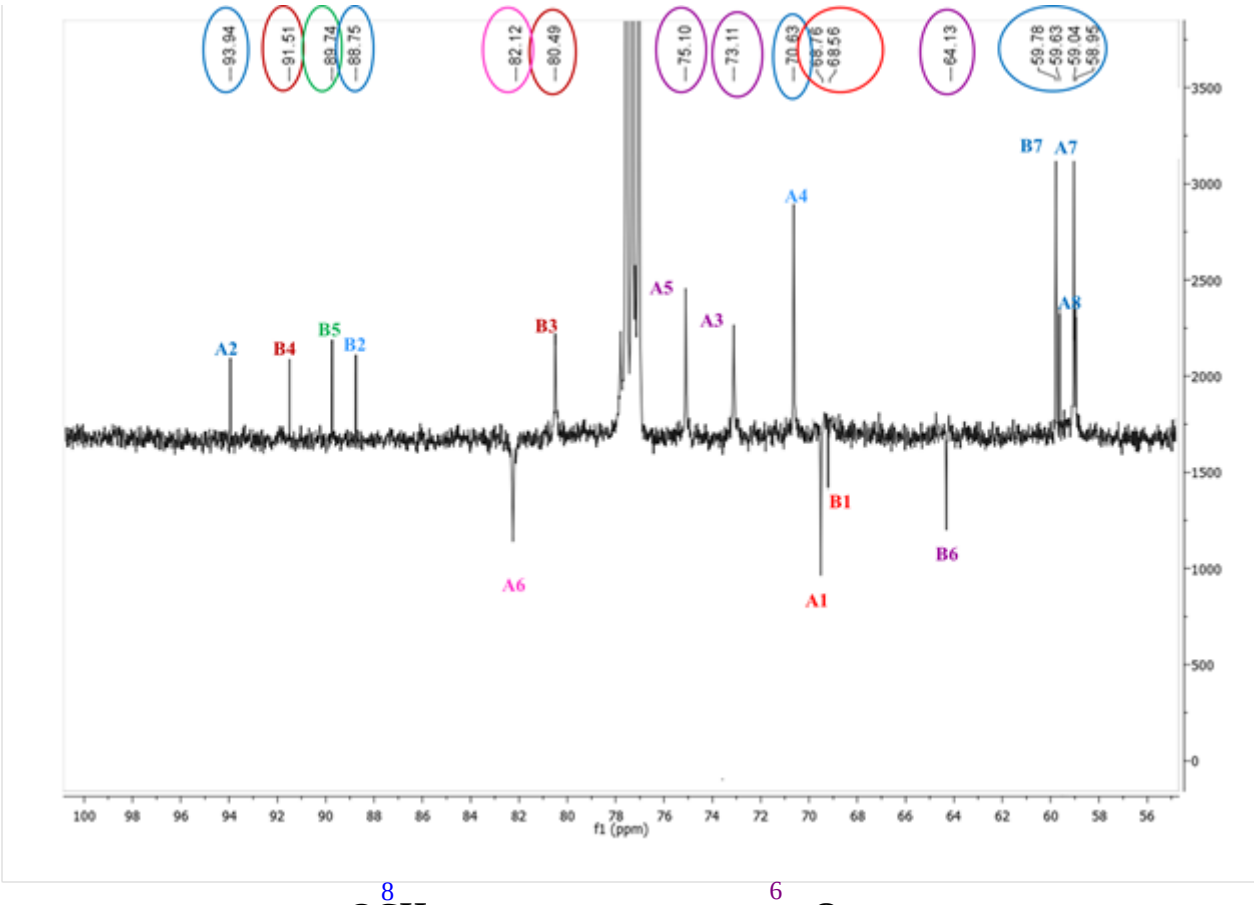

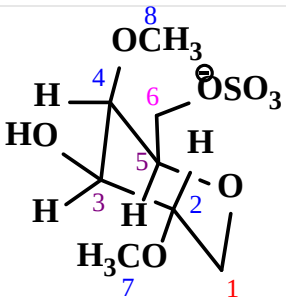

Monomer unit A

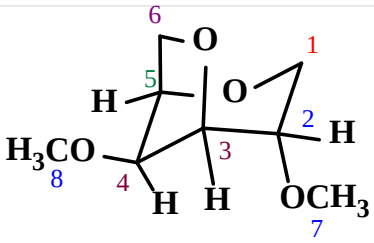

Monomer unit B

Figure 6.21.: DEPT[135] spectrum of methylated polysaccharide analogue after hydrolysis

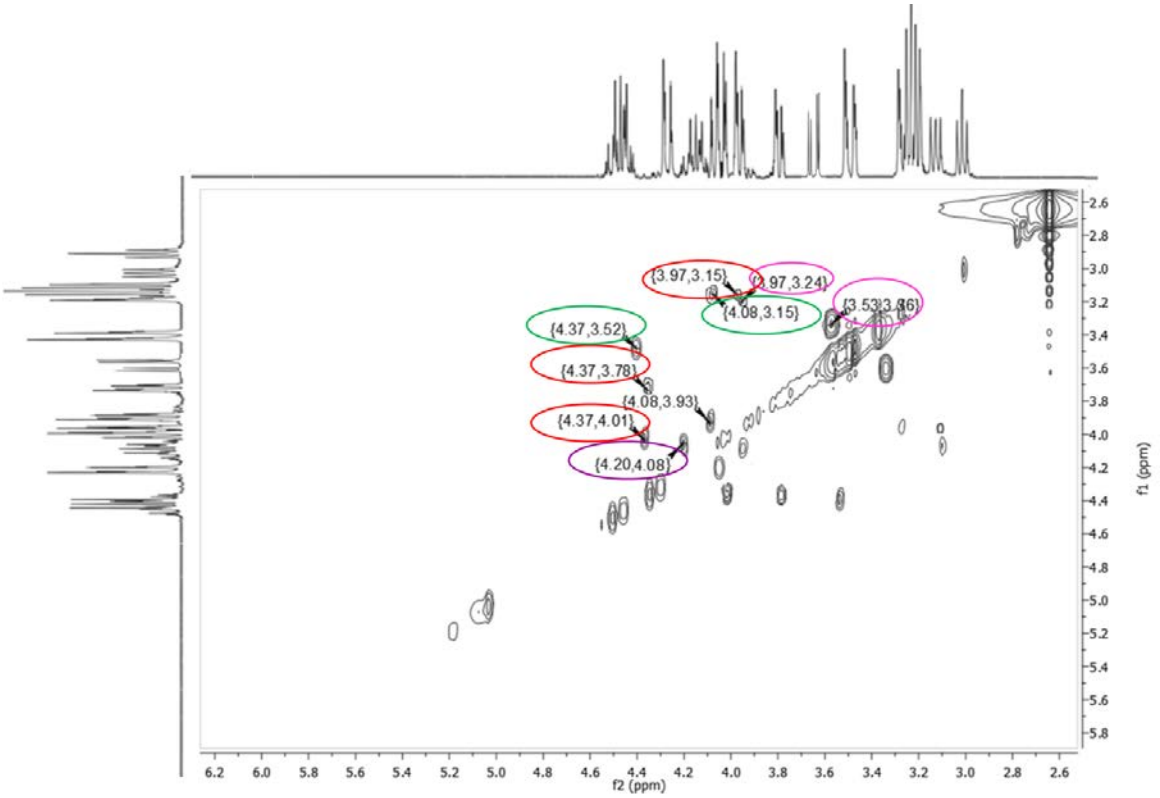

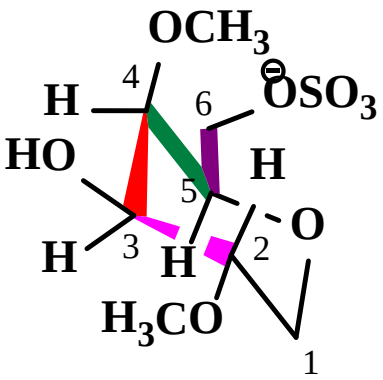

Monomer unit A

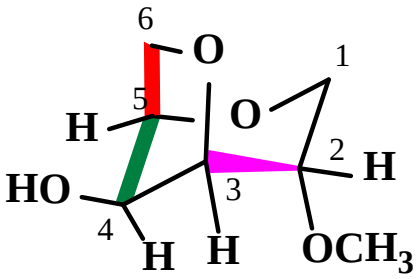

Monomer unit B

Figure 6.22.: ^{1}H-^{1}H COSY NMR spectrum of methylated polysaccharide analogue after hydrolysis

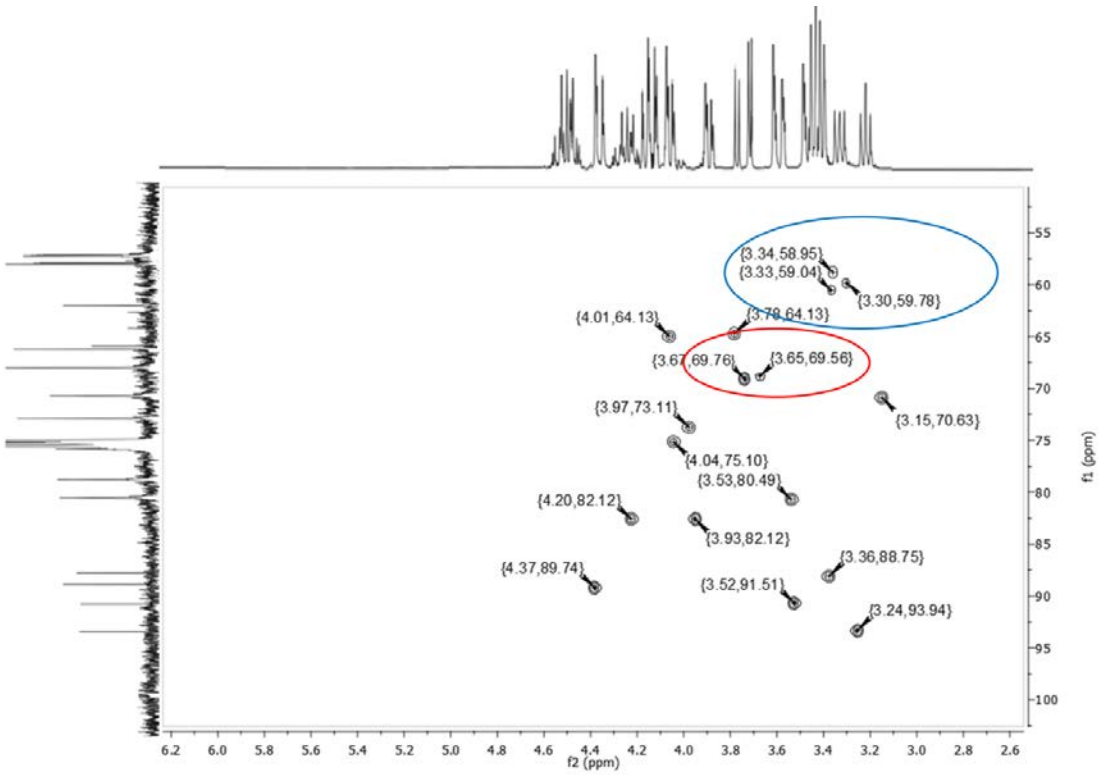

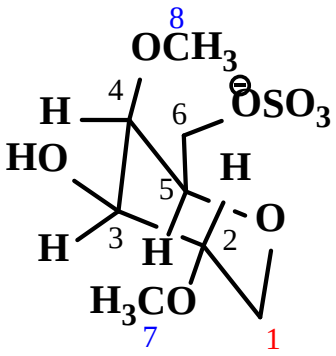

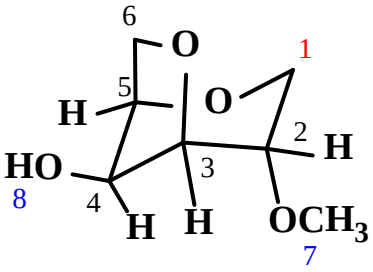

Monomer unit A **Monomer unit B**

Figure 6.23.: HSQC spectrum of methylated polysaccharide analogue after hydrolysis

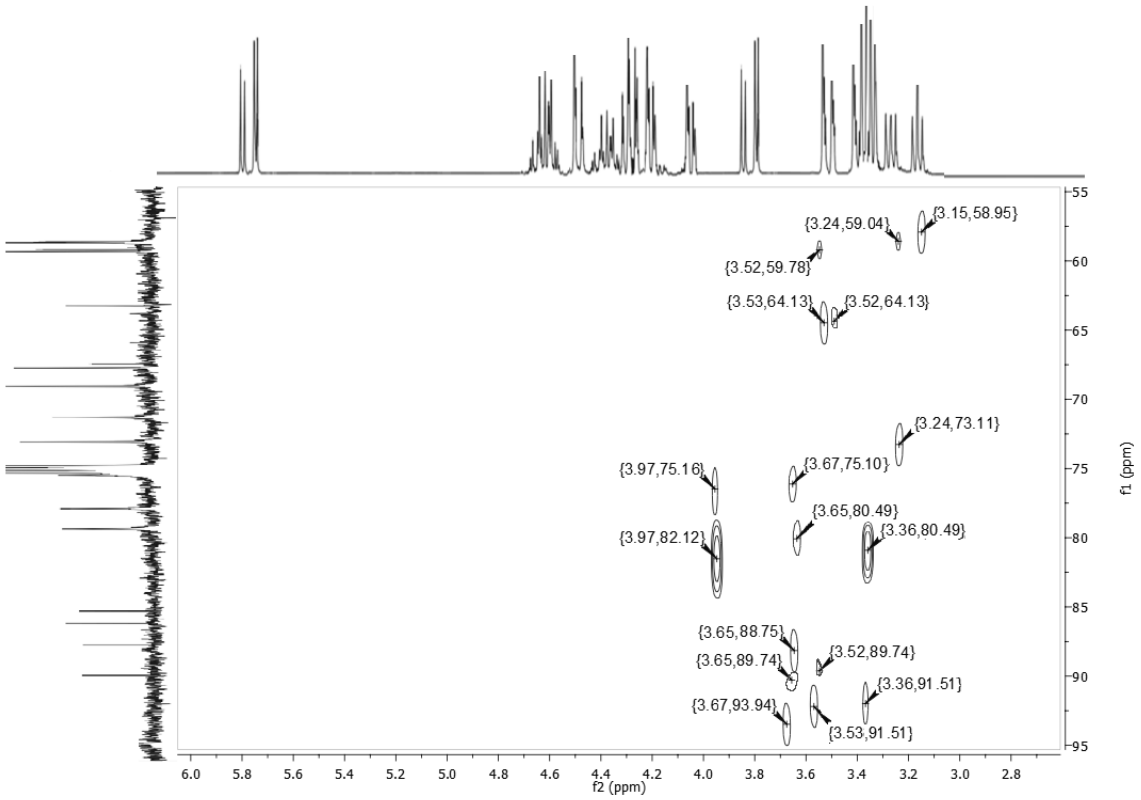

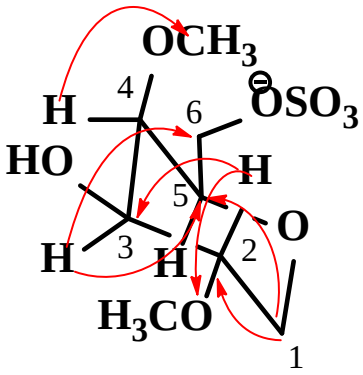

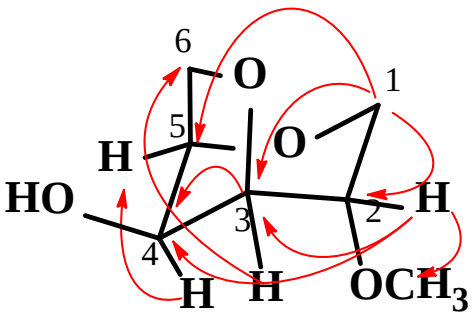

Monomer unit A **Monomer unit B**

Figure 6.24.: HMBC spectrum of methylated polysaccharide analogue after hydrolysis

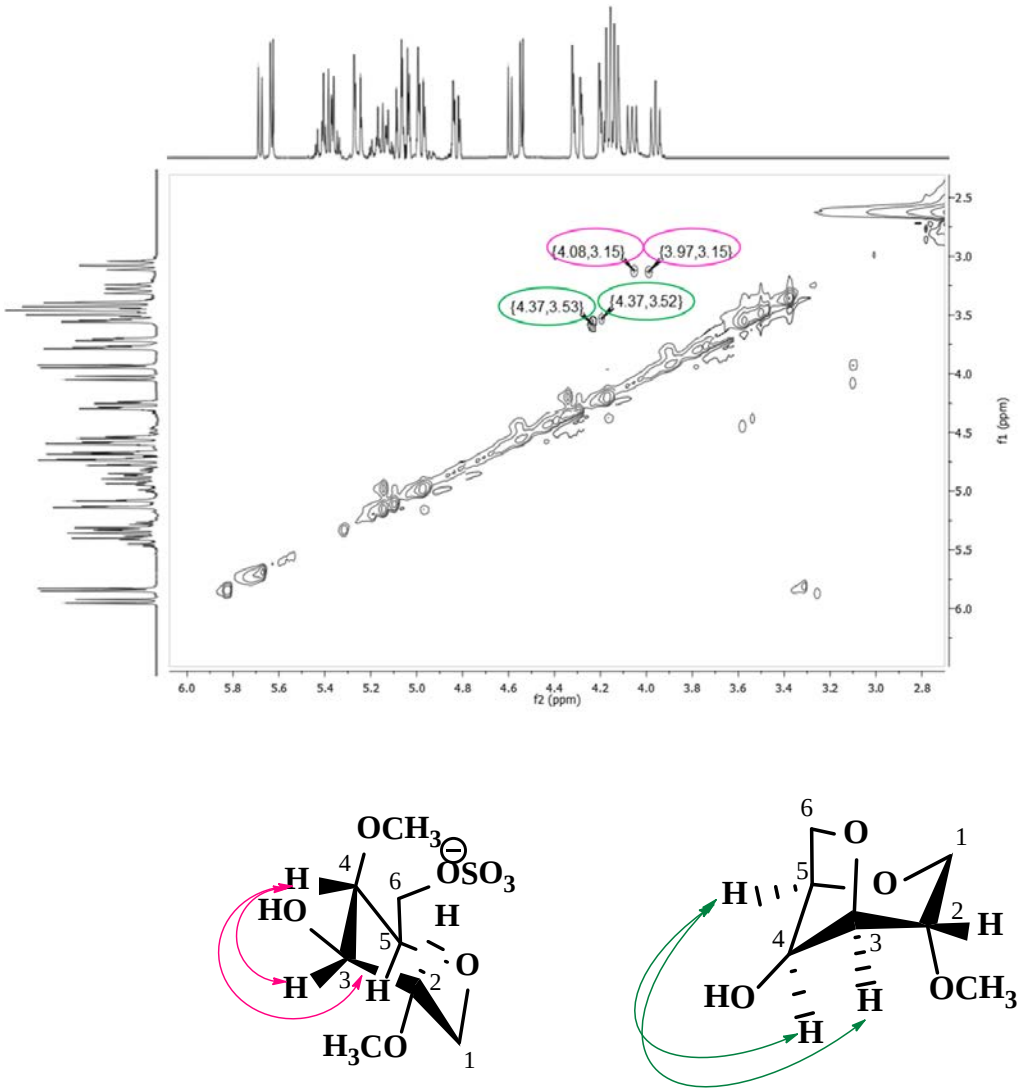

Figure 6.25.: NOESY spectrum of methylated polysaccharide analogue after hydrolysis

Table 6.6.: NMR spectroscopic data[a] of polysaccharide …(1→3)-*O*-6-sulfonato-β-D-galactopyranosyl-(1→4)-3,6-anhydro-α-D-galactopyranose…isolated from the red seaweed *G. salicornia*

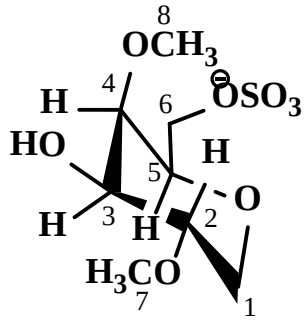

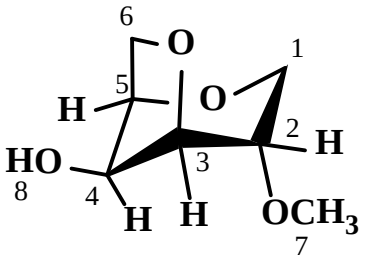

Type of C	C. No.	^{13}C NMR	^{1}H NMR	COSY	HMBC	Type of C	C. No.	^{13}C NMR	^{1}H NMR	COSY	HMBC
Unit A						**Unit B**					
CH_2	A1	69.76	3.67	-	C-A2,A5	CH_2	B1	69.56	3.65	-	C-B2,B3,B5
CH	A2	93.94	3.24	H-A3	C-A7,A3	CH	B2	88.75	3.36	H-B3	C-B3,B7
CH	A3	73.11	3.97	H-A4	C-A5,A6	CH	B3	80.49	3.53	-	C-B6
CH	A4	70.63	3.15	H-A5	C-A8	CH	B4	91.51	3.52	H-B5	C-B5,B6
CH	A5	75.10	4.08	H-A6	-	CH	B5	89.74	4.37	H-B6	-
CH_2	A6	82.12	4.20,3.93	-	-	CH_2	B6	64.13	4.01,3.78	-	-
CH_3	A7	59.04	3.33	-	-	CH_3	B7	59.78	3.30	-	-
CH_3	A8	58.95	3.34	-	-	-	-	-	-	-	-

[a]NMR spectra were recorded using a Bruker AVANCE III 500 MHz (AV 500) spectrometer (Bruker, Karlsruhe, Germany) in MeOH as aprotic solvent at ambient temperature with TMS as the internal standard (δ 0 ppm).

[b]Values in ppm, multiplicity were indicated in parentheses. Multiplicities were allocated by ^{135}DEPT NMR spectrum. The assignments were made with the aid of the COSY, HSQC, HMBC and NOESY experiments.

Furthermore, the COSY correlations H_2 (δ3.24)/H_3 (δ3.97)/H_4 (δ3.15)/H_5 (δ4.08)/H_6 (δ4.20/3.93) framed the fragment as the extension of C_1-C_2; -CH_2-CH-(OCH_3)-CH(O-)-CH(O-)-CH(O-)-CH_2- in (MeA). These fragments were further confirmed by the HMBCs correlations from δ3.24 to δ73.11; δ3.97 to δ75.10 and δ82.12. Moreover, the deshielded signal δ3.97 (H_3) was appeared as triplet at C_3, and which did not show any branching like C_2. Therefore, it was assigned as -CH(OH), while deshielded signal was apparent at δ3.15 (H_4) exhibited an intense HMBC with δ58.95, indicating the presence of methoxyl substitution, CH(-OCH_3). Similarly, the signal at δ4.08 (H_5) was appeared as multiplet, which has connected to a CH_2 functionality via a COSY; H_5 (δ4.08)/H_6(δ4.20/3.93), and they exhibited higher chemical shift due to the presence of oxygen functionality as the part of ring. Finally, the signals at δ4.20 and δ3.93 indicated the presence of sulfated functionality, and these intense deshielded signals were attached to CH_2 group. These results were corroborated by the deshielded signals beyond δ4.00 observed for CH_2 functionalities attached sulfate group in the carrageenan-type of polysaccharides, which were isolated from the red algae (Stortz, et al., 1994). From these results, in MeGal*p*, the positions C_1 was found to be protonated, and C_3 was attached with OH group, thus indicating the presence of (1⋯→3) linkage. Therefore, the methylated Gal*p* was characterized as *O*-6-sulfonato-2,4-dimethyl-β-D-Gal*p* or *O*-6S-2,4-Me_2-β-D-Gal*p* with linkage pattern(1⋯→3).

Similarly, the COSY correlations H_2(δ3.36)/H_3(δ3.53) and H_4(δ3.52)/H_5(δ4.37)/H_6(δ4.01/3.78) framed the fragment as the extension of C_1-C_2; -CH_2-CH-(OCH_3)-CH(O-)-CH(O-)-CH(O-)-CH_2- in (MeB). These fragments were further confirmed by HMBCs correlations from δ3.36 to δ80.49; δ3.52 to δ89.64 and δ64.13. Furthermore, the HMBC signals from δ3.53 to δ91.51 and δ3.52 to δ64.13 along with COSYs at H_4(δ3.52)/H_5(δ4.37)/H_6(δ4.01/3.78) appropriately deduced the presence of furanose ring in MeAnGal*p*. Besides, the deshielded signal δ3.53 (H_3) was appeared as triplet, and did not show any substitution, whereas their higher chemical shift values was due to the presence of directly attached oxygen of furanose ring in MeAnGal*p*. The deshielded signal at δ3.52 (H_4) was connected to C_3 and C_5 via the HMBC correlation H_3 (δ3.53)/C_4(δ91.51) and COSY correlation H_4(δ3.52)/H_5(δ4.37). The signals δ4.37 (H_5), and 4.01/3.78 (H_6) appeared with high chemical shift value due to the connection with oxygen moiety as the part of ring. Thus, in MeAnGal*p*, the positions C_1 and C_4 appeared with lack of methoxy substitutions and C_4 was found to be consisted of OH group, indicating the presence of (1⋯→4) linkage. The methylated AnGal*p* was characterized as 2-methyl-α-D-AnGal*p* or *O*-6S-2-Me-α-D-AnGal*p*. The relative configurations obtained for methylated polysaccharide was depicted in Figure 6.25.

These data confirmed that the sequence of linkage pattern (1⋯→3) and (1→⋯4) in between the alternatively repeating monosaccharides of MeGal*p* and MeAnGal*p*. Therefore, the

polysaccharide was named as (1⋯→3)-*O*-6S-2-Me-β-D-Gal*p*-(1→4)-2-Me-α-D-3,6-AnGal*p*(1→⋯).

6.3.3.5 Structural interpretation of the polysaccharide by acetylation

The reductive cleavage (acetylation) is found as one of the important methods to characterize the linkage pattern and functionalities of the polysaccharide. This includes a series of chemical reactions, such as methylation, reduction and acetylation. Thus, the linkage pattern in polysaccharide was ensured by the incidence of acetyl group on the cleaved glycosidic end of polysaccharide. Like earlier method, initially the polysaccharide was subjected for methylation followed by reduction yielded two methylated sugar residues after the cleavage of polysaccharide. Finally, the free glycosidic ends were substituted with acetyl functionalities. This partially methylated and acetylated polysaccharide were characterized by extensive 1D and 2D NMR spectroscopic analysis (Figure 6.26-6.32, Table 6.7). The proton NMR spectrum of acetylated GSP-2 was depicted in Figure 6.17. As described in the previous section, the acetylated sugar residues were designated as (AcA or AcGal*p*) and (AcB or AcAnGal*p*).

Table 6.7.: NMR spectroscopic data[a] of polygalactan …(1→3)-*O*-6-sulfonato-β-D-galactopyranosyl-(1→4)-3,6-anhydro-α-D-galactopyranose…from the red seaweed *G. salicornia*

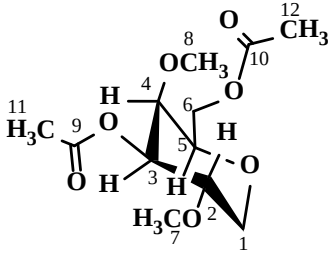

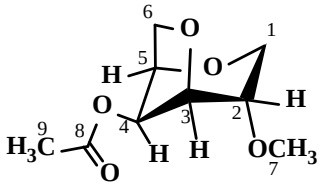

Type of C	C. No.	^{13}C NMR	^{1}H NMR	COSY	HMBC	Type of C	C. No.	^{13}C NMR	^{1}H NMR	COSY	HMBC
Unit A						**Unit B**					
CH_2	A1	69.80	3.72	-	-	CH_2	B1	67.27	3.71	H-2B	-
CH	A2	81.60	3.53	H-3A	C-1A,7A,3A	CH	B2	82.34	3.24	H-3B	C-7B,4B
CH	A3	72.40	4.90	H-4A	C-8A,4A	CH	B3	91.40	4.78	-	C-4B,6B
CH	A4	62.43	3.52	H-5A	C-10A, 6A	CH	B4	82.24	4.67	H-5B	C-8B,6B
CH	A5	81.58	4.54	H-6A	C-1A	CH	B5	88.40	3.78	H-6B	C-1B
CH_2	A6	86.24	4.37,4.08	-	C-10A	CH_2	B6	62.56	4.05,3.75	-	-
O-CH_3	A7	59.76	3.36	-	-	O-CH_3	B7	59.07	3.41	-	-
O-CH3	A8	59.55	3.34	-	-	C	B8	174.27	-	-	-
C	A9	175.24	-	-	-	CH_3	B9	20.90	2.27	-	C-8B
C	A10	174.49	-	-	-	-	-	-	-	-	-
(CO)CH3	A11	22.64	2.37	-	C-9A	-	-	-	-	-	-
(CO)CH3	A12	22.18	2.31	-	C-10A	-	-	-	-	-	-

[a]NMR spectra were recorded using a Bruker AVANCE III 500 MHz (AV 500) spectrometer (Bruker, Karlsruhe, Germany) in MeOH as aprotic solvent at ambient temperature with TMS as the internal standard (δ 0 ppm).

[b]Values in ppm, multiplicity and coupling constants (*J*= Hz) were indicated in parentheses. Multiplicities were allocated by [135]DEPT NMR spectrum. The assignments were made with the aid of the COSY, HSQC, HMBC and NOESY experiments.

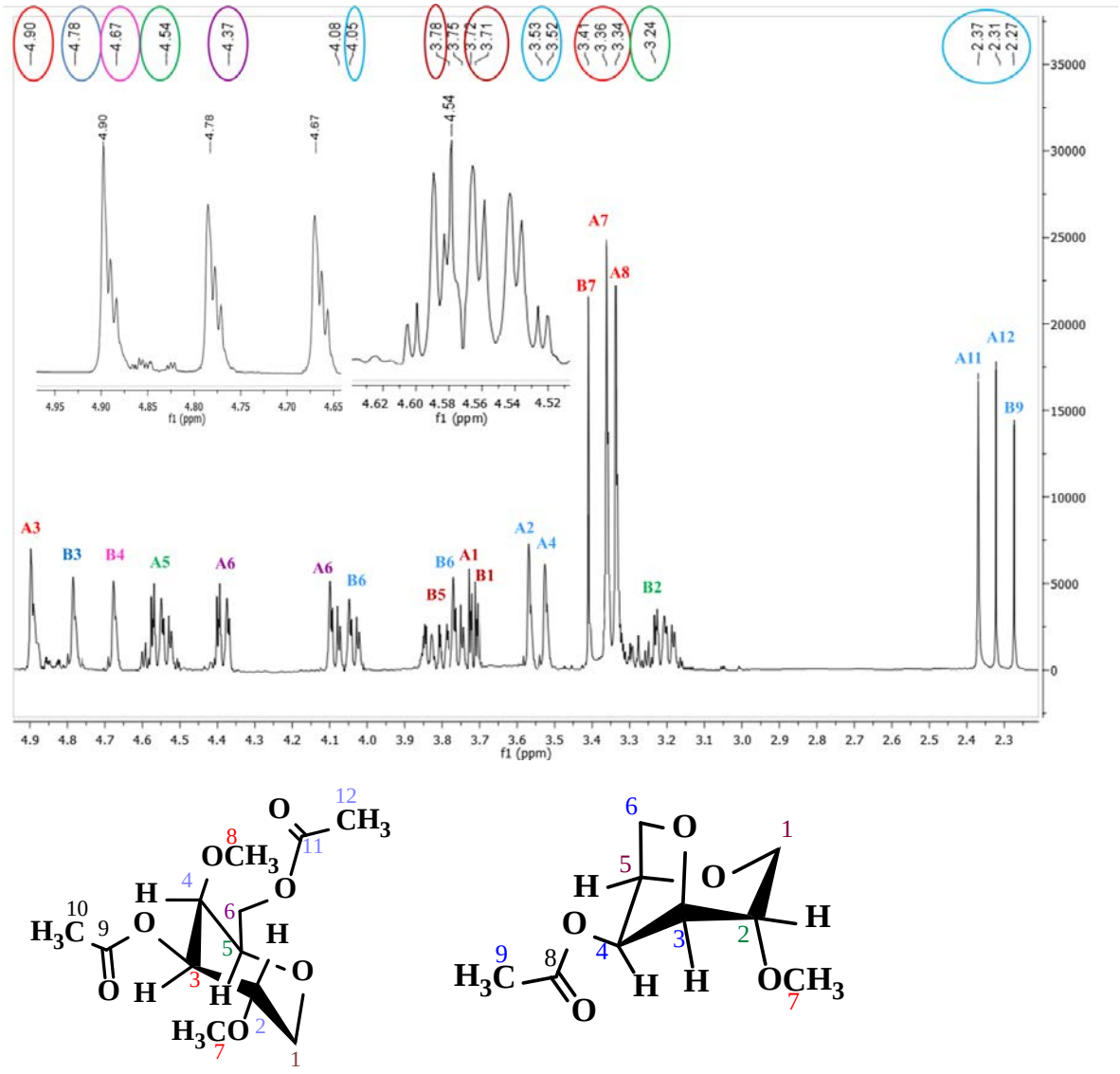

Figure 6.26.: ^{1}H NMR spectrum of the acetylated polysaccharide analogue

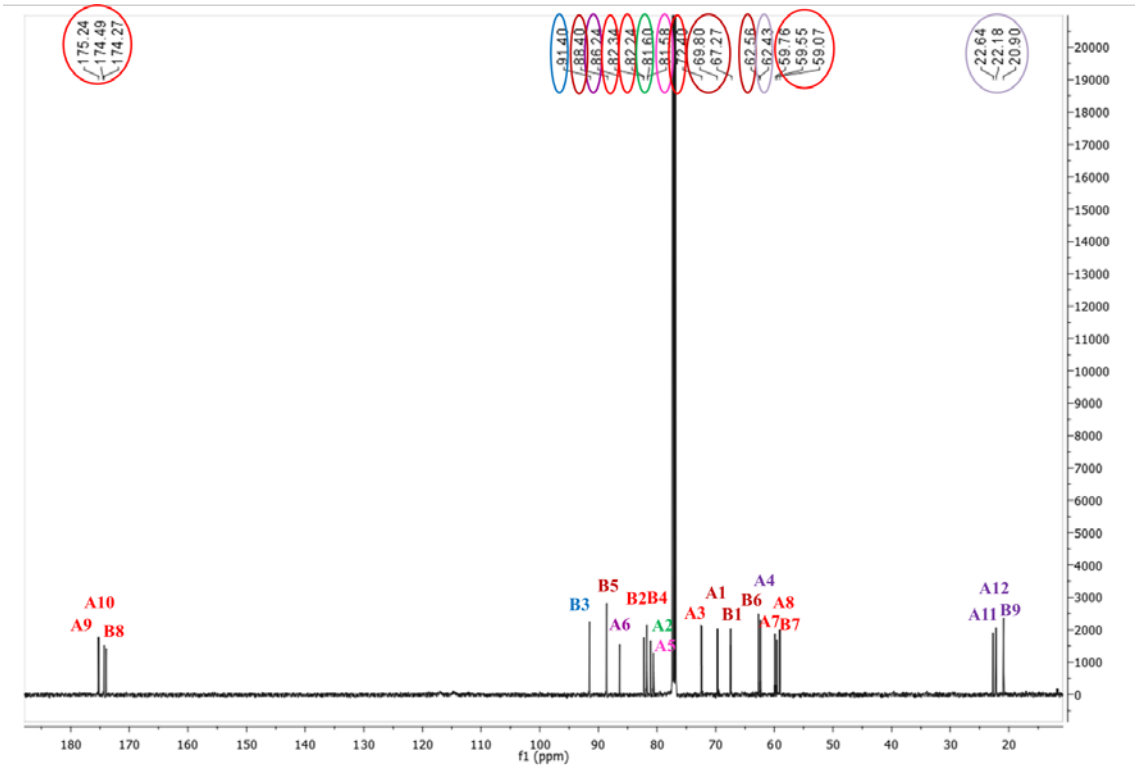

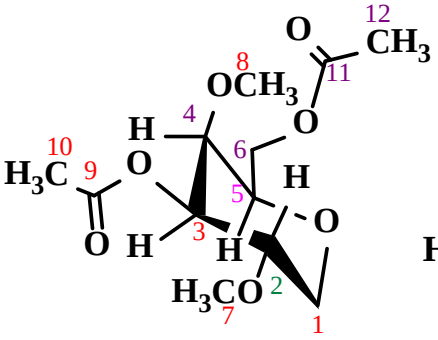

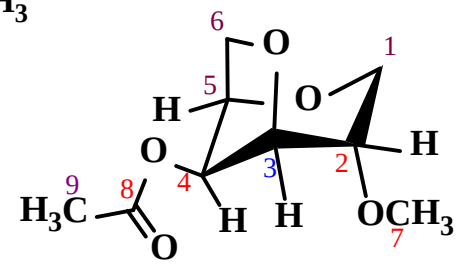

Monomer unit A **Monomer unit B**

Figure 6.27.: ^{13}C NMR spectrum of the acetylated polysaccharide analogue

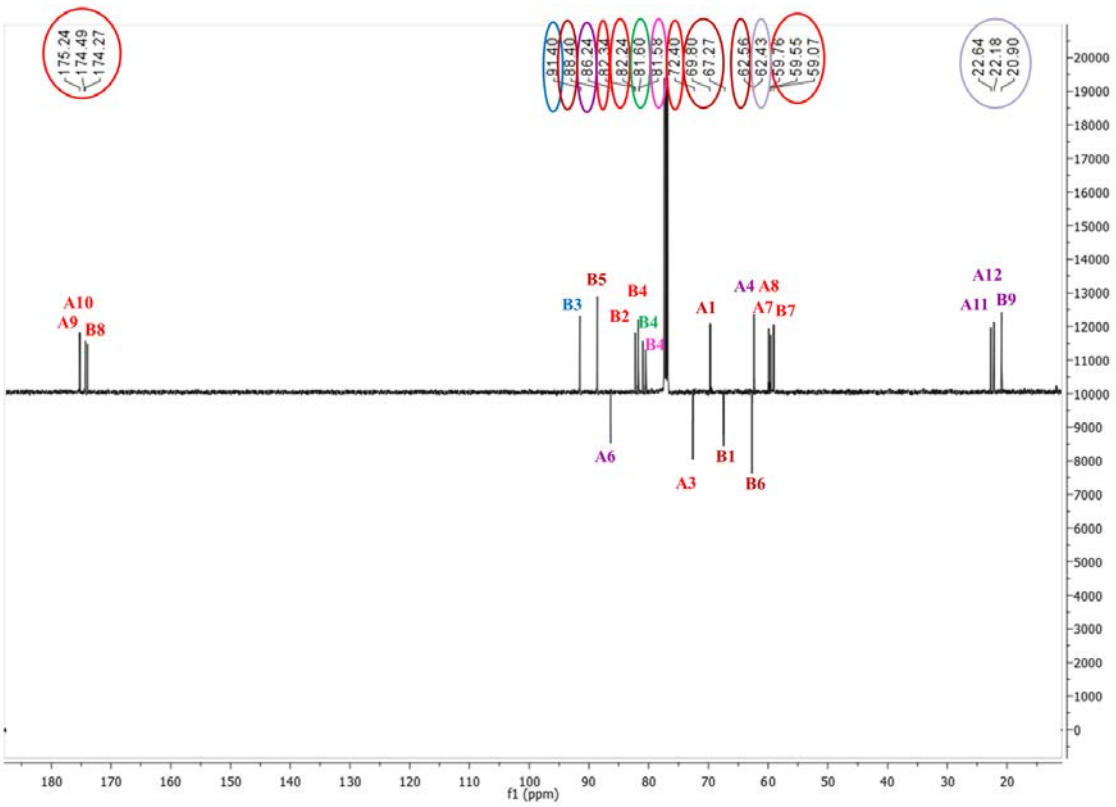

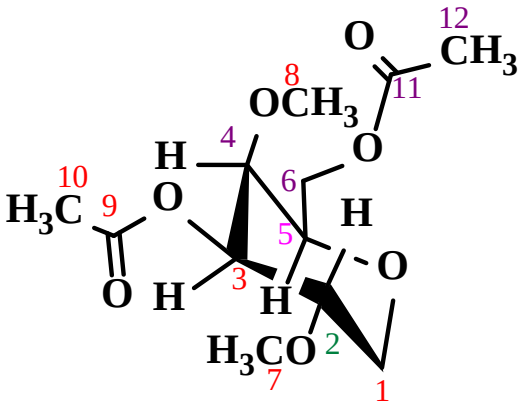

Monomer unit A

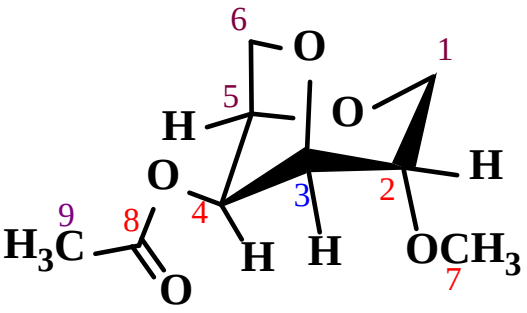

Monomer unit B

Figure 6.28. DEPT[135] spectrum of the acetylated polysaccharide analogue

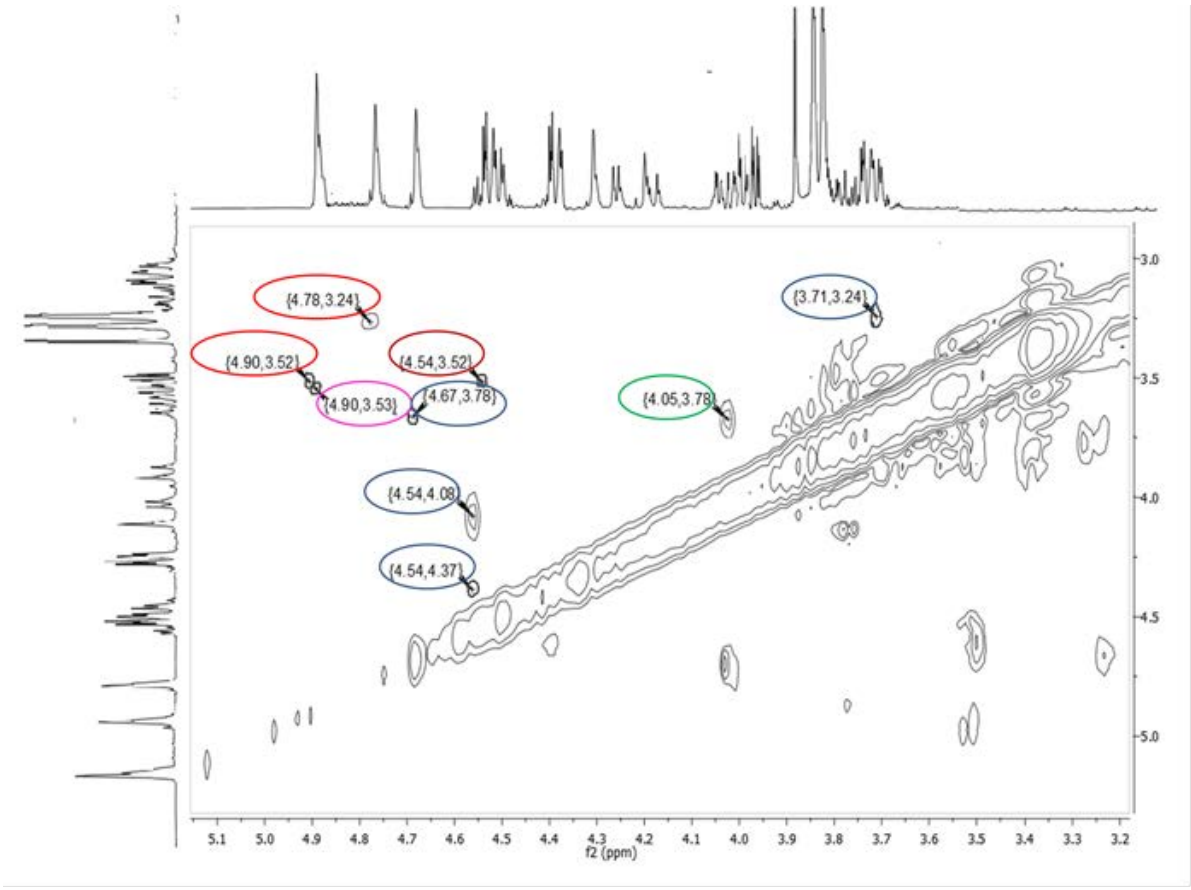

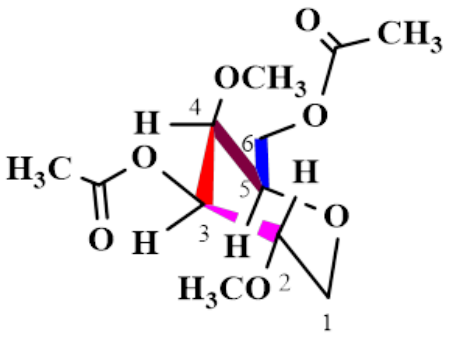

Monomer unit A

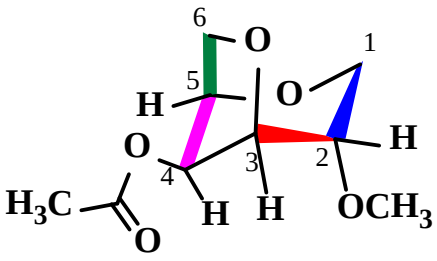

Monomer unit B

Figure 6.29.: COSY spectrum of the methylated polysaccharide analogue

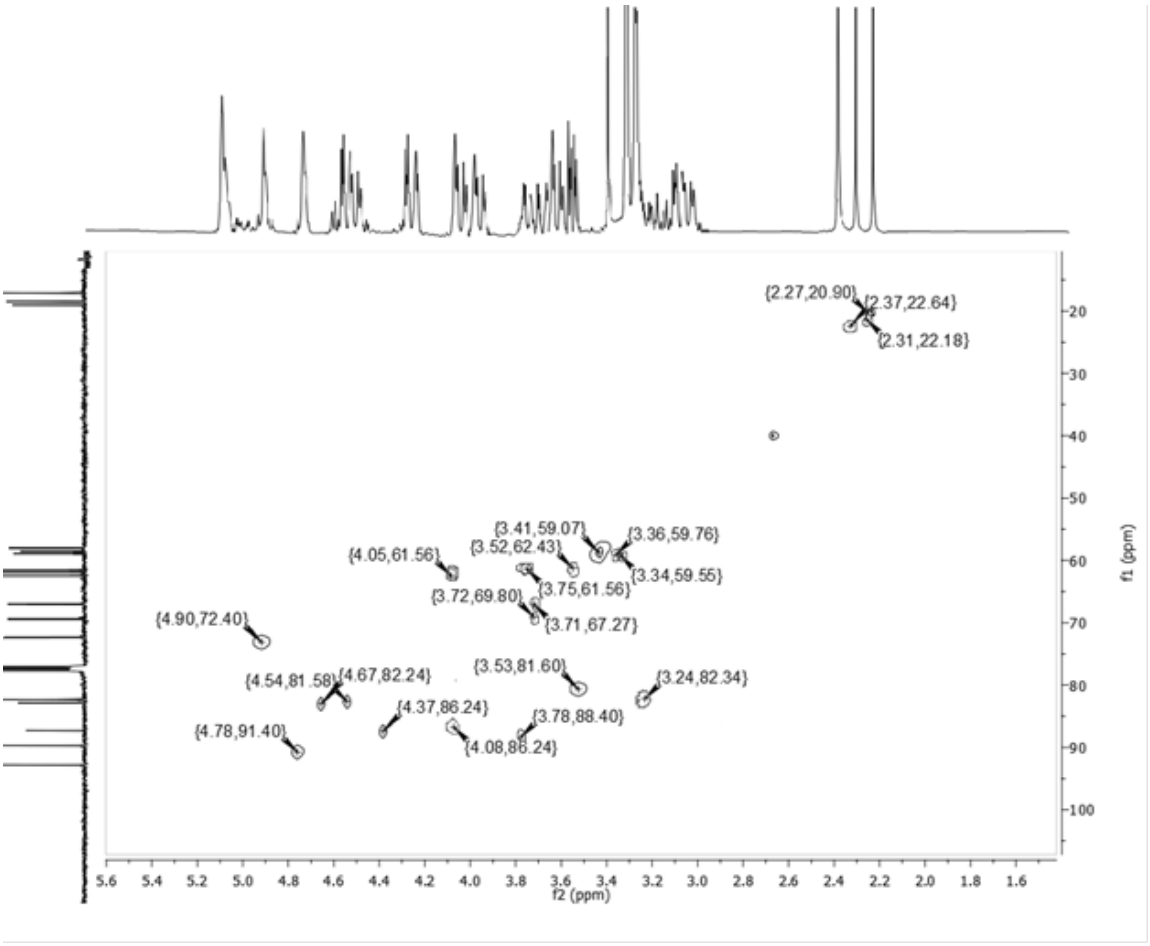

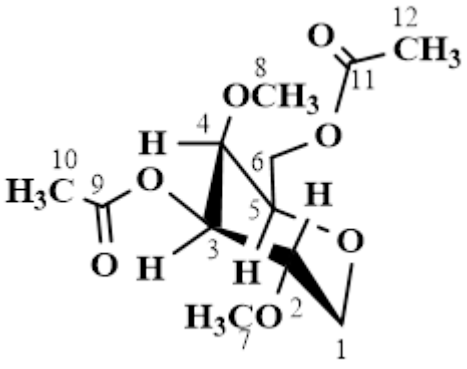

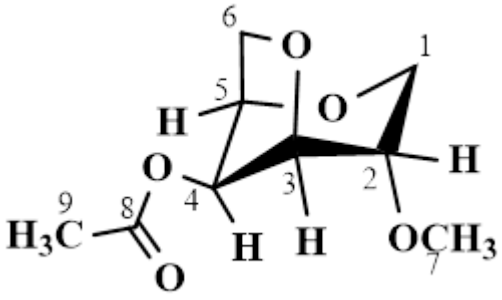

Monomer unit A **Monomer unit B**

Figure 6.30.: HSQC spectrum of the methylated polysaccharide analogue

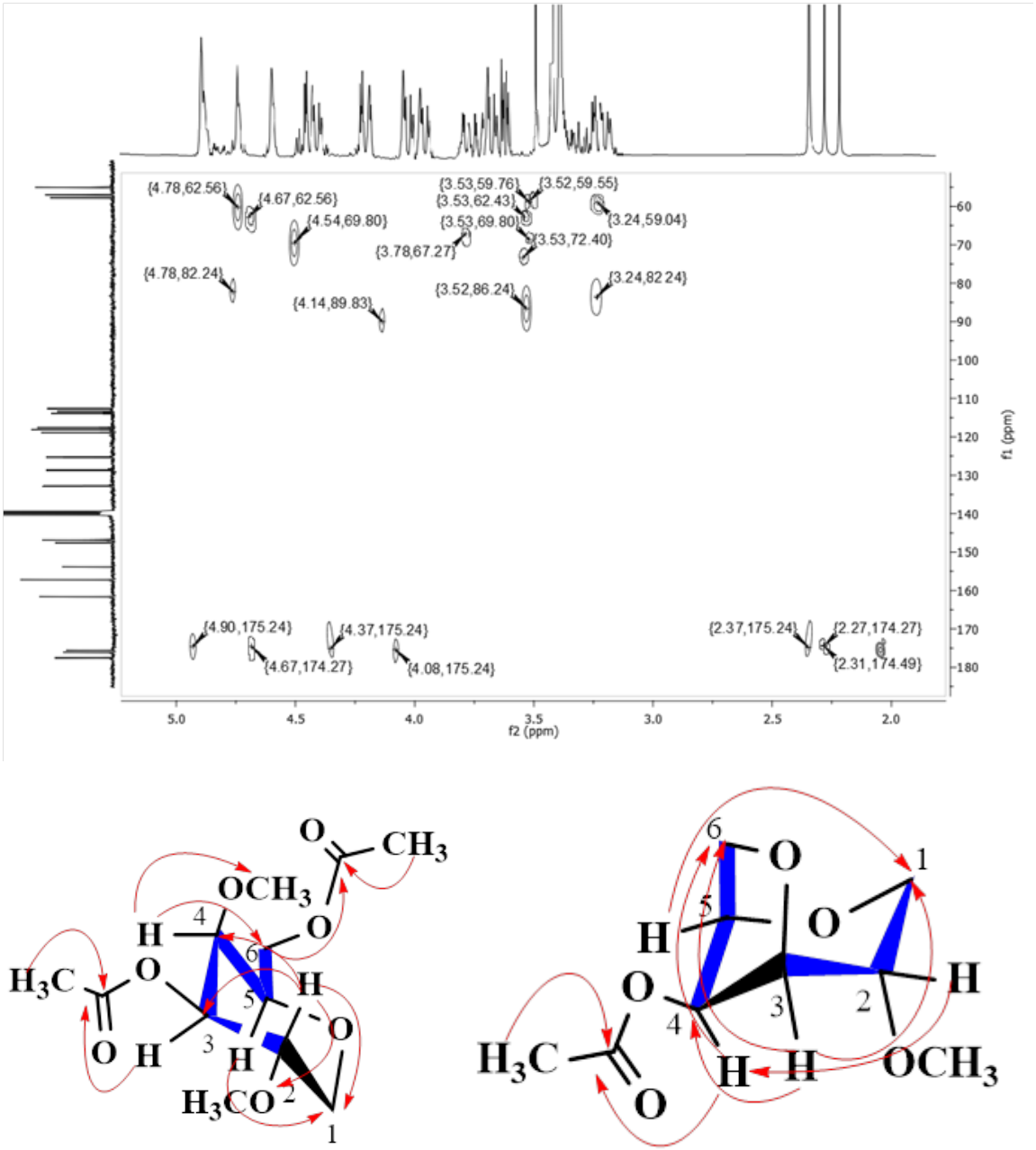

Figure 6.31.: HMBC spectrum of the methylated polysaccharide analogue

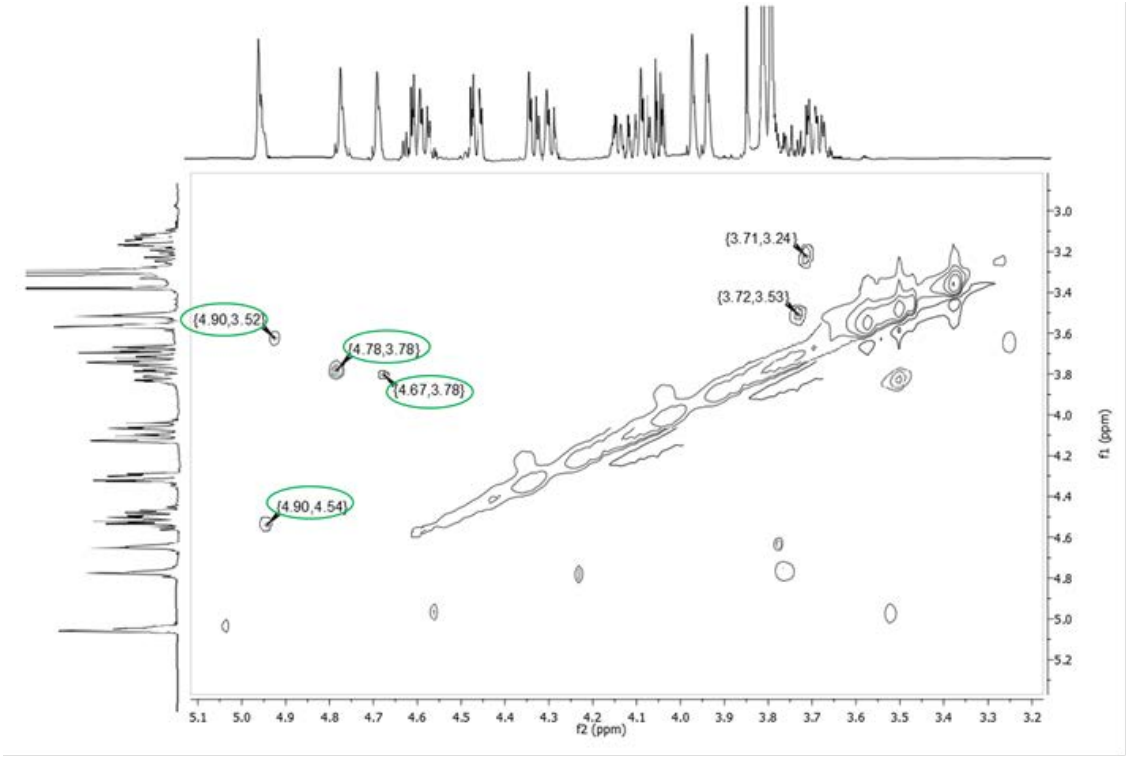

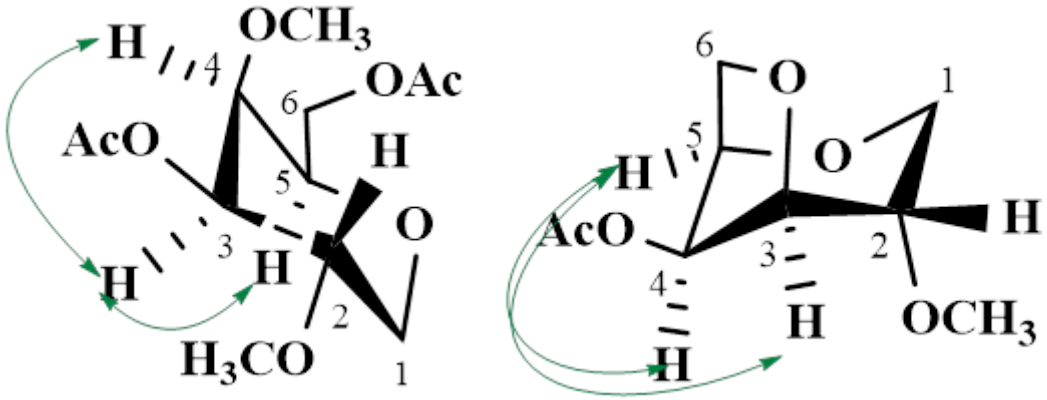

Monomer unit A **Monomer unit B**

Figure 6.32.: NOESY spectrum of the methylated polysaccharide analogue

Three major signals were discernable in the proton NMR in between the region of δ2.0-2.5 and δ3.3-3.5, representing the partially methylated and acetylated sugar residues in the studied polysaccharide, GSP-2. The doublet appeared at δ3.72 and δ3.71 (with same integral) depicted the protonated anomeric region in polysaccharide after cleavage of the glycosidic linkage. The 1D NMR along with HSQC characterized the proton and carbon signals in the acetylated polysaccharide, and the absence of anomeric region in the proton NMR ensured the acetylation of glycosidic residues in GSP-2. Thus, the signals at δ3.72 (δ69.80; CH_2) and δ3.71 (δ67.27; CH_2)

were assigned as C_1 positions of AcGal*p* and AcAnGal*p*, respectively. The signal at δ3.72 (δ69.80; CH_2) was found to exhibit HMBC correlation with δ81.60 (δ3.53), which framed the fragment of -CH_2-CH-(O-); C_1-C_2. The proton signal at δ3.53 displayed HMBC correlation with the carbon at δ59.76 (δ3.36), representing the methoxyl group attached to the C_2 position; -CH-(O-CH_3). The further fragments in the AcGal*p* were framed by the COSY correlation, such as H_2(δ3.53)/H_3(δ4.90)/H_4(δ3.52)/H_5(δ4.54)/H_6(δ4.37/4.08), assigning the fragment of -CH_2-CH-(OCH_3)-CH(O-)-CH(O-)-CH(O-)-CH_2-; C_1-C_6. These fragments were further confirmed by the HMBC correlations, H_2 (δ3.53) to C_3 (δ72.40); H_3 (δ4.90) to C_4 (δ62.43); H_4 (δ3.52) to C_6 (δ86.24), H_5 (δ4.54) to C_1 (δ69.80). The -CH- at δ4.90 (H_3) displayed HMBC correlation with δ175.24, demonstrated the (-C=O) substitution at C_3. At the same time, the HMBC correlation in between δ2.37 and δ175.24 assigned the connection of methyl (-CH_3) to (-C=O) functionality. These correlations represented the substitution of acetyl functionality at C_3; -CH-((-C=O)-CH_3). The -CH- functionality at δ3.52 (H_4) showed the HMBC with δ59.55, indicating the presence of methoxyl functionality at C_4; -CH-(OCH_3). The highly deshielded proton signal at δ4.54 proximal to the oxygen moiety of the pyranose ring with multiplet was found to be correlated with -CH_2- functionality at C_6 via the COSY correlation, H_5(δ4.54)/H_6(δ4.37/4.08). Finally, the HMBC correlations from the signals at δ4.37, δ4.08 and δ2.31 to the δ174.49, revealed the acetyl substitution at C_6. The observations from the acetylation along the methylation (in section 3.3.3) apparently revealed that the sulfated functionality at C_6 was replaced by an acetyl group. Thus, in AcGal*p*, C_2 and C_4 positions were substituted with methyl entities and C_3 and C_6 positions were substituted with the acetyl moieties. Therefore, in AcGal*p*, the positions at C_1 and C_3 confirmed the linkage pattern of (1⋯→3). The partially methylated and acetylated AcGal*p* were characterized as 3,6-diacetyl-2,4-dimethyl-β-D-Gal*p* and 3,6-Ac_2-2,4-Me_2-β-D-Gal*p*, respectively.

Further, the signal at δ3.71 (δ67.27; CH_2) was found to exhibit COSY correlation with δ3.24 (δ82.34), which framed the fragment of -CH_2-CH-(O-); C_1-C_2. The signal at δ3.24 displayed HMBC correlation with δ59.07 (δ3.41), indicating the methoxyl group attached at the C_2 position; -CH-(O-CH_3). Additional fragments in the AcAnGal*p* was framed by the COSY correlations, at H_2(δ3.24)/H_3(δ4.78) and H_4(δ4.67)/H_5(δ3.78)/H_6(δ4.05/3.75) along with HMBC correlations, H_2 (δ3.24) to C_3 (δ82.34); H_3 (δ4.78) to C_4 (δ82.24); H_4 (δ4.67) to C_6 (δ62.56), H_5 (δ3.78) to C_1 (δ67.27), indicating the presence of the fragment -CH_2-CH-(OCH_3)-CH(O-)-CH(O-)-CH(O-)-CH_2-; C_1-C_6. The functionality at δ4.67 (H_4) showed HMBC correlation with δ174.27, indicating the attachment of (-C=O) group at C_4. At the same time, the proton signal at δ2.27 displayed the HMBC with δ174.27. These HMBC correlations together demonstrated the presence of the acetyl functionality at C_4; -CH-((-C=O)-CH_3). The relative configurations obtained for partially methylated and acetylated polysaccharide were depicted in Figure 6.32.

Thus, in AcAnGal*p*, C_2 and C_4 positions were substituted with methyl and acetyl entities, respectively. The C_1 was found to be protonated like AcGal*p*. Therefore, the linkage pattern was confirmed as (1⁻⁻→4). The partially methylated and acetylated AcAnGal*p* was characterized as 4-acetyl-2-methyl-α-D-AnGal*p* or 4-Ac-2-Me-α-D-AnGal*p*. These results together confirmed that the following sequel of linkage pattern of monosaccharide residues were apparent in GSP-2 derived from *G. salicornia*, and were interpreted as (1⁻⁻→3)-*O*-6-sulfonato-2-methyl-β-D-Galactopyranose-(1→4)-2-methyl-α-D-3,6-Anhydrogalactopyranose-(1→⁻⁻) and (1⁻⁻→3)-*O*-6S-2-Me-β-D-Gal*p*-(1→4)-2-Me-α-D-3,6-AnGal*p*(1→⁻⁻) or [2-Me-G6S-2-MeAnG].

6.3.3.6 Linkage pattern analysis of polysaccharide by reductive cleavage method

The modern technique of reductive cleavage was introduced for the determination of linkage pattern and position of rings in polysaccharide. This method forms the basis of a series of chemical reactions, such as methylation, reduction and acetylation analysis; wherein the polysaccharides on partial methylation followed by reduction and acetylation formed partially methylated and acetylated (PMA) sugar residues. These resultant PMA derivatives were further characterized by GC-MS. The PMA-D-hexitols and PMA-3,6-anhydro-D-hexitols having galactose configuration, namely, 3,6-diacetyl-2,4-dimethyl-β-D-Gal*p* and 4-acetyl-2-methyl-α-D-AnGal*p*, respectively, were deduced. The spectrum was found to exhibit signals corresponding to these PMA-D-hexitols and PMA-3,6-anhydro-D-hexitols at *m/z* 274.1 and 200.1, respectively, thereby indicating the molecular weight of these components. Appearance of the peaks in the spectrum revealed differences in the positional-isomers in terms of the presence of some ions, such as $CH_3C{\equiv}O^+$ (*m/z* 43) and their intensity related to the base peak. The signals of some ions, such as *m/z* 243.1, 211.1, 152.0 were detected in the spectrum due to the eliminations of methanol/O-methyl and acetic acid/O-acetyl, wherein those peaks were arosed due to the cleavage of C_2, C_3, C_4 and C_6 from D-hexitols. Similarly, the signals of certain ions, like *m/z* 169.1and 109.0, were ascertained in the spectrum due to the eliminations of methanol/O-methyl and acetic acid/O-acetyl, wherein those peaks arosed due to the cleavage of C_2 and C_3 from anhydro-D-hexitols. The base peak was appeared at *m/z* 94.0.

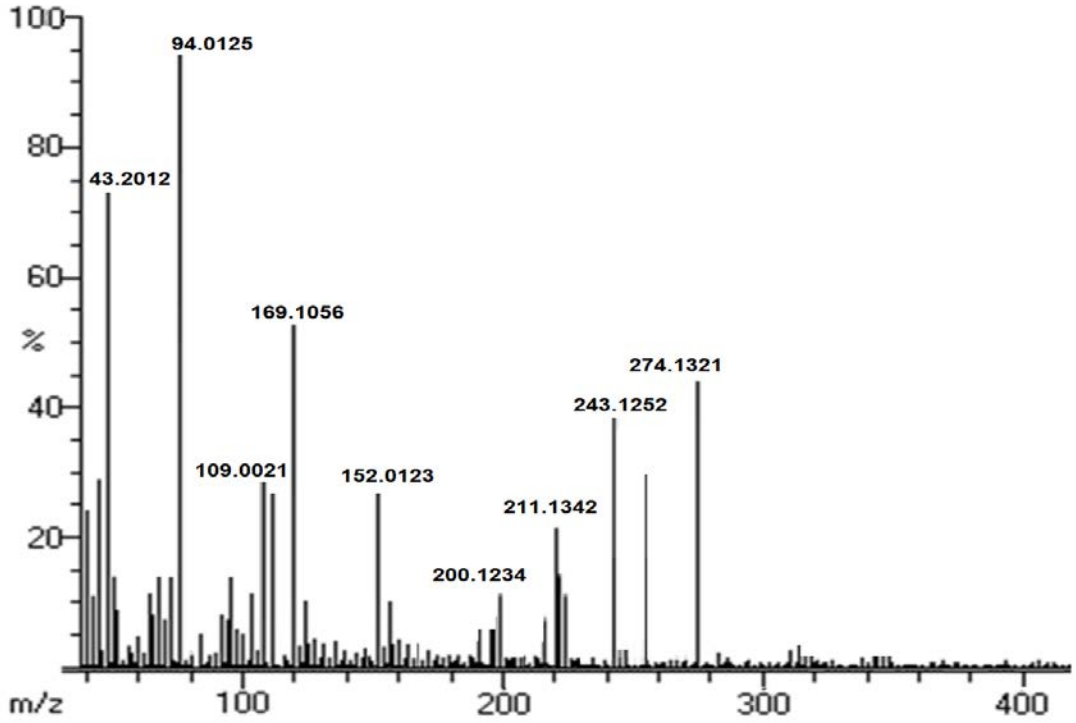

Figure 6.33.: GCMS spectrum of the polysaccharide analogue

6.3.3.6 Structural interpretation of polysaccharide-nano composite (P-AgNPs)

The different concentrations of polysaccharide solutions (0.1, 0.15, 0.2, 0.25, and 0.3 % in a, b, c, d, and e, respectively) were agitated with $AgNO_3$ for the nanoparticle formation. The yields obtained for different concentrations were found to be 0.042 g, 0.063 g, 0.85 g, 0.120 g and 0.158 g, respectively. These were further confirmed by the surface plasmon resonance (SPR) bands observed from the UV chromatogram. These results revealed that the formation of numbers of AgNPs increased with the increasing concentration of polysaccharide. Therefore, the solution of 0.3 % with higher yield was selected for the further analysis and characterization of silver nano composite (P-AgNPC) of polysaccharide.

6.3.3.7 Structural interpretation of polysaccharide-nano composite (P-AgNPCs) by UV

UV-visible spectroscopic data was used to determine the formation of silver nanocomposite (AgNPC) by observing the SPR bands. The absorption spectrum of nano particles (NP_S) depends on their shape, size, and distribution. However, characteristic SPR bands of Ag-NPs were identified around in the region of 402 to 420 nm (Fig. S27), which indicates the formation of Ag-NPs. As shown in Figure 6.34, when the concentrations of polysaccharide in solution increased (0.1, 0.15, 0.2, 0.25, and 0.3 % in a, b, c, d, and e, respectively), the intensity of the SPR peak also regularly increased. The increase in the absorbance was indicative the increasing concentration of

Ag-NPC. Furthermore, with an increase in the concentrations of polysaccharide, the absorbance also increased and shifted to the lower wavelength at 402 nm to blue-shift, which was referred to a decrease in the particle size. Based on Mie's theory (Elsupikhe et al, 2015, 2016), the nanoparticles with different sizes should demonstrate different optical properties due to the difference in the SPR bands. It was observed that the 0.3 % polysaccharide solution had a larger absorbance compared to other samples, indicating the increased concentration of Ag-NPC in 0.3 % polysaccharide solution (Elsupikhe et al, 2015, 2016).

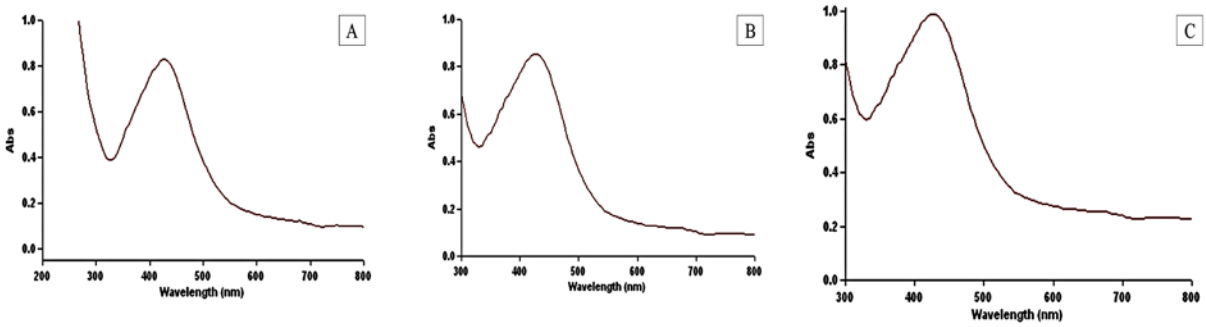

Figure 6.34.: UV chromatogram of polysaccharide-silver nano composite (AgNPC) at different time intervals, (A) 30, (B) 60 and (C) 120 minutes

6.3.3.7 Structural interpretation of polysaccharide-nano composite (P-Ag-NPC) by FTIR

FT-IR spectrum of the polysaccharide silver nanocomposite (P-Ag-NPC) showed absorption bands at 3,385 cm^{-1} and 2,912 cm^{-1} that were characteristics of the O-H stretching and interlayer C-H stretching, respectively. The absorption band at 1,446 cm^{-1} was corresponding to sulfate stretch and absorption at 1,238 cm^{-1} was due to the ester sulfate group. Additionally, the absorption peak at 1,048 cm^{-1} was assigned to the glycosidic linkage and absorption band at 924 cm^{-1} for 3,6-anhydro-D-galactose. The absorption at 847 cm^{-1} assigned the presence of C-O-S axial secondary sulfate on the C-4 group of the galactose (Barros et al., 2013; Knutsen et al., 1994; Usov et al., 2011). However, after adding $AgNO_3$ followed by ultrasonic irradiation resulted a new peak at 1,757 cm^{-1}, which was due to the formation of the carbonyl group (Figure 6.35). This result was reinforced by the carbonyl group resulted from the oxidation of carbohydrate radicals generated inside the polysaccharide (Elsupikhe et al, 2015, 2016). The peaks of polysaccharide after reaction with $AgNO_3$ were narrowed down at 3385 cm^{-1}, indicating the polymeric O-H functional groups of polysaccharide got involved in capping silver nanoparticles. The broad peak in the range 100 to 500 cm^{-1} was related to the Ag-NPs bonding with oxygen from of the hydroxyl groups of the polysaccharide chains (Elsupikhe et al, 2015, 2016). This is according to the presence of van der

Waals forces between the positively charged groups that surround the surface of the inert Ag-NPCs, and negatively charged groups presenting in the molecular structure of the polysaccharide (Figure 6.35). Moreover, the change in the wavenumber in the P-Ag-NPC samples that shifted to the lower wave numbers indicated an interaction between the polysaccharide and Ag-NPC (Elsupikhe et al, 2015, 2016). These FTIR spectral attributions confirmed the interactions of Ag-NPCs with the studied polysaccharide.

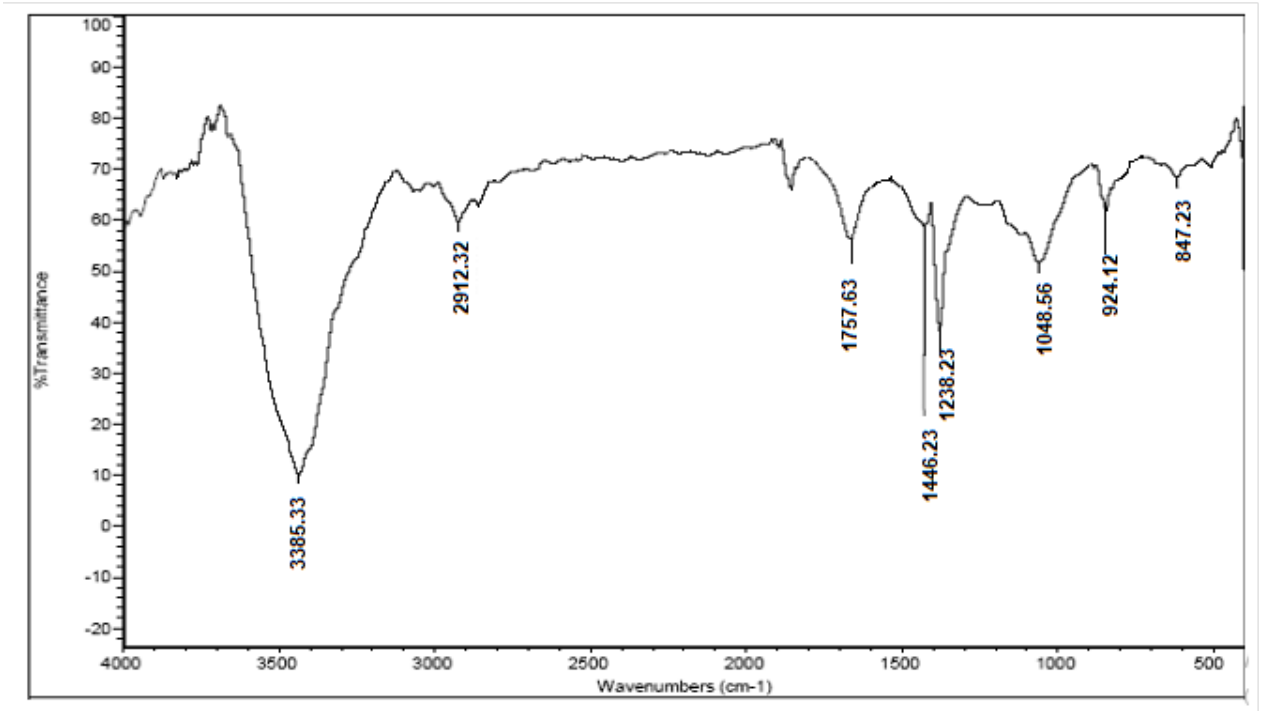

Figure 6.35.: FTIR spectrum of the polysaccharide-silver nano composite (Ag-NPC)

6.3.3.7 Morphological analysis of polysaccharide and polysaccharide-silver nanocomposite (P-Ag-NPCs) by SEM analysis

The polysaccharide (GSP-2) and polysaccharide-silver nanocomposite (P-Ag-NPC) have unique physical and chemical properties owing to their size and shape-dependent effects. Therefore, the morphological features of GSP-2 and P-Ag-NPCs were studied by using SEM experiment (Figure 6.36). The GSP-2 was found to be comprised of spindle-shaped fibrous polymer units. They were of ~1.40 µm length and ~2.50 nm thickness. The appearance and formation of Ag-NPs in 0.3 % polysaccharide solution were analyzed by SEM and EDX experiments (Figure 6.36). The higher percentage of silver along with other elements, such as C, O and S were indicative of their presence in P-Ag-NPC. Higher percentage of silver signals implied the formation of P-Ag-NPCs. The peak of sulfur substantiating the role of polysaccharide sulfate groups in capping P-Ag-

NPs. The P-Ag-NPs were found to appear in spherical shape with the size range of 451 to 551 nm. This solution of 0.3 % was further irradiated with ultrasonicator (750 Watt ultrasonic processor, Sonics, Newtown, CT 06470 USA, and 50/60 Hz) to reduce the size of the particles. Therefore, the 0.3 % solution was subjected to subsequent irradiations with time intervals of 30, 60 and 120 min. The P-Ag-NPC was formed after 30 min interval, and wasappeared as spherical in shape, with the particle size being 110-225 nm.

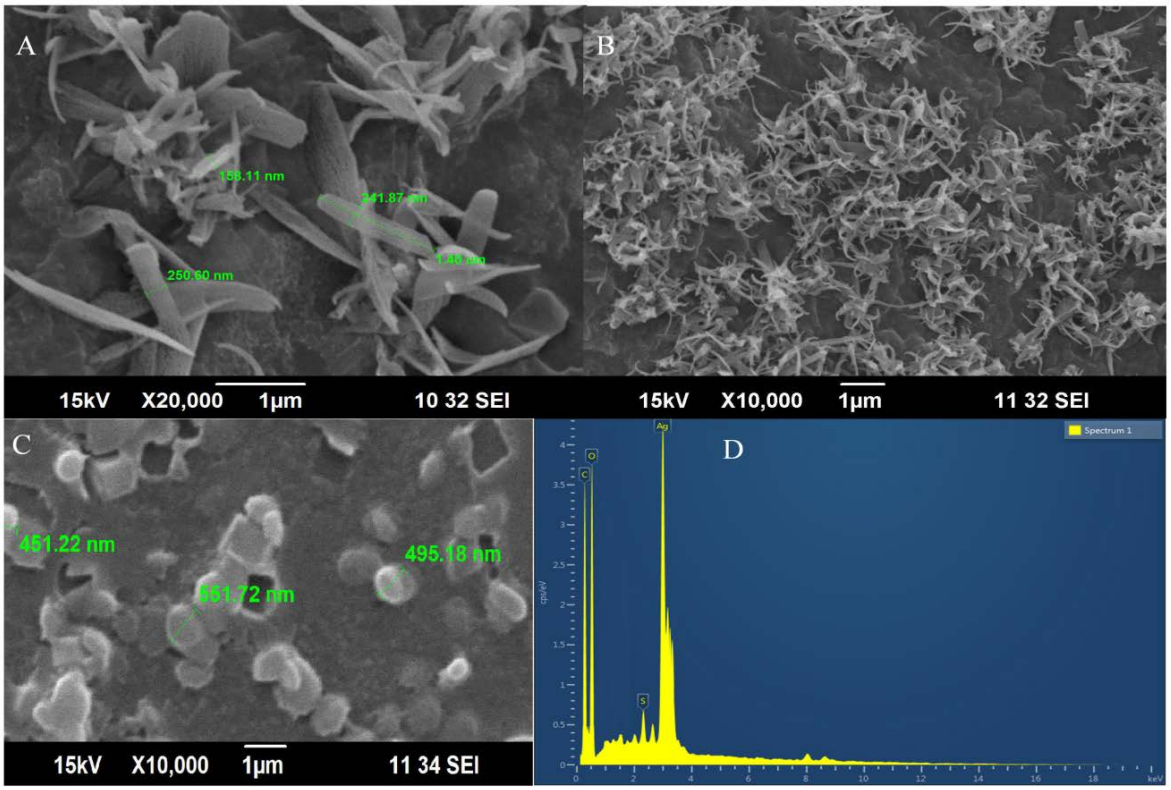

Figure 6.36.: Scanning electron microscopic (SEM) image of the studied polysaccharide, (1⋯→3)-*O*-6-sulfonato-β-D-galactopyranosyl-(1→⋯4)-3,6-anhydro-α-D-galactopyranose-(1⋯→).

Similarly, the uniform distribution of spherical P-Ag-NPC was observed after 60 and 120 min, and which were found to carry the particles of size of 45 nm and 18 nm, respectively (Figure 6.37). SEM micrograph depicted that polysaccharide has a structure filled with intrusions, while a smooth surface was observed for polysaccharide. Therefore, it can be said that the addition of Ag-NPs smoothens the surface of P-Ag-NPC. SEM images of P-Ag-NPC also indicated the change in the surface of Ag-NPC when the concentration of polysaccharide was found to be increased. However, the size of Ag-NPCs became smaller with an increasing concentration of polysaccharide. Moreover, Figure 6.37 exhibited the smallest size and increasing numbers of Ag-

NPsthereby referring that the yields of Ag-NPs (with smaller spherical size) were proportionally increased with the increasing concentration of polysaccharide (Elsupikhe et al, 2015, 2016).

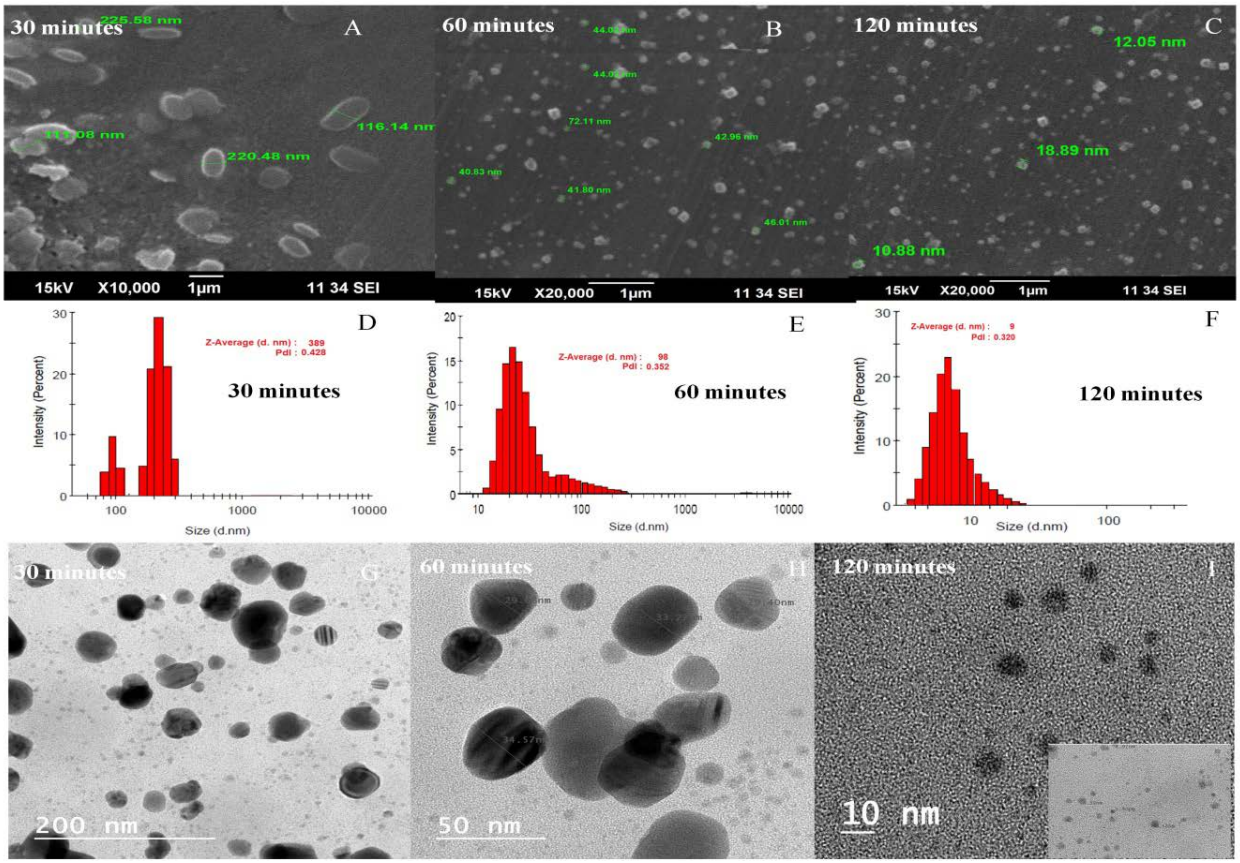

Figure 6.37.: Scanning electron microscopic (SEM) image of polysaccharide-silver nano composite (P-Ag-NPC) after (**A**) 30, (**B**) 60 and (**C**) 120 min of ultra-sonication. Particle size distribution curves of polysaccharide-silver nano composite (P-Ag-NPC) by DLS methods after (**D**) 30, (**E**) 60 and (**F**) 120 min of ultra-sonication. Transmission electron microscopic images of polysaccharide-silver nano composite (P-Ag-NPC) after (**G**) 30, (**H**) 60 and (**I**) 120 min of ultra-sonication.

6.3.3.8 Structural interpretation of polysaccharide-nano composite by XRD analysis

From Figure 6.38, it could be clearly seen that no diffraction peak was observed for the pure polysaccharide, while the Ag^0 polysaccharide-nano composite (P-Ag-NPCs) showed a diffraction peak at = 29.743 and 34.483, of the face centered cubic structure of Ag^0. This faced-centered cubic (fcc) structure indicated that Ag^0 nanoparticles were dispersed in the polysaccharide-nano composite (P-Ag-NPCs), which was confirmed with the SEM image shown in Figure 6.36 & 6.37. These results were mainly due to the strong interaction between the Ag^0 nanoparticles and polysaccharide-nano composite (P-Ag-NPCs).

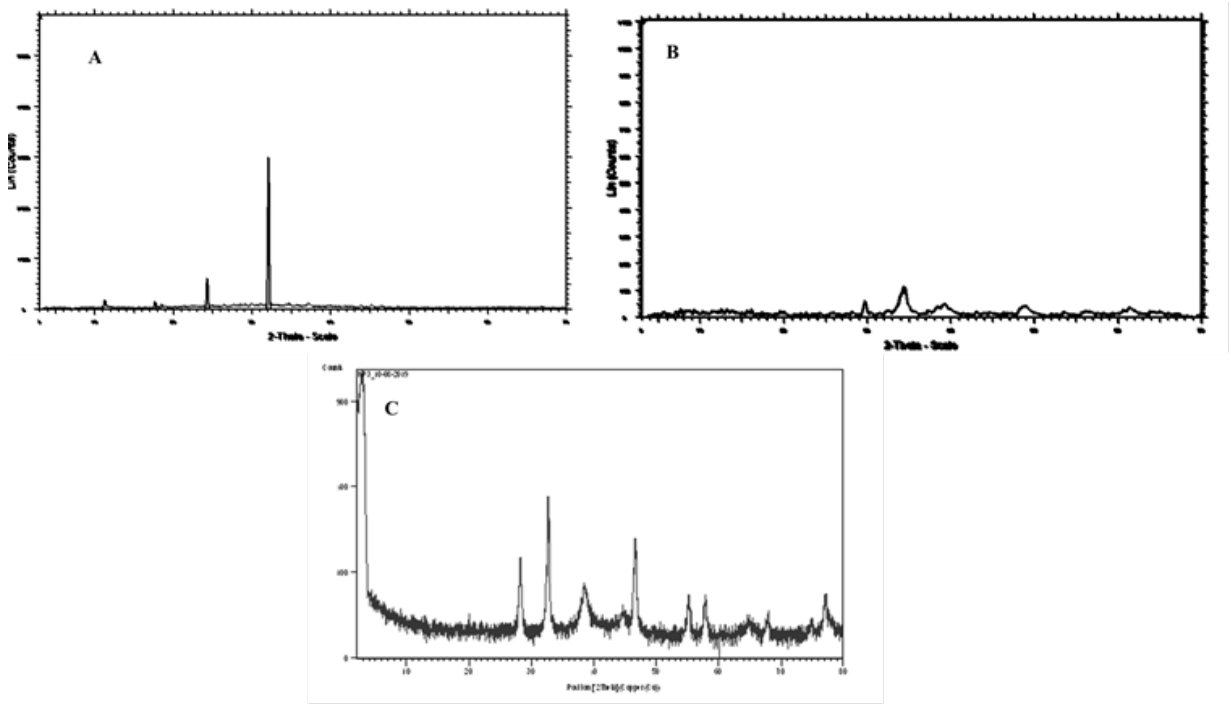

Figure 6.38.: XRD of polysaccharide-silver nano composite (AgNPC) at different time intervals, (**A**) 30, (**B**) 60 and 120 min (**C**)

6.3.3.9 Structural interpretation of polysaccharide-nano composite by TEM analysis

The TEM images of Ag-NPC 0.3 % solution of polysaccharide with different time intervals (30, 60 and 120 min, respectively) were depicted in Figure 6.37. TEM images and their size distributions indicated that the mean diameters and standard deviation of Ag-NPC were about 96.36 ± 24.33, 34.08 ± 3.33, and 4.21 ± 3.91 nm for 30, 60 and 120 min, respectively. The TEM results were in agreement with the UV-vis spectral data, which indicated that when the concentrations of polysaccharide were increased, the size of Ag-NPs decreased with increasing distribution. These results were also corroborated by the SEM images of Ag-NPC formed after time intervals (30, 60 and 120 min, respectively) (Figure 6.37).

6.3.3.10 Structural interpretation of polysaccharide-nano composite by AFM analysis

The P-Ag-NPC was further characterized by atomic force microscopic (AFM) analysis (Fig. 6). AFM provides a three-dimensional surface profile for nanoparticles. The area of polysaccharide analyzed was 1 µm × 1 µm. Although the lateral dimensions were influenced by the shape of the probe, the height measurements could provide the height of nanoparticles with a high degree of accuracy and precision. As shown in the histogram of AFM (Figure 6.39), the size distribution of the P-Ag-NPs was found to be in the range of ~56 nm after 60 min of time interval. The 3D-profile of P-Ag-NPs displayed uniform distribution of the nanoparticles throughout the

surface of the polymer. The white patches observed in the 2D-histogram revealed the spherical shape of P-Ag-NPs.

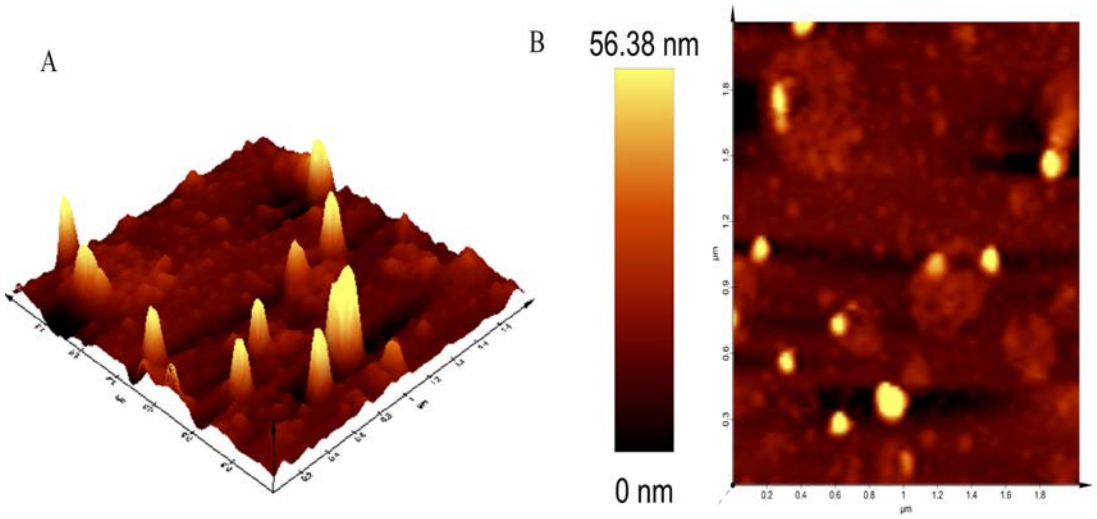

Figure 6.39.: AFM data of polysaccharide-silver nano particle (P-Ag-NPC) composite 2D and 3D images after 60 min (**A**) 2D AFM image of P-AgNPC nanoparticles (**B**) 3D image AFM image of P-Ag-NPC nanoparticles

6.3.3.11 Structural interpretation of polysaccharide-nano composite by Particle size analysis and zeta potential

The particle size analysis has been found as the primary characteristic in the synthesis of nanoparticles and in general, the nanoparticle size ranges of 1-100 nm. The particle size of Ag-NPC was determined by the particle size analyzer (PSA) with the diluent water by using dynamic light scattering (DLS) method. The average particle size of Ag-NPC at different time intervals was depicted in Figure 6.40. The P-Ag-NPC on 30 min of ultrasonic irradiation resulted in the particles with average size in the range of 100-500 nm. After 60 min interval, the size of the Ag-NPs was reduced to ~100 nm. Similarly, the size of the particles was reduced to ~10 nm after 120 min of ultrasonic irradiation. Measurement of the particles using PSA was also obtained by polydispersity index (PDI) value. Measurement of the value of PDI aimed to determine the particle size distribution, which indicated the level of uniformity of the size of the nanoparticles produced. The PDI of P-Ag-NPC composite after 30 min of ultrasonic irradiation resulted in the particles with PDI, 0.428. This was shifted to 0.352, and then 0.320 after 60 min and 120 min of ultrasonic irradiation, respectively. The PDI value below 0.5 indicated the homogeneous dispersion of the particles in the solution, and they were considered as monodispersed system. The monodispersed

systems were found to start from 0.01 up to the value of 0.5-0.7. While the value of PDI of more than 0.7 showed a very wide size distribution, and might contain largeer particles or aggregates. Smaller values of PDI showed narrower particle size distribution and more homogeneous particle size diameter.

Zeta potential is one of the most important nanoparticle characterization tools, which was used to determine the surface charge and give an idea repulsive force among particles of the resulting nanoparticle dispersion system. The interaction between the particles had a prominent role in the stability of the colloidal solution. In general, a dispersion system declared stable if the value of the zeta potential was more positive than +30 mV, or more negative than -30 mV, and were determined based on the electrostatic repulsion. The formula containing polysaccharide nano-composite was found to possess a zeta potential value of -0.23, -0.25 and -0.28, at 30, 60 and 120 min time intervals, respectively. This was influenced by the presence of a sulfate group that could cause increased surface charge and zeta potential value generated.

6.3.4 Molecular docking analysis of the studied polysaccharide from G. salicornia

The attenuation potential of starch degrading enzymes, α-glucosidases and α-amylases inhibition by the studied polysaccharide is an effective procedure to attribute the prospective anti-diabetic properties of the studied compound. The commercially standards acarbose and voglibose have been extensively used to regulate the glucose levels in blood. The derived sulfated polysaccharide analogue was subjected to *in silico* analysis against these carbolytic enzymes (α-amylases and α-glucosidase). The RMSD data were used to evaluate their results. The *in silico* analysis parameters, such as binding energy, intermolecular and torsional free energy, and inhibition constants of polysaccharide were documented (Figure 6.41, Table 6.8). *In silico* molecular docking analysis of the polysaccharide with α-glucosidase with grid box x = 37.224, y = -18.821, z = 28.301, α-amylase with grid box x = -9.251, y = 53.269, z = 29.658 and DPP-IV with grid box x = 28.493, y = -19.821, z = 25.004 displayed the efficient interactions of ligand polysaccharide with the enzyme target sites (Fig. 9). The polysaccharide recorded least binding energy of -5.24 kcal mol^{-1} in interactions with α-glucosidase enzyme target sites. Likewise, the constant of enzyme inhibition (Ki) was 144.49 nM towards α-glucosidase enzyme. Also, intermolecular energy of polysaccharide was -6.43 kcal mol^{-1}. The molecular docking interaction of ligand polysaccharide and α-glucosidase showed four hydrogen bonds (displayed as red and blue coloured lines) to the amino acyl residues of THR^{83}, LYS^{40}, ASP^{34} and ASN^{32} with the bond distances of 2.772, 3.288, 3.054 and 2.806 Å in the active binding site. The polysaccharide recorded least binding energy of -2.44 kcal mol^{-1} in interactions with α-amylases enzyme target sites. Likewise, the constant of enzyme inhibition (Ki) was 16.22 nM towards α-glucosidase enzyme. Also, intermolecular energy of polysaccharide was -3.71 kcal mol^{-1}. The molecular docking

interaction of ligand polysaccharide and α-amylases showed one hydrogen bond (displayed as red and blue coloured lines) to amino acyl residues of HIS^{299} with the bond distances of 3.620Å in the active binding site. The polysaccharide recorded least binding energy of -11.13 kcal mol^{-1} in interactions with DPP-IV enzyme target sites. Likewise, the constant of enzyme inhibition (Ki) was 6.94 nM. Also, intermolecular energy of polysaccharide was -12.40 kcal mol^{-1}. The molecular docking interaction of ligand polysaccharide and DPP-IV showed ten hydrogen bonds (displayed as red and blue coloured lines) to amino acyl residues of THR^{156}, THR^{216}, SER^{106}, ILE^{107}, ARG^{61} with the bond distances of 2.546, 1.603,2.536, 3.198, 2.008, 2.198, 2.350, 2.496, 2.438, 2.666 Å in the active binding site. Likewise, the polysaccharide recorded least binding energy of -6.98 kcal mol^{-1} in interactions with ALP enzyme target sites. The constant of enzyme inhibition (Ki) was 7.68 nM towards the ALP enzyme. Also, intermolecular energy of polysaccharide was -8.22 kcal mol^{-1}. The molecular docking interaction of ligand polysaccharide and DPP-IV showed ten hydrogen bonds (displayed as red and blue coloured lines) to amino acyl residues of ILE^{374}, SER^{373}, PHE^{375}, GLU^{411}, SER^{414} with the bond distances of 3.343, 2.446, (3.266, 3.204), (3.027, 3.196, 2.750), 3.367 Å in the active binding site.

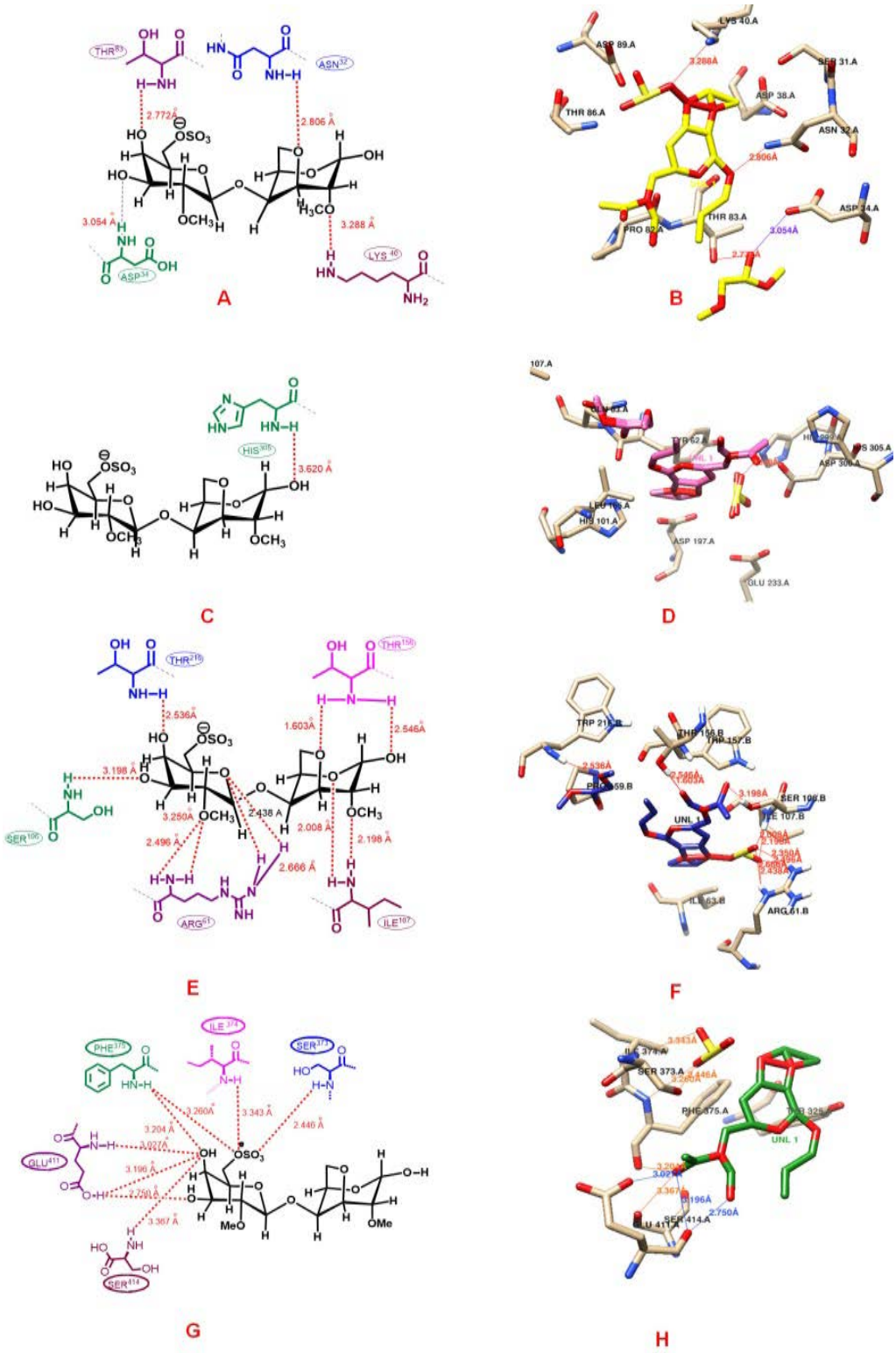

Figure 6.41.: Closer image of molecular docking interactions of polysaccharide in the catalytic site of α-amylase, α-glucosidase, proteolytic DPP-IV and alkaline phosphate (ALP), as obtained by docking experiment. The molecular docking interaction of ligand polysaccharide and α-amylases showed one hydrogen bond (displayed as red and blue coloured lines) to amino acyl residues of

HIS^{299} with the bond distances of 3.620Å in the active binding site. The molecular docking interaction of ligand polysaccharide and α-glucosidase showed four hydrogen bonds (displayed as red and blue coloured lines) to amino acyl residues of THR^{83}, LYS^{40}, ASP^{34} and ASN^{32} with the bond distances of 2.772, 3.288, 3.054 and 2.806 Å in the active binding site. The molecular docking interaction of ligand polysaccharide and DPP-IV showed ten hydrogen bonds (displayed as red and blue coloured lines) to amino acyl residues of THR^{156}, THR^{216}, SER^{106}, ILE^{107}, ARG^{61} with the bond distances of 2.546, 1.603,2.536, 3.198, 2.008, 2.198, 2.350, 2.496, 2.438, 2.666 Å in the active binding site. The molecular docking interaction of ligand polysaccharide and DPP-IV showed ten hydrogen bonds (displayed as red and blue coloured lines) to amino acyl residues of ILE^{374}, SER^{373}, PHE^{375}, GLU^{411}, SER^{414} with the bond distances of 3.343, 2.446, (3.266, 3.204), (3.027, 3.196, 2.750), 3.367 Å in the active binding site.

6.4. Conclusion

The present study demonstrated that the marine-derived polysaccharide and its nano composite (P-Ag-NPs) with the silver particles derivative constituted promising candidates to combat the hyperglycemic conditions. The titled polysaccharide derivatives were found to be effective in attenuating DPP-IV enzyme and carbolytic enzymes such as α-amylases and α-glucosidases. A novel (DPP)-IV inhibiting polysaccharide, A (1⋯→3)-*O*-6-sulfonato-β-D-galactopyranosyl-(1→⋯4)-3,6-anhydro-α-D-galactopyranose-(1⋯→) from red seaweed *Gracilaria salicornia,* was isolated and structurally characterized. The seaweed derived polysaccharide registered greater reduction potentials against proteolytic DPP-IV (IC_{50} 0.63 mg mL^{-1}) and carbolytic enzymes α-amylase and α-glucosidase (IC_{50} 1.48-1.51 mg mL^{-1}), whereas the activities were comparable with those displayed by acarbose (IC_{50} DPP-IV 0.13 mg mL^{-1}, carbolytics IC_{50} 1.38-1.47 mg mL^{-1}). Likewise, the antioxidative potential of the polysaccharide was higher (IC_{50} 0.35-0.48 mg mL^{-1}) than that of commercial standard ascorbic acid (IC_{50} 0.37-0.51 mg mL^{-1}). The presence of chemical constituents in polysaccharide was assessed by the analytical methods, which were corroborated with the bioactivity of polyglactan. The polysaccharides exhibited lower binding energy conformation (-11.13 kcal mol^{-1}) towards the catalytic binding site of DPP-IV, and this was also reinforced with the bioactivity of polysaccharide. Based on the bioactivity, silver-nano-composite of polysaccharide was synthesized for prospective activities against hyperglycemia. The polysaccharide-silver-nano-composite (P-Ag-NP-composite) demonstrated greater inhibition potential against proteolytic (DPP-IV IC_{50} 0.52 mg mL^{-1}) and carbolytic enzyme (α-amylase and α-glucosidase IC_{50} 0.22-0.70 mg mL^{-1}, respectively) than that of the native polysaccharide (≥ 1.0 mg mL^{-1} and ≥ 0.6 mg mL^{-1}, respectively). The nano particle synthesized from polysaccharide was found to be of 4-400 nm size, at different time intervals of 30, 60 and 120 min, and their shape was found to be spherical. The inhibition potential of polysaccharide and its silver nano composite

against DPP-IV along with antioxidant potential suggested the formulation of bioactive leads to reduce the risk of hyperglycemic pathologies.

CHAPTER 7

SUMMARY

Seaweeds have developed an adaptive strategy for their survival in their competitive surroundings by the production of large array of metabolites, and they act as chemically and biologically active defense systems against several life style diseases. Studies on natural product chemistry and chemical defense systems of seaweeds recognized the presence of bioactive leads with prominent pharmacological activities. Phlorotannins and polyphenols from seaweeds have revealed their activities against proliferation of cancer cells and produce some effects on anti-inflammatory and anti-diabetic responses. Bioactive components in seaweeds were recognized to modulate glucose-induced oxidative stress and their ability to control the presence of starch-digestive enzymes. Potential side effects attributed to the synthetic drugs, demanded naturally obtained potential bioactive components for curing of persistent metabolic syndromes. Therefore, consumption and addition of these seaweeds might be increased their food and pharmaceutical applications.

Bioactive constituents of seaweeds also revealed their nutritional and bioactive properties against various life style diseases, which include hypertension, diabetes mellitus and inflammation. Bioactive components of seaweeds also act as the inhibitor of angiotensin-I converting enzyme (ACE), which secrete the angiotensin-II vasoconstrictor. The potential side effects produced by the commercial ACE-inhibitors upsurges the demand of naturally occurring homologues. Specific constituents of seaweeds were found to function as chemical intermediaries, which control the stimulations associated with mammalian defense mechanism and produces inflammatory deregulators.

A total of ten different seaweeds belonging to the subclasses Dictyotophycidae, Rhodymeniophycidae and Corallinophycidae collected from the Gulf of Mannar of Peninsular India were screened for *in vitro* antioxidant, anti-diabetic, anti-inflammatory and anti-hypertensive activities. Among various seaweeds considered in the present study, those belonging to the subclasses Dictyotophycidae and Rhodymeniophycidae displayed considerably greater pharmacological potentials. In particular, the organic extracts of *G. salicornia* and *P. tetrastromatica* registered significantly greater pharmacological properties than those derived from other studied seaweeds. This study also disclosed that the spectral fingerprinting could quickly deduce the signal pattern of the resonances, and conclusions could be drawn as to the likely structural classes involved in the organic extracts of the studied seaweeds. The present study recognized that the seaweeds *G. salicornia* and *P. tetrastromatica* might be promising

candidates to isolate high value compounds for pharmacological use and their application as functional foods.

Bio-assay assisted chromatographical purification of the EtOAc-MeOH extract of *G. salicornia* yielded bioactive secondary metabolites, namely abeo-labdane class of diterpenoid (**TG$_1$**), oleanene class of triterpenoids (**TG$_2$**- **TG$_3$**), drimane-associated quinols (**TG$_4$**- **TG$_6$**), 2*H*-chromenyl compounds (**TG$_7$**- **TG$_8$**), spiro-fused analogues (**TG$_9$**- **TG$_{10}$**), squalene polyether metabolites (**TG$_{11}$**- **TG$_{12}$**), and macrolides enclosing ether functionalities (**TG$_{13}$**-**TG$_{15}$**). The studied compounds exhibited comparable DPPH radical quenching activity as standard antioxidant agent *α*-tocopherol. The first class of compounds in this series abeo-labdene derivative (**TG$_1$**) registered significantly greater activities against pro-inflammatory 5-lipoxygenase than that displayed by non-steroidal anti-inflammatory drug ibuprofen. Its greater selectivity index as compared to that displayed by ibuprofen inferred the higher anti-inflammatory selectivity against pro-inflammatory cyclooxygenase-2.

In second class of metabolites among the isolated compounds, the one with 24(4→23) abeo-oleanene framework (**TG$_3$**) exhibited higher carbolytic enzyme inhibitory activities ($IC_{50} \leq 0.32$ mM) over that bearing 24(4→23), 27(8→26), 30(20→29)-tris-abeo-oleanene moiety (**TG$_2$**) ($IC_{50} \geq 0.34$ mM). The oleanene analogues isolated from *G. salicornia* registered greater radical scavenging potentials against $ABTS^+$ ($IC_{50} < 1.10$ mM) than that exhibited by α-tocopherol ($IC_{50} > 1.69$ mM). Structure-activity relationship analyses showed that higher polarisability and lesser steric bulk of abeo-oleanene (**TG$_3$**) predominantly contributed towards the comparatively greater radical quenching and carbolytic enzyme inhibitory activities than those displayed by its tris-abeo-oleanene analogue (**TG$_2$**). *In silico* molecular modelling studies were performed to designate the α-glucosidase and α-amylase inhibitory mechanism of the abeo-oleanene derivative (**TG$_2$**) exhibiting binding energies of greater than 9.50 kcal mol^{-1}, which substantiated its potential inhibitory activity against the carbolytic enzymes responsible to cause hyperglycaemic disorders. An enzyme-assisted putative biosynthetic cascade leading to the formation of oleanene triterpenoid derivatives were proposed. In particular, the 24(4→23)-abeo-oleanene possessing (12-oxo)-3,5-diene-deconoate moiety (compound **TG$_2$**) was found to be effective dual inhibitors of starch digestive enzymes along with potential antioxidative properties, and therefore, might be utilised as valuable medicinal lead against oxidant species and elevated postprandial glucose levels.

On third series of compounds, the compound (**TG$_4$**) with benzo[*a*]xanthene-4,10,12-triol moiety showed greater pro-inflammatory enzyme inhibitory activities (IC_{50} 1.35-1.72 mM) over other studied drimane quinol chemotypes. Positive correlations between the antioxidant and anti-inflammatory activities were recorded, whereas the compound (**TG$_4$**) displayed greater

oxidant scavenging potentials (IC_{50} 1.33-1.57 mM) than that exhibited by α-tocopherol. Structure-bioactivity correlation analysis showed that lesser hydrophobicity and steric bulk of the compound (**TG_4**) predominantly contributed towards the comparatively greater radical quenching and pro-inflammatory enzyme inhibitory activities than those displayed by its drimane counterparts **TG_5**-**TG_6**. *In silico* molecular modelling studies were performed to designate the 5-lipoxygenase inhibitory mechanism of the compound (**TG_4**) exhibiting binding energy of -12.30 kcal mol^{-1}, which substantiated its potential inhibitory activity against the inflammatory mediators. An enzyme-mediated biosynthetic cascade leading to the formation of drimane sesquiterpenoid quinol derivatives was proposed. The results illustrated the bioactive potential of the natural anti-inflammatory drimane sesquiterpenoid bearing benzo[*a*]xanthene-4,10,12-triol moiety attenuating pro-inflammatory 5-LOX from marine macroalga *G. salicornia.*

In chromenyl derivatives, which were characterised as 4'-[10'-[7-hydroxy-2,8-dimethyl-6-(pentyloxy)-2*H*-chromen-2-yl]ethyl]-3',4'-dimethyl-cyclohexanone (**7**) and 3'-[10'-(8-hydroxy-5-methoxy-2,6,7-trimethyl-2*H*-chromen-2-yl)ethyl]-3'-methyl-2'-methylene cyclohexyl butyrate (**TG_8**) using comprehensive spectroscopic techniques. The compound **TG_8** exhibited higher DPPH radical quenching activity than that displayed by compound **TG_7** and standard antioxidant agent α-tocopherol. The chromenyl derivative registered significantly greater activities against pro-inflammatory 5-lipoxygenase than that displayed by non-steroidal anti-inflammatory drug ibuprofen. Its greater selectivity index as compared to that displayed by ibuprofen inferred the higher anti-inflammatory selectivity against pro-inflammatory cyclooxygenase-2. The newly described chromenyl analogue **TG_8** characterised from the red seaweed *G. salicornia* has potential anti-inflammatory and antioxidant properties for utilisation in pharmaceutical and food formulations.

Among the isolated spiro-compounds, the one with spiro[5.5]undec-2-en framework (**TG_{10}**) exhibited higher pro-inflammatory enzyme inhibitory activities ($IC_{50} \leq 1.91$ mM) over that bearing oxospiro[5.5]undec-4-ene moiety (**TG_9**) ($IC_{50} \geq 2.78$ mM). The spiro analogues isolated from *G. salicornia* registered greater radical scavenging potentials against $ABTS^+$ ($IC_{50} < 1.75$ mM) than that exhibited by α-tocopherol ($IC_{50} > 1.75$ mM). Structure-activity relationship analyses showed that higher polarisability, tPSA and lesser steric bulk of spiro[5.5]undec-2-en (**TG_{10}**) predominantly contributed towards the comparatively radical quenching and proinflammatory enzyme inhibitory activities than those displayed by the oxospiro[5.5]undec-4-en analogue (**TG_9**). Molecular docking analysis inferred that the spiro derivative (**TG_2**) exhibited binding energy of -10.13 kcal/mol with efficient interactions of 5-LOX enzyme, which corroborated its greater inhibitory potential. In particular, spiro[5.5]undec-

2-ene analogue was found to be an effective inhibitor of 5-LOX along with potential antioxidative properties, and therefore, might be utilised as valuable pharmacophore lead against oxidant species and inflammation pathology.

Among unreported polyether analogues, the compound **TG$_{12}$** possessing furanyl-furo[3,2-b]pyran-2*H*-pyran skeleton displayed greater anti-inflammatory properties (IC_{50} < 2 mM) over that exhibited by **TG$_{11}$** bearing pyranyl-10-methylpyrano[3,2-b]pyran-methyleneoxepane moiety (IC_{50} > 2.5 mM). Likewise, the potential anti-radical properties of **TG$_{12}$** (IC_{50} 1.11-1.27 mM) in comparison with **TG$_{11}$** (IC_{50} ~1.65 mM) and α-tocopherol (IC_{50} 1.49-1.69 mM) were reported. Structure-bioactivity-correlation studies displayed that the optimum hydrophobicity (log P_{OW2} < 5), lesser steric hindrance, which along with greater polarisability factors predominantly played significant roles in determining the greater bio-potential of polyether derivative, **TG$_{12}$** over that of **TG$_{11}$**. *In-silico* molecular modeling was analyzed to entitle 5-lipoxygenase inhibitory pathway of compound (**TG$_{12}$**) exhibiting binding energy of -10.96 kcal mol^{-1}, that appropriately attributed its potent inhibitory properties against the inflammatory-mediators.

In the last series of compounds, the undescribed oxabicyclo[21.3.1]heptacosa-ene-diones (compounds **TG$_{13}$**- **TG$_{15}$**) and oxabicyclo[19.3.1]pentacosa-ene-dione (compound **TG$_{15}$**) bearing macrocyclic lactones from the red seaweed, *G. salicornia*. The unprecedented compounds (**TG$_{13}$**- **TG$_{15}$**) displayed significantly higher antioxidative and pro-inflammatory 5-lipoxygense attenuating potential in comparison with the commercially existing antioxidative and anti-inflammation agents. The greater attenuation potential of the 21-membered pyran bearing compound **TG$_{14}$** against 5-lipoxygense was correlated with its respective *in-silico* molecular docking simulations in the binding site of the pro-inflammatory enzyme through the least binding energy (-9.64 kcal mol^{-1}) and inhibitory constant (Ki 85.15 nm). The malonate-S-acyl carrier protein-mediated putative biosynthetic route appropriately corroborated the structural attributions of the studied salicornolides. In particular, the pyran enclosed macrocyclic lactone could be used as prospective natural therapeutic pharmacophore in attenuating the anti-inflammatory disorders and free radical-induced ailments.

Among seven classes of compounds derived from *G. salicornia*, **TG$_{14}$** belonging to macrolide class of chemistries was registered significantly higher anti-inflammatory activity. *In-vitro* antioxidant assays were evaluated by the radical (radicals DPPH and $ABTS^{+}$) quenching abilities of compounds (**TG$_{13}$**- **TG$_{15}$**) against 1, 1-diphenyl-2-picryl-hydrazil (DPPH) and 2, 2'-azino-bis-3-ethylbenzothiozoline-6-sulfonic acid ($ABTS^{+}$), and the antioxidant activities were compared with the standard antioxidative agent, *α*-tocopherol.

Among the titled compounds, **14** showed higher radical scavenging potentials (IC_{50} DPPH 1.10 mM; IC_{50} $ABTS^+$ 1.21 mM) when compared to other studied compounds (**13-15**) (IC_{50} DPPH > 1.38 mM; IC_{50} $ABTS^+$ > 1.42 mM). It is of note that the free radical scavenging potential of the compound (**13-15**) were found to be significantly greater (IC_{50} < 1.50 mM) in comparison with the standard, α-tocopherol ($IC_{50} \geq 1.5$ mM; $P < 0.05$). The greater antioxidative properties against the free radicals were reported for the 12-membered macrocyclic lactone isolated from the seaweed, *S. wightii* (Maneesh and Chakraborty, 2017), a 16-membered macrocyclic bislactone and 10/13-membered macrocyclic lactones from the mollusk, *Amphioctopus neglectus* (Chakraborty et al., 2019). These results further substantiated the antioxidative potential of the studied compounds (**13-15**).

Compound **13** was found to contain two conjugated systems, such as 14-furanyl and 22-benzyl, which could easily transfer H-atoms (by hydrogen-atom transfer) located at C-14 and C-22 positions, respectively of oxabicyclo[21.3.1]heptacosa-11,23,25,27-tetraene-7,18-dione skeleton onto DPPH free radicals to form resonance stabilised 3-acetyl-14-(furan-2(5*H*)-ylidene)-15-(isopentyloxy)-11-methyl-8-oxa-bicyclo[21.3.1]heptacosa-26,11, 22,24-tetraene-7,18-dione. These two positions (C-14 and C-22) could be considered as primary antioxidative reaction centers. Additionally, three more reaction centers related to the ester at C-7, 3-acetyl and 18-keto in the oxabicyclo[21.3.1]heptacosa-11,23,25,27-tetraene-7,18-dione framework, were found for compound **13**. The protons at C-6 (near to ester at C-7), C-3 (acetyl linked carbon) and C-19 (adjacent to keto at C-18) could participate in keto-enol resonance with the nearest >C(=O)< (keto) groups at C-7, C-3^1, and C-18, respectively leading to the generation of -CH=C(-OH)- (enol) functionality via repositioning the protons from C-6, C-3, and C-19, respectively to the DPPH free radical to form a resonance stabilized 14-(furanyl)-3-(1-hydroxyethylidene)-11-methyl-15-(153-methylbutyloxy)-8-oxabicyclo[21.3.1]heptacosa-hexaene-7,18-diol. These five sites of antioxidative reaction centers present in compound $\mathbf{TG_{13}}$ could effectively participate in the resonance stabilization, which in turn, stabilize the DPPH radicals in the biological systems. Compound $\mathbf{TG_{14}}$ exhibited four primary antioxidative reaction sites, which include three keto functionalities and one conjugated olefinic system. The conjugated olefinic groups (-C12=C13-C14=C15-) adjacent to the oxygenated functionality in Compound $\mathbf{TG_{14}}$ could effectively involve in the electron delocalization to form -C11=C12-C13=C14-C15-O-, which in turn, transfer protons from C-11 to radicals through the hydrogen transfer via formation of resonance stabilized 10-acetyl-9-isopentyl-2-methyl-5,16,23^1-trioxa-bicyclo[21.3.1]heptacosa-2,11,13-triene-6,19-dione . The protons at C-7 (near to ester at C-6), C-10 (acetyl linked carbon) and C-20 (adjacent to keto at C-19) could involve in the keto-enol resonance with nearby >C(=O)< groups at C-6, C-10^1 and C-19, respectively resulting in the

formation of -CH=C(-OH)- by replacing the protons from C-7, C-10, and C-20, respectively to DPPH radicals through the genesis of resonance stabilised 10-(1-hydroxyethylidene)-9-isopentyl-2-methyl-5,16,23[1]-trioxa-bicyclo[21.3.1]heptacosa-2,6,10,12,14, 19-hexaene-6,19-diol. These four antioxidative reaction centres might be the predominant reasons for potential radical scavenging properties of Compound **TG_{14}** through the neutralisation of DPPH radical. However, Compound **TG_{15}** possessed only three reaction centres, which include two carbonyls and one hydroxyl functionalities. The free electron pair of -OH of -CHOH group located at C-8 of the macrolide might not efficiently contribute in resonance stabilization due to the weak acidic property of this proton, resulting in the formation of weakly stabilized DPPH radical. The protons at C-9 (near to keto at C-10) and C-22 (adjacent to keto at C-23 in the pyrone ring) could involve in the keto-enol resonance with the nearby >C(=O)< groups at C-10 and C-23, respectively leading to the formation of -CH=C(-OH)- by replacing the protons from C-9 and C-22, respectively to the DPPH radicals. These antioxidative reaction centers resulted in the resonance stabilized form of Compound **TG_{15}**, 20-isobutyl-16-methyl-7,14-dioxa-bicyclo[19.3.1]pentacosa-2,5,9,16,22-pentaene-10,23-triol to neutralize the DPPH free radical . Notably, the compound **TG_{15}** did not hold any extended conjugation as in **TG_{13}** and **TG_{14}**, and hence, it could not effectively transfer H-atom to DPPH, and therefore, displayed weaker antioxidant activity (IC_{50} DPPH 1.42 mM; IC_{50} $ABTS^{+}$ 1.47 mM) than those displayed by Compounds **TG_{13}** and **TG_{15}** (IC_{50} DPPH 1.37-1.40 mM; IC_{50} $ABTS^{+}$ 1.41-1.43 mM).*In-vitro* anti-inflammatory potential of the studied compounds was assessed by their attenuation potential against pro-inflammatory enzymes 5-lipoxygenase (5-LOX) and cyclooxygenase-1 and 2 (COX-1/2). Among the titled compounds, 21-membered pyran-enclosed Compound **TG_{14}** displayed greater attenuation property against COX-2 (IC_{50} 1.13 mM) than those exhibited by the 21-membered aryl Compound **TG_{13}** and 19-membered macrolide **C** (IC_{50} COX-2 ~ 1.2 mM). The attenuating potential of the studied compounds against 5-LOX was significantly greater (IC_{50} < 1.5 mM) than that displayed by ibuprofen (IC_{50} 4.5 mM), whereas the selectivity indices exhibited by macrolides against COX-2 were significantly higher (1.18-1.41, $P < 0.05$) when compared to ibuprofen (SI = 0.43) attributing the greater selectivity profile of the former towards inducible pro-inflammatory mediators than that exhibited by the latter.

The bioactive potentials of the Compound **TG_{13}- TG_{15}** were substantiated with their physico-chemical-parameters. It is relevant to note that the electronic-parameters of 21-membered macrolide derivative (**TG_{13}**) was higher (polarizability, Pl 59.35; topological polar surface area, tPSA 78.9) than that recorded with 19-membered macrolide derivative, **TG_{15}** (Pl 52; tPSA, 72.8), and that could be correlated with the greater bioactivities of the former (Table 4.30). The higher electronic values recorded for Compound **TG_{14}** further supported the possibilities of

greater number of electron-rich centres, which in turn, resulted in its greater bioactive properties. Electronic or polar factors were reported to play important parts to govern the target pharmacological properties (Wang et al., 2007). Notably, the steric bulkiness of the 21-membered aryl macrolide, compound **TG$_{13}$** (molar-volume, MV 565 cm^3 mol^{-1}; parachor, P 1455 cm^3) was significantly greater than the 21-membered pyran enclosed macrolide derivative, Compound **TG$_{14}$** (MV 543 cm^3 mol^{-1}; P 1279 cm^3) and 19-membered cyclohexanone enclosed macrolide derivative, Compound **TG$_{15}$** (MV 465 cm^3 mol^{-1}; P 1109 cm^3). The greater steric hindrance of Compound **TG$_{13}$** due to its bulkier side chains of benzyl/furanyl ring systems could negatively affect its bioactivities, although its electronic parameters recorded higher values (Pl 69.4; tPSA, 78.9). The optimum hydrophobicity/lipophilicity (log P_{ow}) equilibrium of Compound **TG$_{14}$** and **TG$_{15}$** (5.6-6) appeared to contribute towards their greater bioactivities over Compound **TG$_{13}$** that displayed greater lipophilicity (log P_{ow} ~ 7.7). The balanced hydrophilic-lipophilic properties as determined by log P_{ow} was found to control the inter-membrane perviousness including requisite hydrophobic/lipophilic (Lipinski, 2004) relationship and binding of receptors (Huuskonen et al., 2000). Apparently, greater electronic parameters (electron-rich centres) along with optimum steric bulkiness and permissible hydrophobicity-lipophilicity equilibrium of Compound **TG$_{14}$** could result in its greater antioxidative properties and effective interaction with the active site of inflammatory enzymes to impart anti-inflammatory properties compared to other studied compounds (Wang et al., 2007).

At the same time, the abeo-oleanane class of compounds from *G. salicornia* was registered higher anti-diabetic potential. the *in vitro* anti-diabetic potential of the studied abeo-oleanenes (**TG$_2$** and **TG$_3$**) were assessed by their inhibitory properties towards the carbolytics, α-glucosidase and α-amylase that were found to regulate the intestinal carbohydrate absorption, thereby reducing postprandial insulin level (Goldstein et al., 1998). Among the titled abeo-oleanenes, the one with 24(4→23)-abeo-oleanene framework (**TG$_3$**) displayed significantly higher α-amylase and α-glucosidase inhibitory properties (IC_{50} 0.32 and 0.29 mM, respectively) over that bearing 24(4→23), 27(8→26), 30(20→29)-tris-abeo-oleanene moiety (**TG$_2$**) (IC_{50} 0.40 and 0.34 mM, respectively). The higher α-amylase and α-glucosidase inhibitory properties of 24(4→23)-abeo-oleanene framework (**TG$_3$**) (IC_{50} 0.32 and 0.29 mM, respectively) exhibited close resemblance towards the reference carbolytic enzyme inhibitor acarbose (IC_{50} 0.22 and 0.19 mM, respectively mM). *In vitro* radical scavenging assays by $ABTS^+$ and DPPH radicals were employed to deduce the antioxidant properties of studied abeo-oleanenes. The studied compound, **TG$_3$** exhibited greater radical scavenging activities (IC_{50} DPPH 1.33 mM; IC_{50} $ABTS^+$ 1.09 mM), when compared to those displayed by compound **TG$_2$** (IC_{50} DPPH 1.56 mM; IC_{50} $ABTS^+$ 1.24 mM) and standard, *α*-tocopherol (IC_{50} DPPH 1.49 mM; IC_{50} $ABTS^+$

1.69 mM). The isolated abeo-labdane registered significantly lesser potential against pro-inflammatory COX-2 and 5-LOX (> IC_{50} 3.00 mM).

Five previously unreported xenicanes were isolated from the ethyl acetate/methanol extract of *P. tetrastromatica* by extensive chromatographic fractionation, and were characterized by detailed spectroscopic experiments. The xeniolide derivative octahydro-1,7-dihydroxy-4-(4^1-hydroxy-4^2-methylpropyl)-6-(6^1-hydroxy-6^2-propenyl)-10-methyl-cyclonona[*c*]pyran-3(*1H*)-one (**TP_5**) showed potential antioxidant and anti-inflammatory activities, with greater selectivity index pro-inflammatory cyclooxygenase-2 than other studied xenicane derivatives and ibuprofen. Molecular docking analysis inferred that the xeniolide derivative **TP_5** exhibited efficient interactions with 5-lipoxygenase, which validated its greater inhibitory potential against the pro-inflammatory enzyme. In particular, the xeniolide-type diterpenoids with octahydrocyclonona[*c*]pyran-3(1*H*)-one backbone could be potential functional food components for use against inflammatory diseases. The biologically active xeniolides isolated from brown seaweed *P. tetrastromatica* might constitute a promising potential natural alternative to the commercially available synthetic antioxidants and anti-inflammatory agents.

The EtOAc-MeOH extract of *P. tetrastromatica* was fractionated by repeated chromatographic techniques to obtain five unprecedented dolabellane and dolastane analogues, named 6-methoxy-dolabella-8(17),12-diene-10*β*,18-diol (**TP_6**), 3-methoxy-dolabella-12(18)-ene-4*β*-ol **TP_7**), 3-methoxy-dolabella-10,18(19)-diene-5*α*,8*β*-diol (**TP_8**) along with two previously unreported dolastanes 2,7-dimethoxy-14*α*-hydroxy-dolasta-1(15),9-diene (**TP_9**) and 4,7-dimethoxy-9*β*,14*α*-dihydroxy-dolasta-1-ene (**TP_{10}**). This is the first report of isolation of dolabellane and dolastane terpenoids from *P. tetrastomatica*. The structural features of the studied compounds were characterised using comprehensive spectroscopic techniques. The compounds **TP_6** and **TP_{10}** displayed greater inhibitory activities against starch digesting enzymes, and their activities were greater than those exhibited by acarbose. In particular, 4,7-dimethoxy-9,14-dihydroxy-dolasta-1-ene (**TP_{10}**) was found to be an effective dual inhibitors of *α*-amylase and *α*-glucosidase along with potential antioxidative properties, and therefore, could be utilised as potential antioxidant/anti-diabetic pharmacophore in medicinal applications.

Among two classes of diterpene compounds derived from *G. salicornia*, **TG_{14}** belonging to macrolide class of chemistries was registered significantly higher anti-inflammatory activity.

The present study demonstrated that the marine-derived polysaccharide and its nano composite (P-Ag-NPs) with the silver particles derivative constituted promising candidates to

combat the hyperglycemic conditions. The titled polysaccharide derivatives were found to be effective in attenuating DPP-IV enzyme and carbolytic enzymes such as α-amylases and α-glucosidases. Here we have extracted the novel (DPP)-IV inhibiting polysaccharide, A (1⋯→3)-*O*-6-sulfonato-β-D-galactopyranosyl-(1→⋯4)-3,6-anhydro-α-D-galactopyranose-(1⋯→) from red seaweed *Gracilaria salicornia.* The seaweed derived polysaccharide registered greater reduction potentials against proteolytic DPP-IV (IC_{50} 0.63 mg mL^{-1}) and carbolytic α-amylase and α-glucosidase (IC_{50} 0.98-0.87 mg mL^{-1}) were comparable with those displayed by acarbose (IC_{50} DPP-IV 0.13 mg mL^{-1}, carbolytics IC_{50} 1.38-1.47 mg mL^{-1}) whereas the antioxidative potential of polysaccharide was higher (IC_{50} 0.35-0.48 mg mL^{-1}) than that of commercial standard ascorbic acid (IC_{50} 0.37-0.51 mg mL^{-1}). The presence of chemical constituents in polysaccharide was assessed by analytical methods which were corroborated with the bioactivity of polysaccharide. The polysaccharides were exhibited lower binding energy conformation (-11.13 kcal mol^{-1}) towards catalytic binding site of DPP-IV and this was also reinforced with the bioactivity of polysaccharide. Based on the bioactivity, silver-nano-composite of polysaccharide was synthesized to reduce the risk of hyperglycemia. The polysaccharide-silver-nano-composite (P-Ag-NP-composite) was demonstrated greater inhibition potential against proteolytic (DPP-IV IC_{50} 0.22 mg mL^{-1}) and carbolytic enzyme (α-amylase and α-glucosidase IC_{50} 0.52-0.70 mg mL^{-1}, respectively) than that of polysaccharide motif (≥ 1.0 mg mL^{-1} and ≥ 0.6 mg mL^{-1}, respectively) whereas they have exhibited greater antioxidant potentials (IC_{50} 0.32-0.41 mg mL^{-1}) than those displayed by polysaccharide motif. The nano particle synthesized from polysaccharide was found to be covered the range of 4-400 nm in different time intervals of 30, 60 and 120 min, by the X-ray diffraction analysis and their shape was assigned as spherical by SEM-EDX, TEM and AFM morphological analysis. The average size, distribution and the stability of nano particle were assigned by particle size analysis; the average size and zeta potential distribution of nano particle at different time intervals 30, 60 and 120 min were assigned as 389, 98 and 9 nm and -23, -25 and 0.28 respectively. The inhibition potential of polysaccharide and its silver nano composite against DPP-IV along with antioxidant potential suggested the formulation of bioactive leads to reduce the risk of hyperglycemic pathologies.

REFERENCES

A. Maneesh, K. Chakraborty, Previously undescribed fridooleanenes and oxygenated labdanes from the brown seaweed *Sargassum wightii* and their protein tyrosine phosphatase-1B inhibitory activity. Phytochemistry. 144 (2017) 19–32.

A. Wojdylo, J. Oszmianski, R. Czemerys, Antioxidant activity and phenolic compounds in 32 selected herbs. Food Chem. 105 (2007) 940–949.

A. Wojdylo, J. Oszmianski, R. Czemerys, Antioxidant activity and phenolic compounds in 32 selected herbs, Food Chem. 105 (2007) 940–949.

A.G. Gonzalez, J.M. Arteaga, J.J. Fernandez, J.D. Martin, M. Norte, J.Z. Ruano, Terpenoids of the red alga *Laurencia pinnatifida*, Tetrahedron. 40(14) (1984) 2751–2755.

A.L. Lane, L. Mular, E.J. Drenkard, T.L. Shearer, S. Engel, S. Fredericq, C.R. Fairchild, J. Prudhomme, K. Le Roch, M.E. Hay, W. Aalbersberg, J. Kubanek, Ecological leads for natural product discovery: Novel sesquiterpene hydroquinones from the red macroalga *Peyssonnelia sp*. Tetrahedron. 66 (2010) 455–461.

Abad, M.J., Bedoya, L.M., Bermejo, P., 2008. Natural marine anti-inflammatory products. Mini Rev. Med. Chem. 8(8), 740–754.

Abdelgaleil, S., Doe, M., Morimoto, Y., and Nakatani, M., 2006. Rings B, D-seco limonoids from the leaves of *Swietenia mahogani*. Phytochemistry. 67(5), 452–458.

Ahmad Z, Mehmood S, Fatima I, Malik A, Ifzal R, Afza N, Iqbal L, Latif M, Nizami TA (2008) Structural determination of salsolins A and B, new antioxidant polyoxygenated triterpenes from *Salsola baryosma* by 1D and 2D NMR spectroscopy. Magn Reson Chem 46:94-98.

Antony T, Chakraborty K (2018) First report of antioxidant abeo-labdane type diterpenoid from intertidal red seaweed *Gracilaria salicornia* with 5-lipoxygenase inhibitory potential. Nat Prod Res doi:10.1080/14786419.2018.1508150. Online published.

Antony T, Chakraborty K. 2018. First report of antioxidant abeo-labdane type diterpenoid from intertidal red seaweed *Gracilaria salicornia* with 5-lipoxygenase inhibitory potential. Nat Prod Res. Epub ahead of print, doi: 10.1080/14786419.2018.1508150.

Antony T, Chakraborty K. 2018. First report of antioxidant abeo-labdane type diterpenoid from intertidal red seaweed *Gracilaria salicornia* with 5-lipoxygenase inhibitory potential. Nat Prod Res. Epub ahead of print, doi:10.1080/14786419.2018.1508150.

Antony T, Chakraborty K. 2018. First report of antioxidant abeo-labdane type diterpenoid from intertidal red seaweed *Gracilaria salicornia* with 5-lipoxygenase inhibitory potential. Nat Prod Res. Epub ahead of print, doi:10.1080/14786419.2018.1508150.

Antony, T., and Chakraborty, K. 2019. Xenicanes attenuate pro-inflammatory 5-lipoxygenase: Prospective natural anti-inflammatory leads from intertidal brown seaweed *Padina tetrastromatica*. Med. Chem. Res. 28(4): 591-607.

Antony, T., Chakraborty, K., 2018. First report of antioxidant abeo-labdane type diterpenoid from intertidal red seaweed *Gracilaria salicornia* with 5-lipoxygenase inhibitory potential. Nat. Prod. Res. Epub ahead of print, doi: 10.1080/14786419.2018.1508150.

Antony, T., Chakraborty, K., 2019. Pharmacological properties of seaweeds against progressive lifestyle diseases. J. Aquat. Food Prod. T. Epub ahead of print, doi: 10.1080/10498850.2019.1684407.

Atkinson, A.B., and Rovertson, J. 1979. Captopril in the treatment of clinical hypertension and cardiac failure. Lancet. 2: 836–839.

Awad NE, Selim, MA, Metawe HM, Matloub AA (2008) Cytotoxic xenicane diterpenes from the brown alga *Padina pavonia* (L.). Gaill. Phytother Res 22: 1610-1613.

Ayala A, Muñoz MF, Argüelles S (2014). Lipid peroxidation: production, metabolism, and signaling mechanisms of malondialdehyde and 4-hydroxy-2-nonenal. Oxidative medicine and cellular longevity. Article ID 360438, 31 pages.

B.J.M. Jansen, A. de Groot, Occurrence, biological activity and synthesis of drimane sesquiterpenoids. Nat. Prod. Rep. 21 (2004) 449–477.

B.K. Carte, Biomedical potential of marine natural products: Marine organisms are yielding novel molecules for use in basic research and medical applications, Bioscience. 46 (1996) 271–286.

Bansemir A, Blume M, Schroder S, Lindequist U. 2006. Screening of cultivated seaweeds for antibacterial activity against fish pathogenic bacteria. Aquaculture. 252(1):79-84.

Barrento S, Camus C, Sousa-Pinto I, Buschmann AH (2016) Germplasm banking of the giant kelp: Our biological insurance in a changing environment. Algal Res 13: 134-140.

Bartoli A, Rodier F, Commeiras L, Parrain J.L, Chouraqui G. 2011. Construction of spirolactones with concomitant formation of the fused quaternary centre -application to the synthesis of natural products. Nat Prod Rep. 28:763-782.

Baylac S, Racine P (2003) Inhibition of 5-lipoxygenase by essential oils and other natural fragment extracts. Int J Aromather 13:138-142.

Baylac S, Racine P (2003). Inhibition of 5-lipoxygenase by essential oils and other natural fragment extracts, Int J Aromather. 13 138-142.

Baylac S, Racine P. 2003. Inhibition of 5-lipoxygenase by essential oils and other natural fragment extracts. Int J Aromather. 13(2-3):138-142.

Baylac S, Racine P. 2003. Inhibition of 5-lipoxygenase by essential oils and other natural fragment extracts. Int J Aromather. 13(2-3):138-142.

Baylac S, Racine P. 2003. Inhibition of 5-lipoxygenase by essential oils and other natural fragment extracts. Int J Aromather. 13(2-3):138-142.

Baylac, S., and Racine, P. 2003. Inhibition of 5-lipoxygenase by essential oils and other natural fragrant extracts. Int. J. Aromather. 13: 138–142.

Baylac, S., Racine, P., 2003. Inhibition of 5-lipoxygenase by essential oils and other natural fragment extracts. Int. J. Aromather. 13(2-3), 138-142.

Birringer M, Siems K, Maxones A, Frank J, Lorkowski S. 2018. Natural 6-hydroxy-chromanols and chromenols: Structural diversity, biosynthetic pathways and health implications. RSC Adv. 8(9):4803-4841.

Bishara A, Rudi A, Goldberg I, Benayahu Y, Kashman Y (2006) Novaxenicins A–D and xeniolides I–K, seven new diterpenes from the soft coral *Xenia novaebrittanniae.* Tetrahedron 62: 12092-12097.

Blunt JW, Carroll AR, Copp BR, Davis RA, Keyzers RA, Prinsep MR (2018). Marine natural products. Nat Prod Rep 35, 8-53.

Blunt JW, Copp BR, Hu W, Munro MHG, Northcote PT, Prinsep M (2008). Marine natural products. Nat Prod Rep 25, 35-94.

Blunt JW, Copp BR, Hu WP, Munro MHG, Northcotec PT, Prinsep MR (2009) Marine natural products. Nat Prod Rep 26(2): 170-244.

Blunt JW, Copp BR, Keyzers RA, Munro MH, Prinsep MR (2012). Marine natural products. Nat Prod Rep 29 (2), 144.

Blunt JW, Copp BR, Keyzers RA, Munro MH, Prinsep MR (2013). Marine natural products. Nat Prod Rep 30 (2), 237-323.

Blunt JW, Copp BR, Keyzers RA, Munro MH, Prinsep MR (2014). Marine natural products. Nat Prod Rep 31 (2), 160-258.

Blunt JW, Copp BR, Keyzers RA, Munro MHG, Prinsep MR (2017). Marine natural products. Nat Prod Rep 34, 235-294.

Blunt JW, Copp BR, Munro MHG, Northcote PT, Prinsep MR. 2006. Marine natural products. Nat Prod Rep. 23:26-78.

Blunt, J.W., Copp, B.R., Keyzers, R.A., Munro, M.H., Prinsep, M.R., 2013. Marine natural products. Nat. Prod. Rep. 30(2), 237–323.

Brayer GD, Luo Y, Withers SG (1995) The structure of human pancreatic alpha-amylase at 1.8 A resolution and comparisons with related enzymes. Protein Sci 4:1730-1742.

C. Rice-Evans, D. Leake, K.R. Bruckdorfer, A.T. Diplock, Practical approaches to low density lipoprotein oxidation: Whys, wherefores and pitfalls. Free Radic. Res. 25 (1996) 285–311.

C.A. Lipinski, Lead and drug-like compounds: The rule-of-five revolution. Drug. Discov. Today Technol. 1, (2004) 337–341.

C.A. Lipinski, Lead and drug-like compounds: The rule-of-five revolution, Drug Discov. Today Technol. 1(4) (2004) 337–341.

C.E. McNamara, L. Larsen, N.B. Perry, J.L. Harper, M.V. Berridge, E.W. Chia, M. Kelly, V.L. Webb, Anti-inflammatory sesquiterpene-quinones from the New Zealand sponge *Dysidea cf. Cristagalli*. J. Nat. Prod. 68 (2005) 1431–1433.

C.N. Serhan, J. Savill, Resolution of inflammation: The beginning programs the end. Nat. Immunol. 6 (2005) 1191–1197.

C.N. Serhan, J. Savill, Resolution of inflammation: The beginning programs the end, Nat. Immunol. 6 (2005) 1191–1197.

C.S. Vairappan, T. Kamada, W.-W. Lee, Y.-J. Jeon, Anti-inflammatory activity of halogenated secondary metabolites of *Laurencia snackeyi* (Weber-van Bosse) Masuda in LPS-stimulated RAW 264.7 macrophages, J. Appl. Phycol. 25 (2013) 1805–1813.

Cai X-H, Wang Y-Y, Zhao P-J, Li Y, Luo X-D. 2010. Dolabellane diterpenoids from *Aglaia odorata*. Phytochemistry. 71:1020–1024.

Calder PC, (2009). Polyunsaturated fatty acids and inflammatory processes: New twists in an old tale. Biochimie. 91, 791-795.

Cardozo, K.H.M., Guaratini, T., Barros, M.P., Falcao, V.R., Tonon, A.P., Lopes, N.P., Campos, S., Torres, M.A., Souza, A.O., and Colepicolo, P. 2007. Review: Metabolites from algae with economical impact. Comp. Biochem. Physiol. C: Toxicol. Pharmacol. 146: 60–78.

Carroll AR, Copp BR, Davis RA, Keyzers RA, Prinsep MR (2019). Marine natural products. Nat Prod Rep 36, 122-173.

Cen-Pacheco F, Nordstrom L, Souto ML, Martin MN, Fernandez JJ, Daranas AH (2010) Review: Studies on polyethers produced by red algae. Mar Drugs 8:1178-1188.

Chakraborty K (2010a). A process to prepare antioxidant and anti-inflammatory concentrates from brown and red seaweeds and a product thereof. Patent Grant number 294451 (2064/CHE/2010-Indian patent).

Chakraborty K (2010b). A process to prepare antioxidant and anti-inflammatory concentrates from brown and red seaweeds and a product thereof. Patent Grant number 294451 (2064/CHE/2010-Indian patent).

Chakraborty K (2010b). A product containing anti-inflammatory principles from brown seaweeds (Indian patent Appl. no. 5199/CHE/2012-Grant order under Section 43 due).

Chakraborty K (2010c). A product containing anti-inflammatory principles from brown seaweeds (Indian patent Appl. no. 5199/CHE/2012-Grant order under Section 43 due).

Chakraborty K (2010d). A process to concentrate anti-inflammatory principles from green mussel *Perna viridis L*. and a product incorporating these ingredients. Patent Grant number 302803 (2065/CHE/2010-Indian patent).

Chakraborty K and Joseph D (2016). Anti-inflammatory concentrate enriched with substituted oligofucans derived from brown seaweed *Turbinaria conoides* (J. Agardh) Kützing and its safety assessment on wistar rats. J. Aquat. Food Prod. Technol. 25(8), 1323-1338.

Chakraborty K et al (2010a). A product containing anti-inflammatory principles from green mussel *Perna viridis L*. and a process thereof. Patent Grant number 303813 (2066/CHE/2010-Indian patent)

Chakraborty K et al (2015b) A process to prepare antidiabetic concentrates from seaweeds and a product thereof (Indian Patent Appl. no. 3366/DEL/2015)

Chakraborty K et al (2015c). Anti-inflammatory principles in a preparation of brown seaweeds (Indian Patent Appl. no. 4254/DEL/2015)

Chakraborty K et al (2017d). A process to prepare anti-dyslipidemic concentrate from seaweed and a product therof (Indian Patent Appl. no. 201711018741)

Chakraborty K, Antony T (2019a). First report of spiro-compounds from marine macroalga *Gracilaria salicornia*: Prospective natural anti-inflammatory agents attenuate 5-lipoxygenase and cyclooxygenase-2. Nat Prod Res.1608545, 1-12

Chakraborty K, Antony T, Joy M (2019). Prospective natural anti-inflammatory drimanes attenuating pro-inflammatory 5-lipoxygenase from marine macroalga *Gracilaria salicornia*. Algal Res, 39, 101472.

Chakraborty K, Antony T, Joy M (2019b). Prospective natural anti-inflammatory drimanes attenuating pro-inflammatory 5-lipoxygenase from marine macroalga *Gracilaria salicornia*. Algal Res. 39, 101472.

Chakraborty K, Chakkalakal SJ, Joseph D (2014). Response of pro-inflammatory prostaglandin contents in anti-inflammatory supplements from green mussel *Perna viridis L*. in a time-dependent accelerated shelf-life study. J. Funct Foods. 7, 527-540.

Chakraborty K, Dhara S (2019). First report of substituted 2*H*-pyranoids from brown seaweed *Turbinaria conoides* with antioxidant and anti-inflammatory activities. Nat Prod Res.DOI: 10.1080/14786419.1578761

Chakraborty K, Joseph D, Praveen NK (2015a). Antioxidant activities and phenolic contents of three red seaweeds (Division: Rhodophyta) harvested from the Gulf of Mannar of Peninsular India. J Food Sci Technol 52(4), 1924-1935.

Chakraborty K, Joseph D, Vamshi KR (2016). Anti-inflammatory concentrate enriched with substituted oligofucans derived from brown seaweed Turbinaria conoides (J. Agardh) Kützing and its safety assessment on wistar rats. J Aquat Food Prod. T 25 (8), 1323-1338.

Chakraborty K, Joseph D, Vamshi KR (2016.) Anti-inflammatory concentrate enriched with substituted oligofucans derived from brown seaweed *Turbinaria conoides* (J. Agardh) Kützing and its safety assessment on wistar rats. J Aquat Food Prod T 25 (8), 1323-1338.

Chakraborty K, Lipton AP, Paulraj R, Vijayan KK. 2010. Antibacterial labdane diterpenoids of *Ulva fasciata* Delile from southwestern coast of the Indian Peninsula. Food Chem.119:1399-1408.

Chakraborty K, Raola V K (2018) Oxygenated heterocyclic metabolites with dual cyclooxygenase-2 and 5-lipoxygenase inhibitory potentials from *Rhizophora annamalayana*. Med Chem Res 27: 1679-1689.

Chakraborty, K., Antony, T., and Joy, M. 2019. Prospective natural anti-inflammatory drimanes attenuating pro-inflammatory 5-lipoxygenase from marine macroalga *Gracilaria salicornia.* Algal Res. 39: 101472.

Chakraborty, K., Krishnan, S., Joy, M., 2019. Macrocyclic lactones from seafood *Amphioctopus neglectus*: Newly described natural leads to attenuate angiotensin-II induced cardiac hypertrophy. Biomed. Pharmacother. 110, 155–167.

Chakraborty, K., Thilakan, B., Chakraborty, R.D., Raola, V.K., Joy, M., 2017. *O*-heterocyclic derivatives with antibacterial properties from marine bacterium *Bacillus subtilis* associated with seaweed, *Sargassum myriocystum*. Appl. Microbiol. Biotechnol. 101, 569–583.

Chakraborty, K., Thilakan, B., Raola, V.K., 2014. Polyketide family of novel antibacterial 7-*O*-methyl-5′-hydroxy-3'-heptenoate-macrolactin from seaweed-associated *Bacillus subtilis* MTCC 10403. J. Agric. Food. Chem. 62(50), 12194–12208.

Chia YY, Kanthimathi MS, Khoo KS, Rajarajeswaran J, Cheng HM, Yap WS (2015) Antioxidant and cytotoxic activities of three species of tropical seaweeds. BMC Complement Altern Med 15: 339.

Chinou I, 2005. Labdanes of natural origin-biological activities. Curr Med Chem. 12(11):1295-1317.

Cho, M.L., Lee, H.S., Kang, I.J., Won, M.H., and You, S.G. 2011. Antioxidant properties of extract and fractions from *Enteromorpha prolifera*, a type of green seaweed. Food Chem. 127: 999–1006.

Cismas C, Terec A, Mager S, Grosu I. 2005. Six-membered ring spiranes: Carbocycles and heterocycles with oxygen. Curr Org Chem. 9(14):1287-1314.

Costa, P., Gonçalves, S., Andrade, P.B., Valentao, P., and Romano, A. 2011. Inhibitory effect of *Lavandula viridis* on Fe^{2+}-induced lipid peroxidation, antioxidant and anti-cholinesterase properties. Food Chem. 126: 1779–1786.

Cui Y, Luo D (2008). Fucoidan: Advances in the study of its anti-inflammatory and antioxidative effects. Yao Xue Xue Bao [Acta Pharmaceutica Sinica]. 43(12):1186-1189

Curtiss, C., Chon, J.N., Vrobel, T., and Francious, J.A. 1978. Role of the rennin-angiotensin system in the systemic vasoconstriction of chronic congestive heart failure. Circulation. 58: 763–770.

D.J. Faulkner, Marine natural products, Nat. Prod. Rep. 19 (2002) 1–48.

D'Orazio N, Gammone MA, Gemello E, De Girolamo M, Cusenza S, Riccioni G (2012) Marine bioactives: Pharmacological properties and potential applications against inflammatory diseases. Mar Drugs 10: 812-833.

Da Rocha CQ, Vilela FC, Santa-Cecilia FV, Cavalcante GP, Vilegas W, Giusti-Paiva A, Dos Santos MH (2015) Oleanane-type triterpenoid: An anti-inflammatory compound of the roots *Arrabidaea brachypoda.* Rev Bras Farmacogn 25:228-232.

Davyt D, Enz W, Manta E, Navarro G, Norte M. 1997. New Chromenols from the brown alga *Desmarestia menziesii*. Nat Prod Lett. 9(4):305-312.

Davyt D, Fernandez R, Suescun L, Mombru AW, Saldana J, Dominguez L, Coll J, Fujii MT, Manta E. 2001. New sesquiterpene derivatives from the red alga *Laurencia scoparia*. Isolation, structure determination, and anthelmintic activity. J Nat Prod. 64(12):1552-1555.

De Almeida CLF, Falcao HDF, Lima GRDM, Montenegro CDA, Lira NS, de Athayde-Filho PF, Rodrigues LC, de Souza MDFV, Barbosa-Filho JM, Batista LM (2011) Bioactivities from marine algae of the genus *Gracilaria.* Int J Mol Sci 12:4550-4573.

Demetzos C, Dimas, KS. 2001. Labdane-type diterpenes: Chemistry and biological activity. Stud Nat Prod Chem. 25:235-292.

Dewi, M. K., Arsianti, A., Zagloel, C. R. Z., Aziza, Y. A. N., Kurniasari, K.D., Mandasaril, B.K.D., Masita, R., Zulfa, F. R., Azizah,N.N., and Putrianingsih, R. 2018. *In vitro* evaluation of seaweed *Gracilaria verrucosa* for cytotoxic activity against Cervical HeLa Cells. Pharmacogn. J. 10: 1007-1011.

Driggers, E.M., Hale, S.P., Lee, J., Terrett, N.K., 2008. The exploration of macrocycles for drug discovery an underexploited structural class. Nat. Rev. Drug. Discov. 7(7), 608–624.

E. Ibanez, M. Herrero, J. Mendiola, M. Castro-Puyana, Extraction and characterization of bioactive compounds with health benefits from marine resources: Macro and micro algae, cyanobacteria, and invertebrates. In: M. Hayes, (Eds.), Marine bioactive compounds: Sources, characterization and applications (Chapter 2), Springer US, New York, USA, 2012, pp. 55–98.

E. Perez-Garcia, E. Zubia, M.J. Ortega, J.L. Carballo, Merosesquiterpenes from two sponges of the genus *Dysidea*. J. Nat. Prod. 68 (2005) 653–658.

E.S. Silverman, J.M. Drazen, The biology of 5-lipoxygenase: Function, structure and regulatory mechanisms. Proc. Assoc. Am. Physicians. 111 (1999) 525–536.

El-Beih AA, Kato H, Ohta T, Tsukamoto S. 2007. (3R,4aR,5S,6R)-6-hydroxy-5-methylramulosin: A new ramulosin derivative from a marine-derived sterile mycelium. Chem Pharm Bull. 55:953-954.

Esterbauer, H., Pubi, H., and Dieber-Rothender, M. 1991. Effect of antioxidants on oxidative modification of LDL. Ann. Med. 23: 573–81.

F. Makkar, K. Chakraborty, Antioxidant and anti-inflammatory oxygenated meroterpenoids from the thalli of red seaweed *Kappaphycus alvarezii*, Med. Chem. Res. 27 (2018) 2016–2026.

F. Makkar, K. Chakraborty, Highly oxygenated antioxidative 2*H*-chromen derivative from the red seaweed *Gracilaria opuntia* with pro-inflammatory cyclooxygenase and lipoxygenase inhibitory properties. Nat. Prod. Res. (2017) Epub ahead of print. doi:10.1080/14786419.2017.1378209.

F. Makkar, K. Chakraborty, Highly oxygenated antioxidative 2*H*-chromen derivative from the red seaweed *Gracilaria opuntia* with pro-inflammatory cyclooxygenase and lipoxygenase inhibitory properties, Nat. Prod. Res. 32 (2019) 2756–2765.

F. Makkar, K. Chakraborty, Novel furanyl derivatives from the red seaweed *Gracilaria opuntia* with pharmacological activities using different *in vitro* models. Med. Chem. Res. 27 (2018) 1245–1259.

F. Makkar, K. Chakraborty, Novel furanyl derivatives from the red seaweed *Gracilaria opuntia* with pharmacological activities using different *in vitro* models, Med. Chem. Res. 27 (2018) 1245–1259.

F.C. Pacheco, J.A. Villa-Pulgarin, F. Mollinedo, M.N. Martin, J.J. Fernandez, A.H. Daranas, New polyether triterpenoids from *Laurencia viridis* and their biological evaluation, Mar. Drugs. 9(11) (2011) 2220–2235.

F.C. Pacheco, L. Nordstrom, M.L. Souto, M.N. Martin, J.J. Fernandez, A.H. Daranas, Studies on polyethers produced by red algae, Mar. Drugs. 8 (2010) 1178–1188.

Faulkner DJ. 1996. Marine natural products. Nat Prod Rep. 13:75–125.

Faulkner DJ. Marine natural products (1998) Nat Prod Rep 15: 113-158.

Faulkner, D.J. 2002. Marine natural products. Nat. Prod. Rep. 19: 1–49.

Fazeela MBS, Hemalatha S (2017). Characterisation, in silico and in vitro determination of antidiabetic and anti-inflammatory potential of ethanolic extract of *Sargassum wightii*. Asian J. Pharm. Clin. Res.10, 297-301.

Fernandes E, Costa D, Toste SA, Lima JLFC, Reis S (2004). In vitro scavenging activity for reactive oxygen and nitrogen species by nonsteroidal anti-inflammatory indole, pyrrole, and oxazole derivative drugs. Free RadicBiol Med. 37, 1895-1905.

Fernando IPS, Nah JW, Jeon YJ (2016). Potential anti-inflammatory natural products from marine algae. Environ. Toxicol. Pharmacol. 48, 22-30.

Francavilla M, Franchi M, Monteleone M, Caroppo C (2013) The red seaweed *Gracilaria gracilis* as a multi products source. Mar Drugs 11:3754-3776.

Funk, C.D., 2001. Prostaglandins and leukotrienes: Advances in eicosanoid biology. Science 294, 1871–1875.

G. Genta-Jouve, O.P. Thomas, Sponge chemical diversity: From biosynthetic pathways to ecological roles. Adv. Mar. Biol. 62 (2012) 183–230.

G.M. Cragg, D.J. Newman, Natural products as sources of new drugs over the last 25 years, J. Nat. Prod. 70 (2007) 461–477.

G.M. Cragg, P.G. Grothaus, D.J. Newman, Impact of natural products on developing new anti-cancer agents, Chem. Rev. 109 (2009) 3012–3043.

Ganesan P, Chandini SK, Bhaskar N (2008). Antioxidant properties of methanol extract and its solvent fractions obtained from selected Indian red seaweeds. Bioresour Technol 99, 2717-2723.

Garcia DG, Bianco EM, Santos MCB, Pereira RC, Faria MVD, Teixeira VL, Burth P. 2009. Inhibition of mammal Na^+/K^+-ATPase by diterpenes extracted from the Brazilian brown alga *Dictyota cervicornis*. Phytother Res. 23:943–947.

Gaven KMC, Percot A (2010). Alkaloids in marine algae. Mar Drugs. 8(2):269-284

Gilbert NC, Rui Z, Neau DB, Waight MT, Bartlett SG, Boeglin WE, Brash AR, Newcomer ME. 2012. Conversion of human 5-lipoxygenase to a 15-lipoxygenase by a point mutation to mimic phosphorylation at Serine-663. Faseb J. 26:3222-3229.

Gilbert NC, Rui Z, Neau DB, Waight MT, Bartlett SG, Boeglin WE, Brash AR, Newcomer ME. 2012. Conversion of human 5-lipoxygenase to a 15-lipoxygenase by a point mutation to mimic phosphorylation at Serine-663. Faseb J. 26:3222-3229.

Gilbert, N.C., Rui, Z., Neau, D.B., Waight, M.T., Bartlett, S.G., Boeglin, W.E., Brash, A.R., Newcomer, M.E., 2012. Conversion of human 5-lipoxygenase to a 15-lipoxygenase by a point mutation to mimic phosphorylation at serine-663. FASEB. J. 26, 3222–3229.

Goldstein BJ, Ahmad F, Ding, W, Li PM, Zhang WR (1998) Regulation of the insulin signaling pathway by cellular protein-tyrosine phosphatases. Mol Cell Biol 182:91-99.

Groweiss A, Shmueli U, Kashman Y (1983) Marine toxins of *Latrunculia magnifica*. J Org Chem 48: 3512-3516.

Guiry MD, Dhonncha EN. 2003. http://www.algaebase.org.

Guiry MD, Nic-dhonncha E (2003) Algaebase. J Phycol 39: 19-20.

Gulcin, I., Oktay, M., Kirecci, E., and Kufrevioglu, O.I. 2003. Screening of antioxidant and antimicrobial activities of anise (*Pimpinella anisum* L.) seed extracts. Food Chem. 83: 371–382.

H. Andriamanatoanina, G. Chambat, M. Rinaudo, Fractionation of extracted Madagascan *Gracilaria corticata* polysaccharides: Structure and properties. Carbohydr. Polym. 68 (2007) 77–88.

H. Mitome, T. Nagasawa, H. Miyaoka, Y. Yamada, R.W.M. van Soest, A new sesquiterpenoid quinone and other related compounds from the Okinawan marine sponge *Dactylospongia elegans*. J. Nat. Prod. 66 (2003) 46–50.

H. Qi, T. Zhao, Q. Zhang, Z. Li, Z. Zhao, Antioxidant activity of different molecular weight sulfated polysaccharides from *Ulva pertusa* Kjellm (Chlorophyta), J. Appl. Phycol. 17 (2005) 527–534.

H. Shimizu, T. Koyama, S. Yamada, S.A. Lipton, T. Satoh, Zonarol, a sesquiterpene from the brown algae *Dictyopteris undulata*, provides neuroprotection by activating the Nrf2/ARE pathway. Biochem. Biophys. Res. Commun. 457 (2015) 718–722.

Hamdan II, Afifi FU (2004) Studies on the *in vitro* and *in vivo* hypoglycemic activities of some medicinal plants used in treatment of diabetes in Jordanian traditional medicine. J Ethanopharmacol 93:117-121.

Hamdan, I.I., and Afifi, F.U. 2004. Studies on the *in vitro* and *in vivo* hypoglycemic activities of some medicinal plants used in treatment of diabetes in Jordanian traditional medicine. J. Ethnopharmacol. 93: 117–121.

Hanson JR. 2000. Diterpenoids. Nat Prod Rep. 17(2):165-174.

Hanson JR. 2001. Diterpenoids. Nat Prod Rep. 18(1):88-94.

Hanson JR. 2002. Diterpenoids. Nat Prod Rep. 9(2):125-132.

Hara, Y., and Honda, M., 1990. The inhibition of α–amylase by tea polyphenols. Agric. Biol. Chem. 54: 1939–1945.

Hassan EM, Mohammed MMD, Mohamed SM (2012). Two new phorbol-type diterpene esters from *Synadenium grantii* Hook F. leaves. Rec Nat Prod 6:255-262.

Henriksen EJ, Diamond-Stanic MK, Marchionne EM (2011) Oxidative stress and the etiology of insulin resistance and type-2 diabetes. Free Radic Biol Med 51:993-999.

Heo SJ, Yoon WJ (2010). Evaluation of anti-inflammatory effect of fucoxanthin isolated from brown algae in lipopolysaccharide-stimulated RAW 264.7 macrophages. Food Chem Toxicol. 48(8):2045-2051

Hill RA, Connolly JD (2012). Triterpenoids. Nat Prod Rep 29:780-818.

Hu JF, Geng MY, Zhang JT, Jiang HD (2001). An in vitro study of the structure-activity relationships of sulfated polysaccharide from brown algae to its antioxidant effect. J Asian Nat Prod Res 3, 353-358.

Huang R, Zhou X (2010). Diketopiperazines from marine organisms. Chem Biodivers. 7(12):2809-2829

Huang YL, Sachi N, Tanaka T, Matsuo Y, Saito Y, Kouno I (2013) Two new oleanane-type triterpenes isolated from Japanese post-fermented tea produced by anaerobic microbial fermentation. Molecules 18:4868-4875.

Huuskonen JJ, Livingstone DJ, Tetko IV (2000) Neural network modeling for estimation of partition coefficient based on atom-type electrotopological state indices. J Chem Inf Model 40: 947-955.

Huuskonen JJ, Livingstone DJ, Tetko IV (2000). Neural network modelling for estimation of partition coefficient based on atom-type electrotopological state indices. J Chem Inf Comput Sci 40:947-955.

Huuskonen JJ, Livingstone DJ, Tetko IV. 2000. Neural network modelling for estimation of partition coefficient based on atom-type electrotopological state indices. J Chem Inf Model. 40:947-955.

Huuskonen JJ, Livingstone DJ, Tetko IV. 2000. Neural network modelling for estimation of partition coefficient based on atom-type electrotopological state indices. J Chem Inf Model. 40:947-955.

Huuskonen, J.J., Livingstone, D.J., Tetko, I.V., 2000. Neural network modeling for estimation of partition coefficient based on atom-type electrotopological state indices. J. Chem. Inf. Comput. Sci. 40, 947–955.

Hwa JK, Lee BH, Wook CB, Lee H, Shin J. 2005. Chromenes from the brown alga *Sargassum siliquastrum*. J Nat Prod. 68:716-723.

Hyun TK, Eom SH, Kim J-S (2014) Molecular docking studies for discovery of plant-derived α-glucosidase inhibitors. POJ 7:166-170.

I.S. Marcos, A. Conde, R.F. Moro, P. Basabe, D. Diez, J.G. Urones, Quinone/hydroquinone sesquiterpenes. Mini Rev. Org. Chem. 7 (2010) 230–254.

Ioannou E, Quesada A, Rahman MM, Gibbons S, Vagias C, Roussis V. 2012. Structures and antibacterial activities of minor dolabellanes from the brown alga *Dilophus spiralis*. Eur J Org Chem. 2012(27):5177–5186.

Ioannou E, Quesada A, Vagias C, Roussis V. 2008. Dolastanes from the brown alga *Dilophus spiralis*: Absolute stereochemistry and evaluation of cytotoxicity. Tetrahedron. 64:3975–3979.

Ioannou E, Vagias C, Roussis V. 2013. Isolation and structure elucidation of three new dolastanes from the brown alga *Dilophus spiralis*. Mar Drugs. 11:1104–1112.

Ioannou E, Zervoub M, Ismailc A, Ktaric L, Vagiasa C, Roussisa V (2009) 2, 6-Cyclo-xenicanes from the brown algae *Dilophus fasciola* and *Dilophus spiralis.* Tetrahedron 65: 10565-10572.

Ireland C, Faulkner DJ, Finer J, Clardy J. 1976. A novel diterpene from *Dollabella californica*. J Am Chem Soc. 98(15):4664–4665.

Iwashima M, Mori J, Ting X, Matsunaga T, Hayashi K, Shinoda D, Saito H, Sankawa U, Hayashi T. 2005. Antioxidant and antiviral activities of plastoquinones from the brown alga *Sargassum micracanthum*, and a new chromene derivative converted from the plastoquinones. Biol Pharm Bull. 28(2):374-377.

J. Martel-Pelletier, D. Lajeunesse, P. Reboul, J.P. Pelletier, Therapeutic role of dual inhibitors of 5-LOX and COX, selective and non-selective non-steroidal anti-inflammatory drugs. Ann. Rheum. Dis. 62 (2003) 501–509.

J. Martel-Pelletier, D. Lajeunesse, P. Reboul, J.P. Pelletier, Therapeutic role of dual inhibitors of 5-LOX and COX, selective and non-selective non-steroidal anti-inflammatory drugs, Ann. Rheum. Dis. 62 (2003) 501–509.

J.J. Fernandez, M.L. Souto, M. Norte, Marine polyether triterpenes, Nat. Prod. Rep. 17(3) (2000) 235–246.

J.W. Blunt, B.R. Copp, M.H.G. Munro, P.T. Northcote, M.R. Prinsep, Marine natural products, Nat. Prod. Rep. 28 (2011) 196–268.

Jaggi R, Wurgler U, Grandjean F, Weiser M, (2004). Dual inhibition of 5-lipoxygenase/cyclooxygenase by a reconstituted homeopathic remedy; possible explanation for clinical efficacy and favourable gastrointestinal tolerability. J.Inflamm. Res, 53, 150-157.

Jang KH, Lee BH, Choi BW, Lee H-S, Shin J. 2005. Chromenes from the brown alga *Sargassum siliquastrum*. J Nat Prod. 68:716-723.

Ji N-Y, Li X-M, Li K, Ding, L-P, Gloer JB, Wang B-G. 2007. Diterpenes, sesquiterpenes, and a C_{15}-acetogenin from the marine red alga *Laurencia mariannensis*. J Nat Prod. 70(12):1901-1905.

Jimenez-Escrig A, Jimenez-Jimenez I, Pulido R, Saura-Calixto F (2001) Antioxidant activity of fresh and processed edible seaweeds. J Sci Food Agric 81: 530-534.

Joshipura, K.J., Hu, F.B., and Manson, J.E. 2001. The effect of fruit and vegetable intake on risk for coronary heart disease. Ann. Intern. Med. 134: 1106–1114.

Joy M, Chakraborty K (2017a) Nutritional qualities of the low-value bivalve mollusks *Paphia malabarica* and *Villorita cyprinoides* at the estuarine waters of the southwestern coast of India. J Aquat Food Prod T 26(1): 54-70.

Joy M, Chakraborty K (2018). Antioxidative and anti-inflammatory pyranoids and isochromenyl analogues from Corbiculid bivalve clam, *Villorita cyprinoides*. Food Chem. 251, 125-134.

Joy M, Chakraborty K (2018). Specialized oxygenated heterocyclics from *Villorita cyprinoides* with cyclooxygenase-2 and 5-lipoxygenase inhibitory properties. Food Res Int. 106, 164-172

Joy M, Chakraborty K. 2017a. Previously undescribed antioxidative and anti-inflammatory chromenyls bearing 3*H*-isochromenone and furanyl-2*H*-chromenyl skeletons from the venerid clam, *Paphia malabarica* . Med Chem Res. 26(8):1708-1722.

Joy M, Chakraborty K. 2017b. First report of two new antioxidative meroterpeno 2Hpyranoids from short-necked yellow-foot clam Paphia malabarica (family: Veneridae) with bioactivity against pro-inflammatory cyclooxygenases and lipoxygenase. Nat Prod Res. 31(6):615−625.

Joy M, Chakraborty K. 2018. Antioxidative and anti-inflammatory pyranoids and isochromenyl analogues from Corbiculid bivalve clam, *Villorita cyprinoides*. Food Chem. 251:125-134.

Joy M, Chakraborty, K (2017b) Previously undescribed antioxidative and anti-inflammatory chromenyls bearing 3*H*-isochromenone and furanyl-2*H*-chromenyl skeletons from the venerid clam, *Paphia malabarica*. Med Chem Res 26: 1708-1722.

Joy, M., Chakraborty, K., 2017. Previously undescribed antioxidative and anti-inflammatory chromenyls bearing 3*H*-isochromenone and furanyl-2*H*-chromenyl skeletons from the venerid clam, *Paphia malabarica*. Med. Chem. Res. 26(8), 1708–1722.

K. Chakraborty, S.J. Chakkalakal, D. Joseph, Response of pro-inflammatory prostaglandin contents in anti-inflammatory supplements from green mussel *Perna viridis* L. in a time-dependent accelerated shelf-life study, J. Funct. Foods. 7 (2014) 527–540.

K. Chakraborty, T. Antony, M. Joy, Prospective natural anti-inflammatory drimanes attenuating pro-inflammatory 5-lipoxygenase from marine macroalga *Gracilaria salicornia*, Algal Res. 39 (2019) 101472.

K. Hagiwara, J.E.G. Hernandez, M.K. Harper, A. Carroll, C.A. Motti, J. Awaya, H.Y. Nguyen, A.D. Wright, Puupehenol, a potent antioxidant antimicrobial meroterpenoid from a Hawaiian deep-water *Dactylospongia sp*. Sponge. J. Nat. Prod. 78 (2015) 325–329.

K. Seibert, J.L. Masferrer, Role of inducible cyclooxygenase (COX-2) in inflammation, Receptor Spring. 4(1) (1994) 17–23.

K.R.R. Rengasamy, M.G. Kulkarni, W.A. Stirk, J. Van Staden, Advances in algal drug research with emphasis on enzyme inhibitors. Biotechnol. Adv. 32 (2014) 1364–1381.

Kang SM, Lee SH, Heo SJ, Kim KN, Jeon YJ (2011) Evaluation of antioxidant properties of a new compound, pyrogallol-phloroglucinol-6, 6'-bieckol isolated from brown algae, *Ecklonia cava*. Nutr Res Pract 5: 495-502.

Karawita, R., Siriwardhana, N., Lee, K.W., Heo, M.S., Yeo, I.K., and Lee, Y.D. 2005. Reactive oxygen species scavenging, metal chelating, reducing power and lipid peroxidation inhibition properties of different solvent fractions from *Hizikia fusiformis*. Eur. Food Res. Technol. 220: 363–371.

Kaza-owska K, Hsu T, (2010). Anti-inflammatory properties of phenolic compounds and crude extract from Porphyra dentata. J. Ethnopharmacol. 128(1):123-130

Kazlauskas, R., Murphy, P.T., Wells, R.J., Blackman, A.J., 1982. Macrocyclic enolethers containing an acetylenic group from the red alga *Phacelocarpus labillardieri*. Aust. J. Chem. 35, 113–120.

Kim M, Kim K, Park S, Choi H, Park S, Kim J, Jang M, Im M, Ahn D, (2017). Anti-Inflammatory effect of Sargassum patens C. Agardh ethanol extract in LPS-induced RAW264.7 cells and mouse ear edema. Korean J. Microbiol. Biotechnol. 45, 110-117.

Kim SK, Wijesekara I (2010). Development and biological activities of marine-derived bioactives: A review. J Funct Foods 2, 1-9.

Kim, A.R., Shin, T.S., Lee, M.S., Park, J.Y., Park, K.E., Yoon, N.Y. Kim, J.S., Choi, J.S., Jang, B.C., Byun, D.S., Park, N.K., and Kim, H.R. 2009. Isolation and identification of phlorotannins from *Ecklonia stolonifera* with antioxidant and anti-inflammatory properties. J. Agric. Food Chem. 57: 3483–3489.

Kindleysides S, Quek SY, Miller MR (2012) Inhibition of fish oil oxidation and the radical scavenging activity of New Zealand seaweed extracts. Food Chem 133: 1624-1631.

Kindleysides S, Quek SY, Miller MR. 2012. Inhibition of fish oil oxidation and the radical scavenging activity of New Zealand seaweed extracts. Food Chem. 133:1624-1631.

Kito, K., Ookura, R., Yoshida, S., Namikoshi, M., Ooi, T., Kusumi, T., 2008. New cytotoxic 14-membered macrolides from marine-derived fungus *Aspergillus ostianus*. Org. Lett. 10, 225–228.

Koay YC, Wong KC, Osman H, Eldeen I, Asmawi MZ (2013) Chemical constituents and biological activities of *Strobilanthes crispus* L. Rec Nat Prod 7:59-64.

Konig GM, Wright AD, Sticher O. 1991. Diterpenes from the brown alga *Dictyota divaricata*. Phytochemistry. 30:3679–3682.

Koutsaviti A, Daskalaki MG, Agusti S, Kampranis SC, Tsatsanis C, Duarte CM, Roussis V, Loannou E (2019). Thuwalallenes A–E and Thuwalenynes A–C: New C15 acetogenins with anti-inflammatory activity from a Saudi Arabian red sea *Laurencia sp*. Mar Drugs.17, 644

Kuda, T., and Ikemori, T. 2009. Minerals, polysaccharides and antioxidant properties of aqueous solutions obtained from macroalgal beach-casts in the Noto Peninsula, Ishikawa, Japan. Food Chem. 12: 575–581.

Kuda, T., Tsunekawaa, M., Goto, H., and Araki, Y. 2005. Antioxidant properties of four edible algae harvested in the Noto Peninsular, Japan. J. Food Compos. Anal. 18: 625–633.

Kulisic, T., Radonic, A., Katalinic, V., and Milos, M. 2004. Use of different methods for testing antioxidative activity of oregano essential oil. Food Chem. 85: 633–640.

Kumar S, Narwal S, Kumar V, Prakash O (2011) α-Glucosidase inhibitor from plants: A natural approach to treat diabetes. Phcog Rev 5:19-29.

Kumar V, Gill KD (2018). Estimation of urea in serum and urine. In: Basic concepts in clinical Biochemistry: A Practical Guide. Springer, Singapore.

Kwon YI, Apostolidis E, Kim YC, Shetty K (2007) Health benefits of traditional corn, beans and pumpkin: *In vitro* studies for hyperglycemia and hypertension management. J Med Food 10:266-275.

Kwon, Y.I., Apostolidis, E., Kim, Y.C., and Shetty, K. 2007. Health benefits of traditional corn beans and pumpkin *in vitro* studies for hyperglycemia and hypertension management. J. Med. Food. 10: 266–275.

L. Hui, X-M. Li, Y. Liu, P. Zhang, J-N. Wang, B-G. Wang, Chermesins A-D: Meroterpenoids with a drimane-type spirosesquiterpene skeleton from the marine algal-derived endophytic fungus *Penicillium chermesinum* EN-480. J. Nat. Prod. 79 (2015) 806-811.

L. Minale, R. Riccio, G. Sodano, Avarol, a novel sesquiterpenoid hydroquinone with a rearranged drimane skeleton from the sponge *Dysidea avara*. Tetrahedron Lett. 15 (1974) 3401–3404.

L.N. Larsen, E. Dahl, J. Bremer, Peroxidative oxidation of leuco dichloroluorescein by prostaglandin H synthase in prostaglandin biosynthesis from polyunsaturated fatty acids. Biochim. Biophys. Acta. 1299 (1996) 47–53.

L.N. Larsen, E. Dahl, J. Bremer, Peroxidative oxidation of leuco-dichloroluorescein by prostaglandin H synthase in prostaglandin biosynthesis from polyunsaturated fatty acids, Biochim. Biophys. Acta. 1299 (1996) 47–53.

Lanhers MC, Joyeux M, Soulimani R, Fleurentin J, Sayag M, Mortier F, Younos C, Pelt JM (1991). Hepatoprotective and anti-inflammatory effects of a traditional medicinal plant of Chile, Peumus boldus. Planta Med, 57(2):110-5.

Lann KL, Surget G, Couteau C, Coiffard L, Cérantola S, Gaillard F, Larnicol M, Zubia M, Guérard F, Poupart N, Valérie SP (2016) Sunscreen, antioxidant, and bactericide capacities of phlorotannins from the brown macroalga *Halidrys siliquosa*. J Appl Phycol 28: 3547-3559.

Larsen LN, Dahl E, Bremer J (1996) Peroxidative oxidation of leuco dichloroluorescein by prostaglandin H synthase in prostaglandin biosynthesis from polyunsaturated fatty acids. BBA 1299: 47-53.

Larsen LN, Dahl E, Bremer J (1996). Peroxidative oxidation of leuco-dichloroluorescein by prostaglandin H synthase in prostaglandin biosynthesis from polyunsaturated fatty acids, Biochim. Biophys. Acta. 1299 47-53.

Larsen LN, Dahl E, Bremer J. 1996. Peroxidative oxidation of leuco-dichloroluorescein by prostaglandin-H synthase in prostaglandin biosynthesis from polyunsaturated fatty acids. BBA: Lipid Lipid Met. 1299(1):47-53.

Larsen LN, Dahl E, Bremer J. 1996. Peroxidative oxidation of leuco-dichloroluorescein by prostaglandin-H synthase in prostaglandin biosynthesis from polyunsaturated fatty acids. BBA: Lipid Lipid Met. 1299(1):47-53.

Larsen LN, Dahl E, Bremer J. 1996. Peroxidative oxidation of leuco-dichloroluorescein by prostaglandin-H synthase in prostaglandin biosynthesis from polyunsaturated fatty acids. BBA: Lipid Lipid Met. 1299(1):47-53.

Larsen, L.N., Dahl, E., and Bremer, J. 1996. Peroxidative oxidation of leucodichlorofluorescein by prostaglandin H synthase in prostaglandin biosynthesis from polyunsaturated fatty acids. Biochim. Biophys. Acta. 1: 47–53.

Larsen, L.N., Dahl, E., Bremer J., 1996. Peroxidative oxidation of leuco-dichloroluorescein by prostaglandin-H synthase in prostaglandin biosynthesis from polyunsaturated fatty acids. BBA: Lipid Lipid Met. 1299(1), 47–53.

Laszczyk MN (2009) Pentacyclic triterpenes of the lupane, oleanane and ursane group as tools in cancer therapy. Planta Med 75:1549-1560.

Le Cesne A, Blay JY, Bui BN, Bouche O, Adenis A, Domont J(2010). Phase II study of oral masitinib mesilate in imatinib-naive patients with locally advanced or metastatic gastro-intestinal stromal tumour (GIST). Eur J Cancer 46, 1344-1351.

Leal MC, Munro MHG, Blunt JW, Puga J, Jesus B, Calado R (2013). Biogeography and biodiscovery hotspots of macroalgal marine natural products. Nat Prod Rep 30, 1380-1390.

Ledesma, B.H., Alvarez, P.J.M., and Pueyo, E. 2003. Assessment of the spectrophotometric method for determination of angiotensin-converting-enzyme activity: Influence of the inhibition type. J. Agric. Food Chem. 51: 4175–4179.

Lee DY, Yang H, Kim HW, Sung SH (2017) New polyhydroxy triterpenoid derivatives from fruits of *Terminalia chebula* Retz and their α-glucosidase and α-amylase inhibitory activity. Bioorg Med Chem Lett 27:34-39.

Lee, J.C., Hou, M.F., Huang, H.W., Chang, F.R., Yeh, C.C., Tang, J.Y., Chang, H.W., 2013. Marine algal natural products with anti-oxidative, anti-inflammatory, and anti-cancer properties. Cancer Cell Int. 13, 55.

Lee, S.H., Li, Y., Karadeniz, F., Kim, M.M., and Kim, S.K. 2008. α-Glucosidase and α-amylase inhibitory activities of phloroglucinol derivatives from edible marine brown alga, *Ecklonia cava*. J. Sci. Food Agric. 89: 1552–1558.

Leonid GV, Svetlana K, Tatiana NB, Alexandr BE, Valery ST. Sergey VT, Victor NK, Alexey VV. 2012. Novel synthetic route toward benzofuran-pyridine based spirans. Synth Commun. 42(22):3337-3343.

Lipinski C, Hopkins A. 2004. Navigating chemical space for biology and medicine. Nature. 432:855–861.

Lipinski CA (2004) Lead and drug-like compounds: the rule-of-five revolution. Drug Discov Today Technol 1:337-341.

Lipinski CA (2004) Lead and drug-like compounds: The rule-of-five revolution. Drug Discov Today Technol 1(4): 337-341.

Lipinski CA. 2004. Lead and drug-like compounds: The rule-of-five revolution. Drug Discov Today Technol. 1(4):337-341.

Lipinski CA. 2004. Lead and drug-like compounds: The rule-of-five revolution. Drug Discov Today Technol. 1(4):337-341.

Lipinski, C.A., 2004. Lead and drug-like compounds: the rule-of-five revolution. Drug. Discov. Today Technol. 1(4), 337–341.

Liu T, Yip YM, Song L, Feng S, Liud Y, Laid F, Zhang D, Huanga D. 2013. Inhibiting enzymatic starch digestion by the phenolic compound diboside-A: A mechanistic and in silico study. Food Res Int. 54:595–600.

Liu WK, Ling YH, Cheung FWK, Che CT, Stellettin A (2012). Endoplasmic reticulum stress in murine B16 melanoma cells. J Nat Prod 75, 586-590.

Lordan S, Ross RP, Stanton C (2011). Marine bioactives as functional food ingredients: potential to reduce the incidence of chronic diseases. Mar Drugs 9, 1056-1100.

Lorenzo-Morales J, Díaz-Marrero AR, Cen-Pacheco F, Sifaoui I, Reyes-Batlle M, Souto ML, Daranas AH, Piñero JE, Fernández JJ (2019). Evaluation of oxasqualenoids from the red alga *Laurencia viridis* against Acanthamoeba Mar Drugs.17, 420

Lowry OH, Roseborouch NI, Farrand AL, Randal RJ (1951). Protein measurement with the folin-phenol reagent. J Biol Chem, 263-275.

M. Abe, D. Inoue, K. Matsunaga, Y. Ohizumi, H. Ueda, T. Asano, M. Murakami, Y. Sato, Goniodomin A, an antifungal polyether macrolide, exhibits antiangiogenic activities via inhibition of actin reorganization in endothelial cells, J. Cell Physiol. 190 (2002) 109–116.

M. Francavilla, M. Franchi, M. Monteleone, C. Caroppo, The red seaweed *Gracilaria gracilis* as a multi products source. Mar Drugs. 11 (2013) 3754–3776.

M. Murakami, K. Makabe, S. Yamaguchi, S. Konosu, R. Walchi, A novel polyether macrolide from the dinoflagellate *Goniodoma pseudogoniaulax*, Tetrahedron Lett. 29 (1988) 1149–1152.

M. Norte, J. Fernandez, M.L. Souto, New polyether squalene derivatives from *Laurencia*, Tetrahedron. 53(13) (1997) 4649–4654.

M. Saleem, Lupeol, a novel anti-inflammatory and anti-cancer dietary triterpene, Cancer Lett. 285 (2009) 109–115.

M.B. Quin, C.M. Flynn, C. Schmidt-Dannert, Traversing the fungal terpenome. Nat. Prod. Rep. 31 (2014) 1449–1473.

Makkar F, Chakraborty K (2017). Antidiabetic and anti-inflammatory potential of sulphated polygalactans from red seaweeds *Kappaphycus alverizii* and *Gracilaria opuntia.* Int. J. Food Prop. 20(6), 1326-1337.

Makkar F, Chakraborty K (2018a) Novel furanyl derivatives from the red seaweed *Gracilaria opuntia* with pharmacological activities using different *in vitro* models. Med Chem Res 27: 1245-1259.

Makkar F, Chakraborty K (2018a). Previously undescribed antioxidative azocinyl morpholinone alkaloid from red seaweed *Gracilaria opuntia* with anti-cyclooxygenase and lipoxygenase properties. Nat Prod. Res. 32(10), 1150-1160.

Makkar F, Chakraborty K (2018b) Antioxidant and anti-inflammatory oxygenated meroterpenoids from the thalli of red seaweed *Kappaphycus alvarezii*. Med Chem Res 27: 2016-2026.

Makkar F, Chakraborty K (2019). Highly oxygenated antioxidative 2*H*-chromen derivative from the red seaweed *Gracilaria opuntia* with pro-inflammatory cyclooxygenase and lipoxygenase inhibitory properties. Nat Prod Res. 32(23), 2756-2765.

Makkar F, Chakraborty K. 2017. Unprecedented antioxidative cyclic ether from the red seaweed *Kappaphycus alvarezii* with anti-cyclooxygenase and lipoxidase activities. Nat Prod Res. 31(10):1131-1141.

Makkar F, Chakraborty K. 2017a. Unprecedented antioxidative cyclic ether from the red seaweed *Kappaphycus alvarezii* with anti-cyclooxygenase and lipoxidase activities. Nat Prod Res. 31(10):1131-1141.

Makkar F, Chakraborty K. 2017b. Highly oxygenated antioxidative 2*H*-chromen derivative from the red seaweed *Gracilaria opuntia* with pro-inflammatory cyclooxygenase and lipoxygenase inhibitory properties. Nat Prod Res. Epub ahead of print. doi:10.1080/14786419.2017.1378209.

Makkar F, Chakraborty K. 2018a. Antioxidative sulphated polygalactans from marine macroalgae as angiotensin-I converting enzyme inhibitors. Nat Prod Res. 32 (17):2100-2106.

Makkar F, Chakraborty K. 2018a. Highly oxygenated antioxidative 2*H*-chromen derivative from the red seaweed *Gracilaria opuntia* with pro-inflammatory cyclooxygenase and lipoxygenase inhibitory properties. Nat Prod Res. 32 (23):2756-2765.

Makkar F, Chakraborty K. 2018b. Antioxidative sulphated polygalactans from marine macroalgae as angiotensin-I converting enzyme inhibitors. Nat Prod Res. 32 (17):2100-2106.

Makkar F, Chakraborty K. 2018b. Previously undescribed antioxidative azocinyl morpholinone alkaloid from red seaweed *Gracilaria opuntia* with anti-cyclooxygenase and lipoxygenase properties. Nat Prod Res. 32(10):1150-1160.

Makkar F, Chakraborty K. 2018c. Previously undescribed antioxidative azocinyl morpholinone alkaloid from red seaweed *Gracilaria opuntia* with anti-cyclooxygenase and lipoxygenase properties. Nat Prod Res. 32(10):1150-1160.

Makkar F, Chakraborty K (2018b). Antioxidant and anti-inflammatory oxygenated meroterpenoids from the thalli of red seaweed *Kappaphycus alvarezii*. Med Chem. Res. 27(8), 2016-2026.

Makkar F, Chakraborty K (2019a). Highly oxygenated antioxidative 2*H*-chromen derivative from the red seaweed *Gracilaria opuntia* with pro-inflammatory cyclooxygenase and lipoxygenase inhibitory properties. Nat Prod. Res. 32(23), 2756-2765.

Makkar F. Chakraborty K (2018c). First report of dual cyclooxygenase-2 and 5-lipoxygenase inhibitory halogen derivatives from the thallus of intertidal seaweed *Kappaphycus alvarezii*. Med Chem. Res. 27, 2331-2340.

Makkar, F., Chakraborty, K., 2017. Unprecedented antioxidative cyclic ether from the red seaweed *Kappaphycus alvarezii* with anti-cyclooxygenase and lipoxidase activities. Nat Prod Res. 31(10):1131-1141.

Makkar, F., Chakraborty, K., 2018a. Antioxidative sulphated polygalactans from marine macroalgae as angiotensin-I converting enzyme inhibitors. Nat Prod Res. Epub ahead of print, doi: 10.1080/14786419.2017.1363756, 2017, 1-7

Makkar, F., Chakraborty, K., 2018b. Previously undescribed antioxidative azocinyl morpholinone alkaloid from red seaweed *Gracilaria opuntia* with anti-cyclooxygenase and lipoxygenase properties. Nat Prod Res. 32(10):1150-1160.

Makkar, F., Chakraborty, K., 2018c. Highly oxygenated antioxidative 2*H*-chromen derivative from the red seaweed *Gracilaria opuntia* with pro-inflammatory cyclooxygenase and lipoxygenase inhibitory properties. Nat Prod Res. Epub ahead of print, doi: 10.1080/14786419.2017.1378209.

Maneesh A, Chakraborty K (2017b). Unprecedented antioxidative and anti-inflammatory aryl polyketides from the brown seaweed *Sargassum wightii*. Food Research International, 100, 640–649.

Maneesh A, Chakraborty K, Makkar F (2017a). Pharmacological activities of brown seaweed *Sargassum wightii* (Family Sargassaceae) using different *in vitro* models. Int. J. Food Prop. 20, 931-945.

Maneesh A, Chakraborty K (2017) Previously undescribed fridooleanenes and oxygenated labdanes from the brown seaweed *Sargassum wightii* and their protein tyrosine phosphatase-1B inhibitory activity. Phytochem 144:19-32.

Maneesh A, Chakraborty K (2018). Pharmacological potential of sulfated polygalactopyranosyl-fucopyranan from the brown seaweed *Sargassum wightii*. J. Appl. Phycol. 30, 1971-1988.

Maneesh A, Chakraborty K. 2017. Previously undescribed fridooleanenes and oxygenated labdanes from the brown seaweed *Sargassum wightii* and their protein tyrosine phosphatase-1B inhibitory activity. Phytochem. 144: 19-32.

Maneesh A, Chakraborty K. 2017. Previously undescribed fridooleanenes and oxygenated labdanes from the brown seaweed *Sargassum wightii* and their protein tyrosine phosphatase-1B inhibitory activity. Phytochemistry. 144:19-32.

Maneesh, A., and Chakraborty, K. 2017. Previously undescribed fridooleanenes and oxygenated labdanes from the brown seaweed *Sargassum wightii* and their protein tyrosine phosphatase-1B inhibitory activity. Phytochemistry. 144: 19-32.

Maneesh, A., and Chakraborty, K. 2018. Pharmacological potential of sulfated polygalactopyranosyl-fucopyranan from the brown seaweed *Sargassum wightii*. J. Appl. Phycol. 30(3): 1971–1988.

Maneesh, A., Chakraborty, K., 2017. Unprecedented antioxidative and anti-inflammatory aryl polyketides from the brown seaweed *Sargassum wightii*. Food Res. Int. 100, 640–649.

Marsault, E., Peterson, M.L., 2011. Macrocycles are great cycles: Applications, opportunities, and challenges of synthetic macrocycles in drug discovery. J. Med. Chem. 54(7), 1961–2004.

Martel-Pelletier, J., Lajeunesse, D., Reboul, P., Pelletier, J.P., 2003. Therapeutic role of dual inhibitors of 5-LOX and COX, selective and non-selective non-steroidal anti-inflammatory drugs. Ann. Rheum. Dis. 62, 501–509.

Matsukawa, R., Dubinsky, Z., Kishimoto, E., Masaki, K., Masuda, Y., Takeuchi, T., Chihara, M., Yamamoto, Y., Niki, E., and Karube, I.A. 1997. Comparison of screening methods for antioxidant activity in seaweeds. J. Appl. Phycol. 9: 29–35.

Mayer AMS, Lehmann VKB (2000). Marine Pharmacology in 1998: Marine compounds with antibacterial, anticoagulant, anti-inflammatory, anthelmintic, antiplatelet, antiprotozoan, and antiviral activities; with actions on the cardiovascular, endocrine, immune, and nervous systems; and other miscellaneous mechanisms of action, The Pharmacologist, 42 (2), 62-69.

McNally VA, Rajabi M, Gbaj A, Stratford IJ, Edwards PN, Douglas KT, Bryce RA, Jaffar, M, Freeman S (2007) Design, synthesis and enzymatic evaluation of 6-bridged imidazolyluracil derivatives as inhibitors of human thymidine phosphorylase. J Pharm Pharmacol 59(4): 537-547.

McPhee S, Hodges LD, Wright PF, Wynne PM, Kalafatis N, Harney DW, Macrides TA (2007). Anti-cyclooxygenase effects of lipid extracts from the New Zealand green lipped mussel, *Perna canaliculus*. Comparative Biochemistry and Physiology. Part B, Biochemistry & Molecular Biology, 146, 3, 346-356.

Medeiros V, Queiroz K (2008). Sulfated galactofucan from *Lobophora variegata*: Anticoagulant and anti-inflammatory properties. Biochem (Mosc). 73(9): 1018-1024

Meenakshi S, Manicka Gnanambigai D, Tamilmozhi S, Arumugam M, Balasubramanian T (2009). Total flavanoid and in vitro antioxidant activity of two seaweeds from Rameshwaram Coast. Global J Pharmacol 3, 59-62.

Meirer, K., Steinhilber, D., Proschak, E., 2014. Inhibitors of the arachidonic acid cascade: Interfering with multiple pathways. Basic Clin. Pharmacol. Toxicol. 114, 83–91.

Milan M, Mirjana M, Desanka B, Sanja M, Neda N, Vladimir M, Vukovic N, Sukdolak S, Solujic S. 2011. *In vitro* antioxidant of selected 4-hydroxy-chromene-2-one derivatives-SAR, QSAR and DFT studies. Int J Mol Sci. 12(5):2822-2841.

Mishra, B.B., Tiwari, V.K., 2011. Natural products: An evolving role in future drug discovery. Eur. J. Med. Chem. 46(10), 4769–807.

Mohsin S, Mahadevan R, Kurup GM (2014) Free-radical-scavenging activity and antioxidant effect of ascophyllan from marine brown algae *Padina tetrastromatica.* Biomed Preventive Nutr 4: 75-79.

Mohsin S, Mahadevan R, Kurup GM. 2014. Free-radical scavenging activity and antioxidant effect of ascophyllan from marine brown algae *Padina tetrastromatica*. Biomed Prev Nutr. 4:75–79.

Molinski, T.F., Dalisay, D.S., Lievens, S.L., Saludes, J.P., 2009. Drug development from marine natural products. Nat. Rev. Drug Discov. 8(1), 69–85.

Mondol, M. A. M., Tareq, F. S., Kim, J. H., Lee, Ma, Lee, H.-S., Lee, Y.-J., Lee, J.-S., Shin, H. J. (2011). Cyclic ether-containing macrolactins, antimicrobial 24-membered isomeric macrolactones from a marine *Bacillus* sp. J. Nat. Prod. 74(12): 2582–2587.

Mondol, M., & Shin, H. (2014). Anti-bacterial and anti-yeast compounds from marine-derived bacteria. Mar. Drugs. 12(5): 2913–2921.

Mondol, M.A., Tareq, F.S., Kim, J.H., Lee, Ma, Lee, H.S., Lee, Y.J., Lee, J.S., Shin, H.J., 2011. Cyclic ether-containing macrolactins, antimicrobial 24-membered isomeric macrolactones from a marine *Bacillus sp*. J. Nat. Prod. 74(12), 2582–2587.

Monk JM, Jia Q, Callaway E, Weeks B, Alaniz RC, McMurray DN, Chapkin RS (2012). Th17 cell accumulation is decreased during chronic experimental colitis by (*n*-3) PUFA in Fat-1 mice. J Nutr 142, 117-124.

Mullane KM, Kraemer R, Smith B (1985). Myeloperoxidase activity as a quantitative assessment of neutrophil infiltration into ischemic myocardium. J. Pharmacol. Methods, 4(3),157-67.

Murakami, M., Matsuda, H., Makabe, K., Yamaguchi, K., 1991. Oscillariolide, a novel macrolide from a blue-green alga *Oscillatoria sp*. Tetrahedron Lett. 32, 2391–2394.

N. Fuestani, T. Sugawara, S. Matsunago, Potent antitumor metabolites from a marine sponge, J. Org. Chem. 57 (1992) 3828–3832.

Na M, Cui L, Min BS, Bae K, Yoo JK, Kim BY (2006) Protein tyrosine phosphatase-1B inhibitory activity of triterpenes isolated from *Astilbe koreana*. Bioorg Med Chem Lett 16:3273-3276.

Narasimhan M.K., Pavithra, S.K., Krishnan, V., and Chandrasekaran M. 2013. *In vitro* analysis of antioxidant, antimicrobial and antiproliferative activity of *Enteromorpha antenna*, *Enteromorpha linza* and *Gracilaria corticata* extracts. J. Nat. Pharm. Prod. 8: 151-159.

Nastrucci C, Cesario A and Russo P (2012). Recent Patents on Anti-Cancer Drug Discovery 7, 218-232.

Nazaruk J, Borzym-Kluczyk M (2015) The role of triterpenes in the management of diabetes mellitus and its complications. Phytochem Rev 14:675-690.

Newman DJ, Cragg GM (2012). Natural products as sources of new drugs over the 30 years from 1981 to 2010. J Nat Prod 75(3), 311-335.

Ngatu NR, Okajima MK (2012). Anti-inflammatory effects of sacran, a novel polysaccharide from *Aphanothece sacrum*, on 2,4,6-trinitrochlorobenzene-induced allergic dermatitis in vivo. Ann. Allergy Asthma Immunol.108(2):117-122. e2.

Nickavar, B., and Yousefian, N. 2011. Evaluation of α-amylase inhibitory activities of selected antidiabetic medicinal plants. J. Verbr. Lebensm. 6: 191–195.

Nitin K, Sushil K, Himanshu G, Sharma PK. 2012. 3-hydroxy-2(substituted phenyl)-4*H*-chromen-4-one derivatives-synthesis, spectral characterisation and pharmacological screening. World Res J Biochem. 1(1):1-5.

Novoa, A.V., Andrade-Wartha, E.R.S., Linares, A.F., Silva, A.M.O., Genovese, M.I., Gonzalez, A.E.B., Vuorela, P., Costa, A., and Mancini-Filho, J. 2011. Antioxidant activity and possible bioactive components in hydrophilic and lipophilic fractions from the seaweed *Halimeda incrassata*. Rev. Bras. Farmacogn. 21: 53–57.

Oramas-Royo SM, Chavez H, Martin-Rodriguez P, Fernandez-Perez L, Ravelo AG, Estevez-Braun A (2010) Cytotoxic triterpenoids from *Maytenus retusa*. J Nat Prod 73:2029-2034.

Ovenden SPB, Nielson JL, Liptrot CH, Willis RH, Tapiolas DM, Wright AD, Motti CA. 2011. Metachromins U-W: Cytotoxic merosesquiterpenoids from an Australian specimen of the sponge *Thorecta reticulata*. J Nat Prod. 74(5):1335-1338.

P. Cohen, C. Holmes, Y. Tsukitani, Okadaic acid: A new probe for the study of cellular regulation, Trends Biochem. Sci. 15 (1990) 98–102.

P. Torres, J.P. Santos, F. Chow, D.Y.A.C. dos Santos, A comprehensive review of traditional uses, bioactivity potential, and chemical diversity of the genus *Gracilaria* (Gracilariales, Rhodophyta), Algal Res. 37 (2019) 288–306.

Pacienza N, Lee RH, Bae EH, Kim DK, Liu Q, Prockop DJ, Yannarelli G (2018). *In vitro* macrophage assay predicts the *in vivo* anti-inflammatory potential of exosomes from human mesenchymal stromal cells. Mol Ther Methods Clin Dev. 13, 67-76.

Park HY, Han MH (2011). Anti-inflammatory effects of fucoidan through inhibition of NF-IB, MAPK and Akt activation in lipopolysaccharide-induced BV2 microglia cells. Food Chem. Toxicol. 49(8):1745-1752.

Pati MP, Sharma SD, Nayak L, Panda CR (2016). Uses of seaweed and its application to human welfare: a review. Int J Pharm Pharm Sci. 8(10), 12-20.

Peake M, Whiting M (2006). Measurement of serum creatinine-current status and future goals. Clin Biochem Rev. 27(4), 173-184.

Perera PRD, Ekanayake S, Ranaweera KKDS (2013) *In vitro* study on antiglycation activity, antioxidant activity and phenolic content of *Osbeckia octandra* L. leaf decoction. J Pharmacogn Phytochem 2:198-201.

Peters RJ. 2010. Two rings in them all: The labdane-related diterpenoids. Nat Prod Rep. 27(11):1521-1530.

Plaza M, Cifuentes A, Ibanez E (2008) In the search of new functional food ingredients from algae. Trends Food Sci Technol 19(1): 31-39.

R. Kurumbail, Cyclooxygenase enzymes: catalysis and inhibition, Curr. Opin. Struct. Biol. 11 (2001) 752–760.

R.M. McMillan, E.R.H. Walker, Designing therapeutically effective 5-lipoxygenase inhibitors. Trends Pharmacol. Sci. 13 (1992) 323–330.

Reitman S, Frankel S (1957). A colorimetric method for the determination of serum glutamic oxalacetic and glutamic pyruvic transaminases. Am. J. Clin Pathol, 28(1), 56-63.

Ren Q, Siau, W-Y, Du Z, Zhang K, Wang J. 2011. Expeditious assembly of a 2-amino-4*H*-chromene skeleton by using an enantioselective mannich intramolecular ring cyclization-tautomerization cascade sequence. Chem Eur J. 17(28):7781-7785.

Rocha, D.H.A., Seca, A.M.L., and Pinto, D.C.G.A. 2018. Seaweed secondary metabolites *in vitro* and *in vivo* anticancer activity. Mar. Drugs. 16(11): 410-437.

Rodriguez AD, Gonzalez E, Ramirez C. 1998. The structural chemistry, reactivity, and total synthesis of dolabellane diterpenes. Tetrahedron. 54:11683–11729.

Roth BL, Baner K, Westkaemper R, Siebert D, Rice KC, Steinberg S, Ernsberger P, Rothman RB (2002) Salvinorin A: A potent naturally occurring non nitrogenous kappa opioid selective agonist. Proc Natl Acad Sci USA 99:11934-11939.

Ruzicka L (1963) Perspectives of the biogenesis and chemistry of terpenes. Pure Appl Chem 6:493-522.

S. Baylac, P. Racine, Inhibition of 5-lipoxygenase by essential oils and other natural fragment extracts. Int. J. Aromather. 13 (2003)138–142.

S. Baylac, P. Racine, Inhibition of 5-lipoxygenase by essential oils and other natural fragment extracts, Int. J. Aromather. 13 (2003)138–142.

S. Cao, Z. Gao, S.J. Thomas, S.M. Hecht, J.S. Lazo, D.G.I. Kingston, Marine sesquiterpenoids that inhibit the lyase activity of DNA polymerase-β. J. Nat. Prod. 67 (2004) 1716–1718.

Sadaka, M. W. M., 2017. A New Neo-clerodane diterpenoid from *Teucrium polium* Linn. Int. J. Pharmacogn. 4(9): 287–293.

Salas, S., Chakraborty, K., 2018. An unreported polyether macrocyclic lactone with antioxidative and anti-lipoxygenase activities from the Babylonidae gastropod mollusc *Babylonia spirata*. Med. Chem. Res. 27(11-12), 2446–2453.

Saraswati, Giriwono PE, Iskandriati D, Tan CP, Andarwulan N (2019). *Sargassum* seaweed as a source of anti-inflammatory substances and the potential insight of the tropical species: A review, Mar. Drugs. 17, 590

Sasaki T, Li W, Morimura H, Li S, Li Q, Asada Y, Koike K (2011) Chemical constituents from *Sambucus adnata* and their protein-tyrosine phosphatase-1B inhibitory activities. Chem Pharm Bull 59:1396-1399.

Sedlak J, Lindsay RH (1968). Estimation of total, protein-bound, and nonprotein sulfhydryl groups in tissue with Ellman's reagent. Anal. Biochem, 25, 192-205.

Sekar S, Viswanathan KP, Kishnan B, Ganesan KK (2015) Evaluation of anti-hyperglycemic effect of *Gracilaria corticata* extract in normal and streptozotocin-induced diabetic rats. Chem Biol Lett 2:6-11.

Shreadah MA, Abd NM, Moneam E (2018). Phytochemical and pharmacological screening of *Sargassium vulgare* from Suez Canal, Egypt. Food Sci. Biotechnol. 27, 963-979.

Sindhu RK, Sood N, Puri V, Arora S (2017). Various animal models for preclinical testing of anti-inflammatory agents. Int J Pharm Sci Res 8(4), 1550-1557.

Singh M, Pal M, Sharma RP. 1999. Biological activity of the labdane diterpenes. Planta Med. 65(1):2-8.

Stout, E.P., Hasemeyer, A.P., Lane, A.L., Davenport, T.M., Engel, S., Hay, M.E., Fairchild, C.R., Prudhomme, J., Roch K.L., Aalbersberg, W., Kubanek, J., 2009. Antibacterial neurymenolides from the Fijian red alga *Neurymenia fraxinifolia*. Org. Lett. 11(1), 225–228.

Suleria HAR, Gobe G, Masci P, Osborne SA (2016). Marine bioactive compounds and health promoting perspectives; innovation pathways for drug discovery. Trends Food Sci Technol. 50: 44-55.

Suzuki M, Daitoh M, Vairappan CS, Abe T, Masuda M. 2001. Novel halogenated metabolites from the Malaysian *Laurencia pannosa*. J Nat Prod. 64(5):597-602.

Suzuki M, Kurosawa E, Kurata K.1988. Venustanol, a brominated labdane diterpene from the red alga *Laurencia venusta.* Phytochem. 27(4):1209-1210.

Suzuki M, Nakano S, Takahashi Y, Abe T, Masuda M, Takahashi H, Kobayashi K. 2002. Brominated labdane-type diterpenoids from an Okinawan *Laurencia sp*. J Nat Prod. 65(6):801-804.

T. Antony, K. Chakraborty, First report of antioxidant abeo-labdane type diterpenoid from intertidal red seaweed *Gracilaria salicornia* with 5-lipoxygenase inhibitory potential, Nat. Prod. Res. (2018) 1-8. doi: 10.1080/14786419.2018.1508150. Epub ahead of print.

Tahrani AA, Bailey CJ, Del Prato S, Barnett AH (2011) Management of type 2 diabetes: New and future developments in treatment. Lancet 378:182-197.

Tanaka J, Ogawa N, Liang J, Higa T, deNys R, Bowden BF, Carroll R, Coll J, Bernardinelli G, Jefford CW (1994) Helioxenicins A-C: Diterpenes from the blue coral *Heliopora coerulea*, Tetrahedron 50: 9989-9996.

Thanh-Sang, V., Dai-Hung, N., and Se-Kwon, K. 2012. Phospholipase A2: Function and pharmacological regulation. Inflamm. Allergy Drug Targets. 11: 90–101.

Thomas, N.V., and Kim, S.K. 2011. Potential pharmacological applications of polyphenolic derivates from marine brown algae. Environ. Toxicol. Pharmacol. 32: 325–335.

Tran QTN, Wong WSF, Chai CLL. 2017. Labdane diterpenoids as potential anti-inflammatory agents. Pharmacol Res. 124:43-63.

Udenigwe, C.C., Lin, Y., Hou, W., and Aluko, R.E. 2009. Kinetic of the inhibition of renin angiotensin I-converting enzyme by flaxseed protein hydrolysate functions. J. Funct. Foods. 1: 199–207.

Uemura, D., Takahashi, K., Yamamoto, T., Katayama, C., Tanaka, J., Okumura, Y., Yoshimasa, H., 1985. Norhalichondrin A: An antitumor polyether macrolide from a marine sponge. J. Am. Chem. Soc. 107, 4796–4798.

V.K. Sali, R. Malarvizhi, V.M. Manikandamathavan, H.R. Vasanthi, Isolation and evaluation of phytoconstituents from red alga *Acanthophora spicifera* as potential apoptotic agents towards A549 and HeLa cancer cells lines. Algal Res. 32 (2018) 172–181.

Vanderah DJ, Steudler PA, Ciereszko LS, Schmitz FJ, Ekstrand JD, Van der Helm D (1977) Marine natural products. Xenicin: A diterpenoid possessing a nine-membered ring from the soft coral, *Xenia elongata*. J Am Chem Soc 99: 5780-5784.

Vargas P, Oliveira IDB, Stephens PRS, Santos CCC, Paixao CNDP, Ramos FA, Jimenez C, Resende JALC, Teixeira VL, Castellanos L. 2014. Dolabelladienols A-C, new diterpenes isolated from Brazilian brown alga *Dictyota pfaffii*. Mar Drugs. 12:4247–4259.

Veena CK, Josephine A, Preetha SP, Varalakshmi P (2007). Beneficial role of sulfated polysaccharides from edible seaweed *Fucus vesiculosus* in experimental hyperoxaluria. Food Chem 100(4), 1552-1559.

Viano Y, Bonhomme D, Camps M, Briand JF, Ortalo-Magne A, Blache Y, Piovetti L, Culioli G (2009) Diterpenoids from the Mediterranean brown alga *Dictyota sp*. evaluated as antifouling substances against a marine bacterial biofilm. J Nat Prod 72:1299-1304.

Vijayabaskar P, Shiyamala V (2012). Antioxidant properties of seaweed polyphenol from *Turbinaria ornata* (Turner) J. Agardh, 1848. Asian Pac J Trop Biomed 2, S90-S98.

W.A. Wijesinghe, E.A. Kim, M.C. Kang, W.W. Lee, H.S. Lee, C.S. Vairappan, Y.J. Jeon, Assessment of anti-inflammatory effect of 5β-hydroxypalisadin B isolated from red seaweed *Laurencia snackeyi* in zebrafish embryo in vivo model, Environ. Toxicol. Pharmacol. 37 (2014) 110–117.

Wang J, Xie XQ, Hou T, Xu X (2007) Fast approaches for molecular polarizability calculations. J Phys Chem A 111: 4443-4448.

Wang J, Xie X-Q, Hou T, Xu X (2007) Fast approaches for molecular polarisability calculations. J Phys Chem A 111:4443-4448.

Wang J, Xie X-Q, Hou T, Xu X. 2007. Fast Approaches for molecular polarisability calculations. J Phys Chem A. 111(20):4443–4448.

Wang J, Xie X-Q, Hou T, Xu X. 2007. Fast Approaches for molecular polarisability calculations. J Phys Chem A. 111(20):4443-4448.

Wang J, Xu QL, Zheng M-F, Ren H, Lei T, Wu P, Zhou ZY, Wei XY, Tan JW (2014) Bioactive 30-noroleanane triterpenes from the pericarps of *Akebia trifoliata*. Molecules 19:4301-4312.

Wang T, Jónsdóttir R, Liu H, Gu L, Kristinsson HG, Raghavan S (2012). Antioxidant capacities of phlorotannins extracted from the brown algae *Fucus vesiculosus*. J Agr Food Chem, 60(23), 5874-5883.

Wang, J, Xie, X-Q, Hou T, Xu, X. 2007. Fast Approaches for molecular polarisability calculations. J Phys Chem A. 111(20):4443-4448.

Wang, J., Xie, X.Q., Hou, T., Xu, X., 2007. Fast approaches for molecular polarizability calculations. J. Phys. Chem. A 111, 4443–4448.

Wang, T., Jonsdottir, R., Liu, H., Gu, L., Kristinsson, H.G., Raghavan, S., and Olafsdóttir, G. 2012. Antioxidant capacities of phlorotannins extracted from the brown algae *Fucus vesiculosus*. J. Agric. Food Chem. 60: 5874–5883.

Wei X, Rodríguez AD, Baran P, Raptis RG. 2010. Dolabellane-type diterpenoids with antiprotozoan activity from a southwestern Caribbean gorgonian octocoral of the genus *Eunicea*. J Nat Prod. 73(5):925–934.

Wessjohann, L.A., Ruijter, E., Garcia-Rivera, D., Brandt, W., 2005. What can a chemist learn from nature's macrocycles?-A brief, conceptual view. Mol. Divers. 9, 171–186.

W-H. Jiao, T-T. Xu, B-B. Gu, G-H. Shi, Y. Zhu, F. Yang, B-N. Han, S-P. Wang, Y-S. Li, W. Zhang, J. Li, H-W. Lin, Bioactive sesquiterpene quinols and quinones from the marine sponge *Dysidea avara*. RSC Adv. 5 (2015) 87730–87738.

Wijesinghe, W.A.J.P., Athukorala, Y., and Jeon, Y.J. 2011. Effect of anticoagulative sulfated polysaccharide purified from enzyme-assistant extract of a brown seaweed *Ecklonia cava* on Wistar rats. Carbohydr. Polym. 86: 917–921.

Winter JM, Chiou G, Bothwell IR, Xu W, Garg NK, Luo M, Tang Y (2016). Expanding the structural diversity of polyketides by exploring the cofactor tolerance of an inline methyltransferase domain. Org Lett 15, 3774-7.

Wojdylo A, Oszmianski J, Czemerys R (2007) Antioxidant activity and phenolic compounds in 32 selected herbs. Food Chem 105:940-949.

Wojdylo A, Oszmianski J, Czemerys R (2007) Antioxidant activity and phenolic compounds in 32 selected herbs. Food Chem 105: 940-949.

Wojdylo A, Oszmianski J, Czemerys R. 2007. Antioxidant activity and phenolic compounds in 32 selected herbs. Food Chem. 105:940-949.

Wojdylo A, Oszmianski J, Czemerys R. 2007. Antioxidant activity and phenolic compounds in 32 selected herbs. Food Chem. 105(3):940-949.

Wojdylo A, Oszmianski J, Czemerys R. 2007. Antioxidant activity and phenolic compounds in 32 selected herbs. Food Chem. 105(3):940-949.

Wojdylo, A., Oszmianski, J., and Czemerys, R. 2007. Antioxidant activity and phenolic compounds in 32 selected herbs. Food Chem. 105: 940–949.

Wojdylo, A., Oszmianski, J., Czemerys, R., 2007. Antioxidant activity and phenolic compounds in 32 selected herbs. Food Chem. 105(3), 940–949.

Wu C, Huang S, Yen GC (2011) Silymarin: A novel antioxidant with antiglycation and antiinflammatory properties *in vitro* and *in vivo*. Antioxid Redox Signal 14:353-366.

Xie J, Zhang AH, Sun H, Yan GL and Wang XJ (2018). Recent advances and effective strategies in the discovery and applications of natural products. RSC Adv 8, 812-824.

Y.V. Yuan, M.F. Carringto, N.A. Walsh, Extracts from dulse (*Palmaria palmata*) are effective antioxidants and inhibitors of cell proliferation *in vitro*, Food Chem. Toxicol. 43 (2005) 1073–1081.

Yamamoto K, Miyake H, Kusunoki M, Osaki S (2010) Crystal structures of isomaltase from *Saccharomyces cerevisiae* and in complex with its competitive inhibitor maltose. FEBS J 277:4205-4214.

Yan X, Nagata T, Fan X (1998). Antioxidative activities in some common seaweeds. Plant Foods for Human Nutrition, 52, 253-262.

Yan XJ, Fang GM, Lou QX (1999). Studies on free radical scavenging activity in Chinese seaweeds. Part I. Screening results. Chinese Journal of Oceanology and Limnology 17, 240-246.

Yan XJ, Li XC, Zhou CX, Fan X (1996). Prevention of fish oil rancidity by phlorotannins from *Sargassum kjellmanianum*. J. Appl. Psychol, 8, 201-203.

Yang L, Zhang LM (2009). Chemical structural and chain conformational characterization of some bioactive polysaccharides isolated from natural sources. Carbohydr Polym. 76(3):349-361

Yang Z, Yin J, Wang Y, Wang J, Xia B, Li T, Yang X, Hu S, Ji C Guo S (2019). The fucoidan A3 from the seaweed *Ascophyllum nodosum* enhances RCT-related genes expression in hyperlipidemic C57BL/6J mice. Int. J. Biol. Macromol.134, 759.

Yeh, C.-C., Yang, J.-I., Lee, J.-C., Tseng, C.-N., Chan, Y.-C., Hseu, Y.-C., Tang, J-.Y. Chuang, L.-Y., Huang, H-.W, Chang, F.-R. Chang, H.-W. 2012. Anti-proliferative effect of methanolic extract of *Gracilaria tenuistipitata* on oral cancer cells involves apoptosis, DNA damage, and oxidative stress. BMC Complement. Altern. Med. 12: 142.

Yin J, Wang J, Li F, Yang Z, Yang X, Sun W, Xia B, Li T, Song W, Guo S (2019). The fucoidan from the brown seaweed *Ascophyllum nodosum ameliorates* atherosclerosis in apolipoprotein E-deficient mice *Food Funct.* 10, 5124.

Younus H (2018). Therapeutic potentials of superoxide dismutase. IJHS, 12(3), 88-93.

Yu X-Q, Jiang C-S, Zhang Y, Sun P, Kurtan T, Mandi, A, Li X-L, Yao L-G, Liu A-H, Wang B, Guo Y-W, Mao, S-C. 2017. Compositacins A-K: Bioactive chamigrane-type

halosesquiterpenoids from the red alga *Laurencia composita* Yamada. Phytochemistry. 136:81-93.

Zedler S, Faist E (2006). The impact of endogenous triggers on trauma-associated inflammation. Current Opinion in Critical Care.12(6):595-601

Zhang W, Okimura T, Xu L, Zhang LJ, Oda T, Kwak M, Yu Q, Jin JO (2016). Ascophyllan functions as an adju-vant to promote anti-cancer effect by dendritic cell activation. Oncotarget, *7*, 19284-19298.

1. **Tima Antony** & Kajal Chakraborty (2019). Pharmacological Properties of Seaweeds against Progressive Lifestyle Diseases. Journal of Aquatic Food Product Technology, 28(10):1-13. DOI:10.1080/10498850.2019.1684407.
2. **Tima Antony** & Kajal Chakraborty (2019). Xenicanes attenuate pro-inflammatory 5-lipoxygenase: Prospective natural anti-inflammatory leads from intertidal brown seaweed *Padina tetrastromatica*. Medicinal Chemistry Research, 28 (4), 591-607. DOI:10.1007/s00044-019-02322-8
3. **Tima Antony** & Kajal Chakraborty & Minju Joy (2019). Antioxidative dolabellanes and dolastanes from brown seaweed *Padina tetrastromatica* as dual inhibitors of starch digestive enzymes. Natural Product Research, 1-13. E-publication ahead of print; DOI: 10.1080/14786419.2019.1591402
4. **Tima Antony** & Kajal Chakraborty (2018). First report of antioxidant abeo-labdane type diterpenoid from intertidal red seaweed *Gracilaria salicornia* with 5-lipoxygenase inhibitory potential. Natural Product Research, 1-8. E-publication ahead of print; DOI: 10.1080/14786419.2018.1508150.
5. **Tima Antony** & Kajal Chakraborty (2019). First report of antioxidative 2H-chromenyl derivatives from the intertidal red seaweed *Gracilaria salicornia* as potential anti-inflammatory agents. Natural Product Research, 1–13. E-publication ahead of print; DOI: 10.1080/14786419.2019.1579807.
6. Kajal Chakraborty, **Tima Antony** & Minju Joy (2019). Prospective natural anti-inflammatory drimanes attenuating pro-inflammatory 5-lipoxygenase from marine macroalga *Gracilaria salicornia*. Algal Research, 40, 101472. DOI:10.1016/j.algal.2019.101472.
7. Kajal Chakraborty & **Tima Antony** (2019). First report of spiro-compounds from marine macroalga *Gracilaria salicornia*: prospective natural anti-inflammatory agents attenuate 5-lipoxygenase and cyclooxygenase-2. Natural Product Research, 1-12. E-publication ahead of print; DOI: 10.1080/14786419.2019.1608545.
8. Kajal Chakraborty & **Tima Antony** (2019). First report of antioxidative abeo-oleanenes from red seaweed *Gracilaria salicornia* as dual inhibitors of starch digestive enzymes. Medicinal Chemistry Research, 28 (5), 696-710. DOI:10.1007/s00044-019-02328-2
9. Kajal Chakraborty & **Tima Antony** (2020). Salicornolides A-C from Gracilaria salicornia attenuates pro-inflammatory 5-lipoxygense: Prospective natural anti-

inflammatory leads. Phytochemistry, 172, 112259. E-publication ahead of print; DOI: 10.1016/j.phytochem.2020.112259.

10. **Tima Antony** & Kajal Chakraborty (2020). Anti-inflammatory polyether triterpenoids from the marine macroalga Gracilaria salicornia: Newly described natural leads attenuate proinflammatory 5-lipoxygenase and cyclooxygenase-2, Algal Research 46,101791. E-publication ahead of print; DOI: 10.1016/j.phytochem.2020.112259

PAPERS IN CONFERENCES

1. **Tima Antony** & Kajal Chakraborty (2017). Pharmacological properties of seaweeds against lifestyle diseases. Presented a poster in 11th IFAF, November 21-24, 2017, Book of Abstracts. 438-439. Asian Fisheries Society Indian Branch, ICAR- Central Institute of Fisheries Technology. Kochi, Kerala, India
2. **Tima Antony** (2019). First report of anti-oxidative 2*H*-chromenyl derivatives from red seaweed *Gracilaria salicornia* as potential anti-inflammatory agents. Presented a poster in MATCON 2019, March 14-16, 2019. International conference on materials for the millennium. Department of applied chemistry Cochin University of Science and Technology. Kochi, Kerala, India.
3. **Tima Antony** & Kajal Chakraborty (2019). Natural anti-Inflammatory drimanes to attenuate pro-Inflammatory 5-Lipoxygenase from marine macroalga *Gracilaria Salicornia* participated in ICCM-2019, October 17-19, Book of Abstracts. 86-87. International Conference on Advances in Chemical & Materials Sciences (ICCM-2019), Department of Studies in Chemistry Mangalore University, Mangalagangothri - 574 199 Karnataka, India.
4. **Tima Antony** & Kajal Chakraborty (2020). Natural anti-inflammatory compounds isolated from *Gracilaria salicornia*: Attenuate 5-lipoxygenase activity, January 8-10, Book of Abstracts. 440-441. International Symposium Marine Ecosystems Challenges & Opportunities (MECOS 3), Marine Biological Association of India (MBAI), CMFRI, Kochi, Kerala, India